Proceedings of the 21st Seismic Research Symposium: Technologies for Monitoring The Comprehensive Nuclear-Test-Ban Treaty

21-24 September 1999

Las Vegas, Nevada

Volume I

Seismic Regional Characterization and Wave Propagation
Seismic Event Detection, Location, and Identification Methods
Seismic Source Characterization

Approved for Public Release; further dissemination unlimited





LA-UR-99-4700

Dedicated to Dr. Frank F. Pilotte

In appreciation of his support to nuclear test monitoring.

Table of Contents - Volume I

EISMIC REGIONAL CHARACTERIZATION AND WAVE PROPAGATION

Page

guilar-Chang, Julio, Aaron A. Velasco, Hans E. Hartse
Seismic Database in Support of Regional Monitoring Research in Asia 1

aker, G. Eli and Mariana Eneva
Predicting Crustal Phase Propagation from Other Geophysical Parameters 7

onner, Jessie, L., D. Craig Pearson, W. Scott Phillips
Shallow Velocity Structure at the Shagan River Test Site in Kazakstan 18

radley, C. R. and L. E. Jones
Full Waveform Modeling of the Effects of Q and Structure Over Sub-Regional Paths in Western China 28

Chan, Winston and Xiaoxi Ni
Collection and Analysis of Seismic and Ground-Truth Information in Northeastern China 39

Dewey, James W., Ellen Herron, John O. Kork
Recent Calibration Events in the United States 48

Goldstein, Peter, Joydeep Bhattacharyya, Gene Ichinose, Richard Leach
On the Sensitivity of Broad Band Regional Seismic Phases to Multi-Dimensional Earth Structure: Implications for Phase Identification 58

Harris, David, Kevin Mayeda, Keith Nakanishi, Arthur Rodgers, Stan Ruppert, Florianne Ryall, Ken Skinnell, Abdel-Qadar Amrat, Tawfiz Al-Yazjeen, Ahmed Al-Husien, Frederick Simon
Calibration of Seismic Wave Propagation in Jordan 64

Harris, David, Stan Ruppert, Jasem Al-Awadhi, Kevin Mayeda, Arthur Rodgers, Florianne Ryall, Jerry Sweeney, Frederick Simon
Calibration of Seismic Wave Propagation in Kuwait 73

Hartse, Hans, Aaron A. Velasco, Steven R. Taylor
Some Interesting Seismic Events from Western China 82

Hayward, Chris, Brian Stump, Paul Golden, Eugene Herrin, Myung-Soon Jun, Jeong-Soo Jeon,
The Korean Seismo-Acoustic Array 92

Hazler, Shannon, Michael. Pasyanos, William, Walter, Ann Sheehan
Two-Station Phase Velocity Determination for Structure in North Africa 102

Helmberger, Donald V., Sidao Ni, Ji Chen
Modeling Regional Seismograms 111

Herrmann, R. B., C. J. Ammon, J. Julia, T. Mokhtar,
Joint Inversion of Receiver Functions and Surface-Wave Dispersion for Crustal Structure 122

Page

Jordan, Thomas H., Eliza Richardson, Jeffrey J. McGuire, Cedric Wright, Sue Webb, Eldridge Kgaswane, Teresia Nguuri
Characterization of Natural and Human-Related Seismicity in South Africa 130

Kirichenko, Victor V. and Yury A. Kraev
Review of Research Being Performed in the Russian Federation Related to CTBT Seismic Monitoring 131

Koper, Keith D. and Terry C. Wallace
Regional Wave Propagation in Siberia 132

Levshin, Anatoli L., Mikhail P. Barmin, Michael H. Ritzwoller
Evaluation of Uncertainties and Bias in Surface Wave Tomographic Maps and Travel-Time Correction Surfaces 141

Mackey, Kevin and Kazuya Fujita
The Northeast Russia Seismicity Database and Explosion Contamination of the Russian Earthquake Catalog 151

Mooney, Walter D.
Crustal and Upper Mantle Seismic Velocity Structure of the Former USSR 162

Mooney, Walter, D., Gabi Laske, T. Guy Masters, Katharine H. Favret
How Thick is the Earth's Crust? 172

Mooney, Walter D. and Robert G. Coleman
The Crustal Structure in Northwest China 182

Morozov, Igor B., Elena A. Morozova, Scott B. Smithson
Preliminary Characterization of Lg Phase Propagation from Peaceful Nuclear Explosions in Siberia 190

Mykkeltveit, Svein, Frode Ringdal, Conrad Lindholm, Elena Kremenetskaya
Seismic Calibration of the European Arctic 201

Parker, Paul B. and Lane R. Johnson
Regional Characterization from Joint Inversions of Geophysical Data 208

Phillips, W. Scott, Hans E. Hartse, Steven R. Taylor, Aaron A. Velasco, George E. Randall
Regional Phase Amplitude Tomography for Seismic Verification in China 216

Rodgers, Arthur J. and William R. Walter
Complete Regional Waveform Modeling to Estimate Seismic Velocity Structure and Source Parameters 226

Ruppert, Stanley D., Teresa F. Hauk, Jennifer L. O'Boyle, Doug Dodge, Miki Moore, Stephanie Daveler
Lawrence Livermore National Laboratory's Middle East and North Africa Database 234

Saikia, Chandan and Bradley B. Woods
Path Calibration and Source Characterization In and Around India 243

Page

Sandvol, Eric, Alex Calvert, David Steer, Dogan Seber,
Khaled Al-Damegh, Muawia Barazangi,
Regional Travel Time and Amplitude Ratio Correction Surfaces in the Middle East 254

Schlittenhardt, Jorge
Regional Velocity Models for Germany: A Contribution to the Systematic Travel-Time Calibration of the International Monitoring System 263

Stevens, Jeffry L. and David A. Adams
Improved Methods for Regionalized Surface Wave Analysis 274

Thurber, Clifford, Chad Trabant, Florian Haslinger
Testing Event Location Capability and Ground Truth in Kazakstan 283

Walter, William R., Arthur J. Rodgers, Alan Sicherman, William Hanley,
Kevin Mayeda, Stephen C. Myers, Michael Pasyanos
Lawrence Livermore National Laboratory's Seismic Discrimination Research 294

Woods, Bradley B., Chandan K. Saikia, Hong Kie Thio
Extending Regional Waveform Modeling to Shorter Periods to Improve the Location and Identification of Small Seismic Sources 303

Wu, Francis T. and Eric Hetland
Crustal and Upper Mantle Structures Under the Changbai Volcano 312

Xie, Jiakang
Excitation and Attenuation of Regional Waves from Recent Events in China 323

Yang, Xiaoping, Keith McLaughlin, Robert North
Source-Specific Station Corrections for Regional Phases at International Monitoring System Stations 333

SEISMIC EVENT DETECTION, LOCATION, AND IDENTIFICATION METHODS

Anderson, Dale N., Steven R. Taylor, Kevin K. Anderson
Discrimination Information in Phase Amplitude Threshold 334

Antolik, Michael, Gonan Ekstrom, Adam M. Dziewonski, Laop Boschi
Utilizing Three-Dimensional Seismic Velocity Models in Teleseismic Event Location 346

Baumgardt, Douglas R.,
Seismic Characterization of Underwater Explosions and Undersea Earthquakes Using Spectral/Cepstral Modeling and Inversion 352

Bennett, Theron J., Margaret E. Marshall, Ronald W. Cook
Screening of Seismic Events in Rockburst Areas 363

Bernard, Michelle, Delaine Reiter, Shirley Rieven, William Rodi
Development of a 3-D Model for Improved Seismic Event Location in the Pakistan/India Region 374

Page

Bowers, David
Identification of Low-Magnitude Seismic Disturbances Using Regional Observations in the Kara/Barents Sea Region 383

Der, Zoltan A. and Robert Shumway
Automatic Interpretation of Seismic Signals Using the CUSUM-SA Algorithm 393

Drake, Lawrence A. and Rodolfo Anaya
Location of Events in the Region of Bolivia 404

Drob, Douglas P. and J. M. Picone
Statistical Performance Measures of the HWM-93 and MSISE-90 Empirical Atmospheric Models 414

Fan, Guangcho
An Application of Earthquake Detection of Time-Frequency Analysis 418

Federenko, Yury V. and Eystein S. Husebye
Signal Detection in a Wavelet-Transformed Three-Component Station Noise Environment 419

Fisk, Mark, Steven Bottone, Henry Gray, Gary McCartor
Event Characterization Using Regional Seismic Data 427

Golden, Paul, Jessie Bonner, Eugene Herrin, Chris Hayward, Brian Stump, Ileana Tibovleac, David Anderson
Installation of the Mina, Nevada, Seismic and Acoustic Arrays 438

Goldstein, Peter and Douglas Dodge
Depth and Source Mechanism Estimation for Special Event Analysis, Event Screening, and Regional Calibration 449

Henson, Ivan, Xiaoxi Ni, Wilmer Rivers
Seismic Event Location in 3-D Velocity Models Using Initial and Secondary Arrival Times Compared with Dynamic Ray Tracing 460

Husebye, Eystein S. and Yury V. Fedorenko
Picking P- and S-Onsets in Wavelet Transformed Local Seismic Records 466

Jepsen, David and Sprio Spiliopoulos,
Event Screening Procedures at the Prototype International Data Centre 476

Jih, Rong-Song
A Comparative Study of Azimuth-Based Non-Standard Location Methods 487

Khalturin, Vitaly I., Tatyana G. Rautian, Paul C. Richards
A Study of Small-Magnitude Seismic Events During 1961-1989 on and near the Semipalatinsk Test Site, Kazakstan 499

Lay, Thorne, Guangwei Fan, Ru Shan Wu, Xiao-bi Xie
Path Corrections for Regional Phase Discriminants 510

Maggi, Alessia, Delaine Reiter, Keith Priestley
Improved Estimation of Seismic Focal Depths in Iran 520

Page

Mayeda, Kevin, Rami Hofstetter, Arthur D. Rodgers, William R. Walter,
Applying Coda Envelope Measurements to Local and Regional Waveforms for Stable Estimates of Magnitude, Source Spectra, and Energy 527

Murphy, John R., Jamil D. Sultanov, Brian W. Barker, Ivan O. Kitov, Margaret E. Marshall
Application of Soviet PNE Data to the Improvement of Seismic Monitoring Capability 534

Murphy, John R., Jeffry L. Stevens, Theron J. Bennett, Brian W. Barker, Ronald W. Cook,
Development of Improved Magnitude Measures for the International Data Centre 542

Murphy, John R., Ronald W. Cook, William L, Rodi
Improved Focal Depth Determination for Use in CTBT Monitoring 550

Park, Jeffrey, Vadim Levin, Joydeep Bhattacharyya
Multi-Taper Coherence Receiver Functions and P-Wave Scattering Within the Crust 554

Pasyanos, Michael E., William R. Walter, Shannon E. Hazler
Improving mb:Ms Discrimination Using Phase Matched Filters Derived from Regional Group Velocity Tomography 565

Patton, Howard J.
Investigations into Regional Magnitude Scaling: Transportability and Ms:mb Relationships Based on Nuttli's mb(Lg) 572

Pinsky, Vladimir and Avi Shapira
Robust Procedures for Automatic Precise Location of Regional Seismic Events 579

Pulliam, Jay, Cliff Frohlich, Brian Schlottman
Accuracy and Uncertainty in Single-Station Event Locations 589

Reiter, Delaine and Robert Shumway
Improved Seismic Event Depth Estimation Using Cepstral Analysis 599

Ringdal, Frode, E. Kremenetskaya, V. Asming, T. Kvaerna, J. Schweitzer
Research in Regional Seismic Monitoring 607

Ryaboy, Vladislav
Development of 3-D Crustal and Upper Mantle Velocity Models of Northern Eurasia and North America to Refine Location of Regional Seismic Events 616

Schultz, Craig A., Stephen C. Myers, Megan Flanagan, Jennifer Swenson, William Hanley, Michael Pasyanos
Improving Regional Seismic Event Location Through Calibration of the International Monitoring System 626

Shearer, Peter M.
Relocation of Global Events Using the L1-Norm and Source-Specific Station Terms 633

Steck, Lee K., Aaron A. Velasco, Howard T. Patton
Improving Regional Seismic Event Location in China 639

Taylor, Steven, R., Aaron A. Velasco, Hans E. Hartse, W. Scott Phillips, William R. Walter
Amplitude Corrections for Regional Seismic Discriminants 646

Page

Villasenor, Antonio, Michael H. Ritzwoller, Anatoli L. Levshin,
E. Robert Engdahl, Michael Barman, Wim Spakman, Jeannot Trampert
Construction of a 3-D P and S Model of the Crust and Upper Mantle to Improve Regional Locations in Western China, Central Asia, and Parts of the Middle East 656

Wang, Jin, Hans Israelsson, Keith McLaughlin
Signal Detection and Estimation at the New International Monitoring System Array at Mina 666

Woodward, Wayne A., Stephan R. Sain, H. L. Gray
Outlier Testing When Some Data Are Missing 674

Wu, R. S., X. B. Xie, X. Y. Wu
Lg Wave Simulations in Heterogeneous Crusts with Irregular Topography Using Half-Space Screen Propagators 683

SEISMIC SOURCE CHARACTERIZATION

Bonner, Jessie, Brian Stump, Chris Hayward, Eugene Herrin, Paul Golden
Empirical Seismo-Acoustic Studies for Calibration and Identification Capabilities at International Monitoring System Array Sites 694

Gitterman, Yefin and Avi Shapira
Source Characterization of Ground Truth Quarry Blasts in Israel and Calibration of Local Stations 703

Hedlin, Michael A. H.
An Analysis of Low-Frequency Seismic Signals from Large Mining Blasts 713

Kennett, Brian L. N.,
Constraining the Depth and Source Mechanism for Smaller Seismic Events at Far-Regional to Teleseismic Distances 723

Mellors, Robert J., Bernard Minster, William Walter, Dave Harris, Paul S. Earle
Location and Characterization of Mining Activity Using Interferometric Synthetic Aperture Radar 729

Myers, Steven C. and William R. Walter
Using Epicenter Location to Differentiate Events from Natural Background Seismicity 731

Rohay, Alan
Observation and Modeling of Ripple-Fired Explosions at the Centralia Mine, Washington 741

Rohay, Alan, Kenneth F. Sprenke, Michael C. Stickney
Source Characterization of a Large Rock Burst, Coeur d'Alene Mining District, Idaho 750

]
Sammis, Charles G.
Incorporating the Effects of Damage-Induced Secondary Seismic Radiation into Numerical Models for Underground Explosions 759

Page

Stump, Brian W., D. Craig Pearson, Vindell Hsu
Empirical Scaling Relations for Contained Single-Fired Chemical Explosions and Delay-Fired Explosions at Regional Distances 764

Paul Vincent, Bill Foxall and William R. Walter
Analysis, Comparison and Modeling of Radar Interferometry Data of Surface Deformation Signals Associated With Underground Explosions, Mine Collapses and Earthquakes Phase 1: Underground Explosions, Nevada Test Site 775

SEISMIC REGIONAL CHARACTERIZATION AND WAVE PROPAGATION

SEISMIC DATABASE IN SUPPORT OF REGIONAL MONITORING RESEARCH IN ASIA

Julio Aguilar-Chang, Aaron A. Velasco, Hans E. Hartse, Los Alamos National Laboratory

Sponsored by U. S. Department of Energy
Office of Nonproliferation and National Security
Office of Research and Development
Contract No. W-7405-ENG-36

ABSTRACT

The Geophysics Group at Los Alamos National Laboratory (LANL) has successfully developed and implemented a research database in support of regional seismic monitoring research, with the goal of improving our ability to locate, characterize, and discriminate small magnitude events recorded at regional distances. The database contains a wide variety of data (approximately 20 Gigabytes), gathered from a variety of open sources, including the Incorporated Research Institutions for Seismology (IRIS), the United States Geological Survey (USGS), the prototype International Data Centre (pIDC), the International Seismological Centre (ISC), and individual contractors and collaborators.

The types of data that we have collected from these sources include global seismic event catalogs, raw seismic digital waveforms, regional arrival information, and network and station information. Contributions by contractors and collaborators have significantly added to this database. For example, the USGS has provided velocity models for China and GIS information such as topography, moho depth, and mine locations. Woodward-Clyde has provided source studies of events that we now use as depth ground truth. The seismic database also contains information from our own efforts, including processed seismic data, arrival time and amplitude measurements, ground truth information, travel-time tables for regional 1-D models, and processing algorithms.
This regional seismic database is a rich source of information for regional seismic research and has allowed for regional studies on a wide range of topics, including surface-wave studies, propagation studies, magnitude calibration studies, special event studies, location improvements, and discrimination enhancements. We have also created a subset of this large dataset to focus on nuclear test sites in Asia. Not only does the dataset provide seismological information for the nuclear test sites, it also allows for improvements in the detection, location, and discrimination of events near the test sites.

The dataset is also an integrated design, allowing for easy use. That is, reference event waveforms correspond to events in the earthquake catalogs, station information corresponds to the waveforms, and 2-D travel-time correction surfaces are derived from picked travel-time arrivals derived from the catalog events. Future enhancements will include more seismic data, the latest regional discrimination procedures, special event analyses and data, and calibration studies.

Key Words: seismic database, regional, Asia, nuclear test sites

OBJECTIVE

The Geophysics Group at Los Alamos National Laboratory (LANL) has successfully designed and implemented a research database that contains a wide variety of information. Much of the information in the database stems from our efforts to mine open sources of data, which allows us to use this information for our regional seismic research efforts. The database is focussed on regional data, although we include global information when necessary. This database is also being used as a research tool, with the goal of developing methods to improve the detection, location, and discrimination of events recorded at regional distances in Asia. Researchers use the seismic database to access information for reference events, earthquake catalogs, regional station information, digital waveforms, ground truth information, and amplitude measurements. Research that is finalized is then integrated into the seismic research database, making the database a rich source of regional seismic information.

RESEARCH ACCOMPLISHED

Database Design

The seismic data gathered resides in an Oracle™ relational database, which runs on a Sun server. The size of this database is approximately 20 gigabytes and consists of over 200 reference tables. These tables contain data from a wide variety of sources, such as information from the Unites States Geological Survey (USGS), the prototype International Data Centre (pIDC), the International Seismological Centre (ISC), and individual contractors and collaborators. The database is an integrated design, allowing for easy use. That is, reference event waveforms correspond to events in the earthquake catalogs, station information corresponds to the waveforms, and 2-D travel-time correction surfaces are derived from picked travel-time arrivals derived from the catalog events. Future enhancements will include more seismic data, the latest regional discrimination procedures, special event analyses and data, and calibration studies.

The global catalogs from the USGS, pIDC, and the ISC contain event origin information, which is a summary of hypocentral parameters and information describing a derived or reported origin for a particular event. Associated with event origins are tables that contain summary information of seismic arrivals. This is information characterizing a seismic phase observed at a particular station. The phase arrival attributes conform to seismological convention and are listed in earthquake catalogs.

There are auxiliary tables that support origin and arrival information. There is a table that contains network-station affiliations, by which seismic stations may be clustered into networks, as well as tables containing station location and station-channel information. Through the use of these tables, we can obtain station names and locations. The station-channel information available in these tables describes the orientation of a recording channel at a particular site; it also provides information about the various channels that are available at a station and maintains a record of the physical channel configuration at a site. Network and station magnitudes based upon measurements made on specific seismic phases are also available in other tables. All these data can be tied to SAC waveforms by means of a table that contains waveform header file and descriptive information, which provides pointers to waveforms stored on disk.

The tables within the research database contain information on more than 400,000 distinct events, beginning in 1973 to the present. Of these, there are 13,662 events that have 128,120 related SAC waveforms. There have been over 3.5 million amplitude measurements made on 5,287 seismic phases representing 3,593 events with related SAC waveforms.

The research database is being used to store, query, manipulate, and produce reports on the following data:

- event location and confidence bounds
- information on seismic arrivals
- amplitude measurements
- waveform header file and descriptive information
- network and station magnitude
- station location and channel information

Database Content

Earthquake catalogs

We have collected earthquake catalog information from various sources. Most of our processing of waveform data requires an event location, which we take from available reference earthquake catalogs. We have gathered earthquake catalog information from global (United States Geological Survey: USGS) and regional (State Seismological Bureau of China: SSB) sources, and store the information as CSS 3.0 Oracle™ tables. We have also gathered information from the Reviewed Event Bulletin (REB) catalog from the prototype International Data Centre (pIDC). The earthquake catalogs are intended to provide a foundation for storing our regional waveform data. Thus, every waveform will have an origin for which it is associated. The catalogs may also be used for other purposes, such as event location and historical seismicity.

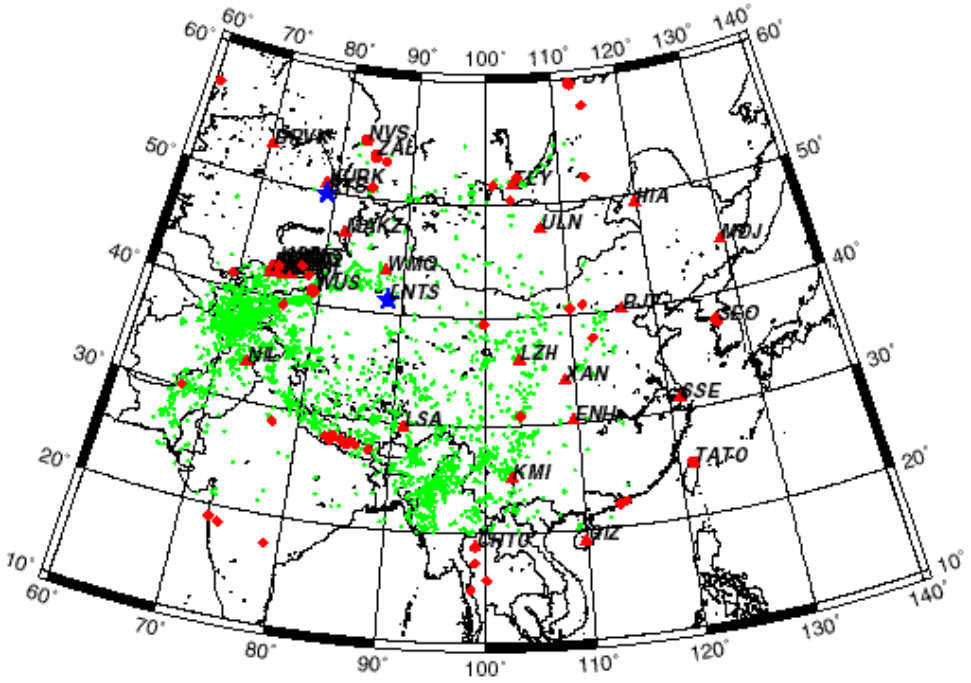


Figure 1: Map showing the Lop Nor (LNTS) and Kazakhstan (KTS) nuclear test sites (stars), USGS catalog events (dots), digital stations for which we have data (triangles), digital stations that are not in this database (circles), and USGS reporting stations that have arrival times in this database (diamonds).

We currently have data from the USGS Preliminary Determination of Epicenters (PDE) catalog between Jan. 1973 and Dec. 1989, the USGS Earthquake Data Report (EDR) catalog between Jan. 1990 and Jan. 1998, the USGS weekly PDE catalog between Feb. 1998 and Feb. 1999, and the State Seismological Bureau of China (SSB) catalog between Jan. 1973 and Dec. 1989. The REB catalog event data covers from May 1993 to Nov. 1998. The EDR catalog contains origin and phase information, and is considered to be the final event location in these USGS catalogs. Event magnitudes for the USGS events are generally above m_b 4.0. Prior to 1990, we use the final PDE origin records, which do not include phase information. For all of 1998, researchers use the weekly PDE data, since the final locations are not yet available. Although these are not the final USGS locations, they allow us to work with new waveform data. We also have loaded into our research database origin information from the State Seismological Bureau of China (SSB) catalog between the years 1973 to 1989. This catalog includes many regional and local events that are not in the global USGS catalogs. The SSB events have local magnitudes (M_L) ranging between 2.0 and 4.5. The REB catalog data were obtained as exported database tables from the Center for Monitoring Research (CMR), who runs the pIDC. These catalogs offer their own quality control for which we have little information. However, our quality control has been to guarantee that the electronic files were converted correctly and input properly into the database. Furthermore, by using primary and unique constraints in the database, we have identified duplicate records and misassociated phases. We have carefully reviewed these duplicates and misassociations and have corrected them in the database.

Waveforms for reference and catalog events

These are segmented digital waveforms from selected events (nuclear explosions and earthquakes) in eastern Asia. The events corresponding to the waveforms are included in the event catalogs. The waveforms are obtained from the Incorporated Research Institutions for Seismology (IRIS) Data Management Center (DMC), and were retrieved using windows defined by the catalog epicenter information. These digital waveforms are used as reference waveforms for the evaluation of regional seismic events in Asia. The waveforms are also used as a historical reference waveform database that can assist with special event analysis.

The events for which we have waveform data occurred between 1974 and 1998. The waveform segments were retrieved from the IRIS database using the event origin information from the United States Geological Survey (USGS) Preliminary Determination of Epicenters (PDE) and Earthquake Data Report (EDR) event catalogs, the Reviewed Event Bulletin (REB) catalog from the prototype International Data Centre (pIDC), or using the Chinese State Seismological Bureau (SSB) catalog. Event magnitudes for USGS PDE/EDR events are generally above mb 4.0, and SSB events range between M_L 2.0 and 4.5. The data are broadband (20 sps), short-period (40 sps), and long-period (1 sps) three-component digital waveforms from stations located in China, Pakistan, Khyrghyzstan, Kazakhstan, Mongolia, Russia, Korea, and Thailand. Data from the 1980's are mostly from the Chinese Digital Seismic Network (CDSN). The waveforms are stored as Seismic Analysis Code (SAC) files, which are binary files with header information. The files can be read using the computer program SAC [Tapley and Tull, 1992]. Furthermore, any tool that reads CSS-3.0-style information (e.g., MatSeis) can read our information. We also store instrument calibration information, which have been calculated for most of the stations in our database.

We have made travel-time picks and amplitude measurements of regional phases on many of the waveforms, and store the travel-time information. Picks were made on broadband channels when available; otherwise, they were made on short-period channels. The associated amplitude measurements from these picks are stored in a custom table. Regional phase amplitudes are measured using time domain techniques following the techniques of Hartse et al. (1997).

Travel-time tables and 2-D correction surfaces

We have developed 1-D travel time tables for regional velocity models in the region. The travel-time tables are stored as flat files, but are read by an event locator that writes results to the research database (see Steck et al., this issue for a review). The velocity models are derived from a number of sources, including the USGS, which are used as base models to compute 2-D travel-time correction surfaces to improve seismic event location. This is a research product that was derived from preliminary information in the seismic research database, and the results were later integrated into the database.

Preliminary ground truth events

We have digital waveform data for 10 Lop Nor nuclear explosions ranging in m_b between 4.7 and 6.5. We have also created a list of 26 events with well-constrained depths located within 1500 km of the Lop Nor test site in western China. Woodward-Clyde has provided source studies for these events using a variety of techniques, and we have looked at a number of other sources (see Steck et al., this issue). The events can be considered as depth ground truth events and are meant to be helpful for identifying reference events. This ground truth earthquake data is not based on epicentral location (such as GT2, which is a ground truth event known to within 2 km). Rather, the list of events is based on well-determined depth estimates using a variety of methods. It is important to emphasize that, in the absence of realistic strategies for gaining ground truth information, this approach of establishing ground truth may be the best means available to verification seismologists for calibrating a region. Furthermore, much can be learned about the performance of seismic techniques from comparative analysis, and such knowledge can be used to design improvements in techniques and/or to identify new data requirements.
Regional magnitude calibration information for station WMQ

Priestley and Patton (1997) developed a list of magnitudes calculated for events recorded at station WMQ, and we have incorporated this information into the database. Regional magnitudes based on regional phases have been shown to be useful for seismic discrimination. A list of regional phase magnitudes calculated for seismic station WMQ and the developed magnitude scale can be used to assist with short-period to long-period discrimination. All of the data and methods are outlined by Priestley and Patton (1997). They studied 27

nuclear tests and 52 earthquakes. One nuclear event occurred at the Lop Nor nuclear test site, while 26 occurred at the East Kazakhstan test site.

Regional station information

Our research database contains station information for all waveform data that has been gathered. We must have accurate station information in order to effectively utilize our waveform data. The station information is used for regional waveform analysis and event location. We have obtained station information from the IRIS database and from the Lawrence Livermore National Laboratory (LLNL) effort. Other information for global catalogs was obtained from the USGS Earthquake Data Report (EDR), which include many stations at teleseismic distances. We have compared the latitude and longitude of each station from different sources and have discovered some discrepancies. For example, stations sometimes have different elevations between the EDR and IRIS sources. Thus, we have kept the two sources separate. Unfortunately, we have little information about the accuracy of the station locations.

We have visually scanned the instrument response information gathered for each station. At this time, the instrument files should have accurate information. The accuracy of this information is dependent on the source of the station information. Some stations listed both by the IRIS database and the EDR differ in latitude, longitude and elevation. For station information, see the on-line Federation of Digital BroadBand Seismographic Network Station Book (FDSN Station Book).

Contextual (GIS) information

The USGS has provided a contextual dataset for China that includes moho depth, mine locations, faults, tectonic regions, and seismicity information. The dataset is stored in a GIS format that can be read and manipulated by users. Much of the interface to this information was developed by colleagues at Sandia National Laboratories, and compliments the seismic information in our dataset.

Utility for Research

The research database can be utilized to perform research on a vast amount of data. For example, in an effort to improve our ability to locate seismic events in western China using only regional data, Steck et al. (this issue) have developed empirical propagation path corrections (PPCs) using the earthquake catalogs within the database. They used travel-time observations available from the USGS Earthquake Data Reports (EDR), the International Seismic Centre (ISC) catalogs, the prototype International Data Centre Reviewed Event Bulletin (REB), and our own travel-time picks from regional data. They also included ground truth events mentioned above that are stored within the database. Another example is the use of extensive regional amplitude measurement for the development of amplitude corrections in 1-D and 2-D (Taylor et al., this issue; Phillips et al., this issue).

CONCLUSIONS

The Oracle™-based regional seismic database designed and implemented by the Geophysics Group at Los Alamos National Laboratory is a rich source of information that has allowed for research on a wide range of regional seismic topics. These include surface-wave, propagation, magnitude calibration, and special event studies, location improvements, and discrimination enhancements. We have also created a subset of this large dataset to focus on nuclear test sites in Asia. Not only does the dataset provide seismological information for the nuclear test sites, it also allows for improvements in the detection, location, and discrimination of events near the test sites.

Researchers have used the seismic research database effectively to store and manipulate large quantities of seismic information. The relational nature of the Oracle™ database helps in the integration of the different types of seismic data needed for research. For example, event information from published catalogs is stored in a table that is linked to tables containing seismic arrival information and pointers to waveforms stored within the operating system. Event origin and seismic arrival data can also be linked directly to phase amplitude information and to network and station magnitude data.

A major advantage of implementing the CSS-style relational database is the ability to use software developed to support CTBT-related research projects, such as MatSeis, a MATLAB-based graphical user interface and toolbox for working with seismic data, developed at Sandia National Laboratories (Harris et al., 1998).

REFERENCES

Hartse, H.E., S.R. Taylor, W.S. Phillips, and G.E. Randall, Regional event discrimination in central Asia with emphasis on western China, *Bull. Seism. Soc. Am*., 87, 551-568, 1997.

Harris, J. Mark, Christopher J. Young, Judy I. Beiriger, New Features in MatSeis, *20th Annual Seismic Research Symposium on Monitoring a CTBT, Abstract Proceedings*, 85, 1998.

Priestley, K. F., and H. J. Patton, Calibration of mb(Pn), mb(Lg) scales and transportability of the Mo : mb discriminant to new tectonic regions, *Bull. Seism. Soc. Am., 8*7, 1083-1099, 1997.

Tapley, W. C. and J. E. Tull, SAC- Seismic Analysis Code, Users manual, revision 4, 1992.

PREDICTING CRUSTAL PHASE PROPAGATION FROM OTHER GEOPHYSICAL PARAMETERS

G. Eli Baker and Mariana Eneva, Maxwell Technologies, Systems Division

Sponsored by U. S. Department of Defense
Defense Threat Reduction Agency
Contract No. DSWA01-97-15746

ABSTRACT

Crustally guided shear and compressional waves, which generally arrive within well-defined group velocity windows, can be important indicators of the ratio of shear to compressional energy at an event source, permitting discrimination between explosions and earthquakes. Differences in the propagation efficiencies of each phase reduce their effectiveness. The objective of this work is to develop a means of accurately predicting Lg and Pg propagation effects in a manner that can be reliably extrapolated to uncalibrated regions. The basis of this effort is the division of the crust into different types, each of which has consistent effects on each phase, but not necessarily the same effects as any other crustal type. The division is based on a variety of geophysical parameters and on observed propagation efficiency.

The initial work used data from the dense southern California seismic network (SCSN), which allowed us to observe changes in phase amplitudes over very short distances. We first review the techniques developed on this data set and results obtained. In a second phase of the work, we use the large global data set of Lg and Pg amplitude measurements reported in the reviewed event bulletin (REB) of the Preliminary International Data Center (PIDC).

To analyze the SCSN data, we employed statistical analysis techniques not commonly applied to geophysical data sets, particularly categorical statistics techniques. These include cluster analyses to separate crustal types and analysis of variance to test hypotheses regarding whether differences in propagation between crustal types are significant. We also constructed models to test the extent to which propagation of each phase is predictable by various statistics of topography, gravity, and velocity structure. Surprisingly, no clear correlations were observed between propagation efficiency and velocity structure, using a detailed 3-D velocity model of southern California. That may however be due to low resolution in the shallowest and deepest crustal layers, which could be the most important for waveguide efficiency. We were able to analyze Lg and Pg propagation separately, as SCSN site amplifications are known and sufficient data exist that we were able to construct a table of known calibration problems. This enables insights into differences between shear and compressional wave propagation in the crust that are not achievable using ratios of phase amplitudes.

To apply these techniques globally, we are using measurements of Lg and Pg amplitudes from the PIDC. Because this is a major new network, much effort is being spent assessing data quality, and it may not yet prove feasible to separately analyze Lg and Pg amplitudes. Even so, the broad extent of coverage and the network's purpose of CTBT monitoring make this the most relevant and useful data set to analyze. We also have collected and merged global data sets of other geophysical parameters that are likely to vary between different lithologies. These include topography, geoid estimates, sediment thickness, crustal magnetization, and crustal thickness estimates where available. We outline the separation of large regions into distinct crustal types, and explore the relationship between propagation efficiency and the crustal types. Specifically, we describe the inverse approach we are developing to assess the effect of each crustal type and the transition between crustal types, based on the length of each path segment in each crustal type for all possible paths in a large region.

Key Words: Lg, Pg, regional propagation

OBJECTIVE

The primary objective of this research program is to improve the accuracy of discrimination of nuclear explosions from earthquakes by developing a transportable path correction algorithm for the Lg/Pg discriminant.

RESEARCH ACCOMPLISHED

Introduction

The transportability of path corrections is difficult to assess or ensure. Good path corrections with well-defined confidence levels can be made in well-calibrated areas based on observed phase amplitudes (e.g. Phillips, 1999). The problem we address is how to provide accurate path corrections in areas with little data. The basis for such corrections is the identification of similar crustal structures that have similar effects on regional propagation. The crustal types are characterized by statistics of geophysical parameters that may vary with lithology. These may include topography, gravity, crustal thickness, sediment thickness, magnetization, age, or heat flow. This approach began with the work of Zhang et al (1994), who demonstrated a correlation between statistics of topography and P- and S-wave amplitude ratios at regional distances. The appearance of significant correlations bolstered the hope that corrections based on such correlations could be used to make path corrections. The difficulty encountered in numerous studies has been that corrections determined for a particular data set do not appear to be useful for data collected in adjacent regions (e.g. Rodgers et al, 1999).

This paper has three distinct sections. In the first, we review the research we have performed on southern California seismic network (SCSN) data, specifically focusing on the novel application of categorical statistical techniques to assess relationships between parameters and propagation, and transportability of the resulting propagation corrections. We address whether differences in the nature of Lg from explosions and earthquakes might inhibit the transportability of path corrections, and use an Israeli data set to further examine that question. Finally, we discuss the use of global IMS data to develop path corrections that will be most useful for the IMS network.

Section 1: Categorical Analyses and Short Propagation Paths

Review of SCSN Data Analysis Techniques and Results:
The data used in this section were described in Baker (1998) and are reviewed only briefly here. The closely spaced short-period vertical seismometers of the SCSN provide 618 recordings with at least one of Lg or Pg having signal-to-noise ratio (S/N) greater than 2, from 10 Nevada Test Site (NTS) nuclear explosions, and 583 such recordings from 5 regional earthquakes. These are used to construct short path segments between stations along the propagation directions. Changes in phase amplitudes along those paths are compared with statistics of topography, crustal thickness, and the isostatic gravity residual along those paths segments.

Previous studies compared regional phase amplitude ratios to statistics of parameters for entire source-receiver paths, which are generally quite long. By analyzing propagation effects along short paths between SCSN stations, we avoid several problems associated with long paths. For example, differences between source S-to-P ratios become irrelevant. Also, parameter values measured along long paths can lose meaning: half of a long path could be through high mountains and half through sedimentary basin, so mean elevation along the path is not representative of any portion of the path. Structure along very short paths is more likely to be homogeneous. Further, by using estimates of site amplifications we are able to examine just changes in Lg, or Pg, without relying on the ratio. We mostly focus on analyses of Lg/Pg ratios here.

Previous studies also relied on linear fits between parameters and amplitude ratios to make corrections. Propagation effects are commonly modeled using $c=ax+b$, where c is an observation, typically a P-to-S-wave amplitude ratio, x is some statistic estimated along the propagation path, such as mean elevation or topographic roughness, and a and b are constants. This empirical approach often has no theoretical basis, but does have the virtue of simplicity and may be justified where it provides reliable prediction. Initial analyses of the transmission efficiency (TE) of Lg and Pg however, indicate that important relationships between TE and the parameters would be missed if we only used general linear models. Instead we employ categorical models and analysis of variance (ANOVA).

We define transmission efficiency as $\log_{10}(A_d/A_u)$, where A_u and A_d are the amplitudes at the *upstream* and *downstream* stations respectively, that is, at the first and second station along a given raypath. Before discussing path corrections, we consider the relationships they are based on and specifically note why not all statistically significant relationships are necessarily useful. A plot of individual Lg TE observations versus median elevation demonstrates that point (figure 1, left). Only when the data are binned is a relationship apparent (figure 1, right). The high variance relative to the trend limits the variance reduction achievable using corrections based on the trend. This example also illustrates the importance of constructing testable hypotheses, since we clearly may be deceived by the manner in which the data are viewed. That is, figure 1 (left) indicates no relationship while 1 (right) does. Further, how we construct the hypotheses merits critical examination, since we are able to state and test more than one hypothesis.

We can simply hypothesize that the least squares fitting line to the data has some meaning. A t-test indicates that such a fit is significant, that is, the slope of the line found is not likely to have occurred if the data were random. This is counter to what one might assume looking at the raw data (figure 1, left). We note however that no hint of a trend is visible in a plot of Lg amplitude loss with distance, although in that case it is reasonable to assume that amplitude decreases with distance. The t-test does also indicate that the slope of Lg amplitude loss versus distance is significant. For any of the relationships considered however, we can make different hypotheses. We could assume that distinctly different types of crust, in regards to their effect on Lg propagation, are distinguished by their median elevation. For example, we can divide the crustal paths into low, medium, and high elevation groups. An examination of path locations provides a means of qualitative classification that separates the paths into geographically, and possibly tectonically, distinct groups (not shown for space considerations). We then use ANOVA to test the null hypothesis that the mean TEs of the groups are the same. ANOVA rejects that hypothesis, with probability 0.002. That we can form such different hypotheses and even find that very different types of relationships hypothesized are statistically significant, emphasizes the importance of not just applying statistical tests, but also assessing how appropriate the hypotheses may be. In this case an inspection of the distribution of paths to see whether the groups of paths are tectonically distinct, helps to make that assessment. Visual inspection of path locations for different groups also lets us avoid a dangerous circularity in the application of ANOVA. That is, we must not choose levels at which to separate the paths into different groups based on which levels provide the greatest separation, as we do not *know* yet whether such a relationship exists.

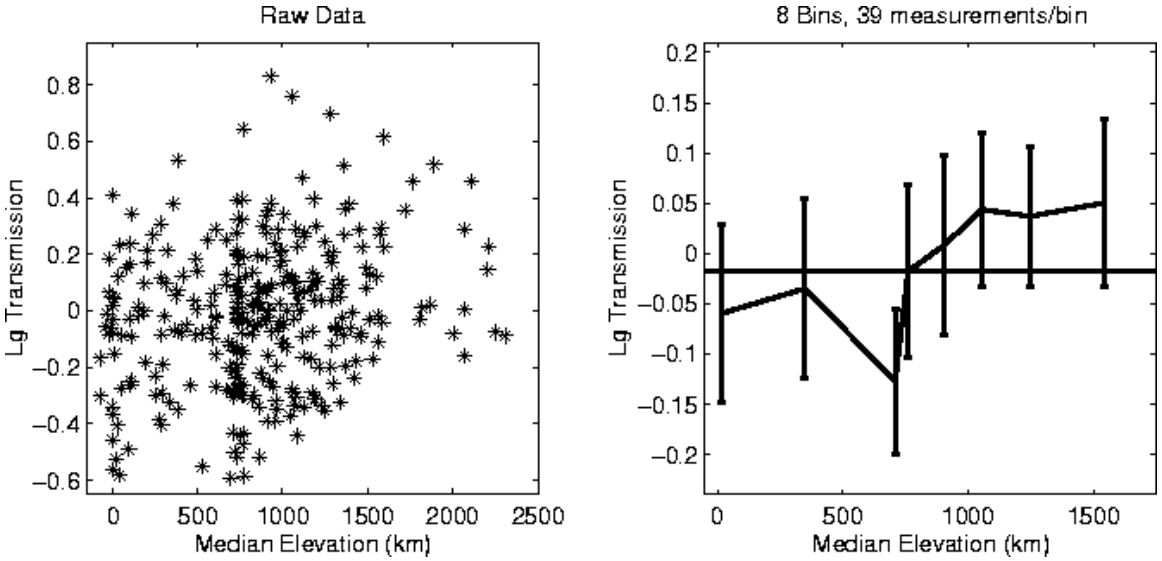


Figure 1: Lg TE vs median elevation along short path segments between SCSN stations.

Variance Reduction and Transportability:
We have systematically tested all possible single and two parameter categorical models, as well as models of crustal types based on cluster analyses of the various combinations of geophysical parameters, to predict Lg, Pg, and Lg/Pg ratio TEs. While we have found many statistically significant relationships, particularly for Lg and the Lg/Pg TEs, we do not include an exhaustive listing, but focus on how useful such models predict the TE of

new data. We first consider the application of corrections to new data in the same well-calibrated region. To assess that, the SCSN Lg/Pg data are divided randomly into 2 subsets of the data, and a model is derived from one of the data subsets. The propagation correction for a particular group is simply the median value of the change in log(Lg/Pg) along all the paths in that group. The corrections provide modest variance reduction for both the data set from which they were derived and to a lesser extent, for second data set, indicating some robustness to the method. All measurements have been normalized to 20 km distance, and variance reduction reported is in addition to any achieved by the distance correction. The separation of the data into two subsets and subsequent application of corrections is repeated 100 times to ensure a robust estimate of the improvement we might typically expect. The results for single parameters are shown in Table 1 for the 1-2 Hz and 2-4 Hz data. The corrections perform better at the higher frequency, with the crustal thickness* estimate and topographic roughness providing the greatest variance reduction. The use of two or more parameters only improves the variance reduction by another 1% to 2% at best.

Table 1: Variance reduction achieved by path corrections based on single geophysical parameters.

		Crustal Thickness*	Topographic Roughness	Steepest Gradient	Isostatic Residual	Isostatic Roughness
1-2 Hz	set 1	11%	6%	7%	5%	8%
	set 2	5%	3 %	4%	3%	3%
2-4 Hz	set 1	13%	15%	8%	5%	4%
	set 2	10%	10%	2%	2%	1%

An important result is that despite complete spatial overlap of the between-station paths of the nuclear explosion and earthquake data, corrections based on the earthquake data provide no variance reduction for the nuclear explosion data. For example, corrections based on the crustal thickness estimate for the 2-4 Hz data, which overall had the best results, reduce the variance by 13% when applied to the earthquake data, but *increase* the variance of the nuclear explosion data by 2%. Similarly, corrections based on topographic roughness achieve a 10% variance reduction for the entire earthquake data set, but cause a 2% variance increase for the nuclear explosion data. We explore this problem in detail in the next section. We assume for now that differences in the Lg/Pg ratio are due to Lg, as that has the greatest variance, but we still must repeat this analysis for Lg alone, rather than the ratio.

Baker (1998) showed that there are statistically significant differences in TE between different types of crust as distinguished by cluster analysis using the parameters of Table 1. We put this information to use in attacking the most difficult, but the most useful to solve problem in path corrections, that of real transportability. That is, the ability to predict propagation effects within reasonable confidence intervals in a region without prior seismicity. As demonstrated above, corrections based on levels of single or multiple parameters are useful in reducing variance of a "new" data set in the same general area.

To test extrapolation of corrections to uncalibrated crust, we apply path corrections based on changes in Lg/Pg amplitude ratios over short paths between stations to the changes that occur over paths between stations at opposite ends of the network (figure 2). The long paths connecting distant stations in the network (distance at least 150 km, and ray paths within 5 degrees of the azimuth between stations) traverse large areas not covered by the short paths (distances from 10 to 60 km). Corrections determined for the short paths may not be applicable to some sections of the crust sampled only by segments of the long paths, because that crust may be of a different type. For example, median elevation paths in the calibrated region may be in foothills, with rough topography, while some of the median elevation paths in the uncalibrated area could be flat, stable, and shield-like. We use the 2-4 Hz passband and test both the crustal thickness estimate and the topographic roughness, as they provided the greatest variance reduction for "new" data in a calibrated region (Table 1). The corrections are not based on median elevation of the entire path, but instead are determined and applied to each 20-km segment of the long paths, based on each segment's median elevation. As before, we divide the short paths into groups based on parameter values and use the median change in the Lg/Pg TE for each group as a correction term for

* Crustal thickness was found to be the single best predictor of TE (Baker, 1998), but is not known over the entire study region. Stepwise regression indicates that the sum of the minimum and maximum elevations along a path provides the best linear combination of the other parameters for predicting crustal thickness; thus this sum provides a crustal thickness estimate used over the entire region.

that group. The corrections reduce the variance of the short paths, as before, but they increase the variance when applied to the long paths. The elevation corrections do not appear to transport out of the area for which they were developed.

Presumably, some of the crust sampled only by the long paths is like that sampled by the short paths, and some is not. If so, cluster analysis should enable better distinction of which portions are similar, as it permits great flexibility in incorporating multiple parameters. We perform a cluster analysis using the minimum, maximum, and median values of topography, gravity, and crustal thickness where available, on all 20-km segments of the long paths together with the short paths. When we separate the crust into six distinct types, only four types have significant numbers of paths in both the short- and long-path groups. We use the median value of the change in Lg/Pg TE for the short paths in each cluster group as a propagation correction term. We hypothesize that these corrections will be appropriate for segments of the long paths in the same cluster group, even if they are in areas not sampled by the short paths, because the cluster analysis will have appropriately clustered similar types of crust. Segments of the long paths that are not in any cluster group with short paths will not have a correction term available. Fifty-four out of the 1292 20-km segments of long paths do not have corrections.

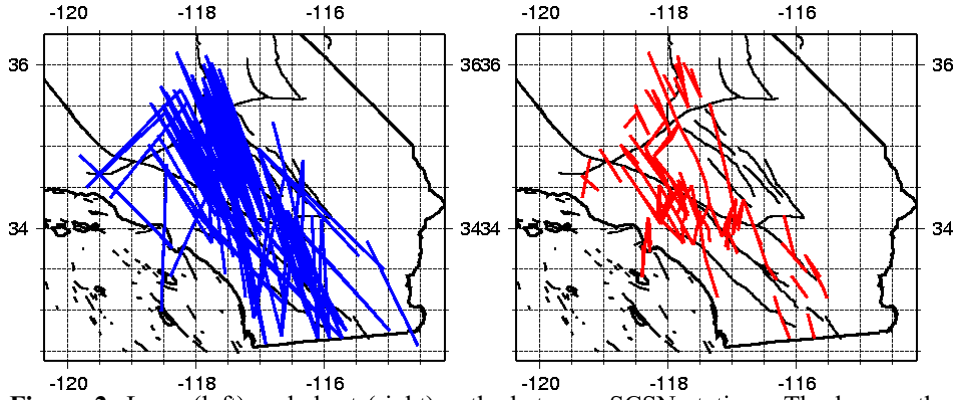


Figure 2: Long (left) and short (right) paths between SCSN stations. The long paths cover much terrain not sampled by the short paths, which have been used to define corrections.

The first attempt to apply these corrections caused a 28% increase in variance, much worse even than occurred with the single parameter based models. However, we also measure the change in the squared Scaled Median Absolute Deviation (SMAD), which provides an estimate of the spread of values which is less sensitive to outliers and so more appropriate in the presence of non-Gaussian errors (SMAD is equivalent to the standard deviation for Gaussian distributed data). The same path corrections that increased the variance when applied to the long paths, caused a 20% decrease in $SMAD^2$. The corrections decrease the residuals of most of the data, but very significantly increase the residuals of a small number of points, producing large outliers. Thus, the corrections are in the correct direction for most data. If we want to reduce the residuals of most of the data (i.e. reduce $SMAD^2$), we can use the corrections as they are. To avoid the creation of occasional large outliers while still reducing the residuals somewhat for most of the data, we tried applying scaled down corrections. Path corrections with the magnitude reduced by half cause a 5% increase in variance for the long paths and a 47% decrease in $SMAD^2$. Corrections reduced in magnitude by 3/4 cause no change in the variance, but still reduce $SMAD^2$ by 39%. Reducing the magnitude of the corrections based on single geophysical parameters does not appear to have a similar dramatic effect. This is a recent realization and its robustness, implications, and application must be much more thoroughly explored. Further work will include examination of which data have increased versus reduced residuals.

Section 2: Do Earthquake and Explosion Lg differ (and if so, how?)

Depth/Source Type Dependence of Lg Travel Times in Southern California:
As discussed above, the TE's of earthquake and nuclear explosion Lg appear not to be sensitive to the same parameters, at least not in the same way. To investigate if and how Lg from explosions and earthquakes differ, we first examine the timing of arrivals. We measure the midpoint of the area under the curve of absolute amplitudes within the Lg windows (3.6-3.0 km/s group velocity). The Lg window length varies from 11 to 29 seconds over the range of distances observed, so the amplitude midpoints are plotted relative to the window length. The mid-

point of nuclear explosion Lg amplitude arrives much later in the Lg window than it does from earthquakes (figure 3, left). The data from one shallow earthquake (2 km depth) at NTS are not shown in figure 3. For that event, the arrival times of energy within the Lg window cluster with those of the explosions. The positions of the first and third quartiles of Lg amplitude indicate no difference in the distribution of energy between explosion and earthquake Lg. The packets simply appear to be delayed in explosion records.

The differences observed in figure 3 may enable depth discrimination and so merit further study, along with our inquiry into differences between wavetypes that make up explosion and earthquake Lg. While no simple solution appears to explain the phenomena, consideration of three possible explanations provides insight into the character of crustal shear waves. First, there may be a difference in wavetype generated by sources at different depths. Shallow sources could excite modes that travel in the upper crust at lower velocity, while deep events could excite modes that propagate deeper in the crust at higher velocity. Another possibility is that the S-waves are generated by scattering from Rg (e.g. Myers, 1999). This is one of the most popular explanations for the generation of shear waves by explosions. In that case, Lg would be delayed by $x(1/V_{Rg}-1/V_S)$, where x is the distance at which Rg scatters to S, and V_{Rg} and V_S are the Rg and S-wave velocities. Differences in velocity structures around the different source regions could provide a third possible explanation, since the explosions and shallow earthquake are at NTS, and the other earthquakes are in other areas. The same analysis for Pg (figure 3, right) as was done for Lg shows no difference between source types. Thus, the differences between source regions would have to be in S-wave velocity structure only, making that explanation somewhat less probable.

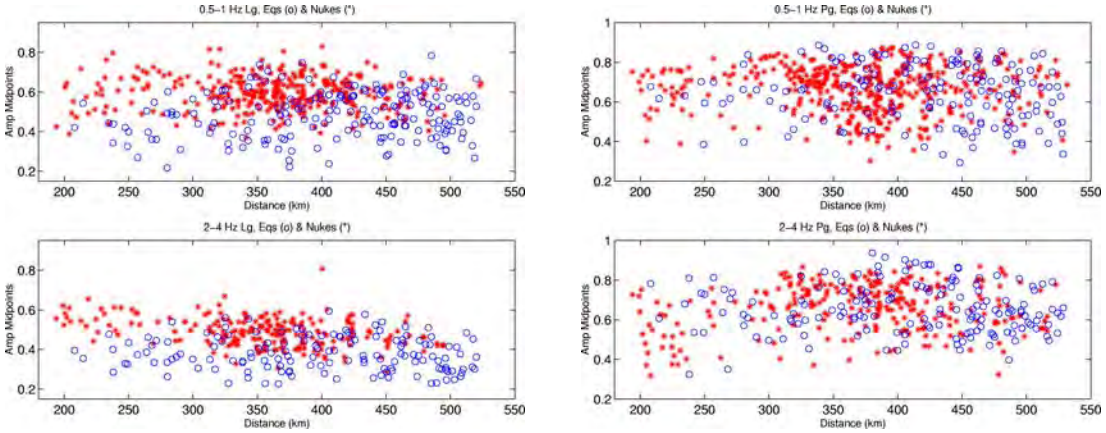


Figure 3: Source-receiver distance versus position within the Lg window of the amplitude midpoint (left column). At 0.5-1 Hz (top) the mean amplitude midpoint within the Lg window for earthquakes (circles) is at 0.48, where total Lg window lengths are normalized to 1.0. The same measure for explosions (asterisks) is 0.59. At 2-4 Hz, the mean amplitude midpoint is at 0.38 and for explosions is 0.49. No difference is apparent in the distribution of amplitudes within the Pg windows between explosions and earthquakes (right column).

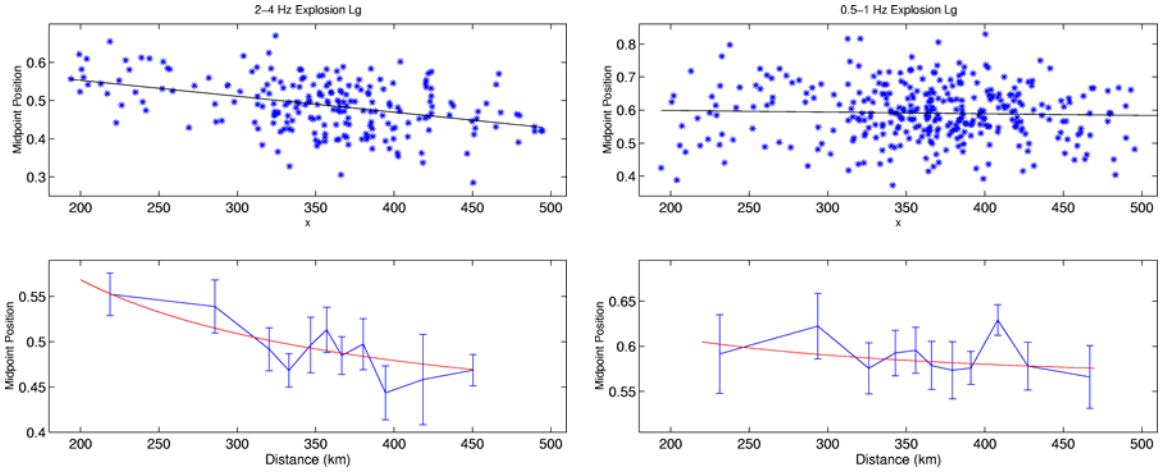


Figure 4: Midpoint position within the Lg window from 2-4 Hz explosion data (left). The upper left plot shows the least squares fitting line to the data. The lower left plot shows the median value in 20 data point bins with 2 SMAD confidence intervals. Lg energy arrives later in the Lg window at the distances less than 300 km, and the position within the Lg window stabilizes at greater distance. The curve is the predicted arrival of Lg energy if the explosion Lg were generated by scattering from Rg at 10 km from the source. The right column shows the same plots for 0.5-1 Hz measurements.

The effect of range is relevant to the second explanation. Energy arrives relatively later within the predicted Lg window at lesser distances. This is the effect of an approximately constant time offset, as the Lg window lengthens with range. In figure 4, we replot the high frequency explosion Lg results with a least squares straight line fit to the data (top plot). The lower plot shows the median position of the amplitude midpoint within the Lg window for successive bins of 20 data points each. That indicates that the arrival time of energy within the Lg window is later at lesser distances, but there is no apparent slope at distances greater than 300 km. A constant time offset of explosion Lg is consistent with explosion Lg being generated by Rg-to-Lg scattering at the surface. The curve superimposed on the lower left plot (figure 4) shows this effect. It assumes a 2-4 Hz Rg velocity of 2.1 km/s, Lg velocity of 3.6 km/s, and scattering at 10 km from the source. The observation of a constant time offset is also consistent with the hypothesis that earthquake and explosion Lg are composed of different modes, as long as the modal structure differences are lost through scattering at less than 200 km. Otherwise, the time offset would increase with distance.

The greater delay in Lg at lesser range is not observed in the 0.5 to 1 Hz explosion data (figure 4). This could be explained by higher Rg velocity at 0.5-1 Hz. If Rg velocity at 0.5-1 Hz were 2.9 km/sec (Revenaugh, 1995), the predicted delay would be much less, as indicated by the curve in the lower plot. We are admittedly employing more parameters (Lg and Rg velocities and the scattering distance) than we have observations. Nonetheless, within a wide range of values for these parameters, the basic observations can be explained.

A Second Data Set:

To try to distinguish better between explanations for the Lg delay for shallow events, we examine an additional data set. Nineteen quarry blasts and twenty-eight earthquakes in the Galilee provided 630 recordings on the local Israeli network (Grant et al, 1999). These data allow us to extend the observations closer to the source, to higher frequencies, and verify them in a different region. As in the SCSN data set, explosion Lg is delayed relative to earthquake Lg. Because these explosions and earthquakes are both distributed across the Galilee, we can rule out as unlikely the possibility that velocity structure differences between source regions cause the delays.

There are only 20 quarry blast and 45 earthquake records from distances greater than 200 km. Most data were recorded closer in, and we concentrate on Sg and Pg arrivals recorded at less than 72 km distance so that mantle phases do not complicate the interpretation. The basic observation that explosion shear waves, in Sg now, are delayed relative to earthquake shear waves, is again duplicated here. There again is no difference in Pg timing for the two source types (figure 5). These observations are consistent at all frequencies up to 22 Hz, which precludes Rg to shear wave scattering contributing to the phase and causing the delay. These observations of Sg

delays are relevant to the Lg delays, since Sg will become Lg with distance. Models that only explain delays of shallow event shear waves in the crust at one range of distances, but not the other, will be less credible. The simplest explanation of the Sg observations is that the predicted times, based on the IASPEI91 model, are too fast at shallow depths. We note however that Lg, and regional distance Pg in southern California, are defined by group velocity windows, so those delays can not be explained by errors in the velocity model based predicted times.

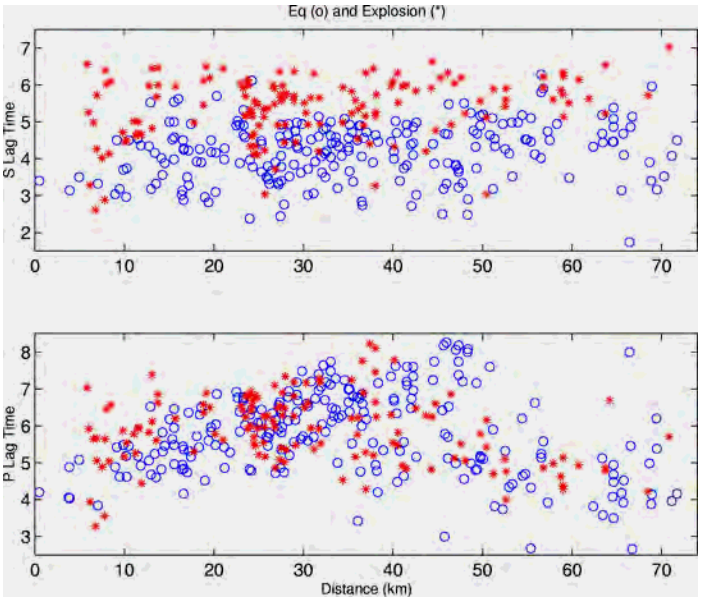


Figure 5: Earthquake (circles) and explosion (asterisks) lag times for Sg (top) and Pg (bottom). Lag time is defined here as the midpoint of amplitude under the curve of absolute amplitudes within the predicted phase windows. The explosion Sg is approximately 2 seconds later than the earthquake Sg, while no difference is observed between the time of Pg arrivals for the two source types.

The Galilee earthquakes had depths from 0 to 23 km, and we use those data to examine the effect of depth on the delay of Sg. Earthquake Pg and Sg travel time residuals based on analysts' picks are comparable for deep events (figure 6). Sg, but not Pg residuals increase however from approximately 12 km depth up to the surface (where they are delayed the same amount as the quarry blast Sg phases). This decrease in Sg travel time residuals with depth is also observed in automatically picked maximum peak times and in the energy midpoint times within theoretical Pg and Sg windows and is observed for all frequencies up to 22 Hz. The increased lag time of all measures of Sg energy down to 12 km depth and at all frequencies is inconsistent with Rg scattering having contributed to the Sg energy and delayed it. Further, there was no observable variation in the Sg/Pg amplitude ratio with depth and frequency such as would be predicted if Rg-to-S scattering contributed significant shear wave energy for the shallow events. Modal structure is not a consideration for these local phases.

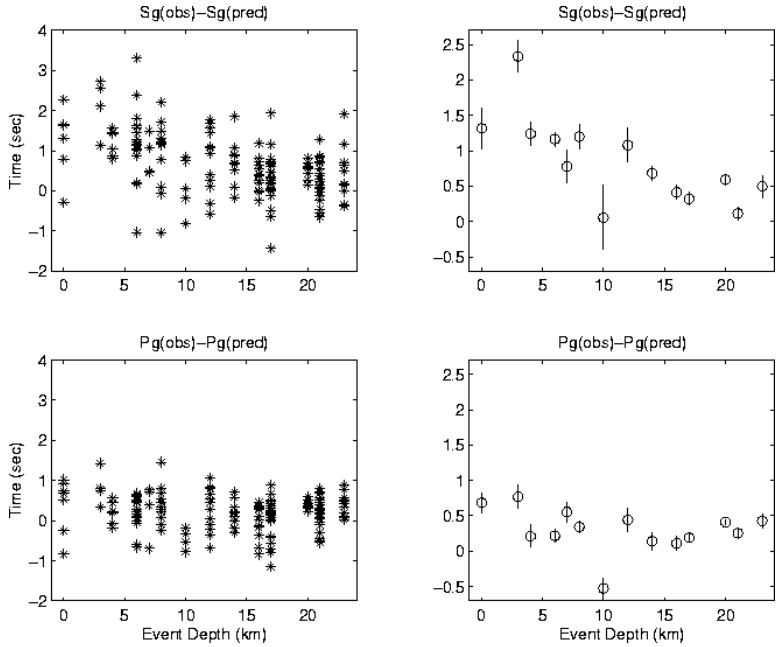


Figure 6: Observed minus predicted times for Sg (top) and Pg (bottom) versus earthquake depth. All the data are shown in the left column. The median and 1 SMAD confidence intervals are shown in the right column.

The rate of amplitude decay after the initial peak indicates that more energy is in the latter part of both the Sg and Pg windows of shallower events, possibly due to more scattering in the shallow layers and at the surface. We see no clear difference between the patterns for the two phases, and so can not conclude that the explosion shear wave energy for these events is due to or preferentially augmented by scattering at some distance from the source.

In summary, the question of whether there is a difference in the wavetypes making up earthquake and explosion Lg remains unresolved, but we have uncovered the potentially useful observation that Lg energy arrives later for explosions than for earthquakes. This is the most significant result of this section. The search for the mechanism is enlightening in that the initial obvious explanations are not altogether consistent with detailed analysis of all the data. The delay and that it is constant with distance are consistent with Rg scattering contributing to the explosion Lg and with differences in modal excitation, if the mode structure does not persist beyond 200 km from the source. Those observations are duplicated in the Galilee data set, but measurements made on near-source Sg from the Galilee data (which could not be observed in the SCSN data) are inconsistent with Rg scattering contributing to the S-wave energy and with the modal explanation. An incorrect S-wave velocity model could explain the Galilee observations, but this is unsatisfying, as it calls on two different explanations for the very similar observations made from both data sets. That is, the crustal S-wave phases from explosions, but not from earthquakes, are delayed relative to their respective P-wave phases. Given that we observe delays in crustal S-waves measured very near the source, it is most reasonable to assume that delays measured at greater distance are simply carried over from that initial delay. A single model that explains both sets of observations would be more credible. Because the arrival time of energy within the Lg window may prove to be a useful depth discriminant, development of such a model will be the focus of further efforts.

Global Application:

We have developed some promising techniques for determining path corrections and transporting them to new, uncalibrated regions. Because the goal is to improve CTBT monitoring using stations of the IMS, we next will apply these techniques, modified as necessary, to IMS data. This may also be one of the most useful data sets for such research, as it provides an extremely large set of global observations. We also will extend the analysis to the mantle phases, Pn and Sn. Because however the IMS network is large, new, and still being implemented, quality control is a concern. We describe below tests we perform to filter out errors in reported phase amplitudes.

We are concerned with both instrument calibration problems and phase identification errors. Evidence of probable calibration problems will prevent us from separately analyzing Lg and Pg, as we did in southern California. We examined 3 Hz IDC data reported between July 1996 and January 1998, when 20,159 regional phase signal and noise peak measurements were recorded. We consider two types of timing problems, chronological inconsistencies (arrival times out of order) and time-window discrepancies (arrivals falling outside theoretical time windows).

We checked for chronological inconsistencies of two types, noise measurements made after signal measurements of the same type (e.g. the Pn noise measurement being made after the Pn signal measurement), and signal arrival times listed out of the proper sequence (Pn, Pg, Sn, Lg, except for small distances where Pg may arrive earlier than Pn). Proper chronological order is violated less than 0.2% of the time, except for Sn. We will not use those data. The Sn arrival times have more problems, with 4% of the Sn measurements made later than the Lg measurements. Sn and Lg traverse very different structures, so for the creation of path corrections, we must ensure that we do not use measurements of misidentified phases.

The percentage of Pg and Lg noise and signal measurements that are made outside of the predicted time windows are shown in Table 1. Phases not being measured for some events causes some rows to sum to less than 100%. We are assessing which identifiable errors render the data unusable.

The worst problem among the four types of arrivals is seen with Sn. 8.7% of the Sn measurements are made within the predicted Lg signal window. Further, close to half of the noise measurements and 20% of the signal measurements were made outside their predicted time windows, mostly late. Some, but not all of these inconsistencies may be due to errors in the depth assumed for the event. These problems combined indicate that the use of at least a tenth of the listed Sn arrivals may be questionable.

We also looked for variations with time of pre-Pn noise, which serves as an indicator of possible problems with the instrument calibration. The median value of pre-Pn amplitude reported for station MJAR, for consecutive 20 point bins is shown in figure 1. Some time intervals appear to have unusually high pre-Pn noise, and the station appears to have been shut down after one of those time periods. This is likely typical, as this is the first station we examined. The reasonable possibility that these are not natural variations in background noise levels, but rather changes in instrument gain, suggest that we use only phase amplitude ratios.

Table 1. Percentages of arrival times within, before and after the predicted time windows.

Phase	in predicted window	before predicted window	after predicted window
Pg noise	91.0	3.0	6.1
Pg signal	97.3	1.0	1.7
Lg noise	94.4	2.0	3.5
Lg signal	99.2	<1	<1

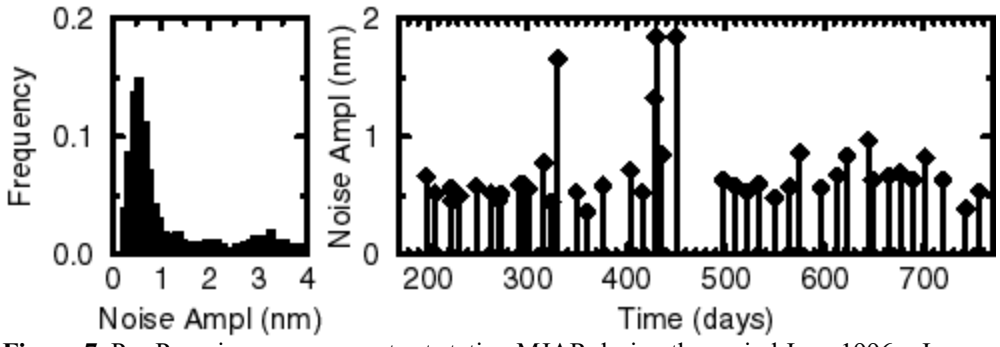


Figure 7. Pre-Pn noise measurements at station MJAR during the period June 1996 – January 1998. Time is counted from the beginning of 1996. The histogram of noise distribution shows a small second peak at 3 mm, rather than a smooth distribution of values (left). On the right are median values of pre-Pn noise amplitude for non-overlapping groups of 20 events each.

CONCLUSIONS AND RECOMMENDATIONS

Analysis of correlations between topography, gravity, and crustal thickness and Lg, Pg, and Lg/Pg ratio propagation in southern California has led to the development of path corrections that are transportable, in that they reduce the distribution of discriminant values for earthquake records for uncalibrated areas. In particular, the identification of distinct crustal types using cluster analysis appears to have the most promise for this task. Earthquake record-based path corrections do not, however, reduce the spread of values for Lg/Pg ratios from nuclear explosions, leading us to examine the differences between Lg phases generated by the two source types.

Southern Californian and Israeli earthquake and explosion data sets were analyzed to assess whether explosion and earthquake Lg differ and so are subject to different propagation effects. Observations made in addressing the question suggest a possible depth discriminant based on the relative Lg-to-Pg travel time residuals. Specifically, energy within the Lg group velocity window and around the predicted arrival times for Sg arrives later for shallower events. The physical basis for this is not clear. Late Lg is consistent with either Rg-to-Lg scattering or excitation of different modes by different depth events. That shear-wave energy measured close to the source for the Galilee data is delayed for shallower events complicates the picture. Because the close in Sg energy presumably contributes to Lg at greater distance, any explanation for Lg delays should be consistent with the Sg measurements. This makes both Rg-to-Lg scattering and excitation of different modes due to event depth less likely reasons for the delay of shallow event Lg. That these initially plausible, and perhaps most obvious explanations are inconsistent with close in shear wave observations is an important result that bears on the generation of S-waves by explosions. The delay of shear wave energy from shallow events should be studied further, as it may prove to be useful in discriminating event depth. The question of whether the wavetypes that make up Lg vary with depth should also be studied further as it is important to the application of path corrections.

The next step in this project will be to apply the techniques developed for the SCSN data to the global data of the IMS. We have shown that careful checking of reported travel times permits identification of some problematic data. The path correction techniques developed for the SCSN data will be modified to deal with long paths. We will also modify the techniques to include censored data, since lack of a signal where one is expected indicates blockage somewhere along the path. We will use a maximum likelihood approach to incorporate such data. We will again use cluster analysis to distinguish crustal types, and use an inverse approach to estimate the effect of each type and transitions between types, based on their contribution to the total path.

REFERENCES

Baker, G.E., 1998, Predicting crustal phase propagation efficiency from topography, gravity, and crustal thickness, in *Proceedings of the 20th Annual Seismic Research Symposium on Monitoring a Comprehensive Test Ban Treaty*, 153-162

Grant, L., F. Ryall, B. Wagner, I. Henson and W. Rivers, 1999, http://es1.multimax.com/~gtdb/index.html

Liu, C. and T. Ahrens, 1998, Wave generation from explosions in cavities in rock, *Proceedings of the 20th Annual Seismic Research Symposium on Monitoring a Comprehensive Test Ban Treaty*, 286-301

Myers, S., W. Walter, K. Mayeda, and L. Glenn, 1999, Observations in support of Rg scattering as a source of explosion S waves: regional and local recordings of the 1997 Kazakhstan depth of burial experiment, *Bull. Seism. Soc. Am.*, 544-549

Phillips, W.S., 1998, Path correction using interpolated amplitude residuals; an example from central China, *Geophys. Res. Lett.*, 2729-2732

Revenaugh, J., 1995, The contribution of topographic scattering to teleseismic coda in southern California, *Geophys. Res. Lett*, 543-546

Rodgers, A., W. Walter, C. Schultz, S. Myers, L. Thorne, 1999, A Comparison of Methodologies for Representing Path Effects on Regional P/S Discriminants, *Bull. Seism. Soc. Am*, 394-408

Zhang, T.R., S. Schwartz, and T. Lay, 1994, Multivariate analysis of waveguide effects on short-period regional wave propagation in Eurasia and its application in seismic discrimination, *Jour, Geophys. Res*., 714-725

SHALLOW VELOCITY STRUCTURE AT THE SHAGAN RIVER TEST SITE IN KAZAKSTAN

Jessie L. Bonner, Southern Methodist University
D. Craig Pearson, W. Scott Phillips and Steven R. Taylor, Los Alamos National Laboratory

Sponsored by U.S. Department of Energy
Office of Non-Proliferation and National Security
Office of Research and Development
Contract No.: W-7405-ENG-36

ABSTRACT

During 1997 and 1998, 12 chemical explosions were detonated in boreholes at the former Soviet nuclear test site near the Shagan River in Kazakstan. These explosions were recorded at local distances by a network of seismometers operated by Los Alamos National Laboratory and the Institute of Geophysics for the National Nuclear Centre (NNC) in Kazakstan. The depths of these explosions ranged from 2.5 to 550 m, while the explosive yield varied from 2 to 25 tons.

Short-period, fundamental-mode Rayleigh waves (*Rg*) were generated by these explosions and recorded at the local stations, and the waves exhibited normal dispersion between 0.2 and 3 seconds. Dispersion curves were generated for each propagation path, and tomographic maps of *Rg* group velocity show a zone of fast velocities (> 2.3 km/sec for 1-second period *Rg*) for the southwestern section of the test site and slow propagation (≤ 2.3 km/sec) for the northeastern section. The two regions are separated by a thin NW-SE trending transitional zone that parallels the tectonic fabric for the study area. The group velocities correlate with spatial patterns of magnitude residuals (Ringdal and Marshall, 1989) from nuclear explosions at the Shagan River Test Site, and may help to evaluate the mechanisms behind those observations. The inversions of the *Rg* dispersion curves show shear wave velocities for the southwestern section that are on average 0.4 km/sec greater than the northeastern zone. At depths greater than 1.5 km, the standard deviations for the models begin to overlap, and the statistical difference between the models is no longer significant. The differences observed in the shear wave velocity structures above 1.5 km, for the various propagation paths, must be considered when making local to near-regional correlations of the explosions.

Key Words: *Rg* dispersion, shear wave velocity structure, Shagan River Test Site

OBJECTIVES

The properties of geological materials change quickly near the earth's surface. If these changes in geologic structure affect seismic generation from shallow (near-surface) and deep (up to 1-km) explosions differently, we may be able to develop techniques to discriminate between large industrial blasts and an underground nuclear test. For the present study, we attempt to determine the lateral variations in the velocity structure at the former Soviet test site near the Shagan River in Kazakhstan (STS) by using the properties of explosion generated *Rg*. *Rg* was observed on the local seismograms near the test site from a series of chemical explosions detonated at varying depths within the upper crust during 1997 and 1998. The purpose of the explosions was for the closure of the unused boreholes at the former test site as part of a joint project between the U.S. Department of Energy (DOE), the U.S. Defense Special Weapons Agency (DSWA), and the National Nuclear Center of the Republic of Kazakhstan (NNC). The explosions were recorded by a dense local network operated by Los Alamos National Laboratory and by a regional network operated by Lamont-Doherty Earth Observatory.

For explosions detonated on or near the earth's surface, *Rg* is often the dominant arrival at local to near-regional distances. *Rg* group velocities are controlled by the velocity variations in the upper few kilometers of crust along the propagation path. The phase is highly attenuated in regions of complex terrain, and is most prominent on paths comprised of low velocity sediments or weathered rock (Kocaoglu and Long, 1993). *Rg* is seldom recorded at distances greater than 300 km thus limiting its usefulness as a depth discriminant. However, the influence of *Rg* scattering into *Lg* coda from explosions has been noted and can make an important contribution to explosion seismograms [e.g. Gupta *et al*., 1992; Patton and Taylor, 1995; Mayeda and Walter, 1996; Meyer *et al.,* 1999].

Because *Rg* group velocities are controlled by the velocity variations in the upper few kilometers of crust, the surface geology of the path can offer insight into the characteristics of the propagation. The former test site has a complex structural and geologic setting created by the interaction of the Siberian and Kazakhstan continental plates and intervening island arcs (Zonenshain *et al.,* 1990). The region has undergone two periods of deformation as a result of the Caledonian and Hercynian orogenies. The Caledonian orogeny (early Paleozoic) is represented by varying degrees of faulting, folding, and metamorphism (Nalivkin, 1960). One of these faults, the Chinrau, dissects the former test site along a NW-SE trend and appears to show evidence of recent offset on SPOT imagery (Leith, 1987). It is the later Hercynian orogeny (Carboniferous) that folded the Carboniferous-aged sedimentary rocks and implaced the granites and granodiorites at the test site (Figure 1). The result of the compressive forces associated with these two orogenies is a NW-SE trending tectonic fabric. Quaternary sediments, including sands, clays, and gravel now cover a large portion of the test site. As can be inferred from Figure 1, the test site is not in a homogenous body of rock. In fact, the site can be divided into two regions--a northeastern (NE) region composed of alluvial and tuffaceous deposits overlying folded and faulted Paleozoic sedimentary rocks and a southwestern (SW) quadrant comprised of a large granodiorite body that intruded into the surrounding sedimentary rocks. This intrusive complex is encountered in boreholes 1327 and 1411, and can be inferred to connect beneath the alluvium. The lithology of this pluton has been referred to as granite and granodiorite (Davis and Berlin, 1992) and granodiorite (Borovikov, 1972). For the purpose of this paper, we refer to the pluton as crystalline rock. The results of this paper show how these variations in the shallow geology cause a large range of *Rg* group velocities.

RESEARCH ACCOMPLISHED

This study involves seismograms from 10 explosions at STS (Table 1). The explosions were conducted to seal the unused boreholes at the test site. The shots at boreholes 1071, 1311, 1349, and 1381 had an explosive weight of 25 tons and were emplaced at depths of 50 m, 50m, 300 m, and 550 m, respectively. At the intervals of the explosives emplacement, neogenic clays (1311) or crystalline rock (1071, 1349 and 1381) were observed. The primary scientific objective of this series of explosions was to determine the effect of depth of burial on the discrimination of nuclear explosions. A secondary objective was to calibrate the Kazakhstan seismic network, with special emphasis on the IRIS GSN station at Makanchi (MAK) and the IMS auxiliary stations Kurchatov (KUR) and Aktyubinsk (AKT). Results of the regional studies can be found in Glenn and Meyers (1997) and Meyers *et al*. (1999).

TABLE 1. EXPLOSION CHARACTERISTICS AT BOREHOLE CLOSURES

Borehole	Latitude	Longitude	Explosive weight (kg)	Depth of charge emplacement from surface (m)	Date	Origin Time (UTC)
1071	49.9810	78.7559	25000	28	9/17/98	07:19:40.551
1311	49.9412	78.7860	25000	50	8/3/97	08:07:20.039
1327	49.9129	78.7871	2028	20	7/14/98	05:11:35.570
1349	49.8794	78.8493	25000	550	08/5/97	07:30:15.126
1381	49.8837	78.8147	25000	300	8/31/97	07:08:39.179
1383	49.8724	78.6477	2028	14	8/15/98	02:40:59.116
1386	49.8801	78.6921	2028	20	7/13/98	10:44:56.363
1389	49.8786	78.7601	2028	9	08/15/98	05:05:11.156
1409	50.0357	79.0114	2028	13	8/14/98	04:28:52.815
1419	50.0576	78.9387	2028	2.5	08/14/98	05:39:24.970

In addition to the DOB study, 8 additional explosive borehole closures were recorded (Table 1). The depth of the explosives emplacement for these closures ranged from 2.5 to 46 meters with 2 ton yields. Boreholes 1071 and 1383 were detonated in granoseyenites, while the six other explosive closures in 1998 were conducted in neogenic clays.

A seismic network was deployed at local distances by Los Alamos National Laboratory to record the explosions, and the network was maintained for the duration of the program by the Institute of Geophysical Research (NNC). Seismograms were recorded on L4-C-3D, three-component, velocity sensors connected to Refraction Technology (REFTEK) data loggers. Origin times for each event were obtained by a GPS-based timing system employed at each hole for shot-break time. The origin times were checked for consistency using an accelerometer and data acquisition system placed near the test borehole. Seven sites were selected at various azimuths to the proposed locations for the DOB experiment (Table 2). For the 1998 series of hole closures, the seismic stations reoccupied the same DOB locales, except for S3 which was relocated because of technical problems. For the REFTEK/L4-C-3D sites, the data was sampled at 500 Hz, and the recorder was set up to use a STA/LTA trigger. The data was then transferred to a workstation at LANL for dispersion processing and analysis. The dispersion curves were generated through use of the Multiple Filter Analysis (Dziewonski *et al*., 1969) and refined by Phase Match Filtering (Herrin and Goforth, 1977).

TABLE 2. COORDINATES FOR THE BALAPAN NETWORK

Station	Latitude	Longitude
S2	49.8636	78.8701
S3[1]	49.8874	78.9087
S3	49.9494	78.7483
S4	49.8766	78.7636
S6	49.8217	78.7531
S7	49.8526	78.9841
S8	49.9777	78.7590
S9	49.9719	78.9587

The dispersion curves for all paths considered in this study are shown in Figure 2. Group velocities range from 1.7 up to 2.9 km/sec, and have periods between 0.2 and 3 seconds. A better way to show the same data is through the use of group velocity tomography maps for individual periods. Tomography was performed assuming straight ray propagation, parameterizing the model with an array of constant velocity circles. We used first-difference regularization to control the effects of noise on the final image.

[1] Location valid for Hole Closures 1311, 1349, and 1381

Regularization parameters were chosen to optimize resolution and covariance; further details may be found in Phillips *et al*. (1999). Tomographic inversion produced variance reduction of 80%, 94%, 78% and 66%, relative to a flat model, for periods of 0.5, 1.0, 1.5 and 2.0 seconds, respectively.

The group velocity tomography maps presented in Figures 3 – 5 show a relatively high velocity region to the southwest (SW), separated from a low velocity region in the northeast (NE) by a thin transition zone. We suspect that the faster velocities in the SW region are related to crystalline rocks at or near the surface. Logs for test hole 1383 (NNC Field Report, 1996) show crystalline rocks to within 5 m of the surface. At shorter periods of 0.5 and 1 sec (Figure 3 and Figure 4), the low velocities associated with the transition zone follow the Shagan River towards the southwest, and may be related to alluvium overlying the intrusive crystalline rocks near this section of the test site. Lithologic logs from boreholes in this region confirm that alluvium and weathered rock with thickness as great as 350 m overlie the crystalline rocks. For all period ranges, a region of low velocities is observed in the northeast. Lithologies for these boreholes include thick sections of alluvium and unconsolidated tuffs that overlie the Paleozoic sedimentary section.

We used least squares inversion technique (Herrmann, 1988) to invert group velocity dispersion curves for the shallow shear wave velocity structure within the different regions of the STS. Paths within each region of the test site were inverted using both differential and stochastic inversions for different starting velocity models. The minimum, maximum, and average shear wave velocity structures from all inversions for paths in the SW and transition regions of the test site are shown in Figure 6. The minimum velocity was obtained by inverting the paths that predominantly sample the rocks for the transition zone between the fast and slow regions (1327 and 1311 to S6, S7, and S4). The maximum velocity curve is the result of the path from shot 1383 to S3 and S8. These paths are confined in the granodiorite and have the greatest group velocities for the entire *Rg* bandwidth. The average velocity structure shows three distinct layers--a 250 m thick section with velocities averaging 2.45 km/sec, a layer between 250 m and 900 m with velocities averaging 2.95 km/sec, and a third layer to a depth of 2.5 km with shear wave velocities of approximately 3.3 km/sec.

Figure 7 shows the results of the inversions in the northeast region. The minimum velocity structure was obtained from the inversion of paths such as 1327 to S9 and 1311 to S9, both having flat, low-velocity dispersion curves. *Rg* along this path is slowed by propagation predominantly within the NE region. However, about 25% of the path occurs in the transition zone, thus creating a velocity structure with greater velocities than the average for the NE. Three distinct layers were noted in the velocity structure for the SW and transitional regions, while the suite of inversions in the NE region show the average velocity structure to be increasing with depth without prominent discontinuities down to a depth of approximately 2 km. Below this depth, the resolution is compromised, as *Rg* waves in this region have smaller wavelengths.

As discussed above, the trends from the tomographic inversion appear to delineate two distinct zones separated by a NW-SE trending boundary. Relatively high velocities are observed to the SW and lower velocities to the NE. The boundary separating the two zones roughly coincides with the Chinrau fault. Sequences of tuffs and alluvium exist to the northeast of this boundary overlying Paleozoic sedimentary rocks and to the southwest, crystalline rock is predominant. Differences between the NE and SW regions have been known for some time on the basis of teleseismic P-wave spectral and waveform differences from nuclear explosions (Marshall *et al*., 1984; Stewart, 1988; Bache *et al*., 1986). Additionally, more recent studies have indicated NE and SW contrasts in *Lg* amplitudes (Ringdal *et al*., 1992; Jih and Wagner, 1992). Specifically, Marshall *et al*., (1984) observed that *P* waves from Shagan Test Site (STS) nuclear explosions fell into two distinct classes. NE STS *P* waveforms are more complex and have higher corner frequencies than those from SW explosions of similar magnitude. The *P* waveforms from the NE explosions exhibit a few cycles of ringing not observed on the simple waveforms from the SW. This is consistent with the observed complexity of the NE *Rg* waves relative to those in the SW discussed earlier (Figs. 3 and 4). The observation of longer duration waveforms in the NE relative to SW STS conflicts with the spectral observations of Marshall *et al*. (1984). However, in comparing spectra for the two different regions at the UK array stations in Bache *et al*. (1986), the difference in the corner frequencies is not strongly apparent. It was suggested that changes in source material properties were the cause of the observed differences, although very little geologic information was available at the time. Stewart (1988) also noted the NE explosion *P* waveforms had a smaller, longer period, first negative pulse (presumably pP) than those from the SW. It was suggested that the greater P-pP times and longer period pP pulses were due to greater scaled depth of burial and/or slower uphole velocities in the northeast.

The spatial variations in velocities from this study (Figure 3-5 and Figures 6 and 7) are consistent with the observations of teleseismic *P* waves and *Lg* waves from STS nuclear explosions. For example, it is expected that explosions detonated in a region having low-velocity sedimentary layers overlying crystalline basement will show *P* waveforms that are more complex and lower frequency than those detonated in crystalline rock. The complex waveforms and larger pP delays are presumably due to near-surface reverberations and lower uphole velocities. The lower corner frequencies are predicted from established explosion-source models (e.g. Mueller and Murphy, 1971). Using a Mueller-Murphy explosion-source model for granite we compute Reduced Velocity Potential (RVP) spectra for two identical explosions. Each explosion had a yield of (150 kT) and near-source compressional velocities of 5 and 3.9 km/s taken from velocity models shown in Figures 6 and 7 (representing the SW and NE portions of the STS, respectively). The results are shown in Figure 8 and it can be seen that just based on simple elastic properties, we expect explosions of identical yields from the NE to have lower corner frequencies than those from the SW. The explosion-source corner frequency is proportional to the decay rate of the pressure-time history acting at the elastic radius, which in turn, is proportional to the compressional velocity at the source. Thus, the lower corner frequencies as evidenced by the longer duration *P* waves for the NE explosions may simply be due to the reduced velocities (e.g. material strength) in the near-source region.

CONCLUSIONS AND RECOMMENDATIONS

The results of this study show that variations in geologic structure have a significant effect on *Rg* group velocities at STS. Tomography maps of *Rg* group velocity show the SW region of the test site is characterized by faster velocities than the NE section. As an example, *Rg* with a period of 1 sec propagates with velocities greater than 2.3 km/sec for the SW section of the test site, while propagating at less than 2.3 km/sec for the NE section. Surface geologic maps and borehole lithology logs for the region show the slow region in the NE section of the test correlates well with sedimentary rocks and tuffaceous deposits overlain by alluvium. A large granodiorite body that has intruded the sedimentary rocks appears to correlate well with the fast velocities in the SW region. The inversions of the *Rg* dispersion curves give shear wave velocities for the SW region that are on average 0.4 km/sec greater than the NE region. At depths greater than 1.5 km the standard deviations for the models begin to overlap, and the statistical difference between the models is no longer significant.

The systematic variation in the relative patterns of *P* wave complexity and *P* and *Lg* source size estimators across the test site (Marshall *et al.,* 1985; Stewart, 1988; Ringdal *et al.,* 1992) correlate with the two geophysically distinct regions obtained from this study. Future studies should focus on the quantification of how the velocity structure at the test site influences the regional and teleseismic nature of *P* and *Lg* wave seismograms.

ACKNOWLEDGEMENTS

The authors wish to thank Brian Stump, Bob Herrmann, and Howard Patton for insightful suggestions concerning the research. We also wish to thank Diane Baker and Los Alamos National Laboratory for providing the raw and instrument corrected data along with details concerning the explosions at the test site. We wish to thank Luke Kluchko of DSWA for his support and expertise. Much of the information about the 1998 borehole closures including borehole lithology and rock properties was provided by the Institute of Geophysical Research of the National Nuclear Center of the Republic of Kazakhstan (NNC), and we wish to thank them for their help with this experiment. The research was sponsored by the Office of Nonproliferation and National Security and the Office of Research and Development for the Department of Energy under contract no. W-7405-ENG-26.

REFERENCES

Bache, T.C., S.R. Bratt, and H. Bungum, (1986). High-frequency P-wave attenuation along five teleseismic paths from central Asia, Geophys. *J. R. astr. Soc*., 85, 505-522.

Borovikov, L.E., 1972, Tectonic map of central and eastern Kazakhstan, scale 1:1000000, Sheet 2.

Davis, P.A., and G.L. Berlin (1992). Geologic mapping of the Semipalatinsk region, eastern Kazakhstan, using land sat thematic mapper and spot panchromatic data, Los Alamos National Laboratory, LAUR-92-310, 15p.

Dziewonski, A., S. Bloch and M. Landisman (1969). A technique for the analysis of transient seismic signals, *Bull. Seism. Soc. Am.* 59, 427-444.

Glenn, L., and S. Myers (1997). Depth of burial experiment at Balapan, Lawrence Livermore National Laboratory, UCRL-JC-128313.

Gupta, I.N., W.W. Chan, and R.A. Wagner (1992). A comparison of regional phases from underground nuclear explosions at East Kazakh and Nevada Test Sites, *Bull. Seism. Soc. Am.* 82, 352-382.

Herrin, E. and T. Goforth (1977). Phase-matched filters: application to the study of Rayleigh waves, *Bull. Seism. Soc. Am.* 67, 1259-1275.

Herrmann, R.B. (1988). *Computer Programs in Seismology.* Vols II-IV, St. Louis University, St. Louis, Missouri.

Jih, R.S., and R.A. Wagner, (1992). Path-corrected body-wave magnitudes and yield estimates of Semipalatinsk explosions, Teledyne-Geotech, TGAL-92-05, Alexandria, Virg., 69pp.

Kocaoglu, A. and L.T. Long (1993). Tomographic inversion of *Rg* wave group velocities for regional near-surface structure, *J. Geophys. Res.* 98, 6579-6587.

Leith, W. (1987). Tectonics of eastern Kazakhstan and implications for seismic source studies in the Shagan River area, in Paper Presented at the 9th annual DARPA/AFGL Seismic Research Symposium, 15-18 June 1987, pp. 34-37.

Marshall, P.D., T. C. Bache, and R. C. Lilwall (1985). Body wave magnitudes and locations of Soviet underground explosions at the Semilpalatinsk test site, AWRE Report No. 0 16/84 (re-issue), HMSO, 87.

Mayeda, K. and W. Walter (1996). Moment, energy, stress drop, and source spectra of western United States earthquakes from regional code envelopes, *J. Geophys. Res.* 101, 11195-11208.

Meyers, S.C., W. R. Walter, K. Mayeda, and L. Glenn (1999). Observation in support of *Rg* scattering as a source of explosion S waves: regional and local recordings of the 1997 Kazakhstan depth of burial experiment, *Bull. Seism. Soc. Am*. 89, 544-549.

Mueller, R.A., and J.R. Murphy (1971). Seismic characteristics of underground nuclear detonations, *Bull. Seism. Soc. Am*., 61, 1675-1692.

Nalivkin, D,V. (1960). The geology of the USSR. A short outline (including a 1:7,500,000 scale geologic map), Pergammon Press, New York, 170p.

NNC Field Report (1996). Unused vertical borholes at the Balapan test field of the former Semipalatinsk test site; review of existing data on the boreholes geology and design, National Nuclear Center of the Republic of Kazakhstan, Kurchatov city, Republic of Kazakstan.

Patton, H.J., and S. R. Taylor (1995). Analysis of *Lg* spectral ratios from NTS explosions: implications for the source mechanisms of spall and the generation of *Lg* waves, *Bull. Seism. Soc. Am.* 85, 220-236.

Phillips, W.S., H. E. Hartse, S. R. Taylor, A. A. Velasco, and G. E. Randall (1999). Regional phase amplitude tomography for seismic verification, PAGEOPH, submitted.

Ringdal, F., P. D. Marshall, and R. W. Alewine (1992). Seismic yield determination of Soviet underground nuclear explosions at the Shagan River test site, *Geophys. J. Int.* 109, 65-77.

Stewart, R.C., (1988). P-wave seismograms from underground explosions at the Shagan River Test Site recorded at four arrays, AWE Report O 4/88, Aldermaston, UK, 249pp.

Thurber, C.H., H. R. Quin, and R. Saleh (1994). Catalog of Locations of Nuclear Explosions at Balapan, Kazakhstan, 1965 to 1985, *Bull. Seism. Soc. Am.,* 84, 458-461.

Zonenshain, L.P., M.I. Kuzmin, and L.M. Natapov (1990). Geology of the USSR: a plate-tectonic synthesis, B.M. Page, Ed., American Geophysical Union Geodynamic Series, 21, 242p.

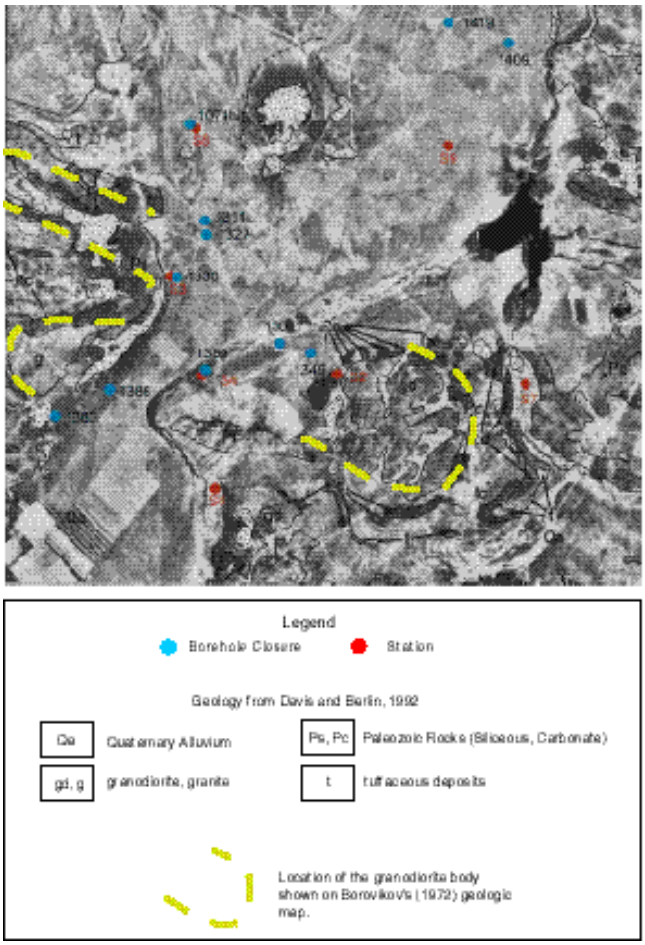


Figure 1. Land Sat image of the STS with superposed geologic units (modified from Davis and Berlin, 1992). The locations of the boreholes and seismic stations for this study are also shown. The approximate outline of the granodiorite body shown on Borovikov's (1972) regional scale geologic map is also shown. The granodiorite body (or similar lithology) is mapped in both 1311 and 1327 boreholes.

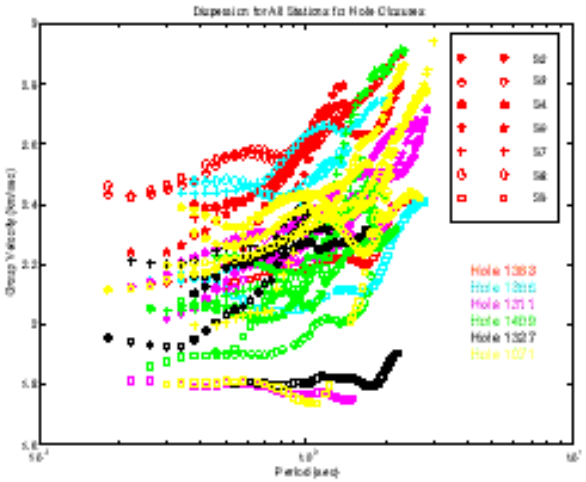


Figure 2. *Rg* group velocity dispersion curves for all station-event pairs processed in this study.

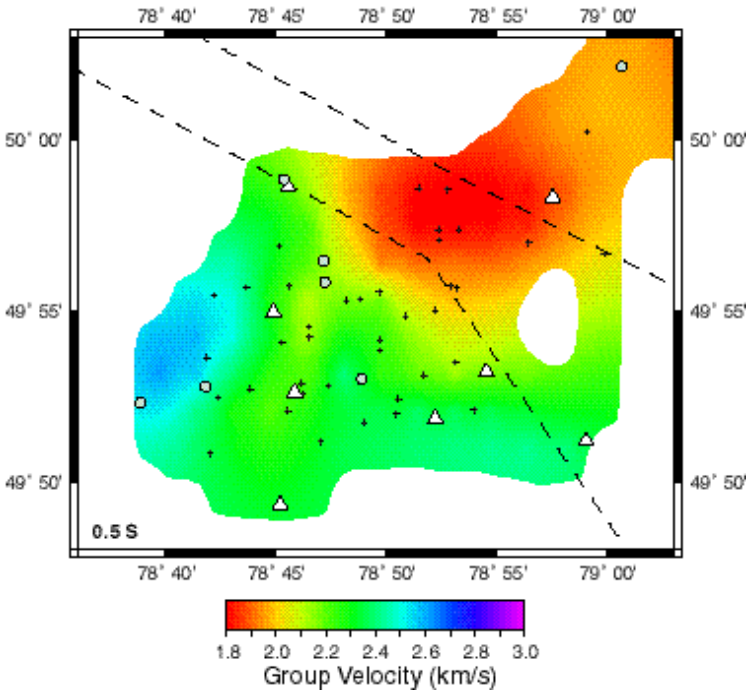


Figure 3. Tomographic map of *Rg* velocities at T=0.5 sec. The stations and explosions are shown by triangles and circles respectively, while the midpoints for each path are shown as plusses. The dashed lines show the subregions of the STS as determined by magnitude residuals (m_b-m_{Lg}) from Ringdal *et al.* (1992).

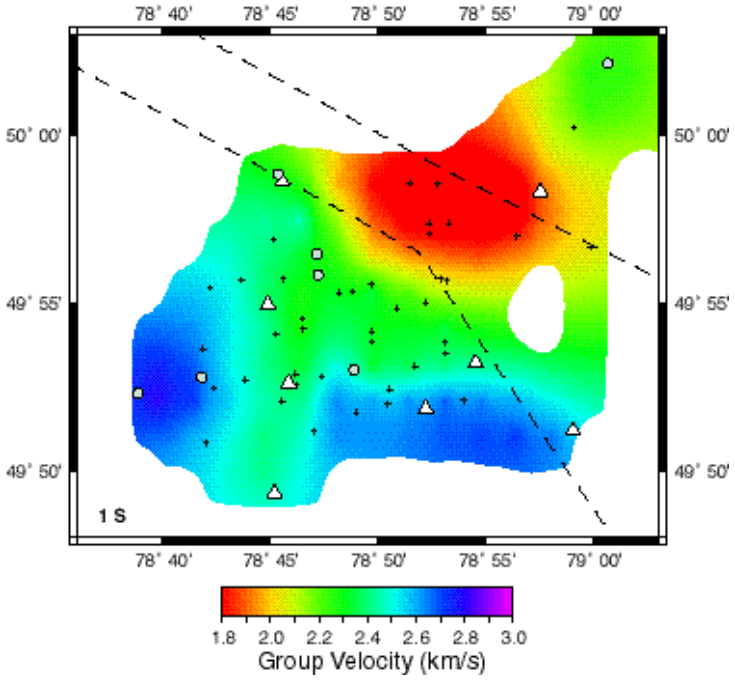


Figure 4. Tomographic map of *Rg* velocities at T=1 sec.

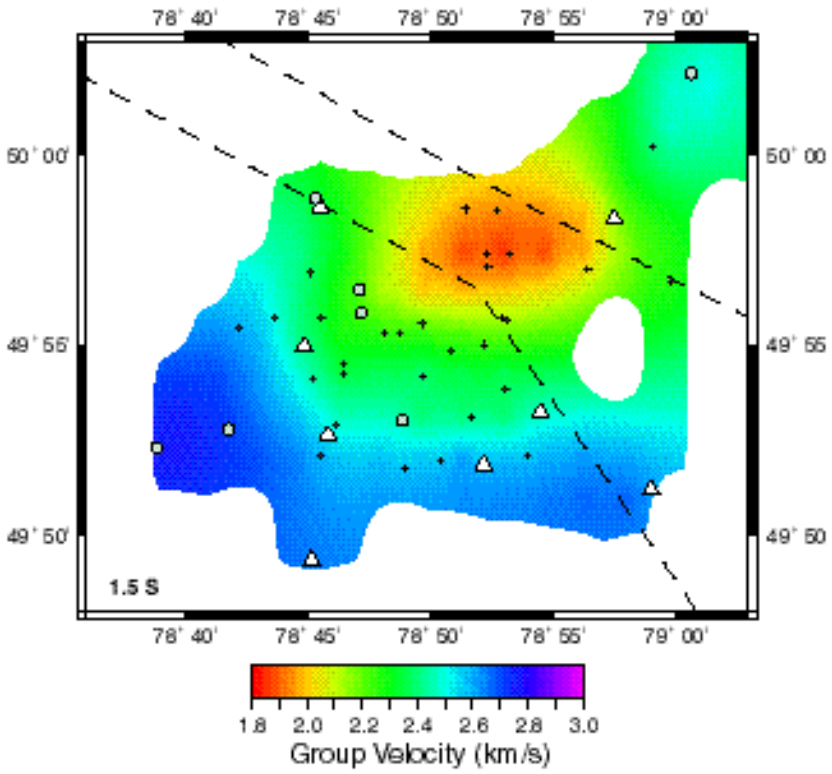


Figure 5. Tomographic map of *Rg* velocities at T=1.5 sec.

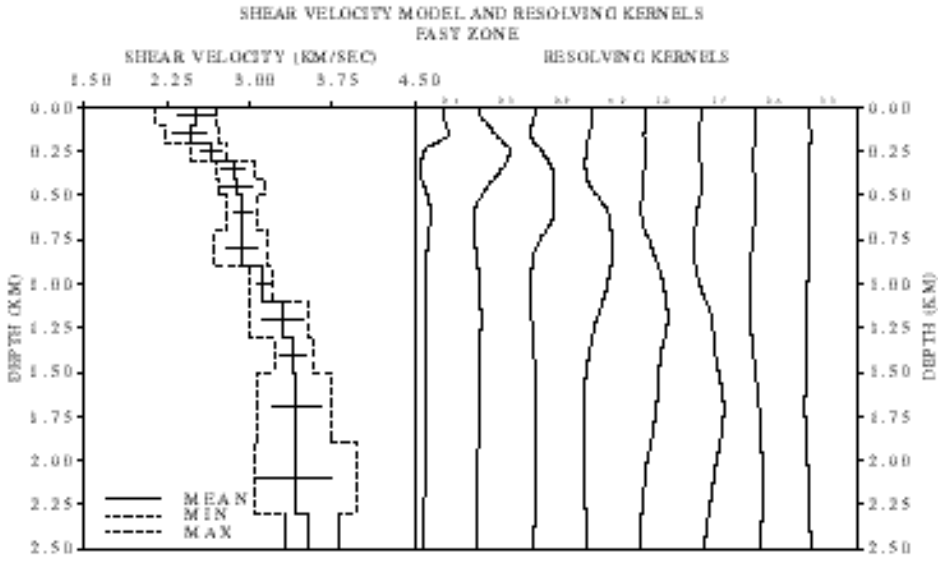


Figure 6. Inversion for shallow shear wave velocity structure in the SW region of the STS. The range of all velocity models that fit the observed dispersion are shown by the dashed lines, and the solid line shows the average velocity structure. The final velocity models show little deviation from the starting model at depths greater than 2.5 km because of loss of resolution as noted in the normalized resolution kernels.

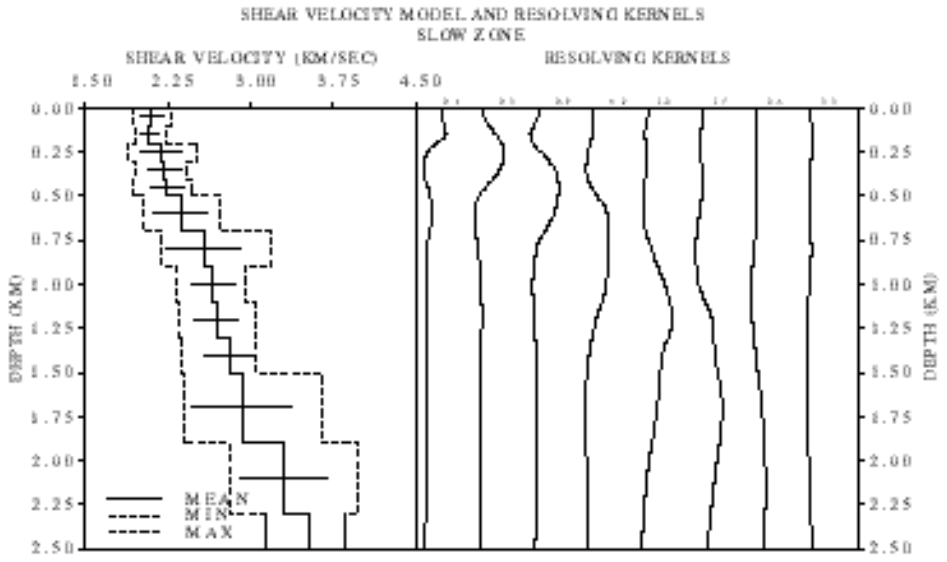


Figure 7. Dispersion results for the inversion of the 1383 to S7 dispersion curve. The observed data is shown as circles with error bars, while the theoretical dispersion from the inversion is shown as the line.

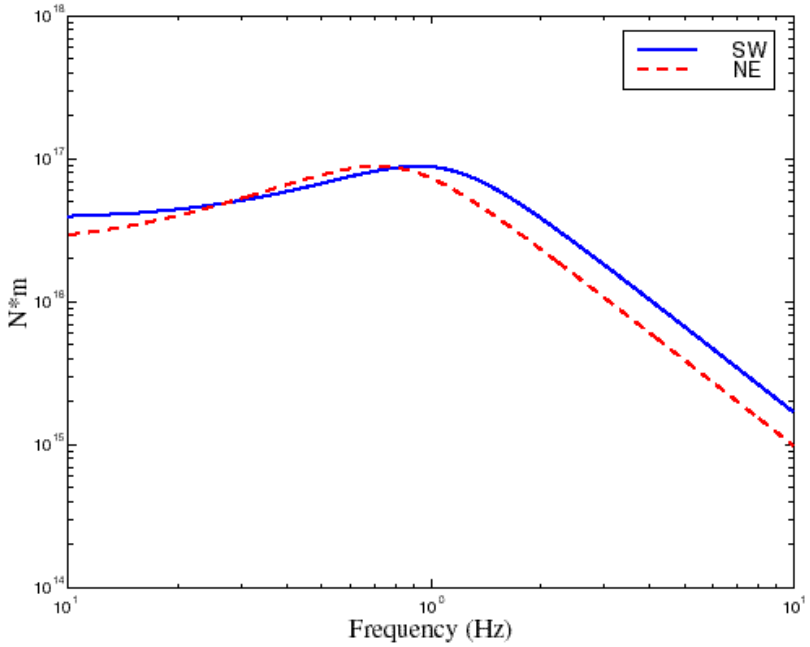


Figure 8. Reduced Velocity Potential (RVP) spectra for two identical explosions in geologic structures representative of the NE and SW regions of STS.

FULL WAVEFORM MODELING OF THE EFFECTS OF Q AND STRUCTURE OVER SUBREGIONAL PATHS IN WESTERN CHINA

Christopher R. Bradley and Laura E. Jones
Los Alamos National Laboratory

Sponsored by U. S. Department of Energy
Project Number: ST482A
Contract Number: W-7405-ENG-36

ABSTRACT

In order to accurately simulate the basin, crust and mantle phases generated from earthquakes and explosions, detailed knowledge of lithospheric structure is required. Inversion for velocity from crustal surface wave phases (Lg and Rg) and subsequent detailed forward modeling may be the best means of recovering three-dimensional regional and subregional structure. Simple, homogeneous three-layer (basin, crust, mantle) models of path-specific structure indicate that more complex models of the crust and upper mantle are required to perform accurate simulations. Simple velocity models are obtained via inversion or forward modeling of surface wave dispersion data from subregional paths because these phases tend to have the greatest signal to noise. After testing the models by forward modeling, models for paths with a nearly common azimuth, but at varying distances, are combined to yield two- and three-dimensional structures.

Considering moderately sized (m_b 4.5 - 6.0) earthquakes in the Lop Nor region (China) we obtain near regional to regional distance group velocity measurements. We use these to construct a family of simple, one-dimensional velocity structures for crustal, lithospheric and uppermost mantle structure in Western China and Tibet, for stations AAK, MAK, LSA and LZH. Finally, we compare results from these simple one-dimensional models with two-dimensional models incorporating basin structure and Moho topography into the original one-dimensional velocity structures.

Key Words: seismic wave propagation, crustal structure, Q

OBJECTIVE

In support of the stated goal of the Comprehensive Nuclear-Test Ban Treaty '*to globally monitor and verify the testing of nuclear weapons'*, we demonstrate the modeling of sub-regional path effects using a recently developed finite difference wave propagation algorithm. Models derived from surface wave data, gleaned from the literature, and obtained from the Cornell Database are together employed in a practical forward modeling method for determining earth structure. We thus obtain valuable insight into the physical basis for discrimination of naturally occurring earthquakes and nuclear explosions. Wave propagation modeling should be used in direct support of

1) the parametric study of source and propagation phenomenology along regional and sub-regional paths for earthquake and explosion sources,

2) analysis and accurate simulation of historic events in areas where sparse recorded data exists to test the robustness of current discrimination techniques,

3) the need for a quick response mechanism for discrimination of seismic events of unknown origin.

Advances in regional empirical discriminants are augmented by numerical models. Modeling can test and validate hypotheses about the basis of these discriminants. There is currently a need for information on sub-regional scales to improve discriminant models. If modeling provides information at such scales to explain the physical basis for why discriminants may work in some areas but not in others, then it is a useful tool for the analyst.

RESEARCH ACCOMPLISHED

Efforts this year have been focused in two directions: 1) developing a method for incorporating observation-based surface wave information into realistic earth models and 2) perfecting a memory efficient 3-D finite difference scheme for modeling both elastic and anelastic wave propagation over regional to subregional distances. The procedure followed includes the following steps: data selection, group velocity measurements, group velocity inversion for one-dimensional models and/or construction of composite models, initial forward modeling, and preliminary interpretation. This paper presents a first test of a new algorithm, preliminary results from our surface-wave inversion to full-waveform modeling scheme, along with a carefully selected data set to be used in future such modeling.

Data selection.
For this study, three component broadband waveforms were assembled for earthquakes recorded at IRIS stations AAK in Kyrgyzstan , MAK in Kazakhstan, and CDSN stations LSA and LZH in China between 1989 and 1996. These earthquakes are distributed across the Tien Shan fold-belt, the Tarim basin and the Tibetan plateau [Figure 1], offering source-receiver paths which cover varied and heterogeneous structure. The events are at subregional to regional distances [roughly 400 to 1400 km epicentral distance] and are of moderate size [M_b 4.5 to 6.0]. Great-circle paths shown indicate source-receiver paths for the test events modeled in this paper. Prior to further analysis, records were corrected for instrument response, rotated and decimated to one sample per second. Record sections [vertical components only] for each station are shown in Figure 2 [panels a – d]. Events modeled in this paper are shown in bold line [Figure 2a].

Group velocity measurements
Fundamental mode Rayleigh wave dispersion curves were obtained using a multiple filter scheme: a narrow band gaussian filter is applied to the displacement seismogram over many different period windows. For each period window, the maximum amplitude of the envelope function is picked. The corresponding arrival time is used to compute group velocity. We obtained group velocity measurements for a select set of vertical and radial waveforms from the above events within the period range of roughly 5 to 50 seconds, when possible. Where fundamental mode group velocity measurements for the vertical and radial components were markedly inconsistent, measurements were discarded. All measurements were made using the **PGSWMFA** [**Pg**plot **S**urface **W**ave **M**ultiple **F**ilter **A**nalysis] software created by Chuck Ammon [St. Louis University]. Dispersion curves for each station are shown in Figure 3 [panels a - d]. Dispersion curves for AAK [panel 3a] show both the effects of propagation through the Tarim Basin [lower thickened curves] and propagation through the thickened crust of the Tien Shan. At station LSA, and to a lesser extent, station LZH [panels 3b and 3c], curves show the 'reverse dispersion' typical of the thickened crust.

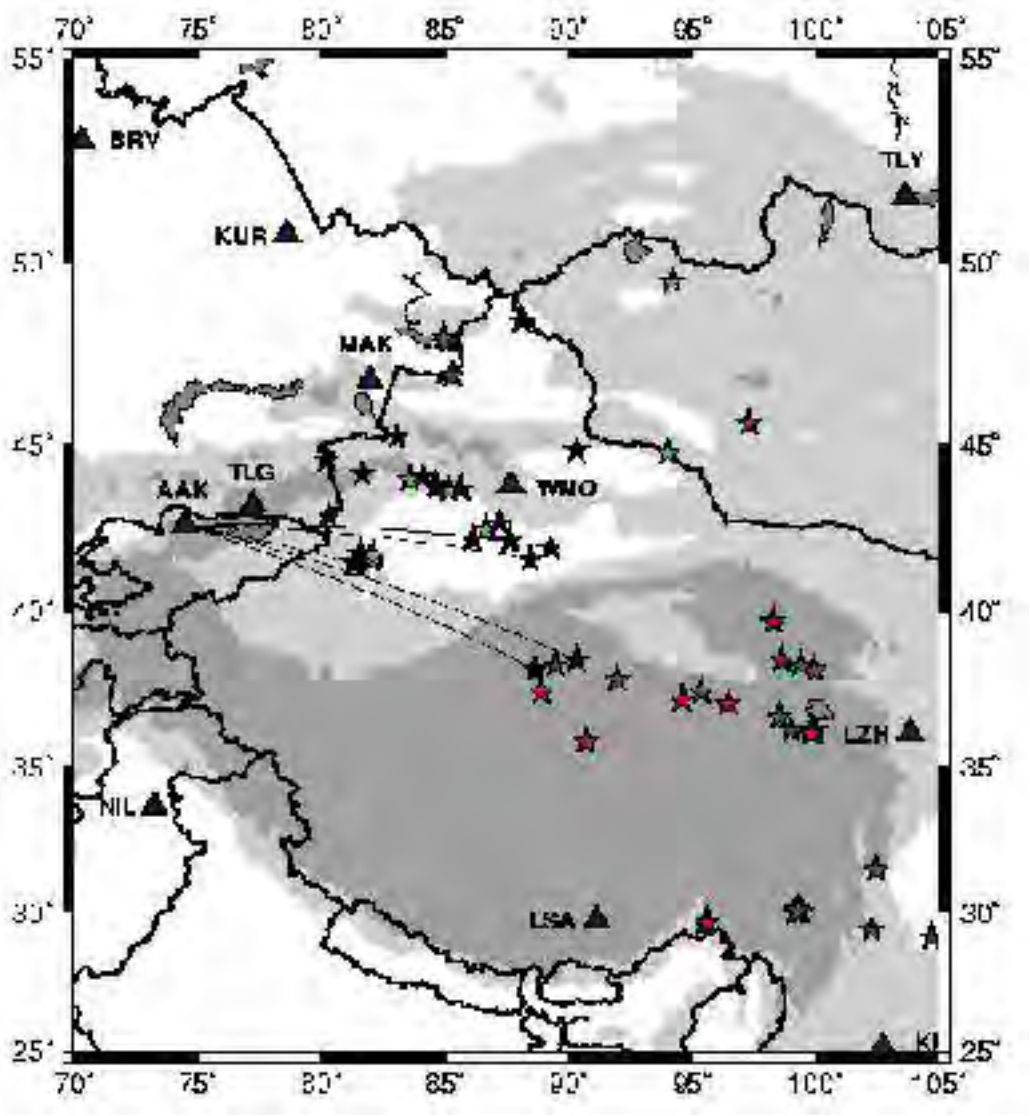


Figure 1: Map of Lop Nor area. Stations are indicated by triangles and events by stars. Solid black stars are events recorded at AAK. Paths modeled in this paper are indicated by great-circle paths.

The Tibetan Plateau. In thick grey line [panels 3b and 3c] are shown Rayleigh dispersion curves for a classic Tibetan plateau model [Romanowitz, 1982]. Dispersion at station MAK suggests the heterogeneity of the structure surrounding it [panel 3d], comprising both basin and fold-belt [Figure 1].

Preliminary Modeling

Two events were chosen to test a new numerical scheme for modeling full waveform anelastic wave propagation in three dimensions (see Appendix). These events were recorded at station AAK and propagated along similar azimuths but traveled different distances to the station. An event from 1991 May 5 (M_b 4.4) propagated 577 km across the Tarim Basin and a second event from 1993 October 2 (M_b 5.6) propagated 1300 km across a portion of the Tibetan Plateau and the Tarim Basin. Both events are shown in Figure 4 (a,b). From the group velocity analysis it is evident that the Rayleigh wave dominates the waveform beyond 175 seconds in the first event and 460 seconds in the second event. In previous studies (e.g. Jones et. al., 1997 and Bradley and Jones, 1998), modeling wave propagation across deep basins has produced a relatively weak Rayleigh wave relative to Lg. This has been attributed to crustal dispersion and high attenuation in the basins. The currently modeled events indicate a shallow source yielding a strong surface wave and higher that average crustal attenuation. Figures 4c

and 4d show the resultant synthetic seismograms from an explosion (4c) and simple double couple source. The model was developed from downloading a lithospheric cross section from the Cornell database. The velocity was adjusted using the arrival times from the actual event data. Rough estimates of Q were made based on previous studies (Bradley and Jones, 1998).

2-D Models

Figure 5a shows snapshots of the P- and S-wave field 100 seconds after the source has been initiated in a simple 3 layer crust. The parameters for the crust are:

	Vp (km/s)	Vs (km/s)	Qp	Qs
Basin	5.6	2.8	200	53
Crust	6.1	3.5	500	219
Mantle	7.7	4.7	1000	419

These values were partially derived from the group velocity analysis [Figure 4] and previous values from earlier modeling. From the comparison, the model under predicts the Rayleigh wave amplitude relative to Lg. This is likely due to the under estimate of Q in this edge of the Tarim Basin. Additionally, the relative strength of the Rayleigh wave indicates a source depth much shallower than the published CMT solution.

3-D Model

As a test of the new algorithm for memory efficient Q, a simple 3-D model of the subregional path from the 2 May 1991 event and AAK was constructed. The model was based on the Cornell data base cross section and extended in the orthogonal dimension symmetrically. Figure 5b shows the P- and S-wave snapshot in the xz-plane (left panel) and the vertical velocity in the xz- and xy-plane (right panel) at 45 seconds after the source initiation. The source focal mechanism is a simple in vertical strike-slip double couple. Results from this model again underestimate the Rayleigh wave amplitude due to the simplistic nature of the model/source and the potentially miss estimated focal depth.

CONCLUSIONS AND RECOMMENDATIONS:

1. **Inversion for Layering and accurate modeling of Q:** Dispersion and scattering are required to distribute energy properly into the respective guided and surface wave modes. Surface waves provide a robust data set from which average 1-D models of velocity and Q can be inverted.

2. **Modeling source properties can be as important as propagation:**. Source depth continues to be vitally important for accurately modeling surface wave phases. Source mechanism and depth can be modeled and improved upon via faster techniques than finite difference, then the improved focal mechanism used in the full waveform modeling.

3. **Fast numerical approximation of Q is a necessary component:** With the realization that 3-D propagation effects are important to the simulation, we find that intrinsic attenuation and scattering are required for accurate modeling. Memory restrictions on most computers require a better method of simulating attenuation. Coarse graining of memory variables used in Q simulation provide this method.

Our future modeling will include more accurate source descriptions, the more memory efficient "coarse grained Q" method and composite velocity models of 1-D (derived from surface wave inversions) and 3-D models (derived from whole earth data set like those in the Cornell data base statistical parameters inverted from coda and topography).

Appendix:

Memory Efficient Finite Difference Modeling of Intrinsic Attenuation (Q):

Finite difference (FD), finite element (FE), and pseudospectral methods are currently able to solve transient three-dimensional seismic wave propagation problems over domains sufficiently large that anelastic attenuation should not be neglected. Realistic treatment of anelastic losses is especially important for simulating the earthquake-induced response of complex geologic structures such as sedimentary basins (e.g., Frankel and Vidale, 1992; Yomogida and Etgen, 1993; Olsen and Archuleta, 1996; Wald and Graves, 1998; Pitarka et al, 1998; Sato et al., 1999). An important component of the ground motion in basins is the trapping of incident

waves at the basin edges, resulting in the excitation of surface waves in the basin sediments (e.g., Field, 1996). These basin-edge induced waves in turn may reverberate within the basin. Numerical simulations which neglect anelastic losses in the sediments may seriously overpredict the amplitude and duration of the ground motion, even if the seismic velocity structure and source are well-modeled. Realistic formulation of anelastic losses is also important in other applications of 3D numerical simulations. These include studies directed at seismic verification of the comprehensive nuclear test ban treaty, modeling of seismic reflection profiles, and global-scale seismic waveform modeling.

In this appendix, we extend the coarse-grained memory variable approach to anelastic wave propagation in three dimensions. We implement the method in a fourth-order finite difference program, demonstrate its accuracy for plane P and S waves. We also outline the extension of the method to power law frequency-dependent *Q*.

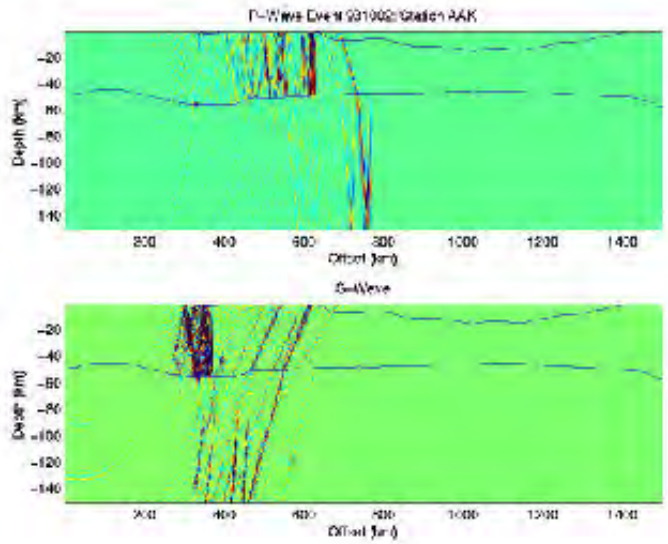
Implementation for acoustic case.
Day, 1998 also gave a practical implementation of coarse graining for the acoustic wave equation discretized on a 3D lattice. To approximate the special case of frequency-independent *Q*, equally spaced on a logarithmic scale, between lower and upper absorption-band cutoffs. All weights w_k were set to 1. In the acoustic case, the appropriate modulus is the bulk modulus and the bulk modulus relaxation is set such that the specified *Q* value,Q_0, will be realized at some prescribed reference frequency (near the center of the absorption band). The appropriate Q is then that which satisfies

$$Q_0^{-1} \approx \frac{\pi\delta\kappa}{2\kappa_u}\left[\ln\left(\frac{\tau_M}{\tau_m}\right)+\frac{\delta\kappa}{\kappa_u}\ln\left(\omega_0\tau_m\right)\right]^{-1}.$$

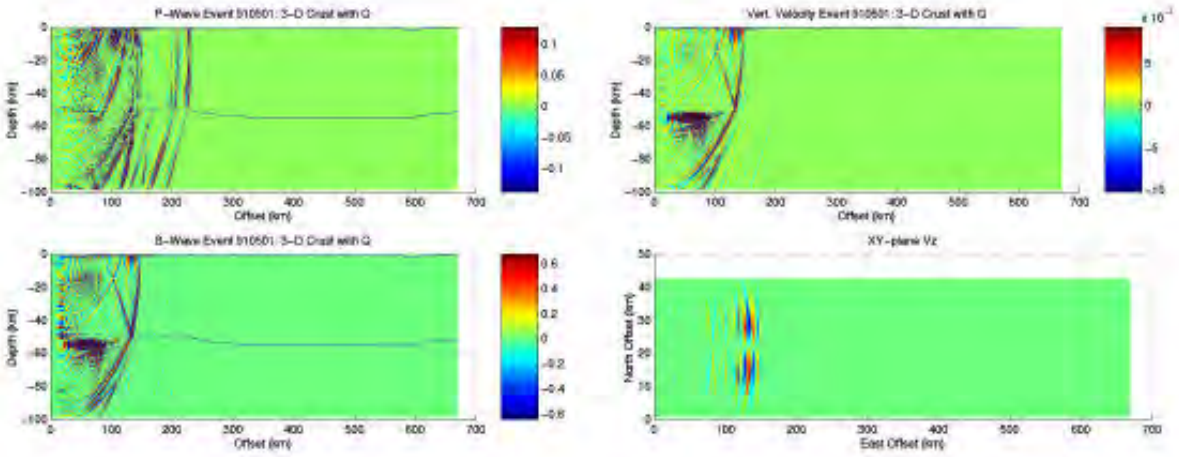
This procedure successfully simulates frequency-independent *Q*, to within 3% tolerance, over 2 orders of magnitude in frequency, yet requires only 1 memory variable per stress node. A limitation of the method is that it produces strong scattering at wavelengths shorter than 4 grid cells (as predicted by the perturbation analysis, and confirmed by numerical experiments). As a result, the method is probably most appropriate for use with low-order finite difference and finite element methods, for which wavelengths shorter than 4 grid cells are already subject to large errors due to numerical dispersion. On the basis of acoustic wave tests, the method appears to be well suited to the fourth-order staggered-grid finite difference method which is now widely used in seismological applications.

ANELASTIC FORMULATION

The coarse grained approach is easily generalized for anelastic models, and the generalization is particularly simple for isotropic anelasticity, to which we limit ourselves here. In the isotropic case, the stress strain relationship can be partitioned into separate relationships for, respectively, the mean stress (in terms of the volumetric strain and a volumetric memory variable), and the deviatoric stresses σ'_{ij} (in terms of the deviatoric strains ε'_{ij} and corresponding memory variables). Considering that only 5 of the 6 deviatoric stress (and strain) components are independent, this formulation leads to one equation for each of 6 memory variables. For example, adding attenuation to a 3D staggered grid FD method (assuming a conventional velocity-stress formulation, e.g., Graves, 1996) requires adding 6 memory variables (one for each stress component) to each unit cell of the grid.



5a)



5b)

Figure 5. In 5a are shown a snapshots of the P- and S-wave field at 100 seconds after initiation of a double couple source for a simple crustal model between AAK and an earthquake 1300 km away. Figure 5b shows the snapshots from a full 3-D computation for the subregional path from the 2 May 1991 event to AAK.

In the above formulation, one could assign different frequency dependence to the compressional and shear Q's. This would be accomplished by using one set weights in the equation controlling the memory variable for mean stress, and a different set in the 5 equations controlling the memory variables associated with the deviatoric stresses. The development is less cumbersome, however, if we make the additional assumption that the $Q_{\cdot s}$ share a common frequency dependence. One advantage of this simplification is that we can avoid partitioning the stress tensor into mean-stress and deviatoric-stress parts. Instead, we form linear combinations of the mean-stress and deviatoric-stress memory variables, choosing combinations that correspond to the usual physical components of the total stress tensor. The above procedure leads to the following set of equations

$$\sigma_{ij} = 2\mu_u \varepsilon_{ij} + \left(\kappa_u - \tfrac{2}{3}\mu_u\right)\varepsilon_{kk} - \xi_{ij}, \quad \text{and}$$

$$\tau \frac{d\xi_{ij}}{dt} + \xi_{ij} = w\left[2\mu_u A_s \varepsilon_{ij} + \left[\left(\kappa_u + \tfrac{4}{3}\mu_u\right)A_p - 2\mu_u A_s\right]\varepsilon_{kk}\delta_{ij}\right],$$

where A_p and A_s are constants that scale with Q_p^{-1} and Q_s^{-1}, respectively. For the special case of frequency-independent Q, these constants are

$$A_p = \frac{2}{\pi} Q_p^{-1}\left(\ln\frac{\tau_M}{\tau_m}\right)\left[1 - \frac{2}{\pi} Q_p^{-1}\left(\ln\omega_0\tau_m\right)\right]^{-1}, \quad \text{and}$$

$$A_s = \frac{2}{\pi} Q_s^{-1}\left(\ln\frac{\tau_M}{\tau_m}\right)\left[1 - \frac{2}{\pi} Q_s^{-1}\left(\ln\omega_0\tau_m\right)\right]^{-1}.$$

STAGGERED-GRID FINITE DIFFERENCE IMPLEMENTATION

We incorporate the anelastic coarse graining in a 3D staggered-grid FD method. The implementation is analogous that used in Day, 1998, for the acoustic case. The underlying elastodynamic code, that of Olsen (1994), approximates spatial derivatives with fourth-order accuracy and time derivatives with second-order accuracy (Graves, 1996, gives a detailed description of the difference equations). Figure 5b shows the result of a subregional test of the 3-D finite difference code with attenuation calculated via coarse graining.

REFERENCES:

Bradley, C. and Jones, E., Modeling propagation effects from explosions in western China and India, 20th Annual Seismic Research Symposium on Monitoring a CTBT, Santa Fe, NM, 1998.

Bradley, C. and Day, S., Elastic Coarse-Graining of Memory Variables: Memory efficient Q simulation for finite difference methods. *Bull. Seis. Soc. Am*., (in Prep), (LA-UR-99-719) 1999.

Day, S., Efficient simulation of constant Q using coarse-grained memory variables. Bull. Seism. Soc. Am., 88(4) 1051-1062, 1998.

Day, S., and Minster, B., Numerical simulation of attenuated wavefields using a Padé approximant method, Geophysical J. Roy. Astr. Soc., 78, 105-118, 1984.

Dziewonski, A., Bloch, A., and Landisman, M., A technique for the analysis of transient seismic signals, Bull. Seism. Soc. Am., 59(1), 427-444, 1969.

Field, E.H. (1996). Spectral amplification in a sediment-filled valley exhibiting clear basin-edge-induced waves, *Bull. Seism. Soc. Am. 86*, 991-1005.

Frankel, A., and J. Vidale (1992). A three-dimensional simulation of seismic waves in the Santa Clara Valley, California, from a Loma Prieta aftershock, *Bull. Seism. Soc. Am. 82*, 2045-2074.

Jones, E., Bradley, C., App, F., Bos, R., and Patton, H., Modeling seismic propagation from large scale structural features in western China. LANL Memorandum, LA-UR-97-4186, 1998.

Kosarev, G., Petersen, N., Vinnik, L., and Roecker, S., Receiver functions for the Tien Shan analog broadband network: Contrasts in the evolution of structure across the Talasso-Fergano fault. J. Geophys. Res., 98(3), 4437-4448, 1993.

Olsen, K.B. (1994). Simulation of three-dimensional wave propagation in the Salt Lake Basin, *Ph.D. Thesis*, University of Utah, Salt Lake City, Utah, 157 pp.

Olsen, K.B., and R.J. Archuleta (1996). Three-dimensional simulation of earthquakes on the Los Angeles fault system, *Bull. Seism. Soc. Am. 86*, 575-596.

Mahdi, H., and Pavlis, G., Velocity variations in the crust and upper mantle beneath the Tien Shan inferred from Rayleigh wave dispersion: Implications for tectonic and dynamic processes. J. of Geophys. Res., 103(B2) 2693-2703, 1998.

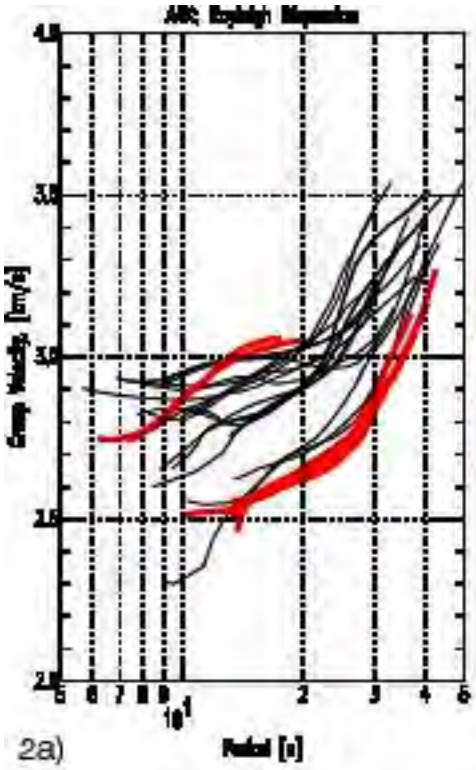
Pitarka, A., K. Irikura, T. Iwata, and H. Sekiguchi (1998). Three-dimensional simulation of the near-fault ground motion for the 1995 Kyogo-ken Nanbu (Kobe), Japan, earthquake, *Bull. Seism. Soc. Am., 88,* 428-440.

Romanowitz, B., Constraints on the structure of the Tibet Plateau from pure path phase velocities of Love and Rayleigh waves. J. of Geophys. Res., 87(B8), 6865-6883, 1982.

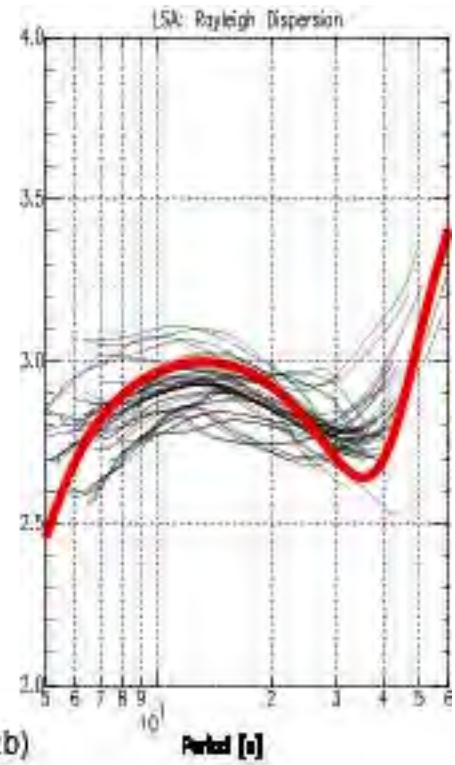
Sato, T., R.W. Graves, and P.G. Somerville (1999). Three-dimensional finite-difference simulations of long-period strong motions in the Tokyo metropolitan area during the 1990 Odawara Earthquake (M_J 5.1) and the Great 1923 Kanto Earthquake (M_S 8.2) in Japan, *Bull. Seism. Soc. Am. 89*, 579-607.

Wald, D.J., and R.W. Graves (1998). The seismic response of the Los Angeles basin, California, *Bull. Seism. Soc. Am. 88*, 337-356

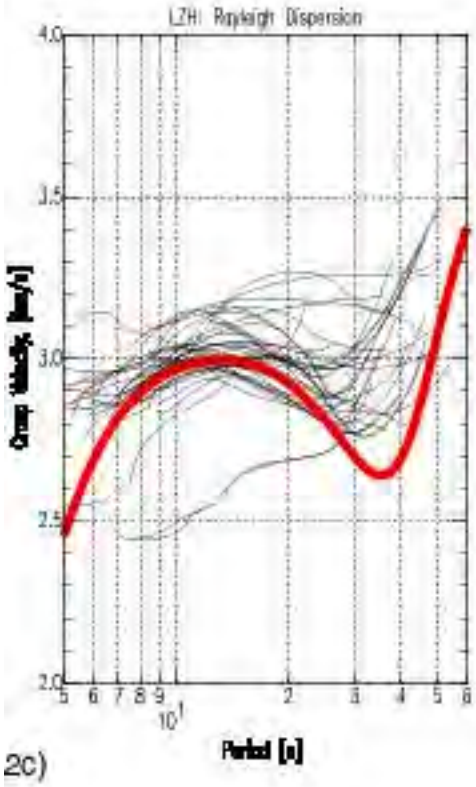
Yomogida, K., and J.T. Etgen (1993). 3D wave propagation in the Los Angeles Basin for the Whittier-Narrows earthquake, *Bull. Seism. Soc. Am. 83*, 1325-1344.



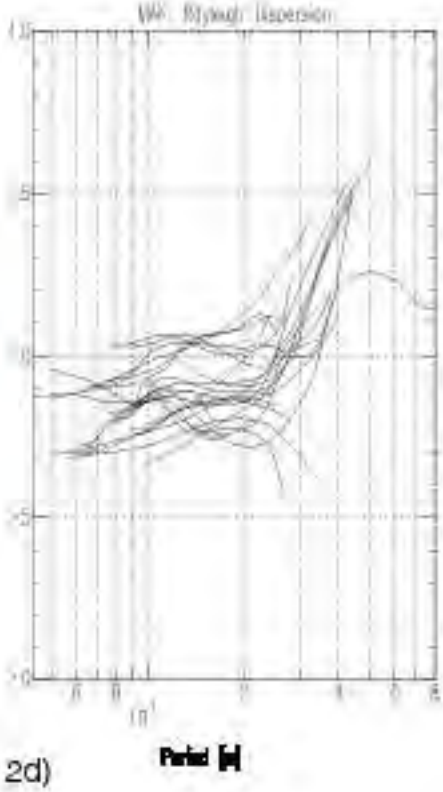
2a)



2b)

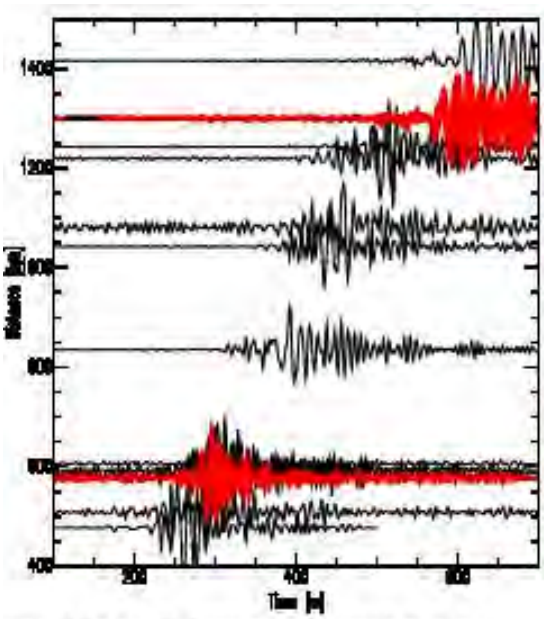


2c)

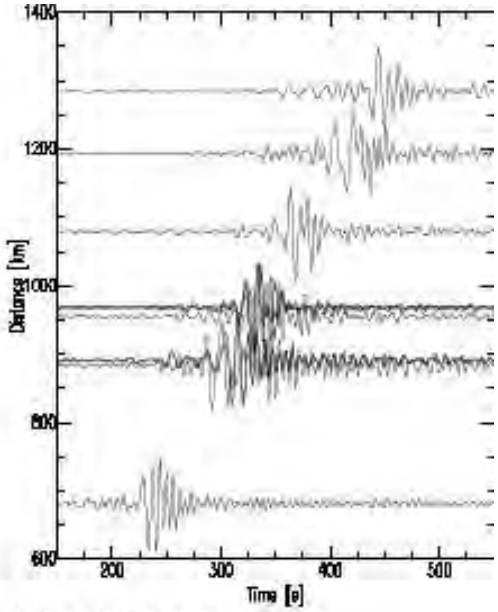


2d)

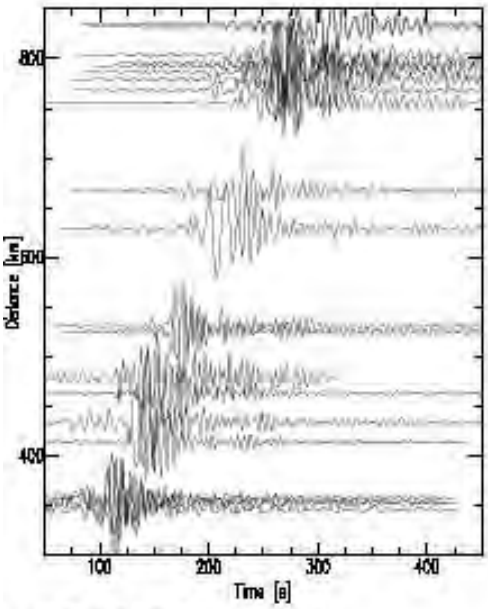
Figure 2) Rayleigh dispersion for stations AAK, LSA, LZH, and MAK.



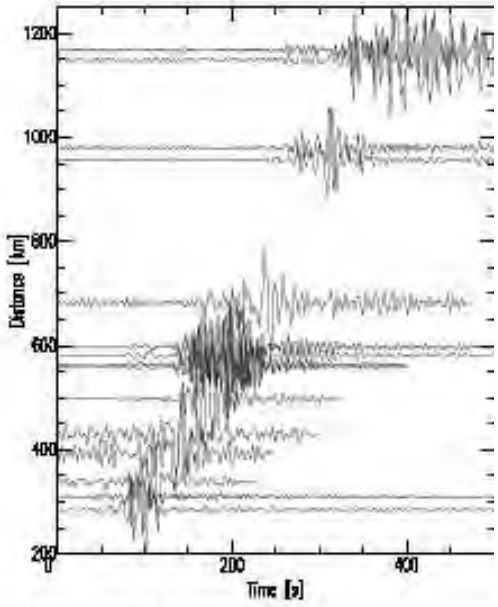
3a) AAK BHZ [Low pass filtered at 5 s] Records modeled in this paper are shown in thick grey line.



3b) LSA BHZ [Lowpassed]



3c) LZH BHZ [Lowpassed]



3d) MAK BHZ [Lowpassed]

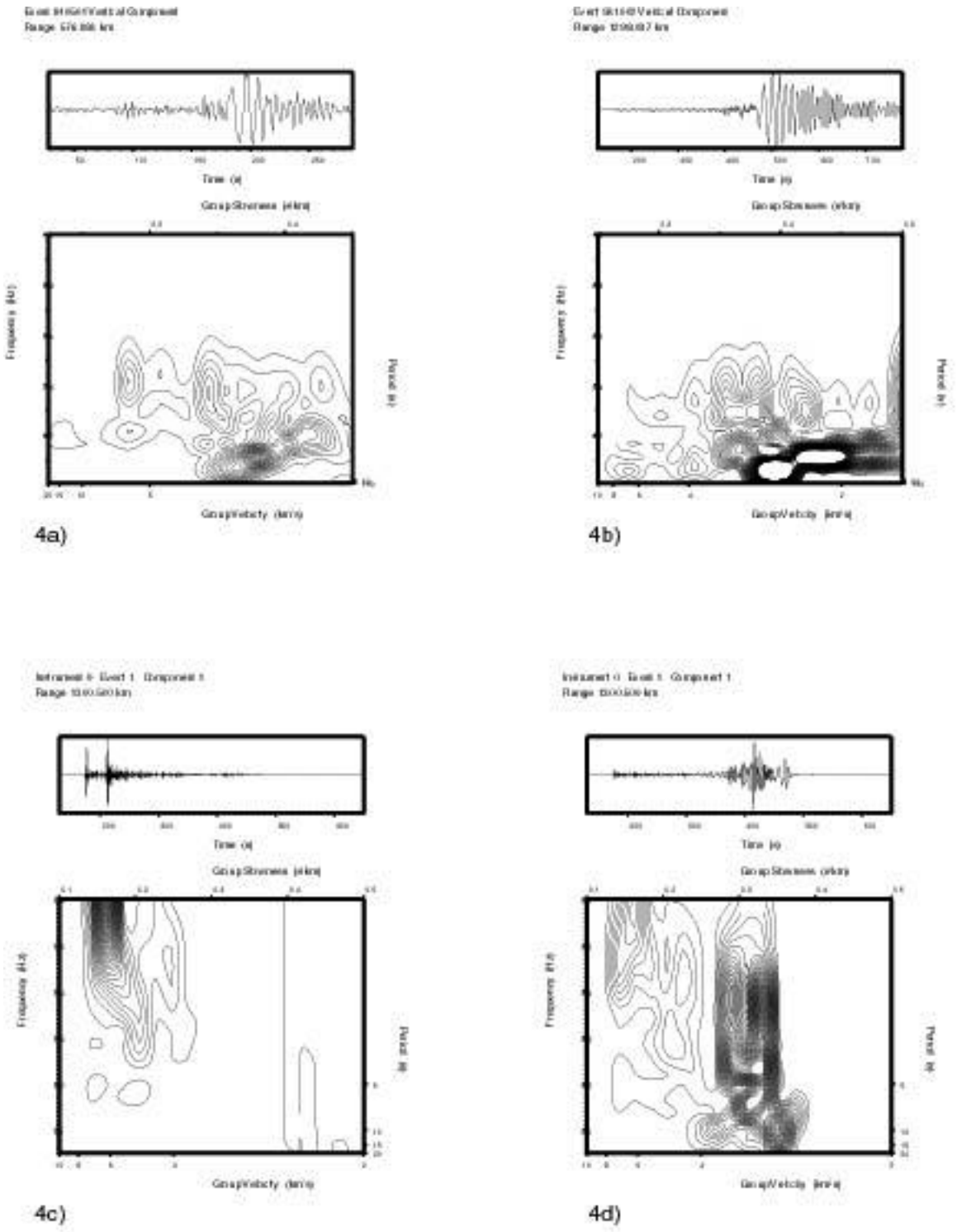


Figure 4. 4a) is a data and group velocity plot from an earthquake at 577 km from station AAK. The Rayleigh wave phase is the dominant arrival. Similarly, in 4b) are shown the data and group velocity plot for and earthquake at similar azimuth but at a range of 1298 km. Figures 4c and 4d are the resultant seismograms from a simple 2-D crust with attenuation for an explosion source and moment tensor respectively.

COLLECTION AND ANALYSIS OF SEISMIC AND GROUND-TRUTH INFORMATION IN NORTHEASTERN CHINA

Winston Chan and Xiaoxi Ni, Multimax, Inc.

Sponsored by U. S. Department of State and U.S. Department of Defense
Defense Threat Reduction Agency
Contract No. DSWA01-97-C-0125

ABSTRACT

This research is aimed at obtaining a database of historical seismological, geophysical, and geological data for East Asia. By obtaining the local Chinese data, better models of the regional crustal structure can be made. We have established a process and procedures for doing this type of reconnaissance and data collection studies.

We have collected the historical earthquake data in northeastern China recorded by the local seismic network and constructed a database of phase arrival times, amplitudes and waveforms. The database consists of nearly 700 seismic events from 1986 to 1999 with over 13,000 entries of seismic phase arrival times and amplitudes. Over 900 analog seismograms were also scanned and stored in JPEG format. The seismic events occurred in northeastern China and the vicinity with an area of over 1,300,000 km^2. The events were recorded by the local seismic network operated by the provincial seismic bureau in northeastern China with over 35 seismic stations that mainly cover Liaoning province and the neighboring provinces. The phase arrival time and amplitude data are verified and validated independently. The location of the events is examined, and re-location is performed on questionable events to correct errors in the raw data. For the events with waveform data available, re-measurement is done to ensure the quality of the phase picks. The data is compiled in MS Excel format with hyperlinks to the seismic waveform data. The historical earthquake data provide a unique seismic database for further refinement of the regional crustal structure.

We performed a 3-D tomographic inversion of the crustal structure in northeastern China utilizing the obtained seismic data. Previous research on the crustal structure in northeastern China is analyzed and summarized to set up a I-D starting model. Both P and S phases are adopted to carry out a tomographic inversion of the crustal velocity structure from the regional seismic events. The results reveal complex lateral heterogeneity of the crustal structure in northeastern China. We find correlation among the velocity structure, the topography and the tectonic structures in the region. The deduced 3-D crustal structure improves the quality of re-location of the seismic events.

Key Words: Ground-truth database, phase arrival time data, waveform data, 3-D tomographic inversion, re-location

OBJECTIVE

At present, regional seismic data is not easily available for East Asia. Without a good seismic database, detection of violations of the Comprehensive Nuclear-Test-Ban Treaty (CTBT) will be extremely challenging. This effort is limited to the collection and analysis of seismological, geophysical, and geological data for East Asia.

The objective of this effort is to obtain a database of historical seismological, geophysical, and geological data for East Asia. By obtaining Chinese data, better models of the Korean Peninsula can be made.

RESEARCH ACCOMPLISHED

Geological Background

The northeastern China region is located at the eastern edge of the Eurasian plate, adjacent to the Pacific plate. The region is divided into two tectonic elements by the Chifeng-Kaiyuan fault. North of the Chifeng-Kaiyuan fault is the Northeastern China tectonic element which is a part of the Tianshan-Xinggan geosynclinal fold belt. South of the Chifeng-Kaiyuan fault is the Northern China tectonic element which lies in the Sino-Korean platform. The two regions are distinctive from each other in geological structure, seismicity, gravity and tectonic stress. The Northeastern China tectonic element undergoes large scale deformation due to the under-thrusting of the Pacific plate into the Heilongjiang plate. It is a region with active deep seismicity and volcanic activity. There are several secondary formations in the region, such as Da Xinggan fold uplift, Jihei fold uplift and Songnen subsidence. The Northern China tectonic element deforms due to the collision between the Northern China plate and the Heilongjiang plate. There are frequent shallow earthquakes within the region. There are also secondary formations in the Northern China tectonic element, such as Yanshan fold belt, Xiaoliaohe fault depression and Liaodong platformal uplift.

Geological structures are abundant in northeastern China, including mountains, basins, faults, volcanoes and hot springs. The gravity anomaly in northeastern China trends in NE direction. The central region has higher gravity than the western and the eastern regions. There are over 350 earthquake faults with lengths greater than 20km in the region. According to historical records and modem observations, over 180 earthquakes with magnitude Ms > 4.75 happened in the region, the greatest among which is the 1975 Haicheng earthquake with Ms = 7.3. Focal mechanism shows that the shallow earthquakes in northeastern China are mainly strike-slip events on nearly vertical faults. The average maximum principal stress is in the NEE-SWW direction.

Previous work

There have been four deep seismic sounding profiles implemented in the northeastern China region. They are Luyang-Haicheng-Donggou profile, Xiongyue-Bengxi profile, Yingkou-Shenyang profile and Dong Ujimqin Qi-Donggou profile. The first three profiles passed the seismogenic zone where the 1975 Ms=7.3 Haicheng earthquake occurred, with a total length of 640 km. The Dong Ujimqin Qi-Donggou profile was a part of the Global Geoscience Transect project. It ran from Dong Ujimqin Qi, Inner Mongolia to Donggou, Liaoning with a length of 960 km. The crustal and upper mantle velocity structure along the profiles were deduced. It is found that the crustal and upper mantle structure are complicated in the region. Typically, three layers are found in the crust (Lu, *et al*., 1991). The thickness of the upper layer is from 13 to 15km and the P-wave velocity within the layer is from 2.0 to 6.3km/s. The middle layer usually consists of two sub-layers. The upper sub-layer in the middle layer has a thickness of 4~9km. The velocity in the layer is from 6.0 to 6.2km/s. The lower sub-layer in the middle layer has a thickness of 2~9km and the velocity in the layer is from 6.3~6.6km/s. The lower layer of the crust has a thickness of 5~10km and the velocity in the layer is from 6.5~7.5km/s. Considerable lateral variation of the velocity in the crust is found in the area. Localized low velocity zones are identified in some regions, e.g., under Haicheng along the Dong Ujimqin Qi-Donggou profile.

The velocity structure deduced from the deep seismic sounding profiles can be utilized for re-location of the earthquakes in northeastern China recorded by the local seismic network. To the best of our knowledge, only 2-D velocity structures along the existing profiles are known in northeastern China. Large scale lateral variations are present in the region. Study of the 3-D velocity structure in northeastern China is important for high precision re-

location of the earthquakes in northeastern China and the Korean Peninsula recorded by the local seismic network.

Ground-truth database

We have collected seismic data in northeastern China from January 1997 to May 1999 plus a limited number of seismic events from 1986-1994. A database has been constructed with over 700 seismic events in northeastern China and North Korea that were recorded by the local seismic network with over 35 stations operated mainly in Liaoning province. For the first time, we were able to obtain a comprehensive listing of over 13,000 seismic phase arrival time picks and amplitude data. Waveform data are also available for 44 events with over 900 analog seismograms. The seismic events cover the area 116W to 130W and 36N to 46N, with magnitudes M1= 1.4~ 4.9 and a maximum depth of 26km. The data listing in the database is raw data information and contains a comprehensive listing of all phases that were detected. The listed information of the earthquakes includes origin time, epicenter location, magnitude, focal depth and precision. Major phase picks, such as Pn, Pg, Sg were reported. The information listed in the station report includes the arrival time, amplitude, station magnitude and epicentral distance. The data is compiled in MS Excel format with hyperlinks to the seismic waveform data. The location of all the seismic events in the database is shown in Figure I along with the seismic stations.

This data set forms the basis of an initial input to a ground-truth database for northeastern China and vicinity. Analysis of the data may be performed to yield preliminary velocity model and event re-location. These data may also be correlated with data obtained from the Chinese Digital Seismic Network (CDSN) to establish ground-truth database information for the region.

We performed quality control on the raw data. The phase arrival time and amplitude data are verified and validated independently. The location of the events is examined, and re-location is performed on questionable events to correct errors in the raw data. For the events with waveform data available, remeasurement is done to ensure the quality of the phase picks. To illustrate the quality of the seismic data, we check the travel time curves for all stations included in the database. Overall, the fluctuations in the travel time curves are small, which shows that the phase pick data are of good quality (Figure 2).

Preliminary Results of 3-D Tomographic Inversion and Re-location

We use the computer code *SPHYPIT90* by Steve Roecker for a 3-D tomographic inversion of the crustal structure in northeastern China. *SPHYPIT90* is a FORTRAN program designed to invert P and S wave arrival times locally recorded and/or P times teleseismically recorded by an array of local to regional dimensions for P and S wave velocities beneath the array (Roecker, 1987; Roecker, 1991). The tomographic method used is based on that of Aki, et a]. (1976) but with many extensions and modifications. The inversion procedure is based on that discussed by Tarantola and Valette (1982). *SPHYPIT90* can analyze locally and/or teleseismically recorded data. In the case of locally recorded data, the velocities determined are those that would be obtained through a joint inversion with hypocenters, but the hypocenters are removed through parameter separation and are relocated in a separate step. The starting model can be either one-dimensional or three-dimensional.

We picked up 226 seismic events with defined depth from the compiled database. The event location, seismic station location and ray path projection are shown in Figure 3. The events were recorded from December 1990 to December 1998 by the local seismic network with over 35 seismic stations. The spatial distribution of the events covers northeastern China in the area 120E-125E, 38N-43N with depths up to 26km. Most of the events were determined with precision 1, the highest confidence in a 4-level precision system employed by the local seismic network. Only a handful of events have precision 2.

A 1-D starting model of the velocity structure of northeastern China was set up according to the previous seismic profiling in the region (Lu *et al*., 1991). The crust in the region was divided into 6 layers (Table 1). The region under investigation is partitioned into 16 by 10 cells in each layer. The resulting P-wave velocity after the 5th iteration of the tomographic inversion is shown in Figure 4. Both lateral heterogeneity and vertical variation are observed through the results. The variation of the P-wave velocity in the first layer trends mainly in the NE direction, which is well correlated with the topography and tectonic settings in the region.

Table 1. Starting model of crustal structure in NE China

Layer	Depth (km)	P-wave velocity (km/s)
1	3.0	4.00
2	9.0	6.10
3	15.0	6.10
4	21.0	6.15
5	24.0	6.45
6	32.0	7.20

The earthquakes adopted in the tomographic inversion are re-located based on the 3-D crustal structure from the inversion (Figure 5). A 73% reduction of variance of the data is achieved after the 5th iteration. The standard error in the re-location of the events is less than 5krn in epicenter and less than 10km in depth. A close look of the Haicheng area shows systematic errors mainly in the east direction (Figure 6), which is evidence that the regionalized 3-D crustal structure is important to the improvement of re-location of the seismic events in the region.

CONCLUSIONS AND RECOMMENDATIONS

A comprehensive database of phase arrival time, amplitude and waveform is compiled for northeastern China, which consists of over 700 events and 12,000 phase arrival times recorded at more than 35 regional seismic stations. The data constitute a ground-truth database for the region and is valuable for study of the crustal structure and re-location of the seismic events in the region.

A 3-D tomographic inversion based on the phase picks data in the database is performed and significant lateral variation in the crustal structure is found in the region. Re-location of the seismic events based on the 3-D crustal velocity structure shows improvement of the location of the events.

A more complete coverage of northeastern China region is desirable for more reliable inversion of the 3-D crustal structure. We will continue to incorporate the newly recorded seismic events in the region and improve the resolution and precision of the 3-D tomographic inversion of the crustal velocity structure and re-location of the seismic events.

REFERENCES

[1] Aki, K. and Lee, W.H., Determination of three-dimensional velocity anomalies under a seismic array using first P arrival times from local earthquakes; 1, A homogeneous initial model, J Geophys. Res. Vol. 81, No. 23, 4381-4399, 1976.

[2] Tarantola, A. and Valette, B., Generalized nonlinear inverse problems solved using the least squares criterion. Reviews of Geophysics and Space Physics, Vol. '-IO, No. 2, 219-232,1982.

[3] Lu, Z., Meng, B. and Li, P., Characteristics of pseudo 3-D crustal structure and seismicity in Haicheng seismogenic zone, Northeastern Seismological Research, Vol.7, No. 4, 1-11, 1991.

[4] Roecker, S.W., Yeh, Y.H. and Tsai, Y.B., Three-dimensional P and S wave velocity structures beneath Taiwan: deep structure beneath an arc-continent collision. J Geophys. Res., Vol. 92, No. B IO, 10,547-10,570, 1987.

[5] Roecker, S.W., Sabitova, T.M., Vinnik, L.P., Burmakov, Y.A., Golvanov, M.I., Mamatkanova, R. and Munirova, L., Three-dimensional elastic wave velocity structure of the western and central Tien Shan. J Geophys. Res., Vol. 98, No. B9, 15,779-15,796,1993.

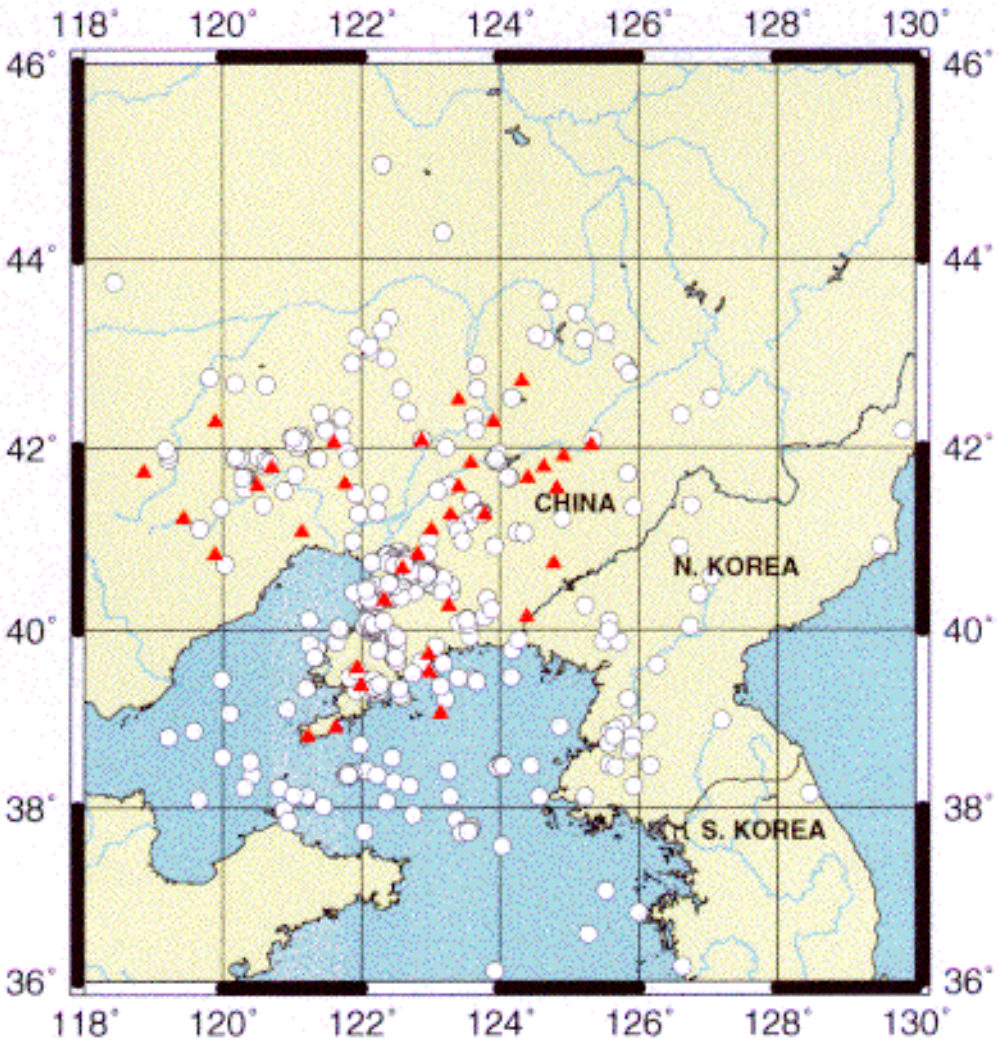


Figure 1. Distribution of earthquakes included in the database (open circles) and the seismic stations (red triangles in the local seismic network in northeastern China.

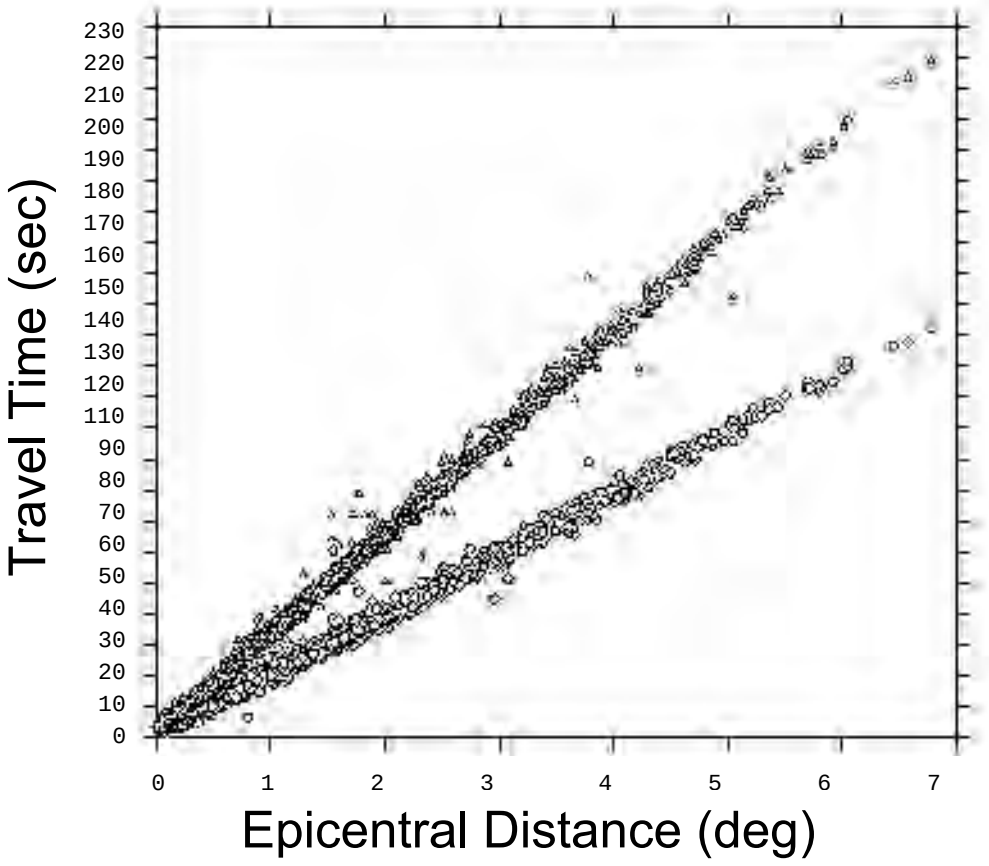


Figure 2. P-wave (open circle) and S-wave (open triangle) travel times observed at all stations in the database.

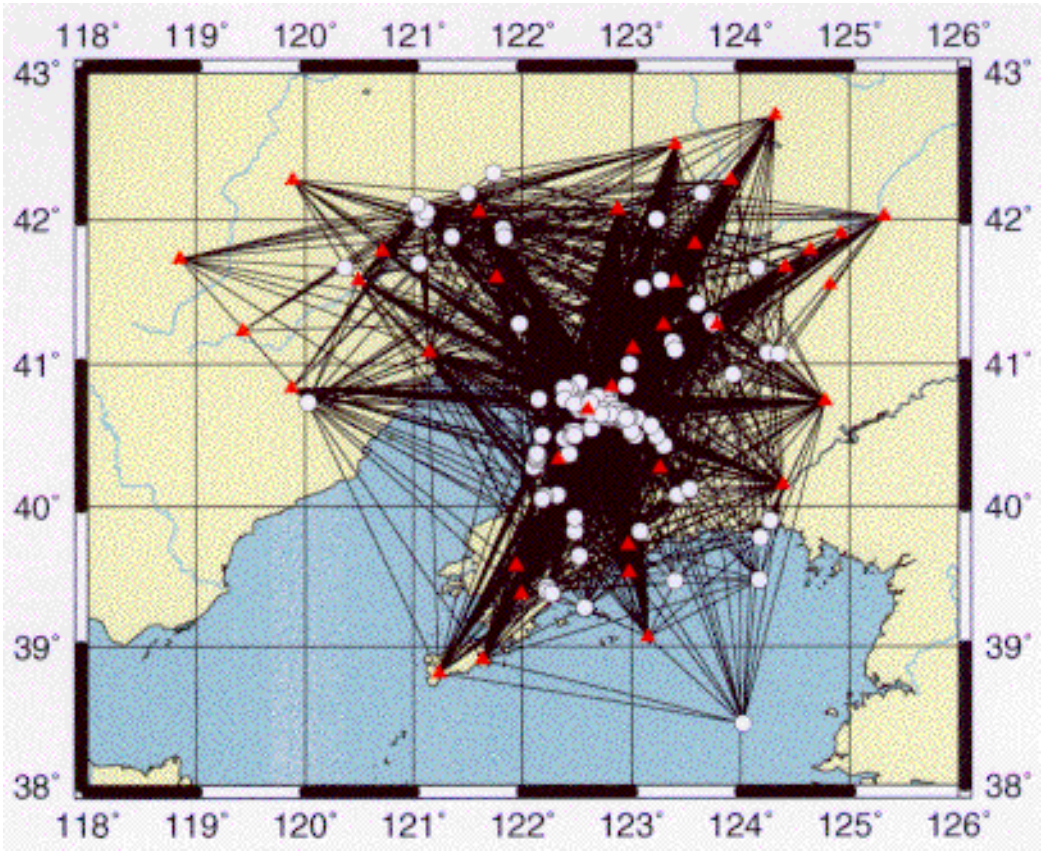


Figure 3. Ray path projection on the earth surface for 226 seismic events used in the inversion. The earthquakes are indicated by open circles and the seismic stations are identified by red triangles.

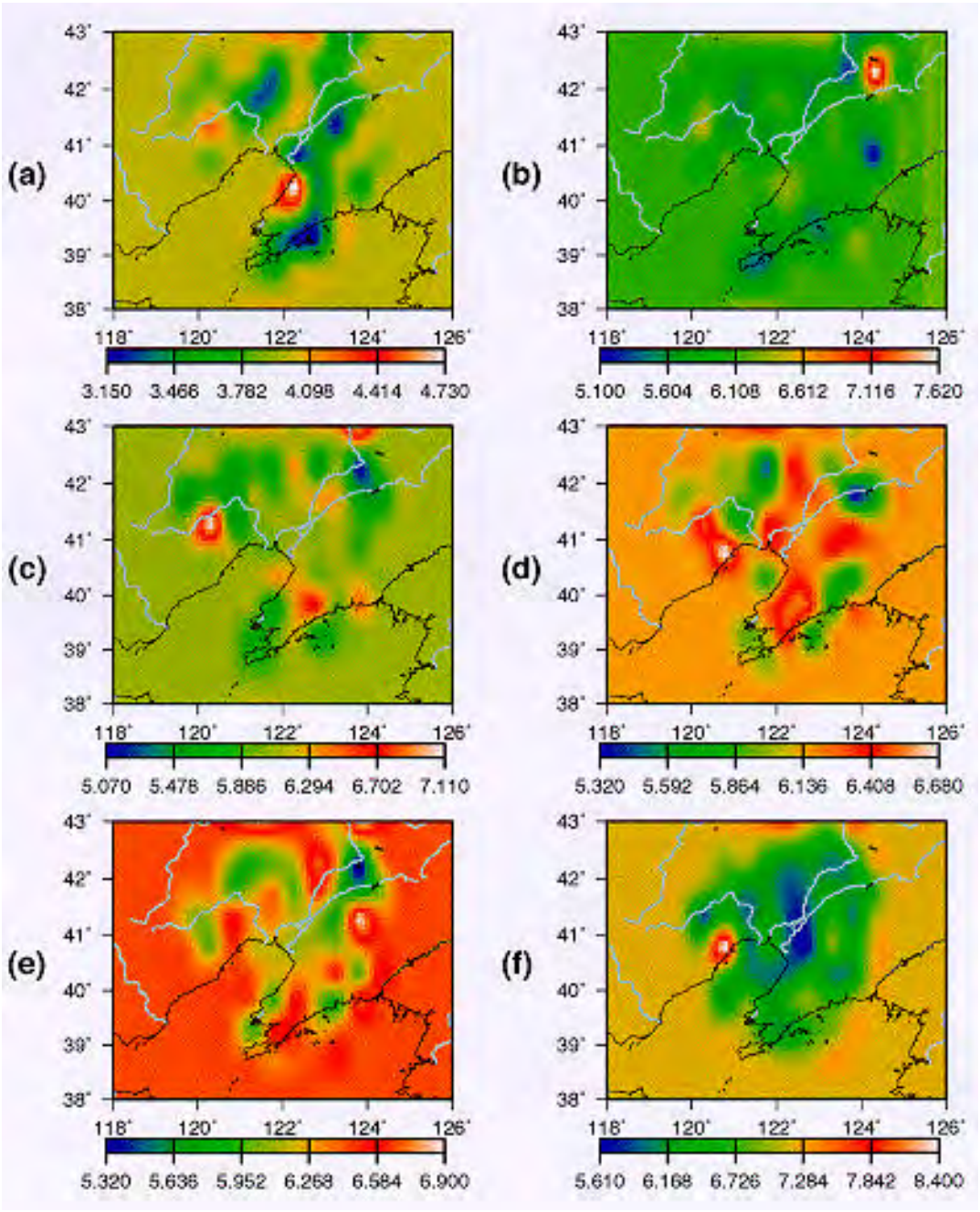


Figure 4. Deduced P-wave velocity after the 5th iteration of 3-D tomographic inversion. Panels (a)-(f) denote layers at different depths corresponding to Table 1.

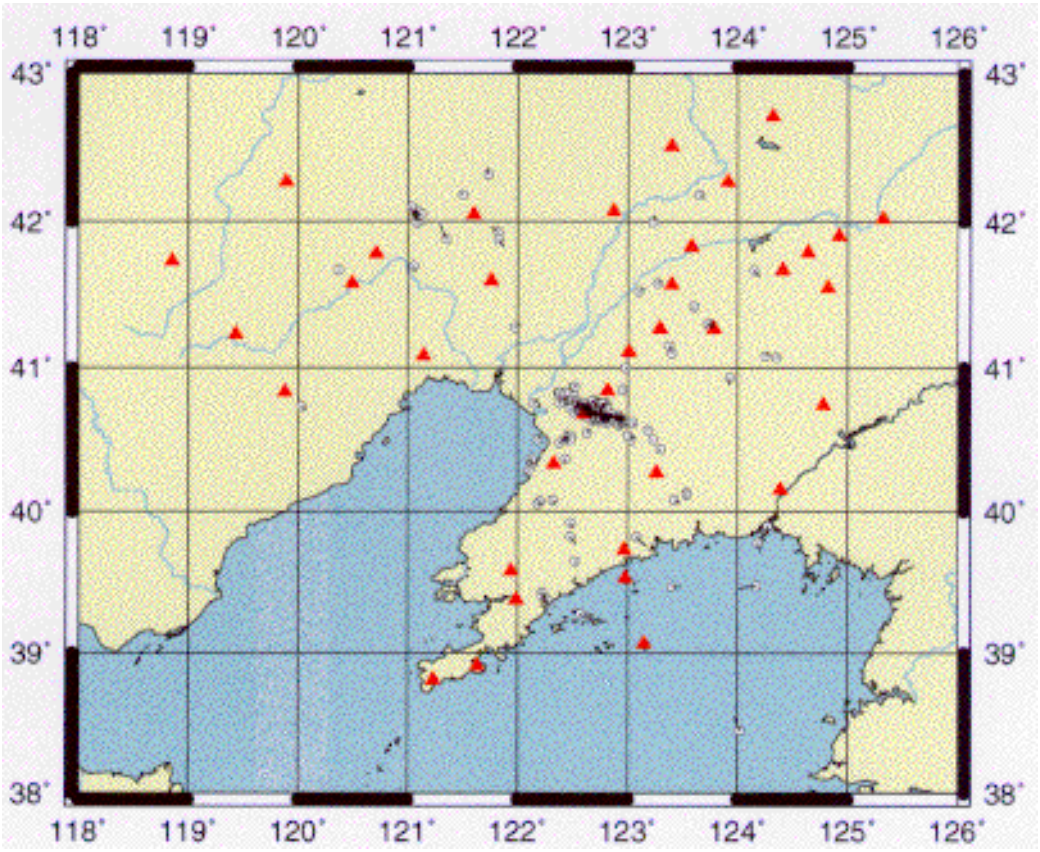


Figure 5. Re-location of the 226 seismic events on the deduced 3-D crustal structure. Short bars represent deviation from the original locations.

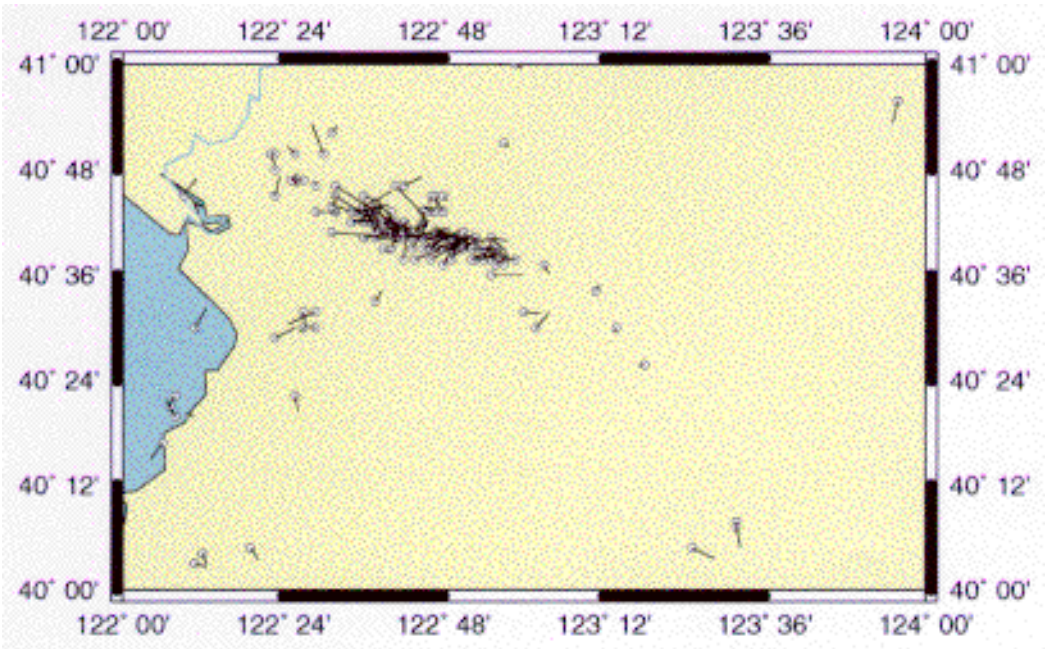


Figure 6. An enlargement of Haicheng area in Figure 5.

RECENT CALIBRATION EVENTS IN THE UNITED STATES

James W. Dewey[1], Ellen Herron[2], and John O. Kork[1]
[1]Adjunct US National Data Center at U.S. Geological Survey (USGS)
[2] U.S. National Data Center at Air Force Technical Applications Center (AFTAC)

Sponsored by United States Air Force
Contract Number: N12FY99000785

ABSTRACT

The United States has agreed to provide calibration information to the Comprehensive Nuclear-Test-Ban-Treaty Organization (CTBTO). As part of this contribution, the U.S. National Data Center (NDC) has identified 64 Calibration seismic events that occurred under U.S. Territory from 1996 -- 1998, a period during which many stations of the International Monitoring System (IMS) have been operating.

The U.S. Calibration events meet three selection criteria: (1) their epicenters are accurate to within 10 km in absolute terms; (2) their magnitudes (USGS m_b or local magnitudes as reported by the USGS) are larger than 3.5; (3) data from IMS stations are excluded from the hypocenter calculation. In order to be judged accurate to within 10 km in absolute terms, the epicenters must be known either independently of arrival-time data (e.g., large mining events) or be associated with well-recorded events for which location errors, due to mistaken phase interpretations or inaccurate velocity models, are minimized (e.g., events occurring within a local or regional seismograph network). Included among the 64 selected Calibration events are 38 events for which we believe the calculated focal depth as well as the epicenter are accurate to within 10 km.

For geographic regions in which many events meet the selection criteria, we selected approximately five Ground Truth events per square degree or per seismotectonic province. These events were selected to provide a variety of source types and event sizes.

Data provided to the CTBTO will include event origins, formal statistical estimates of hypocentral precision, the arrival-time data used to compute the hypocenters, a station-coordinate file, documentation of the velocity models with which the hypocenters are determined, and documentation of how local magnitudes are determined.

In addition, we have used sparse subsets of data randomly selected from a widely recorded event to explore criteria for being confident that events occurring in geographic regions covered by less dense local or regional networks have epicenters that are accurate to within 10 km.

Key Words: location, calibration, seismic regionalization

OBJECTIVE

The purpose of this study is to identify seismic events that have occurred in the United States during the time-period in which a significant fraction of International Monitoring System (IMS) seismographs have been in place, that are large enough that they might be expected to have been detected on IMS stations, and that are well enough located that they may be used to test and improve hypocenter accuracies of events that are located by the International Data Center (IDC). Contribution of such data was suggested in CTBT/Working Group B Sixth Session (WGB-6)/ Conference Room Paper .26 (CRP.26) published in June 1998. The data will be submitted to the Comprehensive Nuclear-Test-Ban Treaty Organization/Provisional Technical Secretariat (CTBTO/PTS).

We required that selected seismic events have the following characteristics: (1), they occurred in 1996-1998; (2), they were assigned magnitudes (m_b or local magnitude) larger than 3.5; (3), their epicenters are accurate to within 10 km when computed without using data from the IMS. For large areas of the U.S., there are no seismic events that have these desired characteristics, either because no sufficiently large seismic events occurred in the areas in 1996-1998 or because there were no means to assure epicenter accuracies to within 10 km. For a few areas, however, there are many seismic events that have the desired characteristics. For the latter areas, we have provided about five events per tectonic province or 1° by 1° area: for such areas, our intention is to provide data from a representative range of seismic-source types and source sizes, without overwhelming the IDC with essentially redundant data. We refer to the selected seismic events as "Calibration" events.

For the US Calibration events, we did not require that focal depths have accuracies within 10 km. The problem of determining accurate focal depths is somewhat decoupled from that of determining accurate epicenters. Highly accurate focal depths of shallow-focus events can commonly be determined with teleseismic waveform modelling and only approximate knowledge of the velocity structure in the hypocentral region, even if the teleseismically determined epicenters are severely biased by lateral velocity heterogeneity. Conversely, highly accurate epicenters can be determined with local arrival-time data and regional velocity models, even in cases when the regional velocity models are not well-enough known to ensure highly accurate focal depths. We will identify events with focal depths that are probably accurate to within 10 km, but these focal depths are more susceptible than the epicenters to bias by minor inaccuracies of the assumed velocity model.

We will provide the CTBTO/PTS with Calibration event origins and formal confidence intervals on epicenter and focal depth, arrival-time data used to locate the events, station-coordinate files, documentation of velocity models used in hypocenter computations, and documentation of procedures used to compute local magnitudes. The event origins and confidence intervals will be based entirely on data from non-IMS stations.

RESEARCH ACCOMPLISHED

Our research focussed on the requirement that the calibration epicenters be within 10 km of the true epicenters. Almost all of the events that we have selected as Calibration events are earthquakes. Their epicenters and focal depths were determined from arrival-time data, and therefore have some uncertainty associated with them. The possible sources of location error are diverse, and the possibility of location error had to be evaluated from several perspectives. We have used a three-stage process to select the Calibration events that we will present to the CTBTO/PTS. First, we selected and relocated candidate Calibration events on the basis of the azimuthal and distance distribution of stations that recorded the events. Second, we required that the epicenter confidence ellipses of the selected events be smaller than a threshold value. Third, we required that the epicenters of the selected events be robust under changes in the assumptions used to calculate the epicenters. The first stage yielded 80 candidate events: the second and third stages resulted in some of the candidates being judged not reliable, so that 64 Calibration events were finally selected. In addition, we use randomly selected, sparse subsets of data from well-recorded events to explore the effects of nonlinearities in the location process, non-Gaussian errors in arrival-time data, and lateral variations in seismic-wave velocities.

Selection of candidates for US Calibration events

The U.S. Geological Survey/National Earthquake Information Center (USGS/NEIC) and the institutions that operate regional networks recorded a large number of shocks of magnitude greater than 3.5 during 1996-1998 (Figures 1 -2). We used formal and informal criteria to select a small subset of these events as candidates for Calibration events. The process of selecting candidates for Calibration events, discussed in this section, resulted in 80 candidate Calibration events. We concluded that 64 of the 80 are located with sufficient confidence that they can be presented to the CTBTO/PTS as Calibration events.

To select most candidate Calibration events, we reviewed data listed in the Earthquake Data Reports (EDR's) of the USGS/NEIC and applied the following "stringent station-distribution criteria:"

A. The candidate Calibration events were recorded by at least 10 stations (excluding IMS Primary or Auxiliary stations) within an epicentral distance of 250 km. The use of ten stations gives redundancy of data, so that a gross error in arrival-time data from one or a few stations can be detected by comparison with data from the other stations. Local and near-regional P-wave arrivals from moderate-sized earthquakes tend to be readable to high precision. For most of the regions studied, local and regional velocity models are available that more closely reflect the true velocities than would global-average velocity models. Finally, for a given percentage error in the velocity model, the absolute error in predicted epicenter-to-station distance will be smaller for a short raypath than for a long raypath.
B. The azimuthal gap in the distribution of non-IMS stations was 90 degrees or less. A wide azimuthal range of observations makes the calculated epicenter less dependent on second-order differences between the true velocity structure and the velocity model used in calculating the hypocenters. In addition, arrival-time observations from all quadrants around the epicenter provide sufficient redundancy of azimuthal coverage that a gross arrival-time error at one of the stations can be detected by its effect on the calculated standard error
C. At least one non-IMS station had to be situated at an epicentral distance of 30 km or less. The presence of arrival-time data from close-in stations is critical for calculating reliable focal depths of earthquakes with arrival time data alone.

The stringent station-distribution criteria drastically reduced the area of the United States for which we were able to identify candidate Calibration events (Figures 1-2). In an effort to broaden the area from which candidate Calibration events might be selected in the future, we have also identified (Figures 1-2) events that, on the basis of the data listed in the EDR's, meet the following "relaxed station-distribution criteria":

i. The events were recorded by at least 5 non-IMS stations situated within 250 km.
ii. The azimuthal gap in the distribution of non-IMS stations within 250 km is 180° or less.

The events satisfying the relaxed criteria are of interest because it may be possible to acquire data for some of these shocks that were not reported to the USGS/NEIC but that, together with the data that are reported to the USGS/NEIC, enable the events to satisfy the stringent criteria. In addition, as will be discussed later, it appears possible to find events that fall short of the stringent criteria but that can still be confidently located to within 10 km. In the present study, we did not select Calibration events from among events that satisfied only the relaxed station-distribution criteria.

Independently of station-distribution criteria that enable a reliable epicenter to be computed from seismographic arrival-time data, we searched the EDR's for human-induced seismic events that occurred in the U.S. in 1996-1998, had magnitudes greater than 3.5, and had locations that were known independently of arrival-time data. We found one such event, a rockburst in northern Idaho.

For territories under U.S. control in the western Pacific, we found no seismic events that met stringent or relaxed station-distribution criteria, or that met criteria for human-induced Calibration events. We identified several events near Puerto Rico that met the relaxed station-distribution criteria, but not the stringent criteria.

In some seismically active areas of California, there were many seismic events that met the stringent station-distribution criteria, and we selected only a few of these events from each tectonic province or 1° by 1° area as candidates for Calibration events. For these regions, we did not apply formal criteria for

selecting the candidate Calibration events from among all events that met the station-distribution criteria. Instead we selected events so as to include a variety of source-types and sizes, so that users of our Calibration events could explore the effects of local source-variations or differing source size on IMS capabilities.

Calculating hypocenters and final selection of US Calibration events

We relocated all candidate Calibration events using the program HYPOELLIPSE (Lahr, 1989), a program for computing hypocenters from local and regional data that is widely used by operators of regional seismograph networks and that is available free of charge. We located earthquakes in each region with one-dimensional velocity models that have been determined for the region in which the earthquakes occurred or for a tectonically similar region nearby. Theoretical travel-times to individual stations were modified by elevation corrections, calculated according to the default procedure of Lahr (1989), but otherwise station-specific adjustments were not applied to the theoretical travel-times. Observational data consisted primarily of first-arriving P-waves recorded at local and regional stations; some S-wave data were used, exclusively for stations situated within 100 km of the epicenters. Arrival-time data were taken from the EDR's of the USGS/NEIC (for earthquakes outside of California), from the Northern California Earthquake Data Center (for earthquakes in Northern California), and from the Southern California Earthquake Data Center (for earthquakes in Southern California).

Confidence regions, reflecting the precisions of the calculated epicenters and focal depths, are based on the assumption that the standard deviation of the P-wave arrival-time observations for a given earthquake is equal to either, (a), the standard error of the travel-time residuals for that earthquake or, (b), a lower-bound standard error (.5 for Alaskan events and .4 for other events), whichever is larger. The lower-bound values for P-wave standard error were taken to be the median values of P-wave arrival-time standard errors that resulted from a preliminary location of the candidate Calibration events in each region. The confidence regions normally computed by HYPOELLIPSE are associated with a 68% level of confidence. We have adjusted the sizes of confidence regions to correspond to a 90% level of confidence.

Hypocenters of most of the events had been earlier computed by the institutions that run regional networks within whose boundaries the events occurred. We relocated the events in order to prepare data files to transmit to the CTBTO/PTS, to be sure that we were correctly describing how the contributed hypocenters were computed, to exclude data from IMS stations that might have been used in the original computations, and to obtain a sense of the stability of each computation.

In our relocation of the candidate Calibration events, we used two different implementations of the "distance-weighting" option of HYPOELLIPSE (Lahr, 1989). We examined the confidence regions computed by HYPOELLIPSE, compared the results of applying the two different distance-weighting procedures, and compared our locations with prior regional network locations when the latter were available.

Our two implementations of the HYPOELLIPSE distance-weighting option apply this weighting to the data after four iterations of the "calculate hypocenter/adjust hypocenter" cycle. Both implementations assign full weight to P-wave readings out to distances of 100 km from the epicenter. Our preferred implementation uses only the close-in data; weights assigned to P-wave readings decrease from full weight at 100 km to zero weight at 110 km. A shallow-focus event epicenter that has been calculated under this weighting scheme and that has a small confidence ellipse is likely to be highly accurate, because the short lengths of the raypaths minimize the amplitude of travel-time biases produced by errors in the assumed velocity model. However, some events, widely enough recorded by stations within 250 km to meet the stringent station-distribution criteria, are not widely enough recorded by stations within 110 km that they can be reliably located with the preferred implementation of the distance-weighting option. In the second implementation of the HYPOELLIPSE distance-weighting option, weights assigned to P-wave readings decrease from full weight at 100 km to zero weight at 250 km. By including the data between 110 km and 250 km, the second implementation of the distance-weighting option greatly extends the azimuthal coverage of some events, but the longer ray-paths make the location more susceptible to bias by errors in the assumed velocity model. In this study, we found that epicenters calculated with the second weighting

option were nearly identical to epicenters calculated with the first weighting option, when the epicenter computed with the first weighting option was well-located (as inferred from the size of the epicenter confidence ellipse). However, for some events the focal depths calculated with the second weighting option differed significantly from the focal depths calculated with the first weighting option. In most cases, these depth differences were apparently due to bias allowed by the second distance-weighting option. A distance-dependent structure in the P-wave residuals, and a consistency in this structure from events within the same small source region, suggested that the Pn-arrivals at distances between 110 km and 250 km were the source of the depth discrepancy. Pn arrivals would be sensitive to incorrect depth to the M-discontinuity in the assumed velocity model.

From the candidate Calibration events, the 64 events that we will present to the CTBTO/PTS will be those for which the 90 percent confidence ellipses on epicentral coordinates have semi-axes less than 5.0 km. In the case of earthquakes lying within a regional network, we also require that our relocated epicenters of the Calibration events be within 5.0 km of the epicenters computed by regional networks. The hypocenters and confidence-regions of events calculated with the preferred distance-weighting option will given if the 90 percent confidence ellipses have semi-axes less than 5.0 km: otherwise, we will give the epicenters, focal depths, and confidence-regions calculated with the weighting option that incorporates observations collected out to distances of 250 km.

For 38 of the 64 selected Calibration events, the 90 percent confidence intervals on focal depth were smaller than 5 km, and the focal depths that we have calculated are within 5 km of the focal depths calculated by the institutions running the regional networks in which the events occurred. The focal depths of most of these events are probably accurate to within 10 km, and we will so label them in the files that we give to the CTBTO/PTS. Focal depths calculated with arrival-times from regional networks are, however, generally more vulnerable than epicenters to biasing effects of slightly inaccurate velocity models. A substantially erroneous focal-depth is more likely than a substantially erroneous epicenter to escape detection by our three-stage procedure for identifying Calibration events.

A random-sampling exploration of station-distribution criteria for selecting candidate Calibration events

Most of the 64 events that we will present as Calibration events were initially identified as candidate events on the basis of the stringent station-distribution criteria discussed in the section, " *Selection of candidates for US Calibration events*." In the present section, we explore the robustness of the station-distribution criteria. It would be well to know if the criteria are too stringent as we currently define them. Demonstration that less stringent criteria are adequate to ensure 10-kilometer accuracy would permit Calibration events to be selected from more of the U.S.

Our testing procedure started with events that were so well recorded that they will be accurately located even in the presence of non-Gaussian errors or large velocity heterogeneity. We randomly selected stations to form sparse subsets of the overall station sets that were used to locate the well-recorded events. We calculated hypocenters for each of the sparse subsets and evaluated how well the calculated hypocenters and confidence regions agreed with the hypocenter that was calculated from all the data.

Figure 3 illustrates epicenters calculated with sparse subsets of stations that recorded a magnitude (mb, USGS) 4.8 earthquake that occurred on the San Andreas fault in Central California. The earthquake occurred in the midst of one of the most spatially dense networks of local seismographs in the world and was recorded by over 80 stations within 110 km. The source region of the earthquake has high lateral variations in seismic wave velocities. If a one-dimensional velocity model is used in computing the hypocenter, these velocity variations can result in hypocenter biases of several kilometers even when all of the local data are used in the location process (Uhrhammer et al., 1999). It might therefore be expected that some epicenters calculated with few stations might be severely biased. Three groups of sparse subsets were selected for testing: subsets consisting of eight stations, subject to the requirement that the azimuthal gap in station distribution be less than 120°; subsets consisting of five stations, subject to the requirement that the azimuthal gap in station distribution be less than 120°; subsets consisting of five stations, subject to the requirement that the azimuthal gap in station distribution be less than 180°. Stations selected were required to be situated within 250 km of the epicenter calculated with all data.

None of the three station-distribution criteria used to select the sparse subsets were sufficient, of themselves, to ensure that errors in epicenters were less than 10 km. However, 31 of the 100 epicenters calculated from the eight-station subsets, with azimuthal gaps less than 120°, had 90% confidence ellipses with semi-axes shorter than 5.0 km; all fall within 10 km of the likely true epicenter (Figure 3). Similarly, 6 of the 100 epicenters calculated from five-station subsets, with azimuthal gaps less than 120°, had 90% confidence ellipses with semi-axes less than 5.0 km; all of these also fall within 10 km of the likely true epicenter (Figure 3). None of the 100 epicenters calculated from five-station subsets with azimuthal gaps as large as 180° had 90% confidence ellipses with semi-axes shorter than 5 km. These results suggest that candidate Calibration events can be identified using station-distribution criteria that are less severe than the stringent station-distribution criteria we have used: it is necessary that additional criteria based on the hypocenter computations, such as the size of confidence intervals, be used to select the Calibration events from candidate Calibration events.

CONCLUSIONS AND RECOMMENDATIONS

The United States National Data Center has identified 64 seismic events that occurred in United States Territory to be provided to the CTBTO/PTS as U.S. Calibration events. The Calibration events occurred in 1996-1998; they were assigned magnitudes (m_b or local magnitude) larger than 3.5; and their epicenters are accurate to within 10 km when computed without using data from the IMS. For areas in which there were many events that met the preceding time, size, and accuracy requirements, we selected a limited number of calibration events so as not to provide redundant data to the CTBTO/PTS. The location of one of the events is known, independently of arrival-time data, because it was a rockburst in a mine. Of the 64 events selected as calibration events, 38 have focal depths that are probably accurate to within 10 km.

Most of the work conducted in this study addresses the requirement that the event epicenters be accurate to within 10 km. The locations of earthquake epicenters that are calculated with phase arrival-times are always susceptible to some error, and, by postulating a bizarre velocity structure and bizarre timing errors, we could probably always develop a scenario under which the epicenter of a well-recorded local earthquake with a small epicenter confidence ellipse might be in error by more than 10 km. We used three general approaches to be confident that our locations would be accurate to within 10 km in the presence of typical sources of location error. First, we identified candidate Calibration events by using stringent station-distribution criteria, which required that the events be computed with data from local and regional stations distributed over a wide range of azimuths. Second, after relocating the candidate Calibration events with the HYPOELLIPSE program and a regional one-dimensional velocity model, we applied conservative criteria to the HYPOELLIPSE-produced confidence intervals to select Calibration events from among the candidate Calibration events. Third, for each candidate Calibration event, we have available at least two hypocenters computed by HYPOELLIPSE with different weighting assumptions, and for most candidate Calibration events we have in addition the hypocenters computed independently by the institutions that run the regional seismic networks in which the events occurred. We compared our hypocenters with the regional-network hypocenters to check the stability of our computed hypocenters under changes in the assumptions used in their calculation. We identified 80 candidate Calibration events on the basis of the station-distribution criteria. The 64 events that will be given to the CTBTO/PTS are those candidate Calibration events that also satisfied both the confidence-interval criteria and the requirement that their epicenters computed with differing starting assumptions be mutually consistent.

The station-distribution criteria that we used to define candidates for Calibration events may be unnecessarily conservative. This possibility is suggested by study of epicenters computed from sparse subsets of data randomly selected from a widely recorded event. Because criteria on the size of confidence regions are also used in the final selection of Calibration events, candidates for Calibration events can probably be identified using less stringent criteria on the number of recording local stations and the size of the azimuthal gap in station distribution.

REFERENCES

Lahr, J. C., 1989, HYPOELLIPSE/Version 2.0: A computer program for determining local earthquake hypocentral parameters, magnitude, and first-motion pattern, U. S. Geological Survey Open-File Report 89-116, 92 p.

Uhrhammer, R., Gee, L. S., Murray, W., Dreger, D., and Romanowicz, B., 1999, The M_W 5.1 San Juan Bautista, California earthquake of 12 August 1998: Seismological Research Letters, v. 70, p. 10-18.

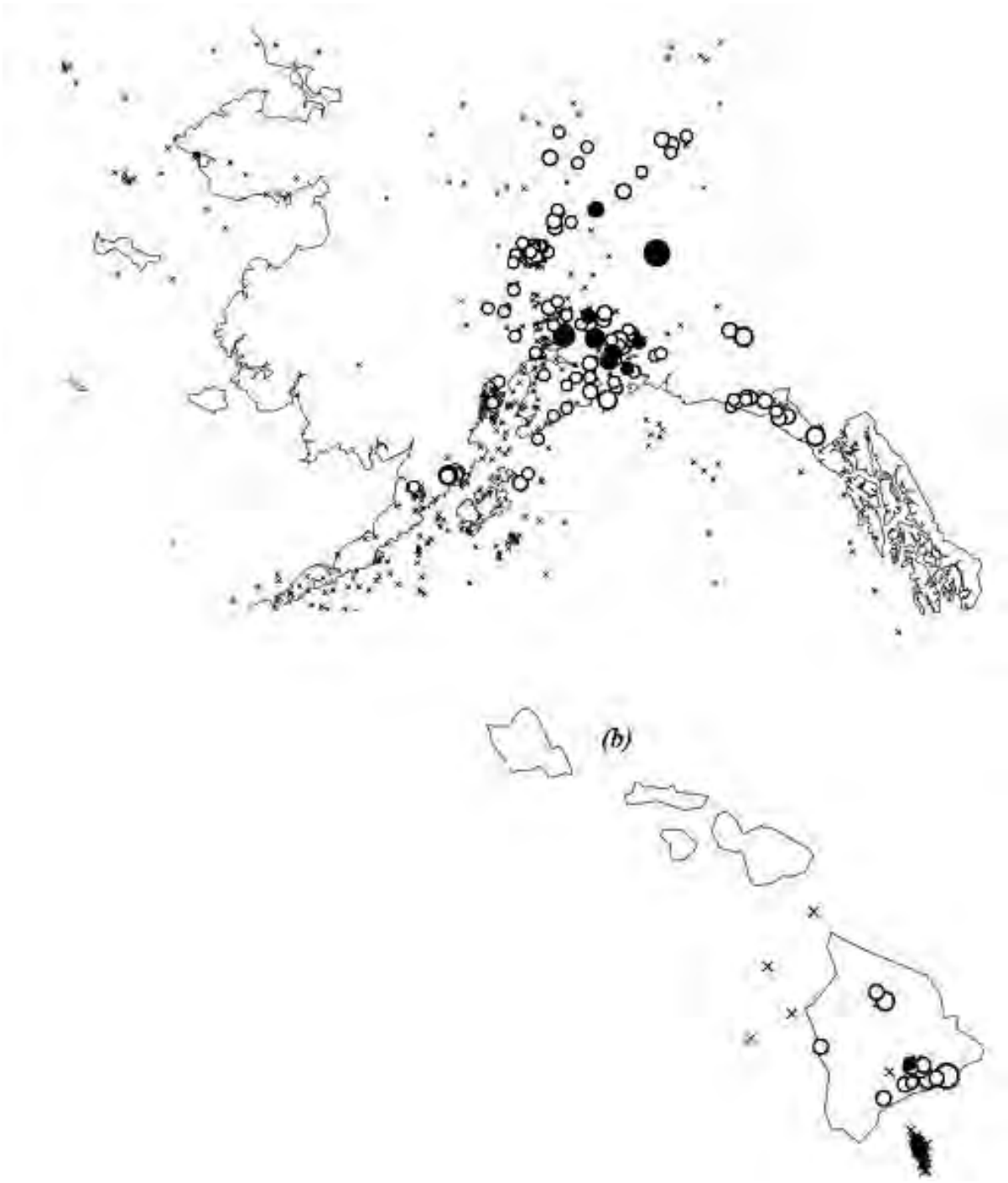


Figure 1. Seismic events of M>3.5 in 1996-1998 in Alaska (a) and Hawaii (b). Black circles denote events whose epicenters and focal depths are both judged accurate to within 10 dm. Gray circles denote events whose epicenters are judged accurate to within 10 km. White circles denote other events for which USGS/NEIC data files show five or more stations that have epicentral distances less than 25o km and that together have an azimuthal gap less than 180 deg.

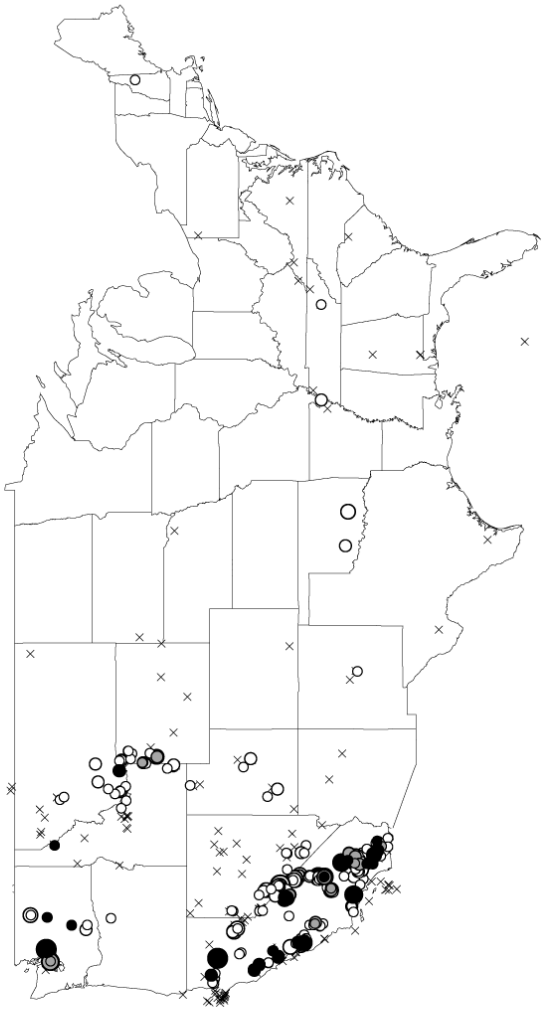


Figure 2. Seismic events of M > 3.5 in 1996-1998 in the 48 contiguous states. Black circles denote events whose epicenters and focal depths are judged accurate to within 10 km. Gray circles denote events whose epicenters are judged accurate to within 10km. White circles denote events for which USGS/NEIC data files show five or more stations that have epicentral distances less than 250 km and that together have an azimuthal gap less than 180 deg, and x's denote other events.

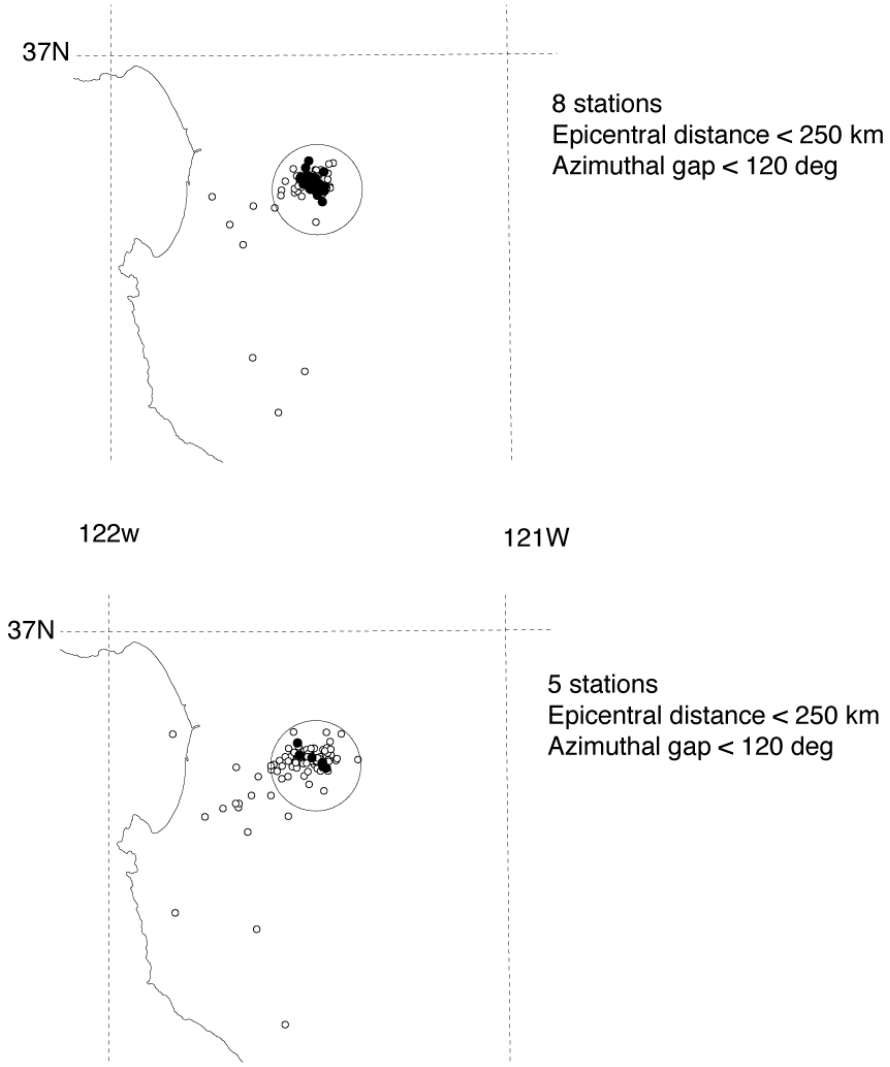


Figure 3. Epicenters of the California earthquake of 1998 August 12, 14:10 UTC, calculated with different, randomly selected, sparse subsets of the entire set of local arrival times. Filled epicenters are those whose 90 % confidence ellipses have semi-axes less than 5 km. Large circle has 10 km radius and is centered on epicenter that is calculated with all data.

ON THE SENSITIVITY OF BROADBAND REGIONAL SEISMIC PHASES TO MULTI-DIMENSIONAL EARTH STRUCTURE: IMPLICATIONS FOR PHASE IDENTIFICATION

Peter Goldstein, Joydeep Bhattacharyya, Doug Dodge, Gene Ichinose,
Richard Leach, Shawn Larsen, Arthur Rodgers
Lawrence Livermore National Laboratory

Sponsored by U.S. Department of Energy
Office of Nonproliferation and National Security
Office of Research and Development
Contract No. W-7405-ENG-48

ABSTRACT

An important challenge for seismic monitoring of nuclear test ban treaties at low magnitude is the development of techniques that use regional phases for detection, location, and identification. Accurate phase identification is a fundamental aspect of this problem. We compare 2-D finite difference synthetics and data for selected events in the Middle East, North Africa and Western US to show how structural features such as deep sedimentary basins, crustal thinning, topography, and high attenuation in shallow structure can have large effects on the timing and amplitude of regional phases.

We use moderate size (Mb~4.5-6) events whose source parameters are well constrained by local and far-regional to teleseismic data. This avoids the possibility of trade-offs between source and path effects. For example, we model the Mb-5.9 October 1992 Cairo, Egypt, earthquake at a station at Ankara, Turkey (ANTO), using a two-dimensional crustal model consisting of a water layer over a deep sedimentary basin with a thinning crust beneath the basin. Despite the complex tectonics of the Eastern Mediterranean region, we find surprisingly good agreement between the observed data and synthetics based on this simple two-dimensional model. We investigate the sensitivity of these synthetics to a number of features including 1) the thickness, velocity, and attenuation of the sedimentary basin, 2) the amount of crustal thinning beneath the basin, 3) the amount of attenuation, and 4) the presence of a water layer. We find that, for this region, the presence of a thick sedimentary basin has the most significant effects on the regional phases. Of particular note, Pg, which appears to have been extinguished in the data and individual synthetics, has actually been significantly delayed far into what is normally considered the Pg coda. The surface waves are dramatically dispersed by the presence of the basin. Sn also appears to have been extinguished in the data and synthetics, however, inspection of successive snapshots of the wavefield indicate that most of Sn has been converted to crustally guided waves that are superimposed on the Lg wavefield.

Crustal thinning beneath the basin also reduces the amplitudes of Pg and Sn, but its effects are less significant. The effects of large-scale attenuation are well approximated by a low-pass filter. The effects of the water layer are small but most noticeable in the surface waves.

These results show that we can use wavefield simulations to understand observed regional wave propagation phenomena and suggest that it may be possible to predict the behavior of regional phases and discriminants when we have an accurate model for the regional seismic structure.

Key Words: Seismic, Wave Propagation Modeling, Phase Identification, Regionalization, Middle East, Mediterranean, Caspian, Sedimentary Basin, Crustal Thinning, Attenuation, Topography.

This work was performed under the auspices of the U.S. Department of Energy by Lawrence Livermore National Laboratory under contract No. W-7405-Eng-48 for the Office of Research and Development, NN-20, within the Office of NonProliferation and National Security, NN-1.

OBJECTIVES

We have been developing the capabilities needed to model regional seismic signals in complex media (e.g., Larsen, 1995; Goldstein, et al., 1996; Goldstein et al., 1997; Goldstein and Dodge, 1999) so that we can help understand the physical basis for and performance of existing monitoring techniques. We also aim to use this improved understanding to help improve location techniques and help develop transportable seismic identification techniques. It may also allow us to predict the behavior of regional phases and discriminants in regions where there is limited data.

In this study, we investigate the sensitivity of regional phases in complex media to features such as deep sedimentary basins, crustal thinning, attenuation, and free-surface topography. We show how these features can affect regional signals and identify those features that have the greatest impact from a monitoring standpoint.

RESEARCH ACCOMPLISHED

The October 1992 Cairo, Egypt, Earthquake

We simulated the October 1992 Cairo, Egypt, earthquake in order to test our predictive modeling capabilities and to investigate the sensitivity of regional phases to complex regional structure, Figure 1. We began by simulating recordings of this earthquake at Ankara, Turkey (ANTO) using the epicentral location determined by the National Earthquake Information Center and a depth and mechanism (Figure 2) determined using broadband modeling of the P-wavetrain (e.g., Goldstein and Dodge, 1999).

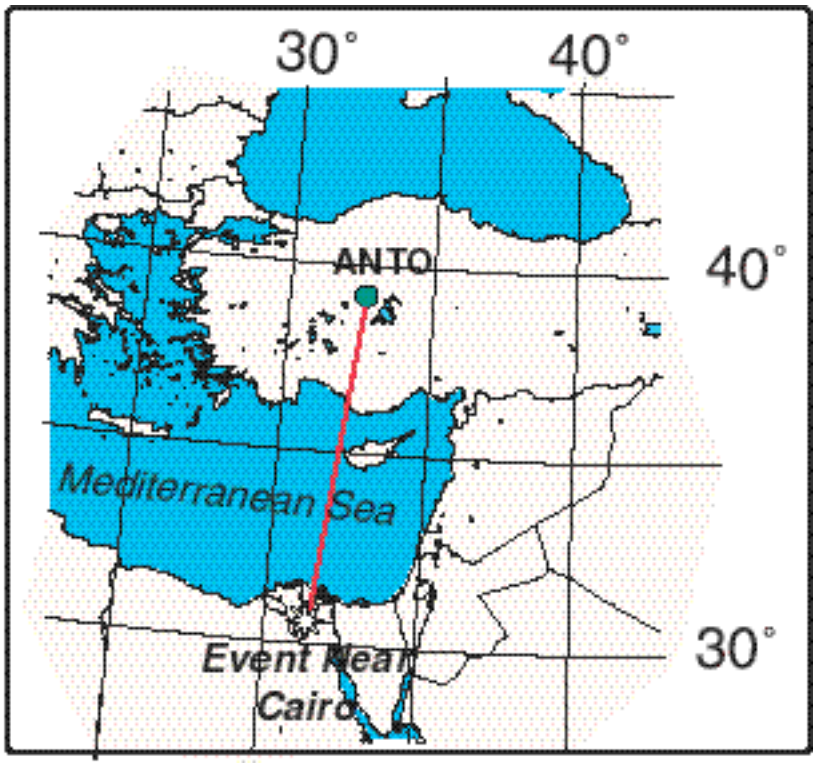


Figure 1. Map showing locations of the Mb-5.9 Cairo, Egypt, earthquake on October 12, 1992, and the seismic station at Ankara, Turkey (ANTO).

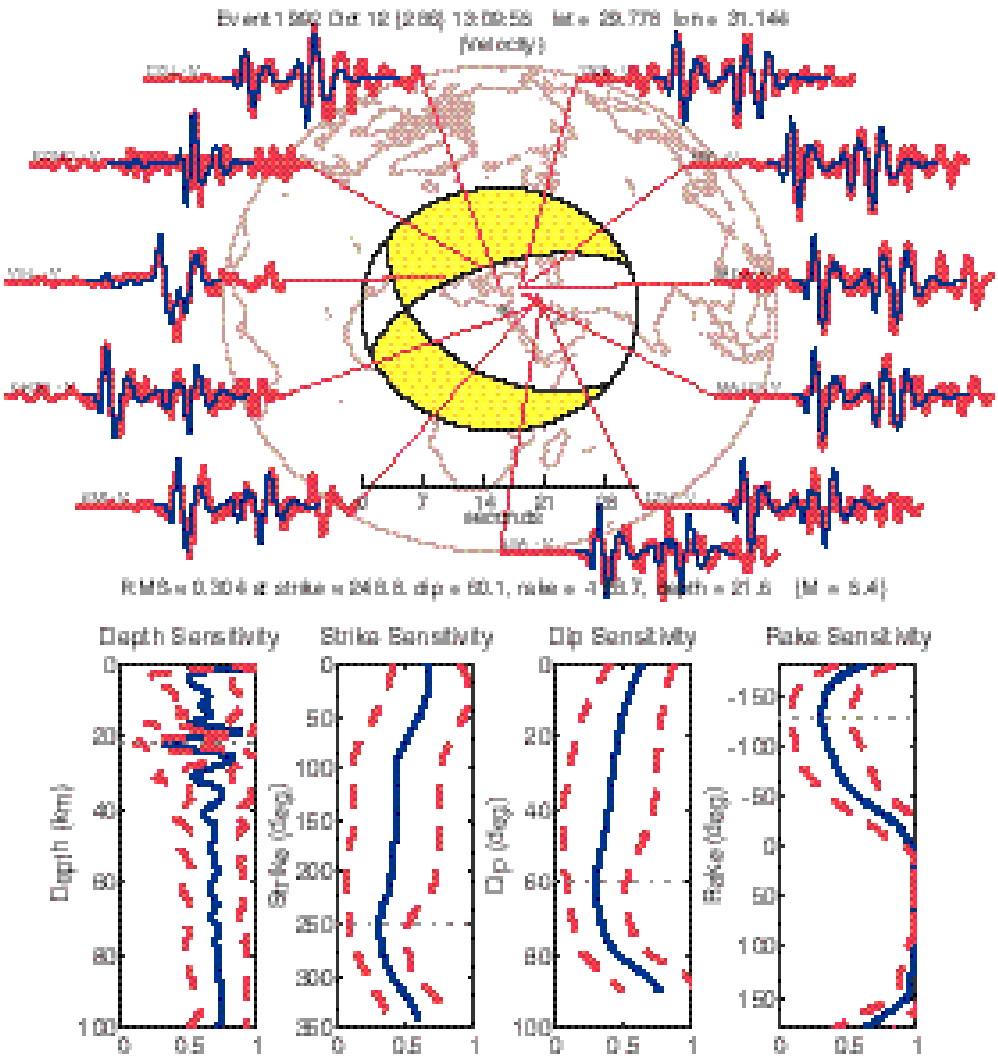


Figure 2. Far regional-teleseismic solution for the depth and mechanism of the October 1992 Cairo Earthquake. The upper part of the figure shows the focal mechanism and the waveform fits to the data. The sensitivity of the preferred solution to depth, strike, dip, and rake are shown in the lower part of the figure.

Based on the depth to basement and crustal thickness given in Cornell University Digital Database for the Middle East and North Africa (Barazangi et al., 1996), we developed a two-dimensional earth structure consisting of three crustal layers, the Mediterranean Sea, a thick sedimentary basin, and deeper crust that thins beneath the sedimentary basin (Figure 3). The upper mantle consists of a uniform velocity gradient extending to a depth of 100 km. At 1000 km, this structure is deep enough to model Pn and Sn but will not include the effects of any upper mantle discontinuities. In Figure 3, we compare the observed data with the simulations based on one- and two-dimensional models. We find excellent agreement between the observed data and the synthetic generated using the two-dimensional structure. In contrast, there are dramatic differences between the flat-layered approximation and the observed data. The excellent agreement between observed data and synthetic based on the two-dimensional model suggest that it may be possible to predict regional waveforms in regions where we have accurate estimates of the seismic velocity structure.

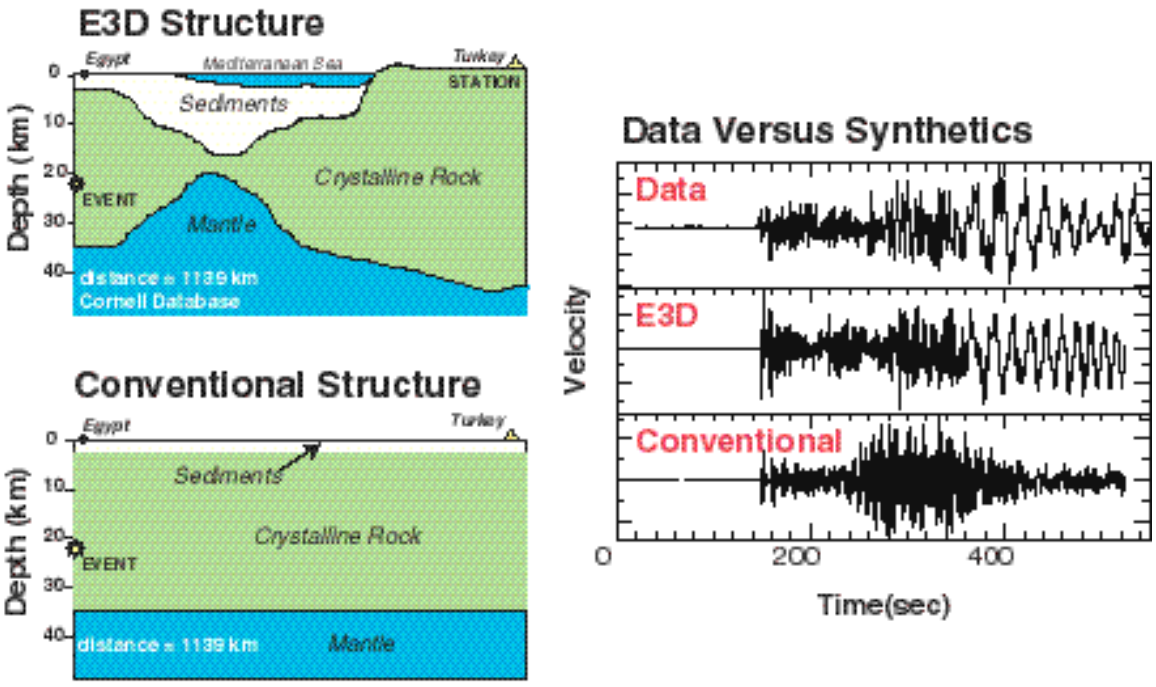


Figure 3 Comparison of one- and two-dimensional models and vertical component data and synthetics for the Mb-5.9 October 1992 Cairo, Egypt, earthquake as recorded at Ankara Turkey. The seismic station ANTO is indicated by the triangle near the upper right corner. The synthetic seismogram based on the laterally varying earth model provides a much better fit to the data.

Sensitivity of Regional Phases to Structure: Implications for Phase Identification

In this section, we describe our investigation of the sensitivity of our simulations of the Cairo, Egypt, earthquake to a number of features of the two-dimensional crustal model including: 1) the thickness and velocity of the sedimentary basin, 2) the amount of crustal thinning beneath the basin, 3) the amount of attenuation, and 4) the presence of a water layer. The effects of many of these features are indicated by the differences in the synthetic seismograms in Figure 4.

The most prominent differences are due to the deep sedimentary basin. Based on differences between simulations with shallow and deep sedimentary basins, this feature is responsible for a dramatic increase in the apparent dispersion of the surface waves. This reduces the amlitudes and significantly delays the Pg and Sn phases. The Lg phase is also enhanced by this feature due to a complex combination of scattering and conversion effects. Crustal thinning can also produce similar changes in Pg and Sn but has relatively minor effects on the surface waves.

An improved understanding of the physical basis for these effects can be obtained by a comparison of snapshots in time of the wavefield as it propagates through the different models (Figure 5). For example, snapshots for the preferred model indicate that the Pg phase doesn't really begin to propagate with significant amplitudes until after it passes the deepest part of the sedimentary basin. This observation is consistent with the idea that the basin absorbs and initially traps most of the P-wave energy with relatively steep incidence angles. This energy is then reradiated at the other end of the basin. Observed signals in the data and synthetics midways through the Pg window are consistent with this hypothesis. Similarly, the

basin also acts like an excellent radiator of surface waves. We hypothesize that these signals, which appear to be dispersed, are actually the result of reverberations of the basin in a fundamental mode.

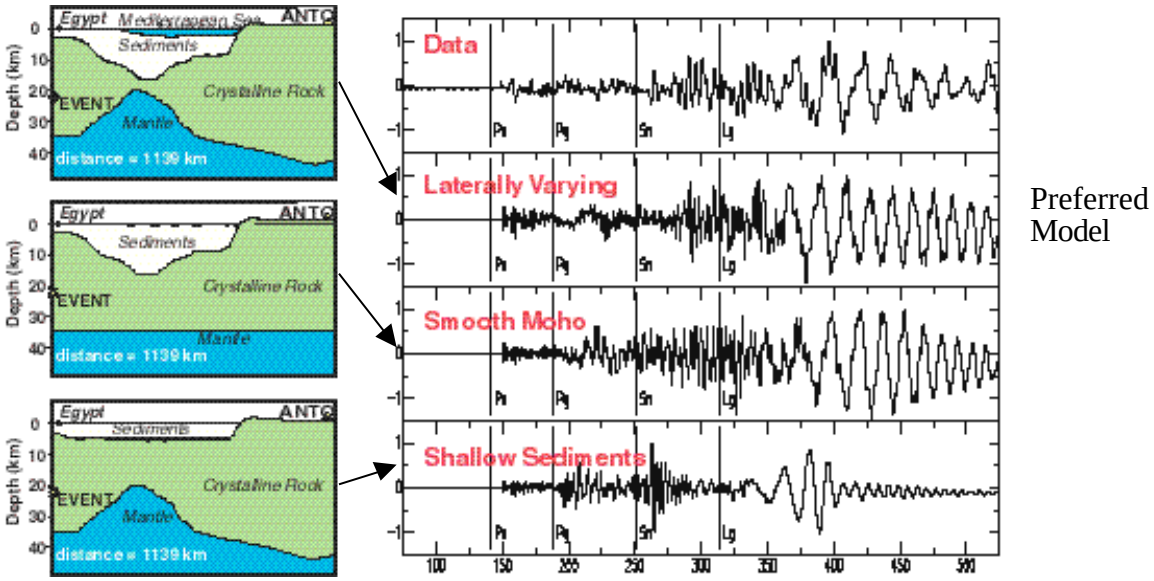


Figure 4. Comparison of vertical component data with synthetics for our preferred model, and models with shallow sediments, a smooth moho, and no water layer. Removing the shallow sediments from the preferred model leads to significant disagreement with the observed data.

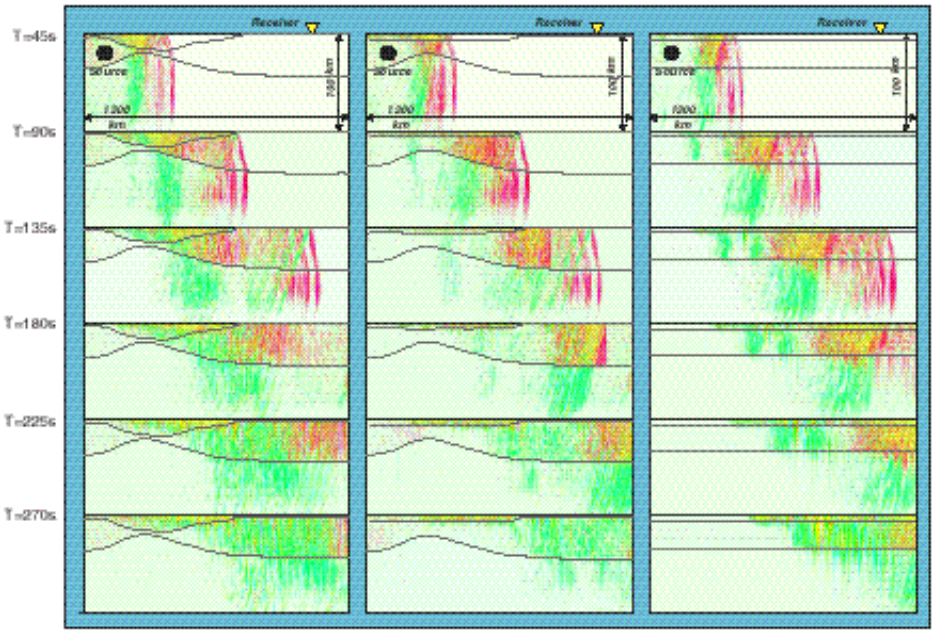


Figure 5. Comparison of snapshots of the wavefield at successive 30 sec time intervals in our preferred model, a model with shallow sediments and a flat layered model. P-waves are red and S-waves are green.

The effects of a variety of other features were also investigated including properties of the water layer, and attenuation. Most of the effects of these features were relatively small, however, as expected, the amount of attenuation in the shallow structure does have significant effects on the amplitudes of the crustal phases.

These result show how we can use simulations to understand regional wave propagation phenomena and suggest that it may be possible to predict the behavior of regional phases and discriminants when we have a reasonably accurate model for the regional seismic structure.

CONCLUSIONS

We have developed and are utilizing state-of-the-art, elastic wave propagation modeling capabilities to understand the physical basis of regional wave propagation phenomena. Understanding the physical basis of these phenomena is essential for developing transportable seismic identification techniques and for predicting the behavior of regional phases in relatively aseismic regions. Based on modeling of data in the vicinity of the Eastern Mediterranean, we find that regional phases (body waves, guided waves, and surface waves) are very sensitive to the existence of deep sedimentary basins. Crustal thinning also affects the regional body and guided waves but to a lesser degree.

REFERENCES

Barazangi, M., D. Seber, E. Sandvol, M. Vallve, 1996, "Digital database development and seismic characterization and calibration for the Middle East and North Africa", PL-TR-96-2222, Phillips Lab., Hanscom AFB, Massachusetts, pp. 63.

Dziewonski, A.M., T.A. Chou, and J.H. Woodhouse, 1981, "Determination of earthquake source parameters from waveform data for studies of global and regional seismicity", J. Geophys. Res., 86, 2825-2852.

Goldstein, P., and D. Dodge, (1999) "Fast And Accurate Depth And Source Mechanism Estimation Using P-Waveform Modeling: A Tool For Special Event Analysis, Event Screening, and Regional Calibration", Geophys. Res. Lett. 8/99.

Goldstein, P., C. Schultz, and S. Larsen, (1997) "The influence of deep sedimentary basins, crustal thinning, attenuation and topography on regional phases; selected examples from the Eastern Mediterranean and the Caspian sea regions", Proceedings of the 19th annual seismic research symposium on monitoring a CTBT, Annapolis, MD, September 23-25, 1997.

Goldstein, P., C. Schultz, S. Larsen, and L. Minner, 1996, "Modeling of regional wave propagation phenomena in the Middle-East and North-Africa and new analysis capabilities in SAC2000", Proceedings of the 18th annual seismic research symposium on monitoring a CTBT, Annapolis, MD, September 4-6, 1995

Larsen, S.C., 1995, 3D MPP simulations in the earth sciences: seismic applications, LLNL Symposium on Distributed Computing and Massively Parrallel Processing.

Rodgers, A., and W.R. Walter, 1997, Regionalization and calibration of seismic discriminants, path effects and signal-to-noise for station ABKT (Alibek, Turkmenistan), submitted to the 19th annual seismic research symposium on monitoring a CTBT, Orlando, FL, September 23-25, 1997

CALIBRATION OF SEISMIC WAVE PROPAGATION IN JORDAN

David Harris, Kevin Mayeda, Keith Nakanishi, Arthur Rodgers, Stan Ruppert, Flori Ryall, Ken Skinnell
Lawrence Livermore National Laboratory[+]
L-205, P.O. Box 808, Livermore, CA 94551

Abdel-Qader Amrat, Tawfiq Al-Yazjeen, Ahmed Al-Husien
Natural Resources Authority of Jordan

Frederick Simon
U. S. Geological Survey

Sponsored by U.S. Department of Energy
Office of Nonproliferation and National Security
Office of Research and Development
Contract No. W-7405-Eng-48

ABSTRACT

The Natural Resources Authority of Jordan (NRA), the USGS and LLNL have a collaborative project to improve the calibration of seismic propagation in Jordan and surrounding regions. This project serves common goals of CTBT calibration and earthquake hazard assessment in the region. These objectives include accurate location of local and regional earthquakes, calibration of magnitude scales, and the development of local and regional propagation models. In the CTBT context, better propagation models and more accurately located events in the Dead Sea rift region can serve as (potentially GT5) calibration events for generating IMS location corrections. The detection and collection of mining explosions underpins discrimination research.

The principal activity of this project is the deployment of two broadband stations at Hittiyah (south Jordan) and Ruweishid (east Jordan). These stations provide additional paths in the region to constrain structure with surface wave and body wave tomography. The Ruweishid station is favorably placed to provide constraints on Arabian platform structure. Waveform modelling with long-period observations of larger earthquakes will provide constraints on 1-D velocity models of the crust and upper mantle. Data from these stations combined with phase observations from the 26 short-period stations of the Jordan National Seismic Network (JNSN) may allow the construction of a more detailed velocity model of Jordan.

The Hittiyah station is an excellent source of ground truth information for the six phosphate mines of southern Jordan and Israel. Observations of mining explosions collected by this station have numerous uses:

- for definition of templates for screening mining explosions,
- as ground truth events for calibrating travel-time models,
- as explosion populations in development and testing discriminants.

Following previously established procedures for identifying explosions, we have identified more than 200 explosions from the first 85 days of recording. In addition, Hittiyah is being calibrated for coda magnitude estimation and is placed favorably to estimate mechanism and magnitude for earthquakes along the Dead Sea Rift and the Gulf of Aqaba.

[+] This work was performed under the auspices of the U. S. Department of Energy by Lawrence Livermore National Laboratory under contract No. W-7405-Eng-48.

OBJECTIVE

The objective of the project is to assemble events occurring in Jordan and surrounding regions suitable for calibrating travel-times for location, screening algorithms, discriminants and magnitude estimators. Two stations have been deployed to maximize coverage of Jordan and surrounding regions.

One research objective of the project is to determine whether observations of many mining explosions can be stacked to extend the range of calibrations. Waveform correlation studies indicate that mining explosions often produce highly reproducible signals, that, in theory, should be susceptible to stacking. In the Middle East and North Africa, the usual shot size is in the 10-25 ton range, and propagation conditions are such that observations beyond 300 kilometers are difficult to obtain even to quiet stations. For this reason, expensive dedicated calibration explosions are being proposed, and would require charges from the range of 5-10 tons in water to several hundred tons in boreholes on land for longer-range observations. The question to be answered is whether 20-100 shots in the 10-25 ton range at a single mine can be combined to extend the range of observation to comparable distances. Several technical hurdles have to be overcome. While explosion waveforms from the same mine often are highly similar, substantial variation is common. Variation can occur because the shots may be spread out over several kilometers at the larger mines. A cluster of mining explosions may constitute a source array where the exact location of the explosions is unknown. The waveforms may decorrelate across the source aperture. These facts complicate the alignment of waveforms for stacking and motivates the search for algorithms that do not require complete knowledge of the waveform moveout or correlation structure to provide stacking gain.

RESEARCH ACCOMPLISHED

Data collected

Figure 1 shows the locations of the Hittiyah and Ruweishid broadband stations that we have operated for approximately one year, as well as the locations of the 26 stations of the Jordan National Seismic Network. The broadband stations consist of three-component Guralp ESP-3T seismometers, Reftek RT72A-08 digitizers and GPS receivers for synchronizing the clocks. Data were collected initially at a 100 Hz sampling rate at both stations; at approximately day 300 in 1998, the sample rate was changed to 50 Hz.

With some breaks, the continuous data have been collected and archived from April, 1998 through March, 1999 for Hittiyah, and August, 1999 through March, 1999 for Ruweishid.

Mining Explosions

The station at Hittiyah is well situated to observe explosions at the large phosphate mines of Jordan and Israel. Figure 2 shows the paths and distances from the station to the 6 major phosphate mines of southern Jordan and Israel. Hittiyah is located only 37 kilometers from the major open pit mine at Shediyah, which simplifies identification of the daily explosions at that mine.

Explosions at the remainder of the mines are identified by previously established waveform correlation techniques [Harris, 1997]. These techniques have been applied to roughly the first 85 days of data recorded at the Hittiyah station to obtain an initial set of 242 correlated waveforms. Single-link cluster analysis was applied to classify these events into 14 clusters, the majority of which appear to be associated with mines. Waveforms from one of the larger clusters are shown in Figure 3. Note the substantial variation in the waveforms. Even though the clustering threshold was set at a correlation value of 0.7, the single-link algorithm can group events that have notable variations. The algorithm requires only that these events be related through a chain of comparisons, each link of which has a high correlation. We believe this algorithm to be appropriate for clustering mining events from extensive open-pit mines, since events distributed across the aperture of a large mine may be linked through a series of intermediaries. The key to

preventing linkage between unrelated events is to insist on a high correlation value for each link, insuring that events involved in each step of the chain are close.

In addition to the Hittiyah work, we have processed a full year of data from EIL, resulting in delivery of waveforms for 155 explosions at the Al Hasa mine to the LLNL discrimination group. These events will be used to test P/S ratio discriminants [Walter, et al., 1999]. At minimum, an additional 200 events will be delivered for the Wadi Al Abyad mine and 100 events for the Shediyah mine.

We have attempted a stack on data from the Ruweishid station, for one of these event clusters, to ascertain whether usable observations can be obtained for calibrating travel time models. Ruweishid is too far from the phosphate mines for clear observation of any individual event. The event cluster we worked with is probably associated with the Al Hasa phosphate mine about 285 kilometers from Ruweishid. Our approach is to use the closer, and, as it happens, quieter Hittiyah station to identify the events and to provide approximate alignment for the Ruweishid signals. The alignment delays are obtained by cross-correlating waveforms recorded at Hittiyah; one event is chosen as a reference for alignment. Corresponding waveform segments are extracted from the Ruweishid data stream, and these segments are aligned using the Hittiyah-derived delays. Because the events are distributed in some unknown fashion over a mine aperture, the Hittiyah-derived delays are correct only for approximate alignment of the signals arriving at Ruweishid. Residual unknown delays exist among the Ruweishid signals due to the fact that the two stations observe the mine with different back azimuths.

We address this difficulty by choosing one of the better-recorded Ruweishid signals as a stacking reference waveform. The waveforms of the remaining events are used to predict the reference waveform by optimizing a finite-impulse-response filter with a range of lags large enough to compensate the residual delays:

$$r[n] \approx \hat{r}_k[n] = \sum_i a_{ik} s_k[n-i]$$

Here, $r[n]$ denotes the reference event waveform and $s_k[n]$ the waveforms of the remaining events. The index k runs over the events. The stack is obtained by summing the reference waveform and the predictions:

$$r[n] + \sum_k \hat{r}_k[n]$$

The result of this operation is shown in Figure 4. All components of the three-component waveform have been stacked. Estimates of arrival times for the four major phases have been overlayed; the times were computed relative to the easily-picked Pg arrival at Hittiyah for the reference event. The P phases appear to be visible in the stack, though not of sufficient quality to be identified or picked.

An interesting problem with this approach is that the effective stacking velocity across the source aperture is not under control because the residual delays are unknown. It appears from Figure 4 that the uncontrolled stacking operation favors the P phases; the secondary phases are suppressed. Nonetheless, we consider this result promising and will attempt it again with improved algorithms and many more (perhaps ~100) stacking events.

Calibration Earthquakes

Another goal of the project is to collect observations of earthquakes that allow calibration of magnitude estimators and propagation models. Figure 5 shows the (predominantly) continental paths from earthquakes of magnitude 5 and greater to the broadband stations for which observations have been collected. These earthquakes are suitable as calibration events for crustal structure through full waveform modelling [Rodgers et al., 1999] and for the coda magnitude estimation [Mayeda et al., 1999].

Figure 5 also shows a reflectivity fit to a Zagros earthquake waveform recorded at Ruweishid made by optimizing an average 1-D velocity model for that path. This path traverses the northern Arabian plate, and shows deep sediments (average 6 km), low crustal velocities and a thinner crust than the southern Arabian peninsula. This analysis is being pursued systematically across the Middle East and North Africa [Rodgers et al, 1999]; the deployments in Jordan improve path coverage particularly in the northern Arabian plate.

REFERENCES

Harris, D. (1997), Waveform correlation methods for identifying populations of calibration events. Proceedings of the 19th Annual Seismic Research Symposium on Monitoring a CTBT, pp. 604-613.

Mayeda, K. , R. Hofstetter, A. Rodgers, W. Walter (1999), Applying coda envelope measurements to local and regional waveforms for stable estimates of magnitude, source spectra and energy. Proceedings of the 21st Annual Seismic Research Symposium on Monitoring a CTBT, this volume

Rodgers, A., W. Walter and T. Bredbeck (1999), Complete regional waveform modeling to estimate seismic velocity structure and source parameters for CTBT monitoring. Proceedings of the 21st Annual Seismic Research Symposium on Monitoring a CTBT, this volume.

Walter et al. (1999), LLNL's regional seismic discrimination research. Proceedings of the 21st Annual Seismic Research Symposium on Monitoring a CTBT, this volume.

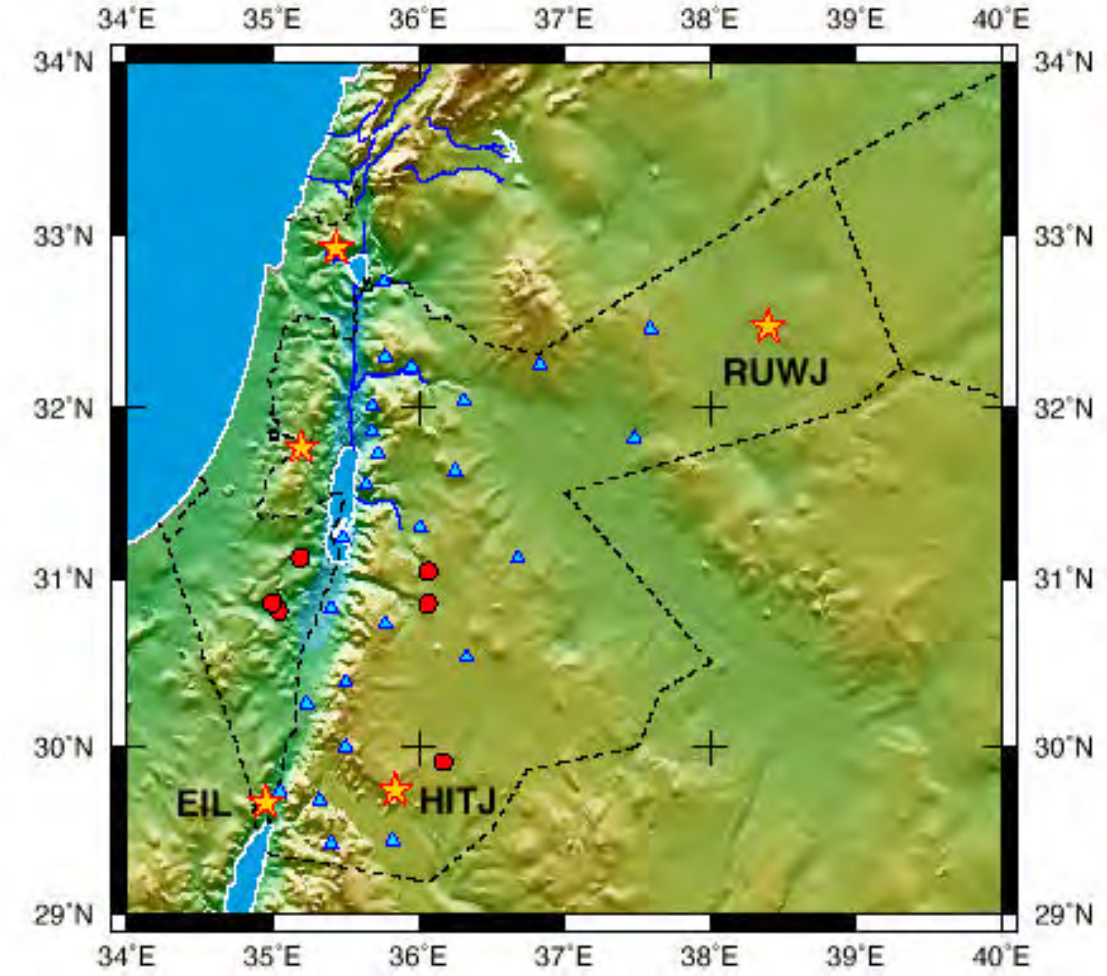


Figure 1 Locations of the two broadband stations (HITJ, RUWJ) operated jointly by the Jordan Natural Resources Authority, the USGS and LLNL. Broadband stations are indicated with stars, the stations of the Jordan National Seismic Network by triangles and the six major phosphate mines as circles. The other broadband station from which a significant amount of data has been collected is EIL in Israel.

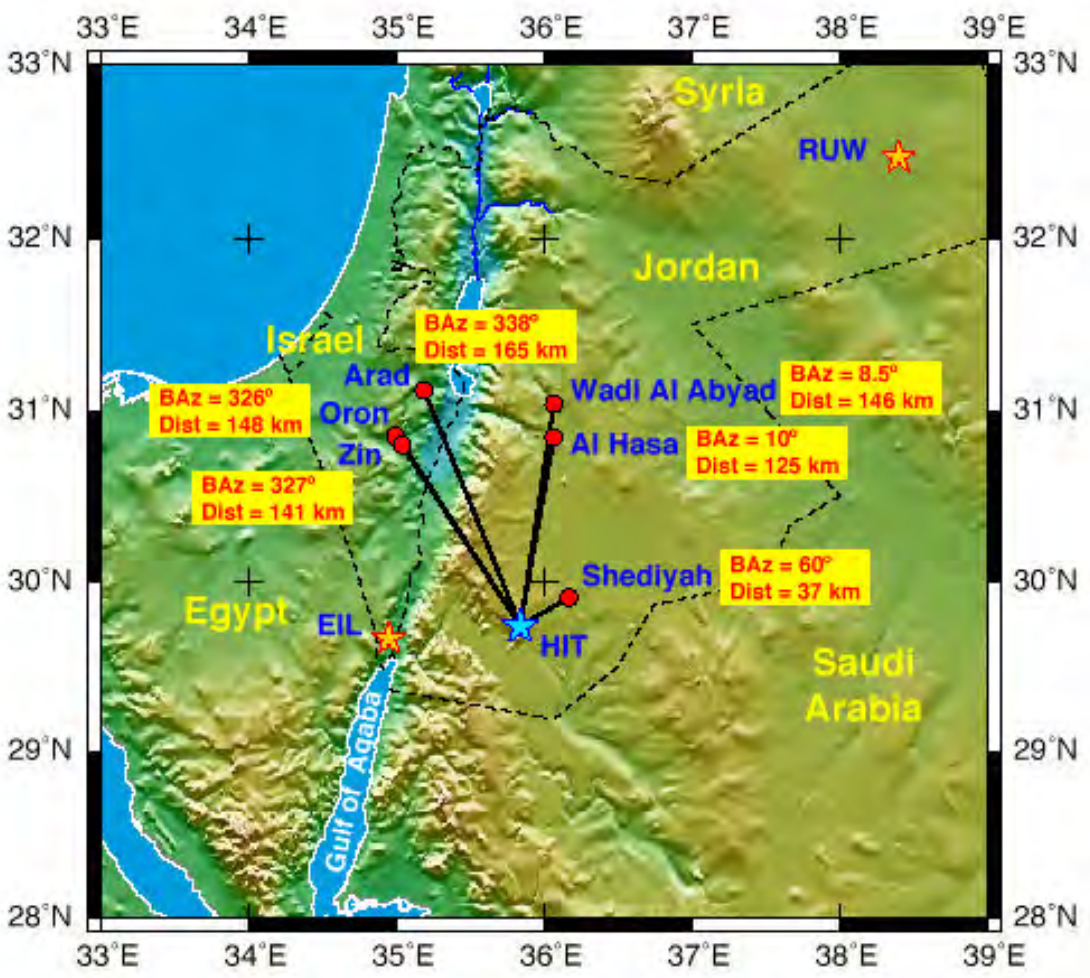


Figure 2 Distances and backazimuths of the major phosphate mines in Israel and Jordan with respect to the broadband station at Hittiyah.

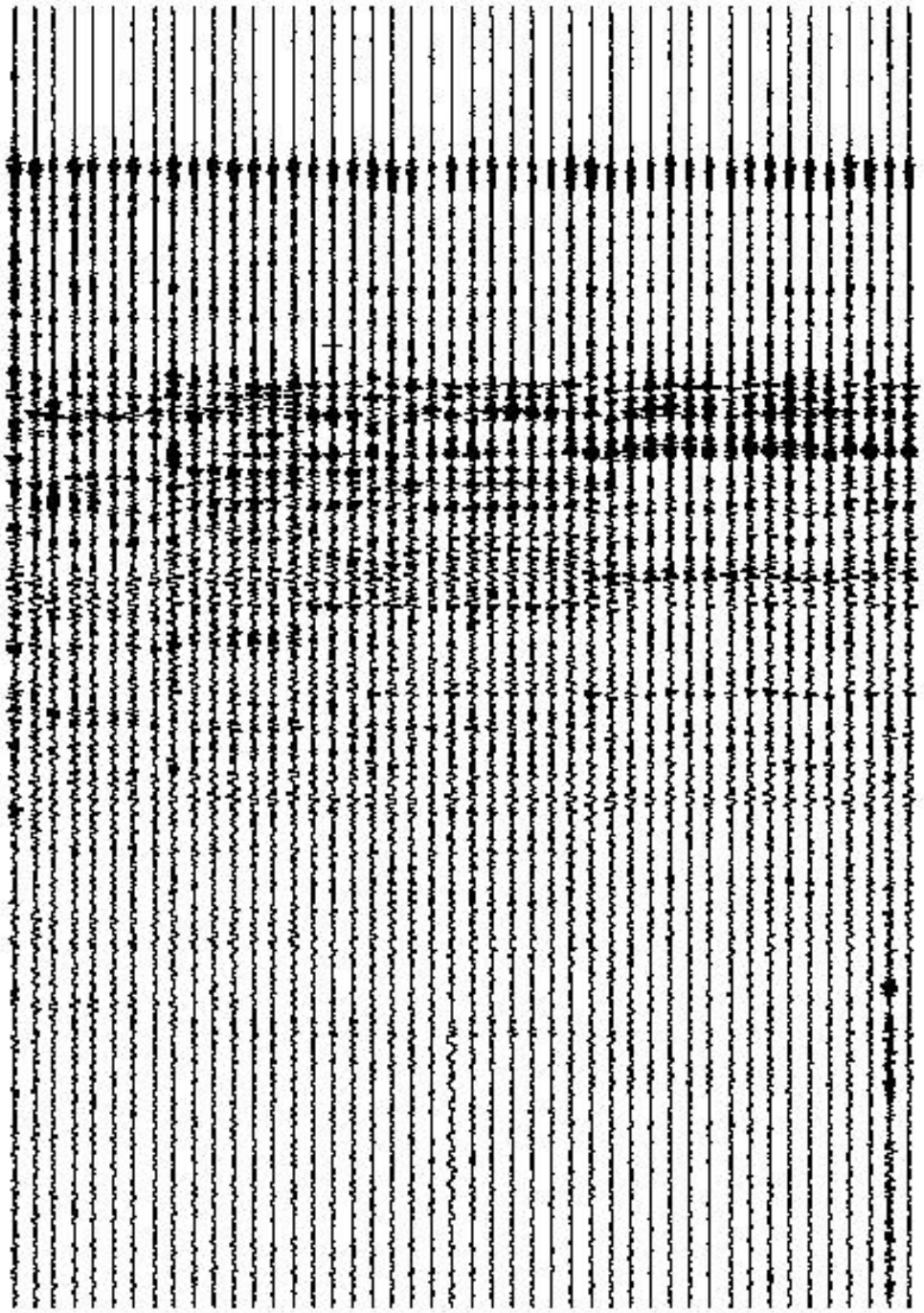


Figure 3 A large number of mining explosions are being obtained from the broadband stations. Using data from Hittiyah recorded from day 119 - day 204, 1998, 242 explosions have been detected; associations to particular mines are pending. The cluster of waveforms shown here was obtained by waveform correlation analysis using a single link algorithm run with a high (0.7) correlation threshold. The substantial waveform variations apparent, particularly in the secondary phases, may be due to migration of the working point within the mine or to the presence of multiple working points. 100 seconds of data are displayed.

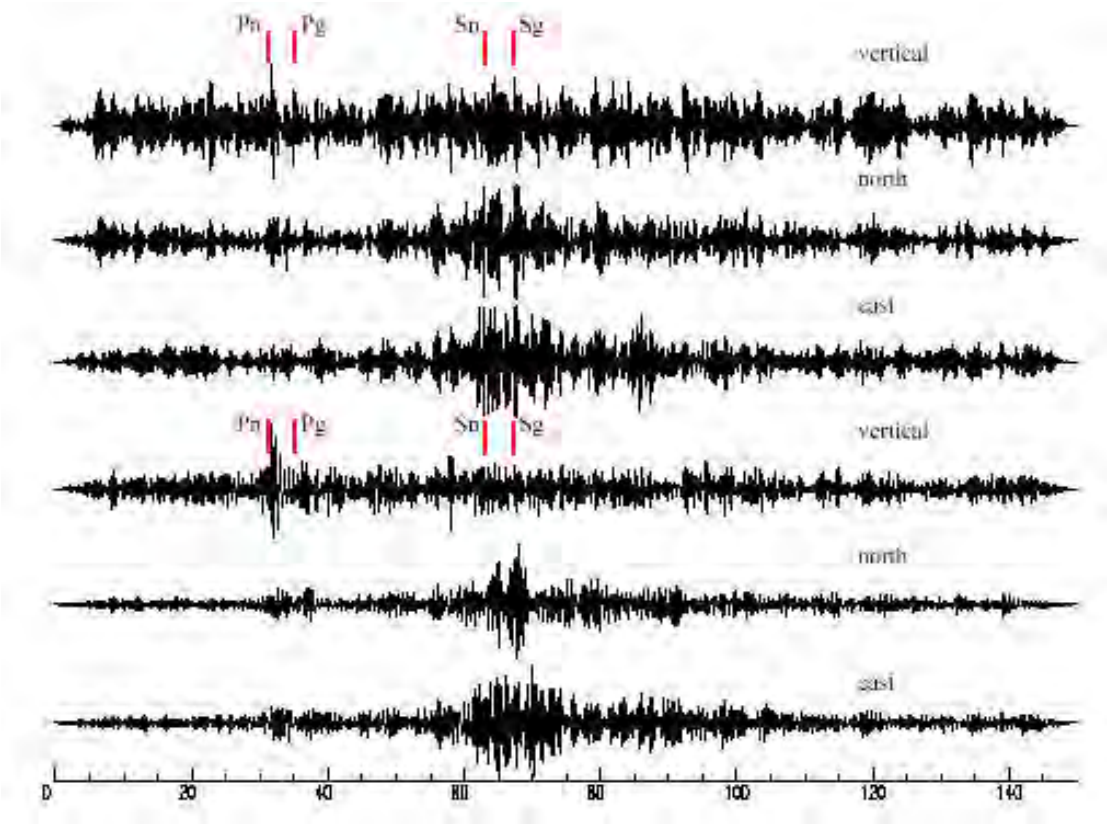


Figure 4 Results of stacking waveforms recorded at Ruweishid for 26 events at (probably) the Al Hasa mine. The top three traces are the original waveforms for the event best recorded at Ruweishid, selected as the reference event (see text) for stacking. The data have been filtered into the 1.5 - 3.5 Hz band. The 26 events were detected at Hittiyah, which provided relative delays for aligning the signals in the Ruweishid data. The bottom three traces are the stack. Arrival times for Pn, Pg, Sn and Sg predicted from the observed Pg arrival time of the reference event at Hittiyah and the AK135 travel time model are superimposed. Pn and Pg may be visible in the stacked traces. The results suggest that usable stacks may be obtained if the number of events is increased by a factor three or four.

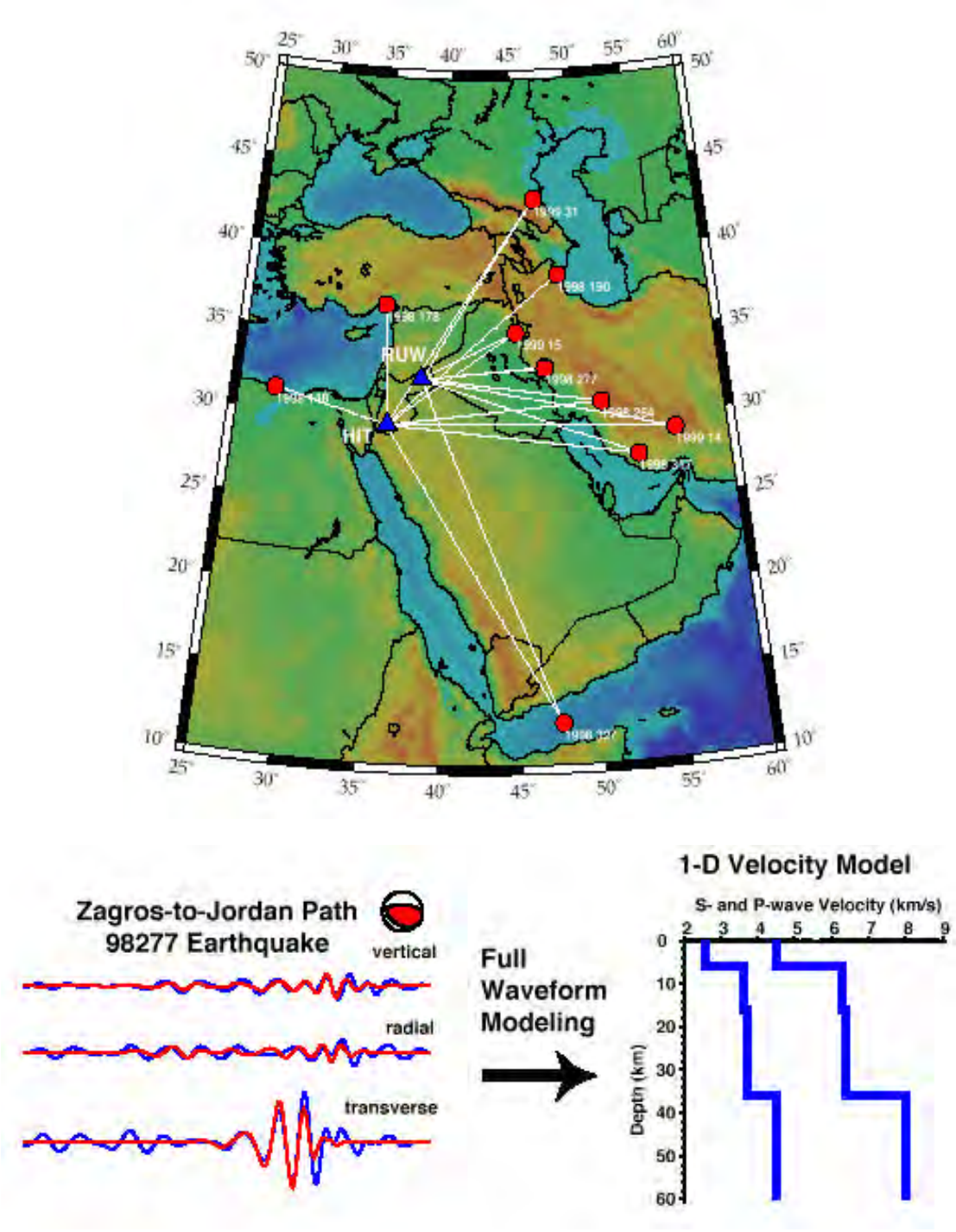


Figure 5 The map at top shows the paths for which observations have been collected at the two broadband stations in Jordan. As shown at the bottom, full waveform synthetics fit to the data provide constraints on crust and upper mantle structure. The model shown here is derived for the north end of the Arabian plate. See Rodgers et al. (1999, this volume) for more detail on waveform modeling.

CALIBRATION OF SEISMIC WAVE PROPAGATION IN KUWAIT

David Harris*, Stan Ruppert*, Jasem Al-Awadhi**, Elliot Endo***, Kevin Mayeda*, Arthur Rodgers*, Flori Ryall*, Jerry Sweeney*, Frederick Simon***
*Lawrence Livermore National Laboratory[+]
L-205, P.O. Box 808, Livermore, CA 94551

**Kuwait Institute of Scientific Research

***U. S. Geological Survey

Sponsored by U.S. Department of Energy
Office of Nonproliferation and National Security
Office of Research and Development
Contract No. W-7405_ENG-48

ABSTRACT

The Kuwait Institute of Scientific Research (KISR), the USGS and LLNL are collaborating to calibrate seismic wave propagation in Kuwait and surrounding regions of the northwest Arabian Gulf using data from the Kuwait National Seismic Network (KNSN). Our goals are to develop local and regional propagation models for locating and characterizing seismic events in Kuwait and portions of the Zagros mountains close to Kuwait.

The KNSN consists of 7 short-period stations and one broadband (STS-2) station. Constraints on the local velocity structure may be derived from joint inversions for hypocenters of local events and the local velocity model, receiver functions from three-component observations of teleseisms, and surface wave phase velocity estimated from differential dispersion measurements made across the network aperture.

Data are being collected to calibrate travel-time curves for the principal regional phases for events in the Zagros mountains. The available event observations span the distance range from approximately 2.5 degrees to almost 9 degrees. Additional constraints on structure across the deep sediments of the Arabian Gulf will be obtained from long-period waveform modeling.

Key Words: Seismic Regionalization, Calibration, Broadband Seismology.

[+] This work was performed under the auspices of the U. S. Department of Energy by Lawrence Livermore National Laboratory under contract No. W-7405-Eng-48.

OBJECTIVE

Calibration objectives for seismic hazard assessment and CTBT monitoring often coincide, especially for event location and the estimation of magnitudes and mechanisms. From the perspective of hazard assessment, the following issues and tasks have high priority:

Assessment of Seismic Hazard from In-Country Earthquakes

- Determine the detection performance of the KNSN.
- Develop a local velocity model with KNSN earthquake observations.
- Construct a seismicity map for the country and territories immediately adjacent.
- Characterize seismic sources within and adjacent to Kuwait.
- Estimate attenuation rates of seismic waves in Kuwait.

Assessment of Seiusmic hazard from Earthquakes in the Zagros Mountains

- Calibrate regional travel times and attenuation.
- Characterize seismic events (moments and mechanisms) in the near Zagros Mountains.
- Estimate the strength of ground motion anticipated from events in the near Zagros at industrial and population centers of Kuwait.

These objectives overlap or support CTBT calibration goals as well. The larger in-country earthquakes, if well-located and well-characterized, can serve as calibration events for stations of the IMS. Although Kuwait is not very active seismically, it has had several events with magnitudes greater than 4.0 in recent years. Travel-time and phase amplitude calibrations for events occuring in Kuwait, and characterization of representative mechanisms, will permit these events to be located and screened with greater reliability. The seismicity of the Zagros mountains is a significant challenge for the IMS. The Zagros are among the most active areas of the Middle East; at least 17 earthquakes with magnitudes greater than 7 have occurred there this century. Figure 1 shows the distribution in a large part of the Middle East of events of the last 23 years with reported Harvard CMT mechanisms (Harvard Centroid Moment Tensor web page). A large fraction of these events, and a large fraction of events that will have to be located and screened by the IMS, are located in the Zagros mountains. The principal CTBT objective of this project is to provide better location, magnitude and mechanism constraints on calibration events in the Zagros region.

RESEARCH ACCOMPLISHED

The network and local hazard assessment

During April, 1999, a team of five seismologists and geophysicists from the USGS and LLNL visited colleagues at the Kuwait Institute of Scientific Research (KISR) to develop research collaborations for implementing objectives of the Kuwait National Seismic Network. The KNSN is a high quality digital network (Figure 2) consisting of seven short period stations (3 component Ranger SS-1 instruments) and one broadband station (with an STS-2 seismometer). The data are digitized by 24-bit Reftek 72A07 DAS's and telemetered digitally to KISR in Kuwait City. The network is synchronized with a GPS receiver at KISR and a heartbeat signal broadcast from the center to the field stations.

Four - six months of continuous data were selected for a detection study. These data will be processed with STA/LTA and matched filter detectors, and the detections screened by an analyst to develop a catalog of events against which the automated detection system at KISR can be evaluated and tuned. This task is expected to improve automated detection of local seismic events by the KNSN, and to assist in classifying local, regional and teleseismic detections.

During the KISR visit, we relocated 6 events (Figure 2) with the default model supplied by the system vendor to check the location performance of the current automated system (which uses just P waves). The relocations were performed with analyst picks for both P and S waves. Events with locations inside the network did not move too much upon relocation, but two events on the margins of the network did relocate

far from the automatic locations. In part, this behaviour suggests that a better velocity model is required. Accordingly, plans have been initiated to develop a better 1-D velocity model by:

- performing joint relocation of local events and velocity model estimation,
- searching for mining explosions as calibration events in the continuous data,
- constraining upper mantle velocities with two-station Pn and Sn differential travel-times,
- constraining crustal thickness / average velocity with receiver functions,
- constraining crustal shear velocities with two-station differential surface wave dispersion measurements
- full-wave synthetic modelling to constrain calibration event depths and mechanisms

An example of the use of full-wave synthetic modelling to constrain depth is shown in Figures 3 and 4. The modeling was performed for the southernmost event in Figure 2, a magnitude 4.2 earthquake (relocated) near the Al Minagish oil field. The waveforms were recorded at the nearby broadband station, and modeled with reflectivity synthetics in the 10-20 second period band using an average Arabian platform model with sediment thickness somewhat increased. Figure 3 shows the waveform fit for an assumed event depth of 7 km. Figure 4 shows the misfit error as a function of depth; the best-fitting mechanism is indicated for each depth. The depth is very sharply constrained by the local recordings, suggesting that when a good model is obtained, high-quality ground truth depths will be developed. This event and one other in 1994 are large enough to serve as calibration events for stations of the IMS.

We also calibrated the broadband station coda envelopes for magnitude estimation (Mayeda et al., 1999). Better estimates of magnitude will improve the estimation of b-values in seismic hazard assessment and detection thresholds for IMS stations.

Zagros Seismicity

Earthquakes in the Zagros mountains pose a potential hazard for the population and infrastructure of Kuwait. Events with magnitudes greater than 5.5 are common within 2-3 degrees of Kuwait City. The objective of hazard research in this context is to determine the likelihood of an event of magnitude greater than 7 in a position to produce strong ground motion in Kuwait in the forseeable future. Moment histograms constructed from ISC and NEIC data can be used to estimate recurrence intervals, but the data show a reporting threshold around 4.7 for the region. The KNSN should provide moment histograms and b-value estimates at lower magnitudes due to its proximity to the Zagros.

Once travel-time models are calibrated, the KNSN should provide good constraints on event locations in the Zagros, and help to improve estimates of the distribution of seismicity. Both P and S phases are well recorded at the broadband station from local distances to almost 9 degrees, as shown in the 16-event waveform sample of Figure 5.

For calibrating propagation from the Zagros to Kuwait and characterizing Zagros seismicity, we plan to:

- estimate recurrence intervals from KNSN detections using coda magnitudes
- calibrate travel time models with observations of ground truth (GT5 - GT20) Zagros earthquakes
- calculate mechanisms for large and medium events by reflectivity modeling
- estimate path models and attenuation rates from larger events with independently-constrained source parameters using reflectivity modeling and coda source spectrum estimates

REFERENCES

Harvard Centroid Moment Tensor Web Page, www.seismology.harvard.edu.

Mayeda, K., R. Hofstetterr, A. Rodgers, and W. Walter (1999), Applying coda envelope measurements to local and regional waveforms for stable estimates of magnitude, source spectra and energy. proceedings of the 21st Seismic Research Symposium: Technologies for Monitoring the Comprehensive Nuclear-Test-Ban Treaty.

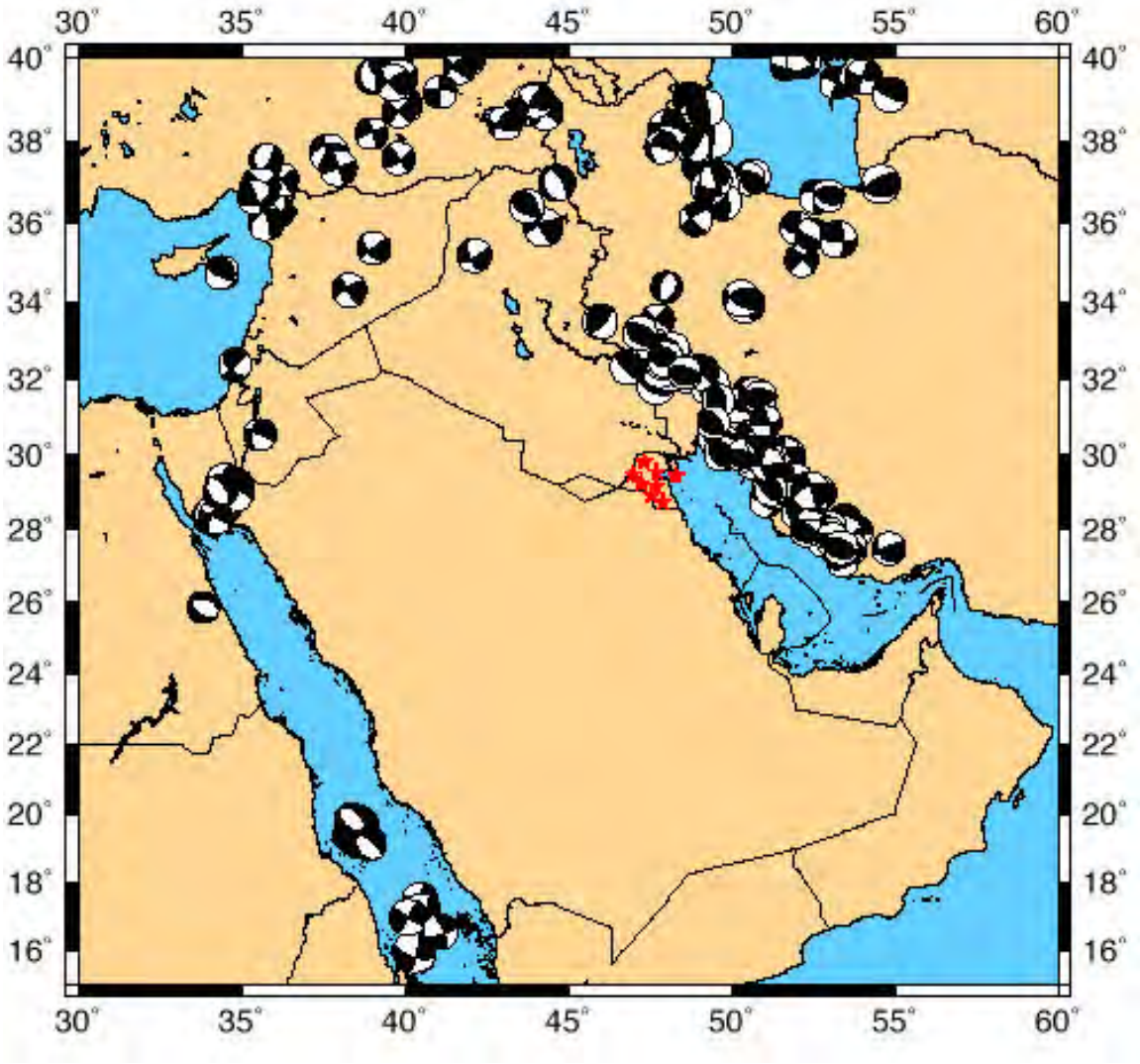


Figure 1 Focal Mechanisms for 23 years of Harvard CMT events from 1976 to 1999. Stations of the Kuwait National Seismic Network are shown as stars. The KNSN is ideally placed to study events in the Zagros mountains.

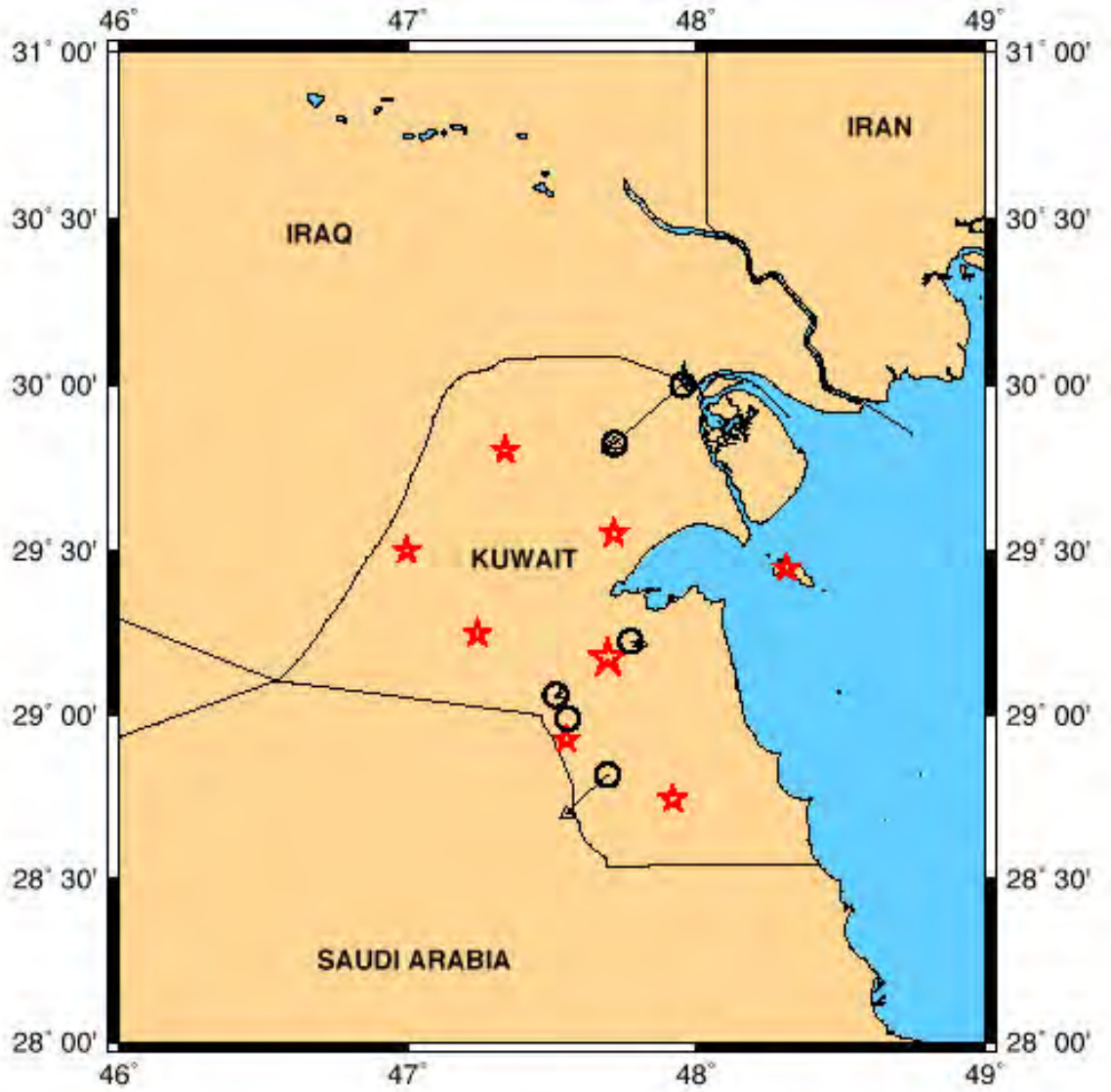


Figure 2 Kuwait is well-covered by the eight stations of the Kuwait National Seismic Network (stars). One of the stations (largest star) has an STS-2 instrument in a cylindrical vault 4 meters deep with three baffles insulating the instrument against wind noise and temperature variations. We have relocated six local events to test a default velocity model. Locations for five of the events made with automatic P picks are shown as small triangles. The corresponding locations with analyst picks using both P and S waves are shown as circles. Large mislocation vectors for two events at the margins of the network suggest the need to calibrate the local velocity model.

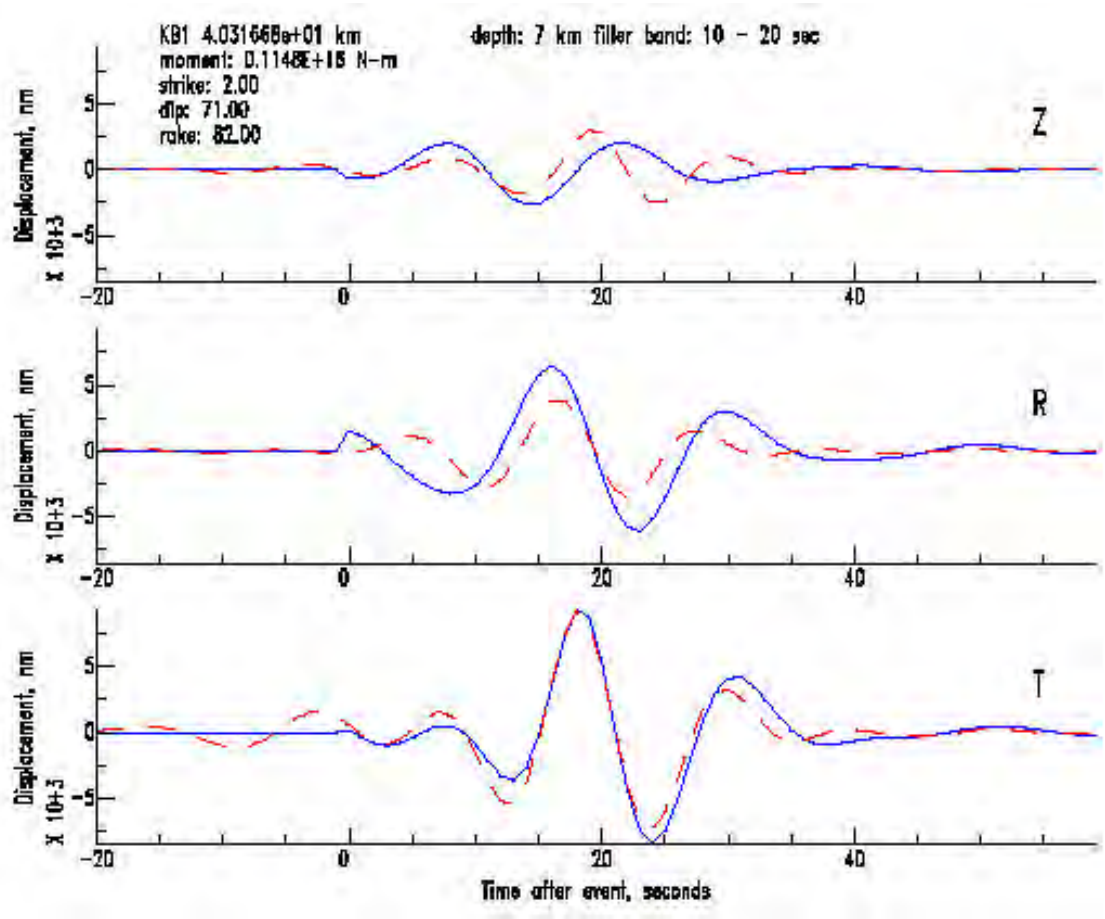


Figure 3 Comparison of broadband (10-20 sec period) reflectivity modeling waveforms with data recorded for the December 30, 1997 magnitude 4.2 event in southern Kuwait by the broadband station KB1 shows a reasonable modeling result. The data are represented by the dashed line and the model waveform by the solid line.

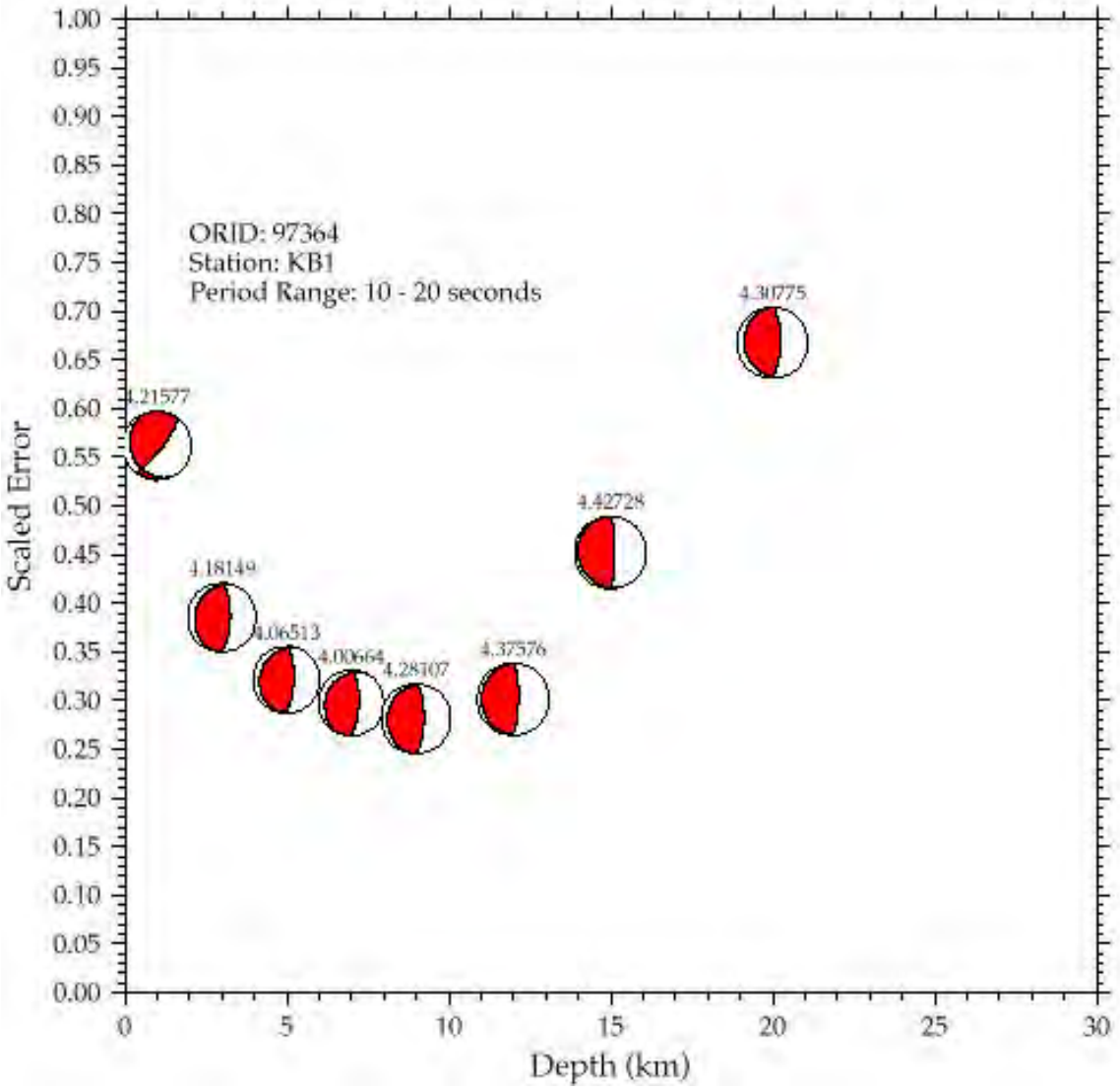


Figure 4 Waveform fitting error as a function of depth and me chanism for the December 30, 1997 earthquake in southern Kuwait shows the value of broadband data for constraining the depth and mechanism of local events in Kuwait.

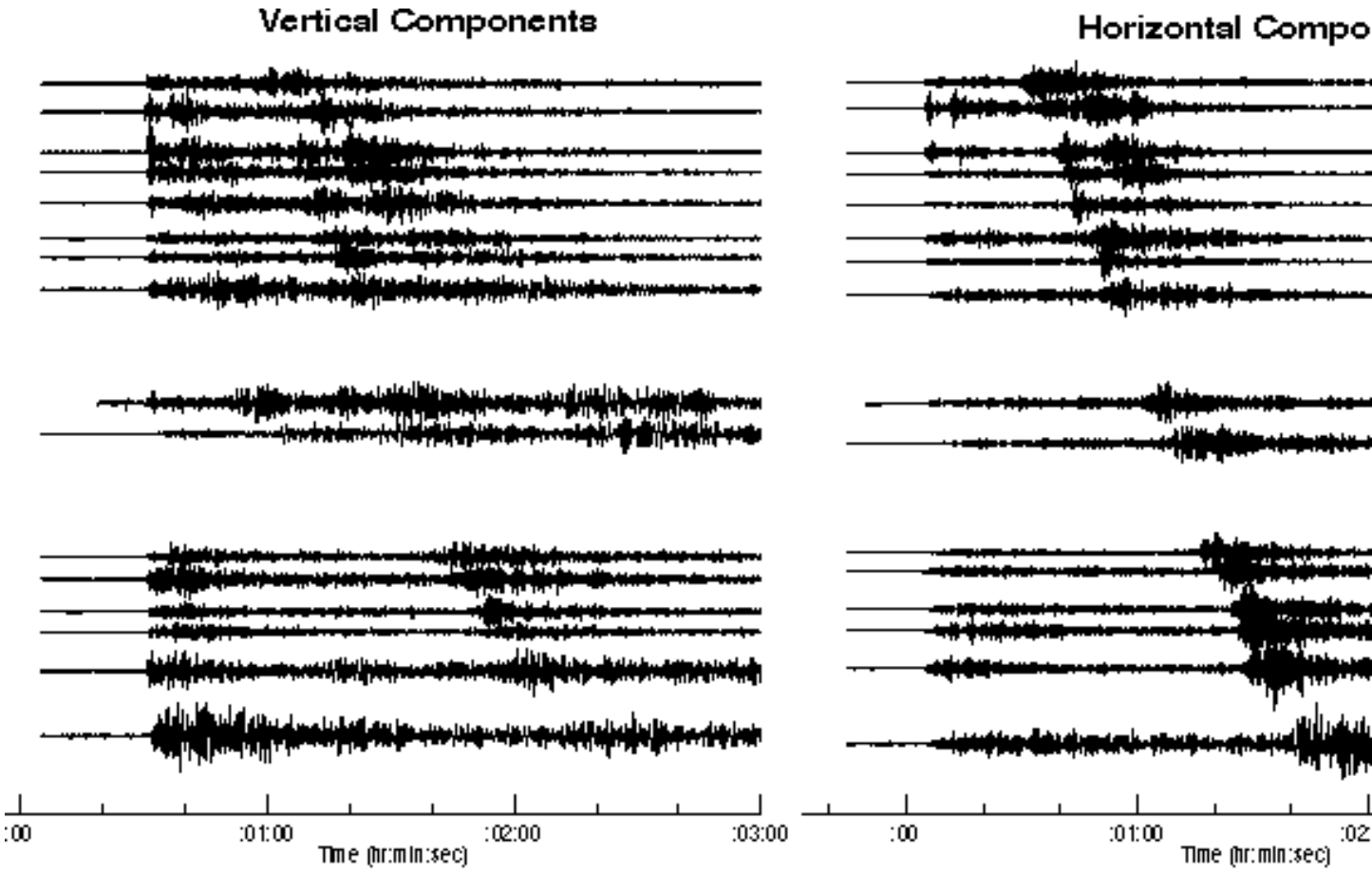


Figure 5 Waveforms of Zagros earthquakes recorded on the broadband instrument (KB1) demonstrate that P and S phases are well recorde particularly well-observed in this area. With sufficient ground truth information, well-calibrated P and S travel-time models should be obtai are plotted vertically from top to bottom with spacing proportional to increasing S-P time (not distance).

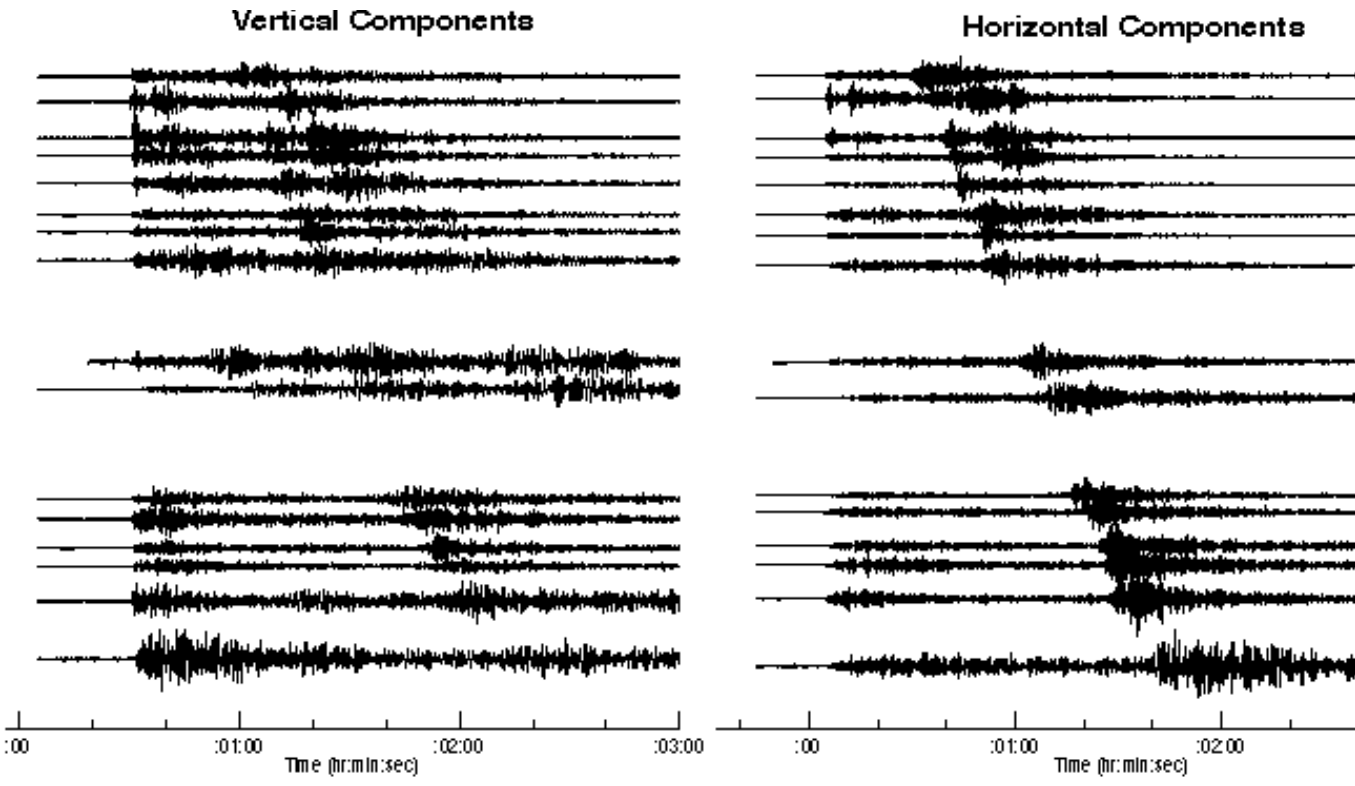


Figure 5 Waveforms of Zagros earthquakes recorded on the broadband instrument (KB1) demonstrate that P and S phases are well recorded. Sn appears to
particularly well-observed in this area. With sufficient ground truth information, well-calibrated P and S travel-time models should be obtained. The event
are plotted vertically from top to bottom with spacing proportional to increasing S-P time (not distance).

SOME INTERESTING SEISMIC EVENTS FROM WESTERN CHINA

Hans E. Hartse, Aaron A. Velasco, and Steven R. Taylor, Los Alamos National Laboratory

Sponsored by U.S. Department of Energy
Office of Nonproliferation and National Security
Office of Research and Development
Contract No. W-7405-ENG-36

ABSTRACT

Over the past year we have investigated some interesting seismic events from western China. We have obtained records of small (about 2 tons), shot-hole chemical explosions from within about 350 km of station WMQ. These events allow us to test Pg/Lg discriminants down to magnitude levels between 2 and 2.5. We have also obtained records at WMQ of a seismic event from Qinghai Province that has an unusually strong Pn arrival. We have not yet identified the source of this event. Finally, we have worked with the late January, 1999 earthquakes from near the Lop Nor test site. Below, we briefly describe each of these investigations.

We have obtained information on shot locations, charge sizes, shot days, and approximate shot times pertaining to crustal-scale refraction profiles conducted in China during the years 1986-1989. We were interested in explosions from the summer of 1988, because these occurred at distances between 200 and 500 km from station WMQ in northwest China. We obtained lists of trigger times at WMQ for the months of July and August 1988 from the IRIS DMC. From the trigger lists, we determined that the 1988 explosions were detonated at the hours of 1700 and 1900 GMT. To date we have obtained WMQ were detonated between about 200 and 350 km from WMQ. We have measured Pg and Lg amplitudes from these chemical explosion records, from many nearby earthquakes, and from the September, 1988 Lop Nor nuclear explosion (mb near 4.6). We find that the single-charge chemical explosions (with mb's between about 2.0 and 2.2) and the nuclear explosion clearly separate from the small earthquakes when Pg/Lg (4-8 HZ) ratios are plotted versus magnitude.

On January 27, 1999 a seismic event from near the Chinese nuclear test site at Lop Nor was detected and located by the PIDC. The PIDC assigned a body wave magnitude of 3.9. On January 30, 1999 a second, larger seismic event from near Lop Nor was detected and located by the PIDC and by the NEIC. The PIDC assigned an mb of 5.3 and the NEIC assigned a preliminary mb of 5.8. We obtained regional waveforms for these events. Using the newly retrieved data and the previously processed events from NIL, we classify these events as earthquakes. We have also used the larger event to design phase-matched filters to enhance the surface waves of the smaller event as recorded at regional distances.

On December 6, 1997 a seismic event with mb near 4.5 occurred in a mountainous region of the east-central Qinghai Province, China. The event was detected and located by the PIDC and by the NEIC. Both organizations fixed the depth when estimating the event's location. The PIDC estimated an mb of 4.2 and an Ms (using only 2 stations) of 3.4. Using the PIDC mb:Ms event screening criteria this event falls within the earthquake population. We obtained regional waveforms for this event. In general, signal-to-noise ratios are poor for body waves at frequencies above about 2 HZ, except at stations WMQ (1350 km NE) and MAKZ (2000 km NE). We merged arrival times from regional stations with times from the NEIC and PIDC bulletins and relocated the event. Our relocation moved the event about 10 km farther south, but we could not constrain depth. Rayleigh and Love waves at periods between about 15 and 25 seconds generally have good signal-to-noise ratios at most regional stations. Because we do observe clear surface waves, we assume the event was not unusually deep. At WMQ we observe that Pn above 1 Hz is unusually strong relative to the shear phases Sn and Lg, and Pn is also unusually strong relative to the Love and Rayleigh waves. We do not know the cause for these observations. Possible explanations could include some combination of these factors: (1) some type of a large mining explosion, (2) an earthquake with an unusual source radiation pattern, (3) unusually strong Sn and Lg attenuation (or phase blockages) along the path to WMQ, (4) unusual focusing of Pn energy due to the geometry of the crust-mantle boundary along the path to WMQ.

Key Words: Special Events, Discrimination, Regionalization

OBJECTIVE

Over the past several years seismic verification research has emphasized the analysis of seismograms recorded at regional distances (between about 200 and 2000 km). The primary objective of this research has been to lower magnitude levels at which events can be detected, located, and identified. Our efforts have been directed at regional event identification in Asia. While conducting research in this field we have come across several interesting seismic events. In this paper we discuss three specific event identification situations, each of which provides unique examples of how regionalization and discrimination research efforts contribute to monitoring nuclear test ban treaties.

In our first example, we obtained records of small (about 2 tons), shot-hole chemical explosions from within about 350 km of station WMQ in northwest China. These events allow us to test Pg/Lg discriminants down to magnitude levels near mb 2.0. We are able to show that the Pg/Lg discriminant does separate explosions from earthquakes as magnitudes drop below mb 4.0. Our second example demonstrates why regionalization research is important in preparing for treaty monitoring. In late January 1999 an earthquake sequence from near the Lop Nor test site was recorded at NIL in Pakistan. We obtained autodrm data in near real time and measured these waveforms. Because we had done earlier regionalization work in this area, we were able to quickly classify the January 1999 events as earthquakes. Our final example shows that there are still regionalization research issues that must be resolved to effectively monitor treaties. We show waveforms from a seismic event that occurred in December 1997 in Qinghai Province, China. At WMQ the short-period records look explosion-like. However, we observe strong regional Love and Rayleigh waves, and we are currently unable to confidently classify this event.

RESEARCH ACCOMPLISHED

Example 1: Small chemical explosions

When approaching the regional identification (or discrimination) problem, seismologists can often assemble data sets of large nuclear explosions ($4.5 < mb < 6.2$). For instance, Hartse et al. (1997) studied large nuclear explosions from the former Soviet test site in Kazakhstan (KTS) and the Chinese test site at Lop Nor by com-paring P/S ratios of the nuclear explosions to ratios of earthquakes. As the tectonically active regions of central Asia have high levels of natural seismicity, digital earthquake data sets that span a wide range of magnitudes ($2.5 < mb < 6.0$) can be assembled for these analyses. Even for regions of relatively low natural seismicity, digital records of at least a few small earthquakes can generally be assembled for discrimination studies (cf. Hartse, 1998). However, regional-distance records of known, low-yield nuclear tests for central Asia are not available. Therefore, it is difficult to assess the performance of the P/S regional discriminants when event size drops below mb 4.5.

We have recently obtained near-regional seismograms, recorded at WMQ, of chemical explosions detonated in 1988. These explosions provided the energy source of crustal-scale refraction profiles conducted in China (Figure 1, top) during the late 1980's (Li and Mooney, 1998; Mooney, 1998). Unlike delay-fired mining explosions, these were single-charge explosions shot in tamped holes. We assume that these single-charge chemical explosions can be treated as surrogate nuclear explosions. Our assumption is primarily based on results of the Department of Energy Non-Proliferation Experiment (NPE) conducted at the Nevada Test Site (NTS) in 1993. This experiment demonstrated that the seismic source functions for single-charge chemical and nuclear explosions are equivalent. (e.g. Denny et al., 1995; Stump et al., 1999). Thus, we expect single-charge chemical explosions to produce nearly identical seismic signatures and discriminants (Walter et al., 1995) as those from similarly-sized nuclear explosions when detonated under similar emplacement conditions.

We obtained all waveforms for our chemical explosion study from the IRIS Data Management Center (DMC). All data were recorded at WMQ, which began digital recording in late 1986. We requested waveforms recorded from late 1986 through mid-1998. All events fall within a box bounded from 34° to 52° north latitude and from 77° to 100° east longitude (Figure 1).

We obtained most of our data from PDE, REB, and SSB (Gao and Richards, 1994) event catalogs. We obtained our catalog of chemical explosions from a report by Mooney (1998) that describes interpretation

of crustal-scale refraction and reflection profiles in China. The report describes the chemical explosions used as the energy source for a refraction experiment conducted during the years 1986-1989. The report lists shot days and shot locations, but describes detonation times only as near midnight, which we assumed to be a local time. In 1988 the BH (20 sps) and the SH (40 sps) components at WMQ were operated in an event-detection mode. We therefore examined lists of WMQ SH and BH trigger times in an attempt to deduce the GMT explosion times. We found that the explosions occurred at near the hours 1900 or 1700 one day before the shot day listed in Mooney (1998). We obtained waveforms from three July explosions with good signal-to-noise ratios (Figure 1, bot-tom). Figure 1 shows example explosion and earthquake waveforms that have been bandpass filtered between 1 and 8 Hz. Note that for both the nuclear and chemical explosion Pg amplitude is about three times greater than Lg amplitude, while for the earthquake Lg amplitude is much greater than Pg amplitude. These basic patterns of relative P and S energy on the explosion and earthquake seismograms allow us to separate the explosions from the earthquakes on our discrimination figures presented below.

Before making any measurements we corrected each seismogram for instrument response into units of displacement in meters. We made time-domain phase amplitude measurements in several one-octave filter bands from 0.5-1 Hz up to 8-16 Hz. For measurements up to 8 Hz we used the BHZ component, whenever available. If BHZ was not available, we used the SHZ component. For all measurements above 8 Hz we used the SHZ component. After manually picking each regional phase arrival, we bandpass filter, cut appropriate data windows, and measure the RMS amplitude (in the LOG10 domain) for Pn, Pg, Sn, Lg, and pre-event noise. More details of our amplitude measurements are given in Hartse et al. (1997). Following amplitude measurements we corrected amplitudes for the effects of source and path using the MDAC method (Taylor et al., 1999).

Using the MDAC-corrected Pg and Lg amplitudes, we tested several ratios as discriminants. We found that the high-frequency Pg/Lg (4-8 Hz) ratio (Figure 1) separates the small chemical explosions from the small earthquakes, just as we had previously shown this discriminant separating larger (mb > 4.5) explosions and earthquakes in Hartse et al. (1997). Although we do not show the example in this paper, we also find that the Pg/Lg cross-spectral ratio separates the small explosions from the earthquakes. In general, the results of this study suggest that the discriminants derived from earthquakes and explosions at larger magnitudes (mb > 4.5) can be extra-polated to smaller magnitudes (mb near 2.0).

Example 2: January 1999 Lop Nor Earthquakes

On January 27, 1999 at near 06:25 GMT a seismic event from near the Chinese nuclear test site at Lop Nor was detected and located by the Prototype International Data Center (PIDC). The PIDC assigned an mb of 3.9 to this event. On January 30, 1999 at near 03:51 GMT a second, larger seismic event from near Lop Nor was detected and located by the PIDC and by the USGS National Earthquake Information Center (NEIC). The PIDC assigned an mb 5.3 to this event and the NEIC assigned a preliminary mb of 5.8. As each event was reported in the seismic bulletins, we used email-based automatic data request manager (autodrm) commands to retrieve broadband waveforms from station NIL in Pakistan. NIL is about 1610 km from Lop Nor. CTBT seismic researchers at Los Alamos had previously retrieved and processed several seismic events from northwest China that were recorded at NIL, including four nuclear explosions from Lop Nor (Figures 2 and 3). Using the newly retrieved data and the previously processed events, we did a quick event identification analysis of the January 1999 events. As we had previously retrieved and processed NIL data for events from near Lop Nor, we were prepared to quickly classify these January 1999 event as earthquakes.

Figure 2 shows a detailed map of events near Lop Nor and a discrimination plot based on events from the region bounded by 35° to 50° N and 80° to 95° E. The discrimination plot uses Pn and Sn phase amplitudes measured in the 4-8 HZ band. The waveform plots (Figure 3, top) show that for the explosions, the earthquakes, and the 27 January event Sn and Lg are barely above noise levels. However, for all of these events, in the 4-8 HZ band, Sn signal does exceed prephase noise levels. Hence, we were able to include all of these events in the discrimination plot shown in Figure 2. The earthquakes and the January 1999 events have Pn/Sn ratios that reach a maximum of about 2.5, while the nuclear explosions have Pn/Sn ratios that reach a minimum of about 6. Based on our experience with regional discriminants, this is very good

separation between the earthquakes and the explosions. Because the January 1999 events have nearly the same ratios as the earthquakes from near Lop Nor, we class the recent events as earthquakes.

We have tested other discriminants (that is, other combinations of phases and bands) using NIL data and obtained similar results. Also, we have tested these same discriminants using data from station AAK in Kyrgyzstan and again obtained similar results. These January 1999 events will prove extremely useful for future discrimination studies, path calibration research of regional body waves and surface waves, event location investigations, and other seismic regionalization efforts now underway at LANL. For example, we measured the group velocities of the larger event and, based on these group velocities designed phase-matched filters to enhance the surface waves of smaller nearby events. Figure 3 (bottom) shows how the phase-matched filter effectively isolates the surface waves of the smaller event as recorded at regional station AAK.

Example 3: An Unusual Seismic Event From Qinghai Province, China
On December 6, 1997 at near 04h53m GMT a seismic event occurred in a mountainous region of the east-central Qinghai Province, China (Figure 4). The event was detected and located by the PIDC and by the NEIC. Both organizations used only teleseismic records when estimating the event's location, and neither organization attempted to estimate an event depth. The PIDC assigned an mb of 4.2 and an Ms (using only 2 stations) of 3.4. The NEIC assigned an mb of 4.5. Using the PIDC mb:Ms event screening criteria, this event falls within the earthquake population.

We analyzed regional waveforms, mostly recorded by the CDSN, for this event. Unfortunately, stations LZH and XAN were not operating on December 6, 1997. In general, signal-to-noise ratios are poor for body waves at frequencies above about 2 HZ, except at stations WMQ (1350 km NE) and MAKZ (2000 km NE) (Figures 4 and 5). At WMQ we see an unusually strong Pn arrival, and the shear wave phases Sn and Lg are weak. Rayleigh and Love waves at periods between about 15 and 25 seconds generally have good signal-to-noise ratios at most regional stations (Figure 5, middle). We merged arrival times from the regional stations with times from the NEIC and PIDC bulletins and relocated the event. Our relocation moved the event about 10 km farther south, but we could not constrain depth. Because we do observe clear surface waves, we assume the event was not unusually deep.

Forming Pn/Sn discrimination ratios using WMQ measurements emphasizes the unusually strong Pn energy of this event (Figure 5, bottom). Note that the 06 December event is high on the ratio plots and within the population of Kazakh Test Site (KTS) explosions. Furthermore, the other presumed earthquakes from the Qinghai area do not display these characteristics. We do not know the cause for these observations. Possible explanations could include some combination of these factors: (1) some type of a large mining explosion, (2) an earthquake with an unusual source radiation pattern, (3) unusually strong Sn and Lg attenuation (or phase blockages) along the path to WMQ, (4) unusual focusing of Pn energy due to the geometry of the crust-mantle boundary along the path to WMQ. Whatever the cause or causes for these observations, this area will require more research effort. We need to calibrate the paths from Qinghai Province out to the regional stations, allowing for estimates of regional mb and Ms. Furthermore, we need to study the geometry of the crust-mantle boundary between the event and the regional stations.

CONCLUSIONS AND RECOMMENDATIONS

We presented three examples of interesting seismic events from western China. Our first example demonstrates that small (1.6 to 2.5 tons), single-charge chemical explosions can be separated from small earthquakes in the mb 2 to 2.5 range using P/S amplitude ratios. We recommend that other crustal-scale refraction survey explosions be used to test discriminants at low magnitudes. Explosions from such surveys may have been recorded at several IMS sites around the world and at other modern digital seismic stations. Our second example, identification of earthquakes from near Lop Nor, demonstrates the importance of regionalization and discrimination research in preparing to monitor the CTBT. Further, because the January 1999, earthquakes occurred close to Lop Nor, they present an excellent opportunity to calibrate regional seismic paths. In our final example, and event from Qinghai Province, we have found a seismic event with some characteristics that indicate an explosion and some characteristics that indicate an earthquake. Our

last example demonstrates the need for more regionalization research. We need to calibrate regional magnitude scales and better under the regional seismic paths in this part of Asia.

REFERENCES

Denny, M., P. Goldstein, K. Mayeda, and W. Walter, Seismic results from DOE's Non-Proliferation Experiment: a comparison of chemical and nuclear explosions, in Monitoring a Comprehensive Test Ban Treaty, NATO ASI Series, Kluwer Academic, Hingham, Massachusetts, 355-364, 1995.

Gao, L. and P. G. Richards, Studies of earthquakes on and near the Lop Nor, China, nuclear test site, *Proceedings of the 16th Annual DARPA/AF Seismic Research Symposium*, 106-112, 1994.

Hartse, H.E., The 16 August 1997 Novaya Zemlya seismic event as viewed from GSN stations KEV and KBS, *Seismol. Res. Let., 69, No. 3,* 206-215, 1998.

Hartse, H.E., S.R. Taylor, W.S. Phillips, and G.E. Randall, Regional event discrimination in central Asia with emphasis on western China, *Bull. Seism. Soc. Am.,* 87, 551-568, 1997.

Li, S. and W.D. Mooney, Crustal structure of China from deep seismic sounding profiles, *Tectonophysics*, 288, 105-113, 1998.

Mooney, W.D., Crustal structure of China and adjacent areas: A final report of the detailed compilation of data and results, *DOE Report DE-A101-97NN20004*, 1998.

Stump, B.W., D. C. Pearson, and R.E. Reinke, Source comparisons between nuclear and chemical explosions detonated at Rainier Mesa, Nevada Test Site, *Bull. Seism. Soc. Am.,* 89, 409-422, 1999.

Taylor, S.R., A.A. Velasco, H.E. Hartse, W. S. Phillips, W.R. Walter, Amplitude corrections for regional seismic discriminants, Los Alamos National Laboratory, Los Alamos, NM, LAUR-99-3040, submitted to *PAGEOPH*, 1999.

Walter W.R., K.M. Mayeda, and H.J. Patton, Phase and spectral ratio discrimination between NTS earthquakes and explosions: Part I: Empirical observations, *Bull. Seismol. Soc. Am.,* **85,** 1050-1067, 1995.

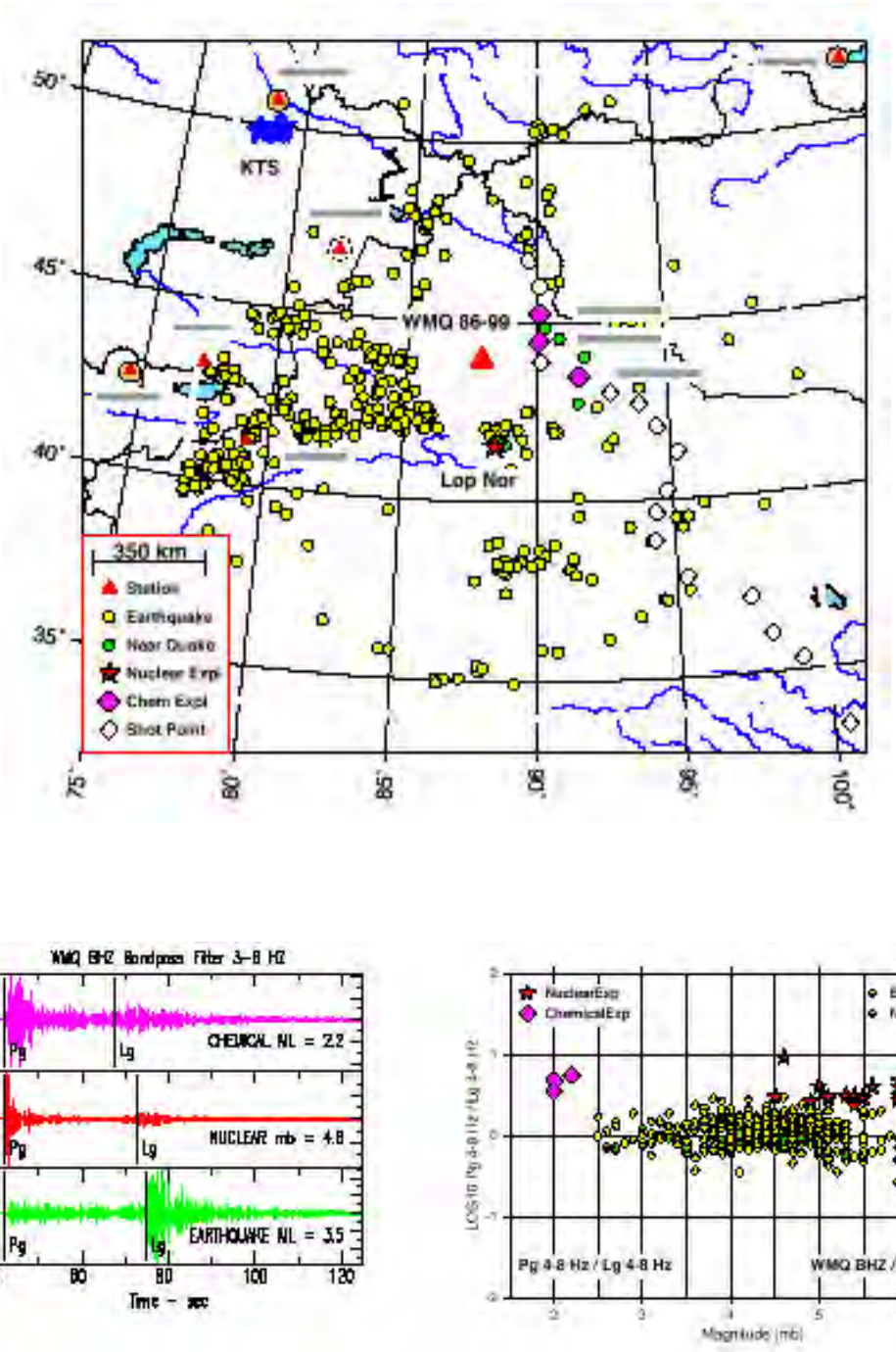


Figure 1. Map showing seismic events from northwest China (top), WMQ seismograms of a regional chemical explosion, a nuclear explosion, and an earthquake (bottom left), and the Pg/Lg (4-8 Hz) discrimination plot (bottom right). The diamonds on the map indicate refraction profile shot point locations and the dark diamonds indicate the explosions with seismic records at WMQ. Note that these small (2 ton), single-charge explosions can be separated from the small earthquakes.

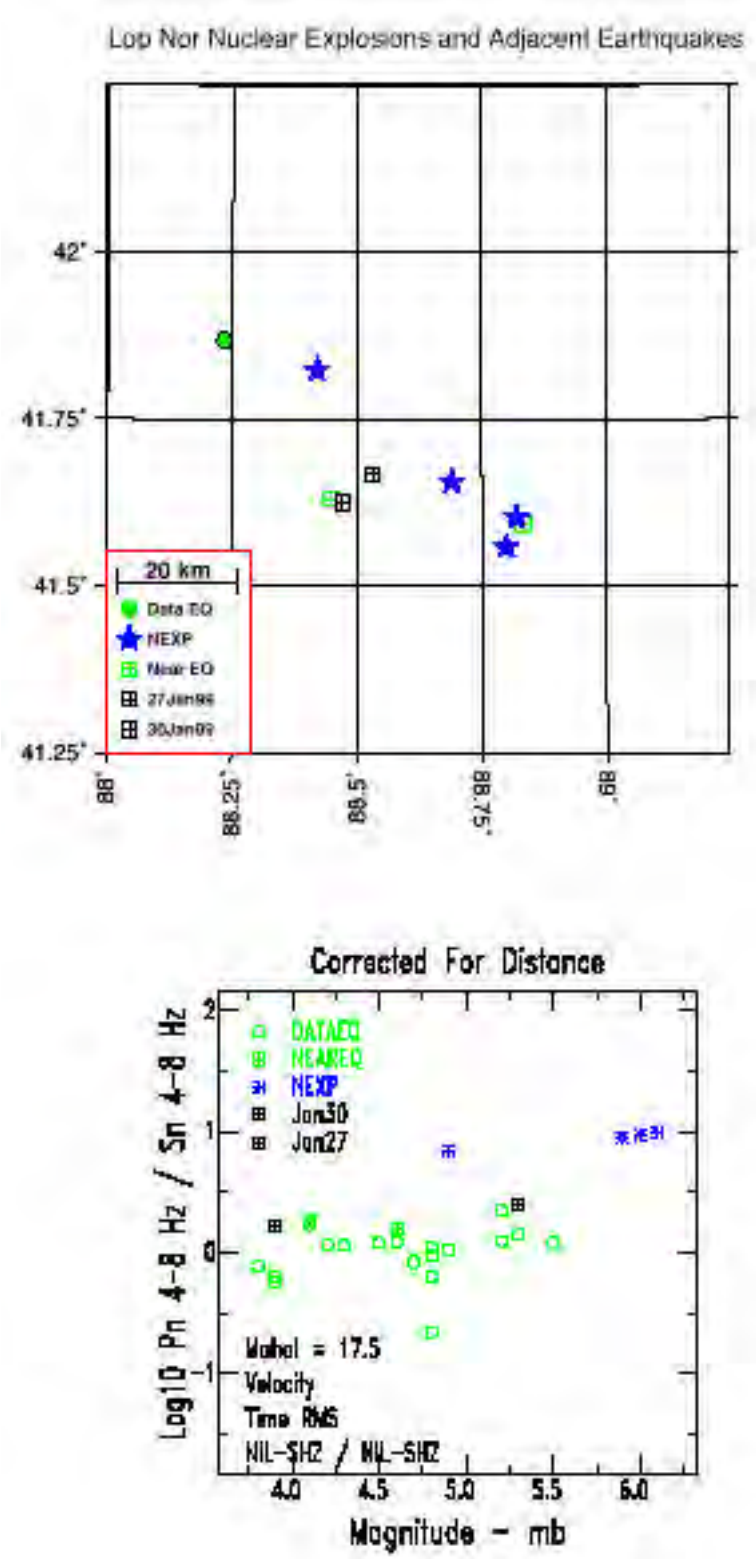


Figure 2. Map of the area around Lop Nor and locations of seismic events that have been recorded at NIL (top), and the Pn/Sn (4-8 Hz) discrimination plot of seismic events from the Lop Nor region (bot-tom). Note that the January, 1999 seismic events fall within the earthquake population. Waveforms are shown in Figure 3.

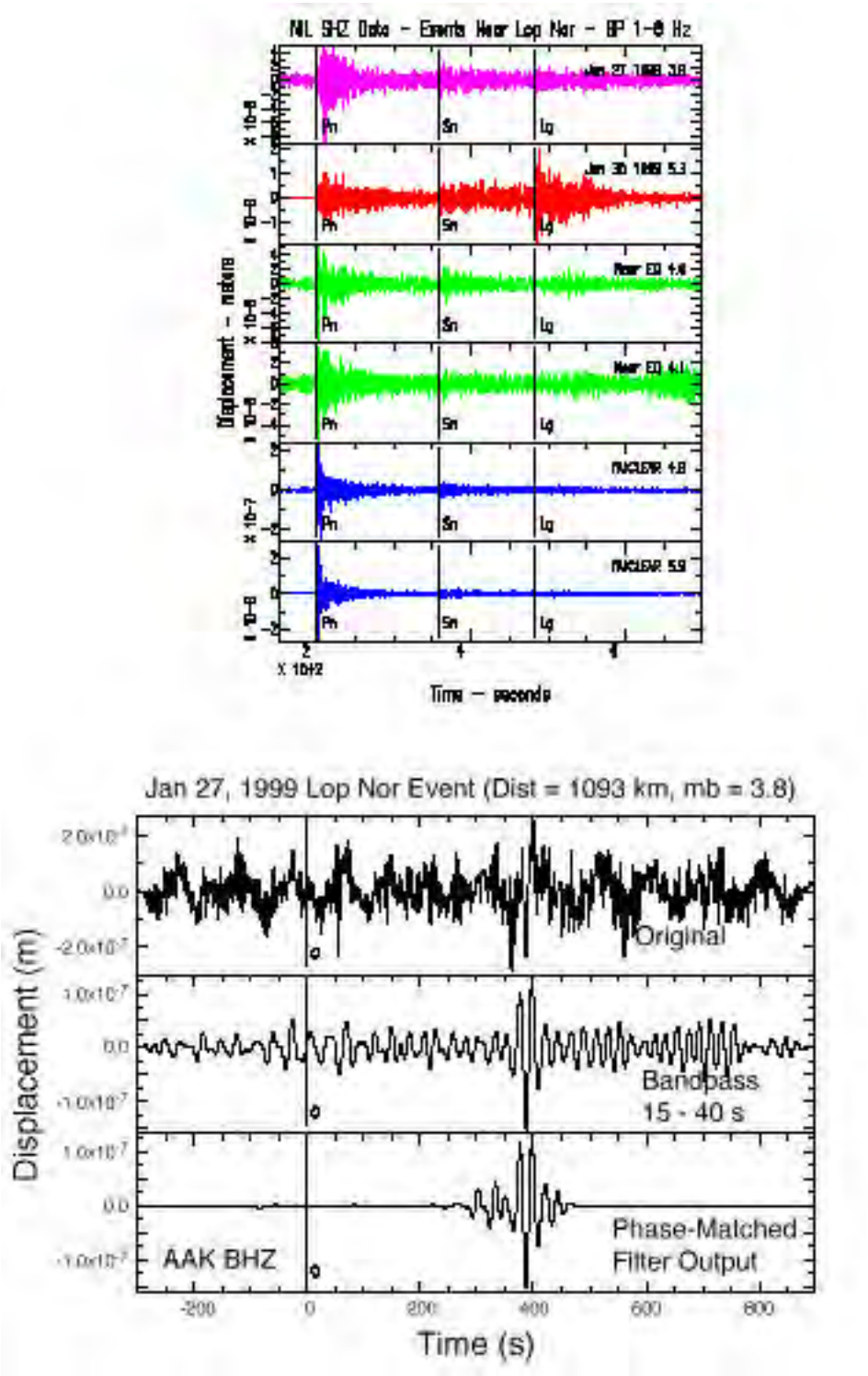


Figure 3. Short-period seismograms of four earthquakes and two nuclear explosions from Lop Nor recorded at NIL (top). The two top traces are the 27 Jan and 30 Jan seismic events. Also, we show the broadband, bandpass filtered, and phase-matched filtered seismograms of the 27 Jan event as recorded at AAK. We designed the phase-matched filter using the large Lop Nor earthquake (mb 5.2) of 30 Jan.

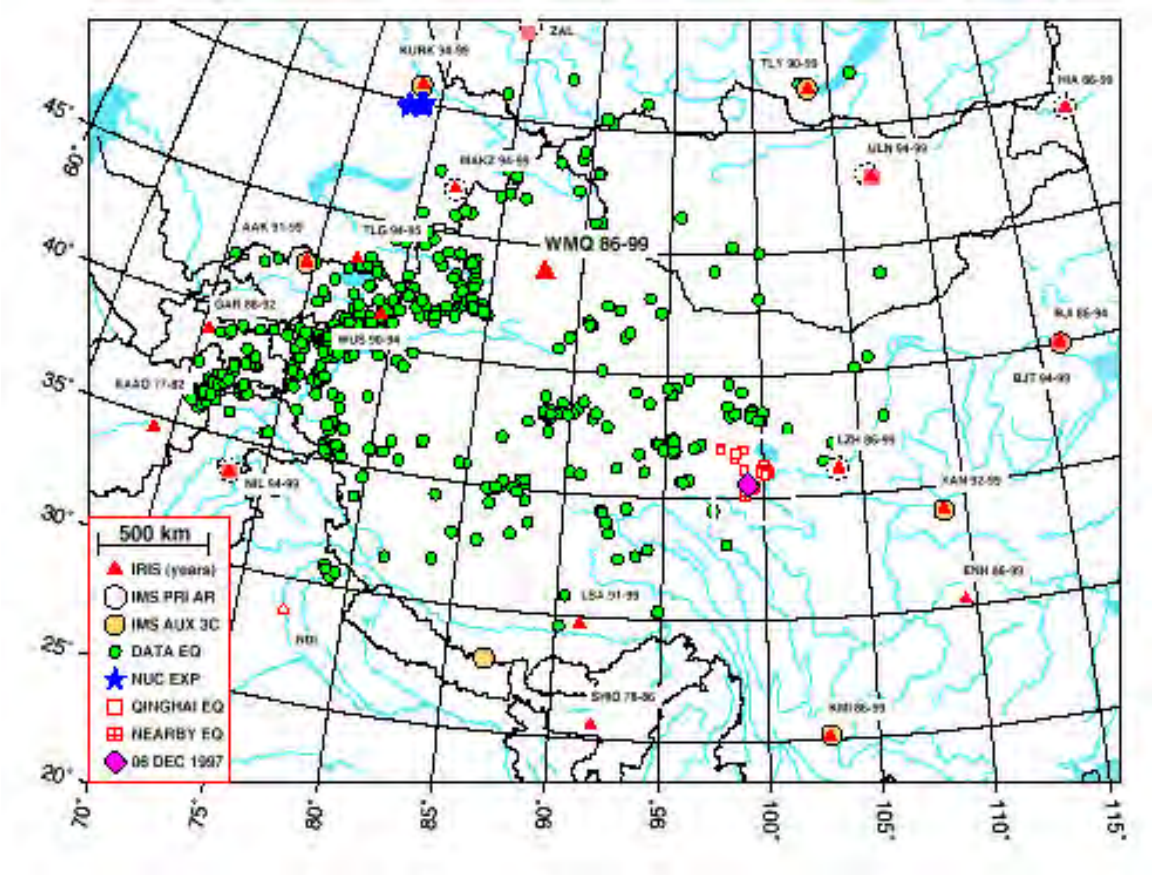


Figure 4. Map of western China showing the location of the 06 Dec 1997 Qinghai seismic event (diamond). The open squares near the diamond are earthquakes that occurred near the 06 Dec event. Waveforms and discrimination plots related to these events are shown in Figure 5.

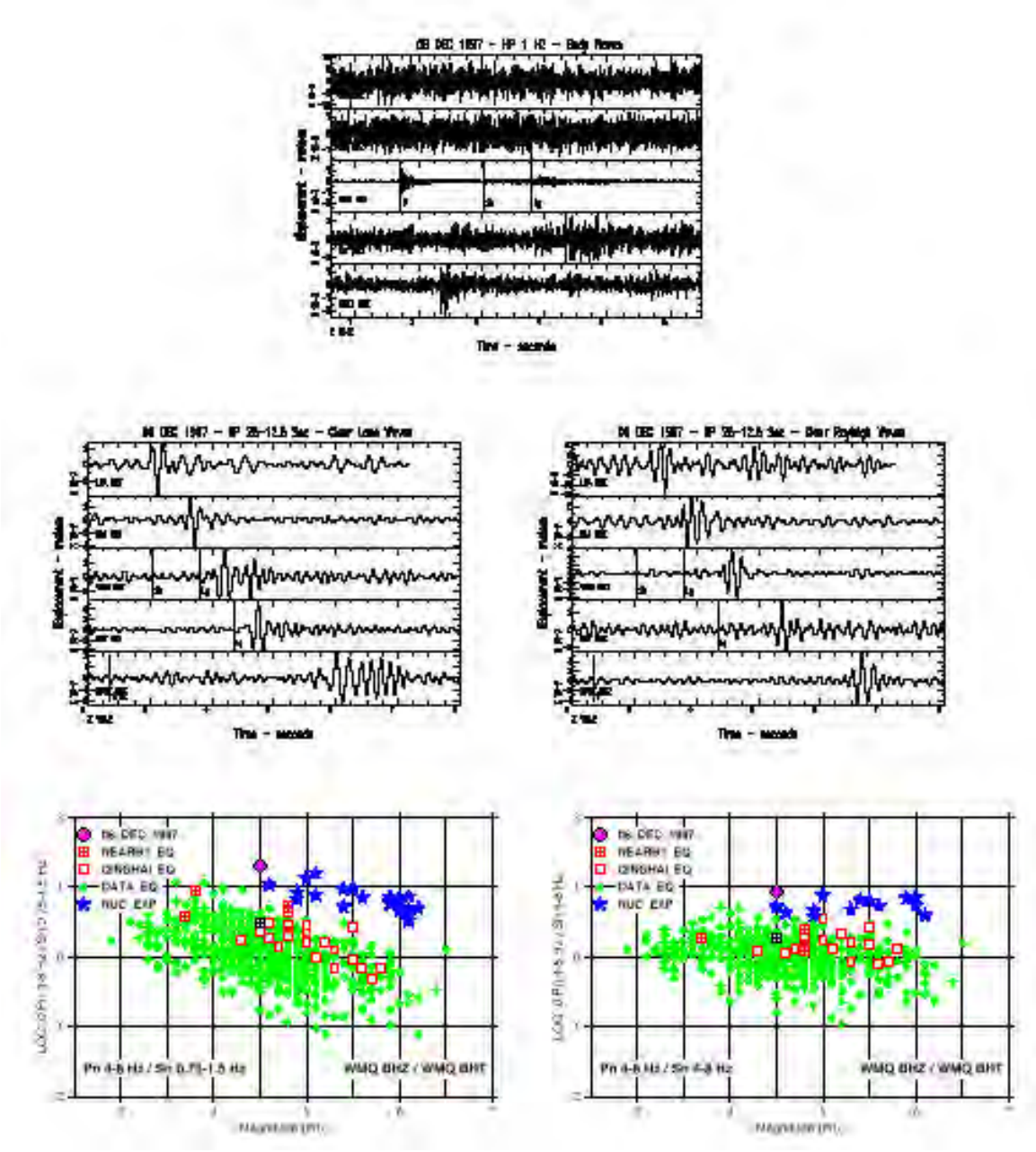


Figure 5. Short-period waveforms (top) and long-period waveforms (middle) of the 06 Dec 1997 Qinghai event recorded at several CDSN stations. The middle trace of each waveform display is data from WMQ. Note the Unusually strong Pn arrival at WMQ. The 06 Dec event is high in the nuclear explosion population on the Pn/Sn discrimination plots (bottom).

THE KOREAN SEISMO-ACOUSTIC ARRAY

Chris Hayward, Brian Stump, Paul Golden, Eugene Herrin, Southern Methodist University
Myung-Soon Jun, Jeong-Soo Jeon, Korea Institute of Geology, Mining and Materials

Sponsored by U. S. Department of Defense
Defense Threat Reduction Agency and Air Force Technical Applications Center
Contract No. DSWA01-98-C-0131

ABSTRACT

The Korea Institute of Geology, Mining, and Materials (KIGAM) and Southern Methodist University (SMU) are jointly installing a four-element 1-km aperture seismo-acoustic array at 85 km northeast of Seoul, Korea, similar to the seismo-acoustic arrays at Lajitas, Texas (TXAR) and at Mina, Nevada (NVAR). This array will be used to identify and locate events associated with industrial blasting. These identified and located events will then be used to form a ground-truth database.

The Korean array uses Geotech Intelligent Communication Processing System Model 59660, similar to the prototype infrasound array at Los Alamos National Laboratory. Significant differences in the new system include the use of 2.4-GHz radios for inter-array communication and a link for the outgoing alpha protocol, use of three-channel digitizers with calibrators rather than single-channel digitizers, use of 40 SPS data, a modified alpha stream for weather data, omission of authenticators, and operation of a complete 12-volt system. Each array element includes solar power supplies, a GS-13 seismometer in a 10-meter borehole, and an infrasonic gauge similar to that used at NVAR.

The system was deployed and operated in a test configuration in McKinney, Texas. The primary purposes of the test were to build confidence in unfamiliar equipment, test installation procedures, and identify remote problem diagnosis procedures. The test deployment also demonstrated the characteristics of the infrasonic gauges and noise reducers under varying wind and weather conditions. Wind speed and temperature are measured at one infrasonic site and included in the data stream.

Infrasonic gauges were built using modified 2.5-inch Validyne DP250 sensors mounted in a 4-inch PVC pipe such that the sensor could be easily installed in the seismic borehole. The infrasound gauge included a backing volume of 1 liter, a fore volume designed to be fed from a _-inch hose, a remotely activated calibrator, thermal insulation of the backing volume, electrical and magnetic shielding of the sensor, and the capability to use long RC time constants in the capillary to push the response beyond 120 seconds.

Tests of the gauges at McKinney included self-noise under field conditions (equivalent to blocked mass seismometer tests), comparison and noise tests of systems driven from no or the same acoustic array, comparison tests of arrays of eleven 25-foot, five 25-foot, and one 25-foot 5/8-inch Moisture Master soaker hose. Initial tests of the remote calibrator were made. An alternative simple static field calibration procedure was also developed.

Final tests at SMU examine the capability of the system to send alpha data via mixed radio and wire telemetry to KIGAM to be forwarded over the internet to SMU.

Key Words: seismo-acoustic, array, industrial blasts, infrasound, noise

OBJECTIVE

The objective of this joint Southern Methodist University (SMU) and Korea Institute of Geology, Mining and Materials (KIGAM) program is to design, procure, integrate, test, install and operate a seismo-acoustic array in the Republic of Korea in order to create a ground truth database as has been done for TXAR.

RESEARCH ACCOMPLISHMENTS

Introduction

KIGAM and SMU are jointly installing and operating a four-element 1-km aperture seismo-acoustic array at Chulwon, 85 km north-northeast of Seoul, Korea (Figure 1). The Chulwon array (CHNAR) is similar to the Lajitas, Texas (TXAR) and Mina, Nevada (NVAR) seismo-acoustic arrays in its choice of sensors and geometry. The digitizer and data system, however, are similar to the LANL infrasound system. Waveforms from CHNAR are used to detect, identify, and locate events associated with industrial blasting. These events are then used to form a ground-truth database.

The cooperative cost sharing and operation of the array has been critical to the success of the project. SMU completed system design, instrument procurement, fabrication, testing, and training. KIGAM developed and tested the power and communication infrastructure, the site civil work, and the data integration into the current KIGAM seismic network processing. A joint KIGAM – SMU team made the site selection and initial installation. KIGAM will continue operation and maintenance of the array receiving real-time alpha data from CHNAR, integrating it into their automatic detection and location routines, and forwarding the alpha data stream and automatic locations to SMU for additional analysis.

The Chulwon Array is situated in an area of faulted metamorphic rocks overlain by quaternary alluvium and basalt flows. Geology of the individual 4 element sites varies from competent schist and gneiss to basalt over alluvium. All sites are remote from heavy traffic, although each site has a unique relation to topography. The central site CHN00 (Figure 2) is at the top of a lightly forested hill. Site CHN01 is within 5 m of a moderately traveled narrow unpaved road. Site CHN02 is near the 5-10 m banks of an entrenched river. Site CHN03 is near a 10 m high vertical wall.

The array hub is 4-5 km from the nearest commercial telephone service in the town of Daema-ri although commercial power service is available at the array hub. An existing concrete building is used to house the hub equipment.

Siting an array that was culturally quiet, was suited to microwave communication, was topographically acceptable, was within a reasonable distance of the acoustic sources, had sufficient land area for a pipe array, and was unfarmed proved to be difficult. The intensive farming of all level ground combined with rugged topography limited site selections. The final selection, near Chulwon, is nearly ideal. It is culturally quiet since there is neither through traffic nor much overhead air traffic. All sites are suited for direct radio communication to the hub. The array is well positioned to examine the industrial events associated with activity near Incheon and when combined with the existing KSAR and INCH stations will be well suited for locating events in the region.

Several minor modifications to the design were made to accommodate site conditions. The weather station, originally telemetered by radio from site 0, was moved to the hub and wired directly to the hub controller. This freed a set of radios such that a radio TCP/IP connection could be made between the hub and the nearby town. The original hose array, a six arm radial array of 50’ porous hoses, was modified to an 11 arm 25’ array to minimize the required land around the sites. Boreholes originally limited to 20’ depth were extended up to 30’ to allow better penetration of the bedrock.

Equipment Description

The overall configuration is a union of a modified LANL digitizer and infrastructure with SMU style sensors and power systems (Figure 3).

Each array element uses a GS-13 at the bottom of a 6-20 m deep borehole similar to the installation at NVAR and TXAR. Unlike NVAR and TXAR which used a poured concrete base at the bottom of the hole, at CHNAR

the casing was closed with a welded steel bottom insuring that the base of the hole would stay dry, flat, and level. This simplified seismometer installation (NVAR required a down-hole camera).

The infrasonic subsystem used SMU style microbarographs, a modified version of the NVAR design. These use a modified Validyne DP250-14 gauge with P55D electronics. The modifications to the model were gauge improvements to allow a stress free mounting of the diaphragm in the down-hole package. The microbarograph is in a simple plastic pipe package 6 feet long and 4" in diameter with connections at the top for a standard 3/4" pipe thread and at the bottom a connector designed to plug into the digitizer. The design is simple with most components constructed from plastic plumbing parts purchased at the local hardware store. Unlike the NVAR package which used a traditional design of a hose connected to a closed bottle for the fore-volume, the CHNAR package uses a partial impedance match to help control hose resonance. Because the frequencies are low, it is difficult to build an ideal match and still maintain a reasonably small fore-volume. However the partial match does reduce the effect of reflections at the microbarograh connection to the pipe array.

To reduce the electronic noise, particularly when the systems were tested in the lab, the pressure sensor was heavily shielded in a three layer mu-metal cylinder and offset by 40-50 cm from the electronics. This also reduced sensor cross talk when multiple sensors must be operated close together (as for coherence measurements).

In addition to the modifications of the fore-volume, the backing volume of the CHNAR sensors was doubled from NVAR to 1 liter. This was then packed with stainless steel wool to increase the thermal mass and heavily insulated. The expanded backing volume helped stabilize the system for small temperature changes and allowed us to add a pump calibrator to the system.

The calibrator is a small impulse metering pump with a manually adjustable displacement. The magnetic and electrical shielding of the sensor was sufficient to eliminate most of the interference cased by pump operation. The pumps are set to produce a nominal signal of 0.6 Pa for each stroke when connected to their normal position at the backing volume. Since the pump may be left connected to the backing volume during normal operation, this permits remote calibrations. The pump impulse is essentially instantaneous (at 40 SPS) and thus produces a calibration step function that is modified by the microbarograph RC constant. The pump is driven through a small microprocessor controlled circuit that takes its input from the standard digitizer calibration signal. Although the calibration pump is only capable of producing a 0.6 Pa step, the driver can selectively operate it as a random binary telegraph spaced step or as multiples of 8, 16, or 64 rapidly pulsed steps. Thus, it is possible for the calibrator to drive the microbarograph at high outputs overriding any noise (or signal) being detected at the fore-volume.

The microbarograph is placed in the shallow borehole about 4 feet below the surface. A 1-inch pipe leading to a 3/4-inch hose connects the microbarograph to an off-the-shelf 12 port manifold. Eleven, 25-foot long soaker hoses are arranged in a radial pattern and connected to the manifold. The hose end caps are sealed with silicon caulk onto the distant ends of the hoses. This was done to prevent the caps from working themselves off as happened at TXAR.

The array uses Geotech Intelligent Communication Processing System Model 59660, similar to the prototype infrasound array at Los Alamos National Laboratory. Modifications to the LANL design were required to support the seismic portion of the seismo-acoustic system, to provide local data archiving for extended periods (up to 2 months), to eliminate the authenticators, and to accommodate the SMU style microbarograph. The following minor modifications were made during the integration and tests at Geotech and at SMU:

1. The system was configured for three digitizer channels per site rather than a single channel. While this was a minor hardware change, it caused a significant impact on parts of the software.
2. The system is sampled at 40 SPS rather than 20 SPS. This increase in sample rate increased the required throughput on the alpha stream and the amount of disk space required for local storage.
3. To accommodate the GS-13 sensor, it was necessary to add an impedance converter board to the digitizer front end and to increase the gain of the seismic channel by 20 dB.
4. A calibrator board was added to calibrate the GS-13. This hardware change required an associated software modification in the alpha sending software.

5. Changes were made to the way weather information is sent in the alpha data stream such that the alpha reader could correctly decode wind speed, direction, and air temperature. In addition, the weather station software was modified at SMU to use metric units.
6. Long distance WAN connections at Chulwon were felt to be uncertain enough that it was desirable to include local data storage for up to 6 weeks. A change in the software allowed us to save waveform files similar to CSS files on the local hard disk.
7. The system was modified at SMU to recover from a power cycle. Local archiving now starts automatically although starting the alpha data stream after power fail still requires manual intervention.
8. A software package to allow remote access to the console was added such that the manual alpha restart and state-of-health monitoring could be done remotely from either KIGAM or from SMU. In addition remote ftp services were added such that it is possible to remotely download or upload data and software.

The hub computer running windows NT4.0 gathers data from all four sites plus the weather station, displays the waveforms, saves it locally to CSS-like waveform files, and formats it to an alpha protocol TCP/IP stream over 10bT. A small Cisco router passes the data stream over a radio link to a second router at a convenient telephone site where it is forwarded to KIGAM and incorporated into the automated processing. KIGAM forwards the alpha stream over the internet to SMU for analysis and use in building the ground truth database. SMU records and archives the data stream with DCC-Lite on a small Sun workstation.

System Tests

Once the system was delivered from Geotech Instruments, two sets of tests were scheduled. One field test at McKinney, Texas was designed to locate problems in fielding the system and to field test the microbarographs. A set of tests at SMU was designed to test the alpha protocol. Field tests at McKinney were terminated after demonstrating successful operation of the microbarographs. Tests at SMU were terminated after demonstrating successful transmission of alpha data from the recording system over the internet to KIGAM and back to SMU's alpha reader.

The system was deployed and operated for six weeks in a test configuration in McKinney, Texas (Figure 4). The test goals were to build confidence in unfamiliar equipment, to test installation procedures, to identify remote problem diagnosis procedures, to make minor changes to the configuration to match field conditions (field tuning), to field test the microbarograph, and to demonstrate the system in a realistic configuration to KIGAM personnel. Results during the McKinney test led to minor changes in hardware (such as correcting the wiring on inverted GS13 cables), changes in hub software (such as correcting the local archiving software so it would function across a month rollover), minor changes in microbarograph design (such as increasing the low cut corner from 600 seconds to 20 seconds and modifying the calibrator logic), familiarity with various field configuration changes that might have to be made during installation (such as radio reconfiguration), and demonstration of the complexity of details involved in fielding even a simple system.

The test deployment also demonstrated the characteristics of the infrasonic gauges and noise reducers under varying wind and weather conditions. Wind speed and temperature are measured at one infrasonic site and included in the data stream. This portion of the test was useful in that it furnished information for analysis.

Tests at SMU were done to insure that alpha data could be sent from the hub to KIGAM and forwarded back to SMU. It required four weeks to reach a successful conclusion. Prior to testing, we had demonstrated that the system was able to transmit alpha data directly to a DCC-Lite system (a commercially available alpha reader) configured at SMU. The alpha tests were done to demonstrate that the system was able to send data to KIGAM's reader and back to SMU.

Tests of the infrasound gauges at McKinney included self-noise under field conditions (equivalent to blocked mass seismometer tests), comparison and noise tests of systems driven from no or the same acoustic array, comparison tests of arrays of 11 25-foot, 5 25-foot, and 1 75-foot 5/8" Moisture Master soaker hose. Initial tests of the remote calibrator were made and a simple alternative static field calibration procedure developed.

Analysis of two microbarographs driven from a Y-connector open to the air (no hose array) demonstrated that the microbarograph high frequency response even when connected to a 50' hose, is coherent and undisturbed to

8 Hz and that the microbarograph noise floor matches the calculations based on previous laboratory tests. The nominal noise floor is plotted in Figure 4a as a horizontal line below –50 dB relative to 1 Pa^2/Hz.

The effect of the 11-arm radial hose array of 25' radius was estimated by comparing the response of a collocated system without the hose array to the hose array. This was done under varying wind conditions. Figure 4a suggests that the hose array attenuates all signals by about 6 dB (since one would expect that the effect of a 25' array would be minimal for long wavelength signals). For signals of 1 Hz the small array offers a 12 dB improvement in the SNR. For the conditions examined, the open system recorded a difference in signal level of 12 dB from nearly 0 to 11 MPH winds. For the hose array, there is little difference in noise levels above 3 Hz for any of the observed wind conditions. For these conditions and frequencies, the array is apparently over sampled. In both cases, the background noise is above sensor noise up to 10 Hz.

Figure 4b shows the transfer function between the open system and hose array. The transfer function was calculated by using only time segments with zero wind. The phase delay is from a difference in the sampling points of the two systems and from the delay caused by propagation in the arms of the hose array. The array appears as a low pass filter with a corner at 3 Hz. Figure 4c shows an example time series of the two systems under zero wind conditions. The open system (lower plot 4c, dotted trace) has wider bandwidth than that of the pipe array and slightly higher amplitude.

A test of the remote calibrator (Figure 4d) demonstrated that the system could be calibrated under normal operate conditions. Five different calibration signals were tried. Under low wind conditions, an individual step calibration of 0.6 Pa is easily visible, but such a signal has insufficient SNR at the low frequency corner to verify the system RC time constant. Multiple pulses (Figure 4d, top three traces) produce enough energy (up to 20 Pa P-P) to be useful under windy conditions. The utility of the random binary calibration signal (Figure 4d, bottom two traces) has not been demonstrated to be superior to the simpler multiple step calibrations at least for the parameters tested. Lower clock rates for the RBT may be more useful in calibrate while operate configurations.

As a check on the calibrations, the absolute DC pressure response of the microbarographs was checked using a simple gravity method. Since the diaphragm is a known mass, inverting the sensor will cause a known equivalent pressure step. Since the gauges used here have a response flat to DC, this is easily read in the field to better than 5% using a multimeter. Although this does not guarantee the dynamic response of the system, it does provide a simple check.

CONCLUSIONS AND RECOMMENDATIONS

A seismo-acoustic array, the first of its particular configuration and design has been designed, tested, and installed in the Republic of Korea by KIGAM and SMU. Data from the array is being sent on the internet in alpha protocol to SMU.

Design, procurement, testing, site selection and installation of the array required approximately one year. Although many of the components were off-the-shelf, significant integration and design issues required field tests. Based on our experience with this array, it is unlikely that a similar design and installation task completed to the same degree of confidence, could be completed in less than 6 months.

Tests of the microbarograph and hose arrays at McKinney have demonstrated that the pipe array used in Korea causes little signal modification below 3 Hz other than an attenuation.

A test of the calibrator has demonstrated that it is possible to do remote calibrations of the microbarograph under normal conditions.

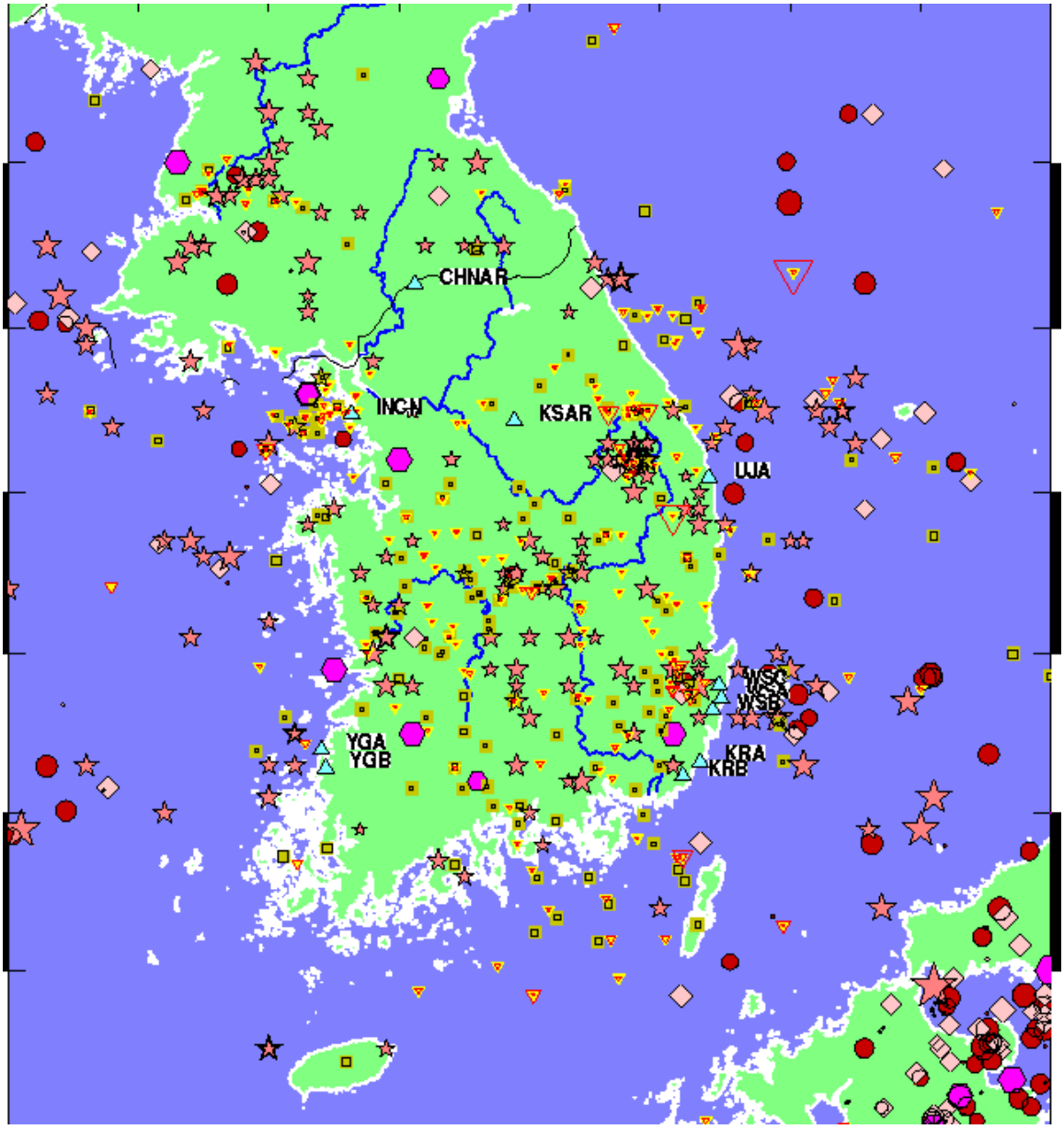


Figure 1. Seismicity of Korea.

Selected stations in the KIGAM network are labeled and shown as triangles. The station CHNAR is the new seismo-acoustic array. Other symbols, for example stars, indicate the epicenters of cataloged earthquakes. Symbol size in proportional to magnitude. The following symbols have been used to plot earthquakes:

Stars	KMA catalog locations from 1990-1999
Circles	USGS PDE locations from 1974
Squares	KSAR automatic locations from Feb 1999 to July 1999
Diamonds	PIDC locations from 1994 to July 1999
Inverted Triangles	KIGAM locations from Feb 1999 to July 1999
Hexagons	NOAA significant events catalog

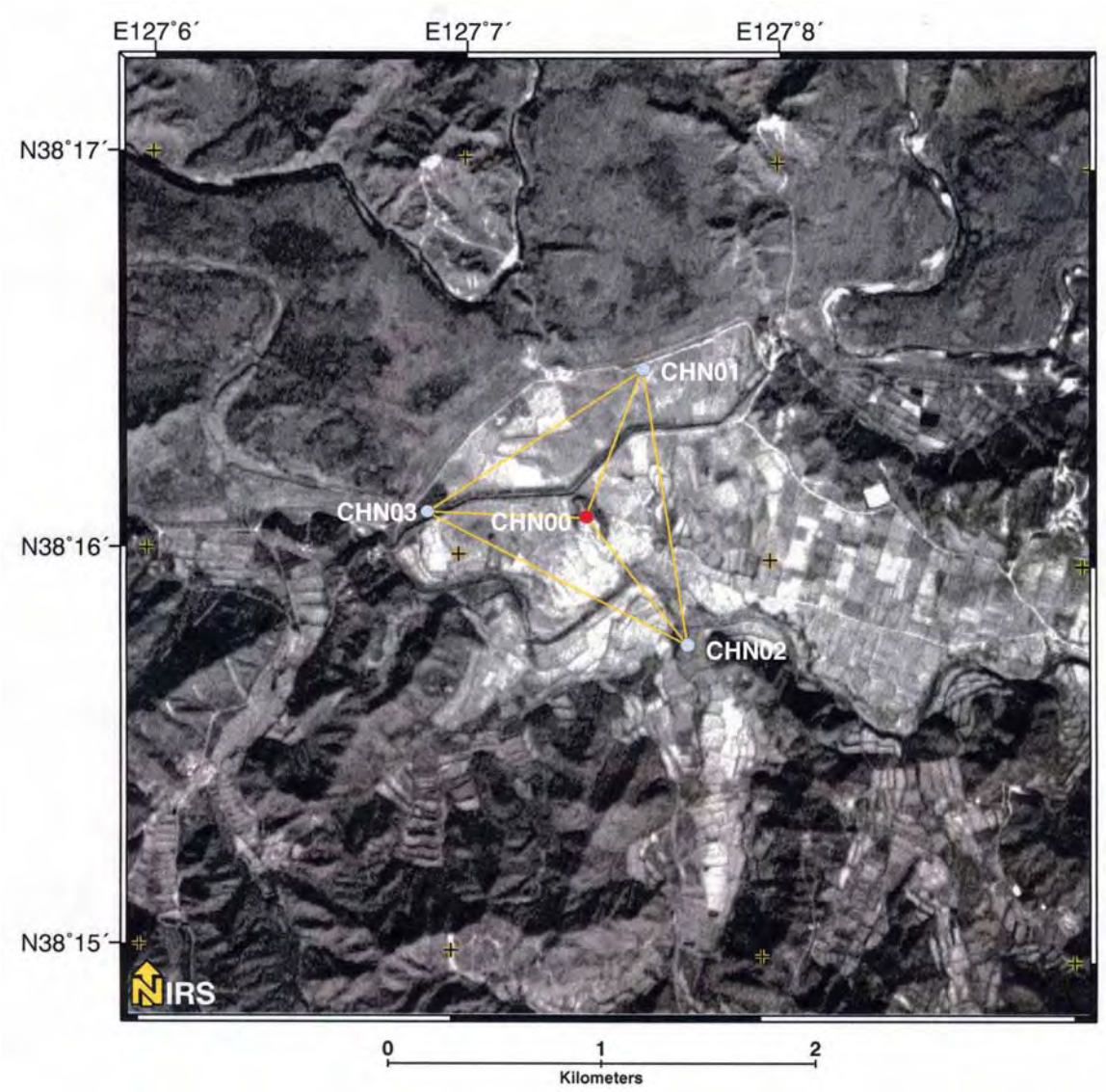


Figure 2. Overhead photo of CHNAR location. The area is in intensive rice farming. Site CHN00 is on top of a forested hill. The array is about 1.2 Km on a side.

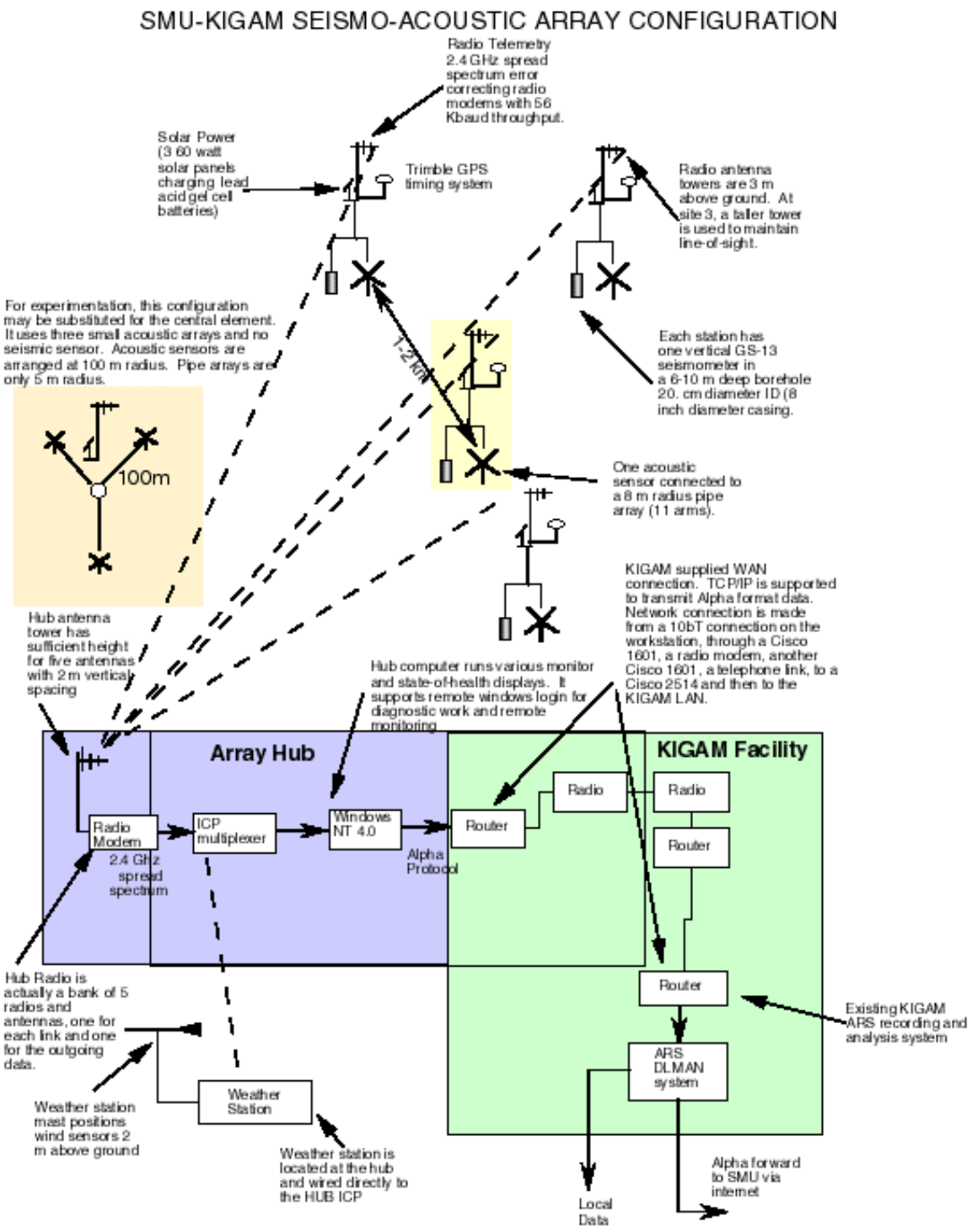


Figure 3. Schematic diagram of Korean array configuration.



Figure 4. Photographs of the McKinney field test. Top, left photo is the hub computer and associated multiplexer and radio bank. Bottom photo is one test site with 5 microbarographs mounted to the solar panel supports for testing. The enclosure contains the digitizer, power supply, and weather station. A second site is visible in the background. Top, right photo shows the hose manifold for the 11 arm hose array.

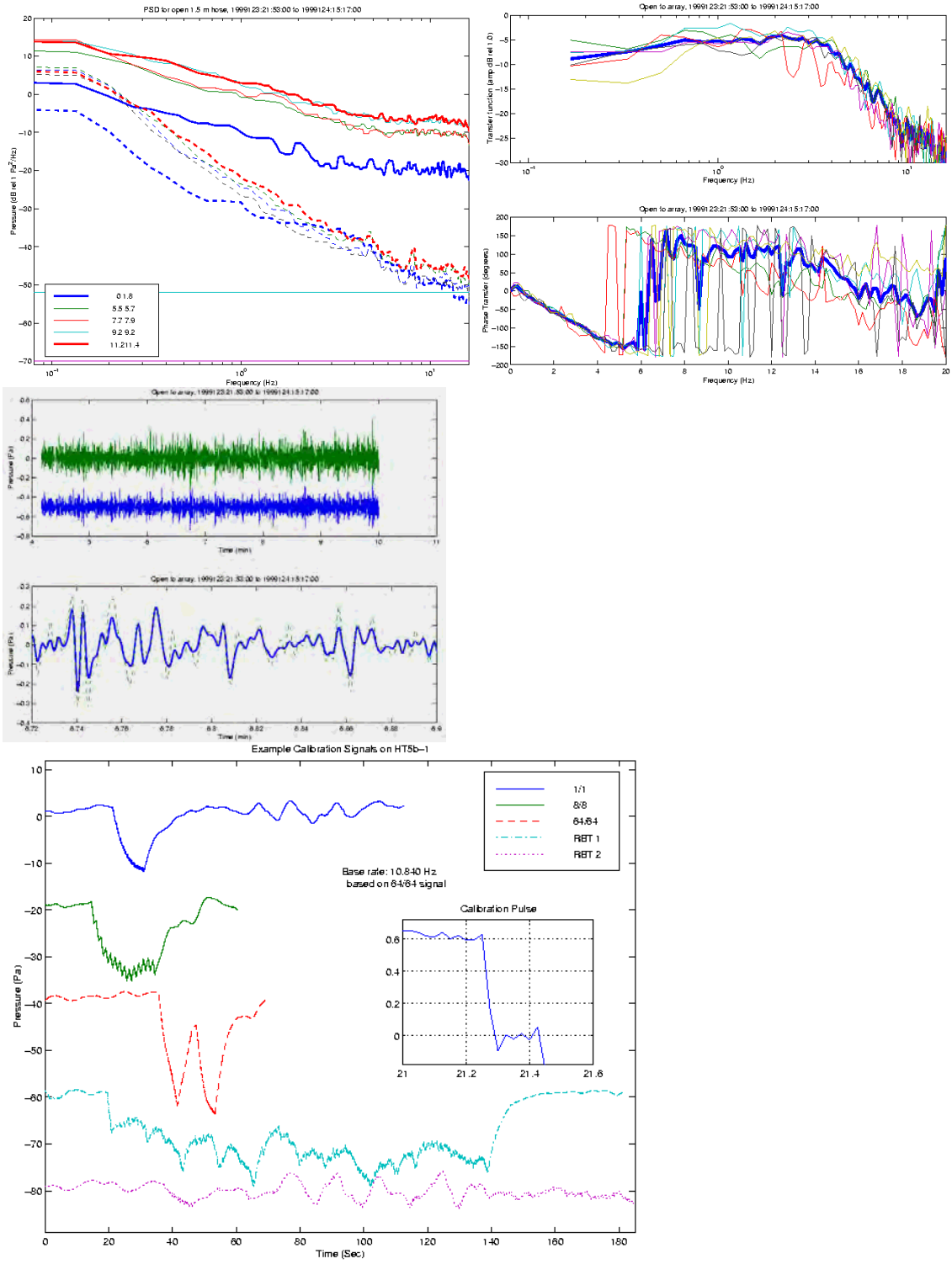


Figure 5. Microbarograph tests at McKinney, Texas. Figure 5a (top left) shows the power spectrum for an infrasound gauge without pipe array and with pipe array under varying wind conditions. Figure 5b (top right) shows the transfer function between the open infrasound gauge and pipe array under dead calm conditions. Figure 5c (middle plot) shows the time series of the two systems under these quiet conditions. Figure 5d (bottom plot) shows example remote calibration signals recorded under field conditions.

TWO-STATION PHASE VELOCITY DETERMINATION FOR STRUCTURE IN NORTH AFRICA

Shannon Hazler*, Michael Pasyanos, William R. Walter, and Anne Sheehan*

Lawrence Livermore National Laboratory
Geophysics and Global Security Division, Livermore, CA

University of Colorado at Boulder*

Sponsored by the U.S. Department of Energy
Office of Nonproliferation and National Security
Office of Research and Development
Contract No. W-7405-ENG-48

ABSTRACT

The seismic structure of North Africa is poorly understood due to the relative paucity of stations and seismicity when compared to other continental regions of the world. A better understanding of the velocity structure in this area will allow improved models of travel times and regional phase amplitudes. Such models will improve location and identification capability in this region, leading to more effective monitoring of the Comprehensive Nuclear-Test-Ban Treaty. Using regional-to-teleseismic Rayleigh and Love waves that traverse the area we can obtain information about the region's seismic structure by examining phase velocity as a function of period. We utilize earthquakes from the tectonically active regions bounding North Africa (Mediterranean, Red Sea, East African Rift, and Mid-Atlantic Ridge) recorded at broadband seismic stations distributed throughout the region. A two-station method is utilized to determine phase velocity information along the interstation segment of the ray path. The two-station method provides particular advantage in this region as it dramatically increases the number of events available to provide pure North African sampling. Bandpass filters are applied to the seismograms so that peaks and troughs may be correlated. The phase is unwrapped and a difference curve computed. The difference curve is then converted to a phase velocity dispersion curve. Phase velocity curves are constructed in the range of 10 to 120 seconds. Rayleigh and Love waves in this period range are most sesitive to the shear velocity structure of the lithosphere and can be used in combination with additional independent seismic observations (e.g. Pn tomography, surface wave group velocity tomography, receiver functions, etc.) to construct reliable velocity models. We compare velocities computed in this study to those generated from well known models for similar tectonic regions throughout the world in order to better define the tectonic setting of North Africa. Results from this study help constrain the regional tectonics of the area and will also be used to better define the seismic characteristics required to verify the CTBT.

Key Words: Surface waves, phase velocity, structure, Africa

Research performed under the auspices of the U.S. Department of Energy by the Lawrence Livermore National Laboratory under contract *W-7405-ENG-48.*

OBJECTIVE

North Africa has been only sparsely sampled both geologically and seismically; yet knowledge of regions such as this is critical for CTBT monitoring purposes. In an effort to fill in the gaps present in our knowledge of the seismic structure of Northern Africa, a study of the shear wave velocity structure beneath this region has been undertaken (Hazler, 1998; Pasyanos et al., 1999). Previous work in this vein has focused on single station group velocity measurements. We have implemented a study of phase velocities in North Africa and the Middle East to augment the knowledge accrued from the ongoing group velocity study at Lawrence Livermore Laboratory. The goals of this phase velocity study are to improve both 1-D models shear velocity versus depth for particular paths as well as the 3-D shear velocity structure of the region. The increased understanding of the regional tectonic setting and shear velocity structure provided by these surface wave studies will better define the seismic characteristics needed to properly monitor the Comprehensive Nuclear-Test-Ban Treaty (CTBT). In particular, increased knowledge of seismic shear wave structure will lead to improved detection, location, and identification capabilities in the region.

RESEARCH ACCOMPLISHED

Paths Chosen

A search was made for pairs of seismic stations whose back azimuths to a given earthquake differed by three degrees or less. Broadband three-component stations from the IRIS/GSN, MEDNET, and GEOSCOPE networks were included in the search. Seismograms from earthquakes between the years 1977-1999 of magnitude 4.5 and greater with great circle paths crossing North Africa or the Middle East were included in the search. A total of 60,559 possible two station pairs were retrieved. Figure 1a depicts the coverage which these paths would provide. A subset of these paths have been examined at this date. The paths presented here are depicted in figure 1b.

Measurement Technique

To make a phase velocity measurement, the raw data are demeaned and detrended, and the instrument response is removed from all seismograms. For each pair of Rayleigh wave records, a Fourier transform is performed, the phase information is unwrapped, and a phase difference curve is computed; the phase difference curve is then converted to a phase velocity curve using the following equation: $\psi_1(\omega) - \psi_2(\omega) = \omega(t_1 - t_2) - \omega(c(\omega))^{-1}(x_1 - x_2) + 2\pi M$, where $c(\omega)$ represents phase velocity, x_1 and x_2 refer to the positions of the stations, t_1 and t_2 refer to the start times of the two records, $\psi_1(\omega)$ and $\psi_2(\omega)$ represent the phase information in each record, and M is an integer describing the number of cycles the surface wave has undergone in its travels. A suite of potential phase velocity curves is computed for several possible values of M and the appropriate dispersion curve is chosen from this suite. For ease of display, phase velocity curves along the same path were averaged and are pictured here with the region bounded by one standard deviation from the average (Figure 3, 4, and 5).

Error Sources

The two factors which have most contributed to the errors inherent in this study are scattering and inaccurate source information. Scattering occurs when an incoming seismic ray encounters a geologic feature, most often crustal, which changes the ray's path so that it deviates from the path predicted by the ray tracing method employed in a given study. The errors associated with this scattering effect are due to the observer's choice of an assumed path which deviates from the true path of the seismic wave. Errors can also result from inaccurate source information particularly origin time and source location. By examining phase velocity curves which demonstrate reversed propagation direction, one can gain insight into the influence of these error sources on the dispersion curve. Seven of the nine two-station pairs examined in this study contain reversed paths. These reversed paths are visually indistinguishable from phase velocity curves representing forward propagation. The repeatability of measurements along a single path can also provide some understanding of the degree to which these error impact phase velocity measurements. An example of the phase velocity curves measured along a single path, TAM to DBIC, is presented in figure 3.

Discussion

Figure 2 depicts generalized geologic divisions in North Africa. The path from TAM to DBIC samples a large amount of shield material, the West African Craton, and lithified sedimentary material [Bertrand-Sarfati et al, 1991; Cahen and Snelling, 1984; Rocci et al, 1991]. Unlithified sediments are minimal along

this path. The phase velocities in figure 3 reflect this geologic setting. The curves obtained along this path display uniformly high velocities which conform to a high velocity shield body. High phase velocities can also be found in figure 4a which depicts the results from the KEG to ATD path. The high velocities at short periods probably reflect travel off the assumed path through the fast oceanic material in the Red Sea. At longer periods, high velocities can be linked to the crystalline material of the Nubian Shield (Goodwin, 1996). Figure 4b depicts results for the KEG to TAM path. This path crosses the East African Craton which is largely covered by the sediments of the Sahara (Condie, 1982). The thickness of these sediments is reflected in the slow phase velocities at short periods. At longer periods, the curves demonstrate the fast velocities common to cratons.

In figure 4c, we move away from cratons and shields and into a regime dominated by old orogenic belts. The path from TAM to BGCA demonstrates slower phase velocities at longer periods than the paths which sample shield material. Low velocities are also displayed at short periods reflecting the unlithified fluvial deposits as well as Saharan sediments (Petters, 1991). Figure 4d shows results from the ATD to BGCA path. This path samples the Central African Belt, the Mozambique Belt, as well as the northern-most extent of the East African Rift (Goodwin, 1996). Again, we see velocities slower than those presented in shield dominated paths. These curves display faster short period results which are indicative of the small amount of unlithified sediment sampled along this path.

Figure 5a depicts the results for the path from ATD to ABKT. This path samples the thick sedimentary basins of Saudi Arabia as well as an active orogenic belt. Both of these features result in strikingly low velocities at short periods. At longer periods, velocities are comparable to those found along the previously discussed shield poor continental paths. Figure 5b examines results from the TAM to PAB path. This path samples a moderate amount of unlithified sediments and minimal amount of shield material. The curves produced along this path return to the pattern established by the other shield poor continental paths. Figure 5c shows results from the DBIC to BGCA path. This path samples shield material, unlithified fluvial sediments, and an old orogenic belt (Cahen and Snelling, 1984). This geologic hodgepodge results in phase velocity curves which appear to be closer to the results from shield poor continental paths than results from paths dominated by shield material.

Figure 5d depicts the results from the path linking ATD and KMBO. This paths samples the edge of the East African Rift. Specifically, the path samples faulted material belonging to the Mozambique Orogenic Belt which dates to the Proterozoic. At the uppermost crustal level, this material is interfingered with largely alkaline volcanics implaced during the rifting process beginning in the mid-Tertiary [Sandvol et al, 1998; Cahen and Snelling, 1984; Tesha et al, 1997]. These extrusive volcanics are believed to be underlain by magmatic intrusions at the middle and lower crustal level (Petters, 1991). Like most of East Africa, this region is covered by Phanerozoic sediments. At longer periods, this path displays the slowest phase velocities found in this study. These velocities are not as slow as those calculated from Priestley and Brune's (1978) model of the Basin and Range. At short periods, (30 seconds and lower) the phase velocities are comparable to those found for non-shield continental regimes.

Knox et al. (1998) demonstrate the potential power of phase velocity information in conjunction with such numerical techniques as the grid search method. Using a grid search method, Knox et al. found a significant negative shear wave velocity gradient at 100 km depth beneath the Afar triangle and linked this low velocity zone to a thermal anomaly. As our phase velocity study proceeds, it is hoped that similar methods will allow our group to develop a coherent picture of the 1-D shear velocity structure which lies beneath the paths described in this paper.

CONCLUSIONS AND RECOMMENDATIONS

In this study we find that phase velocities at short periods are strongly controlled by the presence or absence of sedimentary basins. The variation produced by different amounts of unlithified sediments along a path can be seen in the TAM-DBIC path and the KEG-TAM path. These paths both sample cratonic bodies. The TAM-DBIC path contains little sediment cover and has higher short period phase velocities; while the KEG-TAM path contains substantial amounts of unlithified sediments and has slower short period phase velocities. Our results from the ATD to KMBO path, an active tectonic path, show the slowest long period velocities in this study. This may indicate the presence of a large low velocity body; however, the geometry of this path does not provide optimal sampling of the East African Rift. Results for

paths which sample shield material (TAM-DBIC, KEG-TAM, and KEG-ATD) return the highest phase velocities.

Future work on this project will include an expansion of the dataset so that measured paths may closer reflect the coverage displayed in figure 1a. As crossing path coverage improves, the dataset will be used as the backbone of an inversion for 3-D shear velocity structure. The 3-D inversion will also utilize other datasets such as group velocity data. On a smaller scale, phase velocity information will be inverted with group velocity information to produce a 1-D model of shear velocity.

This work was performed in part under the auspices of the U.S. Department of Energy by the Lawrence Livermore National Laboratory under contract W-7405-ENG-48 and LLNL subcontract B334420 to the University of Colorado.

REFERENCES

Bertrand-Sarfati, J., A. Moussine-Pouchkine, P. Affaton, R. Trompette, and Y. Bellion. (1991), Cover Sequences of the West African Craton, In: *The West African Orogens and Circum-Atlantic Correlatives*, R.D. Dallmeyer and J.P. Lécorché (ed.), Germany: Springer-Verlag, 65-82.

Brune, J., and J. Dorman. (1963), Seismic waves and Earth structure in the Canadian Shield, *Bulletin of the Seismological Society of America*, **53**, 167-210.

Cahen, L., and N.J. Snelling, *The Geochronology and Evolution of Africa*, (Clarendon Press, Oxford 1984).

Condie, K.C., *Plate Tectonics and Crustal Evolution*, (Pergamon Press, New York 1982).

Goodwin, A.M., *Principles of Precambrian Geology* (Academic Press Limited, Great Britain 1996).

Gumper, F., and P.W. Pomeroy. (1970), Seismic wave velocities and Earth structure on the African continent, *Bulletin of the Seismological Society of America*, **60**, 651-668.

Hazler, S.E. (1998), One-dimensional velocity structure of Northern Africa as determined by Rayleigh wave group velocity dispersion, Masters thesis, University of Colorado, Boulder, Colorado..

Knox, R.P., A.A. Nyblade, and C.A. Langston. (1998), Upper mantle S velocities beneath Afar and western Saudi Arabia from Rayleigh wave dispersion, *Geophysical Research Letters*, **25**, 4233-4236.

Pasyanos, M.E., W.R. Walter, and S.E. Hazler. (1999), A surface wave dispersion study of the Middle East and North Africa for monitoring the Comprehensive Nuclear-Test-Ban Treaty, *submitted to Pure and Applied Geophysics*.

Petters, S.W., *Regional Geology of Africa*, (Springer-Verlag , Germany 1991).

Priestley, K., and J. Brune. (1978), Surface waves and the structure of the Great Basin of Nevada and Western Utah, *Journal of Geophysical Research*, **83**, 2265-2272.

Rocci, G., G. Bronner, and M. Deschamps. (1991), Crystalline basement of the West African Craton, In*: The West African Orogens and Circum-Atlantic Correlatives*., R.D. Dallmeyer and J.P. Lécorché (ed.), Germany: Springer-Verlag, 31-61.

Sandvol, E., D. Serber, A. Calvert, and M. Barazangi. (1998), Grid search modeling of receiver functions: Implications for crustal structure in the Middle East and North Africa, *Journal of Geophysical Research*, **103**, 26,899-26,917.

Tesha, A.L., A.A. Nyblade, G.R. Keller, and D.I. Doser. (1997), Rift localization in suture-thickened crust: evidence from Bouguer gravity anomalies in northeastern Tanzania, East Africa, *Tectonophysics*, **278**, 315-328.

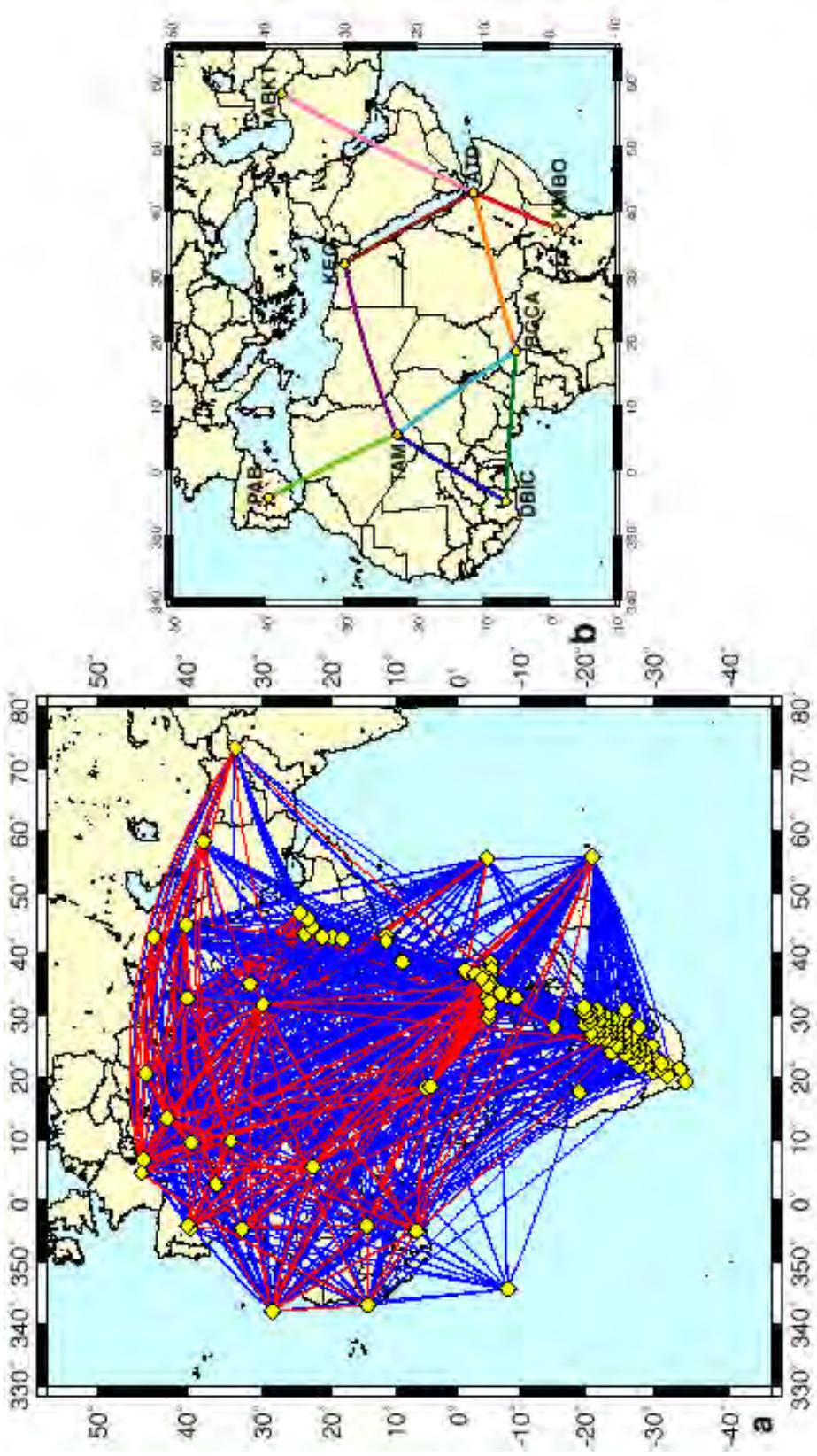


Figure 1. Panel a shows the 60,378 possible two-station pairs which have been orientated by searching against the CMT catalog. Paths which are returned represent two station pairs whose back azimuths to a given earthquake differ by three degrees or less. The search notes the onset of dates to each broadband seismic station in an effort to significantly reduce false returns. Panel b depicts the broadband seismic stations (diamonds) and the great circle paths which are examined in this study.

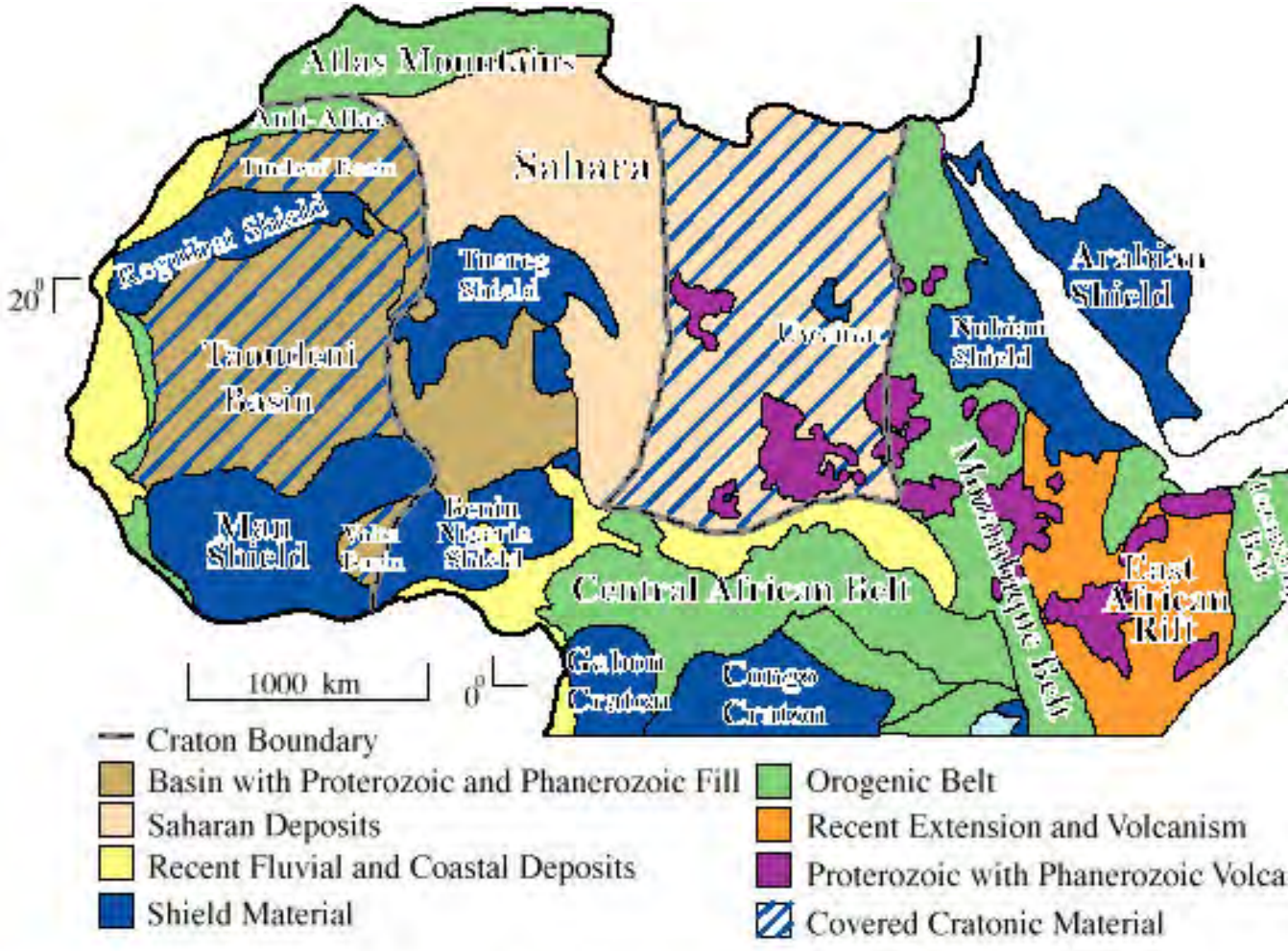


Figure 2. Generalized geologic divisions of North Africa. Major divisions include shield material, covered cratonic material, basins filled and Phanerozoic sediment, Saharan deposits, recent fluvial and coastal deposits, orogenic belts, regions of recent extension, and Proterozo Phanerozic volcanics. After Goodwin (1996).

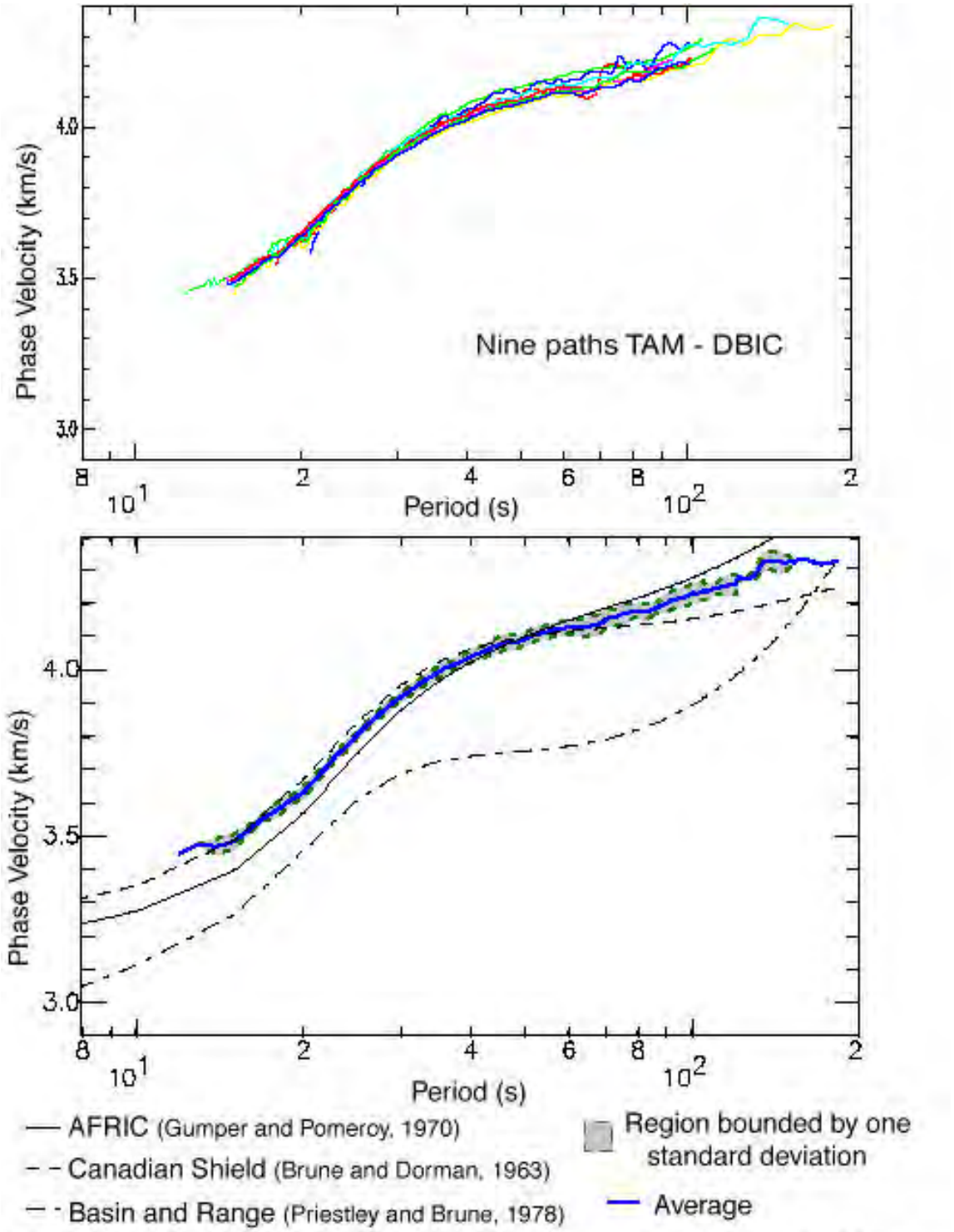


Figure 3. The upper panel shows nine phase velocity curves which were measured along the great circle path between the seismic stations, TAM and DBIC. Three of these curves represent a reversal of propagation direction. The lower panel depicts the average of these curves as well as the region bounded by one standard deviation. The averaged results found in this study are compared to phase velocity curves calculated from three reference models; AFRIC (Gumper and Pomeroy, 1970), Canadian Shield (Brune and Dorman, 1963), and Basin and Range (Priestley and Brune, 1978).

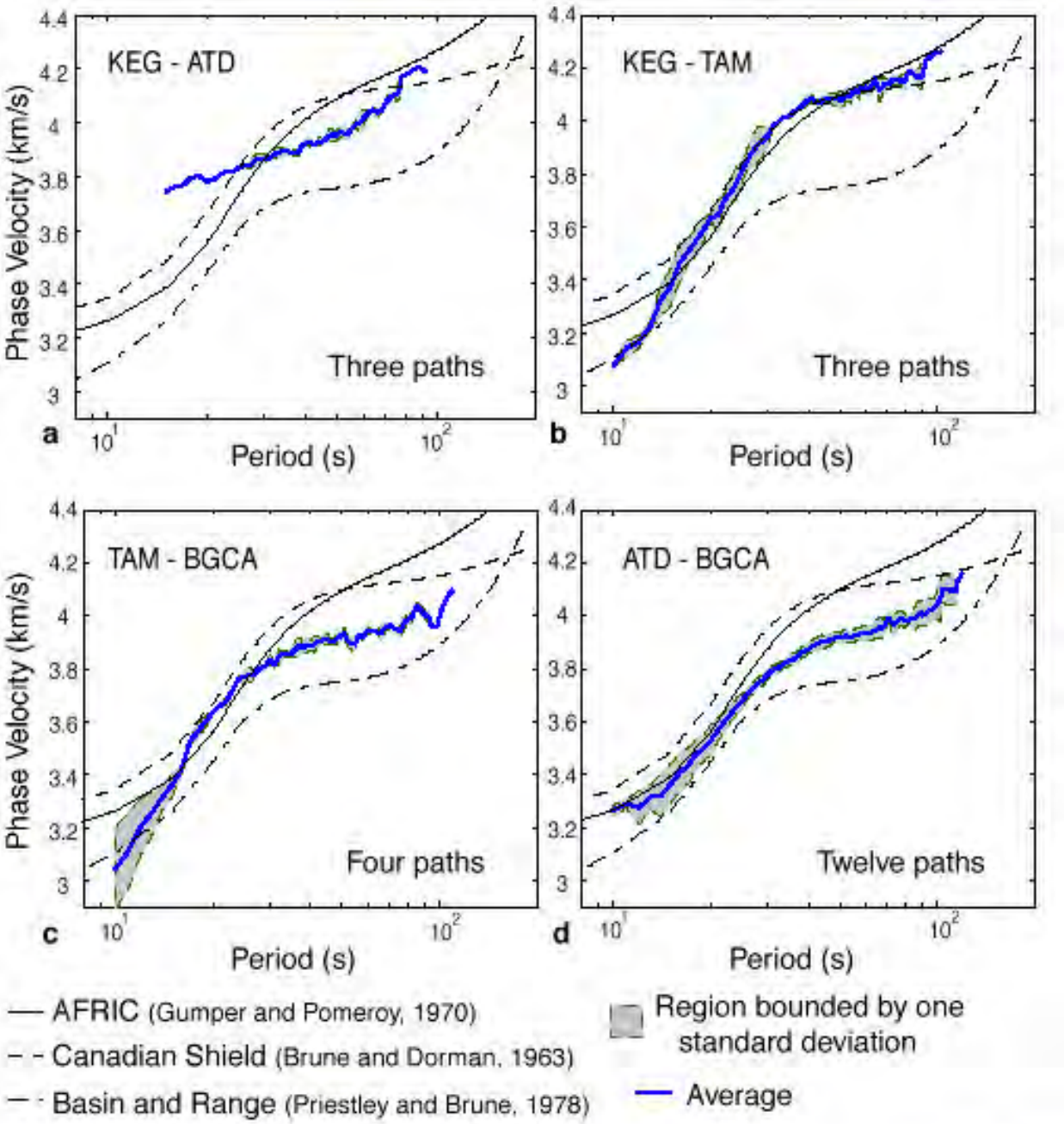


Figure 4. Panel a shows the average of the three phase velocity curves calculated between the broadband seismic stations, KEG and ATD. One of these curves represents a reversal of propagation direction. Panel b depicts the average of the three phase velocity curves calculated between the stations, KEG and TAM. One of these curves represents a reversal in propagation direction. Panel c depicts the average of the four phase velocity curves calculated between TAM and BGCA. Two of these curves represent a reversal of propagation direction. Panel d shows the average of the twelve phase velocity curves calculated between the stations, ATD and BGCA. Five of these curves represent a reversal of propagation direction. The averaged results found in this study are compared to phase velocity curves calculated from three reference models; AFRIC (Gumper and Pomeroy,1970), Canadian Shield (Brune and Dorman, 1963), and Basin and Range (Priestley and Brune,1978)

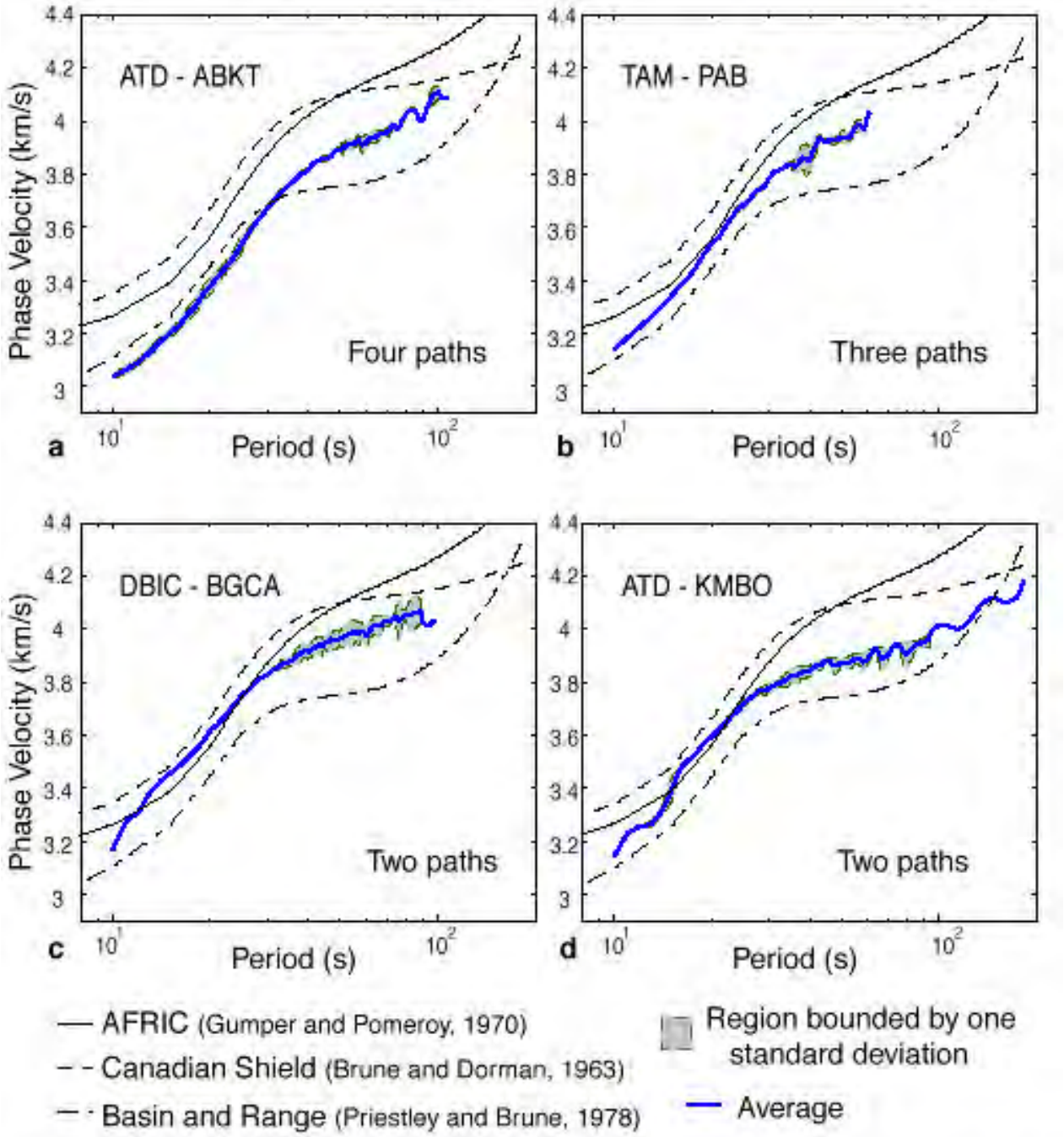


Figure 5. Panel a shows the average of the four phase velocity curves calculated between the broadband seismic stations, ATD and ABKT. Two of these curves represent a reversal of propagation direction. Panel b depicts the average of the three phase velocity curves calculated between the stations, TAM and PAB. None of these curves represent a reversal of propagation direction. Panel c depicts the average of the two phase velocity curves calculated between the stations, DBIC and BGCA. None of these curves represent a reversal of propagation direction. Panel d shows the average of the two phase velocity curves calculated between the stations, ATD and KMBO. One of these curves represents a reversal of propagation direction. The averaged results found in this study are compared to phase velocity curves calculated from three reference models; AFRIC (Gumper and Pomeroy,1970), Canadian Shield (Brune and Dorman, 1963), and Basin and Range (Priestley and Brune,1978)

MODELING REGIONAL SEISMOGRAMS

Don Helmberger, Sidao Ni, and Chen Ji
Geological and Planetary Sciences Division, Seismological Laboratory
California Institute of Technology

Sponsored by U. S. Department of Defense
Grant Number DSWA01-98-1-0010

ABSTRACT

Retrieving source characteristics of moderate-sized earthquakes in sparsely instrumented regions has been made possible in recent years, through the modeling of waveforms at regional distances. The techniques used in such studies model waveforms with some success at long period, using Green's functions for simple ID crustal models. For small earthquakes (M < 4), however, long-period signals are usually noisy and modeling shorter- periods requires refined Green's functions such as used in the empirical Green's functions approach. We are attempting to solve this problem by developing three approaches with varying degrees of empirical versus analytical methodologies. Approach (1), Pseudo Green's functions (Song and Helmberger, *BSSA*, **88**, 1998) uses observations from master events in conjunction with ID Green's functions as calibrations to correct for phase derivations. Approach (2) is more analytical which we call waveform tomography that generates ray responses derived from existing tomographic models. First, the ray paths from the ID layered reference model are used to localize each ray segment, where the anomalous velocities are applied by overlay, as in tomography. Next, new p_i (t_i) (p_i ray parameter, t_i travel time) are computed to satisfy Snell's law along with their numerical derivative ($\delta p/\delta t$), which can be used to construct a synthetic seismogram similar to the WKBJ method, or can be used to construct more exact Cagniard-style 2D synthetics. These individual ray responses are allowed to shift in relative timing and summed to better fit a set of observed waveforms aided by a simulated annealing code to optimize. Approach (3), inputs a profile of waveform data and produces a 2D model by direct inversion using a combination of analytical and numerical propagators (Chen *Ji et al., BSSA*, 1999, in press). This approach addresses complex structures, basins, etc., and requires data coverage. We are testing these methods against examples chosen from the TriNet (Southern California) dataset, 400 events recorded broadband with over 80 stations for some events. Preliminary applications reveal strong lateral variation near the crustal surface (± 20% in upper 3 km) with a particularly strong dependence on geology above the sources and approaching the individual stations.

Key Words: Waveform tomography; Source Inversions; 2D Synthetics; Waveform Modeling.

OBJECTIVE

We are developing methods aimed at providing a systematic means of calibrating paths for small events. The basic idea is to use large events (Masters) where locations and source parameters are reasonably well known to calibrate those particular paths to stations that observe smaller events as well, usually regional. The waveforms at a local station are then used to construct Pseudo-Green's functions which can be used to characterize still smaller events.

In this report, we will discuss efforts conducted on two tasks:
(1) Further development of Pseudo-Green's functions for use with sparce datasets (2 stations).
(2) Automate the comparison of observations with synthetic predictions from Tomographic models (Local and Global).

RESEARCH ACCOMPLISHED

In a recent paper on locating events in Pakistan, Zhu *et al.* (1997), we discuss the problems of locating events between two modern broadband stations (NIL and AAK) by using waveform modeling. The procedure worked well for deep events but became more difficult for shallow events. Here we investigate some of the propagational complexities involved in regional modeling where we have a large set of observations (TERRAscope) so that distortions can be easily assessed.

A relatively large number of regional events (500) have been recorded broadband with the implementation of modern equipment, especially in southern California (80 Stations). This data contains an immense amount of information about source processes (frequency-dependence) and crustal structure, but to unscramble these features proves very difficult. Most efforts to date have concentrated on the recovery of source parameters; namely, the Regional Centroid Moment Tensor (RCMT) solution using long-period surface wave (Ritsema and Lay, 1993). For events larger than M_w>5, it is possible to invert surface wave records for periods greater than 50 seconds assuming the PREM model (Dziewonski and Anderson, 1981) for all the western United States, essentially the standard CMT procedure. At shorter periods, the surface waves show regional variation and corresponding regionalized models are required (see for example, Patton and Zandt, 1991; Thio and Kanamori, 1992).

A second method, Dreger and Helmberger (1990), uses the relative strengths of the observed bodywaves to surface waves compared with synthetics to determine mechanisms, moment, and depth. Often, only one station is sufficient to fix the source parameters, since S and sS (SV and SH) are strongly dependent upon source orientation. By cycling through source depths, the proper timing between P and pP, S and sS, etc. allows accurate depth estimates. This approach works best at periods greater than about 5 seconds to stabilize the inversion. The biggest difficulty with this approach is that local fluctuations in arrival times, especially surface waves, requires highly localized structures. A useful modification (Zhao and Helmberger, 1994) uses a grid search and matches observed broadband seismograms against synthetics over discrete phases so that the beginning portion of records, which contains extended P-waves, can be shifted a few seconds relative to the later arriving surface waves. This approach, called the Cut and Paste method, desensitizes the crustal model used to generate the synthetics. A refinement, Zhu and Helmberger (1996), downweights nodal stations which further stabilizes the technique and allows automated source retrieval. We now determine the source characteristics within 5 minutes of an event occurrence.

An application of the code to Landers aftershocks was recently reported on by Jones and Helmberger (1998), see Fig. 1, where the size of the focal spheres indicates the relative magnitudes. A sample of the waveform fits (tangential component) for some of these events at PFO and GSC are displayed in Fig. 2. Note that only two events, events 24 and 31, are deep which is quite obvious based on the absence of significant surface waves. Other obvious source features are the lowest stress-drop event (19) and the highest (24), as is apparent from their relative long-period nature. Note that these source parameters were determined by the full TERRAscope array.

These synthetics were generated from the Jones model, and contain the various mechanisms and appropriate depths. Many of the fits are quite good with noticeable S_mS and sS_mS phases. The station PFO

has a particularly strong sS_mS relative to S (first arrival) for events 9 and 7, while sS_mS at station GSC is not so obvious. Thus, we need to address the issue of modeling such obvious complexity with some type of automation because of the large number of data becoming available. Developing such a technique is the main objective of this report where we will assume the sources are known and search for a 2D model compatible with observations at GSC and PFO.

Method (Ray-Shifting)

Our waveform modeling approach has been discussed in detail earlier in Song and Helmberger (1998). From the generalized ray theory (Helmberger and Engen, 1980), a synthetic seismogram consists of a series of ray responses that describe energy packets arriving at the receiver along various paths as displayed in Fig. 3. If we allow each ray response to shift in time and to vary in amplitude, synthetic fits to data can be dramatically improved. The more freedom we allow in the process, the better the synthetic fits to data. Our practice is to parameterize the problem so that the travel time of each ray response is associated with a block velocity model. Previous studies have shown that mild changes in model geometry lead to similarly shaped single ray responses (Song and Helmberger, 1996). The travel time of an individual ray is controlled by the integral slowness along its path, which allows relatively coarse model parameterization. The amplitudes of the ray responses, however, are more sensitive to the velocity perturbation and usually depend on very local changes in the velocity model. Changing the amplitude of individual rays, compared to changing their travel time, proves relatively harder to achieve with only a few blocks in the velocity model. To tackle this complexity, we adopt a two-step modeling approach. The first step is to fix the amplitude of each ray response based on the ID model and focus on the timing effect of the model parameterization. Then as we find velocity models that better explain the waveform data based on improvement to the timing of individual rays, we study the amplitude effect with ray synthetics based on the improved, now 2D, velocity models.

Our modeling involves multiple parameters. Event depth, origin time, and model velocity along an individual ray path all contribute to the timing of the ray response. With each set of parameters, individual ray responses are shifted differently in time, with their interference constructing a new synthetic seismogram. The problem is defined in terms of obtaining an optimal set of parameters that minimizes the least square error between data and synthetics. The search is conducted with a simulated annealing algorithm, as discussed in several recent seismological studies (e.g., Sen and Stoffa, 1991; Zhao and Frohlich, 1996). The reconstruction involves shifting back all the surface wave forming rays, a fraction of a second for the first ray, and gradually increasing to over a second for the last ray. The three rays forming S_mS are shifted differentially with the middle trace moving back slightly. These small adjustments produce a relatively good match of synthetic to observed waveform, although the ratio of S to S_mS is too large in the synthetic relative to the observed. The latter feature is difficult to correct without attenuating S or introducing more complex structure along the path.

Since surface multiples can easily overwhelm S_mS and sS_mS, we damp the penalty of misfit with time, thus emphasizing the fit over the time interval particular to the down-going rays. To do this, we applied to both the data and the synthetics a damping factor f (t), defined as a function of time t. f (t) = 1 for $t <= t_0$, and f(t) = e ** $[(t-t_0) / (t_1-t_0)]$ for $t > t_0$ ($t_0<t_l$). Time constants t_0 and t_1 are marked with vertical bars in Fig. 3. With this damping factor, the beginning of the observations is emphasized in the inversion and it places more resolution on the model recovery of the deep crust.

As demonstrated in Fig. 3, a small shift in timing of S_mS relative to direct S can usually improve fits. The flexibility provided by the interference with the two neighboring reflections is also very useful in modeling the S_mS triplication. Adjusting the timing in the surface layer multiple can likewise improve fits, although we have downweighted their contributions to concentrate on the deeper structure.

Results of Numerical Experiments

Preliminary runs revealed a tendency for faster velocities to occur towards the west. Thus, we allowed a separate set of boxes for the section west of the San Andreas although such a boundary cannot be identified precisely. We also experimented with a set of boxes for the surface layer. Results assuming 3 surface layer

sections are given in Fig. 4. Since it is difficult to judge how significant any particular simulation may be, we started by comparing inversion results as a function of the number of events used in the modeling, in particular 7, 19, and 25. The events chosen are indicated in Fig. 1 and have been picked to be representative of the population. The results proved quite stable with very rapid changes in the surface layers ranging over ± 13%. The section enclosing the upper Coachella Valley appears particularly slow which might be expected. Actually the surface variation in this section is quite compatible with local geology as can be seen by comparing with Fig. 1 where the mountainous region appear relatively fast relative to the basins. Numerous other results with different assumptions involving more blocks and allowing the sources to move are discussed in Helmberger *et al.* (1999). (Preprints available at the meeting).

To obtain better modeling results, we need to regenerate these ray responses with the 2D perturbations to move our synthetics closer to data. This approach appears possible using a new analytical method designed for generating 2D synthetics discussed in the next section, Ni *et al.* (1999) and will be pursued in future efforts. To check solutions, we can use a numerical-interfacing code outlined in Fig. 5. Here we demonstrate the method by considering the profile of stations running across the extended Los Angeles Basin starting at the basin edge, XPO, and forming a rough 2D profile across the basin. Particle motions indicate that the seismic field is predominantly SH (tangential) as displayed in the record section (black lines, lower left). For the region outside the basin, we assume a 1D crustal model, upper right) and analytical techniques to propagate the sources to the basin edge where the motions are interfaced to finite-difference technique (Wen and Helmberger). The method absorbs the uncertainties of the source and 1D propagation to fit the first record exactly; this is essentially a calibration so that the synthetic fits XPO by definition. We start by assuming a simply layered model. The three numbers accompanying each trace indicate the goodness-of-fit (synthetic to observation), the amplitude ratio, and the timing shift. For example, at DOW the misfit is (.56), the synthetic is smaller than the data by (.32) and it is late by 2.16 sec. We want to drive these numbers to (0,1,0). To improve the fit, we parameterize the layers with linear dipping segments between the inflection points which are allowed to vary. We generate numerical derivatives and apply a conjugate gradient inversion to refine the structure resulting with a new model. See Chen Ji *et al.* (1999) for details on the new method.

Preliminary Results on Global Models

New seismologic investigations of the Earth are capitalizing on the exponential growth of high quality waveform data. For example, Hendrik van Heijst, Jeroen Ritsema, and John Woodhouse (Spring AGU meeting) have teamed to produce a high order Global model. It contains data from all the networks, over 100,000 higher mode paths along with a huge collection of bodywave travel times, including complex paths (SP, S_cP, and multiples of P and S). This model is just now reaching completion and will be used to predict broadband synthetics in the near future. However, a considerable gap exists between global, large-scale seismological studies and higher resolution regional waveform analysis. For example, most global tomographic inversions do not incorporate triplication data caused by seismic discontinuities in the mantle, essentially attributing any associated travel-time anomalies to volumetric heterogeneity. Similarly, most waveform modeling uses globally averaged 1D seismic reference models focusing on isolated regions without consideration of the significant geographical variations in velocity. This disconnect between seismic inversion techniques often makes it difficult to isolate local structure from broader anomalies distributed along the ray paths. To rectify this, we have introduced physical models based on compositional states where a mapping is performed to infer temperature and the behavior of phase transitions, allowing depth-dependent behavior. Figures 6 and 7 display the application of this procedure to Grand's tomographic model. One such mantle feature in regional models is a seismic travel time triplication attributed to a sharp 2-3% seismic velocity discontinuity about 250 km above the core-mantle boundary, Lay and Helmberger (1983). The primary evidence for the triplication is an additional phase, S*cd*, arriving between the direct, *S*, and core-reflected, *ScS*, shear wave phases in approximately the 65^o-83^o distance range. The relative timing and amplitudes of the three phases experience significant regional variations. In some regions, the triplication is clearly displayed while becoming difficult to detect in others, suggesting an intermittent D" discontinuity, see Wysessions *et al.* (1998). Alternatively, the observed spatial intermittence of the triplication may be attributed to variations of the local seismic velocity gradients accompanying a substantially smaller (≈1%) velocity jump as displayed in Fig. 7. To determine the properties of the model, we compute the differential travel times between the various phases as in Fig. 6b and adjust the

parameterization (Clapeyron slope, percentage phase jump in velocity, etc.) to calibrate to datasets (Lay's differential times in this case). The triangles are stations and stars are events. Thousands of 2D synthetics generated for the various paths are compared against data in an automated fitting procedure, Sidorin *et al*. (1999). In most cases, this physical model predicts better fits to the seismic observations than the original 1D modeling exercises.

CONCLUSIONS AND RECOMMENDATIONS

The present plan of the PIDC is to improve locations by introducing source and stations corrections determined from ground-truth events (GTX). Although this appears to be working well, we will still be faced with particular problem events (New Year's event). In this case, being able to use the whole seismogram and interpret it in terms of travel paths and test what we would expect from the best 3D model for the particular region remains valuable. Another issue is the lack of waveform information use in definitions of ground-truth events for GTX's > 5. At least in Southern California, local modeling is forcing travel-time routines to be modified to yield source locations more compatible with waveform modeling, Luccio *et al.* (1999). In particular, the distribution of SCEC events with depth was (5.6 ± 4.4) while in waveform modeling, it was (11.9 ± 3.7 km). The latter estimates are proving to be the more accurate. Perhaps, a workshop addressing these issues would be helpful.

REFERENCES

Dreger, D., and D. V. Helmberger, Broadband Modeling of local earthquakes, *Bull Seismol Soc. Am*., **80** (5), 1162-1179, 1990.

Dziewonski, A. M., and D. L. Anderson, Preliminary Reference Earth Model, *Phys. Earth Planet. Int*, **25**, 297-356, 1981.

Helmberger, D. V., and G. R. Engen, Modeling the long-period body waves from shallow earthquakes at regional ranges, *Bull Seismol. Soc. Am*., **70**, 1699-1714, 1980.

Helmberger, D. V., X. J. Song, and L. Zhu, Crustal Complexity from Regional Waveform Tomography: Landers Aftershocks, submitted to *JGR,* July 1999.

Ji, Chen, D. V. Helmberger, and D. J. Wald, Basin Structure Estimation by Forward and Inversion Methods, submitted to *BSSA*, May 1999.

Jones, L. E., and D. V. Helmberger, Earthquake Source Parameters and Fault Kinematics in the Eastern California Shear Zone, *Bull. Seismol. Soc. Am.,* **88**, No. 6, 1337-1352, 1998.

Lay, T., and D. V. Helmberger, A lower mantle S-wave triplication and the shear velocity structure of D", *Geophys. J R. astr. Soc.* **75**, 799, 1983.

Luccio, F., L. M. Jones, L. Zhu, E. Hauksson, and D. V. Helmberger, Resolution of focal depth determinations in Southern California, submitted to *BSSA,* 1999.

Ni, S., X. Ding, and D. V. Helmberger, Constructing Synthetics from Deep Earth Tomographic Models, submitted to *GJI,* May 1999.

Patton, H. J., and G. Zandt, Seismic Moment Tensors of Western U. S. Earthquakes and Implications for the Tectonic Stress Field, *J Geophys. Res.,* **96**, 18,245-18,259, 1991.

Ritsema, J., and T. Lay, Rapid Source Mechanism Determination of Large ($M_w \geq 5$) Earthquakes in the Western United States, *Geophys. Res. Lett.,* **20**, 1611-1614, 1993.

Sen, M. K., and P. L. Stoffa, Nonlinear one-dimensional seismic waveform inversion using simulated annealing, *Geophysics,* **56**, 1624-1638, 1991.

Sidorin, I., M. Gurnis, and D. V. Helmberger, Bridging the Gap Between Seismic Tomography and Waveform Modeling: Constraints on the Origin of Structures at the Base of the Mantle, submitted to *Science,* 1999.

Song, X. J., and D. V. Helmberger, Source estimation of finite faults from broadband regional networks, *Bull. Seismol. Soc. Am*., **86**, 797-804,1996.

Song, X. J., and D. V. Helmberger, Pseudo Green's Functions and Waveform Tomography, *Bull. Seismol. Soc. Am.*, **88**, No. 1, 304-312, 1998.

Thio, H. K., and H. Kanamori, Moment Tensor Inversions in Southern California Using Surface Waves recorded by TERRAscope (abstract), *EOS Trans. AGU*, 73,376, 1992.

Wysession, M.E. et al., in *The Core-Mantle Boundary Region*, M. Gurnis, M.E. Wysession, E. Knittle, B. Buffet, Eds., *Geodynamics Series*, Vol. 28 (American Geophysical Union, Washington, DC, 1998), pp.273-297.

Zhao, L.-S., and D. V. Helmberger, Source Estimation from Broadband Regional Seismograms, *Bull Seismol. Soc*. *Am.,* **84**, 91-104,1994.

Zhao, L.-S., and C. Frohlich, Teleseismic body-waveforms and receiver structures beneath seismic stations, *Geophys. J Int*., **124**, 525-549, 1996.

Zhu, L., and D. V. Helmberger, Advancement in source estimation techniques using broadband regional seismograins, *Bull Seismol Soc. Am*., **86**, 1634-1641, 1996.

Zhu, L., D. V. Helmberger, C. Saikia, and B. B. Woods, Regional waveform calibration in the Pamir-Hindu Kush region, *J. Geophys. Res*., **102**, 22,799-22,813, 1997.

Zhu, L., and H. Kanamori, Moho Depth Variation in Southern California from Teleseismic Receiver Functions, submitted to *JGR*, March 1999.

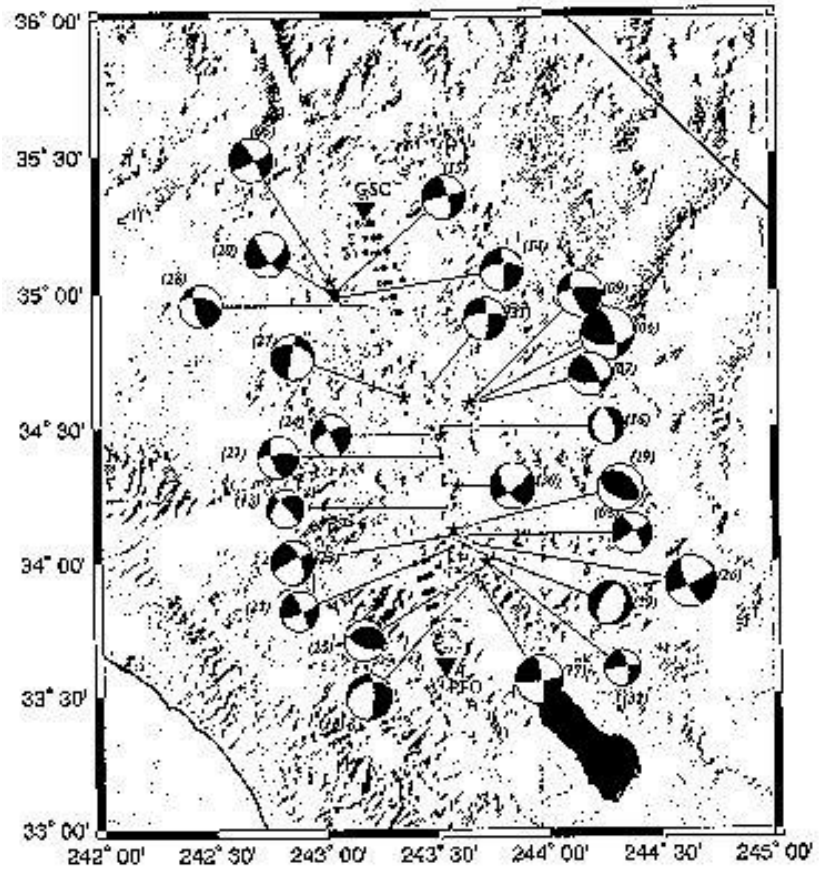


Figure 1. Topographic map of Southern California showing Landers aftershocks as black, white, and gray stars. The source mechanisms are after Jones and Helmberger (1998). The size of the focal spheres is proportional to the event magnitude. Two stations, GSC and PFO, are shown as dark triangles. The small dots indicate surface reflection points of ray paths for sS_mS phases (near events) and surface multiples of up-going S(near stations). The darkness of these dots indicates phase strength relative to a 1D-reference model.

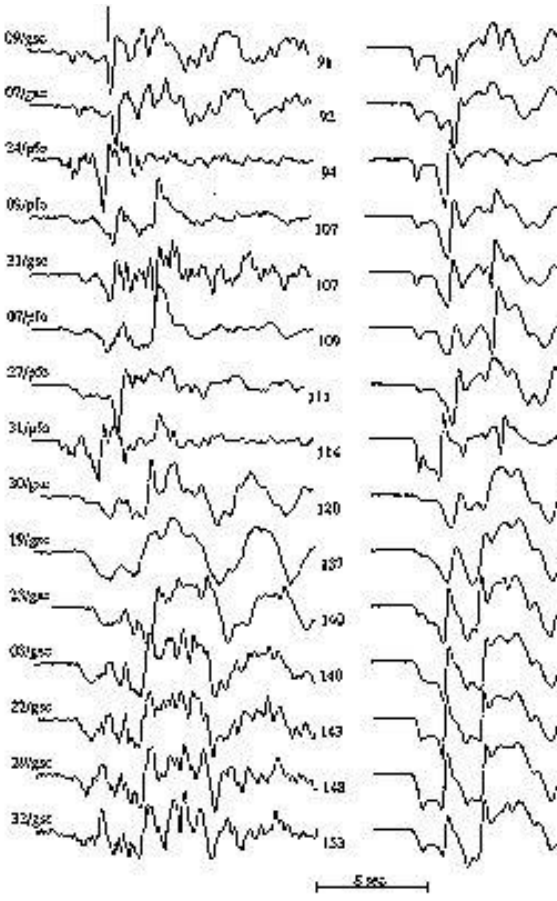
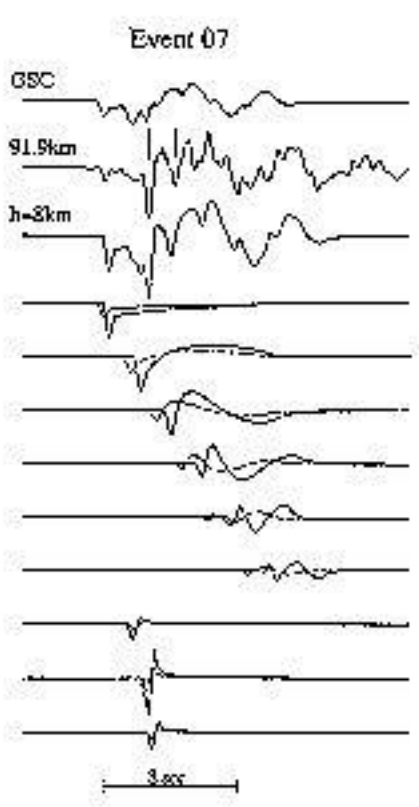


Figure 2. Comparison of observations (left) with sy
predicted from source estimation (Jones and Helmb
have been plotted on a reduced velocity section (t -
time shifts found by the source-shifting procedure. N
arrive early (event 31 at PFO) and shallow events la
The range estimates and depths have been included
the right.



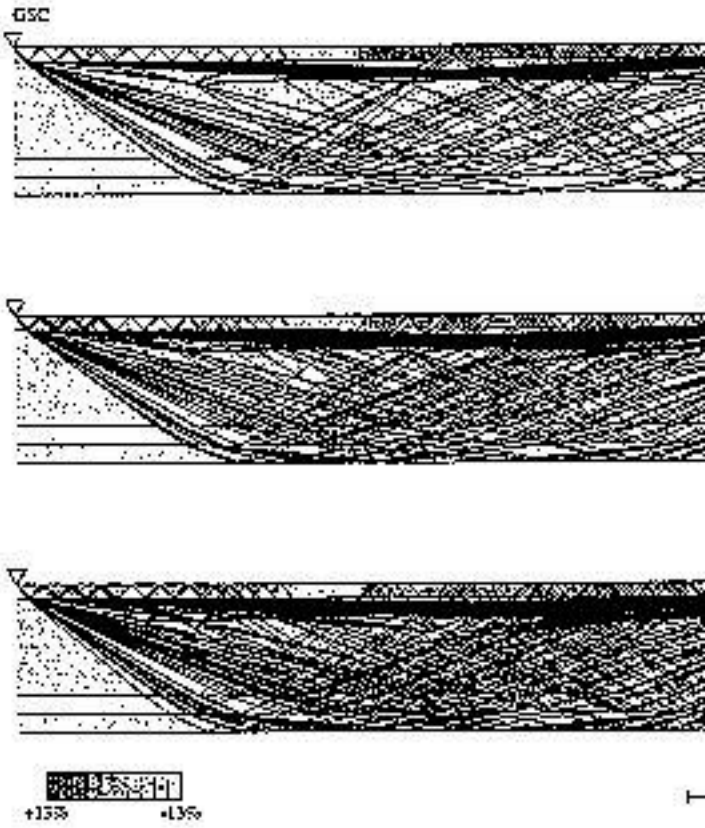


Figure 3. Pseudo-Green's function simulation procedure. The top trace displays the synthetics constructed from 1D Green's function with appropriate mechanism and moment. Middle trace displays data, and lower trace displays the Pseudo-Green's function. An amplification factor has been added to maximize the correlation with the data since the moment estimate comes from the network average and does not necessarily agree with individual observations. The lower set of traces show the shifting of the surface waves (direct plus surface multiples, 6 responses, and the bottom three include the SS rays). Note the small shifts back in time to match the data, dotted (original) and solid (shifted).

Figure 4. Comparison of results as a function of the numb used. Upper panel shows result of inversion using 7 event Fig. 1); middle panel, 19 events (black and white stars); a 25 events (all stars). The upper layer is divided into three lower layers have only one division assumed to be at roug Andreas fault boundary. In these inversions, source depth move by up to 3 km and event origin time can vary by up

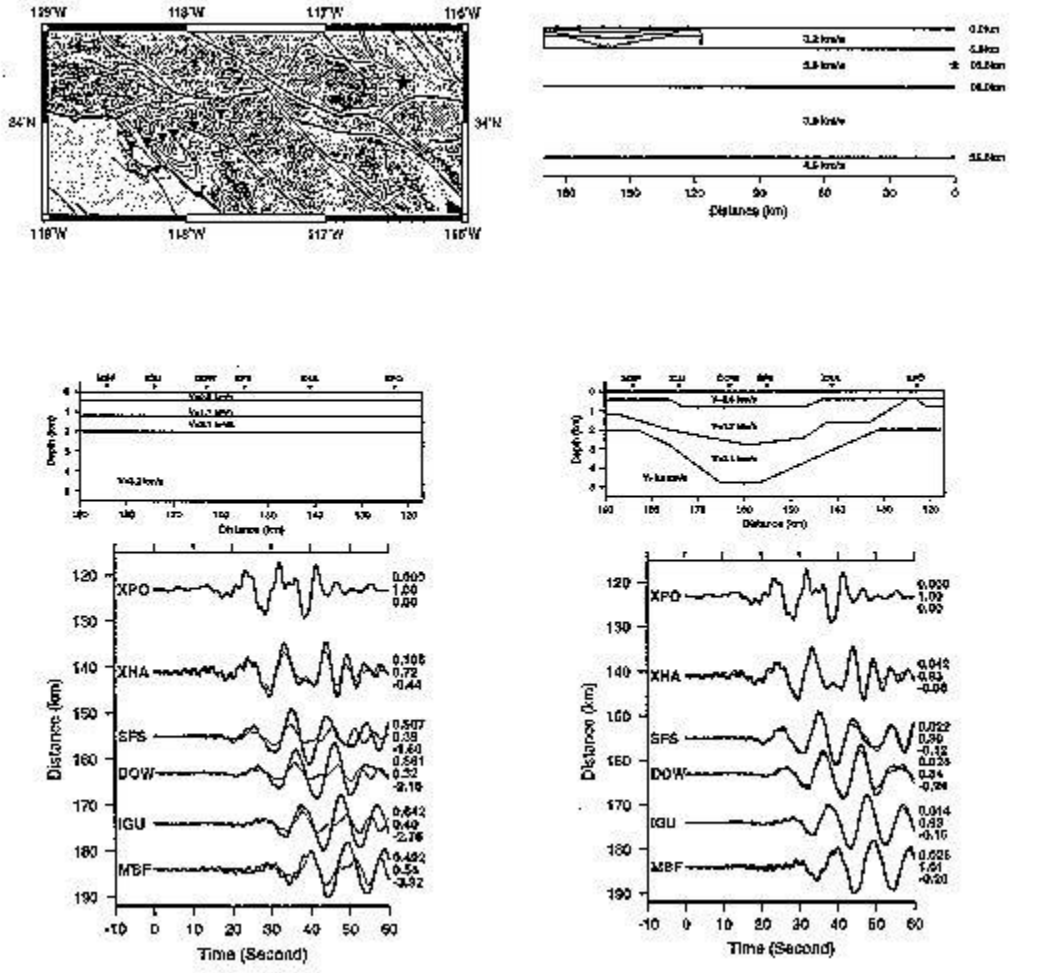


Figure 5. Layout of the waveform inversion procedure. Map of Southern California from Landers (star) to Los Angeles (contours of sediments). The full final model is shown in upper right; the analytical solution is interfaced at the shaded box edge. The initial model along with a comparison of synthetics with observation (black lines) is shown in the lower left. In the lower right, a comparison is made between observed and synthetic seismograms after adding basin structure

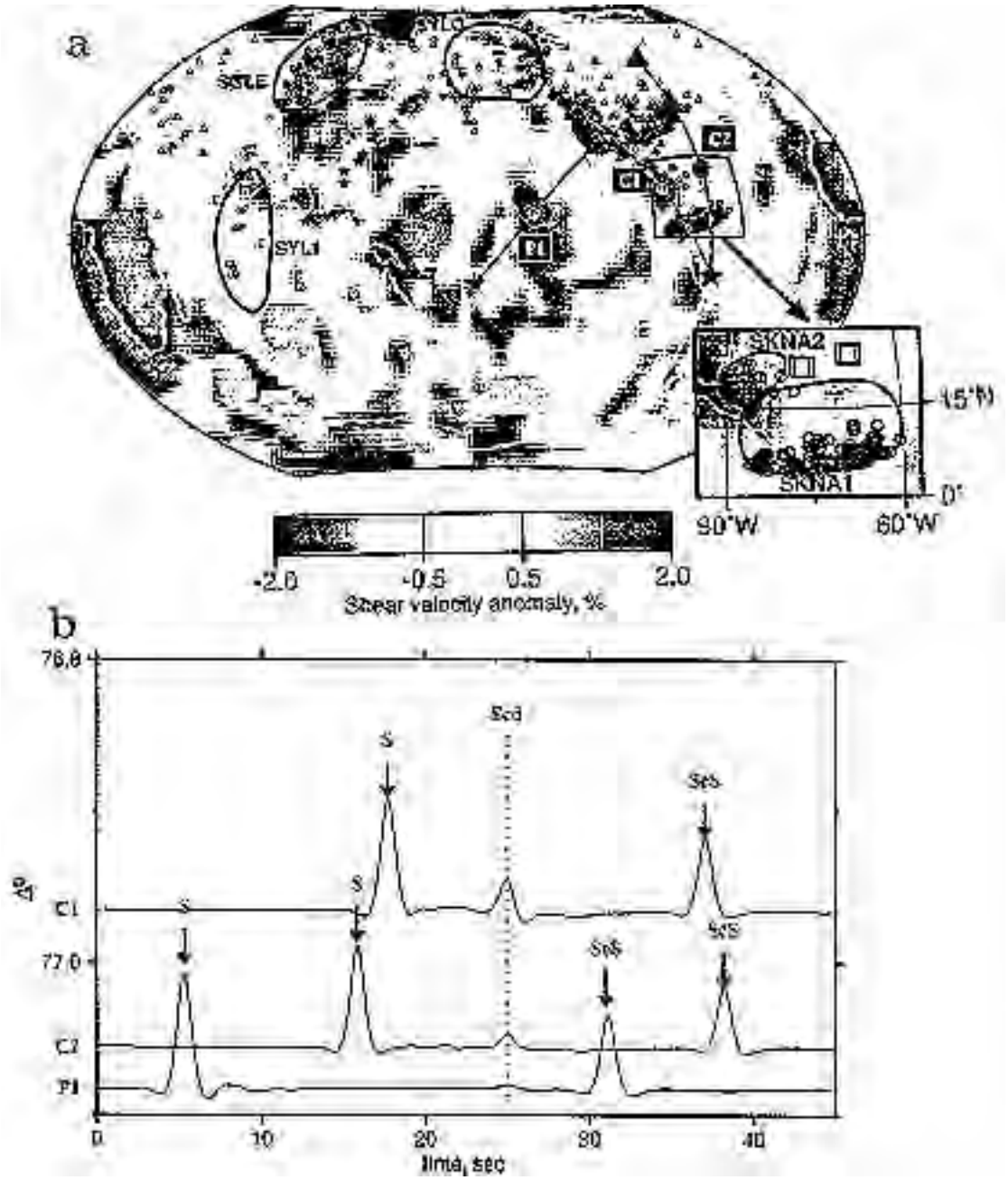


Figure 6a. Seismic observations of the D" triplication: events (stars) and stations (triangles) used in the study by Sidorin *et a1.* 1999). Circles show surface projections of *ScS* bounce points for the paths that are considered. The regions with strong observed D" triplication are shown by heavy contours and the names of the corresponding seismic 1D reference models are given next to the contours. The squares in the inset indicate *ScS* bounce points beneath Central America for ray paths that do not show any evidence for a D" triplication. The three highlighted paths are used in Fig. 7 to illustrate the sampled structure at the base of the mantle and its influence on the predicted seismic waveforms. The background color represents the shear velocity in the lowermost 240 km of the mantle, Grand (1994). **Figure 6b** indicates the relative strength of the D" triplication for central Pacific and Central America predicted by the preferred model. 2D synthetic waveforms (Green's functions from)WKM, Ni *et al.* (1999) computed for paths C1, C2, and P1 (cross-sections along these paths are shown in Fig. 7). The waveforms are normalized by the amplitude of direct S and aligned by the *Scd* peak.

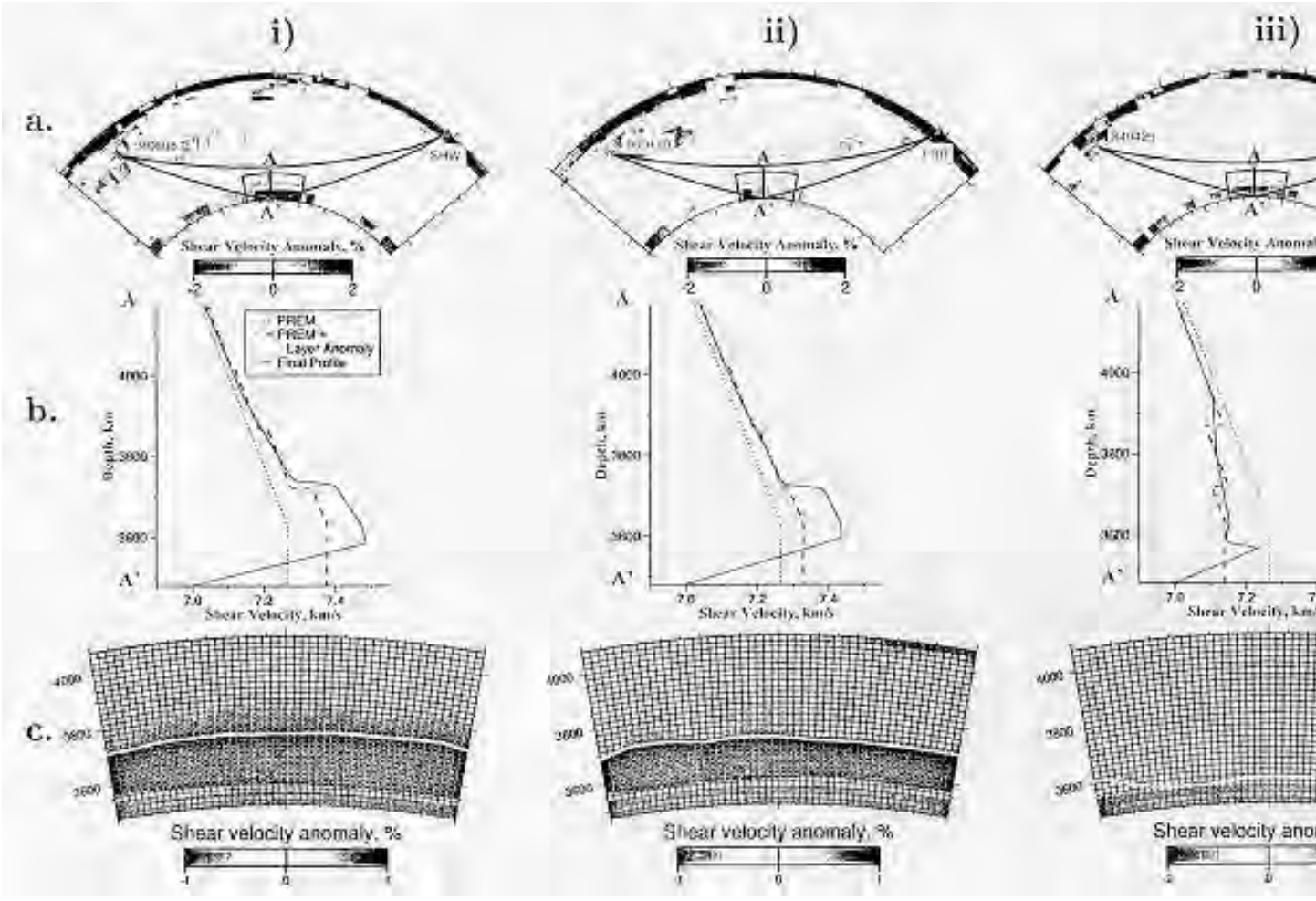


Figure 7. Shear velocity cross-sections along the ray paths highlighted in Fig. 6a. (i) Event 940808 to station SHW (path C1); (ii) even
C2); (iii) event 840425 to station PFO (path P1). (a) Cross-sections through Grand's tomography model. Direct (*S*) and core-reflected (*
Peturbing a vertical column to incorporate a discontinuity using cross-section A-A' indicated in (a) as an example. The gray shade show
tomography model. Dotted line shows PREM; dashed line shows the block anomalies (PREM values with added tomography velocity
line shows the final profile obtained by adding a discontinuity and a compensating negative gradient at the base. (c) Final composite m
respect to PREM) for the region marked in (a). The grid lines of the fine mesh are shown (every other line is plotted horizontally, and
vertically) and the phase boundary is indicated by the white line. The phase transition in (b) and (c) is characterized by h_{ph} = 200 km an

JOINT INVERSION OF RECEIVER FUNCTIONS AND SURFACE-WAVE DISPERSION FOR CRUSTAL STRUCTURE

R. B. Herrmann[1], C. J. Ammon[1], J. Julià[2] and T. Mokhtar[3]
[1]Department of Earth and Atmospheric Sciences, Saint Louis University
[2]University of Barcelona, Barcelona, Spain
[3]King Abdulaziz University, Jeddah, Saudi Arabia

Sponsored by DSWA
Contract No. DSWA 01-98-C-0160

ABSTRACT

A program for joint inversion of teleseismic receiver functions and surface-wave dispersion measurements has been implemented by merging existing inversion programs. The purpose of this effort is the implementation of an algorithm that draws upon the true capabilities of each technique in a manner that complements the imperfections of the other. Inversion of single-mode surface-wave dispersion yields a velocity model that cannot resolve crustal velocity discontinuities; the receiver function technique excels at defining impedance changes and travel times but suffers from tradeoffs between velocity and depth. The combination of the two yields a velocity model that is better constrained.

The inversion program uses an a priori participation factor p such that the end members p = 0 or 1 represents an inversion using only one set of observations (receiver function or surface-wave dispersion). We present a formulation that compensates for the different units of the two classes of observations and the number of observations to yield formal, statistical estimates of model error.

The program is tested using surface-wave group velocity dispersion estimated from a surface-wave tomography study in the Arabian plate and teleseismic receiver functions computed usijng seismograms from permanent and portable broadband stations in the region. Initial results are encouraging. Experiments with synthetic seismograms show great potential for resolving relatively fine-scale vertical structure of the crust and crust-mantle transition.

The tool developed here will be available for use in constraining regional structure at existing and planned broadband stations deployed as part seismic monitoring under the CTBT.

Key Words: Surface wave, receiver function, crustal structure, algorithms

OBJECTIVE

The object of this effort is to develop a stable inversion program that simultaneously extracts constraints on regional crustal structure from both surface-wave dispersion curves and teleseismic receiver functions. This work is similar to that performed by Özalaybey et al (1997) but the bandwidth of surface-wave observations is greater and the surface-wave dispersion estimates are extracted from earlier tomographic imaging results. Separate inversions of the two types of data lead to models that contain artifacts that reflect subjective inversion constraints, such as a minimum length or roughness, rather than actual earth structure.

The research community has almost 40 years of experience with computer assisted inversion of surface-wave dispersion data. We have learned that inversion of fundamental-mode dispersion over a limited frequency band is an underdetermined problem. Models consisting of a few constant velocity layers or models consisting of many thin layers can be found that fit the same observations. One would hope that there is similarity in some gross features of these models. It is our experience that surface-waves can constrain mean crustal velocity to a given depth, but cannot easily resolve velocity discontinuities or gradients.

Teleseismic P-wave receiver function inversion has become a standard tool for crustal structure estimation. The receiver function is most sensitive to impedance contrasts, which give rise to converted phases, and to phase travel times, but allows for substantial tradeoff between the depth and velocity above an impedance change.

Joint inversion of these complementary observations should reap the benefits of each, helping to reduce the imperfections of either. The receiver function will tell us something about the nature of strong changes in impedance, such as at the crust-mantle boundary, and the crustal travel times while the surface-wave crustal velocity estimates will permit mapping these times into depth.

The reason this approach is of value to the CTBT program is that the crustal structure beneath seismograph stations can be defined. Work by Ritzwoller et al (University of Colorado) under previous funding has given the research community regionalized surface-wave dispersion curves for much of Eurasia. As CTBT monitoring stations are installed, teleseismic waveforms can be collected during the initial operation (depending on frequency of worldwide large earthquakes) to provide the receiver functions for an estimate of the crustal structure beneath the station.

In the long run, improved estimates in the crustal structure arising from the joint inversion of receiver function and surface-wave dispersion will help improve event location accuracy. For small event analysis, the incorporation of receiver function observations with longer period (> 15 seconds) surface-wave observations typical of tomographic studies could help produce more accurate filters for signal identification and enhancement and eventual source identification. We also believe that this localized structure will permit waveform inversion of regional signals for source identification. The need for a good crustal structure is required for both.

RESEARCH ACCOMPLISHED

1. Design of Goodness of Fit Criteria

The design of an inversion program relies on the awareness that the data,, dispersion and receiver function, have different units, magnitudes, noise and number of observations. Yet we desire in some sense to give each data set equal influence on the final model.o balance the relative importance of each set of observations, we use a parameter p to control the participation of each data set. For a value of $p=0$, only the receiver function data are used, while a value of $p=1$ will mean that only the dispersion data are used..

Specifically the following goodness-of-fit functional is minimized iteratively:

$$S(\vec{x}) = [(1-p)N + pM]\left\{ \frac{(1-p)}{N} \sum_{i=1}^{N} \left(\frac{y_i - Ax_i}{\sigma_{y_i}} \right)^2 + \frac{p}{M} \sum_{j=1}^{M} \left(\frac{z_j - Bx_j}{\sigma_{z_j}} \right)^2 \right\}$$

In this expression the model perturbation for an iteration is given by **x,** N receiver function and M dispersion residuals are given by **y** and **z** respectively. The A and B matrices contain the partial derivativesof the receiver function and the surface-wave dispersion observations with respect to shear-wave velocity. The σ values are estimates of the data standard errors of each data set. This formulation does a number of things: 1) the normalization by the standard error, accounts for the different units and magnitudes of each data set; 2) the division of the normalized residuals by N and M before the summations corrects for the different number of observations within each data set; 3) the coefficent *[(1-p)N+pM]* forces the expression to equal that expected for a stochastic inverse for the end member cases of $p=0$ and $p=1$. This requirement means that the model variance – covariances are obtained directly from the inverse matrix of the normal equations. The formulation can also be viewed as a weighted least-squares procedure. The σ's can be estimated from residuals of fit at each iteration with a minimum positive value for safety and realism. Note that by construction, $p=0.5$ means that each data set has equal influence on the final model.

The present formulation can be easily extended. For example, we can use a damped inversion scheme for stability. We can also apply a smoothing criteria for the model perturbations. Finally the functional could be generalized more by permitting inversion of other data, such as refraction times or event waveforms.

2. Design of Inversion Program

The joint inversion procedure builds upon two existing programs: *SURF* (Herrmann, 1987) for surface-wave dispersion inversion and *BODY* (Ammon, 1990) for receiver function inversion. Julià (1999) developed the program *JOINT* to connect these procedures. The use of the programs and data flow are given in Figures 2.1-2.3.

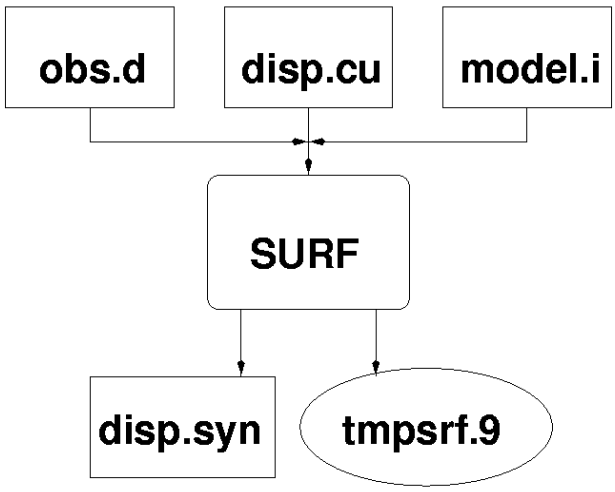


Fig. 2.1. Data flow for the program *SURF*. tmpsrf.9 contains the partial derivatives.

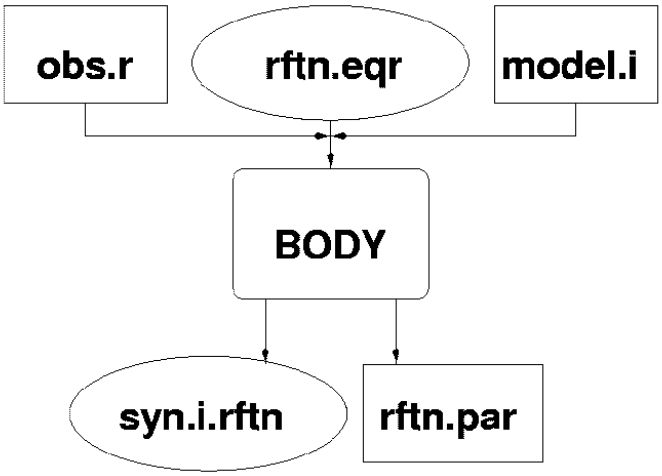


Fig. 2.2. Data flow for *BODY*. Rftn.par contains the partial derivatives

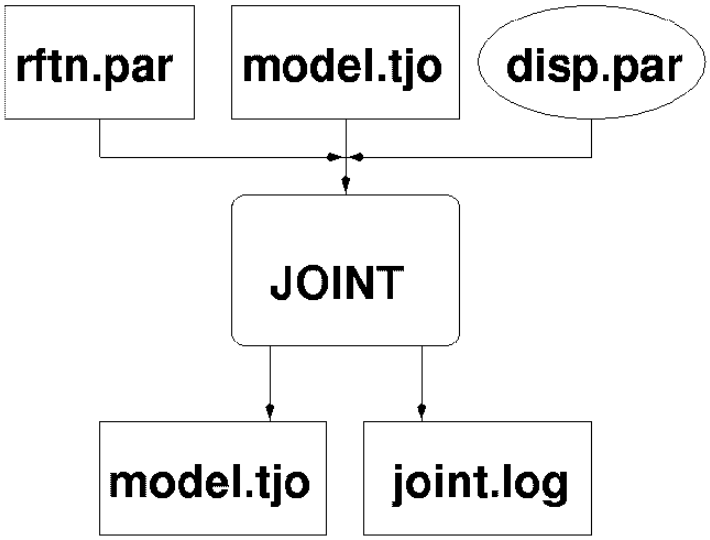


Fig.2.3. Data flow for the program *JOINT*. Model for current iteration is *model.tjo*.

3. Application to Arabian Plate

Seismic wave propagation in the Arabian Plate has been the topic of a number of investigations (Mooney et al, 1978; Sandvol et al, 1999; Mokhtar et al, 1999). To demonstrate the inversion technique we use the surface-wave dispersion observationsof Mohktar et al (1999) and the receiver functions for the station SODA which was part of a special IRIS PASSCAL deployment between November, 1996 and February 1997. Figure 3.1 shows the Arabian plate and the location of the PASSCAL deployment.

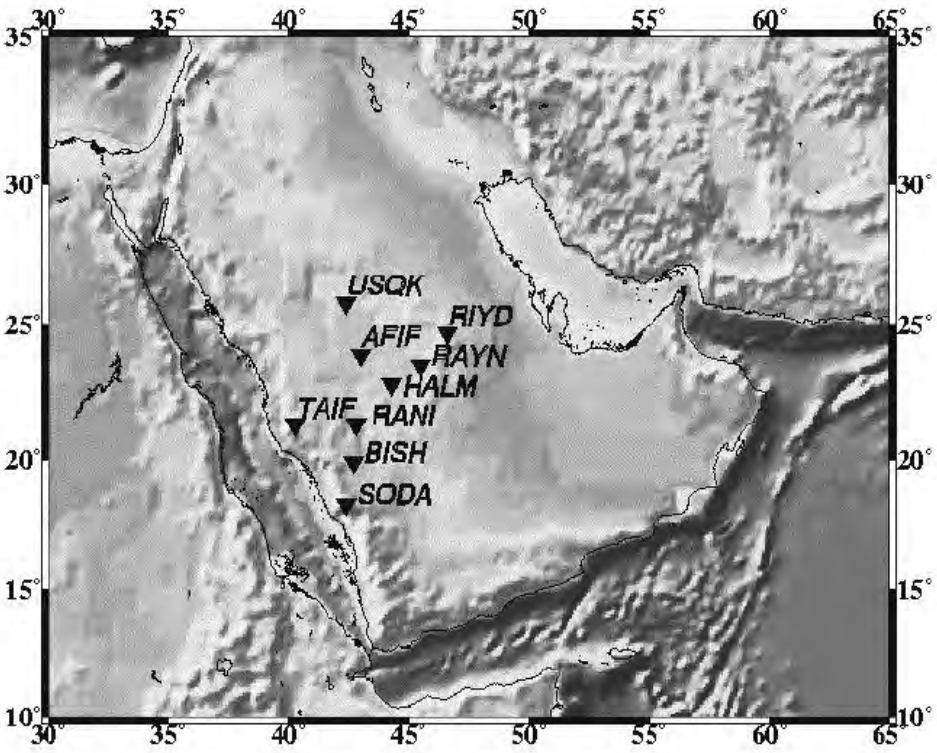


Fig 3.1 Arabian Plate and IRIS station locations.

The station SODA is used for receiver functions since it lies close to the Saudi Arabia refraction line for which crustal models have been published (Mooney et al, 1978). Four teleseisms with magnitudes between 6.1 and 7.0 were used to compute the receiver functions using the methodology of Ammon (1991) and Ammon et al (1990). Mokhtar et al (1999) studied Rayleigh – and Love-wave group velocity dispersion within the Arabian Plate by performing a tomographic inversion using small cells and a spatial smoothing constraint. We use the Rayleigh-wave group velocity dispersion for the cell that contains the station SODA.

Separate inversion were performed using values of $p=0.0$ *(receiver function only and 1.0 (surface-wave dispersion only).* As expected, the fits to each individual observation set were acceptable, but the complementary observations were not matched by the two extremes of the participation factor. In Figures 3.2 to 3.4 we show the inversion results for values of $p=0.1$, $p=0.6$, and $p=0.9$., respectively.

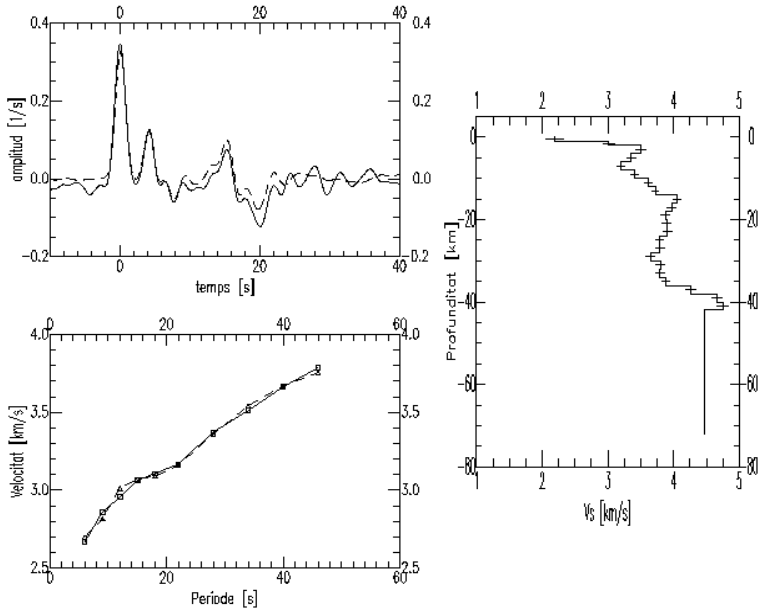


Fig. 3.2. Simultaneous inversion results for *p=0.1.* The receiver function is at the upper left, the surface wave dispersion at the lower right, and the model at the right. The solid line denotes the data and the dashed line the predictions for the model at the right. The fit to both sets of observations is not too bad, but the model has several fluctuations and a rather high mantle velocity

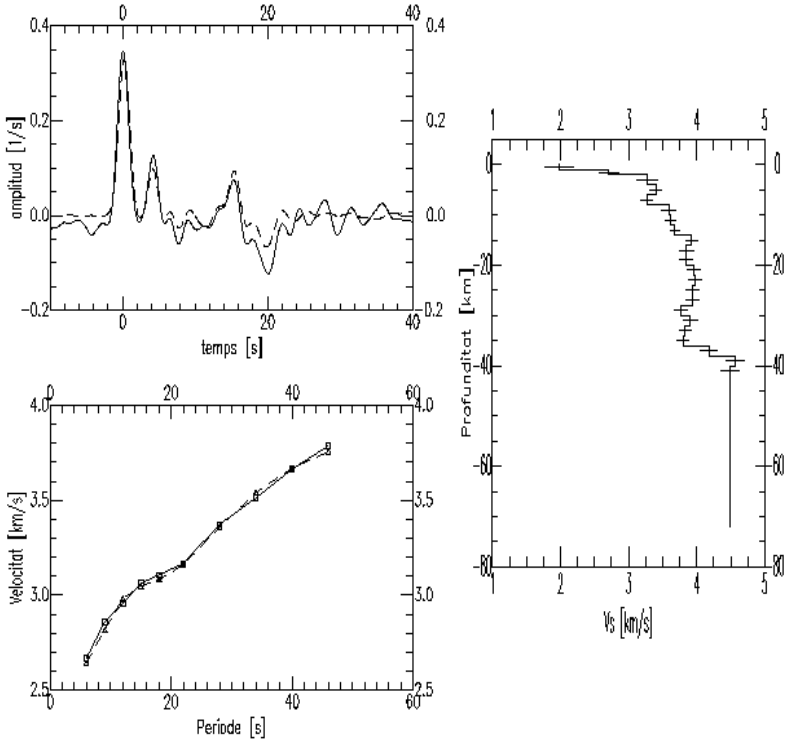
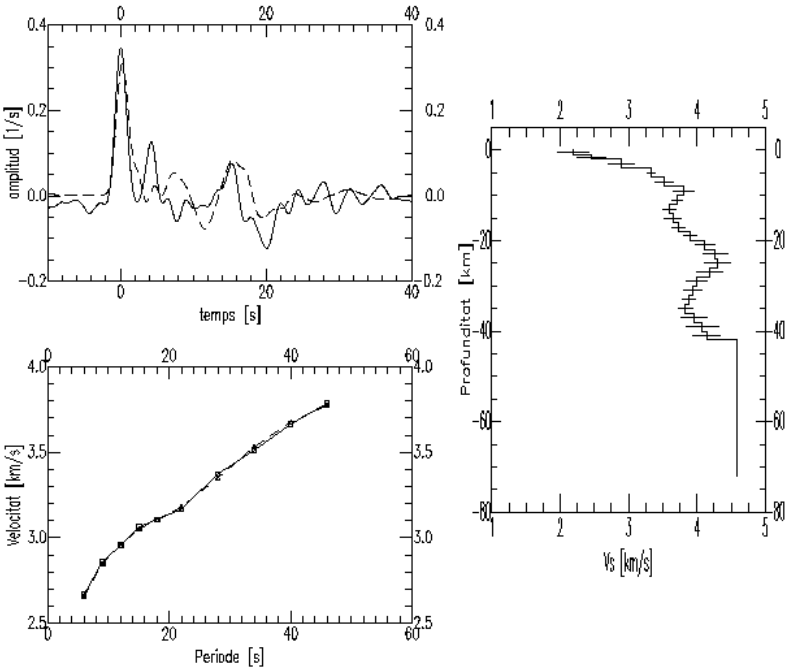


Fig. 3.3. Processing results of *p=0.6* which corresponds to a slightly more favorable weight for the surface-



wave dispersion measurements.

Fig. 3.4. Inversion results for *p=0.9.* For this value, the surface waves are dominant as evidenced by the excellent match to these observations, but a poor match to the receiver function.

In Figure 3.5 we compare the joint inversion results for *p=0.6* with the structure estimated using a refraction profile (Mooney et al, 1978). The results of the joint inversion are very consistent with those obtained in the earlier refraction analysis. Although there are some small fluctuations in the velocity of the thin layers, the overall comparison is quite good. The crustal thickness is particularly consistent, about 40-42 km. Interesting differences are also noticeable. The model from this study has a well-defined, thin near-surface layer with lower velocities and the transition from the crust to mantle appears relatively sharp (which is consistent with the strong P-S conversion in this region seen in the receiver function.

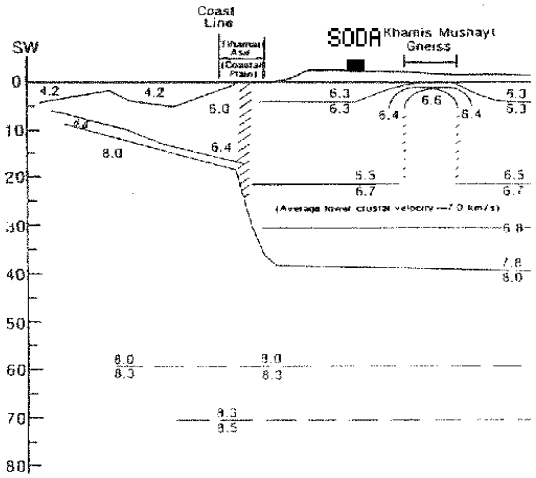
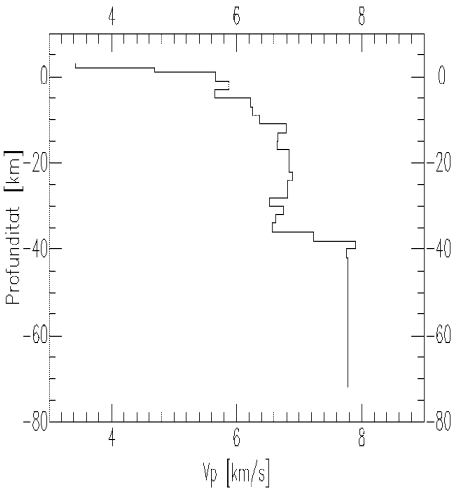


Fig. 3.5 Comparison of $p=0.6$ inversion to Mooney et al (1978) model.



CONCLUSIONS AND RECOMMENDATIONS

This effort has shown that the joint inversion procedure works as expected. Our method differs from that of Özalaybey et al (1997) primarily in the bandwidth of the surface waves and in a goodness of fit criteria, which expilicitly accounts for the different units of the two iobservations (in this case *km/sec* and *sec* $^{-1}$ for the dispersion and receiver function, respectively). We also include an *a priori* parameter thatcontrols which data set has the most influence. In this exercise, many thin layers were used without a differential smoothing constraint. That the $p=0.6$ choice leads to a model that fits the data without perhaps artificial low velocity zones indicates the robustness of the technique.

The success so far supports our initial hypothesis that the joint inversion will produce a more tightly constrained earth model than those arising from separate inversions of either of the two data sets.

During the second year of this effort, Dr. Jordi Julià will join us as a post-doc researcher under another project. He will be available to document the programs and further test the technique with real data sets. The resulting program will be available from the authors as part of their software documentation efforts.

REFERENCES

Ammon, C. J. (1991). The isolation of receiver effects from teleseismic P-waveforms, *Bull. Seism. Soc.Am.,* 2504-2510.

Ammon, C. J., G. E. Randall and G. Zandt (1990). On the nonuniqueness of receiver function inversions, *J. Geophys. Res.,* 95, 15303-15318.

Herrmann, R. B. (1987). *Computer Programs in Seismology,* Saint Louis University, St. Louis, MO.

Herrmann, R. B. (1996). *Computer Programs in Seismology: An overview of synthetic seismogram computation,* Saint Louis University, St. Louis, MO.

Julià, J. (1999).*Inversió Simultània de Funcions Receptores i Corbes de Dispersió,* Doctoral Dissertation, University of Barcelona

Mokhtar, T., C. J. Ammon, R. B. Herrmann and H. A. A. Ghalib (1999). Lithospheric structure beneath Arabia, *PAGEOPH* (submitted).

Mooney, W. D., M. E. Gettings, H. R. Blank and J. H. Healy (1978). Saudi Arabian seismic-refraction profile: A traveltime interpretation of crustal and upper mantle structure, *Tectonophysics* 111, 173-246.

Özalaybey, S., M. K. Savage, A. F. Sheehan, J. N. Louie and J. N. Brune (1997). Shear-wave velocity structure in the northern Basin and Range province from the combined analysis of receiver functions and surface-waves, *Bull. Seism. Soc. Am.* 87, 183-199.

Sandvol, E., D. Seeber, M. Barazangi, F. Vernon and A. Al-Amri (1998). Lithospheric seismic velocity discontinuities beneath the Arabian Shield, *Geophys. Re. Let.* 25, 2873-2876.

CHARACTERIZATION OF NATURAL AND HUMAN-RELATED SEISMICITY IN SOUTH AFRICA

Thomas H. Jordan, Eliza Richardson, Jeffrey J. McGuire
Department of Earth, Atmospheric and Planetary Sciences, Massachusetts Institute of Technology
Cedric Wright, Sue Webb, Eldridge Kgaswane, Teresia Nguuri
Department of Geophysics, University of Witwatersrand, Johannesburg, South Africa

Sponsored by U.S. Department of Defense
Defense Threat Reduction Agency
Contract No. DSWA01-98-C-0158

ABSTRACT

We have begun a two-year collaborative project between the Massachusetts Institute of Technology (MIT) and the University of Witwatersrand to investigate the natural and human-related seismicity of southern Africa. The project is focused on the seismic activity of the Witwatersrand Basin during the two-year period from April 1997, through April 1999. The data for this project come from three principal sources: (a) permanent seismic observatories operated by the South Africa Council for Geosciences, (b) a broadband, 52-element temporary array operated by the Carnegie Institution of Washington and MIT as part of the Kaapvaal Project under the sponsorship of the National Science Foundation, and (c) a number of local arrays operated by companies engaged in deep gold mining.

The project has four principal objectives: (1) to catalog the seismicity of the Witwatersrand Basin and surrounding regions during this two-year period; (2) to calibrate locations in this region using events with hypocenters and origin times precisely determined by in-mine networks, and to use these calibrations to refine three-dimensional crustal and upper-mantle models for the region; (3) to determine moment-tensor solutions and spectral characteristics of a subset of events for the purpose of assessing such information as discriminants among tectonic earthquakes,[1] mine tremors, rockbursts, and chemical explosions; and (4) to employ three-component waveform data from the local events to assess anisotropic propagation effects and wavefield scattering by small-scale crustal heterogeneities.

Project personnel have worked directly with the Council of Geosciences to establish a preliminary catalog for the study period from phases reported by the permanent stations. The seismicity of the region is much higher than most stable cratons, owing to frequency of mining-induced events. In the 10-month period of April to December 1997, for example, there were 557 events locatable by the permanent observatories; 415 of these had local magnitudes of 2.5 or greater. The highest seismicity rates were observed in the Far West Rand and Klerksdorp mining districts, which accounted for 43% and 30% of the seismicity, respectively.

Detailed investigations of the seismicity of the Far West Rand district using in-mine arrays have revealed two populations of mining-induced events, designated as Type A and B, with distinct frequency-magnitude statistics and other characteristics. Type A events are small in magnitude ($M_L<1$) and highly clustered in time and space, usually within 100 m of active stope faces; their spectra are rich in high frequencies, and their mechanisms often involve significant tensional components. We associate these events with new fractures in competent rock induced by dynamic stresses during blasting and quasi-static stress perturbations from the excavation and closure of individual stopes. According to this model, the upper magnitude of these events is limited by the dimensions of the stress-perturbation aureoles around the stopes. Type B events, on the other hand, show distributed locations, spectra depleted in high frequencies, and double-couple mechanisms. In the Far West Rand regions, these events can have large magnitudes (> 4), but they show a distinct lower magnitude cut-off at $M_{min} \approx 0$. Type B events are caused by ruptures on preexisting faults and other weak geological structures, such as dyke faces and bedding planes, and they can be used to place significant constraints on the physics of the faulting process. In particular, their frequency-magnitude statistics and spectral properties are consistent with a rate-and-state friction model in which M_{min} is controlled by a critical slip distance D_c of approximately 10^{-4} meters.

Key Words: seismicity, South Africa, mining activities, earthquakes, discrimination, calibration

[1] The earthquake moment tensors will be used to study the tectonic stress field in the region and its relationship to geological structures.

REVIEW OF RESEARCH BEING PERFORMED IN THE RUSSIAN FEDERATION RELATED TO CTBT SEISMIC MONITORING

Victor V. Kirichenko and Yury A. Kraev, SAIC GT
Sponsored by U.S. Department of Defense

Defense Threat Reduction Agency
Contract No. DSWA01-98-C-0029 and Contract No. N00014-95-C-0044

ABSTRACT

During the last five years a number of research projects under the Russian Monitoring Technologies Program (RMTP) were performed. The major RMTP goal is to improve national and international capabilities to ensure compliance with the Non-Proliferation Treaty, Comprehensive Nuclear-Test-Ban Treaty (CTBT) as well as agreements on Nuclear Material Protection, Control and Accounting. We present some research results of two current projects of the SYNAPSE Science Center and Moscow State Technical University (MSTU).

The SYNAPSE Science Center project is intended to develop and investigate adaptive algorithms and software for data analysis from broad-band three-component seismic arrays, algorithms and software for seismic source identification, algorithms and software for automated data processing from local seismic networks as well as to develop a problem-oriented system for automated data analysis from seismic arrays and local seismic networks. Examples of applications will be presented for the following algorithms: statistically optimal seismic array data processing, extraction of seismic phase waveforms, and estimation of seismic wave arrival parameters based on data from three-component seismic arrays, automated location of small local events by the medium scanning (emission topography) method as well as newly developed methods and procedures of statistical discrimination. The project of the MSTU is intended to develop and investigate statistical procedures and software for nuclear explosion pattern recognition using data from seismic, radionuclide and other monitoring methods, taking into account source data errors. The results of the development of mathematical pattern recognition algorithms for a fixed sample size (parametric and non-parametric models) and mathematical algorithms for sequential pattern recognition methods will be presented.

We present the results of the first year performance on the seismo-acoustic research for the CTBT Monitoring project. This project has been performing by SAIC/SAIC GT and its subcontractors: the Geophysical Survey and the Joint Institute of Physics of the Earth of the Russian Academy of Sciences. These results are related to the calibration of the stations of the International Monitoring System (IMS) at the territory of the Russian Federation. Studies are designed to improve discrimination of seismic sources for the regions of the former Semipalatinsk Test Site, Lop Nor Test Site, North Caucasus, and Baikal Rift Zone as well as collection and analysis of an archive seismic records of earthquakes, rockbursts, chemical and underground nuclear explosions. The newly developed travel-time curves for major regional seismic phases (Pn/P, Pg, Sn/S and Lg) related to the East-European, West-Siberian platforms, Urals Folded Belt, North Kazakstan and North Caucasus regions will be presented. The estimates of uncertainties for these travel-time curves are presented as well as their comparison with the IASPEI-91 tables.

We present results on the continuing development of the Peleduy small aperture seismic array in Southern Yakutiya, Russia. In March 1999, during a three week period, a team of American and Russian specialists installed seismic and communication equipment and thus put into operation the first small aperture seismic array in the territory of the Russian Federation; this is the first Russian array that satisfies the IMS station specifications. During the summer of 1999, all site upgrade efforts should be completed and the small aperture seismic array will be ready for final inspection and acceptance.

This part of the paper will be illustrated with photographs. Also, a short description of the geology of the seismic array site and array's boreholes as well as examples of seismic noise spectrums for the newly installed seismic array will be presented. These examples illustrate the low-level background noise at the Peleduy site.

Key Words: seismic arrays, seismic data processing and analysis, discrimination, location, calibration, seismic station upgrade

REGIONAL WAVE PROPAGATION IN SIBERIA

Keith D. Koper and Terry C. Wallace, Department of Geosciences, University of Arizona

Sponsored by U.S. Department of Defense
Defense Threat Reduction Agency
Grant DSWA01-97-C-0123

ABSTRACT

Monitoring of the Comprehensive Nuclear-Test-Ban Treaty (CTBT) requires the ability to discriminate between low-yield nuclear explosions and small-magnitude earthquakes. Standard discriminants are generally based on the properties of regional seismic phases such as L_g and P_n; however, the character of these phases depends strongly on the geology and tectonic setting along the ray path. Thus, for a discrimination scheme to be successful, the propagation characteristics of regional phases in the area of interest must be well known. Although previous work on the propagation characteristics of regional phases has concentrated mainly on former test site areas, here we present results for Siberia, a region of potential importance that has been under studied.

We use data recorded at 12 broad band stations located either in or adjacent to Siberia. Four of these stations were installed in 1995, and an additional six have been deployed only since 1992-1993. This fact, coupled with the low natural seismicity of the cratonic Siberian platform, leaves us with a sparse data set. Nevertheless, we have assembled waveforms from 427 events, yielding 618 viable ray paths, for analysis. Although the majority of paths cover the border regions of southern Russia, northeastern China, northern Kazakstan, and Mongolia (latitude 50°N) a significant number sample the eastern half of Siberia (longitude 120°E), and a few sample the Siberian platform itself. The events range in size from 3.1 m_b to 7.5 M_s.

Initially, we calculate the magnitude of the L_g phase, $m_b(L_g)$, for each ray path assuming a constant Q_o value of 800. The $m_b(L_g)$ values are compared to values of teleseismic m_b reported by the PDE. A linear regression of the regional and teleseismic magnitudes yields a correlation coefficient of 0.96 and a slope of 0.85. Using different Q_o values in the calculations leaves these values largely unchanged, with only the intercept having significant variation. The difference between the two magnitudes for a given ray path provides a simple estimate of the relative efficiency of L_g propagation. Coherent azimuthal trends in the magnitude differences are observed to correlate well with regional tectonic features. Our results also compare favorably with previous large-scale tomographic models of Q_o for the region, while offering higher resolution and greater spatial sampling in Siberia.

Key Words: CTBT, L_g, magnitude, Siberia

OBJECTIVE

The success of the Comprehensive Nuclear-Test-Ban Treaty (CTBT) depends on the ability of seismologists to monitor the global occurrence of seismic events; of particular importance is the ability to discriminate low-yield nuclear explosions from small-magnitude earthquakes, meteorite impacts, mining blasts, and other man-made chemical explosions. Such discrimination will rely heavily upon the character of the regional distance (source-receiver distances less than 1500-2000 km) wavefield and seismic phases such as P_n, P_g, and L_g. However, these phases travel in the most heterogeneous portions of the Earth, the crust and uppermost mantle, thus their properties have significant regional variation.

Our objective is to characterize the propagation of such regional seismic phases in Siberia [*Wallace and Tinker*, 1998]. By constraining the Earth structure signature in the waveforms we will be better able to infer the source properties of anomalous events in the region. Only in the past decade have enough "open", broadband instruments been deployed in this region to permit such an undertaking. Our specific objectives are (1) to construct a high-quality data base of regional waveforms from the area, (2) to define the spatial and temporal trends of seismicity in the region, and (3) to describe the variation in amplitude and frequency content of the regional phases. The data base will be freely available to researchers in the discrimination community.

RESEARCH ACCOMPLISHED

Construction of Database

We have identified 427 earthquakes that produced well-recorded, regional distance waveforms at one or more of the 12 broadband stations located in or near Siberia (Figure 1). The raw data are freely available and the majority were obtained via the Incorporated Research Institutions of Seismology (IRIS) data management system, the exception being 7 waveforms from station PDY that were obtained via the autodrm at the Prototype International Data Center (PIDC). The earthquakes occurred between December of 1989 and March of 1999, and range in magnitude from 3.1 m_b to 7.5 M_s. The data are currently stored as 600 s-long waveforms in Seismic Analysis Code (SAC) format. We have installed header information, such as event coordinates and origin time, for each waveform and we have constructed a catalog that contains (1) the event hypocenters, (2) the corresponding teleseismic body wave magnitude, $m_b(P)$, (3) the distance, azimuth, and backazimuth of each station which recorded each event, (4) an average Q_o for each ray path based on the model of *Mitchell et al.* [1997], and (5) the corresponding $m_b(L_g)$ values for each ray path. We discuss the calculation and interpretation of the $m_b(L_g)$ values in a later section.

Seismicity Trends

Figure 2 illustrates the time-rate accumulation of "useful" seismic events in Siberia. The number of events is defined as those events that produced at least one high-quality, regional distance ray path to a broadband seismometer in the region. Thus we implicitly account for factors such as station geometry and downtime as well as the actual rate of seismicity in the area. A large number (157) of the cataloged events occurred along the eastern edge of the Kamchatka peninsula where the Pacific plate is subducting beneath the Sea of Okhotsk microplate; ray paths from these events to station PET sample only a small slice of the peninsula (Figure 1) and so they are not included in Figure 2. Since the addition of four stations in 1995 the earthquake total has grown at a linear rate of approximately 50 events per year. From that time period there are ~ 1.5 ray paths per event, so equivalently the data base has been growing by about 75 ray paths per year.

Most of the 461 non-PET ray paths are concentrated in southern Russia and northern Mongolia, however a significant number sample Siberia and eastern Russia. The least sampled tectonic province is the Siberian platform. This is expected since the old Cratonic lithosphere in this region has extremely low seismicity and no stations are located in the deep interior of the platform. We have increased coverage of this region by including paths with lengths of up to 2000 km from events occurring near Lake Baikal and recorded at station NRIL. Although these paths do not produce usable P_n observations, the L_g phases are generally observable.

Unfortunately the coverage of ray paths in the Siberia data base is not expected to increase dramatically in the near future. We anticipate the coverage to continue to be dominated by earthquakes occurring in the Kurile-Kamchatka subduction zone recorded at PET and BILL, and earthquakes occurring in the Inner Asian belt (southern Russia and northern Mongolia) recorded at KURK, TLY, ULN, and HIA. The region most likely to have a significant increase in coverage in the near future is eastern Russian north of ~ 60 N. This region should become much better sampled as events occurring in the Chersky Seismic Belt (CSB, located at the intersection of the North American, European, and Okhotsk plates, see *Mackey et al.*, [1998]) are recorded at stations TIXI, YAK, MA2, and BILL. The northernmost tip of Siberia (latitude > 70°N, 90°E < longitude < 120°E) will also become significantly better sampled as events from the Gakkel Ridge in the Arctic are recorded at NRIL.

The region most likely to remain undersampled given the current station geometry is the western 2/3 of the Siberian platform. The best way to increase coverage of this region would be the installation of a broadband station approximately 800-1000 km due south of NRIL. Such a station would record regional distance events from the Inner Asian belt to the south, the Lake Baikal rift zone to the southeast, the CSB to the east, and possibly the Gakkel rift system to the northeast. As an alternative to the installation of a new instrument in Siberia, increasing the availability of data from station PDY could dramatically improve the coverage of this region. Although this station has been deployed since August of 1993, and is positioned to record regional distance waveforms from the Inner Asian belt, the CSB, and the landward extension of the Gakkel rift system, we were able to obtain only 7 records from PDY.

Calculation of L_g Magnitudes

For each ray path in the data base we calculate a magnitude, $m_b(L_g)$, based on the amplitude of the L_g phase using the method of *Nuttli* [1973] as described by *Priestly and Patton* [1997]. We first deconvolve the instrument response from the observed waveform and convolve in the response for a short period WWSSN instrument. This has the effect of a narrow bandpass filter near 1 Hz. Next we window the L_g phase by combining the source-receiver distance with a velocity bracket of 3.3-3.6 km/s. We take the average of the three largest maxima in this time window, from each of the three components, as the observed amplitude (A) of the L_g phase. Since the frequency content of the data is sharply peaked at ~ 1Hz, estimates of the frequency dependence of Q are unneeded and only Q_o (Q at 1 Hz) is required for the calculation of $m_b(L_g)$.

Given values for A and Q_o it is straightforward to apply the formulas in *Priestly and Patton* [1997] to generate $m_b(L_g)$ estimates; however, it is also important to quantify how errors in A and Q_o are mapped into $m_b(L_g)$ values. We expand the appropriate formula to first order, rewriting $m_b(L_g)$ as m_{bLg} for notational clarity,

$$\ddot{A}m_{bLg}(A,Q_o) = \frac{fm_{bLg}}{fA}\ddot{A}A + \frac{fm_{bLG}}{fQ_o}\ddot{A}Q_o$$

and find,

$$?m_{bLg} = 0.434*\left(\frac{?A}{A}\right) - 0.434*\left(\frac{1}{Q_o}\right)*\left(\frac{?(d-10.0)}{UT}\right)*\left(\frac{?Q_o}{Q_o}\right),$$

where U is the group velocity of the L_g phase, T is the period, and d the source-receiver distance. The expression is dominated by the second term since even an error as large as 25% in the measurement of the amplitude results in an error of only ~ 0.11 in $m_b(L_g)$.

We illustrate the effect of the second term, inaccurate Q_o values, on $m_b(L_g)$ in Figure 3 using U = 3.4 km/s, T = 1 s, and a Q_o of 600. Because Q_o appears in the exponent for the $m_b(L_g)$ expression it is necessary to specify a theoretical value of Q_o, in addition to the percent error of Q_o, when considering $m_b(L_g)$ error estimates. Thus for low-Q_o regions a given percent error in Q_o will have much larger impact than in high-Q_o regions. As an example, if the true Q_o value along a ray path is 600 but a value of 400 is inadvertently used, then at a distance of 1000 km, $m_b(L_g)$ will be overestimated by ~ 0.25 units.

One method that has been used to account for this well-known dependence of $m_b(L_g)$ on Q is that of *Nuttli* [1988]. In this approach the L_g-coda is analyzed to determine Q as a function of frequency along a given ray path, and the Q_o from this relationship is used in the $m_b(L_g)$ computation. A weakness of this method, however, is that the calculated Q_o value may not be a robust estimate of anelastic Earth structure because of source effect biases. Here we adopt two different approaches to the problem of Q_o estimation.

In the first approach, we trace each Siberia ray path through the 3° by 3° L_g coda-Q_o model of *Mitchell et al.* [1997], presented in Figure 4. We take a weighted average of the Q_o values from the cells that are sampled and assume Q_o to be 600 for path segments outside of the model bounds. *Mitchell et al.'s* [1997] Q_o model is the result of a large tomographic inversion and so should provide a robust estimate of Q_o along a given ray path. Second, we assume Q_o is constant over the entire region and use a value of 800 in our $m_b(L_g)$ calculations. Although there will clearly be significant Q_o variations over an area as large as Siberia, by comparing the corresponding $m_b(L_g)$ values to the reported body wave magnitudes ($m_b(P)$ values, which are presumably much less biased by shallow Earth structure) we hope to map out anelastic variability on station by station basis. This will provide empirically determined, azimuthally dependent, relations for $m_b(L_g)$ calculations at a given station.

The resulting $m_b(L_g)$ values for the data set as a whole are plotted against the corresponding body wave magnitudes, $m_b(P)$, in Figure 5. For both Q_o models the $m_b(L_g)$ values are well correlated with the $m_b(P)$ values, having correlation coefficients of 0.97 and 0.96. Linear regression of the binned data indicates that the slopes of the best-fitting lines for the $m_b(L_g)$-$m_b(P)$ relationships are similar (0.94 and 0.85); however, the intercept values are significantly different. Using the regional Q_o model of *Mitchell et al.* [1997] we find the intercept to be 0.18 and for the constant Q_o model we find the intercept to be 0.83.

The fact that the $m_b(L_g)$ values determined with the constant Q_o model are systematically higher than those determined with the *Mitchell et al*. [1997] model is expected since it is simply a reflection of the difference in mean Q_o between the two models. It is more surprising that (1) the two Q_o models provide similar slope values with respect to $m_b(P)$ and (2) the correlation between $m_b(L_g)$ and $m_b(P)$ is not increased by using a laterally varying Q_o model. It may be that in the Siberia region *Mitchell et al.'s* [1997] model lacks the resolution to improve the magnitude correlation compared to a constant Q_o model; however, it may also be that improvement is seen when the magnitudes are compared on a station by station basis as opposed to the data set as a whole.

We investigate this by performing linear regressions between $m_b(L_g)$ and $m_b(P)$, for both Q_o models, on a station-by-station basis. The results of this are shown in Table 1. Just as in the previous case the intercepts from the different Q_o models are substantially different but the correlation coefficients and slope are quite similar. This confirms the idea that model of *Mitchell et al.* [1997], developed to infer continental scale structures, is not sensitive to the fine scale anelastic variations in the Siberia region.

Several of the stations in Table 1 show poor correlation between $m_b(L_g)$ and $m_b(P)$. One possibility for the scatter is that the $m_b(P)$ values are poorly determined in certain cases, either because of anomalous Earth structure at depth, or a sparse number of teleseismic observations. A more important factor, however, is that the $m_b(L_g)$ values are being influenced by laterally varying Earth structure. We present an example of this in Figure 6 for TIXI and NRIL, two stations which show very poor magnitude correlations (Table 1). In the case of TIXI there is an azimuthal trend to the magnitude residuals resulting from ray paths which straddle the eastern edge the Siberian platform. As the earthquake location moves to the west (increasing in azimuth) the ray path to TIXI samples increasingly more of the high-Q_o Siberia platform, generating positive magnitude residuals. In the case of NRIL, all the magnitude residuals from events occurring at the Gakkel ridge (azimuth < 40°) are strongly negative. This is indicative of the low-Q_o nature of the oceanic portion of the ray path for these events. Identifying and accounting for factors such as these greatly increases the correlation between $m_b(L_g)$ and the teleseismic body wave magnitudes.

CONCLUSIONS AND RECOMMENDATIONS

We have assembled a high quality data set of regional distance waveforms which sample the areas in and around Siberia. All the waveforms show clear P_n and L_g arrivals, while the existence of P_g is more sporadic.

The source-receiver paths of the waveforms are concentrated in southern Russia, northern Mongolia, and the eastern portion of the Kamchatka peninsula. Significant coverage of eastern Russia and Siberia is also obtained, however the western 2/3 of the Siberian platform is extremely undersampled. Coverage of this region is not likely to improve in the near future with the current station geometry. The installation of a single broadband seismometer deep in the interior of the Siberia platform, 800-1000 km south of NRIL, would be the ideal way to enhance coverage of this region, since it would be positioned to record data from the Inner Asia seismic belt, including the highly active Lake Baikal region to the south and southeast, the Chersky seismic belt to the east, and the Gakkel Ridge to the north and northeast. An alternative idea, that would in theory be simpler and cheaper, is to increase the availability of data recorded at PDY to the general academic community.

We have calculated $m_b(L_g)$ for all of the paths in the Siberia data base using two distinct Q_o models. The resulting magnitude values are highly correlated with the body wave magnitude estimates as a whole, and, to a lesser degree, on a station by station basis. The effect of the assumed Q_o value is subtle with regard to the slope of the $m_b(L_g)$ vs. $m_b(P)$ relation, however it is more pronounced as a static offset (change in intercept) of the magnitude values. In some cases the scatter in the magnitude residuals can be directly mapped to tectonic features in the region. By analyzing the regional variations in magnitude residuals, we can empirically determine $m_b(L_g)$ station corrections that depend on the azimuth of the ray path as well as a static offset. These relations will provide a higher-resolution view of the anelastic structure of the region than is currently provided by large-scale tomographic models.

REFERENCES

Mackey, K. G., K. Fujita, and L. J. Ruff, Crustal thickness of northeast Russia, *Tectonophysics, 284*, 283-297, 1998.

Mitchell, B. J., Y. Pan, J. Xie, and L. Cong, L_g coda Q variation across Eurasia and its relation to crustal evolution, *J. Geophys. Res., 102*, 22767-22779, 1997.

Nuttli, O. W., Seismic wave attenuation and magnitude relations for Eastern North America, *J. Geophys. Res., 78*, 876-855, 1973.

Nuttli, O. W., L_g magnitudes and yield estimates for underground Novayan Zemlya nuclear explosions, *Bull. Seismol. Soc. Am., 78*, 873-884, 1988.

Priestly, K. F., and H. J. Patton, Calibration of $m_b(P_n)$, $m_b(L_g)$ scales and transportability of the M_o:m_b discriminant to new tectonic regions, *Bull. Seismol. Soc. Am., 87*, 1083-1099, 1997.

Wallace, T. C. and M. A. Tinker, Seismic characterization of Siberia, in *Proceedings of 20th Annual Symposium on Monitoring a Comprehensive Test Ban Treaty (CTBT)*, Santa Fe, New Mexico, 536-541, 1998.

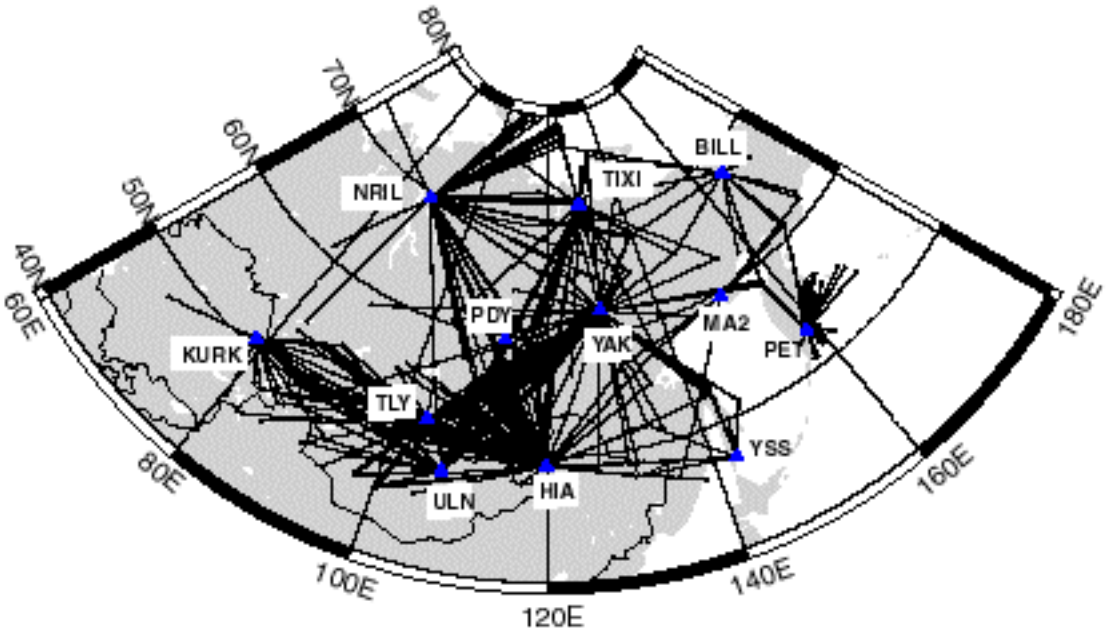


Figure 1. Event-receiver paths of waveforms currently archived in the Siberia data base. We have identified a total of 618 regional paths, from 427 earthquakes, that were well-recorded at one or more of 12 broadband stations which have been installed in the previous decade.

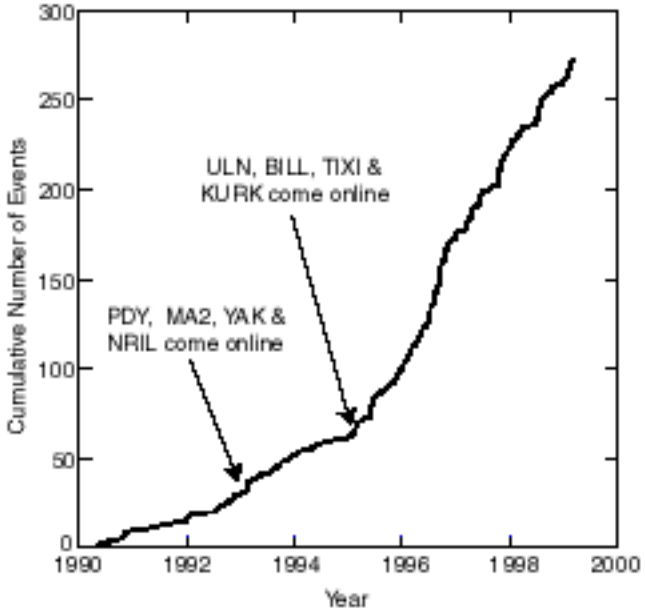


Figure 2. The cumulative number of useful events as a function of time. Events from the Kurile-Kamchatka subduction zone to PET are not included as they sample only a small slice of the Kamchatka peninsula. Since 1995 approximately 50 events per year have occurred which provide useful data.

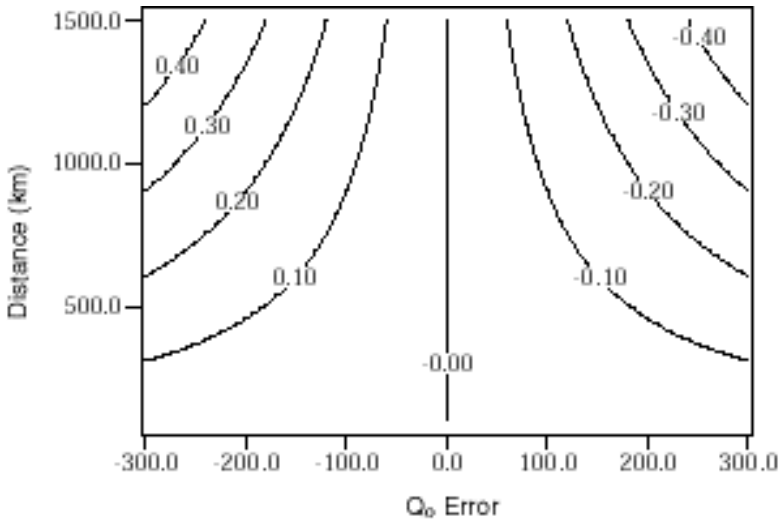


Figure 3. The error in $m_b(L_g)$ as a function of distance and uncertainty in the average, along-path Q_o value. The contours of $m_b(L_g)$ error are in intervals of 0.1. The magnitude errors are negatively correlated with Q_o errors and positively correlated with distance. We assume a theoretical Q_o value of 600 for this calculation.

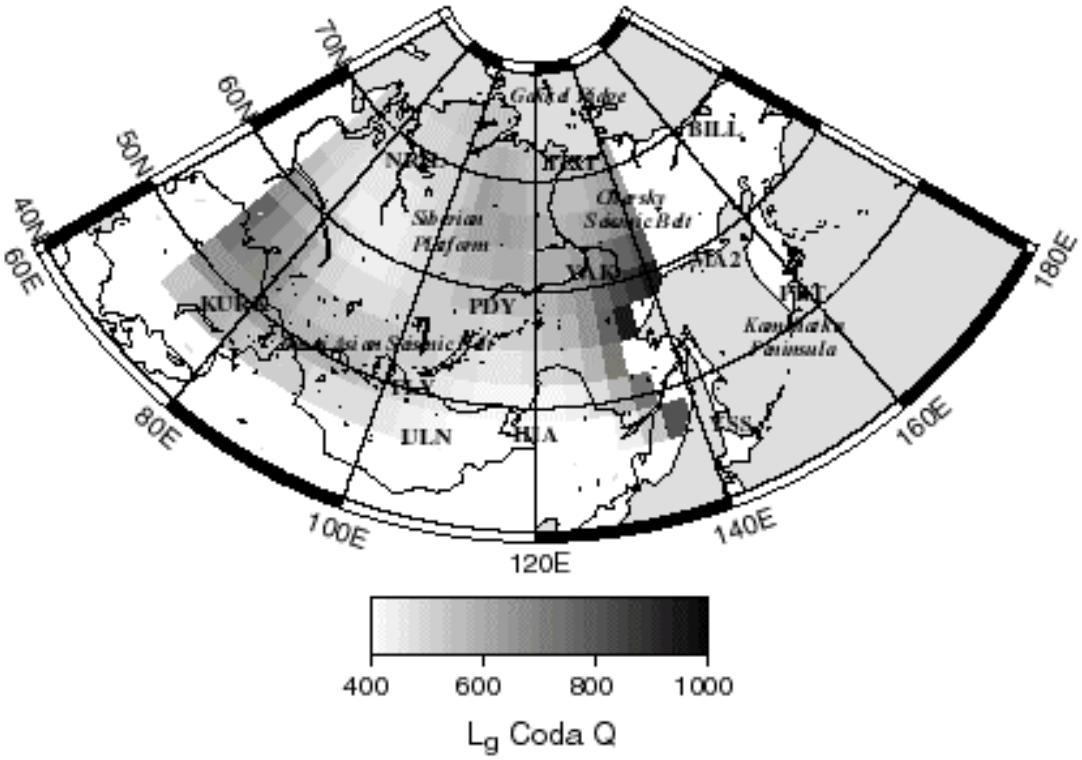


Figure 4. A portion of the coda Q model developed by *Mitchell et al.* [1997]. The model continues to the south and west but is bounded on the east by the 140°E meridian. This model facilitates calculations of L_g magnitudes.

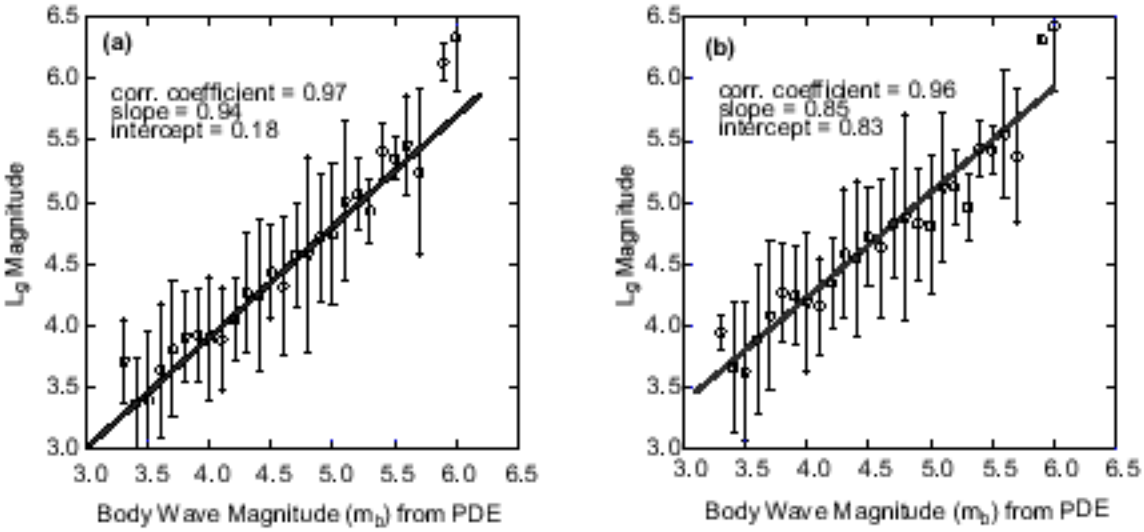


Figure 5. Correlation between magnitudes determined from teleseismic body waves and magnitudes determined from the L_g pulse, for the entire Siberian database, using **(a)** the Q_o model of *Mitchell et al.* [1997], and **(b)** a constant Q_o value of 800. The circles represent the average L_g magnitude for 0.1 bins of m_b; the error bars represent +/- one standard deviation of each bin. In both cases the magnitude values are highly correlated and the best-fitting lines have similar slopes.

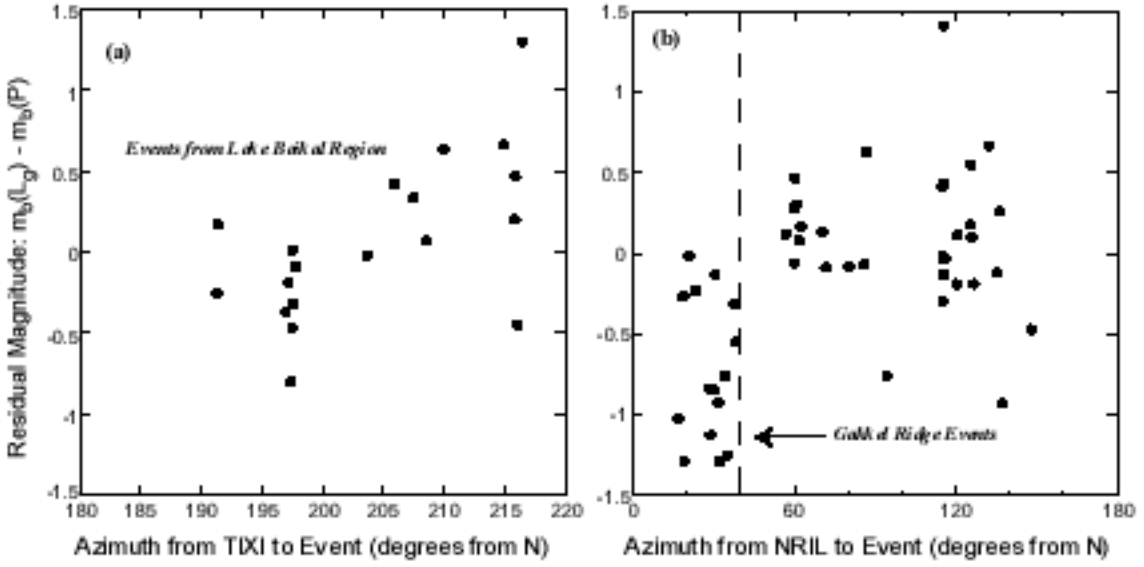


Figure 6. The azimuthal dependence of $m_b(L_g)$ - $m_b(P)$ residuals for **(a)** TIXI and **(b)** NRIL. In both cases we compute $m_b(L_g)$ using the constant Q_o model. In the former case magnitude residuals are shown from a string of events occurring in the Lake Baikal region. The increase of residual with increasing azimuth is due to enhanced sampling of the Siberian platform (a high-Q_o region) as the event location moves to the west. In the latter case, NRIL, events from the Gakkel Ridge (azimuth < 40°) show strongly negative residuals, that are related to the sampling of oceanic lithosphere along the ray path. These effects contribute to the poor $m_b(L_g)$ vs. $m_b(P)$ correlation reported in Table 1.

Station	Number of Observations	Correlation Coefficients	Slopes	Intercepts
BILL	15	0.80,0.78	1.14,1.12	-0.69,-0.44
HIA	91	0.80,0.80	0.98,0.95	0.12,0.69
KURK	25	0.87,0.88	1.13,1.13	-0.21,-0.07
MA2	6	—	—	—
NRIL	49	0.43,0.41	0.42,0.43	2.14,2.55
PDY	7	—	—	—
PET	131	0.43,0.45	1.10,1.06	-0.72,-0.44
TIXI	43	0.47,0.45	0.92,0.97	0.15,0.19
TLY	78	0.69,0.73	0.92,0.94	-0.19,-0.04
ULN	37	0.83,0.84	1.02,1.02	0.00,0.38
YAK	72	0.77,0.68	0.83,0.73	1.02,1.60
YSS	15	0.52,0.53	0.81,0.77	0.13,0.42

Table 1. Linear regressions of magnitudes for each station. The magnitude relationship is of the form $m_b(L_g) = slope \times m_b(body\ wave) + intercept$. We calculate $m_b(L_g)$ using two separate Q_o models: the L_g-coda model of *Mitchell et al.* [1997] and a constant model with Q_o=800. The magnitudes retain the same degree of correlation and slope values independent of which Q_o model is used, though the intercept is much more dependent on the assumed Q_o structure.

EVALUATION OF UNCERTAINTIES AND BIAS IN SURFACE WAVE TOMOGRAPHIC MAPS AND TRAVEL TIME CORRECTION SURFACES

Anatoli L. Levshin, Mikhail P. Barmin, and Michael H. Ritzwoller
Department of Physics, University of Colorado at Boulder

Sponsored by U.S. Department of Defense
Defense Threat Reduction Agency
Contract No. DSWA01-97-C-0157

ABSTRACT

Group velocity travel time correction surfaces (TTCS) are computed easily from group velocity tomographic maps. The TTCSs are then used to create phase-matched filters, designed to detect and extract weak surface wave signals immersed in ambient and signal-generated noise as a basis for spectral amplitude measurements essential to discriminate explosions from earthquakes. A long-standing problem in surface wave tomography is that both TTCSs and group velocity maps would be more useful if their uncertainties could be estimated rigorously. The estimation of formal uncertainties is complicated by the fact that the level of uncertainty depends on the spatial length-scale of the modeled features as well as unknown theoretical errors and unmodeled structures. Our purpose is to take steps toward understanding uncertainties in both the tomographic maps and the TTCS constructed from them. All analyses are based on data coverage for 15 s - 20 s Rayleigh waves in Central and Southern Asia.

We have developed a new method to construct tomographic maps that permits estimation of resolution and scale-dependent amplitude bias corresponding to a given data coverage. Based on the resolution matrix formalism, this method produces more reliable estimates of the quality of the tomographic maps than more popular checkerboard tests.

These estimates do not propagate naturally into uncertainties in predicted travel times. To gain insight into the uncertainties in the TTCSs, we perform two synthetic experiments to determine the effects of limited spatial resolution of the tomographic maps and unmodeled azimuthal anisotropy. In the first, we evaluate how the effects of random noise in measurements and unmodeled sub-scale inhomogeneities present in an input model (e.g., sedimentary basins, Moho topography) distort the TTSCs computed from estimated tomographic maps. We estimate that the accuracy of group velocity maps and TTCSs for the part of the region to the north of 25°N is typically better than 0.03-0.04 km/s. In the second, we estimate errors in the TTSCs produced by azimuthal anisotropy not modeled in the tomographic maps. The effect of unmodeled azimuthal anisotropy across large areas, such as the Tibetan plateau, on group velocity maps and TTCSs is in general small: rms of group velocity errors for the region in the presence of 2% anisotropy is less than 0.025-0.035 km/s.

Key Words: surface waves, group velocity tomography, correction surfaces

OBJECTIVE

This research is dedicated to the study of uncertainties and bias in constructing surface wave travel time correction surfaces (TTCSs) computed from group velocity tomographic maps. TTCSs are necessary for the design of phase matched filters used to detect and extract weak surface wave signals in the CTBT monitoring environment. Knowledge of uncertainties in tomographic maps and TTCSs provide estimates of efficiency of phase matched filtering and accuracy of quantitative evaluation of surface wave signals. To acquire such knowledge, we perform synthetic experiments simulating data analyses for intermediate period surface waves propagating across Central and Southern Asia.

RESEARCH ACCOMPLISHED

Introduction

Estimation of surface wave amplitudes plays an important role in the discrimination of explosions from earthquakes. For small seismic events surface wave signals are often too weak to be directly measured or even detected on seismograms. The most efficient technique for extracting such signals from ambient and signal-generated noise is phase-matched filtering (Herrin & Goforth, 1977; Russel *et al.*, 1988; Stevens & McLaughlin, 1997; Leach *et al.*, 1998; Levshin *et al.*, 1998). Lateral inhomogeneity of the crust typical for tectonically active regions, such as Central and Southern Asia and the Near East, produces a variability in surface wave propagation from seismic sources to recording stations. To design efficient phase-matched filters, it is necessary to account for this diversity by tuning filters to a particular wave path. This can be done for each station using travel time correction surfaces (TTCSs) for a set of intermediate periods (10 - 30 s). TTCS may be constructed using regional group velocity tomographic maps for these periods obtained as a result of the tomographic inversion of numerous surface wave dispersion measurements (Levshin *et al.*, 1996, 1997, 1998; Ritzwoller & Levshin, 1998; Ritzwoller *et al.*, 1995, 1998, 1999; Vdovin *et al.*, 1999). The efficiency of phase-matched filtering based on TTCSs strongly depends on the their quality and the quality of the group velocity maps used for their generation. One of the ways to estimate the quality is to use ground-truth events for which hypocenter parameters are well known (Harkrider *et al.*, 1998). Unfortunately there is only a limited number of ground-truth events located in Central and Southern Asia (Engdahl, 1998). Most of them are nuclear explosions at well known test sites. Subsequently, the azimuthal coverage of wave paths for ground-truth events to the existing network of stations is quite poor, and does not provide sufficient information for verifying TTCSs.

However, it is evident that both TTCSs and group velocity maps would be more useful if their uncertainties could be estimated rigorously. The estimation of formal uncertainties is complicated by the fact that the level of uncertainty depends on the spatial length-scale of the modeled features as well as unknown theoretical errors and unmodeled structures. Our purpose is to take steps toward understanding uncertainties in both the tomographic maps and the TTCS constructed from them. All analyses are based on data coverage for 15 s - 20 s Rayleigh waves in Central and Southern Asia as the region of main CTBT monitoring efforts.

We have developed a new method to construct tomographic maps that permits estimation of resolution and scale-dependent amplitude bias corresponding to a given data coverage. This method will be briefly described below and in more detail in Barmin *et al.* (1999). Based on the resolution matrix formalism, this method produces more reliable estimates of the quality of the tomographic maps than the more popular checkerboard tests.

Unfortunately, these estimates do not propagate naturally into uncertainties in predicted travel times. To gain insight into the uncertainties in the TTCSs, we performed two synthetic experiments to determine the effects of limited spatial resolution of the tomographic maps and unmodeled azimuthal anisotropy. In the first experiment we evaluate how the effects of unmodeled sub-scale inhomogeneities present in an input model (e.g., sedimentary basins, surface or Moho topography) and random noise, which is always present in real measurements, distort the TTSCs computed from estimated tomographic maps. In the second experiment we estimate errors in the TTSCs produced by azimuthal anisotropy unmodeled in the tomographic maps. We plan to continue this study in the future using the latest model of the Central and Southern Asia region (Villasenor *et al.*, 1999).

New technique for a 2-D tomographic inversion of surface wave dispersion measurements.

We developed a new technique to invert regional surface wave group or phase velocity measurements into 2D isotropic and azimuthally anisotropic tomographic maps. Such maps are important for monitoring purposes in two aspects: (1) for constructing 3D velocity models of regions under study that are essential for accurate location of seismic events (Villasenor *et al.*, 1999); (2) for constructing surface travel time correction surfaces for a set of monitoring stations. These correction surfaces then can be used for designing phase-matched filters.

The main features of this technique are:
Geometry: spherical, no flattening approximation is applied.
Parameterization: a nodal model of basic functions to parameterize velocity distribution on a spherical Earth surface is used. This model is defined at a finite number of discrete points and the intervening spaces are determined by a specific interpolation algorithm in the inversion matrix and travel-time accumulation codes. Nodes are spaced at constant distances from one another, interpolation is based on the three nearest neighbors. Typical internodal distances for regional inversions are 100 km or less.
Theoretical Assumptions: surface waves are treated as rays, sampling an infinitesimal zone along the great circle linking source and receiver, scattering is ignored. The method generalizes naturally to non-great circular paths, if they are known, e. g., as a result of ray tracing across preliminary phase velocity maps obtained after the first 3D inversion of group velocity data.
Regularization: application of spatial smoothness (with a specified correlation length) plus model amplitude constraints, both spatially variable and adaptive, depending on data density. The regularization scheme that we have effected involves a penalty function composed of a spatial smoothing function with a user defined correlation length and a spatially variable constraint on the amplitude of the perturbation from a reference state. The absolute weight of each component of the penalty function is user specified. The model amplitude constraint smoothly blends the estimated model into a background reference in regions of low data density. This dependence on data density is also user specified.
Azimuthal Anisotropy: can be estimated with isotropic structure. Both 2ψ and 4ψ terms (Smith & Dahlen, 1973) can be evaluated.

This technique has advantages in comparison with our previously used method by Yanovskaya and Ditmar (1985) in at least in two aspects: (1) there is no spatial bias due to the Earth's flattening; (2) there is more efficient smoothing, depending on data density. Figures 1 and 2 demonstrate new isotropic tomographic group velocity maps for the target region between 15° and 50° N, 25° and 105° E for Rayleigh and Love waves at the 15 s period obtained by this technique from surface wave dispersion measurements described at Ritzwoller & Levshin (1998), Ritzwoller *et al.* (1998). The numbers of independent paths used for the inversion are 3160 for Rayleigh waves, and 2160 for Love waves. The same figures show the path density (defined as a number of rays crossing 2°x 2° bin), estimated spatial resolution of these maps, and amplitude bias resulting from smoothing. We define the amplitude bias as the relative difference (in percents) between the amplitudes of the observed output anomaly and of the input local perturbation of the group velocity. Zero bias corresponds to the undistorted amplitude imaging. We see that the spatial resolution for the territory defined above is quite high. We resolve features of the size 250 - 300 km on Rayleigh wave maps almost everywhere to the north of latitude 30°N, except NW Iran. The resolution on Love wave maps is slightly worse but still better than 300-350 km virtually everywhere in the same territory. We are able to contour even relatively small sedimentary basins, like the Dzhungarian basin and some others, as slow velocity spots on group velocity maps. The amplitude bias characterizing these group velocity maps is rather small, less than ±10%, except the southern part of the region characterized by poor ray coverage. We used these maps as input to construct the travel time correction surfaces for several seismic stations deployed in this region and belonging to the IMS network, namely AAK (Kirgizstan), ABKT (Turkmenistan), BRVK, KURK, MAKZ (all in Kazakstan), LZH, WMQ (China), and TLY (Russia). Examples of TTCSs for four of these stations are shown in Figure 3 for the 15 s Rayleigh wave. These figures show group velocity corrections δU for the path from any point on the map to a given station. The predicted travel time t for a selected path is found using the formula:

$$t = \Delta/(U^\circ + \delta U),$$

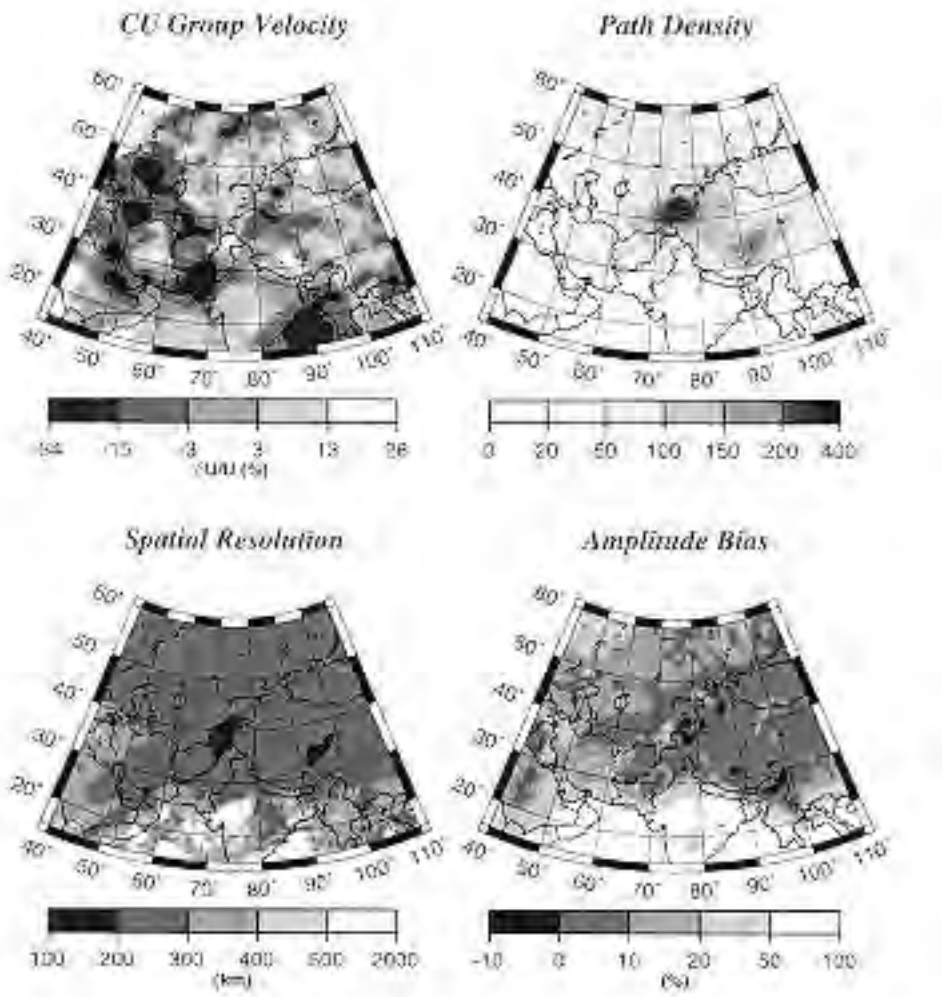


Figure 1. Estimated Rayleigh wave group velocity map and its assessment at the 15 s period. Path density is defined as the number of rays intersecting a 2° square cell.

where Δ is the epicentral distance and U° is the reference value obtained by averaging the group velocities across the input map. Both group velocity maps and TTCSs exhibit significant variations in surface wave group velocities and group travel times across the region.

Synthetic experiments with isotropic tomographic maps.

To estimate uncertainties in tomographic maps and TTCSs constructed from them due to unmodeled sub-scale heterogeneities and random noise in measurements, we performed the following numerical simulations:

(1) the group velocity maps described above were considered as "exact" maps representing the real structure. We traced our set of rays across this model, assuming that waves follow great circle paths, and then introduced the random noise into the resulting average group velocities along each path. The rms of noise was selected to be equal to 0.03 km/s. This noise level is typical for group velocity observations along "clustered" paths (Ritzwoller & Levshin, 1998).

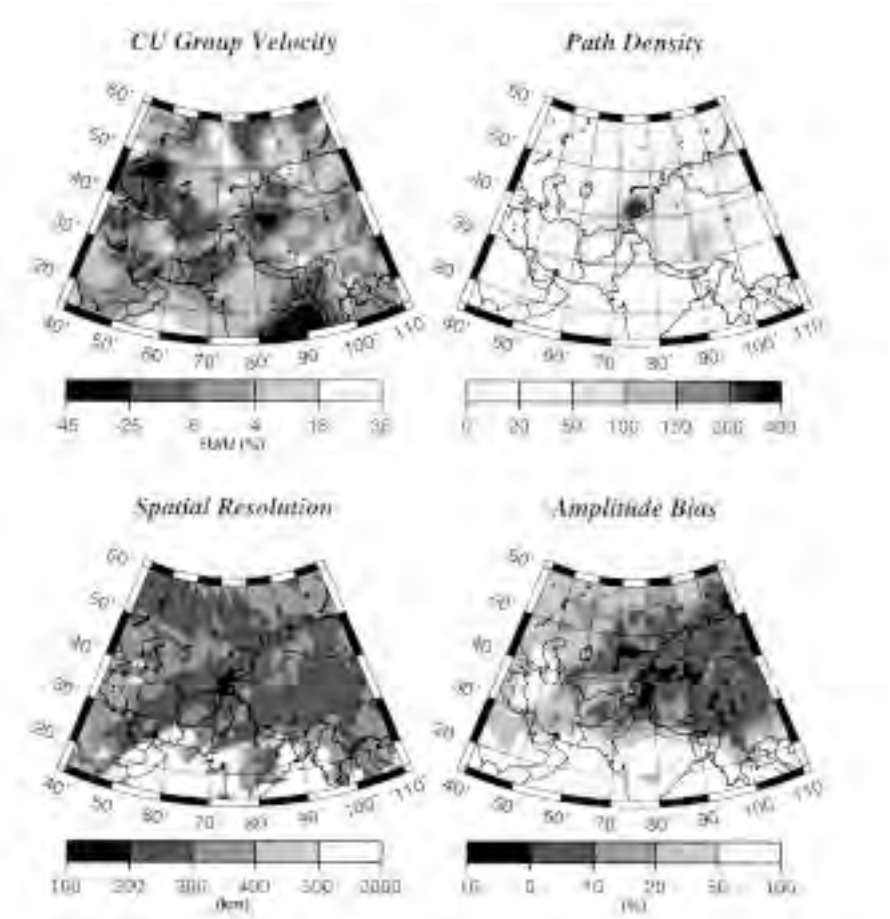


Figure 2. Estimated Love wave group velocity map and its assessment at the 15 s period.

(2) This new set of "data" was then used as the input for the tomographic inversion code. We ran this code several times using different smoothing parameters and different background reference models: "exact" maps and maps predicted by the global crustal model of Mooney *et al.* (1998) . Smoothing parameters were chosen to get slightly "overdamped" tomographic maps. Resulting maps are distorted due to the random noise in input data, unaccounted sub-scale heterogeneity of the medium, and bias caused by the inhomogeneous path density. If we use our "exact" model as the background reference model in constructing the map, the distortion is caused only by the random noise and smoothing. In this case, the bias is minimized due to the rule for a local smoothing imbedded into our code: the less the path density the stronger the penalty for local deviation of a solution from the background model. The rms deviations of obtained maps from the "exact" ones are two or three times higher than the input noise level and slightly decrease with increase of smoothing. The rms deviation of "observed" group velocities from predicted by the constructed model is of the same order as the input noise level. In the realistic case of the absence of a good background model and nonhomogeneous path density, distortions become more significant. Such an example is presented in Figure 4, where we used as the reference models group velocity maps predicted by the crustal global model of Mooney *et al.* (1998). This figure demonstrates difference between the input and constructed maps for the 15 s and 20 s Rayleigh waves and 20 s Love wave. The rms differences between the two maps are much higher than the level of random noise (of the order of 0.1-0.2 km/s), weakly depending on the smoothing parameter. The significant distortions correspond to the parts of the region characterized by poor coverage: the Caspian Sea, NW Iran, Oman Bay. At the same time, for most of the region, including all of Central Asia and Western China where the path coverage is good, the distortions are relatively small (1-2% of velocity values.) Note that the rms deviation of "observed" group velocities along individual paths from those predicted by the constructed model is only slightly higher than the input

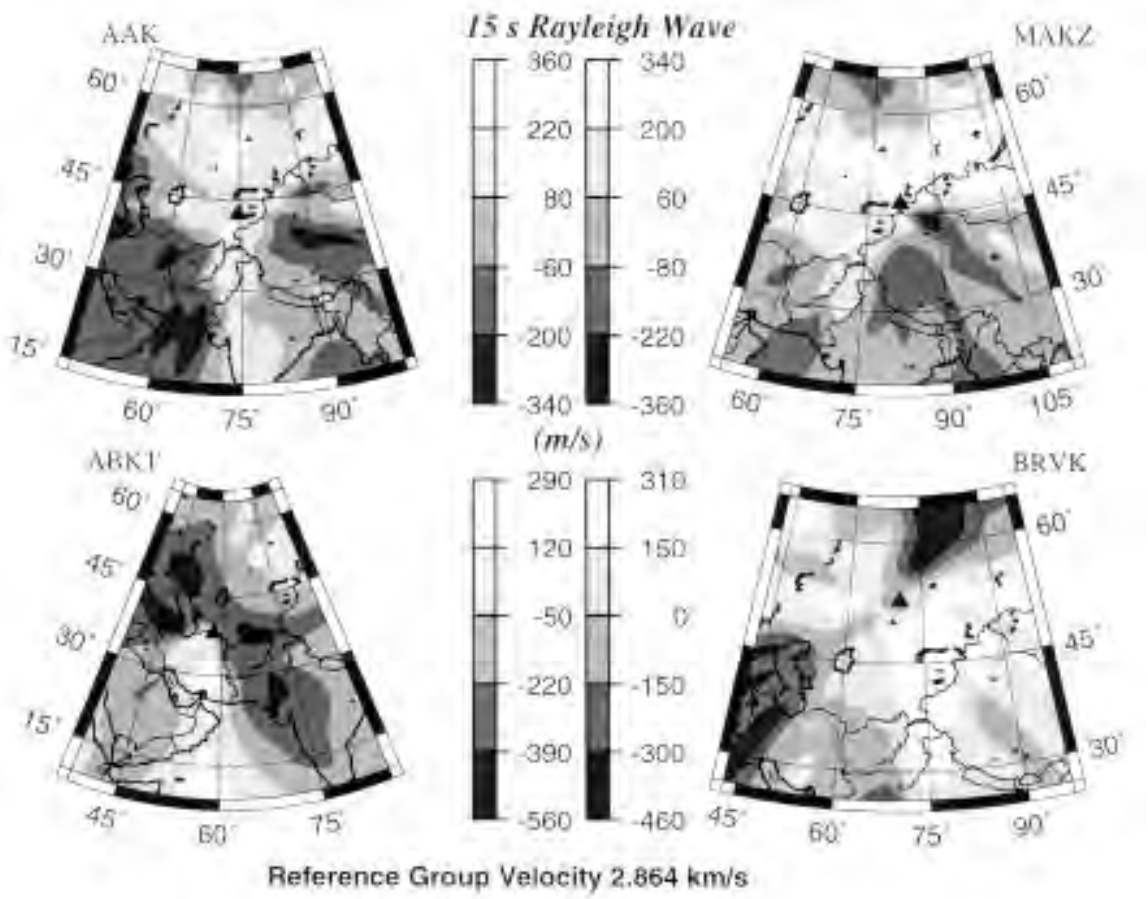


Figure 3. Group velocity correction surfaces for 4 stations in Central and Southern Asia for the 15 s Rayleigh wave. For each geographical point, maps define the group velocity perturbation that should be applied to a 20 s Rayleigh wave observed at a station if an event were located at the chosen point. Perturbations are relative to the reference value of the group velocity.

noise level. This was expected because distortions of the map caused by the poor coverage have almost no effect on group travel times. This example clearly demonstrates the importance of a reliable reference model when the path density is not homogeneous. In the absence of such a model, maps of spatial resolution and of amplitude bias should be used to outline poorly defined areas.

(3) We used these "noisy" and "overdamped" maps for constructing TTCSs, and compared them with TTCSs obtained from "exact" maps. Examples of differential TTCSs are presented in Figure 5. The rms values of differences between predicted and "exact" TTCSs vary from station to station mostly being of the same order of magnitude as the noise level (0.03-0.04 km/s). These values do not change significantly with changes of the smoothing parameters in tomographic inversion. The smallest differences are for the 20 s Rayleigh waves due to the highest density of paths. The largest differences are observed for the station ABKT in Turkmenistan due to the poor coverage of the western part of the region (NW Iran, Figure 5.)

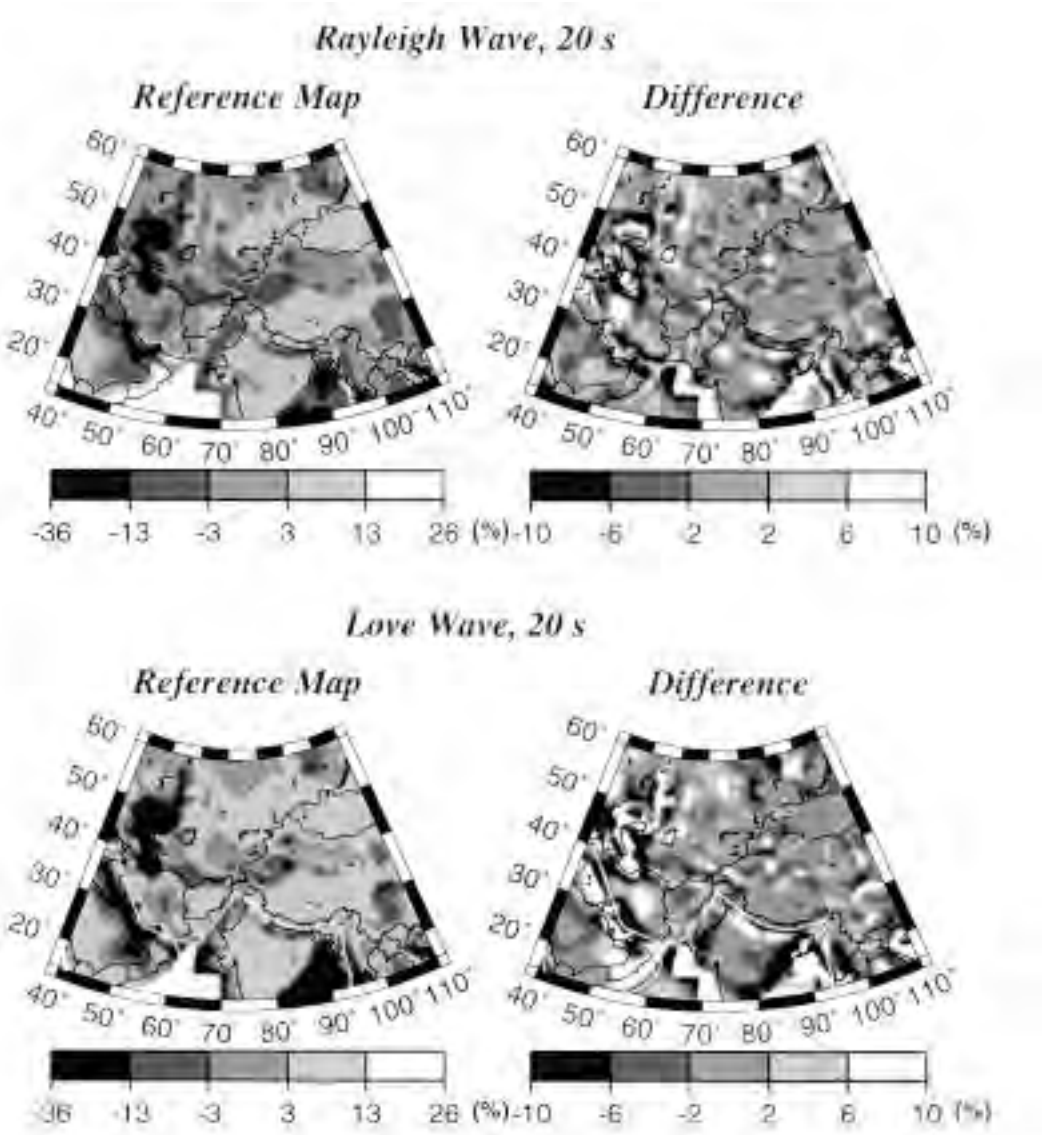


Figure 4 . Synthetic example of errors in the constructed tomographic group velocity map for the 20 s Rayleigh and Love waves. Errors are due to the data noise, path density, and unmodeled sub-scale structures. The left map is an "exact" reference map. The right map is a relative difference (in percents) between the "exact" and constructed maps. The background reference map for the tomographic inversion is predicted by the model CRUST5.1 (Mooney *et al.*, 1998).

Synthetic experiments with anisotropic tomographic maps.

Effects of unmodeled azimuthal anisotropy on tomographic maps and TTCSs were evaluated by the following way:

(1) We introduced 2% of the 2ψ azimuthal anisotropy (Smith & Dahlen, 1973; Trampert & Woodhouse, 1995) into our "exact" maps across the Tibetan plateau , creating "exact anisotropic maps". Then, we traced rays across these maps to get a new "data" set for tomographic inversion.

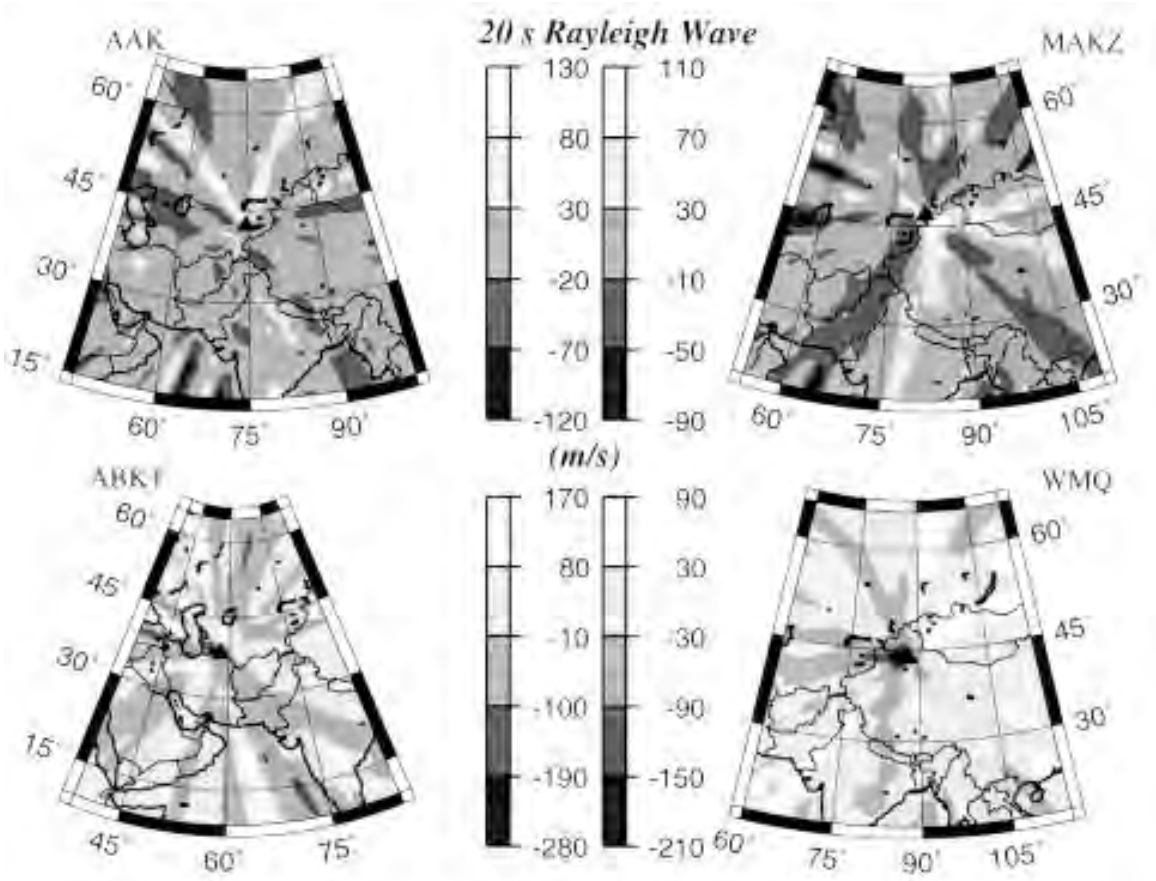


Figure 5. Errors in the travel time correction surfaces for the 20 s Rayleigh wave at four seismic stations. Errors (in m/s) are obtained by subtraction of "exact" correction values of group velocity from values found using the maps shown in Figure 4.

(2) We constructed a new set of *isotropic* tomographic maps using this new set of "data". The resulting maps are distorted due to the unaccounted effect of anisotropy. Differential maps demonstrating the differences between "real" and isotropic tomographic maps are shown in Figure 6. The differences between the "exact" isotropic map and the map constructed from "data" without modeling anisotropy are quite small for all reasonable values of the smoothing parameters. The rms of differences are on the order of 0.025-0.035 km/s, depending on the value of the smoothing parameter used in the inversion. The strongest differences are at some areas around Tibet and the poorly covered southern parts of the region. It is evident from this simulation that azimuthal anisotropy of this level cannot significantly distort the maps and TTCSs.

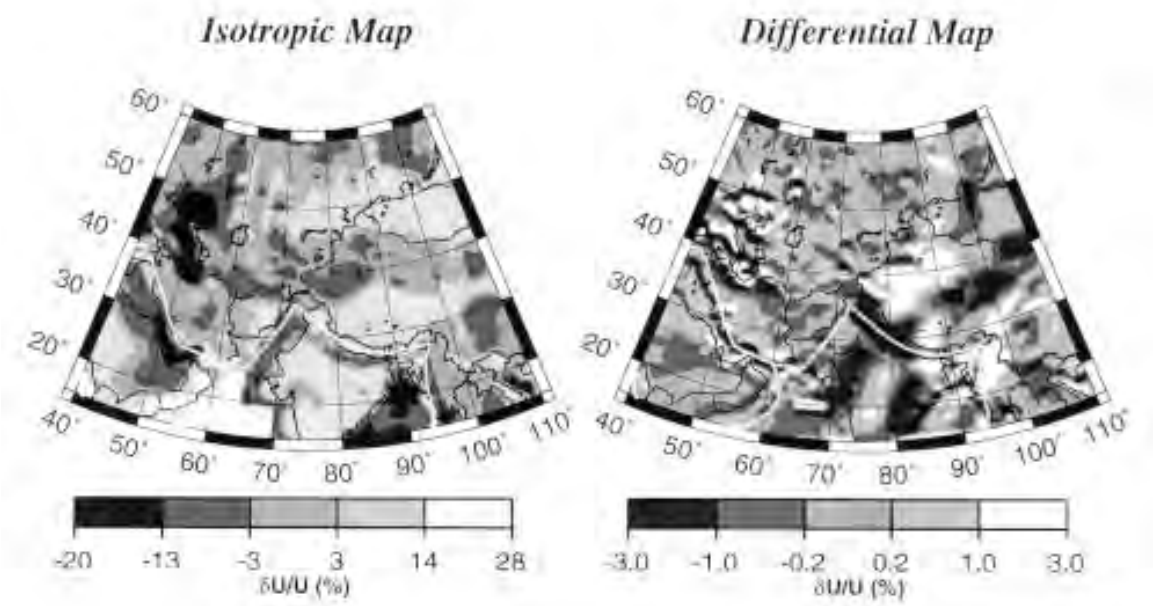


Figure 6. Errors in the group velocity map due to unmodeled azimuthal anisotropy introduced into the isotropic model for the Tibetan plateau. The left map is an "exact" isotropic map. The right map is a relative difference (in percent) between the "exact" and constructed maps.

CONCLUSIONS AND RECOMMENDATIONS

Conclusions

The new technique for tomographic inversion of surface wave dispersion measurements provides necessary means for constructing travel time correction surfaces for selected stations and their assessment in terms of spatial resolution and amplitude bias. The existing set of group velocity measurements across the Central Asia and Western China is sufficient for constructing reliable group velocity maps and TTCSs both for Rayleigh and Love waves at periods 15 s and longer. Synthetic experiments show that in areas with dense ray coverage the spatial resolution of these maps is on the order of 250 - 350 km and the amplitude bias is no more than 10%. We estimate that the accuracy of group velocity maps and TTCSs for the part of the region to the north of 25°N is typically better than 0.03-0.04 km/s. The unmodeled 2% azimuthal anisotropy across such large areas as the Tibetan plateau does not generate significant errors in group velocity maps and TTCSs constructed from them.

Recommendations

This study is based on group velocity measurements for periods above 10 s. To construct efficient phase-matched filters able to extract surface wave signals from events with the *Ms* magnitudes less than 3.5-3.7 it is necessary to broaden the period range of measurements to periods of 6-8 s. Such measurements can be done only for relatively short wave paths of less than 2000 km length. We consider that special efforts should be dedicated to making such measurements across the target region, constructing group velocity maps and travel time correction surfaces, and providing their assessment.

REFERENCES

Barmin, M.P., A.L. Levshin, and M.H. Ritzwoller, Regularized regional surface wave tomography, submitted to PAGEOPH, 1999.

Engdahl, E.R., Development of an archive of seismic ground truth events globally in support of monitoring under the CTBT, *Proceedings of the 20th Seismic Research Symposium on Monitoring a CTBT*, 11 - 15, 1998.

Harkrider, D.G., and N.K. Yacoub, Evaluation of intermediate-period Rayleigh and Love wave global group velocity models, *Proceedings of the 20th Seismic Research Symposium on Monitoring a CTBT*, 453 - 457, 1998.

Herrin, E. and T. Goforth, Phase-matched filters: Application to the study of Rayleigh waves, *Bull. Seismol. Soc. Am.*, **67**, 1259 - 1275, 1977.

Leach, R.R.Jr., D.B. Harris, and W.R.Walter, Phase matched filtering of aftershock sequences to detect Rayleigh waves in low SNR seismograms, *Proceedings of the 20th Seismic Research Symposium on Monitoring a CTBT*, 458 - 465, 1998.

Levshin, A.L. and M.H. Ritzwoller, Characteristics of surface waves generated by events on and near the Chinese nuclear test site, *Geophys.J.Int.*, **123**, 131 - 149, 1995.

Levshin, A.L., M.H. Ritzwoller, and S.S. Smith, Group velocity variations across Eurasia, *Proceedings of the 18th Seismic Research Symposium on Monitoring a CTBT*, 70 - 79, 1996.

Levshin, A.L., M.H. Ritzwoller, L.I. Ratnikova, M. Silitch, R. Kelly, and B. O'Sullivan, Intermediate period group velocity maps across Central Asia and parts of the Middle East, *Proceedings of the 19th Seismic Research Symposium on Monitoring a CTBT*, 67 - 76, 1997.

Levshin, A.L., M.H. Ritzwoller, M.P. Barmin, L.I. Ratnikova, and C.A. Padget, Automated surface wave analysis using phase-matched filters from dispersion maps, *Proceedings of the 20th Seismic Research Symposium on Monitoring a CTBT*, 466 - 473, 1998.

Mooney, W.D., G. Laske, and G. Masters, CRUST 5.1: A global crustal model at 5 degrees by 5 degrees, *J. Geophys. Res.*, **103**, 727 - 748, 1998.

Ritzwoller, M.H. and A.L. Levshin, Eurasian surface wave tomography: Group velocities, *J. Geophys. Res.,* **103**, 4839 - 4878, 1998.

Ritzwoller, M.H., A.L. Levshin, L.I. Ratnikova, and A.A. Egorkin, Intermediate period group velocity maps across Central Asia, Western China, and parts of the Middle East, *Geophys. J. Int.*, **134**, 315 - 328, 1998.

Ritzwoller, M.H., A.L. Levshin, S.S. Smith, and C.S. Lee, Making accurate continental broadband surface wave measurements, in *Proceedings of the 17th Seismic Research Symposium on Monitoring a CTBT*, 482-490, 1995.

Ritzwoller, M.H., O.Y. Vdovin, and A.L. Levshin, Surface wave dispersion across Antarctica and the surrounding oceans: A first look, *Ant. J. U.S.*, in press, 1999.

Russell, D.W., R. B. Herrmann, and H. Hwang, Application of frequency-variable filters to surface wave amplitude analysis, *Bull. Seismol. Soc. Am.*, **78**, 339 - 354, 1988.

Smith, M.L., and F.A. Dahlen, The azimuthal dependence of Love and Rayleigh wave propagation in a slightly anisotropic medium, *J. Geophys. Res.*, **78**, 3321 - 3333, 1973.

Stevens, J.L., Estimation of scalar moments from explosion-generated surface waves, *Bull.Seismol. Soc. Am.*, **76**, 123-151, 1986.

Stevens, J.L. and K.L. McLaughlin, Improved methods for regionalized surface wave analysis, in *Proceedings of the 19th Seismic Research Symposium on Monitoring a CTBT*, 171 - 180, 1997.

Trampert, J., and J. Woodhouse, Global azimuthal anisotropy, *Eur. Geophys. Soc. Newsl.*, **58**, 57, 1996.

Vdovin, O.Y., J.A. Rial, A.L. Levshin, and M.H. Ritzwoller, Group velocity tomography of South America and the surrounding oceans, *Geoph. J. Int'l.*, **136**, 324-330, 1999.

Villasenor, A., M.H. Ritzwoller, A.L. Levshin, E.R. Engdahl, and M.P. Barmin, Construction of a 3-D P and S model of the crust and upper mantle to improve regional locations in W. China, Central Asia, and parts of the Middle East, this volume.

Yanovskaya, T.B., and P.G. Ditmar, Smoothness criteria in surface wave tomography, *Geoph. J. Int*., **102**, 63-72, 1990.

THE NORTHEAST RUSSIA SEISMICITY DATABASE AND EXPLOSION CONTAMINATION OF THE RUSSIAN EARTHQUAKE CATALOG

Kevin G. Mackey and Kazuya Fujita, Department of Geological Sciences, Michigan State University

Sponsored by U. S. Department of Defense
Defense Threat Reduction Agency
Contract No. DTRA-98-C-0168

ABSTRACT

Northeastern Russia (roughly east of 120ºE and north of 55ºN) is one of the most poorly understood regions on Earth from a seismological viewpoint. Even the plate tectonic setting of the region is still a matter of debate. The level of seismicity, epicentral locations, and crustal and upper mantle seismic velocities are poorly characterized. In order to improve our understanding of the baseline seismicity and velocity structure of the region for Comprehensive Nuclear-Test-Ban Treaty monitoring, seismicity data obtained through a cooperative research program between Michigan State University, the University of Alaska, and several institutes in northeastern Russia since 1990, are being analyzed.

The Northeast Russia seismicity database includes epicenter data for approximately 36,000 earthquakes and phase data for 10,000 of these events that occurred in northeastern Russia (Sakha Republic, Magadan District, Chukotka Autonomous District, Amur District; partial coverage of northern Kamchatka, Sakhalin, and Irkutsk Districts) primarily from 1961 to 1999. During this period, several regional networks operated in northeast Russia; however, phase data were not routinely exchanged among the network or with the United States. Sources used to compile the database include the annual *Zemletryaseniya v SSSR* (1961-1992), the International Seismological Center Bulletin (1964-1996), the U.S. Preliminary Determination of Epicenters (1993-1999), *Materialy po Seismichnost' Sibiri* (1970-1990), the Far East Seismic Bulletin (1972-1974, 1985-1988), the epicenter tape from the University of Alaska's Western Alaska regional network (1977-1982), the seismological bulletins of the Russian Yakutsk (1982-1998) and Magadan (1977-1999) regional seismic networks, and phase picks from seismograms.

Included in this database are industrial explosions that have been identified by the Russian regional networks as well as regional micro-earthquakes. The regional seismicity listings include a large number of mining and construction-related explosions, which are listed as earthquakes. In order to determine the level of explosion contamination of these regional catalogs and obtain a better idea of the level of natural seismicity in the region, we analyzed the entire database by examining the temporal variation of events. Since mining and industrial explosions tend to be concentrated during local day, and often to the winter season, extreme temporal biases are indicative of explosion contamination. Regions with such biases can be compared with maps showing placer excavation, roads and railroads, and locations of ore deposits. In this part of Russia, explosions occur in tin, coal, and placer gold mines, and in construction of roads and railroads. Most explosions have magnitudes of about 1.0-2.5 and occur during local day. Placer deposit explosions are concentrated from mid-winter to early spring when frozen placers are broken up for the summer processing season.

Areas with temporal biases indicative of mining or other explosions include the Yana River Delta and Chukotka (placers), southern Amur District (coal mining), the trace of the Baikal-Amur Railroad (construction), Lazo (quarry), south Yakutian gold fields, Omsukchan (tin), other Yakutian gold producing areas, areas of known prospecting (e.g., Lena River Delta), and the Kolyma gold belt. Many of these regions also have a large number of operator-identified explosions. The identification of these explosions indicates that natural seismicity may be of lower level, and not as diffuse, along the plate boundaries in northeast Russia as previously believed. Russian authors have also noted explosions near construction and survey sites for hydroelectric dams along the Kolyma and other rivers.

To obtain further ground truth on explosions, we hope to deploy several digital stations in the Magadan District and investigate waveform characteristics and other discriminants to better understand industrial explosions in the area and to obtain an improved baseline of natural seismicity in the region.

Key Words: explosion discrimination, northeast Russia, mining explosions, seismicity character

OBJECTIVES

Northeastern Russia is very poorly known in terms of its seismicity. Previous studies have focused on the seismotectonics of the region (e.g., Chapman and Solomon, 1976; Riegel et al., 1993), and we now have a better understanding of the plate tectonic setting of the region as a buffer zone between two large continental plates (Fujita et al., 1997). However, the crustal and upper mantle velocity structure, and their implications for earthquake locations from Russian regional network data, remain very poorly known. Mackey et al. (1998) used well located events to perform a first-order analysis of crustal and mantle velocities and determined that a 6.0 km/sec crust overlying an 8.0 km/sec mantle fit well for the region as a whole. They also identified variations in velocities and crustal thicknesses that coincided with pre-Quaternary extension in a broad region in the Verkhoyansk Mountains. In this paper, we report on the assembly of a data base of seismic data on northeastern Russia and the results of preliminary analyses for explosion contamination of the Russian seismicity catalog. Ultimately, we will relocate earthquakes and develop better models for the crustal and upper mantle seismic velocity structure. These will contribute a better understanding of the background seismicity of the region and improve event locations, both of which will support verification of the Comprehensive Nuclear-Test-Ban Treaty (CTBT).

RESEARCH ACCOMPLISHED

Introduction

The study area consists of the region east of 120ºE and north of the Chinese border. We focus on the Sakha Republic (Yakutia), the Magadan District, and the Chukchi Autonomous District, but also encompass the Amur District, northern Khabarovsk District, northern Koryak Autonomous Region, and Sakhalin.

The former Soviet Union operated several analog regional seismic networks in the study area for over 30 years, and significant amounts of data were collected. Of interest here are the former Soviet Magadan, Yakutsk, Amur, and Sakhalin networks, and the American Western Alaska network, as well as portions of the former Soviet Irkutsk and Kamchatka networks. The distribution of network boundaries is shown in Figure 1. As part of a cooperative research program between Michigan State University, the University of Alaska, and several research institutes in eastern Russia, phase and epicentral data from these networks were acquired and are being incorporated into an unified Northeast Russia Seismic Database (NRSD). Although this data base was compiled from Russian analog records, it would take the installation of several tens of permanent digital stations, and a minimum of two decades, to duplicate the database using modern acquisition methods, which is impractical given current economic conditions in Russia.

There are two major sections to the database developed here: A catalog of hypocenters for northeast Russia and western Alaska, and a database of arrival times by combining data from all sources and networks; phase data were not routinely exchanged between the Soviet networks. Other information include industrial explosions and seismic station locations. Approximately 36,000 individual earthquakes have been complied from throughout the region (Figure 1), primarily between 1968-1998. So far, phase data for over 10,000 events (over 100,000 arrival times) have been entered into the NRSD. Historic events and data recorded teleseismically are taken from standard sources such as International Seismological Summary (ISS), International Seismological Centre (ISC) Bulletin, and the United States Geological Survey (NEIC). A few arrivals have also been read from original seismograms.

Russian seismic networks generally report magnitudes (M) for events only of M > 4.0. However, all events have sizes assigned a K-class value, based on the $\log_{10}$ of work release in Ergs. K-class is determined from the maximum amplitudes of the P and S phases using a distance-corrected nomogram calibrated for individual regions (Solonenko, 1974; Pustovitenko and Kul'chitskii, 1974: Gunbina, pers. comm.). Unfortunately, this results in inconsistent size determinations between networks.

Database Sources

The NRSD has been compiled from a large number of sources which report epicentral and phase data. The primary sources, as well as some information on regional network histories, is presented below.

Zemletryaseniya v SSSR (1961-1991; Earthquakes of the USSR) and its successor publication

Zemletryaseniya Severnoi Evrazii (1992; Earthquakes of Northern Eurasia). This annual catalog lists event

parameters for the larger earthquakes which occurred within each regional network. In general, only events of K-class 8.5 and larger are listed, although this varies from year to year and network to network. In addition, the cutoff was often raised for large aftershock sequences. These publications have previously been available in the US and incorporated into other U.S. digital databases (e.g., U.S. Geological Survey CD-ROM).

Materialy po Seismichnost' Sibiri (1970-1990; Data on the Seismicity of Siberia; hereafter *Materialy*). This is a bi-monthly publication with both epicenter lists and phase data for the continental seismic networks in Siberia (Irkutsk, Magadan, Yakutsk, Amur (1979-1990), and Altai). The epicenter list is generally complete, although isolated events found in the Far East Bulletin and in the network bulletins seem to be missing. This bulletin also contains phase data for events of K class 9.5 or greater occurring within a network. This study includes only a small portion of the Irkutsk network (south of 56 N between 120 and 122 E) and none of the data from the Altai network.

Seismologicheskii Byulleten' – Dal'nego Vostoka (Intermittent years obtained; Seismological Bulletin - Far East; hereafter *Far East Bulletin*). This quarterly bulletin is similar in format to *Materialy* and covers the Magadan, Amur, Sakhalin, Kamchatka, and Kurile networks. The epicenter list provided here is generally complete for Magadan and Amur. For the Kamchatka network, only events of K-class larger than 9.0 are listed. Coverage of phase data varies from network to network.

Magadan Network Bulletin (1977-1998). The Magadan Experimental Methodological Seismological Division (EMSD) network was formally established in December, 1979. Earthquakes were located using Pg and Sg time differences. Prior to 1982, locations were computed by hand. In 1982, computers were first used for locations, and the network switched to computer only determinations in the early 1990s. A velocity structure derived from the Magadan – Srednikan refraction profile (Davydova et al., 1968) was used (Pg 6.1 km/sec, Sg 3.5 km/sec). The epicenter lists and phase data for located events are identical to that found in the *Far East Bulletin*; however, the network bulletin contains additional material on explosions and unlocated events.

Yakutsk Network Material (1982-1998). The Yakutsk network was established in the mid-1960s. The Yakutsk network has operated a large number of permanent and temporary seismic stations in Yakutia and adjacent regions. All earthquake locations determined by the Yakutsk network are calculated by hand by drawing arcs on 1:5,000,000 scale maps. Epicentral distances are determined by Sg-Pg time differences for each station. Pg velocities of 6.0 or 6.1 km/sec and Sg velocities between 3.5 and 3.7 km/sec are used depending on location. Explosions with associated arrival times are also given, but are not always located. Data from the 1971 Artyk and 1989 South Yakutia aftershock studies are also included in the database.

Kamchatka Seismicity Catalog (1962-1966). Seismic stations were first opened on Kamchatka peninsula in 1948, with a rapid increase in the number of stations in the 1960s. Earthquake locations were computed by hand up until 1978, when location procedures were computerized (E. Gordeev, pers comm.). Only earthquakes in the region north of 56^{o} N (north of the subduction zone) are included in our database. The relevant epicenters were extracted from the catalog, which contains 55,000 earthquakes. Some phase data were taken from the *Far East Bulletin*.

Western Alaska Network. The Western Alaska Network was operated from 1977 to 1982 (closed for 1980), in the region of the Seward Peninsula, Alaska (Figure 1) (Biswas et al., 1983; Biswas et al., 1980). Focal parameters for 1,010 earthquakes were computer determined using first arrival P times and S-P differences. The epicenter catalog was taken from Biswas et al. (1983) and the complete computerized phase and arrival time listings were downloaded from archive tapes at the Geophysical Institute, University of Alaska, Fairbanks.

Northeast Russia Test Network. In the mid 1960's a number of experimental seismic stations were established throughout northeast Russia to determine background seismicity levels to aid in developing permanent seismic networks (Mishin, 1967). The distribution of seismicity located using the test network was instrumental in site selection for future seismic stations. Most of the temporary stations were deployed for between 6 months and 1 year. Hypocenters obtained from the test network given in Andreev (1967) are included in the database. Phase data for the events are not available.

Seismograms. Supplemental arrival times, mainly for teleseisms, were hand picked from seismograms in Yakutsk and Magadan. In addition, phase data for approximately 50 events from Chukotka were picked from develocorder records for Alaskan network stations. Additional data will be obtained.

Other. Data were also acquired from other publications. Earthquake data for 1920-1999 were obtained from the ISS, the ISC Bulletin, NEIC (Preliminary Determination of Epicenters listings), the Alaska Earthquake Information Center (AEIC), Kondorskaya and Shebalin (1982), and Godzikovskaya (1995).

In compiling the database, numerous phases have been reidentified, and conflicts between the different sources have been resolved. Upon completion of the database assembly, all events will be computer relocated using travel-time curves determined separately for individual regions (generally 1 x 2 degree blocks).

Seismicity Map

The current seismicity map with plate boundaries after Fujita et al. (1997), network boundaries, and seismic stations is shown in Figure 1. Overall, seismicity levels in northeast Russia are much higher than is generally recognized in the literature. Moreover, the seismicity distribution is likely to be biased by station distributions. For example, there is a distinct lack of microseismicity in the northwestern Sea of Okhotsk. This may entirely be a result of the distribution of the regional seismic networks. Note on Figure 1 that this region is near the intersection of the Magadan, Yakutsk, Amur, Sakhalin, and Kurile networks. Although there is microseismicity trending into the region from each of the surrounding networks, the distances to individual stations are high, and combined with the lack of data exchange between neighboring networks, small events occurring in this region are most likely detected by only one or two stations in each network and thus below the detection or location threshold for any individual network. Since data were not exchanged between networks, the region appears aseismic.

Explosion Contamination

The seismicity catalog for Eastern Russia, and therefore Figure 1, is known to be contaminated by a large number of industrial explosions (e.g., Godzikovskaya, 1995; Odinets, 1996). In this part of Russia, explosions occur in tin, coal, and placer gold mines, as well as in prospecting and the construction of roads, railways, and dams. Many of the active mines are located in seismically active regions, which has resulted in misidentification of mine blasts as earthquakes. The contamination of the seismicity catalog with explosions results in an erroneous perception of the level and distribution of natural seismicity.

While analysis of waveform data for all reported earthquakes is desirable, it would require an unrealistic re-examination of several hundred thousand analog seismograms. However, a qualitative estimate of the level of explosion contamination can be obtained by examining the spatial, size, and temporal characteristics of earthquakes located by the regional networks. Thus, we investigated explosion contamination in the study area primarily through temporal analysis of origin times; both time of year and time of day were considered.

Early attempts at explosion filtering from the late 1960's through mid-1970's in the Magadan region simply removed all events within a particular radius of stations in some of the mining regions (V. N. Kovalev, pers. comm.); however, this also removes tectonic events and creates peculiar rings of seismicity (Riegel, 1994). Beginning in the late 1970's, station operators attempted to discriminate close events (up to 50 - 70 km) based on waveform characteristics and information from the mining companies. Unfortunately, not all mining companies provided information on their blasting activities (V. N. Kovalev, pers. comm.), and waveform characteristics tended to vary. Thus, all catalogs containing events of $M < 3.5$ (K-class 11) remain contaminated with explosions.

Previous work on identifying explosion contamination has been undertaken by Godzikovskaya (1995), who identified several regions of explosion contamination in the Amur and Kolyma Districts and Chukotka. Odinets (1996) also determined that a large fraction of earthquakes reported in the central Kolyma region are actually explosions. Industrial explosions locatable by the regional networks have magnitudes of about 1.5 - 3.0 and occur during the local day (Godzikovskaya, 1995; Odinets, 1996). Placer deposit explosions are also concentrated during the late winter and early spring, when frozen ground is broken up for the summer processing season.

The examination of this temporal bias in the seismicity can, in a broad sense, indicate potential regions of

explosion contamination (Agnew, 1990). Unfortunately, unlike standard practice in the United States, blasting in Russia is not confined to a specific time of day, but may occur at any time during the workday. A small, but not statistically significant, number of explosions are also known to occur at night (Godzikovskaya, 1995) since Russian law requires that explosives loaded into boreholes can not be kept overnight, but must be detonated (V. N. Kovalev, pers. comm.). This results in some night blasting, and is supported by a small number of nighttime explosions listed in the network bulletins. In Figure 2, the study area is divided into cells in which the percentages of daytime earthquakes are calculated. Cells containing fewer than ten events were not considered to be statistically significant, and were not analyzed. The 12 hour local "day" has been shifted according to time zones. Dark gray areas represent regions where seismicity is roughly balanced between night and day, and light gray areas are those in which seismicity is concentrated during local night (>65%). There are many areas of nighttime-biased seismicity, most of which are in seismically less active regions and away from seismic stations. This is not unexpected since almost all seismic stations in the area are located in populated areas, and thus have lower cultural noise during the night.

Black areas on Figure 2 represent regions where more than 65% of the seismicity occurs during local "day". Many of the regions with predominantly daytime events are found in discrete clusters or trends of seismicity, most of which can be associated with mining or construction related blasting. Several clusters of seismicity in the Amur region have more than 90% of the events occurring during local day. There are a few cells with predominantly daytime seismicity that we are unable to explain with explosions. These cells are probably a result of random statistics of small numbers as these cells generally are close to the 10 event cutoff. Below, we examine several regions shown in Figure 2 of daytime bias which can be positively related to explosion contamination.

Explosion Contamination by Region

One of the clearest regions of explosion contamination is the **Amur District** (Area 1, Figure 2). Here, the distributions of daytime and nighttime epicenters (Figures 3 and 4 respectively) show distinct differences. We present two examples of the temporal distribution of seismicity. The first (Figure 5) is Area A in the northern part of Figure 3. The seismicity here is believed to be tectonic, as the region is generally unpopulated and thus should not contain any contamination due to mining. This region can therefore be used as a baseline to which other analysis can be compared. The area analyzed contains 399 located earthquakes, with 189 having occurred during local daytime and 210 during local night. This corresponds to a day/night ratio of 0.9, which is essentially the same for the aftershock sequence of the 1989 South Yakutian earthquake.

The second (Figure 6) is an example of a cluster of "day" only seismicity that correlates with the Raychikhinsk coal mining region (Figure 3). Here, and in some other regions, the seismicity also varies by season. Figure 6 shows activity only during winter months and during local "day". However, in the nearby Khingansk mining region (Figure 3), events occur throughout the year but only during the day. There is also industrial activity in the region around Komsomolsk' na Amur. Origin times and times of year for explosions vary from place to place, for example, events in the Raychikhinsk, Khingansk, and Komsomolsk' na Amur center around 05 hours UTC, which corresponds to 1 PM local time. However, the explosion maximum occurs around 05 hours UTC (12 noon local time) in the mines about 5 km to the north of Chegdomyn and there is a bias towards summer months.

The seismicity near Svobodniy is consistent with an anthropogenic origin. However, the existence of mining in this region is unclear from the available maps. Events here show a slight bias toward summer months. Events occur about 40 km northeast of Shimanovsk along the west bank of the Zeya river. Events located in this region occur exclusively during daylight hours, but with a slight bias towards mid winter. Near Oktyabrskiy, extensive placer mining has occurred in the vicinity of the town, primarily to the north and southeast, and along the Gar' River valley to the south. Origin times indicate that almost all blasting occurs during the winter daytime.

Some regions have a mix of natural and anthropogenic seismicity. Prior to 1981, a small number of earthquakes occurred in the Taldan region with no bias in origin times, indicating natural seismicity. In addition, a magnitude 5.0 event occurred during the night of January 31, 1985. Beginning in 1981, however, the number of events rose drastically, and a strong daytime bias was introduced into the origin times. Explosion contamination due to dam construction in the Zeya basin region to the east (near 54^{o}N,

127°E) is discussed at length by Godzikovskaya (1995). The region around Ekimchan is also consistent with a mix of tectonic events and explosions. There are a total of 283 events in this region, with 92 occurring during the nighttime. If we assume that the number of daytime tectonic events is 0.9 of the nighttime level (83 events), then the total number of tectonic events in this region is about 175. Therefore, the number of explosions is 106, representing a 37% contamination of the database.

In the north-central portion of Figure 3, there is a northwest-southeast trend of predominantly daytime and summer seismicity extending several hundred kilometers which correlates with the route of the Baikal-Amur railroad (BAM) and is assumed to be explosions associated with its construction in the 1980's. Note also that most events are located to the west of the track in the central portion, and to the north of the track in the northern portion, indicating systematic errors in the epicentral locations. The region also has some tectonic earthquakes, as there are a reasonable number of nighttime events. A cluster of events south of the railway south of Tynda is likely to be mining associated as the events are biased more towards early winter.

Overall, as the explosion contamination appears to be confined to daylight hours, nighttime seismicity should better reflect the level and distribution of tectonic earthquakes (Figure 4). Compared to the daytime map (Figure 3), a different, more northerly trend appears in the plotted nighttime earthquake epicenters, which probably delineates an active tectonic feature that was previously obscured with clusters and trends of explosions. We also note that the teleseismically located events fall almost entirely within the regions where seismicity occurs in the night. Clusters and trends of primarily daytime events have very few events of magnitude 4 or larger.

Polyarnyi and **Leningradsky** (Area 2, Figure 2) are placer gold deposits located along the coast of the Chukchi Sea, while Plamennyi, slightly inland, is a mercury deposit which was mined from 1967 to 1972 (Pilyasov, 1993). From 1966 to 1982, most of the events located in this area were single station locations obtained by the three-component station at Iul'tin (ILT). A clear bias towards winter and daytime is evident for the events in the mining region. Several events are also located near Plamennyi after closure of the mine and may be due to known continued prospecting or mislocations from Leningradsky and Polyarnyi. Comparison of origin times of ILT-located events with more recent, known, explosions from the same area yields a nearly identical temporal distribution, with blasting primarily in the daylight hours of late winter and spring. The complete lack of teleseismically recorded events around Polyarnyi-Leningradsky-Plamennyi, as compared to an area a few hundred kilometers to the southeast, is also consistent with explosions. Some previous authors (e.g., Lander, 1996) have used the explosions reported here both in tectonic models, and assessment of seismic risk, resulting in erroneous conclusions. Earthquakes located by ILT in eastern Chukotka do not show any temporal bias, and probably represent tectonic events.

A cross of predominantly daytime seismicity lies in the **Kolyma gold mining belt** (Area 3, Figure 2). Tectonically, this region is extremely complex in that it is located just south of the Ulakhan Fault system along which motion between the Okhotsk block and the North American plate is occurring (Riegel et al., 1993). Therefore easy statistical separation of anthropogenic and tectonic sources is difficult. Mining in this region is primarily placer gold, but also includes coal and other minerals. Temporal analysis of a cluster of events northwest of Susuman yields a clear bias towards local day and winter/spring. This is consistent with the distribution of known explosions from the Magadan seismic bulletin for this region. The eastern half of the cluster is composed entirely of explosions, while the western half probably contains some tectonic events. There is also a reduced numbers of nighttime events within a 100 kilometer radius of Susuman, which is also indicative of mining.

The Kolyma hydroelectric dam is located about 200 kilometers southeast of Susuman. Blasting during construction of this dam resulted in contamination of the earthquake catalog (Godzikovskaya, 1995) and there is a an elevated level of daytime seismicity for approximately 100 km upriver from the dam. A second cluster of primarily daytime events exists approximately 120 km to the east in the vicinity of the Ust' Srednikan dam project. Godzikovskaya (1995) also notes explosion contamination there.

A puzzling cluster of seismicity is located south of Susuman near the town of Kulu. This cluster is biased towards winter months, but only slightly towards daylight hours. The events occurred in the 1970's and 1980, with a few events each year. In 1980, when the seismic station at Kulu opened, the earthquakes essentially stopped. This would be consistent with explosions, with the local operator removing explosions from the catalog.

Placer gold deposits around **Ust' Nera** (Area 4, Figure 2) are on the northwest extension of the Kolyma gold belt. Seismicity in the vicinity of Ust' Nera is biased towards daytime, with 10 "day" and 2 "night" events, although statistics of small numbers may be a factor. The region immediately to the southeast and east of Ust' Nera, however, is very active tectonically, and events of up to magnitude 7 have occurred.

Lazo (Area 5, Figure 2) is a gold placer deposit between the Adycha and Nel'gese Rivers at 66.51N, 137.01E. Seismicity here is almost entirely confined to the daytime in the early part of the year, thus they are likely to almost exclusively be explosions. A similar looking cluster of seismicity about 100 km south of Lazo has been suggested to be of mining origin (V. Imaev, pers. comm.), although the temporal variation is more consistent with tectonic activity.

The **Deputatsky** (Area 6, Figure 2) tin mining region is completely biased to winter events, with 13 events reported during winter day and 2 events during winter night. There are no events reported in the summer months, a good indicator of an anthropogenic origin. However, caution must be taken as the number of events is small. A cluster to the north appears to be tectonic in origin.

The region around **Kular** (Area 7, Figure 2) and to the north is an extensive placer gold mining region. Coal has also been mined southeast of Kular along the banks of the Yana River. The coal mining operations closed in the past few years, but in the mid-1990's gold mining operations began south of Severnyi, about 25 km southeast of Kular. Reported seismicity in the Kular region forms an elongated north-south trend, an excellent correlation with explosion locations. Temporal analysis of reported seismicity in the Kular region shows a strong bias to winter and daytime, also consistent with explosions from mining (Figure 2-34).

Reported seismicity in the **Stolb** (Area 8, Fig. 2) region is probably contaminated by daytime explosions. From 1988 to present, the geological survey in Moscow has been conducting explosions in this region along the Lena River looking for placer deposits of diamonds. Although there are only 12 earthquakes that fall within this region, 9 occur during daylight hours, and 8 occur between 1989 and 1994.

Yugorenok (Area 9, Fig. 2) is a mining region along the Yudoma and Allakh-Yun rivers. Of the 25 earthquakes located in the vicinity, 20 occur during winter daytime hours. In addition, there are no large events associated with this cluster of seismicity. Two other small seismicity clusters to the north are both associated with teleseismic events, and do not show any strong temporal biases in their origin times, which suggests tectonic origins.

South Yakutia (Area 10, Fig. 2) is similar to the Kolyma gold belt in that there are tectonic events occurring in the vicinity of mining regions. Several cells in this area show strong daytime biases, each of which is associated with mining. Three regions are of note in the south Yakutia region. Aldan is a mining region with extensive deposits of gold and phlogopite mica (Shabad, 1969). The region is associated with a diffuse cluster of predominantly daytime reported seismicity. Explosions from the Aldan mining region are also located and listed in the Yakutsk bulletin.

Approximately 200 km south of the Aldan is an extensive coal mining region near Chul'man. The Chul'man mining region produces many explosions, some of which are located by the Yakutsk network and identified and listed in the bulletin. The seismic station at Chul'man seems able to identify and filter the explosions, as a plot of the temporal distribution of reported earthquakes shows no bias.

To the northeast of Chul'man is a dense cluster of seismicity near the settlement of Spokoynii. The events show a strong bias towards daytime and winter events, which is consistent with placer mining and Soviet military 1:200,000 scale topographic maps (dated 1986) which show extensive mine workings in the region. The published literature, however, has no mention of any mining activity in this region, nor does the Yakutsk network bulletin identify any explosions in the region. Overall, the nature of activity at this location remains unclear.

Finally, there is one cell in northern Alaska with seismicity predominantly in the summer and fall. This coincides with the location of the **Red Dog Mine** (Area 11, Figure 2) in the western Brooks range. Exploratory work prior to the opening of the mine occurred while the Western Alaska Network was in operation, which probably recorded and located a number of blasts (D. Thurston, pers. comm.).

CONCLUSIONS AND FUTURE WORK

Compilation of the NRSD and based on simplistic temporal analysis thereof, it is evident that the seismicity catalog of northeast Siberia is heavily contaminated with industrial explosions. Identification of these explosions and their removal from the seismicity catalog is essential in studying and understanding the tectonics and associated natural seismicity of the region. Overall, it appears that the majority of contamination in the seismicity catalog results from daytime mine blasts. Using phase data from the NRSD, we plan to derive local travel-time curves, relocate events using them, and further refine crustal and upper mantle seismic velocities in northeast Russia. In addition, several seismic stations were deployed in the Magadan district in the summer of 1999 to obtain digital waveforms and further improve our understanding of local explosions and wave propagation in the area.

REFERENCES

Andreev, T. A., Kravets, I. F., and Mishin, S. V.,1967, On the seismic activity of the Northeast: *Trudy SVKNII*, v. 30, Magadan, p. 159-166 (in Russian).

Agnew, D. C., 1990, The use of time-of-day seismicity maps for earthquake/explosion discrimination by local networks, with an application to the seismicity of San Diego county, *Bulletin of the Seismological Society of America,* v. 80, p. 747-750.

Biswas, N.N., Gedney, L., and Agnew, J., 1980, Seismicity of western Alaska: *Bulletin of the Seismological Society of America*, V. 70, p. 873-883.

Biswas, N. N., Pujol, J., Tytgat, G., and Dean, K., 1983, *Synthesis of Seismicity Studies for Western Alaska*, Final report, contract NA81-RAC00112: Fairbanks, Alaska, University of Alaska Geophysical Institute, 74 p.

Chapman, M. E., and Solomon, S. C., 1976, North America – Eurasian plate boundary in northeast Asia: *Journal of Geophysical Research*, v. 81, p. 921-930.

Davydova, N. I., Shvarts, Ya. B., and Yaroshevskaya, G. A., 1968, Wave patterns in deep seismic sounding along Magadan-Kolyma profile, *in* Deep Seismic Soundings of the Earth's Crust in the USSR: *International Geology Review* - Book Section, v. 10, p. 93-102.

Fujita, K., Stone, D. B., Layer, P. W., Parfenov, L. M., and Koz'min, B. M., 1997, Cooperative program helps decipher tectonics of northeast Russia: *Transactions of the American Geophysical Union (Eos*), v. 78, p. 245, 252-253.

Godzikovskaya, A. A., 1995, *Local Explosions and Earthquakes*: Rossiskoe Aksionernoe Obshchestvo Energy and Electrification "EES Rossii", Moscow, p. 55-66 (In Russian).

Imaev, V. S., Imaeva, L. P., Koz'min, B. M., and Fujita, K, 1994, Active faults and modern geodynamics of the Yakutia seismic belts: *Geotektonika*, p. 59-71 (in Russian).

Kondorskaya, N. V., and Shebalin, N. V., eds., 1982, *New Catalog of Strong Earthquakes in the USSR from Ancient Times Through 1977*: World Data Center A for Solid Earth Geophysics, Report SE-31, xi+608 pp.

Lander, A. V., Bukchin, B. G., Droznin, D. V., and Kiryushin, A. V., 1996, The tectonic environment and source parameters of the Khailino, Koryakia earthquake of March 8, 1991: Does a Beringia plate exist?: *Computational Seismology and Geodynamics*, v. 3, p. 80-96.

Mackey, K. G., Fujita, K., and Ruff, L. J., 1998, The crustal thickness of northeast Russia: *Tectonophysics*, v. 284, p. 283-297.

Materialy po Seismichnost' Sibiri, 1970-1990: Academy of Sciences of the USSR, Siberian Branch, Irkutsk (bi-monthly, in Russian).

Mishin, S. V., 1967, *Experimental Instrumental Seismological Investigations in the Northeast USSR*: Laboratory of Regional Geodynamics, NEISRI, Magadan, 165 pp. (In Russian).

Odinets, M. G., 1996, The problem of polluting the earthquake catalog with industrial blasts in northeastern Russia, *in* Lin'kova, T. I., and Bobrobnikov, V. A., eds., *Geophysical Models of Geologic Processes in Northeast Russia*: NEISRI, Magadan, p. 90-99 (in Russian).

Pilyasov, A. N., 1993, Regularities in the mining-industrial mastery of northeast Russia: *Kolyma*, 1993(8), p. 5-12 (in Russian).

Pustovitenko, B.G., and Kul'chitskii, V.E., 1974, About energy estimates of earthquakes in the Crimea-Black Sea region *in* Kondorskaya, N. V., Nersesov, I. L., Gorbunova, I. V., Rautian, T. G., and Korchagina, T. G., eds*., Magnitude and Energy Classification of Earthquakes v. 2*: IPE AS USSR, Moscow, p. 113-124 (In Russian).

Riegel, S. A., Fujita, K., Koz'min, B. M., Imaev, V. S., and Cook, D. B., 1993, Extrusion tectonics of the

Okhotsk plate, northeast Asia: *Geophysical Research Letters*, v. 20, p. 607-610.
Riegel, S. A., 1994, *Seismotectonics of Northeast Russia and the Okhotsk plate*: M.S. Thesis, Michigan State University, East Lansing, ix + 70 pp.
Seismologicheskii Byulleten' – Dal'nego Vostoka, 1972-1988: Academy of Science of the USSR, Far Eastern Branch, Yuzhno Sakhalinsk (in Russian).
Shabad, T., 1969, *Basic Industrial Resources of the USSR*: Columbia University Press, New York, 393 pp.
Solonenko, 1974, Energy classification of earthquakes of Prebaikalia,. *in* Kondorskaya, N. V., Nersesov, I. L., Gorbunova, I. V., Rautian, T. G., and Korchagina, T. G., eds., *Magnitude and Energy Classification of Earthquakes, v. 2*: IPE AS USSR, Moscow, p. 174-179 (In Russian).
Zemletryaseniya v SSSR, for *1961-1989*: Nauka, Moscow (annual, in Russian).
Zemletryaseniya v SSSR, for *1990-1991*: Russian Academy of Sciences, Moscow (annual, in Russian).
Zemletryaseniya Severnoi Evrazii, 1992: Geoinformmark, Moscow (in Russian).

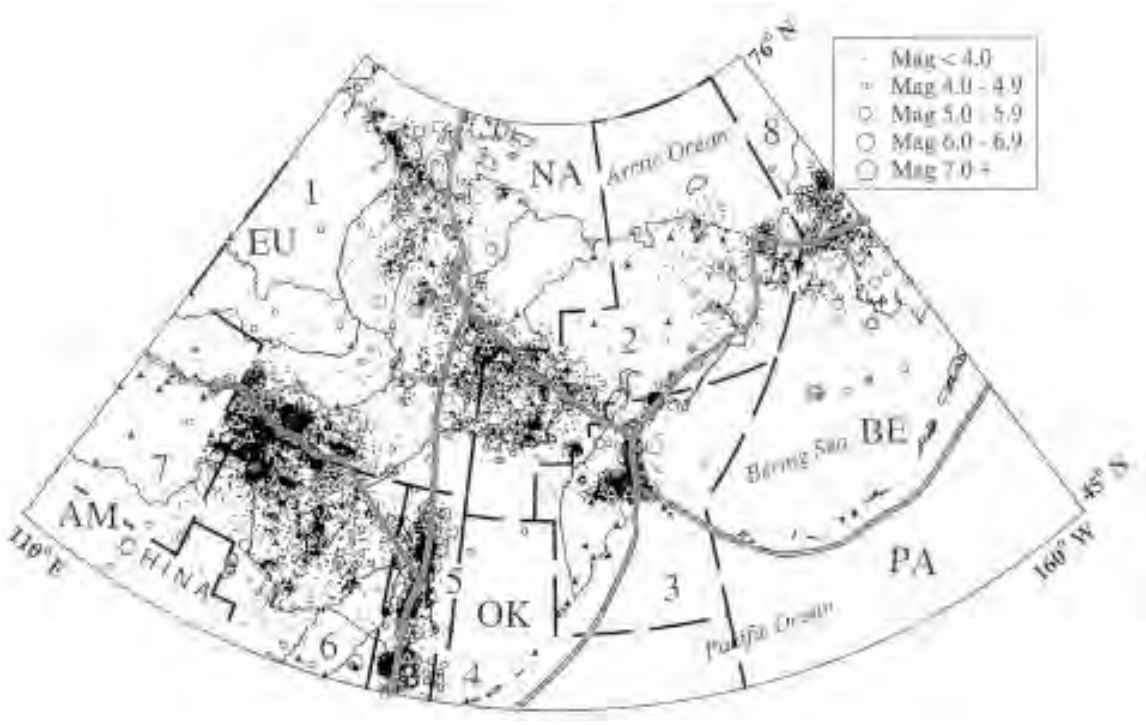


Figure 1. Seismicity map of northeast Russia showing network boundaries (long-dashed lines), plate and block boundaries (stippled lines), and all earthquake epicenters (dots, sized by magnitude). Triangles show locations of regional seismic stations. Abbreviations for plates or blocks are: PA – Pacific; NA – North America; EU – Eurasia; AM – Amur (North China) block; OK – Okhotsk block; and BE – Bering Block). Networks identified by number 1 – Yakutsk; 2 – Magadan; 3 – Kamchatka ; 4 – Kurile; 5 – Sakhalin; 6 – Amur; 7 – Irkutsk; and 8 – Western Alaska.

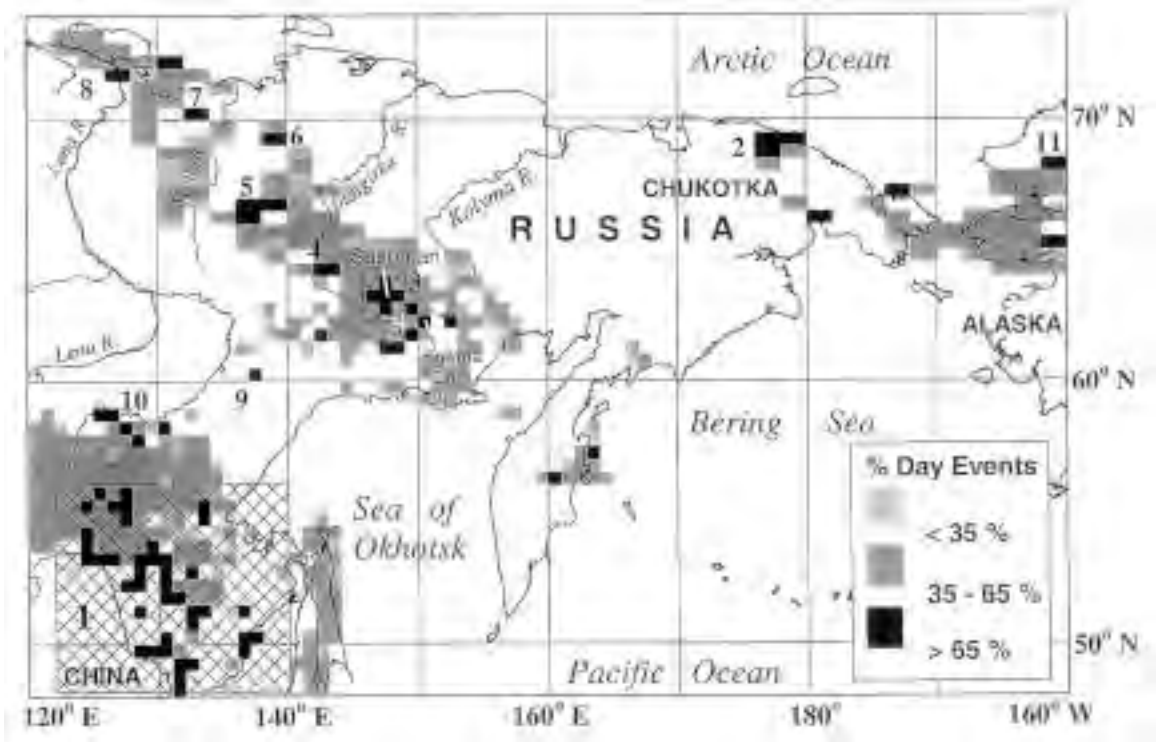


Figure 2. Grid map of northeast Russia showing areas where seismic events are concentrated during local day (black), local night (light gray), or balanced (dark gray). White indicates insufficient data. Numbers denote areas discussed in text; cross hatching denote larger areas.

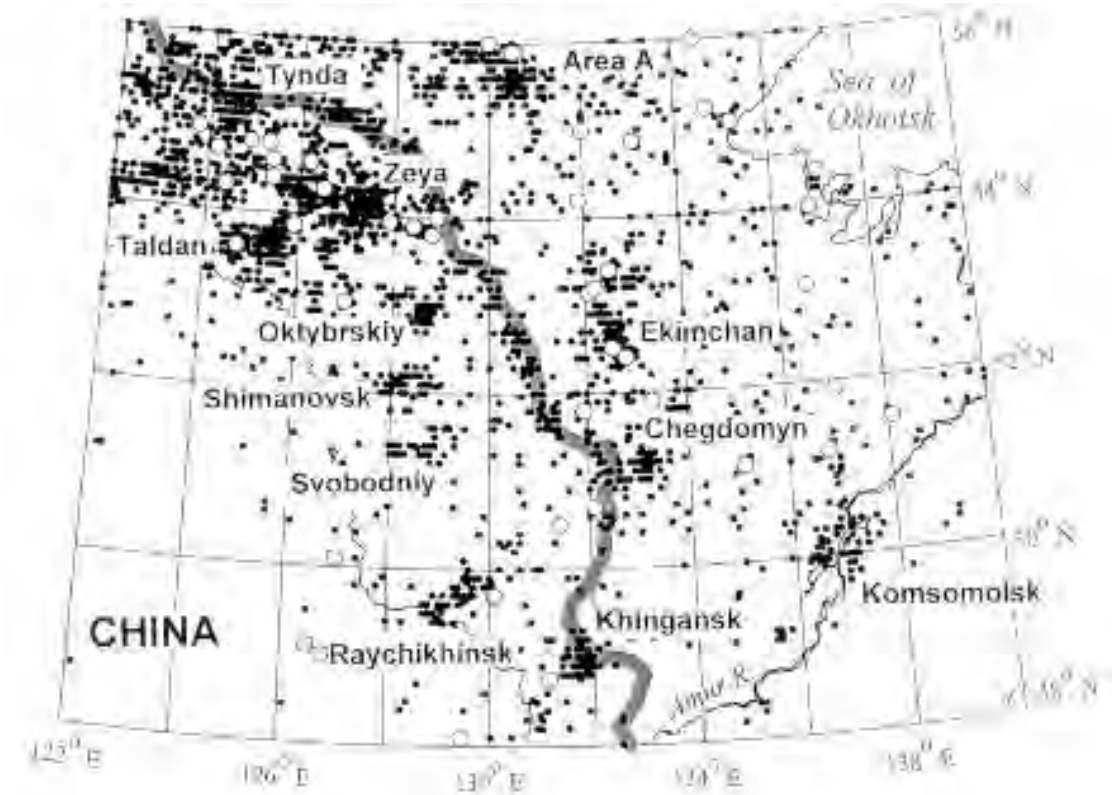


Figure 3. Daytime seismicity of the Amur district and locations discussed in text. Grey line shows Baikal-Amur railroad. Open circles are teleseisms.

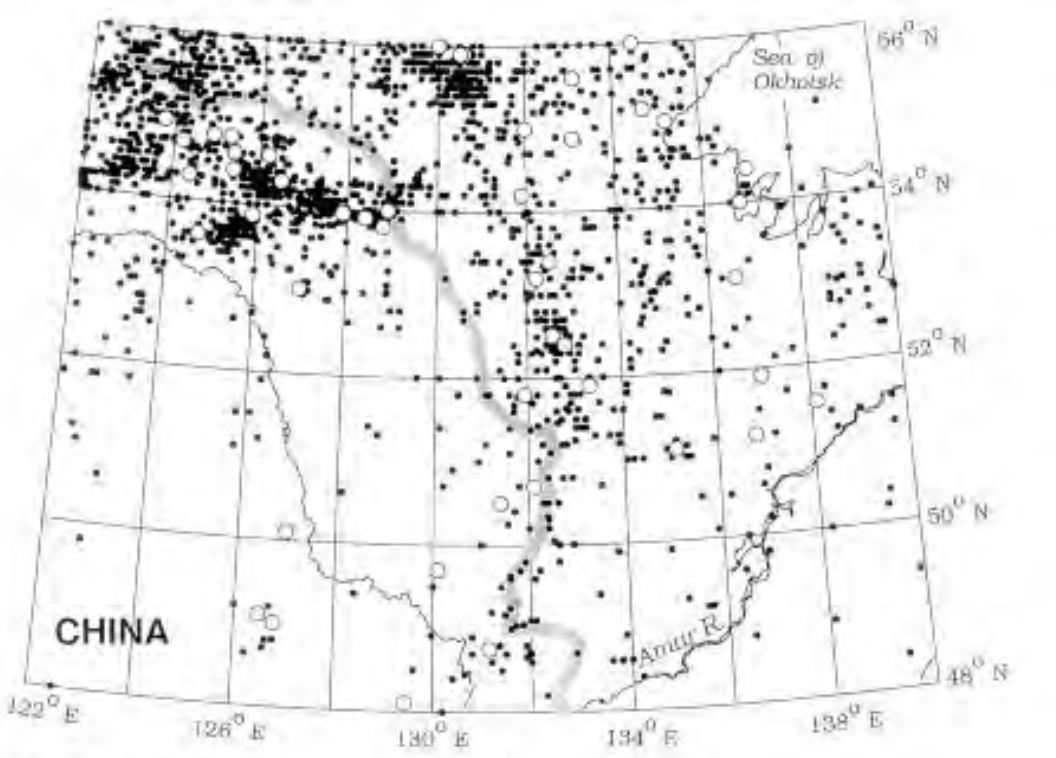


Figure 4. Nighttime seismicity of the Amur district. Key is identical with Figure 3.

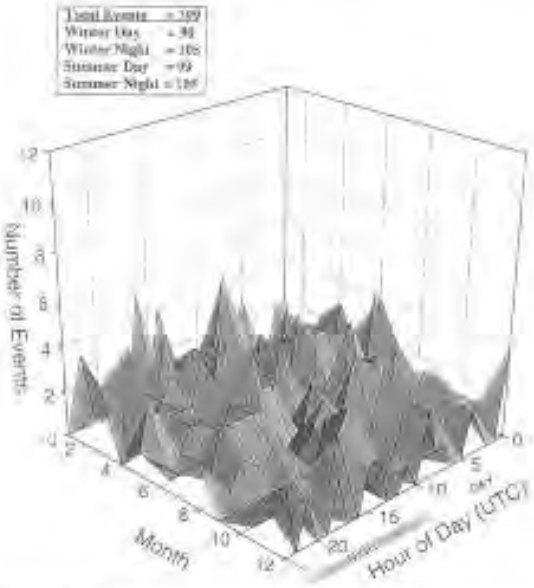


Figure 5. Temporal distribution of earthquakes in "Area A" of Figure 3.

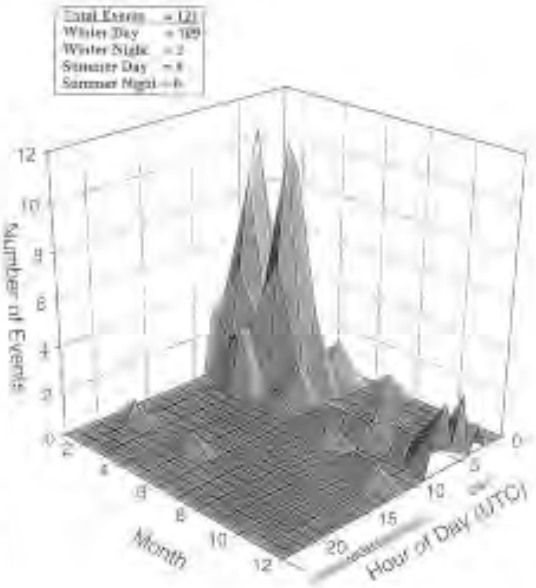


Figure 6. Temporal distribution of earthquakes in the Raychikhinsk coal mining district (Figure 3).

CRUSTAL AND UPPER MANTLE SEISMIC VELOCITY STRUCTURE OF THE FORMER USSR

Walter D. Mooney, U.S. Geological Survey
Menlo Park, CA 94025 USA

Sponsored by U.S. Department of Energy
Office of Nonproliferation and National Security
Office of Research and Development
DOE IA No.: DE-AI04-98AL79758

ABSTRACT

In the past forty years, the Ministry of Geology of the former USSR committed vast funding to investigations of the structure of the continental crust and upper mantle by seismic methods. The former USSR is crisscrossed by a network of seismic profiles that are more detailed than in any other part of the world. There are three kinds of profiles: (1) short-range refraction; (2) Deep Seismic Sounding (DSS) profiles; and (3) ultra-long range seismic profiles using Peaceful Nuclear Explosions (PNEs). The main goal of the short-range refraction work was to image sedimentary cover and basement. Measurements were obtained using 48-60 channel analog instruments with 100 m receiver spacing, and seismograms were recorded on photographic paper by the wiggle trace method. The DSS observations were mainly used for crustal studies. The shotpoint spacing was 30-50 km, and three components of ground displacement were recorded. The refracted compressional (P) and shear waves (S), reflected (P and S) and converted waves were interpreted. Ultra-long range PNE-sourced profiles provided information on the structure of the crust and upper mantle to a depth of 670 km. For PNE profiles, up to 400 short-period (1.5-20 Hz), three-component seismometers were deployed every 5- 10 km to record ground motion. Thirty-nine PNE shots were detonated for these purposes, with intermediate chemical shots spaced at 40-70 km intervals. These chemical shots had charges ranging from 2000 to 5000 kg. The total length of all of these three types of profiles exceeds 80 thousand kilometers. We present a synthesis of these results in the form of new maps of crustal thickness and seismic velocity below the Moho discontinuity.

Key Words: crustal structure, former USSR, seismic refraction, Deep Seismic Sounding, Peaceful Nuclear Explosions

OBJECTIVE

High quality regional models of crustal structure are necessary for accurate seismic locations required by the monitoring of the Comprehensive Nuclear-Test-Ban Treaty (CTBT). This paper presents models of the seismic velocity structure of the lithosphere in the Former Soviet Union.

RESEARCH ACCOMPLISHED

1 Introduction

The properties of the Earth's crust and uppermost mantle are particularly well suited to measurement using seismological data due to the existence of the pronounced variations in seismic wave speeds both with depth and laterally. Seismological studies are capable of imaging high resolution structure to depths of several tens of kilometers, and moderate resolution to depths of 1 00's of kilometers. Here we discuss crustal and uppermost mantle studies from the Former Soviet Union (FSU) that have utilized controlled-source seismic-refraction data, including long-range profiles from nuclear sources. The chief advantages of such data are: 1) the exact time and position of the seismic sources are accurately known; 2) there is no reliance on either local nor teleseismic events that may occur infrequently and/or have an unsuitable spatial distribution; 3) the recording geometry of the seismic investigation may be planned in relation to the specific geologic target.

Since the early 1950's a large number of seismic profiles have been collected in the FSU. Advancing technology has led not only to better instrumentation, but also improved data processing and interpretation techniques. Useful recent reviews of seismic methods for determining crust and upper mantle structure have been provided by Mooney (1989) and Braile et a]. (1995), and Giese et al. (1976) provide older methods of data analysis. Papers that summarize global crustal structure, including the FSU, include Soller et al. (1992), Prodehl (1984), Meissner (1986), Tanimoto (1995), Pavlenkova (1996), and Mooney et al. (1998).

Resolution is a major consideration when discussing seismic data. Because of the variety in seismic techniques, however, general statements about resolution are difficult to make. In seismology, resolution is related both to data quality and physical laws. The quality of a data set is usually considered to be a function of the strength of the signal relative to noise (expressed as signal-to-noise ratio) and the number or density of measurements depending on the number of sources and receivers and their relative spacing. Generally, the more data are available, the higher is the resolution. However, physical laws limit the resolution of even near-perfect data set. The Earth strongly attenuates high frequencies so that signals penetrating deeper will contain relatively low frequencies. Typically, signals traversing the whole crust have peak frequencies of 5-20 Hz resulting in absolute accuracy of depth determination of not better than 2% to 5% of the depth (e.g., 1-2 km for a 40-km-thick crust).

Seismic refraction data provide information on velocities within the continental lithosphere. In many cases it is also of interest to infer the composition of the lithosphere, and for this a comparison can be made with laboratory measurements the speed of sound in specimens of rocks believed to have once resided at depth within the lithosphere. These studies are reviewed in Holbrook et al. (1992) and Christensen and Mooney (1995).

2.1 Main features of crustal structure of the Former Soviet Union

There have been many attempts to synthesize this structure in terms of the most important parameters, including crustal thickness, mean crustal velocity, Pn velocity, Conrad discontinuity (defining the seismic boundary between upper and middle/lower crust), thickness and mean velocities of main crustal layers (sediments, upper, middle and lower crust), and representative crustal cross sections. We have compiled this information for the FSU, but space limitations prevent us from presenting extensive examples.

The basic features of the crustal structure of the FSU were recognized by the 1960's (Ryaboy, 1966; Kosminskaya, 1968; Pavlenkova, 1973). The seismic velocity distributions vary widely in different geographic localities, and crustal models generally consist of two, three or more layers separated by velocity discontinuities or gradients. In relatively stable continental regions, the thickness of the crust, as

defined by depth to Moho, is between 30 and 50 km. Seismic velocities in the upper crustal layer (basement) are usually 5.6-6.3 km/s. At a depth of 10-15 km the seismic velocity increases to 6.4-6.7 km/s. In many stable continental interiors there is a third crustal layer with a velocity of 6.8-7.2 km/s. The seismic velocity below the Moho (Pn velocity) is typically about 8 km/s. The exact nature of the velocity-depth distribution is not always well defined. The evidence for distinct layers within the continental crust almost exclusively depends on the interpretation of second-arrival phases. In some regions, clear evidence of later arrivals confirms that the velocity increases discontinuously through intermediate layers within the crust, in other regions velocity may increase gradually with increasing depth producing no distinct intracrustal reflection.

The compilation of seismic crustal data around the world has also defined the characteristic primary crustal types connected with specific tectonic settings (Fig. 1). These models are well based on data from the FSU. Each primary crustal type was derived by averaging models determined from seismic refraction profiles recorded in crust of specific age or tectonic setting. The existing data are so numerous (Fig. 2) that in this summary paper only a few examples of results can be presented. Figure 3 shows Pn velocity for Western Russia.

2.2 Crustal Cross-Sections

Seismic profiles cover all tectonic structures of northern Eurasia (old and young platforms, shields and deep depressions, orogenic belts of different age and geological history, rifts, marginal and inner seas). In Figures 4 and 5, examples of the deep seismic studies from the FSU are summarized for three long-range profiles: (a) Black Sea - Dnieper-Donetz basin, (b) Baltic Shield - Urals - West-Siberian Plate and (c) West-Siberian Plate - Siberian Craton. The first profile was carried out in the 1960s using continuous profiling with distance between seismometers of 100 m and chemical explosions with 50-60 km interval (Pavlenkova, 1973). The lines from the Baltic Shield across the Urals to the West-Siberian Plate and from the West-Siberian Plate to the Siberian Craton were recorded with 10 km interval between seismic stations and two types of explosions: chemical ones and Peaceful Nuclear Explosions (PNEs). The latter ones enabled to study the upper mantle down to depth of 700 km (Egorkin et al., 1987, Beloussov et al., 1991, Mechie et al., 1993).

The crustal structure can be described by 4 basic layers with seismic mean velocities as follows: 2.0-5.5 km/s (sediments), 5.8-6.4 km/s (upper crust), 6.5-6.7 km/s (middle crust) and 6.8-7.4 km/s (lower crust). The first profile (Fig. 5a) crosses the Black Sea basin, Crimea Mountains, the Sivash basin, the Ukrainian Shield and the Dnieper-Donetz basin. In the Ukrainian Shield the crust has a thickness of more than 40 km and consists of three crustal layers of comparable thickness (I 0- 15 km). Beneath the basins, the Moho (M) is uplifted and the upper crust thins. Such changes become even more dramatic in the Black Sea area where the consolidated crust is only 20 km thick and where the upper and lower crustal layers disappear. The adjacent Crimean mountains have crustal "roots" and a crustal average velocity that is slightly lower than beneath the Ukrainian Shield.

The second profile (Fig. 5b) crosses the Baltic Shield, Western Russian Platform, Timan Ridge, Pechera Platform, Ural Mountains, and the West-Siberian Platform. All these tectonic units have a similar crustal structure, an important exception being the Timan-Pechera block. It is characterized by considerably lower crustal velocities, with the elsewhere present third high-velocity layer ($Vp > 7$ km/s) absent. The Urals have a pronounced "root" in Moho (M) topography, while the Timan Ridge is compensated by an increased thickness of the upper crust. A clear seismic boundary was revealed in the uppermost mantle where strong reflections indicate a velocity discontinuity (N) at depths of 75-105 km. The relief of this boundary shows an opposite correlation with the Moho. Seismic velocities between the two boundaries M and N vary from 8.0 beneath the Pechera and West-Siberian plates to 8.4 beneath the Urals. These changes clearly correlate with heat flow: the lower velocities correspond to higher heat flow areas. An anomalous zone was identified at the boundary between the old Russian plate and the younger Timan-Pechera unit. The thick dashed line in (Fig. 5b) traces this zone from a high-velocity intrusion in the crust to the boundary N where it is subducted beneath the Pechera Plate.

The third profile (Fig. 5c) characterizes the young West-Siberian plate and the Siberian Craton. Though of differing age, both platforms have a similar crustal thickness. The crustal structure changes mainly beneath

deep sedimentary basins. Common features are characteristic for the West-Siberian central basin and the Tunguss basin: in both cases the middle crustal layer remains the same, and the lower crustal thickness increases. The Vilui basin which is younger than the Tunguss basin has a clear uplift of the Moho. The upper mantle velocities hardly change along this profile. The only characteristic feature is the block of lower velocity in the central part of the West-Siberian plate. It corresponds to a large rift zone which crosses the plate from north to south. Another characteristic feature of this cross-section is a velocity inversion zone immediately above the N boundary at a depth of 100 km.

CONCLUSIONS AND RECOMMENDATIONS

Extensive seismic profiling data from the Former Soviet Union, including long-range profiles that were recorded from Peaceful Nuclear Explosions provide a vast geophysical database. Much of this data is now available in digital format, and thus can be re-evaluated in terms of the seismic velocity structure and attenuation of the crust and upper mantle to a depth of 700 km. The improved knowledge of the seismic structure, in turn, will enable significantly improved determinations of seismic source parameters as needed by the Comprehensive Nuclear-Test-Ban Treaty.

REFERENCES

Beloussov, V.V., Pavlenkova, N.I., and Kvjatkovskaya, G.N.(Eds.), 1991. Deep structure of the USSR territory (in Russian). Nauka, Moscow: 234 pp.

Braile, L.W., Keller, G.R., Mueller, S., and Prodehl, C., 1995. Seismic techniques. In: Olsen, K.H. (Editor), Continenal rifts: Evolution, structure, tectonics. Elsevier, Amsterdam, pp.61-92.

Christensen, N.I. and Mooney, W.D., 1995, Seismic velocity structure and the composition of the continental crust: a global view, Journal of Geophysical Research, 100, 9761-9788.

Egorkin, A.V., Zuganov, S.K., Pavlenkova, N.A., and Chernyshev, N.M., 1987. Results of lithosphere studies from long-range profiles in Siberia. Tectonophysics, 140: 29-47.

Giese, P., Prodehl, C., and Stein, A. (Editors), 1976. Explosion seismology in central Europe - data and results. Springer, Berlin-Heidelberg-New York: 429 pp.

Holbrook, W.S., Mooney, W.D., and Christensen, N.I., 1992. The seismic velocity structure of the deep continental crust. In: Fountain, D.M., Arculus, R., and Kay, R.W. (Editors), Continental lower crust. Development in Geotectonics, vol.23, Elsevier, Amsterdam, 1-43.

Kosminskaya, I.P., 1968, The method of Deep Seismic Sounding of the crust and upper mantle, Nauka, Moscow.

Mechie, J., Egorkin, A.V., Fuchs, K., Ryberg, T., Solodilov, L. and Wenzel, F., 1993. P-wave mantle velocity structure beneath northern Eurasia from long-range recordings along the profile Quartz. Phys. Earth Planet. Inter., 79: 269-286.

Meissner, R., The Continenal Crust: A Geophysical Approach, 426 pp., Academic Press, London, 1986.
Mooney, W.D., 1989. Seismic methods for the determining earthquake source parameters and lithospheric structure. In: Pakiser, L.C., and Mooney, W.D. (Editors): Geophysical framework of the continental United States. Geol. Soc. Am. Memoir 172: 11-34.

Mooney, W.D., Laske, G., and Masters, T.G., 1998. Crust 5.1: a global crustal model at 5' x 5'. J. Geophys. Res., 103: 727-747.

Pavlenkova N.I.,1973. Wave fields and crustal models of continental type (in Russian). Naukova Dumka, Kiev, 253 pp.

Pavlenkova, N.I., 1996. Crust and upper mantle structure in northern Eurasia from seismic data. Advances in Geophysics, 37: 1-133.

Prodehl, C., 1984. Structure of the earth's crust and upper mantle. In: K.-H. Hellwege (Editor in Chief),

Landolt B6rnstein New Series: Numerical data and functional relationships in science and technology. Group V, Volume 2a: K. Fuchs and H. Soffel (Editors), Physical properties of the interior of the earth, the moon and the planets, Springer, Berlin-Heidelberg, pp. 97-206. Ryaboy, V.Z., 1966, Crust and upper mantle structure from DSS profile Kapet-Dag-Aral Sea, Soviet Geology 5, 159-162.

Soller, D.R., Ray, R.D., and Brown, R.D., 1992. A new global crustal thickness model. Tectonics, 1; 125-149.

Tanimoto, T., 1995. Crustal structure of the earth. In: Ahrens, T.J. (Editor), Global Earth Physics: A Handbook of Physical Constants. AGU Ref. Shelf, vol. 1, Am. Geophys. Un., Washington, D.C., p. 214-224.

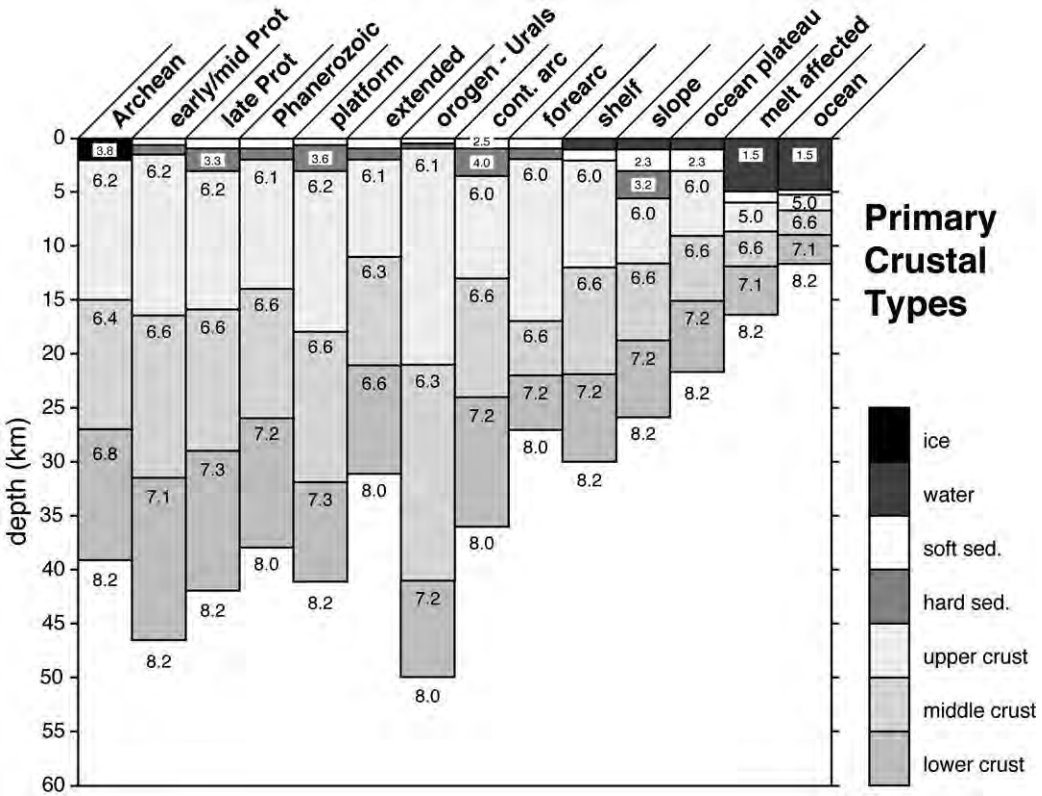


Figure 1. Velocity structure of the primary crustal types developed from seismic refraction data worldwide, including the results summarized here for the Former Soviet Union (FSU). These crustal types represent averages, and specific regions may deviate by as much as 50% in thickness from these values.

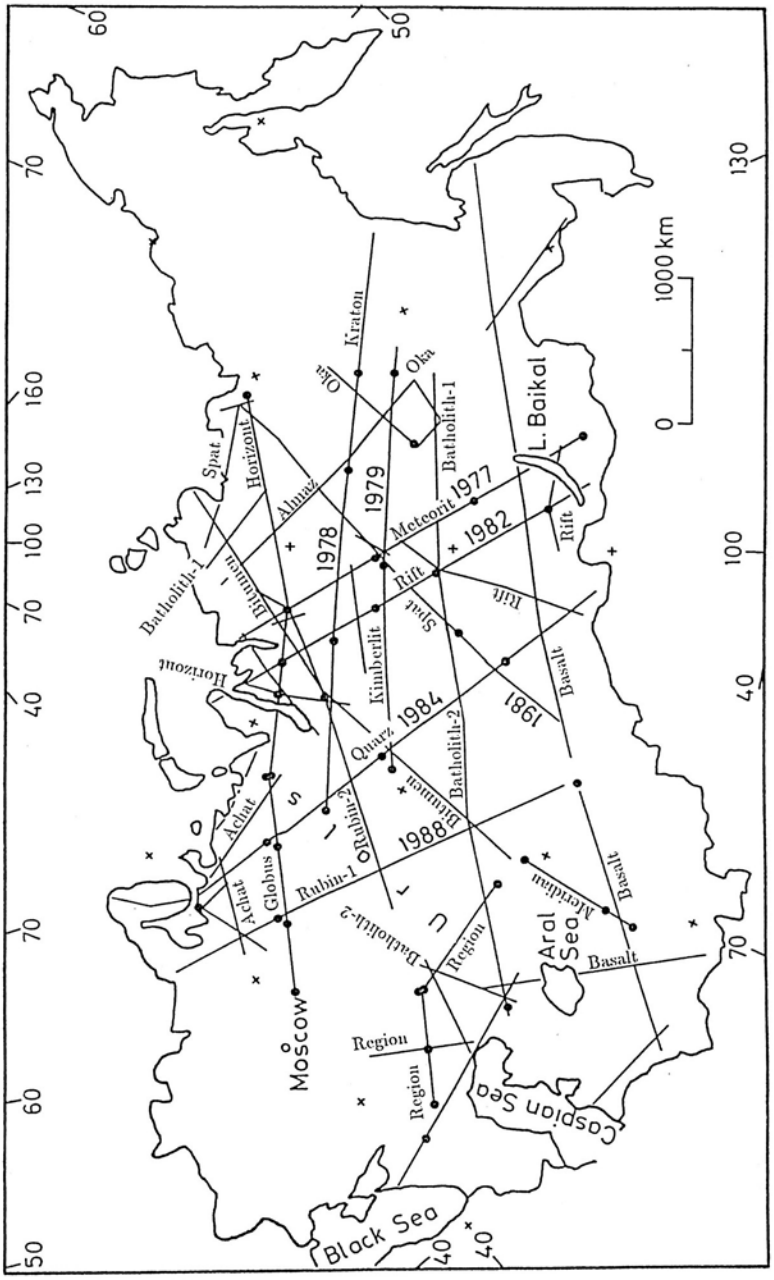


Figure 2. Location of map of long-range profiles completed in the Former Soviet Union using PNE (solid dots) and numerous chemical shots (not included).

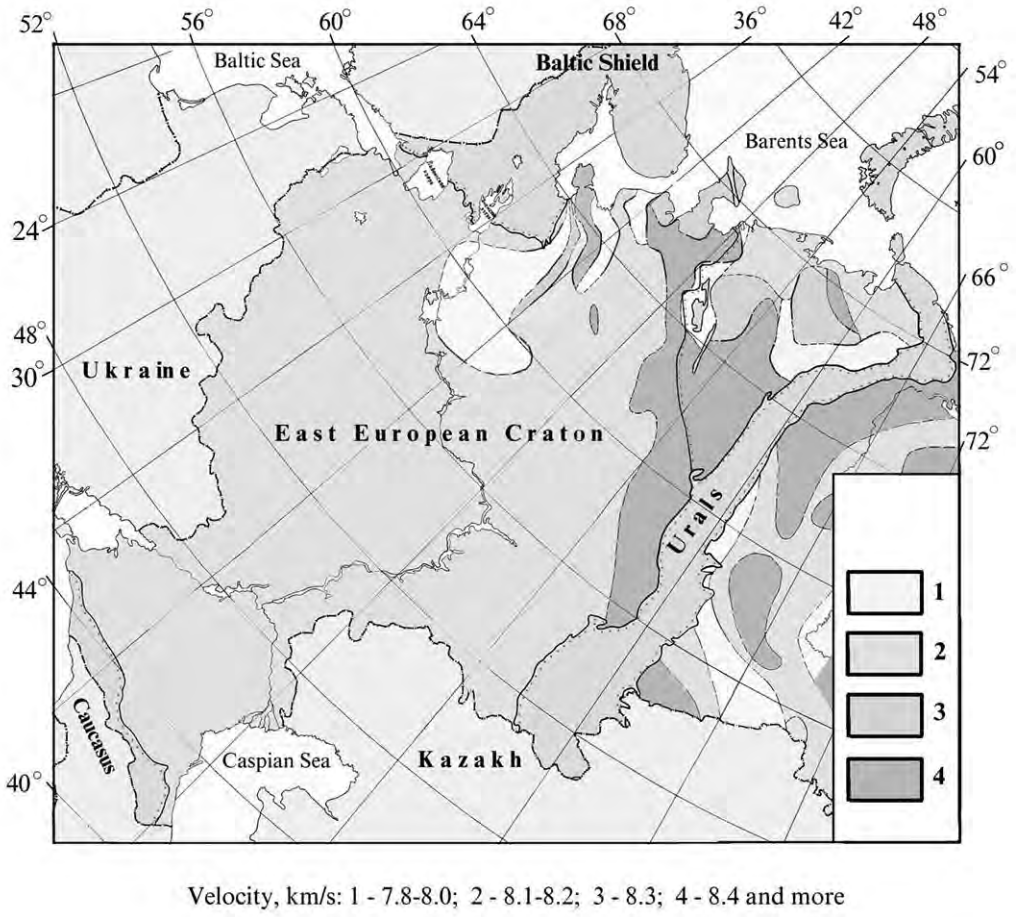


Figure 3. Seismic velocity on the top of the uppermost mantle (Pn velocity) for Western Russia from seismic refraction profiles. The average value is 8.1 km/s, but the individual profiles show values in the range 7.8 to 8.4 km/s due to (1) seismic anisotropy, (2) temperature effects and (3) compositional variations. A map for the entire territory of the Former Soviet Union is presently being prepared by the project.

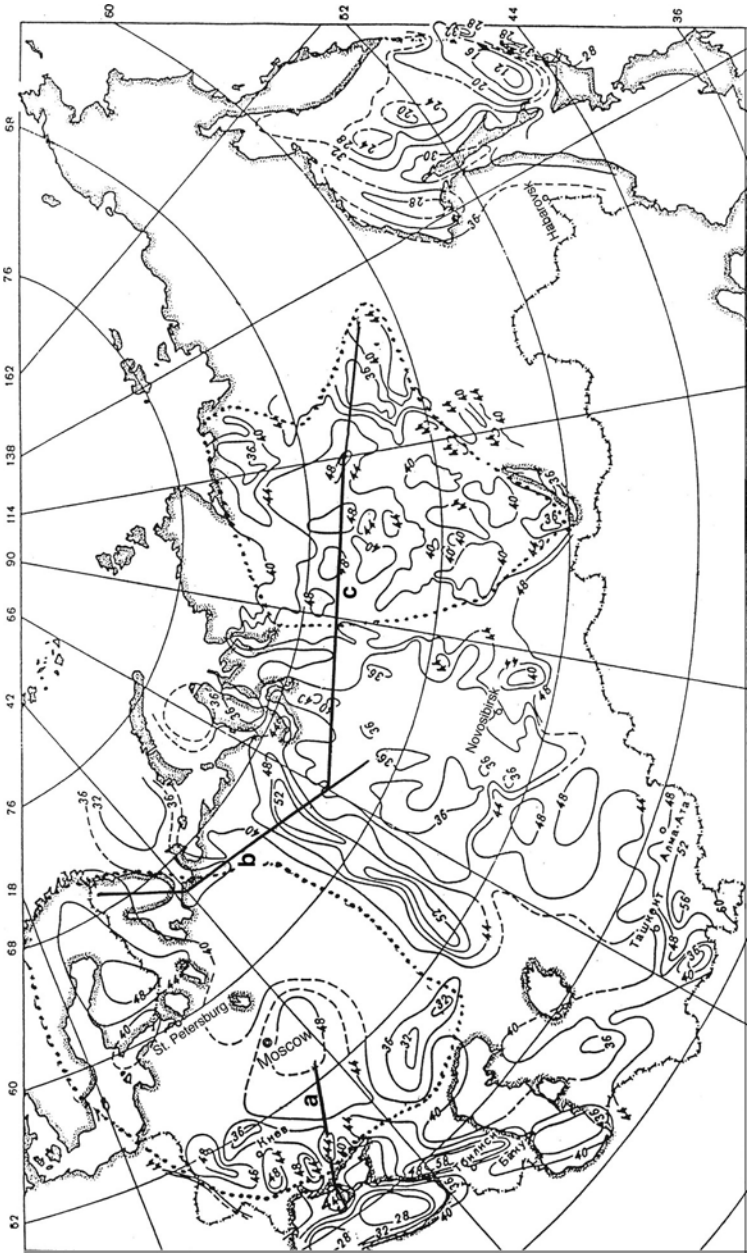


Figure 4. Map of the thickness of the crust of the FSU (thin contour lines) derived from seismic data (Pavlenkova, 1996). Thick lines labeled a, b, c indicate the locations of the three cross-sections in Figure 4

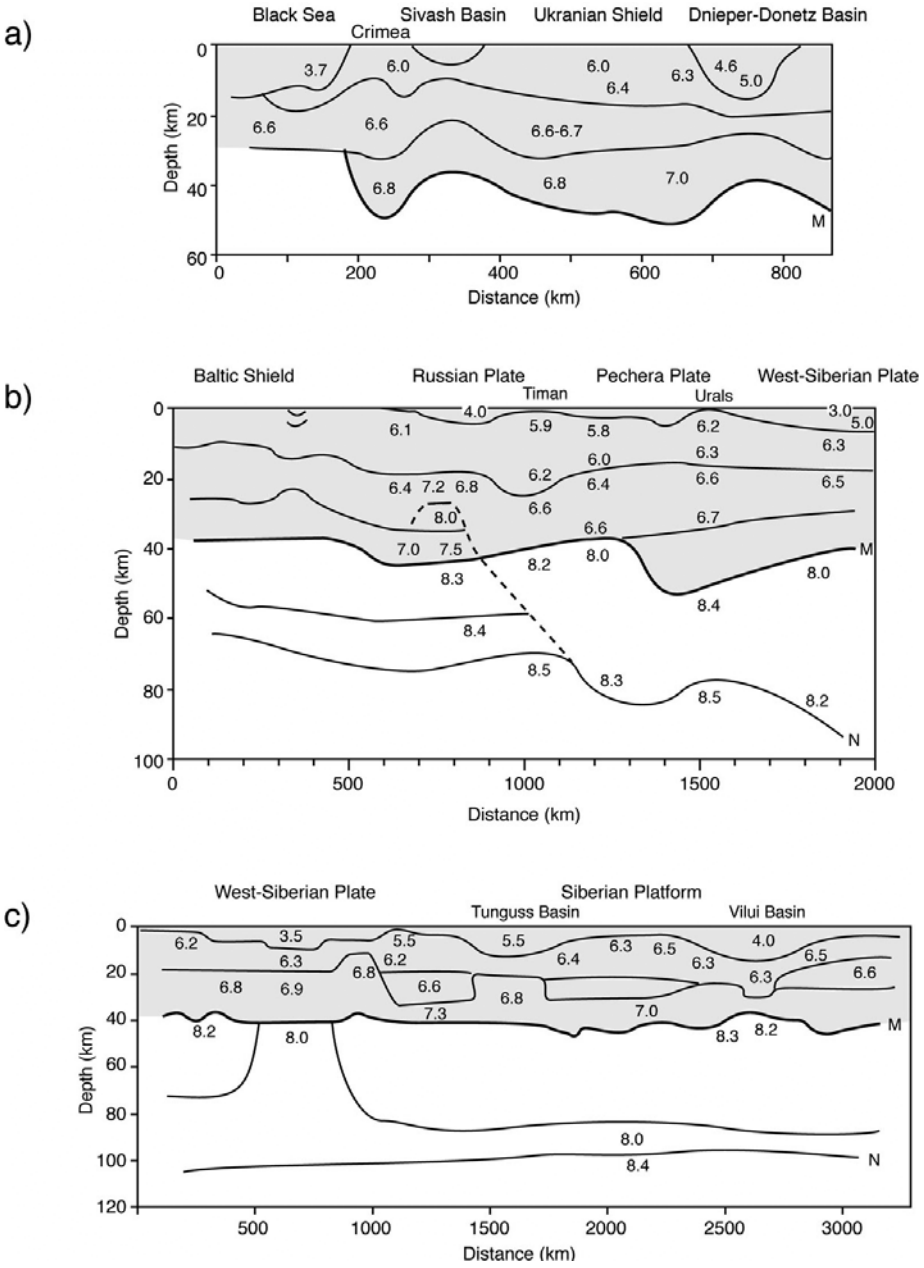


Figure 5. Three cross-sections of the crust and uppermost mantle. Locations indicated in Figure 3. Note that the horizontal scale varies. Cross-sections (b) and (c) are based on both chemical and PNE seismic refraction.

HOW THICK IS THE EARTH'S CRUST?

Walter D. Mooney (1) Gabi Laske (2) T. Guy Masters (2) Katharine H. Favret (1)

(1) U.S. Geological Survey; Menlo Park, CA USA
(2) IGPP Scripps Institution of Oceanography; University of California San Diego CA USA

Sponsored by U.S. Department of Energy
Office of Nonproliferation and National Security
Office of Research and Development
DOE IA No.: DE-A104-98AL79758

ABSTRACT

Thorough knowledge of the Earth's crustal structure is necessary for monitoring the Comprehensive Nuclear-Test-Ban Treaty. We present an updated contour map of the thickness of the Earth's crust using a 10-km contour interval, and the 45-km contour. This contour map was created from a 5° by 5° gridded crustal model (CRUST 5. 1, Mooney et al., 1998) and recently obtained information from Russia and China. The contour map honors all available seismic refraction measurements for features with a dimension greater than 2 degrees. Crustal thickness in Eurasia, North America, and Australia is well constrained by seismic refraction data, whereas Antarctica, South America, Africa, and Greenland are less well constrained. To a first approximation, the continents and their margins are outlined by the 30-km contour. The part of the continental interior enclosed by the 40-km contour and regions with crustal thickness of 45 to 50 km are found on all well-surveyed continents. Continental crust with thickness in excess of 50 km is exceedingly rare and accounts for less than 10% of surveyed continental crust. These observations, now available on a global basis, provide important information to be used for seismic monitoring.

Mooney, W.D., G. Laske and T.G. Masters, CRUST 5. I: A Global Crustal Model at 5° X 5°, J. Geophys. Res., 103:727-747, 1998.

http://quake.wr.usgs.gov/study/CrustalStructure

Key Words: crustal thickness, global, seismic refraction

OBJECTIVE

Monitoring under the Comprehensive Nuclear-Test-Ban Treaty (CTBT) requires accurate locations of questionable events. In order to constrain the area in which an event has occurred, it is necessary to have a good model of the crustal structure. 'Me work summarized in this paper provides one of the most accurate and complete models of the crustal structure of the world.

RESEARCH ACCOMPLISHED

Introduction

Previous global crustal models have provided various levels of detail. Soller et al. (1982) presented a crustal thickness map but did not specify seismic velocities or densities. Hahn et al. (1984) presented a model wherein the crustal structure was described in terms of irregularly shaped regions, each with a uniform structure. More recently, Tanimoto (1995) reviewed the crustal structure of the Earth using a wide range of seismic data, and Nataf and Ricard (1996) presented a model for the crust and upper mantle on a 2° x 2° scale (3SMAC). This latter model was derived using both seismological data and non-seismological constraints such as chemical composition, heat flow and hotspot distribution, from which estimates of seismic velocities and the density in each layer were made.

In this paper, we present a recently published (Mooney et al., 1998) global crustal model (CRUST 5.1) that is based on significantly more data than previous models, and we discuss the model's application as a "crustal correction". Compiling a new global crustal model is timely because of the availability of a large body of new data. Our new global model for the Earth's crust (CRUST 5.1) is based on an extensive compilation of information through the year 1995 (Fig. 1). Published interpretations of the seismic velocity structure of the crust are now numerous enough and cover sufficiently diverse geological settings that it is possible to calculate statistical averages for various geological settings such as Precambrian shields, extended continental crust, and passive margins. These statistical averages define a set of standard crustal sections (referred to here as crustal types). For the vast continental regions where, as yet, no seismic measurements are available, such as large portions of Africa, South America, and Greenland, we predict the crustal structure using the standard crustal types, and present the statistical basis for these predictions.

Our purpose is to create a model for the seismic velocity (Vp and Vs) and density structure of the crust and uppermost mantle that is at a large enough scale to be commensurate with the (non-uniform) global distribution of seismic field observations but that is also at a small enough scale to resolve significant lateral variations in crustal properties. In order to meet these competing goals, we have constructed our model using 5° x 5° tiles that measure 550 km by 550 km at the Equator. In each tile, crustal properties are described by seven layers: (1) ice, (2) water, (3) soft sediments, (4) hard sediments, (5) crystalline upper, (6) middle, and (7) lower crust. An eighth layer is included to describe the elastic properties and density immediately below the Moho since this information is readily obtained from the seismic refraction profiles compiled here. Topography and bathymetry are provided as a separate file. Compressional wave velocity in each layer is based on field measurements, and shear wave velocity and density are estimated using empirical Vp-Vs and Vp-density relationships, as discussed below.

Global Crustal Thickness

The crustal thickness of our model is shown in Fig. 2. In areas with good data coverage, crustal thickness is very similar to existing continental-scale models (e.g., compare Eurasia with Meissner, 1986, and North America with Mooney and Braile, 1989). There is also generally good agreement with the crustal thickness from the model 3SMAC of Nataf and Ricard (1996), who used different data sources for their compilation. The largest differences between their model and ours occur where constraints from seismic refraction data are sparse (e.g. Africa, Greenland, and Antarctica).

The mean Moho depths (with respect to sea level) are 21.8 km (global), 38.0 km (continents) and 12.6 km (oceans, including the water layer of 4.0 km average thickness). The total crustal thickness is clearly bimodal and, in comparison to the crustal thickness our model has substantially higher values for continental regions. The Moho in our model is located at greater depth in some areas than in the model of Soller et al. (1982), especially those areas with poor data coverage such as Africa and South America. Our

crustal thickness (40 km) for the vast shield areas of Africa and South America is in excellent agreement with the global average for shield areas, whereas the thin (30 km) crust in the model of Soller et al. (1982) is clearly inconsistent with these statistics. The data coverage in Australia has increased tremendously since the publication of Soller et al. (1982), and our model displays a slightly deeper (by approx. 5 km) Moho. In northeastern Eurasia, the Moho lies substantially deeper in CRUST 5.1 (as it does in 3SMAC of Nataf and Ricard, 1996) than in the model of Soller et al. (1982). In this part of the continent, the Moho depth is constrained quite well by recently released data so that, again, we have more confidence in our model. On the other hand, based on much new data, the Moho in all of southern Eurasia is shallower in our model than in that of Soller et al., sometimes by over 10 km. Again, our model agrees quite well with 3SMAC, especially in Southeast Asia. The crust in our model is also slightly thinner in North America, where our map is in close agreement with Mooney and Braile (1989).

Large local differences in the oceans are found in the Coral Sea (northeast of Australia) and along the Tonga-Kermadec trench. For the Coral Sea, Soller et al. (1982) refer to results reported by Shor (1967) and Ewing et al. (1970). Shor (1967) reports the Moho at 19 km depth along a profile lying immediately south of the Coral Sea Basin, which has normal oceanic crust (Ewing et al., 1970). North of the Queensland plateau, Shor (1967) also report a significantly thicker crust. However, the contour lines in this area are rather uncertain and are probably overestimated by Soller et al. (1982) who specified 25 km as the crustal thickness. Shor et al. (I 97 1) report crustal thicknesses between I 1 and 15 km along portions of the Tonga Kermadec trench, which may indicate a significant crustal thickening on a 5° x 5° scale. The regional extent of this area of thicker oceanic crust is unknown, and thus has not been included in our model.

The Crustal Model and Mantle Tomography

Seismic tomography has been extensively used in various forms to determine the deviations from a purely radial dependence of seismic velocities within the Earth's mantle. Surface wave and free oscillation data have been used to determine the upper mantle shear wave velocity structure (e.g., Masters et al., 1982; Woodhouse and Dziewonski, 1984; Montagner and Tanimoto, 1991; Trampert and Woodhouse, 1995). Body wave arrivals reported to the International Seismological Center (ISC), or specially picked from seismic records, have been used to determine the P-wave and S-wave structure both on global and regional scales (e.g, Dziewonski, 1984; Inoue et al., 1990; Woodward and Masters, 1991; Pulliam et al., 1993; Zielhuis and Nolet, 1994, Grand, 1994; Vasco et al., 1995; Masters et al., 1996; Alsina et al., 1996). For the majority of these studies, the crust has a significant effect on the observed seismic data but, at the same time, it is too thin to be resolved by these studies. Most authors handle this by applying an assumed "crustal correction" to the data before inverting for mantle structure. Since the inversion techniques can erroneously map crustal structure down to great depth, the application of accurate crustal corrections to the data sets is extremely important.

We will concentrate on effects on phase velocity (not group velocity) in the following. Since surface waves are sensitive to Vp, Vs, and density, a model prescribing all these parameters is essential. When calculating the crustal corrections for global maps of phase velocity we ignore the lateral variations of Vp, Vs and density as specified in layer 8 (uppermost mantle) of CRUST 5.1 so that anomalies displayed in the maps are caused only by variations within the crust itself. For the mantle, we use the reference ID-model PREM (Dziewonski and Anderson, 1981). Global surface wave phase velocity maps are commonly expanded in surface spherical harmonics. We adopt this parameterization and truncate the harmonic expansions as specified in the individual figure captions. For plotting purposes, the spherical averages of the maps have been removed. Crustal structure has the greatest effect on short-period surface waves. The peak-to-peak amplitude in phase velocity anomaly for Rayleigh waves at 40 s is about twice as large as that at 167 s. For Love waves, the crustal effect is more than twice that of Rayleigh waves at the same period. Love waves at 40 s are most sensitive to the S-wave velocity structure in the uppermost 60 km (they are also sensitive to density in the same depth range, although to a much lesser extent). Rayleigh waves at these periods are primarily sensitive to uppermost mantle structure. The sensitivity kernel for S-wave velocity peaks at about 60 km and has a minimum at 20 km depth. However, Rayleigh waves at 40 s are also quite sensitive to variations of P-wave velocity within the shallow most layers of the crust. Hence the large thick sedimentary basins (e.g., in the Arctic ocean or the Gulf of Mexico) cause significant phase velocity anomalies which are not seen in the maps for Love waves at the same period.

When expanded in surface spherical harmonics, continent-ocean-type functions (such as our crustal model) are dominated by harmonic degrees l=1 through 5, but the amplitude is greatest at the first harmonic degree. Surface wave phase velocity maps that have had the crustal signal removed are dominated by contributions from the first harmonic degree in a wide range of periods. Hence, it is very important to obtain an accurate estimate of the structural contrast between continental and oceanic crust in order to ultimately avoid erroneous mapping of the continent-ocean function into greater depth in the upper mantle.

At higher harmonic degrees, the spectra of the crustal corrections roll off roughly as l^a, where a is a negative number between minus one and minus 2. The roll-off of the amplitude spectra plotted on a double-logarithmic scale can then be fit by straight lines where the slope of the lines is a. We find that this parameter is fairly uniform (a=-1.35) for both Love and Rayleigh in the period range between 167 s and 40 s. For Rayleigh waves at 40 s, the roll-off is slightly less (a=-1.19), probably due to the increased sensitivity to the small-scale variations of the P-wave velocity in the thick sedimentary basins.

Figures 3 and 4 show examples of the global phase velocity maps of Laske and Masters (1996) and Ekström et al. (1997) before and after removal of the perturbations due to the crust. For long-period surface waves, lateral phase velocity variations caused by crustal heterogeneities are relatively small. Nevertheless, the crustal correction actually increases the variance of the observed phase velocity. The peak-to-peak amplitude for Rayleigh waves at 167 s is larger after the correction by a factor of roughly 1.3 (Fig. 3a and 3b). The increase in variance is caused by the fact that the signals from the crust and the uppermost mantle are often anticorrelated, e.g., shields have large crustal thickness and low crustal velocities (as compared to the oceans at the same depth) but high velocities in the upper mantle. Obviously, the application of a crustal correction is important for interpreting these long-period surface wave data. However, the fine details of the crustal model used do not appear to be crucial.

The situation is quite different for short period surface waves. In this case, for continental paths, Love waves with a period of 40 s are dominantly sensitive to crustal structure. In fact, Love wave phase velocities at shorter periods (e.g., Ekstr6m et al., 1997) could be used in the future to further refine crustal models where no refraction seismic data are available. The signal in the map (Fig. 4a) is greatly (by a factor of 1.7) by the crustal correction (Fig. 4c). The remaining signal is primarily produced by an age-dependent cooling of the oceanic lithosphere, which is not included in the crustal model. For comparison, we also show the crustal correction for a model (Smith, 1989) used in earlier studies (Fig. 4d). This model includes the Moho variation of Soller et al. (1982) and estimated average seismic velocities and densities for continents and oceans (Smith, 1989) (referred to as the "Soller model" hereafter). It is interesting to note that the resulting map (Fig. 4d) does not display the pronounced high velocity regions beneath the shields that CRUST 5.1 produces, and there are many other regional differences. Since 40 s Love waves are sensitive to upper mantle structure below 60 km, it is to be expected that the high-velocity mantle beneath shields will be clearly evident in the corrected maps. Based on this comparison, we are confident that the crustal corrections from CRUST 5.1 are more accurate than the corrections derived from the Soller model. It is also worth noting that the spectra of the crustal corrections of CRUST 5.1 and the Soller model are similar in shape but that the corrections of CRUST 5.1 have significantly larger amplitudes at harmonic degrees less than l=5 (not shown here). The largest discrepancy is at l=1 where the amplitude of CRUST 5.1 is roughly 1.5 times that of the Soller model. This discrepancy is due to the difference between the average parameters for continents and oceans in the two models. This comparison further stresses the need for accurately estimating seismic velocities and densities at even the longest-wavelength scale (i.e. the contrast in physical properties between continents and oceans).

Rayleigh waves at 40 s sample the Earth quite differently than Love waves at 40 s. As mentioned above, these waves primarily sample the S-wave velocity in the upper mantle, but they are also sensitive to the shallow P-wave velocity and density structure. The overall effect is that crustal corrections for 40 s Rayleigh waves (Fig. 3c) do not change the variance of the anomalies in the maps but redistributes the phase velocity anomalies significantly. High velocities in the mantle beneath shields are much more pronounced after the correction, while the low-velocity anomaly extending from the Afar Triangle through China is decreased significantly (Fig. 3d.). After crustal correction, the previously large low velocity anomaly around the Afar Triangle/Red Sea area is much smaller and concentrates along the Red Sea. This same behavior occurs for both Love and Rayleigh wave phase velocity maps in a large range of frequencies

(down to 167 s) and indicates that the Afar Triangle/Red Sea low velocity anomaly is mostly produced by shallow structure.

CONCLUSIONS AND RECOMMENDATIONS

A contour map based on CRUST 5.1 shows the global variation of crustal thickness (Fig. 2). Because of the 5° x 5° cell size, many interesting but narrow (less then about 250 km wide) features are not evident on this map. The thickest crust (more than 50 kin) is found beneath the Tibetan Plateau, the Andes of South America, and southern Finland. Continental crust (including shelf regions) typically has a crustal thickness of 30-45 km, with a global average of 38 km. Vast regions of oceanic crust have an average thickness of 6-7 km (not including the water layer). A comparison with Figure 1 indicates where crustal thickness has been measured, and where it has been estimated based on tectonic province and crustal age.

We have evaluated the seismological effects of this model by comparing observed short period (40s) Love and Rayleigh wave phase velocities with those predicted by the crustal model. Such a comparison must be approached with caution since these phase velocities are also sensitive to mantle structure. With the global surface wave data currently available, it is not possible to completely isolate the crustal signal. However, this comparison indicates that our model provides a good match to the amplitude and areal extent of phase velocity anomalies that are associated with variations in the thickness of the continental crust and large sedimentary basins. We have applied the crustal correction to observed surface wave phase velocity maps to isolate those features that are due to variations in upper mantle structure. The most obvious features in these corrected maps are the age dependence of oceanic lithosphere and enhanced high velocity anomalies under shields. We also show that an important factor in mapping these features (especially at long periods) is an accurate knowledge of the contrast between continental and oceanic crustal structure.

There are two primary limitations to the CRUST 5.1 model. The first is the cell size (5° x 5°), which measures 550 km by 550 km at the Equator. This cell size is too coarse to permit an accurate model of many important crustal features (e.g., narrow mountain belts or rifts) other than by using a weighted average to account for lateral variations within a cell. A smaller cell size, such as 2° x 2°, would provide approximately six times the resolution of the present model; such a cell size may be needed for many regional studies. However, we feel that the construction and thorough evaluation of a model with a cell size of 5° x 5° is a necessary first step to finer scale models. A second limitation is the means by which we have parameterized the model. This consisted of assigning one of 139 crustal models to each of the 2,592 cells. We found that this parameterization was well suited for the crystalline crust and uppermost mantle but did not provide the desired flexibility for parameterizing the thickness and physical properties of sedimentary accumulations. An alternative approach would be to parameterize the upper layers (ice, water, and sediments) by a grid, and the lower layers (crystalline crust and upper mantle) by crustal types.

As global datasets become more complete and processing techniques evolve, it will be possible to better constrain a crustal model by using observations of short period surface wave dispersion (Ekstr6m et a]., 1997). Such observations will be particularly valuable to constrain those parts of the Earth's crust where the data coverage from seismic refraction studies is likely to remain poor, such as regions at high latitude. For the present, our new model, CRUST 5.1, provides the most accurate mapping of the physical properties of the crust and uppermost mantle available at a 5° x 5° scale. Further refinement will be possible as additional data become available and as additional checks are made by those who apply it to seismological and non-seismological problems.

REFERENCES

Alsina, D., R.L. Woodward, and R.K. Snieder, Shear wave velocity structure in North America from large-scale waveform inversions of surface waves, *J. Geophys. Res., 101*, 15,969-15,986, 1996.

Dziewonski, A.M., Mapping the lower mantle: determination of lateral heterogeneity in P-velocity up to degree and order 6, *J. Geophys. Res., 89*, 5929-5952, 1984.

Dziewonski, A.M., and D.L. Anderson, Preliminary reference Earth model (PREM), *Phys. Earth Planet. Inter., 25*, 289-325, 1981.

Ekström, G., J. Tromp, and E.W. Larson, Measurements and global models of surface wave propagation, *J. Geophys. Res., 102*, 8137-8157, 1997.

Ewing, M., L.V. Hawkins, and W.J. Ludwig, Crustal structure of the Coral Sea, *J. Geophys. Res., 75*, 1953-1962, 1970.

Grand, S.P., Mantle shear structure beneath the Americas and surrounding oceans, *Journ. Geophys. Res.*, *99*, 11.591-11.621, 1994.

Hahn, A., H. Ahrendt, J. Meyer, and J.-H. Hufen, A model of magnetic sources within the Earth's crust compatible with the field measured by the satellite magsat, *Geologisches Jahrbuch, A75*, 125--156, 1984.

Inoue, H., Y. Fukao, K. Tanabe, and Y. Ogata, Whole mantle P-wave travel time tomography, *Phys. Earth Planet. Inter., 59*, 294-328, 1990.

Laske, G., and G. Masters, Constraints on global phase velocity maps by long-period polarization data, *J. Geophys. Res., 101*, 16,059-16,075, 1996.

Masters, G., T.H. Jordan, P.G. Silver, and F. Gilbert, Aspherical earth structure from fundamental spheroidal-mode data, *Nature, 298*, 609-613, 1982.

Masters, G., S. Johnson, G. Laske, and H. Bolton, A shear-velocity model of the mantle, *Phil. Trans. R. Soc. Lond. A, 354*, 1285-1411, 1996.

Meissner, R., The Continental Crust; A Geophysical Approach, 426 pp., Academic Press, San Diego, 1986.

Montagner, J.-P., and T. Tanimoto, Global upper mantle tomography of seismic velocities and anisotropies, *J. Geophys. Res., 96*, 20,337-20,351, 1991.

Mooney, W.D., and L.W. Braile, The seismic structure of the continental crust and upper mantle of North America, in *The Geology of North America, Vol. A, Overview*, edited by A.W. Bally, and A.R. Palmer, pp. 39-52, Decade of North Am. Geol. Project, Geol. Soc. Am., Boulder, Colo., 1989.

Mooney, W.D., G. Laske and T.G. Masters, CRUST 5. I. A global crustal model at 5° X 5°, *J. Geophys. Res., 89*, 727-747, 1998.

Nataf, H.-C., and Y. Ricard, 3SMAC: An a priori tomographic model of the upper mantle based on geophysical modeling, *Phys. Earth Planet. Int., 95*, 101-122, 1996.

Pulliam, R.J., D.W. Vasco, and L.R. Johnson, Tomographic inversions for mantle P wave velocity structure based on the minimization of 1^2 and 1^1 norms of International Seismological Centre travel time residuals, *J. Geophys. Res., 98*, 699--734, 1993.

Shor, G.G. Jr., Seismic refraction profile in Coral Sea Basin, Science, 158, 911-913, 1967. Smith, M.F., *Imaging the Earth's aspherical structure with free oscillation frequency and attenuation measurements*, Ph.D Thesis, Univ. Cal. San Diego, La Jolla, CA, 97 pp., 1989.

Soller, D.R., R.D. Ray, and R.D. Brown, A new global crustal thickness model, *Tectonics, 1*, 125- 149, 1982.

Tanimoto, T., Crustal structure of the Earth, *A Handbook of Physical Constants, Global Earth Physics*, edited by T.J. Ahrens, pp. 214-224, AGU, Washington, D.C., 1995.

Trampert, J., and J.H. Woodhouse, Global phase velocity maps of Love and Rayleigh waves between 40 and 150 seconds, *Geophys. J. Int., 122*, 675-690, 1995.

Vasco, D.W., L.R. Johnson, and J. Pulliam, Lateral variations in mantle velocity structure and discontinuities determined from P, PP, S, SS, and SS-S_dS travel times residuals, *J. Geophys. Res., 100*, 24,037-24,059, 1995.

Woodhouse, J.H., and A.M. Dziewonski, Mapping of the upper mantle: three-dimensional modeling of earth structure by inversion of seismic waveforms, *J. Geophys. Res., 89*, 5953-5986, 1984.

Woodward, R.L., and G. Masters, Global upper mantle structure from long-period differential travel times, *J. Geophys. Res., 96*, 6351-6377, 1991.

Zielhuis, A., and G. Nolet, Shear-wave velocity variations in the upper mantle beneath central Europe, *Geophys. J. Int., 117*, 695-715, 1994.

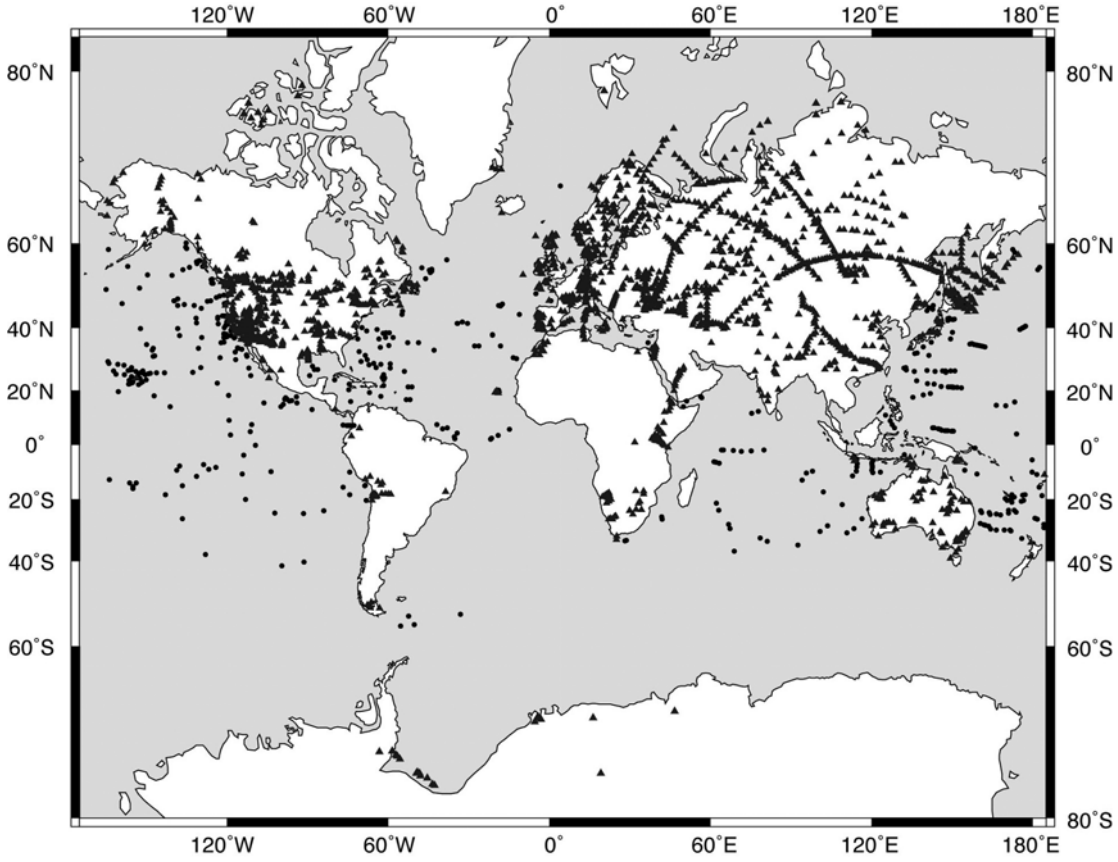


Figure 1. Location of seismic refraction profiles used in this study. Triangles correspond to locations within continents and on margins where a velocity-depth function has been extracted from a published crustal interpretation. These locations are generally at the midpoint between shot points along each profile. These data provide details on the compressional-wave seismic velocity structure and, in about 10% of the cases, also the shear-wave structure of the crust in a wide range of tectonic settings. Sources are cited in Christensen and Mooney (1995). Solid circles are locations of oceanic refraction profiles (Christensen, 1982). A standard crustal model is used for normal oceanic crust, and appropriate models are used for oceanic plateaus and other features. Data selection and interpretation uncertainties are discussed in the text.

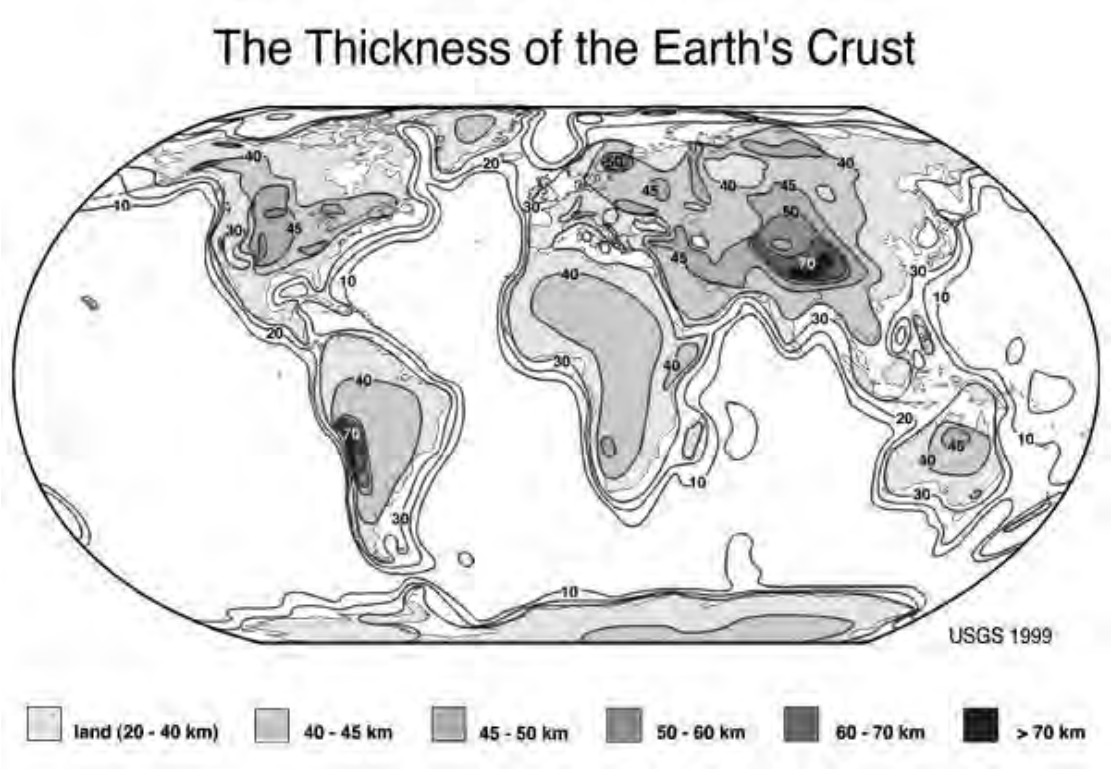


Figure 2. Robinson projection of crustal thickness from CRUST 5.1 (85° N to 80° S latitudes). The normal ocean crust is 6-7 km thick (excluding an average water depth of 4 km). Thin crust at mid-ocean ridges and oceanic fracture zones is not visible, as these and other narrow features (such as the East African Rift) are not resolved by a map based on a 5° X 5° cell size. Stable continental regions typically have crustal thicknesses of 35-45 km, and there are few regions (at the broad scale of this map) with a crustal thickness in excess of 50 km. A comparison with Figure 1 indicates where crustal thickness has been estimated based on tectonic province and crustal age.

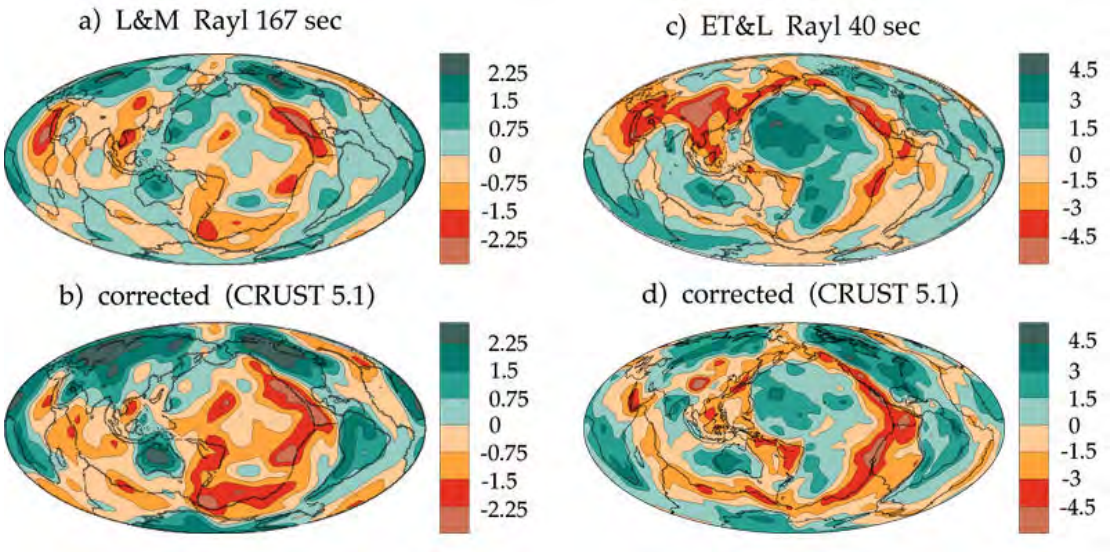


Figure 3. a) Observed phase velocity map for Rayleigh waves at 167 s (Laske and Masters, 1996; "L&M"). The phase velocity perturbation typically varies between -1.5% and 1.5%. b) After the correction for crustal signal, these variations are substantially larger. c) Observed phase velocity map for Rayleigh waves at 40 s (Ekstr6m et al., 1997; "ET&L"). d) Map corrected for crustal signal. The crust correction at this period does not increase the variance but redistributes the anomalies.

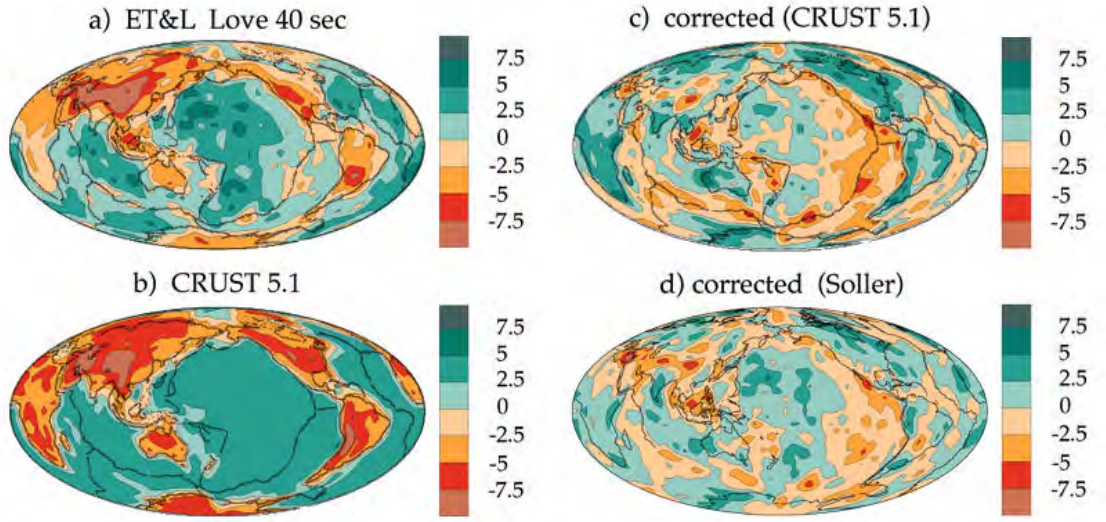


Figure 4. a) Observed phase velocity map for Love waves at 40 s (Ekström et al., 1997). b) Calculated crustal signal in the phase velocity map as predicted by our crustal model CRUST 5.1. c) Observed phase velocity map (a) corrected for crustal signal for the model CRUST 5.1 (b). d) Observed phase velocity map (a) corrected for the crustal signal using Soller's et al. (1982) crustal thickness (see text for details). Note that, while map (c) displays pronounced high velocity anomalies under shields, these anomalies are much smaller in (d).

THE CRUSTAL STRUCTURE IN NORTHWEST CHINA

Walter D. Mooney (1) and Robert G. Coleman (2)

(1) U.S. Geological Survey; Menlo Park, CA USA
(2) Department of Geology and Environmental Sciences Stanford University; Stanford, CA USA

Sponsored by U.S. Department of Energy
Office of Nonproliferation and National Security
Office of Research and Development
DOE IA No.: DE-AI04-98AL79758

ABSTRACT

We have reinterpreted seismic refraction data taken along a geoscience transect recorded in China. The data consists of 3-component seismic data along an 1100 km-long refraction profile in northwest China. The profile crosses the southern margin of the Altay Mountains, the Junggar Basin, the Tianshan Mountains, and the Tarim Basin. P- and S-wave seismic data acquired along this profile were used to model the crustal velocity structure and Poisson's ratio. The average crustal thickness is 50 km, ten kilometers thicker than the global average for continental crust. The largest difference in crustal thickness is located at the northern end of the profile, where, over a distance of <400 km, it varies from 54 km thick under the Altay mountains to 46 km thick under the Junggar basin. On the southern side of the basin, the crustal thickness increases to about 49 km, and it remains this thickness over the rest of the southern portion of the profile, with only slight variation. Poisson's ratios of 0.25-0.28, observed below the Junggar basin, imply either a mafic crystalline Precambrian basement or imbricated Paleozoic accretionary belt, whereas the lower Poisson's ratios of 0.25-0.26, modeled through the crust in the Tianshan Province, imply a granitic composition. Observed Pn velocities vary with tectonic province and include velocities of 7.9 km/s below the Altay Mountains; 7.7 below the thinner crust of the Junggar Basin; 7.8 below the Tianshan Mountains; and 8.0 below the Tarim Basin.

Key Words: crustal structure, China, seismic reflection, seismic refraction

OBJECTIVE

High quality regional models of crustal structure are necessary for accurate seismic locations required by the monitoring of the Comprehensive Nuclear-Test-Ban Treaty (CTBT). This paper presents the first detailed model of P- and S-wave velocity structure of the crust in northwest China created from controlled source data.

RESEARCH ACCOMPLISHED

In 1988, an 1100 km-long, 3-component seismic refraction profile was collected across northwest China (Fig. 1). Seismic energy was provided by twelve shots fired in boreholes. The charge sizes ranged from 1500 to 4000 kg, sufficient to provide clear first arrivals to a maximum offset of 300 km. The shotpoint interval ranged from 63 to 125 km, and the receiver interval was between 2 and 4 km. The profile was recorded along existing roads, which provided three nearly straight profile segments.

In order to aid in the correlation of phases, reduction velocities of 6.0 km/s and 3.46 km/s were used for P- and S-waves, respectively. The time scale used for S-wave record sections was compressed by a factor of 0.58 in order to match the P-wave arrival times. In order to avoid the small time shift that is introduced by digital filters, unfiltered P-wave data were used for phase correlation and traveltime picking. In order to improve the signal-to-noise ratio for phase correlation, the S-wave data were filtered with a 0-6 Hz bandpass.

The first arrivals of the Pg phase were used to invert for the upper crustal velocity structure using a finite-difference tomographic method (Hole, 1992). The reflection phases P_1P, P_LP, P_2P and P_mP were used to determine the approximate velocity structure of the middle to lower crust with the X^2-T^2 method (Giese, Prodehl and Stein, 1976). After establishing an initial crustal P-wave velocity structure, the final P-wave model was determined using 2-D forward raytracing modeling (Cerveny, Molotkov, and Psencik, 1977; Cerveny and Psencik, 1984), amplitude modeling using the reflectivity method (Fuchs and Muller, 1971), and 2-D ray methods. By adjusting the velocities and depths of the boundaries with the raytracing method, the traveltimes of the various phases on the record sections were fit, thus establishing the final P-wave velocity model.

The S-wave velocity structure differs from P-wave velocity structure only in its velocity distribution; the depths of all layer boundaries were kept the same. The upper crust shares similar characteristics to the P-wave structure, and just replacing P-wave velocity with S-wave velocity (assuming Poisson's ratio is 0.25) satisfies these data. Two-dimensional forward modeling was used to fit the remaining S-wave phases. Finally, from the respective P- and S-wave velocity models, the distribution of Poisson's ratio can be calculated.

The accuracy and resolution of the final model is dependent on a large number of factors, including shotpoint interval, receiver density, and lateral variations in near-surface low-velocities. An important factor is the correct identification of the various phases, and the number of ray paths intersecting a particular volume of the model. Perturbation of the velocity model shows that resolution of velocities and interface depths are about 2% and 5%, respectively, depending on the complexity of the model structure and the ray-path coverage.

CONCLUSIONS AND RECOMMENDATIONS

Crustal structure

The depth of sedimentary basins can be determined from these data based on the low seismic velocities of the basin fill. The Junggar, Turpan-Hami, and Tarim basins each have 5-8 km of sedimentary fill despite the overall convergent tectonic setting. The Tianshan, which show evidence for active uplift (Windley et al., 1990), are situated between the Tarim and Turpan-Hami basins. This implies that compressional stresses evident within the Tianshan are applied by the stronger crystalline crust beneath the neighbouring basins. The crystalline crust along this profile consists of three primary layers, with seismic velocities of 6.0-6.3 km/s, 6.3-6.6 km/s, and 6.9-7.0 km/s. The most important features within these layers are: (1) the

Bogdashan arc shows the highest velocities (6.3 km/s) within the upper layer, indicative of higher densities within the upper crust; (2) the seismic velocity within the middle crustal layer is 6.5-6.6 km/s from the Altai Mountains south to the Turpan-Hami basin, but decreases to 6.3 km/s from the Tianshan to the Quidam basin, and a mid-crustal low velocity layer (5.9 km/s) also is present. (3) The thickness of the lower crustal layer reaches a maximum (30 km) beneath the Junggar Accretional belt and the Altai Mountains. A minimum thickness of the lower crust (15 km) is found beneath the Junggar basin.

Such a three-layer stratification of the crust is commonly reported, and the velocities measured here are typical of many continental crustal sections. However, the lower crustal layer (6.9-7.0 km/s) is remarkably thick, with an average of 20 km (40% of the total crustal thickness). The middle crust (6.3-6.6 km/s) has an average thickness of 17 km, and the upper (consolidated) crust has an average thickness of 9 km. (Sedimentary accumulations range from 0 - 8 km in thickness). The average thickness of the entire crust is 50 km; thus the middle and lower crust comprise 74% of the crust.

The seismic velocity of the uppermost mantle (Pn) is less than or equal to the global average (8.05 km/s) in all parts of the study area. The lowest values (7.7-7.8 km/s) occur beneath the Junggar and Turpan-Hami basins. The Pn velocity is 8.0 km/s beneath Altai mountains, Junggar accretional belt, Tianshan accretional belt and Tarim platform.

Crustal thickening

These observations may be compared with global averages for continental crust. The average thickness of continental crust is 39 km. Thus the crustal thickness of NW China is 11 km thicker that the continental average and has likely been thickened by crustal shortening associated with the Tibetan orogeny and/or magmatic additions to the crust. The amount of shortening needed to thicken 39 km thick crust to 50 km is 30%. However, the fact that the upper crust (6.0-6.3 km/s) has only half the thickness of the middle and lower crust suggests that isostatic uplift has led to the erosion of about 10 km of the (shortened) upper crust. If we tentatively accept that 10 km of crust has been removed, then the shortening along the profile amounts to 50%. A major uncertainty in this calculation is the initial crustal thickness.

Alternatively the crust may have been thickened by magmatic additions. If these intrusions were mainly intermediate to mafic in composition, they could have thickened the middle and lower crust, respectively. If the upper crust was also thickened with silicic intrusions, erosion has eliminated the evidence for this thickening. The present geophysical data do not allow us to discern which process, compression or magmatic inflation, has dominated the process of crustal thickening.

Crustal Composition

The interpretation of crustal composition from seismic velocity measurements has recently been reviewed by Holbrook et al. (1992), Rudnick and Fountain (1995), and Christensen and Mooney (1995). We begin our discussion with the measured Vp structure and then discuss the Vp/Vs ratio, or, equivalently, Poisson's ratio.

As mentioned above, the consolidated crust is stratified into three primary layers with seismic velocities of 6.0-6.3 km/s, 6.3-6.6 km/s, and 6.9-7.0 km/s. The average velocity of the consolidated crust is 6.6 km/s, which is significantly higher than the global average of 6.45 km/s (with a standard deviation of 0.21 km/s). This high average velocity is mainly the result of the great thickness (20 km) of the high-velocity lower crustal layer.

Christensen and Mooney (1995) present statistical averages for continental crustal velocities as a function of depth. Upper crustal velocities in the study area are consistent with geological observed meta-sedimentary and felsic intrusive rocks. Measured Poisson's ratios for these rocks (0.25) are consistent with this interpretation. Middle crustal velocities are lower beneath the Tianshan and eastern Tarim basin (6.3 km/s) than those terrains to the north (6.5-6.6 km/s), and Poisson's ratio increases slightly from south (0.25) to north (0.26-0.27). These observations indicate that the bulk composition of middle crust beneath the Tianshan is close to that of a tonalite or granodiorite, and becomes less silicic to the north (equivalent to a diorite). For example, an increase in the abundance of amphibolite in the middle crust from 5% beneath the Tianshan to about 35% beneath the terrains to the north would satisfy the observations (c.f., Figure 18 in

Christensen and Mooney, 1995). The lower crustal seismic velocity (6.9-7.0 km/s) and Poisson's ratio (0.26-0.28) are remarkably uniform along the entire 1,100 km transect. The seismic velocity of the lower crust is consistent with a mafic composition (mafic granulite and mafic garnet granulite), or anorthosite. However, these compositions would provide a Poisson's ratio of 0.29-0.31, which is 0.01-0.05 higher than the reported values. Granulite grade metapelite provides the best fit to the seismic velocity data, but it seems unlikely, based on heat flow constraints, that the lower continental crust is composed of a thick (20 km) layer of metapelite over a distance of 1,100 km. Thus we favor mafic granulite composition.

REFERENCES

Cerveny, V. , I.A. Molotkov, and 1. Psencik. 1977. Ray method in seismology. Prague.: Univerzita Karlova.

Cerveny, V., and I. Psencik, eds. 1984. SEIS83-numerical modeling of seismic wavefield in 2-D laterally varying layered structures by the ray method, in: E. R. Engdahl (editor), Documentation of earthquake algorithms. World data center (A) for solid earth geophysics, Boulder, Colo., Rep. SE-35, 36-40. Edited by E. R. Engdahl. Vol. Rep. SE-35, Documentation of earthquake algorithms. World data center (A) for solid earth geophysics, Boulder, Colo., Rep. SE-35, 36-40. Boulder, Colo.: World Data Center.

Christensen, N. I. and W. D. Mooney, Seismic velocity structure and composition of the continental crust: A global view, J. Geophys. Res., 100,9761-9788, 1995.

Fuchs, K., and G. Muller. 1971. Computation of synthetic seismograms with the reflectivity method and comparison with observations, Geophys. J. R. Astr. Soc. 23:417-433.

Giese, P., C. Prodehl, and A. Stein. 1976. Explosion Seismology in Central Europe. Berlin Heidelberg, New York.: Springer-Verlag.

Holbrook, W.S., W.D. Mooney, and N.I. Christensen. 1992. The Seismic velocity structure of the deep continental crust. In Continental Lower Crust, Elsevier. Developments in Geotectonics, edited by D. M. Fountain, R. Arculus and R. W. Kay: Elsevier.

Hole, J. A., 1992. Nonlinear high-resolution three-dimensional seismic travel time tomography. Journal of Geophysical Research, B, 97 (B5):6553-6562.

Rudnick, R.L., and D.M. Fountain. 1995. Nature and composition of the continental crust: a lower crustal perspective. Reviews of Geopyhsics 33 (3):267-309.

Windley, B.F., M.B. Allen, C. Zhang, Z-Y. Zhao, , and G-R. Wang. 1990. Paleozoic accretion and Cenozoic redeformation of the Chineses Tien Shan Range, central Asia. Geology 18:128-13 1.

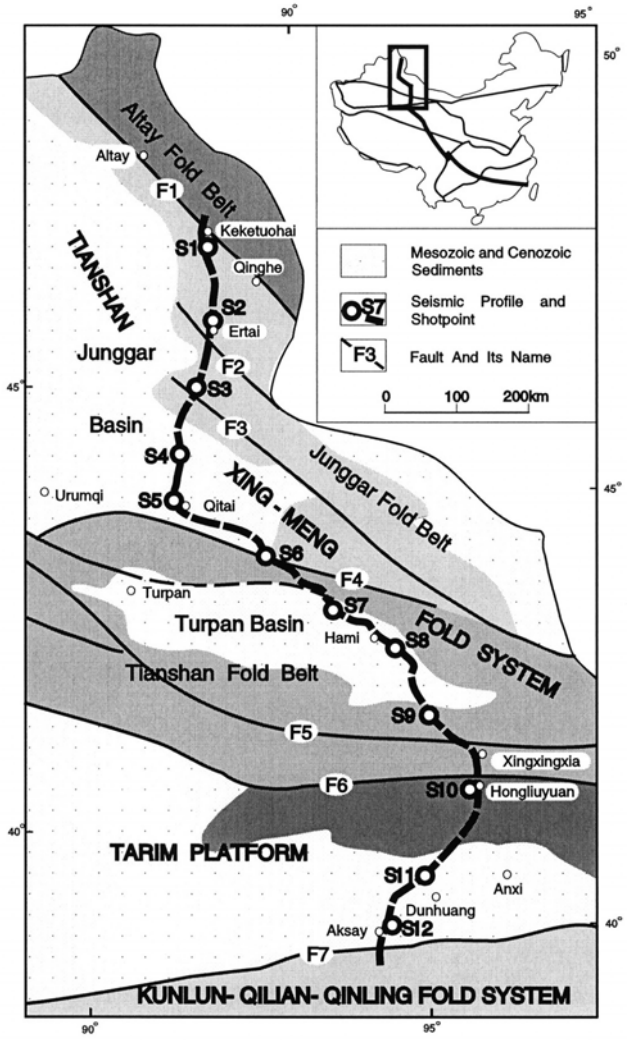


Figure 1. Tectonic setting of China indicating location of Geoscience transect line.

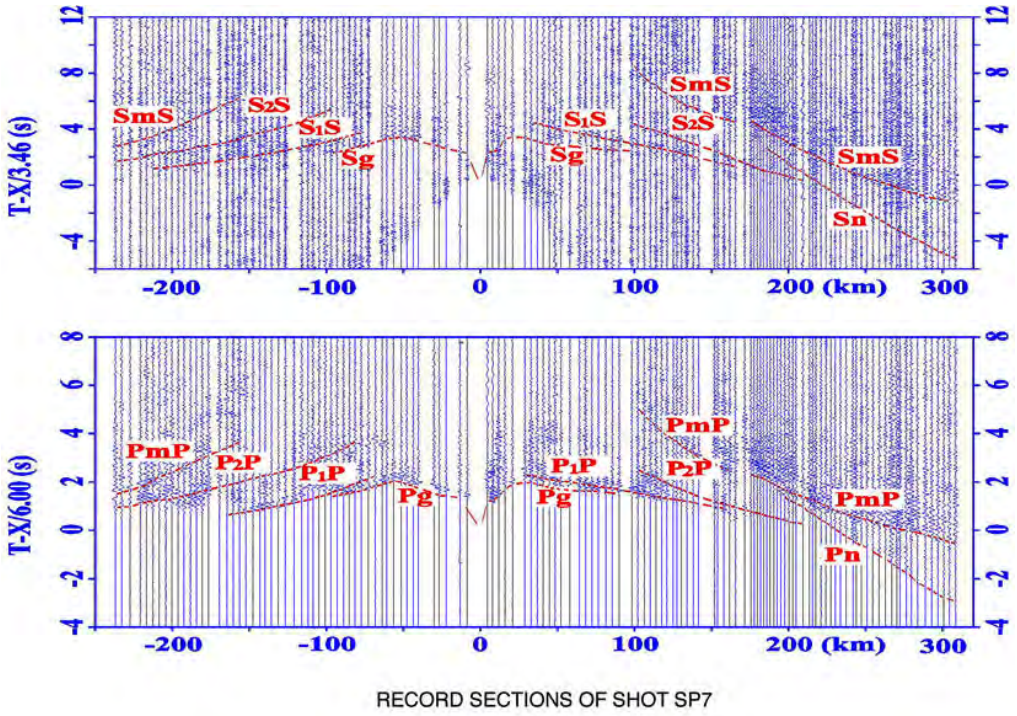


Figure 2. Record sections of shotpoint SP7. (upper: trace-normalized band-pass filtered (0-8 Hz) S-wave record section with a reduction velocity of 3.46 km/s and a factor of 0.58 in time scale with respect to P-wave record section; lower: trace-normalized P-wave record section with a reduction velocity of 6.00 km/s.)

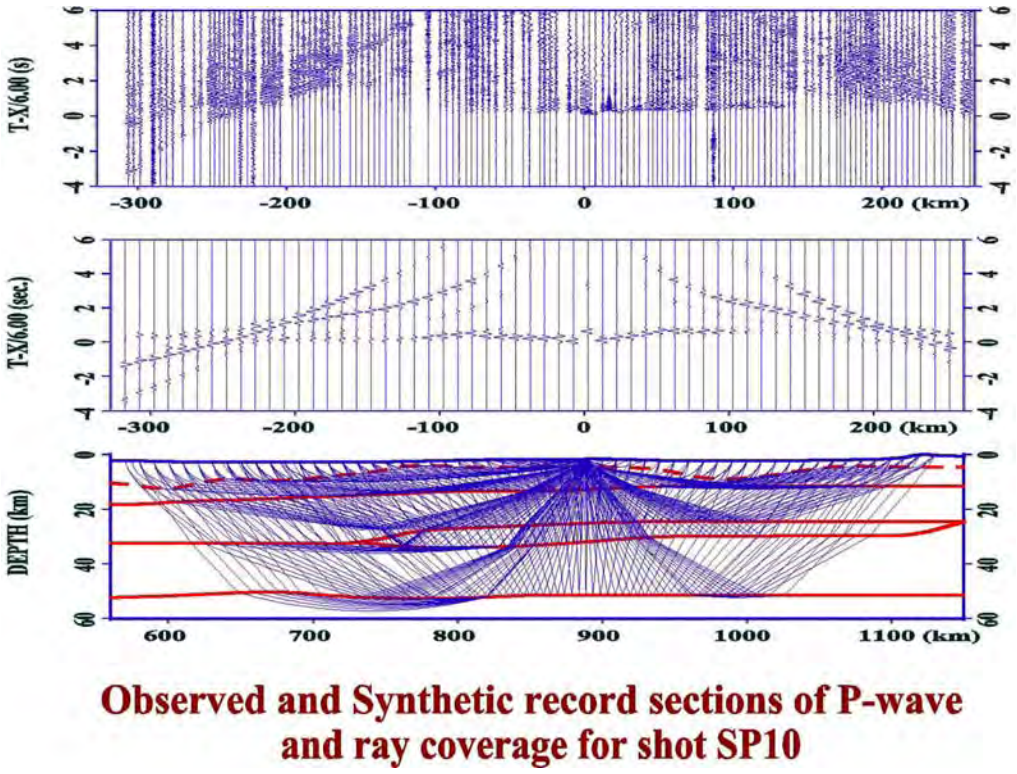


Figure 3. Raypath and sythetic seismogram for shotpoint SPIO

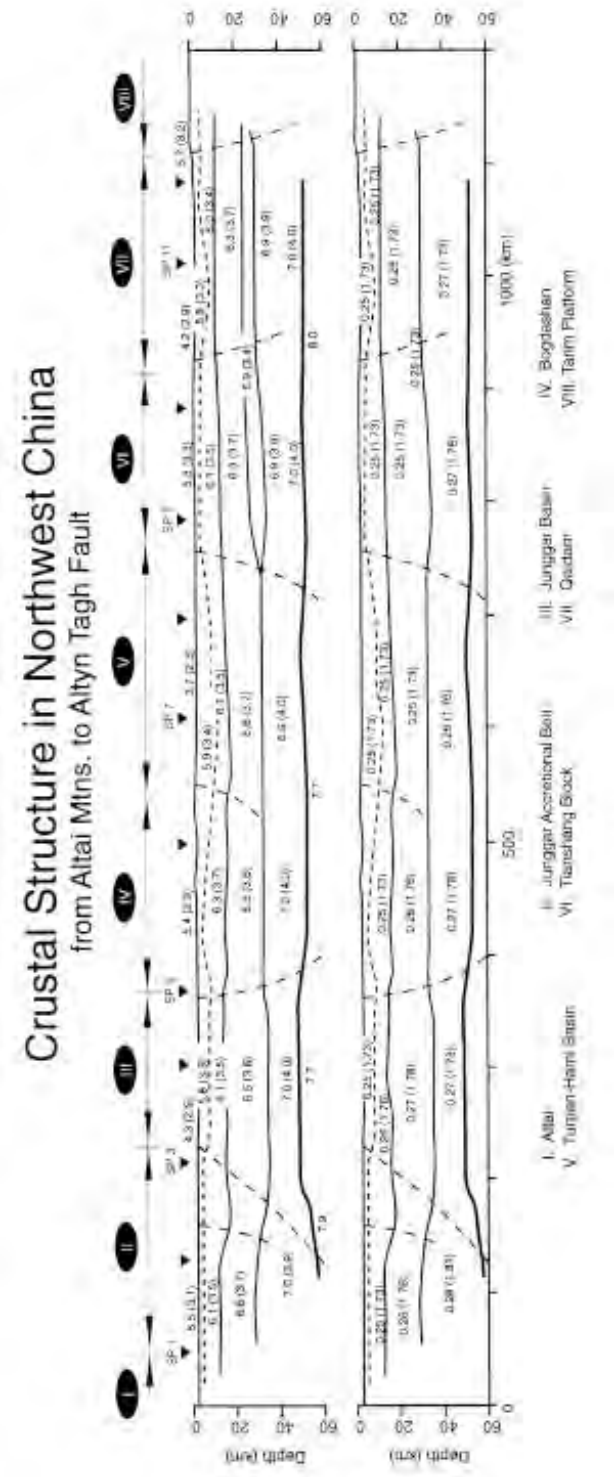


Figure 4. The crustal structure of the profile along the GTTA. (upper: P-wave velocity structure; lower: S-wave velocity structure and Poisson's ratio, where the dashed line indicate the top of basement.)

PRELIMINARY CHARACTERIZATION OF L_g PHASE PROPAGATION FROM PEACEFUL NUCLEAR EXPLOSIONS IN SIBERIA

Igor B. Morozov, Elena A. Morozova, and Scott B. Smithson
Department of Geology and Geophysics, University of Wyoming

Sponsored by U.S. Department of Defense
Defense Threat Reduction Agency
Contract No. DSWA01-98-0015

ABSTRACT

In continuation of our study of L_g propagation from the peaceful nuclear explosions (PNEs) recorded along the Russian ultra-long refraction/reflection profile QUARTZ, we obtained four other PNE profiles: CRATON, KIMBERLITE, RIFT, and METEORITE. This acquisition extends our database to 17 PNEs. Together with QUARTZ, these profiles form a grid traversing the East European Platform, the Ural Mountains, the West Siberian Basin and the Siberian craton in two directions, and the Baikal Rift. The uniqueness of the obtained dataset is in linear, dense (~10 km station spacing), up to 10-min long 3-component recording of seismic phases to over 3000-km distances, with additional control provided by reversed PNEs. Pairs of subparallel and crossing profiles allow correlation of features of wave propagation observed on individual PNE records. The use of PNE profiles provides us with unique opportunities to study large-scale propagation effects of various seismic phases, and especially L_g, across geological and tectonic boundaries.

Preliminary examination of P_g, *S*-wave, and L_g phases in PNE shot gathers reveals strong variations in the character of the phases and poses a number of questions for further interpretation and modeling. L_g broadly varies in velocity (2.2 to 3.8 km/s), in amplitude (from lower to much stronger than the mantle *S* wave) and in propagation range (from around 1000 to 2200 km). Generally, L_g appears to be recorded better by the Siberian profiles than by the profile QUARTZ, where the PNE records show L_g at offset ranges 300-1200 km. Tentatively, these differences, together with the variations between the new PNEs currently being analyzed, can be attributed to the influence of the West Siberian Basin that appears to cause strong L_g attenuation. However, this conclusion requires further assessment of the dynamic character of the wavefield, its correlation with other seismic phases and with the available detailed information about the crustal structure.

This study demonstrates that Russian PNE data provide valuable information for the analysis of the propagation of L_g and other phases for their use in CTBT calibration studies.

Key Words: Nuclear Explosions, Russian Eurasia, Seismic Phase Propagation, L_g

OBJECTIVE

Over the past three decades, Russian scientists acquired a network of dense, linear, long-range, three-component Deep Seismic Sounding (DSS) profiles using conventional and Peaceful Nuclear Explosions (PNEs) over a large territory of Northern Eurasia. Within the framework of the Comprehensive Nuclear-Test-Ban Treaty, these historic data provide unique opportunities to calibrate existing seismic nuclear discrimination techniques by studying regional wave propagation through complex lithospheric structures.

Our work described below focuses on obtaining a representative set of PNE recordings along such profiles and on identification and characterization of the phases relevant for CTBT monitoring. The database of kinematic, spectral, and amplitude parameters of PNE recordings created in this study will result in development of robust amplitude measurement techniques and in correlation of its amplitude characteristics with the tectonic and geologic environment. Also, analysis of the profiles will allow an assessment of a realistic, 2- to 3-D, heterogeneous velocity and attenuation structure of the crust and upper mantle that would enable quantitative analysis of the amplitudes of regional seismic waves. Ultimately, the results of this effort should contribute to improvement of regional seismic event discriminantion techniques and should help calibrate the regional International Monitoring System (IMS) network (**Error! Reference source not found.**).

RESEARCH ACCOMPLISHED

This work continues our recent studies of the 3850-km long DSS profile QUARTZ (**Error! Reference source not found.**) which is one of the best-known profiles of the DSS program (Egorkin, A. V. and A. V. Mikhaltsev, 1990; Mechie et al., 1993). Our

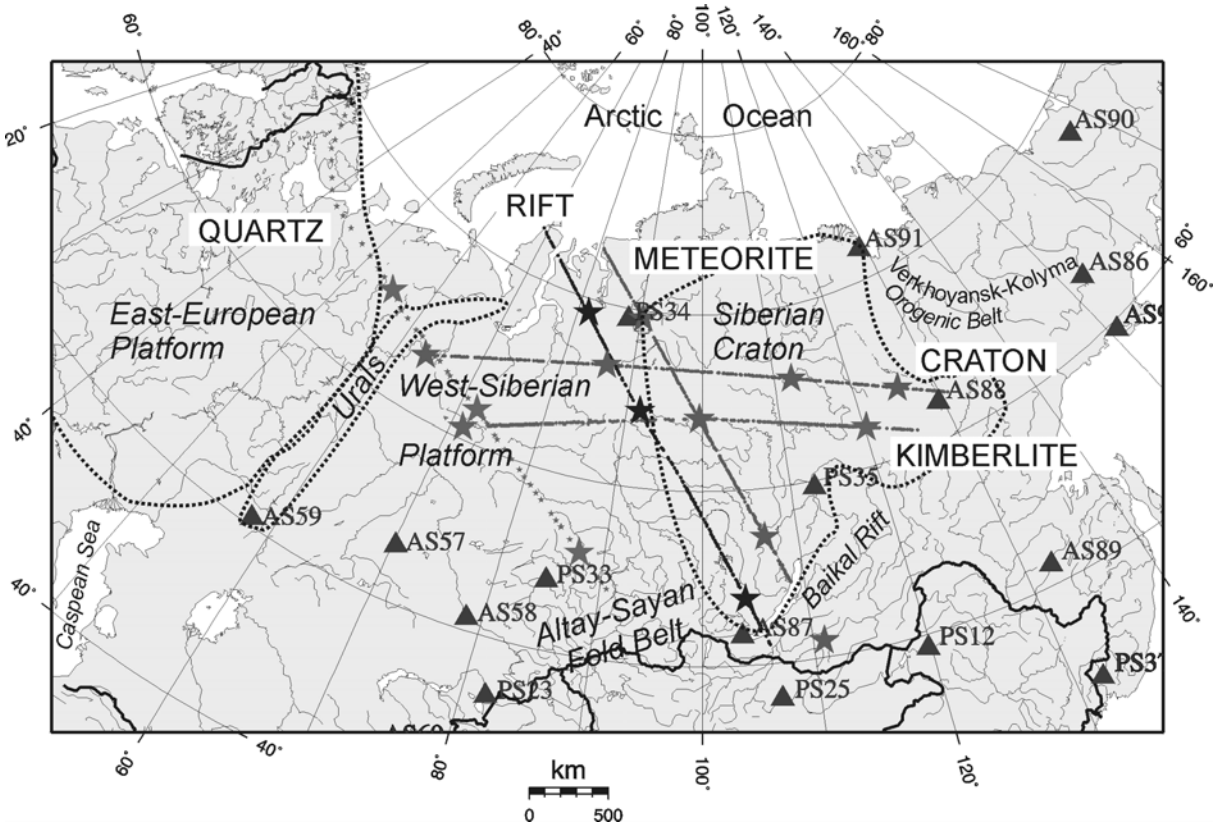


Figure 1 Five DSS PNE profiles under study at the University of Wyoming. Profile QUARTZ has been analyzed previously, profiles CRATON, KIMBERLITE, RIFT and METERORITE were obtained in this study. Large stars are the PNEs, small stars (for profile QUARTZ only) are the chemical explosions. The coordinates and other parameters of the PNEs used in these profiles were

reported by Sultanov et al. (1999). Major tectonic units are indicated. Note the extent of systematic, continuous profiling, with PNEs detonated at the nodes of a 2-D recording grid. Also note that the profiles are close to some of the IMS stations (labeled triangles).

recent, detailed analysis of both PNEs and chemical explosions reveals detailed images of seismic velocity and reflectivity of the crust and upper mantle (Schueller et al., 1997; Morozova et al., 1997 and in press), of seismic attenuation (Morozov et al., 1998b), and provides constraints on the propagation of lithospheric guided waves (Morozov et al., 1998a), and *S*- and *Lg* waves (Morozov et al., 1996, 1997).

Expanding our scientific cooperation with the Center GEON, Moscow, we obtained four other PNE profiles: CRATON, KIMBERLITE, RIFT, and METEORITE (**Error! Reference source not found.**). This acquisition extends our database from 3 to 17 PNEs. Together with the profile QUARTZ, these profiles form a grid traversing the East European Platform, the Ural Mountains, the West Siberian Basin, and the Siberian craton in two directions (**Error! Reference source not found.**). The uniqueness of the obtained dataset is in a linear, dense (~10 km station spacing), up to 10-min long 3-component recording of seismic phases to over 3000-km distances, with additional control on wave propagation provided by the reversed PNEs. Groups of parallel and crossing profiles allow us to correlate features of wave propagation observed on individual PNE records. The use of PNE profiles provides us with unique opportunities to study large-scale propagation effects of various seismic phases and especially L_g, across contrasting tectonic regions.

Our current efforts have concentrated on data reduction for the newly obtained profiles. The original analog recordings were digitized by GEON to the full length of the records of up to 600 s after the onsets of the primary *P*-wave phases. In order to extend the dynamic range of recordings, two sets of records were acquired and digitized at different amplification levels. Further data reduction was performed at the University of Wyoming, where the digital data were converted to a more flexible format used in our lab (Morozov and Smithson, 1997), and an extensive interactive editing of the records used a commercial seismic processing system PROMAX. Our current data editing procedure is based on selecting the best-quality recordings from each recording channel. As an additional data editing option, we are investigating a possibility for combining both low-gain and high-gain channels to increase the dynamic range of the signal while minimizing the instrument noise. This would imply switching from the low-gain channels for first arrivals to high-gain channels for the rest of the records. Such a procedure would correspond to the plotting techniques used at GEON; however, since we intend to preserve the available trace amplitude information, it would also pose a problem of consistency of these two groups of channels, and of their proper scaling in the resulting records.

The data reduction procedures outlined above are completed with an incorporation of the channel amplification information provided by GEON. Averaged spectra of the resulting records from two profiles are shown in Figure 2 and selected record sections of the cross-line component (this component was chosen as containing more *S*-wave energy) are presented in Figure 3.

Preliminary examination of P_g, *S*-wave, and L_g phases in PNE shot gathers reveals strong variations in the character of the phases and poses a number of questions for further interpretation and modeling. L_g broadly varies in velocity (from 2.2 km/s in some branches to 3.8 km/s), in amplitude (from lower to much stronger than the mantle *S* wave) and in propagation range (from around 1000 to 2200 km). Generally, L_g appears to be recorded better by the Siberian profiles than by the profile QUARTZ, where the PNE records show L_g at offset ranges 300-1200 km (Morozov et al., 1997). Tentatively, these differences, together with the variations between the new PNEs currently being analyzed, can be attributed to the influence of the West Siberian Basin that appears to cause strong L_g attenuation. However, this conclusion requires further assessment of the dynamic character of the wavefield, its correlation with other seismic phases and with the available detailed information about the crustal structure.

Recorded amplitude spectra exhibit peaks between 0.5 - 4 Hz, with steeply decreasing amplitudes at higher frequencies. In CRATON records, the usable frequency range is about 0.5 - 10 Hz, with power at 10 Hz about 15 dB lower than between 0.5 - 3 Hz. CRATON-3 shows a broader peak at lower frequencies whereas the white ambient noise appears much stronger (Figure 2). The records from PNE RIFT-1 have a particularly narrow low-frequency energy peak. The records from the profile KIMBERLITE appear most

broad-band, probably usable to 20 Hz. Note that the relatively broad-band KIMBERLITE PNEs and CRATON-3 (Figure 2) also show the best recordings of mantle *S* waves (Figure 3).

Comparison of the observed spectra from the CRATON and KIMBERLITE PNEs detonated at (relatively) close locations suggests a limited correlation with the general tectonic character of the sites. The broad-band shots CRATON-3 and KIMBERLITE-3 and 4 were detonated within the Siberian craton while the low-frequency shots (with an exception of CRATON-4) were located within the West Siberian basin (Figure 1). However, the general difference between the spectra from these two profiles (Figure 2) also suggests a probable difference in the source conditions.

Examination of the *S*-wave and *Lg* phases in the shot gathers reveals strong variations in the character of the phases and poses a number of questions for further interpretation and modeling. *Lg* broadly varies in velocity (2.2 to 3.8 km/s), in amplitude (from lower to much stronger than the mantle *S* wave) and in propagation range (from around 1000 to 2200 km). Below, we present the most characteristic observations available to date.

Pg and *Lg* phases are clear in many of the Siberian PNE records. CRATON-4 shows a remarkably strong *S* wave (especially on component 2 - transverse to the profile), followed by diffuse *Lg* with group velocity of about 3.2 km/s. We can trace *Lg* to about 2000 km but it becomes very weak after about 1700 km. Note that the next shot to the west—CRATON-3 shows a very strong Lg, which becomes much slower (2.5 km/s) when it enters the West Siberian basin (Figure 3). Virtually no *S* wave is recorded to the east from CRATON-2 (Figure 3).

We observe a complex *Lg* pattern west from PNE CRATON-3 (Figure 2). The "primary" *Lg* phase is very strong and compact (~10 - 15 s in duration) throughout the entire offset range of 2200 km (this is the longest *Lg* propagation distance from DSS PNEs that we have observed so far). Two trains of energy appear to separate from *Lg* near offsets of 200 and (probably) 700 km, propagating at about 2.2 km/s apparently corresponding to the Rayleigh wave. To the east of this shot, a similar slow branch emerges near 300 km of offset but terminates near 700 km.

Records from CRATON-2 (and CRATON-4, not shown), show strong *Lg* that is more diffuse and can be traced to about 1500 km (Figure 3). The mantle S wave is not pronounced to the east of the shot but appears to be comparable in amplitude to *Lg* to the west (Figure 3). Strong crustal multiples follow the primary *P*-wave arrivals, but we cannot identify these multiples in the *Lg* wavetrains. *Pg* is also very strong to about 1500 km east of the shot.

CRATON-1 (not shown) generated little *S*-wave or *Lg* energy although its spectral content is not dramatically different from that of CRATON-3. However, this PNE also exhibits significant gaps complicating its interpretation.

The *Lg* from KIMBERLITE-1 (not shown in Figure 3; at the center of the West Siberian basin; Figure 1) to the east is very slow (about 2.4 km/s), reverberative and strong to about 500 km. After 500 km, it appears to decay quickly, similar to *Lg* phases from PNEs 213 (which is located close to KIMBERLITE-1) and from PNE 323 of the profile QUARTZ (Morozov et al., 1996, 1997). This slow propagation suggests that *Lg* in this area is dominated by relatively shallow S-wave phases propagating within the thick sediment cover of the basin.

KIMBERLITE-3 (Figures 1 and 3) shows good *Lg* and mantle *S* waves in both directions. *Lg* appears to be stronger than the *S* (unlike what we had observed from the southern PNE of QUARTZ profile (see Figure 1). *Pg* is strong to 1300 km offset to the east and to about 1000 km to the west. As in other PNE records, close examination of the records indicates strong *P*-wave crustal reverberations; such reverberations might contribute to the diffuse character of *Lg*.

KIMBERLITE-4 also shows strong *S* and *Lg* phases (Figure 3). *Lg* appears to carry somewhat more energy than the *S* wave. Both *S* and *Lg* waves are diffuse but the onset of S waves is clearly marked. As expected, *Lg* separates from *Sn* near 250 km of offset, where high amplitudes of the shear-wave arrivals indicate a near-critical *SmS* reflection.

RIFT data have narrower bandwidth and somewhat lower quality. Yet, *Lg* from RIFT-1 and RIFT-2 can be identified to offsets of about 1600 km, propagating at about 3.8 km/s. A mantle *S* wave, somewhat

scattered in character, can be also observed (Figure 3). A notable difference in the relative amplitudes of the *Pg*, *S*, and *Lg* arrivals east of PNEs RIFT-1 and RIFT-2 (Figure 3) is not explained at present.

Due to instrumental problems, METEORITE recordings are limited in offset coverage (Figure 3). The *P*, *Pg*, *S*-, and *Lg* phases are strong and reliably observed to the ranges of 1200 - 1600 km.

CONCLUSIONS AND RECOMMENDATIONS

Preliminary examination of the newly obtained Russian PNE records from four Siberian DSS profiles demonstrates that the data provide valuable information for the analysis of the propagation of L_g and other phases for their use in CTBT calibration studies. Our further effort in analyzing the data will be focused on a detailed characterization and modeling of the *P*-, *S*-, and *Lg* wave phases critical for nuclear test discrimination.

In the records from the Siberian DSS PNE profiles, we generally find stronger *Lg* propagating to longer distances than recorded by the profile QUARTZ. At the same time, the propagation character of *S* waves and *Lg* shows high variability that is apparent across the contact between the Siberian craton and the West Siberian basin where the observations are more consistent with those from the profile QUARTZ.

In our ongoing research, we will substantiate and quantify these observations in more detail. As a first step, we will perform picking travel-times of the *P*- *S*- wave, *Lg*, and *Rg* seismic phases in the records; and checking for reciprocity between the reversed PNEs. During further stages of this work, we will proceed with further analysis of *Lg* phases, selecting noise correction approaches, spectral estimators, to examine offset dependence of the amplitudes and spectral ratios. This will result in a database of travel-time, velocity, amplitude, spectral, coda *Q*, and other parameters of these phases.

At later stages of this research, we intend to use crustal/uppermost mantle structural models to interpret the resulting database, associating the observed variations in propagation properties of *Lg* with the crustal structure and with the character of other seismic phases identified in the profiles. The crustal velocity and Moho models will be available from previous studies conducted at GEON. At this stage, we will model *Lg* propagation along the profiles in order to test hypotheses about the effects of the crustal and uppermost mantle structure on *Lg* and other regional phases.

REFERENCES

Egorkin, A. V. and A. V. Mikhaltsev, 1990. The Results of Seismic Investigations along Geotraverses, *in* Super-Deep Continental Drilling and Deep Geophysical Sounding, K. Fuchs, Y. A. Kozlovsky, A. I. Krivtsov and M. D. Zoback (Editors), Super-Deep Continental Drilling and Deep Geophysical Sounding, Springer, Berlin, 111-119.

Mechie, J., A. V. Egorkin, K. Fuchs, T. Ryberg, L. Solodilov, and F. Wenzel (1993). P-wave velocity structure beneath northern Eurasia from long-range recordings along the profile Quartz, *Phys. Earth Planet Inter*., 79, 269-286.

Morozov, I. B**.,** and Smithson, S. B., 1997, A new system for multicomponent seismic processing, *Computers & Geosciences,* 23, 689-696.

Morozov, I. B., E. A. Morozova, and S. B. Smithson, 1996. L_g propagation in northern Eurasia recorded by profile "Quartz", *in:* Proceedings of 18 Seismic Research Symposium, PL/DARPA

Morozov, I., B., E. A. Morozova, and S. B. Smithson, 1997. Observation of Lg and S wave propagation along the ultra-long profile "Quartz", Russia, *in:* Fuchs, K. (Ed.) Upper mantle heterogeneities from active and passive seismology, Kluwer, pp. 147-154.

Morozov, I., B., E. A. Morozova, and S. B. Smithson, 1998a. On the nature of the teleseismic *Pn* phase observed in the recordings from the ultra-long profile "Quartz", Russia, *Bull. Seism. Soc. Am.*, 88, 62-73.

Morozov, I., B., E. A. Morozova, S. B. Smithson, and L. N. Solodilov, 1998b. 2-D image of seismic attenuation beneath the Deep Seismic Sounding profile QUARTZ, Russia, *Pure Appl. Geoph*, 153, 311-343.

Morozova, E. A., I. B. Morozov, S. B. Smithson, and L. N. Solodilov, Heterogeneity of the uppermost mantle beneath the ultra-long range profile "Quartz," Russian Eurasia, *J. Geophys. Res*., in press.

Morozova, E. A., Morozov, I., B., and S. B. Smithson, 1997. Heterogeneity of the uppermost Eurasian mantle propagation along the DSS profile "Quartz", Russia, *in:* Fuchs, K. (Ed.) Upper mantle heterogeneities from active and passive seismology, Kluwer, pp. 139-146..

Schueller, W., Morozov, I. B., and Smithson, S. B., 1997**,** Crustal and Uppermost Mantle Velocity Structure of Northern Eurasia along the Profile *Quartz, Bull Seism. Soc.Am.*, 87, 414-426.

Sultanov, D. D., J. R. Murphy, and Kh. D. Rubinstein, 1999. A seismic source summary for Soviet Peaceful Nuclear Explosions, *Bull. Seism. Soc. Am.,* 89, 640-647.

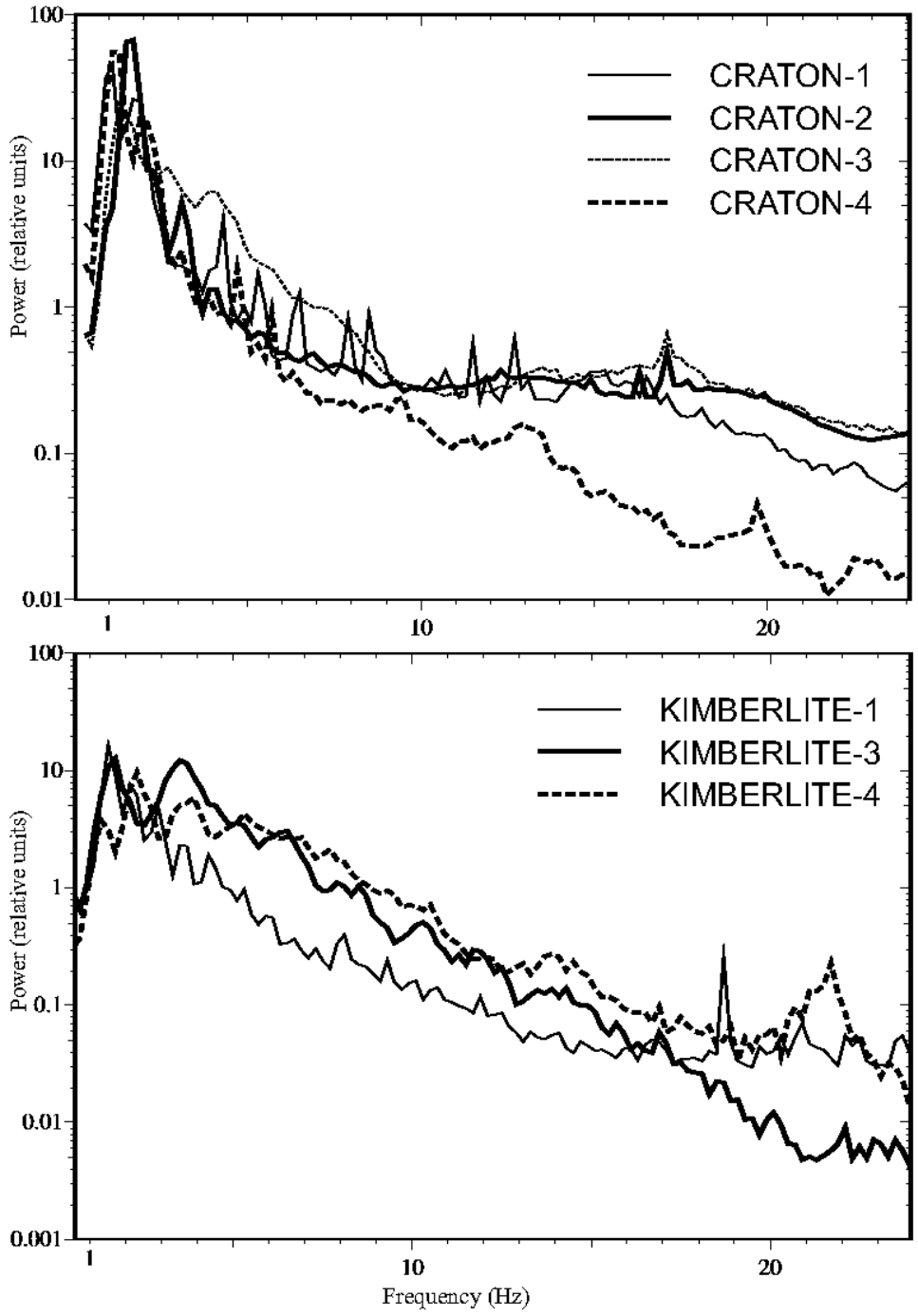


Figure 2. Averaged power spectra of the vertical-component records from profiles CRATON (top) and KIMBERLITE (bottom). To obtain these spectra, record sections were trace-normalized, and the resulting power spectra were averaged within 0.2 Hz intervals over the entire sections. The recorded spectra vary significantly between the shots and between the profiles; however, the PNEs in the cratonic areas (CRATON-3, KIMBERLITE-3 and 4; see Figure 1) generate more high-frequency energy.

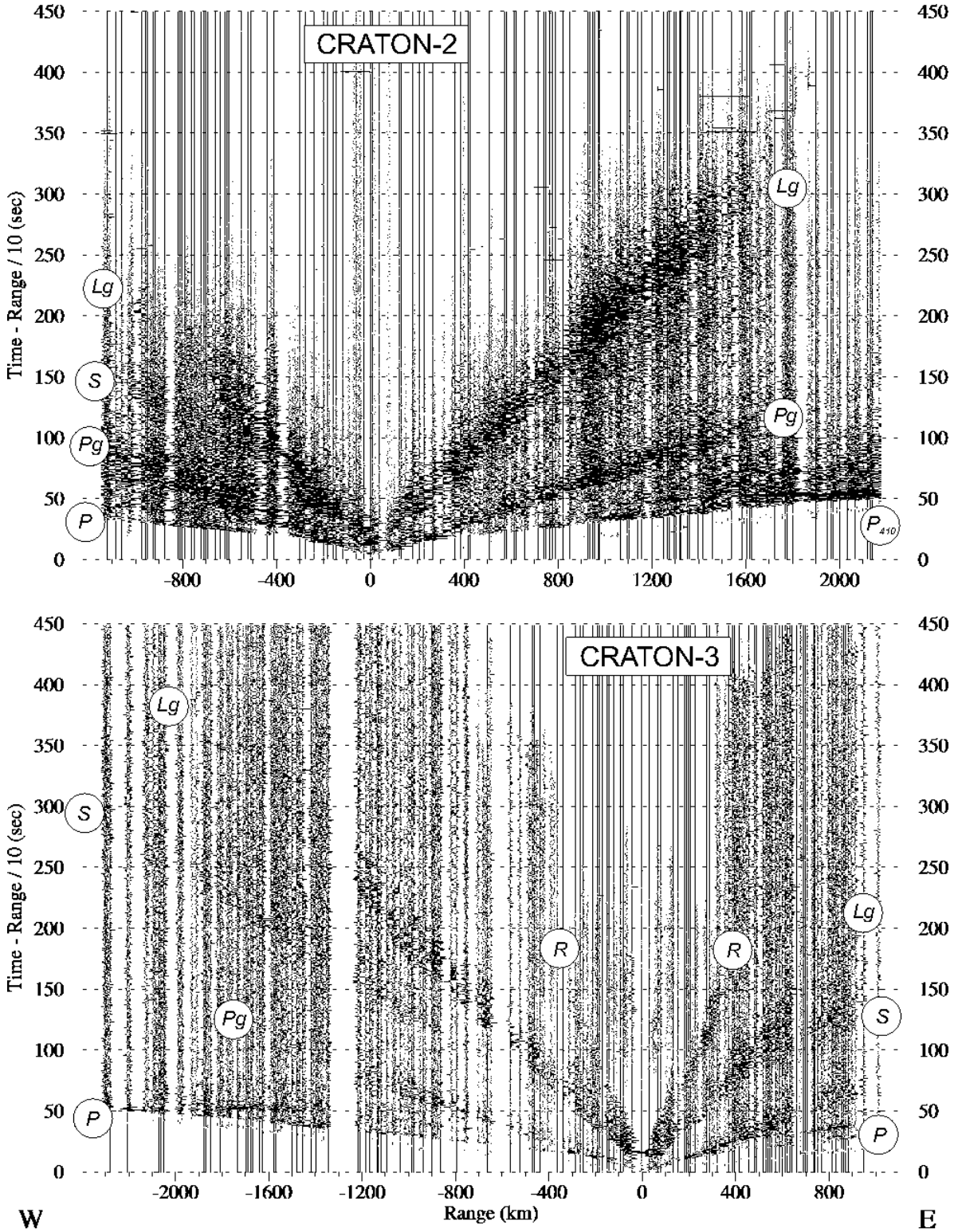


Figure 3. Horizontal component (transverse to the profiles) records from 2 PNEs from each of the newly obtained profiles (Figure 1). Automatic gain control within 100-sec window used for normalization. Note the strong and variable *S*-wave and *Lg* phases.

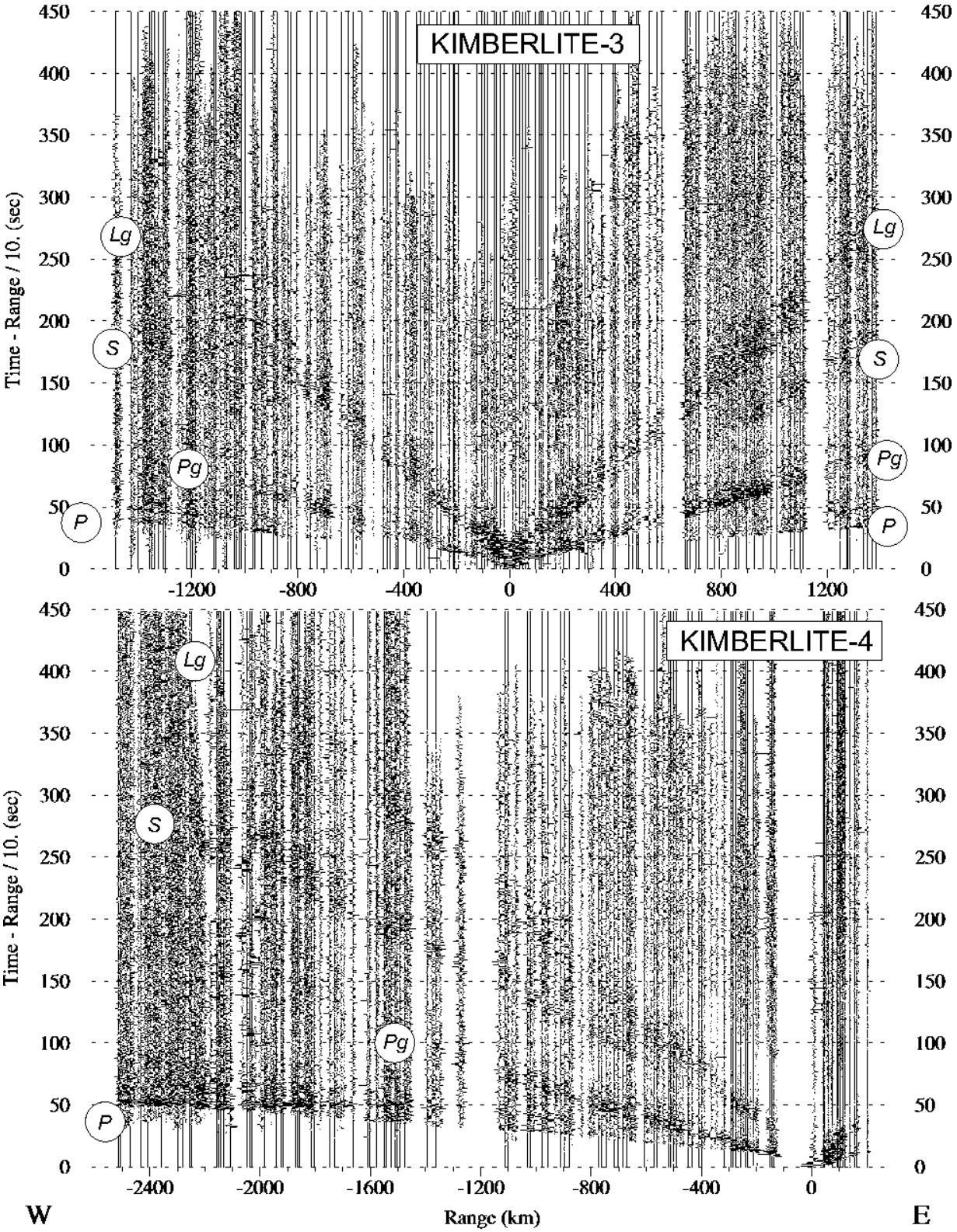


Figure 3 (continued).

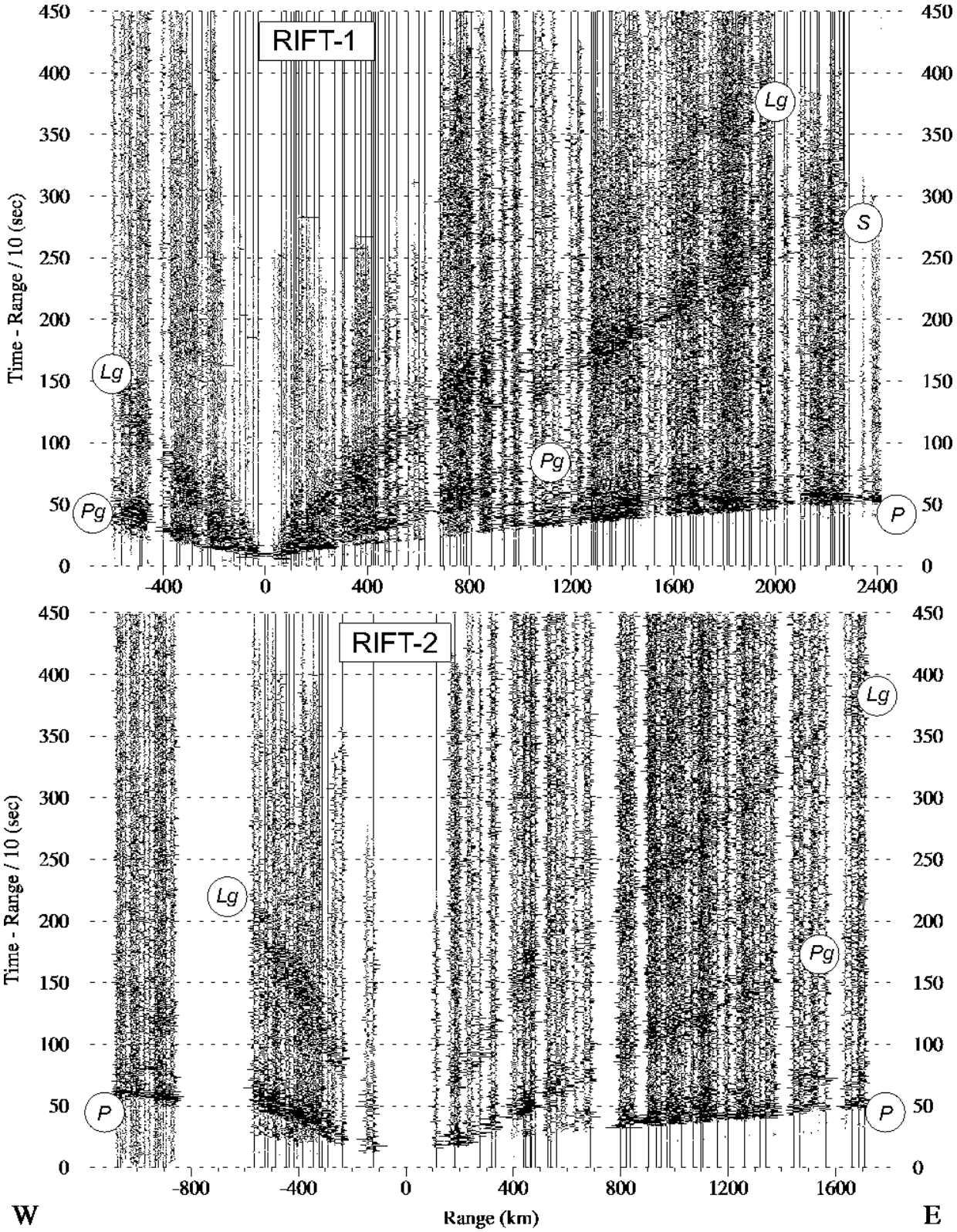


Figure 3 (continued).

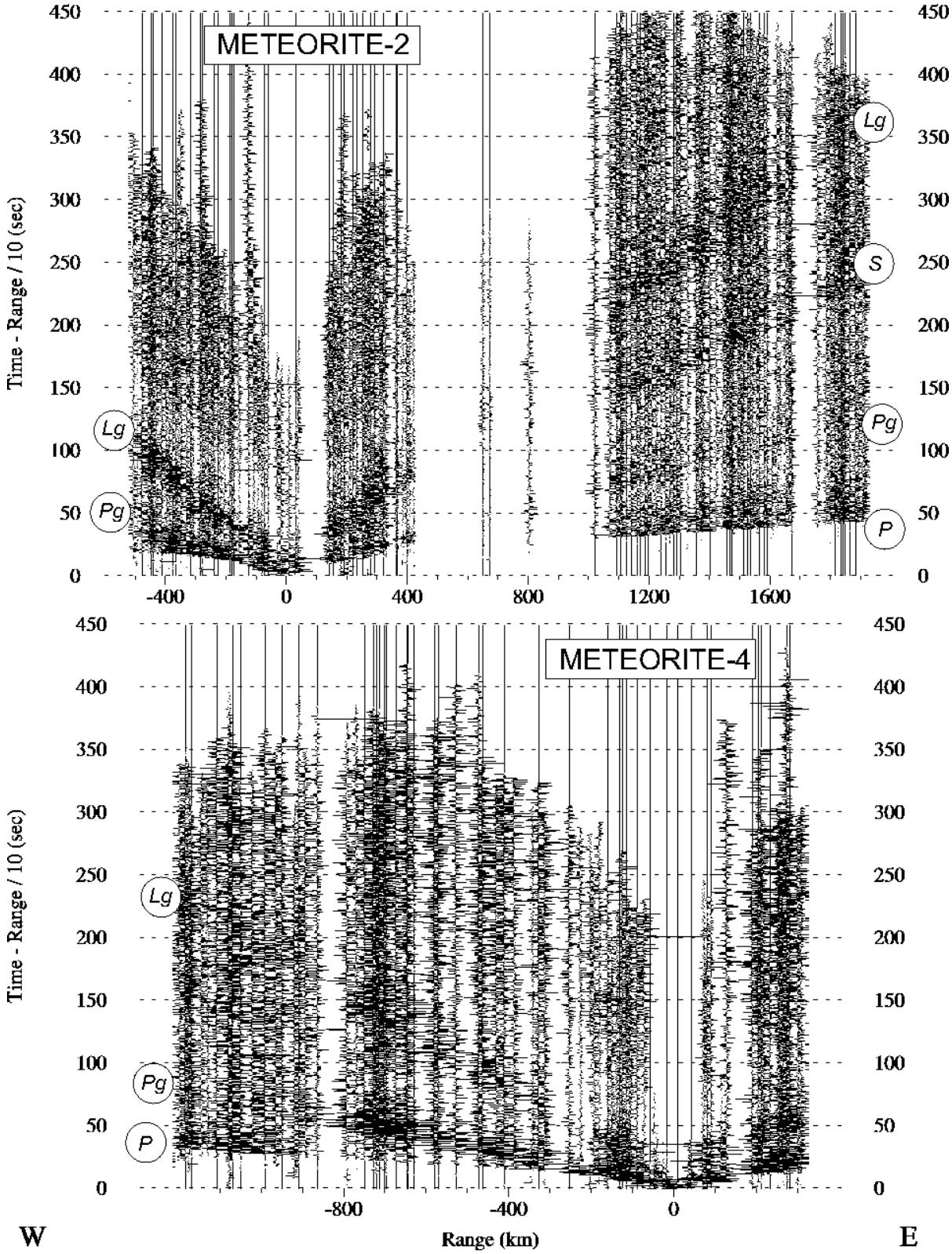


Figure 3 (continued).

SEISMIC CALIBRATION OF THE EUROPEAN ARCTIC

Svein Mykkeltveit, Frode Ringdal, Conrad Lindholm, NORSAR
Elena Kremenetskaya, Kola Regional Seismolgical Centre

Sponsored by U. S. Department of Energy
Office of Nonproliferation and National Security
Office of Research and Development
Contract No. DE-AC04-99AL66001

ABSTRACT

The purpose of this two-year effort, which started on 1 January 1999, is to support the construction of the U.S. Department of Energy (DOE) Comprehensive Nuclear-Test-Ban Treaty Knowledge Base for detecting, locating and identifying seismic events in the area of northern Fennoscandia, the Kola Peninsula, Novaya Zemlya, and the surrounding waters of the Barents and Kara Seas. The main objectives of the effort are to assemble a set of historical seismic observations suitable for characterizing all aspects of seismic wave propagation and seismic sources in this region, to describe the principal seismic phases observed in the seismograms, and to calibrate the region with respect to seismic wave propagation (travel-times and amplitude-distance relations).

The main emphasis during the first year of this contract is on data collection. Waveform data are now being collected for a range of sources in the European Arctic: Nuclear tests at the Novaya Zemlya test site, peaceful nuclear explosions conducted in the area, earthquakes and presumed underwater explosions from 1970 to the present, and representative blasts from mining operations in the Kola Peninsula, northern Norway, Sweden, Finland and adjacent regions of European Russia. Waveform data collected under this effort will be provided in CSS 3.0 format on a set of CD ROMs, with the appropriate metadata included, to DOE through the Lawrence Livermore National Laboratory, to the U.S. Department of Defense through the Center for Monitoring Research and to the U.S. National Data Center.

The project is a collaborative effort between NORSAR and the Kola Regional Seismological Centre (KRSC) of the Russian Academy of Sciences. The main source of data for this project is the historical waveform archives at NORSAR, containing data from the NORSAR teleseismic array and the network of northern European small-aperture arrays. These data will be supplemented with data provided by KRSC for stations AMD and APA in northwestern Russia.

The presentation will provide details on the data being compiled for this project and will summarize the current status of the data collections effort. Representative waveforms for different source types and propagation paths will be shown to illustrative the variability in the characteristics of seismic phases, and some initial results from analysis of the data will be presented.

Key Words: data collection, characterization of seismic phases, seismic calibration

OBJECTIVE

The purpose of this research is to support the construction of the DOE CTBT Knowledge Base for detecting, locating and identifying seismic events in the area of northern Fennoscandia, the Kola Peninsula, Novaya Zemlya, and the surrounding waters of the Barents and Kara Seas. This is done by assembling a set of historical seismic observations suitable for characterizing all aspects of seismic wave propagation and seismic sources in this region, by describing the principal seismic phases observed in the seismograms, and by calibrating the region with respect to seismic wave propagation.

RESEARCH ACCOMPLISHED

The main emphasis during the first year of this contract is on data collection. Waveform data are now being collected for a range of sources in the European Arctic: Nuclear tests at the Novaya Zemlya test site, peaceful nuclear explosions conducted in the area, earthquakes and presumed underwater explosions from 1970 to the present, and representative blasts from mining operations in the Kola Peninsula, northern Norway, Sweden, Finland and adjacent regions of European Russia. We have completed the first phase in generating a list of events for inclusion in this data set, based on systematic searches in regional bulletins covering this area. This work has been carried out in cooperation between NORSAR and the Kola Regional Seismological Centre (KRSC) personnel. The data sources include:

- The bulletin of the International Seismological Centre (ISC)
- The bulletin of the NEIC (USA)
- The IDC Reviewed Event Bulletin
- The NORSAR regional and teleseismic bulletins
- The Kola Regional Seismological Centre regional bulletin

In this work, we have also been able to take advantage of several publications, technical reports, and event lists compiled over the years, containing seismic events for particular sites (like the Novaya Zemlya test sites) or subregions of the European Arctic. The resulting preliminary event list comprises more than 300 seismic events. We will in the next phase of this program go through this list carefully, aiming to extract a subset of about 100 events most relevant to the purposes of the contract.

Table 1 gives an overview of the available digital stations that will form the primary data source for this project. The table specifies the station configuration (array, 3C), its location, the operating organization, and the years during which the station has been in operation.

Station	Station Type	Station Location	Operating Organization	Data Availability (in NORSAR's archives)
NORSAR large-aperture array	Array	60.82˚N 10.83˚E	NORSAR	1971-present
NORESS array	Array	60.73˚N 11.54˚E	NORSAR	1984-present
ARCESS array	Array	69.53˚N 25.51˚E	NORSAR	1987-present
Spitsbergen array	Array	78.18˚N 16.37˚E	NORSAR	1992-present
FINESS array	Array	61.44˚N 26.08˚E	Univ. of Helsinki	1990-present
Apatity array	Array	67.61˚N 32.99˚E	KRSC	1992-present
Amderma array	Array/3C	69.74˚N 61.66˚E	KRSC	1994-present

Table 1. This table gives an overview of available digital stations that will form the primary data source for this project.

We also intend to include some carefully chosen additional digital stations for selected events of special interest. An excellent example is the IRIS station Kevo in Finland. Other potential candidates are KBS in Spitsbergen, EKA in the U.K., and GERESS/Grafenberg in Germany. For all of the stations listed in the table, there are shorter or longer time intervals of system downtime, or degradation of data due to other factors (spikes, channel outages, etc.). Therefore, the years of operation specified in the table must not be taken to mean that data of high quality will be available for every seismic event in this time period. One of the major tasks in the further work will be to analyze the quality of the station recordings for each event and make a selection of a suitable subset accordingly. Given otherwise equal conditions, the event selection will focus upon maximizing the station coverage. In practice, this means that the most recent events are the most important, since this is usually synonymous with having more stations in operation.

Under this contract waveform data in the CSS 3.0 format, with the appropriate metadata information provided in accordance with the specifications given by Carr et al (1998), will be made available on a set of CD-ROMs to DOE through the Lawrence Livermore National Laboratory, to the DOD through the Center for Monitoring Research, and to the U.S. National Data Center. Thus far, a data set of Novaya Zemlya explosions recorded on the large-aperture NORSAR array has been converted from our native format to the CSS 3.0 format, and a CD-ROM containing these data has been distributed.

The data on this CD-ROM comprise all available recordings from 30 explosions on Novaya Zemlya during 1971 - 1990 with ray paths as indicated in Fig. 1. The source-receiver distances are around 20 degrees. The data presented cover all nuclear explosions conducted on Novaya Zemlya during this time interval with the exception of the mb 5.7 explosion on 1978, Sept. 27. The data acquisition systems were out of operation on this date.

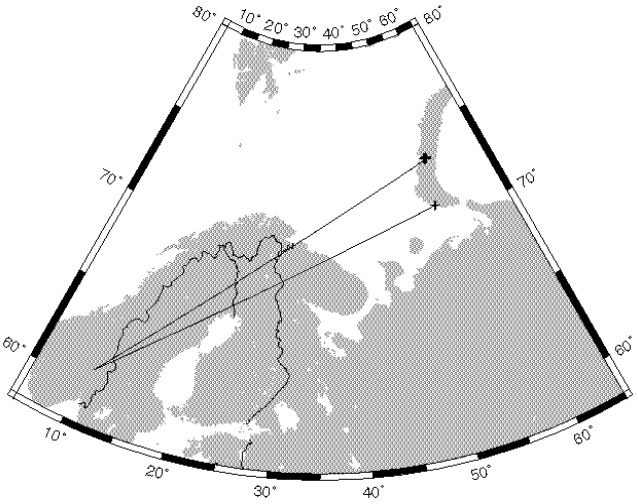


Fig. 1. Ray paths of the data set of Novaya Zemlya explosions during 1971-1990 recorded on the large-aperture NORSAR array.

The data cover a time period of 20 years, in which the instrumentation was largely stable, with the exception that since 1976 some short period channels were equipped with different gain settings and different filter settings over shorter time periods. The data for many of these explosions are saturated for the short period high gain instruments, whereas most of the long period records are recorded on scale. Since 1975 a low gain short period channel has been available, so for all records after that time there is at least one unclipped short period channel available. Figs. 2 to 4 show typical records of events in this data base, and Fig. 5 shows the low gain short period channels for some events recorded during 1975-1979 that have clipped on the other short period channels.

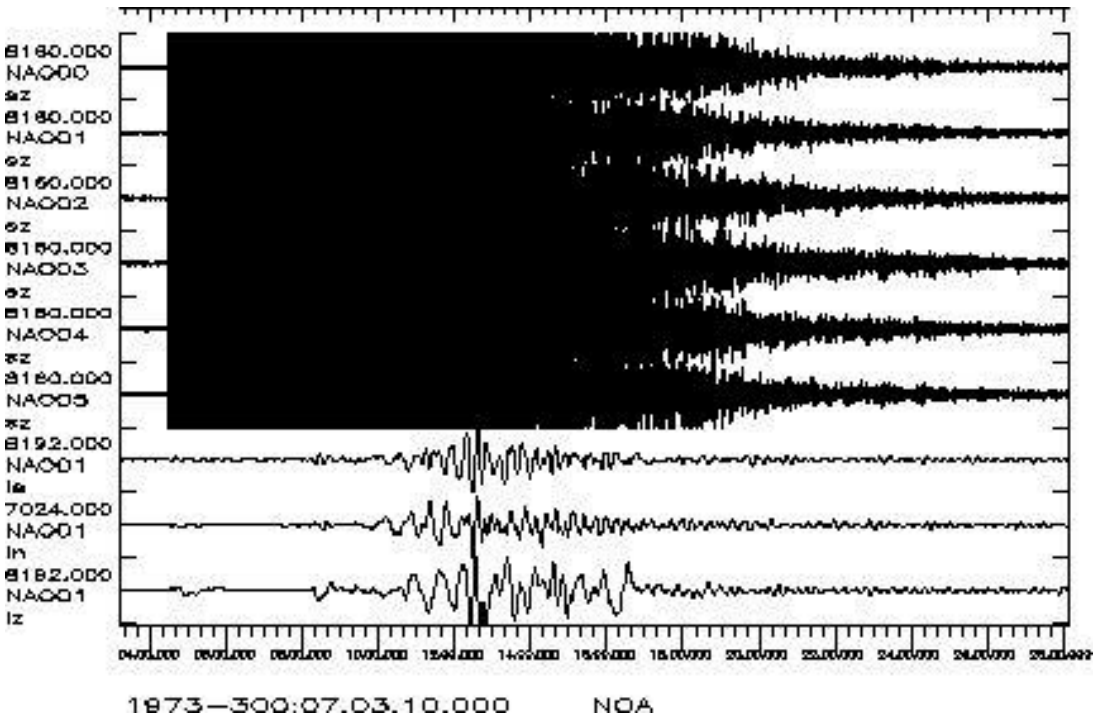


Fig. 2. Data example from the 1973 October 27, magnitude 6.9 explosion with strong clipping of all short period data and slight clipping of long period data

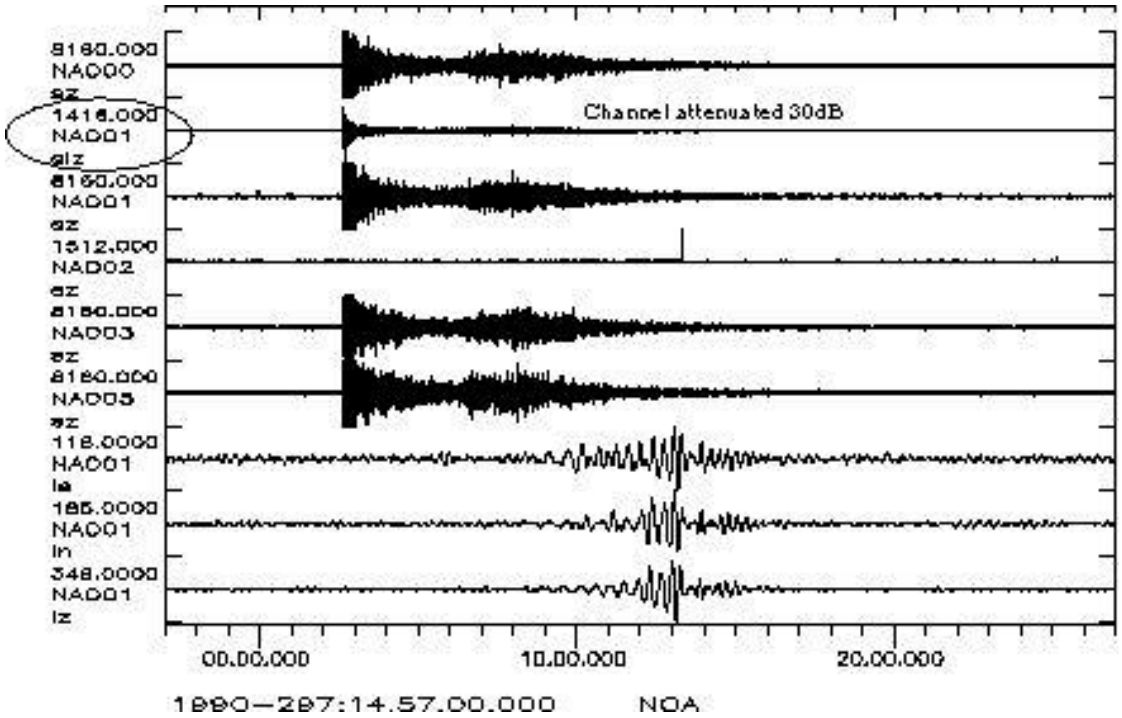


Fig. 3. Data example from the 1990 October 24, magnitude 5.6 explosion with only short period P waves clipped.

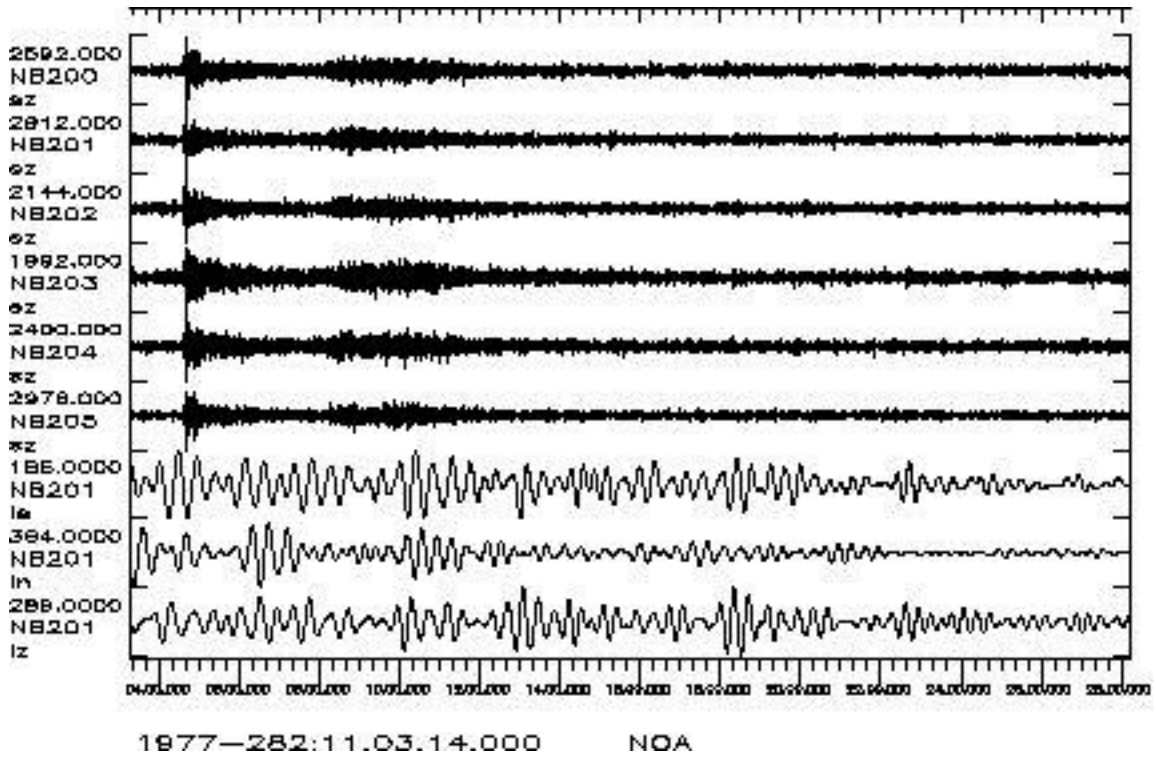


Fig. 4. Data example from the 1977 October 9, magnitude 4.5 explosion with no clipped data.

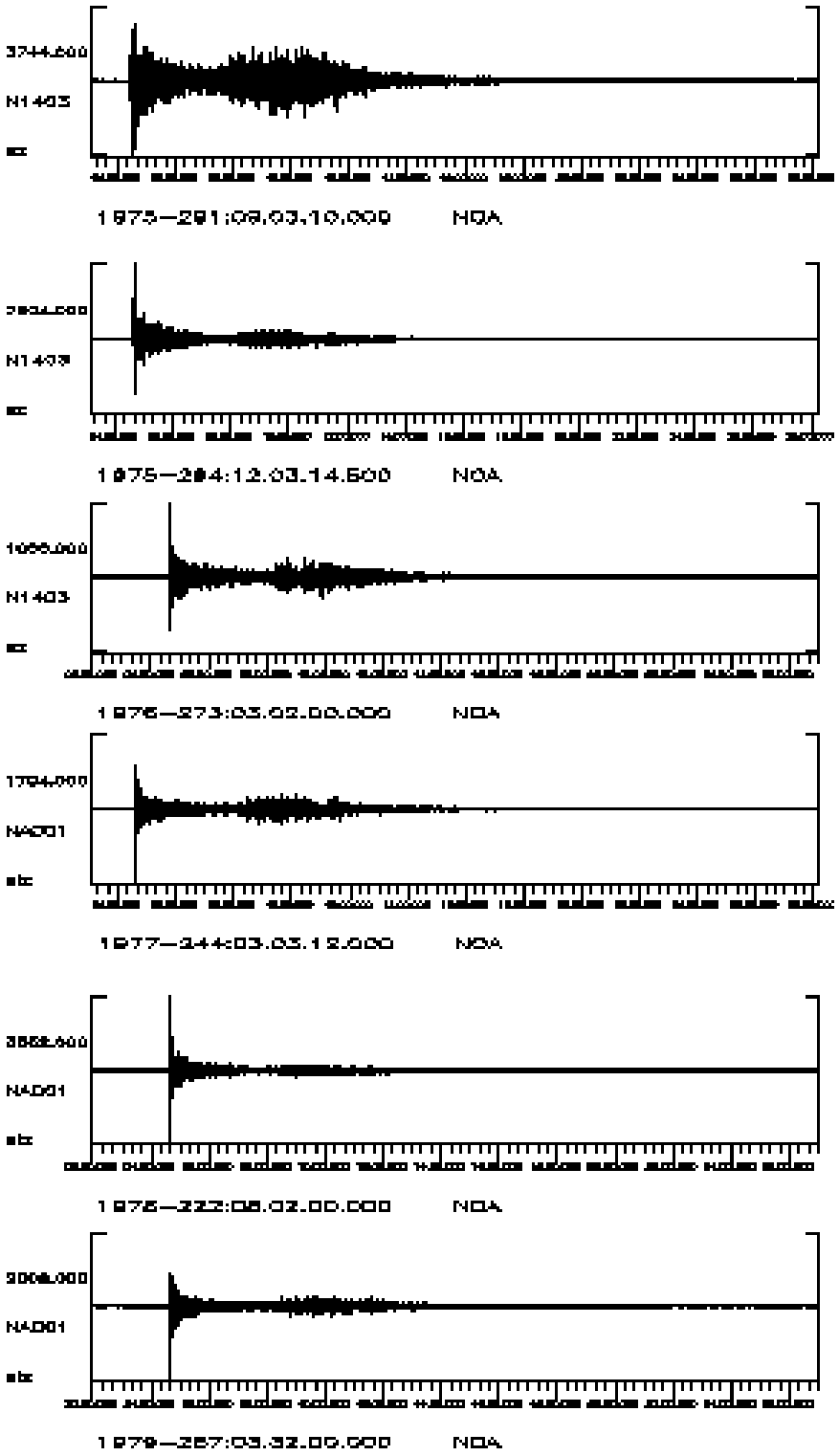


Fig. 5. Data examples of low gain unsaturated short period channels from events where the other short period channels are saturated.

For all data on this CD-ROM, system responses are available in the form of FAP (Frequency-Amplitude-Phase) files. Epicenter information included in the data set is taken from Ringdal (1997).

CONCLUSIONS AND RECOMMENDATIONS

Efforts under this contract so far have resulted in the production of a CD-ROM containing records of Novaya Zemlya explosions recorded on the large-aperture NORSAR array. These data are now available to the research community. For other data, to be made available on CD-ROMs that will appear successively during the course of this two-year effort, we are continuing the extraction of waveforms from our tape library.

The effort will also include analysis of the data in the new data base. This analysis will focus on the following topics:

- Study of the P-to-S amplitude ratio as a function of path, frequency, source type and distance
- Spectrogram analysis of selected presumed underwater explosions and mining explosions at the Kola Peninsula to identify distinguishing characteristics of these events
- Special analysis for a few events with ground truth information using a comprehensive collection of waveform data to include an extended set of stations in the Fennoscandian-northwestern Russia region.

REFERENCES

Carr D., H. Armstrong, T. Edwards, C. Young and R. Keyser (1998): Knowledge base metadata handbook. Draft. Sandia National Laboratories, Albuquerque.

Ringdal F. (1997): Study of low magnitude seismic events near the Novaya Zemlya nuclear test site. Bull. Seism. Soc. Am., 87, pp. 1563-1575.

REGIONAL CHARACTERIZATION FROM JOINT INVERSIONS OF GEOPHYSICAL DATA

Paul B. Parker and Lane R. Johnson, Seismological Laboratory,
University of California Berkeley

Sponsored by U. S. Department of Defense
Defense Threat Reduction Agency
Grant No. DSWA01-97-1-0026

ABSTRACT

A continuing problem in the monitoring of a Comprehensive Nuclear-Test-Ban Treaty is the development of three-dimensional models of the earth's velocity structure which have sufficient resolution to provide accurate locations of seismic events and allow the use of waveform modeling techniques at regional distances. In most cases these velocity models must be estimated on the basis of insufficient data, as both the types and the coverage of the geophysical information is usually quite limited. We have been trying to develop approaches to this problem that use all of the available data in a consistent manner and that obtain solutions to the inverse problems, which are as unrestricted as possible. The data types included so far are structural information from regional geology, regional gravity data, receiver functions at individual seismic stations, and travel times from local and regional seismic events. The inversions for velocity structure are being performed with a genetic algorithm, an efficient stochastic optimization scheme, which mimics Darwinian natural selection in order to find the best fitting models. We are currently applying these techniques to two regions, the Mendocino triple junction region of northern California and the South Island of New Zealand.

In the Mendocino region, receiver functions are available at 6 broad band stations, and it is possible to resolve both the crustal structure and a subducting Gorda plate as having a dip that gradually increases from 3 to 22 degrees with distance from the coast.

In New Zealand, receiver functions are available from the portable broad band stations of the Southern Alps Passive Seismic Experiment (SAPSE). The quality of the data is less than that of the Mendocino region, but it is still possible to resolve crustal thickness' that range between 20 and 40 km which appear to correlate well with distance from the Alpine Fault. Considerable attention is given to the most difficult aspects of these types of problems, the general non-uniqueness of the results, the effects of dipping boundaries, and the effects of anisotropy.

Key Words: seismic velocities, regional structure, inverse problems

OBJECTIVES

The scope of this research effort is concerned with the development of an improved understanding of methods for locating and characterizing seismic events in a heterogeneous earth. The general objective is to investigate how improved models for the generation and propagation of elastic waves can help in the evaluation of methods and models currently being used. The work statement for the research contains two primary tasks:

1) Continue the development of analytical and numerical techniques capable of modeling the physical processes that cause the generation of elastic waves by seismic sources. Also continue the development of three-dimensional models of the earth's velocity structure, which have sufficient resolution to provide accurate locations of seismic events at regional and teleseismic distances.
2) The modeling capability will be validated against existing data bases and any new data which can be acquired by taking advantage of targets of opportunity to perform broad band recording experiments.

During the past year research was conducted in a number of areas related to the objectives listed above, which can be grouped under the following general descriptions:

1) Effect of damage on explosion generated elastic waves
2) Scaling relationships for explosions and earthquakes
3) Use of genetic algorithms in geophysical inverse problems
4) Calculation of waveforms in three-dimensional media
5) Three-dimensional regional velocity structure

This paper will be concerned with the third and fifth topics, the study of improved methods of constructing three-dimensional models for use in regional monitoring.

RESEARCH ACCOMPLISHED

Our recent research on regional velocity structure has concentrated on developing inversion methods that explore the entire range of possible models and permit use of all available geophysical data. Some of the results of this research are described below using the Mendocino area of California as an example. This is a good test of our approach, as it is a region with a fairly complicated structure involving plate boundaries, a triple junction, and a subduction zone. The results included in this paper are primarily those obtained by the analysis of receiver functions obtained at seismographic stations operating in the Mendocino region.

The complex plate geometry of the Mendocino Triple Junction (MTJ) is the focal point of northern California tectonics. Bounded by strike slip faulting to the West and South and subduction to the North, the junction itself has been moving to the North at a rate of approximately 5 cm/yr for the last 5.5 million years (Atwater, 1970). This northward migration (and the oblique convergence of the Juan de Fuca/Gorda Plate) are responsible for many of the significant tectonic events in north America, including (1) volcanism in the Northern Coast Ranges, (2) a broad zone of faulting and deformation in the Coast Ranges, and (3) extinction of arc volcanism to the North of the MTJ (Benz et al., 1992).

The North American Plate in the region of the MTJ is an accretionary complex of Mesozoic to Cenozoic origin (the Franciscan, manifesting itself in the Coast Ranges and Klamath Mountains) which is overlain by the Eel River Basin, a sedimentary forearc basin of Cenozoic origin (Beaudoin and Magee, 1994). Velocities in these crustal units are believed to be relatively uniform, in the range of 5.5-5.8 km/s in the West and 6.0-6.5 km/s in the East (Beaudoin and Magee, 1994; Benz et al., 1992). The subducting Gorda Plate is believed to vary in thickness from 7 km at the Southern end of the MTJ to 10 km in the North, decreasing in velocity from 6.7 km/s to 6.2 km/s at the same time (Beaudoin and Magee, 1994).

Figure 1 is a schematic cross section of the standard model for the tectonic interaction in Northern California as proposed by Benz et al. (1992). The cross section is assumed to be valid for the region between 40 and 41 degrees latitude. The dip associated with the subducting Gorda Plate is a matter of much contention. The most reliable estimates come from east-west cross sections of seismicity, which define a Benioff zone that dips 10^{O} to the east at the coast and up to 25^{O} below the Southern Cascades. Estimates of the velocities V_1, V_2 and V_3 are not as reliable as the estimates of Benioff zone dip. V_1 is likely the least uncertain, typically in the range of 6.3 to 6.5 km/s. V_2 is found to be as low as 6.7 km/s

(Beaudoin and Magee, 1994) and as high as 8.0 km/s (Benz et al., 1992), and the underlying mantle velocity V_3 is usually estimated to be from 8.0 to 8.2 km/s.

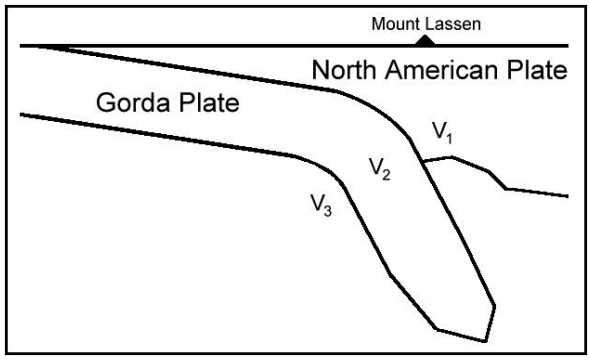


Figure 1. Schematic east-west cross section of standard model for the tectonic interaction in Northern California as proposed by Benz et al. (1992) (not to scale).

Focal mechanisms and seismicity patterns imply a change in the orientation of stress on the Gorda Plate from compression in the North-South direction to down slab extensional beyond 236^{O} east (Dicke, 1998). An obvious consideration with a model in which $V_1 < V_2 < V_3$ is the lack of a driving force for this type of subduction. If $V_2 < V_3$, the Gorda Plate should also be less dense than the underlying mantle material and therefore more buoyant. It is possible that compressional forces associated with spreading from the Gorda Ridge are driving the subduction. In this case there should either be a thickening of the Gorda Plate as it is being subducted or some type of imbrication. Benz et al. suggest that the slab is imbricated in the MTJ region resulting in accreted slab fragments under the North American Plate, but Verdonck and Zandt (1994) find the plate to be intact.

Receiver functions are calculated for 7 teleseismic events recorded at five northern California Broadband stations in the Berkeley Digital Seismic Network (BDSN) (see Table 1). The stations and their spatial relationship to the MTJ can be seen in Figure 2. The teleseismic data used in this investigation consist of 7 events of magnitude 7.0 or greater between -15 and -28 degrees latitude and -173 and -179 degrees longitude (see Table 2). The 7 South Pacific events have travel paths approximately perpendicular to the zone of convergence in the MTJ region.

The data, sampled at 0.05 s, is filtered to remove microseismic noise below 0.15 Hz, cosine tapered and 25% zero padded before being deconvolved with a Gaussian filter coefficient of $\alpha = 2.0$ to produce both radial and tangential receiver functions for each station-event. The stacked receiver functions for the South Pacific events are shown Figure 3. Note that the final 5 seconds of each time series is "wrapped around" to the beginning purposely to give a clearer picture of the first arrival. Because the latter part of the time series was zero padded before deconvolution, the rms amplitudes for the first 5 seconds can give some insight into the amount of noise present.

There is strong similarity between the stacked and the individual receiver function traces. The correlation coefficients ranged from 0.611 to 0.949, with an average of 0.805.

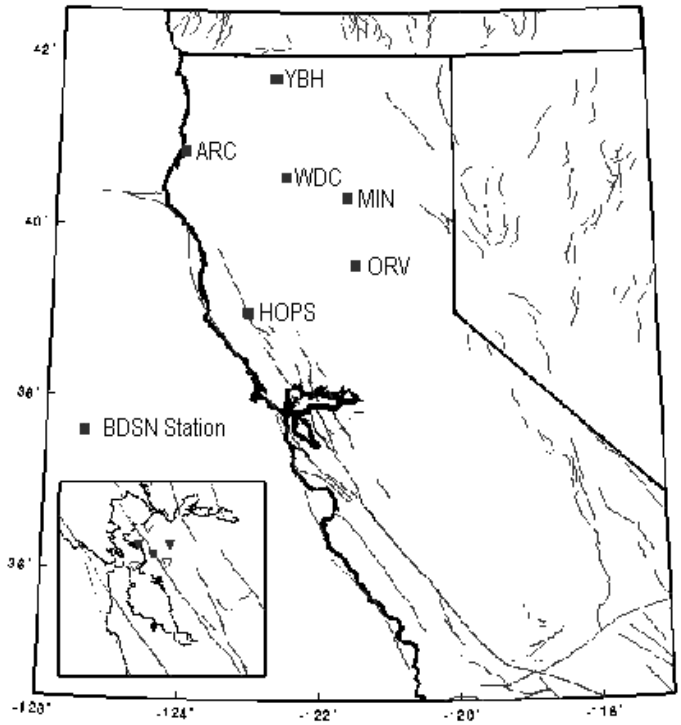


Figure 2. Berkeley Digital Seismic Network (BDSN) stations. YBH, ARC, WDC, MIN and HOPS were used in this study.

Station code	Station name	Latitude	Longitude	Elevation (m)
ARC	Arcata	40.877	-124.075	60
HOPS	Hopland	38.994	-123.072	299
MIN	Mineral	40.345	-121.605	1495
ORV	Oroville	39.556	-121.500	360
WDC	Whiskeytown	40.580	-122.540	300
YBH	Yreka	41.732	-122.710	1110

Table 1. Berkeley Digital Seismic Network (BDSN) broadband stations used in this study.

date	latitude	longitude	depth(km)	M_0	location
03/09/94	-18.039	-178.413	562.5	7.6	South Pacific
04/07/95	-15.199	-173.529	21.2	8.0	South Pacific
07/03/95	-29.211	-177.589	35.3	7.2	South Pacific
08/05/96	-20.690	-178.310	550.2	7.4	South Pacific
09/20/97	-28.683	-177.624	30.0	7.2	South Pacific
10/14/97	-22.101	-176.772	167.3	7.7	South Pacific
03/29/98	-17.576	-179.061	536.6	7.2	South Pacific

Table 2. Locations and magnitudes for the 7 events used in the inversion.

As a first approximation of Moho depth below each station, a simple inversion is performed assuming a constant crustal velocity of 6.5 km/s to find depths for the major amplitude peaks on the stacked receiver functions. On the receiver function for the station at Arcata two amplitude peaks are visible in the first 5

seconds, corresponding to depths of 21.9 km and 32.0 km, respectively. It is likely that the crust is thinnest in this region (Verdonck and Zandt, 1994; Benz et al., 1992), so the first amplitude peak is most likely caused by a P-S conversion at the Moho at 21 km depth. The receiver function determined from the station at Hopland shows amplitude peaks corresponding to 26.4 and 37.1 km depth, and, because, this is still in the Coast Ranges, 26.4 km is the most likely Moho depth. The receiver function for the station at Mineral has a long, flat amplitude peak that begins at 31.1 km and begins to recede at 46.6 km. Sustained positive amplitude on a receiver function is associated with a gradual increase in velocity, so it is possible that there is a slower transition to mantle velocities in this region. The receiver function determined for Oroville has significant amplitude peaks corresponding to 31.4 and 39.7 km. Located in the Sierra foothills, it is likely to overlie a fairly thick crust, so the choice is not as obvious as with the previous ones. The receiver function calculated for Whiskeytown has two obvious amplitude peaks which correspond to 34.2 and 48.0 km in depth. Lastly, the receiver function determined from the station at Yreka has major amplitude peaks which correspond to depths of 32.6 km and 41.4 km, although the peak at 41.4 km is the larger of the two, implying that the conversion at 41.4 km has the largest impedance contrast.

Following Ammon et Al. (1990) the approach that is used here is to model the receiver functions with many thin layers of fixed thickness. However, modeling with too many thin layers can produce unstable solutions. The fit may be quite good, but the model will have many alternating high and low velocity layers that may not be realistic. Because the problem is inherently nonunique it is desirable to minimize the number of degrees of freedom in order to find the simplest model that fits the data. To accomplish this, a minimum roughness constraint is added to the objective function, with the model roughness being calculated using an $||\mathbf{L}_2||$ norm:

$$X_r = \sum_{i=1}^{n} \left[\left(\alpha_{i+1} - \alpha_i \right)^2 \right]^{1/2} \tag{1}$$

where α_i represents the P wave velocity for each layer. The roughness parameter is then multiplied by a normalized weighting factor, which is found through trial and error. A value of 0.4 is used as a weighting factor for the minimum roughness constraint and 0.6 for the receiver function fit.

The inversion of the receiver functions was accomplished with the genetic algorithm (Goldberg, 1989). Genetic algorithms offer an attractive approach for many geophysical inverse problems in that they can explore the entire model space, are not dependent upon an initial estimate, require no derivatives, and are much more efficient than completely random search methods. A general study of this approach was necessary in order to determine how the control parameters of the method influence its performance when applied to realistic geophysical inverse problems. It was found that a particular choice of parameters consistently produced optimal results for a broad range of problem difficulties. At least for problems such as the inversion of receiver functions, the choice of a low mutation rate of about half the inverse of the population size was the most critical factor, with the crossover method and rate having a relatively minor affect upon performance. Tournament selection was found to be the most effective and robust selection method.

The inversion results are shown in Figures 3 and 4. Figure 3 shows the stacked receiver function and their fits. Figure 4 shows the models produced by the fits. The amplitude peak corresponding to the direct arrival on many of the South Pacific receiver functions cannot be fit adequately. Because the height of this amplitude peak is a function of the angle of incidence of the seismic wavefront, it is likely that dipping layers are producing an angle of incidence that is not as steep as the one that is used in the modeling.

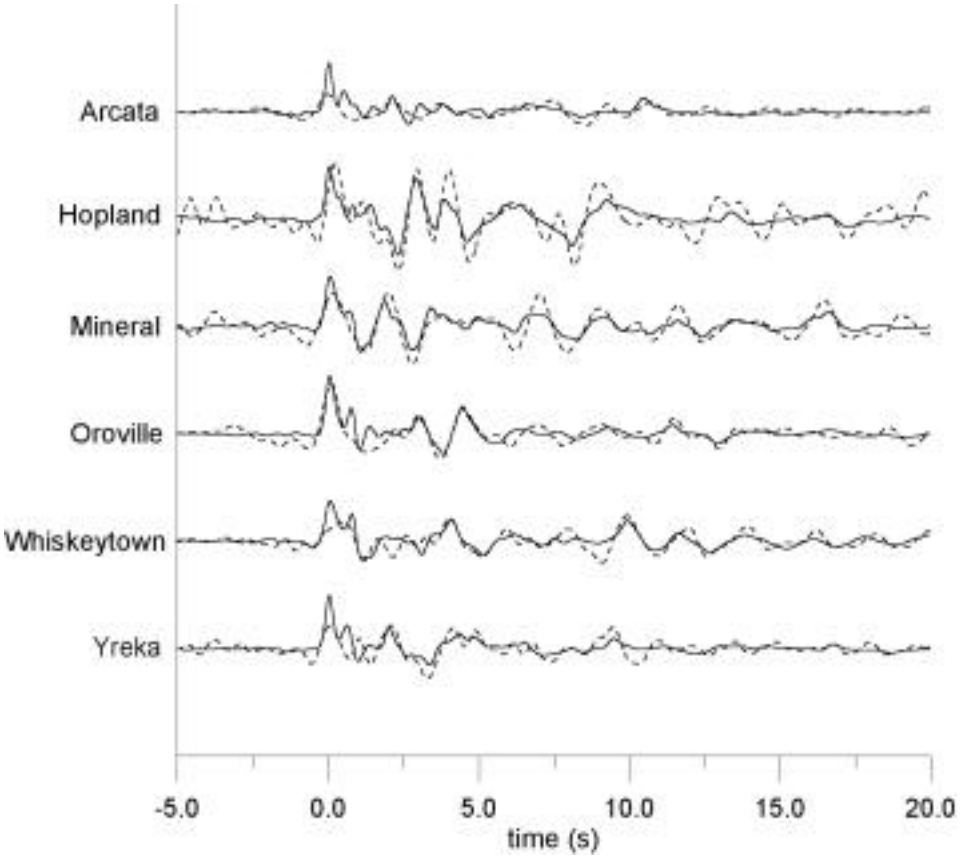


Figure 3. Stacked receiver functions for the 6 BDSN stations and their fits. Note that the last 5 seconds is wrapped around in order to observe the direct arrival more clearly.

Inversions results for the coastal station of Arcata imply a relatively flat velocity structure until 20 km depth, in which velocities jump to 7.4 km/s. Another smaller increase in velocity can be seen at 28 km depth. No consistent low velocity zone can be seen here. It would be interesting to look at receiver functions for a station at the same longitude as Arcata but south of the MTJ to see if there is a low velocity zone where Benz et al. (1992) suggest the existence of a slab window. Inversion results for the stations in the Southern Cascade Range are more interesting. The results derived for the station at Yreka (near the Oregon border) show a steep initial spike indicating a high velocity at about 4-6 km depth, followed by a consistent gradual rise to upper mantle values at about 36 km depth. Inversion results for the station at Whiskeytown show a relatively constant velocity profile down to about 46 km in depth, where the velocity jumps to nearly 8 km/s. Inversion results for the station at Mineral (near Mount Lassen) display a relatively constant velocity structure until 36 km depth, where there is a large increase to near mantle velocities. The results for the station at Oroville (in the Sierra Nevada foothills) are difficult to interpret as there is no obvious Moho conversion. Inversions for the Hopland station suggest a crustal thickness of about 32 km.

In Figure 5, the results from the direct interpretation of the receiver functions are plotted in two dimensions for the purpose of comparison with existing subduction models of the MTJ region. Estimated depths derived from amplitude peaks on the stacked South Pacific receiver functions, which are larger than 50% of the direct arrival peak and fall between 2.3 and 5.8 seconds (corresponding to roughly 20-50 km depth

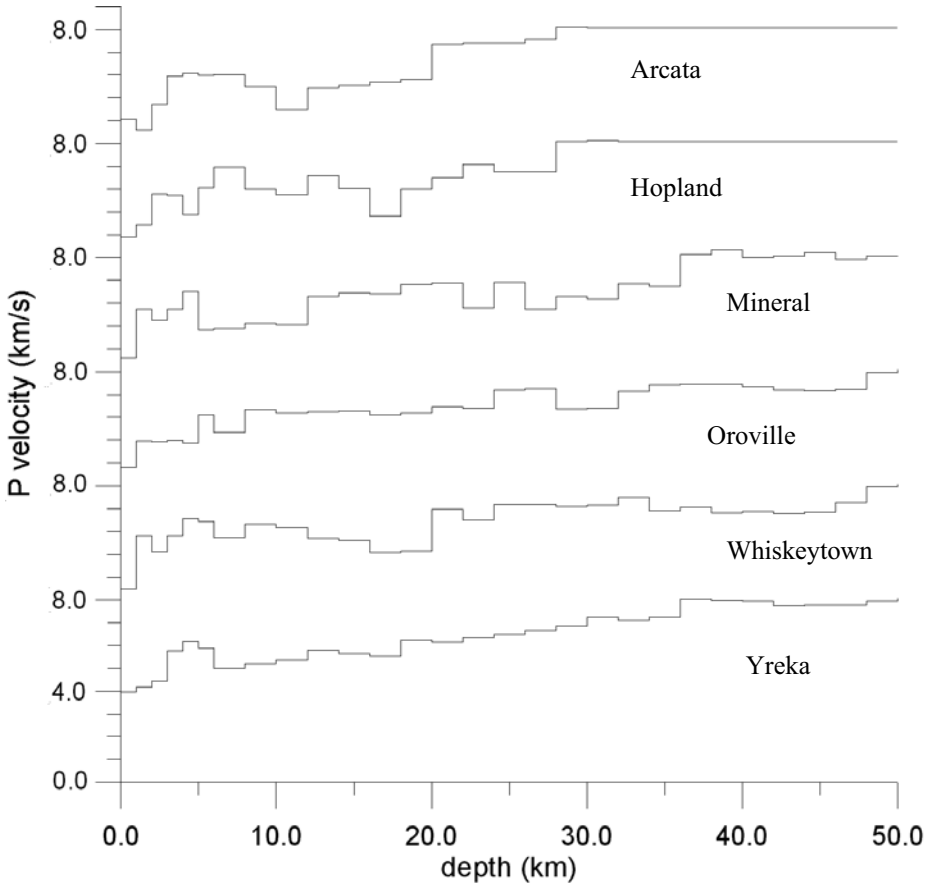


Figure 4. Models produced by the receiver function fits in figure 3. Each tick mark on the vertical axis corresponds to 1 km/s.

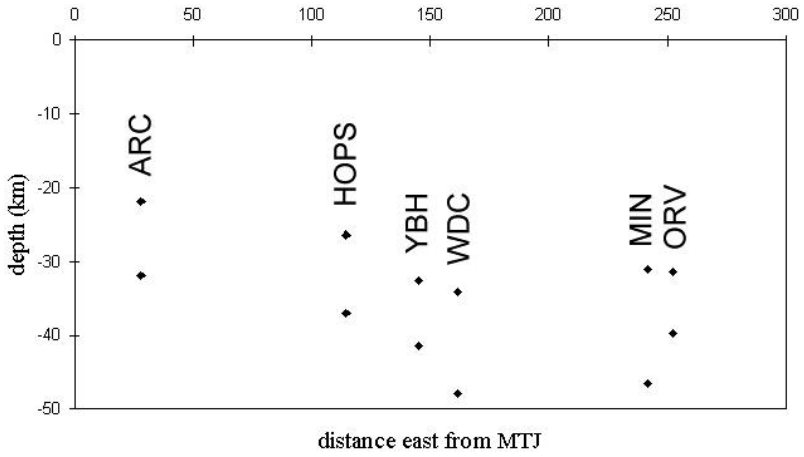


Figure 5. Receiver function conversions inverted for depth

if a constant velocity of 6.3 km/s is assumed for the region), are plotted as a function of one-dimensional distance from the MTJ. The results are consistent with the schematic in Figure 1 for the case where $V_1 < V_2 < V_3$. Assuming the lowest points correspond to conversions originating from the bottom of the Gorda

Plate, the dip on the Gorda Plate can be estimated. Between the stations ARC and HOPS the dip is approximately 3.5^{O}, between HOPS and YBH it is approximately 8.0^{O}, and between YBH and WDC approximately 22.3^{O}. This agrees closely with the estimated dip of the Benioff zone in the region between YBH and WDC but is considerably lower than that for the dip of the Benioff zone near the coast. The two higher points representing conversions for the stations Oroville and Mineral have approximately the same depth at 31 km. If these are Moho conversions, the lower points could be conversions from slab fragments as suggested by Benz et al. (1992). An alternative interpretation for the apparent thickening of the crust is simply the isostatic compensation for the Cascade Range. If this hypothesis is correct then the two lower points in Figure 5 for Oroville and Mineral may be more consistent with Moho depth and the two higher points could be the result of mid-crustal boundaries.

CONCLUSIONS AND RECOMMENDATIONS

Receiver functions are an effective means of obtaining velocity structures for any region that contains seismographic stations. The basic requirement of three-component data from a few teleseismic events is easily met in most cases.

The genetic algorithm can be used for the inversion of the receiver functions to obtain velocity models. With a proper choice of the control parameters, this proves to be an efficient method of exploring the entire range of possible velocity models.

Empirical receiver functions contaminated by noise and/or affected by dipping layers can lead to unrealistic or unstable models with extreme velocity variance. In this case, multiobjective optimization can be used to add a minimum roughness constraint to the objective function. Some amount of experimentation is necessary to find a suitable trade-off between data fit and model smoothness.

In addition to carrying out formal inversion procedures, direct interpretations of receiver functions can provide a great deal of information. Assuming a constant velocity in the crust and then calculating the depths which correspond to significant amplitude peaks on the receiver function can give a rough estimate of the depth and dip of the Moho and other discontinuities.

The receiver functions only provide vertical velocity profiles at the locations of the seismographic stations and it is necessary to use some form of interpolation to obtain models for the intervening regions. We are currently using regional gravity data to help constrain this interpolation.

REFERENCES

Ammon, C., G. E. Randall and G. Zandt, 1990, On the nonuniqueness of receiver function inversions, *J. Geophys. Res.* 95, 15,303-15,318.

Atwater, T., 1970, Implications of plate tectonics for cenozoic tectonic evolution of western North America, *Geol. Soc. Am. Bull*., 81, 3513-3536.

Beaudoin, B., and M. Magee, 1994, Crustal velocity structure of the Mendocino triple junction, *J. Geophys. Res.* 21, 2319-2322.

Benz, H. M., G. Zant, and D.H. Oppenheimer, 1992, Lithospheric structure of Northern California from teleseismic images of the upper mantle, *J. Geophys. Res.,* 97, 4791-4807.

Dicke, M., 1998, Seismicity and Crustal Structure at the Mendocino Triple Junction, Northern California. Master's Thesis, University of California, Berkeley.

Goldberg, D. E., 1989, *Genetic Algorithms in Search, Optimization and Machine Learning*, Reading, MA: Addison-Wesley.

Verdonck, D. and G. Zandt, 1994, Three-dimensional crustal structure of the Mendocino Triple Junction Region from local earthquake travel times, *J. Geophys. Res.* 99, 23843-23858.

REGIONAL PHASE AMPLITUDE TOMOGRAPHY FOR SEISMIC VERIFICATION IN CHINA

W.S. Phillips, H.E. Hartse, S.R. Taylor, A.A. Velasco and G.E. Randall
Seismic Research Center, Los Alamos National Laboratory, Los Alamos, New Mexico

Sponsored by U.S. Department of Energy
Office of Nonproliferation and National Security
Office of Research and Development
Contract No. W-7405-ENG-36

ABSTRACT

We have applied tomographic techniques to amplitude data to quantify regional phase path effects for use in source discrimination and magnitude studies. Advantages of tomography over interpolation (kriging) methods of path correction include extrapolation into inactive regions, as well as increased levels of confidence in the resulting path corrections because of their more physical basis. Disadvantages include the smoothing inherent to tomography, which yields poorer fit to data; however, this can be overcome by incorporating interpolated residuals into the final correction surfaces for use in routine monitoring. Our tomography technique solves for resolvable combinations of attenuation, source-generation, site and spreading terms. First difference regularization is used to remove singularities and reduce noise effects.

In initial tests, the technique was applied to a data set of 1488, 1.0 Hz, P_g/L_g amplitude ratios from 13 stations for paths inside a 30° by 40° box covering western China and surrounding regions. Tomography reduced variance 60%, relative to the power law correction traditionally applied to amplitude ratios. Relative P_g/L_g attenuation varied with geologic region, with low values in Tibet, intermediate in basins and high for platforms and older crust. Comparing with results of prior path effect studies in this region, spatial patterns were most consistent with local earthquake coda-Q of Jin and Aki (1988). Relative spreading was consistent with expected values for P_g and L_g. Relative site terms were similar to one another, yet some tradeoff with attenuation was evident.

Examination of the tomography residuals using a kriging interpolator showed coherent geographical variations, indicating unmodeled path effects. The residual patterns often follow geological boundaries, which could result from attenuating zones or blockages that are too thin to be resolved, or that have anisotropic effect on regional phases. These results will guide efforts to reparameterize tomography models to more effectively represent regional wave attenuation and blockage. Future work will also test combining regionally varying attenuation with source parameter inversion (magnitude-distance amplitude correction, or MDAC; Taylor et al., 1999).

Key Words: Tomography, attenuation, discrimination, regionalization.

OBJECTIVE

Removing the effect of propagation path on regional seismic wave amplitudes is important for isolating source effects and will lead to more effective discrimination between natural and man-made seismic events. This is a crucial effort for extending verification monitoring techniques to small events. Here, we investigate the use of tomographic imaging to obtain amplitude path corrections for use in event discrimination and magnitude determination at regional distances.

RESEARCH ACCOMPLISHED

Background

The quantification of path effects on regional phase amplitudes has received much attention of late. Interpolation has been shown to be the most effective method, in terms of reducing variance in amplitude data (Phillips et al, 1997; Taylor and Hartse, 1998; Phillips et al., 1998; Phillips, 1999; Rodgers et al., 1999). These studies show that interpolated surfaces correlate well with regional geology; thus they reflect path, rather than coherent source radiation effects. Although earlier work was performed with simple, moving window smoothers, we currently prefer the Bayesian kriging interpolator of Schultz et al., (1998). Kriging provides error estimates and continuously differentiable surfaces, while the Bayesian modifications control extrapolation of the surface and errors into regions devoid of calibration events. This allows the inclusion of background models by kriging the model residuals and merging the results with a map of the model predictions.

Models based on correlations of amplitude data with physical data such as topography, basin thickness and moho depth can be used to predict path effects (e.g. Zhang and Lay, 1994; Fan and Lay, 1998). Such models are less effective than interpolation methods in reducing variance in amplitude data (Phillips, 1999; Rodgers et al., 1999), but have the advantage of extrapolating path effects beyond regions where data exist. Phillips (1999) demonstrated the effectiveness of combining the two methods by applying Bayesian kriging interpolation to the model residuals.

Tomographic images of the attenuation of regional phases can also be used to predict path effects (e.g. Singh and Hermann, 1983; Campillo, 1987; Xie and Mitchell, 1990; Campillo et al., 1993; Mitchell et al., 1997; Sandvol et al., 1998). Tomography complements interpolation methods because images can be well resolved in areas where no events occur. In addition, the physical basis of tomography increases our confidence in the derived path corrections. In this study, we test tomography techniques using regional phase amplitude data, with emphasis on the use of results in an automatic monitoring scheme.

In initial tests, we applied tomography techniques to 1 Hz P_g/L_g amplitude ratio data. We chose to start with ratio data because cross-phase relative source and site effects tend to be less dependent on source size, while relative path effects still exhibit large regional variation. This decreases the influence of a possibly error prone m_b that is used to correct for source size and scaling prior to inversion. Of course, using ratios will lead to difficulties in interpreting results because two phases are involved. In addition, monitoring would require a correction surface for every ratio that might be desired, which is a large number if we consider all bands and phases that can be observed. For these reasons, we support the use of single phase correction surfaces for routine monitoring and plan to test single phase tomography in the future.

We have chosen to analyze 1 Hz data in our initial tests. This band is useful for technique development because it offers the most data and coverage; however, 1 Hz ratios perform relatively poorly in discrimination (Walter et al., 1995; Taylor, 1996; Hartse et al., 1997). Results in this band can still be useful for magnitude estimation or for defining geophysically distinct regions that will be useful for assessing performance capabilities. Furthermore, low frequency data can improve the performance of multivariate discriminants (Taylor and Hartse, 1997). As we move to higher frequencies, our hope is that path corrections will lower the frequency threshold at which source types are observed to separate (3 to 4 Hz), allowing the inclusion of smaller and more distant events that might be of poor signal-to-noise in the most effective discriminant bands (6-8 Hz).

In the following, we will outline data reduction procedures for stations in China and surrounding regions, and describe the tomographic method we applied. We will show relative attenuation results that correlate well with geological province as well as spatially coherent, unmodeled data that suggest new avenues of development.

Data

We used the Preliminary Determination of Epicenters (PDE) catalog to guide the collection of regional event data from 13 broadband stations in China and surrounding regions archived at the Incorporated Research Institutions for Seismology, Data Management Center. We retrieved data from all possible, regional distance PDE events occurring between 1986 and 1996 from the now Global Seismic Network stations in China: Enshi (ENH), Lhasa (LSA), Lanzhou (LZH), Urumchi (WMQ) and Xian (XAN), as well as Boravoye (BRVK), Kurchatov (KURK) and Makanchi (MAK) in Kazakhstan; Ala-Archa (AAK), Kirghizstan; Talaya (TLY) and Zalesovo (ZAL), Russia; Nilore (NIL) Pakistan; and Ulan Bator (ULN), Mongolia.

To process the data, we first determined arrival times of the regional phases manually. After correcting for the instrument, RMS amplitudes were obtained for a number of pass bands between 0.5 and 8 Hz using time-domain filtering techniques, aligning windows on picked arrivals if they existed or on preset group velocities if not (Hartse et al., 1997). We use vertical component, P_g/L_g ratios in the band 0.5 to 1 Hz in this study. The preset L_g group-velocity window was 3.6 to 3.0 km/s and the P_g group-velocity window was 6.2 to 5.2 km/s. Requiring paths to lie within a box defined by longitudes 70° to 110° and latitudes 25° to 55°, as well as distances between 300 and 2500 km, event depths less than 50 km and signal-to-noise (pre-Pn) greater than 2 for both phases, reduced the data set to 1488 records. A plot of the raypath distribution shows good coverage over most of the region (Figure 1).

Tomography Method

We solve for resolvable combinations of relative attenuation, site and spreading effects on regional phase amplitude ratios. For a homogeneous propagation model, we express RMS amplitude for a given frequency band,

$$a_{ijk} = c_k \; f(m_b^{\,i}) \; s_{jk} \; x_{ij}^{\,-\beta_k} \; e^{-\alpha_k x_{ij}},$$

where the i, j, k indices represent source, site and phase type, respectively, c_k is a source generation term, f is source scaling, taken as a known function of m_b (Cong et al., 1996; equations 6 and 10), s_j is site effect, x_{ij} is distance, β_k is the spreading coefficient and α_k is the spatial attenuation coefficient. We define a source-corrected amplitude,

$$D_{ijk} = \log_{10} a_{ijk} - \log_{10} f(m_b^{\,i}).$$

Taking logarithms gives,

$$D_{ijk} = \log_{10} c_k + \log_{10} s_{jk} - \beta_k \log_{10} x_{ij} - \alpha_k x_{ij} \log_{10} e.$$

We now discretize attenuation into an array of latitude-longitude centered ellipses of constant α, setting major and minor axes to $\sqrt{2}/2$ of the local grid spacing so ellipses centered on a box of four adjacent grid points meet at a single point in the center. Assuming a great circle path, we take the chord length across each ellipse it intersects and normalize by the total path length in degrees. Thus $\alpha_k x_{ij}$ becomes a sum of products of discretized α_k and normalized ellipse chords. Substituting capital letters for $\log_{10}$, we obtain,

$$D_{ijk} = C_k + S_{jk} - \beta_k X_{ij} - \log_{10} e \, \Sigma m \, \alpha_{km} \, \delta x_{ijm}, \qquad 1.$$

where the new index, m, represents the discretization of the attenuation model and the δx_{ijm} are the normalized ellipse-chord lengths. After taking phase ratios, relative generation, site, spreading and attenuation terms replace those of equation 1,

$$\Delta D_{ij} = \Delta C + \Delta S_j - \Delta\beta \, X_{ij} - \log_{10} e \, \Sigma_m \, \Delta\alpha_m \, \delta x_{ijm}. \qquad 2.$$

Tomographic inversion can be based on these linear equations once we rationalize singularities or tradeoffs between unknown parameters.

We use standard, least squares techniques to solve equations 1 or 2, which can be written in matrix form

$$Ax = d,$$

where d is the data vector, x is the vector of unknowns and A represents the model equations. We apply first difference regularization to reduce the influence of noise on the results and eliminate singularities due to unresolved combinations of model parameters. Second difference regularization is often used in tomographic studies, but the first difference is more powerful in resolving singularities (e.g. Phillips and Fehler, 1991). The least square solution is written,

$$x = (A^tW^tWA + S^t\Lambda^2S)^{-1}\ A^tW^td, \qquad 3.$$

where S represents the regularization equations, Λ is a diagonal matrix containing regularization weights, W is a diagonal matrix representing weights based on estimated data error and superscript t represents the transpose. Resolution and covariance are calculated via,

$$R = (A^tW^tWA + S^t\Lambda S)^{-1}\ A^tW^tWA,$$
$$C = (A^tW^tWA + S^t\Lambda S)^{-1}.$$

We can also estimate predicted data variance along a new path, which will be useful for creating correction surfaces,

$$\sigma_p^2 = a^t\ C\ a,$$

where a is a column vector representing equation 1 or 2 for the new path, similar to a row of A (e.g. Draper and Smith, 1981).

The tomographic calculations have been implemented using a Jacobi conjugate gradient solver (ITPACK). We add switches that eliminate or combine unknown terms in equations 1 and 2 to avoid singularities. For example, the generation term must be combined with the site terms because neither can be resolved uniquely. More subtle tradeoffs can be evaluated by examining the resolution matrix.

We use residual variance to evaluate goodness of fit and model improvement. The trace of the resolution matrix is taken as the number of free parameters in the model (Tarantola, 1987), which is needed to calculate variance. Variance reduction will be quoted relative to a power-law fit with distance, which is the traditional correction for amplitude ratios in discrimination studies (e.g. Hartse et al., 1997).

Results

To parameterize the inversion, we examine residual variance for a range of discretization intervals and regularization parameters. For this study, 1° and 2° attenuation term grids allowed similar fits to data, while a 5° grid was too coarse to fit the data well. Results employing a grid spacing of 2° will be presented here. Regularization parameters must be chosen large enough to control the effects of noise, yet lie below the point where excessive smoothing causes the residual variance to increase rapidly (e.g. Phillips and Fehler, 1991). Our choice of 2.5 for attenuation regularization allowed 58 free parameters in the 2° model, as estimated from the trace of the attenuation portion of the resolution matrix. This number of free parameters is similar to that obtainable with an unregularized 5° grid; however, the finer grid allows more spatial freedom to fit the data. Holding attenuation regularization fixed, the site term regularization parameter was determined to be 0.5, following the same procedure. This regularization constrains poorly resolved site terms to be similar to well resolved site terms and helps to avoid tradeoffs between site and near-station attenuation terms.

We found the standard deviation of residuals after removing a power-law fit with distance to be 0.36, representing the initial scatter in the ratio data. Allowing attenuation, spreading and source generation terms free produced a residual standard deviation of 0.23, or a variance reduction of 59% relative to the power-law fit. Replacing the source generation term with individual site terms resulted in only slight improvement and a variance reduction just over 60%. We plot relative P_g/L_g attenuation, $\Delta\alpha_m$, in grayscale (Figure 2). As the equations are set up, positive $\Delta\alpha_m$ (light gray) indicate P_g attenuates faster than L_g, while negative $\Delta\alpha_m$ (dark gray) indicate the opposite. Color versions of the tomography results, superposed on a topography map for

interpretation purposes, can be found in Phillips et al. (1999). Only well-resolved portions of the image are plotted in Figure 2. Boundaries were placed at the 0.5 contour representing diagonal elements of the resolution matrix, after normalizing by the ratio of the number of grid points to free parameters in the attenuation model. The normalization adjusts for regularization effects, which reduce resolution by smoothing adjacent model parameters.

We find that P_g/L_g attenuation correlates well with geological province. The lowest values (low P_g, high L_g attenuation) fall within the Tibetan plateau. This low is bounded sharply to the north, by the Qaidam basin, and to the east, by the Guangxi platform, associated with the Sichuan basin. Intermediate to low values can be seen in the Qilian Shan and western Tien Shan ranges, as well as the Tarim, Ordos and Junggar basins. Note the sharp transition between the Junggar basin area and the surrounding mountain ranges. Highest P_g/L_g attenuation is found in the stable, platform areas to the north and in the Guangxi platform to the east. Higher values are also found for trans-Himalaya paths to Lhasa (LSA), similar to patterns noted in spectral Q studies of regional phases recorded at LSA (Reese et al., 1998). We expected higher values in the vicinity of station ZAL in Russia; however, the weak L_g observed for paths through the Tien Shan and border ranges, relative to other paths through the northern area, is responsible for the observed pattern of low values.

Relative site terms vary from –0.8 to –0.3 for these data, most clustering about –0.5. The mean can be considered the relative source generation term, which is incorporated into the site terms in this inversion. Including these terms improves the fit to data only slightly, yet adds definition to the attenuation image as site effects are more appropriately accounted for. The similarity between most well resolved site terms may be an advantage of applying tomography to ratio data. However, outlier site terms for KURK (-0.8) and LSA (-0.3) appear to reflect the attenuation from nearby areas, even though these terms are reasonably well resolved.

The relative spreading coefficient, $\Delta\beta$, was estimated to be 0.54±0.11 (standard error). Again, the positive value indicates P_g spreads more quickly than L_g. If we assume L_g spreading is 0.83 (Nuttli, 1973; Campillo et al., 1984), our $\Delta\beta$ of 0.54 implies a P_g spreading coefficient of 1.37, reasonably consistent with a numerical modeling estimate of 1.5 (Campillo et al., 1984). Synthetic calculations generated using the inversion result and including similar levels of Gaussian noise resulted in correct recovery of the results, with some tradeoff evident between spreading and the range of attenuation terms. Based on 100 runs with different realizations of noise, the mean and standard deviation of $\Delta\beta$ was 0.50 ± 0.08.

Discussion

The tomography results are consistent with previous Eurasian path effect studies. If we interpret the variation of P_g/L_g attenuation primarily to be the result of L_g effects, we can qualitatively compare with studies of L_g and L_g coda. Rapine et al. (1997) described of L_g propagation in China, based on regional data from many stations. Most of China is described as efficient for L_g, while the Tibetan plateau is described as inefficient. The boundary between the propagation regions matches our tomographic result very well. We fail to see an extra-low zone along the Tibetan plateau edges, as suggested by McNamara et al (1996); however, the regularization constraints might have smoothed out such a pattern. Mitchell et al. (1997) produced a tomographic map of 1 Hz, L_g coda Q for Eurasia. This map is roughly consistent with ours, except for Mongolia, where we see efficient L_g (high P_g/L_g attenuation) and the L_g coda Q predicts inefficient L_g. However, the L_g coda-Q maps are of significantly larger scale and lower resolution than those presented here. Perhaps the best correspondence, in terms of resolution, is with results of a local earthquake, crustal coda-Q study (Jin and Aki, 1988). The coda-Q measurements are unevenly distributed through China; however, where coverage is dense, such as along the eastern boundary of the Tibetan plateau, the patterns are very similar to ours. This points out the value to discrimination research in performing coda-Q studies in regions of dense station coverage, with care taken to limit the coda lapse times so only crustal materials are sampled (Phillips et al., 1988).

To examine the geographical distribution of inconsistent data, we interpolate tomography residuals, one station at a time. Interpolation is performed with a Bayesian kriging algorithm (Schultz et al., 1998), using a data correlation function appropriate for L_g amplitudes in central China (Anderson and Phillips, 1998). For all stations, we see coherent geographical variations, indicating path effects that are inconsistent with the tomography result. For many stations, such as BRVK (Figure 3), we see residual patterns that follow boundaries between geological regions. For BRVK, a sudden increase in P_g/L_g ratios along the northwest edge of the Tarim basin may indicate a long, thin zone of high L_g attenuation, or a blockage. The high attenuation may be a structural or scattering, rather than an intrinsic, effect. (e.g. Baumgardt, 1990). The blockage may have greater effect on raypaths traveling across the structure than those traveling parallel to the structure. Sub-parallel

raypaths would tend to wash out the high attenuation zone during tomographic inversion. Our smoothing and coarse parameterization contribute to this effect.

CONCLUSIONS AND RECOMMENDATIONS

The inconsistent data patterns suggest directions for future modifications of the tomography methods. We can explore relaxation of regularization constraints in areas of well resolved, high gradients. We can also include anisotropic effects into the model parameterization, as has been done for velocity tomography (Mele et al., 1998), and which may help with blockages. Lateral refraction will also produce inconsistent data, which will be a limiting effect unless we wish to incorporate 2-dimensional effects in the forward model. More general improvement could come from the addition of constraints from censored data into the tomography, as well as realistic data covariance reflecting correlation between data from nearby events. Furthermore, better magnitude estimates will reduce noise introduced by source corrections and facilitate the use of phase amplitude data, rather than ratios. The magnitudes could be improved by accounting for censoring effects on teleseismic amplitudes (e.g. McLaughlin, 1988), or by using regional envelopes or coda (Aki, 1980; Mayeda, 1993). Tomography of phase amplitudes, as opposed to ratios, will be simpler to interpret and to implement into a monitoring scheme. Comparison with ratio tomography results will indicate how well source effects have been accounted for.

The tomographic results can be used to correct for path effects and reduce scatter in discrimination studies. For each station, amplitudes or amplitude ratios, along with errors, can be predicted over a surrounding grid. This grid can be used during the course of routine monitoring. In addition, the tomography can be employed as a background model, and corrections calculated by applying Bayesian kriging to the residuals (Figure 3) to form the final correction surface. The kriging can take the tomography prediction errors into account in creating the correction surface. The final result will reflect the tomography model in areas where events rarely occur and an interpolated version of the data in areas where events do occur.

REFERENCES

Aki, K. (1980). Physical basis for the duration magnitude and recommended practice for coda magnitude determination, *Proc. 17th Assemb. ESC*, Budapest, 73-77.

Anderson, K.K. and W.S. Phillips (1998). A simple procedure for kriging left-censored data, *EOS Trans. Am. Geophys. Union* **79**, F555.

Baumgardt, D. (1990). Investigation of teleseismic L_g blockage and scattering using regional arrays, *Bull. Seism. Soc. Am*. **80**, 2261-2281.

Campillo, M., M. Bouchon and B. Massinon (1984). Theoretical study of the excitation, spectral characteristics and geometrical attenuation of regional seismic phases, *Bull. Seism. Soc. Am*. **74**, 79-90.

Campillo, M. (1987). L_g wave propagation in a laterally varying crust and the distribution of the apparent quality factor in central France, *J. Geophys. Res.* **92**, 12604-12614.

Campillo, M., B. Feignier, M. Bouchon and N. Bethoux, Attenuation of crustal waves across the Alpine range, *J. Geophys. Res.* **98**, 1987-1996.

Cong, L.L, J.K. Xie and B.J. Mitchell (1996). Excitation and propagation of L_g from earthquakes in central Asia with implication for explosion/earthquake discrimination, *J. Geophys. Res*., **101**, 27779-27789.

Draper, N.R. and H. Smith (1981). *Applied Regression Analysis*, Second Edition, John Wiley & Sons, New York.

Fan, G. and T. Lay (1998). Statistical analysis of irregular waveguide influences on regional seismic discriminants in China, *Bull. Seism. Soc. Am.*, **88**, 74-88.

Hartse, H.E., S.R. Taylor, W.S. Phillips and G.E. Randall (1997). A preliminary study of regional seismic discrimination in central Asia with emphasis on western China, *Bull. Seism. Soc. Am.*, **87**, 551-568.

Jin, A. and K. Aki (1988). Spatial and temporal correlation between coda *Q* and seismicity in China, *Bull. Seism. Soc. Am*. **78**, 741-769.

McNamara, D.E., T.J. Owens and W.R. Walter (1996). Propagation characteristics of L_g across the Tibetan plateau, *Bull. Seism. Soc. Am*. **86**, 457-469.

Mayeda, K. (1993). $m_{bLgcoda}$: A stable single station estimator of magnitude, *Bull. Seism. Soc. Am*. **83**, 851-861.

McLaughlin, K.L. (1988). Maximum-likelihood event magnitude estimation with bootstrapping for uncertainty estimation, *Bull. Seism. Soc. Am*. **76**, 855-862.

Mele, G., A. Rovelli, D. Seber, T.M. Hearn and J. Barazangi (1998). Compressional velocity structure and anisotropy in the uppermost mantle beneath Italy and surrounding regions, *J. Geophys. Res*. **103**, 12529-12543.

Mitchell, B.J., Y. Pan, J. Xie and L. Cong (1997). L_g coda Q variation across Eurasia and its relation to crustal evolution, *J. Geophys. Res*. **102**, 22767-22779.

Nuttli, O.W. (1973). Seismic wave attenuation and magnitude relations for eastern North America, *J. Geophys. Res.* **78**, 876-855.

Phillips, W.S., W.H.K. Lee and J.T. Newberry (1988). Spatial variation of crustal coda Q in California, *Pure App. Geophys*. **128**, 251-260.

Phillips, W.S. and M.C. Fehler (1991). Traveltime tomography: A comparison of popular methods, *Geophysics* **56**, 1639-1649.

Phillips, W.S., G.E. Randall, H.E. Hartse, S.R. Taylor and H.J. Patton (1997). Source and path effects on regional phases in China, *Proc. 19th Ann. Seism. Res. Symp.* Orlando, 125-134.

Phillips, W.S., G.E. Randall and S.R. Taylor (1998). Path correction using interpolated amplitude residuals: An example from central China, *Geophys. Res. Lett.,* **25**, 2729-2732.

Phillips, W.S. (1999). Empirical path corrections for regional phase amplitudes, *Bull. Seism. Soc. Am*. **89**, 384-393.

Phillips, W.S., H.E. Hartse, S.R. Taylor, A.A. Velasco and G.E. Randall, Regional phase amplitude ratio tomography for seismic verification, submitted to Pure Appl. Geophys., 1999.

Rapine, R.R., J.F. Ni and T.M. Hearn (1997). Regional wave propagation in China and its surrounding regions, *Bull Seism. Soc. Am.*, **87**, 1622-1636.

Reese, C.C., R.R. Rapine and J.F. Ni (1998). Lateral variation of Pn and L_g attenuation at the CDSN station LSA, *Bull. Seism. Soc. Am*. **88**, 325-330.

Rodgers, A.J., W.R. Walter, C. Schultz, S. Myers and T. Lay, (1999). A comparison of methodologies for representing path effects on regional P/S discriminants, *Bull. Seism. Soc. Am*., in press.

Sandvol, E., D. Seber, M. Barazangi, R. Mohamad, N. Turkelli, C. Gurbuz, E. Zor and R. Gok (1998). Seismological research in the Middle East, *Proc. 20th Ann. Seis. Res. Symp.* Santa Fe, 745-753.

Schultz, C., S. Myers, J. Hipp and C. Young (1998). Nonstationary Bayesian kriging: Application of spatial corrections to improve seismic detection, location and identification, *Bull. Seism. Soc. Am*. **88**, 1275-1288.

Singh, S. and R.B. Herrmann (1983). Regionalization of crustal coda-Q in the continental United States, *J. Geophys. Res.* **88**, 527-538.

Tarantola, A. (1987). *Inverse Problem Theory*, Elsevier, Amsterdam.

Taylor, S.R. (1996). Analysis of high-frequency P_g/L_g ratios from NTS explosions and western U.S. earthquakes, *Bull. Seism. Soc. Am*. **86**, 1042-1053.

Taylor, S.R. and H.E. Hartse (1997). An evaluation of generalized likelihood ratio outlier detection to identification of seismic events in western China, *Bull. Seism. Soc. Am*. **87**, 824-831.

Taylor, S.R. and H.E. Hartse (1998). A procedure for estimation of source and propagation amplitude corrections for regional seismic discriminants, *J. Geophys. Res*. **103**, 2781-2789.

Taylor, S.R., A.A. Velasco, H.E. Hartse, W.S. Phillips and W.R. Walter (1999), Amplitude corrections for regional seismic discriminants, submitted to *Pure Appl. Geophys*.

Walter, W.R., K.M. Mayeda and H.J. Patton (1995). Phase and spectral ratio discrimination between NTS earthquakes and explosions. Part I: Empirical observations, *Bull. Seism. Soc. Am*. **85**, 1050-1067.

Xie, J.K. and B.J. Mitchell (1990). A back-projection method for imaging large-scale lateral variations of L_g coda Q with application to continental Africa, *Geophys. J. Int*. **100**, 161-181.

Zhang, T.R. and T. Lay (1994). Analysis of short-period regional phase path effects associated with topography in Eurasia, *Bull. Seism. Soc. Am*., **84**, 119-132.

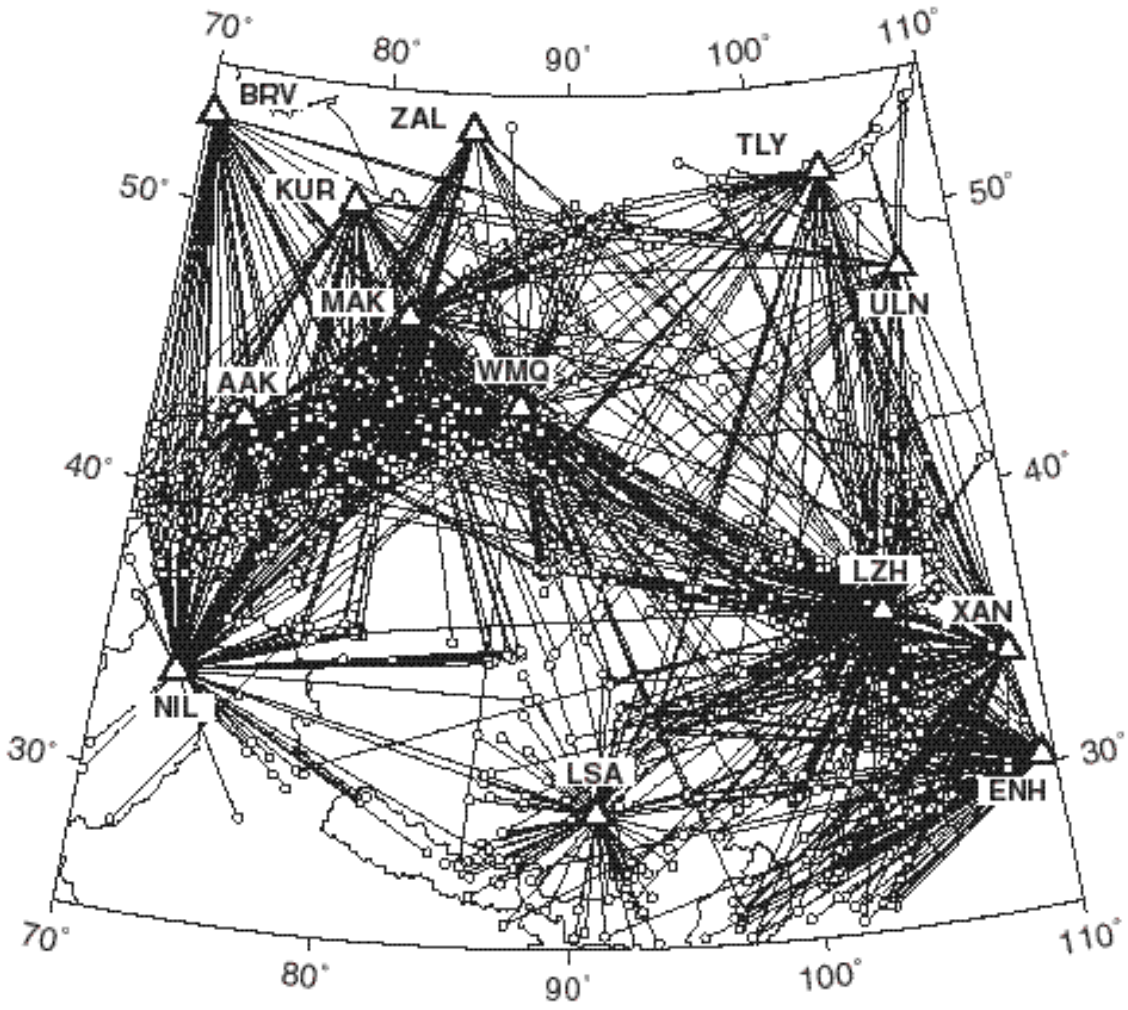


Figure 1. Great circle raypaths representing data used in tomographic inversion. Stations are indicated by triangles and events by circles.

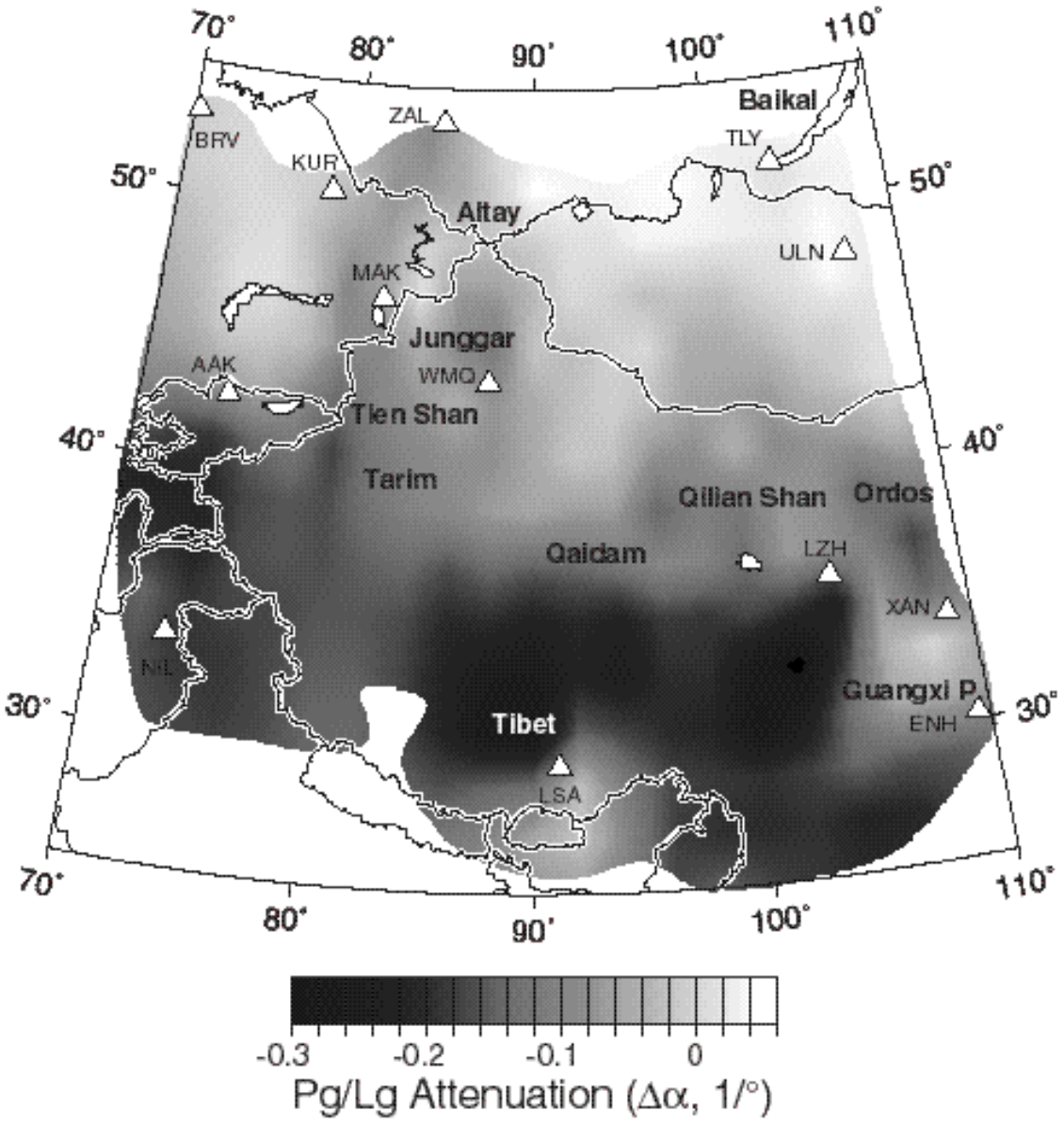


Figure 2. Relative attenuation from tomographic inversion of 1 Hz, P_g/L_g ratios. Light gray represents high relative attenuation (P_g attenuation high; L_g, low); dark gray, vice-versa. Only highly resolved portions of the image are shown. Annotations mark geographical and geological features mentioned in the text. Triangles represent stations that provided data for this study. Color facilitates the interpretation of these results and can be found in Phillips et al. (1999).

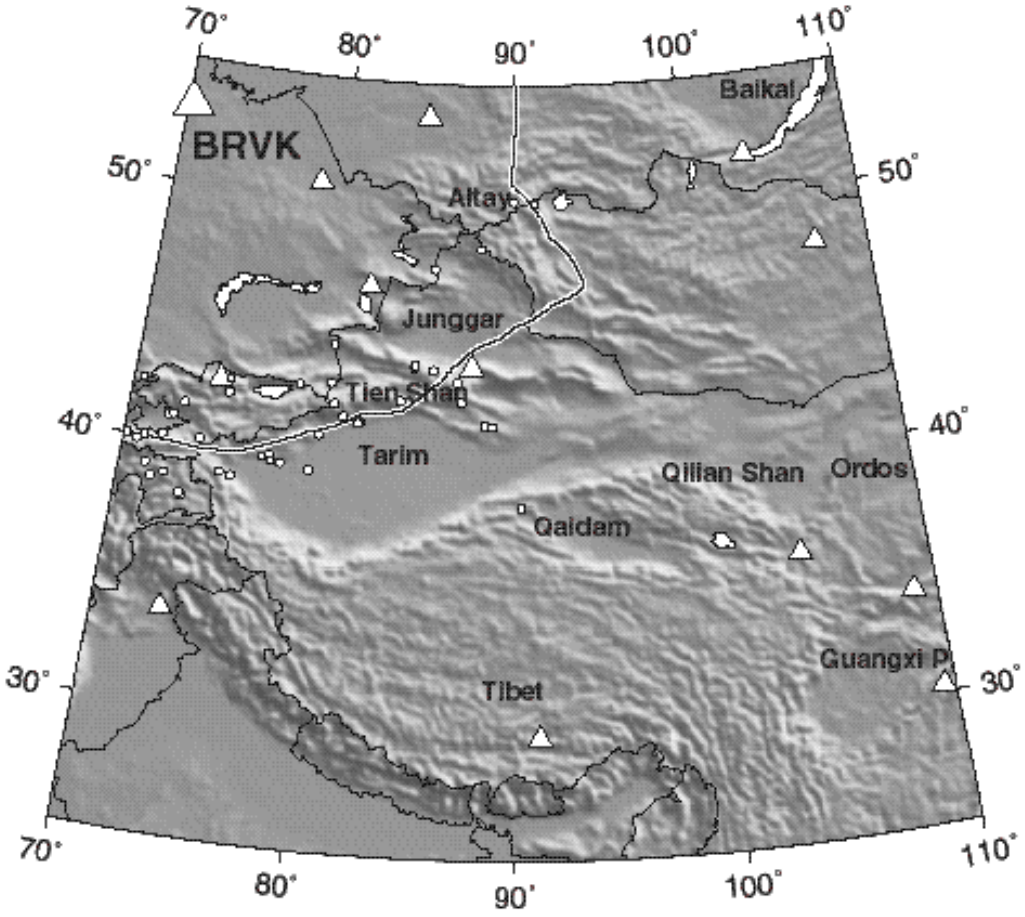


Figure 3. The zero contour of spatially interpolated $\log_{10} P_g/L_g$ residuals (data minus prediction) from station BRVK obtained by kriging (black on white line). Note the well-constrained portion of the contour that parallels the northwest edge of the Tarim basin. Underpredicted values fall to the south and east, overpredicted values to the north and west. Underpredicted data seek lower relative attenuation (darker gray, Figure 1) along their paths through the tomography image, overpredicted data, the opposite. Triangles represent stations providing data for the study.

COMPLETE REGIONAL WAVEFORM MODELING TO ESTIMATE SEISMIC VELOCITY STRUCTURE AND SOURCE PARAMETERS FOR CTBT MONITORING

Arthur J. Rodgers, William R. Walter and Todd M. Bredbeck
Lawrence Livermore National Laboratory, Geophysics and Global Security Division
Livermore, CA 94551 USA

Sponsored by U.S. Department of Energy
Office of Nonproliferation and National Security
Office of Research and Development
Contract No. W-7405-ENG-48

ABSTRACT

Intermediate-period (10-100 s) regional seismic data contain information about the seismic source as well as the velocity structure along the propagation path. Using independently well constrained source parameters we determine averaged one-dimensional velocity models by matching reflectivity generated synthetic seismograms to the observed data. Once the velocity structure along the path is well known, then one can determine the nature of the source for new events (e.g. earthquake, explosion or collapse) as well as accurate estimates of event size and depth. We are modeling regional waveforms to infer velocity structure and source parameters in the Middle East and North Africa.

Complete regional waveforms (body and surface wave amplitudes and phase) are sensitive to the seismic P and S wave velocities in the crust and uppermost mantle. However, there are tradeoffs when using waveform matches to determine both the velocity structure and the depth and focal mechanism of earthquakes, especially when using data from a sparse network in a tectonically complex region. We make use of large (mb>5.5) events with well-constrained mechanisms (e.g. when Harvard CMT and USGS NEIC are available and agree) and well-constrained depths (e.g. depth phases modeled teleseismically) to fix the source and determine the structure. Waveforms are fit using a grid search method where synthetic seismograms for many velocity models are computed and compared to the data. To limit the range of the grid search and speed up the process we often make use of an initial model evaluation by roughly matching the observed Love and Rayleigh wave group velocity dispersion. This narrows the number of models that then need to be compared against the complete waveforms. The resulting velocity models reveal the great geologic and tectonic complexity of our study region. Ideally we model paths that are completely contained within a single tectonic province. We have found this technique is particularly useful for estimating structure in large aseismic, sparsely instrumented regions where structural information is limited, such as North Africa, Arabia and India. We show waveform fits and associated velocity models from each of these regions.

Once velocity structures are determined, we then estimate the source parameters of events with unknown or poorly constrained mechanisms and depths. We sometimes find that smaller Harvard CMT events require significant changes in depth and/or mechanisms to match the regional waveforms. Events of particular CTBT interest are the smaller earthquakes (Mw < 4.5), and explosion and collapse events. An excellent example of the utility of this research is the May 11, 1998 Indian nuclear test. At the regional distance station NIL (Nilore, Pakistan) this nuclear explosion showed a strong Love wave and reversed Rayleigh waves. These observations indicate that there was a strong tectonic release associated with the explosion. We modeled the observed waveforms by adding contributions from both explosion and double-couple sources. Other examples of estimated source parameters and potential pitfalls of these methods are shown.

Key Words: Regional seismic data, seismic velocity models, earthquake parameters

Research performed under the auspices of the U.S. Department of Energy by the Lawrence Livermore National Laboratory under contract W-7405-ENG-48.

OBJECTIVE

Regional waveform modeling fulfills several needs of Comprehensive Nuclear-Test-Ban Treaty monitoring. On a fundamental level, waveform modeling helps us characterize tectonic regions by their seismic velocity and attenuation structure. This information guides regionalization by providing estimates of lithospheric structure such as sediment and crustal thickness. Once velocity models are determined for a given region, waveform modeling is used to estimate seismic moments, focal mechanisms and depths of earthquakes. Seismic moments are used to calibrate the robust *Lgcoda* magnitude scale (Mayeda an Walter, 1996; Mayeda et al., *this volume*). These magnitudes can be estimated from a single regional broadband seismogram. Accurate measurements of event size are crucial for seismic discrimination, particularly small events. Lastly, waveform modeling can be used to characterize the seismic source as an earthquake, explosion or collapse. We modeled regional waveforms to estimate the velocity structure of the crust and upper mantle and the moments, focal depths and mechanisms of earthquakes in the Middle East, Africa and south Asia. Using estimated velocity structures we modeled the tectonic release of the May 11, 1998 Indian nuclear explosion.

RESEARCH ACCOMPLISHED

We worked on several waveform modeling projects during the previous year. These projects are divided into two parts: waveform modeling for earth structure and waveform modeling for source parameters. The following sections describe these efforts.

Structure of the Arabian Peninsula

We estimated seismic velocity structure of the lithosphere (crust and uppermost mantle) from waveform data recorded by the 1995-1997 Saudi Arabian Broadband Deployment (Vernon and Berger, 1998). Whereas the interior of the Arabian Plate is aseismic, the lithosphere of this region can be sampled by earthquakes along the plate boundaries recorded at stations within the interior. Results of waveform analysis for Arabia are presented in Rodgers et al. (1999) and are briefly summarized here.

The temporary stations recorded two moderately large earthquakes (events 95327 and 96145 in Figure 1). The paths for these events provide excellent sampling of the Arabian shield and the Arabian platform. Analysis of the group velocity dispersion reveals significant differences between the structure of these two regions (Figure 2). The group velocities for the shield paths are approximately 10% faster than those for the platform. We modeled the Love and Rayleigh wave group velocities for each path with a grid search scheme. The objective of this procedure is to estimate a suite of velocity models that fit the group velocities and use these models as starting models for waveform modeling. Surface wave group velocities provide constraints on average lithospheric velocities, but suffer from severe trade-offs between layer thicknesses and velocities. Observed waveforms contain surface wave group and phase velocity information as well as body and surface wave amplitude information.

The instrument corrected displacement seismograms were fit using a grid search scheme similar to previous studies (Rodgers and Schwartz, 1998). For this case we used the group velocity modeling results as starting models. Using the United States Geological Survey-Preliminary Determination of Epicenters (USGS-PDE) locations and origin times and the Harvard CMT focal mechanisms we computed reflectivity synthetic seismograms (Randall, 1994). The fits to the observed waveforms and the velocity models are shown in Figure 3. In Figure 2 we show that the group velocities are well fit by the models which we inferred from waveform modeling.

Structure of the Northern Arabian Platform

We estimated velocity structure of the Northern Arabian platform using waveforms recorded in Jordan. Two temporary stations deployed in Jordan by LLNL in conjunction with the Jordanian Natural Resources Authority and the USGS. Figure 1 shows the location of the stations and two earthquakes analyzed with these data (events 98277 and 98264). Using methods similar to those described above we estimated the velocity structure of the lithosphere. Because the temporary stations are band-limited instruments

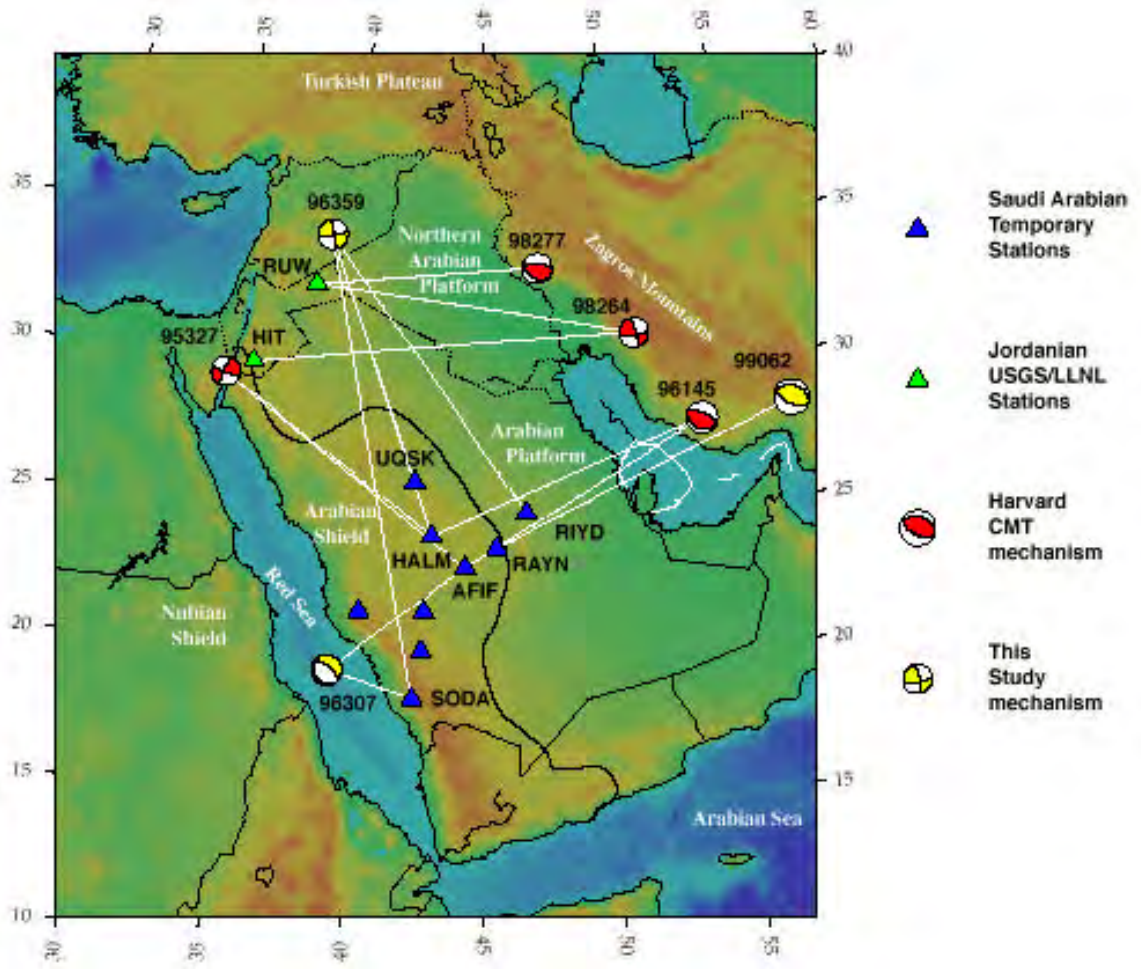


Figure 1. Map of the Arabian Peninsula, events, stations and paths analyzed.

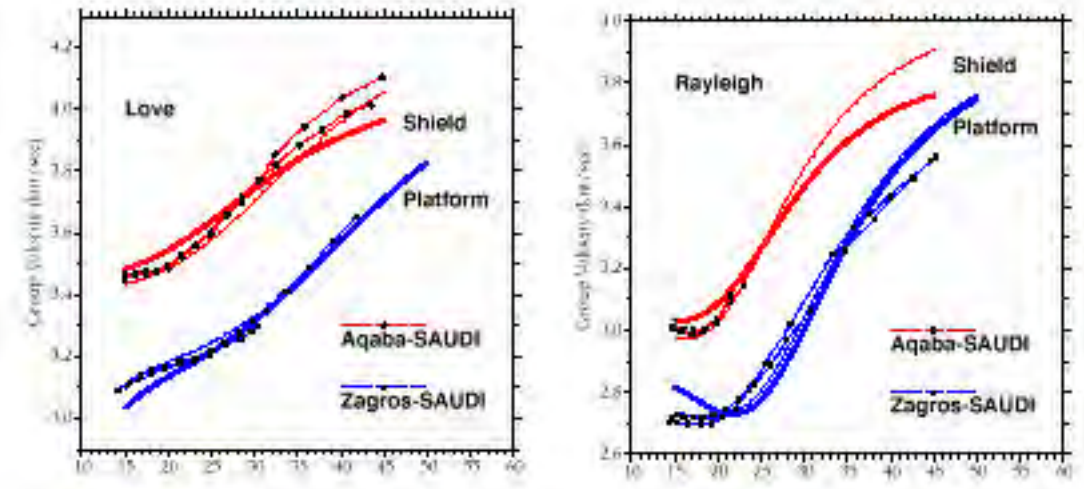


Figure 2. Group velocity dispersion for the 95327 and 96145 events as measured at stations AFIF and HALM. The dispersion curves for the velocity models that best fit the observed dispersion are shown as the light lines. The dispersion curves for the velocity models that best fit the observed waveforms (perfered model) are shown as the heavy lines.

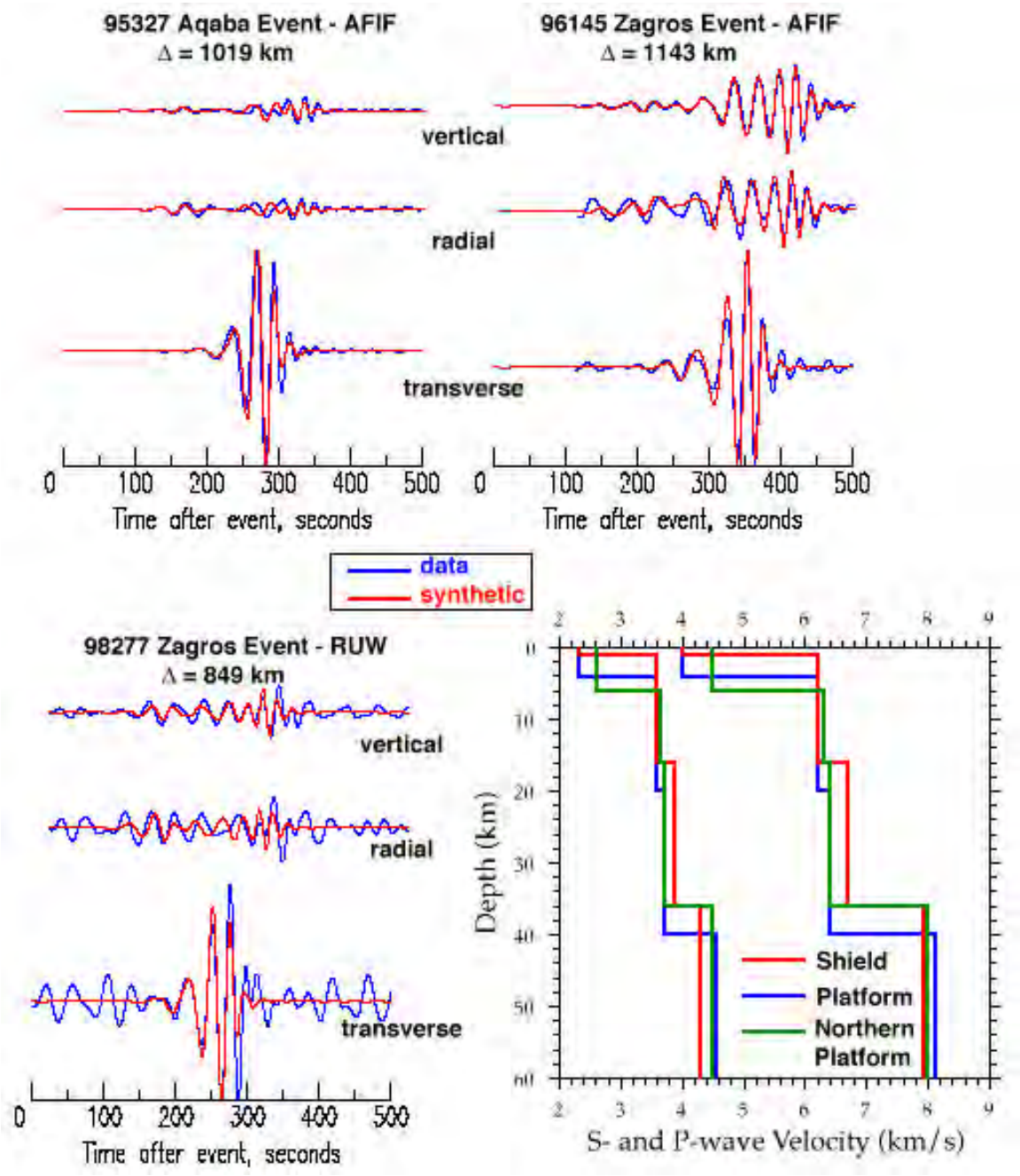


Figure 3. Fits of the synthetic sesimograms for the prefered models to the observed waveforms for the Arabian shield (top left), the Arabian platform (top right) and the Northern Arabian platform (bottom left). Velocity models for the Arabian Peninsula are also shown (bottom right).

(Guralp CGM-3) we could not model periods greater than about 40 seconds. This resulted in limited resolution of the mantle by the surface waves, however the upper parts of the model are well determined. The resulting waveform fits and velocity models are shown in Figure 3. Notice that the model is similar to the Arabian platform model, except that the sediment layer is slightly thicker and the crust is thinner. This is consistent with the Cornell University crustal and sediment thickness models for the region (Seber et al., 1996).

Source Parameters for the November 2, 1996 Red Sea Earthquake

Effective seismic monitoring and discrimination requires accurate estimates of event magnitude. A magnitude scale tied to seismic moment is most useful because it does not saturate at large magnitudes. We estimated seismic moment, focal mechanism and depth for earthquakes in the Middle East by modeling intermediate-period (10-100 s) waveforms. When modeling focal parameters it is essential that the velocity model be well known because of trade-offs between the model and the inferred source parameters.

Using the velocity models obtained for the Arabian shield and platform, we estimated source parameters for the Red Sea (event 96307) and the Zagros (event 99062) earthquakes. Source parameters (seismic moment, depth, strike, dip and rake) were estimated by a grid search algorithm (Walter, 1993). These large events were globally observed and moment tensors were reported by the Harvard CMT project. We found excellent agreement between our regional waveform modeling estimates of source parameters and the Harvard CMT estimates. Figure 4 shows the waveform modeling results for the November 2, 1996 Red Sea event (96307).

We estimated source parameters for a number of events in the Middle East, north and central Africa and south Asia. Some of these focal mechanisms are shown in Figure 1. As we estimate and refine velocity for these regions we will infer seismic moments, focal depths and mechanisms. These results will be used to calibrate the *Lgcoda* magnitude scale (Mayeda et al., *this volume*) and advance efforts to regionalize our study areas.

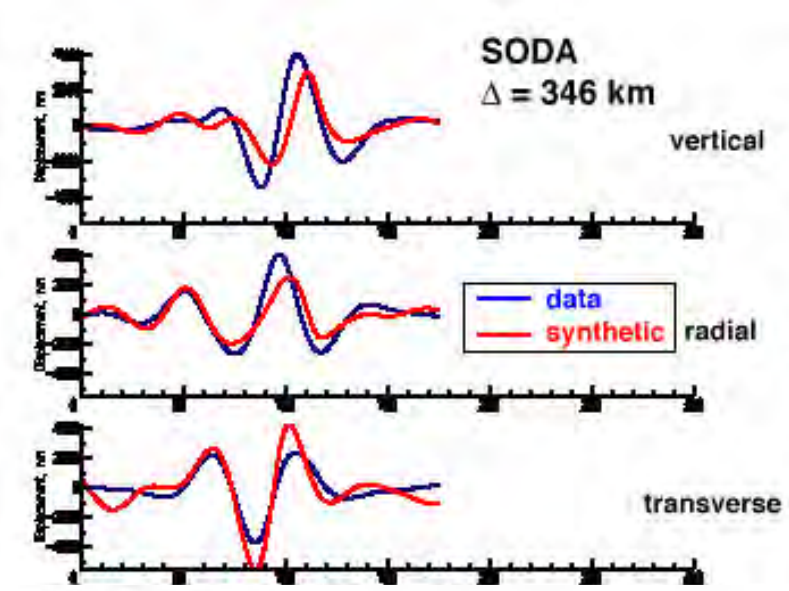
Structure of the Indian Platform

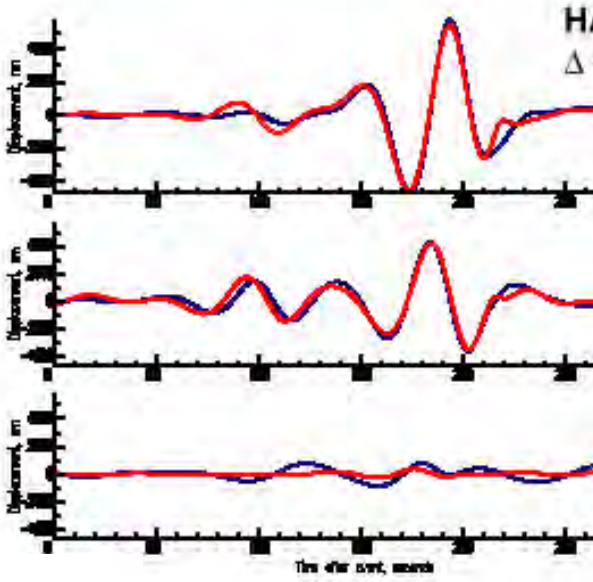
For waveform analysis of the May 11, 1998 Indian nuclear test it was necessary to estimate velocity structures for the region. Figure 5a shows the events, stations and paths analyzed in this region. We began by modeling the May 21, 1997 earthquake. This event has source parameters (moment, depth and focal mechanism) reported in both the Harvard-CMT and USGS-NEIC catalogs. The lower crustal depth is well constrained by depth phases. Because the source parameters agree and fit the long-period filtered data, we feel confident that the source is well modeled. By fixing the source parameters and adjusting the velocity model, we obtained good fits to the observed three-component seismograms (Figure 5b). The inferred velocity structures (Figure 5d) reveal some heterogeneity in the lithospheric structure of the Indian sub-continent. The mantle velocity gradient may not be resolved by the intermediate-period regional data.

Source Parameters for the April 1, 1996 Pakistan Earthquake

A moderately large earthquake occurred in the Thar Desert on April 1, 1996. This event was located by the USGS-PDE at a depth of 43 km. The Harvard CMT catalog reports this event at a depth of 92 km. We used the regional recordings of this event at stations NIL and HYB to estimate the source parameters. The velocity models used for this analysis were slightly modified from those shown in Figure 5d. Synthetics for the CMT solution at station NIL do not fit the data at relatively long-periods (Figure 5c). We solved for the source parameters using the shallower USGS-PDE depth of 43 km and recordings at both NIL and HYB. Our mechanism shows a much improved fit over the CMT solution.

This event demonstrates that source parameters routinely estimated from long-period teleseismic waveform modeling may by in error. Errors in estimated source parameters are probably larger for smaller events because of poor signal-to-noise. Also errors may be larger in regions of heterogeneous or anomalous crustal structure, such as the Alpine-Himalayan Front. This event illustrates the importance of considering both the source and the velocity structure when trying to extract information from intermediate period waveforms.





Event Parameters

strike (deg)	dip (deg)	rake (deg)	depth (km)	moment (dyne-cm)	Mw
150	16	-72	10	1.41e24	5.4 (LLNL solution)
153	20	-68	15	0.99e24	5.3 (Harvard CMT)

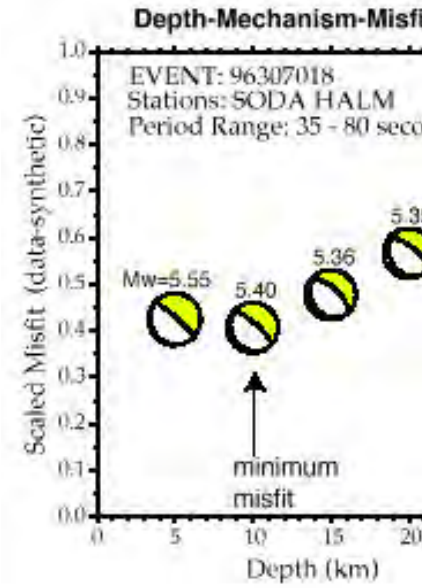


Figure 4. Waveform modeling to estimate earthquake moment, depth and best double-couple focal mechanism for the Red Sea event (96307). (top) Waveform fits to stations SODA and HALM. (right) Depth-mechanism-misfit curve showing the best-fitting depth is 10 km. Our estimated source parameters agree excellently with those reported by the Harvard CMT project. Synthetics were computed using our Arabian shield model (Figure 3) and filtered in the long-period band 35-80 seconds. The misfit of the Rayleigh wave at station SODA probably arises because this path is mostly oceanic while the velocity model is representative of the continental portion of the path.

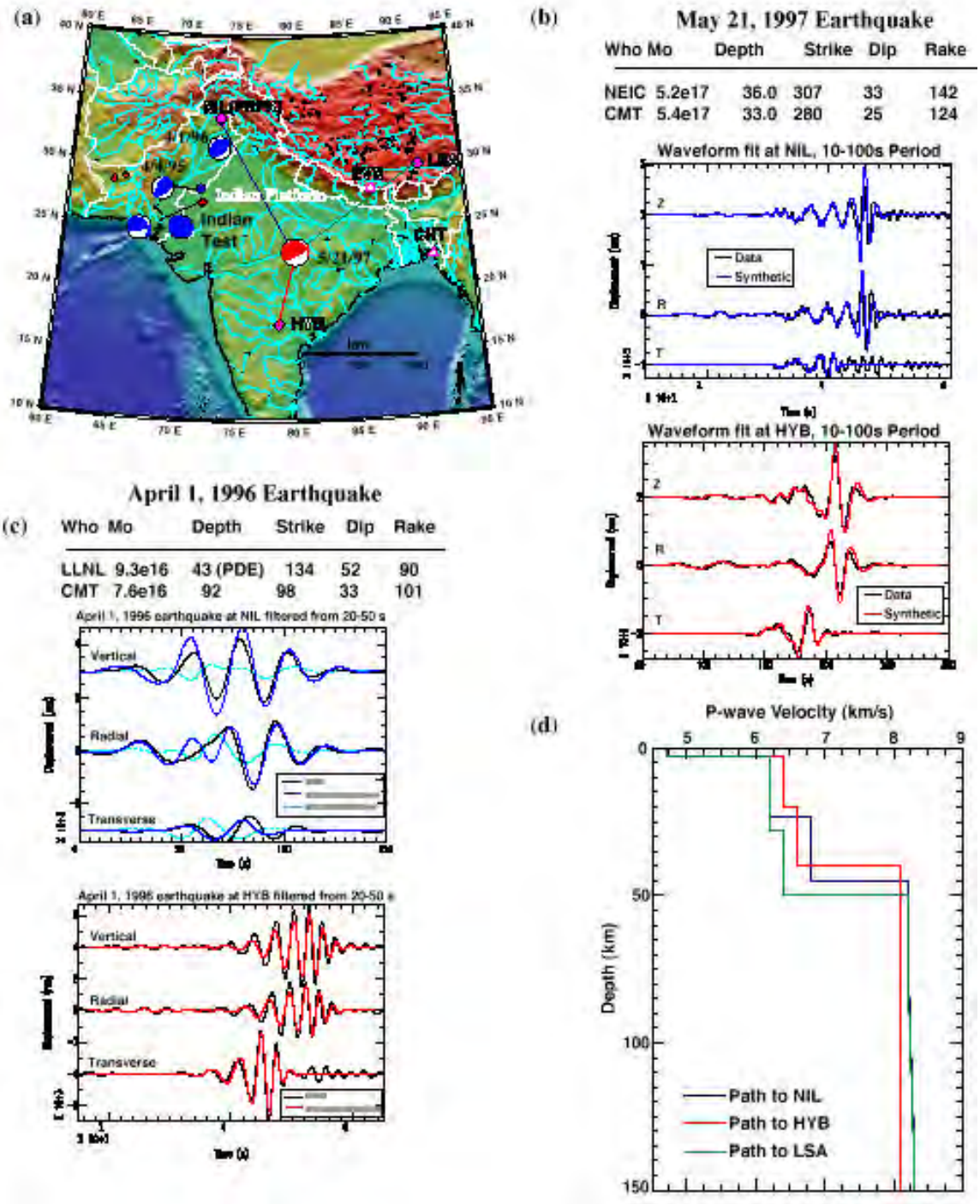


Figure 6. (a) Fits to the April 4, 1995 earthquake at station NIL. The focal mechanism for this event is plotted on Figue 5a. (b) Intermediate-period (10-20 s) three-component waveforms for the May 11, 1998 Indian nuclear test at NIL. Note the strong Love that is not expected from an explosion source. (c) Vertical component Rayleigh wave of the Indian test and a synthetic seismogram for an explosion source. Notice that the synthetic Rayleigh wave (red) has the opposite polarity of the data. (d) Waveform modeling of tectonic release of the Indian nuclear test. The focal mechanism of the tectonic is plotted in Figure 5a.

Magnitude-Distance Amplitude Correction (MDAC; Taylor et al., 1999) to regional body-wave amplitudes for discrimination and calibrating the coda-based magnitude scales.

ACKNOWLEDGEMENTS

Waveform data was collected and organized by Stan Ruppert, Terri Hauk and Jennifer O'Boyle at LLNL. This is LLNL contribution UCRL-JC-134308.

REFERENCES

Mayeda, K., and Walter, W. (1996). Moment, energy, stress drop and source spectra of western United States earthquakes form regional coda envelopes, *J. Geophys. Res*., **101**, 11,195-11,208.

Mayeda, K. Hofstetter, A., Rodgers, A., and Walter, W. (1999). Applying coda envelope measurements to local and regional waveforms for stable estimates of magnitude, source spectra, & energy, *this volume.*

Randall, G. (1994). Efficient calculation of complete differential seismograms for laterally homogeneous earth models, *Geophys. J. Int*., **118**, 245-254.

Rodgers, A., and S. Schwartz (1998). Lithospheric structure of the Qiangtang Terrane, northern Tibetan Plateau, from complete regional waveform modeling: evidence for partial melt, *J. Geophys. Res.,* **103**, 7137-7152.

Rodgers, A., Walter, W., Mellors, R, Al-Amri, A. and Zhang, Y. (1999). Lithospheric structure of the Arabian shield and platform from complete regional waveform modeling and surface wave group velocities, in press *Geophys. J. Int.*

Rodgers, A. and Walter, W. (1999). Seismic discrimination of the May 11, 1998 Indian nuclear test with short-period regional data from station NIL (Nilore, Pakistan), submitted to *Pure. App. Geophys*.

Seber, D., M. Vallve, E. Sandvol, D. Steer and M. Barazangi (1997). Middle East tectonics: applications of geographical information systems (GIS), *GSA Today*, February 1997, 1-5.

Taylor, S., Velasco, A., Hartse, H., Philips, S., Walter, W., and Rodgers, A. (1999). Amplitude corrections for regional discrimination, submitted to *Pure. App. Geophys*.

Vernon, F. and Berger, J. (1998). Broadband seismic characterization of the Arabian Shield, Final Scientific and Technical Report, http://www-ida.ucsd.edu/ANZA/saudi/SAUDI.pdf.

Walter, W. (1993). Source parameters of the June 29, 1992 Little Skull mountain earthquake from complete regional waveforms at a single station, *Geophys. Res. Lett*., 20, 403-406.

LAWRENCE LIVERMORE NATIONAL LABORATORY'S MIDDLE EAST AND NORTH AFRICA RESEARCH DATABASE

Stanley D. Ruppert, Teresa F. Hauk, Jennifer L. O'Boyle, Douglas A. Dodge, R. Miki Moore
Geophysics and Global Security, Lawrence Livermore National Laboratory
University of California

Sponsored by U.S. Department of Energy
Office of Nonproliferation and National Security
Office of Research and Development
Contract No. W-7405-ENG-48

ABSTRACT:

The Lawrence Livermore National Laboratory (LLNL) Comprehensive Nuclear-Test-Ban Treaty Research and Development (CTBT R&D) program has made significant progress populating a comprehensive seismic research database (RDB) for seismic events and derived research products in the Middle East and North Africa (ME/NA). Our original ME/NA study region has enlarged and is now defined as an area including the Middle East, Africa, Europe, Southwest Asia, the Former Soviet Union and the Scandinavian/Arctic region. The LLNL RDB will facilitate calibration of all International Monitoring System (IMS) stations (primary and auxiliary) or their surrogates (if not yet installed) as well as a variety of gamma stations. The RDB provides not only a coherent framework in which to store and organize large volumes of collected seismic waveforms and associated event parameter information, but also provides an efficient data processing/research environment for deriving location and discrimination correction surfaces and capabilities. In order to accommodate large volumes of data from many sources with diverse formats the RDB is designed to be flexible and extensible in addition to maintaining detailed quality control information and associated metadata. Station parameters, instrument responses, phase pick information, and event bulletins were compiled and made available through the RDB. For seismic events in the ME/NA region occurring between 1976 and 1999, we have systematically assembled, quality checked and organized event waveforms; continuous seismic data from 1990 to present are archived for many stations. Currently, over 11,400 seismic events and 1.2 million waveforms are maintained in the RDB and made readily available to researchers. In addition to open sources of seismic data, we have established collaborative relationships with several ME/NA countries that have yielded additional ground truth and broadband waveform data essential for regional calibration and capability studies. Additional data and ground truth from other countries are also currently being sought. Research results, along with descriptive metadata are stored and organized within the LLNL RDB and prepared for delivery and integration into the Department of Energy (DOE) Knowledge Base (KB). Deliverables consist of primary data products (raw materials for calibration) and derived products (distilled from the organized raw seismological data). By combining travel-time observations, event characterization studies, and regional wave-propagation studies of the LLNL CTBT research team for ground truth events and regional events, we have assembled a library of ground truth information, event location correction surfaces, tomographic models and mine explosion histories required to support the ME/NA regionalization program. Corrections and parameters distilled from the LLNL RDB provide needed contributions to the KB for the ME/NA region and will enable the United States National Data Center (NDC) to effectively verify CTBT compliance. The LLNL portion of the DOE KB supports critical NDC pipeline functions in detection, location, feature extraction, discrimination, and analyst review in the Middle East and North Africa.

Key Words: seismic, waveform, database, metadata

This work was performed under the auspices of the U.S. Department of Energy by Lawrence Livermore National Laboratory under contract No. W-7405-Eng-48 for the Office of Research and Development, NN-20, within the Office of Nonproliferation and National Security, NN-1.

OBJECTIVE

The primary objective of the Lawrence Livermore National Laboratory (LLNL) comprehensive seismic research database (RDB) is to help coordinate the LLNL Comprehensive Nuclear-Test-Ban Treaty (CTBT) Middle East and North Africa (ME/NA) regionalization program. Corrections and parameters distilled from the LLNL RDB provide needed contributions to the Department of Energy (DOE) Knowledge Base (KB) for the ME/NA region and will enable the United States National Data Center (NDC) to effectively verify CTBT compliance. The LLNL portion of the DOE KB supports critical NDC pipeline functions in detection, location, feature extraction, discrimination, and analyst review in the Middle East and North Africa. The LLNL RDB provides efficient access to, and organization of, thousands of seismic events and associated waveforms, while also providing the framework to store, organize, and disseminate research results for delivery into the DOE KB (Figure 1). Reference event libraries and ground truth datasets showing space and time clustering of natural earthquake and mine events, phase blockage maps, and event characterization parameters are compiled from the RDB. Sufficient metadata (including measurement procedures, codes, comments and measurement errors) are stored at each step in the analysis process to allow recreation or verification of results at any stage in the processing flow.

DOE Knowledge Base deliverables created using the RDB may be grouped under two major categories: primary data products and derived products. The primary products are those developed in the process of collecting the raw materials for calibration: ground truth data, waveform data, event catalogs, phase pick information, regional station information and instrument responses. The derived products (distilled from the organized raw seismological data) are models and corrections that improve detection, location and discrimination functions. In order for LLNL to calibrate all International Monitoring System (IMS) stations (primary and auxiliary), as well as a variety of gamma stations that experience has shown to be useful, the LLNL RDB must incorporate and organize the following categories of primary and derived measurements, data and metadata:

1) Waveforms and phase picks on high-priority data
2) Waveform metadata (trace quality, properties and processing history)
3) Station and channel parameters
4) Global, regional, and local earthquake catalogs
5) Travel-time models, regional velocity models, kriged corrections surfaces
6) Surface wave group velocities
7) Detection filter bands to optimize signal-to-noise
8) Regional discriminants, phase amplitude and magnitude calibrations
9) Reference archives of waveform and parameter data for special regions of study

RESEARCH ACCOMPLISHED

Data Acquisition

Data collection for the LLNL RDB began in 1996 and continues today. The LLNL study area surrounding the Middle East and North Africa to include Europe, part of the Former Soviet Union, and Central Africa, has been termed the ME/NA region. The region of study spans the area between latitudes 10° South and 60° North and between longitudes 35° West and 85° East. Most of the archived waveforms in the LLNL RDB are from events located within this region and occurring between 1976 and 1999, but we are now expanding our event coverage into the Former Soviet Union and the Scandinavian/Arctic region (Figure 3). The new region, designated ME/NA/FSU, surrounds the mid-ocean ridges and spans 50° West to 90° East and 55° South to the North Pole and also includes an additional region of 65° North to the North Pole and 90° to 145° East to encompass the remainder of the Arctic ridge events. Special datasets are compiled for specific areas of interest or events, such as the Novaya Zemlya test site and the recent India and Pakistan nuclear tests.

Waveforms

We are collecting seismic data from IMS primary and auxiliary stations, as well as surrogate stations (for IMS stations not yet installed) and other stations needed to support calibration in the region of study (Figure 2). We have obtained up to 10 years of continuous data for important ME/NA stations from the Incorporated Research Institute for Seismology (IRIS), Institut de Physique du Globe de Paris GEOSCOPE

program, and the GEO-Forschungs Zentrum/Potsdam, Germany GEOFON program. Current data is being received on a regular basis since June 1998 from several arrays and stations supplied via the Air Force

Technical Applications Center (AFTAC) through cooperation with Sandia Nation Laboratories. Current data is also being supplied by an LLNL joint project with the Jordan Natural Resources Authority from two seismometers deployed in Jordan. We are establishing a similar collaboration with Kuwait. Data for particular events has been obtained from the prototype International Data Center (PIDC). AFTAC and the Center for Monitoring Research (CMR) have provided waveforms for special regions/events, such as the Novaya Zemlya test site.

Data requests are usually made through automated systems provided by networks and seismic data centers, which supply data by email, ftp, or tape. Our current emphasis is on events recorded between 1990 and present, except for IMS surrogate stations no longer in operation or for special events such as nuclear tests. All available channels and components are requested from each station or array. Stations in operation prior to 1990 are typically limited to long period (1 sps) or very long period (0.1 sps) continuous data and short period (40-80 sps), vertical component, triggered data; broadband (20 sps) data exist from very few locations before 1990. Data from IRIS, GEOSCOPE, and GEOFON are provided in SEED format, waveforms from AFTAC and CMR are organized in CSS format, and data from LLNL deployments are recorded in REFTEK format.

The RDB is organized in CSS3.0 (Center for Seismic Studies Version 3.0) format with NDC and LLNL extensions. All data is converted to CSS3.0 format before it is added to the RDB. Waveforms are stored as **.w** files and are referenced through **wfdisc** and **wftag** tables. Additionally, although the continuous data remains archived on tapes, seismic events are extracted from the continuous waveforms. Events used to populate the database are a subset of the (United States Geological Survey) USGS Monthly (Final) Preliminary Determination of Epicenters (PDE) bulletin and consist of events in the ME/NA region from 1990 to early 1999. Originally, the RDB was populated with events of magnitude 4.0 and greater, but the selection has now been enlarged to include all events magnitude 3.5 and above. The list of events has also been altered to include the expanded ME/NA/FSU region. Waveforms are extracted from continuous data based on consistent time window criteria: the waveform begins at the event origin time and ends at the arrival time of seismic waves traveling at 1 km/sec. Due to the size of the region of study, source-receiver distances range from local to teleseismic.

The number of waveforms in the RDB now exceeds 1.2 million, which corresponds to over 11,400 seismic events (Figure 4). There are over 30 stations in the ME/NA region for which we have over 10,000 waveforms for up to 6000 events (Figure 2). We have nearly mined the available historic data supply for open stations in the ME/NA region, but will continue to collect current data from these stations as it becomes available. The data collection process is now being focused on stations in the expanded ME/NA/FSU region. Also, we are augmenting the open historic station data with seismic data from LLNL field deployments and collaborative research efforts established in ME/NA countries.

In addition to individual event waveform segments and continuous data traces managed by the RDB, we also maintain an archive of active and passive seismic data from various field deployments. One example is the archive of very long FSU PNE refraction profiles collected under contract to LLNL by the USGS (Figure 5). Other deployments include IRIS experiments in Tanzania, Pakistan, Caspian, and Geyokcha. These profiles (in SEGY format) collected throughout the ME/NA/FSU region provide critical information for independently determining spatial correlation distances and developing the regional geophysical models necessary to calibrate the many aseismic areas in our study region. Both LLNL and the USGS are jointly analyzing and modeling the refraction profiles to provide both travel time and amplitude information throughout the FSU.

Phase Information

Analyst Flori Ryall and LLNL researchers have made phase picks for over 3000 events to yield over 10,000 travel-time observations available to the LLNL research team for location and discrimination projects. Phase analysis is an ongoing effort since new events and waveforms are continually being added to the RDB. Phase information is recorded in the **arrival** and **assoc** tables. Augmenting the LLNL picks, we added ~5.5 million USGS Earthquake Data Report (EDR) catalog phase pick observations to the RDB

to be used for travel-time correction studies and correction surface generation. Since the EDR picks are available only for 1990-1997, we supplemented the EDR picks with the complete Bulletin of the International Seismological Centre (ISC) phase arrival measurements spanning from 1964-1995. Phase picks have also been entered into the RDB from the Joint Seismic Observing Program (JSOP) and Bob Engdahl's reviewed subset of the ISC bulletin.

Station Parameters

Development of travel-time corrections requires not only accurate source locations and origin times, and quality-controlled waveform data, but also accurate knowledge of station locations. Seismic station information is a metadata requirement needed to support all stages of seismic waveform analysis. This metadata includes such parameters as station operation dates, location and elevation, type of channels and instruments, sampling rates, and instrument responses. Our main source of this information is IRIS "dataless" SEED files, which are provided by each of the networks affiliated with IRIS. These files contain all station parameters and response information and are updated periodically by the networks. Other station information has been obtained through internet station books and AutoDRM systems. **Site** and **sitechan** table entries (listing station location, available channels, sensor orientations, operation dates, etc.) were created for almost all IRIS affiliated networks. This will provide worldwide station information to accommodate any future changes in research needs or the LLNL study region and greatly minimize the need to add or change station entries in the future.

We reviewed all new and existing station and channel information for completeness and coherency before updating the RDB tables. Over 1100 station and array element table entries have been updated, but we still have not located parameter data for many stations (Figure 3). Minimal or inconsistent information has restricted the reliability of certain entries. Often discrepancies arise between multiple information sources for the same station, but IRIS or the network operator is assumed to offer the most complete information in most cases. Network operators have been contacted to resolve significant problems. We maintain a list of sources for each item of station information (**sitesrc, sitechansrc**), since each parameter may be obtained from a different source. **Network** and **affiliation** tables have been created to track the network(s) to which each station is associated. **Instrument** and **sensor** tables are used to document instrument type and response for each station and channel. The IRIS "dataless" SEED files are used to generate instrument response (RESP) files for each station/network/channel/time combination delineated by calibration periods. The RDB **instrument** table contains pointers to the online flatfiles. Frequency-amplitude-phase (FAP) files have been provided by AFTAC and are similarly stored with RDB pointers.

Event Bulletins

Reference event locations and origin time information is necessary in most stages of our seismic processing and research. Bulletin information from many global, local and regional earthquake catalogs has been incorporated into the LLNL RDB. The global catalogs include: USGS Monthly (Final) Preliminary Determination of Epicenters (PDE) catalog, USGS Earthquake Data Report (EDR) catalog with phase arrival information, Bulletin of the International Seismological Centre (ISC) with phase arrival information, Harvard Centroid Moment Tensor (CMT) catalog, and AFTAC PREACH unclassified global catalog. We have also compiled numerous regional and local catalogs from countries in the ME/NA region, including Jordan, Israel, Morocco, and the Joint Seismic Observing Program (JSOP). We have established a number of collaborative agreements with countries and institutes in our study region that are yielding both local seismic catalogs and ground truth information as well as seismic waveform data. We compiled, assembled, and cross-checked several global seismicity catalogs and bulletins of phase arrival measurements in order to create CSS3.0 tables and custom tables in the RDB. Since the catalogs are in a variety of formats, we use a combination of custom filter programs and modified (fixed) DATASCOPE programs to convert all of the bulletins to CSS3.0 table format. In the case of the PDE and CMT catalogs, original bulletin formats are archived in order to retain information not having a CSS3.0 table entry (such as source reference, source parameter information, moment, focal mechanism, etc.). We also reconcile and compare the same bulletin information obtained from different sources in order to create a final quality checked catalog.

Database Organization

Database Format

The LLNL RDB is designed to be flexible and extensible in order to accommodate large volumes of data in diverse formats from many sources in addition to maintaining detailed quality control and metadata. The RDB is comprised of ORACLE relational database software running on a SUN Server accessible from researcher workstations (Figure 6). Data are stored in CSS3.0 format (Center for Seismic Studies Version 3.0 database structure) with NDC and LLNL extensions. These formats provide parameter defined tables for different elements of seismic data, such as event and station information, as well as allowing for customized tables to be developed for specific research needs or results. The CSS3.0 format offers the ability to organize data in a standard format, store metadata necessary for documenting research methods and deliver compatible data to DOE and other researchers. Derived location and amplitude correction surfaces are stored in the standardized LibKBI format for efficient access by location and discrimination software programs.

Table Population

In order to efficiently generate new database entries and update existing tables, it was necessary to develop software to automate these procedures. The following software reduces the time involved with the upkeep of the large amounts of incoming data:

1) UpdateMrg – inserts waveform pointers in **wfdisc** and **wftag** tables for new waveforms, verifies waveforms are not "flat line," and joins all waveform segments related to a single event
2) UpdateResp – determines displacement amplitude responses, calculates nominal calibration values, populates instrument and sensor tables based on calibration epochs in RESP and FAP files
3) UpdateArrival – populates **arrival** and **assoc** tables with phase information obtained from different bulletin formats or analyst picks
4) Catalog Parser – extracts event information from various bulletin formats in order to generate entries for an **origin** table

We are also in the process of developing custom tables (where existing CSS3.0 or NDC tables are inadequate) in order to organize and store research results in a manner that will allow these results to be accessible to the research team and to track metadata related to table entries. Examples of necessary custom tables are analyst comments for phase picks and events, mine explosion statistics and surface wave measurements.

Waveform Quality Assessment

The organization of waveform data into a database with a measure of data quality is fundamental to calibration activity, estimation of errors within other KB products based on waveform analysis, and to future detailed evaluation of special events by analysts at the NDC and elsewhere. The assembly of seismic waveform quality measurements is major task since it involves assessing large quantities of data from numerous waveform sources with several incompatible formats of varying quality. RDB waveforms may contain dropouts, glitches, timing errors or other problems affecting waveform analysis. We have developed an algorithm that analyzes and reports on 18 separate problems in the categories of timing errors, zero slope detection, discontinuity detection, and median filtering. This waveform quality information can be generated while focusing on all or a part of a waveform, examples of which include pre-event noise, the first arrival or event coda. This automated procedure will measure waveform quality in a consistent manner and generate three custom database tables: **wavequal**, **wavequalspt**, **wavequaldisc.** These tables contain the types of problems encountered and pointers to detailed files with the location and frequency of problems encountered. The development of these tables allows researchers and analysts to quickly identify sets of reviewed waveforms, thus reducing the laborious process of previewing each trace.

Data Access

Different researcher needs for data and metadata require that subsets of data must be provided in a format easily accessible to many diverse types of software and analyses tools. Therefore, the RDB access tools have been designed to utilize the power of the relational database to facilitate efficient queries and data retrieval (Figure 6). The Seismic Analysis Code (SAC) software used by LLNL researchers provides direct access to database table information and waveforms and uses the response files to perform instrument response corrections. PL/SQL language can be used to make database queries on contents of any of the available CSS3.0 tables. We are currently developing a GUI interface to the ORACLE database to support

easier access to RDB information; a web tool (Web Application Server) is also available for the ORACLE system. For spatial queries and organization, we have adopted the ESRI product ArcView (Figure 6). Arcview has been linked with the ORACLE database to provide joint spatial and relational queries. Given the large quantity of data now managed by the RDB, emphasis has shifted to produce the efficient "production" level seismic data selection and processing tools necessary to meet programmatic and KB delivery schedules. In addition, data browsers are under development in coordination with Sandia National Laboratory to allow visualization and quick access to both data and delivered research products.

CONCLUSIONS AND RECOMMENDATIONS

Research Product Delivery

Derived Research Products

Corrections and parameters distilled from the LLNL RDB provide needed contributions to the DOE Knowledge Base for the ME/NA region and will enable the USNDC to effectively verify CTBT compliance. The LLNL portion of the DOE KB supports critical NDC pipeline functions in detection, location, feature extraction, discrimination, and analyst review in the Middle East and North Africa. A wide range of research projects required to support the ME/NA regionalization program are being derived from waveforms, station parameters, and bulletin information contained in the LLNL RDB. Current discrimination and location research includes:

1) Mine Atlas: ground truth mine explosions and mine explosion statistics
2) Ground truth depth and mechanism estimates based on waveform modeling
3) Regional phase amplitude measurements and correction surfaces
4) Surface wave group velocities and correction surfaces
5) Regional coda magnitude algorithms
6) Location calibration and travel-time correction surfaces
7) Phase Amplitude correction surfaces and phase amplitude ratio discriminant results for specific regions
8) Important primary data products, reviewed station parameters, supplement these research products
9) Regional assessment & validation maps (preliminary capability studies used to guide LLNL research)

By combining travel-time observations, event characterization studies, and regional wave-propagation studies of the LLNL CTBT research team for ground truth and regional events, we have assembled a library of ground truth information (origin times, locations, depths, magnitudes), event location correction surfaces, tomographic models and mine explosion statistics required to support the ME/NA regionalization program. Future efforts will involve creating customized database tables to store all of the derived data products and related metadata. This will enhance the efficiency in compiling research results for dissemination to the DOE KB.

Knowledge Base Deliveries

LLNL research product submissions during the past year to the DOE KB have included updates for many of the above research products (Specific details of LLNL research products delivered are described in the Research Product Delivery Documents). The research products delivered in the version 2.0 release [Ruppert et al., 1999] represent a significant advance over the initial research products delivery in Spring 1998. In the version 2.0 release, we delivered both reference ground-truth parameters (reference mining event waveforms and Mine Parameter Atlas) and derived location (travel-time) and discrimination (amplitude) correction surfaces for key selected stations within our ME/NA research region. The travel-time correction surfaces are delivered as a framework that allows initial location and performance assessment to be completed within the ME/NA region while also allowing each individual station surface to be easily updated as additional data becomes available. We also delivered completely revised and expanded lookup tables for critical station parameter information (location, response, and other operational characteristics). Surface wave measurements delivered in version 2.0 are completely revised from the version 1.0 spring release, and are integrated with amplitude measurements for two stations that form an integrated package of measurements, discriminants and correction surfaces to support source identification efforts of CTBT monitoring. The algorithms developed and used to create these research products are currently being adapted to efficiently process the additional volume of data necessary to expand these techniques to additional stations necessary to support the next major DOE Knowledge Base delivery scheduled for mid FY 2000.

REFERENCES

Ruppert, S., CTBT R&D Staff, LLNL Middle East and North Africa Research Product Delivery Version 2.0, LLNL, June 1999

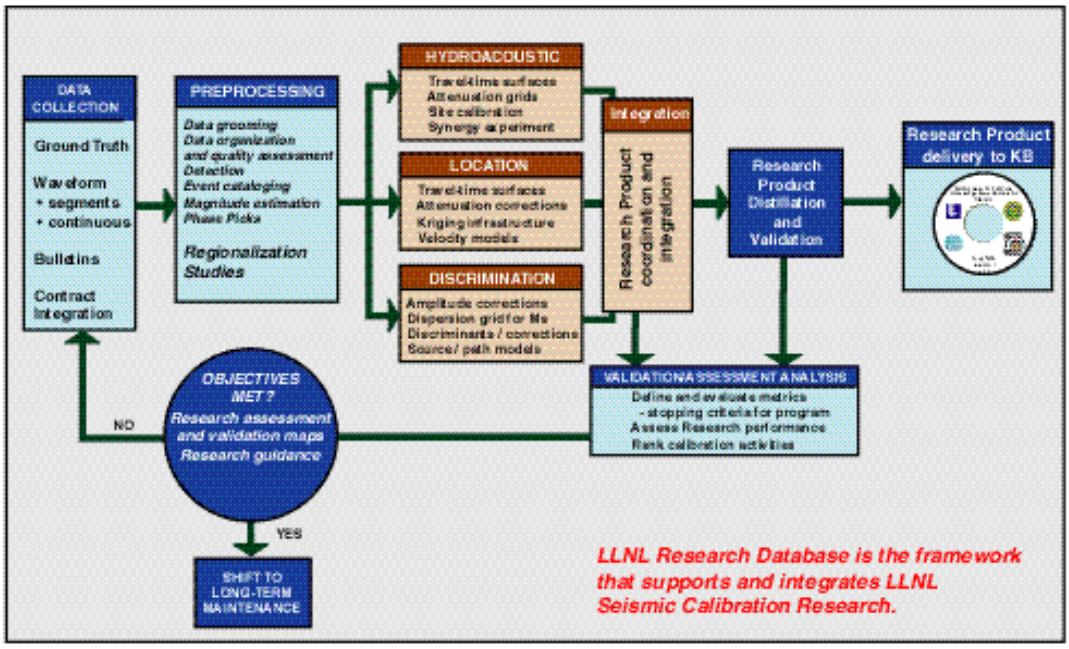


Figure 1: Overview of LLNL research database framework and product production flow.

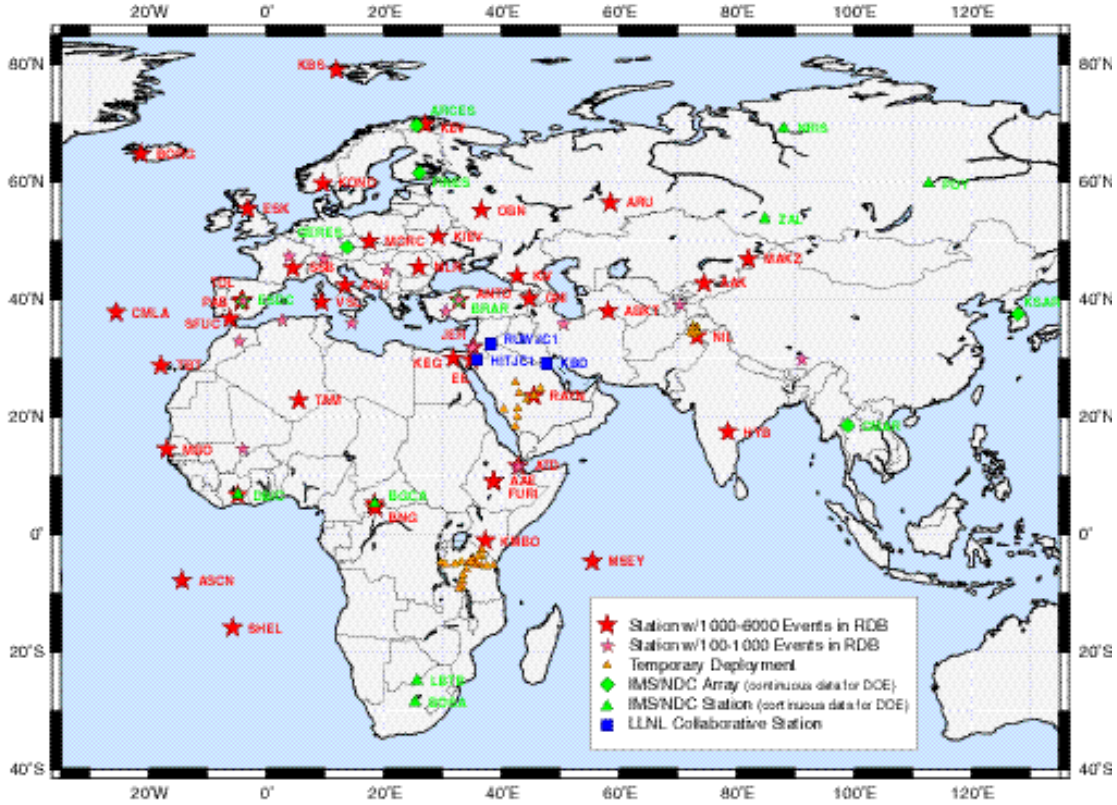


Figure 2: Seismic stations supplying large quantities of seismic event data to the LLNL research database. Data from additional stations is actively being acquired for future addition to the database.

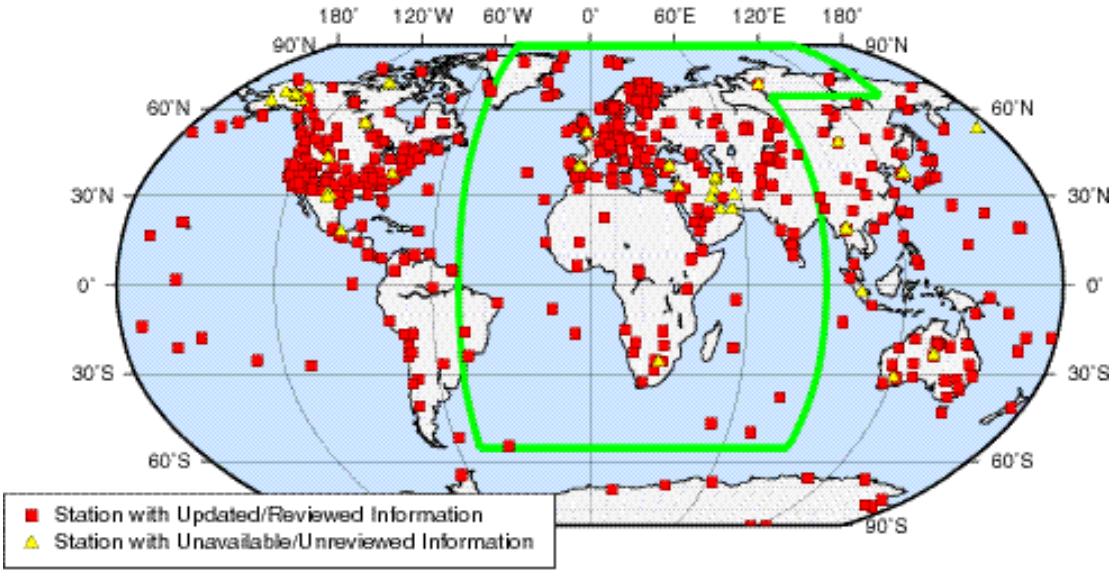


Figure 3: Distribution of all stations contained in the LLNL research database station parameter tables. Station information has been updated and reviewed for completeness and coherency for 1100 station and array element table entries. The outlined region defines the expanded ME/NA/FSU study area, incorporating the Former Soviet Union, Southwest Asia and the Scandinavian/Arctic region, within which seismic events will be collected.

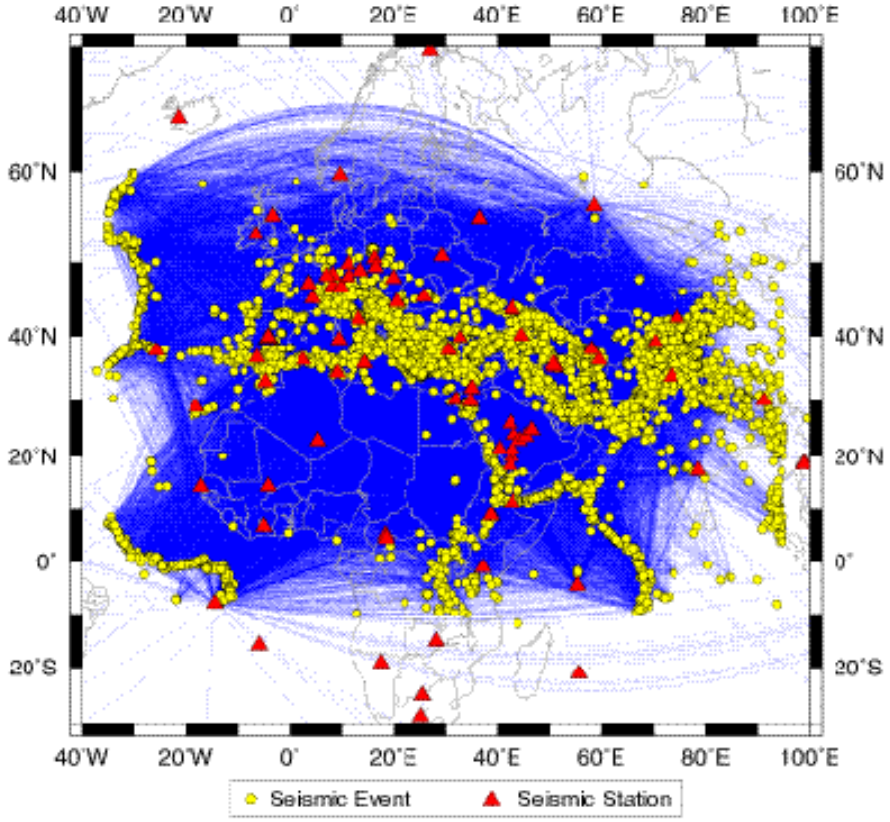


Figure 4: Seismic data available in the LLNL research database. Raypaths show source to receiver coverage for 1.2 million waveforms in the ME/NA region, corresponding to over 11,400 seismic events available to LLNL researchers.

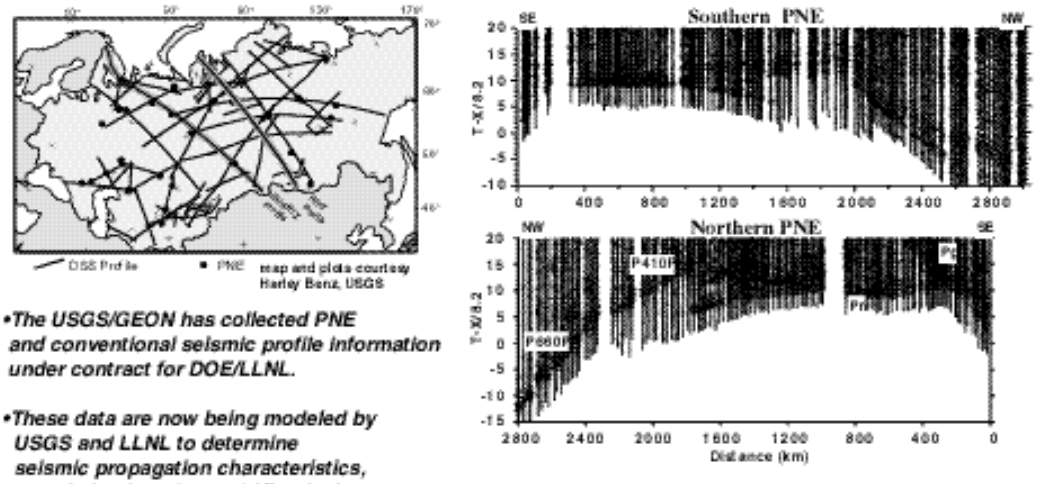


Figure 5: Example of seismic refraction data from FSU QUARTZ profile using PNE's.

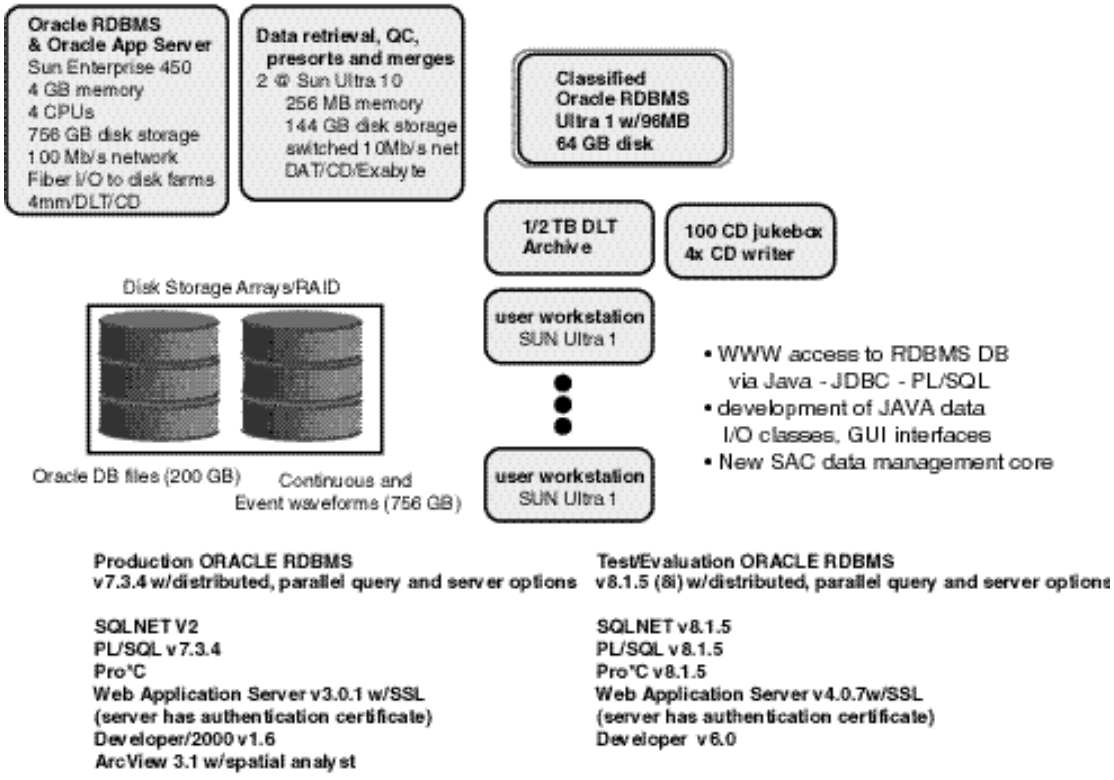


Figure 6: LLNL research database architecture and access tools.

PATH CALIBRATION AND SOURCE CHARACTERIZATION IN AND AROUND INDIA

Chandan K. Saikia*, Lupei Zhu**, Bradley B. Woods* and H-K. Thio*
*URS Greiner and Woodward-Clyde, 566 El Dorado St., Pasadena, CA 91101
**University of Southern California, Earth Science, Los Angeles, CA 90089

Sponsored by Defense Threat Reduction Agency
Contract NO: DSWA-01-98-C-0146

ABSTRACT

Regional path calibration of seismic phases is strongly dependent upon the accuracy of hypocentral locations of seismic events. In general, accurate locations and identification of seismic events based on travel time studies require several stations surrounding each event, which is often difficult to achieve especially for events of magnitude M_w 4.5 or less with a very few regional observations. By analyzing seismic events located in central Asia and Tibet, we find that seismic events move significantly away from the EDR or ISC epicentral locations when they are constrained to depths determined by independent means. For the Tibetan experiment, 7 events' locations met the GT10 criteria (Yang and Romney, 1999) and moved from the ISC epicenters significantly, one of them moved by several degrees. Variation from the reference model within the regional distance also adds to these mislocations. Small earthquakes are plentiful in the Indian sub-continent including its neighboring countries, thus rendering seismic monitoring of the region difficult. To this end, we have made literature survey of available crustal structures and developed models which produce remarkable agreement for events recorded at Hyderabad (HYB) to distances of up to 12°. The model consists of two crustal layers with a P_n velocity of 8.0 km/sec. This model produces detailed features observed in regional waveforms from events occurring in the Pokhran test site, central India and Koyna regions. We have also developed a velocity profile from the NW India to NIL using regional waveforms recorded at HYB and NIL from an earthquake that occurred near the Pokhran test site on April 4, 1995. From the teleseismic depth phase (pP) analysis, we estimated the depth of this event at 15 km, shallower than the 18.7 and 21 km depths reported in the REB and PDE bulletins respectively. We used regional seismograms recorded at HYB to determine its focal mechanism constraining its depth to the teleseismic estimate. Using this focal mechanism and event depth, we then calibrated path towards NIL. This preliminary crustal model from the NW India to NIL consists of four crustal layers; the upper most layer has a thickness of 7 km with velocity relatively lower than the Indian shield region. It also includes a gradient in the upper mantle which helps to account for the strong P_n waves recorded at NIL. The model produces travel times for P, S, Rayleigh and Love waves, including the dispersion recorded in the Rayleigh waves. This model is then used to synthesize explosion seismograms for estimating yield. Knowing better locations and depths of large earthquakes from this area can be useful as they can later be used to calibrate upper-mantle paths towards the NW India and Pakistan. In general, we found that the depths of the events are shallower than the depths reported in the monthly PDE/ISC bulletins and that the CMT solutions are not necessarily optimal in their depth estimates.

Key Words: Regional Wave Propagation, Pokhran Test Site, Tibetan Plateau, GT10, ISC/REB Bulletin

Objectives: The principal objective of this paper is to present results of our on-going study on the path calibration for the entire Indian subcontinent to provide model-based P-wave travel times in the region. To accomplish this goal, it is necessary to establish a catalog of earthquakes with quantitative estimates of uncertainties in their ground truth locations. In general, nuclear explosions (when announced) and quarry blasts provide the best GT0 and GT2 locations respectively. It is, however, difficult to ascertain uncertainties in ground truth locations for earthquakes, especially at low magnitude ($M_w < 4.5$). For the majority of low magnitude earthquakes, depths are often not constrained to their true depths and events are poorly located due to a poor azimuthal coverage by recording stations. An objective of this paper is to demonstrate the effects of errors in depth on the uncertainties of ground truth epicentral locations of earthquakes in various parts of the world, particularly for earthquakes in the neighboring Tibetan Plateau. We shall also summarize briefly crustal wave guides developed in various parts of the Indian subcontinent by local scientists and present an initial map showing the P_g velocity variation and thicknesses of the Moho discontinuity. So far, we have successfully developed crustal structure which can produce remarkable agreement for events recorded at Hyderabad (HYB) to distance of 12° covering the central India and Koyna regions. This model for the Peninsular India was also modified to fit detailed features observed in regional waveforms from events occurring in the Pokhran test site. Results from these preliminary studies are included in this report.

Research Issues: Unlike the former Soviet Union and the United States of America where calibration shots are plentiful and events are available to a GT of 0 to 2 km accuracy, there are a few data in our study region with similar precision except for the recent nuclear explosions in India and Pakistan in 1998 and in India in 1974. In general, establishing ground truth epicentral locations for earthquakes is difficult because the regionally varying crustal structure introduces errors in the reference earth model which together with the mis-identification of seismic phases shift the events from their true locations and depths. To correctly assign ground truth uncertainty on events, especially those of the magnitude (M_w) below 5 which are also recorded by a very few teleseismic stations, it is first necessary to establish the consistencies in events declared to have GTx (where x is accuracy in km) accuracy based on the criteria described at the pIDC (Yang and Romney 1999). It must be determined when an event ($M_w \leq 5$) should be located using either the regionalized model or the iaspei91.

While for the large events located using teleseismic data, the error in depth causes only a trade-off in the origin time (Zhao and Helmberger, 1991), the small events appear to move significantly away from the ISC locations when they are located after establishing their depths and regional models. Thus, knowing the depth well is important in establishing the ground truth locations. Mislocation of depths for seismic events have been encountered in many regions of the world, for example in central Asia (Woods et al., 1998), in the Hindu-Kush (Zhao and Helmberger, 1991; Saikia et al., 1996; Zhu et al., 1997), Egypt and the Western Mediterranean (Thio et al., 1999), and in northeast India (Saikia, Zhu and Helmberger, 1997). In the following paragraphs, we cite further analysis of results from various studies illustrating that depths for small events need to be determined before they are located to assign any ground truth accuracy.

Research Accomplished

Crust-Mantle Structure of the Indian Peninsula

We are continuing our literature survey of available crustal models published by various in-country scientists in India (Gabriel and Kuo, 1966; Kaila *et al.*, 1968, 1987; Bhattacharya, 1971; 1981; Dube *et al.*, 1973; Dube and Bhayana, 1974 and others) in various parts of the Indian Peninsula. These studies are based on the travel times of Pg, P* and Pn waves observed from shallow earthquakes with epicenters in Himalaya, analysis of dispersion in surface waves, and deep seismic sounding (DSS) data. We are in the process of scanning these various profiles and making them available in the geophysical database. These studies suggest that the thickness of the Moho varies between 40 and 45 km. The thickness of the upper crust has a thickness of about 15 km (P-wave velocity reaching 6.3 km/sec) and the lower crust

often consisting of two layers of velocities 6.6-6.9 km/s and 7.3-7.4 km/s. There are several other studies extending towards the northeast India beyond the Indian Peninsula towards the east (Kaila *et al.*, 1992; Kayal and Zhao, 1998; Mukhopadhyay and Krishna, 1991; Mukhopadhyay *et* al., 1997; Singh, 1987). These studies also include refraction and wide-angle reflection data with profiles as long as 140 to 180 km. The path to the east includes the west Bengal basin, which starts west of Bangladesh and extends to northeast India. Within the basin structure, the refraction and wide-angle reflection data indicate presence of prominent refractors (velocities 1.7-2.1 km/s, 2.7-3.2 km/s, 3.7-4.2 km/s and 4.6-5.3 km/s) overlying the crystalline basement with a velocity of 5.8-6.2 km/s. In general, depth to the basement increases from west to east with a maximum depth of around 10 to 11 km at the extreme parts of the east-west trending two profiles where data were collected (Kaila *et al.*, 1992). The depth of the Moho discontinuity is reported to be highly variable, say 36 to 26 km along one profile and 32 to 34 km along the other profile. The region where these profiles were run is highly seismic and earthquakes occurring in this region will have variations in the travel times due to this type of variation in the crustal structure. Figure 1 shows a preliminary summary of these studies which show the various estimates of Pn velocities and the thickness of the Moho interface across the Indian Peninsula.

Epicentral Locations for Small Events (Mw<5) and Depth Accuracy:

Central Asia: Figure 2 shows locations of 26 events for which depths were estimated using separate modeling techniques, such as matching of the surface-wave amplitude, modeling of P_{nl} and surface-wave seismograms using regionalized velocity models, and modeling of teleseismic depth phases (pP and sP) using a crustal model appropriate for the source region. Figure 3a shows a comparison of depths of these events determined from the independent modeling of the P_{nl} and teleseismic waves (Woods et al., 1998), including the depths determined from a surface wave study (Patton, 1998). Dr. A. Velasco of Los Alamos National Laboratory relocated 17 of these events using regional and teleseismic travel times and a regional crustal model that was based on Dr. Walter Mooney's model of central Asia for both fixed (those obtained in our modeling studies) and free depths. Figure 3b shows relative shifts (Δr) of these new relocated epicenters from the EDR locations. For some events, for example events 7 and 16, moved away significantly from the EDR locations for the free depths.

Tibet: Figure 4 shows locations of 49 Tibetan earthquakes, relocated using an effective method developed by Zhu (1998) which does not require an *apriori* velocity model. It starts with a one-layer crustal model and first P arrival timings recorded by stations of a local network like those deployed during the PASSCAL experiments. Figure 5a shows hand-picked timings used for P and S waves plotted as a function of epicentral distances based on the ISC source locations and origin times. This data set consists of 363 P picks and 267 S picks. The large scatter is mostly attributable to the unreliable locations and origin times of the ISC catalog. The scheme used to relocate these events is based an optimization problem in which the best location is obtained by iteratively minimizing the root-mean-squared value of the travel-time residuals (Zhu, 1998). The crustal model is updated and events are relocated until a global minimum is found. Figure 5b shows the travel times after relocation. Of the 49 relocated events, 7 events (squares, Table 1) satisfy the criteria for GT10 events (Yang and Romney, 1999) i.e., they have been recorded by at least 5 stations (actually > 5) within 3° and the largest azimuthal gaps between the stations within 5° is less than 180°. In Figure 6, we compare depths of the ISC and relocated depths for the events and shifts in their epicentral locations relative to the ISC locations as a function of M_w showing that the events indeed moved by about 33 km. Two events which were poorly located in the ISC bulletin due to poor signal-to-noise ratio moved by more than 300 km from the ISC locations. Of these two, one qualified as a GT10 event and moved by about 650 km. ISC located this event using 8 stations of which 5 stations were within an array located at 9.5-10.5° away all lying within an azimuthal aperture of 2°. Actually the final iteration moved the event from the location 31.929°N lat and 94.465°E lon to 27.4°N lat and 97.0°E lon, reducing the RMS from 0.98s to 0.81s. Adding the regional stations not only increased the number of the stations, they also improved the azimuthal coverage. For 5 of the GT10 events, the ISC used picks from many stations distance ranging from 5° to all ranges. Although these stations provided good azimuthal coverage, relocations using augmented regional travel time picks and regionalized

model moved these events up to 20 km from the ISC locations.

Regional Seismogram Modeling

Central India: Our previous report (Saikia et al., 1998) discusses modeling of regional seismograms recorded at HYB from the Koyna region in south western India. To further calibrate the model towards northern India, we applied regional modeling approach to the HYB waveform from an earthquake (M_w 5.8, May 21, 1997) in central India. This event was recorded at many teleseismic stations. Before the path calibration, we have successfully modeled the teleseismic vertical and radial P waves using the inversion to retrieve source mechanism including the depth of this event (Figure 7). We also used this depth to invert the regional broadband seismograms at HYB located at a distance of 645 km (Figure 8, shows synthetics from both regional and teleseismic focal mechanism). Both solutions fit the data, shown in the upper seismograms, well, especially the S and surface waves. The regional solution produces a better fit to the P_{nl} waves. The calibrated model produces travel times of P, Rayleigh and Love waves consistent with the recorded seismograms.

Northwest India: We applied the same technique to model the source parameters of an earthquake which occurred on April 4, 1995 (M_w 4.3) near the Pokhran test site. Although located 100 km from the test site, this event is critical as it was recorded at both NIL in Pakistan and HYB. This is a small earthquake and its teleseismic depth phases could only be seen after processing the broadband seismograms to the equivalent WWSSN short-period records (Figure 9). In this way, we identified four teleseismic stations with observable depth phases (pP) which yielded a depth of 15 km, shallower than the ISC depth by 5 km and REB depth by 3 km. Using this depth, we inverted long-period HYB records (the only seismograms available) to estimate its focal mechanism and seismic moment (Figure 10a). As in the case of May 21 event, we could make the P weak onset times of Rayleigh and Love wave consistent with observations.

Pokhran to NIL: The next step was to model the regional seismograms recorded at NIL. Unlike the explosion data at NIL, this earthquake produced surface wave dispersion and some aspects of these surface waves motivated us to adjust the central India crustal model. The model that we have developed has a 7 km thick layer with lower surface wave velocities for P and S waves. A similar model was also determined at LLNL (Dr. W. R. Walter, personal communication) which has a thickness of about 4 km. Our model predicts recorded seismograms and travel times of P waves within a second (Figure 10b). This crustal model was used to generate the surface waves recorded at NIL from the Indian explosion with its source represented by the displacement potential (Figure 11).

Conclusions and Recommendations: We have presented results illustrating that accurate depths are necessary for establishing ground truth locations of small magnitude earthquakes (M_w<5). A review of many studies demonstrates that errors in depth primarily trade off with the origin times for large events (M_w > 5.5) which yield many teleseismic travel time picks for locations. Variations in the reference crustal model and errors in identification of depth phases result in mislocations of the small magnitude earthquakes presented in various catalogs. Simultaneous inversion of regional crustal structure and travel-time picks of P and S waves of many earthquakes helps to yield good quality locations for earthquakes located within some local network. The locations and crustal structure can be optimized provided that depths for the chosen earthquakes are known by some other independent means before they are used in the analysis. Data collected from PASSCAL experiments of similar arrays can provide the necessary data to establish catalog of high-grade ground truth locations for earthquakes in various regions as we have shown in this report for the Tibet Plateau. Presently, there is no PASSCAL data available from within the Indian sub-continent. So we have calibrated crustal model using earthquakes which are large in magnitude for which the ISC epicentral locations are likely to be adequate. These models may still suffer from some minimal error in the travel times because of the error in depths. The depth we determined fro the earthquake of May 21, 1997 is only 1 km different than the ISC depth and so error in the travel time due to the depth error is expected to be negligible. The earthquake of April 4, 1995 is several km off the ISC depth and it is possible that the travel time of the P waves towards NIL is off by about a second. Our

recommendation for future study in this area is to archive teleseismic broadband and short-period array data from smaller earthquakes (M_w<5) and systemically analyze short-period data for the depth phases so that they can be used in conjunction with establishing the ground truth locations.

References

Bhattacharya, S. N. (1974). The crust-mantle structure of the Indian Peninsula from surface wave dispersion, Geophys. J. R. Astr. Soc., 36, 273-283.

Bhattacharya, S. N. (1981). Observation and inversion of surface wave group velocities across central India, Bull. Seis. Soc. Am., 71, 1489-1501.

Dube, R. K., J. C. Bhayan, and H. M. Cahudhury (1973). Crustal structure of the Peninsula India, Pure and Applied Geophys. 109, 1718-1727.

Dube, R. K. and J. C. Bhayana (1974). Crustal structure in the Gangetic Plains of the Indian subcontinent from body waves, Bull. Seis. Soc. Am., 64, 571-579.

Gabriel, V. G. and J. T. Toro (1966). High Rayleigh wave phase velocities for the New Delhi, India-Lahore, Pakistant profile, Bull. Seis. Soc. Am., 56, 1137-1145.

Kaila, K. L., P. R. Reddy and H. Narain (1968). Crustal structure in the Himalyan foothills area of north India, from P wave data of shallow earthquakes, Bull. Seis. Soc. Am., 58, 597-612.

Kaila, K. L., P. R. K. Murty, D. M. Mall, M. M. Dixit and D. Sarkar (1987). Deep seismic soundings along Hirapur-Mandla profile, central India, Geophys. J. R. Astr. Soc., 89, 399-404.

Kaila, K. L., P. R. Reddy, D. M. Mall, N. Venkateswarlu, V. G. Krishna, and A.S.S.S.R.S. Prasad (1992) Crustal structure of the west Bengal basin, India from deep seismic sounding investigations, Geophys. J. Int., 111, 46-66.

Kayal, J. R. and D. Zhao (1998). Three-dimensional seismic structure beneath the Shillonh Plateau and Assam Velley, northeast India, Bull. Seis. Soc. Am., 88, 667-676.

Mukhopadhyay, M. and M. R. Krishna (1991). Gravity field and deep structure of the Bengal fan amd its surrounding continental margins, northeast indian Ocean, Tectonophysics, 186, 365-386.

Mukhopadhyay, M., R. Chander and K. N. Khattri (1997). Crustal properties in the epicentral tract of the Great 1897 Assam earthquake, northeastern India, Tectonophysics, 283, 311-330.

Patton, H. J. (1980). Bias in the CMT moment tensor for central Asian earthquakes: evidence from regional data, J. Geophys. Res. (Accepted).

Saikia, C. K., L. Zhu and D. V. Helmberger (1997). Relevance of broadband instruments in nirtheast India for seismic hazard mitigation, Symposium on the Great Shillong Earthq, held Nov 18, 1997 in Shillong, India.

Saikia, C. K., B. B. Woods, H-K. Thio, L. Zhu and D. V. Helmberger (1996). Path callibration, source estimation and regional discrimination for Middle East: An application to the Hindu-Kush Region, PL-TR-96-2069, Scientific Report #1, Phillips Lab, MA 130p.

Singh, D. D. (1987). Crust and upper-mantle velocity structure beneath north and central India from phase and group velocity of Rayleigh and Love waves, Tectonophysics, 139, 187-203.

Thio, H-K., X. Song, C. K. Saikia, D. V. Helmberger and B. B. Woods (1999) Seismic source and structure in the western Mediterranean using a sparse broadband network, J. Geophys. Res., 104, B1, 845-861.

Woods, B. B., C. K. Saikia and H-K. Thio (1998). Focal depths and source parameters for earthquakes in northwest China, Tech. Report to Los Alamos National Laboratory.

Yang, Xiaoping and C. Romney (1999). pIDC ground truth events (GT) database, CMR Technical Report, CMR-99/15.

Zhao, L. S and D. V. Helmberger (1991). Geophysical implications from relocations of Tibetan earthquakes: Hot lithosphere, Geophys. Res. Lett., 18, 2205-2208.

Zhu, L., D. V. Helmberger, C. K. Saikia and B. B. Woods (1997). Regional waveform calibration in the Pamir Hindu-Kush region, J. Geophys. Res., 102, 22,799-22,813.

Zhu, L. (1998). Nbroadband waveform modeling and its application to the lithospheric structure of the Tibetan Plateau, Ph.D. Thesis, California Institute of Technology, 141p

Table 1. GT10 locations for 7 earthquakes in Tibetan Plateau
(satisfy criteria of pIDC, Yang and Romney, 1999)

Date	OT(sec) h:m:s	latitude °N	longitude °E	depth h_r km	M_w	m_b	ΔR km	ΔH km isc(h)-h_r
11/19/91	01:04:18.0	32.54	93.82	10.0	3.9	4.2	16.9	23.0
11/26/91	21:16:00.0	34.10	94.22	10.0	4.3	4.2	3.9	22.0
12/02/91	19:45:38.1	32.16	94.53	10.0	4.0	4.2	20.8	47.0
01/08/92	17:41:39.9	30.06	92.30	10.0	3.8	3.9	21.1	14.0
01/23/92	10:26:25.8	34.49	93.18	5.0	4.1	4.3	6.9	4.0
02/03/92	15:44:22.6	34.46	93.20	10.0	4.3	4.5	5.7	0.0
03/30/92	18:29:47.7	32.60	93.79	10.0	3.7	3.9	653.7	13.0



Figure 1. Map showing the variation of the Pn velocities and Moho thickness over the entire Indian subcontinent, including parts of Pakistan, Tibet, and Bangladesh.

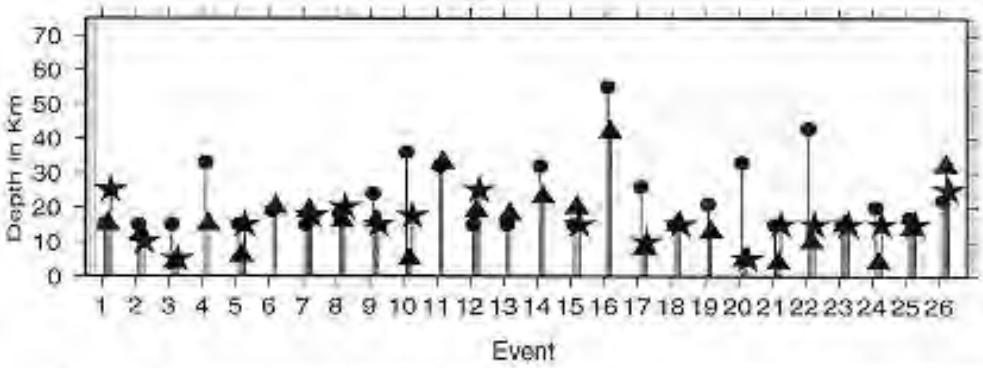


Figure 2. Comparison of depths determined by various methods: surface-waves (Patton, 1998), teleseismic (star) and broadband (triangle, Woods et al., 1998)

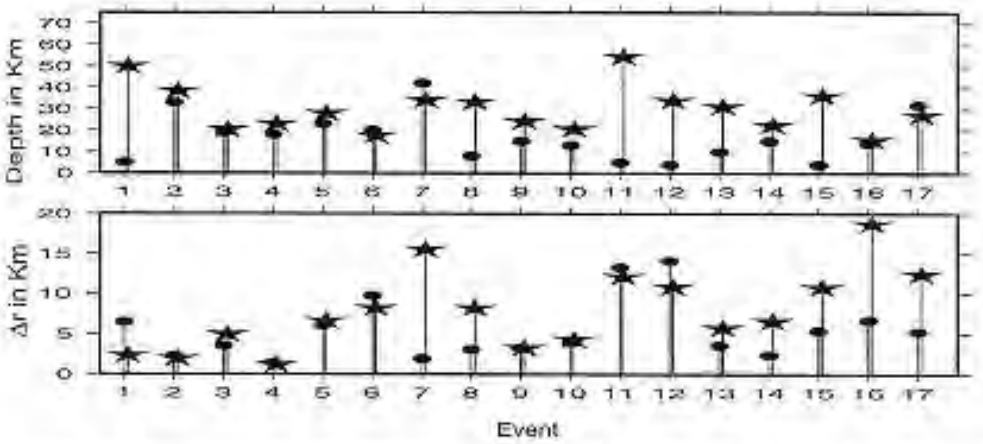


Figure 3. Top panels shows comparison between the broadband modeling depths and the depths determined allowing depth to remain free in the location. Bottom panel shows movement of the epicenters for both fixed and free depths from the EDR locations.

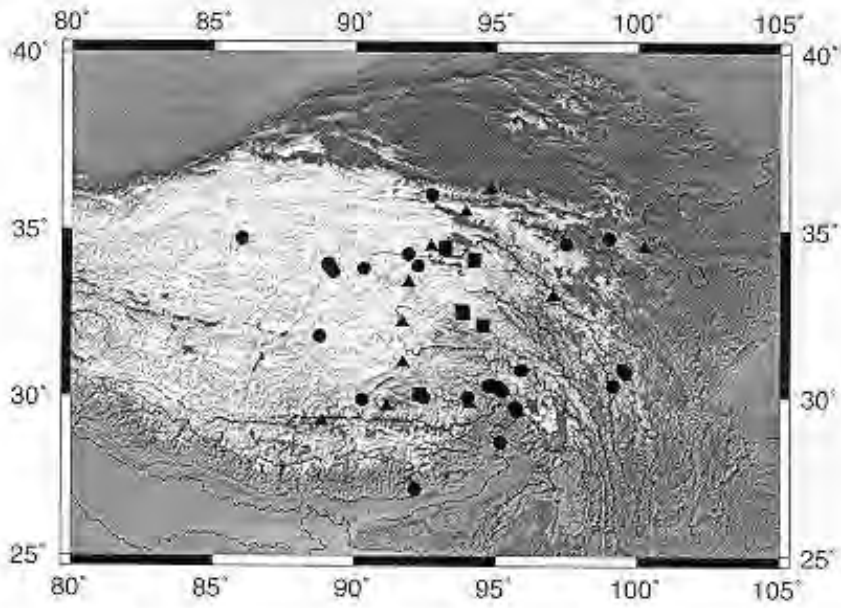


Figure 4. Map of the Tibetan Plateau showing the locations of stations (triangles) deployed during a PASSCAL experiment in 1991. Also shown are the relocated events (circles) and locations of seven GT10 events (squares).

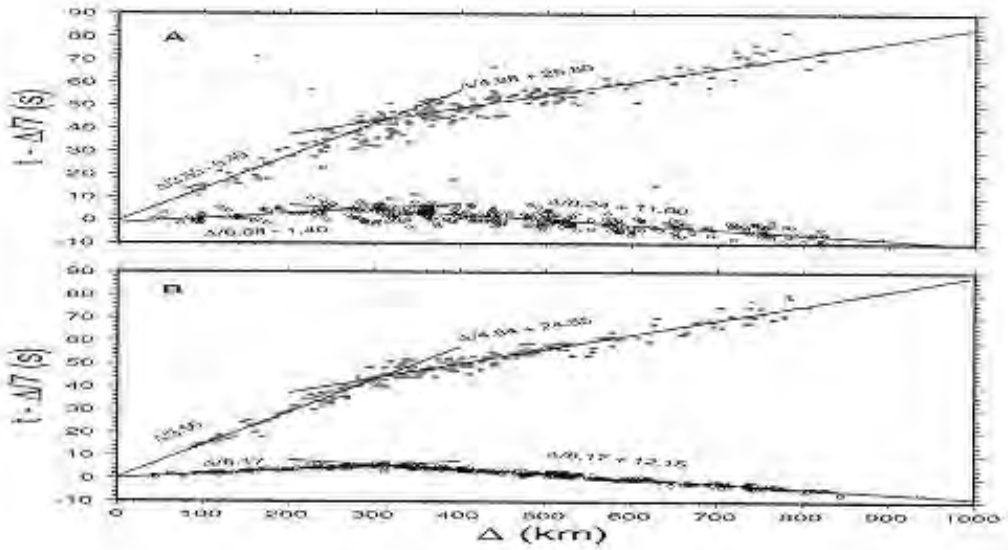


Figure 5A. Shows first P (open circles) and S (gray dots) arrival times as a function of epicentral distance using the ISC source locations and origin times. (B) shows travel times after relocations. The velocities of Pn, Pg, Sn and Sg are presented from the relocation study next to their branches (taken from Zhu, 1998). .

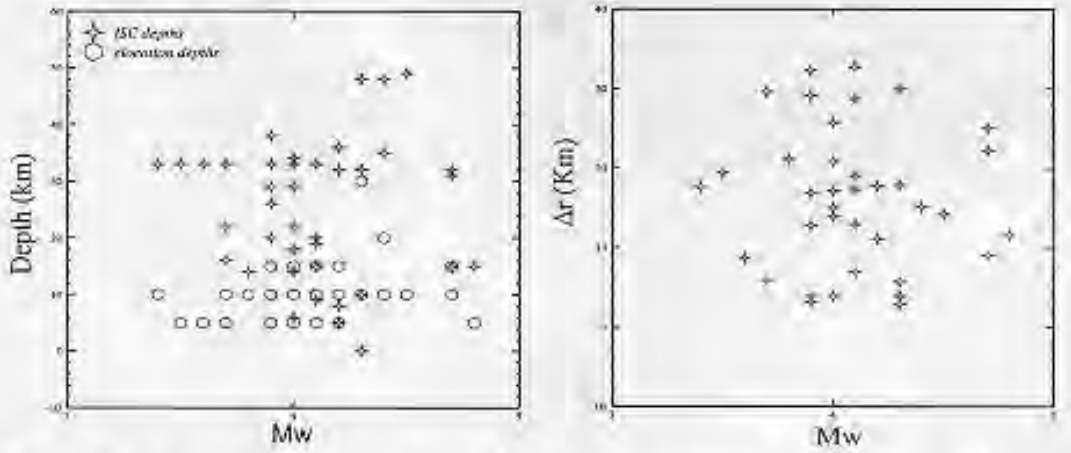


Figure 6. Left panel shows comparison of depths after relocations (open circles) and those reported in the ISC catalog. The majority of events have moved to shallow depths. Right panel shows the relative movement of these events from the ISC's epicentral locations (both panels use data presented in Tables 3.2 and 3.4 given in Zhu (1998).

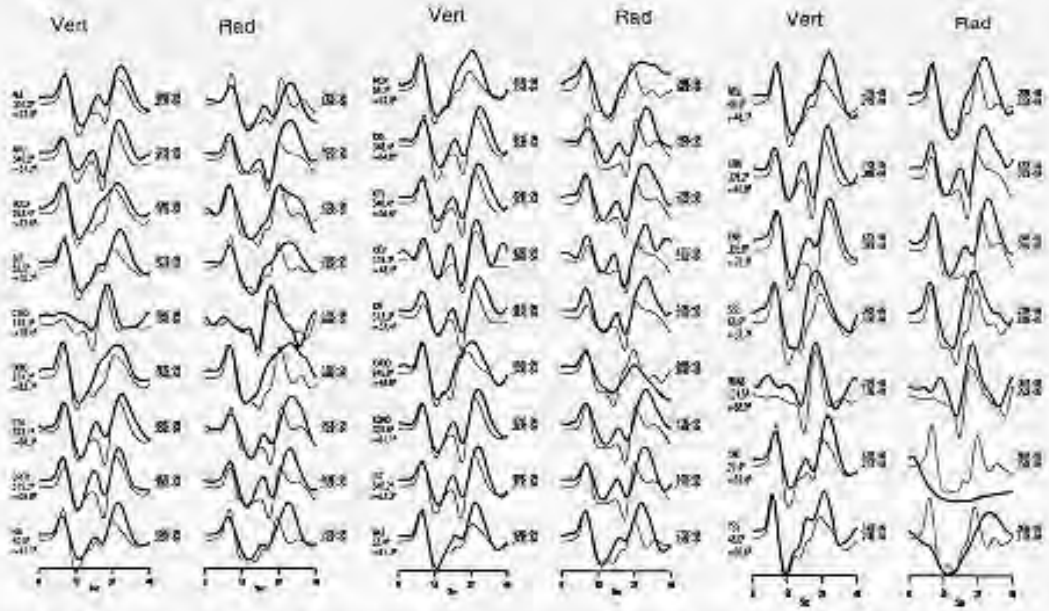


Figure 7. Comparison between data and synthetic seismograms using focal mechanism solution obtained using grid-search technique and both vertical and radial components. The thick waveforms are the recorded data and those in thin lines are synthetics computed using Haskell propagator matrices. We used the same receiver crust for all 27 stations. The peak amplitude of the data should be multiplied by a factor of 100. Station name, azimuth and distance in degrees are printed to the left of the vertical seismograms.

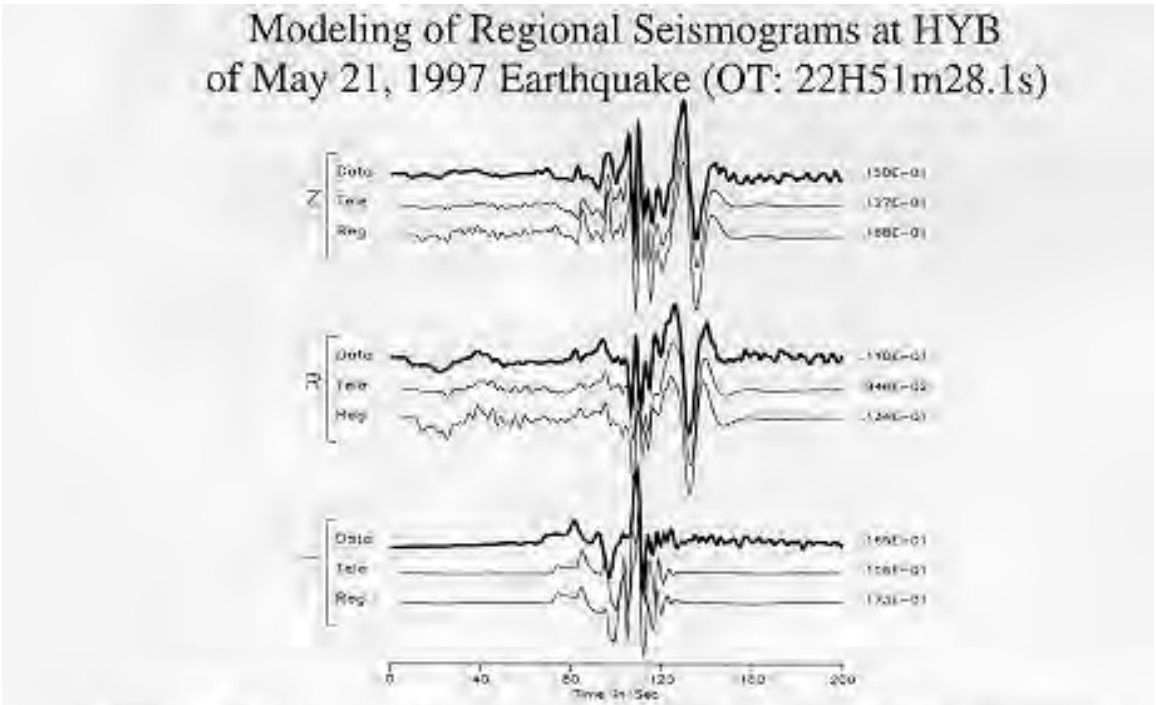


Figure 8. Comparison of data vs synthetic seismograms computed for the teleseismic and regional focal mechsnism. A seismic moment of 5.88x10**24 dyne-cm (Mw=5.9) and depth of 35 km were used. Note the agreement in peak amplitudes,

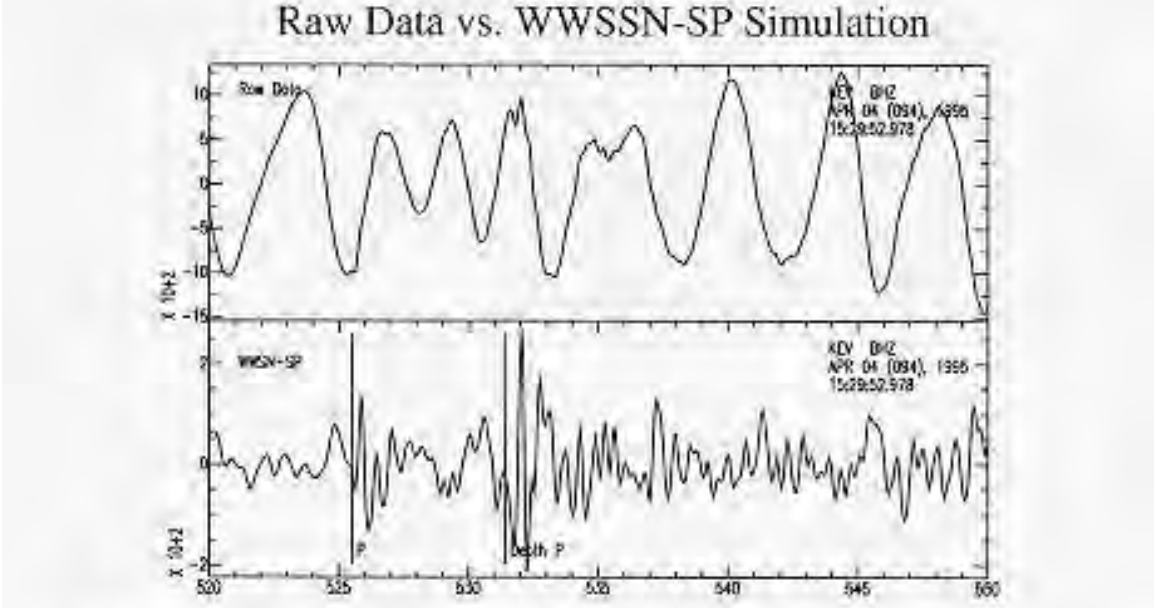


Figure 9. The upper seismogram is the recorded broadband waveform at KEV from the April 4, 1995 earthquake (Mw 4.3) near Pokhran test site. The bottom waveform is a simulation of raw data after convolving with a Wood-Anderson seismogram. No the depth phase relative to P onset.

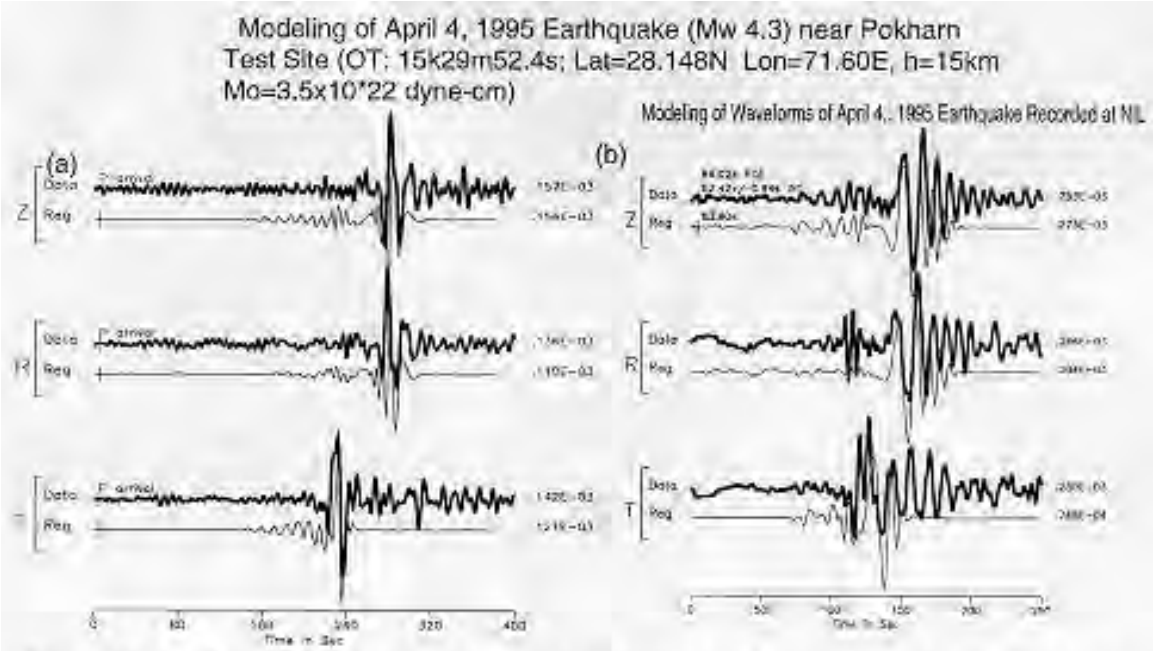


Figure 10. (a) Comparison between data and synthetic waveforms recorded at HYB station. Focal mechanism was obtained using grid-search technique using F-K green's functions computed at a depth of 15 km obtained by modeling depth phases shown in Figure 10. The recorded seismograms are shown by thick lines. (b) Modeling of data at NIL. Crustal model was developed from HYB model to produce dispersion observed in recorded data.

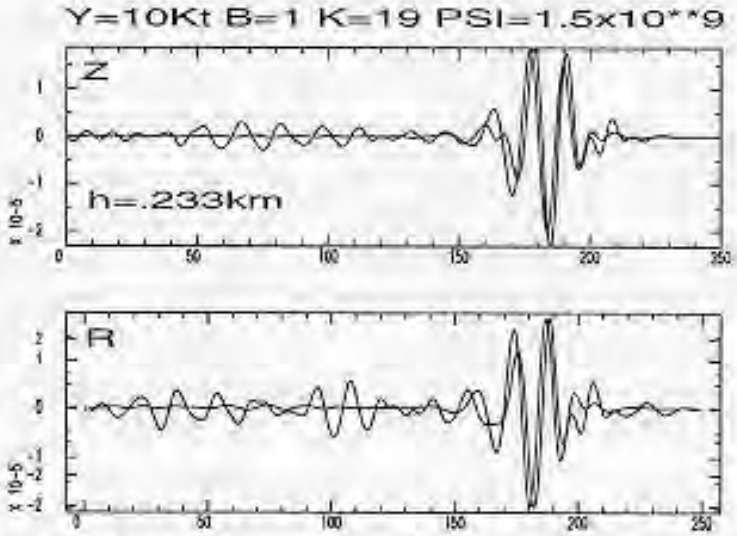


Figure 11. Modeling of Indian nuclear explosion data using the crustal model slightly modified from HYB. The NIL model developed in Figure 11b produces additional dispersion in the surface waves. The top layer is about 4 km thick, 3 km shallower than the model developed for the path in Figure 11b. The source function is represented by a reduced displacement potential and modeling is valid for the 0.05-0.2 Hz frequncy range.

REGIONAL TRAVEL TIME AND AMPLITUDE RATIO CORRECTION SURFACES IN THE MIDDLE EAST

Eric Sandvol, Alex Calvert, David Steer, Dogan Seber,
Khaled AL-Damegh, and Muawia Barazangi
Institute for the Study of the Continents, Cornell University

Sponsored by U. S. Department of Defense
Defense Threat Reduction Agency
Grant No. DSWA 0 1 -97-0006

ABSTRACT

We have begun work on creating travel time correction surfaces in order to significantly improve event locations, and have applied the methodology to two stations in the Middle East. These two stations (BRTR and ABKT in central Turkey and Turkmenistan, respectively) were chosen because our Geographical Information System (GIS) database includes detailed geological and geophysical information for this region. In order to calculate a surface (or volume) of travel time correction values one must first derive a method for calculating the travel time between two arbitrary points in a cross section or volume. A technique was chosen that was originally pioneered by Vidale (1988) and further developed by Matarese (1993) which uses a finite difference technique rather than tracing of rays. This technique essentially propagates wave fronts radially outward from an arbitrarily defined point source location using each timed point as a secondary source for each successive grid point.

This procedure allows us to calculate the travel time of the first arriving P- or S-wave to any point within a given area or volume. This is much more efficient than any two-point ray tracer which would need to propagate rays for each source-station pair in the same volume. Furthermore, the finite difference methodology is able to model diffracted first arrivals that might occur in regions of negative velocity gradients or "shadow" zones; regions in which ray tracers have difficulty in converging to an accurate solution. Our three dimensional regional models were constructed by taking the Moho and basement surfaces and inserting crustal velocities from IASP91 velocity model and Pn velocities from Hearn and Ni (1994) in the upper 220 km of our models. Beneath 220 km we have used the upper mantle model from IASP91. We have found that this 3-D model produces large (up to 4 seconds) travel time corrections with respect to the IASP91 radial velocity model. Such correction surfaces will help reduce systematic location errors at regional distances.

We have also created correction surfaces for selected regional phases in the Middle East. In order to decipher the character and pattern of regional seismic phase propagation we have compiled a large data set of regional and local seismograms recorded in the Middle East. We have mapped zones of blockage, inefficient, and efficient propagation for Lg and Sn. Two tomographic techniques have been developed to objectively determine regions of efficient and inefficient regional phase propagation. Previous observations of regional wave propagation in this region based on data recorded by sparsely distributed stations has indicated that Sn and Lg propagation is very complex; hence the station density from our data set in this region is invaluable. We observe major Lg blockage across the Bitlis suture in southern Turkey and across the Zagros Fold and Thrust Belt, corresponding to the boundary between the Arabian and Eurasian plates. Our observations indicate that in the northern portion of the Arabian plate (south of the Bitlis suture) there is also a zone of inefficient Sn propagation that is not in agreement with prior measurements of Pn velocities. The documented and tomographically mapped lateral variations in attenuation of Sn appear to be related to the complex regional tectonics of the region, and especially to Cenozoic and Holocene volcanism.

Key Words: Travel Time Corrections, Amplitude Ratios, Regional Wave Propagation, Middle East

OBJECTIVE

The CTBT requires the development of credible strategies for effective monitoring, including the ability to detect, locate, discriminate, and characterize any suspect events for any region on earth. In order to accomplish this task necessary models and fundamental observations concerning seismic event location and regional wave propagation are required. Examples of such critical models are travel time models for individual IMS stations that can be used to correct for three-dimensional variations in seismic velocity structure. One dimensional travel time models are not sufficient for regions that contain substantial lateral variations in crustal thickness and uppermost mantle velocity. Furthermore, observations are required for the propagation of several key regional phases in the Middle East and North Africa since current knowledge is insufficient to accurately characterize regional wave propagation in this complex region. New seismological data are required to constrain both travel time and wave propagation models of very low yield events at regional distances. In order to make our final results available to the monitoring community we will include our data and results on the Middle East and North Africa into the Cornell GIS database.

Our objective is to expand the existing geophysical/seismological information and to provide new knowledge of the Middle East and North Africa using data from both short period national networks as well as broadband temporary and global networks. In this paper we give two examples of techniques and observations that are critical to improving seismic event location and discrimination in the Middle East and North Africa.

RESEARCH ACCOMPLISHED

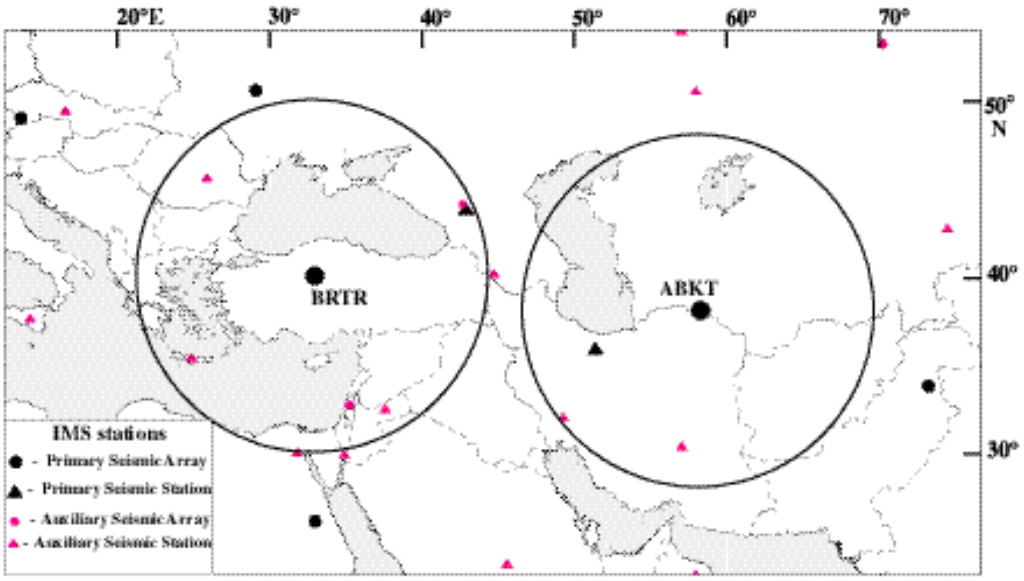


Figure 1. A map showing the two IMS stations used in our travel time correction surface calculations. The circles show the area for which we have calculated a travel time correction surface (radius of 10°).

Travel Time Correction Surfaces

We calculated travel time correction surfaces for two stations in the Middle East (Figure 1). Firbas (1996) demonstrated the importance of using accurate regional models for seismic event location in Europe. We have chosen these two stations such that we have relatively good GIS data coverage that we have collected

in the Middle East. These data sets include depth to basement, depth to Moho, and Pn velocity. All travel time corrections surfaces were calculated relative to IASP91 travel times.

In order to calculate a surface (or volume) of travel time correction values one must first derive a method for calculating the travel time between two arbitrary points in a cross section or volume. We have chosen a technique originally pioneered by John Vidale (Vidale, 1988) which uses a finite difference technique rather than tracing of rays. This technique propagates wave fronts outward from an arbitrarily defined point source location (although in practice it is not difficult to use a linear or planar source rather than a point) using each timed point as a secondary source for each successive grid point. This procedure allows us to calculate the travel time of the first arriving P- or S-wave to any point within a given area or volume. This technique is much more efficient than any two-point raytracer that would need to propagate rays for each source-station pair in the same volume. Furthermore, the finite difference methodology is able to model diffracted first arrivals that might occur in regions of negative velocity gradients; regions in which ray tracers have difficulty in converging to an accurate solution. Such convergence problems are not an issue with the finite difference approach.

Matarese (1993) has extended the original method of Vidale (1988) to include the use of heap-sorting techniques, which speed the travel time calculations up considerably. Also, Matarese (1993) has included stencils in order to find the fast path to each grid point. These modifications have made the finite difference approach even more computationally efficient and accurate when compared to ray tracing algorithms (within 0.1 seconds to 10 degrees). The only computation limitation to this technique is that the entire slowness grid and the travel time grid must be stored in the computer memory cache (RAM) otherwise the problem becomes computationally intractable. This limits the size of the slowness model for which travel time can be computed. However, given the size of RAM memory for state-of-the-art computers (~4 GBytes) travel time calculations for three-dimensional models are feasible.

Due to the limited size of RAM available to us at present we have limited ourselves to 2-D travel time calculations using both Cornell GIS regional velocity models as well as IASP91 velocity models. This allowed us to compare the results of these two different velocity models in 2 dimensions. In order to construct our travel time volumes we have calculated 2-D travel time cross sections for every 1° throughout our 3-D regional velocity model. We then interpolated between all 360° 2-D travel time cross sections to form an evenly spaced travel time volume. The zero depth (or surface) of this volume corresponds, for a particular station, the travel time corrections for surface focus seismic events. In order to obtain the correction surface for different hypocentral depths we simply took a slice at the appropriate depth through our travel time volume.

Our regional velocity models were constructed by taking the IPE Moho and basement surfaces and use the crustal velocities used in the crustal portion of the IASP91 velocity model. We have assigned a linear velocity gradient for the sediments overlying the basement, starting at 4.5 km/s at the surface and reaching 5.8 km/s at the top of the basement. We have assigned the lower crust in our model a 6.5 km/s. We placed the upper crustal and lower crustal velocity contrast (5.8 km/s to 6.5 km/s) half way between the top of the basement and the Moho boundary. We have used the Pn velocities from Hearn and Ni (1994) in the upper 220 km of our models. Beneath 220 km we have used the upper mantle model from IASP91.

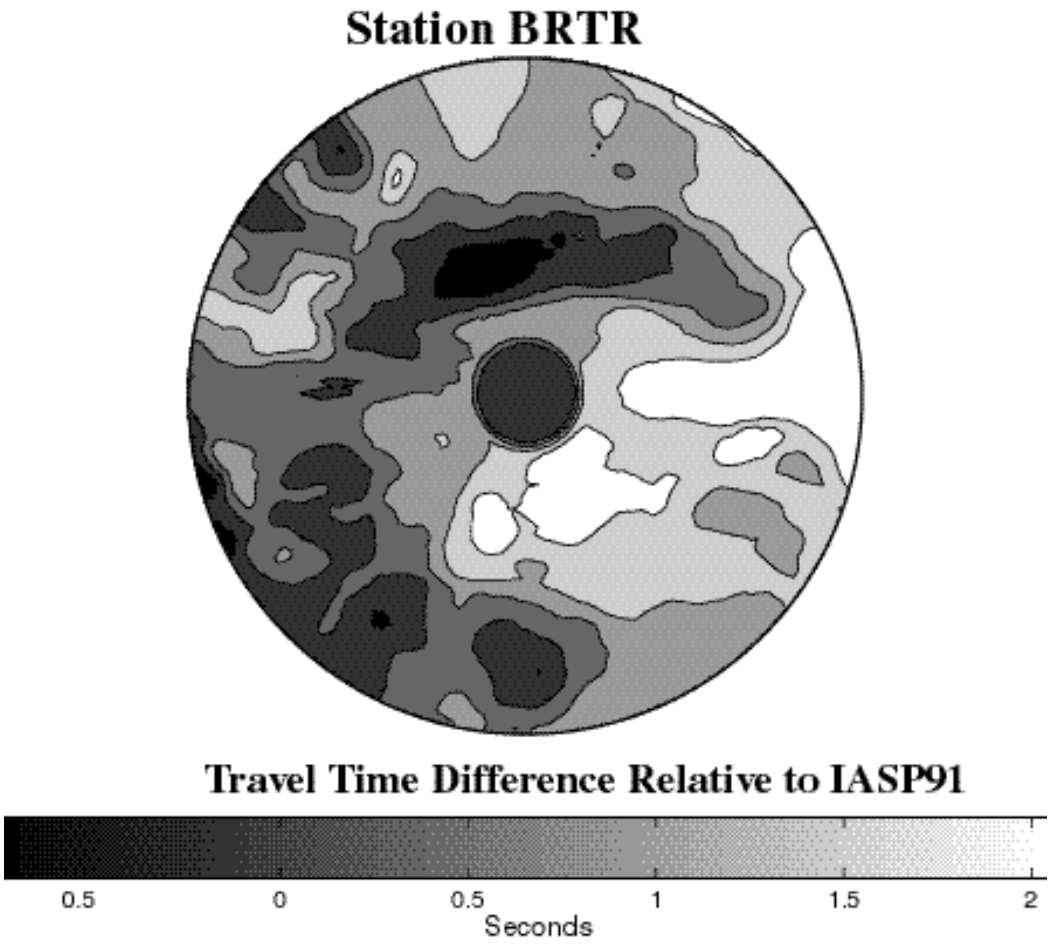


Figure 2. Travel time correction surface for station BRTR in central Turkey for events with no focal depth. The radius of this surface is 10°.

We found significant travel time differences (up to 3 seconds) for calculations using our regional model for the Middle East and IASP91 (Figures 2 and 3). We found the largest discrepancy for paths that crossed regions where crustal thickness exceeded 40 km or where the uppermost mantle was anomalously slow as compared to IASP91 mantle velocities. The largest travel time anomalies for station BRTR occurred in the Anatolian plateau where the uppermost mantle P-velocity is approximately 7.6 km/s (Hearn and Ni, 1994) and IPE Moho depths are between 40 and 50 km. We found that Moho depth was the primary factor responsible for the travel time anomalies for station BRTR (Figure 2). We found similar results for station ABKT in Turkmenistan (Figure 3). Sedimentary basin thickness also affected travel time calculations for station ABKT since the station is located in the southern edge of a large sedimentary basin. At distances larger than 300 km, Moho depth has the most significant impact on the size of the travel time anomalies for this station. Regions where the crust exceeded 60 km in thickness produce very large travel time differences (> 3 seconds) with respect to IASP91.

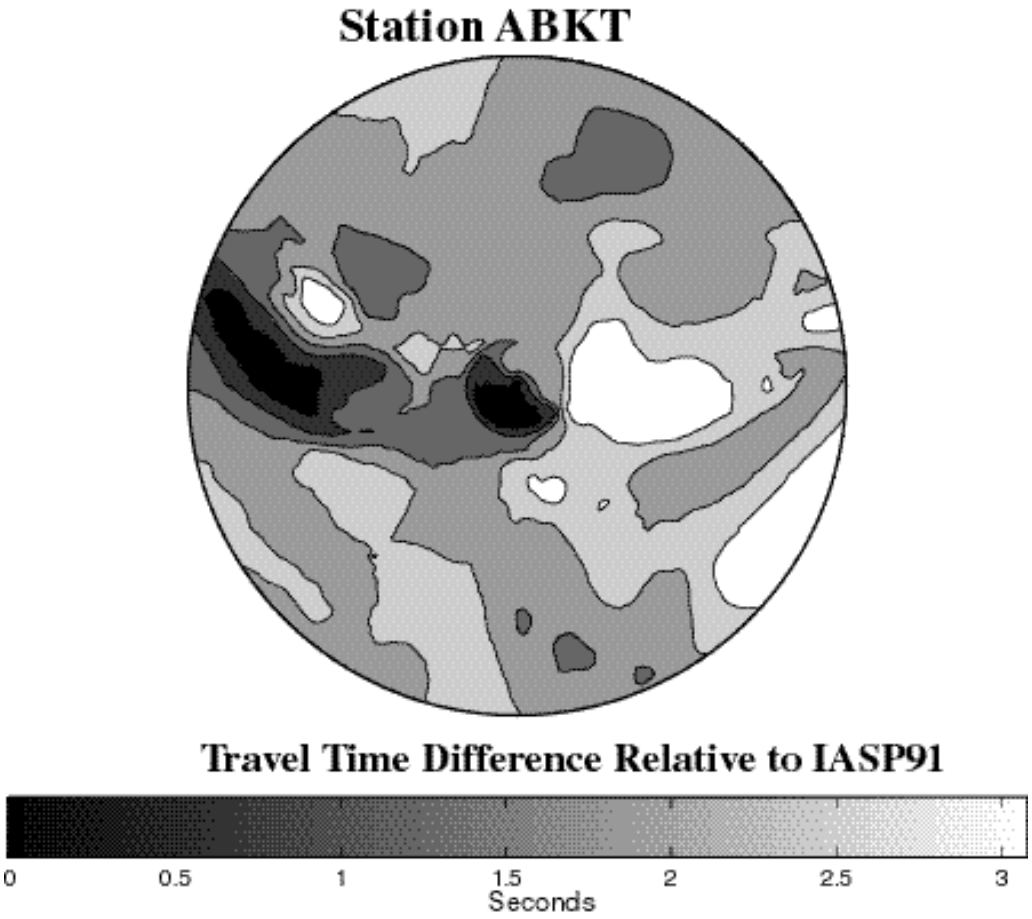


Figure 3. Travel time correction surface for station ABKT in Turkmenistan for events with no focal depth. The radius of this surface is 10°.

Reliable travel time correction surfaces/volumes will be essential for accurately locating small magnitude events, regionally recorded by a sparse network. Travel time corrections will be used to correct for systematic location errors caused by crustal and upper mantle velocity structure. In order to determine accurate travel time correction surfaces reliable regional models must be obtained. Currently in the Middle East there are regions where little is known about the crustal structure, however, we plan over the next years, through collaborative agreements with local scientists, to begin to develop a reliable regional crustal and upper mantle model for the Middle East which will be used to calculate reliable travel time corrections for all IMS stations in the region.

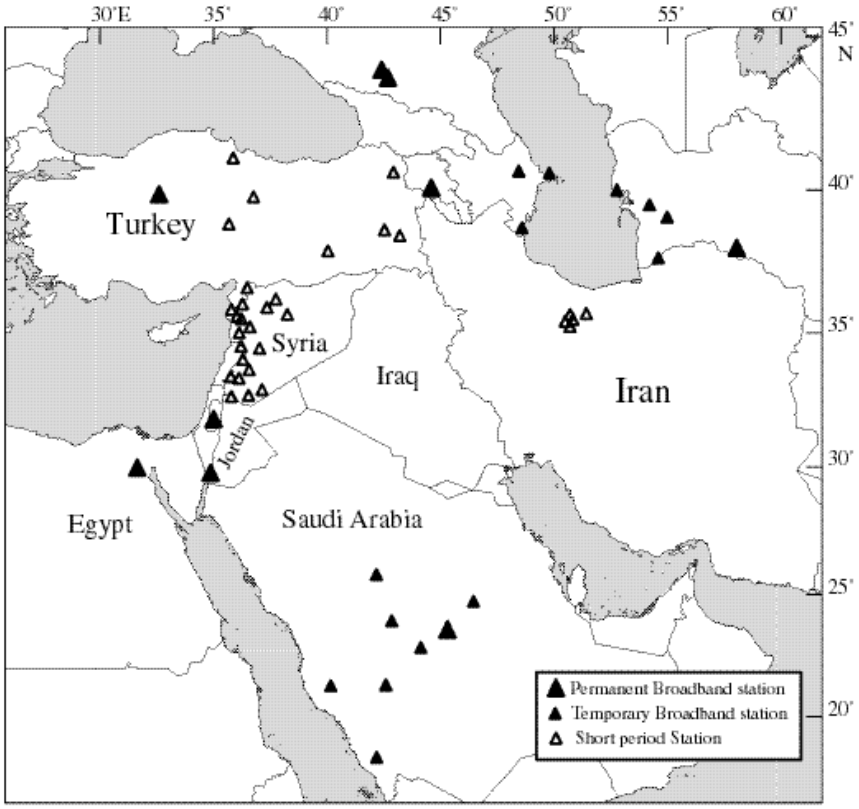


Figure 4. A map of all stations used to characterize Lg and Sn propagation in the Middle East.

Regional Wave Propagation in the Middle East

Observations of regional wave propagation in this region, based on data recorded by sparsely distributed stations have indicated that Sn and Lg propagation is very complex in the Middle East. Therefore, it is necessary to use a large number of seismic stations to accurately characterize regional wave propagation in this region. We have compiled a large data set of regional and local seismograms recorded in the Middle East (Figure 4). This data set is comprised of approximately four years of data from national short period networks in Turkey and Syria, data from temporary arrays in Saudi Arabia and the Caspian Sea region and data from GSN, MEDNET, and GEOFON stations in the Middle East. We have used this data set to decipher the character and pattern of regional seismic wave propagation. We have mapped zones of blockage as well as inefficient and efficient propagation for Lg, Pg, and Sn throughout the Middle East. Two tomographic techniques have been developed to objectively determine regions of lithospheric attenuation in the Middle East. The first technique used Lg/Pg ratios to characterize crustal attenuation as well as to determine the path effects on this commonly used discriminant. The second technique used discrete Sn propagation efficiencies that we defined after examining over 4000 seismograms. This technique allowed us to map the regions of inefficient and efficient Sn propagation in the Middle East.

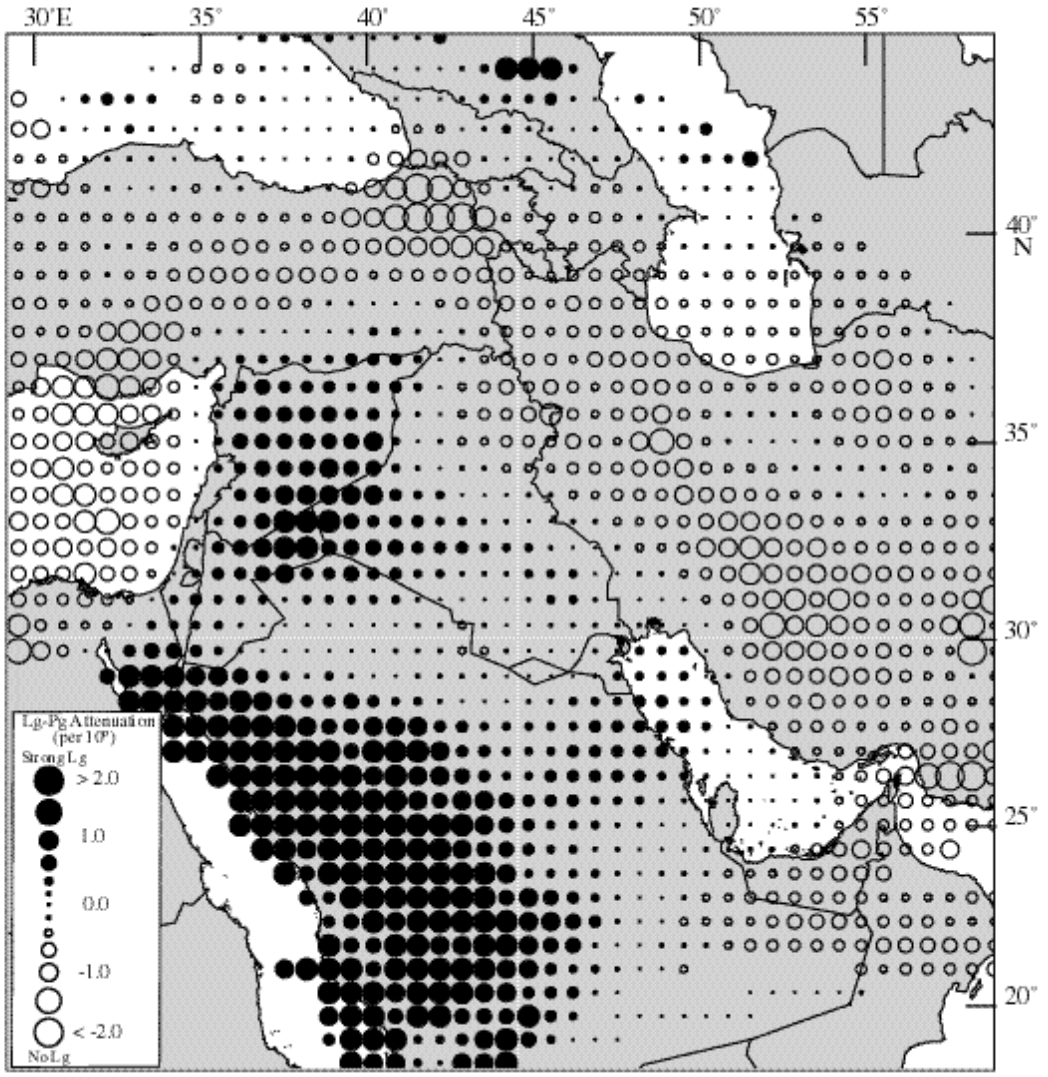
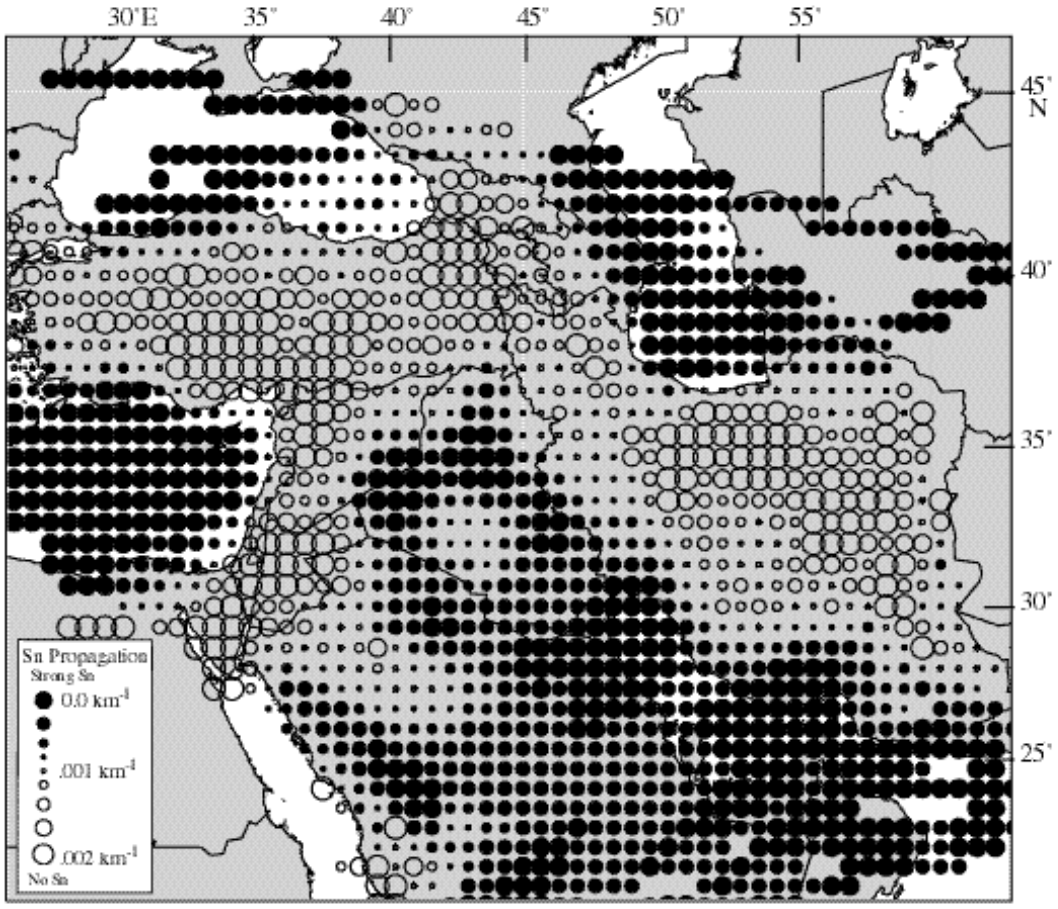


Figure 5. A map showing an image of Lg/Pg ratio tomography in the Middle East. This image is based upon approximately 4400 Lg/Pg waveform observations.

We observe evidence for a significant increase in crustal attenuation across the Bitlis suture and the Zagros fold and thrust belt, corresponding to the boundary between the Arabian and Eurasian plates (Figure 5). Generally Lg was blocked when the ray paths crossed either of these major tectonic boundaries. We also observed Lg blockage in the Mediterranean and southern Caspian Seas. We also observe inefficient Lg propagation, relative to Pg, in the lesser Caucasus and easternmost Anatolia. We also found that within the Middle East, Lg propagation is most efficient in the Arabian Shield and in eastern Jordan and Syria although typically Lg was efficient throughout most of the Arabian Plate. Similarly the Dead Sea fault system had little effect on Lg blockage.

We also observe a zone of inefficient Sn propagation along the Dead Sea fault system (Figure 6) that coincides with low Pn velocities along most of the Dead Sea fault system and with previous observations



of poor Sn propagation in the Gulf of Aqaba (Rodgers et al., 1997). Our observations indicate that in the northern portion of the Arabian plate (south of the

Figure 6. A map showing a tomographic image of Sn propagation efficiency in the Middle East. The model parameters in this tomographic image are the reciprocal of the Sn extinction path length. This image is based on 4200 Sn waveforms.

Bitlis suture) there is also a zone of inefficient Sn propagation that would not have been predicted from prior measurements of Pn velocities. The mapped lateral variations in attenuation of Sn correlate well with the regional tectonics of the region. Regions of Cenozoic and Holocene basaltic volcanism correspond with regions of high Sn attenuation.

CONCLUSIONS AND RECOMMENDATIONS

We found that three-dimensional travel time calculations using a regional velocity model taken from our GIS database in the Middle East produce large variations from the IASP91 travel time tables. These large travel time deviations (as much as 3 seconds) could have very large effects on seismic event location. We also found that in the Middle East crustal thickness is the most important factor in travel time anomalies. Our study of regional wave propagation demonstrates that there are dramatic variations in Lg and Sn propagation in the Middle East. Furthermore using Lg/Pg ratio tomography can, for the most part,

determine the path effects on Lg/Pg ratio calculations and thereby is a method for isolating the source effects on Lg/Pg amplitude ratios.

Our study of travel time correction surfaces for two stations in the Middle East indicate strongly the need to use the best regional models to correct for lateral changes in crustal and upper mantle velocity structure. Also, both of our studies presented in this paper demonstrate that local network data are essential to both calibration and verification of regional travel time models and regional wave propagation models.

We plan to test these models and validate them using very reliable event locations. We will use dense local seismic network locations as well as the GT5 catalog to verify our regional velocity models for each IMS station in the Middle East. Furthermore, we will test and improve our regional models using seismic data we plan to collect to verify the crustal thickness and upper mantle velocity structure in the Middle East.

REFERENCES

Firbas, P., IMS calibration: 3-D travel-time modeling for Europe, Technical Report, CMR-97/02, 1996.

Hearn T. and Ni, J., Pn velocities beneath continental collision zones: The Turkish-Iranian Plateau, Geophys. Int., vol. 117, 273-283, 1994.

Matarese, J., Nonlinear Travel Time Tomography, Ph.D. Thesis, M.I.T, 1993.

Rodgers, A., Ni, J., and Hearn, T., Propagation characteristics of short period Sn and Lg in the Middle East, Bull. Seism. Soc. Amer., vol. 87, 396-413, 1997.

Vidale, J., Finite difference calculations of travel times, Bull. Seism. Soc. Amer., vol. 78, pp. 2062-2076, 1988.

REGIONAL VELOCITY MODELS FOR GERMANY: A CONTRIBUTION TO THE SYSTEMATIC TRAVEL-TIME CALIBRATION OF THE INTERNATIONAL MONITORING SYSTEM

Jörg Schlittenhardt

Federal Institute for Geosciences and Natural Resources (BGR)
Stilleweg 2, 30655 Hannover, Germany

ABSTRACT

The purpose of this investigation was to derive a valid regional traveltime curve to improve seismic event location capability for strong events in Germany within the scope of calibration of the International Monitoring System (IMS) for the verification of the CTBT (Comprehensive Nuclear-Test-Ban Treaty). Onset times from the "Data Catalogues of Earthquakes in the Federal Republic of Germany and Adjacent Areas", published annually by BGR, for seismic phases from 1975–1995 were used to compute 4585 traveltimes for 958 earthquakes and explosions for the stations of the GRSN (German Regional Seismic Network). The advantage of this large data set over data from most active experiments is the unrivaled density and redundancy of the azimuthal coverage with raypaths across Germany. To assure the highest level of precision, only events with independently located epicenters from local networks have been included. The interpretation was carried out by trial-and-error modeling and linear regression of station traveltimes. Four traveltime branches (*Pn*, *Pg*, *Sn, Sg*) are clearly visible in the plot of station traveltimes as a function of distance, despite the large scatter (standard deviation over 2 s for *P* and 3 s for *S*). Other branches, such as *P** (Conrad refracted wave), are not visible. The model obtained by inversion has one layer over a half space. *P*- and *S*-velocities for the layer are 5.9 km/s and 3.5 km/s, respectively. The inferred layer thickness is 30 km, in accordance with the poorly determinable values of intercept time and crossover distance. The sub-Moho *P*- and *S*-velocities are 8.2 km/s and 4.73 km/s, respectively. Tests of the location capability for selected ground truth events (explosions for refraction seismic experiments) in Germany and Poland are presented. The application of the new model distinctly reduces traveltime residuals for the routine determination of epicenters.

Besides inaccurate epicenter parameter values, an azimuthally dependent *Pn* velocity can possibly explain the large scatter of the traveltimes. Due to the abundance of available raypaths, this data set offers a unique opportunity to test models of mantle anisotropy in Central Europe. Subsets are formed of traveltimes for selected pairs of an epicenter and a station in azimuth slices covering all directions. Typically, about 600 raypaths fall into a slice of 30º width. Directions with postulated fast (N30ºE) and slow (N120ºE) sub-Moho velocities found in controlled source experiments (e.g., Enderle et al., 1996) are examined. Although there is a trade-off between source depth and *Pn* velocity, a clear advance of *Pn* arrivals is observed for the fast direction, compared to the traveltimes for the best-fit model. Further results of the *Pn* velocity mapping for different azimuth slices for the region between the Alpine Front in the south and 52ºN will be presented. The study is supplemented with seismic record sections for selected azimuth directions for the magnitude Ml=4.8 rockburst at Teutschenthal near Halle, Germany ("ground truth" event), which was recorded by a number of permanent (GRF/GRSN, GERESS, GOR, LED, SED, etc.) and portable TOR (Teleseismic Tomography TORnquist experiment) digital stations in Germany and adjacent areas.

Key Words: Seismic wave propagation, regional phases, crustal structure, seismic anisotropy, seismic regionalization, IMS, earthquake location, ground truth

OBJECTIVE

The initial motivation for this study came from the GSETT-3 (Group of Scientific Experts Technical Test) experiment of the CD (Conference on Disarmament) in Geneva, where NDC's (National Data Center) were asked to check the location results of the pIDC (prototype International Data Center) for seismic events on their national territory.
The primary objective of this investigation is therefore to derive a valid regional traveltime curve on a large scale to improve seismic event location capability for strong events in Germany within the scope of calibration of the International Monitoring System (IMS) for the verification of the CTBT (Comprehensive Nuclear-Test-Ban Treaty). The derived traveltime curve is intended to be used rather with data from a sparse global network (stations several hundreds of kilometers apart) instead of with data from dense local networks (station spacing tens of kilometers, or less), for which specific models would be needed.

RESEARCH ACCOMPLISHED

The data used in this study stem from the "Data Catalogues of Earthquakes in the Federal Republic of Germany and Adjacent Areas", published annually by BGR (Bundesanstalt für Geowissenschaften und Rohstoffe, (Henger & Leydecker (eds.), 1975)). From this catalogue, onset times for seismic phases from 1975–1995 were used to compute 4585 traveltimes for 958 earthquakes and explosions for the stations of the GRSN (German Regional Seismic Network). To assure the highest level of precision, only events with independently located epicenters from local networks within Germany (University institutes and State Geological Surveys) have been included. The interpretation is carried out by trial-and-error modeling and linear regression of station traveltimes.

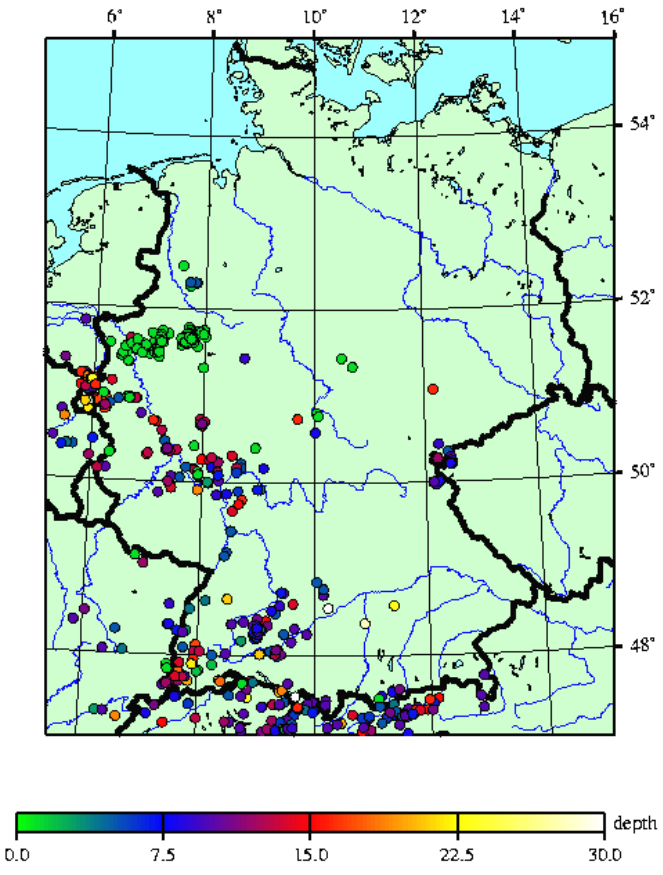


Fig. 1: Map of Germany with the plot of the epicenters of the 958 earthquakes/explosions used in this study. Hypocentral depth is color coded according to the depth scale (km) at the bottom. The seismicity follows essentially the Alpine belt in the south and the north-south trending Rhine Graben. The Swabian

Alb (in the southwest) and the Vogtland area also contribute to the seismicity. Fig. 2 shows a map with a plot of the ray paths from the 958 epicenters to the stations of the GRSN and their predecessor stations.

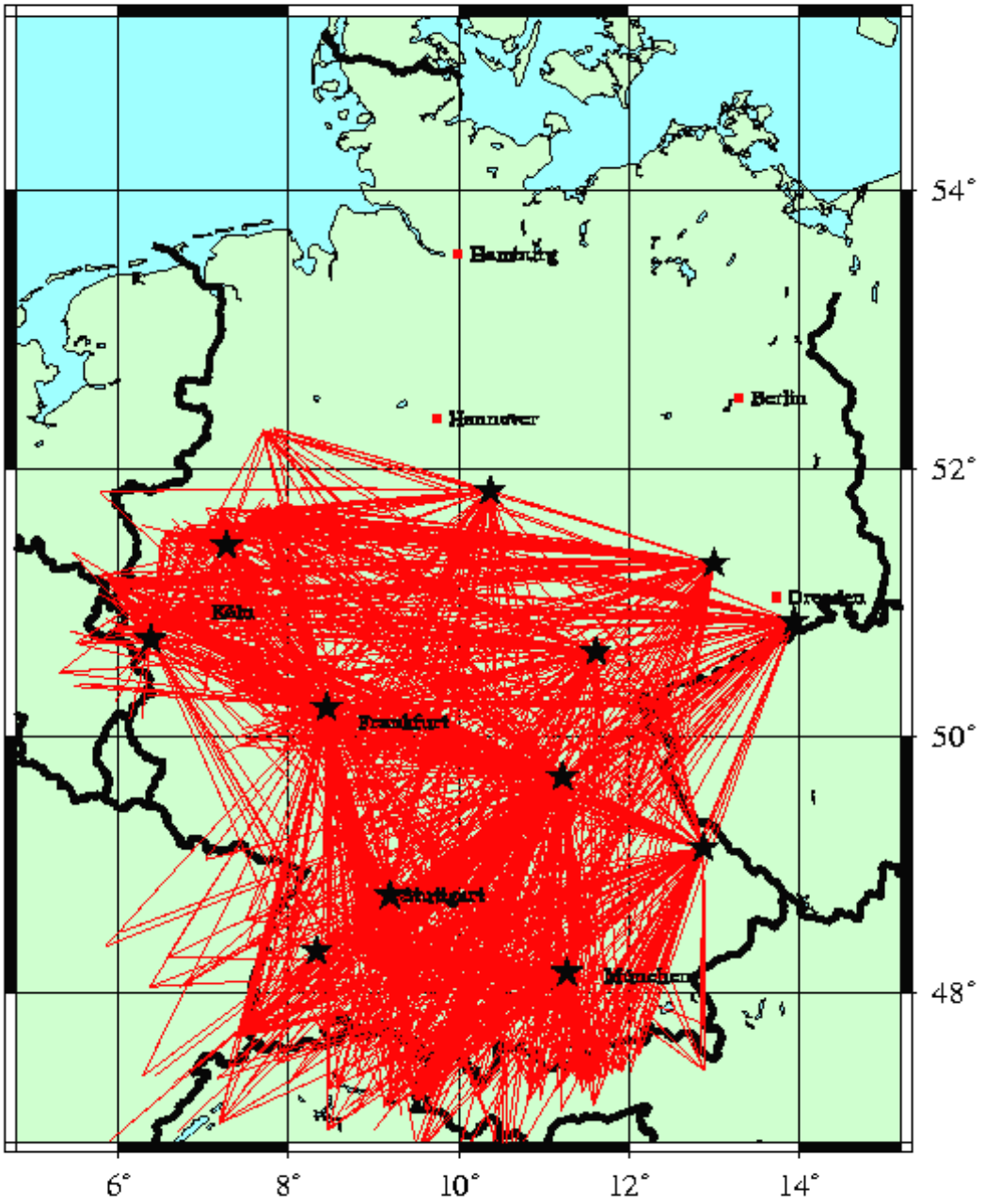


Fig. 2: Map of Germany with the plot of the ray paths (surface projection) from the 958 epicenters to the stations of the GRSN (stars).

The coverage with ray paths south of latitude 52° N in the center and the southern part of Germany is rather well. The north is not covered. The advantage of this large data set over data from most active experiments is the unrivaled density and redundancy of the azimuthal coverage with raypaths across Germany. This is demonstrated in Fig. 3, which shows a uniform distribution of distance and azimuth.

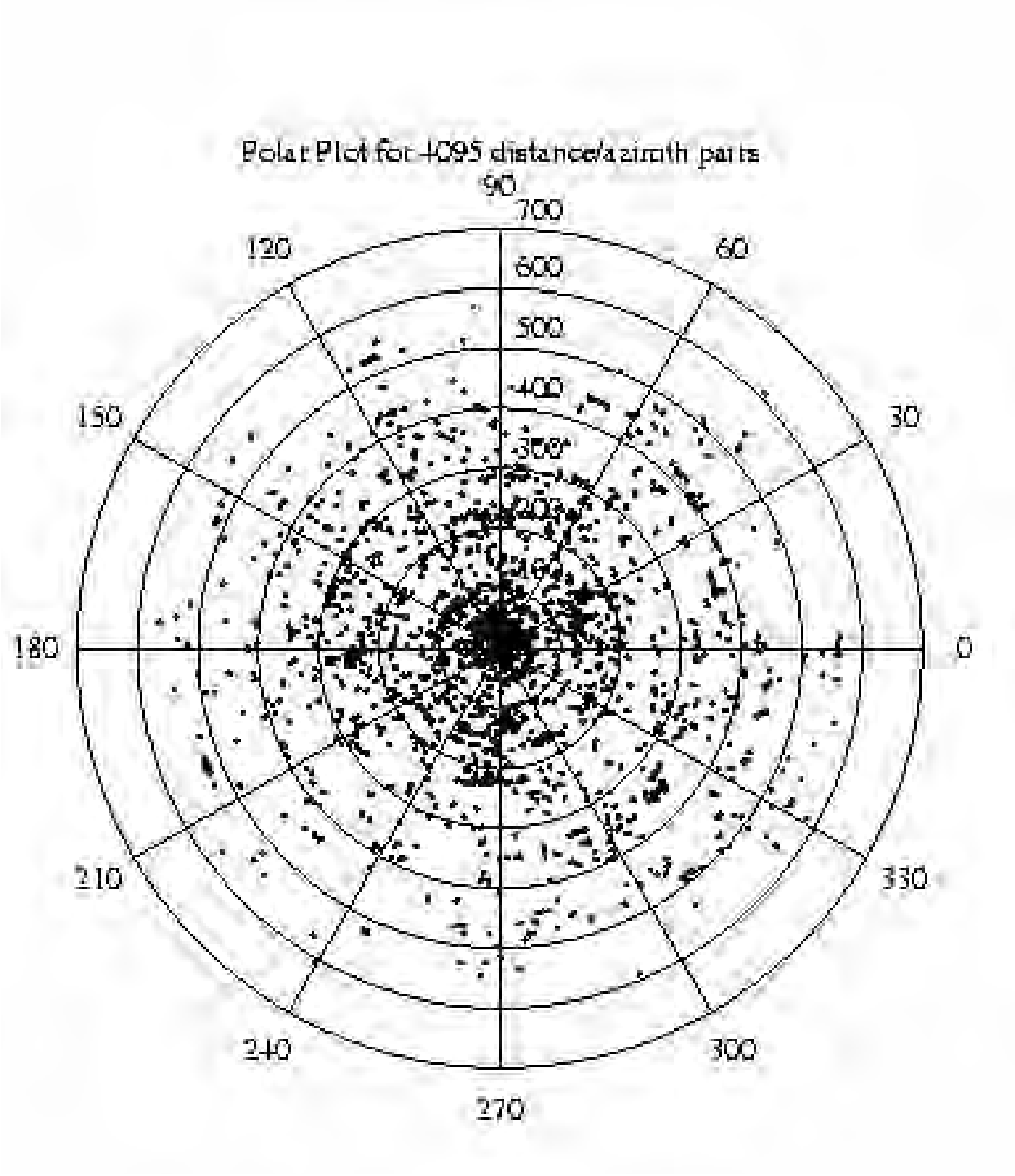


Fig. 3: Polar plot for 4095 distance-azimuth pairs used in this study. Note that azimuth is plotted counter clock wise from north (right). Labels on the concentric circles give distance in kilometers.

Fig. 4 shows a representation of the 4585 station traveltimes as function of epicenter distance. Four traveltime branches (*Pn*, *Pg*, *Sn, Sg*) are clearly visible, despite the large scatter (standard deviation over 2 s for *P* and 3 s for *S*). Other branches, such as *P** (Conrad refracted wave), are not visible.

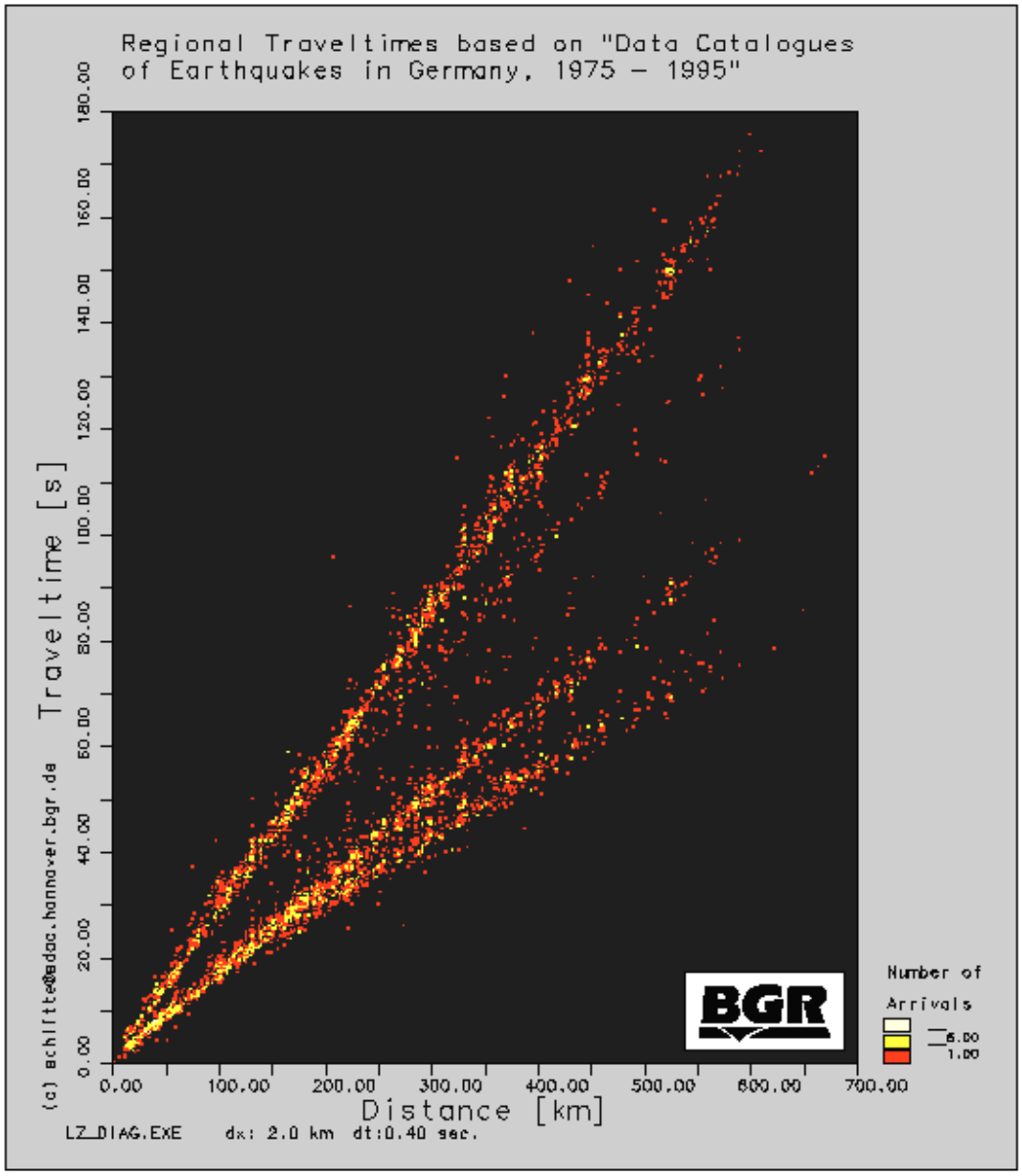


Fig. 4: Representation of the 4585 station traveltimes as a function of epicenter distance. For the plot, the number of arrivals in each bin with a width of dx=2 km and dt=0.4 s is counted and color-coded according to the scale at the right.

Taking into account the large scatter of the data, at first, an adequate interpretation of the traveltimes is achieved by a simple model with one layer over a half space. The interpretation was made interactively graphical as well as by linear regression of station traveltimes. Fig. 5 shows the data from the previous Fig. 4 with reduced traveltimes.

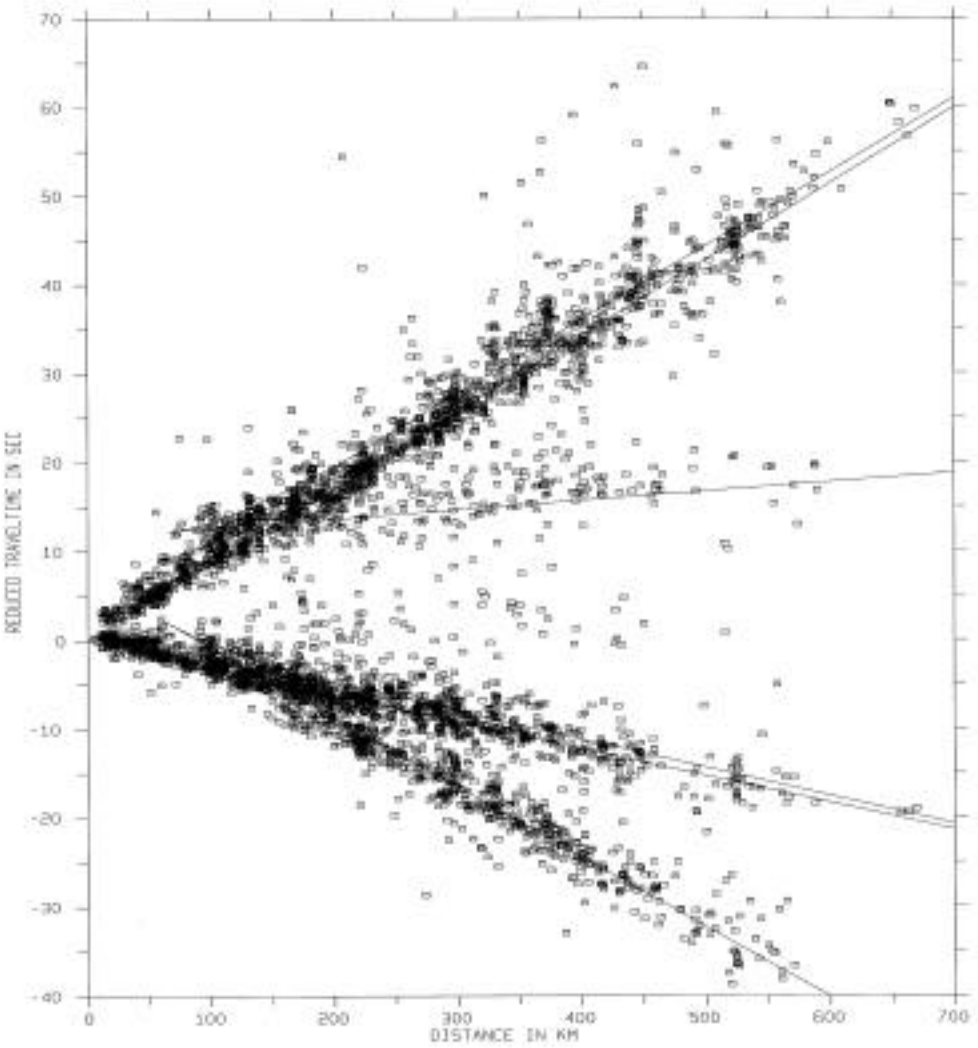


Fig. 5: Reduced traveltime plot of the data from Fig. 4. The reduction velocity (5 km/s) is used to help separate *P*- and *S*-wave traveltime branches. The superimposed theoretical traveltime curves for *Pn*, *Pg*, *PmP, Sn, SmS* and *Sg* stem from the best fitting model.

The reduction velocity of 5 km/s is used to help separate *P*- and *S*-wave traveltime branches. In this representation *P*-wave branches have negative slope, *S*-wave traveltime branches have positive slope. The superimposed theoretical traveltime curves for P_n, P_g, *PmP* and S_n, S_g, *SmS* stem from the best fitting model, which was found by trial-and-error modeling of vertically inhomogeneous velocity depth distributions. The model obtained by inversion has one layer over a half space. *P*- and *S*-velocities for the layer are 5.9 km/s and 3.5 km/s, respectively. The inferred layer thickness is 30 km, in accordance with the poorly determinable values of intercept time and crossover distance. The sub-Moho *P*- and *S*-velocities are 8.2 km/s and 4.73 km/s, respectively. Besides this graphical fitting of the traveltime curves a linear regression of the station traveltimes was made using two approaches. Table 1 shows the apparent velocities of the four main crustal phases as determined by 'using the phase code' and by 'ignoring the phase code', respectively, given in the earthquake catalogue. The apparent velocities for a given phase inferred

Table 1: Apparent velocities and confidence limits (2 σ-level) for the phases Pn, Pg, Sn and Sg as determined by linear regression using two approaches. The results of the trial-and-error modeling are given in the first column in brackets for comparison.

	Using Phase Code		Ignoring Phase Code	
Phase	Velocity (km/s)	2 σ s)	Velocity (km/s)	2 σ (s)
Pn (8.2)	8.04	6.56	8.52	4.20
Pg (5.9)	6.12	(4.21	6.02	1.71
Sg (3.5)	3.51	5.91	3.57	3.86
Sn (4.73)	4.74	8.57	4.93	5.80

from linear regression differ strongly. This result reflects the difficulties encountered selecting appropriate distance-traveltime sections for the regression. The conclusion is to give the trial-and-error modeling results priority over the only apparently more objective regression results.
Fig. 6 shows a comparison of the model derived here with a similarly simple model, namely the IASPEI91 model

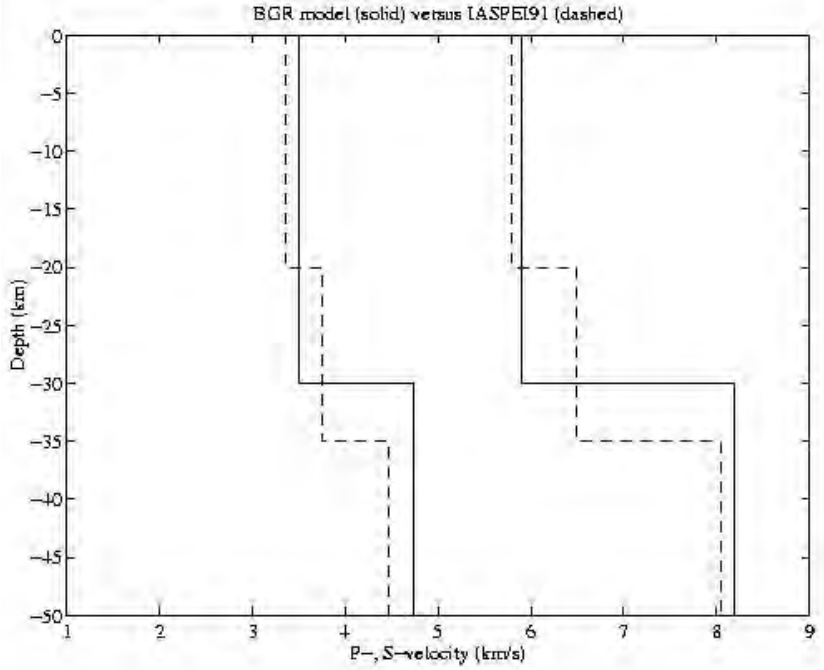


Fig. 6: Comparison of the model derived in this study (solid) with the IASPEI91 model (dashed) used at the IDC. For both models the *P*- and *S*-velocities, respectively, are given.

used at the IDC. Because of the different *Pn* and *Sn*, but also because of the different *Pg* and *Sg* velocities, considerable location differences result. Fig. 7 shows the *Sn-Pn* difference traveltimes for the two models of the previous

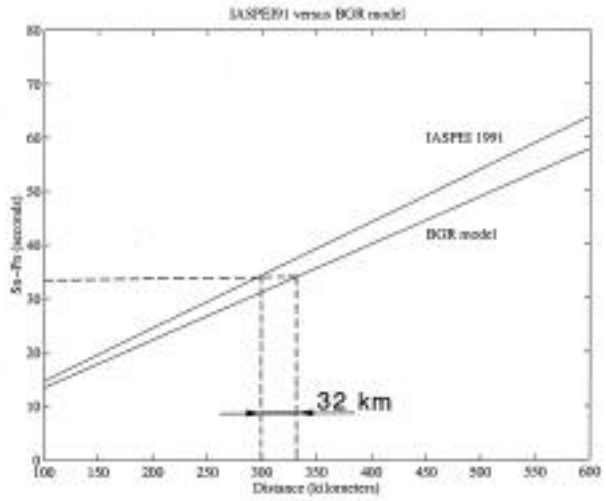


Fig. 7: *Sn-Pn* difference traveltimes for the IASPEI91 and BGR model (see labels**).**

Fig. 6. When using solely *Sn-Pn* difference travel times, for theses two models differences in localization of over 30 km result for observation distances of around 300 km. However, the best possibility to check the reliability of localization procedures and the underlying velocity models is to use so called 'ground truth' events as a reference. Such events are often not easily found. I use here the underground explosions of the seismic experiments GRANU95 and POLONAISE97 as well as the rockburst near Halle, Germany, of September 1996 as ground truth. Stars in Fig. 8 show the location of these events.

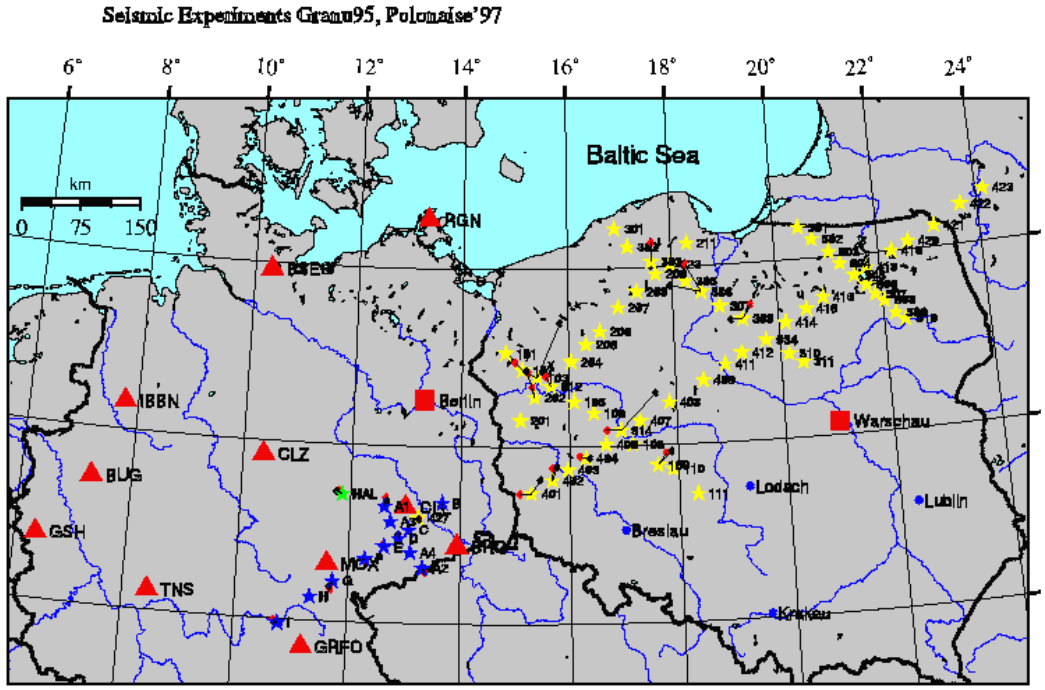


Fig. 8: Shot locations of the seismic experiments GRANU95 (dark stars) and POLONAISE97 (bright stars) in Germany and Poland, respectively. The location of the rockburst at Teutschenthal near Halle (Germany) is marked by a star labeled HAL. Triangles show the locations of GRSN stations**.**
The charge sizes used for these explosions reached from below hundred to thousand kilogram, the corresponding M_L values were in the range 0.5 - ~ 3.0. Fig. 9 shows a detail map of the region shown in Fig. 8

with the seismic localization results for the GRANU95 shots, the rockburst at Teutschenthal near Halle (Germany) and shot '427' of the POLONAISE97 seismic experiment.

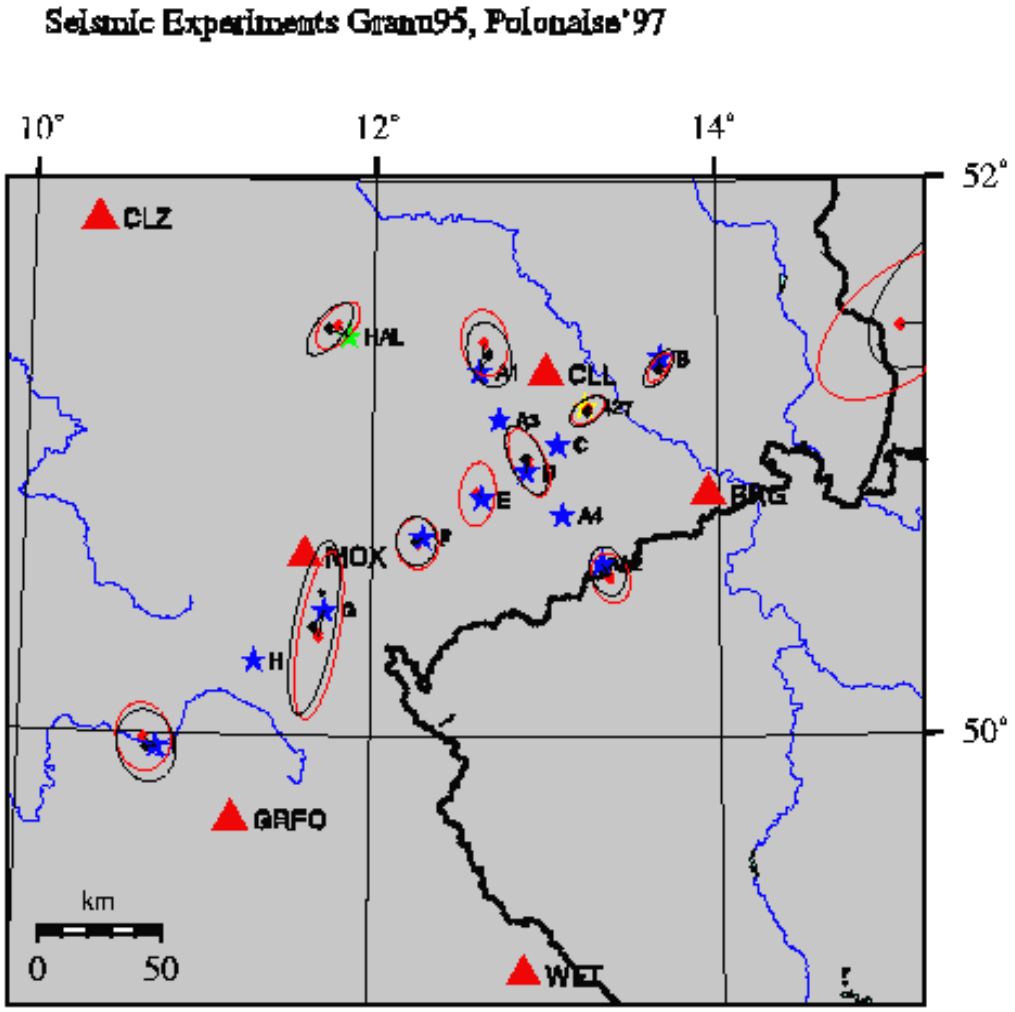


Fig. 9: Detail map of the border region Germany – Czech Republic – Poland showing the seismic localization results for the GRANU95 shots, the rockburst at Teutschenthal near Halle (Germany) and shot '427' of the POLONAISE97 seismic experiment. The dots and ellipses (BGR red; IASPEI91 black) give the locations and error ellipses determined using the two different models. Stars give 'Ground truth' locations. Triangles show the locations of GRSN stations**.**

Red and black dots and ellipses mark the locations determined using the BGR and IASPEI91 model, respectively. There is generally good agreement between the seismically determined locations (dots) and the 'ground truth' locations. With the exception of GRANU95 shot 'I', for all other explosions only *Pg*-phases of the stations BRG, CLL and MOX could be used. The good agreement between the localization results for the two models can be explained by the fact that the *Pg* velocities of the IASPEI91 and BGR model are only slightly different. Shot 'G', which is located outside the three-station subnet BRG, CLL and MOX, clearly shows the largest error ellipse. Fig. 10 shows a detail map of the western part of Poland with the seismic localization results of selected POLONAISE97 shots.

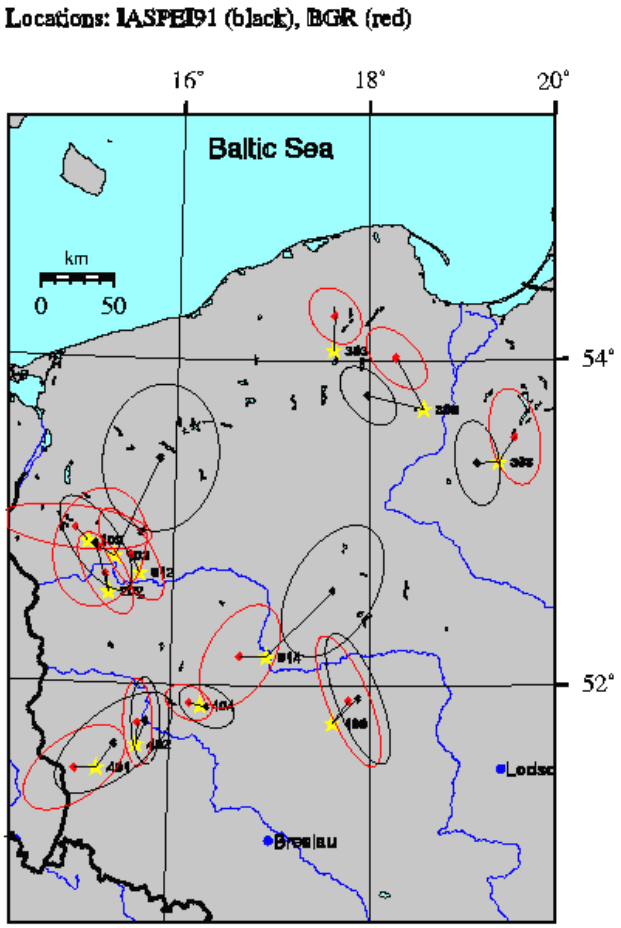


Fig. 10: Detail map of the western part of Poland with the border to Germany at the left showing the seismic localization results for selected POLONAISE97 explosions. The dots and ellipses (BGR red; IASPEI91 black) give the locations and error ellipses determined using the two different models. Stars give 'Ground truth' locations. Note that for some of the explosions (e.g. shot '303') no location was found using the IASPEI91 model.

These examples represent the borderline case were all seismic events are located outside the recording regional network. For the majority of the explosions close to the German border the localizations using the BGR model lie closer to the 'ground truth' locations. For some of the more distant explosions there is no convergence of the Geiger method when the IASPEI91 model is used.

CONCLUSIONS AND RECOMMENDATIONS

The model obtained in this study by inversion of earthquake/explosion bulletin data ("Data Catalogues of Earthquakes in the Federal Republic of Germany and Adjacent Areas") has one layer over a half space. *P*- and *S*-velocities for the layer are 5.9 km/s and 3.5 km/s, respectively. The inferred layer thickness is 30 km, in accordance with the poorly determinable values of intercept time and crossover distance. The sub-Moho *P*- and *S*-velocities are 8.2 km/s and 4.73 km/s, respectively. Tests of the location capability for selected ground truth events (explosions for refraction seismic experiments) in Germany and Poland are presented which confirm the validity of the model. The application of the new model distinctly reduces traveltime residuals for the routine determination of epicenters.
Besides inaccurate epicenter parameter values, an azimuthally dependent *Pn* velocity can possibly explain the large scatter of the observed traveltimes. Due to the abundance of available raypaths, this data set offers a unique opportunity to test models of mantle anisotropy in Central Europe. Subsets are formed of

traveltimes for selected pairs of an epicenter and a station in azimuth slices covering all directions. The results are presented in Fig. 11.

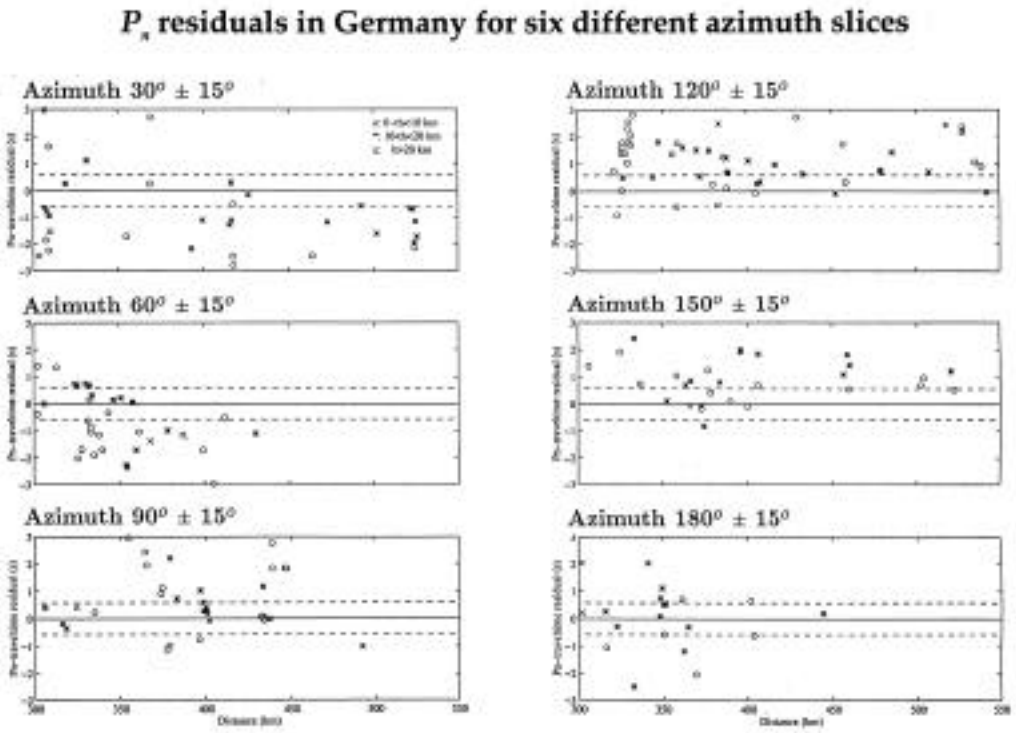


Fig. 11: *Pn* residuals for six different azimuth slices of 30º width (see labels) as a function of distance. The hypocenters of the earthquakes used are from depths *h* within three consecutive intervals of 10 km thickness (symbols in sub-plot top, left). The heavy lines and the two dashed lines correspond to the theoretical residuals for the middle and the top and bottom of the three depth intervals (5±5km, 15±5km, 25±5km), respectively. There exists an azimuth dependence of the residuals, particularly for the postulated fast (30º±15º) and slow (120º±15º)) directions**.**

Typically, about 600 raypaths fall into a slice of 30º width. Directions with postulated fast (N30ºE) and slow (N120ºE) sub-Moho velocities found in controlled source experiments (Prodehl & Giese, 1990; Enderle et al., 1996) can be confirmed (see residuals for the corresponding azimuth in Fig. 11). Although there is a trade-off between source depth and *Pn* velocity, a clear advance of *Pn* arrivals is observed for the fast direction, compared to the traveltimes for the best-fit model. It is recommend to use the unique data set presented in this study for future investigations of anisotropy and 3-D velocity structure (tomography) to further improve localization capabilities.

REFERENCES

Henger, M., Leydecker, G., (Eds.), 1975 (and following years). Data catalogue of earthquakes in the Federal Republic of Germany and adjacent areas, *Data of the Seismological Observatories in the Federal Republic of Germany compiled and edited by the Bundesanstalt für Geowissenschaften und Rohstoffe, Hannover*, Hannover.

Enderle, U., Mechie, J., Sobolev, S., Fuchs, K., (1996). Seismic anisotropy within the uppermost mantle of southern Germany. *Geophys. J. Int.*, **125**, 747-767

Prodehl, C., P. Giese, 1990. Seismic investigations around the EGT in Central Europe, in *The European Geotraverse: integrative studies - results from the 5th Earth Science Study Centre*, R.Freeman, P.Giese, St.Mueller (ed.), 77-97, European Science Foundation, Straßburg.

IMPROVED METHODS FOR REGIONALIZED SURFACE WAVE ANALYSIS

Jeffry L. Stevens and David A. Adams, Maxwell Technologies, Systems Division

Sponsored by U. S. Department of Defense
Defense Threat Reduction Agency
Contract No. DSWA01-98-C-0154

ABSTRACT

The goal of this project is to improve the capability to identify and detect surface waves under a Comprehensive Nuclear-Test-Ban Treaty. This is accomplished through the following tasks: improvement of regionalized station magnitudes through development of improved regionalized phase and group velocity models and other parameters, development of regionalized path-corrected spectral magnitudes, and improvement of automated surface wave detection using phase-matched filtering; development of maximum likelihood network spectral magnitudes and magnitude upper bounds; and optimization of the Ms:mb discriminant using both time domain and spectral magnitudes.

The first objective is to improve the dispersion curves, which are now in use at the International Data Centre (IDC) and were developed in a previous project. The global dispersion data set has been expanded by about 50% and now contains over 164,000 data points including; Eurasian, Antarctic, and South American group velocity measurements from Levshin and Ritzwoller (University of Colorado), phase and group velocity measurements from the Middle East and Saudi Arabia (Herrmann, Mitchell, and Mokhtar at St. Louis University), a model of global low-frequency phase velocities, dispersion curves from historic explosion data sets, and a large number of measurements made from prototype International Data Centre data (Maxwell Technologies). This expanded data set provides extensive coverage of the Middle East and Saudi Arabia, and fills in some important gaps, such as Antarctica, which were poorly constrained in the earlier data set.

This data set is used to perform a global tomographic inversion, which determines the shear velocity as a function of depth in approximately 150 discrete earth models. These earth models are then used to calculate phase and group velocity curves, which are used in automatic detection and identification of surface waves. The current automatic processing system in place at the IDC uses narrow-band filtering to determine group velocities, which are then compared with the predicted group velocities for the path. We expect to be able to replace this with a more robust method based on phase-matched filtering using the improved phase velocity dispersion curves. The earth models are also used to develop path-corrected spectral magnitudes, a type of moment, to regionalize the surface-wave excitation functions as well as surface-wave dispersion.

Key Words: surface wave, dispersion curve, phase matched filter, regionalization, moment

OBJECTIVE

The goal of this project is to improve the capability to identify and detect surface waves under a CTBT in order to improve event screening using the M_s:m_b discriminant. This is being accomplished through development of improved regionalized phase and group velocity models, development of regionalized path corrected spectral magnitudes, and improvement of automated surface wave detection using phase-matched filtering.

RESEARCH ACCOMPLISHED

During the first phase of this project we have concentrated on two tasks:

1. Improvement of regionalized global earth models and dispersion curves.
2. Automatic surface wave identification using phase-matched filtering.

In this paper, we first discuss the motivation for these improvements and the automatic surface wave processing context in which they are used, and then discuss the results to date from the current project.

Surface wave processing at the PIDC and IDC

Surface waves are of primary importance for CTBT monitoring because the M_s:m_b discriminant and its regional variants are among the most reliable means of determining whether an event is an earthquake or an explosion. With the International Data Center (IDC) identifying approximately 20,000 events per year, it is particularly important to be able to unambiguously "screen" as many events as possible (see Fisk et al, 1999). Because of the large volume of data acquired daily from the IMS, it is necessary for the IDC to be as automated as possible. An automatic processor initially performs P-wave phase identification and event location, however considerable analyst review and correction is required to ensure the quality of the results before the REB is published. Surface wave processing in contrast is completely automatic, with no operator review of the results. Consequently it is very important that the surface wave processing procedures be reliable and robust.

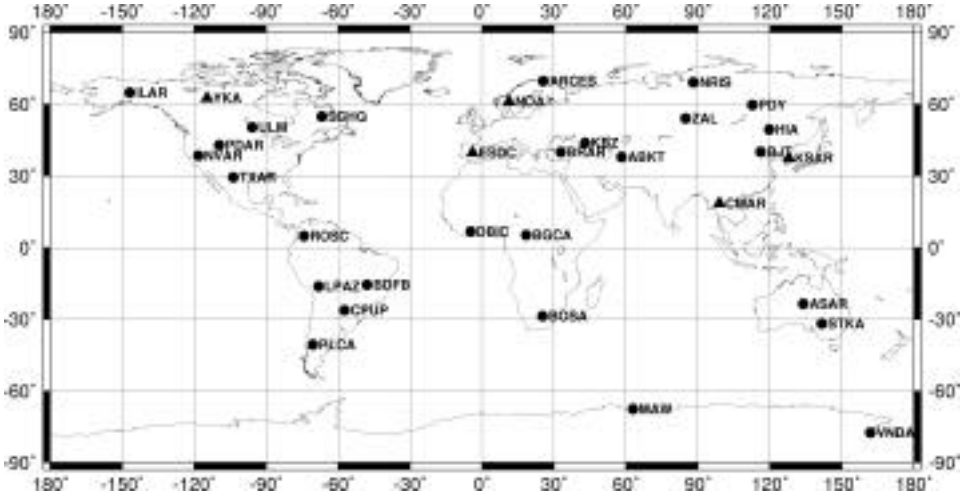


Figure 1. Map showing locations of current IMS stations that produce continuous long period or broadband data. Circles indicate three component stations, triangles arrays.

Surface wave processing at the IDC is performed using the automatic processing program Maxsurf, which has been developed and maintained by Maxwell Technologies. Maxsurf 1.0 was first implemented at the Prototype International Data Center (PIDC) in May 1995, and has been improved in successive releases since that time. Surface wave processing is applied to all continuous long period and broadband data that are received by the IDC. The existing IMS stations that produce this data are shown in Figure 1. There are a total of 32 stations – 5 long period arrays and 27 three component stations. 21 of the three-component stations and all five arrays are currently operational and transmitting data to the IDC. Surface waves are only measured using primary stations; for economic reasons, the IDC does not currently request auxiliary station data in the surface wave arrival time window.

Processing of auxiliary long-period data may be added in the future. Surface waves are processed for all stations within 100 degrees of each event. The PIDC/IDC processing procedures are summarized here, and are described in detail by Stevens and McLaughlin (1999).

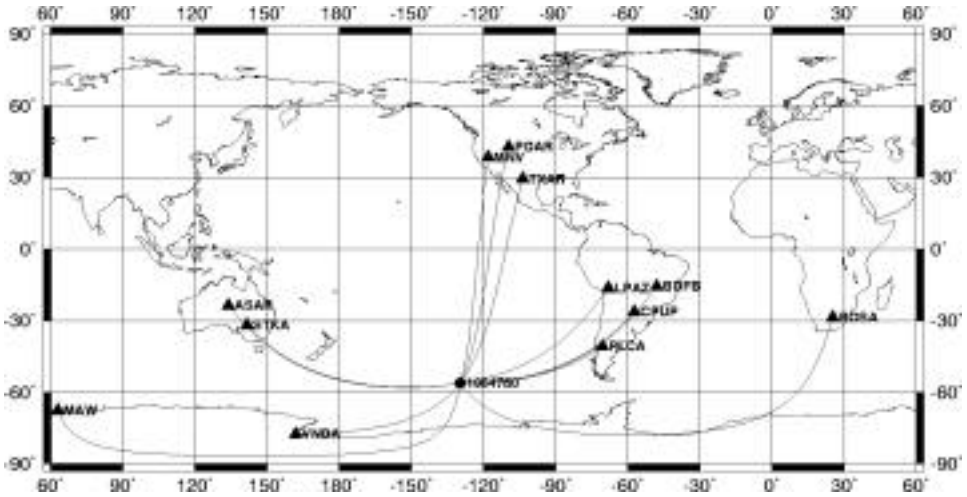


Figure 2. Map showing location of a 1997 South Pacific earthquake and the 12 IMS stations within 100 degrees that recorded the event. Lines are great circle paths.

Maxsurf runs in the processing stream after events have been identified and located. Maxsurf then examines the arrival window where a surface wave would be expected and applies a dispersion test to see if a surface wave can be identified. If so, then the amplitude is measured and stored in the IDC database. We start with an example that illustrates this procedure. Figure 2 shows the location of an m_b 3.9 South Pacific earthquake that occurred on 1997 June 15, together with the 12 IMS stations within 100 degrees that recorded the event, and the great circle paths between the earthquake and the stations.

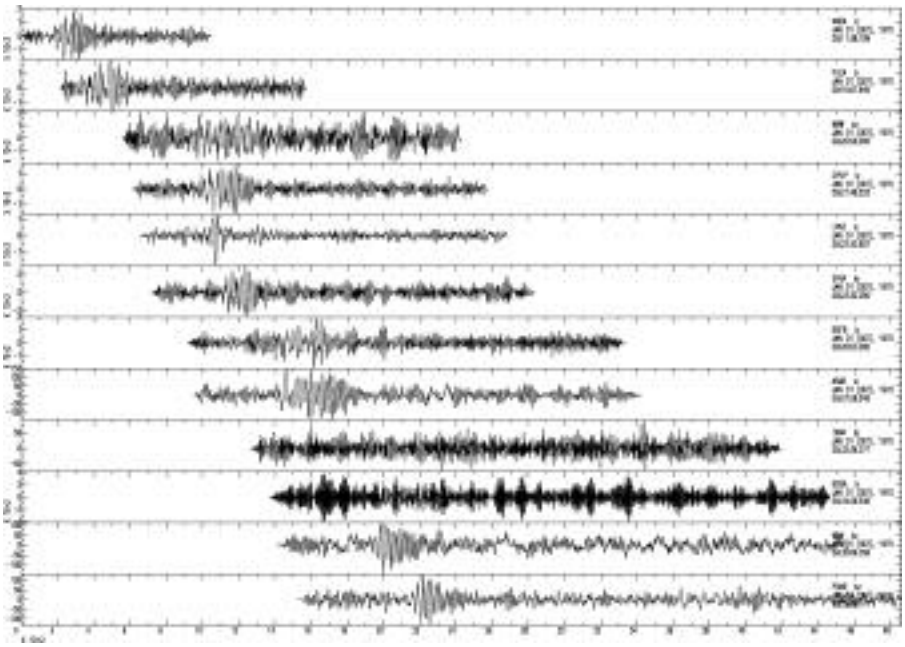


Figure 3. Long period data from the 1997 South Pacific earthquake. Seismograms are ordered by distance from the earthquake. All seismograms have been transformed to a common KS36000 instrument.

Figure 3 shows the data recorded at these stations after conversion to a common (KS36000) instrument. The surface wave is visible at most of the stations, however it is obscured by noise and difficult to see at some of them. Surface

waves are identified in the following way: a set of narrow band filters are applied to the data over a set of 8 frequencies from 0.02 to 0.06 Hz. A long-period or broadband beam is formed at arrays with the expected azimuth and slowness. The arrival times at each frequency are then compared with predicted arrival times generated from the regionalized group velocity model which will be described later in this paper. Figure 4 shows the bounds on the allowed dispersion and the measured group velocities at the 8 frequencies for several stations. The dispersion test requires that 6 of the 8 measured data points lie within the predicted bounds, and all stations except for TXAR pass this test. The marginal data fit at VNDA is due to inaccuracies in the model near Antarctica. The fit is improved significantly by the more recent models discussed later in this paper.

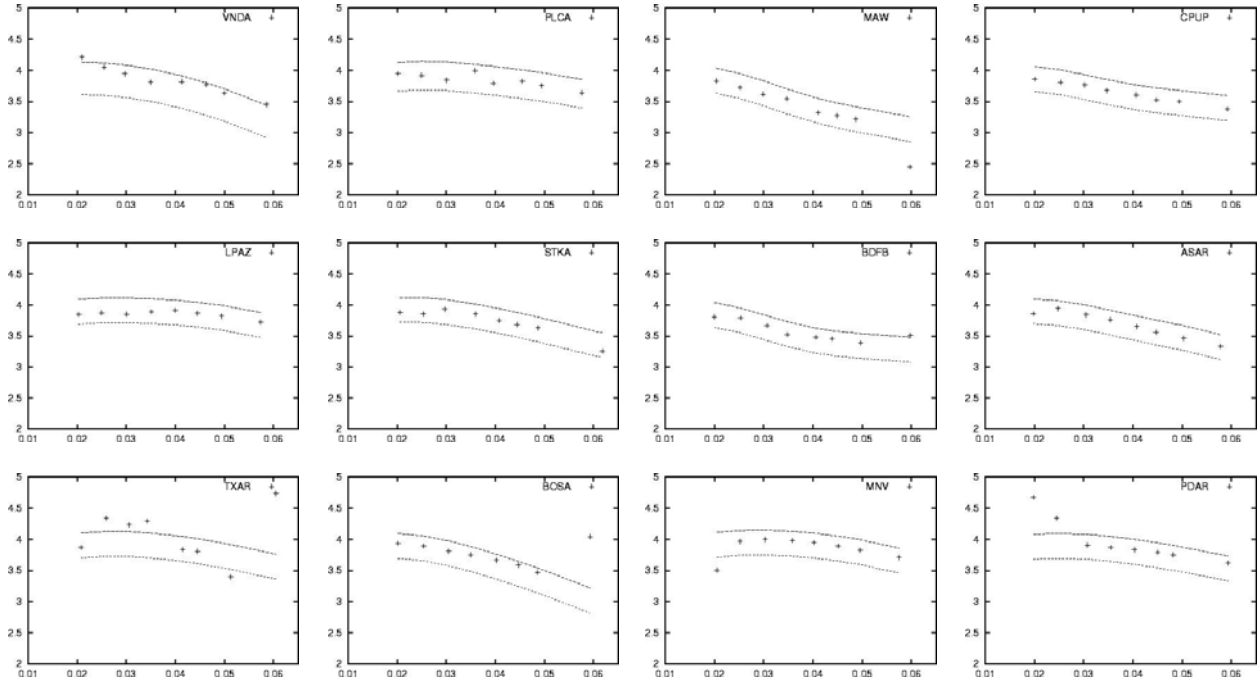


Figure 4. Measurements of group velocity made by narrow band filtering of the seismograms in Figure 3, and the predicted dispersion window. Plus signs indicate measured data. Lines indicate the predicted dispersion curve offset above and below to determine the allowable time window as discussed in the text. The dispersion curves are ordered by increasing source to receiver distance.

Optimization of Surface Wave Processing and Analysis

Surface wave processing can be optimized by defining a path corrected spectral magnitude which can be regionalized to allow for geographic variations in source excitation, attenuation, and dispersion, and can also be measured at different frequency bands in order to optimize signal to noise ratio. To do this, we base the magnitude on the equation for surface waves in a plane-layered structure. This equation can be factored into functions that depend on the source and receiver earth structure and the phase velocity and attenuation integrated over the path. The displacement spectrum for a Rayleigh wave at distance *r* from an *explosion* is given by:

$$U(\omega, r) = M_0' \frac{S_1^x(\omega, h_x) S_2(\omega) \exp[-\gamma_p(\omega) r + i(\varphi_0 - \omega r / c_p(\omega))]}{\sqrt{a_e \sin(r / a_e)}} \qquad (1)$$

S_1^x depends on the source region elastic structure and the explosion source depth. S_2 depends on the receiver region elastic structure, γ_p is the attenuation coefficient that depends on the attenuation integrated over the path between the source and receiver. c_p is the phase velocity integrated over the source to receiver path. φ_0 is the initial phase of the source. a_e is the radius of the earth. $M_0' = \frac{3\beta^2}{\alpha^2} M_0$ where M_0 is the explosion isotropic moment. This definition is introduced so that the function S_1^x does not depend explicitly on the material properties at the source depth.

We can use Equation 1 to define a spectral magnitude corrected for distance and spectral shape. We define, for any event, earthquake or explosion, the scalar moment (Stevens, 1986):

$$M_0' = \left| U(\omega, r, \theta) \Big/ \frac{S_1^x(\omega, h_x) S_2(\omega) \exp[-\gamma_p(\omega) r + i(\varphi_0 - \omega r / c_p(\omega))]}{\sqrt{a_e \sin(r / a_e)}} \right| \tag{2}$$

$\log M_0'$ is then a path corrected spectral magnitude that can be evaluated over any desired frequency band. This is similar to the approach taken by Okal and Talandier (1987) in defining a mantle magnitude M_m, except that they used an averaged earthquake source spectrum that they referred to as the Rayleigh Wave "Excitability" instead of the explosion excitation function S_1^x at the reference depth h_x. Although the imaginary part of the exponential is removed by the absolute value, it is shown here explicitly because in practice the phase is used to generate a phase-matched filter (Herrin and Goforth, 1977) to compress the signal and improve signal/noise ratio prior to taking the spectrum. The spectrum is then averaged over a frequency band to smooth the spectrum and obtain a stable measurement.

For an isotropic explosion source at depth h_x, M_0' is independent of frequency. Equation 2 therefore corrects completely for all frequency dependent and distance dependent factors in the observed spectrum. In general, M_0' for an earthquake is not completely frequency independent, but it is partially corrected for frequency dependence by removal of the path attenuation and receiver structure and similarities in the explosion and earthquake excitation functions in the same source region. The remaining differences mean that the earthquake magnitude will vary somewhat when measured over different frequency bands while the explosion will not. In particular, the spectra of deeper earthquakes will decline more rapidly with increasing frequency, while the path corrected spectra of shallow earthquakes is approximately flat over the frequency band of about 0.01-0.08 Hz.

By defining the path corrected spectral magnitude as the logarithm of Equation 2, we obtain a measure of surface wave magnitude that is independent of range, nearly independent of frequency, and regionalizeable. The functions S_1^x and S_2 depend only on the source and receiver points and can be stored in a simple lookup table. The functions γ_p and c_p depend on the source to receiver path and can be found by integrating along a great circle path between the source and receiver in a regionalized earth model.

Development of Regionalized Earth Models

With a set of regionalized earth models that maps any point on the earth into the earth structure at that point, we can calculate all of the quantities in Equation 4 for any source and receiver point and calculate the path corrected spectral magnitude from any observed seismogram. In addition, we can use the phase velocity for the path to construct phase matched filters, and use the predicted group velocity arrival times as part of an existence test for surface waves in automatic processing as discussed earlier.

Observed surface waves provide strong constraints on earth structure, so development of regionalized earth models can be a self-correcting process. That is, surface wave dispersion and amplitudes can be used to infer earth structure, and earth structure can be used to calculate surface wave dispersion and amplitudes. So with a data center such as the IDC which collects surface wave data on a continuous basis, it is possible to implement a program of continuous improvements in regionalization and surface wave processing using this extensive data set. In the following, we have used dispersion data measured from GSETT3 PIDC data, merged with dispersion data from other studies to develop regionalized global earth models.

Stevens and McLaughlin (1999) describe development of the global earth model with 149 distinct models on a five degree grid that is now used for surface wave identification at the PIDC and IDC. The development used global tomographic inversion of about 90,000 dispersion measurements, using the Crust 5.1 model (Mooney, et al., 1998) as a starting point. We have continued this process further, adding more data points and additional models. The global dispersion data set now contains over 164,000 data points including:

Global surface wave group velocities from earthquakes derived using PIDC GSETT3 data (Stevens and McLaughlin, 1996), augmented with more recent measurements derived from PIDC data.

1. Surface wave phase and group velocity dispersion curves from underground nuclear test sites (Stevens, 1986; Stevens and McLaughlin, 1988), calculated from earth models for 270 paths (test site – station combinations) at 10 frequencies between 0.015 and 0.06 Hz.

2. Phase and group velocity measurements for western Asia and Saudi Arabia from Mitchell et al.(1996) for 12 paths at 17 frequencies between 0.012 and 0.14 Hz.

3. Global phase velocity model of Ekstrom et al. (1996) for 9 periods between 35 and 150 seconds calculated for each 5 degree grid block from a spherical harmonic expansion of order l=40.

4. Group velocity measurements for Eurasia from Ritzwoller et al.(1996) and Levshin et al.(1996) for 20 frequencies between 0.004 and 0.1 Hz with 500 to 5000 paths per frequency.

5. Antarctic and South American group velocity measurements from the University of Colorado (Vdovin et al., 1999; Ritzwoller et al., 1999).

6. A very large set of dispersion measurements from Saudi Arabia provided by Herrmann and Mokhtar at St. Louis University.

This expanded data set provides extensive coverage of the middle east and Saudi Arabia, and fills in some important gaps, such as Antarctica, which were poorly constrained in the earlier data set.

The new shear velocity models obtained by tomographic inversion of this data set are changed primarily in areas that contain additional data. For example, there is now more variation in the shear velocity structure in the Arabian plateau where high frequency dispersion data provides additional information about this structure. This is a good test showing both that the tomographic inversion is responding correctly to new data, and that the previous inversion was stable with respect to the addition of new data in other regions. The current IDC model and the model discussed above as well as calculated dispersion curves and other quantities may be downloaded from the World Wide Web at: http://www.maxwell.com/products/geop/PAGEOPH_CTBT/SurfWave/LP_export.html. We have reviewed the results of this inversion, and are trying to find the optimum ways to improve the results further. What we are trying to find are a set of models that accurately predict the phase and group velocity dispersion, and ultimately the amplitude, for any source and receiver point. There are three basic ways to improve the inversion results, depending on what is causing the inaccuracy in the current model. These are:

1. Add additional model types. The inversion described above, as well as the current IDC models, use 149 distinct models, and each model corresponds to a number of locations in the world with similar crustal types. However, as the data set becomes more complete, and it becomes possible to resolve differences between the same model in different locations, it is necessary to subdivide some of these regions. At some point, we expect to divide the regions into smaller blocks than the current 5 degree grid.

2. Add additional model layers. The current set of models contain only a few layers in the crust, similar in most cases to the Crust 5.1 models that were the starting point for the initial set of inversions. As we get more higher frequency data, we develop additional resolving power in the crust, and it will be necessary to add more layers and allow more variation in the crust.

3. Add new data to fill in gaps. The first two changes above are for regions where there is an abundance of data. However, we still have some regions where the data is limited and may not be adequate to constrain the models sufficiently. In these regions, we need to find additional dispersion data to add to the data set.

We want to accomplish 1 and 2 above without adding new models and layers that do not contribute to improvements in the data fit. We therefore tried to find ways to identify those regions that could not be modeled well with the existing 149 models. We did this in three ways:

1. We identified outliers in the data and plotted the corresponding ray paths color coded according the residuals, to identify poorly modeled regions.

2. We identified clusters of similar ray paths. Such clusters can be used to check the robustness of outlying data. Clusters that have consistently anomalous residuals can be used to make routine path corrections, once a final model is determined.

3. We performed tomographic inversions for specific frequency ranges. The 2D group velocity tomographic inversions were done for 8 frequency bands:- below 0.01 Hz, 0.01 to 0.0167 Hz, 0.0167 to 0.025 Hz, 0.025 to 0.033 Hz, 0.033 to 0.04 Hz, 0.04 to 0.05 Hz, 0.05 to 0.067 Hz, and greater than 0.067 Hz. The inversions were done without smoothing or damping. We selected 84 cells with changes of more than 3% in group velocities and occurring with the same sign at more than two adjacent frequency bands, and with more than 15 ray paths intersecting. From these 84 cells, we found 3 pairs of adjoining cells with similar velocity changes. We associated a single new model type for each pair, thus reducing the total number of new model types to 81. Figure 5 shows the locations of the 84 cells colored coded depending on the change in group slowness for the frequency band 0.025 to 0.033 Hz. The initial structures of each of these 81 cells were the same as the original model types, however they were allowed to adjust independently of the original models during the following shear wave velocity tomography.

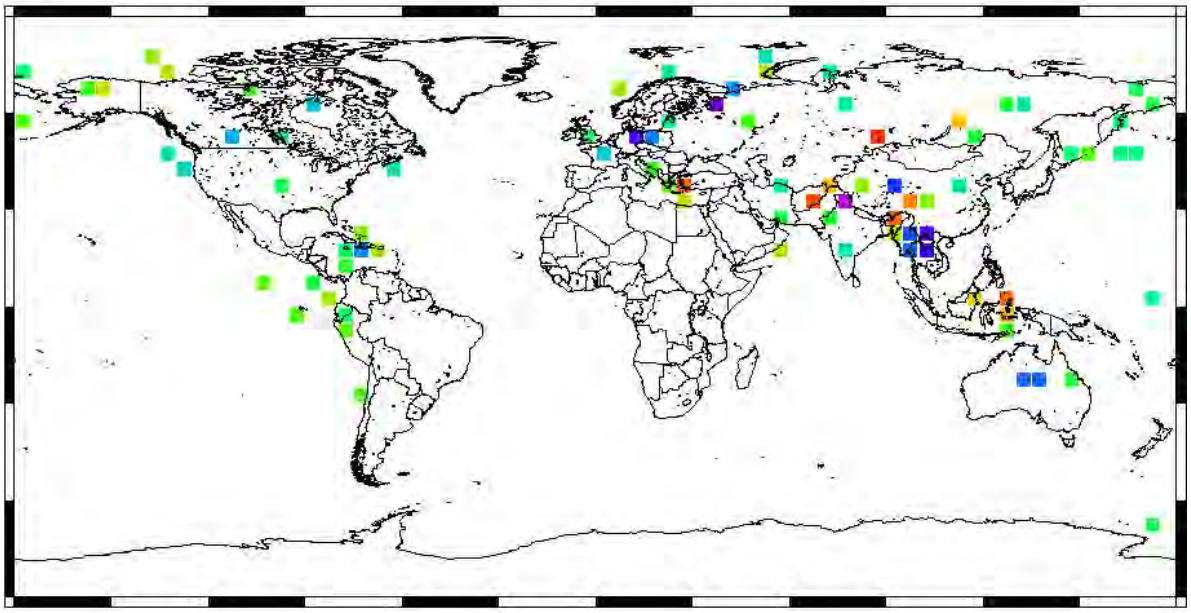


Figure 5. New models added to surface wave tomographic inversion.

This increased the total number of model types from 149 to 230. This reduced the total data variance by about 4%. This relatively small variance reduction reflects the fact that the initial model fit the data quite well over most of the world, and that the improvements occur primarily in the limited regions illustrated in Figure 5. The improvement in data fit is more substantial in these regions

Path Corrected Spectral Magnitudes and Phase-matched Filtering

A second automatic surface wave processing program, Maxpmf, has been developed which is similar to Maxsurf except that it applies phase-matched filtering to seismograms and calculates path-corrected spectral magnitudes in addition to M_s. Maxpmf integrates a regionalized phase velocity model to generate a phase-matched filter and applies amplitude corrections to generate a path-corrected spectral magnitude (log M_0). An advantage of the frequency domain processing is that a spectral magnitude of either signal or noise can always be measured over the specified frequency band, while it may not be possible to measure data in a specified frequency band in the time domain. Maxsurf, for example, will reject a seismogram if it can't find a 20 second arrival within the predicted arrival time window. This often occurs at regional distances and there is no reason for such a restriction for spectral magnitudes. Consequently, moments can be measured for regional seismograms in cases where standard M_s measurements cannot be made.

Figure 6 shows an example of phase-matched filtering derived from the regional phase velocity model applied to the data set discussed earlier and shown in Figure 3. The surface waves are compressed into a narrow time window near zero and amplified relative to the noise.

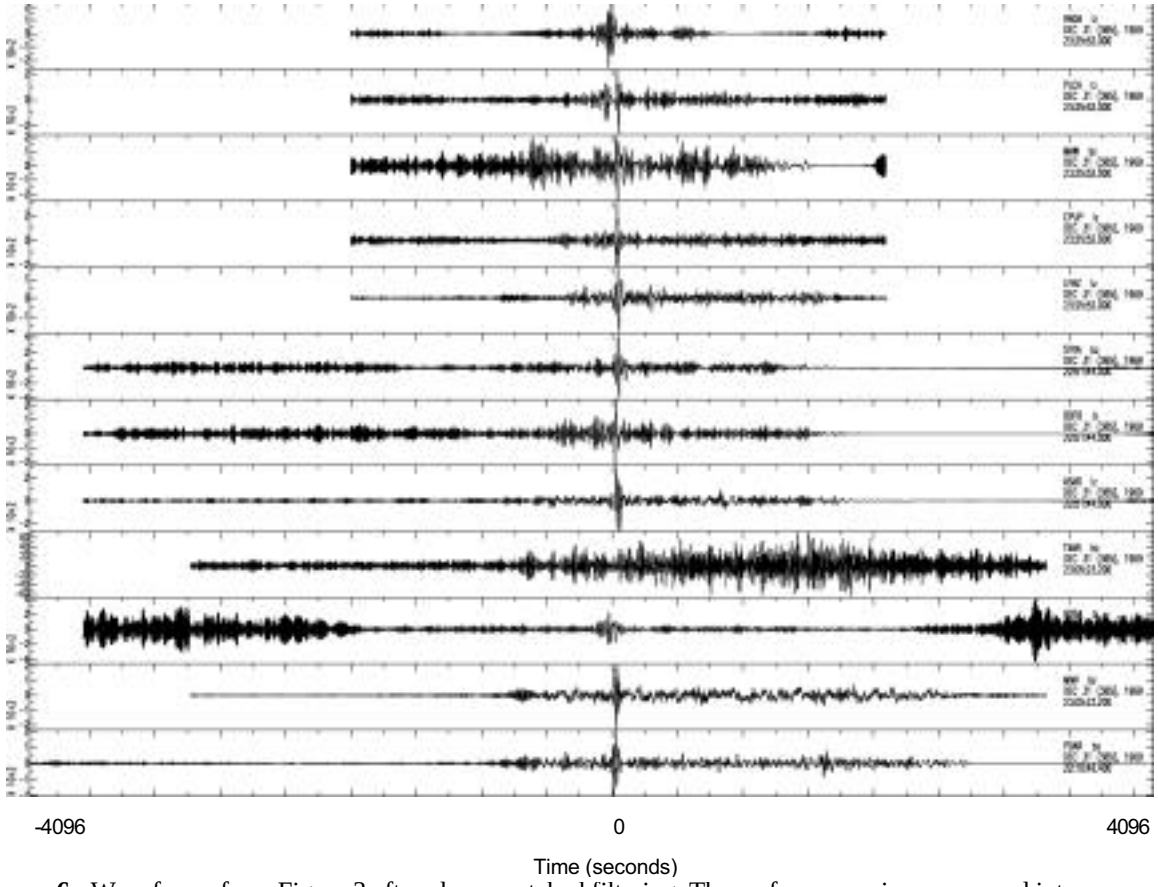


Figure 6. Waveforms from Figure 3 after phase-matched filtering. The surface wave is compressed into a narrow time window near zero.

One of the goals of the current project is to use phase-matched filtering directly for surface wave identification rather than performing narrow-band filtering first, and then using phase-matched filtering for measurement. As can be seen in Figure 6, the improvement in signal to noise ratio derived from phase-matched filtering suggests that the detection threshold could be reduced by eliminating the narrow-band filtering step. However, the narrow-band filter detection procedure now in place has been tested carefully and is mature enough that spurious or incorrect identification of arrivals is relatively rare, so replacement with an alternative procedure requires extensive testing to ensure that improvement in detection does not come at the expense of erroneous detection. We have started this process by running phase-matched filters in a semi-operational mode on PIDC data. We ran Maxpmf on two days of continuous data (approximately 650 waveforms within the correct time and distance windows), and saved a number of parameters from phase-matched filtering. We looked first to see if the signal enhancement alone was sufficient to identify surface waves. That is, we looked at the rms amplitude in the region near zero time, and compared it with the rms amplitude over a longer time window outside of this region. We found that this did, in fact, identify a substantial fraction of the surface waves identified by narrow band filtering, however it is not as reliable and has a higher error rate. We are now investigating narrow-band filtering of the compressed waveform as a potentially more robust method of identifying surface waves in the compressed and enhanced signal.

CONCLUSIONS AND RECOMMENDATIONS

In this paper, we have described procedures for optimization of surface wave processing under a Comprehensive Test Ban Treaty, and described improvements to regionalized dispersion models and phase-matched filtering that are necessary for their implementation. Because the number of events increases rapidly at small magnitudes, a decrease

in the threshold of reliable surface wave detection and measurement can greatly reduce the number of unidentified events. Improved surface wave analysis methods can reduce the surface wave magnitude threshold, improve screening capability, and reduce the likelihood of unnecessary on-site inspections under a CTBT. We are continuing to improve the regionalized models, and to test and implement surface wave identification using phase-matched filtering to reduce the threshold for surface wave identification and measurement further.

ACKNOWLEDGEMENTS

We would like to thank Mike Ritzwoller and Anatoli Levshin of the University of Colorado, Brian Mitchell and Bob Herrmann of St. Louis University, Goran Ekstrom of Harvard University, and their coworkers for the use of their data and models in this project. We thank Keith McLaughlin, Mike Skov and Hans Israelsson for their help in development of these techniques and implementation and testing of this work at the PIDC.

REFERENCES

Ekstrom, G., A. M. Dziewonski, G. P. Smith, and W. Su (1996), "Elastic and Inelastic Structure Beneath Eurasia," in *Proceedings of the 18th Annual Seismic Research Symposium on Monitoring a Comprehensive Test Ban Treaty, 4-6 September, 1996*, Phillips Laboratory Report PL-TR-96-2153, July, pp. 309-318, ADA313692.

Fisk, M. D., D. Jepsen, and J. R. Murphy (1999), "Experimental Event-Screening Criteria at the Prototype International Data Center," submitted to *Pure and Applied Geophysics*.

Herrin, E. and T. Goforth (1977), "Phase-Matched Filtering: Application to the Study of Rayleigh Waves," *Bull. Seism. Soc. Am*., v. 67, pp. 1259-1275.

Levshin, A. L., M. H. Ritzwoller, and S. S. Smith (1996), "Group Velocity Variations Across Eurasia," in *Proceedings of the 18th Annual Seismic Research Symposium on Monitoring A Comprehensive Test Ban Treaty, 4-6 September, 1996*, Phillips Laboratory Report PL-TR-96-2153, July, pp. 70-79, ADA313692.

Mitchell, B. J., L. Cong and J. Xie, (1996), "Seismic Attenuation Studies in the Middle East and Southern Asia", St. Louis University Scientific Report No. 1, PL-TR-96-2154, ADA317387.

Mooney, W., G. Laske, and G. Masters (1998), "Crust 5.1: A Global Crustal Model at 5x5 Degrees," *Journal of Geophysical Research*, v. 103, no. B1, pp. 727-747.

Okal, E. A. and J. Talandier (1987), "M_m: Theory of A Variable-Period Mantle Magnitude," *Geophysical Research Letters*, v. 14, pp. 836-839.

Ritzwoller, M. H., A. L. Levshin, L. I. Ratnikova, and D. M. Tremblay (1996), "High Resolution Group Velocity Variations Across Central Asia," in *Proceedings of the 18th Annual Seismic Research Symposium On Monitoring A Comprehensive Test Ban Treaty, 4-6 September, 1996*, Phillips Laboratory Report PL-TR-96-2153, July, pp. 98-107, ADA313692.

Ritzwoller, M.H., O.Y Vdovin, and A.L. Levshin (1999), "Surface wave dispersion across Antarctica: A first look", *Antarctic J. U.S.*, in press.

Stevens, J. L. (1986), "Estimation of Scalar Moments From Explosion-Generated Surface Waves," *Bull. Seism. Soc. Am.*, v. 76, pp. 123-151.

Stevens, J. L. and K. L. McLaughlin (1996), "Regionalized Maximum Likelihood Surface Wave Analysis," Maxwell Technologies Technical Report submitted to Phillips Laboratory, PL-TR-96-2273, SSS-DTR-96-15562, September, ADA321813.

Stevens, J. L. and K. L. McLaughlin (1999), "Optimization of surface wave identification and measurement," submitted to *Pure and Applied Geophysics*.

Vdovin, O. Y., J. A. Rial, M. H. Ritzwoller, and A. L. Levshin, 1999, "Group-velocity tomography of South America and the surrounding oceans", *Geophys. J. Int.*, 136, 324-330.

TESTING EVENT LOCATION CAPABILITY WITH GROUND TRUTH EVENTS IN KAZAKSTAN

Clifford Thurber, Florian Haslinger, Chad Trabant,
Department of Geology and Geophysics, University of Wisconsin-Madison

Sponsored by U.S. Department of Defense
Defense Threat Reduction Agency
Contract No. DSWA01-98-1-0008

ABSTRACT

We are investigating seismic event location capability in Kazakstan using first-P arrivals from nuclear explosions with exact ground truth information recorded on a sparse network of digital seismic stations. Our first step involves the application of a waveform cross-correlation method to extract higher precision first-P arrival times. Comparison of our revised picks with picks from the International Seismological Centre (ISC) catalog reveals significant discrepancies. Occasional large discrepancies (several seconds) may be due to clock errors (either not incorporated in the digital data or erroneously applied to the ISC data), but most are due to 0.5-second and 1-second round-off at various ISC stations (that is, stations reporting times rounded off to integer seconds or half-seconds), leading to errors up to 0.25 and 0.5 seconds, respectively. Though the round-off problem is not a direct concern for future CTBT monitoring, it does point to one source of error in global relocation and tomography studies.

We are using the improved arrival times to examine several issues regarding location accuracy and precision. Because the true explosion locations are known precisely, we can evaluate both relative and absolute location capabilities. Our initial focus is on relative locations. Aspects we are investigating include relative location accuracy using sparse regional-distance observations, the spatial variability of derived source-specific station corrections (also known as path corrections) to regional versus teleseismic stations, and the influence of source-region heterogeneity.

Relative relocations for most events are extremely accurate using all available picks from digital data. The vast majority of events are relocated within 1 to 2 km of ground truth, consistent with estimated location uncertainties of 1 to 2 km. Restricting the data to stations within 40° cuts the number of stations by a factor of about 3 and the number of observations by a factor of about 4, but both mislocations and estimated uncertainties increase only by modest factors.

For location using path corrections to be accurate and effective in practice, the rate at which the corrections change with changing source location must be relatively modest. We determined sets of path corrections for three subsets of explosions in adjacent regions each about 10 to 15 km in diameter. The sets of corrections are highly correlated, although with systematic differences that we attribute to uncertain origin times. Accounting for the systematic differences, correction differences are generally +/- 0.2 s or less.

The alternative is to use a model-based approach. We will examine the contributions of 3-D structure to mislocation. We will present the results of teleseismic tomography beneath the Kazakstan test site using the explosions as a source array. We will investigate the effect of source-region heterogeneity on the travel times. We will also assess the degree to which a regional or global 3-D velocity model can account for some of the travel time differences that are indicated by the path corrections and their spatial differences.

Key Words: location, ground truth, corrections, calibration, waveform cross-correlation, 3-dimensional structure

OBJECTIVE

We are carrying out investigations of seismic event location capability, using events that have ground truth information to allow a direct assessment of actual location errors and computed precision estimates. The objectives are to determine the most effective approaches for precise and accurate event location for CTBT monitoring purposes. Waveform cross-correlation methods have been applied to determine more accurate relative arrival times for available digital seismic data from nuclear explosions at Shagan River (Balapan), Kazakstan. These arrival times, along with the original bulletin times, are being used for a comparison of two strategies for improving absolute location accuracy and reducing estimated location uncertainty, one "model-based" and the other "calibration-based." The calibration-based approach involves joint hypocenter determination (JHD), including the estimation of path corrections. The model-based approach involves the use of regional and/or global three-dimensional (3D) velocity models to provide improved travel time estimates.

RESEARCH ACCOMPLISHED

Our current region of investigation is the former nuclear testing site at Shagan River, Kazakstan. Ground-truth information for Shagan River has been compiled from publicly available sources: absolute locations for 100 nuclear explosions (NNCRK, 1999) and origin times for 7 of them (Bocharov et al., 1989). This information was used to derive origin time estimates for the other 93 nuclear explosions using International Seismological Centre (ISC) data and JHD, assuming depths of 0 km for all the explosions. The event locations are shown in map form in Figure 1 and the locations and origin time results (including estimated origin time uncertainties) are presented in Table 1.

We analyzed the residuals from the JHD results, characterizing the residual distribution and evaluating the quality of the stations in terms of self-consistency of the estimated travel times (reported arrival time minus estimated origin time). The ISC residuals show a broad distribution with numerous +/- 5 and 10 second residuals. The distribution is well fit by the sum of a Gaussian term with a standard deviation of 0.3 seconds and a smaller non-Gaussian term. It is apparent that using raw ISC data, in this case mainly from reasonably large events, will be problematic for location calibration work as well as for tomography studies (see below), unless outliers are dealt with carefully.

Waveform cross-correlation can significantly improve pick quality (VanDecar and Crosson, 1990). We have applied the Xadjust package (Dodge et al., 1995) to the available digital data for Shagan River explosions (mainly from 1980 on). The cross-correlation technique is particularly valuable for extracting more accurate relative arrival times when some waveforms are noisy - see Figure 2 for an example. Comparing picks from the digital data to the ISC picks (see example in Figure 3) shows the effect of round-off in the reported ISC times (that is, stations reporting times rounded off to integer seconds or half-seconds). In Figure 4 we compare the set of cross-correlation picks to the corresponding ISC times, showing the frequency of time differences. Most of the time differences are less than 0.5 seconds. We attribute much of the scatter to round-off in the times reported to ISC.

Relocation analysis was carried out using JHD for the entire group of events and for 3 subsets (Northeast, Central, West groups). Relative relocations for most events are extremely accurate using all available picks from digital data (fixing one event location and origin time in each case). Many events are located within 1 km of ground truth, and almost all locate within 2 km. Estimated location uncertainties are of the same order. The number of truly regional-distance observations (within 20°) with reliable timing for these events is extremely small. Thus to simulate a regional monitoring situation in a reasonable manner, we relocated the events using stations within 40°; an example is shown in Figure 5.

For location using path corrections to be accurate and effective in practice, the rate at which the corrections change with changing source location must be relatively modest. We determined sets of path corrections for three subsets of explosions in adjacent regions each about 10 to 15 km in diameter. The sets of corrections are highly correlated, although with systematic differences that we attribute to uncertain origin times. Accounting for the systematic differences, correction differences are generally +/- 0.2 s or less.

In order to image the 3D crustal structure beneath the Shagan River test site using teleseismic traveltime residual analysis, we follow the Aki-Christofferson-Husebye (ACH) approach (Aki et al., 1977). The unique characteristic in our case is that the nuclear explosions (seismic events) are treated as a station array and the stations from which arrival time data are available are treated as seismic events. For a general overview and mathematical details of ACH type teleseismic tomography see for example Evans and Achauer (1993); here we will just briefly discuss the peculiarities of the inversion when using events as stations and vice versa.

The travel time residual r_{ij} for a ray traveling from source j to receiver i can be expressed as

$$r_{ij} = dO_j + \sum_{k=1,K} \left(- \int_{base}^{receiver} \frac{1}{V_0^2} \frac{\delta V}{\delta \boldsymbol{m}_k} \, \mathrm{ds} \right) \delta \boldsymbol{m}_k + e_{ij}$$

The integral describes the change in travel time of the ray from the model base to the receiver with respect to change of the seismic velocity V in the K model parameters $\boldsymbol{m}_k$. In our case, as generally in ACH tomography, the model is constructed of blocks of constant velocity. e_{ij} is an error term, and dO_j is a source term which is introduced to account for absolute velocity differences between ray paths outside the model volume and other unresolvable terms (e.g. source location and origin time uncertainties) which may be present in the data. dO_j can be expressed as a weighted average residual travel time between source j and all receivers. Doing so allows to replace the absolute travel time residual r_{ij} by the relative travel time residual rr_{ij}. These relative residuals are the data used in the inversion, and ideally they solely contain the difference between true velocities and initial model velocities within the space of model parameters $\boldsymbol{m}_k$.

Reversing sources and receivers for the inversion does not change the influence of absolute velocity differences outside the model volume, but places all source uncertainties inside the model volume. To account for that, an additional source term would have to be introduced and inverted for. In our case, however, ground truth location information for all sources is available, and origin time uncertainties are in the order of 30 to 50 ms (see above). Source terms are therefore expected to have magnitudes comparable to the station corrections used in 'normal' ACH tomography, and there is no need to introduce extra parameters in the inversion. On the other hand, our 'sources' now are stations at the surface of the earth. Even though their locations are (at least in theory) precisely known, near surface velocity heterogeneities and topography effects will affect the absolute travel time residuals at least as much as source location and origin time uncertainties in normal ACH tomography. Thus in the case of using ground truth event information, the ACH tomographic scheme can be fully retained when reversing stations and receivers.

We use two different data sets to invert for the local 3D P-velocity structure of the crust beneath the Shagan River test site. One is the high quality arrival time data set described above (further referred to as C-C data), the other is the P-arrival data for the explosions reported in the ISC catalogs. In an initial stage the data sets are re-sorted such that every recording station is taken as a seismic event (pseudo-event), and all explosions for which arrival times are reported at this station are taken as pseudo-stations with arrival time information for this pseudo-event. Residuals for all travel time observations are then calculated with reference to the Herrin (1968) travel time tables. As relative residuals will be used in the inversion, and because our study area is very small (approx. 30 by 30 km), the choice of the reference earth model has no effect on the inversion results. Figure 6 shows the distribution of relative residuals sorted by nuclear explosions. Relative residuals are obtained by subtracting the mean residual for each pseudo-event from the single residuals for this pseudo-event. The C-C data set contains 783 relative residuals for P-wave arrival times from 78 nuclear explosions determined at 33 global network stations. The ISC data set contains 13147 relative P-arrival time residuals from 99 nuclear explosions observed at 351 stations, which were selected for azimuthal coverage, quality and number of observations. The difference in data quality is apparent from the comparison of Figure s 6a and b. It is to be expected that the use of the ISC data in an inversion for local structure will be problematic, as the magnitude of the travel time perturbation expected from local velocity heterogeneities is around the same or even smaller than the scattering for relative residuals at each pseudo-station.

Figure 7 shows map distributions of relative residuals for four stations at different azimuths for the C-C data set. On top of rather random fluctuations, distinct local patterns are visible in each map view. These patterns can be regarded as 'shadows' of the regional and local 3D heterogeneities when illuminated by wavefronts from different directions. On one hand they show that the residual distribution in the data set contains a considerable amount of structural signal, on the other hand they can be used to validate the 3D inversion results, which should mirror the observed pattern to some extent.

In the following, the pseudo-stations will be called 'stations', and the pseudo-events 'events'. The velocity model is parameterized with blocks of 3 by 3 km horizontal size in the upper 27 km, and 6 by 6 km horizontal size from 27 to 49 km. Vertical block size (layer thickness) increases from 4.6 km at 2 km depth to 5.8 km at the bottom. We use a special first layer with 2 km thickness to model pseudo-station corrections (Evans & Achauer, 1993). For that layer, every pseudo-station is assigned one inversion block, no matter how closely the pseudo-stations are spaced. The layering and the layer velocities approximately follow the models proposed by Walter & Ammon (1993, unpublished) for two locations in the wider area. The Moho in this region is at about 50 km depth (e.g. Antonenko, 1984), so due to the small aperture of our pseudo-station array we will not be able to resolve Moho topography or sub-Moho velocities.

The damping value for the inversion is empirically selected by analyzing the trade-off between final data variance and model length (Figure 8). The very small decrease in data variance for the ISC data set is again an indication that this data set is probably not suitable for 3D inversion. For the C-C data set a damping value of 1 s^2 is chosen. This results in a total residual data variance improvement of 70%, from 0.11 s^2 to 0.03 s^2, after a one-iteration inversion.

Figure 9 shows the distribution of station corrections (as velocity perturbations in the uppermost layer) and the velocity distribution in the underlying layer (2 to 6.6 km) resulting from this first preliminary inversion. As a coarse estimate of reliability, the regions with resolution matrix diagonal elements larger than 0.5 are depicted with white contours in Figure 9b. No further refinement of the inversion or quality analysis has been undertaken so far, so these results should be viewed as preliminary. Nevertheless, the apparent systematic patterns in Figure 9b suggest that detailed local 3D velocity structure can be imaged with adequate quality using the C-C data set. The pattern of relatively low velocity in the central part of the model and higher velocity to the west is consistent with results from the "depth of burial" at the test site (Pearson et al., 1998). Heterogeneity is much less at greater model depths.

The station corrections (Figure 9a) do not allow us to distinguish a regional pattern. They can be interpreted as combined effects of near-station heterogeneities, differences in shaft depths (all set to 0 elevation initially), and remaining origin time errors. The large positive correction close to the model center is most likely due to a larger origin time error still present in the dataset. An experiment with a different set of origin time estimates (based just on the C-C data) result in very different station corrections, but very similar models in deeper layers.

The maximum variance reduction that can be achieved for the ISC data, on the other hand, is around 10%. This leads to a much larger model length than the C-C data result (see Figure 8), in other words, we are modeling noise. The conclusion is that, at least without substantial editing, ISC catalog data cannot be used to invert for small scale crustal structure.

CONCLUSIONS AND RECOMMENDATIONS

Ground truth information is a key to evaluating seismic event location capability. For the Shagan River explosions, where we have excellent ground truth, the high-quality arrival times from cross-correlation analysis yield excellent relative location results, even from extremely sparse stations at relatively close distances. Path corrections vary modestly for different sub-areas. Tomography using the high-quality picks and treating the explosions as a source array yields a model for the uppermost crust that is consistent with results from a recent on-site study. Significant velocity variations are found only for the very shallow crust, consistent with the lack of path correction variability.

REFERENCES

Aki, K., Christofferson, A., Husebye, E.S., 1977. Determination of the three-dimensional seismic structure of the lithosphere, J. Geophys. Res., 82, 277-296.

Antonenko, A. N., 1984. Structure of the Earth's crust in Kazakhstan, Academy of Sciences of the Kazakh Soviet Republic, Alma-Ata. 222p.

Bocharov, V. S., S. A. Zelentsov, and V. N. Mikhailov, 1989. Characteristics of 96 underground nuclear explosions at the Semipalatinsk test site, Atomnaya Energiya, 67.

Dodge, D. A., G. C. Beroza, and W. L. Ellsworth, 1995. Evolution of the 1992 Landers, California foreshock sequence and its implications for earthquake nucleation, J. Geophys. .Res., 100, 9865-9880.

Evans, J.R. & Achauer, U., 1993. Teleseismic Tomography using the ACH method, in Iyer, H.M and Hirahara, K. (eds): Seismic Tomography, Chapman & Hall, London, 319-360.

Herrin, E. (ed), 1968. 1968 seismological tables for P phases, Bull. Seismol. Soc. Am., 58, 1193-1241.

NNCRK, 1999. Technical documentation, contributed by the National Nuclear Centre of the Republic of Kazakhstan, Oslo Workshop on IMS Location Calibration, Jan 1999.

Pearson, D. C., J. L. Bonner, L. A. Glenn, M. D. Denny, and W. S. Phillips, 1998. The source depth of burial experiment at Shagan River, Kazakstan, 20th Annual Seismic Research Symposium Proceedings, 86-95.

VanDecar, J. C., and R. S. Crosson, 1990. Determination of teleseismic relative phase arrival times using multi-channel cross-correlation and least squares, Bull. Seismol. Soc. Am., 80, 150-169.

Table 1. Absolute locations for 100 Shagan River nuclear explosions (NNCRK, 1999) and our preliminary origin times and their estimated uncertainties (+/- value, 90% confidence). The first 7 events have fixed origin times obtained from Bocharov et al. (1989).

YRMODAHRMN	SEC	+/-	LATITUD	LONGITU	DEP
650115 6 0	0.80	0.00	49.9350	79.0094	0.0
680619 5 559	0.80	0.00	49.9802	78.9855	0.0
691130 33259	.70	0.00	49.9243	78.9556	0.0
710630 35659	.80	0.00	49.9460	78.9804	0.0
720210 5 3	0.00	0.00	50.0243	78.8780	0.0
721102 127	0.20	0.00	49.9270	78.8171	0.0
721210 42710	.00	0.00	50.0270	78.9955	0.0
730723 123	0.16	0.03	49.9689	78.8174	0.0
731214 74659	.67	0.03	50.0438	78.9856	0.0
740416 55259	.84	0.09	50.0244	78.9264	0.0
740531 327	0.02	0.03	49.9606	78.8441	0.0
741016 633	0.14	0.04	49.9875	78.8941	0.0
741227 54659	.49	0.04	49.9658	79.0032	0.0
750427 53659	.78	0.03	49.9375	78.9035	0.0
750630 327	0.25	0.07	49.9856	78.8969	0.0
751029 44659	.89	0.03	49.9539	78.8738	0.0
751225 51659	.67	0.03	50.0439	78.8199	0.0
760421 5 259	.75	0.04	49.9006	78.8307	0.0
760609 3 259	.79	0.04	49.9936	79.0243	0.0
760704 25659	.99	0.03	49.9042	78.8993	0.0
760828 257	0.04	0.03	49.9750	78.9262	0.0
761123 5 259	.84	0.03	50.0131	78.9432	0.0
761207 45659	.98	0.03	49.9439	78.8391	0.0
770529 257	0.13	0.03	49.9465	78.7715	0.0
770629 3 7	0.24	0.04	49.9995	78.8666	0.0
770905 3 259	.96	0.03	50.0556	78.9141	0.0
771029 3 7	4.90	0.04	50.0522	78.9802	0.0
771130 4 659	.94	0.03	49.9673	78.8743	0.0
780611 257	0.14	0.03	49.9133	78.8018	0.0
780705 247	0.05	0.03	49.9000	78.8665	0.0
780915 23659	.97	0.03	50.0061	78.9670	0.0
780829 237	8.85	0.03	49.9283	78.8670	0.0
781104 5 559	.86	0.03	50.0418	78.9471	0.0
781129 433	5.03	0.03	49.9533	78.7952	0.0
790201 413	0.17	0.03	50.0808	78.8532	0.0
790623 257	0.11	0.03	49.9148	78.8456	0.0
790707 34659	.87	0.03	50.0332	78.9891	0.0
790804 35659	.67	0.03	49.9031	78.8876	0.0
790818 25159	.71	0.03	49.9481	78.9187	0.0
791028 31659	.55	0.03	49.9967	78.9949	0.0
791202 437	0.06	0.03	49.9095	78.7843	0.0
791223 457	0.02	0.03	49.9322	78.7527	0.0
800425 357	0.06	0.03	49.9765	78.7593	0.0
800612 327	0.19	0.03	49.9887	78.9910	0.0
800629 233	0.24	0.03	49.9486	78.8180	0.0
800914 24241	.71	0.03	49.9367	78.7974	0.0
801012 33416	.65	0.03	49.9675	79.0224	0.0
801214 347	9.01	0.03	49.9089	78.9184	0.0
801227 4 910	.63	0.03	50.0619	78.9752	0.0
810329 4 352	.58	0.03	50.0182	78.9787	0.0
810422 11713	.91	0.03	49.8989	78.8084	0.0
810527 35814	.88	0.03	49.9869	78.9705	0.0
810913 21720	.84	0.03	49.9133	78.8942	0.0
811018 357	5.22	0.03	49.9281	78.8445	0.0
811129 33511	.20	0.03	49.9019	78.8488	0.0
811227 34316	.72	0.03	49.9332	78.7781	0.0
820425 323	7.99	0.03	49.9170	78.8876	0.0
820704 11716	.68	0.03	49.9587	78.8115	0.0
820831 131	3.19	0.03	49.9142	78.7613	0.0
821205 33715	.12	0.03	49.9309	78.8095	0.0
821226 33516	.67	0.03	50.0631	78.9938	0.0
830612 23646	.12	0.03	49.9250	78.8979	0.0
831006 147	9.17	0.03	49.9247	78.7505	0.0
831026 155	7.42	0.03	49.9126	78.8215	0.0
831120 327	6.90	0.03	50.0508	78.9991	0.0
840219 357	5.92	0.03	49.8962	78.7429	0.0
840307 239	8.86	0.03	50.0501	78.9560	0.0
840329 51910	.75	0.03	49.9112	78.9267	0.0
840425 1 9	6.09	0.03	49.9359	78.8503	0.0
840526 31314	.92	0.03	49.9790	79.0054	0.0
840714 1 913	.08	0.03	49.9095	78.8769	0.0
841027 15012	.52	0.03	49.9347	78.9279	0.0
841202 319	8.94	0.03	50.0062	79.0087	0.0
841216 355	5.19	0.03	49.9458	78.8084	0.0
841228 35013	.15	0.03	49.8803	78.7037	0.0
850210 32710	.07	0.03	49.8993	78.7804	0.0
850425 057	9.10	0.03	49.9268	78.8805	0.0
850615 057	3.21	0.02	49.9086	78.8426	0.0
850630 239	5.13	0.03	49.8644	78.6685	0.0
850720 05316	.98	0.03	49.9498	78.7837	0.0
870312 15719	.63	0.03	49.9353	78.8287	0.0
870403 11710	.36	0.02	49.9181	78.7801	0.0
870417 1 3	7.14	0.03	49.8779	78.6687	0.0
870620 053	7.16	0.02	49.9353	78.7440	0.0
870802 058	9.27	0.03	49.8806	78.8745	0.0
871115 331	9.17	0.03	49.8987	78.7579	0.0
871213 321	7.25	0.03	49.9632	78.7929	0.0
871227 3 5	7.22	0.03	49.8795	78.7248	0.0
880213 3 5	8.28	0.03	49.9367	78.8637	0.0
880403 133	8.21	0.02	49.9083	78.9081	0.0
880504 057	9.15	0.02	49.9495	78.7501	0.0
880614 227	9.00	0.03	50.0189	78.9605	0.0
880914 35959	.77	0.02	49.8779	78.8229	0.0
881112 330	6.27	0.03	50.0431	78.9688	0.0
881217 418	9.24	0.03	49.8820	78.9245	0.0
890122 357	9.06	0.02	49.9395	78.8191	0.0
890212 415	9.26	0.03	49.9187	78.7109	0.0
890708 347	0.09	0.03	49.8679	78.7801	0.0
890902 41659	.85	0.04	50.0058	78.9855	0.0
891019 94959	.90	0.03	49.9223	78.9081	0.0

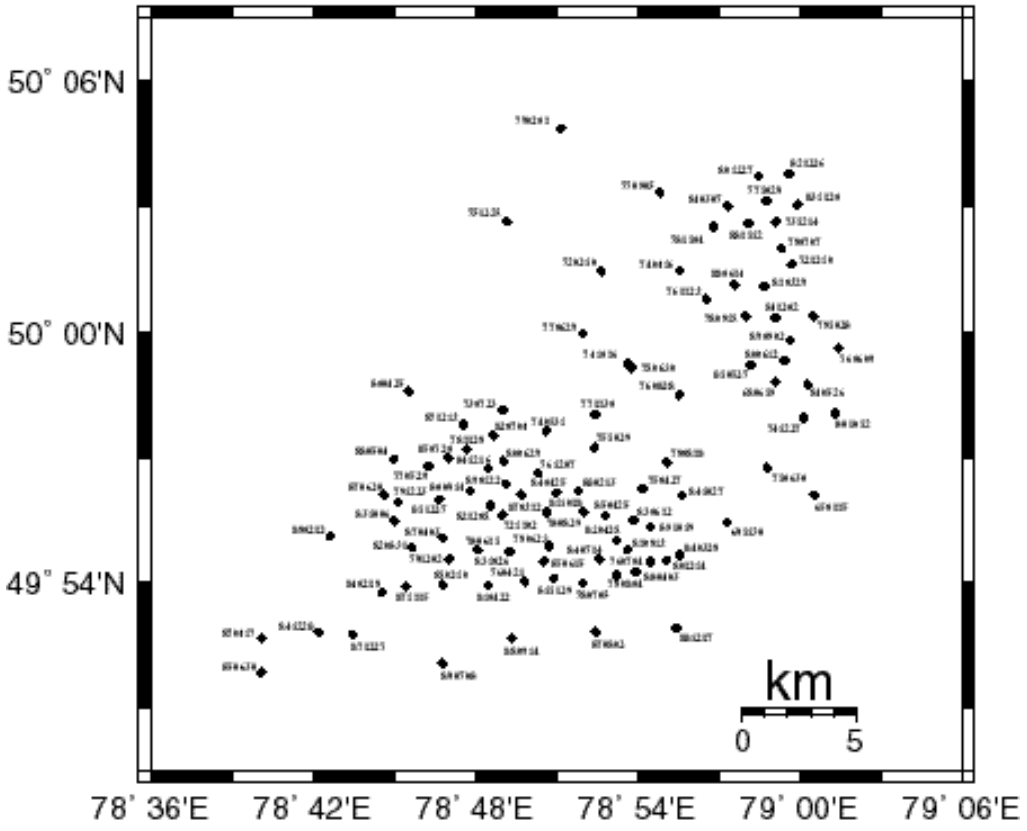


Figure 1. Map of absolute locations of 100 Shagan River nuclear explosions (NNCRK, 1999) used in our analysis.

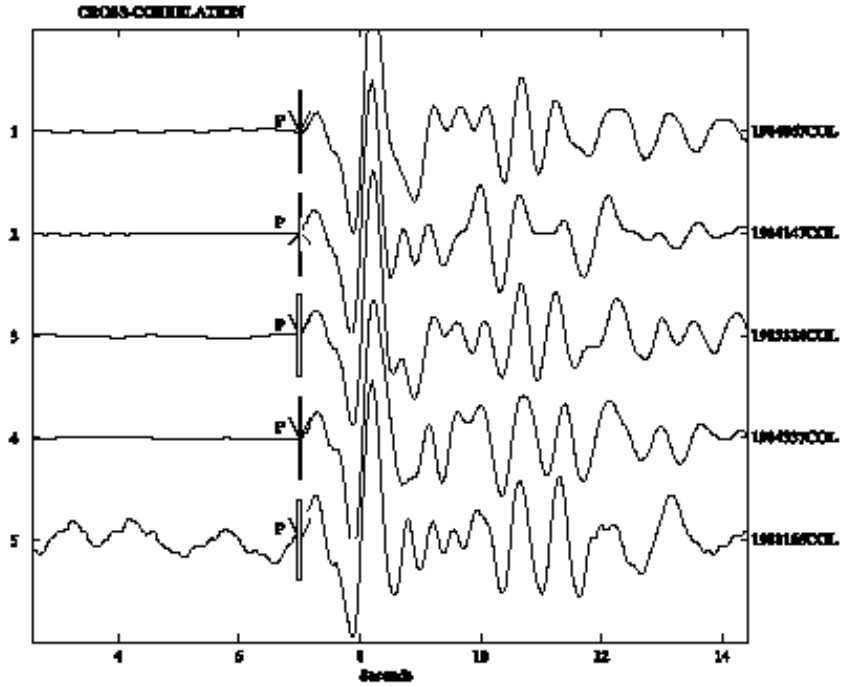


Figure 2. Illustration of cross-correlation arrival time estimation - note alignment of noisy trace at bottom.

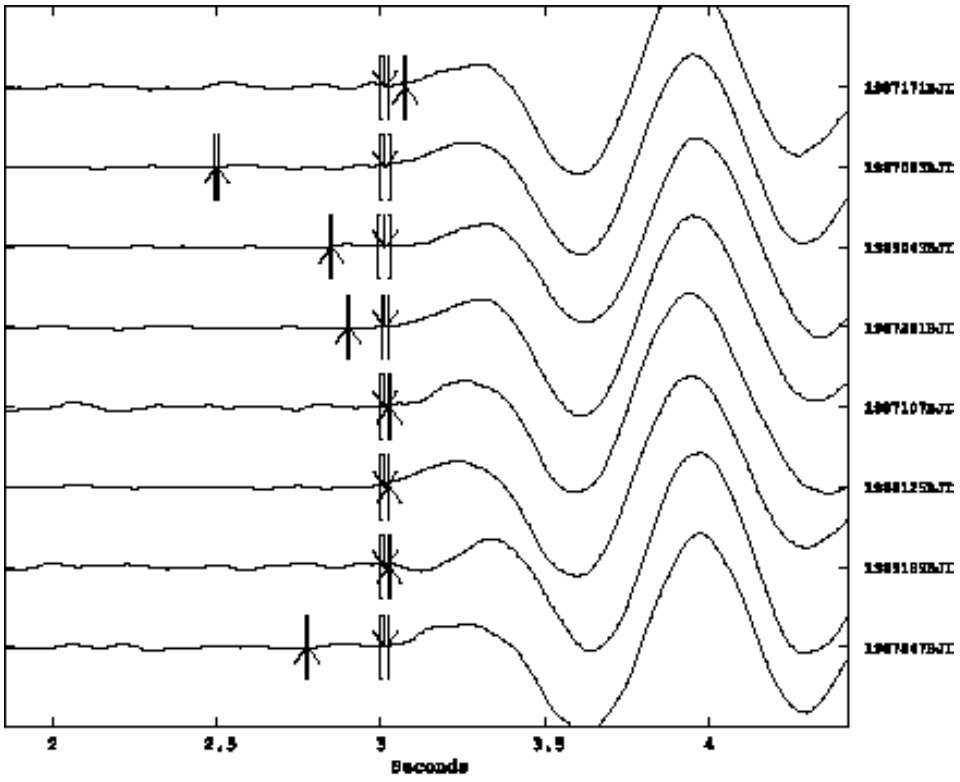


Figure 3. Comparison of arrival times reported by ISC (upward-pointing arrows) to picks determined using cross-correlation analysis (downward-pointing arrows). The differences are due to round-off of the ISC data in this case.

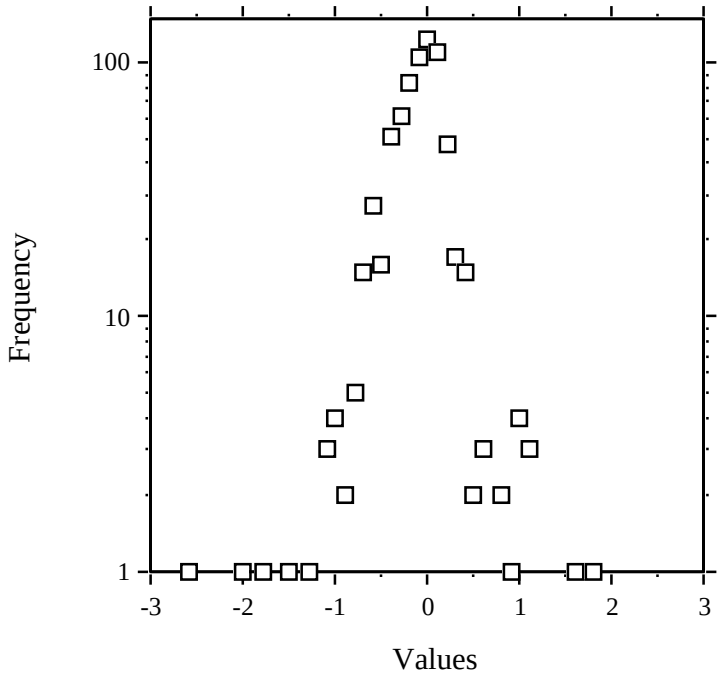


Figure 4. Frequency plot of the differences between ISC and cross-correlation arrival times (values in seconds, in 0.1 s bins). Note the logarithmic frequency scale. Most residuals are with +/- 0.5 s. Some outliers are not shown.

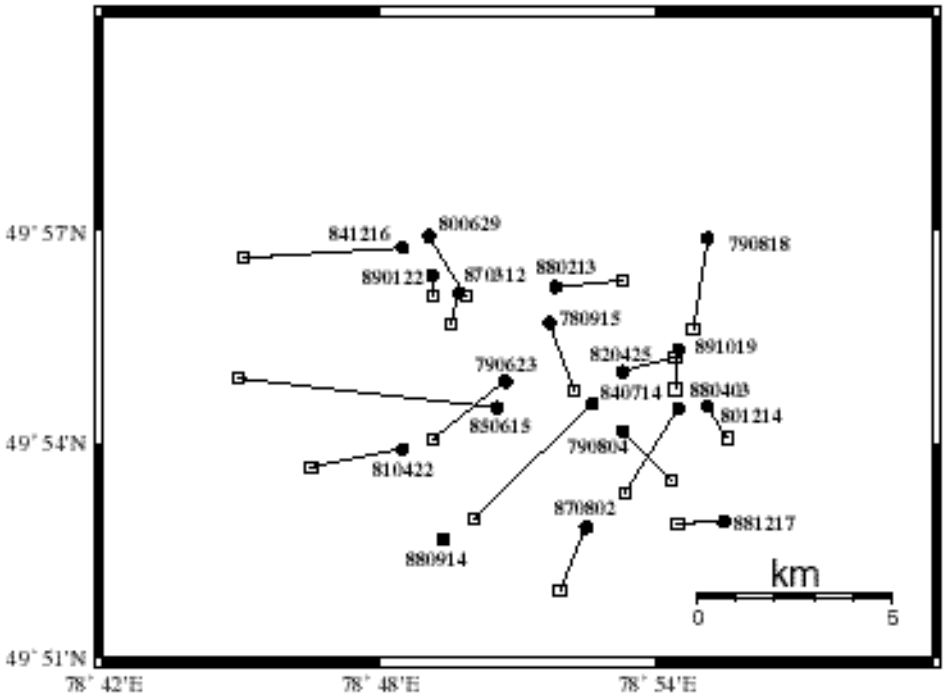


Figure 5. Mislocations (open squares) for explosions from the central Shagan River group using only stations within 40°. The mean mislocation distance is 2.2 km and the mean 90% confidence ellipse area is 8.6 km.

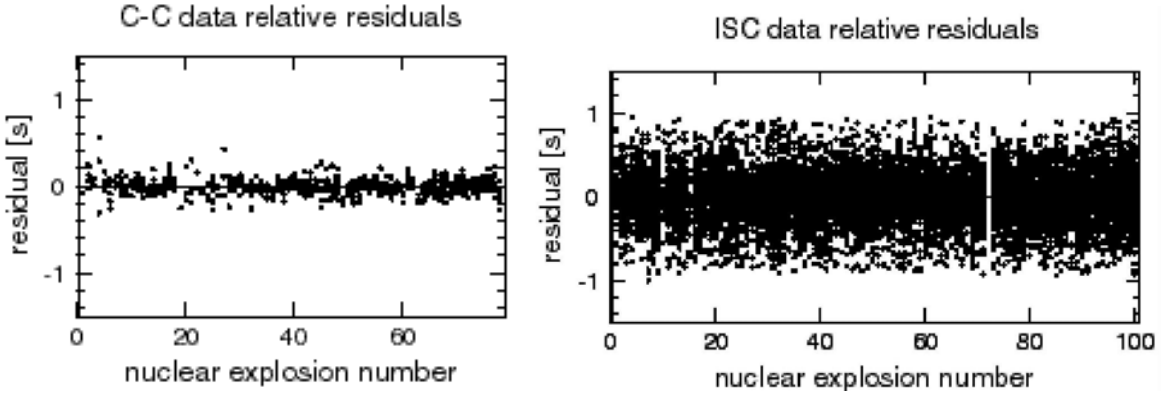


Figure 6. Relative residuals for each nuclear explosion (pseudo-station). Left: repicked (C-C) dataset. Right: ISC catalog dataset. Note the small scatter and apparent systematic variations for the C-C data versus the wide scatter with no apparent trend for the ISC data.

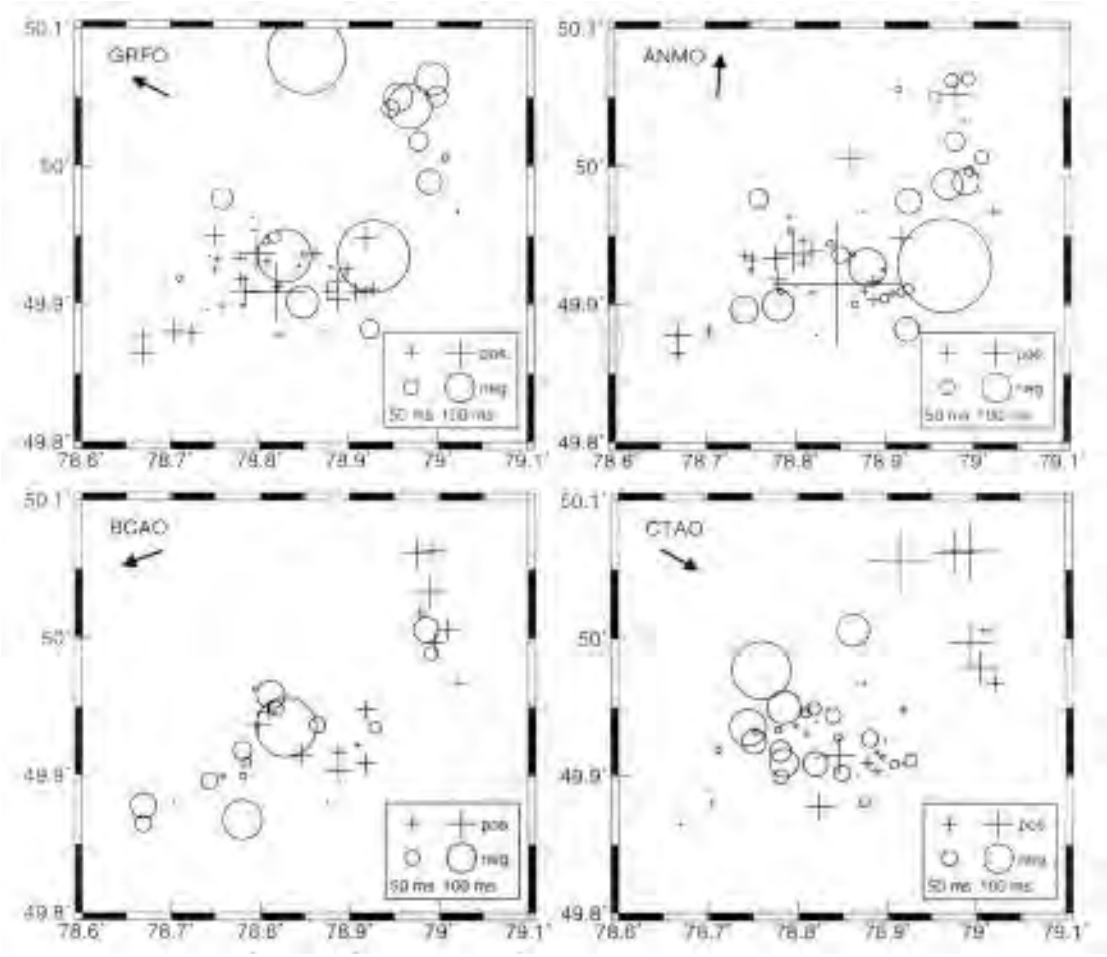


Figure 7. Map views of relative residuals for recording stations (pseudo-events) at different azimuths. Crosses denote negative residuals (i.e. travel times are shorter than average), open circles denote positive residuals (longer travel times). Station name and azimuth to station are given in the upper left corner of each map.

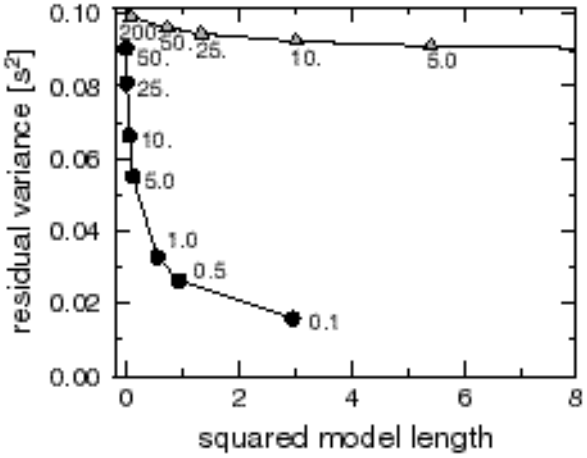


Figure 8. Damping test for the 3D velocity inversion; full circles denote the C-C data, grey triangles the ISC data. A damping of 1.0 was selected for the inversion of the C-C data from this test. The small decrease in residual variance together with the large increase in solution length for the ISC data indicates that this data set may not be adequate for the inversion.

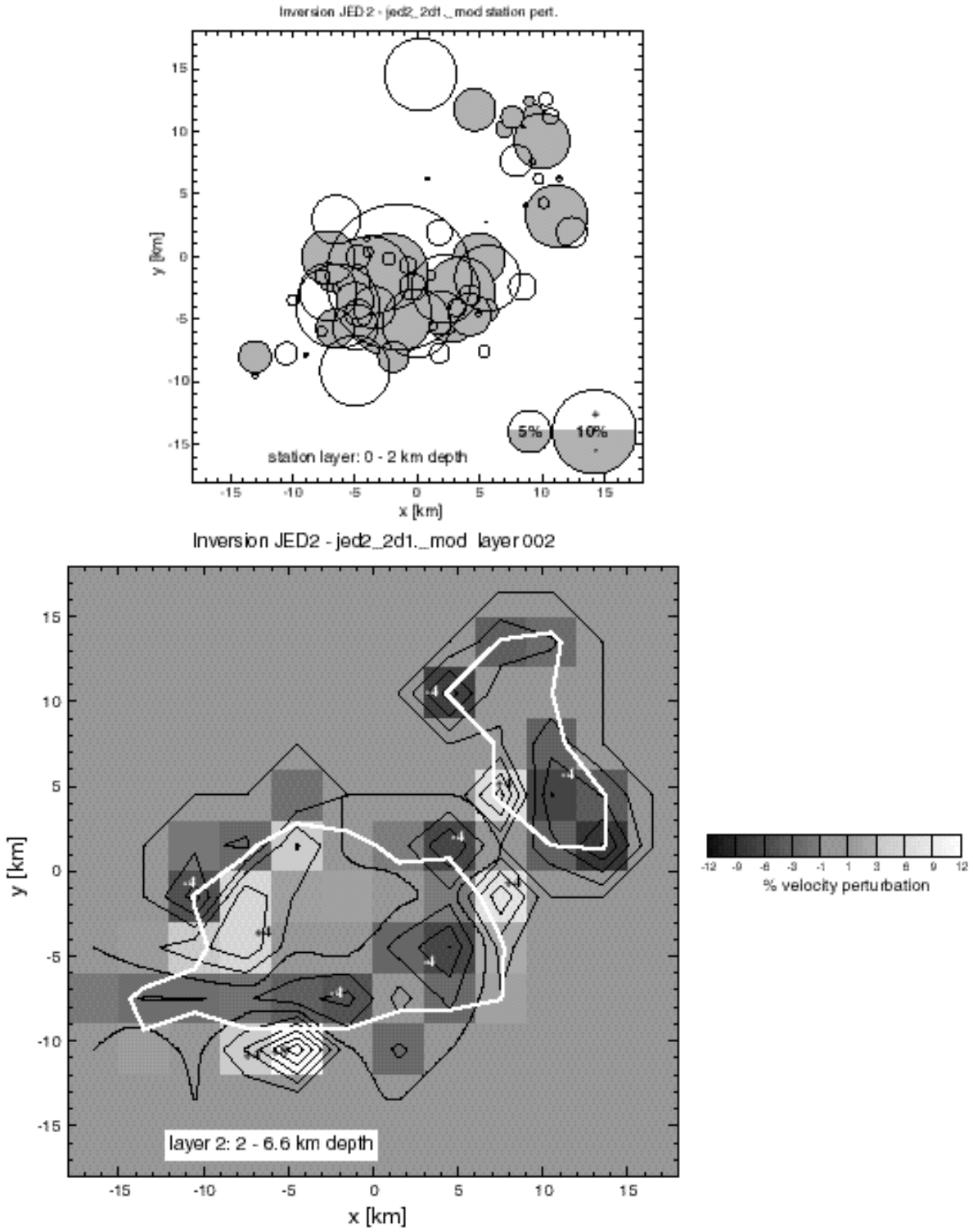


Figure 9. Preliminary 3D tomography results for the C-C dataset. Model center (0, 0) is at 49 57' N, 78 51' E. (a) Top panel: station perturbations (in %). Open circles are positive (faster), filled are negative (slower). (b) Bottom panel: layer 2 (2 - 6.6 km depth) velocity perturbations, shown as shaded blocks and smoothed contours (2% contours). White contouring (smoothed) indicates model areas with diagonal resolution element above 0.5.

LLNL's REGIONAL SEISMIC DISCRIMINATION RESEARCH

William R. Walter, Arthur J. Rodgers, Alan Sicherman, William Hanley,
Kevin Mayeda Stephen C. Myers, and Michael Pasyanos
Geophysics and Global Security Division, Lawrence Livermore National Laboratory

Sponsored by U.S. Department of Energy
Office of Nonproliferation and National Security
Office of Research and Development
Contract W-7405-ENG-48

ABSTRACT

As part of the Department of Energy's research and development effort to improve the monitoring capability of the planned Comprehensive Nuclear-Test-Ban Treaty international monitoring system, Lawrence Livermore Laboratory (LLNL) is testing and calibrating regional seismic discrimination algorithms in the Middle East, North Africa and Western Former Soviet Union. The calibration process consists of a number of steps: 1) populating the database with independently identified regional events; 2) developing regional boundaries and pre-identifying severe regional phase blockage zones; 3) measuring and calibrating coda based magnitude scales; 4a) measuring regional amplitudes and making magnitude and distance amplitude corrections (MDAC); 4b) applying the DOE modified kriging methodology to MDAC results using the regionalized background model; 5) determining the thresholds of detectability of regional phases as a function of phase type and frequency; 6) evaluating regional phase discriminant performance both singly and in combination; 7) combining steps 1-6 to create a calibrated discrimination surface for each stations; 8) assessing progress and iterating. We have now developed this calibration procedure to the point where it is fairly straightforward to apply earthquake-explosion discrimination in regions with ample empirical data. Several of the steps outlined above are discussed in greater detail in other DOE papers in this volume or in recent publications. Here we emphasize the results of the above process: station correction surfaces and their improvement to discrimination results compared with simpler calibration methods.

Some of the outstanding discrimination research issues involve cases in which there is little or no empirical data. For example in many cases there is no regional nuclear explosion data at IMS stations or nearby surrogates. We have taken two approaches to this problem, first finding and using mining explosion data when available, and second using test-site based models to transport earthquake-explosion discrimination behavior to new regions.

Finally an important component of our research is assessing improvement in the ability to discriminate events. By combining the multivariate discriminants with the threshold detection curves for the regional seismic phases used in those discriminants, we have started to make maps of the probability an event will be identified properly. These maps serve a broad range of purposes from demonstrating progress to funding agencies to prioritizing research and calibration efforts.

Key Words: seismic, discrimination, explosion, Middle East, North Africa, India

This work performed under the auspices of the U.S. Department of Energy by the Lawrence Livermore National Laboratory under contract W-7405-ENG-48.

OBJECTIVES

Monitoring of the Comprehensive Nuclear-Test-Ban Treaty (CTBT) requires characterizing seismic events and discriminating between earthquakes, mining activities and banned nuclear tests. LLNL is evaluating and calibrating regional discriminants in the uncalibrated Middle East, North Africa, Southwest Asia, Western Russia and other regions of interest to improve CTBT monitoring capability.

RESEARCH ACCOMPLISHED

As part of the overall Department of Energy CTBT Research and Development program, LLNL is pursuing a comprehensive identification research effort to improve our capabilities to seismically characterize and discriminate banned underground nuclear tests from other natural and man-made sources of seismicity. Over the past several years we have developed, tested, and refined a regional seismic discrimination calibration procedure for seismic regions. Here we will give an overview of the procedure as applied to regional seismic body-wave (Pn, Pg, Sn, Lg, coda) discriminants. Surface-wave discriminant techniques, such as Ms-mb using phase-match filters derived from group velocity tomography results, are described in Pasyanos et al (this volume). The procedure is shown in Figure 1 in flowchart form and described in words in the abstract. We will give a brief description of each part below and summarize the recent progress.

A) Database

The first step in the calibration is to populate a database with independently identified (source ground truth) events to use in calibration and testing. LLNL has created an extensive research database (see Ruppert et al., this volume) of both earthquakes and explosions from public data repositories, catalogs and publications. In addition we have made use of waveform correlation techniques, spatial and temporal clustering and site visits to build up catalogs of ground truth mine blasts (Harris et al., this volume).

B) Regionalization

The Middle East and North African region encompasses the full range of tectonic processes and with a correspondingly heterogeneous lithosphere. This in turn can dramatically affect regional seismic phase producing a large variability in expected amplitudes. In some cases phases such as Lg can be “blocked” (amplitude attenuated to below background noise) due to structural effects. Because relatively small amplitude S-wave phases (Sn or Lg) are potential discriminants it is important to identify when structural rather than source effects reduce their amplitudes in order to avoid false alarms. We developed a new, more quantitative, empirical procedure to better map the efficiency of Lg propagation in the greater Mediterranean region (McNamara and Walter, 1999). The technique plots the maximum observed Lg/Pcoda amplitude in a one by one-degree or smaller cells for several thousand paths in the region. In seismic areas these empirical techniques can be effective, but there are also large aseismic regions (e.g. North Africa, Arabia, India) in our region. To help intelligently extrapolate of empirical calibrations we developed a first-order regionalization for the Middle East and North Africa (Sweeney and Walter, 1998) based on tectonic maps, and a review of published and unpublished literature. There are many ongoing studies to better determine seismic structure in aseismic areas of the Middle East and North Africa both at LLNL (see Rodgers et al., this volume and Hazler et al this volume) and in academia and industry (e.g. Sandvol et al, 1998).

C) Coda Magnitudes

Previous studies have shown the great stability of regional coda magnitudes (Mayeda, 1993; Mayeda and Walter 1996). Regional coda amplitudes show four to eight times less interstation scatter than the amplitudes of direct phases such as Lg and Pn. This means that a single station coda magnitudes can have the same precision as a direct phase magnitude using 16 to 64 station networks. This is particularly useful for characterizing small magnitude events recorded at just a few stations. Coda magnitudes can also be calibrated to give accurate independent seismic moments, which are critical for obtaining accurate source scaling corrections as discussed in the next section. Mayeda et al (this volume) describe how to calibrate regional coda magnitude scales using Middle East stations as examples.

D) Amplitude Corrections

Regional amplitudes are strongly affected by source-size scaling and path propagation effects. Source-size scaling effects include the corner frequency or source dimension effects (e.g. Taylor and Denny, 1991; Walter and Priestley, 1991) and can appear as magnitude dependent discrimination results. Path propagation effects include geometrical spreading and attenuation and can appear as distance dependent discrimination results. Removing these effects allows the comparison of events of different sizes and distances and facilitates combining individual discriminant measures to form more effective multivariate discriminants. For these reasons we are applying a Magnitude and Distance Amplitude Correction (MDAC) technique to the regional measurements (see Taylor et al, this volume; Taylor et al, 1999). The MDAC technique uses a Brune (1970) type source model and simple 1-D path corrections to remove gross magnitude and distance trends from earthquake data at each station. These corrections are then applied to all future measurements at that station. After applying the MDAC process there remain amplitude variations due to heterogeneous structural effects. In a recently completed study (Rodgers et al, 1999) we used a common data set to compare a variety of techniques to correct for 2-D path effects and found that nonstationary Bayesian kriging (Schultz et al., 1998) gave the best results and has particular advantages in the way it handles uncertainties. These results are demonstrated in Figure 2. Phillips (1999) reached similar conclusions. To correct for heterogeneous structure we krig the MDAC residuals and make use of a priori background models to fill in the larger aseismic regions.

E) Detection

To use a regional discriminant with confidence we need to know whether the regional phase amplitudes can be detected at each station. This is particularly important for discriminants that rely on the relatively low amplitude or absence of a phase to identify explosions. We are currently exploring two-dimensional generalizations of a 1-D detectability functions (e.g. Sereno and Bratt, 1989; Taylor and Hartse, 1996) for each phase as a function of frequency.

F) Discrimination

After determining the frequency bands at which regional phase amplitudes can be measured, and correcting for first-order effects of source size and distance, we can examine the combinations of amplitudes separate explosions from earthquakes. The May 11, 1998 Indian tests provide a good underground nuclear explosion data-point to test our calibration procedure and evaluate discriminants. We have recently completed a regional discrimination study using this Indian test (Rodgers and Walter, 1999). We measured 1-2 Hz Pn/Lg amplitudes for several hundred earthquakes recorded at regional distances at the IRIS station NIL (Nilore, Pakistan). Ratios of Pn/Lg have shown good regional discrimination performance at other nuclear test sites (e.g. Walter et al. 1995; Hartse et al, 1997). The 1-2 Hz Pn/Lg values show great variability as a function of location as shown in Figure 3. After correcting for a first-order distance effect we krig the amplitudes giving the correction surface shown on the left-hand side of Figure 3. On the right-hand side of Figure 3 we compare the effect on the separation of the Indian test from surrounding explosions before and after the distance+kriging correction. Note the scatter of the earthquake population is significantly reduced and the explosion separates form the earthquakes more cleanly. In the Assessment section we will quantify this improvement.

G) Station Surfaces

This step combines all the information in steps A-F to create discrimination surfaces for each station. It is important to note that we have developed each of the calibration steps in such a way as to allow this kind of combination. For example the kriging of empirical data can easily be done on top of a background model for regionalization and/or after applying 1-D MDAC corrections. The kriging algorithm can also incorporate a priori boundaries where parameters such as correlation length change to accommodate structural discontinuities.

H) Assessment

After regional discrimination correction surfaces are created for each station we need to be able to assess progress. For example the right-hand side of Figure 3 shows clear improvement in a scatter plot after the calibration corrections are applied. We want to quantify these results and make them more useful to policy

makers and other non-technical people. One standard way to quantify discrimination is using Mahalanobis distance (e.g. Hartse et al, 1997), a measure of separation of the means divided by a sum of the variances, and these numbers are given as D2 on the right-hand side of Figure 3. Bigger Mahalanobis distances are better and we show an improvement of about a factor of three in D2. However these numbers are not intuitively useful by themselves, don't easily allow tradeoffs in error rates and are hard to convey to policy makers and funding agencies. We think a better approach is to use Receiver Operator Characteristic (ROC) curves. We are currently writing up a report documenting these ideas (Sicherman et al., 1999, written communication).

An example of converting the scatter plots shown in Figure 3 into ROC or tradeoff curves is shown in Figure 4. The probability densities of the two population types are calculated and the "decision line" is swept through all possible values tracing out a tradeoff curve as shown in Figure 4. The tradeoff curves plot the two possible error types in identifying events drawn from populations of two types of events against each other. The error types are mislabeling an explosion and an earthquake (missed event) and mislabeling an earthquake as an explosion (false alarm or reported event). This explicitly allows tradeoff of this error type if political or other costs way one type of mislabeling higher than the other. It also easily allows the creation of multiple categories of labels, for example creating a "needs further investigation" label between "earthquake" and "explosion" labels.

In this example, we have only one explosion, and we've assumed the Indian test is the mean of the explosion population and the variance is the same as the earthquakes. Under the equal variance assumption Mahalanobis distance can be explicitly related to the equiprobable point (EPP) on the ROC curve, this is the point where the two errors are equal. So in this example the EPP goes from 19.8% to 8.6%. This also quantifies improvement but in a clearly understandable way, the mislabeling for each event type drops from 19.8% to 8.6% after calibration. It is important to note that 1-2 Hz Pn/Lg is just one discriminant measure and that the EPP value can be reduced much further by combining several discriminant measures.

We are currently developing procedures to combine detection maps, discrimination surfaces and ROC results to map error rates as a function of location for each station. This will allow us to better assess areas that are well calibrated and areas that need more work. Similar work has already been done for the location problem (see Schultz et al., this volume).

I) Iterate

It is important to note that discrimination procedures can always be improved. The assessment process lets us evaluate how we are doing for each station and reallocate resource and priorities in a more cost-effective manner. As stations become calibrated we will continually assess how well they do and how improvements can be made by obtaining new data, doing a calibration experiment or through other means.

CONCLUSIONS AND RECOMMENDATIONS

Regional discrimination algorithms require calibration at each seismic station to be used for CTBT monitoring. LLNL is pursuing a comprehensive discrimination effort in the Middle East, North Africa and other regions of interest. In addition we are engaged in ongoing physical basis studies to understand and model discriminants in new regions. Calibrating seismic stations for monitoring the CTBT is a challenging task and will require processing large amounts of data, and collaboration with government, academic and industry researchers and incorporation of the extensive R&D results both within and outside of DOE.

REFERENCES

Brune, J. (1970). Tectonic stress and the spectra from seismic shear waves earthquakes, *J. Geophys. Res*., **75**, 4997-5009.

Hartse, H., S. R. Taylor, W. S. Phillips, and G. E. Randall, (1997). A preliminary study of regional seismic discrimination in Central Asia with an emphasis on Western China*, Bull. Seism. Soc. Am*. **87**, 551-568.

Mayeda, K., mb(Lgcoda): A stable single station estimator of magnitude, *Bull. Seism. Soc. Am., 83,* 851-861, 1993.

Mayeda, K. M. and W. R. Walter, Moment, energy, stress drop and source spectra of Western U.S. earthquakes from regional coda envelopes, *J. Geophys. Res*., **10***1*, 11,195-11,208, 1996.

McNamara, D. E. and W. R. Walter, Mapping Crustal Heterogeneity using Lg Propagation Efficiency Throughout the Middle East, Mediterranean, Southern Europe and Northern Africa, submitted to PAGEOPH, 1999.

Myers, S. C., W. R. Walter, K. Mayeda and L. Glenn, Observations in support of Rg scattering as a source for explosion S waves: regional and local recordings of the 1997 Kazakhstan depth of burial experiment, *Bull. Seism. Soc. Am. 89*, 544-549, 1999.

Pasyanos, M. E., W. R. Walter, and S. E. Hazler, A surface wave dispersion study of the Middle East and North Africa for monitoring the Comprehensive Nuclear-test-Ban Treaty, submitted to PAGEOPH, 1999.

Rodgers, A. J., W. R. Walter, C. Schultz and S. Myers, A comparison of methodologies for representing path effects on regional P/S discriminants, *Bull. Seism. Soc. Am. 89*, 394-408, 1999.

Rodgers, A. J. and W. R. Walter, Seismic Discrimination of the May 11, 1998 Indian Nuclear Test with Short-Period Regional Data From Station NIL (Nilore, Pakistan), submitted to PAGEOPH, 1999.

Sandvol, E., D. Seber, A. Calvert, M. Barazangi, 1998, Grid search modeling of receiver functions: Implications for crustal structure in the Middle East and North Africa, Journal of Geophysical Research, 103, 26,899-26,918.

Sereno, T.J. and S.R. Bratt, Seismic detection capability at NORESS and implications for the detection threshold of a hypothetical network in the Soviet Union, *J. Geophys. Res.*, 94, 10,397-10,414, 1989.

Schultz, C., S. Myers, J. Hipp, and C. Young, Nonstationary Bayesian kriging: application of spatial corrections to improve seismic detection, location and identification, *Bull. Seism. Soc. Am., 88*, 1275- 1288, 1998.

Taylor, S. R., and Hans E. Hartse, Regional phase seismic phase detection thresholds at WMQ, Los Alamos Report, LAUR-96-395, 1996.

Taylor, S. and M. Denny (1991). An analysis of spectral differences between NTS and Shagan River nuclear explosions, *J. Geophys. Res*., **96**, 6237-6245.

Taylor, S., Velasco, A., Hartse, H., Philips, S., Walter, W., and Rodgers, A. (1999). Amplitude corrections for regional discrimination, submitted to *Pure. App. Geophys*.

Walter, W., and K. Priestley (1991). High-frequency P wave spectra from explosions and earthquakes, in *Explosion Source Phenomenology*, ed. S. Taylor, H. Patton and P. Richards.

Walter, W. R., K. Mayeda, and H. J. Patton (1995). Phase and spectral ratio discrimination between NTS earthquakes and explosions Part 1: Empirical observations, *Bull. Seism. Soc. Am.,* **85**., 1050-1067.

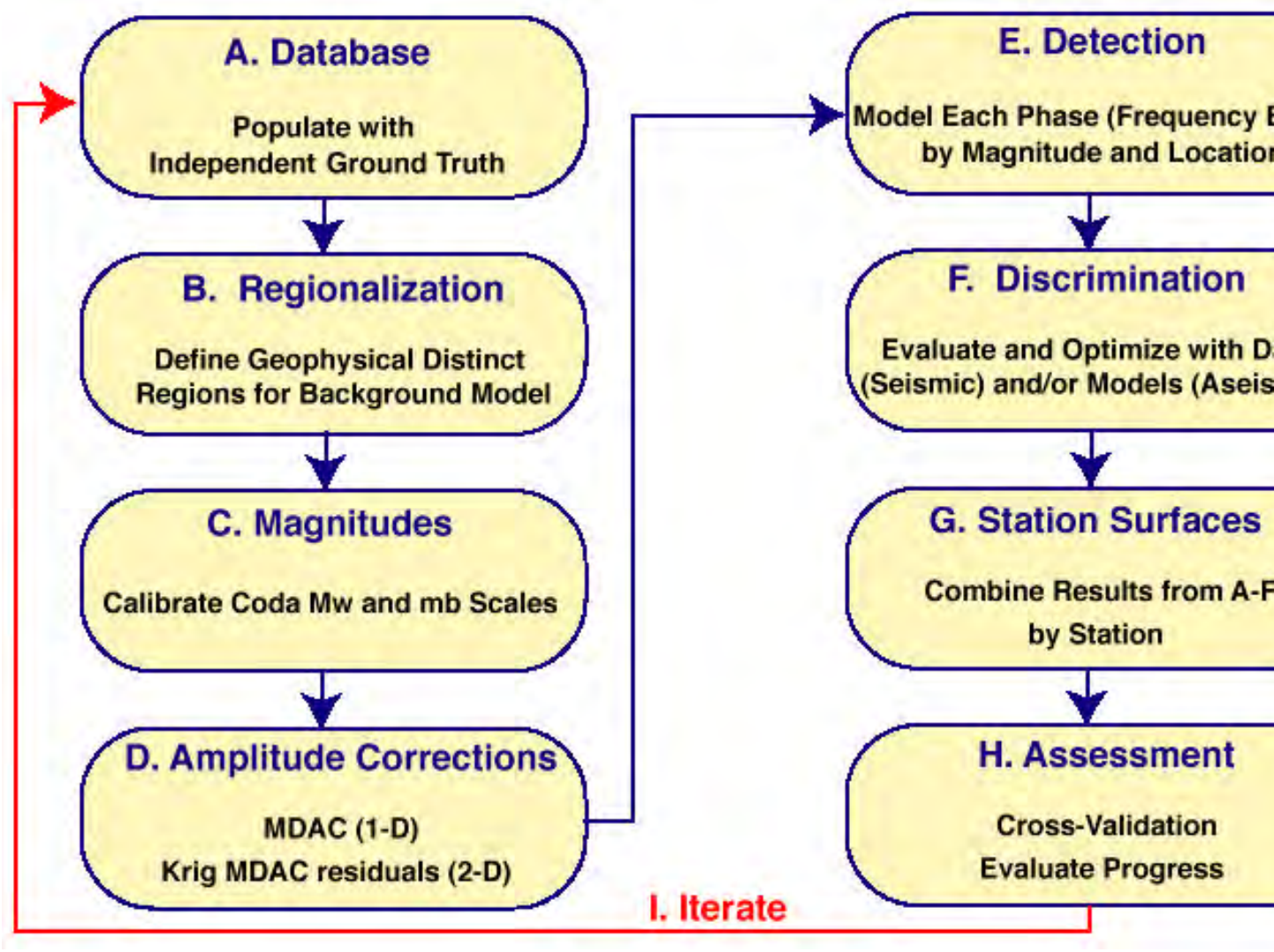


Fig. 1. Flowchart showing regional seismic discrimination calibration procedure as discussed in the text.

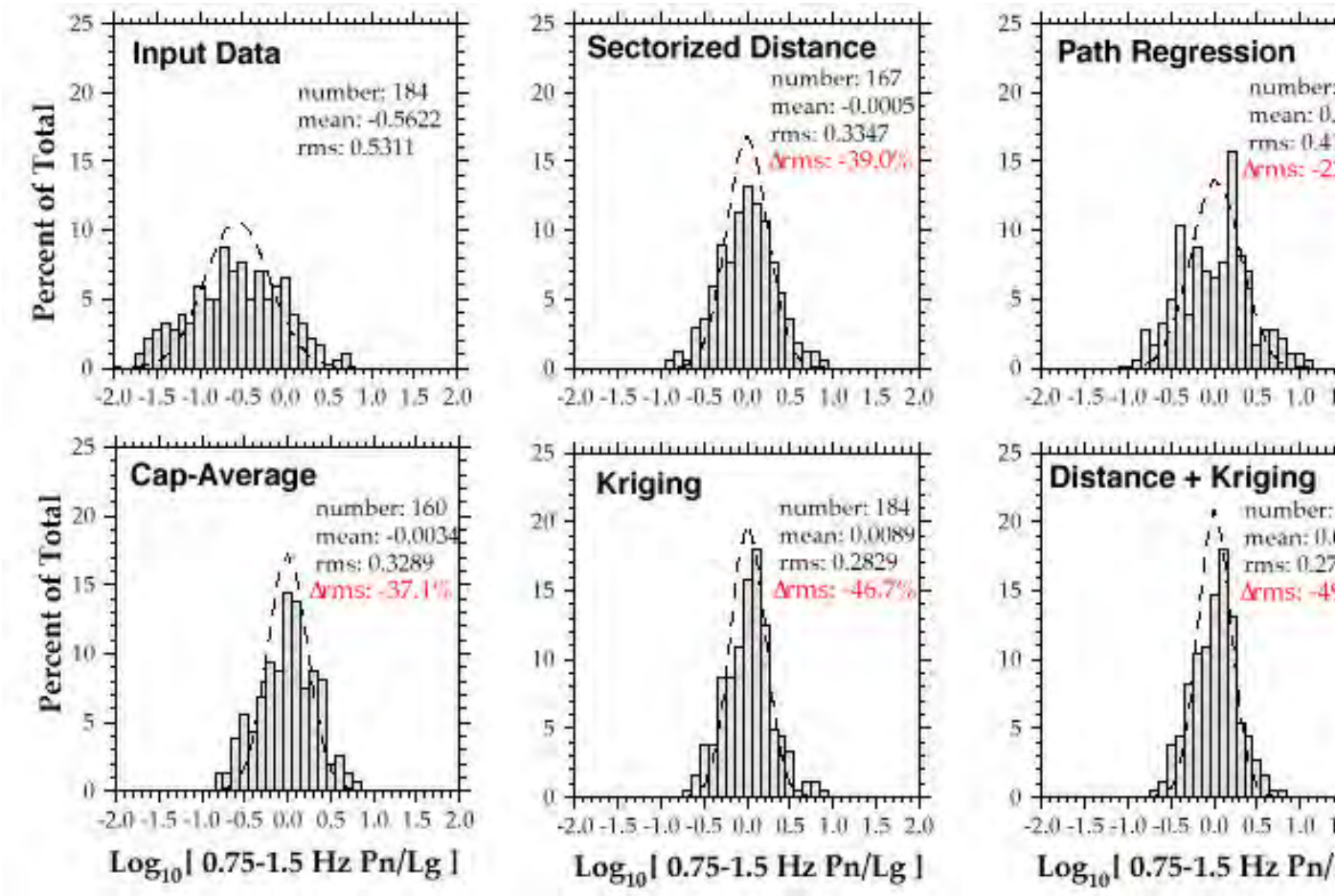


Fig. 2. Comparison of path correction techniques applied to the 0.75-1.5 Hz Pn/Lg regional seismic discrimination measure at the I IMS primary stations GEYT). Upper left shows the uncorrected earthquake population; upper model shows the reduction in scatter corrections sectorized by azimuth were applied; upper right shows scatter after path-specific corrections from the best regression a such as topography and sediment thickness were applied; lower left shows the effect of applying a circular area smoothing process application of the DOE kriging algorithm, and lower right shows the best reduction after kriging is applied to a simple distance cor kriging alone give the best results and that any additional corrections desired (e.g. distance) can be applied prior to kriging. In addi estimates of the error of any point on the surface, (after Rodgers et al., 1999).

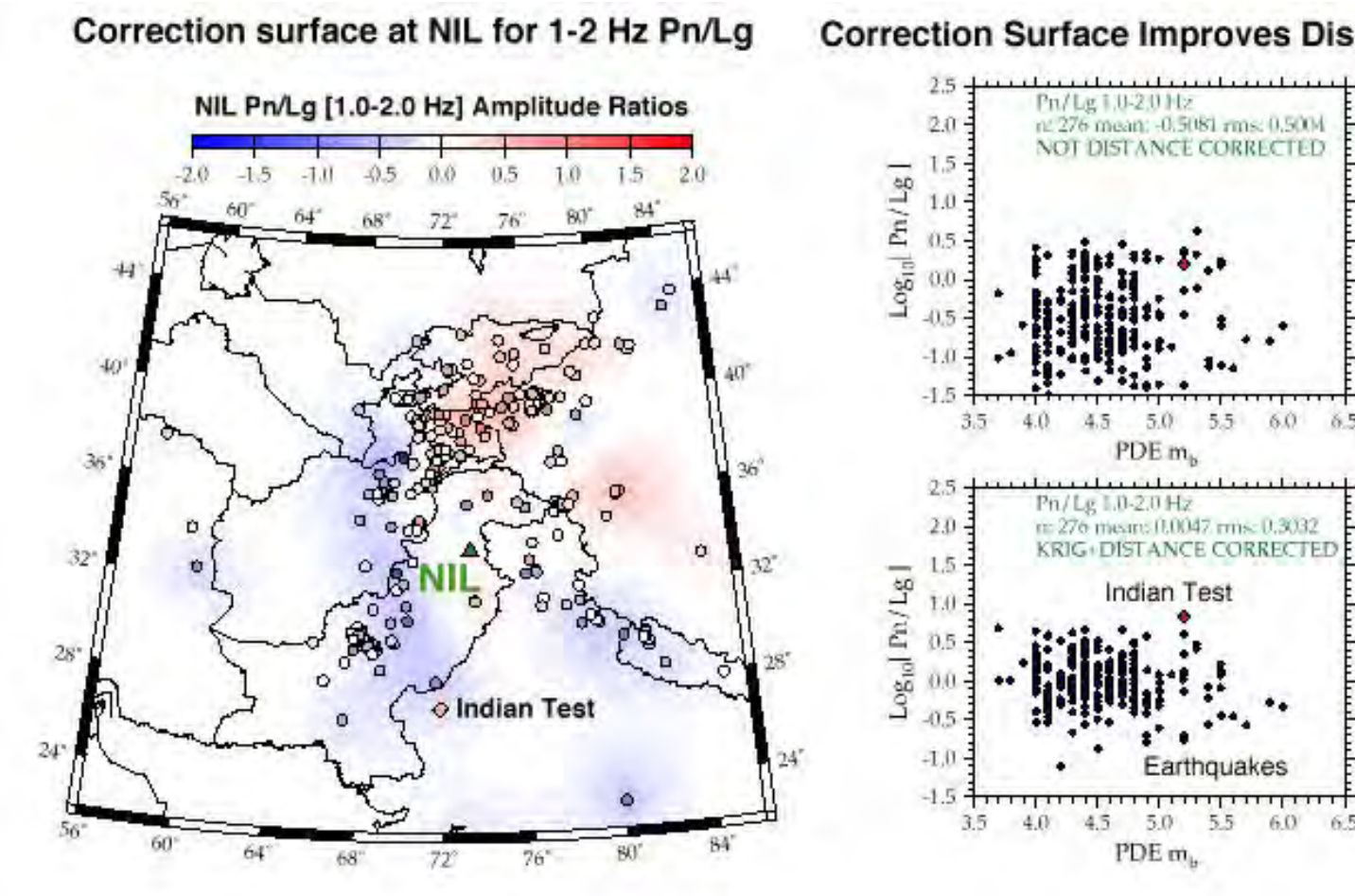


Fig. 3. The left-hand side shows an example of a kriged correction surface for a particular regional seismic discrimination measure (aft
distance effect) at the IRIS station NIL, site of the IMS primary station PRPK. The right hand side shows the improvement in separatin
Indian underground nuclear test from the earthquake population after the distance+kriging correction is applied (after Rodgers and Wal

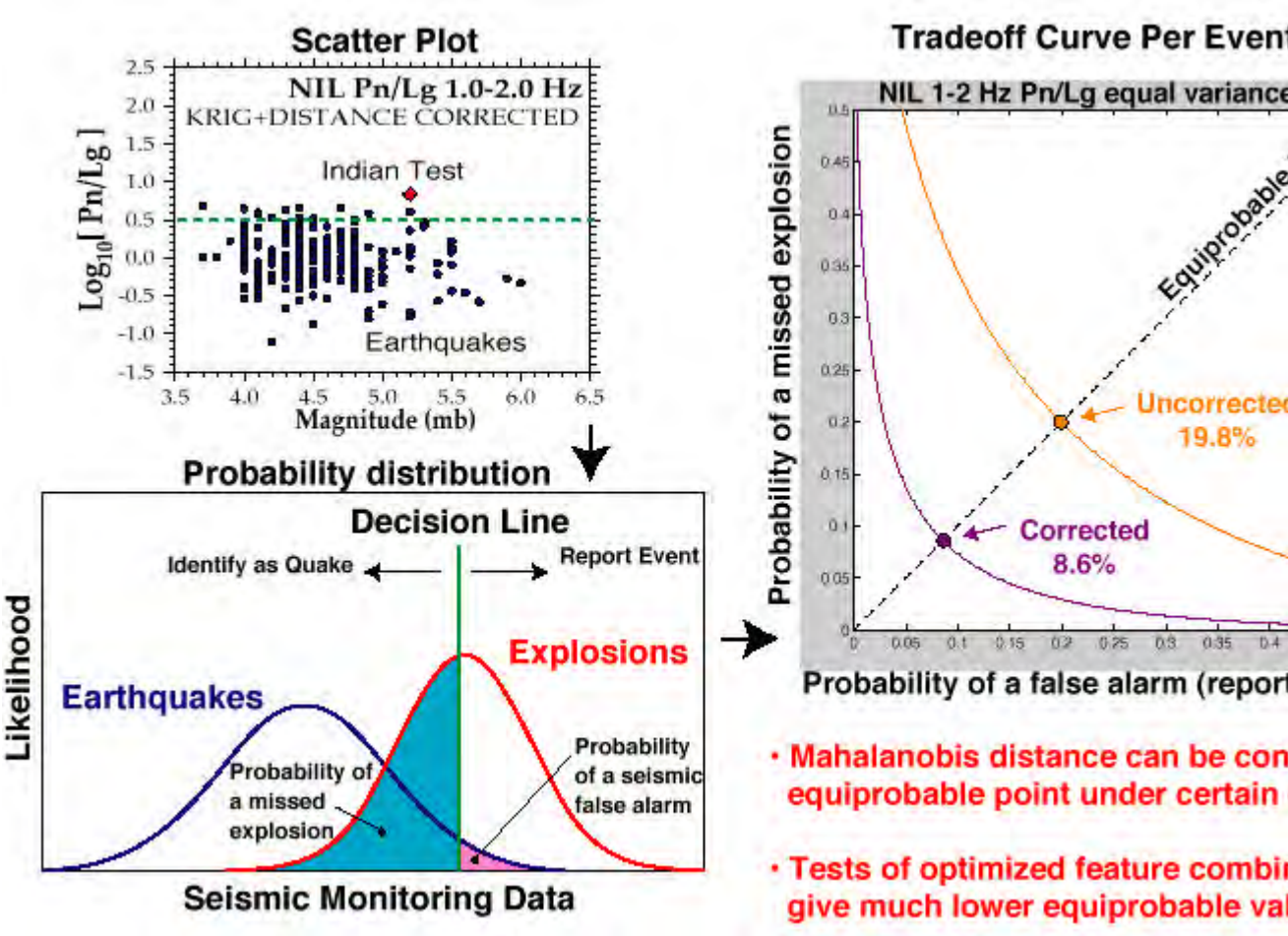


Fig. 4. Example showing how discrimination scatter plots can be converted to Receiver-Operator Characteristic (ROC) curves whi
tradeoff between misidentifying an explosion as an earthquake (missed explosion) and reporting an earthquake as suspicious (false
of these two error types depend on political and other non-technical factors. ROC curves allow these factors to be incorporated and
complete assessment of discrimination potential.

EXTENDING REGIONAL WAVE FORM MODELING TO SHORTER PERIODS TO IMPROVE THE LOCATION AND IDENTIFICATION OF SMALL SEISMIC SOURCES

Bradley B. Woods, Chandan K. Saikia, and Hong Kie Thio
URS Greiner Woodward-Clyde, Pasadena, CA

Sponsored by Defense Threat Reduction Agency
Contract No. DTRA 01-98-C-0151

ABSTRACT

We are developing an interactive analysis system whereby the finer (short period) time-domain features of regional seismograms are modeled. The path calibration for this waveform analysis is being conducted in several steps. First, the best fitting 1-D structure is determined by modeling the broadband waveform features of large (Mw > 5) master events for which source parameters from teleseismic analysis are available. For these events we also determine depth from teleseismic P-wave depth phases. This depth estimate is critical to relocating the event and the relocation is integral to the determining regional velocity model as we have found that using the teleseismic ISC locations result in travel-time discrepancies on the order of 5 sec. in comparison to observations of near-regional distance (200 < R < 400 km) records. Such timing errors, over a 400 km distance, result in P-wave velocity errors on the order of 5% for typical crustal models. We relocate the event using the teleseismic depth in conjunction with the regional P and S travel times and a first-order velocity model. We have developed I-D models for the area surrounding the Lop Nor test site and the region encompassing S. W. Pakistan and N. W. India. With these models, regional source inversions and locations can be performed on smaller events that are still well recorded by 1 or more stations, but which are poorly observed teleseismically, thus lowering the monitoring threshold for the region. We are now refining these models for higher frequency (f > 0.25 Hz) observations. For this, we are applying the method of Pseudo Green's functions to calibrate the finer regional structure. This method has been applied successfully model S waves for events in the southern California and the Hindu Kush region of S. W. Asia. We are extending the method to P waves, which are more important in seismic monitoring practice. These refined Green's functions can then be used to generate realistic short-period seismograms to compare to observations -- particularly for smaller events (M < 4.5) -- for the purpose of characterizing the seismic source.

Key Words: Location, Source Characterization, and Regional Waveforms

OBJECTIVE

We are developing techniques to model the short-period character of regional waveforms in order to improve the analysis of small (mb< 4.5) seismic events which are not well-observed teleseismically for location purposes (Sweeney, 1996) or waveform analysis (Saikia, et al, 1996), as they may only have several usable regional observations. The procedure we use is to first obtain the best-fitting velocity model of the crustal waveguide for long-period waveforms and then refine the model(s) progressively to shorter periods, initially for broadband waveforms and then short-period ones. Particularly for the short-period case, the model is modified to predict the arrival times of prominent regional phases (Pn, Pg, S). For this short-period path calibration in particular, it is essential to have ground truth hypocentral locations for the master events which are large enough to be well recorded teleseismically, so that the P-wave depth phases can be analyzed. We are applying this methodology to regions centered about known test sites, where there is the greatest need and interest to locate and identify small seismic events. In particular our current effort is focused around the Lop Nor test site.

For areas with strong lateral variations, the crustal waveguide model may well have to be sub-regionalized for specific source-receiver paths. As we are only examining specific source regions, only paths for certain distance ranges and azimuths for which regional stations are situated need be modeled, thus limiting the scope of the path calibration. For the fine-timing of the short-period crustal waveguide, we are investigating the application of the pseudo Green's function method (Song and Helmberger, 1998) whereby the 1-D crustal model is broken-up into a 2-D block structure and a genetic algorithm is used to best fit the arrival time and amplitude of specific phases. Thus this modeling requires the identification of the various regional phases.

RESEARCH ACCOMPLISHED

Ground Truth Events

To calibrate the paths from the Lop Nor test site to the various regional stations (see Figure 1), we are modeling the waveforms of master events. Unfortunately, the only event recorded at WMQ, the closest station, with GIO (see Yang and Romney, 1999 for a definition of these criteria) or better location resolution is the 88273 explosion. There are good-sized earthquakes in the vicinity as shown on the map, but none is better than GT25. To develop regional velocity models which yield accurate travel times, event locations need to be well constrained. Therefore their teleseismic locations need to be confirmed or the events need to be relocated using a combination teleseismic depth-phase modeling and regional travel-time data.

Relocation results for 17 earthquakes throughout the Tien-Shan region, including those near Lop Nor, are given in Figure 2 (Velasco, personal communication). The upper box compares the ISC depths (circles) with ours (diamonds) determined from a combination of teleseismic P-wave modeling and regional waveform inversion (Woods et al., 1998) and are in close agreement with results from regional surface-wave spectra inversion (Patton, 1998). In some cases the change in depth is quite significant -- by as much as 50 km. The lower box compares the change in distance, r, between the ISC locations and the regional relocations using free depths (circles) and our constrained depths (diamonds); the events were relocated using a crustal model of central Asia (Mooney and Li, 1997). The constrained-depth relocations tend to move less than the free-depth ones on average, suggesting that the ISC epicentral locations are fairly accurate and that free-depth relocations are susceptible to errors. Thus constraining source depth helps to significantly improve regional event locations.

Figure 3 shows an example of the teleseismic depth-phase modeling for the earthquake 90165. In this case it was possible to model the SH component as well as the P waves; fitting the S waves helps to better constrain the event's seismic moment which, in turn, helps in the modeling of absolute amplitude of the regional phases, thus constraining the attenuation model. Once a reliable depth is determined, the event is relocated with respect to best available regional velocity model as described above.

Modeling Paths

With the best-constrained hypocentral relocations we model regional waveforms. Figure 4 compares observed and synthetic P-SV displacement waveforms, in absolute timing for the 88273 explosion. This model fits the P and S timing well. We are now using this velocity structure to relocate earthquakes near Lop Nor, so that paths from these events to the more distant regional stations (see Figure 1) can be accurately modeled. We also applied this velocity model to events recorded at WMQ from other azimuths. Figure 5 compares broadband (left column) and long-period (right column) observed and synthetic waveforms for the earthquake 90297, west of WMQ. The seismograms are again plotted with respect to absolute time; the synthetics are little slow, requiring a slightly faster model. Otherwise the waveform fits are quite good, suggesting that the model used only needs slight refinements to make it yield accurate travel times for the P and S phases. The large amplitude, ringing nature of the S-wave train, which is also produced in the synthetics, suggests the presence of a gradient in the upper crust at the base of the low-velocity sedimentary layers as was previously observed by Saikia and Burdick (1991) for some regional paths from NTS. Our current model for station WMQ, includes a similar gradient. The refined model for short-period waveforms should include this effect.

Refining Path Models for Short-Period Observations

To refine the regional model for specific azimuths and, in some cases, distances, we are applying the pseudo Green Function (PGF) technique (Song and Helmberger, 1998) whereby the I-D model is broken into blocks and the relative timing of the various regional phases are used to modify this 2-D block model in a fashion similar to waveform tomography. For this procedure the individual phases must be identified. Figure 6 is the anatomy of phases for a set of three-component regional seismograms which we used to identify the major phases recorded at WMQ. For each component the top trace is a generalized ray synthetic and the lower trace is the full waveform generated from F-K integration. The primary rays of interest are Pn, PmP, pPn, pPmP, sPmP, Sn and SmS. Identification of these rays is necessary for the next step in refining the model using pseudo Green's functions.

In the PGF method each ray $R_i(t)$ (determined generalized ray synthetics) is shifted by d_{ti} and amplified by a factor A_i:

$$S(t) = \sum_i A_i R_i(t) * d(t - d_{ti})$$

where i is the index of the ray, in order to best match the composite generalized ray synthetic to the observed waveform. Prior work using the pseudo Green Function method involved modeling only S waves. Figure 7 shows the applicability of the method in which a SH waveform recorded at the TERRAscope station GSC is successfully modeled. The upper left column shows individual rays with their path shown opposite in the right column; the solid trace is for the 1-D model and the dashed trace is the perturbed ray. In the lower left-hand comer are the SH wave displacements records; the top trace is the observed seismogram, the middle trace is the final iteration of the PGF synthetic, and the bottom trace is the 1-D synthetic. The PGF records fits the observed waveform significantly better.

We are currently working on extending the method to P-waves. The idea behind the PGF path calibration is to develop Green's functions for a particular source region using large, well recorded master events. These PGFs could then be used to model records from smaller events from the same vicinity in order to determine information regarding the seismic source, in particular mechanism.

CONCLUSIONS AND RECOMMENDATIONS

For regions with few GTIO (or better) events, locations and source depths, necessary for accurate path calibration, can be better constrained using teleseismic depth phase information. Regional locations with poor azimuthal coverage and no constraint on source depth leads to errors in relocations. A good-fitting regional model has been found for the path from Lop Nor to WMQ. It is now being refined to improve predictions of P and S arrival times.

REFERENCES

Mooney, W. D. and S. Li, 1997. Crustal Structure of China from Deep Seismic Sounding Profiles, Proceedings *19th Annual Seismic Research Symposium Monitoring a Comprehensive Test Ban Treaty*, Orlando, FL, pp. 104 -115.

Patton, H. J., 1998. Bias in the Centroid Moment Tensor for central Asian Earthquakes: Evidence from Regional Surface Wave Data, *J. Geophys. Res*., **103**, 26,963-26,974.

Saikia, C. K. and L. J. Burdick, 1991. Fine Structure of P_{n1}, Waves from Explosions, *J. Geophys. Res*., **96**, 14,383-14,401.

Saikia, C. K., B. B. Woods, H. K. Thio, L. Zhu and D. V. Helmberger, 1996. Path Calibration, Source Estimation and Regional Discrimination for the Middle East: An application to the Hindu-Kush Region, *PL-TR-96-2069, Scientific Report No. 1*, Phillips Laboratory, Hanscomb AFB, MA, 130p.

Song, X. J. and D. V. Helmberger, 1998. Pseudo Green's Functions and Waveform Tomography, *Bull. Seism. Soc. Am*., **88**, No. 1, 304-312.

Sweeney, J. J., 1996. Accuracy of Teleseismic Event Locations in the Middle East and North Africa, *Lawrence Livermore National Laboratory Report*, UCRL-ID-125868, 16p.

Woods, B. B., C. K. Saikia and H. K. Thio, 1998. Focal Depths and Source Parameters for Earthquakes in Northwest China, *URS-Greiner Woodward-Clyde Scientific Report*, WCFS-FR-98, Pasadena, CA.

Yang, X. and C. Romney, 1999. PIDC Ground Truth Database, *CMR Technical Report*, CMR-99/15, Alexandria, VA.

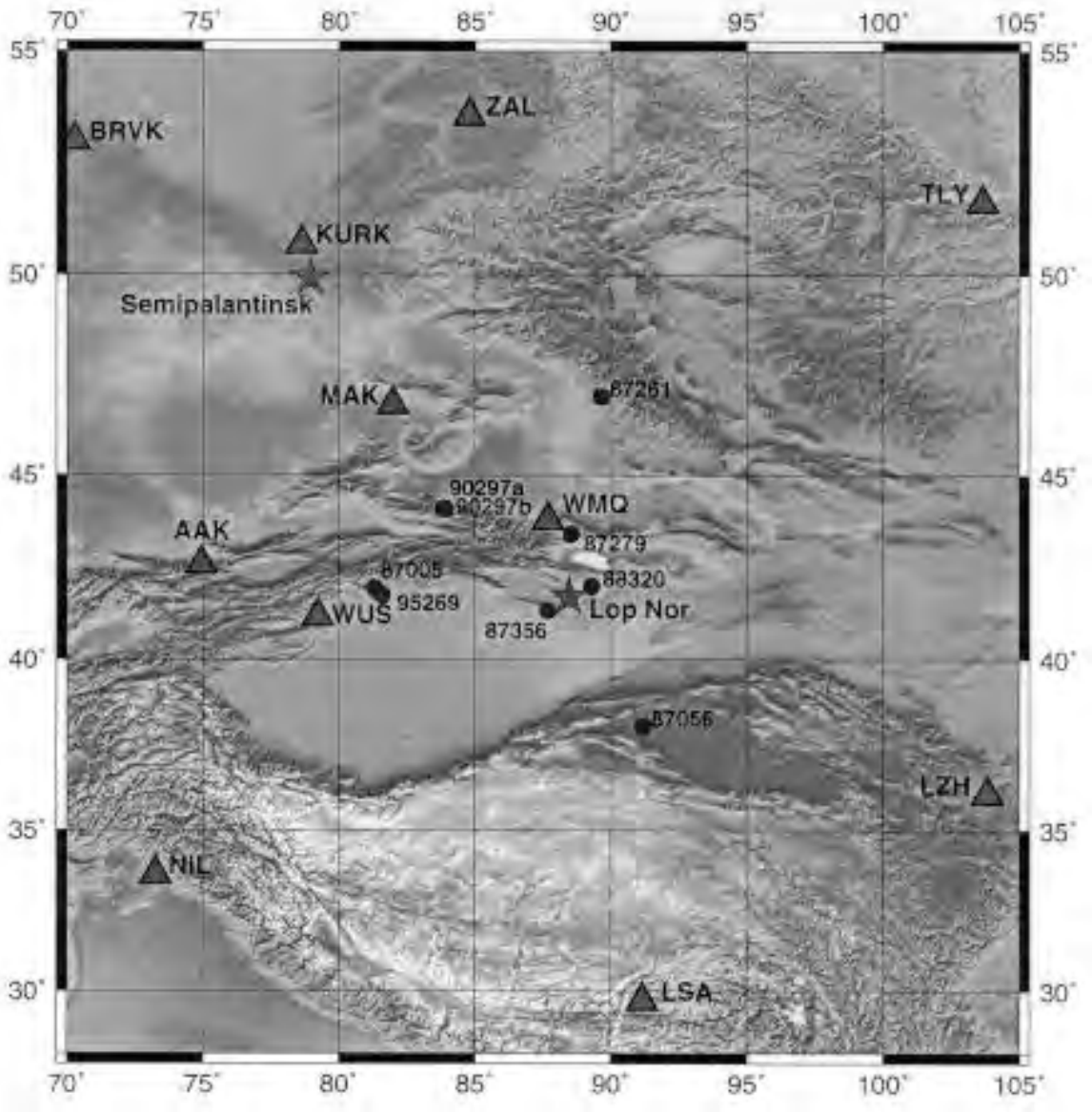


Figure 1. Topographic map of the northwestern border region of China showing the location of earthquakes (circles) and test sites (stars), for which better GT data are available, used to calibrate crustal path models to the regional stations (triangles).

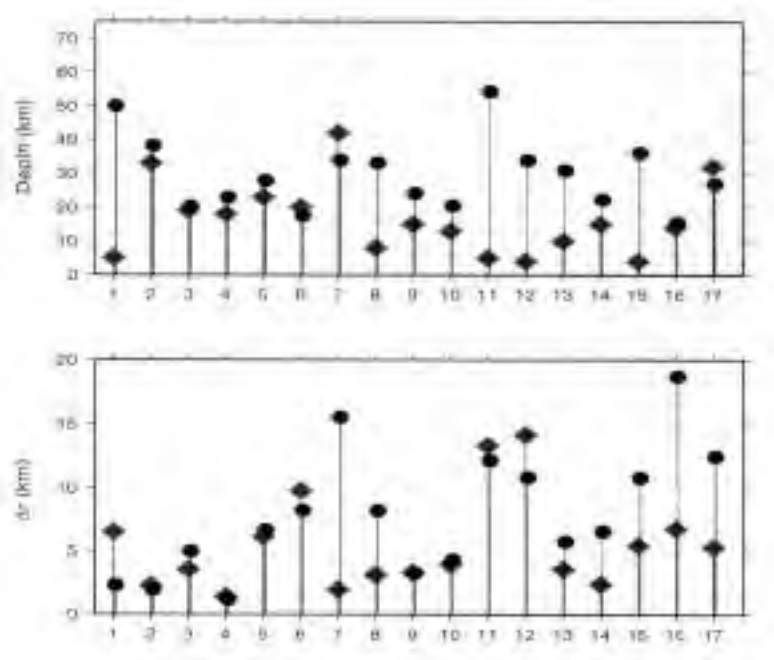


Figure 2. Upper panel: Comparison of ISC (circles) focal depths and those determined from a combination of teleseismic P-wave modeling and regional waveform inversion (diamonds). Lower panel: Change in epicentral location (relative to ISC) for relocations using regional travel times for free-depth (circles) and fixed-depth (diamonds) travel-time inversion; the fixed depth are those determined by Woods et al. (1998).

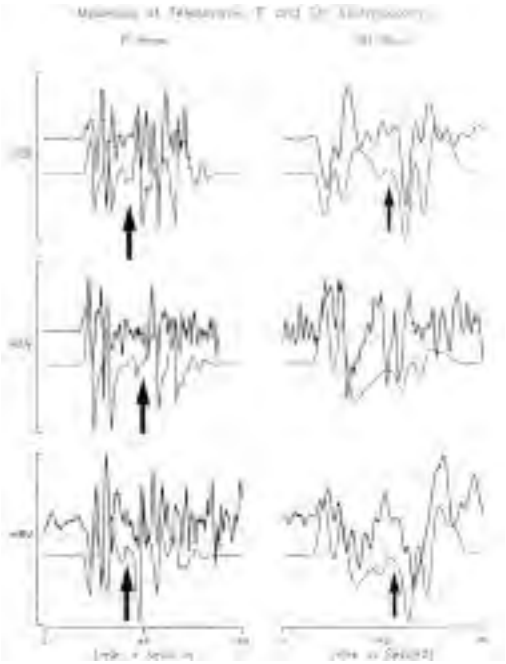


Figure 3. Teleseismic modeling of P and SH waveforms recorded at three stations for the 90165 earthquake. The observed seismograms are the upper (thicker line) trace. Focal mechanism is the Harvard CMT solution. The depth phases are shown by the arrows.

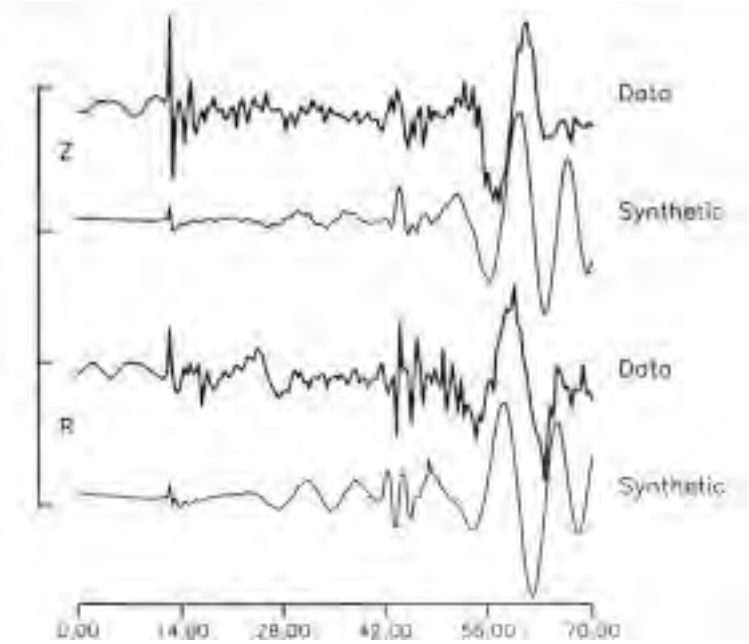


Figure 4. Comparison of observed (upper, thicker trace) and synthetic displacement seismograms for the 88273 Lop Nor explosion recorded at WMQ; both vertical and radial components are displayed.

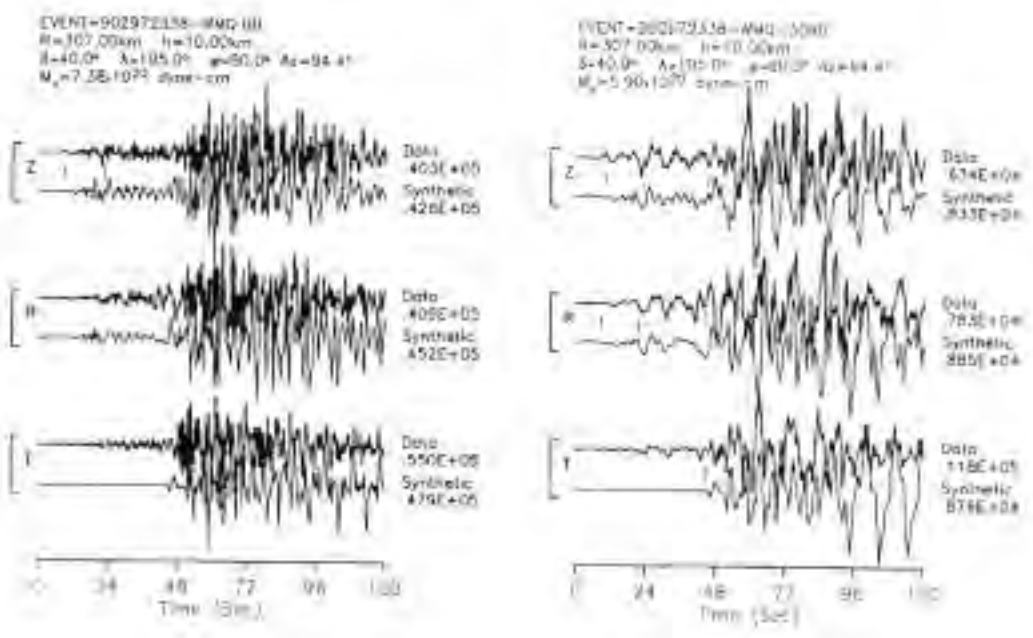


Figure 5. Comparison of observed (upper, darker trace in each pair) and synthetic regional seismograms for the event 90297 recorded at WMQ. The left-hand set of records are the broadband play-outs and the right-hand ones are convolved with a long-period 30-90 instrument.

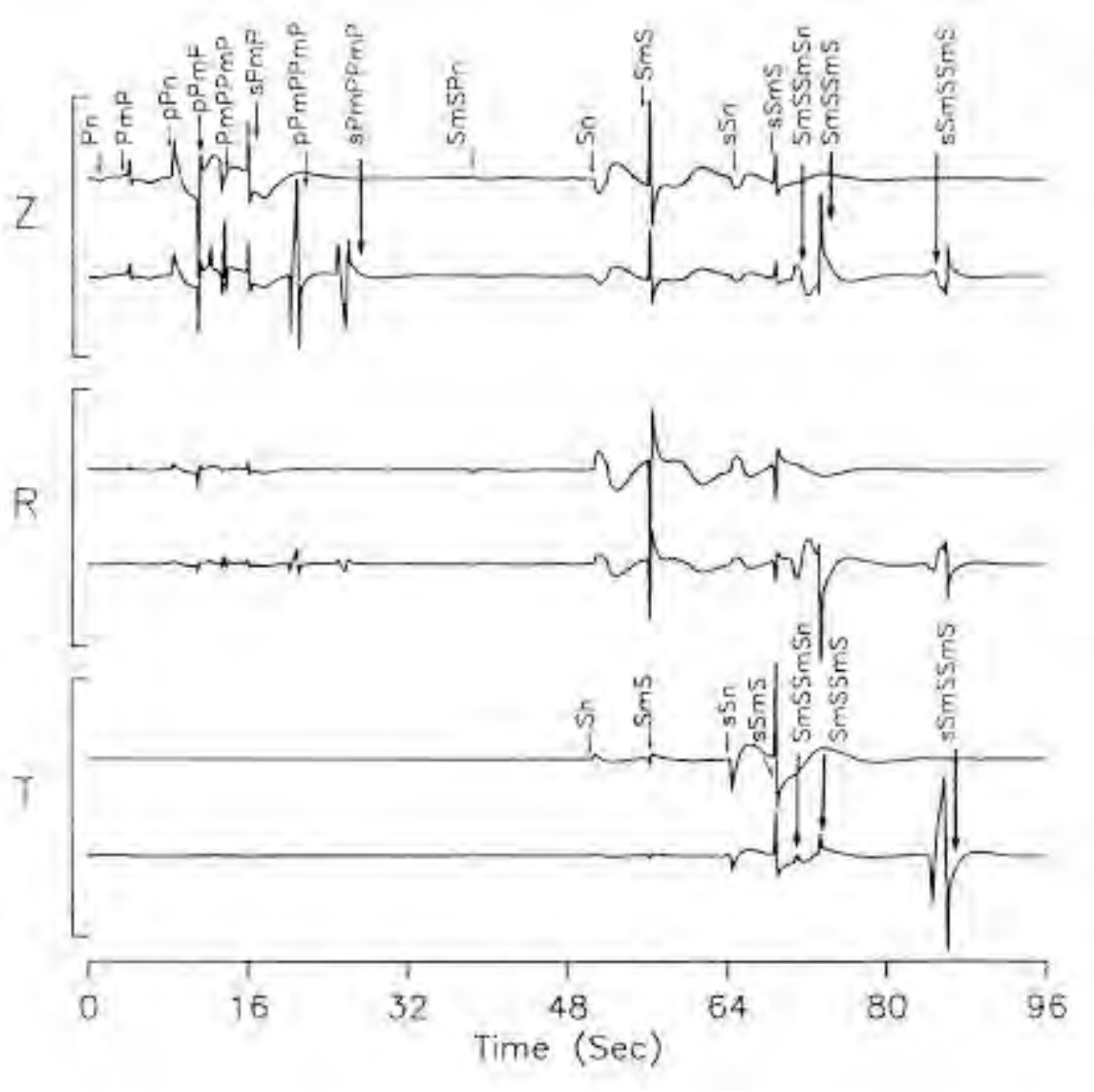


Figure 6. Anatomy of regional seismograms for vertical, radial and tangential components. The top trace in each pair of seismograms is generated with generalized rays, while the lower trace is the full wavefield generated from F-K integration.

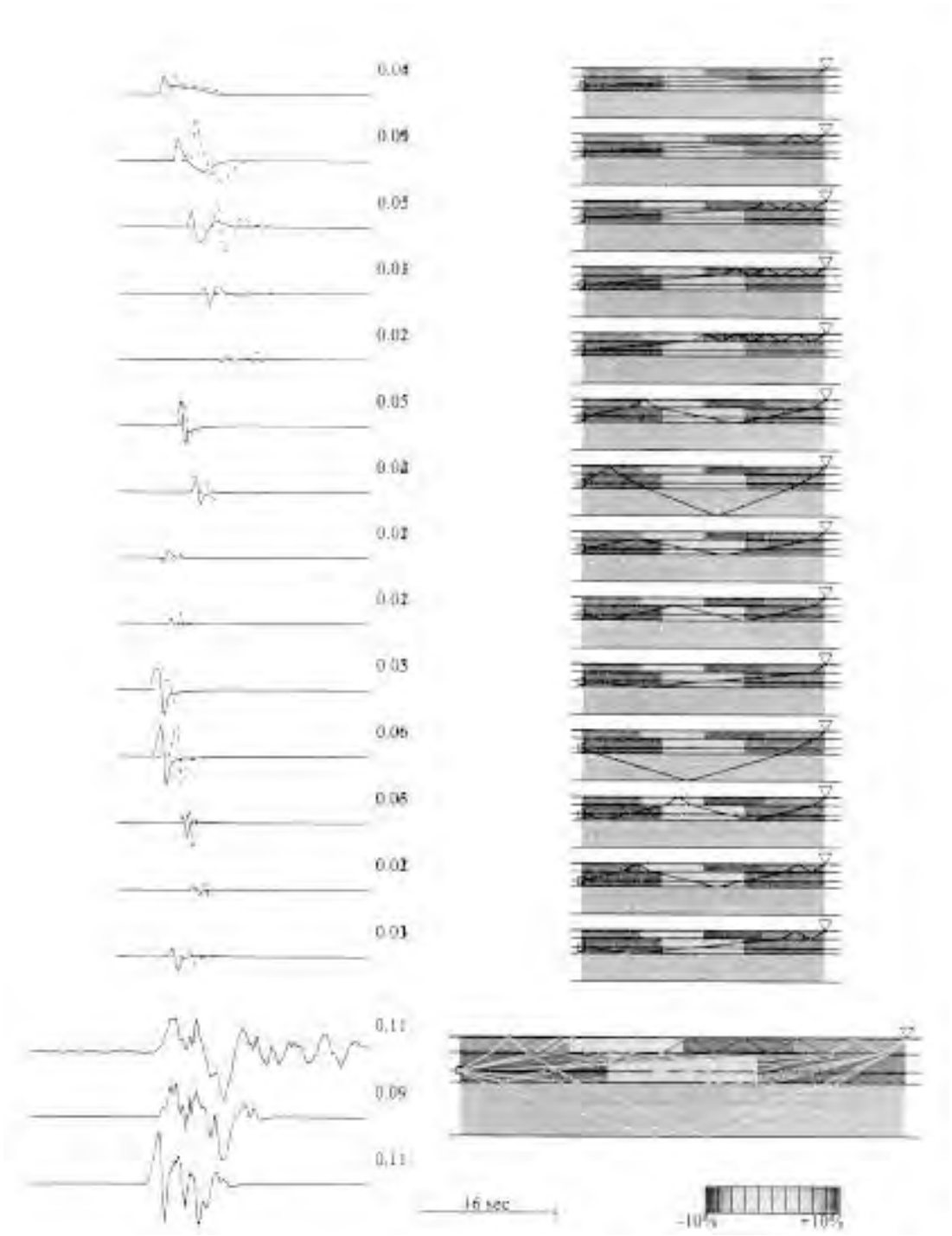


Figure 7. Example of the pseudo Green's function method applied to a tangential component regional record. Each pair of traces in the upper left column is the individual ray contribution corresponding to the ray diagram shown in the right column; the solid trace is for the 1-D model and the dashed-line trace is the perturbed ray in the 2-D block structure (shown in the right column). The number to the right of each pair of traces is the peak amplitude. The three seismograms in the lower left-hand corner are the observed record (top trace), the pseudo Green's function sum of the above rays (middle trace), and the full 1-D F-K synthetic (bottom trace). The full ray diagram in the final 2-2 block model is shown in the lower right-hand corner.

Lg WAVE SIMULATIONS IN HETEROGENEOUS CRUSTS WITH IRREGULAR TOPOGRAPHY USING HALF-SPACE SCREEN PROPAGATORS

R.S. Wu, X.B. Xie and X.Y. Wu, Institute of Tectonics, University of California, Santa Cruz

Sponsored by U.S. Department of Defense
Defense Threat Reduction Agency
Contract No.: DSWA01-97-1-0004

ABSTRACT

This study is aimed at development and application of a new wave propagation and modeling method for regional waves in heterogeneous crustal waveguides using one-way wave approximation. The half-space GSP (generalized screen propagator) has taken the free surface into the formulation and adopts a fast dual-domain implementation. The method is several orders of magnitude faster than finite-difference methods with a similar accuracy for certain problems. It has been used for the simulation of wave propagation for high-frequency waves (1 - 20 Hz) to a regional distance (greater than 1000 km).

In this year we further developed the method in three aspects. First, we extend the GSP method to treat irregular surface topography by incorporating a coordinate transform into the method. Both conformal and non-conformal transformations have been introduced and their relative merits and accuracies have been discussed. Comparison with boundary element integration method showed that the extended method works well for mild topographies. Accuracy improvement for rough topography is still an ongoing research. Second, we developed a hybrid method which couples the fast screen propagator method with a modified boundary element method to treat the problems with severe rough topography. Finally, numerical simulations have been conducted for various crustal waveguide structures, including both deterministic structures and small-scale random heterogeneities and random rough surfaces. Influence of random heterogeneities and rough surfaces on Lg amplitude attenuation and Lg coda formation are shown to be significant. In collaboration with T. Lay, we have investigated the frequency- dependent Lg attenuation and blockage both observationally and numerically. The comparison between the observation and numerical simulations reveals many interesting phenomena and needs more thorough investigation.

Key Words: seismic wave propagation, crustal structure, discrimination

INTRODUCTION

Crustal guided wave Lg provides valuable information for nuclear test monitoring and yield estimation. Lg energy mainly propagates in the crustal wave guide and the uppermost mantle. The low velocity crust provides an ideal channel for Lg propagation. On the other hand, many crustal characteristics, both deterministic structures (e.g., crustal necking, thickening) and stochastic characteristics (e.g., random volume heterogeneities in the crust, random fluctuations at free surface and Moho discontinuity) affect the propagation of the Lg wave. To isolate path effects from the source parameters, a clear understanding of these mechanisms and how they affect the Lg attenuation is crucial. In these investigations, numerical methods for simulating Lg wave propagation based on realistic deterministic and/or stochastic models are often very useful.

The existing methods for calculating synthetic regional phases can be roughly categorized into three groups. (1). Wavenumber integration method (e.g., Bouchon 1981, Campillo 1990). This method originally handles only laterally homogeneous media and is incapable of handling complex 3D structures and heterogeneities. Later developments (e.g., Bouchen et al. 1989; Chen, 1990, 1995) extend the capability of the method to handle large-scale lateral variations, but volume heterogeneities are still excluded. (2). Normal mode approach (e.g. Wang and Hermann 1988). This method works well for layered media, and later development of coupled mode theory (Kennett, 1984) enables it to handle slightly lateral variations, but is limited in its validity for strong lateral variations. (3). Fully discretisized numerical methods, for example finite-difference method (Xie and Lay, 1994; Jih, 1996; Hestholm and Ruud, 1994, 1998) and boundary element method (e.g., Fu and Wu, 1999). In principle, finite-difference method can deal with arbitrarily heterogeneous media including both volume heterogeneities and rough free surfaces. The boundary element method can handle arbitrary free surfaces and interfaces but is not very powerful in dealing with volume heterogeneities. However, under realistic conditions, i.e., complex waveguide with volume heterogeneities and free-surface/interface fluctuations, high frequency and long propagation distances, the ability of all the above mentioned methods is very limited. Yet under over simplified velocity models, lower frequencies and shorter propagation ranges, many practical issues associated with the regional phase propagation can not be properly investigated.

In the crustal waveguide environment, major wave energy is carried by forward propagating waves, including forward scattered waves, therefore neglecting backscattered waves in the propagation will not change the main features of regional waves in most cases. Based on this concept, a generalized screen propagator method (GSP) based on the one-way wave equation has been developed by Wu (1994), Wu, Jin and Xie (1999a) and has been successfully used to simulate SH Lg waves in the complex crustal waveguide and investigate the energy partitioning of Lg waves (Wu, Jin and Xie, 1999b). This method neglects backscattered waves, but correctly handles all the forward multiple-scattering effects, e.g., focusing/defocusing, diffraction, interference, etc. The method is two to three orders of magnitude faster than the finite-difference method for medium sized problems.

In this paper we further extend the GSP method to treat irregular surface topography by incorporating coordinate transforms into the method. Both conformal and non-conformal transforms have been introduced and their relative merits and accuracies have been discussed. Comparison with other exact methods, such as the boundary element integration method, showed that the extended method works well for mild to moderate topographies. Numerical simulations have been conducted for various crustal waveguide structures, including both deterministic structures and random rough surfaces.

CONFORMAL COORDINATE TRANSFORM FOR GSP

General wide-angle formulation. For a 2D SH problem and under the perturbation theory, the frequency domain wave equation for the y-component of displacement field can be written as (Wu, et al. 1999a)

$$(\nabla^2 + k^2)u(r) = -k^2 F(r)u(r) \qquad (1)$$

where $k = \omega / v$ is the wavenumber in the background medium, v is the background S wave velocity defined

by $v = (\mu_0 / \rho_0)^{1/2}$, and μ_0 and ρ_0 are background values of μ and ρ. In the right hand side of (1), $F(\mathrm{r})$ is a perturbation operator

$$F(\mathrm{r}) = \varepsilon_\rho(\mathrm{r}) + \frac{1}{k^2}\nabla\cdot\varepsilon_\mu\nabla \qquad (2)$$

with $\varepsilon_\rho(\mathrm{r}) = \delta\rho(\mathrm{r})/\rho_0$ and $\varepsilon_\mu(\mathrm{r}) = \delta\mu(\mathrm{r})/\mu_0$, where $\delta\rho(\mathrm{r})$ and $\delta\mu(\mathrm{r})$ are purterbations of ρ and μ. Equation (1) is a scalar Helmholtz equation. For flat free surfaces, Wu et al. (1999a) derived a half-space GSP solution for Lg wave propagation. In the case of irregular topography, the global mirror symmetry for the problem no longer

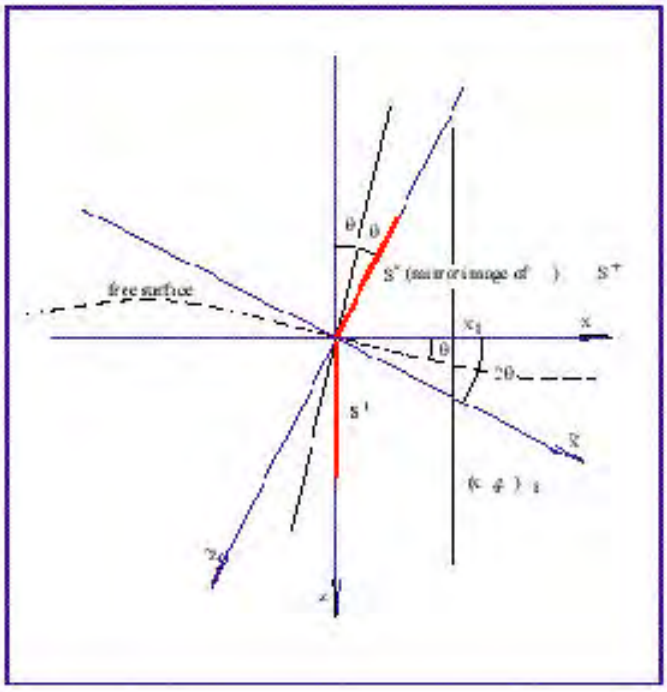


Figure 1: Geometry of the coordinate transform.

exists. However, if a first order approximation (local plane-surface approximation) for the topography is taken, we can modify the mirror image method to a local mirror image method and apply the corresponding coordinate transform to obtain a GSP solution for this case.

Fig. 1 shows the geometry of the derivation. Assume u_0^+ is the incident field on S^+, then u_0^- on S^- is also known as the mirror image of u_0^+ about the local plane surface. The total wavefield composed of S+ and S^- is the sum of the primary field which propagates in the homogeneous background medium and the scattered field which is generated by the local heterogeneities in the thin-slab. The effects of the heterogeneities and the topography can be calculated separately for each step in the GSP method. The effect of the slant free-surface can be incorporated into the propagation integral. Assume $u_t(x, z)$ is the total field including the scattering effect of the volume heterogeneities. The field $u(x_1, z_1)$ in front of the integral surface can be calculated by the Kirchhoff integral

$$\begin{aligned} u(x_1,z_1) &= \int_S ds \left\{ g(x, z; x_1, z_1)\frac{\partial u_t(x,z)}{\partial n} - \frac{\partial g(x,z;x_1,z_1)}{\partial n} u_t(x,z) \right\} \\ &= \int_{S^-} ds\{...\} + \int_{S^+} ds\{...\} \end{aligned} \qquad (3)$$

where $g(.)$ is the Green's function for the full space with homogeneous velocity distribution, S is the integration surface and S^+ and S^- are the lower and upper half surfaces, respectively. The Rayleigh integral can be used to replace the Kirchhoff integral for each half surface integral. For the lower half-space the contribution of S^+ is

$$\begin{aligned} u_t^+(x_1,z_1) &= -2\int_0^\infty dz u_t^+(x,z)\frac{\partial g(x,\ z;\ x_1,\ z_1)}{\partial n} \\ &= \frac{1}{2\pi}\int dK_T e^{iK_T z_1} u_t^+(x_1,K_T) \end{aligned} \tag{4}$$

where

$$u_t^+(x_1,K_T) = e^{i\gamma(x_1-x)}\int_0^\infty dz_1 u_t^+(x,z)e^{-iK_T z_1} \tag{5}$$

Here $u_t^+(x, z)$ is the total field equal to the sum of incident field $u_0^+(x, z)$ and the scattered field $U^+(x, z)$ caused by the heterogeneities within the slab between x and x_1 (see Wu, 1994; Wu et al., 1999a). If we put the slab entrance at $x = x'$ and the field on the screen S^+ at the entrance as $u_t^+(x', z')$, then

$$\begin{aligned} u_t^+(x',z') &= u_0^+(x',z') + U^+(x',z') \\ U^+(x',z') &= k^2\int_{x'}^{x_1} dx e^{i\gamma(x_1-x')}\int_0^\infty dz \{g(x_1,z_1;x,z)\varepsilon_\rho(x,z)u_0(x,z) \end{aligned} \tag{6}$$

$$-\frac{1}{k_2}\nabla g(x_1,z_1;x,z)\ .\ \varepsilon_\mu(x,z)\nabla u_0(x,z)\} \tag{7}$$

For the bent upper half screen, we perform a coordinate transform by clockwise rotation of 2θ to a new coordinate system $(\tilde{x}, \tilde{z})$. Taking the downward direction as positive z-direction, and the rotation angle from x to z as positive, the relation connecting the two systems is

$$\tilde{x} = x\cos 2\theta + z\sin 2\theta \tag{8}$$

$$\tilde{z} = -x\sin 2\theta + z\cos 2\theta \tag{9}$$

In the new system, the surface S^- is parallel to the i-axis, so that

$$u_t^-(\tilde{x}_1,K_T) = e^{i\gamma(\tilde{x}_1-\tilde{x}')}\int_{-\infty}^0 d\tilde{z}' u_t^-(\tilde{x}',\tilde{z}')e^{-iK_T\tilde{z}'} \tag{10}$$

where $u_t^-(\tilde{x}', -\tilde{z}') = u_t^+(x', z')$ The field in the space domain can be obtained by synthesizing the contributions from all the plane waves

$$u_t^-(\tilde{x}_1,\tilde{z}) = \int dK_T e^{i\gamma(\tilde{x}_1-\tilde{x}')}e^{iK_T\tilde{z}}u_t^-(\tilde{x}',K_T) \tag{11}$$

where

$$u_t^-(\tilde{x}',K_T) = \int_{-\infty}^0 d\tilde{z}' u_t^-(\tilde{x}',\tilde{z}')e^{-iK_T\tilde{z}'} \tag{12}$$

Transformed back to the original coordinate system, resulting in

$$u_i(x_1, z_1) = \int_{u_i(\tilde{x}', K_T)} dK_T \exp\left\{ i \left[(\tilde{\gamma}\cos 2\theta - K_T \sin 2\theta)(x_1 - x') + (\tilde{\gamma}\sin 2\theta + K_T \cos 2\theta) z_1 \right] \right\} \tag{13}$$

We can see that in the original coordinate system, the effective transversal and propagating wavenumbers are

$$\begin{cases} \gamma = \tilde{\gamma}\cos 2\theta - K_T \sin 2\theta \\ K_T = \tilde{\gamma}\sin 2\theta + K_T \cos 2\theta \end{cases} \tag{14}$$

If we transform the $(\tilde{k}_T, \tilde{\gamma})$ system into (K_T,γ),

$$u_i(x_1, z_1) = \int dK_T u_i(\tilde{x}', K_T \cos 2\theta - \gamma \sin 2\theta) e^{i(\gamma(x_1 - x') + iK_T z_1)} \tag{15}$$

The total field is a summation of the contributions from both $u^+(x_1, z_1)$ and $u_i^-(x_1, z_1)$

$$u(x_1, z_1) = \int dK_T e^{i\gamma(x_1 - x')} e^{iK_T z_1} \left[u_i^+(x', K_T) + u_i^-(\tilde{x}', K_T \cos 2\theta - \gamma \sin 2\theta) \right] \tag{16}$$

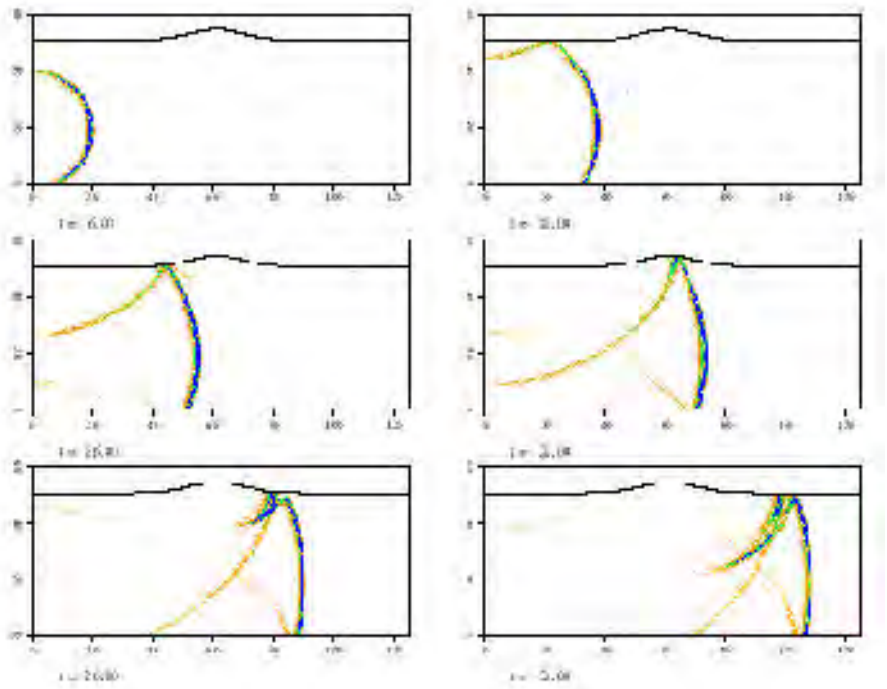


Figure 2: Snap shots of the wave field. the model is a homogeneous half-space with a Gaussian hill on the free surface.

The wavenumber integral can also be done by a FFT.

Narrow-angle approximation When small-angle waves prevail such as in the case of Lg propagation, the spectral interpolation in equation (16), which is tricky and even unstable in some cases, can be avoided and replaced by operations in the space domain using a narrow-angle wave approximation.

From (16), it can be seen that to calculate the reflection response we need to find the spectral components $u_t^+(-\tilde{K}_T)$. We will try to obtain the approximate space-domain operations corresponding to the wavenumber domain interpolation. We know

$$u_t^+(-\tilde{K}_T) = \int_0^\infty dz e^{i(-\tilde{K}_T \cos 2\theta + \gamma \sin 2\theta)z} u_t^+(z) \tag{17}$$

With narrow-angle approximation, $\gamma \approx k$ therefore,

$$u_t^+(-\tilde{K}_T) = \int_0^\infty dz' e^{ik_T z'} \left[\frac{1}{\cos 2\theta} e^{ik(\tan 2\theta)z'} u_t^+(z'/\cos 2\theta) \right] \tag{18}$$

We see that the corresponding operations for wavenumber-domain interpolation in the space-domain are a modulation plus a coordinate stretching.

NON-CONFORMAL COORDINATE TRANSFORM FOR GSP

A non-conformal coordinate transform and the correspondent inverse transform are

$$\begin{cases} x = x \\ \zeta = z - h(x) \end{cases} \quad \text{and} \quad \begin{cases} x = x \\ z = \zeta + h(x) \end{cases} \tag{19}$$

where *h(x)* is the height function of free surface topography. Denote the field and the medium parameters in the new coordinate system as $\hat{u}(x,\zeta)$, $\hat{\mu}(x,\zeta)$ and $\hat{\rho}(x,\zeta)$ respectively. Assuming that μ varies smoothly with *x*, the wave equation for SH wave in the new coordinate system can be obtained as

$$\left(\nabla^2 + k_0^2\right) \hat{u}(x,\zeta) = -k_0^2 \left\{ \hat{F}_m(x,\zeta) + \hat{F}_s(x,\zeta) \right\} \hat{u}(x,\zeta) \tag{20}$$

where
$k_0 = k_0(x,\zeta)$ and the operators $\nabla^2 = \partial^2/\partial x^2 - \partial^2/\partial \zeta^2$ is the Laplacian,

$$\hat{F}_m(x,\zeta) = \hat{\varepsilon}_\rho(x,\zeta) + \frac{1}{k_0^2} \nabla \cdot \hat{\varepsilon}_\mu \nabla \tag{21}$$

is the equivalent force term due to the medium heterogeneities, and

$$\hat{F}_s(x,\zeta) = -\frac{1}{k_0^2} \frac{\hat{\mu}}{\mu_0} \left[h''(x) \frac{\partial}{\partial \zeta} + 2h'(x) \frac{\partial^2}{\partial x \partial \zeta} - (h'(x))^2 \frac{\partial^2}{\partial \zeta^2} \right]$$

is equivalent force term due to the surface topography.

Using local Born approximation, the scattered field generated by the heterogeneities and topographic change of the thin-slab for each step can be written as

$$U(x_1, k_\zeta) = \frac{ik_0^2}{2\gamma} \int_{x'}^{x_1} dx \int_0^\infty d\zeta e^{i\gamma(x_1 - x)} 2\cos(k_\zeta \zeta) \left[\hat{F}_m(x,\zeta) + \hat{F}_s(x,\zeta) \right] \hat{u}_0(x,\zeta) \tag{22}$$

where $\hat{u}_0(x,\zeta)$ is the local incident filed at the slab entrance.

Scattering due to coordinate transformation. Assume that the medium in coordinate (*x, z*) is homogeneous, that is $\hat{F}_m(x,\zeta) = (F_m(x, z) = 0$. The scattered field under the new coordinate system (x, ζ) is only due to the coordinate transformation.

$$U(x_1, k_\zeta) = \frac{1}{2\gamma} \int_{x'}^{x_1} dx e^{i\gamma(x_1 - x)} C \left[2h'(x)A - (h'(x))^2 B + h''(x) D \right] \tag{23}$$

where

$$A = \frac{\partial^2 u_0(x,\zeta)}{\partial\zeta\partial x} = -\mathcal{S}^{-1}\left[k'_\zeta\gamma' e^{i\gamma'|x-x'|}\tilde{u}_0(x',k'_\zeta)\right] \quad (24)$$

$$B = \frac{\partial^2 u_0(x,\zeta)}{\partial\zeta^2} = -\mathcal{C}^{-1}\left[k'^2_\zeta e^{i\gamma'|x-x'|}\tilde{u}_0(x',k'_\zeta)\right] \quad (25)$$

$$D = \frac{\partial u_0(x,\zeta)}{\partial\zeta} = -\mathcal{S}^{-1}\left[k'_\zeta e^{i\gamma'|x-x'|}\tilde{u}_0(x',k'_\zeta)\right] \quad (26)$$

with C [.] and S [.] being the cosine and sine transforms, C^{-1}[.] and S^{-1}[.] as their inverse transforms, and

$$\begin{aligned} u_0(x,\zeta) &= \frac{1}{2\pi}\int_{-\infty}^{\infty} dk'_\zeta e^{ik'_\zeta\zeta} e^{i\gamma'|x-x'|}\tilde{u}_0(x',k'_\zeta) \\ &= \mathcal{C}^{-1}\left[e^{i\gamma'|x-x'|}\tilde{u}_0(x',k'_\zeta)\right] \end{aligned} \quad (27)$$

Narrow-angle approximation. Under the narrow-angle wave approximation, $k_\zeta \approx k'_\zeta \ll \gamma \approx \gamma' \approx k_0$. Also invoking a small slope (or smooth topography) approximation such that $h''(x) \ll 2h'(x)$ and $[h'(x)]^2 \ll 2h'(x)$, the last two terms in equation (23) can be neglected. We obtain

$$U(x_1,k_\zeta) = Z(x_1)e^{i\gamma\Delta x}\int_0^\infty d\zeta 2\cos(k_\zeta\zeta)\frac{\partial}{\partial\zeta}\tilde{u}_0(x',\zeta) \quad (28)$$

where

$$Z(x_1) = \int_{x'}^{x_1} dx h'(x) \quad (29)$$

The total forescattering can be obtained by summing the background field and the scattered field

$$\begin{aligned} u(x_1,k_\zeta) &= e^{i\gamma\Delta x}\int_0^\infty d\zeta 2\cos(k_\zeta\zeta)\tilde{u}_0(x',\zeta) \\ &- e^{i\gamma\Delta x}Z(x_1)\int_0^\infty d\zeta 2\cos(k_\zeta\zeta)\frac{\partial}{\partial\zeta}\tilde{u}_0(x',\zeta) \\ &= e^{i\gamma\Delta x}\int_0^\infty d\zeta 2\cos(k_\zeta\zeta)e^{Z(x_1)\frac{\partial}{\partial z}}\tilde{u}_0(x',\zeta) \end{aligned} \quad (30)$$

where Δx=x1-x1. In the last equation, the Rytov transformation is applied to make the operator unitary.

NUMERICAL EXAMPLES

To test the accuracy and ability of the phase screen method as a propagator for crustal wave guide with rough free surfaces, numerical simulations have been conducted for both conformal and non-conformal methods. The first model is a homogeneous half space with a Gaussian hill. The center of the hill is located at the epicenter distance of 62.5 km, the maximum height of the hill is 4 km and the standard deviation of the Gaussian function is 12.9 km. A SH-wave source is located in the depth of 32 km. The S-wave velocity is 3.5 km/s.

Shown in Fig. 2 are snap shots of the wavefield calculated by the conformal screen method. We can clearly see the incident wave and reflected wave from the free surface. After encountered the Gaussian hill on the surface, the incoming wave split into two arrivals on the ground surface. These interactions complicated the wavefield and provided a test for the new method. Shown in Figs. 3a and 3b are synthetic seismograms for the Gaussian hill model using both conformal and non-conformal methods, respectively. Synthetic seismograms calculated with a more accurate boundary integral method (Fu and Wu, 1999) are used as a reference. In both figures, the solid lines are from the screen method and the dashed lines are from boundary integral method. In Fig. 3a, the conformal screen method uses dx = 0.25 km, dz = 0.25 km and dt = 0.05 sec. The comparisons indicate that the screen method gives a satisfactory result for this model. It correctly modeled waveforms between distances 60 and 70 km, where two reflections from the convex free surface interfere with each other and generate complex waveforms. In Fig. 3b, the non-conformal screen

method uses dx = 0.125 km, dz = 0.25 km and dt = 0.05 sec. in the calculation. Generally speaking, the results are consistent with those from the boundary integral method except there are some minor precursors at distances between 50 and 70 km.

Our next model is for Lg wave propagation in a waveguide with a rough free surface. The model has an average crust thickness of 30 km. A random fluctuation is added to the free surface. The randomness has an exponential power spectrum. Its RMS fluctuation is 0.4 km; horizontal correlation length is 40 km and maximum elevation difference is 1.73 km. These parameters represent the topography of a typical mountain area. A SH-source is located in the depth of 10 km. The conformal transform method is used to calculate the Lg propagation. Parameters used in the calculation are dx = 0.25 km, dz = 0.25 km and dt = 0.05 sec. As a comparison, Fig. 4 gives the snap shots for a crustal wave guide without the surface fluctuation. The figure clearly shows the head wave and multiple reflections between the free surface and Moho discontinuity. All wave fronts are relatively sharp and clear. Fig. 5 gives the snap shots for a crust wave guide with the above mentioned surface fluctuation. With the surface fluctuations, the reflections are combined with randomly scattered waves. These scattered waves blurred the entire wavefield and make part of the energy deflected from its original direction cause the additional Lg attenuation.

CONCLUSION AND DISCUSSIONS

This paper is part of the study aimed at development and application of a new wave propagation and modeling method for regional waves in heterogeneous crustal wave guides using one-way wave approximation. In this paper, two forms of boundary conditions based on conformal and non-conformal coordinate transforms have been developed for taking care of irregular free surfaces for generalized screen propagator. The resulting algorithms can give satisfactory results for models with mild to moderate free surface fluctuations. The comparisons between the method developed here and the more accurate boundary integral method indicate that this method can be used to calculate synthetic seismograms of regional waves for more realistic velocity models, longer propagating distances and higher frequencies.

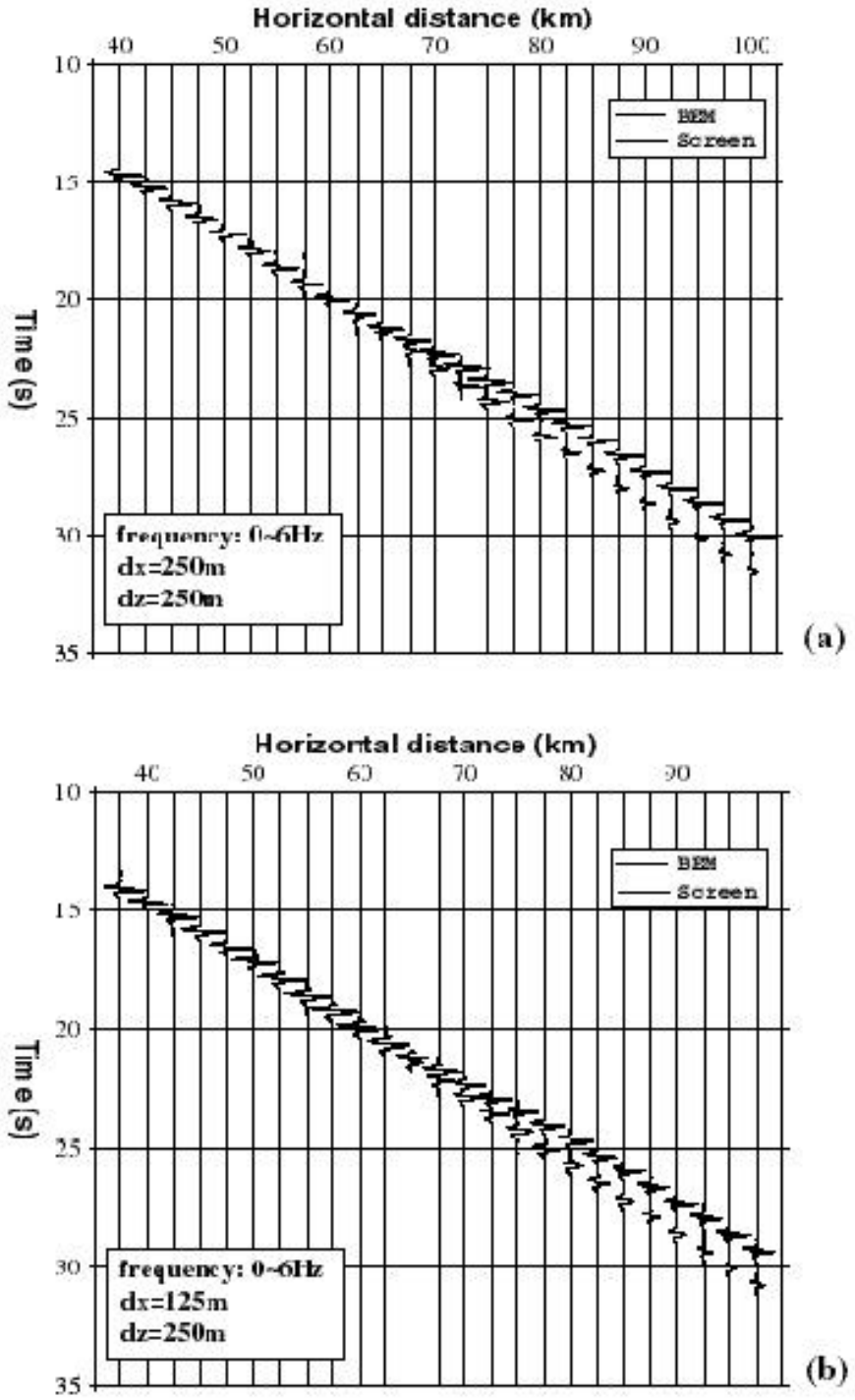


Figure 3: Synthetic seismograms using (a) conformal and (b) non-conformal transform methods, respectively. The solid lines are from the GSP method. The dashed lines are from the boundary integral method, and used as a reference. Details please see the text.

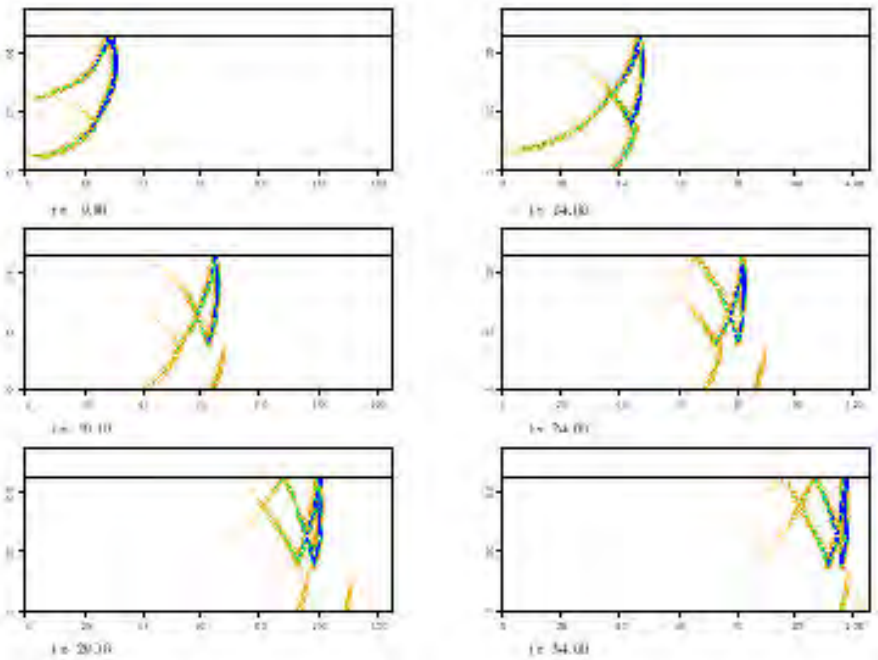


Figure 4: Snap shots of the wave field. the model is a homogeneous crustal wave guide. The depth to the Moho is 30 km. All wave fronts are relatively sharp and clear

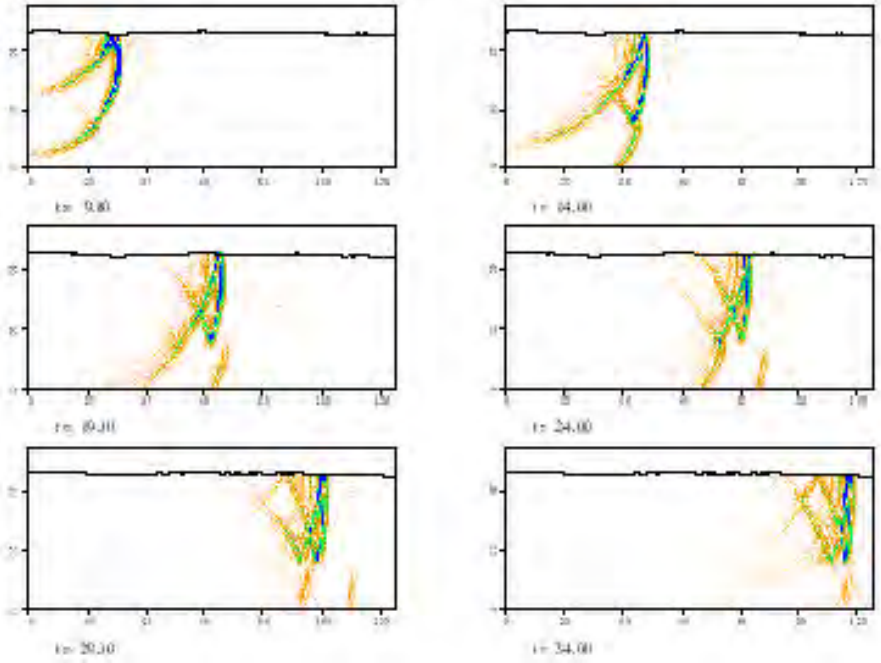


Figure 5: Snap shots of the wave field. the model is a homogeneous crustal wave guide with a rough free surface (for detailed parameters, see the text). With the surface fluctuations, the scattered waves blurred the wavefield.

REFERENCES

Bouchon, M., 1981, A simple method to calculate Green's functions for elastic layered media, *Bull. Seismol. Soc. Am*., 71, 959-971.

Bouchon, M., M. Campillo and S. Gaffet, 1989, A boundary integral equation-discrete wavenumber representation method to study wave propagation in multilayered media having irregular interfaces, *Geophysics, 54*, 1134-1140.

Campillo, M. 1990, Propagation and attenuation characteristics of the crustal phase Lg, *Pure and Appl. Geophys. 132*, 1-19.

Chen, X.F., 1990, Seismogram synthesis for multi-layered media with irregular interfaces by the global generalized reflection/transmission matrices method - Part I. Theory of 2-D SH case*, Bull. Seismol. Soc. Am., 80*, 1694-1724.

Chen, X.F., 1995, Seismogram synthesis for multi-layered media with irregular interfaces by the global generalized reflection/transmission matrices method - Part 11. Applications of 2-D SH case, *Bull. Seismol. Soc. Am*., 85, 1094-1106.

Fu, L.Y. and R.S. Wu, 1999, A hybrid BE-GS method for modeling regional wave propagation, Submitted to *the CTBT special issue*.

Jih, R.S., 1996, Waveguide effects of large-scale structural variation, anelastic attenuation and random heterogeneity on SV Lg propagation: a finite-difference modeling study, *Proc. of the 18th Annual SRS on Monitoring a CTBT*, 182-194.

Kennett, B.L.N., 1984, Guided wave propagation in laterally varying media -I. Theoretical development, *Geophys. J. R. Astr. Soc. 79*, 235-255

Hestholm, S.O. and B.O. Ruud, 1994, 2-D finite-difference elastic wave modeling including surface topography, *Geophysical Prospecting, 42*, 371-390.

Hestholm, S.O. and B.O. Ruud, 1998, 3-D finite-difference elastic wave modeling including surface topography, *Geophysics, 63*, 613-622.

Wu, R. S., 1994, Wide-angle elastic wave one-way propagation in heterogeneous media and an elastic wave complex-screen method, *J. Geophys. Res., 99*, 751-766.

Wu, R.S., S. Jin and X.B. Xie, 1999a, Seismic wave propagation and scattering in heterogeneous crustal waveguides using screen propagators: I SH waves, submitted to *Bull. Seism. Soc. Am*.

Wu, R.S., S. Jin and X.B. Xie, 1999b, Energy partition and attenuation of Lg waves by numerical simulations using screen propagators, submitted to *Phys. Earth and Planet. Inter*.

Xie, X.B. and T. Lay, 1994, The excitation of explosion Lg, a finite-difference investigation, *Bull. Seismol. Soc. Am., 84*, 324-342.

EXCITATION AND ATTENUATION OF REGIONAL WAVES FROM RECENT SEISMIC EVENTS IN CHINA

Jiakang Xie, Lamont-Doherty Earth Observatory

Sponsored by U.S. Department of Defense
Defense Threat Reduction Agency
Contract No. DSWA01-98-1-0006 and DSWA0I-98-1-0009

ABSTRACT

In the past few months I have further improved the method for simultaneous inversion for source spectral parameters and path Q using regional wave spectra. I have implemented a new computerized, non-linear algorithm that can be used for spectral inversion using data from multiple events that are nearly co-located. For example, spectra from swarms or mainshock/aftershock sequences from multiple stations can now be used simultaneously to derive event-variable source seismic moments, comer frequencies and path-variable Q values. This new algorithm can further suppress effects of random and modeling errors in regional wave spectral inversion, and can be jointly used with the previous, single event based algorithms (Xie, 1993; 1998).

I tested the new algorithm by applying it to synthetic, as well as real Pn spectra from several last Lop Nor explosions, originally analyzed by Xie and Patton (1999) using an ad hoc algorithm that lacks generality. In all tests I was able to recover the known source and path spectral parameters in the inversions using the new algorithm. I am currently applying this algorithm to analyze the regional wave spectra from the 1997, Jiashi earthquake swarm (M_W ~ 6) in Xinjiang, and the 1998, Zhangbei earthquake (M_W ~ 6) and its aftershocks in the Hebei province of northern China. Interesting aspects of these events include (1) the magnitude estimated for these events by the USGS and China Seismological Bureau (CSB) differ systematically, with the CSB estimates significantly larger; (2) the Jiashi swarms have mixed focal mechanisms, including strike-slip faulting and normal faulting that is rare in the tectonic environment; (3) some Jiashi events were recorded by strong-motion instruments; data from these recording are now available to the U.S. scientists through the effort of the P.I. and seismologists at University of Nevada.

Estimates of source seismic moments, comer frequencies and path-variable Q using Pn, Lg waves from these events will be presented.

Key Words: Seismic Sources, Q, Seismic Wave Propagation, China

OBJECTIVE

There are two ultimate objectives of this research: (1) We wish to quantify path attenuation of regional waves in continental areas, such as Eurasia, by developing digital, tomographic Q maps. (2) We wish to quantify the difference in the excitations of various regional waves, so that we may achieve better, quantitative understanding and criterion of the P/Lg spectral ratio discriminant of explosions. There proposed research is composed of several tasks. The first is to further improve the inverse method for simultaneous determination of source seismic moment (M_0), corner frequency (f_c) and path-variable Q_0 and η (Q at 1 hz and its power-law frequency dependence, respectively) using regional wave spectra. The second task is to apply the improved inverse method to Lg, Pn, Pg and Sg spectra from many earthquakes and explosions in Eurasia to estimate source M_0, f_c and path Q_0, η. The third task is input the measured Q values to a computerized tomographic algorithm, to obtain laterally varying Q maps for Lg and other regional waves. The fourth task is analyze source spectral scaling and other source spectral characteristics of seismic events, such as the amount of spectral overshoot of explosions, to explore when, how and why the P/Lg spectral ratios can be used to discriminate explosions from earthquakes.

This research provides important input to the implementation of a Comprehensive Test Ban Treaty. The tomographic Q maps can be used for the calculation of source spectral characteristics of any future seismic event to infer the nature and size of the event. These Q maps can also be used for estimating the detection threshold of the existing seismic stations located within the area studied. The source spectral behavior inferred from this study will help to understand if, when and how the P/Lg amplitude ratio can be used to discriminate explosions from earthquakes.

RESEARCH ACCOMPLISHED

Further development of algorithm to study regional wave spectra

In the past several months I have implemented a new version of the non-linear inverse algorithm for estimating source spectral parameters and path-variable Q using regional waves. This is the latest effort in improving the inverse algorithm. Unlike the previous, single-event based algorithm developed and modified by the PI in a series of papers (*e.g.*, Xie, 1993; Xie, 1998; Xie and Patton, 1999), the new version of the algorithm takes regional wave spectra from *multiple* events as the input, and simultaneously estimates the event-variable source M_0, f_c and path-variable Q_0, η values.

The new algorithm is developed for a situation when regional wave spectra from a number of nearly co-located events are available. In this situation the epicentral distance and path Q_0, η values from all events to the same station can be assumed as being constant. Using a stochastic modeling, we may express A_{ijk}, the regional wave spectra observed for the ith station, jth event and kth frequency, as

$$A_{ijk} = S_{jk} G(\Delta_i) \exp\left(-\frac{\pi f_k^{1-\eta} \Delta_i}{V_g Q_0}\right) r_{ijk} \quad . \qquad (1)$$

where f_k is the kth discrete frequency, Δ_i, V_g are the epicentral distance and group velocity. Q_{0j} and η_j are apparent Q at 1 Hz and its power-law frequency dependence. r_{ijk} is the effect of randomness. S_{jk} is the isotropic component of the source spectrum, which is given by

$$S_{jk} = \begin{cases} \dfrac{M_{0j}}{4\pi(\rho_s v_s \rho_c v_c^5)^{1/2}} \dfrac{1}{1 + f_k^2 / f_{cj}^2} & \text{for } \textit{earthquakes} \\ \dfrac{M_{0j}}{4\pi(\rho_s v_s \rho_c v_c^5)^{1/2}} \dfrac{1}{\left[1 + (1-2\beta) f_k^2 / f_{cj}^2 + \beta^2 f_k^4 / f_{cj}^4\right]^{1/2}} & \text{for } \textit{explosions} \end{cases} , \quad (2)$$

where ρ and v are density and wave velocity, with subscript c and s indicating crustal average and source zone values, respectively. The explosion source model in equation (2) is the modified Mueller-Murphy (M.M.M.) model by Sereno *et al.* (1988), with β being the overshoot parameter ($\beta = 0.75$ for a Poisson medium). $G(\Delta_i)$ in equation (1) is the geometrical spreading factor and takes the form

$$G(\Delta_i) = \Delta_0^{-1} (\Delta_0 / \Delta_i)^m \quad , \quad (3)$$

where Δ_0 is a reference distance, and m is the decay rate of A_{ijk} at distances of $\Delta > \Delta_0$. Values of Δ_0 and m can be estimated for 1D velocity models for the study area, using synthetics (*e.g.* Xie, 1996; Xie and Patton, 1999).

If there are I stations, J events and N_d spectral observations, we may define a one dimensional unknown model vector, $\boldsymbol{m}$, as

$$\boldsymbol{m}^T = \left(M_{01}, f_{c1}, M_{02}, f_{c2}, \ldots, M_{0J}, f_{cJ}, Q_{01}, \eta_{01}, \ldots, Q_{0I}, \eta_{0I} \right)^T \quad . \quad (4)$$

where the superscript T denotes transpose. $\boldsymbol{m}$ has a dimension of $N_M = 2 \times J + 2 \times I$ and contains all of the unknown source spectral and path Q parameters to be solved for. We may also map the subscript combination "ijk" into a single subscript, "n", such that n increase from 1 to N_d and has a one-to-one correspondence to the ijk combinations. We may then take the logarithm of equation (1) and write the result into a general form of

$$d_n = \log(A_n) = F_n(\boldsymbol{m}) + \varepsilon_n \qquad (n = 1, 2, \ldots, N_d) \quad , \quad (5)$$

where $F_n(\boldsymbol{m})$ is a non-linear function of $\boldsymbol{m}$, and ε_n is a small, random quantity. Defining a data vector, $\boldsymbol{d}$ and a vector function, $\boldsymbol{F}$, the above equation takes a form of

$$\boldsymbol{d} = \boldsymbol{F}(\boldsymbol{m}) + \boldsymbol{\varepsilon} \quad , \quad (6)$$

where $\boldsymbol{\varepsilon}$ is a small residual vector. Equation (6) is a standard forward relationship between the data and model vectors, $\boldsymbol{d}$ and $\boldsymbol{m}$. It can be used to form a standard non-linear inverse problem in which given a data vector $\boldsymbol{d}$, the unknown vector $\boldsymbol{m}$ can be solved. We use a simple linearization-iteration (Newton-like) method to solve for $\boldsymbol{m}$, which starts with an initial model, $\boldsymbol{m}^0$, and proceeds in a loop (*e.g.*, Aki and Richards, 1980, § 12.3.7). At the $(q+1)$th step of the loop, the estimated model vector $\boldsymbol{m}^q$ is upgraded into $\boldsymbol{m}^{q+1}$ using

$$\boldsymbol{m}^{q+1} = \boldsymbol{m}^q + (\boldsymbol{G}^{q^T} \boldsymbol{G}^q)^{-1} \boldsymbol{G}^{q^T} \boldsymbol{d} \quad , \quad (7)$$

where $\boldsymbol{G}^q$ is the Frechet kernel matrix defined as

$$G_{ni}^{q} = \partial F_n(m)/\partial m_i|_{m=m^q} \tag{8}$$

The loop stops when the calculated residual

$$Res^q = \sqrt{(d - F(m^q))^T (d - F(m^q))/(N_d - N_M)} \tag{9}$$

stops to decrease with increasing q.

The motivation of developing and implementing such an algorithm comes from general, as well as specific considerations. In general, inverting spectra from multiple event increases the number $(N_d - N_M)$, thus making the inverse problem more overdetermined. Specifically, spectral inversion problems suffers significantly from modeling errors, as pointed out by Xie (1998) and Xie and Patton (1999). The modeling errors include those caused by ignoring the site response or non-isotropic source radiation pattern, and by the use of imprecise models describing the source spectra (equation (2)) and path geometrical spreading (equation (3)). If individual source spectra deviate from the idealized source spectral models randomly, the effects of these deviations tend to cancel out when spectra from multiple, co-located events are inverted simultaneously. For example, Xie and Patton (1999) studied Pn spectra from five similar Lop Nor explosions. By inverting the Pn spectra from individual explosions separately, they obtained drastically varying source and path spectral parameters, indicating that the event-based algorithm, when used without sufficient a priori knowledge on source and path spectral parameters, is unstable for Pn spectral inversion. They therefore used an ad hoc method to tackle the instability problem. First they used the event-averaged spectra at all stations to derive the event-averaged M_0 and f_c values together with the estimated standard errors. These were then used as a priori knowledge for event-based inversion, in which M_0, f_c values for each individual events are allowed to vary from the event-averaged values within the estimated standard error. The ad hoc method works satisfactorily only when the source spectra from different events are very similar, thus lacking a generality.

Application to Recent Events in China

The multiple-event based algorithm has been applied to regional wave spectra from some recent events in China. The first application is to Pn spectra from three of the five similar Lop Nor explosions studied by Xie and Patton (1999), as mentioned in the last section. Table 1 compares the source spectral parameters obtained using the new algorithm with those obtained by Xie and Patton. The two sets of the estimated parameters are very similar.

We have also applied the new algorithm to Lg spectra from several recent earthquake sequences in northwest and north China. These include (a) a swarm of moderate and small earthquakes in Jiashi County of the Xinjiang Autonomous Region (Li and Kerr, 1997), (b) the mainshock-aftershock sequence of the Zhangbei earthquake north of Beijing (Lin *et al.*, 1999), and (c) an M_b=5.5 event and its largest aftershock in inner Mongolia in May, 1996 (event 05/03/96 in Table 2). Figure 1 shows the location of these events. Table 2 lists the source parameters of the larger ($M_b \geq 5.4$) events studied, including the M_0 and f_c values estimated using Lg, and the M_0 values from the USGS and Harvard CMT solutions. Figure 3 shows an example of the fit of station-averaged, path-corrected Lg spectra to the synthetic source spectra constructed using the M_0, f_c parameters estimated during the spectral inversion.

Table 1 Estimated Pn M_0 and f_c Values for Three Lop Nor Explosions

Event Date	Origin Time (UT)	M_b	Pn M_0 (10^{16} N m)	Pn f_c (Hz)
10/05/93	01:59:56.6	5.9	1.1†, 1.0‡	2.2†, 2.5‡
10/07/94	03:25:58.1	5.9	10†, 8.7‡	2.6†, 2.8‡
05/15/95	04:05:57.8	5.7	1.1†, 1.1‡	2.5†, 2.6‡

†Estimated by Xie and Patton (1999).
‡Estimated by this study using the multiple-event based algorithm.

Table 2 Moderate Earthquakes With Lg M_0, f_c Estimates

Event Date	Origin Time (UT) (USGS)	M_b (USGS)	M_W (USGS, Harvard)	Location by USGS (°N, °E)	Fixed Half Duration by Harvard (s)	M_0 from USGS, Harvard (10^{17} N m)	Lg M_0 (10^{17} N m)	Lg f_c (Hz)
10/02/93	08:42:32.7	6.2	6.0, 6.1	38.190 88.663	2.7	13,15	4.8	0.21
05/02/95	11:48:11.8	5.5	-, 5.6	43.776, 84.660	1.3	-,2.8	0.7	0.6
05/03/96	03:32:48.0	5.5	5.9, 6.0	40.772, 109.672	2.5	8.3, 12	4.5	0.28
04/11/97	05:34:44.1	5.8	6.1, 6.1	39.504, 76.974	2.6	14, 16	3.9	0.28
04/15/97	18:19:11.5	5.4	5.7, 5.9	39.602, 76.934	2.2	3.8, 8.3	1.8	0.33
01/10/98	03:50:41.5	5.8	5.8, 5.8	41.083, 114.500	1.9	5.5, 6.1	3.2	0.27

The Lg M_0 and f_c values are obtained by Cong *et al.* (1996) for event 10/02/93, and by this study for all other events.

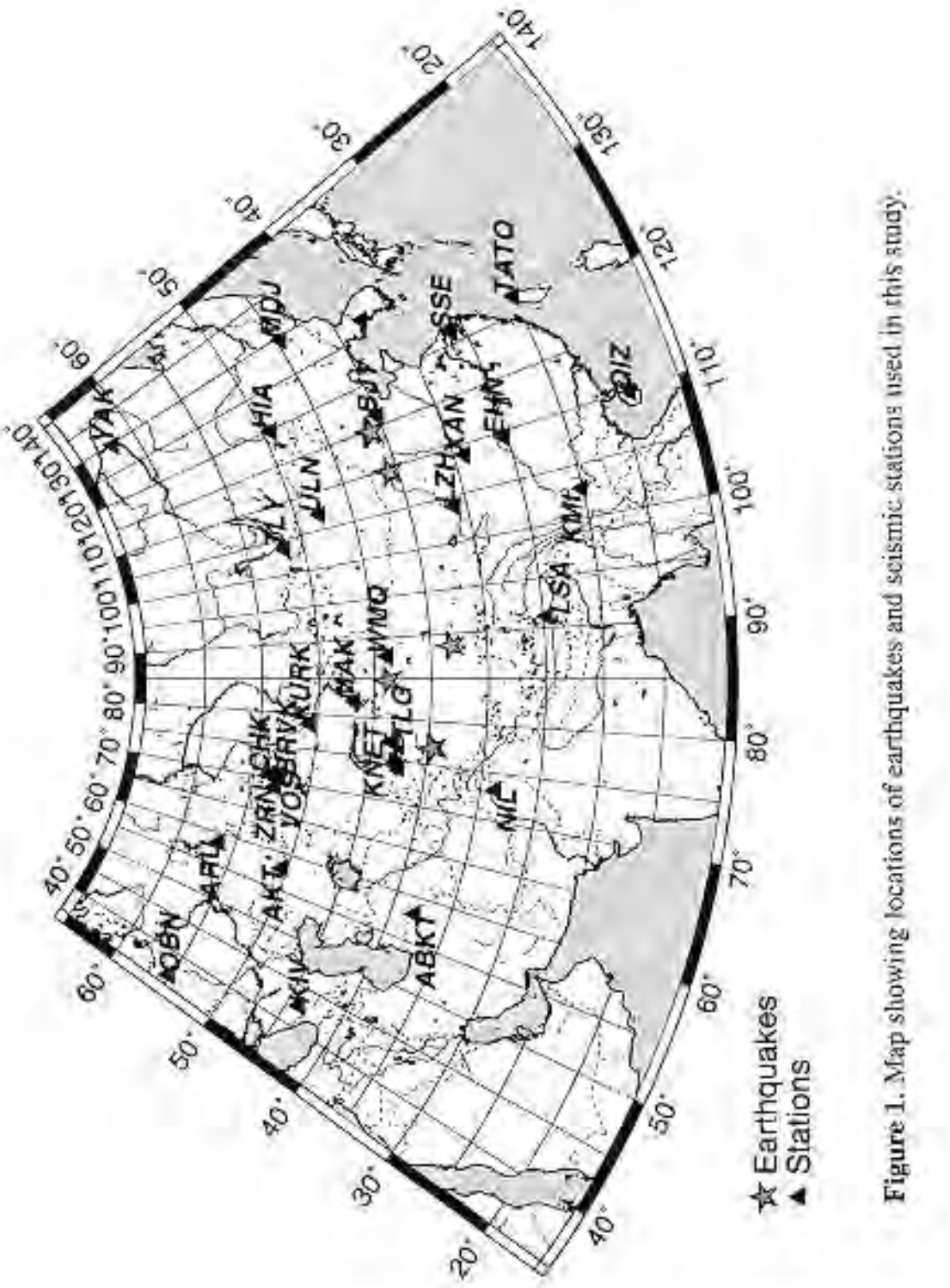


Figure 1. Map showing locations of earthquakes and seismic stations used in this study.



Figure 2. An example of the empirical Green's function deconvolution. Left and middle traces are the Lg waveforms from the 01/10/98 Zhangbei mainshock and an aftershock, observed at station XAN ($\Delta = 956$ km). Deconvolving the left trace by the middle results in the estimated source time function shown on the right, with a rise time reading of about 3.5 s.

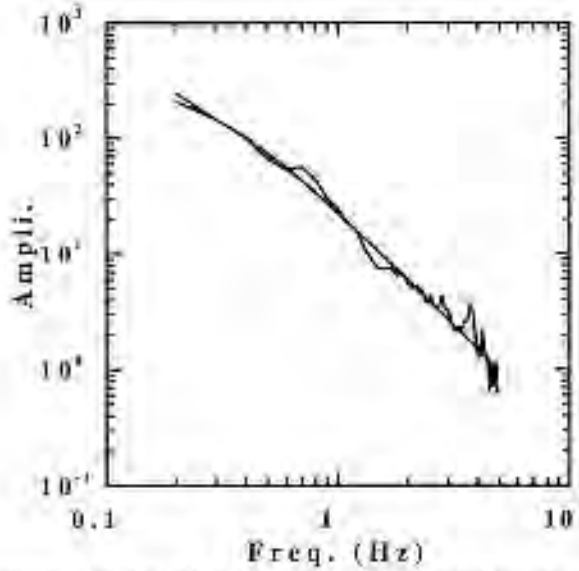


Figure 3 Path-corrected Lg spectra for the 01/10/98 Zhangbei earthquake, averaged over 12 broad-band stations, versus synthetic Lg source spectra constructed using the best-fit source model of ($M_0 = 3.2 \times 10^{17}$ N m, $f_c = 0.27$ Hz). The average Q_0 and η for the 12 stations are estimated to be 443 and 0.4, respectively.

As an independent check of the reliability of our f_c estimates, we estimated the source rise times (which is roughly the inverse of f_c) of the moderate earthquakes using the empirical Green's function (EGF) analysis, whenever co-located small events with similar focal mechanisms are available. Figure 2 shows an example of the EGF analysis. We found that for all larger events that permit the EGF analysis, the estimated Lg source rise times are very similar to the inverse of the Lg f_c values estimated in the spectral inversion.

It is interesting to note that the Lg M_0 values in Table 2 are systematically smaller, by factors of 2 to 4, than the values from the USGS and Harvard CMT solutions, obtained by modeling long-period, teleseismic waveforms. The measured source sizes for Chinese earthquakes by seismologists at different institutions typically differ. For example, it is well known that the magnitude estimates of Chinese earthquakes by the USGS tend to be 0.5 scale lower than those estimated by the China Seismological Bureau (CSB, *e.g.*, Li and Kerr, 1997), and that the estimates of M_0 by the Harvard GMT solution for central Asian earthquakes tend to be lower than those obtained by modeling regional surface waves (Patton, 1998). It is possible that the Lg M_0 values in Table 1 underestimate the real seismic moment because I have used an improper geometrical spreading with the reference distance Δ_0 set at 100 km. Assuming that the Δ_0 values can be as large as 200 km (Kvamme *et al.*, 1995), the Lg M_0 values can be raised by a factor of 1.4, resulting in Lg M_0 values that are lower than the USGS and Harvard estimates by factors of about 1.5 to 3.0. Patton (1998) suggested that for central Asian earthquakes, the Harvard M_0 estimates may be biased low by an average log-unit of 0.27, owing to the unusually thick crust (~ 50 km) unaccounted by the CMT solution. That suggestion appears to be consistent with Table 2, in which the Lg M_0 and the USGS/Havard CMT M_0 values differ more for earthquakes in northwest China (central Asia), where typical crustal thickness is about 50 km, much greater than the typical thickness of 35 to 40 km in north China (*e.g.*, Mooney *et al.*, 1998).

CONCLUSIONS AND RECOMMENDATIONS

We have implemented a multiple-event based, non-linear inverse algorithm for simultaneous determination of event-variable M_0, f_c values, and path-variable Q_0, η values using regional wave spectra. This marks a further improvement of our capability of reliably retrieving source and path spectral parameters using spectra that are subject to various random and modeling errors (Xie, 1998). Applications of the new algorithm to regional wave spectra from various co-located events, including clustered underground nuclear explosions, earthquake swarms and mainshock-aftershock sequences in China have yielded source spectral parameters and path Q for northwest and north China.

A long-standing problem for estimating sizes of seismic events in China has been that the estimates made by various seismological institutions tend to differ significantly. These include systematic differences in magnitude estimates of about 0.5 scale, and systematic differences in moment estimates of more than a factor of two. This poses a fundamental problem for comparative studies of seismic events in China and other regions of the world. In research so far, we have obtained Lg M_0 estimates for several recent, moderate seismic events in China. These estimates are systematically lower than the respective values estimated by the USGS and

Havard CMT solutions. Various causes could have contributed to this discrepancy, including the mis-calibration of the Lg geometric spreading terms in northwest and north China. Revision of this term involves synthetic calculations using more realistic velocity structures. However, it is unlikely that the discrepancy in M_0 estimates comes solely from bias in estimates using Lg. I suspect that the systematic bias in Lg M_0 estimates, if exists, may account for no more than a factor of about 1.4 of the discrepancy. To reconcile the M_0 estimates, efforts will be needed on examining M_0 estimates obtained by modeling long-period, teleseismic surface/body waves, as done by Patton (1998).

It is thus recommend that a special effort be make to select a number of recent, moderate Chinese earthquakes for a joint study, in which seismologists from different institutes in and outside China re-calculate the source parameters using the same broad-band data set, and compare the result. The cause of the discrepancy may be resolved in such a comparison by examining the data processing and source inversion procedures, as well as the velocity/Q structures used in the inversions.

In the next phase of this research, analysis of regional wave spectra from many more events will be conducted. The work will be optimized for achieving the two ultimate goals of this research: (1) development of new tomographic, regional wave Q maps, and (2) quantification of spectral characteristics of excitation of various regional waves, so that better understanding and criterion of the P/Lg ratio discriminants will be obtained.

References

Aki, K. and P.G. Richards P.G., 1980. *Quantitative Seismology: Theory and Methods* W.H. Freeman, San Francisco, Calif., 1980.

Cong, L., J. Xie & B.J. Mitchell, 1996. Excitation and propagation of Lg from earthquakes in Central Asia with implications on explosion/earthquake discrimination, *J. Geophys. Res.*, **101**, 27779-27810.

Kvamme, L.B., R.A. Hansen & Bungum, 1995. Seismic-source and wave-propagation effects of Lg waves in Scandinavia. *Geophys. J. Int.*, **120**, 525-536.

Li, H. and R.A. Kerr, 1997. Warnings precede Chinese temblors, *Science*, **276**, 526.

Lin, A., G. Zhao, G. Zhao and X. Xu, 1999. Inferred seismic fault associated with the 1998 M = 6.2 Zhangbei-Shanyi earthquake, Hebei Province, China. *Bull. Seism. Soc. Am.*, **89**, 550-554.

Mooney, W., G. Laske and T.G. Masters, 1990. CRUST 5.1: A global crustal model at 5°×5°, *J. Geophys. Res.*, **103**, 727-747.

Sereno, T.J., S.R. Bratt and T.C. Bache, 1988. Simultaneous inversion of regional wave spectra for attenuation and seismic moment in Scandinavia, *J. Geophys. Res.*, **93**, 2019-2036.

Xie, J. 1993. Simultaneous inversion of source spectra and path Q using Lg with applications to three Semipalatinsk explosions, *Bull. Seism. Soc. Am.*, **83**, 1547-1562.

Xie, J., 1996. Excitation and propagation of Pn in central Asia, in *Proc. 18h Seis. Res. Symposium on Monitoring a Comprehensive Test Ban Treaty*, edited by J.F. Lewkowicz, J.M. McPhetres, and D.T. Reiter, Air Force Phillips Laboratory, PL-TR-96-2153, pp. 419-428.

Xie, J., 1998. Spectral inversion using Lg from earthquakes: Improvement of the method with applications to the 1995, western Texas earthquake sequence, *Bull. Seism. Soc. Am.*, **88**, 1525-1537.

Xie, J., L. Cong & B.J. Mitchell, 1996. Spectral characteristics of the excitation and propagation of Lg from underground nuclear explosions in Central Asia, *J. Geophys. Res.*, **101**, 5813-5822.

Xie, J. & H. Patton, 1999. Regional Phase Excitation and Propagation in the Lop Nor Region of Central Asia and Implications for the Physical Basis of P/Lg Discriminants, *J. Geophys. Res.*, **104**, 941-954.

SOURCE-SPECIFIC STATION CORRECTIONS FOR REGIONAL PHASES AT INTERNATIONAL MONITORING SYSTEM STATIONS

Xiaoping Yang, Keith McLaughlin, Robert North
Center for Monitoring Research, SAIC

Sponsored by U.S. Department of Defense
Defense Threat Reduction Agency
Contract No. DTRA01-99-C-0025

ABSTRACT

The software at the prototype International Data Centre (pIDC) allows for a hierarchy of calibrations relevant to location improvement. The IASPEI91 global travel-time curves have been used as the default for event location at the pIDC since 1995. A series of corrections can be made, including ellipticity and elevation corrections (for each arrival), Bulk Time Station Corrections (for each station and travel-time phase), and Slowness and Azimuth Station Corrections (for each station and array). Separate regional travel-time curves (distance less than 20 degrees) may be designated for Pn, Pg, Sn, and Lg for each International Monitoring System (IMS) station. It may also use path corrections, or Source Specific Station Corrections (SSSC), to apply corrections relative to IASPEI91 as a function of source location for any station and phase. Where a single model is insufficient for characterizing the regional geology, SSSCs are more appropriate for event locations. The travel-time corrections and modeling errors are specified on a latitude/longitude grid in the pIDC location software. We have adopted an approach developed by Bondár in deriving SSSCs for regional phases. This method is based on regionalization and regional travel times for different tectonic regions surrounding each station. The predicted travel times are calculated as the weighted sum of total travel times in each region along the source-station path. The development and validation of the SSSCs rely on the 1-D regional models/regionalization and the ground truth testing events, respectively. Further development in 1-D velocity models and travel time curves can improve such SSSCs, event locations, and uncertainties. Ground truth events with high location accuracy are essential in demonstrating the expected improvement in event locations when applying SSSCs.

Fennoscandia is the only region where the 1-D travel times (Baltic model) were implemented in location processing at the pIDC. We have developed SSSCs for regional phases at the Fennoscandian stations by interpolating travel times through different 1-D models using Bondár's method. SSSCs for stations NRIS and SPITS are also derived given the fact that paths from both stations to high-latitude events are within the Fennoscandia regionalization as Baltic. Validation testing using ground truth events shows significant reduction in error ellipses by applying the SSSCs (from 3830 to 1120 km^2). When using the SSSCs mislocations have also been reduced for events outside the shield while the improvement within the shield is similar to that using the 1-D Baltic model (9 km improvement on average for GT2 events). The SSSCs for these stations were implemented at the pIDC for Reviewed Event Bulletin (REB) location in April 1999.

Regional SSSCs for North American IMS stations have been developed and have undergone initial testing by Bondár. For ground truth events with location accuracy better than 10 km, the median improvement in location due to SSSCs is 7 km, and the median reduction of error ellipse areas is about 800 km^2 (from 3700 to 2900 km^2). Currently we are evaluating the 1-D travel times and regionalization used in deriving the SSSCs for the North American IMS stations. We are also collecting high-quality ground truth events in North America for further validation testing of the SSSCs.

Key Words: prototype International Data Centre, pIDC, IASPEI91, SSSCs, location, calibration, 1-D model, travel times, Baltic model, Fennoscandia, North America, International Monitoring System, Reviewed Event Bulletin.

OBJECTIVES

Our goal is to improve event locations using regional travel time corrections for IMS stations relative to the IASPEI91 model. Miss-locations and error ellipses have recently been reduced in Fennoscandia region by operational use of regional SSSCs at stations ARCES, FINES, HFS, NOA, NRIS, and SPITS (Yang and McLaughlin, 1999a). Similarly we develop regional SSSCs in North America based on regionalization and 1-D models to reflect the differences in geology and tectonics in eastern and western North America. New regional SSSCs are derived for 21 IMS stations in North America, including ALQ, BBB, DLBC, ELK, FRB, ILAR, INK, KDAK, MBC, MNV, NEW, PDAR, PFO, SADO, SCHQ, SFJ, TKL, TXAR, ULM, YBH, and YKA. Validation testing for regional SSSCs in North America is conducted using ground truth events to verify event location improvement relative to GT and location error ellipse coverage.

TRAVE LTIMES FOR 1-D MODELS IN NORTH AMERICA

We employ regionalized 1D models in deriving the regional SSSCs for the IMS stations in North America (distance less than 20 degrees). The travel time corrections are a weighted sum of the travel times in each region along the source-station path (Bondár et al., 1998; Yang et al., 1998). There are large variations in upper mantle (Moho to 300 km) velocity structures and travel times between the stable central/eastern and the tectonic western North America. The upper mantle velocities are low in the tectonic region and high in the shield/platform region. We collected and compared a number of velocity models/travel times in search of suitable models to use for SSSCs in North America. In the shield/platform region of North America there may be no or only a thin low velocity zone. In contrast, there may be a thick low velocity zone below tectonic western North America. Compared to the IASPEI91 model, the travel times are up to 4 seconds faster in the stable region but are up to 3 seconds slower in the tectonic region than the IASPE91. In this paper we summarize our findings and more details are given in Yang and McLaughlin (1999b).

Western North America. We collected 15 velocity models/travel times for tectonic western North America from the literature and a number of agencies. For instance, Archambeau et al. (1969) constructed P-wave velocity models of the upper mantle, CIT109, CIT110, CIT111, and CIT112 from LRSM profiles running east-southeast and east-northeast from two nuclear explosions (Shoal and Bilby) and an earthquake (Fallon) in Nevada. Their Moho Pn velocities range from 7.72 to 8.048 km/s. Archambeau et al. modeled the arrival times of Pn out to 1200 km and used an upper mantle triplication to explain Pn from 1200 to 2000 km. Their data and models serve as an excellent set of travel times for seismic sections starting in Nevada and ending in the eastern shield and platform regions. The CIT111 model is slow at distances less than 10 degrees and then becomes fast at distances greater than 10 degrees. This model seems particularly suitable for paths across different geology regions in North America. ISC data for six GT0 Nevada nuclear tests and an earthquake at Borah Peak in 1983 (ground truth information is available for all 7 events) generally agree with the CIT111 model, but there are no data beyond 12 degrees. Kovarch and Robinson (1969) derived an S velocity model (STAN3) for the Basin and Range province of western North America using LRSM array data. Their S model (Sn of 4.5 km/s) is compatible with P velocity models of Archambeau et al. (1969). The STAN3 mode is roughly the median of the group of S travel time curves that we compiled for western North America.

Eastern North America. Over 15 velocity models/travel times are collected from the literature and a number of agencies. In general the shield models in North America as well as in other regions are in good agreement with each other; they are all faster than the IASPEI91 model. For instance, Kremenetskaya and Asming (1999) extended the NORSAR model (e.g. Ringdal et al., 1997) for the general Barents Sea region. The median of our compiled travel times for eastern North America are almost identical to those generated using the Barents Sea model. ISC arrival time data for 54 well-located events in eastern North America also generally agree with the shield model. For Sn in

North America, the travel times for the Barents Sea model are within a reasonable range of other curves.

Regionalization. Mooney et al. (1998) compiled crustal data from the literature to produce a 5 degree by 5 degree grid of discrete models for the globe. Their goal was to compile regionalized crustal thicknesses and velocities for inclusion in worldwide tomographic inversions. Compilation of upper mantle Pn velocities was a secondary goal to their study. The 139 discrete models span a range of Pn velocity of 7.9 to 8.2 km/s. Mooney et al. report that this is only a fraction of the worldwide range from 7.6 to 8.6 km/s. Models assigned to stable North America have Pn velocities of 8.0 - 8.2 km/s. Models assigned to western tectonic North America are assigned Pn values of 7.9 to 8.0 km/s. Pn velocities below 7.8 km/s reported by many authors for the region are not represented. Braile et al. (1989) provided a summary on Pn velocity, crustal thickness, and average crustal P velocity in the US and adjacent Canada from the literature. Their contour maps clearly show variations across the continent corresponding to the geological and tectonic features. From the west to the east the medians are about 35 to 40 km in crustal thickness, 7.8 to 8.1 km/s in Pn velocity, and 6.2 to 6.4 km/s in average crustal P velocity. From Braile et al. map of Pn velocities we can see that it is not possible to construct a path greater than 10 degrees from the tectonic west to the stable east without crossing the 8.0 km/s contours.

Pg and Lg. Fewer studies are available for Pg and Lg velocity models and these phase detections are less common than Pn and Sn. We use velocities of 6.2 km/s for Pg and 3.55 km/s for Lg for the tectonic region, and velocities of 6.4 km/s for Pg and 3.6 km/s for Lg for the shield/platform region. The Pg velocities are roughly the medians of the average crustal velocities for the eastern and western North America, respectively, given in Braile et al. (1989). The Pg and Lg modeling errors for the Baltic model were used as guide for the Pg and Lg errors in North America.

Selected Models. Based on our review of the literature and examination of recent data, we chose the Barents Sea model for both Pn and Sn in the shield/platform region, and CIT111 for Pn and STAN3 for Sn for the western tectonic region. We construct modeling errors using the standard deviations of each model relative to the median of each group of our compiled models (10 for Pn and 6 for Sn in eastern North America; 11 for Pn and 7 for Sn in western North America). The modeling errors also account for the expected variations due to the difference in crustal thickness: 0.25 seconds for Pn, assuming a crust thickness of 7 km, and P velocities of 6.5 and 8.2 km/s; 0.4 second for Sn, assuming a crust thickness of 7 km, and S velocities of 3.58 and 4.5 km/s. Figure 1 shows the Pn, Sn, Pg, and Lg travel times and modeling errors for the shied/platform region. Figure 2 shows those for the tectonic region.

The regionalization of North America is shown in Figure 3. For the US (except Alaska) we use the Braile et al. Pn map to outline the tectonic region following contours of ~ 8.0 km/s. We extended this tectonic region slightly further north to include Vancouver Island where reported velocities are low. In this tectonic region the CIT111 and STAN3 models are used for Pn and Sn, respectively. We use faster travel times for the rest of North America, including eastern US, most of Canada, and Alaska. Although Alaska is far more complex than the shield geologically, there are reports that the P velocity in Alaska is higher than 8.1 km/s. However, currently only GT10 events are available in our ground truth data set for validation testing for this region and only one or two IMS stations are within regional distances for each event. The Alaska/Yukon region requires additional study.

RELOCATIONS USING REGIONAL SSSCs AT NORTH AMERICAN IMS STATIONS

We have derived SSSCs for Pn, Sn, Pg, and Lg for IMS stations in North America using Bondár's method. In our regionalization, North America is divided into two regions, stable shield/platform region and tectonic region (Figure 3). We use travel times faster than IASPEI91 for the shield/platform region (Figure 1), and travel times slower than IASPEI91 for the western tectonic region (Figure 2). Modeling errors are also shown in Figures 1 and 2. An example of Pn, Sn, Pg, and Lg SSSCs and modeling errors are given in Figures 4 and 5 for IMS station PDAR.

We relocated events in the same ground truth data set as studied by Bondár et al. (1998). We reassign the 34 P and 4 S defining phases with distances less than 20 degrees to Pn and Sn, respectively. Among the 49 events in the US (excluding Alaska), the testing and validation metrics are as follows:

- 55% of events moved closer to the GT locations with a median improvement of 5.5 km,
- 45% of events moved away from the GT with a median deterioration of 4.2 km,
- 31% of events moved closer to GT by 20% with a median of 10.8 km,
- 33% of events moved away from GT by 20% with a median of 6.3 km,
- error ellipse areas decreased for 92% of events, with a median decrease of 760 (from 1760 to 910),
- the 90% ellipse area coverage decreased by 10% (from 84% to 74%).

Given that most of the validation events are GT10 and the median miss-location distance is 15 km, we would expect the coverage to be significantly less than 90%. Assuming we were comparing to GT0, the sampling statistics would expect coverage between 75% and 100% at the 1 sigma level, and we do not consider the reduction in coverage as statistically significant. The results further emphasize the need for ground truth events better than GT10.

Among the 49 events in the data set, 21 events are GT2 or better (including 4 GT0 events). For these GT0-GT2 events, the median improvement of GT locations is 9.7 km and the median deterioration is 4.7 km; the median improvement and deterioration by 20% are 11.6 km and 8.9 km, respectively. The error ellipses for all these events are smaller by at least 20% with a median improvement of 1740 . Ground truth events with accuracies better than 5 km are vital for validation testing of location improvement using SSSCs.

We further relocated two recent GT2 events at NTS (Figure 6). Both are earthquakes that occurred in January 1999. Using SSSCs both events moved closer to the GT locations. For the event on 01/25/99 the miss-location decreased from 10 km to 6.7 km; for the event on 01/27/99 the miss-location decreased from 14 km to 8.6 km. In particular, the error ellipse for the 01/27/99 event now includes the GT location. In both cases the error ellipses are significantly smaller when using SSSCs.

CONCLUSIONS

SSSCs were implemented for the Fennoscandia region to improve event locations at the PIDC in April 1999. We are currently developing SSSCs for North American IMS stations using regionalized travel times. Validation testing using ground truth events shows that event locations are improved using SSSCs and location error ellipses are significantly reduced. Compared with previous studies using different regionalization and travel times, the location results here show better improvement. In particular, median deterioration is reduced. The validation testing further emphasizes that ground truth events with accuracies better than 5 km are important for validation testing of SSSCs to event locations.

REFERENCES

Archambeau, C. B, E. A. Flinn, and D. G. Lambert (1969), Fine Structure of the Upper Mantle, J. Geophy. Res., 74, 5825-5865.

Bondár, I, X. Yang, K. McLaughlin, R. North, V. Ryaboy, and W. Nagy (1998), Source Specific Station Corrections for regional phases at IMS stations in North America and Fennoscandia, EOS Trans. AGU, 79(45), Fall Meet. Supple., F839.

Braile, L.W., W.J. Hinze, R.R.B. von Frese, and R.G. Keller (1989), Seismic properties of the crust and uppermost mantle of the conterminous United States and adjacent Canada, Memoir-Geol. Soc. Am., 172, 655-680.

Kovach, R.L., and R. Robinson (1969), Upper mantle structure in the Basin and Range province, western North America, from the apparent velocities, Bull. Seismo. Soc. Am., 59, 1653-1665.

Kremenetskaya, E., and V. Asming (1999), Location calibration of the Barents region, Calibration Workshop, January 12-14, Oslo, Norway.

Ringdal, F., E. Kremenetstkaya, V. Asming, and Y. Filatov (1997), Study of seismic travel time models for the Barents region, NORSAR Sci. Rep. 2-96/97, 102-114.

Yang, X., K. McLaughlin, and R. North (1998), SSSCs for regional phases at IMS stations in North America and Fennoscandia, CMR Technical Report, CMR-98/46.

Yang, X. and K. McLaughlin (1999a), SSSCs for regional phases at Fennoscandian and other stations, CCB memo, CCB-PRO-99/03.

Yang, X. and K. McLaughlin (1999b), SSSCs for regional phases at North American IMS stations, CMR Technical Report (in preparation).

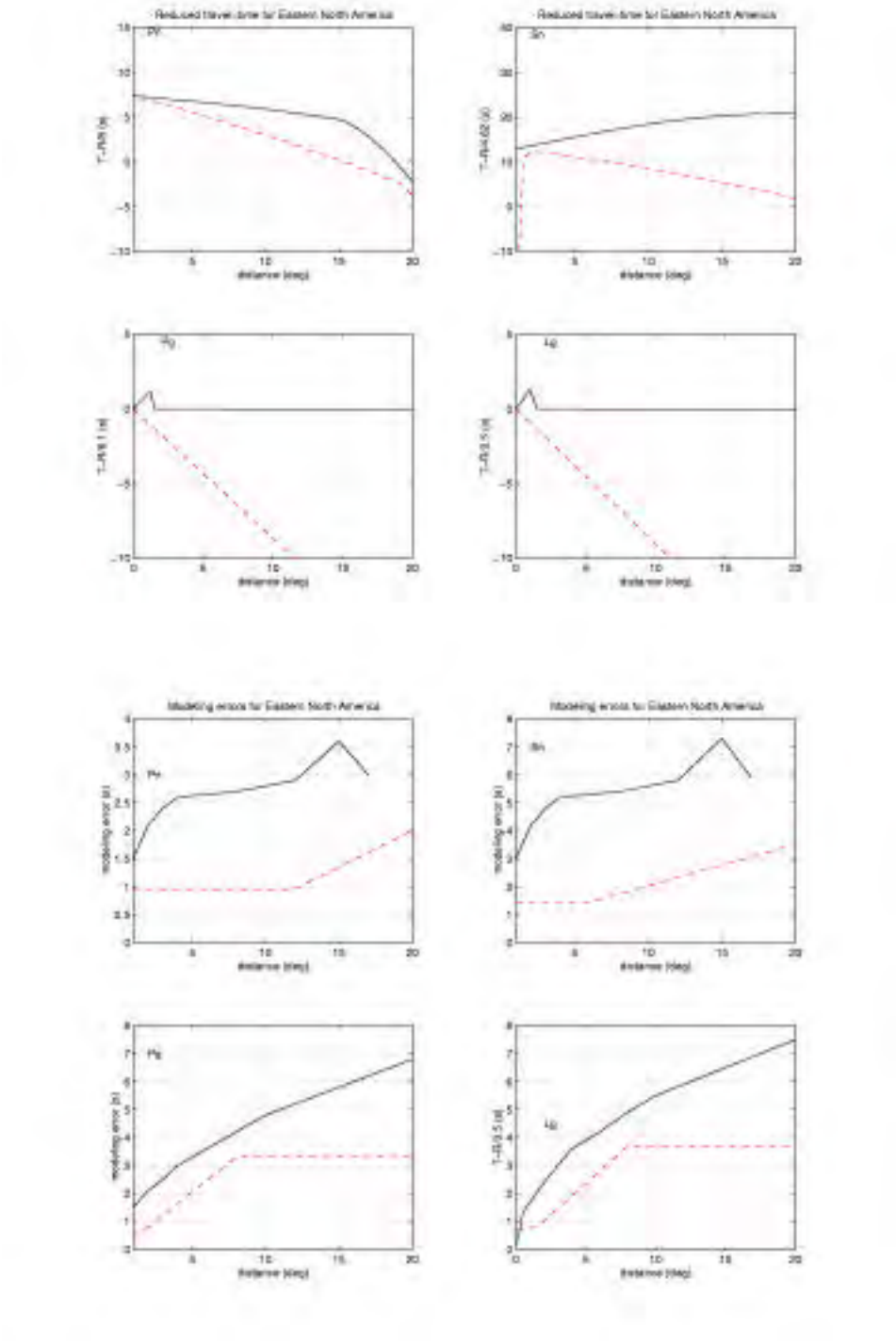


Figure 1. Pn, Sn, Pg, and Lg reduced travel time and modeling errors for eastern North America (dashed line) compared to the IASPEI91 travel times. The Pg and Lg travel times correspond to constant velocities of 6.4 km/sec and 3.6 km/sec, respectively. The Pn and Sn modeling errors are derived from the standard deviation of a suite of travel time curves (10 Pn and 6 Sn), plus expected travel time variations due to variations in crustal thickness (0.25 and 0.4 seconds, respectively). The Pg and Lg modeling errors are default values.

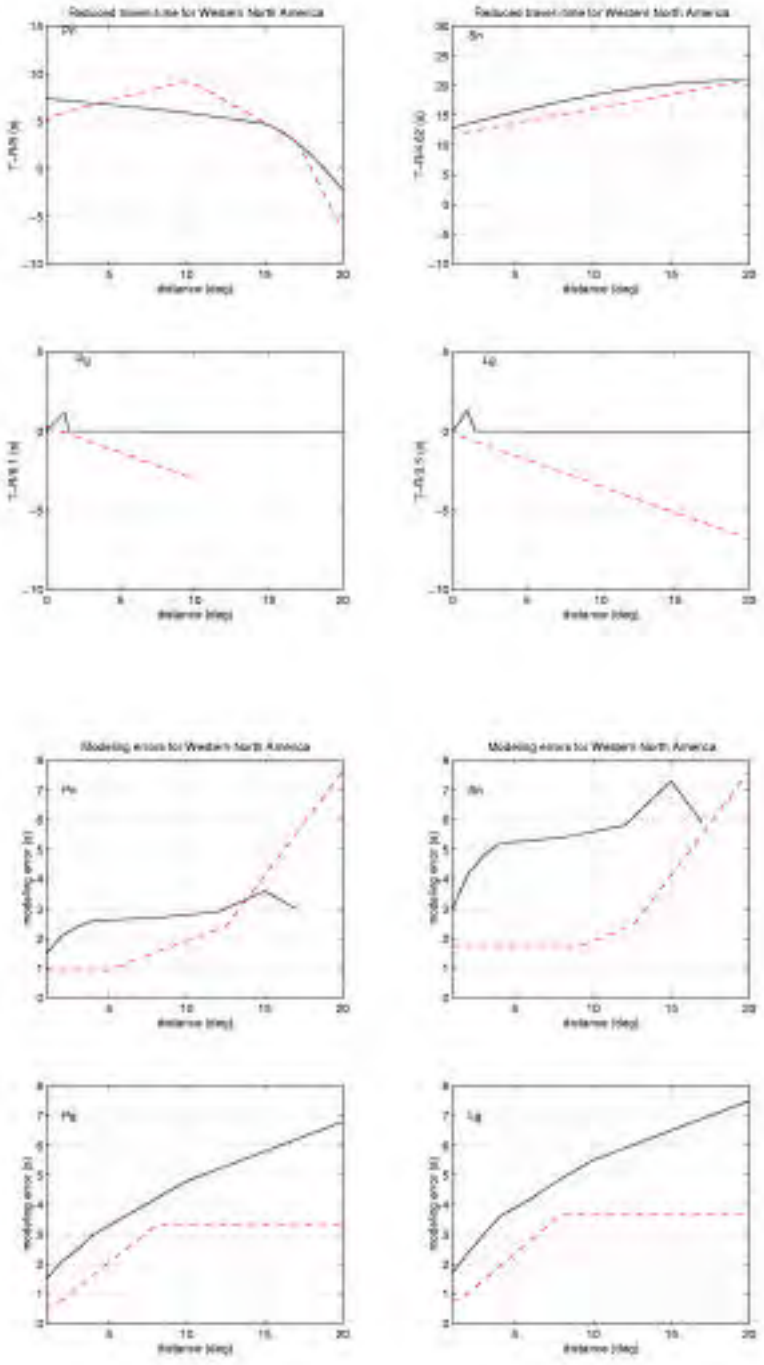


Figure 2. Pn, Sn, Pg, and Lg travel times and modeling errors that are used for SSSCs in western North America (dashed line) compared to the IASPEI91 travel times. The Pg and Lg travel times correspond to constant velocities of 6.2 km/sec and 3.55 km/sec, respectively. The Pn and Sn modeling errors are derived from the standard deviation of a suite of travel time curves (11 Pn and 7 Sn), plus travel time variations due to differences in crustal thickness (0.25 and 0.4 seconds, respectively). The Pg and Lg modeling errors are default values.

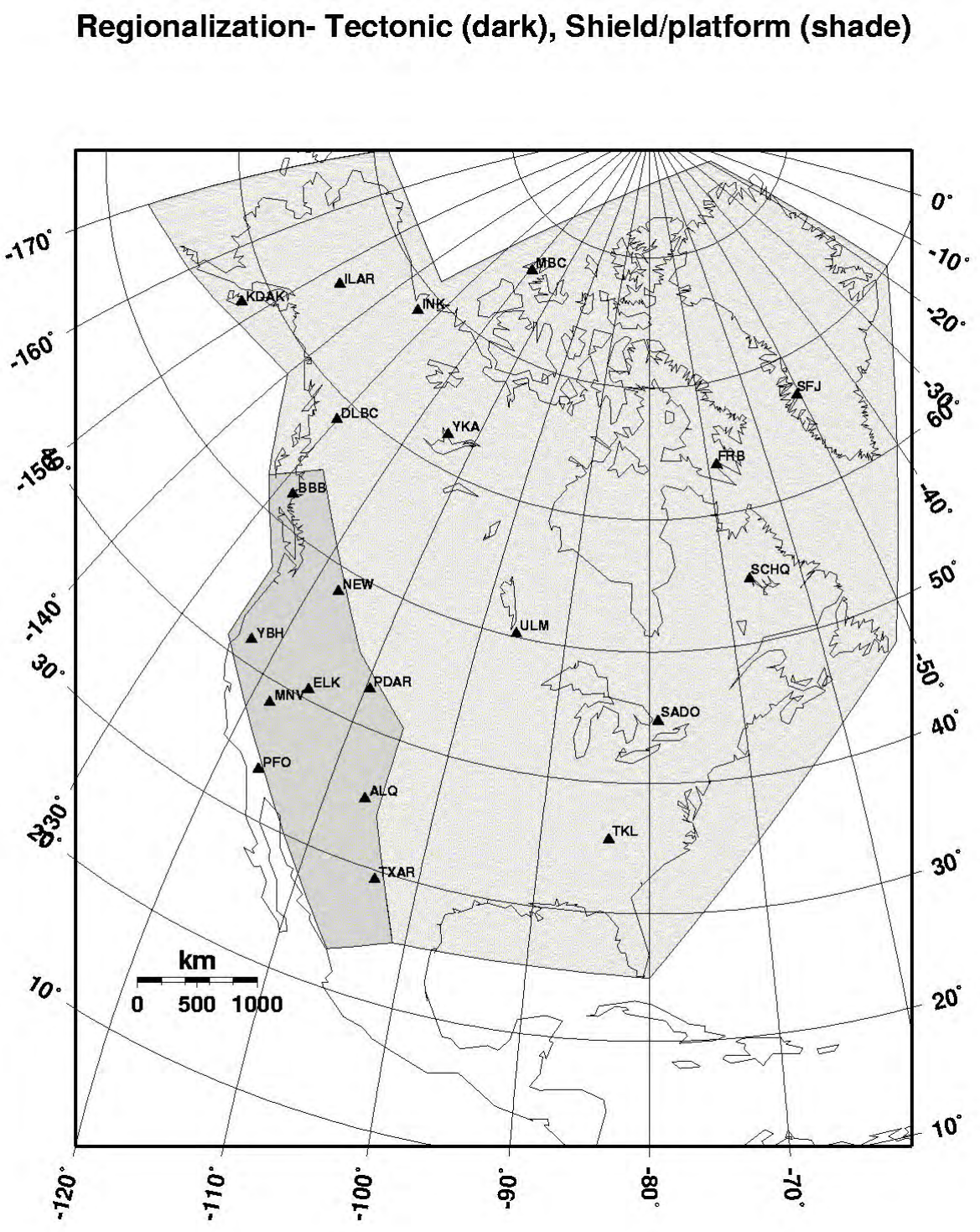


Figure 3. Regionalization of North America. In the tectonic region (dark) the CIT111 P model and the STAN3 S model are used (Figure 2). In the shield/platform region (shade) the Barents Sea model is used (Figure1). The IASPEI91 model is used for the rest of region.

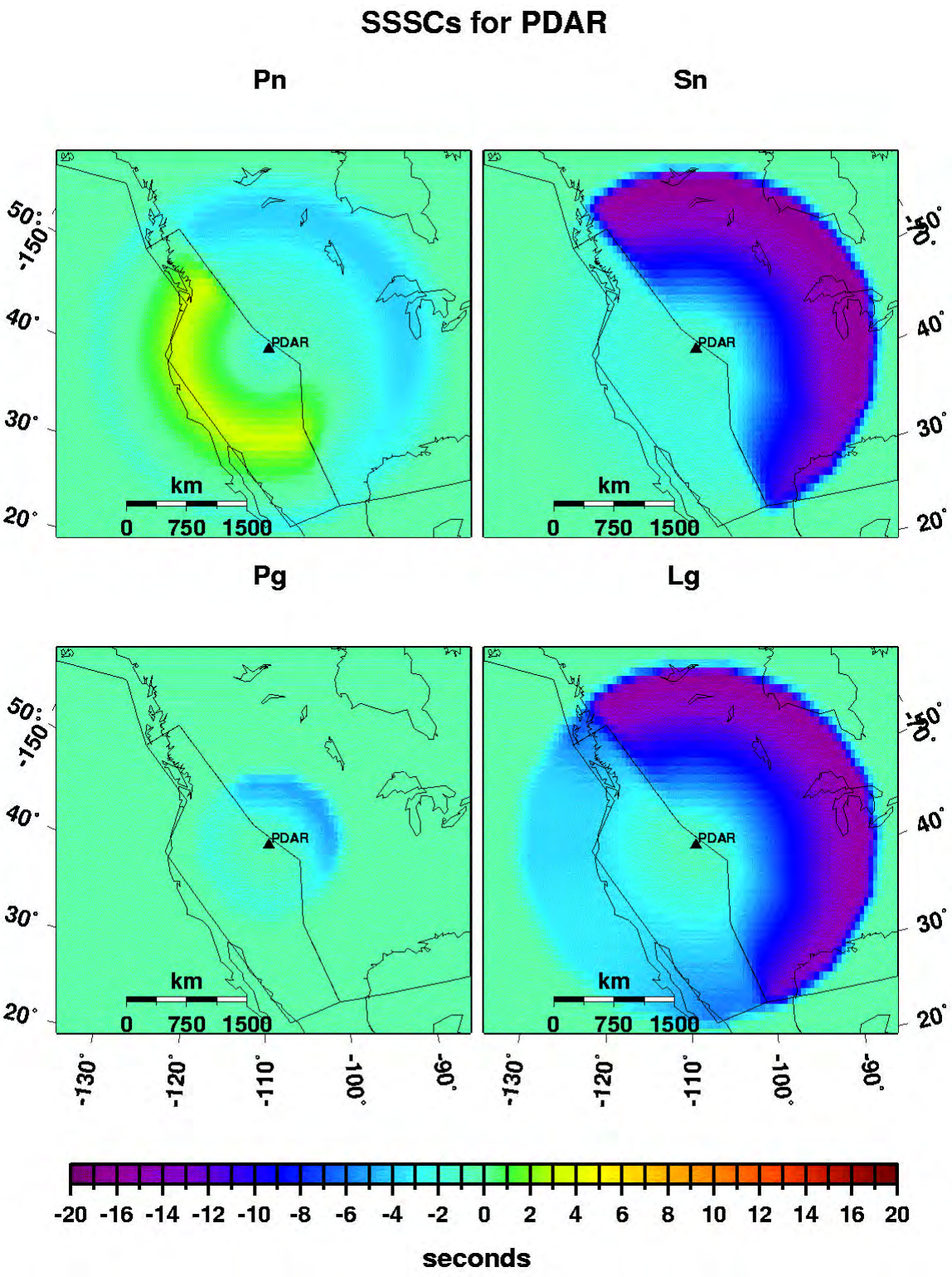


Figure 4. Pn, Sn, Pg, and Lg regional SSSCs for PDAR (Pinedale array) out to 20 degrees. Predicted travel times are fast to the east and slow to the west, so the travel time corrections are negative in the east and positive in the west.

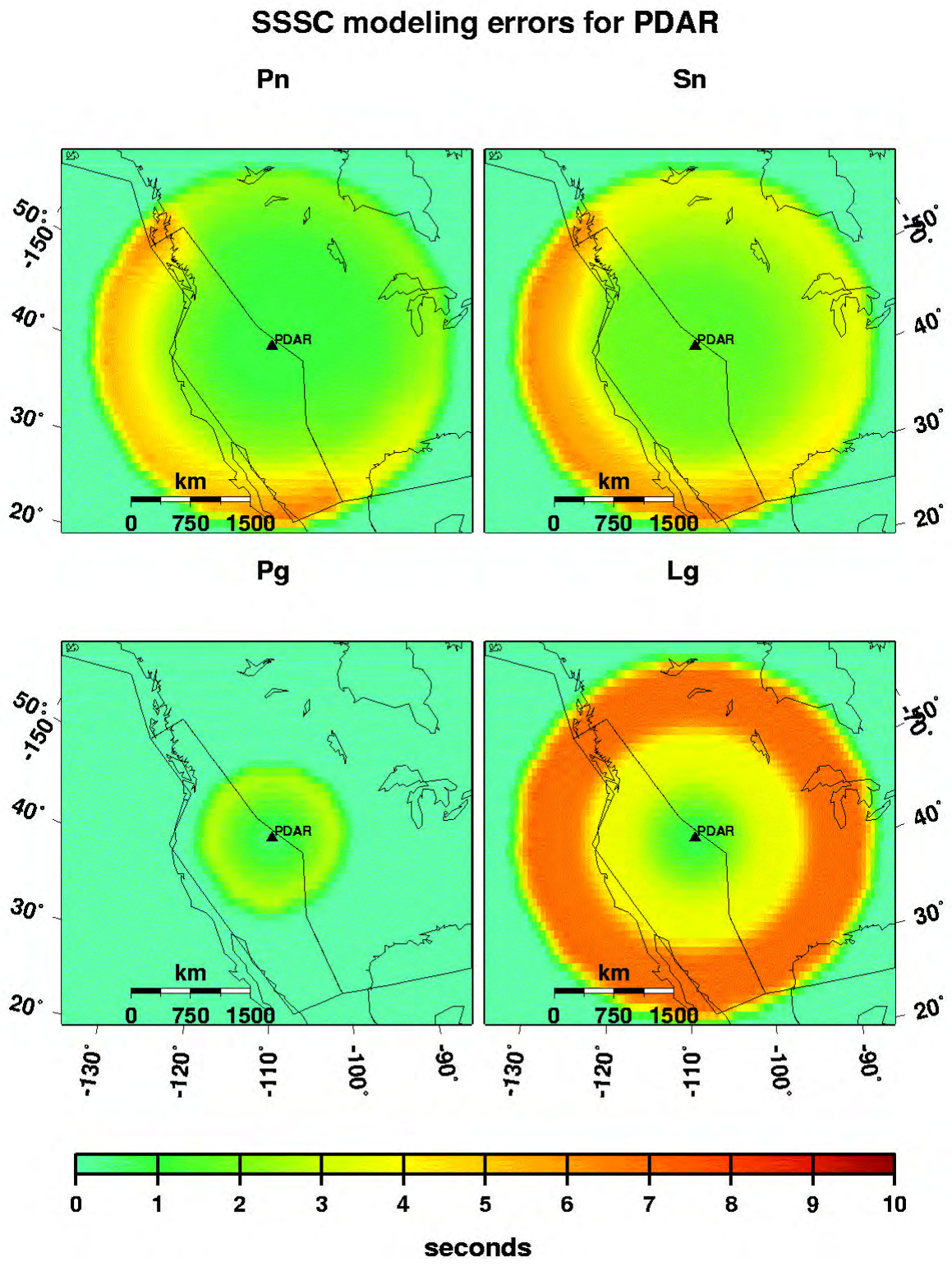


Figure 5. Pn, Sn, Pg, and Lg a-priori modeling errors for PDAR. Modeling errors increase with distances and they are larger in the west than the east for Pn and Sn (see also Figures 1-2).

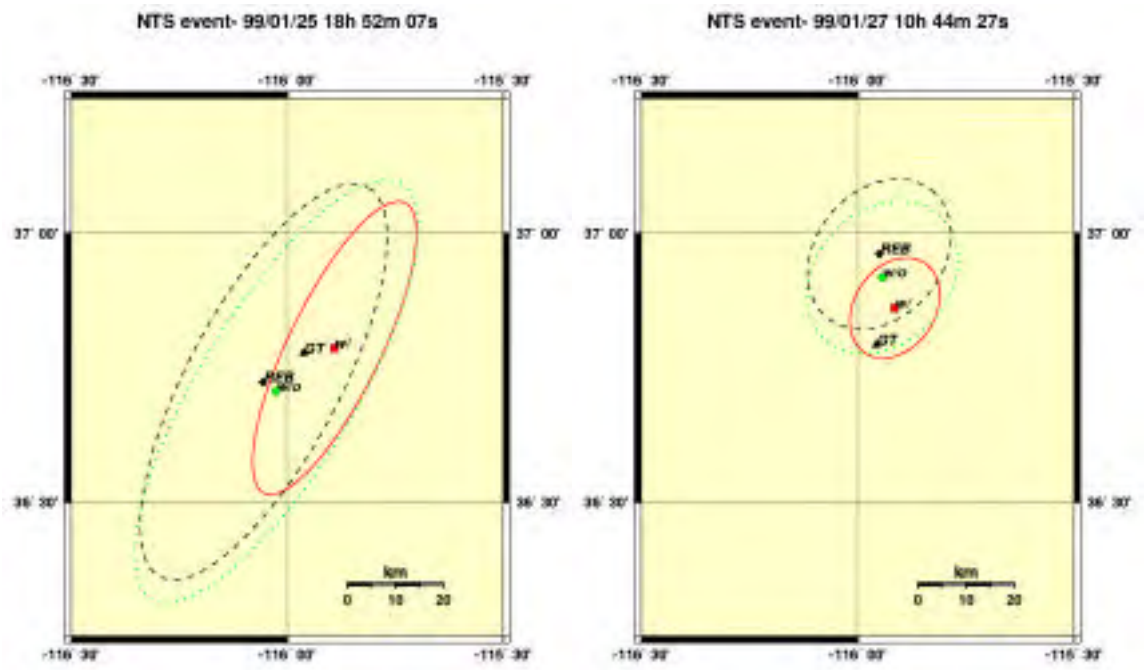


Figure 6. Location comparisons for earthquakes at NTS on 01/25/99 and 01/27/99. The GT locations have accuracy better than 2 km. Locations obtained without SSSCs are not identical to the REB locations due to fixed zero depth. All IMS stations in the REB are used in locations. The distances to GT locations and error ellipses are reduced when using SSSCs. (a) The distance to the GT location is improved 3.3 km using SSSCs (from 10 km without SSSCs to 6.7 km with SSSCs). SSSCs for 3 of the 8 IMS stations are applied, including MNV (Pn, Pg, Sn, Lg), PDAR (Pn), and TXAR (Pn). (b) The distance to the GT location is improved 5.4 km using SSSCs (from 14 km without SSSCs to 8.6 km with SSSCs). SSSCs for 4 of the 16 IMS stations are applied, including MNV (Pn, Pg, Lg), ELK (Pn, Sn, Lg), PDAR (Pn, Pg, Lg), and TXAR (Pn).

SEISMIC EVENT DETECTION, LOCATION, AND IDENTIFICATION METHODS

DISCRIMINATION INFORMATION IN PHASE AMPLITUDE THRESHOLDS

Dale N. Anderson†, Steven R. Taylor§ and Kevin K. Anderson†
†Pacific Northwest National Laboratory, §Los Alamos National Laboratory

Sponsored by U.S. Department of Energy
Office of Nonproliferation and National Security
Office of Research and Development
Contract No. DE-AC06-76RLO 1830

ABSTRACT

We developed a regional seismic discrimination method that uses information inherent in phase amplitudes that are unmeasurable due to small signal amplitudes and/or high noise levels. The method, Quadratic Negative Evidence Discrimination (QNED), is an enhancement to the teleseismic techniques proposed by Elvers (1974), and is extended to regional discrimination. The method is developed for a single seismic station, and makes use of the empirical evidence in the regional Pg vs Lg discriminant (see Pomeroy et al. 1983).

Key Words: negative evidence, phase threshold, discrimination

OBJECTIVE

Events observed at teleseismic distances are effectively identified with the mb vs Ms discriminant because, relative to the compression wave energy (mb) of an event, an earthquake has more shear wave energy (Ms) than an explosion. For some teleseismic events, the magnitude Ms is difficult to measure and is known only to be below a threshold. With Ms unmeasurable, the mb vs Ms discriminant cannot be formed. However, if the Ms threshold is sufficiently small relative to a measured mb, then the event is still likely to be an explosion.

A regional analog to the mb vs Ms discriminant is the Pg vs Lg discriminant (see Pomeroy et al. 1983 for a discussion of regional discriminants). As in the teleseismic setting, the Lg amplitude is difficult to measure for some regional events (especially explosions) and is known only to be below a threshold. With Lg poorly measured, we cannot form the Pg vs Lg discriminant. However, if the Lg threshold is sufficiently small relative to a measured Pg, then the event is still likely to be an explosion. This work develops a mathematical formalization of these ideas.

RESEARCH ACCOMPLISHED

We assume that poor phase amplitude measurements are caused by the noise characteristics of a region, and not by physical-basis causes such as phase blockage or event depth. Four cases of signal censoring are possible. The first case (C1) involves no censoring, that is, both Pg and Lg can be measured. In this case, classical statistical discrimination methods can be used to construct a decision rule to identify seismic events. The second case (C2) is when Pg can be measured but Lg is known only to be below a threshold. The third case (C3) is when Lg can be measured but Pg is known only to be below a threshold. The fourth case (C4) is when both Pg and Lg are buried in noise. We develop a discrimination rule for these four cases and the equations necessary to compute the station-specific missed-explosion and false-alarm error rates. These error rates depend on the required minimum signal-to-noise ratio (S/N), and can be adjusted, within

limits, to desired levels. We also show that these equations are an accurate assessment of the errors in seismic discrimination. We propose that many of the current approaches to assessing seismic discrimination errors are often overly optimistic. For some applications, this disparity can be significant. For an application to Western China regional data (Pg vs Lg (1.5 to 3 Hz)), a widely used estimate of the missed-explosion error rate is 20%, leading to the perception that explosions can be identified with an accuracy rate of 80% (see Anderson (1999)). A proper accounting of the missed-explosion error rate, using Quadratic Negative Evidence Discrimination, shows that explosions can be identified with accuracy rate of only 73%. A detailed presentation of the work can be found in Anderson (1999).

CONCLUSIONS AND RECOMMENDATIONS

QNED is a broadly applicable approach to discrimination, designed to make defensible decisions in the presence of questionable amplitude measurement accuracy. An amplitude measurement is necessary to compute a S/N ratio. However, a poor S/N casts doubt on the accuracy of the amplitude measurement. It is true that a discrimination algorithm can be based on amplitude and noise measurements devoid of S/N considerations. However, interpretability and defensibility of a decision based on such an algorithm will come into question—strong S/N is a well-reasoned requirement for high-quality amplitude measurements. Thus, the power of a QNED approach to discrimination is found in its defensibility, due to agreement with the physical theory of compression versus shear type discriminants in all measurement cases C1, C2, C3 and C4. Some specific conclusions and recommendations on the application of QNED include:
QNED should only be applied to a single geophysically distinct region. As noted above, the QNED method is based on the assumption that poor amplitude measurements are caused by the noise characteristics of a region and not by physical-basis causes such as phase blockage or event depth.
While it is possible to expand QNED methods to more dimensions, the complexity of such a multivariate extension would make clarity and interpretation quite difficult. For example, using 3 amplitudes will involve developing the mathematics for cases rather 4, and 7 OC curves with corresponding parameters. Clarity and physical basis interpretability are extremely important requirements in the seismic discrimination problem. The authors feel that QNED methods should only be applied to a single discriminant (e.g., 2 amplitudes).
The fundamental idea in QNED is the formal modeling and inclusion of the four types of data C1, C2, C3, and C4 into a seismic discrimination method. This idea can be applied to other seismic analyses.

REFERENCES

Anderson, D.N., Taylor, S.R. and Anderson, K.K. (1999) Discrimination Information in Phase Amplitude Thresholds with Application to Western China Regional Data ", *Bulletin of the Seismological Society of America*, Volume 89, No. 3.

Elvers, Eva (1974), "Seismic Event Identification by Negative Evidence", *Bulletin of the Seismological Society of America*, Vol. 64, No. 6, pp. 1671-1683.

Hartse, H.E., Taylor, S.R., Phillips, W.S. and Randall, G.E. (1997), "A Preliminary Study of Regional Seismic Discrimination in Central Asia with Emphasis on Western China", *Bulletin of the Seismological Society of America*, Vol. 87, 551-568.

McLachlan, G.J. (1992*), Discriminant Analysis and Statistical Pattern Recognition*, John Wiley & Sons, New York.

Nelson, W. (1982), *Applied Life Data Analysis*, John Wiley & Sons, New York.

Pomeroy, P.W., Best, W.J. and McEvilly, T.V. (1983), "Test Ban Treaty Verification with Regional Data - A Review*", Bulletin of the Seismological Society of America*, Vol. 72, No. 6, S89-S129.

Taylor, S.R., and Hartse, H.E. (1998), "A Procedure for Estimation of Source and Propagation Amplitude Corrections for Regional Seismic Discriminants", *J. Geophys. Res.*, Vol. 103, 2781-2789.

UTILIZING THREE-DIMENSIONAL SEISMIC VELOCITY MODELS IN REGIONAL AND TELESEISMIC EVENT LOCATION

Michael Antolik, Göran Ekström, Adam M. Dziewonski, and Lapo Boschi
Department of Earth and Planetary Sciences, Harvard University, Cambridge, MA

Ivan Kitov
Institute for the Dynamics of the Geospheres, Moscow, Russia

Sponsored by U.S. Department of Defense
Contract No.: DSWA01-97-C-0124

ABSTRACT

The objective of this project is to develop and improve upon three-dimensional (3-D) seismic velocity models of the Earth and to utilize such models for improving the locations of events recorded at regional and teleseismic distances. In previous research it has been shown that 3-D models, even when parameterized in terms of low-order spherical harmonic functions, can provide significant improvement to teleseismic location accuracy over 1-D models. 3-D models of the Earth's mantle continue to evolve, and many P wave models now exist that are parameterized by constant velocity blocks with dimensions of a few hundred km or less, including one developed as part of this project [*Boschi and Dziewonski*, 1998]. In this paper we compare the accuracy of locations obtained for some of the more detailed models to those obtained from longer wavelength models for a set of globally distributed events with known locations. We find that the new, higher-resolution models do not appear to further improve location accuracy. For many source regions the block models do not predict as well the full range of observed residuals. This may be due to a variety of factors. In addition to assessing location accuracy using the full data set of ISC P wave travel times, we examine location accuracy for small to moderate events by performing multiple location iterations using reduced datasets. Use of the 3-D models produces locations within the stated 1000 km ^{2} accuracy goal of the CTBT for ~70% of location trials using 30 phases but less than half of trials using 8 phases. The performance can be improved using either model-based or ground-truth empirical station corrections in addition to the 3-D model corrections.

Key Words: Event location; seismic tomography; mantle heterogeneity

OBJECTIVE

The aim of this project is to ultimately improve the locations of earthquakes and other seismically recorded events. Our strategy is based on developing new, detailed 3-D models of the mantle, with an emphasis on P wave structure. This involves the construction of global high-resolution models with more detailed resolution in certain areas where particularly good data coverage is available. A second, subsidiary objective concerns the development of additional techniques used in locating events teleseismically and regionally with sparse datasets, and with assessing the improvement in accuracy afforded by the new techniques and models. In this report we describe recent results concerning this second objective.

RESEARCH ACCOMPLISHED

One stated technical goal for monitoring of the Comprehensive Nuclear-Test-Ban Treaty (CTBT) is to locate events of $M \geq 4$ with an estimated uncertainty of 1000 km^2 or less for the purposes of on-site inspection. Because of the lateral heterogeneities present within the real Earth, this goal is usually not achieved using conventional location techniques with standard one-dimensional velocity models. Two general approaches can be used to improve the quality of locations. The first is the application of empirically derived station corrections. While such corrections are calculated only once and then stored, and therefore can be applied extremely quickly in most location algorithms, they are often critically dependent on the source region. Station corrections which are regionally invariant often give little or no improvement in location. Further, the application of source-region dependent corrections depends upon previous sampling of raypaths from all possible source regions. The second approach is the use of a laterally varying Earth model. While this approach does not suffer from the above disadvantage, it requires the calculation of a travel time correction for each ray. In addition, the potential resolution of laterally heterogeneous models is limited by the quality and coverage of the data employed, and also by the computational resources available for their derivation.

Global three-dimensional (3-D) velocity models of the Earth's mantle continue to evolve and become parameterized on an ever finer scale. Models of both compressional and shear wave velocity are now commonly parameterized in terms of constant velocity blocks [e.g., *Vasco and Johnson*, 1998; *Grand et al.*, 1997; *van der Hilst et al.*, 1997] rather than spherical harmonic functions. The model BDP98 [*Boschi and Dziewonski*, 1999a] was developed for an earlier phase of this project. Such "high-resolution" models, using blocks with sizes on the order of a few hundred kilometers, have provided sharper images of coherent smaller scale heterogeneities, in particular fast, sheet-like anomalies presumed to correspond to slabs penetrating into the lower mantle. They should be able to offer a better characterization of P wave residuals for paths through subduction zones or other areas where small-scale lateral heterogeneities are present. However, a number of factors may lead to lower resolution of large-scale, smaller amplitude anomalies in block models. Because of the higher number of unknown parameters, it is still impractical to invert combinations of very large data sets (waveforms and travel times), as is frequently done with spherical harmonic models [*Su and Dziewonski*, 1997; *Li and Romanowicz*, 1996]. This may result in lower resolution in certain areas (particularly the shallow mantle) to which particular data sets are sensitive. In addition, the division into arbitrary, constant velocity blocks may induce an unrealistic shape in long-wavelength anomalies. A lack of correlation between new, high-resolution Earth models and earlier longer wavelength models has previously been noted [*Grand et al.*, 1997]. Another possible factor in this discrepancy may be the use of regularization or damping in the solution of the inverse problem [*Boschi and Dziewonski*, 1999a].

In an earlier phase of this project we have shown that spherical harmonic models of the Earth's mantle are of sufficient quality to be useful in improving the quality of teleseismic locations [*Smith and Ekström*, 1996]. By inverting *P* travel times from a dataset of events with known or very accurately determined "ground-truth" locations, the average mislocation distance was reduced by approximately 40% using the 3-D model S&P12/WM13 (hereafter referred to as SP12) [*Su et al.*, 1993] as compared to PREM or IASP91.

However, only small improvements were obtained for earthquakes occurring in geologically complex areas along plate boundaries, presumably due to the inadequate representation in SP12 of anomalies with wavelengths of a few hundred kilometers or less. On the other hand, this may be due to the fact that most of these latter events are earthquakes with less accurate ground-truth locations.

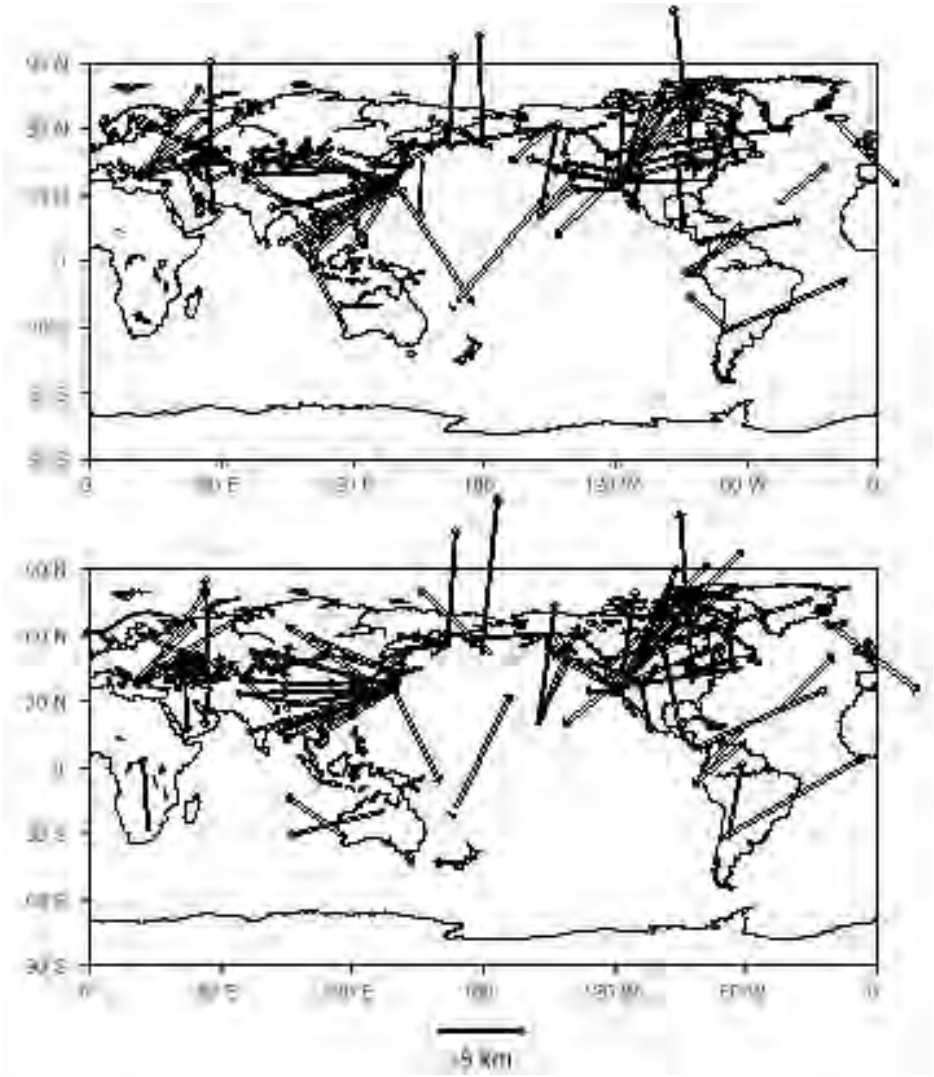


Figure 1: Mislocation vectors for the test events using the complete ISC P wave travel time set, for models SP12 (top) and BDP98 (bottom) without station corrections. Length of the vectors is proportional to the magnitude of the mislocation. The base of each arrow is plotted at the ground truth location and each vector points in the direction of the model-derived location. Explosion events are plotted as the solid vectors and earthquakes as the open vectors. Events located with BDP98 are generally mislocated in the same direction as with SP12, but with a larger error.

Using essentially the same dataset, we tested the improvement which can be obtained in teleseismic event location using the newer block models of mantle P wave velocity compared to model spherical harmonic models and to PREM. In addition to SP12, we also tested a P wave model derived from model MK12WM13 (MK12) [*Su and Dziewonski*, 1997]. *Su and Dziewonski* [1997] obtained a degree-12 spherical harmonic model of bulk sound and shear velocity using a wide variety of direct and differential travel times as well as about 40,000 long-period waveforms. The block models are those of *Boschi and Dziewonski* [1999a] (BDP98) and *van der Hilst et al.* [1997] (HWE97). In addition to the corrections for 3–D mantle structure obtained for the four models, we applied corrections for crustal structure based on

model CRUST5.1 from *Mooney et al.* [1998]. We inverted ISC travel times from 25 to 96 epicentral distance for 112 explosions and earthquakes and found that the locations derived from models BDP98 and HWE97 were generally not as good as those obtained from SP12. Figure 1 compares mislocation vectors for model SP12 to those of BDP98. Locations derived from BDP98 are generally displaced from the true location in the same direction as those derived from SP12, although by larger distances. This suggests that the amplitudes of large velocity anomalies are not as well recovered in BDP98, although the lateral positions of the anomalies are similar to SP12. We have noted previously a tendency for anomalies to be smaller in amplitude in the newer block models than in the spherical harmonic models [*Boschi and Dziewonski*, 1999a; *Ekström et al.*, 1998]. Use of the full CRUST5.1 model results in significant improvement in location accuracy over earlier, less detailed corrections for crustal structure.

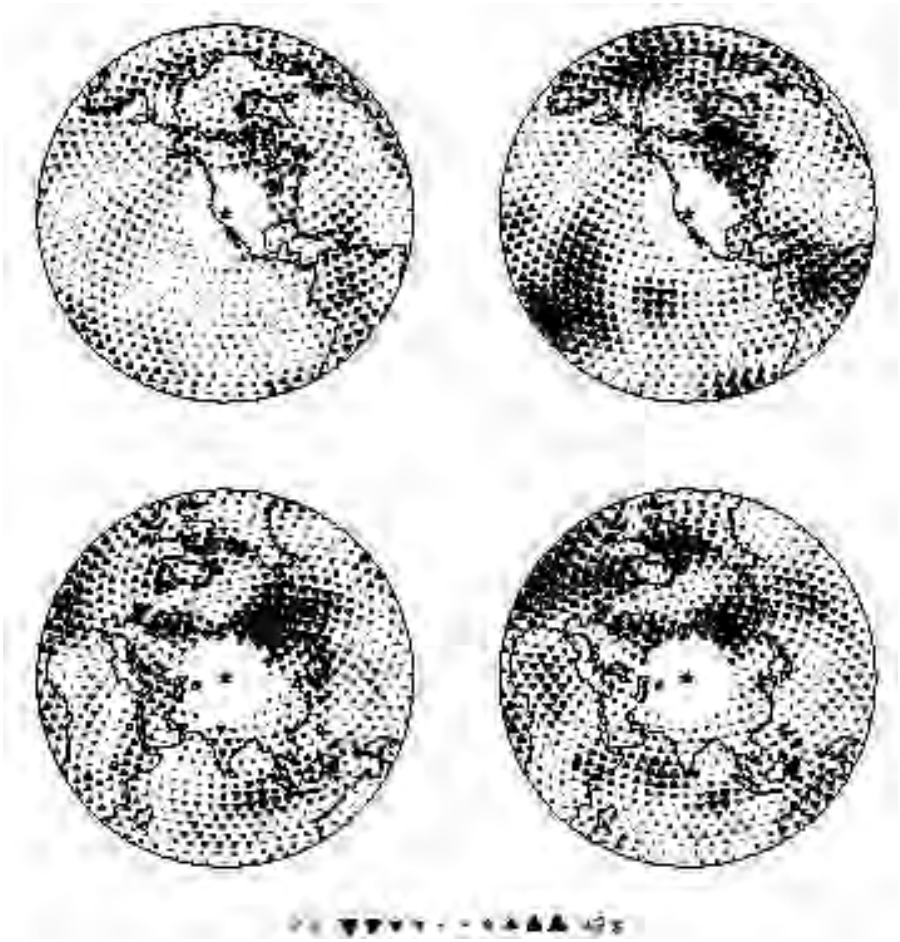


Figure 2: Predicted travel time residuals plotted in 5° x 5° bins for models BDP98 and SP12 for events located at the Nevada and Semipalatinsk nuclear test sites. Each triangle represents the value of the mantle travel time correction in the center of the bin after removal of the mean value over all bins. Top two maps are for an event at the Nevada test site and the bottom two maps are for an event at the Semipalatinsk test site. Maps on the left are for BDP98 and those on the right are for SP12.

One area in which the location difference between BDP98 and SP12 is especially large is in the western United States. It is interesting to compare residuals predicted for these two models for events in this region. Although the areas for which the two models predict particularly large residuals are similar (Figure 2), in general the amplitudes of the residuals predicted by SP12 are larger.

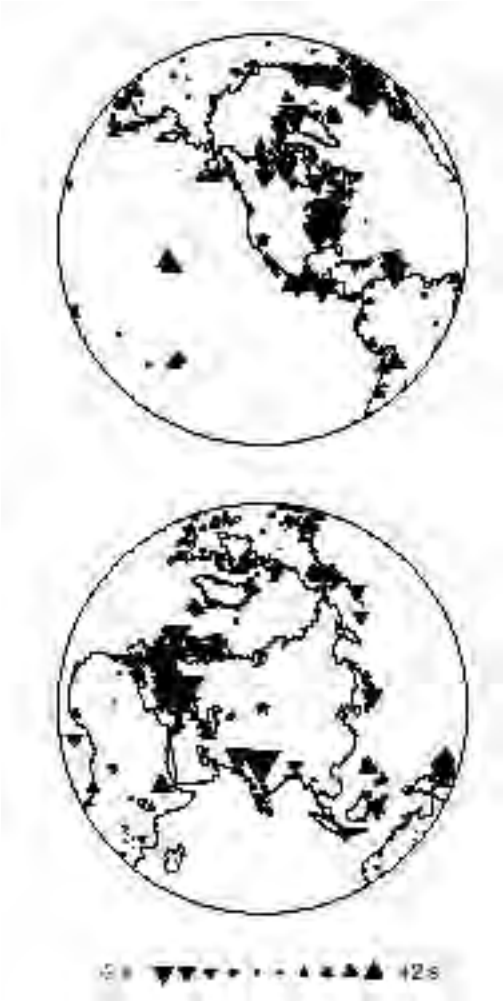


Figure 3: Mean observed P wave travel time residuals for explosions at the Nevada (*top*) and Semipalatinsk (*bottom*) test sites. The value plotted is the difference between the observed travel time and the value predicted for PREM plus all additional corrections except for the mantle correction. The mean of all of the values has been subtracted from each data point. Residuals with a magnitude larger than 5 s have been excluded.

The residual pattern predicted by SP12 much better matches the wide variation in the observed residuals (Figure 3). In contrast, the residuals predicted by both models for events at the Semipalatinsk nuclear test site are much more similar, although some differences (notably in north Africa and Australia) do exist. As a result the locations derived from both models for events in central Asia are quite similar.

Testing 3-D models with sparse datasets

It is important to examine the performance of 3-D models when locating events teleseismically with a limited number of phases. The primary seismic network of the International Monitoring System, for example, is to consist of only 50 3-component stations and arrays worldwide. Station coverage in many areas is therefore sparse.

For each of the test events we randomly selected 30 of the available phases and relocated the event according to the procedure described in *Smith and Ekstr¨om* [1996]. We repeated this procedure 100 times for each event. No consideration with regard to the aziumth or epicentral distance of the reporting station was made when selecting the phases, except that the distance was restricted to between 25° and 96° as

before. A location trial is deemed to be "successful" if it results in a location within the 1000 km^2 area surrounding the actual location specified by the CTBT. We also performed this procedure using 8 phases in each location trial and 250 trials per event.

In addition to relocating the events in this manner using only the model travel time corrections, we computed new empirical station corrections using only the test events. We divided the test events into groups containing three or more events located within 500 km of a central point, and took as the station correction the residual remaining after relocation of the reference event in the 3-D model. These corrections are referred to as "model-based" adjustments. Station corrections were also calculated using the ground-truth location for each event and are referred to as "ground-truth" corrections. Since the stations reporting nearby test events are similar, most of the available stations have a correction for a given event. This allowed computation of station corrections for 69 of the total of 112 test events.

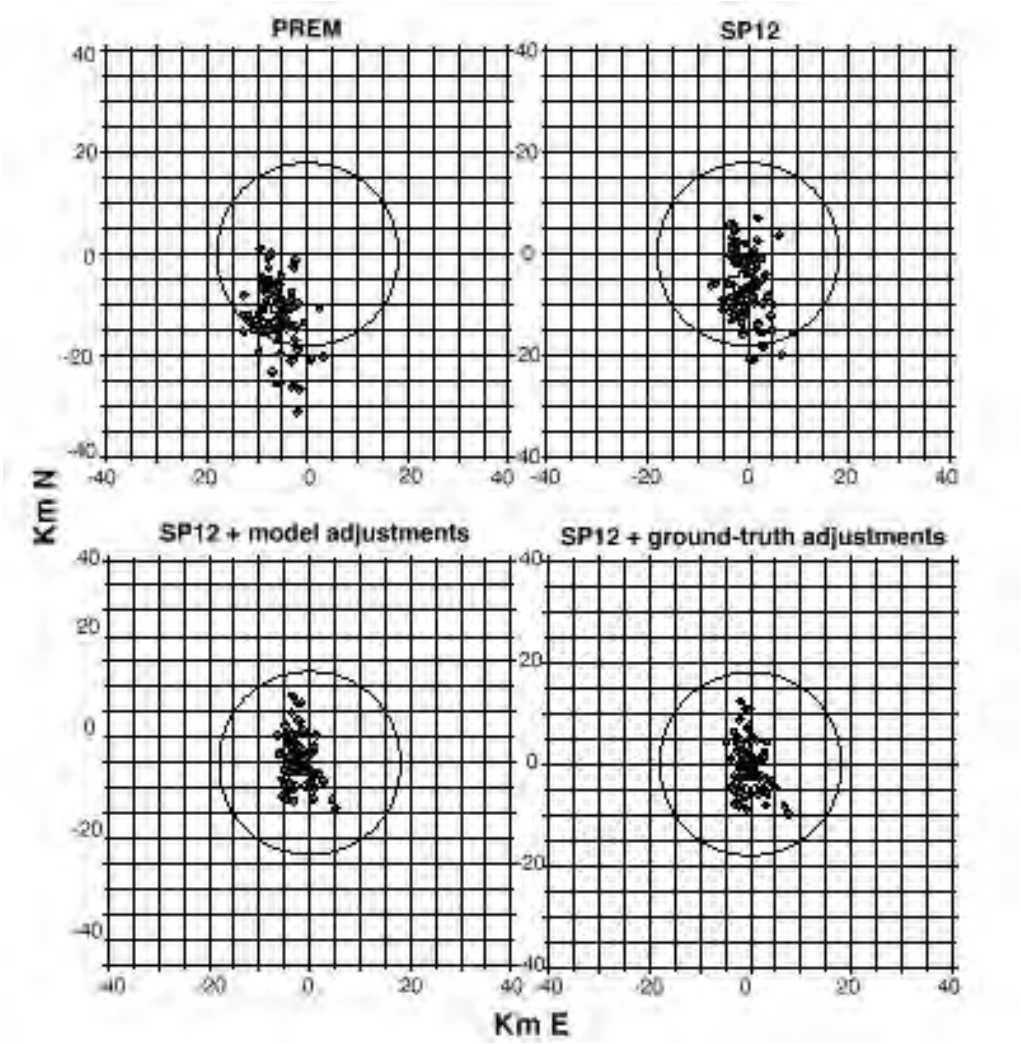


Figure 4: Results of 100 location trials, each using only 30 wave observations, for a single explosion located near the southern Ural mountains. Each grid is a map-view with the ground-truth location denoted by the black cross at the center. The velocity model used for each set of trials is shown at the top of the grid. The grid at top left is for PREM with no station corrections, that at the top right for SP12 with no station corrections, the lower-left grid is for SP12 with model-based station corrections, and the lower-right grid is for SP12 with ground-truth corrections. Each filled circle depicts the location resulting from one of the trials. The white stars indicate the locations obtained from all of the available phases. The black circles delineate an area of 1000 km surrounding the ground-truth location.

SEISMIC CHARACTERIZATION OF UNDERWATER EXPLOSIONS AND UNDERSEA EARTHQUAKES USING SPECTRAL/CEPSTRAL MODELING AND INVERSION

Douglas R. Baumgardt, ENSCO, Inc.

Sponsored by U.S. Department of Defense
Defense Threat Reduction Agency
Contract No. DSWA01-98-C-0157

ABSTRACT

This study has investigated using seismic data to characterize underwater explosions and discriminate underwater blasts from earthquakes. Seismic recordings of underwater blasts can be used to characterize the source itself, based on identification of bubble pulses, and the *in-situ* water depths from mode-converted acoustic signals reflecting in the vicinity of the source. Thus, regional phases from undersea events, such as *Pn*, *Sn*, and *Lg*, may provide more information about the source and *in-situ* characteristics than later arriving T phases, usually recorded hydroacoustically, since the latter signals may be strongly distorted by heterogeneities in the water-column propagation path. Bubble pulses and near-source water column reflections cause time-independent scalloping of the spectra of regional phases that can be analyzed to infer depth and yield of the explosion.

An inversion algorithm has been prototyped in Matlab to characterize the regional-phase cepstra from underwater explosions recorded at seismic stations. The algorithm matches synthetic against observed cepstra for suspected underwater blasts. The observed cepstra are computed for regional phases (e.g., *Pn, Pg, Sn,* and *Lg*) by taking the logarithm of the trend-corrected spectrums for each phase, stacked across a regional array if array data are available, and then taking the inverse Fourier transform of log amplitude spectrum. The result is the so-called signed cepstrum. Each of the individual phase cepstra is then stacked to produce a composite cepstrum for the event. The signed cepstra for regional phases from underwater explosions have negative peaks caused by the reflections of the acoustic wave from the surface and positive peaks from the bubble pulse. Undersea earthquakes may only have the negative water-column reflection peaks or no peaks at all. Cepstra of the background noise to *Pn* are also computed in order to check if the peaks are caused by noise or processing artifact. Synthetic cepstra are computed for assumed minimum-phase wavelets caused by an explosion of specified yield and depth in the water, which can be constrained by known bathymetry. The depth and yield of the underwater blast are determined by finding a synthetic cepstrum that most closely matches the observed cepstrum. Match statistics considered include the cross-correlation coefficient and the L1 and L2 norm of the difference between synthetic and observed cepstra. The algorithm seeks to either maximize the cross-correlation coefficient or minimize the L1 or L2 norms. The best matching cepstrum can be found by optimal search algorithms, which includes the simplex search and simulated annealing. This algorithm can identify undersea events as either blast or earthquake based on the degree of correlation between a best fitting underwater explosion model cepstum and the observed cepstrum.

The algorithm has been tested on offshore events including both earthquakes and suspected underwater chemical blasts. Offshore events have been collected by a survey of the Reviewed Event Bulletins (REB) of the prototype International Data Centre (pIDC). The main focus initially has been on events around Scandinavia, in the Norwegian, North, and Baltic Seas, and the Gulf of Bothnia, recorded at one or more of the Scandinavian arrays. Most of these events appear to be earthquakes. However, at least one previously unidentified underwater blast has been found that occurred in the Norwegian Sea on November 25, 1998. Spectral modulations have been observed in all phases that were likely produced by bubble pulse and a water-column bounce. The event has small *Pn*/*Sn* and *Pn*/*Lg* amplitude ratios because of the large amount of shear-wave energy, relative to the *Pn*, which makes the event look like an earthquake. Large shear waves are unexpected for a pure compressional underwater explosion. Possible origin of the strong shear waves or weak *Pn* from a blast might include scattering in the source region or along the path or reduction of the *Pn* amplitude by spectral scalloping. However, strong scalloping is apparent in the spectra of all phases. Applying the cepstral inversion algorithm to the event, a synthetic cepstrum for an 1800 kg explosion at a depth of 130 m matches the observed cepstrum with a correlation coefficient of 0.73. This algorithm has also been tested on other events suspected of being underwater explosions as well as earthquakes and also synthetic underwater explosion and earthquake waveforms. When completed, the algorithm may have potential for event screening of underwater chemical blasts as well as for special-event analysis of suspected underwater nuclear blasts.

Key Words: underwater explosion, undersea earthquake, discrimination, cepstrum

OBJECTIVE

The problem of the identification of underwater blasts has gained increased interest recently in the context of the monitoring of the Comprehensive Nuclear Test-Ban Treaty (CTBT) which was opened for signature by the United Nations on 24 September 1996. Annex 1 to the Protocol of the CTBT calls for the installation of an International Monitoring System (IMS) including six hydroacoustic stations and five so-called "T-phase" stations. T-phase stations are seismic sensors located near the coast that can detect hydroacoustic phases converted to seismic phases at the coast. Thus, only 11 stations will be available specifically for monitoring underwater events. If an explosion occurs in the ocean, but near the coast outside of the SOFAR channel, long-range propagation of hydroacoustic signals may be blocked, and there is a possibility that the events may not be easily detected by the IMS hydroacoustic and T-phase assets directed toward the underwater explosions. Because of the relatively larger number of seismic stations, 170 primary plus auxiliary stations, called for the CTBT Protocol for the IMS, near-coast seismic stations may have a better chance of detecting and characterizing underwater events on the continental slopes, outside of the SOFAR channel, or in confined seas. Moreover, early-arriving seismic signals, such as *Pn*, *Pg*, *Sn*, and *Lg*, produced by mode conversion of acoustic waves in the water in the vicinity of the source, may carry more useful information about in-situ source conditions than later arriving T phases that may be affected by propagation path effects in the oceanic water column.

Baumgardt and Der (1998) showed numerous examples of underwater explosions recorded at seismic stations and how they can be characterized by spectral and cepstral analysis. A simple model for underwater explosions was developed and synthetic cepstra were produced that reproduced most of the essential features of observed underwater explosion cepstra. The main features were bubble pulses, which produce positive cepstral peaks, and the first surface reflection that produces a strong negative cepstral peak. The timing and relative amplitudes of these cepstral peaks provide useful constraints on the depth and yield of underwater explosions.

The following are the objectives of this study:

1. Collect appropriate seismic data from explosions and earthquakes in water-covered and nearby areas for study, preferably with corresponding hydroacoustic data that may be used to validate results of calculations.
2. Gain an improved understanding of the effects of the water column on the seismic data, and use this understanding to determine parameters such as in the water column/not in the water column, water depth, and others.
3. Develop an algorithm to extract information from seismic records of events in and near water-covered areas to aid in monitoring the CTBT.

RESEARCH ACCOMPLISHED

In this study, we have collected and analyzed events, reported in the Reviewed Event Bulletin (REB), located offshore near the coastlines. In most cases these events have turned out to be earthquakes. However, a number of events have been found that have characteristics of underwater explosions, i.e., spectral scalloping as described by Baumgardt and Der (1998). In this paper, we describe one of these events that occurred on November 25, 1998, and use it to demonstrate a new cepstral characterization method for identifying underwater explosions. We also contrast this event to a nearby earlier event that also has spectral scalloping but of a different nature that indicates that it is a shallow undersea earthquake.

PRESUMED UNDERWATER EXPLOSION NEAR TROMSO

On November 25, 1998, an event occurred off the coast of Norway that appeared in the Reviewed Event Bulletin (REB) for the PIDC with the following event parameters:

EVENT 20230910

Date	Time	Latitude	Longitude	Depth	Ndef	Mag1	N
1998/11/25	11:34:29.5	69.0645	16.4273	0.0 f	12	ML 3.5	4

This event was recorded by 4 seismic arrays, ARCES, FINES, HFS, and NOA and was located just off the coast of Northern Norway in the vicinity of Tromso.

Figure 1 (a) shows a map with the great circle propagation path from the event location reported in the REB to the ARCES array center element. Figure 1 (b) shows part of the bathymetric/topographic data for the first 50 km of the path from the source to the receiver. The bathymetry gives a water depth of 130 m in the vicinity of the source, although the water depth varies from between 50 to 300 m along the path. Also, Figure 1 (b) shows that the event was only within about 13 to 15 km of the land of the offshore islands, which is less than the REB epicenter error ellipse long axis of about 21 km. However, as we will show below, the spectral/cepstral characteristics of the signal are consistent with a water depth of 130 m.

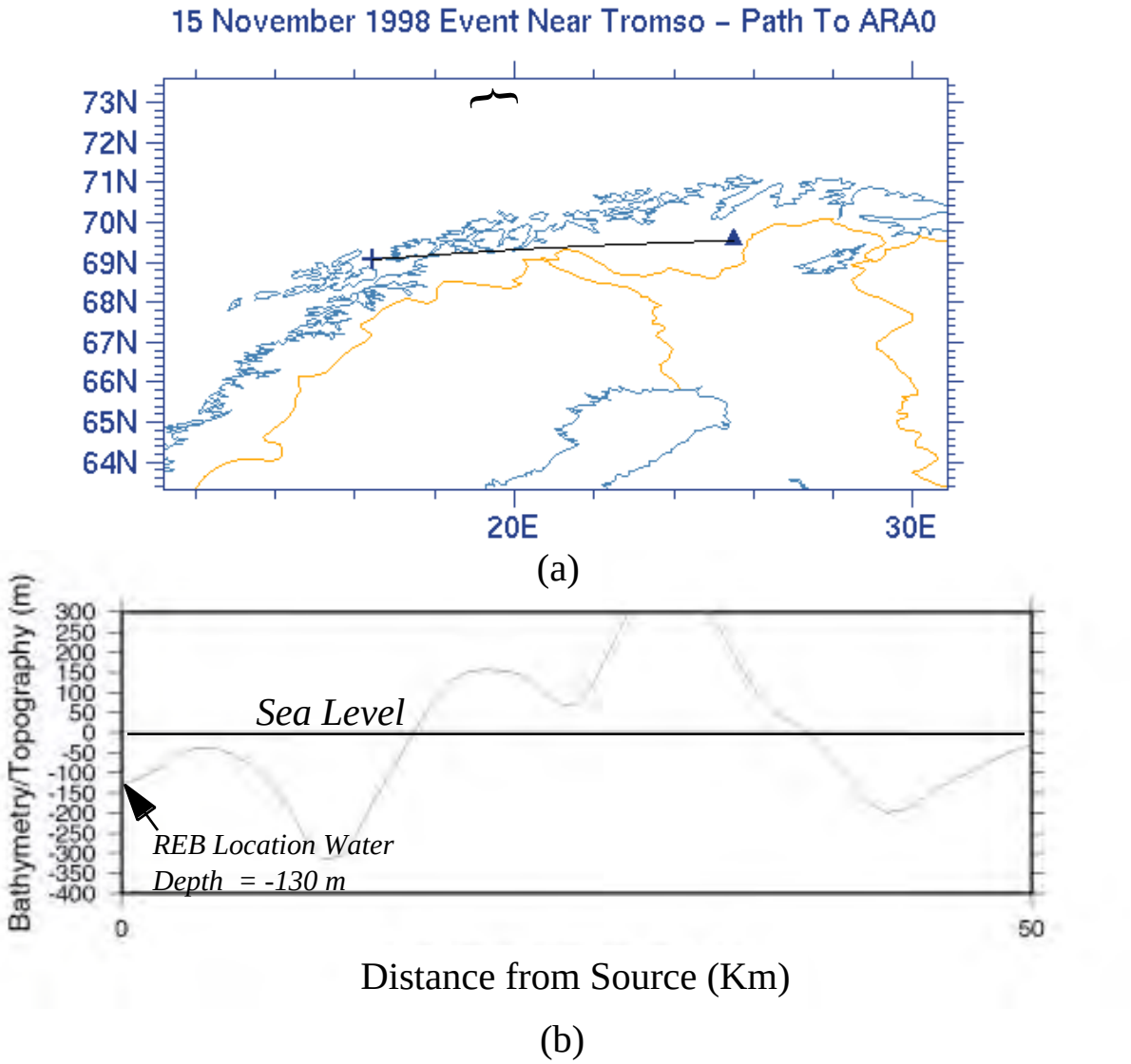


Figure 1: (a) Map showing path from November 25, 1998 event to the ARCES array center element (ARA0). (b) Bathymetric/topographic profile in the vicinity of the source.

Figure 2 shows a 2 Hz high-pass filtered waveform recorded at the ARCES center element, ARA0, indicating the picked phases, *Pn*, *Pg*, and *Lg*. These phase picks were used to set the start points of the windows for spectral analysis.

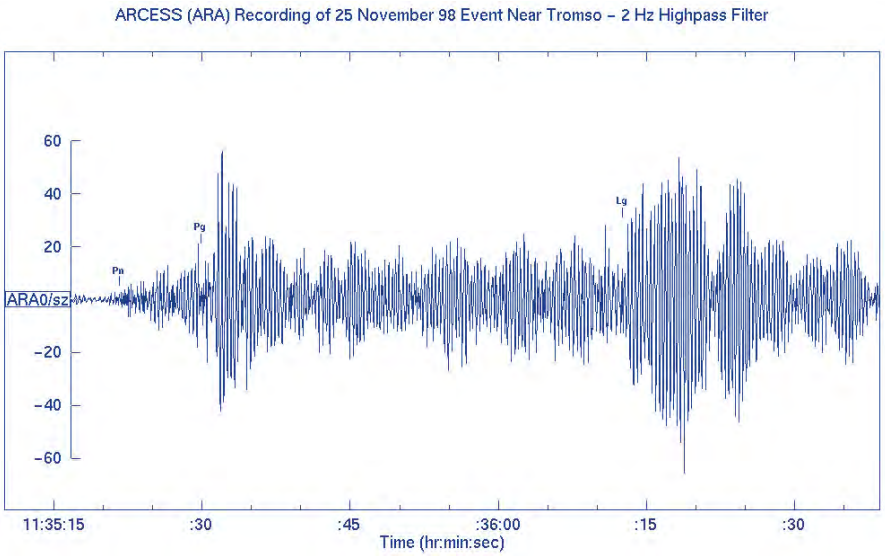


Figure 2: ARA0 vertical-component waveform of the November 25, 1998 event, highpass filtered from 2 Hz, showing regional phase picks.

Figure 3 shows a bandpass filter analysis of the waveform, with frequency bands from 0.5 to 2.5 Hz up to 10 to 16 Hz. The signal-to-noise ratio is quite high through the entire spectral band. The *Pg* and *Lg* phases are notably large throughout the band from 2 to 7 Hz and the first arrival *Pn* is emergent. *Pn*/*Lg* ratios are generally less than 1, except at frequencies above 8 Hz, indicating significant shear-wave excitation. Baumgardt and Der (1998) showed that, under certain circumstances, the *Pn*/*Lg* or *Pg*/*Lg* ratio might discriminate earthquakes and explosions for screening purposes. However, it is doubtful that a *Pn*/*Lg* or *Pg*/*Lg* ratios would confidently screen this event out as an earthquake.

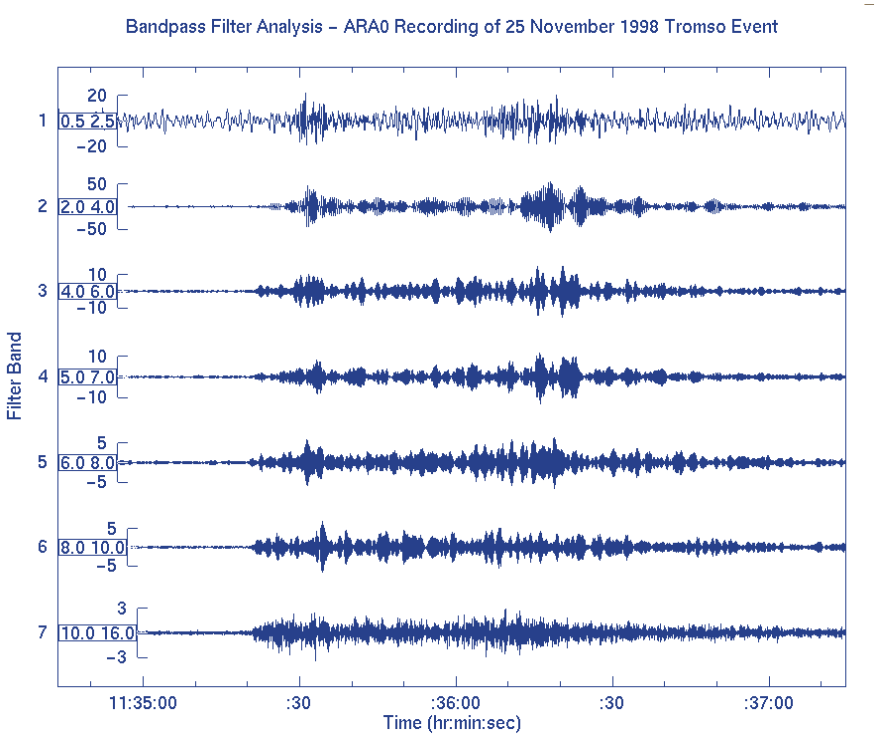
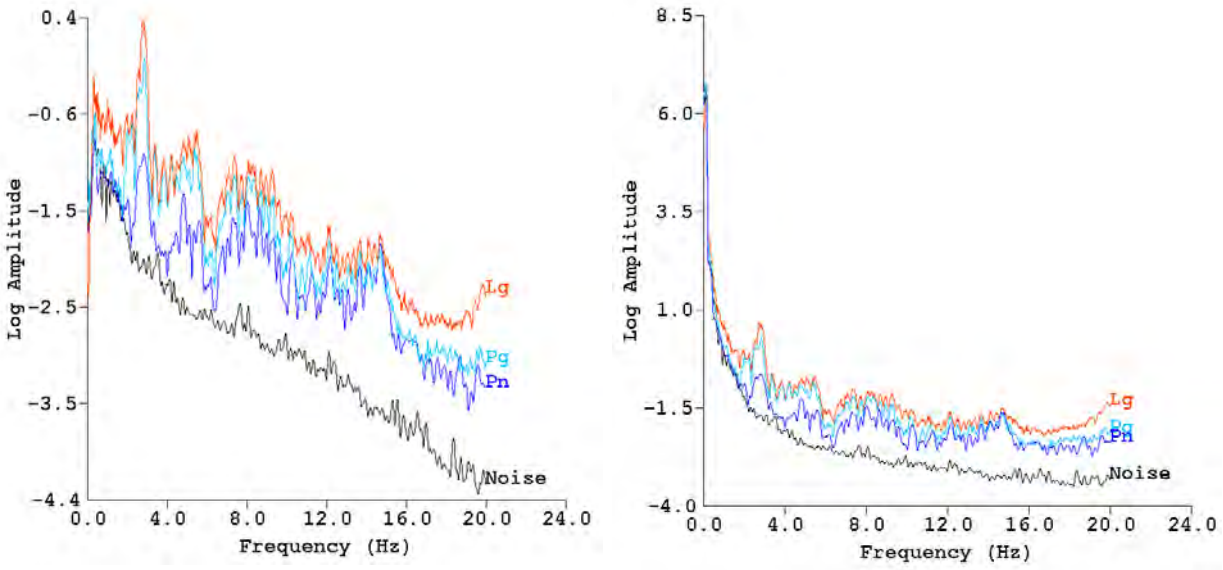


Figure 3: Bandpass filter analysis of the ARA0 vertical-component waveform of the November 25, 1998 event. Strong shear waves at high frequency and the complex coda waves in the 8-16 Hz band are noted.

SPECTRAL/CEPSTRAL ANALYSIS

Figure 4 (a) and (b) show the array-averaged spectra for the different phases and background noise. The spectra are computed on each individual ARCES vertical-component channel by windowing the phases, starting at the time picks shown in Figure 2, for 20 seconds and applying a Parzen window. The spectra for each channel are then averaged across the array, which produces much smoother spectra than the individual channel spectra. The spectra in Figure 4 (b) have had instrument response removed.



(a) (b)

Figure 4: (a) Spectra of the *Pn*, *Pg*, and *Lg* phases and *Pn* background noise. 20 sec time windows smoothed with Parzen window. (b) Spectra after instrument correction.

These figures show a very distinct spectral modulation or scalloping in all phases, and a strong spectral peak at about 3 Hz. None of these features appear in the noise. Spectra of this kind have been shown to be caused by source multiplicity, either due to ripple fire in mine blasts (Baumgardt and Ziegler, 1988) or by water column reverberations and bubble pulses in underwater explosions (Baumgardt and Der, 1998). Since the event occurs off the coast, it is likely to be an underwater explosion, as can be shown by cepstral analysis.

Figure 5 shows cepstra for the three phases, the stack of the three cepstra, and the cepstra of the background noise. The cepstra are computed by removing the trend in the instrument-corrected spectra in Figure 4 (b), using a polynomial fit, taking the log and another Fourier transform of the real part of the original complex spectrum. The resultant cepstra are a function of delay time between the multiple pulses, called "quefrency" in units of time (sec), and are signed. A cepstrum for the noise spectrum is also computed in order to check for cepstral features that may be due to processing artifact rather than source effects. We look for cepstral peaks in the individual phase cepstra that do not appear in the noise cepstra. The cepstra in Figure 5 have been shifted for display purposes and the absolute amplitudes are arbitrary. Positive cepstral peaks indicate pulses which are correlated with the same polarity and negative peaks, or troughs, are produced by pulses with reverse polarity. As shown by Baumgardt and Der (1998), positive peaks are caused by bubble pulses with positive polarity and negative peaks are produced by reflections of acoustic waves off the water-air interface.

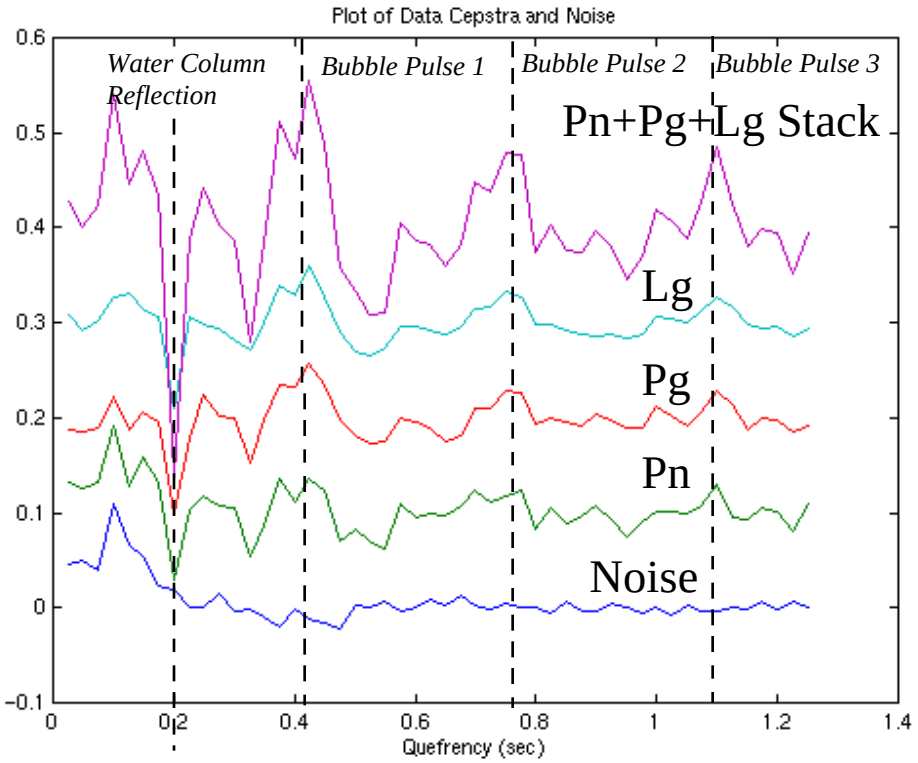


Figure 5: Cepstra of the *Pn*, *Pg*, and *Lg* phases, stack cepstrum, and *Pn* background noise cepstrum. The dashed lines indicate peaks identified in the signal cepstra but do not show up in the noise cepstrum. The first trough is interpreted to be the surface reflection, with reversed polarity, and the subsequent peaks to be caused by bubble pulses.

Figure 5 shows the clear signs of an underwater explosion, as shown in Baumgardt and Der (1998). As in the case of the recent Murmansk explosion (Baumgardt, 1998), the event has a clear negative trough at around 0.2 seconds, which we interpret as the surface reflection, and positive peaks at greater delay time, caused by bubble pulses. In our interpretation of the cepstra in Figure 5, we identify at least 3 bubble pulses. Both the reverberation peak and the bubble pulses are notably stronger on the stack cepstrum than on the individual phase cepstra

CEPSTRAL MODELING AND INVERSION

We have developed a modeling and inversion algorithm for the characterization of cepstra of underwater blasts. Because the cepstrum reflects the correlation structure of the source-produced pulses, it is easier to model than the waveforms themselves. The removal of the polynomial trend in the spectra also eliminates the spectral effects of the propagation path and thus, only the source correlation structure is retained in the cepstra. We showed in our earlier study (Baumgardt and Der, 1998) that modeling cepstra does not require information about the propagation path or receiver function, nor does it even require much information about the source time function. Thus, modeling cepstra requires many fewer parameters that modeling waveforms or spectra.

The modeling techniques described by Baumgardt and Der (1998) are used to interpret this event. The model construction is illustrated in Figure 6. We compute wavelets for the bubble pulse, shown on top, and water column reverberation, shown as the second trace, for a given assumed yield and depth in the water. The theory for calculating bubble pulse wavelets was taken from the literature and is described by Baumgardt and Der (1998). Other parameters that must be specified include average water column depth, that can be obtained from the bathymetry, and the surface and water bottom reflection coefficients, which we assume to be -0.9 and 0.3, respectively. As in the case of water depth, these parameters can be estimated with some degree of accuracy, but it is also conceivable that they can be inferred from the data. We assume that the acoustic waves in the water reflect from first-order discontinuities at the bottom and the surface.

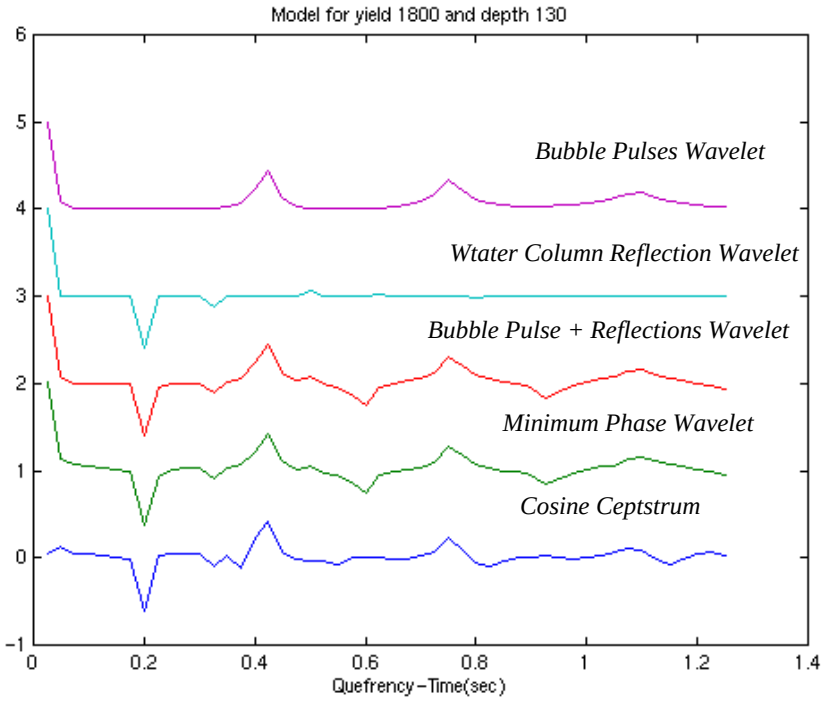
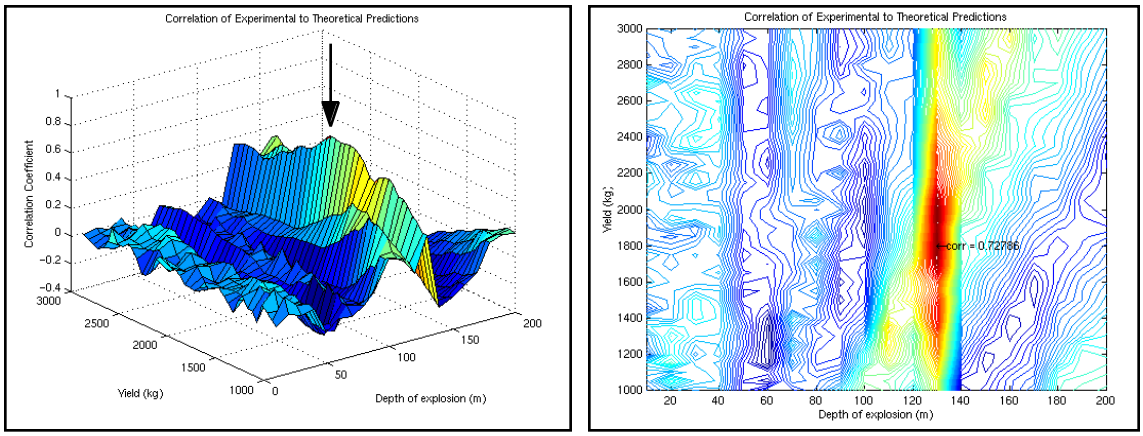


Figure 6: Example of construction of synthetic spectrum for an explosion of 1800 kg detonated at 130 m in the water.

The final synthetic cepstrum is the convolution of the source plus bubble pulse wavelet and reflection wavelet. We then compute the cepstrum of this composite wavelet, which is shown at the bottom of Figure 6. We also show a minimum phase wavelet reconstruction from the cepstrum which is identical to the original wavelet. This shows that our modeling method assumes minimum phase wavelets.

Finally, we seek a synthetic cepstrum that matches the observed cepstrum. For this purpose, we compute the correlation coefficient between the stacked observed cepstrum and the synthetic cepstrum and seek a cepstrum that provides the maximum correlation. (Note: We have also considered the L1 and L2 norms of the difference between the observed and synthetic cepstra as well as the correlation coefficient.) We first have considered an exhaustive search method, where the parameter space of blast yield and depth in the water is gridded and synthetic cepstra are computed for each grid point. Then, we correlate the synthetic cepstra at each grid point and compute a correlation coefficient surface over the depth/yield parameter space and look for the peaks in the depth/yield surface. Optimal search algorithms, such as simplex search and simulated annealing, are also being investigated.

Figure 7 shows he resultant correlation coefficient surface plotted as an object (a) and as a contour plot (b). Both displays have a distinct peak in the correlation, with a maximum correlation coefficient of 0.73, corresponding to a water depth of 130 m and yield of 1800 kg or about 1.98 tons. It is evident in Figure 7 that depth is well constrained but yield is less well constrained. The yield is controlled exclusively by the bubble pulse delay time, although the bubble pulse delay is also a function of depth. However, depth is constrained also by the negative peak delay time, corresponding to the two-way water-column reflection time.



(a) (b)

Figure 7: (a) Correlation surface for synthetic cepstra matched against the observed stack cepstra for the November 25, 1998 event. Arrow indicates the peak of the surface which gives the model with the maximum correlation. (b) Contour plot of the maximum peak.

It is notable that the inferred explosion depth of 130 m is close to the actual water depth of the source location as inferred from bathymetry, shown in the cross section in Figure 1. This suggests that the explosion may have occurred near the bottom or on the bottom. Note, however, that knowledge of the water depth is not actually required to infer the explosion depth in the water, since the reflection from the surface is by far the strongest signal. We actually assumed a water depth of 225 m in our model. Reflections from the bottom may, in principle, be observed and reveal water depth, but they are very weak, as is evident in Figure 6. Because of the roughness of the bottom itself and the extremely low reflection coefficients, it is doubtful that bottom reflections will be observable. However, water depths at given locations in the ocean are usually well known and need not be inferred by this method. However, knowing the maximum water depth is useful because it constrains the required search space.

The sensitivity to yield is illustrated in Figure 8, which shows the correlation coefficient as a function of yield for the depth of 130 m.

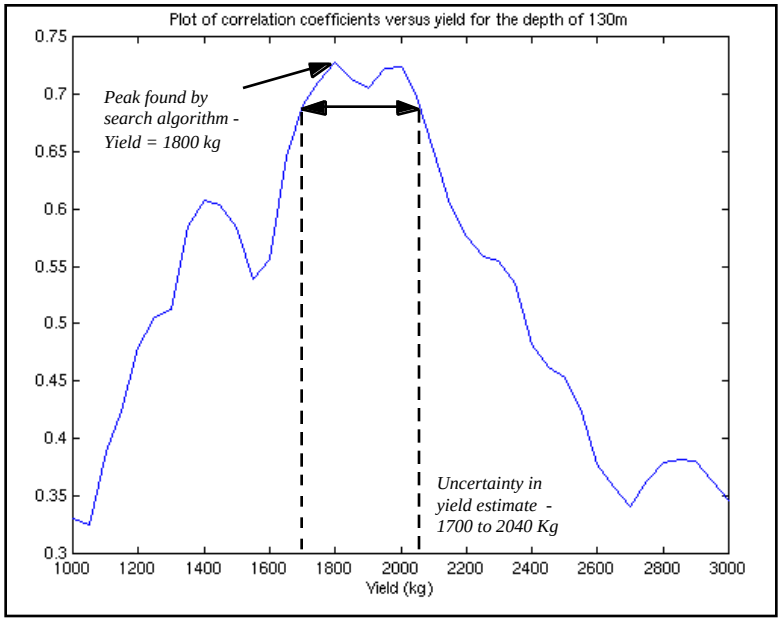


Figure 8: Maximum correlation peak plot at depth of 130 m. Dashed lines indicate that uncertainty of yield given by the peak width.

The maximum peak was at 1800 kg, but another peak of comparable strength appears at closer to 2000 kg. However, the overall broad peak is about 200 or 300 kg in width, which provides an estimate of the resolution of the method to yield. Thus, a better estimate of yield might be 1900 kg + or - 200 kg.

Finally, Figure 9 shows a direct comparison of the observed stack cepstrum and the best-matching synthetic cepstrum.

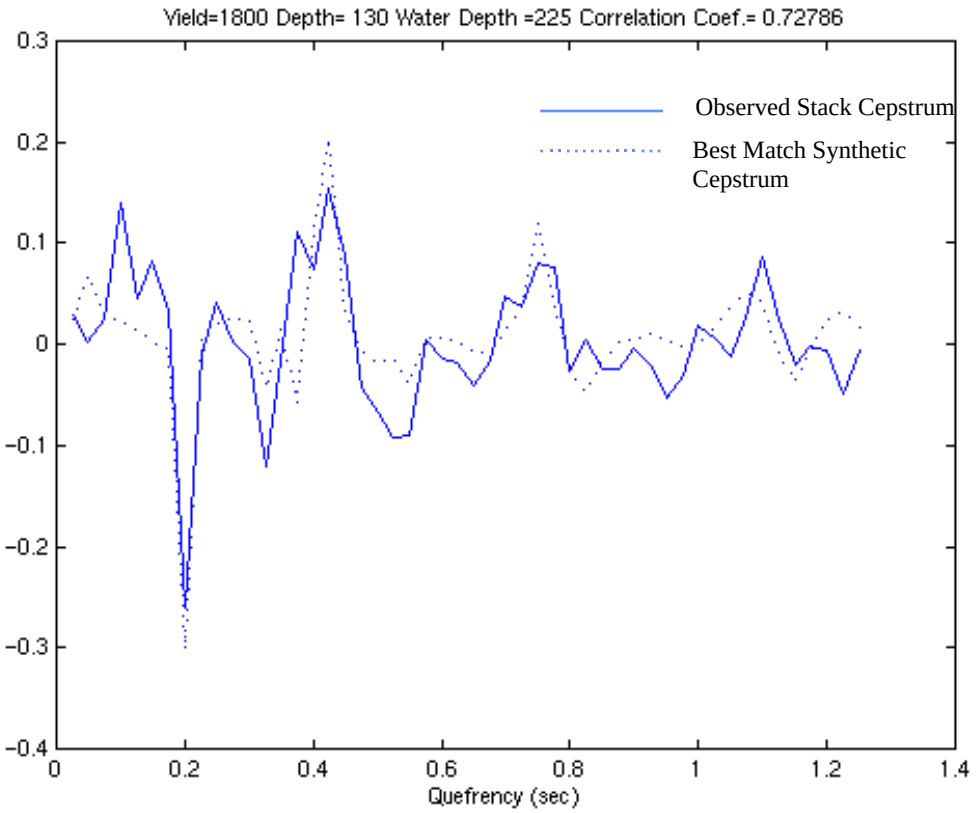


Figure 9: Comparison of the observed stack cepstrum of the November 25, 1998 event and best matching synthetic cepstrum for depth of 130 m and yield of 1800 kg.

This comparison shows that, although the match is not perfect, reasonably good matches of the essential features, the negative peaks of the water column reflection and the bubble pulses, have been attained.

COMPARATIVE EXAMPLE OF AN UNDERSEA EARTHQUAKE NEAR TROMSO

Shallow undersea earthquakes may also produce scalloped spectra if seismic energy is coupled into acoustic energy in the water column. However, the only scalloping possible would be from the water reverberations since no bubble pulses would be expected. An example of this difference can be seen in the February 5, 1993 shown in Figure 10, that occurred near the November 25, 1998 event near Tromso.

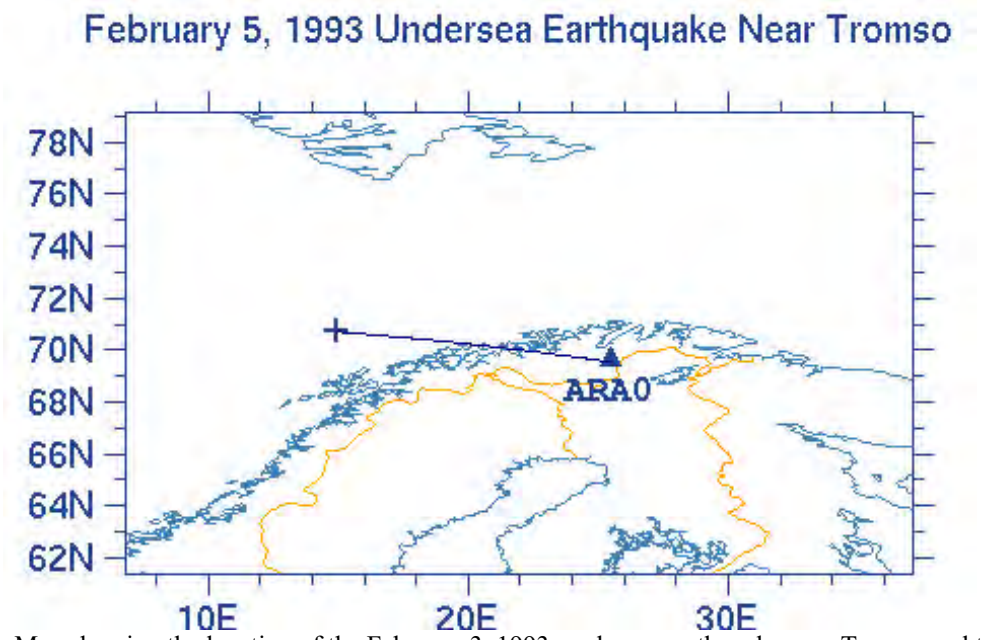
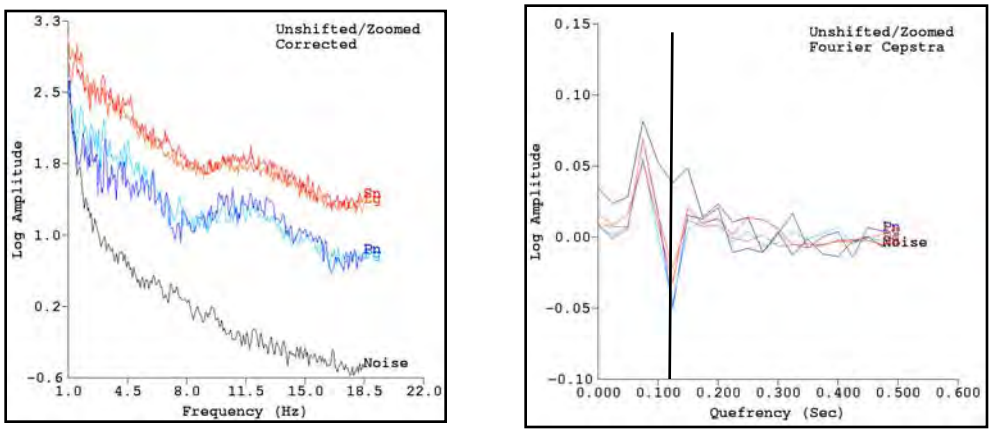


Figure 10: Map showing the location of the February 3, 1993 undersea earthquake near Tromso and the propagation path to ARCES.

The magnitude and distance are similar to that of the November 25, 1998 event, and all four phases, *Pn*, *Pg*, *Sn*, and *Lg* were observed at ARCES. Figure 11 shows the spectra (left) and cepstra (right) of the phases and the background noise.



Delay Time = 0.12 Seconds
Water Depth = 1007 Meters

Figure 11: Spectra (left) and cepstra (left) of the February 5, 1993 undersea earthquake. The spectral scalloping only produces a negative peak in the cepstra, characteristic of an underwater reverberation from depth of 1007 m.

Note that the spectra of the phases are scalloped but the noise is not. This scalloping produces a negative peak (trough) only in the cepstra with a time delay of 0.12 seconds that is consistent with a two-way water reverberation of 1007 meters. No positive peaks, characteristic of bubble pulses, are observed in the cepstra, except for one at low quefrency just before the trough at about 0.06 seconds. However, note that this peak also appears in the noise which suggests it is a processing artifact, not a bubble pulse. The depth of 1007 meters is consistent with water depths from bathymetry of the region near the epicenter. Thus, we interpret this event to be a very shallow undersea earthquake and the spectral scalloping to be consistent with the time delay for a single pass of the acoustic pulse through the water column above the epicenter.

CONCLUSIONS AND RECOMMENDATIONS

This analysis has shown that the recent November 25, 1998 event off the coast of Norway near Tromso has spectral/cepstral features consistent with an underwater explosion. After consulting with NORSAR, there appears to be no confirmation of the event actually being an explosion. However, the region near Tromso has military activities and explosions have occurred in this region in the past. Baumgardt and Der (1998) presented data for a large number of events around the Scandinavian arrays that appear to have been underwater explosions, so blasting underwater for military or geophysical exploration purposes may not be uncommon.

The February 3, 1993 event near Tromso also has spectral scalloping but cepstral analysis shows it to be due to water column reverberations, not bubble pulses. The reverberations give a water column depth of about 1007 m, which is consistent with the bathymetry for the region. This illustrates a means of discriminating between underwater blasts and undersea earthquakes.

The cepstral modeling and matching method described above and demonstrated on the November 25, 1998 event provides a potential method for screening of underwater chemical explosions as well as for identifying larger nuclear explosions. For a given event located offshore, the cepstral modeling and matching algorithm would be run to try to find an explosion model that matches the observed cepstrum. If at match can be obtained, with a correlation coefficient that exceeds some specified threshold, the event would be identified as an underwater blast. If the estimated yield is small, again less than some threshold, the event would be identified as a chemical explosion and screened. If no such match can be attained, the event would be screened as a likely offshore earthquake. Also, additional research is required to determine whether the method could also be used to identify earthquakes. Synergy with location may be possible since the method provides an estimate of depth in the water. This depth must be equal to or less than the bathymetric depth at the location point, and thus provides a check on the estimate of distance of the event from land. This approach could be used for either explosions or earthquakes.

Although the hydroacoustic component of the IMS may be adequate to detect and identify nuclear explosions in the SOFAR channel of the deep ocean, explosions near the coasts of countries, which may occur outside the SOFAR channel, may be harder to detect and characterize by hydroacoustic sensors. For example, the November 25, 1998 event was in a location that all paths to the hydroacoustic stations were blocked and was not detected hydroacoustically. Thus, the seismic stations in the IMS may have to be relied on to monitor for such events.

Analysis of the regional seismic phases, such as *Pn*, *Pg*, *Sn*, and *Lg*, from underwater explosions, provides more in-situ information about the source environment than T phases. Early arriving seismic phases result from the conversion of hydroacoustic to seismic signals that occurs in the vicinity of the source. T phases, on the other hand, may result from long-range propagation of acoustic signals in the ocean before they convert to seismic signals, and thus, the source information in the spectrum may be contaminated by propagation effects.

Therefore, the overall conclusion of this study is that the IMS seismic stations can serve as an important complement to the hydroacoustic network for detecting and identifying underwater explosions. Moreover, in many instances, seismic stations may be better suited for the characterization of underwater explosions, such as those near coastlines, than hydroacoustic or T-phase stations. Thus, automated processing techniques developed for characterizing underwater events, such as the cepstral inversion method described in this paper, should be developed and applied to seismic data as well as to hydroacoustic data from offshore events.

REFERENCES

Baumgardt, D.R. (1998). Anomalies in high frequency P/S ratios: the 16 October 1997 underwater explosion near Murmansk and PNEs recorded at Borovoye, Technical Note submitted to DOD Nuclear Treaty Program Office, May 6, 1998.

Baumgardt D.R. and Z. Der (1998), Identification of presumed shallow underwater chemical explosions using land-based arrays. *Bull. Seism. Soc. Am.*, **88**, 581-595.

Baumgardt, D.R. and K. Ziegler (1988). Spectral evidence of source multiplicity in explosions: application to regional discrimination of earthquakes and explosions, *Bull. Seism. Soc. Am.*, **78**, 1773-1795.

SCREENING OF SEISMIC EVENTS IN ROCKBURST AREAS

Theron J. Bennett, Margaret E. Marshall, Ronald W. Cook, Geophysics Group, Maxwell Technologies, Inc.

Sponsored by U. S. Department of Defense
Defense Threat Reduction Agency
Contract No. DSWA01-98-C-0153

ABSTRACT

Rockbursts present several unique challenges for seismic discrimination and event screening in the Comprehensive Nuclear-Test-Ban Treaty (CTBT) monitoring environment. Rockbursts are located in approximately the same depth range as nuclear tests, so depth discriminants are likely to be ineffective. Some rockburst mechanisms produce relatively weak long-period surface waves which could negate screening based on M_s-vs-m_b. Since many rockbursts are small, their screening is likely to depend heavily on observations from a few regional stations. The current research is directed at identifying rockburst regions with respect to their significance to CTBT monitoring at the International Data Centre (IDC) and at investigating the performance of some promising discriminant measures for use in IDC event screening in those regions.

Based on past experience, we identified 62 areas worldwide in which there have been historical reports of rockbursts associated with mining activity. In our initial efforts under this contract, we have searched the 1995-1999 database at the prototype IDC and found more than 900 events within 50 km of 34 of these mining areas. The majority of these events had magnitudes greater than 3. The most active of these areas were (1) three areas in Poland, (2) an area on the Kola Peninsula in northern Russia, and (3) five areas in South Africa.

We have been systematically reviewing preliminary event screening results from the pIDC and waveforms for events in all the rockburst areas and comparing those to pIDC observations for events outside of rockburst areas. The large majority of events from the historical rockburst areas are not screened out, as earthquakes, by the default screening procedures currently being tested at the pIDC; however, some are. For the three most active rockburst areas noted above, only four events were "screened out"; and those were on the basis of M_s-vs-m_b. The majority of the more than 900 events, from all areas, had "insufficient data" for screening, even though most had $m_b > 3$ and many had $m_b > 4$. In general, the pIDC data are inadequate for screening events from the rockburst areas using the current default screening procedures, which are based on (1) M_s-vs-m_b, (2) source depth, and (3) offshore-vs-onshore.

In an effort to identify more effective screening procedures for use with events from rockburst areas, we have been analyzing waveform data for events in each of the areas. We have retrieved waveform data recorded by the International Monitoring System network stations for the largest events in each of 32 different historical rockburst areas. For even these relatively large events, the teleseismic signals from the events in the rockburst areas are usually weak and are not likely to provide definitive screening. On the other hand, seismic signals from events in these rockburst areas are frequently strong at stations out to about 10º from the source. Measurements based on analyses of regional signals appear, then, to offer the most promise for screening events from rockburst areas.

We have been investigating several specific regional signal measurements to determine their screening potential for events in these areas. We have utilized the frequency-band spectral measurements of P_n, and L_g phases, as currently determined at the pIDC, to get some initial impression of the behavior of regional phase spectral discriminants in screening. There appears to be a preliminary indication from these measurements that events within the rockburst areas (presumed to be predominantly rockbursts) have L_g/P_n ratios in several frequency bands which are systematically larger than events outside the rockburst areas (presumed to be predominantly earthquakes). There also seems to be an indication that the L_g signals from events within rockburst areas have a tendency to be somewhat richer in some higher frequency passbands than the L_g signals from events outside the rockburst areas.

Key Words: seismic, screening, discrimination, regional, pIDC

OBJECTIVE

A Comprehensive Test Ban Treaty (CTBT) prohibiting nuclear weapons testing is expected to broaden the range of seismic events of interest in treaty monitoring to include both smaller events and events in geographic regions which were not previously considered important. Rockbursts present several unique challenges for seismic discrimination and event screening in the CTBT monitoring environment. Rockbursts are located in approximately the same depth range as nuclear tests, so depth discriminants are likely to be ineffective. Some rockburst mechanisms produce relatively weak long-period surface waves which could negate screening based on M_S-vs-m_b. Since many rockbursts are small, their screening is likely to depend heavily on observations from a few regional stations. The current studies will identify rockburst regions with respect to their significance to CTBT monitoring and focus on the performance of three promising discriminant measures for use in IDC event screening in those regions. The research program includes the following elements: (1) systematic collection of IDC data for events in known rockburst areas worldwide, (2) determination of S/P or L_g/P ratios for events from rockburst areas, (3) measurement and analyses of complexity of regional signals from events in rockburst areas, (4) determination of LP surface-wave excitation for events in rockburst areas, (5) relation of the range of behavior of observed signal characteristics to those expected from reported rockburst and other source mechanisms, and (6) prediction of seismic signal and discriminant behavior for significant rockburst areas worldwide.

RESEARCH ACCOMPLISHED

Our initial efforts in this research program have focused on the acquisition of data from the prototype International Data Centre (pIDC). In particular, from prior experience based on review of available technical literature, we have identified 62 areas worldwide in which there have been historical reports of rockbursts associated with mining operations. We searched the Reviewed Event Bulletin (REB) database at the pIDC during the time period from the beginning of 1995 to April of 1999 for events within 50 km of each of the mining areas, which have had historical rockbursts. This search found more than 1000 events in 34 different areas (cf. Figure 1); the REB database contained no events from the remaining 28 areas. Based on the REB data, the most active of the areas, which have had historical rockbursts, were (1) three areas in Poland, (2) an area on the Kola Peninsula in northern Russia, and (3) five areas in South Africa. Although the majority of the 1000 REB events from these areas had magnitudes greater than 3 (cf. Figure 2), the detection thresholds may differ significantly between the different rockburst areas. Some of the reported Polish and Kola events had magnitudes as low as 2, while South African events are seldom smaller than 3.5. In most of the areas which have reported events in the REB, the magnitude thresholds appear to be near 3.5. It seems likely that smaller events associated with mining in some of the other areas, where no REB events were reported, may have been missed because of the pIDC reporting criteria, which require signal detection at multiple International Monitoring System (IMS) stations. We are looking at alternative event lists for selected areas to assess what events from the rockburst areas might have been overlooked by pIDC processing.

We have also been systematically reviewing screening results and waveforms for events in all the rockburst areas. Screening results have been retrieved and compared for all events from the historical rockburst areas for which screening was attempted at the pIDC. Although the majority of events from these areas are not screened out as earthquakes, some are. Of the events in the principal rockburst areas, only four are "Screened Out" by the current pIDC default screening procedures based on (1) M_S-vs-m_b, (2) source depth, and (3) offshore-vs-onshore (cf. Table 1). Approximately 44 events from these areas are categorized as "Not-Screened." A closer look at the screening measurements (cf. Table 2) indicates that the four "Screened-Out" events (three in South Africa and one in Poland) are screened on the basis of M_S-vs-m_b. Figure 3 shows a plot of M_S versus m_b for several historical events including numerous rockbursts, which has been adapted from a prior plot by Bennett and McLaughlin (1997). Where they were available, we have used pIDC magnitude measurements; National Earthquake Information Center magnitudes are used for some of the older events. These events include several of the largest rockbursts (e.g. the 1989 Völkershausen, Germany mine collapse; the 1994 Orange Free State, South Africa mine tremor; the 1995 southwestern Wyoming mine collapse; and the 1995 Urals rockburst in Russia). For reference we also show several decision lines which provide a potential basis for event screening. The four rockburst events, as described above, which are screened out by the preliminary pIDC screening procedures have been circled on this plot. It should be noted that the actual pIDC screening procedure incorporates an estimate of the M_S-m_b uncertainty associated with each event; so that the 3.1 M_S South African

mine tremor is barely screened out at the nominal 97.5% confidence level. Furthermore, based on this screening procedure, many of the other events shown here would not be screened out, except for those that lie well above the line. Several of the "Not-Screened" events in South Africa have low M_S magnitudes and/or large M_S-m_b uncertainties which do not allow them to be screened out. The large magnitude uncertainties can be directly attributed to the small number of IMS stations reporting magnitudes. The relatively low M_S values from rockburst events is probably caused by their mechanisms, as suggested by Bennett and McLaughlin (1997) and by Pechmann et al. (1995). If the source mechanisms of mine collapses and some other types of rockbursts may be represented as closing of a shallow, horizontal tension crack, we would expect the kind of reduced long-period surface wave excitation and low M_S relative to m_b which is observed from many of these events.

We also looked more closely at the "Not-Screened" events and found that events which are "Not-Screened" in Poland often show what appear to be erroneous indications of depth. While the depths determined from the unconstrained pIDC location procedures for these Polish events are often greater than 10 km, the associated uncertainties are large; so that these events are not screened out based on their depths. Because these events are induced by the mining activity and are clearly shallow, any depths greater than a few kilometers determined from the location scheme are suspect, and probably erroneous. Therefore, event focal depths cannot provide reliable screening out of events from rockburst areas, except for a few areas where some natural earthquake activity may also be present and occurring at greater depths in the crust.

The remainder of the more than 900 events have "Insufficient Data," even though most have $m_b > 3$ and many have $m_b > 4$. As can be seen in Table 2 and as we would expect from their locations, none of the events from the three principal rockburst areas are categorized as "Offshore." It is, in fact, remarkable that some of these events are categorized as "Mixed." This is probably indicative of a large location uncertainty, which overlaps offshore areas, for some of these events. Although some of the historical rockburst areas are located along coasts or on islands (as can be seen in Figure 1 above), it is unlikely that any rockbursts can be categorized as "Offshore."

We are continuing to look at the other historical rockburst areas; but, in general, the pIDC data are inadequate for screening events from the principal rockburst areas based on the current default screening procedures. In particular, observations from predominantly teleseismic stations and the related discriminant measures, which rely on those observations, do not appear to be useful for screening most events from rockburst areas. We have, therefore, begun looking into alternative screening procedures for characterizing events from the historical rockburst areas, with particular emphasis on screening based on regional signal observations. These investigations have focused on (1) retrieval and analyses of waveform data from REB events in each of the areas; (2) analyses and comparisons of routine parametric measurements, which are currently being made at the pIDC, for use in screening of events within historical rockburst areas and outside those areas; and (3) investigation of selected regional phase signal characteristics for events from the rockburst areas. We have retrieved waveform data from each station which reported seismic signals from the largest of the REB events in each of the 34 areas. In addition, we have retrieved waveform data from additional REB events for several of the rockburst areas. This should enable analyses of the variability of the regional signals from within these rockburst areas. Past studies (cf. Bennett et al., 1994, 1995) have suggested remarkable consistency in the regional phase signals between events from individual rockburst areas. However, we also know that variations in mining practice can produce some differences in focal mechanisms (cf. Hasegawa et al., 1989; Gibowicz and Kijko, 1994; Bennett and McLaughlin, 1997) which can cause regional signal changes. It is anticipated that these observations of the variability for regional phases within selected rockburst areas will lead to better understanding of the uncertainty associated with potential discriminant measures based on the regional signal characteristics. The recorded signals will be used to determine discriminant measures, as described above, and to determine their reliability for future event screening in these areas.

With regard to the waveform data, we note that even the largest events from the rockburst areas are usually not very well recorded by the existing IMS network. The recorded signals are often weak and near the background noise level, particularly for stations beyond about 10°, for most of the events. This is illustrated in Figure 4 for a pIDC event of magnitude 4 M_L from a known rockburst area in southern Utah. The top part of Figure 4 shows, for the passband 2-4 Hz, the strong regional signals at the pIDC stations from 1.9º to 6.9º. However, beyond 11.4º the signal character for this event severely deteriorates, as can be seen in the bottom part of Figure 4. Even though the pIDC has managed to pick some phases at the more distant stations, the signal-to-noise

level is often not very good. This behavior is fairly typical of the pIDC station waveforms for magnitude 3-4 events from the various rockburst areas. Figures 5 and 6 show the regional signals at pIDC stations, out to 10º, for events in two other rockburst areas. For the magnitude 3.8 M_L Polish rockburst in Figure 5, there are clear and strong P_n, P_g, and L_g phases at stations in northern Europe over a distance range from 2.2º to 9.8º. The magnitude 3.9 M_L South African rockburst, in Figure 6, shows good P_n, P_g, S_n, and L_g phases at the available pIDC regional stations between 2.7º and 8.9º. Although some IMS teleseismic stations may occasionally contribute to observations for use in event location, screening procedures for events in rockburst areas are likely to require higher quality signals and will probably depend on good regional signals observed over a sparse station network.

We are currently in the process of performing systematic analyses on the waveforms recorded at the regional stations for the largest events from each of the 34 rockburst areas for which we have retrieved pIDC data. We are determining L_g/P ratios as a function of frequency for these events and comparing with our past experience from other source types and with events from other rockburst areas. We have defined a regional signal complexity measure and have begun making a series of measurements on the regional P phases for the pIDC events, which we will compare to similar measurements for explosions and earthquakes. We are also attempting to look more closely at the character of regional long-period surface waves from these rockburst area events, by filtering the broadband records to enhance the low-frequency signals.

We have also reviewed results from some of the routine parametric measurements currently made at the pIDC to obtain some initial assessment of their potential use in event screening. In particular, we have been looking at measurements from events within historical rockburst areas compared to events outside the known rockburst areas. There appears to be a preliminary indication from these measurements that the observed seismic signals for events within the rockburst areas (presumed to be predominantly rockbursts) may be systematically different than those for events outside the rockburst areas (presumed to be predominantly earthquakes). Figure 7 shows that, for the distribution of L_g/P_n ratios in the frequency band 2-4 Hz, the ratios appear to be somewhat larger for events within rockburst areas than outside rockburst areas. We see similar systematic differences in each of the frequency bands for which the parametric measurements are available (viz. 4-6 Hz, 6-8 Hz, and 8-10 Hz). These observations suggest that the rockbursts are more efficient in generation of high-frequency shear waves (or less efficient in generating regional P) than earthquakes. We have also found differences in the L_g/P_g, S/P_n, L_g spectral ratios, and SP/LP ratios between pIDC events inside and outside rockburst areas. These results look rather interesting and need to be investigated more closely to understand their implications for event screening at the IDC.

CONCLUSIONS AND RECOMMENDATIONS

Over the past four years the pIDC has reported about 1000 REB events from more than half of the 64 known historical rockburst areas worldwide. Approximately 85% of these events had magnitudes greater than 3. Less than 1% of these events are screened out by the default screening procedures which are currently in use at the pIDC. In general, screening procedures based on focal depth, M_S-vs-m_b, and offshore-vs-onshore location are not likely to be effective for event screening in rockburst areas; in most cases IMS data from teleseismic stations are insufficient to obtain the measurements required to perform the screening. Screening of events in rockburst areas is likely to require the use of discriminant measures based on signal observations at regional stations. We have been looking at L_g/P, S/P, L_g spectral ratios, regional P complexity, and at regional long-period surface waves from events in rockburst areas. We have found that there appear to be some systematic differences in the regional signals between events inside and outside rockburst areas. Preliminary results suggest that rockbursts may be more efficient in generation of high-frequency regional shear waves than earthquakes.

REFERENCES

Bennett, T. J., and K. L. McLaughlin (1997). "Seismic Characteristics and Mechanisms of Rockbursts for Use in Seismic Discrimination," in Rockbursts and Seismicity in Mines, Gibowicz and Lasocki (editors), Balkema, Rotterdam, pp. 61-66.

Bennett, T. J., M. E. Marshall, B. W. Barker, and J. R. Murphy (1994). "Characteristics of Rockbursts for Use in Seismic Discrimination," Phillips Laboratory Report PL-TR-94-2269.

Bennett, T. J., K. L. McLaughlin, M. E. Marshall, B. W. Barker, and J. R. Murphy (1995). "Investigation of the Seismic Characteristics of Rockbursts," Phillips Laboratory Report PL-TR-95-2169.

Gibowicz, S. J., and A. Kijko (1994). An Introduction to Mining Seismology, Academic Press, San Diego.

Hasegawa, H. S., R. J. Wetmiller, and D. J. Gendzwill (1989). "Induced Seismicity in Mines in Canada – An Overview," Pageoph, 129, pp. 423-453.

Pechmann, J. C., W. R. Walter, S. J. Nava, and W. J. Arabasz (1995). "The February 3, 1995, ML 5.1 Seismic Event in the Trona Mining District of Southwestern Wyoming," Seism. Res. Lett., 66, pp. 25-34.

Sykes, L. R., J. F. Evernden, and I. L. Cifuentes (1983). Conference Proceeding 104, American Institute of Physics, pp. 85-133.

Working Group B (1998). Report on the IDC Technical Experts Meeting on Event Screening 5-9 June 1998, Preparatory Commission of the CTBT, CTBT/WGB-6/TL-2/10.

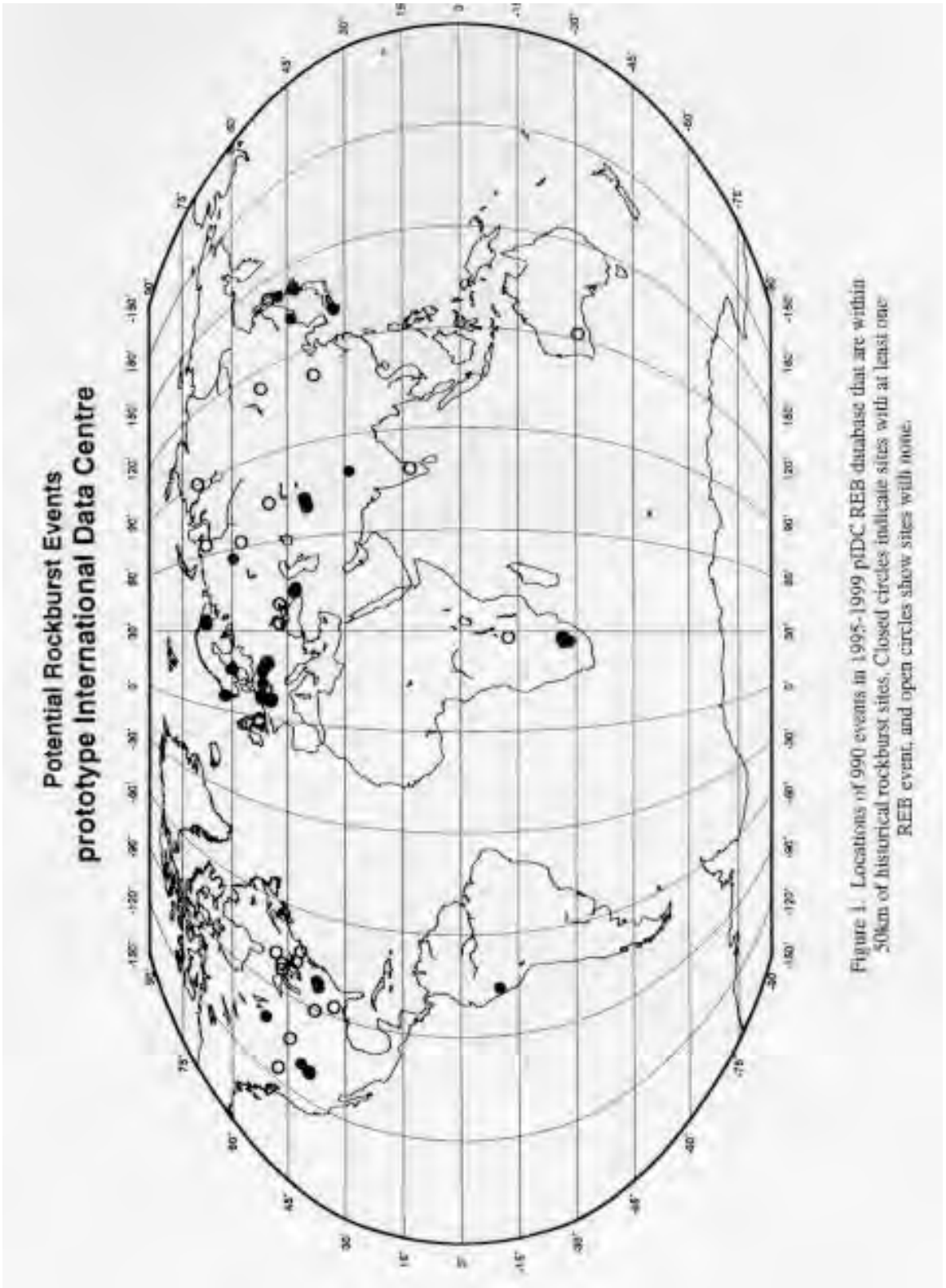


Figure 1. Locations of 990 events in 1995-1999 pIDC REB database that are within 50km of historical rockburst sites. Closed circles indicate sites with at least one REB event, and open circles show sites with none.

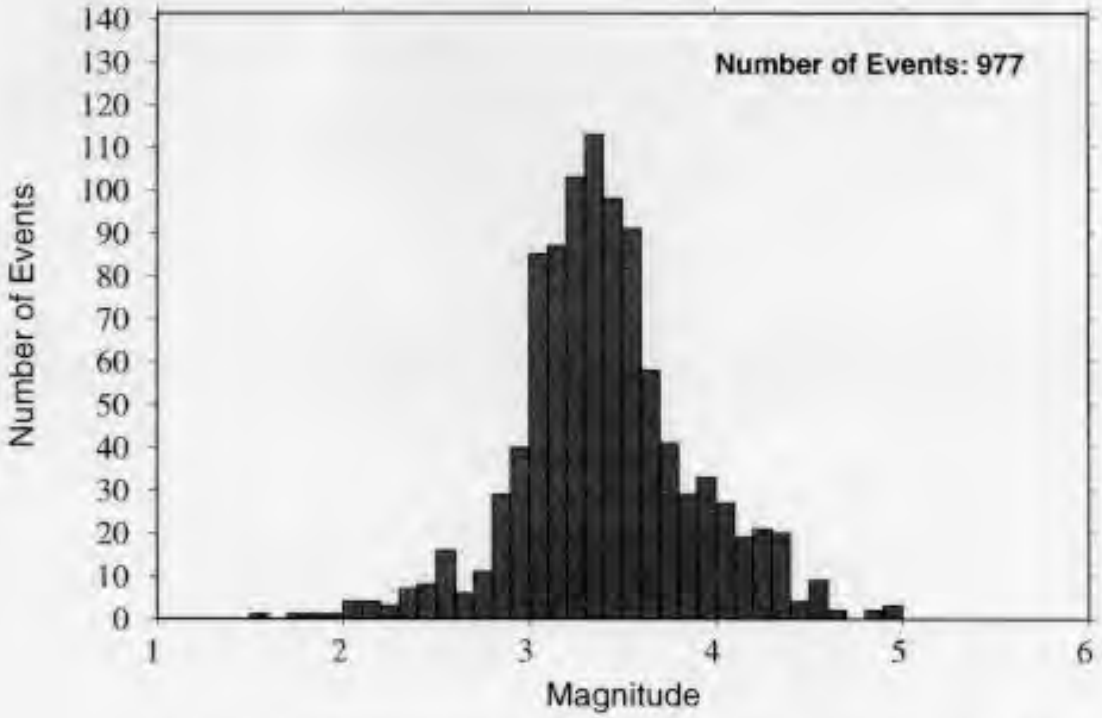


Figure 2. Distribution of potential rockburst events with respect to REB magnitude (m_b or M_L).

Table 1. PIDC preliminary screening results for the three principal rockburst areas.

Rockburst Region	Screened	Not-Screened	Insufficient Data
Poland	1	33	618
Kola Peninsula	0	5	161
South Africa	3	6	104

Table 2. Basis for plDC preliminary screening results for the three principal rockburst areas.

Rockburst Region	m_b, M_S Measured	$1.25m_b - M_S + 2\sigma_M < 2.2$	Depth > 0	$D - 2\sigma_D > 10$	Offshore
Poland	1	1	33	0	0
Kola Peninsula	0	0	5	0	0
South Africa	8	3	1	0	0

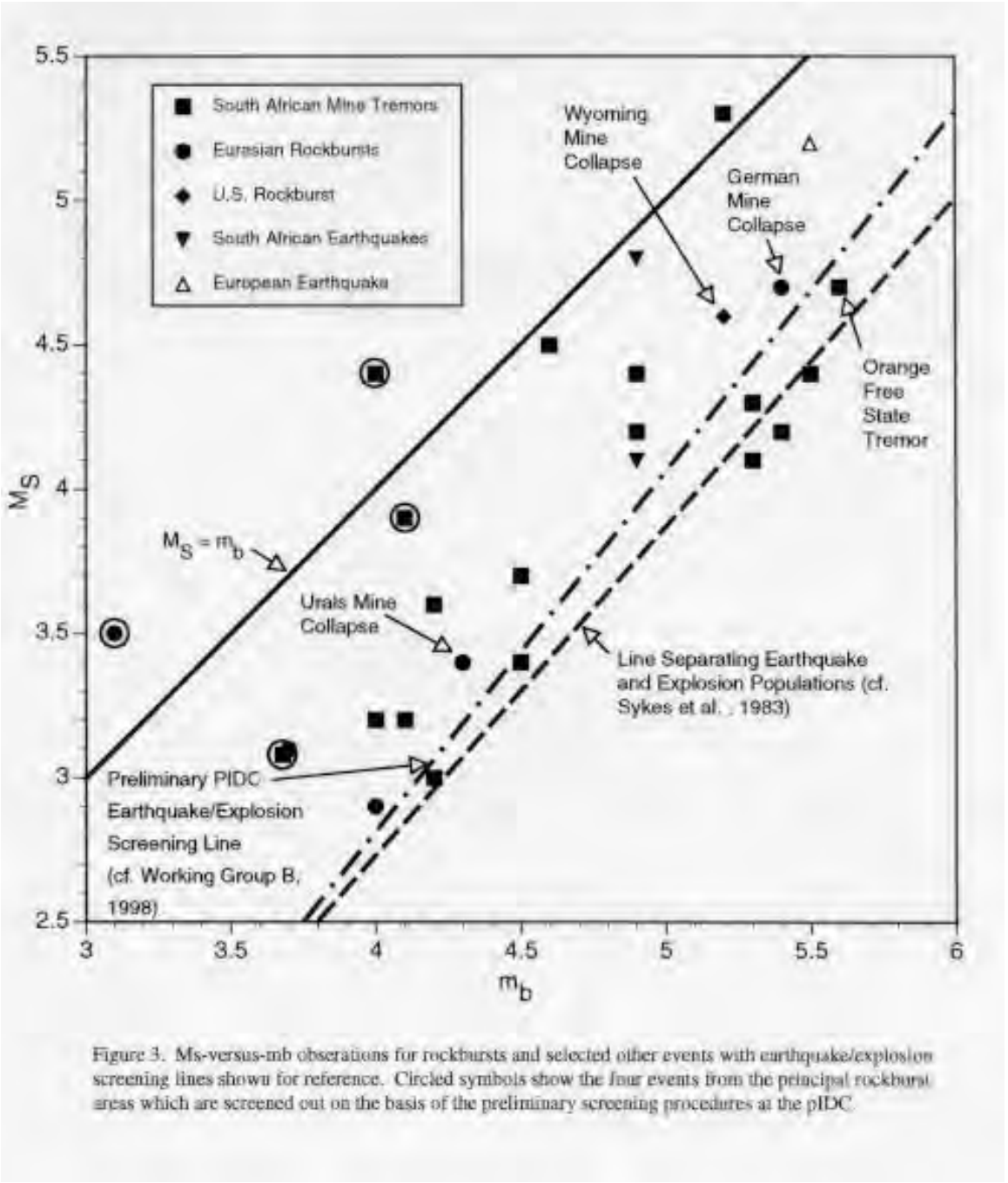


Figure 3. Ms-versus-mb observations for rockbursts and selected other events with earthquake/explosion screening lines shown for reference. Circled symbols show the four events from the principal rockburst areas which are screened out on the basis of the preliminary screening procedures at the pIDC.

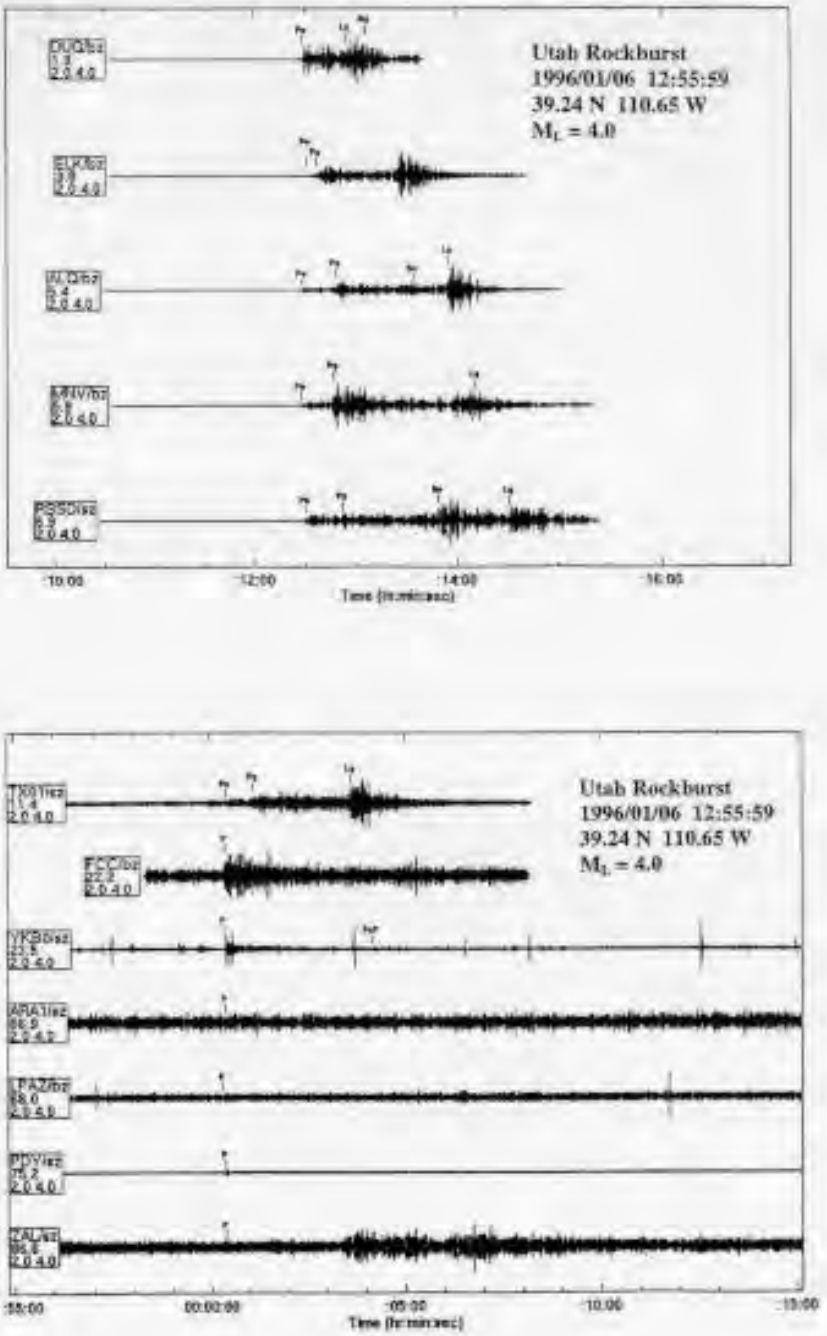


Figure 4. Seismic signals at pIDC stations from event in southwestern Utah rockburst area. Top – 5 stations at distances within 10°; Bottom – 7 stations at distances beyond 10°.

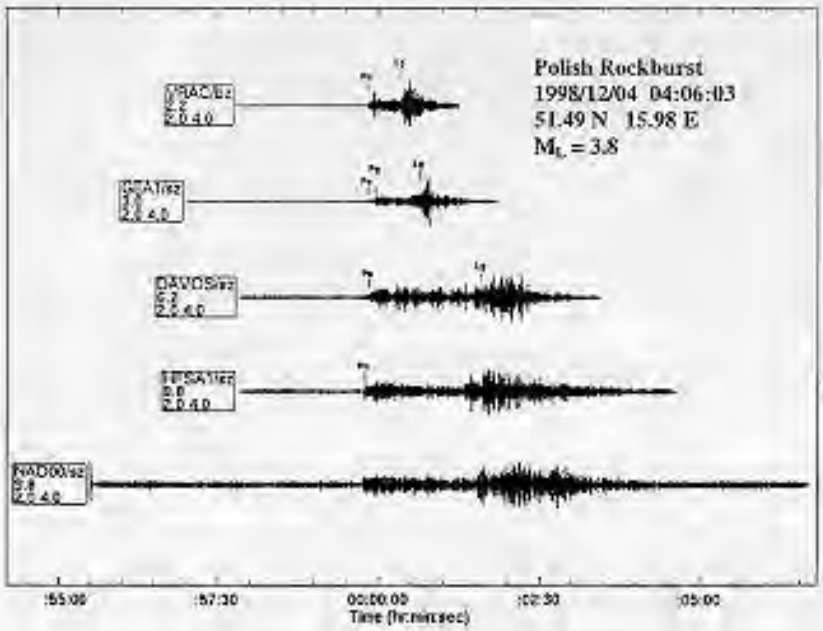


Figure 5. Seismic signals at 5 pIDC stations within 10° of event in Polish rockburst area.

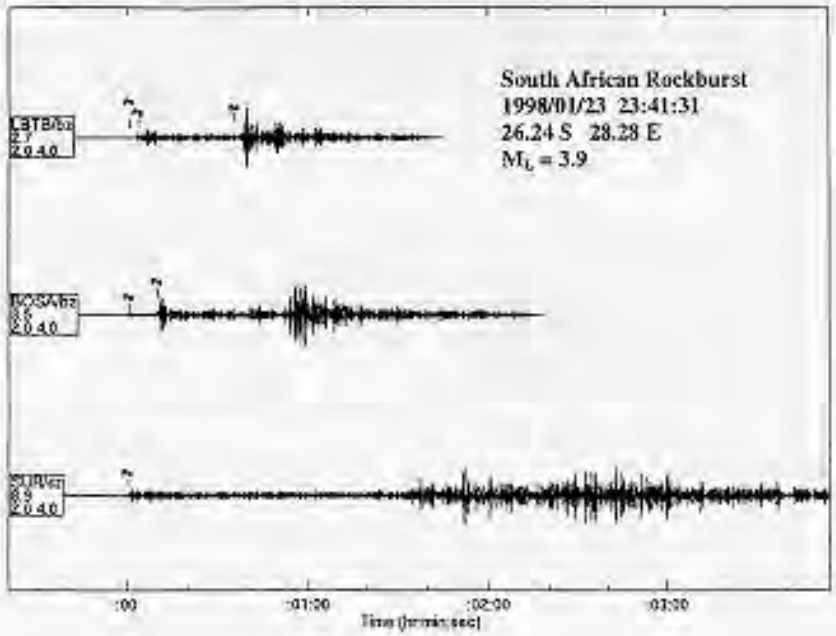


Figure 6. Seismic signals at 3 pIDC stations within 10° of event in South African rockburst area.

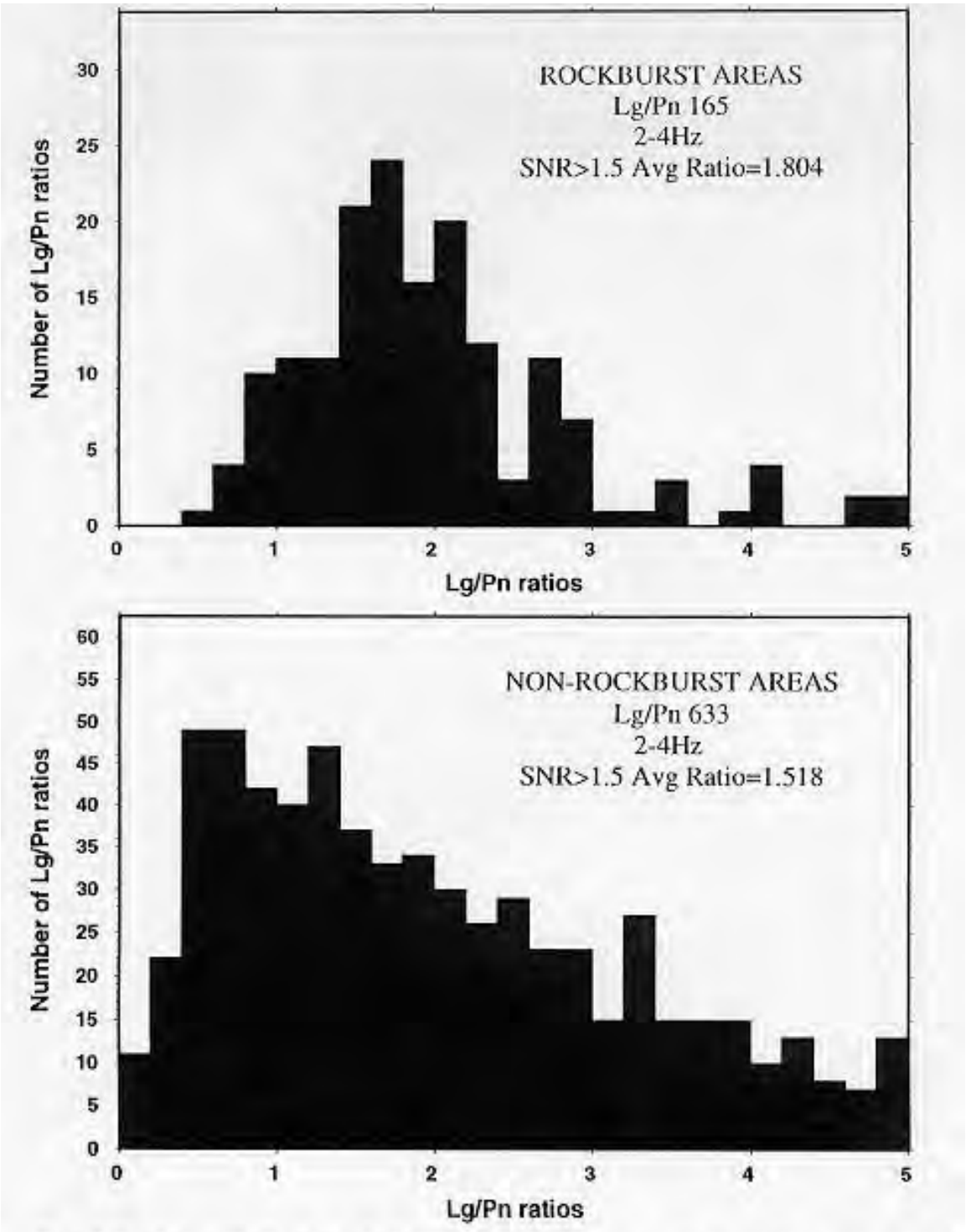


Figure 7. Distribution of Lg/Pn ratios in the 2-4Hz passband for pIDC events within the rockburst areas compared with event sample from outside rockburst areas.

DEVELOPMENT OF A 3-D MODEL FOR IMPROVED SEISMIC EVENT LOCATION IN THE PAKISTAN/INDIA REGION

Michelle Bernard, Delaine Reiter, Shirley Rieven, Weston Geophysical Corporation
William Rodi, Carolynn Vincent, Earth Resources Laboratory, Massachusetts Institute of Technology

Sponsored by U.S. Department of Defense
Defense Threat Reduction Agency
Contract No. DSWA01-98-C-0143

ABSTRACT

The ability to accurately perform location calibration in regions of monitoring concern depends heavily on an understanding of the crust and upper mantle velocity structure in the region. Our project is focused on developing a 3-D model of Pakistan and surrounding regions for the purpose of improving seismic event location. During the initial portion of the study, we have developed a preliminary 3-D model of the region and a regional seismic event database as a foundation for performing tomographic inversion and event location.

We constructed the preliminary velocity model by synthesizing data from references that contained both direct and indirect information about the velocity structure, geology, and tectonics throughout the region. The sources of data for the velocity model vary in spatial coverage, resolution, and the number of constraints; consequently, the model varies in a similar manner. Developing a unified 3-D model has allowed us to obtain constraints on the large-scale variations in the depth to the crust-mantle interface (Moho discontinuity) across the region. For example, the Moho is approximately 25 km deep near the coast in the Makran region of southwestern Pakistan where the Afghan plate is being subducted beneath the Eurasian plate (Byrne *et al.*, 1992). In contrast, the Moho reaches great depths beneath the Pamir region in northern Pakistan, where it dives to 70 km depth at the interpreted meeting point of subducted Asian continental lithosphere with the under-thrusting Indian lithosphere (e.g. Fan *et al.*, 1994). Our composite 3-D velocity model illustrates the large range of crustal thickness in the Pakistan region, a factor that could result in significant error in travel-time calculations based upon models (such as IASPEI91) with a constant 35-km thick crust.

In addition to developing the preliminary velocity model, we have also constructed a partial database of phase arrival times and waveforms for local, regional, and near teleseismic events. The principal objective of the event database is to provide as much ray coverage through our 3-D model as possible. We have identified permanent and temporary seismographic stations for the time period between 1989-1998, and have found that at least 12 organizations have operated as many as 159 regional and local seismographic stations in the region. We referred to multiple data collection sources to construct our database, including the prototype International Data Centre's (pIDC) reviewed event bulletin (REB) archives, the International Seismological Center (ISC), National Earthquake Information Center (NEIC), and the Incorporated Institutes for Research in Seismology (IRIS). From these online sources, we were able to obtain phase arrivals from 61 of 159 of the potential stations. Additional offline efforts will be required to obtain times from the remaining 98 stations. Nevertheless, the acquired data provides 6096 phases including P, Pn, P*, pP, PP, PcP, S, Sn, SS, and exhibit an azimuthal coverage which approaches that estimated for the full complement of 159 stations.

We have completed the development of both the preliminary velocity model and a partial database of seismic phases and are currently beginning the tomographic inversion effort. Two initial tasks prior to performing a full tomographic inversion include comparing travel times calculated using the IASPEI91 or other regional 1-D models versus those computed using our model, and performing event relocations with the preliminary 3-D model and a grid-search location method.

Key Words: seismic, 3-D velocity model, location, Pakistan

OBJECTIVE

Seismic calibration of regions of monitoring concern requires the development and validation of 3-D models of regional seismic velocity that improve the location of events. We are working on a multi-year project to develop such a model, along with improved event locations, for a region centered on Pakistan that extends into eastern Iran, southern states of the Former Soviet Union, and western India. The first year of the project has focused on the development of a preliminary 3-D model and the foundations of a seismic event database. We have also begun the development of our joint tomography and location technique, with the ultimate purpose of providing validated source station specific corrections (SSSCs) to the pIDC for International Monitoring System (IMS) stations in the Pakistan/India region.

RESEARCH ACCOMPLISHED

Preliminary 3-D Regional Velocity Model

There are several preliminary steps that must be completed prior to performing tomographic inversion and relocation of events in the Pakistan region. As a first step, we have developed a preliminary 3-D regional velocity model (see Figures 1 and 2) to serve as a starting point for the tomographic inversion. Our model is bounded by 55-80^{o} east longitude and 25-45^{o} north latitude. This is an expansion of our originally proposed model boundaries (60°-75°E, 25°-40°N) to allow for adequate data coverage of the region. This enlarged area includes portions of India, Pakistan, Afghanistan, China, Tajikistan, Kyrgystan, Uzbekistan and Turkmenistan. We defined the preliminary velocity model on a grid of one-degree latitude by one-degree longitude blocks and 5 km depth intervals from 0 to 75 km. We constructed the velocity model by synthesizing data from 27 published references that contained information about the velocity structure throughout the region. To derive a reasonable estimate of the gross velocity structure in regions where direct velocity measurements were lacking, we compiled information indirectly related to velocity from over 50 sources pertaining to the geology and tectonics of the Pakistan area. The sources of data for the velocity model vary in spatial coverage, resolution

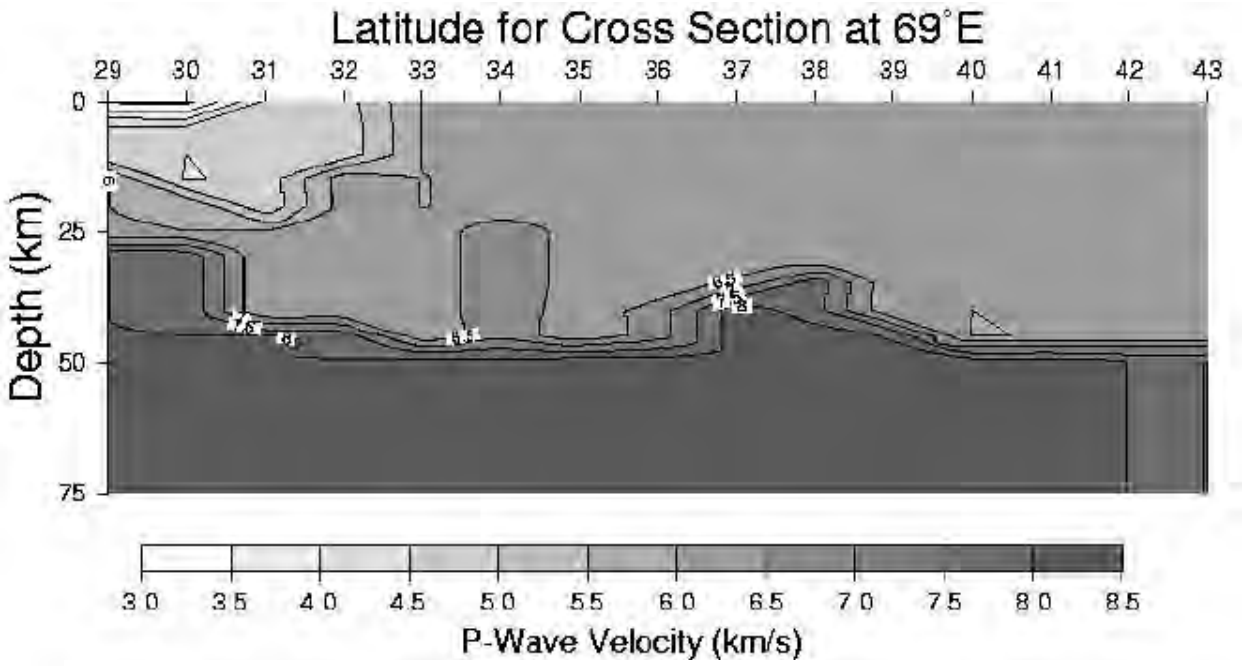


Figure 1. Latitudinal cross section of the preliminary velocity model at 69°E. This cross section cuts through part of the Sulaiman Lobe and continues north across the Tadjik Depression. Note the presence of thick low velocity material in the Sulaiman region (~15 km of sediments) overlying a shallow Moho. The Moho deepens quickly to the north, and then shallows once again beneath the Tadjik Basin (~37°N). This figure demonstrates the effects of merging the results of many studies that have varying resolution on different depth intervals. For example, there have been numerous research studies on the shallow structures in the Sulaiman region as opposed to other areas where more detailed data for shallow structures are lacking. These attributes are subsequently reflected in the velocity model.

and the number of constraints; consequently, the model varies

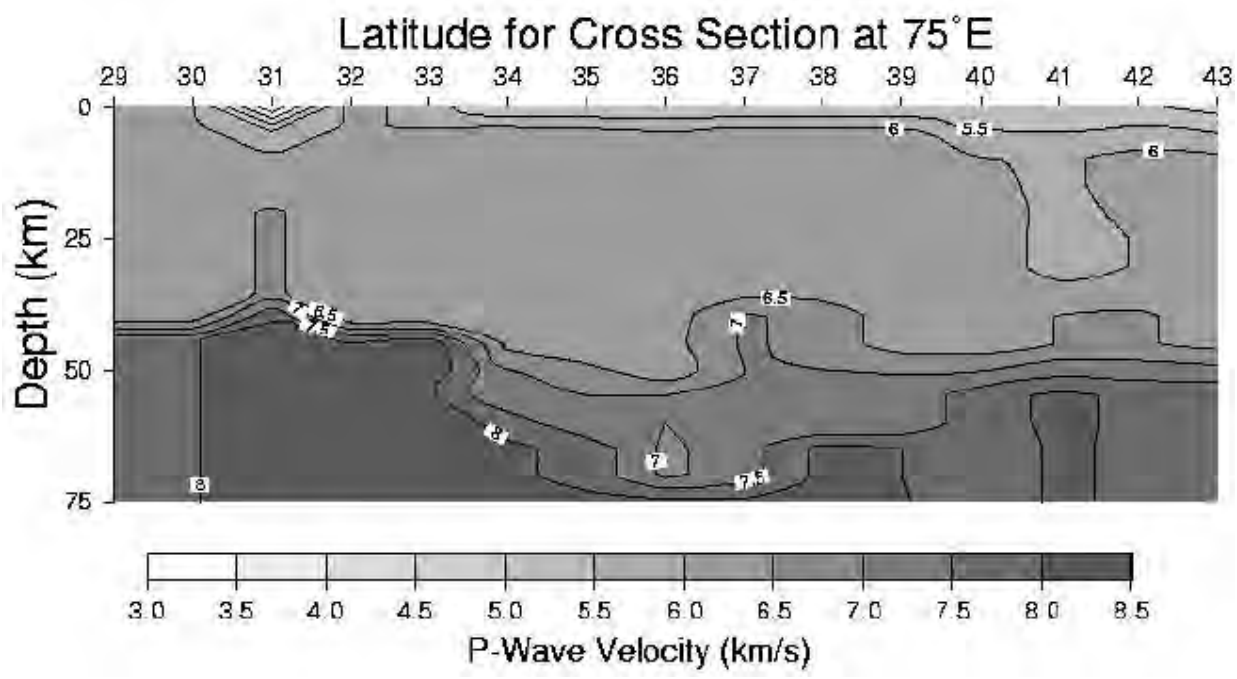


Figure 2. Latitudinal cross section of the preliminary velocity model at 75°E. This cross section is further to the east where the southern part of Indian sub-continent has near-average crustal thickness. Note how the Moho deepens considerably and then shallows again (near 36° N, observing the 7.5-8.0 km/s contour interval) as the cross section passes through the Karakoram and the Pamir regions to the north (e.g. Fan *et al.*, 1994). Other smaller features must be carefully interpreted, because the blending of data from studies of varying resolution scales may lead to certain artifacts in the model.

in a similar manner. We have appended the IASPEI91 model (Kennett and Engdahl, 1991) to the base of the preliminary velocity model, beginning at 80 km depth and extending to 400 km depth, since raypaths of certain event-station pairs within our region travel into the upper mantle. If the need arises, we will compile information on the mantle velocity structure between 80-400 km depth, so that we can replace the IASPEI91 model with one more appropriate to the Pakistan region.

Compiling past and current research into a unified 3-D model has resulted in constraints on the large-scale variations in the depth to the crust-mantle interface (Moho discontinuity) across the region. Due to the complexity of crustal deformation across the region, variations in depth to the Moho are significant (see Figure 3). Any understanding of the nature of these variations is a great improvement from the currently used IASPEI91 model that assumes a constant crustal thickness of 35 km. For example, the Moho is approximately 25 km deep near the coast in the Makran region of southwestern Pakistan where the Afghan plate is being subducted beneath the Eurasian plate (Byrne *et al.*, 1992). In contrast, the Moho reaches great depths beneath the Pamir region in northern Pakistan, where it dives to 70 km depth at the interpreted meeting point of subducted Asian continental lithosphere with the underthrusting Indian lithosphere (e.g. Fan *et al.*, 1994). Travel time calculations based on a constant 35-km thick crust will produce significant error in the Pakistan region, where there is a large range of crustal thickness.

Other large-scale features of note in the Moho surface include the following:

- A slight rise in the Moho beneath the Sulaiman (~32 km depth) before the Moho dips sharply to the northwest at the Chaman fault. At this point the Moho becomes considerably deeper (~57 km depth) beneath the Afghan block (Jadoon and Khurshid, 1996).

- A rise in the Moho beneath the south Caspian Sea (~33 km depth) in the northwest part of our study region (Mangino and Priestley, 1998; Priestley, 1997). Moho depth increases to ~47 km away from this shallow section.

- Shallow Moho (~35 km depth), compared with surrounding regions, beneath the Tadjik Depression located in the region surrounding 37°N, 68°E (e.g. Mellors *et al.*, 1995).

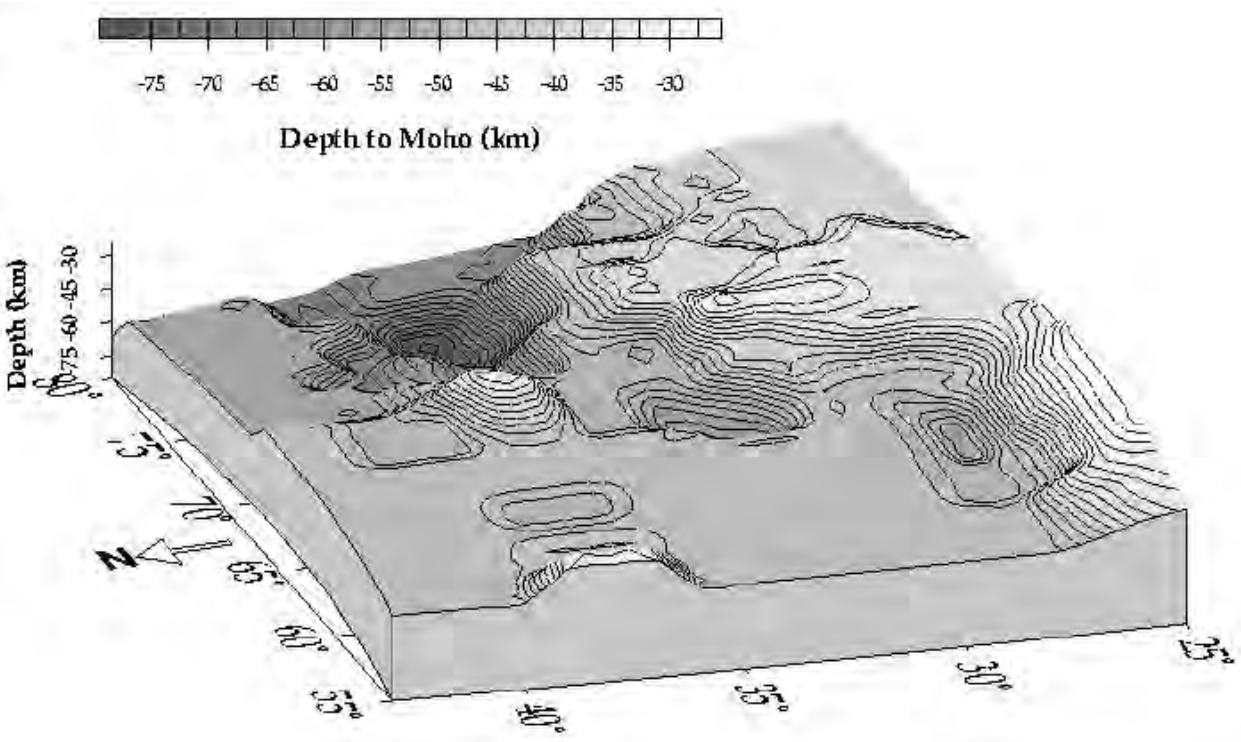


Figure 3. Contoured and smoothed surface plot depicting variations in depth to the Moho boundary determined by data synthesis of approximately 27 published references

Seismic Event Database

Another important step in building a 3-D velocity model of the Pakistan region is to collect a large seismic event database. The information stored in our database is intended to serve multiple purposes. The principal and initial purpose for the database is to provide the arrival time data used to develop our 3-D tomographic model. The database must contain regional phase arrival times for ray paths with enough azimuthal and depth coverage to adequately sample the modeled volume. Additionally, the arrival times must be reliable enough to support the highest quality tomographic results. We are attempting to include only quality arrival times, and so we have started compiling the database by incorporating data from major seismological data-serving organizations. These include the pIDC, the ISC, IRIS, and the NEIC. As our database expands, we intend to increase our list of information sources so that we may improve the available ray coverage for tomography purposes and expand the suite of phase types in our holdings.

A secondary purpose for compiling an event database is to provide useful seismological information for future studies of the India/Pakistan region. We are investigating which seismological data, beyond just the arrival times, will be most useful for CTBT projects, and how this data should best be organized, stored, accessed and shared with outside interested parties.

We are developing the database in three phases, an initial assessment and design phase (already completed), a data collection phase (in progress), and a quality assessment and control phase (upcoming).

Phase One: Geographic Coverage, Station Lists and Event Bulletins

To provide adequate coverage at the edges of our originally proposed model (60°-75°E, 25°-40°N), we populated our database using an expanded grid (Figure 4). We included stations and events from an area 5 degrees larger on the west, north, and east sides of our modeling area and 10 degrees on the southern edge bringing our expanded grid boundaries to 55-80 ^{o} E longitude and 15-45 ^{o} N latitude.

Due to the interesting and complex tectonics of the region, our area of study encompasses a region in which at least 12 seismographic networks have operated more than 159 seismographic stations since the early 1960's (see Figure 4). The temporal availability of data from this set of stations is, of course, variable and we are

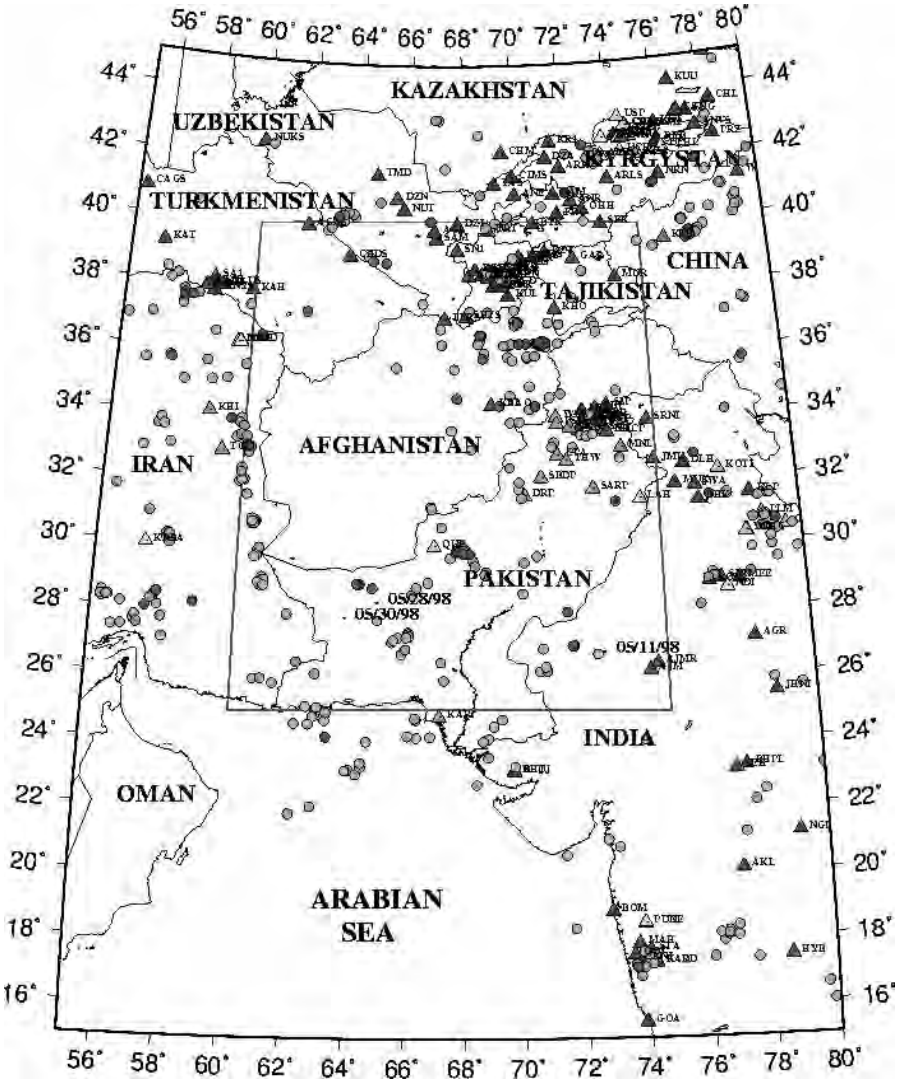


Figure 4. Map of study area showing location of all known seismographic stations and hypocenters for 441 seismic events.

conducting an ongoing investigation to identify additional networks and stations. Our current list of organizations that have operated networks in the area includes: Institute of Physics Moscow (MOS) and

Institute of Physics Moscow Regional Networks (MOSR), the Pakistan Institute of Nuclear Science and Technology (PINS), the Pakistan Meteorological Department Quetta Network (QUE), the India Meteorological Department (NDI), the Wadia Institute of Himalayan Geology, Dehra Dun, India (WHIG), the Institute of Geophysics, Beijing (BJI), Ferdowski University, Iran (MUI), the University of Tehran (THE), the National Institute of Earthquake and Seismology, Tehran, Iran (THR), Lamont Doherty Network(s) (PAL), and Cambridge University.

Currently, our database contains arrival time data from 61 of the 159 known stations. Stations that contribute phase arrivals for the 441 events currently held in our database include: AAA, AAK, ABKT, AGL, AJM, AKL, ANR, ASH, BHJ, BHK, BOM, BZN, CEP, CGT, CHCP, CPA, DDI, DRP, DSH, DZE, DZI, DZT, FRG, FRU, GAR, GOA, HYB, JHNI, JMU, KAD, KAT, KHO, KRU, KSH, KUL, LNA, MAIO, MHI, MUR, NAM, NDI, NIL, NRN, NUT, OBG, POO, PRZ, PTH, QUE, RGR, SAM, SARP, SBDP, SEH, SHTS, SRNI, TAS, THW, TLG, URT, and VAN (see Figure 4). We have identified over 3600 events in our target region for which data is available from the major online sources. Currently, our holdings include 441 of the "best" events. We defined "best" as any event with a relatively higher magnitude than the other available events in the same hypocentral region and a hypocenter location that optimizes the spatial distribution of ray coverage.

The events in our current catalog were recorded during the decade 1989—1999. This time span was chosen to allow more rapid online data retrieval. It is our intent, however, to supplement this catalog with additional data from events recorded prior to this period, provided that the data can be efficiently and accurately incorporated. This effort will include data collection from offline sources and may require selective digitization of waveforms from paper record archives, if particular rays are needed to enhance the tomographic modeling results.

Phase Two: Data Collection

Our database currently contains all of the phase arrivals reported by the source organizations for each of the 441 events mentioned above. We have extracted a subset of these arrivals for further study and possible inclusion in our tomographic inversion. Figure 5 presents the ray coverage available given one possible subset of 6096 regional phase arrivals. The phases represented include P, Pn, P*, pP, PP, PcP, S, Sn, and SS. The rays included in this subset of arrivals provide excellent azimuthal coverage of the area to be modeled. Incorporation of both near and far regional phases and arrivals from events at various depths will provide maximum ray coverage as a function of depth.

We are currently populating our database with both arrival time data and digital waveform data. Our initial priority has been to collect the phase arrival travel times that are needed for the 3-D modeling and tomography. Waveform data collection, while important, is linked primarily with the process of quality assessment and control of the arrival time data. As our phase arrival time database volume increases, we will obtain digital waveform data for each of the events contributing arrival times to our modeling effort. These waveforms will be used to confirm the arrivals incorporated into the modeling and will also be important for future assessment of regional phase characteristics.

Phase Three: Quality Assessment and Control

The events currently held in our database have had hypocentral parameters estimated by all of the agencies from which we obtained our data records. The accuracy of the estimates generated for these events varies according to the number of arrivals used by the particular agency, the quality of those arrivals, the station distribution, the algorithm and the input velocity model. We have attempted to include events with the best hypocentral estimates available, incorporating many events from the pIDC's ground truth databases (GT0,GT1,GT2,etc.) and the Calibration Event Bulletin (CEB). We have reviewed the events listed in the Ground Truth and Calibration event databases and determined that one GT0 event is located in our region, along with an additional five GT1 events (Yang *et al.*, 1999). There are no GT2 or GT5 events, and we are currently conducting a cross-reference of our database holdings with the GT10 and higher database listings. Forty-nine of our events are pIDC CEB events (many of which are anticipated to also be included in the GT10 database event list), 112 are pIDC REB listed events, 211 were obtained from the ISC bulletins and the remaining 64 were obtained from the IRIS and other online sources.

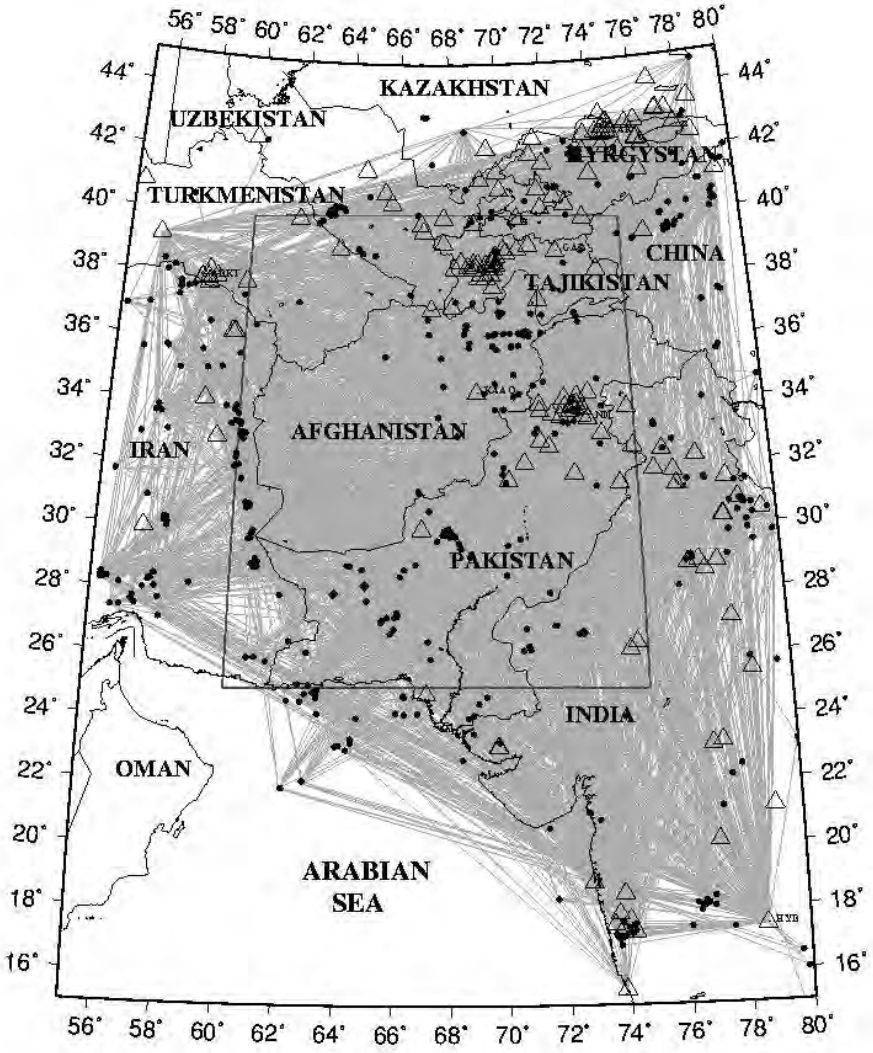


Figure 5. Map of study area showing azimuthal ray coverage for a subset of regional phase arrivals from 441 events recorded at 61 seismographic stations.

3-D Grid Travel-Time Calculations and Event Location

We have completed the development of both the preliminary velocity model and a partial database of seismic phases in preparation for the tomographic inversion effort. During the next phase of the study we will begin to invert the travel time data for updates to the preliminary model and locations of events. One initial task prior to performing a full tomographic inversion includes comparing travel times calculated using the IASPEI91 or other regional 1-D models versus those computed using our model. Presently we are using a 3-D travel time eikonal equation method to calculate travel times through the preliminary model (Podvin and Lecomte, 1991). This method relies on a finite difference approximation of Huygen's principle, which explicitly takes into account the existence of different propagation modes (e.g. transmitted and diffracted body waves, head waves). A great advantage the method has over traditional ray-tracing methods is that it is designed to compute the travel time from a source to every point on a 3-D grid. Further, the method does not require the model to have only smooth velocity variations; it can deal with discontinuities and high velocity contrasts.

The eikonal finite-difference algorithm requires our velocity model to be discretized onto a square, 3-D grid. To maintain reasonable file sizes, we have modified the grid of our model to cover 10 km intervals in latitude, longitude and depth. This required losing some resolution with depth and producing finer grid spacing laterally through linear interpolation. We have calculated travel times to every point in a grid of our preliminary velocity model from the location of the station at Nilore, Pakistan (NIL). We also created a similar pair of velocity and travel time grids using the IASPEI91 model, which we adapted into the correct format for the 3-D travel time algorithm. By subtracting the resultant grid of travel times for the IASPEI91 model from the grid of travel times for our preliminary velocity model, we predict travel time residuals that are consistent with other observations for this region (e.g. Murphy *et al.*, 1998). These results for the surface layer of the grid are shown in Figure 6, where the residuals are on the order of 4 to 6 seconds for shallow events in regions where the Moho is quite deep (the Hindu-Kush, Pamir, and the Karakoram). This residual shrinks to near zero for deep events, which is to be expected since our model currently merges with the IASPEI91 model below 80 km. These

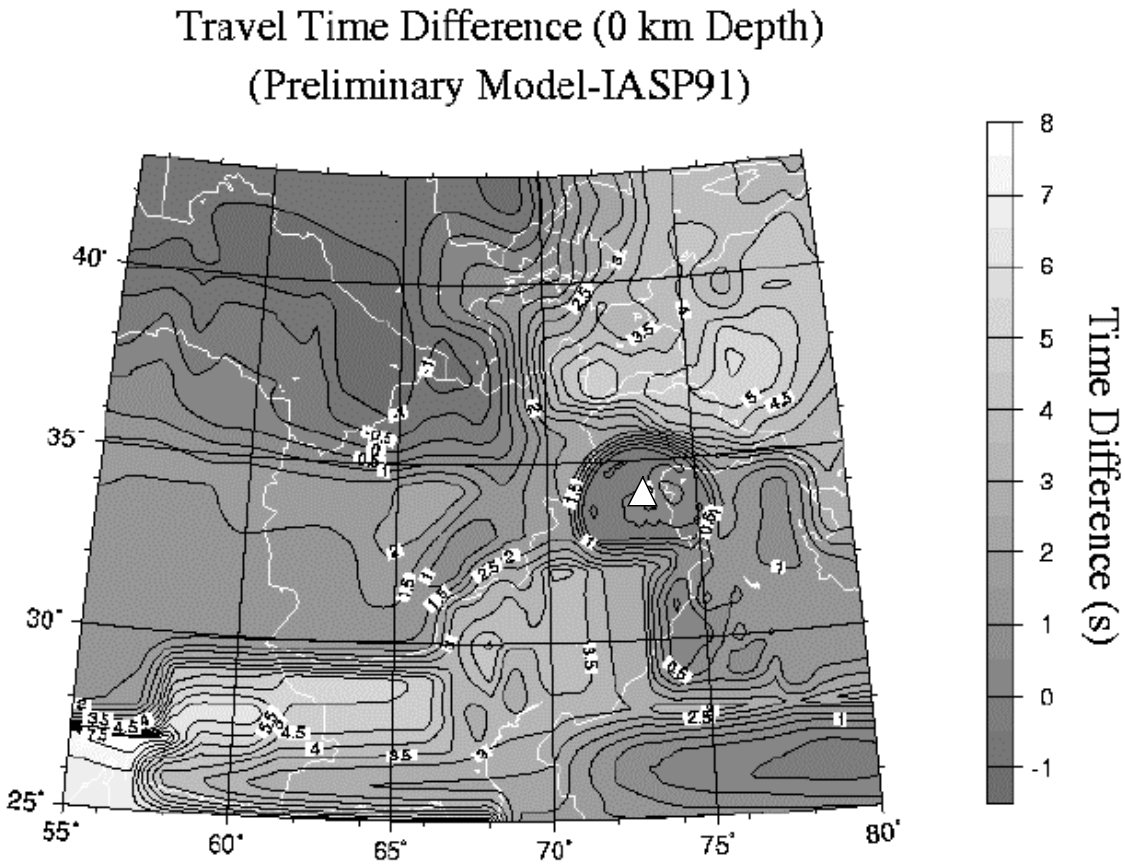


Figure 6. Travel-time differences calculated for station NIL between our preliminary velocity model and the IASPEI91 model at 0km depth. The triangle at 33.65 ^{o} E, 73.25 ^{o} N represents the location of station NIL.

results are encouraging, as they indicate our preliminary model is reasonable. The travel time grid also represents a rudimentary, though unvalidated, form of source station specific corrections (SSSCs) surrounding station NIL. As a subsequent task, we have begun performing event relocations with the preliminary 3-D model and a grid-search location method. This will allow us to estimate the reduction in travel time residuals and determine the tomographic signal we will use to update the velocity model.

CONCLUSIONS

During the first nine months of this study, we have completed the development of a preliminary velocity model of the Pakistan region and a partial database of seismic phases. We are currently beginning the joint tomographic inversion and relocation effort using 3-D, eikonal finite difference methods and a grid-search location method. The first phase of that work will involve identifying the tomographic signal that will be used to update our velocity model from our current database of seismic phase arrival times. We are encouraged by the spatial distribution of ray coverage provided by our preliminary database of seismic phases, and feel we will be able to improve on our preliminary velocity model significantly. Development of our India/Pakistan database will continue as an ongoing effort, and we anticipate including as many of the current catalog of 3600 events as possible. The data collection will be tailored to optimize available ray coverage and arrival time quality, and we hope that the database will serve as an excellent source of data for both current and future investigations in the region.

REFERENCES

Byrne D. E., L. R. Sykes, and D. M. Davis (1992), Great thrust earthquakes and aseismic slip along the plate boundary of the Makran Subduction Zone, *J. Geophys. Res*., 97 (B1), p. 449-473.

Fan G., J. F. Ni, and T. C. Wallace (1994), Active tectonics of the Pamirs and Karakorum, *J. Geophys. Res*., 99 (B4), p. 7131-7160.

Jadoon I. A. K. and A. Khurshid (1996), Gravity and tectonic model across the Sulaiman foldbelt and the Chaman fault zone in western Pakistan and eastern Afghanistan, *Tectonophysics*, 254, p. 89-109.

Kennett B. L. N. and E. R. Engdahl (1991), Traveltimes for global earthquake location and phase identification, *Geophys. J. Int.,* 105, p. 429-465.

Mangino S. and K. Priestley (1995), The crustal structure of the southern Caspian region, *Geophys. J. Int.,* 133, p. 630-648.

Mellors R. J., G. L. Pavlis, M. W. Hamburger, H. J. Al-Shukri, and A. A. Lukk (1995), Evidence for a high-velocity slab associated with the Hindu Kush seismic zone, *J. Geophys. Res.,* 100 (B3), p. 4067-4078.

Murphy J. R., R. W. Cook, and W. L. Rodi (1998), Improved focal depth determinations for use in CTBT monitoring, Proceedings of the 20th Annual Seismic Research Symposium on Monitoring a Comprehensive Test Ban Treaty, p. 255-264.

Podvin, P. and I. Lecomte (1991), Finite difference computation of traveltimes in very contrasted velocity models: a massively parallel approach and its associated tools, *Geophys. J. Int*., 105, p. 271-284.

Priestley K. (1997), An integrated study of lithospheric structure, regional seismic wave propagation, and seismic discrimination capability in the Middle East, Final Technical Report PL-TR-97-2161.

Yang X. and C. Romney (April 1999), pIDC Ground Truth (GT) Database, Technical report, Center for Monitoring Research, CMR Technical Report CMR-99/15.

IDENTIFICATION OF LOW-MAGNITUDE SEISMIC DISTURBANCES USING REGIONAL OBSERVATIONS IN THE KARA/BARENTS SEA REGION

David Bowers, AWE Blacknest

Sponsored by United Kingdom Atomic Weapons Establishment

ABSTRACT

Earthquakes have been identified successfully by demonstrating that the *P*-seismograms, observed at long range (>3000 km), are consistent with the radiation pattern expected from a double-couple moment tensor. However, for small seismic disturbances, the only signals available will be those recorded at local and regional distances (<3000 km). Seismograms recorded at regional distances are generally difficult to interpret as the propagation path through the heterogeneous crust and upper mantle results in complex signals. Thus, the radiation pattern can rarely, if ever, be inferred from regional observations. We have calculated mean *P* and *S* amplitude spectra by stacking the spectra at each element of the array at SPITS (Spitsbergen, Norway, distance 1270 km) using signals from the 16 August 1997 seismic disturbance in the Kara Sea (OT 02:10:59.7 UTC, 3.2mb, PDE). The spectra show clear signal-above-noise in the frequency range 2 to above 15 Hz. Assuming an ω^{-2} source spectrum, the spectra show a slower fall-off with frequency than that predicted by "shield" regional attenuation models for *Pn*, such as those determined by Sereno *et al.* (1988) for Scandinavia [who assume frequency-independent geometrical spreading, with $Q_{Pn}(f) = 325\, f^{0.48}$], and by Chun *et al.* (1989) for the Canadian Shield [who assume both attenuation and geometrical spreading are frequency dependent, with *Pn* amplitude decaying as Δ^{-n}, where $n = 2.17 + 0.022\, f$]. Thus, attenuation across the Barents Sea is much lower than for these models. We obtain a reasonable fit to the observed spectra, using frequency-independent *Q* values of $Q\alpha = 9000$, and $Q\beta = 4000$. We have also examined the spectra of *P* and *S* recorded at KEV (Kevo, Finland) from the 16 August disturbance and find that attenuation is also low for this path. *Pn* and *Sn* on the vertical, radial, and transverse components at SPITS, KEV and AMD (Amderma) show weak cross-component scattering. Thus, *P* and *S* propagate efficiently in the Kara/Barents Sea region, suggesting that the radiation pattern may be inferred for the 16 August 1997 disturbance. We apply a grid-search method to identify moment tensors that are consistent with the observed three-component seismograms at SPITS, KEV and AMD, and with the *P*-seismograms observed at the array stations HFS (Hagfors, Sweden) and NORES (Norway). We conclude that the observed relative *S*-amplitudes (*SV/SH*) and *P* first-motions (positive at HFS and NORES) are consistent with a double-couple moment tensor.

Key Words: regional *Pn* and *Sn* attenuation, Kara/Barents Sea Region, focal mechanisms

OBJECTIVE

To develop a discriminant for the Kara/Barents Sea region, based on the differences in P and S radiation patterns from earthquakes and explosions, to determine whether the 16 August 1997 3.3 m_b OT 02:11 UTC seismic disturbance can be positively identified as an earthquake.

RESEARCH ACCOMPLISHED

Introduction

At around 02:11 UTC on 16 August 1997 there was a small seismic disturbance (3.3 m_b) in the vicinity of the northernmost test site at Novaya Zemlya (NNZ). The epicentre of the disturbance (e.g., Israelsson *et al.* 1997) is in the Kara Sea, about 100 km from NNZ (Fig. 1), thus the disturbance is likely to have been an earthquake. However, initial reports in the press (e.g., Washington Times, 28 August 1997) suggested that the disturbance has 'explosion-like characteristics' that may indicate a Russian low-yield nuclear test at NNZ. Such reports of possible low-yield tests at NNZ are not uncommon (e.g., van der Vink and Wallace, 1996; Ryall *et al.*, 1996). Thus, it seems that identification with high confidence of small ($M_L < 4.0$) seismic disturbances in the vicinity of known nuclear test sites is an important issue in the context of monitoring compliance with the Comprehensive Nuclear-Test-Ban Treaty (CTBT).

Unfortunately, signals from small ($M_L < 4.0$) seismic disturbances are too weak to be detected at long range (teleseismic distances), so an alternative to common teleseismic discriminants, such as $m_b : M_s$, is required. This led to a major research effort, especially by the United States, directed at developing methods of identifying small seismic disturbances using seismograms recorded at regional distances where signals are typically detected from $M_L > 2.5$ disturbances at distances of up to 2000 km (see Blandford (1996) for a recent review).

Blandford (1996) concludes that S/P ratios at high frequencies ($f > 2$ Hz) are a promising discriminant (where S refers to the group of phases arriving at, and after, S_n). However, each regional phase needs to be corrected for path (distance Δ) and station effects before phase ratios can be applied as a discriminant. These corrections are usually a complicated function of frequency, predominantly due to heterogeneity in the crust and upper mantle. High-frequency signals are also desirable as decoupling factors (the muffling of an explosion by detonation in a large gas-filled cavity) are typically an order of magnitude lower at 20 Hz than at 1 Hz (e.g., Sykes, 1996).

Several authors have identified the 16 August 1997 disturbance as an earthquake using both the location and high-frequency S/P ratios measured from the vertical component (Richards and Kim, 1997, Hartse, 1998, Baumgardt, 1998). Bowers *et al.* (1998) also argue that the 16 August 1997 disturbance is an earthquake on the basis of high-frequency S/P ratios measured from three-component seismograms recorded at KEV (Kevo, Finland) and SPITS (Spitsbergen), and from a comparison of P_n waveforms recorded at NORSAR (southwest Norway) from an earthquake on 1 August 1986 in the Kara Sea (Marshall *et al.*, 1989), and a small explosion (4.2 m_b) on 26 August 1984 at NNZ. However, Ringdal and Kremenetskaya (1999) present evidence that the high-frequency S/P discriminant is unreliable in the Kara/Barents Sea region (although they only analyse S/P ratios from the vertical component) and thus claim that the 16 August 1997 disturbance cannot be identified using seismological observations.

Here, we take a different approach and show that, because P_n and S_n propagation is efficient within the Barents/Kara Sea region, the radiation pattern from the 16 August 1997 disturbance may be inferred. Thus, we can test if the seismograms observed at KEV, SPITS, HFS (Hagfors, Sweden) and NORES (Norway) are consistent with a double couple (earthquake) source.

Observations of P_n and S_n at SPITS and KEV

Fig. 2 shows the results of passing the seismogram recorded at SPA0, within the small-aperture SPITS array, from the 16 August 1997 disturbance, through a bank of bandpass filters. The signal-to-noise ratio remains reasonably constant with increasing frequency, suggesting that the spectral amplitude of the seismic noise at high frequencies is falling off at a similar rate to that of P_n. Also S_n is observed above the noise (P_n coda) at least up to frequencies of 14 Hz.

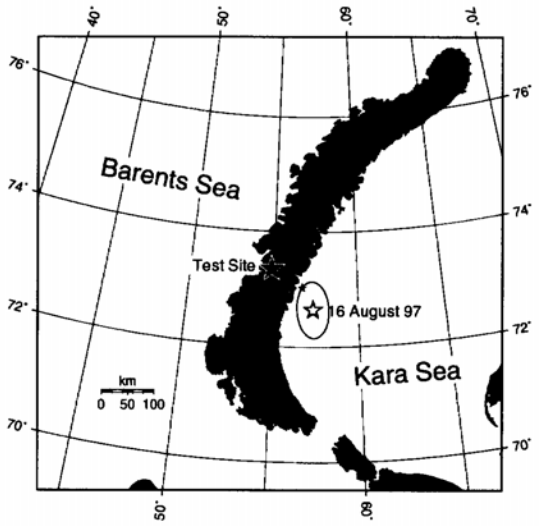


Figure 1: The preferred location of Israelsson *et al.* (1997) for the 16 August 1997 disturbance [72.645°N, 57.369°E]. This is about 50 km from a 4.3 m_b earthquake that occurred on 1 August 1986 (small star). The ellipse marks the 90% confidence interval, and suggests that the 16 August disturbance is located in the Kara Sea (water depth about 250 m), at least 60 km from the NNZ test site.

Fig. 2 also shows time windows containing P_n, S_n and noise samples. Since the amplitudes of P_n and S_n do not appear to vary significantly within each time window we follow Chael (1987) and assume that P_n and S_n are approximately stationary, and that at a distance of 1280 km P_g and S_g do not contribute significantly to P_n and S_n in the defined windows. We then calculate power spectra using a 5% Hanning tapered window of 1024 points (25.6 sec. duration) for each element of the array. We then follow Bache *et al.* (1985) and estimate the average normalised amplitude spectrum, by smoothing each power spectrum with a three-point moving average, calculating the mean of the power spectra, and taking the square-root. The resulting normalised amplitude spectra for P_n, S_n and noise samples are shown in Fig. 3.

The large signal-to-noise ratio of P_n above 5 Hz in Fig. 3 suggests that, (1) SPITS is a low noise site at high frequencies (this is consistent with noise spectra calculated by Anonymous (1995) for SPA0), and (2) there appears to be little attenuation of P_n from the Kara Sea to SPITS. We show the second point quantitatively in Fig. 3 by comparing the observed spectra with theoretical spectra calculated assuming the w-square earthquake source model and published estimates of P_n attenuation.

Fig. 3 shows the spectral decay above the corner frequency (assumed to be 4 Hz) predicted by the w-square source model, along with the spectral decay due to the source model and three attenuation models: (1) a constant Q_{P_n} (frequency-independent attenuation operator) of 9000 (Evernden *et al.*, 1986), (2) the frequency-dependent attenuation operator $Q_{P_n}(f) = 325f^{0.48}$ obtained by inversion of P_n spectra recorded in Scandinavia by Sereno *et al.* (1988), and (3) the spectral decay of P_n due to the combined effects of frequency-dependent attenuation and geometrical spreading ($\Delta^{-(2.17+0.022f)}$) determined by Chun *et al.* (1989) for the Canadian shield.

The spectra in Fig. 3 suggest that P_n attenuation along the path from the 16 August 1997 epicentre in the Kara Sea to SPITS is effectively negligible – a remarkable observation given the epicentral distance of 1280 km. Fig. 3 shows the observed S_n spectral decay along with the w-square model, and a constant Q_{S_n} of 4000. Baumgardt (1998) claims that there is strong S_n attenuation along the path from the Kara

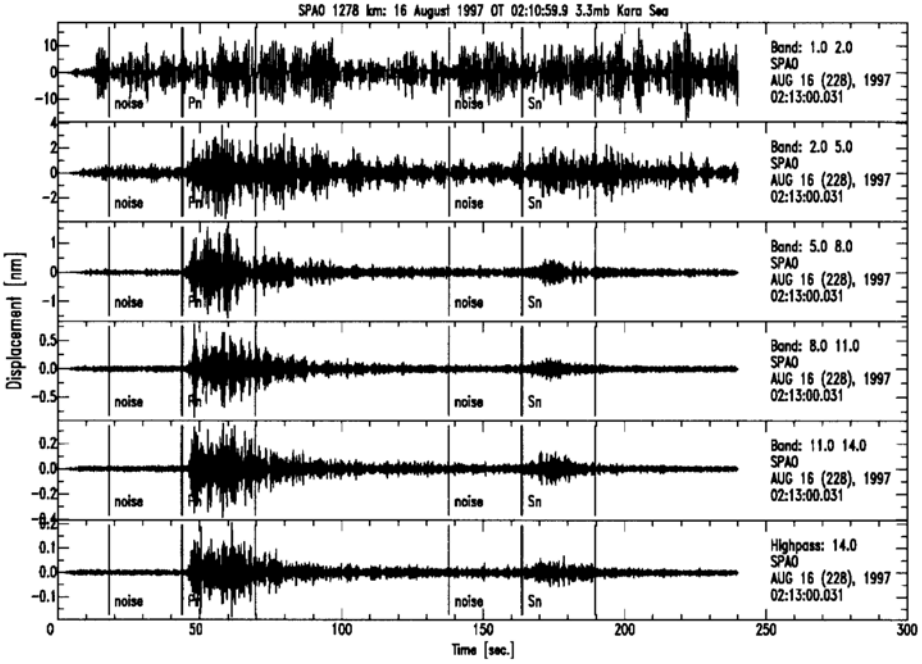


Figure 2: Bandpass filtered seismograms recorded at SPA0 from the 16 August 1997 disturbance. The response of the Guralp CMG3ES seismograph has been deconvolved to give estimates of the vertical component of ground displacement (within the passband of each 5-pole Butterworth filter)

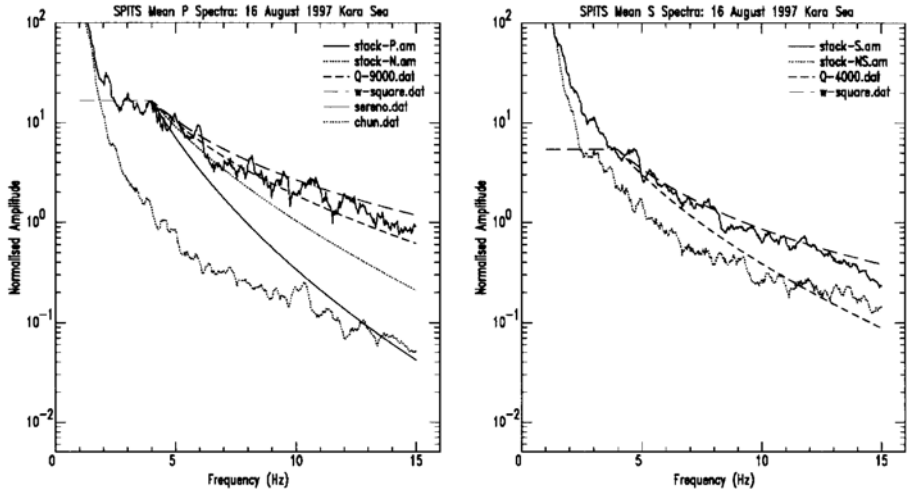


Figure 3: P_n, S_n and noise spectra calculated for the SPITS array, compared with attenuation models discussed in the text.

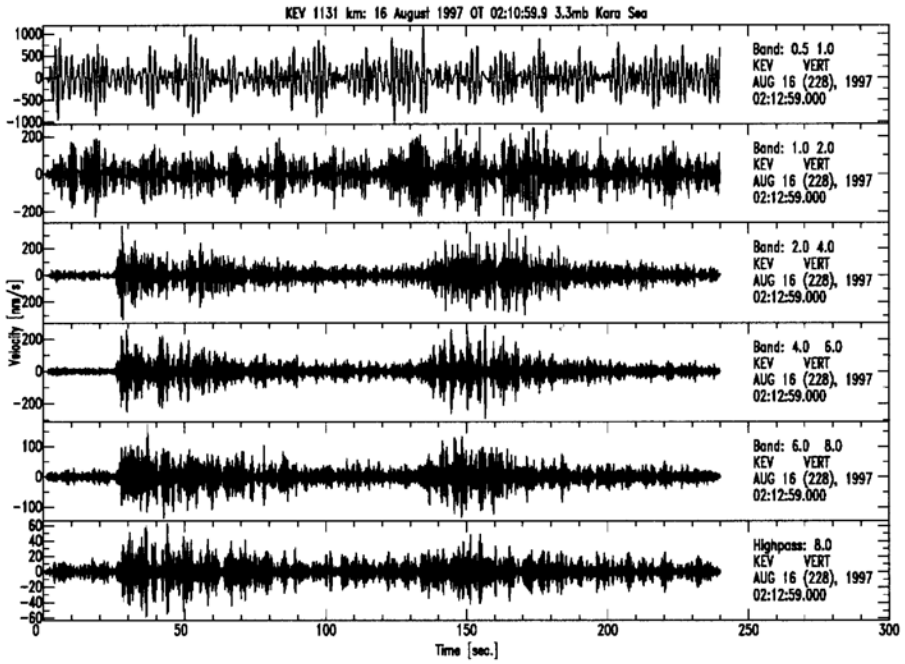


Figure 4: Bandpass filtered seismograms recorded at KEV from the 16 August 1997 disturbance.

Sea to SPITS. However, the spectra in Fig. 3 suggest weak attenuation of S_n with $Q_{S_n} > 4000$.

Fig. 4 shows the results of passing the vertical-component seismogram recorded at KEV ($\Delta = 1130$ km) through a bank of bandpass filters. While the Nyquist frequency is at 10 Hz, there is still significant P_n and S_n energy in the above 8 Hz passband, indicating weak P_n and S_n attenuation along the path from the Kara Sea to KEV.

Free-Surface Corrected Three-Component Seismograms at SPITS and KEV

We correct the three-component seismograms recorded at KEV and SPB4 (within the SPITS array) for the effect of the free surface in order to recover estimates of P, SV and SH at the receiver. Kim *et al.* (1997) give expressions to derive P, SV and SH from the vertical, radial and transverse components. These require the P and S angles of emergence and the ratio of the S and P wave speeds (β/α).

The frequency-wavenumber spectra for P_n and S_n at the SPITS array (between 2.5 and 3.5 Hz), calculated using the high resolution method of Capon (1969), suggest a P_n slowness of 0.13 s km^{-1}, and an S_n slowness of 0.18 s km^{-1}. The amplitude of S_n at SPB4 is weak on the vertical component compared with the radial, implying a small S_n angle of emergence. Thus, S/P ratios measured from the vertical component at SPITS will be much lower than S/P from the free-surface corrected three-component seismograms at SPB4. The relative amplitude of S_n on the vertical and radial components at SPB4, and the observed S_n slowness at SPITS, suggest low wave-speeds within the surface layer. We assume $\alpha = 2.5$ km s^{-1} and $\beta = 1.2$ km s^{-1}; this gives estimates of the P_n and S_n emergent angles of 19° and 12° respectively.

At KEV we cannot measure the P_n and S_n slownesses directly, so we apply the approximate free-surface corrections for P_n and S_n derived by Kennett (1991). We use the P_n-slowness to calculate the free-surface corrections for the portion of the seismograms with group velocities greater than 5.0 km s^{-1}, and the S_n-slowness for the corrections to the remaining portion of the seismograms.

Figures 5 and 6 show the complex envelopes of the resulting free-surface corrected seismograms. At

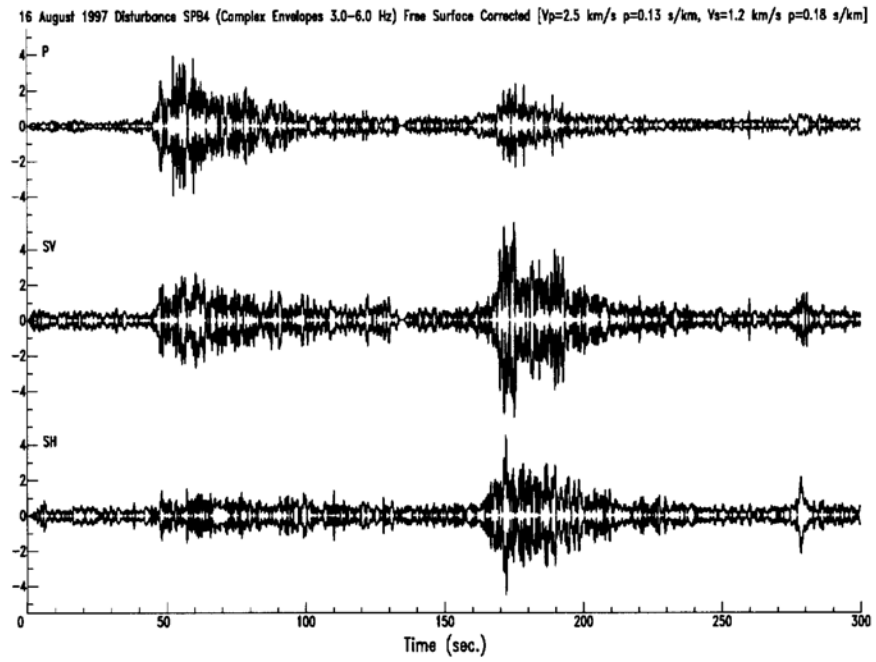


Figure 5: Complex envelopes of free-surface corrected three-component seismograms recorded at SPB4

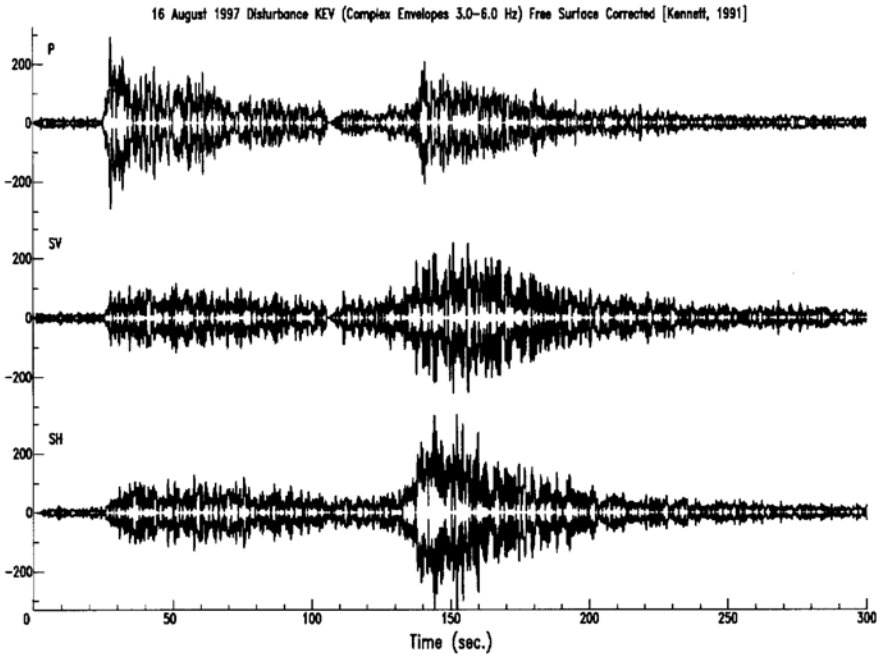


Figure 6: Complex envelopes of free-surface corrected three-component seismograms recorded at KEV.

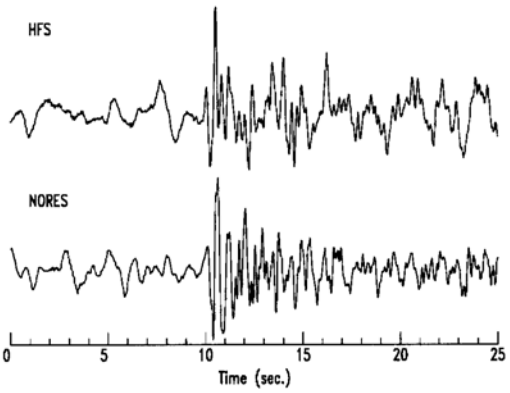


Figure 7: Beamformed P-seismograms recorded at HFS and NORES showing clear positive first-motion (P-onset is at 10 sec.).

about the P_n arrival time there is little P-energy on the SV and SH components. This indicates that cross-component scattering along the paths to SPB4 and KEV is weak, which combined with the weak attenuation demonstrated above, shows that P_n and S_n propagation is efficient in the Kara/Barents Sea region. Thus, we conclude that the relative amplitudes of the SV and SH complex envelopes relate to S-radiated by the 16 August 1997 disturbance, and so can be used to infer the source radiation pattern.

Inversion for the Focal Mechanism

We test if there is an orientation of the double-couple (earthquake) source that is consistent with the observations, and thus determine if the data from the 16 August disturbance are consistent with an earthquake given reasonable assumptions about the source structure.

We measure the maximum amplitude of the complex envelopes in Figures 5 and 6 to estimate the relative amplitudes of SV/SH at SPB4 and KEV (Schwartz, 1995). We also measure the amplitude of P at HFS and NORES (Fig. 7), and note that there are no arrivals with amplitude greater than P, thus we conclude that the pP and sP amplitude at the station is smaller than P. The first-motion of P at HFS and NORES is positive (compressional).

Table 1 gives the amplitude bounds we have placed on our measured amplitudes to account for uncertainties in our measurements (Pearce, 1977). We calculate frequency-wavenumber spectra for P_n at HFS and NORES, and estimate the slownesses as 0.09 s km^{-1} and 0.08 s km^{-1} respectively. We calculate the take-off angles of P and S, using our estimated slownesses, assuming a Poisson source layer with

	Slowness (s km^{-1})		Pol.	Min.	Max.	Pol.	Min.	Max.	Pol.	Min.	Max.
	P_n	S_n		P			pP			sP	
HFS	0.09		+	8.0	10.0	U	0.0	8.0	U	0.0	8.0
NORES	0.08		+	8.0	10.0	U	0.0	8.0	U	0.0	8.0
				SV			SH				
SPB4	0.13	0.18	U	4.4	5.2	U	3.5	4.3			
KEV	0.11	0.22	U	3.2	4.0	U	4.4	5.2			

Table 1: The relative amplitude bounds of the SV, SH, P, pP, and sP phases. The polarity of each phase is: + compression, U unknown. The take-off angle is calculated using the slowness assuming a Poisson source layer with a P-wave speed of 6.5 km s^{-1}.

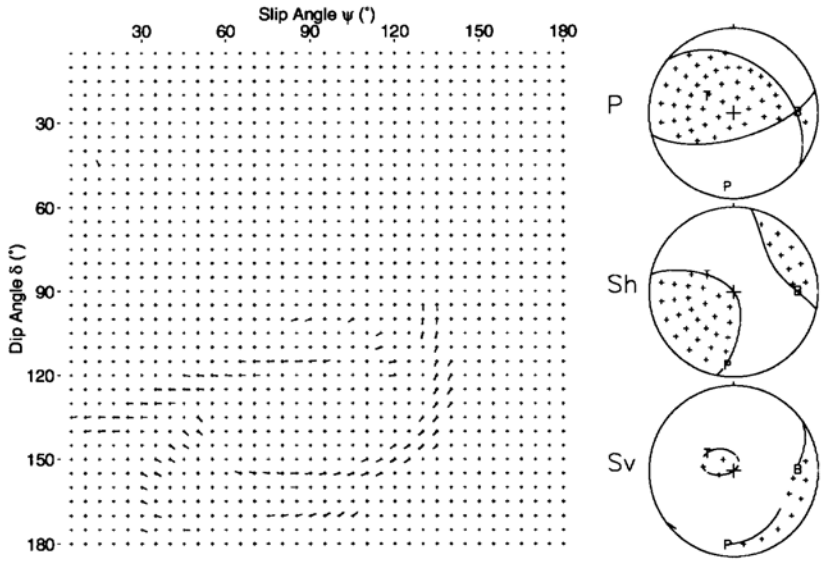


Figure 8: [left] Vectorplot of Pearce (1977) showing the orientation (σ strike measured clockwise from north, δ dip angle, ψ slip angle) of double couples that are consistent with the SV, SH, P, pP and sP bounds in Table 1. [right] Lower hemisphere focal plots showing the P, SV and SH nodal planes of our preferred focal mechanism ($\sigma = 255°$, $\delta = 115°$, $\psi = 120°$).

$\alpha = 6.5$ km s^{-1} (Table 1). While these take-off angles are reasonable for a source located in the middle of a continental-type crust, we acknowledge there is probably large uncertainty in these values. We then grid-search for orientations of the double couple that are consistent with the amplitude bounds in Table 1, using increments of 5° in strike (σ), dip (δ) and slip (ψ), calculating SV/SH, pP/P and sP/P amplitude ratios at each grid-point. This procedure is a modification of the relative amplitude method of Pearce (1977, 1980).

Fig. 8 shows the orientations of a double couple that are consistent with the amplitude bounds in Table 1 plotted on a vectorplot (Pearce, 1977) ($\delta > 90°$ indicates reverse-type faulting). The vectorplot allows the whole range of consistent solutions to be displayed, and shows both the fault and auxiliary planes of the double couple (the two are indistinguishable as we assumed a point source when calculating the P, SV and SH radiation patterns).

Consideration of the P, SV and SH radiation coefficients of the solutions in Fig. 8 suggests that a reasonable fit to the observed relative amplitudes is obtained with $\sigma = 255°$, $\delta = 115°$, $\psi = 120°$ (Fig. 8). This solution is similar to that determined by Marshall *et al.* (1989) for the 1 August 1986 Kara Sea earthquake (their model II solution is $\sigma = 253°$, $\delta = 130°$, $\psi = 147°$). Also, the P-radiation coefficient for our preferred focal mechanism is 0.04 to NRI (Norilsk, Russia, $\Delta = 1180$ km, Az. = 95°), suggesting that the emergent P_n, with poor signal-to-noise ratio, reported for this station (Baumgardt, 1998) can be explained by weak P-radiation, rather than by poor P_n propagation across the Kara Sea. The P-radiation coefficients to HFS and NORES are 0.65 and 0.74 respectively, perhaps explaining why clear P_n signals are observed at these far-regional stations from the 16 August 1997 disturbance.

CONCLUSIONS AND RECOMMENDATIONS

Our analysis of high-frequency three-component P_n and S_n at SPITS and KEV, from the 16 August 1997 disturbance, shows that P_n and S_n propagation across the Kara/Barents Sea is efficient. A comparison of S_n amplitudes on the vertical and radial components at SPB4, suggests that the S_n emergent angle is small. Thus, S/P ratios measured from the vertical component at SPITS will be smaller (more explosion-like) than S/P measured from free-surface corrected three-component seismograms. We have calculated the complex envelopes of free-surface corrected three-component seismograms at SPB4 and KEV to estimate P, SV and SH at each station. We use the maximum amplitude of the complex envelopes of SV and SH at SPB4 and KEV, along with P_n at HFS and NORES, to determine a range of focal mechanisms (double couples) that are consistent with the observed relative amplitudes of SV/SH, pP/P and sP/P. After consideration of the radiation coefficients of P, SV and SH our preferred solution ($\sigma = 255°$, $\delta = 115°$, $\psi = 120°$) is similar to that determined by Marshall *et al.* (1989) for the 1 August 1986 Kara Sea earthquake. The P-radiation coefficient to NRI is 0.04, suggesting that the reported emergent nature of P_n at NRI from the 16 August 1997 disturbance can be explained by weak P-radiation to this station, rather than by poor P_n propagation across the Kara Sea.

Digital three-component data exists for AMD (e.g., Ringdal and Kremenetskaya, 1999), but has yet to be released. We eagerly await the release of these data, in order to refine the focal mechanism determined above, and to verify that the corner frequency of 4 Hz, assumed to determine the attenuation at SPITS, is reasonable.

REFERENCES

Anonymous (1995). Conference room paper/243 Norway. Group of Scientific Experts: Volume Three Facilities.

Bache, T.C., P.D. Marshall, and L.B. Bache (1985). Q for teleseismic P waves from Central Asia. *J. Geophys. Res.*, **90**, 3575–3587.

Baumgardt, D.R. (1998). Special event discrimination analysis: the TEXAR blind test and identification of the August 16, 1997 Kara Sea event. Technical Report AFRL-VS-RA-TR-98-0049.

Blandford, R.R. Regional seismic event discrimination. In Husebye, E.S. and A.M. Dainty, editors, *Monitoring a Comprehensive Test Ban Treaty*, pages 689–719. Kluwer, London, 1996.

Bowers, D., H. Trodd, and A. Douglas (1998). The Novaya Zemlya seismic disturbance of 16 August 1997. AWE Report No. O-1/97. HMSO, London.

Capon, J. (1969). High-resolution frequency-wavenumber spectrum analysis. *Proc. IEEE*, **57**, 1408–1418.

Chael, E.P. (1987). Spectral scaling of earthquakes in the Miramichi region of New Brunswick. *Bull. Seism. Soc. Am.*, **77**, 347–365.

Chun, K.Y., R.J. Kokoski, and G.F. West (1989). High frequency P_n attenuation in the Canadian shield. *Bull. Seism. Soc. Am.*, **79**, 1039–1053.

Evernden, J.F., C.B. Archambeau, and E. Cranswick (1986). An evaluation of decoupling and underground nuclear test monitoring using high frequency seismic data. *Rev. Geophys.*, **24**, 143–215.

Frohlich, C. (1996). Cliff's nodes concerning plotting nodal lines for P, SH and SV. *Seism. Res. Lett.*, **67**, 16–24.

Hartse, H.E. (1998). The 16 August 1997 Novaya Zemlya seismic event as viewed from GSN stations KEV and KBS. *Seism. Res. Lett.*, **69**, 206–215.

Israelsson, H., M.D. Fisk, X. Yang, and R.G. North (1997). The August 16, 1997 event in the Kara Sea. Technical Report CMR-97/38.

Kennett, B.L.N. (1991). The removal of free surface interactions from three-component seismograms. *Geophys. J. Int.*, **104**, 153–163.

Kim, W.-Y, V. Aharonian, L. Lerner-Lam, and P.G. Richards (1997). Discrimination of earthquakes and explosions in Southern Russia using regional high-frequency three-component data from the IRIS/JSP Caucasus network. *Bull. Seism. Soc. Am.*, **87**, 569–588.

Marshall, P.D., R.C. Stewart, and R.C. Lilwall (1989). The seismic disturbance on 1986 August 1 near Novaya Zemlya: a source of concern? *Geophys. J.*, **98**, 565–573.

Pearce, R.G. (1977). Fault plane solutions using relative amplitudes of P and pP. *Geophys. J. R. astr. Soc.*, **50**, 381–394.

Pearce, R.G. (1980). Fault plane solutions using relative amplitudes of P and surface reflections: further studies. *Geophys. J. R. astr. Soc.*, **60**, 459–487.

Richards, P.G. and W.-Y. Kim (1997). Testing the nuclear test-ban treaty. *Nature*, **389**, 781–782.

Ringdal, F. and E. Kremenetskaya (1999). Observed characteristics of regional seismic phases and implications for P/S discrimination in the Barents/Kara Sea region. NORSAR Sci. Rep. 2-98/99.

Ryall, A.S., D.R. Baumgardt, M.D. Fisk, and F. Riviere-Barbier. Resolving regional discrimination problems: some case histories. In Husebye, E.S. and A.M. Dainty, editors, *Monitoring a Comprehensive Test Ban Treaty*, pages 721–741. Kluwer, London, 1996.

Schwartz, S. (1995). Source parameters of aftershocks of the 1991 Costa Rica and 1992 Cape Mendicino, California, earthquakes from inversion of local amplitude ratios and broadband waveforms. *Bull. Seism. Soc. Am.*, **85**, 1560–1575.

Sereno, T.J., S.R. Bratt, and T.C. Bache (1988). Simultaneous inversion of regional wave spectra for attenuation and seismic moment in Scandinavia. *J. Geophys. Res.*, **93**, 2019–2035.

Sykes, L.R. Dealing with decoupled nuclear explosions under a Comprehensive Test Ban Treaty. In Husebye, E.S. and A.M. Dainty, editors, *Monitoring a Comprehensive Test Ban Treaty*, pages 247–293. Kluwer, London, 1996.

van der Vink, G.E. and T.C. Wallace (1996). The political sensitivity of earthquake locations. *IRIS Newsletter*, **15**, 20–23.

Wessel, P. and W.H.F. Smith (1991). Free software helps map and display data. *EoSTrans., AGU.*, **72**, 441, 445–446.

Acknowledgements

Waveform data were kindly provided by the prototype International Data Center, Arlington, and by Matti Tarvainen (University of Helsinki). The Seismic Analysis Code (LLNL), the GMT mapping package (Wessel and Smith, 1991) and Cliff Frohlich's 'nodes' program (Frohlich, 1996) were used to prepare the figures. I thank Alan Douglas for many useful discussions.

AUTOMATIC INTERPRETATION OF REGIONAL SEISMIC SIGNALS USING THE CUSUM-SA ALGORITHMS

Zoltan A. Der and Matthew W. McGarvey, Ensco Inc

Robert H. Shumway, University of California at Davis

Sponsor; Defense Threat Reduction Agency
Contract DSWA01-98-C-0155

ABSTRACT

Automatic onset estimation is a desirable goal facilitating the rapid location and discrimination of seismic events, automation also relieves the human operator from onerous repetitive tasks. At regional distances onsets of seismic phases are associated with gradual, rather than sudden, changes in the statistical properties of the seismic time series, i.e. changes in autoregressive models and mean square amplitudes. The work presented combines two aspects of the onset time estimation, the detection of the onset as a change in the trend of the cumulative sum (CUSUM) of a suitable test statistic, and a randomized search for its location, simulated annealing (SA). The latter is applied repeatedly thus resulting in multiple onset time estimates. These typically form clusters around the arrival times of the know seismic phases, but there are some scattered values as well that have to be discarded. The uncertainties in the onset times estimated can be quantified in terms of the spread in the values of the best defined clusters. Various standard cluster analysis methods can be applied to define individual clusters.

During past work we have used cumulative sums of the absolute amplitudes of the trace amplitudes after suitable prefiltering. We have found that for determining Pn onset times the method performed comparable to a human analyst. We have also been successful in picking later regional arrivals, even though many of these were emergent and poorly defined. In the followup work we have changed to the iterative cumulative sum of squares (ICSS), developed by Inclán and Tiao (1996), and applied to suitably prewhitened time series. This method has a better theoretical foundation because it can be justified on the basis of a Gaussian time series model. Our tests showed that it performs comparably to the previously described approach. We are extending this approach to the CUSUM of other time-variable statistics of single and multiple (three-component) time series. The system is presently developed using MATLAB, utilizing its graphical user interface capabilities.

Key Words: onset times, location, discrimination

OBJECTIVE

The objective of this work is to develop automated methods for interpreting regional seismograms.

INTRODUCTION

Automatic phase arrival time estimation is of considerable interest because of the need for rapid location and identification of numerous seismic events by networks monitoring natural and man-made seismic activity. Times of seismic 'phase' arrivals can be defined as time instants where some visible characteristic, such as amplitude, frequency content or wave polarization changes in some recording. Typically, regional arrivals are high frequency, broadband, emergent wave groups containing numerous cycles. Later arrivals generally have no clear, impulsive waveforms and are preceded by the codas of earlier ones and their onset times can only be defined to within a few cycles. Besides locating events from multiple Pn times, onset time estimation is useful in facilitating location using multiple arrivals in the same seismogram and in automated application time and frequency domain discriminants.

GENERAL STATISTICAL BACKGROUND.

There are numerous statistical approaches in the literature to determining the arrival time of 'phases'. Onsets of packets of seismic energy associated with various paths, i.e. seismic phases, are usually associated with sudden changes in amplitudes, spectra, polarization and slowness. Generally it is assumed that it is known that the change occurs somewhere in a predefined time interval and that the statistical model of the time series changes abruptly. It is usually assumed that the time series are stationary before and after such a change and that the statistical distributions are multivariate Gaussian (e.g. Basseville and Nikiforov 1993). A popular approach is to test for changes in single- or multi-channel autoregressive models to the data of the form

$$\mathbf{x}(t) = \sum_{k=1}^{p} \mathbf{A}_k \, \mathbf{x}(t-k) + \mathbf{e}(t)$$

where $\mathbf{x}(t)$ is the multidimensional time series, the constants in matrix $\mathbf{A}_k$ are regression coefficients and $\mathbf{e}(t)$ is a stationary noise vector process. The number of channels p in various applications may be one (a single seismic channel), three (three component station) or many (a seismic array). In this process the autoregressive parameters $\mathbf{A}_k$ will have to be estimated (Pisarenko et al 1987). The determination of the onset times is based on residuals $\mathbf{r}$ of the autoregressive models computed by using the estimated autoregressive parameters

$$\mathbf{r}(t) = \mathbf{x}(t) - \sum_{k=1}^{p} \overline{\mathbf{A}}_k \, \mathbf{x}(t-k)$$

Depending on the autoregressive models applied one may test for spectral and amplitude changes (single channnel model), slowness changes (multichannel model applied to array sensor outputs) or polarization (three-channel model) as described by Kushnir (1996). The model fitting can be performed for each guess of the onset time (Taylor et al 1992, Takanami 1991) or the fit to two fixed models fitted at each side of the possible arrival times may be used (Kvaerna 1966a,b). The minimum of the summed residuals occurs when two models are fitted such that the boundary of the fitting regions correspond to the onset time. In any case the estimation process decreases the degrees of freedom in the process, thus decreasing the stability and its sensitivity. Common to all these methods is the assumption that the time interval where the phase onset occurs is known and there are sufficient segments of the time series preceding and following the onset for effect the estimation models.

The approach described above is quite general and is applicable to many kind of problems involving changes in time series. Regardless what kind of test statistic is used for detecting changes a steplike change can be detected easier if a cumulative sum (CUSUM) of it is computed (Der and Shumway 1999, Iclan and Tiao 1994, Basseville and Nikiforov 1993, Shumway 1998), after the application of appropriate prefilters. After imposing a linear trend to the CUSUM, a repetitive onset time estimation is performed, locating the minima of the resulting function, by simulated annealing. The clustering in the multiple onset time

estimates provides a means to assess the reliability of the process and the significance of each major arrival. In practical tests the method has outperformed those based testing for changes in autoregressive models.

The approaches based on the cumuative sum statistics are simple to apply and can be automated for applications in a CTBT monitoring environment. Inclan and Tiao (1996) developed a properly centered and normalized CUSUM test statistic and tabulated critical points for testing of significance. Furthermore, they developed an Iterative Cumulative Sum of Squares (ICSS) algorithm that allows sequential identification of multiple changepoints in a white noise series. In this paper we have tested their approach on a set of regional seismic data.

Suppose first that a single channel time series xt, t=1,2,….n is observed and we have a possible changepoint that is to be detected using a CUSUM type statistic. Assume that the time series xt has been prewhitened and has a zero mean, so that the change in regime can be modeled simply by a change in the variance of the white noise process. Inclan and Tiao (1996) proposed using the centered and scaled cumulative sum of the squared amplitudes. First define the sum of squares function over the interval [t1 t2] of length T=t2-t1+1 points as

$$S(t_1,t_2)=\sum_{t=t_1}^{t=t_2} x_t^2$$

The scaled and normalized CUSUM statistic over the interval $[t_1\ t_2]$ at the point $t_1<t<t_2$ is defined as

$$D(t_1,t)=\sqrt{T/2}\left|\frac{S(t_1,t)}{S(t_1,t_2)}-\frac{t}{T}\right|$$

The F statistic for testing for a change of variance at time t is

$$F_{T-t,t}=\left(\left(C_T-C_t\right)/(T-t)\right)\left(C_t/t\right)$$

This is, of course the standard power detector. With no change in variance in the time interval $t1<t<t2$ $D(t_1,t)$ is a monotone function if t. If the variance increases $D(t_1,t)$ will have a maximum at the change point.

If we assume that the x_i are normally distributed with mean 0 and variances σ then we can obtain the likelihoods for testing one change against no change and let $NT=1$ represent one change. The likelihood for $NT=0$ is

$$l\left(N_T=0;x\right)=-\frac{T}{2}\log(2\pi)-\frac{T}{2}\log\left[S(t_1,T)/T\right]-\frac{T}{2}$$

The likelihood function for NT=1, change at point t is

$$l\left(t,N_T=1;x\right)=-\frac{T}{2}\log(2\pi)-\frac{t}{2}\log\left[S(t_1,t)/t\right]-\frac{T-t}{2}\log\left[\frac{S(t_1,T)-S(t_1,t)}{T-t}\right]-\frac{T}{2}$$

The best estimate of the change point is where the likelihood ratio is maximized

$$LR_{0,1}=-\max_t\left\{-\frac{t}{2}\log\left[1+\frac{T}{2}D(t_1,t)-\frac{T-t}{2}\log\left[1-\frac{T}{T-t}D(t_1,t)\right]\right]\right\}$$

The function puts more weight on the middle of the time series. This is not a serious disadvantage since

prior to applying the algorithm one has a fairly good idea where the main regional phases are (from standard detection algorithms and F-K analyses).

The iterative version of the CUSUM algorithm uses a repetitive application of the approach described above for subintervals of the first time interval. The method applies the following steps;

1) Calculate D(t1,tn) from the start to the endpoint of the initial time segment
2) Search for a significant maximum as defined by equation (3). If one is found at t2 then
3) Search the time interval t1<t<t2 for another significant maximum
4) Similarly search the t2<t<tn intervals for a significant maximum
5) Continue the same procedure in other subinterval until no more significant maxima are found.

PRE-FILTERING ISSUES.

Subtle changes in the frequency content in noisy records often give clue to a human indicating the onset of a seismic phase arrival. On the other hand, when such human capabilities are needed it simply indicates a failure of applying appropriate frequency domain prefiltering that could produce an enhanced amplitude contrast between the noise and the arrival. Appropriate prefiltering in frequency is a prerequisite for further onset time determination regardless of the method (Kvaerna 1996a,b). Various schemes for optimum pre-filtering were suggested and most of these seem to work well in practice and the exact nature of filter is not critical as long as they are reasonably close to the optimum S/N^2 shape (averages of signal amplitude spectrum divided by the squared noise amplitude spectrum). Minimum phase filters based on Kvaerna 's definition of "usable bandwidth" (Kvaerna 1995, 1996a), those shaped according to S/N^2 or noise-adaptive predictive filtering all enhance the amplitude contrast between the noise background preceding the onset of the signal. Empirical fixed 'optimum' filters defined for a given region being monitored or path type seem to work as well. Such filters for regional signals will reduce the amplitude of the low frequency noise below 2 Hz, emphasize the band where the S/N is nearly constant, in the 3-10 Hz range, and reduce the low S/N portions of the spectra at very high frequencies. This enhancement of the signal amplitude happens at the expense of decreasing the visible frequency contrast between the signal and noise. This happens because both regional seismic signals and noise have similar spectral shapes in the 3-10 Hz band, they both fall off with frequency.

The CUSUM-based onset time estimation

The CUSUM algorithms described in Basseville and Nikiforov (1993) were designed for pinpointing the time of a change in a system and have their primary applications in quality control and machine diagnostics. The basic idea is detecting *changes in the trends* of the cumulative sum of some suitable statistic that abruptly changes with time as the properties of the time series changeIt is much easier to see and quantify a change in a trend, than to pinpoint the exact time of the first point where the change occurred (such as picking the first large value of a trace processed by a unit-distance predictive filter). The CUSUM-based methods have indeed been used for determining P onset times in the past (Nikiforov and Tikhonov 1986, Nikiforov et al 1989). In this paper we rely on the approach of Inclan and Tiao (1996).

F TESTS.

F tests are standard tools for verifying the arrival of a new package of energy from the source, i. e. a phase arrival. In this work we pick the arrival time from the modified CUSUM D(t) and test whether the variances on both sides of this arrival are indeed different. **Figure 1** shows two examples of this approach as applied to two Kola peninsula events observed at ARCESS. In these examples amplified noise samples were superposed on otherwise clean signals to simulate various S/N ratios. In making F tests appropriate adjustments must be made to account for the effective bandwidths of the signals.

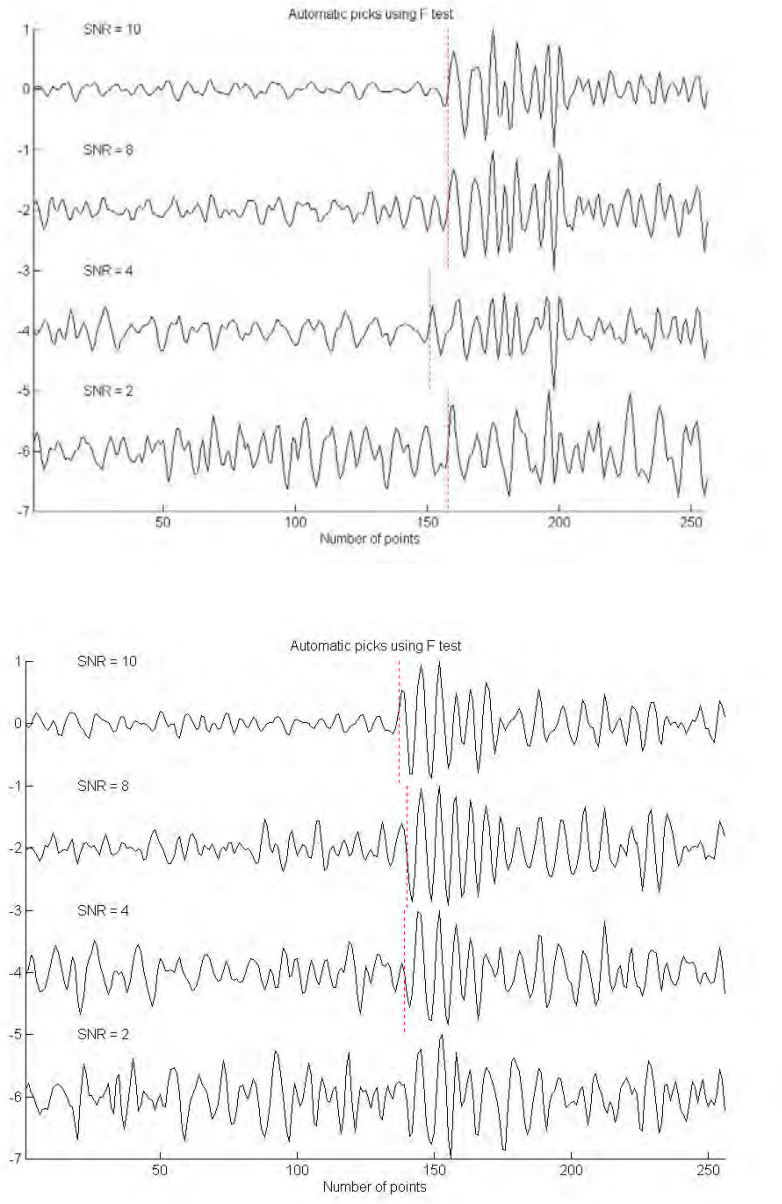


Figure 1. Two examples of F detection of signals under various noise conditions. Amplified noise samples were superposed on otherwise clean signals to simulate various S/N ratios. The F test was applied to the two sides of the window separated by the minimum of the normalized CUSUM statistic D(t). The picks are marked with vertical lines. Only one phase arrival with low S/N was missed.

SIMULATED ANNEALING.

Instead of finding an absolute minimum in the CUSUM-linear trend sum the minimum can also be located by randomized search methods. In the work we have used the method of simulated annealing (SA). SA was designed to find global minima of irregular functions where many local minima may exist. It tends to disregard minor local minima and converge to the lowest points. It uses the randomized Metropolis search algorithm which is based on a thermodynamic analogy (Press et al 1986). Initially it allows the search using large steps in the independent variables which may even be associated with increased values of the function. This allows the solution to "jump out" from local minima and resume search for other minima. As "cooling" occurs such steps are accepted less and less and finally the solution will settle in broad global minima. Repeated application of SA with random starting points will give rise to *populations* of onset time estimates that can be used for evaluation of the efficiency and accuracy of the method.

CLUSTER ANALYSIS.

The multiple application of SA searches automatically provides means for assessing the stability and accuracy of the onset estimates derived from the SA method. Starting out with numerous randomly chosen positions for the onset time within a search window these will converge into positions of prominent CUSUM minima and form a varying number of tight clusters. Besides these there will be hopefully much fewer scattered 'solutions' that are obviously spurious and thus must be discarded. This approach was not pursued much in our recent work but it has a considerable potential (Der and Shumway 1999).

PRACTICAL EXAMPLES OF THE APPLICATIONS OF THE METHODOLOGY.

PERFORMANCE OF THE CUSUM PROCEDURE FOR ESTIMATING PN ONSET TIMES.

In the following we show evaluations of the performance of the CUSUM minimum and the combined CUSUM-SA procedure for picking onset times of first-arriving Pn phases. The evaluation is based on comparing the performance of **a)** human analysts **b)** picking the absolute minimum of normalized CUSUM and keeping the arrival if the F tests is passed **c)** picking the median of multiple picks using SA on the CUSUM and taking the median of these, but discarding the result if the SA arrivals are highly scattered.

Prefiltering preceded all the data processing. The two kinds of prefilters applied to the seismograms were 2-7 Hz Butterworth band-pass filters and minimum phase filters designed by taking the S/N^2 spectral ratio such that the maximum was set at unity and cutoffs were placed at the values at 0.24. The latter are similar to the filters that define "useful bandwidth". We have seen little difference in the performance of these filters in accordance with the comments made by Kvaerna (1996a). The events used had originally very high S/N ratios, especially on the prefiltered traces. To provide a "true" onset time the practically noise-free original trace was picked by the analyst after he has gone through all the noisy examples presented to him. In order to construct noisy data we have fitted a 15-th order AR model to the noise prior to the signal arrival and this model was used to construct independent noise samples by filtering Gaussian white noise. The noise sampled were added to the signal (mean removed) with various signal-to-noise ratios. The differences between this value and the other onset time estimates were plotted for all the three methods against the logarithms of SNR values, with the random time shifts corrected for, of course. This is the same kind of evaluation method as the one used by Kvaerna (1996a,b) and Yokota et al (1981) and Maeda (1985).Examples of results from these procedures are shown in.

The surprising finding of these tests is that most automatic onset times at SNR levels above 2 were comparable in quality to that of the analyst, although the relative
performance of these methods varies from event to event.

APPLICATION OF THE ITERATIVE VERSION OF NORMALIZED CUSUM METHOD TO SEGMENT COMPLETE REGIONAL SEISMOGRAMS.

The iterative method of Inclan and Tiao (1996) was applied to regional seismograms. Typically, three iterations were used. During the first iteration, the largest arrival was commonly picked. In the succeeding iterations the smaller arrivals were identified

Figure 4 and 5 show examples of the onset time determinations by the automatic algorithm described

above as applied to the events from the Ground Truth Data Base assembled by Multimax.

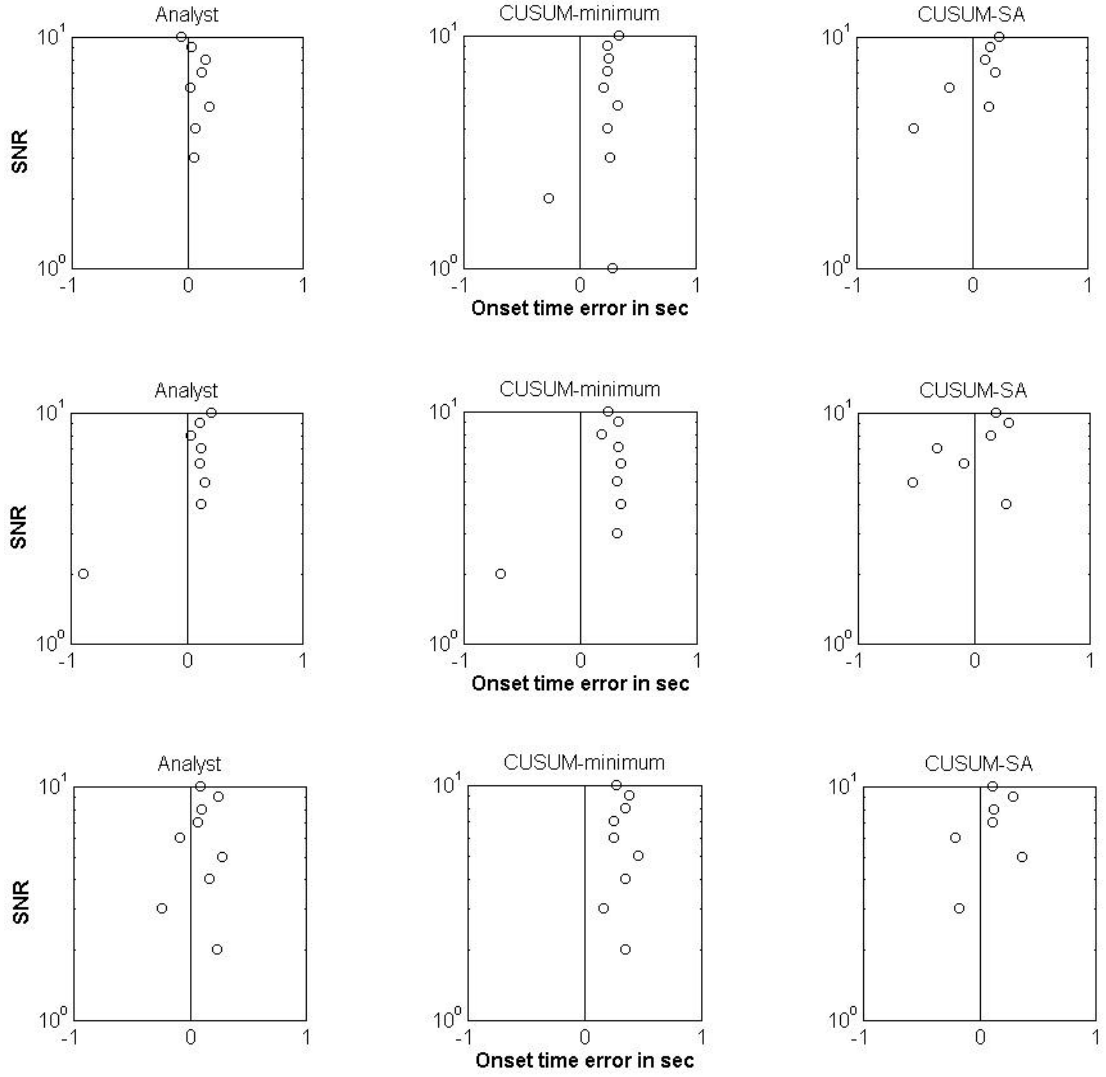


Figure 2. Comparison the Pn onset picks with various S/N ratios. The picks on the left were made by an analyst, those in the middle were CUSUM minimum picks accepted only if the F-test was passed. Those on the right were made by a CUSUM-SA combination, and were accepted only if _ of the trials were less than .5 sec near the median. Even though the analyst has the best performance, the second method come fairly close. Automatic picks tend to be somewhat later than the analyst. These picks were made for the events K2054, K2066 and K2110 listed by Der and Shumway (1999).

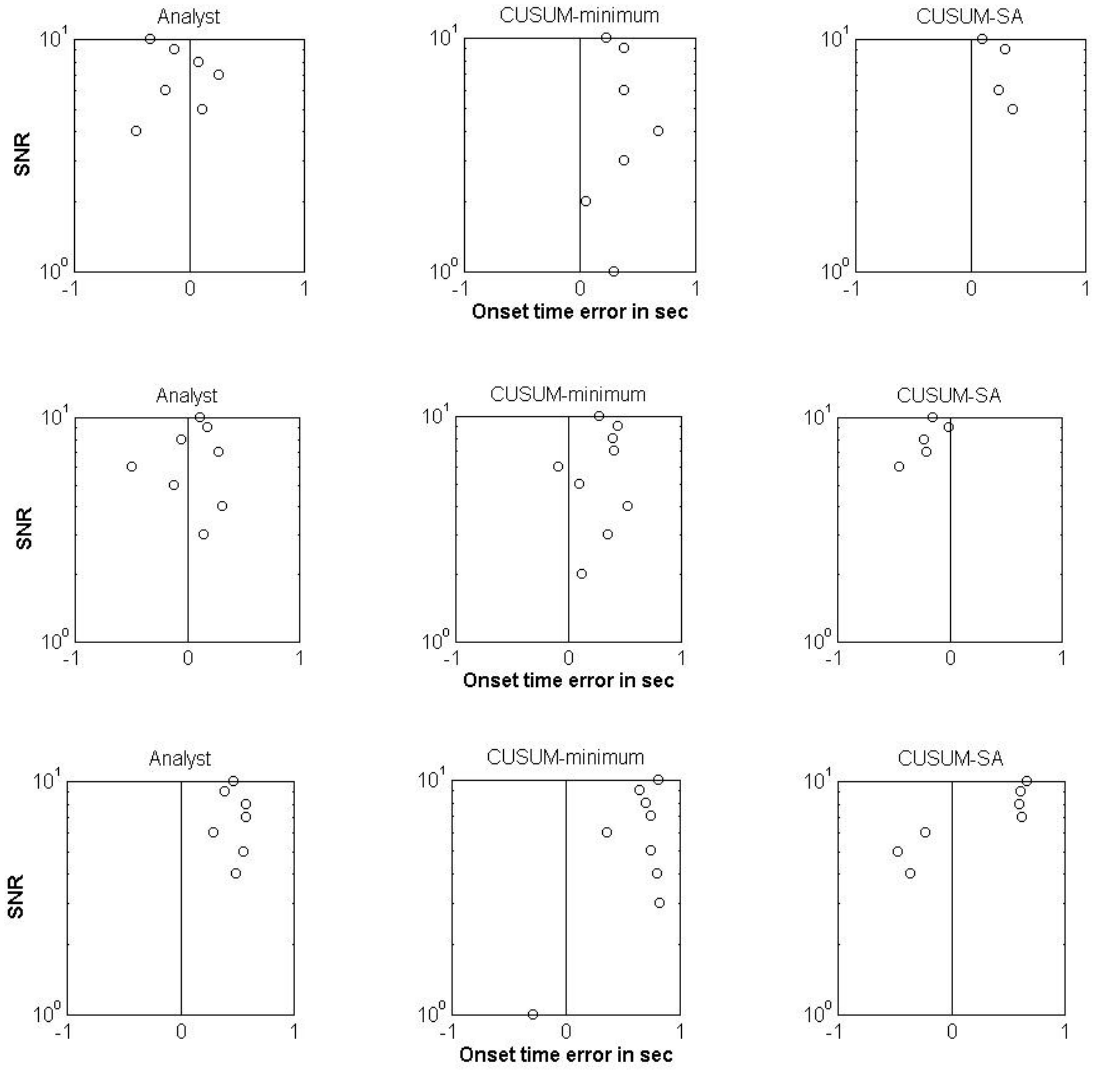


Figure 3. Comparison the Pn onset picks with various S/N ratios. The picks on the left were made by an analyst, those in the middle were CUSUM minimum picks accepted only if the F-test was passed. Those on the right were made by a CUSUM-SA combination, and were accepted only if _ of the trials were less than .5 sec near the median. Even though the analyst has the best performance, the second method come fairly close. Automatic picks tend to be somewhat later than the analyst. These picks were made for the events K2285, K4130 and K5040 listed by Der and Shumway (1999).

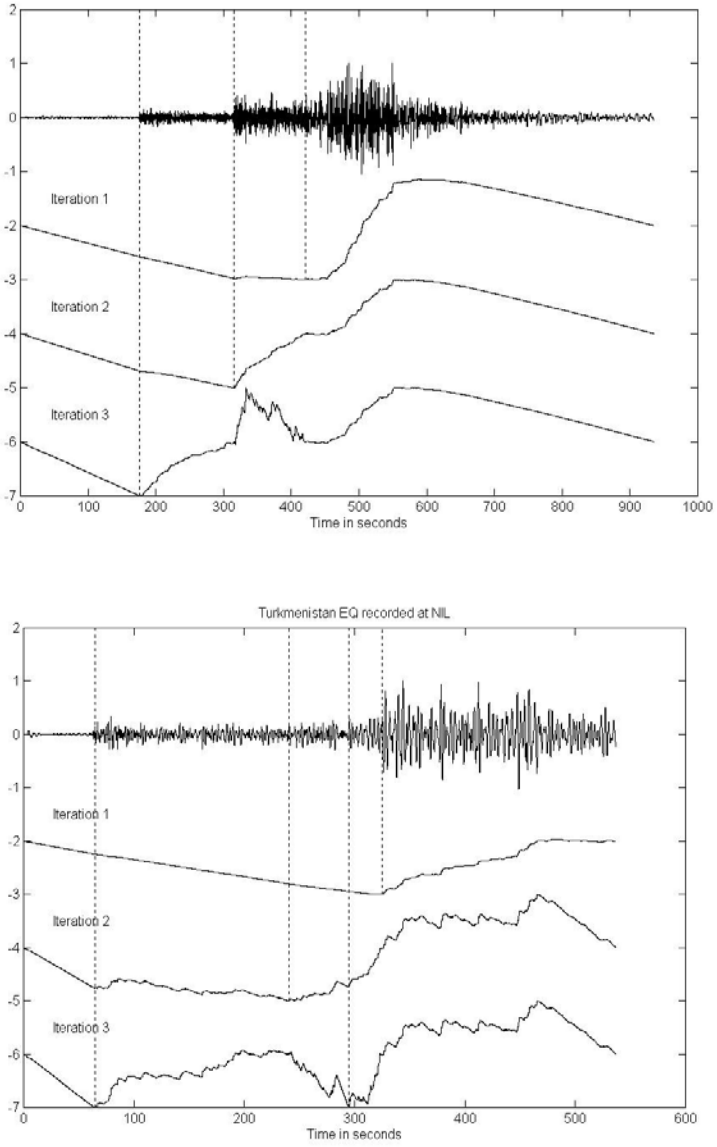
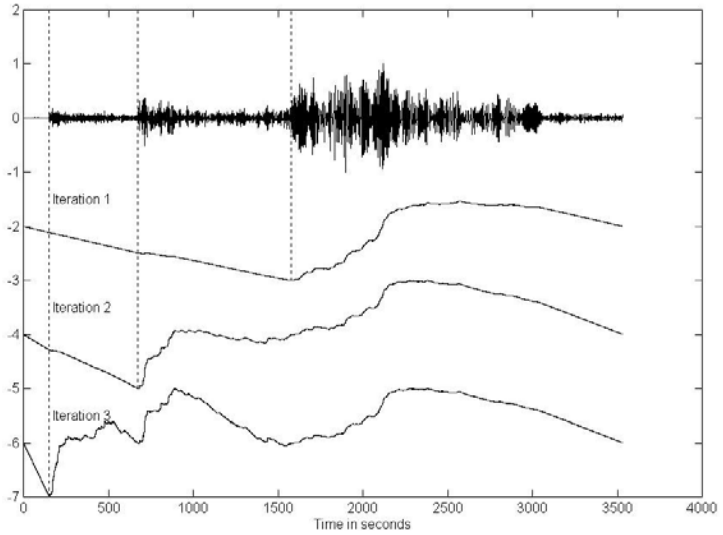


Figure 4. Examples of seismogram segmentation using the iterative CUSUM procedure of Inclan and Tiao (1996). In these figures we plot the raw trace (top) followed by the segmented CUSUM functions between the previously found arrivals. The final onset time picks are the vertical thin lines. Minima that failed the F tests were discarded. The figure shows the results for the stations KIV and NIL recording a Turkmenistan event.



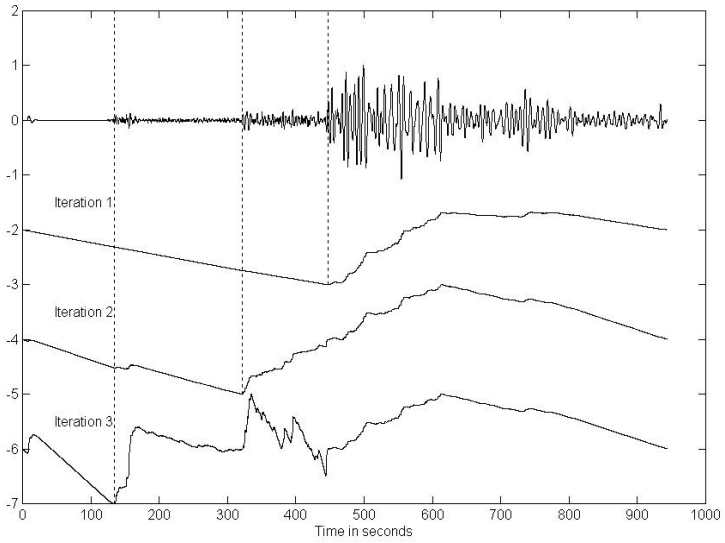


Figure 5. Examples of seismogram segmentation using the iterative CUSUM procedure of Inclan and Tiao (1996). In these figures we plot the raw trace (top) followed by the segmented CUSUM functions between the previously found arrivals. The final onset time picks are the vertical thin lines. Minima that failed the F tests were discarded. The figure shows the results for the stations DBIC and RAYN recording a Northern Iran event.

CONCLUSIONS AND FUTURE PLANS.

CUSUM-based methods seem to be quite suitable for processing regional seismograms since these consist of long wavetrains and have emergent phase onsets. Since CUSUM methods emphasize changes in the properties of signals over several cycles this kinds of methods can be used to segment regional seismograms. CUSUM-based methods to pick seismic phase onset times can also be developed based on a variety of statistics that are diagnostic of polarization, slowness, and spectral changes (Jurkevics 1988, Der et al 1993). Other candidates may include instantaneous relative phase differences among components, adaptive slowness estimates or their combination.

A completely new application of these methods in a CTBT could be the timing of T phase, oceanic seismic and infrasonic wave groups. Upon visual inspection signals of these types do not appear much different in nature than regional seismic signals and the methodology clearly could be used for them. Often such signals contain contributions from multiple raypaths through the atmosphere and the oceans.

REFERENCES

Basseville, M. and I.V. Nikiforov (1993), Detection of Abrupt Changes: Theory and Application. Prentice Hall Information and System Science Series, Prentice Hall, Englewood Cliffs, NJ.

Der, Z.A., Baumgardt,D.R. and R.H. Shumway (1993), The nature of particle motion in regional seismograms and its utilization for phase identification. Geophys. J. Int., 115, 1012-1024.

Der, Z. A. and R. H. Shumway (1999), Phase onset time estimation at regional distances using the CUSUM-SA algorithm. Phys. Earth and Planet. Int., 113,227-246..

Inclán, C., and G. C. Tiao (1994), Use of cumulative sums of squares for retrospective detection in the changes of variance. J. Amer. Statist. Assoc., 89,, 913-923.

Jurkevics, A. (1988), Polarization analysis of three-component array data. Bull. Seism. Soc. Am., 78, 1725-1743.

Kushnir, A. F. (1996), Algorithms for adaptive statistical processing of seismic array data. In 'Monitoring a Comprehensive Test Ban treaty', E. S. Husebye and A. M. Dainty Eds., Kluwer Academic Publishers.

Kvaerna, T. (1995), Automatic onset time estimation based on autoregressive processing. Semiannual Technical Summary, 1 April-30 September 1995. NORSAR, Sci. Report No. 1-95/96, Kjeller, Norway.

Kvaerna, T. (1996a), Quality assessment of automatic onset times estimated by the autoregressive method. Semiannual Technical Summary, 1 April-30 September 1995. NORSAR, Sci. Report No. 1-95/96, Kjeller, Norway.

Kvaerna, T. (1996b), Time shifts of phase onsets caused by SNR variations, Semiannual Technical Summary, 1 October 1995-31 March 1996. NORSAR, Sci. Report No. 2-95/96, Kjeller, Norway.

Maeda, N. (1985), A method for reading and checking phase time in auto-processing ssystem of seismic wave data (in Japanese with English abstract), J. Seismol. Soc. Jpn., 38, 365-379.

Nikiforov, L.V. and Tikhonov, I. N. (1986), Application of change detection theory to seismic signal processing. In "Detection of Abrupt Changes in Signals and Dynamical Systems " M. Basseville and A. Benveniste Editors. Lecture Notes in Control and Information Sciences, LNCIS 77, Springer, New York.

Nikiforov, L.V., Tikhonov, I.N., and Mikhailova, T.G. (1989), Automatic on-line oricessing of seismic data- Theory and applications. Far Eastern Dept. of USSR Academy of Sciences, Vladivostok, USSR (In Russian).

Press, W.H., Flannery, B.P., Teukolsky, S.A. and W.T. Vetterling (1986), Numerical Recipes: The Art of Scientific Computing. Cambridge University Press.

Pisarenko, V. F., Kushnir, A. F. and Savinn, I. V. (1987), Statistical adaptive algorithms for estimation of onset moments of seismic phases. Phys. Earth. Planet Int., 47, 4-10.

Shumway, R. H. (1998), An iterative cumulative sum of squares algorithm for phase onset estimation. ENSCO Technical Memo.

Takanami, T. (1991), A study of detection and extraction methods for earthquake waves by autoregressive models. J. Fac. Sci. Hokkaido, U., Ser VII, 9, 67-196.

Taylor, D. W. A., Ghalib, H. A. A. and Kimmel, R. H. (1992), Autoregressive analysis for seismic signal detection and onset time estimation. ENSCO Technical Report DCS-92-90.

Yokota, T., Zhou, S., Mizoue, M., and Nakamura, I. (1981), An automatic measurement of arrival time of seismic waves and its application to an on-line processing system (in Japanese with English abstract), Bull. Earthquake. Res. Inst. Univ. Tokyo, 55, 449-484.

LOCATION OF EVENTS IN THE REGION OF BOLIVIA

Lawrence A. Drake and Rodolfo Ayala, Observatorio San Calixto, Bolivia

Sponsored by U. S. Department of Defense
Defense Threat Reduction Agency and Air Force Technical Applications Center
Contract No.: F49620-97-1-0214

ABSTRACT

A fully decoupled nuclear explosion of 10 kT has a magnitude m_b of approximately 3.4. Although a cavity from a previous explosion is needed to fully decouple such an explosion, 3.4 is a useful reference magnitude for the Comprehensive Nuclear-Test-Ban Treaty. There are five principal difficulties in locating events of this magnitude (to ± 18 km) in Bolivia. First, the distance between the primary seismic station in Bolivia, LPAZ, and the auxiliary station, SIV (San Ignacio de Velasco), is approximately 7° and, at this distance, for events of magnitude 3.4, it is easy to misidentify Pg as Pn. The resulting error is approximately 30 s and accurate location is impossible. Second, the Andean crust beneath LPAZ has a thickness of approximately 65 km, whereas the crust beneath SIV has a thickness of approximately 40 km. The higher mantle velocity at a depth of 50 km in the region of SIV moves locations of events in Bolivia toward SIV, unless a three-dimensional location model is used. We have found that for the earthquake near Totora in central Bolivia, 22 May 1998, locations with the three-dimensional program (with grid spacings of 10 km, and then 5 km) are within a carefully studied and closed meizoseismal area. Third, even a three-dimensional model of the Andean region in Bolivia is so different from the reality (and the seismic stations are so widely spaced) that the computed residuals (especially that of depth) indicate only that the location is consistent with the model and the observed arrival times of the P and S phases. At least one S phase is required to control approximately the distance and depth of the hypocenter, but the arrival time of an S phase in Bolivia is usually difficult to observe, because there is rapid subduction of the Nazca plate and volcanism in the west, and a décollement by the Brazil Shield in the east. Fourth, because S is difficult to observe, we do not have much information about S velocities and we use in our three-dimensional models a constant P to S velocity ratio (1.76) for the whole region at all depths; we are correcting this. Finally, international hypocentral determinations in Bolivia have a bias toward the northwest, presumably because the wave paths to central American and North American seismic stations pass once or twice through the higher velocity regions of the Nazca and Cocos subducting plates.

Key Words: Bolivia, earthquake location, subduction.

OBJECTIVES

The objectives of this study were: i) to compare the location of seismic events in the region of Bolivia by horizontally layered models, by three-dimensional models and by international agencies; ii) to check the sensitivity of the primary seismic station in Bolivia (PS 06, LPAZ) of the International Monitoring System (IMS) of the Comprehensive Nuclear-Test-Ban Treaty (CTBT) in distance, depth and azimuth with respect to the magnitudes m_b given by the Prototype International Data Centre (PIDC).

TABLE 1. SEISMIC STATIONS OF BOLIVIA OPERATED BY OBSERVATORIO SAN CALIXTO

NAME	CODE	DATE	LATITUDE S	LONGITUDE W	ALTITUDE m	COMPONENT
La Paz, Millani	LPAZ	1993-,,	16°17'16.6" (16°.2879)	68°07'50.4" (68°.1307)	4740	BB-Z-NS-EW; SP-Z
Zongo	BOA	1972 -....	16°16'09.7" (16°.2694)	68°07'26.5" (68°.1240)	4397	SP-Z-NS-EW
Banderani	BOB	1975-....	16°08'39.6" (16°.1443)	68°07'58.4" (68°.1329)	3960	SP-Z
Gloria	BOD	1986 -....	16°38'14.6" (16°.6374)	68°35'53.2" (68°.5981)	4230	SP-Z
Chanca	BOE	1982 -....	16°48'45.7" (16°.8127)	67°58'55.6" (67°.9821)	4325	SP-Z
Collana	BOF	1993 -....	16°57'14.4" (16°.9540)	68°20'16.8" (68°.3380)	4480	SP-Z
San Ignacio de Velasco	SIV	1990 -....	15°59'28.7" (15°.9913)	61°04'19.9" (61°.0722)	520	SP-Z-NS-EW
Mochara	MOCB	1993 -....	21°15'01.5" (21°.2504)	65°38'16.8" (65°.6380)	3580	SP-Z-NS-EW
Warizata	BOG	1999-....	15°56'57.9" (15°.9494)	68°32'43.2" (68°.5453)	4970	SP-Z
Bombeo	BBO	1998-....	17°39'27" (17°.6575)	66°27'27" (66°.4575)	3821	SP-Z-NS-EW
Apacheta	APC	1998-....	17°21'32" (17°.3589)	66°01'30" (66°.0250)	3676	SP-Z-NS-EW
Cri. Ichu Kkollu	IKK	1998-....	17°15'02" (17°.2506)	66°19'32" (66°.3256)	4612	SP-Z-NS-EW
Col. Juan XXIII		1998-....	17°22'30" (17°.3750)	66°11'34" (66°.1928)	2496	CENTRAL STATION

RESEARCH ACCOMPLISHED

A fully decoupled nuclear explosion of 10 kilotons (kT) has a magnitude m_b of approximately 3.4. Nuclear explosions of yields of a few kT with large decoupling factors are feasible only in cavities in salt domes formed by previous nuclear explosions, and no country is known to have evacuated the brine from a very large cavity formed by solution mining and then conducted a decoupled nuclear explosion it it (Sykes, 1996). However, 3.4 is a useful reference magnitude for monitoring the CTBT. A possible on-site inspection area of 1000 km^2 corresponds to an epicenter location accuracy of approximately plus or minus 18 km.

There are five principal difficulties in locating seismic events of this magnitude with this accuracy in Bolivia.

The first difficulty is that the distance between the primary seismic station of the IMS in Bolivia (LPAZ) and the auxiliary seismic station, San Ignacio de Velasco (AS 08, SIV), is approximately 7° (Table 1; Figure 1), and, at this distance, for seismic events of magnitude 3.4, it is easy to misidentify Pg as Pn. The resulting error is approximately 30 s and location to plus or minus 18 km is impossible.



Figure 1. Seismic stations and the proposed infrasound station in Bolivia operated by Observatorio San Calixto.

The seismic stations and the proposed infrasound station in Bolivia operated by Observatorio San Calixto (OSC) are tabulated in Table 1 and shown in Figure 1. We plan to move the short period vertical component of the historically important station Zongo to Warizata (15°.9494 S, 68°.5453 W, 4970 m above sea level), north of the planned infrasound array (IS 08) near Peñas (Figure 1), and the two short period horizontal components to Mocharà. The three stations constituting the seismic net around Cochabamba, tabulated in Table 1 (Crr. stands for Cerro and Col. for Colegio) and shown in Figure 1, are at present being calibrated. It is clear from Figure 1 that there are still big spaces between Cochabamba and the seismic stations SIV to the east and Mocharà to the south, to say nothing of the space further east and southeast. Location of seismic events of magnitude 3.4 with an accuracy of plus or minus 18 km in this region will be challenging.

Figure 2 shows part of the crustal section of Schmitz (1993; Romanyuk et al., 1999) at 21° S. The seismic station Mocharà is a few kilometres north of Tupiza (21°.45 S, 65°.72 W). Distances of the section (km) are measured horizontally from 13 km west of the Chile Trench and vertically from sea level. Curiously, the most

interesting figure, the maximum thickness of the Andean crust, 75 km, is uncertain, because Wigger and his coworkers (1994) failed to get a clear Moho reflection east of Ollagüe (21°.23 S, 68°.27 W; 265 km W of Tupiza; Figure 2).

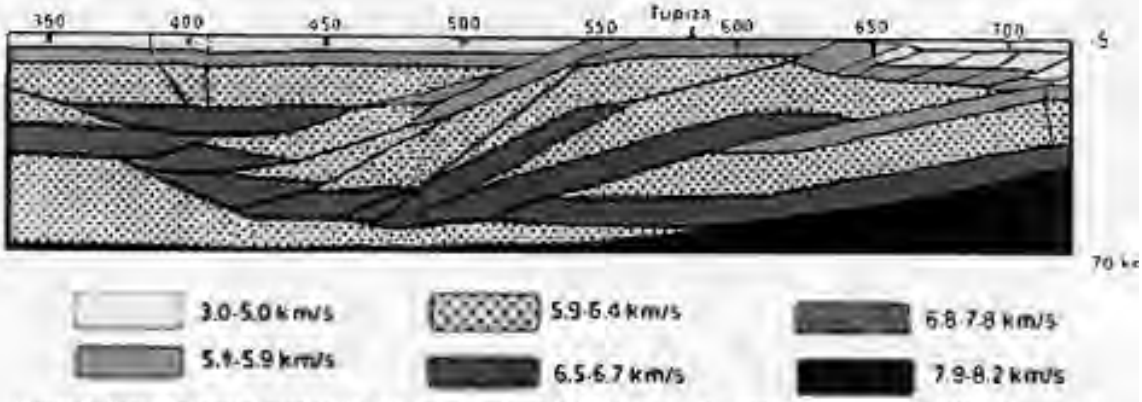


Figure 2. Part of a crustal section (E-W) at approximately 21° S (Schmitz, 1993; Wigger et al., 1994; Romanyuk et al., 1999); distances of the section are measured horizontally from 13 km west of the Chile Trench and vertically from sea level.

Dorbath and her coworkers (1993) estimated a maximum thickness of the Andean crust in the region of La Paz to be 60 km below the Altiplano (cf. Figure 1; 17°.4 S, 68°.4 W). However, these workers note that observed P arrival time residuals from teleseisms are accounted for by depth variations of the sedimentary fill and by variations of the Moho depth: there are basically two unknowns, velocity and depth, and it is difficult to fix the depth of the Moho without detailed knowledge of the velocities in the layers above it. Dorbath and Granet (1996) returned to the problem and found a depth to the Moho under theAltiplano of 66 km; they used the same seismic profile as in 1993, but, in 1996, sources in the Nazca plate subduction zone.

Beck and her coworkers (1994; 1996) used, by receiver function analysis (Ammon et al., 1990), the P to S conversion at the Moho (Ps) and a P that reflects from the free surface and converts to an S wave at the Moho beneath the station (PpPms) to determine the P to S velocity ratio (V_p/V_s). These workers found maximum thicknesses of 70-74 km under the Cordillera Occidental and Cordillera Oriental; these thicknesses thin to 32-38 km, 200 km east of the Andes in the Chaco Plain; the central Altiplano at 20° S has crustal thicknesses of 60 to 65 km. The crust also appears to thicken from north (16° S, 55-60 km) to south (20° S, 70-74 km) along the Cordillera Oriental. However, Beck and her coworkers note that there is a tradeoff between average crustal velocities (V_p and V_s) and crustal thickness, the same problem encountered by Dorbath and her coworkers.

Zandt and his coworkers (1996) used, also by receiver function analysis, an upgoing SV wave that converts to a P wave at the free surface and becomes trapped in the crust owing to its reflection at the Moho beyond its critical angle (sPmP; Langston, 1996); this whole family of P waves can easily be mistaken for S and, at longer period, constitutes a leaky mode (S leaks back into the mantle), similar to the PL phase (Aki and Richards, 1980; p. 460). Zandt and his coworkers (1996) found in the Altiplano a low mean P wave velocity of 6.0 km/s, a low Poisson's ratio of 0.25 and a crustal thickness of 65 km. Again, Zandt and his coworkers encounter the tradeoff problem mentioned above.

Myers and his coworkers (1998) developed a three-dimensional, lithospheric-scale model across the Bolivian Andes at approximately 20° S, based on tomographic images of velocity and attenuation for both P and S waves. Observations of travel time and attenuation for the study of these workers were from regional earthquakes in the mantle and the subducted Nazca plate. The shallow mantle under the Altiplano from approximately 18° S to approximately 21° S has high velocity (approximately V_p = 8.3 km/s, V_s = 4.7 km/s) and moderately high Q (approximately Q_p = 500, Q_s = 200), which suggests lithospheric mantle. High velocity material under the Altiplano extends to a depth of approximately 125-150 km. The shallow mantle of the Cordillera Occidental is characterized by high V_p/V_s (approximately 1.83), which suggests a correlation between V_p/V_s and arc volcanism. Seismic velocities under the Cordillera Occidental are, on average, only slightly reduced from global averages, but velocity and attenuation anomalies are locally strong (approximately V_p =7.8 km/s, V_s = 4.3 km/s.

Finally, Chmielowski and his coworkers (1999), again by receiver function analysis, have found, at a depth of approximately 19 km, a very low velocity layer of thickness approximately 0.8 km, with P velocity of approximately 3.5 km/s and S velocity of approximately 0.45 km/s. These velocities correspond to a Poisson's ratio of 0.4916. Thus, this layer almost certainly represents a large sill-like magma body. It has an area of approximately 50,000 km^2, west for approximately 150 km from an approximately north-northwest line joining the points (20° S, 68° W) and (23° S, 67° W); Ollagüe (21°.23 S, 68°.27 W; 265 km west of Tupiza; Figure 2), is near the center of this region. It represents an additional complexity in the crustal structure shown in Figure 2 (Schmitz, 1993; Wigger et al., 1994; Romanyuk et al., 1999).

TABLE 2. CRUSTAL MODEL FOR MOCHARA

Layer thickness km	Compress. velocity km/s	Shear velocity km/s	Density g/cm^3	Poisson's ratio	Quality factor
4.10	5.50	3.19	2.620	0.2474	250
24.30	6.15	3.55	2.724	0.2506	350
9.80	7.30	4.21	2.908	0.2506	450
14.90	6.15	3.55	2.724	0.2506	350
10.80	7.30	4.21	2.908	0.2506	450
63.90	8.05	4.48	3.360	0.2763	600

Table 2 presents a crustal model, based on these observations, for the region of the seismic station Mochará, in the Cordillera Oriental. The layer thickness shown for the half-space below the Moho is the total thickness of the crust of the model (63.90 km, 58.90 km below sea level; cf. the region of Tupiza in Figure 2). The region of the primary seismic station of the IMS of the CTBT, LPAZ, also in the Cordillera Oriental, though further north, can be expected to be over a crustal thickness of approximately 65 km. The seismic station Gloria (Table 1, Figure 1), near the western edge of the Altiplano, can be expected to be over a greater thickness of crust. Values of Poisson's ratio and of Q are taken from the IASPEI (1991) model and from the Preliminary Reference Earth Model (Dziewonski and Anderson, 1981) and values of density are consistent with the Nafe-Drake curve (Grant and West, 1965, p. 200).

TABLE 3. CRUSTAL MODEL FOR REGION OF COCHABAMBA

Layer thickness km	Compress. velocity km/s	Shear velocity km/s	Density g/cm^3	Poisson's ratio	Quality factor
13.10	5.50	3.19	2.620	0.2474	250
14.10	6.15	3.55	2.724	0.2506	350
5.70	5.50	3.19	2.620	0.2474	250
14.70	6.15	3.55	2.724	0.2506	350
8.60	7.30	4.21	2.908	0.2506	450
56.20	8.05	4.48	3.360	0.2763	600

Similarly, Table 3 presents a crustal model for the seismic stations in the region of Cochabamba and Table 4 presents a crustal model for the region of the auxiliary seismic station of the IMS of the CTBT, SIV. Obviously, if horizontally layered models with seismic stations over these different types of crust are used to locate earthquakes in the region of Bolivia, the higher velocities in the mantle at depths of 45-60 km in the region of SIV will bias the location of the events toward SIV.

Table 5 and Figure 3 show, for the earthquake near Totora in central Bolivia, 22 May 1998, the location by the PIDC, the location according to the Preliminary Determination of Epicenters (PDE), the location according to

the method of the Harvard central moment tensor (HVD), and locations by Observatorio San Calixto. These latter locations included: i) carefully observed and closed isoseismals, with a depth found by the formula of Kövesligethy (Papazachos and Papaioannou, 1997; Drake and Vega; 1998; Drake et al., 1999); ii) routine location, mainly with the use of French seismic stations in Bolivia and with a model of one horizontal layer over a half-space (Table 6); iii) location with a model of four horizontal layers and the program HYPOCENTER (Table 7; Lienert et al., 1986); iv) location by the three-dimensional program 3DGRIDLOC with a grid spacing of 10 km (Ayala, 1997; Ayala and Drake, 1997; 1998; Podvin and Lecomte, 1991; Tarantola and Valette, 1982; Vidale, 1988; 1990; Wittlinger et al., 1993) ; v) location by the three-dimensional program 3DGRIDLOC with a grid spacing of 5 km.

TABLE 4. CRUSTAL MODEL FOR SAN IGNACIO DE VELASCO

Layer thickness km	Compress. velocity km/s	Shear velocity km/s	Density g/cm^3	Poisson's ratio	Quality factor
9.73	4.00	2.32	2,380	0.2474	180
5.26	5.50	3.19	2,620	0.2474	250
15.34	6.15	3.55	2,724	0.2506	350
9.67	7.30	4.21	2,908	0.2506	450
40.00	8.05	4.48	3,340	0.2763	600

TABLE 5. LOCATIONS OF AN EARTHQUAKE BY THE PROTOTYPE INTERNATIONAL DATA CENTER, ACCORDING TO THE PRELIMINARY DETERMINATION OF EPICENTERS, ACCORDING TO THE HARVARD CENTRAL MOMENT TENSOR METHOD AND BY OBSERVATORIO SAN CALIXTO

Source	Time h m s	Latitude °S	Longitude °W	Depth km
PIDC	04 48 48.2	17.54	65.14	34
PDE	04 48 50.4	17.731	65.431	24
Harvard CMT	04 49 02.9	17.600	65.070	15
3DGRIDLOC	04 48 46.2	17.810	65.100	1
3DGRIDLOC, 5km	04 48 45.2	17.920	65.180	1
OSC, French	04 48 44.8	17.883	65.050	9
OSC, Lienert	04 48 43.6	17.804	65.057	13
Isoseismals		17.850	65.160	11

TABLE 6. LAYER OVER HALF-SPACE MODEL FOR CENTRAL BOLIVIA

Layer thickness km	Compress. velocity km/s	Shear velocity km/s	Poisson's ratio
65.0	6.2	3.580	0.25
	8.0	4.619	0.25

TABLE 7. FOUR LAYER MODEL FOR CENTRAL BOLIVIA

Layer thickness km	Compress. velocity km/s	Shear velocity km/s	Poisson's ratio
10.0	5.0	2.8090	0.2694
15.0	6.0	3.3708	0.2694
35.0	6.6	3.7079	0.2694
120.0	8.0	4.4944	0.2694

The locations the by the PIDC and according to the method of the Harvard central moment tensor (HVD) appear to be approximately 35 km too far north, and the location according to the PDE appears to be about 30 km too far northwest. As expected, the locations with the horizontally layered models are pulled toward SIV. The locations by the three-dimensional program 3DGRIDLOC are within the meizoseismal area

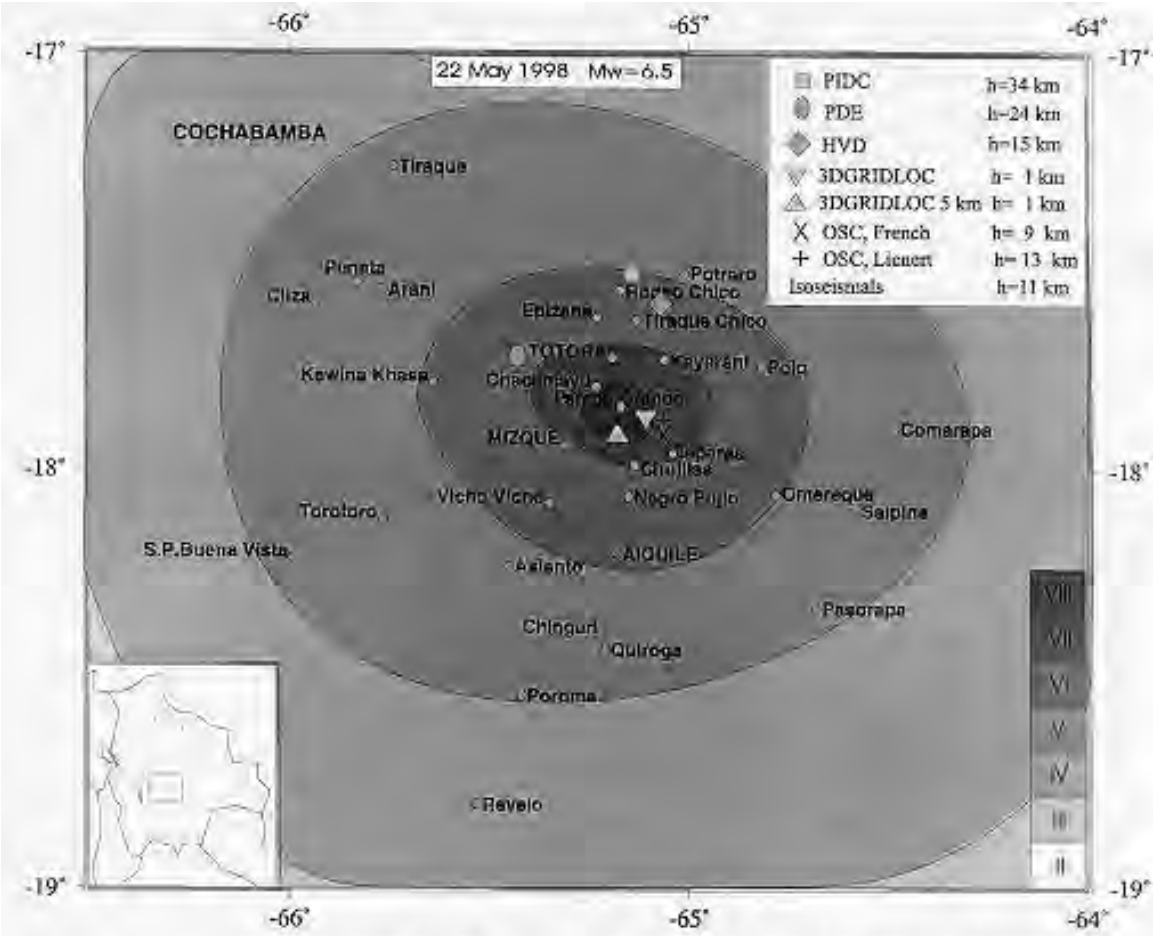


Figure 3. Isoseismals for the earthquake of 22 May 1998 near Totora in central Bolivia, together with locations by the PIDC, by the PDE, by the Harvard central moment tensor method (HVD) and by Observatorio San Calixto.

The third principal difficulty with the accurate location of earthquakes in Bolivia is that even a three-dimensional model of the region is so different from the actual structure of the earth beneath the Bolivian Andes and the seismic stations are so widely spaced that the computed residuals (especially that of depth) indicate only that the location is consistent with the model and the observed arrival times of the P and S phases. At least one S phase is required to control approximately the distance of the hypocenter from the seismic stations (especially its depth). However, the arrival time of an S phase in Bolivia is usually difficult to observe, because there is rapid subduction of the Nazca plate and volcanism in the west (Gordon, 1995; Norabuena et al., 1998; Kendrick et al., 1999), and a décollement by the Brazil Shield in the east (Sempere et al., 1988; Gubbels et al., 1993; Iacobshagen et al., 1998; Lamb and Hoke, 1997; Lamb et al., 1997). The S phase from the approximately north-south bands of deep earthquakes in Peru-Brazil (6°.5 S, 71°.5 W to 11°.5 S, 70°.8 W) and in Bolivia-Argentina (19°.0 S, 63°.5 W to 28°.5 S, 63°.0 W), and also from the region of Totora (17°.60 S, 65°.15 W) in Bolivia, is comparatively clear. However, S from southern Peru (e.g. Arequipa, 16°.40 S, 71°.55 W) and Chile is likely to be confused with the more conspicuous R_g. Also, in the region of Bolivia, PpPms (Beck et al., 1996), sPmP (Zandt et al., 1996) or a trapped low velocity phase (Chmielowski et al., 1999) can be mistaken for S.

The fourth principal difficulty with the accurate location of earthquakes in Bolivia is that, because S is difficult to observe, we do not have much information about S velocities. Our three-dimensional models of the region

used in the programs 3DGRIDLOC use a constant V_p/V_s ratio of 1.76 for the whole region at all depths, which is not realistic. We are correcting this.

Finally, the fifth principal difficulty with the accurate location of earthquakes in Bolivia is that international hypocentral determinations in Bolivia have a bias toward the northwest. This occurs possibly because the wave paths to central American and North American seismic stations pass once or twice through the higher velocity regions of the Nazca and Cocos subducting plates. Under central America at a depth of 150 km there appears to be a low S velocity region, but at a depth of 550 km the S velocity is more normal (Dziewonski, 1989). Because errors of location of earthquakes by the PIDC clearly depend on which seismic stations are used, the practices of kriging (interpolation of location corrections relative to reference "ground truth" events; Schultz et al., 1998) and of plotting error vectors of arrays or stations relative to supposed "correct" locations of the PIDC (Koch and Kradolfer, 1999) are no substitute for close azimuthal cover in the accurate location of earthquakes (Lienert et al., 1986).

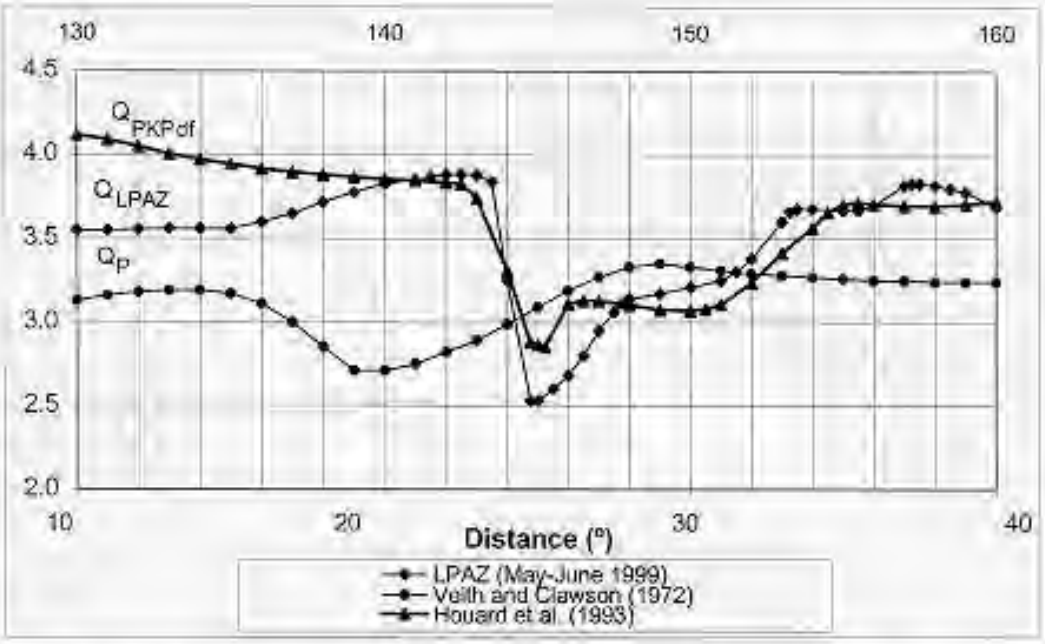


Figure 4. Q for the IMS primary seismic station LPAZ from 130° to 160° for May and June 1999 compared with Q for PKP_{df} and PKP_{bc} (Houard et al., 1993) and with Q for P from 10° to 40° (Veith and Clawson, 1972).

The promptness of the PIDC preliminary locations has now enabled seismologists to obtain locations of earthquakes before they see seismograms. Figure 4 shows the sensitivity (approximate Q) of the IMS primary seismic station LPAZ between distances of 130° and 160° compared with the Q values derived for the phases PKP_{df} and PKP_{bc} for the model 1066B (Gilbert and Dziewonski, 1975; Houard et al., 1993) and the Q values of Veith and Clawson (1972) for events between distances of 10° and 40° (at a depth of 15 km). The approximate LPAZ values are derived from amplitudes observed in May and June of 1999, without distinction of period, depth or azimuth; the apparently low Q between distances of 130° and 140° appears to be from the phase PKiKP. The apparently sharp decrease in Q shown for the phase PKP_{df} between distances of 142°.8 and 154°.8 is from the phase PKP_{bc} (Houard et al., 1993). The IMS seismic station LPAZ appears to be more sensitive to events between distances of 144° and 151° than to events between distances of 10° and 16°.

CONCLUSIONS AND FUTURE PLANS

Location of seismic events in Bolivia to plus or minus 18 km, with control of depth, needs close azimuthal cover of seismic stations, an appropriate earth model and observation of at least one S phase. At present the three-dimensional models 3DGRIDLOC do not include appropriate S values and we need to correct these. S is usually

difficult to observe in Bolivia and we need to examine methods of detecting it. Finally, we can look more at the effect of period, depth and azimuth on amplitudes of phases observed at the IMS primary seismic station LPAZ of the CTBT.

REFERENCES

Aki, K. and P.G. Richards, 1980. *Quantitative Seismology*, Freeman, San Francisco.

Ammon, C.J., G.E. Randall and G. Zandt, 1990. On the nonuniqueness of receiver function inversions. *J. Geophys. Res.* **95**, 15,303-15,318.

Ayala, R., 1997. Seismotectonique des Andes de Bolivie et rôle de l'Orocline bolivien. *PhD thesis*, Institut de Physique du Globe de la Université Louis Pasteur, Strasbourg, France.

Ayala, R. and L.A. Drake, 1997. Earthquake location with a 3-D velocity model for the region of the Bolivian Andes. In *Proceedings of the 19th Annual Research Symposium on Monitoring a Comprehensive Test Ban Treaty*, 23-25 September 1997, pp. 191-200.

Ayala, R. and L.A. Drake, 1998. Shape of the Nazca plate beneath northern Chile from earthquake locations with a 3-D velocity model. In *20th Annual Seismic Research Symposium on Monitoring a Comprehensive Test Ban Treaty (CTBT)*, 21-23 September 1998, pp. 233-240.

Beck, S.L., P.G. Silver, G. Zandt, T.C. Wallace, S.C. Myers, R. Kuehnel, S. Ruppert, L.A. Drake, E. Minaya, P. Soler, P. Baby, S. Barrientos, J. Telleria, M. Tinker and J. Swenson, 1994. Across the Andes and along the Altiplano: a passive seismic experiment. *IRIS Newsletter* **13**, No. 3, 1-3.

Beck, S.L., G. Zandt, S.C. Myers, T.C. Wallace, P.G. Silver and L.A. Drake, 1996. Crustal-thickness variations in the central Andes. *Geology* **24**, 407-410.

Chmielowski, J. and G. Zandt, 1999. The central Andean Altiplano-Puna magma body. *Geophys. Res. Lett.* **26**, 783-786.

Dorbath, C. and M. Granet, 1996. Local earthquake tomography of the Altiplano and the Eastern Cordillera of northern Bolivia. *Tectonophys.* **259**, 117-136.

Dorbath, C., M. Granet, G. Poupinet and C. Martinez, 1993. A teleseismic study of the Altiplano and the Eastern Cordillera in northern Bolivia: new constraints on a lithospheric model. *J. Geophys. Res.* **98**, 9825-9844.

Drake, L.A. and A. Vega, 1998. Seismic hazard in Bolivia. In *Modern Preparation and Response Systems for Earthquake, Tsunami and Volcanic Hazards*, 27-30 April, Santiago, Chile, Instituto Geográfico Militar, p. 203.

Drake, L.A., R. Ayala and A. Vega, 1999. The Comprehensive Test Ban Treaty in the region of Bolivia. *Seism. Res. Lett.* **70**, 214.

Dziewonski, A.M., 1989. Earth structure, global. In *The Encyclopedia of Solid Earth Geophysics* (D.E. James, ed.), Van Nostrand-Reinhold, New York, pp. 331-359.

Dziewonski, A.M. and D.L. Anderson, 1981. Preliminary Reference Earth Model. *Phys. Earth Planet. Inter.* **25**, 297-356.

Gilbert, F. and A.M. Dziewonski, 1975. An application of normal mode theory to the retrieval of structural parameters and source mechanisms for seismic structure. *Phil. Trans. Roy. Soc. London* A, **278**, 187-269.

Gordon, R.G., 1995. Present plate motions and plate boundaries. In *Global Earth Geophysics: a Handbook of Physical Constants* (T.J.Ahrens, ed.), American Geophysical Union Reference Shelf 1, pp. 66-87.

Grant, F.S. and G.F. West, 1965. *Interpretation Theory in Applied Geophysics*, McGraw-Hill, New York.

Gubbels, T.L., B.L. Isacks and E. Farrar, 1993. High-level surfaces, plateau uplift, and foreland development, Bolivian central Andes. *Geology* **21**, 695-698.

Houard, S., J.L. Plantet, J.P. Massot and H.C. Nataf, 1993. Amplitudes of core waves near the PKP caustic, from nuclear explosions in the South Pacific recorded at the "Laboratoire de Détection et Géophysique" network, in France. *Bull. Seism. Soc. Am.* **83**, 1835-1854.

IASPEI, 1991. *Seismological Tables* (B.L.N. Kennett, ed.), Research School of Earth Sciences, Australian National University, Canberra.

Jacobshagen, V., D. Mertmann, J. Müller and S. Tawackoli, 1998. The Eastern Cordillera of southern Bolivia: geotectonic evolution in Mesozoic and Cenozoic times. *Zbl. Geol. Paläont. Teil* I, **1997**, 571-579.

Kendrick, E.C., M. Bevis, R.F. Smalley, O. Cifuentes and F. Galban, 1999. Current rates of convergence across the central Andes: estimates from continuous GPS observations. *Geophys. Res. Lett.* **26**, 541-544.

Koch, K. and U. Kradolfer, 1999. Determination of mislocation vectors to evaluate bias at GSETT-3 primary stations. *J. Seism.* **3**, 139-151.

Lamb, S. and L. Hoke, 1997. Origin of the high plateau in the central Andes, Bolivia, South America. *Tectonics* **16**, 623-649.

Lamb, S., L. Hoke, L. Kennan and J. Dewey, 1997. Cenozoic evolution of the Central Andes in Bolivia and northern Chile. In *Orogeny Through Time* (J.-P. Burg and M. Ford, eds) Geol. Soc. Spec. Publ. 121, 237-264.

Langston, C.A., 1996. The SsPmp phase in regional wave propagation. *Bull. Seism. Soc. Am.* **86**, 133-143.

Lienert, B.R., E. Berg and L.N. Frazer, 1986. HYPOCENTER: an earthquake location method using centered, scaled, and adaptively damped least squares. *Bull. Seism. Soc. Am.* **76**, 771-783.

Myers, S.C., S. Beck, G. Zandt and T.C. Wallace, 1998. Lithospheric-scale structure across the Bolivian Andes from tomographic images of velocity and attenuation for P and S waves. *J. Geophys. Res.* **103**, 21,233-21,252.

Norabuena, E., L. Leffler-Griffin, A. Mao, T. Dixon, S. Stein, I. Selwyn Sacks, L. Ocola and M. Ellis, 1998. Space geodetic observations of Nazca-South America convergence across the central Andes. *Science* **279**, 358-362.

Papazachos, C. and Ch. Papaioannou, 1997. The macroseismic field of the Balkan area. *J. Seism.* **1**, 181-201.

Podvin, P. and I. Lecomte, 1991. Finite difference computation of travel times in very contrasted velocity models: a massively parallel approach and its associated tools. *Geophys. J. Int.* **105**, 271-284.

Romanyuk, T.V., H.-J. Götze and P.F. Halvorsen, 1999. A density model of the Andean subduction zone. *The Leading Edge* **18**, 264-268.

Schmitz, M., 1993. Kollisionsstrukturen in den Zentralen Anden: Ergebnisse refraktionsseismischer Messungen und Modellierung krustaler Deformationen. *Berliner Geowissenschaftliche Abhandlungen*, Reihe B, **20**, 1-127.

Schultz, C.A., S.C. Myers, J. Hipp and C.J. Young, 1998. Nonstationary Bayesian kriging: a predictive technique to generate spatial corrections for seismic detection, location and identification. *Bull. Seism. Soc. Am.* **88**, 1275-1288.

Sempere, T., G. Herail and J. Oller, 1988. Los aspectos estructurales y sedimentarios del orocline boliviano. *I° Congreso Geológico Chileno*, 1, A127-A142, Santiago.

Sykes, L.R., 1996. Dealing with decoupled nuclear explosions under a comprehensive test ban treaty. In *Monitoring a Comprehensive Test Ban Treaty* (E.S. Husebye and A.M. Dainty, eds), Kluwer, Dordrecht pp. 247-293.

Tarantola, A. and B. Valette, 1982. Inverse problems = quest for information. *J. Geophys.* **50**, 159-170.

Veith, K.F. and G.E. Clawson, 1972. Magnitude from short-period P-wave data. *Bull. Seism. Soc. Am.* **62**, 435-452.

Vidale, J., 1988. Finite-difference calculation of traveltimes. *Bull. Seism. Soc. Am.* **78**, 2062-2076.

Vidale, J., 1990. Finite-difference calculation of traveltimes in three dimensions. *Geophys.* **55**, 521-526.

Wigger, P.J., M. Schmitz, M. Araneda, G. Asch, S. Baldzuhn, P. Giese, W.-D. Heinsohn, E. Martinez, E. Rietaldi, P. Roewer and J. Viramonte, 1994. Variation in the crustal structure of the southern central Andes deduced from seismic refraction investigations. In *Tectonics of the Southern Central Andes* (K.-J. Reutter, E. Scheuber and P.J. Wigger, eds), Springer-Verlag, Berlin, pp. 23-48.

Wittlinger, G., G. Herquel and T. Nakache, 1993. Earthquake location in strongly heterogeneous media. *Geophys. J. Int.* **115**, 759-777.

Zandt, G., S.L. Beck, S.R. Ruppert, C.J. Ammon, D. Rock, E. Minaya, T.C. Wallace and P.G. Silver, 1996. Anomalous crust of the Bolivian Altiplano, central Andes: constraints from broadband regional seismic waveforms. *Geophys. Res. Lett.* **23**, 1159-1162.

STATISTICAL PERFORMANCE MEASURES OF THE HWM-93 AND MSISE-90 EMPIRICAL ATMOSPHERIC MODELS

Douglas P. Drob and J. M. Picone, Upper Atmospheric Physics Branch,
E.O. Hulburt Center for Space Research, Naval Research Laboratory

Sponsored by the U.S. Department of Energy,
Office of Nonproliferation and National Security,
Office of Research and Development
Contract Number: DE-AT04-98AL79800, DE-AT04-99AL66330

ABSTRACT

An enforceable Comprehensive Nuclear-Test-Ban Treaty (CTBT) regime will require accurate detection and location of low-yield (1 kT or less) nuclear detonations. For reliable infrasonic detection and location of candidate events, a thorough knowledge of the upper atmosphere and advanced modeling techniques is required. Currently, a near-real-time global specification of the atmosphere extends to only about 55 km from the surface. This is insufficient for CTBT monitoring purposes. A near-real-time global specification will have to be developed that covers the region that is 45 ±10 km to 150 ± 20 km above the surface for infrasonic detection and location of nuclear detonations.

The Naval Research Laboratory maintains both the Mass Spectrometer and Incoherent Scatter Radar Model (MSISE-90) and Horizontal Wind Model (HWM-93). These empirical models employ meteorological data assimilation techniques and draw upon a forty-year, multi-instrument database of satellite- and ground-based research measurements. These models produce global atmospheric state estimates in the region of interest from day-of-year, time-of-day, latitude, longitude, altitude, and solar and geomagnetic activity indices using a set of harmonic coefficients. These models provide a framework for organizing and disseminating measurements of density, temperature, and wind data.

It is important to have statistical performance measures of the MSISE-90 and HWM-93 models to evaluate their performance, determine potential error, and enable adjustment for that error. The models' limitations stem from two types of uncertainties – statistical and systematic errors. Statistical errors are introduced by unresolved random fluctuations in the upper atmosphere. Systematic errors are introduced by observation and modeling biases. The measurement database that was used to construct the models and seven newer comprehensive data sets are used in calculating these statistical performance measures. Limitations of the models can be quantified and understood through this methodology. A database of standard deviations and mean biases is being developed for these models. The database will be organized to facilitate assessment of the models and validation of current source location error ellipses. The resulting data will then be made available to the infrasound community for use in error correction.

Key Words: infrasound, atmospheric models, statistical performance

OBJECTIVES

Source location algorithms require global winds and temperatures from the ground to approximately150 km. Currently, operational near-real time global specification of the atmosphere is only available for the region below 55-km. Above this region near-real time atmospheric specification remains an active scientific research topic. The purpose of this task is to advance Naval Research Laboratory (NRL) upper atmospheric empirical models; the Mass Spectrometer and Incoherent Scatter Radar (MSISE-90) model and Horizontal Wind Model (HWM-93) for infrasonic measurement applications. The objective of this work is to understand and reduce uncertainties in the models using newly available upper atmospheric observations in order to provide the best information possible for infrasound source location and characterization.

RESEARCH ACCOMPLISHED

Our models (henceforth HWM/MSIS) provide an elegant solution for infrasound monitoring applications and research. They are publicly available at http://uap_www.nrl.navy.mil/models_web. Given day-of-year, time-of-day, latitude, longitude, altitude, and solar and geomagnetic activity indices the end-user FORTRAN subroutines produce global atmospheric state estimates from the ground to 500 km using a set of harmonic coefficients that have been optimally estimated from the database of historical measurements. Dr. Alan Hedin of the NASA Goddard Spaceflight center developed the HWM/MSIS models over a twenty-year period. They employ meteorological data assimilation techniques and have been produced from a forty-year, multi-instrument database of satellite and ground-based research measurements. Mathematical details of the models and the underlying measurement databases can be found in Hedin *et al.* (1991, 1996) and references therein. These models and our supporting software tools provide an extremely powerful and readily available framework for organizing and making widely available measurements of density, temperature, and wind data from satellite missions, rocket flights, and ground-based observations. Furthermore, now that global near-real time measurements are becoming available above 35 km, these tools are being considered for adaptation to produce near real-time specifications of the atmosphere from the ground to 120 km for use in infrasound monitoring activities.

It is important to consider the uncertainties in the background atmospheric field in order to understand uncertainties in infrasound propagation solutions. Uncertainty estimates and model bias are currently not provided as standard model output. The subsequent production and distribution of these statistical measures will serve two very important purposes for the CTBT and infrasound community. First, these statistical measures can be used to effectively assess the overall performance of the models and the subsequent impact and infrasound source location and characterization. Secondly, once this statistical knowledge is obtained it can be used to upgrade the models.

Data Collection and Organization

The data sets collected for model analysis and improvement effort are shown in Table 1. This table also illustrates the regions of parameter space covered by the data. It is important to note that while certain data sets may extend over several years, observations may have only been collected a small fraction of the time. Each of these diverse data sets was provided different format. Therefore, an investment has been made to reformat, organize, and understand them. A sets of software routines was developed so that each data set can be read from disk and stored in common database format for subsequent analysis.

Statistical Model Performance

The majority of the dominant fluctuations in the upper atmosphere, which are driven by solar heating and periodic wave processes, are generally repeatable from day-to-day and year-to-year and are parameterized in the empirical models. There are, however, some classes of waves and fluctuations that are purely random or even pseudo-random, which cannot be resolved or predicted given the current set of historical

Table 1. Upper atmospheric data sets collect to evaluate HWM/MSIS model performance.

Data type	Measurement kind	Altitude Range	Instrument Name	Dates	Location	Time Coverage
Meteorological Analysis Products	Wind, Temperature Geopotential Height	1000 - .35 mb (0 - 55 km)	United Kingdom Meteorology Office (UMKO) – UARS correlative analysis	1993 – 1994 1996 – 1997	Global 2.5º x 2.5º Grid	12:00 UTC
		10 - .4 mb (35 – 55 km)	Navy Fleet-Numeric STRATOI	Spring 1999	Global 1º x 1º Grid	0:00 and 12:00 UTC
NASA Upper Atmosphere Research Satellite (UARS)	Winds and Temperature	10 – 35 km and 50 – 110 km	High Resolution Doppler Imager (HRDI) (level 2b and 3a version 11)	1991 to present	Near Global +/- 60º	Daytime and 93 km during nighttime
MF Radars	Winds	70 – 110 km	Christmas Island	1993 - 1994	2 N – 157 W	24-hr coverage
			Briebe Island	1996	28 S – 153 E	
Airglow Interferometers	Wind and Temperature	87 and 97 km	Peach Mountain, MI	1995 to 1996	40 N - 83 W	Night
LIDAR	Temperature	80 – 100 km	Colorado State	1993 to present	41 N - 105 W	Night (No cloud cover)
			Urbana, IL	1997 - 1998	40 N - 88 W	

observations. Thus current limitations of the HWM/MSIS models stem from two types of uncertainties – statistical and systematic errors. The statistical occurrence of these fluctuations can however, be estimated given our current models and the newly collected data sets. At times these waves represent a significant source of uncertainty in our models. Several examples of statistical comparisons with the underlying historical data sets are given in Hedin *et al.* (1991, 1996). Several recent papers have also focused on HWM/MSIS model biases using newly collected scientific data sets (see for example Fleming *et al.*, 1996). To date, however, there are no published studies directly involving the calculation of comprehensive statistical measures for these models and the subsequent impact on infrasound source estimation.

Figure 1 shows a histogram analysis of hourly Medium Frequency (MF) radar wind measurements and HWM model predictions for a 3-month period over Christmas Island during spring at an altitude of 90 km. The solid lines indicate the distribution of HWM model predictions. The dashed line indicates the measurement distribution of the zonal wind component. Variance in the HWM model predictions is due to the modeled climatological changes in zonal mean flow and the dominant diurnal and semi-diurnal tidal wind components. The differences in the mean value of the histogram distribution indicate a systematic bias between the MF radar measurements and the HWM model. During this period the HWM model under predicts the magnitude of the zonal mean wind component by approximately 20 m/s. This comparison does not imply that the model is biased everywhere. Furthermore, Figure 1 shows that the MF radar winds exhibit a much broader range of values. This is due to the inability to deterministically model fluctuations on time scales less than 8 hours. The magnitude these short time scale fluctuations in the atmosphere depends highly on altitude, latitude, and season.

To access model performance a variety statistical measures will be calculated. These include model bias, standard deviation, and anomaly correlation (error covariance). Together these measures determine the limitations of the models and parameterize the natural variability of the upper atmosphere.

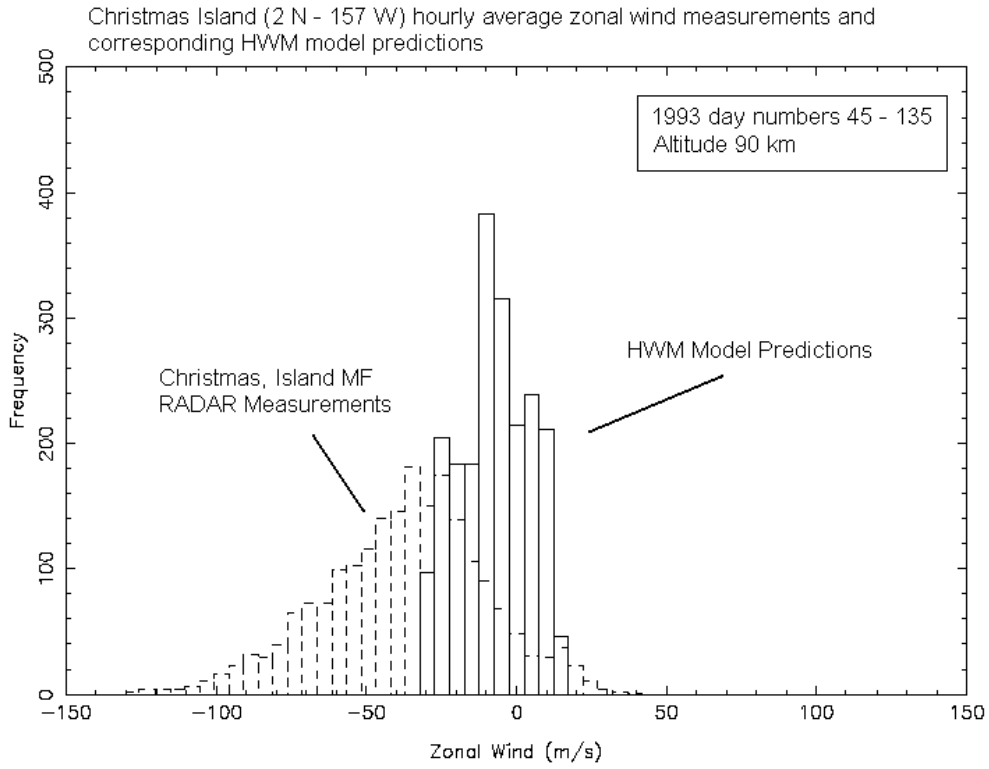


Figure 1. Hourly average wind measurement made at Christmas, Island and the corresponding HWM predictions over a 3-month period indicating a region where model improvement is needed.

CONCLUSIONS AND RECOMMENDATIONS

Application of our models and the pending statistical performance database requires careful consideration, because there are many regions where knowledge may be incomplete. Bias in the current HWM/MSIS models are known to exist. Additional work is needed to understand the impact of atmospheric estimate uncertainties on infrasound source location and characterization. Using the data recently collected for this effort, a better characterization of departures of the HWM/MSIS empirical models from the true state of the atmosphere is being made.

REFERENCES

Hedin, A.E., Extension of the MSIS thermosphere model into the middle and lower atmosphere, *J. Geophys. Res.*, 96, 1159, 1991.

Hedin, A. E., —, Reviesed global model of upper thermospheric winds using satellite and ground-based observations, *J. Geophys. Res.*, 96, 7657-7688, 1996.

Fleming E., —, Climatolgical mean wind observations from the UARS high-resolution doppler imager and wind imaging interferometer: comparison with current reference models, *J. Geophys. Res.,* 101, 10455, 1996.

AN APPLICATION OF EARTHQUAKE DETECTION OF TIME-FREQUENCY ANALYSIS

Guangchao Fan, Northwest Institute of Nuclear Technology

Sponsored by Northwest Institute of Nuclear Technology, China

ABSTRACT

The method of STA/LTA is a conventional automatic detection and timing of earthquakes on a single seismic trace. With comparing the amplitudes of signal and noise level, an event is declared when the ratio of STA/LTA exceeds a given threshold; however, the method can't lead to satisfactory results when Signal-to-Noise Ratio has low level.

We consider applying the method of Time-Frequency Analysis to conventional STA/LTA detection. With analysis of the variance of signal in different frequency bands on a single seismic trace, some CF (characteristic function) can be used, then applying to STA/LTA, an event can be declared. It may be a more effective detection method.

Key Words: detection, STA/LTA, CF, time-frequency analysis

SIMULATING SEISMIC SIGNAL DETECTORS

Yu. V. Fedorenko[1, 2] and Eystein S. Husebye[1]

1. Institute of Solid Earth Physics, University of Bergen, Norway
2. Institute of North Ecology Problems, Kola Science Center Russian Academy of Sciences

Sponsored by U.S. Department of Defense
Defense Threat Reduction Agency
Grant DSWA01-98-C-0159

ABSTRACT

x

The initial, critical step in Comprehensive Nuclear-Test-Ban Treaty (CTBT) International Monitoring System (IMS) seismic monitoring is that of detecting signals in ambient noise at many stations deployed globally. A commonly used detector is the STA/LTA, which is tied to an almost continuous comparison of 'rectified' or RMS trace power in two windows of short (STA) and long (LTA) durations. Moreover, for enhanced performance, the records are pre-filtered in suites of frequency bands for noise suppression prior to the detection process itself. As well-established observationally the noise vary on a diurnal basis; nearly monochromatic during nights and week ends since microseisms dominate while more white during day time due to the influx of high-frequency cultural noise from traffic, running machinery etc. For a fixed STA/LTA threshold, the false-alarm rate is higher during night time. This empirical example serves to illustrate a major problem, highly relevant in the context of CTBT/IMS monitoring, namely how to quantify performances of signal detectors of various designs? We have explored this problem through synthetic but realistic modeling.

Firstly, artificial noise traces are generated via the Gaussian probability density function (p.d.f) for all three sensor (3C) components for which noise is presumed uncorrelated. Processing in terms of noise suppression is achieved through wavelet transform discarding FIR and Butterworth kinds of bandpass filtering (Fig. 1). Test statistics are of the STA/LTA and Kolmogorov-Smirnov (K-S) types defined for four different types of 3C sensor "power-rectified amplitude" combinations. Using the Monte Carlo Method we addressed critical detector design issues through numerical simulations. We started with estimations of confidence intervals for detector performance statistics for given false alarm rates. STA/LTA proved better than K-S types test statistics in terms of variances of critical false alarm levels. The STA/LTA detector is also best if noise is free of spikes and/or other artificial interferences. It can recognize signals with signal-to-noise ratio down to 1.0 given moderate false alarm and missing signal rates of 0.001 and 0.1 respectively. However. inserting spikes with both flat time and amplitude p.d.f.s gave that the STA/LTA detector performances degrades while K-S type detectors are insensitive to spikes. In particular STA/LTA power detectors perform poorly. Likewise, K-S detectors unlike STA/LTA ones have relatively poor performances for "sharp" signals like those generated by WKBJ synthetics but excellent performances for "flat" signals like Pn, volcanic tremors and the like. We have also considered single sensor versus 3C combinations; the latter have better performances for large to moderate angles of incidence ($i > 20°$). Finally, this study is complementary to (Hysebye and Fedorenko, 1999, ibid) because its relevance to seismic stations designed in order to solve real-time phase-picking and event recognizing problem.

Key Words: Signal detectors, STA/LTA, Kolmogorov-Smirnov, test statistics, spike degrading, 3C enhancement.

OBJECTIVE

The objective of this research is to simulate realistically signal detector designs and the corresponding performances for typical operational scenarios for 3-component (3C) stations. The noise is presumed Gaussian while signals are generated by WKBJ synthetics and relative component amplitudes made a function of incident angles. Four different test statistics are considered i) | Z |, ii) Z^2, iii) (Z^2; $N^2 + E^2$) and iv) $Z^2 + N^2 + E^2$ where Z, N and E are respective seismometer components. Two signal detectors are currently tested, namely the popular STA/LTA and the non-parametric Kolmogorov-Smirnov (K-S) detectors in one- and two-dimensional sample space. Preliminary synthetic results are as follow; rectified power STA/LTA detectors have better performances than K-S type detectors. However, for spike prone recordings STA/LTA detector performances degrade in particular for power test statistics while the K-S detectors are insensitive to such irregularities. Most interesting and promising results so far is that including horizontal components in the test statistics gives enhanced signal detection performances for signal incident angles exceeding 20° relative to Z-components on a stand alone basis. Despite moderate testing on real data one result stands out; so-called unexplainable missed signal detections are probably due to blinding of the STA/LTA detector caused by spikes. This is not an entirely uncommon phenomenon in many local network operations where signals are missed by the digital detector but clearly seen visually in the analog seismograms.

RESEARCH ACCOMPLISHED

The advent of digital recording in seismology also introduced the problem of detecting relatively weak signals in ambient noise; strong signals do not pose any problem in this context. The most popular and widely used signal detector is the so-called STA/LTA or variants hereof which is a power ratio measured over two separate windows. The Short Term Average (STA) is measured over windows being 1 - 3 sec while the Long Term Average (LTA) is measured over long windows exceeding minutes. For Gaussian noise the STA/LTA detector is approximately optimum explaining the general popularity of this simple detector in array and network monitoring (Ruud *et al*., 1993). There has also been some "competition' in designing the best signal detector; best in the sense of detecting the largest number of events within a given time period for a given data set. Such contests have never proved conclusive since close to the STA/LTA threshold the number of false alarms increases steeply while the probability of earthquake occurrence only increase linearly according to the earthquake recurrence relation. Besides there is no simple way of confirming the presence of marginal signals from other stations. Also in a CTBTO/IMS context of global seismic monitoring detector design is of considerable interest since only about 50-70 percent of reported signal detections are associated with time-space matching signal detections from other stations as required for acceptable epicenter locations.

A peculiarity of network operations is that most stations are equipped with 3-component seismometers while only vertical recordings are used for detection purposes. In this paper we first discuss briefly the logic of signal detector design and then present different signal diagnostics including joint usages of both vertical and horizontal recordings. The detector performances for various designs and noise conditions would be simulated in a realistic manner and in this context we discuss the redundancy of non-associated signal detections.

Basic logic of signal detector design

From the point of view of statistical hypotheses testing any signal detector perform the same task. It compares current recordings with the previous ones forming the equivalent of the STA/LTA ratio. Depending on the specific value of this ratio, larger or smaller than a prespecified threshold value Y,, the choice is one of two alternative hypotheses. If smaller than Y,, then Ho or the null hypothesis is true that is current data is noise. The alternative or Hi hypothesis is true for exceedance of Y,, that is current data is signal or more correctly (signal + noise). To choose between Ho and HI statistically, we need to translate these two hypotheses from qualitative into quantitative terms. Usually this is done by specifying a probability distribution for the parameters describing the data (often denoted "test statistics"). For example, the STA/LTA detector uses the STA/LTA ratio as test statistics. If this ratio exceeds the threshold level, H_o is rejected that is, H_1 is accepted meaning that a signal is detected.

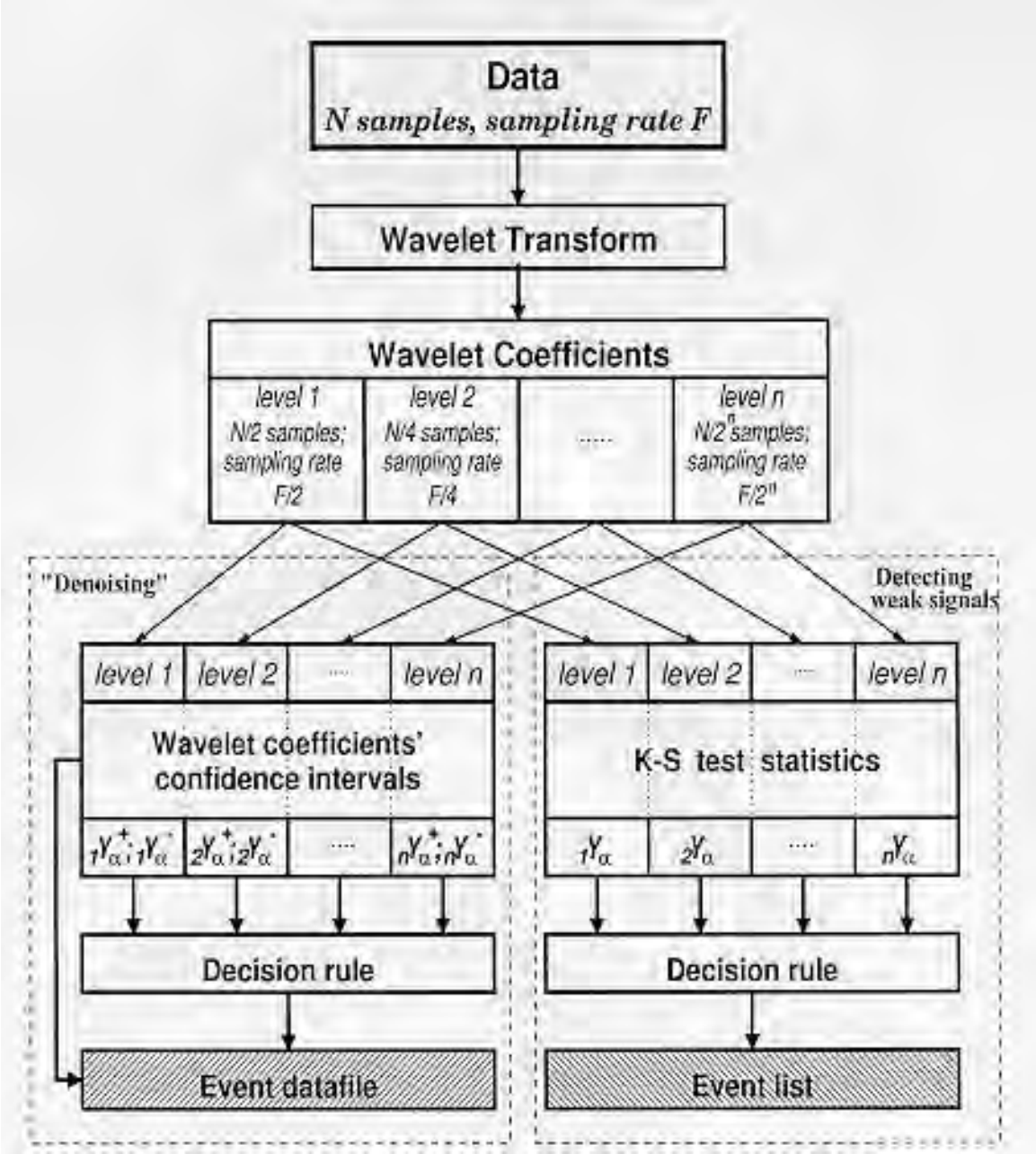


Fig. 1. Dataflow chart. N data samples, sampling rate F are subject to wavelet transform that results in wavelet co-efficients of n hierarchy levels, $n = \log_2 N$. Sampling rate at each level k is $F_k = F/2^k$. "De-noising" algorithm processed wavelet co-efficients at each level for each component independently obtaining estimates for upper and lower critical values ${}^{i}_{k}Y_a^{+}$ and ${}^{i}_{k}Y_a^{-}$ (confidence interval boundaries). Here i = 1,2,3 is component number, k = 1, . . , n is wavelet co-efficients' hierarchy level, α is confidence level. If the number of wavelet co-efficients that fell outside of confidence interval $\left[{}^{i}_{k}Y_a^{+} \; , \; {}^{i}_{k}Y_a^{-} \right]$ exceeds some threshold value, to say 30 to 50%, data are written to the hard disk together with ${}^{i}_{k}Y_a^{+}$ and ${}^{i}_{k}Y_a^{-}$. Latter parameters will be used later for "de-noising" of seismic traces as shown in (Husebye and Fedorenko, ibid). Algorithm responsible for detecting of weak signals has been described in details above.

In general, decision rules may lead to two types of errors: H_0 when H_0 is true and H_0 accepted when H_0 is false. These are called "Type I" and "Type II" errors, respectively. In our case Type I errors are called "false alarm" and Type II errors are called "missing signal," which is easier to understand. There is no way to know for sure whether our decision is incorrect, but it is possible to evaluate the probability of making an incorrect decision. The probability of a "false alarm" or Type I error is referred to as the test's level of significance and is denoted by α. The probability of "missing signal or Type II error is denoted by β. If we know or presume the probability density function (p.d.f.) for the test statistics we can compute the "false alarm" and "missing signal" critical values Y,, and Y,3 which in turn completely determine the decision-making process. Since we aim at designing detection algorithms not using any assumption on the p.d.f. of the test statistics, we use data in the reference time window to obtain the critical value Y_α. How to assess Y_α, is demonstrated below using synthetic signal and noise data. Firstly, we assume that that current data are in short windows (STA equivalent, denoted below as STW) of 2- to 5-sec length. Duration of reference (LTA equivalent, LTW) window is arbitrary and chosen to be some 30 to 60 min. The LTW choice is long enough to reduce test statistics variance and short enough to adapt to changes in the noise structure. Note, that seismic noise exhibits diurnal variations; nearly monochromatic during nights due to dominance of microseism while more white during daytimes due to human activities like fast running machinery etc. Anyway, using a sliding procedure each STW is compared with LTW and the resulting test statistics Y_i, i = 1,.., N are sorted and stored in descending order. Obviously Y_α, = Y_k, where $k = \alpha N$ and N is large. The estimator Y_α, is a function of the random data so Y_α, itself is a random variable and its behavior is described by the presumed p.d.f. Its quality depends on whether or not the estimator's p.d.f. is suitably centered over its expected value. In other words, Y_α, must be unbiased. Another important estimator feature is precision implying that its p.d.f. dispersion should be as small as possible. The precision measure is used for choosing between several estimators.

To study the estimator Y_α, we assume that i) Y_α, has Gaussian distribution with $\sigma = 1$; and ii) Y_α has Kolmogorov-Smirnov distance p.d.f. for N_1, = 32 and N_2 = 4096 where N_1, and N_2 are numbers of samples in STW and LTW, respectively. Exploring case i) is of practical interest because many distributions converge asymptotically to Gaussian. Case ii) is important because, as to be shown later, Kolmogorov-Smirnov "distanc" D has several advantages versus other detector test statistics. For instance, extensive Monte Carlo integrations have shown that the distribution of D is nearly identical for quite different distributions (Press et al., 1993), so the Kolmogorov-Smirnov test does not require the assumption that the noise is normally distributed. Monte Carlo techniques were used to evaluate Y, mean values and confidence intervals for α = 0.1, 0.01 and 0.001. Successive Gaussian random deviates are produced by routines from the Numerical Recipes library (Press et al., 1993), while K-S random deviates are obtained by the "rejection" method. Here the K-S distribution for D is approximately $p_D(x) = dQ_D/dx$, where $Q_D(x) = 2\sum_{j=1}^{a}(-1)^{j-1} e^{-2j_2x_2}$ then $p_D(x) = -8x\sum_{j=1}^{a}(-1)^{j-1j^2e-2j^2x^2}$ (Press et al., 1993) . When x is distributed according to the $p_D(x)$, distance $D = x(\sqrt{N} + 0.12 + 0.11/\sqrt{N})$ for one-dimensional K-S test (which was applied to $|Z|$, Z^2 and $Z^2 + N^2 + E^2$); however $D = x\sqrt{N}[1 + \sqrt{1- r^2}\ (0.25 - 0.75/\sqrt{N})]$ for two-dimensional K-S test which was applied to [Z^2; $N^2 + E^2$]) and r2 = $(r_1^2 + r_2^2)$ / , r_1 and r_2 are correlation coefficients between Z^2 and $N^2 + E^2$ in STW and LTW. Fast algorithm ($n$log$n$) for calculating the two-dimensional K-S test distributed under Gnu GPL and written by Andrew Cooke has been used.

The results in Figs. 2 and 3 imply that the above method for estimating critical "false alarm" value Y, can be used successfully in real-time detectors. In order to obtain stable results about 5000 test statistics samples should be stored which in turn corresponds to 2.5 - 6 hours of recording and hence is representative of daily noise variations. In addition, the $\rho_D(\chi)$ virtue of being almost independent of the actual noise distribution so asymptotic approximation of the p.d.f. may be used in cases of a small α.

Simulating signal detector performance.

As mentioned above, using 3-component (3C) seismic recordings in network operations it may be worthwhile to use all 3 components in the detection process. There are many possible ways to construct such detector test statistics but our preference are for the 4 combinations i) Z; ii) Z^2; iii) (Z^2 ; N^2+ E^2) and iv) Z^2 ; N^2+ E^2 where Z, N, and E are respective seismometer components. Below Z, N, and E are also used

as component indices. Anyway, our signal $s(t)$ and noise $n(t)$ models have zero mean Gaussian p.d.f. $\rho_s(\chi)$ and $\rho_n(\chi)$

$$p_s(x) = \exp(-x^2/s_s^2)/\sqrt{2ps}_s;\ p_n(x) = \exp(-x^2/2s_n^2)/\sqrt{2ps_n}$$

where σ_s^2 and σ_n^2 are signal and noise variances and signal-to-noise ratio (SNR) is σ_s^2/σ_n^2. Vertical n_z, North n_N, and East n_E noise components are independent; $< n_N^2 + n_E^2 + n_Z^2 > = < n^2 >$ and $< n_N^2 > = < n_E^2 > = < n_Z^2 >$ where angular brackets imply averaging.

CONCLUSIONS AND FUTURE PLANS

Our extensive experiments in simulating 3-component seismic signal detections in realistic operational environments are instructive for their designs and workings. Somewhat surprising is how easily poor data like spiky records can ruin performances for STA/LTA type of detectors. The non-parametric Kolmogorov-Smirnov detector is insensitive to such irregularities since rank testing is used for declaring signal presence. The other significant result obtained so far is that utilizing also the horizontal components in the signal detection process performances will improve even at teleseismic ranges $i > 20^o$. The above results reflect extensive synthetic experiments for in our opinion realistic noise and signal conditions. Practical experiences confirm these results. For example, the often puzzling missing signal detections when the signal *per se* is clearly seen in analog records are obviously due to the 'blinding' of the detector due to spike occurrences. This is a persistent problem in some national seismograph networks but far less so for CTBT/IMS stations due to the high technical standard of the latter. Regarding horizontal components our results here reflect the common observation that at local ranges the strongest signal amplitudes are often on the EW- or NS-component. Signal shape is also important in detector design where the STA/LTA detector favor sharp onsets while the K-S detectors are relative insensitive to such signals and spikes as well. On the other hand, signals with gradually growth like Pn are sometimes missed by STA/LTA detectors and the later detected Sg/Lg-phase will then initially be identified erroneously as Pn. This point to likely advantages by operating signal detectors of different design properties to better match variations in signal shapes and durations for different distant ranges and tectonic environments.

Our future plans aim at running both STA/LTA and Kolmogorov-Smirnov detectors in parallel for local 3C stations and naturally for various kinds of test statistics. We will also investigate detector differentiations (phase identifications) between P- and S-arrivals at local distance ranges which is not much of a problem using seismic array data through inherit spatial resolution here. Up to now most of our practical tests have been tied to local (Norwegian) network data while in a CTBT context IMS network data should be used not at least in view of the uniform high technical quality of IMS stations.

REFERENCES

Husebye, S. E. and Yu. V. Fedorenko, 1999. First Breaks - Automatic Pickings of P- and S-offsets, ibid.

Press, W. H., S. A. Teukolsky, W. T. Vetterling and B. P. Flannery, 1992. Numerical Recipes in C: The Art of Scientific Computing, 2nd Edition, Cambridge University Press, MA, USA.

Ruud, B. 0. and E. S. Husebye, 1992. A New Three-Component Detector and Automatic Single-Station Bulletin Production. Bull. Seism. Soc. Am., **82**, 221-237.

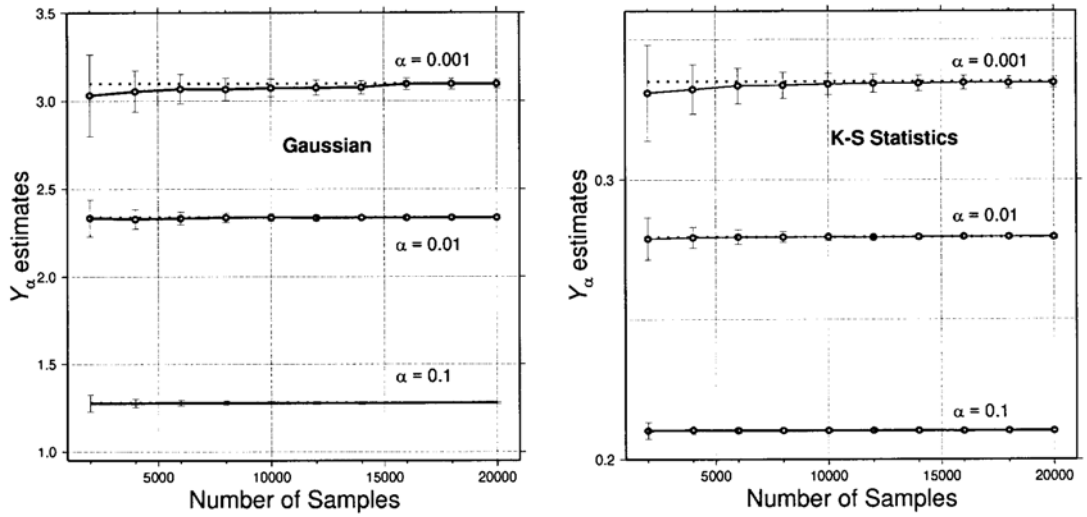


Fig. 2. Y_α estimator mean value versus N (number of samples). Error bars indicate 90% confidence intervals. Dot lines show theoretical values for Y_α. Estimators are consistent but have a small biases for $\alpha = 0.001$ and $N < 10000$.

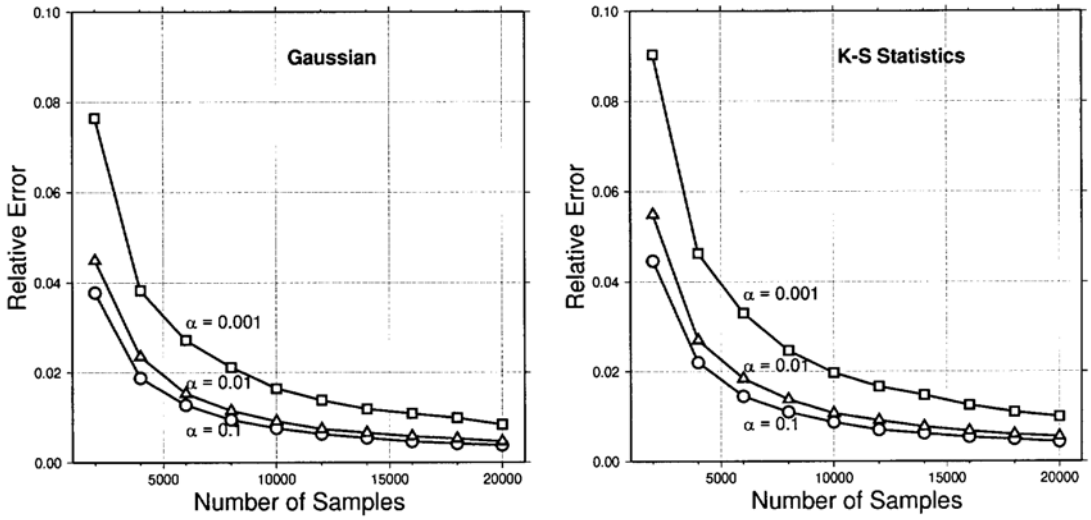


Fig. 3. Relative errors of estimator Y_α versus N (number of samples). Error values calculated as $\delta Y_\alpha = \Delta Y_\alpha / (\overline{Y}_\alpha - Y_{\alpha=0.5})$ where ΔY is 90% confidence interval, $\overline{Y}_\alpha$ is mean value for given α's and $Y_{\alpha=0.5}$ is median value. The Gaussian p.d.f. median value $Y_{\alpha=0.5} = 0$ while K-S p.d.f. median $Y_{\alpha=0.5} = 0.1422$ for $N_1 = 32$ and $N_2 = 4096$. The K-S estimator has smaller confidence intervals ΔY_α but its relative error δY_α is larger than that of the Gaussian.

Seismic signals are modeled as upgoing P-wave with apparent incidence angle ϕ and azimuth θ;

$$[s_N,\, s_E,\, s_Z]^T = [\sin\phi\cos\theta,\, \sin\phi\sin\theta,\, \cos\phi]^T s$$

where $\tan\phi = F\tan i$, i is "true" angle of incidence and F is :

$$F = \frac{2\cos i\cos j}{1 - 2\beta_0^2\sin^2 i/\alpha_0}, \quad \frac{\sin j}{\beta_0} = \frac{\sin i}{\alpha_0}$$

where α_0 and β_0 are surface P- and S-wave velocities. The STW contains $M_s = 32 = N_1$ samples of signal+noise, $S_i = s_i + n_i$, $s_i = s(t_i)$, $t_i = (i-1)/f_{sampl}$, $i = 1, .., M_s$, f_{sampl} is sampling rate while the LTW contains $M_n = 4096 = N_2$ samples of pure noise n_i, $i = 1, .., M_n$. Note that the azimuth parameter is excluded from the test statistics above.

Spikes occurrences in seismic data are not entirely unusual and in particular seismic stations in towns are occasionally spike prone. In order to investigate the influence of spikes on signal detector performance

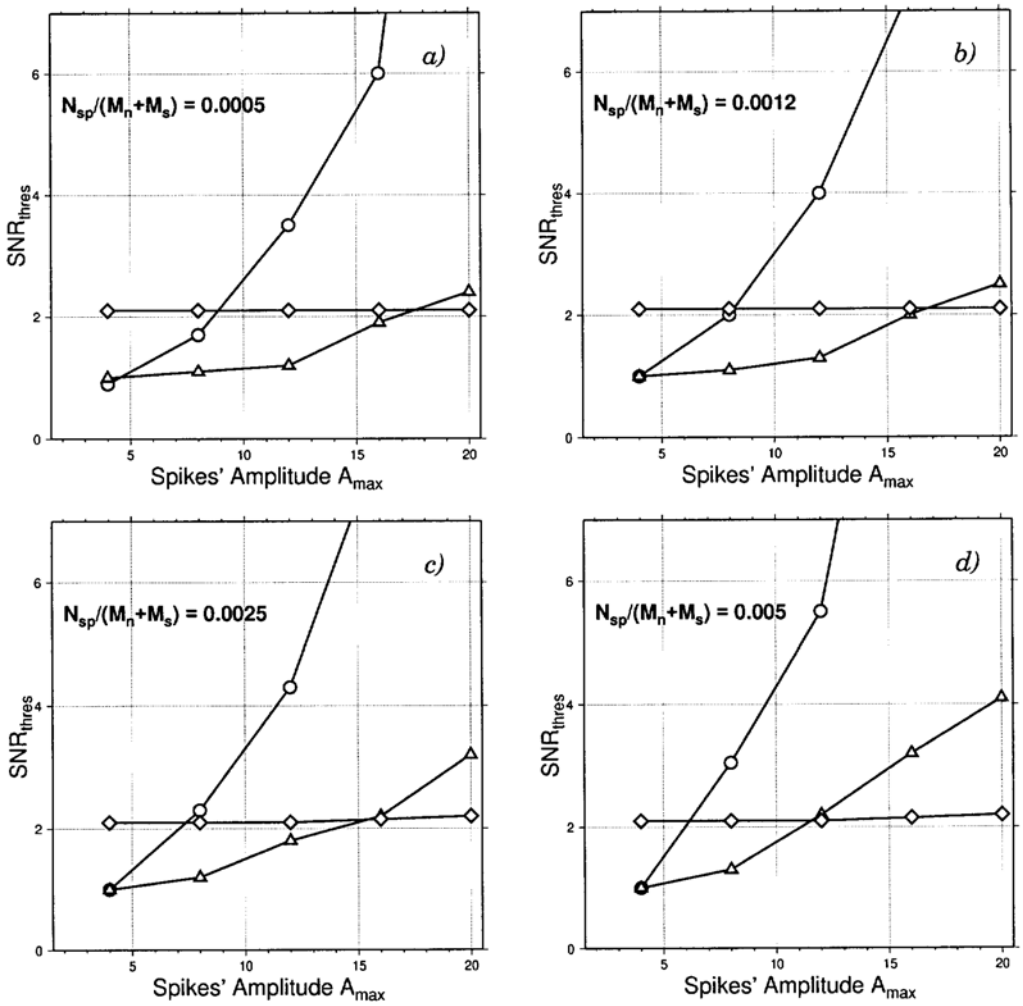


Fig. 4. Spike $A_{\max}$ influence to detector performance for different rates $N_{sp}/(M_n + M_s)$ that is the relative number of spike occurrences. Circles indicate SNR_{thres} for STA/LTA detector test statistics (eq. 2), triangles - for "rectified" STA/LTA (eq. 1), diamonds - Kolmogorov-Smirnov D-statistics (eq. 3). STA/LTA that used power ratio is very spike dependent, on the other hand "rectified" STA/LTA is superior to K-S for small spikes' amplitudes and rates but it is also spike dependent. The K-S D-statistics has poorest performance when noise is pure Gaussian, but on the other hand it is not spike dependent. The latter is not unexpected because D-statistics uses ranks of samples while STA/LTA detectors use amplitudes of samples.

we proceeded in the following manner. Firstly, spikes are modeled as N_{sp} independent single samples uniformly distributed in time with p.d.f. $p^t_{sp}(x) = 1/(M_n + M_s)$, $N_{sp} \ll M_n + M_s$. Likewise the amplitude of spikes also supposed to be uniformly distributed with p.d.f. $p^A_{sp}(x) = 1/A^{\max}_{sp}$. To summarize, the N_{sp} and $A^{\max}_{sp}$ parameters define spikes appearances in the modeled seismic records.

Three types of detector test statistics were studied at this stage, all of them include the 3 seismometer components;

$$R_1 = \frac{\sum_{j=1}^{M_s}(|S_{Nj}| + |S_{Ej}| + |S_{Zj}|)}{\sum_{j=1}^{M_n}(|n_{Nj}| + |n_{Ej}| + |n_{Zj}|)} \quad (1)$$

$$R_2 = \frac{\sum_{j=1}^{M_s}(S_{Nj}^2 + S_{Ej}^2 + S_{Zj}^2)}{\sum_{j=1}^{M_n}(n_{Nj}^2 + n_{Ej}^2 + n_{Zj}^2)} \quad (2)$$

$$D_2 = D_2([S_{Zj}^2,\ S_{Nj}^2 + S_{Ej}^2];\ [n_{Zk}^2,\ n_{Nk}^2 + n_{Ek}^2]),\ j = 1,..,\ M_s;\ k = 1,..,\ M_n \quad (3)$$

where R_1 is the "rectified" STA/LTA detector, R_2 is the conventional STA/LTA detector and D_2 is two-sample Kolmogorov-Smirnov test statistics. In our modeling we set $\beta = 0.1$ which means that 10% of seismic signals with SNR_{thres} will be missed. Fig. 4 shows the results of modeling.

Kolmogorov-Smirnov detectors

Above we have demonstrated that STA/LTA is the best detector test statistics while detector input is free of spikes and noise p.d.f. close to Gaussian. We concentrate further more on K-S detectors because they are not conventional in seismology and otherwise exhibit some useful features. For K-S detectors we summarize from above:

- by direct numerical simulation we have shown that detector performances for all 4 combinations of 3C seismometers are azimuth independent. This is not obvious because of non-linear mixture of noise and signal but demonstrated by simulations to be valid.
- sensor combination iv) being subject to one-sample K-S test shows poorer performances than iii) being subject to two-samples K-S test. In the latter case vertical Z^2 and horizontal $(N^2 + E^2)$ form two-dimensional distribution while $(Z^2 + N^2 + E^2)$ is a one-dimensional random variable;
- test statistics (3) and statistics

$$D_1^i = D_1(S_{Zj}^2;\ n_{Zk}^2),\ j = 1,..,\ M_s;\ k = 1,..,\ M_n \quad (4)$$

were investigated with respect to P-wave angle of incidence. Results obtained (Fig. 5) clearly show

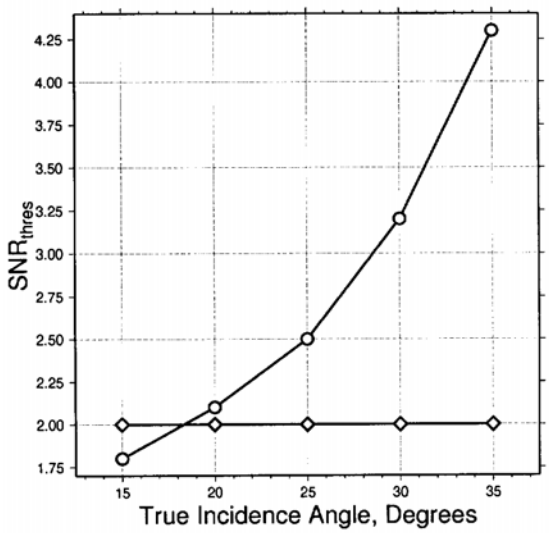


Fig. 5. SNR dependence on the "true" incidence angle. Diamonds represent $D_2(Z^2,\ N^2 + E^2)$, circles - $D_1(Z^2)$. For small incidence angles $D_1(Z^2)$ has better performance but much poorer for large incidence angles.

EVENT CHARACTERIZATION USING REGIONAL SEISIMIC DATA

Mark Fisk and Steven Bottone, Mission Research Corporation
Henry Gray and Gary McCartor, Southern Methodist University

Sponsored by U. S. Department of Defense
Defense Threat Reduction Agency
Contract No. DSWA01-98-C-0152

ABSTRACT

This effort focuses on collecting and analyzing regional seismic data for earthquakes and underground explosions to improve seismic event characterization capabilities with regard to monitoring the Comprehensive Nuclear-Test-Ban Treaty (CTBT). Digital data have been acquired and processed for 227 regional recordings of 148 underground nuclear explosions. Nearly 5800 regional waveforms, recorded by existing seismic stations of the International Monitoring System (IMS), for 3794 presumed earthquakes above mb 3.5 have also been processed at the prototype International Data Center (pIDC). Maximum amplitude measurements of Pn, Pg, Sn and Lg have been computed in several frequency bands ranging from 2 Hz up to 14 Hz (depending on the Nyquist frequency of a given station). The data for the presumed earthquakes have been used to estimate region-specific attenuation corrections for Pn/Sn and Pn/Lg ratios in the 2–4, 4–6, and 6–8 Hz frequency bands. Since Sn or Lg propagate more efficiently in various regions and it is difficult to map all such regions and/or paths, Pn/Smax has been tested in the event characterization analysis, where Smax = max(Sn,Lg). Distance-corrected Pn/Smax measurements from multiple regional stations are averaged for applicable events.

A hypothesis test is applied which fixes the significance level with respect to misclassifying explosions. A score for each event is computed such that events with negative scores are not screened out at the specified significance level. The significance level used here is set such that none of the available underground explosions are screened out. Events with scores greater than zero are screened out (i.e., are considered to be inconsistent with the hypothesis that the event belongs to the explosion population). Screening rates for earthquakes above mb 3.5 are compared for various regions.

Key Words: CTBT monitoring; regional seismic data; event characterization; underground explosions

OBJECTIVE

This effort focuses on collecting and analyzing regional seismic data for underground explosions and earthquakes to improve seismic event characterization capabilities with regard to monitoring the Comprehensive Nuclear-Test-Ban Treaty (CTBT). Key aspects of this effort include: (i) acquiring regional seismic recordings for underground explosions and earthquakes; (ii) processing the waveforms to measure Pn, Pg, Sn and Lg amplitudes in various frequency bands; (iii) evaluating optimum processing techniques for regional amplitude ratios; (iv) developing a regional event-screening capability, which includes establishing necessary region-specific training sets and distance corrections; and (v) evaluating optimum screening criteria for various regions and comparing explosion and earthquake characteristics in an effort to understand how regional event characterization parameters and screening criteria can be transported to regions for which no explosion data exist.

This work is motivated by the fact that, although depth and Ms:mb are essential methods in the characterization of seismic events, the experimental depth and Ms:mb screening criteria being tested at the prototype International Data Center (pIDC) currently screen out less than 50% of the presumed earthquakes above mb 3.5 in the Reviewed Event Bulletin (REB) (e.g., Fisk et al., 1999). However, there are a significant number of events in the REB with regional seismic data that can provide additional event-screening performance. Many studies have indicated that ratios of high-frequency, regional seismic phase amplitude ratios can provide adequate separation between underground explosions and earthquakes to aid in monitoring the CTBT (see Fisk et al., 1996, and references therein).

We describe data that have been compiled and processed for 227 regional recordings of 148 underground nuclear explosions (UNE's). These explosions are compared to over 5800 regional waveforms, recorded by existing seismic stations of the International Monitoring System (IMS), for 3794 presumed earthquakes, above mb 3.5, processed at the pIDC. We then describe how region-specific distance corrections are derived and applied to Pn/Sn and Pn/Lg values in various frequency bands. To characterize the events, we use distance-corrected, network-averaged Pn/Smax in the 4–6, and 6–8 Hz bands, where Smax = max(Sn,Lg). We apply a hypothesis test to these data sets to assess whether an event is consistent with the explosion population, at a fixed significance level with respect to incorrectly screening out an explosion. A *score* is computed such that events with positive scores are screened out, i.e., are inconsistent with the hypothesis that the event belongs to the explosion population. Events with scores less than or equal to zero are not screened out. At the 0.005 significance level, none of the available explosions are screened out. We also compare the regional screening approach to that of Ms:mb and discuss some applicability issues.

RESEARCH ACCOMPLISHED

Regional Explosion Data

We have compiled 227 regional seismic recordings for 148 UNE's; some events were recorded by more than one station within 20 degrees. Table 1 summarizes our current database of regional UNE recordings. Stations that are part of the IMS network have an asterisk next to the station code. Recordings by NORES and NORSAR are for NZ events beyond regional distances (i.e., > 20 degrees) and are not used in this study. Regional amplitude measurements that have been computed for these recordings using software at the pIDC are indicated by "Yes" entries in the last column of Table 1. The regional measurements for the NTS explosions recorded by MNV and KNB were provided by LLNL (Patton and Walter, 1994) and the PNE data recorded by BRVK were provided by Jack Murphy (1998).

The processed data consist of regional phase amplitudes, Pn, Pg, Sn and Lg in the 2–4, 4–6, 6–8, and 8–10 Hz bands. Not all events have complete sets of amplitude ratios. Six of the UNE's conducted on Novaya Zemlya (NZ) were recorded by station KEV and three were recorded by ARCES. Pn/Sn was measured for these nine waveforms in all frequency bands; Pn/Lg was not measured due to Lg blockage. Five UNE's occurred at the Lop Nor test site, two recorded by ULN and BRVK, one by NIL and ZAL, one by just NIL, and one by WMQ. All amplitude ratios were computed for these events. Two chemical explosions in Kazakhstan, recorded by ZAL, and one UNE in India, recorded at NIL, also have complete data sets. Sixteen UNE's at the Balapan test site have complete data sets based on WMQ recordings. Eight additional Balapan UNE's, recorded by WMQ,

did not meet our signal-to-noise criterion (Pn-SNR > 2) and were not used in this study. There are 99 NTS explosions, 84 of which have recordings at both MNV and KNB, 8 at MNV only, and 7 at KNB only. Most of these events have Pn/Lg in the 4–6 and 6–8 Hz bands, although a few have only Pn/Lg(4–6 Hz). Last, there are 19 Peaceful Nuclear Explosions (PNE's) conducted by the Former Soviet Union with recordings by BRVK. At this time, only values of Pn/Lg(6–8 Hz) are available.

Regional Earthquake Data

Over 5800 regional waveforms that were recorded by 46 IMS seismic stations and processed at the pIDC are used in this study. These recordings correspond to 3794 distinct REB events above mb 3.5 that are presumed to be earthquakes. The restriction to mb > 3.5 is used to reduce the possibility of mining blasts contaminating the earthquake data sets. We also limit the events to those with distances beyond 3 degrees to avoid problems of distinguishing Pn and Pg, and less than 17 degrees, although regional phase amplitudes are computed at distances upto 20 degrees at the pIDC. In addition, we limit this study to data from IMS stations that have at least 20 or more recordings so that useful training sets may be formed. Accordingly, only data from 24 primary and 22 auxiliary stations are used here. Figure 1 shows the locations of the 3794 presumed earthquakes and the 148 explosions used in this study. The locations of the 46 IMS stations and 4 non-IMS stations (KEV, WMQ, BRVK and KNB) are included.

Maximum amplitudes of Pn, Pg, Sn and Lg have been measured at the pIDC in the 2–4, 4–6, 6–8, 8–10 and 10–12 Hz bands (depending on the Nyquist frequency of the instrument). For this study, we use Pn/Sn and Pn/Lg in the 4–6 and 6–8 Hz bands that satisfy the signal-to-noise criterion of Pn signal divided by pre-Pn noise greater than 2.0.

In addition to the pIDC data, the earthquake data set also includes 60 recordings by MNV and 75 by KNB of Pn/Lg in the 4–6 and 6–8 Hz bands for earthquakes near NTS, processed by LLNL in the same way as the 99 UNE's. These earthquakes are necessary to properly calibrate stations MNV and KNB.

Table 1: Summary of Regional Underground Nuclear Explosion Data

Station	Distance	Magnitude	Test Site	Explosion Dates	Processed?
KEV	9.4 3.1-19.5	5.52–5.90 4.70-5.50	NZ PNE's	821011, 841025, 870802, 880507, 881204, 901024 5 (820904-850718)	Geotool
ARCES*	9.9	5.60–5.90	NZ	880507, 881204, 901024	ISEIS
NORES	20.4	5.60-5.90	NZ	841025, 870802, 880507, 881204, 901024	No
NORSAR*	20.5	3.80-6.04	NZ	761020, 771009, 840826	No
ZAL*	12.2 6.2, 6.0	4.71 3.95, 3.80	Lop Nor Kazakhstan	960729 970803, 980822	Yes Yes
NIL*	14.5 6.7	5.69, 4.71 5.00	Lop Nor India	960608, 960729 980511	Yes Yes
ULN*	14.3	5.73, 5.54	Lop Nor	950515, 950817	Yes
WMQ	8.6 2.2	4.6–6.1 4.7	Balapan Lop Nor	21 (1987-1989) 880929	Yes
BRVK	17.0 7.2-17.2	5.73, 5,54 4.5-5.8	Lop Nor PNE's	950515, 950817 19 (730815-880906)	No
MNV*	1.7–2.2	2.4–5.5	NTS	92 Explosions	LLNL
KNB	2.5–2.8	2.6–5.5	NTS	91 Explosions	LLNL

Distance Corrections

The unequal rates of attenuation with distance between regional P and S phases necessitates a correction for distance if amplitude ratios recorded at different distances are to be compared (see Sereno, 1990, Bottone et al., 1997, and Fisk et al., 1998). Figure 2 plots Pn/Lg(6–8 Hz) values as a function of distance from the recording station for the REB events and explosions worldwide (the BRVK PNE data have been excluded here, but will be considered below). The P/S distance dependence is modeled by a three-parameter equation of the form

$$\log (P/S) = \alpha + \beta \log (\Delta/\Delta_0) + \gamma\Delta \qquad (1)$$

where α, β, and γ are parameters depending on the particular amplitude ratio (Pn/Lg or Pn/Sn) and the frequency band, is the epicentral distance, and the constant Δ_0 is a reference distance that is set at 1500 km, roughly the mean epicentral distance of the all REB regional events.

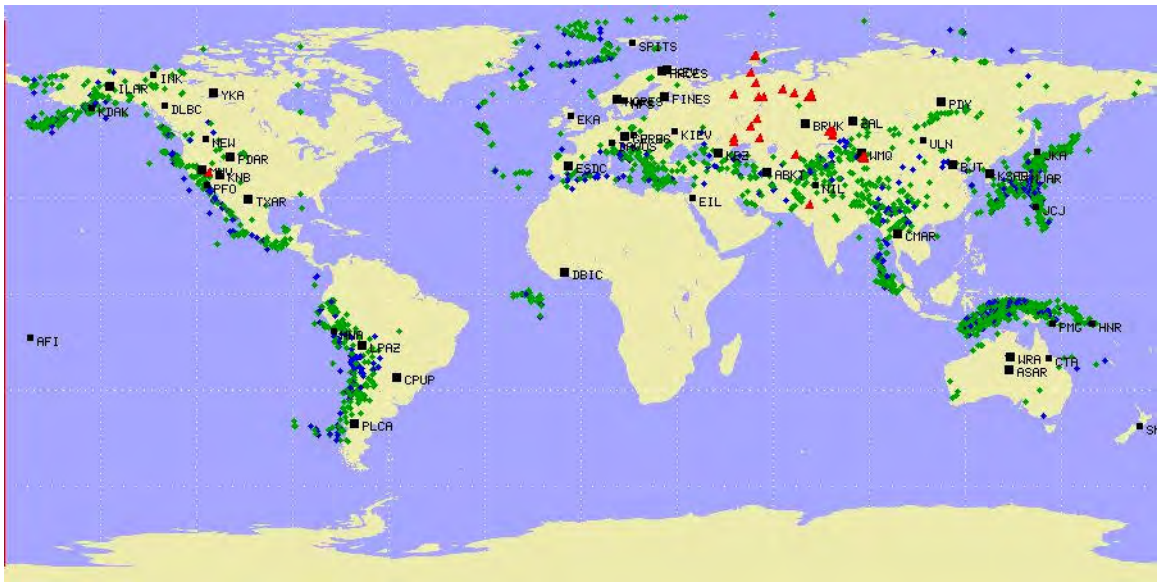


Figure 1. Locations of 148 nuclear explosions (triangles) and 3794 REB earthquakes with mb 3.5 and above. Locations of 46 IMS stations and 4 stations with explosion recordings (KEV, WMQ, BRVK, and KNB) are also shown.

Equation (1) is represented by the solid curve in Figure 2, with the three parameters estimated to minimize the sum of the squared residuals of the REB data points from the curve. It is clear from the plot that if this amplitude ratio for the explosions recorded at MNV and KNB, which have propagation paths only 200 to 300 km in length, are to show separation from the entire sample of all REB events at all distances, then distance corrections will be necessary. In general, amplitude ratios at short distances, 200–500 km, have smaller P/S ratios for both explosions and earthquakes, as demonstrated in Figure 2, and, therefore, distance corrections are most important at these distances.

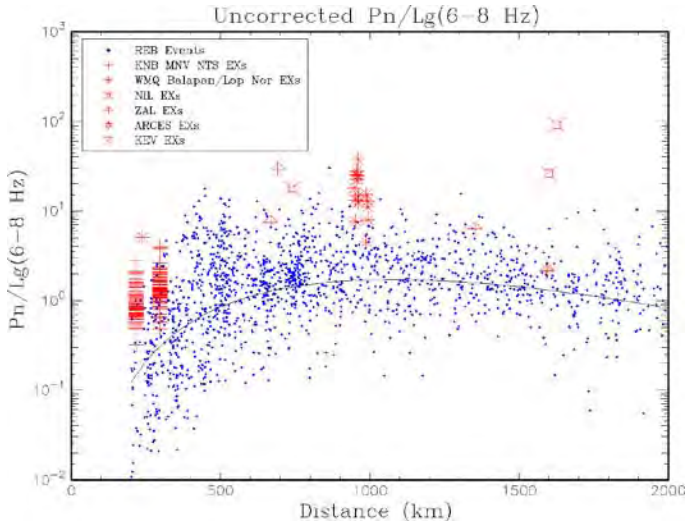


Figure 2. Uncorrected Pn/Lg(6–8 Hz) versus distance for all REB events and explosions worldwide. The solid curve is a best-fit, three-parameter estimate of the distance dependence.

While Figure 2 indicates the general distance dependence of regional amplitude ratios, it is necessary to estimate distance corrections for each station to account for region-specific variations in attenuation. We have investigated several ways of computing distance corrections for a given region and station. We have found that the overall event-screening results are not sensitive to which method is used. The approach we adopt in the remainder of this paper follows Jenkins et al. (1998), in which we divide the world into eleven tectonic regions and estimate b and g in each region using all data available in that region. For each station in a particular tectonic region, a is then estimated using data from that station only. Thus, the distance-correction curves for each station in the same tectonic region have the same shape, but are adjusted to best fit the mean of the data for that station. In our study, two of the regions, eastern North America and Africa, have inadequate data to compute distance corrections, leaving nine regions.

An example of the distance corrections is shown in Figure 3, where Pn/Lg and Pn/Sn values in the 4–6 and 6–8 Hz bands are plotted versus distance for ZAL in the central Asia region. The solid line is the distance-correction curve fit to the ZAL earthquake data. For comparison, the dashed curve is the worldwide-average curve. For ZAL, the two sets of curves are fairly similar. Also plotted are the values of the P/S amplitude ratios for three explosions recorded by ZAL. These three events are clearly separated from the earthquakes. This separation will be quantified below.

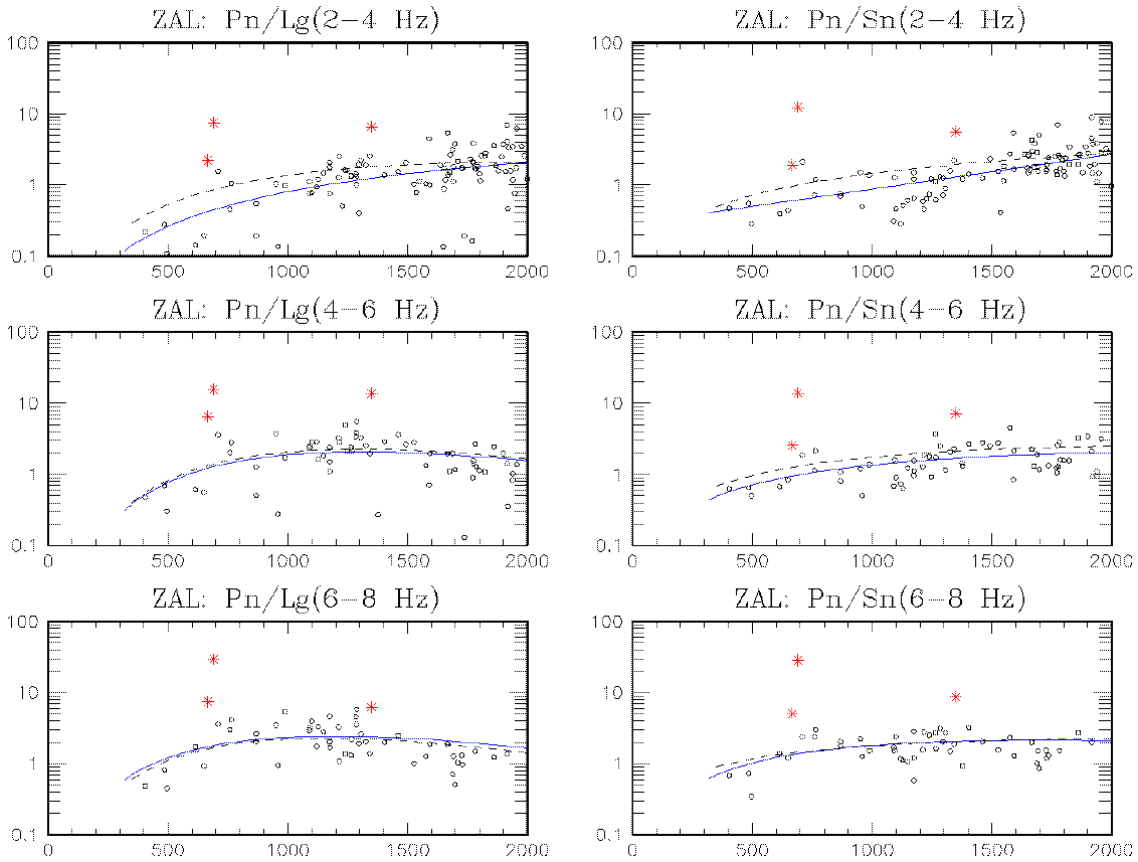


Figure 3. Regional P/S versus distance (km) at ZAL. The solid lines are the distance-correction curves.

Event Characterization Parameters

Pn/Lg and Pn/Sn amplitude ratios are computed, using the same frequency band for the P and S wave amplitude measurements (to minimize source size effects). A problem with using all combinations of the P/S values is that Lg or Sn are severely attenuated or blocked for some paths. For example, Lg is typically blocked along many oceanic or other thin crustal paths and Sn is severely attenuated in the western U.S. and the Middle East. Since

it is difficult to map all such paths, we use Pn/Smax values (in each frequency band), where Smax is the maximum of Lg and Sn (i.e., Smax is the Lg or Sn phase which propagates more efficiently in a given region).

Higher frequency bands generally provide better separation between explosion and earthquake populations (e.g., Fisk et al., 1996; Kim et al., 1997; Walter et al., 1995). However, signals at frequencies above 8 Hz are often below noise levels. We have found that the best overall performance of the hypothesis test presented below is provided by using the 4–6 and 6–8 Hz bands. Thus, we use two event characterization parameters, distance-corrected log[Pn/Smax(4–6 Hz)] and log[Pn/Smax(6–8 Hz)]. Taking the logarithm of each amplitude ratio usually results in populations that are more normally distributed (Bottone et al., 1997), allowing a simpler statistical treatment.

Of the nearly 3800 regional events recorded at 46 IMS stations used in this study, about 25% of these events have regional data recorded at more than one station. About 7% of the events are observed at three or more stations. Our current treatment is to average the regional measurements for those events with multi-station data. We have found that network averaging provides good screening performance, without screening out any explosions, but may not necessarily be the best approach for combining multi-station data. We plan to investigate this problem further. Averaging is performed on the distance-corrected values of log(P/S) for each type of amplitude ratio. If a particular amplitude ratio is missing (e.g., due to low signal-to-noise), it is not included in the averaging.

Figure 4 is a plot of Pn/Smax(6–8 Hz) versus distance after distance corrections and network averaging have been performed. The legend associates the marker types with the various events. It can be seen that the majority (about 80%) of the Pn/Smax(6-8 Hz) values for the REB earthquakes are below the lowest value for the explosions.

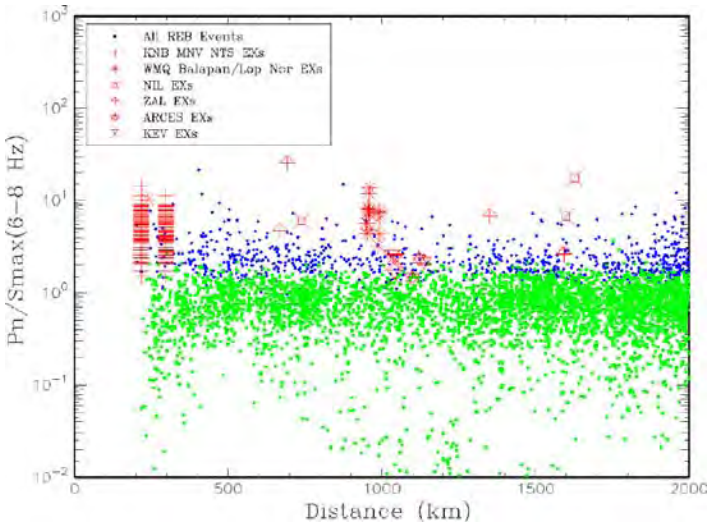


Figure 4. Pn/Smax(6–8 Hz) versus distance after applying distance corrections and network averaging.

Experimental Event-Screening Criterion and Score

A screening criterion may be defined as a hypothesis test, based on a linear discriminant function (see Anderson, 1984), with a fixed significance level with respect to incorrectly screening out an explosion. More precisely, let
$\mathbf{x} = (x_1, x_2)'$, where x_1 and x_2 are the distant-corrected, network-averaged values of log[Pn/Smax(4–6 Hz)] and log[Pn/Smax(6–8 Hz)]. Assuming the data have normal distributions and the covariance matrices for the explosions and earthquakes are equal, the optimal linear combination of x_1 and x_2 is given by

$$\lambda = (\mathbf{u}_{EX} - \mathbf{u}_{EQ})' \Sigma^{-1} \mathrm{x}, \qquad (2)$$

where $\mathbf{u}_{EX}$ and $\mathbf{u}_{EQ}$ are the vector means of $\mathbf{x}$ for the explosion and earthquake populations, respectively, and Σ is the covariance matrix. Under the null hypothesis that $\mathbf{x}$ is an element of the explosion population, λ is also normally distributed with mean u_λ and $\sigma_\lambda^2 =$ variance, where

$$u\lambda = (\mathbf{u}_{EX} - \mathbf{u}_{EQ})' \Sigma^{-1} \mathbf{u}_{EX} \tag{3}$$

and

$$\sigma_\lambda^2 = (\mathbf{u}_{EX} - \mathbf{u}_{EQ})' \Sigma^{-1} (\mathbf{u}_{EX} - \mathbf{u}_{EQ}) \tag{4}$$

We define a screening criterion, to fix the probability of screening out an explosion to be a, given by

$$\lambda < u_\lambda - z_\alpha \sigma_\lambda, \tag{5}$$

where z_α is the (1–α)-percentile of the standard normal distribution with zero mean and unit variance. A *score* may be defined such that an event is screened out at the α significance level, if the score is greater than zero:

$$\text{Score} = \frac{u_\lambda - \lambda}{z_\alpha \sigma_\lambda} - 1. \tag{6}$$

Unbiased sample estimates of the means and covariance matrix are computed from the explosion and earthquake data sets described above and are used in Equations (2)–(6).

The scores for 129 explosions and 3794 earthquakes are represented by the histograms in Figure 5. The significance level, α, is chosen to be 0.005, corresponding to $z_\alpha = 2.576$. In this case, the scores for all the explosions are less than zero and, thus, none are screened out. Typically we should expect one out of 200 explosions to be screened out at this significance level. About 79% of the earthquakes have scores greater than zero and, thus, would be screened out. This gives an estimate of the power of the test, which is the probability that an earthquake will be screened out.

In cases where one of the two discriminants is not available the test described above based on a single frequency band is applied. In this case, the explosion error will still be the same, approximately 0.005, however, the probability of screening out earthquakes will change, depending on which event characterization parameter is available and the relative separation of the explosion and earthquake populations in that case.

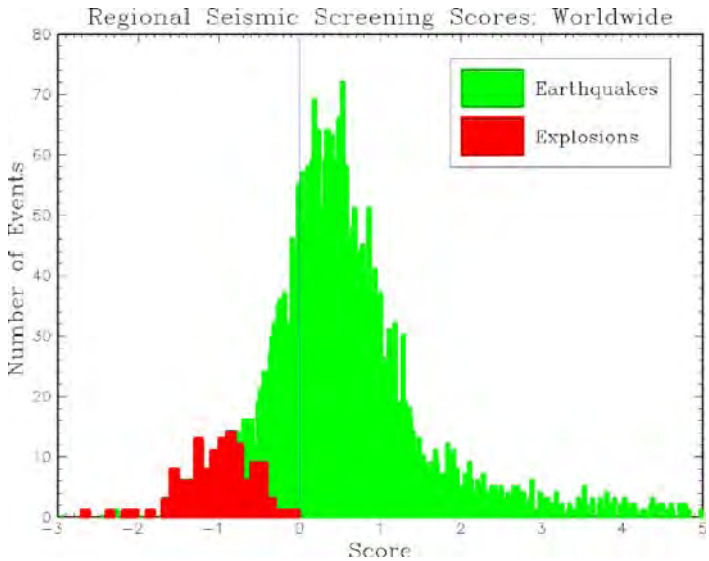


Figure 5. Histograms of regional screening scores for 129 explosions (left) and 3794 earthquakes (right).

None of the explosions are screened out (all have scores less than zero using a significance level of 0.005), while 79% of the REB earthquakes are screened out (scores greater than zero).

Comparison to Ms:mb

The difference of body and surface wave magnitudes (Ms:mb) has long been used to characterize seismic events. In the current implementation at the pIDC, a seismic event above mb 3.5 and having an Ms measurement is screened out if the 97.5% confidence interval of 1.25mb–Ms is less than 2.2 (Fisk et al., 1999). There are a number of similarities between the Ms:mb and regional event-screening criteria. Both procedures utilize the difference of the logarithm of seismic amplitudes measured in appropriate frequency bands. Distance corrections are required for both methods. In addition, the regional variation for distance-corrected Pn/Lg between NTS and Balapan events is similar to that of Ms:mb. The regional and Ms:mb screening criteria are both defined empirically so that no available explosions are screened out. Figure 6 indicates that the performance of the regional and Ms:mb screening criteria are similar. On the left is a plot of the regional score, scaled to the original values of log(Pn/Smax), versus mb for the regional events. The plot on the right shows 1.25mb–Ms versus mb for a similar sets of events. In each case, the percentage of REB earthquakes screened out is about 80%, while no explosions are screened out.

While there is some theoretical basis for the ability of regional P/S to characterize seismic events, it is not as firm as for Ms:mb. Regional phases usually exhibit greater sensitivity to path variations as well. For these reasons, among others, Ms:mb is generally more reliable. However, there are many events of interest which do not have Ms and, thus, the Ms:mb screening criterion cannot be applied. In particular, none of the explosions below mb 4.5 in our data sets have Ms measurements, while many of these events have regional data, allowing the regional screening analysis to be applied. In fact, about 70% of the events in the REB with useful regional phases do not have Ms:mb.

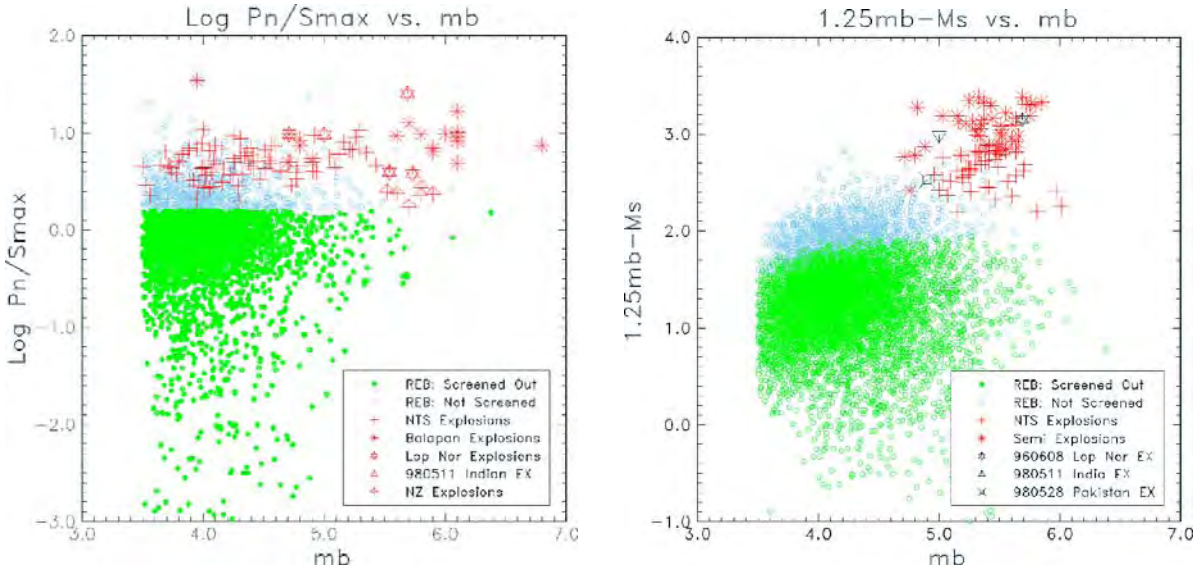


Figure 6. Comparison of the regional Pn/Smax (left) and Ms:mb (right) screening criteria versus mb. In both cases, no explosions are screened out while about 80% of the REB earthquakes are screened out.

Borovoye Data

The 19 Soviet PNE's recorded by Borovoye (BRVK) were not included in our analyses because only Pn/Lg values in the 6–8 Hz band are currently available. For the analysis to be consistent, Pn/Sn is also needed because earthquake data recorded by BRVK suggests that Smax is Sn. Also, having P/S in the 4–6 Hz band usually improves the screening performance. Although using Smax can only reduce the Pn/Smax ratio for the PNE's, there may be an even larger reduction for the earthquakes. This can only be determined with consistent

measurements of all available waveforms. Nevertheless, there appear to be one to three problematic explosions in the BRVK data set.

Figure 7 is similar to Figure 2, showing a plot of Pn/Lg(6–8 Hz) versus distance, with the 19 PNE's included. There is one PNE at about 1200 km from BRVK whose Pn/Lg(6–8 Hz) value is below the distance-correction curve. If Pn/Lg(6–8 Hz) were the only feature and only events with Pn/Lg(6–8 Hz) less than this PNE could be screened out, then the screening rate for earthquakes would be less than 50%. Two other events, at about 800 km and 1200 km, are barely above the distance-correction curve and could also present difficulties. All three events are located north of the BRVK, where there are virtually no earthquake data to compare to the PNE's.

Figure 8 shows plots of Pn/Lg(6–8 Hz) on the left and Pn/Sn(6–8 Hz) on the right versus distance for 18 earthquakes, two Lop Nor UNE's, and the 19 PNE's (Pn/Lg(6–8 Hz) only) recorded by BRVK. Distance-correction curves (solid lines) that were fit to the 18 earthquakes are included in each plot. For comparison, the average distance-dependence curves for central Asia are also plotted (dashed lines). Note that the fit to the BRVK Pn/Lg data is much higher than the central Asia curve, indicating that earthquakes recorded by BRVK typically have values of Pn/Lg above the central Asia average, while the fit to the BRVK Pn/Sn data is lower than the central Asia curve. Note also that for the two Lop Nor explosions, for which there are both Pn/Lg and Pn/Sn, the values of Pn/Sn are further above the distance-correction curve than is the case for Pn/Lg. Neither of these Lop Nor UNE's were screened out using the regional screening procedure. This example indicates the need for a full evaluation of this BRVK PNE data.

Applicability Issues

Although none of the available explosions at the Nevada, Lop Nor, Balapan, Indian and Novaya Zemlya test sites were screened out, as shown in Figure 5, it should be emphasized that the effectiveness of this experimental procedure is unknown for regions without calibration data. For example, northern Russia is relatively aseismic. The PNE data recorded by BRVK indicate possible difficulties in such aseismic regions. Although none of the six NZ underground nuclear explosions were screened out, calibration data are limited in this region.

It should also be noted that all explosions used in this study were underground. Some actual and simulated examples of in-water explosions indicate that they may generate relatively large S waves (e.g., Baumgardt and Der, 1998), depending on the boundary condition at the liquid/solid interface, which would reduce the effectiveness of the current screening procedure. Thus, the regional screening criterion cannot be applied confidently to offshore events at this time. Note that by restricting the procedure to onshore events above mb 3.5, it would not be applied to any of the events in the Novaya Zemlya region since 1990. In the future, it may be possible to combine regional seismic data with other seismic and hydroacoustic characteristics to develop a useful screening procedure for offshore events.

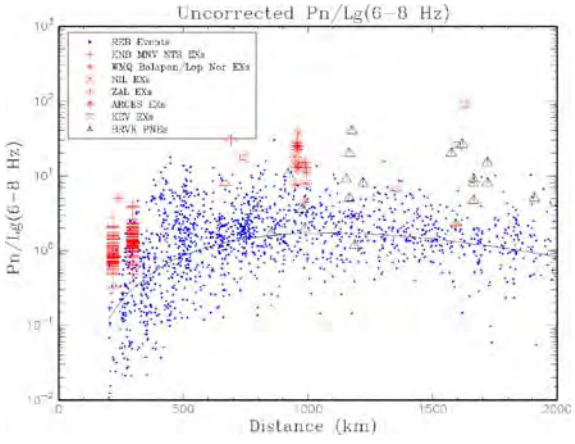


Figure 7. Uncorrected Pn/Lg(6–8 Hz) versus distance for REB events and explosions worldwide, including 19 Soviet PNE's.

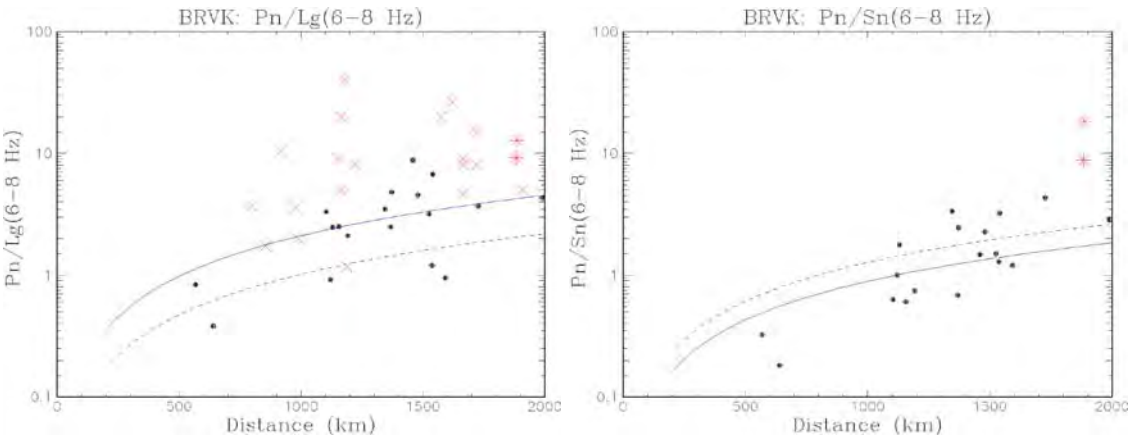


Figure 8. Pn/Lg(6–8 Hz) and Pn/Sn(6–8 Hz) values versus distance for BRVK. Solid lines represent best-fit distance-correction curves for BRVK; dashed lines indicate the average central Asia curves.

CONCLUSIONS AND RECOMMENDATIONS

High-frequency, regional seismic P/S amplitude ratios have potential utility to augment the seismic event-screening procedures based on event depth and Ms:mb. Using the screening procedure described in this paper, no available underground explosions were screened out at the Nevada, Lop Nor, Balapan, Kazakhstan, Indian, or Novaya Zemlya test sites, while about 79% of onshore REB events above mb 3.5 and with Pn-SNR > 2.0 can be screened out. This screening performance compares favorably with that of Ms:mb. The experimental depth and Ms:mb screening criteria at the pIDC currently screen out less than 50% of REB events above mb 3.5 and about 70% of REB events that have applicable regional data are relatively shallow and do not have an Ms measurement.

One to three of the 19 PNE's recorded by BRVK indicate potential difficulties with applying the procedure to regions with insufficient calibration data. Additional BRVK data are needed to complete this evaluation. A possible approach to treating aseismic regions, such as northern Russia where these PNE's were located, is to simply not apply the regional screening criterion in such regions where the performance is uncertain. Since there are few events to consider in aseismic regions, the overall screening rate of earthquakes would not be significantly affected.

In addition to regions without adequate calibration data, screening performance for offshore events is also uncertain. All of the explosions in this study were conducted underground and some evidence suggests that in-water events may generate relatively large S-wave amplitudes, adding to the uncertainty of applying the regional screening procedure to such events. This issue should be investigated further. In the future it may be possible to combine the regional seismic data with other seismic and hydroacoustic characteristics to develop a useful screening procedure for offshore events.

There are several potential ways to improve the regional screening performance. Currently, the pIDC measures regional phase amplitudes only on vertical components. Although P/S ratios measured on vertical components show reasonable power for separating earthquakes from explosions, Kim et al. (1997) showed that P/S spectral ratios of rotated, three-component (3-C) records improve the power. Since most IMS seismic stations have 3-C broadband sensors, the horizontal components should also be considered for event characterization. Also, a small percentage of the automatic regional phase amplitudes measurements suffer from poor data quality (e.g., noise spikes, clipping, drop-outs). Improved methods of flagging such data are needed. Difficulties measuring regional phase amplitudes also exist for events recorded at distances less than about 3 degrees, and so have not been used in this study. More careful analysis at these near regional distances is necessary so that the screening procedure can be applied to these, potentially important, events. Processing additional explosion data, including the BRVK PNE data, should help improve the calibration of corresponding regions. Complicated geological regions may need to be divided into subregions to improve the performance of the procedure.

REFERENCES

Anderson, T. W. (1984). An Introduction to Multivariate Analysis, Second Edition, John Wiley and Sons, Inc., New York.

Baumgardt, D. R., and Z. Der (1998). Identification of presumed shallow underwater chemical explosions using land-based regional arrays, Bull. Seism. Soc. Am., **88**, 581-595.

Bottone, S., M. D. Fisk, H. L. Gray, G. D. McCartor and R. J. Carlson (1997). Initial Regionalization Efforts for the IMS Seismic Network, PL-TR-97-2090, Phillips Laboratory, Hanscom AFB, MA.

Fisk, M. D., S. Bottone, R. J. Carlson, H. L. Gray and G. D. McCartor (1998). Event Characterization Development and Analysis at the Prototype IDC, MRC-R-1548, Mission Research Corporation, Santa Barbara, CA, Phillips Laboratory, Hanscom AFB, MA.

Fisk, M. D., H. L. Gray and G. D. McCartor (1996). Regional discrimination without transporting thresholds, Bull. Seism. Soc. Am., **86**, 1545-1558.

Fisk, M. D., D. Jepsen, and J. R. Murphy (1999). Experimental seismic event-screening criteria at the Prototype International Data Center, submitted to Pure and Applied Geophysics.

Jenkins, R. D., T. J. Sereno and D. A. Brumbaugh (1998). Regional Attenuation at PIDC Stations and the Transportability of the S/P Discriminant, AFRL-VS-HA-TR-98-0046, Air Force Research Laboratory, Hanscom Air Force Base, MA.

Kim, Y. K., V. Aharonian, A. L. Lerner-Lam and P. G. Richards (1997). Discrimination of earthquakes and explosions in southern Russia using regional high-frequency three-component data from IRIS/JSP Caucasus Network, Bull. Seism. Soc. Am., **87**, 569-588.

Murphy, J. R. (1998). Private communication.

Patton, H. J., and W. R. Walter (1994). Private communication.

Sereno, T.J. (1990). Attenuation of Regional Phases in Fennoscandia and Estimates of Arrival Time and Azimuth Uncertainty using Data Recorded by Regional Arrays, SAIC-90/1472, Science Applications International Corporation, San Diego, California.

Walter, W. R., K. M. Mayeda, and H. J. Patton (1995). Phase and spectral ratio discrimination between NTS earthquakes and explosions. Part I: Empirical observations, Bull. Seism. Soc. Am., **85**, 1050-1067.

INSTALLATION OF THE MINA, NEVADA, SEISMIC AND ACOUSTIC ARRAYS

Paul Golden, Jessie Bonner, Eugene Herrin, Ileana Tibuleac,
Jack Swanson, Gordon Sorrells, Chris Hayward, Brian Stump, and David Anderson
Department of Geological Sciences, Southern Methodist University

Sponsored by U. S. Department of Defense
Defense Threat Reduction Agency
Grant No.: DSWA01-97-I-0024

ABSTRACT

The Mina, Nevada, seismic array (NVAR) was installed in the Garfield Hills of west central Nevada, in December 1998, by the Southern Methodist University (SMU) Geophysics Laboratory. The array is a primary seismic station of the International Monitoring System (IMS) at 38.4°N and 118.2°W, as described in Annex I of the Protocol to the Comprehensive Nuclear-Test-Ban Treaty. The central site (NV01) of NVAR is located at 38.43°N and 118.3°W and is 11.3 km from the treaty coordinates. IMS Certification of the array is scheduled for August 1999. A complementary four-element acoustic array was collocated with sites NV01-04 in February 1999.

The short-period seismic array has an aperture of 4 km and consists of ten short-period Geotech GS-13 velocity sensors. Each element is powered by three 64-watt solar panels charging a 12-volt, 220-amp hour battery. The analog data are digitized at 40 samples/sec and authenticated using the AIMs and AIMAs that are part of the AQUINAS™ system designed and integrated by Science Horizons, Inc. Each site has intrusion alarms that alert both the authenticator and digitizer when the wellhead terminal or vault door is opened. Intra-array communication is accomplished by 900-MHz spread-spectrum radios and includes two repeaters atop mountain ranges between the SP array and the central recording facility (CRF) at Mina, NV. The array is polled from the CRF and the data are transmitted to Southern Methodist University by VSAT for processing and archiving. Alpha data are transmitted by land-line to the U.S. National Data Center.

The IMS-required broadband site for the array is collocated with station MNV in the Black Butte Mine northwest of Mina, Nevada, and consists of a three-component long-period (LP) sensor (Guralp CMG-3T) and three Geotech GS-13 short-period (SP) sensors. The combination of the LP and SP sensors meets the IMS requirements for a three-component broadband station for the Black Butte Mine. The array also consists of two LP sites (Geotech KS-54000s) that along with the BB site make up a tripartite array surrounding the SP sites.

Research efforts using data from NVAR are concentrated in three areas. The first is the identification of all events on or near the Nevada Test Site using array beam-forming techniques. The events are analyzed and cataloged and will soon be published on a web page. The second area of research is the creation of a ground truth database for Nevada and the surrounding states using seismic and acoustic data in an attempt to identify sources of man-made seismic and acoustic signals. Also underway, is the back-azimuth and phase velocity calibration of the array using regional and teleseismic earthquakes and explosions.

Key Words: seismic arrays, seismo-acoustic, data communications

OBJECTIVES

Annex I to the protocol of the Comprehensive Nuclear Test Ban Treaty (CTBT) calls for the construction of a primary seismic array near 38.4°N and 118.2°W. The Defense Threat Reduction Agency contracted the Southern Methodist University Geophysics Lab to install the array. SMU objectives were to: 1) Plan, design, and install the seismic array, integrate a four element infrasound array at the site, and prepare the seismic array for certification as an International Monitoring System primary seismic array; 2) Operate and maintain the array; 3) Calibrate the arrays; and 4) Construct regional ground truth databases using seismic and acoustic synergy.

RESEARCH AND DEVELOPMENT ACCOMPLISHED

Installation of Mina, NV Array

The Mina, Nevada, seismic array (NVAR) was installed in the Garfield Hills of west central Nevada, in December 1998, by the Southern Methodist University (SMU) Geophysics Laboratory. Table I shows the timeline for the installation of the array.

Event	Date
Noise Survey (Figure 1)	August 1997
Site Survey (Figure 2)	April 1998
BLM Application/Acceptance	May 1998/October 1998
Factory Acceptance of Data Acquisition Equipment (Figure 3)	November 1998
Borehole Drilling	November 1998
Central Recording Facility Civil Works (Figure 4)	November 1998
SP Array Installation (Figure 5) and NV32	December 1998
BB Installation at NV31/NV11 (Figure 6)	February 1999
Infrasound Sensor Installation	February 1999
Weather Station Installation	June 1999
Differential GPS Survey (Table II)	June 1999
NV33 Installation	Planned for August 1999
Mock Certification	Planned for August 1999
IMS Certification	Planned for Fall 1999

Table I. Timeline showing major events in the installation of the NVAR array.

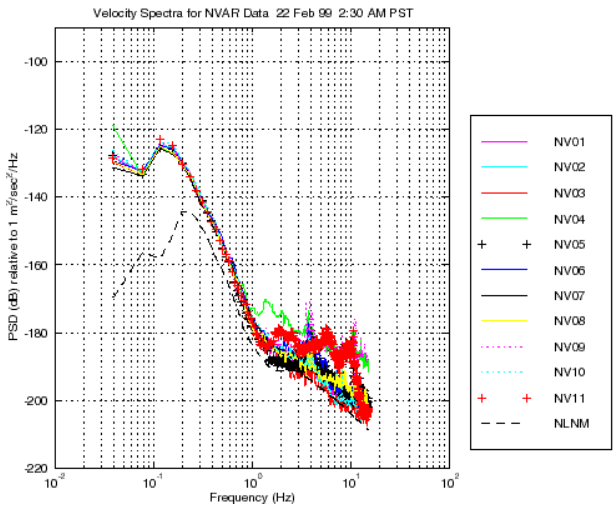


Figure 1. Velocity spectra for noise at NVAR. The spectra show data collected after the installation of the array that were calculated using a 1024 point Welch block averaging method with a Bartlett window

using 10 blocks with 50% overlap. The data are plotted in dB relative to the appropriate units, and for comparison, Peterson's (1993) New Low Noise Model is shown as the dashed line.

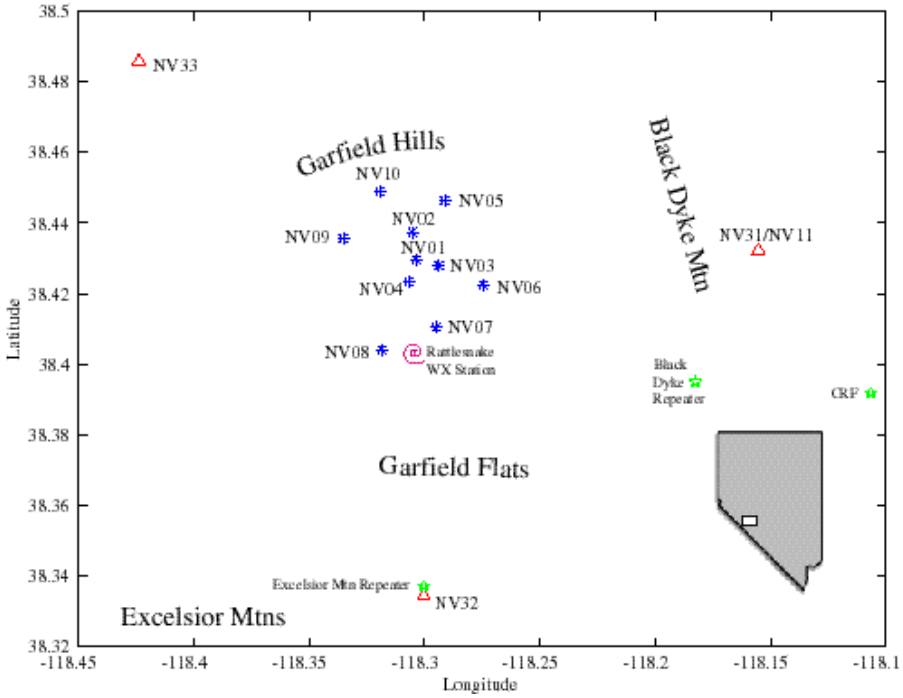


Figure 2. Map showing the elements of the NVAR array. Sites NV01-NV10 make up a 4 km aperture short-period array collocated with an infrasound array at sites NV01-NV04. Sites NV11, NV31, NV32, and NV33 comprise a broadband tripartite array. Also shown are the communication relay points, weather station, and Central Recording Facility (CRF).

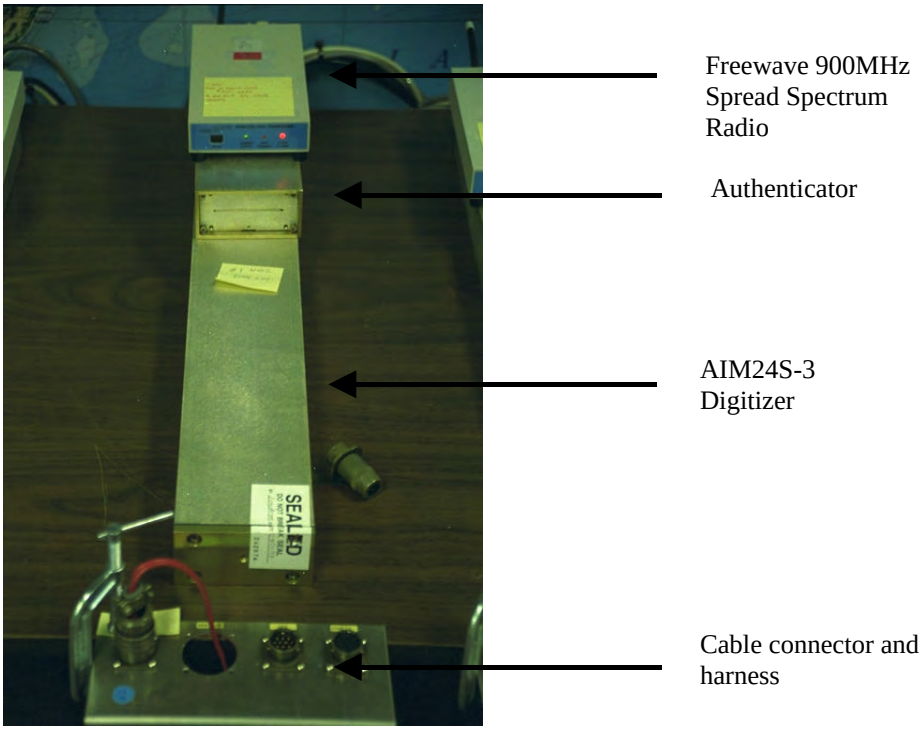


Figure 3. Field components for the AQUINAS™ System from Science Horizon, Inc., including cable connector, digitizer (AIM), data authentication unit (AIMA), and Freewave 900 MHz Spread Spectrum Radio.



Figure 4. The Mina, NV Municipal Building serves as the Central Recording Facility for NVAR. Data from the remote sites are polled by a CIM II (Science Horizons, Inc) using 900 MHz spread spectrum radios. Alpha data is then sent via land-line to the United States National Data Center and data is also sent to SMU for monitoring purposes via VSAT.



Figure 5. SP Array element. Each element is powered by three 64-watt solar panels charging a 12-volt, 220-amp hour battery. The analog data are digitized at 40 samples/sec and authenticated using the AIMs and AIMAs that are part of the AQUINAS™ system designed and integrated by Science Horizons, Inc. Each site has intrusion alarms that alert both the authenticator and digitizer when the wellhead terminal or vault door is opened. Intra-array communication is accomplished by 900-MHz spread-spectrum radios and includes two repeaters atop mountain ranges between the SP array and the central recording facility (CRF) at Mina, NV.



Figure 6. BB Array Element. The IMS-required broad band site for the array is collocated with station MNV in the Black Butte Mine northwest of Mina, Nevada, and consists of a three-component long-period (LP) sensor (Guralp CMG-3T) and three Geotech GS-13 short-period (SP) sensors. The combination of the LP and SP sensors meets the IMS requirements for a three-component broad band station for the Black Butte Mine.

Site	Site Info	Longitude (W)	Latitude (N)	Elevation (m)
NV01	sz, IS	118.303547	38.429609	2029.4
NV02	sz, IS	118.304863	38.437356	2094.3
NV03	sz, IS	118.293709	38.427909	1978.5
NV04	sz, IS	118.306792	38.423245	1983.5
NV05	sz	118.291255	38.446372	2186.6
NV06	sz	118.274397	38.422413	1935.5
NV07	sz	118.294853	38.410503	1849.0
NV08	sz	118.318444	38.404099	1798.2
NV09	sz	118.335177	38.435455	1918.1
NV10	sz	118.319363	38.448782	2132.6
NV11/NV31	sz,se,sn,bz,be,bn	118.155349	38.432049	1509.0
NV32	bz,be,bn	118.300299	38.334192	1783.8
NV33	bz,be,bn	118.423774	38.485762	1939.8

Table II. Locations for the elements of the NVAR array obtained by a differential GPS survey. The elevation listed is the elevation of the seismometer in the borehole or vault.

Calibration Studies

Currently, several studies are underway to calibrate NVAR for travel times, phase velocity, and back-azimuth. However, station corrections are needed due to large elevation differences before calibration studies can be completed. The elevation difference of the vertical elements at NVAR is up to 0.4 km for some elements of the array. Delays caused by elevation difference can be as large as 4 sample points (0.1 s) for a phase velocity of 4 km/s (at a sample rate of 40 samples/sec) therefore an elevation correction is necessary. The elements of the array are also located on different lithologies.

We analyzed 57 arrivals with steep incidence angles (core phases: PcP, PKP, PKKP, Pdiff) coming up to the NVAR array from events located by Prototype International Data Center between March and July 1999. The events had magnitudes $m_b \geq 4.0$ and were recorded at more than 10 stations.

Correction for elevation difference is made by subtracting the time required for waves to travel the vertical distance between the reference station (NV08 - lowest elevation) and each one of the other stations from the total time residual at each station. In order to obtain the matrix of raw time delays between the waveforms we applied the Cross-Correlation Method (Tibuleac and Herrin, 1997) for all the vertical channels but NV11. We used the calculated azimuth and the theoretical slowness to find the time correction for horizontal propagation of the waveforms across the array. We added this time correction to the raw time residuals and obtained the median of time residuals due only to elevation for each station. The resulting time residuals function of the elevation relative to NV08 are presented in Figure 7. The stations NV09 and NV05 are unusually fast compared to NV08. After ruling out a possible misalignment of the clocks, the reason could be variations in geology beneath the stations. Also, NV09 has a higher noise level than any other station.

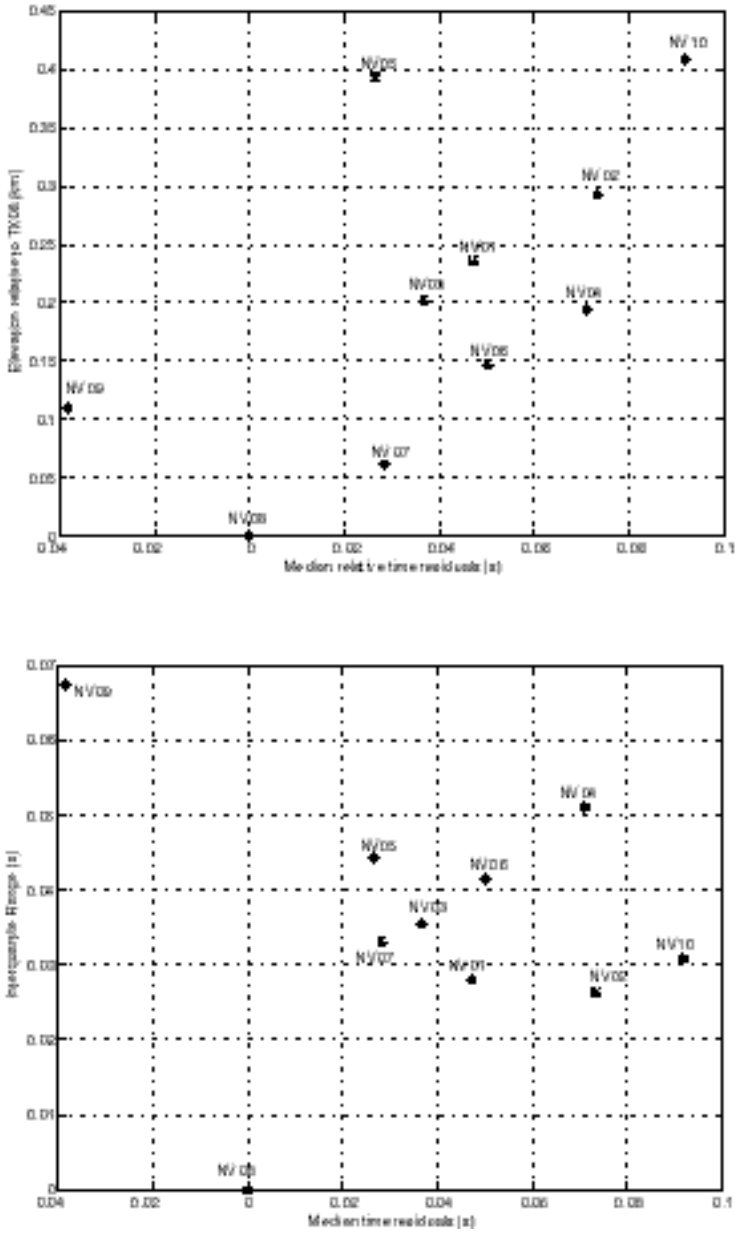


Figure 7. (Top) Elevation as a function of time corrections relative to NV08. (Bottom) Interquartile range as a measure of data dispersion (spread) as a function of time residuals.

As a measure of the data dispersion (spread) we chose the interquartile range (Figure 7). Because a stable replacement velocity cannot be calculated for all stations because of derivatives from a straight line relation between elevation and median correction (e.g. NV09, NV05), time corrections for each station will be used instead, as presented in Table III. The time correction for NV08 is zero seconds as it is the reference station.

Station	**NV01**	**NV02**	**NV03**	**NV04**	**NV05**	**NV06**	**NV07**	**NV09**	**NV10**
Time corr. (sec)	0.047	0.073	0.038	0.072	0.027	0.050	0.028	-0.038	0.092
Interquartile range (sec)	0.028	0.026	0.035	0.051	0.044	0.041	0.033	0.067	0.031

Table III. Time corrections and interquartile range for vertical elements at NVAR relative to NV08

NVAR Ground Truth Data Base Development

Two projects are currently underway using NVAR data for ground truth database development. The first is the complete analysis of seismic events on or near the Nevada Test Site. The analysis of these events can be found on *http://www.geology.smu.edu/~nts_events*.

The second project underway at the SMU Geophysics Laboratory involves the creation of a regional ground truth database. This database will be representative of the seismic activity caused by mine blasts located at regional distances from NVAR. The objective of the project is to create a database that will provide the information necessary to calibrate regional S-P and Lg-P time differences for NVAR and to evaluate the capabilities of the seismo-acoustic method to identify mine blast sources. At its completion, the database will contain definitive information about several hundred mine blast events from known sources located at regional distances from NVAR. A preliminary study has been undertaken to bench mark the data processing level of effort and resources required for the completion of the database. The seismological results of the benchmarking investigation are briefly summarized in the following paragraphs.

The NVAR seismic records were scanned continuously for a one month interval beginning 01 APR 99 to time the arrivals and measure the amplitudes of the phases of events that satisfied the following constraints:

- The event must occur during local daylight hours, Monday through Saturday, inclusively;
- The P signal to noise ratio must be greater than 2:1;
- The horizontal phase velocity of the P phase must be less than 10 km/s.

During the month of April 1999, 299 events were found to satisfy these constraints. This data set was then examined to identify possible mine blast events. It was shown that the association of an infrasound signal with a seismic event uniquely identifies the source of both as a vented explosion (Sorrells *et al.,* 1997). If, in addition, a population of vented explosive sources cluster in both time and space then it may be safely inferred that they are the products of active mining operations. Consequently, NVAR records were scanned for infrasound signals that could be associated with seismic events in the bench mark population. This search resulted in the identification of a subset containing 16 vented explosive sources. The epicentral distribution of the events in the subset is shown in Figure 8. The absence of obvious spatial clustering is attributed to the small size of the subset and the wide azimuthal dispersion of the vented explosive sources. As seen in Figure 9, this subset is characterized by significant temporal clustering. The histogram seen in this figure illustrates the frequency of occurrence distribution for the origin times of the events in the subset as referenced to local daylight savings time. Notice that the distribution is skewed and possibly bimodal. The activity increases dramatically after about 1300 hours and again after 1700 hours local time. These times typically coincide with the end of the lunch break and the end of the work-day for most commercial enterprises. This type of temporal clustering is a common characteristic of the seismic activity associated with active mining operations. Consequently, the members of the vented explosion subset are tentatively identified as mine blasts.

The frequency of occurrence distribution for the origin times of all the events in the bench mark population is seen in Figure 10. Notice that it resembles the distribution seen in Figure 9. From this resemblance, it is inferred that mine blasts account for a fairly significant fraction of the seismic events in the bench mark population. Further evidence supporting this inference is found in Figure 11. The data shown in this figure are the epicenters of the events occurring in the 1300-1500 hour and 1600-1800 hour local time periods. Notice that during these two high activity time periods, spatial clustering is seen in one area northeast of NVAR (presumed to be the gold mines of the Battle Mountain complex).

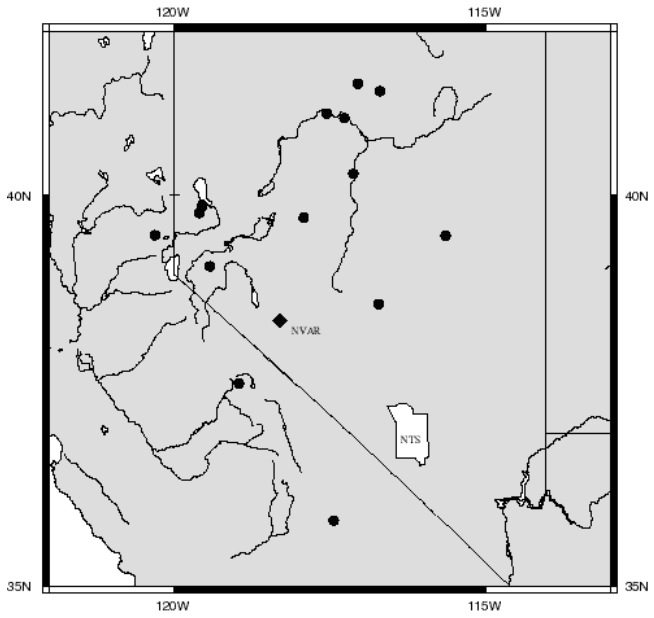


Figure 8. Locations of events for which seismic and acoustic signals were associated.

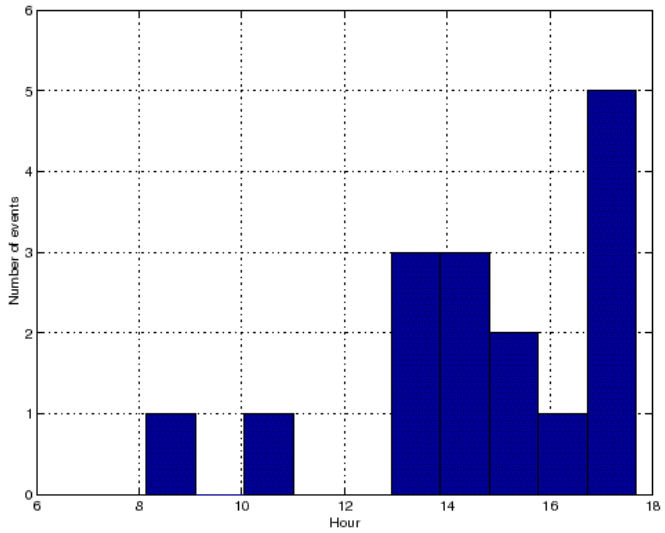


Figure 9. Local origin times of seismo-acoustic events recorded at NVAR for April 1999.

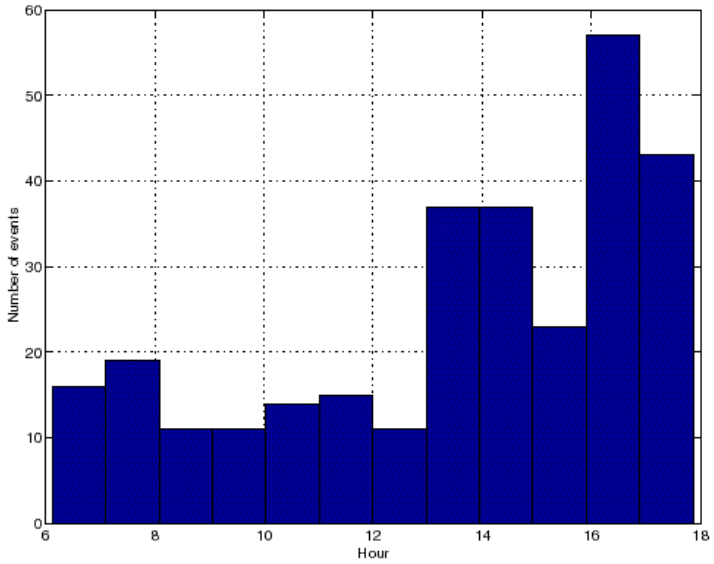


Figure 10. Occurrence of all events recorded at NVAR in April 1999.

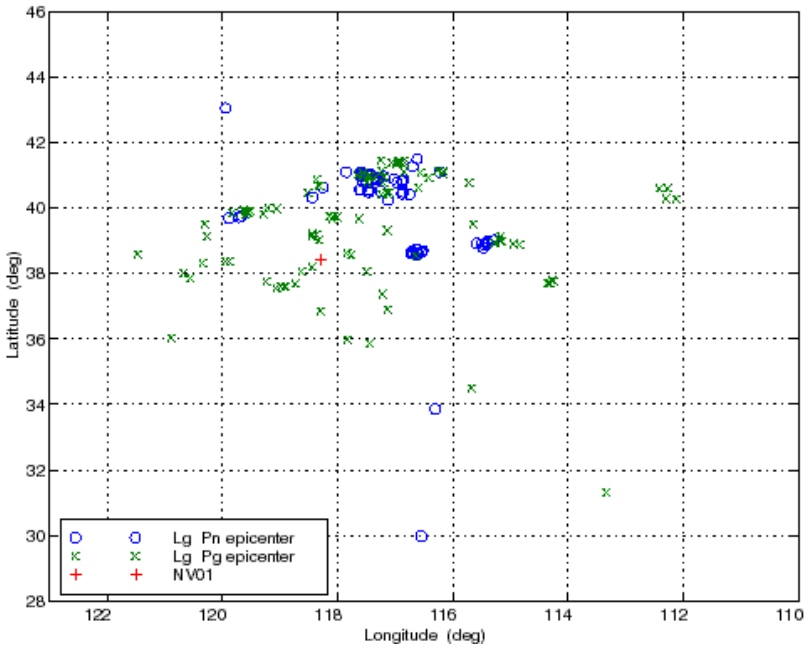


Figure 11. Epicenters for events located at NVAR occurring in the 1300-1500 hour and 1600-1800 hour local time periods.

CONCLUSIONS AND RECOMMENDATIONS

SMU Geophysics Laboratory installed the NVAR seismic array near Mina, NV and began operations in December 1998. The array fulfils a United States obligation for the Comprehensive Nuclear Test Ban treaty and consists of 10 short-period seismometers (Geotech GS-13s) with an aperture of 4km. The inner ring of array elements is collocated with a four element infrasound array. The broadband site for the array is located in the Black Butte Mine northwest of Mina, NV and consists of three GS-13s (Z,N,E) along with a Guralp CMG3-T. This station is also a site in a broadband tripartite that surrounds the short-period array.

Authenticated data from the borehole or vault is transmitted to a Central Recording Facility (CRF) using spread spectrum radios. From the CRF, the data is forwarded via land-line to the USNDC and to the SMU Operations and Maintenance center where the data is monitored for quality assurance, archived, and processed. Calibration and ground-truth data base development is currently underway using NVAR seismic and acoustic data. We hope to fully certify NVAR as an IMS array in the Fall of 1999.

ACKNOWLEDGMENTS

The authors wish to thank Scot and Cheryl Chamberlain for continued support at NVAR. We also appreciate the support offered by the engineers at Science Horizons both during and after the installation. We also wish to thank Don Rock and Marv Denny (Lawrence Livermore National Labs) for their support in installing the BB station at the Black Butte Mine and Randy Rembold and Dick Kromer (Sandia National Labs) for their help during the certification process.

REFERENCES

Sorrells, G.G., E.T. Herrin, and J.L. Bonner, 1997. Construction of regional ground truth databases using seismic and infrasound data, *Seism. Res. Lett.,* **68***,* 743-752.

Tibuleac, I.M. and E. T. Herrin, 1997. Calibration studies at TXAR, *Seism. Res. Lett.,* **68***,* 353-365.

DEPTH AND SOURCE MECHANISM ESTIMATION FOR SPECIAL EVENT ANALYSIS, EVENT SCREENING, AND REGIONAL CALIBRATION

Peter Goldstein and Doug Dodge, Lawrence Livermore National Laboratory

Sponsored by U.S. Department of Energy
Office of Nonproliferation and National Security
Office of Research and Development
Contract No. W-7405-ENG-48

ABSTRACT

We present an overview of methods for estimating depth and mechanism and summarize our recent efforts to use waveform modeling based depth and mechanism estimates for special event analysis, event screening, and regional calibration. We summarize the strengths and limitations of a variety of techniques and describe our on-going efforts to develop accurate high-resolution depth and mechanism estimates by extending existing techniques and integrating methods that use different types of seismic data.

We describe a new tool that we've developed and validated that provides fast and accurate estimates of depth and mechanism based on far-regional to teleseismic (20^0 to 90^0) P-waveform modeling. Significant features of this tool include: its ability to provide accurate, high-resolution depth estimates ($\delta z<2$km) using a small number of stations. It also works well over a large range of depths including events that are very shallow ($z<1$km). It is applicable over a broad band of frequencies ($0\leq f\leq 2$ Hz) and magnitudes ($mb\geq 4.5$) and provides constraints on event mechanism including isotropic contributions. It also provides estimates of random and model errors and can be used to test hypotheses and investigate sensitivity to and trade-off between model parameters.

We illustrate the utility of this technique for regional calibration, special event analysis, and event screening by comparing estimated depths and mechanisms of events in the Middle East and North Africa with those of the NEIC and by comparing our depth and mechanism estimates for selected events such as the May 11, 1998 India nuclear explosion and a November 8, 1991 earthquake that occurred in the same region.

We illustrate the advantage of combining different techniques for estimating depth and mechanism by comparing broadband (0-2Hz) far-regional and teleseismic body waveform modeling estimates of depth and mechanism with those obtained using intermediate to long period estimates based on regional data. We show that the broadband body waves provide strong constraints on source depth and that both the broadband body waves and the intermediate to long period regional waves help constrain source mechanism.

Key Words: depth estimate, source estimate, event screening

OBJECTIVE

Introduction and Overview of Techniques

Depth and mechanism estimates for small- to moderate-size seismic events are useful for a number of reasons including special event analysis, event screening, and improved regional calibration for test ban treaty monitoring, improved understanding of regional earth structure and tectonics, and for characterization of regional wave propagation phenomena.

A variety of techniques have been used to estimate both depth and mechanism. Techniques that are primarily focussed on depth estimation include travel-time analysis of depth phases (e.g., Engdahl et al., 1998), cepstral analysis (e.g., Alexander and Yang .,1997), and observations of Rg waves (e.g., Bath, 1975, Kafka, 1990). Techniques that focus primarily on mechanism include first motion studies (e.g., Reasonberg and Oppenheimer, 1975) and studies of relative amplitudes of P and S phases (e.g., Pierce, 1980). Extensive work has been done on the development and utilization of techniques for estimating depth and mechanism from body and surface waveform modeling [e.g., *Dziewonski et al.*, 1981; *Wallace and Helmberger*, 1982; *Romanowicz and Guillemant*, 1984; *Lay et al.*, 1994; *Sipkin*, 1994; Goldstein and Dodge, 1999].

Although these studies have significantly improved our ability to estimate depth and mechanism of seismic events there is still significant work to be done, particularly for small to moderate magnitude events at regional distances. Table 1 summarizes some of the advantages and disadvantages of many of the techniques for estimation of depth and or mechanism. While each of these techniques has their advantages, there is currently no technique that can consistently be used to obtain accurate depths and mechanisms for small magnitude events.

The most common problems are due to limitations of the data, such as, poor SNR or limited resolution in the bandwidth available, inadequate coverage or significant restrictions on station coverage, and large uncertainties due to significant trade-offs between parameters and sensitivity to earth structure. The empirical nature of some techniques can also make it difficult to assess their transportability and sensitivity to or trade-off with other parameters. Sensitivity to magnitude and source complexity are generally only an issue for relatively large events.

Table 1. Advantages and disadvantages of depth and mechanism techniques

Techniques	Advantages	Disadvantages
Broadband body waves	Accurate, high-resolution depth. Mechanism includes isotropic term Random and model errors estimates Sensitivities and trade-offs Works with small # of stations	Far-regional to teleseismic No near source and receiver structure Sensitive to station coverage
Depth phase picking	Simple to apply	Difficult to identify phases
Measurements of Rg	Indicator of shallow depth	Near-regional Depends on Earth structure No mechanism
Cepstra	High resolution depth	Need high frequencies Sensitive to source mechanism No mechanism
First motion	Simple to apply	Difficult to measure Need many stations and good azimuthal coverage
Relative phase amplitudes	Probabilities for different mechanisms	Difficult to correctly identify phases. No Depth or model errors
Global moment tensor inversion	Extensive validation for large events. Depth and mechanism	Mb>~5.5. Limited depth resolution especially for shallow depths.
Regional moment tensor inversion	Accurate source mechanism including non-double couple. Applicable at relatively small magnitudes. Works with small # of stations	Limited depth resolution. Significant sensitivity to Earth model. Sensitive to station coverage

In this rest of this paper, we describe an approach for accurate high resolution depth estimation based on modifications of the well known technique of modeling the direct P-wave and free surface reflections (e.g., Stein and Wiens, 1986). We describe a new, interactive tool and show that it provides fast and accurate estimates of depth and mechanism, with well defined random and model errors, to magnitudes as low as mb ≅ 4.5. We summarize our use of this tool to obtain "ground-truth" estimates of depth and mechanism for a set of earthquakes in the Middle East and North Africa. We illustrate the potential of this technique for special event analysis and event screening by comparing estimated depths and mechanisms of the May 11, 1998 India nuclear explosion and a November 8, 1991 earthquake that occurred in the same region. Finally, we show that a combination of this technique and longer period full waveform modeling can provide significant constraints on source parameters.

Method

We employ a very efficient, modified version of the well-known technique of modeling the initial P-wave bundle, consisting of P, pP, and sP [e.g., *Pearce*, 1980; *Stein and Wiens*, 1986]. This technique is very well suited for estimating depth because the relative timing of the direct P-wave and the surface reflections pP and sP are linearly dependent on source depth h (e.g., $t_{pP} - t_P = 2\ h/\alpha$). Relative amplitudes of these phases are linearly related to the moment tensor elements and provide significant constraints on source mechanism (Figure 1).

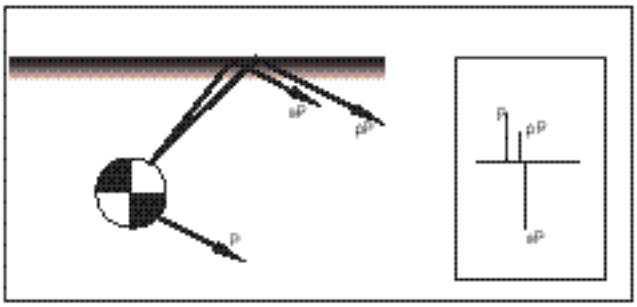


Figure 1. Relative timing of the direct P-wave and the free-surface reflections pP and sP constrain depth. Relative amplitudes of these phases help constrain mechanism.

The speed and accuracy of our technique are obtained via an extremely efficient implementation of the generalized ray synthetic algorithm [*Langston and Helmberger*, 1975]. Our implementation can calculate thousands of P-wave synthetics per second, so it is feasible to conduct exhaustive grid searches and to interactively experiment with different models.
Synthetics are calculated as a convolution of an attenuated source pulse with an impulse train consisting of appropriately delayed and scaled P, pP, and sP pulses:

$$S(t) = \mathbf{P} * [U^{P}\delta(t - t_p) + U^{pP}R^{pP}\delta(t - t_{pP}) + U^{sP}R^{sP}\delta(t - t_{sP})] \qquad (1)$$

Here U^{P}, U^{pP}, and U^{sP} are source amplitudes, R^{pP}, and R^{sP} are reflection coefficients, t_p, t_{pP}, and t_{sP} are travel times, and **P** is the attenuated source pulse.
The source pulse is a triangle function with a rise time corresponding to that of an expanding circular crack with an adjustable prespecified stress drop (usually 30 bars) and moment (Mo) determined from the moment-magnitude relationship of [*Kanamori and Anderson*, 1975]. Magnitude is calculated using the median corner frequency from all the data. Corner frequencies are estimated from the maximum in the instrument-corrected, velocity power spectra. The user can also prespecify magnitude based on other data. Attenuation is accounted for by convolving an [*Futterman*, 1962] attenuation pulse with the source pulse.

To solve for a best-fit depth and mechanism, our tool evaluates a misfit function between data and synthetics on a grid of depths and mechanisms and chooses the combination with the lowest residual as the solution. Further refinement of the solution is carried out using the simplex algorithm. The misfit function is:

$$R = \sum [1 - C_{max}(\text{data}_i, \text{synthetic}_i)]\ SNR_i / SNR_{avg} \qquad (2)$$

where the sum is over N stations, $C_{max}(x,y)$ is the maximum of the normalized cross correlation of x and y, SNR_i is the ratio of mean signal amplitudes in user-set windows before and after the first arrival, and SNR_{avg} is the mean SNR for all the stations.

Our minimization strategy (Table 2) is extremely efficient because it computes synthetics by reading and multiplying precalculated terms from lookup tables. Separate tables are generated for source independent (R^{pP}, R^{sP}, t_p, t_{pP}, and t_{sP}) and path independent (U^P, U^{pP}, and U^{sP}) terms. The source amplitudes are of the form $U^{Phase} = \gamma_k^{\dagger}\ \mathbf{M}\ \gamma_l / c^3$. Where $\mathbf{M}$ is the moment tensor, γ_k is a direction vector of a phase along the ray at the source, and c is the velocity at the source.

Table 2. Outline of minimization strategy.

1.	Compute table of P- and S-wave direction vectors at the source.
2.	Compute table of travel times and reflection coefficient.
3.	For each moment tensor $\mathbf{M}$,
a. Compute the source amplitudes U^P, U^{pP}, and U^{sP}.	
b. Compute synthetics at multiple depths.	
c. Cross correlate with data to find depth with smallest residual.	

Uncertainties due to random errors are estimated using bootstrapping [*McLaughlin*, 1988]. Bootstrapping is used to estimate the mean and standard deviation of model parameters by treating random subsets of the modeled data as different realizations. Model parameters are estimated for each realization, and the mean and standard deviation of the model parameters are estimated from the distributions of model parameters. We restrict our bootstrapping analysis to a maximum of 30 realizations because it can be a very time consuming process. With this restriction, bootstrapped estimates of uncertainties can be obtained in less than ten minutes on a Sun Sparc Ultra 1 workstation.

Model error contributions to uncertainties in depth are relatively easy to calculate. Depth estimates (Z) are linearly related to the medium velocity (V) above the source, $Z = V*(t_p - t_{pP})/2$. Therefore, uncertainties in depth (δZ) are also linearly related to uncertainties in velocity (δV).

$$\delta Z = \delta V*(t_p - t_{pP})/2 \quad \text{or} \quad \delta Z = \delta V*Z/V \qquad (3)$$

If we assume uncertainties in velocity above the source are typically less than 15%, a fairly conservative estimate, model errors should be less than 15% of the estimated depth. We assume that errors in depth due to complexities in source time function [*Christensen and Ruff*, 1985] will usually be small for the small- to moderate-size events of interest to this study. Although laterally varying velocity structure could contribute systematically to uncertainties in depth, we expect that such complications are second-order effects.

Estimating potential systematic errors in mechanism is much more difficult. The primary measurements that determine mechanism are the relative amplitudes of the reflected waves pP and sP to P,

$$A_{pP-P} = [\gamma_2^{\dagger}\ \mathbf{M}\ \gamma_2] * R^{pP} / [\gamma_1^{\dagger}\ \mathbf{M}\ \gamma_1] \qquad (4)$$

$$A_{sP-P} = [\mathbf{P}^{\dagger}\ \mathbf{M}\ \gamma_3] * R^{sP}\ \alpha^3 / [\gamma_1^{\dagger}\ \mathbf{M}\ \gamma_1]\ \beta^3 \qquad (5)$$

Gamma and $\mathbf{P}$ are the radial and transverse direction vectors. The numerical subscripts correspond to (1) downgoing P-wave, (2) upgoing P-wave, and (3) upgoing S-wave. As indicated by these equations, mechanism is a complex function of the direction vectors and velocities at the source and the free-surface reflection coefficients. Given realistic estimates of near-source velocity variations, it should be possible to

use a Monte Carlo analysis of the above equations to estimate potential systematic errors in mechanism. This is a subject of our ongoing work.

A Fast and Accurate Interactive Tool

Our new tool for estimating depth and mechanism (Figure 2) has a number of significant features. Foremost are its speed, validated accuracy, uncertainty estimates, improved depth resolution, and extended performance to smaller magnitudes. The tool is also integrated with an automated network magnitude estimator and easy-to-use, interactive filtering and first-arrival picking tools. It can also be run in batch mode. A user can interactively test hypotheses with a variety of source parameters and investigate the sensitivity of the solution to variations in individual source parameters.

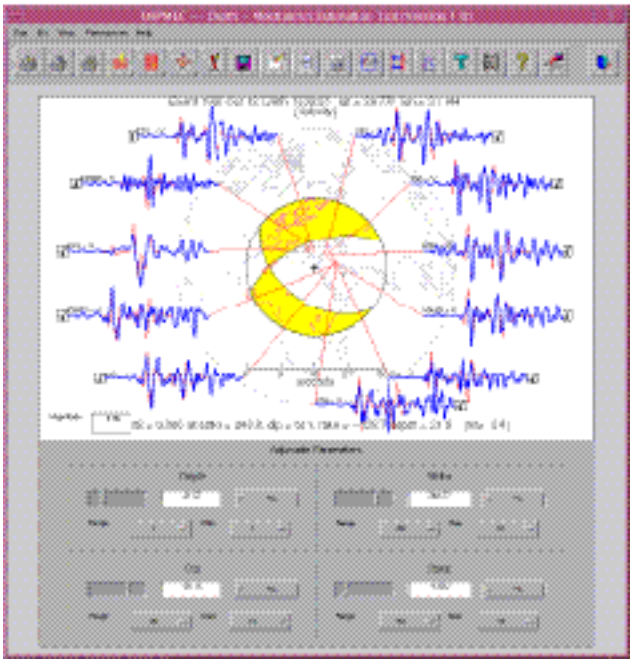


Figure 2. Main window of our new, interactive depth and mechanism estimation tool. Rapid estimates of depth and mechanism are obtained using grid search and simplex algorithms. Uncertainties are estimated using a bootstrapping procedure.

Based on experience thus far, this tool works well with data at far regional and teleseismic distances and can be applied to relatively high-frequency data (up to ~2 Hz). We have also successfully applied it to events with relatively low magnitude (mb ≅ 4.5). As part of our ongoing work, we will extend the capabilities of this tool to regional and near regional distances.

We have successfully analyzed events with tens of stations and as few as three stations; however, uncertainties are typically larger with a smaller number of stations. Solutions include an estimate of depth and the best double couple with an option to estimate an isotropic component of the moment tensor. Our error analyses indicate that depth can usually be estimated to an accuracy of a few km. Although complete mechanisms are sometimes poorly constrained, we usually find that at least two out of three of the mechanism parameters (strike, dip, rake) are well constrained.

Validation with "Ground-Truth" Data

In this section, we demonstrate that body waveform modeling is an accurate technique for estimating depth and mechanism by comparing results from our tool with estimates of depth and mechanism from well-

calibrated local, regional, and global networks (Figure 3). We begin by comparing our estimated depths and mechanisms with those of a set of 15 "ground-truth" events (◆) whose depths and mechanisms were constrained by well-calibrated local and regional networks. These data include shallow explosions, a mine collapse, and earthquakes. We find excellent agreement between our estimated depths and mechanisms and those estimated from the local and regional network data (Figure 4). Since all of the events in our "ground-truth" data set were shallower than 20 km, we applied our tool to an additional set of 25 deeper events (■) whose depths had been constrained with global network data and a global probability model for identifying secondary phases such as pP and sP [*Engdahl et al.*, 1998]. We find generally good agreement between our estimated depths and those obtained by Engdahl et al., (1998). In most cases where there are discrepancies, synthetics based on our depth and mechanism provide a much better fit to the data. However, the waveforms of a small number of events show evidence of source or path complexity that is not modeled very well by any depth and mechanism or by our simple source and earth structure model.

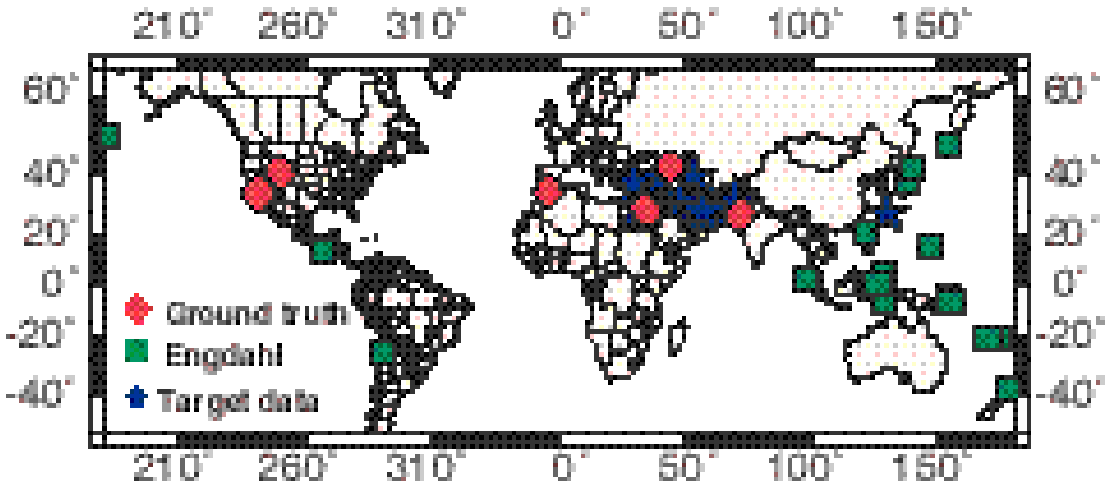


Figure 3. Map indicating the locations of our ground-truth events (◆), Engdahl et al., (1998) data subset (■), and Middle East and North Africa events (★).

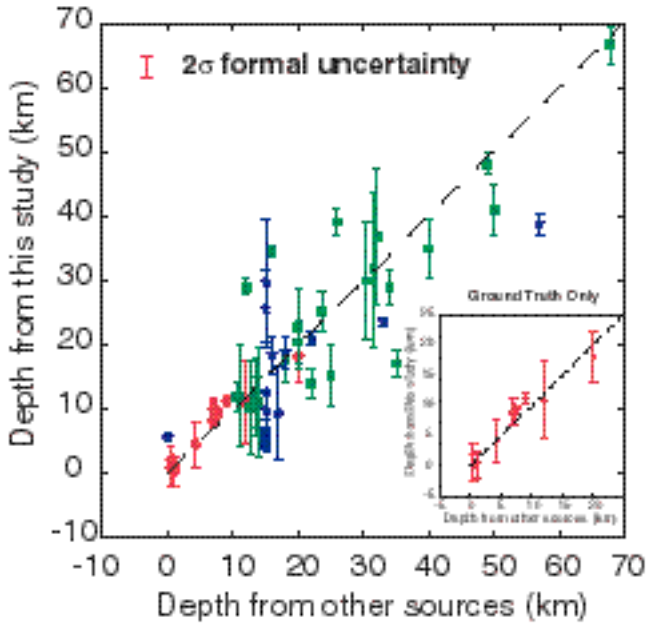


Figure 4. Comparison of our estimated depths with "ground-truth" depths (◆), Engdahl et al.'s (1998) estimated depths (■), and PDE depths (★). The excellent agreement between our depths and those of our "ground-truth" events (inset) suggests that this technique can be used to develop "ground-truth" when depth estimates from local and regional data are not available.

Developing "Ground-Truth" for Regional Calibration

The above results indicate that our new depth and mechanism estimation tool can provide accurate estimates of depth over a broad depth range. For well-recorded events, uncertainties in depth are relatively small (less than a few km). Based on these results, we apply this tool to a set of events in the Middle East and North Africa (■) and obtain estimates of depth and mechanism that should be useful as "ground-truth" for future monitoring-related research in this area. Estimated depths for these data are compared with those from NEIC preliminary determination of epicenters catalog in Figure 4.

Special Event Analysis and Event Screening for a CTBT

The ability to confidently state that a seismic event was not a man-made explosion is an important part of a CTBT monitoring system. Such screening capabilities are important for dealing with unusual or suspect events and are essential given the large number of events that it will be necessary to process. One of the fundamental parameters for event screening is depth. Tools such as the one we describe in this paper should be particularly useful for such screening because they can provide accurate estimates of depth, and it is unlikely that events with depths greater than a certain threshold, say 5 km, would be explosions. As examples, we compare the May 11, 1998 nuclear explosion in India and a November 8, 1991 earthquake from the same region (Figure 5). Our analysis indicates a very shallow depth for the May 11, 1998 event. If this event had not been announced, results from such an analysis would have been strong motivation for additional investigation. In contrast, the November 8, 1991 earthquake is much deeper and would have been of relatively little concern from a monitoring standpoint.

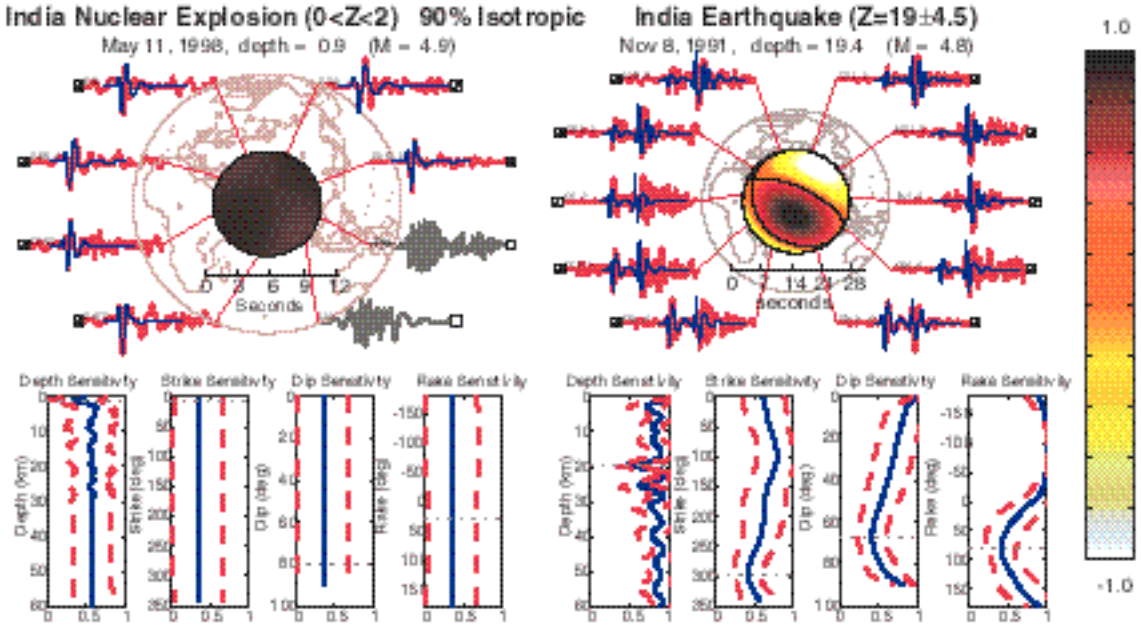


Figure 5. Comparison of waveforms and synthetics for a nuclear explosion (top left) and an earthquake (top right) in India. The sensitivity of the minimized residuals (solid line) and its variance (dashed lines) due to changes in the estimated parameters are shown at the bottom of each plot. The focal mechanism first motion, relative amplitudes are indicated by color beach ball plots. If the nuclear test (left) had not been announced, the estimated shallow depth ($Z < 2$ km) and large isotropic component of the moment tensor would have been strong motivation for additional analysis. In contrast, the earthquake (right) is much deeper and of relatively little concern from a monitoring standpoint.

Combining Techniques

In this section, we compare results from broadband body waveform modeling and intermediate period full waveform modeling and show that they provide complementary constraints on source depth and mechanism. We compare solutions for the Mb 5.5, April 14, 1995 Western Texas event. Even though both methods provide excellent fits to the data, we show that each method is has greater sensitivity to selected parameters. For example, body waveform modeling is particularly sensitive to depth and provides a depth estimate of 18 km with a combined random and model uncertainty of less than 2 km (Figure 6). Uncertainties in strike dip and rake are approximately 100^0, 20^0, and 40^0, respectively.

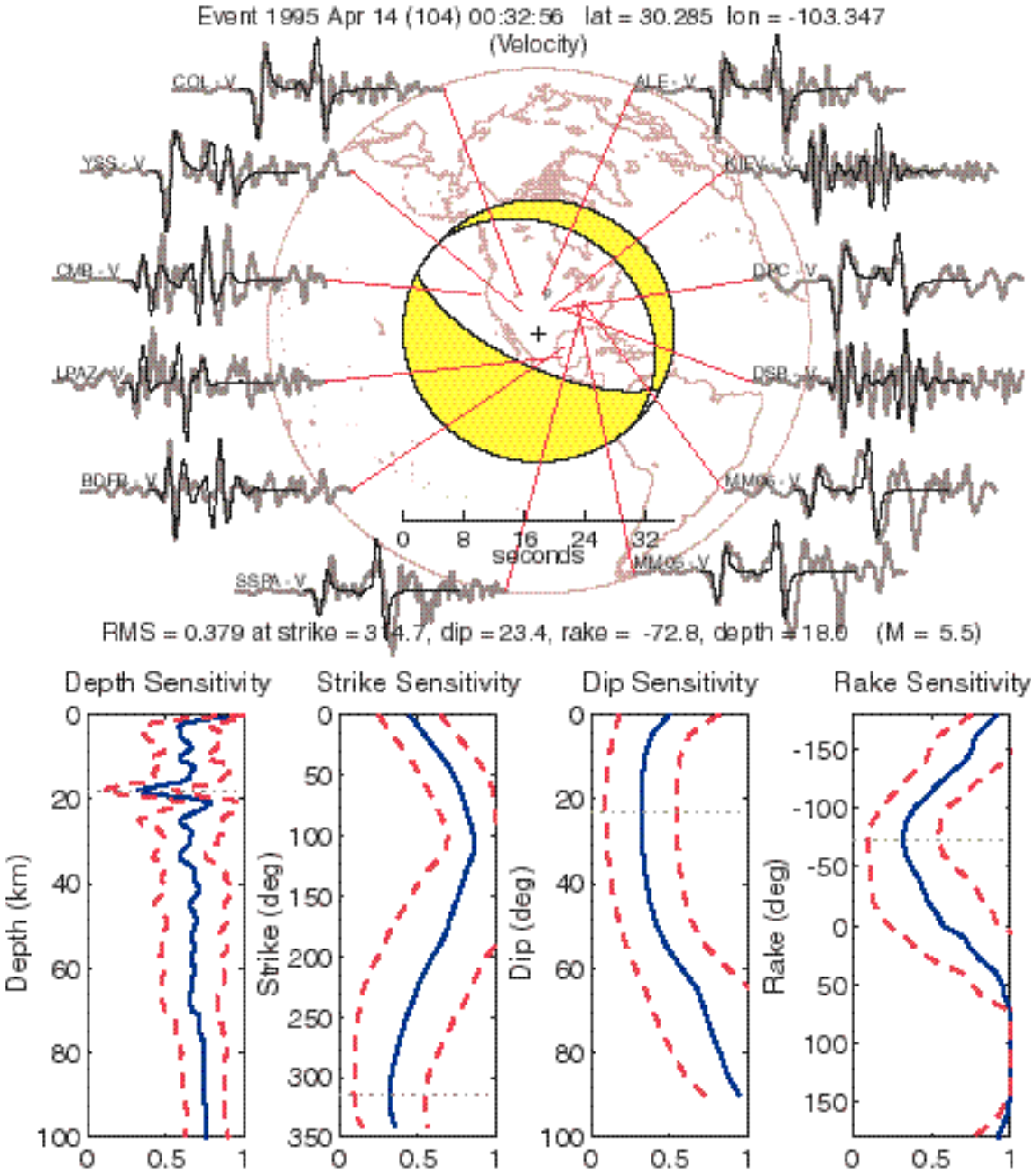


Figure 6. Broadband body waveform modeling solution for depth and mechanism of the April 14, 1995 Western Texas event.

Results from the intermediate-period, regional waveform modeling (Figure 7) are also consistent with a depth of around 20 km but have limited resolution of this parameter. In contrast, the sensitivity of the residuals to strike and rake suggest that these parameters are well resolved. Dip is poorly constrained. Further work is needed to develop complete error estimates for the regional solutions.

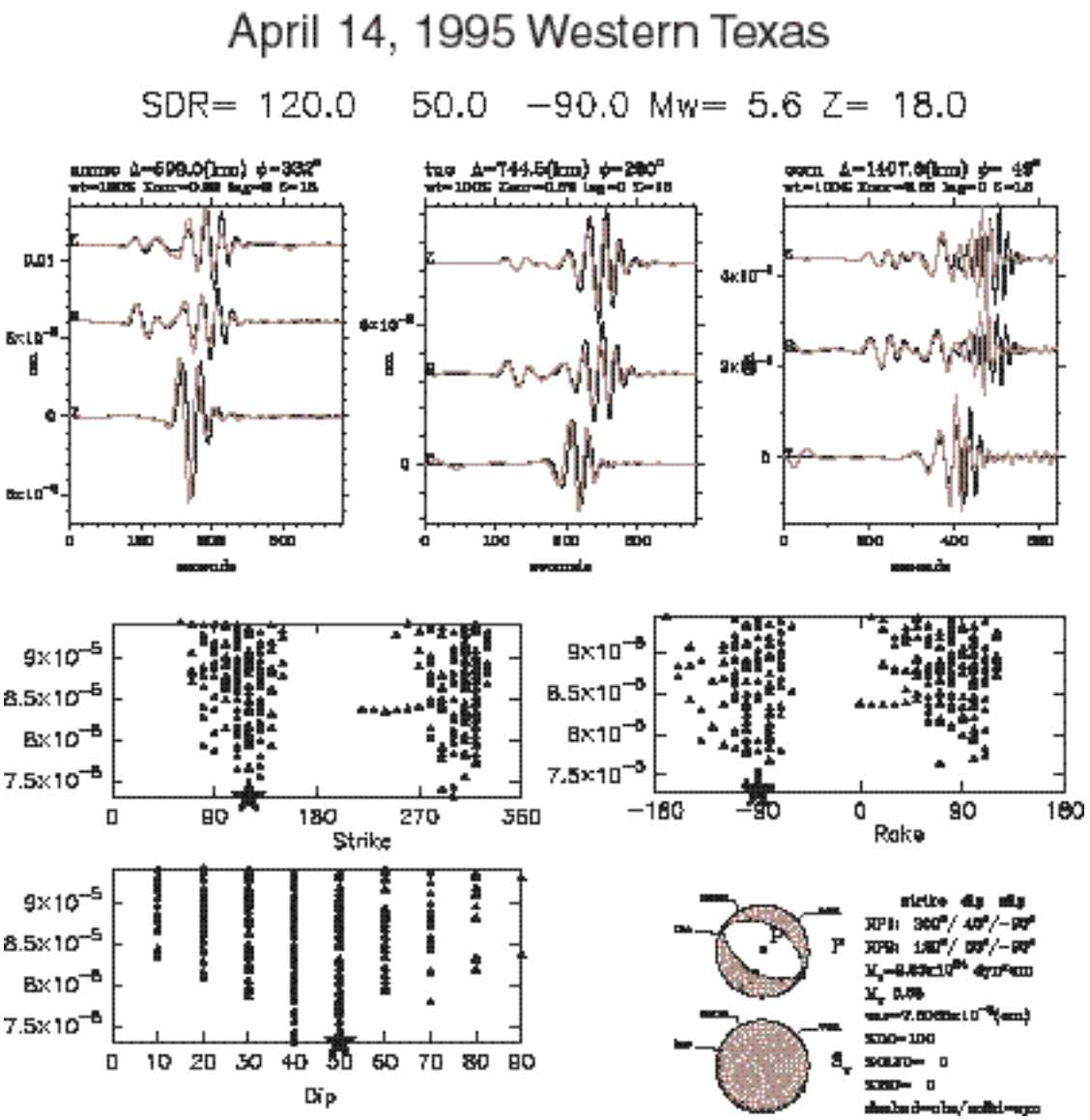


Figure 7. Intermediate period, regional waveform modeling solution for depth and mechanism of the April 14, 1995 Western Texas event.

CONCLUSIONS AND RECOMMENDATIONS

We have summarized the advantages and disadvantages of a variety of techniques for depth and mechanism estimation and suggest that significant work remains to be done for events with magnitudes of interest for test ban monitoring. We also describe a new, waveform modeling-based tool for fast and accurate, high-resolution depth and mechanism estimation. Significant features of this tool include its speed and accuracy and its applicability at relatively high frequencies. These features allow a user to rapidly determine accurate, high-resolution depth estimates and constraints on source mechanism for relatively small magnitude (mb~4.5) events.

Based on the accuracy of depth estimates obtained with this tool, we conclude it is useful for both the analysis of unusual or suspect events and for event screening. We also find that this tool provides significant constraints on source mechanism and have used it to develop "ground-truth" estimates of depth and mechanism for a set of events in the Middle East and North Africa. These "ground-truth" depths and mechanisms should be useful for regional calibration.

Finally, we compare our far-regional to teleseismic body waveform modeling results with those from intermediate period regional data and show that a combination of such methods can provide significant improvements in source parameter estimation capabilities.

Acknowledgements

We thank Arthur Rodgers and Shawn Larsen for their suggestions and contributions to this work and Jim Hannon and Marv Denny for their careful reviews. This work was performed under the auspices of the U.S. Department of Energy by Lawrence Livermore National Laboratory under contract No. W-7405-Eng-48 for the Office of Research and Development, NN-20, within the Office of NonProliferation and National Security, NN-1.

REFERENCES

Alexander, S.S., and C.C. Yang, “Accurate depth determinations and other diagnostic event characteristics in near-real time from regional signals”, Proceedings of the 19th annual seismic research symposium on monitoring a CTBT, Annapolis, MD, September 23-25, 1997.

Bath, M., Short-Period Rayleigh-Waves From Near-Surface Events, *Physics of the Earth and Planetary Interiors, 10* (4), 369-376, 1975Christensen, D. H., and L. J. Ruff, "Analysis of the Trade-Off Between Hypocentral Depth and Source Time Function", *Bull. Seis. Soc. Am., 75* (#6), 1637–1656, 1985.

Dziewonski, A. M., T. A. Chou, and J. H. Woodhouse, "Determination of Earthquake Source Parameters from Waveform Data for Studies of Global and Regional Seismicity," *J. Geophys. Res., 86* (#B4), 2825–2852, 1981.

Engdahl, E. R., R. Vanderhilst, and R. Buland, "Global Teleseismic Earthquake Relocation With Improved Travel-Times and Procedures For Depth Determination", *Bull. Seis. Soc. Am., 88* (#3), 722–743, 1998.

Futterman, W. I., "Dispersive Body Waves," *J. Geophys. Res., 67* (#13), 5279–5291, 1962.

Goldstein, P., and D. Dodge, (1999) “Fast And Accurate Depth And Source Mechanism Estimation Using P-Waveform Modeling: A Tool For Special Event Analysis, Event Screening, and Regional Calibration”, Geophys. Res. Lett. 8/15/99.

Kafka, A.L., Rg As a Depth Discriminant For Earthquakes and Explosions - a Case-Study in New-England, *Bulletin of the Seismological Society of America, 80* (2), 373-394, 1990Kanamori, H., and D. L. Anderson, "Theoretical Basis of Some Empirical Relations in Seismology," *Bull. Seis. Soc. Am., 65* (#5), 1073–1095, 1975.

Langston, C. A., and D. V. Helmberger, "Procedure For Modeling Shallow Dislocation Sources," *Geophysical Journal of the Royal Astronomical Society, 42* (#1), 117–130, 1975.

Lay, T., J. Ritsema, C. J. Ammon, and T. Wallace, "Rapid Source-Mechanism Analysis of the April 29; 1993 Cataract Creek (Mw = 5.3); Northern Arizona Earthquake," *Bull. Seis. Soc. Am., 84* (#2), 451–457, 1994.

McLaughlin, K. L., "Maximum-Likelihood Event Magnitude Estimation with Bootstrapping for Uncertainty Estimation," *Bull. Seis. Soc. Am., 78* (#2), 855–862, 1988.

Pearce, R. G., "Fault Plane Solutions Using Relative Amplitudes of P and Surface Reflections: Further-Studies", *Geophysical Journal of the Royal Astronomical Society, 60* (#3), 459–487, 1980.

Romanowicz, B., and P. Guillemant, "An Experiment in the Retrieval of Depth and Source Mechanism of Large Earthquakes Using Very Long-Period Rayleigh-Wave Data," *Bull. Seis. Soc. Am., 74* (#2), 417–437, 1984.

Sipkin, S. A., "Rapid-Determination of Global Moment-Tensor Solutions", *Geophys. Res. Lett., 21* (#16), 1667–1670, 1994.

Stein, S., and D. A. Wiens, "Depth Determination For Shallow Teleseismic Earthquakes: Methods and Results," *Reviews of Geophysics, 24* (#4), 806–832, 1986.

Wallace, T. C., and D. V. Helmberger, "Determining Source Parameters of Moderate-Size Earthquakes from Regional Waveforms," *Phys. Earth Planet Inter., 30* (#2-3), 185–196, 1982.

SEISMIC EVENT LOCATION IN 3-D VELOCITY MODELS USING INITIAL AND SECONDARY ARRIVAL TIMES COMPUTED WITH DYNAMIC RAY TRACING

Ivan Henson, Xiaoxi Ni, and Wilmer Rivers

Multimax, Inc.

Sponsored by U.S. Department of Defense
Defense Threat Reduction Agency

Contract No. DTRA01-99-P-0015

ABSTRACT

The objective of this project is to develop a seismic event location procedure that utilizes initial and secondary arrivals computed with dynamic ray tracing. We are developing software to compute travel times for complex three-dimensional velocity structures based on the dynamic ray tracing method that is used to compute Gaussian beam seismograms. Travel times for regional phases, such as Pg, Sg, Pn and Sn will be computed efficiently with the paraxial ray approximation, which requires ray tracing only to a point near the source or receiver. The derivatives of the travel-time field with respect to Cartesian coordinates can easily be determined from a single paraxial ray. We will use these derivatives in a standard least-squares iterative inversion for the event location. It will be determined whether the use of later phases improves on the location from first arrivals alone. We are designing this location code to be fast and easily automated. It will be available as a separate program and as an extension to the location program LocSAT.

Key Words: event location, 3-D models

OBJECTIVE

Reliable event location is an essential part of the Comprehensive Nuclear-Test-Ban Treaty (CTBT) monitoring effort. The objective of this project is to develop a seismic event location procedure that utilizes initial and secondary seismic arrival times computed with the Gaussian beam method. Software to compute travel times based on the dynamic ray tracing method that is used to compute Gaussian beam seismograms for complex three-dimensional velocity structures will be developed. This software will be integrated with existing hypocenter inversion software to produce new event location programs. The project will use the iterative least-squares inversion method.

RESEARCH ACCOMPLISHED

Significance of the Problem

High confidence event location plays a critical role in the identification and characterization of seismic sources. It is also an area of ongoing research, since the goal of routinely locating events to within an area of 1000 km^2, the maximum practical area for timely onsite inspections, has not been achieved for all regions and event sizes. The location of low magnitude events remains a technological challenge. Low threshold events can only be recorded at regional distances. Thus their seismic waves spend relatively more time in the crust and upper mantle, where the lateral changes in seismic velocities can significantly affect travel times. In addition, smaller events are frequently recorded only at higher frequencies, where crustal reverberations and the interference of surface reflections make phase identification more difficult. Researchers are constantly improving velocity models by incorporating more complex structure, including laterally heterogeneous velocities and detailed Moho topography. In response, location programs have begun to take advantage of these new high-resolution three-dimensional models.

These location programs have to compute travel times between an event hypocenter and the recording stations for seismic phases traveling through the three-dimensional models. A common approach is the finite-difference method. By finite-differencing the eikonal equation of ray tracing, wave fronts and travel times can be extrapolated from point to point throughout a three-dimensional grid. After travel times from all possible source locations to all recording stations have been computed, the grid is searched for the event location that minimizes the difference between the computed and the observed travel times, using one of several norms. Only the first arrivals at the recording stations are used in the inversion for the hypocenter.

The program QUAKE3D [1] is an example of this type of a finite difference location program. It computes the first arrival only from all possible hypocenters, whether it is a geometric ray, refraction, or diffraction. The source location is found that minimizes the difference between the observed and computed first arrival times, using either the root-mean-square (L2) norm or the absolute value (L1) norm. The program 3DGRIDLOC [2] uses the same finite difference method to compute the travel times, but instead of the L1 or L2 norm, it uses the non-linear inversion algorithm of Tarantola and Valette [3] to find the best hypocenter.

Ray tracing is an alternative to the finite-difference method of computing travel times for three-dimensional velocity models for use in location programs. A technique called the shortest path ray tracing algorithm [4] has been used to compute travel times for a location program [5]. This method computes the first arrivals by tracing rays from all grid points to all recording stations. Then the inversion method of Tarantola and Valette is used to find the hypocenter.

A major drawback of these three programs is that no information about secondary arrivals is included in the location algorithm. The first arrivals calculated might not always be observed. Secondary arrivals that could help determine the event depth, an important parameter in discriminating between earthquakes and explosions, are not used.

A third method of computing travel times for three-dimensional velocity models is the reflectivity method. The reflectivity method computes complete seismograms with all secondary arrivals. Kennett [6] has recently used this method to constrain source depths and source mechanisms for small events. Although this technique shows

promise for determining source depth and mechanism, it is not meant to determine the complete hypocenter. The computations are also very time-consuming compared to finite-differencing or ray tracing.

Clearly, a location method that uses initial and secondary arrival times for three-dimensional velocity models would complement the existing location programs. We are developing such a method by combining the paraxial approximation, which is used in Gaussian beam ray tracing techniques, with a standard hypocenter inversion method.

Accomplishments

We are developing a seismic event location program that computes travel times for a three-dimensional velocity model using the Gaussian beam ray tracing method of Cerven_ [7]. These travel times are used in the nonlinear iterative least square inversion method of Jordan and Sverdrup [8] to compute the hypocenter. This is the inversion method used in the location program LocSAT, which is used by the Center for Monitoring Research. We will add an option to this program to use travel times and travel time derivatives computed by Gaussian beam ray tracing.

The Gaussian beam technique [9] can compute accurate seismograms for isotropic Earth models of varying complexity. It combines the ray concept with elements of wave theory. Instead of solving numerically the full wave equation or the eikonal equation as in finite differences or finite elements, a high frequency approximation is made to the equations of motion to obtain the parabolic wave equation whose solutions include Gaussian beams. The technique is at least an order of magnitude faster than the reflectivity method, the finite element technique and the finite difference method, especially when it is applied to models incorporating complicated lateral structures. Like WKBJ, it is possible to code in individual seismic phases separately, and therefore it is well adapted for use in inversion methods. It matches the widely distributed WKBJ code in speed without suffering the pitfalls at caustics that WKBJ encounters.

Since classical ray tracing fails at caustics, it would be very difficult to utilize it in a location procedure that

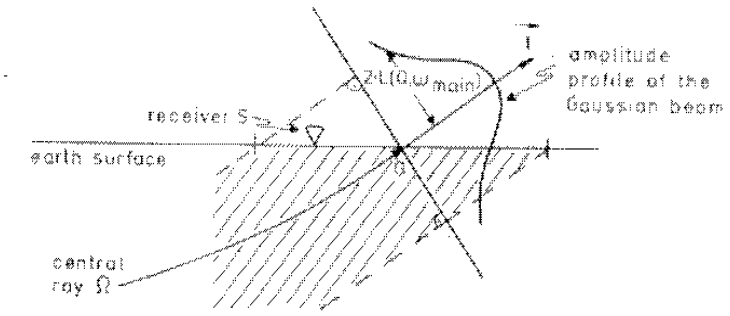


Figure 1. The region around the central ray (shaded area) within which a receiver obtains a contribution from the beam. Adapted from Weber (1998).

requires derivatives of travel time. The Gaussian beam method does not fail at caustics or triplications, since it forms phase arrivals from bundles of nearby rays instead of a single ray. This also means that there is no need for time-consuming iterations to find the exact ray from source to receiver. The beam is valid for any receiver that is within the beam width. (See Figure 1.) The travel times and the derivatives of travel time with respect to hypocenter coordinates are computed numerically from the Gaussian beam, instead of from a single ray, to insure that the location procedure is stable in the vicinity of caustics.

Another advantage the Gaussian beam method has over ray tracing is that it is capable of producing refractions or head waves. The technique can always compute the arrival time of head waves, such as Pn and Sn. In slowly varying media, the beams can be broad and the amplitude of head waves can also be computed. Figure 2 shows

an example seismic-section of Gaussian beam synthetics for a homogeneous three layer moho model. The head

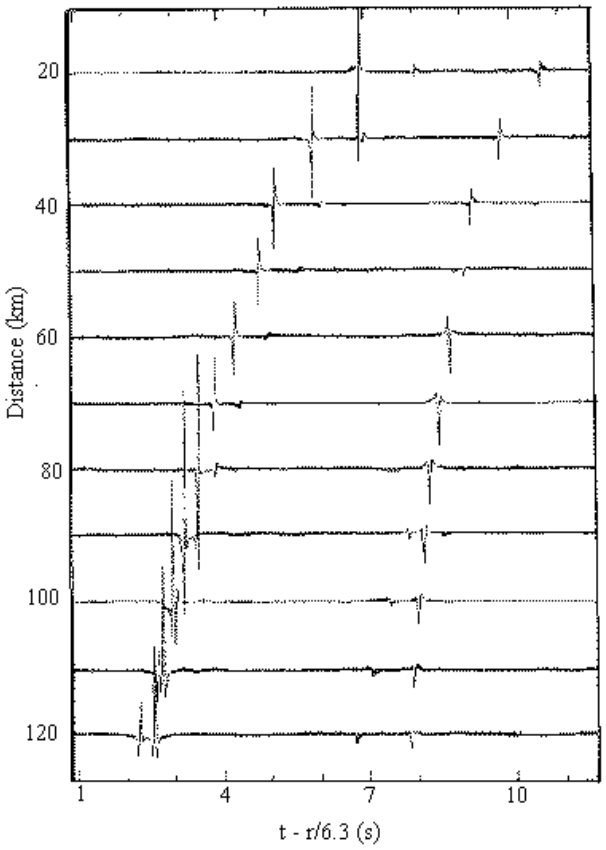


Figure 2. Gaussian beam synthetic seismograms for an explosive source in a two-layer crust plotted with a reducing velocity of 6.3 km/3. Phases include reflections off the crustal interfaces as well as converted phases, but not the direct P wave.

waves become apparent at the larger distances. This amplitude information will be very useful for the seismic analyst.

As a major part of this project, we have developed codes to compute travel times and travel time derivatives based on the dynamic ray tracing method that is used to generate Gaussian beam synthetic seismograms for three-dimensional structures. This task is a straight-forward implementation of the three-dimensional method of Cerven_ [7], starting with the two-dimension Gaussian beam program of Weber [10], as rewritten by Davis and Henson [11]. In the two-dimensional code, the velocites V_p and V_s, the density ρ and the attenuation constants Q_p and Q_s are defined at each vertex of a grid of triangles. The analytical solution to the differential equations describing the behavior of the beam inside each triangle is used to trace the beam from source to receiver. In a similar manner, the three-dimensional model is a grid of tedradedra, and the velocities, density and attenuation constants are defined at each of the four vertices.

The travel time along a ray is computed by adding the contributions from each tetrahedron that the ray passes through. The equations for general three-dimensional dynamic ray tracing are given by Cerven_ [7]. We use dynamic ray tracing to efficiently compute the ray and travel time between two points in the model. To

determine the ray from the source to the receiver, we start with an initial guess for the slowness vector at the source, trace the resulting ray and then use dynamic ray tracing to adjust the slowness vector. The convergence to the correct slowness vector is very rapid.

For the second technical objective of this project, we have extended the graphical interface that has been developed for the two-dimension Gaussian beam software [11] to display the input three-dimension models and display the ray paths that make up the beams. The OpenGL library, which is available on most computer platforms, including SGI, SUN and Windows95, is used to construct the 3-D displays. This work is essential to confirm the correct operation of the ray tracing and the gridding of the three-dimensional velocity structures.

The final objective of this project is to integrate the Gaussian beam software with the LocSAT location program. This program uses the iterative least-squares method of inverting for the hypocenter and therefore requires the partial derivatives of travel time with respect to hypocenter coordinates. Software for numerically computing these derivatives for the Gaussian beams will be developed along with routines to interface with the LocSAT code.

CONCLUSIONS AND RECOMMENDATIONS

There are several results from this project. The first result is a program that computes travel times and travel time derivatives based on the dynamic ray tracing method that is used to compute body-wave Gaussian beam synthetic seismograms for three-dimensional velocity structures. The input to the program is a three-dimensional Cartesian grid of velocities, density and attenuation constants that describe the velocity structure. Also input is a list of seismic phases, specified either using standard terminology (pP, etc.) or by specifying the travel path (transmitted, reflected, refracted, converted, etc.) Finally, the source location, the source moment tensor and the receiver location is input. The output from the program is written in CSS3.0 format.

The second result from this project is a graphical interface which is a modified version of the program Xgbm [11], that displays the input 3-D velocity grid and the ray paths from source to receivers. The user is able to display ray paths for selected phases and also design custom ray paths.

The third result of this project will be a modified version of the location program LocSAT that is linked to a library containing the 3-D Gaussian beam travel time components. There will be an option to LocSAT to use the Gaussian beam travel times and travel time derivatives instead of the IASPEI tables. Both types of travel times will be available, i.e. the user will be able specify that individual phases use either the IASPEI tables or the Gaussian beam travel times for the hypocenter inversion. The Gaussian beam travel times and derivatives will be dynamically computed from the input 3-D grid at each iteration of the hypocenter location.

REFERENCES

[1] G.D. Nelson and J.E. Vidale, Earthquake locations by 3-D finite difference travel times, *Bull. Seismol. Soc. Am.*, **80**, pp. 395-410, April, 1990.

[2] R. Ayala and L.A. Drake, Earthquake location with a 3-D velocity model for the region of the Bolivian Andes, in *Proceedings of the 19th Annual Seismic Research Symposium on Monitoring a Comprehensive Test Ban Treaty*, Orlando, USA, PP. 191-200, September, 1997.

[3] Tarantola and B. Valette, Inverse problems = quest for information, *J. Geophys*., **50**, pp. 159-170, 1982.

[4] T.J. Moser, Shortest path calculation of seismic rays, *Geophysics*, **56**, pp. 59-67, 1991.

[5] T.J. Moser, T. van Eck and G. Nolet, Hypocenter Determination in Strongly Heterogeneous Earth Models Using the Shortest Path Method, *J. Geophys. Res*., **97**, pp. 6563-6572, May, 1992.

[6] B.L.N. Kennett, Constraining the depth and source mechanism for smaller events at far-regional to teleseismic distances, in *Proceedings of the 20th Annual Seismic Research Symposium on Monitoring a Comprehensive Test Ban Treaty (CTBT)*, Sante Fe, New Mexico, pp. 248-254, September 1998.

[7] V. Cerven_, Ray synthetic seismograms for complex two-dimensional and three-dimensional structures, *J. Geophys*., **58**, pp. 2-26, 1985.

[8] Thomas H. Jordan and Keith A. Sverdrup, Teleseismic location techniques and their application to earthquake clusters in the South-Central Pacific, *Bull. Seismol. Soc. Am.*, **71**, pp. 1105-1130, August, 1981.

[9] V. Cerven_, M.M. Popov and I. Psencík, Computation of wave fields in inhomogeneous media—Gaussian beam approach, *Geophys. J.R. astr. Soc.*, **70**, pp. 109-128.

[10] Michael Weber, Computation of body-wave seismograms in absorbing 2-D media using the Gaussian beam method: comparison with exact methods, *Geophys. J.*, **92**, pp. 9-24, February, 1988.

[11] J. Peter Davis and Ivan H. Henson, Development of an X-Windows tool to compute Gaussian beam synthetic seismograms, TGAL-93-03, Phillips Laboratory, Kirtland AFB, NM, 23pp, 1993.

FIRST BREAKS - AUTOMATIC PICKINGS OF P- AND S- ONSETS IN SEISMIC RECORDS

Eystein S. Husebye[1]) and Yu. V. Fedorenko[2])

1) Institute Solid Earth Physics, University of Bergen, Norway
2) Institute North Ecology Problem, Kola Science Center RAS, Russia

Sponsored by the Defense Treat Reduction Agency
Department of Defense, U.S.A.

Grant DSWA0I-98-C-0159

ABSTRACT

With an ever increasing number of seismic stations deployed worldwide partly under the IMS/CTBTO/UN umbrella there is an obvious need to automate seismic phase pickings. The problem is naturally most acute for local event records since they are most numerous and besides are most complex. We have previously addressed this problem in terms of easily picking maxima in envelope transformed records (Husebye et al., BSSA, 1999) which proved efficient for picking Lg-phases. As a needed improvement to this analysis tool, we have developed, validated and tested a versatile processing scheme for picking with confidence P- and S- onsets in local records. Out of 300 events analyzed accurate phase arrival times were picked for 90% of these recordings. Essential ingredients in the processing scheme were i) prewhitening, ii) wavelet transform, iii) polarization filter, iv) envelope transform and v) model function fitting by a simulated annealing method for picking first breaks in an optimal manner in approximately noise free envelope records. Automatic signal analysis implies extraction of a failure diagnostic for activating manual record inspections when need be. Ours are tied to relative energy distributions in the records and despite its simplicity work well. Our P- and S-pickings were converted to epicenter distances using a simple crustal model and then compared to corresponding estimates derived from the local bulletins. A qualitative comparison to analyst (bulletin) results were obtained for 2 separate a priori known explosion sites; our epicenter exhibited less scattering than those of the analyst. Out of the 10 % events classed as picking failures, a few were due to corrupted records while others were too messy even for manual analysis. However, the majority was due to processing errors and the reason being mainly that the function fitting algorithm picked secondary ripples on the dominant S/Lg-envelope. In view of the success in picking P- and S- arrival times for local events we are now adapting concept for picking in an automatical manner also teleseismic P-arrival times.

Key Words: Phase pickings, wavelet transform, polarization, envelope, function fitting, simulated annealing.

OBJECTIVE

The objective of this research is to facilitate to the extent possible automatic pickings of P- and S-phases in seismic records. This remains an outstanding problem in observational seismology and particularly in the context of CTBTO/IMS global seismic monitoring since such tasks still are somewhat manual. The very efficiency of the IMS global monitoring system requires that feature extractions in terms of phase arrivals, signal amplitudes and so forth are automated to the extent of minimum analyst interference. The major element in the research strategy chosen, was to tie analysis to slowly varying signal envelopes and not to the fast varying signals typical of the original waveform records. To achieve this objective, essential ingredients in seismic record analysis are i) prewhitening, ii) wavelet transform, iii) polarization, iv) envelope transform and v) function fitting by a simulated annealing method for picking first breaks in approximately noise free envelope records. The initial research stage our efforts are focused on P- and S-picking in local records which are more complex that those for teleseismic distances.

RESEARCH ACCOMPLISHED

A persistent and outstanding problem in observational seismology is that of confidentially picking P- and S-phases in local event records. These records are not only complex in view of the "sensitivity" of high frequency waves to small scale crustal heterogeneties but also because it is not always clear which phase arrivals are actually present in the records. Ambient noise often tends to mask the first cycle of the P- onset so picking errors are non-Gaussian. Such problems are more adverse for S- signals which arrive in the tail of the P- coda and besides have a more complex propagation path including phase conversions and scattering contributions (Hestholm et al., 1993; Sato and Fehler, 1998). The aim of this study was to develop a more robust and reliable phase picking scheme and in this regard discard the conventional waveform phase picking approach. Instead we focused on signal envelope processing schemes since both P- and S- envelope appear far more stable and recurrent than their respective original waveform segments (Husebye et al., 1998). An additional advantage with signal envelopes is that phase arrival times are tied to the envelope peak where SNR is good in comparison to the P- onset in the original waveform segment. Other approaches are to stack envelope transferred records from a network of stations thus mimicking seismic array beamfoming (Ryzhikov et al., 1997, Kushnir et al., 1999). Most of these processing schemes are often simplistic and seems to ignore a basic feature of envelopes which may be visualized via WKBJ synthetics for laterally homogeneous media. The characteristic features here are sharp P- and S- onsets and after being transformed into envelopes look like pulses of short duration. Another characteristic feature is exponential P- and S- coda decays that are typical of real seismograms (Sato and Fehler, 1998). Taking this into account we may expect that the shape of an envelope of real waveform will be close to that shown in Fig. 1.

Data used in analysis stem from segmented event recordings in the 30-300 km range from the 3-component (3C) station Hoyanger (HYA) in western Norway (Fig. 2). The original records (example in Fig. 3a) are our raw material and is not useful for further analysis unless refined. With refinement is meant suppressing ambient and signal generated noise and then envelope phase shaping as implied in Fig. 1. To achieve this we introduced a waveform processing sequence comprising 4 steps; i) prewhitening, ii) wavelet transform, iii) polarization filtering and iv) envelope smoothing and v) functional fitting. The various processing techniques used, are detailed below and besides illustrated in Fig. 3. Our research accomplishments are tied to analysis of 300 local events recorded at a station on the west coast of Norway. The epicenter distance range is 25 - 250 km ensuring the full complexity of local event recordings and thus taken intuitively to be representative of local events anywhere. Below, analysis procedures are described in some detail and starting with 'record prewhitening' as our first step here.

Raw traces and prewhitening

The prewhitening has a dual purpose of removing low-frequency part of ambient noise and producing an approximate white noise spectrum as desired for the subsequent wavelet transform. With basis in many spectral studies we may use a simple linear noise spectrum representation that is inverse proportional to frequency ω. Ambient noise exhibit at least in coastal areas strong seasonal variations in levels but not in form for $f >$ I Hz so the "inverse ω" shape provides a robust and versatile spectrum representation. Using

this noise feature we can easily transform initial seismic traces into traces with "white" seismic noise simply by differentiation. The fastest numerical procedure is to apply FFT to the initial traces, multiply resulting spectra by $i\omega$ $\left(i = \sqrt{-1}\right)$ in frequency domain and then transform it back to time domain. Alternatively, we may use the so-called IIR high-pass filter of order 1 with cut-off frequency close to Nyquist frequency for prewhitening. The latter is more flexible because we can apply sequentially different filters to suppress "hump" in the noise spectra often observed for $1 < f < 2$ Hz. Anyway, raw traces are shown in Fig. 3a while those obtained after prewhitening are shown in Fig. 3b. The striking gain in SNR was not unexpected as the local noise is dominated by surf on the nearby coast. By bandpass filtering or optimal variants hereof (Kushnir at al., 1999) better noise suppression may be obtained. However, "gain" depends on both noise and signal spectra which makes bandpass filtering not suitable for our purpose.

Wavelet transform.

Like the Fourier transform (FT), the wavelet transform (WT) is a linear operator on a data vector whose length usually is an integer power of 2, transforming it into a numerically different vector of the same length. In the wavelet domain basis functions $\psi(\tau, s; t)$ are somewhat complicated and have fanciful names like 'mother functions' and 'wavelets'. WT can be thought of as $X(\tau, s) = \int x(t)\, \psi_{\tau s}(t)dt$ where $\psi_{\tau s}(t) = (1/\sqrt{s})\, \psi)[(t - \tau)/s]$. In the WT domain the axes are scale s or inverse frequency and τ which is time shift as the wavelet slides through the signal window. Physically this means that low scales which is the high frequency part of the signal has good time resolution while high scales are low frequencies with good frequency resolution. Hence, most of the usefulness of wavelet operation rests on the fact that $X(\tau, s)$ can be severely truncated (Press et al., 1992) thus removing weakly represented scattering and noise contributions. The choice and corresponding length of the wavelet function does not appear to be overly critical; after much experimenting with wavelets of the types Daubechies 4, 12 and 20, we settled for Daubechies 20 (Daubechies, 1988; Press et al., 1992). In practical seismogram analysis we expect that in the case of pure noise with approximately flat spectra after prewhitening the wavelet transform will also be flat so wavelet coefficients for different s and τ will possess similar amplitudes which may be removed without substantial distortion of the seismic signal.

To test this hypothesis and assess the truncation threshold level we computed empirical probability density function (p.d.f) of wavelet coefficients for pure noise samples. According to this p.d.f the truncation at threshold level of 20 must remove 99.9% of wavelet coefficients corresponding to noise. Testing of real data is illustrated in Fig. 3c; the noise preceding incoming P- and S- waves is not only reduced - it is literally wiped out. The P- and S- signals as such are not much distorted except that small "ripples" have been removed so more smooth signals and shorter codas appearances have been obtained.

Polarization filter

To enhance P and S onsets and to suppress various kinds of coda waves we applied polarization filtering. Following Christoffersson et al. (1988) and Jepsen and Kennet, (1990), we assume that seismic signal $s(t)$ $[{}^{s}N(t), {}^{s}E(t), {}^{s}D(t)]^{T}$ containing both P and S waves may be represented as

$$s(t) = [\sin\phi \cos\theta, \sin\phi \sin\theta, \cos\phi]^{T} s(t)$$

Here, $s(t)$ is the plane wave amplitude, θ - azimuth and ϕ apparent angle of incidence on the free surface. The relation between "true" and apparent incident angles are $\tan\phi = F \tan i$ where F is surface correction factor. The latter is given by $F = 2 \cos i \cos j | (1 - 2\sin^2 j)$ where i would be the actual angle to the vertical made by the normal to the plane wave front, and j is the true propagation angle for SV wave which is related to i via Snell's law. If the angle of incidence j is greater than the critical angle j_c, surface displacement for SV waves may be written as

$$s(t) = [i \sin\phi \cos\theta, i \sin\phi \sin\theta, \cos\theta]^{T} s(t)$$

This expression is also appropriate for higher and fundamental mode Rayleigh waves, but here ϕ = arctan e where |e| is the eccentricity of elliptical motion. We used Hilbert transform to make complex traces $\hat{s}_i$ from real traces s_i and to produce complex covariance matrix $C_{ij} = \hat{s}_i \hat{s}_j^*$ where i, j = 1, 2, 3 and an asterisk means "complex conjugate". The expression for polarization filtering P(t) used in this study is:

$$P(t) = \frac{(C_{13}^2 + C_{23}^2)(C_{11} + C_{22} + C_{33})}{(C_{11} + C_{22})C_{33} + \gamma} \qquad (1)$$

where γ is a small number to ensure numerical stability. As may be easily shown, P (t) has following properties: i) Re [P (t)] does not depend explicitly on ϕ and θ, ii) if the seismic signal is pure linearly polarized, Re [Prect(t)] =|s(t)|^2> 0, iii) if the seismic signal is pure elliptically polarized, Re[Pell(t)] = - s(t), ^{s}E(t) ^{s}D(t) elements are uncorrelated, < Re[P (t)] > $\rightarrow$ 0,

These properties make the filter operator P(t) useful for enhancing P and S arrivals as demonstrated in Fig. 3d. The imaginary part of P(t) appears if and only if the seismic signal is a mixture of linearly and elliptically polarized components, which is always the case with ambient noise and coda waves present. For both pure linear and pure elliptical polarization Im[P(t)] = 0. The latter properties of the polarization filter operator (1) were of no use in our analysis. Important, our polarization filtering approach allows us to exclude time domain averaging in record analysis so the original sharp P- and S- onsets are retained which in turn are essential for improving (at least maintaining) phase picking accuracy.

Nonlinear smoothing.

Picking of P- and S- onsets directly from the polarization filter would obviously not be a good idea in view of the spiky and irregular appearances of the output records (Fig. 3d). To make phase picking more robust we apply nonlinear smoothing to the polarization filter output E(t_i) by the recursive formula:

$$E(t_i) = \begin{cases} E(t_i) & \text{if } E(t_i) > E(_{ti\text{-}1}) \\ E(_{ti\text{-}1}) \exp(-\lambda \Delta t), & \text{if } E(t_i) < E(_{ti\text{-}1}) \end{cases}$$

where i = 1, ..., N, N is number of samples in the polarization filter output, Δt sampling interval, in our case Δt = 0.02 s, t_i = (i - 1) Δt + t_b, t_b is UT of recording triggering, parameter λ controls the decay of resulting envelope. The choice of λ was a compromise between 2 extremes; if λ small a spiky record would produce boxlike envelopes while too large the polarization records would be retained without too much distortions. Our choice of λ = 0.05 produced envelope shapes like that shown in Fig. I and besides being sensitive enough to preserve a weak S-wave onset. Naturally this λ - decay is similar to that characterizing observational S-coda roll-off (Sato and Fehler, 1998). Anyway, at this processing step it may be instructive to compare the prototype in Fig. 1, original raw traces in Fig. 3a and the corresponding envelope variant in Fig. 3e; phase picking should be easier in the latter case.

Function fitting - phase fitting.

Due to the simplistic shape of the polarization envelope it may be tempting to read onset times manually but an automatic manner is naturally preferable. Our starting point here was the Fig. 1 envelope which

served as the prototype for the 'record processing end product' or last processing step. On analytical form the Fig. 1 functional representation is:

$$F_e(t) = \begin{cases} 0; & t \in [t_0, t_1) \\ A_1 (t - t_1), & t \in [t_1, t_2) \\ h_1 \exp [\alpha_1 (t - t_2)], & t \in [t_2, t_3) \\ A_2 (t - t_3) + B_2, & t \in [t_3, t_4) \\ h_3 \exp [\alpha_2 (t - t_4)], & t \in [t_4, t_5) \end{cases}$$

Here $A_1 = h_1 / (t_2 - t_1)$, $\alpha_1 = log (h_1 / h_2) / (t_3 - t_2)$, $A_2 = (h_3 - h_2) / (t_4 - t_3)$,

$B_2 = (h_2 t_4 - h_3 t_3) / (t_4 - t_3)$, $\alpha_2 = log (h_3 / h_4) / (t_5 - t_4)$ with the obvious constraints $t_1 < t_2 < t_3 < t_4 < t_5$, $h_4 < h_3$. Using this prototype we can formulate the problem of seismic phases fitting as finding the global minimum $\left[t_1^{min}, t_2^{min}, t_3^{min}, t_4^{min}, h_1^{min}, h_2^{min}, h_3^{min}, h_4^{min}\right]$ of the objective function:

$$\Phi(t_1, t_2, t_3, t_4, h_1, h_2, h_3, h_4) = \sum_{k=1}^{N} F_e((i-1) * \Delta t) - E_i)^2 \qquad (3)$$

Finding the global minimum is always a difficult problem. In our case we have tested almost all numerical quasi-Newton methods which failed apparently because of convergence towards local minima in (3). The method of simulated annealing in Press et al., (1992) proved adequate to find a global minimum for Φ (...) in eq. 3. A good initial guess is important for optimization problem. There are two possibilities to start the optimization process - either to estimate P-onset using the STA/LTA detector triggering time that is t_1^{min} or to find the maximum E_i and estimate t_2^{min} or t_4^{min}. Using maximum of envelope appears to be more robust than seeking for the P-onset but in the former case we must differentiate between t_2^{min} or t_4^{min} to know whether P-onset is larger than S. To resolve this problem we considered the following diagnostic:

$$D = \frac{S_r - S_l}{S_r + S_l}$$

with $S_l \sum_1^{i_{max}-1} E_i$, $S_l = \sum_{i_{max}}^{N} E_i$ where E_i is the smoothed polarization filter output and i_{max} being index for dominant envelope peak. For large S-phase (P weak) $D > 0.65$ implied failure while for P large (S weak) $D < 0.85$ implied failure. In other words, the above D-diagnostic prove reliable in 'triggering' analyst inspection of records and processing results.

Processing scheme summary.

The first 3 steps are straightforward while those of polarization envelopes and functional fitting proved rather cumbersome. The reason for this was our emphasis on robustness in processing without restoring to a multitude of alternative schemes in order to incorporate local seismogram oddities. Of course it would be feasible to modify scheme for picking teleseismic P-onsets including a search for depth phases like pP and sP - we are actively working on this now. Other application will be signal detection (no functional fitting) to use explosion envelopes as multidimensional source features for explosion site recognitions (Fedorenko et al., 1998, 1999).

Bulk analysis of local events.

The 303 events subjected to analysis occurred in 1996 - 1997 and their real distribution is shown in Fig. 2. The raw traces for the Hoyanger (HYA) station were extracted from segmented event files and then processed without human interferences in the manner described in the previous section. The measure used for testing performances was estimated epicenter distances derived by converting (t_S - t_P) times using a

simple crustal model. These distance estimates were in turn compared to those for HYA in the local bulletins as shown in Fig. 4. More than 63 % of the automatically processed events were within 10 km of those in the bulletin while the remaining ones differ in extreme by 90 km. The bulletin epicenter solutions are not error free not at least because the network configuration is much elongated in the N-S direction giving poorer E-W resolutions. Hence, a more objective performance test was to compare 'absolute' distances since we had at hand ground truth information from 2 explosion sites at Geiranger and Mongstad respectively (Fig.2; Fedorenko et al., 1999). Not too surprising our automated distance estimates exhibit lesser scattering than those in the bulletins (Fig. 4 caption). The small distance biases of ca 4-5 km seen here is of little interest since the crust is not entirely homogeneous. In Fig. 4 events with distance differences exceeding 20 km are of special interest - what went wrong? Close examinations of these outliers gave that 3 was caused by corrupted records, a few reflected large bulletin errors but most processing failures. The reason here was that the function fitting algorithm picked secondary ripples on the dominant envelope as an independent P- or S-phase so large distance errors ensued. For 7 events the fitting algorithm was not activated because *D*-diagnostic fell into the uncertain range $0.65 < D < 0.8$. In 4 of these cases the P-envelope was very weak (P-onsets correct!) while in the 3 other cases both us and the fitting algorithm were confused. The above results give that our new processing and phase picking scheme handle approximately 90 % of events analyzed in a most satisfactorily manner.

CONCLUSIONS AND FUTURE PLANS

Automating seismogram analysis has been a prime research topic for more than 3 decades but progresses have been moderate in contrast to interactive seismogram analysis. The main reasons for this appear to be the inherited complexities in local P- and S-wavefield recordings with signal correlations decreasing rapidly between stations being located even less than a kilometer apart. As demonstrated here, signal envelopes have a rather simplistic shape and as such can successfully be used for very accurate pickings of both P- and S-arrival times for 300 local events (Fig. 2 and 4). Our success rate of 90% for the event analyzed and with a performance matching or even better than that tied to manual analyst analysis. These results are indeed encouraging and the next step is joint analysis of all network recording stations in order to demonstrate that the ultimate goal of automated bulletin production perhaps is achievable. However, analyst inspections and event verifications are likely to be needed for the foreseeable future but he/she may be triggered into actions by specific acceptance criteria as also attempted by us. So far we have limited our research work to local events (most complex) but foresee few problems in extending analysis to teleseismic phases like P, pP and sP. Finally, any seismograph station represents a partly unique recording environment so our processing sequences and associated parameterizations albeit robust and flexible are not obviously transportable.

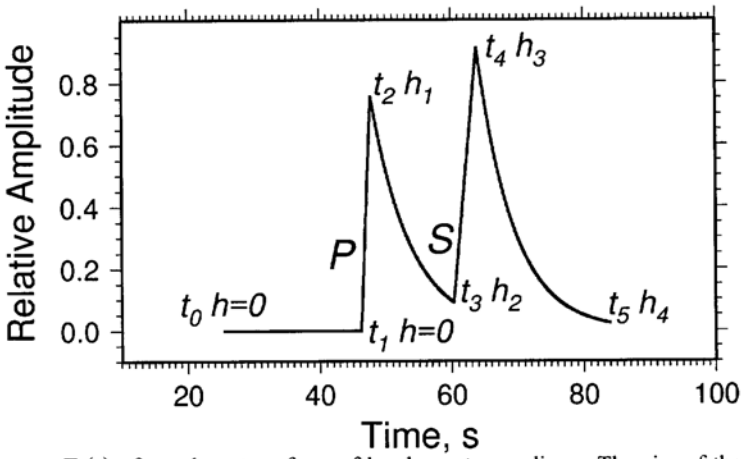


Fig. 1. Prototype $F_e(t)$ of envelope transform of local event recordings. The aim of the record processing sequences is to produce such envelopes. The h- and t- parameter mark extremes of the envelope prototype (definitions in eq. 2), and t_1 and t_3 would be equivalent to P- and S- phase arrival times. The actual picking of t_1 and t_3 is through functional fitting (simulated annealing) and is discussed in text.

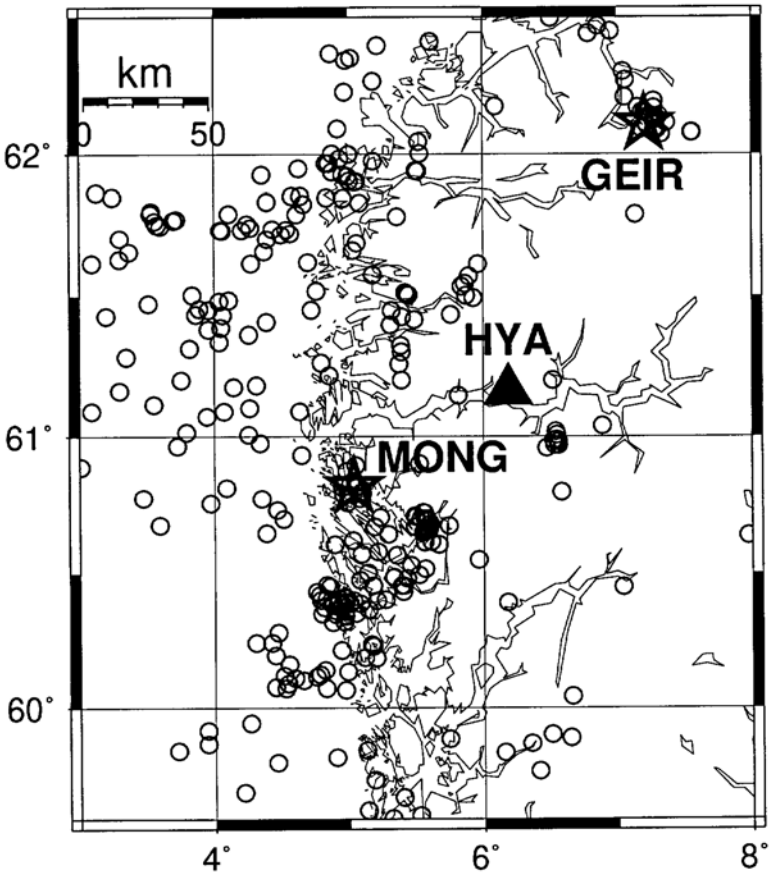


Fig. 2. Map showing the epicenters for all 300 events subjected to automatic P- and S-pickings. The 3-component station Hoyanger (HYA) is special marked and likewise the 2 explosion sites for which ground truth information were avaiable (GEIR=Geiranger; MONG=Mongstad).

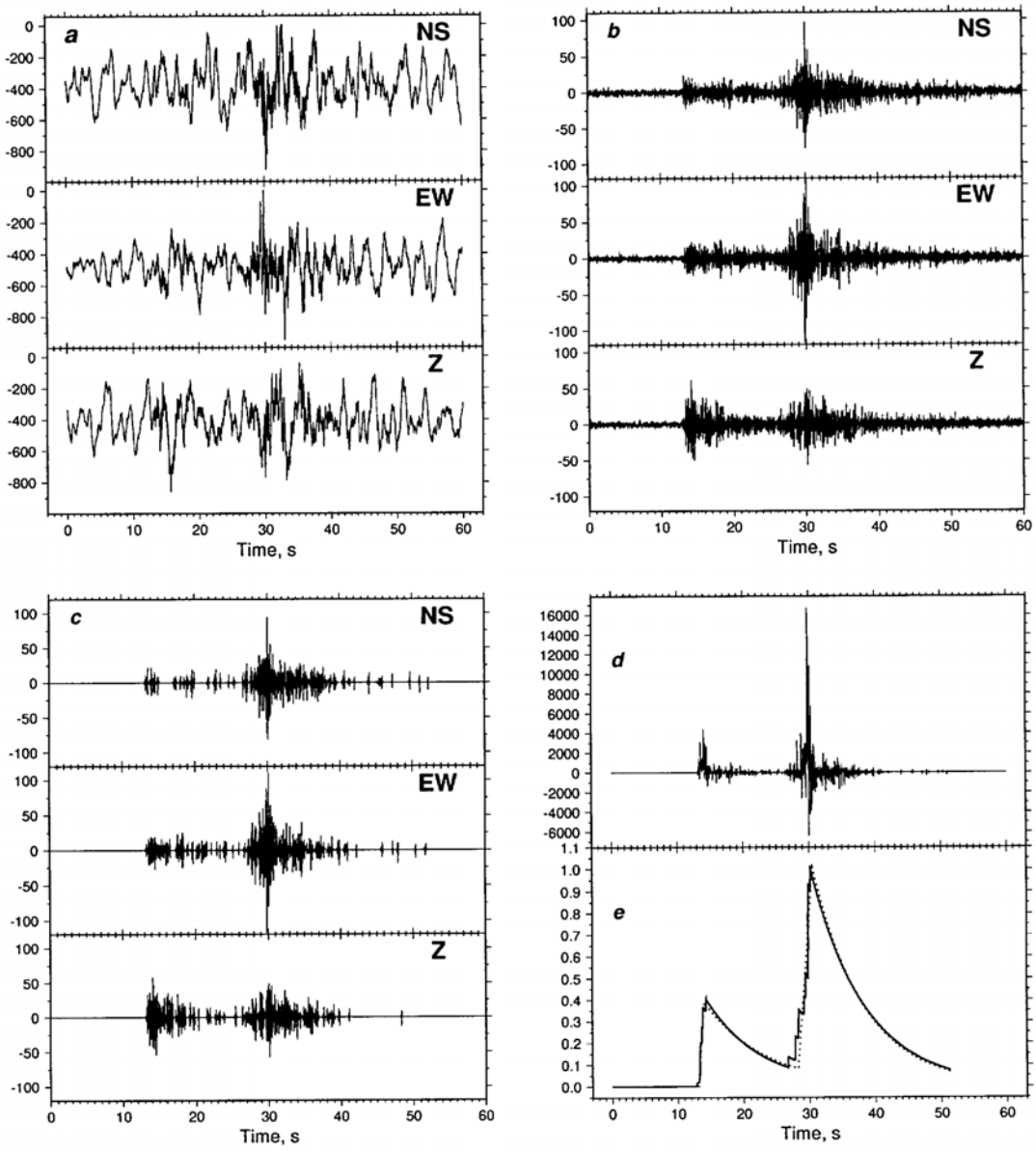


Fig. 3. Original waveform processing. Fig. 3a: Raw waveforms that is unfiltered Hoyanger (HYA) 3-component (3C) recording of an arbitrarily chosen event in our data base. Focal parameters are: Date 12/03/96, OT 14/09/46.0, 60.13 N 4.99 E, H = 0.0, ML = 1.5; Fig. 3b: Same event as in 3a but after prewhitening filtering; noise suppression is significant. Fig. 3c: Same event as in 3a but after wavelet transform operation; preceeding noise has been wiped out while the signal segments remain largely unscatched. However, the later parts of both the P- and S-coda, mainly attributed to multiscattering wavelets, are effeciently suppressed; Fig. 3d: Same event as in 3a but after polarization 'filtering', both P- and S-wave trains are cleaner implying contributions from out-of-plane reflections and refractions in the original waveforms; Fig. 3e: Same event as in 3a but after evelope transform and function fitting (dotted line); P- and S-phase pickings at 'start time' for the 2 envelopes as detailed in Fig. 1.

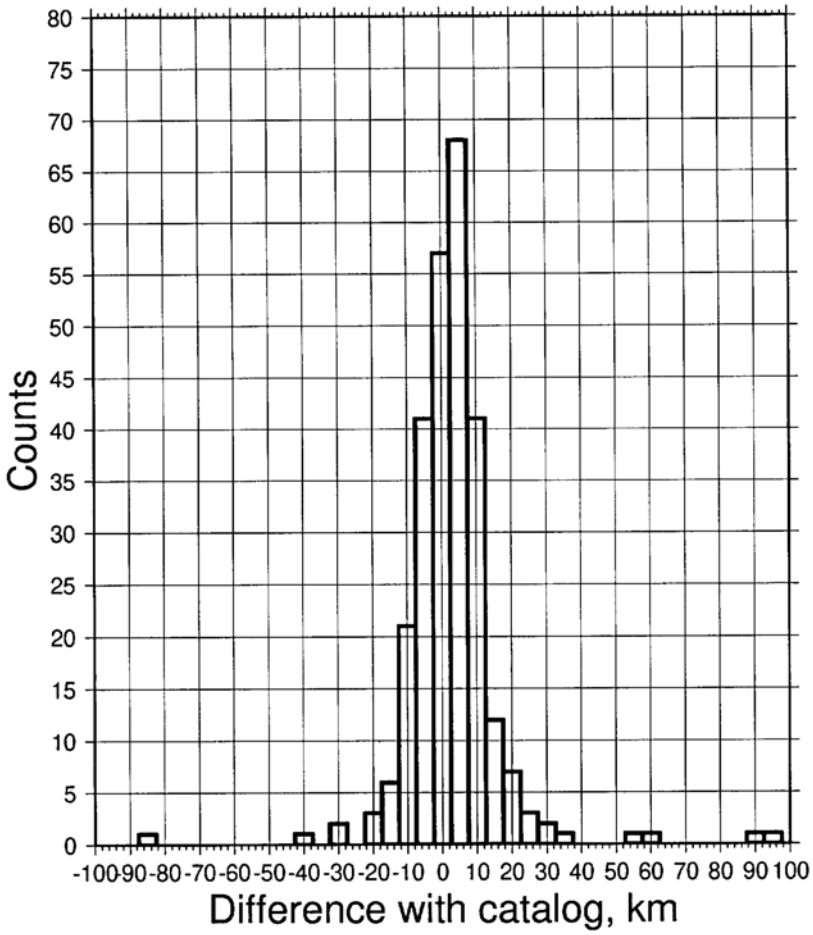


Fig. 4: Performance of the automatic phase picking algoritm for the 300 local events analyzed (Fig. 2). The $t_S - t_P$ differential times were converted to epicenter distances using a simple crustal model and then compared to Hoyanger epicenter distances as listed in the local bulletins. For the known explosion at sites Mongstad and Geiranger (Fig. 2) our distance estimates were more consistent than those in the bulletins that is within bounds of ±2 km (ours) versus ±4 km (bulletin) for a total of 20 explosions. Most of the outliers in the figure, differences exceeding 20 km, were caused by minor (10%) pecularities in the phase pickings as detailed in text.

REFERENCES

Christoffersson, A., E. S. Husebye and, S. F. Ingate, 1988. Wavefield decomposition using ML probabilities in single site 3-component records. Geophys. J. 93, 197-213.

Daubechies, I. 1988. Communications on Pure and Applied Mathematics, vol. 41, pp. 909-996.

Fedorenko, Yu. V, E. S. Husebye, B. Heincke and B. O. Ruud, 1998. Recognizing explosion sites without seismogram readings: neural network analysis of envelope-transformed multistation SP recordings 3-6 Hz. Geophys. J. Int. 133, F 1-F6.

Fedorenko, Yu. V, E. S. Husebye and B. O. Ruud, 1999. Explosion site recognition; neural net discriminator using three-component stations. Phys. Earth Planet. Int., June 1999 issue.

Hestholm, S. O., E. S. Husebye and B. O. Ruud, 1994. Seismic wave propagation in complex crust-upper mantle media using 2-D finite difference synthetics. Geoph. J. Int. 118, 643-670.

Husebye, E. S., B. O. Ruud, and A. M. Dainty, 1998. Fast, robust and reliable epicenter determinations: envelope processing of local network data. Bull. Seismol. Soc. Am. 88, 284-290.

Jebsen, D. C. and B. L. N. Kennett, 1990. Three-component analysis of regional seismograms. Bull. Seismol. Soc. Am., 80, 2032 - 2052.

Kushnir, A. F., E. V. Troitsky, , L. M. Haikin and A. M. Dainty, 1999. Study of statistical classification approach to discrimination between weak earthquakes and chemical explosions recorded by the Israel local seismic network. Phys. Earth Planet. Int., June 1999 issue.

Press, W. H., S. A. Teukolsky, W. T. Vetterling and B. P. Flannery, 1992. Numerical Recipes in C: The Art of Scientific Computing, Chap. 13, 2nd Edition, Cambridge University Press, MA, USA.

Ryzhikov, G.A., M. S. Biryulina and E. S. Husebye, 1997. A novel approach to Automatic Monitoring of Regional Events. IRIS Newslett. 15, 12 - 14.

Sato, H. and M. C. Fehler, 1998. Seismic Wave Propagation and Scattering in the Heterogeneous Earth. Springer-Vertag, Berlin, pp. 308.

EVENT SCREENING PROCEDURES AT THE PIDC

David Jepsen and Spiro Spiliopoulos

Australian Geological Survey Organisation

Sponsored by Defense Threat Reduction Agency

Contract No. DTRA01-99-C-0002

ABSTRACT

Event screening is defined as the process of filtering out events that are considered to be consistent with natural or non-nuclear man-made phenomena, leaving a pool of ambiguous events that may require further examination. An experts working group representing many States Parties has been established to recommend appropriate screening guidelines for use at the International Data Centre (IDC). Event screens, which have been constructed from the key global discriminants: location, depth and Ms:mb, are capable of screening approximately 70% of the events in the REB. It is expected that there will be significant progressive enhancements to the screening procedures over time as the International Monitoring System (IMS) expands and becomes calibrated, and as additional discriminants are evaluated and included into the screening system. Other discriminants suggested for use in event screening (in Annex 2 to the Protocol of the CTBT) have been investigated. Preliminary results of their application and effectiveness are reported.

To assist in this work, the nuclear explosion database at the prototype IDC (pIDC) is being extended, with new seismic waveform data and the addition of phase arrival time information and event characterization measurements. In the future this dataset, including measurements, will be available through the World Wide Web.

Key Words: Event Screening, Discrimination, Groundtruth

OBJECTIVE

In Annex 2 to the protocol of the Comprehensive Nuclear-Test Ban Treaty (CTBT), a set of discriminants have been suggested for use in event screening. Our first goal is to investigate the capability of these discriminants in a global monitoring system and to develop event screening guidelines that can be implemented into the IDC processing system. Our second objective is to augment the nuclear explosion database at the pIDC with new seismic waveform data, the addition of phase arrival time information and event characterization measurements. The extended database will assist in the development of event screening procedures and be a useful data source for those working in the field of seismic event discrimination.

RESEARCH ACCOMPLISHED

Research has been undertaken in three areas. The principal focus has been on further developing and obtaining agreement on event screening criteria to be tested and implemented into Release 3 of the IDC software. Further, a preliminary assessment of screening with other discriminants has been performed and a summary is given of the groundtruth data that has been collected and processed. Each area of research is described below.

1. Event Screening

An experts working group representing many States Parties has been established to recommend appropriate event screening guidelines for use at the IDC. At the second Event Screening Workshop in Vienna, June 1998, the working group agreed upon a set of provisional event screening criteria to be tested and implemented into Release 2 of the IDC software. The initial screening criteria which consisted of both Ms:mb and depth, was approved by Working Group B, and was installed at the IDC during June 1999. Since that meeting, work has progressed with a third meeting held in May 1999 to build upon the existing criteria and procedures. A summary of the currently recommended event screening criteria and event scoring procedures to be tested at the pIDC for the Release 3 version of the event-screening system (installation date: mid 2000), is provided below. The recommendations are conservative in their approach and are thought to be robust in their application. It is expected that there will be significant progressive enhancements to the screening procedures over time as calibration information is added to the applications software, as more experience is gained in the operation of the IMS, as additional stations are added to the IMS, and as additional event characterization parameters are evaluated and included in the screening system.

1.1 Provisional Event Screening Criteria

To date, the event screening criteria are a combination of the discriminants: Ms:mb, depth and joint seismic-hydroacoustic locations. The recommended screening criteria for each discriminant is detailed below.

1.1.1 Ms:mb

Ms:mb has proved to be the most robust teleseismic discriminant for shallow seismic events and is based on the well-documented observation that nuclear explosions generate less surface wave energy than equivalently sized earthquakes. Taking into account differences in NEIC and pIDC magnitude estimates, Murphy (1997) showed from his analysis of 96 underground nuclear explosions and a set of earthquakes in the REB during the period 1996-1998 (see figure 1), that the discriminant line 1.25mb – Ms = 2.20 separates the earthquake and nuclear explosions populations well. It should be noted that this line is set at a level so as to ensure that no nuclear explosions would fall on the upper side of the line and be screened out.

As a result, the following Ms:mb provisional screening criteria was adopted in Release 2. It was recommended that an event be screened out if.

$$1.25\overline{m}_b - \overline{M}_s + 2\sigma_M < 2.20$$

Where

$$\sigma_M^2 = 1.25^2 \frac{\sigma_b^2}{N_b} + \frac{\sigma_s^2}{N_s}$$

$\overline{m}_b and \overline{M}_s$ are the network averaged estimates of mb and Ms from N_b and N_s stations respectively, and σ_b and σ_s are the standard deviations of the single-station mb and Ms measurements, respectively. Determination of uncertainties for Ms and mb estimates is still under development. At present, conservative values of $\sigma_b = \sigma_s =$ 0.3 are used. It was recommended that the Ms:mb screening criterion be applied to all events in the Reviewed Event Bulletin (REB) for which mb >= 3.5 and which have a Ms value. This criterion, including the two-sigma term, is equivalent to requiring that the 97.5% one-sided confidence interval for 1.25mb-Ms is entirely less than 2.20.

Recently, Murphy (1999) has derived preliminary mb station corrections for the IMS network of 89 seismic stations that are currently operational. The corrections lead to an average reduction of more than 40 percent in the variance and an average increase of nearly 0.2 magnitude units in the network-averaged mb values. Murphy indicated that the Ms:mb screening threshold would need to be refined (from 2.20 to 2.45), if these preliminary mb station corrections are used.

These results have stimulated a debate regarding the best way of estimating unbiased station corrections, given that: (1) the IMS network is evolving; (2) mb estimates depend on which, if any, auxiliary stations are used; and (3) the method of estimating mb may need improvements. For Release 3, it was recommended that potential biases in the preliminary mb station corrections be investigated and that the Ms:mb screening criterion be refined appropriately, pending resolution of this issue and results of further testing.

1.1.2 Depth

Events that are confidently deeper than a depth threshold for which it is feasible with existing technology to test an underground nuclear explosion, are very likely to be of natural seismic origin. A provisional screening criterion based on the depth confidence interval, is being tested at the pIDC to screen out such events.

The recommended depth screening criterion to be tested in the Release 3 software is as follows. Let $\hat{D}$ be the hypocentre depth estimate and s_{zz} be the variance of the depth estimate that are reported in the REB. It was recommended that an event be screened out if:

where

$$\hat{D} - 2\sigma_D > 10km$$

The value of k depends on whether depth phase criteria are met:

$$2\sigma_D = 2\sqrt{s_{zz}} + k,$$

k = 0km if number of depth phases >= 3 and ΔT(pP-P) >= 1.5 sec for stations between 25 & 100º
k = 20km otherwise

It was recommended that the depth screening criteria be applied to all events in the REB with mb >= 3.5 and for which depth estimates were not constrained by an analyst. This criterion, including the two-sigma term, is equivalent to requiring that the 97.5% one-sided confidence interval is entirely deeper than 10km.

Comparisons of REB depth estimates with those of the PDE and local bulletins has shown that REB depth estimates exhibit significant regional biases and that the depth uncertainties do not adequately reflect all of the model and random errors. As an interim approach, a constant term k has been introduced to account for errors not adequately represented by s_{zz}. It has been shown by Jepsen and Fisk (1999) that the value of k=40km in Release 2 could be reduced to 20km and would still provide the appropriate coverage at the specified level of confidence.

1.1.3 Joint Seismic-Hydroacoustic Location Event Screening

Hydroacoustic data is sometimes required to assist in screening out events whose epicentres are on the water.

Oceanic seismic events which are confidently located, in water depths for which it is infeasible to install and test explosions in sub-oceanic material and with no associated hydroacoustic bubble pulse or high frequency energy (e.g., above 32 Hz), are very likely to be natural phenomena.

-- The following screening criteria were recommended for testing. The screening criteria would only be applied to events detected and located by seismic data and for which:
  - The minimum water depth (*min_water_depth*) within the 90% location error is ellipse at least 500 meters, based on the two-minute bathymetry grid, in the latitude range of ±72 degrees (the latitude range over which the Smith and Sandwell (1997) grid is valid); and
  - The entire 90% location error ellipse does not overlap or contain any onshore portions of an appropriate high-resolution coastline grid.

-- Such events without a detected hydroacoustic signal are to be screened out if:
  - The entire 90% location error ellipse has a clear path to at least one IMS hydrophone, based on signal blockage grids currently used at the prototype IDC; and
  - Hydrophone(s) without predicted signal blockage are operating properly at the predicted detection time interval; and
  - The noise level in the 32-64 Hz band during the predicted arrival time interval is less than three standard deviations above the long-term average noise level for the hydrophone.

-- Such events with associated hydroacoustic signals are to be screened out if:
  - There are no *significant* cepstral peaks in any of the associated signals from IMS hydrophones (indicating the absence of a bubble pulse); and
  - The total energy in the 32-64 Hz band (TE7) is less than 20 dB above the long-term average noise level in the same band (AN7) at each IMS hydrophone with an associated signal and with a Nyquist frequency greater than 64 Hz (i.e., TE7–AN7 < 20 dB for all single hydrophones with an associated hydroacoustic signal); and
  - The pre-signal noise level in the 32-64 Hz band is not greater than three standard deviations above the long-term average noise level for the associated IMS hydrophone.

1.2 Event Scoring

It was recommended that individual scores be computed for each event to numerically indicate the degree to which that event does, or does not, meet the depth, Ms:mb, and joint seismic-hydroacoustic location event-screening criteria. The following individual scores were recommended for testing:

$SCORE_{Depth}$ $= (\hat{D}$ – 10.0 km)/$2\sigma_D$ – 1.0; if the depth estimate is unconstrained
= –999.0; if the depth is constrained to the surface

$SCORE_{Ms:mb}$ $= [2.20 - (1.25\overline{m}_b - \overline{M}_s)] / 2\sigma_M - 1.0$
= –999.0; if an Ms measurement was not computed

$SCORE_{Hydro}$ = +1.0 – (TE7 – AN7)/20.0 dB; if TE7 is above the detection threshold
= +1.0; if the *min_water_depth* > 500 m, there is no predicted signal blockage, and TE7 is below the detection threshold
= –999.0; if the *min_water_depth* <= 500 m or there is predicted hydroacoustic signal blockage

It was recommended that an event be screened out if $SCORE_{Depth}$ or $SCORE_{Ms:mb}$ or $SCORE_{Hydro}$ is greater than zero, unless there are conflicting Ms:mb and hydroacoustic screening results. Note that the explicit expression for $SCORE_{Ms:mb}$ may be modified, as appropriate, depending on the resolution of issues regarding mb station corrections and the results of further testing.

Table 1 summarizes the recommended event-screening categories and the corresponding criteria to be tested. Each event in the REB will be assigned to one of the five screening categories in Table 1. Only events in the "Screened Out" category are to be screened out.

Table 1. Summary of recommended standard event-screening categories and criteria.

Screening Category	Screening Criteria
Not Considered	mb < 3.5
Insufficient Data	$SCORE_{Depth}$ = -999.0 and $SCORE_{Ms:mb}$ = -999.0 and $SCORE_{Hydro}$ = -999.0
Not Screened Out	$SCORE_{Depth}$ <=0.0 and $SCORE_{Ms:mb}$ <=0.0 and $SCORE_{Hydro}$ <=0.0, and at least one score is greater than –999.0
Conflicting Evidence	($SCORE_{Ms:mb}$ > 0.0 and –999.0 < $SCORE_{Hydro}$ <=0.0) or (-999.0 < $SCORE_{Ms:mb}$ <=0.0 and $SCORE_{Hydro}$ > 0.0)
Screened Out	$SCORE_{Depth}$ > 0.0 or $SCORE_{Ms:mb}$ > 0.0 or $SCORE_{Hydro}$ > 0.0, unless there are conflicting Ms:mb and hydroacoustic scores

1.3 Results

Application of Release 2 Ms:mb and depth event screening criteria on all REB events during 1998 was performed. It was found that a total of 46% of events of mb >= 3.5 were screened out. Figure 2 shows the breakdown of screening by category versus the magnitude of the event. It is evident that the Ms:mb and depth screening criteria complement each other very well, as a majority of the screened events are individually screened by either depth or Ms:mb. The physical basis for this is that Ms:mb is generally applicable to shallow events, whereas the depth criterion is intended to screen out deep earthquakes where Ms:mb is ineffective. Ms:mb provides the main contribution to the screening of events above mb 4.5, and in combination with depth, almost manages complete screening of earthquakes of mb 5.0 and above. It is expected that as the IMS system evolves, the screening capability based on the global discriminants alone will be able to meet the coupled 1KT explosion target (around mb 4.2). About 45% of the events not screened (30% of the total) are confidently located offshore. It is expected that future testing will demonstrate that most of these events will be screened out by the joint seismic-hydroacoustic location screening criteria. This would take the total number of screened events up towards the 70% mark.

2.0 Other discriminants for event screening

There are numerous other discriminants listed in the treaty to be tested for use in event screening. Algorithms for most of them have been written and implemented into the pIDC system (see Jepsen and Spiliopoulos, 1997). In this section a preliminary assessment of the global discriminants: teleseismic complexity, first motion and third moment of frequency are discussed. These discriminants have been in existence for decades but are currently not in favor for screening events worldwide. Issues that will be addressed are: will they help with the screening of natural phenomena and non-nuclear man made events? Do they complement the present screening criteria? How much do they add? Should future work of these discriminants be prioritized?

2.1 Teleseismic complexity

The measure of complexity follows the energy ratio technique of Douglas (1980). In this method the coherent beam of the P signal is filtered in the band 0.8 to 2.0Hz, squared and smoothed with an exponential window. Complexity is then computed as:

$$\text{Complexity} = \frac{S(5\text{-}35\text{sec} - N)}{S(0\text{-}5\text{sec} - N)}$$

except in following two cases:
If S(0-5) – N < 0, complexity = -1
If S(5-35) – N <= 0, complexity = 0

Complexity fell out of favor when complex signals from underground nuclear explosions were observed. Modeling by Bowers (1996) however, has suggested that a network averaged measure of complexity may prove to be viable. The basis for this is that simple sources, such as nuclear explosions, should be observed as simple recordings at many points on the earth and a network averaged value will make use of this. One useful network averaged measure is taking the average of the five lowest complexity measurements of the event. Figure 3 shows the network averages of a set of nuclear explosions from 7 test sites and all REB events during 1998 with at least five complexity measurements with SNR >=4. As expected, the nuclear explosions are in general less

complex than the shallow earthquakes. As a first step, an average network complexity of 1 could be used as the screening criterion and any event with a larger value would be screened out. Such a value ensures that no nuclear explosion would be screened out. Deep earthquakes are generally less complex and will not be screened out using this complexity screen. This is of no concern as the process only intends on screening out events that are more complex than the most complex nuclear explosion, and there are other discriminants such as depth that will help with screening these events. Of the 17299 events in the REB, the network averaged complexity could only be calculated for 1984 events, of which 1200 (60%) would be screened out with this criteria. However in conjunction with Ms:mb and depth, only an additional 180 events (1% of the total) would be screened out by complexity alone. It is expected that as the regional variability of complexity is investigated, and as other methods of calculating complexity are considered, complexity will provide a greater contribution to event screening.

2.2 First Motion

First motion is traditionally difficult to measure and is normally only possible with recordings from large events or events within a close regional network. This imposes a severe constraint on its use for event screening and so it is not expected to add any extra capability to the present screening criteria. The first motion algorithm implemented at the pIDC searches for the first maxima or minima after the onset and then assigns the appropriate direction. However, when this was implemented into the pIDC system it was found that many of the first motions were incorrect, indicating that this measurement is difficult to automate reliably. Analysis of the three nuclear explosions on the Indian sub-continent in 1998 showed that the analysts were incorrectly picking the onsets from many recordings, and hence the first motion were inaccurate. In addition, disagreement was found when Australian NDC analyst picks were compared with automatically calculated pIDC first motions for events recorded at ASAR, WRA and STKA during the first 3 months of 1999. It is of concern that the first motion onsets differ remarkably (see figure 4). Many of the events are emergent, so in these cases a first motion estimate is meaningless. Of the remaining events at least one-third of the impulsive recordings were in disagreement. Using a SNR criterion to resolve this problem is currently not a solution because there is a vast overlap between the SNR ranges of those events that the analysts agreed or disagreed with. As a result, first motion, in the way it is currently implemented, can not be used for event screening.

2.3 Third Moment of Frequency

The TMF measure follows that of Weichart (1971) and is calculated as

$$TMF = \left\{ \int_{0.5}^{5.0} f^3 sig(f) df \Big/ \int_{0.5}^{5.0} sig(f) df \right\}^{1/3}$$

where the signal has been corrected for noise. This measure gives more weight to high frequencies, so events with a greater proportion of high frequency energy will have higher TMF values.

Due to the small source dimension of a nuclear explosion compared to an equivalently sized earthquake, it would be expected that nuclear explosions would have higher frequency content than earthquakes, and so have higher TMF values. A comparison of TMF values of earthquakes in the REB and nuclear explosions (figure 5), shows no separation between the two source types and implies that no global screening criterion can be developed. These observations can be largely explained by the fact that attenuation of seismic energy differs dramatically in different regions of the world. A preliminary analysis of Lop Nor explosions on a station by station basis shows some separation, indicating that TMF could be used as an event screening tool for some source-receiver paths. However, since the TMF measure requires that the signal is significantly greater than the noise in the frequency band of interest, and can only be calculated for large events, it is certain that it will not contribute greatly to screening out additional events.

2.4 Regional Discriminants

Regional phase amplitudes have been studied extensively. Recently, Fisk (1999) has drawn upon many of these studies to devise a preliminary, systematic, global approach using P/S amplitude ratios for screening regional events. Baumgardt (1988), Hedlin et al. (1998) and Sereno & Wahl (1993) have found spectral techniques to be effective in discriminating ripple fired events from other source types. It has been demonstrated that the most successful applications of these techniques occur in areas of low attenuation and with recordings of events out to

10 degrees. Regional equivalents of mb:Ms, such as SPLP energy ratio (Woods and Helmberger, 1997), Ml:Mo and mb:Mo (Patton and Walter, 1993; Woods et al. 1993) have been successfully used to discriminate small regional events in the western US. Application of these discriminants has been limited to specific regional areas, and much work needs to be performed on a global basis before they can be successfully imported into some systematic screening mechanism. We are currently in the data gathering phase, collecting groundtruth data and making routine measurements. It is envisaged that a detailed event screening analysis using each discriminant will be made in the future.

2.5 Prioritization

The prioritization of future work on discriminants that are not currently part of the existing screening criteria was discussed at the 3rd Event Screening Workshop. Prioritization was based on the degree to which the discriminant could contribute to event screening, taking into account current progress and perceived limitations. It was recommended that investigations in terms of event screening should continue with regional phase amplitudes, spectral methods, regional Ms:mb measures and teleseismic complexity. It was agreed that further development of first motion and third moment of frequency should not be pursued in the near future.

3.0 Groundtruth

A Ground Truth data set consisting of seismic waveform data, phase arrival times, event characterization measurements and other associated source information from seismic events with known source type is under construction. This data set is and will be used to develop the event screening methodologies to be employed at the CTBT IDC.

The starting point for this data set was the Nuclear Explosion Database developed at the Center for Monitoring Research (CMR) (Yang et al, 1999). This database consists primarily of a table of origin data for 2041 distinct nuclear explosions. Waveform data for at least 742 of these events is also available. The data set was incomplete for our purposes in that phase arrival time information was not always available with the seismic waveform data, instrument calibration information was required and extensive quality control of the waveform data needed to be undertaken. Consequently only the waveform data from the CMR dataset was used.

The data from the CMR database has been augmented with seismic waveform and ancillary data from a number of other sources. These include:

- The Balapan data set assembled by Jack Murphy, which consists of data from explosions at the former Balapan Test Site.
- Data from the chemical calibration explosions detonated at the Semipalatinsk Test Site in 1997 and 1998.
- Data from IRIS of seismic recordings of nuclear explosions that are not contained in the CMR waveform data set.

Data has been obtained from as many seismic stations as possible and has not been limited to those stations that comprise the International Seismic Monitoring (IMS) network. This has been done in order to sample as many paths as possible for the purpose of possibly investigating the transportability of discriminants. In addition to the CMR and Balapan datasets, some 4000 extra waveform segments have been collected. Also 2600 arrivals have been analyzed and their associated waveforms have been checked for quality control. Figure 6 shows the locations of explosions (nuclear and chemical) from which data is available.

These data are currently being reviewed by a seismic analyst who is checking for quality control and also picking the arrival times of phases. After the data is reviewed, the waveform data, arrival times and calibration information are loaded into the pIDC database and event characterization measurements are made. In the future it is anticipated that this dataset will be available through the World Wide Web.

4.0 CONCLUSIONS AND RECOMMENDATIONS

Event screening criteria recommended by the working group are based on Ms:mb, depth and joint seismic-hydroacoustic location. The criteria are believed to be conservative and robust in their application. Results of testing Release 2 criteria on REB events during 1998 showed that 46% of the earthquakes (mb >=3.5) could be screened out and it is expected that many more earthquakes will be screened (up to 70%) by the Release 3

screening criteria. Further progressive enhancements to the screening criteria will be achieved as the existing screening criteria are improved and as regional and other global discriminants are tested and implemented into the screening system. For many discriminants a single screening criterion will not be possible and it may require defining criterion based on regions or specific source-receiver paths.

A major contribution to the event screening task will be the continual testing on groundtruth data. It is therefore strongly recommended that the collection of groundtruth data should continue and be made accessible to the community.

REFERENCES

Baumgardt, D. R. and K. A. Ziegler (1988). Spectral evidence for source multiplicity in explosions: applications to regional discrimination of earthquakes and explosions, *Bull. Seis. Soc. Am.*,**78**, 1773-1795.

Bowers, D. (1996). On the Probability of Mistaking an Earthquake for an Explosion Using the Simplicity of P, *Bull. Seis. Soc. Am.*, **86**, 1925-1934.

Douglas, A. (1980). Seismic Source Identification: A Review of Past and Present Research Efforts, *Identification of Seismic Sources – Earthquake or Underground Explosion*, E. S. Husebye and S. Mykkeltveit (eds), 1-48.

Fisk, M. D. (1998). Status of PIDC Seismic Event Screening Capabilities, *Proceedings of the IDC Technical Experts Meeting on Seismic Event Screening*, 5-9 June 1998, Vienna, Austria.

Fisk, M. D. (1999). An Experimental Event-Screening Approach using Regional Seismic Data, *Proceedings of the IDC Technical Experts Meeting on Seismic-Acoustic Event Screening*, 21-25 May 1999, Vienna, Austria.

Hedlin, M. A. H. (1998). A Global Test of a Time-Frequency Small-Event Discriminant, *Bull, Seis. Soc. Am.*,**88**, 973-988.

Jepsen, D. and M. D. Fisk (1999). Evaluation of PIDC Depth Estimates, *Proceedings of the IDC Technical Experts Meeting on Seismic-Acoustic Event Screening*, 21-25 May 1999, Vienna, Austria.

Jepsen, D. and S. Spiliopoulos (1997). Seismic Event Characterisation Parameters at the pIDC, *Proceedings of the Event Screening Workshop*, 4-7 November 1997, Beijing, China.

Murphy, J. R. (1997). Calibration of IMS Magnitudes for Event Screening Using the Ms/mb Criterion, *Proceedings of the Event Screening Workshop*, 4-7 November 1997, Beijing, China.

Murphy, J. R. (1999). Improvements to Seismic Magnitude Estimation with Implications for Event Screening, *Proceedings of the IDC Technical Experts Meeting on Event Screening*, 5-9 June 1998, Vienna, Austria.

Patton, H. J. and W. R. Walter (1993). Regional moment : magnitude relations for earthquakes and explosions, *Geophys. Res. Lett.*, **20**, 277-280.

Sereno, T. J. and D. D. Wahl (1993). A fuzzy Logic Approach to Regional Seismic Event Identification: Application to the Novaya Zemlya Event on 32 December 1992, *SAIC-93/1156*.

Smith, W. H. F. and D. T. Sandwell (1997). Global Sea Floor Topography from Satellite Altimetry and Ship Depth Soundings, *Science*, **277**, 1956-1962.

Weichart, D. H. (1971). Short period spectral discriminant for earthquake and explosion differentiation, *Z Geophys*, **37**, 147-152.

Woods, B. B., S. Kedar and D. V. Helmberger (1993). Ml:Mo as a regional seismic discriminant, *Bull, Seis. Soc. Am.*,**83**, 1167-1183

Woods, B. B. and D. V. Helmberger (1997). Regional Seismic Discriminants Using Wave-Train Energy Ratios, *Bull, Seis. Soc. Am.*,**87**, 589-605.

Yang, X., R. North and C. Romney (1999). PIDC Nuclear Explosion Database (Revision 2), *CMR Technical Report CMR-99/16*.

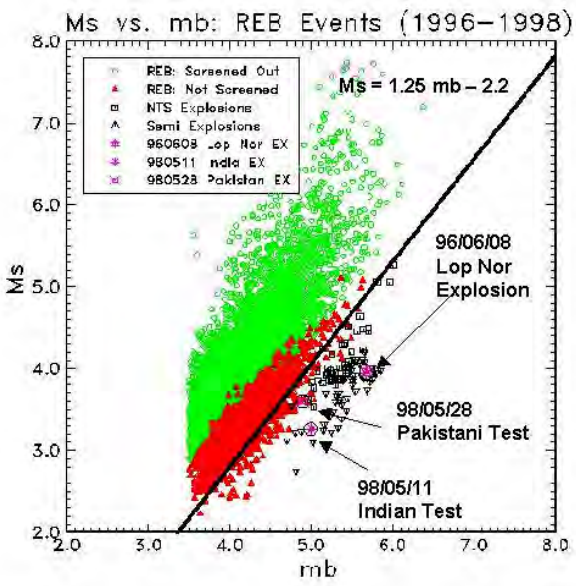


Figure 1: Ms versus mb values for 8608 REB events from 1996 to 1998 and a total of 96 underground nuclear explosions at the Nevada, Semipalatinsk, Lop Nor, Indian, and Pakistan test sites (from Fisk, 1998).

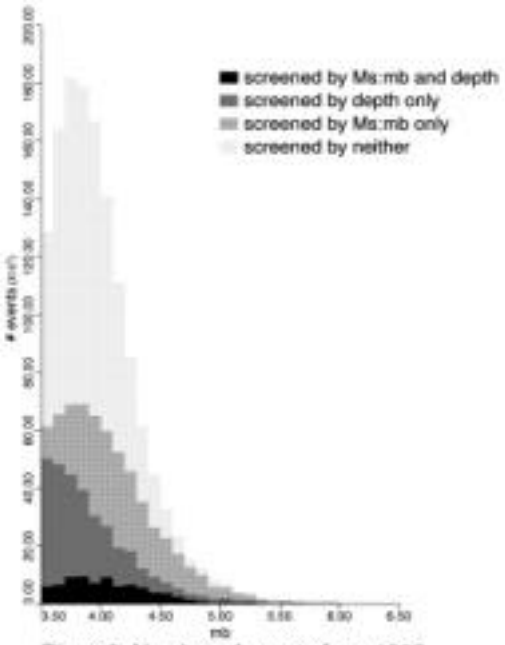


Figure2: Number of events from 1998 REBs screened by Ms:mb, depth or both versus magnitude.

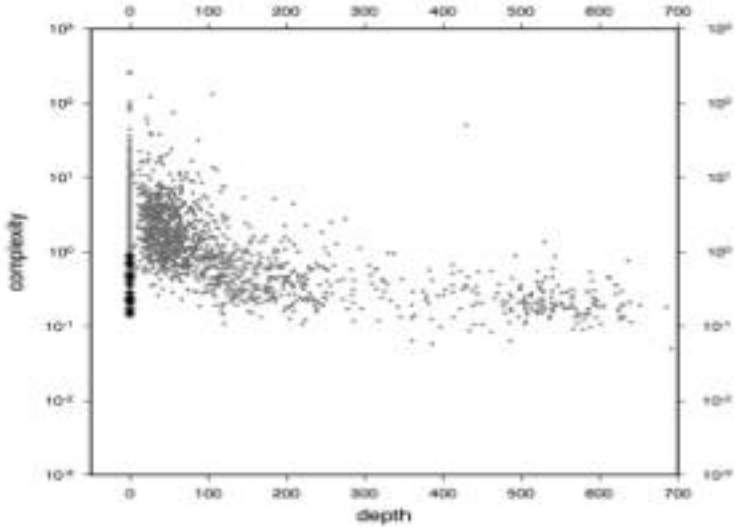


Figure 3: Network averaged complexity (of lowest 5) versus depth for 1998 REB events (grey) and nuclear explosions (black) where snr >=4.

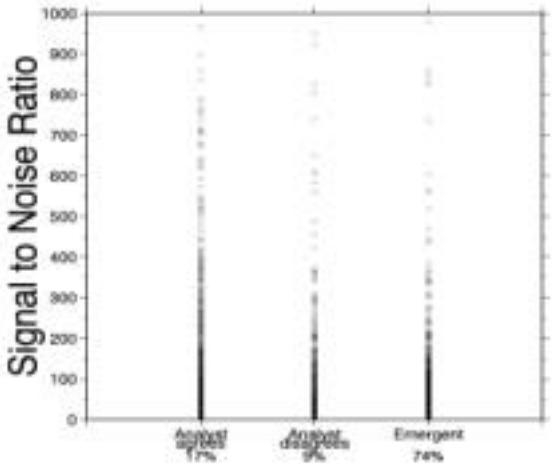


Figure 4: Comparison of analyst first motion picks with pIDC automatic first motion picks as a function of SNR.

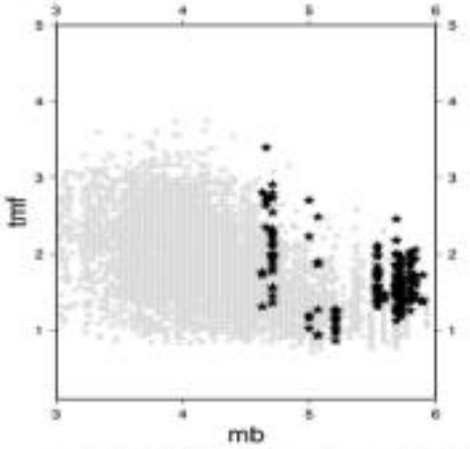


Figure 5: Third moment of frequency versus magnitude for earthquakes (grey) and nuclear explosions (black) in the REB

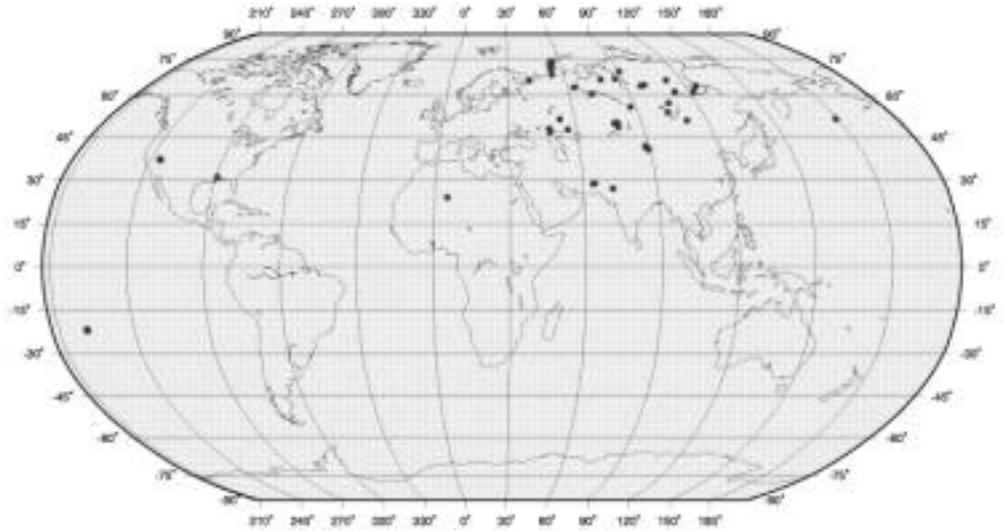


Figure 6: Location of explosions (nuclear and chemical) for which Ground Truth data is available.

A COMPARATIVE STUDY OF TWO AZIMUTH-BASED NON-STANDARD LOCATION METHODS

Rong-Song Jih, Defense Threat Reduction Agency

Sponsored by U. S. Department of Defense
Defense Threat Reduction Agency

ABSTRACT

In this study, two non-standard location procedures are reviewed, implemented and evaluated. Though independently developed, these two methods appear to be extremely similar in concept. Through azimuthal triangulation, Asian seismic network operators have been locating earthquakes for several decades using the "Induced Perpendicular Bisectors" (IPB), long before computers were invented and introduced to seismologists. The underlying simple principle can be best illustrated with the following extreme case. If two seismographs happen to record identical arrival times of the same seismic phase, then to the extent the 1-D structure applies to the region, the hypocenter should lie on the perpendicular bisector of the line segment or the great circle which connects these two specific seismographs. Depending on the epicentral distances, the perpendicular bisector itself could be a great circle along the Earth's surface or a normal section cutting through the Earth. If two or more such perpendicular bisectors are available, then the hypocenter or epicenter can be determined via triangulation. The merit lies in how the perpendicular bisector is derived in a more general setting, when the arrival time varies from station to station, which is typically the case in reality; and when waveform data are not available, which renders techniques based on full waveforms (such as polarization analysis and frequency-wave number (FK) technique) not applicable. The so-called "Yin Zhong Xian" algorithm, hereafter the YZX method, is an Oriental version of IPB-based procedure. It computes one IPB (via interpolation) for each group of three seismographs.

Also relying on the azimuthal triangulation for seismic location, Jih (1999) proposes a procedure, J0, to derive the back azimuth with a large-aperture network where all seismographs are on one side of the event. Any standard Geiger-type of least-squares inversion routine can be applied to determine the back azimuth easily. Two or more such skewed networks would suffice to derive two back azimuths for triangulation purpose. It has been demonstrated in Jih (1999) that this simple, hybrid procedure is particularly suitable for the seismic location problem at regional distances when [1] the crustal model is not known, [2] the seismic network is not calibrated, and [3] the azimuthal coverage of recording stations is poor. In this paper the procedure J0 is compared against the YZX method, to relocate earthquakes and explosions of known or well-constrained locations. It is shown that, at regional distances, the J0 algorithm performs better than does the YZX method, because the back azimuth derived with J0 is more reliable and stable. This is not surprising, as the YZX tends to be more susceptible to the small-scale lateral heterogeneity, which is often present in the crust. At local distances, however, the two methods seem to perform equally well.

Key Words: location, triangulation, back azimuth, calibration.

OBJECTIVE

To develop *ad hoc* algorithms which can effectively tackle the seismic location problem under the following difficult yet realistic situations often encountered in earthquake monitoring for the purposes of hazard reduction as well as for the CTBT verification: [1] the crustal model is not known, and hence an arbitrary global model (such as IASP91) will be sued; [2] the seismic network is not calibrated, and hence the phase arrivals will be used as they are - without any correction; and [3] the azimuthal coverage of recording stations is poor.

RESEARCH ACCOMPLISHED

1 Background

Epicenter remains as one of a few important source parameters that need to be promptly determined with sufficient accuracy and confidence whenever a natural - or man-made - seismic event of concern occurs. Over the years the computer-based Geiger-type least-squares inversion and its variations have become the standard means in solving the location problem.

If the ground-truth location of a nearby seismic event is known, the arrival readings of the new event at each seismograph can be individually "calibrated" to match the predicted travel-time curves of some pre-selected velocity model. It has been long established that, with the station corrections, locations of new seismic events in the vicinity around the ground-truth event can be significantly improved. This is the standard approach of ``calibration''. In a special application of this technique, travel-time residuals are obtained from a least-square location routine which is run with the depth constrained to the known ``true'' value. When these residuals are used as travel-time corrections in the same program run depth-free, nearby events can be located with smaller errors in depth. An elaboration of this specific application has been denoted the SRST (Source-Region-Station-Time) technique by Veith (1975) (see also Blandford, 1975). Alternatively, a postulated 1D crustal velocity model can be adjusted so that the estimated hypocenter would perfectly match the ground-truth event. Thus, the fine-tuned velocity model can be used to determine the location of nearby events without the need of establishing residual corrections for individual stations. Both the SRST and the model-tuning procedures require at least one ground-truth event.

There are cases where no nearby event of known location is available. Furthermore, there are cases where not only the crustal model is not well known, the seismic stations could be sparse or even spread in a very skew geometry. Jih (1999) presents a procedure, J0, which could be particularly suitable for these disadvantageous situations. In this study, J0 and another azimuth-based non-standard location procedure are reviewed and compared.

2 Adaptive Location Methods J0 and YZX

The most commonly used triangulation procedure for location is the "radial triangulation" which is based on intersection of several arcs drawn at respective epicentral distances. The epicentral distances can be individually estimated at each seismograph if, for instance, [1] the differential arrival (such as S-P) is available and [2] the P- and S-wave velocity structure around the seismograph is known. In the case only one common phase, say, the initial P, is available, then each pair of seismographs can jointly determine a hyperbola which passes through the epicenter – provided that, again, the P-wave velocity is known. Lacking the knowledge of the crustal structure, the location derived from radial triangulation could be severely biased when the number of seismograph is limited. The Geiger-type least square inversion using arrival times would inherently suffer from the same drawback and limitations.

Through "azimuthal triangulation", Asian seismic network operators have been locating earthquakes for several decades using the "Induced Perpendicular Bisectors" (IPB), even before computers were introduced to seismologists. The underlying simple principle can be best illustrated with the following extreme case. If two seismographs happen to record identical arrival times of the same seismic phase, then to the extent the 1D structure applies to the region, the hypocenter should lie on the perpendicular bisector of the line segment or the great circle which connects these two specific seismographs. Depending on the epicentral distances, the perpendicular bisector itself could be a great circle along the Earth's surface or a normal

section cutting through the Earth. If two or more such perpendicular bisectors are available, then the hypocenter or epicenter can be determined via triangulation. The merit lies in how the perpendicular bisector is derived in a more general setting when the arrival time varies from station to station, which is typically the case in reality; and when waveform data are not available, which renders techniques based on full waveforms (such as polarization analysis and frequency-wavenumber (FK) technique) not applicable.

The so-called "Yin Zhong Xian" algorithm, hereafter the YZX method, is an oriental version of IPB-based procedure. Given three arrivals, t1 < t2 < t3, at three seismographs S1, S2, and S3, respectively, the YZX method finds a point S4 which lies on the great circle connecting S1 and S3 such that the arrival time at S4 would be approximately t2. S2 and S4 then determine one IPB. The search of S4 (through interpolation) requires a priori knowledge about the velocity structure. In reality, simple interpolation procedures are often used, which inevitably introduce additional uncertainty into the derived back azimuth, and hence the location would be affected as well.

Also relying on azimuthal triangulation for seismic location, Jih (1999) proposes a procedure J0 to derive the back azimuth with a large aperture network where all seismographs are on one side of the event. The basic idea of J0 method is to decompose the recording network into (at least) two sub-networks so that each sub-network is comprised of stations spread over only one side of the postulated epicenter. That is, each sub-network should have a very large azimuthal gap and preferably a large aperture as well. Any standard Geiger-type of least-squares inversion routine can be applied to determine the bac kazimuth easily. Two or more such skew networks would suffice to derive two back azimuths for triangulation.

In this paper the procedure J0 is compared against the YZX method, to relocate earthquakes and explosions of known or well-constrained locations. It is demonstrated that, at regional distances, the J0 algorithm performs better than does the YZX method, because the back azimuth derived with J0 is more reliable and stable. This is not surprising, as the YZX tends to be more susceptible to the small-scale lateral heterogeneity which is often present in the crust. At local distances, however, the two methods seem to perform equally well (not shown).

3 Example 1: The Salmon Explosion of October 22, 1964

Salmon, an underground nuclear explosion in Mississippi, was seismically recorded throughout North America and at some teleseismic stations. The 5-kt explosion was detonated at 16h 00m 00.0s UT on October 22, 1964, at a depth of 828.1 meters. The epicenter is 31°08'31.57"N, 89°34'11.8"W, in the Taut salt dome in Hattiesburg, Southern Mississippi. Extensive studies have been conducted for this event to validate crustal profiles toward different directions (Jordan *et al.,* 1966; Springer, 1966; Warren *et al.,* 1966). Jordan *et al.* (1966) published phase picks recorded at 143 stations for Salmon explosion. Thirty six arrivals from those stations within 10º are used in this example.

Figure 1 shows 21 "induced bisectors", each derived with the YZX method from three sites of the 36-station regional network. Figure 2 is the same as Figure 1, except that 25 back azimuths are determined using the method J0 in conjunction with a global continental average model, IASP91 (Kennett, 1991). The IASP91 model is arbitrarily chosen to mimic the situation where the true crustal structure of a region of interest may not be available, and seismic analysts would have to use a possibly erroneous crustal model to start with (Figure 2). The method J0 gives tightly converged rays, with the majority intersecting in the vicinity of the ground-truth location. The dashed circle in Figures 1, 2, 3, 4, and 6 has a radius of 18.73 km, which encircles an area of 1,000 km_ .

4 Example 2: The Taiwan Strait Earthquake of September 16, 1994

The September 16, 1994, Taiwan Strait earthquake caused significant damages to southeast China. Though at equal distance to Taiwan, its damage to Taiwan was relatively minor. Paths to the mainland China apparently had a weaker attenuation in ground motion. Fifteen pairs of Pn and Sn arrival times have been published by the Fujian Provincial Seismological Bureau [FSB], China (Yeh, 1995; Huang et al., 1998.) Yeh (1995) selected five sets of IPBs and suggested that YZX would lead to a solution consistent with the conventional triangulation results using solely S-P times (c.f. Figures 2 and 3 of Yeh, 1995). In an attempt to duplicate Yeh's result, it is found that the YZX method degrades somewhat as additional IPBs are drawn from different combinations of FSB seismographs (Figure 3). It should be noted that, however, the station

coordinates of FSB seismographs used in this re-location exercise are not exact, as they were digitized from geographic maps, which certainly have added extra random errors to the location, with an effect equivalent to those of larger phase picking errors or stronger lateral heterogeneities in the crust.

If the same 1-dimensional model is assumed for paths to Taiwan and mainland China, then combining FSB phase picks with those measured at Taiwan's Central Weather Bureau [CWB] leads to a location with large offset (See the yellow diamond in Figure 4). The 1-second difference between FSB and CWB clocks, as speculated by Huang *et al.* (1998), can not count for this dramatic shift of location. It appears that paths to Fujian region may have a velocity faster than that of the IASP91model, whereas paths to Taiwan may be much slower. This is evidenced by Figure 4 (bottom) in which FSB and CWB underestimate and overestimate, respectively, the epicentral distances when the IASP91 model is used. Nevertheless, the individual back azimuths determined by FSB and CWB networks are not severely biased in direction. Thus applying the adaptive method J0 would lead to a triangulation result extremely close to the ISC and USGS/NEIC solution, which are based on hundreds of stations spread over all directions. The adaptive method is less sensitive to the choice of crustal model. Changing the crustal model from IASP91 to the southeast China model, which is in routine use at FSB (Fan *et al.,*1989; see also Jih, 1998), does not seem to affect the triangulation result (Table 1). This is yet another indication that the adaptive method J0 is robust.

Table 1. Comparison of Epicenters of September 16, 1994 Event

Network/Bulletin	φ° (N)	λ° (E)	Remark
Fujian Network	22.60	118.68	Yeh (1995), Southeast China model
Fujian + Canton	22.70	118.75	Yeh (1995), Southeast China model
CSB Preliminary	22.60	118.73	(China Seismological Bureau)
CSB RRSN	23.00	118.50	(CSB Rapid Reporting Seismograph Network)
Taiwan CWB	22.43	118.47	(Taiwan Central Weather Bureau)
USGS / NEIC	22.53	118.71	
ISC	22.52	118.75	
Adaptive Method J0	22.48	118.73	This study: Fujian+Taiwan, SE China model
Adaptive Method J0	22.48	118.72	This study: Fujian+Taiwan, IASP91 model

5 Example 3: The Kara Sea Event of August 16, 1997

Figure 5 illustrates how the method J0 can be applied to derive the location of Kara Sea event of August 16, 1997. A sub-network “A” comprised of 6 stations (KBS, SPITS, KEV, SDF, KAF, and FINESS), 11 phase picks, are fed into the LocSAT program (Figure 5, top) as described in Jordan and Sverdrup (1981) and Bratt and Bache (1988). The semimajor axes of the seven error ellipses are nearly the same, all pointing to the east – roughly 100º from the north (Figure 6). A second sub-network ``B'' is formed with 7 stations all spread to the south of Novaya Zemlya, which includes NRI, ARU, PKK, JOF, VAF, SUF, and KJN. There are 10 phase picks reported by these stations. Seven different continental crustal models produce nearly identical “optimal” back azimuths, pointing to the north (Figure 5, bottom). Using the IASP91 model, the two rays intersect at a location 11 km to the west of pIDC's REB location published in Israelson *et al.* (1997) (Figure 6). If the two networks were combined and the conventional location algorithm applied, the resulting location is 24 km to the south of the REB location (unfilled star in Figure 6). In-depth reviews addressing both the technical and political aspects of this event can be found in Sykes (1997) and Richards and Kim (1997).

DISCUSSION AND CONCLUSIONS

Two azimuth-based location techniques, J0 and YZX, have been implemented and tested to relocate earthquakes and explosions of known or well-constrained locations. It is shown that, at regional distances, the J0 algorithm performs better than does the YZX method, because the back azimuth derived with J0 is more reliable and stable. This is not surprising, as the YZX tends to be more susceptible to the small-scale lateral heterogeneities which are often present in the crust. At local distances, however, the two methods seem to perform equally well.

An interesting question raised by Prof. Thorne Lay at the 1st Event Screening Workshop (November 1997, Beijing) was that, if both the staged location procedure (like J0) and the conventional Geiger inversion are using virtually the same amount of information, would the staged approach offer advantages over the conventional procedure? In the case of simple crustal structure, indeed both methods could perform equally. Figure 2 exhibits a tight clustering of back azimuths derived from the adaptive method J0, resulting a well-constrained epicenter. This can certainly be achieved with all the phase picks lumped in one single Geiger inversion. This is not the case in general, however. As shown in Figure 4, lumping phase picks from Fujian and Taiwan seismic networks into one least-squares inversion would lead to a disastrous location, unless the difference in lateral difference in crustal velocities is accounted for. This is the intrinsic drawback of the conventional location procedure. In the case of staged procedure such as J0, each back azimuth is determined with a skew sub-network. The skew geometry of the sub-network would inevitably lead to large uncertainty in location and large error in epicenter. However, the method J0 does not use the epicenter information in the second stage of the process. The only piece of information – which is the best constrained piece – utilized by J0 is the semi-major axis, or equivalently, the back azimuth. As a result, the J0 method is practically using several back azimuths – each one being better constrained in the process - for triangulation. This explains why J0 is not equivalent to the conventional Geiger inversion.

A side remark on seismic data should be made. Seismic data have multiple uses – quick and accurate location of damaging earthquake so as to permit rapid emergency response, studies of the interior of the earth and the physics of the earthquake source, and nuclear test verification (Sykes, 1997). The field of seismology, which has been involved in earthquake studies for nearly 100 years, has a long tradition of international data exchange, much like that for weather information. It would be a tragedy if a major earthquake disaster strikes and response to the disaster were delayed because seismic data were not available. Example 2 clearly illustrates the advantages and importance of sharing the phase readings between China and Taiwan. China Seismological Bureau [CSB] has been promptly sharing phase readings of large earthquakes with Russia and Cuba. It is not surprising that the performance of CSB's RRSN [Rapid Reporting Seismograph Network] in earthquake location has greatly benefited from the data exchange. News has it that CSB and the Central Weather Bureau [CWB] of Taiwan have recently started negotiating a possible “seismic cooperation”, hopefully that could lead to an agreement on routine seismic data exchange between the two sides of the Taiwan Strait.

A lesson learned from Example 2 (Figure 4) is that phase picks from different tectonic regions must be combined in a judicious manner, if the conventional Geiger inversion is to be applied. One way to do so is to take into account the difference in crustal structures and apply the path-dependent travel-time tables - or equivalently, path-dependent corrections - prior to lumping the phase picks together for inversion. If adaptive methods (such as the method J0) are utilized, however, then the improvement in location can be immediately achieved without the need to wait for the time-consuming ``calibration research'' is conducted. This can be regarded as an *ad hoc* measure.

V. References

Blandford, R. R. (1975). Use of Source-Region-Station Time corrections at NTS for depth estimation, *Report SDAC-TR-75-4,* Teledyne Geotech, Alexandria, VA.

Bratt, S. R. and T. C. Bache (1988). Locating events with a sparse network of regional arrays, *Bull. Seism. Soc. Am.*, **78,** 780-798.

Fan, Y.-L., J.-Z. Lin, R.-H. Hu, and Z.-N. Luo (1989). Compilation of near-regional travel-time tables for South China, in ``*Development of regionalized travel-time tables in China*'' (J.-G. Xiu, C. Zhang, and K.-X. Qu, Edt.), Monitoring and R&D Department, State Seismological Bureau, Beijing.

Huang, B.-S., G.-C. Chen, H.-Y. Yan, and Z.-X. Yao (1998). Re-examination of the epicenter of September 16, 1994, (magnitude 6.5) earthquake in the Taiwan Strait *(unpublished manuscript).*

Israelson, H., M. D. Fisk, X. Yang, and R. G. North (1997). The August 16, 1997 event in the Kara Sea, *CMR Technical Report CMR-97/38*, Center for Monitoring Research, Arlington, VA.

Jih, R.-S. (1998). Location calibration efforts in China, in *Proceedings of the 20th Seismic Research Symposium*, 21-23 September, 1998, Santa Fe, New Mexico. 44-55.

Jih, R.-S. (1999). Epicenter estimation using erroneous crustal model(s) and skew regional networks*, Phys. Earth Planet. Inter.,* **113**, 303-319.

Jordan, J. N., W. V. Mickey, W. Helterbran, and D. M. Clark (1966). Travel times and amplitudes from the Salmon explosion*, J. Geophys. Res.,* **71-14,** 3469-3482.

Jordan, T. and K. A. Sverdrup (1981). Teleseismic location techniques and their application to earthquake clusters in the South-central Pacific, *Bull. Seism. Soc. Am.,* **71,** 1105-1130.

Kennett, B. (editor) (1991). *IASPEI 1991 Seismological Tables*, Research School of Earth Sciences, Australian National University, 167 pp.

Richards, P. G., and W.-Y. Kim (1997). Testing the nuclear test-ban treaty, *Nature,* **389** (23 Oct 1997), *781-782.*

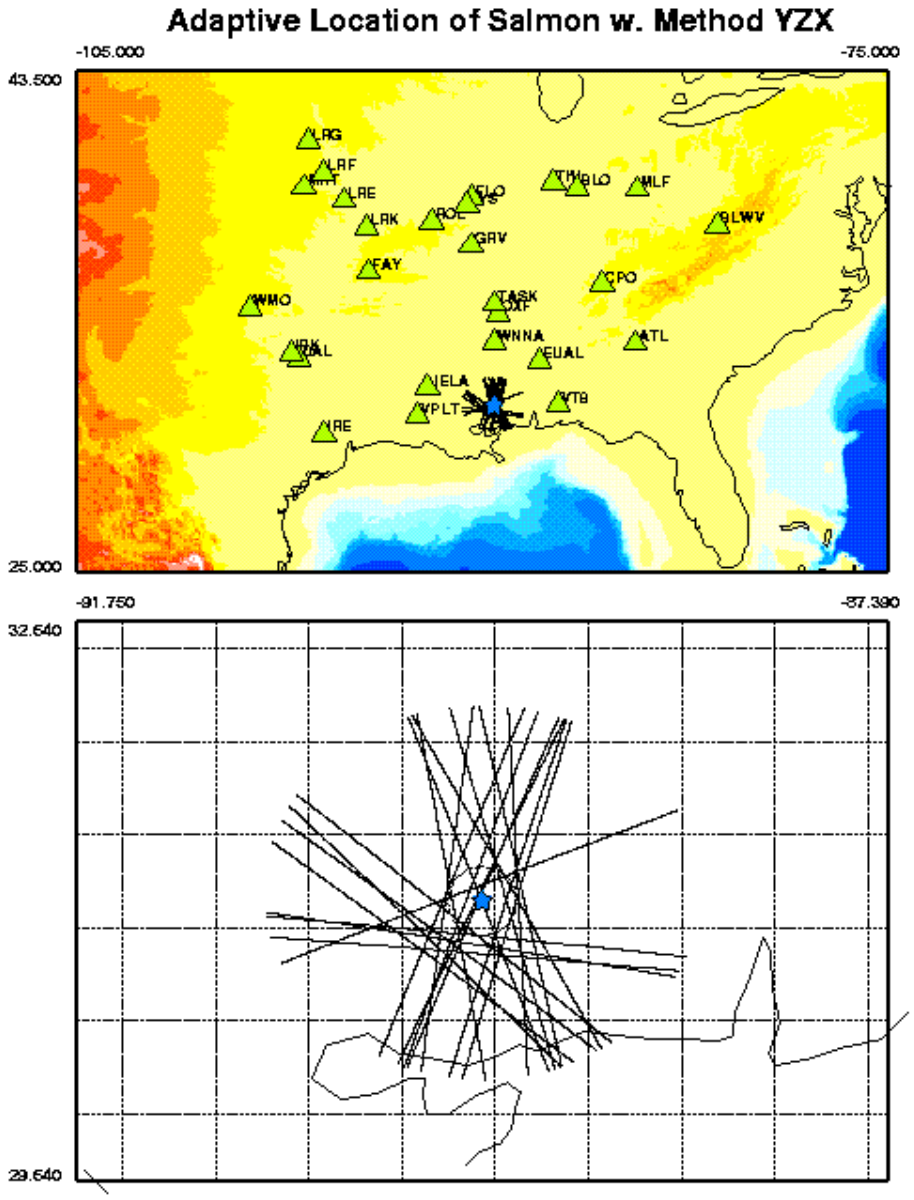
Springer, D. L. (1966). Calculation of first-zone P wave amplitudes for Salmon event and for de-coupled sources, *J. Geophys. Res.,* **71-14**, 3459-3467.

Sykes, L. R. (1997). Small earthquake near Russian nuclear test site leads to U.S. charges of cheating on Comprehensive Test Ban Treaty, *J. Fed. of Am. Scientists.* **50-6,** 1-12.

Veith, K. F. (1975). Refined hypocenters and accurate reliability estimates, *Bull. Seism. Soc. Am.,* **75,** 1199-1222.

Warren, D., J. H. Healy, and W. H. Jackson (1966). Crustal seismic measurements in southern Mississippi, *J. Geophys. Res.*, **71-14,** 3437-3458.

Yeh, W.-Y. (1995). Preliminary study of the epicenter of September 16, 1994, (magnitude 7.3) earthquake in the Taiwan Strait, *Fujian Seismology*, **11-1,** 110-114.



G.T. location= 31.142N -89.570W 0.828
21 "induced bisectors" used, each derived from a 3-station subnetwork

Figure 1

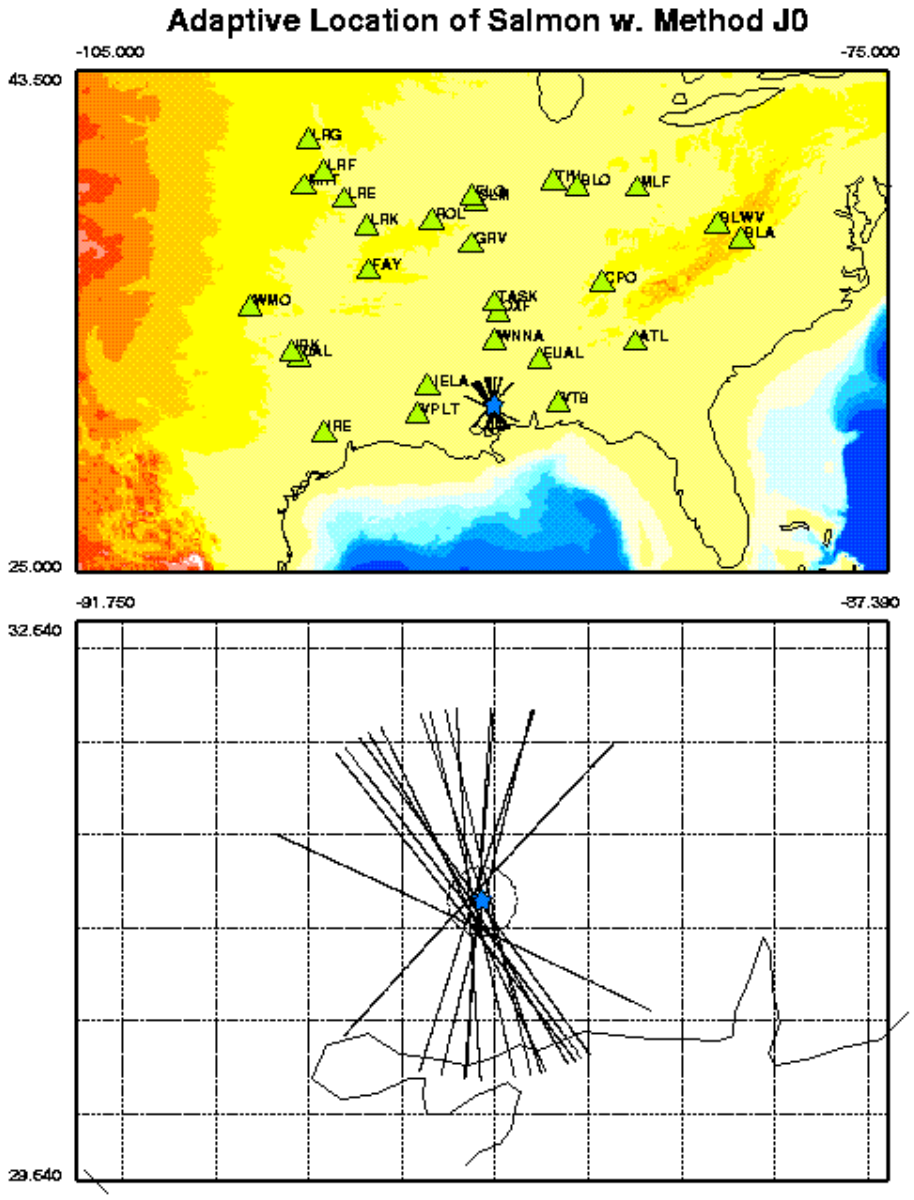
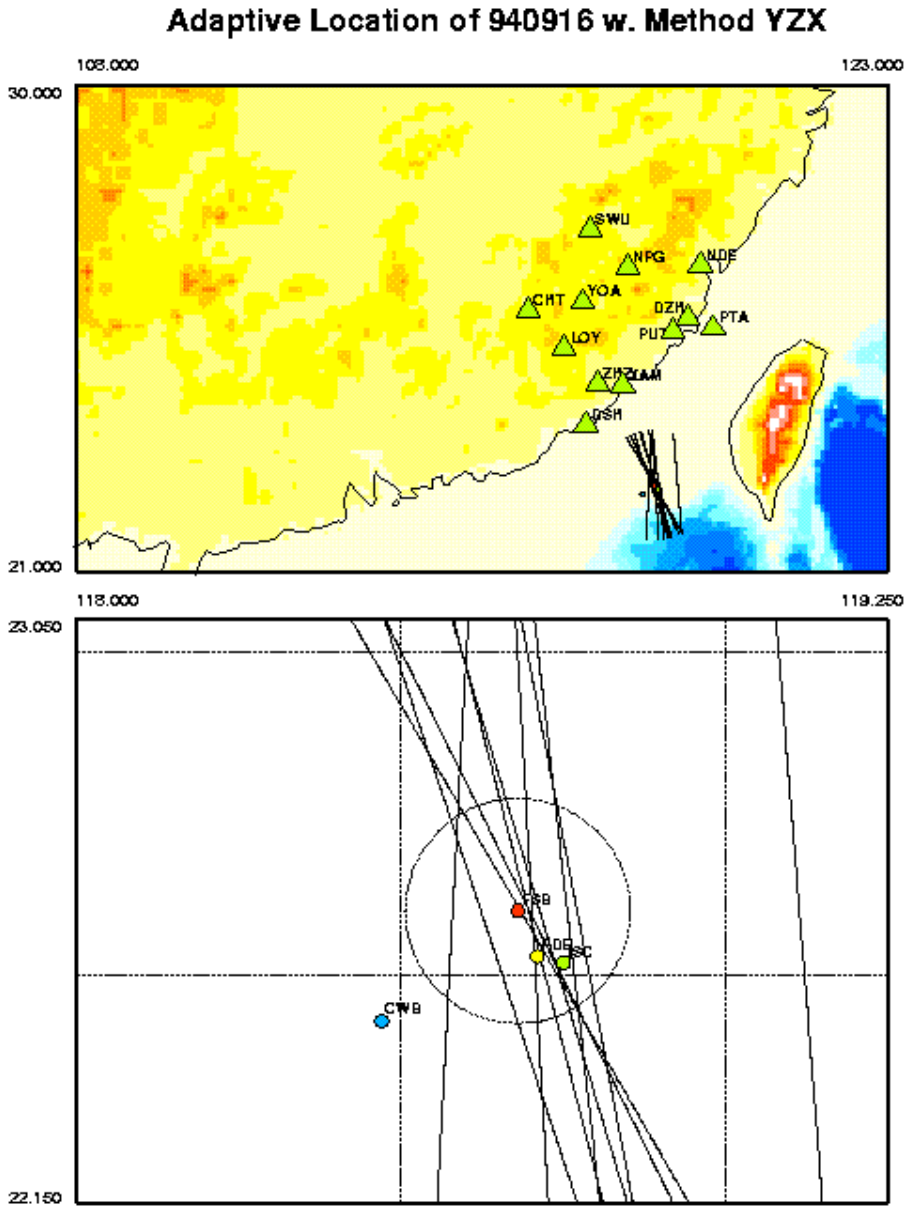
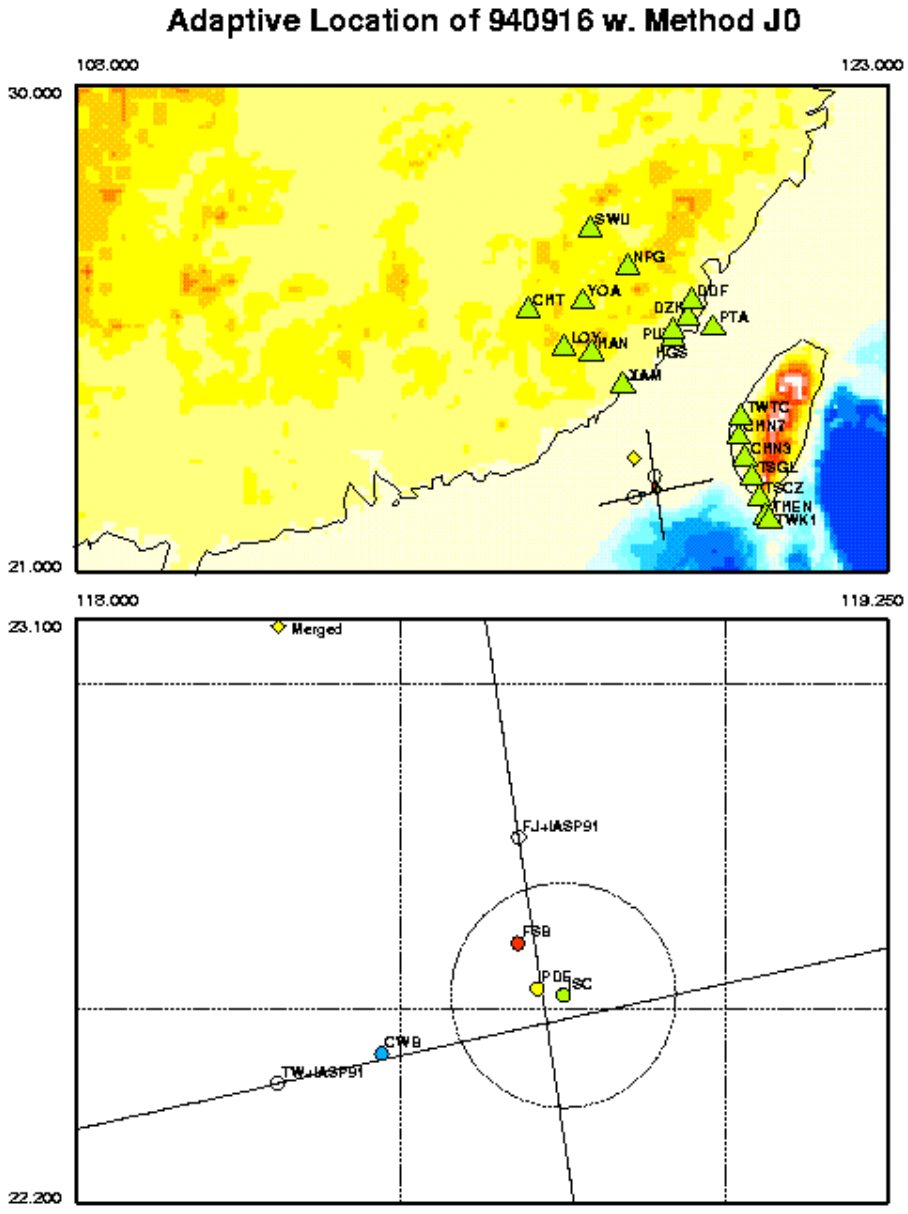

Adaptive Location of Salmon w. Method J0
-105.000
-75.000
43.500
25.000
LRG
LRF
LRE
LRK
ROL
GRV
FAY
WMO
CPO
ATL
ELA
VPLT
VTB
MLF
BLO
BLA
-91.750
-87.390
32.640
29.640
G.T. location= 31.142N 89.570W 0.828km
IASP91 model used for all subnetworks

Figure 2



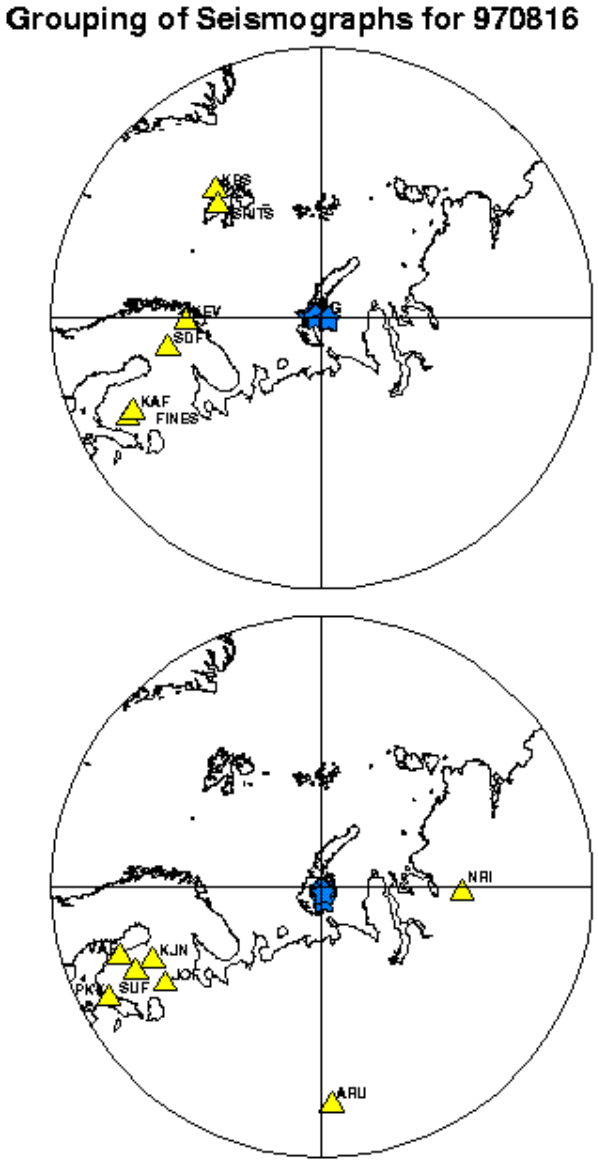
10 "induced bisectors" used, each derived from a 3-station subnetwork
NEIC = 0620 18.7 22.53N 118.71E 13km, ISC = 22.52N 118.75E 13km
CWB = 0620 15.62 22.43N 118.47E 19km; FSB = 22.60N 118.68E 10km

Figure 3



IASP91 model used for all subnetworks
NEIC = 0620 18.7 22.53N 118.71E 13km, ISC (REF) = 22.52N 118.75E 13km
CWB (Taiwan) = 0620 15.62 22.43N 118.47E 19.1km
FSB = 22.10 22.60N 118.68E 10.0km

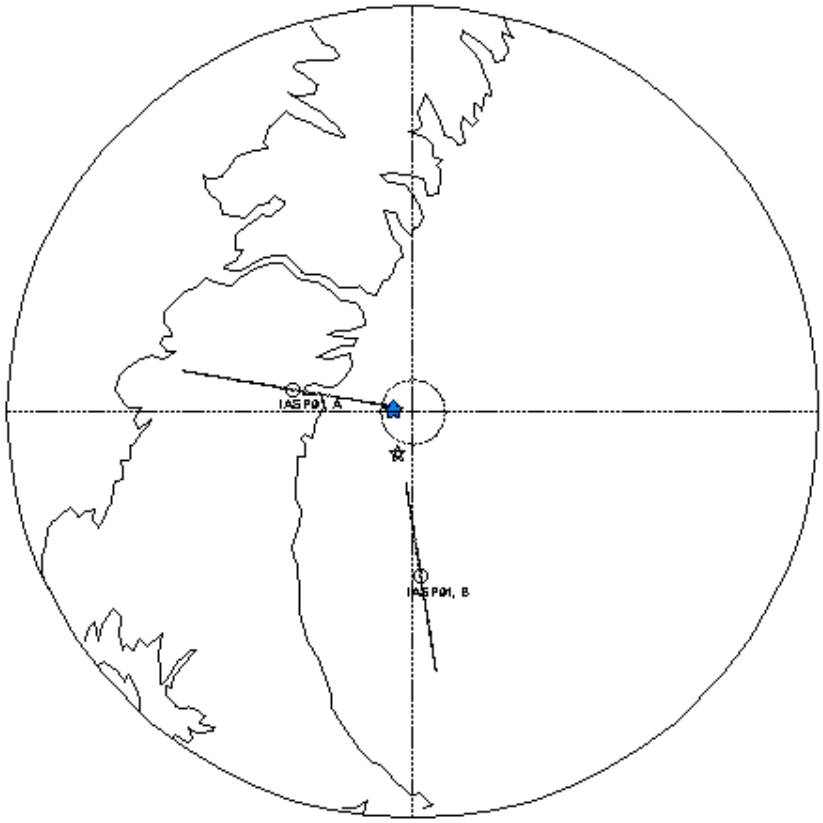
Figure 4



Network A= FINES KAF KBS KEV SDF SPITS
Network B= ARU JOF KJN NRI PKK SUF VAF

Figure 5

Locations of 970816, Conventional vs. Adaptive [J0]



REB location = 72.6484 57.3517 [depth set to 0]

IASP91, 11 picks ==> OT=2:11:5.281, 72.750 55.358 0.000, Offset= 57.2
(Network A=FINES KAF KBS KEV SDF SPITS)
IASP91, 10 picks ==> OT=2:11:4.357, 71.839 57.472 55.559, Offset= 90.4
(Network B=ARU JOF KJN NRI PKK SUF VAF)

IASP91 + J0 method => 72.657 57.033, Offset=10.7, Ang=71.29
IASP91 + all picks combined => 72.445 57.104, Offset=24.2

Figure 6

A STUDY OF SMALL-MAGNITUDE SEISMIC EVENTS DURING 1961 - 1989 ON AND NEAR THE SEMIPALATINSK TEST SITE, KAZAKSTAN

Vitaly I. Khalturin, Tatyana G. Rautian, and Paul G. Richards, Lamont-Doherty Earth Observatory

Sponsored by U. S. Department of Defense
Defense Threat Reduction Agency
Contract No. DSWA01-97-C-0156

ABSTRACT

Official Russian sources in 1996 and 1997 have stated that 340 underground nuclear tests (UNTs) were conducted during 1961-1989 at the Semipalatinsk Test Site (STS) in Eastern Kazakstan. However, only 279 of these nuclear tests appear to have been described with well-determined coordinates, in the openly available technical literature; and only 271 have both good locations and magnitudes. Thus, good documentation has been lacking for 69 UNTs at STS.

We have used regional data from 52 stations to detect, locate, and assign magnitudes for as many of these 69 UNTs as possible. Thus, for 8 previously located events with unknown magnitudes, we have assigned magnitudes. We identify 12 pairs of concurrent UNTs where one of the paired events had not been separately detected. We give another pair of almost simultaneous UNTs where both events had been undetected, and we have been able to detect one of the UNTs but not the other. For the total of 13 event pairs where one event has now been detected but not the other, we presume detection would have been possible if the undetected event had occurred alone. We find seismic detections and locations for an additional 30 nuclear tests at STS. Their magnitude ranges from 2.7 up to 5.1 (an event in 1965 that was often obscured at teleseismic stations by signals from earthquakes in the Aleutians).

Most of the 31 newly detected and located events were sub-kiloton. We note that for the remaining undetected 17 UNTs that did not occur at the time of another UNT, the announced yield is less than one ton and thus seismic detections would not be expected. Only two UNTs remain, for which the announced yield exceeds one ton and we have been unable to find any signals.

For 17 small UNTs at STS during 1964-1988, we compare the locations (with their uncertainty) that we had earlier determined in 1994 from analysis of regional seismic waves, with ground truth information obtained in 1998 on tunnel locations at the Degelen sub-area of STS. The average error of the seismically determined locations is only about 4 km, and the ground truth location is almost always within the predicted small uncertainty of the seismically determined location.

We also report the origin time, location, and seismic magnitude of 29 chemical explosions and 3 earthquakes on or near STS during the years 1961 - 1989.

Our new documentation of STS explosions is important for purposes of evaluating the detection, location, and identification capabilities of teleseismic and regional arrays and stations.

Key Words: nuclear explosions, ground truth data, chemical explosions, seismic discrimination, Semipalatinsk Test Site

OBJECTIVE

The overall goal of this project is to improve our understanding of the capability of modern and future monitoring networks. We do this, by learning from past experiences with monitoring a test site at which hundreds of underground nuclear explosions actually occurred; and by building up the archive of information on nuclear tests.

RESEARCH ACCOMPLISHMENTS

It has been reported in recent official Russian publications (Mikhailov et al., 1996; USSR Nuclear Tests, 1997) that a total of 340 underground nuclear tests (UNTs) were carried out on the Semipalatinsk Test Site (STS) from 1961 to 1989. Only 279 of them had been included in previously published lists of Soviet underground nuclear explosions that included purportedly accurate origin times and locations (specifically, the lists contained in Bocharov et al., 1989, Ringdal et al., 1992; and Lilwall and Farthing, 1990). For eight of these 279 explosions, the magnitudes have not been available. So accurate epicenter parameters of 61 UNEs and the magnitudes of 69 UNEs appear not to been given previously for this test site (STS).

The main goal of this paper is to estimate the origin time and location, and to assign the magnitude, for as many of the 69 hitherto undocumented UNTs at STS as possible. Our analysis is based principally upon seismic observations using regional stations located in Kazakstan and elsewhere in Central Asia. We also evaluate the accuracy of locations for small UNTs at STS, as determined from regional seismic signals.

Besides underground nuclear explosions, we have obtained information about chemical explosions and earthquakes which have been detected on and near the area of STS. Their parameters also were obtained from data of regional stations, and in some cases teleseismically. It is of interest, that some of these earthquakes and chemical explosions were included in some lists of Soviet underground nuclear explosions published in the West in the mid 1980s before Russian announcements about Soviet nuclear explosions were made beginning in 1992.

It is important to develop thorough documentation of all nuclear explosions, and especially for small explosions, as an aid in evaluating the detection and identification capability of monitoring stations. Of course, explosion monitoring in the present and the future will typically be done using stations that differ from those we have used to document small explosions at STS. Nevertheless our database of small explosions (chemical and nuclear), and nearby earthquakes, can provide guidance in estimating the capability of current networks, which can be expected to be better than the capability that was available for much of the period of active nuclear testing.

In the following sections, first we summarize the information from Russia officially available on STS UNTs. Second we identify those explosions that had not been assigned accurate epicenter and magnitude parameters. Third we describe our regional seismic detections of small events on and near STS. Fourth and fifth we give the newly-determined epicenter and magnitude parameters for 31 small UNTs at STS, and discuss the accuracy of their seismically-determined locations by making comparisons with ground truth information given by Leith (1998).

1. Summary of available official information about UNTs from STS

The 340 UNTs at STS listed by Mikhailov et al. (1996) and USSR Nuclear Tests (1997) were each associated with one of three sub-areas of the test site. Thus, 209 UNTs were in the Degelen sub-area, 106 at Balapan (sometimes referred to as Shagan), and 25 at Murzhik (sometimes referred to as Konystan). These explosions covered a wide range in yield, from less than 1 ton up to 165 kilotons (kt). Among 96 UNTs with magnitude *mb* less than 5.0, 84 were at Degelen, only 7 at Balapan, and 5 at Murzhik, so about 88% of the smaller yield events were in tunnels at Degelen.

The origin time and coordinates (latitude, longitude and depth) of STS UNTs have so far been announced by Soviet/Russian sources only for a group of 96 events that were conducted during a period from October 1961 to December 1972 (Bocharov et al., 1989; see also Vergino, 1989). Among these 96 UNTs, 6 were small and were not mentioned by Lilwall and Farthing (1990), or by Ringdal et al. (1992). With the official Russian announcements of 1996 – 1997 it became clear that 20 small magnitude tests at STS during this 1961 – 1972 time period had not been included in the list of Bocharov et al. (1989).

In 1992, the Russian Federation declassified information about the dates on which Soviet UNTs had occurred, the number of tests and number of nuclear explosions carried out within one nuclear test, the yield range, the sub-area, and the purpose of these UNEs. But the origin time, coordinates, and yield of most Soviet UNEs are still unavailable; and their magnitudes as determined from Soviet or Russian studies have not been announced, either from the network operated by scientists, known as ESSN, or from the military network, known as SSK.

Apart from the explosion locations given by Bocharov et al. (1989), Soviet and Russian publications have not listed UNT coordinates. But within the framework of Kazakstan – US cooperation, coordinates of tunnel portals at Degelen have become available (Leith, 1998). Separately, the coordinates of Balapan shafts have been obtained through fieldwork conducted by the National Nuclear Centre of the Republic of Kazakstan, and these locations are also now available (NNCRK, 1999). We use ground truth information in Tables below whenever these locations are available for specific explosions. When ground truth is absent (for example for chemical explosions) we give coordinates determined by seismological methods — whose accuracy is demonstrated in a later section of this paper.

2. Small UNTs at STS previously undocumented by Western seismologists

In this section we identify 61 UNTs at STS, out of the 340 now officially announced, for which accurate location information has not been given in openly available publications so far as we are aware; and we identify 69 for which accurate magnitude information has not been given. We assign each of these 69 UNTs to a category that indicates why their documentation has been poor (for example, low yield, or occurrence at the same time as another UNT). The following sections then report our own efforts to acquire and generate additional information, including locations and magnitudes, for as many of these 69 UNTs as possible.

Thus, the International Seismological Centre (ISC) has reported the seismically-determined location and magnitudes of 271 UNTs at STS. The ISC relies upon volunteered reports of seismic wave arrival times and amplitudes from thousands of stations around the world, and publishes its estimated locations and magnitudes together with the reported data used to derive them. Many researchers have carried out additional levels of analysis based upon ISC data for subsets of the STS events listed by the ISC. One of the largest such efforts, by the British Atomic Weapons Establishment (AWE), has applied the Joint Epicenter Determination method described by Douglas (1967) to ISC data, using several UNTs at STS as master events for which ground truth information was given by Bocharov et al. (1989). The AWE location estimates are given by Lilwall and Farthing (1990). AWE has also obtained maximum likelihood *mb*'s for 239 STS UNTs and has made them widely available on an informal basis. AWE *mb*'s for 100 UNTs and one chemical explosion in the Balapan sub-area were published by Ringdal et al. (1992). An additional 8 UNTs, not mentioned by Lilwall and Farthing (1990) or Ringdal et al. (1992), are given with locations but not magnitudes by Bocharov et al. (1989) and Vergino (1989).

Table 1. The list of weak UNTs at STS with Y < 1 ton, which could not be detected even at typical regional distances

N	#	Date	N	#	Date
1	283	1968 May 23	9	517	1979 Apr 10
2	317	1970 Feb 18	10	520	1979 Jun 12
3	359	1972 Apr 20	11	543	1980 Mar 14
4	387	1973 Sep 20	12	567	1981 Mar 25
5	397	1974 Feb 28	13	572	1981 Jun 04
6	484	1978 May 24	14	581	1981 Oct 16
7	486	1978 Jun 02	15	607	1983 Mar 11
8	516	1979 Mar 23			

Using information from the official Russian publications, we can tentatively give three reasons why many UNTs were not included in lists of events accurately located by seismic methods. First, some UNTs have now been announced as having had yield less than 1 ton; such tests would generally be too small for either regional or teleseismic detection. Second, some UNTs were carried out at essentially the same time as another UNT and only one test was reported. Third, some UNTs have now been announced as having had yield greater than 1 ton, but they may still have been too weak for teleseismic detection with high confidence, given the networks in operation at the time. For these events, we can inquire as to the possibility of regional detection as discussed in the following sections. Let us now list events in these three categories.

2.1. Weak UNTs with yield Y announced as less than 1 ton

This category consists of the 15 UNTs listed in Table 1. They would not be detected by standard instruments at distances more than 100 – 150 km. One of these small UNTs, with yield *Y* less than 1 ton, was carried out at Balapan (#387); the other 14 were carried out in the Degelen sub area. The number preceding the date corresponds to the numeration of UNTs in official Russian lists. We use the same numbering system throughout this paper.

2.2. Pairs of UNTs exploded simultaneously

This category is concerned with pairs of tests carried out within a short time interval, or even simultaneously, but with a spatial and/or temporal interval that requires them to be listed as different tests. As origin times and locations have not been officially announced, our discussion of which tests occurred in pairs, such that one test obscures another, has to be tentative. [Note: each UNT can include multiple explosions provided they are close enough in space and time — as specified in the 1990 revised protocol to the Threshold Test Ban Treaty.]

Table 2. 17 pairs of UNTs at STS which were exploded simultaneously or with a short time interval

Date	Subarea	Test numbers	Detected test: test no.	mb	Undetected test: test no.
1970 Jun 28	Both Degelen	321 & 322	321	5.7	322
1970 Sep 06	Both Degelen	325 & 326	?	5.4	325 or 326
1971 Mar 22	Both Degelen	333 & 334	333	5.7	334
1971 Dec 30	Both Degelen	353 & 354	354	5.7	353
1972 Jun 07	Both Degelen	360 & 361	?	5.4	360 or 361
1972 Dec 10	Degelen	376	376	5.6	-
	Balapan	377	377	6.0	-
Both tests were detected, with a 10 sec interval					
1975 Feb 20	Both Degelen	417 & 418	?	5.7	417 or 418
1976 Dec 07	Both Balapan	454 & 455	454	5.9	455
1977 Mar 29	Degelen	457	457	5.4	-
	Murzhik	458	not detected	-	458
1977 Oct 29	Degelen	473	473	5.6	-
	Balapan	474	474	5.6	-
Both tests were detected, with a 4.9 sec interval					
1977 Dec 26	Both Degelen	479 & 480	?	4.9	479 or 480
1978 Aug 29	Degelen	493	493	5.2	-
	Balapan	494	494	5.9	-
Both tests were detected, with a 8.8 sec interval					
1978 Nov 29	Degelen	507	507	5.3	-
	Balapan	506	506	5.9	-
Both tests were detected, with a 4.8 sec interval					
1979 Jul 18	Murzhik	524	524	5.2	-
	Degelen	525	not detected	-	525
1980 Dec 05	Both Degelen	561 & 562	-	-	561 and 562
Both tests were undetected					
1983 Nov 29	Both Degelen	629 & 630	?	5.4	629 or 630
1987 Apr 03	Balapan	671	671	6.1	-
	Degelen	672	not detected	-	672

In the last columns of Table 2 are shown the numbers of the 14 UNTs unreported by the ISC. These are events ## 322, 325 (or 326), 334, 353, 360 (or 361), 417 (or 418), 455, 458, 479 (or 480), 525, 561 and 562, 629 (or 630) and 672. These double tests can be the object of special investigation. Only one pair of UNTs from this table — 561 and 562 — was unreported by the ISC, so one event from this pair potentially can be detected.

Thus, we note that in the official lists there are 19 pairs exploded on the same day. Two of them were on the same day but are known to be separated by a long time interval: ## 414 and 415 (December 16, 1974, Degelen) with more then three hours time interval; and ## 440 and 441 (April 21, 1976, at Degelen and Balapan and hence with a significant spatial separation) with a four minutes interval.

The last 17 pairs of UNTs at STS (Table 2) were carried out on the same day with a small time interval, presumably not more then several seconds. Only for four pairs were both tests detected and reported as separate explosions in the standard western publications. The time intervals between the two tests in each of these four pairs varied from 4.8 to 10 s. For 12 other pairs only one test (for each pair) was reported by the ISC. For one pair — ##561 & 562 — neither test was reported.

2.3. Small UNTs with yield more than 1 ton, not reported by the ISC

These events, listed in Table 3, are most interesting for us because potentially they can be detected at regional distances. They are the main object of our investigation.

Table 3. List of 33 separate UNTs (Y > 1 ton) which were not reported in standard western publications, but which potentially can be detected at regional distances

N	##	Date	Sub area	N	##	Date	Sub area
1	#224	1964 Jun 06	Deg	18	#404	1974 Jul 29	Bal
2	#226	1964 Aug 18	Deg	19	#412	1974 Nov 28	Mur
3	#228	1964 Sep 30	Deg	20	#424	1975 Jul 15	Deg
4	#232	1965 Feb 04	Deg	21	#429	1975 Oct 05	Deg
5	#234	1966 Mar 27	Deg	22	#437	1976 Mar 17	Deg
6	#259	1966 Oct 29	Deg	23	#439	1976 Apr 10	Deg
7	#260	1966 Nov 19	Deg	24	#447	1976 Aug 04	Mur
8	#271	1967 Sep 02	Deg	25	#476	1977 Nov 12	Bal
9	#292	1968 Oct 29	Deg	26	#477	1977 Nov 27	Deg
10	#298	1969 Apr 04	Deg	27	#551	1980 Jun 25	Deg
11	#299	1969 Apr 13	Deg	28	#559	1980 Oct 23	Deg
12	#310	1969 Oct 30	Deg	29	#561	1980 Dec 05	Deg
13	#311	1969 Nov 27	Deg	30	#627	1983 Nov 02	Deg
14	#332	1971 Jan 29	Deg	31	#664	1985 Jul 11	Deg
15	#336	1971 Apr 09	Deg	32	#665	1985 Jul 19	Deg
16	#393	1973 Nov 04	Bal	33	#707	1988 Dec 28	Deg
17	#395	1973 Dec 31	Deg				

We note that a total of 61 previously undocumented UNTs are given in Tables 1, 2, and 3, namely, 15 UNTs with yield less than 1 ton; 13 UNTs that occurred at essentially the same time as another UNT, including one of the pair ##561 and 562; and 33 UNTs which potentially can be detected at regional distances, including the other of the pair ## 561 and 562. In the next section we report our locations and magnitudes, based on regional detections, for most of these 33 UNTs.

3. Detection of small events from STS from regional recordings in Central Asia

Our work on this subject was carried out in two stages. The first, in late 1993, resulted in a technical report (Khalturin et al., 1994), produced prior to the publication of the first Russian preliminary list of Soviet UNTs (Gorin et al., 1994). Information about the dates on which UNTs occurred, and ground truth locations, were not then available for us. We used regional data, and tried to detect and locate all seismic events at STS which could be UNTs, chemical explosions or earthquakes. The second stage was carried out in 1997 – 99, in light of official information on UNT dates and acquisition of ground truth locations.

Our results are based mainly on seismic data acquired by the Complex Seismological Expedition (CSE) of the Institute of the Physics of the Earth, Russian Academy of Sciences. Also we used bulletins of other regional stations of Central Asia including the Altai region. In total we used the records or bulletins of more than 50 seismographic stations. Most useful for detecting and locating small magnitude UNTs, were seismograms of narrow-band short period instruments installed in several stations by CSE in North Kazakstan at distances of 500 km to 1200 km from STS. Long-term CSE observations in this region show that high-frequency regional phases propagate very efficiently.

The seismographic network operated by CSE was used to acquire observations in the Kazakstan region throughout the period of UNT activity at STS — from 1961 to 1989. During the long-term monitoring effort, besides the well-known intermediate and large magnitude UNTs from STS, several tens of small magnitude events were detected that were not mentioned by Lilwall and Farthing (1990), or Ringdal et al. (1992). These events can be UNTs, or they could be chemical explosions used for military experiments and for construction. Few of these signals can be from earthquakes, which are very rare in the Semipalatinsk region since it is located on the far western flank of the Altai seismic zone.

Our first stage of study (Khalturin et al., 1994) examined data for 57 of these events that were on or near STS; estimated their coordinates, origin time, and magnitude; and made a preliminary identification as to the nature of each event (nuclear or chemical explosion, or earthquake). We now know that these 57 events consisted of 19 UNTs, 27 chemical explosions, 8 small magnitude UNTs known from Bocharov et al. (1989), and three earthquakes. Our first stage identified all of the UNTs and earthquakes correctly, but wrongly listed two of the chemical explosions as UNTs, and two other chemical explosions as "either UNE or chemical explosion".

Our second stage of study, in this paper, done following the release of UNT date information, has examined data for 71 events on or near STS, and has resulted in estimates of the origin time and magnitude of an additional 12 small UNTs which were missed in the first stage. So, from the 33 previously undocumented UNTs of Table 3, our first stage of study uncovered 19 UNTs and the present paper documents another 12.

Magnitude estimation of small known UNTs

Among the analysed signals were 8 small UNEs known from Bocharov et al. (1989) but listed there without magnitudes. Four of these events had been reported using teleseismic signals by Sykes and Ruggi (1986, 1989), who also listed a magnitude for three of the events.

For these 8 events the energy class K is known from regional records at several stations, allowing us to give the value of $mb(K)$ as in Table 4, using the relation $mb(K) = 0.46\,K - 0.64$ (Khalturin et al., 1998).

Table 4. 8 known UNTs for which we can now assign magnitudes

Date	Time (to nearest s)	K	mb(K)	mb**	Comment
1961 Oct 11	07:40:00	11.8	4.78	-	A
1962 Feb 02	08:00:00	13.6	5.63	-	B-1
1965 Jul 29	06:00:00	10.7	4.28	4.5	B-2
1965 Oct 14	04:00:00	10.7	4.28	-	A
1968 Oct 21	03:52:00	10.2	4.05	-	A
1968 Nov 12	07:30:00	10.6	4.24	-	A
1970 May 27	04:03:00	10.3	4.20	3.8	B-3
1972 Dec 28	04:27:00	11.4	4.60	4.9	B-4

**mb from Sykes and Ruggi (1989).

4. Detection of small underground nuclear explosions from STS

All but two of the small UNTs shown in Table 3 were detected regionally at temporary and permanent stations of CSE. Their parameters are listed in Table 5. Origin times were estimated for all 31 of them.

For the 19 largest of these small events, we give location estimates, K values, and mb(K). For the 12 smallest events we give estimated mb(Lg) values, which range from 2.2 to 3.7.

One relatively large UNT, with *mb*(*K*) 5.1 (February 4, 1965), was not reported by standard western publications as it was obscured teleseismically by a swarm of Aleutian earthquakes. We can be sure this was a coincidence rather than an effort to obscure the event, because the origin time (06:00:00) was typical for UNTs of the mid-1960s. But even if we exclude this large event, the *mb* value (calculated from *K*) for missed events ranges up to 4.55, and during 1964 – 1989, about 10 Soviet UNTs at STS, with magnitude 4.0 or more, had teleseismic signals that were too weak or too noisy to lead to publication of good location estimates. Some of these events were detected teleseismically at particular arrays (Ringdal, 1990).

Table 5. Small announced UNTs studied in this paper

No.	Date	Time	Subarea	(Lat.,	Long.)	K	mb(K)	mb(Lg)	m(NOR)	Note
224	1964 Jun 06	00:00:00	Deg	49.7747	77.9881	11.0	4.42	-	-	
226	1964 Aug 18	06:00:00	Deg	49.0206	78.0819	8.5	3.27	-	-	
228	1964 Sep 30	Not detected								
232	1965 Feb 04	06:00:00	Deg	49.7731	77.9914	12.5	5.10	-	-	A
234	1965 Mar 27	06:30:00	Deg	49.7747	77.9881	8.4	3.22	-	-	
259	1966 Oct 29	03:58:00	Deg	49.7847	77.9994	9.0	3.50	-	-	
260	1966 Nov 19	03:58:00	Deg	49.8297	78.0575	8.7	3.36	-	-	
271	1967 Sep 02	04:04:00	Deg	49.7419	78.0256	10.3	4.10	-	-	
292	1968 Oct 29	03:54:00	Deg	49.8333	78.0928	10.8	4.33	-	-	
298	1969 Apr 04	04:57:00	Deg	49.7533	78.0536	9.2	3.60	-	-	
299	1969 Apr 13	04:04:00	Deg	49.7356	78.1047	11.3	4.55	-	-	
310	1969 Oct 30	Not detected								
311	1969 Nov 27	05:02:00	Deg	49.8367	78.0597	10.3	4.10	-	-	
332	1971 Jan 29	05:03:00	Deg	49.8053	78.1686	11.1	4.47	-	-	
336	1971 Apr 09	02:33:00	Deg	49.8322	77.9994	9.6	3.78	-	-	B
393	1973 Nov 04	03:57:00	Bal	50.0716	78.9362	-	-	2.6	-	
395	1973 Dec 31	04:03:00	Deg	49.7394	78.0863	10.6	4.24	-	4.0	
404	1974 Jul 29	03:28:00	Bal	n/a		-	-	3.3	-	
412	1974 Nov 28	05:57:00	Mur	n/a		-	-	2.8	-	
424	1975 Jul 15	02:57:00	Deg	49.7914	78.0944	-	-	3.3	-	
429	1975 Oct 05	04:27:00	Deg	49.7831	78.0867	10.7	4.28	-	4.0	SR1
437	1976 Mar 17	02:57:00	Deg	49.7556	78.0992	-	-	2.2	-	
439	1976 Apr 10	05:03:00	Deg	49.7550	78.0475	-	-	3.0	-	
447	1976 Aug 04	02:57:00	Mur	49.87	77.7	10.5	4.20	-	3.8	SR2
476	1977 Nov 12	05:11:00	Bal	n/a		-	-	2.8	-	
477	1977 Nov 27	03:57:00	Deg	49.7544	78.0503	9.9	3.92	-	3.4	
551	1980 Jun 25	02:27:00	Deg	49.8258	78.0994	-	-	3.7	-	
559	1980 Oct 23	03:57:11	Deg	49.7517	78.1317	-	-	2.5	-	
561	1980 Dec 05	04:17:16	Deg	49.7517	78.1317	-	-	3.6	-	
627	1983 Nov 02	04:18:54	Deg	49.7792	78.1247	-	-	3.0	-	
664	1985 Jul 11	02:57:02	Deg	49.7506	78.0492	10.2	4.05	-	3.5	SR3
665	1985 Jul 19	04:00:08	Deg	49.8011	78.0686	-	-	2.5	-	
707	1988 Dec 28	05:28:10	Deg	49.8011	78.0686	9.5	3.74	-	3.63	C

First column is the explosion identifying number used by Mikhailov et al.(1996). Time, *K* and *mb*(*Lg*) are based on regional observations of CSE. (Lat., Long.) on Degelen Mountain are from Leith (1998). Event #447 is assigned to the Balapan sub-area in USSR

Nuclear Tests (1997), whereas in our opinion it took place in Murzhik. *mb*(*K*) — calculation of *mb* from *K* using the relationship: $mb(K) = 0.46\,K - 0.64$. *m*(NOR) — from F. Ringdal (pers. comm., 1994), based on teleseismic signals at NORSAR.

Comments on Table 5:
A — This event was obscured by many Aleutian earthquakes, up to *mb* 6.4 on that day.
B — The yield of this explosion has been announced as 0.23 kt (USSR Nuclear Tests, 1997)
C — This event was mentioned by Ringdal (1990). SR# — These three events are listed by Sykes and Ruggi (1986, 1989) with the following coordinates and *mb*:
1. 55.8N and 75.1E; *mb* = 4.6. 2. 49.9N and 77.7E; *mb* = 4.1. 3. 50.0N and 78.0E; *mb* = 4.0.

5. Comparison of ground truth and seismologically-determined locations, for small UNTs

Our earlier study (Khalturin et al. 1994) determined coordinates of 18 small-magnitude UNTs (one additional UNT was detected only by one station) on the basis of arrival times of regional waves, and estimated the location uncertainty, which was typically an area of the order of 100 km^2. One of those UNT was at Balapan for which we do not yet know the ground truth coordinates. For 17 UNTs (magnitudes 3.8-4.6), which occurred at Degelen, we can now compare the seismically-located epicenters with ground truth recently obtained for that sub-area by Leith (1998).

For these small UNTs, regional signals were acquired at CSE stations located at distances in the range 500 – 1400 km from STS. We mostly used data from bulletins but did read waveforms ourselves in some cases. Thus for these 17 UNTs we had 20 records and 49 station bulletin data from stations to the south; and 37 station bulletin data from stations to the east or west. So on average for the location of one event we had about one record and about three pieces of data from station bulletins located to the south of STS, and about 2 data from stations located to the east or west. On each record, 2 or 3 regional phases were measured (typically *Pn*, *Sn*, *Lg*). To obtain a preliminary estimate of location and origin time, we usually used (if they were available) three values of time intervals such as $t(Lg) - t(Sn)$; $t(Lg) - t(Pn)$ and $t(Sn) - t(Pn)$ from each station record or bulletin. Having estimated the origin time (t_0) in this way, the next step for location was to use time intervals such as $t(Pn) - t_0$; $t(Sn) - t_0$ and $t(Lg) - t_0$.

For event location we used travel times of regional phases as given by Nersesov and Rautian (1964), based on a Pamirs-Baikal profile, and observations slightly adapted by Khalturin for Northeast Kazakstan. Our locations, and the comparison with ground truth information, are given in Table 6. On average, the seismically-determined location error was only about 4 km. The ground truth location was found to lie within the interval specified by Khalturin et al. (1994) as the location uncertainty in almost all cases, and only marginally outside that interval in the few cases where it was outside. The average of absolute errors for all 17 UNTs is only 3.2 km in latitude, and 4.4 km in longitude. The average of signed errors is only 0.53 km in latitude and 0.45 km in longitude (i.e., real epicenters systematically lie 0.53 km south and 0.45 km west of our estimated locations). Since the average length of the seismic paths was 750 km, the systematic error is remarkable small — about 0.07%, corresponding to an error in velocity of about 0.005 km/s.

We have thus been able to demonstrate the utility of regional seismic waves for purposes of accurate estimation of UNT locations, even when only a few records are available per event. The location uncertainty is so small in our case, because of the availability of travel-time tables appropriate to the region.

Table 6. Comparison of seismically-determined locations based on regional phases (Khalturin et al., 1994) and ground truth locations (Leith,1998), for small UNTs at the Semipalatinsk Test Site.

Date	Latitude		Δ Lat	Longitude		Δ Long
	Seism.	G.T.	km	Seism.	G.T.	km
1964 Jun 06	49.79	49.774	1.8	78.00	77.988	0.9
1964 Aug 18	49.81	49.820	-1.1	78.10	78.082	1.3
1965 Feb 04	49.78	49.773	0.8	78.12	77.991	9.2
1965 Mar 27	49.82	49.775	5.0	78.00	77.988	0.9
1966 Oct 29	49.74	49.785	-5.0	78.07	78.000	5.0
1966 Nov 19	49.70	49.730	-3.3	78.20	78.058	10.2
1967 Sep 02	49.79	49.742	5.3	78.02	78.026	-0.4
1968 Oct 29	49.84	49.833	0.8	78.14	78.105	2.5
1969 Apr 13	49.70	49.736	-4.0	77.92	78.105	-13.3
1969 Nov 27	49.79	49.837	-5.2	78.20	78.060	10.0
1971 Jan 29	49.77	49.805	-3.9	78.11	78.169	-4.2
1971 Apr 09	49.88	49.832	5.3	78.02	78.039	-1.4
1973 Dec 31	49.75	49.739	1.2	78.04	78.086	-3.3
1975 Oct 05	49.81	49.783	3.0	78.10	78.087	0.9
1977 Nov 27	49.80	49.754	5.1	78.06	78.050	0.7
1985 Jul 11	49.78	49.750	3.3	77.90	78.049	-10.7
1988 Dec 28	49.80	49.801	-0.1	78.06	78.069	-0.6

6. General discussion

A longer version of this paper, with the same title and authors, has been submitted for publication in the journal Pure and Applied Geophysics (special volumes on CTBT monitoring). The longer version lists 29 chemical explosions on and near STS, as well as several earthquakes; shows the magnitude distribution of all observed UNTs (it appears more than 40 were sub-kiloton); and shows that the yield estimated for each UNT on the basis of its magnitude *mb* is in good agreement with the officially announced total yield on UNTs for each year at STS.

CONCLUSIONS AND RECOMMENDATIONS

The most important point to draw from our study is that detection capability has been very good for recent decades in Central Asia, since all but two UNTs at the Semipalatinsk Test Site with yields announced as greater than 1 ton have now been associated with regional detections. Detections have also been very good using only teleseismic data. But for accurate location and confident identification, additional data is often needed. In practice, such additional data can often be provided by regional stations. When regional travel times are well calibrated, they can be used to proved accurate locations even when few stations are available.

Now that we have documented an almost complete list of UNTs at the main test site of the former Soviet Union, we recommend that efforts be supported to build up the database of waveforms, particularly for the small events, since these are the types of signal the IMS must be designed to detect and identify. A waveform database for these events can be an important training set, as well as a basis for comparison with problem events in the future.

REFERENCES

Bocharov, V.S., Zelentsov, S.A., and Mikhailov, V.I. (1989), *Characteristics of 96 underground nuclear explosions at the Semipalatinsk test site*, Atomnaya Energiya, **67**, 210 – 214.

Bolt, B.A. (1976), *Nuclear explosions and earthquakes: the parted veil*, W.H. Freeman and Co., San Francisco.

Douglas, A. (1967), *Joint epicentre determination*, Nature, **215**, 47 – 48.

Gorin, V.V, Krasilov, G.A., Kurochkin, A.I., Kurkin, A.I., Maltsev, A.L., Matushenko, A.M., Orlov, S.L., Pichugin, A.V., Smagulov, S.G., Strukov, V.G., Fillipovsky, V.I., Kharitonov, K.V., and Chernishev, A.K., (1994), *Semipalatinsk Test Site: Chronology of underground nuclear explosions and their primary radiation (1961-1989)*. Bulletin of the Center of Public Information, #4, pp 21 – 32, Moscow, Central AtomInform Institute.

Khalturin, V.I., Rautian, T.G., and Richards, P.G. (1994), *A study of small explosions and earthquakes during 1961-1989 near the Semipalatinsk Test Site, Kazakhstan*, technical report for subcontract B239589 with Regents of Univ. of Calif., 64 p.

Khalturin, V.I., Rautian, T.G., and Richards, P.G. (1998), *The seismic signal strength of chemical explosions*, Bull. Seism. Soc. Am., **88**, 1511 – 1524.

Leith, W. (1998), Degelen Nuclear Test and Tunnel Data, Technical Memorandum dated June 26, 1998 to the Defense Threat Reduction Agency, US Geological Survey; and Technical Reports to the Defense Threat Reduction Agency (formerly Defense Special Weapons Agency; formerly Defense Nuclear Agency), under Contract DNA001-95-C-1079.

Lilwall, R.C., and Farthing, J. (1990), *Joint epicentre determination of Soviet underground nuclear explosions 1973-1989 in Eastern Kazakhstan*, AWE Report No. O 12/90, H.M. Stationery Office, London.

Mikhailov, V.N. (editor) and 14 co-authors, (1996), *USSR Nuclear Weapons Tests and Peaceful Nuclear explosions, 1949 through 1990*, RFNC-VNIIEF, Sarov, 96 p.

Nersesov, I.L., and Rautian, T.G. (1964), *Kinematics and dynamics of seismic waves at epicentral distances less than 3500 km*, Proceedings (Trudy) of the Institute of Physics of the Solid Earth, Academy of Sciences of the USSR, #32.

NNCRK (1999), Technical documentation, contributed by the National Nuclear Centre of the Republic of Kazakhstan, Oslo Workshop on IMS Location Calibration, Jan 1999.

Ringdal, F. (1990), *Teleseismic event detection using the NORESS array, with special reference to low-yield Semipalatinsk explosions*, Bull. Seism. Soc. Am., **80**, 2127 – 2142.

Ringdal, F., Marshall, P.D., and Alewine, R.W. (1992), *Seismic yield determination of Soviet underground nuclear explosions at the Shagan River test site*, Geophys. J. Int., **109**, 65 – 77.

Sultanov, J.J., Adushkin, V.V., Danilova, T.V., Kaazik, P.B., Kuznetsov, O.P., Nedoshivin, N.I., and Rubinshtein, N.D. (1995), *Completion of data base of PNE and large-scale chemical blasts conducted inside the territory of FSU and analysis of characteristics of seismic waves in order to improve the methods of seismic event identification*. Institute for Dynamics of Geospheres Report to IRIS, subcontract 201, 144 p.

Sykes, L. and Ruggi, S. (1986), *Soviet Nuclear Testing.* Natural Resources Defense Council, Working Paper NWD 86-4, November 1986.

Sykes, L. and Ruggi, S. (1989), *Soviet Nuclear Testing.* Chapter 10, pp. 332 – 375 in *Nuclear Weapons Databook*, Vol. IV, edited by Cochran, T.B., Arkin, W.M., Norris, R.S., and Sandes, J.I.

USSR Nuclear Tests (1997), Mikhailov, V.N. (editor) and 29 co-authors, UZDAT Publishing House, Moscow, 248 p.

Vergino, Eileen S. (1989), *Soviet Test Yields*, EOS, **70**, 1511 – 1513 (with corrections and additions, EOS, **70**, 1569).

PATH CORRECTIONS FOR REGIONAL PHASE DISCRIMINANTS

Thorne Lay, Guangwei Fan, Ru-Shan Wu, Xiao-bi Xie

Earth Sciences Department and Institute of Tectonics
University of California, Santa Cruz

Sponsored by Defense Threat Reduction Agency

Contract No. DSWA01-98-C-0161-P00001

ABSTRACT

In order to utilize regional seismic phases for reliable source identification, it is essential to account for wave propagation effects that may obscure the subtle differences in source radiation for distinct source types. Recent work has established three main approaches to the problem of characterizing and correcting regional phases for propagation effects: empirical methods based on parametric dependence on path properties such as pathlength or crustal waveguide parameters, interpolation methods such as cap-averaging and kriging for station-dependent source region correction surfaces, and waveform modeling methods based on complete waveform synthesis for two-dimensional or three-dimensional crustal models. Our research program is exploring all three approaches, seeking to establish relative merits of each strategy for different situations. In a recent publication we compare the reduction in scatter for regional P/S amplitude ratios for station ABKT for distance correction, waveguide parameter regressions, cap-averaging, and kriging (Rodgers et al., 1999), finding that kriging has some distinct advantages over other methods. We have further explored kriging and waveguide parameter regressions for two International Seismic Monitoring Stations, NIL and ZAL. Frequency dependent regional phase amplitude ratio measurements at these stations for earthquakes and underground nuclear explosions, obtained from the Comprehensive Nuclear-Test-Ban Treaty prototype-International Data Center, have a large amount of scatter, most of which is attributed to wave propagation effects in the heterogeneous crustal waveguide. Interpolation of the anomalies using a Kriging algorithm achieves significant variance reduction, but provides little insight into the nature of the path effects. Linear regressions indicate that the phase ratios are correlated with topographic features along the paths, providing an empirical means for reducing path effects beyond conventional distance corrections. Topography variations appear to provide a proxy for structural complexity of the crustal waveguide, which influences the reverberations and energy partitioning in the regional wavefield in a way that can be statistically isolated. Using available high-resolution topography data, correction of regional P/S ratios for the best models obtained from multivariate regressions systematically reduces the data variance relative to path length corrections alone, as has been observed for other data sets. The reduced scatter in the measurements increases the separations between earthquake and explosion populations in most cases, enhancing the regional discriminant performance. The path-corrected discriminants work better at station NIL than at station ZAL, even though the explosion sources are located in a common source area. The laterally varying characteristics of the waveguide structure for different sets of paths can apparently overwhelm intrinsic source differences, complicating discrimination when small numbers of observations are available. While always desirable, corrections for heterogeneous path effects may prove inadequate in some cases, notably when phase blockage occurs or when strong attenuation reduces the diagnostic high frequency energy. Our modeling approach is based on breakthrough developments by our group in long-range high frequency regional wave synthesis, using half-space screen propagators. We analyze Lg signals for paths traversing the Tibetan Plateau using spectrograms to characterize the frequency dependent transmission effects, and then synthesize two-dimensional seismograms for plausible crustal models. An observed increase in Lg spectral ratios for the 3-6Hz/0.75-1.5Hz bands with propagation distance within the Plateau can be explained if we assume that small-scale random heterogeneity and/or random rough topography at the surface and layer interfaces is present. The complex-screen propagator method is used to generate synthetic Lg up to 10 Hz over paths as long as 1000 km.

Key Words: seismic discriminants, regional seismic phases, amplitude corrections, regional wave propagation

OBJECTIVE

One of the major challenges confronting seismic monitoring of the Comprehensive Nuclear-Test-Ban Treaty (CTBT) is discriminating the seismic signals of small underground explosions from those produced by other sources. There is tremendous regional variability in short-period signals from all sources, and the characteristics that define the source type may be subtle, easily overwhelmed by propagation complexities in the heterogeneous crust. Reliable regional seismic discriminants must have sufficiently small scatter in the background earthquake population that rare single-shot explosion events will produce diagnostic outlying measurements. That component of the scatter caused by propagation effects can be reduced by path corrections of varying sophistication. We are seeking to develop and test various approaches to reduce the scatter in regional discriminant populations, using numerous observations in Eurasia (China, Russia, and Southeast Asia, in particular) and the Middle East collected under this and a previous PL/DOE-funded effort. Multi-variate regressions of various path attributes (to assess which parametric path characterizations are significant), spatial representations of the path influences such as kriging (to enable interpolation to a unique path for a suspect event), and tests of significance of the corrections (ability to tighten up scatter in discriminant measures to a useful extent) are all being considered in our effort to develop a unified strategy for discriminant calibration that will transport into the operational regime and lead to high confidence discrimination.

RESEARCH ACCOMPLISHED

Our first year of research has addressed improving the performance of short-period regional seismic discriminants by applying propagation corrections to regional P/S amplitude ratios observed at two seismic monitoring stations in Asia, NIL (Nilore, Pakistan) and ZAL (Zalesovo, Russia), which are part of the ISMS. The regional phase amplitude ratios recorded at these stations are correlated with regionally-averaged distance effects as well as path-specific effects parameterized by measures of surface topography. A high-resolution topographic database is used because the most reliable waveguide parameters available for any path are those involving surface topography. We consider path-integrated properties (e.g., mean altitude, average surface roughness, etc.) because regional wave propagation effects are likely to involve significant lateral averaging. For comparison, ordinary Kriging, which involves multiple regression on spatial parameters, is utilized to estimate path corrections and to visualize the systematic regional path effects. We test whether the reduced scatter in the regional seismic discriminant measures for NIL and ZAL using the topographic models actually yields better separation between earthquake and explosion populations. We also explore whether regionally distinctive characteristics of waveguide structure and geologic setting influence source discrimination performance.

Central Asia is a region of significant interest for monitoring the CTBT. Diffuse seismicity, sparse seismic instrumentation, acute crustal heterogeneity, and recent nuclear testing prioritize the area as a target for calibration of regional discriminants. Observed broadband waveforms for paths in Eurasia display great complexity (e.g., Zhang *et al.*, 1994), presumably caused by a combination of lateral heterogeneity in waveguide structure and source radiation effects. Our data set involves broadband vertical component recordings at ISMS stations NIL and ZAL for Eurasian earthquakes with magnitudes of $3.5 \leq m_b \leq 6.0$ that occurred between 1995 and 1998. Hypocenter parameters are those determined by the CTBT prototype-International Data Center (pIDC). The sparse ISMS station coverage and the complexity of the crustal and upper mantle structure in the region result in large uncertainties for hypocenter parameters, especially for focal depth, thus many smaller events assigned zero depth in the pIDC location are not well-constrained. We only consider shallow events, with pIDC focal depth estimates less than 50 km. The locations are otherwise deemed sufficient for the path property measurements used in this study, and the location uncertainties are typical of those for discriminant calibration efforts in all regions.

We use the amplitude measurements routinely made by the pIDC. The pIDC algorithm processes regional phases using the Detection and Feature Extraction (DFX) code, computing many amplitude measurements for a variety of filtered traces for specified time windows. Time windows are based on either a predicted travel time for a specific phase, a fixed group velocity window, or some combination of the two. The Pn amplitude is calculated within a window starting 8 s before the theoretical arrival time and ending at a group velocity of 6.4 km/s; the Sn window starts 5 s before the theoretical arrival time and has a duration of 20 s. The P_g and Lg windows are between group velocities of 6.3 to 5.8 km/s and 3.7 to 3.0 km/s, respectively. The precise pIDC windows differ from the corresponding windows used in many prior studies of regional discriminants (e.g., Walter *et al.*, 1995; Hartse *et al.*, 1997; Fan and Lay, 1998a, b), so some caution in comparison of results is warranted. The default windows can result in some spurious amplitude measurements in regions of strong crustal heterogeneity as well as varying proportion of coda contribution with distance, but one of our objectives was to exercise the database

generated routinely by the pIDC, as this will ultimately underlie operational applications. In particular, at small epicentral distances there is great difficulty in regional phase isolation, thus only signals at distances greater than 280 km were analyzed. Measurements out to 2100 km were used, recognizing that upper mantle P and S wave triplications overprint true regional guided wave energy at distances larger than 1400 km. We find that the high frequency signals vary gradually with distance, so the effects of this are subdued, and the number of data is still too limited to further restrict the distance range.

For each phase, we consider measurements in four frequency bands: 2 to 4 Hz, 4 to 6 Hz, 6 to 8 Hz, and 8 to 10 Hz. The instrument response was corrected at the center frequency of each passband for all of the phase amplitude measurements. Previous studies have established that rms measures of regional phases like Lg have remarkable stability due to the averaging of multiple arrivals (Gupta *et al.*, 1992; Rodgers *et al.*, 1997a), so we use the pIDC rms amplitude measurements. Noise levels are computed at the pIDC using predicted time and/or group velocity windows around pre-phase noise. In this study only pre-Pn noise is considered as a criterion for selecting the data; events with Pn signal-to-noise ratios greater than two for the frequency bands of interest are retained. This is fairly conservative, given that Pn is usually the weakest regional phase in the data, except when strong Lg blockage occurs (which we do not want to exclude). The number of the selected observations varies with the type of regional phase amplitude measurement observed at each station, ranging between 97 to 109 for NIL, and 66 to 69 for ZAL. The database is growing steadily, and we view our results here as preliminary testing of possible operational implementations with larger data sets.

The paths traversed by our data sample a large area of the Asian continent. Figure 1 shows epicentral locations for the events, station locations, and surface topography in the region. The topographic relief data are from a global digital elevation model developed at the U.S. Geological Survey's EROS Data Center. This database provides a spatial resolution of 30 arc-second (one-km) and an overall vertical accuracy of 70 m (Gesch *et al.*, 1999). Many of the paths traverse mountain ranges such as the Tien Shan, Pamirs and Hindu Kush, high plateaus such as the Iranian and Tibetan Plateaus, or sedimentary basins such as the Tarim Basin. Areas of Lg blockage, inefficient Sn propagation, and low Pn velocities have been reported within our region (e.g., Ni and Barazangi, 1984; Rapine et al., 1997; Rodgers *et al.*, 1997b). Despite the likelihood that internal crustal structure plays an important role in shaping regional seismic phases (Fan and Lay, 1998a,b,c), the available crustal thickness and sediment thickness models for this region were not utilized because they are very low resolution and involve gross extrapolations. We rely on the high resolution topography data to characterize individual path properties. Although variable isostatic compensation and smoothing effects of sedimentation prevent topography from reflecting details of internal crustal structure, to first order topography does indicate gross tectonic features of the crust, with high topography in areas of tectonically thickened crust, and laterally variable topography in areas of rapidly changing crust and mantle structure.

The strategy of empirical correction for parametric path effects is very straightforward. Observed frequency-dependent amplitude ratio measurements for each event recorded by a single station are correlated with various path measurements. High correlations with individual parameters suggest causal influences, but strong covariance amongst parameters mandates a multivariate regression approach to developing a final corrective model. Linear regressions, indicate individual path parameter correlations for Pn/Lg and Pn/Sn ratios measured in different frequency bands at NIL and ZAL. Both amplitude ratios show significant distance dependence, with correlation coefficients ranging between 0.1 and 0.8 at frequencies below 8 Hz. The correlation coefficients and slopes of the linear regressions decrease as frequency increases. The average path parameters considered here are mean elevation (Mean H), topographic variance (Roughness), mean topographic slope (Slope), and the second moment of topography (Skewness) (Zhang *et al.*, 1994). NIL exhibits correlations with these path parameters that can be as strong or stronger than correlations with distance. Mean elevation, average roughness, and, for the higher frequencies, mean slope have linear correlation coefficients of 0.3 to 0.6. ZAL has lower correlations in corresponding cases. NIL has strong negative correlations with skewness of topography, similar to observations at WMQ (Fan and Lay, 1998a,b), while weak positive correlations are found at station ZAL. These correlations in motivate a multivariate regression analysis to account for any collinearity of the path properties.

Assuming an empirical model that minimizes the variance in the data, a best set of predictor variables can be determined from a set of parametric path properties. In practice, the initial list of variables includes the path length and the four path-averaged parameters of topography considered above. Elimination of variables is based on two common criteria: (1) the mean square error (MSE) criterion and (2) the C_p-statistic criterion (Fan and Lay, 1998a). In addition, statistical F-tests help to ensure that the final models have satisfactory estimates of all model coefficients at a high confidence level. Details of this multivariate regression analysis can be found in Fan and Lay (1998a, b, c).

The regression analysis yields models that involve from one to four path parameters. Path length and mean path elevation appear in most of the models, as was found for observations at WMQ (Fan and Lay, 1998 a,b), with surface roughness and rms slope giving some contribution to variance reduction. Figure 2 shows variance

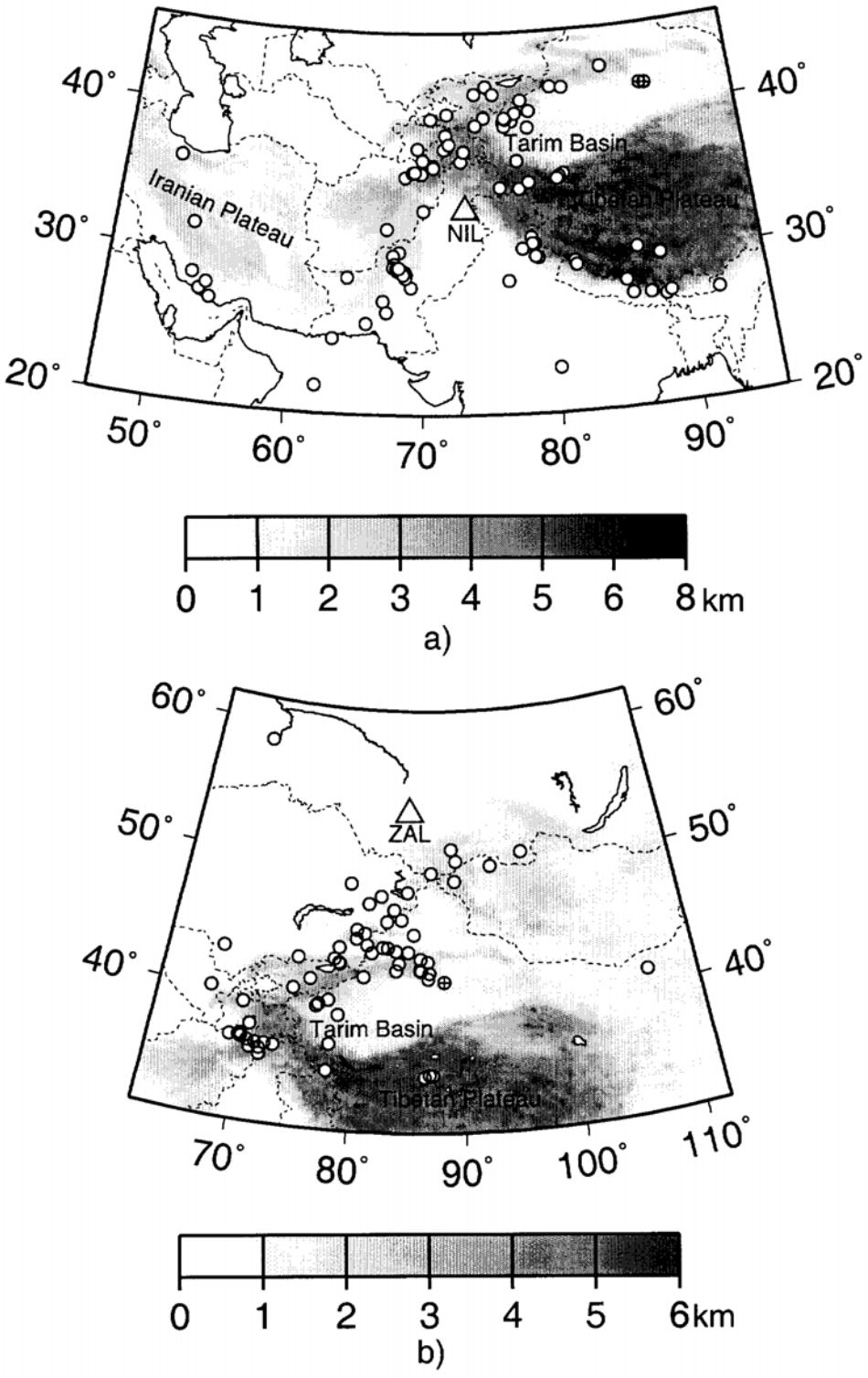


Figure 1. Surface topography in the vicinity of ISMS seismic stations (a) NIL and (b) ZAL. Open circles represents of earthquakes used in this study; circles with a cross are sites of explosions.

reductions achieved by path corrections relative to the raw measurements for NIL and ZAL for four regional discriminant ratios. Known nuclear test signals were omitted. The data for NIL were considered as an entire set (Figure 2a), and in an azimuthal sector spanning azimuths of 0° to 140° (not shown), which straddles the azimuth to the Lop Nor test site. Variance reduction for models involving just distance correction are compared to models with the optimal set of path parameters amongst those considered. It is possible to reduce scatter beyond what is achieved by just distance corrections. For the NIL data, increases in variance reduction by 10-20% beyond distance correction alone are achieved for Log(Pn/Lg), Log(Pn/Sn), and Log(Pg/Lg) amplitude ratios, and there is a few percent improvement for the Log(Pg/Sn) ratios. The azimuthal subset for NIL shows somewhat stronger distance correction effects than for the whole data set, but there are still significant improvements with the multivariate model. ZAL data experience less variance reduction relative to distance correction alone, involving an extra few percent to 15% (see Figure 2b). The higher frequency windows generally exhibit less dependence on path properties, but path corrections may prove useful across the passband. The low signal-to-noise ratio 8-10 Hz band was found to have very little correlation with topographic parameters, and results for that frequency band are not shown.

Kriging involves spatial multiple regression using a covariance function model Isaaks and Srivastava (1989), and this approach can characterize propagation effects without the need for any information about the waveguide. A spatially damped Bayesian kriging (Schultz *et al.*, 1998) has been used successfully as a predictor of arrival time corrections, with the advantage that it controls estimates in extrapolation zones and allows great flexibility in damping. Rodgers *et al.* (1999) have applied this algorithm to regional phase amplitudes, finding that it outperforms parametric regression approaches. A widely available ordinary kriging algorithm is applied to our data, with the constant mean value being replaced by the location-dependent estimate. An advantage of ordinary kriging is that the sum of the weights is constrained to equal to 1 so ordinary kriging does not require a priori knowledge of the stationary mean for building an estimator, yet it remains unbiased for unsampled values. When applied within a moving data neighborhood, ordinary kriging is a nonstationary algorithm, and it corresponds to a nonstationary random function model with varying mean but stationary covariance. The ability to locally rescale the random function to a different mean value makes ordinary kriging robust. However, extrapolation to poorly sampled areas produces plateaus of varying levels determined by proximate date. Since extrapolation is problematic for all kriging algorithms, this is not seen as a major problem.

We applied ordinary kriging using the Log[Pn/Lg] amplitude ratios in the 2-4 Hz frequency band observed at NIL and ZAL. Equal-weighted histograms and cumulative probability plots were created for the Pn/Lg amplitude ratios at each station. Asymmetry of the data histograms suggests that an assumption of normality would be rejected, while the cumulative probability plots indicate that the amplitude ratios are lognormally distributed because the cumulative frequencies plot as a straight line. Kinks in the cumulative probability plots represent changes in the characteristics of the data over different intervals and may be caused by path effects, as suggested by previous studies in which regional discriminants show better normality in distribution after making multivariate path corrections (Fan and Lay, 1998a, b; Rodgers *et al.*, 1999).

The key to successful kriging estimation is choosing a variogram or a covariance that captures the structural pattern of spatial continuity in the data. We first constructed three types of variograms: semivariogram, covariance and correlogram. These variograms typically have been used to describe how spatial variability changes as a function of distance and direction. Variograms were calculated for three experimental directions at angles of 30°, 60° and 90° clockwise from north. The covariance and correlogram display spatial continuity in the data and have few fluctuations because they are resistant to data sparsity, clustering and outlier values. Based on the behavior of these variograms near the origin we select a variogram model for the omnidirectional experimental variogram. The spherical and exponential correlation models are commonly used. We adopt a spherical model to match the experimental variogram for its linear behavior at small separation distances near the origin and its flattening out at larger distances. Isotropic models with a range between 800 and 1200 km resemble the observed semivariograms. Because the range has a relatively minor effect on ordinary kriging weights (Isaaks and Srivastava, 1989), a range of 1000 km is a good choice for our variogram model. The covariance and correlogram also reach a plateau at this distance, confirming that it is appropriate for our data set.

Based on the selected isotropic model, ordinary kriging was performed by searching a regional grid net. To compare estimated values with observed values, we used the cross-validation procedure. As a result of the smoothing effect of kriging, significant variance reduction is achieved. The variance was reduced by 47.1% for the NIL data, and 51.4% for the ZAL data, representing an improvement of 2% (for NIL) and 10% (for ZAL) in comparison to the parametric multiple regression. In addition, the kriging residuals of Log[Pn/Lg] for each data set are close to normally distributed populations.

The Log[Pn/Lg] ratios clearly display regional coherence, as expected for regionally varying path effects. For NIL low Pn/Lg amplitude ratios are found in Kashmir, close to the seismic station, while high Pn/Lg amplitude ratios are located in the eastern part of the Tibetan Plateau, where strong Lg attenuation or blockage is

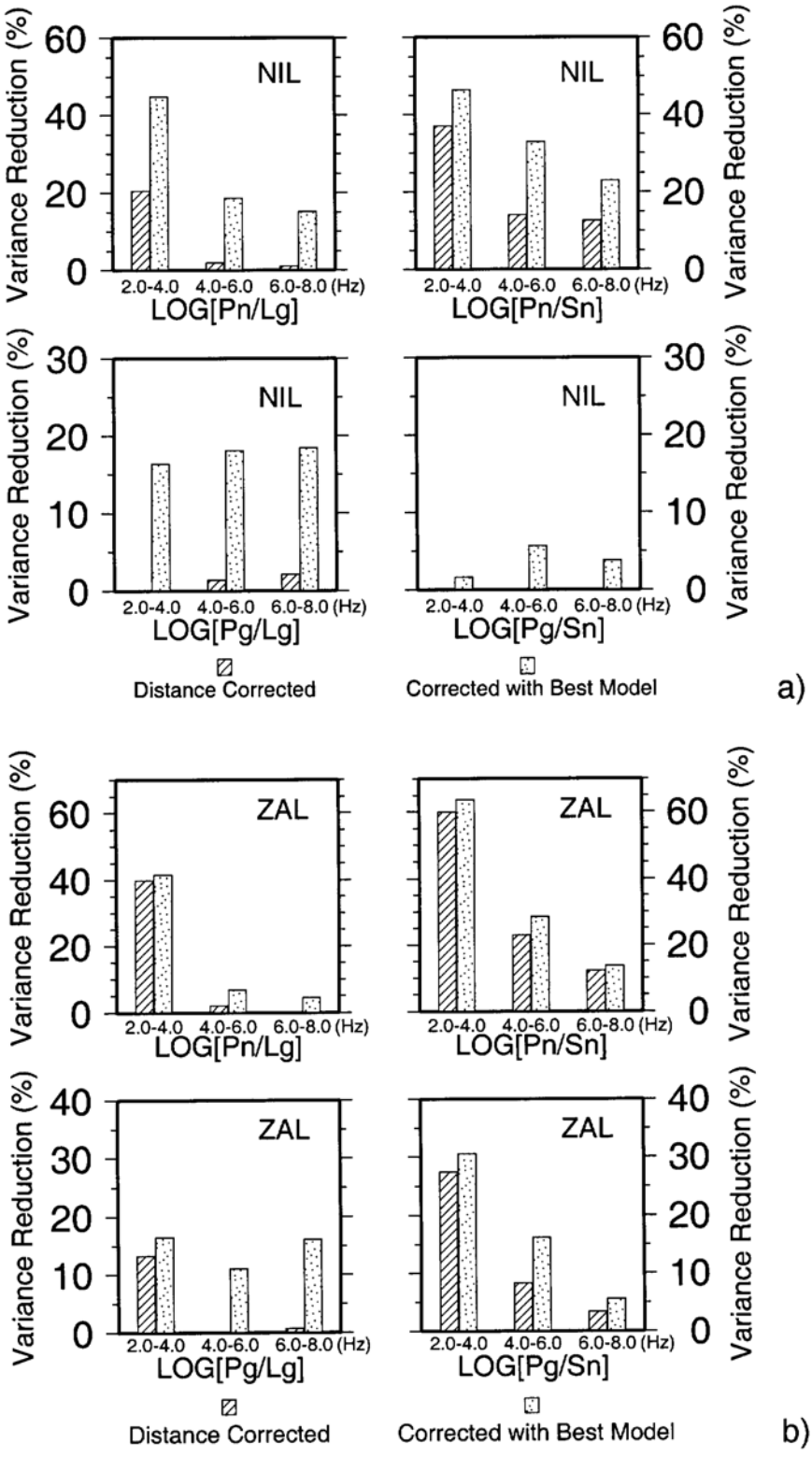


Figure 2. Variance reduction for the Pn/Lg, Pg/Lg, Pn/Sn, and Pg/Sn amplitude ratios achieved at (a) NIL; (b) ZAL. Variance reductions are calculated using corrections for path length only or for the optimal set of parameters in three frequency passbands.

observed (Rapine *et al.*, 1997). A small area between Pakistan and Iran also shows higher Log[Pn/Lg] amplitude ratios. In contrast, at ZAL high Pn/Lg amplitude ratios are found for events in Kashmir, the Pamirs, Hindu Kush, and western Tibet. Low ratios are especially evident for observations from Mongolia and the Baikal rift; these are also regions with low Pg/Lg ratios at LZH (Phillips, 1999). The contrast between regions indicates that the amplitude ratios are controlled by path effects rather than by localized source region effects. This emphasizes the difference in emphasis on path properties between kriging approaches and parametric regressions. Kriging interpolation can predict the value at any point within the grid net based on knowledge of the covariance and values at neighboring points. We expect this to work better for cases where there are many earthquake data near a suspect event, as would be the case here for ZAL, but not NIL. Caution is needed because kriging variance is independent of the data values and usually is not a measure of local estimation accuracy (Journel, 1986).

We now explore whether the separation between earthquake and explosion populations changes after correction for path length and/or other waveguide parameters, i.e., whether the performance of the regional discriminants improves. For our data sets the most effective source discrimination was found for Pn/Lg ratios at NIL. Figure 3 shows Log(Pn/Lg) values as a function of event magnitude for three frequency passbands. Two explosion events at the Lop Nor test site in China are well isolated in the 2-4 Hz and 6-8 Hz frequency bands. In the 4-6 Hz band an earthquake overlaps the explosion group. This event is an outlier of the earthquake population, and is located south of the Tibetan Plateau with a path traveling along the Plateau margin. Distance corrections result in reduced variance as shown in the middle row of Figure 3, but there is little influence on the separation between the earthquake and explosions populations (given the small number of explosion observations, we do not attempt to apply statistical tests, but simply rely on visual separation). Path correction using the best models from multivariate regression analysis (lower row of Figure 3) provides further improvement in variance reduction and better source discrimination in all three passbands in this case. This is the ideal goal for path corrections, to tighten up the scatter in the reference earthquake population while enhancing the separation of the explosion population.

Similar behavior is observed for the Log(Pg/Lg) measurements at NIL. Complete sample separation between earthquake and explosion populations is only found for the frequency band of 2-4 Hz, but the path corrections do give significant improvement in population separation in the two higher bands. The regional discriminants that involve Lg at NIL are more effective for source discrimination at lower frequency. Path corrections for the Log(Pn/Sn) ratios also provide significant variance reduction, however, better separation of earthquake and explosion populations is found at higher frequencies.

While not shown here, the discrimination performance for NIL is enhanced by considering the azimuthally restricted subset. Despite the fact that the overall variance reduction of path corrections is no stronger, there is clearer separation of earthquake and explosion populations than for the complete data set. We believe that there are two factors responsible for this. One is that several earthquakes with particularly strong path effects involving Lg blockage were excluded in the azimuthally limited data. Another factor is that by restricting the azimuthal coverage the data experience more similar travel paths, resulting in more effective path corrections.

Discriminant measurements at ZAL do not perform as well as those at NIL, even though the available explosion sources are located in the same source region. Figure 4 shows the observations for Log(Pn/Lg). The substantial overlap between earthquake and explosion populations is presumably a result of strong path effects. Correction for path length reduces the overlap, but does not achieve separation between earthquake and explosion populations. Using the best parametric regression provides slight further improvement in source discrimination for Log(Pn/Sn), but has little effect on Log(Pn/Lg). Other stations, such as AAK also do not provide clean discrimination (Hartse et al., 1998). In some instances kriging may do better than the parametric regressions, but this involves a large extrapolation for station NIL, and the coverage is very one-sided for ZAL.

CONCLUSIONS AND RECOMMENDATIONS

In this study we made path corrections for regional seismic discriminants observed at two CTBT monitoring stations in Asia. Correction of the path effects is based on empirical models derived from multivariate regression analysis and ordinary kriging. The parametric multiple regression uses a high-resolution topographic database to develop corrections involving path length and/or other topographic parameters. The corrections reduce the variance in the regional discriminants, particularly at lower frequencies. Kriging outperforms the multivariate regression approach in terms of reducing the eathquake population variance. For station NIL, the path corrections enhance discrimination effectiveness for a small set of explosions, while for station ZAL there is improvement, but still substantial overlap of the populations. This variation in discriminant performance presumably reflects acute waveguide heterogeneity that is not captured in the parameteric regression analysis. Accumulating larger data sets, with improved sampling of the paths traversed

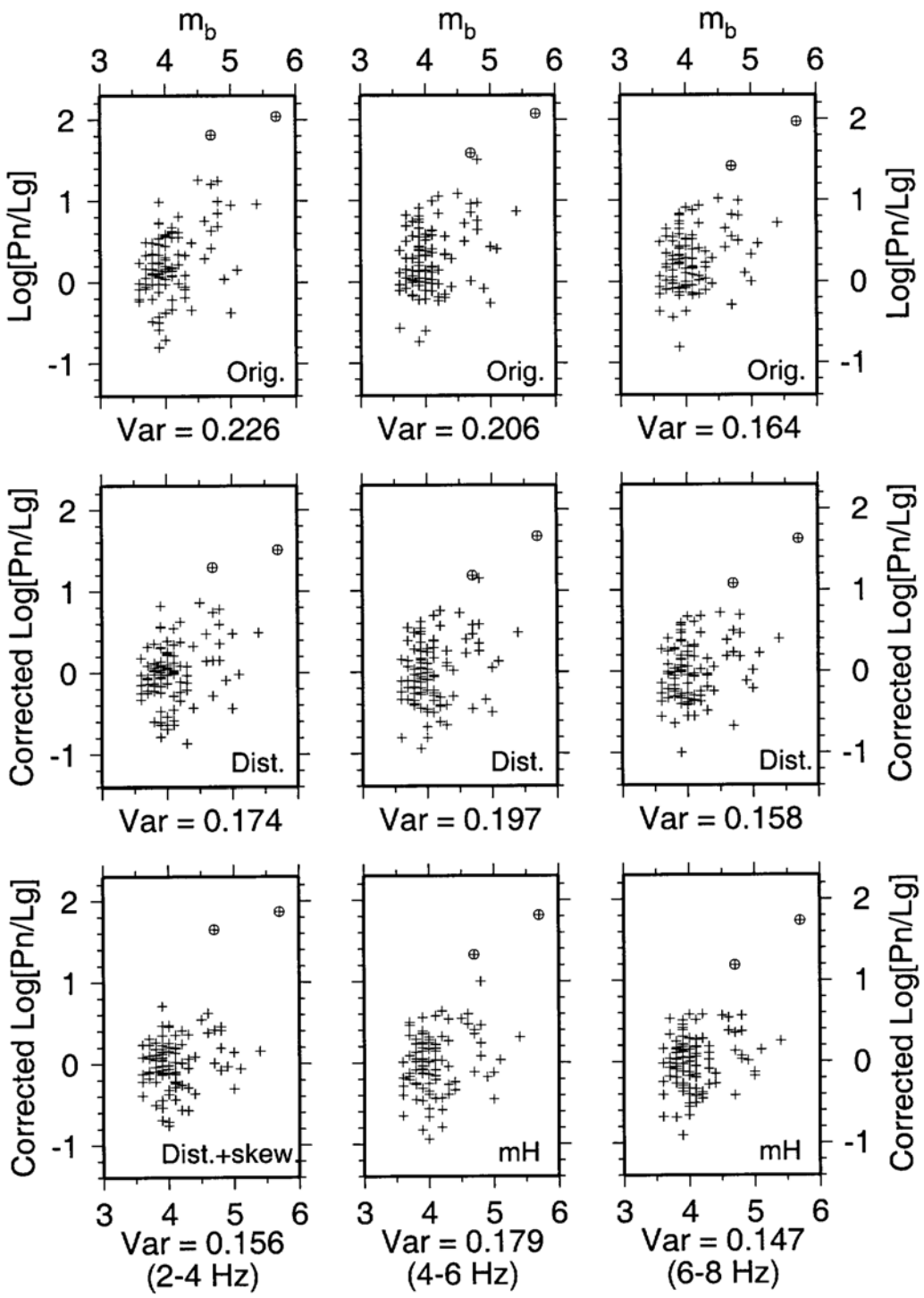


Figure 3. Log[Pn/Lg] measurements observed at NIL as a function of event magnitude in uncorrected form (top row) compared with those measurements corrected for path length (middle row) or for the optimal set of topographic parameters (bottom row) in three frequency passbands. Orig., observed data; Dist., corrected for path length; mH, corrected for mean altitude; Dist.+skew., corrected for a two-parameter model involving distance and skewness of topography.

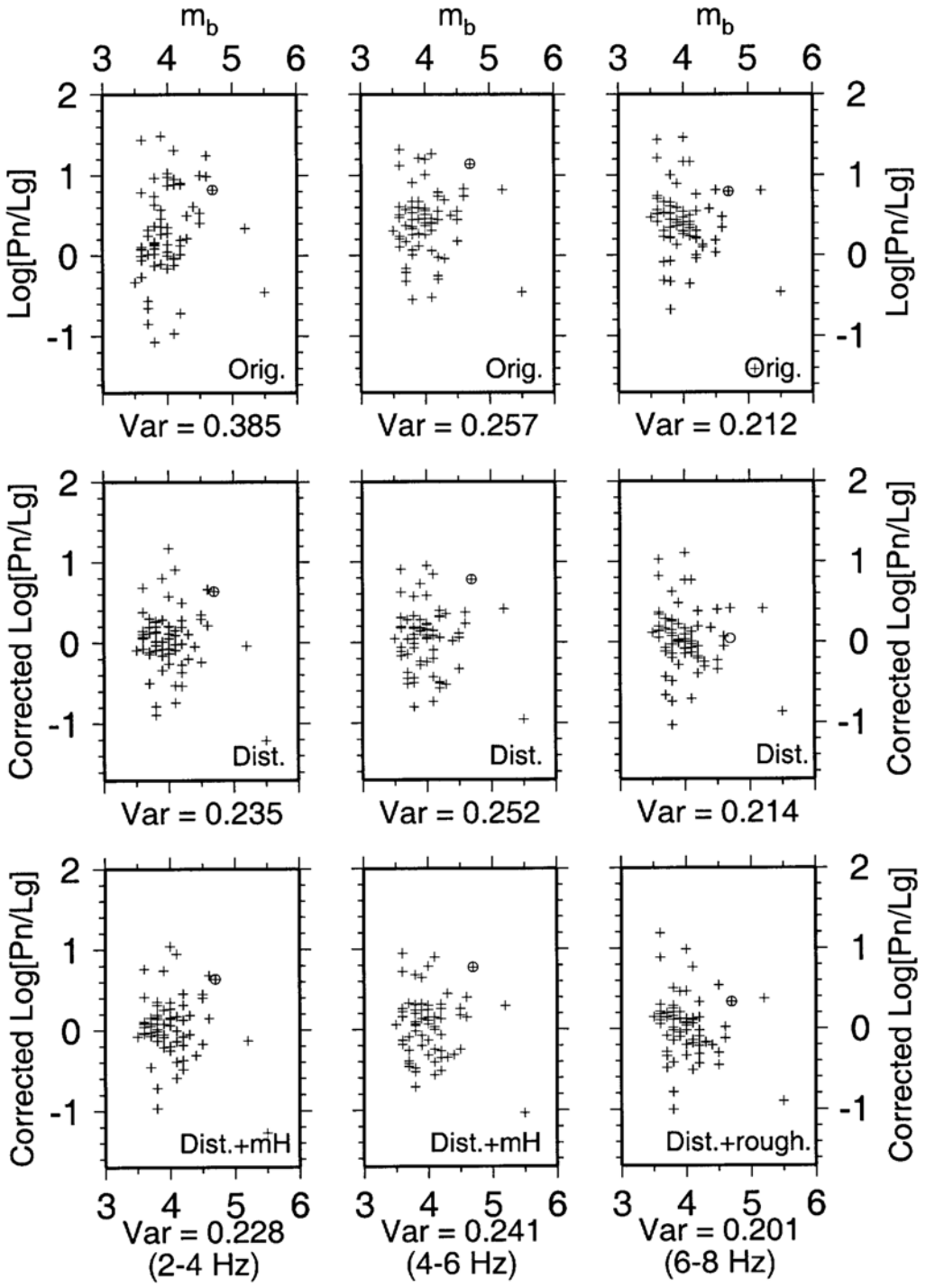


Figure 4. Log[Pn/Lg] measurements observed at station ZAL, plotted as a function of event magnitude, for uncorrected form (top row), distance corrected data (middle row) and multivariate regression corrected data (bottom row). Dist.+mH, corrected for a two-parameter model involving distance and mean path elevation along the path; Dist.+rough., corrected for a two-parameter model involing distance and average topography roughness.

by explosion signals, would likely lead to superior performance for both stations. Improved coverage would also reduce the degree of extrapolation currently required for the kriging analysis to be applied to the specific explosion source region in western China. Overall, there is a promising indication that application of propagation corrections is beneficial for these regional discriminants, but further work is needed to establish a preferred operational approach.

REFERENCES

Fan, G.-W., and Lay, T., (1998a), Statistical analysis of irregular waveguide influences on regional seismic discriminants in China, *Bull. Seism. Soc. Am., 88*, 74-88.

Fan, G.-W., and Lay, T., (1998b), Regionalized versus single-station wave-guide effects on seismic discriminants in western China, *Bull. Seism. Soc. Am., 88*, 1260-1274.

Fan, G.-W., and Lay, T., (1998c), Statistical analysis of irregular waveguide influences on regional seismic discriminants in China: additional results for Pn/Sn, Pn/Lg and Pg/Sn, *Bull. Seism. Soc. Am., 88*, 1504-1510.

Gesch, D.B., Verdin, K.L., and Greenlee, S.K., (1999), New land surface digital elevation model covers the Earth, *EOS Trans., AGU*, 80, 69-70.

Gupta, I.N., Chan, W.W., and Wagner, R.A., (1992), A comparison of regional phase from underground nuclear explosions at East Kazakh and Nevada test sites, *Bull. Seism. Soc. Am., 82*, 352-382.

Hartse, H.E., Flores, R.A., and Johnson, P.A., (1998), Correcting regional seismic discriminants for path effects in western China, *Bull. Seism. Soc. Am., 88*, 596-608 .

Isaaks, E.H., and Srivastava, R.M. (1989), *An Introduction to Applied Geostatistics*, Oxford University Press, New York.

Journel, A.G. (1986), Geostatistics: Models and tools for the Earth sciences, *Math. Geol., 18*, 119-140.

Ni, J., and Barazangi, M., (1983), High-frequency seismic wave propagation beneath the Indian Shield, Himalayan Arc, Tibetan Plateau and surrounding regions: high uppermost mantle velocities and efficient S_n propagation beneath Tibet, *Geophys. J. R. astr. Soc., 72*, 665-689.

Phillips, W.S., (1999), Empirical path corrections for regional phase amplitudes, *Bull. Seism. Soc. Am., 89*, 384-393.

Rapine, R.R., Ni, J. F., and Hearn, T.M., (1997), Regional wave propagation in China and its surrounding regions, *Bull. Seism. Soc. Am., 87*, 1622-1636.

Rodgers, A.J., Lay, T., Walter, W.R., and Mayeda, K.M., (1997a), A comparison of regional phase amplitude ratio measurement techniques, *Bull. Seism. Soc. Am, 87*, 1613-1621.

Rodgers, A.J., Ni, J.F., and Hearn, T.M., (1997b), Propagation characteristics of short period S_n and L_g in the Middle East, Bull. Seism. Soc. Am., 87, 396-413.

Rodgers, A.J., Walter, W.R., Schultz, C.A., Myers, S.C., and Lay, T., (1999), A comparison of methodologies for representing path effects on regional P/S discriminants, *Bull. Seism. Soc. Am, 89*, 394-408.

Schultz, C.A., Myers, S. C., Hipp, J., and Young, C.J., (1998), Nonstationary Bayesian Kriging: A predictive technique to generate spatial corrections for seismic detection, location and identification, *Bull. Seism. Soc. Am., 88*, 1275-1288.

Zhang, T.-R., Schwartz, S., and Lay, T., (1994), Multivariate analysis of waveguide effects on short-period regional wave propagation in Eurasia and its application in seismic discrimination, *J. Geophys. Res., 99*, 21,929-21,945.

IMPROVED ESTIMATION OF SEISMIC FOCAL DEPTHS IN IRAN

Alessia Maggi, Delaine Reiter* and Keith Priestley
Bullard Laboratories, University of Cambridge, United Kingdom
*Weston Geophysical Corporation

Sponsored by U. S. Department of Energy
Office of Nonproliferation and National Security
Office of Research and Development
Contract No. F19628-95-K-0017/NA

ABSTRACT

Accurate estimates of seismic focal depth and mechanism are important for event identification and empirical calibration of regions of monitoring concern. We have used 1-D raytracing of teleseismic body waves to estimate hypocentral depths of recent, moderate-size earthquakes in Iran. The waveform modeling involves matching the shape and amplitude of the direct P and SH arrivals together with the pP, sP and sS surface-reflected phases. This form of waveform modeling can constrain the focal depth to within 2-5 km. Our results, and the results of several earlier studies of Iranian earthquakes using waveform modeling, show that most (94%) of the events in the magnitude range Mw 5.3 to 6.3 in the Zagros Mountains of Iran lie within the uppermost 20 km of the crust. Many of our well-constrained focal depths are significantly shallower than the focal depths for these events reported by Engdahl, van der Hilst, and Buland (1998). We are using the cepstral depth estimation procedure of Reiter and Shumway (1999) to provide an independent estimate of the focal depth these Iranian earthquake results. The cepstral analysis technique detects the delay times of pP-P and sP-P through straightforward signal-processing methods, and assigns statistical significance to the measured delays. Tests to date show that the cepstral method and the body waveform modeling results agree exceptionally well for these moderate size earthquakes. We are now extending our tests to smaller events that cannot be recorded teleseismically. We are using the waveform modeling results for the moderate size earthquakes to calibrate the propagation paths to digital seismographs located in the Caspian region north of Iran. We will then use these results to model the regional waveforms recorded at the Caspian stations for smaller events, and verify the depths of the smaller events using cepstral analysis.

Keywords: seismic focal depth, waveform modeling, cepstral analysis, Iran, Caspian Sea

OBJECTIVE

The primary objective of this research is to accurately determine the depths of small magnitude earthquakes in Iran from seismograms recorded at regional distances. To accomplish this we are using well-located, moderate-size earthquakes to calibrate regional seismic stations in the Middle East. The focus of our work to date has been on building a database of well-located events whose source parameters have been determined by teleseismic waveform modeling with an independent focal depth determination using the cepstral F-statistic method (Reiter and Shumway, 1999). Some of these events have additional source information from field studies. We use the results from the moderate-size earthquakes to calibrate the regional seismographs. Once calibrated, the cepstral depth estimation technique can be applied to regional seismograms to estimate focal depths of small magnitude events. This work will result in a database of well-located, moderate-size events in Iran, a catalogue of small magnitude Iranian events whose focal depths are accurately known, and a calibrated procedure for depth determination in the region. We feel that a combining teleseismic waveform modeling and the cepstral F-statistic method to estimate and validate our depth estimates can improve the regional calibration of events in Iran.

RESEARCH ACCOMPLISHED

Regional path calibration of seismic phases depends on the accuracy of hypocentral locations of seismic events. While moderate-size events present no challenge for seismic identification and discrimination, the study of the waveform characteristics of larger magnitude events can provide information necessary for regional path corrections that are important for the identification and discrimination of small magnitude events. We have used well-located, moderate-size events in Iran to calibrate regional seismic stations. We then use data from regional seismic stations to estimate focal depths of small magnitude events.

Waveform Analysis

We analyze P- and SH-waveforms taken from the Global Digital Seismic Network (GDSN) and GEOSCOPE stations to constrain the source parameters of moderate-size earthquakes in Iran. Source parameters are determined using McCaffrey and Abers' (1988) version of Nabelek's (1984) waveform inversion program. This method minimizes, in a least-squares sense, the misfit between the shape and amplitude of the observed and synthetic P- and SH-waveforms. The synthetic seismograms are computed for a point source embedded in a simplified Earth structure by combining the direct arrival (either P or S) with the near-source reflections (pP and sP, or sS) and near-source multiples. Amplitudes are corrected for geometrical spreading, and for anelastic attenuation using a Futterman Q operator with a t* value of 1.0 s for P and 4.0 s for SH waves. This procedure is now routine, and detailed descriptions can be found in McCaffrey and Abers (1988).

The inversion method minimizes the misfit between the observed and synthetic waveforms by varying the strike, dip, slip, centroid depth, seismic moment, and source time function. To avoid complications introduced by the upper mantle triplication or core phase interference, we restricted the body waveform inversion to P-waves in the 30^o to 90^o distance ranges and S-waves in the 35^o to 84^o distance range. Because of their large amplitudes, SH seismograms were given only 50% of the weight of the P-wave seismograms in the inversion process, and all seismograms were azimuthally weighted; that is, seismograms from stations clustered together in azimuth were given lower weight than seismograms from isolated stations. For these moderate size events we assumed that all slip occurs at the same point in space (centroid location), but the source time function is distributed in time. The source time function is described by a series of overlapping isosceles triangles (Nabelek, 1984).

A minimum misfit set of source parameters is found by the inversion routine. Priestley et al. (1994) have performed tests to evaluate the effects of the unknown velocity structure in the source region. They find that reasonable variations in crustal velocity structure do not result in significant changes in strike, dip, and rake, but can affect centroid depth, moment, and the source time function. Uncertainties in t* lead to uncertainties in source duration and seismic moment, but have only a small effect on centroid depth and source orientation. Uncertainties in the source parameters were estimated in two ways. First we computed the formal errors in these parameters in the inversion procedure, but our past experience has shown that

these uncertainty estimates are overly optimistic. Consequently, we also performed a series of tests to assess more realistic uncertainties and examine trade-offs between the various parameters. Our test procedure is to fix the source parameter being examined at a series of values that bracket the minimum misfit value, then reinvert the waveform data to examine what effect variations in the fixed parameters have on the free parameters. We then visually inspected the fit of the observed and synthetic waveforms to see if there was any deterioration in the fit. We continued this procedure, adjusting the value of the free parameter away from the minimum misfit value until the fit between the observed and synthetic waveforms was noticeably worse, and thereby estimated a more realistic bound on that source parameter. Our tests showed that the strike, dip, rake, and centroid depth are relatively independent of each other. That is, when one parameter was held fixed at a value within a few degrees or kilometers of its minimum misfit value and the waveforms reinverted, the resulting values of the free parameters were close to their minimum misfit values. From these tests we estimate the uncertainty bounds on the centroid depth are ± 3 km, the strike ± 15°, the dip ± 4°, and the rake ± 20°. These uncertainties are of similar magnitude to those noted in comparable studies in other regions (e.g. Molnar and Lyon-Caen, 1989; Baker et al., 1993; Priestley et al., 1994).

We have modeled the waveform of the Zagros Mountains earthquake of July 31, 1994 in the Iran region (Figure 1). The results from the waveform analysis are shown in Figures 2 and 3. This moderate size (International Seismological Centre (ISC): m_b 5.2, M_S 5.3) earthquake occurred on July 31 1994 in the western Zagros Mountains (32.58 ± 0.027°N, 48.37 ± 0.020°E). The focal depth is given as 43 km by the National Earthquake Information Center (NEIC), 44 ± 2.4 km by the ISC and 45 km by Engdahl et al. (1998). We analyzed 22 P- and 18 SH- digital waveforms obtained from the GDSN and GEOSCOPE networks. Figure 2 shows the match between the observed seismograms and synthetic P and SH seismograms computed for the minimum misfit solution. The minimum misfit solution, a low angle thrust, is not typical for the Zagros Mountains, which mainly have high angle reverse or strike-slip mechanisms. The focal depth is 14 km and the source time function is a simple pulse with a total (95%) duration of 2.5s.

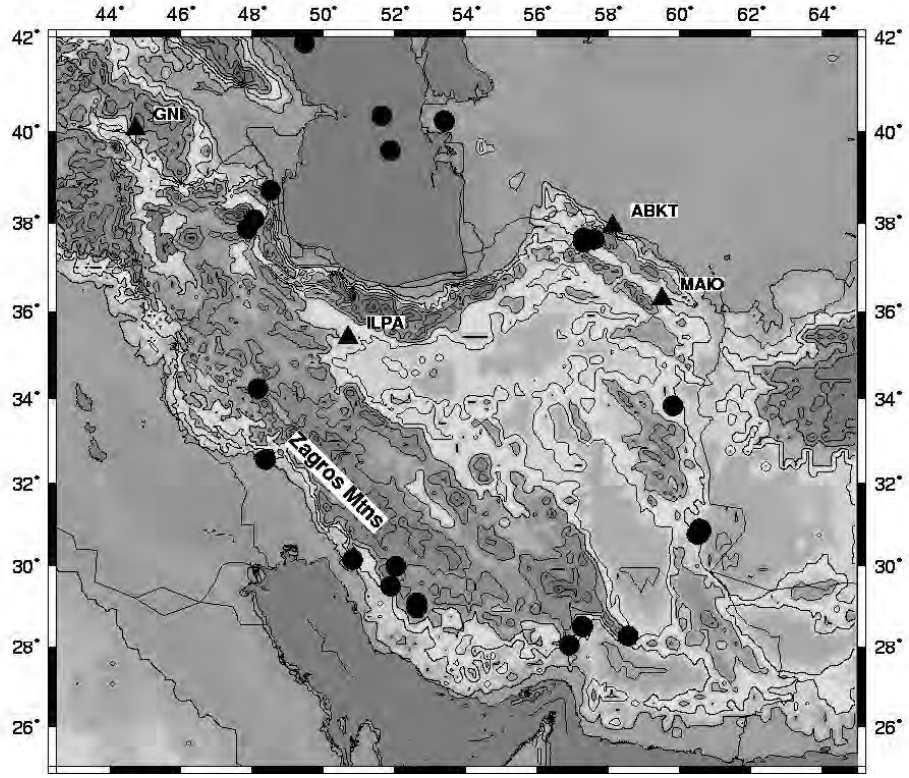


Figure 1. A topography map showing the area of study. The earthquakes under analysis for our study are represented by black dots, and nearby stations are denoted by triangles. The July 31, 1994 earthquake analyzed in the body of the paper is in the western Zagros Mountains (32.58 ± 0.027°N, 48.37 ± 0.020°E).

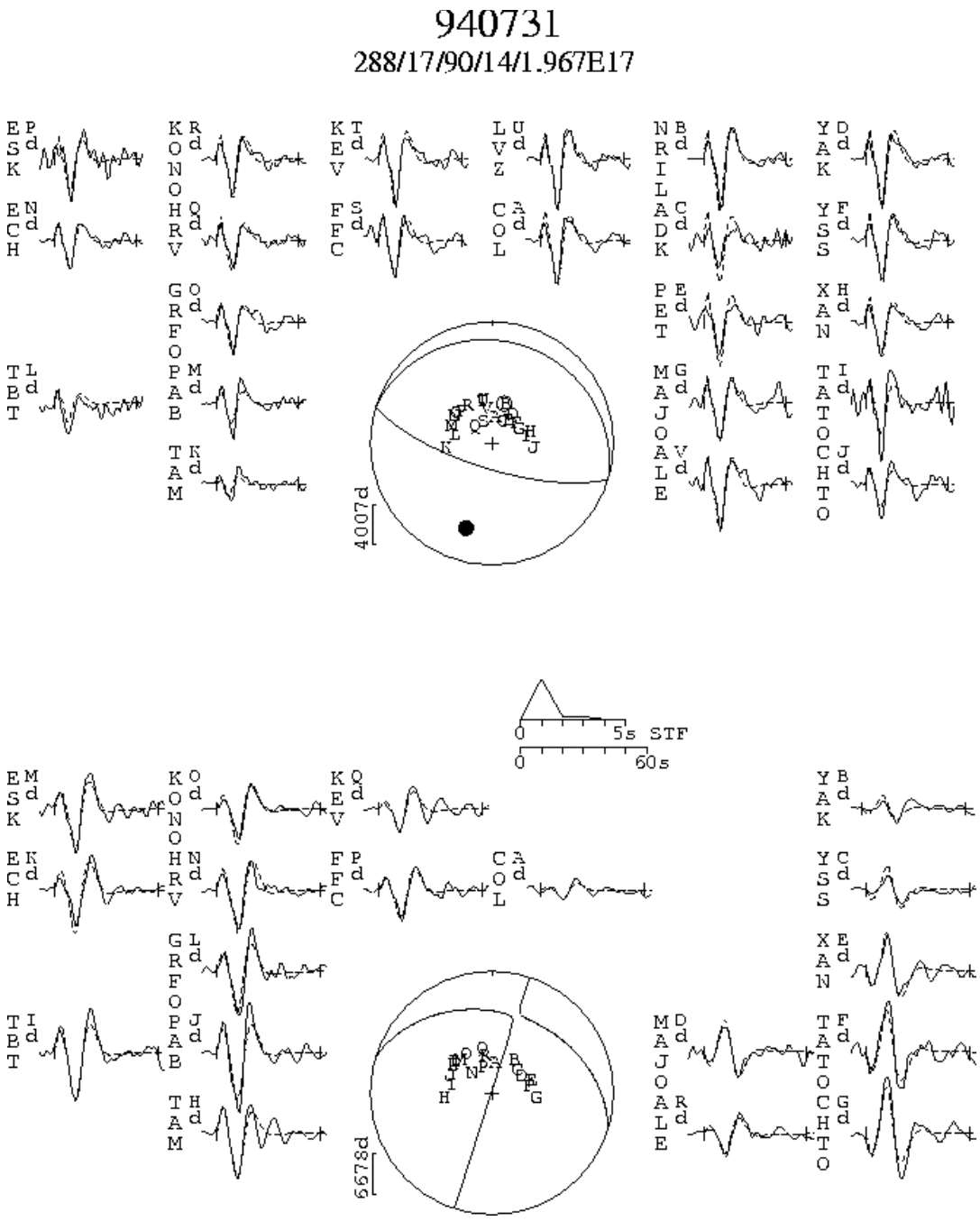


Figure 2. The P and SH radiation patterns of the minimum misfit solution for the Zagros Mountains earthquake of July 31, 1994. The values beneath the event header give strike, dip, rake (in degrees), the depth (in km) and the seismic moment (in units of 10^{18} Nm. The focal spheres are shown with the P and SH nodal planes in lower hemisphere projections. The solid and open circles mark the P and T axes, respectively. Surrounding the focal sphere, the observed P and SH waveforms (solid lines) are compared with synthetic waveforms (dashed lines) computed for the minimum misfit solution. These are ordered clockwise by azimuth. A letter corresponding to its position within the focal sphere accompanies the station code by each waveform. Solid bars at either end of the waveform mark the inversion window. The source time function is shown below the P-wave focal sphere, with the waveform time scale below this. Waveform amplitude scales are to the left of the focal sphere. This solution was obtained using a 10 km thick layer (Vp=6.00 km/s, Vs=3.47 km/s, ρ=2.69 kg/m^3) over a half-space (Vp=6.50 km/s, Vs=3.76 km/s, ρ=2.85 kg/m^3).

This solution was calculated using a velocity model consisting of a 10 km thick layer with Vp =6.00 km/s, Vs=3.47 km/s, and ρ=2.64 kg/m^3 over a half space with Vp=6.50 km/s, Vs=3.76 km/s, and ρ=2.85 kg/m^3. The observed waveforms are well matched by the synthetic waveforms for the first 60 seconds.

Figure 3 shows tests made of the source parameters. The figure compares selected P- and SH- waveforms of the minimum misfit solution (top line) with an inversion computed using the published CMT fault plane solution (s d r) and the Engdahl et al (1998) depth. The solution showed is a minimum in dip, depth, source time function and moment space, but is a much poorer fit than the minimum misfit solution shown in the first line. The third and fourth lines of Figure 2 show the effect of fixing the depth of the minimum misfit solution at 19 and 11 km. These fits are significantly worse than the match of the minimum misfit solution, leading to a depth uncertainty of ± 3 km.

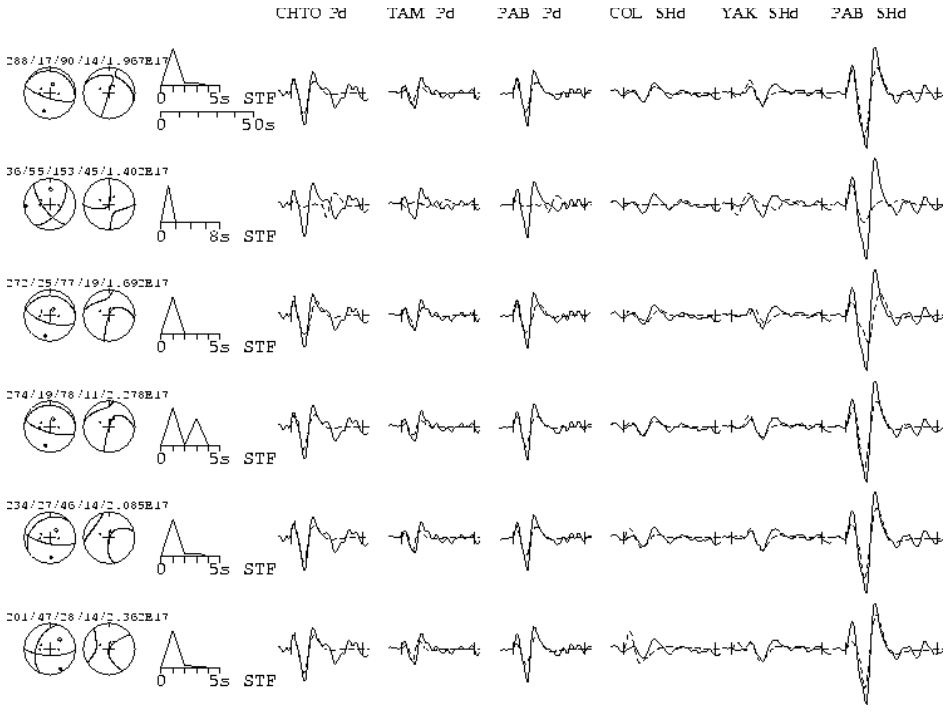


Figure 3. Waveform tests for the Zagros Mountains earthquake of July 31, 1994. (a) minimum misfit solution, (b) results for the inversion of the test of the Engdahl et al (1998) depth, (c) test of 19 km focal depth, (d) test of 11 km focal depth, and (e) and (f) test of the dip.

Cepstral Analysis

Another method used to determine depths that does not rely on waveform modeling is cepstral analysis. This method is based on an estimation of the spectrum of the log spectrum of windows of seismic data (called the *cepstrum*), and peaks in the cepstrum can be directly related to the event depth. As long as a seismic signal has sufficient bandwidth, cepstral analysis can be used to detect the delay times between P and depth phases such as pP and sP. We are using the cepstral F-statistic method (Reiter and Shumway, 1999) to estimate the depths of the same teleseismic events in Iran for which we have depth estimates from waveform modeling. The cepstral F-statistic method for depth estimation attaches statistical significance to peaks in the cepstrum through a signal-to-noise ratio computed from the beam cepstrum and the sum-stacked cepstrum. This is an advantage over traditional cepstral analysis because it allows us to assign validity to peaks in the calculated cepstrum. We estimate individual cepstra from windows of data that contain the P arrival and its coda, and the F-statistic is formed by dividing the beam (mean) cepstrum by the error between the beam and the sum-stacked cepstrum. This analysis can be performed on both array and single three-component station data. To be valid, peaks at possible depth phase delay times must appear in both the beam cepstrum and the F-statistic estimate and must be stable over varied processing

parameters such as window length, start time and overlap. In addition, we window the signal portion of the log spectrum prior to calculating the cepstrum and performing peak detection. This is done to decrease the strong influence of out-of-band noise on the cepstrum and F-statistic. For more details about the method, please see Reiter and Shumway (1999).

We processed the data from the July 31, 1994 earthquake in the Zagros Mountains using a subset of the stations from the waveform analysis. This was based on distance from the earthquake and signal-to-noise ratios. Table 1. provides a list of the stations used, along with their epicentral distance, the number of windows input to the cepstral analysis algorithm and cut-off frequency in the detrended log spectrum. The results indicate a depth of 18 km (± 4km). We derived this result by assuming that the earlier peaks at stations ABKT, LVZ and KEV are due to the pP-P delay time and the later peaks at stations ABKT, WUS and GRFO are due to the sP-P time. Further analysis is necessary to confirm these results, but initial indications are that they agree fairly well with the waveform modeling results.

Table 1.

STATION	Δ	# Windows	Cut-off Freq (Hz)
ABKT	9.62	4	1.2
WUS	25.9	4	1.8
GRFO	32.4	4	2.1
LVZ	36.2	4	.95
KEV	39.1	4	2.0

CONCLUSIONS

In this study we are attempting to calibrate regional seismic stations in the Middle East using well-located moderate-size earthquakes. We are building a database of well-located events whose source parameters have been determined by teleseismic waveform modeling. Depth estimates of moderate-size earthquakes in Iran can be determined to ±3 km from this modeling analysis. The cepstral F-statistic method is being applied to provide an independent focal depth estimate. For the moderate-size earthquakes we have analyzed to date, the cepstral F-statistic method for hypocenter determination agrees well with the hypocentral depths found from the teleseismic waveform modeling.

Once we have developed a database of well-located events in the region, we will use the results from the moderate-size earthquakes to calibrate the regional seismographs. This work will result in a database of well-located, moderate-size events in Iran, a catalogue of small magnitude Iranian events whose focal depths are accurately known, and a calibrated procedure for depth determination in the region. We will also extend the cepstral method to smaller magnitude events in Iran and determine the minimum magnitude for reliable source depth.

REFERENCES

Baker, C., J. Jackson, and K.F. Priestley (1993), Earthquakes on the Kazerun line in the Zagros Mountains of Iran: strike-slip faulting within a fold-and-thrust belt, *Geophys. J. Int.*, **115**, p. 41-61.

Engdahl, E. R., R. van der Hilst and R. Buland (1998), Global teleseismic earthquake relocation with improved travel times and procedure for depth determination, *Bull. Seismo. Soc. Am.,* **88**, p. 722-743.

McCaffrey, R. and G. Abers, G. (1988), SYN3: A program for inversion of teleseismic body wave forms on microcomputers, Air Force Geophysics Laboratory Technical Report, AFGL-TR-88-0099, Hanscom Air Force Base, MA, 50p.

Molnar, P., and Lyon-Caen, H. (1989), Fault plane solutions of earthquakes and active tectonics of the Tibetan Plateau and its margin, *Geophys J. Int.*, 99, p. 123-153.

Nabelek, J. (1984), Determinations of earthquake source parameters from inversion of body waves, *Ph.D. thesis*, M.I.T., Cambridge, MA.

Priestley, K.F., C. Baker, and J. Jackson (1994), Implications of earthquake focal mechanism data for the active tectonics of the south Caspian basin and surrounding regions, *Geophys. J. Int.*, **118**, p. 111-141, 1994.

Reiter, D. T. and R. H. Shumway (1999), Improved Seismic Event Depth Estimation Using Cepstral Analysis, this volume.

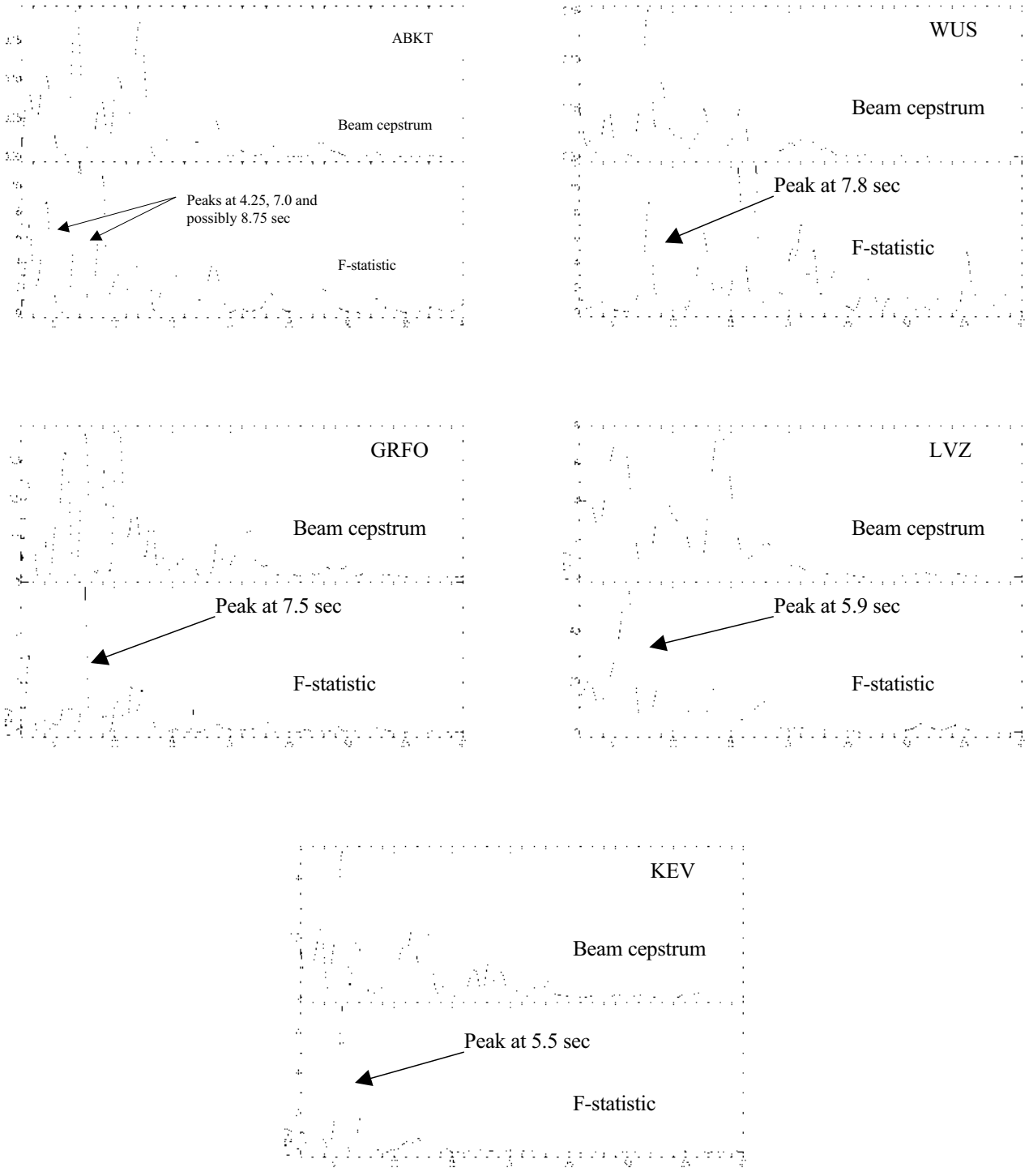


Figure 4. Results from cepstral analysis of the July 31, 1994 earthquake in the Zagros Mountains of Iran. We processed a subset of the stations used in the waveform analysis that had fairly high signal-to-noise ratios. Peaks in the beam cepstra and F-statistics indicate a depth of 18 km (± 4 km). This result was derived by assuming that the earlier peaks at stations ABKT, LVZ and KEV are due to the pP-P delay time, and the later peaks at stations ABKT, WUS and GRFO are due to the sP-P delay time.

APPLYING CODA ENVELOPE MEASUREMENTS TO LOCAL AND REGIONAL WAVEFORMS FOR STABLE ESTIMATES OF MAGNITUDE, SOURCE SPECTRA, & ENERGY

Kevin Mayeda, Rami Hofstetter*, Arthur Rodgers, & William Walter
Lawrence Livermore National Laboratory, and Geophysical Institute of Israel*

Sponsored by the U.S. Department of Energy
Office of Nonproliferation and National Security
Office of Research and Development
Contract No. W-7405-ENG-48
UCRL-JC-134307

ABSTRACT

Magnitude estimation forms an integral part in any seismic monitoring endeavor. For monitoring compliance of the Comprehensive Nuclear-Test-Ban Treaty, regional seismic discriminants are often functions of magnitude such as mb :Mo , high-to-low spectral ratios, and nuclear yield estimation. For small-to-moderate magnitude events that cannot be studied by a large regional or global network of stations, there is a need for stable magnitudes that can be obtained from as few as one station. To date, magnitudes based on coda envelopes are by far the most stable because of the coda's averaging properties. Unlike conventional magnitudes which utilize the direct phases such as P (Pn , Pg) or S (Sn , Lg), or Ms , a coda envelope magnitude is not as sensitive to the undesirable effects of source radiation pattern, 3-D path heterogeneity, and constructive/destructive interference near the recording site. The stability of the coda comes from a time-domain measurement made over a large portion of the seismogram thereby averaging over the scattered wavefield. This approach has been applied to earthquakes in the western United States where it was found that a single-station coda magnitude was approximately equivalent to an average over a 64 station network which used only the direct waves such as Lg (Mayeda & Walter, JGR, 1996).

In this paper we describe in detail our calibration procedure starting with a broadband recording, correlation with independent moment estimates, formation of narrowband envelopes, coda envelope fitting with synthetics, and finally the resultant moment-rate spectra. Our procedure accounts for all propagation, site, and S-to-coda transfer function effects. The resultant coda-derived moment-rate spectra are then used to estimate seismic moment (Mo), narrowband magnitudes such as mb or ML , and total seismic energy. For the eastern Mediterranean region a preliminary study was completed for earthquakes in the Gulf of Aqaba region using two regional broadband stations, KEG and BGIO. As was found in the western U.S., a significant reduction in magnitude scatter was achieved when using the coda. This procedure provides a means of unbiased, unsaturated magnitude estimation that will be tied to a physical measure of earthquake size (seismic moment), unlike conventional magnitudes such as mb , ML , MD , and MS . We outline a calibration procedure that can be used in software codes such as SAC on both UNIX and PC platforms. This paper describes the calibration technique and the application to regional stations of the IMS.

Key Words: Regional Magnitude, coda, source spectra, earthquake parameters

Research performed under the auspices of the U.S. Department of Energy by the Lawrence Livermore National Laboratory under contract S-7405-ENG-48.

OBJECTIVE

Regional magnitudes for small-to-moderate sized crustal events using Pn , Pg , and Lg all suffer from source and path heterogeneity. As a consequence multi-station averaging is necessary to reduce the amplitude variability. Under the CTBT however, the average station spacing is larger than 1000 km and thus the ability to measure a stable magnitude becomes difficult because of limited stations over which to average. Because small-to-moderate sized events cannot be measured teleseismically, we need a stable single-station measure of earthquake size. Over the past several years we have developed and applied a magnitude based on the Sn and Lg coda envelope which is significantly less affected by source anisotropy and 3-D path heterogeneity. We have found that the amplitude of the time domain coda envelope can provide a far more stable amplitude measure than the more conventional methods that measure the direct arrivals. For small regions such as the Nevada Test Site (see Mayeda, 1993) and aftershock zones (this study) we find that a single-station coda magnitude is equivalent to roughly a 16 station network using direct waves. For larger regions (such as the western U.S.) the crustal averaging properties are equivalent to a 64-station network (Mayeda and Walter, 1996). In this paper we outline a procedure and discuss new software codes that have been developed to process broadband waveforms for coda-based Mw and mb given a set of calibration parameters. The calibration procedure is applied to a small set of earthquakes in the region which are large enough to be modeled using 1-D velocity models.

Method

Unlike conventional magnitudes which measure peak or RMS amplitude our coda magnitude procedure fits a Green's function envelope to the actual narrowband coda envelope and measures the amplitude relative to a fixed level. We then tie the coda measurements (taken in time-domain) to an absolute scale by correcting the frequency dependent effects of S-to-coda transfer function, path attenuation, site response, and finally instrument response. Once these corrections are known, we find that our magnitudes (whether Mw or mb) are remarkably stable and accurate. Furthermore, these magnitudes are transportable and not subject to regional bias as is often the case for the conventional magnitudes such as mb(Pg), mb(Pn), mb (Lg), Ms etc. The amplitude measurements can be done with either synthetic or empirical Green's function envelopes. We have found a simple functional form that can fit regional narrowband coda envelopes over a broad range of frequency bands (~0.03 to 10 Hz). For speed and simplicity, synthetic envelopes of the form shown below were the easiest to handle where Ac is the coda
amplitude, f is the center frequency of the band, and t is the time in seconds measured from the origin time, $Ac(f,t) = Ao\, t^{-\gamma} \exp(-bt)$ where γ and b are functions of frequency and distance. Note that the above functional form is similar to the single-scattering formulation of Aki(1969), where b is related to the coda Q. For our purposes however, we search for the best parameters for each narrow frequency band and allow them to change as a function of epicentral distance. We found that this was necessary perhaps because of the larger source-to-receiver distances, waveguide effects and/or multiple scattering that are not accounted for in virtually all scattering models. Therefore, for a particular region we determine as a function of distance, x; $\gamma(x)$, b(x) as well as the S-wave and surface wave group velocities for each of the frequency bands. Unlike most other magnitudes, our procedure operates on absolute source spectra and thus is transportable and will not suffer regional bias. We accomplish this by tying our time-domain coda envelope measurements to moments derived from long-period regional waveform modeling results. Since the waveform modeling results are not as sensitive to structure and site effect (at long periods (> ~10 seconds) we feel confident in using these as calibration events. What makes our procedure more attractive is its stability and ability to extend Mw down to much smaller events than can be accurately waveform modeled (< ~Mw 3.5).

SAC Command

We have developed a SAC command that will read an ASCII flatfile of calibration information and automatically processes the waveform data that will then output moment-rate spectra, Mw and mb . The two horizontal broadband traces are read into SAC by the tool. Averaged log10 envelopes are formed for consecutive narrow frequency bands (the number and exact frequency bands are specified in the calibration flatfile). Using the epicentral distance in the SAC headers, the synthetic envelopes for each frequency band are generated and used to measure (in an L-1 sense) the observed envelopes in time-domain (Figure 1).

Typically we use 12 frequency bands but again, this can be changed in the calibration inputfile. Each of the discrete time-domain amplitude measurements are then corrected for path, site, and instrument effects resulting in a completely corrected S-wave source spectra. The result is a plot of the source spectra and an ASCII output file with diagnostic information. To make the code automated the tool checks for degenerate cases such as aftershocks in the coda, drop-outs, and minimum coda length.

Application

We have previously calibrated two broadband stations in the eastern Mediterranean region, BGIO and KEG, for the Gulf of Aqaba mainshock and its associated aftershocks. In Figure 2 we show mb (Lg) and mb (Pg) compared to mb (coda) using stations KEG and BGIO for a subset of the Gulf of Aqaba aftershock sequence. We see that the coda-based magnitude is 4 times less variable which is equivalent to a 16 station network using the conventional magnitudes. Figure 3 shows coda-derived S-wave spectra for two aftershocks. The November 23, 1995 event is nodal for S at BGIO, however the coda spectra at both BGIO and KEG are virtually identical, confirming that the coda is averaging over the source radiation pattern. Finally, figure 4 compares the coda-derived Mw against those obtained using 1-D regional waveform modeling. As was found in the western U.S., the coda-derived Mw is in excellent agreement with conventional methods. The advantage of the coda is its ability to extent the Mw measure to much smaller events and is more stable. We then compared the performance of our new tool with our old research-mode SAC macro which at best can be described as “clunky” (it utilizes C-shells and FORTRAN subroutines). The spectral and magnitude results were identical and the only major difference was that the new SAC tool is roughly 20 times faster and significantly more robust.

CONCLUSION

We have developed a new SAC command that can be used in both research-mode and large scale data processing for stable coda magnitude estimation. The success of this procedure has been demonstrated in numerous regions but is difficult to apply for those that are uninitiated. With the development of this new tool, the application to other regions by other researches should be significantly easier. In addition, we are working with Sandia National Laboratory to code a more robust version to be used in an operational setting. Currently, the calibration is handled by a set of SAC macros that operate on a small calibration dataset that have independent moment estimates. The current example in the Gulf of Aqaba region is now being extended to other neighboring regions.

REFERENCES

Aki, K., Analysis of the seismic coda of local earthquakes as scattered waves, *JGR*, **74**, 1969, 615-631.

Mayeda, Kevin, mb(LgCoda): A stable single station estimator of magnitude, *BSSA*, **83**, 1993, 851-861.

Mayeda, Kevin, & William Walter, Moment, energy, stress drop, and source spectra of western United States earthquakes from regional coda envelopes, *JGR*, **101**, 1996, 11195-11208.

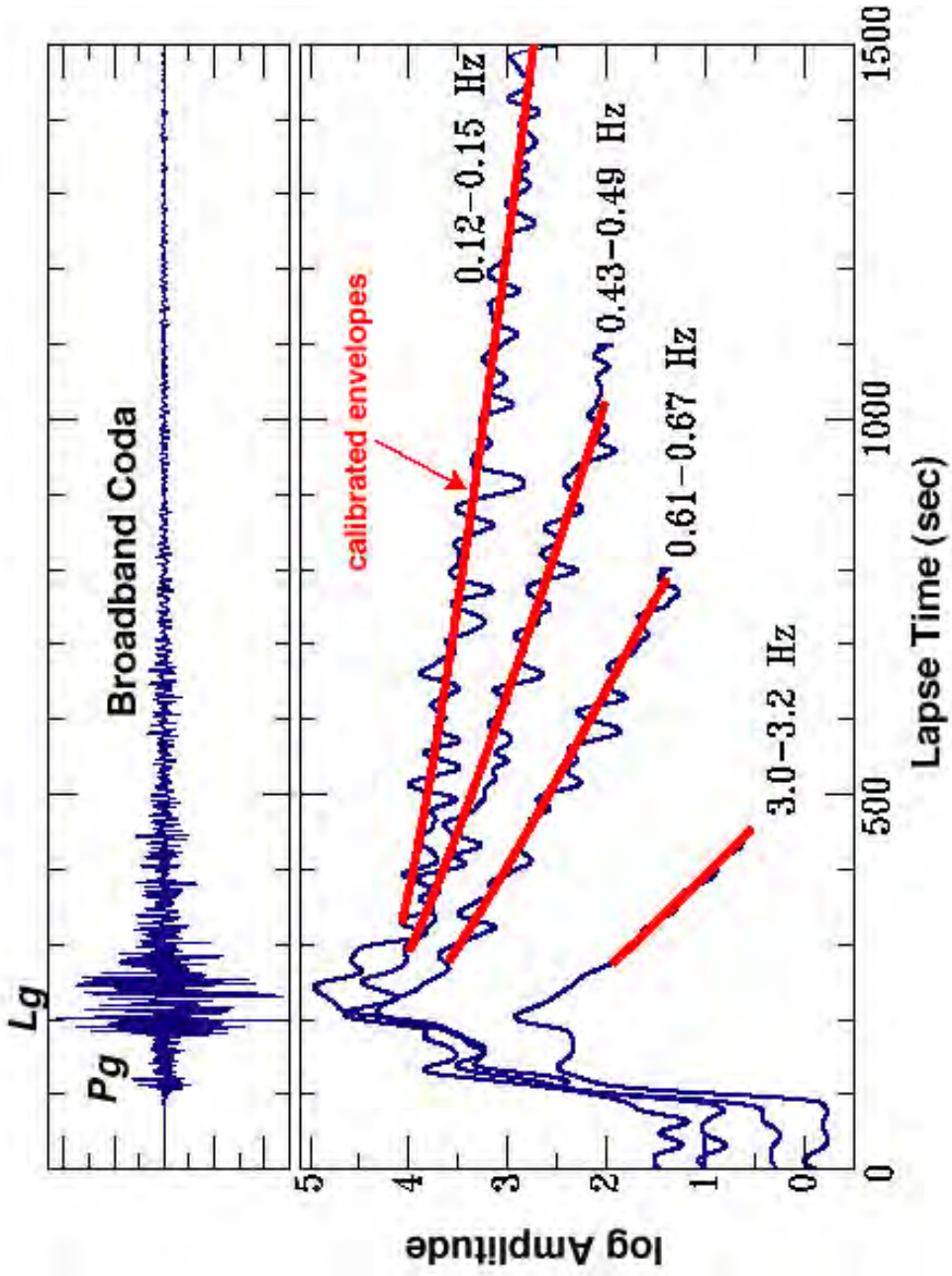
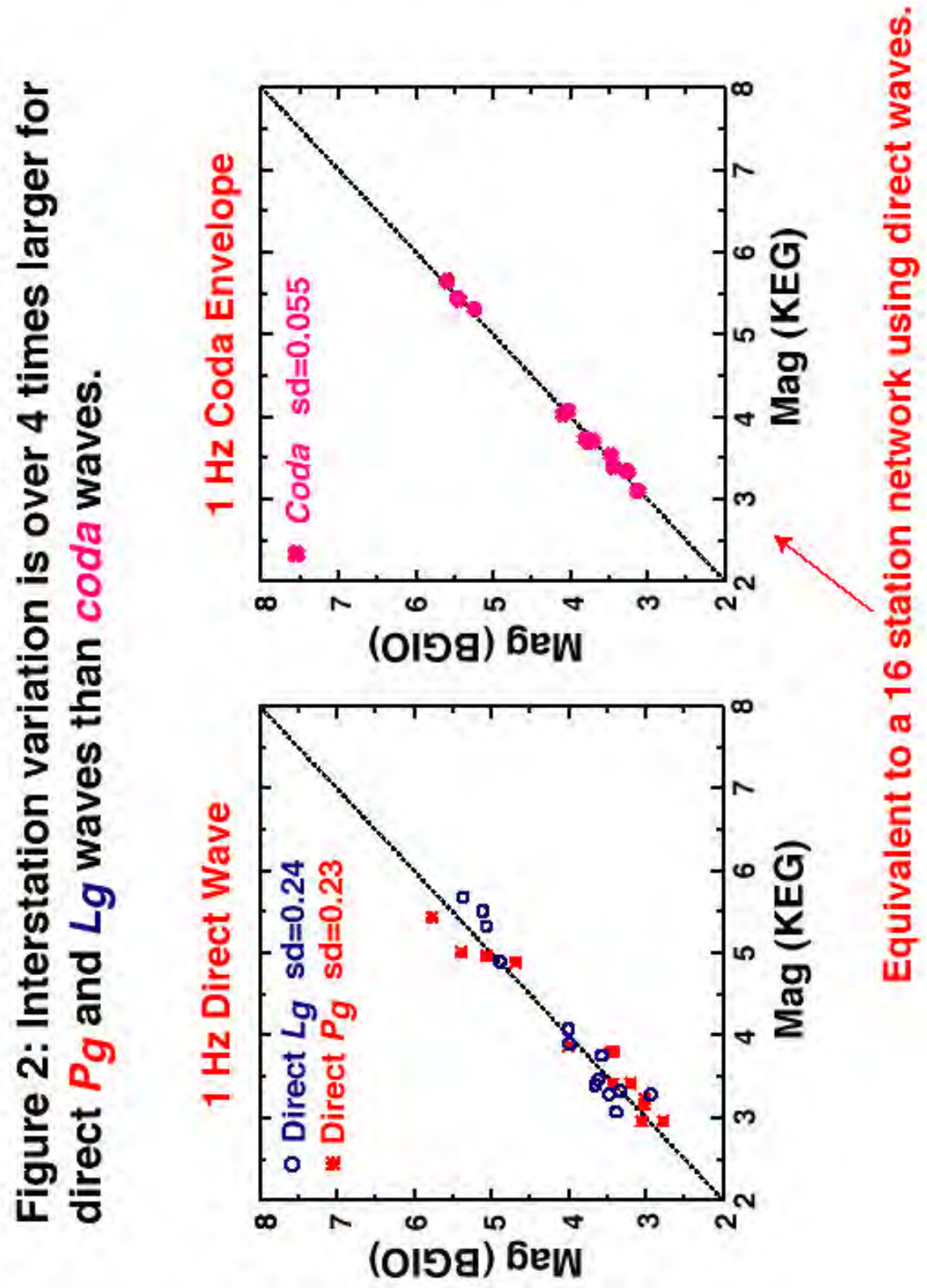


Figure 1: Example of coda envelope amplitude measurements for four narrow frequency bands.


Figure 2: Interstation variation is over 4 times larger for direct Pg and Lg waves than coda waves.
1 Hz Direct Wave
Direct Lg sd=0.24
Direct Pg sd=0.23
Mag (BGIO)
Mag (KEG)
1 Hz Coda Envelope
Coda sd=0.055
Mag (BGIO)
Mag (KEG)
Equivalent to a 16 station network using direct waves.

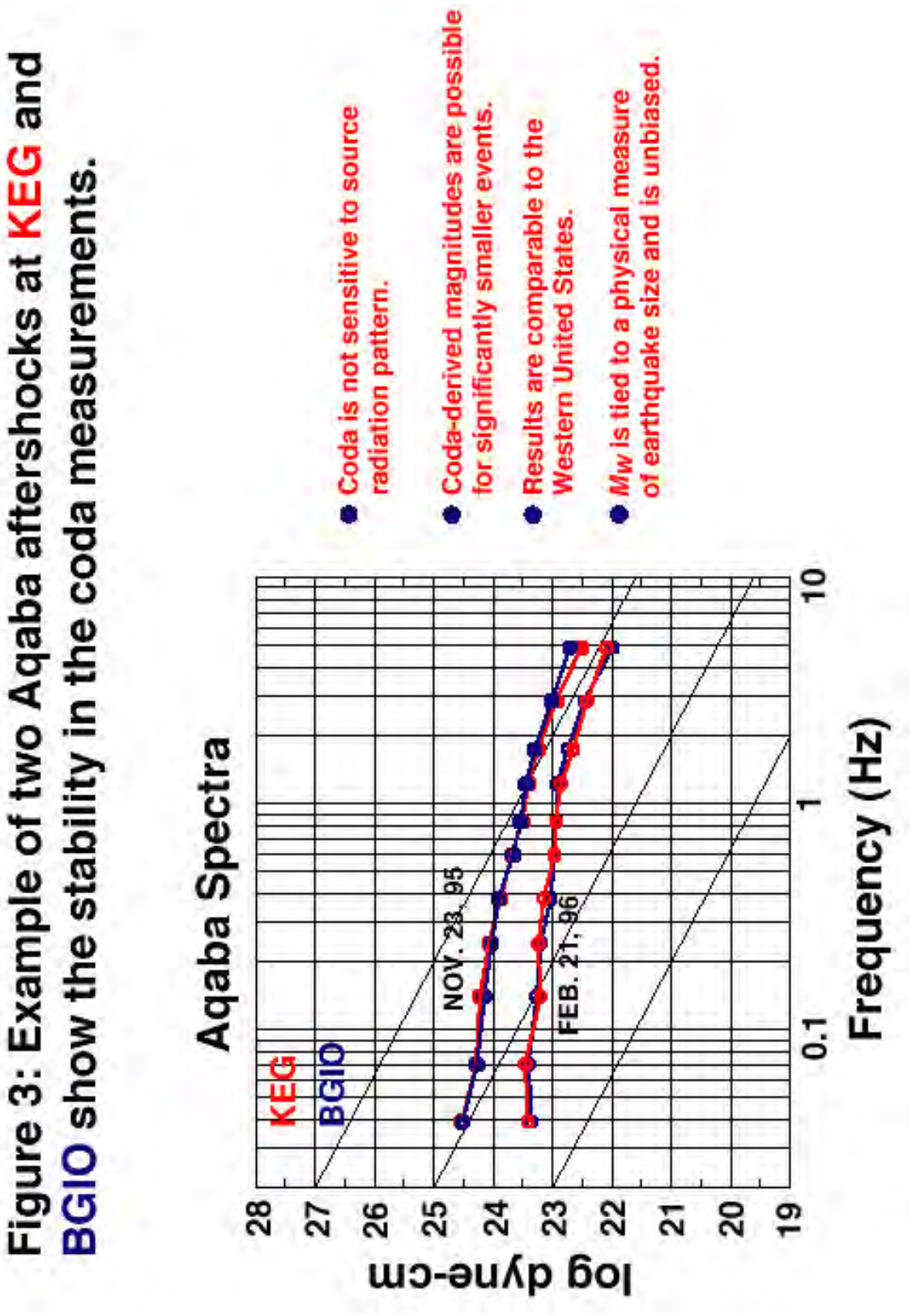


Figure 3: Example of two Aqaba aftershocks at KEG and BGIO show the stability in the coda measurements.

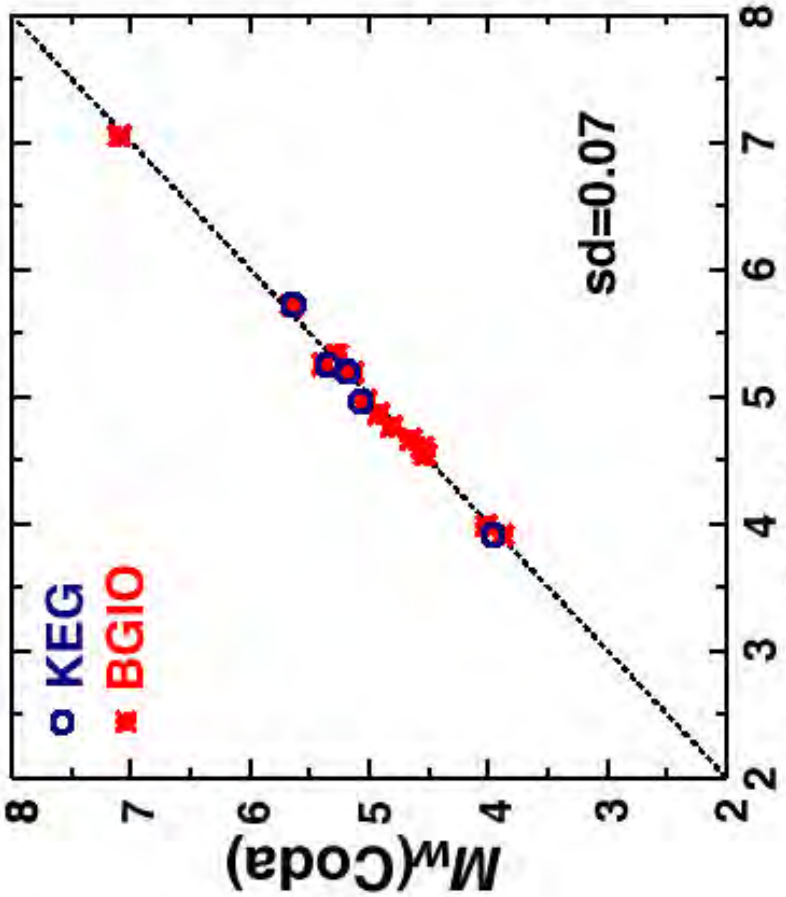


Figure 4: Single station coda moment magnitudes, M_W(coda), agree with 1-D waveform modeling results.

Note: 3-D path variation and source anisotropy do not affect the coda measurement.

APPLICATION OF SOVIET PNE DATA TO THE IMPROVEMENT OF SEISMIC MONITORING CAPABILITY

John R. Murphy, Jamil D. Sultanov*, Brian W. Barker, Ivan O. Kitov*, Margaret E. Marshall
Geophysics Group, Maxwell Technologies, Inc.
*Institute for Dynamics of the Geospheres, Russian Academy of Science

Sponsored by U. S. Department of Defense
Defense Threat Reduction Agency
Contract No. DSWA01-97-C-0126

ABSTRACT

In order to discriminate the regional seismic signals produced by underground nuclear explosions from those produced by earthquakes, rockbursts, and conventional mining explosions of comparable magnitude, it is necessary to know the ranges of signal variations that can be expected as a function of source type and propagation path conditions over the entire ranges of these conditions which may be encountered in global test monitoring of the Comprehensive Nuclear-Test-Ban Treaty. For this reason, Maxwell Technologies and the Russian Institute for Dynamics of the Geospheres (IDG) have been working on a joint research program to improve regional discrimination capability through analyses of seismic data recorded from Soviet Peaceful Nuclear Explosion (PNE) events. During the past year this effort has focused on the compilation of a seismic source summary for Soviet PNE tests and on discrimination analyses of regional seismic data recorded from Soviet PNE tests and nearby events reported in the Reviewed Event Bulletin (REB). A seismic source summary has now been completed which contains all currently available information regarding the source parameters for 122 Soviet PNE tests conducted during the 1965 to 1988 time period. The data presented include detonation times, locations, explosion yields and depths of burial, as well as summary information regarding the explosion configurations and source emplacement media. The discrimination analysis has focused on regional seismic data recorded at the Borovoye station from 28 Soviet PNE tests and 24 prototype International Data Centre REB events located at comparable distances from Borovoye. These selected events sample a magnitude range extending from 3.7 to 5.7 and a distance range extending from 5.2 to 19.1 degrees. The Borovoye data have now been processed for estimates of the RMS spectral amplitude levels in the group velocity windows corresponding to the P_n, P_g, S_n, and L_g phases. Associated spectral ratios L_g/P_n, S_n/P_n, L_g/P_g, S_n/P_g, have been computed and averaged over the 2- to 5-Hz frequency band for each event. In addition, L_g spectral ratio discriminant values based on the average spectral amplitude levels in the 0.50- to 1.25-Hz and 2.00- to 5.00-Hz passbands have been estimated for each event. Following normalization for observed effects of event magnitude and epicentral distance, the effectiveness of each of these five potential discriminants has been evaluated. It has been found that, though the traditional S/P type spectral ratio discriminants provide some average separation of source type for this sample of events, there is significant overlap of the values from the two populations for each of these four discriminants. Better separation of source type is provided by the L_g spectral ratio discriminant. However, for this sample of events, L_g shows larger low- to high-frequency spectral ratio values for earthquakes than for explosions, which is inconsistent with prior western U.S. experience. These results indicate that the various proposed regional discriminants will have to be carefully calibrated on a station-by-station basis.

Key Words: seismic, discrimination, regional, Soviet PNE, Borovoye

OBJECTIVES

Under this research program, scientists from Maxwell Technologies, Inc. and the Russian Institute for Dynamics of the Geospheres (IDG) are using seismic data recorded from Soviet Peaceful Nuclear Explosions (PNE) and nearby Central Asian earthquakes and chemical explosions to better define the limitations of existing operational capabilities with respect to the global seismic monitoring required by the Comprehensive Test Ban Treaty (CTBT). The objectives of this program are to expand our recently completed analysis of regional seismic data recorded from Soviet PNE events to incorporate seismic data from nearby earthquakes and large chemical explosions, and to use these data to directly test the utility of different regional discriminants over the widest possible ranges of source and propagation path conditions.

RESEARCH ACCOMPLISHMENTS

During the past year, work has focused on the finalization of a seismic source summary for Soviet PNE events and on a detailed discrimination analysis of broadband seismic data recorded at the Borovoye Observatory in Central Asia from samples of Soviet PNE and PIDC REB events located at regional distances from that station. With regard to the PNE source summary, a paper has now been published (Sultanov et al, 1999) listing the best currently available source parameters for 122 Soviet PNE experiments conducted between 1965 and 1988. The data presented include detonation times, locations, explosion yields and depths of burial, as well as summary information regarding the explosion configurations and source emplacement media. Exact origin times and locations are currently available for 69 of these 122 explosions. Exact locations and seismically determined origin times with estimated accuracy's of ±0.5 sec are available for an additional 8 explosions. Thus, the paper lists source parameters for some 77 widely dispersed Soviet PNE tests that are accurate enough for highly detailed seismological investigations. Hopefully, future studies encompassing analyses of satellite imagery and regional seismic data, perhaps supplemented by GPS determinations from visits to selected sites, will eventually provide accurate locations for all the other explosions in this unique data set.

The discrimination analysis of the Borovoye regional seismic data recorded from Soviet PNE tests and other source types has focused on comparisons with PIDC REB events located within 20 degrees of the Borovoye station. Data recorded at the IRIS station at Borovoye from a selected sample of such REB events were recovered from the IRIS database and previewed for signal quality, resulting in a sample of 28 REB events (including 2 Chinese Lop Nor underground nuclear explosions) with good signals at Borovoye for the time interval extending from 1/1/95 to 4/1/98. The map locations of these events are shown in Figure 1, together with the locations of previously analyzed Soviet PNE events. It can be seen that, although there is some overlap in location between the two sets of events, the majority of the Soviet PNE tests are located to the north of the Borovoye station, where few REB events have been detected. Therefore, even though the data to be analyzed were recorded at a common station, the regional propagation paths are generally not common for the different source types. This, of course, is representative of the general CTBT monitoring problem in that there will be many IMS stations for which there will be no regional recordings of previous underground nuclear explosions which can be used as a calibration reference.

Data recorded at Borovoye from these selected REB events have been processed through a series of narrowband filters to obtain estimates of the spectral composition of the signals in the group arrival windows associated with the P_n, P_g, S_n and L_g phases, using exactly the same procedures which were previously applied to the corresponding Borovoye PNE data (Murphy et al, 1997). The regional phase spectral ratios L_g/P_n, Lg/P_g, S_n/P_n, S_n/P_g were then computed from these narrowband filter amplitudes and averaged over the frequency band extending from 2-5 Hz, for which the signal-to-noise ratios are generally good for all these Borovoye data. In addition to these interphase spectral ratios, an Lg spectral ratio of the average amplitude level in the 0.50-1.25 Hz band to that in the 2.00-5.00 Hz band was also computed. Review of these various spectral ratio data revealed that they all showed some trends with epicentral distance (Δ) and magnitude (m_b). Consequently, for each ratio type, the PNE and REB spectral ratio values were separately analyzed in multivariate regression analyses in which the data for each phase ratio type *p* were fit to a functional relation of the form.

$$R_p = K_p \cdot 10^{n_p m_b} \cdot \Delta^{m_p}$$

The regression analysis results for the L_g/P_n spectral ratio data are shown in Figure 2 for the PNE and REB data sets. It can be seen that the variations with both distance and magnitude are quite similar for the two event groups in this case. This was found to be true for all the other phase spectral ratios as well and, consequently, the statistically derived n_p and m_p scaling exponents for the PNE and REB samples were averaged for each spectral ratio type and these average exponents were used to scale all the observed spectral ratio values to the sample mean distance and magnitude levels (i.e. $\Delta = 12.5°$, $m_b = 4.6$). Note that since the PNE and REB data are normalized in exactly the same way for each phase ratio type, no average bias between event groups is introduced by this scaling procedure.

The resulting normalized discriminant values for the L_g/P_n and L_g/P_g spectral ratios are shown in Figure 3, where it can be seen that, while there is some average separation between the underground nuclear and other source types, there is also considerable intermixing of the spectral ratio values for the different source types. In particular, as has been noted previously, although the L_g/P_n discriminant generally provides the best separation of source types along common propagation paths, the P_n amplitudes show much greater variability as a function of propagation path differences than do the corresponding P_g amplitudes and, consequently, the L_g/P_n spectral ratios show considerably more scatter than do the L_g/P_g spectral ratios. Note also from Figure 3 that, while the Lop Nor explosions are very consistent with the Soviet PNE population with respect to their L_g/P_n ratio values, the corresponding Lop Nor L_g/P_g ratio values fall closer to the mean of the REB population. This suggests that a multvariate discriminant will provide better resolving power than any single spectral ratio discriminant.

Results of some preliminary analyses of the Borovoye PNE data indicate that the intermingling of the 2-5 Hz band L_g/P_n spectral ratio discriminant values shown in Figure 3 persists at higher frequencies as well. Thus, for example, Figure 4 shows a comparison of the 6-8 Hz band P_n/L_g ratio values estimated for that subset of the Borovoye PNE data having usable signal-to-noise ratios in that band with comparable ratios computed for a large sample of REB events and explosions at other test sites using the prototype PIDC P_n/L_g discriminant (personal communication, Mark Fisk, 1999). It can be seen from this figure that a number of the Borovoye PNE values fall within the population of REB values and that, in fact, they contribute several of the lowest explosion values observed with respect to the corresponding REB mean values at those distances. It appears most likely that these anomalously low explosion values are due primarily to propagation path effects, although it is possible that the unusual source environments of the PNE tests may be contributing to some extent. That is, as was noted previously, these PNE tests were predominately low-yield, overburied explosions in hardrock, quite unlike the typical nuclear weapons tests represented by the other explosion values on Figure 4. In any case, these results indicate that the L_g/P_n spectral ratio discriminant will have to be carefully calibrated for applications at previously untested sites.

Somewhat surprisingly, it was found that the best separation of Borovoye PNE and REB events was provided by the L_g spectral ratio discriminant. This robustness is documented in Figure 5 where it can be seen that the mean values of this discriminant for the two event groups are separated by nearly a full order of magnitude, with very little intermingling of the two populations. Unfortunately, the sense of the observed difference is opposite to that found by Murphy and Bennett (1982) for NTS explosions, which indicates that the performance of this discriminant can be expected to vary significantly as a function of source and propagation path conditions. It follows that, in the absence of a quantitative theoretical model which can be used to predict this variability, it will be necessary to empirically calibrate any such L_g spectral ratio discriminant on a station by station and region by region basis. However, it may well be worth such an effort in regions where the separation of source types is as powerful as that shown in Figure 5.

CONCLUSIONS AND RECOMMENDATIONS

A seismic source summary for Soviet PNE events has now been published (Sultanov et al, 1999) which lists the best currently available source parameters for 122 Soviet PNE experiments conducted between 1965 and 1988. These data represent a unique resource for seismic calibration studies of the vast territories of the former Soviet Union. The discrimination analysis of regional seismic data recorded at the Borovoye station in Central Asia from Soviet PNE events and PIDC REB events located within 20° of that station has revealed important new information regarding the variability of regional phase spectral ratio discriminants. In particular, it has been shown that some of the Soviet PNE tests can't be reliably identified as nuclear explosions using the nominal L_g/P_n spectral ratio disciminant, at least with the currently available calibration information. An alternate L_g spectral ratio discriminant was found to work

well to separate the different source types at Borovoye, but a quantitative theoretical understanding of this discriminant is currently lacking, and more research will be required to determine whether it can be calibrated well enough to be generally applicable at the wide variety of IMS stations.

REFERENCES

Murphy, J. R. and T. J. Bennett (1982), "A Discrimination Analysis of Short-Period Regional Seismic Data Recorded at Tonto Forest Observatory," *Bull. Seism. Soc. Am.*, *72*, pp. 1351-1366.

Murphy, J. R., D. D. Sultanov, B. W. Barker, I. O. Kitov and M. E. Marshall (1997), "Further Analyses of Regional Seismic Data Recorded From the Soviet PNE Program: Implications With Respect to CTBT Monitoring," PL-TR-97-2141.

Sultanov, D. D., J. R. Murphy and Kh. D. Rubinstein (1999), "A Seismic Source Summary For Soviet Peaceful Nuclear Explosions," *Bull. Seism. Soc. Am., 89*, pp. 640-647.

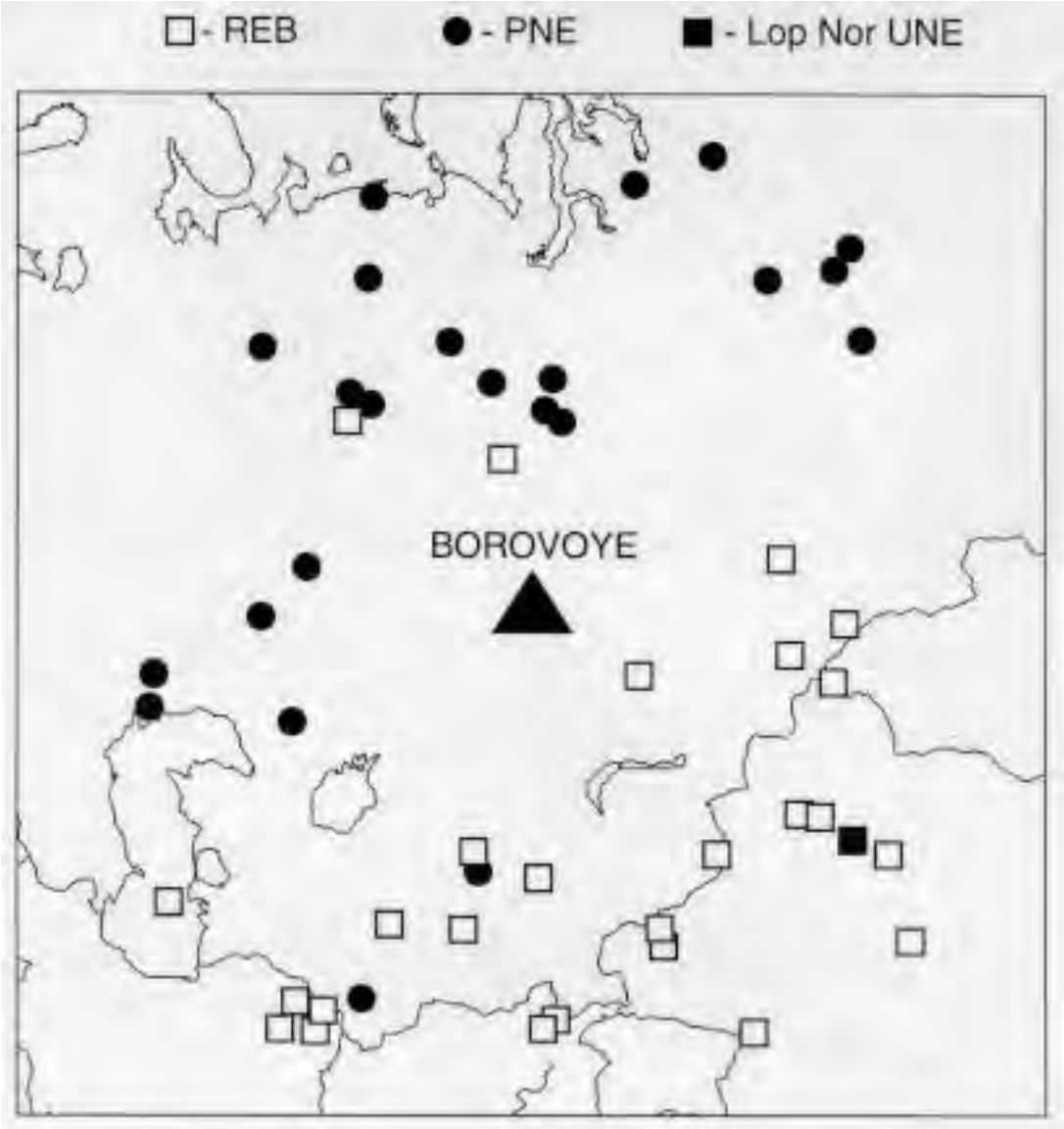


Figure 1. Map locations of Soviet PNE tests and selected REB events located within 20° of the Borovoye station in Kazakhstan.

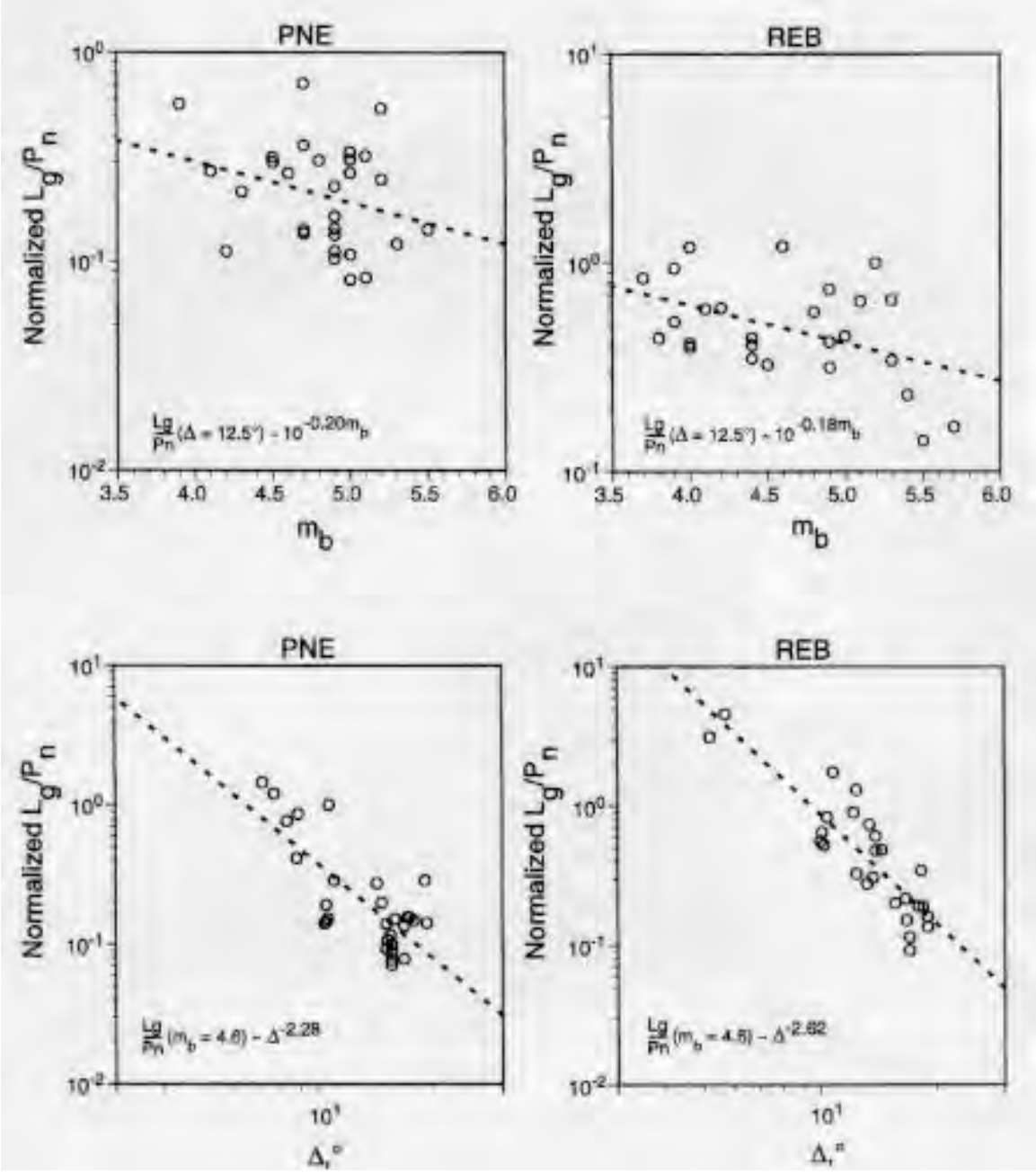


Figure 2. Comparison of estimated magnitude dependence (top) and distance dependence (bottom) for the Borovoye PNE and REB Lg/Pn spectral ration data.

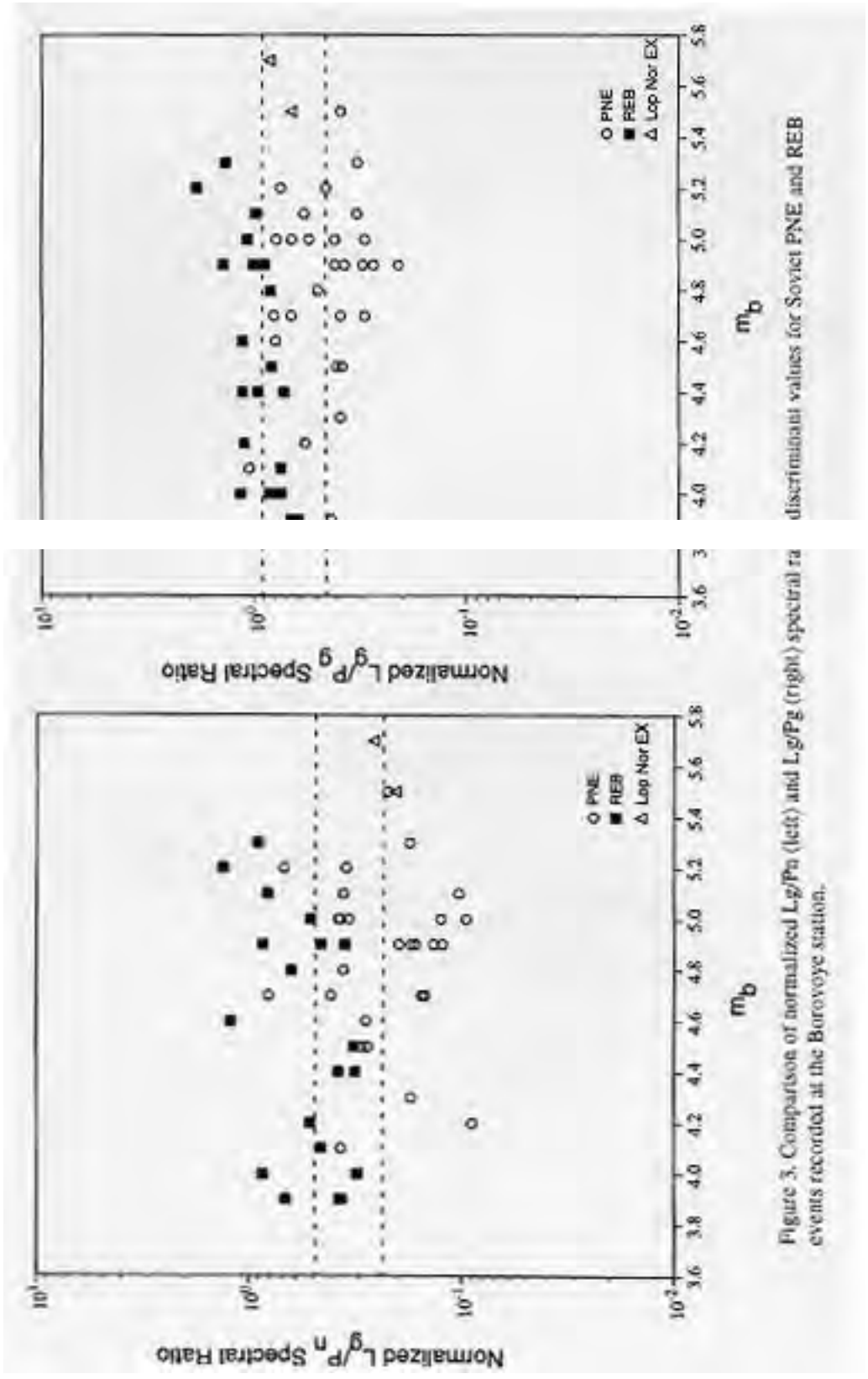


Figure 3. Comparison of normalized Lg/Pn (left) and Lg/Pg (right) spectral ra
events recorded at the Borovoye station.

discriminant values for Soviet PNE and REB

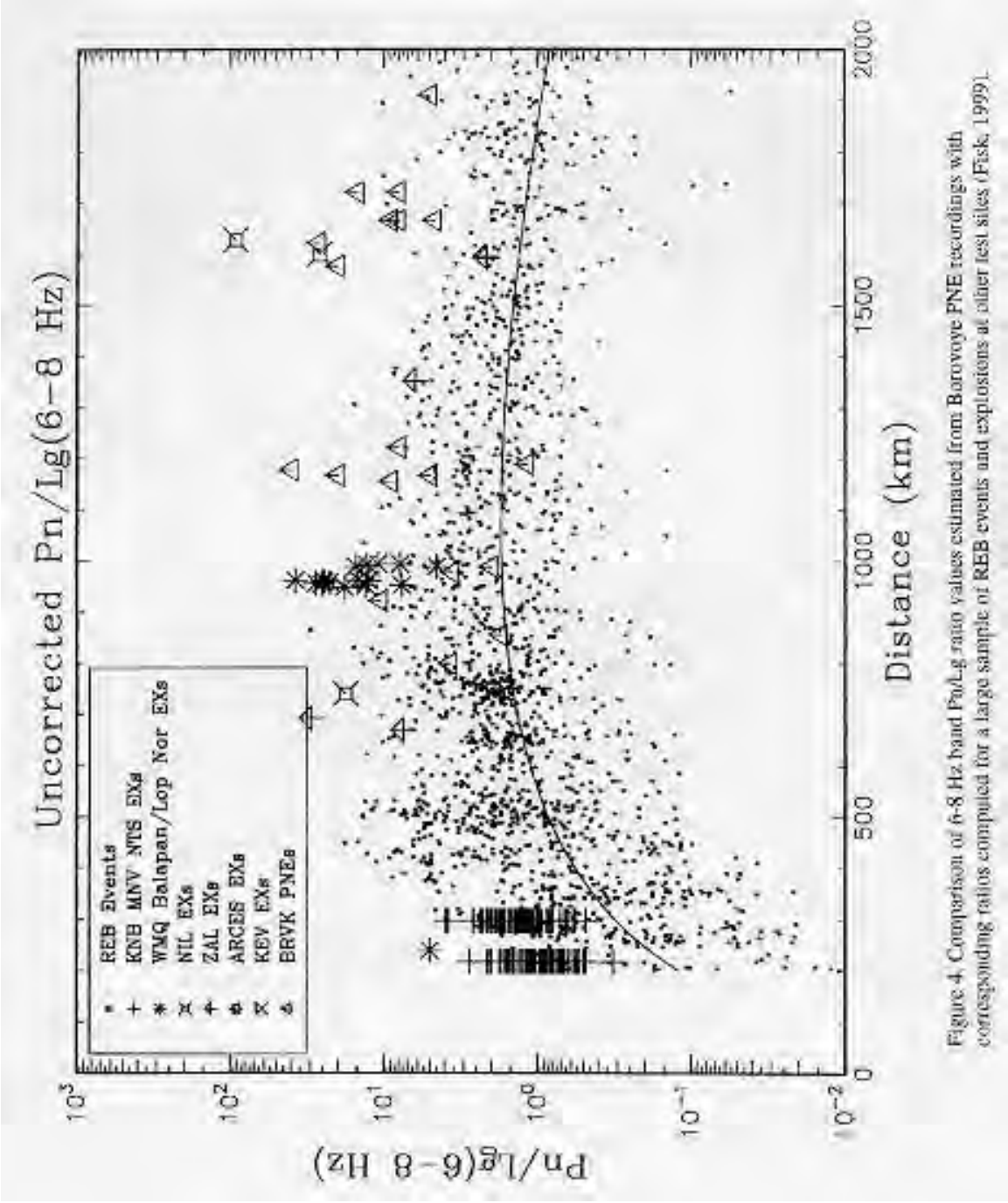


Figure 4. Comparison of 6-8 Hz band Pn/Lg ratio values estimated from Borovoye PNE recordings with corresponding ratios computed for a large sample of REB events and explosions at other test sites (Fisk, 1999).

DEVELOPMENT OF IMPROVED MAGNITUDE MEASURES FOR THE INTERNATIONAL DATA CENTRE

John R. Murphy, Jeffry L. Stevens, Theron J. Bennett, Brian W. Barker, Ronald W. Cook
Geophysics Group, Maxwell Technologies, Inc.

Sponsored by U. S. Department of Defense
Defense Threat Reduction Agency
Contract No. DASG 60-96-C-0039

ABSTRACT

Many of the most important issues in nuclear test monitoring at the International Data Centre (IDC), such as event screening, depend critically on the details of the definitions of the various magnitude measures to be employed by the IDC and their relations to the classical National Earthquake Information Center, International Seismological Centre, and Air Force Technical Applications Center magnitude measures, which have historically been used to assess seismic verification capability. Therefore, it is important that these IDC magnitude measures be well understood and carefully calibrated. During the past year, we have been continuing to refine the IDC m_b and M_S magnitude measures, as well as the associated M_S/m_b event screening criterion. A database of approximately 220,000 single station m_b observations recorded from some 25,000 earthquakes reported in the prototype IDC (pIDC) Reviewed Event Bulletin (REB) have now been statistically analyzed to obtain revised corrections for epicentral distance, focal depth, global station corrections for a prototype International Monitoring System network consisting of 89 currently operational stations and distance weighting factors for use in the estimation of a new, generalized m_b magnitude measure which incorporates both teleseismic and regional P wave data. The results of this statistical analysis indicate that the Veith/Clawson corrections for epicentral distance and focal depth employed at the pIDC are remarkably accurate in the teleseismic distance range, where they are clearly superior to the corresponding Gutenberg/Richter corrections, at least for events with focal depths of less than about 400 km. Furthermore, it has been found that application of the associated m_b global station correction factors leads to an average reduction of more than 40% in the variance of the network-averaged m_b values, which indicates that these derived corrections have a high degree of statistical significance. The application of these station correction factors also produces an average increase in the network-averaged m_b values of nearly 0.2 magnitude units, due to the fact that the REB m_b determinations are dominated by data from primary and array stations, which generally have positive station correction factors with respect to the prototype network average. It follows that the recommended M_S/m_b event screening criterion for use with the station-corrected, generalized m_b measure, m_b, is

$$M_S(\mathrm{IDC}) = 1.25\, m_b(\mathrm{IDC}) - 2.45$$

Key Words:: Seismic, Magnitude, IDC, Event Screening

OBJECTIVE

The IDC has the responsibility to characterize and measure seismic sources detected by the global network of stations of the IMS used to monitor the CTBT. Characterization of the size of detected events is important to many aspects of CTBT monitoring, including determination of detection thresholds, event screening (e.g. M_S-versus-m_b), and yield estimation for explosion sources. Furthermore, because of the large volume of events recorded by the IMS, IDC monitoring should be facilitated and made more consistent by automating magnitude measurement procedures. Therefore, the objective of this research program has been to expand and improve the magnitude measurement procedures used to characterize seismic sources at the IDC. We have been seeking to ensure that the magnitudes reported by the IDC are consistent with the definitions of seismic magnitudes and with previous magnitude measures and that they are free of regional biases and biases associated with measurement procedures. We have also been attempting to evaluate new magnitude measures which can help extract as much information as possible about the seismic sources in an automated processing environment. To accomplish these objectives, our efforts have been directed at improving the standard m_b, M_S, and regional magnitude measures currently employed at the IDC and at implementing and testing alternative source characterization procedures including moment tensor inversion, spectral magnitude estimation, and a generalized magnitude, combining teleseismic and regional P-wave amplitude measurements.

RESEARCH ACCOMPLISHED

During this past year, the effort on this project has focused primarily on revisions to the m_b estimation procedures, with particular emphasis on the development of improved corrections for epicentral distance and focal depth and the derivation of preliminary global m_b station correction factors for a subset of 89 currently operational pIDC stations which are scheduled to be included in the final IMS network. The data used in this study consisted of approximately 220,000 single station m_b observations from some 25,000 selected events reported in the pIDC REB. The distribution of these selected events with respect to m_b is shown in Figure 1, where it can be seen that it is approximately normal, with a mean value of about m_b = 3.8, with the overwhelming majority of the events falling in the range $3 < m_b < 5$.

The statistical model which has been used to analyze these magnitude data is a General Linear Model (GLM) in which the single station magnitude values $m_b(i,j,k)$, are represented as a general linear combination of the form (cf. Murphy and McLaughlin, 1998):

$$m_b(i,j,k) = m(i) + sta(j) + db(k) + e(i,j,k) \qquad (1)$$

where

m(i)	=	event magnitude
sta(j)	=	station correction
db(k)	=	correction to the specified dependence on epicentral distance (either Veith/Clawson or Gutenberg/Richter)
e(i,j,k)	=	error term

The system of equations (1) is solved using the Expectation Maximization Algorithm to minimize the residual error, subject to the constraints:

$$\sum_j sta(j) = 0$$

$$\sum_k db(k) = 0 \qquad \text{for } 23^\circ < D < 92^\circ \qquad (2)$$

The constraints (2) are employed to retain the average absolute levels of the event magnitudes for comparison purposes. That is, since the absolute levels of the single station magnitudes are set by arbitrary convention, any constant value could be added to all the single station magnitudes without affecting the

error term in (1) in any way and, therefore, it is necessary to constrain the absolute levels of the correction terms for comparison purposes.

As an initial step in evaluating the m_b distance corrections, GLM analyses were conducted using single station magnitudes for the subset of shallow focus (h < 50 km) events obtained using both the Veith/Clawson (V/C) and Gutenberg/Richter(G/R) corrections for epicentral distance. The resulting perturbations to these two standard sets of distance corrections (i.e. db(k) in equation (1)) obtained from the GLM analyses are compared in Figure 2 over the teleseismic distance range extending from 23 to 92 degrees over which the corrections are constrained to average to zero in both cases. It can be seen from this figure that the corrections to the V/C factors are remarkably small over this range (i.e., generally less than ±0.05) and, more specifically, that they are significantly smaller than the corresponding correction to the G/R factors determined using the same data set. We conclude from these results that the V/C corrections for epicentral distance employed at the pIDC are remarkably accurate on average, and superior to the corresponding G/R corrections employed by the U.S.G.S. and ISC for the estimation of m_b, at least in this teleseismic distance range for shallow focus events.

The V/C corrections are found to be less satisfactory at distances less than and greater than those shown in Figure 2. This fact is illustrated in Figure 3 where the derived corrections to the V/C factors are displayed over the entire distance range extending from 2 to 100 degrees. It can be seen that these corrections are greater than 0.2 magnitude units near the 20 degree upper mantle triplication range and are as large as –0.5 magnitude units at the closest distances. Based on the results of Figures 2 and 3, we recommend retaining the V/C corrections for the epicentral distance range 23 to 92 degrees and have smoothed the corrections of Figure 3 for smaller and larger distances using a three point smoothing operator to obtain the final proposed corrections to the V/C factors for shallow focus events shown in Figure 4.

At the present time, a non-traditional regional magnitude measure based on initial P wave amplitudes in the 2-4 Hz passband observed at distances less than 20 degrees is being estimated at the pIDC and published in the REB as a local magnitude, M_L. However, the observed high degree of variability of the M_L magnitude measure with respect to the corresponding REB m_b values, together with its inconsistency with some of the more conventional regional magnitude measures published by the various countries participating in GSETT-3, has produced considerable confusion. This led Bennett et al. (1998) to investigate the feasibility of defining a new, generalized m_b measure that incorporates both regional and teleseismic observations. This is an attractive alternative for the IDC because, since an event must be detected by at least three primary station to be reported in the REB, most events incorporate at least some teleseismic data; and, in fact, m_b values were reported for more than 95% of the REB events during 1997.

In order to specify an optimum algorithm for combining teleseismic and regional observations to obtain a generalized m_b value, it is necessary to first examine the uncertainties in the derived epicentral distance correction factors as a function of distance. For example, the standard errors of estimate associated with the GLM shallow focus event distance correction estimates of Figure 3 are displayed as a function of epicentral distance as a dashed line in Figure 5. It can be seen that this measure of uncertainty is essentially constant, with an average value of about 0.28 in the teleseismic range extending from 23 to 92 degrees, and that it increases at shorter and larger distances. Therefore, we have constrained the standard error of estimate to the average constant value of 0.28 in the range 23 to 92 degrees and have smoothed the GLM results at shorter and longer distances to obtain the final epicentral distance dependence of the uncertainty represented by the solid line in this figure. Based on these results, a generalized network-averaged magnitude measure, m_b, has been defined as an inverse variance weighted average of the single station magnitude estimates. Note that for events recorded exclusively at teleseismic distances, where the weights are constant, the definition of the network-averaged magnitude value is unchanged from current practice, and the results will be identical to the existing REB m_b values. As is illustrated in Figure 6, it has been found that this generalized mb measure correlates better with the corresponding REB values than does the current pIDC M_L measure, even for events for which the number of regional observations equals or exceeds the number of teleseismic observations. On the basis of these results, we conclude that this generalized m_b magnitude measure can provide useful magnitude estimates for events which are not well-recorded by the available network of teleseismic stations, at least until such time as a more robust regional magnitude measure is defined and implemented at the pIDC.

Since the station correction factors are designed to be used in the estimation of generalized m_b values, a GLM analysis of the shallow focus event data was carried out with the distance corrections constrained to the revised Veith/Clawson factors obtained from the final, smoothed corrections of Figure 4. The resulting m_b station correction factors were found to range from approximately –0.7 to +0.5. Application of these correction factors to the observed single-station m_b values produces a significant reduction of more than 40% in the variance about the resulting network-averaged m_b values. Thus, it can be concluded that the derived corrections have a high degree of statistical significance.

Somewhat surprisingly, application of these station correction factors also produces a significant change in the absolute levels of the estimated m_b values. This fact is illustrated in Figure 7 which shows a histogram of the differences in m_b values computed with and without station corrections. It can be seen that the application of the station correction factors increases the resulting network-averaged m_b values by more than 0.18 magnitude units, on average. This offset seems puzzling at first glance, since by equation (2) the station corrections are determined under the constraint that they must sum to zero. That is, events recorded by all or most of the 89 station would be expected to have station-corrected m_b values which are the same on average as the corresponding uncorrected values. In fact, however, not all stations are equally represented in the REB. That is, for reasons of economy, data are not routinely recovered from secondary stations and the m_b determinations are dominated by data from the primary and array stations. The significance of this sampling bias with respect to the resulting network-averaged m_b values is indicated in Figure 8, which shows the station correction factors color-coded to distinguish between primary and secondary stations. Note that the station corrections for the primary stations are predominantly positive, averaging to a value of about +0.15, while those for the secondary stations are predominantly negative, with an average value of about –0.11. It follows that, since data from the primary stations dominate the REB m_b determinations, the application of the derived station correction factors generally increases the network-averaged m_b values, leading to the systematic offsets observed in Figure 7.

CONCLUSIONS AND RECOMMENDATIONS

A careful statistical analysis of a large sample of approximately 220,000 pIDC single-station m_b observations has been conducted in an attempt to formulate improved procedures for estimating network-averaged m_b values at the IDC. This analysis has led to the derivation of revised corrections for epicentral distance and focal depth, global m_b station corrections for a prototype IMS network consisting of 89 currently operational stations and distance weighting factors for use in the estimation of a new, generalized m_b magnitude measure which incorporates both teleseismic and regional P wave data. A notable result of this investigation has been the finding that the application of the derived global m_b station correction factors produces an average increase in the network-averaged m_b values of nearly 0.2 magnitude units with respect to the original REB values. This results from the fact that the REB m_b determinations are dominated by data from primary and array station which generally have positive station correction factors with respect to the prototype network average.

REFERENCES

Bennett, T. J., J. R. Murphy, R. W. Cook and B. W. Barker (1998), "Development of a Generalized m_b Magnitude Measure Incorporating Regional and Teleseismic P Wave Amplitude Observations from the IDC," Technical Memorandum to NTPO, May.

Murphy, J. R., and B. W. Barker (1996), "An Evaluation of the IDC/NEIS m_b Anomaly," Technical Memorandum to NTPO, September.

Murphy, J. R., B. W. Barker and M. E. Marshall (1997), "Event Screening at the IDC Using the M_S/m_b Discriminant," Technical Memorandum to NTPO, October.

Murphy, J. R. and K. L. McLaughlin (1998), "Comment on 'Empirical Determination of Depth-Distance Corrections for m_b and M_W from Global Seismograph Network Stations' by Guust Nolet, Steve Krueger and Robert M. Clouser," Geophys. Res. Lett., 25, 4269.

Veith, K. F., and G. E. Clawson (1972), "Magnitude From Short-Period P-Wave Data," Bull. Seism. Soc. Am., 62, 435-452.

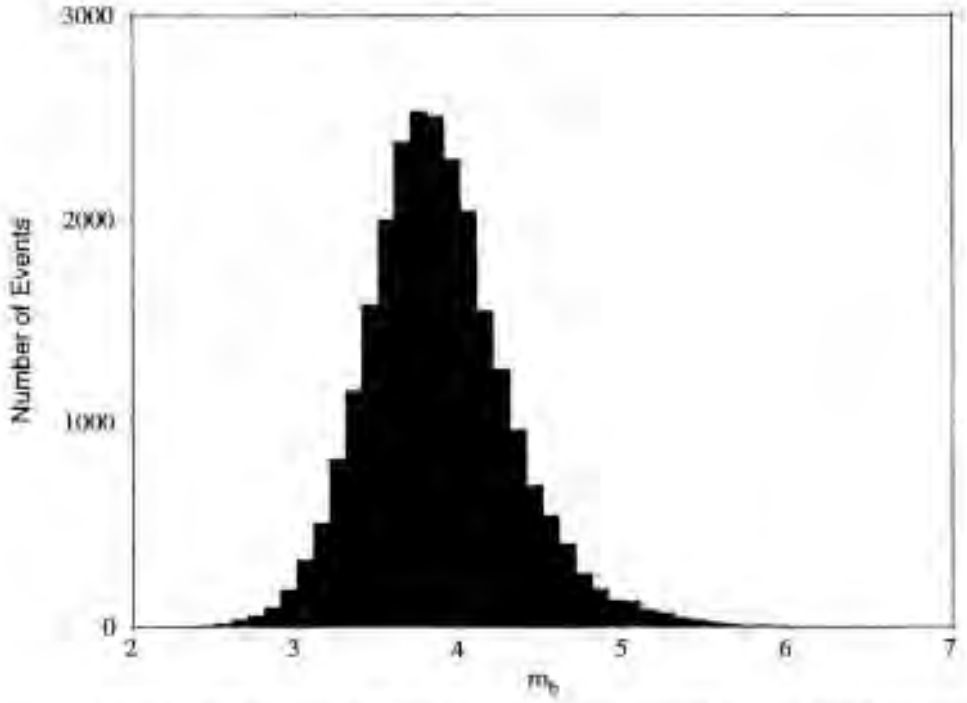


Figure 1. Distribution of the selected sample of events with respect to REB mb value.

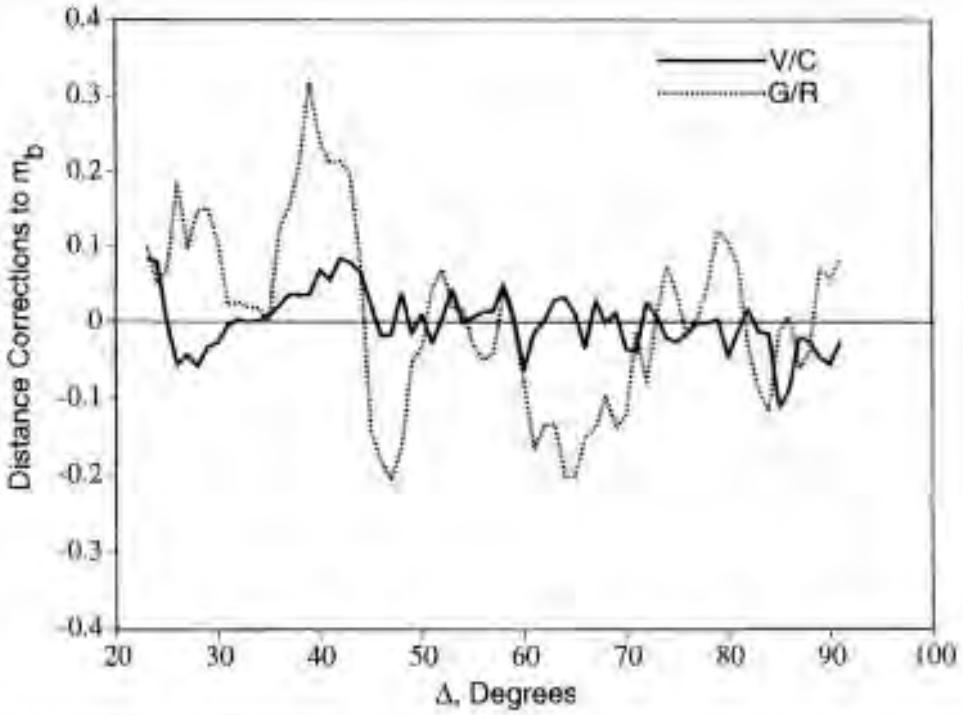


Figure 2. Comparison of corrections to V/C and G/R epicentral distance factors derived from GLM analyses of the same large sample of REB data recorded from shallow focus (h < 50 km) events, 23° < Δ < 92°.

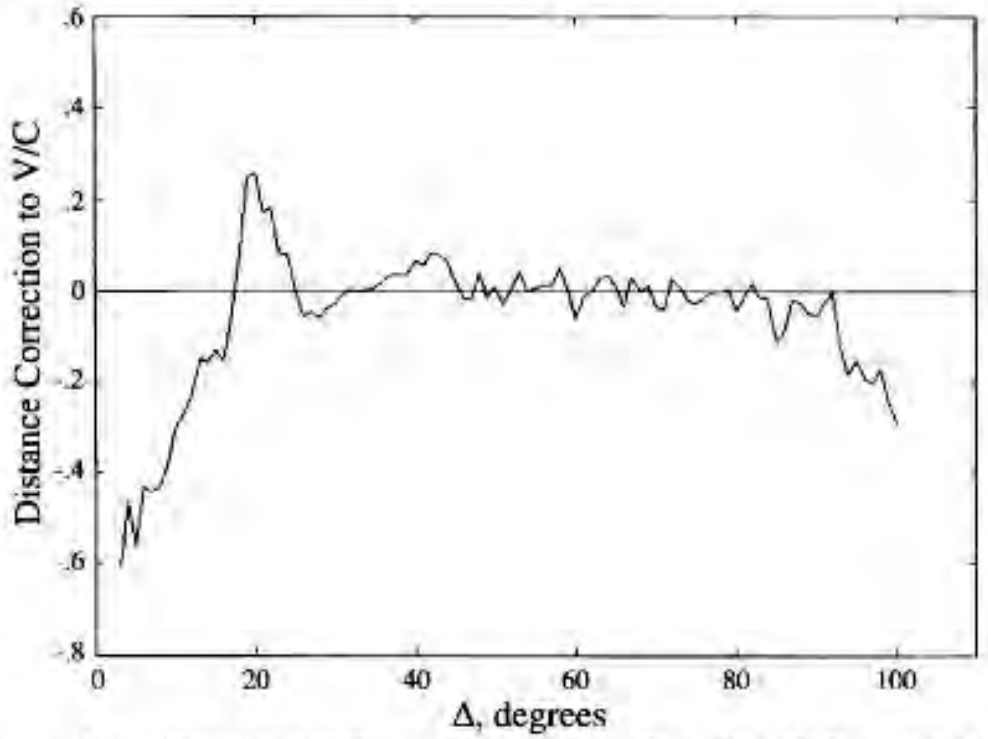


Figure 3. Corrections to V/C epicentral distance factors derived from a GLM analysis of a large sample of REB data recorded from shallow focus (h < 50 km) events, $2^{\circ} < \Delta < 100^{\circ}$.

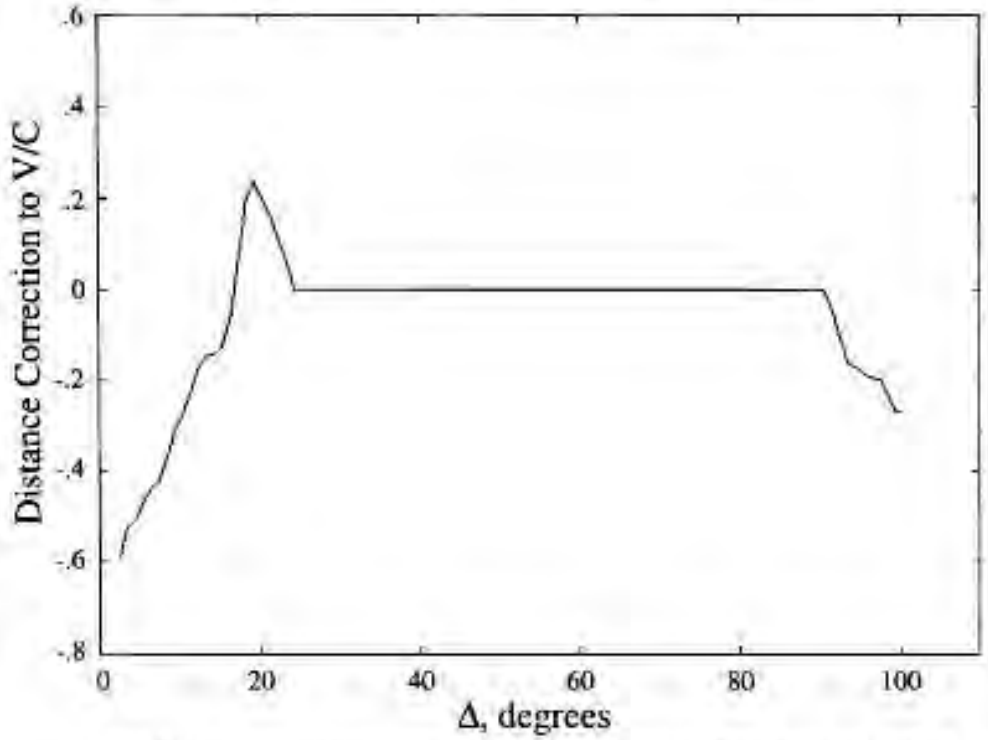


Figure 4. Final smoothed corrections to the V/C epicentral distance factors for shallow focus (h < 50 km) events, $2^{\circ} < \Delta < 100^{\circ}$.

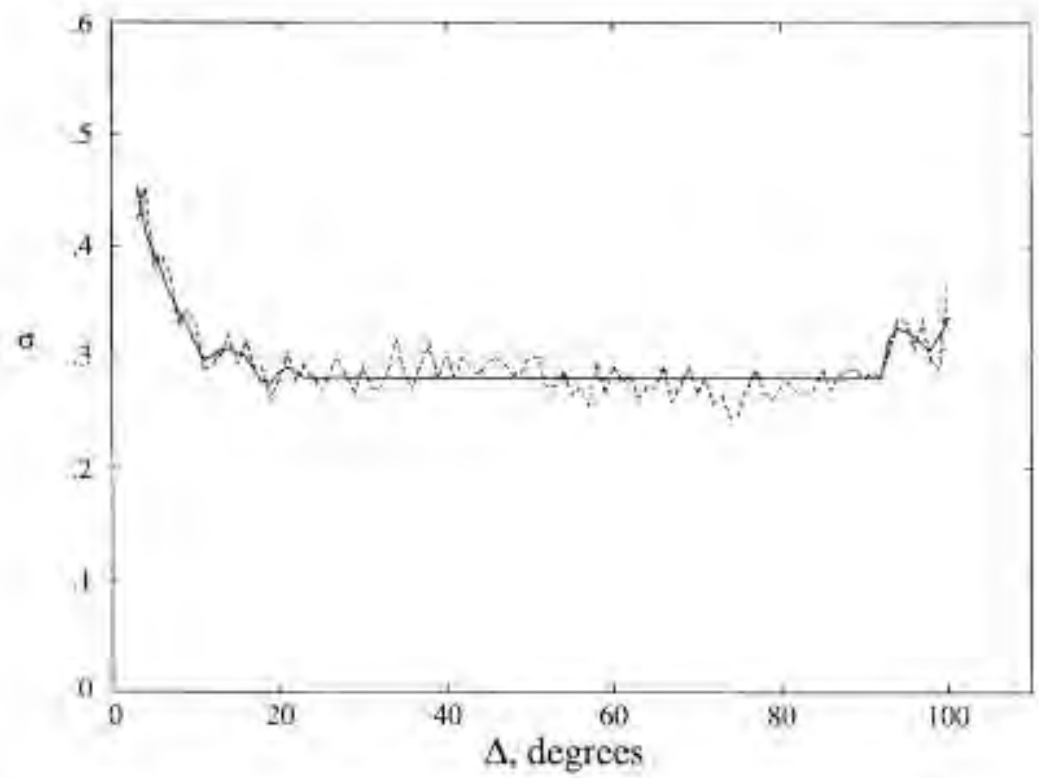


Figure 5. Standard errors of estimate (σ) as a function of epicentral distance for shallow focus events. The dashed line denotes the original GLM results, while the solid line denotes the final smoothed version adopted for generalized magnitude estimation purposes.

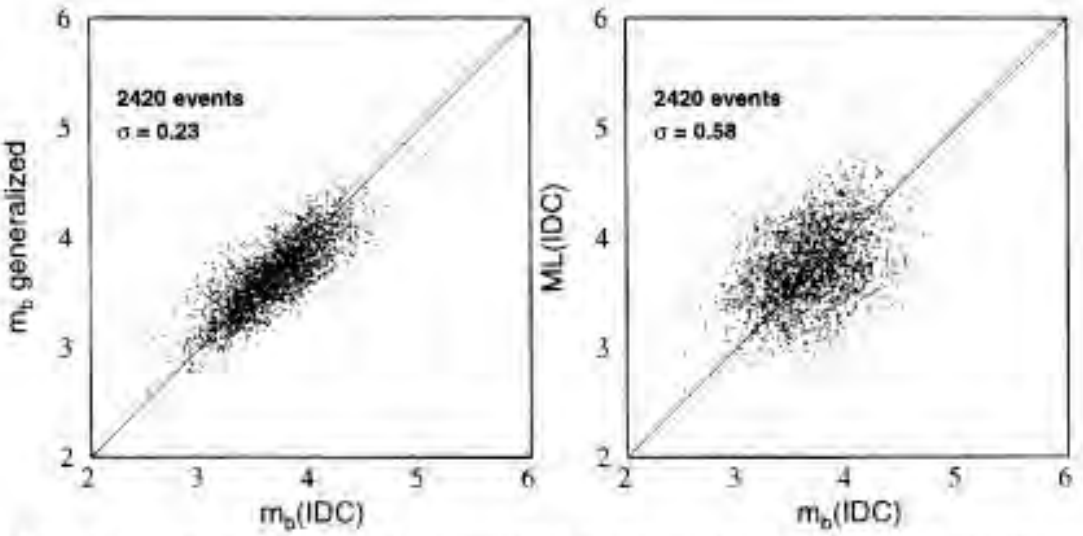


Figure 6. Comparison of generalized mb versus REB mb (left) with REB M_L versus REB mb (right) for a set of common events for which the number of regional observations equals or exceeds the number of telesesmic observations.

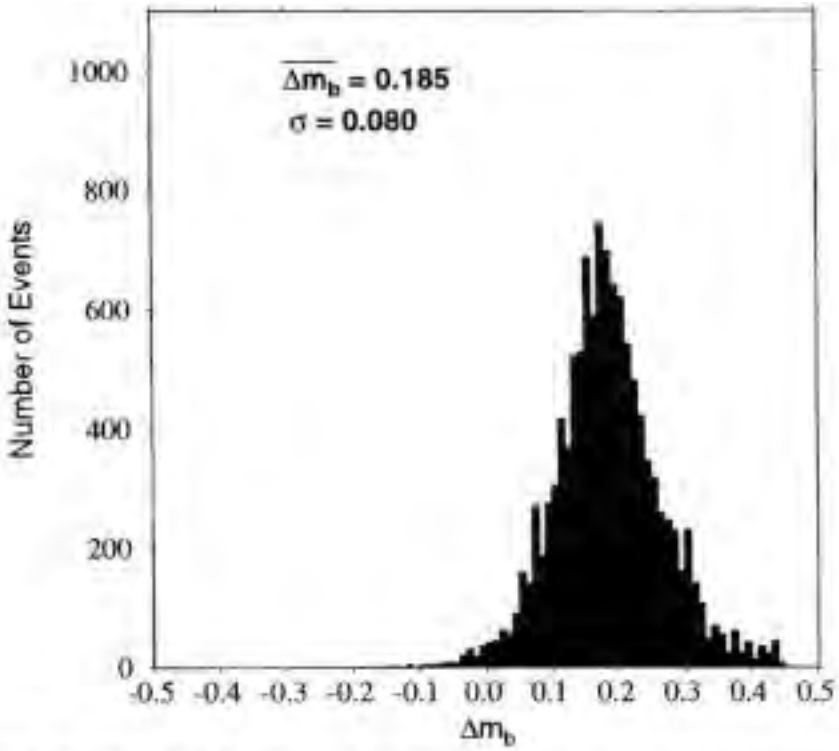


Figure 7. Distribution of differences in individual event network-averaged teleseismic mb values computed with and without station corrections, h < 50 km.

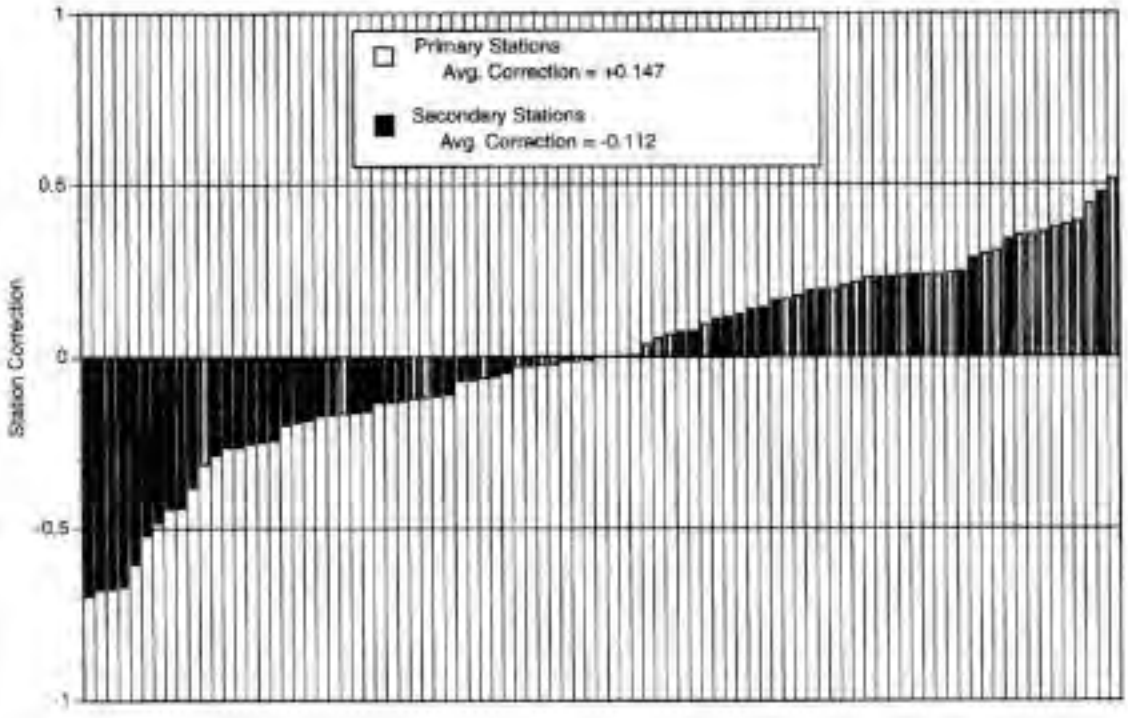


Figure 8. Estimated mb station correction factors for the 89 stations of the prototype IMS network color-coded to distinguish between primary and secondary stations.

IMPROVED FOCAL DEPTH DETERMINATION FOR USE IN CTBT MONITORING

John R. Murphy and Ronald W. Cook, Geophysics Group, Maxwell Technologies, Inc.
William L. Rodi, Earth Resources Laboratory, Massachusetts Institute of Technology

Sponsored by U. S. Department of Defense
Defense Threat Reduction Agency
Contract No. DSWA01-97-C-0127

ABSTRACT

Seismic event location remains as one of the most important discriminants for separating natural tectonic and explosive events. However, in order to be useful for discrimination purposes, the uncertainties associated with seismic locations must be well defined and reliable, and this has proven to be difficult to accomplish to the required degree of accuracy. In particular, high-confidence estimation of focal depths remains as an outstanding monitoring problem. During the past year, we have continued to pursue a research program which is directed toward the development of improved detection and identification procedures for the depth phases pP and sP, as well as with the formulation of a new algorithm for computing more reliable confidence intervals on focal depth estimates determined from P-wave first arrival times. With regard to depth phase identification, we have been investigating the potential utility of a fully automated network stacking procedure based on an algorithm originally proposed by Israelsson (1994). In this approach, post-P detection times in the prototype International Data Centre (pIDC) automatic detection file for each station for a given event are mapped into functions of depth using the pP-P and sP-P delay times predicted by the IASPEI travel-time tables for the various station distances. These functions of depth for the selected event are then added together for all the stations in the detecting network to identify arrivals consistent with the predicted depth phase move-outs over the entire range of potential source depths. The results of preliminary tests of this algorithm on a sample of about 30 Hindu Kush earthquakes with m_b > 4.0, and depths in the 200- to 250-km range have been encouraging, in that most of the network detection stacks show candidate depth phase peaks near the corresponding published Reviewed Event Bulletin depth values for these events. In addition, a new algorithm for computing formal confidence intervals associated with seismic focal depth estimates has been formulated and implemented. This new algorithm is general in that it does not require the conventional linearity assumptions and allows for both random and systematic errors in the arrival time data that may be characterized by different distribution functions. In such cases, there is no simple analytic solution for the confidence regions, and it is necessary to define them numerically. In the present case, Monte Carlo simulations are being used to map out the values of an appropriate likelihood ratio on a grid surrounding the maximum likelihood hypocenter solution, and these likelihood ratio values are then used to define precise confidence regions corresponding to the generalized model assumptions. This model is also being evaluated using data from Hindu Kush earthquakes for which the focal depths are well constrained by verified depth phase observations.

Key Words: seismic, focal depth, discrimination, prototype International Data Centre, Hindu Kush

OBJECTIVES

The objectives of this research program are to determine more reliable estimates of the uncertainties associated with the different focal depth estimation procedures and to increase the number of events which can be identified as earthquakes on the basis of focal depth through the implementation of new and improved analysis tools. This is being accomplished through the development of improved procedures for identifying and using the teleseismic depth phases pP and sP, the incorporation of regional S-P based origin time constraints into an improved depth estimation algorithm and the development of more robust statistical hypothesis tests for use in event screening.

RESEARCH ACCOMPLISHMENTS

High confidence estimation of focal depths remains as an outstanding seismic monitoring problem. If accurate focal depths could be determined for the majority of earthquakes deeper than 5, or even 10km, the event screening problem would be much easier. However, despite intensive efforts by relatively well-trained and experienced analysts, more than two-thirds of the PIDC Reviewed Event Bulletin (REB) events are currently being assigned artificially constrained depths of zero. Moreover, the cited accuracies of even the few freely determined focal depths are questionable, particularly in the light of the ground truth evidence which indicates that the corresponding epicentral uncertainties are generally underestimated by the hypocentral location algorithm employed at the PIDC. These results indicate that all of the sources of error have not been properly accounted for in the existing statistical location models and, consequently, the prototype PIDC focal depth event screening criterion currently incorporates a crude, empirically derived correction to the formal focal depth uncertainty estimates which significantly limits its applicability.

During the past year, work on this project has focused on the development of improved tools for detection and identification of the depth phases pP and sP and on the continuation of the evaluation of a new algorithm for computing more reliable confidence intervals on focal depth estimates determined from P wave first arrival times alone. With regard to depth phase identification, we have been analyzing IMS data recorded from a sample of Hindu Kush events with REB focal depths in the 200 to 250 km range. The map locations of these REB events are shown in Figure 1 where it can be seen that they occur in a very compact band, which is controlled by the regional tectonic forces acting at this continental collision zone. Surprisingly, depth phase observations from these events are relatively rare, even for the larger, well-recorded events. Thus, for example, depth phase observations are reported in the REB for only about 35% of the subset of these events for which arrival time data are reported from 12 or more IMS stations. One of the principal reasons for this failure to more consistently identify depth phases from such events is illustrated in Figure 2, which shows the vertical component recordings at station MBC ($\Delta \approx 70°$) from a series of these events covering an REB depth range extending from 207 to 248 km. Note that even for these closely-spaced events in a narrow depth range, the variation of the observed pP/P and sP/P amplitude ratios is very large. This kind of variation can presumably be explained by differences in focal mechanisms between these events, but such effects make it much more difficult for the analyst to consistently identify depth phases, even for such closely-spaced events.

In an attempt to overcome such difficulties in single station depth phase identification, we have been investigating the potential utility of a fully automated network stacking algorithm which employs signal analysis procedures similar to those originally proposed by Israelsson (1994) and more recently applied to a sample of Canadian data by Woodgold (1999). In this approach post-P arrivals observed at each station for a given event are mapped from functions of delay time to functions of source depth using the pP-P or sP-P delay times predicted by the IASPEI travel time tables for the various station distances. These functions of depth for all the stations in the detecting network are then added together to identify arrivals consistent with the predicted depth phase moveouts over the entire range of potential source depths. This transformation is illustrated in Figure 3, which shows the predicted pP moveout with respect to P as a function of source depth for two different epicentral distances. Using such predicted moveout curves, the observed delay times of all post-P arrivals with respect to P can be translated into equivalent focal depths under the hypotheses that they are either pP or sP arrivals. Those arrivals which are consistent with such hypotheses should then show up as peaks on the stacked network depth function.

As was noted by Woodgold (1999), one of the difficulties of applying the above algorithm directly to the recorded short-period seismic data is that the depth phase waveforms and dominant frequency contents for a given event can show substantial variability across the network, and this significantly degrades the effective gain of the network stacking procedure. Consequently, we have adopted a modified method in which only the post-P detection times in the PIDC automatic file for each station are used. That is, the observed post-P arrival times and their associated uncertainties (currently assumed to be ±1 sec for pP and ±2 sec for sP) are used to define boxcar functions of unit amplitude centered on the automatic detection time and these boxcars as functions of time are mapped into equivalent boxcars as functions of source depth using predicted IASPEI movement curves such as those shown in Figure 3. It is these simplified functions of depth which are then stacked over the network to identify candidate depth phase consistent with pP or sP.

The results of applying this processing procedure to the automatic detection files for the Hindu Kush earthquake of 02/14/98 are shown in Figure 4, where the functions of depth derived under the hypothesis of pP arrivals are shown for each of the 31 stations which recorded this relatively large (m_b≈5.0) event, together with the network stacking results for the specified candidate depth range extending from 50 to 700km. The dashed vertical line on this figure denotes the reported REB depth, and it can be seen that there is a strong peak in the network detection stack corresponding to this depth which would be identified as a candidate pP phase by the automatic process. Similar examples for several smaller earthquakes from the selected Hindu Kush data set are shown in Figures 5 and 6. In Figure 5 it can be seen that there is again a strong peak in the network detection stack which is consistent with the REB depth of 204 km for this event, and which would be readily identified as a candidate depth phase. Figure 6 shows the corresponding results for the much smaller (m_b ≈4.0) earthquake of 04/08/96, and it can be seen that in this case there is a pronounced peak in the network detection stack which is close to the REB depth estimate of 248 km, but which does not quite encompass it. It is interesting to note that, in this case, no depth phases were reported in the REB and, consequently, the REB depth estimate is based on P wave first arrival times alone. Therefore, it is not surprising that the two independent depth estimates are not in exact agreement given the uncertainties in both estimates. In any case, the automatic process has identified candidate depth phases which, if validated, could be incorporated into the hypocentral inversion to obtain a more robust estimate of source depth.

Of course, because of focal mechanism variations such as those illustrated in Figure 2, as well as other effects, the interpretation of the network detection stacks is not always as unambiguous as for the examples shown in Figure 4-6. For example, Figure 7 shows the pP detection stack for the Hindu Kush earthquake of 12/11/98. It can be seen from this figure that in this case there are a number of peaks at different depths, which are as large or larger than that coinciding with the reported REB depth of 248 km for this event. However, as is illustrated in Figure 8, a sum of this pP network stack and that for the corresponding sP network stack produces a function of depth which shows a maximal value at the REB depth. Data from a sample of 30 of those Hindu Kush earthquakes with m_b>4.0 and focal depths in the 200-250 km range have now been processed using this algorithm, and the results have been quite encouraging in that more than 80% of the resulting network stacks have been found to show significant peaks corresponding to candidate depth phases which are consistent with the REB depth estimates. The procedure is currently being further tested using samples of Hindu Kush events encompassing a wider range in focal depths.

With regard to focal depth estimates based on P wave first arrival times alone, we are continuing with the development of rigorous methods for computing confidence intervals on focal depth and hypothesis tests that can be used as focal depth discriminants. The following complexities are being addressed in our approach:

- Nonlinearity of the travel time vs. hypocenter forward model, especially nonlinearity with respect to event depth.
- Uncertainty in the variance of arrival time picks.
- Uncertainty in travel time corrections for regional stations. (This is in contrast to the standard practice or treating station-correction uncertainty as an additional random error in the data.)

Our statistical formulation uses likelihood ratio tests to define confidence regions and hypothesis tests – for either the vector hypocenter or event depth. The likelihood function is based on a Gaussian error model.

We maximize likelihoods over "nuisance parameters" which are not the target of a test, including origin time, error variance, unknown station corrections and, when focal depth is the target parameter, event epicenter. Given the generality of our formulation, the test statistic used in a given test is not necessarily chi-squared or F distributed, as is usually assumed. Moreover, its probability distributions (needed to define critical values of the test statistic) depend on the problem parameters themselves. To address these complications, we have developed numerical techniques based on Monte Carlo simulation and grid search to calculate confidence regions on hypocenters, confidence intervals on focal depth, and significance levels for focal depth hypothesis tests. We are currently applying these algorithms to events in the Hindu Kush region in an attempt to derive confidence regions and discriminants that are in better agreement with the results of our observational studies.

CONCLUSIONS AND RECOMMENDATIONS

During the past year, the effort on this project has focused on the development of improved tools for detection and identification of depth phases and on the continuation of the evaluation of a new algorithm for computing more reliable confidence intervals on focal depth estimates based on P wave first arrival times alone. A new, fully automatic process has been implemented for stacking network detection data to identify candidate depth phases for further review by the analyst. This procedure has now been tested on a sample of 30 Hindu Kush earthquakes with REB focal depths in the 200 to 250 km range, and it has been shown to provide useful diagnostic information on depth phases for events with REB $m_{b.}$ values as low as 4.0. More specifically, candidate depth phases were identified for more than 80% of these test events, as opposed to the 35% of those events for which analyst determined depth phase observations were reported in the REB. We conclude that this new automatic processing procedure holds promise for providing a useful tool which could be used by the IDC analysts to make more frequent and more reliable depth phase picks. With regard to the determination of improved confidence intervals on depth, a more rigorous statistical method based on Monte Carlo simulation and grid search has now been implemented as is currently being evaluated using data recorded from Hindu Kush earthquakes with well-constrained focal depths.

REFERENCES

Israelsson, H. (1994), "Stacking of Waveforms for Depth Estimation," Center for Seismic Studies Final Report C95-02

Woodgold, C.R.D. (1999), "Wide Aperture Beamforming of Depth Phases by Timescale Contraction." Bull. Seism. Soc. Am., 89, pp.165-177.

MULTI-TAPER COHERENCE RECEIVER FUNCTIONS AND P-WAVE SCATTERING WITHIN THE CRUST

Jeffrey Park, Vadim Levin, Joydeep Bhattacharyya,
Department of Geology and Geophysics, Yale University

Sponsored by U. S. Department of Defense
Defense Threat Reduction Agency
Contract No. DSWA01-98-011

ABSTRACT

Teleseismic P-waves are followed by a series of scattered waves, particularly P-to-S converted phases, that form a coda. The sequence of scattered waves on the horizontal components is represented by the receiver function (RF) for the station, and may vary with the approach angle and azimuth of the incoming P wave. This coda can be generated via side-scattering from topographic features. However, at teleseismic frequencies (<2 Hz) many, if not most, converted phases in the first few seconds after P are generated via forward scattering from seismic interfaces within the crust and uppermost mantle, where density and elastic properties undergo discontinuity. P-coda on the transverse horizontal component indicates either the presence of dipping interfaces, the presence of anisotropy, or 3-D structures. The three different cases can be distinguished, given sufficient data, by the move-out of scattered waves with back-azimuth and incoming phase velocity. Comparing RFs for different records can be misleading if the frequency content of different P waves varies greatly. Popular methods for RF-generation include deconvolution and spectral division, with damping to avoid numerical instabilities. Deconvolution operators are often biased towards the frequencies where signal is strongest, similar to spectral-division schemes with constant water-level damping. Worse, estimates of uncertainty are scarce, which impedes developing a weighted average of RF-estimates from multiple events.

We have developed a frequency-domain RF inversion algorithm using multi-taper coherence estimates instead of spectral division, using the pre-event noise spectrum for frequency-dependent water-level damping. The multi-taper spectrum estimates are leakage resistant, so low-amplitude portions of the P-wave spectrum can contribute usefully to the RF estimate. The coherence between vertical and horizontal components can be used to obtain a frequency-dependent uncertainty for the RF. Tests of this technique using teleseismic data from PET (Petropavlovsk-Kamchatsky, Russia) show excellent RF retrieval for signals up to f=2.0Hz. Several crustal P-SH conversions can be seen in the transverse RF, as well as a “derivative pulse” signal with extreme move-out that we interpret as a wave scattered at the top of the Kamchatka slab. The “derivative pulse” character of this and other signals in the transverse RF suggests interfering P-S conversions at closely spaced interfaces. We will report RF sweeps from PET and other permanent broadband stations.

Key Words: P waves, receiver function
UR-99-384 or UCRL-ID-132897.
location, source mechanism, waveform inversion, depth phases, phase detection

OBJECTIVE

Proper detection and discrimination of seismic waves from suspected clandestine explosions is best accomplished when the wave-propagation characteristics of the Earth between the source and the seismometer are well-known. Teleseismic body waves from earthquakes and explosive sources experience scattering as they travel upwards through the uppermost mantle and crust. Similarly, regional body waves experience scattering as they travel through the crustal waveguide. The objective of this research project is to use variations in the elastic anisotropy of the crust and uppermost mantle to describe the scattering that is observed in seismic data. Most models for seismic scattering invoke a statistical 3-D distribution of small-scale anomalies in isotropic P and S seismic velocities e.g., the phase-screen approach (Wu, 1994) or finite-difference computations (e.g. Levander and Hollinger, 1992). The motivation for using anisotropy is threefold. First, fairly modest fluctuations in anisotropic properties can cause significant conversion of P (compressional) motion to S (shear) motion in propagating seismic waves. Second, numerical experiments have shown that flat-layered anisotropic media can cause large scattered wavetrains in both surface waves (Park, 1996) and body waves (Levin and Park, 1997a; 1998). Third, elastic anisotropy, as a material property of rocks, seems to be the rule rather than the exception, caused by aligned cracks (Hudson, 1981), by lattice-preferred mineral orientation within rocks (Babuska and Cara, 1991), and by fine-layering (Helbig, 1994). Large-scale 3-D velocity structures are not necessary to create a P-coda or an extended surface-wave signal, at least in theory. If a 1-D anisotropic seismic-velocity structure can usefully represent much of the scattered seismic energy in an incoming signal at a particular seismic observatory, there are practical benefits. An analyst, faced with a complex seismic signal to interpret, would likely need to know fewer parameters of earth structure local to the station, and may run simpler synthetic seismogram codes to reproduce the data.

A key objective of this research is to determine whether layered anisotropy is pervasive in the crust and has a strong influence on body-wave coda. To do this, we estimate the scattering of teleseismic P waves as they travel upwards through the crust, using a modification of familiar receiver-function techniques (Langston, 1977; Ammon, 1991; Abers, et al 1995). Computational modeling (Cassidy, 1992; Kosarev et al 1994; Levin and Park, 1997a; 1998; Savage, 1998) demonstrates that both anisotropy and dipping interfaces cause predictable variations in P-to-S scattered energy, dependent on the incoming direction of the P-wave -- its angle of incidence (or equivalently, its "slowness" p), and its back-azimuth angle ϕ. The P-to-SH energy scattered to the transverse-horizontal component of motion is particularly diagnostic, as its amplitude is predicted to reverse from positive to negative, and vice versa, in a lobate pattern with back-azimuth ϕ. We therefore analysed seismic data from representative permanent seismic observatories to study the back-azimuth dependence of receiver functions. A dipping interface and a 3-D scatterer can be distinguished from flat-layered anisotropy by examining the "moveout" of the scattered wave. The radial- and transverse-horizontal scattered waves arrive later for waves that approach updip a slanted interface, relative to waves that approach downdip. The timing of a wave generated by an isolated 3-D scatterer also depends strongly on the back-azimuth of the incoming P wave. By contrast, a P-to-S scattered wave experiences very little moveout, if any, from a horizontal interface between layers of anisotropic rock. If receiver functions from a particular seismic observatory exhibit a lobate amplitude pattern in the transverse component, and there is negligible moveout with back-azimuth in the delay time, a flat-layered anisotropic crust gains respect as a good model to represent scattering at that location.

Although this research focusses on developing anisotropic models for crustal seismic velocities, the receiver functions themselves may be useful in the verification and monitoring activities associated with a Comprehensive Nuclear-Test-Ban Treaty (CTBT). Receiver functions represent empirically the scattering at particular seismic stations. They are useful to the extent that they are reproducable in many seismic records, even if no simple earth-structure model can explain them.

RESEARCH ACCOMPLISHED

Early in the fiscal year we studied P-to-S scattered waves in seismograms recorded at the Southern California Seismic Network (SCSN) station JRC, a broadband seismic observatory sited within the Coso

geothermal field. We constructed an anisotropic crustal model to fit this data using the genetic-algorithm tools developed by Levin and Park (1997a). In this model we find a low-velocity zone in the mid-crust, presumably related to the heat source of the geothermal activity. P-SH scattering effects in the RFs can be modeled with a 15-km anisotropic (2%) mid-crustal layer and a highly anisotropic (6%) thin surface layer that has fast axes (N60°W) aligned near the NE-SW direction of shear in regional seismicity.

Later in the first year of our project we improved our algorithm for determining the receiver functions (RFs) that describe P-to-S scattering by the shallow layers of the Earth, with particular emphasis on P-to-SH scattering that appears on the transverse horizontal component. Receiver functions are easy to define, but much more difficult to compute in a reliable, robust manner. The receiver function describes the tendency of an upward-travelling P-wave to set off a chain of subsidiary waves, mostly S waves, that arrive after the main P wave. Favored methods to compute receiver functions use the record of vertical vibration on the seismogram, which contains mostly P-wave motion, to predict the records of radial- and transverse-horizontal seismic motion. The simplest way to accomplish this is by spectral division: form a ratio of the Fourier transforms of the different components: $H_R(f) = R(f)/Z(f)$ and $H_T(f) = T(f)/Z(f)$. Here Z(f), R(f), and T(f) are the Fourier spectra of the vertical, radial and transverse seismic components, respectively. The spectral-domain receiver functions $H_R(f)$ and $H_T(f)$ can be transformed into a "prediction filter" of P-to-S scattered waves by performing the inverse Fourier transform on them.

Although simple to apply, spectral division is a bad method. It is numerically unstable near the zeroes of Z(f). It also fails to account for seismic noise. To circumvent this, a modified spectral division is preferred, using a "water level" to avoid the zeroes of Z(f) (e.g. Ammon, 1991). Alternatively, one can deconvolve the horizontal seismic records from the vertical record in the time domain (e.g. Abers et al 1995) to compute the scattering "prediction filter" directly. Each of these techniques has shortcomings, as each tends to be bandlimited. The "water level" in spectral division obscures low-amplitude spectral components. Similarly, time-domain deconvolution tends to be dominated by the Fourier components with largest amplitude. In practice this has limited many RF-studies to use data low-passed at f~0.5 Hz. This has led to some spectacular images of upper-mantle discontinuities at 420 and 670-km depth (e.g., Dueker and Sheehan, 1997), but is problematic for probing fine-layered crustal structure.

We developed a technique that appears to overcome the problems of typical RF estimation. The technique is a spectral-domain method, using the complex-valued multiple-taper spectral cross-correlation, rather than spectral division, as a more robust estimator of the causal relation between the horizontal and vertical seismograms. We use a frequency dependent water-level to damp the inversion, using the spectrum of the pre-event noise as a scaling factor. We use multiple-taper spectral estimation (Thomson, 1982; Park et al, 1987; Vernon et al, 1991) to ensure that the estimates of water-level and coherence are minimally contaminated by spectral leakage. This allows us to estimate spectral ratios at frequencies where the signal is low, but the signal-to-noise ratio is still high. Estimating $H_R(f)$ and $H_T(f)$ using coherence has an additional advantage. At frequencies where the coherence between vertical and horizontal seismic components is low, one can presume that either background noise or signal-generated noise has obscured their relationship. In the RF-estimation examples we show below, the vertical-radial-transverse coherences vary up and down with frequency, in a manner largely unpredictable from visual perusal of the data. We developed a frequency-dependent uncertainty estimate for the receiver functions $H_R(f)$ and $H_T(f)$ that varies inversely with coherence C(f). The uncertainty is small when C(f) near unity, and large for smaller C(f). The formal uncertainty estimate offers a way to form composite RFs from different seismic records in a weighted linear combination. We use the inverse-variances of the individual RFs as weights, so that poorly constrained estimates influence the weighted sum less than do H(f) with smaller uncertainty.

We compute time-domain receiver functions by inverting the Fourier-domain RFs $H_R(f)$ and $H_T(f)$. To avoid ringing in the RF, we taper the spectrum up to a user-specified cutoff frequency with a cosine-squared function. For example, RFs with a frequency cutoff of 2 Hz include significant information only up to ~1.3 Hz, with half-amplitude at 1 Hz. In the frequency domain, error bars indicate the uncertainty of the RFs. In the time domain there are no formal error bars, but fluctuations in the RF at negative times offer a visual assessment of uncertainty in the wiggles that follow. When frequency-domain RFs from multiple

data records are combined in a weighted average, this spurious precursory portion of the prediction filter tends to decrease in the composite time-domain RF.

The advantages of our new RF-estimation technique can be assessed with examples from seismic data. Figure 1 shows P waves from two earthquakes recorded at station PET (Petropavlovsk-Kamchatsky, Russia) of the Global Seismographic Network (GSN). Neither P wavetrain is an ideal candidate for receiver-function estimation. Both P-waves are extended in time, rather than impulsive, and the 10/5/93 record has a low signal-to-noise ratio in the unfiltered time domain. The signal and pre-event spectra are compared in Figure 2, and show that the signal-to-noise ratio is high at frequencies f>1 Hz, even though the P-waves are both dominated by frequencies f<0.7 Hz. The coherences are variable, but often near unity even where the spectrum has low amplitude. The water-level damping technique would erase this information. Figure 3 demonstrates that the radial RFs for these two P-waves are reassuringly similar. For the 9/6/93 record, a sequence of 3-4 pulses spaced at ~2-sec intervals is reconstructed from a signal that is dominated by energy at significantly longer period. The transverse RFs agree less well, but this is reflected in the spectral-domain error bars in Figure 3. The peak in $H_T(f)$ at 0.3 Hz coincides with the microseism peak at PET, and so is not retrieved well for the 10/5/93 record.

We have estimated distance- and back-azimuth dependent receiver functions for the permanent broadband seismological stations PET, RAYN (Ar Rayn, Saudi Arabia) and ARU (Arti Settlement, Russia). PET lies above the active, steeply dipping (55º) Kamchatka subduction zone (Gorbatov et al, 1997). RAYN lies within stable continental shield. ARU lies above an ancient (Paleozoic) continental suture zone, marked by the north-south trending Ural Mountains.

We had identified a strongly anisotropic lower-crustal layer beneath ARU in a previous study (Levin and Park, 1997b). Using the new RF-estimation technique, we were able to utilize 1989-98 data from 442 seismic events with M=6.3 or greater, including 112 core-refracted high-frequency PKP and PKiKP phases from events more distant than 95 degrees from ARU. Frequency-domain RFs from individual records are bin-averaged in overlapping 10º intervals of either epicentral distance or back-azimuth. The bins are spaced at 5º intervals. When the radial-component composite RF for ARU is plotted against epicentral distance (Figure 4), the moveout of the P-to-S converted wave at the Moho (~4-5-sec time delay) is clearly evident. The delay is greater for closer events, because the P-wave incidence angle is more shallow, and the converted wave must travel a longer path from the base of the crust to the seismometer. One can also observe a distance-dependent modulation in the amplitude of the radial RF $H_R(t)$ at t=0. The largest $H_R(0)$ is found for closer events, in which the incoming P-wave has shallow incidence and a substantial radial projection. The minimum radial RF amplitude occurs at epicentral distances beyond 100º, where PKP waves are steeply incident. The back-azimuth sections for radial and transverse composite RFs (Figure 5) confirm the anisotropic crustal model of Levin and Park (1997b): a strong negative pulse on the radial RF at 2-sec delay indicates a mid-crustal seismic low-velocity zone of some kind, and is a strong derivative-pulse on the transverse RF that suffers an amplitude polarity reversal with back-azimuth. Levin and Park (1997b) modeled this feature with a strongly anisotropic lower crustal layer with seismic velocity suggestive of a steeply-tilted fine-layered mixture of crust and mantle rocks.

Although only two years of data are available for RAYN, an estimate of crustal reverberation structure can be made at this low-noise station from 65 events (not shown), even though only PKP waves are available at most back-azimuths. A clear polarity reversal in the transverse RF for pulses at 5- and 8-sec delay is seen. This suggests an interface between anisotropic layers and not a simple dipping interface, because there is no accompanying radial-RF pulse at 8-second delay. It is possible that the transverse signals are actually reverberations of some kind, but the lack of similar set of pulses in the radial RF argues against a simple reverberation.

We computed receiver functions from 241 data traces recorded at station PET, but data is sparse and/or poor in several sectors of back-azimuth e.g. 275º-360º. Nevertheless, abundant earthquakes illuminate PET from the east, south and southwest. For back-azimuths between 150º and 200º, a strong transverse-component scattered wave moves out from 7-sec delay to 10-sec delay (Figure 7). This delay suggests an interface

much deeper than the Moho, and that the interface is strongly tilted. We identify it with the top of the Pacific plate as it subducts (as a "slab") into the mantle along the east coast of Kamchatka. At shorter delay times (1-3 sec), the transverse RF flips polarity at roughly 200° back-azimuth, that is, for P waves that arrive roughly parallel to the strike of the dipping slab. Dipping geologic interfaces that are aligned with the downgoing slab are not good candidates to explain this behavior. The transverse RF polarity reversal might be better explained by a shallow interface that dips with strike perpendicular to the Kamchatka trench. Alternatively, a strongly anisotropic surface layer with a symmetry axis sub-parallel to the trench could cause the polarity switch.

Analysis for stations ARU, RAYN and PET demonstrates that the radial and transverse RFs do not often correlate peak to peak, as would be expected from a set of solitary waves deflected from a collection of isolated interfaces or obstacles. Instead, the transverse- and radial-component scattered waves are often shifted in phase by 90°, so that one resembles the derivative of the other. The slab-converted phase at PET has a "derivative pulse" shape on the transverse RF, and is as large as on the radial RF. This implies the phase is generated by interference between multiple scattered waves e.g. conversions at the top and bottom of a thin oceanic crust at the top of the subducting slab. Within the crust, the phase lag between radial and transverse RFs persists as the cutoff frequency increases to f=3.0 Hz and beyond. This suggests that the pulses are caused by the interference of numerous P-to-S converted phases caused by fine-scale layering of anisotropic rock units.

CONCLUSIONS AND RECOMMENDATIONS

Seismic stations ARU and RAYN appear both to lie atop a horizontally layered structure that nevertheless generates strong P-SH scattered energy on the transverse component. A 1-D anisotropic model of seismic velocity may therefore adequately describe wave-propagation effects near these stations. For station PET the situation is more complicated. RF estimates show clear evidence of the steeply-dipping subducting slab in the mantle. Tilted interfaces in the upper crust are suggested by perusal of Figure 8, especially at the 3.0-Hz cutoff, where the midcrustal 3.5-sec-delay conversion appears to arrive early for nearby earthquakes, but later for distant earthquakes, in an trend opposite to that of the Moho P-to-S conversion. This suggests a weakly-dipping mid-crustal interface. More analysis is needed to determine the total departure of this region from a horizontally-layered earth model, but significant 3-D structure appears necessary to model the crustal reverberations at PET in detail.

We recommend continued use of back-azimuth and range-dependent receiver functions to characterize scattering at broadband seismic monitoring stations within the verification system of the Comprehensive Nuclear-Test-Ban Treaty (CTBT). Data analysis from our preliminary suite of stations suggests that a 1-D anisotropic crustal structure is appropriate for modeling a significant portion of crustal scattering in teleseismic signals. Even where significant 3-D structure is evident (PET), 3-D effects are superimposed on strong scattering from what appears to be finely-spaced horizontal, or gently dipping, layers.

REFERENCES

Abers, G. A., X. Hu, and L. R. Sykes, Source scaling of earthquakes in the Shumagin region, Alaska: Time-domain inversions of regional waveforms, **Geophys. J. Inter., 123**, 41--58, 1995.

Ammon, C. J., The isolation of receiver effects from teleseismic P waveforms, **Bull. Seism. Soc. Amer., 81**, 2504-2510, 1991.

Babuska, V., and Cara, M., **Seismic Anisotropy in the Earth**, Kluwer Academic, Dordrecht, 1991.

Bostock, M. G., Anisotropic upper-mantle stratigraphy and architecture of the Slave craton, **Nature, 390**, 393-395, 1997.

Cassidy, J. F., Numerical experiments in broadband receiver function analysis, **Bull. Seism. Soc. Amer., 82**, 1453--1474, 1992.

Gorbatov, A., V. Kostoglodov, G. Suarez, and E. Gordeev, Seismicity and structure of the Kamchatka subduction zone, **J. Geophys. Res., 102**, 17883-17898, 1997.

Helbig, K., **Foundations of Anisotropy for Exploration Seismics**, Pergammon/Elsevier Science, Oxford, 1994.

Hudson, J. A., Wave speeds and attenuation of elastic waves in material containing cracks, **Geophys. J. Roy. Astron. Soc., 64**, 133--150, 1981.

Kosarev, G. L., Makeyeva, L. I. and Vinnik, L. P., Anisotropy of the mantle inferred from observations of P to S converted waves, **Geophys. J. Roy. Astron. Soc., 76**, 209--220, 1984.

Langston, C. A., The effect of planar dipping structure on source and receiver responses for constant ray parameter, **Bull. Seism. Soc. Amer., 67**, 1029--1050, 1977.

Levander, A. R., and Hollinger, K., Small-scale heterogeneity and large-scale velocity structure of the continental crust, **J. Geophys. Res., 97**, 8797--8804, 1992.

Dueker, K. D., and A. F. Sheehan, Mantle discontinuity structure from midpoint stacks of converted P to S waves across the Yellowstone hotspot track, **J. Geophys. Res., 102,** 8313-8327, 1997.

Levin, V., and J. Park, Crustal anisotropy beneath the Ural mtns foredeep from teleseismic receiver functions, **Geophys. Res. Letts, 24**, 1283-1286, 1997**.**

Levin, V., and J. Park, P-SH conversions in a flat-layered medium with anisotropy of arbitrary orientation, **Geophys. J. Int., 131**, 253-266, 1997**.**

Levin, V., and J. Park, A P-SH conversion in layered media with hexagonally symmetric anisotropy: A cookbook, **Pure and Applied Geophysics, 151**, 669-697, 1998**.**

Owens, T. J., and Crosson, R. S., Shallow structure effects on broad-band teleseismic P waveforms, **Bull. Seism. Soc. Amer., 77**, 96-108, 1988.

Park, J., Lindberg, C. R., and F. L. Vernon III, Multitaper spectral analysis of high-frequency seismograms. **J. Geophys. Res., 92**, 12675--12684, 1987.

Park, J., Surface waves in layered anisotropic structures, **Geophys. J. Int., 126**, 173-184, 1996.

Savage, M., Lower crustal anisotropy or dipping boundaries? Effects on receiver functions and a case study in New Zealand, **J. Geophys. Res., 103**, 15069-15087, 1998.

Thomson, D. J., Spectrum estimation and harmonic analysis, **IEEE Proc., 70**, 1055-1096, 1982.

Vernon, F. L., J. Fletcher, L. Carroll, A. Chave and E. Sembrera, Coherence of seismic body waves from local events as measured by a small-aperture array, **J. Geophys. Res., 96**, 11981--11996, 1991.

Wu, R.-S., Wide-angle elastic wave one-way propagation in heterogeneous media and an elastic wave complex screen method, **J. Geophys. Res., 99**, 751--766, 1994.

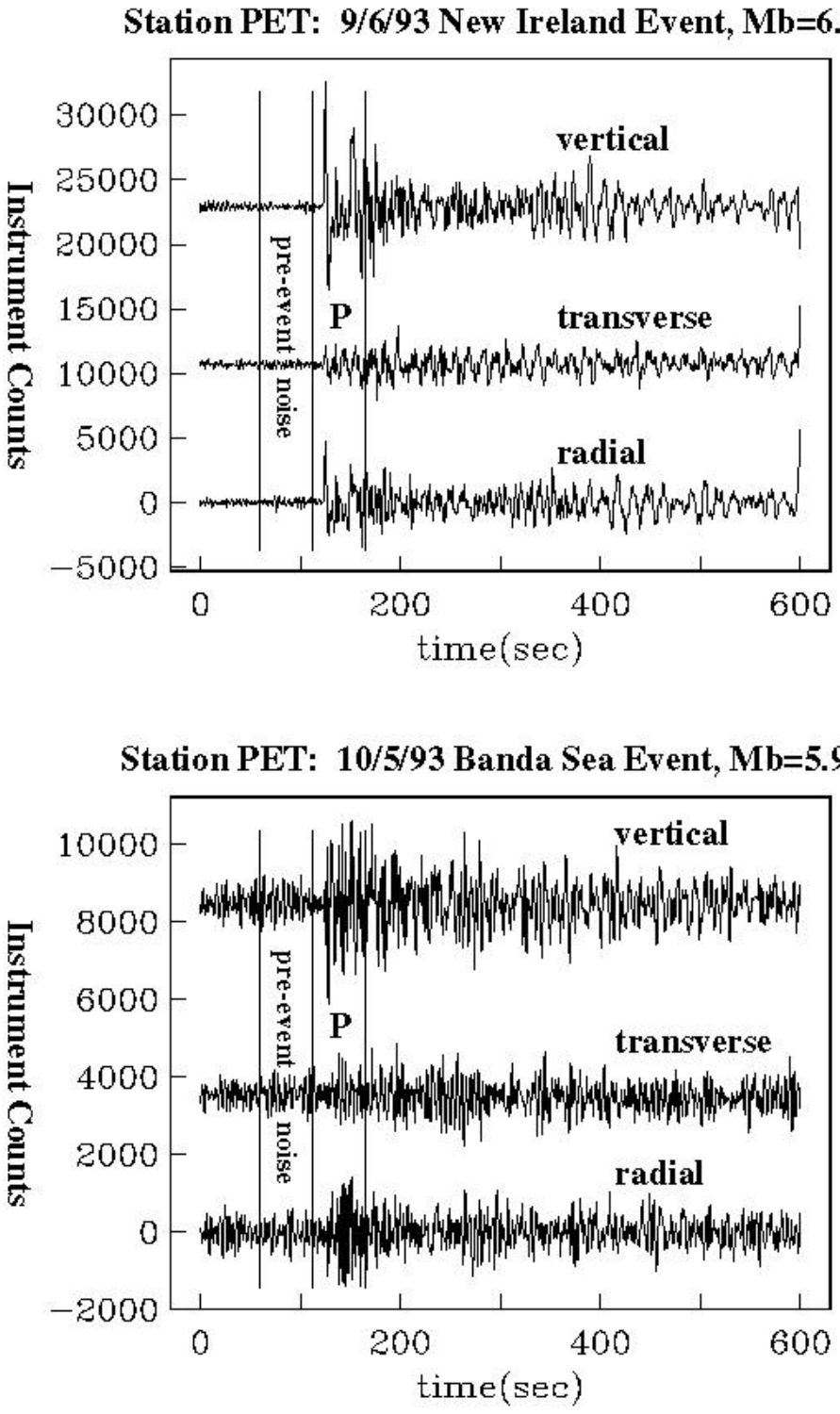


Figure 1. P-waves recorded at PET (Petropavlovsk-Kamchatsky, Russia). Data windows for spectral receiver-function analysis are indicated.

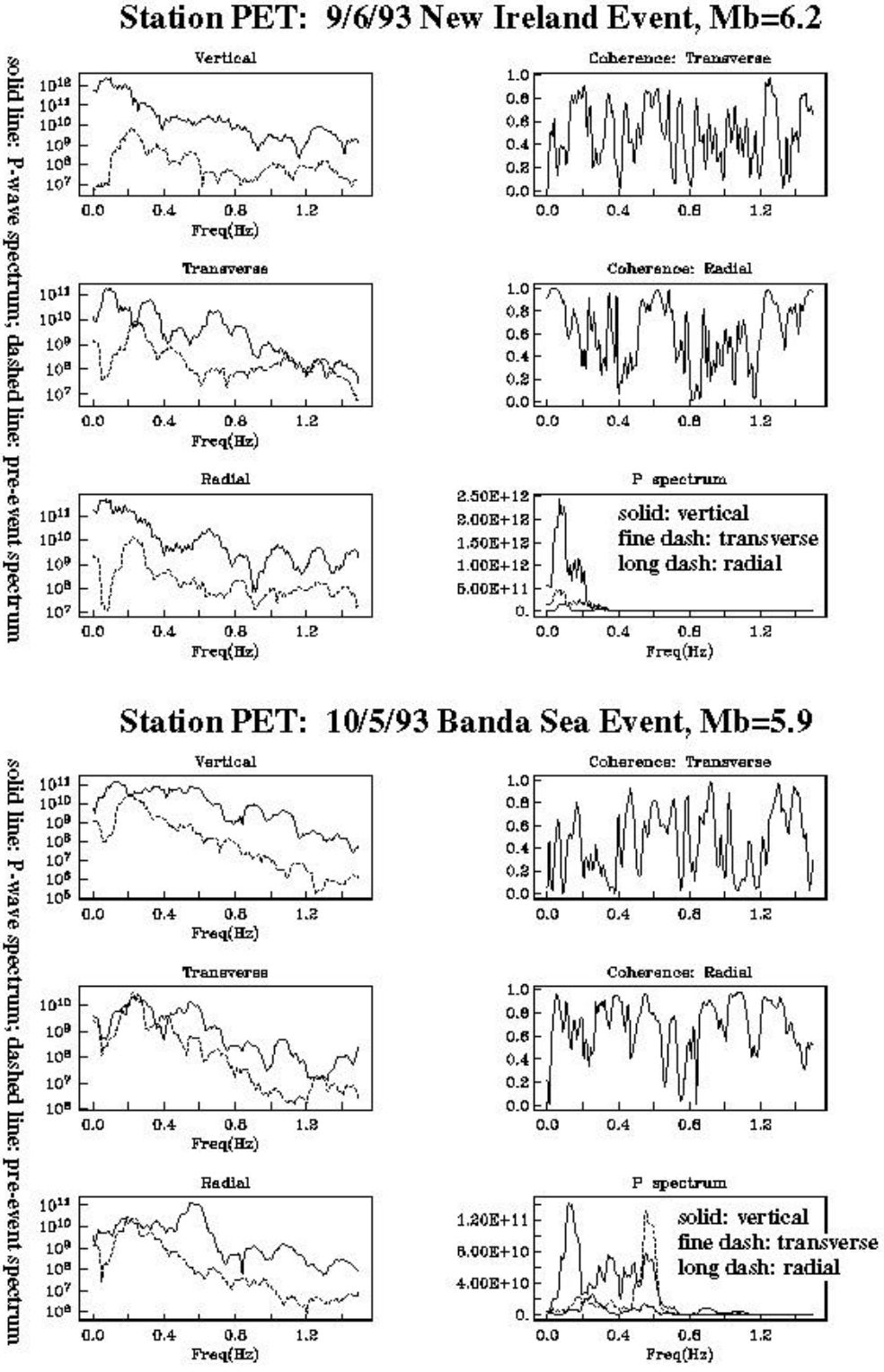


Figure 2. Multitaper spectral-correlation receiver function analysis: computations. Left-column plots compare the signal and pre-event noise of different components. Right-column plots show the coherences of radial and transverse seismic motion with the vertical motion. Note that both P waves have weak signal above 0.7 Hz.

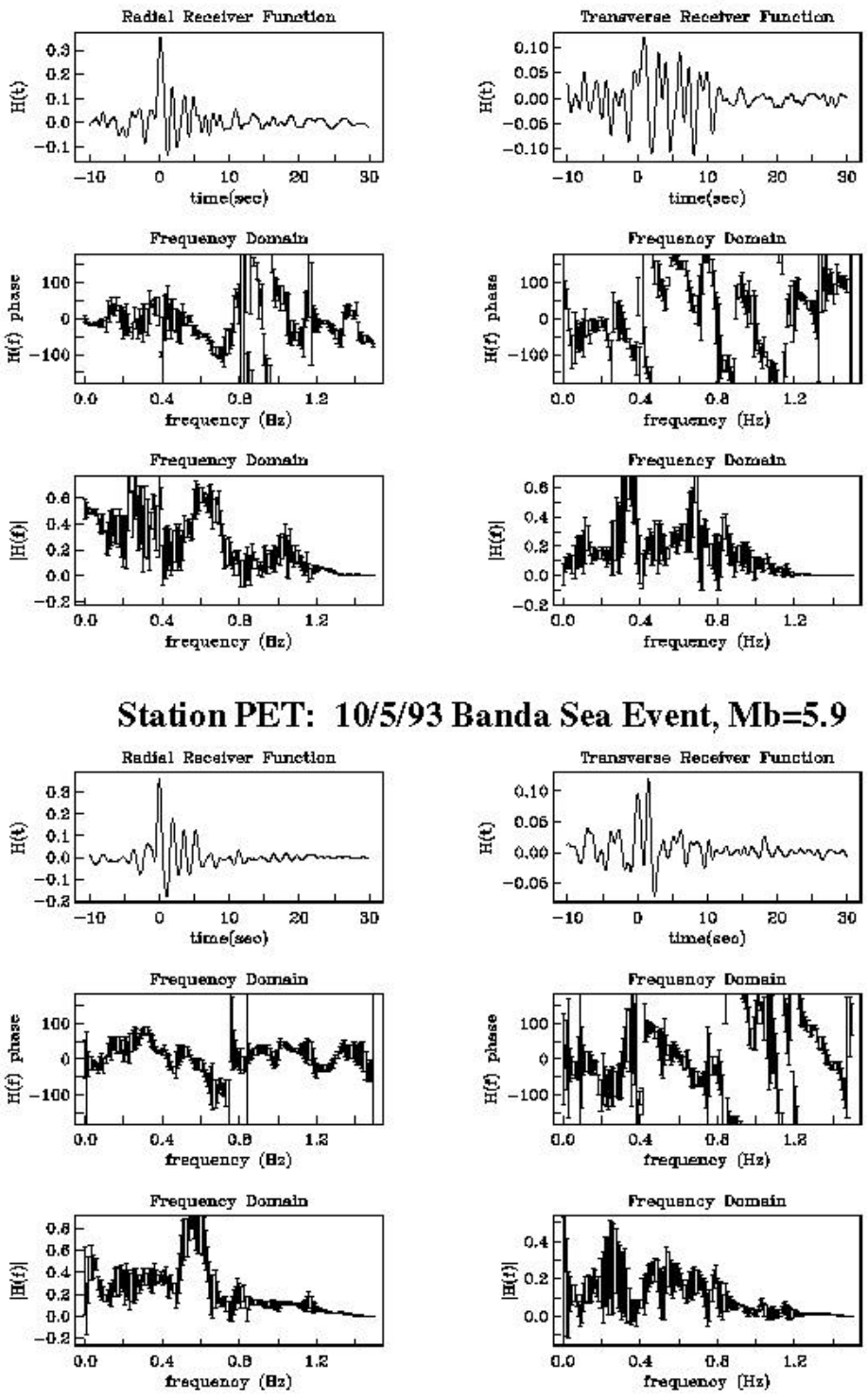


Figure 3. Multitaper spectral-correlation receiver function analysis: results. Left-column plots show radial-component RFs in both time and frequency domains. Right-column plots show transverse-component RFs. Oscillations in the time-domain RFs at negative times are diagnostic of the RF uncertainty.

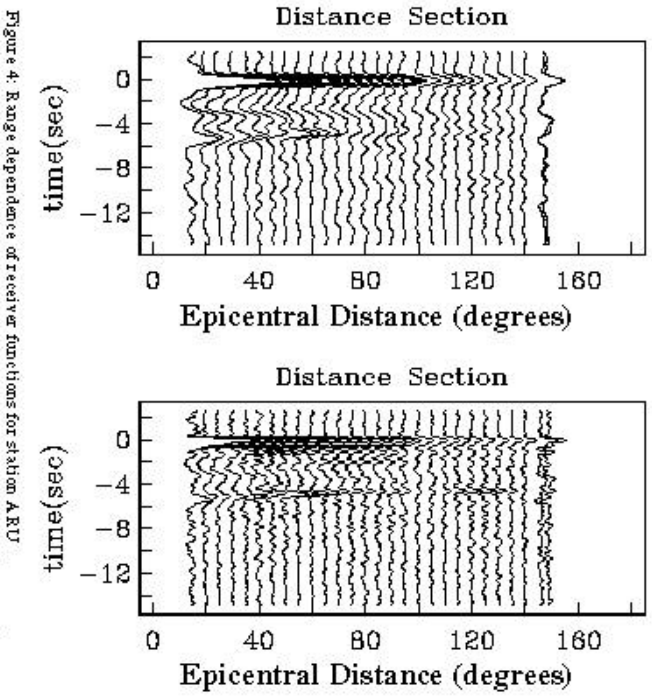


Figure 4: Range dependence of receiver functions for station ARU (Arti Settlement, Russia). RF sections for 1.5-Hz and 3.0-Hz cutoff frequencies are plotted. The composite section uses 442 seismic events. Note that several crustal-scattered waves, including the prominent Moho Ps phase at 5-sec delay, can be traced through nearly all of the 3.0-Hz section, suggesting strong horizontal layering.

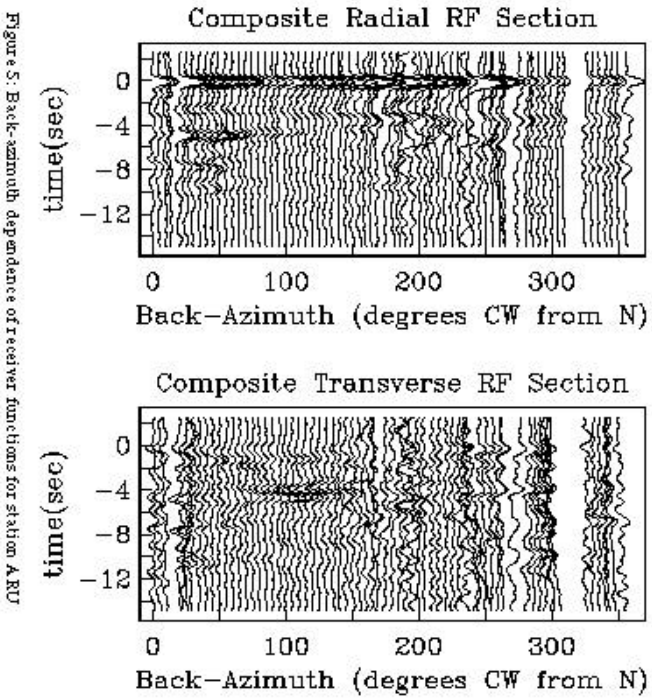


Figure 5: Back-azimuth dependence of receiver functions for station ARU (Arti Settlement, Russia). Note the strong transverse pulses at 4-5-sec delay. These pulses centered on 120° and 280° back-azimuth have reversed polarity. This can be modelled with a strongly anisotropic layer (>10%) in the lower crust. Transverse RF amplitude is boosted by factor of two for visual comparison.

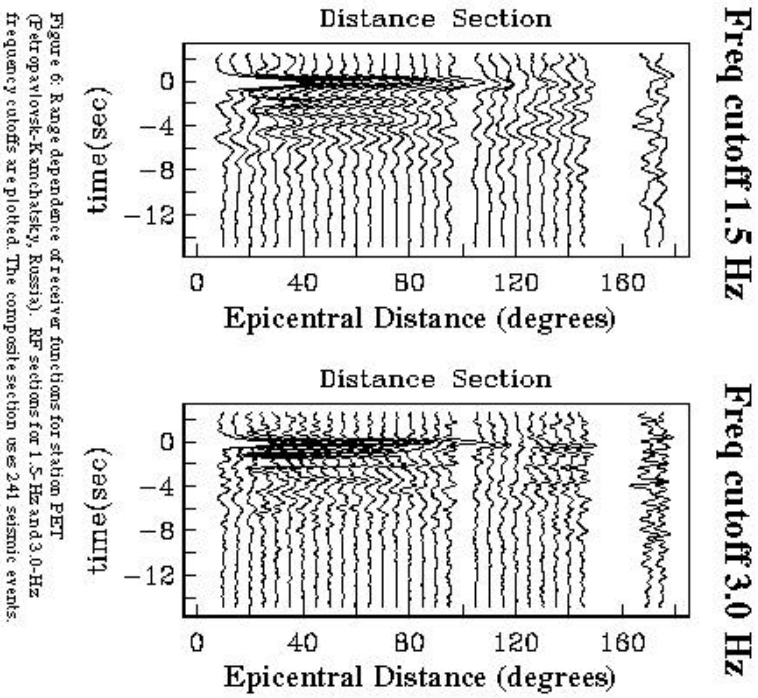


Figure 6: Range dependence of receiver functions for station PET (Petropavlovsk-Kamchatsky, Russia). RF sections for 1.5-Hz and 3.0-Hz frequency cutoffs are plotted. The composite section uses 241 seismic events.

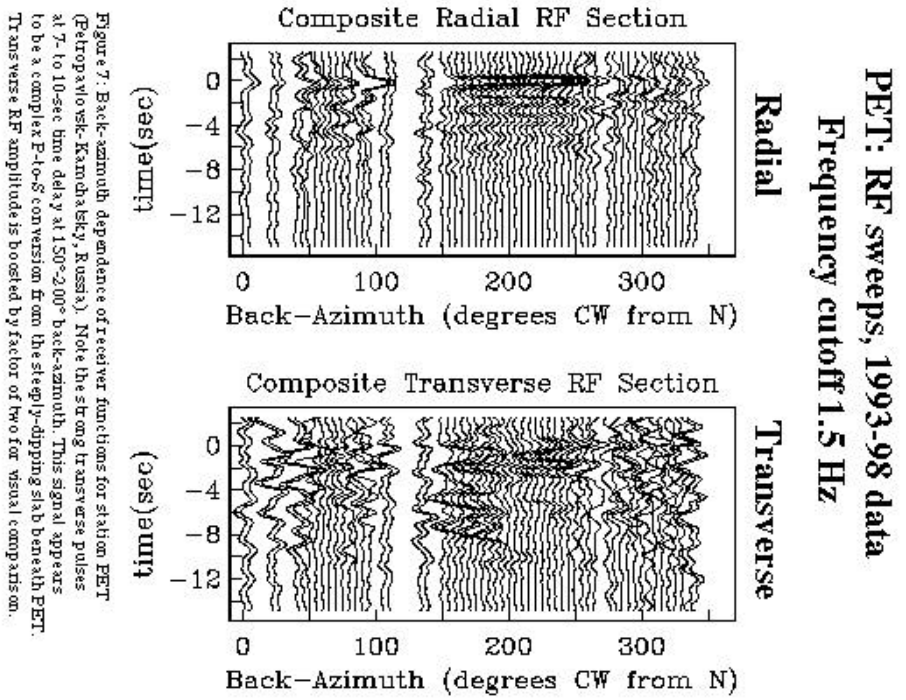


Figure 7: Back-azimuth dependence of receiver functions for station PET (Petropavlovsk-Kamchatsky, Russia). Note the strong transverse pulses at 7- to 10-sec time delay at 150°-200° back-azimuth. This signal appears to be a complex P-to-S conversion from the steeply-dipping slab beneath PET. Transverse RF amplitude is boosted by factor of two for visual comparison.

IMPROVING m_b:M_S DISCRIMINATION USING PHASE MATCHED FILTERS DERIVED FROM REGIONAL GROUP VELOCITY TOMOGRAPHY

Michael E. Pasyanos, William R. Walter, and Sean R. Ford
Lawrence Livermore National Laboratory, Geophysics and Global Security Division

Shannon E. Hazler
Department of Geology and Geophysics, University of Colorado, Boulder

Sponsored by U.S. Department of Energy
Office of Nonproliferation and National Security
Office of Research and Development
Contract No. W-7405-ENG-48

ABSTRACT

This study reports on the ongoing investigation of surface wave group velocity dispersion across the Middle East and North Africa. Using broadband data gathered from various sources, we have measured group velocity using a multiple narrow-band filter method. To date, we have examined over 13,500 seismograms and made quality measurements for about 6500 Rayleigh and 3500 Love wave paths. A conjugate gradient method is used to perform the group velocity tomography at several periods. There is excellent agreement between short period structure and large known sedimentary features. Longer period structure is sensitive to crustal thickness, particularly the contrast between continental and oceanic regions and thicker crusts found beneath orogenic zones. We also find slow upper mantle velocities along rift systems. Correlation between the inversion results and known major tectonic features gives us confidence in our surface wave group velocities.

Accurate group velocity maps can be used to construct phase matched filters. The filters can improve weak surface waves by compressing the dispersed signal. We are particularly interested in using the filters to calculate regionally determined M_s measurements, which we hope can be used to extend the threshold of m_b:M_s discriminants to lower magnitude levels. A preliminary analysis of surface wave data processed using phase matched filters indicates a significant improvement in increasing the signal-to-noise ratio and improving magnitude estimates. Where signal-to-noise is very poor, phase matched filtering can still be useful in lowering the upper bound on M_s measurements. We propose a series of tests in order to analyze the utility of phase matched filters. Goals of the study include determining at what distance and magnitude ranges we can expect to see improvement using the filters and the overall effect of the filters on discrimination capability. We also propose to look at seismic velocity models of the Middle East and North Africa region in order to test the discrimination performance achieved using the various models.

Research performed under the auspices of the U.S. Department of Energy at the Lawrence Livermore National Laboratory under contract number W-7405-ENG-48.

Key Words: surface waves, group velocity, discrimination, tomography, Middle East, North Africa

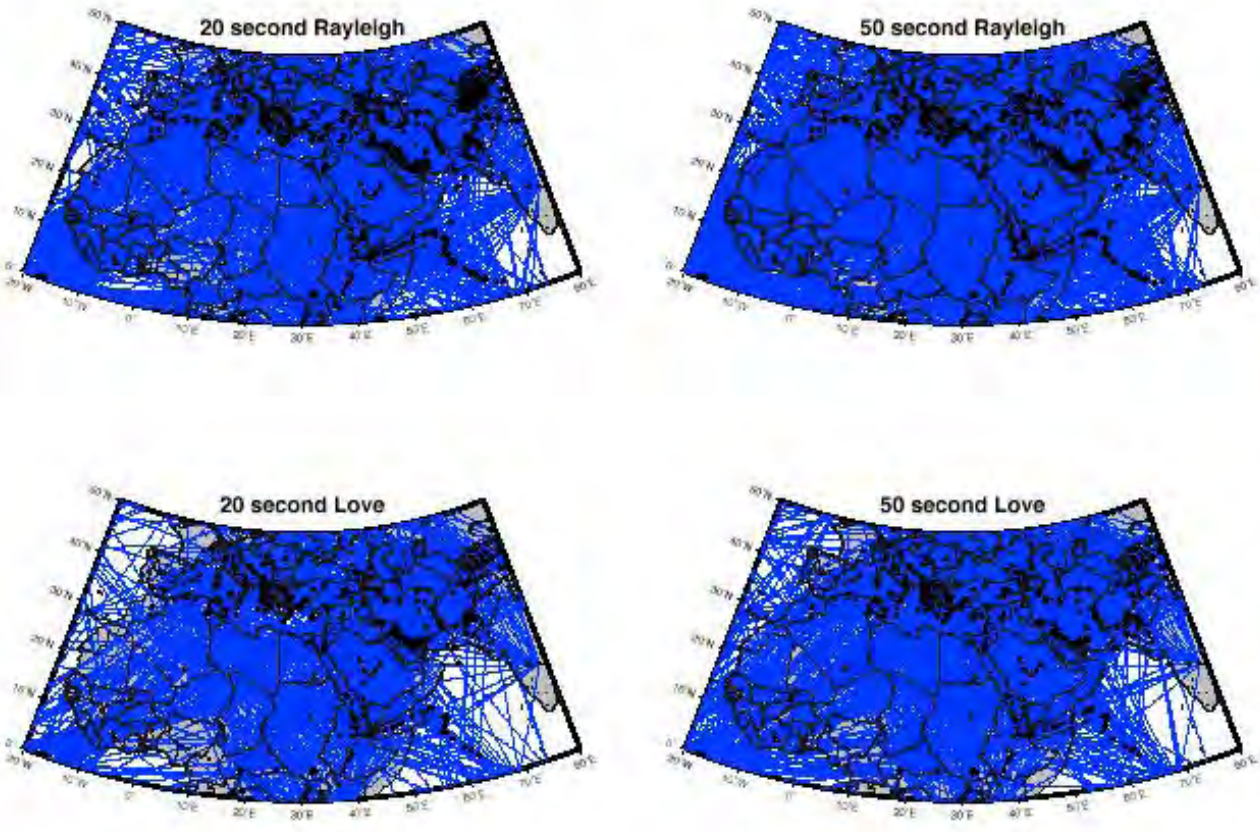


Figure 1 - Surface wave path maps for group velocities recorded for 20 sec Rayleigh waves, 50 sec Rayleigh waves, 20 sec Love waves, and 50 sec Love waves. Circles show earthquake locations, triangles show station locations.

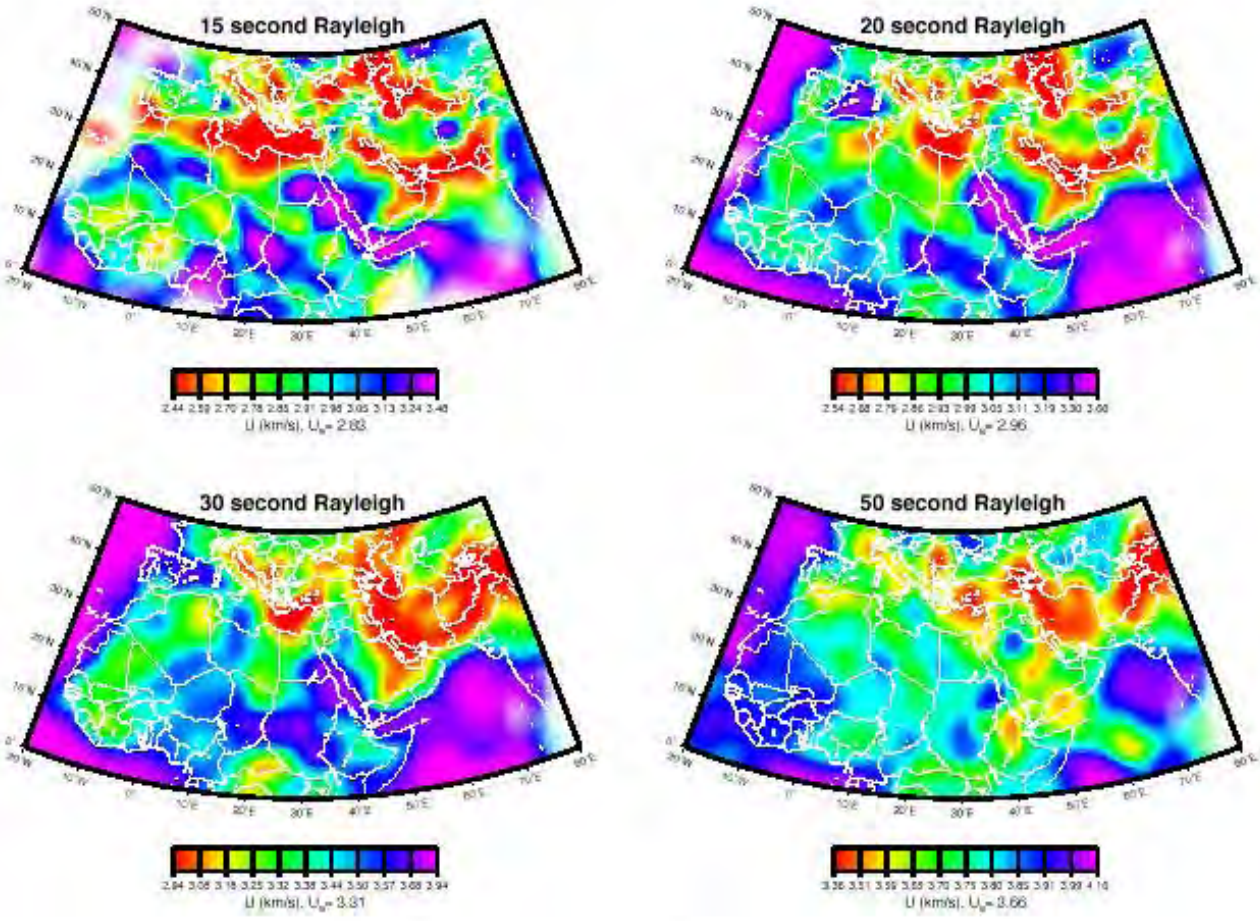


Figure 2 - Group velocity tomography for 15, 20, 30, and 50 sec Rayleigh waves. Velocities are indicated by the accompanying scale bars.

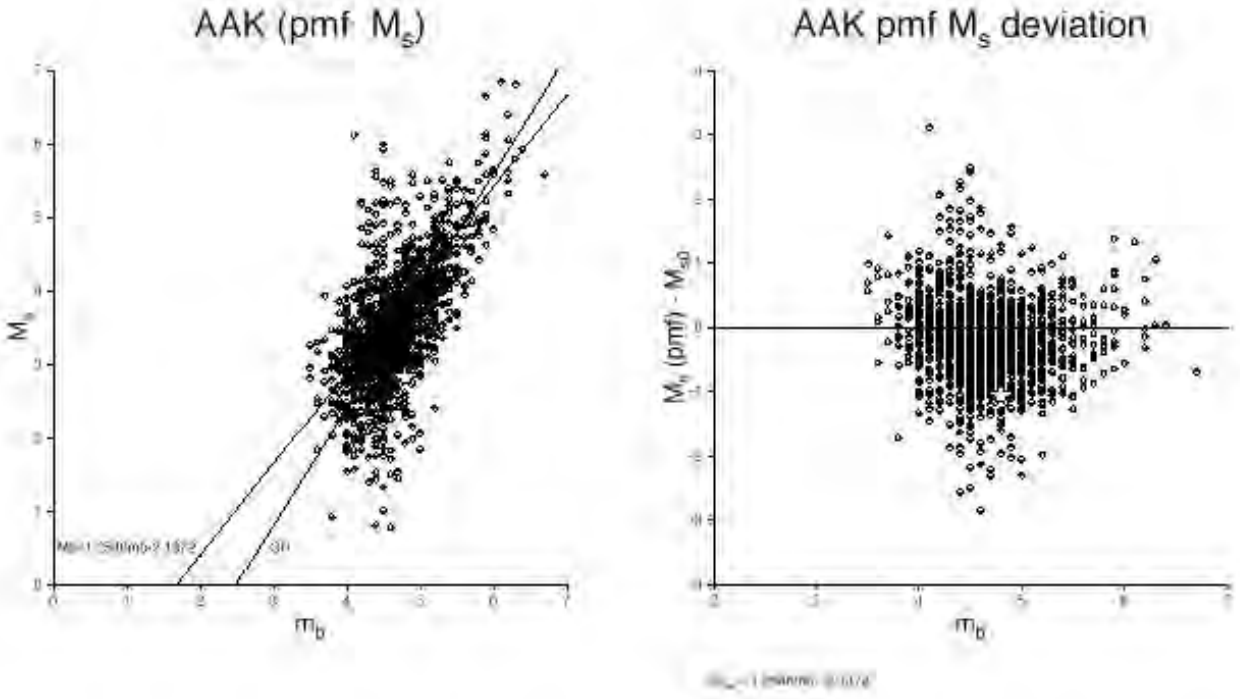


Figure 5 - a) Surface wave magnitudes at station AAK calculated with a phase-matched filter and plotted as a function of body wave magnitude
b) The difference between surface wave magnitudes calculated with and without use of the filter, also as a function of body wave magnitude

OBJECTIVE

The purpose of this research is 1) to improve surface wave group velocity maps and lithospheric shear wave velocity models for the Middle East and North Africa, and 2) use the group velocity results in phase-matched filters in order to lower M_s thresholds and improve m_b:M_s discrimination. M_s is an important discriminant measure and phase-matched filters could help identify smaller magnitude events. Improved shear velocity should improve event location capabilities throughout the region. Both improved identification and location capabilities are important to monitoring the Comprehensive Nuclear-Test-Ban Treaty. This work is on-going and to date we have concentrated on measuring Rayleigh and Love wave group velocities for paths in the region and tomographically inverting the measurements. We are currently starting to focus more on the discrimination aspect of this research.

RESEARCH ACCOMPLISHED

Group Velocity Measurements and Inversion

Using broadband data gathered from various sources, we have measured group velocity using a multiple narrow-band filter method. To date, we have examined over 13,500 seismograms and made quality measurements for about 6500 Rayleigh and 3500 Love wave paths. Path maps for a number of periods are shown in Figure 1. In general, we have the most paths for periods between 40 and 60 seconds, with the number of paths dropping off at both shorter and longer periods. We also have about twice as many Rayleigh waves as Love waves at a particular period. In Figure 1, for example, we have 3000 paths for 20 second Rayleigh waves, 5000 paths for 50 second Rayleigh waves, 1700 paths for 20 second Love waves, and 2100 paths for 50 second Love waves.

A conjugate gradient method is used to perform the group velocity tomography at several periods. We perform the group velocity inversions for both Rayleigh and Love waves between 10 and 100 seconds at 5 second intervals at periods shorter than 30 seconds and at 10 second intervals beyond. A more complete analysis of the inversion method, uncertainty, resolution and damping is given in Pasyanos, et al [1999]. Results for several periods between 15 and 50 seconds are shown for Rayleigh and Love waves in Figures 2 and 3, respectively.

Results

There is excellent agreement between short period structure and known large-scale sedimentary features. Rayleigh wave maps between 10 and 15 seconds and Love wave maps between 10 and 20 seconds highlight shallow sedimentary basins (i.e. whole Mediterranean Basin, northern Indian Ocean). Meanwhile, Rayleigh wave maps between 20 and 30 seconds and Love wave maps between 25 and 40 seconds emphasize only the deepest basins (i.e. Eastern Mediterranean, Caspian Basin, Persian Gulf, Mesopotamian Foredeep). In some cases, we can see a great likeness between Rayleigh and Love wave maps. For example, at 20 second Rayleigh waves and 30 second Love waves, which are both sensitive to deep sedimentary features, the maps are quite similar.

Longer period inversions (40 - 50 second Rayleigh waves and 50 - 60 second Love waves) are sensitive to crustal thickness, particularly the contrast between continental and oceanic regions and thicker crusts found beneath orogenic zones. At the longest periods in our study (> 60 second Rayleigh waves and > 70 second Love waves), our inversions are increasingly sensitive to the mantle, such as the slow upper mantle velocities along rift systems. Correlation between the inversion results and known major tectonic features gives us confidence in our surface wave group velocities, as does the correspondence between Rayleigh and Love wave maps. Additionally, our group velocity maps are very similar to those performed in Eurasia (Ritzwoller and Levshin, 1998) in regions where the two studies overlap.

The group velocity maps can be used to invert for shear wave structure in the Middle East and North Africa. In addition, the group velocity tomography can be combined with other data, such as P_n tomography and phase velocity tomography (see Hazler, et al, this volume) to reduce non-uniqueness in the model and develop the most complete P-wave and S-wave structure of the region. This is especially important in aseismic regions, where surface waves are one of the only methods of studying the area. The resulting three-dimensional velocity model would be useful for improving location of seismic events, as well as for characterizing the propagation of regional phases (i.e. L_g) which are useful for discrimination.

Phase Matched Filters

Phase-matched filters can improve weak surface wave signals by compressing the dispersed signals (Herrin and Goforth, 1977). The compressed signals can be cleaned to exclude noise sources such as microseismic noise, multipathing, body waves, higher order surface waves, and coda. With this methodology it is possible to extract surface wave signals from noisy measurements, calculate regionally determined M_s measurements, and lower the threshold on surface wave magnitude measurements. Much research has already been performed on surface wave analysis using phase-matched filters. For example, Stevens and McLaughlin, [1997] focused on using a 5 degree by 5 degree model to improve magnitude estimates globally. In our study the emphasis is on using our high-resolution surface wave tomography in the filters in order to make regional surface wave magnitude estimates in our region. These, in turn, can be combined with m_b to form one of the best known discriminants of earthquakes and explosions. Using phase matched filters derived from our high-resolution tomography, we hope to more accurately get at smaller events in our area and lower the m_b:M_s discriminant to even lower magnitude levels.

We can construct group velocity correction surfaces for a station, wavetype (i.e. LR, LQ), and period. A background velocity model for the correction surface is produced by integrating slownesses for the appropriate period and wavetype from the station to all points on the grid. We then employ the kriging methodology to create the correction surfaces (Schultz, et al 1998). The surface is made by kriging residuals formed from comparisons between the measurements made at that station and the tomographically-derived background velocity model. The kriged residuals are then added back to the velocity model back to produce the final correction surface. For a given station and source location, we can simply look up the group velocities to use in the phase-matched filter. An example of a correction surface for 50 second Rayleigh waves at station ABKT (Alibek, Turkmenistan) is shown in Figure 4.

Filter Performance

A preliminary analysis of surface wave data processed using phase-matched filters indicates a significant improvement in increasing the signal-to-noise ratio and making more robust magnitude estimates. Where signal-to-noise is very poor, phase matched filtering can still be useful in lowering the upper bound on M_s measurements. We intend to test discrimination performance by examining the m_b:M_s discriminant for the Indian and Pakistani nuclear tests at nearby stations. Figure 5a shows single-station M_s measurements made at station AAK (Ala Archa, Kyrgyzstan) using a phase-matched filter. In this case, the phase-matched filters were derived from only the surface wave tomography, without the addition of kriging. The M_s measurements are compared to m_b estimates from the PDE. The trend between the two sets of magnitudes are shown by the dotted line. In addition, we plot the theoretical relation between the two magnitudes predicted by equilibrating the Gutenburg and Richter energy relationships for m_b and M_S. There is a variation of about one magnitude unit around the trend that is probably due to a combination of factors, but is likely most attributable to variations in surface wave radiation caused by the source mechanism.

Figure 5b shows the difference between the M_s measurements made using the phase-matched filter and the measurements made without it. In general, use of the phase-matched filter results in lowering the measured M_s, with the greatest improvement seen for $m_b < 5.0$. There is still some improvement from the use of the filter up to m_b 5.5 for events with longer epicentral distances ($\Delta > 20°$). There is a significant portion of the data (events with excellent signal-to-noise) in which the use of the filter has little or no effect on M_s. We propose to conduct a series of tests in order to analyze the utility of phase-matched filters. Goals of the study include determining at what distance and magnitude ranges we can expect to see improvement using the filters and the overall effect of the filters on discrimination capability.

The phase-matched filters used in Figure 5 were derived using group velocities from our surface wave tomography. If the phase-matched filters were derived from another model, we would get different results. We propose to look at seismic velocity models of the Middle East and North Africa region in order to test the discrimination performance achieved using the various models. For example, in general how sensitive are our results to the base velocity model. How significant are any improvements between one-dimensional and two-dimensional models or between different two-dimensional models? Figure 6 shows one way of trying to assess model performance.

Figure 6a plots the surface wave magnitude that was determined for events both with and without phase-matched filters derived from the global model PREM (Dziewonski and Anderson, 1981), a model which we would not expect to have group velocities that are appropriate for the Middle East and North Africa. In general, there is an offset of about a half of a magnitude unit between the two measurements. Even for the largest events, we note a difference between the surface wave magnitudes calculated with and without the phase-matched filters. In this case, the reason for the difference is that the inappropriate model is unable to predict the correct group velocity and a significant portion of the surface wave energy is coming in outside of the window. Since we are unable to recover the magnitude for the largest events, we have no confidence in the filter performance for the smaller events.

Figure 6b shows a similar magnitude plot determined with and without a phase-matched filter derived from the surface wave tomography. For the largest events, there is not much of a difference in the M_s value determined using the filters indicating that, since the events had such good signal-to-noise ratio, the filters had little or no effect on the waveform. More importantly, it means that along all of these paths the envelope of group velocities predicted from the tomography was able to successfully predict the arrival time of the surface wave energy. For smaller magnitude events, starting around M 4.5, we can see that the magnitudes that were determined using the filter generally had smaller magnitudes. Unlike the previous case, where we were testing an inappropriate model, we can conclude that the lower magnitude levels are presumably due to a reduction in the noise that was contaminating the surface wave signal.

CONCLUSIONS AND RECOMMENDATIONS

We have made group velocity measurements of thousands of paths across the Middle East and North Africa. By tomographically inverting our measurements, we find that the Love and Rayleigh group velocities correlate well with tectonic structures, such as sedimentary basins, variations in crustal thickness, and upper mantle features. Over the whole period range examined, we find significant lateral variations of group velocities that diverge significantly from global models. As such, it is obviously inappropriate to use globally derived group velocity models as the basis for the phase-matched filters. We have found that the use of tomographically-derived background models produce suitable correction surfaces for the filters. The addition of kriging on top of these background models will further improve the correction surfaces. Having established an appropriate model to use as a basis for the phase-matched filters, we can now test the performance of the filters over a range of distances and magnitudes, ultimately assessing the overall improvement of our discrimination capability. High-resolution tomography models in the region can allow us to look at smaller magnitude events at shorter regional distances.

REFERENCES

Dziewonski, A. and D. Anderson (1981), Preliminary Reference Earth Model, *Phys. Earth Planet. Inter.,* **25,** 297-356.

Herrin, E. and T. Goforth (1977*),* Phase-matched Filters: Applications to the Study of Rayleigh Waves, *Bull. Seism. Soc. Amer.*, **67,** 1259-1275.

Pasyanos, M.E., W.R. Walter, S.E. Hazler (1999), A surface wave dispersion study of the Middle East and North Africa for Monitoring the Comprehensive Nuclear-Test-Ban Treaty, *submitted to Pure and Applied Geophysics.*

Ritzwoller, M.H., and A.L. Levshin (1998), Eurasian surface wave tomography: group velocities, *J. Geophys. Res.,* **103,** 4839-4878.

Schultz, C., S. Myers, J. Hipp, and C. Young (1998), Nonstationary Bayesian kriging: a predictive technique to generate corrections for detection, location, and discrimination, *Bull. Seism. Soc. Amer.,* **88**, 1275-1288.

Stevens, J.L. and K.L. McLaughlin (1997), Improved methods for regionalized surface wave analysis, Maxwell Technologies Technical Report to Phillips Laboratory, PL-TR-97-2135.

INVESTIGATIONS INTO REGIONAL MAGNITUDE SCALING: TRANSPORTABILITY AND M_s : m_b RELATIONSHIPS BASED ON NUTTLI'S m_b(Lg)

Howard J. Patton
Los Alamos Seismic Research Center
Earth and Environmental Sciences Division
Los Alamos National Laboratory

Sponsored by U. S. Department of Energy
Office of Nonproliferation and National Security
Office of Research and Development
Contract No. W-7405-ENG-36

ABSTRACT

Datasets of m_b(Pn) and m_b(Lg) measurements are presented for three continental regions to investigate magnitude scaling and issues related to event discrimination at small magnitudes. Compilations of published measurements are provided for eastern North America and central Asia, while new measurements are reported for earthquakes located in western United States, significantly increasing the number of previously reported m_b(Lg) and m_b(Pn) observations for this region. Transportability of regional magnitudes between tectonic provinces is investigated by statistical tests of scaling relationships for all three regions. While m_b(Pn) failed these tests, the m_b(Lg) scale of Nuttli (1973) is shown to be transportable and scales similarly for earthquakes with M_w ~4.2 - 6.5 and nuclear explosions with M_w 3.5 - ~5.5. Below M_w 4.0, m_b(Lg) scales differently for earthquakes in eastern North America and western United States. Scaling coefficients for m_b(Pn) and m_b(Lg) have values near 1.0, scaling as ~ $2/3 \cdot \log M_o$ (seismic moment) based on linear regressions of earthquakes with M_w ~3.9 - 6.5. For nuclear explosions, m_b(Pn) scales at a significantly higher rate than m_b(Lg), and this could be related to differences in "effective" source functions for Pn and Lg waves. Observed differences in scaling coefficients can be explained by (1) over-shoot in the reduced displacement potential affecting Pn amplitudes and (2) generation of 1-Hz Lg by near-field Rg-to-S scattering.

M_w:m_b(Lg) scaling relationships are converted to M_s:m_b(Lg) using published scaling laws between log M_o and M_s. Explosions conducted in weak materials and releasing tectonic stress by strike-slip faulting lie ~0.4 m_b units closer to earthquakes than explosions conducted in hard rock with thrust tectonic release. M_s:m_b(Lg) relationships scale as 0.69 and 0.78 for earthquakes and explosions respectively. Earthquakes are separated from hard-rock explosions by 1 – 1.25 m_b units for M_s greater than ~3.0; for M_s 1.5, the separation is reduced to ~0.7 m_b units in stable continents. Estimates of m_b(P) bias are made by comparing M_s:m_b(P) observations with M_s:m_b(Lg) relationships derived in this study. Results of these comparisons for earthquakes suggest that m_b(P) bias is significant, averaging about –0.4 m_b units, for tectonic regions of southern Asia.

Key Words: Seismic magnitude, source scaling, discrimination, regionalization

OBJECTIVE

The objective of this work is (1) to develop regional magnitude scales for CTBT monitoring purposes, (2) to apply these scales in regions of interest, (3) to evaluate the performance of regional M_s:m_b discriminants at small magnitudes, and (4) to develop relationships between regional magnitudes and teleseismic m_b for the characterization of regional m_b bias.

M_s:m_b is an important discriminant with a long history of success in teleseismic applications and a firm physical basis. Application of M_s:m_b to small magnitude events requires extensions to regional data. It is highly desirable for regional magnitude scales to exhibit stability and robustness, to be effective at small magnitudes and over the entire regional distance range, and finally to be transportable. Transportability is a key feature because of the wide range of geologies and tectonics of monitoring environments. This work focuses on research and development necessary to assure successful extension of M_s:m_b to regional applications.

RESEARCH ACCOMPLISHED

The first part of this work focuses on the problem of transportability. Teleseismic magnitude m_b(P) has long been known to be non-transportable. A classic example is the western U. S., where seismologists have long known of differences between this region and eastern U. S., e.g., m_b(P;west) ≈ m_b(P;east) – 0.33 (Chung and Bernreuter, 1981). Another example is from monitoring the Threshold Test Ban Treaty, where test site bias for the Nevada Test Site (NTS) and test sites of the former Soviet Union was an important issue. It was found that the NTS m_b(P) - yield curve for well-coupled shots does <u>not</u> apply to explosions at other test sites because m_b(P) is not transportable between test sites. In both examples, anomalous P-wave attenuation in the upper mantle under western U. S. is commonly accepted as the cause of non-transportability of teleseismic m_b (Douglas and Marshall, 1996).

A standard practice in developing regional magnitudes scales is the stage where the scale is “tied to” or “calibrated against” teleseismic magnitude. Since magnitude is an arbitrary construct, this practice simply puts the regional magnitude on the same “baseline” as m_b(P). Typically this calibration is performed on a region by region basis (for an example, see the paper on calibration of m_b(Pn) scale for western U. S. by Denny et al., 1987). It is important to note that a regional magnitude scale so calibrated will <u>not</u> be transportable because biases in m_b(P) data used for calibration will be transferred to the new scale by the calibration procedure.

The regional magnitude m_b(Lg) devised by O. Nuttli is tied to teleseismic m_b in central U. S. (Nuttli, 1973). In 1986, Nuttli applied a more generalized formulation of m_b(Lg), still tied to m_b in the central U. S., to NTS explosions for the purpose of improved yield estimation (Nuttli, 1986a). Subsequent studies were carried out to estimate m_b(Lg) for Soviet explosions detonated at test sites in Kazakhstan (KTS) and Novaya Zemlya (Nuttli, 1986b; 1987; 1988). In addition to their usefulness for yield estimation, measurements of m_b(Lg) provided a means for computing test site bias by direct comparison of m_b(P) and m_b(Lg) for explosions with both measurements. The important results in this

series of papers required that m_b(Lg) is transportable, an assertion Nuttli made repeatedly. Why should this scale be transportable and other regional scales are not?

Examining Nuttli's 1986 formulation, it can be seen that m_b(Lg) is tied to m_b(P) once and only once (for the central U. S., as mentioned above) by the calibration equation,

$$m_b(Lg) = 5.0 + \log_{10} [\, A(10) / 110. \,],$$

where

$$A(10) = A(\Delta) \cdot (\Delta/10)^{1/3} \cdot [\sin (\Delta/111.1) / \sin (10/111.1)]^{1/2} \cdot \exp[\gamma \cdot (\Delta - 10)],$$

and Δ is epicentral distance, γ is attenuation coefficient, and "exp" is the exponential function. $A(\Delta)$ is Lg amplitude measured near 1 Hz off regional seismograms recorded on short-period WWSSN instrumentation. This amplitude is corrected for Airy phase propagation, geometrical spreading, and attenuation back to a reference distance of 10 km. The calibration equation states that *an earthquake in central U. S. with m_b(P) 5.0 will produce a "hypothetical" 1-Hz Lg wave 10 km from the source of 110 microns amplitude.* For m_b(Lg) to be transportable, two conditions must be met: (1) the hypothetical calibration amplitude of 110 microns is valid from one region to the next and (2) accurate path corrections for attenuation are available for Lg waves. Another way to state condition (1) above is that 1-Hz Green's function responses for Lg waves are invariant in continental structures and for seismogenic depths confined to the crust.

While Nuttli's results for nuclear explosions support his claim of transportability, the claim has never been tested rigorously on datasets of earthquakes located in structurally/tectonically diverse regions. In this study, I present the results of statistical tests for transportability comparing m_b(P), m_b(Pn) and m_b(Lg) scaling relationships for earthquakes located in eastern North America (ENA), western U. S. (WUS), and central Asia (CA). The results confirm non-transportability of m_b(P) and also demonstrate non-transportability of m_b(Pn). However, m_b(Lg) is transportable and scales similarly for earthquakes with M_w ~4.2 - 6.5 and for nuclear explosions with M_w 3.5 - ~5.5. Below M_w 4.0, m_b(Lg) scales differently for ENA and WUS.

Figure 1a summarizes m_b(Lg) observations for all earthquakes and all nuclear explosions analyzed in this study. The nuclear explosions were detonated at continental test sites around the world in a wide variety of emplacement conditions. Regression lines are shown for 1st-order scaling models (there is no evidence for magnitude saturation of m_b(Lg) for events in this dataset up to M_w 6.5). Earthquake scaling in stable regions is based on data for ENA, while scaling in tectonic regions is based on WUS and CA data. The "unified" M_w:m_b(Lg) scaling relationship was derived using earthquake data from all three regions for M_w 4.2 - 6.5, and it is arguably transportable to any continental

region. Also shown in Figure 1a is the scaling relationship for nuclear explosions.

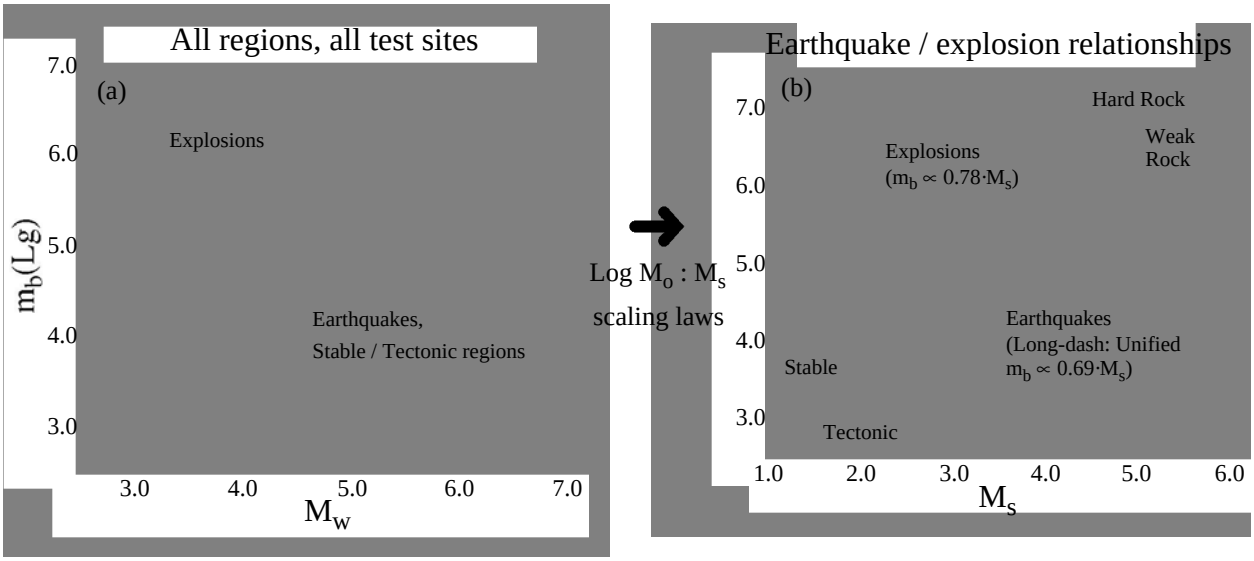


Figure 1. mb(Lg) scaling relationships for earthquakes and explosions. (a) Explosion data are compilations for NTS, KTS, and Novaya Zemlya. One relationship fits all explosion data. Earthquake data are divided into stable (ENA) and tectonic (WUS + CA) regions. Above M_w 4.2, a "unified" relationship (dash line) satisfies data from all regions. (b) Log M_o:M_s scaling laws were used to derive M_s:m_b(Lg) scaling relationships

M_s:m_b(Lg) relationships were obtained from 1st-order scaling models by the use of log M_o:M_s scaling laws for earthquakes and explosions. The global scaling law of Ekstrom and Dziewonski (1988) was used for continental earthquakes. For nuclear explosions, two relationships between isotropic M_o and M_s were drawn upon: one is based on surface wave observations for NTS (Stevens and McLaughlin, 1997), where media is characterized by low velocities, low strength and tectonic release in the form of strike-slip faulting; the other is based on surface wave observations for KTS (Ekstrom and Richards, 1994; Sykes and Cifuentes, 1984), where hard rocks (granites) prevail and tectonic release is typically reverse dip-slip faulting.

The results of applying log M_o:M_s scaling laws are shown in Figure 1b. There are two M_s:m_b(Lg) relationships for explosions: the "weak rock" case is based on NTS experience and plots ~ 0.4 magnitude units (mu) closer to earthquakes. Both relationships scale as $0.78 \cdot M_s$, while earthquake relationships scale as 0.64, 0.75, and 0.69 for stable, tectonic, and unified models, respectively. Convergence of explosion and earthquake populations at small magnitudes is most pronounced for stable continental regions, while the populations are nearly parallel for tectonic regimes. M_s:m_b(Lg) relationships are separated by 1.0 - 1.25 mu for M_s greater than ~3.0, and converge to ~0.8 mu or less at M_s 2.0 depending on tectonic region and geologic/tectonic nature of the test site. A research goal in the near future is to experimentally confirm these M_s:m_b(Lg) relationships for key monitoring regions. Some results should be available by the time of the symposium.

Having established transportability of m_b(Lg) for continental regions, I investigate ways in which the results pre-

sented above could be used to quantify both size and regional variations of m_b(P) bias for monitoring regions. I present results based on two methods: (1) extension of Nuttli's test site method to earthquakes using direct comparison of m_b(P) and m_b(Lg) for events with both measurements, and (2) a new approach comparing M_s:m_b(P) observations with M_s:m_b(Lg) relationships developed above. Summarizing the results from (1), I find that the average difference, E[m_b(P) – m_b(Lg)], for ENA (New Madrid seismic zone only), WUS (California and Basin and Range areas only), and CA is –0.06 ± .03, –0.33 ± .03, and –0.12 ± .04 mu, respectively, where uncertainty is one standard deviation (1·σ) and m_b(P) values were taken from EDR or ISC bulletins. Ideally, the difference should be zero for the New Madrid seismic zone since Nuttli's calibration was originally performed for this region. It is not different from zero at the 95% confidence level (2·σ). Results for California and the Basin and Range are consistent with previous bias estimates for western U. S. (Chung and Bernreuter, 1981) and with Nuttli's estimate of test site bias for NTS (Nuttli, 1986a; –0.31 ± .02 mu). While the bias estimate for Tien Shan and neighboring regions of CA is smaller than WUS, I find significant variations when the region is sub-divided: e.g., 15 earthquakes located in eastern Tarim Basin, close to the Lop Nor test site, yield E[m_b(P) – m_b(Lg)] of –0.37 ± .05 mu while observations for earthquakes in or near the Tien Shan mountains show large scatter and average values not significantly different from zero.

The results of a new approach, which can be used to survey m_b bias for large areas, are summarized in Figure 2.

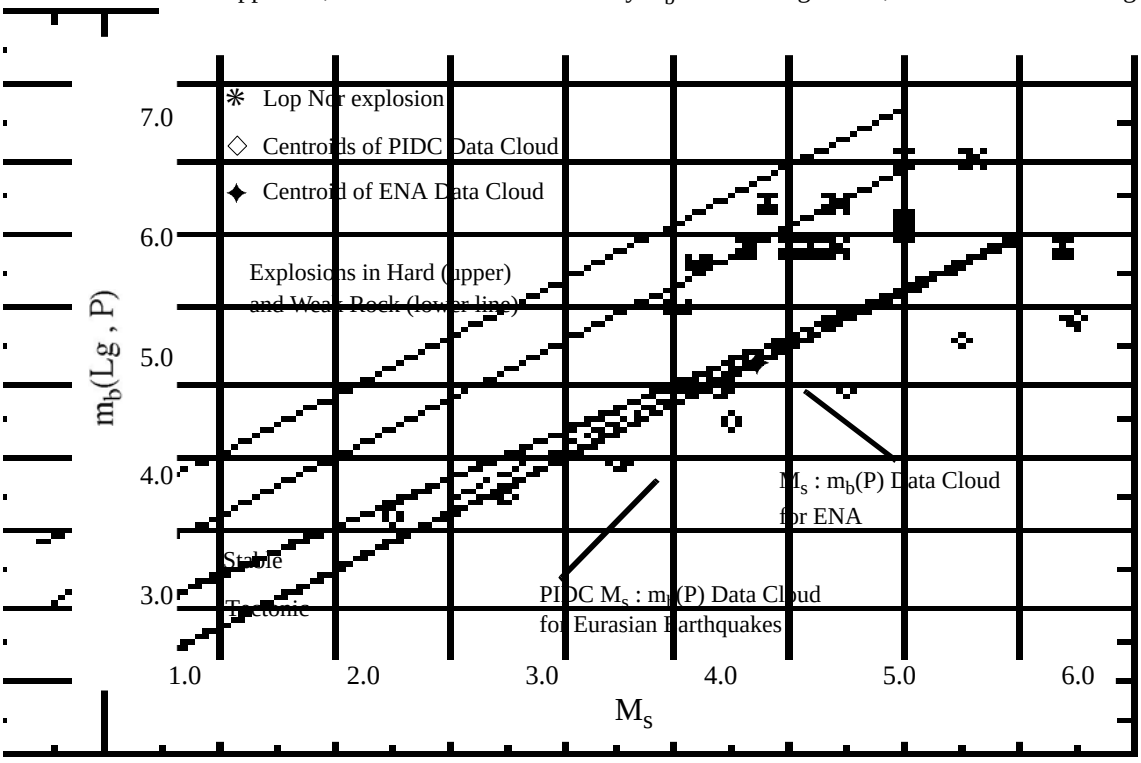


Figure 2. Comparisons of M_s:m_b(Lg) relationships with selected datasets of earthquake and explosion

This figure shows M_s:m_b(Lg) relationships for earthquakes and explosions developed above and several datasets of M_s:m_b(P) observations from published catalogs. Data published by the Prototype International Data Center (PIDC) in Reviewed Event Bulletins (REBs) are shown as dark-gray data cloud representing the distribution of ~800 M_s:m_b

observations for Eurasian events in a ~33 month reporting period. A vast majority of these events are located in tectonic regions of southern Asia. Open diamonds are centroid m_b(P) values obtained by binning M_s data in intervals of 0.5 mu. The smaller, light-gray data cloud is the distribution of 26 M_s:m_b(P) data points for a much smaller dataset of earthquakes located in ENA with $3.8 < M_s < 4.7$. This range was selected because it avoids problems with m_b saturation for larger events and the effects of data censoring on m_b estimates for smaller events. The solid diamond is the centroid of the ENA data cloud.

In this paper I assert that m_b differences between M_s:m_b(P) observations and the unified M_s:m_b(Lg) relationship for earthquakes in the M_s 3.8 - 4.7 range are mainly caused by regional m_b(P) bias. Residuals with respect to the unified relationship were computed for all 26 M_s:m_b(P) observations in the ENA dataset. The mean residual is $-0.11 \pm .06$ mu which is equivalent to the difference in m_b units between the centroid of the ENA data cloud and the unified relationship drawn as a long-dashed line in Figure 2. This result compares favorably with the results from method (1) above; the mean of 52 [m_b(P) – m_b(Lg)] observations for earthquakes located throughout ENA is $-0.07 \pm .03$ mu.

In the case of the Eurasian data cloud, comparison of the centroid plotted at M_s 4.2 with the unified M_s:m_b(Lg) relationship suggests that m_b(P) bias is significantly larger for tectonic regions of southern Asia. The m_b difference is about –0.4 mu, six times larger than the difference for ENA. Keeping in mind evidence for spatial variations of [m_b(P) – m_b(Lg)] observations in CA discussed above, significant lateral variations in m_b differences are expected across southern Asia, and one of the objectives of this work is to map spatial variations. Preliminary maps will be presented at the symposium.

Turning to M_s:m_b(P) observations for Lop Nor explosions in Figure 2, I applied method (2) once again to make an estimate of m_b(P) bias for the test site. For this application, the question of which M_s:m_b(Lg) relationship to use must be addressed. The source medium at Lop Nor is generally characterized by granite, similar to the former Soviet test site at KTS. On the other hand, studies of tectonic release for Lop Nor explosions (Gao, 1993) find that the mode of tectonic release is strike-slip, which is more the style of large NTS explosions. Thus, log M_o:M_s scaling laws for Lop Nor may represent something of a hybrid between NTS and KTS scaling, and I assumed an M_s:m_b(Lg) relationship with the same slope but midway between the weak and hard rock models in Figure 2. Computing residuals for all data points except the largest explosion (M_s 5.7, which is a significant outlier and plots well above the range of applicability of the models) and taking the mean, the result is $-0.35 \pm .06$ mu. This estimate of the test site bias for Lop Nor agrees very well with direct observations of [m_b(P) – m_b(Lg)] for earthquakes located in eastern Tarim Basin close to the test site (see results for method (1) above).

CONCLUSIONS AND RECOMMENDATIONS

The importance of m_b(Lg) transportability for treaty monitoring cannot be over-stated. The results of studies that exploit transportability may well lead to improved understanding of discrimination at small magnitudes and to better

monitoring capabilities. Among the results of this study are: (1) unified (or global) M_w:m_b(Lg) scaling relationships for continental earthquakes and nuclear explosions; (2) M_s:m_b(Lg) scaling models for discrimination at small magnitudes; and (3) development of methods for estimating both size and regional variations of m_b(P) bias. Future work will focus on further test and application of these results for successful extension of M_s:m_b technologies to regional data.

REFERENCES

CHUNG, D. H. and BERNREUTER, D. L. (1981), *Regional relationships among earthquake magnitude scales.* Rev. Geophys. Space Phys. *19*, 649-663.

DENNY, M. D., TAYLOR, S. R. and VERGINO, E. S. (1987), *Investigation of m_b and M_s formulas for the western United States and their impact on the M_s/m_b discriminant*. Bull. Seismol. Soc. Am. *77*, 987-995.

DOUGLAS, A. and MARSHALL, P. D. (1996), *Seismic source size and yield for nuclear explosions.* In *NATO Proc. on Monitoring a Comprehensive Test Ban Treaty* (eds. Husebye, E. S. and Dainty, A. M.), Kluwer Academic Publishers, Hingham Massachusetts, 309-353.

EKSTROM, G. and DZIEWONSKI, A. M. (1988), *Evidence of bias in estimations of earthquake size.* Nature *332*, 319-323.

EKSTROM, G. and RICHARDS, P. G. (1994), *Empirical measurements of tectonic moment release in nuclear explosion from teleseismic surface waves and body waves.* Geophys. J. Int. *117*, 120-140.

GAO L. (1993), *Seismotectonics, and the mechanics of faulting inferred from seismic body wave inversions.* Ph.D. Thesis, University of Arizona, Tuscon, Arizona.

NUTTLI, O. W. (1973), *Seismic wave attenuation and magnitude relations for eastern North America.* J. Geophys. Res. *78*, 876-885.

NUTTLI, O. W. (1986a), *Yield estimates of Nevada Test Site explosions obtained from seismic Lg waves.* J. Geophys. Res. *91*, 2137-2151.

NUTTLI, O. W. (1986b), *Lg magnitudes of selected east Kazakhstan underground explosions.* Bull. Seismol. Soc. Am. *76*, 1241-1251.

NUTTLI, O. W. (1987), *Lg magnitudes of Degelen, east Kazakhstan, underground explosions.* Bull. Seismol. Soc. Am. *77*, 679-681.

NUTTLI, O. W. (1988), *Lg magnitudes and yield estimates for underground Novaya Zemlya nuclear explosions.* Bull. Seismol. Soc. Am. *78*, 873-884.

STEVENS, J. L. and MCLAUGHLIN, K. L. (1997), *Improved methods for regionalized surface wave analysis.* Maxwell Technologies Final Report No. *MFD-TR-97-15887*, Phillips Laboratory Report No. *PL-TR-97-2135*.

SYKES, L. R. and CIFUENTES, I. L. (1984), *Yields of Soviet underground nuclear explosions from seismic surface waves: Compliance with the Threshold Test Ban Treaty.* Proc. Natl. Acad. Sci. USA *81*, 1922-1925.

ROBUST PROCEDURES FOR AUTOMATIC PRECISE LOCATION OF REGIONAL SEISMIC EVENTS

Vladimir Pinsky and Avi Shapira

Seismology Division, Geophysical Institute of Israel
P.O. Box 2286
Holon 58122, Israel

Sponsored by the U.S. Department of Defense
Defense Threat Reduction Agency
Contract No. DSWA01-97-C-0151

ABSTRACT

Coordinates YY,H of seismic source and origin time T are routinely determined through P and S phases manual picking and an optimization procedure minimizing the discrepancy between model arrival times and network observations. The proposed procedure has two main steps: preliminary rough location and final, accurate location. Preliminary location is based on the computation of **seismogram envelopes** for each station and finding the envelope maximums **Pmax** and **Smax**. This is followed by estimation of the epicenter X,Y and the origin time T, using travel time curves (lines) for propagation of P and S seismic energy and a **grid search robust optimization** procedure. The method has already been presented and its accuracy demonstrated, DX, DY~6 km for the epicenter coordinates, and T~1 Sec for the origin time. Values of X, Y, T estimated in the first step are used together with a local velocity model to approximate P and S on-set times for each station and improved in the second step using **likelihood-maximum estimation**. For increased reliability additional P and S pickings are provided due to intersection of the corresponding envelope fronts with noise level. This last procedure is applied to the parts of the seismogram corresponding to the intervals containing the hypothetical P and S arrivals. Finally, a grid-search **robust optimization** procedure (60X60X25km3, ±10 sec), based on the local P and S velocity model, is used to provide accurate location. This procedure is based on maximization of the target function equal to the sum of the "bell-like" functions (equals 1when discrepancy is 0 and equals ~ 0 at infinity), accounting for good pickings and ignoring bad ones. Due to the robustness, the package does not require pre-selection of seismograms for events recorded with relatively good quality by at least several stations, even if the others are noisy or do not contain any signal at all. The quality of location is indicated by the value of the target function (≈ equal to the number of "good" stations) and/or the usual confidence ellipsoid estimation. The procedure was checked using records of the Israel Seismic Network from four calibration quarry blasts at the Arad quarry close to the Dead Sea, providing location accuracy of 0.3 to 1.7 km and, in all the cases, better than a qualified analyst. This was then applied to a data set of 61 earthquakes and quarry blasts occurring in Israel with an overall 80% accuracy of DX, DY ~3 km, DH~ 7 km and DT~0.7 sec.

Key Words: seismic event location, envelopes, maximum likelihood on-set estimation, grid search optimization.

OBJECTIVE

Within the general framework of improving the monitoring capabilities of the CTBT in the Middle East, this research is focused on implementation of innovative, automatic and robust location procedures intended to improve accuracy and enhance efficiency of regional network performance on the basis of data collected by the Israel Seismic Network (ISN).

RESEARCH ACCOMPLISHED

Automation of regional event location using ISN recordings is one of the tasks of our diverse research program initiated under the DSWA contract. This paper describes the continuation of the research first reported at the previous symposium presents the main aspects of our approach and the initial results of the prototype automatic location procedure.

INTRODUCTION

The routine source location of regional and local events is based on picking the onsets of P (first) and S (second) phases on the seismogram. These are then converted into the corresponding geographical source coordinates, depth and time, using the given travel time model as determined by the velocity structure. In doing this, we need to remove noise, spikes and sporadic simultaneous events. In such cases, analysts must rely on their view of the seismogram and previous experience. Our task was to imitate the performance of the analyst.

In the first stage of our investigation, we simplified the problem by picking not first arrivals, but maxima of energy of the corresponding phases having a better signal-to-noise (SNR) relation. The physical basis for this is that the energy of the P and S seismic phases obeys the law of diffusion and propagates in the stratified medium at a constant velocity. Based on this, Ryzhikov et al. (1996) derived a theoretical function over the observed envelopes of seismic phases which has a maximum pointing to the source epicenter. Further to this premise, and in parallel with Shoubik et al. (1997) and Husebye et al. (1998), we developed a procedure for estimating source epicenters, X,Y (no depth) and time, T, using specific envelopes of the seismogram (Pinsky and Shapira, 1998). This procedure utilized automatic picking of maxima Pmax and Smax from the envelopes and a robust search inversion method. The automatic algorithm yielded an accuracy for X,Y of ~6 km (local coordinates) and T ~1 sec on the data set from pre-selected seismograms (with clear seismic phases) from the ISN data base of 150 earthquakes and quarry blasts. However, it did not achieve the location accuracy (~2 km for X,Y; ~3 km for H and T ~0.3 sec) as set out in the bulletin. This is probably due to the relatively large variation in Pmax and Smax times around theoretical values, while the P and S first arrivals seem to be more stable, at least for earthquakes.

In view of this, we returned to the location method based on first arrival time estimation, but with reasonable preliminary estimates of X,Y and T from the envelope location procedure. There is a variety of automatic methods for finding first phase arrivals on seismograms. We tested one method based on maximum likelihood ratio (Pisarenko, et al (1987)) which was shown convincingly by Kushnir, (1996) to be equivalent to, or even better than, manual picking and another inspired by the envelope processing algorithm of Fedorenko and Husebye (1999). Both require a specified time interval, assumed to comprise phase arrival. We placed it on the time axis according to the preliminary X,Y,T and theoretical travel time computations for P and S phase first arrivals. Finally, source coordinates, time and depth are estimated through a grid search using a robust optimization procedure based on M-estimates developed by Huber (1972) and tested for seismic location by Andersen (1982).

The data used in this study are presented in the short period seismograms (50 Hz sampling rate with efficient bandwidth 0.5-12 Hz) of the Israel Seismic Network (~30 stations) telemetered to a Hub via radio FM link. The data include 61 earthquakes, M_L=1.0-2.8 at distances of 15-310 km and four calibration quarry blasts exploded in the Arad quarry with precisely known GMT coordinates and ignition time (see Table 1.). Event epicenters, station and quarry locations are presented in Fig. 1.

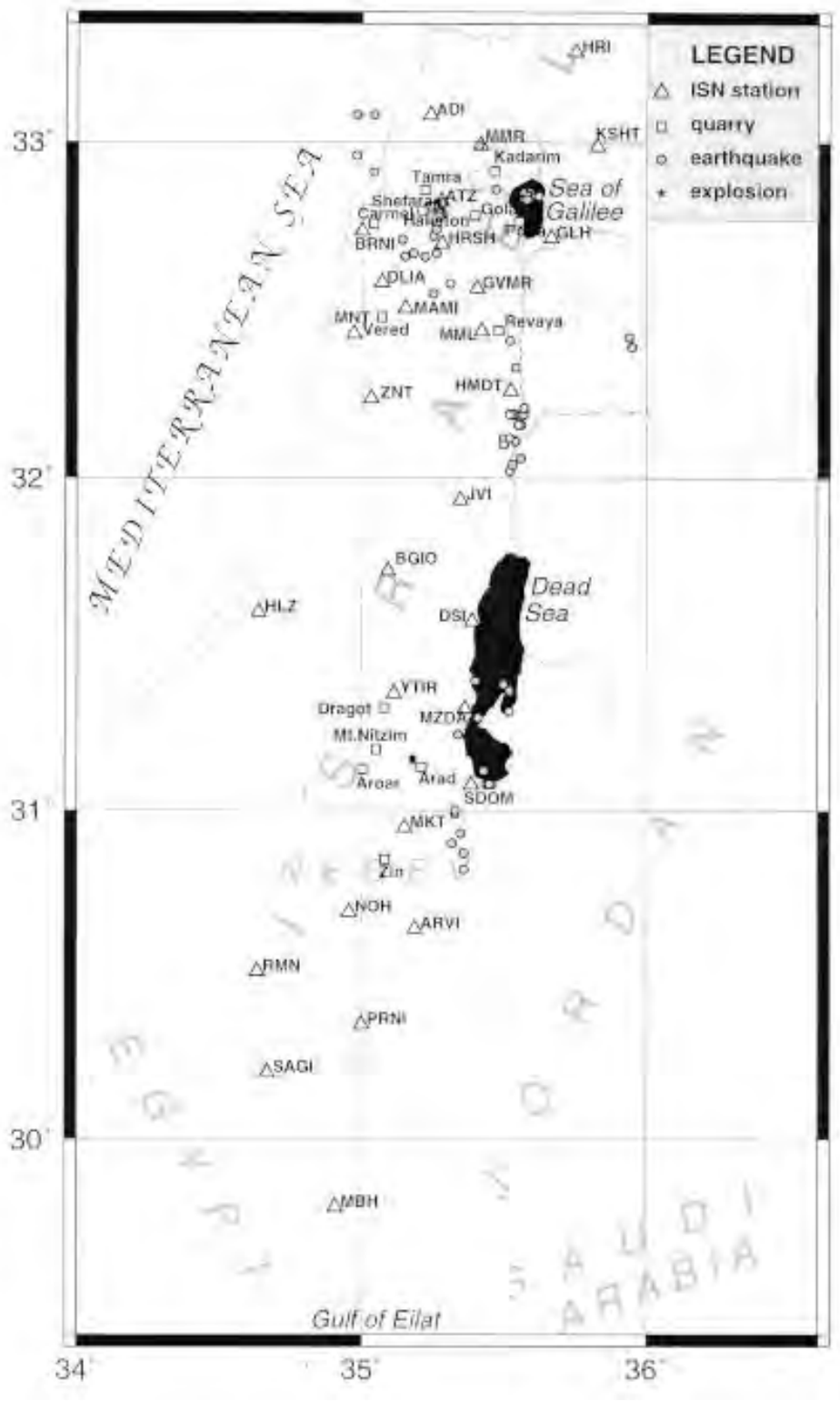


Fig. 1 Map of Israel and adjacent area, showing the data base region, earthquakes, quarries and explosions.

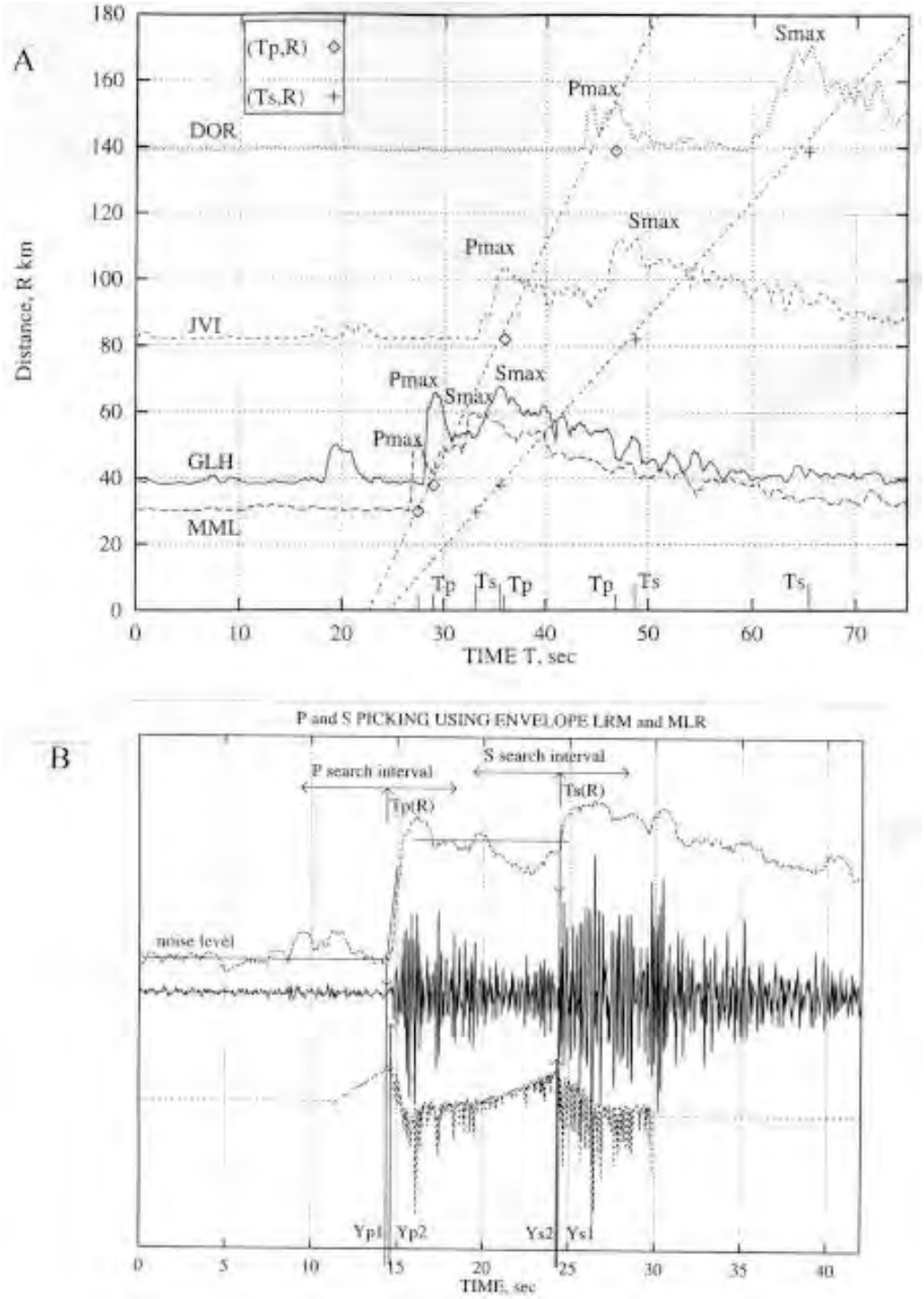


Fig 2. Automatic P and S phases picking using a) time picks Tp and Ts, corresponding to the local maximums of Pmax and Smax of the envelope curves and using b) time picks Ypi, Ysi, i=1,2 provided by the maximum likelihood ratio (lower curve) and linear regression method of the envelope (upper curve) front. The Tp and Ts time picks are compared to the travel time curves of the maximum of energy for the P and S phases. The Yp and Ys time picks are found inside P and S search intervals, guided by Tp(R) and Ts(R) theoretical travel times, where R is the distance from preliminary epicenter to the given station.

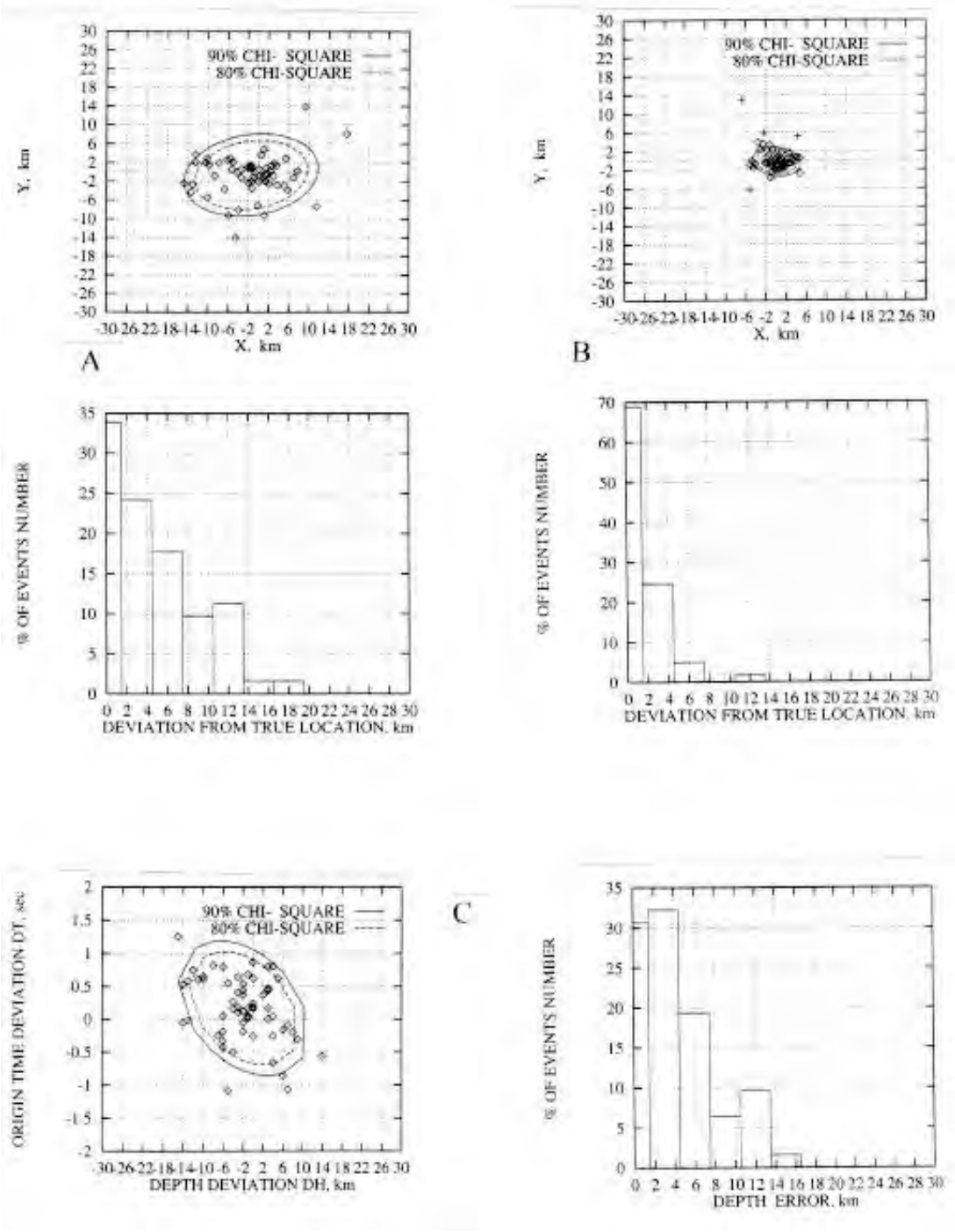


Fig. 3. Maps and histo grams of the 61 earthquake automatic locations relative ISN bulletin, provided by the a) envelope method of preliminary epicenter estimations due to the automatic on-set pickings.

METHOD

The method used comprises four main stages; (i) preprocessing; (ii) preliminary epicenter location; (iii) P and S onset picking and (iv) final hypocenter location.

Preprocessing: this includes despiking and band pass filtering of the seismograms in an appropriate frequency band and automatic selection of the traces with appropriate signal-to-noise ratio (SNR). The records used are often marred by spikes or noise outbursts caused by radio pulses or industrial and micro-seismic noise that cause inaccurate interpretation. It is, therefore, crucial to the success of a procedure based on detecting seismic signals, that records are clean. A spike is assumed to be "thin" and "high", thus we perform a simple de-spiking by cutting the whole trace into a series of intervals (2 sec. each) and comparing average noise level with its current value inside the interval. Naturally, some of the channels may suffer partial distortion of the signal front as a result of this procedure. The next step is to calculate seismogram envelopes for each station which are used for preliminary **epicenter location** by the **envelope location method** (Pinsky, 1999). Two different types of envelope are computed, both characterized by abrupt fronts and sharp energy maxima, even for rather weak seismic phases; thus providing, in most cases, a clear separation between P and S phases even at short distances. The envelopes have local maximums P_{max}, S_{max} at time points T_p and T_s which are coincident with P and S arrivals in the original non-transformed records. The quality of a trace is characterized by the SNR=P_{max}NL ratio, where NL is the noise level of the envelope. The traces with low SNR are omitted to give a clearer result, thus providing automatic selection of channels for further processing. Additional selection criteria are - closeness of T_p or T_s picks between the two types of envelopes, checking whether $dt_{\alpha\beta} = |T_\alpha - T_\beta| < dt0$, at least for one α, β pair, where $\alpha, \beta \in \{p, s\}$; dt0 meanwhile is chosen as equal to 2 sec. Those traces that are left after trace selection as described above, are arranged according T_p time, the first having the minimum T_p among M channels, having the largest SNR. In this way it is possible to estimate the station which is probably closest to the source.

PRELIMINARY EPICENTER LOCATION is provided by the mentioned above **envelope location method**, based on fitting time-distance (T_p,R) , (T_s, R) pairs to the travel time curves presented in this case by the two lines: $T_{\mathbf{p}} = T_{0\mathbf{p}} + R/V_{\mathbf{p}}$, $T_{\mathbf{s}} = T_{0\mathbf{s}} + R/V_{\mathbf{s}}$, which characterize propagation of maximum of energy for the regional P and S seismic phases (see Fig. 2a) correspondingly. The parameters of the two equations, estimated through a least squares fitting for a set of earthquakes and quarry blasts, are as follows V_p=6.0, V_s=3.5, T_{0p}=2.5, T_{0s}=3.5. The $T_{\mathbf{p}}$ and $T_{\mathbf{s}}$ estimates, found by triggering the envelopes with the following maximum determination are not especially reliable. However, for the case where we have sufficient stations (NS > 10) with good SNR, true $T_{\mathbf{p}}$ and $T_{\mathbf{s}}$ are the expected majority and, therefore, a robust optimization that ignores false observations may provide a satisfactory source location. The optimization procedure of such a class was specified by Huber, 1972 as M-estimators. The task is to maximize (minimize) target function

$$F(\theta) = \sum_r w_r f(\Delta_r(\theta)) \qquad (1)$$

with a gain (loss) function **f**(Δ) of residuals Δ (Δ =[observations minus model]). The usual and, in many cases efficient, procedure for location is a least-squares technique in which the solution is due to minimization of a sum of squares of the residuals $\Delta_{ai} = T_a - T_a(R_i) - T_0$, a = P,S. for a number of stations, where T_0 is the source time. If, however, the observations include random outliers of the time T_a then this procedure is inefficient and, besides, may cause large errors in location. We observe, that many P identifications give S travel time and vice versa by mistake; so a random T_a variable for the fixed a should bi-modal or even multi-modal distribution. This feature should be taken into account in the specialized location scheme since the conventional least-squares procedure is not applicable in this case.

In such cases residuals appear as

$$\Delta_{aci} = T_a - T_c(R_i) - T_0 \qquad (2)$$

Next, instead of one station's residuals Δ_{aci} we shall consider two station residuals $\Delta_{abcij} = \Delta_{aci} - \Delta_{bcj}$, ij=1,N, *a*, *b*, *c* = P, S, which do not depend on origin time T_0, thus, reducing the number of unknown variables from 3 to 2. From the "picker" above we obtain two time picks T_p and T_s for each channel, but the "picker" is not aware to which phase: P, S, or Rg they belong. To distinguish between correct and incorrect identifications we use a gain function in Eq. (1)

$$f(\Delta) = (|\Delta| + \varepsilon)^{-1} \qquad (3)$$

deviations Δ (instead of the usual $\mathbf{f(\Delta)=\Delta^2}$), "voting" for true pickings for its large values and against false pickings for its small values respectively. Thus it is reasonable is to estimate epicenter X,Y by maximization of the F(θ) function (1), which is provided by computing the F(θ) value at each of the grid points (say, 60X60 km of 1 km step).

Consequently, the procedure unites in one the two tasks: the location with the phase identification, where majority of "good" pickings, close to P or S track, would guarantee successful solution. The control parameter ε >0 helps to avoid possible zeroes of the residuals Δ_{abcij}, thus providing robustness of the X_{max}, Y_{max} estimator, which maximize the F(θ). After that we estimate origin T_0 providing a maximum to F(θ) with f(Δ) due to (3) and fixed X= X_{max}, Y= Y_{max}. and Δ determined by (2). The parameter ε is selected automatically as ε=0.1+k*2., k=l,..,5 according to the empirical criterion that for more than N/2 stations there is at least one combination of *a*, *b*, *c*, *i* and *j* that ($|\Delta_{abcij}|$+ε)<3.

P and S ONSET PICKINGS are provided by estimating P and S first arrivals $\mathbf{Y_p}$ and $\mathbf{Y_S}$, which seems more stable than T_p and T_s for good SNR conditions. For the automatic $\mathbf{S_p}$ and $\mathbf{Y_s}$ estimation we chose a statistically optimal algorithm proposed by Kushnir (1994) and shown to be efficient for seismic phase picking. The procedure is based on statistical testing of the hypothesis, that time series before and after signal arrival are two different autoregreessive time-series in the chosen time interval [T1,T2], possibly containing the point of interest T0. The two autoregressive models are approximated using "noise" and "signal" recordings corresponding to the opposite edges of the interval. The point T0 is estimated as a maximum likelihood ratio (MLR) by scanning through the interval (see Fig. 2b). Another approach, demonstrated in Fedorenko & Husebye (1999) is to look for the point where signal energy starts to grow. This comprises two steps: (1) linear regression of the envelope front in the neighborhood of a trigger point **Tr** and (2) computation of the intersection point **Ti** of the line obtained with the noise level, which provides us with an estimate of a seismic phase onset time (see Fig. 2b) and the inclination angle **A** . Let us call this the Linear Regression Method (LRM). Both methods require determination of the time interval [T1,T2] inside which the onset time T0 is expected. The interval is computed as T1=T(R)-dtl, T2=T(Ri)+dt2, where T(R) denotes P or S travel time determined by the preliminary epicenter location and by the local velocity model. The values of dt1 & dt2 are set at 5 and 4 sec, correspondingly for both P and S phases.

HYPOCENTER LOCATION is a robust grid search procedure based on maximization of a type (1) function equal to the linear combination of the "bell-like" gain functions **f**(Δ) (equal to 1 when the discrepancy is 0 and equal to ~0 at infinity). The algorithm is comprised of two steps: first, the P arrivals $\mathbf{Y_p}$ provided previously by the two onset estimators, MLR and LRM, are used in computing:

$$\Delta_{ip} = Y_p - Y_p(R_i,H) - T_0 \qquad (4)$$

where i=1,...,N is a channel index, $\mathbf{Y_p(R_i,H)}$ - is a local travel time model for the first P phase arrivals at station number **i**, $\mathbf{T_0}$ -origin time,

$$\begin{aligned} f(\Delta) &= \exp(-|\Delta|), && |\Delta| < 0.5 \\ f(\Delta) &= 0. && |\Delta| > 0.5 \end{aligned} \qquad (5)$$

The scanning grid is (60x60x25 kM^3, ±10 sec) with a relatively large step dx,dy,dh=2 km, dt=0.5 sec. The algorithm using gain function (5), ignores all observations **S**, deviating more than 0.5 seconds from the model. When the optimum is found, it tries to reach higher accuracy. For this purpose it continues computations on a smaller grid (5x5x25 km^3, ±3 sec), dx,dy=0.3 km, dh=l km, dt=0.l sec., using (4) for computation of Δ_{ip} and Δ_i. (with index s substituting p) but using gain function due to

$$\begin{aligned} f(\Delta) &= \exp(-|\Delta|), & |\Delta| &< 0.5 \\ f(\Delta) &= 0. & |\Delta| &> 0.7 \end{aligned} \qquad (6)$$

Weighting coefficients $\mathbf{w_r}$ in (1) are set $\mathbf{w_r=l. -exp(-Tg(A_r))}$, where $\mathbf{A_r}$ is the envelope inclination angle determined above. Thus, abrupt onsets are highlighted and overly slow onsets neglected. Reliability of location is determined by the maximum value of the F(θ) function close to the number of donating channels. Accuracy is determined by its sharpness in the R? space, or as usual by the error ellipsoid.

RESULTS

Under the supervision of the Geophysical Institute of Israel a series of four calibration explosions was performed at the Arad quarry (see Fig. 1) with controlled source parameters: coordinates, time of ignition, charge, delays etc. The seismograms of the explosions were recorded by the ISN stations and processed by the analysts.

In Table 1 we compare the results of the analysts' location with those provided by the fully automatic procedure. From the table we see that though preliminary estimates provided by the envelope processing algorithm are less accurate than those provided by the analysts, the final automatic decision is the best and is very close to the real source location. We applied the developed automatic algorithm to a data set of 62 earthquakes from the Galilee, Gilad and Dead Sea areas. Our epicenter locations results in Figs. 4 and 5 1D by histograms of deviations R from X_0,Y_0 and 2D by plots of points (X-X X_0,Y- Y_0). Here X_0, Y_0 are presumed true source coordinates as reported in bulletins. The 80% and 90% error ellipsoids are presented on the corresponding plots. From Fig. 3a we see that preliminary epicenter estimates provided by the envelope processor STA+OD are sometimes rather rough. Nevertheless, epicenters demonstrated in Fig. 3b are significantly improved by the MLR+RLM procedure and in many cases are equivalent to the bulletin solutions, showing 80% of epicenters "mislocation" dR < 3 km (assuming bulletin solution true) and standard deviation α(dR)=2.1 km. Fig. 3c depicts 2D estimates of origin time T0 and depth by MLR+RLM procedure and shows that T0 is well done; the depth estimates, however, often deviate considerably from those in the bulletin.

CONCLUSIONS AND RECOMNLUENDATIONS

The above results appear promising for atomization of local seismicity monitoring. Our new procedure performed well providing robust and accurate solutions for earthquake epicenters in the different geological regions of Israel; the Galilee, Gilad and Dead Sea areas, as well as for the four calibration explosions in the Arad quarry. There are some locations which deviate from the results of standard processing , but usually these events are qualified in the bulletin as having "low reliability" and, as such, are difficult to judge as ground truth. The same remark is true for the depth estimates which are known to be poor in the bulletin quite often due to the low resolution of the existing system of surface observations. We also tried to apply this technique to the local quarries. For many of them the results were very accurate. But almost 10% of the events proved problematic for analysis most of them due to the failure on the preliminary location stage. The reason is that this kind of signal source causes strong excitation of the Rg surface waves, propagating with low velocities in the range of 1-3 km/sec. This may, in turn, result in too late pickings of the true P and S phases. Another factor is scattering and multi-pathing due to heterogeneity of the uppermost part of the crust. The local seismicity is 99.9% represented by quarry blasts and earthquakes, hence our suggestion that earthquakes/quarry blast automatic discrimination be carried out before the automatic location as shown to be reliable in Gitterman et al. (1998) with around 98% reliability. If an event is classified as an earthquake it can automatically be located by the procedure developed. On the other hand, if it is a quarry blast, it is

possibly easier to identify the source quarry among the set of known quarries using pattern recognition approach as in Joswig, 1990 or, Fedorenko et al, 1998.

Table 1. Results of Location of the Four Calibration Explosions by Routine and Automatic Techniques

			ROUTINE PROCESSING			**AUTOMATIC PROCESSING**					
			SEIS			**Envelope Processing**			**Onset Estimation**		
1	**2**	**3**	**4**	**5**	**6**	**7**	**8**	**9**	**10**	**11**	**12**
Event N date	Estim. Coord	GPS	Analyst	**Error km**	N St.	STA+ OD	**Error km**	N St.	MLR+ LRM	N St.	**Error km**
N1 30.07.98	X Y	167.9 57.0	167.3±2.0 55.0±2.3	**2.1**	15	167.0	**3.1**	13	167.2	15	**1.737**
N2 26.01.99	X Y	168.0 57.0	167.1±1.3 57.1±0.8	**0.9**	21	167.0 59.80	**3.0**	15	167.8 56.4	19	**0.63**
N3 26.01.99	X Y	168.0 57.6	166.3±1.2 58.1±1.5	**1.77**	37	166.5 55.8	**2.34**	24	167.7	35	**0.36**
N4 27.01.99	X Y	168.0 57.5	170.3±5.3 56.4±2.7	**2.55**	10	168.6 62.1	**4.64**	11	167.2 57.7	16	**0.82**

ACKNOWLEDGMENT

We would like to thank Eystein Husebye for suggesting this research and careful assistance in the period of study, Boris Gurevich and Yefim Gitterman for fruitful discussions. This study is supported by the U.S. Department of Defense, Contract Number DSWA01-97-C-0151.

REFERENCES

Andersen K.R.(1982). Robust earthquake location using M-estimates. *Phys. Earth Plan Inter*., .**30**, 119-130.

Fedorenko, Yu., E.S. Husebye, B. Heincke and B.O. Ruud (1998) Recognizing explosion sites without seismogram readings: Neural network analysis of envelope transformed multistation SP recordings 3-6 Hz. *Geoph J Int*., **133**, F1.

Fedorenko, Yu.V., E.S. Husebye, 1999. First breaks-Automatic pickings of P- and S- onsets in seismic records. Geoph. Res. Let., submitted for publication.

Y.Gitterman, V. Pinsky & A. Shapira.(1998). Spectral Classification Methods in Monitoring Small Local Events by the Israel Seismic Network. J. Seismology 2, p. 237-256.

Huber, P.J. (1972). Robust statistics: a review. Ann.Math.Stat.,**43**:1041-1067.

Husebye, E.S., B.O.Ruude.and A.M. Dainty (1998). Fast Robust and Reliable Epicenter Determinations: Envelope Processing of Local Network Data. . *Bul. Seism. Soc. Am*., **88**, pp. 284-290.

Joswig,. M. (1990). Pattern recognition for earthquake detection. *Bul. Seism. Soc. Am.* **80**, pp. 170-186.

Kushnir, A.F. (1995). Algorithms for adaptive statistical processing of seismic array data. In Monitoring Comprehensive Test Ban Treaty Ed. E.S. Husebye abd A.M. Dainty, NATO ASI Series. Series E: Applied Sciences - Vol. 303.

Ryzhikov, G.A., MS. Birulina and E.S. Husebye. (1995). Automatic event location using local network data. pp. 393-399 Proceedings of the 17th Annual Seismic Research Symposium on Monitoring a Comprehensive test Ban Treaty, 12-15 September 1995.

Shoubik, B.M., A.F.Kushnir, L.M. Haikin, A. Dainty (1996). SCANLOC: Automatic seismic event location based on local seismic network data. Proceedings of the 18th Annual Seismic Research Symposium on Monitoring a Comprehensive test Ban Treaty, 4-6 September 1996, pp.7 74-781.

Pinsky, V. and A. Shapira. Regional Events Location Using Seismic Energy Time-Space Distribution, Proceedings of the 20th Annual Seismic Research Symposium on Monitoring a Comprehensive Nuclear Test Ban Treaty, Santa Fe, September 21-23, 1998, p.265-274.

Pinsky V. I. (1999). An Approach to Automatic Location of Regional Events. PEPI ELSEVIER- Accepted for publication 7 July 1998.

Pisarenko, V.F., A.F. Kushnir and I.V. Savin (1987) Statistically adaptive algorithms for estimations of onset moments of seismic phases, Phys. Earth. And Planet. Interiors, 47, 888-900.

ACCURACY AND UNCERTAINTY IN SINGLE-STATION EVENT LOCATION

Jay Pulliam, Cliff Frohlich, and R. Brian Schlottmann
Institute for Geophysics, The University of Texas at Austin

Sponsored by the Defense Threat Reduction Agency
Contract No. DSWA-01-97-0016

ABSTRACT

To monitor compliance the Comprehensive Nuclear-Test-Ban Treaty it is desirable to locate and/or determine focal depths for seismic events with magnitudes of three or less; these events are often recorded by too few stations to locate them using conventional travel-time based methods. The principal objective of our research is to develop location and depth-determination methods that utilize signals from a single, three-component seismic station.

Success of waveform correlation methods for estimating focal depths depends on the accuracy of the crustal model used. Our efforts to constrain crustal models continue to exploit a receiver function method that employs a variant of the simulated annealing global search algorithm (SORVEC). Through a series of synthetic modeling experiments we are trying to determine the method's sensitivity to focal mechanism and depth, data frequency content, and the usefulness of models produced via teleseismic receiver functions in modeling regional seismic phases. An important question is whether the models determined by receiver functions, which utilize high-angle-of-incidence teleseismic signals as input, provide a reasonable basis for modeling seismic sources recorded at regional distances. The experiment described herein indicates that regional synthetics determined using the models provided by SORVEC are essentially similar to the "true" seismic signals, even when the SORVEC models are somewhat less complex than the "true" models.

We continue to investigate optimum methods to determine event-station bearings using single-station, three-component records of regional seismic events having magnitudes between 3.0 and 4.5. Since many such events do not have impulsive phase arrivals with high signal-to-noise ratios, it is not always feasible to determine azimuth using narrow time windows. We get much more reliable results using the entire P-to-Sn time window, which contains both P and P-to-Sv converted energy. Our present approach is to determine event-station bearing in two steps; initially we utilize horizontal components only to determine the event-to-station azimuth mod 180 degrees; then identify the proper direction from an analysis of the vertical-component and rotated horizontal component signals. Even for relatively small earthquakes that lack impulsive P arrivals, preliminary results indicate that we are determining event-station bearings with errors of about 10 degrees or less. Moreover, the uncertainties determined from statistical analysis are approximately equal to the observed error.

Keywords: single-station location, focal depth determination, regional seismology

OBJECTIVE

Monitoring compliance with the Comprehensive Nuclear-Test-Ban Treaty (CTBT) provides the immediate impetus for improving single-station location (SSL) methods, as recent studies have indicated that monitoring decoupled explosions at the one-kiloton level would require detecting and identifying all quakes with mb above 3.0 or less. Travel-time based location methods are ineffective for small events since with the seismic station network currently in place for monitoring compliance to the CTBT, 82% of the earth's surface doesn't have three or more stations within 10°, and 99% doesn't have three within 5° (Frohlich and Pulliam, 1999). The situation is somewhat better for land areas, and would be very much better if we required only one station to obtain a location; in particular, only 7% of the land area has no stations within 10°, while 45% has none within 5°. Moreover, travel-time based location methods are notoriously inaccurate when the number of stations is small or when the epicenter is controlled by arrivals at a few 'key' stations. Finally, focal depths determined by traveltime-based methods are notoriously unreliable even when phase arrival times are numerous and properly identified. For CTBT purposes, it is desirable to obtain focal depths even if it isn't possible to determine an epicenter since any seismic event deeper than a few km is an unlikely candidate for a nuclear explosion.

RESEARCH ACCOMPLISHED

Estimating Focal Depths at Regional Distances with a Single Station

We conducted a synthetic experiment to determine the usefulness of waveform correlation methods for determining focal depths in cases where the crustal structure is known only approximately. Our strategy has been to find the 1D crustal structure beneath a seismographic station with the SORVEC receiver function method (Zhao and Frohlich, 1996; Zhao et al. 1996), which conducts a global search using a modified simulated annealing algorithm, called Very Fast Simulated Annealing (VFSA). While the SORVEC method is quite successful at retrieving a crustal model that accurately predicts teleseismic phases, it is not obvious that the SORVEC model should also predict the regional phases that are most useful in constraining focal depths. The teleseismic phases used by SORVEC, including phases internally-reflected in crustal layers, are steeply propagating, while regional phases interact with the crustal layers at more oblique angles. Small discrepancies in model velocities, impedance contrasts, and depths to layer interfaces can result in large differences in regional waveforms.

To conduct a synthetic test of our waveform correlation method, we first computed teleseismic waveforms (30<delta<70) with the reflectivity method for both shallow (h<30 km) and deep (h>300 km) sources. These "data seismograms" were computed for various focal mechanisms and contain energy up to 5 Hz. Our input model consisted of eight crustal layers over the PREM mantle. Next, using the SORVEC method we determined the best-fitting crustal models having three, four, five, six, seven, and eight layers over a half-space (Fig. 1). While the synthetic "data" were computed with reflectivity, SORVEC uses a truncated generalized ray expansion to compute seismograms, evaluating on the order of 100,000 models to obtain the best-fitting model.

In all cases, the bulk properties of the crust--vertical travel times and crustal thickness-- were determined to within 4% of those of the input model. This result bodes well for attempts to use phases reflected at the Moho and the Earth's surface to constrain focal depths. However, depths to internal layers and layer velocities were more variable. S travel times were more accurate than P travel times in every case. Also, in some parameterizations, e.g., the 5-layer model, SORVEC determined velocities at the limits of the search bounds for some layers, indicating that the search bounds should be widened to allow a more complete search of model space.

Comparisons between the “true” radial synthetic seismograms (Fig. 2, solid lines) and the best-fitting radial seismograms computed by SORVEC indicate that the increasing model complexity beyond about five layers is not warranted in terms of error reduction alone. On the other hand, experiments with overparameterization--using 4 and 5 layers to model the "data" produced with three layers over PREM--indicate no serious consequences to high model complexity. In that case, two or more layers in the

SORVEC crustal model were so similar that a simple inspection would lead one to combine them. Note also that SORVEC's seismograms generally match the initial arrivals well, while later arrivals which often represent energy reflected between internal layers is modeled less well. This pattern carries through to the models, which generally show less accurate internal structure than bulk properties.

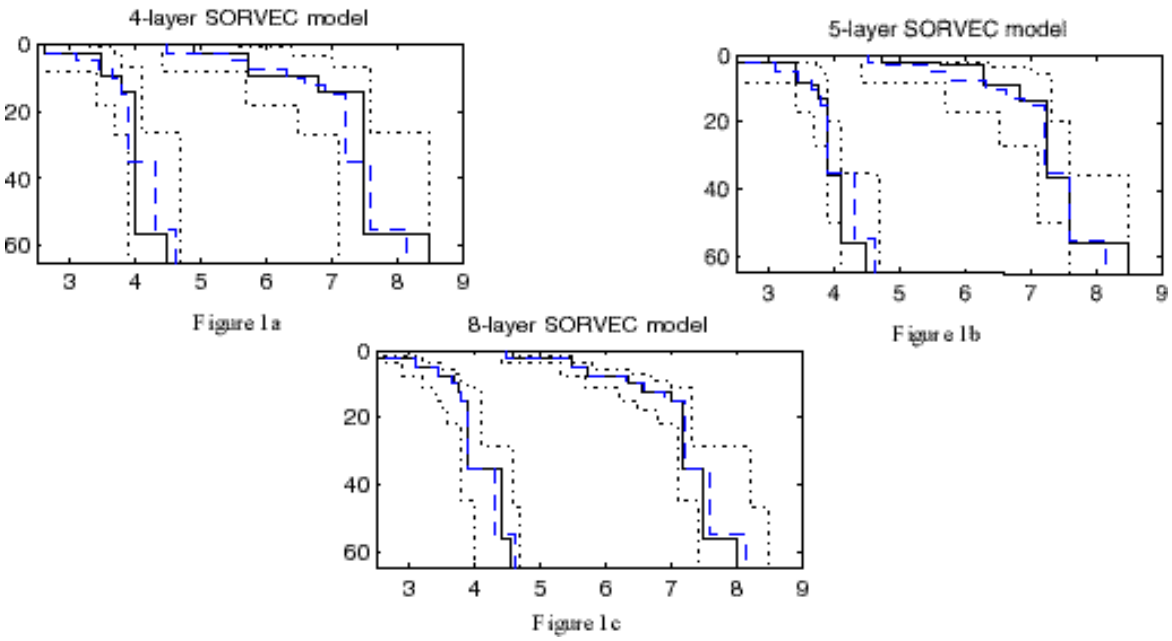


Fig. 1. Crustal velocity models produced by SORVEC using synthetic teleseismic seismograms (solid lines), the 8-layer velocity model used to compute these seismograms (dashed lines), and the search bounds input to SORVEC for each of three parameterizations (dotted lines). Each panel shows results when model is constrained to a different number of layers: (a) 4 layers, (b) 5 layers, (c) 8 layers. In each panel results for modeling S velocities are on the left, while P velocities are on the right.

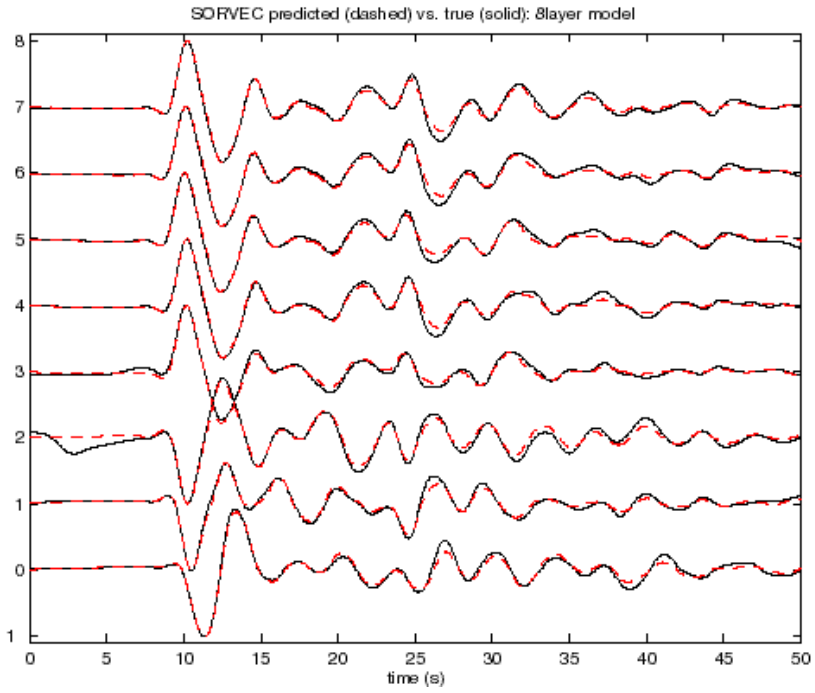


Fig. 2. Radial seismograms predicted by SORVEC for the best-fitting 5-layer velocity model (dashed lines) compared to the synthetic teleseismic "data" seismograms (solid lines). The fit was only slightly better for the best-fitting SORVEC seismograms for models having 8 layers.

Using the "true", eight-layer crustal model we computed seismograms for a focal depth of 5 km, distances of 200, 400, and 600, and various focal mechanisms (e. g., Figs. 3 and 4). With the five-layer SORVEC model, produced by fitting teleseismic synthetics to the eight-layer input model, we computed suites of radial and vertical seismograms for various focal depths (0-15 km depth in 2.5 km intervals) and distances of 200, 400, and 600 km (e. g., Fig. 5). Rather than assuming a single fault orientation, we compute seismograms for three fundamental faults (45 degree dip-slip, vertical dip-slip, and vertical strike-slip), which can be combined linearly to produce any double-couple source. Fault orientation essentially controls the energy emitted into any given phase in a direction that will reach the recording station. Some phases will not appear at a station that is situated on a source's nodal line. By computing each fundamental fault, and then attempting to correlate "data" synthetics with each, we automatically search for finite occurrences of every phase. We essentially assume that retrieving fault orientation in addition to focal depth using just a single station is unrealistic. Waveform correlation to fundamental faults is a strategy for simplifying the problem of single-station estimation of focal depths.

A second strategy for simplifying the correlation is to further minimize the effects of varying source orientations by computing and comparing energy envelopes (e. g., Fig. 4), rather than actual synthetics, which include positive and negative swings of the trace as determined by the focal mechanism. We find that pulses in energy envelopes are broadened by the combination of both positive and negative signals. In theory this broadening will decrease resolution. However, in practice it serves to make the procedure more robust. For demonstration purposes we have used focal depth increments of 2.5 km. Depth increments smaller than 2.5 km are generally indistinguishable when the procedure is applied to real data, so the slight loss of resolution with energy envelopes is insignificant.

Finally, we correlate the vertical "data" energy envelopes, computed for a distance of 200 km, with the vertical "fundamental fault" seismograms and plot the combined correlation function (Fig. 6). A clear peak can be seen at the expected 5 km focal depth, which indicates that the seismograms computed from the approximate (SORVEC) crustal model are sufficiently similar to those from the true (input) model to admit modeling of the regional phases that are most essential for determining focal depths. Fig. 7 shows a similar result for a distance of 400 km. However, distances of 600 (Figure 8) and 800 km did not work well, which suggests that the effects of model discrepancies become relatively more important with distance. This, in turn, implies that successful applications of single-station location methods may be limited to several hundred kilometers.

Determining the Station-Event Bearing

Our previous investigations focused on determining station-event bearing for small ($3 < M < 4.5$), regional (100 km < distance < 1000 km) events and on developing methods that were applicable to records from stations in a broad variety of tectonic environments (Pulliam and Frohlich, 1998). This research established that most reliable station-event azimuth information was obtainable from 1) the P-to-S time window; and 2) the high-frequency portion of the signal, i. e., we obtained best station-event azimuths when we high-pass filtered the three-component broadband signal with a corner frequency of 0.5 Hz. However, we were able to determine bearings only within about ±20° using conventional methods to determine bearing.

We have modified our approach to fully exploit the fact that the signal arriving between P and S combines both direct P arrivals and converted P-to-Sv arrivals. These have polarization directions 180° apart, which degrades the determination of azimuth if we employ the usual method of finding the bearing of the largest eigenvector of the 3-D covariance matrix. Instead, we now: 1) determine an initial bearing α from the 2-D covariance matrix formed from the E and N horizontal components; 2) rotate the horizontal-component signal along this bearing, and form the 2-D covariance matrix from this H- and the vertical Z-component signal; and 3) inspect this H-Z covariance to choose whether true signal bearing is α or $\alpha+180°$. This is theoretically similar to the 2-D method employed previously by Magotra et al. (1987) and Walck and Chael (1991). However, they applied this method to relatively impulsive signals in short (2 sec) time

windows, while here we evaluate rather noisy signals with well-developed codas in time windows of 25-100 sec duration.

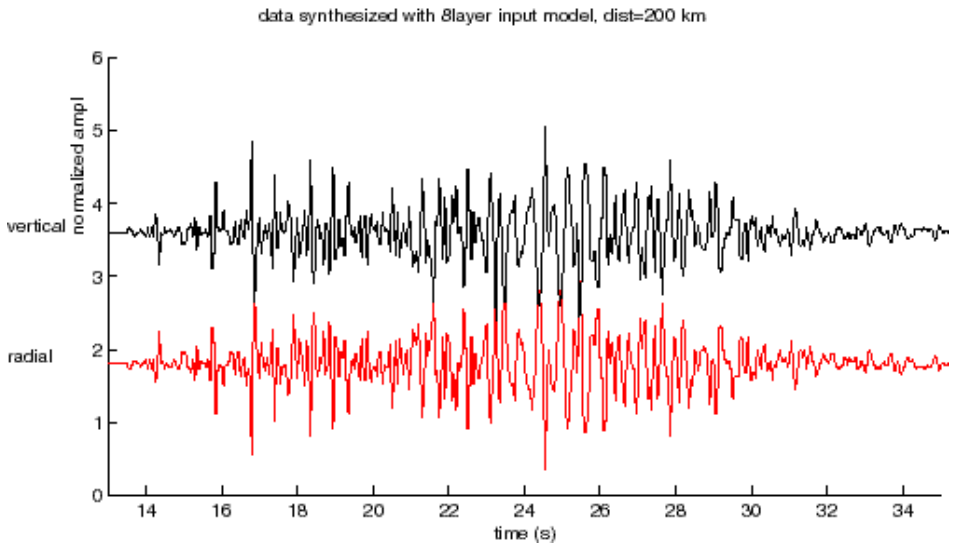


Fig. 3. Data synthesized with the eight-layer input model using a reflectivity method. The focal depth is 5 km; the distance is 200 km.

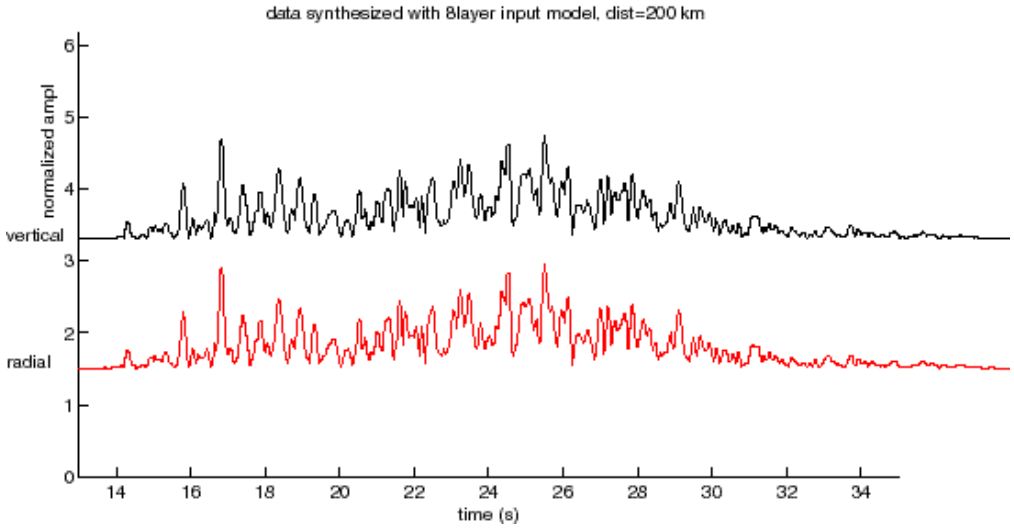


Fig. 4. Energy envelopes for the seismograms shown in Fig. 3.

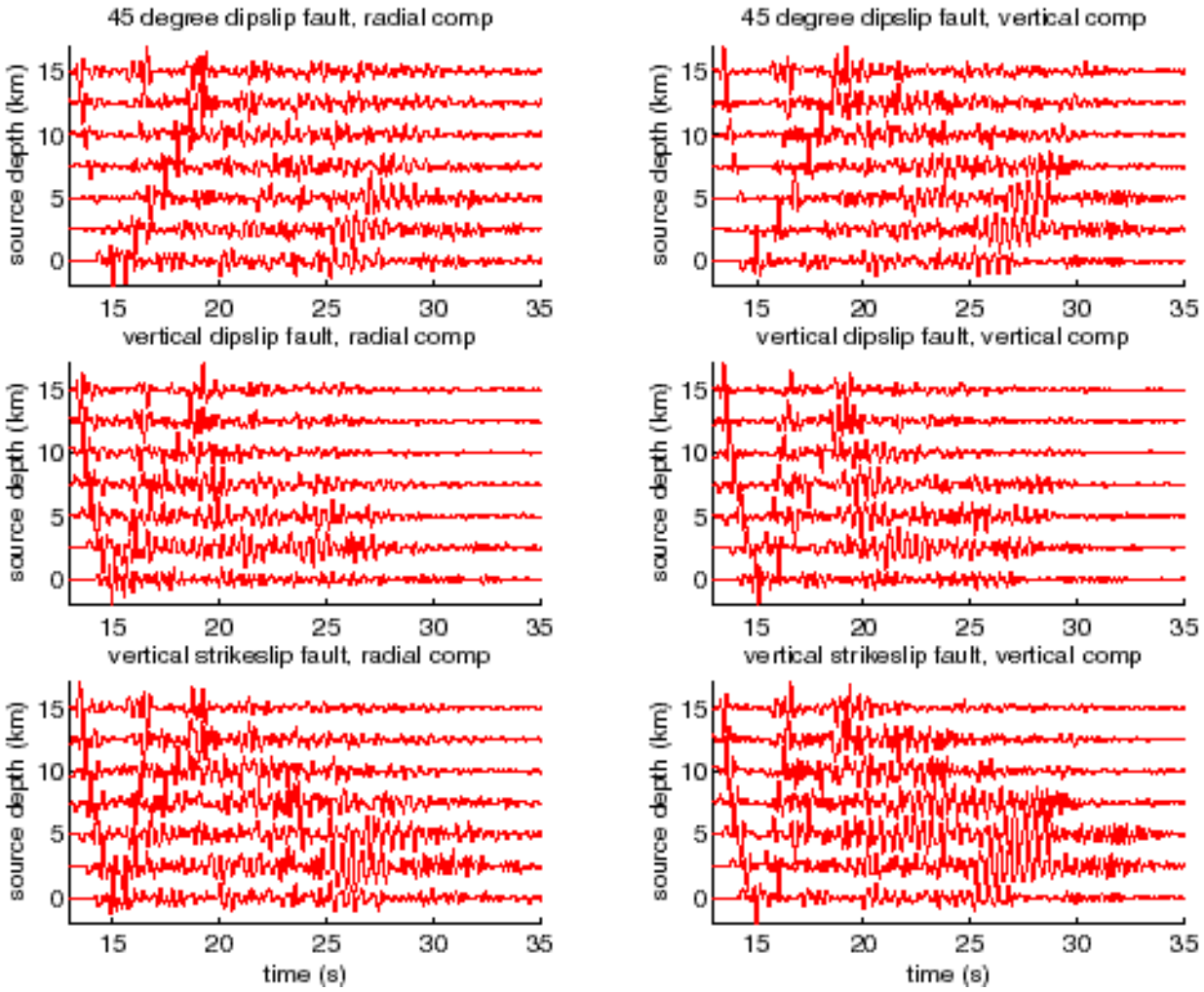


Fig. 5. Suites of synthetic seismograms computed for source depths of 0, 2.5, 5, 7.5, 10, 12.5, and 15 km at an epicentral distance of 200 km. The velocity model used was the best-fitting 5-layer model found by SORVEC.

`

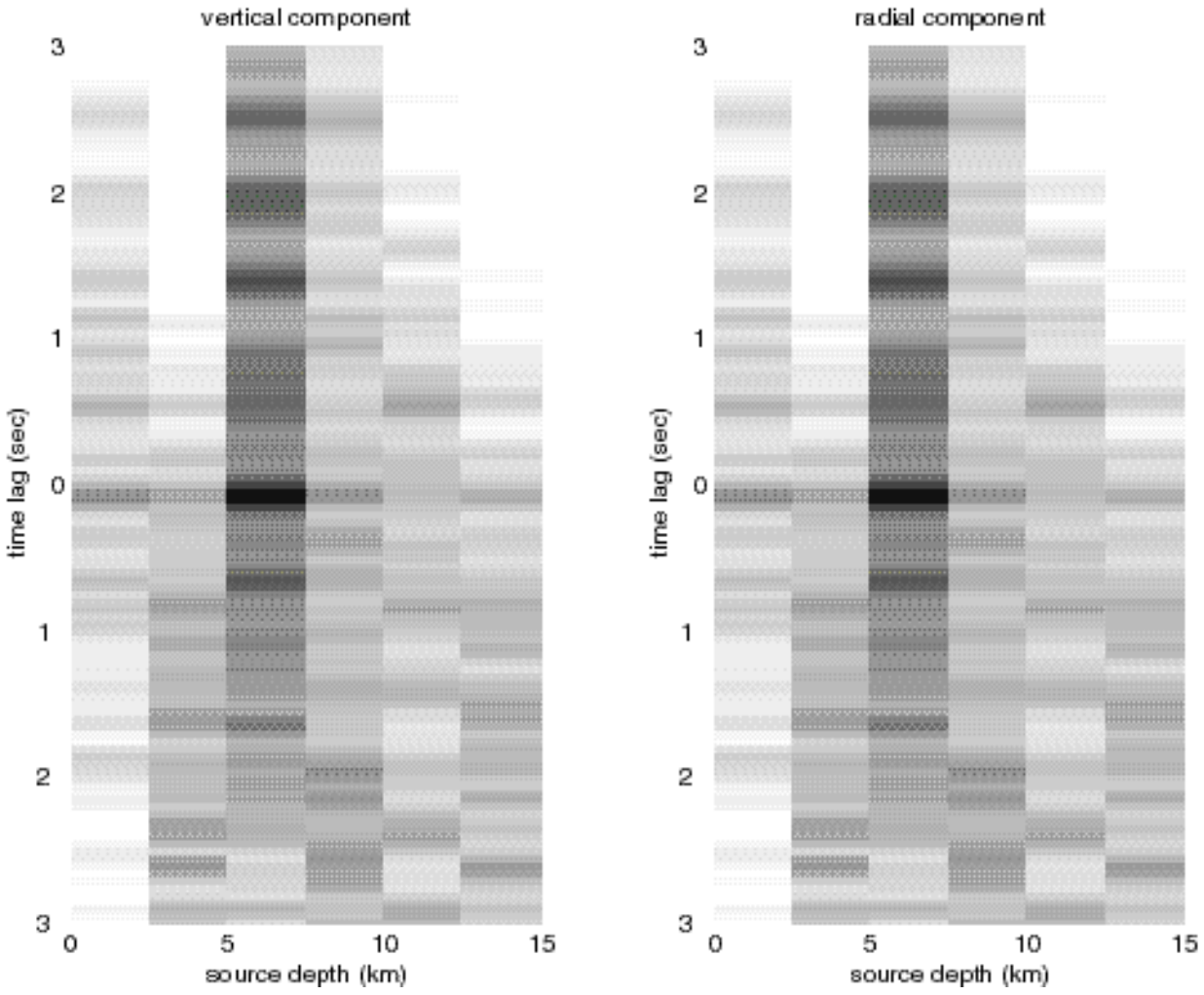


Fig. 6. Combined correlation functions for the vertical (left) and radial (right) data seismograms with the suites of synthetics computed with SORVEC's best five-layer model at 200 km epicentral distance. Note the peak at zero time lag and 5 km source depth, which indicates the correct source depth.

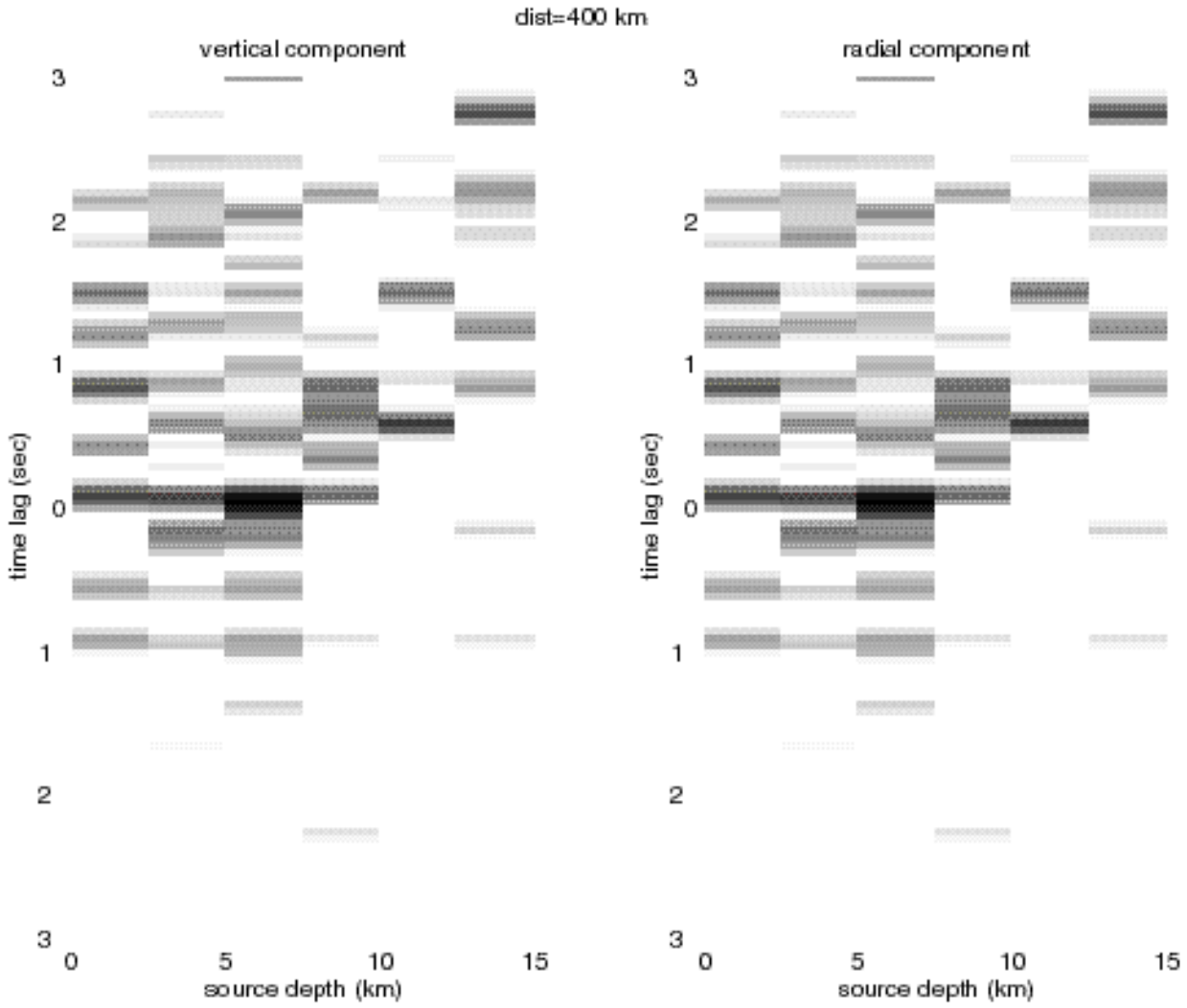


Fig. 7. Combined correlation functions for the vertical (left) and radial (right) data seismograms with the suites of synthetics computed with SORVEC's best five-layer model at 400 km epicentral distance. Note the peak at zero time lag and 5 km source depth, which indicates the correct source depth.

Our preliminary results indicate that the modified approach gives results that are similar to those obtained with to the previously-used method. In particular, the differences between the true bearing and the bearing determined by the modified approach are typically ±10° or less when the method is applied to signals with signal-to-noise ratios of 2.0 or more. Moreover, the differences between true and observed bearing are of approximately comparable size to our statistical estimates of the error, determined from the ratio of eigenvalues of the 2-D covariance matrix. This is important for CTBT concerns, as it suggests that we have some knowledge of the bearing uncertainty even for signals where the true bearing is unknown.

CONCLUSIONS AND RECOMMENDATIONS

Most practical single-station location methods rely heavily on comparing real seismic signals recorded at regional distances to synthetics determined assuming a reasonably accurate crustal model. The present research demonstrates that crustal models determined using teleseismic signals and receiver-function methods are accurate enough. However, while our synthetic test is realistic in many respects, it fails to reproduce several types of real-world complexity, including laterally-varying crustal structure, surface topography, complicated source time functions, and non-stationary noise. We note that the waveform correlation scheme does not require that SORVEC be used to model the crust. While SORVEC finds a 1D model directly beneath the station and the waveform correlation assumes that that model represents structure between the source and the receiver, other, yet-to-be-determined methods for determining crustal structure may well produce a better average model between the source and receiver.

The most popular methods for determining event-station bearing rely on evaluating the 3-D signal covariance over a time window that contains an impulsive phase arrival, and generally has a duration of a few seconds or less. Our preliminary results suggests that if we use data from the entire P-to-S time window, we can obtain relatively bearing angle information with an uncertainty of ±10° or less for small events even though they lack an impulsive P and even though signal-to-noise ratios are low. Our ongoing research is focused on determining whether this conclusion will hold up for station-event pairs in a broad variety of tectonic environments. When the true event location is known, we are also investigating whether the statistical estimates of the error in bearing provide a meaningful estimate of the discrepancy between true and observed bearing.

REFERENCES

Frohlich, C. and J. Pulliam. Single-station location of seismic events: A review and a plea for more research, *Phys. Earth Planet. Int. 113*, 277-191, 1999.

Magotra, N., N. Ahmed and E. Chael. Seismic event detection and source location using single-station (three-component) data, *Bull. Seis. Soc. Am., 77*, 958-971, 1987.

Pulliam, J., and C. Frohlich. Case studies of event location with a single station, *Proc. 20th Annual Seismic Research Symp.*, pp. 275-285, 1998.

Walck, M. C. and E. P. Chael. Optimal backazimuth estimation for three-component recordings of regional seismic events, *Bull. Seis. Soc. Am., 81*, 643-666, 1991.

Zhao, L.-S. and C. Frohlich. Teleseismic body waveforms and receiver structures beneath seismic stations, *Geophys. J. Int., 124*, 525-540, 1996.

Zhao,. L.-S., M. K. Sen, P. Stoffa and C. Frohlich. Application of very fast simulated annealing to the determination of the crustal structure beneath Tibet, *Geophys. J. Int., 125*, 355-370, 1996.

IMPROVED SEISMIC EVENT DEPTH ESTIMATION USING CEPSTRAL ANALYSIS

Delaine T. Reiter, Weston Geophysical Corporation
Robert H. Shumway, University of California, Davis

Sponsored by U.S. Department of Defense
Defense Threat Reduction Agency
Contract No. DSWA01-98-C-0142

ABSTRACT

The objective of cepstral analysis is to detect echoes in a signal using simple signal processing methods. In principle, cepstral analysis should be capable of detecting the delay times of seismic depth phases, which could then be used to accurately estimate event depth. Cepstral techniques have been utilized in the past for seismic depth determination with some success (Alexander, 1996; Bennett et al., 1989; Kemerait, 1982). However, the results have been mixed, at best, and the operational capability of the method has never been established. To address some of the negative aspects of the method, we have formulated a cepstral F-statistic (Shumway et al., 1998) that attaches statistical significance to peaks in the cepstrum through a signal-to-noise ratio computed from the beam cepstrum and the sum-stacked cepstrum. We estimate the cepstra from windows of data, which contain the P arrival and its coda. The F-statistic is then formed by dividing the beam (mean) cepstrum by the error between the beam and the sum-stacked cepstra. Peaks at possible depth-phase delay times must appear in both the beam cepstrum and the F-statistic estimate. Appropriate F-statistics for both arrays and single 3-component stations have been developed.

Initial results indicate that out-of-band noise in the signal severely degrades the estimate of the depth phase delay times. To address this problem, we are experimenting with both tapering and filtering ('liftering' in the cepstral literature) the detrended log spectrum of each window of data prior to forming the cepstrum. The improvement in peak detection capability from the cepstral F-statistic is significant using even a simple taper on the detrended log spectrum, and we anticipate that more sophisticated filtering methods will further improve the results. Results are presented from events from regions of monitoring concern, with an emphasis on events that have teleseismic depth phases, but confusing regional signals.

Key Words: seismic focal depth, cepstral analysis, depth-phase delay times, F-statistic

OBJECTIVE

The primary objective of this research is to establish the operational usefulness of cepstral techniques to determine the depth of a seismic event. To accomplish this objective, we have developed a statistical criterion to accompany cepstral estimates of seismic depth phase delay times. This statistical measure, or cepstral F-statistic, provides a measure of the significance of a particular peak in the cepstrum. We have applied the technique to both synthetic and Reviewed Event Bulletin (REB) data with initial results that are promising.

RESEARCH ACCOMPLISHED

Accurate determination of the focal depth of seismic events continues to be an important seismic monitoring problem. If the depth of an event can be confidently found to be more than a few kilometers beneath the surface, further event processing becomes unnecessary. However, robust techniques for determining depth from both teleseismic and regional data continue to be elusive. Depth phase signals (pP and sP) are the best indicators of depth, but they can be difficult to detect in seismic data due to path effects, focal mechanism and coda complexity. Some of the currently available techniques to determine the depth of an event from available depth phase data include body-wave modeling (Goldstein and Dodge, 1998), beamforming (Woodgold, 1999), and cepstral techniques (Alexander, 1995). In our project we are investigating a modified cepstral technique to conclusively determine its operational capability to estimate focal depths.

Cepstral techniques are used to detect echoes in a signal using simple Fourier transform processing methods. They have been used in such diverse applications as speech analysis, image processing and radar data analysis (Bogert et al., 1963; Childers et al., 1977). The cepstrum is defined as the Fourier transform of the log of the spectrum of a time domain signal (Oppenheim and Schafer, 1975), and was designed to help analyze the periodicity that occurs in the power spectrum when echoes are present in the original signal. In principle, cepstral analysis can be used to detect the periodicity of scalloping in the seismic spectrum that is due to the interference of the direct (P) and depth (pP and/or sP) phases. This periodicity is directly related to the depth phase delay time, which is in turn directly related to focal depth. Cepstral techniques have been utilized in the past for seismic depth determination (Alexander, 1996; Bennett et al., 1989; Kemerait, 1982), but the results have been mixed, and the operational capability of the method has never been established. To improve the method, we have formulated a cepstral F-statistic (Shumway et al., 1998) that attaches statistical significance to peaks in the cepstrum. The F-statistic is found using a classical approach to detecting a signal in N stationarily correlated time series (Shumway, 1971). Testing the hypothesis $S(d) = 0$, where S is the signal transform at delay time d, leads to an F-statistic given by

$$F_{2,2(N-1)}(d) = (N-1)\frac{SCB(d)}{SCE(d)},$$

which can be interpreted as a signal-to-noise ratio. The subscripts refer to an F distribution with 2 and 2(N-1) degrees of freedom. In this instance, the signal consists of the spectrum of the stacked log spectra, or *beam cepstrum (SCB),* defined as

$$SCB(d) = \sum_{j=1}^{N} N\left|\overline{Q}(d)\right|^2,$$

where

$$\overline{Q}(d) = N^{-1}\sum_{j=1}^{N} Q_j(d),$$

is the mean Fourier transform of the log spectra. The noise is defined as the *error cepstrum (SCE):*

$$SCE(d) = \sum_{j=1}^{N}\left|Q_j(d) - \overline{Q}(d)\right|^2$$

$$= SCT(d) - SCB(d),$$

where *SCT(d)* is the *total stacked cepstrum*,

$$SCT(d) = \sum_{j=1}^{N} \left| Q_j(d) \right|^2 .$$

The error cepstrum is a measure of the extent to which the individual channel or window transforms differ from the mean transform. The beam and total cepstra are computed from multiple windows of data, which can be extracted from elements in an array or from sliding windows in a single seismogram. Note that the total stacked cepstrum (*SCT(d)*) is equivalent to the sum-stack proposed by Alexander et al. (1995), which is computed by simply adding up the cepstra of individual windows. Our tests have shown that the sum-stack will not reflect the common signal components as well as either the beam cepstrum or the F-statistic.

In practice the individual cepstra require some additional processing in order for peaks that correspond to the depth phases to be detected. Figure 1 illustrates a simple flow chart of the algorithm. The log-power spectrum is calculated from each window of data. The log spectrum is then detrended with a cubic spline to remove the Fourier component of the log-power spectrum that is not due to the depth-phase echo. In the standard version of cepstral peak detection, each individual detrended log spectrum is used to form the beam and total cepstrum necessary for peak detection with the F-statistic. However, we have found that noise in the high frequency portion of the detrended log spectrum obscures peaks in the cepstrum that are due to true signal echoes. To illustrate this effect,

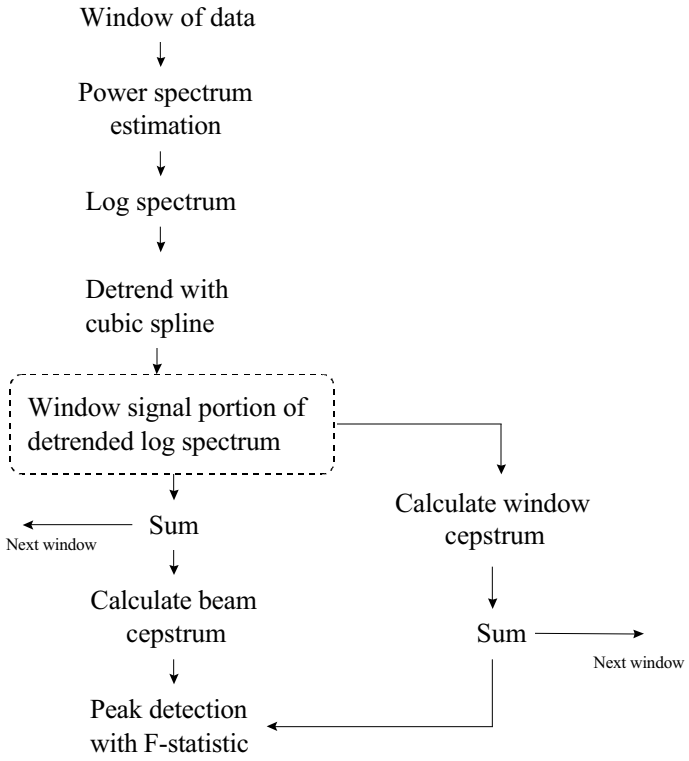


Figure 1. Flow chart illustrating the cepstral F-statistic algorithm. The solid, squared-off boxes denote steps in the algorithm that are traditional in cepstral analysis techniques. The traditional method is highly sensitive to noise in the seismic signal, which is magnified in the detrended log spectrum. Therefore, we have added a modification denoted by the dashed, rounded box, in which we window the signal portion of the detrended log spectrum prior to cepstrum estimation and peak detection.

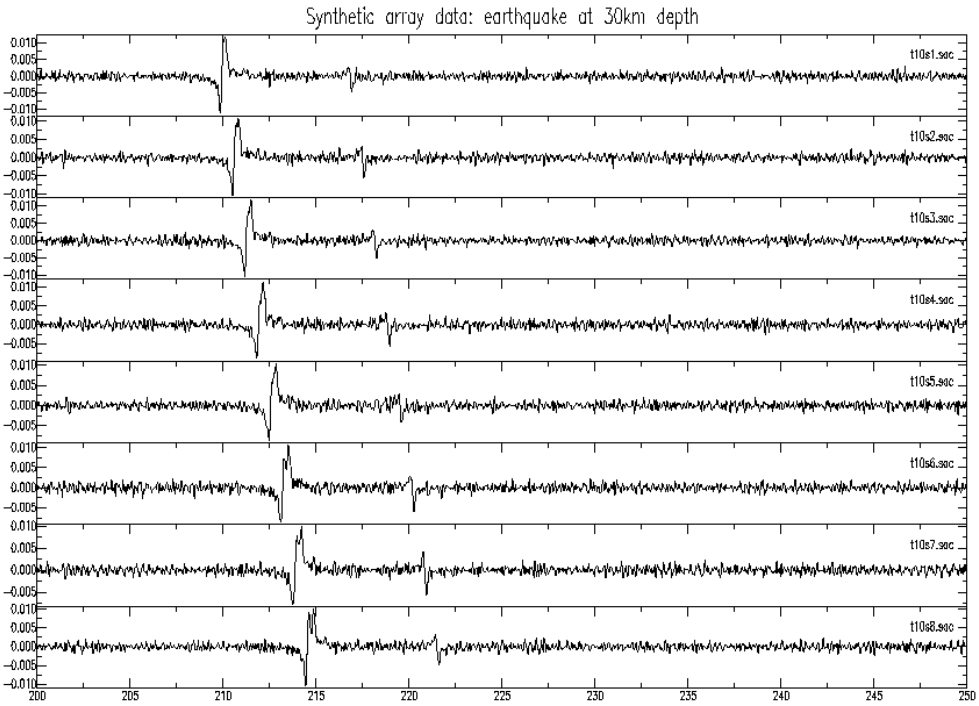


Figure 2. Synthetic data calculated using WKBJ theory. The earthquake was modeled at a depth of 30 km through the IASPEI91 velocity model. An array of eight linearly configured stations was positioned starting 15° from the epicenter with a total aperture of 39 km. Bandlimited Gaussian noise was added at a signal to noise (SNR) ratio of 10.

we modeled some noisy synthetic data using a WKBJ raytracing package (Chapman et al., 1991); the resulting seismograms are shown in Figure 2. An earthquake depth of 30 km depth and the IASPEI91 model (Kennett and Engdahl, 1991) were used to synthesize just the P and pP phase arrivals. We placed an array of eight linearly configured stations starting 15^o from the epicenter, with a total aperture of approximately 39 km. After producing the seismograms, we added bandlimited Gaussian noise to the synthetic data at a signal-to-noise ratio (SNR) of 10. The delay time between the P and pP phases is approximately 6.8 seconds. We then processed the data using the cepstral technique illustrated in Figure 1, but left out the step outlined by the dashed line. The results are shown in Figure 3, where we display the beam cepstrum and total cepstrum in the top two panels. We have included the total cepstrum in the results to illustrate the superiority of the beam cepstrum and F-statistic for peak detection. The cepstral F-statistic, shown in the bottom panel, provides a statistical level of significance for the various peaks. At a false alarm rate of .05 (dashed line), multiple peaks are significant, even though only one of them corresponds to the true depth phase delay time. At a higher confidence level, none of the peaks is significant. This is a discouraging result, since the pP phase is clearly visible in the seismic signal, and the SNR is higher than might be expected for many typical earthquakes.

The noisiness in the beam cepstrum and F-statistic is due to high frequency noise in the detrended log-power spectrum. To alleviate the effect of this noise, we have begun experimenting with windowing the low frequency portion of the log spectrum prior to performing cepstrum estimation and peak detection. The dashed box in the flow chart of Figure 1 depicts this modification to the algorithm. The results from processing the data using the modified technique are shown in Figure 4. We windowed the log spectrum of each array component at 2 Hz. The noisiness in both the beam and total cepstrum is significantly reduced, and the F-statistic now clearly detects the correct pP-P delay time with a false alarm rate of .001. Further tests of the method indicate that out-of-band noise in the signal severely degrades the ability to estimate depth phase delay times using straightforward cepstral analysis. Our simple modification to the algorithm improves peak detection capability significantly, using even a simple taper on the detrended log spectrum, and we anticipate that more sophisticated filtering methods will further improve the results.

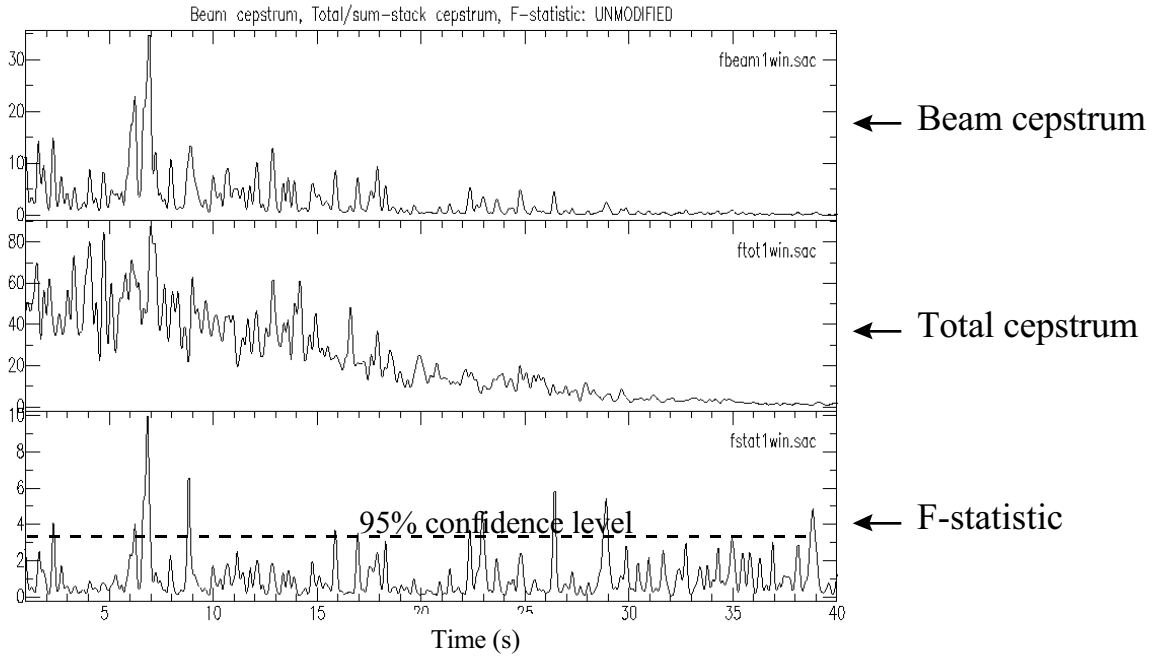


Figure 3. The results from processing the noisy synthetic data using a traditional cepstral analysis with peak detection. The beam cepstrum (top), total (sum-stack) cepstrum (middle) and cepstral F-statistic (bottom) are all noisy, with multiple peaks obscuring the true pP-P delay time (approximately 6.8 seconds).

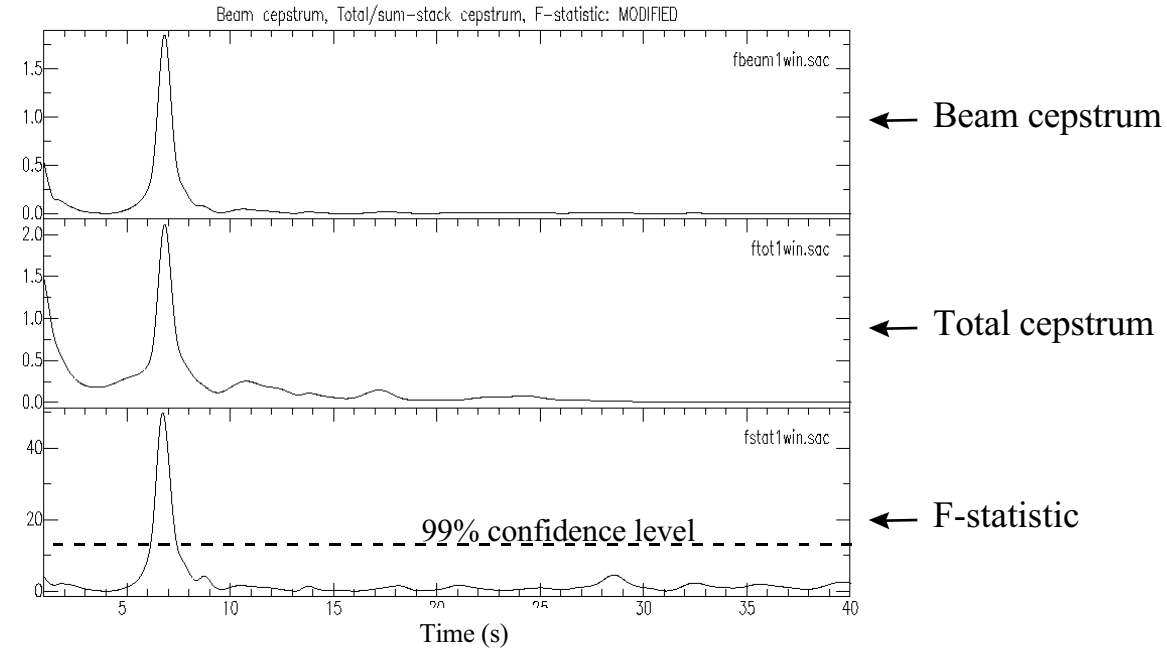


Figure 4. The results from processing the noisy synthetic data using a modified cepstral analysis with peak detection. The modification to the algorithm involves windowing the signal portion of the detrended log spectrum prior to cepstrum estimation and peak detection. The effect of noise on the beam cepstrum, total (sum-stack) cepstrum and cepstral F-statistic is significantly decreased, and the true pP-P delay time is easily detected with high confidence.

We have begun testing our method on a variety of seismic events. For example, we processed the data from an earthquake that appeared in the Reviewed Event Bulletin (REB). This event (EVID 20058461, m_b=4.3) occurred on 19 Aug 1998 in Northern Xinjiang, China. Processing at the International Data Centre (IDC) indicated an event depth of 20.2 km (+-2.2km), and both pP and sP phases were detected at several teleseismic stations. We used a subsample of reporting stations that had higher signal-to-noise ratios, all of which were in the far regional to near-teleseismic range. Table 1 lists the stations used in the cepstral analysis, with the distance from the event, number of windows and length of window for each station provided. For each station, we windowed the detrended log spectra at corner frequencies between 1.3 – 2.0 Hz, depending on where the signal power dropped off. The results are shown in Figure 5 for all five stations used in the analysis. Delay times of approximately 7.2 seconds for pP-P and 10.5 seconds for sP-P results in an estimated depth of 25 km,

Station	Dist	N	Length (s)
NIL	14.37	4	50
BJT	22.42	4	45
PDY	22.54	4	50
FINES	39.04	12	50
ARCES	39.73	15	40

Table 1. Stations and parameters used in cepstral analysis.

which agrees fairly well with the IDC estimate. Note that it is important to see stable peaks in both the beam cepstrum and the F-statistic before interpreting them as actual depth phase delay times (or as any other common signal component). Stable in this case means repeatable over varied processing parameters, such as window length, taper width and passband in the detrended log spectra.

CONCLUSIONS

During the first year of this effort, we have formulated a cepstral focal depth estimation technique that provides a statistical estimate of the significance of peaks in the stacked cepstrum. This significance measure has been missing in previous cepstral estimates of focal depth. The method can be used on both teleseismic and regional data, provided there is sufficient bandwidth and signal strength. We have found that the original formulation of the cepstral F-statistic method is highly sensitive to out-of-band noise, which is amplified in the detrended log spectrum formed prior to cepstrum estimation and peak detection. We have modified the technique by windowing in the detrended log spectrum, and have shown that this modification significantly decreases the influence of noise on the cepstral estimation and peak detection portion of the method.

Future work in the remainder of the effort will include the development of more sophisticated methods to window the signal portion of the detrended log spectra. We also will continue testing different forms of the F-statistic specifically designed for different regimes, such as regional 3-component stations or teleseismic arrays. Application to REB events from regions of monitoring concern is a high priority for future testing, with specific concentration on events with teleseismic depths phases but confusing regional signals. Another important avenue to investigate is the use of preprocessing techniques to further improve the results. These could include well-known signal processing techniques such as band-pass filtering, spectral smoothing and time domain envelope normalization. We are also investigating the use of methods to enhance the depth phase prior to cepstral processing. Our continued major priority during the second year of the effort will be on the operational potential of the method for seismic depth estimation.

REFERENCES

Alexander, S. S. (1996), A new method for determining source depth from a single regional station, *Seismic Res. Ltrs*., **67**, p. 63.

Alexander, S. S., R. C. Hsu, S. L. Karl, I. N. Gupta and D. H. Salzberg (1995), New techniques for estimating source depth and other diagnostic source characteristics of shallow events from regional observations of P, Lg and Rg signals, Report No. PL-TR-95-2108, Phillips Laboratory, Directorate of geophysics, Air Force Materiel Command, Hanscom AFB, MA 01731-3010. ADA 310037.

Bennett, T. J., B. W. Barker, K. L. McLaughlin, and J. R. Murphy (1989), Regional discrimination of quarry blasts, earthquakes and underground nuclear explosions, Final Report GL-TR-89-0114, Geophysics Laboratory, Hanscom Air Force Base, MA.

Bogert, B. P., M. J. R. Healy and J. W. Tukey (1963), The quefrency analysis of time series for echoes: cepstrum, pseudo-autocovariance, cross-cepstrum and saphe cracking, in *Proceedings of a Symposium on Time Series Analysis*, ed. M. Rosenblatt, John Wiley and Sons, Inc., New York.

Chapman, C. H., J.-Y. Chu, and D. G. Lyness (1988), The WKBJ Seismogram Algorithm, Chapter 1.2 in *Seismological Algorithms*, ed. D.J. Doornbos, Academic Press.

Childers, D. G., D. P. Skinner, and R. C. Kemerait (1977), The cepstrum: a guide to processing, *Proc. of the IEEE*, **65**, p. 1428-1443.

Goldstein, P. and D. Dodge (1998), Depth and mechanism estimation using waveform modeling, in Proceedings of the 20th Annual Seismic Research Symposium on Monitoring a Comprehensive Test Ban Treaty (CTBT), p. 238-247.

Kemerait, R. C. and A. F. Sutton (1982), A multidimensional approach to seismic event depth estimation, in *Geoexploration*, **20**, p. 113-130.

Kennett B. L. N. and E. R. Engdahl (1991), Traveltimes for global earthquake location and phase identification, *Geophys. J. Int.,* **105**, p. 429-465.

Oppenheim, A. V., and R. W. Schafer (1975), *Digital Signal Processing*, Prentice Hall, New York.

Shumway, R. H. (1971), On detecting a signal in N stationarily correlated noise series, *Technometrics*, **10**, p. 523-534.

Shumway, R. H., D. R. Baumgardt and Z. A. Der (1998), A cepstral F-statistic for detecting delay-fired seismic signals, *Technometrics*, **40**, p. 100-110.

Woodgold, C. R. D. (1999), Wide-aperture beamforming of depth phases by timescale contraction, *Bull. Seis. Soc. Am*., **89**, p. 165-177.

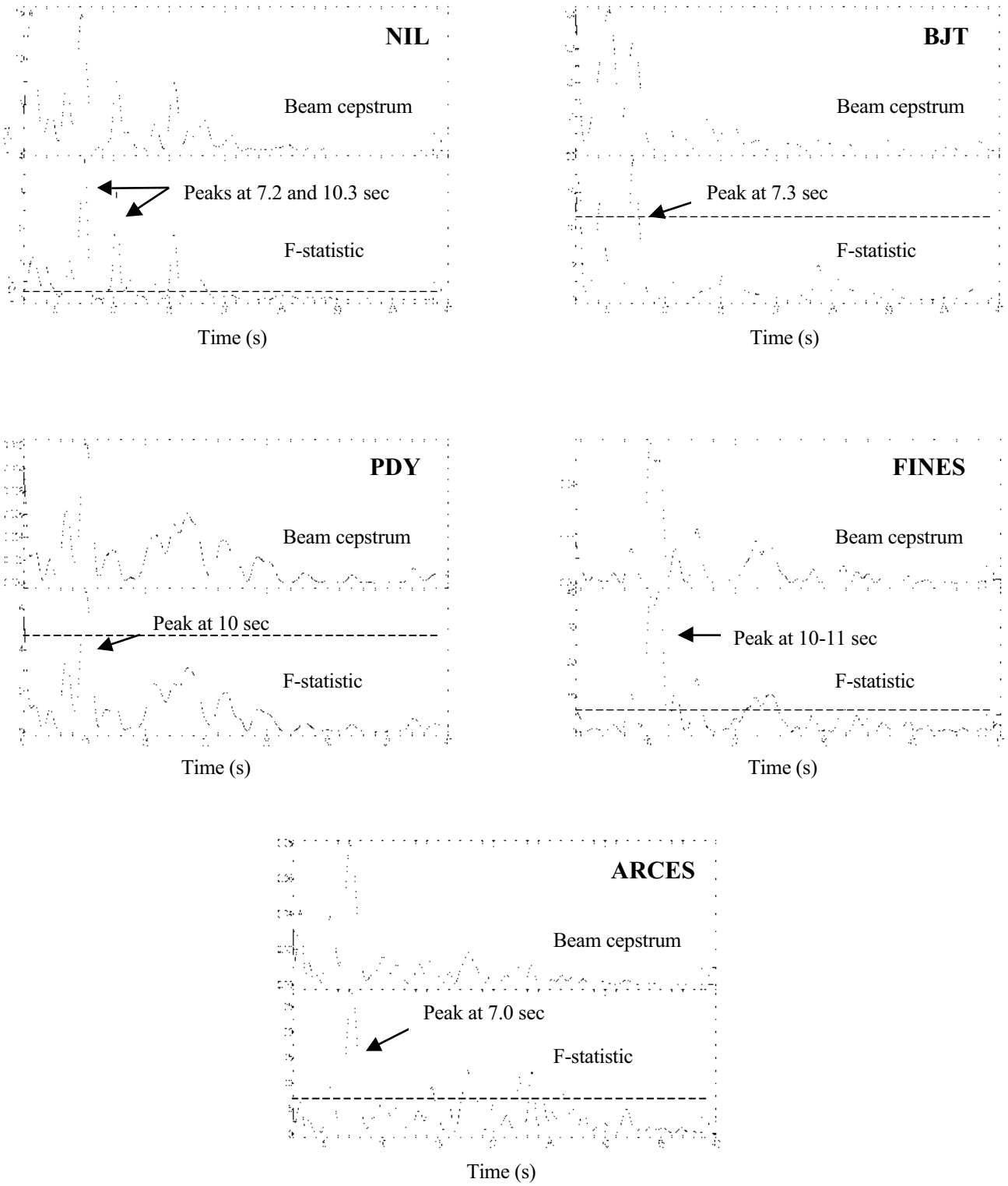


Figure 5. Results from processing data using cepstral analysis from an REB earthquake (evid 20058461, 19 Aug 1998) that took place in Northern Xinjiang, China. Delay times of approximately 7.2 sec for pP-P and 10.5 sec for sP-P result in an estimated depth of 25 km. The dashed lines indicate which peaks are significant at a false alarm rate of .01, except for PDY, which has the line drawn at a false alarm rate of .05.

RESEARCH IN REGIONAL SEISMIC MONITORING

Frode Ringdal, Tormod Kværna and Johannes Schweitzer, NORSAR
Elena Kremenetskaya and Vladimir Asming, Kola Regional Seismological Centre

Sponsored by U.S. Department of Defense
Defense Threat Reduction Agency
Contract No. F08650-96-C-0001

ABSTRACT

During the last decade, a network of sensitive regional arrays has been installed in northern Europe in preparation for the global seismic monitoring network under the Comprehensive Nuclear-Test-Ban treaty (CTBT). This regional network, which comprises stations in Fennoscandia, Spitsbergen and northwestern Russia provides a detection capability for the European Arctic that is close to $m_b = 2.5$, using the Generalized Beamforming (GBF) method for automatic phase association and initial location estimates.

We have implemented some new improvements to the regional GBF processing system currently used at NORSAR. Among the improvements are inclusion of the SPITS array in the GBF procedure, expansion of the beam grid coverage, increased density of the beampacking grid to allow more accurate epicenter determinations and improved detector and f-k recipes for six of the arrays used in GBF. As a result, the processing coverage of the European Arctic is significantly improved, with a much larger number of valid detected events and correspondingly better locations. Primarily, this improvement is due to the inclusion of the very sensitive SPITS array. Using various criteria to reduce the occurrence of spurious phase associations, we conclude that there are significant improvements in the detection and location performance in all regions covered by the regional network. We note that the NORSAR GBF system is capable of detecting and locating seismic events up to one order of magnitude smaller than the automatic association process currently used by the prototype International Data Center, This is due to a combination of better regional array coverage and less strict event definition criteria.

We have continued our studies to use data from the regional networks operated by the Kola Regional Seismological Centre (KRSC) and NORSAR to study the seismicity and characteristics of regional phases of the Barents/Kara Sea region. These studies have encompassed the traditional M_S:m_b discriminant, using surface waves recorded at regional distances, as well as short-period regional discriminants such as the P/S ratio. We have applied these discriminants to events with known source type as well as "unknown" events. The regional M_S: m_b results are encouraging, whereas the short-period discriminants will need further research, and will probably only be effective after extensive regional calibration and in combination with detailed station-source corrections.

A workshop was held in Oslo, Norway during 12-14 January 1999 in support of the global seismic event location calibration effort currently being undertaken by the Preparatory Commission's Working Group B in Vienna. Among the contributions were recent results provided by NORSAR and KRSC of our joint regional calibration effort in the European Arctic, which has resulted in much improved travel-time models for this region. We show by examples that significant improvements in event location precision can be achieved compared to using the IASPEI model, and we use the regional model to calculate locations of some recent small seismic events in the Novaya Zemlya region of interest in a CTBT monitoring context.

Key Words: detection, location, discrimination, seismic data analysis

OBJECTIVE

This work represents a continued effort to study earthquakes and explosions in the Barents/Kara Sea region, which includes the Russian nuclear test site at Novaya Zemlya. The overall objective is to characterize the seismicity of this region, to investigate the detection and location capability of regional seismic networks and to study various methods for screening and identifying seismic events in order to improve monitoring of the Comprehensive Nuclear-Test-Ban Treaty.

RESEARCH ACCOMPLISHED

NORSAR and Kola Regional Seismological Centre (KRSC) of the Russian Academy of Sciences have for many years cooperated in the continuous monitoring of seismic events in North-West Russia and adjacent sea areas. The research has been based on data from a network of sensitive regional arrays which has been installed in northern Europe during the last decade in preparation for the CTBT monitoring network. This regional network, which comprises stations in Fennoscandia, Spitsbergen and NW Russia (see Figure 1) provides a detection capability for the Barents/Kara Sea region that is close to $m_b = 2.5$ (Ringdal, 1997).

The research carried out during this effort is documented in detail in several contributions contained in the NORSAR Semiannual Technical Summaries. In the present paper we will limit the discussions to some recent results of interest in the context of applying the P/S discriminant to seismic events in the Barents/Kara Sea region.

The Kara Sea seismic event on 16 August 1997 that was reported by the prototype International Data Center has caused a considerable and renewed interest in the seismicity of the region surrounding the Novaya Zemlya islands. Historically, registered earthquake activity in this region has been virtually nonexistent, with the exception of one presumed earthquake in the Kara Sea close to the Novaya Zemlya coast on 1 August 1986 (Marshall et al, 1989). The event on 16 August 1997 (m_b =3.5) has been studied by several investigators (Richards and Kim, 1997; Hartse, 1998), with particular attention to the P/S ratio observed at high frequencies.

This paper addresses the possibilities and limitations of utilizing the P/S ratio to characterize seismic events at low magnitudes in this region. We note that the P/S and other similar discriminants (e.g. Pn/Lg) have been extensively studied in many areas of the world, but at present there is no consensus on the applicability of such discriminants on a global basis.

Data

The seismicity of the Barents/Kara Sea region has previously been discussed by Ringdal (1997). Nuclear and chemical explosions were conducted at Novaya Zemlya until 1990, but the availability of regional data for these events is quite limited because most of the high-quality regional arrays in Fennoscandia and adjacent areas were established after this time. In addition, the Novaya Zemlya explosions were generally large, except for two smaller nuclear explosion in 1977 and 1984, and two chemical explosions in 1978 and 1987. A small presumed earthquake (Marshall et al, 1989) occurred on Novaya Zemlya near the nuclear test site in 1986. To our knowledge, there is no available digital recordings at near-regional distances (less than 12 degrees) for any of the abovementioned smaller events. Although there has been several low-magnitude seismic events detected near Novaya Zemlya in recent years, they are difficult to use for establishing or testing regional discriminants, since there is no confirmed evidence available as to their source type.

In other parts of the European Arctic, there is a quite good selection of reference earthquakes and mining explosions. For example, there are some well-known mining areas in the Kola Peninsula and Vorkuta south of Novaya Zemlya. The seismic event occurrence is also very high in the Spitsbergen area and offshore Norway (to the north and west). These events are presumably mostly earthquakes.

We have made a selection of known nuclear explosions, known earthquakes and some unknown events as a basis for this study. The events are listed in Table 1 and shown in Figure 1 together with the station network. Some of the smaller events have been located by Kremenetskaya et. al. (1999).

Date/time	Location	m_b	Comment
04.09.72/ 07.00.00	67.75 N, 33.10 E	4.3	Nuclear explosion, Kola Peninsula
09.10.77/ 10.59.58	73.414 N, 54.935 E	4.5	Nuclear explosion, Novaya Zemlya
10.08.78/ 07.59.58	73.293 N, 54.885 E	6.0	Nuclear explosion, Novaya Zemlya
27.08.84/ 06.00.00	67.75 N, 33.00 E	4.3	Nuclear explosion, Kola Peninsula
01.08.86/ 13.56.38	72.945 N, 56.549 E	4.3	Located by Marshall et.al. (1989) (presumed to be an earthquake)
16.06.90/ 12.43.28	68.52 N, 33.09 E	4.0	Earthquake, felt in the Murmansk region
24.10.90/ 14.57.58	73.360 N, 54.670E	5.6	Nuclear explosion, Novaya Zemlya
23.02.95/ 21.50.00	71.856 N, 55.685 E	3.5	Located by Kremenetskaya et. al. (1999)
31.01.97/ 04.23.53	67.3 N, 60.6 E	2.5	Mining explosion — Vorkuta region
16.08.97 02.11.00	72.510 N, 57.550 E	3.5	Located by Ringdal et al (1997)
16.08.97 06.19.10	72.5 N, 58 E	2.6	Probably co-located with preceding event
14.02.98/ 00.49.37	67.34 N, 62.9 E	2.4	Mining explosion — Vorkuta region

Table 1: List of seismic events used in this study.

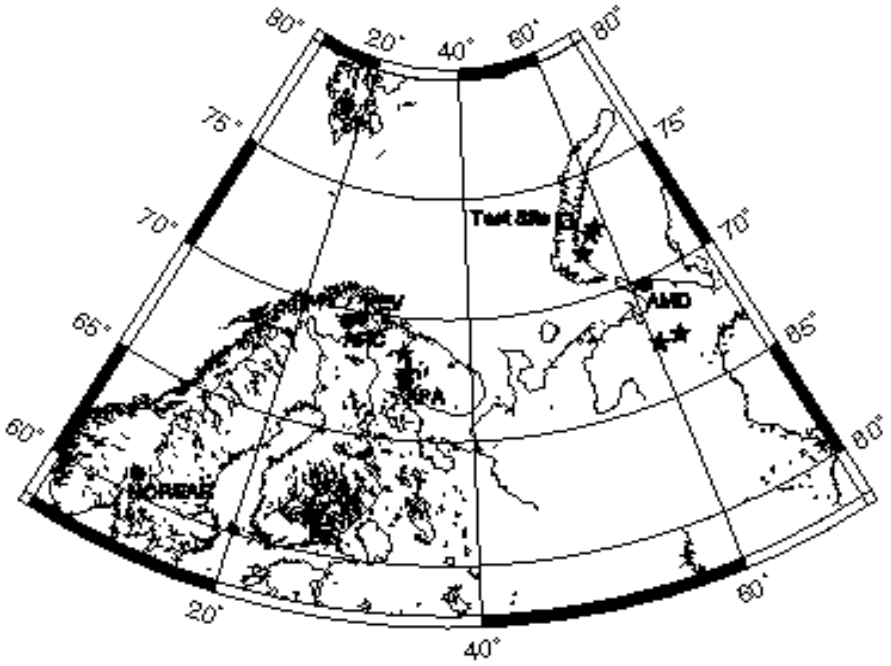


Fig. 1. Regional network of seismic stations and seismic events analyzed in this study. The location of the Novaya Zemlya nuclear test site is indicated.

P/S Ratios Observed at NORSAR

Novaya Zemlya events

The NORSAR large array (Bungum et. al., 1971) has an extensive database of recordings from events near Novaya Zemlya, including some nuclear explosions of magnitudes similar to those of the 16 August event and the nearby presumed earthquake of 1 August 1986. The large aperture of NORSAR makes it possible to study the spatial variability of signal characteristics for the same seismic event over an area extending up to 100 km across. Ringdal et. al. (1998) made the following observations for the 1-3 Hz filter band:

- The P/S ratios show very large variability (about an order of magnitude) across the array.
- This variability is dominated by strong P-wave focusing effects across NORSAR

They concluded that the P/S ratio in the 1-3 Hz frequency band is not a very promising discriminant when using data recorded at a single station. They noted, however, recent studies for Central Asia (Hartse et al, 1997), which have shown that the P/S discriminant for that region appears effective at frequencies above 4 Hz, but has a poor performance for frequencies below 4 Hz. At NORSAR, there is almost no significant S-wave energy above 4 Hz, so we are confined to consider the lower frequencies for Novaya Zemlya events.

Source scaling of the P/S ratio

The NORSAR array data base includes digital recordings of both large and small nuclear explosions from Novaya Zemlya. It is instructive to study the P/S pattern of these explosions as a function of the event size. In order to accomplish this, we have used the one NORSAR sensor (01A01) that has dual gain recording (the usual high-gain channel and a channel that is attenuated by 30dB). The attenuated channel has been available since 1976, and therefore provides a good data base of unclipped short period recordings of Novaya Zemlya explosions.

Figure 2 a-b shows the P/S ratio as a function of magnitude m_b (world-wide as well as NORSAR) for 16 Novaya Zemlya nuclear explosions for which attenuated channel data were available. A magnitude-dependent trend can be clearly seen, and can be approximated by:

$$\log(P/S) = 1.35 m_b + c$$

The slope is similar in the two plots, whereas the value of the constant c is slightly different due to the NORSAR bias relative to world-wide m_b. This indicates that source-to station specific P-wave focusing effects at NORSAR are not a dominant cause of the trend. There could be other possible explanations, such as systematic differences in depth of burial or source corner frequency effects, but for our purposes, it is sufficient to note that comparing the P/S ratios of large and small events could easily give misleading conclusions.

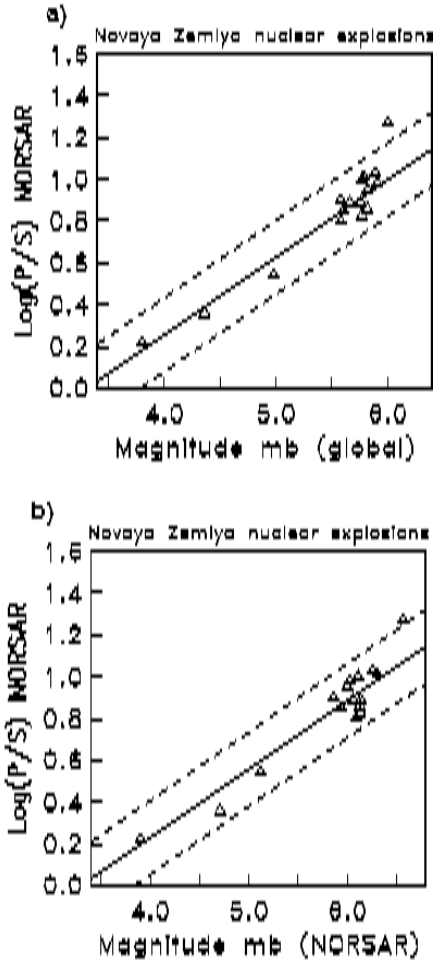


Fig. 2. NORSAR P/S ratios (seismometer 01A01) in the 1.5-2.5 Hz filter band for a suite of 16 Novaya Zemlya nuclear explosions. Parts a) and b) show log(P/S) as a function of world-wide m_b and NORSAR m_b, respectively. Note the similar trend for the two cases.

Recordings of Kola nuclear explosion and earthquake

In order to illustrate the behavior of the P/S discriminant at higher frequencies (3-5 Hz), we show in Figure 3 selected NORSAR traces for an earthquake in the Kola Peninsula in 1990 (felt in the Murmansk district) and a Kola nuclear explosion in 1984 (colocated with the 1972 explosion discussed by Ringdal et. al. (1998)). Both are at an epicentral distance of between 11 and 12 degrees. It appears that the P/S ratio is slightly higher for the explosion, but the difference is not very significant in view of the relative variation in P/S ratios for each event. On the other hand, a similar figure for recordings at the Kevo station (Figure 4) shows a clear difference in the P/S ratio between the two events. Thus, it is indicated that the P/S ratio discriminant could be effective at high frequencies if a good azimuthal distribution of recordings is available, but more data will be required for further assessment of its discrimination potential.

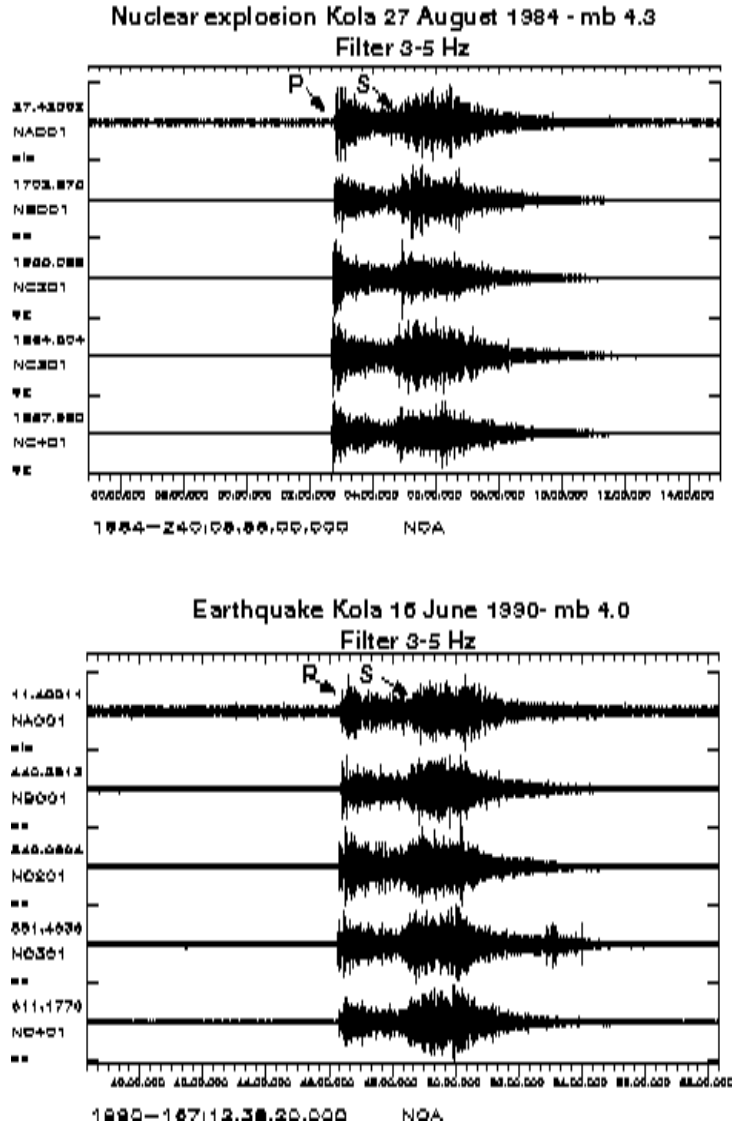


Fig. 3.Selected NORSAR traces for an earthquake in the Kola Peninsula in 1990 (felt in the Murmansk district) and the Kola nuclear explosion in 1984. Both are at an epicentral distance of between 11 and 12 degrees. The data have been filtered in the 3-5 Hz band.

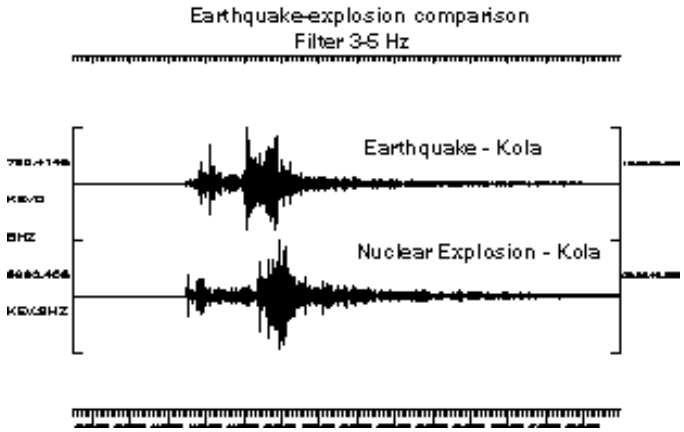


Fig. 4. Recordings by the Kevo station in Finland for the same earthquake and explosion shown in Fig. 3. The epicentral distance is 2-3 degrees, and the data have been filtered in the 3-5 Hz band. Note the significantly greater P/S ratio for the explosion.

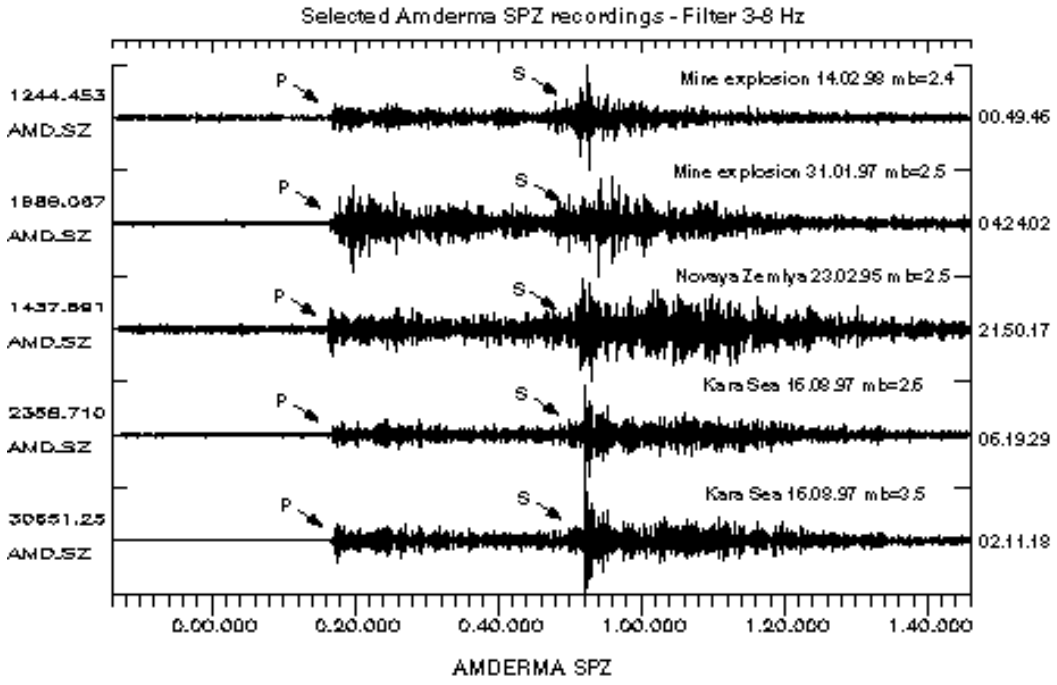


Fig 5. Amderma vertical component recordings of five seismic events at a similar epicentral distance from the station (about 300 km). The data have been filtered in the 3-8 Hz band. The five events are the two Kara Sea events on 16 August 1997, two mining explosions in Vorkuta south of the station, and a small event at the coast of Novaya Zemlya in 1995. The scaling factor in front of each trace is indicative of the relative size of the events.

The 16 August 1997 Event

On 16 August 1997, the CTBT prototype International Data Center in Arlington, Va. reported a small seismic disturbance located in the Kara Sea, near the Russian nuclear test site on Novaya Zemlya. The event caused considerable interest, since initial analysis indicated that the seismic signals had characteristics similar to those of an explosion.

NORSAR and KRSC worked together on locating this event, each carrying out independent analysis. Since some phase onsets were very difficult to read, this was quite useful, and the results were very consistent. We were very quickly able to confirm beyond doubt that the 16 August 1997 event was located in the Kara Sea, at least 100 km from the Novaya Zemlya nuclear test site.

Perhaps the best indication of an earthquake source would be the presence of several aftershocks, if such could be found. We have carried out a detailed search for aftershocks of the 16 August 1997 event, using both Spitsbergen array data and data that later have become available at KRSC from the Amderma station south of Novaya Zemlya.

Our search of Spitsbergen data, which was conducted by detailed visual inspection of the array beam, enabled us to find a second (smaller) event from the same site a little more than 4 hours after the main event. This second event had Richter magnitude 2.6, and could be quite clearly seen to originate from the same source area (Ringdal et. al., 1998).

This conclusion was supported when Amderma data became available at KRSC some weeks later. In spite of very careful analysis of both Spitsbergen and Amderma data, we have not been able to identify additional aftershocks during the two weeks following the main event.

P/S ratios of regional events recorded at Amderma

Figure 5 shows Amderma vertical component recordings of five seismic events at a similar epicentral distance from the station (about 300 km). The data have been filtered in the 3-8 Hz band. The five events are the two Kara Sea events on 16 August 1997, two mining explosions in Vorkuta south of the station, and a small event at the coast of Novaya Zemlya in 1995 (Kremenetskaya et. al.,1999).

The recordings are quite instructive. As can be seen by the scaling factor in front of the traces, the events vary in size by about an order of magnitude. It is noteworthy that the two Vorkuta explosions have very different P/S ratios, and encompass the range of P/S ratios for the other three events. This should however, not be taken as an indication of explosive sources for the other events, since we have demonstrated that the P/S ratio does not have sufficient stability to provide confident source identification. Unfortunately, we do not have any confirmed earthquake recordings at Amderma at a similar epicentral distance.

It is of interest to note that for both the event in 1995 and the first event in 1997, the estimated origin times (assuming zero depth) are almost exactly on the minute. These origin times have been calculated by using the Barents travel time model (Kremenetskaya et. al., 1999) , and are estimated to be accurate to within less than 1.0 seconds. This could be taken as indicators that one or both of these two events were man-made. However, it should be noted that the second event on 16 August 1997 did not occur on the entire minute. In any case, our waveform analysis does not support any assertion about the nature of the 16 August event either as an earthquake or as an explosion.

CONCLUSIONS AND RECOMMENDATIONS

We conclude from this study that the P/S ratio is currently unproven as a seismic discriminant, and should be applied with great caution when attempting to identify the source type of seismic events. Case studies for the Barents/Kara Sea region, some of which are discussed briefly in this paper, have demonstrated that the P/S ratio, even at high frequencies, is rather unstable and should not at present be relied upon for regional event discrimination.

The Kara Sea events on 16 August 1997 provide an interesting case study for the Novaya Zemlya region. It highlights the fact that even for this well-calibrated region, where numerous well-recorded underground nuclear explosions have been conducted, it is a difficult process to reliably locate and classify a seismic event of approximate m_b 3.5.

Our conclusion from this study is that the 16 August 1997 events cannot be positively identified as earthquakes on the basis of seismological evidence. On the other hand, neither is there any evidence based on the observed waveforms to confidently classify these events as explosions. Therefore, the source type of these two events remains unresolved on the basis of available seismological evidence.

It is clear from this study that more research is needed on regional signal characteristics in the European Arctic and the application of additional discriminants, such as M_S:m_b at regional distances. It would be a particularly useful exercise to carry out a small chemical calibration explosion, in order to improve the seismic calibration of Barents/Kara Sea region. Such an explosion, even if not recorded teleseismically, would provide valuable additional information for future studies.

REFERENCES

Bungum, H., E.S. Husebye and F. Ringdal (1971). The NORSAR array and preliminary results of data analysis, Geophys. J.R. Astr. Soc. 25, 15-26.

Hartse, H.E. (1998). The 16 August 1997 Novaya Zemlya Seismic Event as Viewed from GSN Stations KEV and KBS, Seism. Research Letters 69, No.3, 206-215.

Hartse, H.E., S.R. Taylor, W.S. Phillips and G.E. Randall (1997). A preliminary study of regional seismic discrimination in Central Asia with emphasis on western China, Bull. Seism. Soc. Am. 87, 551-568.

Kremenetskaya, E.Asming, V. and F. Ringdal (1999). Seismic location calibration of the Barents region. Semiannual Technical Summary 1 October 1998 - 31 March 1999, NORSAR Sci. Rep. 2-98/99, Kjeller, Norway.

Marshall, P.D., R.C. Stewart and R.C. Lilwall (1989): The seismic disturbance on 1986 August 1 near Novaya Zemlya: a source of concern? Geophys. J., 98, 565-573.

Richards, P.G. and Won-Young Kim (1997). Test-ban Treaty monitoring tested, Nature, 389, 781-782.

Ringdal, F. (1997): Study of low-magnitude seismic events near the Novaya Zemlya nuclear test site, Bull. Seism. Soc. Am. 87 No. 6, 1563-1575.

Ringdal, F., E.Kremenetskaya, V.Asming, T.Kvœrna, J. Fyen, J. Schweitzer (1998). Seismic monitoring of the Barents/Kara Sea Region. Proceedings from the 20th Annual Seismic Research Symposium on CTBT Monitoring, September 21-23, 1998

Ringdal, F., T.Kvœrna, E.Kremenetskaya, V.Asming (1997). The seismic event near Novaya Zemlya on 16 August 1997. Semiannual Technical Summary 1 April - 30 September 1997, NORSAR Sci. Rep. 1-97/98, Kjeller, Norway.

DEVELOPMENT OF 3-D CRUSTAL AND UPPER MANTLE VELOCITY MODELS OF NORTHERN EURASIA AND NORTH AMERICA TO REFINE LOCATION OF REGIONAL SEISMIC EVENTS

Russian Federation / United States Calibration Working Group
Contact Person: Vladislav Ryaboy

Center for Monitoring Research
1300 N, 17th Street, Suite 1450, Arlington, VA 22209

Sponsored by Defense Threat Reduction Agency, USA
Contract No. DSWA01-98-C-0032

ABSTRACT

This paper reports research performed by the Russian Federation (RF) / United States (US) Joint Research Program of Seismic Calibration of the International Monitoring System (IMS) in Northern Eurasia and North America. This program was signed between the Nuclear Treaty Programs Office (NTPO), Department of Defense, USA and the Special Monitoring Service (SMS) of the Ministry of Defense, Russian Federation. To date the Joint Program has focused on collection and interpretation of data from large chemical and nuclear explosions with known location and origin time to improve regional seismic event location. A RF/US working group has been established to coordinate the joint research program; the current membership is given below.

Seismic event locations based on regional 1-D velocity-depth sections can be biased by travel-time variations within different tectonic provinces and by ray-paths crossing boundaries between tectonic provinces. Seismic event locations based on 3-D velocity models have the potential to overcome these limitations. This paper summarizes preliminary results for calibration of IMS for North America and Northern Eurasia using 3-D crustal and upper mantle velocity models. Initial 3-D velocity models were tested against maps of Pn travel-time residuals for selected calibration explosions; corrections to the 3-D model were made to fit the observed residuals. The goal was to find 3-D crustal and upper mantle velocity models capable of predicting Pn travel-times with an accuracy of 1.0 - 1.5 seconds (r.m.s.). The 3-D velocity model for North America that gave the best fit to the observed travel-times was used to produce maps of regional distance Source-Specific Station Corrections [SSSCs(3-D)]. These SSSCs(3-D) with their estimated modeling errors, were applied to relocate an independent set of large chemical and nuclear explosions (with known locations and origin times) detonated within various tectonic provinces of North America.

We are testing location accuracy using the SSSCs(3-D) for Pn derived from our 3-D models in comparison both with locations based on the IASPEI-91 travel times and locations based on regionalized travel-time tables. Our test events are GT0 and GT2 events (announced chemical explosions and mine blasts) from the prototype International Data Center (PIDC) Ground Truth database that was not used in the derivation of the 3-D models. Preliminary results indicate that the 3-D model-derived SSSCs improved location accuracy and decreased error ellipse area for some, but not all, tested events. This might indicate that the relocation results may be also influenced by other factors such as phase misidentification, low signal to noise ratios, and underestimated errors of arrival time measurements. This analysis is continuing, and similar experiments are in progress for events in Northern Eurasia.

The RF members of the calibration working group (WG): Colonel Vyacheslav Gordon (chairman); Dr., Prof. Marat Mamsurov, and Dr. Colonel Vladimir Belov.

The US members of the WG: Dr. Anton Dainty (chairman), Dr. Douglas Baumgardt, Mr. John Murphy, Dr. Robert North, and Dr. Vladislav Ryaboy.

Key Words: location, calibration, 3-D modeling, Pn waves.

OBJECTIVE

This paper reports research performed by the Russian Federation (RF) / United States (US) Joint Research Program of Seismic Calibration of the International Monitoring System (IMS) in Northern Eurasia and North America. The International Monitoring System (IMS) is being developed for global monitoring under the Comprehensive Nuclear-Test-Ban Treaty (CTBT). To fulfill this task, seismic events should be located with high accuracy. The globally averaged IASPEI-91 seismological travel-time tables have been used by the prototype International Data Center (PIDC) to locate seismic events. To achieve the CTBT goal of 1000 km^2 location accuracy the IMS has to be calibrated to correct travel times for bias caused by 3-D heterogeneities in the Earth's structure (Firbas, Peshkov, and Ryaboy, 1997). The most precise data that can be used to calibrate the IMS are large chemical and nuclear explosions with known locations and origin times. Deep Seismic Sounding (DSS) data, long-range seismic profile observations, well located mine explosions and earthquakes can also make important contributions to IMS calibration (RF/US, 1997, 1998, 1999). This paper builds upon the methodology of a feasibility study for 3-D modeling presented in (Firbas, 1997a, 1997b, 1999; Firbas, Fuchs, and Mooney, 1998; Ryaboy, Baumgardt, Firbas, and Dainty, 1999). The effort is focused on calibration of IMS stations in North America and Northern Eurasia using 3-D crustal and upper mantle velocity models developed for these regions. The main objectives of this study are the following:

- Analysis of Pn travel-time data collected and exchanged between US and RF;
- Investigation of the feasibility of 3-D modeling for location of regional seismic events in North America and Nortern Eurasia;
- Demonstration for North America of improvements achieved in location accuracy when 3-D models are used.

RESEARCH ACCOMPLISHED

The 3-D approach for the IMS calibration includes the following main steps:

- Regionalization based on tectonic data, travel-times, and crustal and upper mantle velocity structures;
- Collection and analysis of Pn travel-times;
- Collection and analysis of 1-D crustal and upper mantle velocity-depth sections;
- Development of a 3-D crustal and upper mantle velocity model;
- Computation of Station-Source Specific Corrections [SSSCs(3-D)] for seismic stations using the derived 3-D crustal and upper mantle velocity model;
- Regional seismic events relocation to demonstrate the improvement in location accuracy.

These steps have been applied to a preliminary study of the continental US, and similar studies are in progress in Northern Eurasia. These steps are briefly described further in this paper.

Tectonic maps of North America (King, 1977) and Northern Eurasia (Belousov, 1989; Zonenshain, Kuzmin, and Natapov, 1990; Pavlenkova, 1996) were taken as starting points for delineating various tectonic provinces. Maps of crustal thickness and Pn velocity compiled for the US and RF territories were digitized by Cornell university and used for this study. These data and a regionalized upper mantle seismic model (Gudmundsson and Sambridge, 1998) provided a preliminary regionalization based on tectonic and seismic data. Several large explosions with known location and origin time were selected to serve as reference events for location calibration. Figures 1 and 2 show maps of location of peaceful nuclear explosions (PNEs) and large chemical explosions within the US and RF territories, respectively, used for the IMS calibration and location experiments (RF/US, 1998; Ryaboy, Baumgardt, Firbas, and Dainty, 1999).

Pn travel-times recorded from the calibration events were collected and carefully evaluated. Data from many seismic stations were used in this study to derive maps of Pn travel-time deviations from the IASPEI-91 travel-times. These maps were used to study Pn travel-time variations as a function of distance and azimuth within different geological provinces of North America and Northern Eurasia. Abrupt and unreasonable variations of travel-times from reversed and overlapping observations were used as criteria to identify outliers. All available Pn travel-time observations along the Fennolora long-range profile in Scandinavia (Hauser and Stangl, 1990) were also used in this work.

Analysis of seismic observations of explosions in North America and Northern Eurasia shows that the Pn travel-time variations are caused by lateral inhomogeneities of the Earth's crust and upper mantle velocity structure, both on large and small scales. Pn travel times for the ancient Pre-Cambrian provinces (North American and East European platforms, including the Canadian, Baltic, and Ukrainian shields) are up to 5 sec early compared to the IASPEI-91 tables for the distance range 1,000 - 2,000 km. The tectonically active regions of the Western US are characterized by substantially slower Pn travel times, up to 5 sec late in comparison with the IASPEI-91 tables. Pn travel time residuals relative to the IASPEI-91 tables for the southern regions of the European part of the RF, including the Alpine tectonic zone, are approximately +/-(1.0-2.0) sec.

The computer program "sssc" (Firbas, 1997b, 1999), was used to compute Source-Specific Station Corrections (SSSCs) for Pn travel-times by utilizing 3-D velocity Earth models. The parametrization of the 3-D model employs an approach that allows combination of the best velocity information available from multiple sources. An advantage of this approach is that the number of parameters varied in an iterative search to improve the base model can be small and these parameters have a clear physical interpretation. The "sssc" algorithm combines the ray-shooting (interval ray-tracing) and linearization approach. In the global background model, each branch of any travel-time curve is represented by a unique code. The ray reaching the station is found by paraxial approximation, bending (morphing) the particular ray by the Fermat principle, and in the last stage, applying linearization to get the best estimate of the travel-time. The IASPEI-91 travel times are also calculated by the program "sssc" and are accurate to at least several hundredths of a second. When the IASPEI-91 travel time is subtracted from the full travel time in the 3-D velocity model, the deviation or SSSC(3-D) is obtained.

The goal of our effort was to define a 3-D crustal and upper mantle velocity model of US territory and the European part of RF capable of predicting Pn travel times with accuracy of approximately 1.0-1.5 sec (r.m.s.). The simplest 3-D velocity models were sought from a family of 3-D models that simultaneously fit the observed Pn travel times for all calibration events used. To develop 3-D models we used in this work eight calibration explosions for US territory and eight calibration explosions for the European part of the RF. The first steps of testing different 3-D velocity models revealed that the crustal model and the Moho depth surface variation had only minor effects on travel times. We fixed the 3-D crustal velocity model (Mooney, Laske, and Masters, 1998) and the Moho depth in further iteration steps and changed the 3-D upper mantle velocity models only.

A total of 45 iterative 3-D velocity models were developed and evaluated for North America. The current model (revision 4.5) fits the observed travel times with an average precision of 1.0 - 1.5 sec r.m.s. Figure 3A shows 1-D velocity models for P-waves derived by this process in comparison with the IASPEI-91 model. Figure 3B shows upper mantle regionalization; numbers on the map of Figure 3B refer the velocity models Figure 3A. Figures 4A and 4B show 1-D velocity models and upper mantle regionalization for Northern Eurasia. Figures 4A and 4B include a 3-D model developed for Europe by P. Firbas (Firbas, 1999). A total of five iterative 3-D velocity models were developed and evaluated for Northern Eurasia. Differences between calculated Pn travel times for the current model (revision 1.4) and observed data for some regions of Northern Eurasia are up to 2-5 sec. The revision 1.4 is a preliminary model for Northern Eurasia which should be improved.

Figures 5 shows as an example a map of the difference between observed and calculated Pn travel times for the Early Rise explosions (Iyer et al., 1969). The differences are mainly within +/- 1 sec, increasing in some relatively small areas to +/- 2.0 sec. Figure 6 compares of observed and calculated Pn travel-time curves for the Fennolora long-range profile (3-D model revision 1.4) for shot point B (southern Baltic shield). Figure 6 shows that observed Pn travel times for southern Baltic shield fit Pn travel times calculated for 3-D model (revision 1.4) rather well. However, similar calculations showed that observed Pn travel times for the northern Baltic shield (Fennolora profile, shot point I) are up to 2-3 sec faster in comparison with the Pn travel times calculated for the 3-D model.

The 3-D velocity model developed for the USA territory (revision 4.5) was used to produce maps of SSSCs for all IMS stations and other stations needed for the relocation experiments. The purpose of the relocation experiments was to evaluate the influence of SSSCs on the accuracy of location of seismic events recorded at regional distances and thus to test the usefulness of the 3-D model. The 3-D model residuals fit the observed residuals in the US to within 1.0-1.5 sec r.m.s. The average r.m.s. value for all calibration explosions is approximately 1.0 sec. The value of 1.0 sec was therefore used as the modeling error in relocation experiments. The calculated SSSCs with the

estimated modeling error (1.0 sec) and the estimated measurement error (0.5 sec) were first applied to locate the eight mentioned calibration events used to derive the 3-D velocity model. This step can be also viewed as a test of the internal consistency of the 3-D model process development. As an independent test, four large chemical explosions with good signal to noise ratio and with known locations and origin times, not used in the model development, were also relocated using derived SSSCs and "surrogate networks" to the IMS network.

As example Figure 7A shows the results of the relocation experiment for the Rockville Dam chemical explosion (LRSM Rockville Dam Report, 1966) using 6 stations placed within the North American platform (2 stations) and the western US (4 stations). The distance between the ground truth epicenter and the estimated location (mislocation) decreased from 20.7 km, in the case using the IASPEI-91 travel times, to 9.0 km using SSSCs(3-D). The calculated error ellipse for the location based on SSSCs(3-D) is substantially smaller than for the IASPEI-91 solution and includes the ground truth epicenter. Mislocation based on the International Seismological Center (ISC) Bulletin solution using 25 stations is 7.1 km. The main results of the relocation experiments are summarized in Figure 7B which shows a boxplot to display the distribution of mislocation values obtained for three methods of location. Locations using SSSCs(3-D) are characterized by the smallest average mislocation and by the smallest width of the mislocation distribution, i.e. they are most accurate and most robust of the three approaches. However, preliminary results of similar relocation experiments for small explosions with low signal to noise ratio (explosions detonated along Deepprobe and Lithoprobe long-range profiles, and mine explosions) showed that using of SSSCs(3D) did not improve location accuracy for all tested events. This might indicate that relocation results may be also influenced by other factors such as phase misidentification, low signal to noise ratio, and underestimated errors of arrival time measurements. This analysis is continuing and similar experiments are in progress.

CONCLUSIONS AND RECOMMENDATIONS

This paper presents the development of 3-D crustal and upper mantle velocity models for the US and RF territories to improve location of regional seismic events carried out within the framework of the RF/US Joint Research Program of Seismic Calibration of IMS in Northern Eurasia and North America. The main results of the study as follows:

1. Preliminary calculations made for Northern Eurasia show that it may be feasible to use for this region a 3-D modeling approach to fit the measured travel-time anomalies of Pn waves and then calculate SSSCs from a 3-D velocity model.

2. The application of SSSCs(3-D) with an estimated modeling error of 1.0 second derived from a preliminary 3-D velocity model led to a clear improvement in seismic event location accuracy and substantial decrease in error ellipse area compared to locations based on the IASPEI-91 travel times and locations based on two regional travel-time curves (1-D velocity models).

The next steps to be made should include: (1) development and evaluation of the 3-D velocity model for Northern Eurasia including relocation experiments using SSSCs(3-D) for events with known location and origin time, (2) continued collection and exchange between RF and US travel times major regional phases recorded from calibration events, (3) extension of the 3-D model developed for US territory to cover the areas north of latitude 55 degrees N, (4) calculations of SSSCs(3-D) for other major regional phases (Pg, Sn, and Lg) for the IMS stations located in North America, and (5) continuation of relocation experiments for calibration events.

REFERENCES

Belousov, V.V. Fundamentals of Geotectonics. Moscow, Nedra Publishing House, 382 p., 1989 (in Russian).

Firbas, P., A.B. Peshkov, and V. Ryaboy. From IASP-91 global model to a 3-D model for CTBT monitoring. In: Upper mantle heterogeneities from active and passive seismology (Edited by K. Fuchs), Kluwer, 199-214, 1997.

Firbas, P. IMS Calibration for Europe, Technical report CMR-97/02, Center for Monitoring Research, 44 p., 1997a.

Firbas, P. Program SSSC for computation of station-source specific time corrections for 3-D velocity models, Technical report CNR-97/08, Center for Monitoring Research, 31 p., 1997b.

Firbas, P., K. Fuchs, and W. Mooney. Calibration of Seismograph Network May Meet Test Ban Treaty's Monitoring Needs, vol. 79, No. 35, 413, 1998.

Firbas, P. Calibration based on ground truth data and 3-D modeling: framework and feasibility study for Western Europe, manuscript submitted for publication in Pure and Applied Geophysics, 1999.

Gudmundsson, O., and M. Sambridge, A regionalized upper mantle (RUM) seismic model, J. Geophys. Res., 103, B4, 7121-7136, 1998.

Hauser F. and R. Stangl. The structure of the crust and the lithosphere in Fennoscandia derived from a joint interpretation of P- and S-wave data of the FENNOLORA refraction seismic profile. In Proceedings of the 6-th European geotraverse (EGT) project (Edited by R. Freeman and St. Mueller), 71-92, 1990.

Iyer, H.M., L.C. Pakiser, D.J. Stuart, and D.H. Warren. Project Early Rise: Seismic probing of the Upper Mantle, J. Geophys. Res., vol. 74, No. 17, 4409-4441, 1969.

King, P.B., The Evolution of North America, Princeton Univ. Press, 197 p., 1977.

LRSM Rockville Dam Report. VELA-UNIFORM project, 19 August 1966.

Mooney, W.D., G. Laske, and T.G. Masters, Crust 5.1: A global crustal model at 5^0 x 5^0, J. Geophys. Res., 103, B1, 727-747, 1998.

Pavlenkova, N.I. Crust and upper mantle structure in Northern Eurasia from seismic data. In Advances in Geophysics, vol. 37, Academic Press, 1-133, 1996.

RF/US Calibration Working Group, Joint RF/US Research Program of Seismic Calibration of the International Monitoring System in Northern Eurasia and North America, In Proceedings of the 19th Annual Seismic Research Symposium on Monitoring the Comprehensive Nuclear-Test-Ban Treaty, 152-161, 1997.

RF/US Calibration Working Group, Evaluation of the IMS location accuracy of large chemical and nuclear explosions in Northern Eurasia and North America using regional and global Pn travel-time tables. In Proceedings of the 20th Annual Seismic Research Symposium on Monitoring the Comprehensive Nuclear-Test-Ban Treaty, 92-101, 1998.

RF/US Calibration Working Group, Analysis of the IMS location accuracy in Northern Eurasia and North America using regional and global Pn travel-time tables, manuscript submitted for publication in Pure and Applied Geophysics, 1999.

Ryaboy, V., D.R. Baumgardt, P. Firbas, and A.M. Dainty, Application of 3-D crustal and upper mantle velocity model of North America for location of regional seismic events, manuscript submitted for publication in Pure and Applied Geophysics, 1999.

Zonenshain, L.P., M.I. Kuzmin, L.M. Natapov (B.M. Page, Editor). Geology of the USSR: A Plate-Tectonic Synthesis. Geodynamics Series, vol. 21, American Geophysical Union, 242 p., 1990.

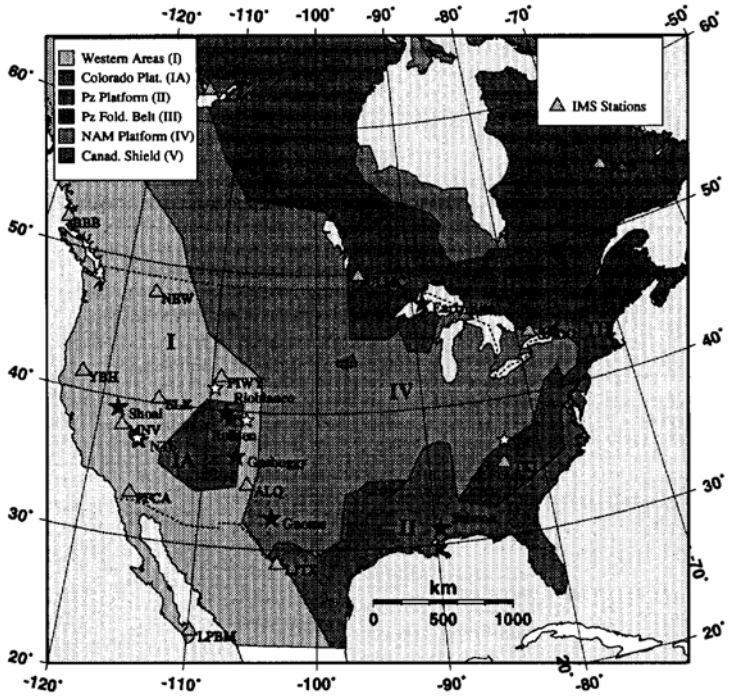


Figure 1. Location of large explosions used for the IMS calibration and location experiment in US. Solid stars are calibration explosions used for the IMS calibration and relocation experiments, and open stars are explosions used only for relocation experiments. In the background the simplified tectonic map is shown.

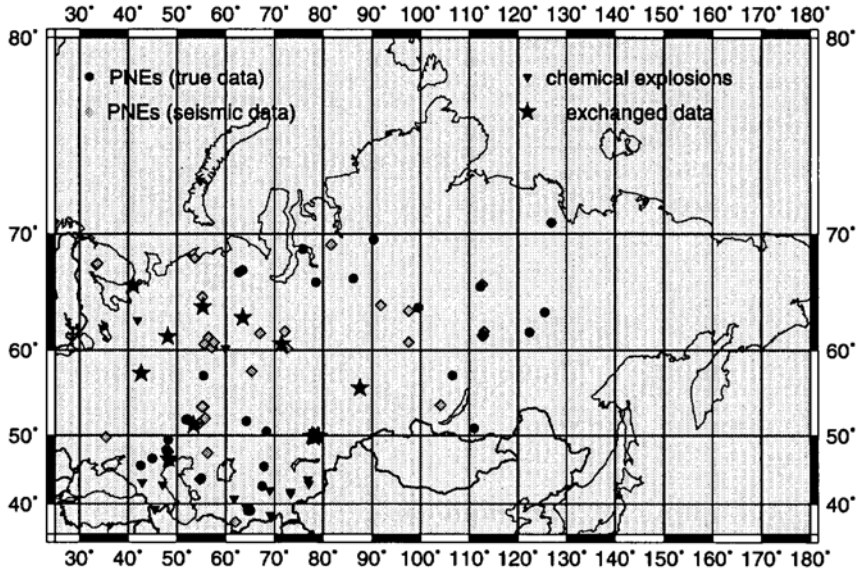


Figure 2. Location of nuclear and large chemical explosions within RF.
PNEs - Peaceful Nuclear Explosions located using seismic data and true data.

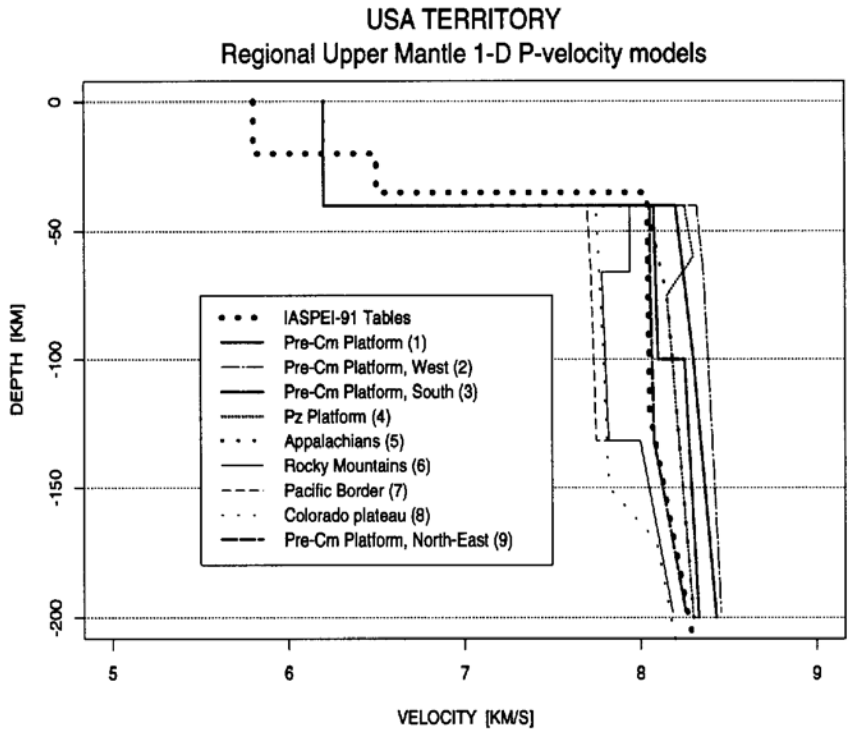


Figure 3A. Regional upper mantle 1-D P-velocity models of the USA territory and neighboring regions of Canada.

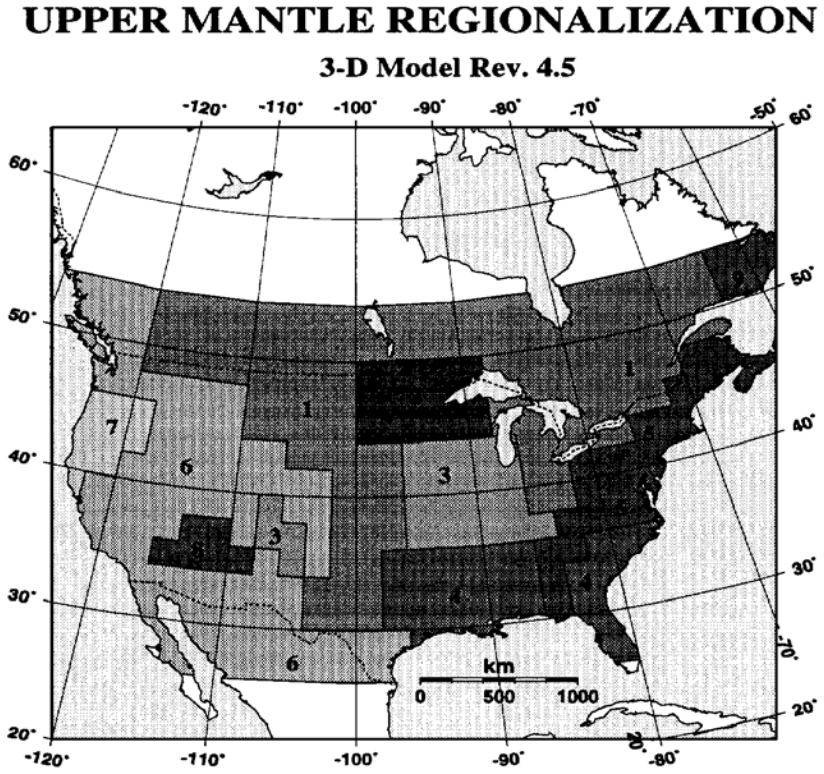


Figure 3B. Upper mantle P-velocity regionalization of the USA territory and neighboring regions of Canada (3-D model, revision 4.5).

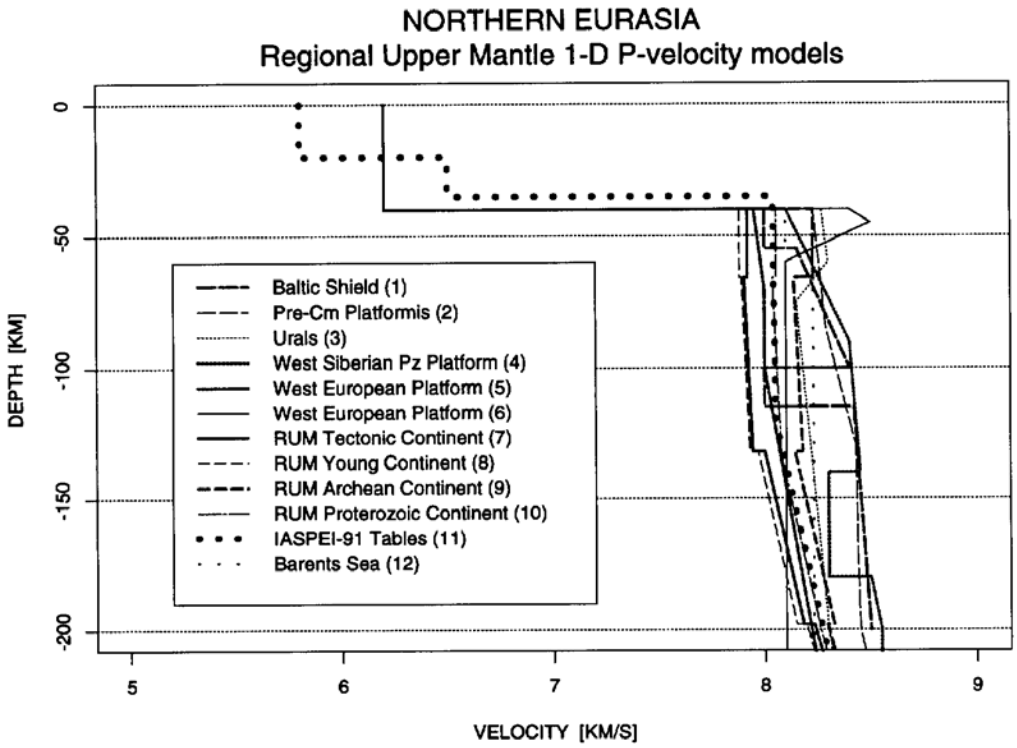


Figure 4A. Regional upper mantle 1-D P-velocity models of Northern Eurasia.

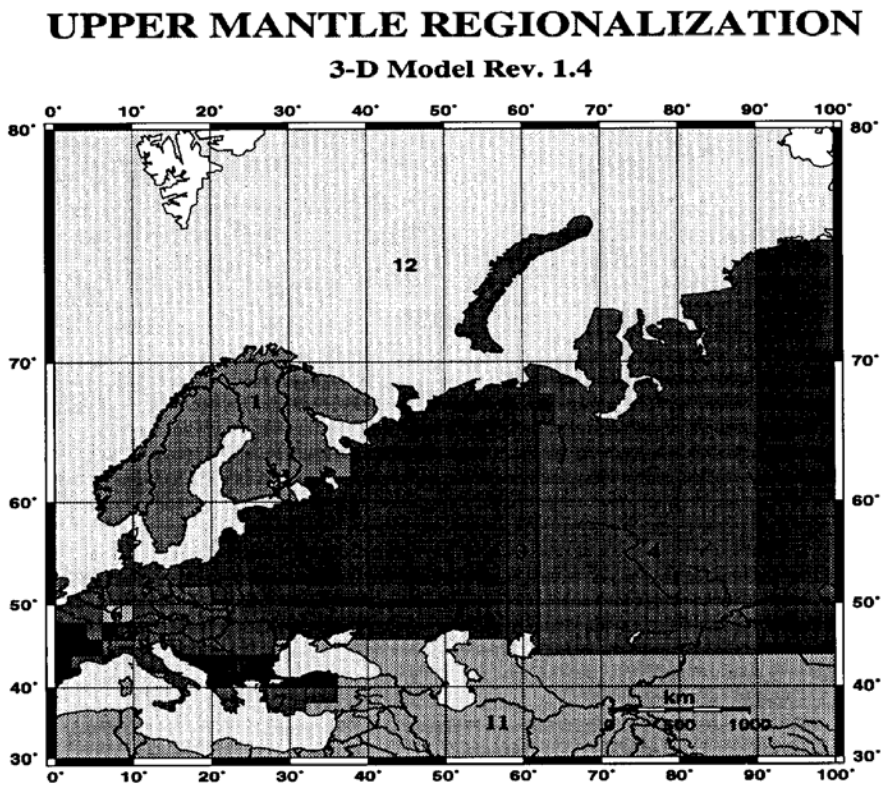


Figure 4B. Upper mantle P-velocity regionalization of Northern Eurasia (3-D model, revision 1.4).

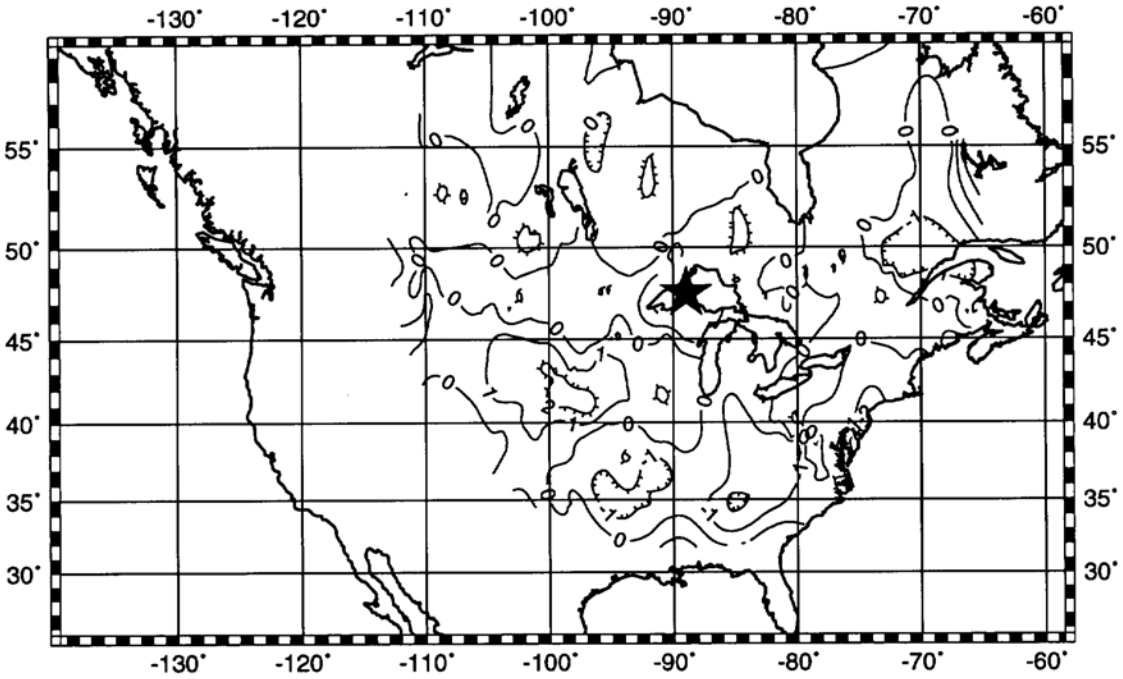


Figure 5. Early Rise experiment (solid star is a shot point). Map of difference between observed and calculated Pn travel-times (in sec) for 3-D model, revision 4.5.

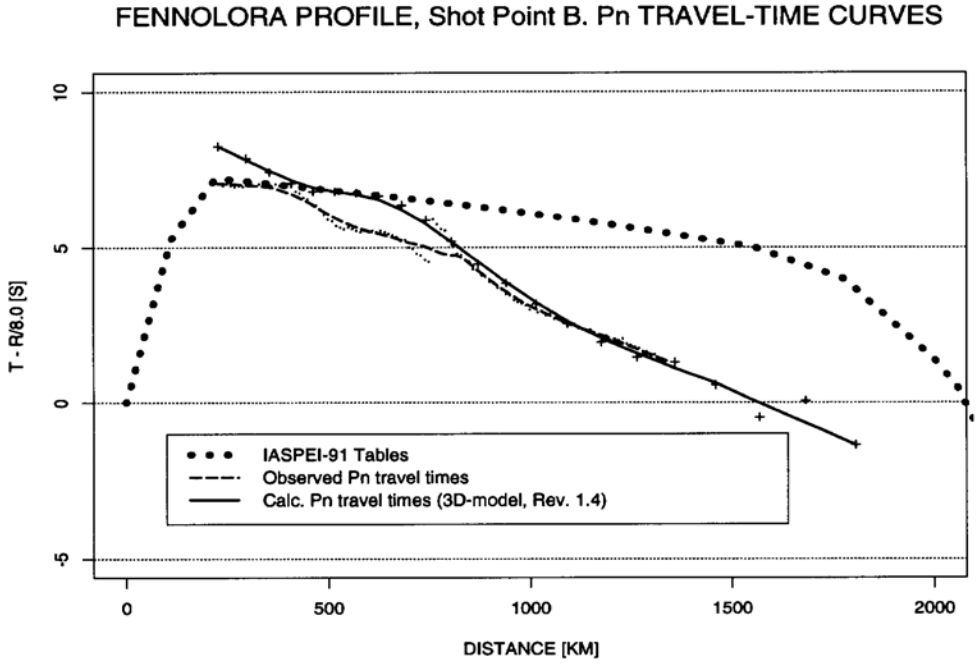


Figure 6. FENNOLORA profile. Comparison of Pn travel-time curves observed (shot point B), calculated (3-D model, revision 1.4), and IASPEI-91.

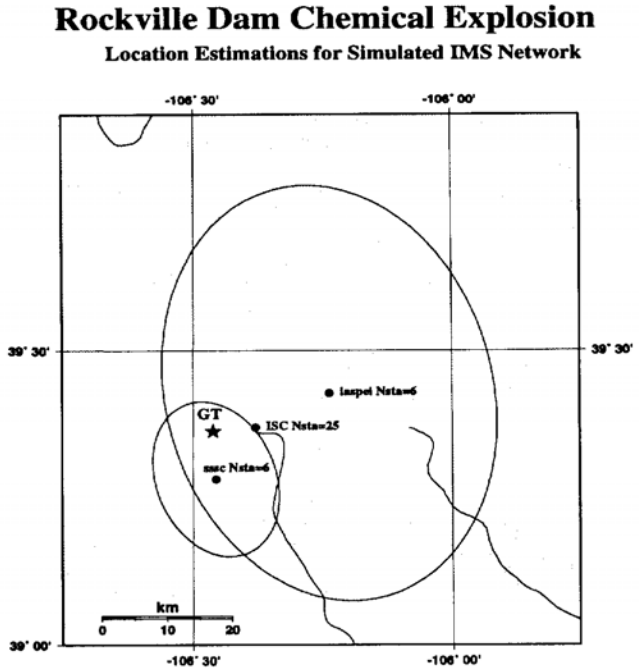


Figure 7A. Locations of the Rockville Dam Chemical Explosion using 6 stations (Nsta=6). Locations: ground truth (GT), iaspei (IASPEI-91 tables, sssc (SSSCs(3-D)).

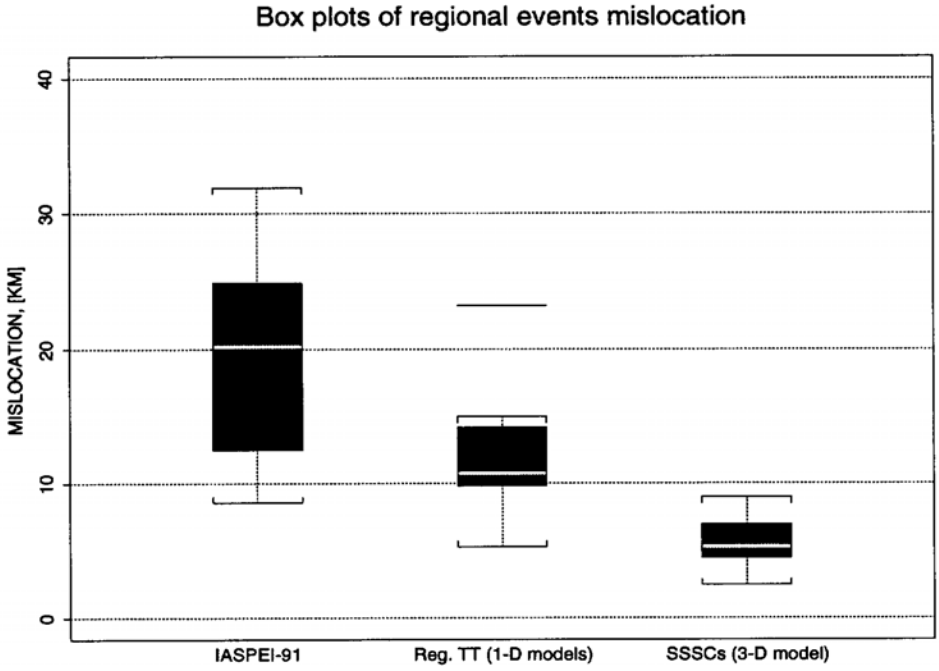


Figure 7B. Box plots of mislocation of large explosions detonated within US. Locations using: IASPEI-91 tables (IASPEI-91) (12 events), two 1-D regional models (Reg. TT) (1-D models) (5 events), SSSCs(3-D) (Source-Specific Station Corrections inferred from the 3-D velocity model of the Earth crust and upper mantle) (12 events).

IMPROVING REGIONAL SEISMIC EVENT LOCATION THROUGH CALIBRATION OF THE INTERNATIONAL MONITORING SYSTEM

Craig A. Schultz, Stephen C. Myers, Megan Flanagan, Jennifer Swenson, William Hanley, Micheal Pasyanos
Geophysics and Global Security, Lawrence Livermore National Laboratory

Sponsored by U.S. Department of Energy
Office of Nonproliferation and National Security
Office of Research and Development
Contract No. W-7405-ENG-48

ABSTRACT

At Lawrence Livermore National Laboratory (LLNL), we are working to help calibrate the 170 seismic stations that are part of the Comprehensive Nuclear-Test-Ban Treaty (CTBT) monitoring network, in order to enhance the network's ability to locate small seismic events. These low magnitude events are likely to be recorded by only the closest of seismic stations, ranging from local to near teleseismic distances. At these distance ranges, calibration statistics become highly nonstationary, challenging us to develop more general statistical models for proper calibration.

To meet the goals outlined above, we are developing a general nonstationary framework to accurately calibrate seismic travel-time predictions over the full distance range, from local, to regional, to teleseismic distances. The objective of this framework is to develop valid region-specific corrections for the Middle East, North Africa, and portions of the Soviet Union, to assess our progress towards meeting calibration goals, and to perform cost-benefit analysis for future calibrations. The framework integrates six core components essential to accurate calibration. First, is the compilation and statistical characterization of well located reference events, including aftershock sequences, mining explosions and rockbursts, calibration explosions, and teleseismically constrained events (Harris et al., SSA 1999; Hanley et al., SSA 1999). Second, is the development of generalized velocity models based on these reference events (McNamara et al., SSA 1998; Pasyanos, SSA 1999). Third, is the development of nonstationary spatial corrections (nonstationary Bayesian kriging) that refine the base velocity models (Schultz et al., SSA 1998). The fourth component is the development of a detection model on a station-by-station basis. The fifth component is the cross-validation of calibration results to ensure internal consistency along with the continual benchmarking of our nonstationary model where event locations are accurately known (Myers and Schultz., SSA 1999). Finally, the sixth component is the development of location uncertainty maps, demonstrating how calibration is helping to improve location accuracy across both seismically active and aseismic regions. Together, these components help us to ensure the accurate location of events, and just as important, help to ensure the accurate representation of bias uncertainty and random uncertainty in the predicted error ellipses.

Key Words: assessing progress, location, kriging, discrimination, detection, cross-validation

OBJECTIVES:

Seismic monitoring requires the accurate detection, location and identification of seismic events as they occur regionally, both in seismic and aseismic regions. Enhancement in these areas can come from the application of geophysical corrections to various properties of the seismic waveform such as travel-time, magnitude, amplitude, attenuation and dispersion measurements. Given *a priori* information about the velocity structure, corrections can be developed to improve estimates of travel-time prediction in aseismic regions. In seismically active regions historic sets of events, for which the source location parameters are well constrained, can be used to develop corrections that improve on travel-time predictions.

The goal of the location project at LLNL is to provide an innovative statistical framework for seismic location (both in seismic and aseismic regions) that can be used to propagate uncertainties accurately from model predictions and empirical corrections to our confidence in a specific location. To meet these goals we are developing a general nonstationary framework to accurately calibrate seismic travel-times over the full range, from local, to regional, to teleseismic distances. The objectives of our work are to develop valid region-specific corrections for the Middle East, North Africa, and portions of the Soviet Union, to assess our progress towards meeting monitoring goals, and to perform cost-benefit analysis for future calibrations.

RESEARCH ACCOMPLISHED

The Challenge: Regional Calibration

Regional variation in the propagation of seismic waves is the largest source of uncertainty for seismic monitoring of the CTBT (Figure 1). Unlike the Threshold Test Ban Treaty, which banned nuclear explosions larger than 150 kt, the CTBT bans all nuclear explosions. Thus the emphasis has shifted from estimating yields of large, easily identified nuclear explosions from the data recorded at numerous stations throughout the world to detecting, locating, and identifying nuclear explosions using data recorded at a few stations located at regional distances (less than about 2000 kilometers) from the explosions. The CTBT monitoring challenge is further complicated by the many earthquakes and mining explosions that generate tens of thousands of seismic signals annually, some very similar to the signals generated by nuclear explosions.

Detection, location, and identification of small seismic events all require a region-specific understanding of the effects of the path between the sources and the recording stations, because the heterogeneity of the earth's crust and upper mantle have significant effects on the properties of their seismic signals. Thus, we are developing a DOE Knowledge Base (KB) of regional seismic properties to help meet monitoring goals. This KB characterizes regional variations in the travel-times, amplitudes, and frequency content of the seismic waves generated by small, shallow sources. In addition, we are developing new methods that use this information to discriminate between nuclear and non-nuclear sources.

Location Research

To account for variations in regional structure, we have developed and continue to refine our comprehensive statistical framework that accounts for the dramatic variations in travel-times and amplitudes that occur over relatively short distances in the crust - variations that can lead to significant errors in event location and identification. Figure 2 gives a general overview of how we accurately account for these errors. We have catalogued the majority of well constrained - both in terms of location and source characteristics - historic earthquakes and explosions into the DOE KB and we use these events to spatially map their amplitude and travel-time changes as a function of geographic coordinate. We are continuing to use this information to refine our models of the earth's velocity structure. These refined models can be used to account for the travel-time and amplitude fluctuations when a potential clandestine nuclear test occurs. As more events occur over time, the velocity models are continually refined and our ability to account for crustal effects is improved. However, one quickly realizes that model prediction will never be perfect. By its very nature, a model of the earth is underdetermined by the observational data and, thus, gives only an average estimate of the true earth structure. More precisely, if one tried to predict the travel-time or amplitude of an event that was used to develop the model, one could not recover its exact characteristics. To provide an accurate characterization, we have developed a set of innovative statistical techniques and algorithms that work together with the model to empirically predict the travel-time or amplitude correction.

At the heart of our approach is the nonstationary Bayesian kriging (NBK) technique. This technique accounts for the nonstationarities in the correction surface that exist between geophysically distinct regions and allows for the introduction of the tomography models through *a priori* distribution. In addition, this technique allows for interpolation and extrapolation and provides robust error estimates in the predictions. Using this technique, we have demonstrated that we can provide the full correction when a new event is co-located with an historic event in the region. In the case that the new event is not co-located, but instead is located near a set of historic events, we can provide a robust estimate of the event correction based on the spatial correlation of seismic attributes for nearby events. We have continued to evaluate and improve upon this technique during the last year, and all comparison studies at Livermore and Los Alamos National Laboratories have shown that combining optimal velocity models with NBK approach outperforms other approaches.

During this last year, we have demonstrated the benefit of this calibration framework using accurately located aftershock sequences and well constrained explosions at former nuclear test sites, as shown in Figure 3 (Myers and Schultz, 1999). Using what we have learned from these focused studies, we have been applying this method to broad areas of North Africa, the Middle East and the former Soviet Union. More specifically, we have developed and refined a procedure which involves a number of specific steps, including: 1) collecting all available seismic data; 2) defining geophysical boundaries where propagation characteristics change abruptly; 3) using collected seismic data to develop refined 3D tomographic models of the earth's crustal and upper mantle structure; 4) calibrating the magnitude scale; 5) applying magnitude and distance relations; 6) determining detection capability for each seismic phase; 7) evaluating and optimizing seismic location measures, and 8) establishing independent source information to avoid circularity in testing location and identification performance. Although each step in this calibration procedure requires much effort, once calibrated, we have been able to integrate all the information into a station correction surface using NBK to interpolate and extrapolate corrections to a new event of interest.

CONCLUSIONS AND RECOMMENDATIONS

The Department of Energy effort is entering a new phase where field calibration projects are increasingly becoming more critical to its CTBT mission. As discussed above, we have collected the majority of readily available historic data in the Middle East, North Africa and the former Soviet Union and are incorporating much of these into our current calibrations. As this work is completed the primary improvements to monitoring will come from the installation of stations and the realization of dedicated calibration experiments. Station installations may include new IMS stations coming on line and other supporting stations that may further enhance the IMS network. Calibration experiments include controlled explosions where the location, origin time, and source characteristics are well known. Experiments can also include the careful monitoring of known mining areas, local deployments to obtain accurate locations for aftershocks and the deployment of stations to better constrain the crustal structure in a region. Given such a broad variety of calibration opportunities and a limited level of funding, it is essential that we provide an objective tool to plan and, thus, prioritize future station installation and calibration experiments based on their combined benefit and cost.

In response to this need, we have utilized our framework above to develop a planning tool. This planning tool draws on the entire CTBT R&D KB and can accurately reflect our current state of the art techniques, algorithms, and calibrations. In the location case, we assess our progress by generating the travel-times for seismic events spanning a given region. This is accomplished by estimating optimal picking and model error processes and their distributions. We then relocate these events and estimate the location uncertainty across the entire region as shown in Figure 4. As an added benefit this tool allows us to objectively measure and report progress as we proceed. With these tools in hand and with our effort in the continued development of new innovative techniques in location and identification, we feel that we are well poised to meet our mission goals in the year 2000 and beyond.

REFERENCES

Schultz, C.A., S.C. Myers, J. Hipp and C.J. Young (1998). Nonstationary Bayesian Kriging: A Predictive Technique to Generate Spatial Corrections for Seismic Correction, Location and Identification. *Bulletin of the Seismological Society of America (BSSA),* 88(5): 1275-1288.

Invited Paper. Schultz, C.A., S.C. Myers, J. Hipp and C.J. Young (1998). Nonstationary Bayesian Kriging: A Predictive Technique to Generate Spatial Corrections for Seismic Correction, Location and Identification. *IASPEI Special Issue: advanced techniques in CTBT monitoring,* 113, 321-338.

Myers, S.C. and C.A. Schultz (1999). Improving Sparse-Network Seismic Location with Bayesian Kriging and Teleseismically Constrained Calibration Events. *Bulletin of the Seismological Society of America*, UCRL-JC-132355.

Schultz, C.A., R.A. Hansen and D.E. McNamara (1998). Pn Velocity Structure from South Western Europe to Western Asia. Seismological Society of America, Boulder, CO, March 16-18, 1998, Abs.

*SSA references are from Seismological Society of America Meeting, 1998, 1999.



Figure 1: (a) Seismic signals from nuclear tests prior to the Comprehensive Test Ban Treaty (CTBT) would usually propagate through the simpler structure of the deep mantle and were recorded by a global network of seismic stations. Seismograms associated with these events were relatively simple. (b) Under the Comprehensive Test Ban Treaty, a country may detonate a smaller nuclear test to evade the treaty. In such cases, the explosion may only be recorded seismically at a sparse set of nearby stations. The paths for these events are quite complex as they travel predominantly through the structures of the crust and upper mantle. As part of the DOE CTBT R&D effort, Livermore is working to calibrate the CTBT seismic monitoring network for these complexities.

Input Representation Goal

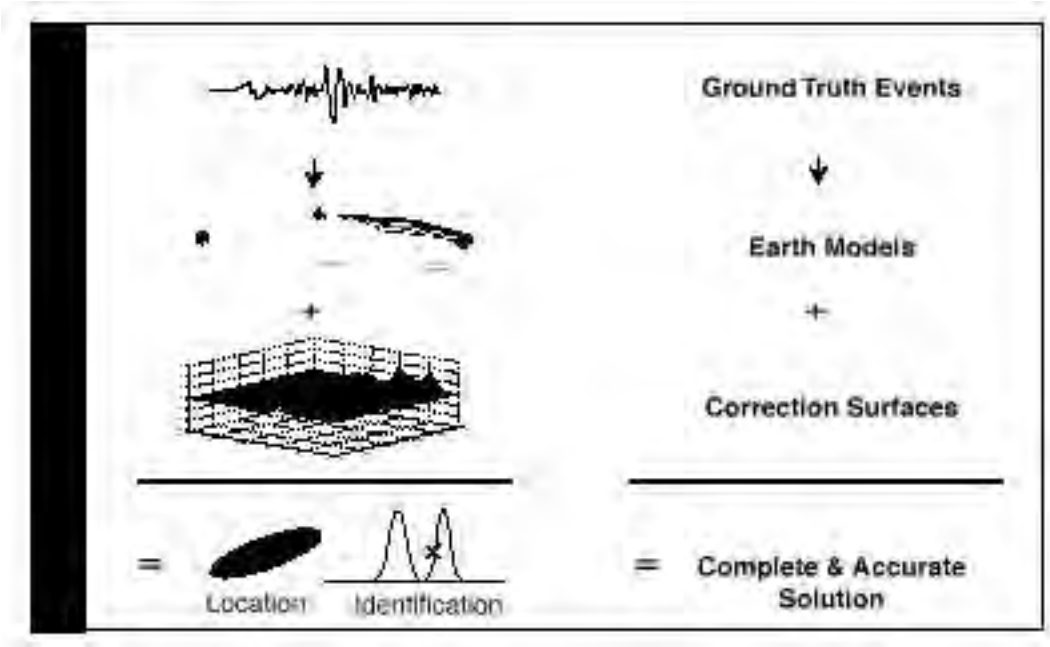
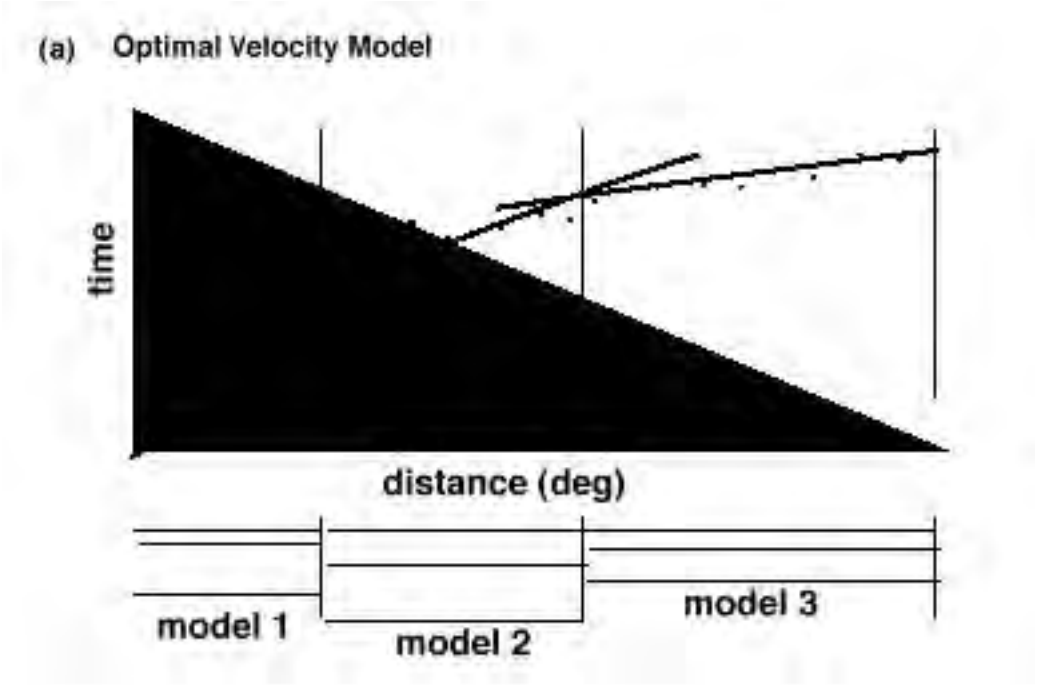


Figure 2: Our goal is to accurately identify and locate clandestine nuclear explosions. This requires us to separate explosion and natural event populations based, in part, on the explosions seismic signature. However, bias uncertainties can cause locations to be in error. To correct for these travel-time biases, we utilize the above statistical framework. Ground truth events are cataloged in our database and then used to refine earth models that can be used to predict travel-time and amplitude anomalies for seismic phases. However, models by their very nature average the data, leaving errors in predictions. We account for these errors by adding correction surfaces to the models through nonstationary Bayesian kriging technique - a technique developed this last year at Livermore. This maximum likelihood technique robustly interpolates and extrapolates corrections spatially and can provide an accurate representation of the error in its prediction.



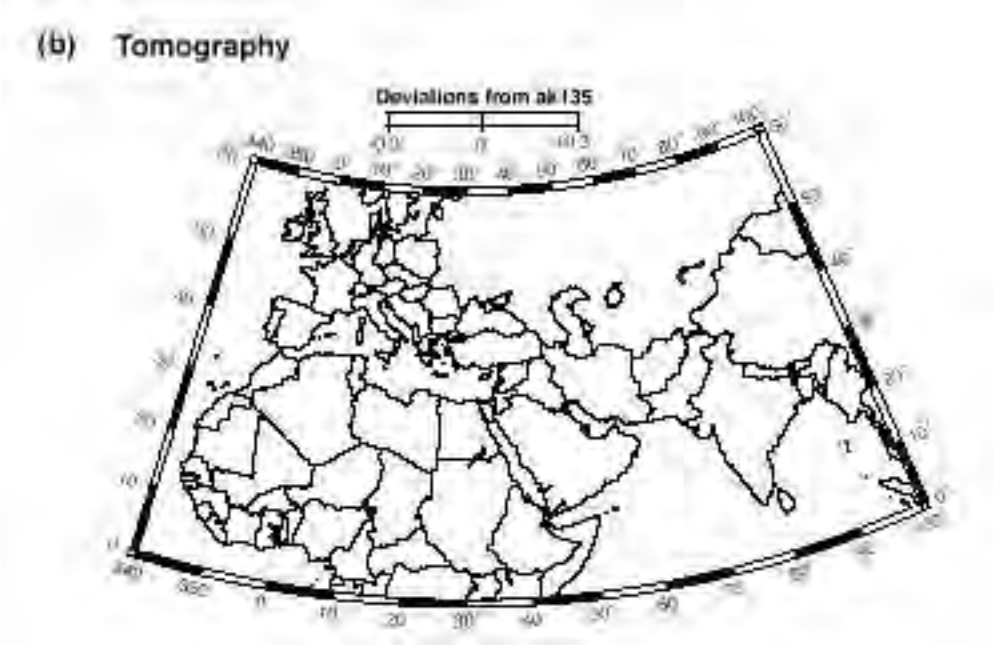


Figure 3: We have developed a comprehensive framework to improve the location of clandestine nuclear tests using the IMS. (a) We are developing optimal two dimensional velocity models for all stations. (b) Where ray path coverage is dense enough we are utilizing 2D and 3D tomography of the crust and upper mantle to further refine our models.

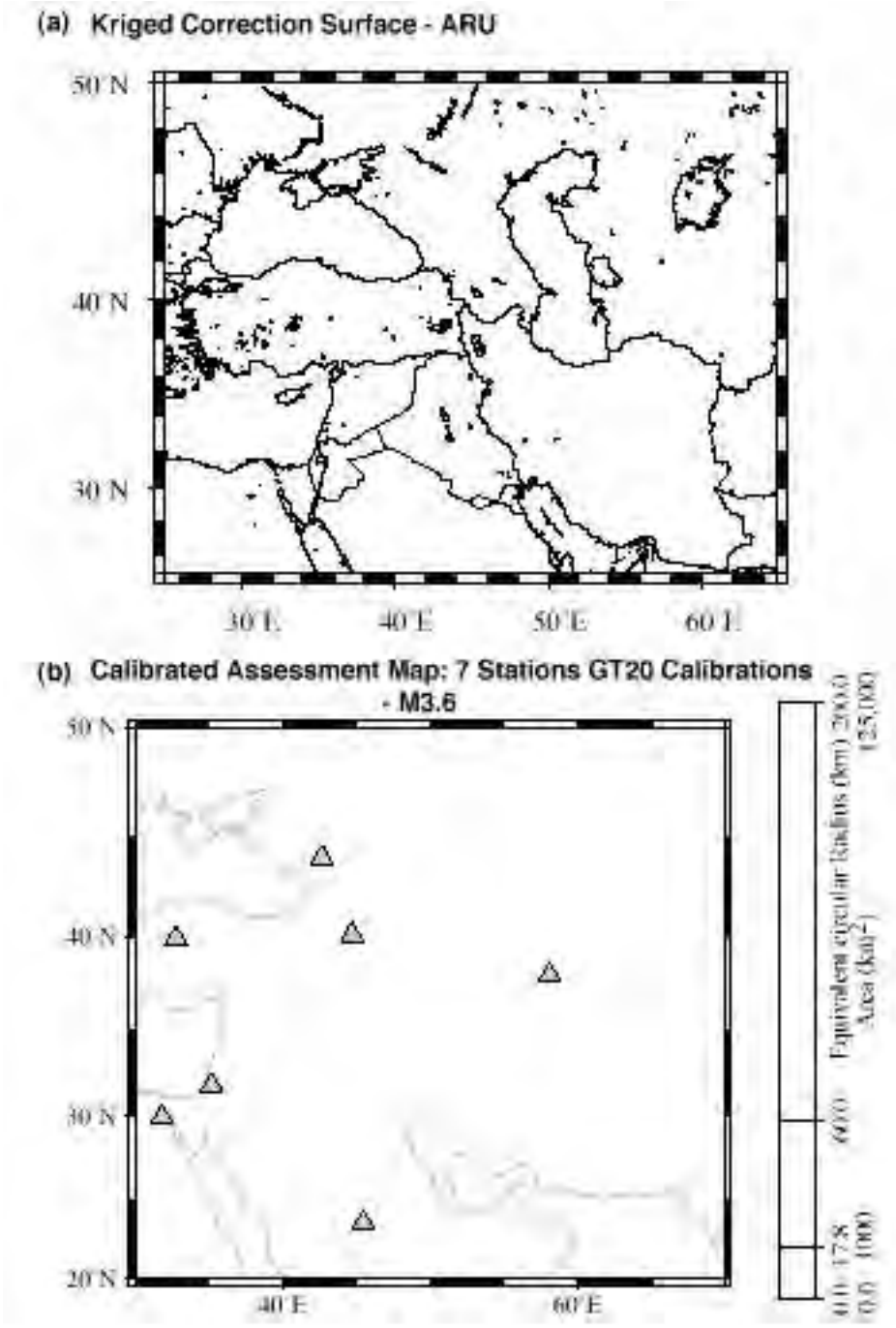


Figure 4: We have developed a planning tool to aid future calibration efforts in location. (a) A kriged correction surface is generated for each station and then used to account for the inaccuracies in our model. (b) Utilizing kriging, we propagate uncertainties in our seismic location. This framework allows us to estimate the actual location performance across a given region. In addition to planning, this performance tool allows us to measure the impact of our calibration effort over time and communicate it to our sponsor.

RELOCATION OF GLOBAL EVENTS USING THE L1-NORM AND SOURCE SPECIFIC STATION TERMS

Peter M. Shearer

Institute of Geophysics and Planetary Physics
University of California, San Diego
pshearer@ucsd.edu

Sponsored by Defense Special Weapons Agency
Grant No. DSWA01-98-1-0005

ABSTRACT

We relocate 99,715 global seismic events from 1964 to 1998 using the L1-norm and the source-specific station term method of *Richards-Dinger and Shearer* (1999). We use both regional and teleseismic P, *S*, *pP*, *PwP* and *sP* phase picks from the International Seismological Centre (ISC) as reassociated and corrected by *Engdahl et al.* (1998). Data from over 13 million picks are converted to a special compressed format that permits rapid storage and retrieval. Locations are obtained using an iterative grid-search method based on the L1-norm that is robust with respect to data outliers. We apply empirical corrections for three-dimensional velocity structure by computing spatially varying station terms using an iterative procedure in which travel time residuals at each station are smoothed over adjacent events. We compare our results to previous catalogs and to selected events of known location.

Key Words: seismic event location, grid-search methods

OBJECTIVE

To develop and implement new methods for locating global and regional seismic events with improved location accuracy and reliability. More accurate event locations will help to discriminate between earthquakes and explosions and will reduce the required search area for possible on-site inspections associated with monitoring of the Comprehensive Nuclear-Test-Ban Treaty.

RESEARCH ACCOMPLISHED

Introduction

Earthquakes are routinely located by comparing observed arrival times of *P* and *S* phases with those predicted by a reference velocity model and identifying the best-fitting event locations and origin times. Inaccuracies in the assumed velocity model will introduce systematic errors into the locations; these errors are typically more significant than the mostly random errors caused by phase timing uncertainties. For example, lateral velocity variations related to three-dimensional Earth structure will bias event locations derived using a one-dimensional velocity model. These errors can be divided into two different categories: (1) absolute location errors in individual events, and (2) relative location errors among nearby events. Addressing the problem of absolute location errors requires solving for an improved velocity model; this is the approach used in joint-hypocenter-velocity (JHV) inversions.

Improvements in relative locations among events, however, can be achieved without solving for a new velocity model. This has been accomplished using a variety of techniques, including joint epicenter determination, station term, and master event methods [e.g., *Douglas*, 1967; *Evernden*, 1969; *Lilwall and Douglas*, 1970; *Frohlich*, 1979; *Jordan and Sverdrup*, 1981; *Smith*, 1982; *Pavlis and Booker*, 1983; *Viret et al.*, 1984; *Pujol*, 1988]. These methods are most effective when applied to a relatively compact cluster of events, so that the travel-time perturbation to each station is approximately constant among the different events. Of these approaches, perhaps the simplest and most widely applied is to solve iteratively for a custom set of station timing corrections (commonly called "station terms"); this is the method described by *Frohlich* [1979].

For localized clusters of events, these techniques often lead to a dramatic improvement in relative location accuracy (although the absolute location of the entire cluster remains poorly constrained). As the events become more distributed, however, these methods become less
effective because a single set of station terms can no longer adequately describe the full effect of the three-dimensional velocity variations. For optimal results, a different set of station terms is required for each source region. Researchers studying ways to improve earthquake locations have given these terms various names, such as "source specific site corrections" (SSSC), and "correction surfaces." If calibration events of known location are available, then improvements in absolute location accuracy can be achieved by suitable spatial interpolation of these terms [e.g., *Cogbill and Steck*, 1997; *Schultz et al.*, 1998].

Here we experiment with a new method for computing source-specific station terms (hereafter termed SSSTs) that we first applied to relocate earthquakes in southern California [*Richards-Dinger and Shearer*, 1999]. The method is capable of simultaneously locating large numbers of earthquakes and achieving, on a local scale, relative location accuracy comparable to master event techniques even when uniformly applied over a large area. Essentially our approach is to compute station terms for each event by smoothing the residuals from nearby events, and then iterating until a stable set of locations and station terms is achieved.

We apply our method to relocate nearly 100,000 earthquakes in the *Engdahl, van der Hilst and Buland* [1998] catalog (here termed the EHB catalog). Our preliminary results are not dramatically different from the EHB locations, although in some areas our relocated earthquakes show a greater tendency to group into clusters and align into linear and planar features. The absolute location accuracy, as measured by comparison to over 100 "ground truth" events, is not significantly different than that obtained by EHB.

Data and Processing

We use as our starting point the reassociated ISC phase picks of *Engdahl et al.* [1998], consisting of about 13.5 million *P*, *Pn*, *pP*, *pwP*, *S* and *sP* phases from 99,715 events (1964 to 1998). Before further

processing, we convert the arrival time information to a special binary format that saves disk space and I/O time. The processed data set consumes 227 Mbytes and can be read into memory in 25 s on a typical workstation.

We relocate each event using a grid-search method based on the L1-norm [*Shearer,* 1997; *Richards-Dinger and Shearer*, 1999]. The L1-norm has the advantage of being more robust with respect to bad picks than conventional least-squares (L2-norm) techniques. We use the EHB corrections for ellipticity, bounce-point topography and water depth, and patch-averaged station terms. We exclude *S* arrivals at ranges beyond 80° to avoid confusion with *SKS*. Source-specific station terms (SSSTs) are obtained iteratively according to the following steps:

(1) Set the SSST for each event-station-phase combination to zero.

(2) Locate the events using the L1-norm and the appropriate SSSTs.

(3) For each event-station-phase combination, identify the closest *N* events that have picks from the same station-phase combination. Calculate the SSST for the event-station-phase combination by computing the median residual over the *N* adjacent events.

(4) Repeat steps (2) and (3) until convergence is achieved (i.e., there is no significant change in either the locations or the SSSTs.

In this way, we obtain station correction surfaces that vary smoothly as a function of source location (in both position and depth), with the degree of smoothing determined by the choice of *N*. The SSSTs so computed will adapt naturally to event density, averaging over larger volumes where seismicity is sparse and over smaller volumes in regions of dense seismicity. Our results presented here are for $N = 20$.

Relocation Results

We have obtained preliminary results for SSST relocations of the EHB data following four iterations for the location and station terms. Differences between these results and the EHB catalog are generally fairly small. In some areas, however, it appears that the SSSTs are successful in reducing the scatter in the locations, as illustrated by events near the Mendocino Triple Junction and the Tonga Trench (Figures 1 and 2). In each case the relocated seismicity shows a greater tendency to align into linear features. Since there is nothing in the algorithm that would cause this behavior, it is therefore likely that the method is providing a more accurate image of the actual seismicity patterns.

It should be emphasized, however, that these improvements are in relative location accuracy among nearby events. The absolute location accuracy is not affected by the SSST method. Analysis of 104 "ground truth" events of known locations [explosions and earthquakes obtained from *Kennett and Engdahl*, 1991; *Smith and Ekstrom*, 1996] indicates that the RMS location error is unchanged from the EHB catalog (approximately 21 km RMS).

CONCLUSIONS AND RECOMMENDATIONS

We have obtained preliminary results for a new global location scheme based on the L1-norm and source-specific station terms (SSSTs). Application of the method to the EHB catalog of reassociated ISC phase picks produces results comparable to the EHB locations, although in some cases the relative location accuracy appears improved as shown by reduced scatter in the positions of nearby events. Significant improvements in the absolute location accuracy of the method will require calibrating the SSSTs with ground truth events or incorporating three-dimensional velocity models.

REFERENCES

Cogbill, A.H. and L.K. Steck, Use of propagation path corrections to improve regional event locations in western China, *EOS*, *78*, Fall Meet. Suppl., F445, 1997.

Douglas, A., Joint epicentre determination, *Nature*, *215*, 47--48, 1967.

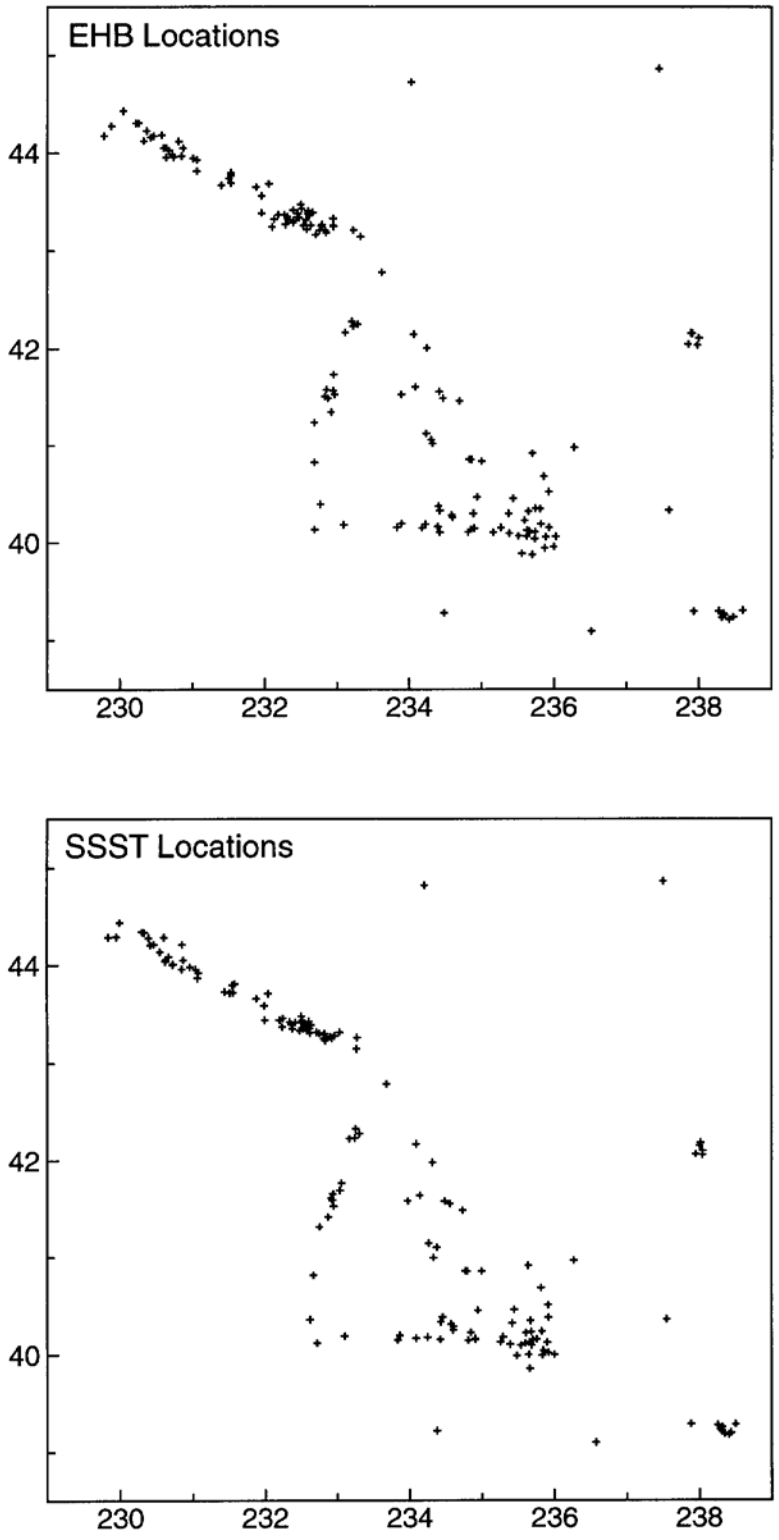


Figure 1. A comparison between EHB locations [*Engdahl et al.*, 1998] and SSST locations for 157 events near the Mendocino Triple Junction, offshore Northern California. Note the reduced scatter in the SSST locations.

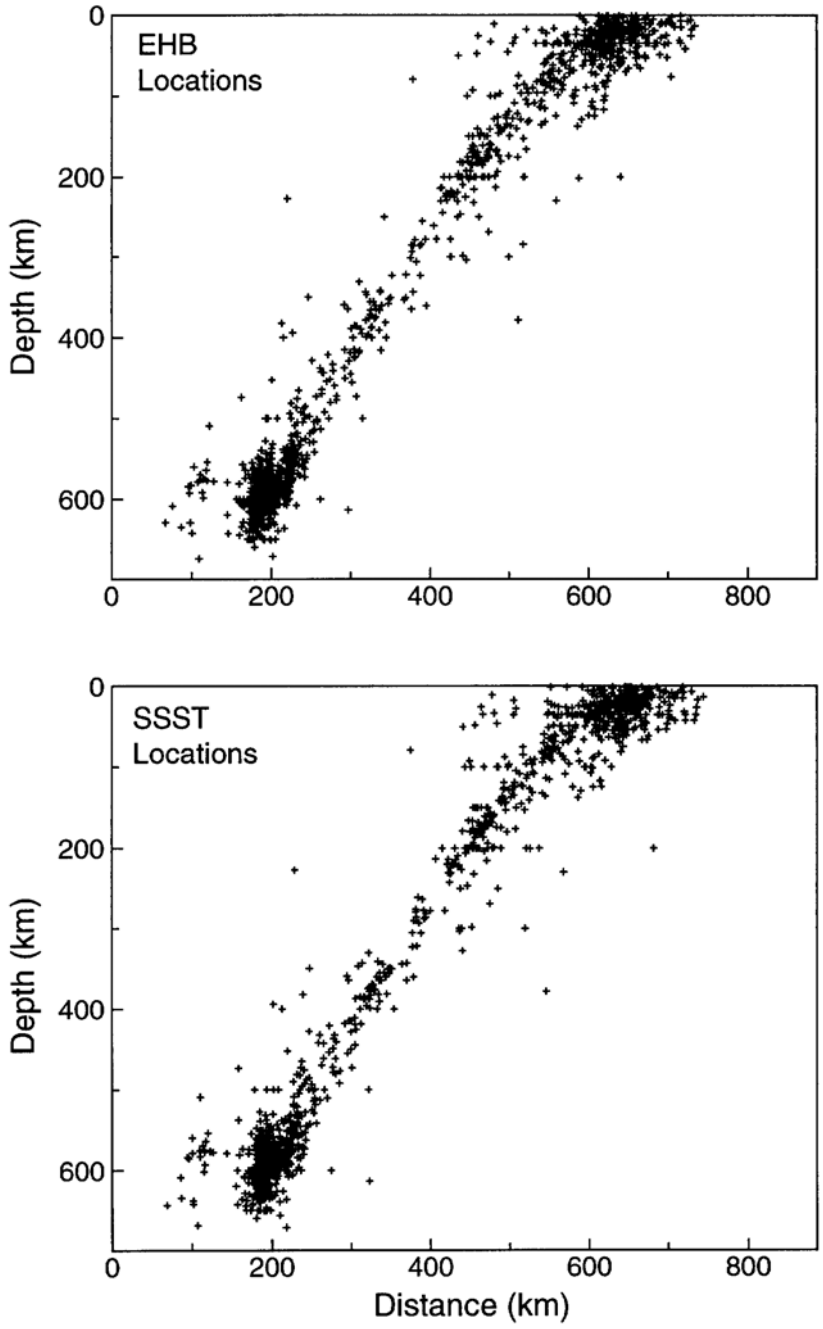


Figure 2. A comparison between EHB locations [*Engdahl et al.*, 1998] and SSST locations for 1385 events in the Tonga subduction zone. Endpoints are at (21°S, 179°E) and (24°S, 187°E); events are included that are within 1° of the cross-section.

Engdahl, E.R., R. van der Hilst and R. Buland, Global seismic event relocation with improved travel times and procedures for depth determination, *Bull. Seismol. Soc. Am., 88*, 722-743, 1998.

Evernden, J.F., Precision of epicentres obtained by small numbers of world-wide stations, *Bull. Seismol. Soc. Am., 59*, 1365-1398, 1969.

Frohlich, C., An efficient method for the joint hypocenter determination for large groups of earthquakes, *Computers and Geosciences, 5*, 387-389, 1979.

Jordan, T.H. and K.A. Sverdrup, Teleseismic location techniques and their application to earthquake clusters in the south-central Pacific, *Bull. Seismol. Soc. Am., 71*, 1105-1130, 1981.

Kennett, B.L.N. and E.R. Engdahl, Travel times for global earthquake location and phase identification, *Geophys. J. Int., 105*, 429-465, 1991.

Lilwall, R.C. and A. Douglas, Estimation of *P*-wave travel times using the joint epicentre method, *Geophys. J. R. Astron. Soc., 19*, 165-181, 1970.

Pavlis, G.L. and J.R. Booker, Progressive multiple event location (PMEL), Bull. Seismol. Soc. Am., 73, 1753-1777, 1983.

Pujol, J., Comments on the joint determination of hypocenters and station corrections, *Bull. Seismol. Soc. Am., 78*, 1179-1189, 1988.

Richards-Dinger, R.B. and P.M. Shearer, Earthquake locations in southern California obtained using source-specific station terms, *J. Geophys. Res.*, submitted, 1999.

Schultz, C.A., S.C. Myers, S.D. Ruppert, J. Hipp, and C.J. Young, Nonstationary Bayesian Kriging: application of spatial travel-time corrections to improve seismic location, *Seismol. Res. Lett., 69*, 156, 1998.

Shearer, P.M., Improving local earthquake locations using the L1 norm and waveform cross correlation: application to the Whittier Narrows, California, aftershock sequence, *J. Geophys. Res., 102*, 8269-8283, 1997.

Smith, E.G.C., An efficient algorithm for routine joint hypocentre determination, *Physics Earth Planet. Int., 30*, 135-144, 1982.

Smith, G.P. and G. Ekstrom, Improving teleseismic event locations using a three-dimensional Earth model, , *Bull. Seismol. Soc. Am., 86*, 788-796, 1996.

Viret, M., G.A. Bollinger, J.A. Snoke, and J.W. Dewey, Joint hypocenter relocation studies with sparse data sets-a case history: Virginia earthquakes, *Bull. Seismol. Soc. Am., 74*, 2297--2311, 1984.

IMPROVING REGIONAL SEISMIC EVENT LOCATION IN CHINA

Lee K. Steck, Aaron A. Velasco, Allen H. Cogbill, and Howard J. Patton
Los Alamos Seismic Research Center
Earth and Environmental Sciences Division
Los Alamos National Laboratory

Sponsored by U. S. Department of Energy
Office of Nonproliferation and National Security
Office of Research and Development
Contract No. W-7405-ENG-36

ABSTRACT

In an effort to improve our ability to locate seismic events in western China using only regional data, we have developed empirical propagation path corrections (PPCs) and applied such corrections using traditional location routines. Thus far, we have concentrated on corrections to observed P arrival times for crustal events using travel-time observations available from the U.S. Geological Survey Earthquake Data Reports, the International Seismic Centre catalogs, the prototype International Data Center Reviewed Event Bulletin, and our own travel-time picks from regional data. Location ground truth for events used in this study ranges from 25 km for well-located teleseismic events, down to 2 km for nuclear explosions located using satellite imagery. We also use eight events for which depth is constrained using several waveform methods. Using the EvLoc algorithm, we relocate events from a region encompassing much of China (latitude 20°-55°N; longitude 65°-115°E). Using *iasp91* as our base model, we find that travel-time residuals exhibit a distance-dependent bias. For this reason, we have developed a new 1-D model for China, which removes a significant portion of the distance bias.

For individual stations having sufficient P-wave residual data, we produce a map of the regional travel-time residuals from all well-located teleseismic events. Residuals are used only if they are smaller than 10 seconds in absolute value and if the seismic event is located with an accuracy better than 25 km. From the residual data, PPC surfaces are constructed using modified Bayesian kriging. Modified Bayesian kriging offers us the advantage of providing well-behaved interpolants, but requires that we have adequate error estimates associated with the travel-time residuals. For our P-wave residual error estimate, we use the sum of measurement and modeling errors, where measurement error is based on signal-to-noise ratios when available, and on the published EDR estimate otherwise. Our modeling error comes from the variance of travel-time residuals for our 1-D China model. We calculate PPC surfaces for 74 stations in and around China, including six stations from the International Monitoring System. The statistical significance of each PPC surface is evaluated using a cross-validation technique. We show PPC relocation results for a Tibetan earthquake that has been located using InSAR. The use of PPC surfaces in regional relocations significantly reduces seismic event mislocations, and eliminates distance bias in travel-time residual curves.

Key Words: location, calibration, seismic regionalization, kriging

OBJECTIVE

Seismic detection and location of small events remains a key issue for effectively monitoring the Comprehensive Nuclear-Test-Ban Treaty (CTBT), which has an implicit goal of locating seismic events within a contiguous area smaller than 1000 km^2. In China, where station coverage is sparse and crustal structure is strongly heterogeneous, this goal presents a significant challenge. Our objective is to improve regional seismic location in China, by developing spatially varying corrections to P-wave travel-time observations for shallow events. We have chosen the propagation path correction approach both because the limited seismicity makes three-dimensional inversion for velocity structure difficult, and because the pIDC and the U. S. National Data Center both utilize this method in their standard analysis proceedures. For our study we use bulletin data from the United States National Earthquake Information Center Earthquake Data Reports (EDRs), the International Seismological Centre (ISC) bulletin, the prototype International Data Center's (pIDC) Reviewed Event Bulletin (REB), and our own travel-time picks from regional data. We have chosen to locate events within a region defined from 20º-55º N latitude and from 65º-115º E longitude, using the EvLoc algorithm (Bratt and Bache, 1988; Nagy, 1996). While our intent is to calibrate all regional seismic stations in Asia, many of the stations of interest, particularly those of that will be part of the International Monitoring System (IMS), have not been in operation long enough to acquire sufficient data for our empirical approach. To circumvent this problem we use data from stations reporting to the EDR and ISC as surrogates for those of the IMS.

RESEARCH ACCOMPLISHED

For the China region, we have gathered an extensive database containing both traveltime information and waveforms for regional stations located in China, Pakistan, India, Kyrghyzstan, Kazakhstan, Mongolia, Russia, Korea, and Thailand. For the years between 1986 and 1989, we use data from the ISC bulletin. Between 1990 and January 1998, we use the EDRs. P-wave residual means and variances at stations reporting to both catalogs are similar, which suggests that we are not introducing any additional biases by combining these data sets. We supplement these data with travel-time picks from the REB, and our own travel time picks from regional data. Our digital waveforms were retrieved from the IRIS database using the event origin information from the global catalogs mentioned above, and are the result of a large regionalization effort (Hartse et al., 1997). Travel-time picks and amplitude measurements of regional phases have been made on broadband channels when available; otherwise, short-period channels are used (Hartse et al., 1997). For the locations, we use only first-arriving P travel-times, and have added about 6800 of these picks to our data set. We base the quality of the pick on the signal-to-noise ratio (SNR) of each phase, using the convention of Nagy (1996). These same criteria are used to define measurement error for REB picks. We begin our analysis using the global velocity models *ak135* (Kennett et al., 1995) and *iasp91* (Kennett and Engdahl, 1991). However, as discussed below, our research has expanded to incorporate analysis using 1-D regional models for China.

A critical element of our location effort lies in improving our ability to accurately estimate the errors in travel-time measurements. This is important both for determining the location confidence region, and for providing accurate estimates of travel-time for interpolation. To aid in this, we have refined estimates of modeling and measurement errors. Modeling error is defined as the travel-time variance of a particular model as a function of distance, while the measurement error is defined as the picking error associated with each phase. Optimally, SNR should be used to determine the measurement error, and we use this when available. When SNR is not available, we use a uniform measurement error of 2 s^2, as is done in the EDRs Modeling error is the more difficult of the two types of error to determine. We begin by using estimates of the modeling error developed from arrivals compiled by the pIDC for *iasp91* (Swanger, personal communication). This estimate of modeling error does not account for intrinsic biases present in our locations, arising from differences in network geometry and from using a 1-D base model when the true structure is laterally variable. Steck et al. (1998) show that for distances < 20º, travel-time residuals exhibit a distance trend, suggesting that standard global velocity models do not adequately reflect the crustal structure of China.

To properly construct the travel-time residual surfaces, we must remove this trend. For this reason, we have attempted to develop unbiased, 1-D, regional velocity models for China before PPC surface construction. The

three models we look at are based on data from Li and Mooney (1998), Kosarev et al. (1993), and Jih (1998), and we call them *China_LM*, *Asia*, and *China_RSJ*, respectively. The *China_LM* model is developed by averaging seven crustal models based on deep seismic sounding results for China (Li and Mooney, 1998). Our strategy was to assume a three-layer crust with each layer having the average crustal thickness and velocity of the three thickest layers of each of the seven models. Thin sedimentary layers and anomalous mid-crustal zones were eliminated. For these regional 1-D models, we place their crustal structure on top of the *iasp91* mantle structure. Figure 1a shows the P-wave models used in this study.

Travel time residuals from our 1-D models show a slight reduction in distance bias (Figure 1b), with the *China_LM China_RSJ* models providing the most improvement. Figure 1c shows the standard deviation of the residuals, which represents the modeling error for each of the models. Also plotted is the original estimate of modeling error from *iasp91* P-waves (Swanger, personal communication). The global and regional 1-D model errors appear to be consistent at regional distances, where modeling errors are largest. At teleseismic distances, all of our models are consistent with each other, but the errors are on the order of 0.4 s larger than that provided by the pIDC. At regional distances, the modeling error differences between all regional 1-D models are not significant, but we obtain a slightly higher modeling error for *iasp91.* The primary impact of applying these new modeling errors will be to change the error ellipse sizes. When we compare our iasp91 locations with the new and old modeling error differences, we find that that the error ellipses grow on average by only 0.4 ± 0.7 km for the semi-major axis and 0.3 ± 0.5 km for the semi-minor axis. Note that none of the 1-D models is able to completely eliminate the distance bias in the residuals. Cogbill and Steck (1997) show that by applying PPCs, most remaining bias can be removed.

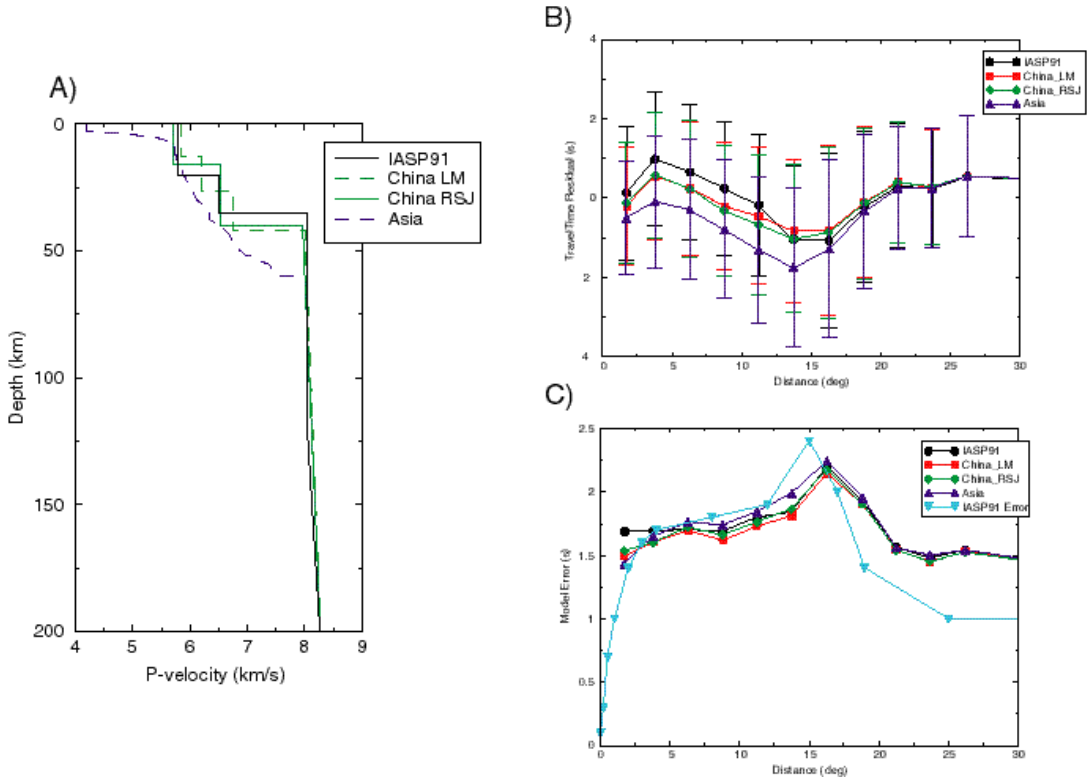


Figure 1. See text for discussion

Seismic Event Relocations

We perform our initial relocations using 9500 events with over 300,000 P-wave arrivals spanning 11 years. We

relocate all events using the four velocity models described above, letting the algorithm remove outliers based on travel-time residual size. To ensure high quality locations to be used in our 2-D correction surfaces, events must have been recorded by at least 30 stations, have maximum azimuthal gap < 180°, and have a sum of depth plus depth error less than the moho depth of the model. Applying these criteria reduces the number of useable events to 705, 915, 907, and 1074 for the *iasp91*, *China_LM*, *China_RSJ*, and *Asia* models, respectively. From these sets of events we then gather residuals by station, discarding residuals larger than 10 s in absolute value. Thus, our data set is teleseismically constrained. By employing the previous two criteria, we restrict ourselves to residuals from events located with an accuracy of about 25 km (E. R. Engdahl, personal communication). Average epicentral differences between the various models are less than a fraction of a kilometer, while origin times and depth vary depending on the routine practices applied at the locating institution and on the relative speeds of model used. For nuclear explosions that were located by Gupta (1995) and Thurber et al. (1993), we constrain the latitude, longitude, and depth and invert only for origin time. We do this for all velocity models. For our depth-constrained events, we set the depth and let the program invert for latitude, longitude, and origin time. While the main effect of constraining depth is to more accurately determine origin time, we expect some improvement in epicentral location as well.

Ground Truth

To test and validate our travel-time corrections and relocation algorithms, ground truth information is needed. The best-constrained ground truth information available for the region is that from nuclear explosions. We include explosions from two test sites: the Chinese test site at Lop Nor and the former Soviet Union test site at Balapan, Kazakhstan. Gupta (1995) relocated many Lop Nor nuclear explosions using satellite imagery and a relative location algorithm. Thurber et al. (1993) obtained locations for 20 explosions at Balapan, Kazakhstan, also using a joint epicentral determination (JED) technique in conjunction with SPOT satellite images. Because the origin times for these events are not known, these events are considered to be accurate within 2 km.

Our ground truth database also includes surface rupture information obtained for a large earthquake (M_w = 7.5) that occurred on Nov. 8, 1997, approximately 750 km south of the Lop Nor nuclear test site. The mainshock is a shallow, strike-slip, intraplate event (Velasco et al., 1999). Velasco et al. (1999) obtain a consistent source model over a wide range of frequencies, from a wide variety of seismic data. However, mapping of the actual ground rupture was obtained from InSAR data for the mainshock (Peltzer, personal communication). The rupture length is approximately 180 km, showing a very linear fault (Figure 4). Because the mainshock is an east-west striking fault, we can use the mainshock rupture as a guide for validating our path correction surfaces since the depth and latitude are well-constrained.

Finally, we have looked at using 26 central Asian seismic events that have independent depth constraints as ground truth. While perhaps not as valuable as epicentrally-constrained ground truth for calibration purposes, these data never-the-less offer an improvement over events for which the depth is poorly constrained. This approach of establishing ground truth is sometimes the best means available to verification seismologists for calibrating a region. Furthermore, much can be learned about the performance of seismic techniques from comparative analysis, and such knowledge can be used to design improvements in techniques and/or to identify new data requirements. Focal depths from a variety of methods are reported in Patton (1998) and Woods et al. (1998). There are nine depth estimates for the 26 events, from (1) ISC hypocenter determination, (2) pP - P travel time delays, as reported by the ISC, (3) hypocenter determinations in the NEIC Preliminary Determination of Epicenter (PDE) and EDR, (4) simultaneous focal depth and moment tensor determination reported by the NEIC based on Sipkin's method (Sipkin, 1982), (5) Harvard centroid moment tensor catalog, (6) pP - P modeling from Woods et al. (1998), (7) broadband modeling of regional seismograms in the time domain from Woods et al. (1998), (8) modeling regional surface-wave spectra (Patton, 1998), and (9) depth phase determinations from Engdahl et al. (1998). We compute focal depth by taking the weighted average of all estimates available for each event, except those from the centroid moment tensor-- they seem to be bounded at 15km.

The largest variance from the weighted mean focal depth is found for regional surface-wave estimates (RSS), while the depth estimates from the NEIC moment tensor inversion have the smallest variance. Their variances

translate into standard deviations of 14.0 km and 2.0 km, respectively. The other standard deviations are: 11.5 km for the ISC location, 5.5 km for the ISC pP, 7.7 km for the NEIC PDE, 2.0 km for the NEIC moment tensor, 8.7 km from the Harvard moment tensor, 12.0 km for the Woods et al. (1999) pP, 11.0 km for the Woods et al. (1999) regional body wave, and 4.9 for the depth phase solutions of Engdahl et al. (1998). In selecting depth-contrained events for use as ground truth, we check the difference between the free- and fixed-depth solutions for hypocentral location. For models *iasp91, China_LM, China_RSJ*, we find 8 events within 5 km depth for the fixed and free depth solution. The latitudes and longitudes are also within 0.1 km of each other for these solutions. Thus, we use these eight events for our 2-D surfaces below. For the Asia model, we find 11 events that meet our criteria.

Propagation Path Correction Surfaces

Propagation path correction surfaces are created by interpolating the residuals onto 2-D surfaces using modified Bayesian kriging (Schultz et al., 1998) for 68 stations reporting to the ISC and/or EDR catalogs, plus 6 of the pIDC stations. Unfortunately, the limited phase data available from the pIDC stations, due to their more recent installation, makes construction of correction surfaces for these stations of reduced value at this stage. Using modified Bayesian kriging, the value of the PPC surface goes to zero at distances greater than a specified correlation length away from the data points, and an estimate of the variance associated with the surface is calculated based on user-supplied residual variances and an estimate of the background variance. We use 5^o for both the model and data correlation lengths.

To explore the validity of the kriged surfaces, we apply a method called cross-validation. There are two principal questions we wish to address: how well do the kriged surfaces describe the data, and how well can kriging predict surface values at data points that have been left out? Our approach is to perform a leave-one-out scenario, whereby for each surface we sequentially recalculate the surface, deleting a different data point each time for all points in that surface. We then determine the mean and variance of the differences between the value of the cross-validated surface at the deleted point and the value at that point for the original surface. The averages of these means and variances are 0.1 s and 1 s^2, respectively, suggesting that the surfaces are robust. For comparison, the average variance of the input residual data is about 5 s^2. The kriged surfaces reduce the variance of the data significantly (an average of 65%) and the average variance reduction of the surfaces themselves from the data is about the same, 70%. In areas were data are plentiful, there is good correlation between the cross-validated surface and the original kriged surface. Where data points are isolated, there is little correlation. Eliminating stations where a cross-validated surface has low correlation with the original surface is unnecessary, because the kriging process itself accounts for the relative accuracy of the input data points.

To illustrate the effect of the PPCs on epicentral location, we show a relocation of the Tibetan earthquake whose surface rupture was identified with InSAR. Figure 2 compares the NEIC epicenter to the relocation using PPCs in EvLOC. Generally, the use of PPCs has two effects. The first is that location bias is reduced, and the second is that the EvLoc algorithm is more likely to converge successfully to a solution. When teleseismic data are used along with PPCs to locate large nuclear explosions, the solutions tend to be dominated by the more plentiful distant data, and the positive effects of using PPCs are much reduced. While this result shows that PPCs can greatly reduce mislocation errors, we have very little other ground truth in the China region. Therefore, the applicability of our correction surfaces cannot be assessed in other geographical provinces. We have found that relocations using a mixture of PPC and non-PPC stations are not successful.

CONCLUSIONS AND RECOMMENDATIONS

We have developed empirical P-wave propagation path corrections for 74 seismic stations in and around China. Some distance dependence is observed in our correction surfaces when locations are performed with the *iasp91* velocity model. To remove this bias we have developed a simple 1-D model for China. Application of PPCs based on our average China model successfully eliminates all remaining bias, except at distances less than 2.5^o. We have shown that these corrections improve regional event location for an earthquake in Tibet; we find similar results for nuclear tests at the Balapan and Lop Nor nuclear test sites. Because of sparse seismicity in some areas of China, and a lack of data at some critical stations, we have begun looking at alternative methods of predicting PPCs. We suggest that efforts be undertaken to generate 3-D velocity models in order to be able to predict PPCs in areas where no data is available.

ACKNOWLEDGMENTS

We thank IRIS/DMC for the data used in this study, and G. Peltzer for providing us with his InSAR results.

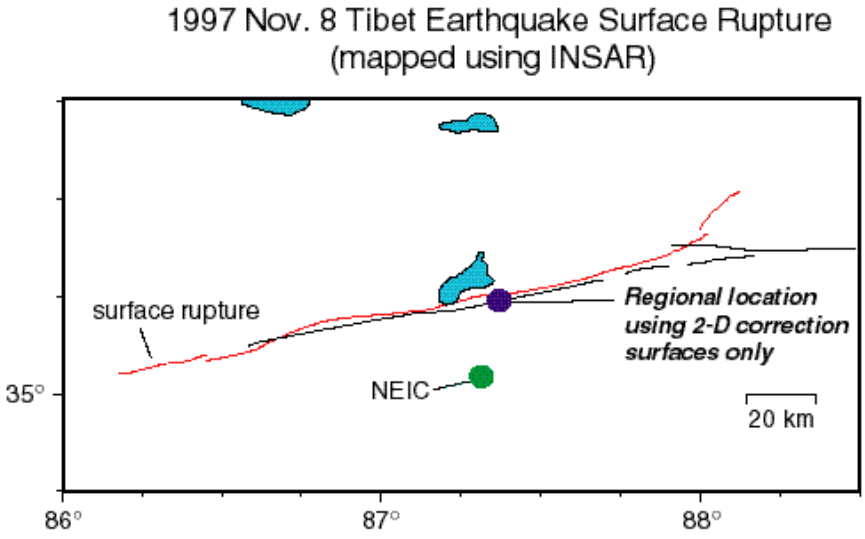


Figure 2. See text for discussion (courtesy of Gilles Peltzer).

REFERENCES

Bratt, S. R., and T. C. Bache, 1988. Locating events with a sparse network of regional arrays, *Bull. Seism. Soc. Am.*, **78**, 780-798.

Cogbill, A. and L. K. Steck, 1997. The use of propagation path corrections to improve seismic event location in Western China, *Los Alamos National Laboratory report*, LA-UR-97-4876.

Engdahl, E. R., Van der Hilst, R., Buland, R., 1998. Global teleseismic earthquake relocation with improved travel times and procedures for depth determination, *Bull. Seism. Soc. Am.*, 88, 722-743.

Gupta, V., 1995. Locating nuclear explosions at the Chinese test site near Lop Nor, *Science and Global Security*, **5**, 205-244.

Hartse, H.E., S.R. Taylor, W.S. Phillips, and G.E. Randall, 1997. Regional event discrimination in central Asia with emphasis on western China, Bull. Seism. Soc. Am., **87**, 551-568.

Jih, R.-S., 1998. Location calibration efforts in China, in *Proceedings for the 20th Annual Seismic Research Symposium*, 12pp.

Kennett, B.L.N. and E.R. Engdahl, 1991. Traveltimes for global earthquake location and phase identification, *Geophys. J. Int*, **105**, 429-465.

Kennett, B.L.N., E.R. Engdahl, and R. Buland, 1995. Constraints on seismic velocities in the earth from travel-times, *Geophys. J. Int*, **122**, 108-124.

Kosarev, G.L., N.V. Petersen, L.P. Vinnik, and S.W. Roecker, 1993. Receiver functions for the Tien Shan analog network: Contrasts in the evolution of structure across Talasso-Fergana fault, *J. Geophys. Res.*, **98**, 4437-4448.

Li, S. and W. D. Mooney, 1998. Crustal structure of China from deep seismic sounding profiles, *Tectonophysics*, **288**, 105-113.

Nagy, W., 1996, New region-dependent travel-time handling facilities at the IDC: Functionality, testing, and implementation details, *Tech Rep. SAIC-96/1179*, 57 pp.

Patton, H. J., 1998. Bias in the centroid moment tensor for central Asian earthquakes: Evidence from regional surface wave data, *J. Geophys. Res.*, **103**, 26963-26974.

Schultz, C. A., S. C. Meyers, J. Hipp, and C.J. Young, 1998. Nonstationary Bayesian kriging: A predictive technique to generate spatial corrections for seismic detections, location, and identification, *Bull. Seismol. Soc. Am.*, **88**, 1275-1288.

Sipkin, S. A., 1982. Estimation of earthquake source parameters by the inversion of waveform data: synthetic waveforms, *Phys. Earth Planet. Int.*,**30**, 242-259.

Steck, L. K., A.H. Cogbill, and A.A. Velasco, 1998. The use of propagation path corrections to improve regional seismic event location in western China, in *Proceedings for the 20th Annual Seismic Research Symposium*, 10pp.

Thurber, C.H., H.R. Quin, and P.G. Richards, 1993. Accurate locations of nuclear explosions in Balapan, Kazakhstan, 1987 to 1989, Geophys. Res. Letts., **20**, 399-402.

Velasco, A. A., S. L. Beck, and C. J. Ammon, 1999. Broadband source modeling of the November 8, 1997 Tibet (Mw = 7.5) earthquake and its tectonic implications, in preparation for *J. Geophys. Res*.

Woods, B. B., C. K. Saikia, and H. K. Thio, 1998. Focal depths and source parameters for earthquakes in northwest China, Final Scientific Report, Woodward-Clyde Federal Services, Pasadena, CA.

AMPLITUDE CORRECTIONS FOR REGIONAL SEISMIC DISCRIMINANTS

Steven R. Taylor, Aaron A. Velasco, Hans E. Hartse, W. Scott Phillips
Seismic Research Center, Los Alamos National Laboratory
Los Alamos, NM 87545

William R. Walter and Arthur J. Rodgers
Lawrence Livermore National Laboratory
Livermore, CA 94551

Sponsored by U.S. Department of Energy
Office of Nonproliferation and National Security
Office of Research and Development

ABSTRACT

We present an update on seismic event identification methodologies being investigated as part of the Department of Energy CTBT R&D program. A fundamental problem associated with event identification lies in deriving corrections that remove source and path effects on regional phase amplitudes used to construct discriminants. Our goal is to derive a set of physically based corrections that are independent of magnitude and distance, and amenable to multivariate discrimination by extending the technique described in Taylor and Hartse (1998). For a given station and source region, a number of well-recorded earthquakes are used to estimate source and path corrections. The source model assumes a simple Brune (1970) earthquake-source that has been extended to handle non-constant stress drop. The propagation model consists of a frequency-independent geometrical spreading and frequency-dependent power-law Q. A grid search is performed simultaneously at each station for all recorded regional phases over stress-drop, geometrical spreading, and frequency-dependent Q to find a suite of good-fitting models that remove the dependence on m_b and distance. Seismic moments can either be inverted for or fixed and are tied to m_b through two additional coefficients. Once a set of corrections is derived, effects of source scaling and distance as a function of frequency are applied to amplitudes from new events prior to forming discrimination ratios. Thus, all the corrections are tied to just m_b and distance and can be applied very rapidly in an operational setting. Moreover, phase amplitude residuals as a function of frequency can be spatially interpolated (e.g. using kriging) and used to construct a correction surface for each phase and frequency. The spatial corrections from the correction surfaces can then be applied to the corrected amplitudes based only on the event location.

Key Words: seismic, discrimination, identification, nuclear

OBJECTIVE

The objective of this work is to outline a methodology for correction of regional amplitudes used to construct discriminants for earthquake source and path effects using simple physical models. The methodology produces discriminants that are multivariate normal and can be rapidly applied in an operational setting.

RESEARCH ACCOMPLISHED

We have outlined a procedure for simultaneously correcting for both propagation and source effects to seismic amplitudes prior to forming amplitude ratios. Correcting amplitudes offers several advantages over correcting ratios. First, correcting amplitudes using simple physical models offers much flexibility in that all information is retained as opposed to partial censoring of data by pre-selecting ratios. Also, because of hidden correlation structures of different ratios, it is difficult to *a priori* select a set of discriminants that will give optimum performance. The best discrimination performance is not necessarily achieved by pre-selecting the best amplitude ratios. In fact, combining a discriminant that by itself does not work well with one that does, may lead to improved overall performance (e.g. Taylor and Hartse, 1997). The problem is exacerbated if little or no explosion calibration information is available, which is the case for most stations that will be used in monitoring the CTBT. Additionally, preselected ratios may be highly interdependent leading to a false impression of discrimination capability. It has been observed that seismic discriminants can show significant regional variability that is a function of factors such as crustal velocity structure and explosion-source material properties. Thus, in areas where little or no calibration information from explosions is available, it may not be prudent to pre-select ratios.

We illustrate that the amplitude-correction parameters can be based on simple physical models which can be difficult to do with ratios because of tradeoffs between different parameters. Thus, in uncalibrated or poorly calibrated regions, reasonable corrections can be obtained using expert opinion or extrapolation from geophysically similar regions. Further, we will show that for a given station and source region, the residuals from the one-dimensional model can be spatially interpolated for each phase and frequency band (e.g. using kriging) to account for lateral variations in propagation. It has been shown that geographical interpolation can be used to create correction surfaces that significantly reduce scatter in discriminants. The corrections appear to be particularly effective at low (1 Hz) frequencies (e.g. Taylor and Hartse, 1998, Phillips *et al.,* 1998).

We have developed a methodology for removing m_b and distance trends from regional seismic amplitudes (MDAC – Magnitude and Distance Amplitude Corrections). MDAC is an improved version of the SPAC (Source and Path Amplitude Corrections) discussed by Taylor and Hartse (1998) and Taylor and Velasco (1998). Improvements over SPAC include the inclusion of a grid search over trial values of stress drop, geometrical spreading, and attenuation parameters. We have also established a tie between m_b and $\log M_0$ using the earthquake source model (rather than a linear relationship as assumed in Taylor and Hartse, 1998).

The MDAC method combined with spatial interpolation of amplitudes (e.g. kriging) represents a station-specific approach for computing discriminants that are multivariate normal for a given source region. For a given station and source region, six MDAC parameters (Q_0, η, γ, σ_b, F_{mb}, A_{mb}) are derived for each regional phase. The first three terms are the Q values at 1 Hz (Q_0), the geometric spreading coefficient (η) and the power law coefficient (γ) for frequency-dependent attenuation and control the path corrections. The fourth term is the Brune stress drop (σ_b). The last two terms (F_{mb}, A_{mb}) control the scaling between the seismic moment and magnitude (m_b) and control the source scaling. The MDAC-corrected amplitudes can be spatially interpolated using kriging (e.g. Schultz *et al.,* 1998) to derive a correction surface for each phase as a function of frequency. These surfaces can be used to reduce scatter in the corrected amplitudes and improve discrimination performance. The MDAC parameters and kriged surfaces can be developed offline and entered into an online database for rapid pipeline processing. Once a new event is located and a m_b is calculated, the regional phases can be windowed and Fourier transformed. The MDAC-corrected amplitudes for each phase and frequency can be computed using only the distance and m_b. The spatial corrections from the kriged surfaces can then be applied to the corrected amplitudes based only on the event location. At this point, a set of multivariate-normal corrected amplitudes is available for event identification.

Estimation of Source and Path Parameters Using MDAC

In this section we briefly describe the method we use for inverting for source and path parameters and forming a set of frequency-dependent amplitude corrections for each phase recorded at a given station. In our formulation, we follow a modification of the techniques of Sereno *et al.,* (1988), Taylor and Hartse (1998) and Taylor and Velasco (1998).

At a particular station and source region, we assume the instrument-corrected amplitude spectrum for a given phase, $A_i(f)$, for source *i*, is given by

$$\log A_i(f) = \log G(r_i, r_0) + \log S_o^{(i)} - \log\left[1 + \left(\frac{f\left(S_o^{(i)}\right)^{\kappa}}{c}\right)^2\right] - \frac{\pi \log e}{Q_0 v} f^{1-\gamma} r_i + \log P(f) \qquad (1)$$

where the first term on the right controls the geometrical spreading, the second two terms the source scaling, the fourth term the frequency-dependent attenuation, and the last term is a phase site/excitation factor (for details, see Taylor *et al.,* 1999). We perform a combination grid search and inversion to determine the main MDAC parameters given above.

Application of MDAC to Western China Data Recorded at MAKZ

As an illustration of the MDAC methodology, we present results from the IRIS GSN station MAKZ (Makanchi, Kazakhstan). All seismograms were obtained from the IRIS Data Management Center (DMC). The data are from 4 Lop Nor nuclear explosions and 412 earthquakes located in a region around Lop Nor extending between 35° and 50° N latitude and 80° and 100° E longitude (the Lop Nor box; Figure 1). As discussed by Hartse *et al.,* (1997), we measured RMS amplitudes taken in 8 different 1 octave frequency bands ranging from 0.5 to 8 Hz. Because the methodology discussed above is for a spectral inversion, we convert the RMS amplitudes to pseudo-spectral amplitudes using Parseval's Theorem for the discrete Fourier. We first computed 6 MDAC parameters including moment for the Lg amplitudes. A grid search was performed for each phase for six logarithmically spaced stress drops between 0.1 and 30 MPa, 50 points each for η, Q_0, and γ, between 0.5 and 1, 300 and 800, and 0 to 1, respectively resulting in 750,000 combinations of parameters.

The next step involves examining the best-fit solutions to see if they adequately remove trends with m_b and distance. To do this we select a specified number of the best-fit solutions and regress the corrected amplitudes versus both m_b and linear distance. At this stage, we go though and recorrect the amplitudes based on the m_b – $\log M_0$ scaling relationship.

Figure 2 shows an example of Lg parameters and fits to our selected model. Because we used Lg to invert for $\log M_0$, the site/excitation factors are small (upper left portion of Figure 2). The numerous tradeoffs between the different parameters make it not difficult to get a good fit to the observed spectrum as seen by the upper right portion of Figure 2.

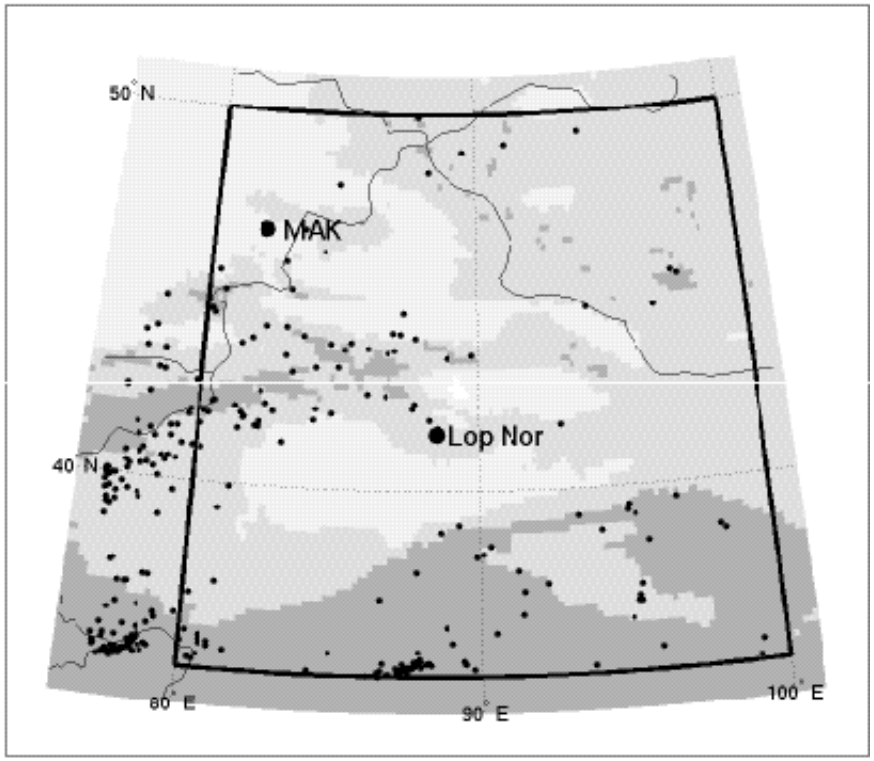


Figure 1. Map showing events used in this study within box surrounding Lop Nor.

We then corrected all amplitudes that passed the signal-to-noise cutoff of 1 using pre-phase noise including the 4 Lop Nor nuclear explosions. Figure 3 shows the corrected log amplitudes for each phase as a function of frequency for all four phases. We have also identified four earthquakes occurring within 50 km of the Lop Nor test site.

As expected, the corrected amplitudes for the earthquakes are very close to zero mean, and χ^2 goodness-of-fit tests show most frequency bands are normally distributed. The explosions show a significantly different pattern than the earthquakes. This is not unexpected, since we are using an earthquake model to fit the data. The misfit is particularly severe for Pn as can be seen by the high residuals at intermediate and high frequencies. As will be further illustrated below, the plot in Figure 3 is interesting in that it can be used as a guide in selecting individual discriminants that provide good separation between earthquakes and explosions. For example, it can be seen that a high frequency Pn to low-frequency Sn or Lg cross spectral ratio will give excellent separation between the earthquakes and explosions (as noted by Hartse *et al.*, 1997). Additionally, a Pn, Pg, or possibly even an Sn spectral ratio will provide good separation. These observations reinforce our earlier comments about the potential restrictions on discrimination performance by *a priori* selecting ratios.

At this point we can directly make traditional discrimination plots from the corrected amplitudes shown in Figure 3 by simply taking differences (log ratios) using any combination of phase and frequency. This is illustrated in Figure 4 where we show the high-frequency (4-8 Hz) Pn to low-frequency (0.75-1.5 Hz) cross-spectral ratio plotted versus both distance and magnitude.

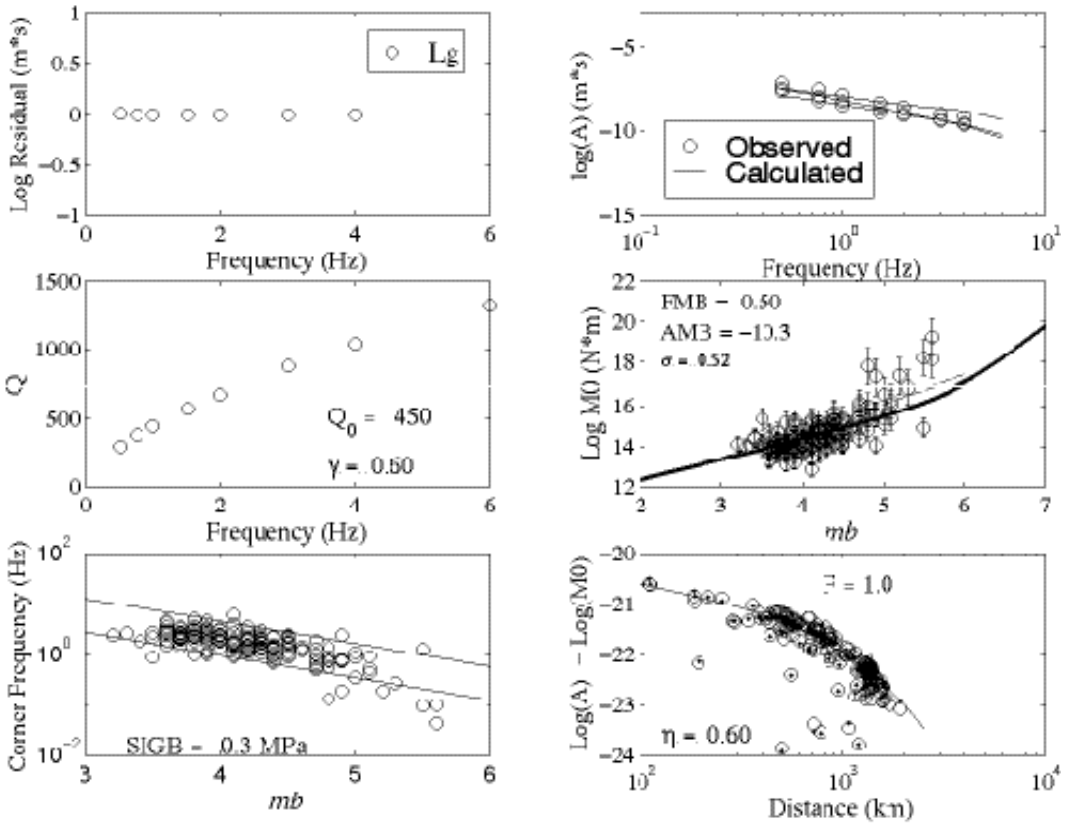


Figure 2. Plots illustrating various parameters for Lg MDAC model. Moving clockwise from upper left (UL): Site/excitation factors (equation 1, *P(f)*). (Upper right) Example of three fits to three randomly chosen events. (Middle right) Moment/magnitude relationship and estimated moments and 95% confidence limits. Dashed line is from universal moment-magnitude scaling (Priestley and Patton, 1997). (Bottom right) Observed (open circle) and calculated (dot) amplitude normalized by moment versus distance at 1 Hz versus distance and theoretical scaling for $\eta = 0.6$. (Lower left) Estimated corner frequency versus m_b for average stress drop of 0.3 MPa. Upper and lower lines are theoretical curves for 0.1 and 10 MPa (1 and 100 bar) stress drop. (Middle left) Q versus frequency using power law model.

From Figure 4 it can be seen that the trends in the ratio are removed with both distance and magnitude. The separation between the earthquakes and explosions is quite good (including the Lop Nor earthquakes). Further examples of various discrimination ratios computed from the MDAC-corrected amplitudes are shown in Figure 5. Note that in all cases the discrimination performance is excellent and trends are removed with magnitude. The separation between the Lop Nor explosions and earthquakes is very good indicating that the discriminants are based on source or very near-source differences between the two different source types.

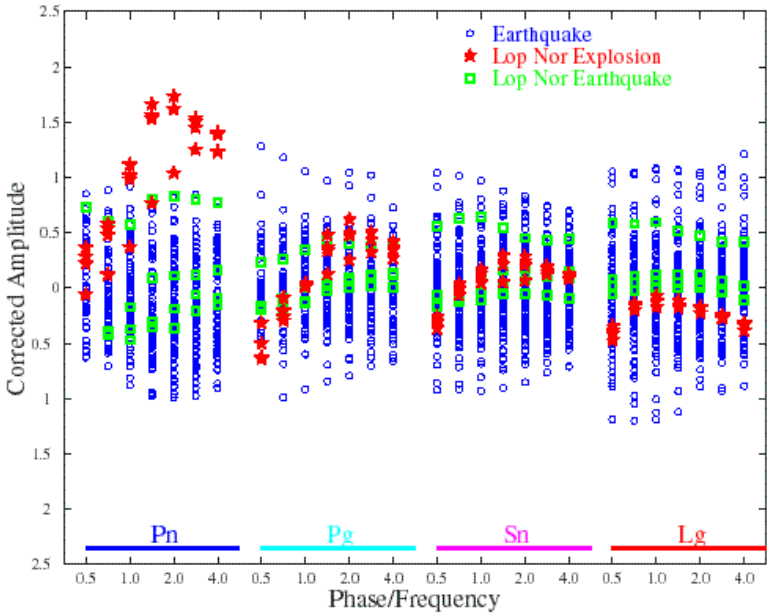


Figure 3. MDAC-corrected log amplitudes for each phase as a function of frequency using the parameters shown in Figure 2 including the 4 Lop Nor nuclear explosions. Four earthquakes within 50 km of Lop Nor are also identified.

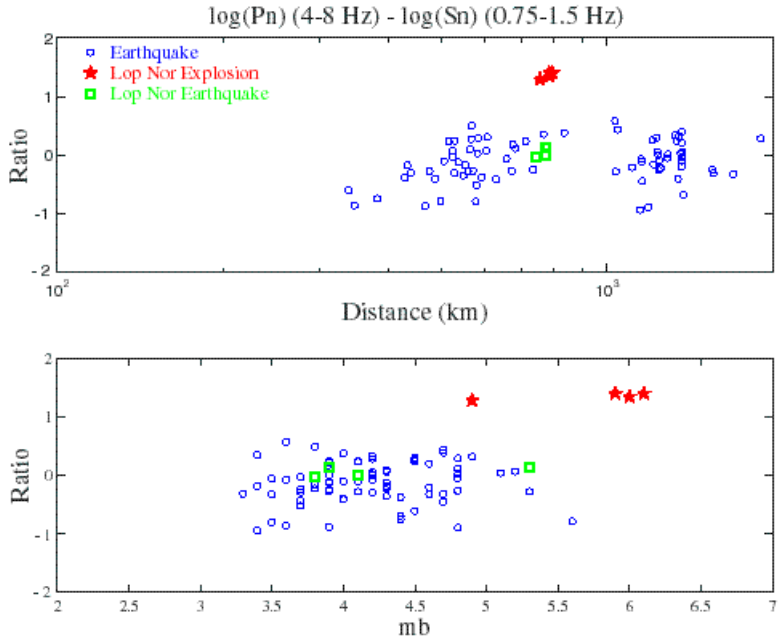


Figure 4. High-frequency Pn (4-8 Hz) to low-frequency (0.75-1.5 Hz) Sn cross-spectral ratio plotted versus log distance (top) and magnitude (bottom).

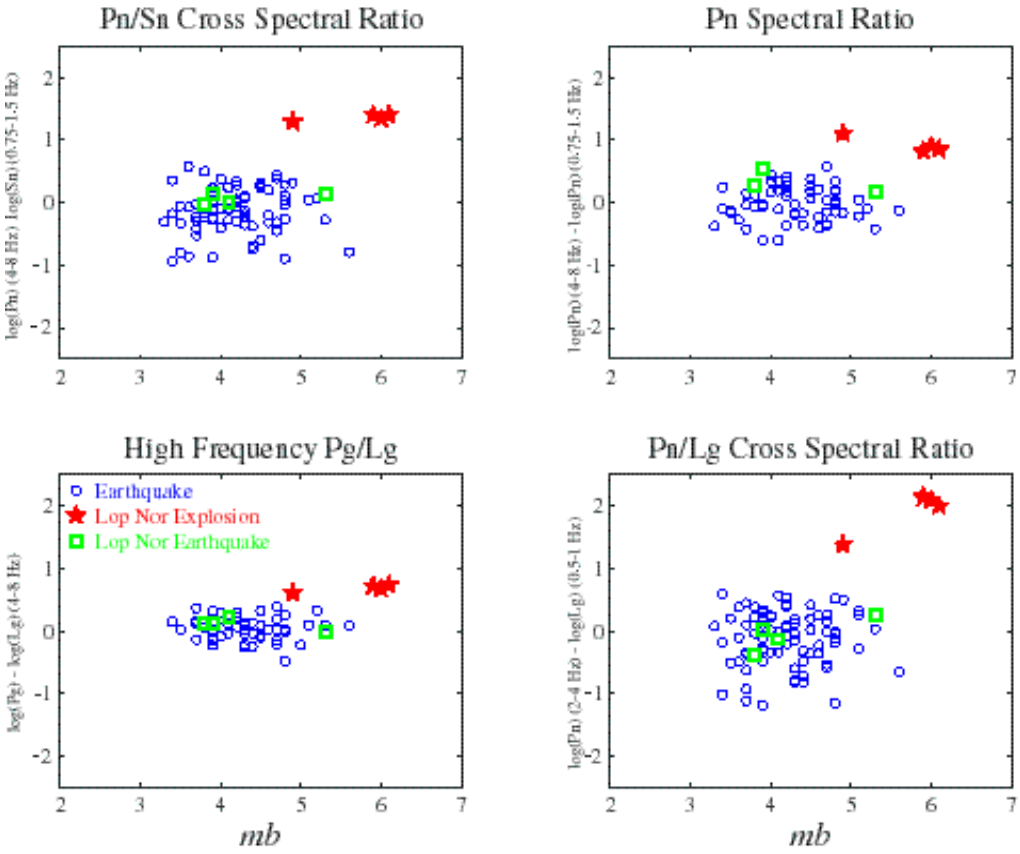


Figure 5. Examples of four discriminants computed from the MDAC-corrected amplitudes shown in Figure 3. Upper left is the Pn/Sn cross-spectral ratio (shown in Figure 4). Upper right is a Pn spectral ratio. Lower right is a Pn/Lg cross-spectral which from Figure 3 was judged to have the most separation between earthquakes and explosions. Lower left, high-frequency Pg/Lg ratio.

The discriminants in Figure 5 illustrate that one-dimensional models for a given station and source-region can lead to good discrimination performance. However, as suggested by Taylor and Hartse (1998) and Phillips *et al.*, (1998), the residuals to the one-dimensional model can be spatially interpolated to account for regional variations in attenuation further reducing the scatter in the discrimination plots. Phillips (1999) and Rodgers *et al.*, (1999) have suggested kriging (e.g. Schultz *et al.*, 1998) as a viable method to spatially interpolate amplitudes.

Using leave-one-out, we corrected the amplitudes and recomputed the Pn to Sn cross-spectral ratio shown in Figure 4. The results are shown in Figure 6 along with the original MDAC-corrected spectral ratio with just a simple distance correction (Hartse *et al.*, 1997). In each plot, we show the estimate of the variance of the earthquake population and an estimate of the univariate Mahalanobis distance between the earthquake and explosion populations, Δ^2 (Hand, 1981). For the lower two plots we show the variance reduction relative to the preceding plot. For the DCR shown in the top portion of Figure 6, we can still see the source scaling effect on the cross-spectral ratio.

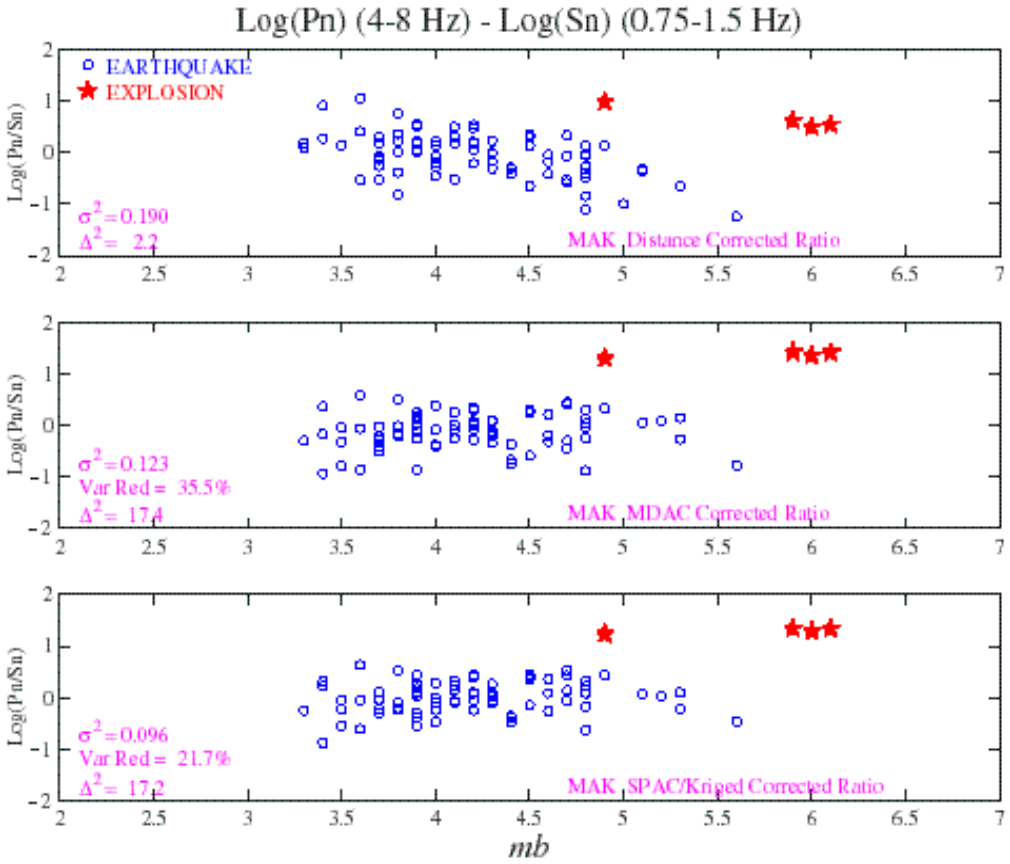


Figure 6. Examples of high-frequency Pn to low-frequency Sn cross spectral ratio versus magnitude with estimated variance for earthquakes and Mahalanobis distance. (top) Distance corrected. (middle) MDAC-corrected ratio (bottom) Results from application of kriged surface corrections to individual MDAC-corrected amplitudes and recomputation of ratio.

The middle plot on Figure 6 shows the MDAC-corrected ratio (same as Figure 4) showing a variance reduction over the DCR of 35.5%. The Δ^2 value has also increased significantly because of the removal of the ratio versus magnitude trend resulting in better discrimination performance. The bottom portion of Figure 6 shows results from application of kriged surface corrections to individual MDAC-corrected amplitudes and subsequent recomputation of the ratio. The variance has been reduced an additional 21.7% over the MDAC ratio (49.5% over the DCR). Although the variance of the earthquakes has been reduced significantly, the Mahalanobis distance has not changed significantly because the correction has moved the two populations slightly closer together due to the nature of the corrections in the vicinity of Lop Nor. Thus, although the one-dimensional models can be used to correct discriminants and obtain good performance, the spatial surface corrections can be used to improve discriminants even further by reducing the scatter in the earthquake population.

The MDAC methodology presented in this paper can be easily incorporated into an operational pipeline. The concept is illustrated in Figure 7. The MDAC parameters and kriged surfaces can be developed offline and entered into an online database for pipeline processing. Once a new event is located and a m_b is calculated, the regional phases can be windowed and Fourier transformed. The MDAC-corrected amplitudes for each phase and frequency can be rapidly computed using only the distance and m_b. The spatial corrections from the kriged surfaces can then be applied to the corrected amplitudes based only on the event location. At this point, a set of multivariate-normal corrected amplitudes is available for event identification.

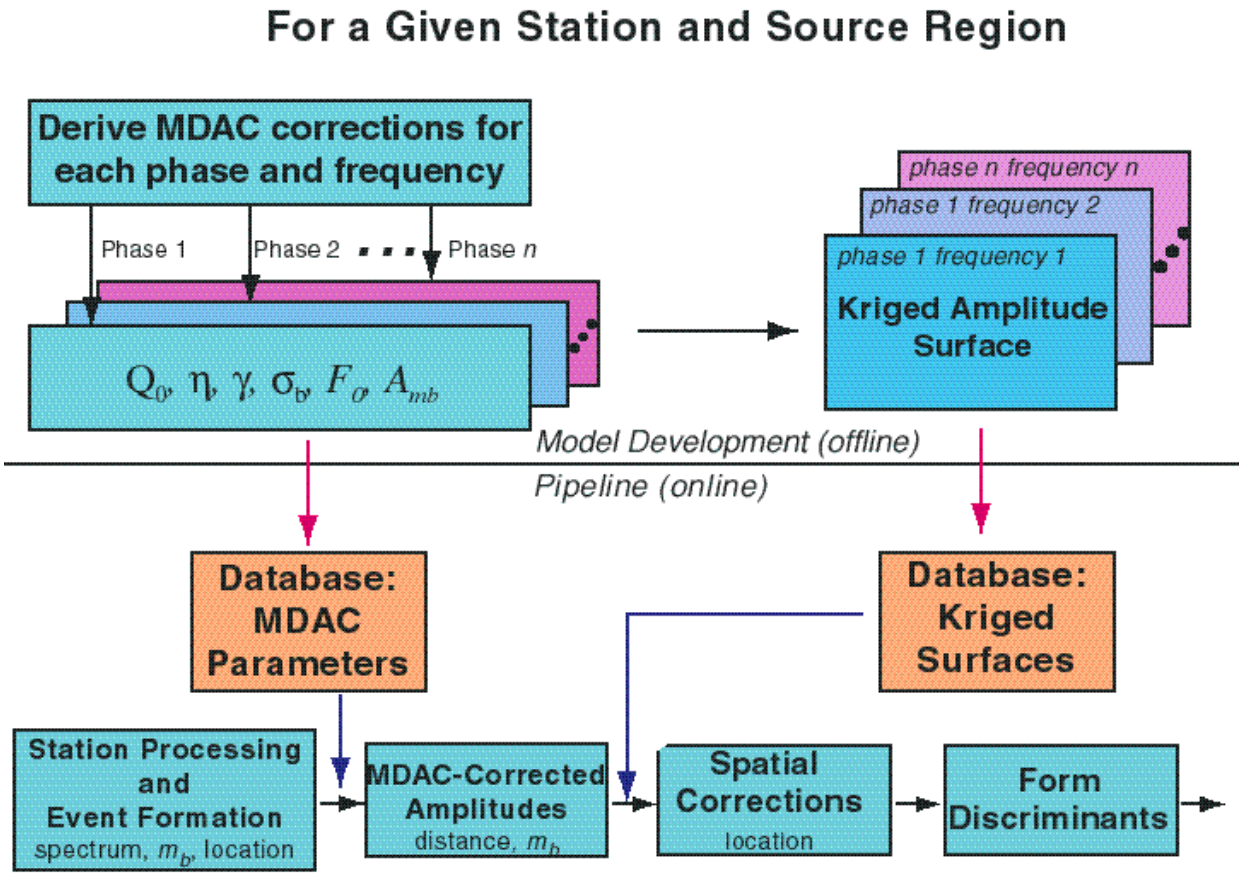


Figure 7. Example flowchart illustrating how the MDAC method could be combined with spatial interpolation (e.g. kriging) to develop database parameters to provide amplitude corrections for regional event identification in near-real time. These parameters can easily be incorporated into an operational pipeline to correct amplitudes from a new event for identification purposes.

CONCLUSIONS AND RECOMMENDATIONS

We have presented the MDAC methodology for correcting regional seismic amplitudes for source scaling and propagation using simple physical source and propagation models. The resulting corrected amplitudes are independent of m_b and distance and amenable to multivariate discrimination analysis. The amplitudes are corrected using a simple one-dimensional propagation model and the Brune (1970) dislocation source model modified to handle non-constant stress drop. The discrimination power in the corrected amplitudes lies in the assumption that the earthquake model will provide a poor fit to the signals from an explosion. Observations of explosions from many different regions have shown significant variability in performance of different discriminants presumably due to the strong effect of linear and nonlinear material-dependent phenomenology acting in the near-source region (e.g. Taylor and Denny, 1991). However, it is expected that there will always be some, possibly unpredictable, differences between earthquake and explosion sources. This fact is the basis for our preference for deriving a set of corrections for seismic amplitudes rather than preselecting traditional amplitude ratios. In an uncalibrated region, it is very difficult to predict *a priori* which combination of discriminants will provide the best performance. Correcting amplitudes allows for much flexibility in the subsequent event identification procedures (Figure 7) because all of the information is retained. Dealing with amplitudes involves a new set of problems (e.g. the m_b bias problem) not encountered as strongly with ratios. However, we feel the advantages outweigh the disadvantages in terms of the flexibility amplitudes give to the source identification problem.

ACKNOWLEDGMENTS

Helpful discussions with Howard Patton and Dale Anderson are greatly appreciated. This work is performed under the auspices of the U.S. Department of Energy by Los Alamos National Laboratory under contract W-7405-ENG-36.

REFERENCES

Brune, J.N., Tectonic stress and spectra of seismic shear waves from earthquakes, *J. Geophys. Res.*, 75, 4997-5009, 1970.

Hand, D.J., *Discrimination and Classification*, Wiley, New York, 218pp, 1981.

Hartse, H.E., S.R. Taylor, W.S. Phillips, and G.E. Randall, Regional event discrimination in central Asia with emphasis on western China, *Bull. Seism. Soc. Am.*, 87, 551-568, 1997.

Priestley, K.F. and H.J. Patton, Calibration of m_b(Pn), m_b(Lg) scales and transportability of the M_0:m_b discriminant to new tectonic regions, *Bull. Seism. Soc. Am.*, 87, 1083-1099, 1997.

Phillips, W.S., G.E. Randall, and S.R. Taylor, Regional phase path effects in central China, *Geophys. Res. Lett*., 25, 2729-2732, 1998.

Phillips, W.S., Empirical path corrections for regional-phase amplitudes, *Bull. Seism. Soc. Am.*, 89, 384-393, 1999.

Phillips, W.S, H.E. Hartse, S.R. Taylor, A.A. Velasco, and G. E. Randall, Regional phase amplitude ratio tomography for seismic verification, Los Alamos National Laboratory, LAUR-99-1904, submitted to PAGEOPH, 1999.

Rodgers, A.J., W.R. Walter, C.A. Schultz, S.C. Myers, and T. Lay, A comparison of methodologies for representing path effects on regional P/S discriminants, *Bull. Seism. Soc. Am.*, 89, 394-408, 1999.

Schultz, C., S. Myers, J. Hipp, and C. Young, Nonstationary Bayesian kriging: application of spatial corrections to improve seismic detection, location and identification, *Bull. Seism. Soc. Am.*, 88, 1275-1288, 1998.

Sereno, T.J., S.R. Bratt, and T.C. Bache, Simultaneous inversion of regional wave spectra for attenuation and seismic moment in Scandinavia, *J. Geophys. Res.*, 93, 2019-2035, 1988.

Taylor, S.R. and M.D. Denny, An analysis of spectral differences between NTS and Shagan River nuclear explosions, *J. Geophys. Res.*, 96, 6237-6245, 1991.

Taylor, S.R., and H.E. Hartse, An evaluation of generalized likelihood ratio outlier detection to identification of seismic events in western China, *Bull. Seis. Soc. Am*., 87, 824-831, 1997.

Taylor, S.R., and H.E. Hartse, A procedure for estimation of source and propagation amplitude corrections for regional seismic discriminants, *J. Geophys. Res.*, 103, 2781-2789, 1998.

Taylor, S.R., and A.A. Velasco, User's manual for SPAC 1.0: A MATLAB program for computing source and path amplitude corrections, *Los Alamos National Laboratory, Los Alamos, NM*, LAUR-98-4363, 1998.

Taylor, S.R., A.A. Velasco, H.E. Hartse, W. S. Phillips, W.R. Walter, and A.J. Rodgers, Amplitude corrections for regional seismic discriminants, *Los Alamos National Laboratory, Los Alamos, NM*, LAUR-99-3040, submitted to PAGEOPH, 1999.

CONSTRUCTION OF A 3-D P AND S MODEL OF THE CRUST AND UPPER MANTLE TO IMPROVE REGIONAL LOCATIONS IN W. CHINA, CENTRAL ASIA, AND PARTS OF THE MIDDLE EAST

Michael H. Ritzwoller, Mikhail P. Barmin, Antonio Villasenor, Anatoli L. Levshin, E. Robert Engdahl
Department of Physics, University of Colorado at Boulder

Wim Spakman, Jeannot Trampert
University of Utrecht, The Netherlands

Sponsored by Defense Threat Reduction Agency
Contract No. DTRA0I-99-C-0019

ABSTRACT

Our overall goal is to assess the capabilities of three-dimensional (3-D) velocity models of the crust and upper mantle to improve the location of small seismic events within a regional monitoring environment. By "regional" we mean using data with path lengths confined to be less than about 2500 km. Our concentration is on the region bounded by latitudes 15° N to 55° N and longitudes 40° E to 100° E. We are now taking the first steps in this direction by constructing and testing a new 3-D S-model of the crust and upper mantle beneath the region of study and comparing it with the P-model of Bijwaard et al. (1998). Our S-model is a regional model of the crust and upper mantle, currently on a 2° x 2° grid, obtained by simultaneous inversion of broadband group velocity (e.g., Ritzwoller and Levshin, 1998; Ritzwoller et al., 1998) and phase velocity dispersion measurements (e.g., Trampert, and Woodhouse, 1996) constrained to fit a priori information about crustal and mantle structures. We find that most of the data used in the inversion can be well fit with a simple model of the crust and mantle that remains faithful to the a priori information. Crustal and mantle structures, with a few exceptions, demonstrate remarkable agreement with tectonic features and S-anomalies in the mantle agree favorably in both distribution and magnitude with the P-model of Bijwaard et al., (1998). In the crust, the tectonically deformed areas are typically slow (e.g., Turkey, Zagros in W. Iran, Hindu Kush in Afghanistan, Tibet, etc.) and shields and other stable regions are fast. Sedimentary basins are underlain by high velocities. The S-model between Moho and 220 km depth is transversely isotropic. The transverse isotropy is pervasive and, on average, somewhat stronger than that in PREM with the strongest anisotropy beneath tectonically deformed regions and shields. Consistent with PREM, vsh is almost everywhere faster than vsv and a low velocity zone typically arises for vsh across most of Eurasia but only rarely occurs for vsv.

Capabilities for computing Travel Time Correction Surfaces (TTCS) from 3-D models using 3-D ray tracing are now in place and we show examples TTCSs from our S-model and the P-model of Bijwaard et al. (1998). We demonstrate the relative importance of the crustal and mantle components of the TTCSs. Because crustal and mantle contributions may anticorrelate (e.g., Tibet), in order to predict regional travel time corrections accurately requires good 3-D models of both the crust and the upper mantle.

Due to different data and inversion methods, the P and S models display different and complementary strengths and weaknesses. The hybrid model that we will construct will be designed to exploit the strengths of the different data sets and inversion methods. The future combination of the P and S models will be facilitated by a new data base of P and S station corrections compiled for the region of study. The figure of merit in this hybridation will be the ability to improve the locations of Ground Truth events.

Key Words: Earth models, correction surfaces, event location, regional monitoring, path calibration

OBJECTIVE

The objective is to provide accurate P- and S-wave path calibrations rapidly and efficiently for the region of study. The method relies on the development, validation, and application of a 3-D model of the crust and upper mantle from which travel time correction surfaces (TTCS) can be computed for arbitrary body wave phases and event and station coordinates. The predicted TTCSs are intended for use within a hierarchy of information to improve path calibrations which are integral to the accurate location of small events with regional data alone. Model predictions are particularly useful in interpolating and extrapolating empirical information, in otherwise uncalibrated regions, for uncalibrated phases, and for newly installed stations.

RESEARCH ACCOMPLISHED

Introduction: The Problem

We approach model-based path calibration in three stages: (1) model construction, (2) model verification and calibration, and (3) validation and Ground Truth Event relocation. We report here only on aspects of the first stage, the construction of a model of the crust and upper mantle for much of the interior of Asia ranging from about 25° E to 120° E and 10° N to 70° N, with particular concentration on the region bounded by latitudes 15° N to 55° N and longitudes 40° E to 100° E. The second stage will comprise careful tests and the modification of the model using regional seismic data. We will also bring to bear information that is not easily applied during model construction; for example crustal velocities from individual refraction profiles. In the final stage, we will characterize the ability of the model to improve the relocation of Ground Truth Events in the region of study.

The challenge at the model construction stage is to develop a model that fits a broad class of seismic data and a priori information, particularly about the crust. We discuss the data, a priori information, and model parameterization in the next three subsections. We conclude by showing aspects of the crustal and upper mantle components of our preliminary S-model, comparing the model with the P-model of Bijwaard et al. (1998) in the upper mantle, and displaying TTCSs for the auxiliary IMS station AAK in Kyrghyzstan.

The Data

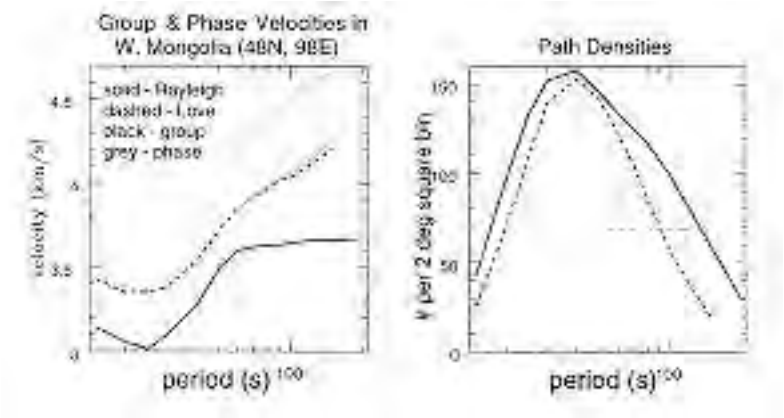


Figure 1. (LEFT) Example of the estimated group and phase velocity curves at a point in W. Mongolia. Rayleigh waves are plotted as solid lines and Love waves as dashed lines. Group velocities are black and phase velocities are grey. (RIGHT) Path densities at the same location with the same color scheme. Path densities are defined as the number of rays intersecting the 2° x 2° cell (~50,000 kM^2) surrounding the spatial point. Phase velocity path densities are independent of period due to the automation of the measurements.

We used the following data to construct the preliminary S-model: (1) intermediate and long period Rayleigh and Love wave group velocity maps from 15 s to 200 s period for Rayleigh waves and from 15 s

to 150 s for Love waves (e.g., Ritzwoller and Levshin, 1998; Ritzwoller et al., 1998; ciei.colorado.edu/geophysics/eurasia.dir/eurasia.html) and (2) long period Rayleigh and Love wave phase velocity maps (e.g., Trampert and Woodhouse, 1995, 1996) from 50 s to 150 s period. Figure 1 shows dispersion curves constructed from these maps at a point in W. Mongolia together with the path densities for each data type at each period. There are other notable sources of measured phase and group velocities and estimated maps, both regional and global, that we have not yet utilized (e.g., Curtis et al., 1998; Ekstrom et al., 1997; Larson and Ekstrom, 1999; Laske and Masters, 1996). We also utilize the P-wave model of Bijwaard et al. (1998) computed from groomed ISC travel times. One of the key ingredients that we are missing at the outset is data to constrain P-velocities in the crust. This is a problem that we will address in Stage 2 of the investigation. As discussed later, accurate crustal velocities are nearly as important as mantle velocities in computing TTCSs for shallow events at regional distances in the region of study.

A Priori Information

Table 1. Summary of Sources of A Priori Information

Structural Type	**Source**
Topography and Bathymetry	ETOP05 (NOAA/NGDC/World Data Center A)
Sedimentary Thickness & Velocities	Laske and Masters, 1997
Crustal Velocities	Mooney et al., 1998 (CRUST5.1)
Moho	Kunin et al., 1987 (IPE) Seeber et al., 1997 Laske and Masters, 1999 Mooney et al., 1998 (CRUST5.1)
Upper Mantle Velocities	Masters et al., 1996 (Sl6B30) Bijwaard et al., 1998
Lower Mantle Velocities	Masters et al., 1996 (Sl6B30)

The inverse problem is characterized by strong trade-offs between crustal and mantle structures and among various crustal structures. These trade-offs are not easily resolved by adding more data of the types described above, although the use of short period Rayleigh and Love wave group velocities does help in this direction. Rather it is necessary to constrain the space of models by applying a priori information about the crust, in particular, in the inversion. Because surface wave sensitivity kernels depend on the unknown structure, the inversion is non-linear and the inferred model depends on the starting model. Thus, an accurate starting model and the application of constraints on allowed perturbations during inversion are necessary ingredients to ensure that a high quality model will emerge from the inversion.

Fortuitously, efforts by several researchers have yielded information about crustal and upper mantle structures across parts of Eurasia in an organized form. We have used information from the sources listed in Table 1. Our input model is based on topography and bathymetry from ETOPO5, sedimentary thickness and velocities from the 1° x 1° compilation of Laske and Masters (1997), crustal velocities below the sediments from the 5° x 5° model CRUST5.1 of Mooney et al. (1998), Moho topography from the sources listed in Table 1 with a specified precedence ordering (Laske and Masters, 1999; Kunin et al., 1987; Mooney et al., 1998), and upper mantle velocities from the istotropic spherical harmonic degree 16 model S16B30 of Masters et al. (1996). We are currently investigating conversion of P to S in order to use a smoothed version of the model of Bijwaard et al. (1998) as a starting mantle model. These models have resolutions ranging from ~10^2 km to >10^3 km and there are variable accuracies within and between the models. Constraints on the structural perturbations allowed during inversion must attempt to account for these differences.

Model Parameterization and Inversion

We have attempted to find a simple, albeit entirely ad hoc, parameterization of the model that will allow us to fit the observed data while remaining faithful to the a priori information discussed in the previous subsection. At each spatial point the group and phase velocity data are inverted iteratively by perturbing the variables displayed

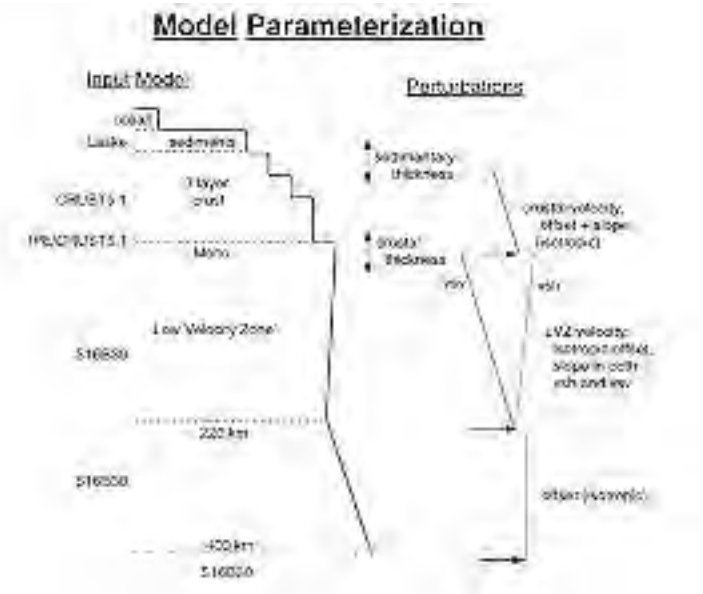


Figure 2. Schematic representation of the parameterization of the model. The left column depicts the form of the isotropic input model which is divided into the following layers: an ocean, two-layer sediments, three-layer crust, the Low Velocity Zone extending between the Moho and 220 km depth, and a layer between 220 km and 400 km depth. Surface topography, ocean bottom bathymetry, sediment thicknesses and velocities, crustal velocities, Moho depths, and mantle shear velocities are taken from sources described above. The right column depicts the estimated perturbations: depth shifts in the sediment bottom and Moho, offsets in the average shear velocity of the crust and the mantle from Moho - 220 km and 220 km - 400 km, and changes in the vertical gradient of shear velocity in the crust and from Moho - 220 km.

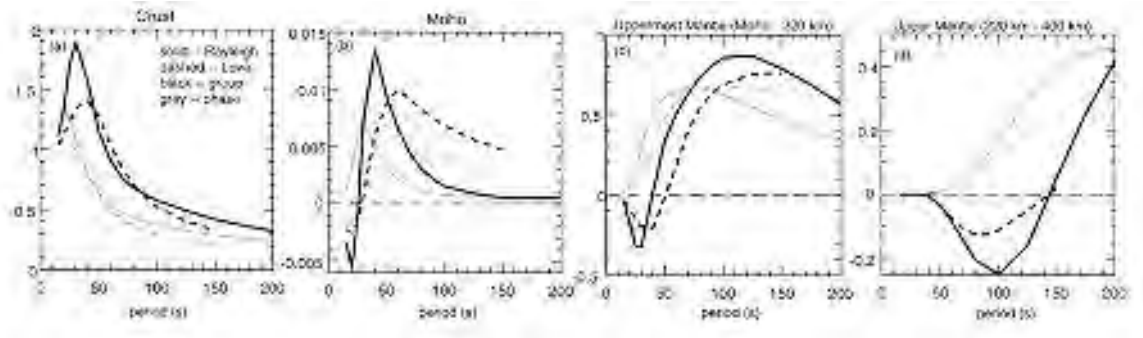


Figure 3. Partial derivatives of Rayleigh and Love wave group and phase velocities with respect to four of the structures in the current parameterization of our S-wave model: (a) constant crustal vs perturbation, (b) topographic perturbation to Moho, (c) constant mantle isotropic vs perturbation between Moho and 220 km, and (d) constant mantle vs perturbation between 220 km and 400 km. Solid lines are Rayleigh waves, dashed lines are Love waves, black is group velocity, and grey is phase velocity. In general, phase velocities sample deeper than group velocities and Rayleigh deeper than Love at each period. Thus, partial derivatives for phase velocities peak at shorter periods than group velocities and Rayleigh at shorter periods than Love. The group velocity partials change sign.

schematically in Figure 2. We recompute the partial derivatives on each iteration and iterate until convergence, usually 5 - 8 iterations. Figure 3 displays examples of partial derivatives for a number of model variables computed in W. Mongolia. This figure demonstrates the importance of the long period phase velocities in improving the sensitivity to shear velocities below 200 km and the importance of the short and intermediate period group velocities in constraining crustal structures. Data weights based on path density and residuals are applied during inversion and structural tolerances are chosen automatically depending on the data distribution. For example, if short period data are missing crustal tolerances are tightened and if long period information is missing mantle tolerances are tightened. For the model displayed in the next subsection, we have allowed perturbations to the input sedimentary thickness and Moho depth of no more than +/-5 km but have allowed much more generous perturbations to crustal and mantle velocities which we believe are more poorly known in the input model.

An important observation is that we are not able to fit both the long period Rayleigh and Love wave data simultaneously without a transversely isotropic uppermost mantle. This is the reason we have introduced the anisotropy between Moho and 220 km depth. In addition, we found it necessary to perturb not only the average velocity of the crust, but also to allow a change in the vertical gradient of the crustal shear velocities.

If the data warrant, the resulting parameterization contains eight variables, which is beyond the capacity of current data to estimate simultaneously. We damp the inversion on each iteration and allow the algorithm to choose the subset of variables to perturb and to resolve the trade-offs given the constraints we place on the inversion.

Figure 4 presents an example of the results of the inversion in Western Mongolia. The group and phase velocity data can be well fit simultaneously across most of Eurasia. Exceptions have motivated our parameterization. There remain problems, however, with discrepancies between the Rayleigh and Love wave maps and between the group and phase velocity maps that arise due to different intrinsic resolutions between the different data types. The inversion algorithm recognizes these discrepancies, chooses a subset of the data to fit, and tightens tolerances when this problem arises.

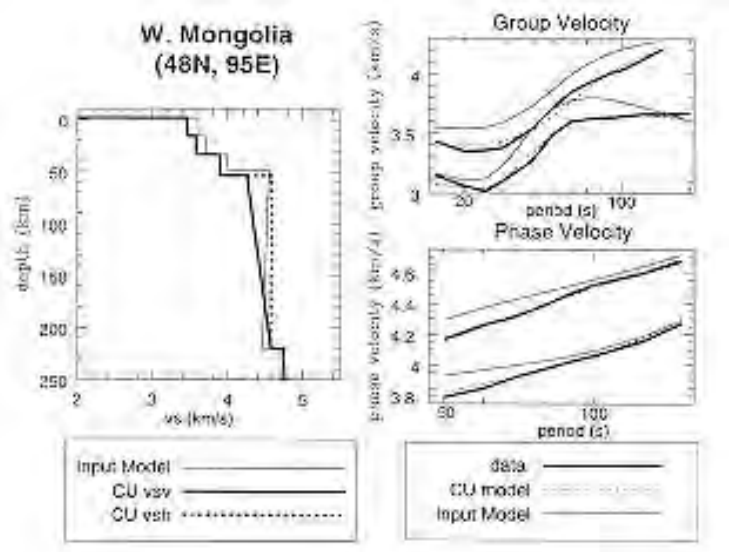


Figure 4. (LEFT) Estimates and input shear velocity profiles under the specified point. The input profile is the thin solid line and is isotropic, as defined above. The estimated profile is the thick solid and dashed lines and is transversely isotropic between Moho and 220 km depth and isotropic elsewhere. Typically vsh > vsv and a low velocity zone is evidenced between Moho and 220 km in vsh but not in vsv. (RIGHT) Comparison between observed group and phase velocities and predictions from the input and estimated models. The data are the thick solid lines whereas the thin solid lines and the dashed lines are the prediction from the input model and the estimated model, respectively.

Our S-model is currently produced on a 2° x 2° degree grid, but we will soon move to 1° x 1°.

Preliminary Shear Velocity Model

Figure 5 presents aspects of the crustal model across the studied region. The sedimentary thickness and Moho depths have been constrained to lie within 5 km of the input model and thus contain little new information. The crustal velocities, however, represent large perturbations from the input model. The upper crust, in particular, displays very strong tectonic correlation. The tectonically deformed areas are typically slow (e.g., Turkey, Zagros in W. Iran, Hindu Kush in Afghanistan, Tibet, etc.) and shields and other stable regions are fast. Sedimentary basins are underlain by high velocities. Clearly, there remain problems; e.g., we have lost the Moho depression under the Zagros and it remains an open question how to estimate crustal P from the crustal S-model. These are questions for on-going research.

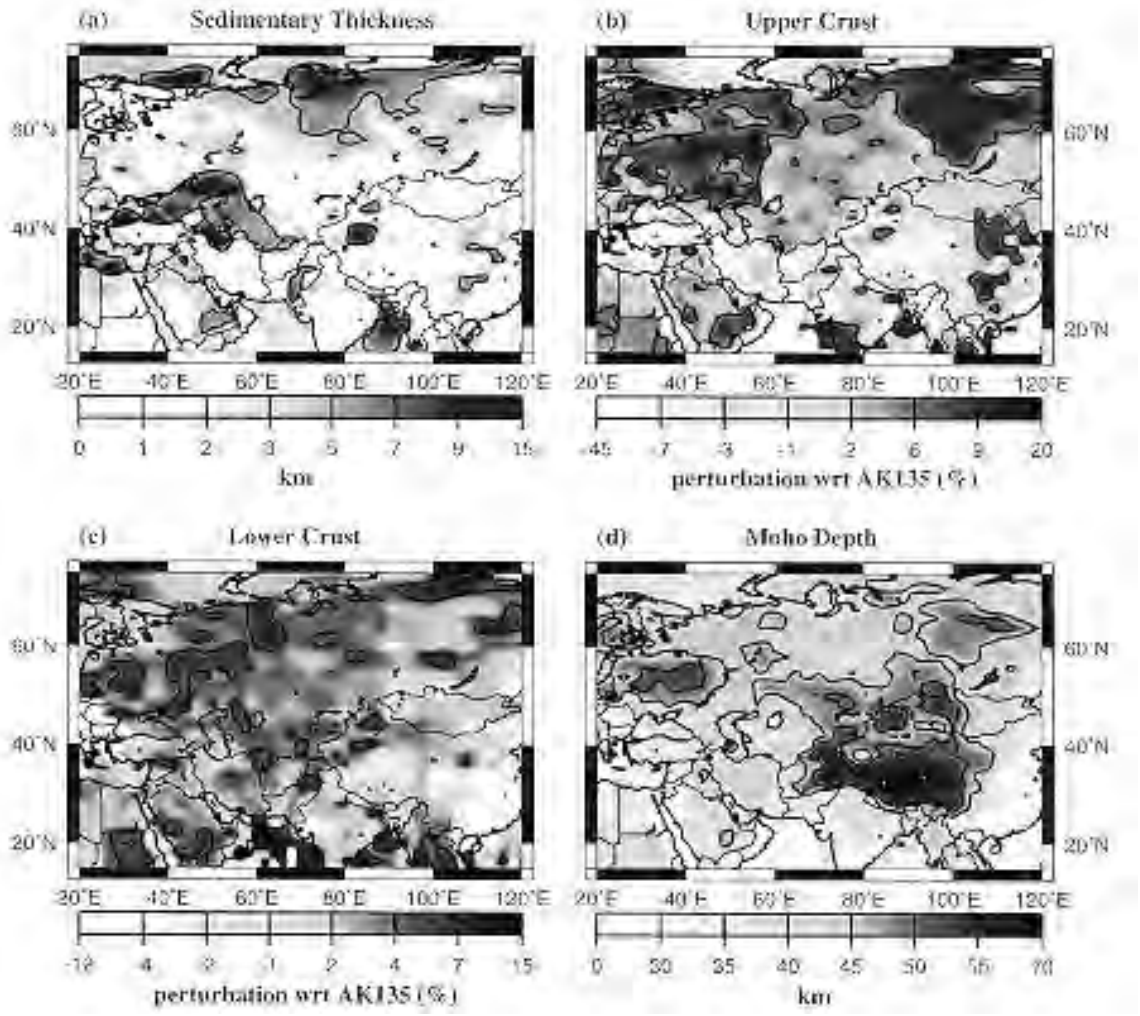


Figure 5. The estimated model of the crust. (a) Sedimentary thickness in km. The 5 km contour is displayed. (b) Upper crustal shear velocity as percent pertrubation relative to AK135 (3.46 km/s). The +5% and -3% contours are displayed. (c) Lower crustal shear velocities relative to AK135 (3.85 km/s). The +5% and -2% contours are displayed. (d) Moho depth below the geoid in km. The 45 km and 50 km contours are displayed.

The upper mantle velocity variations demonstrate somewhat larger scale features than the crustal anomalies because they arise to fit the longer wavelength intermediate and longer period surface wave data. The model between the Moho and 220 km depth is transversely isotropic. The transverse isotropy is pervasive and, on average, somewhat stronger than that in PREM with the strongest anisotropy beneath tectonically deformed regions and shields. As evidenced in Figure 4 and consistent with PREM, vsh is almost everywhere faster than vsv. Also consistent with PREM, a low velocity zone typically arises for vsh across most of Eurasia but only rarely occurs for vsv.

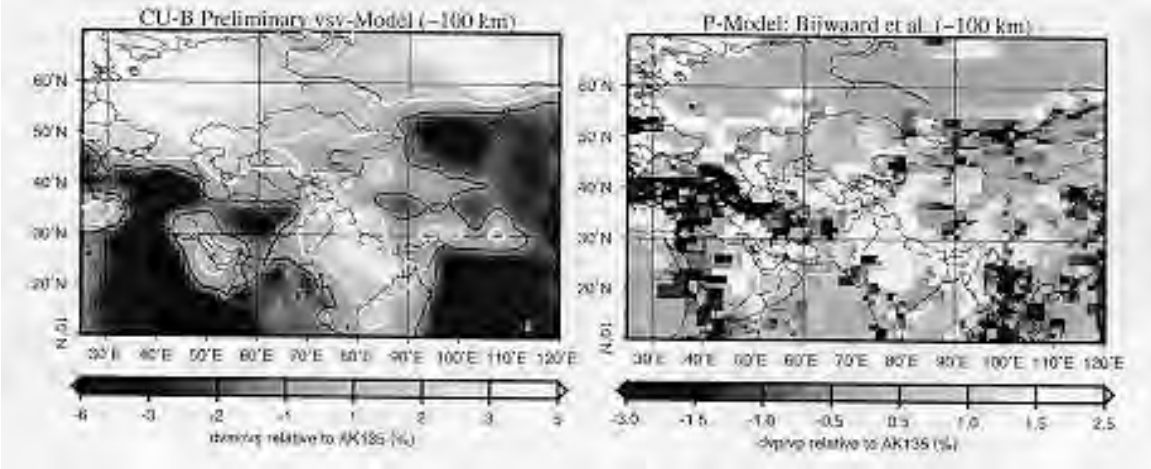


Figure 6. Comparison at about 100 km depth between our estimated S-model (vsv) and the P-model of Bijwaard et al. (1998). The S-model is presented as percent perturbation to S-velocity from AK135 (4.5 km/s) and the P-model is relative to P-velocity from AK135 (8.05 km/s). In the left plot, the +/-I% contours are shown as white and black lines, respectively.

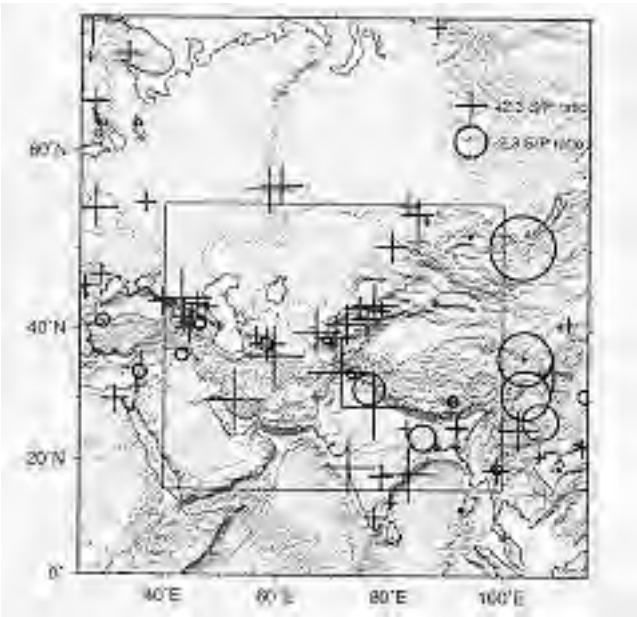


Figure 7. S/P ratios of station residual medians. Pluses correspond to correlated P and S station corrections and minuses to anticorrelated station corrections. Most stations show a positive correlation and the slope of the P- correction to S-correction graph is 2.3. Anticorrelations cluster, however, and are probably physically meaningful. The cause of the anticorrelations is not yet clear.

Figure 6 presents a comparison between our preliminary S-model at 100 km depth in the upper mantle and the P-model of Bijwaard et al. (1998) at approximately the same depth. It is important to recognize that at this depth, the P-model is poorly resolved over large areas characterized by little seismicity and few historical stations (e.g., Russian Platform, Siberian shield, Kazakh Platform, Egypt/Sudan, Arabian Sea, Bay of Bengal, S. China Sea, and other areas). These areas are indicated by larger block sizes in the P-model, but are difficult to see in Figure 6. In the regions with adequate coverage by both P-waves and surface waves the agreement is very good, however.

These observations encourage interconversion of the P variations to S variations and conversely in order to take advantage of the relative strengths and weaknesses of the two models. The P-model displays better lateral resolution than the S-model, but the S-model has more homogeneous coverage. In addition, we have an S-model for the crust but no P-model, but the P-model improves with depth below 200 km and the S-model loses its resolution rapidly below this depth. Figure 7 shows P/S ratios from station corrections computed from the groomed ISC data base across the region of study. Although there are occasional anticorrelations, most stations demonstrate correlated P and S station corrections in both amplitude and azimuthal distribution with a slope of about 2.3.

Preliminary Travel Time Correction Surfaces (TCCS)

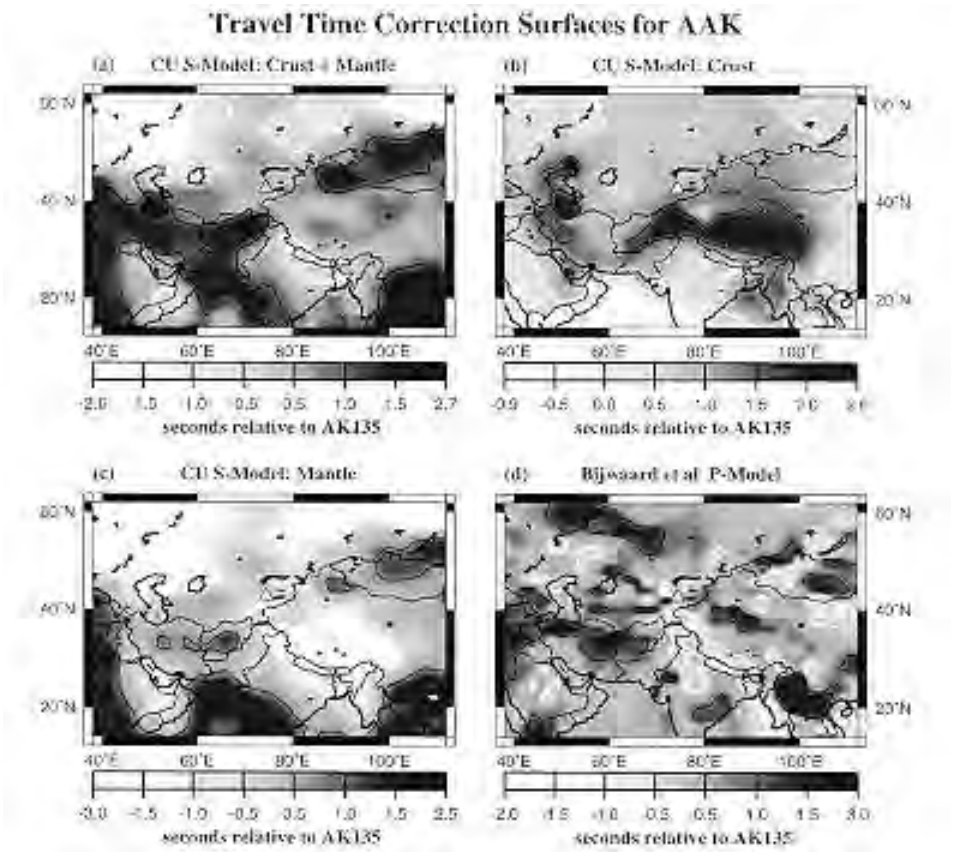


Figure 8. Predicted travel time correction surfaces for the station AAK for a surface event. The value on the map is the specified first arriving body wave travel time relative to the prediction from the laterally homogeneous model AK135. (a) S-wave correction surface for our S-model. The -0.5 s and 1.0 s contours are shown with white and black lines, respectively. (b) S-wave correction surface for the crustal component of our S-model. The 0.5 s and 1.5 s contours are displayed. (c) S-wave correction surface for the mantle part of our S-model. The -0.5 and 0.75 s contours are shown. (d) P-wave correction surface for the P-model of Bijwaard et al. (1998). The -0.25 s and 1.0 s contours are shown.

The computation of a TTCS for a given station from a 3-D model is straightforward. A fictitious event is placed at each geographical position at a given depth. Here we use the geoid as the hypocentral depth in dry continental areas and the solid surface in wet continental and oceanic areas. We trace a 3-D ray from the hypocenter to the station (placed at the geoid here) for each fictitious event using the 3-D ray tracing code described by Pulliam and Snieder (1998). The fictitious events are moved systematically around the region of study. We reference each 3-D travel time to the travel time predicted from the laterally homogeneous model AK135 (Kennett et al., 1995) and define a travel time correction as the difference between the travel time through the 3-D model and the AK135 time. Thus, positive residuals are slow and negative residuals are fast in the usual way.

Figure 8 shows a set of such TTCSs for the auxiliary IMS station AAK. Figures 8a - 8c are computed using the preliminary S-model described above. Several observations are worth noting. First, the travel time corrections are simply related to the features of the model displayed in Figures 5 and 6. On average, tectonically deformed regions produce slow travel times and shields and plate boundaries characterized by thickened lithosphere are fast. Comparison of Figures 8b and 8c reveals that in these regions the crustal and mantle contributions to the corrections correlate and add constructively. Indeed, for shallow events the crustal and mantle contributions are of nearly the same expected magnitude and in these regions the crustal contribution only affects the total travel time correction by changing the amplitude of the prediction from the mantle model. Crustal and mantle contributions frequently anticorrelate, however, as exemplified by the Tibet region. Thus, to predict regional travel time corrections accurately requires both good crustal and mantle models.

Figure 8d, computed similarly for the P-model of Bijwaard et al. (1998), compares most favorably with the mantle part of our S-model. (This comparison, as in Figure 6, must be informed by knowledge of the regions poorly constrained by the P-model; e.g., much of N. Asia, Arabian Sea, Bay of Bengal.) This is expected due to the lack of a crustal component in this P-model. By combining the S-model and the P-model to take advantage of the strengths of each, we plan to produce a hybrid model that will improve the TCCSs for both S and P. The figure of merit in this hybridation is the ability to improve the locations of Ground Truth events.

CONCLUSIONS AND RECOMMENDATIONS

We present here some of the preliminary results that have emerged concerning the new S-model across the studied region. The potential for the use of this and related models for path calibration is encouraging. Most of the data used in the inversion can be well fit with a simple model of the crust and mantle that remains faithful to a priori information. Crustal and mantle structures, with a few exceptions, demonstrate remarkable agreement with tectonic features and S-anomalies in the mantle agree favorably in both distribution and magnitude with a recent P-model of the mantle (Bijwaard et al., 1998). Capabilities are now in place to compute Travel Time Correction Surfaces (TTCS) from this or other models of the region of study. Problems remain that we are continuing to address. Perhaps most significantly, we possess constraints only on crustal shear velocities and must convert the crustal S-model to a P-model. Inspection of P and S station corrections and comparison between the S-model and the P-model of Bijwaard et al. (1998), however, encourage us to investigate the interconversion between the P and S models to take advantage of their complementary strengths and weaknesses.

We anticipate completion of the combined P- and S-model in several months. The verification and further development of this model with local and regional seismic data is an important next step in this research. All developments of the model occur within the framework of improving regional location capabilities within the area of study.

REFERENCES

Bijwaard, H., W. Spakman, and E.R. Engdahl, Closing the gap between regional and global travel time tomography, J. Geophys. Res., 103, 30055 - 30078, 1998.

Curtis, A., J. Trampert, R. Snieder, and B. Dost, Eurasian fundamental mode surface wave phase velocities and their relationship with tectonic structures, J. Geophys. Res., 103, 26919 - 26947, 1998.

Ekstrom, G., J. Tromp. And E.W.F. Larson, Measurements and global models of surface wave propagation, J. Geophys. Res., 102, 8137 - 8158, 1997.

Kennett, B.L.N., E.R. Engdahl, and R. Buland, Constraints on seismic velocities in the Earth from travel-times, Geophys. J. Int., 122, 108 - 124, 1995.

Kunin, N.Y., et al., Eurasian Moho relief map, Inst. of Phys. of the Earth, Acad. of Sci., Minist. of Geol. of the Russ. Fed., Moscow, 1987.

Laske, G. and G. Masters, Constraints on global phase velocity maps from long-period polarization data, J. Geophys. Res., 101, 16059 - 16075, 1996.

Laske, G. and G. Masters, A global digital map of sediment thickness, EOS Trans. AGU, 78, F483, 1997. (mahi.ucsd.edu/Gabi/sediment.html)

Laske, G. and G. Masters, A global digital map of crustal thickness, unpublished, 1999.

Larson, E.W.F. and G. Ekstrom, Global models of surface wave group velocity, submitted to Pageophys., 1999. Masters, G., S. Johnson, G. Laske, and H. Bolton, A shear-velocity model of the mantle, Phil. Trans. R. Soc. London, Ser. A., 354, 1385 - 1411, 1996.

Mooney, W.D., G. Laske, and G. Masters, CRUST5. I: A global crustal model at 5' x 5', J. Geophys. Res., 103, 727 - 747, 1998. (mahi.ucsd.edu/Gabi/crust.html)

Pulliam, J and R. Snieder, Ray perturbation theory, dynamic ray tracing, and the determination of Fresnel zones, Geophys. J. Int., 135, 463 - 469, 1998.

Ritzwoller, M.H. and A.L. Levshin, Eurasian surface wave tomography: Group velocities, J. Geophys. Res., 103, 4839 - 4878, 1998.

Ritzwoller, M.H., A.L. Levshin, L.I. Ratnikova, and A.A. Egorkin, Intermediate period group velocity maps across Central Asia, western China, and parts of the Middle East, Geophys. J. Int., 134, 315-328, 1998. Seeber, D., M. Vallve, E.A. Sandvol, D.N. Steer, and M. Barazangi, Middle East tectonics; applications of geographic information systems (GIS), GSA Today, 7, 1 - 6, 1997.

Trampert, J. and J.H. Woodhouse, Global phase velocity maps of Love and Rayleigh waves between 40 s and 150 s period, Geophys. J. Int., 122, 675 - 690, 1995.

Trampert, J. and J.H. Woodhouse, High resolution global phase velocity distributions, Geophys. Res. Let., 23(l), 21-24, 1996.

SIGNAL DETECTION AND ESTIMATION AT THE NEW INTERNATIONAL MONITORING SYSTEM ARRAY AT MINA

Jin Wang, Hans Israelsson, Keith McLaughlin
Center for Monitoring Research, SAIC

Sponsored by U.S. Department of Defense
Defense Threat Reduction Agency
Contract No. DTRA01-99-C-0025

ABSTRACT

The Mina seismic array, NVAR, in Nevada was recently put into operation and added to the so International Monitoring System (IMS). NVAR includes two seismic subarrays, one with 10 and one with 3 elements. With a diameter of about 5 km and equipped with short period vertical instruments, the 10 element subarray is designed primarily for detection of regional phases and teleseismic P phases. The 3 element subarray lends itself to processing of surface waves with its three-component broad band instruments. It has a diameter of about 20 km and is symmetrically centered around the smaller 10 element array. An additional three component element (NV11) provides, by virtue of its co-location with the conventional station MNV, continuity with historic data.

In this paper we assess the performance of NVAR during its initial few months of operation as part of the IMS using data forwarded to and processed real-time at the Prototype International Data Center (PIDC). Beamforming, signal detection, frequency-wavenumber (f-k) analysis and other types of processing were initially set up according to standard procedures developed at the PIDC.

During the period Feb. 19 - May 18, 1999, an average of 60 signals/day were detected by the automatic processing for NVAR. About one quarter of the detections were subsequently associated with seismic events of the Reviewed Event Bulletin, REB, published by the PIDC, whereas about only 3 signal/day, were missed by the automatic system, had to be added during analyst review for NVAR. This performance is quite comparable to that of similar arrays, like the Pinedale array in Wyoming and the TXAR array in Texas, which have been operating for some time and have benefited from tuning of their processing. Furthermore, the number of signals associated with events in the REB for NVAR almost doubled compared with that of the conventional station MNV.

The slowness and azimuth estimation of detected signals, based on f-k analysis, shows large systematic bias, of up to 3 sec/degree, throughout the slowness plane for NVAR. This can be attributed to the relatively large range in elevation (about 500 m) spanned by array elements and the assumption of co-planar location of array elements in the f-k algorithm. The PIDC processing scheme does, however, allow for removal of slowness bias by applying corrections to observed slowness. Development of such corrections for NVAR is currently in progress, which together with evaluation of other aspects of the NVAR real-time processing will likely lead to fine-tuning of several processing configurations. This will, in turn, most probably enhance the performance of NVAR, which already in its initial few months of operation shown encouraging results with the default configuration.

Key Words: CTBT, Array Detection, Signal Processing

INTRODUCTION

The Nevada Array (NVAR) is the last and newest IMS primary station to be added to North America and the closest primary IMS station to the historically important US Nevada Test Site (NTS). The IMS network is almost complete for North America. NVAR began contributing to the PIDC Reviewed Event Bulletin (REB) on February 17, 1999. The site includes the three-component (3C) Mina Nevada (MNV) station which ceased contributing to the REB on April 14, 1999. This paper reports on preliminary evaluation of the first few months of NVAR operation. The upgrade from MNV to NVAR was anticipated to improve detection and location in North America. IDC automatic processing depends heavily upon arrays to form initial events. The automatic detection, phase identification, and association of array signals is critical to this processing. Arrays generally have lower detection thresholds, higher SNR, better phase identification, and contribute more reliable back-azimuths for association, and location.

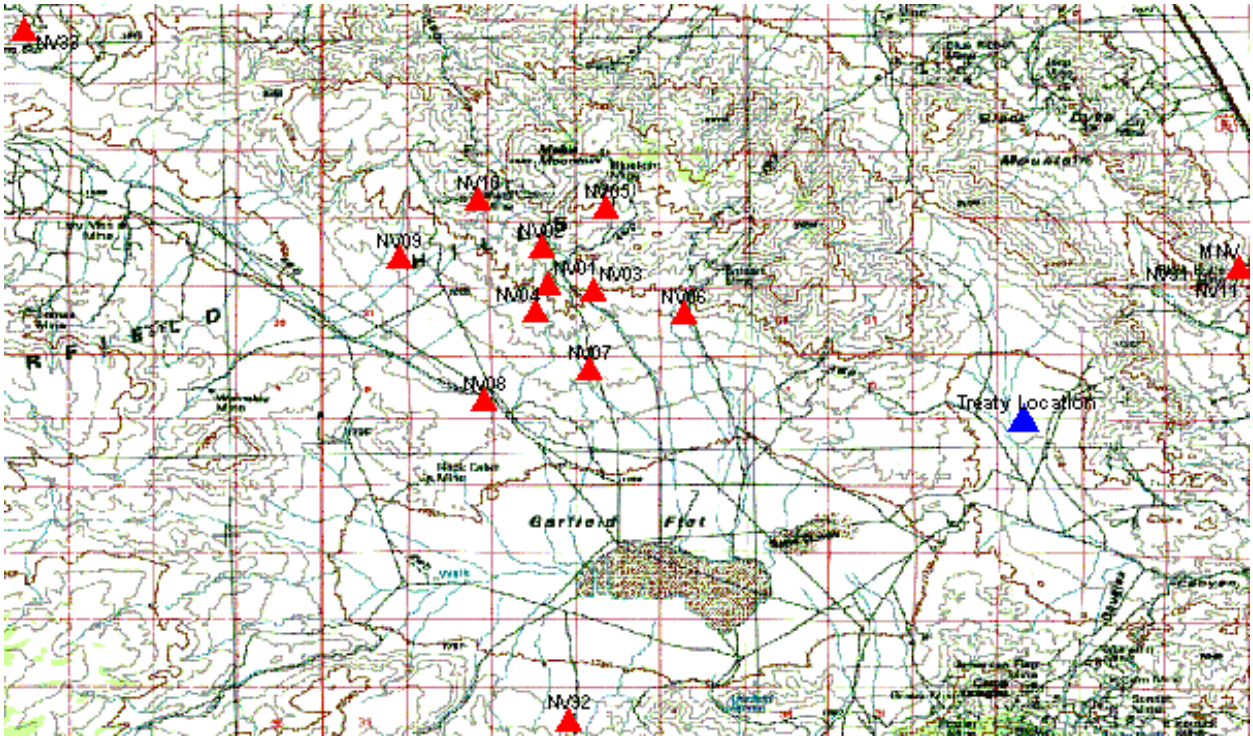


Figure 1. Map of the Nevada Array (NVAR) showing the inner 10 element short period array and the outer 3 element broadband array. The inner 10 element array is built upon the side of a mountain with elevation differences of almost 500 meters.

ARRAY CONFIGURATION

Figure 1 is a topographic map of the array NVAR. From the map we can see that NVAR includes two seismic subarrays, one with 10 and one with 3 elements. With a diameter of about 5 km and equipped with short period vertical instruments, the 10 element subarray is designed primarily for detection of regional and teleseismic P phases. The 3 element subarray lends itself to processing of surface waves with its three-component broad band instruments. It has a diameter of about 20 km and is symmetrically centered around the smaller 10 element array. An additional three component element (NV11) provides, by virtue of its co-location with the conventional 3 component station MNV, continuity with historic data.

Figure 2 shows the instrument displacement response curves for the short-period and broadband instruments installed in NVAR. The curves are normalized at 1 Hz frequency. The broadband KS54000M101 is flat to acceleration up about 5 Hz. The short period GS-13 instrument is flat to velocity above 1 Hz.

The beamforming detectors of NVAR were configured using a systematic approach previously developed at the PIDC (Wang et al., 1996). This approach takes into account array geometry, slowness and frequency distribution of seismic signals, and coherency properties between sensor sites. Figure 3 shows the positions of steered-beams in the slowness plane for signal detection.

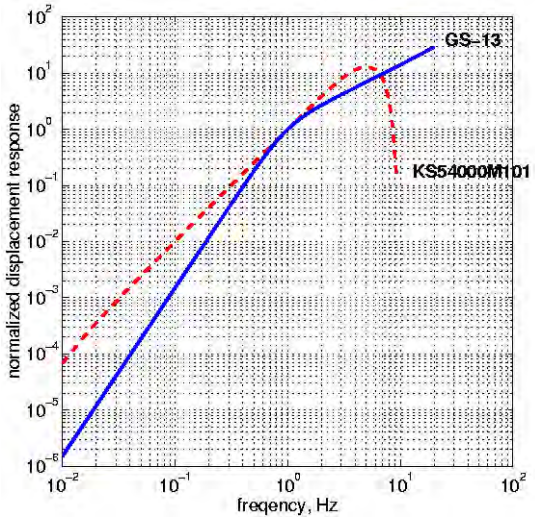


Figure 2: Instrument response at NVAR. The solid line shows the displacement response of the short-period seismometer GS-13. The dashed-line shows the displacement response of the broadband seismometer KS54000M101. The GS-13 anti-alias filter is not included.

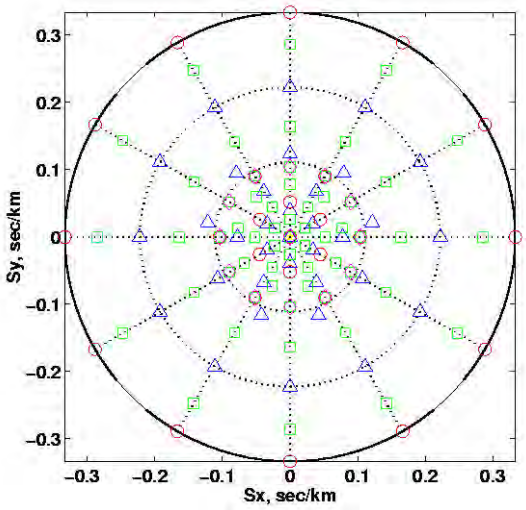


Figure 3: Detection beam deployment at NVAR in the slowness-azimuth plane. Different symbols represent the slowness positions in different frequency bands (circles: 0.75-2.25 Hz; triangles: 1.0 to 3.0 Hz; squares: 2.0-4.0 Hz; diamonds: 3.0-6.0 Hz; pentagrams: 4.0-8.0 Hz).

SIGNAL DETECTION AND ASSOCIATION

The IDC software performs STA/LTA detection on each individual beam. Each beam has a threshold to declare detections. Based on previous experience with other stations, the current initial thresholds at NVAR range from 3.5 to 5.5. These thresholds are tunable after a period of operation. Table 1 shows metrics for detection performance of NVAR for a period of three months (from February 19, 1999 to May 18, 1999). For comparison, the performances for the three-component station MNV, which is co-located with the sensor NV11, of three months (from December 19, 1998 to March 18, 1999) and for three similar arrays, GERES, PDAR, and TXAR are also listed in Table 1. In the table, "# of detection/day" represents the average number of detections per day by the automatic system (Standard Event List 3, SEL3). It should be mentioned that most of the automated detections were identified as 'noise' detections by the automated system. Those 'noise' detections would not be further processed by the automated system. The second row shows the average number of 'signal' detections (total detections excluding 'noise' detections) per day. The third row represents the average number of detection associated in the final Reviewed Event Bulletin (REB). The fourth row represents the number of phases, that were missed by the automatic system, and added during analyst review. The fifth row represents the number of detections, that were incorrectly associated by the automatic system, and removed by analysts. From the table we see that NVAR outperforms the 3C station MNV on each statistic, and has comparable detection performance to that of other similar arrays.

Table 1. Detection performance of NVAR and comparison with other stations

Metric	MNV	NVAR	GERES	PDAR	TXAR
# of detection/day	342.2	281.4	368.9	269.1	285.4
# of signal/day	218.6	64.7	235.1	194.9	135.5
# of associated in REB/ day	6.5	16.9	17.3	17.5	15.7
# of added/day	0.9	3.2	2.1	3.1	4.2
# of dis-associated/day	11.4	9.0	22.4	26.8	18.5

Table 2 compares initial phase identification and event association for NVAR, MNV, GERES, PDAR, and TXAR. The first row represents the performance of initial phase identification. The automatic system at the PIDC uses rules for arrays and default neural networks for 3-C stations to classify initial phase types. From the table we can see that NVAR outperforms the 3-C station MNV for initial phase identifications but performs less well than the other three arrays. We believe this is because of bias in slowness estimation at NVAR, which is discussed in the next section. For event formation and detection, NVAR detected 83.5% and 40.0% of regional events and teleseismic events, respectively, while MNV detected only 62% and 19% of regional events and teleseismic events, respectively. Detection at three or more primary station are required for an event to appear in the REB. The last row of Table 2, 'contribution to 3- station-events', compares the contribution to such three-station events for NVAR and the other stations. Without detections at NVAR, 9 of the 387 events during the three month period would not have appeared in the REB, whereas no event was critically dependent on detection at MNV.

Table 2. Association performance of NVAR and comparison with other stations

Metric	MNV	NVAR	GERES	PDAR	TXAR
% of unchanged initial phase type	72.7	78.3	92.9	97.2	97.2
% of regional events detected	62.0	81.0	68.0	72.0	76.0
% of teleseismic events detected	19.0	44.0	37.0	50.0	55.0
contribution to 3-stations events (associated/total)	0/433	9/387	10/387	14/387	25/387

SLOWNESS AND AZIMUTH ESTIMATION

Seismic arrays usually have better slowness and azimuth estimation than 3-C stations. However, NVAR has a larger systematic bias than MNV, with a median slowness residual of 3.0 sec/degree as shown in Table 3.. It also has larger slowness bias than the other similar arrays. Figure 4 shows the slowness-azimuth error vector map in the slowness-azimuth plane for all NVAR associated phases. To limit the effect of small signal-to-noise ratio (SNR) on the analysis, Figure 5 shows slowness-azimuth error vectors for NVAR associated phases with SNR>=8. From this figure we can see that there are two major trends for the error vectors. One is southeast and another is southwest. These biases are clearly not caused by low SNR. The IDC software can remove slowness bias by applying Slowness-Azimuth Station Corrections (SASC). They are usually derived from observed slowness and azimuth residuals (Bondár, 1998). As a new station, NVAR has no SASC available at this time. Table 3 demonstrates the SASCs have reduced estimation biases at MNV and other three similar arrays.

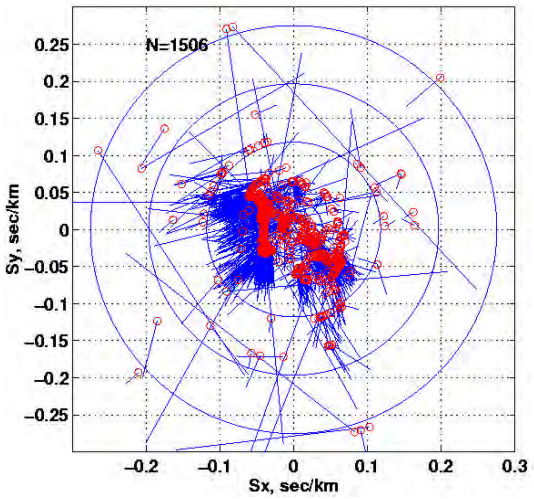


Figure 4. Slowness-Azimuth error vector map in the slowness-azimuth plane for all NVAR associated phases in REB. Circles represent predicted values and tails represent observed values.

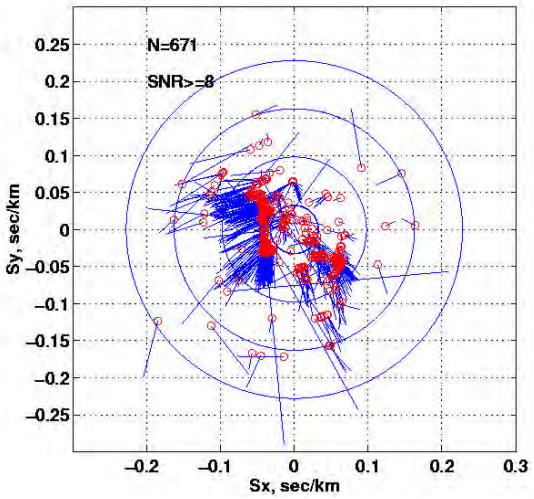


Figure 5. Slowness-Azimuth error vector map in the slowness-azimuth plane for NVAR associated phases in REB with SNR>=8. These vectors show two trends of biases. One in southeast and the other is southwest.

Table 3. Slowness-Azimuth estimation of NVAR and comparison with other stations

	MNV	NVAR	GERES	PDAR	TXAR
Median of slores, sec/deg	-1.29	3.00	-0.24	-1.10	-0.29
Std of slores, sec/deg	2.83	2.48	1.26	2.05	2.11
Median of slores with SASC, sec/deg	-0.51	N/A	-0.11	-0.54	-0.18
Std of slores with SASC, sec/deg	3.04	N/A	1.23	1.47	1.08
Median of azires, deg	3.3	-2.8	2.3	-9.0	-12.8
Std of azires, deg	35.0	21.8	14.5	28.1	26.6
Median of azires with SASC, deg	3.3	N/A	1.7	-0.6	-0.6
Std of azires with SASC, deg	34.4	N/A	14.5	15.5	9.6

ELEVATION EFFECTS AND CORRECTIONS

The current beamforming and f-k analysis algorithms at the PIDC assume that all elements of an array are located in the same horizontal plane so that time delays among all sensors are determined by their horizontal locations. There are no elevation corrections made to the beams. For most IMS arrays, the algorithm works fine because of small elevation differences. However, the relatively large range in elevation at NVAR (about 500 meter difference over 5000 meters aperture) has significant effects on signal propagation and processing.

Assuming all elements are in the same plane, the time delay of the signal at the *i*-th sensor with respect to a reference sensor will be:

$$\tau'_i = (x_i * s_x + y_i * s_y), \qquad (1)$$

where (x_i, y_i) are the 2-D spatial coordinates of the i-th sensor with respect to the reference sensor, and (s_x, s_y) are slowness components in x, y directions, respectively. However, the actual time delay because of elevation differences is:

$$\tau_i = x_i * s_x + y_i * s_y + z_i * s_z , \qquad (2)$$

where z_i is the elevation difference with respect to a reference sensor, and s_z is the vertical slowness component which is constrained by phase velocity, V, of the propagating signal:

$$V^{-1} = \mathrm{sqrt}(s_x^2 + s_y^2 + s_z^2) \qquad (3)$$

Figure 6 shows the array response, or so-called beam-pattern, of NVAR for a vertically incoming signal (s_x = 0 and s_y = 0) at frequency 1 Hz, taking into account elevation differences and assuming V = 4.0 km/sec. The contours are normalized with respect to the maximum at 0.1 intervals. If the array is in a perfect horizontal plane, the peak of the response will be located at the center. From figure 6 we can see that the peak of the elevation effect beam pattern is shifted to the south direction. It also can be noticed from Figure 6 there are two local maxima. One local maximum is greater than 0.7 of amplitude of the main peak. The system may pick the second maximum as the slowness position of incoming signals, which is shifted to the southwest. It should be mentioned that the beam-pattern shown in Figure 6 was computed for all 11 'sz' sensors in NVAR. Figure 1 shows NV11 is far from the other 10 'sz' sensors and it should not be included in the signal processing (beamforming and f-k analysis) because of lacking signal coherence with the other 10 'sz' sensors. Beamforming can be computed with any sensor group and the current initial beamforming group consists of the 10 closely spaced sensors. For F-k analysis, however, the automatic system only can group sensors by their instrument type, that is to say, all 11 'sz' channels in NVAR are used for f-k analysis. This beam-pattern explains the two bias trends in figures 4 and 5. Figure 7 shows the elevation effected beam-pattern of NVAR with only 10 closely spaced sensors. It shows that the local maxima have disappeared but it is still biased by 0.035 sec/km (or 3.9 sec/deg) to the south.

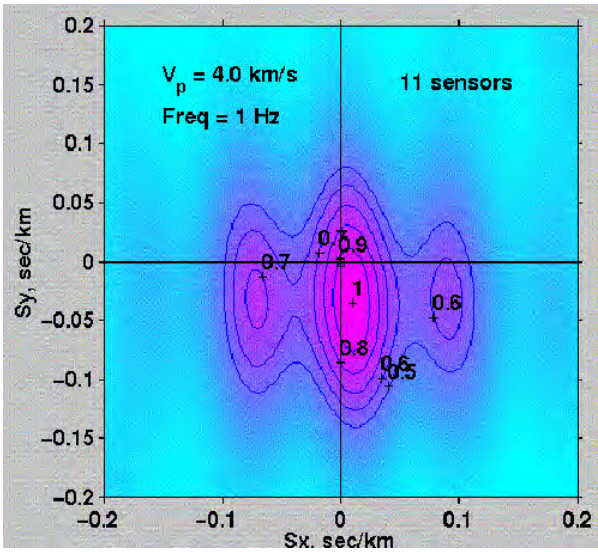


Figure 6. Beam pattern of NVAR with all 11 short-period sensors. It shows the main peak is shifted toward south direction because of elevation differences. It also shows there is one local maximum which is greater than 0.7 in the southwest direction.

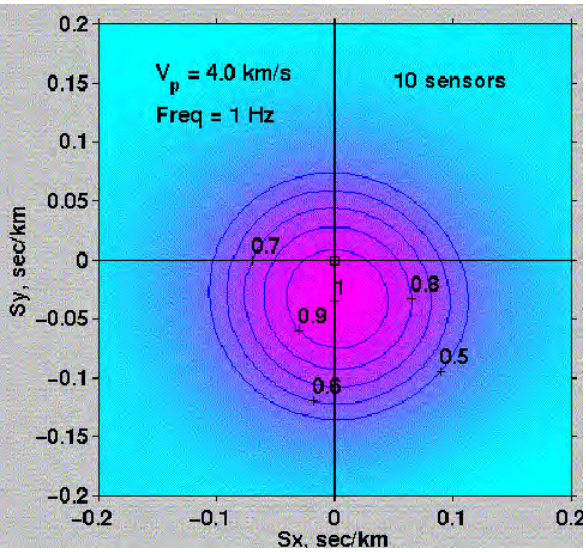


Figure 7. Beam pattern of NVAR with 10 short-period sensors which are closely located. It shows the main peak is shifted toward the south direction and the contours become simple concentric circles.

We can estimate slowness and azimuth residues introduced by ignoring the elevation differences at NVAR. In the current f-k algorithm, the peak in the f-k spectrum indicates the best matched time delays which are used to derive the slowness and azimuth of a signal across the array. By assuming signal phase velocity Vp, the relation between the true slowness vector and observed vector is given by:

$$\begin{matrix} x_1 & y_1 & z_1 \\ x_{i=2,3} & y_{i=2,3,\ldots} & z_{i=2,3,\ldots} \\ x_N & y_N & z_N \end{matrix} \begin{matrix} \\ \left\langle \right. \\ \\ \end{matrix} \begin{matrix} s_x \\ s_y \\ s_z \end{matrix} = \begin{matrix} x_1 & y_1 \\ x_{i=2,3} & y_{i=2,3,\ldots} \\ x_N & y_N \end{matrix} \begin{matrix} \\ \left\langle \right. \\ \\ \end{matrix} \begin{matrix} s_x' \\ s_y' \end{matrix}$$

(4)

where N is the number of sensors, (s_x, s_y) are true slowness and (s_x', s_y') are observed slowness when ignoring elevation effect. Figure 8 shows the predicated slowness-azimuth residue vectors induced by elevation effects at NVAR. The circles represent the true incoming slowness-azimuth, the tails represent observed slowness-azimuth. The residues vary with incoming slowness and azimuth values in a systematic way.

Not only do the elevation differences yield distorted array response, but they also cause reduced array gain because of mismatched delays. The differences between τ_i and τ'_i are called mismatched delays. Mismatched delays reduce the signal-to-noise ratio at the beamforming output, thereby reducing the array gain. The array gain in the case of mismatched delays can be estimated if we assume the signal is a monochromatic plane wave (Johnson and Dudgeon, 1993). Figure 9 shows the array gains normalized by the gain at a perfect matched delay for a 10-sensor subarray of NVAR. It shows the theoretical array gain drops quickly for high frequency bands, and also drops with decreasing slowness. For 0.01 sec/km slowness, the effectiveness of the array at 2 Hz is reduced to 70% and 30% at 4 Hz by the elevation effects alone.

Given the large predicted effects of elevation on array gain we have experimented with elevation corrections for beamforming at NVAR on observed signals. In these experiments, time delays are determined by equation (2) assuming the predicated slowness and azimuth in REB are the true values and the phase velocity of signals underneath the NVAR is 4.0 km/sec. The preliminary results show no significant improvement of SNR for real data because of elevation corrections.

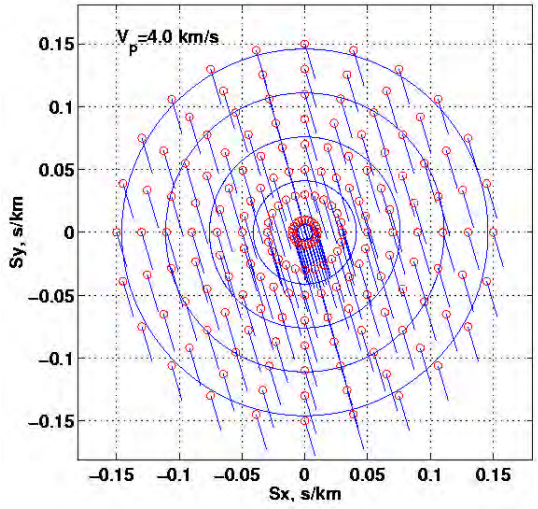


Figure 8. Predicted slowness-azimuth residue vectors induced by ignoring elevation differences at NVAR. Circles represents true values and tails represent observed values.

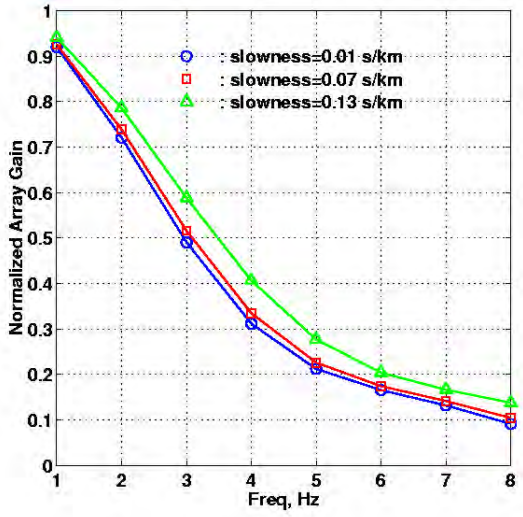


Figure 9. Normalized array gain relative to the ideal array gain at NVAR if elevation differences are ignored. A large reduction in SNR is predicted at frequencies above 2 Hz.

CONCLUSIONS

In this paper we assess the performance of NVAR during its initial few months of operation as part of the IMS using data forwarded to and processed real-time at PIDC. From the standpoint of detection and identification of phases and event location, the array NVAR shows superior performance to its predecessor, the 3-component station MNV. The performance at NVAR is quite comparable to that of similar arrays, like GERES, PDAR and TXAR arrays, which have been operating for some time and have benefited from tuning of their processing.

Preliminary analysis of the new seismic array NVAR suggests that distortion observed in the f-k analysis may be associated with elevation differences across the array. The PIDC processing scheme does, however, allow for removal of slowness biases by applying corrections to observed slowness through SASC's. Development of such corrections for NVAR is currently in progress, which together with evaluation of other aspects of the NVAR real- time processing will likely lead to fine-tuning of several processing configurations.

While predicted elevation effects on beam gain are significant, we have yet to demonstrate that elevation corrections would significantly improve beamforming gain with real data. The observed decay of beam gain with increasing frequency appears to be primarily controled by other factors than elevation.

ACKNOWLEDGEMENTS

We thank Paul Galjan, David Mason and Pierre Caron for their kind assistance.

REFERENCES

Bondár, I., Teleseismic slowness-azimuth station corrections (SASC) for the IMS network, CMR-PRO-98/01, 1998.

Johnson, D. H. and Dudgeon, D. E. (1993). Array signal processing, Prentice-Hall, Inc., Englewood Cliffs, New Jersey.

Wang, J, Israelsson, H. and Carter, J. (1996). A systematic approach to designing detectors for diverse seismic arrays, Seism., Res. Let. 60, No. 2, p60.

OUTLIER TESTING WHEN SOME DATA ARE MISSING

Wayne A. Woodward*, Stephan R. Sain*, H.L. Gray*, and Mark D. Fisk**

* Southern Methodist University
** Mission Research Corporation

Sponsored by Defense Threat Reduction Agency
Contract No. DTRA01-99-C-0018

ABSTRACT

We consider the problem of multivariate outlier testing for purposes of distinguishing seismic signals of underground nuclear events from training samples based on non-nuclear seismic events when some of the data are missing. We first consider the case in which the training data follow a multivariate normal distribution. Suppose that such a training set of n observations based on k features is available but that some of the observations are missing. The approach currently used in practice is to perform the outlier testing using a generalized likelihood ratio test procedure based only on the data vectors with full data. Critical values for this test are usually obtained using Hotelling's T^2 distribution. When large amounts of data are missing, use of this strategy may lead to loss of valuable information. An alternative procedure is to incorporate all n of the data vectors using the EM algorithm to appropriately handle the missing data. In this case, the Hotelling's T^2 procedure no longer applies, and resampling methods are used to find appropriate critical regions. We use simulation results and analysis related to seismic data to compare these two strategies for dealing with missing data.

In some cases it may be best to model the non-nuclear events in the region using a mixture-of-normals model (e.g. when the events come from a variety of sources or the data are substantially non-normal). We describe an EM-algorithm based procedure for using the modified likelihood ratio test to test for outliers when the training data follow a mixture distribution and when some of the observations are missing. In this setting, we again use simulations and analysis of seismic data to compare the use of the EM algorithm on the entire data set with the use of only the complete data vectors. We also consider a new alternative to the likelihood ratio test that provides a useful reduction in the computational complexity.

Key Words: outlier testing, missing data, mixture model, EM algorithm

OBJECTIVE

The objective of this research is to develop and implement statistical methodology for outlier testing when some data are missing. In particular we examine the use of the EM algorithm in the case of missing observations and compare its use with that of only using those data vectors for which complete data are available.

RESEARCH ACCOMPLISHED

BACKGROUND

Several authors have considered the problem of outlier testing for purposes of distinguishing seismic signals of underground nuclear events from training samples based on non-nuclear seismic events such as earthquakes, mining explosions, etc. Fisk, Gray, and McCartor (1996) considered the problem of using a likelihood ratio test for detecting outliers from a multivariate normal (MVN) distribution fit to the training data. They applied the method to a variety of seismic data sets and demonstrated excellent results. Taylor and Hartse (1997) also successfully applied this procedure to seismic data from the WMQ station in western China. These papers, however, require complete or non-missing data. That is, if k features are selected for use on a training sample of n events, then these results assume that all $k \leftrightarrow n$ observations are available. When some of the features for some of the events are missing, then the question arises concerning the optimal method for analyzing the data in such a way as to make the best use of the available data. One common technique for dealing with this issue is to use only those events in the training sample for which all k features were observed. It should be noted that such a procedure can result in a substantial loss of data and associated information. For example, consider the case in which 25% of the data are missing at random from a training sample of size $n = 50$ events. If, for example, we want to use four features, then the expected number of events for which all four features are observed is 16. Intuitively, however, it seems that we should not "throw away" the partial data on the other 34 events. In this research we compare the use of the "complete vector" approach which uses only these 16 vectors of complete data with the use of the Expectation-Maximization (EM) algorithm (see Dempster, Laird, and Rubin, 1977) which attempts to make optimal use of all data observed. These analysis strategies are compared via detection probabilities. Another problem can occur if there are no cases or only a very few cases in which all k of the features are observed. If the "complete-vector" strategy is used, then some key features may need to be removed before analysis can be done.

In some cases it may be best to model the non-nuclear events in the region using a mixture-of-normals model (e.g. when the events come from a variety of sources or the data are substantially non-normal). In this case, the training data can be considered to be a sample of size n from a mixture distribution whose density is given by

$$f(\mathbf{x}) = \sum_{i=1}^{m} p_i g_i(\mathbf{x}; \boldsymbol{\mu}_i, \boldsymbol{\Sigma}_i) \qquad (1)$$

where m is the number of components in the mixture, $g_i(\mathbf{x}; \boldsymbol{\mu}_i, \boldsymbol{\Sigma}_i)$ is the MVN density associated with the ith component, the p_i, $i = 1, \ldots, m$ are the mixing proportions, and $\mathbf{x}$ is a d-dimensional vector of feature variables. Wang, Woodward, Gray, Wiechecki, and Sain (1997) developed a modified likelihood ratio test that is applicable to the mixture and non-mixture settings and, in essence, requires no distributional assumptions concerning the outlier distribution. These authors demonstrated via simulations that the modified likelihood ratio test can be used successfully for outlier detection when m is known and at least some of the training data are labeled. Sain, Gray, Woodward, and Fisk (1999) extend these results to the case in which no data are labeled and in which the number of components in the mixture is unknown. They demonstrated their results using simulations similar to those of Wang, et al. (1997) and showed little or no loss of power when no training data are unlabeled. Sain, et al. (1999) obtained excellent results using their procedure on actual seismic data from the Vogtland region near the Czech-German border and from the WMQ station in western China. Using the China data, the authors demonstrated that a mixture model may be preferable to the use of a single multivariate model even when there are not any identifiable groups of event types represented in the training data.

However, the mixture-model results described above also make the assumption that there is no missing data (except for missing labels.) That is, the assumption is made that all k features are observed on all of the n events in the training sample. Again, because of the fact that it is very common for the seismic data

collected for events in a training sample to contain some missing data, it is important in this setting to also consider the issue of optimal handling of missing feature data. For further discussion of outlier testing in the presence of missing data see Miller, Gray, and Woodward (1993), Miller, Woodward, Gray, Fisk, and McCartor (1994), and Woodward, Sain, Gray, and Fisk (1999).

MODIFIED LIKELIHOOD RATIO TEST

The training sample is denoted by

$$\boldsymbol{X}_1, \ldots, \boldsymbol{X}_n \sim \Pi,$$

and it is a sample of size n from the population (Π) of non-nuclear events in the region of interest. A new observation, $\boldsymbol{X}_{n+1}$, is obtained, and given the training sample we wish to test the hypotheses

$$H_0: \boldsymbol{X}_{n+1} \sim \Pi$$
$$H_1: \boldsymbol{X}_{n+1} \not\sim \Pi.$$

The classical likelihood ratio test statistic is the ratio of the maximized likelihood functions under H_0 and H_1. We let $L_0(\theta) = \prod_{s=1}^{n} f(\mathbf{X}_s;\theta) f(\mathbf{X}_{n+1};\theta)$ denote the likelihood function under H_0 (i.e. under the assumption that $\boldsymbol{X}_{n+1} \sim H_0$) where θ is an unknown vector-valued parameter associated with the distribution of $\boldsymbol{X}$ under H_0. We also let $\tilde{L}_1(\theta) = \prod_{s=1}^{n} f(\mathbf{X}_s;\theta)$ denote the likelihood based only on the training sample $\boldsymbol{X}_1, \ldots, \boldsymbol{X}_n$ from the mixture. Wang, et al. (1997) and Sain, et al. (1999) used the modified likelihood-ratio test statistic

$$W = \frac{\sup_{\theta \sim \Theta} L_0(\theta)}{\sup_{\theta \sim \Theta} \tilde{L}_1(\theta)}. \qquad (2)$$

The usual likelihood ratio would have involved another factor in the denominator consisting of the likelihood function associated with the outlier population. However, we use the form in (2) because of the fact that little is known about the outlier population from which we have only one observation, $\boldsymbol{X}_{n+1}$. It is easily seen in (2) that if $\boldsymbol{X}_{n+1}$ does not belong to Π, this will tend to make W smaller. Hence the rejection region is of the form $W \leq W_\alpha$ for some W_α picked to provide a level α test. The null distribution of W has no known closed form in the case of a training sample from a multivariate normal or a mixture of normals, so we use a bootstrap procedure (see Efron and Tibshirani, 1993) to approximate it. The algorithm is given in Sain, et al. (1999).

A SIMPLIFIED TEST

As part of our research effort, we have considered an alternative approach, which is less computational than the modified likelihood ratio testing procedure and is asymptotically equivalent to it (see Wang, et al., 1997). Specifically, in the new approach we fit a density (mixture or non-mixture depending on the situation) to the training data and estimate the parameters (using the EM algorithm if some data are missing). We denote the estimated density as $\hat{f}$. We then simply evaluate this estimated density at the potential outlier point, i.e. we find $\hat{f}(\mathbf{X}_{n+1})$. Obviously, the smaller the value of $\hat{f}(\mathbf{X}_{n+1})$, the more "outlier-like" the new event is. In order to find the distribution of the density function under the null hypothesis $H_0: \mathbf{X}_{n+1} \sim \Pi$, we use a bootstrap procedure analogous to that used for W. This procedure is much faster and avoids the necessity of calculating the likelihood function in the numerator of (2).

THE EM ALGORITHM

The EM algorithm is a very general procedure for obtaining maximum likelihood estimates when some data are missing, and it is applicable to the mixture-of-normals case considered here. Actually, the EM algorithm may be thought of as a formal procedure for performing the following intuitively appealing approach to dealing with missing data: (a) estimate missing values using the current parameter estimates, (b) revise parameter estimates using the available data and the estimates of the missing values, and (c) iterate on (a) and (b) until convergence of parameter estimates is obtained.

The EM algorithm is directly tied to maximizing the likelihood function. As such, it is often not necessary to actually estimate missing data values but rather is only necessary to estimate the sufficient statistics (based on missing and available data) that are needed in the evaluation of the likelihood function. The EM algorithm thus has two steps: (1) the *expectation step (E-step)* in which the conditional expectation of the sufficient statistics given available data and the current estimates of the parameters are calculated, and (2) the *maximization step (M-step)* in which the log-likelihood function (based on sufficient statistics calculated in Step 1) is maximized to give revised parameter estimates. For more details concerning the use of the EM algorithm in these settings, see Miller, et al. (1993, 1994), and Woodward, et al. (1999).

SIMILATION RESULTS

Consider the situation in which the event in question is measured at three feature variables which we want to simultaneously use in the outlier testing. The question is whether it is preferable to do the outlier testing: (i) using only those data vectors in the training set for which all three features were observed, or (ii) using all data vectors for which at least one of the three feature variables was observed.

Consider the case in which a training sample of size $n = 40$ is obtained from the multivariate normal population with mean μ and covariance Σ. Further suppose that the new event comes from a population that is multivariate normal with mean μ_0 covariance Σ_0. In Table 1 we show results for two separate scenarios. In the table we show the empirical powers based on 1000 replications. We show results using the modified likelihood ratio test and the simplified test based on $\hat{f}$. The first column of each table corresponds to the case in which only complete data vectors are retained and the second column corresponds to the case in which the EM algorithm is used on the complete data set consisting of all observations for which at least one of the three features is available. The rows in the table correspond to the missing data scenarios in which the probability, p_m, of a missing feature takes on the values 0 (i.e. there is no missing data), .38, and .5. In the simulations each data item has a p_m probability of being declared missing. However, if all three features are declared missing then the procedure is repeated until at least one of the observations is declared non-missing. Using this procedure, the expected number of complete vectors out of the 40 observations in the data set is 10 and 6 for p_m equal to .38 and .5 respectively. For the first column in Table 1, training samples of size indicated in parentheses (i.e. 40, 10, or 6) are generated with no missing data. This corresponds roughly to the situation in which the analysis is run only on the vector observations with complete data. The second column in the table corresponds to the case in which all observations, some of which may contain missing features, are analyzed using the EM algorithm. The numbers given in the body of the table are empirical detection probabilities, i.e. they are the proportion of the 1000 replications for which the outlier was detected. The EM entry in the second column of the first row is not given since there is no missing data, and obviously, in this case the EM algorithm requires no iteration and would produce the results given in the first column of this row. Additionally, in parentheses below the detection probabilities are given estimated false alarm rates. That is, in this case we generated the "outlier" from the population of the training data, i.e. MVN(μ, Σ), and we are interested in the proportion of times for which the test (incorrectly) detected an outlier. The test in the simulations is designed to have a false alarm rate of .05, so the empirical false alarm rates provide information concerning whether the actual false alarm rate is near .05. The standard error for detection probabilities shown in this report is .016 while the standard error for the false alarm rates is .007.

From the left-hand column of the table it can be seen that, as would be expected, the presence of missing data has reduced the detection probability both for the modified likelihood ratio test and the test based on $\hat{f}(\mathbf{x}_{n+1})$. Also, in the eight cases shown in the table for which a direct comparison can be made between

the use of the EM algorithm and the use of only the complete vectors, the detection probabilities using the EM-algorithm are always higher, and for p_m =.5 the improvement is substantial. It can also be seen that the detection probabilities for the modified likelihood ratio test and the test based on $\hat{f}(\mathbf{x}_{n+1})$ are similar. It should also be noted that the false alarm rate for both tests have a tendency to be elevated, especially for the case of smaller sample sizes. This phenomenon has been previously observed by Wang, et al. (1997) and Sain, et al. (1999).

OUTLIER TESTING BASED ON WMQ DATA

We next consider the application of these outlier tests in settings dictated by actual seismic data. In particular we consider simulations based on data from the WMQ station in western China (see Hartse, et al., 1997). This distance corrected data consists of n = 134 events which are primarily earthquakes. Data is also available on a few nuclear events observed at WMQ. Our analysis will be based on the three features corresponding to log(Pg/Lg) ratios in the frequency bands 0.5-1, 1.5-3, and 4-8 Hz. There is no missing data on these three features in the data set that was analyzed. Using the three features, a multivariate normal fit to earthquake training data has mean $\mu_{EQ} = (-.024,.016,.015)'$, where the features are in the order 0.5-1, 1.5-3, and 4-8 Hz respectively, and covariance

$$\Sigma_{EQ} = \begin{pmatrix} .0468 & .0268 & .0134 \\ .0268 & .0319 & .0170 \\ .0134 & .0170 & .0188 \end{pmatrix}.$$

Additionally, the multivariate normal fit to the nuclear explosions has mean $(.035,.557,.679)'$ and covariance

$$\Sigma_0 = \begin{pmatrix} .068 & -.004 & .033 \\ -.004 & .017 & .003 \\ .033 & .003 & .019 \end{pmatrix}.$$

The explosion population is so far removed from the training data that detection is essentially assured using any reasonable approach. We follow the approach of Sain, et al. (1999) and Woodward, et al. (1999) and artificially move the outlier population closer to the training data. Specifically, in the simulations given here we consider the outlier population to be multivariate normal with mean $\mu_0 = (.015,.337,.358)'$ and with covariance Σ_0 given above.

In Table 2 we report the results of a simulation study based on the multivariate normal distribution fit to the earthquake training data with the outlier population being the multivariate normal distribution with mean and covariance given by μ_0 and Σ_0 above. While there was no missing data in the original data set analyzed by Sain, et al. (1999), we are able to ascertain the effect of missing data in this situation by simulating training samples from the distribution fit to the earthquake data and randomly assigning some of the observations to be missing. In Table 2 we give the empirical detection probabilities based on 1000 replications with B = 199 in the bootstrap-based outlier test. We consider three training sample sizes, n = 50, 100, and 150, and we again consider the cases in which p_m takes on the values 0, .38, and .5. We give separate tables for the modified likelihood ratio test and the simplified test based on $\hat{f}(\mathbf{x}_{n+1})$. In the table we see that in every case, the use of the EM algorithm improves the detection probability over the use of only the complete vectors. Not surprisingly, this improvement is more apparent when the percent missing is higher and when the original sample size is smaller. As in Table 1, it can be seen that the results using the test based on the modified likelihood ratio and those using the test based on $\hat{f}(\mathbf{x}_{n+1})$ are similar. Of particular interest is the fact that for n = 100 and n = 150, the use of the EM algorithm with p_m = .38 and p_m = .50 yields detection probabilities very similar to those given in the first row of the table for the case in which no data are missing. It can also be seen that the observed false alarm rates were somewhat elevated in some cases. Current investigation by these authors deals with understanding and properly adjusting for these somewhat elevated levels.

APPLICATION TO THE MIXTURE MODEL

We briefly consider the use of the EM algorithm in the mixture model for the case in which the training data are from the model in (1) with $m = 2,\ p_1 = p_2 = 05$ and in which $f_1(x)$ and $f_2(x)$ are multivariate normal densities with

$$\mu_1 = (-25,\ 0)',\ \ \Sigma_1 = \begin{matrix} 1 & -.75 \\ -.75 & 1 \end{matrix}$$

and

$$\mu_2 = (25,\ 0)',\ \ \Sigma_2 = \begin{matrix} 1 & .75 \\ .75 & 1 \end{matrix}.$$

Additionally, we assume that the outlier population is MVN(μ_0, I) where $\mu_0 = (0,2)'$ and *I* is the 2 *x* 2 identity matrix. We consider the cases p_m = 0, 1/3, and .50. In Table 3 we show the results of the outlier test for the case in which, as before, the results are based on 1000 repetitions. The results shown here are for the simplified test based on $\hat{f}(\mathbf{x}_{n+1})$. In the simulations, we let AIC select the number of components with the restriction that $m = 1$ or 2. (See Sain, et al., 1999).

In the table it can be seen that for the p_m = .33 case, the use of the EM algorithm resulted in a marginal decrease in detection probability whereas in the case of p_m = 0.5 there was a marked improvement using the EM algorithm. Other simulations (not shown here) also show that observed false alarm rates may be high, especially in the cases of smaller number of available data values. Our experience has shown that much care must be exercised in applying the EM algorithm in this setting. It is a computationally difficult problem to require estimation of the number of components and parameters of each component in the case in which a fairly substantial amount of data are missing. Further investigation in this area is needed.

CONCLUSIONS AND RECOMMENDATIONS

Our results indicate that when the training data can be reasonably modeled as a multivariate normal, then the use of all available data using the EM algorithm provides improved detection probability over that obtained using only those data vectors for which we have complete data. Our results also show that the use of the simplified outlier test based on $\hat{f}(\mathbf{x}_{n+1})$ should be considered since it is computationally faster and gives detection probability results similar to those obtained using the test based on the modified likelihood ratio. Initial results indicate that the use of the EM algorithm may be plausible when the training data can be modeled as a mixture of normals, but further work is required in this area. When the training data cannot be reasonable well fit using a multivariate normal, possible modifications include using a mixture approach in which it is assumed that the covariance matrices are equal or possibly using some sort of nonparametric kernel density estimator.

REFERENCES

Dempster, A.P., Laird, N.M., and Rubin, D.B. (1977). Maximum Likelihood Estimation from Incomplete Data via the EM Algorithm (with discussion), *Journal of the Royal Statistical Society* B39, 1-38.

Efron, B. and Tibshirani, R.J. (1993). *An Introduction to the Bootstrap*. New York: Chapman and Hall.

Fisk, M.D., Gray, H.L., and McCartor, G. (1996). Regional Event Discrimination without Transporting Thresholds, *Bulletin of the Seismological Society of America*, 86, 1545-1558.

Hartse, H.E., Taylor, S.R., Phillips, W.S., and Randall, G.E. (1997). A Preliminary Study of Regional Seismic Discrimination in Central Asia with Emphasis on Western China, *Bulletin of the Seismological Society of America* 87, 551-568.

Little, R.J.A. and Rubin, D.B. (1987). *Statistical Analysis with Missing Data*, New York: John Wiley and Sons, Inc.

Miller, J.W., Gray, H.L., and Woodward, W.A. (1993). Discriminant Analysis and Outlier Testing when Data are Missing, Phillips Laboratory Technical Report, ARPA F29601-91-K-DB25.

Miller, J.W., Woodward W.A., Gray, H.L., Fisk, M.A., and McCartor, G.D. (1994). A Hypothesis-Testing Approach to Discriminant Analysis with Mixed Categorical and Continuous Variables when Data are Missing," Technical Report No. SMU/DS/TR-273, Department of Statistical Science, Southern Methodist University.

Sain, S.R., Gray, H.L., Woodward, W.A., and Fisk, M.D. Outlier Detection when Training Data are Unlabeled, *Bulletin of the Seismological Society of America* 89, 294-304.

Taylor, S.R. and Hartse, H.E. (1997). An Evaluation of Generalized Likelihood Ratio Outlier Detection to Identification of Seismic Events in Western China, *Bulletin of the Seismological Society of America*, 87, 824-831.

Wang, S., Woodward, W.A., Gray, H.L., Wiechecki, S., and Sain, S.R. (1997). A New Test for Outlier Detection from a Multivariate Mixture Distribution, *Journal of Computational and Graphical Statistics*, 6, 285-299.

Woodward, W.A., Sain, S.R., Gray, H.L., and Fisk, M.D. (1999). Outlier Testing when Some Data are Missing, submitted to *Pure and Applied Geophysics*.

Table 1. Empirical Detection Probabilities for 2 Simulated Models

(a) Training sample of size $n = 40$ from MVN(μ,Σ) where $\mu = (0,\ 0,\ 0)'$ and $\Sigma = \begin{bmatrix} 1 & .2 & .2 \\ .2 & 1 & .2 \\ .2 & .2 & 1 \end{bmatrix}$

Outlier from MVN(μ_0, Σ) where $\mu_0 = (25,\ 25,\ 25)'$

	Modified Likelihood Ratio Test			Test based on $\hat{f}(X_{n+1})$	
p_m	Complete Vectors	EM		Complete Vectors	EM
0.50	.829 (40) (.046)	---		.836 (40) (.066)	---
0.38	.684 (10) (.073)	.790 (.060)		.622 (10) (.068)	.781 (.074)
0.50	.523 (6) (.096)	.790 (.069)		.332 (6) (.042)	.730 (.063)

(b) Training sample of size $n = 40$ from MVN(μ,Σ) where $\mu = (0,\ 0,\ 0)'$ and $\Sigma = \begin{bmatrix} 1 & -.7 & -.7 \\ -.7 & 1 & .7 \\ -.7 & .7 & 1 \end{bmatrix}$

Outlier from MVN(μ_0, Σ_0) where $\mu_0 = (1,\ 1,\ 1)'$ and $\Sigma_0 = \begin{bmatrix} 1 & 0 & 0 \\ 0 & 1 & 0 \\ 0 & 0 & 1 \end{bmatrix}$

	Modified Likelihood Ratio Test		Test based on $\hat{f}(X_{n+1})$	
p_m	Complete Vectors	EM	Complete Vectors	EM
0.00	.666 (40) (.058)	—	.672 (40) (.053)	—
0.38	.582 (10) (.059)	.605 (.059)	.516 (10) (.070)	.628 (.074)
0.50	.442 (6) (.093)	.613 (.083)	.311 (6) (.059)	.606 (.086)

Table 2. Empirical detection probabilities using the models fit to the WMQ data

Modified Likelihood Ratio Test

	$n = 50$		$n = 100$		$n = 150$	
p_m	Complete Vectors	EM	Complete Vectors	EM	Complete Vectors	EM
0.00	.950 (50) (.057)	---	.968 (100) (.049)	---	.955 (150) (.052)	---
0.38	.856 (13) (.079)	.934 (.088)	.915 (25) (.067)	.956 (.043)	.932 (38) (.057)	.962 (.056)
0.50	.675 (7) (.113)	.856 (.076)	.846 (14) (.078)	.945 (.061)	.894 (21) (.055)	.953 (.072)

Test Based on $\hat{f}(X_{n+1})$

	$n = 50$		$n = 100$		$n = 150$	
p_m	Complete Vectors	EM	Complete Vectors	EM	Complete Vectors	EM
0.00	.939 (50) (.059)	---	.959 (100) (.065)	---	.962 (150) (.041)	---
0.38	.813 (13) (.054)	.943 (.084)	.909 (25) (.044)	.947 (.060)	.922 (38) (.060)	.954 (.063)
0.50	.481 (7) (.068)	.906 (.093)	.824 (14) (.066)	.948 (.101)	.883 (21) (.063)	.971 (.071)

Table 3. Detection Results in the Mixture Case Described in the Text

p_m	Complete Vectors	EM
0.00	.922 (50) (.043)	---
0.33	.872 (20) (.053)	.792 (.049)
0.50	.576 (13) (.040)	.722 (.068)

Lg WAVE SIMULATIONS IN HETEROGENEOUS CRUSTS WITH IRREGULAR TOPOGRAPHY USING HALF-SPACE SCREEN PROPAGATORS

R.S. Wu, X.B. Xie and X.Y. Wu, Institute of Tectonics, University of California, Santa Cruz

Sponsored by U.S. Department of Defense
Defense Threat Reduction Agency
Contract No.: DSWA01-97-1-0004

ABSTRACT

This study is aimed at development and application of a new wave propagation and modeling method for regional waves in heterogeneous crustal waveguides using one-way wave approximation. The half-space GSP (generalized screen propagator) has taken the free surface into the formulation and adopts a fast dual-domain implementation. The method is several orders of magnitude faster than finite-difference methods with a similar accuracy for certain problems. It has been used for the simulation of wave propagation for high-frequency waves (1 - 20 Hz) to a regional distance (greater than 1000 km).

In this year we further developed the method in three aspects. First, we extend the GSP method to treat irregular surface topography by incorporating a coordinate transform into the method. Both conformal and non-conformal transformations have been introduced and their relative merits and accuracies have been discussed. Comparison with boundary element integration method showed that the extended method works well for mild topographies. Accuracy improvement for rough topography is still an ongoing research. Second, we developed a hybrid method which couples the fast screen propagator method with a modified boundary element method to treat the problems with severe rough topography. Finally, numerical simulations have been conducted for various crustal waveguide structures, including both deterministic structures and small-scale random heterogeneities and random rough surfaces. Influence of random heterogeneities and rough surfaces on Lg amplitude attenuation and Lg coda formation are shown to be significant. In collaboration with T. Lay, we have investigated the frequency- dependent Lg attenuation and blockage both observationally and numerically. The comparison between the observation and numerical simulations reveals many interesting phenomena and needs more thorough investigation.

Key Words: seismic wave propagation, crustal structure, discrimination

INTRODUCTION

Crustal guided wave Lg provides valuable information for nuclear test monitoring and yield estimation. Lg energy mainly propagates in the crustal wave guide and the uppermost mantle. The low velocity crust provides an ideal channel for Lg propagation. On the other hand, many crustal characteristics, both deterministic structures (e.g., crustal necking, thickening) and stochastic characteristics (e.g., random volume heterogeneities in the crust, random fluctuations at free surface and Moho discontinuity) affect the propagation of the Lg wave. To isolate path effects from the source parameters, a clear understanding of these mechanisms and how they affect the Lg attenuation is crucial. In these investigations, numerical methods for simulating Lg wave propagation based on realistic deterministic and/or stochastic models are often very useful.

The existing methods for calculating synthetic regional phases can be roughly categorized into three groups. (1). Wavenumber integration method (e.g., Bouchon 1981, Campillo 1990). This method originally handles only laterally homogeneous media and is incapable of handling complex 3D structures and heterogeneities. Later developments (e.g., Bouchen et al. 1989; Chen, 1990, 1995) extend the capability of the method to handle large-scale lateral variations, but volume heterogeneities are still excluded. (2). Normal mode approach (e.g. Wang and Hermann 1988). This method works well for layered media, and later development of coupled mode theory (Kennett, 1984) enables it to handle slightly lateral variations, but is limited in its validity for strong lateral variations. (3). Fully discretisized numerical methods, for example finite-difference method (Xie and Lay, 1994; Jih, 1996; Hestholm and Ruud, 1994, 1998) and boundary element method (e.g., Fu and Wu, 1999). In principle, finite-difference method can deal with arbitrarily heterogeneous media including both volume heterogeneities and rough free surfaces. The boundary element method can handle arbitrary free surfaces and interfaces but is not very powerful in dealing with volume heterogeneities. However, under realistic conditions, i.e., complex waveguide with volume heterogeneities and free-surface/interface fluctuations, high frequency and long propagation distances, the ability of all the above mentioned methods is very limited. Yet under over simplified velocity models, lower frequencies and shorter propagation ranges, many practical issues associated with the regional phase propagation can not be properly investigated.

In the crustal waveguide environment, major wave energy is carried by forward propagating waves, including forward scattered waves, therefore neglecting backscattered waves in the propagation will not change the main features of regional waves in most cases. Based on this concept, a generalized screen propagator method (GSP) based on the one-way wave equation has been developed by Wu (1994), Wu, Jin and Xie (1999a) and has been successfully used to simulate SH Lg waves in the complex crustal waveguide and investigate the energy partitioning of Lg waves (Wu, Jin and Xie, 1999b). This method neglects backscattered waves, but correctly handles all the forward multiple-scattering effects, e.g., focusing/defocusing, diffraction, interference, etc. The method is two to three orders of magnitude faster than the finite-difference method for medium sized problems.

In this paper we further extend the GSP method to treat irregular surface topography by incorporating coordinate transforms into the method. Both conformal and non-conformal transforms have been introduced and their relative merits and accuracies have been discussed. Comparison with other exact methods, such as the boundary element integration method, showed that the extended method works well for mild to moderate topographies. Numerical simulations have been conducted for various crustal waveguide structures, including both deterministic structures and random rough surfaces.

CONFORMAL COORDINATE TRANSFORM FOR GSP

General wide-angle formulation. For a 2D SH problem and under the perturbation theory, the frequency domain wave equation for the y-component of displacement field can be written as (Wu, et al. 1999a)

$$(\nabla^2 + k^2)u(r) = -k^2 F(r)u(r) \qquad (1)$$

where $k = \omega / v$ is the wavenumber in the background medium, v is the background S wave velocity defined

by $v = (\mu_0 / \rho_0)^{1/2}$, and μ_0 and ρ_0 are background values of μ and ρ. In the right hand side of (1), $F(\mathrm{r})$ is a perturbation operator

$$F(\mathrm{r}) = \varepsilon_\rho(\mathrm{r}) + \frac{1}{k^2}\nabla\cdot\varepsilon_\mu\nabla \tag{2}$$

with $\varepsilon_\rho(\mathrm{r}) = \delta\rho(\mathrm{r})/\rho_0$ and $\varepsilon_\mu(\mathrm{r}) = \delta\mu(\mathrm{r})/\mu_0$, where $\delta\rho(\mathrm{r})$ and $\delta\mu(\mathrm{r})$ are purterbations of ρ and μ. Equation (1) is a scalar Helmholtz equation. For flat free surfaces, Wu et al. (1999a) derived a half-space GSP solution for Lg wave propagation. In the case of irregular topography, the global mirror symmetry for the problem no longer

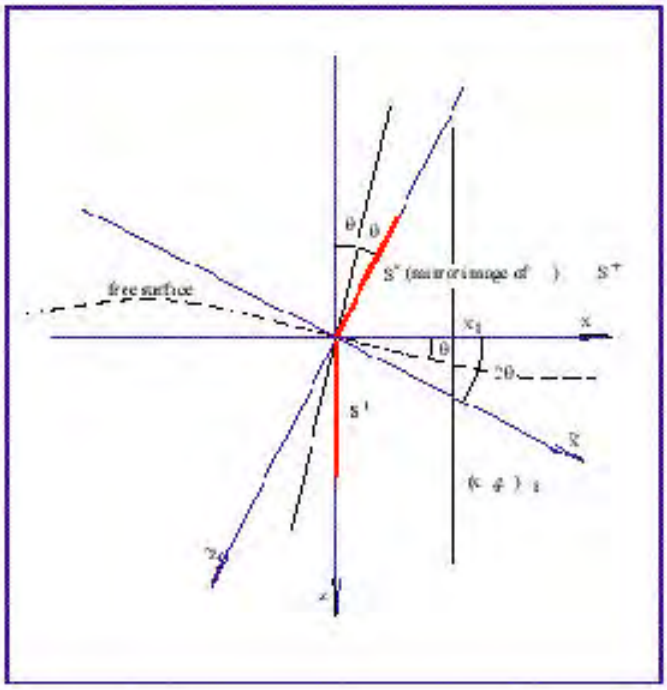


Figure 1: Geometry of the coordinate transform.

exists. However, if a first order approximation (local plane-surface approximation) for the topography is taken, we can modify the mirror image method to a local mirror image method and apply the corresponding coordinate transform to obtain a GSP solution for this case.

Fig. 1 shows the geometry of the derivation. Assume u_0^+ is the incident field on S^+, then u_0^- on S^- is also known as the mirror image of u_0^+ about the local plane surface. The total wavefield composed of S+ and S^- is the sum of the primary field which propagates in the homogeneous background medium and the scattered field which is generated by the local heterogeneities in the thin-slab. The effects of the heterogeneities and the topography can be calculated separately for each step in the GSP method. The effect of the slant free-surface can be incorporated into the propagation integral. Assume $u_t(x, z)$ is the total field including the scattering effect of the volume heterogeneities. The field $u(x_1, z_1)$ in front of the integral surface can be calculated by the Kirchhoff integral

$$\begin{aligned} u(x_1,z_1) &= \int_S ds \left\{ g(x, z; x_1, z_1)\frac{\partial u_t(x,z)}{\partial n} - \frac{\partial g(x,z;x_1,z_1)}{\partial n} u_t(x,z) \right\} \\ &= \int_{S^-} ds\{\ldots\} + \int_{S^+} ds\{\ldots\} \end{aligned} \tag{3}$$

where $g(.)$ is the Green's function for the full space with homogeneous velocity distribution, S is the integration surface and S^+ and S^- are the lower and upper half surfaces, respectively. The Rayleigh integral can be used to replace the Kirchhoff integral for each half surface integral. For the lower half-space the contribution of S^+ is

$$\begin{aligned} u_t^+(x_1,z_1) &= -2\int_0^\infty dz u_t^+(x,z)\frac{\partial g(x,\ z;\ x_1,\ z_1)}{\partial n} \\ &= \frac{1}{2\pi}\int dK_T e^{iK_T z_1} u_t^+(x_1,K_T) \end{aligned} \tag{4}$$

where

$$u_t^+(x_1,K_T) = e^{i\gamma(x_1-x)}\int_0^\infty dz_1 u_t^+(x,z)e^{-iK_T z_1} \tag{5}$$

Here $u_t^+(x, z)$ is the total field equal to the sum of incident field $u_0^+(x, z)$ and the scattered field $U^+(x, z)$ caused by the heterogeneities within the slab between x and x_1 (see Wu, 1994; Wu et al., 1999a). If we put the slab entrance at $x = x'$ and the field on the screen S^+ at the entrance as $u_t^+(x', z')$, then

$$u_t^+(x',z') = u_0^+(x',z') + U^+(x',z') \tag{6}$$

$$U^+(x',z') = k^2\int_{x'}^{x_1} dx e^{i\gamma(x_1-x')}\int_0^\infty dz \{g(x_1,z_1;x,z)\varepsilon_\rho(x,z)u_0(x,z) - \frac{1}{k_2}\nabla g(x_1,z_1;x,z)\cdot\varepsilon_\mu(x,z)\nabla u_0(x,z)\} \tag{7}$$

For the bent upper half screen, we perform a coordinate transform by clockwise rotation of 2θ to a new coordinate system $(\tilde{x}, \tilde{z})$. Taking the downward direction as positive z-direction, and the rotation angle from x to z as positive, the relation connecting the two systems is

$$\tilde{x} = x\cos 2\theta + z\sin 2\theta \tag{8}$$

$$\tilde{z} = -x\sin 2\theta + z\cos 2\theta \tag{9}$$

In the new system, the surface S^- is parallel to the i-axis, so that

$$u_t^-(\tilde{x}_1,K_T) = e^{i\gamma(\tilde{x}_1-\tilde{x}')}\int_{-\infty}^0 d\tilde{z}' u_t^-(\tilde{x}',\tilde{z}')e^{-iK_T\tilde{z}'} \tag{10}$$

where $u_t^-(\tilde{x}', -\tilde{z}') = u_t^+(x', z')$ The field in the space domain can be obtained by synthesizing the contributions from all the plane waves

$$u_t^-(\tilde{x}_1,\tilde{z}) = \int dK_T e^{i\gamma(\tilde{x}_1-\tilde{x}')}e^{iK_T\tilde{z}}u_t^-(\tilde{x}',K_T) \tag{11}$$

where

$$u_t^-(\tilde{x}',K_T) = \int_{-\infty}^0 d\tilde{z}' u_t^-(\tilde{x}',\tilde{z}')e^{-iK_T\tilde{z}'} \tag{12}$$

Transformed back to the original coordinate system, resulting in

$$u_i(x_1, z_1) = \int_{u_i(\tilde{x}', K_T)} dK_T \exp\left\{ i \left[(\tilde{\gamma}\cos 2\theta - K_T \sin 2\theta)(x_1 - x') + (\tilde{\gamma}\sin 2\theta + K_T \cos 2\theta) z_1 \right] \right\} \tag{13}$$

We can see that in the original coordinate system, the effective transversal and propagating wavenumbers are

$$\begin{cases} \gamma = \tilde{\gamma}\cos 2\theta - K_T \sin 2\theta \\ K_T = \tilde{\gamma}\sin 2\theta + K_T \cos 2\theta \end{cases} \tag{14}$$

If we transform the $(\tilde{k}_T, \tilde{\gamma})$ system into (K_T,γ),

$$u_i(x_1, z_1) = \int dK_T u_i(\tilde{x}', K_T \cos 2\theta - \gamma \sin 2\theta) e^{i(\gamma(x_1 - x') + z_1 K_T)} \tag{15}$$

The total field is a summation of the contributions from both $u^+(x_1, z_1)$ and $u_i^-(x_1, z_1)$

$$u(x_1, z_1) = \int dK_T e^{i(\gamma(x_1 - x') + z_1 K_T)} \left[u_i^+(x', K_T) + u_i^-(\tilde{x}', K_T \cos 2\theta - \gamma \sin 2\theta) \right] \tag{16}$$

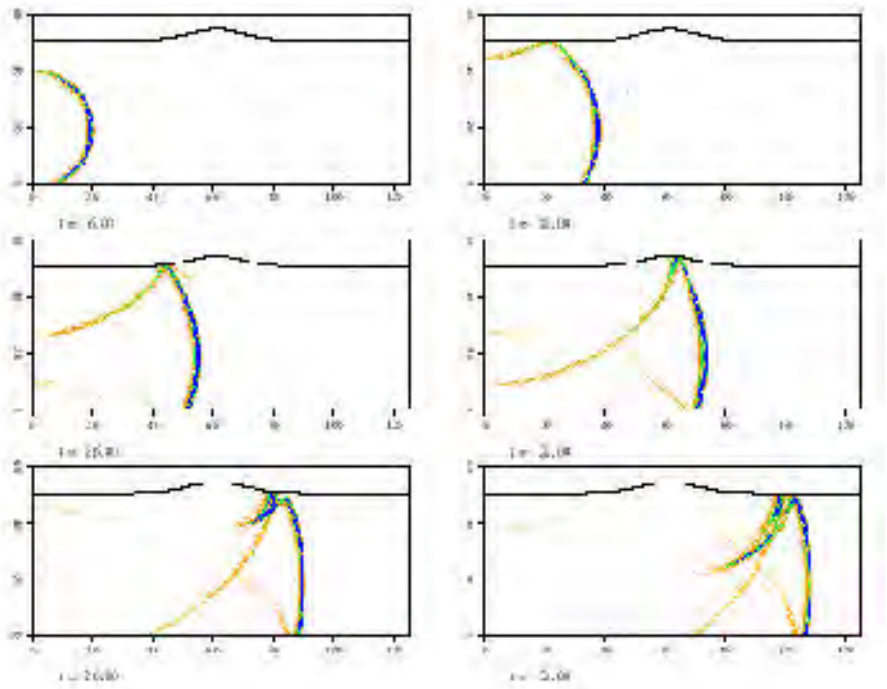


Figure 2: Snap shots of the wave field. the model is a homogeneous half-space with a Gaussian hill on the free surface.

The wavenumber integral can also be done by a FFT.

Narrow-angle approximation When small-angle waves prevail such as in the case of Lg propagation, the spectral interpolation in equation (16), which is tricky and even unstable in some cases, can be avoided and replaced by operations in the space domain using a narrow-angle wave approximation.

From (16), it can be seen that to calculate the reflection response we need to find the spectral components $u_t^+(-\tilde{K}_T)$. We will try to obtain the approximate space-domain operations corresponding to the wavenumber domain interpolation. We know

$$u_t^+(-\tilde{K}_T) = \int_0^\infty dz e^{i(-\tilde{K}_T \cos 2\theta + \gamma \sin 2\theta)z} u_t^+(z) \tag{17}$$

With narrow-angle approximation, $\gamma \approx k$ therefore,

$$u_t^+(-\tilde{K}_T) = \int_0^\infty dz' e^{ik_T z'} \left[\frac{1}{\cos 2\theta} e^{ik(\tan 2\theta)z'} u_t^+(z'/\cos 2\theta) \right] \tag{18}$$

We see that the corresponding operations for wavenumber-domain interpolation in the space-domain are a modulation plus a coordinate stretching.

NON-CONFORMAL COORDINATE TRANSFORM FOR GSP

A non-conformal coordinate transform and the correspondent inverse transform are

$$\begin{cases} x = x \\ \zeta = z - h(x) \end{cases} \quad and \quad \begin{cases} x = x \\ z = \zeta + h(x) \end{cases} \tag{19}$$

where *h(x)* is the height function of free surface topography. Denote the field and the medium parameters in the new coordinate system as $\hat{u}(x,\zeta)$, $\hat{\mu}(x,\zeta)$ and $\hat{\rho}(x,\zeta)$ respectively. Assuming that μ varies smoothly with *x*, the wave equation for SH wave in the new coordinate system can be obtained as

$$\left(\nabla^2 + k_0^2\right) \hat{u}(x,\zeta) = -k_0^2 \left\{ \hat{F}_m(x,\zeta) + \hat{F}_s(x,\zeta) \right\} \hat{u}(x,\zeta) \tag{20}$$

where
$k_0 = k_0(x,\zeta)$ and the operators $\nabla^2 = \partial^2/\partial x^2 - \partial^2/\partial \zeta^2$ is the Laplacian,

$$\hat{F}_m(x,\zeta) = \hat{\varepsilon}_\rho(x,\zeta) + \frac{1}{k_0^2} \nabla \cdot \hat{\varepsilon}_\mu \nabla \tag{21}$$

is the equivalent force term due to the medium heterogeneities, and

$$\hat{F}_s(x,\zeta) = -\frac{1}{k_0^2} \frac{\hat{\mu}}{\mu_0} \left[h''(x) \frac{\partial}{\partial \zeta} + 2h'(x) \frac{\partial^2}{\partial x \partial \zeta} - (h'(x))^2 \frac{\partial^2}{\partial \zeta^2} \right]$$

is equivalent force term due to the surface topography.

Using local Born approximation, the scattered field generated by the heterogeneities and topographic change of the thin-slab for each step can be written as

$$U(x_1, k_\zeta) = \frac{ik_0^2}{2\gamma} \int_{x'}^{x_1} dx \int_0^\infty d\zeta e^{i\gamma(x_1 - x)} 2\cos(k_\zeta \zeta) \left[\hat{F}_m(x,\zeta) + \hat{F}_s(x,\zeta) \right] \hat{u}_0(x,\zeta) \tag{22}$$

where $\hat{u}_0(x,\zeta)$ is the local incident filed at the slab entrance.

Scattering due to coordinate transformation. Assume that the medium in coordinate (*x, z*) is homogeneous, that is $\hat{F}_m(x,\zeta) = (F_m(x, z) = 0$. The scattered field under the new coordinate system (x, ζ) is only due to the coordinate transformation.

$$U(x_1, k_\zeta) = \frac{i}{2\gamma} \int_{x'}^{x_1} dx e^{i\gamma(x_1 - x)} C \left[2h'(x)A - (h'(x))^2 B + h''(x) D \right] \tag{23}$$

where

$$A = \frac{\partial^2 u_0(x,\zeta)}{\partial\zeta\partial x} = -\mathcal{S}^{-1}\left[k'_\zeta\gamma' e^{i\gamma'|x-x'|}\hat{u}_0(x',k'_\zeta)\right] \quad (24)$$

$$B = \frac{\partial^2 u_0(x,\zeta)}{\partial\zeta^2} = -\mathcal{C}^{-1}\left[k'^2_\zeta e^{i\gamma'|x-x'|}\hat{u}_0(x',k'_\zeta)\right] \quad (25)$$

$$D = \frac{\partial u_0(x,\zeta)}{\partial\zeta} = -\mathcal{S}^{-1}\left[k'_\zeta e^{i\gamma'(x-x')}\hat{u}_0(x',k'_\zeta)\right] \quad (26)$$

with C [.] and S [.] being the cosine and sine transforms, C^{-1}[.] and S^{-1}[.] as their inverse transforms, and

$$\begin{aligned} u_0(x,\zeta) &= \frac{1}{2\pi}\int_{-\infty}^{\infty} dk'_\zeta e^{ik'_\zeta\zeta} e^{i\gamma'(x-x')}\hat{u}_0(x',k'_\zeta) \\ &= \mathcal{C}^{-1}\left[e^{i\gamma'(x-x')}\hat{u}_0(x',k'_\zeta)\right] \end{aligned} \quad (27)$$

Narrow-angle approximation. Under the narrow-angle wave approximation, $k_\zeta \approx k'_\zeta \ll \gamma \approx \gamma' \approx k_0$. Also invoking a small slope (or smooth topography) approximation such that $h''(x) \ll 2h'(x)$ and $[h'(x)]^2 \ll 2h'(x)$, the last two terms in equation (23) can be neglected. We obtain

$$U(x_1,k_\zeta) = Z(x_1)e^{i\gamma\Delta x}\int_0^\infty d\zeta 2\cos(k_\zeta\zeta)\frac{\partial}{\partial\zeta}\hat{u}_0(x',\zeta) \quad (28)$$

where

$$Z(x_1) = \int_{x'}^{x_1} dx h'(x) \quad (29)$$

The total forescattering can be obtained by summing the background field and the scattered field

$$\begin{aligned} u(x_1,k_\zeta) &= e^{i\gamma\Delta x}\int_0^\infty d\zeta 2\cos(k_\zeta\zeta)\hat{u}_0(x',\zeta) \\ &- e^{i\gamma\Delta x}Z(x_1)\int_0^\infty d\zeta 2\cos(k_\zeta\zeta)\frac{\partial}{\partial\zeta}\hat{u}_0(x',\zeta) \\ &= e^{i\gamma\Delta x}\int_0^\infty d\zeta 2\cos(k_\zeta\zeta)e^{Z(x_1)\frac{\partial}{\partial z}}\hat{u}_0(x',\zeta) \end{aligned} \quad (30)$$

where Δx=x1-x1. In the last equation, the Rytov transformation is applied to make the operator unitary.

NUMERICAL EXAMPLES

To test the accuracy and ability of the phase screen method as a propagator for crustal wave guide with rough free surfaces, numerical simulations have been conducted for both conformal and non-conformal methods. The first model is a homogeneous half space with a Gaussian hill. The center of the hill is located at the epicenter distance of 62.5 km, the maximum height of the hill is 4 km and the standard deviation of the Gaussian function is 12.9 km. A SH-wave source is located in the depth of 32 km. The S-wave velocity is 3.5 km/s.

Shown in Fig. 2 are snap shots of the wavefield calculated by the conformal screen method. We can clearly see the incident wave and reflected wave from the free surface. After encountered the Gaussian hill on the surface, the incoming wave split into two arrivals on the ground surface. These interactions complicated the wavefield and provided a test for the new method. Shown in Figs. 3a and 3b are synthetic seismograms for the Gaussian hill model using both conformal and non-conformal methods, respectively. Synthetic seismograms calculated with a more accurate boundary integral method (Fu and Wu, 1999) are used as a reference. In both figures, the solid lines are from the screen method and the dashed lines are from boundary integral method. In Fig. 3a, the conformal screen method uses dx = 0.25 km, dz = 0.25 km and dt = 0.05 sec. The comparisons indicate that the screen method gives a satisfactory result for this model. It correctly modeled waveforms between distances 60 and 70 km, where two reflections from the convex free surface interfere with each other and generate complex waveforms. In Fig. 3b, the non-conformal screen

method uses dx = 0.125 km, dz = 0.25 km and dt = 0.05 sec. in the calculation. Generally speaking, the results are consistent with those from the boundary integral method except there are some minor precursors at distances between 50 and 70 km.

Our next model is for Lg wave propagation in a waveguide with a rough free surface. The model has an average crust thickness of 30 km. A random fluctuation is added to the free surface. The randomness has an exponential power spectrum. Its RMS fluctuation is 0.4 km; horizontal correlation length is 40 km and maximum elevation difference is 1.73 km. These parameters represent the topography of a typical mountain area. A SH-source is located in the depth of 10 km. The conformal transform method is used to calculate the Lg propagation. Parameters used in the calculation are dx = 0.25 km, dz = 0.25 km and dt = 0.05 sec. As a comparison, Fig. 4 gives the snap shots for a crustal wave guide without the surface fluctuation. The figure clearly shows the head wave and multiple reflections between the free surface and Moho discontinuity. All wave fronts are relatively sharp and clear. Fig. 5 gives the snap shots for a crust wave guide with the above mentioned surface fluctuation. With the surface fluctuations, the reflections are combined with randomly scattered waves. These scattered waves blurred the entire wavefield and make part of the energy deflected from its original direction cause the additional Lg attenuation.

CONCLUSION AND DISCUSSIONS

This paper is part of the study aimed at development and application of a new wave propagation and modeling method for regional waves in heterogeneous crustal wave guides using one-way wave approximation. In this paper, two forms of boundary conditions based on conformal and non-conformal coordinate transforms have been developed for taking care of irregular free surfaces for generalized screen propagator. The resulting algorithms can give satisfactory results for models with mild to moderate free surface fluctuations. The comparisons between the method developed here and the more accurate boundary integral method indicate that this method can be used to calculate synthetic seismograms of regional waves for more realistic velocity models, longer propagating distances and higher frequencies.

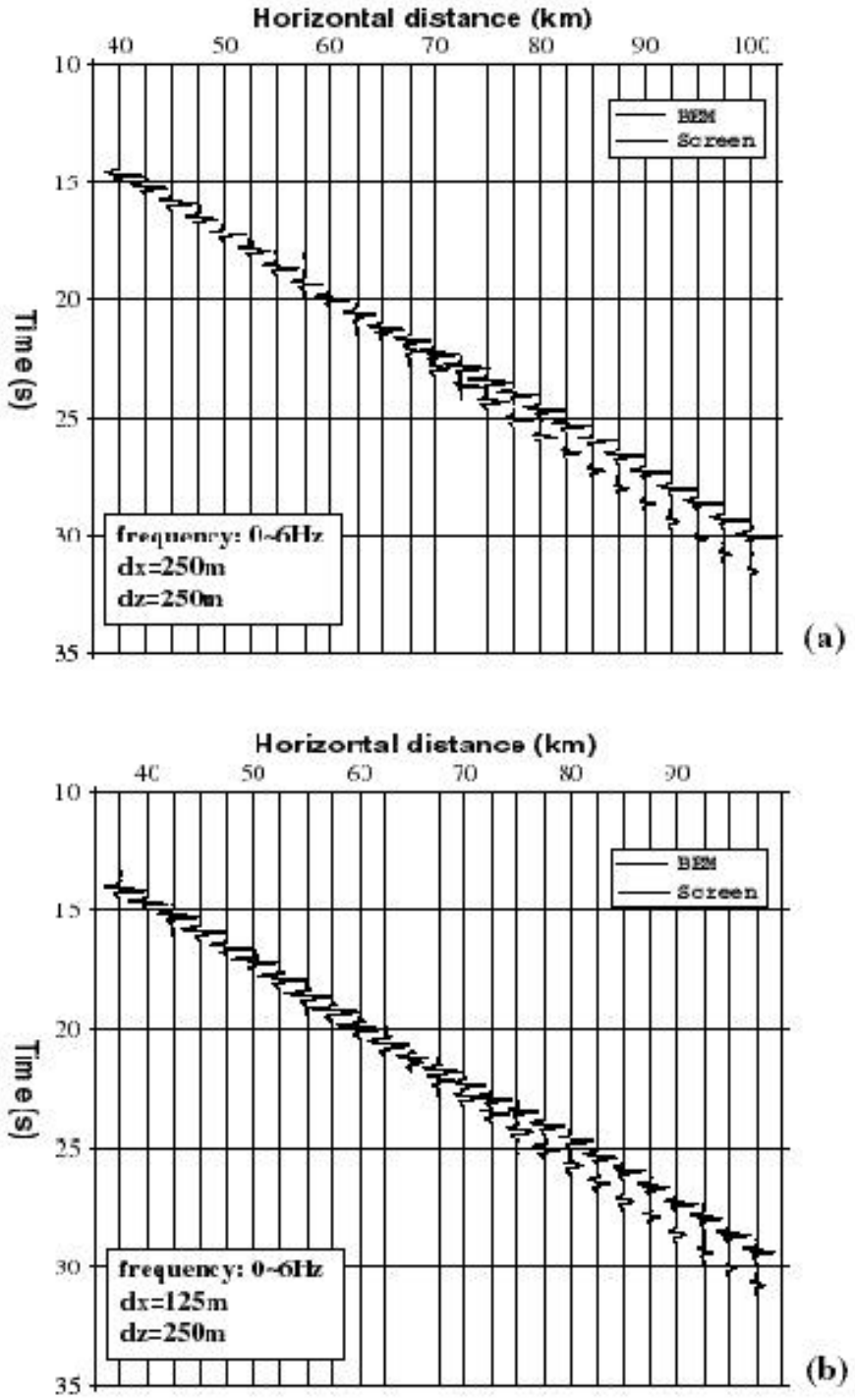


Figure 3: Synthetic seismograms using (a) conformal and (b) non-conformal transform methods, respectively. The solid lines are from the GSP method. The dashed lines are from the boundary integral method, and used as a reference. Details please see the text.

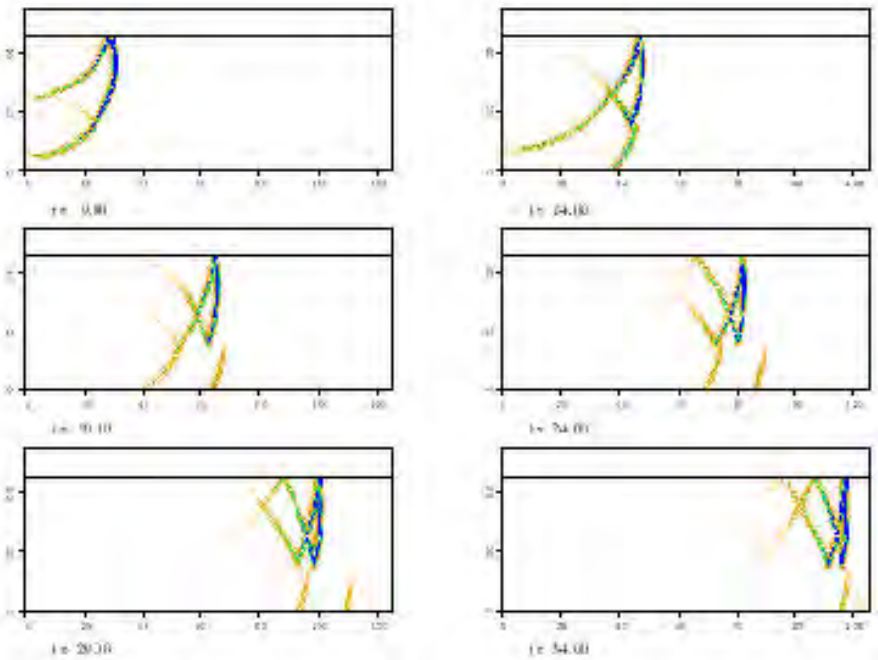


Figure 4: Snap shots of the wave field. the model is a homogeneous crustal wave guide. The depth to the Moho is 30 km. All wave fronts are relatively sharp and clear

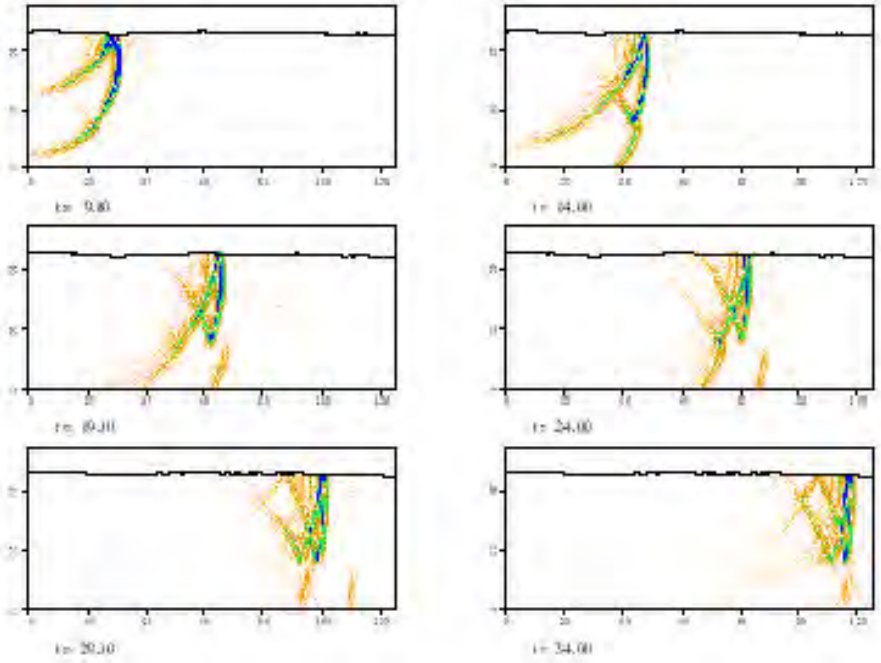


Figure 5: Snap shots of the wave field. the model is a homogeneous crustal wave guide with a rough free surface (for detailed parameters, see the text). With the surface fluctuations, the scattered waves blurred the wavefield.

REFERENCES

Bouchon, M., 1981, A simple method to calculate Green's functions for elastic layered media, *Bull. Seismol. Soc. Am*., 71, 959-971.

Bouchon, M., M. Campillo and S. Gaffet, 1989, A boundary integral equation-discrete wavenumber representation method to study wave propagation in multilayered media having irregular interfaces, *Geophysics, 54*, 1134-1140.

Campillo, M. 1990, Propagation and attenuation characteristics of the crustal phase Lg, *Pure and Appl. Geophys. 132*, 1-19.

Chen, X.F., 1990, Seismogram synthesis for multi-layered media with irregular interfaces by the global generalized reflection/transmission matrices method - Part I. Theory of 2-D SH case*, Bull. Seismol. Soc. Am., 80*, 1694-1724.

Chen, X.F., 1995, Seismogram synthesis for multi-layered media with irregular interfaces by the global generalized reflection/transmission matrices method - Part 11. Applications of 2-D SH case, *Bull. Seismol. Soc. Am*., 85, 1094-1106.

Fu, L.Y. and R.S. Wu, 1999, A hybrid BE-GS method for modeling regional wave propagation, Submitted to *the CTBT special issue*.

Jih, R.S., 1996, Waveguide effects of large-scale structural variation, anelastic attenuation and random heterogeneity on SV Lg propagation: a finite-difference modeling study, *Proc. of the 18th Annual SRS on Monitoring a CTBT*, 182-194.

Kennett, B.L.N., 1984, Guided wave propagation in laterally varying media -I. Theoretical development, *Geophys. J. R. Astr. Soc. 79*, 235-255

Hestholm, S.O. and B.O. Ruud, 1994, 2-D finite-difference elastic wave modeling including surface topography, *Geophysical Prospecting, 42*, 371-390.

Hestholm, S.O. and B.O. Ruud, 1998, 3-D finite-difference elastic wave modeling including surface topography, *Geophysics, 63*, 613-622.

Wu, R. S., 1994, Wide-angle elastic wave one-way propagation in heterogeneous media and an elastic wave complex-screen method, *J. Geophys. Res., 99*, 751-766.

Wu, R.S., S. Jin and X.B. Xie, 1999a, Seismic wave propagation and scattering in heterogeneous crustal waveguides using screen propagators: I SH waves, submitted to *Bull. Seism. Soc. Am*.

Wu, R.S., S. Jin and X.B. Xie, 1999b, Energy partition and attenuation of Lg waves by numerical simulations using screen propagators, submitted to *Phys. Earth and Planet. Inter*.

Xie, X.B. and T. Lay, 1994, The excitation of explosion Lg, a finite-difference investigation, *Bull. Seismol. Soc. Am., 84*, 324-342.

SEISMIC SOURCE CHARACTERIZATION

EMPIRICAL SEISMO-ACOUSTIC STUDIES FOR CALIBRATION AND IDENTIFICATION CAPABILITIES AT INTERNATIONAL MONITORING SYSTEM ARRAY SITES

Jessie Bonner, Brian Stump, Chris Hayward, Eugene Herrin, Paul Golden,
Department of Geological Sciences, Southern Methodist University

Sponsored by U. S. Department of Defense
Defense Threat Reduction Agency
Contract No. DSWA01-98-C-0176

ABSTRACT

Location and identification of small- to intermediate-magnitude seismic events utilizing regional waveforms will be critical to the success of the Comprehensive Nuclear-Test-Ban Treaty (CTBT). Mine-related seismicity has been detected and located by the prototype International Data Center (PIDC). Identification of mine-related events is important for purposes of calibration as well as avoiding false alarms. We report on the development of a portable seismo-acoustic technology that can be utilized for characterizing and constraining a physical understanding of the seismo-acoustic signals generated by these man-made sources. This instrumentation is also used to gather information necessary for calibration of location procedures. The instrumentation and procedures are being tested in the western United States where mine-related events are detected and located using the three regional arrays, TXAR, PDAR, and NVAR.

Portable instruments that are deployed at regional distances consist of a Refraction Technology 72A 6-channel 24-bit high-resolution seismograph interfaced with a Refraction Technology 114 remote access computer, which allows modem access of the data. Seismic sensors include Geotech S-13, Guralp CMG-3T and Streickheisen STS-2. In addition to three-component seismic instrumentation at each regional site, a three-element infrasound array with approximate 100-m station spacing will be deployed. The infrasound gauges are the Chaparral Physics Model 2 with flat response from 10 s to 300 Hz.

Close-in (10 m to 10 km) seismic, acoustic, and video instrumentation will be deployed in cooperating mines for purposes of quantifying shot times to within 0.1 s and shot location to within 100 m. These data will also be critical to the constraint of physical processes that accompany the mining explosions and are important in the generation of regional seismic and infrasonic signals.

Two preliminary experiments have been undertaken for purposes of calibration and source constraint.

The first experiment consisted of two cast blasts at the Peabody Western Coal Company Black Mesa mine near Kayenta, Arizona. The origin of the sequence of explosions (1.57 and 1.61 million pounds of ANFO/Emulsion mix) occurred at 21:07:31.36 UTC on 24 March 1999 and 21:10:38.69 on 25 March 1999. The precise origin time and location allows the classification of this event as a GT0 Ground Truth Data Base (GTDB) event. The event was recorded at several regional stations as well as the IMS array in Wyoming (PDAR). By using the two casts, the back-azimuths and phase velocities for a small range of back-azimuths at PDAR have been calibrated. Traditional Fourier filtering and beaming techniques could not extract analyzable signals out of background seismic noise from the NVAR and TXAR arrays. This most likely results from the propagation paths through the highly attenuating Basin and Range (NVAR) and Rio Grande Rift structures (TXAR).

The second experiment consisted of a reconnaissance visit to the Phelps Dodge Copper Mine in Morenci, Arizona. Mining operations at this mine as well as mines in Tyrone, New Mexico, and Chino, New Mexico, were reviewed. Preliminary information of shooting practices was exchanged and compared to regional observations at the three western U.S. arrays. Regional observations of hard rock fragmentation explosions from these mines were observed at TXAR but not NVAR and PDAR. The variability of these signals is attributed to the complex propagation paths in the western U.S. and illustrates that event identification may often rely on single-station analysis. A simple M pulse, similar to observations from cast blasts, characterizes near-source acoustic signals from delay-fired explosions.

Key Words: seismo-acoustic, mine seismicity, infrasound

OBJECTIVES

The International Monitoring System (IMS) is being developed to detect and locate seismic events down to small magnitudes. Seismic and infrasonic signals associated with mining explosions are detected at the smallest magnitudes. These events must be characterized as distinct from a nuclear explosion, possibly detonated in an evasive manner. Measurements made by SMU at TXAR suggest that the ability to observe infrasonic signals may be useful in developing ground truth data bases of mining explosions (Sorrells, Herrin and Bonner, 1997). However, questions remain as to how explosion source design, seasonal wind variations, and other factors affect seismo-acoustic propagation at regional distances. The objectives of our current study include: (1) Refinement of the physical models of mining explosions and the generation of regional seismic data; (2) Development of a comprehensive data base of acoustic and infrasonic measurements from a variety of types of mining explosions for which the explosive parameters are well known; (3) Investigation of a new approaches for utilizing combined seismic and infrasonic data sets for event location and identification; (4) Development of a procedure for calibrating problematic monitoring regions will be established; (5) Quantification of mining practices in the western US that might produce signals observable by the IMS.

RESEARCH ACCOMPLISHED

Seismic and Acoustic Instrumentation Design

SMU has developed a portable seismo-acoustic instrumentation capability that can be deployed from close-in around the source out to regional distances. The purpose of the instrumentation is to provide a characterization of the initiation and development of the seismic and acoustic/infrasonic wavefields from mining explosions. This data will be used in quantifying these sources as seen at IMS Primary and Auxiliary stations. The data is intended to provide constraints on physical models of the source processes and the associated signal propagation. These models provide the mechanism for the interpretation and understanding of similar signals observed at IMS stations in other parts of the world which might not be directly accessible. Additionally the source studies will provide the physical basis for development of regional discriminants that can be transported to new regions. This approach builds on expertise and results developed by groups at SMU, LANL, UC San Diego, DSWA and AFTAC (Hedlin *et al*., 1999; Stump *et al.*, 1999) over the last several years. The systems have been tested and are ready for deployment in Fall '99.

Included in the instrumentation is special purpose near-source acoustic instrumentation and video documentation that includes accurate time. The acoustic instrumentation development for quantifying close-in signals follows the work of Bob Reinke at DSWA. The introduction of the time stamp to video is new in our field but has been previous implemented by videographers so that multiple cameras can be correlated on frame by frame basis. In this application a video camera with accurate time can provide source location and timing information.

Experiment Design

SMU has established a working relationship with the blasting engineers of the Phelps Dodge mines of western New Mexico and eastern Arizona and these mines have agreed to allow us on-site access to monitor their explosions. Experimental design is centered around the key IMS array TXAR, with complementary data from either NVAR and PDAR (Figure 1). These deployments of portable instrumentation have four goals:

(1) Close-in seismic, acoustic and video instrumentation of a number of different types of mining shots during the experiment. Mining engineers at Phelps Dodge are already cooperating with SMU providing shot time and characterization data. This data will provide empirical quantification of actual delay times, degree of confinement, material cast, and acoustic venting. The acquisition of geophysical and geological site characterization information around a limited number of shots will be needed for constraint of the resulting source models. Material cast into the pit (when appropriate), pit geometry and explosive array configuration can result in azimuthally varying radiation of seismic data. An azimuthal array of instruments at 10 to 20 km from the explosions is planned to assess these effects during the experiment.
(2) Development of a prototype of a system that could be deployed in a mining region for six months for the purposes of obtaining high frequency ground truth information. The mining district in SE Arizona and SW New Mexico has several active mines including Morenci, Tyrone, Chino and Santa Rita. This

configuration is similar to many mining districts in the world where a number of source locations might provide regional signals.

(3) Dial-up seismic stations will be deployed in this region. Queries of these portable instruments will be triggered by near-real time analysis of the TXAR data stream. A simple phone call to the data logger will retrieve the data. Cellular phones can be used in conjunction with the portable instrumentation for this purpose. This portable installation will allow the approach to be assessed with possible application to other mining regions.

(4) Critical to the interpretation of the signals at the permanent IMS arrays is a quantification of the regional signals as they propagate to these distances and beyond. Both seismic and acoustic instruments will be deployed along a radial to TXAR and beyond. The seismic instruments will include three-component broadband instruments while the each acoustic installation will consist of three acoustic sensors with pipe/hose arrays in a small array. We anticipate that 5-10 such stations will be deployed and data acquired over a 2 to 3 month time period.

Ground Truth Data Collection

Black Mesa Mine, Northern Arizona

During the past year, we have collected ground truth data and site specific information from the mining regions that will be monitored for this study. The first of these studies was carried out at the Peabody Western Coal Company Black Mesa mine near Kayenta, Arizona. The purpose of the experiment was to investigate the utilization of in-mine multiple sensor data (seismic, acoustic and video) in constraining important blast related phenomena. A second goal of the experiment was the establishment of the relationship between these source processes and seismic and infrasound data recorded at regional distances (100-1000 km). The casts occurred at 21:07:31.36 UTC on 24 March 1999 and 21:10:38.69 on 25 March 1999. The 24 March event had an explosive yield of 1.57 million pounds of ANFO/Emulsion mix as compared to 1.61 million pounds for the 25 March event.

A third goal of this experiment was to use these cast blasts as GT0 events for the calibration of the IMS arrays TXAR, NVAR, and PDAR (Table I and Figure 1). Both cast blasts were recorded at PDAR while no data from either event was recorded at TXAR. The regional phases *Pg* and *Lg* were recorded for the 24 March 99 event at NVAR, but the low SNR inhibits any attempts at calibration. No phases were recorded at NVAR for the second cast on March 25. A possible reason for the lack of analyzable signals at NVAR and TXAR is a result of the small size of the events. This can not explain the lack of good SNR data at NVAR since the array-to-source distance is only 30 km greater than PDAR, where *Pn*, *Pg*, *Lg*, and *Rg* were recorded with significant SNR. An alternate explanation is related to the propagation path through the Basin and Range, a broad region of extension characterized by a thin crust (~30 km) and highly-attenuating mantle (Koch and Stump, 1995). We feel that the thin, inhomogenous crust in the Basin and Range acted to attenuate *Lg* propagation. In addition, the low-velocity upper mantle beneath the Basin and Range attenuated *Pn* propagation as well. A similar explanation can explain the lack of signals at TXAR as a result of the Rio Grande Rift structure of central New Mexico. The cold, thick crust and upper mantle that comprises the Colorado Plateau and adjacent provinces along the source-to-array path to PDAR provides an excellent medium for the propagation of *Pn*, *Pg*, *Lg*, and *Rg*. In fact, *Rg*, fundamental mode, short-period Rayleigh waves, with a dominant period of 4 seconds was recorded at PDAR from both events and can be seen in Figure 2. The preliminary results of the calibration of PDAR using these GT0 events is presented in Table II. Results thus far show that the observed *Pn* backazimuths are 11 degrees off from the true azimuth, while the observed *Lg* azimuths only slightly deviated from the true great circle path (approximately 1 degree). Incoming *Rg* at PDAR is refracted by more than 18 degrees towards the southeast possibly around the Uinta Mountains. In addition to the IMS array data, regional seismic recordings of the cast from various networks were studied for phase comparison and travel time calibration. Using this data, we have observed significant dipolar radiation patterns in the *Rg* generated from both explosions that may be related to the direction of casting during the shot (Figure 3).

	March 24		*March 25*	
Station	Distance (km)	Back-Azimuth	Distance (km)	Back-Azimuth
PDAR	697.9	186.1	698.2	186.2
NVAR	731.3	104.5	730.2	104.5
TXAR	1014	323.5	1014.7	323.4

Table I. Array-to-source backazimuths for the Black Mesa shots.

24 March 1999	25 March 1999
Parameter: Observed **(True)**	
Pn arrival: 21:09:10.4	*Pn* arrival: 21:12:17.8
Lg arrival: 21:10:57.6	*Lg* arrival: 21:14:07.2
Lg-P (sec): 107.19	*Lg*-P (sec): 109.40
Distance (km): 703.4 **(697.9)**	Distance (km): 717.2 **(698.2)**
Pn BAZ: 174.6 **(186.1)**	*Pn* BAZ: 174.8 **(186.2)**
Pn Phase Vel: 8.1 **(8.1)**	*Pn* Phase Vel: 7.8 **(8.1)**
Lg BAZ: 187.9 **(186.1)**	*Lg* BAZ: 185.7 **(186.2)**
Lg Phase Vel: 4.1	*Lg* Phase Vel: 4
Rg BAZ: 168.5 **(186.1)**	*Rg* BAZ: 166.7 **(186.2)**
Rg Phase Vel: 3.4	*Rg* Phase Vel: 3.5

Table II. Preliminary results of the calibration analysis of the PDAR array using the Ground Truth Database Events from Black Mesa, Arizona.

Morenci Mine, Southeastern Arizona

Another array calibration study was carried out for the IMS arrays using explosions from the open-pit Phelps-Dodge Morenci copper mine in southeastern Arizona. On 18 May 1999, we visited the mine to learn about blasting practices and shooting schedules. During the visit, we installed temporary seismic, acoustic, and videographic instrumentation to record five fragmentation shots. The seismic and acoustic recordings of each are shown in Figure 4, while the an image from the video of a fragmentation shot at a similar coal mine is shown in Figure 5. Two of the fragmentation shots were detonated simultaneously and were separated by less than 600 m. Careful comparison of the near-source P-waves from these shots illustrates significant differences. In particular, the P waves from the multiple event produces a simple impulsive P wave while the other shots yielded P waves more representative of their delay pattern. At our recording distance of 6 km, we were unable to separate the two explosions using the P wave records. We were able to separate the two explosions using the acoustic recordings which show each blast is characterized by a simple M shaped pulse. The shape of this pulse is similar to observations from cast blasts and will be the focus of our future research efforts aimed at learning how a simple M shaped pulse convolves with the atmosphere to create complex acoustic signals at regional distances. We observed no acoustics for these events at TXAR due to the zonal wind direction during the experiment.

Regional observations of the fragmentation explosions from these mines were observed at TXAR but not NVAR and PDAR. The variability of these signals is attributed to the complex propagation paths in the western US and illustrates that event identification may often rely on single station analysis. Results of the TXAR back-azimuth and phase-velocity calibration for these events are shown in Table III.

	Pn Phase Vel	*Pn* BAZ	*Pg* Phase Vel	*Pg* BAZ	*Lg* Phase Vel	*Lg* BAZ
MEAN	8.2	294.7	6.9	317	3.6	305.3
STD	0.3	7.5	0.0	2.3	0.1	5.5
TRUE	8.1	305.9	6.1	305.9	3.5	305.9
RESIDUAL	0.1	-11.2	0.8	11.1	0.1	-0.6

Table III. Phase velocity and back-azimuth calibration results for *Pn*, *Pg*, and *Lg* for the 18 May 99 fragmentation shots at Morenci, AZ.

Additional Calibration Explosions

Explosions were conducted at the Phelps Dodge Tyrone mine as part of the DEEP PROBE experiment in August 1995. The parameters for the explosions are shown in Table IV. The explosions were detonated simultaneously underwater and were recorded at TXAR (Figure 6) and used as Ground Truth Database events. The results of back-azimuth and phase velocity calibration of these explosions are shown in Table V.

Date	Latitude	Longitude	Time	Size (kg)
09 Aug 95	32.6324	32.3878	11:00:00	16329
17 Aug 95	32.6324	32.3878	11:00:00	16000

Table IV. Shot point information for the DEEP PROBE sources at Tyrone, NM.

09 August 1995	17 August 1995
Parameter: Observed **(True)**	
Pn arrival: 11:01:19.85	*Pn* arrival: 11:01:19.78
Pg arrival: 11:01:35.62	*Pg* arrival: 11:01:35.50
Lg arrival: 11:02:44	*Lg* arrival: 11:02:43.87
Distance to TXAR: 578.8 km	Distance to TXAR: 578.8 km
Pn BAZ: 297.5 **(307.8)**	*Pn* BAZ: 298.9 **(307.8)**
Pn Phase Vel: 8.8 **(8.0)**	*Pn* Phase Vel: 9.3 **(8.0)**
Pg BAZ: 302.5 **(307.8)**	*Pg* BAZ: 302.8 **(307.8)**
Pg Phase Vel: 7.1 **(6.0)**	*Pg* Phase Vel: 7.2 **(6.0)**
Lg BAZ: 310 **(307.8)**	*Lg* BAZ: 310.2 **(307.8)**
Lg Phase Vel: 3.7 **(3.4)**	*Lg* Phase Vel: 3.7 **(3.4)**

Table V. Data for regional calibration of the TXAR array using the Ground Truth Database Events from Tyrone, NM.

CONCLUSIONS AND RECOMMENDATIONS

This paper represents the initial reconnaissance for our field based study that will attempt to understand the physics of seismic and acoustic sources from hard rock fragmentation blasts. As part of this study, we will also examine the propagation of the signals from these blasts to regional distances in an attempt to develop ground truth databases for IMS array calibration. We have used explosions in the western United States to acquire calibration data for TXAR and PDAR for various azimuths at regional distances. The data shows large azimuth and phase velocity deviations that must be explained through additional data acquisition and modeling. Our results show that various propagation characteristics for physiographic provinces such as the Basin and Range and Rio Grande Rift will often create the need for single array location and identification, thus increasing the need for additional calibration and ground truth database development in the western United States. Our results thus far show that the Phelps Dodge Morenci mine is the optimum mine for use in the initial phase of the project. This is based upon our working relationship with the blasting engineers at the mine who have agreed to cooperate in the study. Based upon the variability observed in the seismic recordings of Morenci fragmentation shots at the IMS arrays, we have decided to study seismic and acoustic propagation to TXAR for the first phase of this study. This phase will begin in the Fall of 1999 when zonal winds are favorable for the path from Morenci to TXAR.

ACKNOWLDEGMENTS

We wish to thank the engineers at the Black Mesa, Tyrone, Morenci, and Santa Rita mines, with special thanks to Steve Blomberg, James Hansen, Nick Hickson, Colin Sharpe, and Mike Wheat. We wish to thank Ileana Tibuleac of SMU along with C. L. Edwards, Diane Baker, Craig Pearson, and Hans Hartse of Los Alamos National Laboratory for help in the collection of the in-close and regional data.

REFERENCES

Hedlin, M.A.H., B.W. Stump, D.C. Pearson and X. Yang, 1999. Identification of Mining Blasts at Mid- to Far Regional Distances Using Low Frequency Seismic Signals, submitted Pageoph.

Koch, K. and B.W. Stump, 1995. Implications for upper mantle structure in the Western United States from complete far-regional seismograms, *Bull. Seism. Soc. Am.* **85,** 1432-1444.

Sorrells, G.G., E.T. Herrin, and J.L. Bonner, 1997. Construction of regional ground truth databases using seismic and infrasound data, *Seism. Res. Lett.,* **68***,* 743-752.

Stump, B.W, M.A.H. Hedlin, D.C. Pearson and V. Hsu, 1999. Characterization of Mining Explosions at Regional Distances, in review, Reviews of Geophysics.

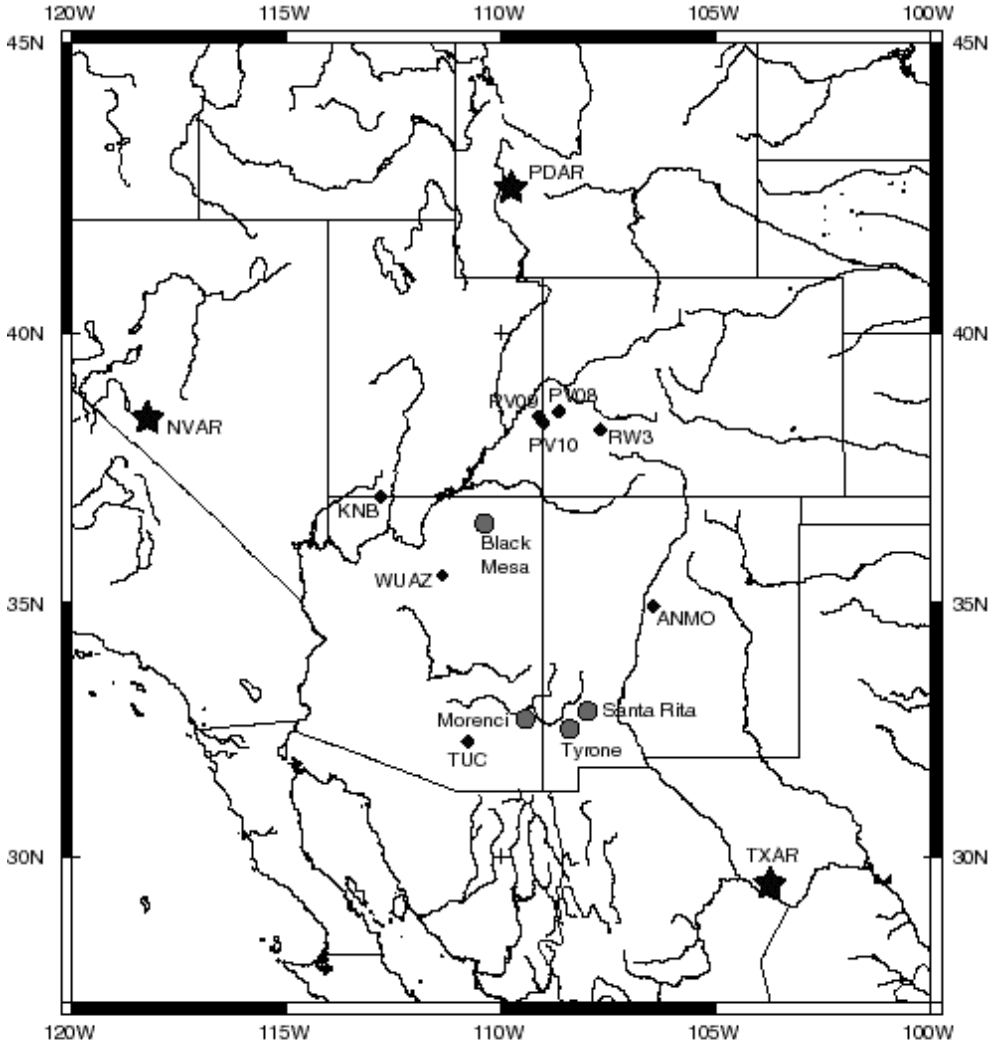


Figure 1. Locations of the mines where calibration events were recorded. Also shown are the locations of the IMS arrays PDAR, TXAR, and NVAR. Additional regional stations used in these studies are marked by small diamonds.

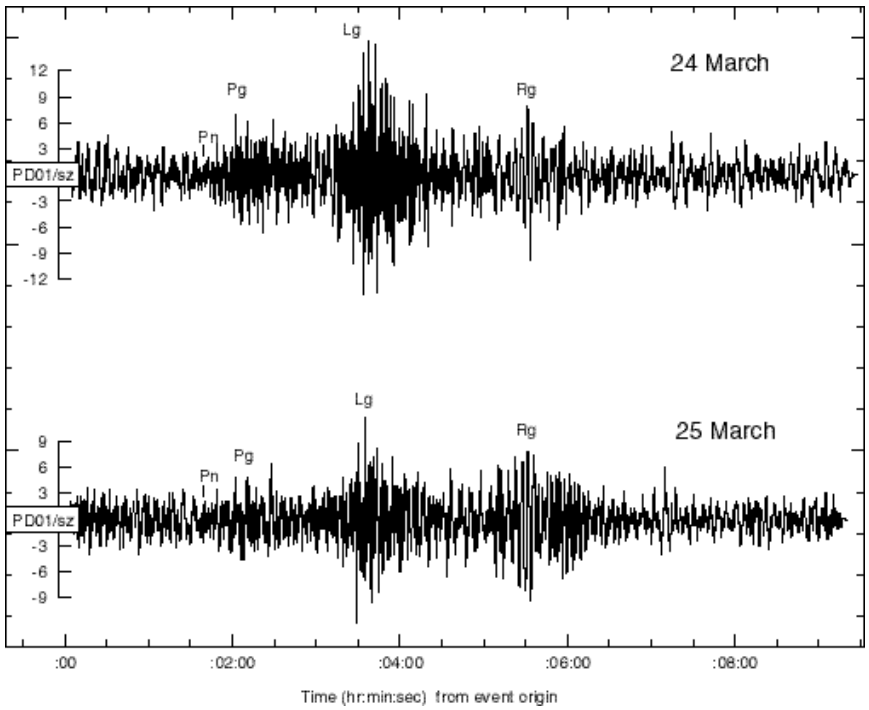


Figure 2. Unfiltered PDAR recordings of the Black Mesa cast blasts.

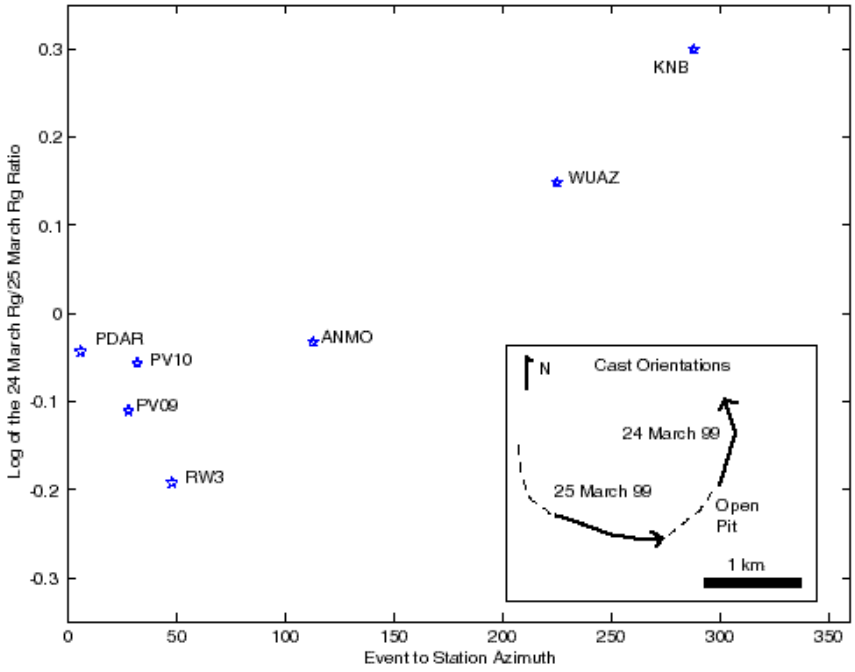


Figure 3. *Rg* ratios observed for the Black Mesa cast blasts. The ratios can be explained by dipolar radiation patterns oriented parallel to the direction of cast propagation. The solid arrows in the inset represent direction of detonation parallel to the free face.

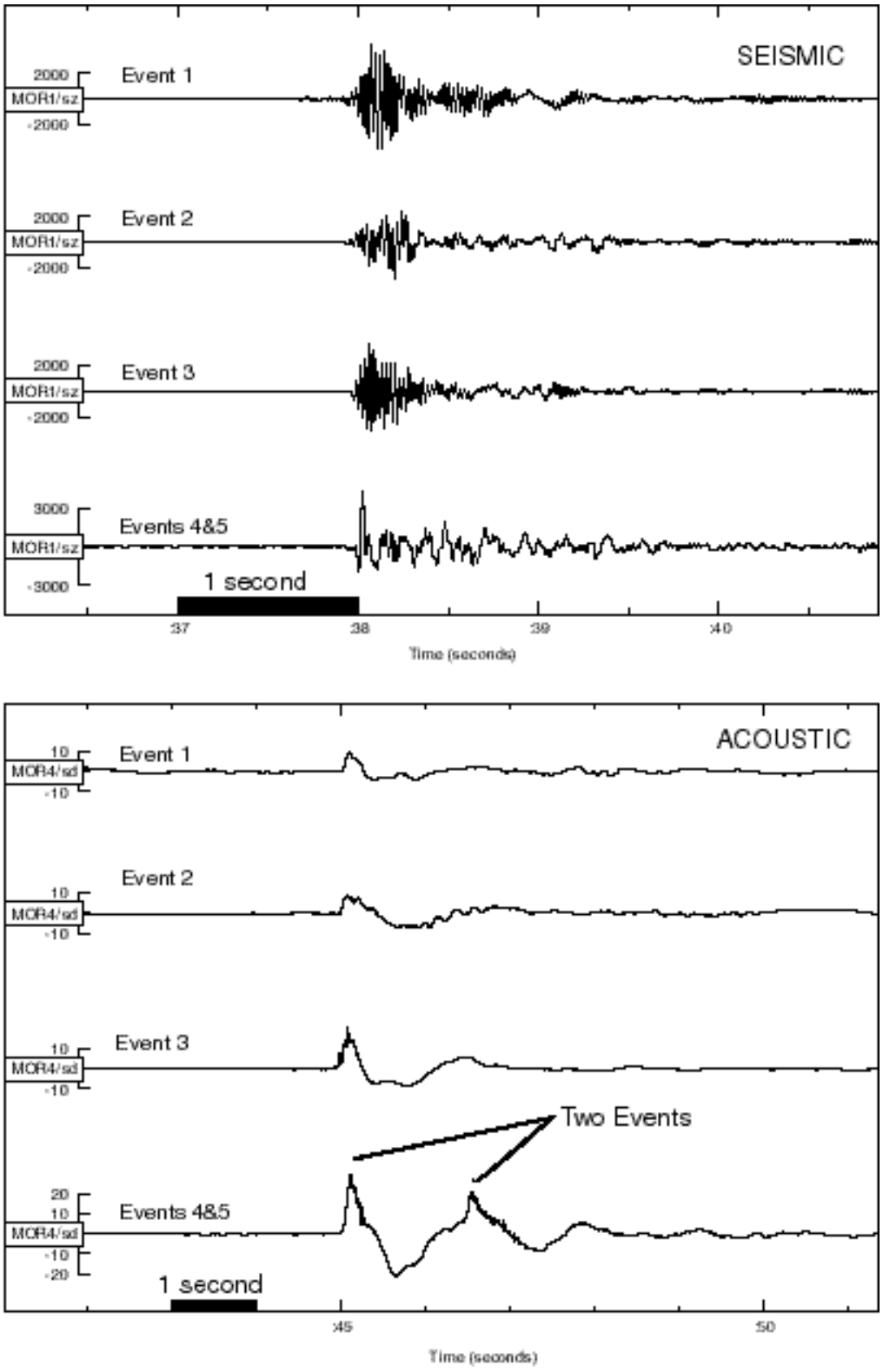


Figure 4. In-close seismic and acoustic monitoring of fragmentation blasts at the Phelps Dodge Morenci open pit copper mine on 18 May 99.



Figure 5. Image of a rock fragmentation blast at copper mine in the southwestern United States.

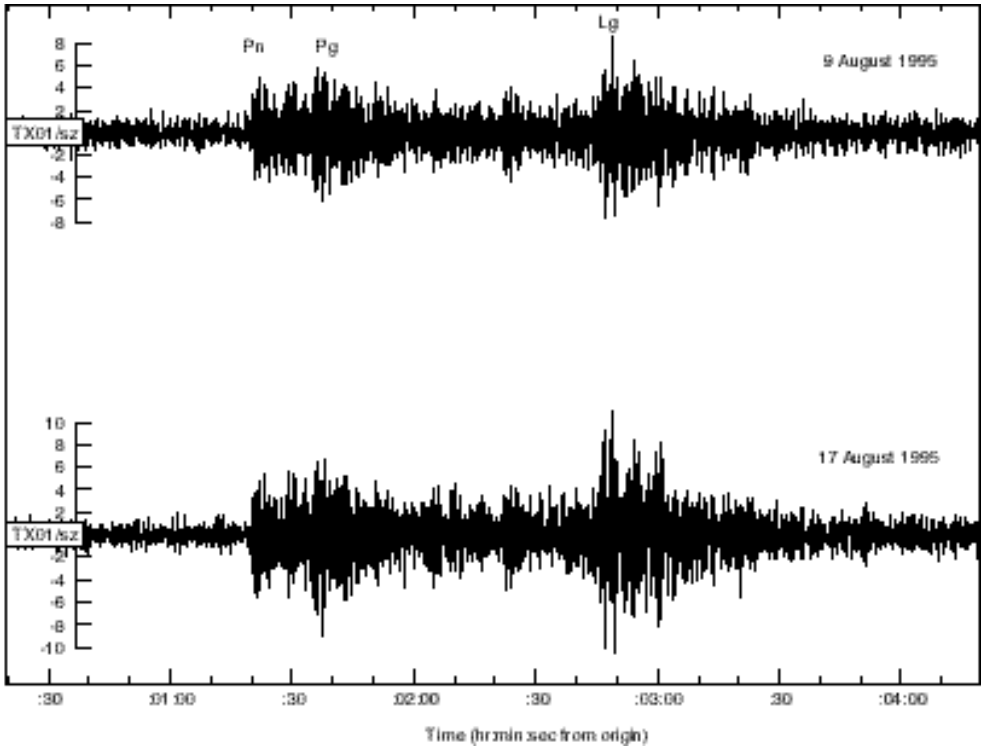


Figure 6. TXAR recordings of the Tyrone, NM DEEP PROBE explosions (BP Filtered 0.6 to 4 Hz).

SOURCE CHARACTERIZATION OF GROUND TRUTH QUARRY BLASTS IN ISRAEL AND CALIBRATION OF LOCAL STATIONS

Yefim Gitterman and Avi Shapira

Seismology Division, Geophysical Institute of Israel

Sponsored by the U.S. Department of Defense,
Defense Threat Reduction Agency

Contract No. DSWA01-97-C-0151

ABSTRACT

Four recent calibration ripple-fired explosions at the Arad phosphate quarry in the Negev desert were recorded by the ISN short period (SP) and Broad Band (BB) EIL and MRNI stations. Two accelerometers were also installed in close proximity (a few hundred meters) to the explosions to provide better source characterization. Location coordinates and origin times were known to within ±50m and ±20 msec, respectively. The blast pattern parameters were also known. These data constitute calibration shots with Ground Truth category GT0. We analyzed correlation of signal features (in both time and frequency domains) and blast patterns as well as travel time curves.

The explosions were conducted a few hundred meters apart using routine (40 msec for EX. 1 and 2) and specially requested (12 msec for EX. 3 and 80 msec for EX. 4) time delays between borehole rows. Total charge weights were 8.0, 10.5, 14.3 and 12.0 tons. The results of the preliminary analysis can be summarized as follows:

1. The yield of EX. 3 was only 19% more than EX. 4; however, it produced far more seismic energy. We attribute this to the shorter delay times in the detonation process. The peak amplitude ratio for the two explosions showed a factor of 2 at short distances (e.g. SP MZDA, r=28 km), increasing with distance to 3 at remote stations (e.g. BB EIL, r=161 km). Similar to EX. 4 amplitudes are observed for EX. 1 and 2 that had much lower yields.

2. The spectral curves show a distinct low-frequency spectral modulation, coherent at different ISN stations. We observed a number of outstanding interference features such as the first null at 5.2 Hz for EX. 1 and the strong main maximum at 14.5 Hz corresponding to the largest time delay in EX. 4.

3. Spectral discriminants, namely Energy Ratio (1-3 Hz/6-8 Hz) and Semblance (1-12 Hz), averaged for a number of ISN stations or for three components of the BB EIL station, showed similar results corresponding to the explosion population. Relatively low ISN ratios and semblance values for EX. 4 could be the result of interference suppression of low frequency energy due to large time delays.

4. High-frequency wave features, which are not available on seismic station recordings, were observed in close-in accelerograms. The strong motion records provided data for the radiation pattern analysis and design of planned larger calibration quarry shots.

5. Observed travel time curves for stations in the 30-250 km range demonstrate a regular time shift of about +2 sec relative to the IASPEI91 model up to 180 km. Far better results were obtained for a local model used by GII for earthquake location where tie residuals do not exceed ±0.5 sec. We identified an outlying station (SP HRI at 240 km) with a lag of about 1 sec.

The data obtained provide the basis for station correction and improvement of crust models used in the region, and contribute to calibration of two auxiliary IMS stations EIL and MRNI.

Key Words: ground truth GT0 quarry blasts, interference phenomena, spectral discrimination, travel time calibration

Table 1. Parameters of controlled ripple-fired quarry blasts in Israel (Hole diameter 200 mm, hole depth 8.5-9 m).

Location and origin time data provided by GPS. O.T. refers to the measured detonation time of the first hole.

#	Date	Origin time (O.T.), GMT	Coordi-nates	Total yield, tons	Delay, msec		No. of del.	No. of rows	No. of holes	Comments
					Nomi-nal	Real				
1	30.07 1998	08:18:51.91	31.10439N 35.18801E	8	40	32	5	6	70	Nearly-regular blast pattern, almost equal rows (9, 13, 14, 13, 13, 8 holes)
2	09.09 1998	10:00:03.22	31.10416N 35.18880E	10.5	40	31.3	8 (7)	9 (8)	75	Non-regular pattern with variable row length (1-15 holes)
3	26.01 1999	11:46:02.41	31.10968N 35.18914E	14.34	12	-	10	11	120	Non-regular pattern with variable row length (4-13 holes)
4	27.01 1999	10:01:00.64	31.10894N 35.18936E	12.0	80	68.5	9	10	76	Non-regular pattern with variable row length (3-9 holes)

Table 2. Local magnitudes and peak amplitudes of the analyzed quarry blasts.

No. of expl.	Mag. M_L	Vertical peak amplitudes at different stations, micron/sec					
		MZDA r=28 km north	YTIR r=29 km north	YASH r=170 km south	HRI r=245 km north	BB EIL r=161 km south	BB MRN r=212 km north
1	2.6	6.2	9.7	0.59	0.57	0.127	-
2	2.7	11.2	8.5	0.79	0.40	0.122	-
3	2.9	17.9	19.6	3.08	2.04	0.389	0.541
4	2.7	8.5	7.8	1.26	-	0.135	0.217

Table 3. Waveform correlation of the quarry blasts at different stations (relatively to EX.1).

Station	Distance, km	Azimuth, deg	Time window, sec	Maximum of the cross-correlation function				Comments
				EX.1	EX.2	EX.3	EX.4	
MZDA	29	35	20	1	0.64	0.32	0.42	-
			35	1	0.63	0.31	0.40	whole signal
YTIR	31	348	10	1	0.39	0.43	0.33	P-waves
			35	1	0.81	0.52	0.37	whole signal
PRNI	84	192	64	1	0.73	0.48	0.61	
			15	1	0.42	0.20	0.20	P-waves
SAGI	110	206	35	1	0.28	0.17	0.25	whole signal
MBH	146	190	45	1	0.55	0.20	0.18	
			15	1	0.61	0.44	0.38	P-waves
			15	1	0.49	0.24	0.20	S-waves
YASH	170	190	15	1	0.41	0.14	0.14	P-waves
			40	1	0.34	0.30	0.22	whole signal

OBJECTIVE

Our research program is aimed at improving monitoring of the CTBT in the Middle East. An important part of the research is the execution and analysis of calibration explosions, currently lacking in the region, including controlled quarry blasts with Ground Truth Information of rank GT0. The data obtained recently are used in the following analysis:

1. An improved understanding of quarry blast phenomenology and characterization of near-field ground motions and waveforms at local and regional distances.
2. Correlation between blast pattern parameters and the amplitude and spectral features of the seismic signal.
3. Discrimination procedures by application of spectral discriminants (semblance and energy ratio) to records of multiple network stations and single BB stations.
4. Travel times and estimation of station corrections for the local and IASPEI91 models.

RESEARCH ACCOMPLISHED

Data

Four routinely-based ripple-fired explosions at the Arad phosphate quarry in the Negev desert were recorded by vertical short period (SP) and 3C Broad Band (BB) stations of the Israel Seismic Network (ISN), at distances of 28-245 km. The stations used in the analysis and the explosion locations are presented on the map in Fig. 1, EIL and MRNI are auxiliary stations of the IMS. The explosions are located a few hundred meters apart, EX.3&4 were adjacent at the same bench. Total charge weights were 8.0, 10.5, 14.3 and 12.0 tons. Routine blasts at this quarry are usually conducted with delays 40 msec between rows of holes (EX.1&2). In the case of EX.3&4 Nonel PETN down-hole delays of 500 ms were used, which can introduce an additional ±3.5 msec scatter in the delay times between rows (Rohay, 1999). At our request, two explosions were conducted with blast patterns a little different from routine techniques, i.e. with smaller (12 msec for EX.3) and larger (80 msec, consisting of two 40 msec devices, for EX.4) time delays. These delay values are nominal. As discussed in the following, spectral analysis of seismograms shows that actual quantities were lower. Explosions coordinates and origin times relating to the first blasting hole were measured by GPS with an accuracy better than 50 m and 20 msec, respectively. The summary of the explosion parameters is presented in Table 1. These data constitute calibration shots with Ground Truth category GT0. Two 3C accelerometers (A-800 by Geotech, USA) were also installed in close vicinity of the explosions (within few hundred meters) for better source characterization.

Correlation between Blast Parameters and Signal Features

Seismic strength. Local magnitudes based on coda duration measurements and peak amplitudes (as an indication of seismic signal strength) of the analyzed blasts are presented in Table 2. The total yield of EX 3 was only 19% more than that of EX 4, however, it produced far more seismic energy. The peak amplitude ratio for the two explosions showed a factor of 2 at short distances (e.g. MZDA, r=28 km), increasing with distance to 3 at more remote stations (e.g. BB EIL, r=161 km). We attribute this effect to the role of delay times in the detonation process. EX 3 with small delays of 12 msec seems to be similar to that of instantaneous blasting with the strongest seismic effect. EX 4 with large delays of 80 msec decreased seismic energy due to destructive interference phenomenon and corresponds approximately to the one-row blast. The effect of delay times is observed also for EX 1&2 with intermediate delays of 40 msec. These blasts have much lower total yields than EX 4, but produced similar amplitudes. An example of signal amplitude comparison is shown on Fig. 2.

Compared to those of EIL, signal amplitudes for EX 3&4 are enhanced at MRNI, that is located closer at the opposite azimuth (see Table 2, Fig. 1). Such an "azimuth effect" was not observed at the SP stations, e.g. HRI and YASH (see map in Fig. 1 and Table 2). It cannot, therefore, be attributed to the source effect like direction of blast sequencing or orientation and position of the free face; however, it is likely to be associated with path and site effects.

Local duration magnitudes correlate well with peak amplitudes and correspond approximately to the upper limit of the yield-magnitude relationship of ripple-fired quarry blasts (Gitterman, 1998, Khalturin et al., 1998). Records of EX 3 (with delays of 12 msec) are exceptional, as this explosion has a source function more similar to instantaneous blasts.

Waveform correlation. We studied waveform correlation from the explosions to check for similarity, i.e., that events from the same mine produce highly repeatable waveforms which, in turn, can be used for event clustering and source identification (e.g. Harris, 1997). Indeed, when comparing normalized seismograms at a specific station (see e.g. Fig. 3), one can observe a conformity in the shape of some phases. Table 3 shows cross-correlation maximal values between EX 1 and the other explosions at several close and remote stations for different time windows. The correlation values decrease significantly with distance (more complicated waveforms and lower signal-to-noise ratio) and increase for larger windows containing the whole wavetrain.

The results demonstrate rather low correlation, although all the blasts were located in a small area of about 0.5 km radius. The highest correlation is between seismograms of EX 1 and EX 2, both having similar blast patterns and delays of 40 msec and spaced about 100 m apart. EX 3&4, with different delays and placed a little further away (500 m), show very low correlation with EX 1, especially at distances greater than 100 km. Similar results were obtained recently by Stump et al. (1999) when regional waveforms from single-fired explosions in a single mine separated by a few kilometers, lost coherency above 1 Hz. All these observations suggest limited applicability of correlation analysis for identifying blasts from a large-scale mine.

Spectral modulation. The most characteristic feature of ripple-fired explosions is the spectral modulation in all wave phases (see also Stump and Reinke, 1988, Chapmen et al., 1992, Gitterman and van Eck, 1993). Availability of Ground Truth parameters for the analyzed quarry blasts and relatively simple blast patterns provide a good chance to check the correlation between blast parameters and seismic wave features. We also examine the correspondence between theoretical predictions, based on the linear interference theory, and experiments, for local mining practices and geological settings.

The main ripple-fired source features are explained by constructive (main maximum at f_m) and destructive (first spectral null at f_{01} and multiples f_{0k}) interference of seismic waves from inter-shots with millisecond delays (not by source finiteness in space or time, or total blast duration). For a regular blast pattern the frequencies depend on delays τ, and number of delays n (Gitterman, 1982):

$$f_m = 1/\tau \quad (1)$$

$$f_{01} = 1/[(n+1)\times\tau] = f_m/(n+1); \quad f_{0k} = k\times f_{01}, \; k = 1, 2, \ldots, n \quad (2)$$

Any random variation of delay time or charge per delay, or any other non-regularity in the blast pattern not to mention anelastic absorption of high-frequency energy with distance, can destroy the spectral modulation features, most significantly at high frequencies (greater than 10-15 Hz). The spectral null features occur at frequencies lower than the main maximum and so can be useful in identifying ripple-fired quarry blasts at regional distances. Based on numerous observations of quarry blasts in Israel and the simple theoretical analysis mentioned above, we found it better to reveal and analyze spectral modulation at low frequencies (<15 Hz) using smoothed spectra of the whole signal for several stations at different azimuths (Gitterman and van Eck, 1993). Advantage of the low-frequency approach is presented also in Hedlin, 1998, Carr and Garbin, 1998.

Amplitude spectra of the whole signal (20-30 sec window) recorded at different SP and BB stations were smoothed in the 0.5-0.7 Hz window. The spectral shapes showed high coherency and clear modulation (except for EX 3 with too small delays of 12 msec) for all stations including spectral null and main maximum features (Figs. 4-6). According to Eq. (1), EX 4 with delays of τ=80 msec should produce a main maximum at the frequency f_m=12.5 Hz. Spectral curves at different ISN stations, presented in Fig. 4, show clear modulation and outstanding maximum at 14-15 Hz, highly coherent at different stations (Fig. 4a). From the average spectral curve (Fig. 4b) we estimated an empirical value f_m^*=14.6 Hz. This maximum is rather strong, in spite of: (a) non-regularity of the blast pattern (different number of hole charges in rows), (b) well-known strong attenuation of high-frequency seismic energy in the region (Q=50-100) with widespread unconsolidated sediments in the upper crust, and (c) the restricted recording band (0.5-12.5 Hz) at ISN stations. This f_m feature is first observed for quarry blasts in the region, because existing mining practices in Israel and Jordan usually include delays of τ<50 msec. These delays produce main maxima at f_m>20 Hz which cannot be observed at local seismic stations for reasons (b) and (c) mentioned above. In some geological settings such as shields, e.g. in the eastern USA, with low anelastic absorption, the maxima were observed at frequencies up to 40 Hz (Kim et al., 1994).

The 2Hz-shift of f_m cannot be explained by a Doppler-like effect caused by specific orientation of detonation between charge rows and azimuth to a station (Chapmen et al., 1992), because the estimate f_m^* is obtained through averaging of several stations covering the whole azimuth range (see Fig. 1). The most natural reason for the shift is the well-known in mining practices variability of short-time delay systems where actual delays can differ from nominal values by 10-20%. Inverted calculations from Eq. (1) give a reasonable assessment of the actual delay: $\tau^*=1/f_m^*$=68.5 msec (i.e. about 34 msec on average for a separate delay device which was doubled for this explosion). Moreover, application of the obtained delay for estimation of the first spectral null by Eq. (2), results in a value of $f_{01}^*=1/[(n+1)\times\tau^*]\approx$1.5 Hz, which corresponds well to the observed minimum at this frequency on the average spectral curve (Fig. 4b), where the second (2.9 Hz), and the fifth (8 Hz) spectral nulls can also be identified.

In the case of EX. 1 (τ=40 msec, n=5) a distinct first spectral null is observed for ISN stations at f_{01}^*=5.2 Hz (Fig. 5a) as compared to the theoretical value of f_{01}=4.2 Hz in Eq. (2). Supposing reduced (as in the case of EX. 3) delays, we estimated actual values $\tau^*=1/[(n+1)\times f_{01}^*]\approx$32 msec. Broad band EIL records (80 Hz sampling rate) from EX. 1 were also analyzed. All three components showed the same LOW-FREQUENCY spectral modulation features (Fig. 5b), and the spectra average corresponds well to the average based on ISN stations. The HIGH-FREQUENCY modulation and the potential main maximum at $f_m\approx$25-30 Hz, which could be observed in the band-pass filtered 0.5-40 Hz seismograms, were not found owing to the steep descent of spectra after 10 Hz associated with the above-mentioned local strong attenuation of signal high frequencies. The

modulation features for EX. 2 were also observed in ISN records, but less obvious than for EX. 1 owing to the non-regularity of the blast pattern.

Discrimination Procedures

Spectral discriminants, namely Energy Ratio of low (1-3 Hz) to high (6-8 Hz) frequency bands and semblance of spectral shapes in (1-12 Hz) band (Gitterman et al., 1996) were applied to seismograms obtained in time windows containing the whole signal. For a given event, the discriminants were averaged for a number of ISN stations (covering a broad azimuth range) or for three components of a single BB station.

Both multi and single station estimates verified the results previously obtained from the Galilee and Negev local data sets (Gitterman et al., 1996): the new controlled quarry blasts also demonstrated higher values of energy ratio and spectral semblance than nearby earthquakes and corresponded to the explosion population (see Table 3). Relatively low energy ratios and semblance values for EX. 4, estimated from ISN records, could be the result of interference suppression of low frequency energy due to large time delays. We found that, for a given explosion, semblance estimates from a single 3C station are higher than those obtained from ISN stations. Such a relation may also be expected for earthquakes. Indeed, for an earthquake from the Galilee dataset (April 15, 1994, 01:20, M_L=2.4), a multi-station ISN semblance estimate was 0.45 (see Gitterman et al., 1996), and for the single 3C ISN station ZNT we now obtained a value of 0.776 which is still much lower than for explosions.

Near-Field Observations

Strong motions for EX 2,3 and 4 were recorded by two A-800 accelerographs at distances of 200-500 m. EX. 3 and EX. 4 yielded approximately equal horizontal Peak Ground Accelerations of 0.3g at about 360 m (Fig. 6a), despite much higher amplitudes and magnitude for EX. 3 at remote seismic stations, as mentioned above. Analysis of the blast patterns and accelerograph locations showed that, for the strong EX. 3, the PGA value was recorded at the free face side in the opposite direction to the detonation sequence, whereas for the weak EX. 4 a sensor was placed along the bench with an azimuth perpendicular to the detonation direction.

Accelerogram spectra demonstrated some high-frequency source features which are not available in seismic station recordings with limited frequency range. Using accelerograms we can observe a main maximum $f_m \approx 26$ Hz for EX. 1 (Fig. 6b) and multiple main maxima at about 30 Hz and 45 Hz for EX. 4 (Fig. 6c), which could not be found in recordings of ISN stations.

Travel Time Analysis

Based on the Ground Truth origin times from the controlled quarry blasts and measured first arrival times, we obtained accurate P-waves travel time empirical curves in the 30-250 km range. The curves demonstrate a regular time shift of about +2 sec when compared to the IASPEI91 model, up to 180 km (Fig. 7a). A much better fit is observed with respect to the local model used by GII for earthquake location where the residuals are less than ±0.5 sec (Fig. 7b). We identified an outlying station (HRI at Mt. Hermon at 240 km) with a lag of about 1 sec.

CONCLUSIONS AND RECOMMENDATIONS

The data and results obtained based on Ground Truth information will contribute to a better understanding of ripple-fired quarry blast phenomenology. The observed correlation between blast pattern parameters, waveform amplitudes and spectral features is useful in the identification of seismic events. Using precisely known parameters of actually routine quarry blasts we can predict the basic spectral modulation features and vice-versa from the observed spectra we can estimate actual blast parameters, namely time delays different from nominal values. The application of spectral energy ratio and semblance discriminants to network stations and 3-component BB recordings provided both multi- and single-station estimates relating to the explosion population. Low correlation of near-regional signals from closely spaced routine quarry blasts suggests limited applicability of the waveform correlation analysis or "master event" approach to the discrimination problem. The data obtained provide the basis for station correction and improvement of crust models used in the region and contribute to calibration of two auxiliary IMS stations EIL and MRNI. The strong motion records provided data for design of planned larger calibration quarry shots, including instantaneous explosions.

REFERENCES

Carr, D.B and H.D. Garbin, 1998. Discriminating ripple-fired explosions with high-frequency (>16 Hz) data, Bull. Seis. Soc. Am., 88: 963-972.

Chapmen, M.C., G.A. Bollinger, and M.S. Sibol, 1992. Modeling delay-fired explosions spectra at regional distances, Bull. Seis. Soc. Am., 82: 2430-2447.

Gitterman, Y., 1982. Assessment of dynamic parameters of seismic and air shock waves from multiple shot systems, Ph.D. Thesis, Institute of Mining, Academy of Sciences of the USSR, Novosibirsk.

Gitterman, Y. and T. van Eck, 1993. Spectra of quarry blasts and microearthquakes recorded at local distances in Israel, Bull. Seis. Soc. Am, 83: 1799-1812.

Gitterman, Y., 1998. Magnitude yield correlation and amplitude attenuation of chemical explosions in the Middle East. In Proceedings of the 20th Annual Seismic Research Symposium on Monitoring a CTBT, 302-311.

Gitterman, Y., V. Pinsky and A. Shapira, 1996. Discrimination of seismic sources using the Israel Seismic Network, Report No.1, PL-TR-96-2207, 98 pp.

Hedlin, M.A.H., 1998. Identification of mining blasts at all regional distances using low-frequency seismic signals, in Proceedings of the 20th Annual Seismic Research Symposium on Monitoring a CTBT, 335-344.

Harris, D.B., 1997. Waveform correlation methods for identifying population of calibration events, in Proceedings of the 19th Annual Seismic Research Symposium on Monitoring a CTBT, 604-613.

Khalturin, V., T. Rautian and P. Richards, 1998. The seismic signal strength of chemical explosions, Bull. Seis. Soc. Am., 88, 1511-1524.

Kim, W.Y., D.W. Simpson and P.G. Richards, 1994. High-frequency spectra of regional phases from earthquakes and chemical explosions, Bull. Seis. Soc. Am., 84, 1365-1386.

Rohay, A.C., 1999. Modeling ripple fired explosions from the Centralia mine, Southwestern Washington, Abstracts of the 94th Annual Meeting of SSA, Seism. Res. Lett., 70, p.228.

Stump, B.W. and R.E. Reinke, 1988. Experimental confirmation of superposition from small scale explosions, Bull. Seis. Soc. Am, 78, 1059-1073.

Stump, B.W., D.C. Pearson and V. Hsu, 1999. Empirical scaling relations for contained single-fired chemical explosions and delay-fired mining explosions at regional distances, Abstracts of the 94th Annual Meeting of SSA, Seism. Res. Lett., 70, p.212.

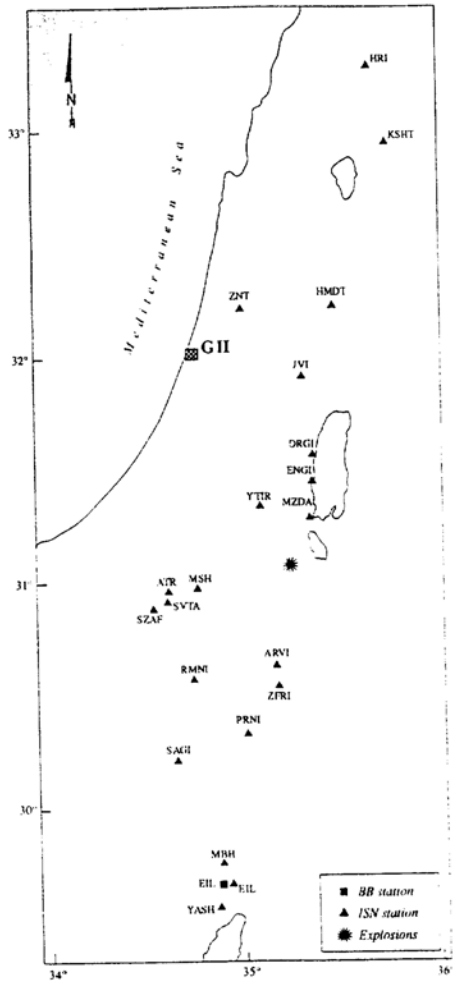


Figure 1. Location of the controlled quarry blasts and seismic stations used in the analysis.

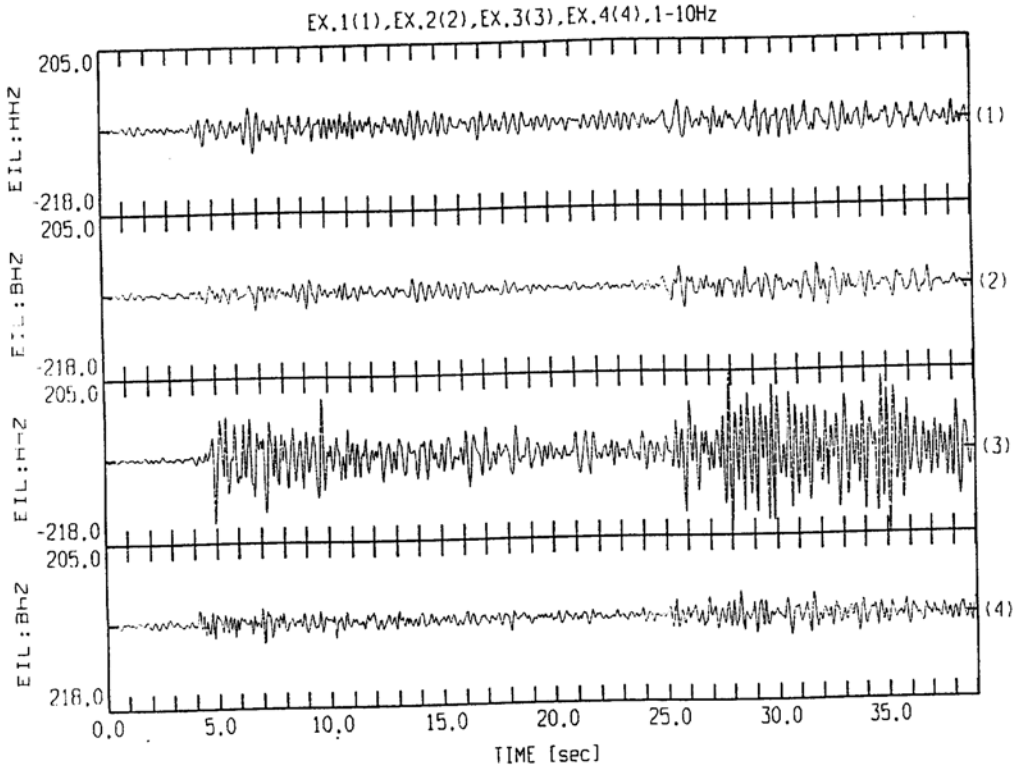


Figure 2. Comparison of amplitudes for the blasts at BB EIL station (vertical component).

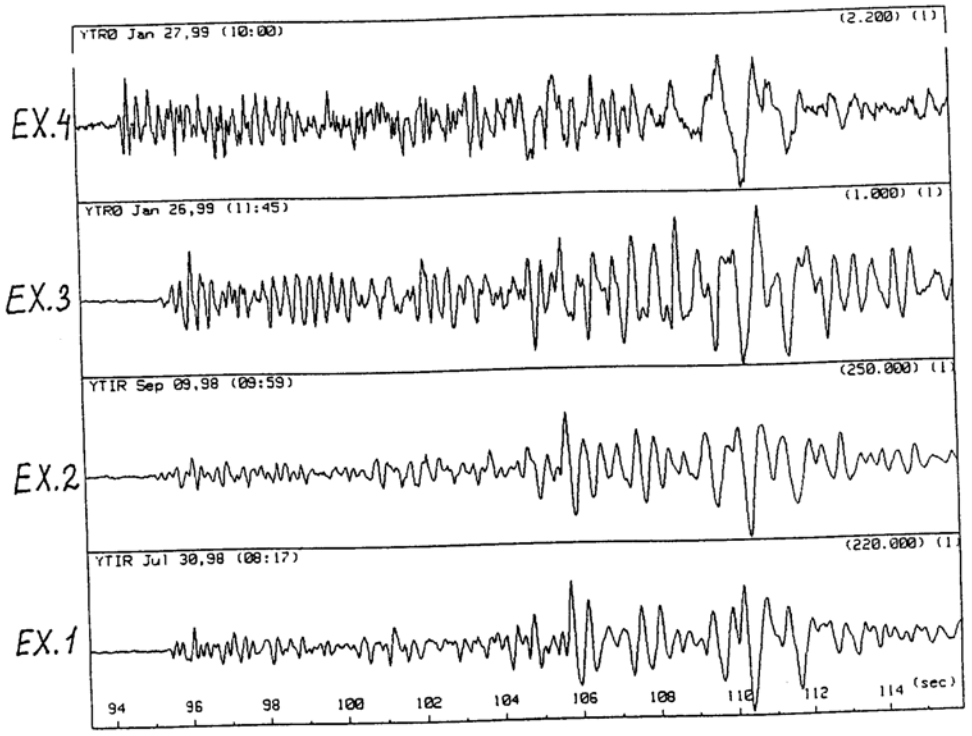


Table 4. Discrimination results for the controlled (calibration) ripple-fired quarry blasts.

No. of expl.	Seismic system	Energy ratio (1-3Hz)/ (6-8Hz)	Semblance in range (1-12 Hz)	Number of stations (ISN), comments
1	SP ISN Vert.	41.0	0.89	11 (ATR, EIL, KER, MBH, MSH, MZDA, PRNI, RMNI, SAGI, YASH, YTIR)
	BB EIL 3C	56.3	0.98	trigger at 80 Hz, filter 0.5-40 Hz
2	SP ISN Vert.	63.3	0.81	11 (DRGI, ENGI, KER, MSH, PRNI, RMNI, RTMM, SVTA, SZAF, YTIR, ZFRI)
	BB EIL 3C	179.4	0.98 (1-10 Hz)	continuous recording at 20 Hz, filter 0.5-10 Hz
3	SP ISN Vert.	15.8	0.78	15 (ATR, DRGI, EIL, ENGI, HMDT, HRI, JVI, MSH, MZDA, PRNI, SAGI, SVTA, SZAF, YASH, ZFRI)
	BB EIL 3C	28.3	0.97	trigger at 80 Hz, filter 0.5-40 Hz
	BB MRN 3C	10.3	0.90 (1-8 Hz)	continuous recording at 20 Hz, filter 0.5-10 Hz
4	SP ISN Vert.	5.6	0.64	9 (ARVI, DSI, MBH, MZDA, PRNI, RMN, SAGI, YASH, YTIR)
	BB EIL 3C	11.2	0.93 (1-8 Hz)	continuous recording at 20 Hz, filter 0.5-10 Hz
	BB MRN 3C	3.9	0.89 (1-8 Hz)	continuous recording at 20 Hz, filter 0.5-10 Hz

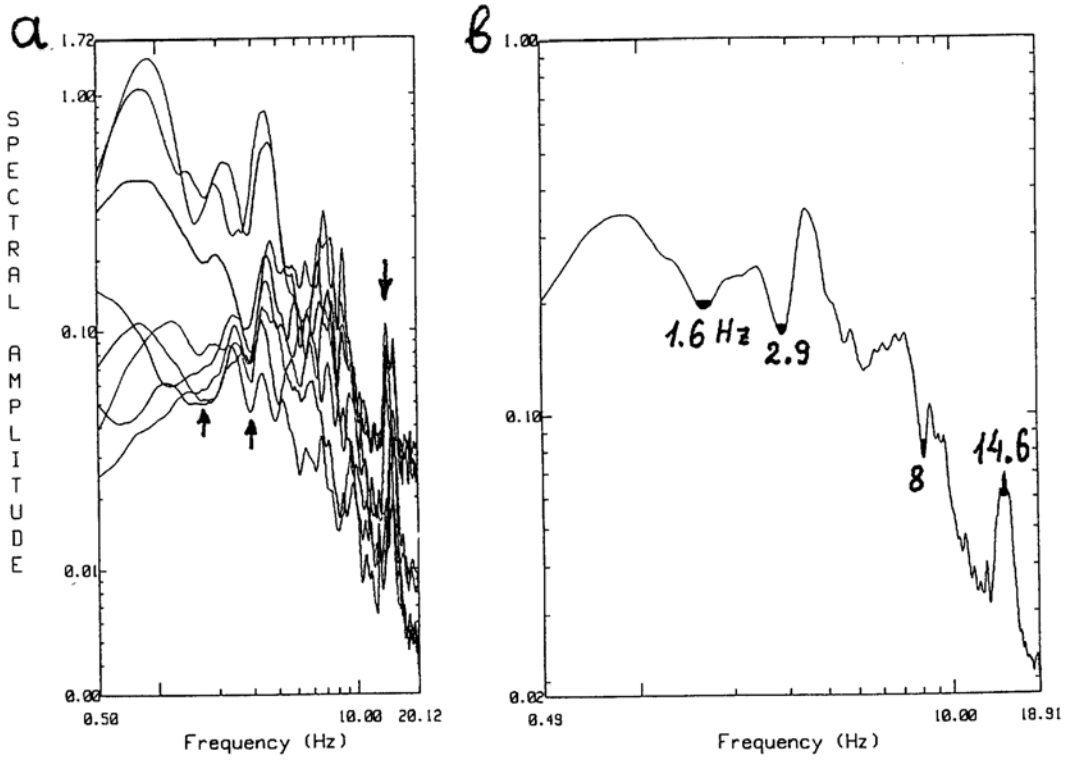


Figure 4. Spectral modulation and the main maximum for EX.4 at ISN stations (a), and the average curve (b).

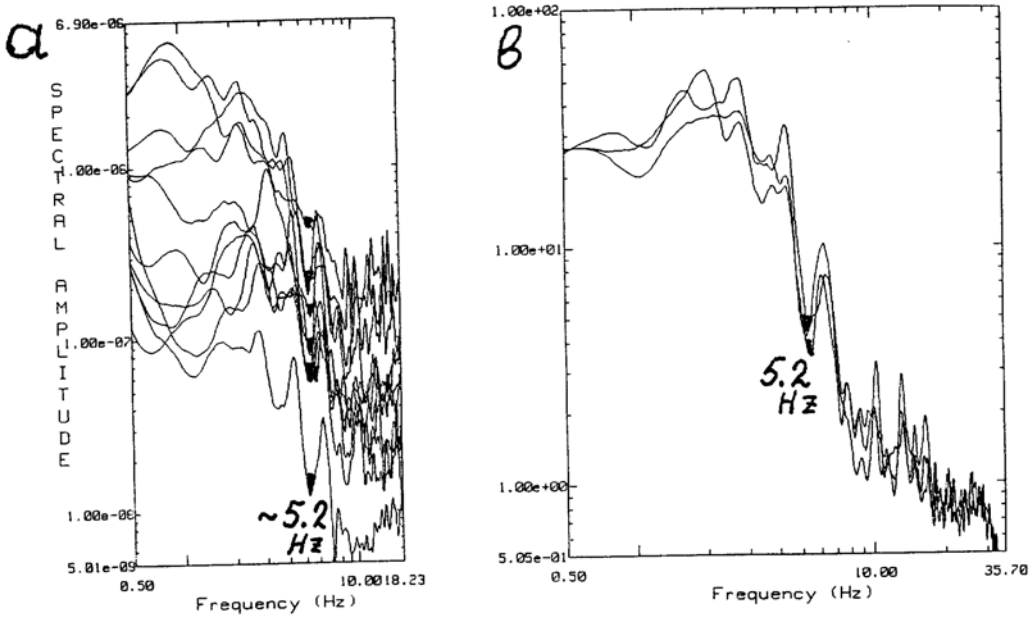


Figure 5. Spectral modulation and the first spectral null feature for EX.1 at ISN stations (a) and at BB EIL 3C station, band-pass filter 0.5-40 Hz (b).

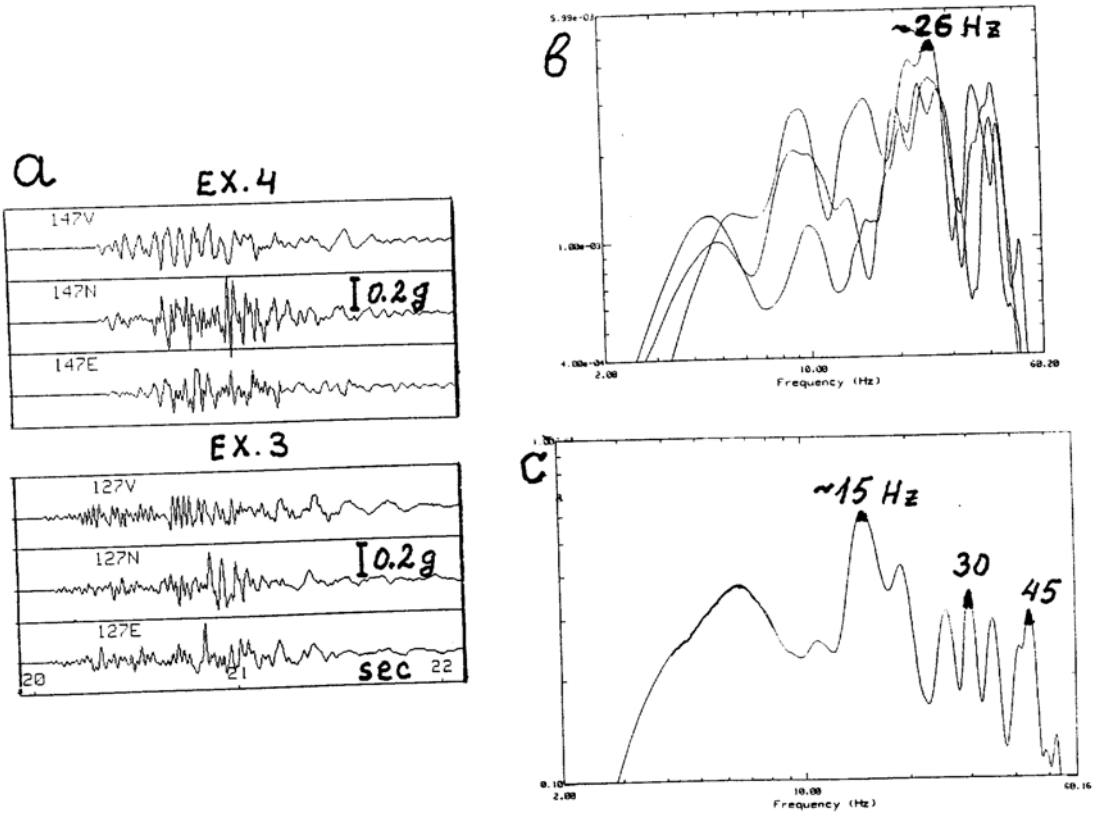


Figure 6. Near-field observations of the blasts: (a) 3-component accelerograms; (b) spectra for EX.2;

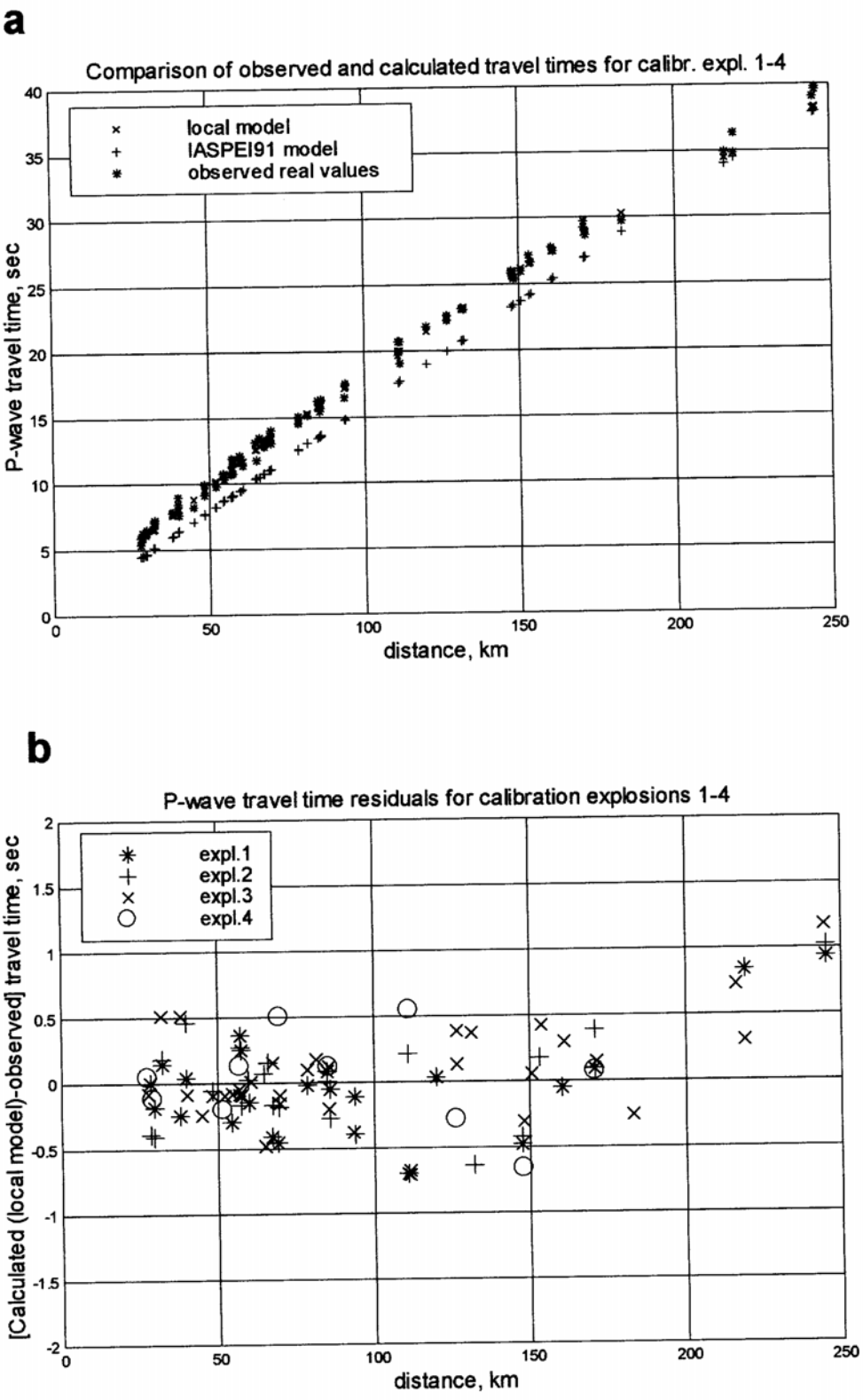


Figure 7. Travel time analysis: (a) observed values for different blasts compared with IASPEI91 and local models; (b) time residuals (observed – calculated) for the local model.

AN ANALYSIS OF LOW FREQUENCY SEISMIC SIGNALS FROM LARGE MINING BLASTS

MICHAEL A.H. HEDLIN

INSTITUTE OF GEOPHYSICS AND PLANETARY PHYSICS
UNIVERSITY OF CALIFORNIA, SAN DIEGO

SPONSORED BY DEFENSE THREAT REDUCTION AGENCY
CONTRACT NO. DSWA01-97-C-0153

ABSTRACT

The worldwide standard mine blasting practice involves a cascade of shots which are used to effectively fracture the rock. It is well established that this delay-fire shooting practice causes interference of the individual wavefields that will introduce artifacts (such as spectral modulations) into the regional seismic wavefield that can be diagnostic indicators of blasting and therefore useful for discriminating these events from earthquakes and nuclear tests. Source intershot delay times are typically on the order of 35 msec and therefore the most obvious interference effects are seen at 30 Hz or above. As the standard IMS station samples at 40 Hz, and because of rapid attenuation of high frequencies during propagation, these artifacts will not commonly be seen under typical CTBT monitoring conditions. This paper explores low-frequency (0.1 to 10 Hz) signals produced by the most important - the largest - mining blasts.

Kiloton class mine blasts are not uncommon in numerous regions worldwide such as Wyoming, Kentucky and, at least historically, the Kuzbass mining region in Russia. Our focus has been on large cast blasts in the Powder River Basin in Wyoming and in the Kuzbass. A recent regional experiment in Wyoming has produced evidence that large cast blasts commonly produce spectral modulations at frequencies from 1 to 10 Hz. Source modeling of these extremely complex events does not reproduce the exact spectral character but indicates the modulations are due to long inter-row delays and source finiteness. Recordings of instantaneous calibration shots exhibit no such modulations and indicate this spectral character should be useful for distinguishing these events from nuclear tests at IMS stations.

The experiment also provided further evidence that these events produce unusually large surface waves between 2 and 10 s. Physical modeling of these events indicates that the surface waves are due mainly to the extended source duration and to a lesser extent to the slap-down of spalled material. Recordings made at 9.1° exhibit both the spectral modulations and surface waves and attest to the utility of these signals for characterizing these events using the IMS.

Recordings of large blasts in the Kuzbass mining region exhibit significant spectral modulations below 20 Hz however surface waves are not routinely produced by these events.

Key words: Spectral modulations, attenuation, surface waves, remote source characterization

OBJECTIVE

To develop high- and low-frequency seismic techniques to characterize mining explosions and discriminate these events from single explosions and earthquakes. The focus is on mining explosions that detonate as planned and on mining explosions which contain significant detonation anomalies. Our focus has been on spectral modulations and surface waves that will commonly propagate beyond near-regional distances to stations in the IMS monitoring network. We use physical modeling to identify the source processes that give rise to these signals.

This paper summarizes our research on low-frequency signals produced by significant (> 1 kT) mining explosions in Wyoming. We also report preliminary results from our analysis of Altai-Sayan mine blasts and earthquakes recorded since January 1, 1995 by the IMS seismic station ZAL near Zalesovo, Russia.

RESEARCH ACCOMPLISHED

Wyoming Kiloton-class Blasts

We have focused on blasts in Wyoming for several reasons. The largest blasts in the Powder River Basin (PRB) coal mining trend in NE Wyoming (Figure 1) delay fire several million pounds of ANFO to fracture and to displace near-surface rock to expose the coal seam. IMS seismic stations occasionally detect these cast blast events. Blasts in this area are carefully documented and have been the subject of several studies (incl. Stump and Pearson, 1997; Stump et al.,

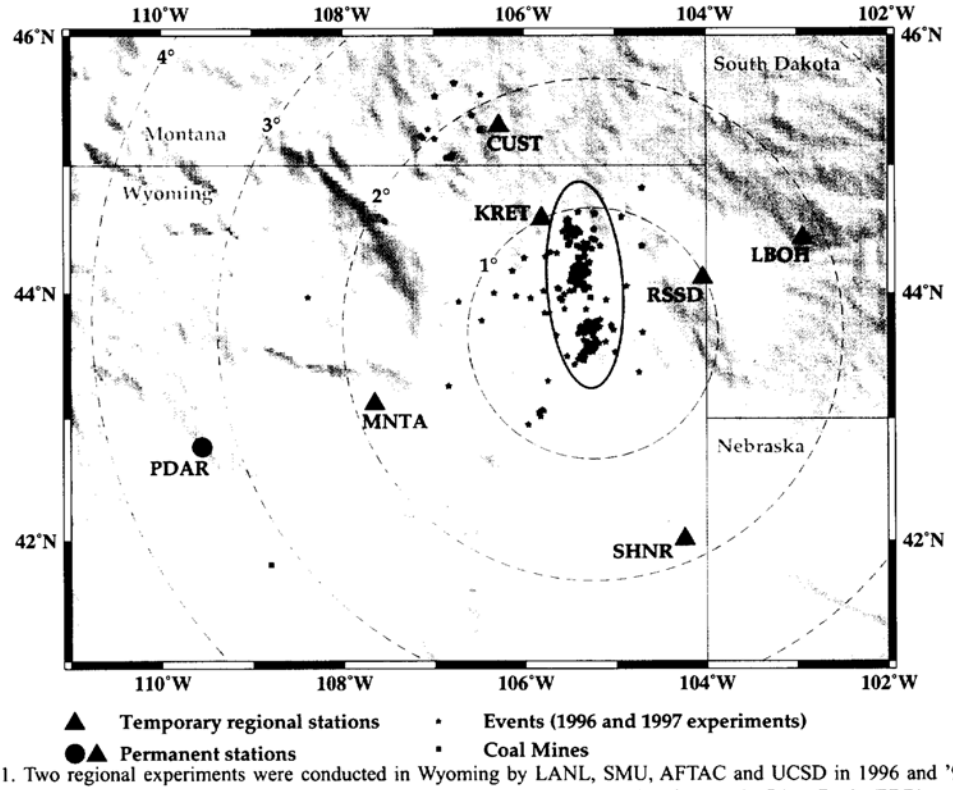


Figure 1. Two regional experiments were conducted in Wyoming by LANL, SMU, AFTAC and UCSD in 1996 and '97. Four broadband seismic stations (3-component STS2's) were deployed in a ring surrounding the Powder River Basin (PRB) at a range of 200 km from the Black Thunder coal mine. A fifth station (KRET) was deployed at a range of 100 km. Permanent seismic stations are located at PDAR and RSSD. Infrasound sensors were deployed at MNTA. Mining explosions detected by the temporary seismic stations during 49 days in 1996 and 1997 are plotted and correlate well with known mines. The slight northward bias is likely due to the 1D model. The oval indicates approximate limits of the PRB.

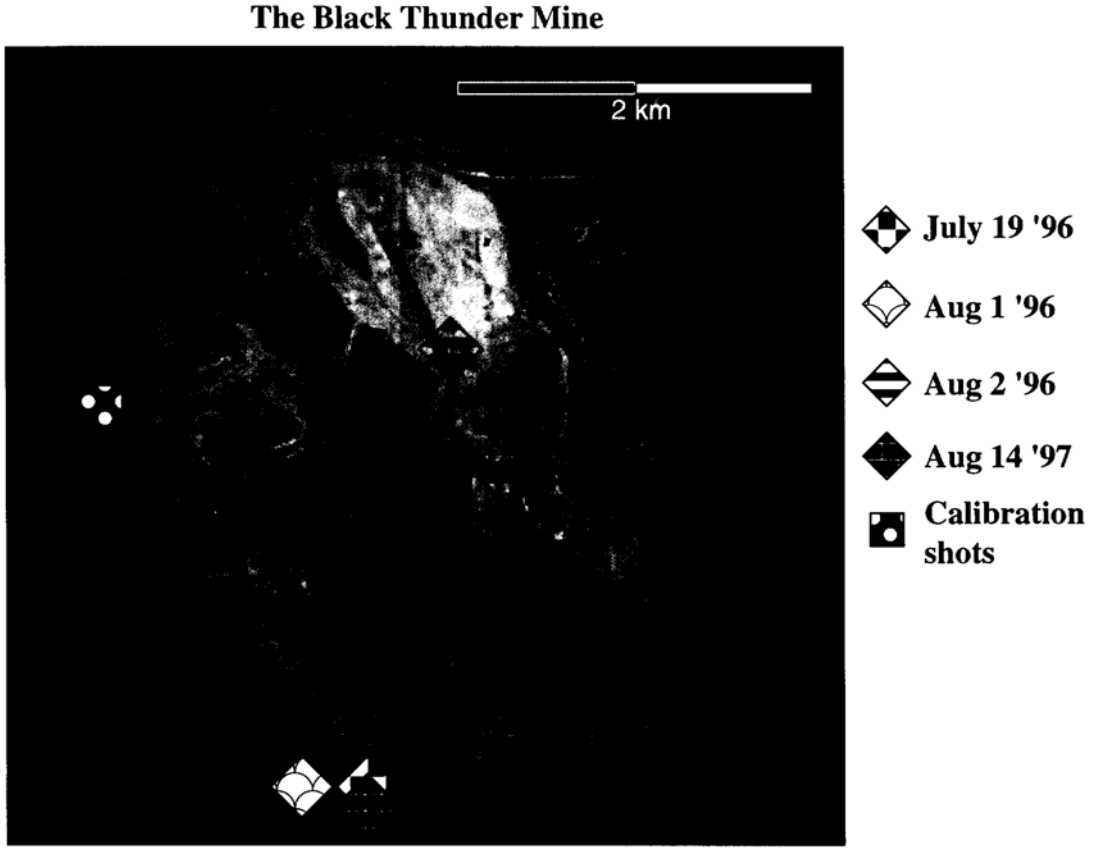


Figure 2. A satellite photo of the Black Thunder Coal mine in Wyoming. The symbols give approximate locations of the major events considered in this paper. The 1996 and 1997 experiments produced recordings of 4 significant cast blasts in the Black Thunder coal mine. The July 19, Aug 1.96 and Aug 14.97 blasts occurred at the west end of the south pit. The west end of the Aug 1 blast is believed to have detonated simultaneously. In the July 19, Aug 1, Aug 2 (all 1996) and Aug 14 (1997) cast blasts 4.5, 2.5, 2.8 and 7.0 million pounds of ANFO were detonated. The two largest calibration tests involved 12,000 and 16,000 pounds of ANFO.

1998). Shot specifications are readily available and thus these events can be modeled and used to better understand how large mine blasts can be distinguished from all other seismic events.

Field Experiments

The results in the present study came from recordings made by temporary seismic stations deployed in 1996 and 1997 at near-regional distances from the PRB (Figure 1). The field experiment was a collaborative effort with B. Stump (SMU/LANL), C. Pearson (LANL) and V. Hsu (AFTAC). The experiment was funded by LANL under the contracts 1973USML6-8F and F5310-0017-8F. The analysis was a collaborative effort involving these scientists and X. Yang (LANL). The results are reported in detail in Hedlin et al., (1999). The events of greatest interest to us occurred in the Black Thunder mine and are depicted in Figure 2. The largest cast mine blast occurred in the south pit and involved 7 million pounds of ANFO. The 1997 experiment produced records of this event and several instantaneous calibration shots that ranged in yield from 5000 to 16000 pounds.

The regional experiments were conducted to examine the dependence of low frequency (10s to 10 Hz) signals from the large mine blasts on range and azimuth. Previous studies (incl. Stump and Pearson, 1997, Anandakrishnan et al., 1997) found significant surface waves produced by the cast blasts in recordings made by the Pinedale seismic array

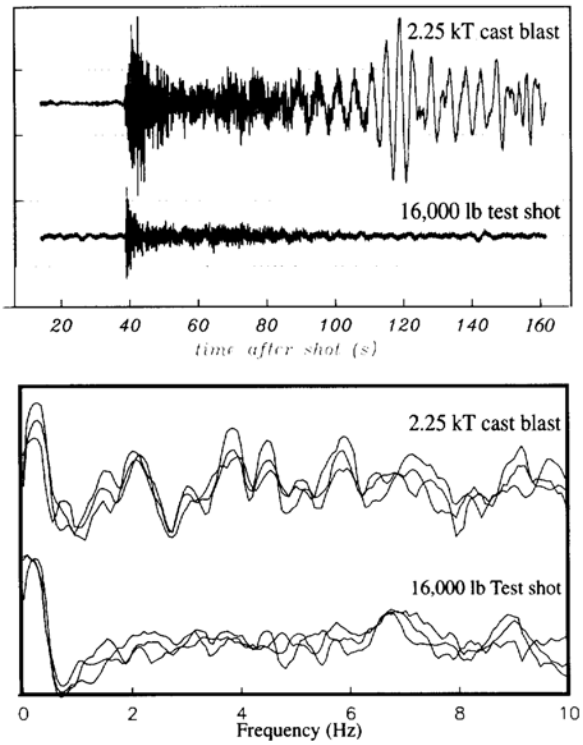


Figure 3. In the upper panel we show unfiltered vertical component recordings of the July 19, 1996 Black Thunder cast blast (top trace) and a 16,000 calibration shot made at CUST (Figure 1). In the lower panel we show spectra taken from the 3 components recorded at CUST. The cast blast is the only event that produced a significant surfae wave and clear spectral modulations below 10 Hz.

(PDAR; Figure 1).Stump (personal communication) found evidence for weak spectral modulations at high frequency at local distances from these events. The absence of strong modulations that normally are produced by millisecond delay-fired events such as these is likely due to source effects (e.g. shot scatter) and propagation losses.

As reported in earlier papers (Hedlin, 1998a,b; Hedlin et al., 1999) the regional recordings indicate that these events produce very energetic surface waves and significant spectral modulations below 10 Hz (Figure 3). These signals were recorded by all stations in the regional network and were seen as far away as the IMS station ULM at a range of 9.1°.

The utility of the surface waves for characterization of the mine blasts is suggested by Figure 4. In this figure we display peak amplitudes in two frequency bands , 1 to 10 Hz and from 2 to 10 s, of signals produced by the cast blasts and instantaneous explosions and recorded by the stations in the outer ring of the regional network. We plot single station amplitudes and unweighted network average amplitudes. The body waves produced by the calibration shots and the cast blasts are not markedly different with the exception of the August 1, 1996 cast event which has elevated body wave amplitudes due to the unplanned near-simultaneous detonation of a portion of the shot grid. The time-domain feature that clearly separates the two event types is the surface wave amplitudes. The calibration shots produced no mid-period surface waves above noise whereas significant surface waves were produced by each of the cast blasts.

Physical Modeling

To give these basic observations a physical basis we turn to synthetics. The synthesis of extraordinarily complex mining explosions has become relatively easy given the early work of BARKER ET AL. (1990, 93) and MCLAUGHLIN ET AL. (1994) and recent work by X. Yang who has modified the linear elastic algorithm of ANANDAKRISHNAN ET AL. (1997) and packaged it into an interactive MATLAB package (MineSeis; YANG, 1998). The algorithm assumes the linear superposition of signals from identical single-shot sources composed of isotropic and spall components. Both shooting delays and location differences among individual shots are taken into account in calculating delays of the superposition, although the Green s functions are assumed to change slowly so that a common Green s function is used for all the single shots. We used a reflectivity method to calculate the Green s functions. A 1-dimensional velocity model was used (PRODEHL, 1979; ANANDAKRISHNAN ET AL., 1997).

To model the July 19 cast blast we used a blast report issued by the Black Thunder Mine. The blast consisted of 7 rows and a total of 620 decked shots with a total yield of 4.5 million pounds. In a decked shot, more than one charge is detonated in the same hole. In this event, each hole contained two charges separated by 50 to 200 msec. Although the number of shots in each row varied from 85 to 93, for simplicity we assumed each row had 89 shots and that each decked shot had a total yield of 0.0033 kt. We assumed that all rows were spaced by 9.1 m and that all adjacent shots in the same row were 10.4 m apart. Intershot delays were 35 msec, interrow delays ranged from 200 to 275 msec. We assumed each decked shot spalled 20 kt of material that was cast at an angle 10° above the horizontal and fell 20 m. SOBEL (1978) estimated that 9.6 x 10^9 kg of material is spalled by each kt detonated. In our experiment, each decked

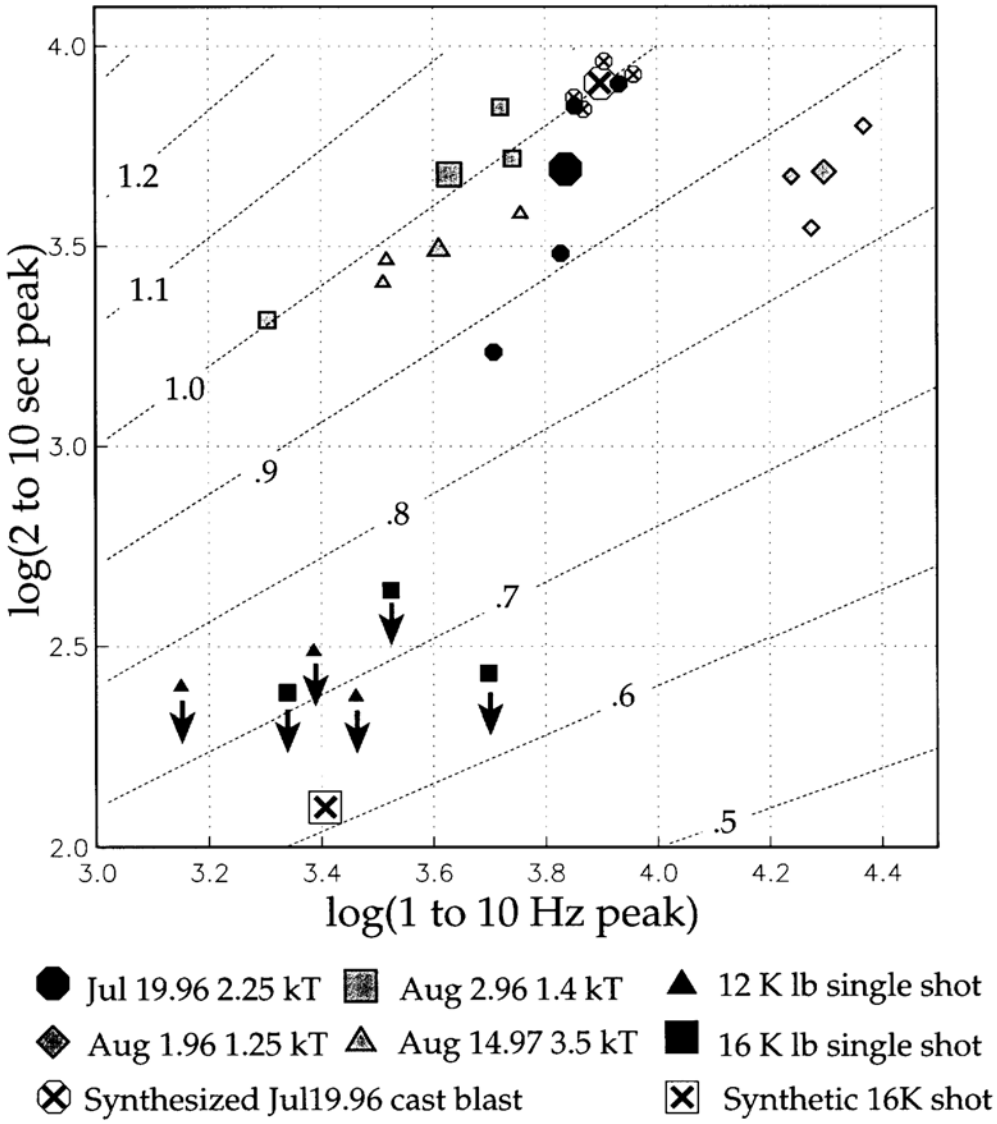


Figure 4. A comparison of 2 to 10 second surface wave and 1 to 10 Hz P wave peak amplitudes using recordings made at a range of 200 km by MNTA, CUST, LBOH & SHNR (Figure 1). All events occurred in the Black Thunder coal mine. Each trace is filtered, converted to an envelope and adjusted downward by an amount determined by pre-onset noise. Above are displayed the logarithms of the individual station peak amplitudes. The large symbols represent the network average for each event. Each labeled curve indicates a constant ratio of surface wave to *P* wave amplitude [*i.e.* log(2to10s peak)/log(1to10Hz peak)]. As expected the calibration shots yield essentially no surface wave energy above noise. The downward arrows indicate that the maximum *P* wave amplitude is well constrained but the surface wave amplitude lies below noise. For this reason, no network averages are displayed for these events. The Aug 1.96 cast shot appears as being somewhat explosion-like due to the sympathetic detonation. The sympathetic detonation greatly boosted P wave amplitudes but left the surface waves untouched. Unadjusted amplitudes are plotted as all stations are at the same range from the mine. We also display peak amplitudes from a synthetic version of the July 19 cast blast and from a synthetic 16,000 pound calibration shot. The energy partitioning from the synthetic events is in agreement with observations.

shot had a total yield of 0.0033 kt and thus the Sobel relation gives ~31 kt of spalled material. For the July 19 Black Thunder event we found this figure yielded surface waves that were more energetic than those that were recorded and so we reduced the spall figure to 20 kt. This discrepancy can be due to the incomplete conversion of spalled kinetic energy into seismic or to inadequacy of the velocity model.

The peak amplitudes of the point source and the July 19, 1996 cast blast synthetics at a range of 200 km have been calculated for the 4 outer stations in the regional network and are displayed in Figure 4 with the observed amplitudes from the recorded events. Despite the assumptions listed above, we found the surface and body wave amplitudes produced by the synthetic event were consistent with the recorded waves at MNTA and CUST. The other two stations (LBOH and SHNR) yielded broadly dispersed surface waves that had lower peak amplitudes in the frequency band from 2 to 10 seconds. This pronounced mismatch is not due to unmodeled source effects but results from the propagation of the energy through a crust that differs significantly from the 1-dimensional Prodehl model. The azimuthal dependence that is seen in the synthetics is due to source directivity.

Experiments in Varying Source Parameters

Although we have reproduced the relative peak amplitudes of body and surface waves generated by the July 19 cast blast, several important questions remain unanswered. We have yet to determine which of the many source parameters included in the model play a leading role in generating the energetic surface waves. We need to gauge the sensitivity of the observed signals to changes in source parameters and to assess the utility of these signals for source characterization. ANANDAKRISHNAN ET AL. (1997) considered the effect of changes in several source parameters on regional waveforms. In this paper, we conduct a similar exercise however we are most interested in how these changes affect the partitioning of energy between the surface and body waves. We focus on the frequency bands considered in Figure 4. We consider a broad suite of mine blasts. The blasts we synthesize are all the same as the presumed correct one reviewed in the previous section except one source parameter is allowed to vary while the others are held fixed. In turn, we vary the spalled mass, individual shot yield, and the duration of the blast. In a separate experiment we also allowed shot times to deviate from the planned 35 msec delays. All synthetics are calculated for CUST, the station located 200 km to the north of the mine.

We consider peak amplitudes in two filtered versions of the synthetic traces. We filter the synthetic traces between 2 and 10 s, and between 1 and 10 Hz and calculate the log of the peak amplitude in each trace. In Figure 5, we display the ratio of the peak amplitude in the low frequency trace to that in the high-frequency trace. We display the ratios obtained from synthetic events in which a significant source parameter has been varied between 2.5% and 500% of the standard value. The filled circles in Figure 5 represent the result of varying individual shot yield. This effect is seen to be relatively minor as varying the yield over more than 3 orders of magnitude (from 182 to 36,300 pounds) changes the body-surface ratio by ~ 10%. This ratio change results from variations in both the surface and body wave amplitudes.

Varying the spalled mass has the opposite effect. When the spalled mass is varied from 0.5 kt to 80 kt (from 2.5% to 400% of the standard) the surface-body wave ratio changes from ~ 0.9 to 1.13 (filled triangles in Figure 5). The change in this ratio results from the effect spalled mass has on the surface waves as the spalled mass is predominantly a source of low-frequency energy. Changing the spalled mass had little effect on the body wave amplitudes. Although the production of surface waves is reduced when essentially no material is spalled into the pit, the restricted blast still produces surface waves that are significantly more energetic than those produced by the single shot.

The most significant changes in the waveform result from variations in the total duration of the blast. To vary the blast duration we scaled both the number of rows and the number of shots in each row. The standard blast had 7 rows and 89 shots in each row and lasted a total of ~ 4.8 s. The largest blast grid we considered had 10 rows, each with 200 shots. The extended blast spanned ~ 9.5 s - ~ 200% of the actual duration and had a total yield of 14 million pounds. The reduced blast grids consisted of 5 rows, 50 shots per row; 4 rows, 40 shots per row; 3 rows with 30 shots per row; 2 rows with 20 shots per row and 1 row with 10 shots. To reduce the blast further we decreased the number of shots in the final row to 5 shots and then to 3. The duration of these reduced blasts ranged from 3.1 s (for the blast with 5 rows and 50 shots per row) to 70 msec (for the smallest blast). As we see in Figure 5, extending the blast beyond the standard one that was used on July 19 yielded essentially no change in the surface-body wave amplitude ratio. However reducing the scale of the grid has a significant effect on the partitioning of energy between surface and body waves. Reducing the scale of the blast has a modest effect on body-wave amplitudes but the surface waves are strongly dependent on this source attribute. The ratio drops most rapidly when the blast duration is reduced below 2/10 of the actual duration

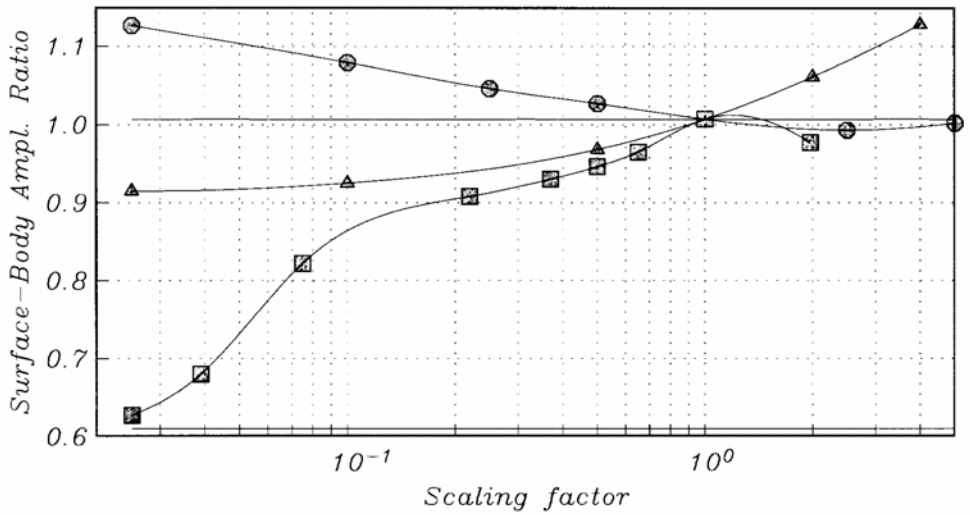


Figure 5. We display the surface-body wave ratios for a suite of blasts in which a single source parameter is varied while all others are held fixed at levels believed to be appropriate for the July 19, 1996 cast blast. The filled circles represent sources in which individual shot yield is varied from 182 to 36300 lb. The filled triangles represent blasts in which the spalled mass per shot is varied from .5 kt to 80 kt. The squares represent blasts grids that range from a single row with 3 shots to a 10 row blast with 200 shots in each row. Varying blast duration clearly has the most significant impact on energy partitioning. Only the severely restricted grid partitions energy like the synthetic 16,000 pound shot (represented by the horizontal line at a ratio of 0.61). All of these simulations assumed the subshots detonated exactly when planned.

(down to ~ 0.5 s from 4.8 s). The production of 2-10 s surface waves is reduced significantly when the blast duration is reduced below 2 seconds. When the blast duration extends much beyond 5 seconds, production of these surface waves is not increased substantially. Of all the blasts considered, just the brief blast resembled the single shot (which is represented by the horizontal line at a ratio of 0.61).

Spectral Modulations

The Wyoming events typically produce strong modulations that are independent of recording direction and time. These modulations are typically seen below 10 Hz and are seen beyond 9° from the source. Physical modeling by Hedlin et al. (1999) reproduces the general character of the modulations (the enhanced spectral roughness) however the fine details of the modulations has not been reproduced for any of the 4 events considered in this study. This is in spite of the fact that excellent shot information is available for the events. There are a number of reasons for the mismatch. Resonance is ever present and will cause additional spectral modulations. We know the spectral modulations we observe are not due to resonance as similar modulations are not seen in the spectra of instantaneous events (Figure 2). The modeling exercise has made a number of assumptions about the events. It is assumed that all shots have equal yield and adhere perfectly to the planned shooting times. Any deviations from the planned shot times will complicate the interference of the wavefields and will change the spectral modulations. If shot yield varies, and given variable coupling of the energy to seismic this is inevitable, the modulation pattern will be dominated by the few shots that have the largest effective yield.

The fine spacing of the modulations requires long delays at the source. We have concluded that these modulations result from long interrow delays (200 to 275 msec) and source finiteness (Hedlin et al., 1999).

Altai-Sayan events

The mines in the Altai-Sayan region in western Siberia produce 100 to 200 blasts each year with a magnitude of 3.5 or above (Khalturin et al., 1997). Of these, ~ 2 each year have a magnitude above 4.0 (Khalturin et al., 1997). This region includes the Kuzbass mine (~ 200 km SE of Novosibirsk) and the Abakan mine. These statistics rank this region as a leader in producing events that are detected by IMS stations (Khalturin et al., 1997). The mines are believed to be

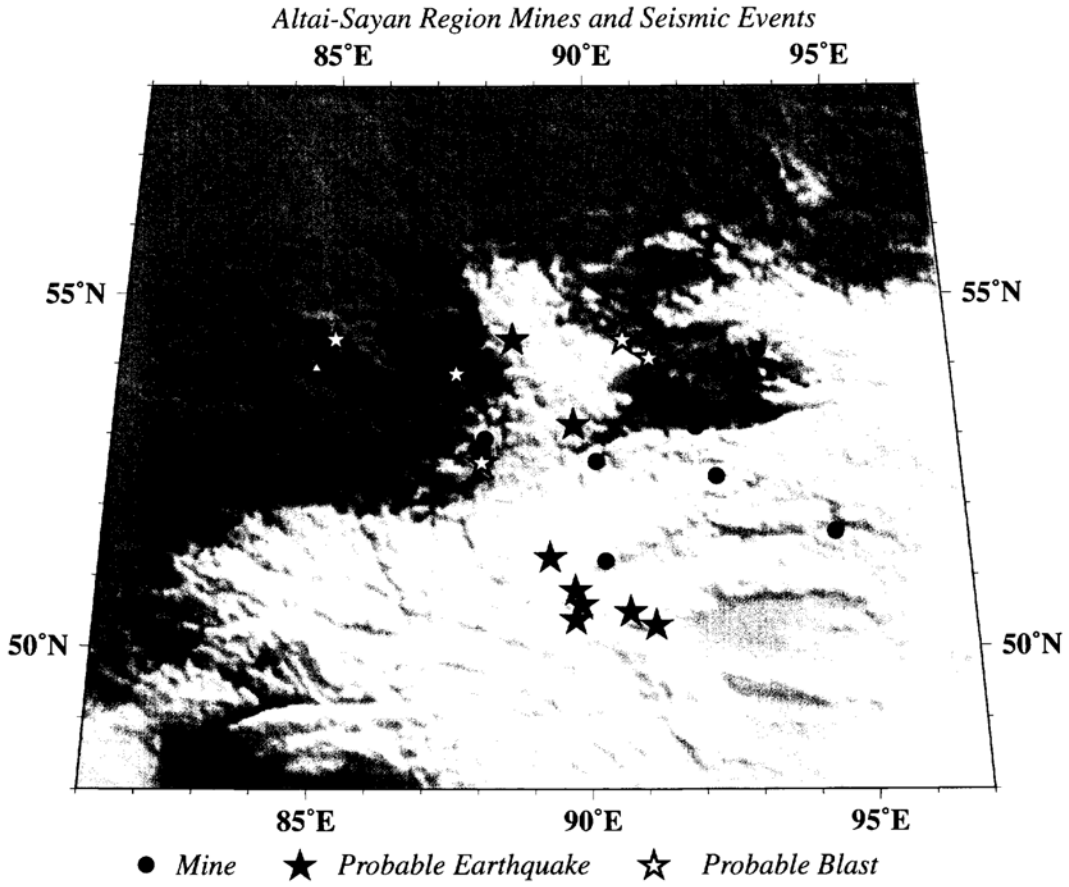


Figure 6. Altai-Sayan region mines, blasts and earthquakes. The event locations were taken from the REB catalog obtained from the PIDC web site www.pidc.org. Mine locations were taken from Khalturin et al. (1996).

extracting coal. The high magnitudes likely result from shooting entire rows of shots with no delay in each row (Paul Richards pers. comm.).

Despite having essentially no ground truth information we have examined events in this region to determine if the methods that appear to be effective in Wyoming also work here. What follows is a preliminary study of 14 events that were recorded at the IMS station ZAL from Jan 1, 1995 to July, 1999. Event and mine locations are shown in Figure 6.

Our preliminary study of events in this region has produced mixed results. In Figure 7 we display 2 to 10 second filtered vertical component records from the IMS station ZAL. Although the blasts shown here had magnitudes above 3.0, and are on par with the Wyoming blasts considered earlier, just one produced a significant mid-period surface wave. This event occurred at a range of 2.35° from ZAL and was assigned an mb of 3.6. Although definitive conclusions are not possible given the lack of detailed information about how these blasts were detonated it is likely that these events have high magnitudes due to the shooting of rows with no delays in each row. The absence of significant 2 to 10 second surface waves in most blasts suggests that the overall shot duration is < 2 seconds.

The mine blasts however do produce significant spectral modulations below 20 Hz (Figure 8). The modulations are typically spaced at ~ 5 Hz and suggest an interrow time spacing of ~ 200 msec.

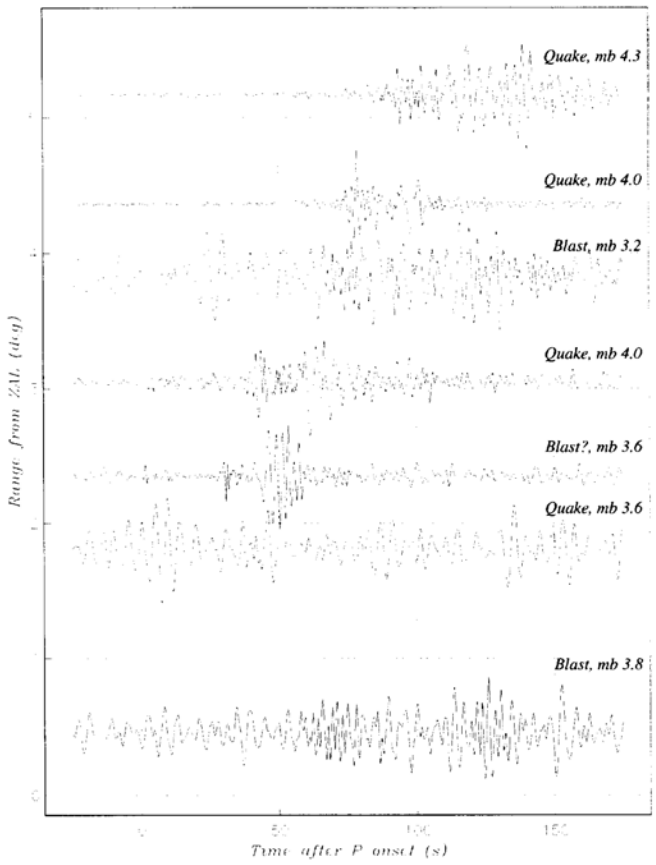


Figure 7. Vertical component (MHZ) recordings made by the IMS station ZAL near the Altai-Sayan mining region in western Siberia. The records have been filtered to 2 to 10 s. Two of three blasts shown here did not produce surface waves above noise in this band.

CONCLUSIONS AND RECOMMENDATIONS

Although virtually all large mining blasts worldwide involve delay-firing, the fine details of how individual shots are delayed with respect to one another depends on the exact practical needs at each location. Shooting practice is highly variable and thus there is a very complex relationship between event magnitude and the kinds of seismic signals that will be produced.

In Wyoming, where millisecond shot delays are used with longer delays between rows and between decks, the large blasts (> 1 kt of explosives) routinely generate significant mid-period surface waves and obvious spectral modulations below 10 Hz. Physical modeling indicates that the surface waves are due mainly to the extended duration of these events. The modulations appear to be due to long interrow and interdeck delays and source finiteness.

Events in the Altai-Sayan mining region in western Siberia have similar seismic magnitudes but are otherwise markedly different. The occasional blast in this region produces significant 2 to 10 second surface waves. Most mine blasts produce significant spectral modulations spaced at ~ 5 Hz. Although we cannot make definitive conclusions regarding the sources due to the lack of ground truth data, we conclude that the spectral modulations are due to long (~ 200 msec) interrow delays. The lack of mid period surface wave energy indicates that most, if not all, mine blasts in this region have a duration of < 2 seconds.

Unannounced mining events that include significant simultaneous explosive energy releases are problematic for several reasons. Such blasts are unwanted by the mining community as these events have both reduced rock-fracturing efficiency and increased seismic efficiency. Some of these blasts will trigger the IMS and cause some to question whether the anomalous energy release was chemical in nature. Effective characterization techniques, which rely on remote IMS observations, will reduce the need for on-site inspections. Our preliminary analysis suggests that such events can be identified using spectral modulations and the relative strength of surface and body wave seismic energy. A fuller analysis of errant blasts will be the subject of a forthcoming paper.

REFERENCES

Anandakrishnan, S., Taylor, S.R., and Stump, B.W. (1997), Quantification and characterization of regional seismic signals from cast blasting in mines: A linear elastic model, *Geophysical Journal International,* **131**, 45-60.

Barker, T.G., and Day, S.M. (1990), A simple physical model for spall from nuclear explosions based upon two-dimensional nonlinear numerical simulations, PL report SSS-TR-93-13859.

Barker, T.G., McLaughlin, K.L., Stevens, J.L., and Day, S.M. (1993), Numerical models of quarry blast sources: the effects of the bench, *PL semiannual report, SSS-TR-93-13915.*

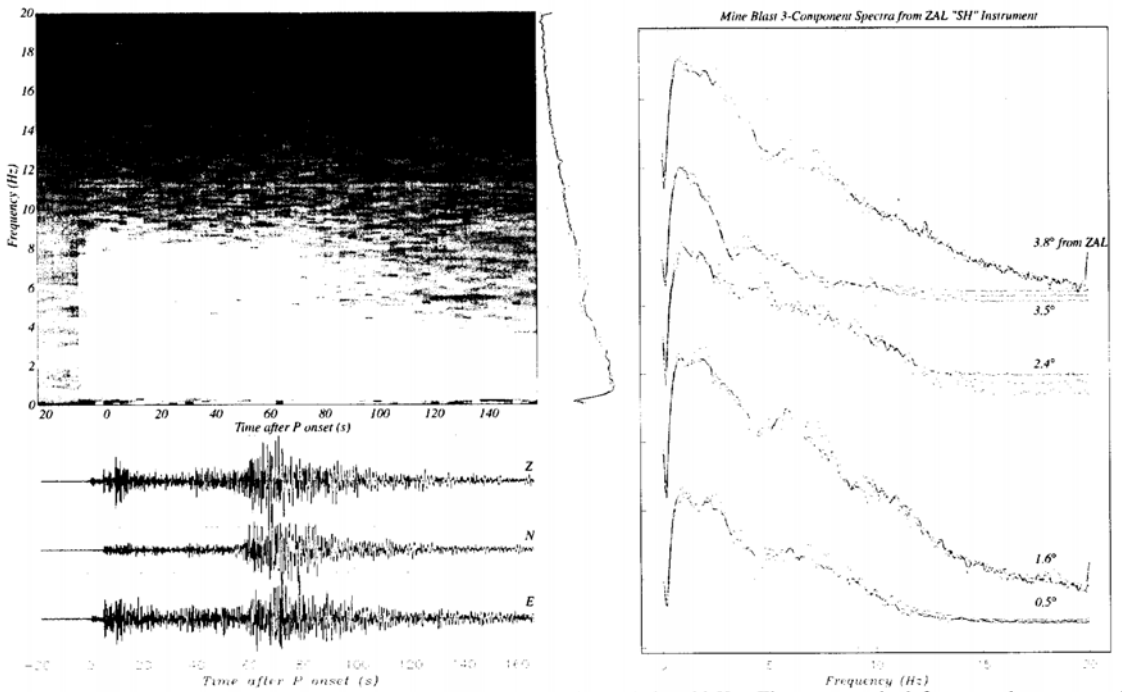


Figure 8. Altai-Sayan mine blasts routinely produce spectral modulaions below 20 Hz. The event on the left occurred at a range of 3.83° from ZAL. A clear spectral notch is present at 5 Hz. No modulations above noise are seen above 10 Hz. On the right we show five events believed to be mine blasts as a function of range. The event at 2.4° occurred during the day at one of the mines shown in Figure 6. The waveform has a sharp P wave onset however the classification of this event as a mine blast is questionable as only a weak spectral modulation can be seen. This event is also shown in Figure 7.

Hedlin, M.A.H. (1997), A global test of a time-frequency small event discriminant, *AFTAC/DOE/DSWA Seism. Res. Symp.*, **19**, 390-399.

Hedlin, M.A.H. (1998a), Identification of Mining Blasts at all Regional Distances using Low-Frequency Seismic Signals, *20th Annual Seismic Research Symposium,* **20**, 335-344.

Hedlin, M.A.H. (1998b), A global test of a time-frequency small-event discriminant, *Bull. Seism. Soc Am., **88**, 973-988.*

Hedlin, M.A.H., Minster, J.-B., and Orcutt, J.A. (1989), The time-frequency characteristics of quarry blasts and calibration explosions recorded in Kazakhstan, U.S.S.R., *Geophys. J. Int.*, **99**, 109-121.

Hedlin, M.A.H., Stump, B., Pearson, D.C., and Yang, X. (1999), Identification of mining blaslts at mid- to far-regional distances using low-frequency seismic signals, *in review with PAGEOPH.*

Khalturin, V.I., Rautian, T.G., Richards, P.G., and Kim, W.Y. (1996), Evaluation of chemical explosions and methods of discrimination for practical seismic monitoring of a CTBT, *Phillips Lab Report PL-TR-96-2172.*

Khalturin, V.I., Rautian, T.G., Richards, P.G., and Kim, W.Y. (1997), Evaluation of chemical explosions and methods of discrimination for practical seismic monitoring of a CTBT, *Phillips Lab. draft Final Report.*

McLaughlin, K.L., Barker, T.G., Stevens, J.L., and Day, S.M. (1994), Numerical simulation of quarry blast sources, PL final report SSS-FR-94-14418.

Prodehl, C. (1979), Crustal structure of the western United States, *US Geological Survey Professional Paper,* 1034.

Sobel, P.A. (1978), The effect of spall on mb and Ms, *Teledyne Geotech Rept.,* **SDAC-TR-77-12**, Dallas, TX.

Stump, B.W., and Pearson, D.C. (1997), Comparison of single-fired and delay-fired explosions at regional and local distances, *19th annual Seism. Res. Symp.* 668-677.

Stump, B.W., Hedlin, M.A.H., Pearson, D.C., and Hsu, V. (1999a), Characterization of Mining Explosions at Regional Distances, *Reviews of Geophysics - in review.*

Stump, B.W., Pearson, D.C., and Hsu, V. (1999b), Empirical scaling relations for contained single-fired chemical explosions and delay-fired mining explosions at regional distances, 1999 SSA meeting.

Yang, X. (1998), MineSeis - A Matlab GUI Program to Calculate Synthetic Seismograms from a Linear, Multi-Shot Blast Source Model, *20th annual Seism. Res. Symp.* 755-764.

Constraining the Depth and Source Mechanism for Smaller Events at Far-regional to Teleseismic Distances

B.L.N. Kennett
Research School of Earth Sciences, Australian National University,
Canberra ACT 0200, Australia

Grant: DSWA01-97-10023
Sponsored by: DOE

ABSTRACT

Techniques for source mechanism inversion are well established for using long period recordings for large events. The challenge for extending such methods to smaller events is to ensure that sufficiently accurate synthetic seismograms are available for comparison with observed records which include the interference with surface multiples and appropriate crustal reverberations.

An effective approach for teleseismic synthetics has been developed for both P and S arrivals which can allow for different crustal structures at the source and receiver with a full allowance for shallow multiples and conversions. Core reflections and refractions, which can become important in different distance ranges, can also be included. With the aid of these full synthetics it is possible to test different levels of approximation. For P waves at least we can reproduce much of the behaviour using simplified approximations.

The simplified synthetics are being used to develop a systematic nonlinear inversion scheme linking a travel-time location scheme and waveform inversion (including depth phases) to constrain both depth and source mechanism. Both the location and waveform inversion procedures make use of the Neighbourhood Algorithm developed by Sambridge (1999).

Because location using a sparse network is most effective when arrivals of different character can be employed, an effort has been made to develop systematic means of detecting and identifying seismic phase, particularly in the far-regional to near teleseismic regime. The combination of a range of methods using amplitude, frequency character and correlation properties can indicate the presence of arrivals even in the presence of significant noise. Polarisation measures can then help to assign phase character and thus aid identification. The phase information can then be used in the nonlinear location scheme.

Key words: Event location, source mechanism, waveform inversion, depth phases, phase detection

B.L.N. Kennett

OBJECTIVE

The prime objective of this work is to provide procedures which can exploit the character of seismic observations at far-regional to teleseismic distances and so transfer analysis of both source-mechanism and depth based on waveform inversion to smaller events.

Such analysis is regularly applied for large events using long-period seismograms, but for smaller events has to be carried out on shorter period information. In consequence it is necessary to make a careful development of the propagation model, including realistic models of crustal and uppermost mantle at both source and receiver. The work is directed to the far-regional to near-teleseismic interval (12°-50°) for which there is usually moderately good recording of P and on broad-band recordings, often reasonable S. The details of structure in the mantle become less important as the range increases. Waveform inversion will be focussed on simplified propagation models but full calculations of synthetic seismograms will be needed as a check on the results.

The inversion procedure builds on information from location using travel times yielding latitude, longitude and origin time and then employs a range of depths to try to exploit the interference between the direct arrivals and their surface multiples as a depth control. Feedback is required between the depth and source mechanism inversion and the primary location estimates.

The accuracy of event location is enhanced if multiple seismic phases can be employed and so a further objective is to develop techniques which can help seismic analysts to recognise and exploit later seismic phases.

The primary utility of this research in promoting discrimination of seismic events lies in the effort to enhance the quality of location estimates and to provide constraints on the source mechanism. The source depth should be better constrained and therefore more useful as discriminant by isolating events beyond the depth of penetration by man-made activities. The extent to which a source mechanism is compatible with an isotropic (explosive) component will also be significant.

RESEARCH ACCOMPLISHED

The approach which we are pursuing depends on being able to exploit selected segments of observed seismograms using information derived from synthetic seismogram calculations. Detailed matching depends on the availability of a good estimate of the source location and particularly the depth, as well as a fair estimate of the source mechanism.

Synthetic seismogram generation and utilisation

Full response

Our object is to construct synthetic seismograms at teleseismic distances and we do this by an adaptation of the reflectivity method (Kennett 1983, 1988a,b). We build the response of a stratified medium in the frequency-slowness (ω, p) domain in terms of the reflection and transmission properties of different parts of the structure.

We construct the response in a form which allows the introduction of different structures in the vicinity of the source and receiver above z_J and a simple mantle structure below extending down to a level z_L. The surface ground motion for a source at a level z_S is then

$$\begin{aligned} \boldsymbol{w}_0^{tel} \;=\; & \mathbf{W}_U^f[\mathbf{I} - \mathbf{R}_D^{0J}\mathbf{R}_U^f]^{-1}\,\mathbf{T}_U^{0J}\cdot && (r) \\ & \cdot\mathbf{R}_D^{JL} && (m) \\ & \cdot\mathbf{T}_D^{SJ}[\mathbf{I} - \mathbf{R}_U^{fS}\mathbf{R}_D^{SJ}]^{-1}\,(\boldsymbol{\Sigma}_D^S + \mathbf{R}_U^{fS}\boldsymbol{\Sigma}_U^S), && (s) \end{aligned} \qquad (1)$$

where we have written the expression in a way that emphasises the different parts of the propagation process. The propagation elements (s) represent the radiation from the source and reverberations in the structure near the source, the middle term (m) represents the mantle contribution and the first group of terms (r) correspond to the contribution from structure in the neighbourhood of the receiver.

For receiver ranges between 3500 km and 9500 km it is common to represent the PP, SS or HH elements of the mantle reflection matrix $\mathbf{R}_D^{JL}$ via approximations such as

$$(\mathbf{R}_D^{JL})_{PP} \sim \exp\{i\omega\tau_m(p) - i\tfrac{\pi}{2}\}Q(\omega), \qquad (2)$$

where $\tau_m(p)$ is the phase delay for the mantle below the separation level z_J and we have also included an allowance for attenuation.

The surface ground motion can be recovered from the frequency-slowness response by making use of the vector surface harmonic representation of the seismic wavefield. We can achieve good results by using a discrete representation of the slowness integral using a bundle of slownesses centred on the geometric slowness for the *P* or

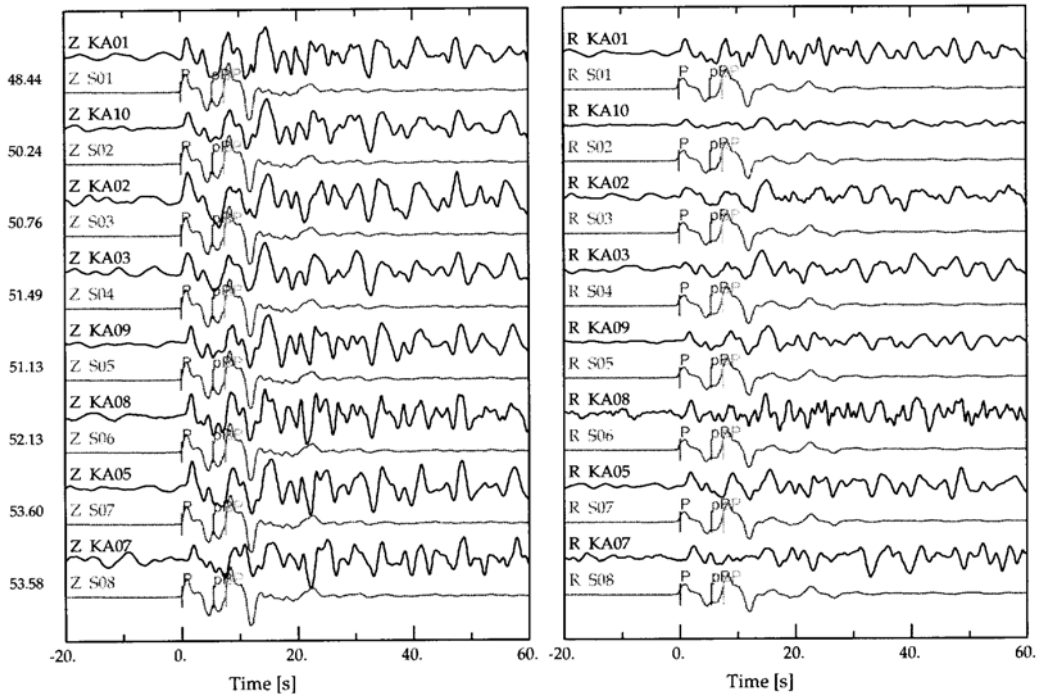


Figure 1. Comparison between observed and synthetic *P* wave seismograms for the Fiji event 1997 day 220, for the vertical (left) and radial (right) components. The black traces are the observed seismograms, and the grey traces are the synthetic seismograms in both cases. The traces are aligned on the theoretical *P* arrival, and the theoretical travel time curves are superimposed on the synthetic seismograms. The epicentral distances are indicated on the left-hand scale.

S arrival, at each frequency ω. In this way we can cover the surface multiples and crustal reverberations through the structure of the (ω, p) response without explicit calculations of the individual contributions.

For shallow events, most of the character of the interference packet comprising *P*, *pP* and *sP* can be reproduced by simpler approximations which are then suitable for use in a nonlinear inversion scheme.

Comparison with observations

As a illustration of the synthetic seismogram calculations at teleseismic distances, we synthesise the records of an event in the Fiji Islands region recorded in northwestern Australia, at epicentral distances of around 50°. The stations are fairly close together, therefore we can illustrate how the seismogram character varies over a small distance range. The source depth (17 km) and mechanism were taken from the Harvard CMT catalog. The event has an estimated moment magnitude of 6.6, and so the records have a noticeable long-period component.

Figure 1 compares the observed and synthetic seismograms for the vertical and radial components of the *P* wave. We have employed a trapezoidal far-field source-time function is used, with empirical time segments for the positive, zero and negative slopes of 1.25 s, 2.50 s and 1.25 s. The synthetics were calculated using the *ak135* velocity model, with the corresponding attenuation profile of Montagner and Kennett (1996). With a small time shift applied to the synthetics, to compenstae for the difference between the onset and centroid times, we can achieve a good fit for the first part of the *P* wave seismograms (*P*, *pP*, *sP*) in figure 1. The estimated source depth of 17 km, obtained from the Harvard CMT catalog, provides a good fit to the relative arrival times of the direct *P* wave and its surface reflections.

Source inversion

Our major effort is now directed towards inversion for hypocentral parameters and source mechanism exploiting the Neighbourhood Algorithm of Sambridge (1998,1999) which we have already shown to be very effective for arrival

time location. This nonlinear inversion scheme provides a means of "zooming" in on the best fitting regions in a multi-dimensional parameter space.

We envisage the following steps in the procedure for source mechanism and source depth inversion:

(1) Invert for source location, given by the four parameters Δ, ϕ, h, t_o. The seismogram depends non-linearly on these parameters through the Green's tensor elements. We will use the Neighbourhood Algorithm as a non-linear location procedure with arrival time information to get an estimate of the hypocentral parameters

(2) Invert for the source mechanism using the hypocentral parameters obtained from step 1, and a range of source depths based around the estimated depth. A simple approach for calculating P, pP, sP and S, pS, sS will be best as we need to be able to perform calculations very rapidly in order to make inversion feasible. We will use a simplified synthetic seismogram scheme with an approximation to the interference packets produced by the direct waves and their surface reflections (similar to the approach adopted by Goldstein and Dodge, 1998). We intend to use a envelope matching procedure which will concentrate on relative amplitudes of arrivals, as well as using the cross-correlation between observed and synthetic seismograms to match the detail of waveforms. Inversion for source depth is non-linear and we will employ a full non-linear scheme with a moment tensor representation of the source.

For discrimination purposes it will be necessary to allow for an isotropic component in the source estimate. The source inversion could be done in two ways. Firstly, restricting the source mechanism to a shear dislocation (with no isotropic component), and secondly, with no restriction on the isotropic component (allowing for a moment tensor with non-zero trace). The fit of the two types of inversions can then be compared in order to estimate the significance of any isotropic component.

(3) Once the best fitting source depth and source mechanism have been obtained from the previous step we can try to relocate the event. The improved depth constraints can be fed back into the source location procedure in order to refine the estimate of the hypocentral parameters. If necessary these refined source location parameters could then be used again in step 2 again to obtain an updated estimate of the source mechanism.

(4) The final step will be to compute full synthetic seismograms using the best estimate of the hypocentral parameters and source mechanism. This will be used as a cross-check for the match to the full range of phases including the core reflections and core phases. These calculations would also provide a check in case of misidentification of phases, for example if crustal reverberations have been misidentified as a surface reflection.

Phase detection and characterisation

We have continued to develop techniques which are suitable for automated phase detection and characterisation of the detected arrivals. Many methods have been devised for event picking and each of these is based on the separation of signal and noise in a particular domain and so can not ensure consistent onset time picking under all source, receiver, path and noise conditions. However, a combination of four methods based on differing aspects of the seismic wavefield can be used to provide automated and consistent onset time picking and event location using a single three-component record. This approach is suitable for real-time use. For arrival detection, a combination of energy analysis, the differences in instantaneous frequency and the nature of the coefficients in an auto-regressive representation of the seismic record are used to develop an algorithm for robust picking of phase arrivals. The phase characterisation is aided by using a number of wavefield measures based on polarisation analysis using complex traces (based on Vidale 1986). These measures help to separate S and P wave phases.

The detection procedure is based on combining information on the changing amplitude of the seismic traces, the current frequency content of the trace and the correlation properties of the wavetrain. These three approaches are based on recognising the differing content of noise and signal in different domains, and we have further extracted three different measures from each method. For energy analysis, the three measures are the total energy (E_3), the vertical energy (Z_e) and the energy in the horizontal plane (H_e); for instantaneous frequency analysis, the three measures are FQ1, FQ2 and FQ3 based on different combinations of the 3-component records; for auto-regressive coefficient analysis (Leonard & Kennett, 1999), the three estimates are derived from the low order correlation coefficients (AR1), the medium order correlation (AR2) and the high order correlation coefficient (AR3).

The 9 attribute estimates from the three different methods are used construct an algorithm for phase recognition and onset time picks. Firstly, for for each of the attribute estimates from the different methods, we set a token equal to unity when the STA/LTA ratio surpasses a pre-set value, otherwise, the token is set equal to zero. Secondly, we declare a recognition or detection trigger when the combination of the nine attribute tokens exceeds a pre-specified value. We have used two different ways to combine such information and so follow the changes in the nature of the noise and signal. In the first approach (equal weighting – COM) we are only concerned with the sum of the tokens rather than the contributions of different methods. In the second (equal content – CM) we attempt to equalise the contribution from the different methods. Whichever process is used we specify two different pre-set thresholds for the combination. When the lower threshold is exceeded we represent the detection by a "small flag" and when the higher threshold is also reached we set a "big flag".

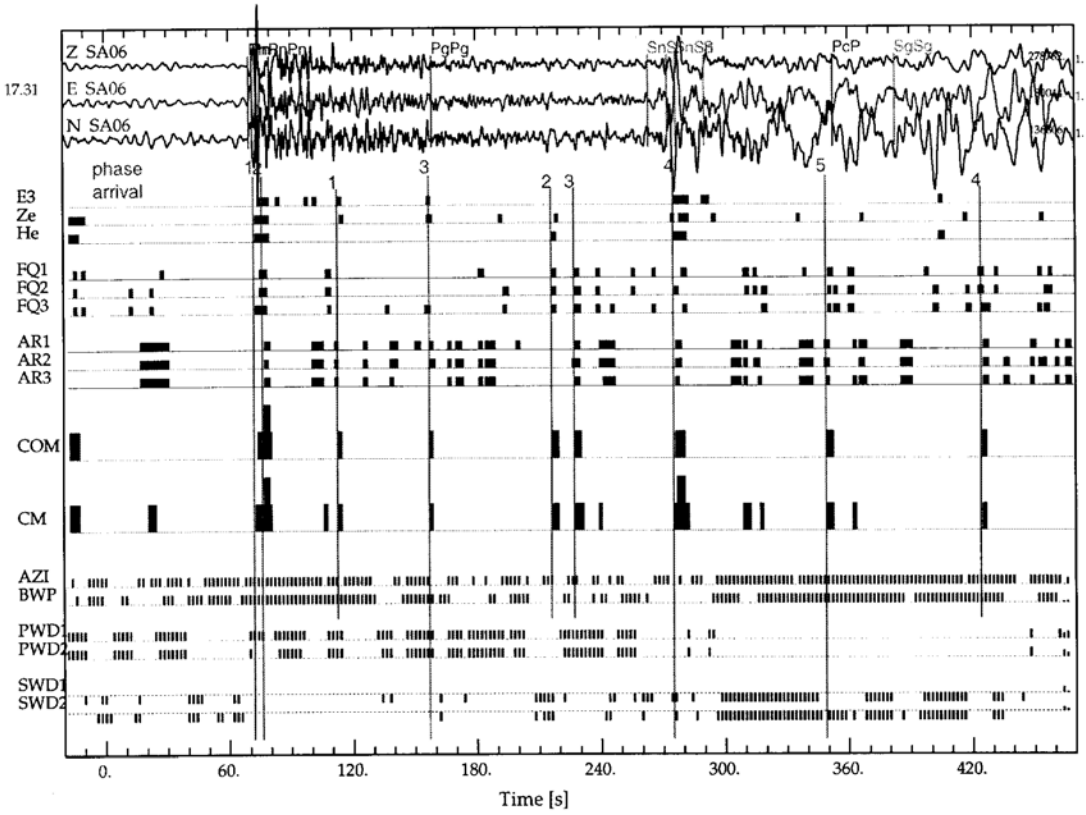


Figure 2. An example of the application of the multi-attribute algorithm to a far-regional record. The upper three traces represent the 3-component seismic records without rotation, with the superimposition of the predicted times of arrivals using the *iasp91* travel time tables for the event parameters. E_3, Z_e, H_e are the total, vertical and horizontal energy ratio of current value to long-term trend. FQ1, FQ2 and FQ3 represent different styles of detectors for instantaneous frequency. AR1, AR2 and AR3 are the detectors on the low-order, medium-order and high-order AR coefficients. COM and CM represents different styles of combining information from the detection processes. The measures AZI and BWP together provide a separation of body wave from background noise; PWD1 and PWD2 are detectors for *P* phases, and SWD1 and SWD2 are the detectors for *S* phases. The long vertical bar from the top to the bottom of the frame represents the case where both the *iasp91* travel times and the combination algorithm both indicate the arrivals, denoted as phases $1, 2, ...n$. A shorter vertical bar indicates where only the combination algorithm recognises the phases, denoted as arrivals $1, 2, ...n$.

In fig 2 we display the results of the multi-attribute analysis for an event at far-regional distance. From fig 1, it is clear that the performance of the combination algorithm is better than the performance of any single method.The energy attributes can only pick the strong seismic phases (*Pn*, *PgPg* and *SnSn*) by means of energy content if at least two attributes have a raised flag. The instantaneous frequency approach not only can pick strong phases (*Pn* and *SnSn*), but also can indicate weaker seismic phases (e.g. *PcP*) not indicated by the energy analysis. The use of the AR coefficients can indicate nearly all the phases (*Pn*, *PnPn*, *PgPg*, *SnSn* and *PcP*) which are indicated by using the *iasp91* travel time tables (Kennett and Engdahl, 1991). The combination algorithm can separate successive arrivals (such as *Pn* and *PnPn*).

For those detections that are indicated by the travel time tables, phases 1,2,3 can be distinguished as *P* wave arrivals with the linear polarisation property of body wave; phase 4 can not be definitely identified as an *S* wave phase due to uncertainty in the polarisation features of the body wave. Phase 5 has also uncertain style of P or S wave, because it is immersed in the S wave segment. However the *P* and *S* wave segments of the record can be clearly separated from the behaviour of the measures PWD1, PWD2 and SWD1, SWD2. Besides these five main phases, there are 4 other detections ('arrivals') which do not correspond to phases expected from the *iasp91* travel time tables using the event parameters.

The multi-attribute approach works well with unfiltered broad-band records even with relatively high noise levels

and such a display could present an analyst with a useful complement to more traditional methods of phase detection and recognition.

CONCLUSIONS AND RECOMMENDATIONS

A computational scheme for synthetic seismograms at teleseismic distances in which separate allowances are made for the crustal and upper mantle structure beneath source and receiver can be made both efficient and flexible. By using a representation in terms of the reflection and transmission properties of portions of the media it is possible to control the class of propagation processes included in the seismogram. The crustal reverberations and surface multiples can be calculated with correct relative amplitudes with a slowness bundle approach. A limited integration in slowness about the geometric slowness for the primary arival is undertaken at each frequency, so that the expense of a full reflectivity treatment is avoided by concentrating attention on the specific expected arrivals. Such an approach can be linked closely to any form of travel time corrections and should incorporate all available information about the structure beneath individual stations.

The full response can be used to calibrate approximate methods with shorter computation time, which can be employed in non-linear waveform inversion for source mechanism and depth. A very fast and effective non-linear location scheme has been developed for arrival time location using the Neighbourhood Algorithm and this same approach is now being developed to handle source parameter inversion by fitting the onset of *P* and, possibly, *S* waveforms.

The quality of location procedures depends heavily on the arrival time picks and for a sparse network of stations will be much enhanced if multi-phase information can be employed. Often even moderate quality later phase data can place strong constraints on an event location. With the combination of a number of different styles of phase detection we are able to provide an aid to analysts which not only flags potential phase arrivals but also provides an indication of their character. The multi-attribute approach works quite well even in the presence of significant noise and could be usefully employed in combination with selective filtering.

References

Goldstein, P. & Dodge, D., 1998. Depth and mechanism estimation using waveform modelling, in *Proceedings 20th Annual Research Symposium on Monitoring a Comprehensive Test Ban Treaty*, 250–259.

Kennett, B.L.N., 1983. *Seismic Wave Propagation in Stratified Media*, Cambridge University Press, Cambridge.

Kennett, B.L.N., 1988a, Systematic approximations to the seismic wave field, 237–259, in *Seismological Algorithms*, D. Doornbos ed., Academic Press, London.

Kennett, B.L.N., 1988b, Radiation from a moment tensor source, 427–441 in *Seismological Algorithms*, D. Doornbos ed., Academic Press, London.

Kennett, B.L.N., & Engdahl, E.R., 1991. Traveltimes for global earthquake location and phase identification, *Geophys. J. Int.*, **105**, 429–465.

Kennett, B.L.N., Engdahl E.R. & Buland R., 1995. Constraints on seismic velocities in the Earth from travel times, *Geophys J Int*, **122**, 108–124.

Leonard, M. & Kennett, B.L.N., 1999. Multi-component auto-regressive techniques for the analysis of seismograms, *Phys. Earth Planet. Inter.*, In press.

Montagner, J-P & Kennett, B.L.N. 1996. How to reconcile body-wave and normal-mode reference Earth models?, *Geophys. J. Int*, **125**, 229–248.

Sambridge M.S., 1998. Exploring multi-dimensional landscapes without a map, *Inverse Problems*, **14**, 427–440.

Sambridge M.S., 1999. Geophysical inversion with a neighbourhood algorithm, part I: searching a parameter space, *Geophys. J. Int.*, in press.

Vidale, J.E., 1986. Complex polarization analysis of particle motion. *Bull. Seism. Soc. Am.*, **76**, 1393-1405.

LOCATION AND CHARACTERIZATION OF MINING ACTIVITY USING INTEFEROMETRIC SYNTHETIC APERTURE RADAR

Robert J. Mellors, San Diego State University and Cecil and Ida Green Institute of Geophysics and Planetary Physics, Scripps Institute of Oceanography
Bernard Minster, Cecil and Ida Green,
Institute of Geophysics and Planetary Physics, Scripps Institute of Oceanography
William Walter and Dave Harris, Lawrence Livermore National Laboratory
Paul S. Earle, University of California, Los Angeles

Sponsored by the
Institute of Geophysics and Planetary Physics and
Lawrence Livermore National Laboratory
Mini-grant 97-1458

ABSTRACT

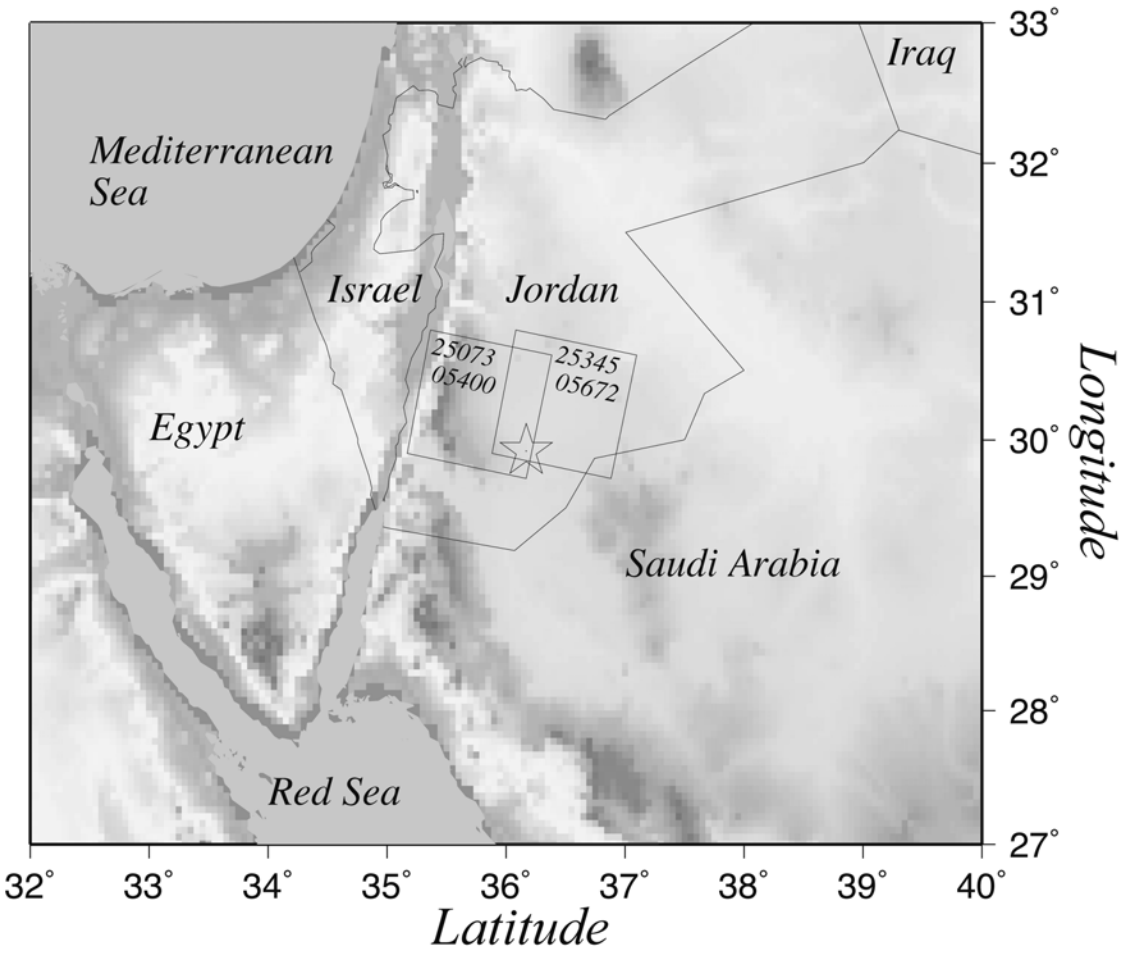
We test the use of satellite-based interferometric synthetic aperture radar (INSAR) to detect, locate, and monitor surface mining at a large phosphate quarry in Jordan. INSAR is a technique that uses radar to create highly accurate digital elevation models (DEM) and can measure small changes in surface deformation. We construct two DEMs of the quarry using two pairs of commercially available tandem images from the ERS-1 and ERS-2 satellites (C band; frame 2997 from May 1 and 2, 1996, and on May 20 and 21, 1996). The region around the quarry is relatively flat and arid, which allows for high coherency between images and high-quality phase information. The quarry is the site of frequent large-scale blasting operations.

The synthetic aperture radar processing uses a range-Doppler algorithm and publicly available orbit information. After aligning and compensating for differences in satellite position, we calculated the correlation and phase difference between the two image pairs. We tested two approaches to phase unwrapping: a least-squares approach and integration. The integration approach produced superior results when converted to topography and compared with ground-truth data. The detailed structure of the quarry is visible on a scale of tens of meters. The quarry's size and location determined from the radar-generated DEMs compare favorably with ground-truth data. Differences observed between the two sets of images may indicate blasting and removal of material during the 19 days between data takes. However, contamination from data artifacts remains a possibility. Currently, we are experimenting with different filters and pixel averaging schemes to determine the robustness of the elevation features.

We also are testing the use of the interferometric phase gradient for detection of subtle features. In addition to the quarry, cultural features such as buildings and power line towers are clearly observed. The quarry is also clearly seen on the correlation images between the different scenes.

We have ordered data and plan to analyze images from the 1998 India and Pakistan tests as well.

Key Words: interferometric synthetic aperture radar, space-borne monitoring


Iraq
Mediterranean Sea
Israel
Jordan
25073
05400
25345
05672
Egypt
Saudi Arabia
Red Sea
33°
32°
31°
30°
29°
28°
27°
Longitude
32°
33°
34°
35°
36°
37°
38°
39°
40°
Latitude

USING EPICENTER LOCATION TO DIFFERENTIATE EVENTS FROM NATURAL BACKGROUND SEISMICITY

Stephen C. Myers and William R. Walter
Geophysics and Global Security
Lawrence Livermore National Laboratory
L-205, P.O. Box 808, Livermore, CA 94551

Sponsored by U.S. Department of Energy
Office of Nonproliferation and National Security
Office of Research and Development
Contract No. W-7405_ENG-48

ABSTRACT

Efforts to more effectively monitor the Comprehensive Nuclear-Test-Ban Treaty (commonly referred to as the CTBT) include research into methods of seismic discrimination. The most common seismic discriminants exploit differences in seismic amplitude for differing source types. Amplitude discriminants are quite effective when wave-propagation (a.k.a. path) effects are properly accounted for. However, because path effects can be exceedingly complex, path calibration is often accomplished empirically by spatially interpolating amplitude characteristics for a set of calibration earthquakes with techniques like Bayesian kriging (Schultz et al., 1998). As a result, amplitude discriminants can be highly effective when natural seismicity provides sufficient event coverage to characterize a region. However, amplitude discrimination can become less effective for events that are far from historical (path-calibration) events. It is intuitive that events occurring at a distance from historical seismicity patterns are inherently suspect. However, quantifying the degree to which a particular event is unexpected could be of great utility in CTBT monitoring. Epicenter location is commonly used as a qualitative discriminant. For instance, if a seismic event is located in the deep ocean, then the event is generally considered to be an earthquake. Such qualitative uses of seismic location have great utility; however, a quantitative method to differentiate events from the natural pattern of seismicity could significantly advance the applicability of location as a discriminant for source type. Clustering of earthquake epicenters is the underlying aspect of earthquake seismicity that allows for an epicenter-based discriminant, and we explore the use of fractal characterization of clustering to characterize seismicity patterns. This fractal relationship can be combined with the Gutenburg-Richter relationship to form a complete seismicity model as a function of magnitude and distance from any point. Such a model can then be fit to seismicity catalogues and extrapolated down to the small magnitudes of concern to CTBT monitoring, where global catalogues are often incomplete. By characterizing the magnitude-spatial distribution of earthquakes, we can evaluate the likelihood that an event at any given location and magnitude is drawn from the background population. The use of this technique can help to identifying events that are inconsistent with historic seismicity, complementing more conventional methods that are applicable in situations where seismic amplitudes from nearby events can be directly compared.

Key Words: Location, Seismic Regionalization, Calibration, Crustal Structure.
This work was performed under the auspices of the U.S. Department of Energy by Lawrence Livermore National Laboratory under contract No. W-7405-Eng-48 for the Office of Research and Development, NN-20, within the Office of NonProliferation and National Security, NN-1.

OBJECTIVE

This study aims to better quantify the use of seismic location to assess source type. Qualitative assessments of seismic source type derived from source location can be useful; however, these qualitative guidelines are generally applied to situations where the physical conditions at the source preclude underground nuclear testing procedures (e.g. under thousands of meters of water). There is considerable utility in further developing seismic location as a more general indicator of source type, and we propose a location-based method that examines the probability that an event was drawn from the magnitude-location population of earthquakes. We characterize the magnitude-location population using a fractal model of spatial clustering in concert with the Gutenburg-Richter magnitude distribution. Using this fractal model, events occurring

far from natural seismicity, where amplitude discriminants are less well calibrated, can be identified as outliers to the background population of earthquakes. Of course this technique does not discriminate between the various types of man-made explosions, but the ability to assess the fit of an event into the natural pattern of seismicity can be useful for monitoring. This study focuses on source identification applications of the proposed fractal method; however, we find that this technique has a wide range of possible applications. For example it may provide a better spatially varying map of the expected seismicity rate for small events than a typical b-value extrapolation. Other possible applications are given brief mention below.

RESEARCH ACCOMPLISHED

Parameterization of the magnitude-location distribution

The joint magnitude-spatial distribution of earthquakes is difficult to assess across a broad magnitude range, due to limitations of seismicity catalogues. Low magnitude events are often under represented, due to network detection limitations, and large magnitude events are poorly sampled, due to long recurrence intervals and the short time span covered by catalogues. Likewise, the spatial distribution of earthquakes in low seismicity regions is often poorly characterized, due to the same seismicity catalogue limitations. It is common practice to parameterize the magnitude distribution of earthquakes using the Gutenburg-Richter relationship (Gutenburg and Richter, 1944):

$$\log(N) = a - bM \qquad [1]$$

N is the number of events; M is the magnitude; *a* and *b* are constants. Parameterization enables the magnitude distribution to be estimated beyond the empirically characterized segment of the distribution. Therefore, parameterization is used (albeit with great caution) to estimate both the recurrence time of large earthquakes and the large number of small events that are undetected. Like the magnitude distribution, the spatial distribution can be parameterized. The spatial distribution of earthquakes is well characterized by fractal-clustering models (e.g. Henderson et al., 1994; Oncel et al., 1996).

There are a number of fractal models that can be used to characterize the clustering of earthquake epicenters, but use of the "correlation dimension" (equations [2] and [3]) is particularly robust due to the cumulative nature of the methodology. The fractal correlation function (as outlined in Henderson et al., 1994) is defined as:

$$C_p(r) = \sum_{i=1}^{k} H(r - \|x_p - x_i\|) \qquad [2]$$

where K is the number of points (events in the seismicity catalogue); r is the radial distance under consideration; H is the Heavyside function that is 0 when the arguments evaluate to less then 0, and H is 1 otherwise; the variable *x* holds the location of each event in the seismicity catalogue, with *xp* representing the point at which the correlation function is evaluated. The double bars represent the scalar distance between points. Equation [2] is just the number of events in the catalogue within a distance *r* from the point *p*. Making use of the correlation function, we use a fractal model of the following form to characterize the spatial distribution of epicenters:

$$\log(C(r)) = c + D\log(r) \qquad [3]$$

where *c* and *D* are constants. *D* is commonly referred to as the fractal dimension of the data set, which is simply the linear slope of [3] in log space. In the case of earthquake clustering analysis, the constant *c* determines the overall rate of seismicity. Figure 1 shows the fractal relationship of epicenters relative to three locations with distinctly different seismicity rates. The fractal model is seen to be a good

parameterization of the spatial distribution in all three instances, but the fractal dimension and rate of seismicity are seen to be dependent on the point under consideration (i.e. fractal characterization of seismicity is spatially non-stationary).

We use the fractal model of equation [3] in concert with the Gutenburg-Richter (G-R) relationship [1] to characterize the joint magnitude-spatial distribution. Both the magnitude and spatial distributions are log-linear relationships for the expected number of events at specific magnitudes and locations, respectively, and we use this commonality to join the two distributions into the following relationship:

$$\log(N) = A + bM + D\log(r) \qquad [4]$$

where A is a new constant and the other variables are defined above. Equation [4] describes a plane that can be used to model the expected number of earthquakes with magnitude M within a distance r from a given location. We note that the Gutenburg-Richter relationship has been shown to be a fractal relationship (Turcotte, 1989), making [4] a double fractal.

Figure 2 shows the joint magnitude-spatial distribution at the same three points that are shown in Figure 1.

Figure 1 illustrates that the slope of each plane in the spatial dimension is distinctly different. The slope in the magnitude direction is more stationary with a value of about one. Figure 2 shows that the expected number of events at a given magnitude and distance from each point can be estimated by using the joint magnitude-spatial fractal characterization, and this provides a means to assess the surprise associated with the occurrence of an event with a given magnitude and location. We present some examples of CTBT application of this technique below, and we now focus on the fit of the joint fractal distribution and its predictive capabilities.

Data fit and predictability of the joint fractal distribution

In this study we make use of the relocated ISC catalogue presented in Engdahl et al. (1998). This catalogue provides good data coverage for globally located events from 1964 through to the present; however, we make use of the 1964-1996 portion of the catalogue in this study. The inclusion of other catalogues, particularly catalogues that are complete to lower magnitude, will be important in the future development and testing of the joint fractal parameterization.

The planar fractal model fits the magnitude-spatial distribution of earthquakes well. For the example locations shown in Figure 2 the correlation coefficients between the fractal models and the catalogue data range between 0.78 and 0.88. The high degree of correlation agrees with the qualitative assessment of the planar nature of the empirical magnitude-spatial distribution. We also found that higher-order terms are statistically significant in fitting the data; however, the correlation coefficients were only marginally improved when higher-order terms were included. Detailed analysis of the empirical data leads us to believe that the curvature of the surfaces has to do with the preferential binning of events into integer number magnitudes, which causes a periodic peak at integer-valued magnitudes (Figure 2).

By parameterizing the joint magnitude-spatial distribution at regularly spaced points that cover a region, the expected number of events in that region can be calculated by summation. The expected number of events in a region is commonly calculated by arbitrarily bounding the region and characterizing the magnitude distribution therein with the Gutenberg-Richter relationship. This method assumes that the rates of seismicity within the region are stationary, and this assumption is commonly violated. Alternatively, a fractal model can be developed on a grid of points within the region, and the expected number of earthquakes at each point can be summed to provide an estimate of the expected number of events in the region. The grid spacing can be adjusted to suite the degree of non-stationarity in the region. Figure 3 shows a map of the expected number of earthquakes within 2° of grid points in a portion of the Middle East. The widely varying values on the map demonstrate the highly non-stationary seismicity rates (see figure caption). Using this map we can sum the contribution of each point to estimate the seismicity rate in the whole region. Figure 4a shows that summing the fractal-model predictions at each point agrees with the seismicity rate in the region. Therefore, decomposing the seismicity catalogue into point-specific fractal

representations and summing the fractal models reproduces the seismicity rate. This is a circular test of the method, but it does demonstrate the validity of representing seismicity with fractal models. A more rigorous test is shown in Figure 4b, where the fractal summation method is used to predict the seismicity rates for a period of time following the catalogue that was used to construct the fractal models. The expected number of events in Figure 4b is in good agreement with observed seismicity rates, demonstrating the predictive capability of the fractal technique.

The example in Figure 4b suggests that the seismicity rate is temporally stationary in a large region. However, temporal stationarity may not hold in local areas where an aftershock sequence, for example, could temporarily boost the seismicity rate. Temporal clustering of earthquakes has also been characterized with fractal models (e.g. Smalley et al., 1987), and this temporal dependence should be accounted for when the study area is local in scale.

The ability to estimate the magnitude distribution within an arbitrary region is of fundamental utility in seismology. Well-defined portions of the seismicity catalogue can be used to constrain the parameters of the fractal model, and predictions can then be made for the number of potentially damaging (large) earthquakes.

Quantifying the expected number of earthquakes of a given magnitude is at the core of earthquake hazard analysis, and we are applying the fractal method to these problems. While hazard studies focus on large earthquakes, seismic monitoring focuses on the other end of the magnitude distribution, which can be just as poorly sampled. Some of the monitoring applications of this technique are: 1) estimating the event-occurrence rate in a specific area as a function of monitoring threshold, 2) identification of mine blasts by their non-fractal magnitude distribution, and 3) assessing the surprise associated with the occurrence of an event with a certain magnitude and location. We devote the remainder of this discussion to the third application mentioned.

Fractal characterization as a location disciminant

How much of a surprise is the occurrence of an event with some magnitude and location? This question is at the heart of using location to identifiy source type, and fractal parameterization can help to quantify this level of surprise. Figure 4 shows the expected number of events at the location of three known nuclear tests verses the number of expected events in a 30 year time period at the locations of similar-sized events in the global catalogue. The bar graphs show the distribution of expected numbers of events at locations where global-catalogue events actually occurred. This gives an empirical distribution of the background pattern of seismicity. The number of expected events (also for a 30 year time period) at the location of the nuclear test is calculated and compared to the global distribution.

Fractal characterization of the global distribution of earthquakes indicates that, taken together, the magnitude and location of the three nuclear tests is uncommon. In other words, the occurrence of these events is surprising. In the case of the 1964 French test (North Africa), the event is seen to be exceedingly unusual.

Based on the location-outlier analysis this event is quite suspicious and would warrant further investigation. The 1998 Indian and Pakistani tests are also outliers, but they are not as unusual as the French test. This is not surprising, considering that the Pakistani test is in a zone of increased seismicity and the Indian test is relatively nearby. Nonetheless, even the Pakistani test, which is in an active tectonic region, is an outlier to the global population of earthquakes, demonstrating the applicability of the fractal methodology. We used the entire ISC catalogue for these tests of the fractal method, and the ISC reports all seismic events including other nuclear explosions. We are currently working to cull non-earthquake events from the ISC catalogue, which is likely to put the example explosions shown in Figure 5 further out on the tails of the distribution.

The examples presented above suggest that using location and magnitude together to identify non-earthquake seismic event is promising. However, more testing of this method is warranted. Of particular interest is the performance of this technique at lower magnitudes. At lower magnitudes the expected

number of earthquakes grows exponentially, and there is some threshold below which an event of a given magnitude is not surprising anywhere on the globe.

CONCLUSIONS AND RECOMMENDATIONS

The joint distribution of earthquake magnitude and location can be characterized with a double fractal model (Equation 4; Figure 2). The examples presented above demonstrate that a seismicity catalogue can be decomposed into point-specific fractal models (figures 2 and 3), and that summing the expected number of events at regularly spaced points agrees with the starting seismicity rates in the region (Figure 4a). In a more rigorous test, summing the expected number of events at each point agrees with the seismicity rate for a subsequent portion of the catalogue that was not used to construct the fractal models (Figure 4b).

Fractal characterization of the joint magnitude-spatial distribution of earthquakes provides a promising means to identify non-earthquake sources. We demonstrate the degree to which three nuclear tests are outliers to the global magnitude-location distribution of earthquakes (Figure 5). An explosion in North Africa is identified as an extreme outlier to the earthquake population. Additionally, the 1998 nuclear tests in India and Pakistan are also identified as outliers, although the 1998 tests are not as unusual as the North African test. Despite the success of the examples shown here, there is a magnitude below which an event will not be distinguished from the earthquake population. This threshold magnitude is important to identify, and we are working to map out this threshold value. The fractal method does not attempt to discriminate between man-made sources; because, there is no reason to believe that these sources are characterized by a fractal distribution.

Nonetheless, the ability to identify events that are inconsistent with the population of earthquakes, which makes up the largest number of seismic events, is of great utility for monitoring purposes. The fractal method relies heavily on complete seismicity catalogues and we are currently working to apply the fractal methodology using regional and local catalogue information. Use of more complete catalogues will allow us to better constrain the fractal models over a wider range of magnitude and distance. I n addition to source characterization for CTBT monitoring, we are adapting the fractal methodology to numerous other seismological problems, including: hazard analysis, estimation of event-occurrence rate as a function of monitoring threshold, and identifying mining activity by its distinct magnitude-spatial distribution.

Acknowledgements

We thank Bill Hanley for providing statistical analysis and interpretation of the data fit. This work was performed under the auspices of the U.S. Department of Energy by Lawrence Livermore National Laboratory under contract No. W-7405-Eng-48 for the Office of Research and Development, NN-20, within the Office of NonProliferation and National Security, NN-1.

REFERENCES

Engdahl, E.R., R. van der Hilst, and R. Buland (1998). Global teleseismic earthquake relocation with improved travel time and procedures for depth determination, *Bull. Seismol. Soc. Am*, **88**, 722-743.

Gutenburg, R., and C.F. Richter (1944). Frequency of earthquakes in California, *Bull. Seismol. Soc. Am*, **34**, 631-644.

Henderson, J., I.G. Main, R.G. Pearce, and M. Takeya (1994). Seismicity in north-eastern Brazil: fractal clustering and the evolution of the b value, *Geophys. J. Int*., **116**, 217-226.

Oncel, A.O., I. Main, O. Alptekin, P. Cowie (1996). Spatial variations of the fractal properties of seismicity in the Anatolian, *Tectonophysics*, **257**, 189-202.

Schultz, C. A., S.C. Myers, J. Hipp, C.J. Young (1998). Nonstationary Bayesian Kriging: a predictive technique to generate spatial corrections for seismic detection, location, and identification, *Bull. Seismol. Soc. Am*, **88**, 1275-1288.

Smalley, R.F., J.-L. Chatelain, D. L. Turcotte, and R. Prevot (1987). A fractal approach to the clustering of earthquakes: applications to the seismcity of the New Hebrides, *Bull. Seismol. Soc. Am*, **77**, 1368-1381.

Turcotte, D.L. (1989). A fractal approach to probabilistic seismic hazard assessment, Tectonophysics, **167**, 171-177

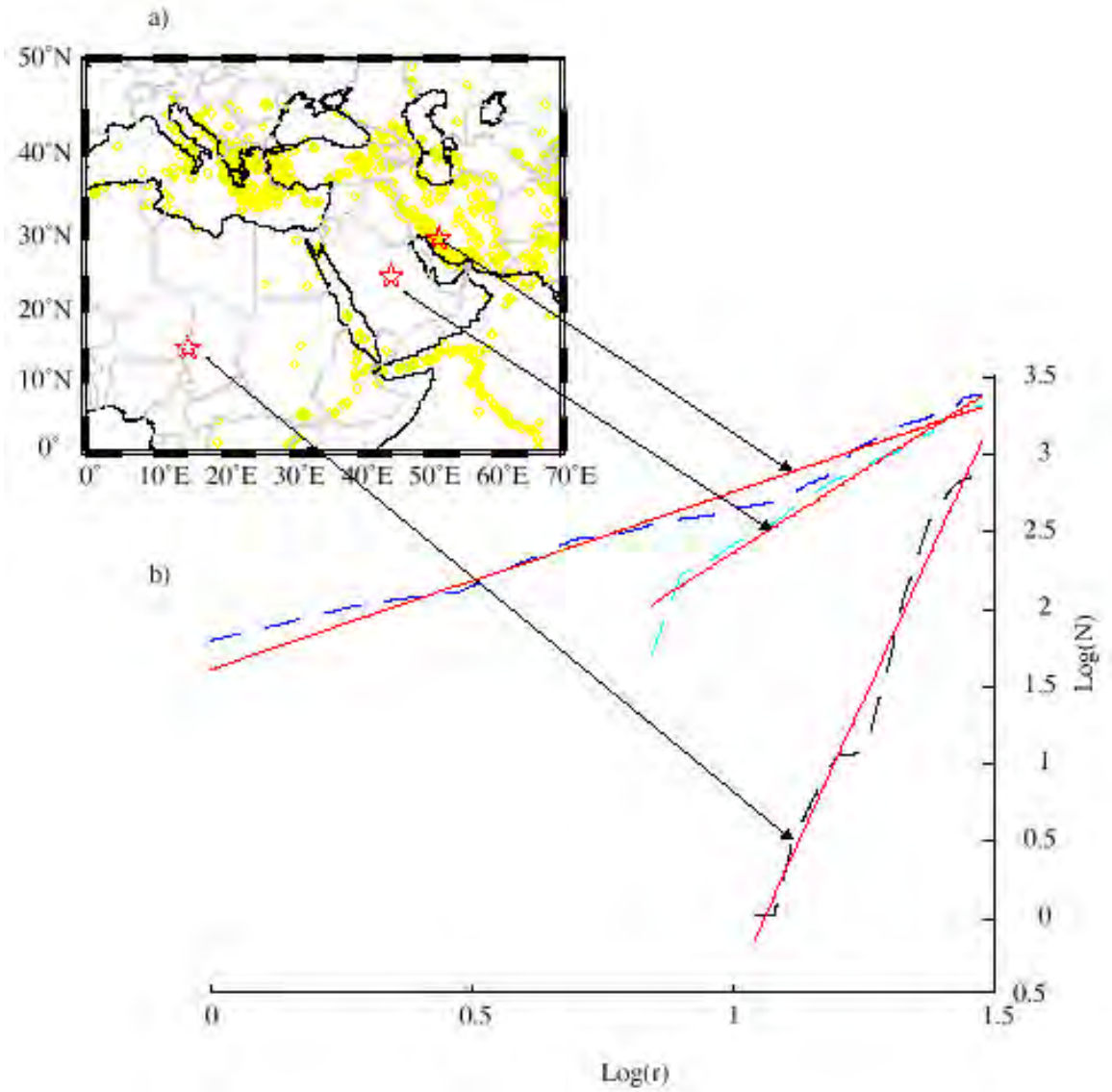


Figure1. Example of fractal models of earthquak e epicenters at three locations with distinctly different seismicity rates. a) Circles are epicenters of catalogue events between magnitude 5 and 6 over a 30 year period. Example locations are shown by stars. b) Fractal models for the three example points. The variable r is the great-circle distance (degrees) from the example point, and N is the number of events occurring inside a disc with radius r. Dashed lines are data curves and straight lines are fractal parameterizations. Note the good fit of the model to the data and the distinctly different slope (fractal dimension) and intercept (overall rate of seismicity) at each of the points.

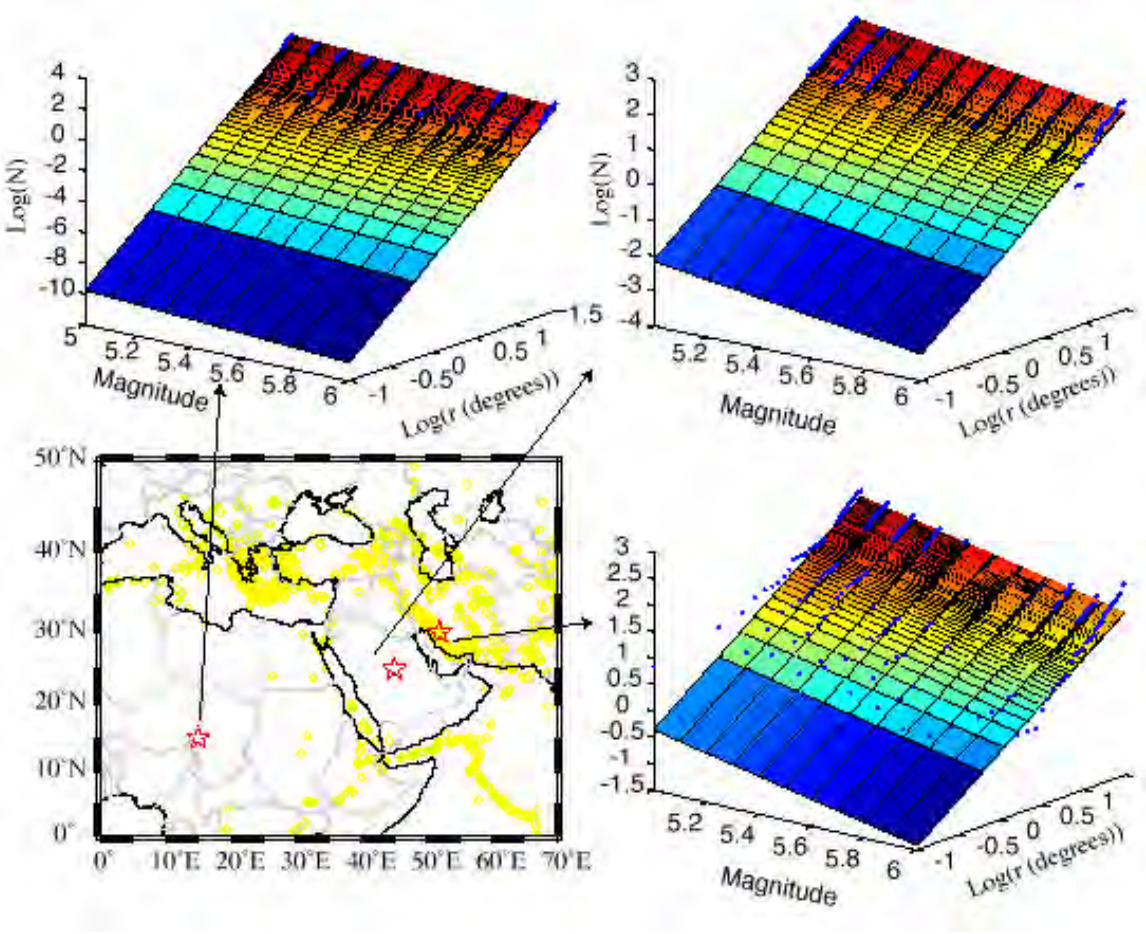


Figure2. Example of joint magnitude-spatial fractal dristrib utions at three locations with distinctly different seismicity rates. The map is the same as Figure 1. Each of the 3- dimensional planes is a fractal model with independent variables of magnitude and distance from the example point. The dependent variable (N) is the number of events occurring inside a disc with radius r at each magnitude. The plotted points are the observations to which the plane is fit. Note the good fit of the model to the data and the vastly differing numbers of events predicted at each example location.

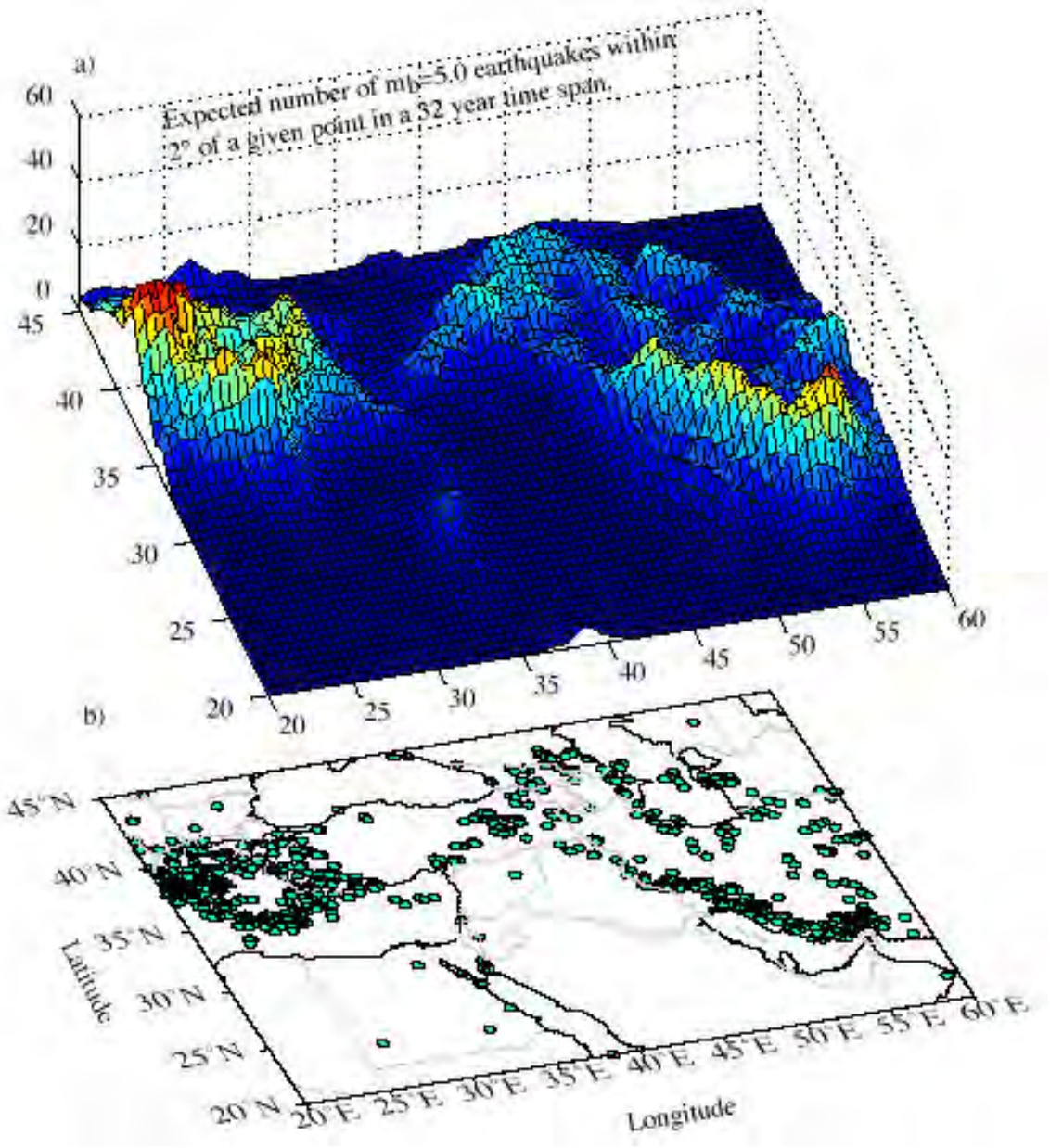


Figure 3. Using fractal models, a map sho wing the expected number of earthquakes of a given magnitude occurring within a given radius from each point can be constructed. a) This map is constructed using the ISC catalogue between 1964 and 1990. The large expected value on the west side of the map area is attributed to Aegean seismicity. The Zagros seismicity is seen as the linear trend in the eastern portion of the map. b) Seismicity in the ISC catalogue that was used to construct the map shown in section (a).

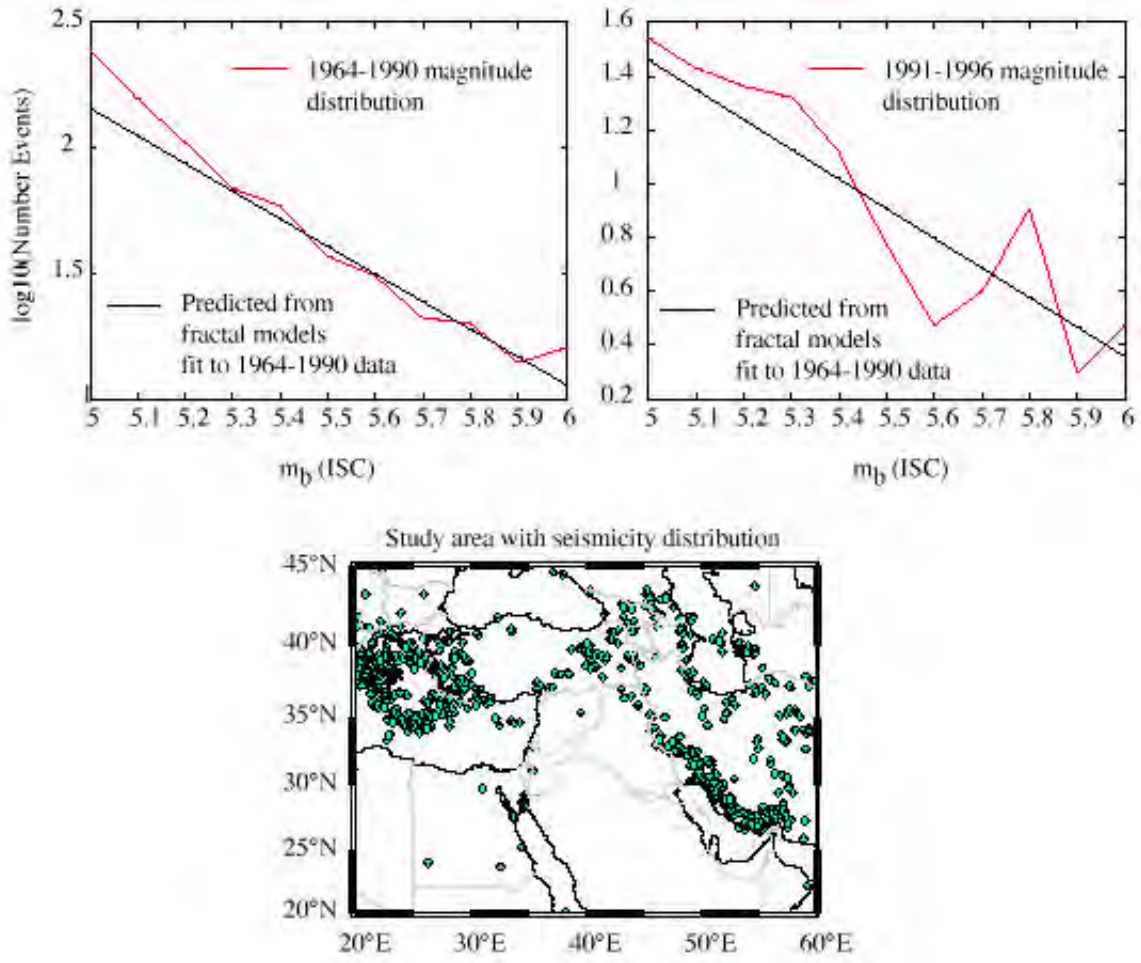


Figure 4. The number of e vents in a region is well matched by determining fractal models on a grid of points that covers the region and summing the number of events predicted at each node. In this procedure the seismicity catalogue is broken down into fractal models at each grid point (Figure3). Then the expected number of events at each point is summed to reconstruct that magnitude distribution. a) The summing procedure fits the data used to produce the fractal models. (b) Summing also predicts the numbers of events in subsequent years. c) The study area for this example is shown in the bottom panel.

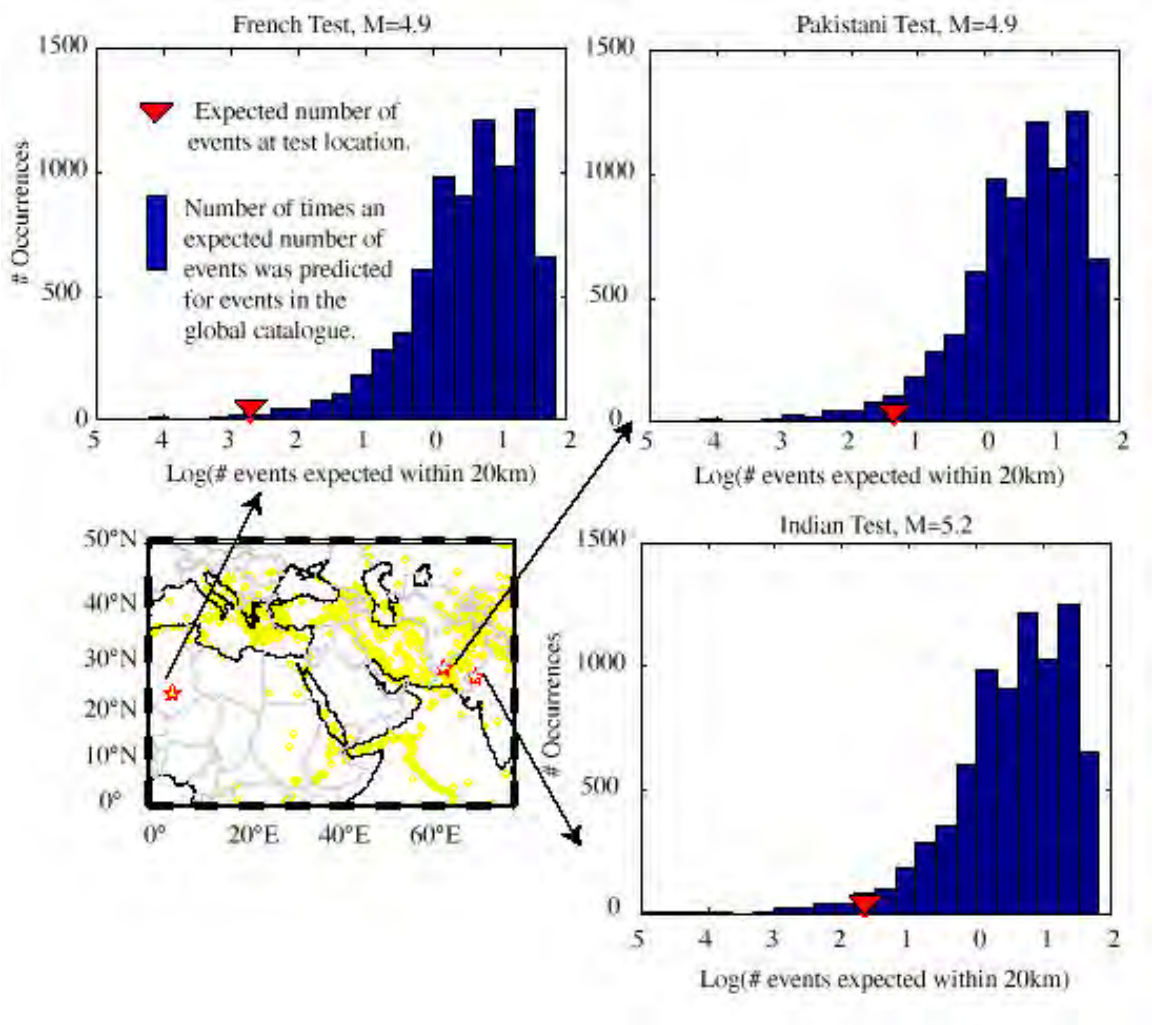


Figure 5. Example of outlier characterization for three nuclear tests. The bar graphs are constructed by: 1) using all the events in the global catalogue (30 years of data) with magnitude equal to the nuclear test, 2) calculating the expected number of earthquakes (with magnitude equal to the nuclear test) within 20 km (arbitrary) of each catalogue epicenter, 3) binning the number of occurrences of the predicted values. This provides an empirical distribution of the variation in fractal model predictions in cases where an event actually occurred. The number of events predicted within a 20 km radius of the nuclear test is then plotted on the distribution for comparison.

SOURCE CHARACTERIZATION OF A LARGE ROCK BURST, COEUR D'ALENE MINING DISTRICT, IDAHO

Alan C. Rohay, Battelle Memorial Institute, Pacific Northwest Division
Kenneth F. Sprenke, University of Idaho, College of Mines
Michael C. Stickney, Montana Tech, Earthquake Studies Office

Sponsored by U. S. Department of Defense
Defense Threat Reduction Agency
DSWA01-97-C-1024

ABSTRACT

Characterization of mining-related seismic events is critical to the implementation of the Comprehensive Nuclear-Test-Ban-Treaty monitoring system. Mine seismicity from uncontrolled sources is particularly troublesome, with magnitudes up to 4 or 5, producing signal strengths comparable to 1- to 10- kiloton contained nuclear explosions. In this study, ground motions from four surface stations and one underground station were inverted to determine the complete moment tensor of a relatively large rock burst in the Coeur d'Alene Mining District in northern Idaho. Many rock bursts, induced by the mining process, show implosional source mechanisms, a feature that should be useful to discriminate mining-related events from underground explosions. The rock burst analyzed in this study yielded seismograms with a moment tensor solution involving a significant volumetric component. The moment tensor was decomposed into isotropic and deviatoric components from which the volumetric closure and total shear deformation were estimated for comparison with in-mine co-seismic damage. The magnitude 3.1 burst occurred 7.5 hours after routine daily blasting in the mine. The event represented the result of deep underground mining combined with sliding on nearby bedding planes or faults. The implosional characteristic may prove to be a useful parameter for fingerprinting seismic events from deep hard rock mines.

Key Words: moment tensor, rock burst

OBJECTIVE

Mining activities world-wide produce seismic events, some of which may be visible to monitoring for the Comprehensive Test Ban Treaty (CTBT). Mine seismicity from uncontrolled sources are particularly troublesome, with magnitudes as high as 4 to 5, producing signals equivalent to 1-10 kiloton contained nuclear explosions. Rock bursts in deep underground mines are in this latter category. These events, however, may have characteristics unlike either explosions or earthquakes that might be used to "fingerprint" specific mines for discrimination purposes. In this light, we are investigating seismic signals from one of the most rock burst-prone hard rock mining areas in the world: the Coeur d'Alene Mining District of northern Idaho.

In a review of mining-induced seismicity, Gibowicz and Kijko (1994) note that such events generally fall into two types: those directly associated with mining operations and those associated with movement on major geological discontinuities. Rock bursts in the Coeur d'Alene District are not so easily categorized. While the events clearly are associated with mining rate (Sprenke and others, 1991) and stope geometry (Jung et al., 1995), they have long been known to be the result of failure on faults and bedding planes (Scott, 1990). These structures are associated with the Osburn Fault, part of the Lewis and Clark Line megashear that strikes north-northwest through the district. An underhand-longwall system of mining, implemented in the late 1980s at the Lucky Friday Mine, has greatly reduced rock burst problems at that mine, illustrating the influence of mining geometry on rock bursts. A district-wide network operated in the early 1990s (Jung et al., 1995) showed that those shear events that could be fit by a double couple solution were consistent with a regional tectonic stress with a northwesterly oriented seismic P-axis and a northeasterly seismic T-axis. This is an orientation particularly deleterious for slip on the north-northwesterly oriented vertical faults and steeply dipping bedding parallel to the Osburn Fault. Apparently, mining operations in the Coeur d'Alene district are releasing pent-up strain, strongly affected by local geology and tectonics. Not unlike deep mines world-wide, the seismicity in this district are affected by depth of mining, production rate, mining geometry, geologic structure, and geologic discontinuities.

Although blasting often triggers rock bursts instantaneously, many rock bursts, particularly large damaging events in deep underground mines, occur spontaneously and unexpectedly, despite the fact that they are caused by stress changes associated with the mining process. This interaction of mine geometry and geological structure suggests that rock bursts in deep underground mines may often be of a shear-implosional nature, involving both co-seismic opening closure and shear failure in the surrounding strata (e.g. McGarr, 1992). Seismograph networks (Stickney and Sprenke, 1992; Jung et al., 1995) demonstrated that well-constrained all-dilatational P-wave first motions for about half of the events in the Lucky Friday Mine indicated a significant implosional component.

RESEARCH ACCOMPLISHED

For this project, we have investigated the seismic signals from a damaging rock burst in the Lucky Friday Mine that occurred at 6:09 August 29, 1998 UTC (11:09 p.m. August 28 PDT). The local magnitude of the event was 3.1 as measured at Butte, Montana. It was recorded on the Montana and Washington regional networks. Predominantly dilatational first motions for this event from our five local stations and several regional stations suggested that this event had an implosional component. To test this hypothesis, we are performing a moment tensor inversion using the signals from five strong motion accelerometers that were deployed in the immediate area of the mine (Figure 1).

The seismic signals used in this experiment were collected as part of a local network deployment of five strong motion accelerometers and one broadband seismometer from May 6 to September 2, 1998 in the immediate vicinity of the Lucky Friday Mine (Rohay et al., 1998). The August 28 rock burst was the largest seismic event recorded in that period. One accelerometer was located in an abandoned adit; the remaining stations were surface stations. The source location was provided by the in-mine geophone array operated by the mine.

The quality of the strong motion accelerometer data was found excellent by comparison with the broadband seismograph record. Both instruments produced virtually identical records of ground motion (Figure 2). The broadband had a GPS time receiver; however the strong motions did not record absolute time. However, because an independent source location was provided by the in-mine geophone array, the lack of absolute timing was not a problem.

The horizontal ground motion signals from the five triaxial accelerometers were rotated to a north and east orientation conforming to a vertical, north, and east coordinate system. Polarities were confirmed to correspond to positive amplitudes for ground motion in the up, north, and east directions. These signals are then again rotated to a radial-transverse-vertical system with radial axis away from the source toward the respective receiver. The seismograms showed reasonably clear P, SH, and SV pulses plus oscillations, particularly on the horizontal components that decay with time, perhaps representing trapped waves in the strata. The oscillations were not the same on all the stations, indicating some degree of heterogeneity about the mine area. The underground station, closest to the workings, shows considerable more high frequency than the others, indicating potential attenuation and near-surface effects.

The moment tensor of the rock burst is estimated in the far field using a linear inversion method in the time domain:

$$\mathbf{U} = \mathbf{G}\,\mathbf{m} \qquad (1)$$

where **U** consists the n sampled observations of ground displacement at the various stations, **G** is an n x 6 matrix containing the Green's functions calculated by the appropriate algorithm and earth model, and **m** = (M11, M12, M22, M13, M23, M33), a vector containing the six moment tensor elements to be determined (Gibowicz and Kijko, 1994).

The data we are using are the maximum displacement amplitudes of the P, SV, and SH waves as recorded at the five three-component strong motion stations surrounding the site. Low frequency noise was removed by filtering below 1 Hz before integrating the time series from acceleration to velocity and displacement. The amplitudes of the P, SH, and SV phases were measured at each of the five stations, and corrected for the free surface effect. These become the 15 observations we will use to estimate the 6 unknowns in the moment tensor.

Green's functions have been formulated in a simple manner using the displacement vectors for far field P, SV, and SH wave radiation (Pujol and Herrmann, 1990) at each of the five stations. A synchronous source in the form of a step function was used to estimate displacements. Based on observations by Stickney and Sprenke (1993), we assumed an isotropic and homogeneous velocity model with a P-wave velocity of 5.74 km/s, and S-wave velocity of 3.47 km/s. A density of 2.7 was assumed for the metasedimentary rocks in the mine area. To estimate the moment tensor elements, we are following a least squares procedure outlined by McGarr (1992).

CONCLUSIONS

We expect that the moment tensor estimates for the M3.1 Coeur d'Alene Mining District rock burst of August 29, 1998 will be dominated by negative diagonal components, indicating a dominantly implosional source. We will use the same procedures for the many smaller events recorded on the acceleromter array and determine whether there are several characteristic types of events that can be classified. We also expect that our results will be similar to those obtained for a group of events studied by McGarr (1992) from deep hard rock mining districts in South Africa. This could indicate that implosional events may be characteristic of a type of event that may fingerprint such mines for CTBT purposes. We will also evaluate regional seismic signals for a catalog of large rock bursts from the Couer d'Alene mining district to evaluate the effect of such implosional events at distances useful for treaty verification monitoring.

REFERENCES

Gibowicz, S.J. and A. Kijko, 1994. An Introduction to Mining Seismology. Academic Press, Inc., San Diego.

Jung, S.J., P.B. Lourence, and K.F. Sprenke, 1995. Fault plane solutions of mining-induced seismicity, Lucky Friday Mine, northern Idaho. Exploration Mining Geology, 4, 65-71.

McGarr, A., 1992. Moment tensors of ten Witwatersrand mine tremors, PAGEOPH, 139, 781-800.

Pujol, J. and R.B. Herrmann, 1990. A students guide to point sources in homogeneous media. Seismol. Res. Letters, 61, 209-224.

Rohay, A.C., K.F. Sprenke, and M.C. Stickney, 1998, Source characterization and regional discrimination of northern Idaho Rockbursts and Explosions. Proceedings, 20th Annual Seismic Research Symposium on Monitoring a Comprehensive Test Ban Treaty (CTBT), pp. 411-416.

Scott, D.F., 1990. Relationship of geological features to seismic events, Lucky Friday Mine, Mullan, Idaho. In Rockbursts and Seismicity in Mines (C. Fairhurst, ed.), 401-405, Balkema, Rotterdam.

Sprenke, K.F., M.C. Stickney, D.A. Dodge, and W.R. Hammond, 1991. Seismicity and tectonic stress in the Coeur d'Alene Mining District, BSSA, 81, 1145-1156.

Stickney, M.C. and K.F. Sprenke, 1993. Seismic events with implosional focal mechanisms in the Coeur d'Alene Mining District, northern Idaho. Journal of Geophysical Research, 98, p. 6523-6528

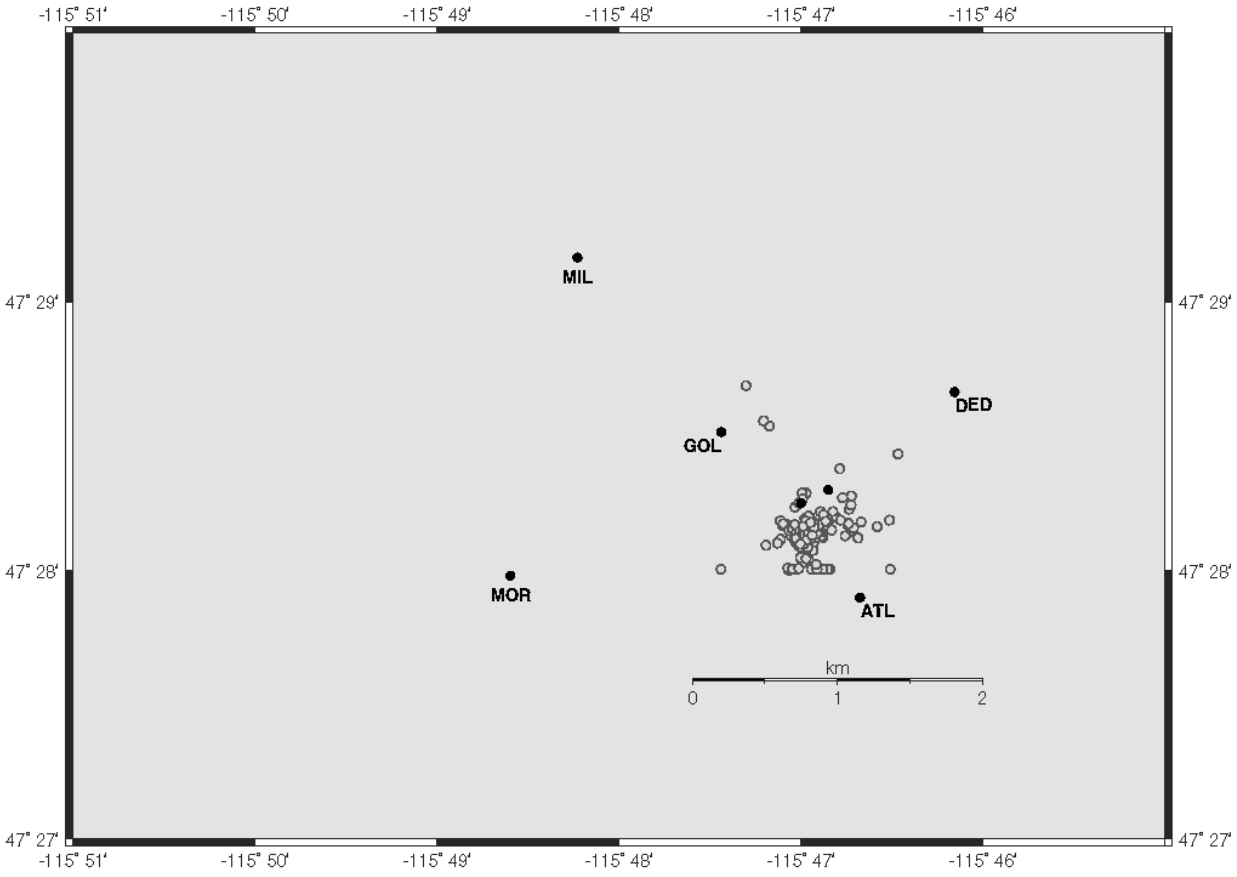


Figure 1. Rockburst locations from the Hecla Mining Company's Lucky Friday mine, and the location of the strong motion accelerometers. The two unlabeled black dots show the locations of the Silver shaft and Number 2 shaft.

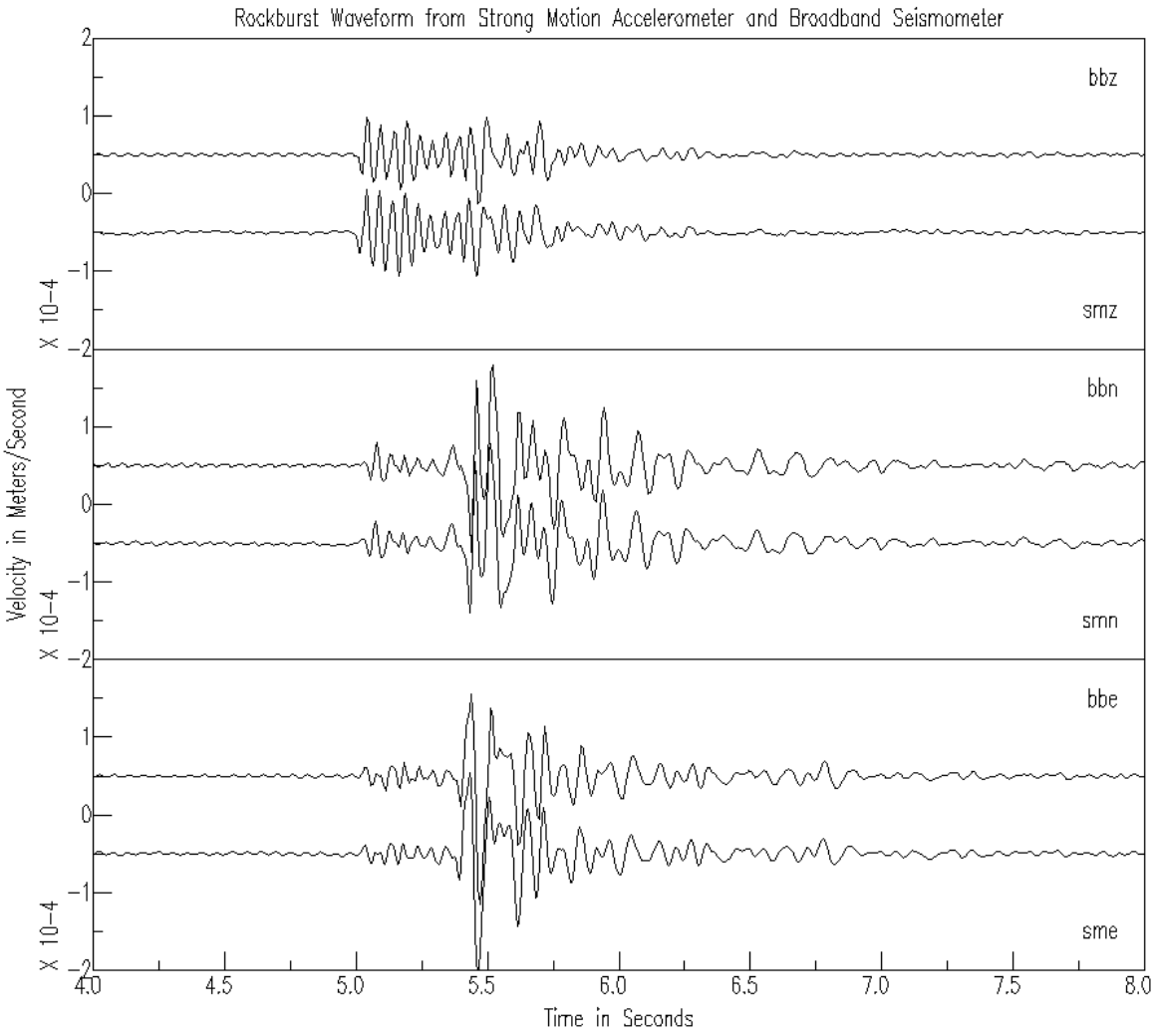


Figure 2. Comparison between three-component broadband velocity records from CMG 40 system (bbz, bbn, bbe) and the result of integrating the strong motion accelerometer records to velocity (smz, smn, sme). The comparison is made at station MOR where the two systems were co-located. This record is for a smaller event than shown in Figure 3 because the magnitude 3.1 event clipped the recording system for the broadband instrument.

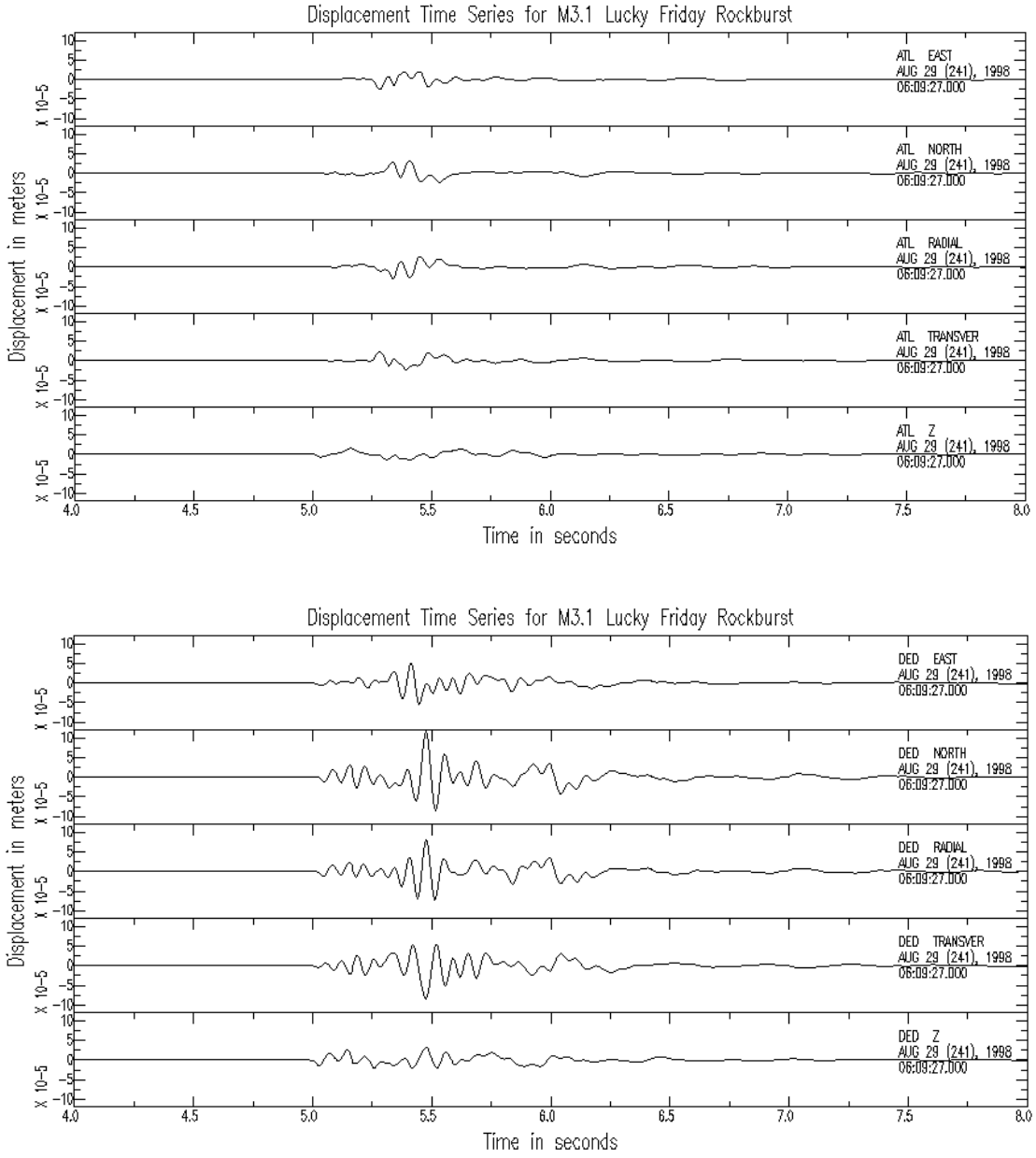


Figure 3. Displacement time series for the five strong motion accelerometers, having the north, east, and up positive convention and the radial (positive outward) and transverse (90 degrees clockwise) convention. Note that the polarity of the first motion is negative on the radial and vertical components (towards the source) at five all stations.

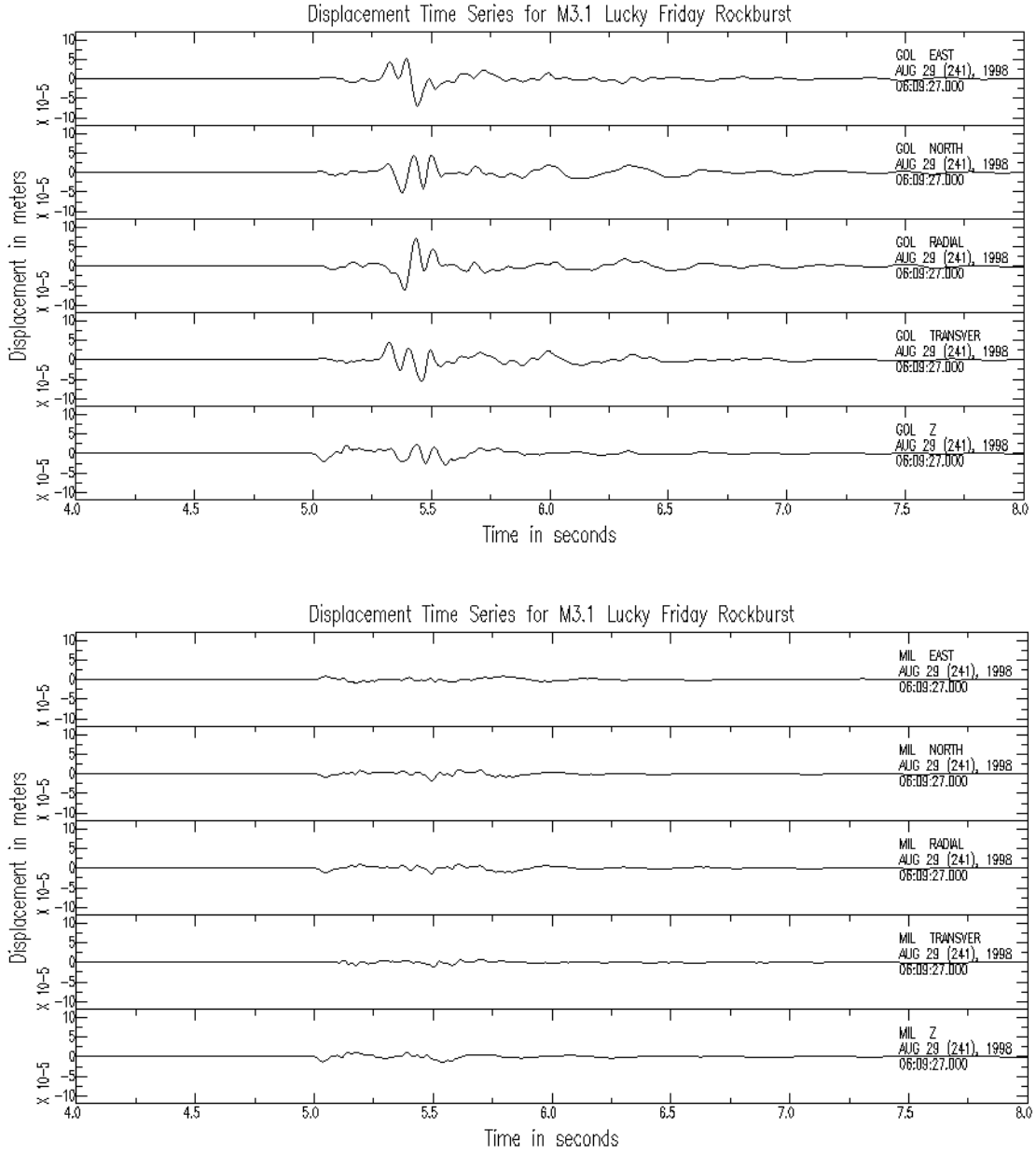


Figure 3 (continued).

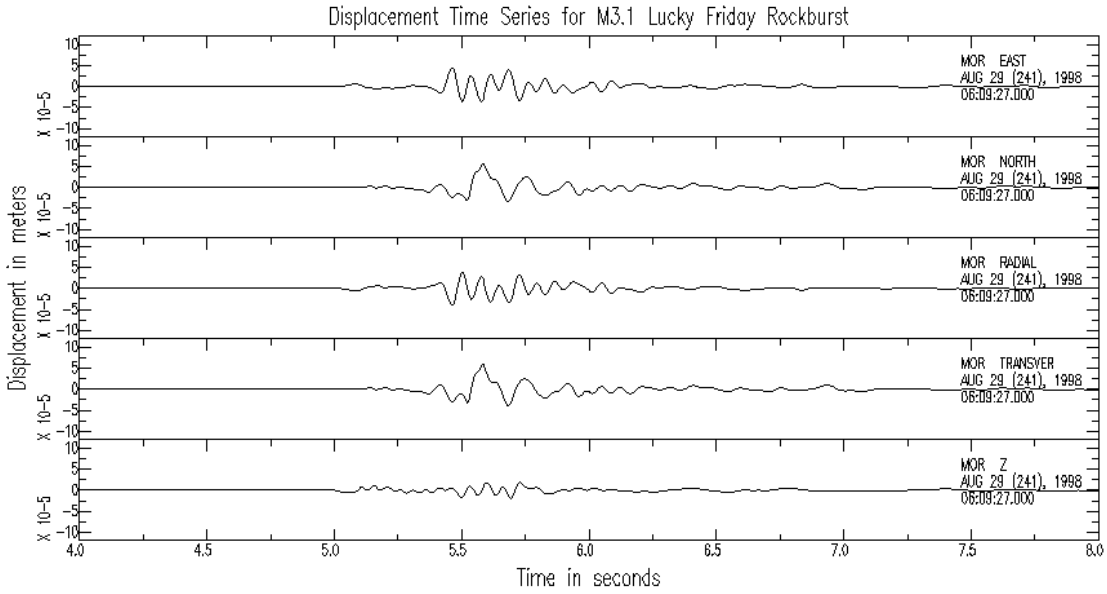


Figure 3 (continued).

OBSERVATION AND MODELING OF RIPPLE-FIRED EXPLOSIONS AT THE CENTRALIA MINE, WASHINGTON

Alan Rohay, Pacific Northwest National Laboratory

Sponsored by U.S. Department of Energy
Office of Nonproliferation and National Security
Office of Research and Development
Contract No. DE-AC06-76RLO 1830

ABSTRACT

One of the issues associated with the Comprehensive Nuclear-Test-Ban Treaty (CTBT) is the discrimination of large mining explosions from nuclear tests.

The Centralia coal mine is a significant source of seismic events in southwestern Washington. Some of the mine explosions have reported magnitudes as large as 3.5. We have assembled a set of waveform data from these explosions, derived from the Pacific Northwest Seismic Network and from broad band stations operated near the mine. These same stations also recorded nearby single explosions from the PASSCAL Southwest Washington Reflection/Refraction Experiment.

Detailed information on the geometry and delay pattern of the explosions was used to simulate the mine signals. The most common set of delays was 25 and 84 ms within and between rows, respectively. This leads to a spectral reinforcement at 12 and 40 Hz. The use of 500-ms down-hole delays introduces an additional $\pm$3.5-ms scatter in the delay times, reducing but not eliminating the spectral peaks in the simulations.

The blast simulations also predict spectral modulations resulting from the total blasting duration and the aspect ratio of the blast geometry (square vs. rectangular). A similar spectral modulation is observed in binary spectrograms and cepstra of many of the mine-generated signals. These spectral characteristics occur at lower frequencies than those related to the delay times, and so could be useful in identifying ripple-fired explosions at regional distances.

An additional important source of low-frequency spectral modulation in the simulation is the ballistic duration of a spall source (material being lifted and re-impacting the surface). Properly modeling the spall source requires additional information about the explosion's effect on the blasted material that is difficult to document given the information typical in blasters' logs. Video documentation of the spall source may be the only way to accurately estimate the parameters of the spall source. Seismic signals from apparently very different source geometries sometimes have very similar waveforms, and additional information such as charge weight, hole depth, and free-face orientation are being examined for their relation to groups of similar-appearing explosion sources.

Key Words: discrimination, seismic sources, mining practices, ground truth

OBJECTIVE

The objective of this study is to develop a relationship between the details of ripple-fired explosions at the Centralia coal mine in southwestern Washington and characteristics of regional seismic signals. These characteristics include the amplitudes of body waves and surface waves (particularly Rg) and spectral scalloping.

The Centralia mine source has reported magnitudes as high as magnitude 3.5 as measured by the coda-length method used by the Pacific Northwest Seismic Network (PNSN), but these magnitudes are over-estimates of the true magnitude of the events. These magnitudes do not appear to be well related to the total amount of explosive used, nor to measures of the maximum explosive charge rate (Figure 1). One of the objectives is to develop an amplitude-based magnitude scale that measures the amount (or rate) of explosives being detonated, to provide a better estimate of the size of these explosions.

The mine operators have been very cooperative in providing to us the details of the spatial and temporal delay pattern and the location and orientation of the blasts, and these data are being used to compare the amplitudes and spectral characteristics of the explosions. Many of the explosions have a relatively simple geometry, square to rectangular, and usually have delays between shots in a row of 25 ms and either 42 or 84 ms between rows. Previous studies (e.g. Hedlin et al., 1990; Hedlin, 1998) have shown that inter-hole time delays can produce spectral peaks in spectra and spectrograms, here at 40, 24, and 12 Hz, respectively. In the western U.S., and western Washington in particular, there is relatively high attenuation and such frequencies are not easily observable at distances of 100 km and further, and this will also be true in the CTBT setting for other regions with high attenuation.

However, it has also been observed that there are spectral modulations from mining explosions at lower frequencies that can be propagated to farther ranges (e.g. Carr and Garbin, 1998) that may be diagnostic of the explosion source. Such modulations have been suggested to be the result of the finite but extended duration of the total sequence of shots (Chapman et al., 1992). Low frequency spectral modulation is usually evident for explosions at the Centralia mine. A second major objective is to understand how different geometric and temporal characteristics (or other parameters) of the explosions produce spectral scalloping at the frequencies seen in the recorded data.

RESEARCH ACCOMPLISHED

We have assembled a data set of seismic waveforms recorded by broadband instruments operated near the mine, regional seismic stations of the PNSN and, for one mine explosion, mine signals recorded on a regional U.S. Geological Survey refraction profile that passed just south of the mine. The single-hole explosions used as sources in the refraction profile were also recorded on the broadband and regional stations and provide a comparison of a significantly different type of explosion.

The data from the mine operators has been analyzed, summarized, and tabulated in terms of whether the explosions had a simple geometry and constant delay time, in which area and level of the mine they occurred, and the geometry of the explosion relative to a free face, if any. In discussions with the mine blasters, they indicate that there is a 3.5 ms scatter in the delay devices, primarily from down-hole delays of 0.5 seconds. The surface delays that sequence the down-hole delays add somewhat to this estimate. We have simulated this scatter in the delay firing system, and determined that this should not cause a total loss of spectral reinforcement at frequencies determined by the spacing (along the free face) or burden (perpendicular to the free face) delay firing. The shot holes are closely spaced for these explosions, (8-10 m) and the propagation delay between holes is small. The propagation delay is calculated at the apparent velocity of the recorded seismic phase. For compressional waves travelling to stations at 5 km/s, this is a maximum of 2 ms/hole. This can only change the frequencies at which spectral nulls occur by 10% as a function of azimuth.

Simulation of the explosions consists of superimposing a sequence of delta functions corresponding to the time delay for each shot hole. As a more realistic representation of the explosion source, or simply to simulate a band-limited reception of the signal, the impulse sequence can be high-cut filtered. This generates a progressive

reinforcement of combined signal amplitude as more and more explosions are detonating closely spaced in time (Figure 2). There is often a ramp up, a steady plateau, and a ramp down. If the duration in the burden and spacing directions is comparable, this leads to a triangular pulse (the steady plateau is very short). If the duration in one direction is significantly different from the other, then the shape of the pulse is trapezoidal (ramp up, plateau and ramp down). Note that it is not the actual distance in each direction that determines the duration for these explosions. As before, the propagation delays that result from the spatial pattern are much smaller than the timing delays. This is true either between two adjacent holes or across the entire blasting area.

According to this model of the explosion sequence, there can actually be two characteristic durations that lead to low frequency spectral scalloping, for relatively simple patterns of explosions. The mine operators logs have been used to simulate several different, but simple, explosions for comparison to spectra and spectrograms measured from the seismic waveforms. This has to date been a discouraging comparison, and led to attempts to simulate a third possible effect that may have a predictable characteristic duration, the effect of spall (e.g. Anandakrishnam, 1997).

The spall source results from the blasted material being lifted from the surface, and after a time of ballistic flight, re-impacting the ground. This may be a larger and more coherent movement than the superposition of individual explosions attains. In fact, because this is the primary intent of the blasting process (to break up and "bulk" the material for removal), this may be a logical result of the experience and skill of the mine operators. The Centralia mine does not attempt "cast" blasting, where the explosions are designed to throw the material into a pit below the free face. Visual observations at the Centralia mine indicate that the duration of the spall source is relatively short, comparable to the duration of the blasting sequence itself. It is possible that there may be some unexamined parameters that are available in the blasting logs (e.g. hole diameter and depth, amount of tamping) that may indicate (in a relative way) the mass of material and how long it is ballistic. The strength and density of the material being blasted are variable, not currently available, and may be important, and the material being blasted interacts in a complicated way. It seems that direct observation of the spall process is needed in this situation, for example with high-speed video recording. In the case of the Centralia mine, where material is being "bulked", even this information may not be sufficient.

As an alternative to the "forward" modeling of similar or dissimilar explosions based on the blasting logs, seismic signals are being sorted for similar amplitude ratios, presence of and frequencies of spectral nulls etc. It is hoped that by approaching the classification of blasts by their seismic signals, that one or more of the controlling parameters producing such features can be explained.

CONCLUSIONS

The Centralia coal mine provides an opportunity to examine a type of ripple-fired explosion that is typical of many open-pit mines. High-frequency spectral reinforcement is difficult to observe in this region and will be in other areas of high attenuation. The use of long time delays relative to the spacing of the holes leads to a conclusion that the spatial extent of the explosions is much less important than the temporal duration of the shot sequence. The temporal duration of the blast sequence can be described as having two characteristic durations, resulting in two sets of low frequency spectral nulls in spectrograms from regional seismic stations. This type of explosion may be effective at producing a spall source, which generates strong surface waves. These surface waves may result in overestimates of energy based on signal duration. The spall source may not be easily parameterized in a way that spectral modulations expected from the duration of the spall can be predicted.

REFERENCES

Anandakrishnam, S., S.R. Taylor, and B.W. Stump, 1997. Quantification and characterization of regional seismic signals from cast blasting in mines: a linear elastic model, Geophys. J. Int. 131, pp. 45-60.

Carr, D.B., and H.D. Garbin, 1998. Discriminating ripple-fired explosions with high-frequency (>16 Hz) data. Bull. Seismol. Soc. Am. 88, pp. 963-972.

Chapman, M.C., G.A. Bollinger, and M.S. Sibol, 1992. Modeling delay-fired explosion spectra at regional distances. Bull. Seismol. Soc. Am. 82, pp. 2430-2447.

Hedlin, M.A.H., 1998. A global test of a time-frequency small-event discriminant. Bull. Seismol. Soc. Am. 88, pp. 973-988.

Hedlin, M.A.H., J.B. Minster, and J.A. Orcutt, 1990. An automatic means to discriminate between earthquakes and quarry blasts. Bull. Seismol. Soc. Am. 80, pp. 2143-2160.

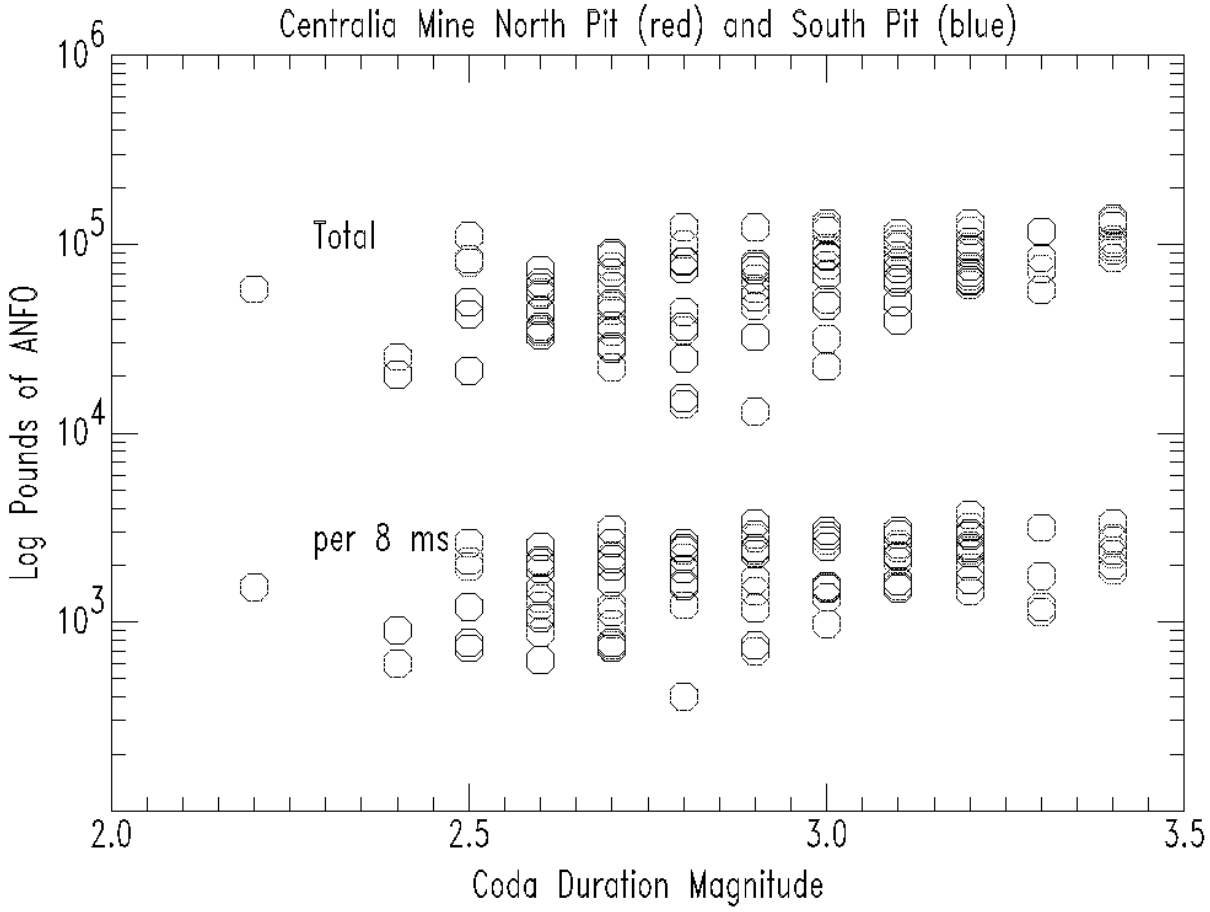


Figure 1. Comparison of PNSN magnitudes with total yield and yield within 8 ms. The latter is used by the mine to estimate peak amplitudes at surrounding points. (Note color is not reproduced in this presentation.)

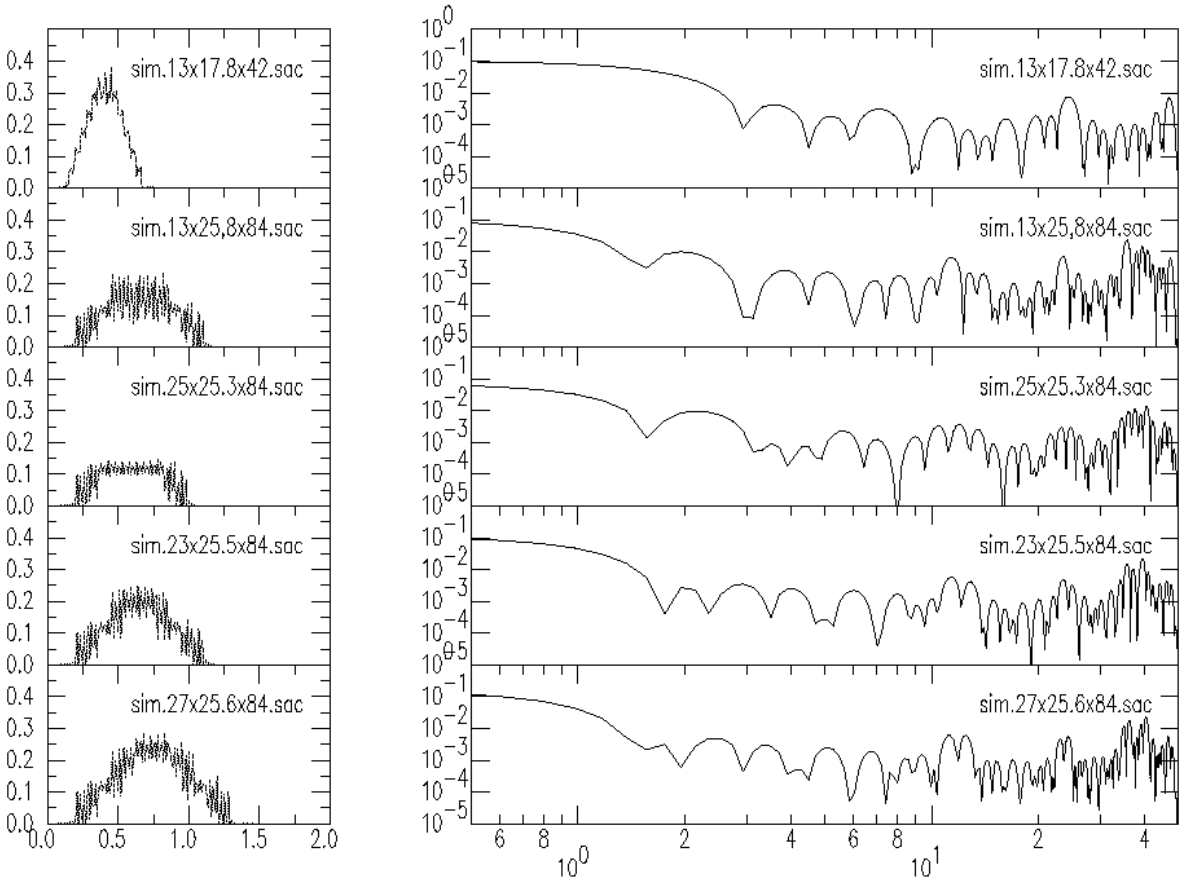


Figure 2. Example source time histories and spectra showing range of source shape and spectral modulations. The source function varies from triangular to trapezoidal depending on how different the total delay are in the spacing and burden directions.

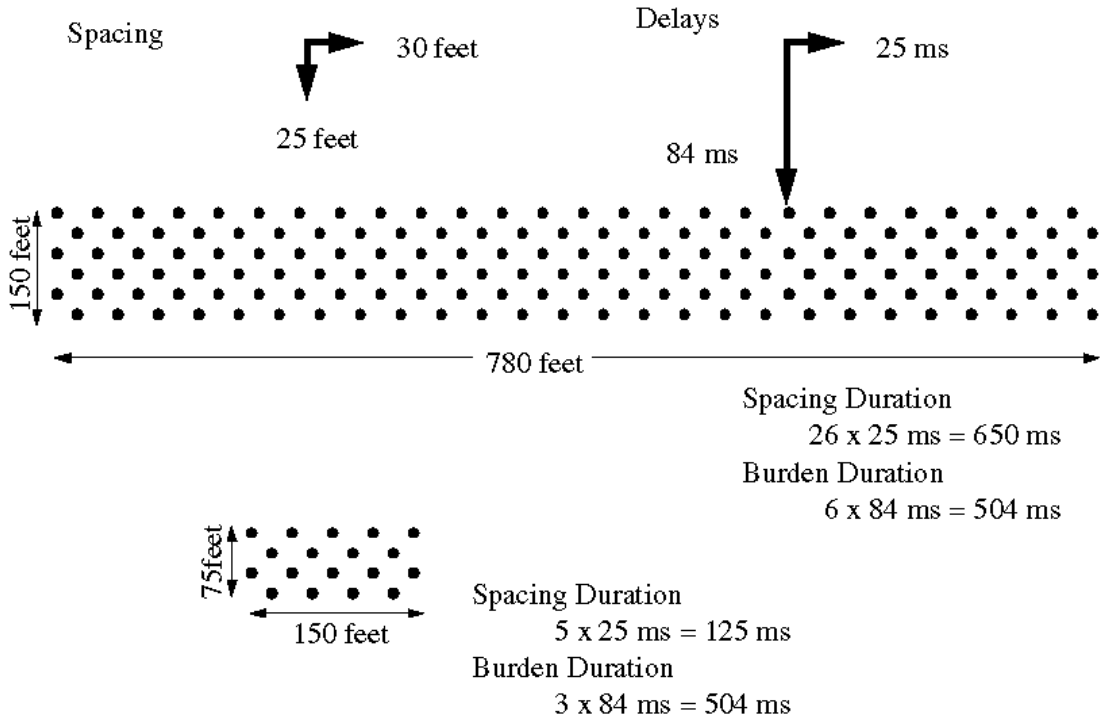


Figure 3. A diagram of two highly different but simple blasting patterns from the Centralia mine blaster's logs.

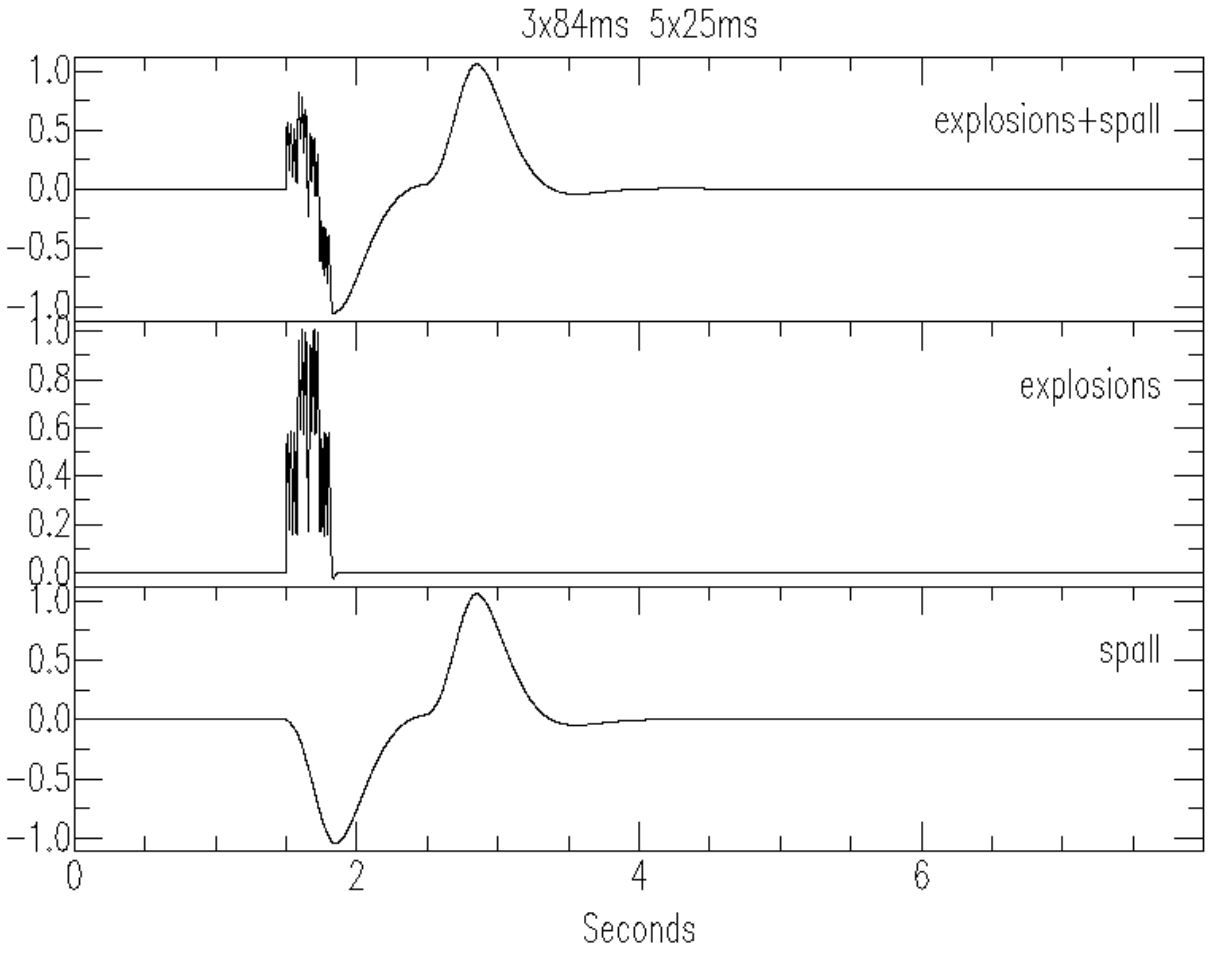


Figure 4. Simulation of the shorter source function of the two blasting patterns in Figure 3. Spall duration is assumed to be 1 second.

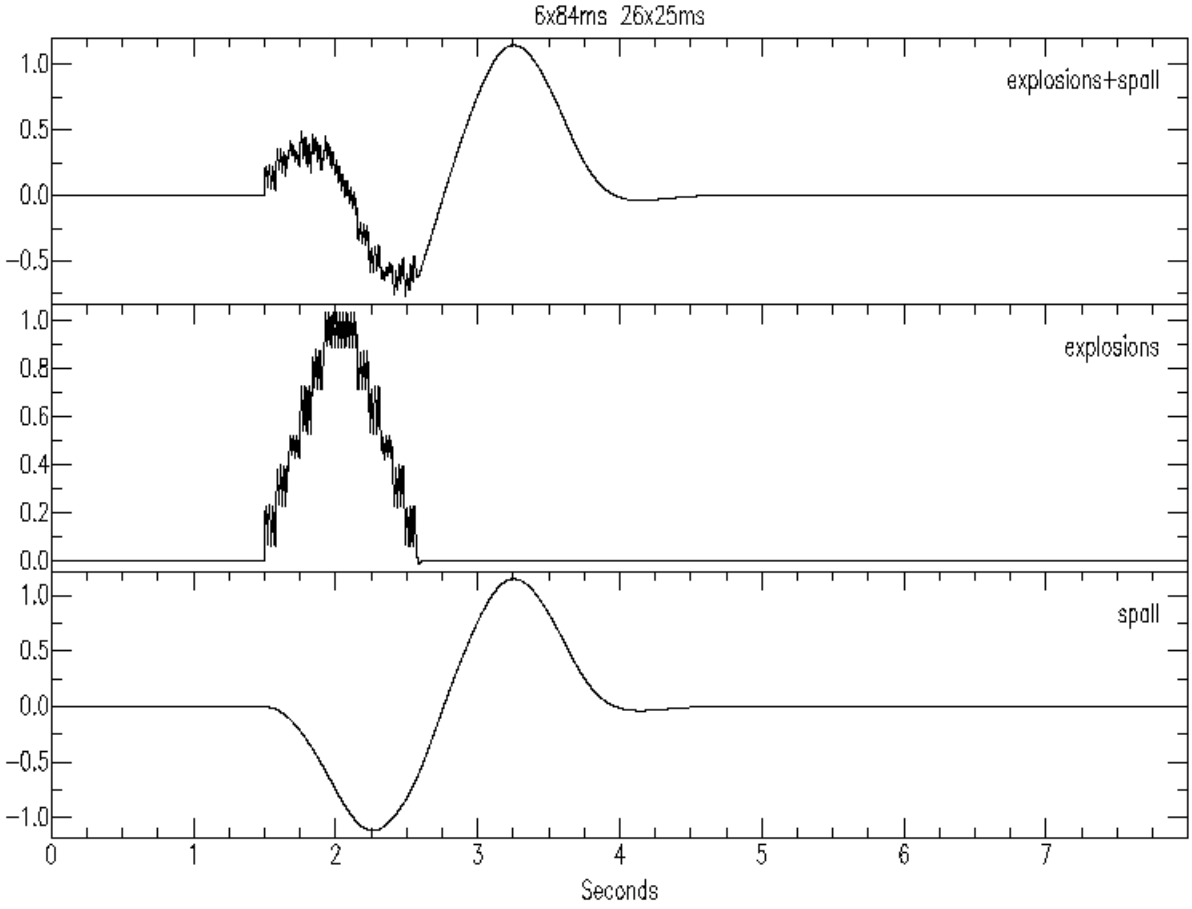


Figure 5. Simulation of the longer source function for the two blasting patterns in Figure 3. Spall duration is assumed to be 1 second.

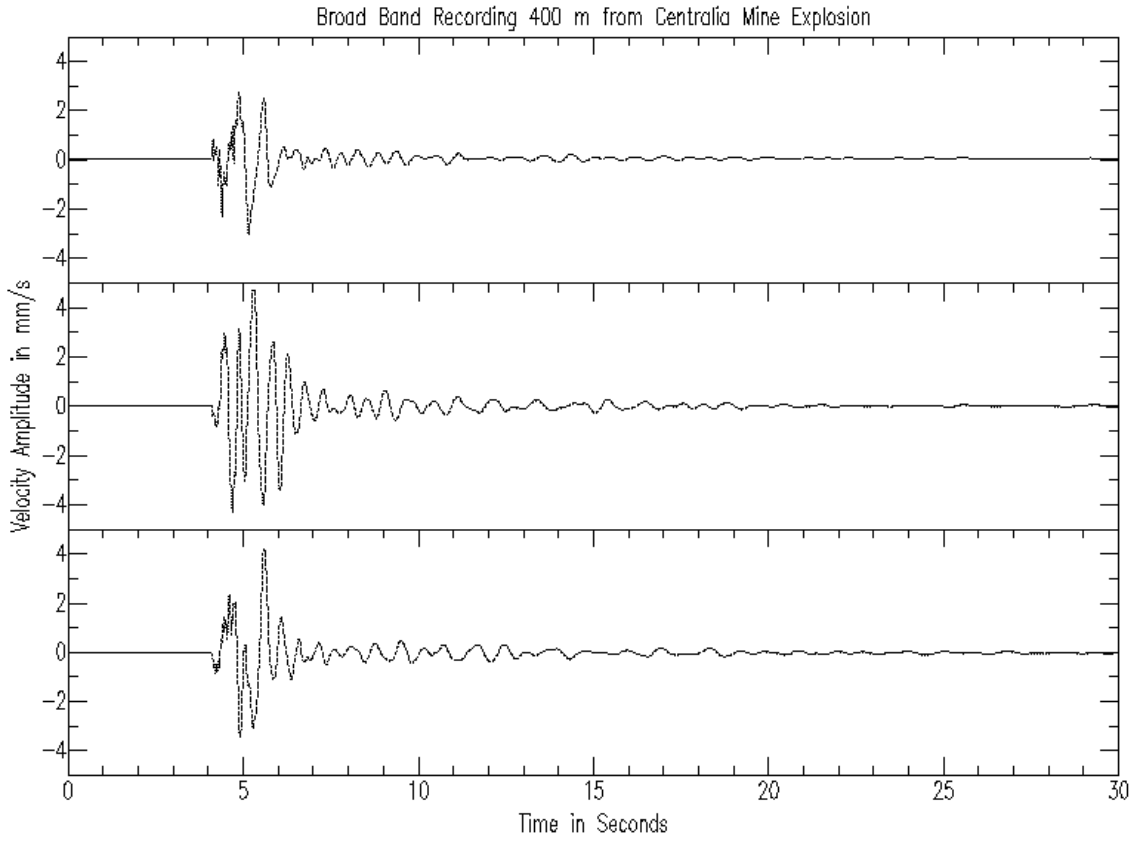


Figure 6. Recorded time series using broadband recorder 400m from Centralia mine blast. This is similar to the longer blast simulated in Figure 5.

INCORPORATING THE EFFECTS OF DAMAGE-INDUCED SECONDARY SEISMIC RADIATION INTO NUMERICAL MODELS FOR UNDERGROUND EXPLOSIONS

Charles G. Sammis
Department of Earth Sciences
University of Southern California
Los Angeles, CA 90089-0740

Sponsored by DoD (DTRA)
Grant No. DSWA01-97-1-0005

ABSTRACT

Secondary seismic radiation is generated by rock fracture in the "damage zone" of an underground nuclear source and by frictional sliding on preexisting fractures in the "non-linear elastic zone" at larger distances from the shot point. This radiation is important for two reasons: (1) Johnson (1997, 1998) has shown that it can make an important contribution to the far-field seismic signal, and (2) Sammis (1998) has argued that it can significantly weaken the granulated rock behind the shock front in the damage zone. This weakening is due to a mechanism called acoustic fluidization originally proposed by Melosh (1979) to explain long-run-out landslides, the fluid morphology of extraterrestrial impact craters, and the low coefficient of effective friction inferred for the San Andreas fault. Such weakening has been shown to be necessary if computer models are to simulate the pulse-broadening observed in the near-field of nuclear explosions in hard rock (Rimer et al., 1987; Rimer et al., 1998). This paper outlines a procedure to incorporate acoustic fluidization into the numerical codes used to simulate underground explosions.

Key Words: seismic sources, discrimination.

OBJECTIVE

The objective of this research project is to understand the physics of rock fragmentation and subsequent deformation in the source region of a nuclear explosion detonated in crystalline rock. Rock fragmentation in the source region is relevant to research in support of the Comprehensive Nuclear-Test-Ban Treaty because it directly affects the seismic radiation observed in both the near and far field in at least two important ways:

1) The fragmentation process itself generates secondary high-frequency P and S waves that may affect seismic discrimination and yield estimates which use high-frequency local crustal phases.

2) Fragmentation behind the advancing shock front leaves a weakened region that is thought to produce the pulse-broadening observed in seismic radiation. A quantitative understanding of this observed pulse broadening is important if the frequency content of the seismic signal is to be used for discrimination and yield estimates.

RESEARCH ACCOMPLISHED

Generation of secondary radiation by the damage process has been modeled by Lane Johnson and the author [Johnson, 1996,1997; Sammis, 1998; Johnson and Sammis, 1999]. We found that secondary seismic energy approaches 10% of the primary radiation.

The micromechanical damage mechanics developed by Ashby and Sammis [1990] has been successfully integrated into the spherically symmetric numerical simulation code at s-cubed through a collaboration between Rimer, Stevens and the author [Rimer et al, 1998] Although these simulations gave a good description of the extent of the fracture damage near the source (as evidenced by Russian fracture measurements at their hard rock sites), they were unable to explain the observed seismic pulse broadening.

The problem is that the Ashby and Sammis [1990] damage mechanics is not applicable in the post-failure regime where the rock fractures and granulate. While it gives a good description of damage nucleation and failure surface, it breaks down and does not give an adequate description of the post-failure behavior of the damaged rock. In the s-cubed simulations [Rimer et al., 1998], we assumed that once an element failed, its strength fell to the level given by friction. This assumption was based on the behavior of granular layers tested under simple shear in the laboratory which are observed to deform according to a simple frictional rheology [Dieterich, 1981; Biegel et al., 1989; Marone and Kilgore, 1993; Sammis and Steacy, 1994;]. However, in order to simulate the observed pulse broadening, Rimer et al.[1998] found that they had to reduce the coefficient of friction in the granulated rock to μ=0.02, far below the value of μ=0.6 commonly observed in the laboratory. The problem may lie in the fact that the laboratory measurements of friction in granular layers are made at very low sliding velocities on the order of microns per second whereas deformation rates in the nonlinear region of a nuclear source are very high and dynamic effects may be important.

A physical solution to this dilemma may lie in the "acoustic fluidization" of the granulated rock in the source region [Sammis, 1998]. Acoustic fluidization is a phenomenon proposed by Melosh [1979] to explain long run-out landslides on earth and the fluid-like morphology of large extraterrestrial impact craters. Melosh [1996] has recently proposed acoustic fluidization as the mechanism which explains the "heat flow paradox" in which the absence of a heat flow anomaly on the San Andreas fault implies that it slips at a very low effective coefficient of friction. This interpretation is supported by recent computer simulations of faulting in a granular medium by Mora and Place [1998].

Acoustic fluidization occurs when high-frequency acoustic energy produces sufficiently large fluctuation in the normal stress between grains that local slip between grains becomes possible at a very low value of the applied stress. The theory developed by Melosh [1979] is necessarily statistical in nature since the stress fluctuations are spatially and temporally distributed throughout the granular medium. The central equation describing the rheology of a fluidized granular medium is

$$\dot{\varepsilon} = \frac{\tau}{\rho\lambda c}\left[\frac{1 - erf\left(s_c / 2^{1/2}\sigma\right)}{1 + erf\left(s_c / 2^{1/2}\sigma\right)}\right] \tag{1}$$

where:

τ = applied shear stress
ρ = density of the granulated rock
λ = wavelength of the acoustic energy
c = P wave velocity in the granulated rock
S_c = critical pressure amplitude in the P wave acoustic field to relieve the overburden pressure ρgh and allow sliding
= $\rho gh - \tau/\mu$
σ = variance of the normally distributed random acoustic P wave field.

Note that the strain rate is linear in the applied stress τ so the fluidized granular rock behaves as a Newtonian fluid with viscosity

$$\eta = \frac{\rho\lambda c}{2}\left[\frac{1 + erf\left(s_c / 2^{1/2}\sigma\right)}{1 - erf\left(s_c / 2^{1/2}\sigma\right)}\right] \tag{2}$$

In a strong acoustic field, $\sigma \approx s_c$ and

$$\eta \approx \rho\lambda c \tag{3}$$

Note that the viscosity is lowest for short wavelength acoustic energy (small λ) and that the low value of the P wave velocity (c) in the highly damaged rock also contributes toward lowering the fluidized viscosity.

There are two questions which must be answered before acoustic fluidization can be considered a viable process in the source region: 1) is a fully fluidized granulated layer weak enough to produce the observed pulse broadening and 2) is the acoustic field strong enough to fully fluidize this layer? We begin with question (1). As a preliminary estimate, take ρ = 3 gm./cm^3 and c = 1 km/s as typical values for granulated rock. Assume that the wavelength of the acoustic waves are of the same order as the flaw size that generates them and take λ = 1 cm. If the damaged rock is fully fluidized, the effective viscosity will be $\eta \approx \rho\lambda c = (3)\left(10^5\right)(1) = 3x10^5 P$. The hoop strain during the Hardhat explosion at a distance of r=200 m. from the shotpoint was about 7.5x10^{-3} [Rimer et al., 1987]. Since the inflation lasts for about 0.15 s., the strain-rate is about $\dot{\varepsilon} = 5x10^{-2}$ sec^{-1}. If the rock is fully fluidized, the stress required to produce this strain rate is:

$$\sigma = \eta\dot{\varepsilon} = (3x10^5)(5x10^{-2}) = 1.5x10^4 \text{ dynes/cm}^2,$$

or about 0.015 bars. Since this is well below the stress level in the granulated layer, we can conclude that full acoustic fluidization can weaken the granulated layer sufficiently to produce the pulse broadening observed in Hardhat.

The second question is more difficult to answer and is the current focus of our research. In a recent paper [Johnson and Sammis, 1999] we have integrated the seismic moments (shear and dilatational) generated by the myriad of small flaws in the damage regime and shown that they make a significant contribution to the far-field seismic radiation provided that a) there is a preferred orientation to the preexisting flaws or b) there

is a non-isotropic prestress, or both. We now need to calculate the integrated contribution of all the flaws to the acoustic field in the granulated zone inside the growing damage front as illustrated in Figure 1. Johnson and Sammis [1999] showed that the damage front moves out with a velocity between the P and S velocity. The bulk of the returning radiation should be trapped in the granulated zone by strong scattering thus extending the time during which the material is fluidized, but this has yet to be quantified. If there were no attenuation, then one can make the following simple geometrical argument that the dilatation will be strong enough to overcome lithostatic pressure. Dilatational stresses at the source must be strong enough to overcome the overburden since dilatational "wing cracks" are formed. At any point inside the spherical damage front (e.g., point P in Figure 1), the radiation from a spherical damage front at r will be independent of r. This is because the $1/r^2$ decrease in pressure is exactly compensated by the r^2 increase in source area. Since the pressure at the source is sufficiently strong, so will be the waves from any subsequent spherical shell. An historical note: this is the same argument used by Olbers in 1823 against a uniform infinite static distribution of stars, and argument subsequently invalidated by the red shift associated with the expanding universe. A quantitative evaluation of the effects of scattering and attenuation on this argument are a current focus of our research program.

Incorporation of acoustic fluidization into the source model requires that failed elements are assigned the viscosity given by eqn. (2) or (3). This is very different from our previous assumption that the strength falls to friction which amounts to specifying a yield surface and relaxing the displacement field by radial-return to this surface. One interesting consequence of a viscous model is that the standard scaling relations no longer necessarily hold.

CONCLUSIONS AND RECOMMENDATIONS

Our recent success in incorporating micromechanical damage mechanics into numerical simulations of explosions in crystalline rock [Rimer et al., 1998] has demonstrated that the weakening associated with crack growth and fragmentation is not sufficient to produce the pulse broadening observed in the seismic radiation. Last year, we [Sammis, 1998] proposed that acoustic fluidization [Melosh, 1979] of the fragmented rock behind the shock front might produce the additional weakening required to fit the observed radiation. We show here that preliminary estimates of the effective viscosity of the fully fluidized fragments are consistent with the stress and strain-rates in the nonlinear regime of the Hardhat explosion calculated by Rimer et al. [1987].

The one remaining question is whether there is sufficient acoustic energy in the granulated rock to achieve full fluidization. In a recent paper [Johnson and Sammis, 1999], we have developed the methodology to calculate the secondary seismic radiation generated by the myriad of small growing fractures which comprise the "damage" in damage mechanics. The next step is to calculate the amplitude of this secondary radiation behind the shock front taking into account scattering and attenuation. A simple geometrical argument suggests that there should be sufficient acoustic energy. Equations (2) and/or (3) can then be used to assign a viscosity to the failed elements.

REFERENCES

Ashby, M.F., and C.G. Sammis, The damage mechanics of brittle solids in compression, PAGEOPH, 133, 489-521, 1990.

Biegel, R.L., C.G. Sammis, and J.H. Dieterich, The frictional properties of a simulated gouge having a fractal particle distribution, J. Structural Geology, 11, 827-846, 1989.

Dieterich, J. H. (1981) Constitutive properties of faults with simulated gouge, in *Mechanical Behavior of Crustal Rocks*., *Geophysical Monograph 24*. American Geophysical Union, 108-120.

Johnson, L.R., The effect of damage on explosion generated waves, Proc. 18th Ann. Seismic Res. Symp, pp 195-198, 1996.

Johnson, L.R., The generation of S waves by explosions, Proc. 19th Ann. Seismic Res. Symp., pp 625-631, 1997.

Johnson, L.R., and C.G. Sammis, Effects of rock damage on seismic waves generated by explosions, PAGEOPH, accepted for publication, 1999.

Marone, C. and Kilgore, B. (1993) Scaling of the critical slip distance for seismic faulting with shear strain in fault zones, *Nature*, **362**, 618-621.

Melosh, H.J., Dynamical weakening of faults by acoustic fluidization, Nature, 379, 601-606, 1996.

Melosh, H.J., Acoustic fluidization: A new geologic process, J. Geophys. Res., 84, 7513-7520, 1979.

Melosh, H.J., and E. S. Gaffney, Acoustic fluidization and the scale dependence of impact crater morphology, Proc. 13th Lunar and Planet. Sci. Conf, J. Geophys. Res., 88, supplement, A830-A834, 1983.

Melosh, H.J., E.V. Ryan, and E. Asphaug, Dynamic fragmentation in impacts: hydrocode simulation of laboratory impacts, J. Geophys. Res., 97, 14735-14759, 1992.

Mora, P. and D. Place, Numerical simulation of earthquake faults with gouge: an unflawed explanation of the heat flow paradox, J. Geophysical Res., submitted, 1998.

Rimer, N., J.L. Stevens, and S.M. Day, Effect of pore pressure, fractures, and dilatancy on ground motion in granite, S-Cubed Report SSS-R-87-8670, 1987.

Rimer, N., J.L. Stevens, J.R. Murphy, and G.G. Kocharyan, Estimating seismic source characteristics of explosions in hardrock using a micro-mechanical damage model, Proc. of the 20th Annual Seismic Research Symposium on Monitoring a Comprehensive Test Ban Treaty (CTBT), pp379-386, 1998.

Sammis, C.G., and S.J. Steacy, The micromechanics of friction in a granular layer, PAGEOPH, 142, 777-794, 1994.

Sammis, C.G., Observational constraints on non-linear source models in the damage regime, Proc. 19th Ann. Seismic Res. Symp., pp 662-667, 1997.

Sammis, C.G., Acoustic fluidization in the damage regime of explosions in crystalline rock, Proc. of the 20th Annual Seismic Research Symposium on Monitoring a Comprehensive Test Ban Treaty (CTBT), pp403-407, 1998.

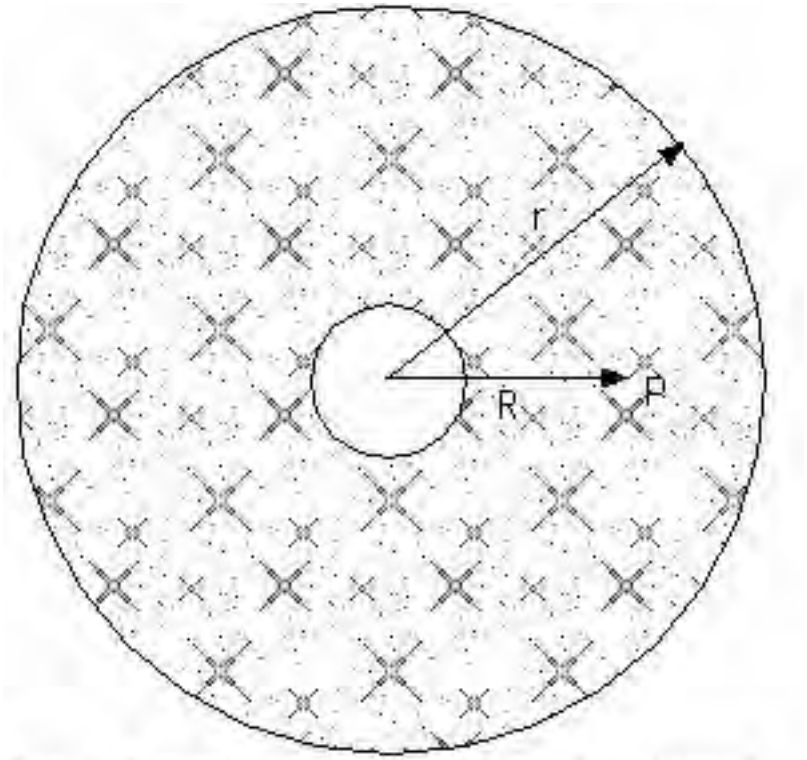


Figure 1. Geometry of fragmented zone. Field point P is at distance R from the shotpoint. The active damage front is at a distance r(t) from the shotpoint at time t.

Empirical Scaling Relations for Contained Single-Fired Chemical Explosions and Delay-Fired Mining Explosions at Regional Distances

Brian W. Stump, D. Craig Pearson, and Vindell Hsu,

Southern Methodist University, Los Alamos National Laboratory, Air Force Technical Applications Center

Sponsored by U.S. Department of Energy
Office of Nonproliferation and National Security
Office of Research and Development

Contract No. W-7405-ENG-48

ABSTRACT

Mining blasts are typically composed of numerous individual explosions that are detonated in a complex spatial and temporal pattern. For purposes of monitoring the Comprehensive Nuclear-Test-Ban Treaty (CTBT), the signals from delay-fired mining explosions must be distinguished from those of a possible nuclear explosion. The similarity of seismic waveforms from contained chemical and nuclear explosions suggests that contained, single-fired chemical explosions can be used to calibrate the International Monitoring System. In order to address these issues, a series of experiments were designed and implemented in which single-fired explosions ranging in size from 5500 to 50000 lb. were detonated. The spatial separation of the individual explosions ranged from 30 m to over 4 km. Seismograms from the single-fired explosions were recorded within the mine (near-source) as well as at the IMS regional array PDAR (~360 km). Peak amplitudes for Pg, Pn and Lg phases at PDAR increased linearly with yield for the fully detonated single-fired explosions. In contrast, peak amplitude measurements from production coal and cast shots in the same mine show no trend of peak amplitude with explosive weight. Maximum amplitudes of the near-source data followed the same trends as the regional data suggesting that measures developed to limit in-mine ground motion might account for the lack of any increase in regional amplitudes with yield for the production blasts. Coherency estimates provide the opportunity to investigate how the waveforms compare as a function of frequency and wavelength. All elements of PDAR were used in estimating an average P wave coherence. The coherence is near 1 to high frequency (12 Hz) for two shots separated by 20 m. The coherence for two shot separated by approximately 350 m decays above 6 Hz. Finally, for the sources separated by nearly 4 km the coherence rises only slightly before decaying. These observations suggest limited applicability of coherency for identifying events from a single mine if it is large. Spectral ratios were used to investigate source scaling relations for the different yield explosions. Four similarly prepared shots with total explosive weights between 5500 and 6000 lb. were detonated to investigate source repeatability. Spectral ratio analysis identified two of the four shots as only partially detonating resulting in a reduction of long period spectral level by factors of 10 and 50. These long period reductions were accompanied by increases in source corner frequency. Production mining explosions can consist of hundreds of individual detonations. Most modeling of such blasts assume that each of the explosions performs in an identical manner. These results suggest that this assumption may need reconsideration.

Key Words: contained explosion, mining explosion, regional, calibration

OBJECTIVE

The IMS is designed to provide observational data that can be used to locate and identify events. The identification of different event types relies on the determination of characteristics that are particular to each. The signing of the CTBT has been accompanied by a cessation of nuclear testing. It has been previously shown (Denny, 1994) that contained single-fired chemical and nuclear explosions produce seismic waves that are similar. Contained, single-fired chemical explosions could therefore be used to calibrate discriminants designed for nuclear explosions. Details of moderate to small sized chemical explosions conducted in a mine are reported in order to investigate this suggestion.

Explosives are used around the world for recovering minerals and energy resources (Richards *et al.,* 1992; Heuze and Stump, 1999). Typically these explosions are delay-fired, meaning that they consist of many small explosions spread out in space and time. The monitoring system must be able to distinguish these types of explosions from a single-fired, contained explosion. The second point of relevance in this work is the quantification of observational similarities and differences between the single-fired explosions and standard mining explosions designed to move and fracture rock.

The goals of this empirical study can be broken into five elements:

1. Determination of the effect of explosive weight or yield on coupling into the regional phases Pn, Pg and Lg.
2. Empirical determination of reproducibility of regional seismograms from explosions.
3. Characterization of coherence in regional waveforms from closely spaced explosions.
4. Constraint of the source time function for single-fired, contained chemical explosions.
5. Quantification of the similarities and differences between single-fired explosions and typical delay-fired mining explosions.

A series of experiments were conducted in a mine in Wyoming on order to address these goals. Regional seismograms that are used for identifying sources are strongly affected by both the source of the waves and the regional structure through which the waves propagate. In order to eliminate propagation path effects in this study, the contained, single-fired explosions were conducted in a mine that was also conducting standard delay-fired explosions. Figure 1 illustrates the location of the cooperating mine as well as Primary IMS array, PDAR, that provided the regional seismic data for this investigation.

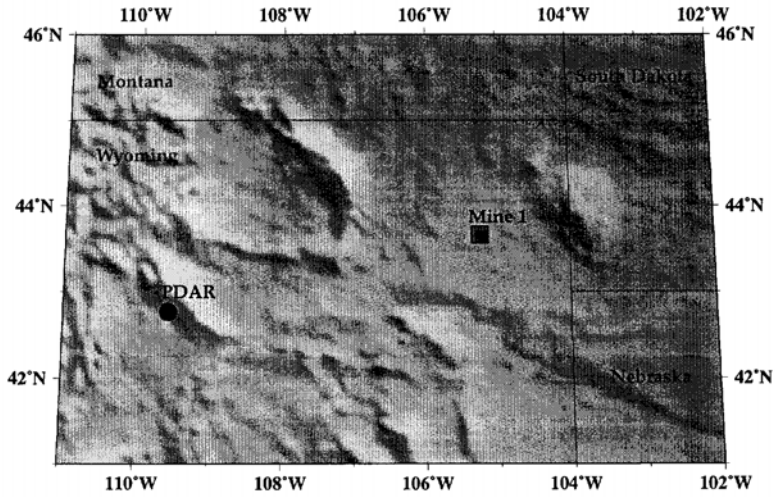


Figure 1: The experiment location. The mine is located in the Powder River Basin in NE Wyoming. The IMS Primary Array at Pinedale, Wyoming (PDAR) provides the regional data for this study.

There were seven contained, single-fired explosions with total explosive weight ranging from 5500 to 50000 lb. The number of individual boreholes in any one explosion was between 1 and 10. The spatial separations of the explosions were between 30 and 3850 m. The source characteristics are summarized in Table 1. The explosives for the contained, single-fired explosions were emplaced with a technique that was similar to that used for production shots in the mine. Boreholes were drilled to a depth of approximately 140 ft., filled with explosives and then backfilled with 40-60 ft. of stemming material. The amount of stemming was increased from that typically used in production shots (20-30 ft.) in order to assure that the event was contained. All the boreholes were drilled away from the mine free-face so that there was no relief from this surface. A single borehole configured in this manner accommodates between 4000 to 6000 lb of explosives. Multiple boreholes fired simultaneously were used for the higher charge weight shots. In these cases the boreholes were spaced approximately 32 ft apart and wired to detonate simultaneously.

Table 1: Shot Characteristics

SHOT	SIZE (lb)	Number of BOREHOLES	Distance to S1 (m)
S1	5500	1	-
S2	5500	1	30
S3	5500	1	70
S4	6000	1	90
S5	12000	3	390
S6	16000	4	420
S7	50000	10	3820

Overhead SPOT imagery of the mine illustrates the spatial distribution of the explosions relative to production activities in the mine. As illustrated in Figure 2, the mine encompasses an area that is approximately 5 km by 7 km. Shots 1 through 6 were detonated in relatively close proximity to one another. Because of its increased size, Shot 7 was detonated in the south of the mine far from the production facilities that were sensitive to close-in ground motions.

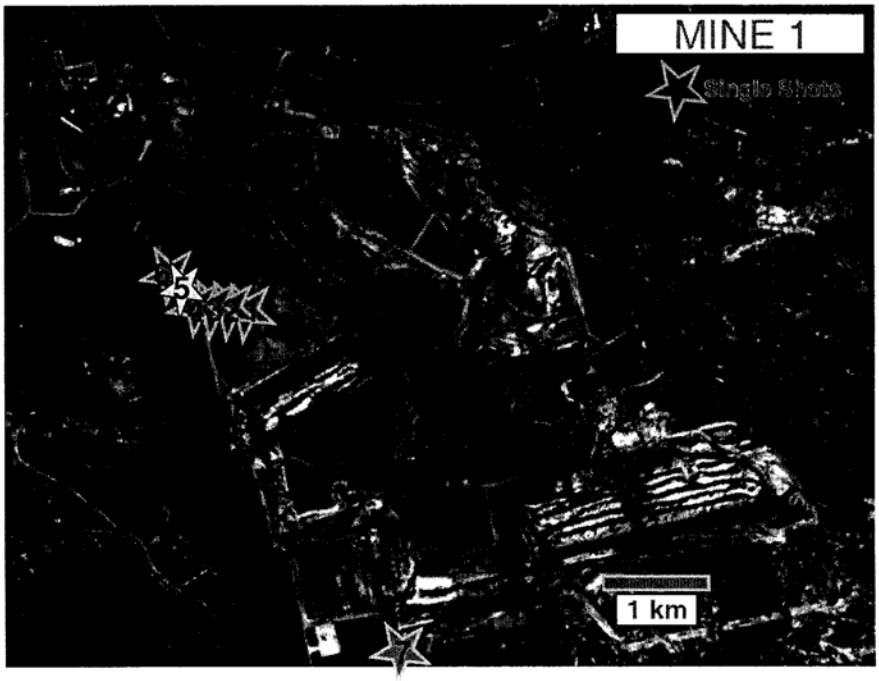


Figure 2: Overhead SPOT image of the mine along with the locations of the single-fired explosions listed in Table 1.

RESEARCH ACCOMPLISHED

1. *Determination of the effect of explosive weight or yield on coupling into the regional phases Pn, Pg and Lg.*
2. *Empirical determination of reproducibility of regional seismograms from mining explosions.*

The vertical component of motion at PDAR (PD03) from each of the seven, single-fired, contained explosions are compared in Figure 3. The relative weight of explosives in each shot is represented by the diameter of the hexagon to the right of each waveform. Each waveform is scaled to its peak in the figure with the absolute peak amplitude represented by the vertical bar to the far right. Despite the first four explosions having nearly identical explosive weight, there is over an order of magnitude variation in peak regional amplitude. Small peak amplitudes from the first two shots, S1 and S2, suggest that these two explosions did not fully detonate. Low order detonation was further substantiated by visual observations of the shot.

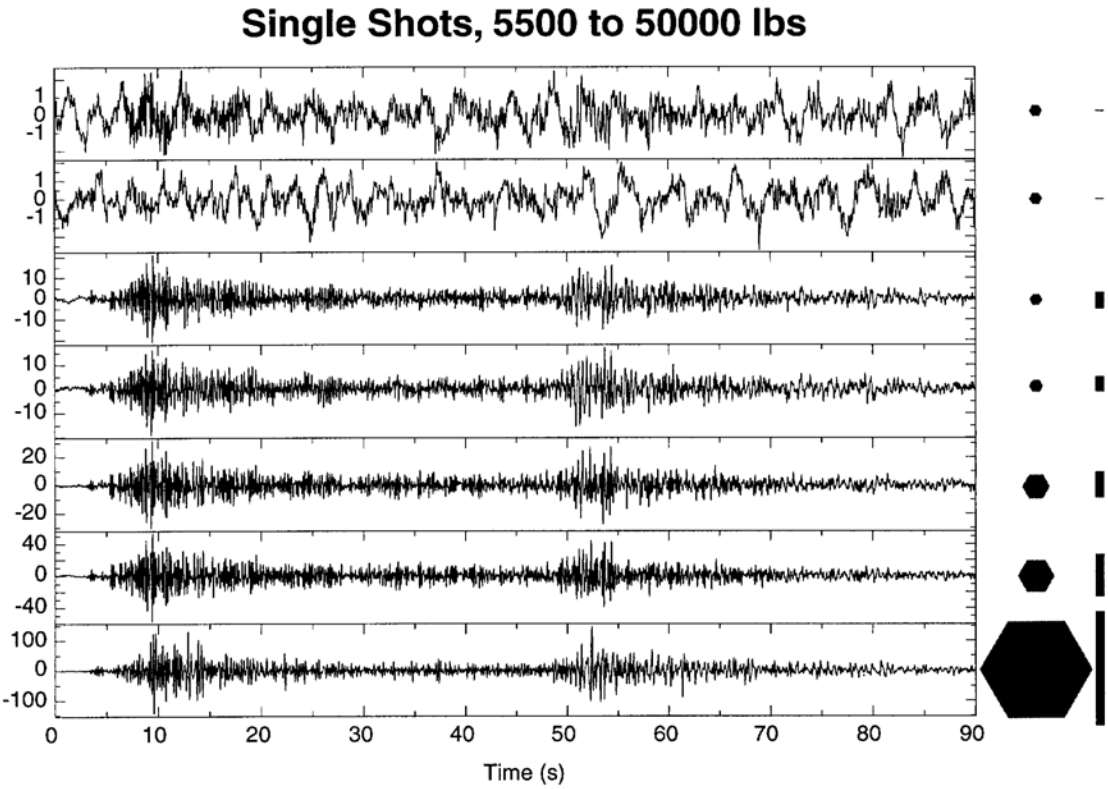


Figure 3: Relative comparison of single array element of PDAR (PD03) for the seven, single-fired explosions described in Table 1. The relative sizes of the explosions are illustrated by the size of the hexagon while the peak amplitudes of the waveforms are represented by the vertical bars to the right of each waveform.

The amount of explosives and delay pattern in a mining explosion is dependent upon both the specific mining application as well as a desire to minimize close-in ground motions to near-by buildings. These requirements limit the largest explosions in a particular application and may be responsible to some extent for a maximum expected regional magnitude from mining explosions. In order to test this hypothesis, close-in velocity measurements (7-11 km from source) were made for the single shots that could be compared to the regional measurements at PDAR. The close-in waveforms are reproduced in Figure 4. The relative comparisons of peak amplitudes for the close-in data are consistent with the regional observations. In both data sets, the first four shots, despite having the same amount of explosives, have nearly a factor of 50 variation in amplitude. The correlation between the regional and

close-in amplitudes is supportive of the idea that blasting practices imposed to limit ground motion within the mine may be reflected in the regional observations.

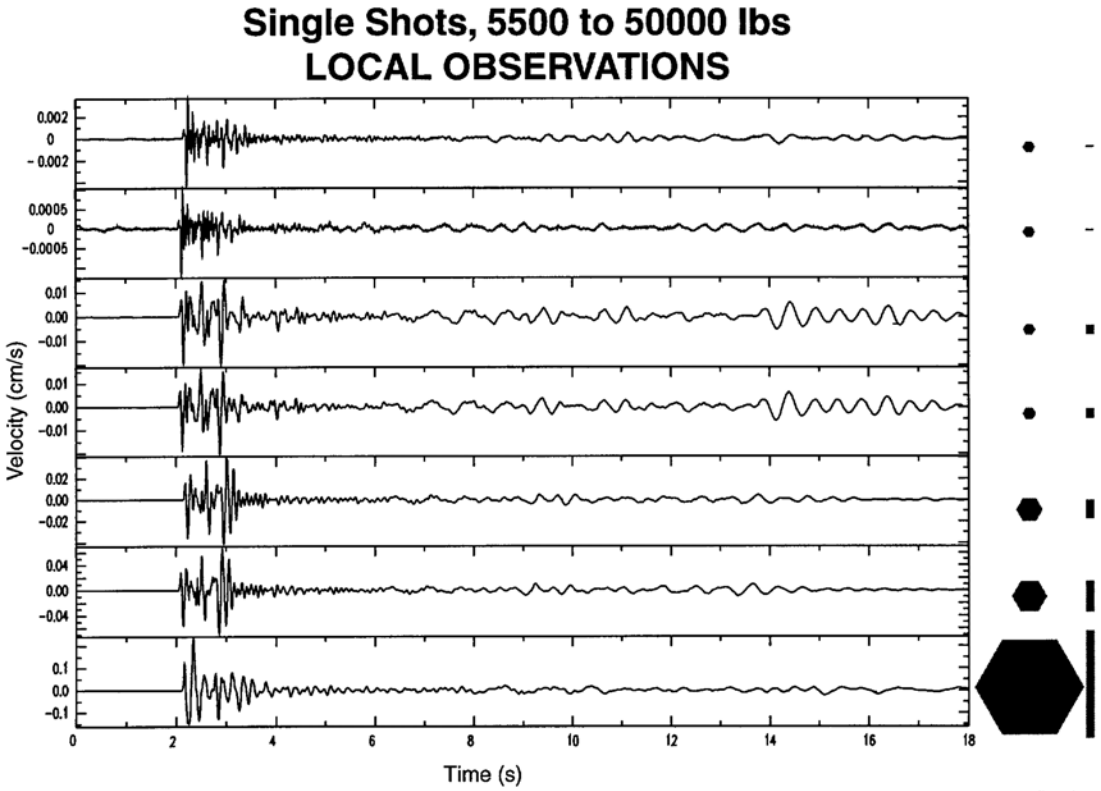


Figure 4 Relative comparison of close-in (7-11 km from source) vertical velocity records for the seven single-fired explosions described in Table 1. The relative sizes of the explosions are illustrated by the size of the hexagon while the peak amplitudes of the waveforms are represented by the vertical bars to the right of each waveform.

The first two of the four similar sized calibration explosions did not fully detonate as reflected in the peak amplitudes close-in and at regional distances. Not only is the amplitude smaller for the first two shots but the close-in data illustrates that the data is characterized by a higher source corner frequency also consistent with a low order detonation. All four of these shots were prepared in a similar manner and illustrate that one might expect significant variations in explosion performance among holes in a typical mine production shot.

Peak P_n, P_g, and L_g amplitudes were measured for each of the single-fired explosions at PDAR. Discarding the first two events, which appear to have detonated anomalously, the peak amplitudes for each of the regional phase increase with total explosive weight (Figure 5). The increase in P_g and L_g amplitudes with explosive weight is nearly identical. P_n has a much reduced amplitude at these ranges (~360 km) and increases with explosive weight at a reduced rate. These results suggest that for this path that one would have to call upon a different magnitude-yield relation for the different regional phases. The P_n amplitudes are small but are above background noise although the small size of these events may result in different components of the wave being used in the peak amplitude measurement. This effect might lead to problematic estimates for this phase.

The apparent linear relation between explosive weight and peak regional amplitudes for single-fired explosions was compared to data from delay-fired mining explosions. The mine in which the single-fired explosions were conducted routinely detonated delay-fired explosions for the purposes of removing overburden (cast blast) and for fracturing coal after removal of overburden (coal shots). The cast shots use the largest amount of explosives with

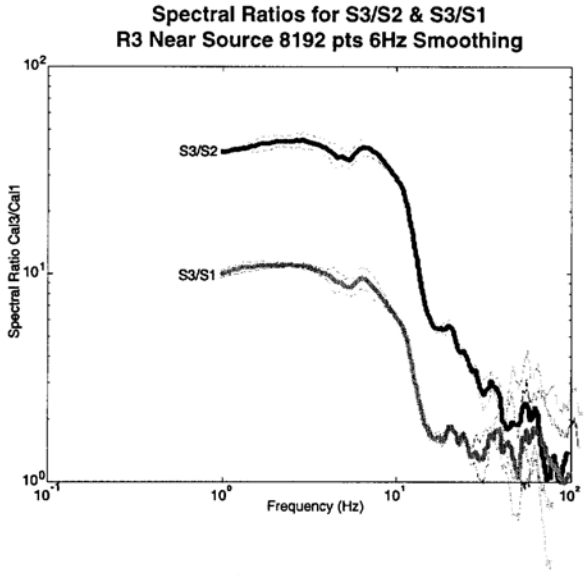


Figure 9: Average spectral ratios using close-in data for sources S1, S2 and S3

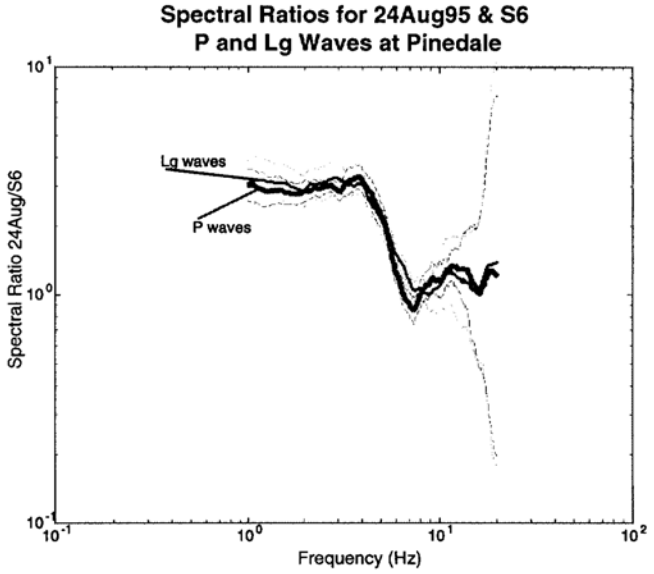


Figure 10: Spectral ratios between S7(24Aug95, 50000 lb.) and S6 (16000 lb.). Spectral ratios were estimated using PDAR and P and Lg waves.

5. *Quantification of the similarities and differences between single-fired explosions and typical delay-fired mining explosions.*

The primary difference between the single-fired explosions and the delay-fired explosions that has been illustrated is the different dependence of peak amplitude on yield. The peak amplitudes of regional Pn, Pg and Lg waveforms

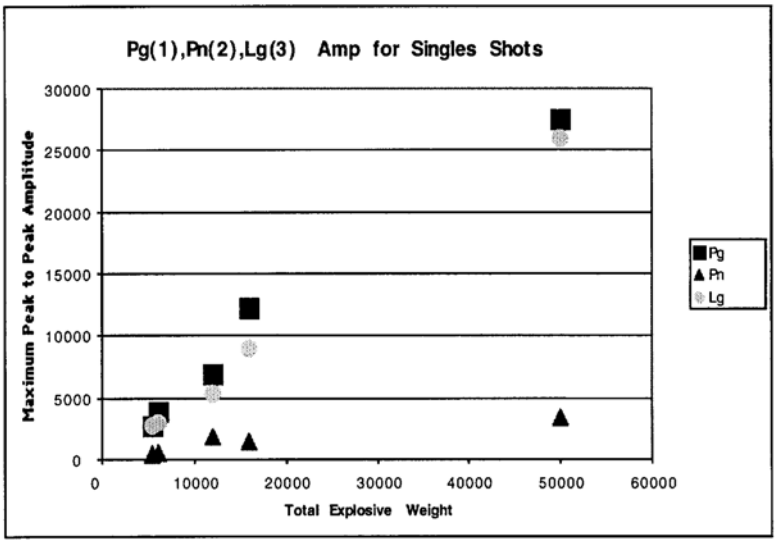


Figure 5: Peak amplitudes of the regional phases P_n, P_g, and L_g at a single array element of PDAR for each of the single-fired explosions that fully detonated as determined from close-in observations. These amplitudes are plotted against total explosive weight.

the highest powder factors. Peak amplitudes from both cast and coal shots were measured on vertical seismograms at PDAR for comparison to the single-fired shots thus allowing the effects of delay-firing on regional amplitudes to be assessed. Peak amplitude comparisons for P_g are reproduced in Figure 6.

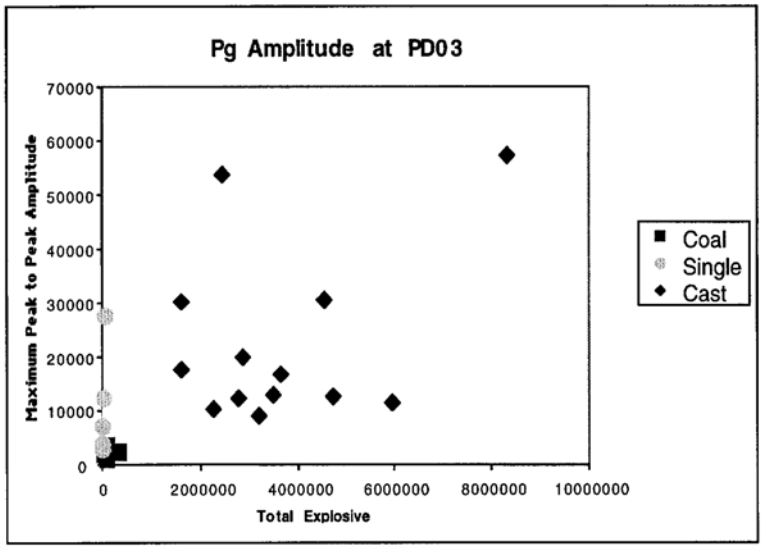


Figure 6: Peak amplitudes of P_g for the single-fired explosions (circles), large cast shots (diamonds) and the smaller coal shots (squares). The linear relation between explosive weight and peak amplitude is only observed for the single-fired explosions.

The coal shots (squares in Figure 6) with their low charge weight to coal mass (low powder factor) produce the smallest amplitudes and unlike the single-fired explosions show no increase in amplitude with explosive weight. The cast shots (diamonds in Figure 6) although quite large (several million lb.) produce peak amplitudes similar to the largest single-fired explosion (50,000 lb.). The delay-firing eliminates any relation between explosive weight

and peak amplitude. These results suggest that mining explosions as observed at regional distances may produce magnitudes that are not correlated with the explosive weight of the entire explosion.

3. Characterization of coherence in regional waveforms from closely spaced explosions.

The spatial distribution of the single-fired explosions (30 m to nearly 4 km) provides the opportunity to investigate the decrease in cross-correlation or coherency in regional waveforms with increasing source separation. The map in Figure 2 illustrates the spatial distribution of the sources. We focus on coherency estimates as they provide an opportunity to investigate how the waveforms compare as a function of frequency and wavelength. Estimates of coherency are dependent upon the product of the bandwidth of smoothing (B) and the time window (T) used for estimating the spectrum (Harris, 1991). All the elements of PDAR were used to make a mean coherency estimate and a standard error determination for each comparison. Figure 7 compares the coherency for S4 & S3 with a source separation of 30 m, S6 & S3 with a source separation of 350 m and S7 & S3 with a source separation of nearly 4 km.

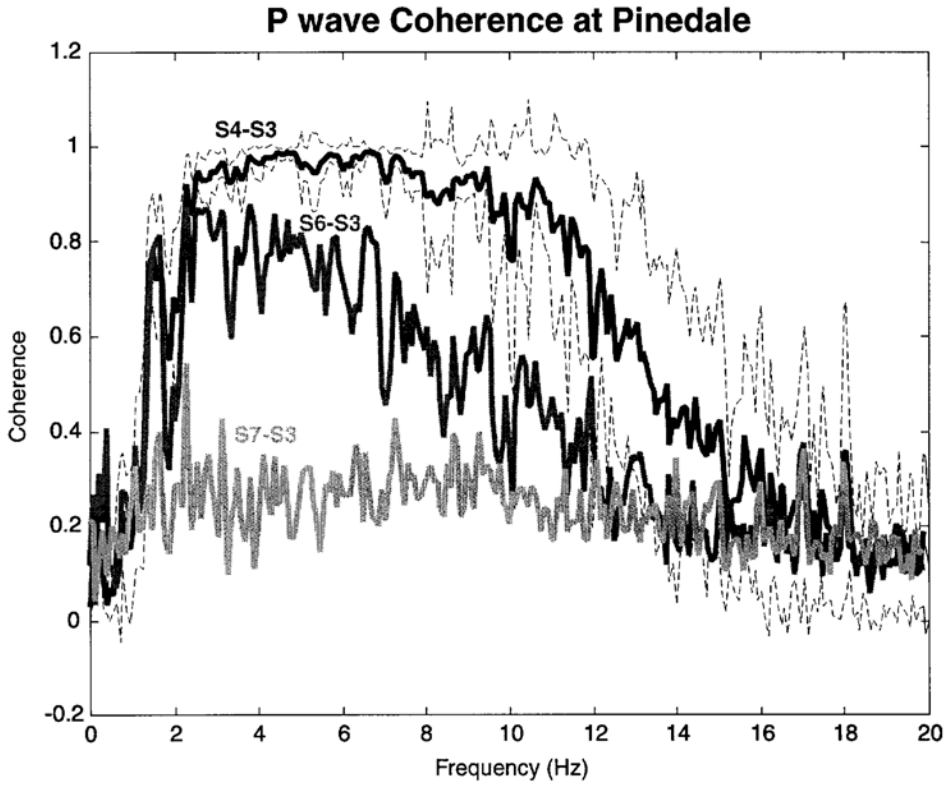


Figure 7: Coherence estimates for P waves at PDAR. Dotted lines represent plus or minus one standard deviation. Sources S4 & S3 are separated by 30 m, S6 &S3 by 350 m and S7 & S3 by 4 km.

Coherence is nearly 1 to high frequency (12 Hz) for the two closely spaced shots. The intermediate spaced shots (350 m) produce a coherence that is large to 6 Hz and then decays. The coherence for the two shots separated by nearly 4 km is small across the entire bandwidth. With P velocities ranging between 6 and 8 km/s, the results suggest that coherence decay at sub wavelength source separations. The spatial dimension at which this decay becomes significant is equal to or less than the spatial dimension of the mine where these experiments were conducted.

4. Constraint of the source time function for single-fired, contained chemical explosions.

Simple spectral ratios utilizing the spectra from the individual single-fired explosions provides a mechanism for quantifying variations in spectral shape that can be attributed to the source function (Stump *et al.,* 1999). The modulus of the spectral estimate from each explosion is compared, eliminating the phase and its variation identified in the coherency estimates. The first example is for two sources (S4 & S3) of identical yield. Spectral ratios were estimated for each array element at PDAR and a mean formed (Figure 8). Additionally spectral ratios were estimated using a single, three-component station in the near-source region. This provides the opportunity to compare near-source and regional source estimates and extend the source comparison to higher frequency.

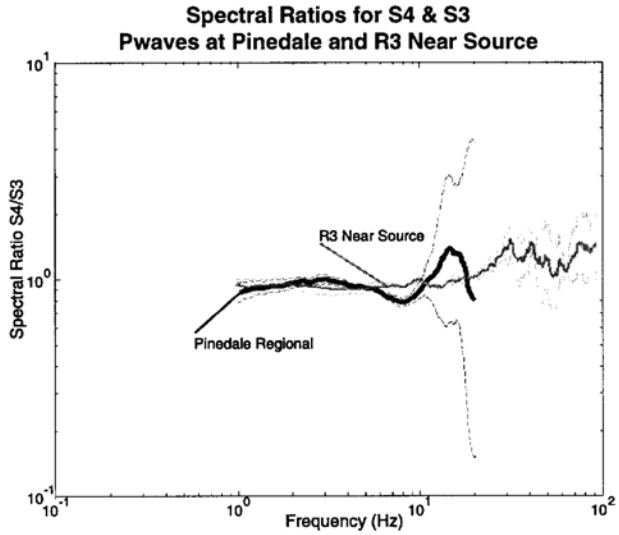


Figure 8: Spectral ratios between two identical single-fired shots (S4 &S3). The thick line is the spectral ratio estimated using the array elements at PDAR. The thin line is the spectral ratio using a single, three-component station from within the mine.

The spectral ratios at local and regional distances in Figure 8 are consistent. They both indicate that the spectra from the two shots are nearly identical (ratio of 1). The rise in spectral ratio above 10 Hz for the regional data is accompanied by an increase in standard deviation. The higher bandwidth close-in data indicates that the ratio remains flat to higher frequencies.

The close-in data can be used to investigate the characteristics of the two single-fired shots that produced the small amplitudes (S1 & S2) illustrated earlier in Figure 3 and 4. Spectral ratios for these shots compared to S3 are given in Figure 9. These spectral ratios suggest that S1 was reduced by a factor of 10 (~500 lb.) and S2 was reduced by a factor of 50 (~100 lb.). It is interesting to note that only two of four identically prepared boreholes produced maximum seismic energy. A single mining explosion consists of hundreds of such boreholes and typical modeling assumes each borehole performs in an identical manner.

In each of the previous examples, the sources used in the comparison were of similar size. In Figure 10, S6 (16000 lb.) is compared to S7 (50000 lb.). The spectral ratios for both P and Lg provide similar estimates of the source differences. The ratios are flat at long periods with the relative size indicative of the factor of three difference in absolute source size. The corner frequency of the larger explosion is below 4 Hz where the ratio begins to decay and then reached a plateau at the second corner of 7 Hz.

from the single-fired explosions were found to reflect the total weight of explosives whereas peak amplitudes for delay-fired explosions did not.

Additional work has been undertaken to investigate other differences in the waveforms from single-fired and delay-fired explosions that might be useful for identification purposes (Hedlin *et al.,* 1999). Both the single-fired explosions and the delay-fired explosions are rich in high frequency P energy. At intermediate frequencies, Lg energy dominates from both source types. It is only at the longest periods (4-10 s) that there is significant differences between the single-fired and cast shots with the cast shots generating intermediate frequency surface waves and the single-fired shots producing none.

CONCLUSIONS AND RECOMMENDATIONS:

The conclusions that can be drawn from this empirical study are four.

1. Over an order of magnitude variation in explosive performance is observed from four identically prepared boreholes. This variation may effect the modeling of delay-fired mining explosions which often assumes linear superposition and similar coupling among sources.
2. Scaling of peak motions observed near-source and at regional distances for single-fired explosions are consistent. Since mines are constrained to control ground motions within the mine, this result suggests that peak motions at regional distances may be similarly controlled.
3. Significant decreases in correlation of P waves for closely spaced sources observed at regional distances were observed. The decrease is sub wavelength and suggests that significant differences can be expected for shots distributed across large mines.
4. Single-fired explosions produce an apparent linear increase in peak amplitude with explosive weight. Delay -fired explosions produce no such trend. Relatively modest sized contained single-fired explosions (50,000 lb.) produce regional signals comparable or greater to production mining explosions including millions of pounds.

The results of this study provide a basis for design and implementation of calibration explosions under a CTBT using typical emplacement and detonation equipment available at a mine.

REFERENCES:

Denny, M.P., ed.,1994. *Proceedings of the Symposium on the Non-Proliferation Experiment (NPE): Results and Implications for Test Ban Treaties,* April 19-21, 1994, Rockville, Maryland: Lawrence Livermore National Laboratory, Livermore, CA, CONF-9404100.

Harris, D.B., 1991. A waveform correlation method for identifying quarry explosions, *Bull. Seism. Soc. Am. 81,* 2395-2418.

Hedlin, M.A.H., B.W. Stump, D.C. Pearson and X. Yang, 1999. Identification of mining blasts at mid- to far-regional distances using low frequency seismic signals, submitted to *Pageoph.*

Heuze, F. and B. Stump, eds., 1999. *Mine Seismicity and Comprehensive Nuclear-Test-Ban Treaty,* Los Alamos National Laboratory, LA-UR-99-384 and Lawrence Livermore National Laboratory, UCRL-ID-132897.

Richards, P., D.A. Anderson, D.W. Simpson, 1992. A survey of blasting activities in the United States, *Bull. Seism. Soc. Am. 82,* 1416-1433.

Stump, B.W., D.C. Pearson and R.E. Reinke, 1999. Source comparisons between nuclear and chemical explosions detonated at Rainier Mesa, Nevada Test Site, *Bull. Seism. Soc. Am. 89,* 409-422.

ANALYSIS, COMPARISON AND MODELING OF RADAR INTERFEROMETRY DATA OF SURFACE DEFORMATION SIGNALS ASSOCIATED WITH UNDERGROUND EXPLOSIONS, MINE COLLAPSES AND EARTHQUAKES PHASE 1: UNDERGROUND EXPLOSIONS, NEVADA TEST SITE

Paul Vincent, Bill Foxall and William R. Walter
Geophysics and Global Security Division, Lawrence Livermore National Laboratory

Sponsored by U.S. Department of Energy
Office of Non-Proliferation and National Security
Office of Research and Development
Contract No. W-7405-ENG-48

ABSTRACT

We have previously presented simple elastic deformation modeling results for three classes of seismic events of concern in monitoring the CTBT – underground explosions, mine collapses and earthquakes. Those results explored the theoretical detectability of each event type using synthetic aperture radar interferometry (InSAR) based on commercially available satellite data. In those studies we identified and compared the characteristics of synthetic interferograms that distinguish each event type, as well the ability of the interferograms to constrain source parameters. These idealized modeling results, together with preliminary analysis of InSAR data for the 1995 m_b5.2 Solvay mine collapse in southwestern Wyoming, suggested that InSAR data used in conjunction with regional seismic monitoring holds great potential for CTBT discrimination and seismic source analysis, as well as providing accurate ground truth parameters for regional calibration events.

In this paper we further examine the detectability and "discriminating" power of InSAR by presenting results from InSAR data processing, analysis and modeling of the surface deformation signals associated with underground explosions. Specifically, we present results of a detailed study of coseismic and postseismic surface deformation signals associated with underground nuclear and chemical explosion tests at the Nevada Test Site (NTS). Several interferograms were formed from raw ERS-1/2 radar data covering different time spans and epochs beginning just prior to the last U.S. nuclear tests in 1992 and ending in 1996. These interferograms have yielded information about the nature and duration of the source processes that produced the surface deformations associated with these events. A critical result of this study is that significant post-event surface deformation associated with underground nuclear explosions detonated at depths in excess of 600 meters can be detected using differential radar interferometry. An immediate implication of this finding is that underground nuclear explosions may not need to be "captured" coseismically by radar images acquired before and after an event in order to be detectable. This has obvious advantages in CTBT monitoring since suspect seismic events-which usually can be located within a 100 km by 100 km area of an ERS-1/2 satellite frame by established seismic methods-can be imaged after the event has been identified and located by existing regional seismic networks.

Key Words: InSAR, SLC images, interferogram, synthetic interferogram, ERS-1/2 frame, phase unwrapping, DEM, coseismic, postseismic, source parameters.

This work is performed under the auspices of the U.S. Department of Energy by the Lawrence Livermore National Laboratory under contract W-7405-ENG-48.

INTRODUCTION

Synthetic aperture radar interferometry (InSAR) is rapidly becoming a new standard geodetic technique to map surface deformation signals from a variety of sources. InSAR is capable of mapping sub-centimeter vertical deformation signals over a 100 x 100 km area and has a resolution (pixel size) of about 20 meters. Although most applications published to date have been to high-rate deformation fields over short time periods, it has recently been shown that low-rate deformation fields can be imaged over time periods in excess of 4.5 years depending on orbital baseline distances, vegetation cover and the climate of the region imaged [Rosen, et al, 1997, Vincent, et al, 1997, Vincent, 1998]. As part of an effort to determine whether InSAR can be used to help discriminate between different types of seismic events, we previously showed that the expected signals from the simplest elastic models of three source types (mine collapses, explosions and small, shallow earthquakes) give very different expected surface deformation signals [Foxall et al, 1998]. In order to better understand the surface deformation produced by underground explosions, we investigate in this paper actual surface deformation signals associated with underground nuclear and chemical explosion tests at the Nevada Test Site. These surface deformations were imaged by processing raw ERS-1/2 satellite data collected over the site from 1992 through 1996 (see Figure 1) and creating deformation maps.

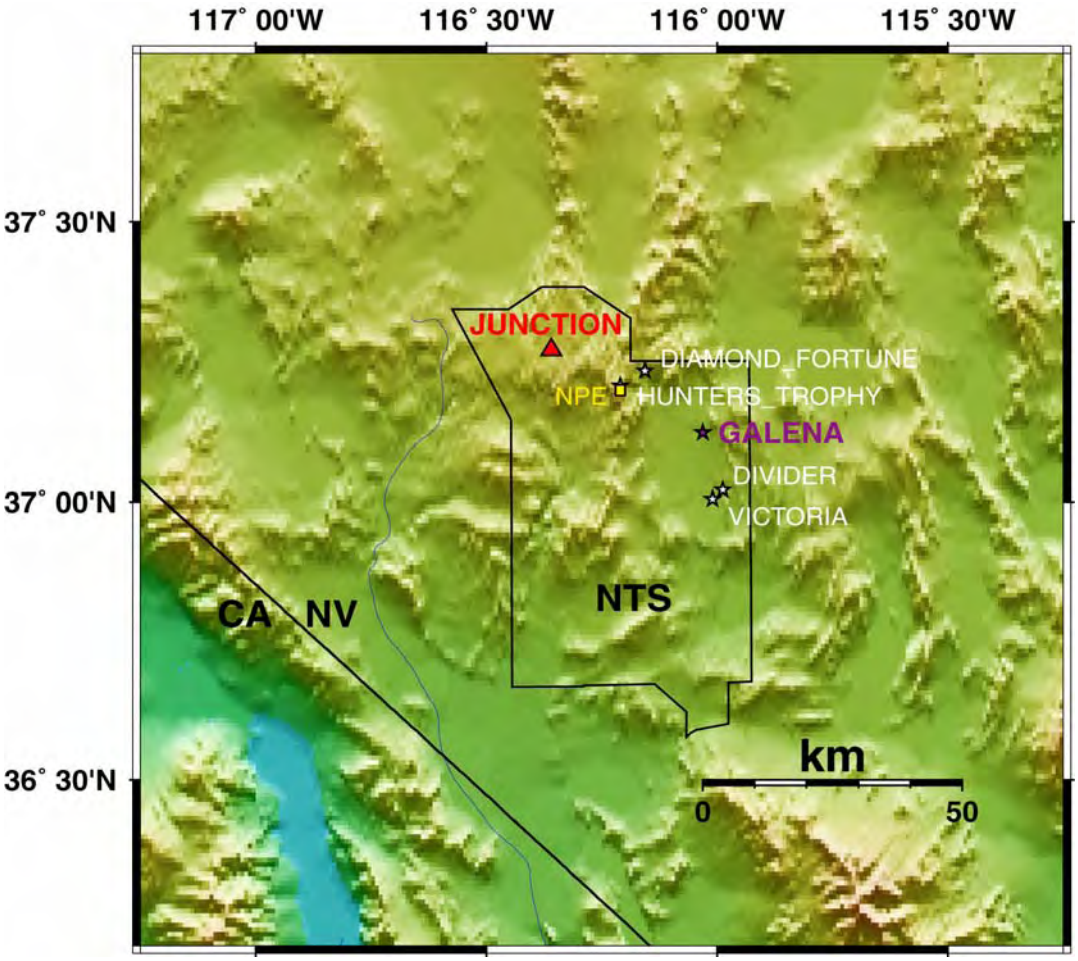


Figure 1. Shaded relief map of the Nevada Test Site showing the location of underground nuclear tests from April 1992 to the last test done in September 1992 (stars). Also shown are the Non-Proliferation Experiment (NPE) a large underground chemical test (square), and JUNCTION the last large Pahute Mesa underground nuclear test done in March 1992 (triangle). Of all the explosions shown, only GALENA produced a surface crater.

Differential InSAR Method

Figure 2 shows the basic imaging geometry of three repeat orbit passes imaging the same region on the ground. The first (reference) satellite position is denoted by A_1 and the second (repeat) orbit position is denoted A_2 (orbit direction is into the page). The relative distance between the two satellite positions at their respective scene acquisition times is referred to as the orbital baseline B. The baseline can be decomposed into perpendicular and parallel components—the parallel component is the relative satellite separation toward or away from the ground parallel to the satellite-to-ground or line-of-sight (los) vector and the perpendicular component is the relative satellite separation perpendicular to this direction. It is the perpendicular component of the baseline that determines the degree of parallax between the two imaging positions and hence the fringe rate—the larger this separation the higher the interference fringe rate will be in a resulting interferogram. When the phase value of each ground pixel viewed from two repeat orbit positions are combined interferometrically and subtracted, the resulting phase values or fringes are proportional to the topography of the ground region imaged. This is because the phase is proportional to the round trip distance between a ground point (pixel) and the imaging satellite—topographic highs will have a lower phase value then topographic lows. If any ground deformation occurs between the repeat orbits, then the phase will be proportional to the sum of the topographic phase signature plus a deformation phase signature. To isolate the desired deformation phase signature the topographic phase must be removed. This can be accomplished in one of two ways. One way is to construct another interferogram using another orbit pair imaging the same ground frame but with minimal time between scene acquisitions to minimize the possibility of any ground deformation occurring between orbit passes. The phase from this second interferogram will be proportional to the topography only and this can be resampled to the first (deformation) pair to remove the topographic phase from the first orbit pair. The second way to do this is to simulate a Digital Elevation Map (DEM) into the radar coordinates of the first (deformation) pair and subtract the simulated topographic phase from the deformation pair to remove topographic phase. Both these methods are referred to as *differential* interferometry. Figure 2 depicts the "3-pass" method whereby a second topography pair is formed by sharing one common orbit with the first pair (A_1-A_2'). Once the topographic phase is removed, the remaining fringes will be proportional to the ground surface deformation plus any atmospheric artifacts and other noise sources. Typically, atmospheric noise terms (both tropospheric and ionospheric noise sources) have a recognizable signature and can usually be isolated from small concentrated deformation signals similar to those seen in this study [e.g., see Massonnet and Feigl, 1998; Vincent, 1998].

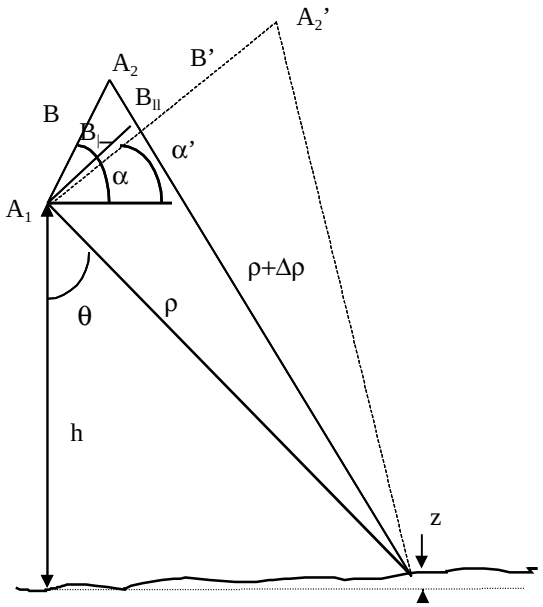


Figure 2. Radar imaging geometry. The solid lines show line-of-sight (los) vectors for the first interferometric pair formed by satellite positions at A_1 and A_2. Dashed lines show paths for a second interferometric pair (A_1-A_2') used to remove topographic phase from the first. Parallel and perpendicular components of the orbital baseline are shown. Path of satellite is into the page.

Data Selection

The ERS data chosen for this study are shown in Table 1. The pairs were chosen based on two criteria. The first was to obtain pairs which had the minimum perpendicular baseline component available (to minimize temporal decorrelation) and the second was to obtain orbit pairs of different time spans and epochs in order to capture both co-event and post-event signals as well as short and long-term deformation signals. Table 2 lists the interferometric orbit pairs of data from Table 1, along with relevant interferometry parameters described above. The ambiguity height is the amount of topographic change across the image required to produce the observed fringe rate seen in a deformation interferogram where topography either has not been removed or it has been removed imperfectly leaving residual topographic fringes. The larger this number, which is inversely proportional to the perpendicular baseline component, the less ambiguous the phase signal is between representing topography and representing change in topography with time (i.e., deformation).

Table 1. Raw ERS SAR data acquired for Nevada Test Site Study

Image #	Satellite—Orbit	Frame	Acquisition Date
1	ERS-1 --4051	2853	Apr 24, 1992
2	ERS-1 –8560	“	Mar 5, 1993
3	ERS-1 –10063	“	Jun 18, 1993
4	ERS-1 –20427	“	Jun 11, 1995
5	ERS-1 –25437	“	May 26, 1996

Table 2. InSAR orbit pairs formed and relevant parameters

Image Pair	Sensors	Epoch	Time Span	Perp. Baseline	Ambig. Height
1/2	ERS-1	920424-930305	315 days	50m	184m
1/3	ERS-1	920424-930618	420 days	41m	224m
3/4	ERS-1	930618-950611	723 days	66m	139m
1/5	ERS-1	920424-960526	1492 days	20m	462m

Raw Data Processing

All of the SAR data listed in Table 1 represents raw unprocessed data. These data sets were processed using the Jet Propulsion Laboratory (JPL) IntSoft software suite. The raw data were processed to zero (compensated) Doppler, slant range projection, phase-preserved single-look complex (SLC) images. These focused images have pixel dimensions (resolution) of about 20m in ground range (cross-track direction) by 22.5m in azimuth (along-track direction). The SLC images are paired according to favorable (smallest) orbital baselines to form the interferograms.

InSAR Processing

The second SLC image in each interferometric pair (shown in Table 2) was coregistered and resampled to the first to sub-pixel precision and the phase difference was computed to form the raw interferogram. The raw interferograms were then “flattened” by removing orbital and earth curvature phase artifacts from the raw interferograms. The phase in the interferograms are modulo 2__and must be unwrapped to obtain absolute phase values. The phase was unwrapped using the residue-branch cut method of phase integration by [Goldstein, et al., 1988]. The unwrapped phase was then converted to range change using an average ERS-1/2 incidence (look angle) of 23 degrees from vertical.

Topographic phase was removed from the interferograms by constructing a Digital Elevation Map (DEM) using U.S. Geological Survey 1 degree (83 meter pixel size resolution) DEMs covering the imaged frame. DEMs ‘goldfield-e’, ‘caliente-w’, ‘death_valley-e’, and ‘las_vegas-w’ were mosaiced and cropped to overlay the ERS image frame centered over the Nevada Test Site.

RESULTS AND ANALYSIS

Figure 3 shows the radar amplitude image of the study area. The boxes enclose the locations of events JUNCTION (920326-- Pahute Mesa) and GALENA (920623-- Pahute Mesa). Deformation maps of the boxed areas are shown in Figures 4-6. Figure 4 shows the four deformation maps derived from the four interferograms

of the boxed areas around event JUNCTION. Figure 5 shows profile plots done along the major and minor axis of the deformation signal associated with JUNCTION captured in orbit pair 1/3 (920424-930618). Figure 6 shows the map and W-E profile plot of the coseismic (i.e., captured by before and after-event orbit passes) deformation signal produced by event GALENA, which formed a crater.

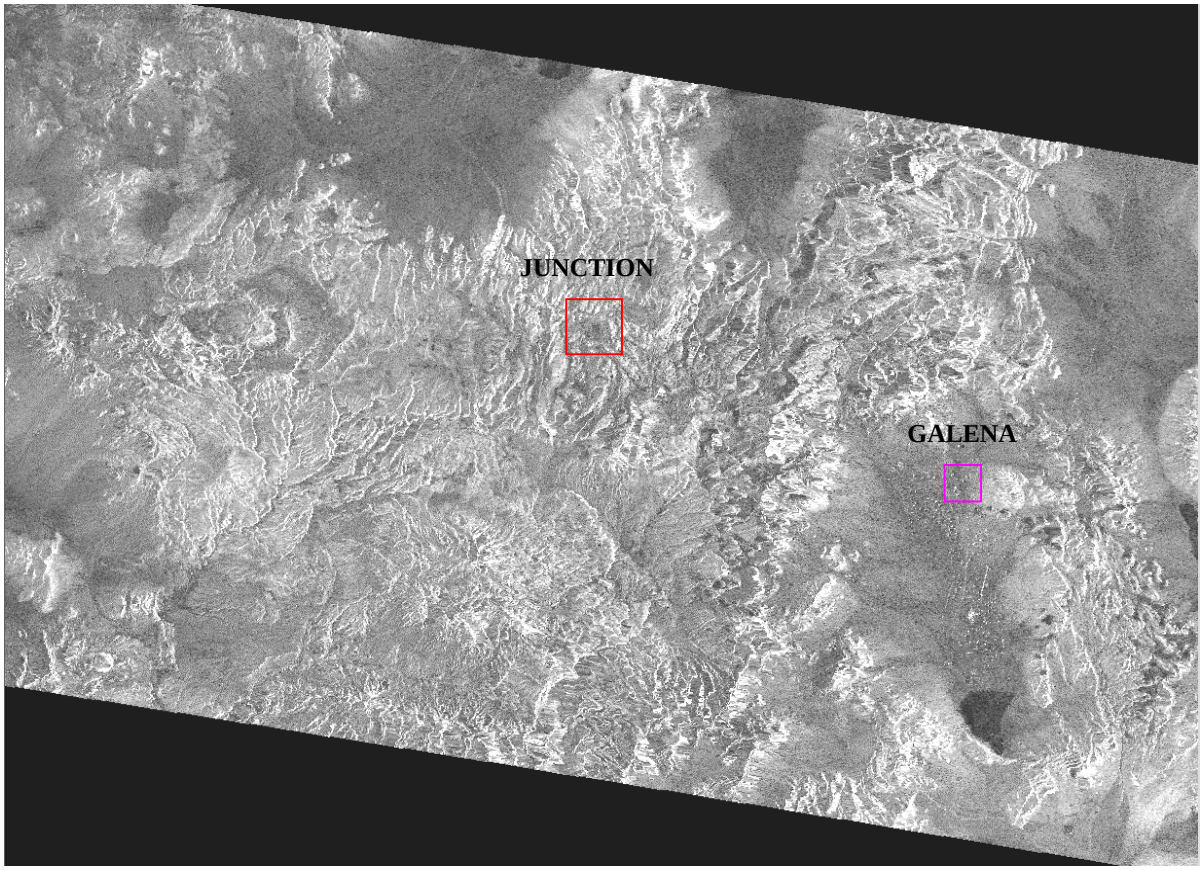
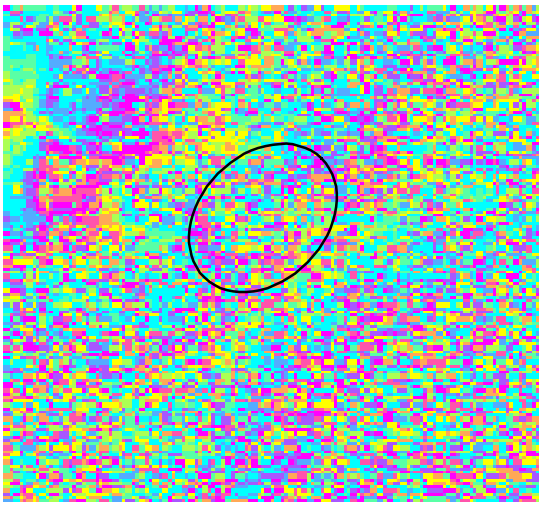


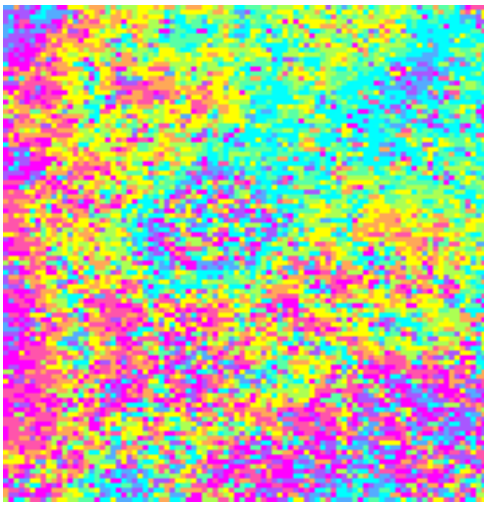
Figure 3. Geocoded radar amplitude image of ERS frame 2853 centered over the Nevada Test Site. Red box shows the location of event JUNCTION , the last large Pahute Mesa test, and the purple box shows the location of event GALENA.

JUNCTION

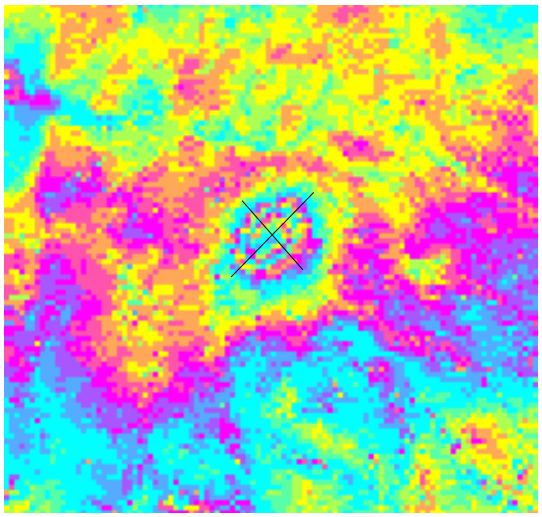
The interferogram/deformation map for image pair 1/2 (920424-930305) is mostly decorrelated in the higher mountainous regions of the imaged frame. This is most likely due to winter weather (possibly snow cover in the highest elevations in the image) contaminating the radar reflectivity function of orbit 8560 which was acquired in mid-winter (930305). This can be deduced from the fact that image pair 1/3 (acquired in spring and summer months) which has image #1 in common with image pair 1/2, has excellent correlation, has a comparable orbital baseline and a longer temporal baseline. Image pair 1/3 shows post-JUNCTION event deformation since the date of the first orbit in that pair (920424) post-dates the JUNCTION event (920326) by one month. Image pair 3/4 shows a notable *absence* of any deformation signal over the JUNCTION test location. This observation puts an upper bound on the duration of the post-seismic signal associated with JUNCTION of 420 days. The postseismic deformation signal seen in image pair 1/5 is remarkably similar to that in image pair 1/3, which also suggests that the post-seismic signal is limited in duration to less than 420 days after the event. The relatively long time baseline of this pair (1492 days) is the reason for the increased decorrelation compared to image pair 1/3. Black ellipses are drawn over the same region in each deformation map to show the location of the JUNCTION event in each map. Profiles



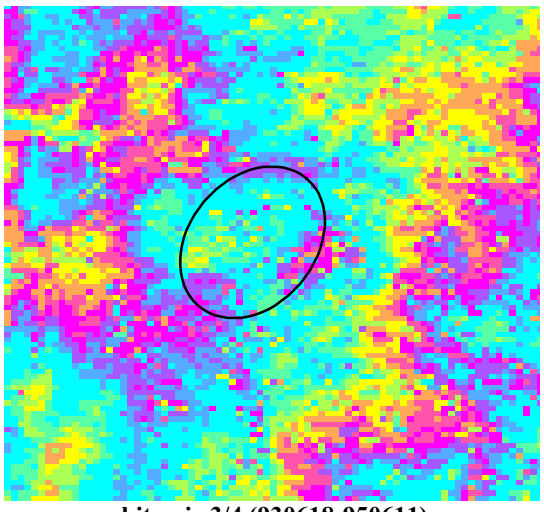
orbit pair 1/2 (920424-930305)



orbit pair 1/5 (920424-960526)



orbit pair 1/3 (920424-930618)



orbit pair 3/4 (930618-950611)

Figure 4. Deformation maps showing post-seismic surface deformation signals collocated with the JUNCTION nuclear test of March 26, 1992 (red box shown in Figure 3). Counterclockwise from upper left corner: orbit pair 1/2, 920424-930305 (mostly decorrelated); orbit pair 1/3, 920424-930618 (post-seismic signal clearly visible); orbit pair 3/4, 930618-950611 (no deformation signal visible); orbit pair 1/5, 920424-960526 (post-seismic signal visible but degraded by temporal decorrelation). Upper bound on duration of post-seismic deformation signal associated with the Junction event is 420 days (most likely less—see text). Cross-hairs denote profile locations for major and minor axis of deformation ellipse signal. shown in Figure 5. Black ellipses show the corresponding location of the JUNCTION signal in each deformation map where no signal is detected.

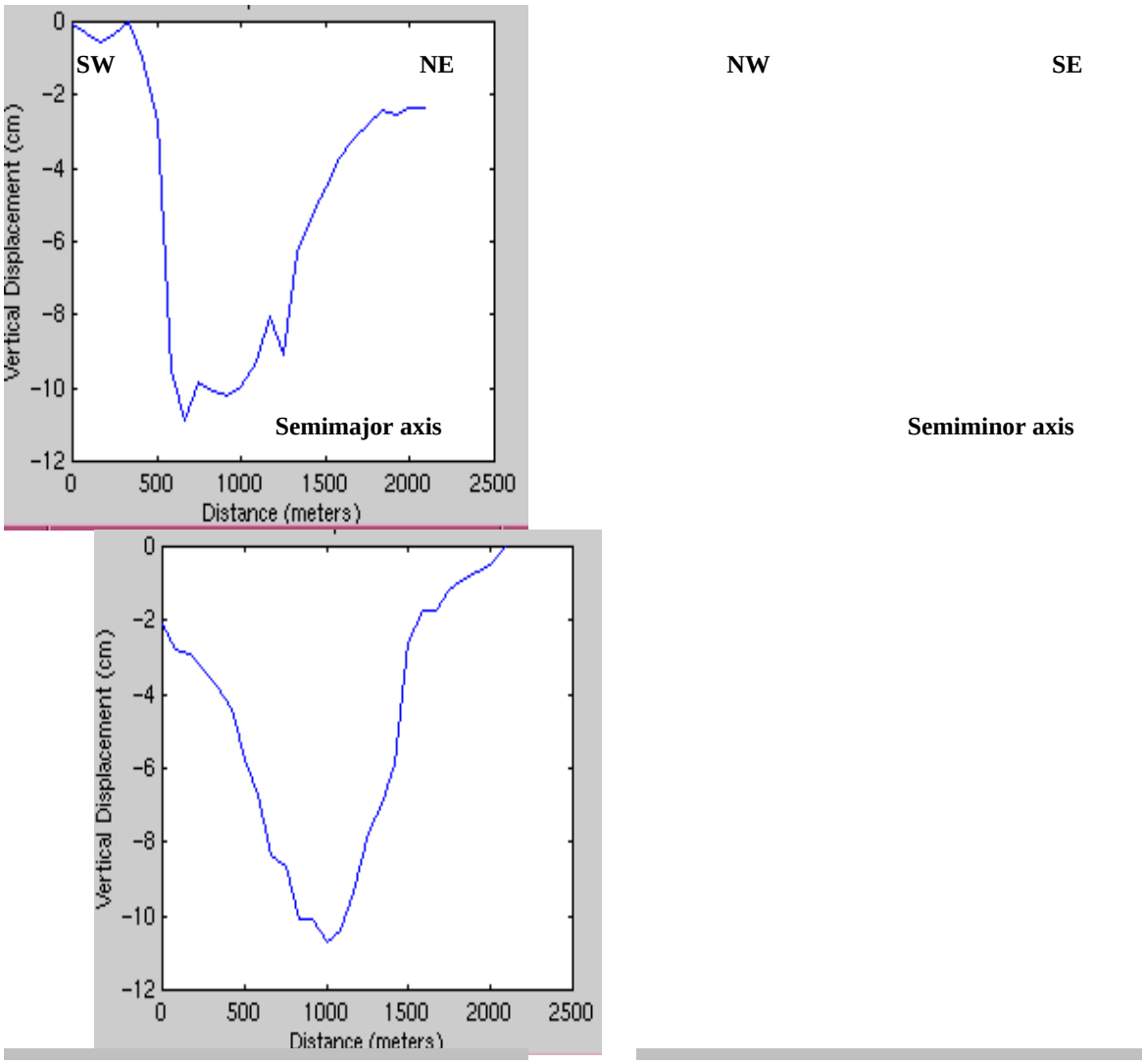


Figure 5. Profiles along major (left) and minor (right) axis of elliptical post-seismic deformation pattern above the JUNCTION test site location (see text).

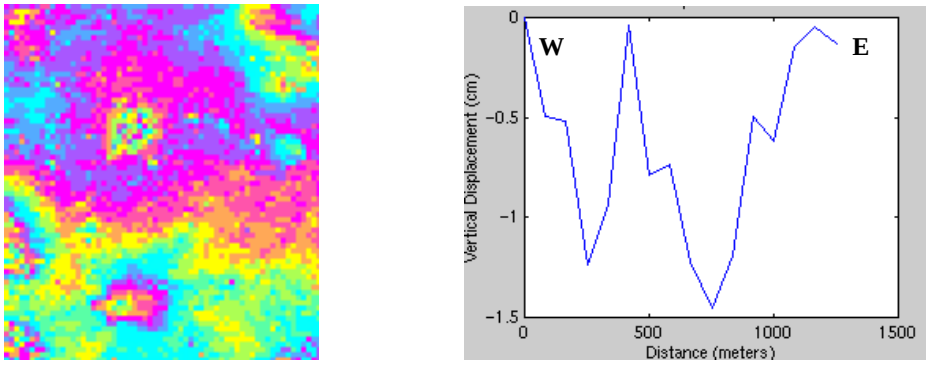


Figure 6. Deformation map (left) and profile across west to east (right) of coseismic deformation associated with the GALENA nuclear test of June 23, 1992 (purple box shown in Figure 3). Image is from orbit pair 1/2

(920424-930305). [Note: Event GALENA is the only event shown in Figure 2 that cratered and shows no significant post-seismic deformation signal in any of the interferograms shown.

were done across the major and minor axes of the deformation ellipse visible in image pair 1/3 (shown in Figure 5 above) and show approximately 10 centimeters of subsidence during the 420 days between images. It is not known whether this subsidence signal occurred over a shorter period but we suspect so and plan to purchase additional orbit pairs to further constrain both the duration and timing of this signal. Both profile plots across the deformation signal show an apparent diameter of about 2 km. The profile taken from SW to NE (the major axis) shows an approximately 800 meter flattened center, while the profile taken from NW to SE does not show a flattened center region. In addition, the outer region of the strain ellipse is tilted down slightly to the north as can by seen on the northeast and northwest ends of the profile plots. The center region, however, has a subtle *relative* uplifted flank on the northern interior of the strain ellipse. This asymmetry suggests a complicated deformation source for the observed signal.

GALENA

Figure 6 shows image pair 1/2 which captures a coseismic deformation signal over event GALENA (see Figures 2 and 3). GALENA formed a coseismic crater 134 meters in diameter and 8 meters deep 17 minutes after the test [LLNL Containment Data Base]. The W-E profile across this feature from (Figure 6) shows two abrupt subsidence regions separated by an (offset) central peak of near-zero net deformation. It is important to note that the profile shown in Figure 6 (as well as other similar profiles done of this feature) does not accurately measure actual crater formation, but instead captures the peripheral deformation of the ground immediately surrounding the crater. The reason for this is that the relatively small radius and large magnitude of the actual cratering event prevent coherent detection and measurement by C-band (5.6 cm wavelength) InSAR methods. Other "stereo" interferometric techniques whereby high resolution inteferometric topographic images before and after an event can be combined stereoscopically to image this type of large deformation signal [Jackowitz, 1999, personal communication].

Source Characterization and Modeling

The majority of NTS events produce either a crater or immediate post-shot (generally minutes to days) subsurface collapse regardless of whether the shot is detonated within alluvium, tuff or rhyolite lava. The post-shot data [W. Brunish, LANL, personal communication] indicate that JUNCTION caused a subsurface collapse up to a depth of about 300m approximately 29 hours after detonation. In general, the dominant post-shot collapse mechanism is chimneying, in which the explosion cavity void migrates upwards as blocks of fractured rock fall to fill in the cavity below. A crater is formed if the chimney reaches the free surface. The volume of the domed 'apical' cavity above the chimney will, in general, decrease as the chimney propagates upward, since chimneying creates pore volume due to mismatch between the fallen blocks of rock, a process referred to as 'bulking'. Chimneying usually takes place over the span of a few seconds.

There are several possible mechanisms for delayed or continued subsidence of like that imaged by the InSAR data following the main collapse. These include: (1) Either abrupt or slow closure of the chimney apical void, including settlement of chimney rubble; (2) gravitational settlement of a possibly larger detached (uplifted) zone possibly from spall; and (3) dip-slip on nearby faults reactivated by the shot or post-shot movement. We carried out preliminary elastic modeling to investigate mechanism (1) as a possible source of the subsidence imaged by the InSAR data. Apical cavity closure was modeled as a closing rectangular horizontal tension crack centered at 300 m in an elastic half-space having Poisson ratio and rigidity of 0.3 and 2.3×10^9 Pa, respectively (representative of the overburden of Pahute Mesa). Dislocation dimensions ranged from 120m to 180m; this is estimated to be a reasonable range of for the width of the chimney at 300m depth based on an explosion cavity radius of 60m estimated from the m_b vs yield relationship of Murphy [1996] together with the scaled cavity radius vs. overburden pressure curves of Terhune and Glenn [1977]. All of the apical cavity models produced calculated surface subsidence troughs that are too narrow to fit the observations (Fig. 5). A closing crack model at a depth of about 600m, close to the source point, with a displacement of about 5m is required to produce even a reasonable fit to the magnitude of the subsidence signal but does not reproduce its elliptical shape. This possibility appears to be precluded, in any case, by the main post-shot collapse.

We also carried out preliminary elastic modeling to investigate mechanism (2) as a possible source. The best-fit model in this case is a 12 centimeter dislocation on a 300 meter deep closing horizontal crack with dimensions

800 meters wide by 1100 meters long oriented N40E. Figure 7 shows profile plots for the data and synthetic interferograms along the major and minor axis of the deformation signal . This model fits both the overall magnitude and the orientation of the elliptical signal but does not reproduce the asymmetry and steep gradients seen in the interferogram. The steep northern side and flat bottom of the trough in the NE-SW (major axis) profile suggests that part of the subsidence might be associated with a down-dropped block between two faults. We are continuing to investigate these and the other possible mechanisms. The elliptical shape and orientation of the subsidence imaged by InSAR are consistent with the results reported by Ellis and Snyder [1974]. These authors showed that the majority of shots in bedrock under Yucca Flats form craters having ellipticities of 1.1 or greater and major axes preferentially oriented within the range N50E-N70E.

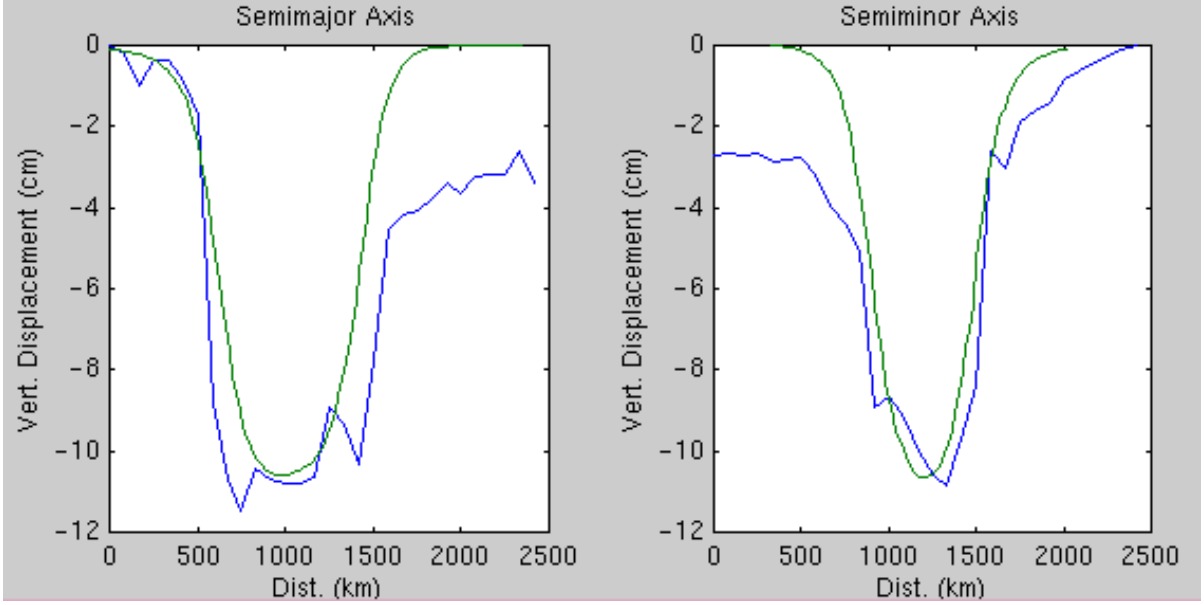


Figure 7. Comparison plots between model and data interferograms for source hypothesis #2 (see text).

Discussion and Conclusion

InSAR holds great promise in helping to identify and characterize shallow events under the CTBT. Shallow events include "false alarms" that that produce anomalous seismic signals, such as shallow earthquakes and the failure of underground cavities (e.g., mine collapses) that need to be distinguished from banned underground nuclear tests. In an effort to begin to understand the range of complex surface deformation signals possible from underground explosions, including complicating effects such as spall, post-event cavity collapse and cratering, we have begun to investigate the surface deformation produced by well studied U.S. nuclear tests at the Nevada Test Site. While we have not yet fully investigated all parameters surrounding these tests, and there is more site information to gather to better constrain our models, important conclusions can be drawn from this study that have important ramifications for CTBT verification efforts. The results presented here yield new information about the detectability of underground explosions and demonstrate that by using differential SAR interferometry in conjunction with established seismic detection methods the following may be obtained:

1) Possible identification of underground explosions *after* they happen with no need for a "before" image.
2) Locations of suspect events to within a hundred meters. This is true even for fully contained tests that do not crater and that have no visible surface traces.
3) The dimensions, shape and amount of surface deformation associated with an event.

An important caveat to these findings are that event JUNCTION was a relatively large m_b=5.6 event and this is most likely the reason that it can be detected and characterized using differential InSAR. Although decorrelation and orbital phase flattening problems may have obscured the smaller events in our interferograms, the detection of smaller test events including the NPE chemical explosion event appears to be much more difficult. However, we are optimistic that we will be able to improve the signal-to-noise ratio of our images,

acquire additional data and begin to capture some of these smaller test events in future interferograms. We are confident that we will be able to gain significant additional information such as independent estimates of source depth, yield and the presence or absence of large underground cavities by using a combination of seismic and InSAR methods.

REFERENCES

Ellis, W.L., and R.P. Snyder, Asymmetry of collapse sinks in Yucca Flat, Nevada Test Site, Nevada, Report USGS-474-180 prepared by the U.S. Geological Survey, Denver, for the U.S. Atomic Energy Commission, Nevada Operations Office, 20 p., 1974.

Foxall, B., J.J. Sweeney, W. R. Walter, Identification of Mine Collapses, Explosions and Earthquakes using INSAR: A Preliminary Investigation, , 1998.

Goldstein, R.M., Zebker, H.A., Werner, C.L., Satellite Radar Interferometry: Two dimensional Phase Unwrapping, Radio Science, 23, No. 4, 1988.

Murphy, J., Types of seismic events and their source descriptions, in Monitoring a Comprehensive Test Ban Treaty, editors E. S. Husebye and A. M. Dainty, Kluwer Academic Publishers, Dordrecht, 225-246. 1996.

Rosen, P.A., C. Werner, E. Fielding, S. Hensley, S. Buckley, P. Vincent, Aseismic creep along the San Andreas fault northwest of Parkfield, CA, measured by radar interferometry, Geophys. Res. Lett., 25, 825-228, 1998.

Terhune, R.W., and H.D. Glenn, Estimate of Earth media shear strength at the Nevada Test Site, UCRL-52358, Lawrence Livermore National Lab., 29 p., 1977.

Vincent, P., J.B. Rundle, J. Fernandez, S.M. Buckley, SAR-constrained models of coseismic and interseismic deformation, EOS trans., AGU, 78, 46, 1997.

Vincent, P., Application of SAR Interferometry to Low-Rate Crustal Deformation Fields, Ph.D. Thesis, University of Colorado, 1998.

Vincent, P., J.B. Rundle, R. Bilham, S.M. Buckley, Aseismic creep along the San Andreas and Superstition Hills faults with uplift at Durmid Hill, southernmost San Andreas fault, CA measured by radar interferometry, EOS trans., AGU, 79, 45, 1998.

Proceedings of the 21st Seismic Research Symposium: Technologies for Monitoring The Comprehensive Nuclear-Test-Ban Treaty

21-24 September 1999

Las Vegas, Nevada

Volume II

Hydroacoustic Monitoring
Infrasound Monitoring
Radionuclide Monitoring
Data Processing and Analysis
Status of the International Monitoring System

Approved for Public Release; further dissemination unlimited





LA-UR-99-4700

Table of Contents - Volume II

HYDROACOUSTIC MONITORING

Blackman, Donna
Calibration of T-Phase Recordings at Ascension Island: Signatures of Natural and Man-Made Sources 1

deGroot-Hedlin, Catherine and John Orcutt
Comparison of T-Phase Observations at Northern California Seismic Stations and the Point Sur Hydrophone 8

deGroot-Hedlin, Catherine and John Orcutt
Hydroacoustic Event Location Using T Phases 17

Eneva, Mariana, Jeffrey L. Stevens, Jack Murphy, Boris D. Khristoforov, Ivan Kitov
Analysis of Russian Hydroacoustic Experiments for CTBT Verification 25

Harben, Philip, E., Donna Blackman, Don Rock, Arthur J. Rodgers
The Ascension Island Hydroacoustic Experiment: Purpose, Data Set Features and Plans for Future Analysis 36

Okal, Emile A.,
Converted T Phases Recorded on Hawaii from Polynesian Nuclear Tests 47

Orris, Gregory J., Laurie T. Fialkowski John S. Perkins
Hydroacoustic Model Validation and the Site Calibration Experiment at Ascension Island 48

Pulli, Jay J., Ted Farrell, Rob Gibson
Characterization and Utilization of Hydroacoustic Signals Reflected from Continents and Bathymetric Features 49

Pulli, Jay J., Robert Bieri, Eugene Dorfman
Modeling Hydroacoustic Waveform Envelopes: Implications for Test-Ban-Treaty Monitoring 57

Rodgers, Arthur J. and Philip E. Harben
Modeling the Conversion of Hydroacoustic to Seismic Energy at Islands and Continental Margins: Preliminary Analysis of Ascension Island Data 66

Stevens, Jeffrey J., G. Eli Baker, Ron W. Cook, Gerald D'Spain,
Lewis P. Berger, Steven M. Day,
Empirical and Numerical Modeling of T-Phase Propagation from Ocean to Land 76

INFRASOUND MONITORING

Page

Brown, David J., Charles N. Katz, Ronal LeBras, Jin Wang, Anna Gault
Infrasonic Processing at the Prototype International Data Centre 86

Garces, Milton and Henry Bass
Results of the Infrasonic Site Survey for CTBT Station IS59, Hawaii 96

Garces, Milton, Roger Hansen, Kent Lindquist, Douglas Drob, and Michael Picone
Variability of the Lower Atmosphere and its Effect on the Propagation of Infrasonic Waves 105

Gibson, Robert, David Norris, Ted Farrell
Development and Application of an Integrated Infrasound Propagation Modeling Tool Kit 112

Hagerty, Michael T., Won-Young Kim, Pasha Martysevich
Characteristics of Infrasound Produced by Large Mining Explosions in Kazakstan 123

Ham, Frederic M., Nizar A. Faour, Joseph C. Wheeler
Infrasound Signal Separation Using Independent Component Analysis 133

Hedlin, Michael A. H., Frank L. Vernon, Jon Berger
Surveying Infrasonic Noise on Oceanic Islands 141

Mutschlecner, J. Paul and Rodney W. Whitaker
Thermospheric Infrasound Signals 151

Norton, Guy V., Wayne A. Kinney, William M. Sanders, Dan J. Ramsdale, Rodney W. Whitaker
Adaptation of an Underwater Acoustic Propagation Model to Infrasonic Atmospheric Propagation 159

Olson, John V. and Charles R. Wilson
Simultaneous Comparison of Three Co-Located Pipe Systems for Wind-Noise Reduction for Use with Model #4 Chaparral Infrasonic Microphones at Fairbanks, Alaska 169

Shumway, Robert H. and Sung-Eun Kim
Estimation and Location Using Multiple Infrasound Arrays 175

Stevens, Jeffrey L., David A. Adams, G. Eli Baker, Heming Xu, John R. Murphy, Igor Divnov, Ivan Kitov,
Infrasound Scaling and Attenuation Relations from Soviet Explosion Data and Instrument Design Criteria from Experiments and Simulations 185

Whitaker, Rodney W., Philip E. Harben, Thomas D. Sandovol, Don Rock
An Introduction to the Ascension Island Synergy Experiment 195

RADIONUCLIDE MONITORING

Biegalski, Kendra M. F., Steven R. Biegalski, Dwight LeRoi Williams
Medical Industry Interference with CTBT Monitoring of Atmospheric Radionuclides 202

Page

Biegalski, Steven R., John Bohner, Leon R. Mason
Cesium-137 Distributions and Trends at CTBT Radionuclide Monitoring Stations and their Implications on CTBT Monitoring 211

Biegalski, Steven R.
Distribution and Trends of Natural Radionuclide Concentrations at CTBT Radionuclide Monitoring Stations 221

Bowyer, Ted W., Justin I. McIntyre, Paul L. Reeder
High-Sensitivity Detection of Xenon Isotopes via Beta-Gamma Coincidence Counting 231

Cavallo, Alfred and Colin G. Sanderson
A Tagged Aerosol Generator for Testing CTBT Radionuclide Aerosol Samplers 242

Dreicer, Mona, Roland Draxler, Michel Jean
Integrating The Radionuclide Data into the International Verification Regime 248

Hayes, James C., Keith H. Abel, Theodore W. Bowyer, Tom R. Heimbigner, Mark E. Panisko, Paul L. Reeder, Justin I. McIntyre, Robert C. Thompson, Lindsay C. Todd, Ray A. Warner
Operations of the Automated Radioxenon Sampler/Analyzer – ARSA 249

Miley, H. S., R. J. Arthur, E. A. Lepel, S. L. Pratt, C. W. Thomas
Evaluation of Fission Product Isotopes for Field or Laboratory Detection 261

Miley, H. S., R. J. Arthur, E. A. Lepel, S. L. Pratt, C. W. Thomas
Evaluation of Laboratory Detection Systems for Fission Product Detection 267

DATA PROCESSING AND ANALYSIS

Agarwal, Deborah A.
Using Multicast in the Global Communications Infrastructure for Group Communication 275

Anderson, Kevin K. and W. Scott Phillips
A Simple Procedure for Kriging Left-Censored Data 283

Carr, Dorthe B., Chris J. Young, Richard C. Aster, Xioabing Zhang,
Cluster Analysis for CTBT Seismic Event Monitoring 285

Chael, Eric, Mark Harris, Chris Young, Kevin Mayeda, William Walter, Steve Taylor, Aaron Velasco,
Prototyping Regional Discrimination Tools with MATSEIS 294

Der, Zoltan A., Matthew W. McGarvey, Robert H. Shumway
Probabalistic Integration of Seismic, Hydroacoustic, and Infrasonic Data Using the Dempster-Shafer Rules for Combining Evidence 300

Firpo, Mike, Doug Dodge, Peter Goldstein
Recent Developments in SAC2000: Enhanced Processing, Database Interaction, and Compatibility with Other Tools 311

Page

Hagedorn, Dan. N., Charles A. LoPresti, Robert F. O'Brien, Stacey A. Hartley, Brett G. Amidan,
Assessment of Data Quality of Selected Data Sets in the DOE/CTBT Knowledge Base 318

Harris, Mark, Pres Herrington, Harry Miley, Edward Ellis, David McKinnon, Devon St. Pierre,
Data Authentication Demonstration for Radionuclide Stations 331

Henson, Ivan, Indra N. Gupta, Robert A. Wagner
A Ground Truth Database for Regional Seismic Research 338

Hipp, James R., Chris J. Young, Randall W. Simons
The Knowledge Base Parametric Grid Interface 348

Knapik, Jerzy F. and Mary L. Girven
Scientific Meetings Database: A New Tool for CTBT-Related International Cooperation 358

Kvaerna, T., L. Taylor, F. Rindgal, J. Swhweitzer
Optimized Threshold Monitoring 374

LeBras, Ronal, Jerry A. Guern, Doug A. Brumbaugh, Jeff A. Hansen, Tom J. Sereno,
Integration of Seismic, Hydroacoustic, Infrasound, and Radionuclide Processing at the Prototype International Data Centre 385

Mangino, Stephen G.
Operation and Recent Development of the Prototype International Data Centre 395

Steer, David N., Dogan Seber, Eric Sandvol, Christine Orgren, Carrie Brindisi, Mauwia Barazangi,
Research and Development of a Geographical Information System (GIS) for Nuclear Treaty Monitoring 399

STATUS OF THE INTERNATIONAL MONITORING SYSTEM

Christie, Douglas R.,
Status of the Infrasound Component of the International Monitoring System, Comprehensive Nuclear-Test-Ban Treaty 406

Davies, J. Alwyn
Working Group B Task Leader International Monitoring System Task Leader View From Vienna 407

Given, Holly
Status of the Seismic Networks of the International Monitoring System, Comprehensive Nuclear-Test-Ban Treaty 411

Newton, John
Status of the Hydroacoustic Network of the International Monitoring System, Comprehensive Nuclear-Test-Ban Treaty 412

Schulze, Joachim
Status of the Radionuclide Component of the International Monitoring System, Comprehensive Nuclear-Test-Bay Treaty 413

HYDROACOUSTIC MONITORING

CALIBRATION OF T-PHASE RECORDINGS AT ASCENSION ISLAND: SIGNATURES OF NATURAL AND MAN-MADE SOURCES

Donna K. Blackman, Scripps Institution of Oceanography

Sponsored by U.S. Department of Energy
Office of Nonproliferation and National Security
Office of Research and Development
Contract No. W-7405-ENG-48 (LLNL-B502679 to UCSD)
and
Provisional Technical Secretariat
Comprehensive Nuclear-Test-Ban Treaty Organization
Contract Number CTBTO/99/30/6001

ABSTRACT

The Ascension Island experiment in May 1999, comprised several elements, each contributing new information about the propagation and coupling of T-phases around an island slope and the subsequent attenuation of seismic energy during propagation to on-shore receivers. Off-shore sensors for which data acquisition was successful include the three bottom-moored (MILS) hydrophones, monitored in real-time, and three temporary, autonomous hydrophones (one deployed on the seafloor northwest of the island, two moored at about the depth of the sound channel axis - one each northeast and southwest of the island). Initial analysis of data from two of these temporary hydrophones is the main focus of this paper.

Three types of source were available during the experiment: airgun shots, an imploding sphere, and numerous natural events that fortuitously occurred during the 3-5 day recording period. These natural events occurred at regional distances to the south of the island and generated T-phases that are clear in both off-shore and on-shore records. The frequency of the arrivals can exceed 50 Hz, suggesting that that a volcanic gas phase may have been released. These are ideal sources for calibration of T-phase coupling at the ocean/island interface for a limited range of southern azimuths, so we will quantify the character of representative T-waves as a function of off-shore location and seafloor topography. These parameters will then be available for comparison to the onshore recordings of the seismic phases whose character will reflect the nature of the slope where acoustic-seismic conversion occurs as well as any losses due to crustal heterogeneity.

One of our goals was to assess the azimuthal dependence of acoustic-to-seismic coupling of T-phases that encounter the rough slopes of a volcanic island. The 6000 cubic inch airgun array towed by the RRS James Clark Ross provided large, impulsive signals, but the 20-m depth of this source is not ideal for generating phases that propagate mainly within the sound channel. The rough seafloor does scatter energy into the sound channel so the extent to which these signals can be used for calibration purposes will be illustrated. The clear advantage of the airgun source is that it can be located at any desired range and, in the short time available, we were able to complete a track pattern that encircled the island.

Key Words: T phase, hydrophone, hydroacoustic monitoring

OBJECTIVE

Island T-stations are an integral part of the monitoring system for the nuclear-test-ban treaty verification. A blast that occurs in the ocean, just above the seasurface, or onshore but near a steeply sloping shoreline, will produce an acoustic wave that can travel long distances in the oceanic sound channel. Ideally this sort of test would be detected by a network of monitoring hydrophones but the cost of deploying cables and maintaining real-time data streams from offshore instruments is significant. Alternatively, seismic stations on remote islands can provide recordings of the acoustic wave after it has been converted to seismic phases at the ocean-island interface and this information can be used to help locate and, perhaps, characterize the event. Detection of converted T-phases from natural events (earthquakes and volcanic sources) has been demonstrated for volcanic island seismic stations (e.g. Hanson, 1998; Talandier and Okal, 1998). The goal of this project at Ascension Island is to begin a systematic, quantitative study of the amount and nature of the losses that occur during the acoustic-seismic conversion. Increased understanding of this process should lead to an improved level of information extraction from the T-station data and, therefore, additional contribution to the IMS.

RESEARCH ACCOMPLISHED

The Ascension Island experiment comprised onshore and offshore deployments of instruments during a one-week period of May, 1999, within which we conducted 3-days of airgun shooting along tracks that surround the island (Figure 1). The British Antarctic Survey ship RRS James Clark Ross was returning from the field season in Antarctica and we were able to contract the ship for 4 days to conduct a combined tomographic and hydroacoustic experiment. Tim Minshull instigated the project with the aim of characterizing the crustal structure of the island after earlier studies (Minshull and Brozena, 1997) suggested the presence of a low elastic strength region at fairly shallow levels which could be interpreted as a magma reservoir. In an effort to follow-up on issues of data access and quality for both the IDA seismic station (ASCN) and the U.S. Air Force MILS hydrophones offshore , Tim contacted me and we established a collaboration for the project with the additional goal of attempting to use the airgun signals to calibrate the degree of signal reduction and alteration due to coupling of the acoustic wave to seismic waves at the island slope. The project was expanded to include deployment by Lawrence Livermore National Labs of portable seismic stations on the island so that changes in the waveform of the converted T phases with distance from the shoreline could be measured. Differences in the coupling mechanism associated with differences in the geologic character of the slope as a function of source-receiver azimuth would be measured as the ship towed the airgun array around the island.

Two of the MILS hydrophones (ASC23 and ASC24) are moored in the sound channel about 50 km off the south shoreline of the island and within about 5 km of each other. These data, as well as that from ASC26 about 100 km further south, are routinely archived at the PIDC. For this project the Center for Monitoring Research put special effort towards real-time monitoring of the data quality and compilation of the continuous data throughout the experiment. The data were then made available in an ftp site shortly after the study.

Four temporary hydrophones were deployed from the JC Ross. Two were Scripp's LCHEAPO instruments that were moored in the sound channel to provide source characterization. Due to their age, the instrument response of the MILS phones is not well known. The PTS underwrote this part of the experiment. The LCHEAPOs (named 'maggie' and 'lisa') were deployed in locations that extended the main NE/SW profile of seismic stations onshore. Two Cambridge University, U.K., ocean bottom hydrophones (OBH27 and OBH29) were deployed to the NW and SE of the island. Unfortunately we failed to recover OBH29 at the end of the experiment when its pressure case leaked and it sank permanently.

The airgun array was quite large (6186 cu inch) and contained 11 individual guns tuned to optimize source impulsiveness. Shooting for the main part of the experiment commenced on Julian day (jd) 134 at 02:30 and, after an initial testing period, continued at 1-minute intervals firing at 50 msec after the even minute until jd 137 at 16:00. A final series of 8 shots were made at 5-minute intervals until 16:40 with the intent to allow complete dissipation of shot energy in the water column between these shots.

The data quality on the LCHEAPOs is good and we can accomplish our goals with it. There are intermittent spikes that occurred when the instrument thought it was being acoustically interrogated (as it

normally is during deployment and recovery) and it pinged in response. Since the ping response was not disabled after deployment, whenever a fairly impulsive, broadband signal was received by the instrument it essentially immediately responded and the sound of its own ping swamps whatever the incoming signal was. The only time this is a problem is when the glass sphere imploded 8 km from instrument maggie. The spike provides a useful time stamp for the implosion but we cannot determine the source signature in this case. The spikes occur most commonly when the ship is in the vicinity of the instrument but are infrequent overall and do not interfere with analysis of the airgun shots. We are continuing to investigate the times of the ping responses so that we can make sure they were not caused by something other than just ship noise. Several of the natural events are well recorded by the LCHEAPOs although several times more of these events are seen in the MILS data. This may be due to the exact position within the sound channel that the instruments were moored.

Ocean currents can cause the LCHEAPO to drift a few hundred meters from the position at which it enters the water column at the seasurface and the position that the anchor settles on the seafloor. Such mislocation is large enough to bias inversion of body-wave travel-times (in the crustal tomography part of the experiment) so we relocated the instruments. The position and timing of the airgun shots is well known (to msec accuracy) and the crossing track pattern is optimal for a seafloor instrument relocation. In our case, the mooring line can continue to move somewhat in the tidal current so we expect a higher level of uncertainty than the usual several-msec values obtained for seafloor relocations. The arrival time of the water wave was picked out to ranges ~10km on each of the three local lines for Lisa and Maggie. These travel-times formed the data vector for a least-squares inversion in which up to five parameters could be varied: x, y, depth, average speed of sound, static time shift. The latter was held constant to account for the 50 msec shift between the airgun trigger and actual fire after initial tests showed this value was stable as expected. The starting position was set to the GPS coordinates at the drop site and the difference in seafloor depth and mooring line length. Starting water velocity was 1501 m/s based on the annual sound velocity profile from the World Ocean Atlas 1° model. Hydrophone depth could vary up to ~100 m given the mooring line lengths and expected currents so we inverted for this parameter as well as letting average water velocity vary if the inversion required it. Maggie, to the NE of the island appears to have drifted ~150m to the north and ~80 m east; Lisa, SW of the island, appears to have drifted ~30 m north and ~150 m west. The preferred depth for both instruments was 10-30 m greater than the simple difference between seafloor and mooring line length predicted. The change from starting to preferred average water velocity was small (1500 m/s preferred at Maggie; 1491 m/s preferred at Lisa). The RMS travel-time residuals for the water wave arrivals were reduced significantly for the relocated positions

Table 1. Information for LCHEAPO Hydrophones on Cruise JR42

Latitude	Longitude	Sensor Depth	Mooring Height	Record (jday/hr:min) Start - stop	Original Residual	Inverted Residual	Name
8° 2.39'S	14° 31.11'W	923 m	730 m	134/14:30 - 137/20:00	63 msec	21 msec	Lisa
7° 50.35'S	14°12.66'W	1347	1460	134/22:00 - 137/20:00	100	26	Maggie

Examples of LCHEAPO recordings of the natural events and the airgun shots are shown in Figures 2 and 3 for shot-receiver ranges of about 25 kms. The airgun shots often have a sharp onset but there are periods in which the water-borne energy is more spread out in time. For some near-source seafloor morphologies, body-waves couple into T-waves at local highs ('radiators') in the sound channel and these arrivals precede the phase that is solely water borne. Systematic study of these situations is underway but initial analysis shows that this clearly happens when the airgun source is near small, isolated highs. The airgun source has high energy in the 5-50 Hz frequency band. In the 2-7 Hz band, the natural events have more energy (Figure 3). This difference will provide interesting comparison of the efficiency of acoustic-seismic

coupling at the island slope. The airgun array shots clearly produce a decent sized signal at sound channel depths for ranges up to at least 40 kms. Some of this energy is reverberating between the sea surface and the seafloor rather than being guided completely within the sound channel. Again, this will provide interesting comparison with the natural events where essentially all the energy is guided so incidence angles should be closer to horizontal.

Initial analysis of the T-wave arrival times at the MILS and LCHEAPO hydrophones suggest that the natural events could have occurred on the Mid-Atlantic Ridge just north of a small right-lateral transform fault at 9° 45'S. The difference in arrival times between ASC26 and the hydrophones closer to Ascension Island is consistently 70 s (Figure 4) but the difference between the near island hydrophones is noisier (although arrivals at Maggie are consistently later than at the rest). More detailed analysis will be required to completely rule out other possible source locations for the natural events. T-phases for 41 events were picked on the MILS data for the time period jd 133-137. All but two of them appear to have come from this same source area.

CONCLUSIONS AND RECOMMENDATIONS

The Ascension Island experiment was successful. More complete analysis to determine just how well the airgun shots can be used to characterize T-phase coupling at a rough island slope is underway. For the meeting, absolute calibration of the shot source signature should be complete and characterization of the natural event T-phases as they approach the island will have been achieved. With this information we can begin the modeling the coupling mechanisms using the onshore seismic data as a guide.

REFERENCES

Hanson, Seismic and hydroacoustic investigations near Ascension Island, Ph.D. Thesis, Scripps Institution of Oceanography, 1998.

Minshull, T.A. and J.M. Brozena, Gravity anomalies and flexure of the lithosphere at Ascension Island, Geophys. J. Intl. 131, 347-360, 1997.

Talandeir, J. and E.A. Okal, On the mechanism of conversion of seismic waves to and from T waves in the vicinity of island shores, Bull. Seismol. Soc. Amer. 88, 621-632, 1998.

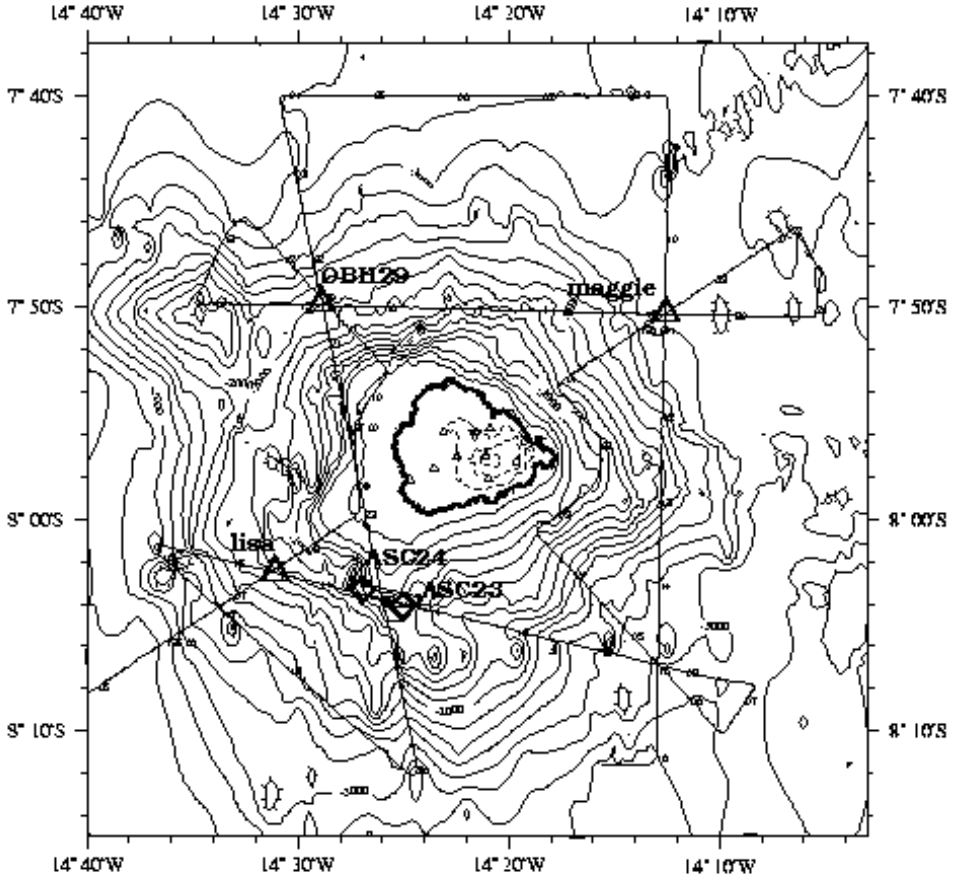


Figure 1. Instrument locations and airgun shotlines for the Ascension Island Experiment in May 1999. Diamonds show the 2 MILS hydrophones (ASC26 is ~100 kms further south); Large triangles show temporary hydrophones: OBH29 was deployed on the seafloor; the Scripps hydrophones lisa and maggie were moored in the sound channel. Onshore seismic stations are shown by small triangles; Inverted triangle shows permanent station ASCN. Airgun shots were fired at 1-minute intervals along the tracks shown. Time (Julian day and hour) is indicated along the track. Bathymetric contours, and dotted topographic contours onshore, are at 200 m intervals.

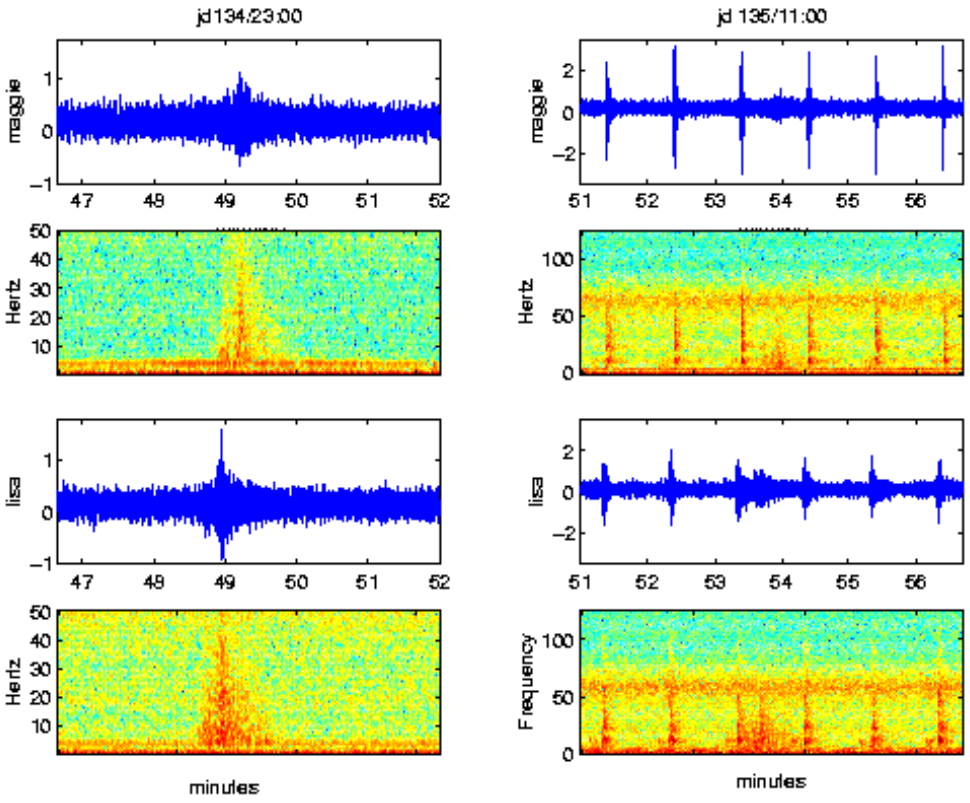


Figure 2. Examples of T-waves and airgun shots recorded on the LCHEAPO hydrohphones. Left panels show a regional natural event with unfiltered record sections above corresponding spectrograms. Ship noise shows up in the 3-5 Hz band. Right panels show both a series of airgun shots and a natural event in the center of the section. Man-made 60 cycle noise is evident in these spectrograms. The airgun shots have significant energy up to 100 Hz.

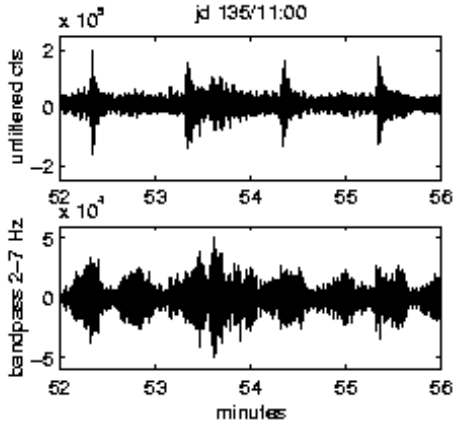


Figure 3. Illustration of the frequency content of the airgun signals vs the natural events. Same section as in right panels of Figure 2. Natural events have more energy than the shots in the 2-7 Hz range.

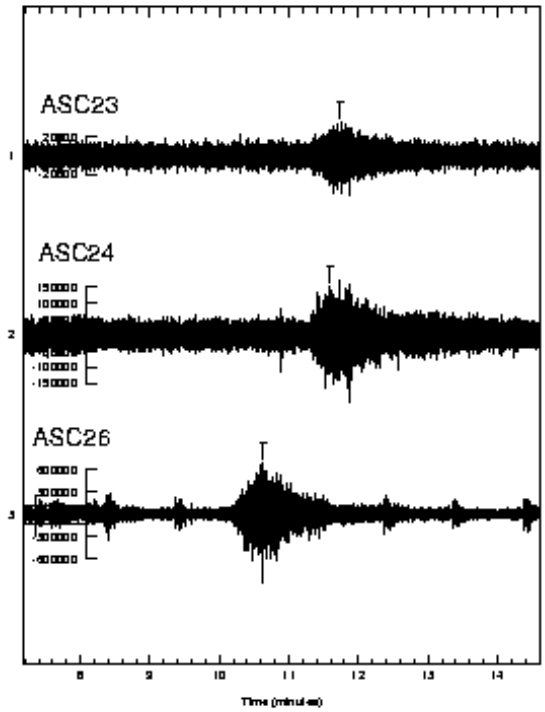


Figure 4. Record sections of the same natural event shown in left panels of Figure 2 from MILS hydrophones. A bandpass filter of 2-20 Hz has been applied.

COMPARISON OF T-PHASE OBSERVATIONS AT NORTHERN CALIFORNIA SEISMIC STATIONS AND THE PT SUR HYDROPHONE

Catherine deGroot-Hedlin and John Orcutt
Scripps Institution of Oceanography, La Jolla CA 92093-0225

Contract # DSWA-01-98-1-0004

ABSTRACT

Plans for a hydroacoustic network intended to monitor compliance with the CTBT call for the inclusion of five T-phase stations situated at optimal locations for the detection of seismic phases converted from ocean-borne T-phases. We examine factors affecting the sensitivity of land-based stations to the seismic T-phase. The acoustic to seismic coupling phenomenon is modeled as upslope propagation of an acoustic ray impinging at a sloping elastic wedge. We examine acoustic to seismic coupling characteristics for two cases; the first in which the shear velocity of the bottom is greater than the compressional velocity of the fluid (i.e. $v_p > v_s > v_w$), the second is a weakly elastic solid in which $v_s << v_w < v_p$. The former is representative of velocities in solid rock, which might be encountered at volcanic islands; the latter is representative of marine sediments. For the case where $v_s > v_w$, we show that acoustic energy couples primarily to shear wave energy, except at very high slope angles. We show that the weakly elastic solid (i.e. $v_s << v_w$) behaves nearly like a fluid bottom, with acoustic energy coupling to both P- and S-waves even at low slope angles.

We examined converted T-wave arrivals at northern California seismic stations for a series of earthquakes near the Hawaiian islands. The characteristics of the T-phase arrivals varied between stations but were consistent from event to event within the event cluster. The seismic T-phases consisted of both P- and S-wave arrivals, consistent with the conversion of acoustic to seismic energy at a gently sloping sediment-covered seafloor. hi general, the amplitudes of the seismic T-phases were highest for stations nearest the continental slope, where seafloor slopes are greatest, however noise levels decrease rapidly with increasing distance from the coastline, so that T-wave arrivals were observable at distances up to several hundred kilometres from the coast. Signal to noise levels at the seismic stations are lower over the entire frequency spectrum than at the Pt Sur hydrophone nearby, and decreased more rapidly with increasing frequency, particularly for stations furthest from the coast.

Key word: hydroacoustics

OBJECTIVE

The planned hydroacoustic network designed to monitor compliance with the Comprehensive Test Ban Treaty (CTBT) will eventually consist of four hydrophones and five T-phase stations located on ocean islands. The plan is to located T-phase stations, each consisting of a single vertical component seismometer, at optimal sites for detecting seismic phases generated by the coupling of acoustic T-phases into compressional (P) or shear (S) waves. Since seismic phases are much more severely attenuated than ocean-borne acoustic energy, the T-phase stations are expected to be less sensitive to T-phases acoustic energy excited by nuclear tests and low atmospheric explosions than hydrophones are. However, their anticipated lower cost makes their use desirable. The rationale behind locating T-phase sensors close to a shoreline is that T-waves are expected to undergo less attenuation, particularly at high frequencies, at these locations. The ability to detect T-waves over a broad frequency band is an essential feature of a T-phase station, as naturally-occurring events often have different spectral characteristics than explosions.

In this paper, we examine factors affecting the sensitivity of land-based stations to the seismic T-phase. In the next section, we examine the physics of acoustic to seismic coupling at a sloping wedge for an acoustic bottom and for two types of elastic bottoms; a Poisson solid with a shear velocity (v_s) that is higher than the acoustic velocity (v_w) of the fluid above, and a semi-elastic solid with a shear velocity much lower than v_w. In the following section, we examine T-phase arrivals at seismic stations in northern California for two event clusters. The first is a series of shallow events that occurred near the Hawaiian islands in July 1996; the second is a series of nuclear tests conducted by the French in the Tuamoto archipelago from September 1995 to January 1996. Both types of events generated T-waves that were recorded at a Pt Sur hydrophone as high amplitude, short duration (15-20 see), broadband arrivals. However, each type of event yielded characteristic T-phase recordings at the seismic stations that were repeatable within each, but distinct between clusters.

RESEARCH ACCOMPLISHED

T-phase coupling at an elastic bottom

Long range acoustic propagation in the SOFAR channel can be described in terms of adiabatic normal mode theory (*eg.* Heaney *et. al*., 1991). At any given frequency, a mode may be represented by an equivalent pair of upgoing and downgoing rays that propagate at an angle or phase velocity giving rise to constructive interference (Officer, 1958). The propagation angle is constant for a range-independent ocean, with higher modes propagating at steeper angles than low modes. As the acoustic wavefield approaches a sufficiently shallow, upward sloping seafloor, a ray trapped in the SOFAR channel becomes bottom interacting, and steepens by twice the seafloor inclination at each cycle of bottom and surface reflections. As the angle becomes steeper than the critical angle, part of the energy is transmitted into the seafloor at each successive bottom bounce. Parabolic equation modeling indicates that, for a fluid over a fluid wedge, acoustic energy is radiated into the bottom in discrete beams at approximately the depths predicted by normal-mode theory, (Jensen and Kuperman, 1980). Thus, for a fluid bottom, the acoustic T-phase would couple into P energy at discrete segments along the slope, defined by the cutoff depths.

The mode cutoff depth is dependent on both mode number and frequency. At any given frequency low modes have the shallowest cutoff depth; for any given mode, the highest frequencies have the shallowest cutoff depth. The lowest modes and highest frequencies are therefore predicted to have the longest oceanic travel path and to couple into seismic energy nearest to the shore. The depth dependence of the acoustic to seismic coupling thus translates to a time separation between coupling points. However, separate T-wave arrivals corresponding to individual mode cutoffs are expected only for highly impulsive sources. In general, for shallow slopes, we predict seismic T-phases with much longer duration than the incident acoustic phase due to the greater lateral separation between the mode cutoff depths. For steeper slopes, mode cutoff depths are more closely spaced, so the seismic T-phase would be expected to have a much more impulsive arrival, yielding T-phases with greater SNR than for shallow slopes.

So far we have discussed only the fluid over fluid case, where the S-wave velocity in the bottom is assumed to be zero. If instead we consider an elastic bottom, with non-zero shear velocity, the coupling problem is

modified by the fact that there are now two critical angles, $Ø_s$, corresponding to the critical angle for transmission of shear waves into the bottom, and $Ø_p$ corresponding to transmission of compressional waves. Since P velocities are always greater than S velocities by at least a factor of $\sqrt{2}$, the critical angle for S waves is less steep than that for P waves. Therefore, ray theory predicts that supercritical incidence is reached first for the S-wave, then for the P-wave after several more bottom reflections.

The partitioning of energy into P and S-waves in strongly dependent upon both the slope and the velocity structure of the elastic bottom. Energy flux densities for transmission and reflection of an acoustic wave incident on an elastic solid, computed using equations (4.2.24 - 4.2.36) of Brekhovskikh and Godin (1990), are shown in Figure 1 at a range of incident angles for three elastic wedge models. The velocities and densities, listed in the figure caption, are typical for solid rock near the Earth's surface. For a ray incident on a shallow elastic wedge, the propagation angle with respect to the vertical decreases by twice the slope inclination at each bottom bounce until it falls below critical incidence for the shear wave in the bottom. A portion of the acoustic energy then couples into S-wave energy in the solid at each bottom bounce until the critical angle for the P-wave is reached. Any remaining acoustic energy then couples into both the P- and S-wave as the angle of incidence continues to decrease. Overall, the introduction of a non-zero shear velocity "softens" the boundary, that is, the total impedance of the solid is less than that of a equivalent liquid with identical velocity and density values, thus the reflection coefficient in the liquid is reduced (Brekhovskikh and Lysanov, 1991). This is indicated by the grey lines in the left panel of Figure 1, which show reflection and transmission coefficients for a liquid with identical density and compressional velocities as those for the solid. For $Ø < Ø_p$, the reflection and transmission coefficients vary more with angle of incidence than for the equivalent solid.

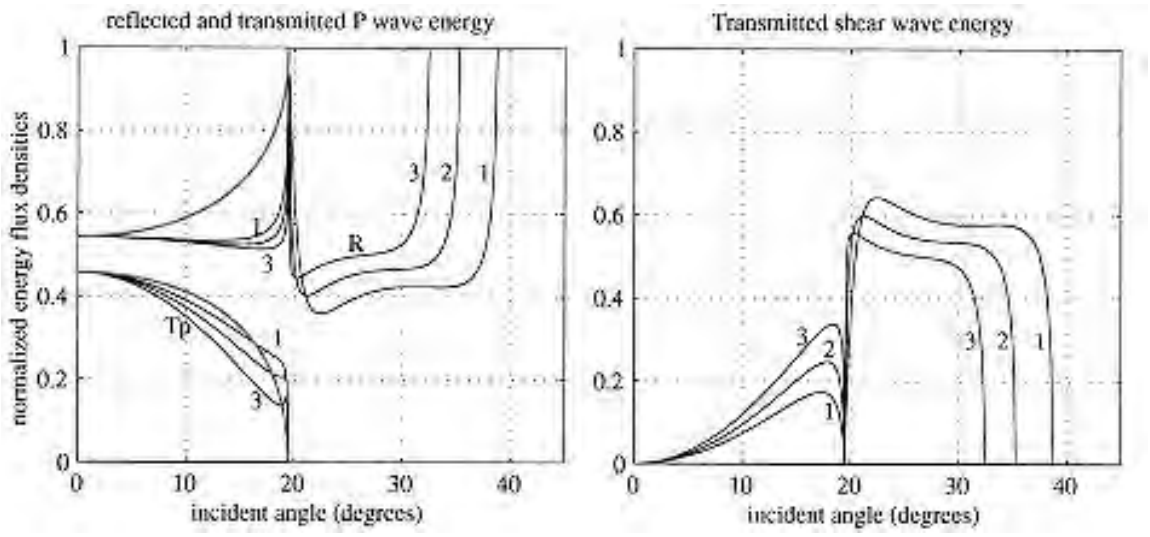


Figure 1: Energy flux densities for transmission and reflection of an acoustic ray incident on an elastic solid. The ratio of compressional velocities from solid to fluid is 3: 1, corresponding to a P-wave velocity of 4.5km/sec and a water velocity of 1.5km/sec. The density contrast from solid to liquid is 2.2. Curves were computed for three values of S-wave velocity: (1) 2.4km/sec, (2) 2.6km/sec (corresponding to a Poisson solid), and (3) 2.8km/sec. In the left panel, the curves labelled R are the reflected energy fluxes in the fluid; those labelled Tp are the transmitted P-wave energies. Transmitted S-wave energy flux densities are shown in the right panel. Velocities and densities for the elastic solid are typical for those of solid rock. Grey lines indicate corresponding values for an equivalent liquid, i.e. one with identical compressional velocity and density

For a slope with inclination ß, a ray goes through approximately $(Ø_s - Ø_p)2ß$ bottom bounces between reaching the critical angles for S- and P-waves. Part of the acoustic energy is transformed into shear wave energy in the bottom at each bounce, thus a shallower slope results in more bounces during which acoustic energy can be transformed to shear waves. This may account for the observations of Talandier and Okal (1998) that for Polynesian shield islands (*i.e.* regions where the seafloor is composed of recent volcanics or

coral reefs) T->P waves are the dominant arrivals only at very steep slopes (*i.e.* slopes greater than 50º), and that the energy couples instead to shear waves at 20º slopes.

Also, parabolic equation modeling confirms that acoustic energy couples into S-wave energy for shallow slopes (Collins, 1993), for the case where the bottom shear velocity is greater than the water velocity. As indicated in Figure 1, the transmission factor for the S-waves increases as shear velocity decreases (for constant P velocity), and conversely, the amount of energy reflected at each bounce decreases. Furthermore, $Ø_s - Ø_p$ increases for decreasing shear velocity so that the range of incident angles over which acoustic energy is transmitted into S-waves increases. Thus, for this range of velocities and densities, the percent of energy coupling into S-waves increases with decreasing shear velocities and decreasing slope.

For typical marine sediments, the shear velocity of the elastic bottom is less than the compressional velocity of the fluid above (Hamilton, 1980), so that an incident T-phase is post-critical with respect to the bottom S-waves at all angles. Thus T->S conversion takes place whenever the seafloor intersects the SOFAR velocity channel. Energy flux densities for transmission and reflection of an acoustic wave incident on an elastic solid with velocities and densities corresponding to those of marine sediments are shown in Figure 2. As shown, for angles of incidence $Ø_p$ such that $Ø < 0 < Ø_P$ the transmission factors for S-waves increase with increasing shear velocity, with most of the energy reflected at each bottom bounce. Once $Ø_p$ is reached, most of the energy is transmitted into P-waves thus, in this case, the percentage of energy coupling into S-waves increases with increasing shear velocity. Again, we predict that the relative partitioning of energy between P- and S-waves will depend on the slope, with coupling into shear waves increasing with decreasing slope. For a shear velocity of zero, the problem reduces to acoustic transmission only and the acoustic energy couples into P-waves in the bottom.

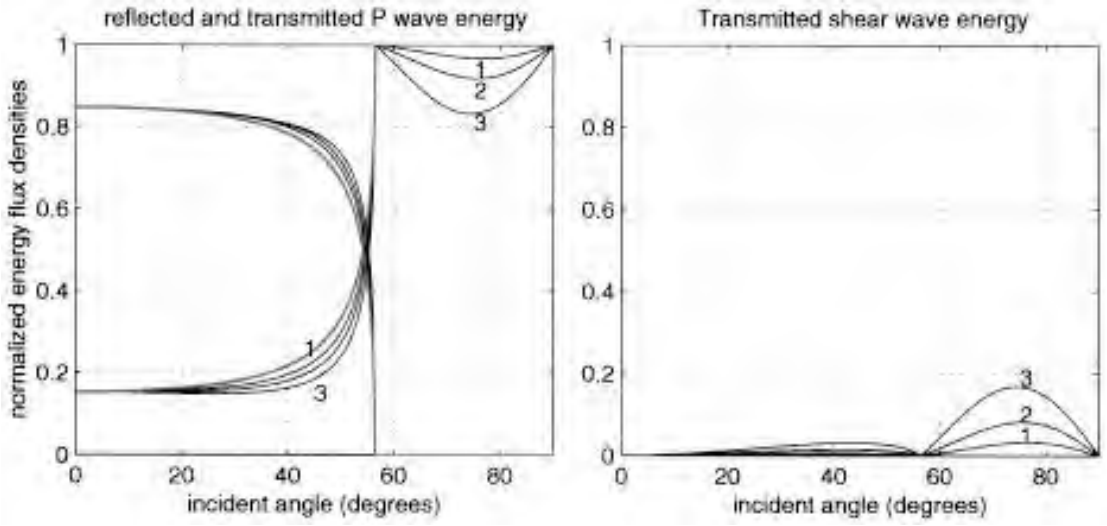


Figure 2: As for Figure 1, but for an elastic solid with velocities and densities corresponding to those of marine sediments. The P-wave velocity of the solid is 1.8km/sec, the density contrast from solid to liquid is 1.9. Curves were computed for three values of S-wave velocity: (1) 0.3km/sec, (2) 0.4km/sec, and (3) 0.5km/sec. The grey lines represent values for an equivalent fluid.

Transmission and reflection coefficients for an equivalent liquid bottom are shown by the grey lines in Figure 2. As indicated, the reflection and transmission coefficients for $Ø < Ø_P$ are almost identical to those of the typical marine sediments, thus for low angles of incidence, the physics of T->P coupling are almost identical to that of the fluid over fluid wedge. As shown by Jensen and Kuperman (1980), for a fluid over fluid wedge with low velocity contrast, the water-borne energy is radiated into downward-going P-waves in the bottom. This suggests that there may be a shadow zone for T->P coupling, with the extent of the shadow zone being dependent on the P velocity gradient. Since shear velocities in the bottom are much lower than the water velocity, acoustic energy coupled into shear energy will also be refracted downward

into the bottom, creating a T->S shadow zone. Hence T->S or T->P phases may be absent for stations located near the coast.

Comparison of acoustic and seismic T-phase recordings

A map of the seismic stations used in this study is shown in Figure 3, along with the off-shore bathymetry in the region. The seismic stations on land, which form part of the Berkeley seismic array, are equipped with three-component accelerometers with a 20Hz sampling rate. The hydrophone at Pt Sur measures pressures at a 200Hz sampling rate. The continental slope in this region is fairly gradual, with average slopes of about 5º between 200m and 3.2km depth. The seafloor off California consists of enormous coalescing fans (the Delgada Fan and the Monterey Fan) that cover the continental shelf and slope, and transgress over the abyssal hills province (Seibold and Berger, 1996). Reflection profiles and drill logs recovered at DSDP sites 32 (McManus et.al, 1970), and 33 (McManus *et. al*., 1970) in central California, and 467 (Yeats *et. al*., 1981) in southern California, indicate that the sediment column is several hundreds of metres thick in the deep water of the continental rise but is well over 1km thick on the continental slope. Compressional velocities in these marine sediments range from 1.5-1.6km/sec in the top 500m, increasing to 3km/sec at a depth of 1km, and densities grade from 1600kg/m^3 to 2300kg/m^3. Waveform fitting of interface waves indicates that shear velocities range from 30m/sec at the surface to 450m/sec at a depth of 150m(Nolet and Dorman, 1996).

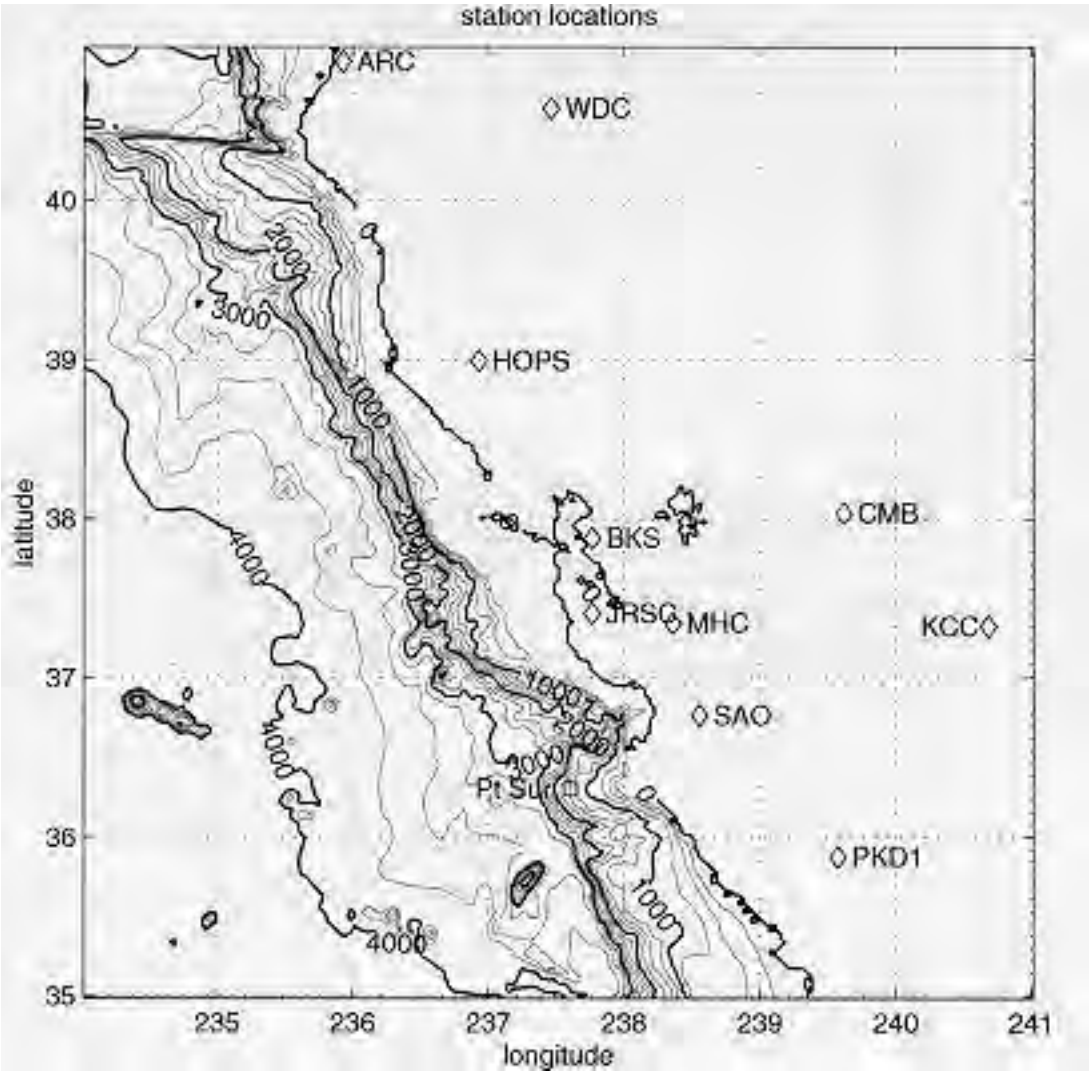


Figure 3: Map of stations used in this study. The locations of the seismic stations, which form part of the Berkeley seismic array, are indicated by diamonds; the location of the Pt. Sur hydrophone is marked by a

square. Contour lines show the bathymetry (from Smith and Sandwell, 1997) near the shoreline. The heavy lines show contours every I km from 0 to 4km depth; the thinner grey lines show contours every 250m.

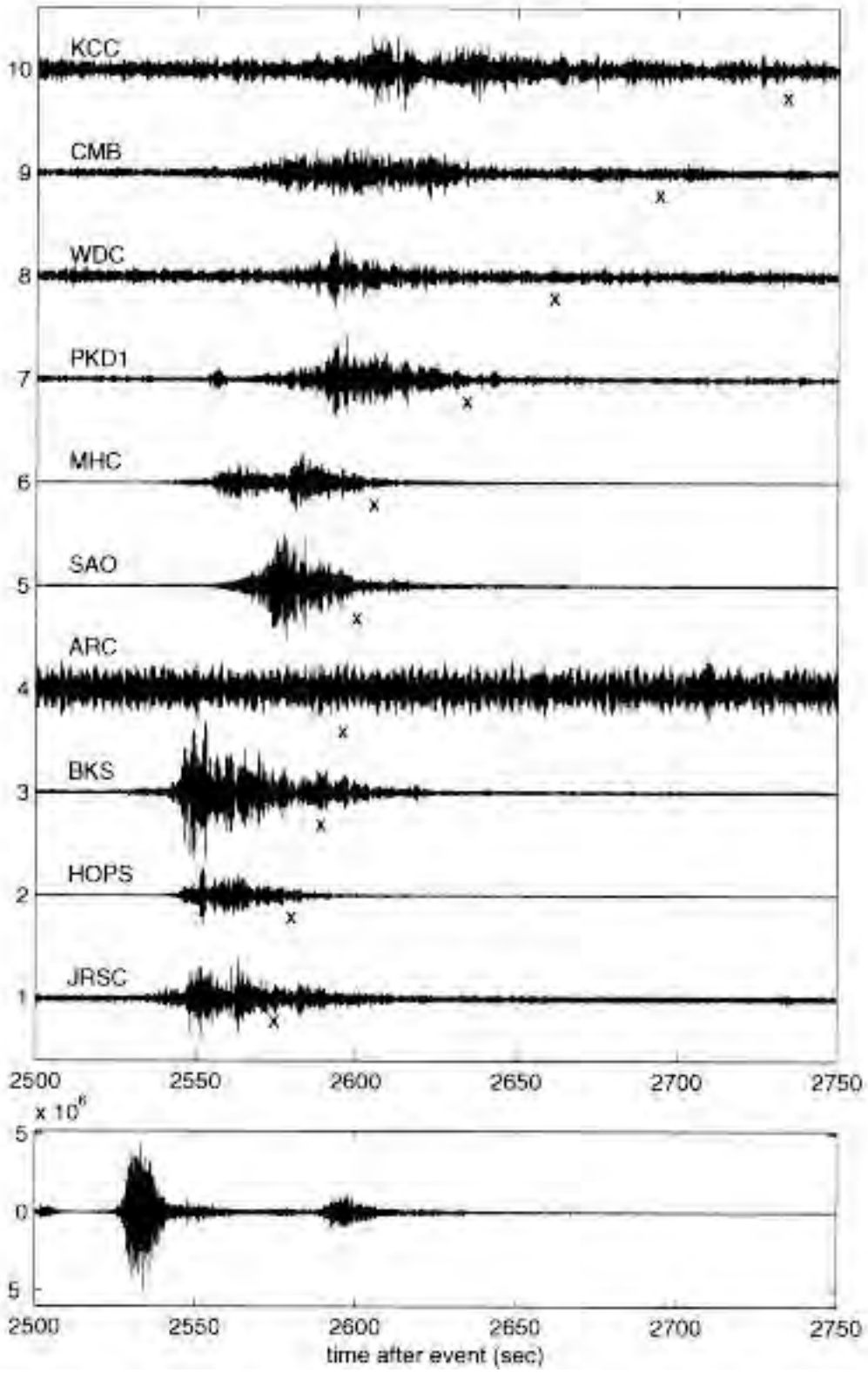


Figure 4: Top - vertical records from the Berkeley array, high-pass filtered over 2Hz, for an mb 5.0 event at 18.83, 155.32W. The 'x'es denote the travel time for purely oceanic propagation. The first 7 records are

shown at a uniform scale; the top 3 records, for stations furthest inland, are shown magnified 10x with respect to the others. Bottom pressure data from Pt Sur, bandpassed from 2-10Hz.

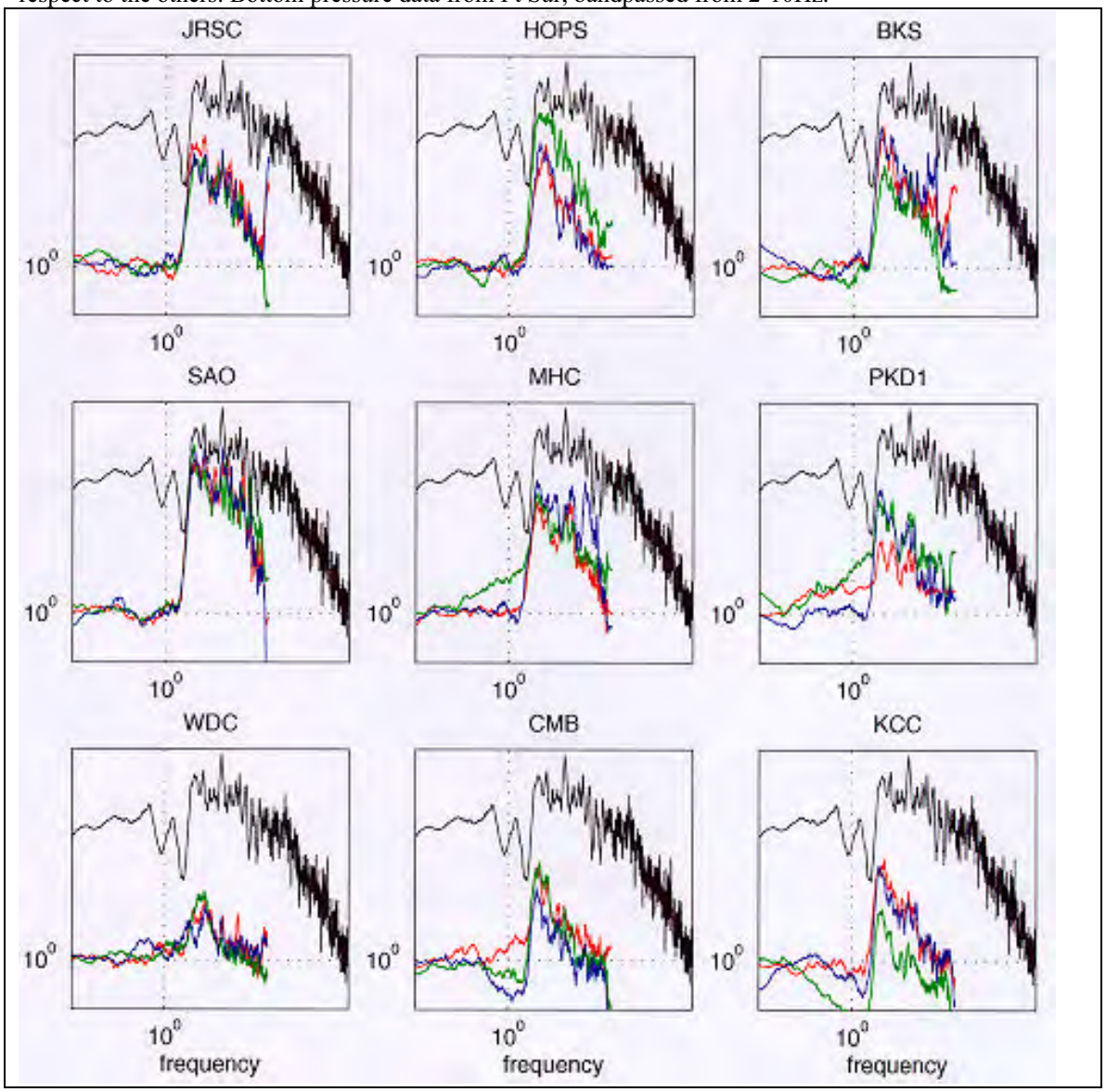


Figure 5: Signal to noise power ratios (SNRs) computed for each station over the entire T-wave arrival. SNRs for the East-West (red), North-South (green), and vertical components (blue) are shown compared to the SNR at Pt Sur (black).

Vertical component recordings of the seismic T-waves, high pass filtered above 2Hz, are shown in the top panel of Figure 4 for a magnitude Mb 5.0 event, one of the largest of the Hawaiian event clusters of July-August 1996. The characteristics at each station, *i.e*. duration, frequency content, and relative amplitudes, are nearly uniform for events within the cluster. The first seven recordings are shown on a uniform physical scale, with the top three recordings, from stations further inland (WDC, CMB, and KCC), shown magnified 10 times with respect to the others. The Pt Sur recording is shown for comparison in the bottom panel. Two stations, JRSC and MHC show two distinct arrivals, whereas signals at other stations appear to consist of several overlapping arrivals. The arrivals at MHC and JRSC have velocities of 4.8-5.7km/sec for the first arrival, and 2.1-2.4km/sec for the second arrival, consistent with crustal P-wave and S-wave velocities, respectively. For stations further inland, amplitudes decrease with distance from the coast. In general, noise levels also decrease with distance inland, so that arrivals are observable as far inland as CMB and KCC.

Spectral ratios were computed over the entire T-wave arrival for each component at each seismic station, and compared to those at Pt Sur as shown in Figure 5. All seismic recordings show lower signal to noise than for the hydrophone at all frequencies. T-phases recorded at Pt Sur for the Hawaii cluster peak at 2-4 Hz, and drop off gradually to background levels at 50Hz. The T-waves at the seismic stations peak at about 2Hz, then drop off more rapidly with increasing frequency. Since the sampling rate at the seismic stations is only 20Hz, compared to 200Hz at Pt Sur, high frequencies cannot be examined but for most stations the spectral ratios suggest that the seismic T-phases decrease to background levels at 9Hz. SAO is a notable exception, with a relatively slow decrease in power with increasing frequency. As expected, recordings at stations located over 100km inland (WDC, CMB, and KCC) are much more attenuated than for stations close to the coast, and the dropoff in signal level with increasing frequency is greater. However, stations closest to the coast (JRSC, BKS, ARC) do not exhibit the highest signal-to-noise, suggesting that there is a tradeoff between noise levels and T-phase amplitudes for stations within several tens of kilometres from the coast.

DISCUSSION AND CONCLUSIONS

Current plans call for several T-phase stations to be located on volcanic shield islands and for one at the edge of a continental margin (on Queen Charlotte Island, Canada). Seafloor slopes at volcanic islands are quite steep (12º-20º), and velocities are high, such that $v_s > v_w$ (*eg*. Piserchia *et.al*., 1998). At continental margins, the sediment-covered seafloor is characterized by very gentle inclinations (3º-6º) at the continental slope. Reflection and transmission energy flux densities computed for $v_s > v_w$ indicate that most acoustic energy will couple into S-waves at volcanic islands, except at very steep slopes. This is consistent with the observations of Hanson (1998) at Ascension Island, of Koyanagi *et.al.* (1995) at Hawaii, and of Talandier and Okal (1998) at Polynesian shield islands. At the edge of a continental margin, T-waves convert to both P and S-waves as observed in this study, and by Shapira (1981), and Cansi and Bethoux (1985).

A marine sediment-covered seafloor has similar acoustic properties to that of an equivalent fluid, i.e. one with identical density and compressional velocity. Thus coupling is expected to occur at distinct cutoff depths corresponding to modal cutoff depths. In this study, we do not discern distinct arrivals corresponding to each mode coupling point, and would not expect to, as the incident T-phases have durations of 15-20 seconds, which is greater than the travel time between mode coupling points. The largest amplitude arrivals occur at stations with propagation paths crossing steep portions of the continental slope near the station, where delay times between cutoff points are minimal and the propagation through land is minimal. The largest arrivals thus likely correspond to the nearly simultaneous arrival of several converted modes. Therefore information in the acoustic wavefield is lost in coupling to seismic energy. Variations in the duration of the seismic T-phase arrivals between stations thus can be attributed to variations in the bathymetry nearest each station.

Noise levels generally decrease with increasing distance from the coast so that seismic T-phases can be detected as far as several hundred kilometres inland. Comparison of T-phase signal to noise ratios over a 0.1-10Hz band at the Berkeley array to those observed at Pt Sur indicate that the seismic T-phase signal is lower at all frequencies than the acoustic T-phase arrival. Furthermore, signal strengths decrease more rapidly with increasing frequency, especially at stations located several hundreds of kilometres from the coast. The relatively high SNR at SAO, compared to the other seismic stations, may be attributed to the fact that the continental shelf is unusually narrow at this point, thus the low mode coupling points lie closer to SAO than at the other sites. This implies that optimal sites for T-phase stations will be at locations where the continental slope lies close to the coastline. For slopes covered by marine sediments, acoustic to seismic coupling is efficient for slopes as low as 5º.

REFERENCES

Brekhovskikh, L.M., and O.A. Godin, Acoustics of layered medial plane and quasi-plane waves Springer-Verlag, 1990.

Brekhovskikh, L. M., and Y.P. Lysanov, Fundamentals of Ocean Acoustics, Springer-Verlag, 1991.

Cansi,Y., and N.Bethoux, T waves with long inland paths:synthetic seismograms, J Geophys. Res., **90**, 5459-5465, 1985.

Collins, M.D., An energy-conserving parabolic equation for elastic media, *J.Acoust. Soc*. Am, **94**, 975-982, 1993.

Hamilton, E.L., Geocoustic modeling of the sea floor, J Acoust.Soc. Am , **68,** 1313-1340, 1980.

Hanson, J.A., Seismic and hydroacoustic investigations near Ascension Island Ph.D. thesis, UCSD, 1998.

Heaney, K.D., WA. Kuperman, and B.E. MacDonald Perth-Bennuda sound propagation (1960): Adiabatic mode interpretation, *J Acoust.Soc.* Am., **90,** 2586-2594, 1991.

Jensen, F.B. and W.A. Kuperman, Sound propagation in a wedge-shaped ocean with a penetrable bottom, *J Acoust .Soc. Am.,* **67,** 1564-1566,1980.

Koyanagi, S., K. Aki, N. Biswas, and K. Mayeda, Inferred attenuation from site effect-corrected T phases recorded on the Island of Hawaii, PureAppl.Geophys., **144,**1-17,1995.

McManus,D.A., R.E.Bums, C. von der borch, R. Goll, E.D.Milow, R.K.Olsson, T.Vallier O.Weser, Site 32, *Init.Repts.* D.S.D.P., **5**,15-56,1970.

McManus, D.A., R.E. Bums, C. von der borch, R.Goll, E.D. Milow, R.K. Olsson, T. Vallier, O.Weser, Site 33, *Init.Repts. D.S.D.P.,* **5,** 57-80, 1970.

Nolet, G., and L.M. Dorman, Waveform analysis of Scholte modes in ocean sediment layers, *Geophys*.J *Int.,* **125**, 385-396, 1996.

Officer, Charles B., Introduction to the theory of sound transmission, with application to the ocean McGraw-Hill, 1958.

Piserchia, P.-F.; Virieux, J.; Rodrigues, D.; Gaffet, S., and J. Talandier, Hybrid numerical modelling of T-wave propagation: application to the Midplate experiment., *Geophys.J Int.,* **133,** 789-800, 1998. Seibold, E. and W.H. Berger, The Sea floor, Springer-Verlag, 1996.

Shapira,A.,T Phases from underwater explosions off the coast of Israel, *Bull. Seism. Soc. Am.,* 71, 1049-1059, 1981.

Smith, W.H.F., and Sandwell, D.T., Global sea floor topography from satellite altimetry and ship depth soundings, *Science,* **277,** 1956-1962, 1997.

Talandier, J. and E.A. Okal, On the mechanism of conversion of seismic waves to and from T waves in the vicinity of Island Shores, *BULL Seism. Soc. Am.,* **88**, 621-632, 1998.

Yeats, R.S, B.U. Haq, J.A. Barron, D. Bukry, J.K. Crouch, C. Denham, A.C. Douglas, V.I.grechin, M.Leiner, A.R.Neim, S.Pal, K.A.Pischiotto, R.Z.Poore, T.Shibata, andR.Wolfart, Site 467: SanMiguel gap, *Init.Repts. D.S.D.P*, **63**, 23-50, 1981.

HYDROACOUSTIC EVENT LOCATION USING T-PHASES

Catherine deGroot-Hedlin and John Orcutt
Scripps Institution of Oceanography, La Jolla CA 92093-0225

Contract # DSWA-01--97-C-0162

ABSTRACT

In this study, we examine the use of T-wave arrivals in pinpointing earthquake locations for sources with epicenters in the ocean basins. Our database consists of a set of events listed in the IDC's Reviewed Event Bulletin (REB), for which arrivals were recorded at the Wake Island and Pt. Sur hydrophones. Most of these events had accurate epicentral location estimates; the given event mislocations were 30km or less. Misfits between the T-phase picks and the predicted arrival times were as large as 120sec, far larger than could be accounted for given the size of the epicentral error ellipse. Since T-phase generation occurs over a broad region of the seafloor, the T-phase onset time is usually not associated with excitation at the epicenter. Hence the accuracy of source location depends on both the method used for picking T-phase onset times, as well as the velocity model. We find that the seasonal variability in the phase velocities is on the order of 4 mm/sec - too small to account for the observed time residuals. Comparing predicted T-phase arrival times with observed T-phase arrivals, we demonstrate that by picking the T-phases in a high frequency band (8-32Hz) improved estimates of source location may be obtained.

We also examine whether waveform matching can be used to improve hypocentral estimates. We show that for arrivals with multiple peaks, the time separation between peaks depends on the distance between T-phase source regions. For well-located series of events east of Honshu, Japan, we determined that a seismic velocity of between 2.2km/sec-3.9km/sec would yield waveforms with peaks showing approximately the correct delay time. Our preliminary interpretation is that the S-wave is coupling into T-phase energy.

Key word: hydroacoustics

OBJECTIVE

Hypothetically, the slow phase velocity (less than 1.5km/sec) and low attenuation characteristics of the T-phase should allow for highly precise estimates of event location. In practice, T-phase source location is often not coincident with earthquake epicentral location, since the efficiency of seismic to acoustic coupling is dependent on water depth(de Groot-Hedlin and Orcutt, 1999), therefore T-phase source locations are often biased toward bathymetric promontories in the vicinity of the hypocenter (Walker, 1992). Moreoever, acoustic velocities are seasonally variant which may yield mis-estimates of predicted T-phase travel times. In this study, we compute seasonal variation s in the acoustic velocitiy for deep ocean paths. We compare results of picking T-phase arrivals in different frequency bands and examine whether waveform fitting can aid in event location estimates.

RESEARCH ACCOMPLISHED

T-phase residuals for Pacific events

Figure 1 shows a map of events that had identifiable T-phases at at least three hydrophones. The locations of the hydrophones at Pt. Sur and the two near Wake Island (WK30 AND WK31) are marked by asterisks. The T-phases are auxiliary phases, that is, they are not used in estimating event locations. The size of the major axes of the error ellipses ranges from 10 to 38 km, that is, the events are located quite accurately by the seismic phases. The size of the circles is proportional to the size of the error ellipse.computed as the square root of the product of the minor and major axes. Since the events are well located this set can serve as a good test set to determine the accuracy needed in both the velocity model, and the most accurate way to pick the T-phase arrival.

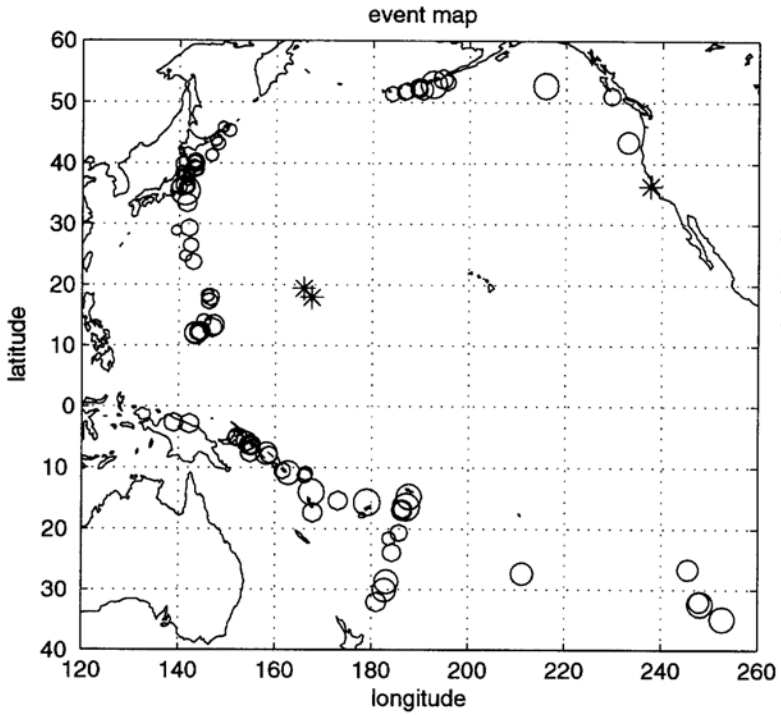


Figure 1: Map of events which had identifiable T-phases at WK30, WK31, and Pt Sur. The size of the circles increases with the size of the location error ellipse.

A comparison of the size of the error ellipse vs. the absolute time difference between the T-phase pick in the REB and the expected T-phase arrival is shown in figure 2. The predicted T-phase arrival times are based on modal velocities

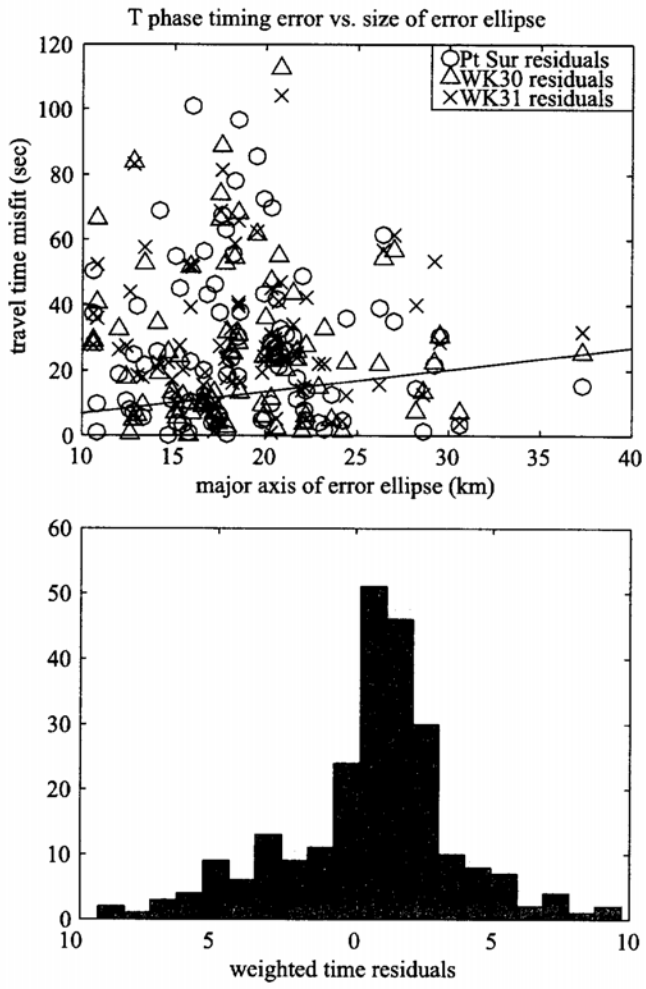


Figure 2 : top - size of T-phase time residuals vs. size of error ellipse. bottom - histogram of weighted time residuals.

computed along geodesic travel paths from source to receiver. T-phase arrivals are based on a "probability weighted time" (Hanson et.al, 1999) and are picked in the frequency band with the highest signal level. The probability weighted time is a weighted sum of the peak time and the mean energy time. For a location error ellipse oriented with its major axis parallel to the direction of propagation, the maximum expected timing residual is given by the length of the major axis divided by the T-phase velocity (about 1.5km/sec). The solid line in this figure represents the maximum expected timing misfit. As indicated, a large number of points fall well above this line, suggesting a problem either with the velocity model used, or with the method of picking T-phase arrivals. We define the weighted time residual as the time residual supplied in the REB, divided by the travel time across the major axis of the error ellipse.A histogram of the weighted time residuals is shown in the bottom panel. The time residuals have a net positive bias, with a mean weighted error of 0.57sec. The time residuals are randomly distributed geographically.

Seasonal variations in T-phase velocity

Since we don't have direct velocity measurements we use a nine term formula (Mackenzie,1981) relating salinity, temperature, and depth to sound velocity. Temperatures and salinity profiles are derived from the WOA database (Levitus and Boyer, 1994). Surface temperatures, and to a lesser extent, salinities, vary over the year thus the acoustic velocity model is a function of time. In figure 3, we examine acoustic velocity profiles and group velocities for each month at 50N, 180E. As shown in the top left panel both the SOFAR channel velocity and depth vary over the year. Below approximately 500m, velocities are constant. Mode shapes, shown in the top right panel of figure 3, are nearly constant over the year. Ocean-borne sound energy propagates at the modal group velocities (Heaney et.al., 1991), plotted for the first few modes for f=5Hz, left, and f=10Hz, right. Velocity variations over the year are only on the order of nearly 4mm/sec, which translates to a time difference of 9 sec over a 5000km path. Thus seasonal variations in travel time are small, and not a significant source of location error. Note that the above computations were done for a deep water at a nearly polar latitude. Velocity variations at equatorial latitudes are less severe, due to less severe variations in surface temperature. On the other hand, seasonal velocity variations in shallow water are slightly greater, since the modal propagation is confined to the upper, more variable part of the ocean column.

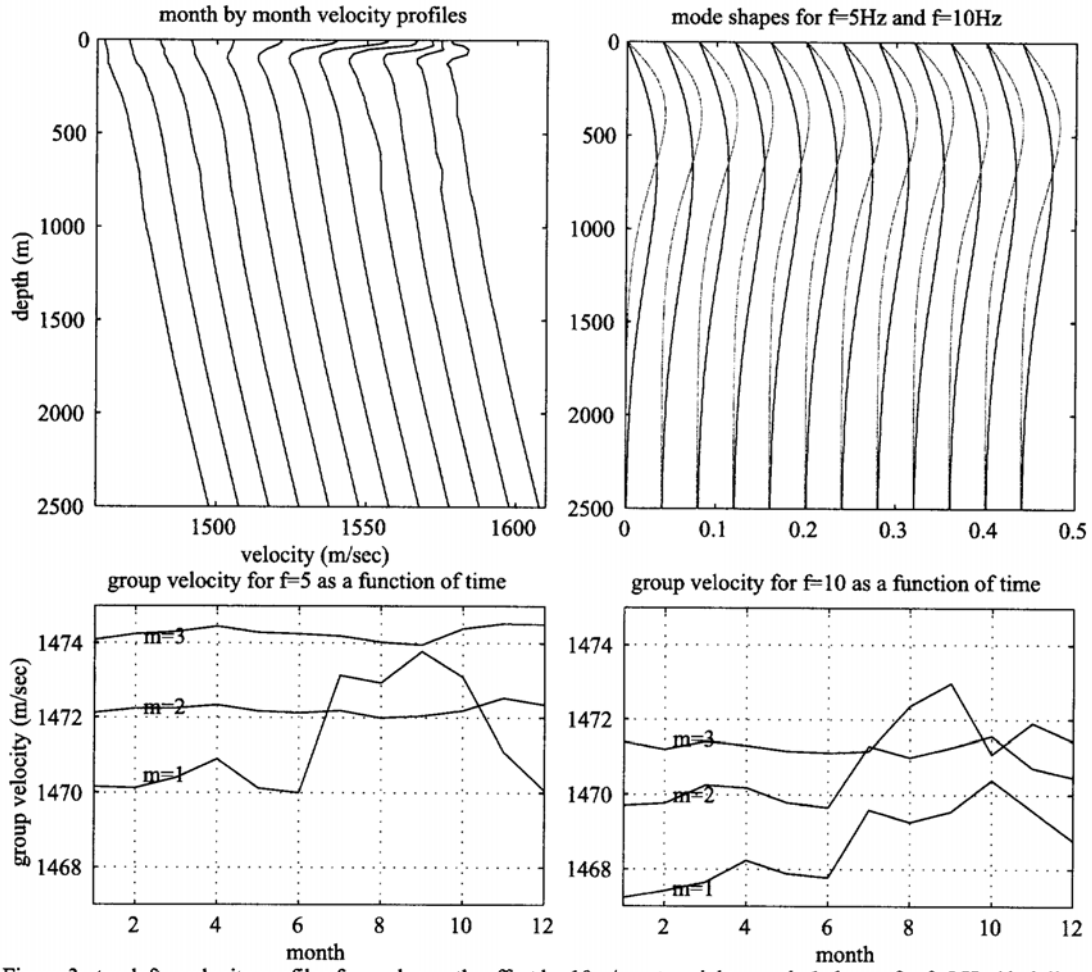


Figure 3: top left - velocity profiles for each month, offset by 10m/sec. top right - mode 1 shapes for f=5 Hz (dark line and f=10Hz (light line). bottom left - variations in group velocities over a year at f=5Hz for the first 3 modes. bottom right - variations in group velocity for f=10Hz.

Accuracy of T-phase picks

For some events, large T-phase time residuals may be attributed arrivals with low signal to noise ratios. However, in many cases, the T-wave recordings consist of a number of distinct peaks, and the large residual is due to the ambiguity in picking one of these as the arrival corresponding to the epicentral location. In figure 4, we show sonograms and waveforms for an event with high signal to noise ratios at all three hydrophones, which nevertheless had timing residuals of 80-90 seconds. The epicenter was located east of Honshu, Japan at 40N, 143E, about 100km east of the coastline where the water depth is nearly 2km, that is, far below the SOFAR velocity minimum. There are two distinct arrivals at WK30 and WK31, the first with travel times corresponding to excitation at the epicenter, and the second with travel times suggesting excitation near the coastline. The latter peak, generated about 100km from the epicenter, has a higher signal to noise ratios and was picked as the T-phase arrival by the automatic picking routine at the IDC, yielding the large time residuals. We identify the latter peak as a slope phase, usually characterized by a high amplitude phase with peak frequency at 5Hz; the first arrival is an abyssal T-phase, usually characterized by lower amplitudes which peak at

For T-phase arrivals with two or more distinct peaks, the arrival time chosen by an automated picking routine often depends on the frequency band used in picking. To examine the frequency dependence of the T-phase picks, we bandpass T-wave recordings at WK30 and WK31 for a series of events off Honshu, Japan. Earthquake epicentral locations, plotted on a bathymetry map as shown in figure 5, are mainly offshore so that at least two peaks are evident in the T-phase recordings of the events. Waveforms bandpassed from 2-8 Hz and 8-16Hz are shown in Figure 6 for most of these events. As indicated, the relative amplitude of each arrival is dependent upon the frequency band, with the amplitude of the abyssal phase dominating the high frequency band. Since abyssal phases are associated with excitation at the epicentral location, T-phase picks made in a high frequency band will likely yield more accurate location estimates. However, this method fails if high frequencies are absent or very weak at frequencies greater than about 8Hz (as in the T-phase recording at Pt Sur shown in figure 4).

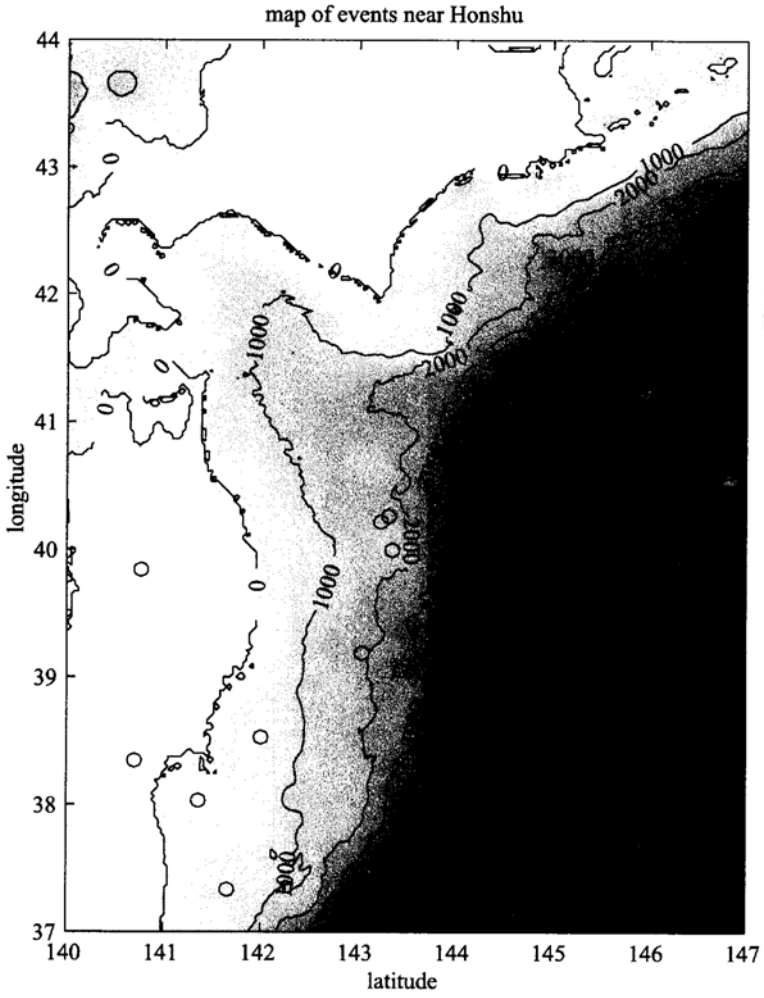


Figure5: Event locations and bathymetry east of Honshu, Japan

Finally, we note that the shape of the T-waveform is dependent on source location, with clustered events all having similar amplitude, duration, and frequency characteristics. This suggests that waveform fitting may aid in event location. For events with both an abyssal phase and a slope phase, the time separation of these phases depends on the distance between the epicenter and nearby bathymetric highs where seismic energy can be scattered energy into the ocean column (deGroot-Hedlin and Orcutt, 1999). As shown in figure 6, the time separation between the two types of

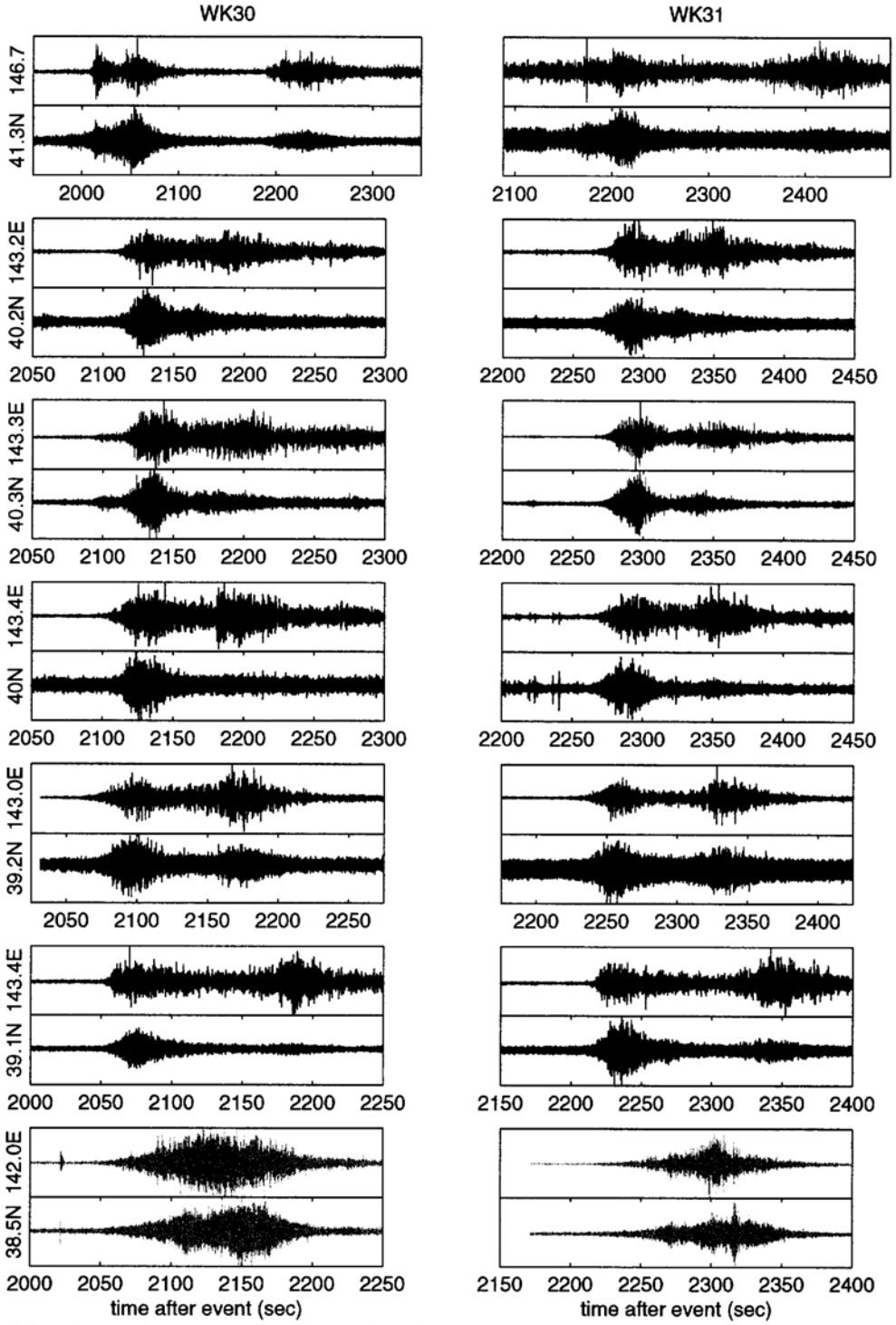


Figure 6: Bandpasses T-wave recordings for a series of events off Honshu, Japan. WK30 recordings are shown at left; WK31 recordings at right. For each recording pairs of waveforms bandpassed from 2-8Hz (top) and from 8-32Hz (bottom) are shown. Note that the first event is on a different time scale.

frequencies of 10-20Hz.. In this case the differences in the frequency content and amplitude of these two arrivals is relatively insignificant at Pt Sur. At WK30 and WK31, there is a greater falloff with increasing frequency for the second arrivals (the "slope" phase), than for the first (the abyssal phase).

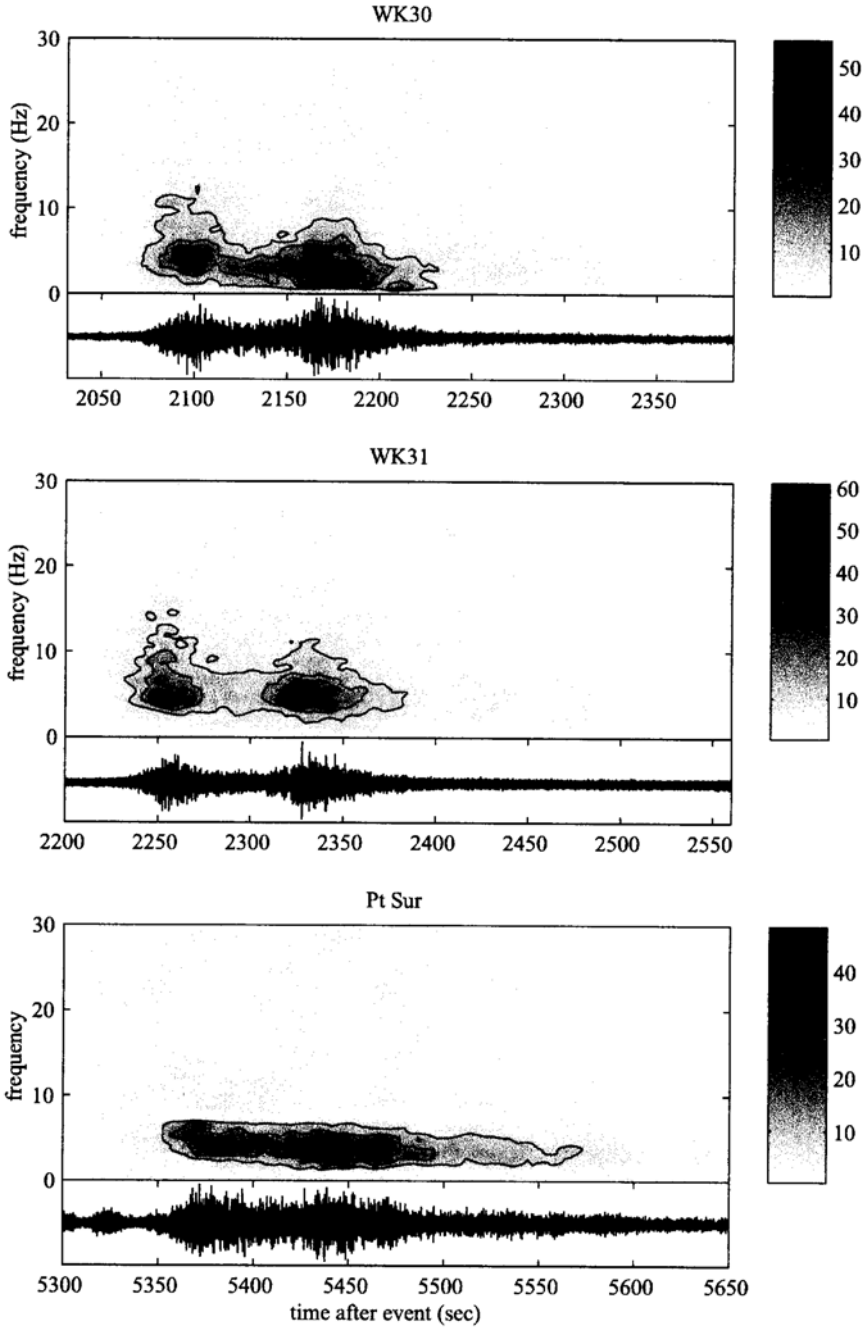


Figure 4 Waveforms and spectral ratio sonograms for an event at 40N, 143E, formed by dividing sonograms for each time slice by average noise powers computed for quiet intervals before the T-phase arrivals, for hydrophones located in the Pacific Ocean. The waveforms are bandpassed from 1-30Hz for WK30 and WK31; from 1-10Hz at Pt Sur.

T-phase increases with increasing distance from the shore. We estimated the crustal velocity for each event of figure 5 by finding the distance from the epicenter to the shallow region where the slope phase is generated, and determining the difference in the crustal portion of the traveltime. The crustal portion of the travel time is given by

$$dt_{crust} = dt_{meas} - dt_{ocean}$$

where dt_{meas} is the observed travel time difference between the slope and the abyssal phase, and dt_{ocean} is the difference in the computed travel paths through the ocean from epicenter to reciever and from the shallow region to the receiver. We found that crustal velocities ranged from 2km/sec to 3.9km/sec. We attribute the large variation in the crustal velocities to the difficulty of picking a precise travel time for each arrival, and to the fact that all but one of the events was within 100km of the coastline, so that high precision in the picks was required. However, we can state that the seismic velocities are low, suggesting that S-wave energy, not P-wave energy converts to acoustic energy at the slope. Thus, given the arrival times of both the high and low frequency T-phase arrivals (which correspond to the abyssal and slope phases, respectively), a reasonably accurate epicentral source location estimate may be made.

CONCLUSIONS

Seasonal velocity variations yield variations in travel times on the order of less than 10 seconds, which correlates to a hypocentral misestimate of about 15km. The major difficulty in using T-phases to estimate epicentral location is that many arrivals are excited at bathymetric peaks in the vicinity of the epicentre, rather than at the epicenter itself. We found that picking T-phase arrivals in a high frequency passband (8-32Hz) yielded travel times corresponding to exciation at the epicenter. We also found that the velocity of the seismic phase which couples into T-phases is on the order of 2.2-3.9km/sec, corresponding to the velocity of a shear wave. Given this approximately known seismic velocity, and the accurately known acoustic velocities, T-phases with multiple peaks may be correlated with bathymetric highs to give an estimate of epicentral location.

REFERENCES

de Groot-Hedlin, C.D., and J.A. Orcutt, Synthesis of earthquake-generated T-waves, *Geop. Res. Lett.*, **26**, 1227-1230, 1999.

Hanson, J., R. Le Bras, P. Dysart, D. Brunbaugh, A. Gault, and J. Guern, Operational processing and special studies of hydroacoustics at the Prototype International Data Center, submitted *to Pure Appl. Geoph.*, 1999.

Levitus and Boyer, World Ocean Atlas 1994, *NOAA Atlas NESDIS 4*, Washington, D.C., 1994.

Mackenzie, Nine term equation for sound speed in the oceans, *J. Acoust. Soc. Am.*, **70**, 807, 1981.

Walker, D.A., C.S. McCreery and Y. Hiyoshi, T-phase spectra, seismic moments, and tsunamigenesis, *Bull. Seismol. Soc. Am*, **82**, 1275-1305, 1992.

ANALYSIS OF RUSSIAN HYDROACOUSTIC DATA FOR CTBT VERIFICATION

M. Eneva, J. L. Stevens, and J. Murphy
Maxwell Technologies, Systems Division

B. D. Khristoforov and V. V. Adushkin
Institute for Dynamics of the Geospheres, Russian Academy of Sciences

Sponsored by the U. S. Department of Defense
Defense Threat Reduction Agency
Contract No. DSWA01-97-C-0166

ABSTRACT

As part of a collaborative research program for the purpose of monitoring the Comprehensive Nuclear-Test-Ban Treaty (CTBT), we are in the process of examining and analyzing hydroacoustic data from underwater explosions conducted in the former Soviet Union. We are using these data as constraints on modeling the hydroacoustic source as a function of depth below the water surface. This is of interest to the CTBT because although even small explosions at depth generate signals easily observable at large distances, the hydroacoustic source amplitude decreases as the source reaches the surface. Consequently, explosions in the ocean will be more difficult to identify if they are on or near the ocean surface. We are particularly interested in records featuring various combinations of depths of explosion, and distances and depths of recording.

Unique historical Russian data sets have now become available from test explosions of 100-kg TNT cast spherical charges in a shallow reservoir (87 m length, 25 m to 55 m width, and 3 m depth) with a low-velocity air-saturated layer of sand on the bottom. A number of tests were conducted with varying water level and charge depths. Pressure measurements were taken at varying depths and horizontal distances in the water. The data available include measurements of peak pressures from all explosions and digitized pressure-time histories from some of them. A reduction of peak pressure by about 60-70% is observed in these measurements for half-immersed charges as compared with deeper explosions. In addition, several peak-pressure measurements are also available from a 1957 underwater nuclear explosion (yield < 10 KT) in the Bay of Chernaya (Novaya Zemlya).

The 100-kg TNT data were compared with model predictions. Shock wave modeling is based on spherical wave propagation and finite element calculations, constrained by empirical data from U. S. underwater chemical and nuclear tests. Modeling was performed for digitized pressure-time histories from two fully-immersed explosions and one explosion of a half-immersed charge, as well as for the peak-pressure measurements from all explosions carried out in the reservoir with water level at its maximum (3 m). Although the modeling had been calibrated to independent data sets from explosions under different conditions, the predictions match the Russian data well.

Peak-pressure measurements and pressure-time histories were simulated at 10 km distance from hypothetical 1-KT and 10-KT nuclear explosions conducted at various depths in the ocean. The ocean water was characterized by a realistic sound velocity profile featuring a velocity minimum at 700 m depth. Simulated measurements at that same depth predict about a tenfold increase in peak pressures from explosions in the SOFAR channel as compared with explosions shallower than 100 m. The observations and the modeling results were also compared with predictions calculated at the Lawrence Livermore National Laboratory using a different modeling approach. The results suggest that although the coupling is reduced for very shallow explosions, a shallow 1-KT explosion should be detectable by the IMS hydroacoustic network.

Key Words: Hydroacoustic, Russian tests, modeling, shallow underwater explosions

OBJECTIVE

The objective of this work is to analyze and model a unique historical set of Russian hydroacoustic data measured from underwater explosions. The Russian data are used as constraints on modeling the hydroacoustic source as a function of depth below the water surface. The results are expected to contribute significantly to the understanding of the difference in coupling from deep underwater explosions versus shallow and surface explosions of interest to the CTBT.

RESEARCH ACCOMPLISHED

Introduction

As part of a collaborative research program for the purpose of monitoring the Comprehensive Nuclear-Test-Ban Treaty (CTBT), we are in the process of examining and analyzing hydroacoustic data from underwater explosions conducted in the former Soviet Union. The CTBT hydroacoustic network consists of 11 stations that monitor the oceans for underwater explosions, as well as for atmospheric explosions conducted close to the ocean surface. The reason such a small network can monitor the whole world is that hydroacoustic waves propagate very efficiently in the acoustic waveguide known as the SOFAR channel. Since a significant portion of the energy from an underwater explosion couples to this channel as acoustic waves, even kilogram-sized explosions at depth generate signals easily observable at large distances. For example, Stevens et al (1999) discuss hydroacoustic signals from four-pound charges detonated off the coast of San Francisco that were recorded as far away as Wake Island, a distance of about 7,000 km.

Understanding the effects of underwater explosions is largely based on measurements and modeling of shock waves. The coupled energy is the energy transferred from the source to the water, manifested as a point-source explosion generating an initially spherically divergent underwater shock wave. The amount of energy coupled to the water depends strongly on the explosion depth. Of interest to the CTBT are shallow and surface sources, as the explosion energy from such tests would be significantly decoupled from the ocean. In light of the above, we are particularly interested in records featuring various combinations of depths of explosion, and distances and depths of recording. Historical Russian hydroacoustic data have become available recently that consist of a number of such measurements. The usefulness of these data lies in the possibility of understanding better the coupling for shallow and surface explosions, and how they differ from deeper, fully coupled explosions. Thus we are using these data as constraints on modeling the hydroacoustic source as a function of depth below the water surface.

The focus in this work is on analyzing and modeling uniquely comprehensive hydroacoustic data from relatively small-scale explosions in a shallow reservoir. The available measurements feature shock-wave parameters (peak pressure, duration and impulse) and pressure-time histories. This data clearly demonstrates that underwater shock waves from explosions at or near the water surface depend strongly on the amount of energy coupled to the water in the source region and peak pressures are significantly diminished by comparison with deeper explosions (by 60-70%). Several measurements from an underwater nuclear explosion in shallow water are also examined. Scaling rules can be applied to relate smaller HE explosions to the nuclear explosions of interest to the CTBT. Additional hydroacoustic data from Russian nuclear underwater explosions are becoming available at time of writing, to be analyzed in a future work.

The modeling in the present work uses a numerical code known as REFMS (Britt et al., 1991; Britt, 1985; Britt, 1999 – personal communication) that models surface reflections, bottom reflections and refraction due to sound velocity gradients. Many of the measurements in the Russian experiments are predicted remarkably well, given that the REFMS code had been previously validated on the basis of U. S. data only. REFMS was also used here to simulate pressure-time histories and maximum peak pressures from 1-KT and 10-KT nuclear sources detonated in the ocean, using a realistic sound-velocity profile.

Data

Unique historical Russian data have become available recently, among them a variety of hydroacoustic measurements. These include data from 100-kg TNT explosions in a shallow reservoir, explosions of 136-kg bombs

in the deep waters of the Sea of Okhotsk, detonation of a 500-m long cord at depth 1 m in the Black Sea, and some underwater nuclear explosions in Novaya Zemlya. The focus here is on the comprehensive data set from the 100-kg TNT explosions in shallow water. Preliminary modeling of data from an underwater nuclear explosion is also discussed.

100-kg TNT Explosions in Shallow Water

Twenty nine explosion experiments were conducted in a shallow reservoir in the former Soviet Union (Kozachenko and Khristoforov, 1970; Korobeinikov and Khristoforov, 1976). The radius of the 100-kg TNT cast spherical charges was about 0.25 m. Charge depth varied from surface (0 m, or half-immersed) to 2.75 m (charge on the bottom) and water level from 0.25 m to 3 m. The bottom of the reservoir consisted of 1-m thick layer of air-saturated sand with a very low sound velocity of 270 m/s. Figure 1 schematically represents the dimensions of the reservoir and the experimental setup of the explosions.

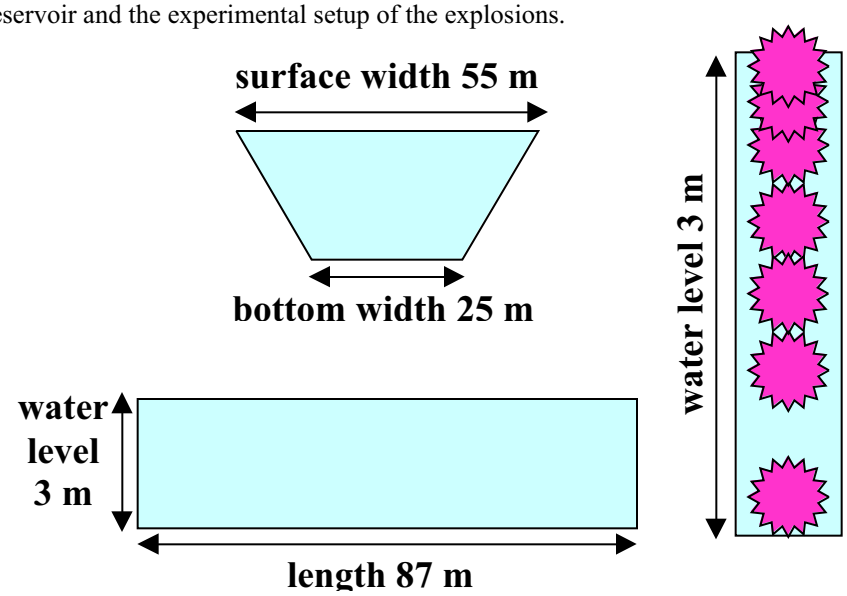


Figure 1. Schematic representation of the reservoir and the experiments with underwater explosions. Left – cross-sections of the reservoir (dimensions not to scale). Right - explosions were carried out featuring various combinations of water levels (0.25 m to 3 m) and charge depths (0 m to 2.75 m). Charge radius is 0.25 m.

Measurements from these explosions were made with piezoelectric gauges suspended at various distances (7.5 m to 30 m) and depths (0.25 m to 2.75 m) in the water. 26 digitized pressure records (pressure-time histories) from two fully immersed explosions (1-m charge depth, 3-m water level) and 14 such records from one half-immersed charge (0-m charge depth, 3-m water level) are now available. In addition, peak-pressure measurements are available from all 100-kg TNT explosions. Figure 2 below shows pressure-time histories from the fully immersed charges along with modeling results to be discussed in the next section. The available pressure-time histories from the half-immersed charges are shown in Eneva et al. (1999). The peak pressures measured at depth of 1.5 m from half-immersed charges are reduced by 60% at a distance of 15 m and 70% at 30 m by comparison with the fully immersed explosions. Peak pressures measured at sensor depth of 1.5 m (mid-pool) in this comparison can be assumed to be least affected by surface and bottom reflections.

Underwater Nuclear Explosion in Novaya Zemlya

Three underwater nuclear explosions were carried out in the Bay of Chernaya, Novaya Zemlya (70.70^0N, 54.67^0E) in the period 1955-1961 (*USSR Nuclear Weapons Tests and Peaceful Nuclear Explosions 1949 through 1990*, 1996). These explosions were conducted in shallow water, as the bottom in the Bay of Chernaya is 60 m to 100 m deep. The purpose was to test torpedo launches with various nuclear charges and to study their effects on military equipment, such as ships, submarines, and buildings on the coast.

The hydroacoustic data available at present consist of seven peak-pressure measurements (see Eneva et al., 1999) at a distance of 235 m from the second of the three underwater tests, conducted on October 10, 1957. The reported yield of this explosion is 10 KT, but the modeling performed below indicates a lower yield.

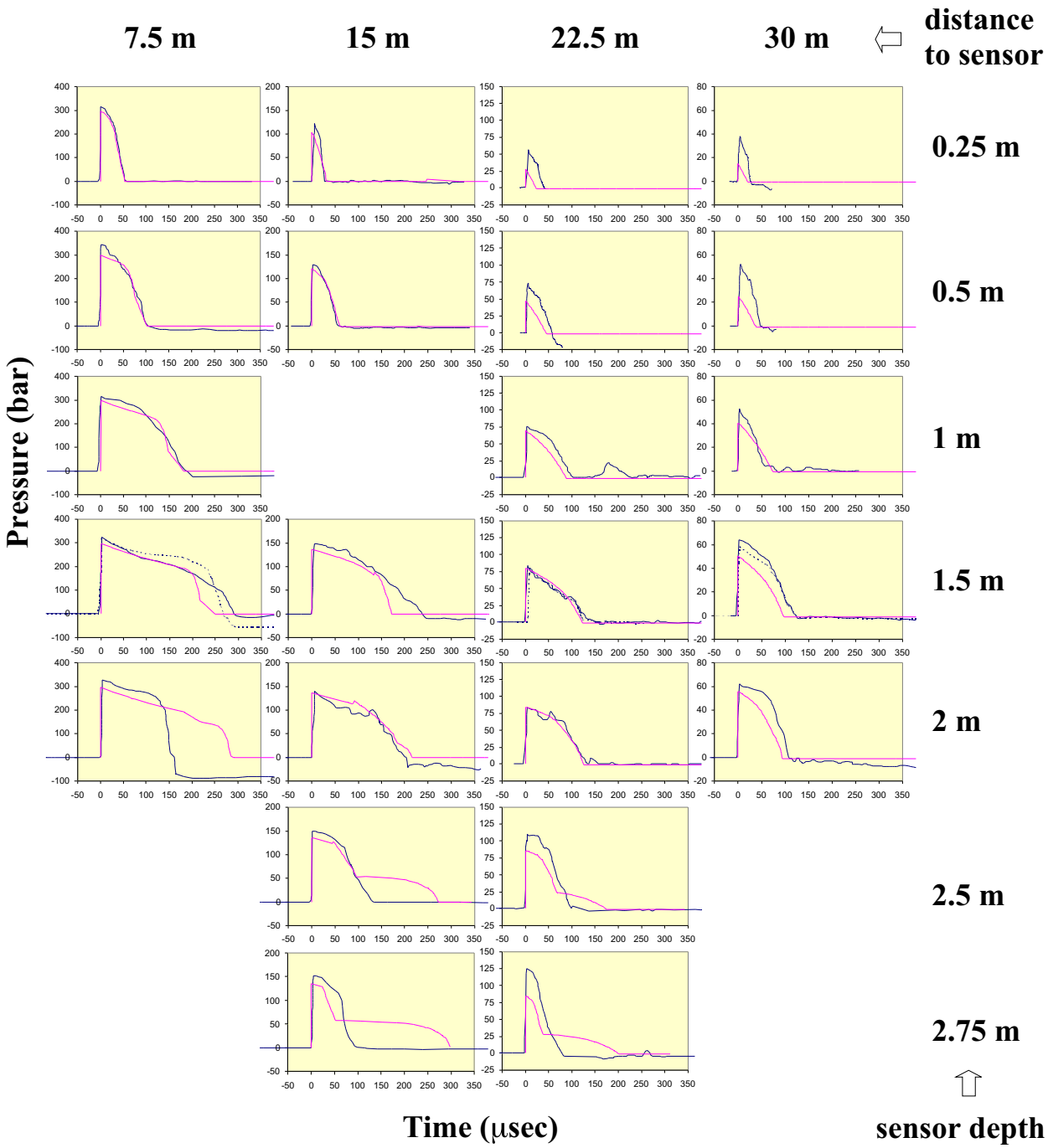


Figure 2. Observed and modeled pressure-time histories for fully immersed charges (charge depth 1 m, water level 3 m). Modeled – gray solid lines (red in color); observed – black solid lines (dark blue in color), with dashed lines indicating additional measurements at sensor depth 1.5 m.

The measurements were taken at various depths using up to six sensors at any given location. The observed peak pressure is between 300 and 320 bars, with one exception of a lower measurement (<260 bars) at 40-m depth. The pressure drop may be due to either a measurement error or a shadowing effect.

Modeling Results

The modeling of the shock waves in the present work was performed using one of the codes, Underwater_Shock, included in the so-called DNA (former Defense Nuclear Agency) Computational Aids (e.g., Stephens and Kelly, 1995). This particular computer program is a modified and simplified Windows version of the ray-tracing code, known as REFMS, that continues to undergo improvements (Britt et al., 1991; Britt, 1985; Britt, 1999 - personal communication). REFMS in turn is the newer version of a numerical code known originally as REFM (Reflection and Refraction in Multi-Layered Ocean/Ocean Bottoms).

REFMS is a computer program for predicting shock-wave parameters from underwater explosions. It includes major aspects of near-source wave propagation from underwater explosions, such as direct shock waves and in-water refraction and bottom and surface reflection. Of the reflected waves, the surface-reflected and the bottom-reflected waves are particularly important, with an effect comparable to and sometimes greater than that of the direct wave. In addition to the reflected waves, if gradients are present in the water sound velocity, the code also handles refraction calculated through the consideration of up to 150 discrete layers in the water and the bottom, each having a constant sound velocity and density. The computational tools in the REFMS modeling include two main features: (1) use of spherical wavefronts and (2) finite-element calculations taking into account deviations from acoustic propagation. The former is based on the acoustic spherical wave reflection theory formulated by Cagniard et al. (1962). The second feature is needed because finite-amplitude effects, not considered in the regular acoustic approximation, become increasingly important with increasing incident pressures and incidence angles (e.g., greater than 170 bars and 85^0, respectively).

The REFMS code has been extensively calibrated. The finite-amplitude surface reflection calculations have been validated with a series of HE experiments. Predictions were very good with the exception of some discrepancies at the shallowest gauges. In terms of refraction, the code is in good agreement with data from underwater nuclear explosion tests (Wigwam, Wahoo, Umbrella, and Swordfish), as well as from HE experimental series performed on a laboratory scale, in flooded quarries, and in the ocean (e.g., Britt e al., 1991; Brockhurst et al., 1961).

We used this code to calculate peak pressures and pressure-time histories. The term “pressure” in this context refers to overpressure (pressure above hydrostatic) as compared to the hydrostatic pressure at the points of observation (gauge, or sensor, locations). More details of the modeling are discussed by Eneva et al. (1999).

100-kg TNT Explosions in Shallow Water

Figure 2 shows the observed pressure-time histories from the explosions of fully immersed charges together with the predicted signals using the REFMS modeling. The modeling was done assuming a constant sound velocity in water of 1500 m/s (i.e., no velocity profile). All other parameters in the modeling matched exactly the configuration of the explosions (depth 1 m, water level 3 m) and the sensors (depth 0.25 m to 2.75 m, horizontal distance from explosion 7.5 m to 30 m), with one exception. Because of limitations of the used version of the code, the bottom layer of 1-m thickness could not be modeled with the original very low sound velocity (270 m/s). This low velocity was likely used so as to not destroy the reservoir in these experiments, and its effect on the measurements was comparable to that of the air above the water surface. The minimum allowed velocity in the modeling (1220 m/s), is higher than the original one, but it matches qualitatively the real low-velocity bottom (i.e., sound velocity in the bottom is lower than the sound velocity in the water). This is the likely cause of the discrepancies between predicted and observed signals at larger sensor depths in Figure 2 (e.g., see the pressure-time histories for sensor depths 2.5 m and 2.75 m at distances 15 m and 22.5 m, and sensor depth 2 m at distance 7.5 m). As to the discrepancies seen at smaller sensor depths (0.25 m and 0.5 m) at larger distances (22.5 m and 30 m), they may be due to an “overinterpretation” of the nonregular surface reflection, with the observations not supporting the predicted spatial extent of such a region in this case. With the above exceptions, the predicted signals in Figure 2 match the observed ones very well, even in what can be considered as essentially the source region of the explosions (at small distances of 7.5 m and sensor depths smaller than 2 m). Predictions are also very good for larger distances at intermediate sensor depths.

Half-immersed explosions are much more difficult to model and larger discrepancies are to be expected. Model parameters in this case followed the test configuration in the same manner as for the fully immersed explosions above, with one additional exception. Charge depth could not be put at 0 m, but a depth of 3 cm was used instead, as the minimum allowed by this version of the code. It is assumed that no significant problems are caused by this discrepancy. Given the difficulty of modeling surface explosions, good agreement between observed and predicted pressure-time histories was obtained in this case as well (see Eneva et al., 1999), although inferior to the modeling of pressure-time histories from the fully-immersed charges. Figure 3 depicts the observed and the predicted relationship between peak pressures and sensor depth for the surface explosion. For sensor depths close to the surface, the modeling probably exaggerates the effect of nonregular reflection and the predicted peak pressures underestimate the observations. The mismatch between the real and model sound velocities in the bottom apparently cause discrepancy at larger sensor depths closer to the source (15 m), but not further (30 m). Model predictions, however, are satisfactory around intermediate sensor depths for both distances. Of the peak pressure measurements available from the 100-kg TNT explosion tests, we further show observed and predicted values for the 11 explosions conducted in the reservoir with water level of 3 m. The effect of explosion depth is depicted in Figure 4 for a fixed sensor depth of 1.5 m. Agreement is very good except for two measurements of explosions on the reservoir bottom.

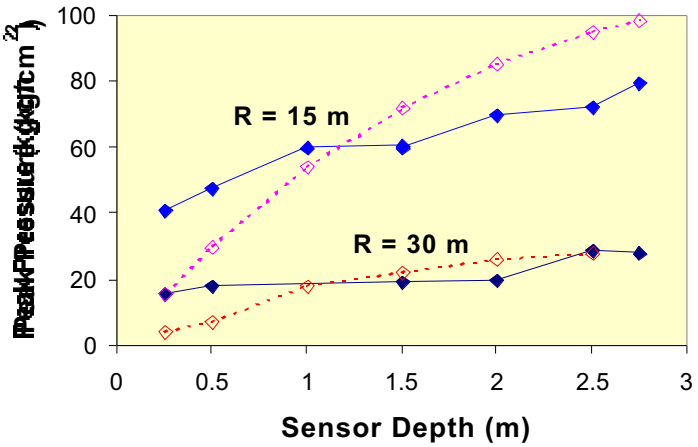


Figure 3. Observed and modeled peak pressures for a half-immersed charge (explosion depth = 0 m), water level 3 m. Measured – solid lines and filled symbols, modeled – dashed lines and empty symbols. Horizontal distance to sensor, as indicated (15 and 30 m).

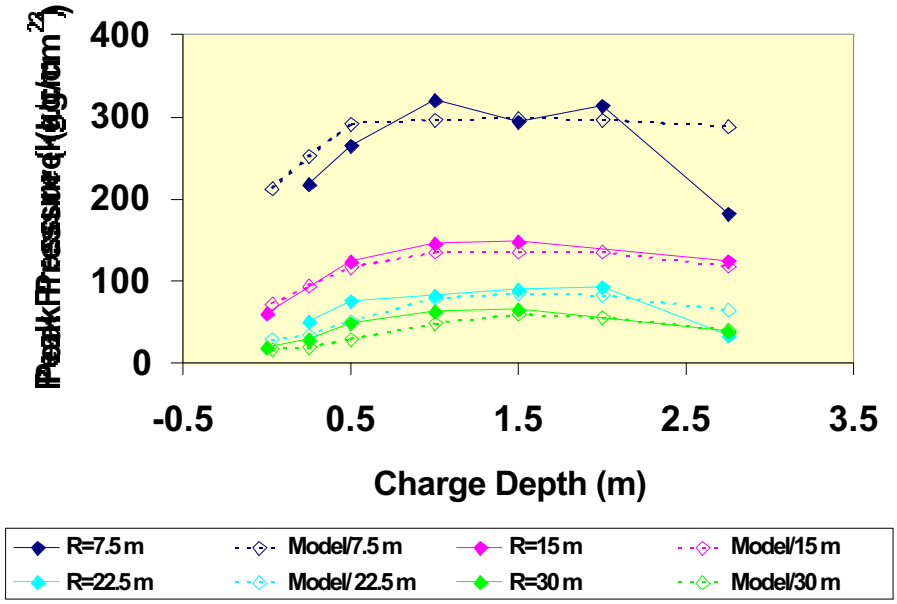


Figure 4. Example of effect of charge depth on peak pressure measured at sensor depth 1.5 m. Observed peak pressures – bold lines and filled symbols; modeled peak pressures – dashed lines and empty symbols. From top to bottom – horizontal ranges 7.5 m, 15 m, 22.5 m, and 30 m, as indicated in legend.

Underwater Nuclear Explosion in the Bay of Chernaya

REFMS was used to model the seven peak-pressure measurements at 235 m from the 1957 underwater nuclear explosion in Novaya Zemlya. The test was conducted in shallow water, with the bottom not deeper than 60 m. No other bottom specifications or sound velocity profile in the water are available at this time. Thus, a constant sound velocity in water (1500 m/s) was used in the modeling, while various reasonable bottom velocities and densities, different yields and variable explosion depths were tried. This limited modeling revealed that the yield of the explosion was probably not much larger than 5 KT and its depth was around 30 m to 40 m. This yield estimate is smaller than the reported yield of 10 KT (*USSR Nuclear Weapons Tests and Peaceful Nuclear Explosions 1949 through 1990*, 1996).

The lower yield estimate above is further confirmed by the similarity between the peak-pressure measurements at 235 m from the 1957 nuclear explosion and the 100-kg TNT at a distance of 7.5 m (Figure 2), which are between 300 and 350 bars in both cases, regardless of sensor depth. Thus a scaling factor of about 235/7.5=31.33 may be applicable, which leads to 100 kg X 31.33^3=3.08 KT TNT-equivalent when the cube-root scaling rule is applied. Taking into account the difference between HE and nuclear sources, the yield estimate becomes 3.08/0.667= 4.62 KT.

Simulated 10-KT Underwater Nuclear Explosion

We would like to use the data and the available modeling capabilities to predict the variations in the hydroacoustic signals that would be observed at the IMS stations. These might differ from peak-pressure measurements in the strong-shock regime in the near field. In the absence of any more detailed observations from real underwater nuclear explosions, modeling results were obtained for the realistic case of a 10-KT yield detonated in an ocean with a velocity profile modeled with 29 different layers, as shown in Figure 5. This profile (Stevens et al, 1999) features a minimum velocity at a depth of 700 m, consistent with the SOFAR channel in the ocean. An additional layer was used to model the bottom, starting at 3350-m depth, with sound velocity 6100 m/s, density 2750 kg/m^3, and thickness 10,000 m. Pressure-time histories were calculated at a hypothetical depth of 700 m (i.e., in the SOFAR channel) and a 10 km distance from the explosion. This distance is outside the nonlinear region and expected to be a reasonable approximation to the signal that would propagate further with low at-

tenuation to the IMS stations. Figure 5 shows examples of the modeled pressure-time histories for two different explosion depths.

More examples of modeled peak-pressure histories are shown by Eneva et al. (1999). The results from this modeling showed that peak pressures increase up to ten-fold between explosion depths 3 m and 800 m, after which they slowly decrease. Thus the predicted features are consistent with channeling expected in the SOFAR channel (the largest peak-pressures are calculated for explosion depths of 700-800 m). In addition, it was demonstrated (Eneva et al., 1999) that in the presence of realistic sound-velocity profiles, changes in peak pressures with explosion depth may be quite complex (see Figure 6 below).

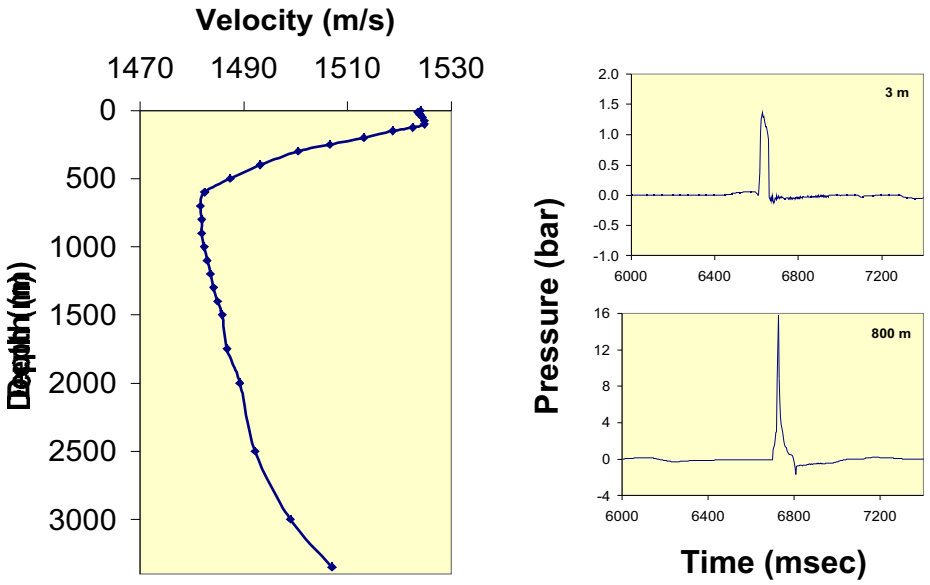


Figure 5. REFMS simulation of a 10-KT nuclear explosion. Left – sound velocity profile used in the simulations. Right – examples of pressure-time histories for two different explosion depths (3 m and 800 m).

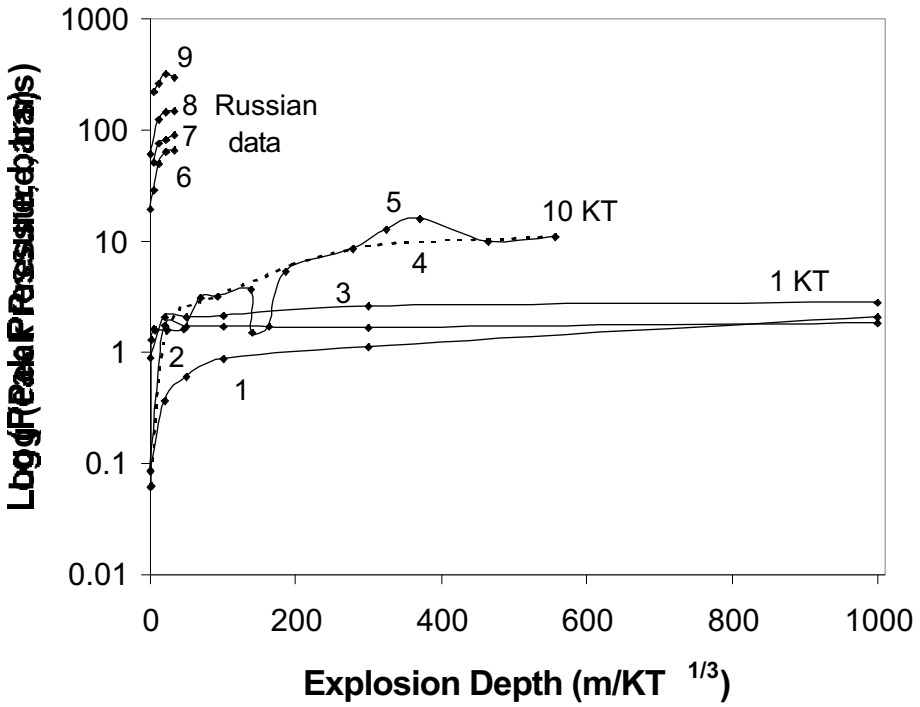
Discussion

The relevance of the Russian small-scale experiments to larger explosions can be determined on the basis of commonly used scaling relationships, relating distances and times with the cube root of the yield (Cole, 1948). That is, the peak-pressure measurements at a distance of 30 m from a 100-kg TNT charge detonated at 1 m depth in a 3 m deep reservoir should be comparable, for example, with measurements (1) at a distance of 646 m from a 1-KT TNT explosion at 22 m depth above a 65 m deep bottom, (2) at a distance of 1400 m from a 10-KT TNT explosion at 46 m depth above a 140 m deep bottom, or (3) at a distance of 30 km from a 100-KT TNT explosion at 1000 m depth above a 3000 m deep bottom. Factors of 21.5 = (1 KT/100 kg)$^{1/3}$, 46.4 = (10 KT/100 kg)$^{1/3}$, and 1000 = (100 KT/100 kg)$^{1/3}$ respectively, are used in this comparison. The scaling in (3) above is the only one somewhat approximating the ocean environment; however, the sound velocity in water was constant in the reservoir, unlike the real sound-velocity profiles in the ocean.

We would further like to compare the Russian observations, REFMS modeling results obtained here, and LLNL modeling results reported by Clarke et al. (1995). Direct comparison is not possible, because the Russian measurements were taken at much smaller scaled distances (160 m/KT$^{1/3}$ to 646 m/KT$^{1/3}$) than the distance in the LLNL modeling (10,000 m/KT$^{1/3}$). This was dictated by the limited dimensions of the reservoir. The difference between homogeneous and refractive water is another complication. However, some general conclusions can be still drawn. In their modeling of a 5000-m deep ocean with a mid-latitude sound velocity profile, without incorporating bottom interactions, Clarke et al. (1995) combined two numerical codes. The first code, CALE, is a LLNL hydrodynamic code used for the strong-shock calculations. The second code, NPE, is a Naval Research

Laboratory (NRL) code used to model weak-shock propagation. The coupling factor was estimated by calculating the energy of the shock waves at a 10-km range from a 1-KT nuclear source for a variety of explosion depths below the ocean surface (0 m to 1000 m) and heights above it. In particular, the total acoustic energy at 10 km range from a fully-coupled reference explosion with depth 1000 m was calculated to be 31.3 T, while for explosions at depths 20 m and 0 m (on the surface), this energy is 2.1 T and 174 kg, respectively. We can then deduce that the energy coupling ratios in the LLNL simulations are about 1:14 for a 20-m explosion depth and 1:180 for a surface explosion and thus the total wave energy from the 1-KT shallow bursts at these depths should be equivalent to that of about 71.4 T and 5.6 T TNT, respectively, detonated at 1000 m depth. In view of this, since even kilogram-size HE explosions can be detected under the right conditions, the LLNL modeling shows that the IMS hydroacoustic network should not miss 1-KT explosions detonated at any depth in the ocean, including on the surface.

Figure 6. Summary of observed and simulated peak pressures. 1 - LLNL simulation of a 1-KT nuclear source, scaled distance 10,000 m/KT$^{1/3}$, mid-latitude sound-velocity profile. 2 and 3 - REFMS simulations, scaled distance 10,000 m/ KT$^{1/3}$, sound velocity profile shown in Figure 5: 2 – 1-KT nuclear source; 3 – 1-KT TNT source. 4 and 5 – 10-KT nuclear source, scaled distance 4,640 m/KT$^{1/3}$, sound velocity profile shown in Figure 7: 4 – smooth (dashed line); 5 – detailed (solid line). 6 to 9 – largest observed peak pressures (at sensor depth of 1.5 m) from the Russian experiments, explosion depths $\leq$ 32 m/KT$^{1/3}$ (1.5 m), at the following scaled distances:



6 – 646m/ KT$^{1/3}$ (30 m); 7 – 485 m/KT$^{1/3}$ (22.5 m); 8 – 323 m/KT$^{1/3}$ (15 m); 9 – 162 m/KT$^{1/3}$ (7.5 m).

To compare with Clarke et al.'s simulations, we performed REFMS modeling of a 1-KT explosion using the sound-velocity profile shown earlier in Figure 5. To address the possible difference in the way coupling of energy to water changes with depth for HE and nuclear explosions, 1-KT nuclear and 1-KT TNT sources were modeled. The REFMS predictions in both cases (HE and nuclear) were calculated for explosions with varying charge depth, at 10 km distance and 700 m depth. The explosion depths in these REFMS simulations matched those used by Clarke et al. (1995). Figure 6 shows the peak-pressure predictions from the LLNL (Clarke et al., 1995) and REFMS modeling of 1-KT explosions, together with the previously performed modeling of 10 KT and the most representative Russian observations in this context.

The Russian data appear in a separate cluster in Figure 6 as they represent measurements much closer to the source, for much shallower explosion depths. The REFMS predictions for a 1-KT nuclear source match the LLNL modeling for surface (0 m) and deep explosions (1000 m) quite well; about 95% decrease with depth is

found in both cases. However, the REFMS change is much steeper for subsurface explosion depths. That is, in the REFMS modeling of the nuclear source, full coupling is approached much faster than in the LLNL modeling. Otherwise, the 1-KT TNT REFMS predictions remain above the predictions for the nuclear source by a factor of 0.667, as expected (Cole, 1948). The REFMS predicted change in peak pressure is much smaller for the HE source (67.5%) than for the nuclear source (95%), when explosion depths of 0 m and 1000 m are compared. In addition, the change in the HE case is more gradual. In fact, the rate of change in coupling for shallow explosion depths suggested by the LLNL modeling is closer to the REFMS curve for the 1-KT TNT than to the REFMS curve for the nuclear source. Although our sound-velocity profile may be somewhat different from the profile used by Clarke et al. (1995), the discrepancies are more likely due to differences in the modeling than to differences in the water profiles.

The 10-KT predicted values in Figure 6 are shown in two versions – a smooth curve using only calculations for explosion depths similar to the ones used by Clarke et al. (1995) and higher-resolution predictions including calculations at more explosion depths (Eneva et al., 1999). It is obvious that changes in coupling as explosions approach the ocean surface may be much more complicated than a smooth decrease.

Figure 7 illustrates the shallow depths, showing together the 1-KT predictions, the observations in the shallow reservoir at a sensor depth of 1.5 m, and averaged data from the 1957 underwater nuclear explosion.

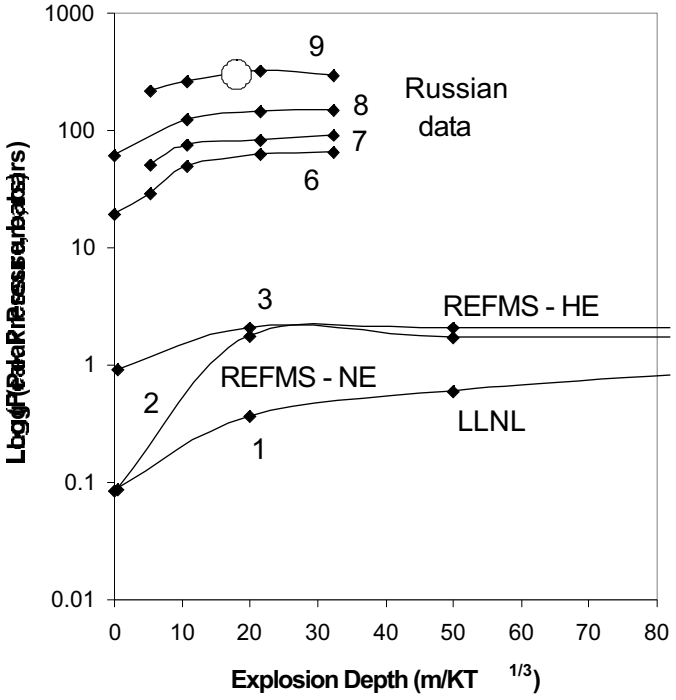


Figure 7. Russian observations and 1-KT simulations from Figure 6, with focus on small explosion depths. Circle shows the peak pressure averaged over various sensor depths (300 bars) measured at 235-m distance from the 1957 underwater nuclear explosion. A yield in the range 3 KT to 6 KT translates into a scaled distance of 160 m/KT$^{1/3}$ to 130 m/KT$^{1/3}$ (see text for details). This fits well the scaled range of 162 m/KT$^{1/3}$ (real distance 7.5 m) for curve 9 of the small-scale observations, on which the circle falls.

The scaled distance for the nuclear explosion in Figure 7 is between 130 and 160 m/KT$^{1/3}$, if an yield between 3 KT and 6 KT is assumed. The rates of change in the small-scale observations agree very well with the rates in the REFMS predictions of the HE source and some of the estimates in the LLNL modeling. As an example, there is 58.6% (at a distance of 15 m) to 71% (at 30 m) decrease in observed peak pressures when explosions on the surface are compared with explosions at mid-pool depths (e.g., 1.5 m), for which the largest peak pressures were measured in the Russian experiments. This matches very well the 67.5% decrease predicted by REFMS for the 1-KT TNT explosion when an explosion on the surface is compared with an explosion at 1000 m depth,

and is predictably smaller than the 95% decrease for the nuclear sources in both the REFMS and the LLNL modeling.

CONCLUSIONS AND RECOMMENDATIONS

The REFMS modeling performed in this work made it possible to make detailed predictions directly relevant to the experimental setup of the Russian tests. The good agreement between predictions and measurements provides a further validation of the REFMS code, previously performed only with U. S. data. Given the inherent limitations of comparing near-field measurements with far-field simulations, and the additional shortcomings of comparing homogeneous, but severely bounded water, with sound-velocity profiles characteristic for the real ocean, the above results and discussion lead us to conclude that a reasonable agreement exists between the Russian observations and both the REFMS and the LLNL predictions. Thus the reservoir experiments and the REFMS modeling performed here can be considered as an additional confirmation that a 1-KT TNT explosion detonated at any depth in the ocean will be detected by the existing IMS network. Further work is needed to address in more detail the relevance of small-scale HE tests in the study of energy decoupling from underwater nuclear explosions.

ACKNOWLEDGEMENTS

We thank Bob Britt (SAIC, St. Joseph, Louisiana) for discussions and suggestions related to the applications of the REFMS code, Chuck Wilson (Maxwell Technologies) for helping identify the relevant literature and available DNA tools, Norton Rimer and John Pritchett (Maxwell Technologies) and Gerald D'Spain (Marine Physical Lab, Scripps Institution of Oceanography, San Diego, CA) for reviewing the manuscript, and Y.V. Poklad (IDG) for assisting with providing the hydroacoustic data.

REFERENCES

Britt, J.R., Application of Cagniard theory to reflection and refraction of explosion shock waves in soil and water, in *Proceedings II 9-th Int. Symposium on Military Applications of Blast Simulations, Oxford, England, 23-27 September 1985*, 1985.

Britt, J.R., R.J. Eubanks, and M.G. Lumsden, *Underwater Shock Wave Reflection and Refraction in Deep and Shallow Water. Volume I – A User's Manual for the REFMS Code (Version 4.0)*, SAIC (Science Application International Corporation), DNA-TR-91-15-VI, June 1991 (U).

Brockhurst, R.R., J. Bruce, and A.B. Arons, Refraction of underwater explosion shock waves by a strong velocity gradient, *J. Acoust. Soc. Am.* **33**, 452-456, 1961.

Cagniard, L., E.A. Flinn, and C.H. Dix, *Reflection and Refraction of Progressive Seismic Waves*, McGraw-Hill, New York, 1962.

Clarke, D.B., J.W. White, and D.B. Harris, *Hydroacoustic Coupling Calculations for Underwater and Near-Surface Explosions*, Lawrence Livermore National Laboratory, UCRL-ID-122098, 1995.

Cole, R.H., *Underwater Explosions*, Princeton University Press, Princeton, New Jersey, 1948.

Eneva, M., J.L. Stevens, B.D. Khristoforov, J. Murphy, and V.V. Adushkin, Analysis of Russian hydroacoustic data for CTBT verification, submitted to *Pure Appl. Geophys.*, 1999.

Korobeinikov, V.P. and B.D. Khristoforov, Underwater explosions, *Hydromechanics* **9**, 54-119, 1976 [in Russian].

Kozachenko, L.S. and B.D. Khristoforov, Shock waves in a shallow-water reservoir, *J. Appl. Mech. Tech. Phys.* **4**, 166-171, 1970 [in Russian].

Stephens, T. and C.S. Kelly, DNA updates Computational Aids, *Science & Technology Digest*, September, 29-30, 1995.

Stevens, J.L., G.E. Baker, R.W. Cook, G. D'Spain, L.P. Berger, and S.M. Day, Empirical and numerical modeling of T-phase propagation from ocean to land, submitted to *Pure Appl. Geophys.*, 1999.

USSR Nuclear Weapons Tests and Peaceful Nuclear Explosions 1949 through 1990, Ministry of the Russian Federation for Atomic Energy, ISBN 5-85165-062-1, pp. 63, 1996.

THE ASCENSION ISLAND HYDROACOUSTIC EXPERIMENT: PURPOSE, DATA SET FEATURES AND PLANS FOR FUTURE ANALYSIS

Philip E. Harben, Don Rock, and Arthur J. Rodgers
Geophysics and Global Security Division, Lawrence Livermore National Laboratory

Sponsored by U.S. Department of Energy
Office of Nonproliferation and National Security
Office of Research and Development
Contract No. W-7405-ENG-48

ABSTRACT

Calibration of hydroacoustic and T-phase stations for Comprehensive Nuclear-Test-Ban Treaty (CTBT) monitoring will be an important element in establishing new operational stations and upgrading existing stations. Calibration of hydroacoustic stations is herein defined as precision location of the hydrophones and determination of the amplitude response from a known source energy. T-phase station calibration is herein defined as a determination of station site attenuation as a function of frequency, bearing, and distance for known impulsive energy sources in the ocean. To understand how to best conduct calibration experiments for both hydroacoustic and T-phase stations, an experiment was conducted in May 1999 at Ascension Island in the South Atlantic Ocean. The experiment made use of a British oceanographic research vessel and collected data that will be used for CTBT issues and for fundamental understanding of the Ascension Island volcanic edifice.

The Ascension Island calibration experiment established 11 temporary seismic stations on the island, 4 temporary hydrophone stations at sea, and archived the data from the 3 operational hydrophones that send data to the prototype International Data Center (pIDC). During the 4-day experiment the British ship towed an 11-element airgun array on tracks around the island that extended from 1 – 45 km from shore. The airguns were fired every 60 seconds at a depth of 20 meters. Imploding sphere sources were also tested as a potential method to couple hydroacoustic energy directly into the Sound Fixing and Ranging (SOFAR) channel (2000 feet depth) without the use of explosives. A six-station seismic line across the island was a primary focus line, with imploding sphere tests, temporary hydrophone stations, and extended ship tracks all along the ocean extensions of the SW-NE trending line. An infrasound station and one of the 11 seismic stations form the basis of a synergy experiment left behind on the island and currently in operation.

Future data analysis will focus on: (1) determination of precise locations of hydrophones ASC23, ASC24, and ASC26; (2) comparison of three-dimensional hydro/T-phase conversion modeling with data set results; and (3) a calibration model for an Ascension Island T-phase station that shows coupling/attenuation dependence on frequency, source bearing, and source distance. In addition, the data will be analyzed by other experiment participants not affiliated with any CTBT agencies to determine a 3-D seismic velocity model for the Ascension volcanic edifice. The synergy experiment just put into operation will be archiving continuous recordings of seismic, hydroacoustic, and infrasound data for the next 2 years.

Key Words: T-phase, hydroacoustic

OBJECTIVE

Hydroacoustic monitoring for the Comprehensive Nuclear Test Ban Treaty has made use of some existing hydroacoustic stations that were not necessarily intended to be used for the purpose of CTBT monitoring. Some of these systems are very old with poor knowledge of the sensor calibrations and location in the ocean. The calibrations of T-phase stations -- seismic stations on an island that conduct hydroacoustic monitoring for the CTBT through T-phase signals -- are also poorly understood, making it difficult to utilize such stations effectively in a network of monitoring stations. Finally, although many recognize the possible benefits of joint analysis of different monitoring technologies such as seismic, hydroacoustic, and infrasound, little effort has been expended on this topic, in part because there is not much data of this type to analyze and in part because it is not clear exactly how to analyze it.

The Ascension Island Experiment was an attempt to gather data that could be used to understand all of these technical issues. The experiment would specifically locate and calibrate the CTBT hydroacoustic monitoring station at Ascension Island, help determine how to calibrate T-phase stations, and would leave behind a continuous monitoring system consisting of nearly co-located seismic, hydroacoustic, and infrasound stations. It represented an experiment of opportunity through collaboration and cost sharing. Participant institutions included Cambridge University, Naval Research Laboratory, Scripps Institute of Oceanography, Los Alamos National Laboratory, and the Provisional Secretariat. This paper outlines the specifics of the experiment, features of the data set collected, and plans for future data processing and analysis.

RESEARCH ACCOMPLISHED

Ascension Island is located in the middle of the South Atlantic Ocean at about 8 degrees south latitude (see Figure 1). It was chosen as the location for a hydroacoustic experiment because of an existing hydroacoustic monitoring station on the island, characteristics typical of T-phase stations, and a ship of opportunity with cost sharing potential that would transit the region. The Ascension island experiment was conducted in May-99 after an intensive but relatively short planning period that began in December-98 at a small workshop held at LLNL. The experiment consisted of a sea-based and land-based operation. The sea-based operation (Minshull, 1999) made use of the J.C. Ross, a British icebreaker class oceanographic research vessel returning from a season in the Antarctic via Ascension Island (see Figure 2). The ship was equipped with an array of airguns and hired for four days of airgun shooting and instrument deployment around the waters of Ascension Island. The ship track for the duration of the experiment is shown in Figure 3. A single airgun was deployed for the hydrophone calibrations but the bulk of the experiment utilized an 11-element array of airguns with a total firing chamber size of over 6000 cubic inches. Two temporary hydrophone systems were deployed by Scripps and one by Cambridge. Cambridge also deployed numerous sonobouys during the experiment. In addition several imploding sphere sources were tested.

The land based operation consisted of continuous recording from ten temporary seismic stations deployed on the island for the duration of the airgun shooting. The seismic stations were sited and permitted on an earlier site-survey visit to the island. Concrete pads were poured to provide good coupling and a stable surface for seismometer leveling and the seismometers were buried below ground level. A Sprengnether S-6000 3-component 2 Hz seismometer was emplaced at each station site and recorded continuously at 250 samples/sec with 24 bit digitization using a Reftek data acquisition box. The distribution of stations on the island is shown in Figure 4. The station locations represent a compromise between having multiple lines of stations crossing the island and siting in areas of good relative coupling to competent formations.

HYDROACOUSTIC CALIBRATION:

The three hydrophones currently utilized by the pIDC as the Ascension Island hydrophone monitoring station are ASC26, ASC23 and ASC24. ASC26 is located about 100 km south of the island while ASC23 and ASC24 are within 3 km of each other and only a few km south of the island. The J.C. Ross approached Ascension Island from the south and consequently conducted a calibration of ASC26 during the journey to Ascension Island. A single towed 1000 cubic inch airgun was fired every minute at 5 meters depth as the ship sailed on two orthogonal tracks over the nominal coordinates of ASC26. The data set selected for analysis and the corresponding signals recorded by ASC26 is shown in Figure 5. Each open circle represents a shot and the

corresponding waveform is shown. The data will be used to determine the precise location of the hydrophone at the time of the experiment to about 20 meters accuracy. It is clear from the moveout on the waveform traces that the nominal latitude of ASC26 agrees well with the data but that the nominal longitude is somewhat to the east of what the data indicates.

In the same way as data was acquired over ASC26, data was collected over ASC23 and ASC24. The ship tracks and firing locations are shown in Figure 6. The accuracy of the location determinations of ASC23 and ASC24 at the time of the calibration is expected to be about 20-50 meters. Although the bulk of the experiment had a fully deployed 11-element array of airguns firing, a single 1000 cubic inch airgun was used for the hydrophone calibrations. The reasons were to minimize the source distribution and to fire a consistent source near each hydrophone. In addition, two calibrated Scripps hydrophones were temporarily deployed during the experiment and the single airgun was fired over these instruments. This data will be used to characterize the source pressure amplitude spectrum which in turn will allow us to determine the unknown amplitude response spectrums for ASC23, ASC24, and ASC26. Data records show clipping of the direct path signal when the source is very close to the ASC hydrophones which will also allow us to determine the clip levels of the ASC hydrophones.

T-PHASE STUDIES:

The T-phase studies have yet to be accomplished. The 11-element airgun array fired every minute for about 2.5 days, over 3500 events in all. The nominal 20 meter depth of the towed airgun array was constrained by equipment limitations and operational procedures. This depth is very shallow for good coupling to the SOFAR. Consequently, the relatively poor coupling of the airgun events into the SOFAR and the relatively high background seismic noise levels typically encountered on islands may make it difficult to use the airgun as a signal source for T-phase coupling-to-land studies. A plot of the seismic station SBC recordings over a one hour time period during the full airgun array shooting is shown on Figure 7.

A simple model based on the bathymetry and sound speed profile at Ascension Island predicted that for a shallow source, the convergence length for optimal detection of the signal in the SOFAR channel is 45 km. The ship tracks were chosen to provide a few straight line paths from 45 km or more towards a land sesimic station and a MILS hydrophone so that the convergence length can be measured. These data will be compared to model predictions.

During the short duration of the experiment several apparent volcanic events were recorded by the MILS hydrophones, the temporary hydrophones, and the seismometers on the island. An example of the events as recorded on the MILS hydrophones is shown in Figure 8. The events are rich in high frequency energy (above 30 Hz) and are also recorded on land with significant energy above 30 Hz. These events, therefore, will be ideal to address two of the T-phase research issues: 1) How well do the high frequencies in an explosive generated T-phase couple into land? and 2) What is the attenuation of high frequency T-phase energy across an island? The volcanic events recorded appear to be part of a volcanic cycle noticed on the MILS hydrophones about a month before the experiment, a cycle that may correlate with a large fish kill and temperature rise in the waters around Ascension Island during the same time period.

IMPLODING SPHERE SOURCES:

Use of explosives aboard the J.C. Ross was not allowed, consequently there was no commercially viable way to get sources at the SOFAR channel depth (nominally 750 meters) for optimal T-phase signal generation. This left few alternatives since airgun and other seismic marine sources are designed for use only at shallow depths. The result was a rushed attempt to develop an imploding sphere source that could be initiated at a prescribed depth, nominally 750 meters. Imploding spheres have long been recognized (Issacs, 1952 and Orr, 1976) as an effective source at mid-ocean depths and below, however, they have not been reliable: either failing well below or above the desired depth or not failing catastrophically at all (Sauter, 1996).

We designed and tested a prototype smashing system (Boro, 1999) that would initiate sphere failure at a desired depth. The system firmly held the sphere in place and in contact with a 4 inch diameter piston. A 1/4 inch diameter ram connected to the center of the piston passes through a small O-ring sealed hole in the cap confining the piston and abutting the glass sphere. The ram initiates failure by punching a hole through the glass

sphere. The end cap on the cylinder confining the piston and opposing the ram end cap tapers to a one inch diameter opening with a rupture disk sealed to it. The rupture disk is calibrated to fail within 5% of the calibrated failure pressure, 1000 psi in our tests. Failure of the rupture disk results in an inrush of high pressure water into the air-filled piston chamber, driving the piston -- and attached ram -- towards the glass sphere.

The smashing system was tested on 4 occasions and reliably actuated every time at the nominal rupture disk failure pressure of 1000 psi. The system also successfully punched a hole in a Benthos flotation sphere on each test, however the Benthos did not fail catastrophically except when tested in the lab without the water pressure acting on the body of the sphere. These rugged flotation spheres are too thick-walled to be reliable sources at SOFAR depths (nominally 2,500 ft.) since they do not tend to fail catastrophically. Tests were also conducted with a thinner walled glass sphere made from a standard 22 liter boiling flask. This sphere was not expected to survive to the depths and pressures desired but deep water tests showed the sphere survived to 1600 meters. The combination of this thinner-walled sphere with the smashing mechanism results in a reliable implosive source at a desired depth and with no associated safety concerns in transport or deployment. During the Ascension Island Experiment, only one sphere implosion was initiated, at a depth of 1600 meters. The implosion signal should be recorded on a temporary Cambridge Univ. OBH. The data will be available soon.

SYNERGY:

An operational synergy experiment was left behind on the island after the airgun shooting. Two new stations were established: a high frequency seismic station and an infrasound station. A level cement pad was poured on top of an old cement antenna anchor that extended over two meters into the ground. An S-6000 seismometer was mounted on the cement pad and buried. A nearby Reftek data acquisition system records continuous 3-component data at 250 samples/second and 24 bits resolution. Data tapes are mailed bi-monthly to LLNL.

In the same part of the island -- near Butt Crater -- an infrasound station was established. This station consists of four sensor elements about 100 meters apart in a tetrahedron formation. Each sensor is an aneroid microbarometer with a manifold allowing for six microporous hose extensions. The data is recorded on a Reftek unit identical to that used for the seismic station. A wind speed and direction indicator will be added to give a total of 6 data channels. These data are recorded to DAT tapes and mailed to LLNL on the same schedule as the seismic data.

The continuous data from the three monitoring technologies will be archived. Selected time periods containing noise and events of interest will be extracted with window lengths that span all three technologies for any known event location. These selected time periods will form a data base that will be analyzed for joint noise statistics and specific joint monitoring analysis studies that use two or more of the technologies to improve overall location or identification capabilities.

CONCLUSIONS AND RECOMMENDATIONS

Calibration of existing hydrophone stations using a ship-towed airgun with precision GPS timing and location provides accurate location of hydrophones at sea. It can also determine the amplitude response and clip levels of the hydrophones provided care is taken to characterize the airgun source and the source pressure pulse is sufficient to saturate the hydrophones at close range. The airgun data taken at Ascension Island will be used to locate and calibrate the three hydrophones that are currently recorded at the pIDC.

The data collected at Ascension Island will allow us to determine if an airgun array is an adequate source for T-phase calibrations at an island station. The primary concern with using an airgun for T-phase signal generation is that the airgun needs to be fired at relatively shallow depths and this does not result in good signal coupling into the SOFAR channel. Luckily, during the short deployment at Ascension Island, there were volcanic events recorded that will allow us to investigate the issues of coupling and of T-phase attenuation across the island even if we determine the airgun sources to be inadequate for T-phase studies.

The use of small explosive sources at the SOFAR channel depth is an ideal way to effectively couple acoustic energy into that channel and provide a good source for T-phase studies. It was clear during the planing phase of this experiment that complying with the required procedures necessary to meet most civilian ship explosives

handling safety plans is costly and problematic, if indeed permission can be obtained at all. Imploding spheres circumvent these problems and provide an acoustic source at SOFAR channel depths. They are clearly useful for experimentally investigating local hydroacoustic propagation and blockages as well as longer range acoustic travel times. It remains to be determined if the signal amplitude and bandwidth from imploding spheres are adequate for T-phase coupling research and calibration.

The synergy experiment is underway and will collect continuous data from hydroacoustic, seismic and infrasound stations on or near Ascension Island for the next two years. The data collected will provide a large database of background noise and events for the three monitoring technologies.

Hydroacoustic monitoring research has started to focus on calibration and ground truth issues to try to improve event location and identification, as seismic monitoring has effectively done. The data collected at Ascension Island will be a rich source of ground truth data for the topics summarized above and will help determine how to best conduct future hydroacoustic and T-phase calibrations while collecting hydroacoustic ground truth data for the knowledge base.

REFERENCES

Boro, C. and P.E. Harben, 1999, Sphere Implosion Initiation Device, Record of Invention IL-10551, University of California, LLNL Patent Group.

Isaacs, J.D. and Maxwell, A.E., 1952, The Ball-breaker, A Deep Water Bottom Signalling Device, J. Marine Res., V 11, pp. 63-68.

Minshull, T. A.,1999, Cruise Report for the RRS James Clark Ross 42: A Seismic Tomographic and Hydroacoustic Study of Ascension Island, Univ. of Southampton School of Earth Science Report, Southampton Oceanography Center, European Way, Southampton SO14 3ZH.

Orr, M. and M. Schoenberg, 1976, Acoustic Signatures From Deep Water Implosions of Spherical Cavities, J. Acoust. Soc., V 59, pp. 1155-1159.

Sauter, A., L. Dorman, E. Canuteson, 1996, Development of a Seismo/Acoustic Implosive Source, Am. Geophys. Union, Proc. fall meeting.

ACKNOWLEDGEMENTS

A large number of individuals and institutions made the Ascension Island Experiment possible. Special thanks to Tim Minshull, now at Southampton University, England for planning and coordinating the ship use, the airgun configuration and operation, and the overall specifics of the cruise. Thanks to Vicki Childers and John Brozena from the Naval Research Laboratory for partial financial support of the cruise and for assistance in the field. Thanks to Marta Galindo and Martin Lawrence of the PTS for financial support for the temporary OBH deployments and for field assistance. Thanks to Rod Whittaker and Tom Sandoval of LANL for siting and installation of the infrasound station for the synergy experiment. Thanks to Jay Pulli and Ted Farrell of BBN Inc. for assistance with MILS data quality during the cruise, collaboration with imploding sphere investigations, and for the use of one figure in this report. Thanks to Crispin Hollinshead of Scripps for field support and Jeff Hanson of SAIC for insightful suggestions during the planning phase of the experiment. Finally, thanks to Jenny Hollfelder of LLNL for assistance with ship track file corrections and report figures.



Figure 1) The location of Ascension Island is shown by the red dot. Ascension Island is one of the most remote islands in the Atlantic Ocean.



Figure 2) The J.C. Ross was the sea based platform for the airgun array. The ship is an icebreaker class oceanographic research vessel commissioned in the early 1990's.

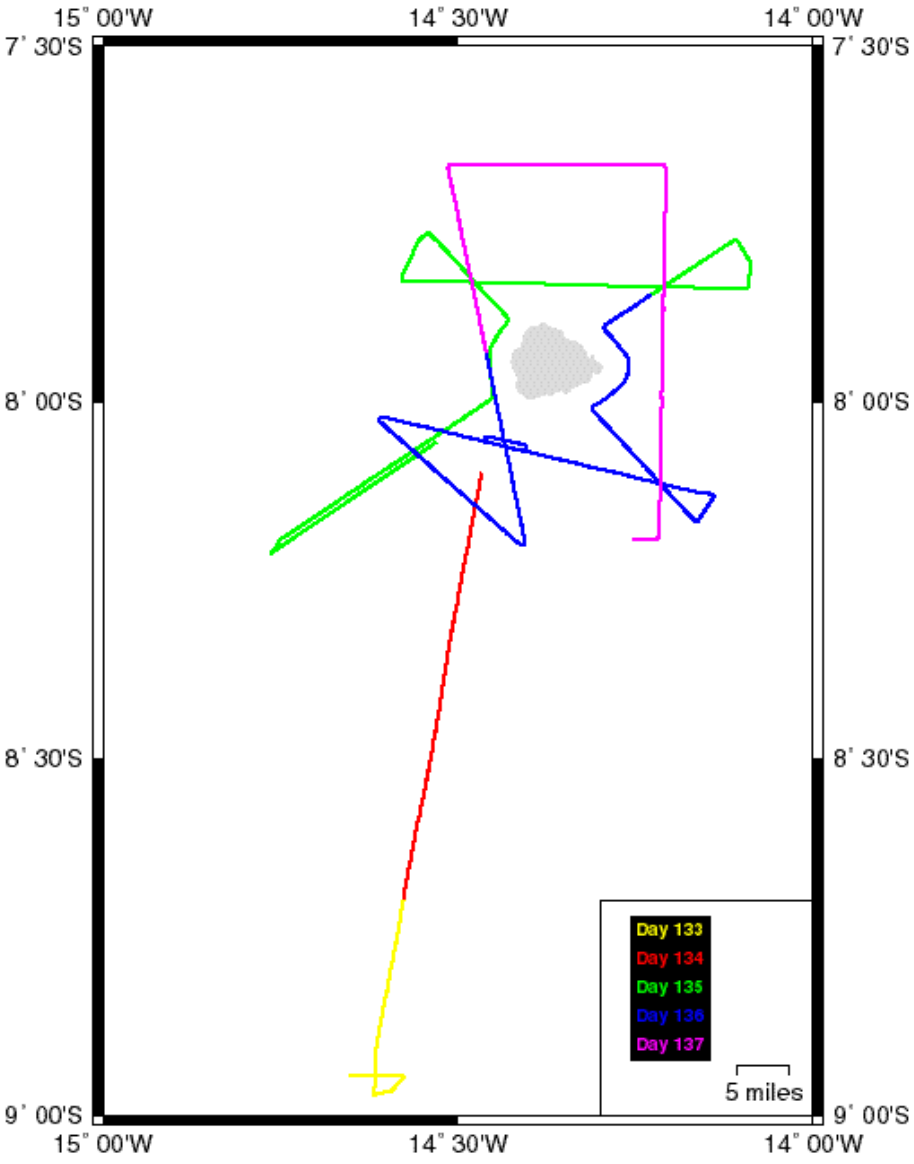


Figure 3) The ship track of the J.C. Ross during the Ascension Island experiment color coded by day. Note that on day 134 the track abruptly ends. This coincides with the end of the single airgun firing followed by a pickup of crew at Ascension Island. The track resumes on day 135 outbound on the southwest extension of the seismic line to 45 km followed by a return on the same track.

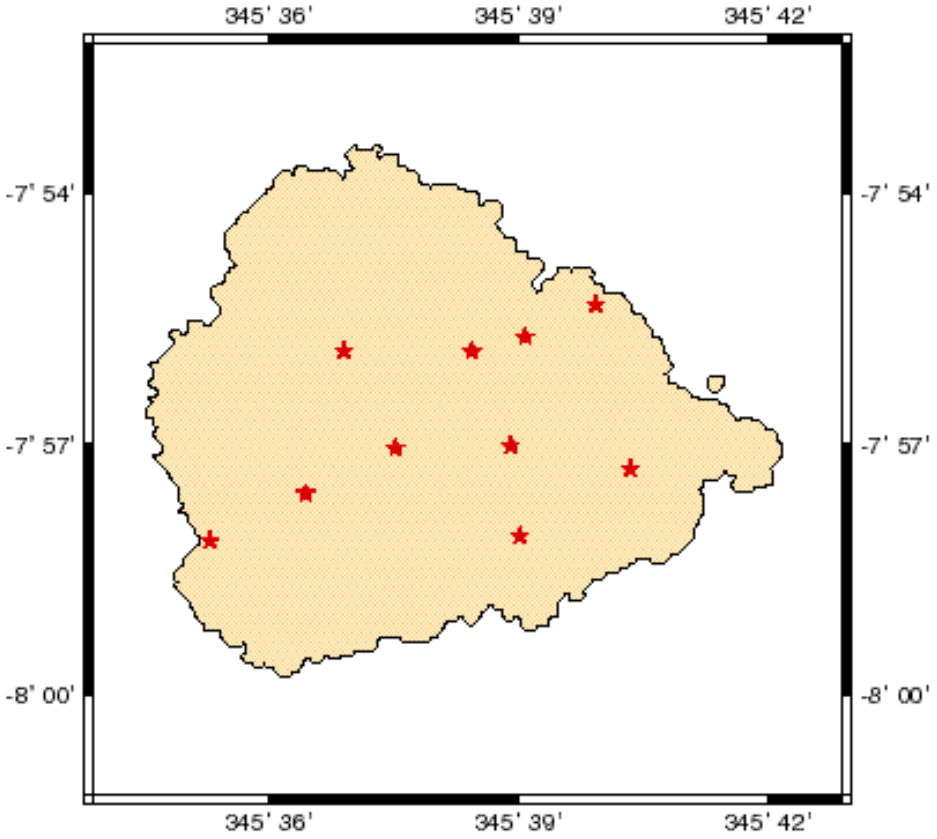


Figure 4) The location of the ten temporary seismic stations on Ascension Island. Note the southwest - northeast trending line of stations that coincide with the extended ship track lines.

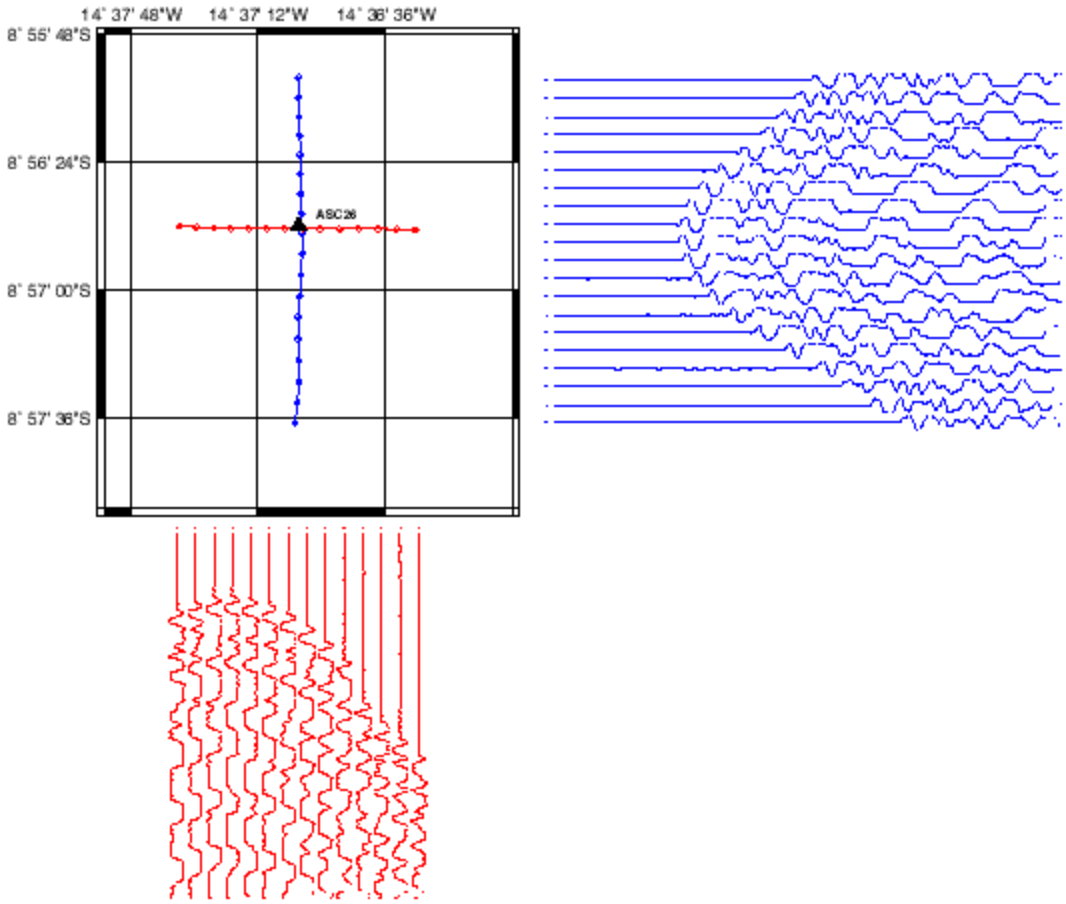


Figure 5) The ship tracks near the nominal location of ASC26 are shown with each shotpoint indicated by an circle. The associated waveforms recorded by ASC26 for each shot are also shown. Note that the data agrees well with the nominal location on the north-south track but the east-wast location of ASC26 is west of the location indicated by the data.

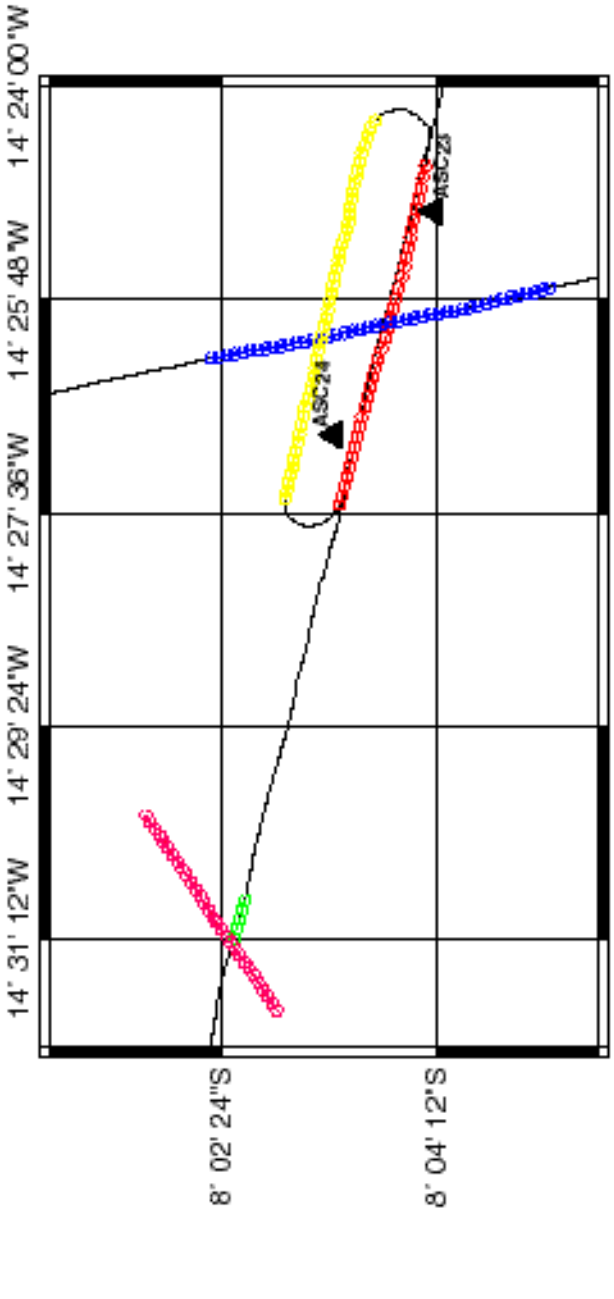


Figure 6) The ship tracks that will be used in the calibration of ASC23 and ASC24 are shown color coded according to day as shown on the ship track file in Figure 3. Note that the tracks displayed to the west are the tracks over the Scripps OBH that will be used to characterize the source.

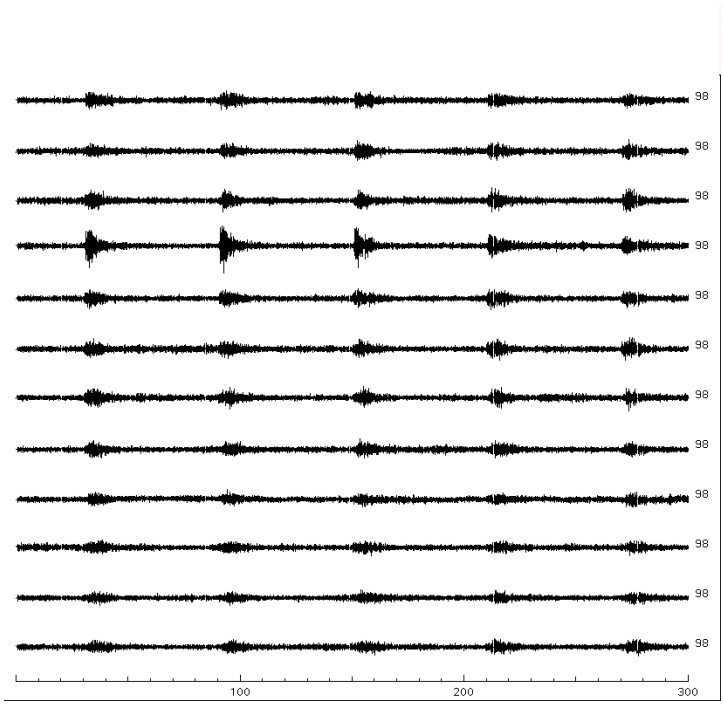


Figure 7) One hour of recordings from seismic station SBC during full array airgun shootings.

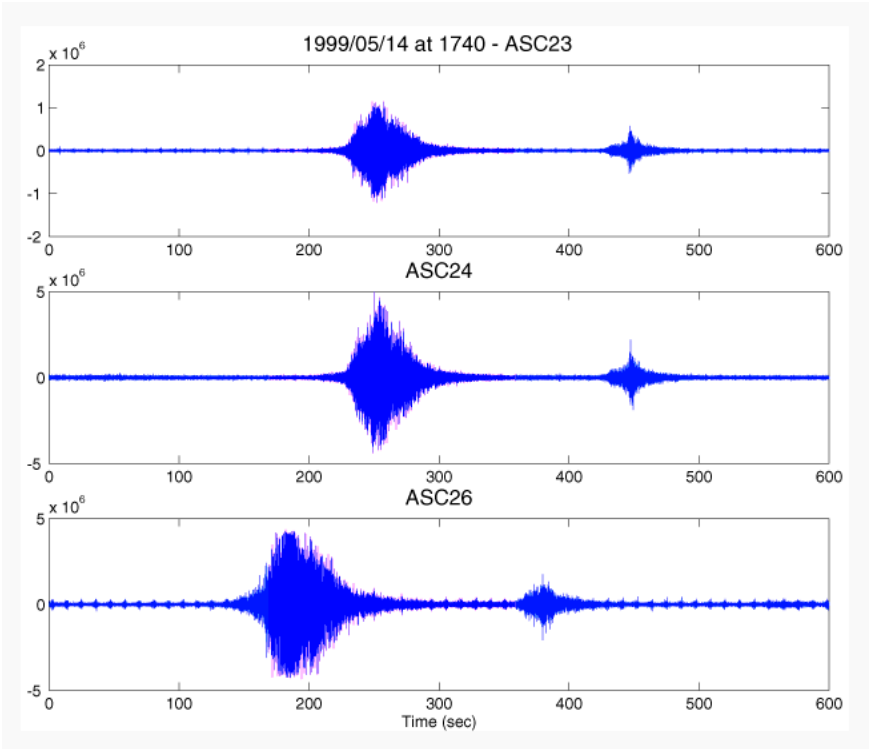


Figure 8) An apparent volcanic event recorded by the MILS hydrophones.

CONVERTED T PHASES RECORDED ON HAWAII FROM POLYNESIAN NUCLEAR TESTS

Emile A. Okal, Department of Geological Sciences, Northwestern University

Sponsored by U. S. Department of Defense
Defense Threat Reduction Agency
Grant No. DSWAOI-98-1-0007

ABSTRACT

We present a preliminary study of T waves from Polynesian nuclear tests at Mururoa, recorded on digital stations of the Hawaii Volcano Observatory network, following their conversion to seismic waves at the southern shore of the Island of Hawaii, and subsequent propagation to the recording stations. We show that seismograms are composed of several packets, which can be interpreted as resulting from T ∅ P and T ∅ S conversions, and which feature distinct spectral characteristics. At Station HUL, located 7 km away from the
conversion point, the P ∅ T wavetrain can be further decomposed into several arrivals corresponding to propagation through the various crustal layers. The energy of the P ∅ T wave packet is peaked at 5-7 Hz. The
S ∅ T arrival is generally of larger amplitude, but peaked at only 3 Hz. It is followed by low-frequency energy (between 2 and 4 Hz) propagating inside the island structure as a surface or guided wave.
As the station is moved inland, the relative importance of the several wave packets changes; a prominent shadow for T ∅ P is found at 8-12 km from the shore. The T ∅ P conversion re-emerges as a fast high-frequency
(6 Hz) arrival at 18 km. This pattern is generally verified at other locations along the coast of the island, but its details are affected by the local crustal structure, which reflects the three-dimensional volcanic
structure under the island. In a favorable case, propagation in deep, low-attenuation layers results in a clear record of 3- to 4-Hz energy on the Northeastern flank of Mauna Kea, 76 km from the shoreline. Finally, we verified that these results are generally robust and affected only moderately by a change of location of the source inside Mururoa Atoll.

Key Words: T waves, acoustic-to-seismic conversion, Polynesian nuclear tests

HYDROACOUSTIC MODEL VALIDATION AND THE SITE CALIBRATION EXPERIMENT AT ASCENSION ISLAND

Gregory J. Orris, Laurie T. Fialkowski, John S. Perkins, Naval Research Laboratory

Sponsored by U.S. Department of Energy
Office of Non-proliferation and National Security
Office of Research and Development
Contract No. DE-A101-95IS20011

ABSTRACT

The ability of any given hydrophone of a monitoring station to successfully detect a Comprehensive Nuclear-Test-Ban Treaty violation will depend to a large extent on the acoustics of two different scales; global and local. At global distances, acoustic propagation within the ocean sound channel is dominated by the effects of acoustic modal refraction/reflection from variances in the oceanic sound channel, i.e., environmental effects on the local sound speed. On smaller scales, in particular close to the receiver, the local geo-acoustic environment will ultimately determine whether a propagation path between source and receiver exists: However, quite often this type of environmental data is not known to the precision and/or detail necessary to calculate accurate acoustic blockage charts. Further complicating matters is the deep sediment penetration of the relatively low-frequency (10 Hz) content of probable source characteristics. We address the problems and their ramifications in site calibration studies caused by the limitations of the environmental databases. As a specific case we consider the acoustic blockage for the hydrophones in the vicinity of Ascension Island that are to be used as the basis of one of the International Data Centre's monitoring sites. A regional/local acoustic propagation model that appropriately accounts for local variations in the environment is employed in this investigation to calibrate each hydrophone as a function of frequency and azimuth. This model is then compared to a representative sample of the data collected from the recent calibration experiment conducted near Ascension Island.

Key Words: hydroacoustic monitoring, hydrophone, acoustics

CHARACTERIZATION AND UTILIZATION OF HYDROACOUSTIC SIGNALS REFLECTED FROM CONTINENTS AND BATHYMETRIC FEATURES

Jay J. Pulli, Ted Farrell, & Rob Gibson
GTE/BBN Technologies, 1300 N 17th St, Suite 1200, Arlington, VA 22209

Sponsored by U.S. Defense Threat Reduction Agency
Contract No. DSWA01-97-C-0164

ABSTRACT

The objective of this research is to establish an understanding of the hydroacoustic signals that reflect from continents and bathymetric features so that these signals may be utilized as part of the hydroacoustic component of CTBT monitoring. This understanding is important because long-range propagation modeling predicts that some direct source-receiver paths are either blocked by bathymetric features or do not exist because of horizontal refraction. In these cases, reflections may be the only observable signal from a source, and may provide important information for localization and source type estimation.

In our research we have identified, acquired, and analyzed numerous historical and contemporary databases of hydroacoustic signals for sources with known origins. These include the Chase ship scuttling exercises in the 1960's and 70's; French nuclear tests in the southwest Pacific; the Japanese crustal exploration explosions in 1996; and signals generated during the May 1999 Ascension Island experiment. Results to date indicate that hydroacoustic reflections can be consistently seen at specific receivers for repeated events in a given source area. For example, the Chase explosions off the US eastern seaboard produced signals that reflected off the Guianna Plateau off the coast of South America and were recorded at Ascension Island. The locations of these reflecting features can be determined either from their arrival times at multiple receivers or by beamforming hydroacoustic array data (when available) and combining the back azimuth estimation with the time difference between the direct and reflected signals. Reflections that are 30 dB lower in power than the direct arrivals can be seen from the Japanese exploration explosions recorded at WAKE, but only for the largest events. For the smaller events with lower SNR, these reflections are below the ambient noise and hence not observed.

Information about the source also appears to be preserved in the reflected signals. For example, both the direct and reflected signals from the Chase 22 explosion recorded at Ascension show spectral scalloping in the band 5-30 Hz, unlike the signals from the nearby Chase 21 explosion, which have smoother spectra.

Key Words: Hydroacoustics, reflections, long-range propagation, bearing estimation

OBJECTIVE

The objective of this research is to establish an understanding of the hydroacoustic signals that reflect from continents and bathymetric features so that these signals may be utilized as part of the hydroacoustic component of CTBT monitoring. This understanding is important because long-range propagation modeling predicts that some direct source-receiver paths are either blocked by bathymetric features or do not exist because of horizontal refraction. In these cases, reflections may be the only observable signal from a source, and may provide important information for localization and source type estimation.

RESEARCH ACCOMPLISHED

Databases Examined

We have examined numerous historical and contemporary databases of hydroacoustic signals for sources with known origins. Historical data were provided to us by LLNL and AFTAC, and include:

- The Chase ship scuttling explosions of the 1960's and 70's which occurred in both the Atlantic and Pacific Oceans. These include Chase 2, 3, 4, 5, 7, 12, 16, 17, 18, 19, 20, 21, & 22.
- Nuclear tests in the Aleutians, such as Longshot in 1965 and Milrow in 1969.
- The IITRI explosions conducted off the coast of California in 1968.
- French nuclear tests conducted in the south Pacific from 1971-78.

These historical databases have the advantage that the sources were large and thus produced large signals, but in many cases the direct arrivals are clipped because of the limited dynamic range of the old analog recording systems. In addition, station and origin information is often difficult to track down for these events. Instrument calibration factors are generally not available. The authors would appreciate hearing from anyone with information or references on the Chase explosions.

Contemporary databases examined include:

- The French nuclear tests conducted at Mururoa during 1996-96.
- The Japanese ocean crustal exploration explosions in September 1996
- The Ascension Island airgun experiment of May 1999

These contemporary databases were obtained online at the PIDC and AFTAC via AutoDRM requests.

Examples

Because hydroacoustic signals propagate at relatively low speeds (~1.49 km/sec), can propagate for long distances, and still retain high-frequency information (on the order of 100 Hz), data streams that include reflections can be very large (on the order of an hour). A convenient way of examining and processing this data is to transform the time series to an envelope. The data are first rectified, then smoothed, and then resampled to a frequency on the order of the length of the smoothing window. Smoothing windows are typically 1-second long. The data can also be bandpass filtered before processing to examine the relative spectral contribution between the direct and reflected signals. Shipping noise and electrical interference often contaminate the signals, and bandpass filtering is often necessary to mitigate these effects.

Figure 1 shows waveform data for the IITRI-1 explosion of February 16, 1968 recorded at the WAKE Island array. This is an example of one of the better recordings from the historical database; the signals are not clipped or saturated, and there is little electrical interference. This was a 12-ton TNT-equivalent explosion detonated at a depth of 1825 ft near Long Beach, CA (Kos and Kennedy, 1969 report on the IITRI program, though not this particular test). The figure shows both the full waveform recording and the processed waveform envelope. Numerous reflections after the first arrival can be seen in the envelope; prominent reflections arrive approximately 2 minutes and 16 minutes after the direct.

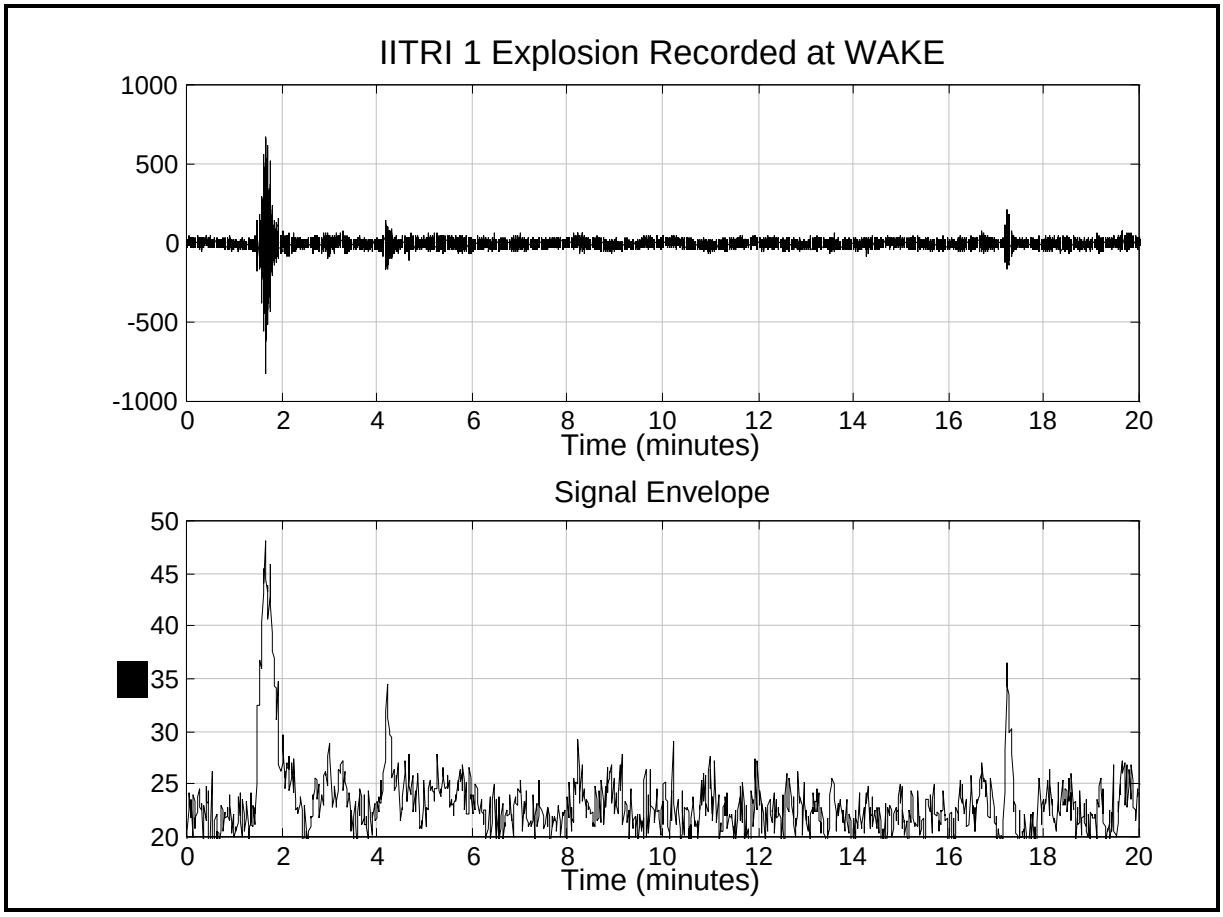


Figure 1. The IITRI-1 explosion of February 16, 1968 off Long Beach, CA recorded at WAKE Island. The full waveform recording at 200 s/sec is shown at the top. The signal is then filtered, rectified, integrated over a 1-second smoothing window, resampled at 1 s/sec, and plotted in dB at the bottom. Numerous reflections after the first arrival can be seen; prominent reflections arrive approximately 2 minutes and 15 minutes after the direct.

Figure 2 is an example from contemporary databases. The data are from one of the 138 marine seismic exploration explosions conducted off Japan in September 1996 (Brumbaugh and Le Bras, 1998). This particular explosion (Event 58) had a yield of 400 kg, and no further explosions were detonated for 1 1/2 hours (other explosions in this series were detonated every 15 minutes). Thus Event 58 provides an opportunity to examine potential reflections without having to account for additional sources which may be detonated at times on the order of the reflection delays. *Figure 2* shows the signal envelope at WAKE Island. The large direct arrival is followed by 3 arrivals within about 3 minutes and a prominent reflection 25 minutes after the direct. The amplitude of this reflection is 30 dB below that of the direct, which means that the signal-to-noise ratio must be at least 30 dB for this late reflection to be seen. Indeed, for most of the Japanese exploration explosions, which are either 20 or 40 kg (rather than 400), the signal-to-noise ratio is too low for this late reflection to show up.

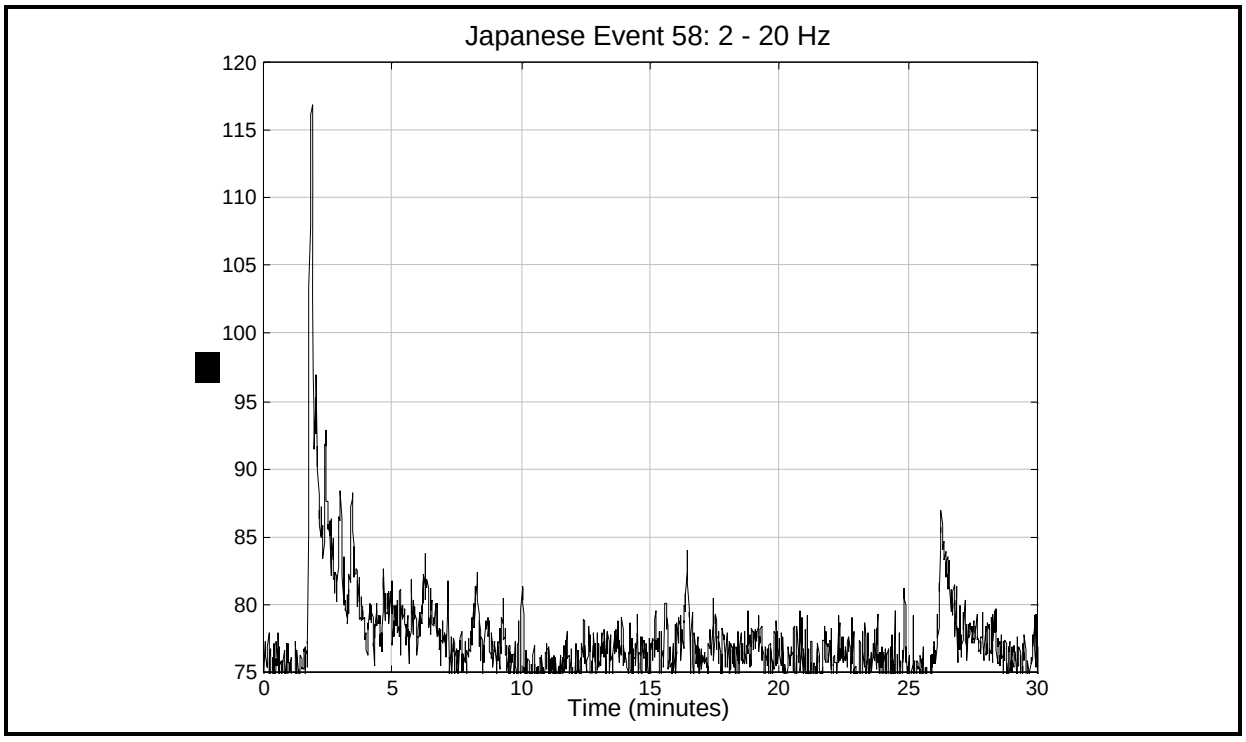


Figure 2. Envelope of the WAKE Island recording of the Japanese marine exploration explosion on September 8, 1996. The reflection, which is observed 25 minutes after the direct, is approximately 30 dB smaller than the direct and thus is only, observed for the largest of these explosions.

Localization of a Bathymetric Reflector - the Guiana Plateau

In order to gain an understanding of the nature of hydroacoustic reflections, we must be able localize and identify the bathymetric feature responsible for the signals. If enough recordings of the reflected signal are available over a range of azimuths, then we can time and locate the source, much in the same way as we locate earthquakes with a network of seismometers. However, hydroacoustic stations are sparse in distribution and the scattering properties of the bathymetric feature may not be azimuthally uniform. Reflections may often only be observed at preferential azimuths. An alternative method is possible when we have an array of recordings and can take advantage of their directional response to determine the back azimuth of the arriving signal. This back azimuth, when combined with the time difference of arrival between the direct and reflected signals, will provide both a bearing and range for localization. We now illustrate this procedure with recordings of the Chase 21 and Chase 22 explosions, detonated off the coast of New Jersey and recorded at the Ascension Island array.

Figure 3 shows the envelopes of the recordings at Ascension for the two events. The signals consist of a strong direct arrival and a prominent reflected arrival (or set of arrivals) about 8 minutes later. Since recordings are available for five array elements (and the array geometry is know), we can window each arrival and beamform (stack) the envelopes based on the theoretical travel time differences between array elements. In this case, we used a propagation velocity of 1.49 km/sec. *Figure 4* shows the beam amplitudes as a function of azimuth for the direct and reflected arrivals. The back azimuth of the direct arrivals is 319 deg. This matches the back azimuth computed from the known source location and provides a point of confirmation of the method. The back azimuth of the reflected arrival is 290 deg. The travel time from the source origin to the measured reflected arrival defines a travel distance and thus an ellipse of possible locations of the reflecting features. When this ellipse is combined with the back azimuth projection, we find that this intersection is at the site of the Guiana Plateau off the coast of Brazil.

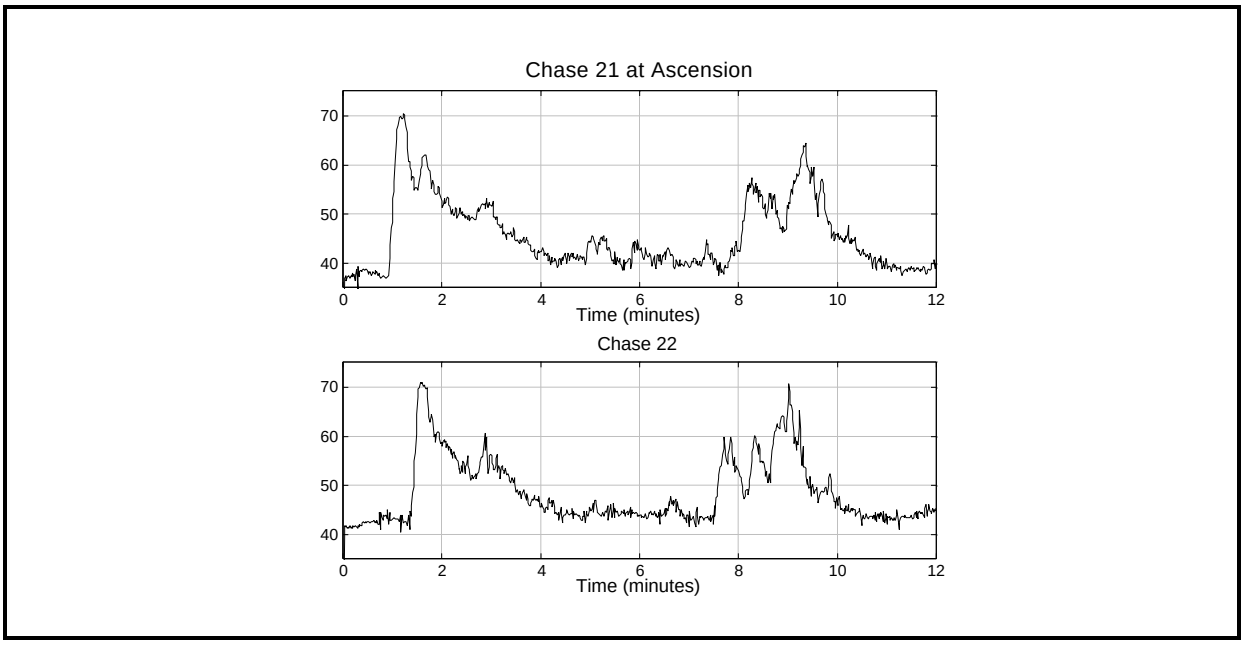


Figure 3. Envelope of the Ascension Island recording of the Chase 21 and Chase 22 ship scuttling explosions off the coast of New Jersey. The signals contain both a direct arrival and a strong reflected arrival about 8 minutes later.

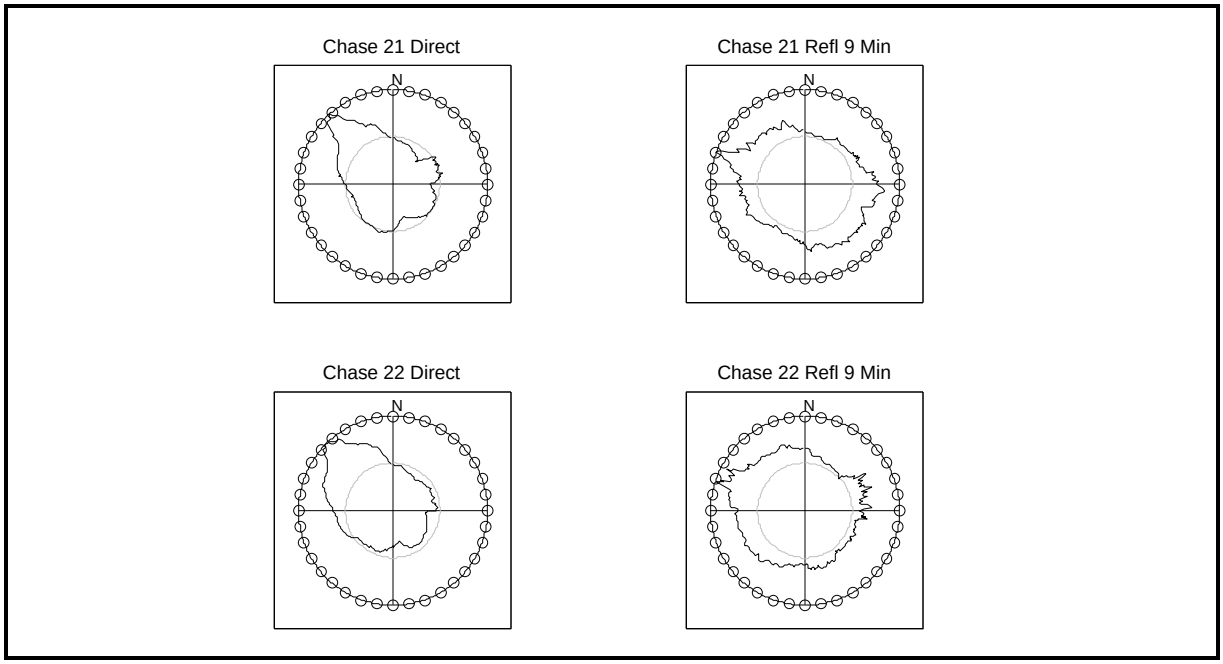


Figure 4. Bearing scans at the Ascension Island array for the Chase21 (top) and Chase 22 (bottom) explosions off the coast of New Jersey. For both recordings, the back azimuth computed for the direct arrival (319 deg) points to the known source locations. For the reflected arrivals 9 minutes later, the back azimuth (290 deg) points to the Guiana Plateau.

Spectral Characteristics of Reflected Hydroacoustic Signals

One of the reasons why an understanding of hydroacoustic reflections is important is that in some circumstances, these reflections may be the only observed signal. For example, the direct signal may be blocked by bathymetry or its ray path may be refracted away from a receiving station. The localization procedure described above provides us with a means of identifying and utilizing the reflected ray path, but an additional question is "what information about the source is contained in the reflected signals"?

Let us first examine the spectra of the arrivals at WAKE Island for the IITRI underwater explosion first shown *in Figure 1*. In this example, both the direct and reflected arrivals are clear and simple, unlike the reflected arrivals for the Chase explosions shown earlier. *Figure 5* shows the spectra of the direct arrival and the reflected arrival observed some 16 minutes later. Modulation of the spectra are caused by the interference of the primary explosion with the signals generated by the bubble pulses. Although the peaks and valleys of each spectra do not always track identically, it is apparent that the spectra of both arrivals are indicative of an underwater explosion. The differences in the spectra may be explained by the additional interference effect of complex reflection at the scattering bathymetric feature.

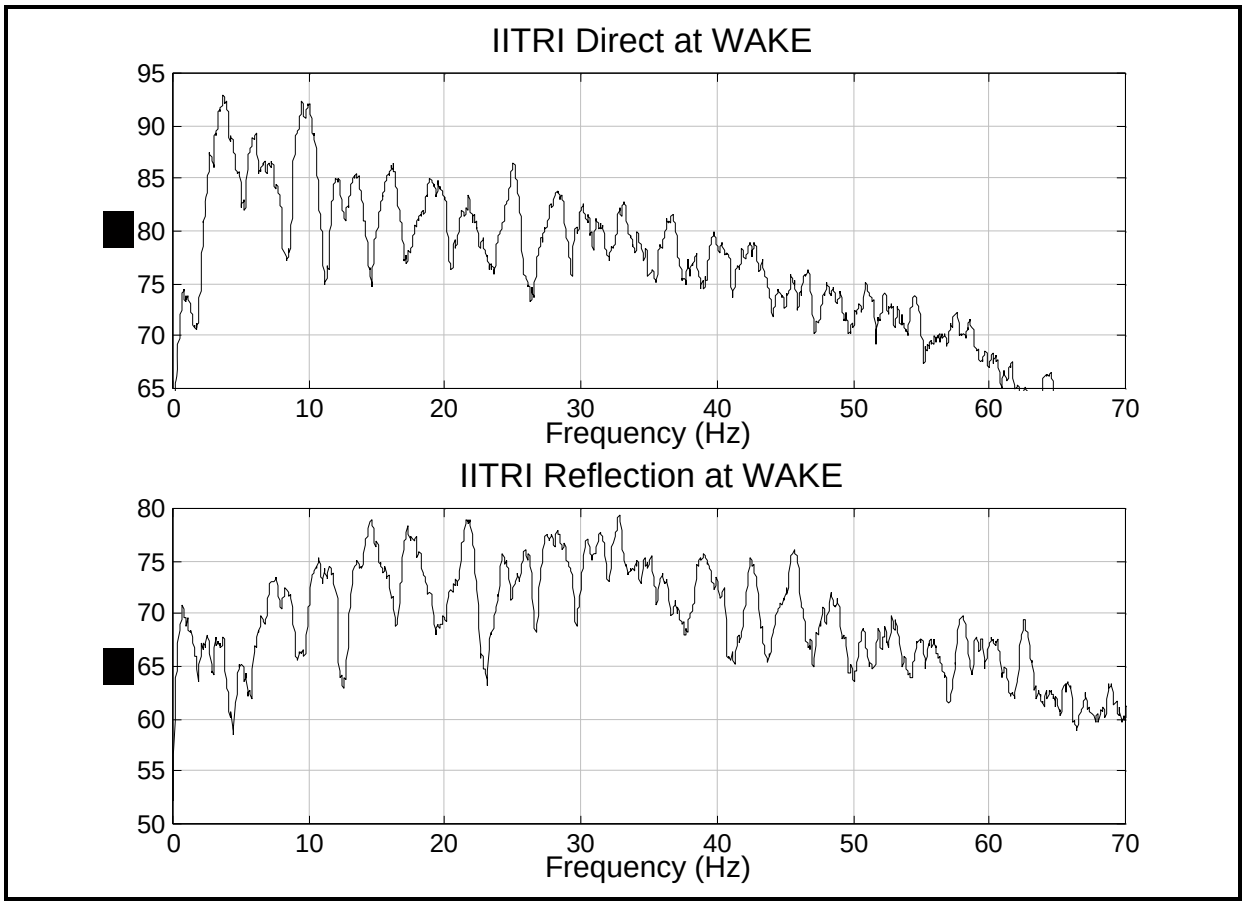


Figure 5. Spectra of the direct (top) and reflected arrival at WAKE Island for the IITRI underwater explosion off the coast of Long Beach, CA.

Figure 6 shows another example, this time for the Chase 22 explosion recorded at Ascension Island. Here we use the time-frequency representation to illustrate the similarity of spectral features because the arrivals are not

cleanly separated, and in the case of the reflected arrival, actually consists of three separate signals. In this case, the spectral modulation is remarkably similar for the arrivals. Additionally, note that the spectra of the scattered energy after the direct arrival and between the reflected arrivals also maintain these same spectral features.

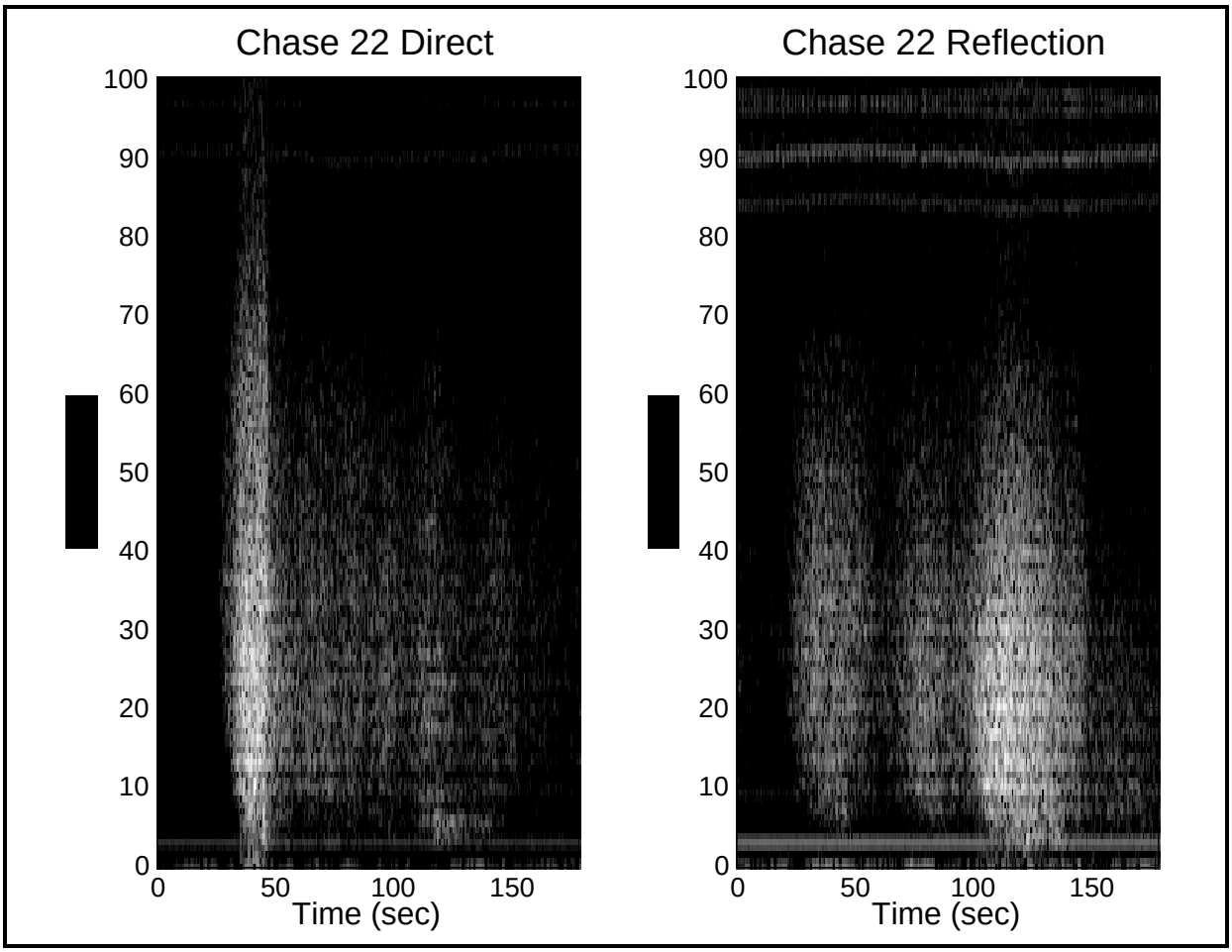


Figure 6. Time-frequency diagrams of the direct and reflected signals from the Chase 22 explosion recorded at Ascension Island. Note the similarity in spectral modulation between the two arrivals, as well as the scattered energy after the direct arrival and between the three reflected arrivals.

CONCLUSIONS AND RECOMMENDATIONS

We have examined a number of historical and contemporary recordings of underwater explosions as a means of understanding the nature of hydroacoustic reflections. We have found that reflections are observed for many source-receiver combinations, and that these reflections are visible for repeated events in the same source area. When an array recording is available, beamforming can be used to estimate the back azimuth of the arrival. This back azimuth, when combined with the travel time ellipse defined by the source and receiver locations defines a point on the globe that can be associated with the source of the reflection. An examination of the bathymetry at this location provides information on the likely features, which produce the reflection. Additionally we have found that the spectral characteristics of the source can be seen in both the direct and reflected arrivals. Our next step is to develop a simple scattering model to further explain the reflected arrivals, which will be used to predict where in a particular ocean reflected signals are likely to be produced.

REFERENCES

Brumbaugh, D.A. and R.J. Le Bras (1998), Hydroacoustic signals from a ground-truth data set of marine explosions, SAIC Report No. 98/3008, 27 pp.

Kos, D.W. and J.E. Kennedy (1969), Development of a system to deliver and detonate large explosive charges undersea, IIT Research Institute Report J6034-25, 97 pp.

MODELING HYDROACOUSTIC WAVEFORM ENVELOPES: IMPLICATIONS FOR TEST BAN TREATY MONITORING

Jay J. Pulli, Robert Bieri, and Eugene Dorfman[†]
GTE/BBN Technologies, 1300 N 17th St, Suite 1200, Arlington, VA 22209
[†]GTE/BBN Technologies, 70 Fawcett St, Cambridge, MA 02140

Sponsored by U.S. Department of Energy
Office of Nonproliferation and National Security
Office of Research and Development

Subcontract Number B344846

ABSTRACT

Test ban treaty monitoring in the world's oceans is aided by the fact that the ocean environment is known to a degree of detail that is much finer than in the solid earth. Raypaths, traveltimes, and amplitudes can thus be accurately predicted. But additional information about the source and path may be contained in the received waveform envelope. This modeling effort has been undertaken to determine whether or not it is practical to extract information such as source depth and type from the waveform envelope, and how this may be used in a CTBT context.

To compute the waveform envelopes, a truncated set of normal modes is summed over a finite bandwidth to obtain an approximate time series. The normal mode code KRAKEN is used to compute modal shapes and wavenumbers for a set of frequencies, and the time series is then recovered using the Fast Fourier Transform. The model has been used to illustrate the factors that contribute to the shape of the received hydroacoustic waveform envelope, including the locations of the source and receiver with respect to the sound channel axis, the bottom conditions, and the bathymetry.

As expected, the largest amplitude is produced when both the source and receiver are in the middle of the sound channel axis. In this situation, path bathymetry determines the number of trapped (low loss) modes. As expected for typical SOFAR sound speed profiles, a buildup of signal energy with time is predicted, culminating in the large mode 1 arrival (this signal shape is often called "classic SOFAR"). Higher order modes are increasingly important as the source and/or receiver are moved away from the SOFAR axis. Bottom conditions are only an issue for the case of a bottom mounted hydrophone.

Modeling results are presented for a number of events, including the Chase21 ship scuttling explosion on June 25, 1970 off the New Jersey coast; nuclear explosions on Mururoa Atoll; and Japanese exploration explosions.

Key Words: Hydroacoustics, long-range propagation, modeling, normal modes

OBJECTIVE

Test ban treaty monitoring in the world's oceans is aided by the fact that the ocean environment is known to a degree of detail that is much finer than in the solid earth. Raypaths, traveltimes, and amplitudes can thus be accurately predicted. But additional information about the source and path may be contained in the received waveform envelope. This modeling effort has been undertaken to determine whether or not it is practical to extract information such as source depth and type from the waveform envelope, and how this may be used in a CTBT context. These capabilities have now been integrated into the program HydroCAM, which has been developed under DOE funding (Farrell and LePage, 1996) to estimate the performance of hydroacoustic networks for the CTBT. In this study, we are interested in the gross features of the waveform envelope, such as its duration, rise time, and shape (skewness). Ranges of interest are on the order of thousands of kilometers; frequencies are less than 100 Hz.

RESEARCH ACCOMPLISHED

Theory

The long-range propagation of sound in the ocean is usually described in terms of normal mode theory (Brekhovskikh and Lysanov, 1991). In normal mode theory, the far field pressure p at a range r and depth z_r due to a point source located at (r=0, z=z_s) is given by the coherent mode sum

$$p(t,r,z) = \sum_{n=1}^{\infty} p_n(t,r,z)$$

Modal pressure $p_n(t,r,z)$ is given by

$$p_n(t,r,z) = \sqrt{\frac{2\pi}{k_n r}}\, e^{i\pi/4} \int_{-\infty}^{\infty} P_s(\omega)\Psi_n(\omega,z_s)\Psi_n(\omega,z_r) e^{i\omega t - ik_n(\omega)r}\, d\omega$$

where Ψ_n and k_n are the shape and wavenumber of mode n, respectively, and $P_s(\omega)$ is the source spectrum. For a point source we have

$$p_n(t,r,z) = \frac{1}{2\pi}\,\frac{1}{\rho(z_s)\sqrt{8\pi k_n r}}\, e^{i\pi/4} \int_{-\infty}^{\infty} P_s(\omega)\Psi_n(\omega,z_s)\Psi_n(\omega,z_r) e^{i\omega t - ik_n(\omega)r}\, d\omega$$

The corresponding pressure level PL is

$$PL = 20\log\frac{\langle p^2 \rangle}{p_{ref}^2}$$

In long range propagation, environmental fluctuations (sound speed changes) result in pressure level fluctuations around the mean value PL_0. In this case, the average received pressure and mean pressure level are often modeled as an incoherent sum, which is

$$p_{RMS}^2 = \sum_{n=1}^{\infty} p_{n,RMS}^2(\omega,r,z)$$

Normal mode shapes and wavenumbers were computed using the program KRAKEN (Porter, 1995) for a frequency band of 1-100 Hz and a frequency increment of 1 Hz. To increase the efficiency of the calculation, we use a grid of modal parameters created once using the program KRAKEN (Porter, 1995); these modal parameters are stored and used for all subsequent calculations. We also use interpolation, since the modal wavenumbers are generally smooth functions of frequency. These are computed and stored for a sparse grid of frequencies, then interpolated to a denser frequency grid to prevent aliasing.

Overview of the Model

The computation of the waveform envelope can be broken down into nine steps (see *Figure 1*):

- The first step is to calculate the path based on the source and receiver locations. This is accomplished within the framework of HydroCAM using the bent ray approach (refraction included)
- Next the modal wavenumbers are extracted
- Next the time interval of the waveform envelope is computed (since we do not want the entire time series from the origin time to the receiver time)
- Transfer functions for each of the modes are then calculated
- Each transfer function is multiplied by the source spectrum
- Then we extract the mode shape at the source and receiver
- Modal amplitudes are then used to scale each modal transfer function
- An inverse Fourier transform is taken to compute the modal time series
- Finally the modes are summed to compute the waveform envelope

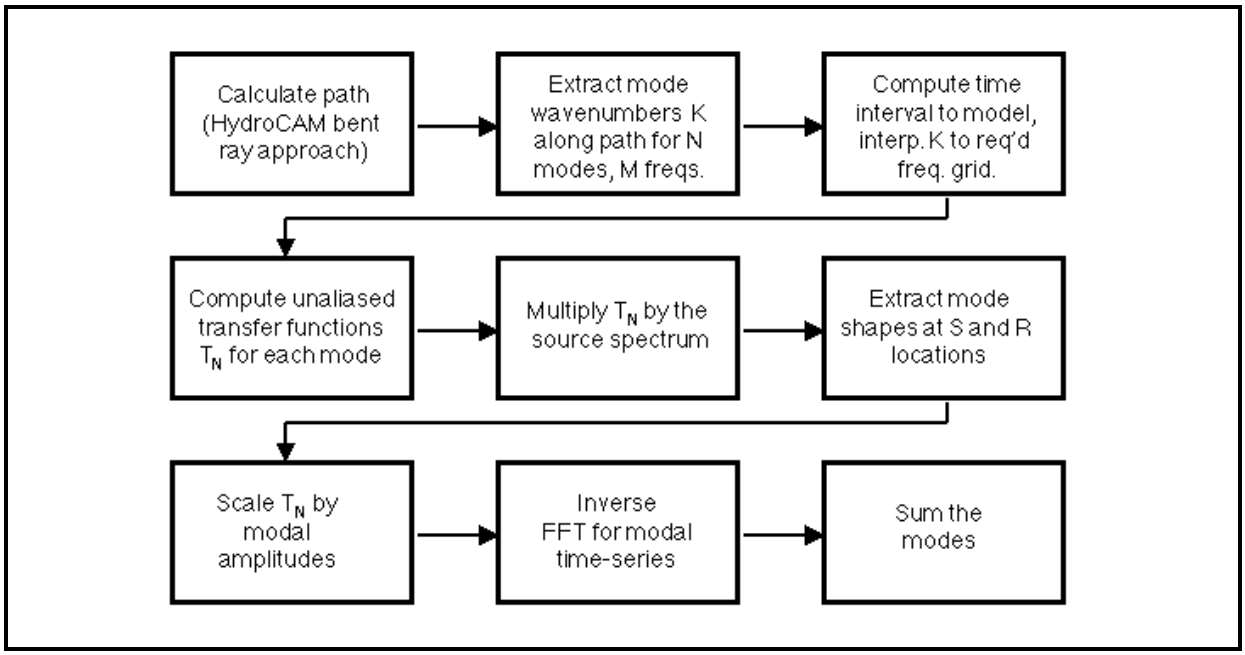


Figure 1. Flowchart of the waveform envelope modeling procedure.

Running the Model

The waveform modeling is accomplished from within the framework of HydroCAM and thus uses the same graphical user interface structure. The first interface is that of the Environment Form, shown in *Figure 2*. Here we select the bathymetric database to be used, the sound speed profile database (tied to the season), and the bottom conditions.

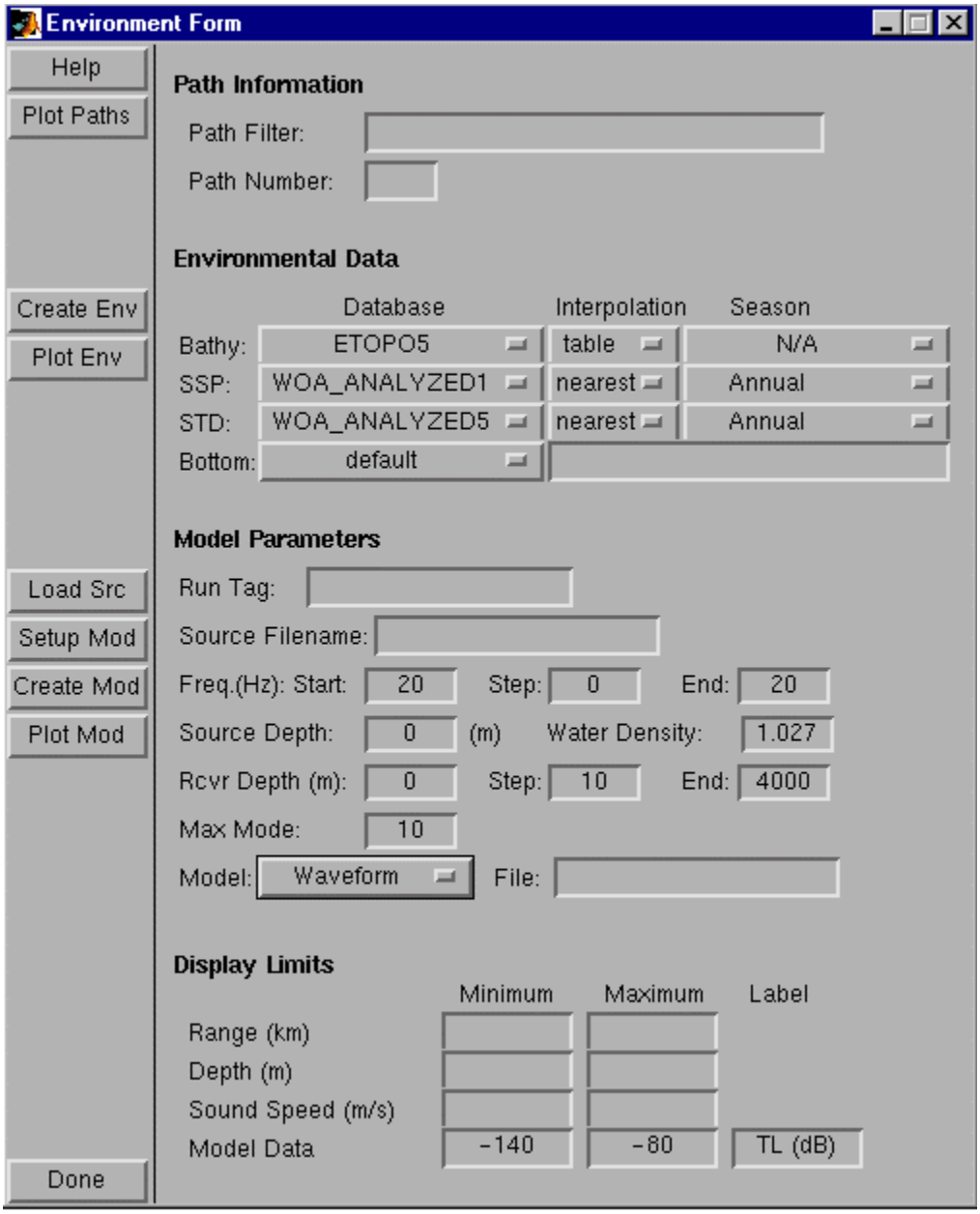


Figure 2. The path environment form used to select the databases and to create the environment (bathymetry and sound speed).

We then switch to the Kraken Parameter form, shown in *Figure 3*. This is where we set type of interpolation for the sound speed profiles, the surface and bottom conditions, the attenuation, phase speed limits, and maximum range.

When these are loaded, we return to the first panel (*Figure 2*) to load the source parameters, source depth, and receiver depth. Calculations are then begun. Results are saved in CSS Version 3 format, controlled under the Waveform Plot panel, shown in *Figure 4*. The user can specify origin information (times, station code, database prefix) as well as the frequency range and number of modes. Modes are saved separately and as a sum (envelope).

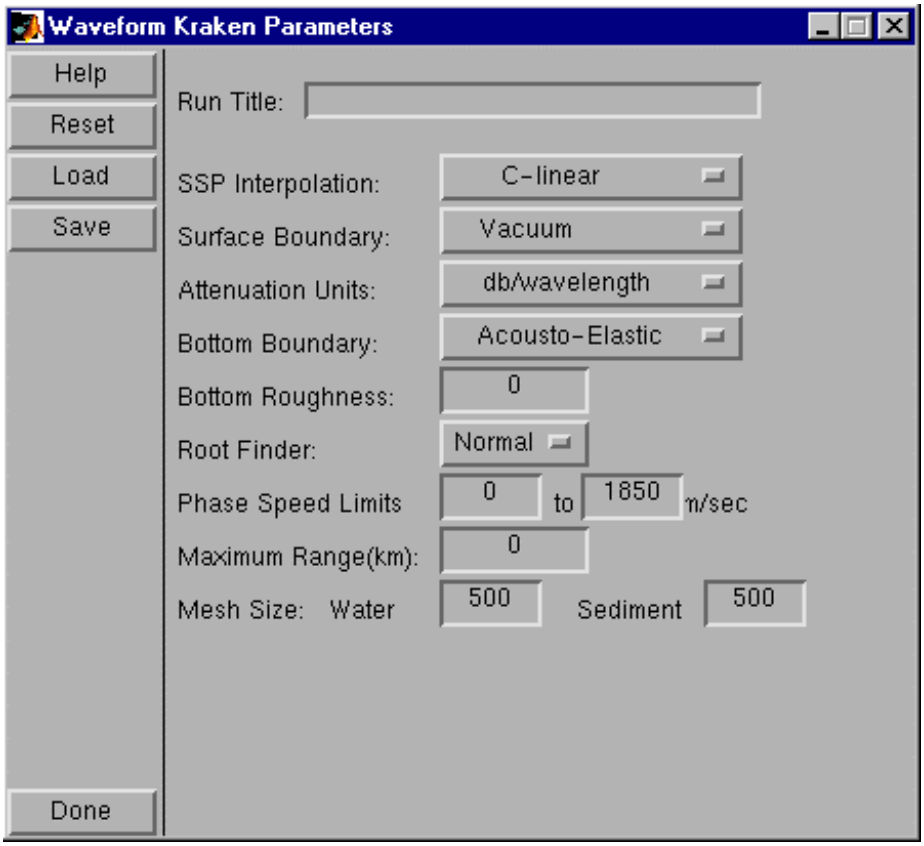


Figure 3. Kraken run options form. Options include sound speed interpretation, attenuation, and bottom conditions.

Examples

Figure 5 shows the results of a simple deep-water long range path calculation. In all three cases, the source was located on the sound channel axis (SCA), which provides the largest excitation of modal amplitudes. The waveform envelopes for three receiver locations are shown. When the receiver is also located on the SCA, large mode 1 amplitudes are observed in the waveform envelope. When the receiver is located above the SCA, higher modes begin to contribute to the waveform envelope and the entire waveform envelope is of lower amplitude. Very little energy is propagated below the SCA and the signal amplitude is greatly diminished.

Figure 6 shows the relative modal contribution to the waveform envelope for the path from Mururoa Atoll to Point Sur, CA. This is a case where only the first few modes contribute to the waveform envelope. It is a deep water path at a long range, and thus the low order modal contributions provide little sensitivity to determining the source depth from the waveform envelope. *Figure 7* illustrates an example where there is a greater sensitivity to source depth. This is the path from the Chase 21 explosion off the coast of New Jersey to the Ascension Island receiving station. The source was relatively shallow, on the continental shelf, and as the figure illustrates, there are numerous higher order modes excited from this shallow source. For comparison, a modal excitation plot is also shown for a deep source at this site. Only the lower order modes are excited in this case.

Source duration (as well as source time function) can be specified in the model. *Figure 8* shows the effect of source duration on the resulting waveform envelope for the Chase21 to Ascension path. A simple 3-cycle overshoot source is used with the source duration varying from 0.1 to 0.3 seconds. The longer source duration not only produces a larger signal (more source energy) but also contributes to more higher mode energy reaching the receiver. This increases the duration of the received signal.

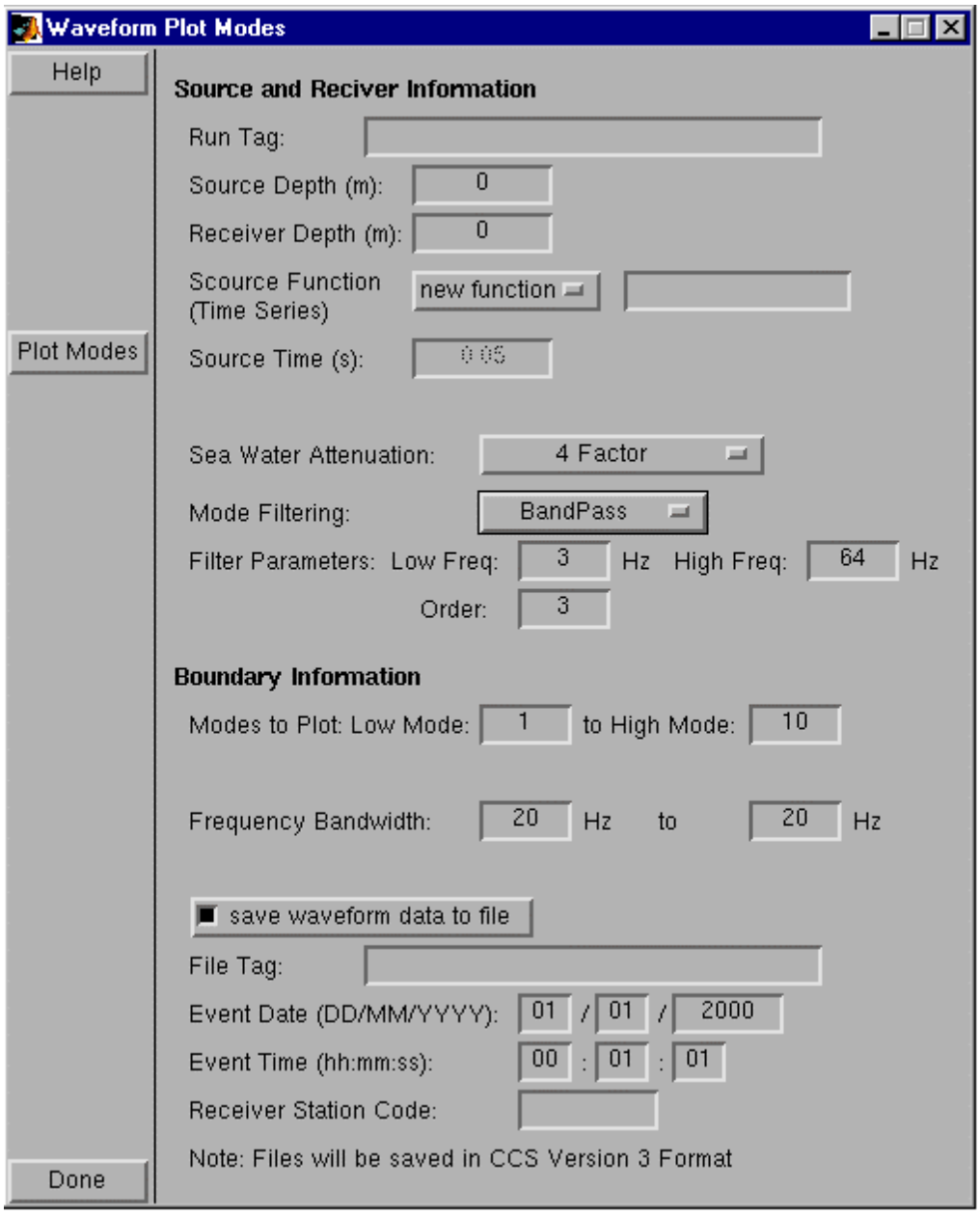


Figure 4. Waveform analysis option and plotting form. Here you input source and receiver depth, source functions, attenuation models, and output prefix for the CSS database.

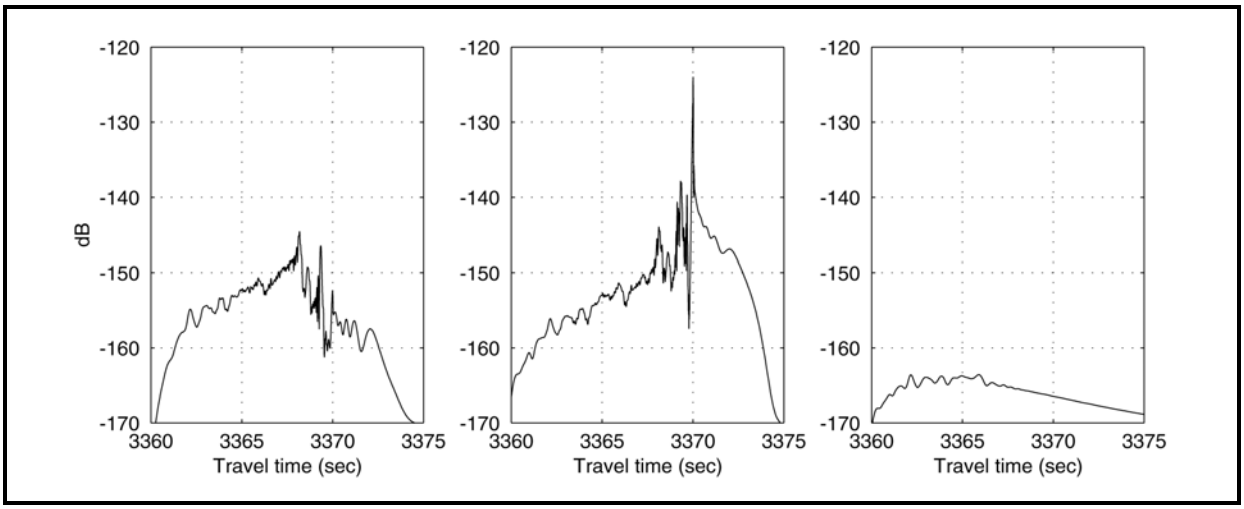


Figure 5. Sample calculation for a deep water path, source on the sound channel axis (SCA). The waveform envelope is shown for three receiver depths: above the SCA (left), on the SCA (middle) and below the SCA (right).

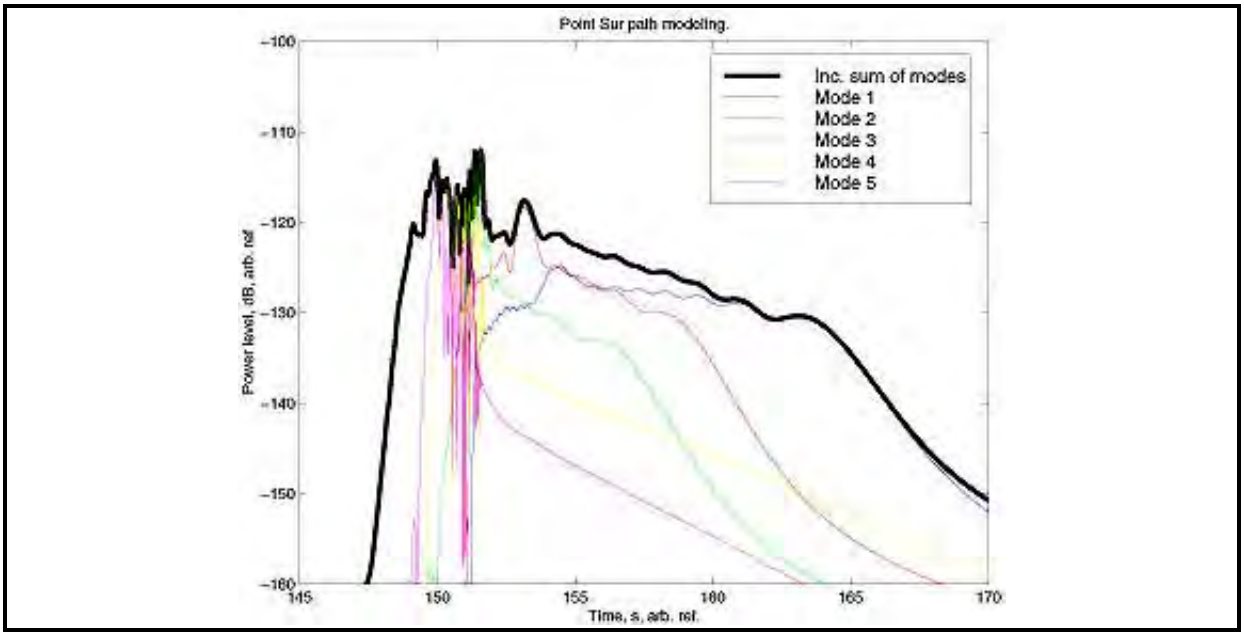


Figure 6. Modal contributions for the path from Mururoa Atoll to Point Sur, CA.

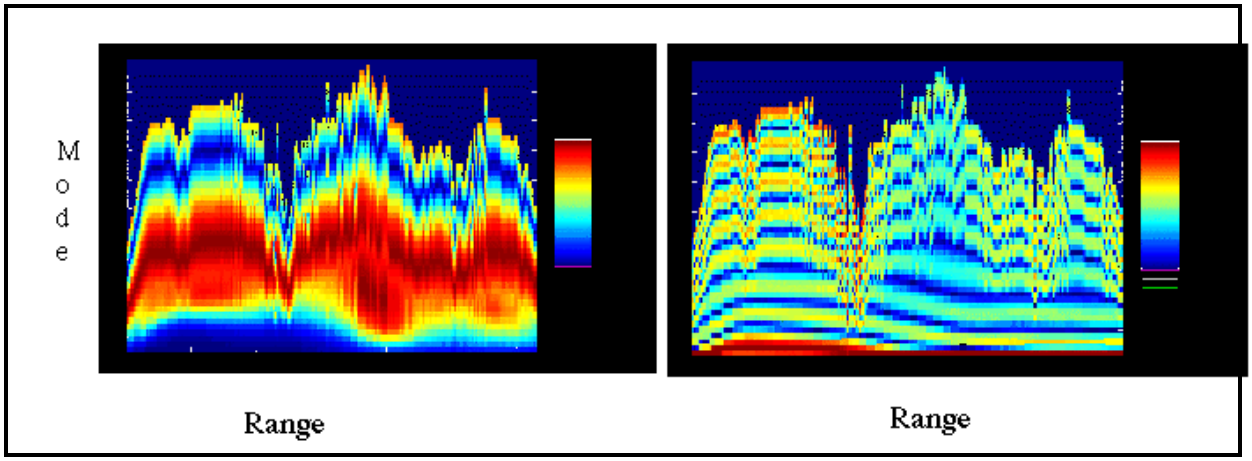


Figure 7. Modal excitation as a function of range for the path from the Chase 21 explosion off the coast of New Jersey to Ascension Island. The plot on the left shows the modal excitation of a shallow source (higher modes excited) whereas the plot on the right is for a deep source, which excites primary the lower order modes.

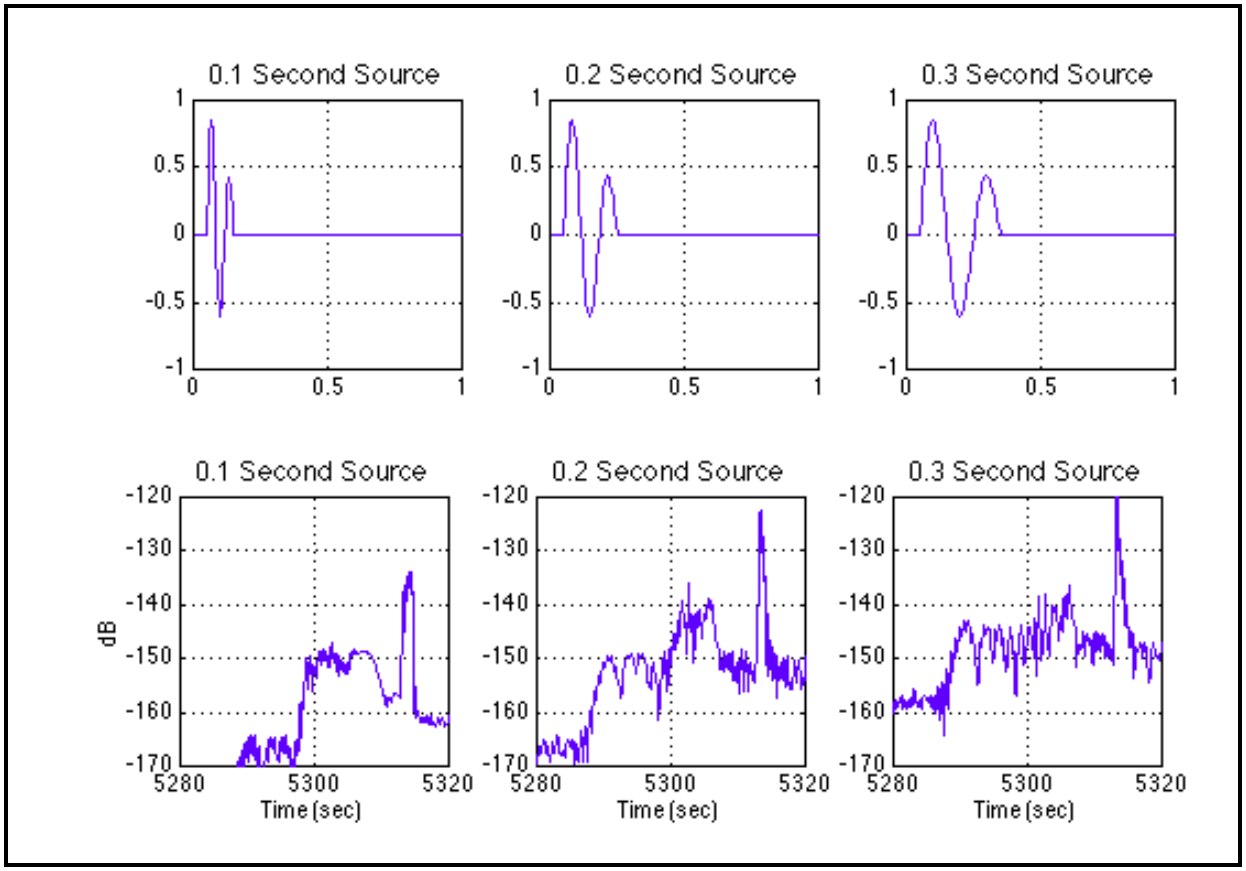


Figure 8. Effect of source duration on the waveform envelope for the Chase 21 to Ascension Island path.

CONCLUSIONS AND RECOMMENDATIONS

We have added a waveform envelope modeling capability to the program HydroCAM, which will now allow the utilization of waveforms as well as arrival times in the analysis of hydroacoustic events. Until now, we have compared the calculations with recordings of events that occurred in complicated environments, or may be seismic events which couple to waterborne acoustic energy (T-waves). Efforts are now underway to validate the calculations using sources in the ocean, which are not only simpler but more appropriate for the model. The modeling capability opens for study numerous effects such as absorption, bottom conditions near the source and receiver, mode coupling, source size region, etc. Eventually, a worldwide grid could be calculated and stored which would be used to examine the waveform envelopes of any source/receiver pair, and enable the user to

REFERENCES

Farrell, T. and K.D. LePage (1996), Development of a Comprehensive Hydroacoustic Coverage Assessment Model (HydroCAM), Proc. 18th Annual Seismic Research Symposium, PL-TR-96-2153.

Porter, M.B. (1995), The KRAKEN Normal Mode Program, SACLANT Undersea Research Centre Report of October 30, 1995

MODELING THE CONVERSION OF HYDROACOUSTIC TO SEISMIC ENERGY AT ISLANDS AND CONTINENTAL MARGINS: PRELIMINARY ANALYSIS OF ASCENSION ISLAND DATA

Arthur J. Rodgers and Philip E. Harben
Geophysics and Global Security Division, Lawrence Livermore National Laboratory

Sponsored by U.S. Department of Energy
Office of Nonproliferation and National Security
Office of Research and Development
Contract No. W-7405-ENG-48

ABSTRACT

Seismic stations at islands and continental margins will be an essential component of the International Monitoring System (IMS) for event location and identification in support of Comprehensive Nuclear-Test-Ban Treaty (CTBT) monitoring. Particularly important will be the detection and analysis of hydroacoustic-to-seismic converted waves (T-phases) at island or continental margins. Acoustic waves generated by sources in or near the ocean propagate for long distances very efficiently due to the ocean sound speed channel (SOFAR) and low attenuation. When ocean propagating acoustic waves strike an island or continental margin, they are converted to seismic (elastic) waves.

We are using a finite difference code to model the conversion of hydroacoustic T-waves at an island or continental margin. Although ray-based methods are far more efficient for modeling long-range (> 1000 km) high-frequency hydroacoustic propagation, the finite difference method has the advantage of being able to model both acoustic and elastic wave propagation for a broad range of frequencies. We are performing simulations of T-phases to relatively high frequencies (≥10 Hz). Of particular interest is to identify factors that affect the efficiency of T-phase conversion, such as the topographic slope and roughness at the conversion point and elastic velocity structure within the island or continent. Previous studies have shown that efficient T-phase conversion occurs when the topographic slope at the conversion point is steep (Cansi and Bethoux, 1985; Talandier and Okal, 1998). Another factor impacting T-phase conversion may be the near-shore structure of the sound channel. It is well known that the depth to the sound channel axis decreases in shallow waters. This can weaken the channeled hydroacoustic wave. Elastic velocity structure within the island or continent will impact how the converted seismic wave is refracted to recording stations at the surface and thus impact the T-phase amplitudes.

For this meeting we will focus on modeling T-phases observed by the May 1999 Ascension Island Experiment. A network of broad-band seismometers on Ascension Island recorded a large number of off-shore airgun shots. The shots occurred at all azimuths around the island and at ranges from 1-45 km. Measurements of signal amplitude and duration will be made to understand the variability of T-phase behavior on Ascension Island. The sensitivity to topographic slope and island structure will also be investigated.

Key Words: T-phase, hydroacoustics

OBJECTIVE

Hydroacoustic monitoring for the Comprehensive Nuclear Test Ban Treaty has made use of some existing hydroacoustic stations that were not necessarily intended to be used for the purpose of CTBT monitoring. Some of these systems are very old with poor knowledge of the sensor calibrations and location in the ocean. The calibrations of T-phase stations -- seismic stations on an island that conduct hydroacoustic monitoring

for the CTBT through T-phase signals -- are also poorly understood, making it difficult to utilize such stations effectively in a network of monitoring stations. Finally, although many recognize the possible benefits of joint analysis of different monitoring technologies such as seismic, hydroacoustic, and infrasound, little effort has been expended on this topic, in part because there is not much data of this type to analyze and in part because it is not clear exactly how to analyze it.

The Ascension Island Experiment was an attempt to gather data that could be used to understand all of these technical issues. The experiment would specifically locate and calibrate the CTBT hydroacoustic monitoring station at Ascension Island, help determine how to calibrate T-phase stations, and would leave behind a continuous monitoring system consisting of nearly co-located seismic, hydroacoustic, and infrasound stations. It represented an experiment of opportunity through collaboration and cost sharing. Participant institutions included Cambridge University, Naval Research Laboratory, Scripps Institute of Oceanography, Los Alamos National Laboratory, and the Provisional Secretariat. This paper outlines the specifics of the experiment, features of the data set collected, and plans for future data processing and analysis.

RESEARCH ACCOMPLISHED

Ascension Island is located in the middle of the South Atlantic Ocean at about 8 degrees south latitude (see Figure 1). It was chosen as the location for a hydroacoustic experiment because of an existing hydroacoustic monitoring station on the island, characteristics typical of T-phase stations, and a ship of opportunity with cost sharing potential that would transit the region. The Ascension island experiment was conducted in May-99 after an intensive but relatively short planning period that began in December-98 at a small workshop held at LLNL. The experiment consisted of a sea-based and land-based operation. The sea-based operation (Minshull, 1999) made use of the J.C. Ross, a British icebreaker class oceanographic research vessel returning from a season in the Antarctic via Ascension Island (see Figure 2). The ship was equipped with an array of airguns and hired for four days of airgun shooting and instrument deployment around the waters of Ascension Island. The ship track for the duration of the experiment is shown in Figure 3. A single airgun was deployed for the hydrophone calibrations but the bulk of the experiment utilized an 11-element array of airguns with a total firing chamber size of over 6000 cubic inches. Two temporary hydrophone systems were deployed by Scripps and one by Cambridge. Cambridge also deployed numerous sonobouys during the experiment. In addition several imploding sphere sources were tested.

The land based operation consisted of continuous recording from ten temporary seismic stations deployed on the island for the duration of the airgun shooting. The seismic stations were sited and permitted on an earlier site-survey visit to the island. Concrete pads were poured to provide good coupling and a stable surface for seismometer leveling and the seismometers were buried below ground level. A Sprengnether S-6000 3-component 2 Hz seismometer was emplaced at each station site and recorded continuously at 250 samples/sec with 24 bit digitization using a Reftek data acquisition box. The distribution of stations on the island is shown in Figure 4. The station locations represent a compromise between having multiple lines of stations crossing the island and siting in areas of good relative coupling to competent formations.

HYDROACOUSTIC CALIBRATION:

The three hydrophones currently utilized by the pIDC as the Ascension Island hydrophone monitoring station are ASC26, ASC23 and ASC24. ASC26 is located about 100 km south of the island while ASC23 and ASC24 are within 3 km of each other and only a few km south of the island. The J.C. Ross approached Ascension Island from the south and consequently conducted a calibration of ASC26 during the journey to Ascension Island. A single towed 1000 cubic inch airgun was fired every minute at 5 meters depth as the ship sailed on two orthogonal tracks over the nominal coordinates of ASC26. The data set selected for analysis and the corresponding signals recorded by ASC26 is shown in Figure 5. Each open circle represents a shot and the corresponding waveform is shown. The data will be used to determine the precise location of the hydrophone at the time of the experiment to about 20 meters accuracy. It is clear from the moveout on the waveform traces that the nominal latitude of ASC26 agrees well with the data but that the nominal longitude is somewhat to the east of what the data indicates.

In the same way as data was acquired over ASC26, data was collected over ASC23 and ASC24. The ship tracks and firing locations are shown in Figure 6. The accuracy of the location determinations of ASC23 and ASC24 at the time of the calibration is expected to be about 20-50 meters. Although the bulk of the experiment had a fully deployed 11-element array of airguns firing, a single 1000 cubic inch airgun was used for the hydrophone calibrations. The reasons were to minimize the source distribution and to fire a consistent source near each hydrophone. In addition, two calibrated Scripps hydrophones were temporarily deployed during the experiment and the single airgun was fired over these instruments. This data will be used to characterize the source pressure amplitude spectrum which in turn will allow us to determine the unknown amplitude response spectrums for ASC23, ASC24, and ASC26. Data records show clipping of the direct path signal when the source is very close to the ASC hydrophones which will also allow us to determine the clip levels of the ASC hydrophones.

T-PHASE STUDIES:

The T-phase studies have yet to be accomplished. The 11-element airgun array fired every minute for about 2.5 days, over 3500 events in all. The nominal 20 meter depth of the towed airgun array was constrained by equipment limitations and operational procedures. This depth is very shallow for good coupling to the SOFAR. Consequently, the relatively poor coupling of the airgun events into the SOFAR and the relatively high background seismic noise levels typically encountered on islands may make it difficult to use the airgun as a signal source for T-phase coupling-to-land studies. A plot of the seismic station SBC recordings over a one hour time period during the full airgun array shooting is shown on Figure 7.

A simple model based on the bathymetry and sound speed profile at Ascension Island predicted that for a

shallow source, the convergence length for optimal detection of the signal in the SOFAR channel is 45 km. The ship tracks were chosen to provide a few straight line paths from 45 km or more towards a land sesimic station and a MILS hydrophone so that the convergence length can be measured. These data will be compared to model predictions.

During the short duration of the experiment several apparent volcanic events were recorded by the MILS hydrophones, the temporary hydrophones, and the seismometers on the island. An example of the events as recorded on the MILS hydrophones is shown in Figure 8. The events are rich in high frequency energy (above 30 Hz) and are also recorded on land with significant energy above 30 Hz. These events, therefore, will be ideal to address two of the T-phase research issues: 1) How well do the high frequencies in an explosive generated T-phase couple into land? and 2) What is the attenuation of high frequency T-phase energy across an island? The volcanic events recorded appear to be part of a volcanic cycle noticed on the MILS hydrophones about a month before the experiment, a cycle that may correlate with a large fish kill and temperature rise in the waters around Ascension Island during the same time period.

IMPLODING SPHERE SOURCES:

Use of explosives aboard the J.C. Ross was not allowed, consequently there was no commercially viable way to get sources at the SOFAR channel depth (nominally 750 meters) for optimal T-phase signal generation. This left few alternatives since airgun and other seismic marine sources are designed for use only at shallow depths. The result was a rushed attempt to develop an imploding sphere source that could be initiated at a prescribed depth, nominally 750 meters. Imploding spheres have long been recognized (Issacs, 1952 and Orr, 1976) as an effective source at mid-ocean depths and below, however, they have not been reliable: either failing well below or above the desired depth or not failing catastrophically at all (Sauter, 1996).

We designed and tested a prototype smashing system (Boro, 1999) that would initiate sphere failure at a desired depth. The system firmly held the sphere in place and in contact with a 4 inch diameter piston. A 1/4 inch diameter ram connected to the center of the piston passes through a small O-ring sealed hole in the cap confining the piston and abutting the glass sphere. The ram initiates failure by punching a hole through the glass sphere. The end cap on the cylinder confining the piston and opposing the ram end cap tapers to a one inch diameter opening with a rupture disk sealed to it. The rupture disk is calibrated to fail within 5% of the calibrated failure pressure, 1000 psi in our tests. Failure of the rupture disk results in an inrush of high pressure water into the air-filled piston chamber, driving the piston -- and attached ram -- towards the glass sphere.

The smashing system was tested on 4 occasions and reliably actuated every time at the nominal rupture disk failure pressure of 1000 psi. The system also successfully punched a hole in a Benthos flotation sphere on each test, however the Benthos did not fail catastrophically except when tested in the lab without the water pressure acting on the body of the sphere. These rugged flotation spheres are too thick-walled to be reliable sources at SOFAR depths (nominally 2,500 ft.) since they do not tend to fail catastrophically. Tests were also conducted with a thinner walled glass sphere made from a standard 22 liter boiling flask. This sphere was not expected to survive to the depths and pressures desired but deep water tests showed the sphere survived to 1600 meters. The combination of this thinner-walled sphere with the smashing mechanism results in a reliable implosive source at a desired depth and with no associated safety concerns in transport or deployment. During the Ascension Island Experiment, only one sphere implosion was initiated, at a depth of 1600 meters. The implosion signal should be recorded on a temporary Cambridge Univ. OBH. The data will be available soon.

SYNERGY:

An operational synergy experiment was left behind on the island after the airgun shooting. Two new stations were established: a high frequency seismic station and an infrasound station. A level cement pad was poured on top of an old cement antenna anchor that extended over two meters into the ground. An S-6000 seismometer was mounted on the cement pad and buried. A nearby Reftek data acquisition system records continuous 3-component data at 250 samples/second and 24 bits resolution. Data tapes are mailed bi-monthly to LLNL.

In the same part of the island -- near Butt Crater -- an infrasound station was established. This station consists of four sensor elements about 100 meters apart in a tetrahedron formation. Each sensor is an aneroid microbarometer with a manifold allowing for six microporous hose extensions. The data is recorded on a Reftek unit identical to that used for the seismic station. A wind speed and direction indicator will be added to give a total of 6 data channels. These data are recorded to DAT tapes and mailed to LLNL on the same schedule as the seismic data.

The continuous data from the three monitoring technologies will be archived. Selected time periods containing noise and events of interest will be extracted with window lengths that span all three technologies for any known event location. These selected time periods will form a data base that will be analyzed for joint noise statistics and specific joint monitoring analysis studies that use two or more of the technologies to improve overall location or identification capabilities.

CONCLUSIONS and RECOMMENDATIONS

Calibration of existing hydrophone stations using a ship-towed airgun with precision GPS timing and location provides accurate location of hydrophones at sea. It can also determine the amplitude response and clip levels of the hydrophones provided care is taken to characterize the airgun source and the source pressure pulse is sufficient to saturate the hydrophones at close range. The airgun data taken at Ascension Island will be used to locate and calibrate the three hydrophones that are currently recorded at the pIDC.

The data collected at Ascension Island will allow us to determine if an airgun array is an adequate source for

T-phase calibrations at an island station. The primary concern with using an airgun for T-phase signal generation is that the airgun needs to be fired at relatively shallow depths and this does not result in good signal coupling into the SOFAR channel. Luckily, during the short deployment at Ascension Island, there were volcanic events recorded that will allow us to investigate the issues of coupling and of T-phase attenuation across the island even if we determine the airgun sources to be inadequate for T-phase studies.

The use of small explosive sources at the SOFAR channel depth is an ideal way to effectively couple acoustic energy into that channel and provide a good source for T-phase studies. It was clear during the planing phase of this experiment that complying with the required procedures necessary to meet most civilian ship explosives handling safety plans is costly and problematic, if indeed permission can be obtained at all. Imploding spheres circumvent these problems and provide an acoustic source at SOFAR channel depths. They are clearly useful for experimentally investigating local hydroacoustic propagation and blockages as well as longer range acoustic travel times. It remains to be determined if the signal amplitude and bandwidth from imploding spheres are adequate for T-phase coupling research and calibration.

The synergy experiment is underway and will collect continuous data from hydroacoustic, seismic and infrasound stations on or near Ascension Island for the next two years. The data collected will provide a large database of background noise and events for the three monitoring technologies.

Hydroacoustic monitoring research has started to focus on calibration and ground truth issues to try to improve event location and identification, as seismic monitoring has effectively done. The data collected at Ascension Island will be a rich source of ground truth data for the topics summarized above and will help determine how to best conduct future hydroacoustic and T-phase calibrations while collecting hydroacoustic ground truth data for the knowledge base.

REFERENCES

Boro, C. and P.E. Harben, 1999, Sphere Implosion Initiation Device, Record of Invention IL-10551, University of California, LLNL Patent Group.

Isaacs, J.D. and Maxwell, A.E., 1952, The Ball-breaker, A Deep Water Bottom Signalling Device, J. Marine Res., V 11, pp. 63-68.

Minshull, T. A.,1999, Cruise Report for the RRS James Clark Ross 42: A Seismic Tomographic and Hydroacoustic Study of Ascension Island, Univ. of Southampton School of Earth Science Report, Southampton Oceanography Center, European Way, Southampton SO14 3ZH.

Orr, M. and M. Schoenberg, 1976, Acoustic Signatures From Deep Water Implosions of Spherical Cavities, J. Acoust. Soc., V 59, pp. 1155-1159.

Sauter, A., L. Dorman, E. Canuteson, 1996, Development of a Seismo/Acoustic Implosive Source, Am. Geophys. Union, Proc. fall meeting.

ACKNOWLEDGEMENTS

A large number of individuals and institutions made the Ascension Island Experiment possible. Special thanks to Tim Minshull, now at Southampton University, England for planning and coordinating the ship use, the airgun configuration and operation, and the overall specifics of the cruise. Thanks to Vicki Childers and John Brozena from the Naval Research Laboratory for partial financial support of the cruise and for assistance in the field. Thanks to Marta Galindo and Martin Lawrence of the PTS for financial support for the temporary OBH deployments and for field assistance. Thanks to Rod Whittaker and Tom Sandoval of LANL for siting and installation of the infrasound station for the synergy experiment. Thanks to Jay Pulli and Ted Farrell of BBN Inc. for assistance with MILS data quality during the cruise, collaboration with imploding sphere investigations, and for the use of one figure in this report. Thanks to Crispin Hollinshead of Scripps for field support and Jeff Hanson of SAIC for insightful suggestions during the planning phase of the experiment. Finally, thanks to Jenny Hollfelder of LLNL for assistance with ship track file corrections and report figures.



Figure 1) The location of Ascension Island is shown by the red dot. Ascension Island is one of the most remote islands in the Atlantic Ocean.



Figure 2) The J.C. Ross was the sea based platform for the airgun array. The ship is an icebreaker class oceanographic research vessel commissioned in the early 1990's.

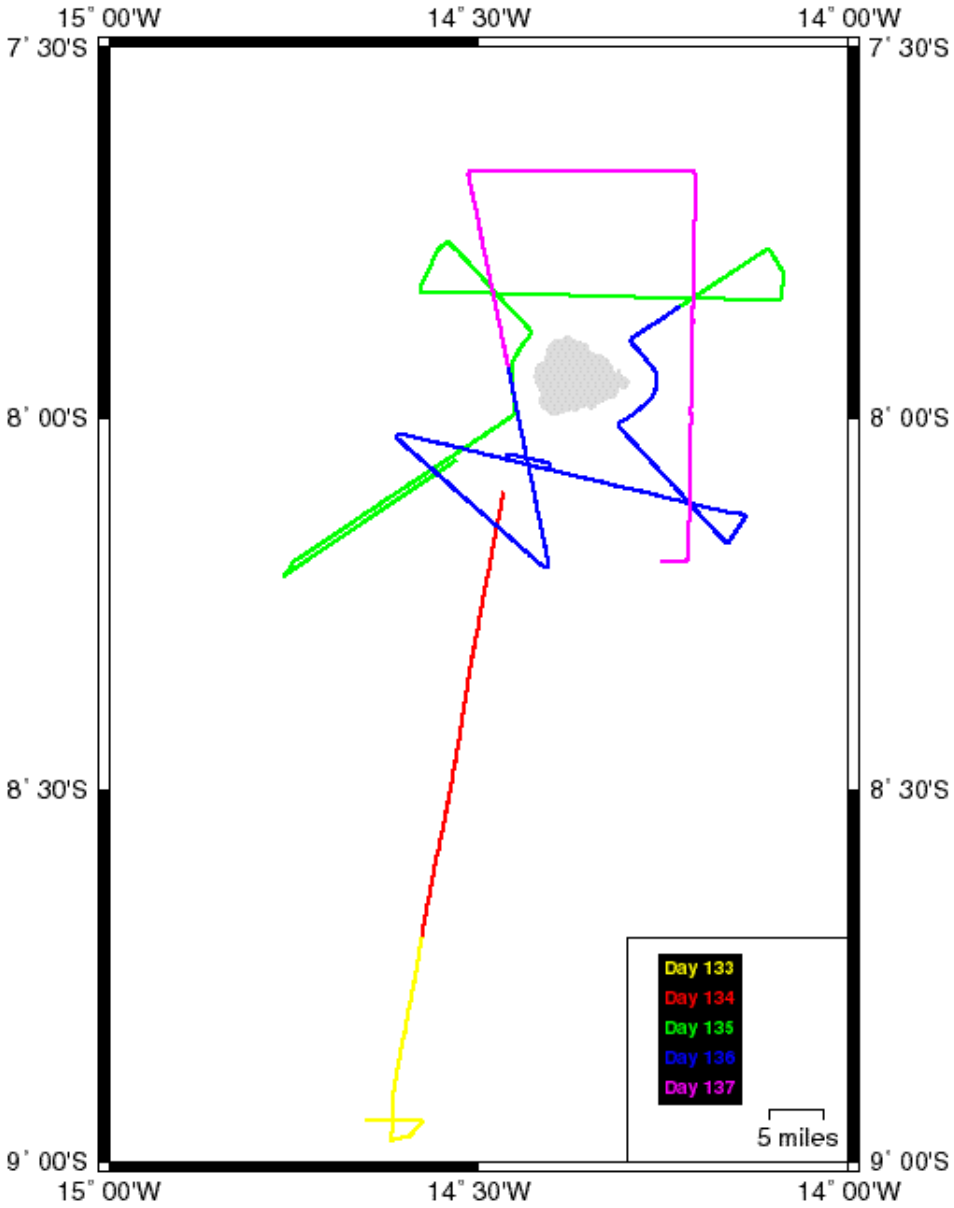


Figure 3) The ship track of the J.C. Ross during the Ascension Island experiment color coded by day. Note that on day 134 the track abruptly ends. This coincides with the end of the single airgun firing followed by a pickup of crew at Ascension Island. The track resumes on day 135 outbound on the southwest extension of the seismic line to 45 km followed by a return on the same track.

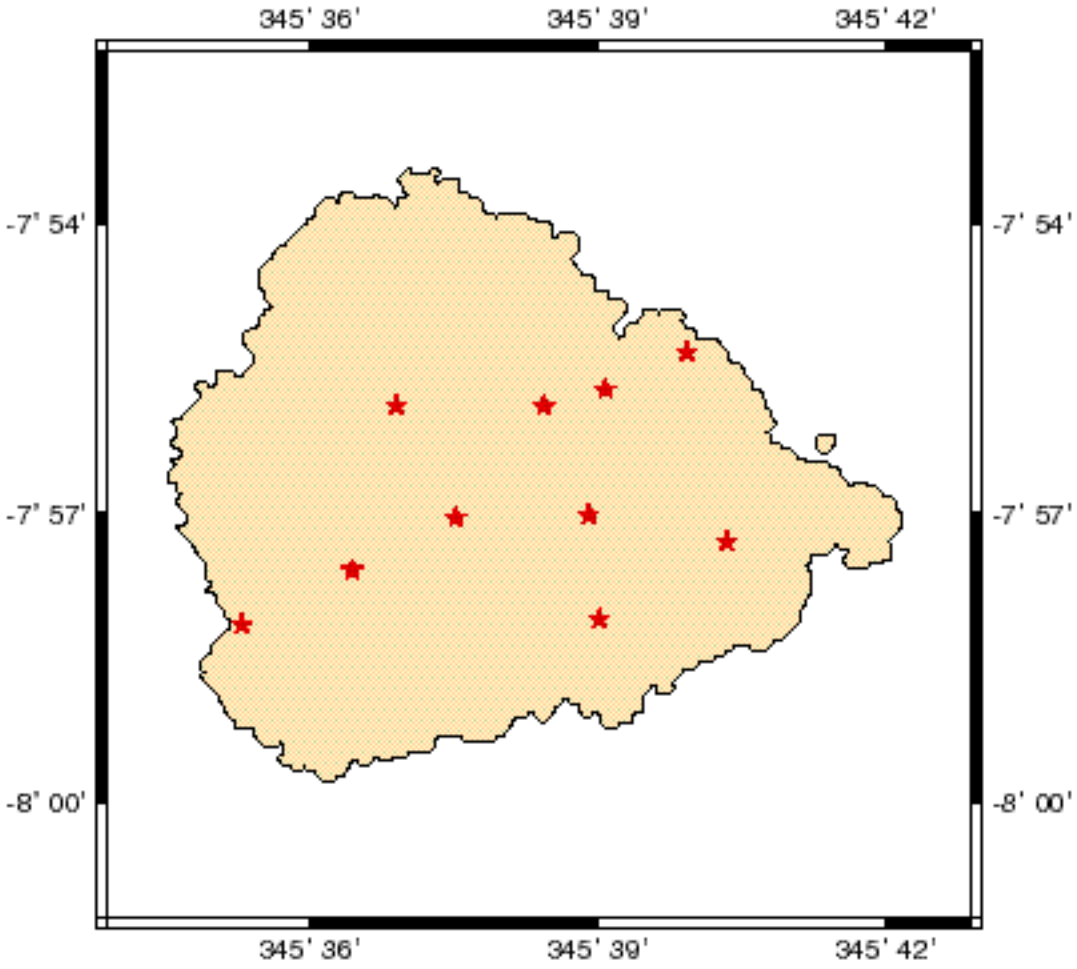


Figure 4) The location of the ten temporary seismic stations on Ascension Island. Note the southwest - northeast trending line of stations that coincide with the extended ship track lines.

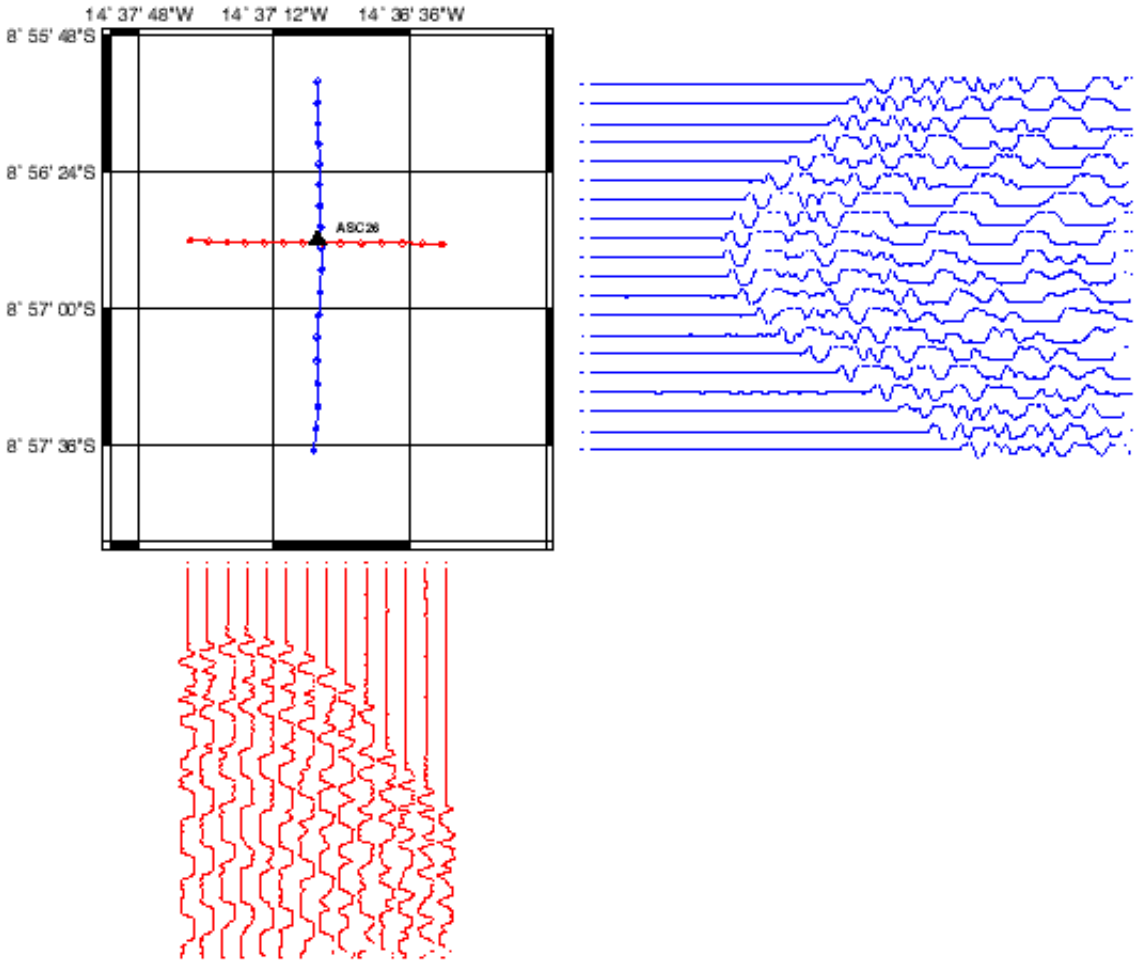


Figure 5) The ship tracks near the nominal location of ASC26 are shown with each shotpoint indicated by an circle. The associated waveforms recorded by ASC26 for each shot are also shown. Note that the data agrees well with the nominal location on the north-south track but the east-wast location of ASC26 is west of the location indicated by the data.

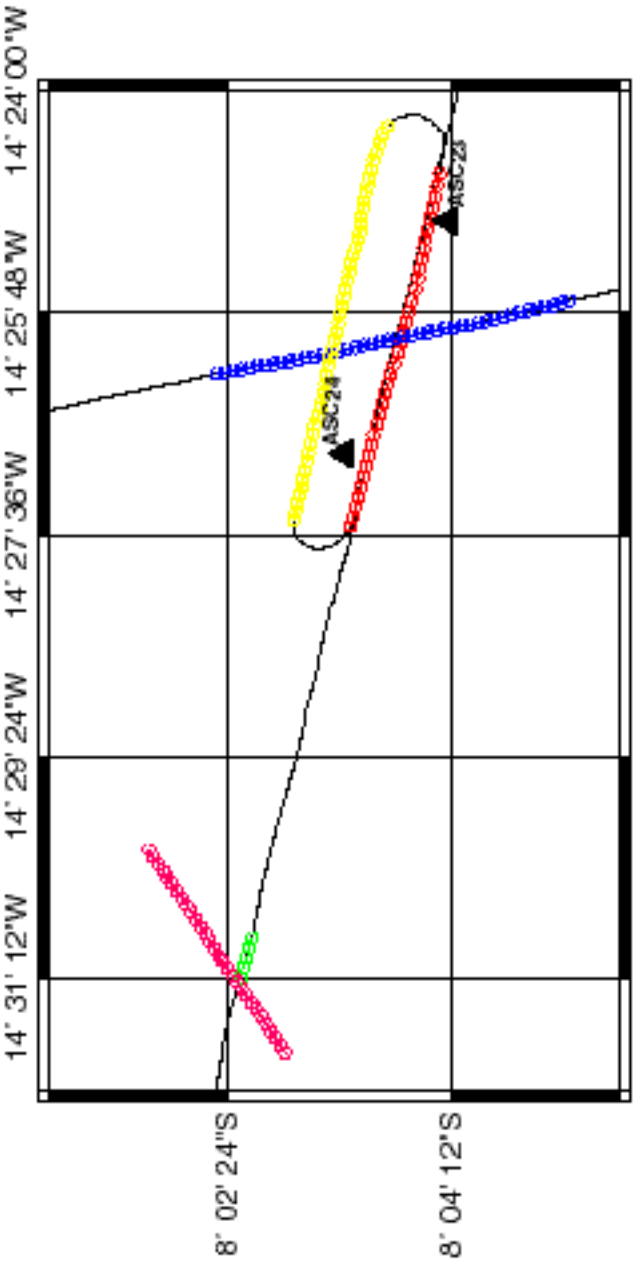


Figure 6) The ship tracks that will be used in the calibration of ASC23 and ASC24 are shown color coded according to day as shown on the ship track file in Figure 3. Note that the tracks displayed to the west are the tracks over the Scripps OBH that will be used to characterize the source.

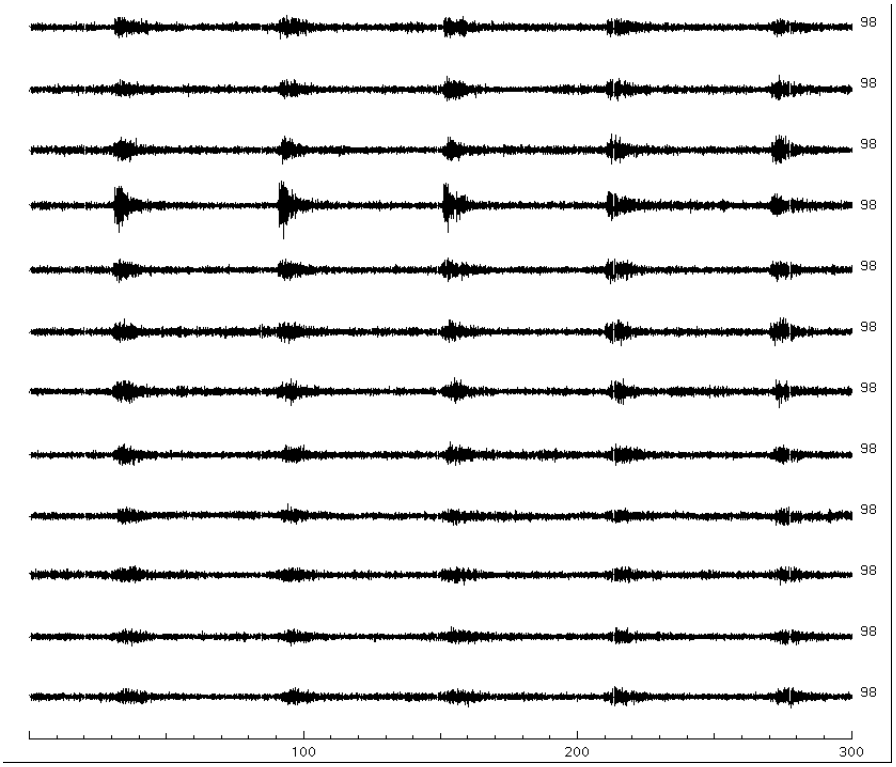


Figure 7) One hour of recordings from seismic station SBC during full array airgun shootings.

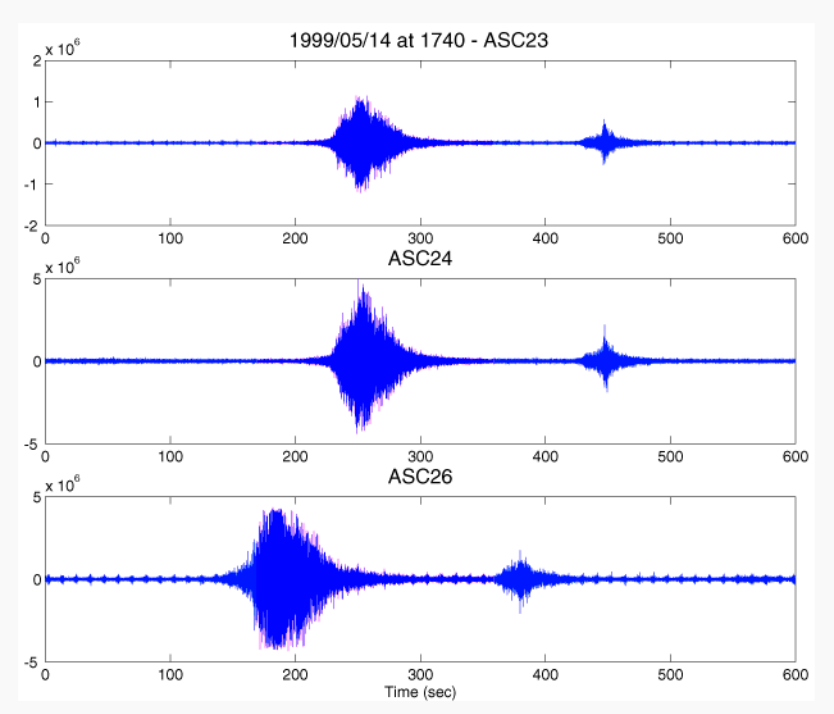


Figure 8) An apparent volcanic event recorded by the MILS hydrophones.

EMPIRICAL AND NUMERICAL MODELING OF T-PHASE PROPAGATION FROM OCEAN TO LAND

Jeffry L. Stevens, G. Eli Baker, and Ron W. Cook
Maxwell Technologies, Systems Division
Gerald D'Spain and Lewis P. Berger
Marine Physical Laboratory, Scripps Institution of Oceanography
Steven M. Day
San Diego State University

Sponsored by the Defense Threat Reduction Agency

ABSTRACT

T-phase propagation from ocean onto land is investigated by comparing data from hydrophones in the water column with data from the same events recorded on island and coastal seismometers. The threshold level for hydroacoustic signals measured in the SOFAR channel is much lower than the threshold for T-phases observed on island and coastal seismic stations. Because nearly half of the future hydroacoustic network of the International Monitoring System is made up of T-phase stations on land, it is important to understand T-phase propagation onto land in order to evaluate the capability of the hydroacoustic network to monitor the oceans. To estimate the transfer function, it is necessary to find events with large enough T-phases to be measurable over an acceptable frequency band at land-based stations near a hydroacoustic station.

A particularly good data set has been obtained for the series of events from the emerging seamount Loihi, located southeast of Hawaii. These events generated very large amplitude T-phases that were recorded at both the IMS hydrophone stations and land based stations near the northern California coast and over 100 km inland from the coast. We have obtained data from the preliminary IMS hydrophone station at Point Sur, from land based stations operated by U. C. Berkeley along the coast of California, and from the PG&E coastal California seismic network, and used this data set to estimate the T-phase transfer functions for all of these paths.

The transfer function and predicted signal from the Loihi events are modeled with a composite technique using normal mode based numerical propagation codes to calculate the hydroacoustic pressure field and an elastic finite difference code to calculate the seismic propagation to land-based stations. The modal code is used to calculate the pressure field in the ocean off of the California coast, which is used as input to the finite difference code TRES to model propagation onto land. Animations were created from the finite difference calculations to help visualize the complex conversion process.

We also look at the nature of T-phases after conversion from ocean to land by examining far inland T-phases. We find that T-phases propagate primarily as P-waves once they are well inland from the coast, and can be observed in some cases hundreds of kilometers inland from the coast.

Key Words: Hydroacoustic, T-phase, Finite Difference, IMS, Loihi

OBJECTIVE

The objective of this project is to better understand the propagation of T-phases from ocean to land, and the performance of T-phase International Monitoring System (IMS) stations, through empirical and numerical methods. The empirical study uses data from pressure sensors in the ocean and coastal and island seismometers to examine the T-phase transfer function. The numerical study uses finite difference calculations to model propagation of T-phases from ocean to land.

RESEARCH ACCOMPLISHED

The International Monitoring System (IMS) hydroacoustic network is a relatively sparse network consisting of 6 underwater hydroacoustic stations and 5 land-based seismic T-phase stations. The hydroacoustic stations are much more sensitive to underwater signals than the T-phase stations and have a higher sampling rate and broader frequency range. The broader frequency range is important for identifying explosions, which are characterized by higher frequency content than other sources. Because of these limitations, it is important to understand the efficiency of T-phase conversion in order to assess the capabilities of the IMS network for detection and identification of underwater sources. Currently, only part of the hydroacoustic network is in place, and an additional hydroacoustic station at Point Sur is acting as part of the IMS network. Figure 1 shows the location of the two hydroacoustic and one T-phase stations which are currently operating in and adjacent to the Pacific Ocean, and the location of the emerging seamount Loihi, which has been the source of strong T-phases.

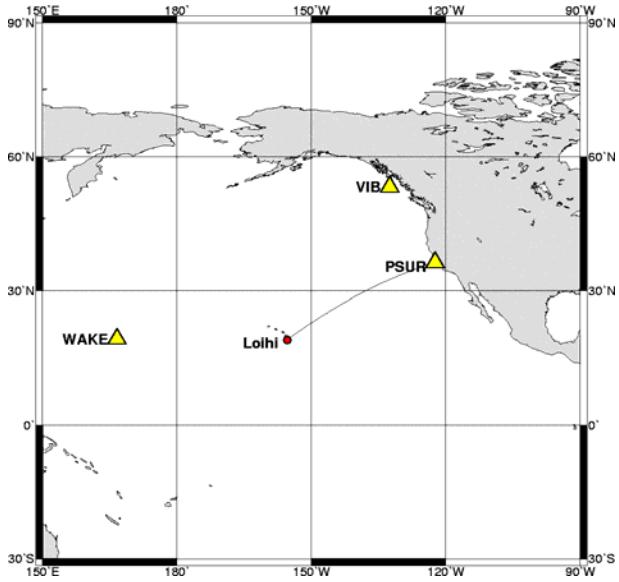


Figure 1. Hydroacoustic network stations in the current International Monitoring System in the Pacific Ocean. VIB is a T-phase station. Point Sur and Wake are underwater hydroacoustic stations. "Loihi" marks the location of strong T-phase sources south of Hawaii used in this study. The great circle path from Loihi to Point Sur is also shown.

Transmission of T-phase Energy from the Ocean onto Land

We have gathered data sets from events that were recorded on both underwater and coastal seismic stations for the purpose of directly measuring T-phase conversion. Several earthquakes from the emerging seamount Loihi and on the island of Hawaii generated very strong T-phases that impacted the California coast. We have collected recordings of these events from the Point Sur (PSUR) hydroacoustic station, the Pacific Gas and Electric Central Coast seismic network (PG&E), and the Berkeley broadband digital seismic network (BDSN). The location of these stations and the bathymetry of the California continental shelf are shown in Figure 2. This is a nearly optimal situation for study of T-phase conversion because the hydroacoustic waves impact the coastline almost perpendicular to the coast as shown by the ray path on Figure 2.

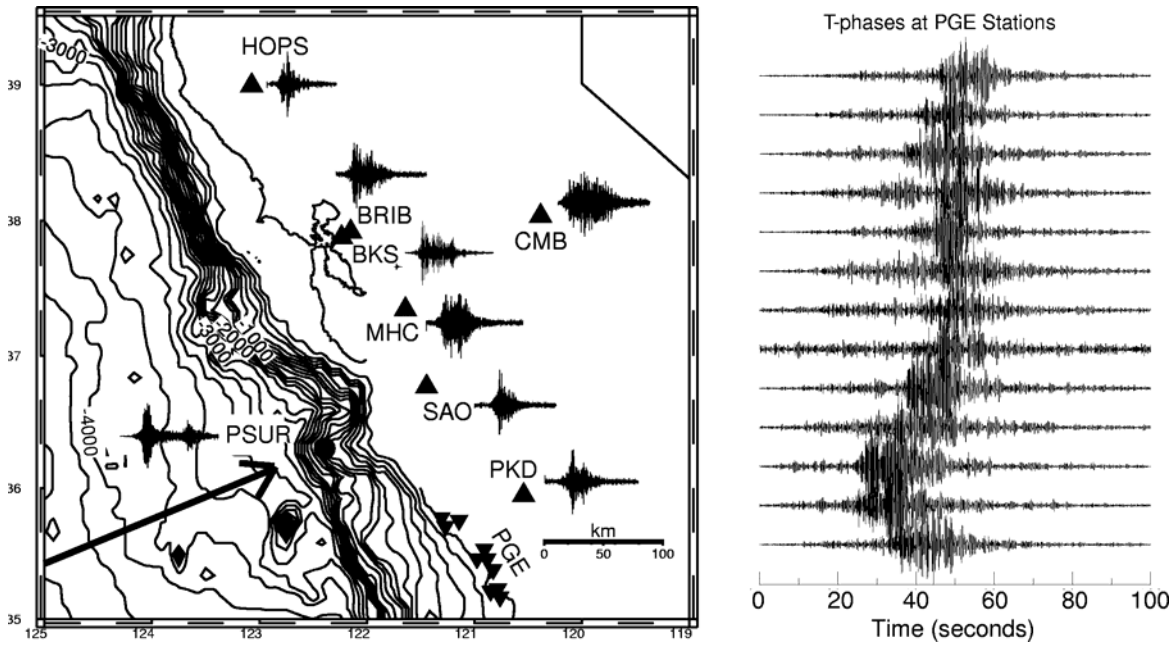


Figure 2. Records from the 1997 June 30 Loihi event and station locations. The propagation direction is indicated by the arrow, which points to the hydroacoustic station PSUR (indicated by the circle). 150 seconds of the T-phase record is shown to the station's left. The BDSN stations (large triangles) and corresponding records are included on the map on the same scale. The PG&E station locations are indicated by inverted triangles and their waveforms are shown to the right, in order of increasing distance from bottom to top. The arrival times do not correspond well to total distance because the distance from the conversion point varies. The bathymetry is contoured in 200 m intervals.

The sampling rate and instrumentation are different for each of the three networks. Point Sur is sampled at 200 samples per second and the instrument response is approximately proportional to frequency at frequencies less than 25 Hz. Data in the BDSN network is sampled at 20 samples per second. BDSN instrument responses are approximately flat to velocity in the 1-10 Hz frequency band. The PG&E network consists of S-13 seismometers with a sampling rate of 100 samples per second, and is flat to velocity from 2-25 Hz. We have relative gain corrections for each of the instruments, however the absolute gain for the PG&E stations is uncertain. Because of the differences in instrumentation, the usable frequency band for obtaining T-phase transfer functions from this complete data set is about 2 to 9 Hz.

We have calculated T-phase transfer functions for this data set by taking the ratio of the instrument corrected vertical component velocity spectral amplitudes of the seismic stations to the instrument corrected Point Sur pressure spectra for all good quality data at the PG&E stations and the 6 coastal BDSN stations (CMB was excluded because it is much farther inland). The spectral ratios were averaged for all events for each station. The resulting spectral ratios are shown in Figure 3. There is a clear decline in amplitude with frequency for both networks, but it is particularly pronounced for the BDSN network. This is likely due to greater attenuation of the higher frequencies because of the longer paths to the BDSN stations. Simulations discussed later in this paper indicate that much of the energy in the hydroacoustic wave is transmitted to land at approximately 200 m bathymetry, which corresponds to the contour line (Figure 2) nearest the coast. The crustal paths from the conversion point to the PG&E stations are only 5 to 20 km long, while paths to the BDSN stations are 40-75 km.

Although the transfer function can only be calculated by numerical methods, we can estimate an approximate upper bound on the transfer function by considering the simple case of a plane acoustic wave travelling in the ocean and propagating into a solid at normal incidence. This is an approximate upper bound in the sense that any scattering or other boundary effects will reduce the amplitude below this level, although conversion to shear waves or focusing could conceivably cause amplitudes to exceed this value. For propagation of a plane wave at normal incidence from a fluid into a solid, the transmission coefficients for velocity and pressure are given by:

$$T_{v_f \blacklozenge v_s} = \frac{2\rho_f \alpha_f}{\rho_s \alpha_s + \rho_f \alpha_f} \qquad T_{P_f \blacklozenge v_s} = \frac{2}{\rho_s \alpha_s + \rho_f \alpha_f}$$

where ρ and α are the density and compressional velocity and the subscript s indicates solid and f indicates fluid.

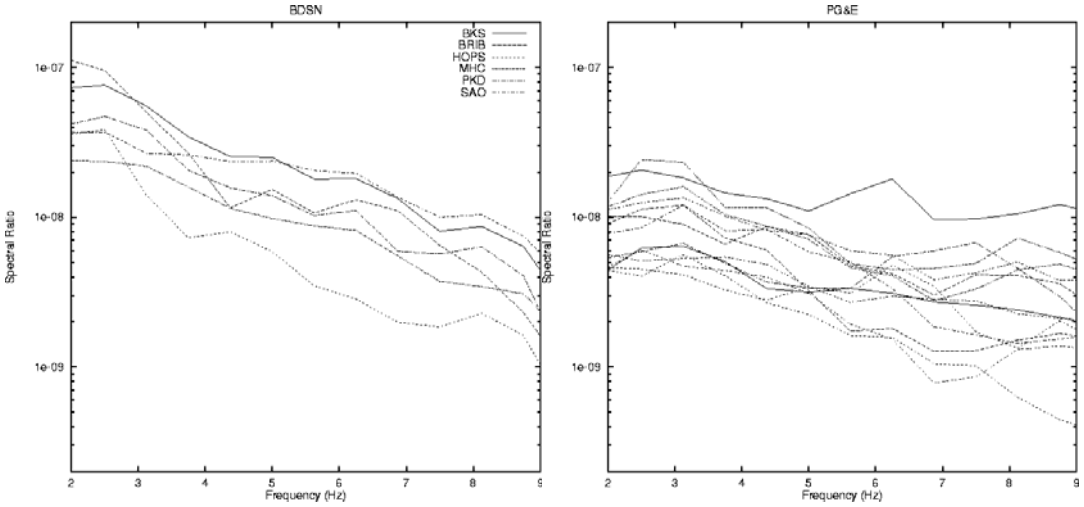


Figure 3. Ratios of seismic spectra at stations in California that recorded the Loihi events, divided by the Point Sur spectra. These are T-phase transfer functions converting pressure to vertical velocity. The frequency band shown here is from 2-9 Hz. the left figure shows BDSN stations and the right figure shows PG&E stations. There is some uncertainty about the absolute amplitude of the PG&E records, however the amplitude of the BDSN records, and the spectral shape of both sets of curves, are accurate. Spectral ratios are in MKS units (meters/second/Pascal).

Depth (m)	P velocity (m/s)	S velocity (m/s)	Density (kg/m^3)
500	3400	1500	2200
1500	5000	2900	2500
11000	6100	3484	2750
21000	6300	3503	2800
31000	6600	3464	2900
×	8000	4260	3300

Table 1. Velocity model for the California coast.

Table 1 lists a velocity model for the California coast near Point Sur from Mooney et al (1998) with the shear velocity as modified by Stevens and McLaughlin (1997). Using a typical water velocity and density of 1480 m/s and 1000 kg/m^3, respectively, we can estimate upper bounds on the velocity transfer function of 0.21 and 0.36 for the top two layers of the coastal California earth model. The pressure to velocity transfer function for each layer has an upper bound of 1.4×10^{-7} and 2.4×10^{-7} meters/second/Pascal. At 2 Hz, the average of the BDSN spectral ratios is 0.6×10^{-7}, about a factor of 3 less than the estimate given above, which gives a numerical estimate of the efficiency of T-phase transmission into the coast. That is, the BDSN records show that at low frequencies the transfer function is reduced by complex coastal interactions by a maximum of about a factor of 3. The spectra of the BDSN records fall off by an order of magnitude over the 2-9 Hz frequency band. The PG&E records show that for stations close to the coast, the maximum attenuation with frequency is a factor of 3-4 over the 2-9 Hz frequency band.

Far Inland T-phases

The ocean hydroacoustic phase may convert to a variety of complex phases due to the interaction with the coast. We can get some insight into the type of conversion that occurs by looking at far inland T-phases, and examining the propagation speeds of these waves. The T-phase from the 1997/06/30 event was large enough to be observed as much as 200 km inland from the coast. Figure 4 shows two sets of seismograms recorded along two (approximate)

great circle paths. The paths are from SAO to KCC and from JRSC to MHC to CMB. Since the waveform is dispersed, there is some uncertainty about when to pick the arrival, however if we use the peaks of each wave train, then we get a velocity between SAO and KCC of 6.8 km/sec, and a velocity along the path of the other three stations of 5.6 km/sec. These velocities correspond to P-wave speeds, so the T-phases must be travelling as P-waves over this range.

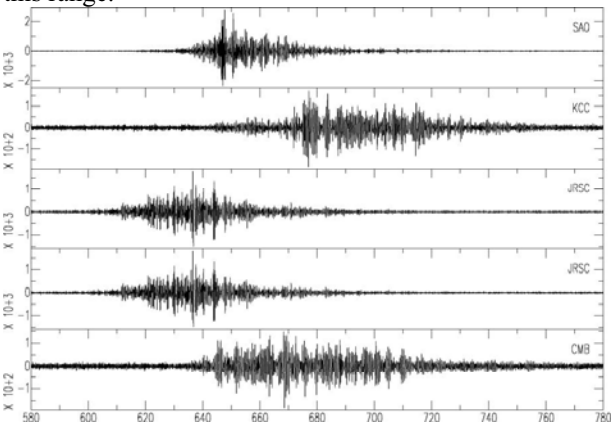


Figure 4. T-phases recorded near the coast and far inland from the 1997 June 30 Loihi event. The top two seismograms are from stations located along one great circle path and the bottom three seismograms lie along a second great circle path. The horizontal axis is time in seconds. The data has been high pass filtered at 2 Hz.

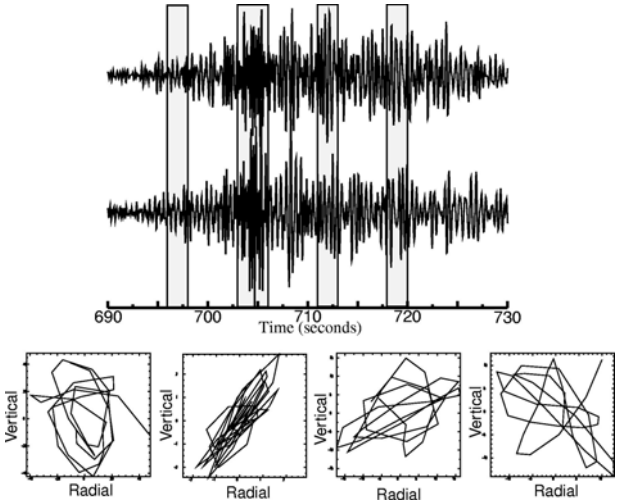
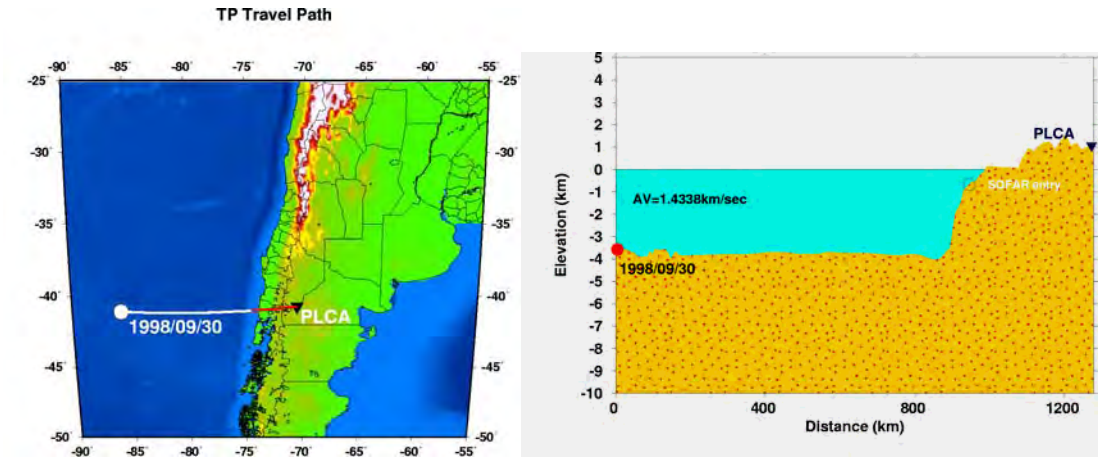


Figure 5. Vertical (top trace) and radial (lower trace) component seismograms from SAO for the 1997 June 30 event. Particle motions for four time windows outlined by shading are shown below the seismograms. The linear motion of the second time window indicates dominance by body waves, and the elliptical motion of the first time window suggests that the early part of the wave train is composed of surface waves.

Particle motion provides an independent means of assessing wave type. Figure 5 shows that the particle motion for the largest part of the record, near the front of the T-phase, is strongly linear. This part of the record is clearly dominated by body waves, most likely P-waves, in agreement with the conclusion from travel times. Linearity decreases later in the record, although it's not clear whether that is due to the arrival of later scattered P-wave energy, surface wave arrivals, or a mixture of phases. The particle motion of the earliest part of the T-phase is elliptical and retrograde, suggesting that this part of the wave train is composed of Rayleigh waves. This is consistent with the simulations shown later in this paper, which indicate that surface waves can precede the P-wave near the coast, due to earlier conversion of the T-phase in water to surface waves.



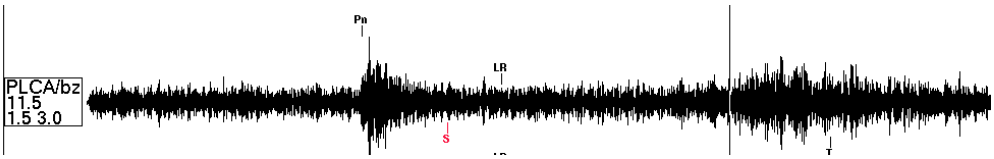


Figure 6. Map (left) and bathymetry/topography (right) for the path of T-phases from the 1998/09/30 earthquake recorded at PLCA. At the bottom is the seismogram recorded at PLCA with the phases marked.

Cook and Stevens (1998) collected a number of examples of T-phases recorded far inland from the coast. We show one example of these here. Figure 6 shows a T-phase from an earthquake in the eastern South Pacific ocean recorded in Argentina, on a path that traveled through the Andes and over a distance of approximately 300 km on land. The velocity labeled "AV" on the plot is the apparent velocity in the water after subtracting the travel time for propagation on land. This apparent velocity acts as a consistency check and should be close to the velocity of water if the T-phase is traveling on land at Pn speeds. This is additional evidence that T-phase propagation on land, at least once the wave has propagated well inland from the coast, consists of P-waves. Far inland T-phases have very peculiar travel times because they travel very slowly (~1.4 km/s) in the ocean, and very fast (up to 8 km/sec) as P-waves on land. Consequently, the T-phase starts out far behind the other seismic phases, but will eventually catch up to the Rayleigh wave if it travels far enough. Because of this, there is some danger in a semi-automated processing system like the IDC that T-phases could be misidentified as other phases.

Numerical simulations of T-phase Transfer functions

In order to better understand the T-phase transfer functions, and the nature of the seismic T-phase as compared the direct hydroacoustic signal, we have performed numerical simulations of the waveforms and the transition process. A more detailed description of this work is given by Stevens et al. (1999). Because of the excellent data set for the Loihi events, we are modeling waveforms that travel from Loihi to the California coast traveling through the location of the Point Sur hydroacoustic station. The map in Figure 1 shows the locations of the Loihi seamount southeast of the Hawaiian Island chain and the Pt. Sur station on the continental slope just to the southwest of Monterey Bay on the central California coast. The two locations are separated by a distance of 3745 km. Bottom bathymetry data along the path was obtained from the National Geophysical Data Center. The water depth is nominally 5000 m along the propagation path until the continental slope along the west coast of California is reached. In the region being modeled near Point Sur, a single typical profile having a sound speed of 1525 m/sec at the surface and 1482 m/sec at the sound channel axis at 700 m depth was used. 9 distinct temperature profiles were used to model the path between Loihi and Point Sur.

Kraken, a normal mode code written by M. Porter, was used to calculate the hydroacoustic wave field off the coast of California. Kraken can be obtained through the Ocean Acoustics Library web site at http://oalib.njit.edu/. To model the range dependence, the propagation path has been divided into 48 consecutive range-independent segments. The range intervals for the segments are determined by the places where the bottom bathymetry contours change by 100 m. 18 segments were used on the first 3710 km of the path, to the point where the solution was transferred to the finite difference calculation. The ocean bottom for the in-water propagation calculations is modeled as a lossy fluid layer of 1 km thickness with a compressional velocity of 2100 m/sec and density of 2100 kg/m^3 overlying a lossy fluid halfspace with velocity 6000 m/sec and density 2700 kg/m^3. The T phase source is modeled as a single omnidirectional point at a depth of 1 km, corresponding to the depth of the peak of the Loihi seamount.

The adiabatic approximation has been used in the normal mode numerical modeling to model propagation through the deep ocean. The problem is transferred to a finite difference code at the point where the ocean depth begins to decrease rapidly. The ocean water depth in this part of the calculation is shown in Figure 7, together with the number of modes that can exist at each integral frequency from 1 to 10 Hz over this range. As the ocean waveguide becomes progressively shallower, the water depth where a given mode at a given frequency reaches cutoff determines the location along the continental slope where that mode's energy couples into the land seismic field. Almost all of the modes couple into the bottom over the 80 km range from 3710 to 3790 km, with the majority of the higher order modes coupling in over the 35-km interval from 3715 to 3750 km, and the lower order modes in the 20-km interval from 3765 to 3785 km. It is over the corresponding depth interval for this latter range, i.e., depths shallower than 1000 m, that the elastic properties of the continental slope are most critical in modeling the ocean-

acoustic-to-land-seismic field coupling. A more detailed discussion of modal propagation in the ocean and modal coupling is given in D'Spain, et al (1999).

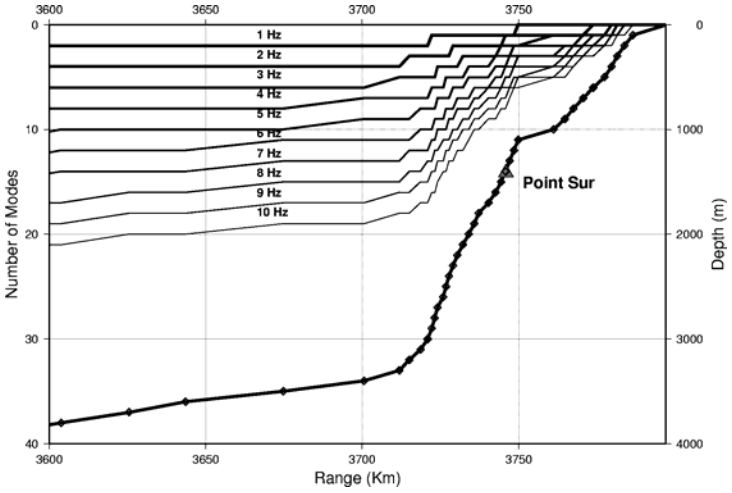


Figure 7. Number of in-water propagating modes at each frequency versus range. The bottom bathymetry also is shown as a set of connected diamonds. Each curve corresponds to a different frequency. The top curve corresponds to a frequency of one Hz, the second to two Hz, etc. At 10 Hz, 21 modes are supported at the deepest depth, while only two modes exist at 1 Hz.

Two-dimensional finite difference calculation of propagation onto land

We use the two-dimensional finite difference code TRES2D to model the propagation of hydroacoustic waves onto the coast. The Kraken normal mode solution in the ocean at a distance of 3710 km from Loihi was used as the source in the finite difference calculation. The first step in this process is to convert the modal spectra to time domain displacements and pressures at each node point. The first 20 seconds of the pressure waveforms at two depths are show in Figure 8. At 1005 meters depth, the fundamental mode is much larger than the other modes, however at 2160 meters depth, the second mode is larger then the fundamental. The modes have been filtered in a band pass of 1.0 to 4.5 Hz, consistent with the spectral resolution of the finite difference calculation.

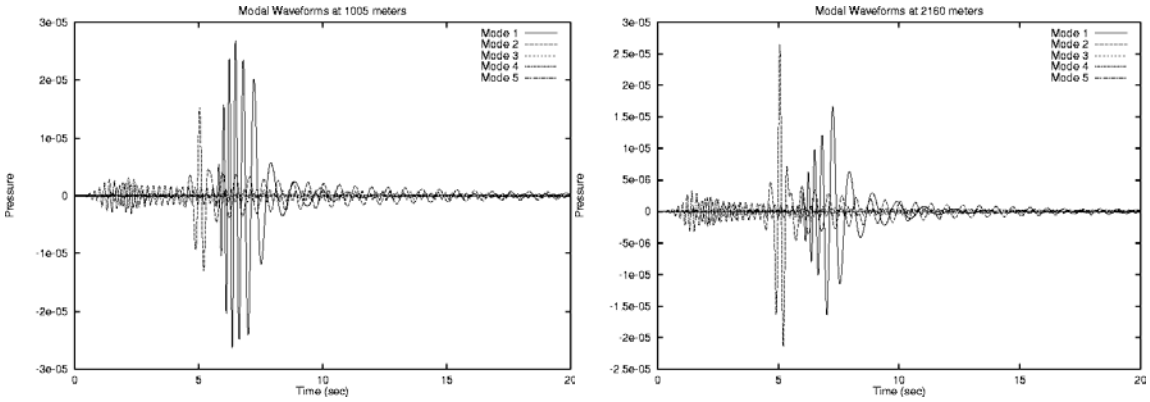


Figure 8. Input waveforms for first five modes at depths of 1005 (left) and 2160 (right) meters.

Even though this is a two-dimensional problem, it requires a very large calculation because the distances of interest are large, about 100 km, the wave speed in the water is slow, and we are interested in frequencies higher than 1 Hz. The velocity model is the California coastal model discussed earlier and listed in Table 1. The ocean model is based on the bathymetric profile along the path from Loihi through Point Sur and the water velocity profile in the ocean near Point Sur. We used a grid with a uniform spacing of 67 meters per grid cell, dimensions of 1500x500 grid blocks, and a time step of 0.005 seconds. The calculation was run for 20,000 cycles to obtain a duration of 100

seconds. The calculation should be accurate throughout the grid to at least 2.5 Hz. We expect to see some numerical dispersion in the 2.5-4.5 Hz frequency band in the lower velocity parts of the grid.

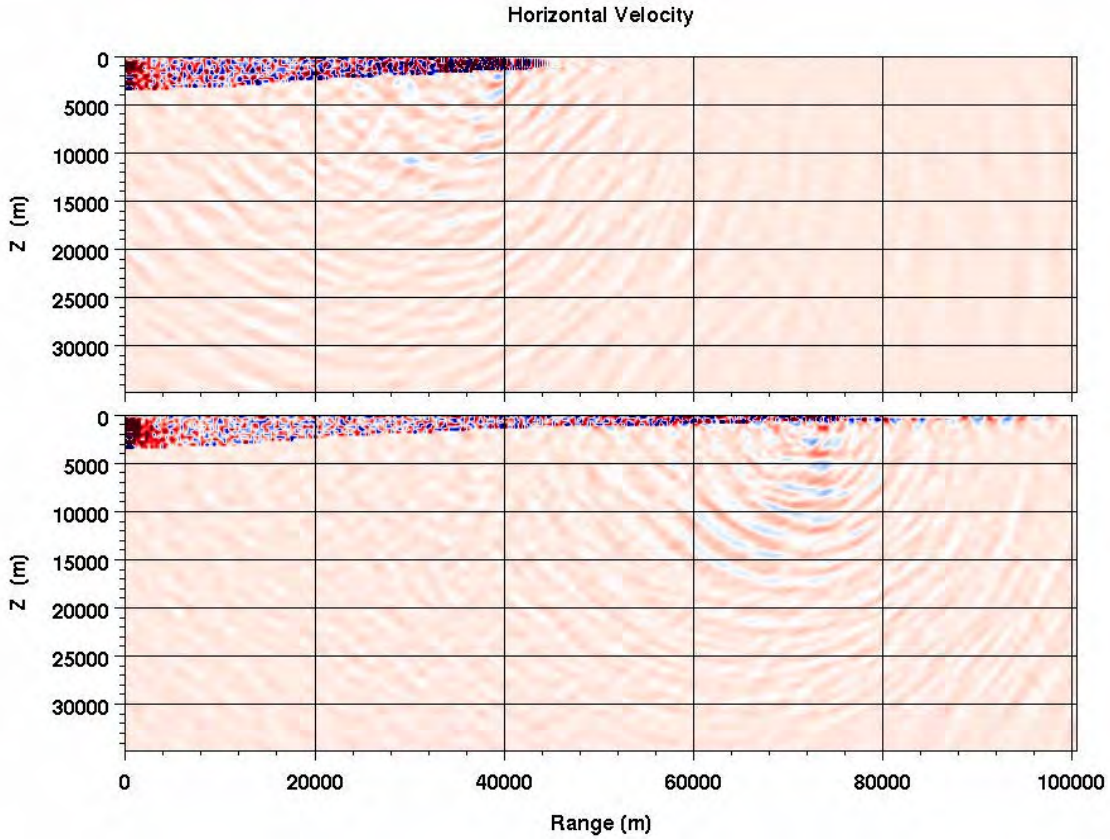


Figure 9. Snapshot of the calculation at 35 seconds (top) and 65 seconds (bottom). In the bottom figure, the dominant hydroacoustic arrival has reached a depth of 200 meters. At this point there is a burst of energy transferred as body waves from the ocean into land. Zero range corresponds to the point 3710 km from Loihi (see Fig. 18). The ocean/land interface at the surface is at location 87368.

Two calculations were performed, one with only the fundamental mode and one with the first 5 modes. Velocities for the full grid were saved for each second of time in the calculation, and these were used to create images and animations to help visualize the evolution of the velocity field. The results with a single mode and with five modes are very similar. There is a gradual decay of the hydroacoustic wave as it travels upslope, with body waves emitted continuously with varying amplitudes into the earth below, and a surface wave that gradually forms along the ocean bottom. At sharper bathymetric gradients the transmission is increased, and when the hydroacoustic wave reaches an ocean depth of 200 meters, there is a burst of energy much larger than anywhere else along the path. Strong surface waves are present on land from the edge of the ocean to the boundary of the calculation. Figure 9 shows snapshots of the fields at 35 seconds and 65 seconds. The second figure shows the burst of energy at 200 meter depth. Color animations of both calculations can be viewed online at http://www.maxwell.com/products/geop/Movies/hydro.htm. The calculated T-phases have some very odd properties. As can be seen in Figures 9 and 10, a strong surface wave develops quite early and can be seen on land at 65 seconds, which is the same time that the burst of body waves occurs. Consequently the surface wave appears in the wave train before, and simultaneous with, the body waves generated by the final decay of the hydroacoustic wave. The T-phase near the coast is therefore a mixture of seismic phases, similar to what was observed in Figure 5.

The results of the calculation were saved with a much finer time resolution at selected locations along the surface, and at a depth of 740 meters in the center of the sound channel. Figure 10 shows the calculated horizontal velocity in the water at 47235 m, which corresponds approximately to a location above the Point Sur hydroacoustic station. Also shown are the horizontal and vertical components of the waveform on the surface at location 87904 m, which is on land close to the coast. The amplitude ratios between the velocity on land and in the water are about 0.2, which

is consistent with our earlier estimates of the upper bound of the transfer function. The waveforms on land are complex and longer in duration than the underwater waveform, and are dominated by surface waves.

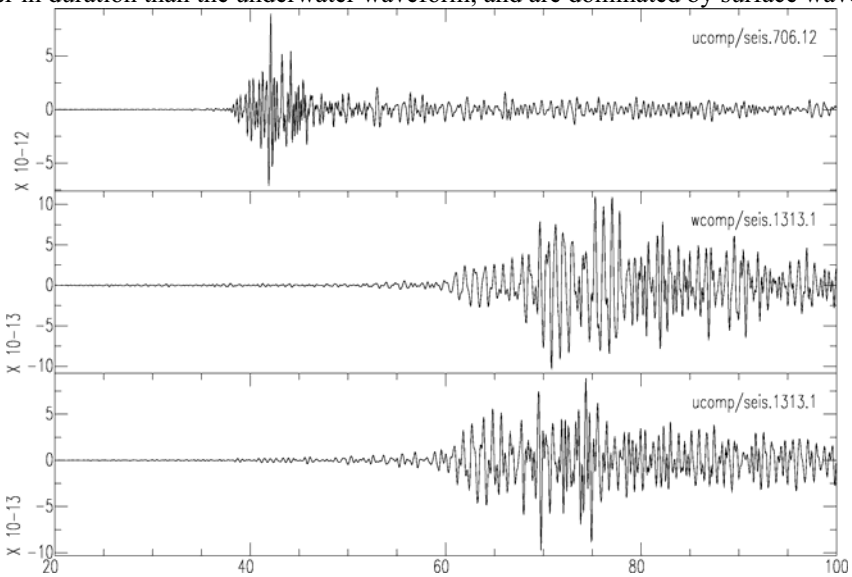


Figure 10. Calculated horizontal velocity at a depth of 740 meters in water at the location of the Point Sur station (top) and vertical (mid) and horizontal (bottom) components of the velocity on land close to the coast. Horizontal axis is time in seconds since the start of the calculation.

Figure 11 shows the spectral amplitude of the horizontal velocity in the 1-4 Hz frequency band underwater at the Point Sur location and the vertical velocity at a station on land close to the coast. The underwater spectrum is nearly flat across this frequency band. The spectra on land, however, exhibit a significant decline in amplitude with frequency, similar to the spectral decline observed for the coastal California stations. This suggests that during transmission from water to land, the higher frequencies are scattered more strongly than the lower frequencies, leading to a decline in high frequency content in the coastal waveforms.

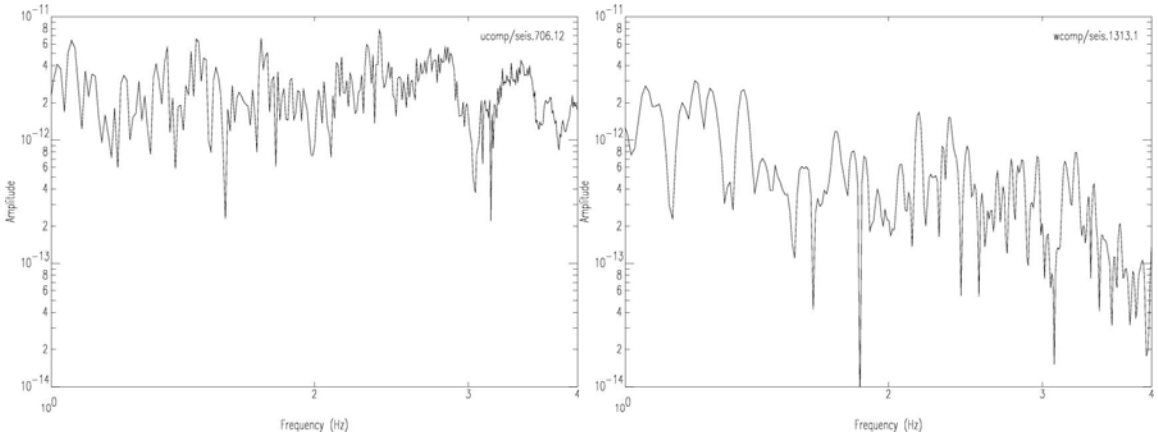


Figure 11. Calculated spectral amplitudes of the horizontal velocity at a depth of 740 meters underwater (top) and the vertical velocity at the surface on land near the coast (bottom).

Discussion

We have used T-phase observations in water and on land together with numerical calculations of T-phase propagation from water to land in order to understand the nature of T-phase conversion. The results are complex and at first glance contradictory. Whereas T-phases are observed to travel at P-wave speeds on land, the calculations show strong surface waves near the coast. However, the calculations also show lower amplitude body wave arrivals even very close to the coast, and strong body waves propagated away from conversion points along the ocean

bottom. Some of this body wave energy will return farther inland as Pg and Pn phases. The high frequency surface waves, on the other hand, can be expected to attenuate away very quickly and will not propagate to large distances. We therefore expect to see strong surface waves and smaller P-wave arrivals near the coast, with the surface waves dying out and the P-waves becoming dominant as the wave travels inland. The strong surface waves seen in this case may be somewhat anomalous, since they are formed in the ocean and propagate up the ocean bottom onto land. In a real earth with bottom sediments, these would be more strongly attenuated.

A similar study was performed by Piserchia et al (1998), in which they modeled T-phase conversion from an explosive source in the ocean, observed on the islands of Mururoa and Fangataufa in the South Pacific Ocean. They used ray tracing instead of a modal solution, and calculated Green's functions along a vertical boundary in order to propagate the source onto the islands. They found that the T-phase on land consisted of two P waves followed by two Rayleigh waves, where the multiple arrivals are identified as coming from different conversion points. The calculation was performed for a dominant frequency of 6 Hz, and the calculated P and Rayleigh waves were found to be comparable in size. Talandier and Okal (1998) studied conversion of T-phases on steep island slopes using data from the Polynesian Seismic Network and found from the observations and ray tracing arguments that the T-phase consisted primarily of P-waves at distances greater than 9 km from the conversion point. At closer distances, they found that the T-phase was more complex and composed primarily of S-waves and surface waves. They also suggested that only surface wave conversion would occur for slopes with angles of less than 16 degrees.

CONCLUSIONS AND RECOMMENDATIONS

We have used observations of T-phases underwater and on land to directly measure the transmission of energy from ocean to land, and have performed numerical simulations of T-phase propagation from ocean to land to obtain a better understanding of this process. The observations show that there is a significant decline in spectral amplitude with frequency on land compared to observations in the ocean. The observations also show that T-phases propagate primarily as P-waves once they are well inland. The numerical simulations provide considerable insight into the phenomena that occur when hydroacoustic waves propagate onto land. The calculations reproduce the spectral degradation observed in Coastal California stations. The calculations also suggest that strong surface waves may be present in T-phases observed near the coast while body waves may be the dominant phase farther inland.

ACKNOWLEDGEMENT

We thank Marcia McLaren of Pacific Gas and Electric for the use of her data and for pointing out to us the large T-phases from the Loihi events.

REFERENCES

Cook, R. W. and J. L. Stevens (1998), "TP Phase Observations at the pIDC," Transactions of the American Geophysical Union, v. 79, P. F558, November.

D'Spain, G. L., L. P. Berger, W. A. Kuperman, J. L. Stevens, and G. E. Baker (1999), "Normal mode composition of earthquake T-phases," submitted to Pure and Appl. Geophys.

Mooney, W. D., G. Laske and T. Guy Masters (1998), "Crust 5.1: A global crustal model at 5ºx5º," Journal of Geophysical Research, 103, 727-747.

Piserchia, P. F., J. Virieux, D. Rodrigues, S. Gaffet and J. Talandier (1998), "Hybrid numerical modelling of T-wave propagation: application to the Midplate experiment," Geophys. J. Int., V. 133, pp 789-800.

Stevens, Jeffry L., G. Eli Baker, Ron W. Cook, Gerald D'Spain, Lewis P. Berger, and Steven M. Day (1999), "Empirical and Numerical Modeling of T-Phase Propagation from Ocean to Land", submitted to Pure and Applied Geophysics.

Stevens, J. L. and K. L. McLaughlin (1997), "Improved Methods for Regionalized Surface Wave Analysis," Maxwell Technologies Final Report submitted to Phillips Laboratory, MFD-TR-97-15887, September.

Talandier, J. and E. A. Okal (1998), "On the mechanism of conversion of seismic waves to and from T waves in the vicinity of island shores," Bull. Seism. Soc. Am., V.88, pp. 621-632.

INFRASOUND MONITORING

INFRASONIC PROCESSING AT THE PROTOTYPE INTERNATIONAL DATA CENTER

David J Brown, Jin Wang, Charles N Katz, Anna Gault, Ronan LeBras,
SAIC, Center for Monitoring Research, Arlington, VA

Sponsored U.S. Department of Defense, DTRA
Contract No.DTRA01-99-C-0025

ABSTRACT

The PIDC has been developing an automatic and interactive data processing system to provide spatial and temporal source location information for highly-impulsive sources in any terrestrial environment. Here we review several recent refinements that have been made to the infrasonic data processing system. This system has been processing infrasonic data automatically since April 1998 and interactively since December 1998.

Improvements to the infrasonic data processing system are currently being implemented in a number of different areas.

First, we are incorporating seasonal travel-time information into location processing. A 3D propagation model based on the Eikonal equations for acoustic-gravity waves, which uses a seasonal atmospheric model to provide ambient wind and temperature information, is used to provide a set of azimuthally varying travel-time tables for each microbarographic array site.

The second area of improvement is in detector tuning. Sophisticated event detectors such as the infrasonic event detector under development at the PIDC require a significant number of tunable parameters, which can be written succinctly as a vector {P}. A comprehensive set of procedures for determining the optimal vector {P} have been established. These procedures involve determining a set of curves which yield the probability of detection (PD) as a function of signal to noise ratio (SNR) at a given false alarm rate for a specified vector {P} = {P0}. By varying {P} it is possible to determine the curve that yields the Minimum Detectable Level (MDL), i.e. the smallest SNR that gives a specified PD = PD0. In conjunction with efforts at the Los Alamos National Laboratory, tuning activities have focussed on the IMS prototype infrasonic array in New Mexico (DLIAR), but will culminate in a set of procedures that can be used to tune the detector for any IMS infrasonic array when the data becomes available.

Third, we have investigated the azimuth and slowness deviations due to the relative heights of the sensors. Our research indicates that significant errors in slowness, azimuth and signal power can be introduced into the signal feature extraction procedure if sensor height differences are not accommodated. Deviations in azimuth of up to several degrees, and a power loss of 10% seems to be possible if these factors are not accounted for.

Fourth, we have improved procedures for the interactive processing of infrasonic data. These procedures allow for infrasonic source locations based on two intersecting azimuths, and also provide rudimentary means for inferring source to receiver distance based on signal frequency composition. In addition, these procedures also provide event definition criteria in the case where an event is formed from a combination of seismic, hydroacoustic and infrasonic arrivals.

Keywords: Infrasound, Detector-tuning, infrasonic travel-times

OBJECTIVES

The infrasonic processing subsystem at the Prototype International Data Center (PIDC) in Arlington, VA, forms part of a larger system currently under development at the PIDC where seismic, hydroacoustic, radionuclide and infrasonic methods are used to detect and locate impulsive sources with a yield of at least 1-kT in any terrestrial environment. The infrasonic processing subsystem gives the PIDC the ability to estimate the temporal and spatial source location for impulsive sources that couple in some part to the atmosphere. The infrasonic automatic data processing system is being completed in stages. Release two (of four releases) of the system is currently in operation at the PIDC. It is anticipated that the final version of the system will be operational by mid 2001.The objective of this current research is to enhance performance of the operational system and has four main aims. The first objective is to improve the traveltime information currently used in the infrasonic source location algorithm. The second aim is to 'tune' the detector so as to optimize its performance for events of interest (1-kT explosions located within approximately 3000 km from the receiver). The third objective is to determine the magnitude of errors in observed azimuth and slowness that occur due to relative height differences among the sensors in an infrasonic array.The fourth objective is to determine accurate interactive procedures for infrasonic analysis. It is intended that the completed system will process continuously transmitted data from the full 60-station International Monitoring System (IMS) infrasound network. It will therefore be necessary that reasonably accurate automatic event processing take place prior to any interactive analysis and production of the Reviewed Event Bulletin, the final product of the PIDC.

RESEARCH ACCOMPLISHED

1.0 Travel-time information

Standard IMS array geometry implies that observed azimuth may be measured quite accurately for many recorded infrasonic signals (see Fig. 1).

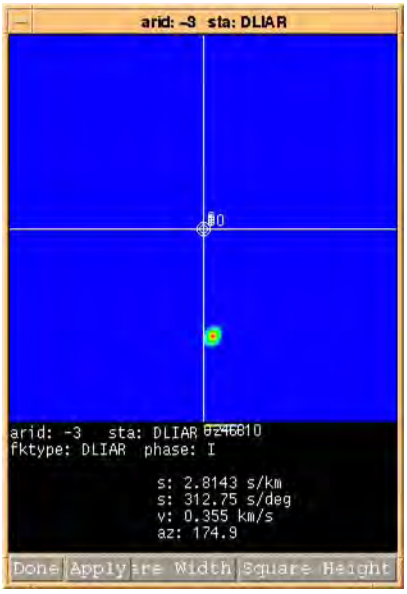


Figure 1: *XfkDisplay* output showing the slowness plane location of an infrasonic source. Diagram indicates zero slowness at the center and 5 sec/deg at the domain boundaries.

In view of the relatively poor constraint one has on the predicted travel-time for infrasonic arrivals, it is reasonable, therefore, to make observed azimuth the primary source location parameter for infrasonic sources. Travel-times still need to be estimated, however, for the purpose of temporal source location and refinement of spatial location, as well as preventing causal violations.

The infrasonic travel-time model presently in use at the PIDC is particularly crude as it assumes that all signals have horizontal speeds across the ground of 320 m/s. This obviously necessitates the inclusion of large variances on the travel-time.

In order to refine the determination of infrasonic travel-times, a more sophisticated propagation model is being introduced. An eikonal ray-tracing algorithm for acoustic waves in an atmosphere with seasonal variations in wind and temperature is being used to provide travel-time information for infrasonic signals recorded at each infrasonic array. The philosophy at the present time is to incorporate only seasonal influences in the determination of travel-times. The refined seasonal travel-time information will be introduced in stages. In its final form, the automatic processing system will attempt to identify all infrasonic arrivals based on a hypothesized propagation path. As an interim measure, however, only a single possible infrasonic phase-type will be used. The ray-tracing algorithm will be used to infer travel-times for each arrival at an infrasonic array. Based on the behavior of a multitude of rays emanating from a given source with a given azimuth of departure, the time and range of each bounce will be noted. A single interpolating curve, which focuses on the stratospheric arrival when it exists and the dominant thermospheric arrival otherwise, will be calculated for each operational array, for every 1 degree of azimuth and for each season. In its final form, the source location algorithm will use a separate interpolating curve for each of the different phase types (tropospheric, stratospheric and thermospheric). In the event that a predicted arrival type doesn't exist, a generic curve will be used. An example of such a set of curves is indicated in Fig. 2.

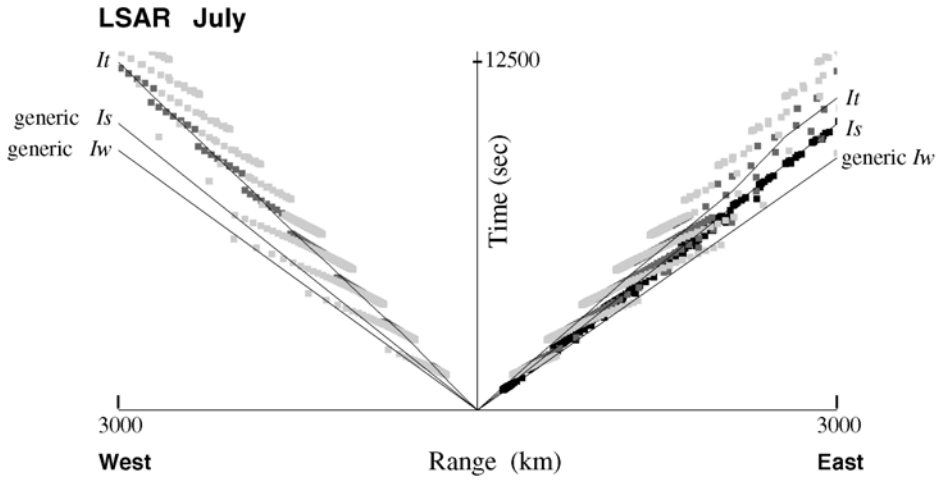


Figure 2: Theoretical bounce-point locations determined via an Eikonal ray-tracing model for acoustic waves propagating in an atmosphere with seasonal variation in wind and temperature. Travel-time curves for the three different arrival types have been shown. (Adapted from Brown et al. (1999))

It will ultimately be necessary to accommodate the wind-generated azimuthal deviations in the source location algorithm. It has been shown (Brown, *In preparation*) that these effects can be quite significant, at least 5-6 degrees in some circumstances.

2.0 Deviations in observed azimuth and slowness due to relative height differences of the sensors.

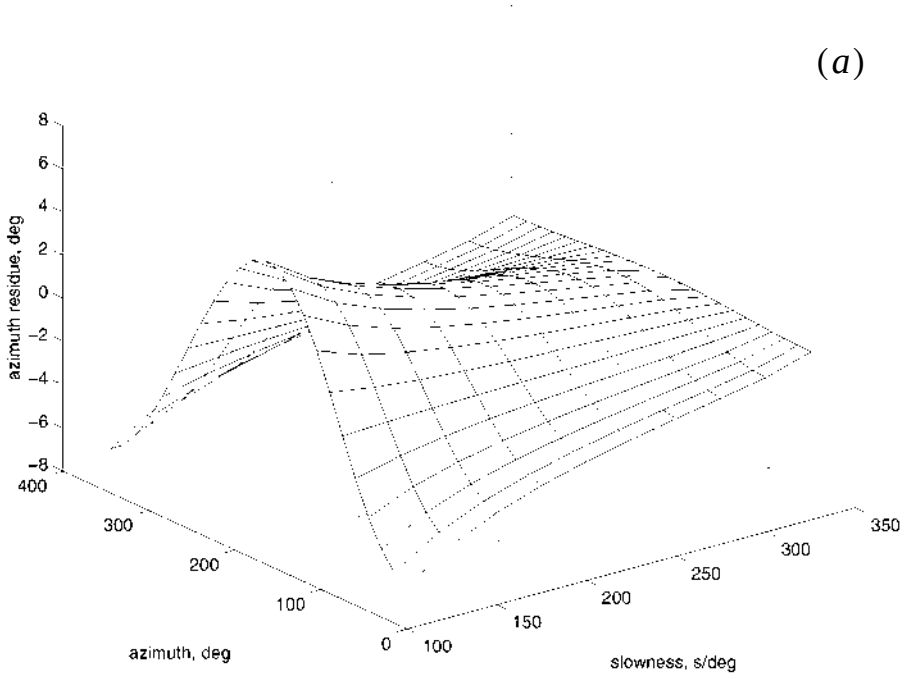
One aspect of infrasonic signal processing that has received little or no attention in recent years is the influence that sensor height differences have on the estimated azimuth and slowness of infrasonic signals impinging on an array. With the commencement of the installation of the International Monitoring System (IMS) infrasonic network, and subsequent processing of the array data, it becomes important to investigate the magnitude of these effects.

Table 1 shows the relative heights of the sensors comprising the DLIAR infrasonic array.

element	Northerly deviation rel. to center (m)	Easterly deviation rel. to center (m)	height rel. to center (m)
North	728.5	151.7	-11.9
East	-437.7	789.0	-24.8
Center	0.0	0.0	0.0
West	-226.2	-534.3	16.0

Table 1: DLIAR array sensor locations.

Figure 3 shows the deviation in observed azimuth and slowness that will occur at the DLIAR infrasound array due to the relative height differences of the 4 sensors (Wang et al, 1999 provide details on the algorithm used).



.

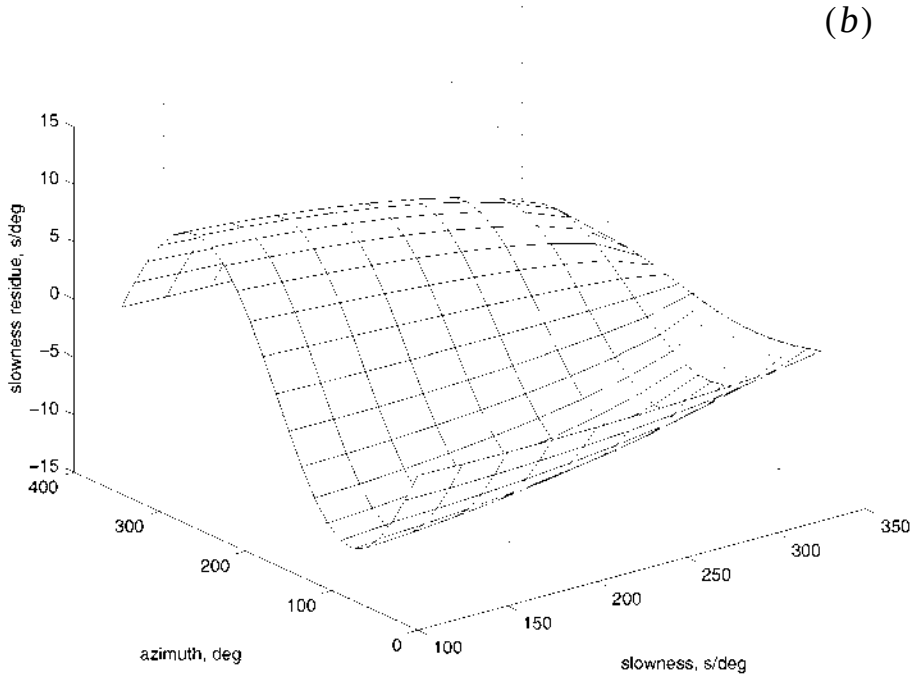


Figure 3: azimuth and slowness residues due to sensor elevation differences at the DLIAR array. (a) azimuthal deviation (deg)., (b) slowness deviation (s/deg)

Figure 3a. shows a steady increase in maximal azimuthal deviation from about 0.2 degrees at 340 m/s and 180 degrees, to about 2.0 degree at 500 m/s and 180 degrees. Similarly, Fig 3b. shows a steady increase in maximal speed deviation from about 1.2 m/s at 340 m/s and 250 degrees, to about 17.6 m/s at 500 m/s and 250 degrees. These values are significant and need to be accommodated in the feature extraction algorithm.

3.0 Detector Tuning

The infrasonic processing system at the PIDC has had to be developed largely in the absence of IMS quality data. Nevertheless, the infrasonic signal detector needs to be 'tuned' for the events of interest (i.e., a 1-kT source located up to 3000 km from the receiver). With LANL involvement, a substantial and sophisticated tuning exercise using synthetic waveforms that represent signals of interest is being undertaken. The tuning exercise, which at the time of writing is far from complete, consists of the following steps:

1. Approximately 100 hours of data from the DLIAR array (an IMS-type array) are selected. This data is chosen to represent the complete set of possible ambient conditions, from quiescent to windy, with and without microbarom clutter. The time interval chosen is from Feb 21, 1998 00:00:00 to Feb 25, 1998 00:00:00 and appears to be relatively free of highly-impulsive signals.
2. The waveform data is scanned, both manually and with the detector set to a low detection threshold, to determine where all possible signals are located; these areas are to be avoided as much as possible in the subsequent analysis. Due to the ubiquitous nature of the microbaroms, however, it may be impossible to avoid coherent energy due to the microbaroms. Although the microbaroms tend to come from a restricted direction at DLIAR, the side-lobe energy generate by the sensor locations may not be insignificant. Figure 4 shows the array response for a source with frequency 0.33 Hz, due West of the array with an apparent speed of 340 m/s. When considering a band of possible arrival azimuths, it becomes obvious that it will be nearly impossible to avoid the microbarom activity or dominant side-lobe activity. It is, of course, of interest to perform the tuning exercise at some stage with a strong microbarom presence, but in the early stages of the tuning exercise it is desirable to reduce the microbarom influence as much as possible.

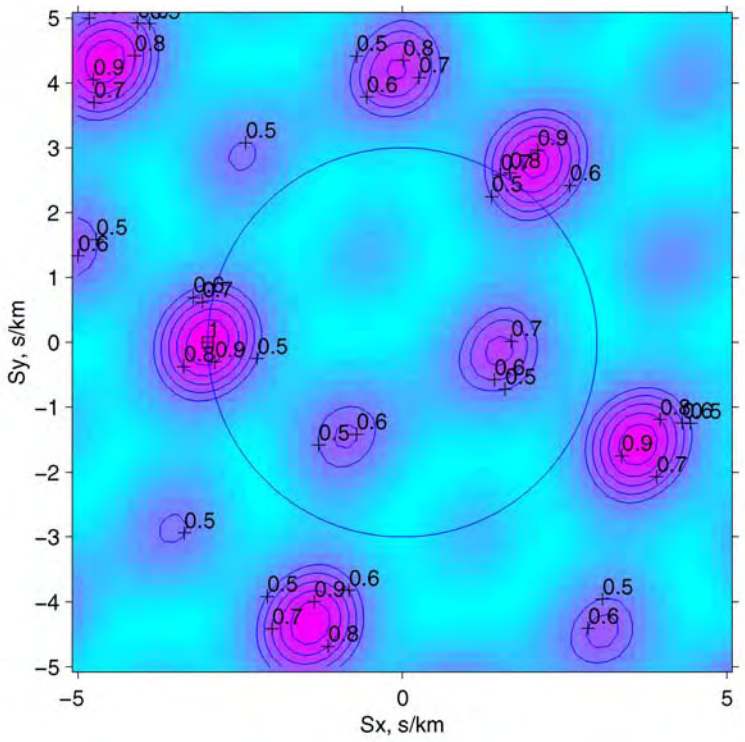


Figure 4: Array response for DLIAR array at 0.33Hz for signal travelling at 340 m/s from an azimuth of 270 degrees.

Manual scanning of the slowness plane in the frequency band 0.125 Hz to 0.333 Hz with 8-pole tapering for the 100 hours of data, yields the distribution of coherent SNR, observed azimuth, and speed as a function of time that is shown in Fig. 5. This figure provides information about the quiet times for microbarom activity and are the desirable locations for the initial implantation of the signals.

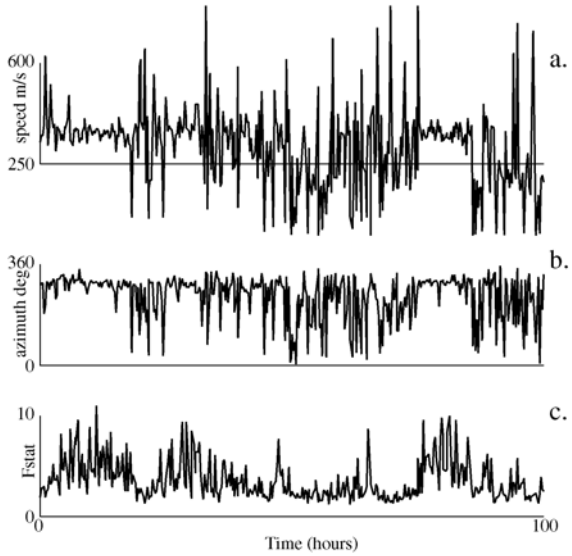


Figure 5: Microbarom activity for the 100 hours of test data. a.) speed versus time. b.) azimuth versus time. c.) Fstat versus time.

3. A signal of interest is chosen to implant into the background data. It is intended to use an artificially generated signal, designed to represent the signal from a 1-kT explosion located 2000 km away from the sensor. The synthetic signal decided on is that described by Dighe at al (1998) in relation to the modeling of infrasonic signals from low yield sources up to distances of several thousand kilometers. A representative signal is shown in Fig. 6, and represents the signal recorded down-wind from a hypothesized source located 2500 km away.

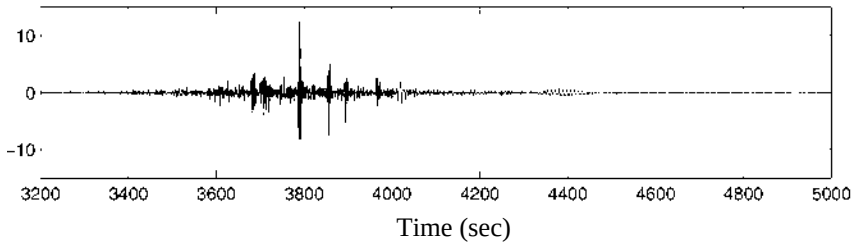


Figure 6: Representative synthetic waveform used in the detector tuning exercise. Units are pressure in dynes/cm^2 [adapthed from Dighe et al, 1998]

The down-wind signal is used because it predicts both stratospheric and thermospheric arrivals.

4. The signal is treated so that it matches the various properties of the background data and so that when duplicated across the channels, the correlation is physically realistic. Additionally, the multipathing character of the signal is preserved.
5. An acceptable False Alarm Rate (FAR0) is selected, and the detector passed over the background data a number of times with the set of tuning parameters changed each time until the FAR0 level is achieved.
6. Approximately 100 representations of the signal with varying SNR are implanted randomly throughout the data so as to avoid the regions with signals. The set of tuning parameters are systematically changed so that the same FAR0 value is obtained on the data free of implanted signals. As the SNRs of the implanted signals vary from very small to very large, certain signals will be detected and some will not. In this way a probability of detection versus SNR curve can be obtained. For a given probability of detection, PD0, and the prescribed false alarm rate FAR0, we seek the arrangement of the tuning parameters which yields the smallest SNR. This is known as the Minimal Detectable Level (MDL).

4.0 Interactive Review of Infrasonic Data

Analysts have been reviewing infrasound data at the Prototype International Data Centre (PIDC) since December, 1998. The last of the technologies to be integrated into the PIDC interactive system, infrasound has necessitated some modifications to the existing analysis interface, and to analysis procedures.

4.1 Analyst Review Station

Analysts perform their review on an interactive display known as the Analyst Review System (ARS) (Fig. 7). Compliments to this interface include a slowness determination tool (*XfkDisplay)* -which also indicates the level of spatial coherence of the most coherent arrival, and a spectral analysis tool (*SpectraPlot*).

ARS is the main interface through which all time-series technologies are analyzed. Operational analysts typically review infrasound data at approximately 12 hours behind real time. Although future plans include the evaluation of all infrasound detections, analysts currently examine only those infrasound events that have been detected by the automatic processing, shallow terrestrial events for possible infrasound associations, and shallow oceanic events for possible infrasound associations.

The functionality in ARS includes the ability to display waveforms, add phases, evaluate and modify phases, and to save events to several databases. For the integration of infrasound into ARS, which was formally used for seismic and hydroacoustic data evaluation, new functionality had to be added to handle this new technology. Most important is the

inclusion of an *mx* trace along with the waveform display. The *mx* trace is a beam that indicates the level of signal coherence across the elements of a given array. ARS also now has the ability to retrieve six hours of data from the calculated event time, in order for the comparatively late-arriving infrasound data to be included in the event.

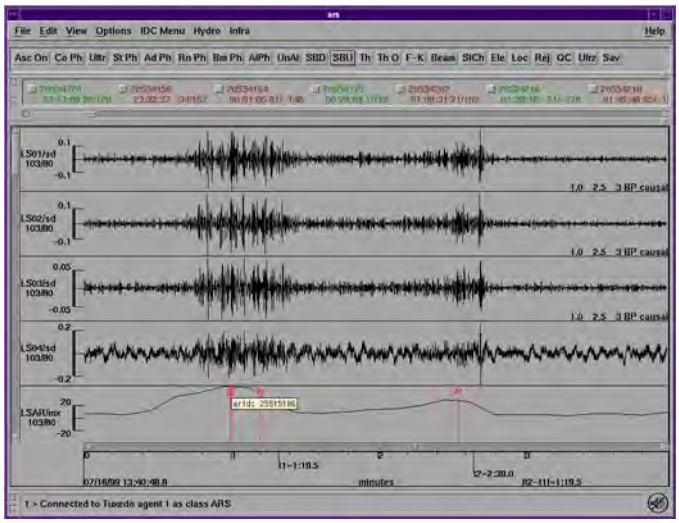


Figure 7: Analyst Review Station display

Besides filtering, the two most powerful tools that analysts use to evaluate infrasound data are the *XfkDisplay* tool and the *SpectraPlot* tool.

The *XfkDisplay* tool computes the apparent velocity recorded at an array and, as such, can provide an indication of the steepness of the vertical incidence angle. This is what analysts use to judge relative heights of the atmospheric layers at which the signals are refracted, and hence provide an idea of the phase of the arrival. Analysts use an increasing apparent velocity through multiple arrivals to suggest a single source.

SpectraPlot provides a visual display of the total power of the sampled energy at a given frequency. Analysts use *SpectraPlot* to determine if signals recorded at different stations belong to the same event by looking for decreasing dominant frequencies as distance from the event increases.

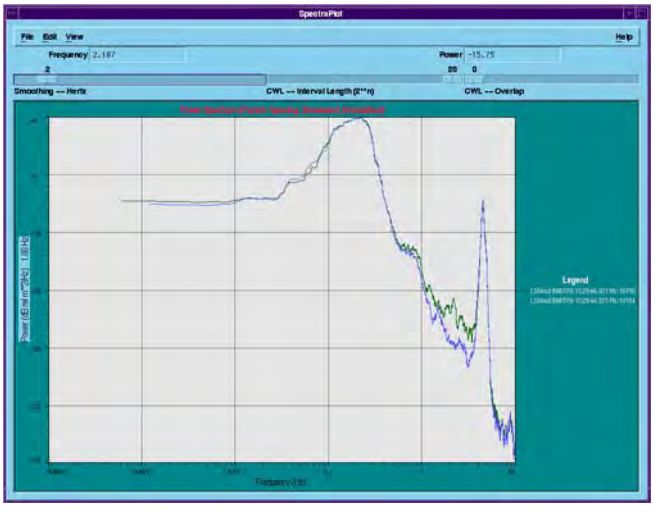


Figure 8: *SpectraPlot*

Analysts apply a number of narrow-band filters to waveforms when performing their analysis. The recommended initial filter is set at 1-3 Hz for the shorter baseline arrays, and 0.1-2 Hz for the IMS-type arrays. However, analysts have been cautioned against becoming too familiar with data from the smaller infrasound arrays, as signal characteristics at these arrays are considerably different than those recorded at the larger, IMS standard arrays. Other than the special microbarom analysis band [0.125-0.333 Hz], analysts have also been alerted to the risk of using filter bands below 0.5 Hz on small arrays; below this frequency, most energy appears to be spatially coherent.

To the extent that waveform data is available at the PIDC, a significant number of infrasound events have been recorded. These include a swarm of events from early December 1998, a number of chemical explosions, shuttle launches, and bolides. Since the automatic pipeline started processing infrasound data in April 1998, there have been 460 automatically associated detections and 18 analyst-reviewed detections used to build infrasound events.

Since infrasound is still in the early stages of being used operationally, strict event definition criteria have been imposed until more results are studied. Restrictions on event definition include the following:

1. I-phases must be seen on at least 2 stations for the event to be saved to the Late Event Bulletin (LEB), but must be seen on at least 3 stations to be saved to the Reviewed Event Bulletin (REB). The difference between the two bulletins is subtle. The LEB contains the results of analyst review, and is mostly used internally as a research tool. The REB is the official PIDC published bulletin. It was decided by development and operations staff that more defining parameters be required for the published bulletin until more events are analyzed and archived.

2. Time and azimuth are the only defining parameters, that is; time and azimuth contribute to the event time and location calculations, whereas slowness does not.

3. For time to be a defining parameter, we currently allow the very loose criteria of a 30 minute time residual. The azimuth residual must not be greater than 15 degrees. No seismic events with estimated depth greater than 40 km may have infrasonic associations.

CONCLUSIONS AND RECOMMENDATIONS

In this paper we present refinements to the PIDC infrasonic processing system that are currently being implemented. The first, improved travel-time information, will improve the knowledge of the spatial and temporal location of a source. The second, detector tuning has never been performed prior to this exercise and will yield optimal detection parameters for the events of interest. In the absence of sources of interest to the IMS/IDC it is suggested that these studies be used as a basis for detector tuning procedures for the individual IMS arrays as they come online. Procedures along similar lines can be used to test source location procedures as the IMS infrasonic net is progressively installed. The third refinement deals with the errors in observed azimuth and slowness that can occur simply because the array sensors don't all lie in the same horizontal plane. The studies indicate that significant errors can occur and should be accommodated in the feature extraction part of the detection algorithm. The fourth refinement concerns the development of interactive procedures for the examination of infrasonic signals. Although at an early stage of development, these analyst procedures have allowed infrasonic associated events to contribute to the Reviewed Event Bulletin.

ACKNOWLEDGEMENTS

The authors would like to thank Dr Rod Whitaker of Los Alamos National Laboratory for his assistance with various aspects of this project.

REFERENCES

Brown, D.J., Katz, C.N., Le Bras, R., Flanagan, M.P., and Gault, A.K., (1999) I*nfrasonic Signal Detection and Source Location at the Prototype International Data Center,* pageoph, submitted.

Dighe, K.A., Whitaker, R.W., and Armstrong, W.T., (1998) *Modeling Study of Infrasonic Detection of 1 kT Atmospheric Blast.* In, *Proceedings, 20th Annual Seismic Research Symposium On Monitoring a Comprehensive Test Ban Treaty, Santa Fe NM, September 21-23*, 571-578.

Wang, J. Israelsson, H., and McLaughlin, K.(1999), *Signal Detection and Estimation at the New IMS Array at Mina*. In, *proceedings of the 21st annual Seismic Research Symposium, Las Vegas, Nevada, September 21-24, 1999*

RESULTS OF THE INFRASONIC SITE SURVEY AT CTBT STATION IS59, HAWAII

Milton Garcés[1], Hawaii Institute of Geophysics and Planetology
University of Hawaii, Manoa
[1]Also at the University of Alaska, Fairbanks

Henry Bass, National Center for Physical Acoustics, University of Mississippi

Sponsored by the U.S. Department of Defense
Contract No.: DASG60-99-0018

ABSTRACT

An infrasonic site survey for station IS59 in the island of Hawaii was performed from June 2 to June 16, 1999. Instruments were deployed at two prospective sites. The first site, in the Kulani forest, was located at a mean elevation of 1.7 km on the windward side of the island, approximately 10 km downhill from the Northeast rift zone of Mauna Loa Volcano. The second site was located in the Kahalu'u forest at a mean elevation of 1 km on the leeward, drier side of the island. Comparison of infrasonic noise levels recorded at the candidate sites demonstrated that the Kahalu'u forest was the quieter of the two sites.

Key Words: Infrasound, site survey, IS59, Hawaii

OBJECTIVE

The primary purpose of the site survey at Hawaii is to determine a suitable location for a CTBT infrasonic array (IS59) with the lowest possible background noise level. This paper presents a comparison of infrasonic noise levels observed at two candidate sites in opposite sides of the island.

RESEARCH ACCOMPLISHED

1. Introduction

A site survey for infrasound array station IS59 in the International Monitoring System (IMS) was carried out on the island of Hawaii over the period from June 2 to June 16, 1999. The survey was conducted by the University of Hawaii in collaboration with the Infrasound Section of the International Monitoring System Division of Comprehensive Nuclear-Test-Ban Treaty Organization. The survey was conducted in accordance with the infrasound site survey requirements described in the Preparatory Commission guidelines.

Hawaii is the largest island in the chain with dimensions of approximately 150 km (N to S) by 130 km (E to W), and a total land area of 10,433 km^2. A map showing the topography of the island is shown in Figure 1. The IMS coordinates are within 3 km of the Kulani site (Figure 2). The Kulani survey area is at high elevation (1.7km) in the windward, rainy side of the island, hosts a variety of endangered flora and fauna, and is close to two of the most active volcanic areas in the world. The Kahalu'u survey area (Figure 3) is at a lower elevation (1 km) in the leeward, dry side of the island, where trade winds are absent. Volcanic risk at the Kahalu'u site is minimal.

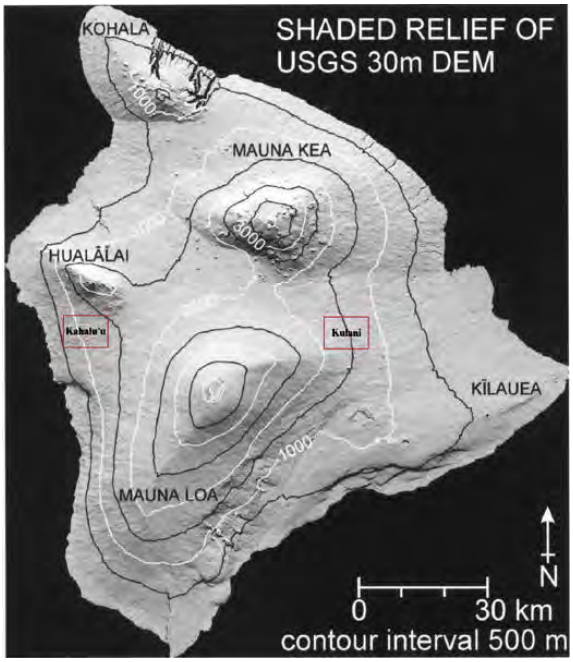


Figure 1. Shaded digital elevation map of Hawaii, showing the extreme topography of the island and the five main volcanoes. The two survey sites in the Kulani and Kahalu'u forests are demarcated by boxes. The IMS coordinates for IS59 (19.6N, 155.3W) are contained within the Kulani area. (DEM image provided by Scott Rowland, University of Hawaii, Manoa)

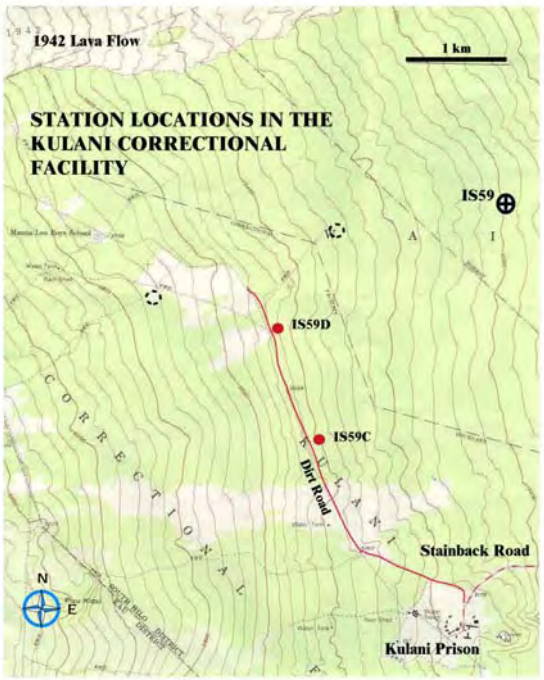


Figure 2. Site survey area on the Kulani Correctional Facility, and designated station coordinates for IS59. Solid dots mark the locations of survey stations, and dashed dots represent two additional elements required to complete a 4-element array.



Figure 3. Site survey area on the Kahalu'u Forest. Solid dots mark the locations of survey stations.

2. Experimental Equipment and Procedure

Observations of background micropressure noise, wind speed, wind direction and temperature were made using four sets of Orion portable field recorders, Vector Instruments anemometers, Skye Instruments temperature sensors and MB2000 microbarometers. Unless otherwise stated, all microbarometers had porous hoses. The campaign strategy consisted of two distinct stages. The initial stage involved the deployment two stations in the Kulani site and two stations in the Kahalu'u site in order to record simultaneously at both prospective sites. Comparison of the infrasonic data recorded during this first stage of the survey showed that the Kahalu'u site provided a better location for IS59. This decision led to the second stage of the campaign, where all stations were established in the Kahalu'u site and located as close as possible to the proposed IMS array configuration.

From June 1 to June 2 the absolute pressure microbarometers were reset for sea level, and a huddle test was performed to check the sensors and digitizers. On June 2, three stations were deployed at Kulani (Figure 2): one with porous hoses (C), a second station (H) with an open port co-located with station C, and a third station (D) at a different location. On June 3, station H was removed, and stations C and D were left to record continuously until June 8. On June 4, two stations were installed at Kahalu'u (stations A and B, Figure 3), which recorded continuously until June 16. On June 7, data was downloaded from all Kahalu'u and Kulani stations, and a comparison of the noise levels demonstrated that Kahalu'u was quieter. On June 8 the two stations in Kulani were removed, and an open-port microbarometer (K) was co-located with site A in Kahalu'u. On June 9, site K was removed, and two new stations were deployed in the Kahalu'u site (stations E and F). A 4-element array with an aperture of approximately 1.85 km recorded continuously from June 9 to June 16 in Kahalu'u.

This paper describes the results of the infrasonic noise survey during the fist part of the filed campaign, when simultaneous measurements were made at the Kahalu'u and Kulani sites from June 4 to June 8, 1999. During this time period, stations A and B recorded in the Kahalu'u forest while stations C and D recorded in the Kulani forest.

3. Results of Noise Survey

3.1 General Description of Noise Characteristics

The average infrasonic noise characteristics in Hawaii will be determined by the diurnal heating and cooling cycle, the thermal interaction between the relative large landmass of the island and the ocean, and the flow of the ever-present Northeasterly trade winds around the extreme topography of the island. Since the Kahalu'u forest is completely protected form the trade winds and incoming weather by Mauna Loa, Mauna Kea, and Hualalai Volcanoes, this site is expected to be acoustically quieter than the Kulani site. The following section illustrates in more detail how this intuitive argument is corroborated by infrasonic data.

3.2 Evaluation of Noise Levels

The noise characteristics at individual potential array sites may be evaluated by comparing the power density spectra of micropressure data from the various sites recorded over the same time interval. Most of the analysis described in this report has, been carried out using a modified version of MATLAB programs developed by Dr. Manfred Henger and Dr. Gernot Hartmann (Henger et al., 1998). Power spectra, in Pa^2/Hz, are estimated by Welch's method using a non-overlapping Hanning window of 4096 samples (204.8 s) and averaged over an integer number of hours.

During the IS59 site survey, average wind velocities were lower than 1 m/s. Due to the unresponsiveness of the anemometers to such low-wind conditions, wind measurements were not useful during most of the survey.

3.3 Daytime Noise Conditions

Averaged power spectral density for the 12 hours of the day (6AM to 6 PM local time) of June 5 and 6 are shown in Figure 4 for all sites. The microbarom peak at approximately 0.23 Hz is present at both the Kahalu'u and Kulani stations, although the microbarom peak appears slightly stronger in Kulani. Array processing of microbarom signals recorded during the second stage of the campaign suggest that this microbarom frequency may be associated with swells driven by the ever-present Northeasterly trade winds. This would be consistent with the higher microbarom peak observed at Kulani, on the Eastern side of the island. For frequencies between 0.2 Hz and 2 Hz, noise levels have similar slopes at all stations, but levels are higher by a factor of two or more at the Kulani site. For frequencies below 0.2 Hz, the difference between the Kahalu'u and Kulani sites is more severe, with noise levels about an order of magnitude higher at the Kulani site. No clear interpretation has been given for this difference in spectral levels at low frequencies, although it is possible that Mauna Loa and Mauna Kea volcanoes block westward-propagating eddies that may travel with the trade winds.

A small spectral peak near 0.12 Hz was observed at the Kahalu'u site on June 6. This peak, well below the noise floor of the Kulani site, vanished after a few days. Analysis of secondary microbarom peaks observed during the second stage of the site survey suggest that these secondary peaks may be associated with low-pressure systems in the Pacific Ocean.

3.4 Nocturnal Noise Conditions

Averaged power spectral density for the 12 hours of the night (6PM to 6 AM local time) of June 5 and 6 are shown in Figure 5 for all sites. Spectral features are similar those of Figure 4 in the frequency band between 0.2 Hz and 2 Hz, with small variations in the noise levels. At frequencies below 0.2 Hz, noise levels are slightly reduced in Kulani during the night, although they are still higher than at Kahalu'u. On June 6, the slope of the mean nocturnal spectrum at Kahalu'u changed noticeably when the 0.01 Hz level dropped. Diurnal noise levels fluctuations at the Kahalu'u site are most pronounced in the 0.01 to 0.1 Hz band, as will be discussed in the next section.

3.5 Mean, Maximum, and Minimum Noise Levels

Averaged power spectral density for all 24 hours of June 5 and 6 are shown in Figure 6 for all sites. It is evident that the Kahalu'u stations have lower average noise levels than the Kulani stations. The diurnal variability in noise levels for all sites during the 24 hours of June 6 are shown in the upper panel of Figure 7. Each gray line represents a one-hour average, and the solid line represents the mean spectrum, as shown in Figure 6. Figure 7 shows that he Kulani site does not show much diurnal variability, possibly because its noise characteristics are determined by the dominant trade winds, which are quite stable. Maximum and minimum noise levels at Kulani may correspond to the evening slackening of the trade winds. In contrast, the Kahalu'u site shows a strong variability for frequencies below 0.1 Hz. Since the trade winds are completely absent in the Kahalu'u site, it is likely that its noise characteristics are determined by local effects which may be driven by ocean-land thermal interaction. The relatively small variability and low noise floor of high-frequency noise levels at all stations reflects the low wind conditions encountered at both sites.

The lowest noise level shown in the first panel of Figure 7 occurred in Kahalu'u between 0 and 2 UT of June 6, which corresponds to 2 and 4 PM local time of June 5. It is possible that during this time, clouds and mist forming in the mountain created a stable, thermally equilibrated layer with no wind. However, the rogue spectral peak at 0.12 Hz prevented this episode from producing the lowest levels. The lowest noise levels observed during the site survey occurred on June 11, 1999, after the installation of a 1.85 km aperture array in the Kahalu'u site (Figure 3). The minimum noise levels for all the array elements are shown on the lower panel of Figure 7. The times correspond to the seven-hour period between 5 PM and midnight. The formation of a stable layer on the mountain slopes during the late afternoon may also explain the exceptionally low noise levels at this site. Because of the low noise floor, it was possible to observe the formation of a secondary microbarom peak, which steadily grew in amplitude until the end of the survey

(June 16). This secondary microbarom peak may be associated with the formation and evolution of a low pressure system in the Aleutian arc.

3.6 Summary of Infrasonic Noise Conditions

The analysis of the survey data has shown that noise conditions at Hawaii exhibit some diurnal variations, specifically in the Kahalu'u site. Most of this variability occurred at frequencies lower than 0.1 Hz, and may be driven by local effects. The survey has shown that noise levels are lower at the Kahalu'u site, where an infrasound station with very good detection capability can be established.

CONCLUSIONS AND RECOMMENDATIONS

The site survey demonstrated that the Kahalu'u site is superior to the Kulani site for the installation of IS59. The Kahalu'u site has a lower volcanic risk, is less humid, has less environmental impact and land access restrictions, and most importantly, has lower infrasonic noise levels than the Kulani site. The installation of IS59 in the Kahalu'u forest is recommended.

REFERENCES

Henger, M., G. Hartmann, T. Grasse, B. Stork, R. Schiewe, and K. Kock, *Report on a site survey in the area of the IMS Infrasound Station IS26, Freyung, Bavarian Forest, Germany*, Federal Institute for Geosciences and Natural Resources, Hannover, Germany, 1998.

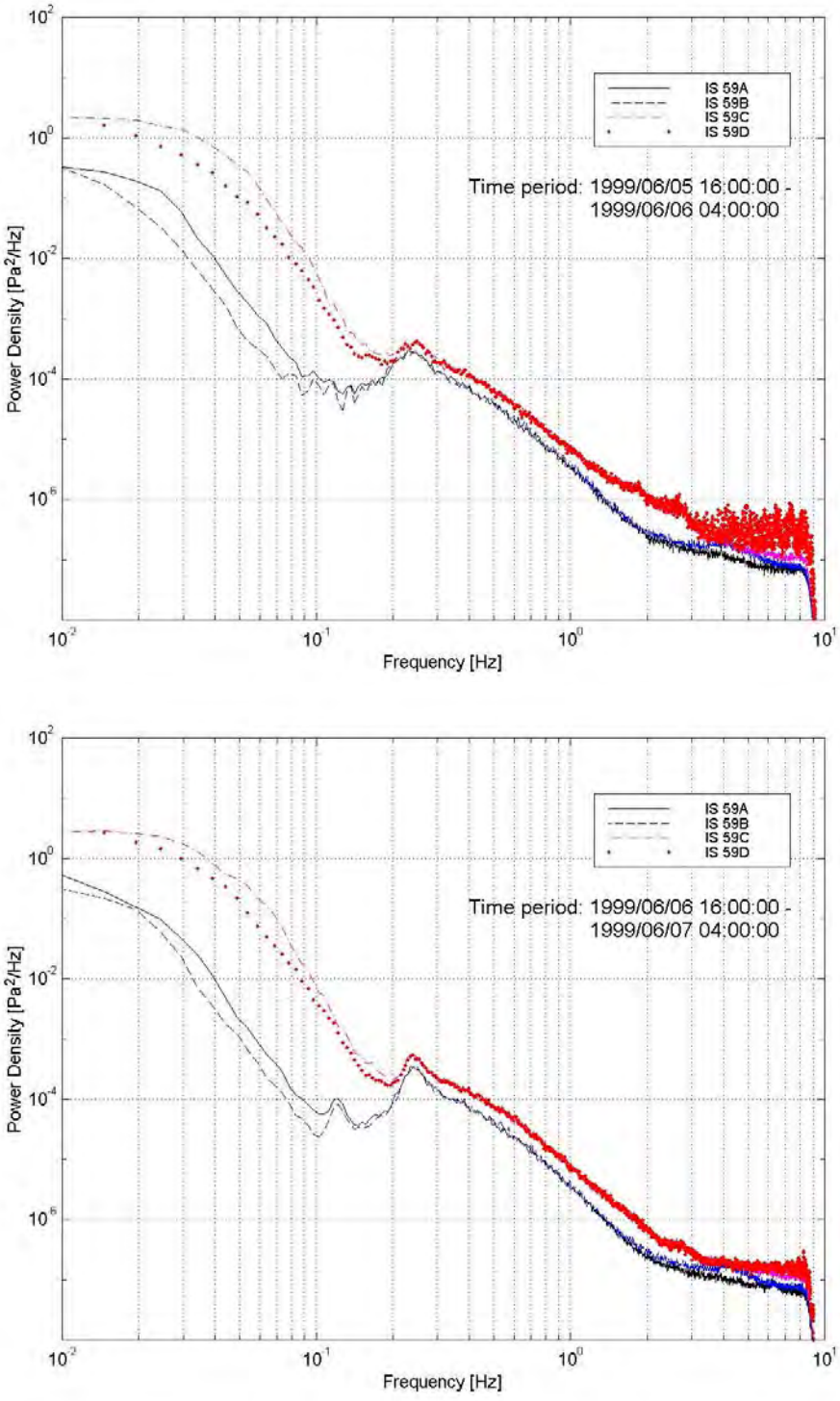


Figure 4. Power spectral density as a function of frequency for the Kahalu'u and Kulani sites averaged from 16 to 4 UT, or 6 AM to 6 PM local time (daytime). The Kahalu'u stations are quieter at all frequencies.

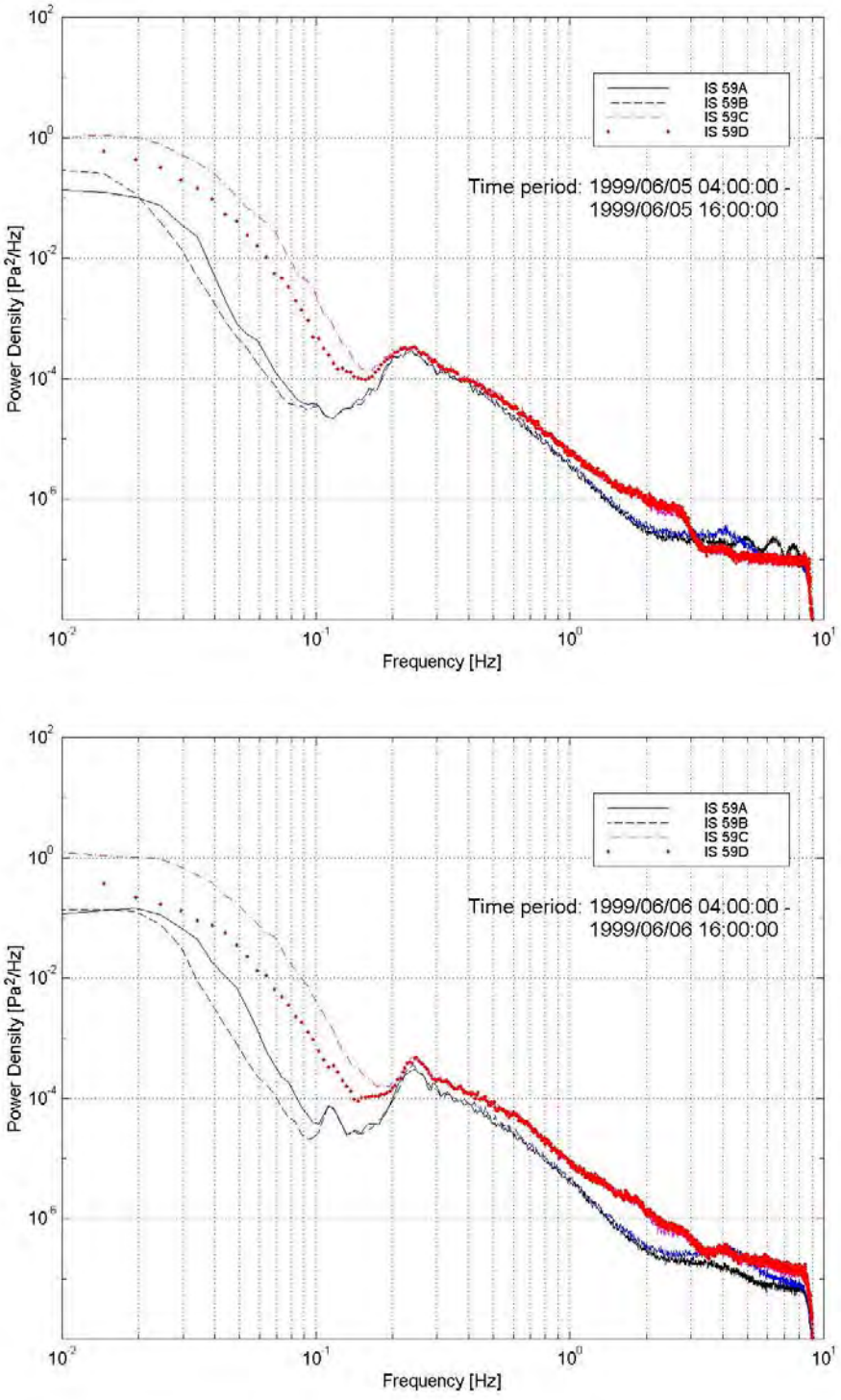


Figure 5. Power spectral density as a function of frequency for the Kahalu'u and Kulani sites averaged from from 4 to 16 UT, or 6 PM to 6 AM local time (night time). The Kahalu'u stations are quieter at all frequency lower than 3 Hz. The sharp change in slope at 3 Hz in the Kulani stations suggests a local source of low-frequency noise.

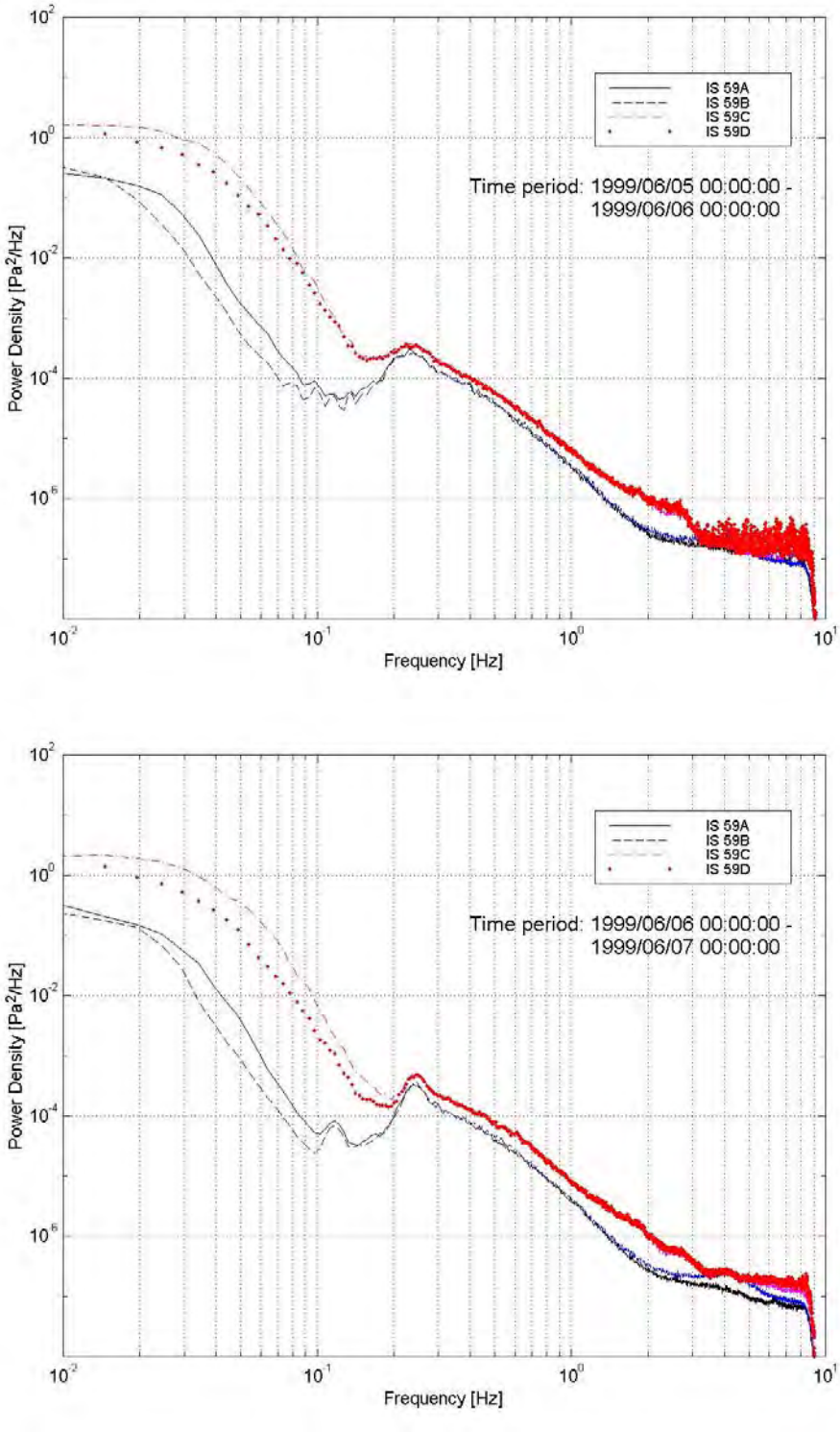


Figure 6. Twenty-four hour power spectral density averages for all sites on June 5 (upper panel) and June 6 (lower panel). The Kahalu'u sites are quieter at all frequencies.

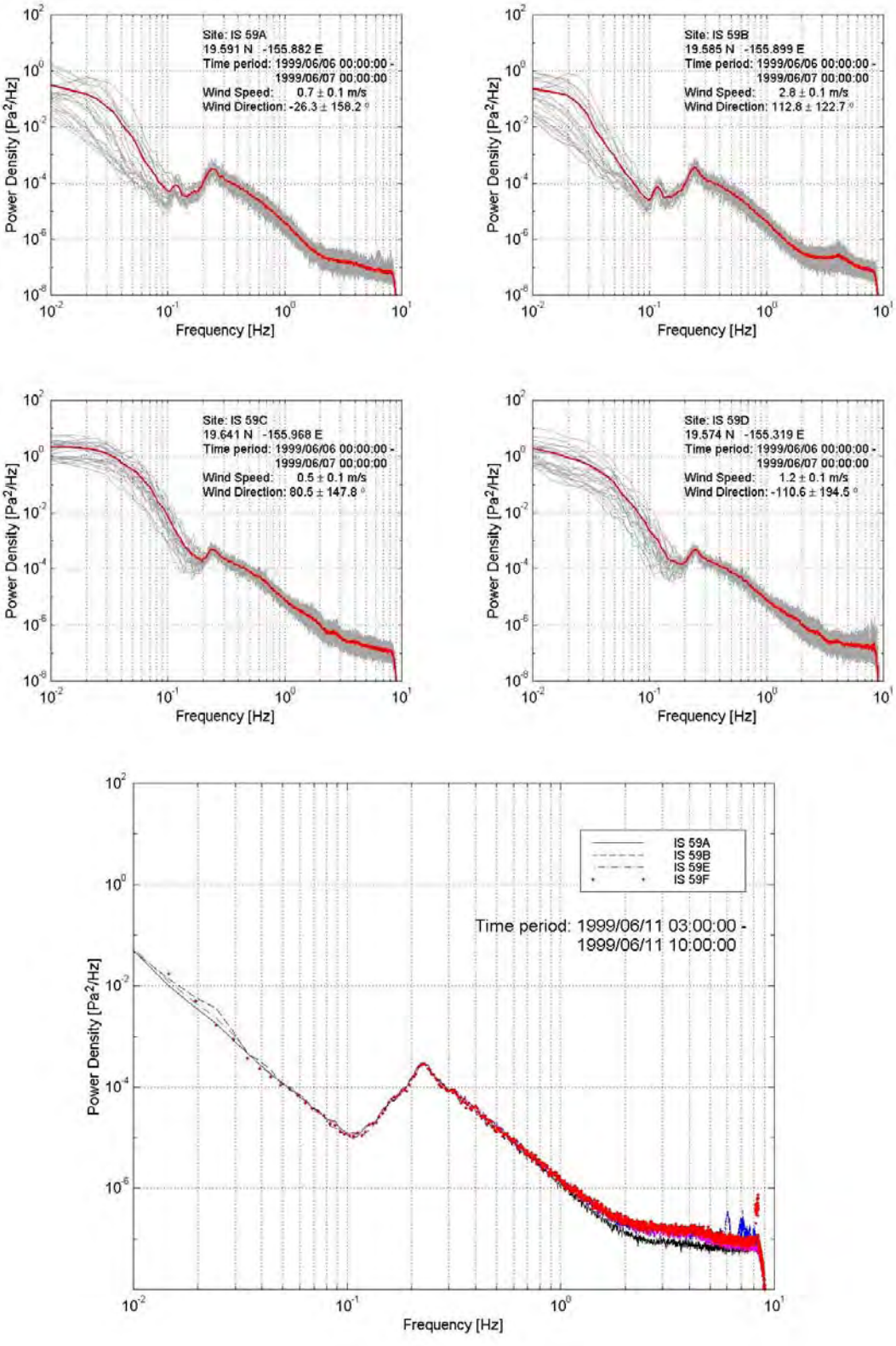


Figure 7. The upper panel shows the range of micropressure noise levels observed during the 24 hours of June 6. These levels are representative of the maximum and minimum noise levels observed from June 3 to June 8, 1999. The lowest noise levels in this time period occurred from 0 to 2 UT. The lowest noise levels recorded during the site survey occurred in the Kahalu'u forest on June 11, and are shown in the lower panel. After June 12, a low pressure system in the Aleutian arc increased the microbarom peak to a peak level of approximately 2×10^{-3} Pa^2/Hz at 0.15 Hz.

VARIABILITY OF THE LOWER ATMOSPHERE AND ITS EFFECT ON THE PROPAGATION OF INFRASONIC WAVES

Milton Garcés[1], Roger Hansen, and Kent Lindquist
Geophysical Institute, University of Alaska, Fairbanks

[1]Also at the University of Hawaii, Manoa

Douglas Drob and Michael Picone
Naval Research Laboratory, Upper Atmospheric Physics Branch

Sponsored by the U.S. Department of Energy
Contract No.: DE-FC04-98AL79801

ABSTRACT

Previous work focused on infrasonic wave propagation effects in the Mesosphere and Lower Thermosphere (MLT), which is strongly affected by solar tides, geomagnetic storms, and solar EUV radiation. The present work integrates acoustic wave propagation models, NRL's MSIS90 and HWM93 atmospheric models, and the United Kingdom Met Office (UKMO) Correlative Analyses to investigate in detail the effects of stratospheric variability on the propagation of infrasonic waves over Hawaii and Alaska. Below 55 km heights, the UKMO data, which is based on radiosonde data and NOAA satellite temperature profiles, captures planetary waves with periods of 2, 5, 10, and 16 days. The augmentation of the HWM and MSIS models with the UKMO dataset dramatically alters the acoustic propagation medium and therefore the predicted travel time curves and azimuth deviations of infrasonic waves.

Key Words: Infrasound, Travel Times, Atmospheric Models, Source Location, Alaska, Hawaii

OBJECTIVE

The objective of the project is to improve the source location capabilities of the Alaska and Hawaii CTBT infrasonic arrays. The deliverables of this part of the project are predicted infrasonic wave travel time curves and azimuth corrections at the arrays, based on the best available atmospheric models and data.

Introduction

Infrasonic waves originating near the Earth's surface may be refracted back to the ground by atmospheric conditions in the troposphere, stratosphere, and thermosphere. Wave energy is trapped between the ground and the turning points at each layer, thus creating well-defined ducts. These ducts define distinct infrasonic phases, which may be recorded by pressure sensors and utilized to locate infrasonic sources. According to ray theory, the tropospheric and stratospheric ducts are only generated along the dominant wind directions. However, the thermosphere will frequently have two turning regions, and thus support two distinct phases.

Previous work (Garces et al., 1999a-c) investigated the effects of geomagnetic activity and solar EUV flux variations on the propagation of infrasonic waves in the atmosphere. In that study, we used the Naval Research Laboratory Horizontal Wind Model (HWM) and Mass Spectrometer and Incoherent Scatter (MSIS) models to produce atmospheric data for Fairbanks, Alaska (146.9^{o}W, 64.8^{o}N) and the Big Island, Hawaii (155.3^{o}W, 19.6^{o}N). Atmospheric profiles for the temperature, mean molecular mass, zonal winds, and meridional winds from the ground up to 180 km were computed every three hours for the season of Winter (November 1 to January 31). Waves propagating to heights greater than 180 km were not considered because of the high attenuation encountered by sound waves in these rarefied layers of the ionosphere. Using the atmospheric data, 50 rays were launched along specified directions to compute theoretical travel time curves, azimuth deviations, tau surfaces, and turning heights (Garces et al., 1998). Tropospheric-ducted waves only occur during strong tropospheric winds, which may be irregular. Since the HWM and MSIS models are obtained from 15 year averages, they do not reproduce these irregular weather patterns in the troposphere. The HWM and MSIS models predict Winter stratospheric phases occur only

for waves propagating towards the Eastern quadrant in Hawaii and the Southeastern quadrant in Alaska, along the dominant stratospheric wind direction. These trends reverse in Summer, and the stratospheric phase may completely vanish in parts of Spring and Fall. In contrast, thermospheric phases are present year round. During most of Winter, there were two thermospheric branches, defined by turning points below 120 km and above 150 km. Solar tides created diurnal fluctuations in the azimuth deviations, ray density, and turning points. Furthermore, it was found that strong geomagnetic fluctuations during the solar maximum may induce a wind component that can dominate over the tidal component, and alter the partitioning of energy between the upper and lower thermospheric ducts.

The present work extends previous studies by augmenting NRL's MSIS90 and HWM93 atmospheric models with the UK Met Office (UKMO) Correlative Analyses dataset. We use the enhanced atmospheric models to investigate in detail the effects of stratospheric variability on the propagation of infrasonic waves over Hawaii and Alaska during the 89 days of Spring (February 1 to April 30). The UKMO data is based on radiosonde data and NOAA satellite temperature profiles, extends up to 55 km, and captures planetary waves with periods of 2, 5, 10, and 16 days. The UKMO data was used for all heights below 55 km, and was patched with the NRL model outputs using a general weighted and constrained least squares fitting method to non-uniform rational B-splines (NURBS). In contrast to usual interpolation, where a curve is constructed to satisfy the data precisely, in the least squares approximation the constructed curves capture the general shape in a statistical sense (L. Piegl and Tiller, 1997).

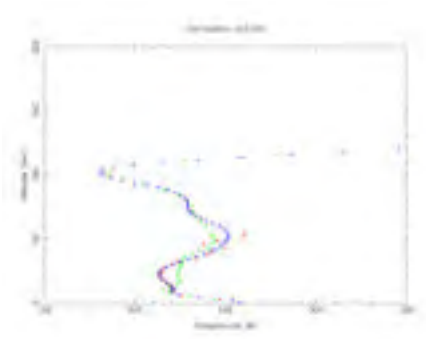


Figure 1. Profiles obtained from NRL models, UKMO data, and the interpolated line. The next number stands for UARS day number 2700, or February 1, 1999. Green points correspond to the MSIS or HWM output, red to UKMO, and blue to the NURB fit (Cammpfire - Combined Atmospheric Measurement and Model Profiles For Infasound Range Estimation.)

The enhancement of the HWM and MSIS models with the UKMO dataset dramatically alters the acoustic propagation medium and therefore the predicted travel time curves and azimuth deviations. In addition to the predictable variability introduced by the tides in the Mesosphere and Lower Thermosphere (MLT), planetary waves and weather disturbances in the lower atmosphere add significant unpredictable variability. Thus, infrasonic wave propagation models would have to access updated atmospheric data for the troposphere and stratosphere in order to produce accurate locations.

Salient Results

We wish to investigate the effect of stratospheric perturbations on the propagation of infrasonic waves. We build on our previous studies of the upper atmosphere, where the HWM and MSIS are robust. The thermosphere is significantly affected by the tides (Forbes, 1995), leading to a diurnal variability in the azimuth deviation and turning points of propagating phases. During periods when the upper thermosphere winds blow counter to the wave propagation, the steep rays are lost to the thermosphere, thus making shallower rays turn at a higher level. This means that shallower rays spend more time in the turning region, leading to extreme azimuth deviations as high as 10 degrees. However, in general, only the thermospheric branches with the highest turning point suffer such high deviations, and stratospheric phases and low thermospheric branches have relatively small deviations, usually less than 3-5 degrees(Garces et al., 1999a-c). This theoretical result is in agreement with historical field observations.

The atmospheric conditions for Alaska during the season of Spring (February 1- April 30, or days 32 to 120) obtained with the MSIS and HWM models are shown in Figures 2.

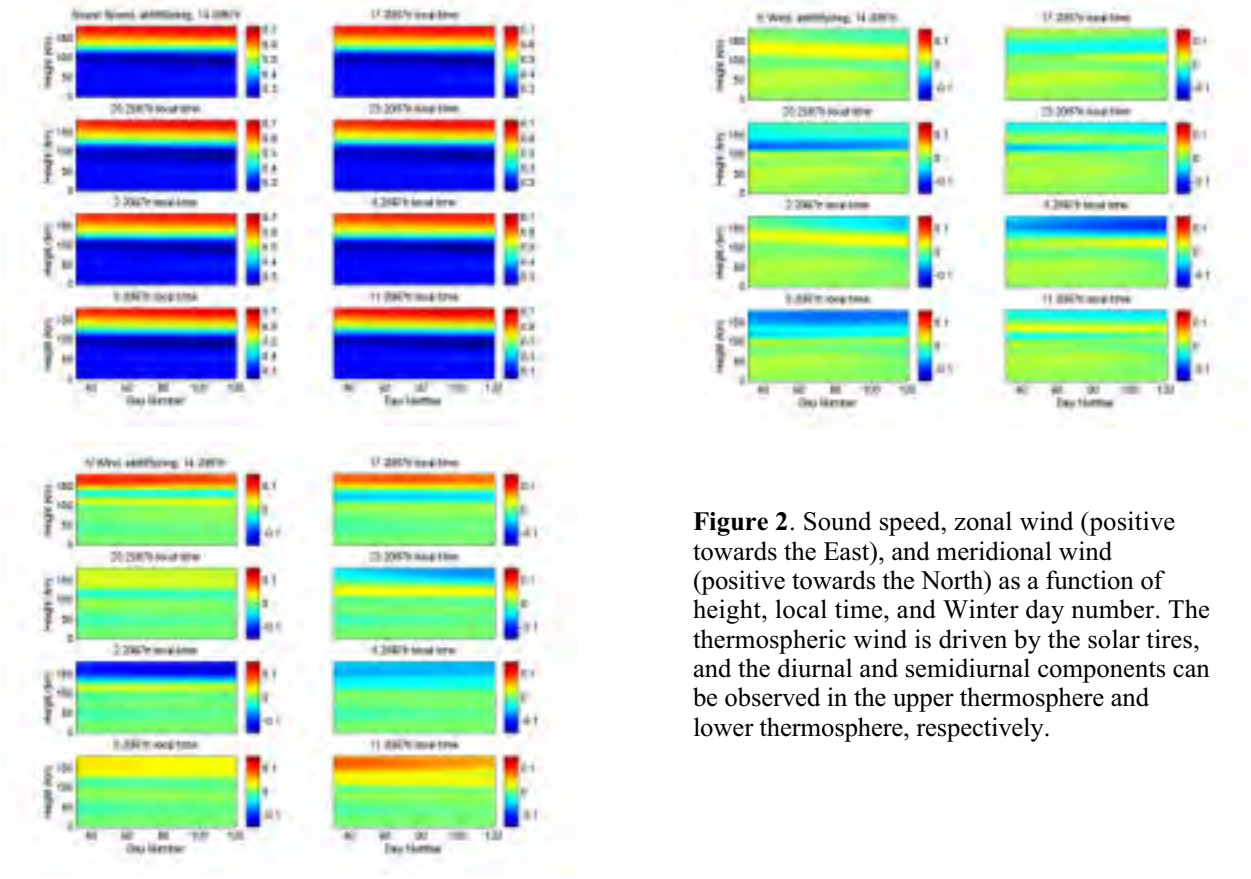
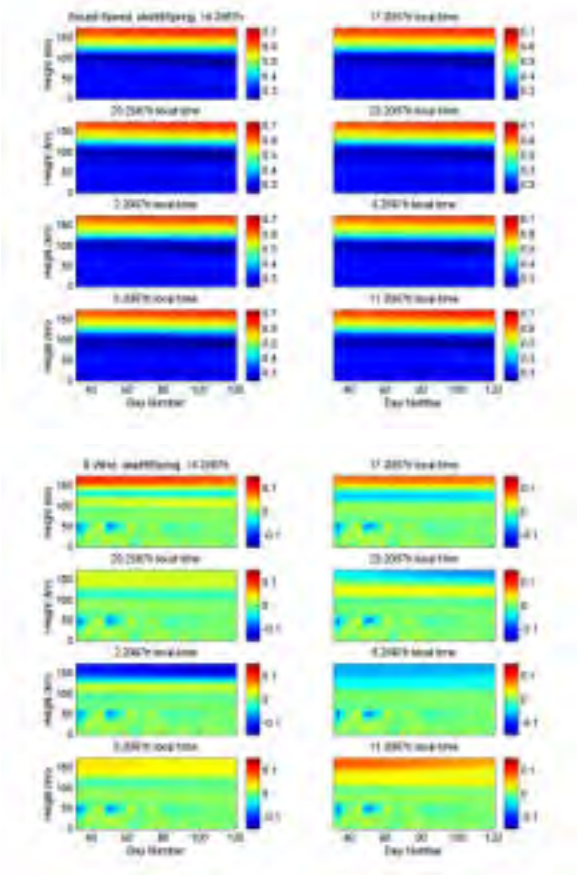


Figure 2. Sound speed, zonal wind (positive towards the East), and meridional wind (positive towards the North) as a function of height, local time, and Winter day number. The thermospheric wind is driven by the solar tires, and the diurnal and semidiurnal components can be observed in the upper thermosphere and lower thermosphere, respectively.

The weakening of the stratospheric winds occurs quite late in the season. As previously noted, thermospheric variability is driven by the solar tides. The conditions for the same region at the same time, but with the UKMO data enhancement, are shown in Figure 3. The greatest discrepancy between the climatologies occurs during strong jet stream events, which the MSIS and HWM models do not incorporate. A notable example is the drastic increase in zonal wind jet velocities at the beginning of the season, from days 32 to 50. This event may be caused by oscillations in the Arctic Polar Vortex due to large scale planetary waves . This feature is well defined in Antarctica (due to free ocean) but new evidence suggests that it is becoming stronger in the Northern hemisphere due to global warming. The contrast between the raw NRL model output and the enhanced climatologies in Hawaii is still significant, but not as dramatic as in Alaska.



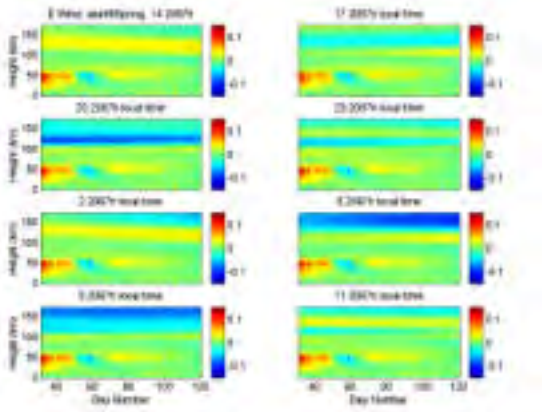


Figure 3. Sound speed, zonal wind (positive towards the East), and meridional wind (positive towards the North) as a function of height, local time, and Winter day number. The UKMO enhancement of the HWM and MSIS models provides atmospheric models which are a step closer to reality.

Figure 4 shows the predicted travel time curves for waves arriving from the West after propagating through the raw MSIS and HWM (AK, Figure 2) and the UKMO augmented (AKA, Figure 3) model atmospheres. The most noticeable difference is the filling in of the shadow zone for the stratospheric phase. Note that Figure 4 shows a superposition of all travel time curves for all selected days, and that there will be a shadow zone when the stratospheric phase is absent. Figure 5 shows the superposition of the azimuth deviations for all selected days, as in Figure 4. The azimuth deviations for model AK can be identified with the phases on Figure 4, in sharp contrast with the scattered deviations corresponding to model AKA. The azimuth deviation and turning height as a function of apparent phase speed, local time, and day number are shown on Figures 6 and 7, respectively. These last two figures are intended to be utilized with array processing algorithms. A detected arrival will possess a specific horizontal phase speed and direction. Figure 6 provides the correction needed to obtain the true azimuth, and Figure 7 provides the height in the atmosphere corresponding to that specific return. Figure 7 is also valuable in identifying specific phases. Turning points below 50 km correspond to stratospheric phases (Is), returns below ~140 km correspond to the thermospheric return with the larger slope on the travel-time curve (Ita) and returns above ~140 km correspond to the thermospheric return with the lower slope (Itb). The results of the AK run shown in Figure 6 are as in the work of Garces et al. (1999a-c), where azimuth deviations are relatively small for the stratospheric and low-turning thermospheric phases, and only the most far-reaching thermospheric returns show deviations as large as 10 degrees.

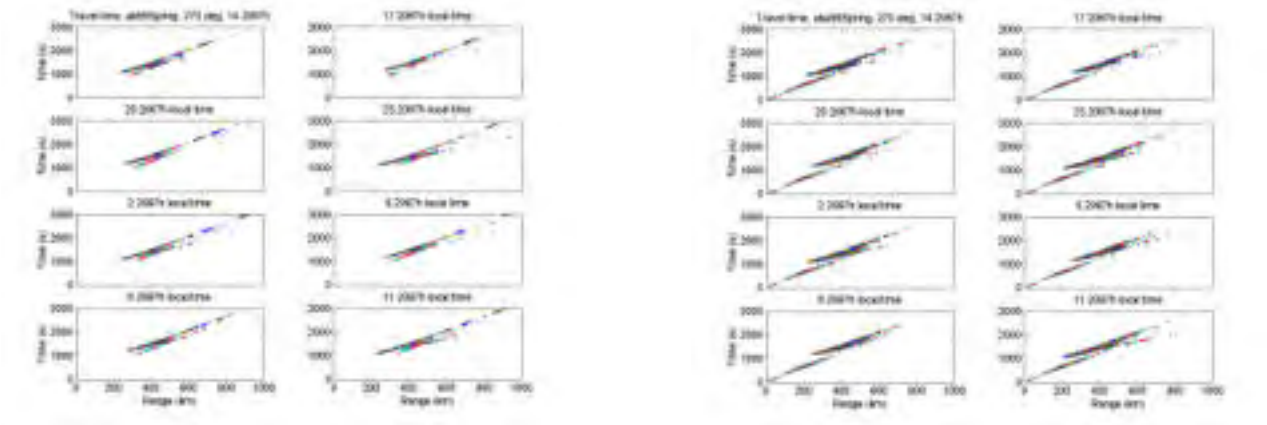


Figure 4. Travel time curves for infrasonic waves arriving from the West for the AK (left) and AKA (right) models. All the travel time curves for the selected time period are superposed. Each line corresponds to a distinct phase and to different reflection levels in the atmosphere. The stratospheric phase in the AKA model is much better defined, and the thermospheric phases are significantly modified.

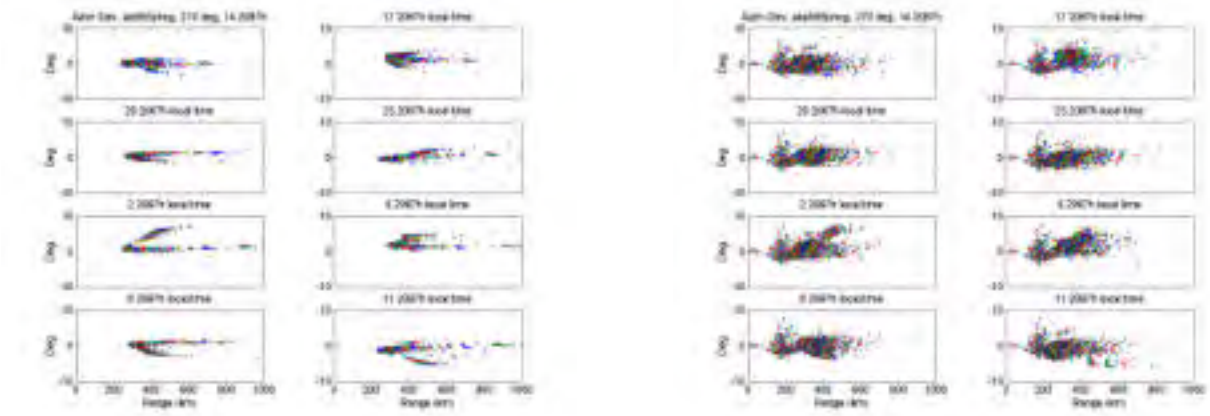


Figure 5. Azimuth deviations for infrasonic waves arriving from the West for the AK (left) and AKA (right) models. All the deviations for the selected time period are superposed. A positive deviation corresponds to a deflection towards the right along the direction of propagation. Seen from the receiving array, a positive deviation corresponds to an angular correction towards the right of the arriving incidence angle.

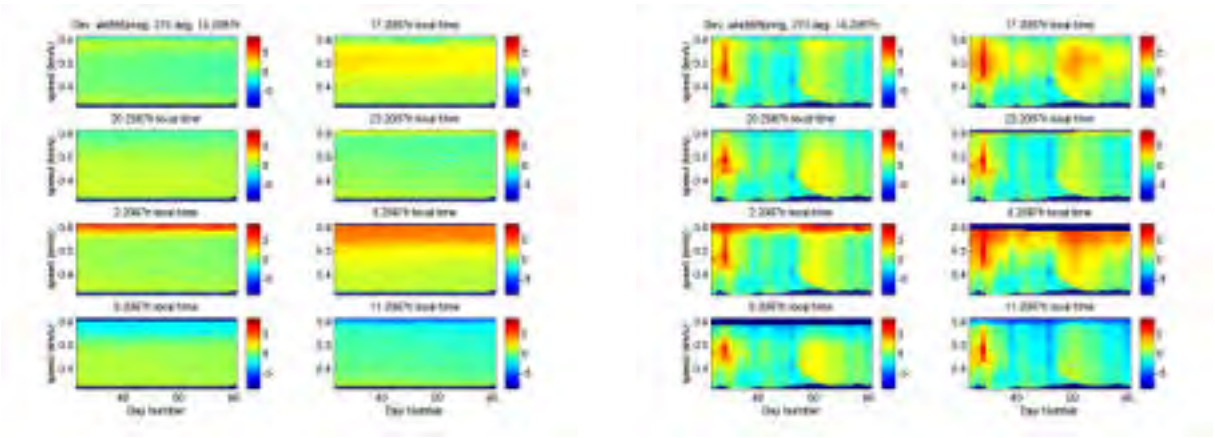


Figure 6. Azimuth deviation as a function of apparent phase speed (trace velocity), local time, and day number. Infrasonic waves are impinging from the West through the AK (left) and AKA (right) atmospheric models. The steepest rays (highest speeds) have the largest deviations, and stratospheric phases have small deviations.

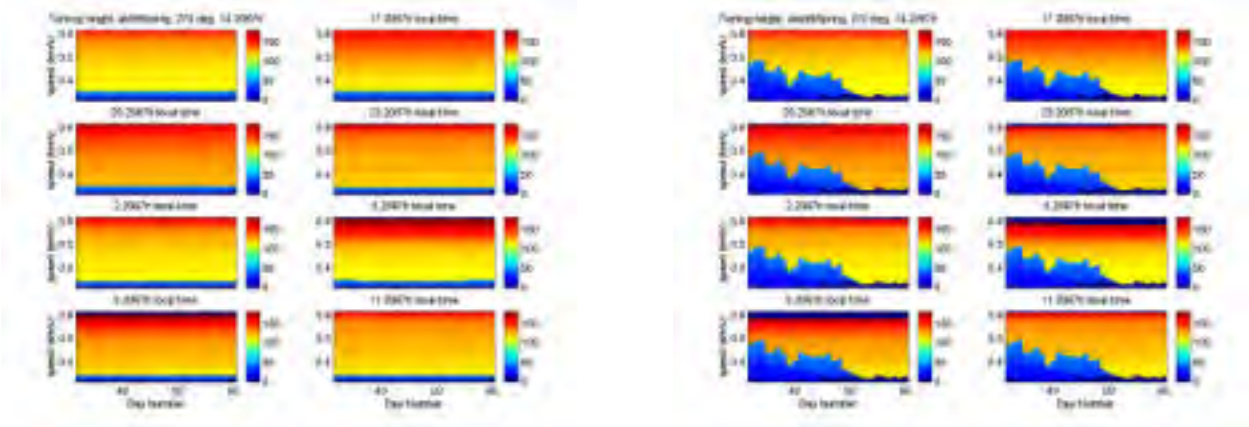


Figure 7. Turning height as a function of apparent phase speed (trace velocity), local time, and day number. Infrasonic waves are impinging from the West through the AK (left) and AKA (right) atmospheric models. The steepest rays (highest speeds) turn at the highest levels.

The runs for model AKA show more varied results. There is more energy going into the stratospheric phase as some of the steeper rays are refracted in the stratosphere by the strong wind speed of the arctic jet (Figure 7). In contrast to the AK run, the AKA model yields azimuth deviations of approximately 5 degrees associated with the stratospheric returns. These returns correspond to rays that turn during periods of strong transverse (Southward, Figure 3) winds, thus producing a significant deflection towards the right of the propagation direction. However, large deviations are still associated with the far-reaching rays refracted in the upper thermosphere during strong tidal winds, although some of these rays are now lost. Another noteworthy difference is that the AK runs predict a stratospheric arrival throughout the month of February (days 32 to 60), whereas the AKA runs predict that this phase may vanish during the zonal wind reversal at the end of the month.

CONCLUSIONS AND RECOMMENDATIONS

Stratospheric disturbances introduce significant variability on the arrival times and azimuth deviations of propagating infrasonic waves. Although the NRL HWM and MSIS models are useful for the study of fundamental principles of infrasonic wave propagation in time-varying atmospheres, these models do not accommodate sufficient variability in the troposphere and stratosphere to provide precise results. More realistic infrasonic propagation models can be obtained from the fusion of the NRL models, whose strength is in the upper atmosphere, with finer-scale lower atmosphere datasets such as the UKMO Correlative Analyses.

The integration of meteorological data with atmospheric models will continue throughout the rest of this project, with the aim of improving the robustness and accuracy of the resulting infrasonic propagation models. After completing a detailed study of the propagation characteristics in Alaska and Hawaii over the yearly cycle, studies should focus on solving the inverse problem for infrasonic source locations using the most realistic propagation models available.

REFERENCES

Forbes, J. M. (1995). *Tidal and planetary waves*, in The Upper Atmosphere and Lower Thermosphere: A Review of Experiment and Theory, Geophysical Monograph 87, AGU.

Garcés, M., D. Drob, and M. Picone (1999a). *A theoretical study of the effect of geomagnetic fluctuations and solar tides on the propagation of infrasonic waves in the atmosphere*. Geophys. J. International (submitted).

Garcés, M., D. Drob, and M. Picone (1999b). *Geomagnetic and solar effects on thermospheric phases during Winter*. EOS, Trans. Am. Geophys. Union, 80, S71.

Garcés, M., K. Lindquist, R. Hansen, D. Drob, and M. Picone (1999c). *Temporal variability in the propagation on infrasonic waves over Hawaii and Alaska during Winter*. J. Acous. Soc. Am., 105, 1104.

Garcés, M. A., R. A. Hansen, K. Lindquist (1998). *Travel times for infrasonic waves propagating in a stratified atmosphere*. Geophys. J. International, 135, 255-263.

L. Piegl and R. Tiller (1997). *The NURBS book*. 2nd ed., Springer Verlag.

DEVELOPMENT AND APPLICATION OF AN INTEGRATED INFRASOUND PROPAGATION MODELING TOOL KIT

Robert Gibson, David Norris, Ted Farrell, GTE/BBN Technologies

Sponsored by U. S. Department of Defense
Defense Threat Reduction Agency
Contract No. DSWA01-97-C-0160

ABSTRACT

Infrasound propagation models and upper-atmospheric characterizations have been integrated into a single software tool kit that allows for user-friendly model execution and data visualization. The tool kit, called InfraMAP, for Infrasonic Modeling of Atmospheric Propagation, can be applied to predict travel times, bearings, and amplitudes from potential event locations worldwide. Temporal and spatial variability of the atmosphere is addressed by allowing range-dependent sound speed and winds to be incorporated with the propagation models. The ability to predict propagation characteristics necessary for localization is therefore enhanced. The integrated software has been used to conduct sensitivity analyses and to model infrasound propagation corresponding to historical events of interest. Results from these analyses and comparisons of predictions with measurements are discussed.

InfraMAP integrates three types of research-grade propagation models with two empirically based atmospheric models. The baseline set of acoustic propagation models consists of a three-dimensional ray theory model (HARPA), a WKB version of Pierce's normal mode model, and a continuous-wave, two-dimensional parabolic equation model. The baseline empirical atmospheric models are the Horizontal Wind Model (HWM) and the Extended Mass Spectrometer - Incoherent Scatter Radar (MSIS or MSISE) temperature model. Wind, temperature, and densities are modeled from the surface into the thermosphere and include spatial, diurnal, and seasonal effects. The InfraMAP tool kit provides a common user interface that allows researchers to use these models efficiently for investigating issues of interest for CTBT monitoring.

Key Words: infrasound, long-range propagation, database, atmosphere

OBJECTIVE

Verification of the Comprehensive Nuclear-Test-Ban Treaty (CTBT) will require the ability to detect, localize, and discriminate nuclear events on a global scale. Verification systems such as the International Monitoring System (IMS) rely on several sensor technologies to perform these functions. The current IMS infrasound system design includes a network of low-frequency atmospheric acoustic sensor arrays, which contribute primarily to the detection and localization of atmospheric nuclear events.

The technical challenges involved in monitoring the CTBT using infrasound include the proper consideration of the effects of upper atmospheric dynamics on propagation. Because of the temporal and spatial variability of the atmosphere, there are no stable, reliable, simply predictable propagation paths that can be used in standard back-azimuth and time-of-arrival localization approaches. Uncertainties inherent in propagation modeling techniques and in characterizations of temperature and wind can result in location errors. The approximations currently in use operationally are expected to result in localization performance significantly worse than the monitoring network design goal of 1000 sq. km [Clauter and Blandford, 1996].

It is anticipated that the ability to identify infrasound phases, and to include the appropriate travel-time and bearing refraction corrections for each arrival into localization procedures, would dramatically improve localization performance. Reducing uncertainties in location estimates from the infrasound network will also improve the ability to associate detected events with hydroacoustic and seismic signals. In addition, improved predictions of infrasound waveform amplitude will aid in the determination of detection thresholds and observability of individual phases; these predictions can be used in source discrimination, in particular for yield estimates.

Infrasound analysts and researchers require tools that will allow them easily to model propagation through realistic characterizations of the atmosphere. Furthermore, operational processing and interpretation of infrasonic data will require computation of a knowledge database that contains accurate atmospheric characteristics, travel times, bearings, path amplitudes and ultimately spectral characteristics of received waveforms. The primary objective of this effort is to develop modeling software that can be used to support these requirements and to improve source localization. The specific goals for this effort are:

1) Develop an integrated software system capable of: (a) defining the state of the atmosphere, such as temperature and wind speed profiles, as required for infrasound propagation modeling; (b) predicting the phases, velocities, travel times, azimuths and amplitudes of atmospheric explosions measured by infrasound sensors; (c) supporting prediction of localization area of uncertainty and detection performance, by quantifying environmental variability and propagation sensitivity.

2) Conduct sensitivity studies to determine the effects of environmental variables on infrasound propagation, and validate that the modeling software techniques are consistent with measured data.

3) Prepare a users' manual and documentation describing the models.

Progress toward these goals is discussed in the following section.

RESEARCH ACCOMPLISHED

Approach

An integrated software package for infrasound modeling has been developed by BBN. The software contains tools for modeling infrasound propagation through a dynamic atmosphere and for visualizing modeled propagation results and atmospheric characteristics. The atmospheric models, acoustic propagation codes, and display functions are integrated in a common software environment that allows for user-friendly data access and model execution. The tool kit, called InfraMAP, for Infrasonic Modeling of Atmospheric Propagation, can be applied to predict travel times, bearings, and amplitudes from potential event locations worldwide.

The development of the infrasound software tool kit followed an approach analogous to that used for the Hydroacoustic Coverage Assessment Model (HydroCAM) [Farrell and LePage, 1996], which was developed under the Department of Energy's CTBT R&D program. The HydroCAM software contains the best available seasonal databases of the ocean environment from the US Navy, the National Oceanic and Atmospheric Administration (NOAA) and other institutional sources, and is used to predict hydroacoustic travel time, amplitudes, travel time variances and network performance throughout the world's oceans.

InfraMAP was rapidly prototyped to develop a baseline functional capability. Following testing and evaluation of each baseline capability, additional functions were then added. The software design philosophy was to use existing models, databases and access software whenever possible. Models and databases were identified and prioritized for integration by using a benefit/cost tradeoff. The benefits included the ability to meet operational requirements and acceptance by the infrasound research community. The cost included the estimated integration effort and computational requirements. As integration of the modeling components progressed, enhancements were added to the software to simplify and speed execution. The graphical user interface (GUI), including forms and data display formats, was designed and implemented using MATLAB®. In addition to the forms contained in the GUI, models can also be exercised at the command line in script mode.

Figure 1 shows the default topographic display and the user interface for selecting the principal menus. Menus are organized by task for the most common operations, and are divided into the categories of "Environment" and "Propagation." Additional functions such as printing, zooming, adding overlays, and defining networks of sensors for analysis are available on separate menu bars (not shown). An overlay of the IMS infrasound network is shown.

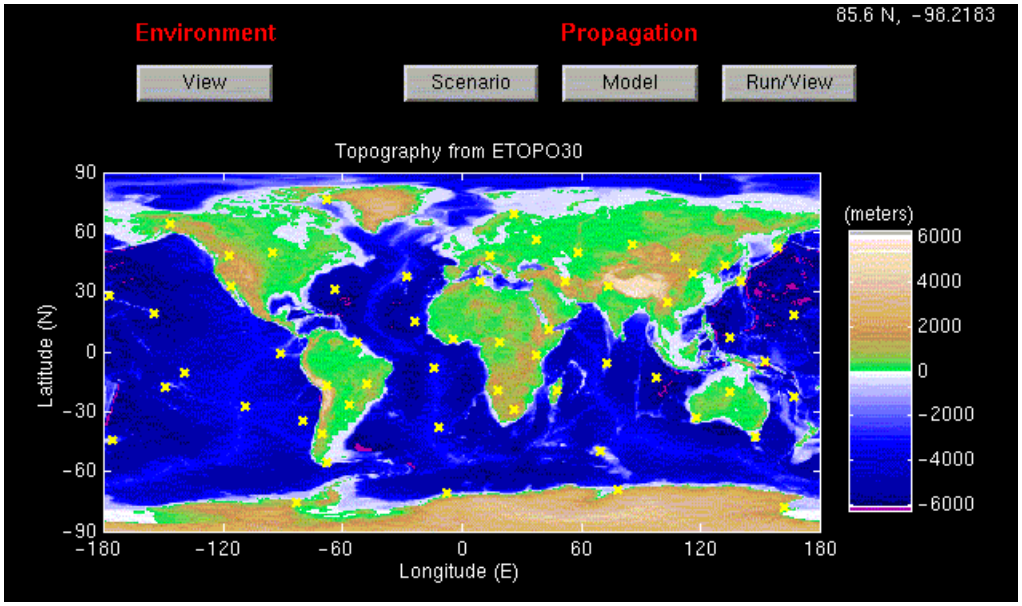


Figure 1: InfraMAP Main Menu and User Interface

Selection of the View Environment menu allows the user to visualize the atmospheric characterizations. From the View menu, the user then makes a number of choices: the environmental database or model, the variable of interest, temporal and spatial parameters, resolution, and the type of data plot desired. Atmospheric characteristics, such as temperature or wind speed, can be presented in a variety of views, e.g., as a function of a spatial or temporal variable or as a function of an environmental model parameter.

A set of propagation menus allows the user to define and execute InfraMAP's integrated modeling capabilities. First, via a Scenario menu, source and receiver locations, event date and time, and environmental parameters are chosen. Second, a Model menu is used to select the propagation model and its required input parameters. Default values of model parameters are provided automatically but may be modified by the user. Third, a Run/View menu is used to commence model execution and to display results upon completion of the run. Model results are automatically stored and can be recalled later for analysis or display. A range of display options is available. In addition to propagation model results, the atmospheric characteristics used in the run can also be viewed.

The software design enables a user to run propagation models quickly and efficiently via the pre-defined menus, and simultaneously provides flexibility both in the choice of model parameters and by allowing user-defined manipulation of data via the command line input. The remainder of the section describes the models in more detail and presents examples of the tool kit's capabilities.

Environmental Characterization

The existence of multiple atmospheric layers and large spatial and temporal variability of the atmospheric temperature and wind speed produces a very complicated infrasound propagation environment in which sound speed varies with time, location and altitude. Lower, middle and upper atmospheric temperature and wind data, required for predicting infrasound propagation paths, are currently available in a variety of formats at varying temporal and spatial resolutions, but no one data source contains all of the required environmental parameters at all locations and altitudes. Multiple atmospheric databases and models have been evaluated for use in InfraMAP, with consideration given to spatial and temporal resolution, coverage, and ease of implementation.

Two empirical atmospheric models, developed at NASA and currently maintained by the Naval Research Laboratory, have been integrated with the propagation models in InfraMAP. They are:

1. the Horizontal Wind Model (HWM) [Hedin *et al.*, 1996] and
2. the Extended Mass Spectrometer - Incoherent Scatter Radar (MSIS or MSISE) temperature and density model [Picone *et al.*, 1997].

HWM provides zonal and meridional wind components, and MSISE provides temperature, density and atmospheric composition. These environmental models, which extend from the ground into the thermosphere, were constructed using observed data from a variety of sensors (e.g., satellite, rocket, ground-based radar) as constraints on a set of low-order spherical harmonics. The models produce the mean estimate of the atmospheric parameters at a particular time and location, and they incorporate spatial, diurnal and seasonal effects. Other databases are being used to estimate variances in atmospheric data for incorporation in studies of propagation variability and localization.

Examples of output from the environmental models are presented in Figures 2 and 3. Figure 2 shows a global image of wind magnitude at a fixed altitude of 120 km, with wind vectors superimposed. Figure 3 displays temperature profiles at 500 km increments along a great circle path from the equator to the north pole.

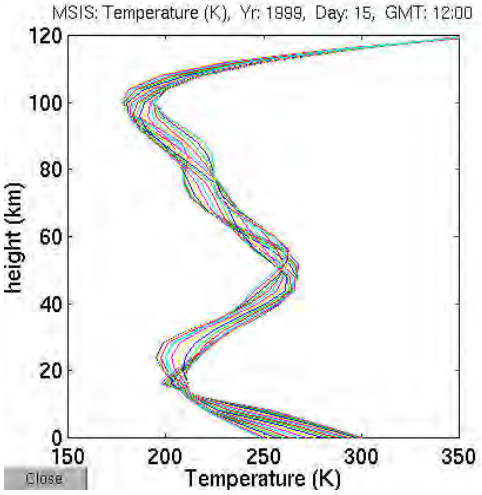
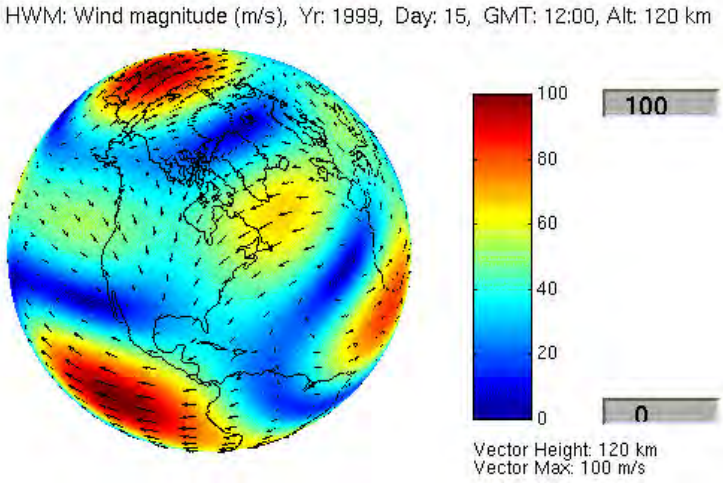


Figure 2: Global Display of Wind Magnitude at Fixed Altitude (from HWM)



Propagation Models

A range of modeling capabilities is required in order to meet the CTBT monitoring objectives of predicting travel time, azimuth, amplitude, and ultimately waveform or spectral characteristics. No one model is sufficient for predicting all essential features. The baseline set of acoustic propagation models contained in InfraMAP consists of:

1. a three-dimensional ray theory model [Jones *et al.*, 1986],
2. a WKB version [Dighe *et al*., 1998; Hunter and Whitaker, 1997] of the normal mode model [Pierce and Kinney, 1976; Pierce *et al.*, 1973; Pierce and Posey, 1970], and
3. a continuous-wave, two-dimensional parabolic equation (PE) model [Jensen *et al.*, 1994; West *et al.*, 1992].

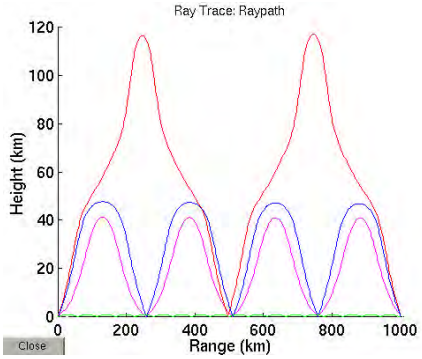


Figure 4: Vertical Projection of Ray Paths (Eigenrays)

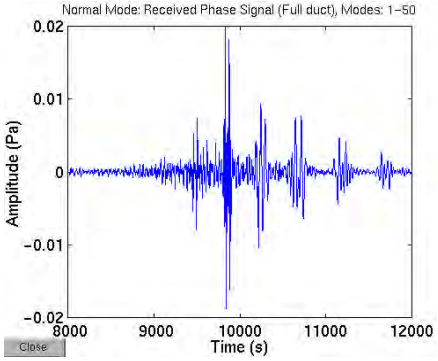


Figure 5: Waveform Predicted Using Normal Modes

A sample of output from each of the three models is shown in Figures 4 through 6.

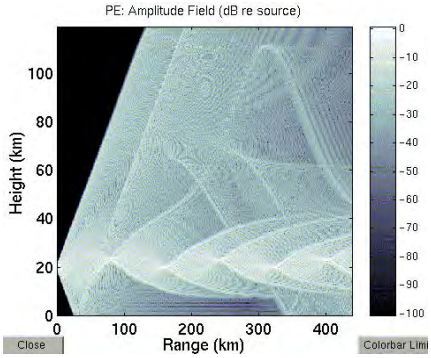


Figure 6: Amplitude Field From Parabolic Equation Model

The 3-D ray tracing code, developed at NOAA, is capable of incorporating a range-dependent atmosphere in propagation calculations. In addition to vertical and horizontal refraction, the model accounts for horizontal translation of the ray path due to the moving medium. It is well established that horizontal refraction and translation can cause significant azimuth biases in the propagation path [Georges and Beasley, 1977]. Azimuth and elevation angles, travel time, and absorption can be readily calculated at each point along a ray path. The ray tracing technique is capable of stepping either forward from a source or backward from a receiver. In InfraMAP, an algorithm has been implemented for finding eigenrays, rays that connect a source and a receiver to within a tolerance of a user-defined distance.

A version of Pierce's normal mode code, modified to determine propagation of higher frequency modes, was provided to BBN by Los Alamos National Laboratory and has been integrated into InfraMAP. The model uses the Wentzel-Kramer-Brillouin (WKB) method to calculate a dispersion curve, which in turn is used to predict received waveforms at a given range and azimuth. Only range-independent environments are supported. The environmental profiles can be retrieved from the source location, receiver location, or from averaged values along the entire path. InfraMAP automates the selection of the waveform time window, based upon the signal velocity and range. In addition, the special case of dual-duct propagation is identified and automatically processed; in which case the full waveform solution is a linear sum of those for the upper and lower ducts.

An implementation of the wide-angle finite-difference PE model was developed internally at BBN for use in InfraMAP. The PE technique steps forward from a source, which is characterized by a starter field, and calculates an attenuation field useful for predicting amplitudes along a vertical slice of the atmosphere. The 2-D model can accommodate a range-dependent atmosphere, but does not account for horizontal refraction and therefore cannot provide predictions of azimuth deviation.

Validation Studies

Data describing a number of historical infrasound events have been reviewed and compared with modeled results using InfraMAP. One important aspect of these investigations is assessment of the utility of three-dimensional ray tracing for predicting infrasonic travel time and azimuth resulting from impulsive events in the atmosphere. Comparisons between observations and predictions are presented here for one event: the meteor-fireball, or super-bolide, of 9 October 1997 above Horizon City, Texas, near El Paso, as observed at TXAR.

Infrasound from the bolide was observed at the two arrays at Los Alamos, NM and at the TXAR array in West Texas [ReVelle *et al*., 1998; Armstrong, 1998; Herrin *et al*., 1998]. The atmospheric explosion was determined to have occurred at 18:47:15 UTC at the location 31.8° N, 106.1° W, and an altitude of 28-30 km, based on visual observations, satellite data and seismic signals [ReVelle *et al*., 1998]. Four separate arrivals were associated with this event at both Los Alamos [Armstrong, 1998] and TXAR [Herrin *et al*., 1998]. Ray tracing comparisons with the Los Alamos observations (at a range of 453 km and a back azimuth of 177°, corresponding to near-northward propagation) have been published previously [Gibson *et al*., 1998].

InfraMAP was used to identify eigenrays from the source location, at a height of 29 km, to the TXAR array location on the ground (at a range of 359 km and a back azimuth of approximately 320°). A tolerance, or miss-distance, of 5 km was allowed for each ray at the receiver. The HWM and MSISE models were used to characterize the environment. Vertical projections of five ray paths resulting from range-dependent propagation modeling through the empirically modeled atmosphere are shown in Figure 7. Two stratospheric rays (channeled below approximately 50 km) and three thermospheric rays (passing above approximately 90 km), two of which include a ground reflection, were identified. The rays represent distinct infrasonic "phases," or separate bundles of energy that could constitute separate observed arrivals.

Table 1 presents the modeled travel time and modeled deviation from the geodesic azimuth for each ray and also presents corresponding data for the observed arrivals [Herrin *et al*., 1998]. The main arrival at 1239 seconds is well modeled as a stratospheric path. The arrival at approximately 1465 seconds is also well modeled as a thermospheric path with a ground bounce. The weak first phase was observed to arrive approximately 6% earlier than predicted. The predicted thermospheric phase at 1365 seconds was not reported as observed. The modeled azimuth deviations are within 1 degree of the observed deviations.

Travel Time (seconds)		Azimuth Deviation (degrees)	
Observed	**Modeled**	**Observed**	**Modeled**
1139		+1.8	
	1211		+1.7
1239	1233	+1.2	+1.1
	1365		+3.4
1464 1466	1475 1476	+4.0 +4.0	+3.2 +3.2

Table 1: Comparison of Observed and Modeled Arrivals at TXAR Array

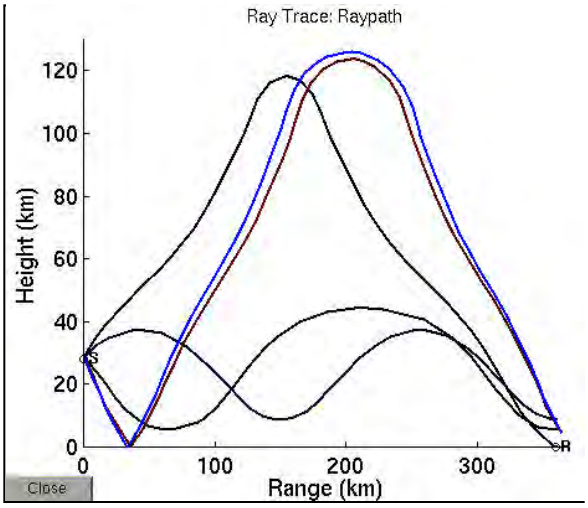


Figure 7: Modeled Eigenrays from El Paso Bolide to TXAR Array

Sensitivity Analyses

The InfraMAP tool kit allows sensitivity analyses to be conducted readily. Model parameters can be varied systematically in order to compare results from a range of propagation scenarios. Such studies are useful for assessing the accuracy, flexibility, and robustness of different modeling approaches and for defining spatial and temporal resolutions required for accurate predictions of infrasound travel times, bearings, and amplitudes. They can also be used to identify systematic biases in travel time and azimuth that it may be possible to eliminate in a localization technique.

Results from one sensitivity study are presented here. InfraMAP was used to evaluate the effect of diurnal variability of atmospheric winds and temperature on ray paths. The environmental models HWM (for wind) and MSISE (for temperature) were used to model the diurnal changes. The effect on eigenrays calculated for several representative scenarios was studied. Specific attention was given to azimuthal deviation and travel time, as these ray parameters impact localization algorithms.

Example results from the modeling are shown, as a function of event time, in Figures 8 and 9. For this event scenario, the source was located in Central Asia (50.5 N, 78.0 E), and the receiver was due West at a range of 2500 km. The time of year was mid-September. Five eigenrays were identified and all had turning points within the thermosphere at altitudes in the range 110-130 km. Over the 24-hour period of the sensitivity study, the travel time variability was up to 2.3% and the change in azimuthal deviation was up to 4.3 degrees. The diurnal variability in temperature was small and found to have a negligible impact on the eigenrays. However, changes in the zonal and meridional winds were significant; winds at the source location are shown in Figures 10 and 11. The greatest variability occurs above 100 km, where the effects of the semi-diurnal solar tide are apparent.

The travel along a ray path is directly influenced by the projected wind along the path; the wind subtracts or adds to the effective sound speed depending on wind direction. This property is observed in the high correlation between the zonal wind and travel time. For example, the ray travel times reach a maximum for events at 10-11 UT. This correlates with the minimum extreme in the eastward zonal wind above 100 km. Westward ray paths at this time of day encounter a headwind with a maximum speed of 60 m/s at their turning points. Similar observations can be made regarding the azimuthal deviations. The crosswind along a ray path acts to translate and/or refract the path, resulting in a change in the observed azimuthal deviation at the receiver. Maximum azimuthal deviation in the negative direction occurs for events at 6 UT. This correlates with the maximum in the meridional winds above 100 km. Ray paths at this time of day encounter a maximum crosswind of 60 m/s at their turning points.

In summary, it is concluded from the diurnal sensitivity study that modeled diurnal changes in the winds can generate observable changes in travel time and azimuthal deviations for ray path solutions over fixed source-receiver geometries. These changes correlate strongly with the wind at the ray turning points. Only thermospheric rays are discussed here. Similar, although weaker, diurnal effects were also found to hold for stratospheric rays [Norris and Gibson, 1998].

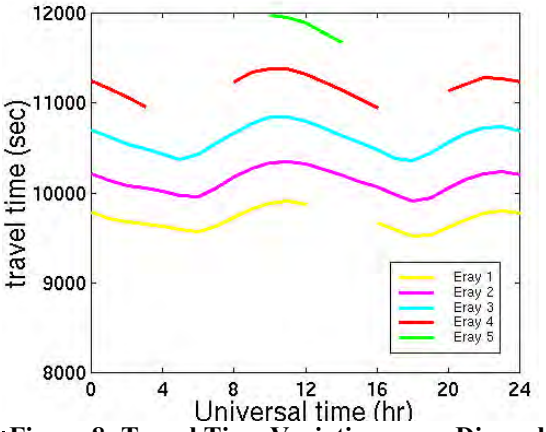


Figure 8: Travel Time Variations over Diurnal Cycle; 2500 km Path

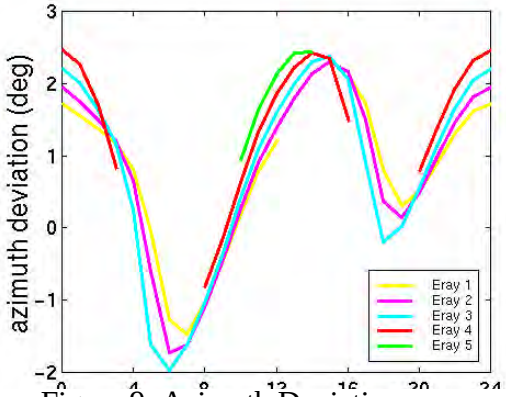


Figure 9: Azimuth Deviations over Diurnal Cycle; 2500 km Path

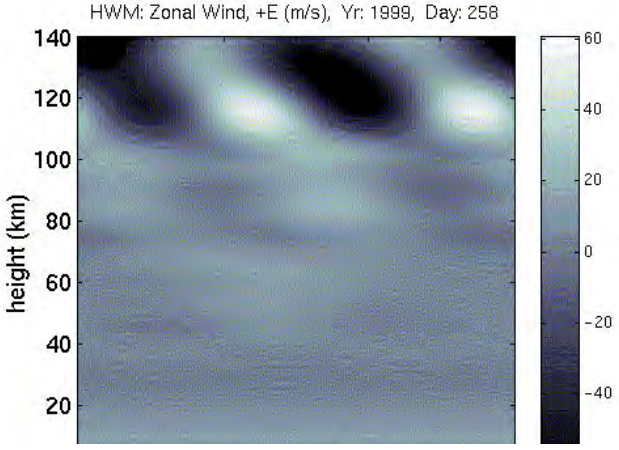


Figure 10: Zonal Wind Variations over Diurnal Cycle; Central Asia (+Eastward)

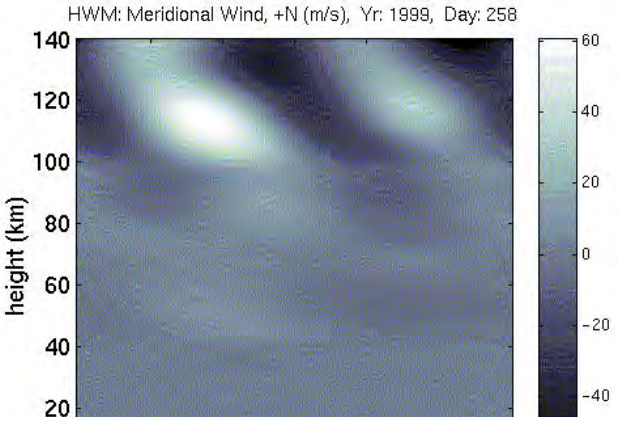


Figure 11: Meridional Wind Variations over Diurnal Cycle; Central Asia (+Northward)

CONCLUSIONS AND RECOMMENDATIONS

Atmospheric characterizations (worldwide temperature and wind profiles) and infrasound propagation models (ray tracing, normal mode and parabolic equation) have been integrated in a single software package. The software incorporates a common user interface for accessing the various models and for viewing output data. Prior to the development of the InfraMAP tool kit, the component models were used primarily in basic research, were individually exercised on a case-by-case basis, and were often restricted by assumptions such as range-independence or a windless, constant sound speed. The integrated set of models allows for higher fidelity propagation modeling by offering features such as the inclusion of range-dependent sound speed and winds and the identification of eigenrays that connect a source and receiver. The ability to predict the critical infrasound propagation characteristics (travel time, azimuth, amplitude) that affect localization and network performance is therefore enhanced.

The functionality of the software is directed toward application to problems of interest in CTBT monitoring. The tools allow the research community to model or evaluate the performance of infrasound localization and detection algorithms. They also allow studies of network performance to be conducted. Use of the InfraMAP tool kit is anticipated to lead to increased efficiency and effectiveness of CTBT operational and research components.

Systematic sensitivity analyses and validation studies are being conducted to understand the effect of environmental and model parameters on accurate modeling of long range infrasonic propagation. These investigations serve to identify specific areas where additional infrasound research and further development of modeling capabilities are needed. The CTBT research community will benefit from improved understanding of modeling issues (e.g., confidence bounds on predictions, need for *in situ* atmospheric data or synoptic models, relative importance of temporal and spatial parameters).

InfraMAP provides the software infrastructure to incorporate improved propagation and localization models, as they are developed, and updated atmospheric characterizations, as available. These upgrades may be needed to improve the estimate of current propagation conditions in order to help the operational monitoring community reduce the area of uncertainty in infrasound source location. Furthermore, the capabilities of the tool kit can be leveraged to generate an accurate infrasound knowledge database for use in CTBT monitoring.

REFERENCES

Armstrong, W.T., 1998: Comparison of infrasound correlation over differing array baselines. Los Alamos National Laboratory Report LA-UR-98-2742, in *Proceedings of the 20th Annual Seismic Research Symposium*, Santa Fe New Mex.

Clauter, D. A., and R. R. Blandford, 1996: Capability modeling of the proposed International Monitoring System 60-station infrasonic network. *AGU Fall Meeting*, San Francisco, Ca.

Dighe, K. A., R. W. Whitaker, and W. T. Armstrong, 1998: Modeling study of infrasonic detection of a 1 kT atmospheric blast. *Proceedings of the 20th Annual Seismic Research Symposium*, Santa Fe, New Mex.

Farrell, T., and K. LePage, 1996: *Development of a Comprehensive Hydroacoustic Coverage Assessment Model.* Air Force Phillips Laboratory Technical Report PL-TR-96-2248, BBN Technical Report No. W1275, Arlington, Va.

Georges, T. M., and W. H. Beasley, 1977: Refraction of infrasound by upper-atmospheric winds. *J. Acoust. Soc. Am.*, **61**, 28-34.

Gibson, R., R. Bieri, and T. Farrell, 1998: *Application of Three-Dimensional Ray Tracing to Infrasonic Propagation in the Atmosphere: The October 1997 El Paso Bolide*. BBN Technical Memorandum No. W1332, Arlington, Va.

Hedin, A. E, E. L. Fleming, A. H. Manson, F. J. Schmidlin, S. K. Avery, R. R. Clark, S. J. Franke, G. J. Fraser, T. Tsuda, F. Vial, and R. A. Vincent, 1996: Empirical wind model for the upper, middle, and lower atmosphere. *J. Atmos. Terr. Phys*., **58**, 1421-1447.

Herrin, E., J. Bonner, P. Golden, C. Hayward, G. Sorrells, J. Swanson, and I. Tibuleac, 1998: Reducing false alarms with seismo-acoustic synergy. *Proceedings of the 20th Annual Seismic Research Symposium*, Santa Fe, New Mex.

Hunter, J. H., and R. W. Whitaker, 1997: Numerical modeling of long range infrasonic propagation. *Infrasound Workshop for CTBT monitoring*, Santa Fe, New Mex.

Jensen, F. B., W. A. Kuperman, M. B. Porter, and H. Schmidt, 1994: *Computational Ocean Acoustics*. AIP Press, New York.

Jones, M. J., J. P. Riley, and T. M. Georges, 1986: *A Versatile Three-Dimensional Hamiltonian Ray-Tracing Program for Acoustic Waves in the Atmosphere above Irregular Terrain*. NOAA Special Report, Wave Propagation Laboratory, Boulder, Co.

Norris, D.E. and R. Gibson, 1999: Diurnal variability in the atmosphere and its effect on ray paths. *Spring Annual Meeting of the American Geophysical Union*, Boston, Mass.

Picone, J. M., A. E. Hedin, S. L. Coffey, J. Lean, D. P. Drob, H. Neal, D. J. Melendez-Alvira, R. R. Meier, and J. T. Mariska, 1997: The Naval Research Laboratory program on empirical models of the neutral upper atmosphere. In *Astrodynamics: Advances in the Astronautical Sciences*, Vol. 97, edited by F. R. Hoots, B. Kaufman, P. J. Cefola, and D. B. Spencer, American Astronautical Society, San Diego, Ca.

Pierce, A. D., and J. W. Posey, 1970: *Theoretical Prediction of Acoustic-Gravity Pressure Waveforms Generated by Large Explosions in the Atmosphere*. Technical Report AFCRL-70-0134, Air Force Cambridge Research Laboratories, Bedford, Mass.

Pierce, A. D., C. A. Moo, and J. W. Posey, 1973: *Generation and Propagation of Infrasonic Waves*. Technical Report AFCRL-TR-73-0135, Air Force Cambridge Research Laboratories, Bedford, Mass.

Pierce, A. D., and W. A. Kinney, 1976: *Computational Techniques for the Study of Infrasound Propagation in the Atmosphere*. Technical Report AFGL-TR-76-56, Air Force Geophysics Laboratories, Hanscom AFB, Mass.

ReVelle, D.O., R.W. Whitaker, and W.T. Armstrong, 1998: Infrasound from the El Paso Super-Bolide of October 9, 1997. Los Alamos National Laboratory Report LA-UR-98-2893, in *Characteristics and Consequences of Space Debris and Near-Earth Objects, SPIE*.

West, M., K. E. Gilbert, and R. A. Sack, 1992: A tutorial on the Parabolic Equation (PE) model used for long range sound propagation in the atmosphere. *Applied Acoustics,* **37**, 31-49.

CHARACTERISTICS OF INFRASOUND PRODUCED BY LARGE MINING EXPLOSIONS IN KAZAKSTAN

Mike T. Hagerty, Won-Young Kim and Pavel Martysevich[1]

Lamont-Doherty Earth Observatory of Columbia University, Palisades, NY
[1]Institute of Geophysical Research, National Nuclear Center, Semipalatinsk-21, Kazakstan

Sponsored by U.S. Department of Defense
Defense Threat Reduction Agency
Contract No. DSWA01-97-C-0156

ABSTRACT

Since October, 1997, we have recorded infrasonic signals at the Kurchatov Observatory in Kazakstan from large mining blasts in Kazakstan and Siberia. The Kurchatov Observatory is an ideal site for research on infrasound and application of synergistic (seismic and acoustic) methods of event discrimination as it operates a 21-element short-period seismic cross-array and a three-component broadband seismographic station, and because of its close proximity to several large (100+ton) mining operations.

In September, 1998, we installed two additional infrasound sensors to form a three-element triangular array with 2-4 km spacing. Two of the elements consist of Globe microphones connected to noise reduction hose and pipe arrays, while the third is actually a small array comprised of several Soviet built, low-frequency microphones (K-301A) connected to various noise-reducing pipe configurations. We have compiled and analyzed infrasound signals from mine blasts for 1997 and 1998 in order to understand the character of infrasound signals produced by regional mine blasts and the nature of infrasound propagation at high latitudes. We are currently analyzing signals from 1999 recorded by the new large array.

Several large mines in the region routinely generate explosions that are detected seismically and with infrasound. The mines range in distance from 80 to 750 km from the infrasound array. The Ekibastuz mine, 250 km west of the array, regularly produces 4-6 seismic detections per day. The corresponding number of infrasound detections is found to be dependent upon the season and the local winds. During the winter months, when the direction of the zonal component of the stratospheric wind is from west to east, a strong stratospheric duct develops between Ekibastuz and Kurchatov and the number of infrasound detections is high. During this period the infrasound signal consists of two arrivals separated by about 60 s.

A preliminary interpretation of these signals, based on ray-tracing through an atmospheric model that includes a mean zonal wind model for mid-latitude, northern hemisphere winter and is modified below 15 km to account for an observed tropospheric duct, is that the first arrival at 250 km distance propagates through the troposphere and is followed 60 s later by a stratospheric arrival. During the summer months, when the zonal winds reverse direction, the number of infrasound detections is low.

Preliminary analysis of signals recorded during spring, 1999, by the larger aperture array suggests that the larger array results in improved infrasound detection of Ekibastuz mine blasts and improved discrimination of non-acoustic noise. During this period the second infrasound arrival follows the first by 90 s and is found to consist of two pulses separated by about 10 s. The larger array also confirms identification of infrasound signals believed to be produced by events in the Kuzbass mining region of Siberia, over 700 km away.

Key Words: Infrasound, ray-tracing, mine explosion, atmosphere, Kazakstan

OBJECTIVE

In order to meet the monitoring requirements of the Comprehensive Nuclear-Test-Ban Treaty (CTBT), three technologies - seismic, hydroacoustic, and infrasonic - will be relied upon to detect acoustic waves produced by nuclear explosions detonated on land, in the sea, and in the air. While seismic and hydroacoustic technologies are sufficiently evolved to meet the monitoring needs of the CTBT, in its current state, infrasonic technology, is not. There are several reasons why development of the infrasound component lags behind the other two. Temperatures in the atmosphere vary on time scales of hours to months, and wind speeds (up to 100 m/s) are a significant fraction of the average sound speed (~330 m/s). The result is that the acoustic propagation channels in the atmosphere are highly variable. This variability must be quantified for infrasonic monitoring to meet the needs of the CTBT.

There is currently an acute lack of reliable infrasonic observations that can be utilized to examine the effects of time-dependent variations in atmospheric properties on the delectability and characteristics of infrasound signals. This is particularly true for infrasound generated from smaller explosions, which the CTBT aims to monitor, but which are likely to be recorded by only a few (1-3) of the nearest IMS stations. We are constructing a database of infrasound waveforms from the mine explosions in order to examine the variability of observed infrasound characteristics (delectability, arrival time, waveform) throughout the year. In addition, we are evaluating the performance of several adaptive filtering techniques designed to suppress wind noise and enhance infrasound detection.

RESEARCH ACCOMPLISHED

Installation of Kurchatov Infrasound System

Since October, 1997, we have conducted infrasound observations at the Kurchatov Geophysical Observatory in Kazakstan using available microphones coupled with existing noise reduction systems in order to address some of the infrasound monitoring issues outlined above. The Kurchatov Observatory (Figure 1) is an ideal site for research on infrasound and on the application of synergistic (seismic and acoustic) methods of event discrimination as it operates both a 21-element short-period seismic cross-array (Figure 2) and a three-component broadband seismic station, and because of its close proximity to several large (100+ton) mining operations (Figure 1). In addition, conditions appear to be favorable for long-range infrasound propagation in Kazakstan, where infrasound signals have been detected out to 2,000 km distance [Al'Perovich et al., 1985].

Three types of noise reduction configuration are utilized in this study from fall of 1997 through January 1998 at the central recording site Figure 2: 1) six, 70 m long underground pipes extending radially from a central chamber and referred to as "East-" and "West-" spiders; 2) a single, 30 m long pipe with an outlet at the center of the length; and 3) an "H-pipe" array consisting of two, 300 m long pipes joined at their centers by a 100 m long pipe. The 300 m long pipes are raised 1 m above the ground and have sampling nozzles spaced at 3 m intervals located on their undersides, facing the ground. The internal diameter of the 300 m long pipes varies from 1/2 inch at the ends to 2 inches in the middle. The 30 m long pipe is raised 0.5 m above the ground and has sampling nozzles spaced at 0.5 m intervals. We presume that these systems, which were constructed during the Soviet era, were designed to be functional during the severe local winters, when snow covers the ground for five months each year and prohibits the use of conventional plastic hoses.

Two types of capacitor microphone - Globe and Soviet K301 - have been utilized with the pipe arrays described above. The K301s were originally installed at Kurchatov in the early 1970's by the Russian Ministry of Defense and recorded on paper. Since February, 1995, the analog signal from a K301 sensor has been digitized and recorded by a 16-bit A/D system together with the seismic channels from the cross array. Since October, 1997, 4-8 microphones connected to the various noise reduction systems have been simultaneously recorded, forming a small aperture acoustic array.

Fall 1997, Winter 1998 Small Array Infasound Observations

Between October, 1997 and January, 1998, we detected infrasound signals generated by 26 Ekibastuz mine events. The location and origin time of each event were determined from the seismic cross-array and are

listed in Table 1. Ekibastuz comprises a number of coal mines centered about (51.67N, 75.40E) as determined by satellite



Figure 1: Map of Kazakstan and southwestern Siberia showing locations of broadband seismic stations in Kazakstan (solid triangles), active mining areas (diamonds), Kuzbass and Abakan mining areas (shaded squares), the Balapan nuclear test site, and the Kurchatov Geophysical Observatory (KUR), where the seismic and infrasonic observations were made.



Figure 2: Plan view of the 21-element seismic borehole array (cross array) at Kurchatov and location of infrasound sensors. All are located within the Kurchatov Geophysical Observatory compound, which also houses the central recording unit for the cross array and a three-component broadband seismometer installed in a 25m shaft. Infrasound noise reduction systems (pipe arrays) utilized in this study are located at the central recording site (circled triangle).

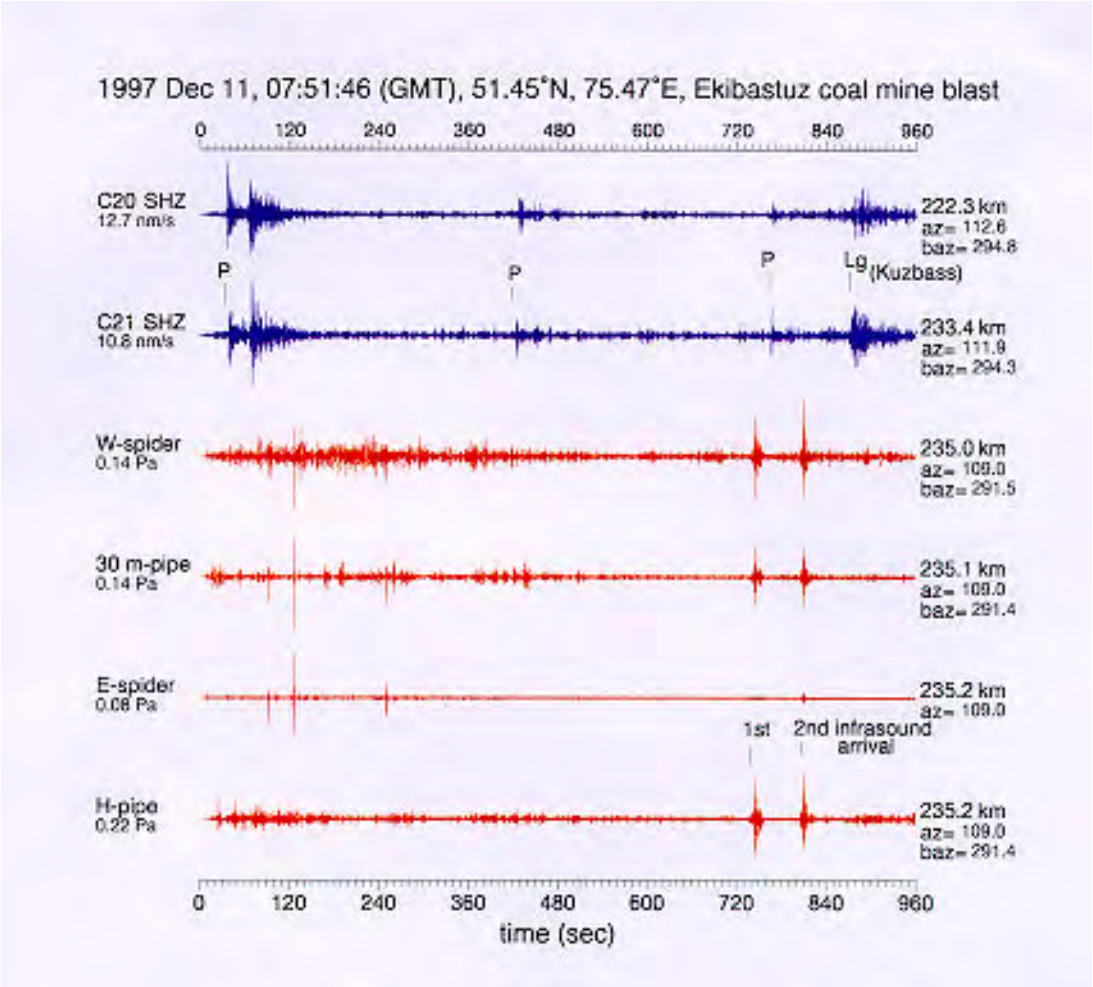


Figure 3: Selected cross-array seismic channels (top two traces) and infrasound signals recorded with four different noise reduction systems (Figure 2) for an Ekibastuz coal mine blast on Dec. 11, 1997. The first infrasound arrivals show phase velocity=0.38 km/s and back-azimuth=267º.

photographs [Thurber et al., 1990].

The infrasound wavetrain generated by Ekibastuz explosions during this period can be classified into two categories. The first, shown in Figure 3, consists of 1 or 2 simple pulses, with travel times of approximately 740 and 810s with respect to the seismically estimated origin time. The second arrival is observed in about 60% of the events (18) from Ekibastuz; when present, it generally follows the first by 50-70 s, though this can range anywhere from 24 to 85 s (Table 1). The travel time of the first arrival exhibits great variation and probably reflects varying atmospheric conditions such as transient propagation ducts.

We applied a beamforming procedure to the acoustic traces to estimate the apparent phase velocity (0.38 km/s) and back-azimuth (2670). The estimated back-azimuth is 30'off that predicted from the seismic location (2970). The large discrepancy likely reflects the small aperture of the small infrasound array; the back-azimuth estimated by the large aperture array, discussed below, is extremely close to the predicted value.

The second type of infrasonic wavetrain associated with Ekibastuz events, shown in Figure 4, consists of a series of pulses of growing amplitude lasting some 20-30 s. The event shown in Figure 4 is actually two

explosions closely spaced in time. While the seismic waves from the two explosions overlap, making it difficult to resolve two events, the lower phase velocities and shorter durations of the infrasonic waves allow the two events to be distinguished (Figure 4). For this reason, infrasound observations may be crucial for detecting a shallow nuclear test hidden in the seismic coda of an earlier event.

Table 1: **List of infrasound signals from mining blasts at Ekibastuz, Kazakstan**

Id	Origin time		Magnitude	Phase	Travel time	Group velocity	Amplitude
no.	mm/dd/yy	hh:mm:sec		id	(s)	(m/s)	(Pa)
01	10/16/97	08:16:13	2.1	S1	820	303	0.22
02	10/16/97	08:28:43	2.6	S1	810	307	0.23
03	10/16/97	08:34:39	2.3	S1	825	301	0.11
04	10/17/97*	11:39:14	2.2	S1	646	325	0.13
				S2	731	287	0.06
05	11/19/97	09:37:57	2.2	S1	730	341	0.09
06	11/19/97	10:20:07	2.5	S1	793	313	0.13
07	11/27/97	07:43:17	2.2	S1	763	326	0.29
08	11/27/97	09:47:45	1.9	S1	788	315	0.16
09	11/27/97	09:53:18	2.4	S1	765	325	0.54
10	11/28/97	08:34:14	2.5	S1	763	326	0.13
11	11/28/97	08:58:06	2.4	S1	761	327	0.19
12	11/28/97	09:30:49	2.3	S1	757	328	0.45
13	12/02/97	08:48:11	1.9	S1	734	339	0.29
				S2	793	313	0.17
14	12/02/97	09:23:38	1.6	S1	756	329	0.08
				S2	794	313	0.05
15	12/02/97	09:27:25	2.0	S1	746	333	0.41
				S2	786	316	0.22
16	12/02/97	10:29:01	2.1	S1	743	335	0.13
				S2	779	319	0.08
17	12/11/97	07:51:46	2.4	S1	739	336	0.23
				S2	809	307	0.29
18	12/11/97	07:57:43	1.9	S1	718	346	0.04
				S2	799	311	0.03
19	12/11/97	08:36:50	2.8	S1	747	333	0.09
				S2	809	307	0.05
20	12/11/97	08:58:22	2.5	S1	750	332	0.19
				S2	812	306	0.17
21	12/11/97	10:49:47	2.2	S1	737	337	0.09
				S2	798	312	0.06
22	01/14/98	07:02:34	2.0	S1	796	312	0.26
				S2	827	301	0.49
23	01/14/98	08:13:40	2.4	S1	795	313	0.26
				S2	829	300	0.31
24	01/14/98	09:16:47	2.6	S1	815	305	0.17
				S2	839	296	0.25
25	01/28/98	07:31:04	3.0	S1	753	330	0.15
				S2	777	320	0.08
26	01/28/98	08:15:21	2.4	S1	764	325	0.25
				S2	788	315	0.27

There is no evidence for multiple cast firing within either of the two seismic events, hence, the multiple phases observed in the infrasound data must be produced by propagation effects.

During the observation period, three infrasound signals from events in the Kara-Zhyra coal mine in the Balapan former Soviet nuclear test site were identified (Table 2); their detection at such short range (Δ=80 km) suggests that a favorable tropospheric duct exists.

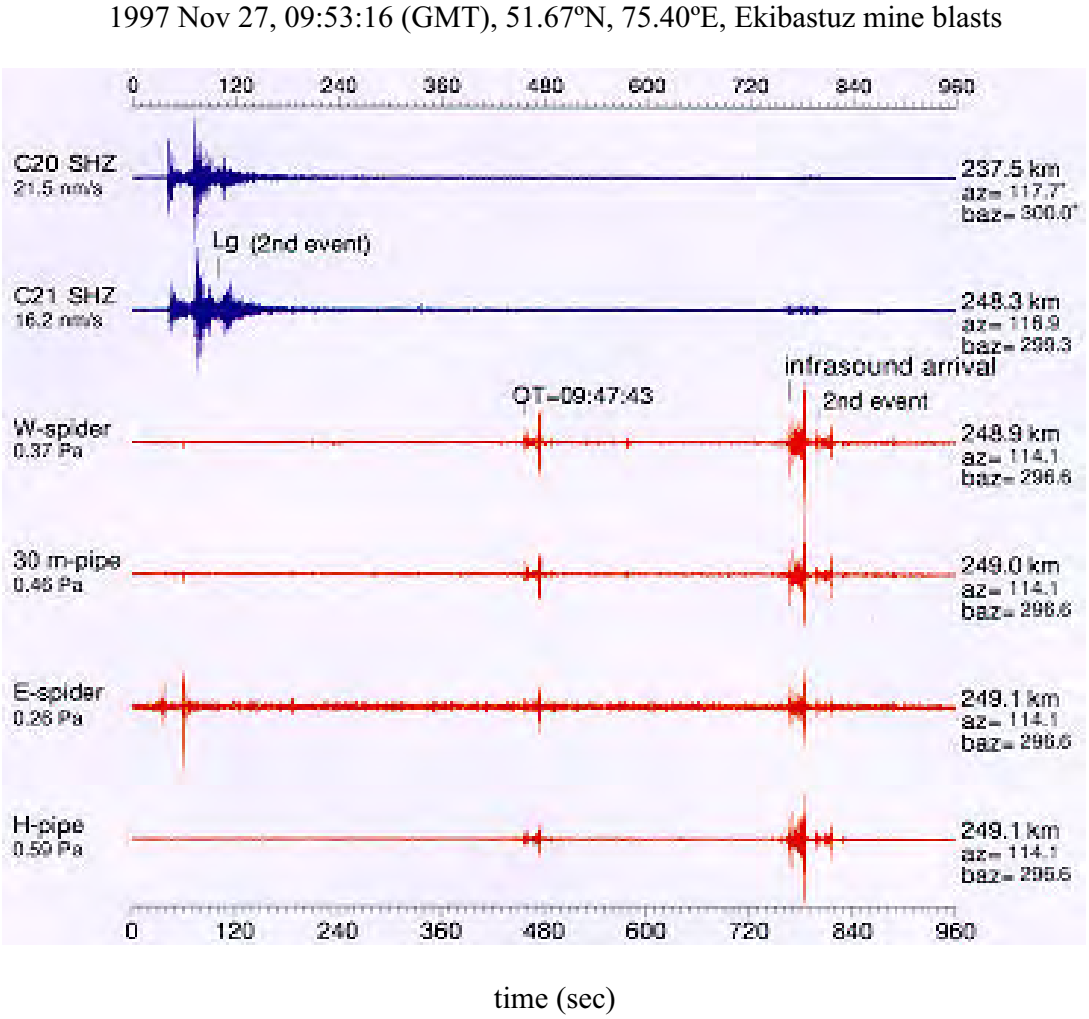


Figure 4: Same as Figure 3 for Ekibastuz mine blast on Nov. 27, 1997. This event is actually two closely spaced explosions which produce overlapping Lg phases in the seismic channels but produces separate infrasound arrivals. An additional infrasound arrival at t~460 s is from an earlier Ekibastuz event. Each event is seen to consist of a sequence of pulses of increasing amplitude lasting 20-30 s.

Modeling of winter infrasound signals

In order to identify the infrasound arrivals, we ray traced through various suitable atmospheric models. Figure 5 shows the sound speed (c) as a function of height in the atmosphere derived from mid-latitude (45N) temperature profiles for January and July [Valley, 1965] and the well-known theoretical relation $c(T) = 20.1\sqrt{(TK)}$, where T is the temperature in degrees Kelvin. In Figure 5 a mid-latitude zonal wind models for winter adapted from Georges and Beasley [1977] is shown. Ray tracing through the winter temperature model alone confirms that in the absence of wind, no rays are predicted return to the Earth's surface at distances less than 280 km. Beyond 280 km, the first arrivals turn in the thermosphere, at altitudes of ~150 km, followed by secondary arrivals that turn at ~125 km; no energy is returned from the stratosphere (40-80 km). Thus, in the absence of wind, no favorable propagation paths are predicted to exist between Ekibastuz and Kurchatov (Δ=250 km).

Figure 5 shows ray paths for the winter model including the winter zonal winds. The first rays arriving at 220-250 km have turned in the stratosphere (h~38 km). The predicted travel time and phase velocity match the observed values at Ekibastuz reasonably well, however, the second observed arrival is not predicted by this model. In order to produce two arrivals with the observed time separation (~70 s) at Δ=250 km, a tropospheric duct must exist between Ekibastuz and Kurchatov. This is supported by the observation of a direct (tropospheric) arrival from Kara-Zhyra explosions, 80 km away and well within the shadow zone

Table 2: **List of infrasound signals from other mining blasts**

Id	Origin time mm/dd/yy	Origin time hh:mm:sec	Lat. (°N)	Long. (°E)	Magnitude	Phase id	Travel time (s)	Group velocity (m/s)	Amp (Pa)
				Novotaubinka near Semipalatinsk					
1	11/19/97	09:24:38	49.80	80.85	0.5	D	624	302	0.10
				Kara-Zhyra mine in Balapan					
1	11/19/97	10:28:27	50.01	78.80	3.7	D	252	317	0.58
2	12/11/97	11:58:10	49.99	78.59	1.8	D	232	234	0.39

predicted by models with no tropospheric duct. The existence of a tropospheric duct implies an increase in the effective sound speed between the surface and the tropopause (0-15 km); we cannot distinguish whether this is caused by a temperature inversion or a westerly jet, however, we prefer the former as the duct must exist in both the easterly and northerly directions. Support for a winter temperature inversion can be found in a study on infrasound reception of explosions detonated at 1 km height in the atmosphere in southern Kazakstan [A1'Perovich et al., 1985]; direct arrivals observed out to distances of 200 km were linked with meteorological measurements in the troposphere that confirmed a temperature inversion between the surface and 2-4 km.

Spring 1999 Large Array Observations

Preliminary analysis of signals recorded during spring, 1999, by the large aperture acoustic array indicate an improved ability to detect mine events and to reject non-acoustic "noise" compared with use of the small array alone. An example 1 hour window of data recorded during peak mining hours (07:00-10:00 GMT) is shown in Figure 6. During this hour we are able to identify 7 Ekibastuz events in the seismic channels; for all but one of these we can also identify associated infrasound signals. The first infrasound arrival for each event has a travel time of 760 s and is followed 90 s later by a second arrival that consists of two pulses separated by 10 s. The estimated back-azimuth for these arrivals is 302°, close to the expected value. The character of the infrasound arrivals is so regular on this day, that we are able to identify two Ekibastuz events (one of these is indicated by the "?" in Figure 6), for which no seismic detection was made, solely on the basis of the infrasound detections. During this period we are also able to identify infrasound signals generated by mine explosions near the Kuzbass region in Siberia (Figure 1), over 700 km away. Since August, 1998, we have operated a broadband seismometer near the town of Eltsovka, close to the Kuzbass region, in order to aid identification of Kuzbass events.

CONCLUSIONS AND RECOMMENDATIONS

We have presented here an initial interpretation of the characteristics of infrasound propagation observed in northern Kazakstan and Siberia. During the winter, the infrasound signals associated with Ekibastuz events can be classified into two types. The first type consists of two pulses spaced 50-70 s apart, while the second type consists of multiple pulses arriving within about a 20-30 s window. Infrasound arrivals from both Ekibastuz (Δ=250 km) and Kara-Zhyra(Δ=80 km) explosions support the existence of a tropospheric duct, produced by a temperature inversion and/or a westerly jet in the troposphere. The multiple arrivals characteristic of the second type of infrasound wavetrains likely result from strong positive sound speed gradients in the troposphere and, especially, in the upper stratosphere. The large variability in the character of infrasound signals generated by Ekibastuz events over short time scales (hours to days) is indicative of the rapidity of atmospheric fluctuations.

Measurements of the back-azimuth of different infrasound arrivals have the potential to resolve some of the ambiguity that exists in using infrasound to infer the horizontal wind structure in the atmosphere. However, much more accurate back-azimuth estimates than can be obtained by a small aperture array are required. For this reason, we have extended the small array at Kurchatov into a larger triangular array with 2-4 km sides. In addition, we intend to install a second three-element infrasound array at Borovoye, 377 km NW of Ekibastuz (Figure 1), in order to examine the seasonal effects of the stratospheric winds both upwind and downwind from the source. These improved infrasound arrays will provide unique data that may be used to advance the infrasound technology used for CTBT monitoring.

REFERENCES

A1'Perovich, L. S. et al., The acoustic wave of an explosion, *Izvestiya Academy of Sciences USSR, Physics of the Solid Earth (USA)*, **21**(**11**),835-842,1985.

Georges, T. M., and W. H. Beasley, Infrasound refraction by upper-atmospheric winds, *J. Acoust. Soc. Am*., **61** (1), 28-34, 1977.

Thurber, C., H. Given, and J. Berger, Regional seismic event location with a sparse network: application to Eastern Kazakstan, USSR, *J. Geophys. Res*., **94**, 17,767-17,780, 1989.

Valley, S. L. (editor), *Handbook of Geophysics and Space Environments*, McGraw-Hill, New York, 1965.

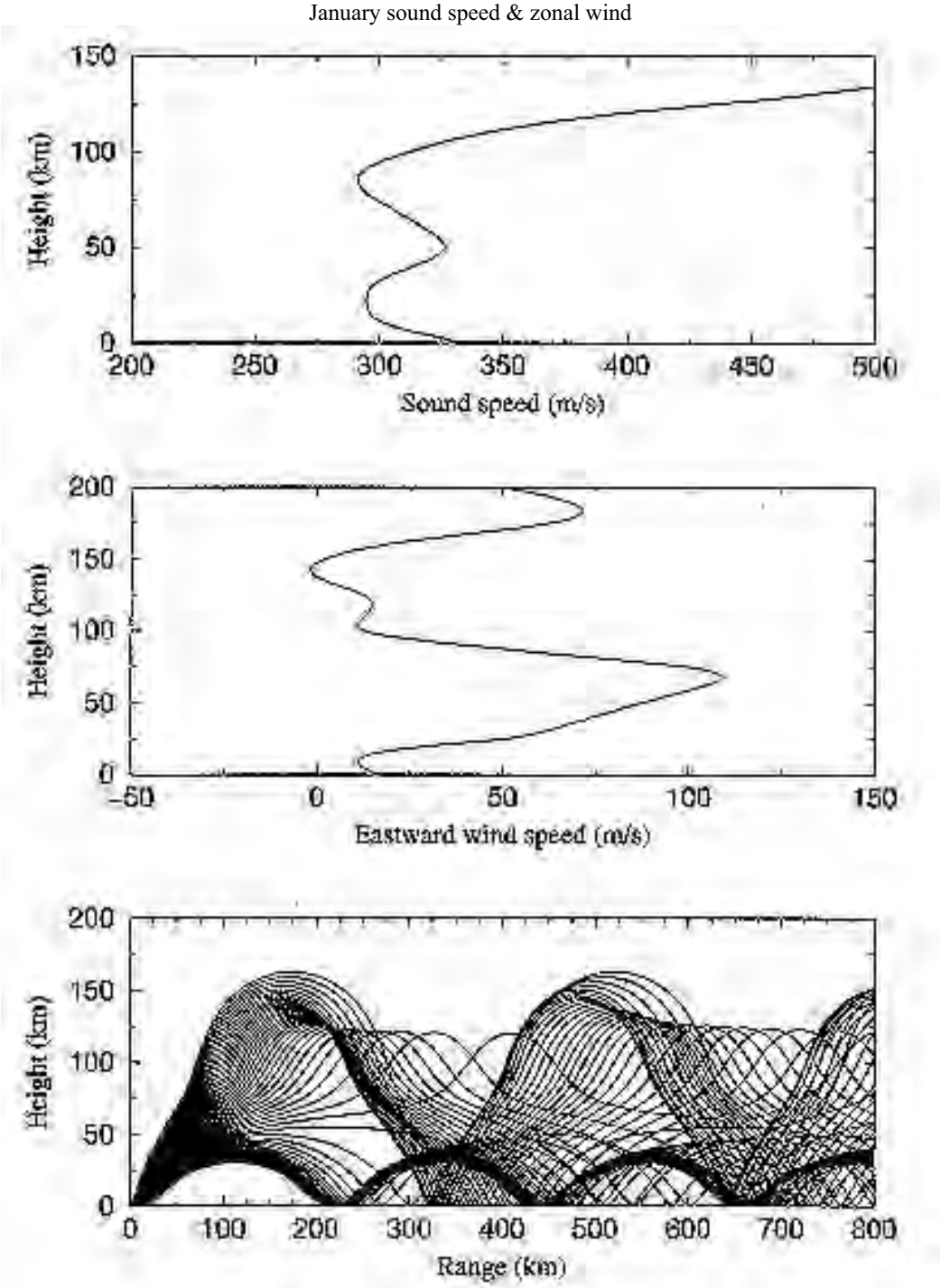


Figure 5: (a) January and July sound-speed profiles derived from the 1962 U.S. Standard Atmosphere midlatitude (45N) temperature profiles [Valley, 1965]. (b) January and July midlatitude zonal winds taken from Georges and Beasley [1977]. Also shown for comparison are zonal winds measured by the high-resolution doppler imager aboard the Upper Atmosphere Research Satellite (UARS) [Fleming et al., 1996]. (c) Results of ray tracing through a sound speed profile given by the 1962 U.S. Standard Atmosphere midlatitude temperature profile and the January zonal wind model. Ray paths computed for the exact method.

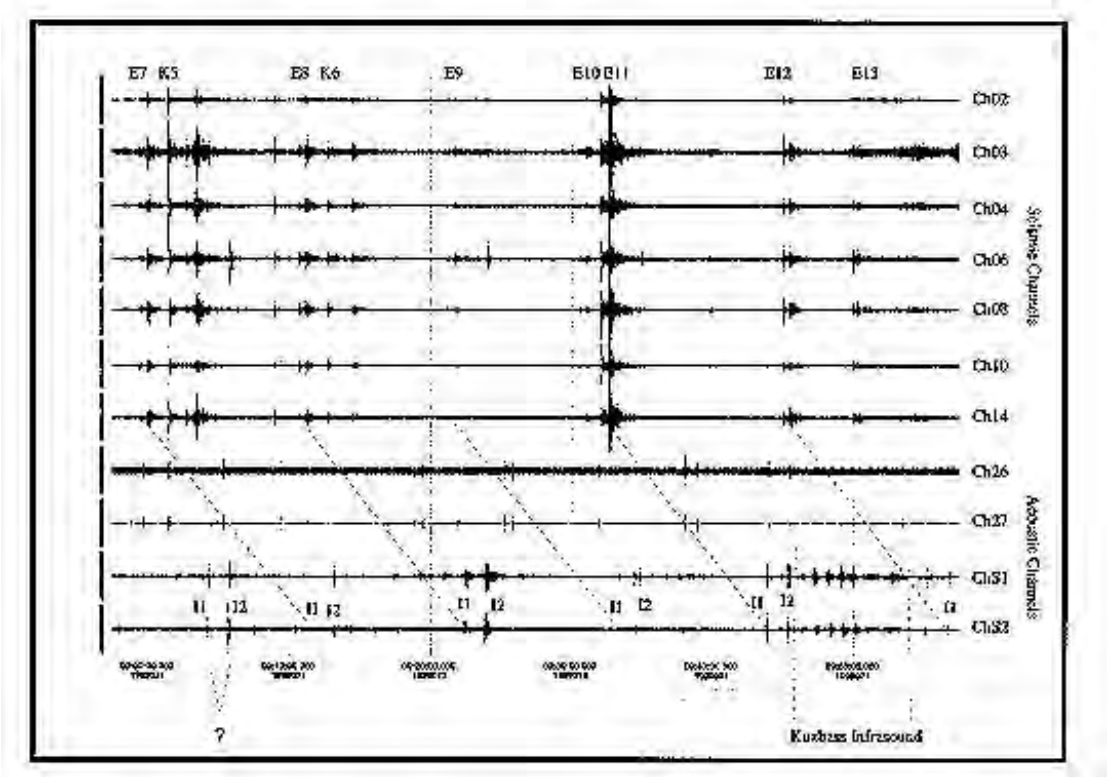


Figure 6: Example data from the Kurchatov seismic cross-array and acoustic triangle array for spring, 1999. During the one hour period shown are 7 Ekibastuz events with associated infrasound arrivals (?) believed to be produced by an Ekibastuz event that did not generate a seismic signal, and infrasound arrivals from a Kuzbass mine event, 700 km away.

INFRASOUND SIGNAL SEPARATION USING INDEPENDENT COMPONENT ANALYSIS

Fredric M. Ham and Nizar A. Faour, Florida Institute of Technology
Joseph C. Wheeler, The Boeing Company

Sponsored by The Boeing Company
Contract No. 7M210007

ABSTRACT

An important element of monitoring compliance of the Comprehensive Nuclear-Test-Ban Treaty (CTBT) is an infrasound network. For reliable monitoring, it is important to distinguish between nuclear explosions and other sources of infrasound. This will require signal (event) classification after a detection is made. We have demonstrated the feasibility of using neural networks to classify various infrasonic events. However, classification of these events can be made more reliably with enhanced quality of the recorded infrasonic signals. One means of improving the quality of the infrasound signals is to remove background noise. This can be carried out by performing signal separation using Independent Component Analysis (ICA). ICA can be thought of as an extension of Principal Component Analysis (PCA). Using ICA, noise, and other events that are not of concern, can be removed from the signal of interest. This is not a *filtering* process, but rather a technique that actually *separates* out the background noise from the signal of interest, even if the signals have overlapping spectra. Therefore, not only is the signal of interest *recovered*, but so is the background noise. The higher fidelity signal of interest (compared to any one sensor channel signal from the infrasound array before separation) can be presented to an event classifier (e.g., a neural network), and the background noise can also be further scrutinized.

We show two examples of infrasound signal separation using ICA. The ICA is performed using a neural network approach, i.e., an unsupervised nonlinear PCA subspace learning rule. The first example involves artificially mixing three different infrasonic signals from three separate events using a random mixing matrix, these mixed signals are then used to recover the original event signals. The second example is in the true spirit of ICA, i.e., the separation is performed blindly. From four channels of an infrasound array, these four inputs are used in the ICA to separate two signals, i.e., one "signal" the other "noise." The mixing matrix is not known, however, the separated *signal* of interest is shown to be the infrasound signal of a volcano eruption, and the separated *noise* is shown to contain characteristics of a microbarom signal. Moreover, in spite of overlapping spectra between the output signals of the ICA, separation of the signals is possible.

Key Words: Infrasound, independent component analysis, signal separation, neural network, nonlinear principal component analysis, overlapping spectra.

OBJECTIVE

The proposed International Monitoring System (IMS), for verifying compliance of the Comprehensive Nuclear-Test-Ban Treaty (CTBT), includes an infrasound network that will be capable of detecting nuclear explosions. In the past, the primary interest in monitoring infrasound waves from nuclear explosions was to detect low-frequency signals associated with large (megaton) yield nuclear events. The main emphasis for monitoring compliance of the CTBT is the ability to detect and classify kiloton-size nuclear explosions. Infrasound signals from these events have a much higher frequency content than those from larger yield nuclear explosions. The infrasound signals received at a single station (multi-sensor array) can contain multiple events that can overlap in frequency and make reliable detection and classification of a nuclear explosion difficult. Therefore, the objective of this paper is to show how Independent Component Analysis (ICA) [1-4] can be used to separate infrasonic signals, in spite of overlapping spectra, recorded on a multi-sensor array. The ICA is performed using a neural network approach, specifically, an unsupervised nonlinear Principal Component Analysis (PCA) subspace learning rule. The purpose of the signal separation process is to separate the signal of interest from the background noise. It is assumed that there is one *dominant* event recorded along with background noise (which can consist of multiple, less dominant, components, including noise). The separated signal of interest will be higher quality compared to any one sensor channel signal from the infrasound array before separation. This high fidelity separated signal of interest can then be presented to an event classifier, e.g., a neural network [5, 6], and the background noise can also be further evaluated.

RESEARCH ACCOMPLISHED

A succinct presentation of ICA is given first followed by a brief discussion of how ICA can be carried out using neural networks. Finally, two examples of signal separation using a neural network ICA approach is presented.

Independent Component Analysis

Independent component analysis (ICA) can be thought of as an extension of PCA [7]. It is used primarily to separate unknown source signals from their linear mixtures, this is known as the blind source signal separation problem. The characteristics of the transmission channel does not have to be known to separate the source signals from a set of noisy observable (measured) signals. Moreover, even when the source signals have overlapping spectra, separation of the signals is possible. Blind source separation techniques can be applied to array processing, medical signal processing, communications, speech processing, and image processing, to name a few. The main difference between PCA and ICA is that instead of the uncorrelatedness property associated with standard PCA, in ICA the coefficients of the linear expansion of the data vectors must be mutually independent, or as independent as possible. What this means is that higher-order statistics [8, 9] must be used to determine the ICA expansion. In standard PCA, second-order statistics provides only decorrelation. Higher-order statistics are useful when dealing with non-Gaussian processes, non-minimum phase problems, colored noise, or even nonlinear processes [8]. Therefore, it is not surprising that nonlinearities must be used in the learning phase, even though the final input/output mapping is linear [10]. Neural network structures have been developed to perform ICA [10].

We assume that there exist *q zero-mean* wide-sense stationary source signals $s_1(k), s_2(k), \cdots, s_q(k)$ for $k = 1, 2, \cdots$ (the discrete time index or for images the pixels), that are scalar-valued and mutually statistically independent for each sample value *k*. The independence condition can be formally defined by stating that the joint probability density of the source signals is equal to the product of the marginal probability densities of the individual signals, i.e.,

$$p[s_1(k), s_2(k), \cdots, s_q(k)] = p[s_1(k)]\, p[s_2(k)] \cdots p[s_q(k)] = \prod_{i=1}^{q} p[s_i(k)] \qquad (1)$$

The individual source signals are also assumed to be unknown (unobservable), however, we do have access to a set of *h* noisy linear mixtures of the unknown signals, $x_1(k), x_2(k), \cdots, x_h(k)$. These measured signals are given by

$$x_j(k) = \sum_{i=1}^{q} s_i(k) a_{ij} + n_j(k) \qquad (2)$$

for $j = 1, 2, \cdots, h$, the elements a_{ij} are assumed to be not known, and $n_j(k)$ is additive measurement noise. We can now define the following, $\boldsymbol{x}(k) = \begin{bmatrix} x_1(k) & x_2(k) & \cdots & x_h(k) \end{bmatrix}^T$, $\boldsymbol{x}(k) \in \Re^{h\text{x}1}$, $\boldsymbol{s}(k) = \begin{bmatrix} s_1(k) & s_2(k) & \cdots & s_q(k) \end{bmatrix}^T$, $\boldsymbol{s}(k) \in \Re^{q\text{x}1}$ (the *source vector* consisting of the q independent components), and $\boldsymbol{A} = \begin{bmatrix} \boldsymbol{a}_1 & \boldsymbol{a}_2 & \cdots & \boldsymbol{a}_q \end{bmatrix}$, $\boldsymbol{A} \in \Re^{h\text{x}q}$ (the *mixing matrix*), where the column vectors of $\boldsymbol{A}$ are the *basis vectors* of the ICA expansion. Equation (2) can now be written in vector-matrix form as

$$\boldsymbol{x}(k) = \boldsymbol{A}\boldsymbol{s}(k) + \boldsymbol{n}(k) = \sum_{i=1}^{q} s_i(k)\boldsymbol{a}_i + \boldsymbol{n}(k) \qquad (3)$$

referred to as the ICA expansion. We will assume the mixing matrix $\boldsymbol{A}$ contains at least as many rows as columns ($h \geq q$), and it has full column rank, i.e., $\rho(\boldsymbol{A}) = q$ (i.e., the mixtures of the source signals are all different).

Independent Component Analysis Using Neural Networks

This discussion pertaining to the neural network approach for blind source separation using ICA follows the presentation by Karhunen *et al.* [10]. Figure 1 shows the basic neural architecture to perform the separation of source signals (i.e., estimate the independent components), and estimate the basis vectors of the ICA expansion, [i.e., estimate the column vectors of the mixing matrix $\boldsymbol{A}$ in (3)].

Error! No topic specified.

Figure 1. The ICA network. The three layers perform whitening, separation, and estimation of the basis vectors. The weight matrices that are necessary to determine are $\boldsymbol{V}$, $\boldsymbol{W}^T$, and $\boldsymbol{Q}$.

Prewhitening Process

The whitening process that proceeds the separation step (i.e., prewhitening) is a critical procedure. This process normalizes the variances of the observed signals to unity. In general, separation algorithms that use prewhitened inputs often have better stability properties and converge faster. However, whitening the data can make the separation problem more difficult if the mixing matrix $\boldsymbol{A}$ is ill-conditioned or if some of the source signals are relatively *weak* compared to the other signals [11, 12]. The input vectors $\boldsymbol{x}(k)$ are whitened by applying the transformation

$$\boldsymbol{v}(k) = \boldsymbol{V}\boldsymbol{x}(k) \qquad (4)$$

where $\boldsymbol{v}(k)$ is the kth whitened vector and $\boldsymbol{V}$ is the whitening matrix. The whitening matrix can be determined in two ways: (i) using a batch approach, or (ii) neural learning. For the batch approach, PCA is used to determine the whitening matrix, it is given as

$$\boldsymbol{V} = \boldsymbol{D}^{-1/2}\,\boldsymbol{E}^T \qquad (5)$$

where $\boldsymbol{V} \in \Re^{qxh}$, $\boldsymbol{D} = \text{diag}\begin{bmatrix} \lambda_1 & \lambda_2 & \cdots & \lambda_q \end{bmatrix} \in \Re^{qxq}$, and $\boldsymbol{E} = \begin{bmatrix} \boldsymbol{c}_1 & \boldsymbol{c}_2 & \cdots & \boldsymbol{c}_q \end{bmatrix} \in \Re^{hxq}$, with λ_i : ith largest eigenvalue of the covariance matrix $\boldsymbol{C}_x = \text{E}\left\{\boldsymbol{x}(k)\boldsymbol{x}^T(k)\right\} \in \Re^{hxh}$, and $\boldsymbol{c}_i$ for $i = 1, 2, \cdots, q$ are associated (principal) eigenvectors. Therefore, the transformation in (4) actually consists of two steps, i.e., compression and whitening. The compression step consists of selecting the proper value for q (the number of source signals). Therefore, the PCA described above for the whitening can also be used to select (i.e., estimate) the number of source signals (q) to be recovered (or the number of independent components) if the noise term $\boldsymbol{n}(k)$ in (3) is assumed to be zero-mean Gaussian white noise with covariance matrix $\text{E}\left\{\boldsymbol{n}(k)\boldsymbol{n}^T(k)\right\} = \sigma^2\boldsymbol{I}_h$. In the noise covariance matrix, σ^2 is the conjoint variance of the components of the noise vector $\boldsymbol{n}(k)$. The noise vector is assumed to be uncorrelated with

the sources $s_i(k)$, for $i = 1, 2, \cdots, q$. Given these assumptions, the covariance matrix of the data vectors $\boldsymbol{x}(k)$ is given by

$$\mathrm{E}\left\{\boldsymbol{x}(k)\boldsymbol{x}^T(k)\right\} = \sum_{i=1}^{q} \mathrm{E}\left\{s_i^2(k)\right\}\boldsymbol{a}_i\boldsymbol{a}_i^T + \sigma^2\boldsymbol{I}_h \tag{6}$$

The q largest eigenvalues of the covariance matrix in (6), i.e., $\lambda_1, \lambda_2, \cdots, \lambda_q$, are some linear combination of the source signal powers $\mathrm{E}\left\{s_i^2(k)\right\}$ added to the noise power σ^2. Therefore, the remaining $h - q$ eigenvalues correspond to only noise (theoretically these eigenvalues are equal to σ^2). The q largest *signal* eigenvalues will be distinctly larger than the remaining *noise* eigenvalues if the signal-to-noise ratio is large enough. In practice, the eigenvalues of the input covariance matrix are determined from the time-average of the covariance matrix over the available data vectors given by

$$\boldsymbol{C}_x \cong \frac{1}{N}\sum_{i=1}^{N} \boldsymbol{x}_i(k)\boldsymbol{x}_i^T(k) \tag{7}$$

where N is the total number of input vectors. A stochastic approximation algorithm to *learn* the whitening matrix is given by

$$\boldsymbol{V}(k+1) = \boldsymbol{V}(k) - \mu(k)[\boldsymbol{v}(k)\boldsymbol{v}^T(k) - \boldsymbol{I}]\boldsymbol{V}(k) \tag{8}$$

where it is recommended to adjust the learning rate parameter according to

$$\mu(k) = \frac{1}{\dfrac{\gamma}{\mu(k-1)} + \|\boldsymbol{v}(k)\|_2^2}, \quad 0 < \gamma \le 1.0 \tag{9}$$

where $\|\cdot\|_2$ is the L_2 or Euclidean norm of a vector, and γ is the forgetting factor. When the whitening (orthogonal) transformation $\boldsymbol{V}$ is applied to the inputs as in (4), the resulting whitened outputs $\boldsymbol{v}(k)$ will possess the whiteness condition, i.e.,

$$\mathrm{E}\left\{\boldsymbol{v}(k)\boldsymbol{v}^T(k)\right\} = \boldsymbol{I}_q \tag{10}$$

Separation Process

The separation process can be carried out by using many different methods [4, 11, 13]. Approximating contrast functions, maximized by separating matrices, have been developed [4]. Contrast functions typically require extensive batch computations using estimated higher-order statistics of the data and lead to very complicated adaptive separation algorithms. However, it is sufficient to use the kurtosis (fourth-order cumulant) of the data. Another class of separation methods involves using neural networks to perform the separation of the source signals [12]. In Fig. 1, the second stage of the architecture is responsible for the separation of the whitened signals $\boldsymbol{v}$. The linear separation transformation is given by

$$\boldsymbol{y}(k) = \boldsymbol{W}^T\boldsymbol{v}(k) \tag{11}$$

where $\boldsymbol{W} \in \Re^{q \times q}$ ($\boldsymbol{W}^T\boldsymbol{W} = \boldsymbol{I}_q$) is the separation matrix. Thus the separated signals are the outputs of the second stage, i.e., $\hat{\boldsymbol{s}}(k) = \boldsymbol{y}(k)$. An interesting observation is once the source signal $\boldsymbol{s}(k)$ has been estimated, this means that the pseudo-inverse of $\boldsymbol{A}$, i.e., $\boldsymbol{A}^+$, must have been also "blindly" determined [refer to (3)].

One very straightforward neural learning method to determine the separation matrix is based on the nonlinear PCA subspace learning rule [14-16] given by

$$\boldsymbol{W}(k+1) = \boldsymbol{W}(k) + \mu(k)[\boldsymbol{v}(k) - \boldsymbol{W}(k)g\{\boldsymbol{y}(k)\}]g\{\boldsymbol{y}^T(k)\} \tag{12}$$

where $\boldsymbol{v}(k)$ is the prewhitened input vector given in (4), and the function $g(\cdot)$ is a suitably chosen nonlinear function usually selected to be odd in order to ensure stability and for separation purposes. It is

recommended that the learning rate parameter $\mu(k)$ be adjusted according to the adaptive scheme given in (9), with $\boldsymbol{v}(k)$ replaced by $\boldsymbol{y}(k)$. Also, for good convergence, it is best to select the initial weight matrix $\boldsymbol{W}(0)$ to have as columns a set of orthonormal vectors. Typically, the nonlinear function $g(\langle)$ is chosen as

$$g(t) = \beta\tanh(t / \beta) \tag{13}$$

where $g(t) = \dfrac{df(t)}{dt}$ and $f(t) = \beta^2 \ln[\cosh(t / \beta)]$, the logistic function. This is not an arbitrary choice for the nonlinearity in the learning rule of (12). It is motivated by the fact that when determining the ICA expansion *higher-order statistics* are needed. This can be seen by observing another neural learning rule to perform separation of unknown signals. This learning rule is called the *bigradient algorithm* [10, 17, 18] given by

$$\boldsymbol{W}(k+1) = \boldsymbol{W}(k) + \mu(k)\boldsymbol{v}(k)g[\boldsymbol{y}^T(k)] + \gamma(k)\boldsymbol{W}(k)[\boldsymbol{I} - \boldsymbol{W}^T(k)\boldsymbol{W}(k)] \tag{14}$$

where $\gamma(k)$ is another *gain* parameter, typically about 0.5 or one. This is a stochastic gradient algorithm that maximizes or minimizes the performance criterion

$$J(\boldsymbol{W}) = \sum_{i=1}^{q} \mathrm{E}\{f(y_i)\} \tag{15}$$

under the constraint that the weight matrix $\boldsymbol{W}$ must be orthonormal. The orthonormal constraint in (15) is realized in the learning rule in (14) in an additive manner. With the appropriate function $f(\langle)$ in (15), the performance criterion would involve the sum of the fourth-order statistics (fourth-order cumulants) of the outputs, i.e., the *kurtosis* [8]. Therefore, the criterion would be either *minimized* for sources with a *negative kurtosis* and *maximized* for sources with a *positive kurtosis*. Source signals that have a *negative kurtosis* are often called *sub-Gaussian* signals and sources that have a *positive kurtosis* are referred to as *super-Gaussian* signals. In (15) the expectation operator would be dropped because we only consider instantaneous values. We now write the logistic function $f(t) = \ln[\cosh(t)]$ (for $\beta = 1$) in terms of a Taylor series expansion

$$f(t) = \ln[\cosh(t)] = t^2 / 2 - t^4 / 12 + t^6 / 45 - \cdots \tag{16}$$

The second-order term $t^2 / 2$ is on the average constant due to the whitening. The nonlinearity would then be given by $g(t) = \dfrac{df(t)}{dt} = \tanh(t) = t - t^3 / 3 + 2t^5 / 15 - \cdots$, and the cubic term will be dominating (an odd function) if the data are prewhitened.

Estimation of the ICA Basis Vectors

This is the last stage in Fig. 1. Two basic methods can be used to estimate the ICA basis vectors, or the column vectors of the mixing matrix $\boldsymbol{A}$ in (3). The first method is a "batch" approach where the estimate of $\boldsymbol{A}$, i.e., $\hat{\boldsymbol{A}}$, is given by

$$\hat{\boldsymbol{A}} = \boldsymbol{E}\boldsymbol{D}^{1/2}\boldsymbol{W} \tag{17}$$

where $\boldsymbol{D}$ is the eigenvalue matrix shown in (5), $\boldsymbol{E}$ has columns that are the associated eigenvectors shown in (5), and $\boldsymbol{W}$ is the separation matrix. The second method is a neural approach for estimating the ICA basis vectors. From Fig. 1, the last stage gives an estimate of the observed data as

$$\hat{\boldsymbol{x}} = \boldsymbol{Q}\boldsymbol{y} \tag{18}$$

Comparing (18) with (3) for $\boldsymbol{n}=\boldsymbol{0}$ (i.e., $\boldsymbol{x} = \boldsymbol{A}\boldsymbol{s}$), we see that $\boldsymbol{Q} = \hat{\boldsymbol{A}}$ since $\boldsymbol{y} = \hat{\boldsymbol{s}}$. Therefore, the columns of the $\boldsymbol{Q}$ matrix are estimates of the columns of $\boldsymbol{A}$, the ICA basis vectors. A neural learning algorithm can be derived from a representation error performance measure given by

$$J(\boldsymbol{Q}) = \frac{1}{2}\|\boldsymbol{x} - \hat{\boldsymbol{x}}\|_2^2 = \frac{1}{2}\|\boldsymbol{x} - \boldsymbol{Q}\boldsymbol{y}\|_2^2 \tag{19}$$

Taking a steepest descent approach given by $\boldsymbol{Q}(k+1) = \boldsymbol{Q}(k) - \mu \nabla_{Q} J(\boldsymbol{Q})$, the neural learning rule for estimating the ICA basis vectors is

$$\boldsymbol{Q}(k+1) = \boldsymbol{Q}(k) + \mu(k)[\boldsymbol{x}(k) - \boldsymbol{Q}(k)\boldsymbol{y}(k)]\boldsymbol{y}^{T}(k) \tag{20}$$

where $\mu > 0$ is the learning rate parameter that can be adapted during learning using (9) with $\boldsymbol{v}(k)$ replaced by $\boldsymbol{Q}(k)\boldsymbol{y}(k)$.

Simulation 1

This example involves separating three different *artificially mixed* infrasonic signals. These infrasonic signals were recorded from a single station, 4-sensor (F-array), infrasound array in Windless Bight, Antarctica as separate events. The three signals are shown in Fig. 2(a), and are (i) an infrasonic signal from a volcano eruption at Galunggung, Java (recorded in 1982), (ii) a mountain associated wave originating from New Zealand (recorded in 1983), and (iii) and an internal atmospheric gravity infrasound wave (recorded in 1983). The three signals are *artificially* mixed using a random mixing matrix given by

$$\boldsymbol{A} = \begin{matrix} 0.3050 & 0.9708 & 0.4983 \\ 0.8744 & 0.9901 & 0.2140 \\ 0.0150 & 0.7889 & 0.6435 \\ 0.7680 & 0.4387 & 0.3200 \end{matrix} \tag{21}$$

Therefore, four observed mixed signals are generated from $\boldsymbol{x}(k) = \boldsymbol{A}\boldsymbol{s}(k)$, for $k = 1, 2, \cdots, 768$, and are shown in Fig. 2(b). The eigenvalues of the estimated covariance matrix of the observed data, given by (7), are $\lambda_1 = 2.1346$, $\lambda_2 = 0.1976$, $\lambda_3 = 0.0434$, and $\lambda_4 = -3.7772\text{x}10^{-16}$. The fourth eigenvalue is considerably smaller than the first three. Therefore, only the first three largest ones need to be retained, and from (5) the whitening matrix $\boldsymbol{V} \in \Sigma^{3\text{x}4}$ provides both whitening of the observed data and compression. So $h = 4$ and $q = 3$ (the number of source signals to be recovered). The nonlinear PCA neural learning rule in (12) is used to compute the separation matrix $\boldsymbol{W} \in \Sigma^{3\text{x}3}$, and the nonlinearity $g(\langle)$ is selected as the derivative of the logistic function as shown in (13) with $\beta = 1$. The initial weight (separation) matrix $\boldsymbol{W}(0)$ is selected randomly, however, the columns of the matrix are constrained to be orthonormal. The learning rate adjustment scenario in (9) is used with $\boldsymbol{v}(k)$ replaced by $\boldsymbol{y}(k)$, and the forgetting factor is set at $\gamma = 0.9$. It required 250 training epochs for the neural network weights to converge. Fig. 2(c) shows the resulting three separated signals. Because we know what the source signals are, the correlation coefficient can be computed for each of the separated signals with respect to the known (actual) source signals. These correlation coefficients are shown in Fig. 2(c). The correlations of the separated signals with respect to the actual source signals are almost perfect. The negative correlation coefficient indicates that a 180^{0} phase shift has occurred in the output of the ICA separation process.

Error! No topic specified.

Figure 2. (a) Three original infrasonic source signals. (b) "Observed" mixed infrasound signals. (c) Separated infrasonic source signals using the nonlinear PCA subspace learning rule.

Simulation 2

The second example involves processing four infrasound signals from a large volcano eruption in Galunggung, Java in 1982. The signals analyzed were recorded from a single station, 4-sensor (F-array), infrasound array in Windless Bight, Antarctica. Fig. 3(a) shows the four recorded signals after beamforming [5] is applied to time align the signals to a common reference in the sensor array. The nominal sampling frequency is 1 Hz, and 590 time samples were retained from each signal record for analysis. It is assumed that the number of source signals is two, i.e., a signal of interest and noise. Therefore, in the ICA, q=2 and n=4, the number of observed signals, i.e., the measured signals that are shown in Fig. 3(a) (which are the inputs to the ICA). The inputs are first prewhitened using the batch approach given in (4) and (5). Only the first two (largest) eigenvalues are retained along with the associated eigenvectors. Therefore, the whitening matrix $\boldsymbol{V} \in \Sigma^{2\text{x}4}$ computed using (5) provides both whitening of the observed data and compression. The nonlinear PCA neural learning rule in (12) is used to compute the

separation matrix $\boldsymbol{W} \in \Sigma^{2x2}$, and the nonlinearity $g(\langle)$ is selected as the derivative of the logistic function as shown in (13) with $\beta = 1$. The initial weight (separation) matrix $\boldsymbol{W}(0)$ is selected randomly, however, the columns of the matrix are constrained to be orthonormal. The learning rate adjustment scenario in (9) is used with the forgetting factor is set at $\gamma = 0.9$. It required 50 training epochs for the neural network weights to converge. Fig. 3(b) shows the two separated signals. The signal in the top graph appears to be the volcano infrasound signal and the signal in the bottom graph has the semblance of "noise." Figure 4(a) shows the first separated signals superimposed on the four input signals. The correlation coefficient computed for each input signal with the first separated signal is relatively high. Figure 4(b) shows the first separated signal superimposed on the average of the four input signals. In this case, the correlation coefficient is very high compared to the individual channel signals and the separated signal. This is due to reducing some of the noise in the signals from the simple averaging of the four input signals. Figure 5(a) shows the Power Spectral Density (PSD) of the four input signals, and Fig. 5(b) shows the PSD of the averaged input signal in the top graph and the PSD of the first separated signal in the bottom graph. The PSDs shown are an estimate of the respective signal's power spectrum based on the periodogram of the signals. Figures 4(a) & 4(b) give strong evidence that the first separated signal is the volcano signal. This is further evidenced in Fig. 5(b) by comparing the shape of the PSD of the average of the four input signals with the PSD of the first separated signal.

Error! No topic specified.Figure 3. (a) Four volcano infrasound signals recorded on a four-sensor, single station, array in Windless Bight, Antarctica in 1982 (inputs to the ICA). (b) Two separated signals (outputs of the ICA).

Figure 6(a) shows the second ICA separated signal in the top graph and a typical microbarom signal in the bottom graph. The microbarom signal was recorded at Windless Bight, Antarctica on a T-array (3-sensor) infrasound array (the nominal sampling frequency is 4 Hz). In Fig. 6(b), the top graph is a rescaled version of the PSD of the first separated signal show in the bottom graph of Fig. 5(b), and bottom graph is the PSD of the microbarom signal. Figure 6(c) shows the PSD of the second separated signal in the top graph, and the PSD of the microbarom signal in the bottom graph, and Fig. 6(d) is a rescaled version of Fig. 6(c). Comparing the top and bottom graphs in Fig. 6(b), there is no evidence of the microbarom signal in the first separated signal. However, when comparing the top and bottom graphs in Fig. 6(d) we see that there is evidence of a microbarom signal *buried* in the second ICA separated signal. Specifically, in the 0.1 to 0.2 Hz region there are two spectral peaks in both PSDs. Probably more profound is the observation made when comparing the bottom graph in Fig. 5(b) for the first separated signal, to the top graph in Fig. 6(c) for the second separated signal. Upon first glance when comparing these two spectra, they appear to be almost the same. However, when they are rescaled, shown in the top graph in Fig. 6(b) for the first separated signal, and the top graph in Fig. 6(d) for the second separated signal, the differences in the spectra can be seen. In fact, the correlation coefficient computed between the two time-domain signals is very low, specifically, 1.7992×10^{-4}. But more importantly is the overlapping spectra that exists between the two signals in the frequency range from 0.01 Hz to 0.02 Hz. In spite of this spectral overlap, ICA can separate the signals.

Error! No topic specified.

Figure 4. (a) First ICA separated signal superimposed on the four input signals. (b) First ICA separated signal superimposed on the average of the four input signals.

Error! No topic specified.Figure 5. (a) PSD of the four ICA input signals. (b) Top Graph: PSD of the average of the four ICA input signals, and Bottom Graph: PSD of the first ICA separated signal.

Error! No topic specified.

Figure 6. (a) Top Graph: Second ICA separated signal, Bottom Graph: microbarom infrasound signal recorded on the T-array. (b) Top Graph: PSD of the first separated signal, and Bottom Graph: PSD of the microbarom signal. (c) Top Graph: PSD of the second separated signal, and Bottom Graph: PSD of the microbarom signal. (d) Top Graph: Rescaled PSD of the first separated signal, and Bottom Graph: Rescaled PSD of the microbarom signal.

CONCLUSIONS AND RECOMMENDATIONS

We have shown the feasibility of applying Independent Component Analysis (ICA), using a neural learning algorithm, to single station infrasound signals for the purpose of separating signal from noise. The second

example presented showed that infrasound signals recorded on a 4-sensor array (F-array) could be separated into a signal of interest (volcano event) and background noise. The signal of interest was shown to be the volcano infrasound signal. It was also discovered that the background noise contained a microbarom component. This was determined by observing the noise signal in the frequency domain (i.e., its PSD) compared to the PSD of a typical microbarom signal. It was also observed that the two separated signals had overlapping spectra. In spite of this, the ICA was able to separate the signals. Further research in this area will involve investigating other infrasound recordings from the historical database [19, 20] for other types of events. When enough separated signals are generated for different infrasound events, this data set will be used to train and test a neural network classifier.

REFERENCES

[1] C. Jutten and J. Herault, "Independent component analysis (INCA) versus principal components analysis," in *Signal Processing* IV: *Theories and Applications*, Proc. *EUSIPCO*-88, J. Lacoume, *et al.,* Eds., Amsterdam, The Netherlands, Elsevier, pp. 643-646, 1988.

[2] C. Jutten and J. Herault, "Blind separation of sources, Part I: An adaptive algorithm based on neuromimetric architecture," *Signal Processing*, **24**, pp. 1-10, 1991.

[3] P. Comon, "Independent component analysis," in Proceedings of the *International Signal Processing Workshop on Higher-Order Statistics,* Chamrousse, France, pp. 111-120, 1991. [Republished in *Higher-Order Statistics*, J.L. Lacoume, Ed., Amsterdam, The Netherlands, Elsevier, pp. 29-38, 1992.]

[4] P. Comon, "Independent component analysis-A new concept?," *Signal Processing*, **36**, pp. 287-314, 1994.

[5] F.M. Ham, T.A. Leeney, H.M. Canady, and J.C. Wheeler, "Discrimination of Volcano Activity Using Infrasonic Data and a Backpropagation Neural Network," In Proceedings of the *SPIE Conf. on Appl. and Sci. of Compt. Intel. II*, Eds. K.L Priddy, P.E. Keller, D.B. Fogel, and J.C. Bezdek, Orlando, FL, **3722**, pp. 344-356, 1999.

[6] F.M. Ham, T.A. Leeney, H.M. Canady, and J.C. Wheeler, "A Radial Basis Function Neural Network for Classification of Infrasonic Events for the CTBT IMS," *American Geophysical Union Conference, EOS Transactions, AGU*, vol. 80, no.17, Boston, MA, June 1-4, (Abstract A52A-01), p. S71, 1999.

[7] I.T. Jolliffe, *Principal Component Analysis*, New York: Springer-Verlag, 1986.

[8] J. M. Mendel, "Tutorial on higher-order statistics (spectra) in signal processing and system theory: Theoretical results and applications," *Proc. of the IEEE*, **79**, pp. 278-305, 1991.

[9] C.L. Nikias and J.M. Mendel, "Signal processing with higher-order spectra," *IEEE Signal Processing Mag.,* **10**, pp. 10- 37, 1993.

[10] J. Karhunen, E. Oja, L. Wang, R. Vigario, and J. Joutsensalo, "A class of neural networks for independent component analysis," *IEEE Trans. on Neural Networks*, **8**, pp. 486-504, 1997.

[11] J.-F. Carduso and B.H. Laheld, "Equivariant adaptive source separation," *IEEE Trans. on Signal Processing*, **44**, pp. 3017-3030, 1996.

[12] J. Karhunen, "Neural approaches to independent component analysis and source separation," In *Proc. 4th European Symp. Artificial Neural Networks, ESANN'96*, Bruges, Belgium, pp. 249-266, April 1996.

[13] A. Hyvärinen, "Fast and robust fixed-point algorithms for independent component analysis," *IEEE Trans. on Neural Networks*, **10**, pp. 626-634, 1999.

[14] E. Oja, H. Ogawa, and J. Wangviwattana, "Learning in nonlinear constrained networks," in *Artificial Neural Networks Proc. ICANN-91*, T. Kohonen, *et al.* Eds., Amsterdam, The Netherlands, North-Holland, pp. 385-390, 1991.

[15] J. Karhunen and J. Joutsensalo, "Representation and separation of signals using nonlinear PCA type learning," *Neural Networks*, **7**, pp. 113-127, 1994.

[16] J. Karhunen and J. Joutsensalo, "Generalizations of principal component analysis, optimization problems, and neural networks," *Neural Networks*, **8**, pp. 549-562, 1995.

[17] L. Wang and E. Oja, "A unified neural bigradient algorithm for robust PCA and MCA," *Int. J. Neural Syst.,* **7**, pp. 53-67, 1996.

[18] L. Wang, J. Karhunen, and E. Oja, "A bigradient optimization approach for robust PCA, MCA, and source separation," In *Proc. 1995 IEEE Int. Conf. on Neural Networks,* Perth, Australia, pp. 1684-1689, Nov. 1995.

[19] C.R. Wilson, J.V. Olson, and R. Richards, "Library of typical infrasonic signals," Report Prepared for ENSCO (subcontract no. 269343-2360.009) **1-4**, 1996.

[20] K.D. Hutchenson, "Acquisition of historical infrasonic data," Final Technical Report, Contract No. F08650-95-D-0033, ARS-97-012, ENSCO, Melbourne, FL, 1997.

SURVEYING INFRASONIC NOISE ON OCEANIC ISLANDS

MICHAEL A.H. HEDLIN, JON BERGER AND FRANK VERNON

INSTITUTE OF GEOPHYSICS AND PLANETARY PHYSICS
UNIVERSITY OF CALIFORNIA, SAN DIEGO

SPONSORED BY DEFENSE THREAT REDUCTION AGENCY
CONTRACT NO. DSWA01-97-C-0163

ABSTRACT

An essential step in the establishment of an International Monitoring System (IMS) infrasound station is the site survey. The survey seeks a location with relatively low infrasonic noise and the necessary logistical support. This paper reports results from our surveys of three of the oceanic sites in the IMS - the Azores, Cape Verde and Ascension island. Each survey sampled infrasonic noise, wind velocity, air temperature and humidity for ~ 3 weeks at 4 sites near the nominal IMS locations. The surveys were conducted on Sao Miguel (the main island in the Azores) and Maio (Cape Verde) as well as Ascension. Infrasonic noise was measured using the French MB2000 microbarometer.

During our 3 week experiment in January the trade winds at Cape Verde varied little from an azimuth of 60°. Because of the unvarying wind azimuth, the experiment gave us an opportunity to examine the effectiveness of a forest at reducing both wind speed and infrasonic noise. We find that the thick Acacia forest on Maio reduces wind speeds at a 2 m elevation by more than 50% but does not reduce infrasonic noise at frequencies below 0.25 Hz. This forest serves as a high-frequency filter and clearly does not reduce long period noise levels which are due to large-scale turbulence in the atmospheric boundary layer above the forest. This is consistent with our observations in the Azores and on Ascension island where the relationship between infrasonic noise and wind speed is more complex due to frequent changes in wind azimuth.

In Cape Verde, wind speed and infrasonic noise are relatively constant. The diurnal variations are clearly seen but the microbarom is only rarely sensed. In the Azores, during our 3 week experiment in November and December of 1998, wind speed and infrasonic noise change rapidly. At this location, daily noise level swings of 40 to 50 dB at 0.1 Hz are not uncommon in the early winter and are due to changes in wind speed and atmospheric turbulence. The effectiveness of an infrasound station in the Azores will be strongly dependent on time during the winter season.

Our surveys have identified locations on each of these island where noise levels are relatively low and there is enough flat terrain to deploy infrasound arrays ranging in aperture from 1 to 3 km. We recommend 2 km aperture arrays at each location. Due to high winds at each location we further recommend augmented arrays of 7 elements. We recommend that 3 of the 7 elements in each array be deployed in a micro-array spanning 300 meters at the center of the larger array.

Key words: Atmospheric turbulence, infrasonic noise, noise reduction

OBJECTIVE

Our objective is to record infrasonic noise, wind velocity and air temperature and humidity on 3 islands in the Atlantic to identify the location on each island which is subject to the lowest infrasonic noise levels and is most suitable as a site for a station in the IMS infrasound network. In addition we seek the array and noise filter designs that are most appropriate for each site.

RESEARCH ACCOMPLISHED

Overview

The island stations in the planned global IMS infrasound network are essential, as they provide much needed coverage in oceanic areas, but are not ideal in other respects. Stations located on islands will, in general, be subject to strong winds (Figure 1) and thus high infrasonic noise levels. Strong trade winds dominate in the tropics. In latitudes above 30°N and below 30°S the prevailing westerly winds dominate although local winds can be strongly influenced by local pressure cells. Some islands (e.g. Ascension) are small (relative to the size of a 2-3 km aperture infrasound array) and rugged . Some islands (e.g. Cape Verde archipelago) receive limited rainfall and are sparesely vegetated.

The Provisional Technical Secretariat (PTS) calls for an infrasonic noise survey of the vicinity of each nominal infrasound station to find the most suitable location for a standard infrasound station (an array of 4 sensors with an aperture of 1 to 3 km). The noise survey for each station is to be conducted simultaneously at 4 locations in the vicinity of each nominal station location. Infrasonic noise is to be collected with wind velocity and temperature. With these requirements in mind this project has 4 main elements: Site selection, data collection, analysis and final recommendations regarding the location and design of the infrasound array at each of the 3 IMS sites. Four temporary stations were established on each of the three islands. All sites on each island were occuppied concurrently for 3 or more weeks.

At each site we deployed an infrasound sensor equipped with a 30 m aperture Daniels filter composedof porous hose. We have used the MB2000 infrasound sensor fabricated by the D partement Analyse et Surveillance de l Environnement (DASE). These sensors provide a filtered signal between 0.01 and 27 Hz. We used RefTek 6x24 bit digitizers and sampled the infrasound data at 20 Hz. The Atlantic site surveys were preceeded by calibration tests in the field at the Pinon Flat Observatory (PFO) in southern California, and in the laboratory at IGPP in La Jolla, California. The tests were conducted to ensure all field systems were robust and yielded equal digitized signals for equal input.

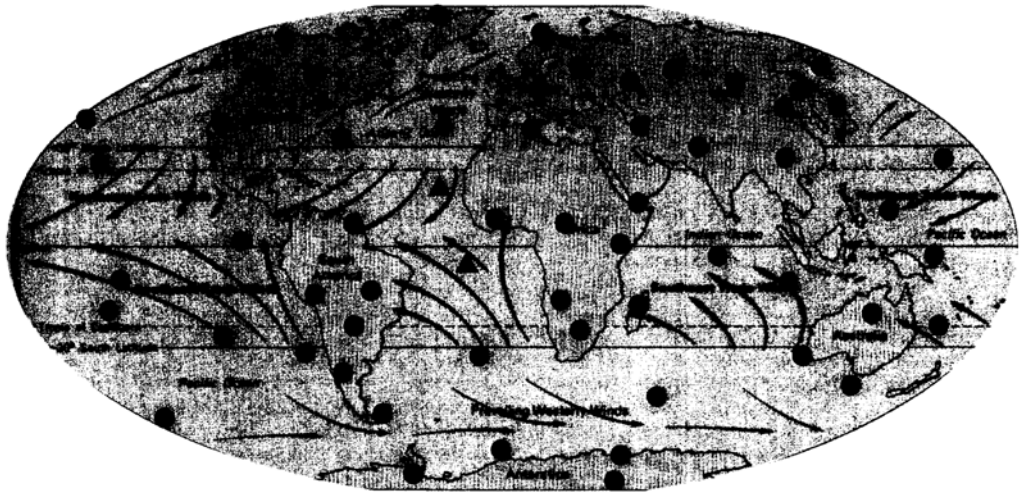


Figure 1. The planned IMS infrasound network. Stations located on islands will, in general, be subject to the strongest winds. The strong trade winds dominate in the tropics. In latitudes above 30°N and below 30°S the prevailing westerly winds dominate although local winds can be strongly influenced by local pressure cells. The 3 considered in this study are indicated by triangles. The Azores lie in the northern westerlies, Cape Verde and Ascension lie in the trades.

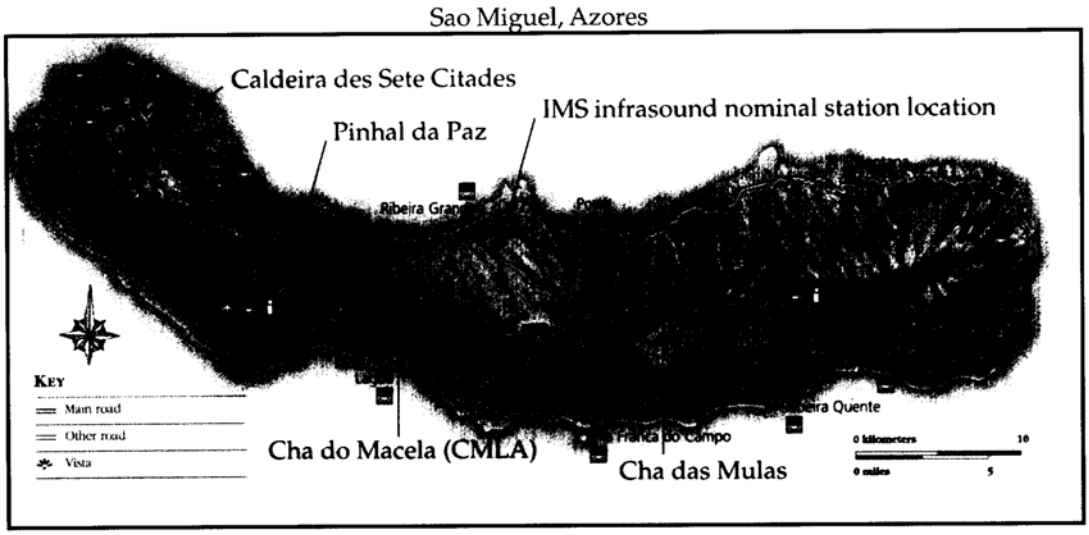


FIGURE 2. Sao Miguel, Azores and the 4 survey locations. The western site is located in a calderra. The two central sites are located in dense forests. Cha das Mulas is located on a plateau which has a rich low-level ground cover. Most of the original forest has been cleared. Most trees are in long rows and are used to decrease wind speed. The nominal station is located near the second largest city on the island, Ribeira Grande, in an active hydrothermal area. The recommended IMS infrasound array is at Cha das Mulas. One possible configuration is indicated by the triangle.

Preliminary Site Selection

In the Azores, Cape Verde and on Ascension meteorological data have been collected for decades. These data together with ground cover, topography and infrastructure maps guided us in our selection of survey sites. In the Azores, meteorological data from the past 30 years indicates that winds on the main island, Sao Miguel, are relatively weak. We selected 4 sites on this island that sampled different means of reducing infrasonic noise. One site was located in a large calderra (Figure 2). Two sites (Pinhal da Paz and Cha da Macela) were located in thick forests. The fourth, eastern, site was located on a broad blateau between long rows of criptomeria trees.

The Cape Verde archipelago comprises 9 major islands. All but one are unsuitable for infrasound. The western islands are relatively young and rugged. The extreme example is Fogo, a 2829 m high active volcano. The eastern, relatively flat, islands have little vegetation and are subject to high trade winds from the northeast. The exception is Maio which is sparsely populated, has a substantial forest and a line of site to the largest island, Santiago, where telecommunications infrastructure is located. All 4 survey sites were located on this island in the forest in a 3 km aperture centered equilateral triangle (Figure 3). Forests reduce wind speeds and thus will attenuate atmospheric noise. The thickness of the forest on Maio is variable. We have chosen sites at which the forest comprises mature, closely spaced, Acacia trees (MAO2) and sites where the trees are either broadly spaced (MAO1 and MAO3) or very young (MAO4). There is essentially no ground cover at any of these sites. A comparison of measurements made at these dissimilar locations will allow us to gauge the utility of Acacia forests for reducing wind speeds and noise in the infrasonic band between 0.02 and 5 Hz.

Ascension island (Figure 4) offers few options for siting infrasound sensors. In this survey, all sensors were located near the center of the island in an equilateral triangle. None of the sites are located in a well developed forest. The central site has a low ground cover. The site near the GSN station has mature, broadly spaced, pine trees.

Preliminary results from the surveys

The 4 survey points on Sao Miguel, Azores were occupied in November, 1998. After 19 days of simultaneous recording at all sites, the equipment was moved to Cape Verde (Figures 1 & 4) for an additional 3 weeks of recording in January, 1999. The Ascension survey occurred in April to June, 1999.



FIGURE 3. The island of Maio, Cape Verde has little vegetation except in an Acacia tree forest in the north. The island covers ~ 310 square km - roughly 4 times the size of Ascension island, the site of another nominal IMS infrasound station. The 4 survey points are in a forest of Acacia trees.

Fifteen minutes of pressure and meteorological data from the Azores experiment are shown in Figure 5. The unfiltered pressure timeseries from the station at Cha das Mulas exhibits 30 s period fluctuations superimposed on substantially longer period energy. The shorter period variations dominate the filtered record (second panel). In this time period, minor wind velocity fluctuations are constant. The temperature and humidity vary relatively slowly. The detailed structure of the filtered pressure record results from the superposed contributions of myriad atmospheric phenomena. Our study is concerned primarily with the dependence of the noise on frequency and the exact location of the sensor and thus we will focus on the spectral properties of the noise.

To examine the spectral content of the filtered data we used Welch s method (Welch, 1967) which yields a single power spectral estimate from an average of several taken at regular intervals in the time range of interest. The spectral estimates we have used in this study were derived from an average of 4 estimates, each taken from consecutive 204.8 s intervals. The power spectral density taken from the filtered record (Figure 6) shows a decay in power levels from the peak at 30 s to the corner of the anti-aliasing filter at 9 Hz. A strong microbarom peak is centered at 0.2 Hz. The overall spectral shape is due to a well known phenomena in the atmosphere which receives a major input of energy at ~ 0.1 to 1 mHz. Energy from large scale eddies cascades into smaller eddies, and thus into higher frequencies, as the large eddies are broken up (Kaimal and Finnigan, 1994).

From the full 3 weeks of recording at all 4 sites we calculated power spectral denstiy at 454 time intervals. Each interval began at the turning of the hour and spanned 15 minutes. Tenth, 50th and 90 percentile noise levels at all frequencies from 0.005 Hz to 10.0 Hz are shown in Figure 6. At times of relatively low noise the microbarom peak is obvious at Cha das Mulas. This figure shows that the interval displayed in Figure 5 was a time of relative quiescence. From this figure it is evident that the longer periods depend more strongly on time. For example, the spread between the 10th and 90th percentiles is 50 dB at 0.1 Hz and just 20 dB at 1.0 Hz.

The same spectral character is seen at all four sites (Figure 7). Median noise levels between 0.03 and 0.1 Hz are 5 to 10 dB lower in the calderra and in the forest at Pinhal da Paz than on the plateau at Cha das Mulas and at Cha do Macela. A other frequencies the noise levels are comparable. The noise spikes at 3.5 and 7.0 Hz at Pinhal da Paz are likely due to infrequent industrial activity. That survey point is near several quarries.

At Cape Verde, the wind azimuth is relatively constant and there exists a simple dependence of infrasonic noise levels on wind speed (Figure 8). As wind speeds at Cape Verde are relatively constant, the most significant source of variability in infrasonic noise levels is the diurnal effect which is predominantly due to day-night variations in the speed of the trade winds. Infrasonic noise levels are highly correlated with this effect and thus at any time of day, noise levels are quite easily predicted.

During our experiment in the early winter, wind speed and noise levels in the Azores varied strongly with time(Figure 9). The experiment in Nov. and Dec. occurred at a time of advancing inclement weather. Toward the end of the experiment wind speed at Cha das Mulas could increase from 1 to 6 m/s in a few hours.

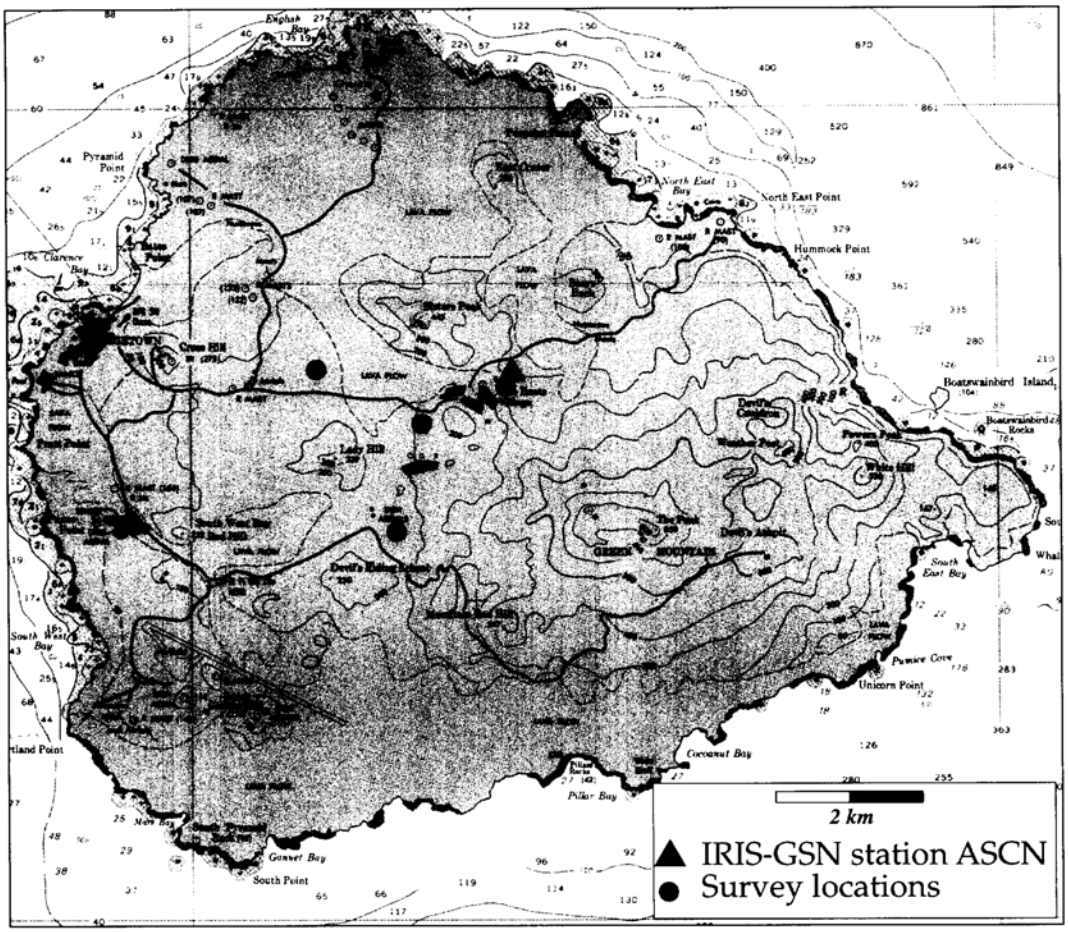


Figure 4. Ascension island topography and the GSN station (ASCN) and the 4 infrasound survey sites we occupied in early 1999.

CONCLUSIONS AND RECOMMENDATIONS

Forests and Infrasonic Noise Reduction

Cape Verde is perhaps the ideal place to study the generation and suppression of infrasonic noise. The archipelago is located at 16°N where northeast trade winds are dominant. During the 3-week experiment in January, the mean wind azimuth was 63° with a standard deviation of 9.6°. The wind-topography interaction is relatively time invariant when the wind azimuth remains constant. These wind tunnel conditions produce a simple scaling between wind speed and wind noise at all frequencies from 0.02 to 5 Hz (Figure 8).

With azimuthal considerations effectively nullified it is possible to address the issue of the effectiveness of a forest for reducing infrasonic noise in the frequency band between 0.02 and 5 Hz. The Acacia forest on Maio is thickest at MAO2. At this location the trees were planted in the 1950 s and are ~10 to 15 m high. The forest is less mature, the trees are smaller (5 to 10 m) and more broadly spaced, at MAO1 and MAO3. MAO4 was located in a grid of recently planted ~ 5 m tall Acacia trees. As we see in Figure 8, wind speeds (at an elevation of 2 m) at MAO2 are reduced sharply. The maximum wind speed at this location is ~ 1.4 m/s wheras at MAO1 and MAO4 the wind speed reached 2.7 m/s and 2.5 m/s respectively and at MAO3 the wind speed reached 3.1 m/s. As we see in Figure 8, at frequencies below

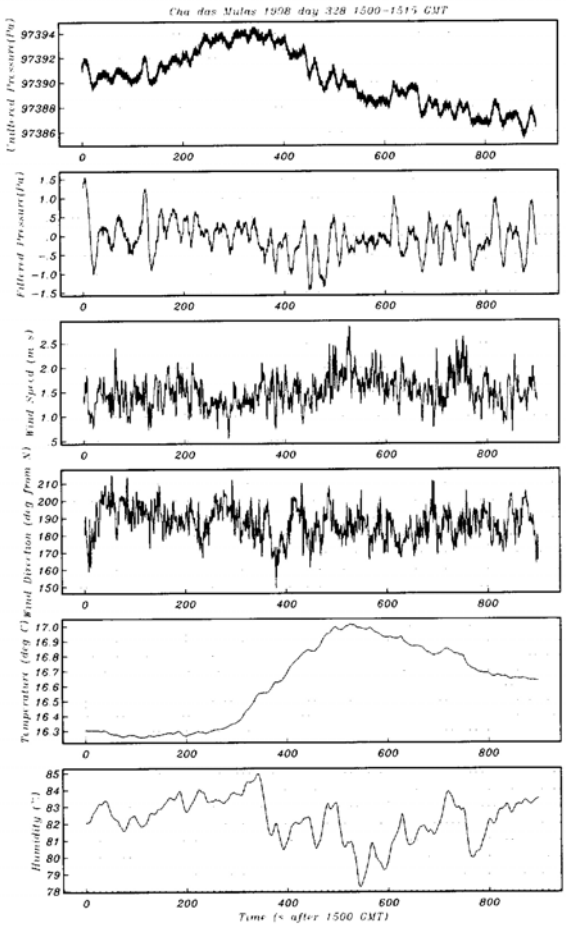


FIGURE 5. Atmospheric pressure and meteorological data from a 15 minute interval starting at 15:00 GMT at Cha das Mulas. Raw and filtered pressure data are shown in the upper two panels. Wind speed, direction, temperature and humidity are shown below. As shown in the next figure, this is a time of relatively low infrasonic noise.

0.25 Hz there is no reduction in noise levels. For example, at all locations infrasonic noise at a period of 20 s ranges from .01 Pa^2/Hz when there is no wind to 50 Pa^2/Hz when wind speeds are highest. It is apparent that infrasonic noise at frequencies below 0.25 Hz is not dependent on wind speed at 2 m elevation within the forest. Noise at these long periods depends on turbulence that is common to all sites - that which exists in the boundary layer above the trees. The thick forest at MAO2 is clearly reducing noise levels at frequencies between 0.25 and 5.0 Hz. The noise estimates at MAO2 become progressively lower than at the other sites as the wind speeds increase. At times when the wind speed is near the maximum, noise levels in this frequency band at this site are 5 to 10 dB lower than at the other sites. Although the forest is reducing high-frequency infrasonic noise levels, the reduction is not complete. A comparison of noise levels at the maximum speed of 1.4 m/s at MAO2 with noise levels at the other sites at the same wind speed indicate that at frequencies at and above1 Hz, noise levels in the thick frorest are 5 to 15 dB higher than elsewhere. When wind speeds are low, the noise suppression within the thick forest extends to 0.1 Hz (Figures 8).

Noise levels within a calderra

Wind flow over a two-dimensional ridge is laminar upwind of the ridge crest and becomes turbulent on the lee side (Kaimal and Finnigan, 1994). The turbulence results when the wind flow, which is compressed and accelerated at the ridge crest, decompresses on the lee side. A separation bubble forms at the location where some air flows in the opposite direction, back to the ridge, and is followed by a turbulent wake. The site in the calderra on Sao Miguel island was chosen for our survey to determine if this turbulence would contribute noise in the band between 0.05 and 1.0 Hz or if, overall, the walls of the calderra would deflect the wind away from the site and reduce noise levels. Figure 7 indicates that noise levels are clearly increased at .02 Hz and suggests the presence of unusually energetic large-scale turbulence in this area. It is difficult to make definitive conclusions about noise levels at higher frequencies because of the scatter in the noise estimates. However it is apparent that although the calderra is effectively reducing wind speeds, noise levels at 0.05 Hz and above are not clearly reduced when wind speeds are high. When the wind is near-average, the calderra noise levels between 0.05 and ~ 0.15 Hz are comparable to those in the forest at Pinhal da Paz and 5 to 10 dB lower than at the other two sites (Figure 7). As discussed in the previous section, at times of elevated winds, the calderra walls reduce wind speed but no notable reduction in infrasonic noise levels results.

The best site in the Azores

The primary objective of our field program is to identify the location on each island that is most suitable for a permanent IMS infrasound array. The paramount factor is infrasonic noise however our selection must be guided by practical considerations. A site that offers low infrasonic noise but gives few options for siting a permanent array might

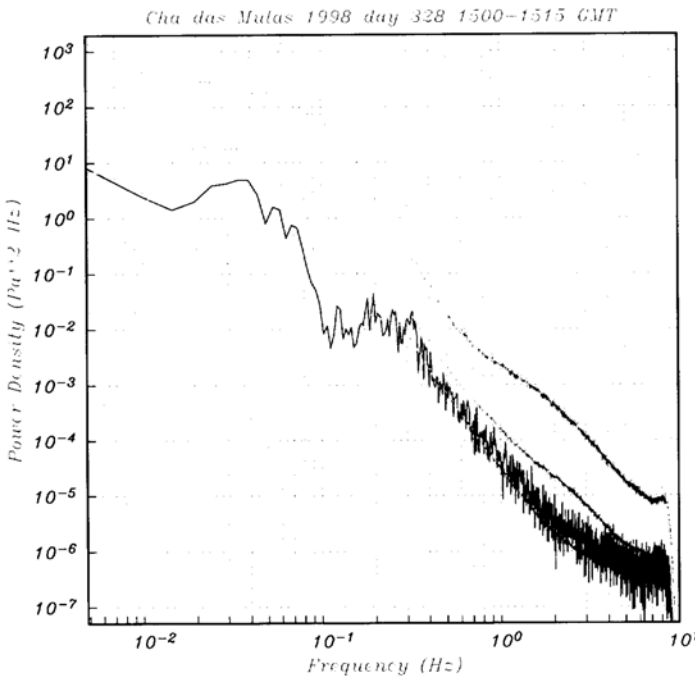


Figure 6. Noise power density at Cha das Mulas. In black is shown a single power density estimate taken from the filtered pressure data displayed in figure 5. The colored curves are the 10th, 50th and 90th percentile noise levels from the entire experiment. These curves are based on 454 noise level estimates taken at 1 hour intervals. Each estimate is taken from 15 minutes of data. The 5 second microbarom is not observed at times of high noise.

not be optimal. The ideal site is large enough to allow any array configuration from 1 to 3 km aperture to be considered. On Sao Miguel, the Cha das Mulas site is the only one that could accommodate *any* IMS array design. From every perspective other than the most important one, noise, the plateau is clearly the best site and it will serve as the standard against which all other sites in the Azores will be judged. In addition to plenty of space to deploy array elements at the same elevation, there are unobstructed views to the horizon from most points. There is little cultural activity and the site is relatively far from the ocean. Most of the plateau is covered by a lush grass. Long rows of trees interrupt the flow of wind.

Median noise levels in the calderra on Sao Miguel are comparable to those at Cha das Mulas at all frequencies except between .03 and .1 Hz where the median noise levels in the calderra are 5 to 10 dB lower (Figure 7). Most signals of interest lie between 0.05 and 1.0 Hz (PTS summary) and so this discrepancy could be important. Because of short duration of the survey (~ 3 weeks) it is not clear if this noise spread is significant and indicates relative noise levels throughout the year. The calderra is large enough to accommodate an IMS infrasound array and could be an excellent site however it offers few options for array configurations. Two large lakes and a village lie within the calderra. Just one array configuration is possible - 4 elements in an isosceles triangle 2 1/2 km tall and 1 1/2 km at the base. As shown in Figure 7, noise levels at long periods are elevated - probably due to wind flow across the rim of the calderra. For these reasons, and because of the potential for signal blockage at some azimuths due to the walls of the calderra, this location is not preferred over Cha das Mulas.

The second site, Pinhal da Paz, lies in a dense Criptomeria forest on the axis of the island. This site is near several quarries but has median noise levels that are on par with those in the calderra (Figure 7). This site lies in rolling hills and, like the calderra, offers few options for array design. Elements in any array deployed at this location would be separated vertically by ~ 50 m. If full-scale (70 m aperture) Daniel s filters are required, it would be difficult to keep all ports at the same elevation. This site is also not preferred over Cha das Mulas for these reasons and because there is more cultural activity in this area. The third site, Cha da Macela, also lies in a dense forest but is subject to high winds directed through the central, low, part of the island (Figure 2). Although median noise levels are comparable to those at Cha das Mulas, 90th percentile noise levels are high. Despite the proximity to the GSN station CMLA and the nominal infrasound coordinate (Figure 2) this site is also not preferred.

Our survey indicates that the best site in the Azores is at Cha das Mulas. This broad plateau is large enough to accommodate any array configuration. Our brief survey indicates that this area is subject to substantial noise level swings (Figure 9) however comparable noise swings occurred at all sites on Sao Miguel (and presumably at all other islands in the Azores). Any infrasound monitoring station located in the Azores will offer a highly variable performance - particularly during the winter when storms are not uncommon.

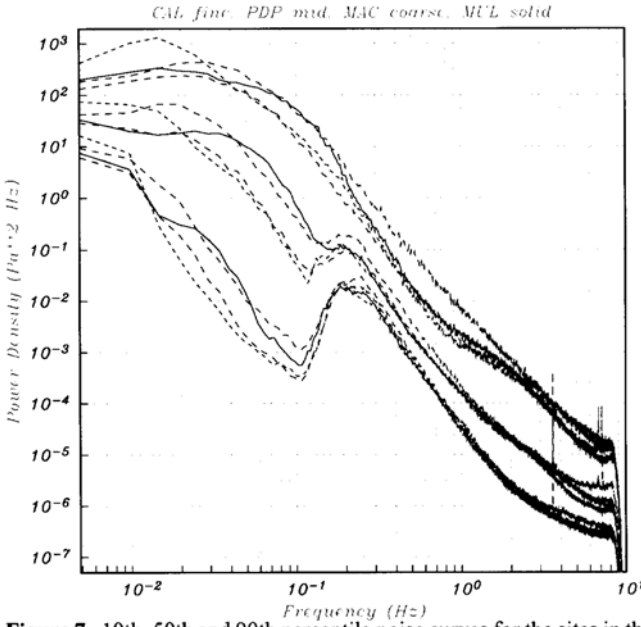


Figure 7. 10th, 50th and 90th percentile noise curves for the sites in the Azores. Cha das Mulas noise is represented by the solid curves. The other sites are identified at the top of the figure.

The best site in Cape Verde

Due to limited options, the Cape Verde survey points were all located together on the same island - Maio. Because of topograpy, cultural activity or a lack of ground cover the other islands are clearly unsuitable for an effective infrasound deployment. This micro deployment was in the configuration of a standard IMS array (a 3 km aperture centered equilateral triangle) in the event that all sites were shown to be adequate and all could be chosen to be sites for the permanent installation. All sites appear to be adequate however this configuration lies at the upper limit of the allowable range for IMS infrasound arrays and might not be appropriate for this rather windy site. Our survey revealed thick forest reduces wind speed however, just as in the the calderra in the Azores, the wind noise was not reduced substantially at long periods. We recommend that the IMS array be deployed in the oldest, thickest, part of the Acacia forest near the site MAO2.

Recommended arrays in the Azores, Cape Verde and Ascension Island

On the Azores and in Cape Verde the array designs are still not finalized. Due to the strength of the microbarom and the presence of high noise due to winds the best array designs will likely have an aperture of ~ 2 km with extra 3 sensors in a microarray at the center. The location in Cape Verde is in a state park and there are no logistical limitations on array design. At some locations the forest is not mature and additional high-frequency noise suppression might be advisable. Some locations might require additional ground cover and trees. In the Azores, the final array design is pending as not all local landowners have been contacted.

Both array locations are near small hills which have existing road access and could serve as central processing stations. In Cape Verde, telecommunications infrastructure is located on Monte Babosa on Santiago island. This facility is ~ 52 km from Monte Vermhelo and will be used to transmit data from the GSN station, SACV, located just west of the capital, Praia. In the Azores, telecommunications facilities are situated on Pico de Barrosa - the 947 m high peak located 15 km west of Cha das Mulas.

The Ascension array design is still pending as the data have just recently been retrieved from the field.

The utility of infrasound site surveys

Because of limited resources and manpower, the standard infrasound site survey lasts just 2 to 3 weeks. This gives just a glimpse of the full range of meteorological conditions that will occur in a typical year. Is it fair to assume that the brief period sampled is representative of the entire year and the survey will lead the surveyer to recommend the best site or is a 2 to 3 week survey too brief to be useful? For a brief survey to be ineffective, climactic conditions at the time of the survey would have to be out of the ordinary and tilt the balance of infrasonic noise so that the relative noise levels at the sites are not representative of the yearly average. Intuitively, this seems rather unlikely and easy to check. The chief source of infrasonic noise is turbulence due to wind flow over topography. If wind direction changes in such a way that the wind-topography interaction at the time of the survey is unusual and, as a result, anomalously little turbulance is generated at certain sites, or excessive turbulence is generated at others, the brief survey taken at that time would be misleading. It should be possible to rule out this scenario by comparing wind velocity measurements made during the

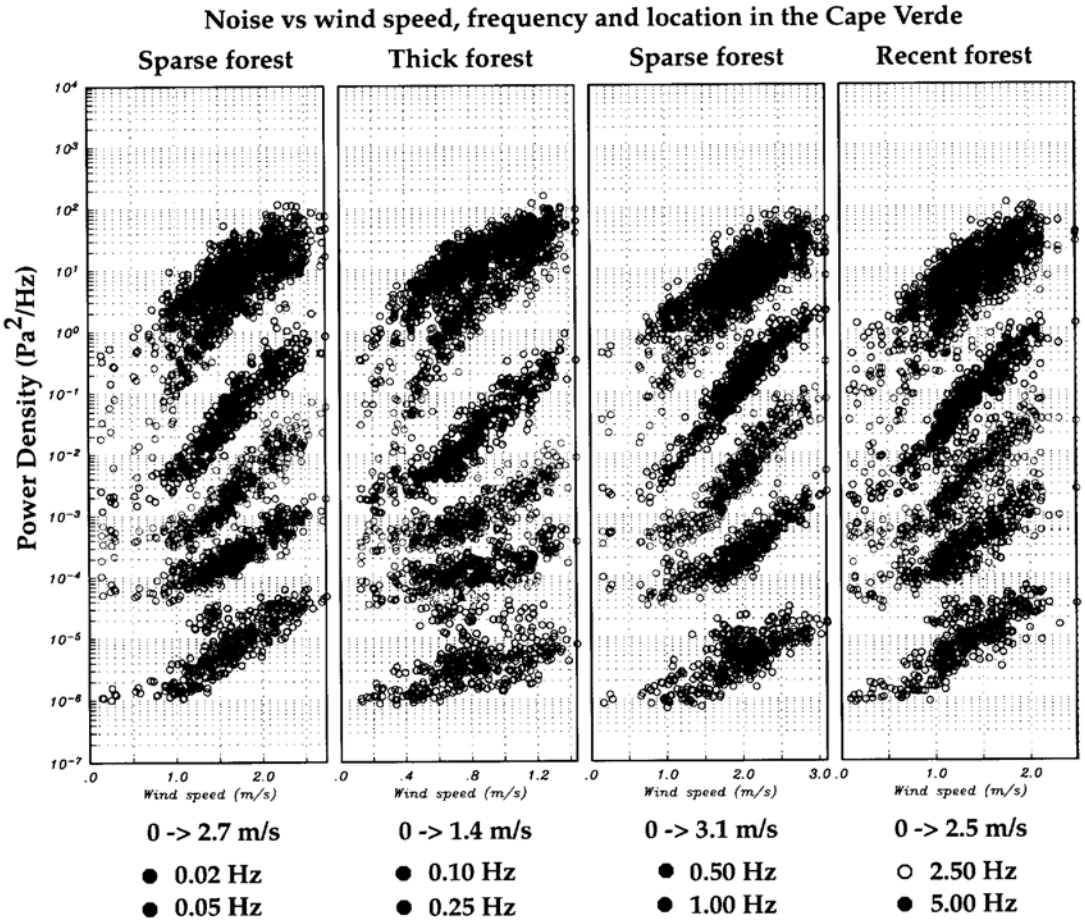


Figure 8. The four panels above show the strong dependence of infrasonic noise on wind speed and frequency at the four sites in Cape Verde. From top to bottom in each panel is noise power at 0.02 Hz (black); 0.05 Hz (red); 0.1 Hz (green); 0.25 Hz (dark blue); 0.5 Hz (light blue); 1.0 Hz (pink); 2.5 Hz (yellow); and 5.0 Hz (black). Wind speeds in the thickest forest on Maio, which at MAO2, are lower than elsewhere however noise power is not reduced at frequencies lower than 0.25 Hz. Winds are weakest in the thickest part of the forest at MAO2. Noise power has a relatively simple dependence on wind speed.

survey with those from long-term meteorological observations. A significant discrepancy in wind speed or direction combined with azimuthally dependent topography would be cause for concern. The winds observed during the Azores, Cape Verde and Ascension surveys appear to be in line with long term observations. These surveys occurred at times of elevated winds, but these winds were as expected from historical data. There is no reason to believe that these winter surveys are misleading.

The utility of oceanic sites.

There are numerous requirements for a good infrasound station (Christie, 1998). The exceptional island might meet all of them. Noise is the most important consideration. There are a plethora of noise sources - wind noise is the paramount concern. As we have seen, wind in the Azores, in the early winter at least, is capricious. This is not a trait of just oceanic sites but it is reasonable to expect such conditions to be more common on islands. Changes in wind speed of 5 to 6 m/s in a few hours appear to be common in the early winter in the Azores. No infrasound station deployed in

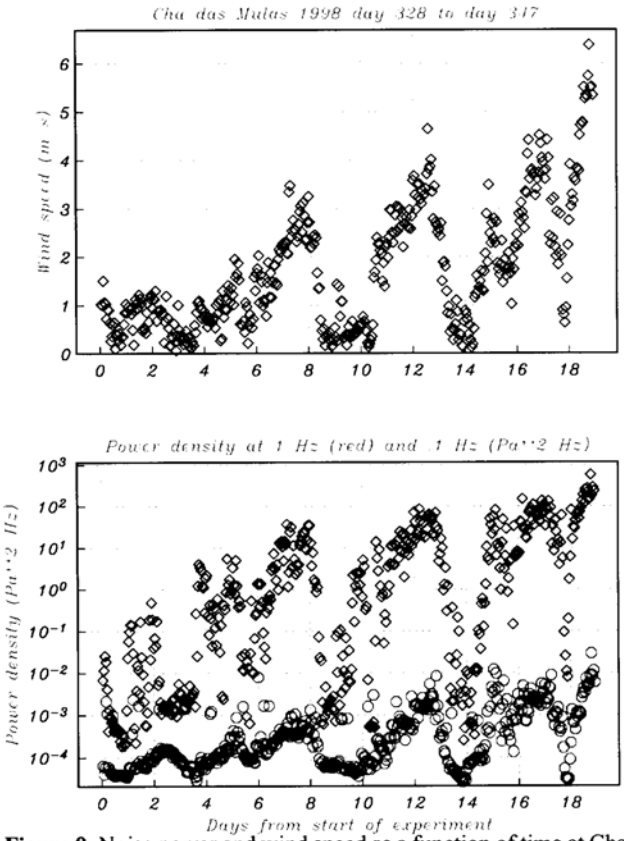


Figure 9. Noise power and wind speed as a function of time at Cha das Mulas in the Azores. In the Azores, wind noise at 0.1 Hz (upper sequence of points in the lower panel) and at 1.0 Hz closely track the wind speed. Severe winds during a storm near the conclusion of the Azores experiment lead to substantial swings in the noise level.

such a setting can be expected to deliver invariant performance through the year. At times of high wind, such a station will be rendered ineffective for sensing all but the most energetic signals. There are several options for improving signal to noise levels. It is well known that Daniels filters reduce noise and the effectiveness of these filters is strongly dependent on the design. It might be necessary to design the filters to suit local needs at each of the windy sites. The standard IMS infrasound array has 4 elements. Additional elements, located in a microarray at the center, will improve the performance of the overall array. In some areas flat ground will be unavailable and the best noise suppression scheme, beyond vegetation, will likely be spatially limited wind fences (e.g. ReVelle and Whitaker, 1999).

The oceanic sites will make an important contribution to global monitoring but it is clear that the effectiveness of a typical oceanic, or continental, site will be highly dependent on local meteorological conditions. Global detection thresholds will be strongly dependent on time at all locations (Trost, 1997). Recent research by Clauter and Blandford (1997) indicates that detection 90% confidence level two station detection levels will be between 0.1 kt and 0.3 kt over most continental areas and between 0.3 and 0.7 kt over most oceanic regions. Advances in empirical atmospheric wind models (e.g. Drob, 1999) and improvements in modeling the propagation of acoustic waves through a non-stationary medium (e.g. Collins, 1993; Norris and Gibson, 1999) should lead to improved estimates of global monitoring thresholds as a function of time.

REFERENCES

Christie, D. (1998), Requirements for IMS Infrasond Station Site Surveys, issued by the Preparatory Commission forf the comprehensive nuclear-test ban treaty organization, CTBT/PC/III/WBG/PTS/INF.3

Clauter, D., and Blandford, R. (1997), Capability Modeling of the Proposed International Monitoring System 60-Station Infrasound Network, *proceedings of the Infrasound Workshop for CTBT Monitoring, Santa Fe, NM, Aug 25-28, 1997,* pp. 227-236.

Collins, M.D. (1993), The adiabatic mode parabolic equation, *J. Acoust. Soc. Am.*, **94**, 2269-2278.

Daniels, F.B. (1959), Noise-Reducing Line Microphone for Frequencies Below cps, J. Acoust. Soc. Am., **31**, 529.

Drob, D.P. (1999), The atmosphere from 35-160 km: Moving from Climatology to Nowcast, *Informal session on Infrasound at spring AGU, Boston, June 2, 1999.*

Gossard, E.E., and Hooke, W.H. (1975), Waves in the Atmosphere, Elsevier Scientific Publishing Co., New York.

Kaimal, J.C., and Finnigan, J.J. (1994), Atmospheric Boundary Layer Flows: Their Structure and Measurement, *Oxford University Press.*

Norris, D.E., and Gibson, R.G. (1999), Diurnal Variability in the Atmosphere and its effect on ray paths, *EOS, Transactions, American Geophysical Union 1999 Spring Meeting,* **80**, S71.

ReVelle, D.O., and Whitaker, R.W. (1999), Infrasonic noise reduction using shelters/windbreaks, *EOS, Transactions, American Geophysical Union 1999 Spring Meeting,* **80**, S68.

Trost, L.C. (1997), High altitude wind effects on infrasound network performance, *proceedings of the Infrasound Workshop for CTBT Monitoring, Santa Fe, NM, Aug 25-28, 1997*, pp 271-284.

Welch, P.D. (1967), The use of fast Fourier transforms for the estimation of power spectra: a method based on time averaging over short modified periodograms, *Trans IEEE **AU-15**, 70-73.*

THERMOSPHERIC INFRASOUND SIGNALS

J. Paul Mutschlecner, Comforce Technical Services
Rodney W. Whitaker, Los Alamos National Laboratory

Sponsored by U.S. Department of Energy
Office of Nonproliferation and National Security
Office of Research and Development
Contract No. W-7405-ENG-48

ABSTRACT

The primary signals considered for the detection of explosions by infrasound are stratospheric, that is, signals received after reflection from stratospheric layers near 50 km in height. However, thermospheric signals may also be an important means of detection. Thermospheric signals are produced by reflections from atmospheric layers at about 110 to 130 km.

An analysis has been carried out of thermospheric signals from atmospheric nuclear tests at the Nevada Test Site out to distances of about 250 km. Stratospheric signal amplitudes are very dependent upon stratospheric winds and hence have a seasonal variation. In contrast it is found that thermospheric signal amplitudes have little or no seasonal variation. This is because the sound velocities at thermospheric heights are always sufficient to produce signal returns. As a result, thermospheric signals are more easily interpreted since no correction for the effects of wind are required.

It is found that thermospheric amplitudes may be very competitive with stratospheric amplitudes during a portion of the year and, in fact, will dominate during conditions of strong stratospheric counterwind conditions. Thus thermospheric signals should also be considered in the operational methods for detection of explosions in the atmosphere. We have detected thermospheric signals out to at least 500 km for which the attenuation law appears to follow that for stratospheric signals. Further work will be needed to determine the range attenuation for greater distances. Current predictions indicate that thermospheric signal amplitudes will be about 1μ bar at 2000 km for a 1-kT nuclear event

Because of the much greater height of the return layer for thermospheric signals, their average travel velocities are much smaller than for stratospheric signals. Here average velocity is defined as the surface distance to the source divided by travel time. Typical stratospheric velocities are about 290 m/s, whereas thermospheric velocities are only about 220 m/s. As a result the arrival times of thermospheric signals may be considerably later than those of stratospheric signals. For example, at a distance of 500 km the interval between the signals is about nine minutes.

For circumstances where both stratospheric and thermospheric signals are detected at a station two useful determinations can be made: (1) the value of the directed stratospheric wind speed that is neeed for normalization of stratospheric signal amplitudes and (2) an estimate of distance to the source.

Key Words: infrasound signal propagation, thermosphere, stratosphere, atmospheric wind

I. Introduction and Background

Stratospheric (S) infrasound signals, that is, those returned from the stratospheric region of the atmosphere by refraction, are generally expected to be the primary signal from medium to small size explosions in the atmosphere and many other sources. Thermospheric (T) signals also may be returned to earth from thermospheric regions of the atmosphere at about 110 to 130 km in height or more. T signals can be shown to be highly competitive with, or even exceed S signals in amplitude, during favorable periods of the year. Thus it is important to understand the general characteristics of the T signals and to search for these signals along with the conventional search for S signals as a part of CTBT monitoring activities.

We have used a data set of signals from NTS atmospheric nuclear tests for a preliminary assessment of the characteristics of T signals. The NTS data were reported by Reed (1969) and have been analyzed in depth by Mutschlecner et al (1999). The observations were made at several stations surrounding NTS. In the present report we utilize the data taken at a station at Bishop, California, to provide examples. Bishop is at an average distance of about 211 km from NTS and at an azimuth of 278^{o} from NTS. Others stations in the data set give general confirmation of the Bishop results.

II. T Signal Velocities

Figure 1 compares the average velocity of the observed S and T signals at Bishop. Average velocity, *V,* is defined at the great circle distance from source to receiver on the surface divided by the signal transit time. In this example it is seen that the S signals have *V* from about 270 to 300 m/s. We believe, from a more detailed study of all stations, that there is a seasonal dependence of the S signal velocities. By contrast the T signals show much lower values of *V* ranging from about 200 to 250 m/s. On occasion, even lower values are seen and an example is seen in the figure at about 150 m/s. The comparatively low values of *V* for T signals compared to S signals can be understood as a result of the much higher return altitude for T rays as illustrated in Fig. 1.

Of course, the consequence of the lower values of *V* for T signals is that the arrival times will be later than for S signals from an event. Figure 2 gives an illustration of the time delay between S and T signals as a function of distance. The upper line indicates the time delays for downwind conditions (i. e. signals propagating in the direction of stratospheric wind flow) and the lower line for counterwind conditions. Notice that the time delays can be very large, reaching, for example, about 19 minutes for a distance of 1000 km. While Fig. 2 provides general guidance, a more exact calculation should be made for any specific case. The possible large time delay between the S and T signal arrivals suggests that in many instances T signals inadvertently may be ignored after a large S signal has been detected. Observers should be aware of this and attempt to detect T signals as well.

III. T Signal Amplitudes

Figure 3 shows the yield-scaled amplitude of the atmospheric nuclear explosions for S signals at Bishop versus day of the year. Several years of data are contained in this plot. Yield scaling is done by dividing the peak-to-peak amplitudes by the factor W^n where n= 0.456. Further details of the scaling are given by Mutschlecner et al (1999). There is a very large seasonal dependence in the scaled amplitude--over three decades of variation. This effect is caused by the seasonal stratospheric wind variation. For comparison Fig. 4 shows the yield-scaled amplitudes of T signals for Bishop. Here we see a much smaller variance--about one decade. Data from all of the stations suggest that there is no seasonal variation in the T signals. We adopt a value of 1.29 for log of the T signal peak-to-peak amplitude (_b) of a 1-kT nuclear explosion at a distance of about 215 km (one bounce from the source).

Figure 5. compares seasonal predictions for S and T amplitudes. The calculation is for a 1 kT explosion at a distance of 500 km propagating toward an azimuth direction of 270^{o}. The S signal amplitude, A_S, in _b is given by

$$log\ A_s = 1.36 + 0.016\ V_d \qquad (1)$$

where V_d is the component of wind speed (m/s) at an average height of 50 km directed towards the observer from the source. A statistical model is used for the winds at mid northern latitudes. Further details of this formulation are given by Mutschlecner et al (1999). The figure indicates that the predicted T signal will be larger than the S signal during a significant portion of the year. Similar calculations have been made for a series of azimuths. The results are given in Figure 6 which shows the percentage of a year in which T signals will be competitive with S signals in amplitude versus azimuth. We arbitrarily define "competitive" as meaning that a T signal amplitude is at least 1/2 of the S signal amplitude. Notice that there is strong asymmetry between east and west, with the west showing considerably greater T signal competition than does the east. Figure 6 demonstrates that T signals may be of importance during significant parts of the year. Of course this example is specifically for mid-northern latitudes and is statistical in nature. For other locations of interest appropriate calculations could be made.

IV. <u>Range Determination from S and T Signals</u>

If both S and T signals are observed from the same source at a station, it is possible to determine a distance to the source from the difference, _*t,* in the arrival times of the two signals. This procedure is of course in common usage for seismic signal analysis. The distance,*R*, is given by

$$R = \Delta t \left(\frac{1}{V_t} - \frac{1}{V_s} \right) \qquad (2)$$

where V_t and V_s are the average velocities for T and S signals respectively. The difficulty in this determination of R is that the values of the two average velocities vary with propagation conditions which may be a function of location and time of the year.

To illustrate this use of S and T signals we use a simple approximation of 219 m/s for V_t and for V_s : 294 m/s for downwind conditions and 285 m/s for counterwind conditions. These values were obtained from our general analysis of data from all stations. Figure 7 shows the absolute value of the percentage error between the true distance and the distance given by Eqn. 2 for Bishop. The average error is about 17 percent. Presumably better accuracy could be given by an improvement in the ability to predict the best values for V_t and V_s . Ultimately, with an increasing data base from CTBT monitoring and other sources this improvement should be possible. The ability to estimate a distance that is independent of triangulation using multiple station detections may be a very useful tool in some instances.

V. <u>Determination of the Directed Wind Component from T and S Signals</u>

When both S and T signals are observed from a source the local value of V_d may be obtained. It can be shown that the use of the amplitudes A_s and A_t from S and T signals respectively gives

$$V_d = \frac{1}{k} \left[\left(log\ A_s - log\ A_t \right) - \left(log\ A_{cs} - log\ A_{ct} \right) \right] \qquad (3)$$

where *k* is the wind effect normalization parameter for S signals taken here as 0.019 s/m. log *Acs* and logA_{ct} are respectively the values of S and T signal log amplitudes for one kT and zero stratospheric wind; their values are taken as 1.87 and 1.29. These parameter numbers are for a first-bounce distance and are derived by Mutschlecner et al (1999). The values will be somewhat different for larger distances. The expression assumes that the attenuation with distance is the same for S and T amplitudes. Figure 8 shows the values of V_d derived from Eqn 3 for Bishop from pairs of S and T signals compared with the wind from a statistical model appropriate to that location. There is good general agreement between the derived values and the statistical model. Of course the derived values of V_d reflect actual stratospheric conditions at the time of each event while the model values represent a statistical average which can vary by significant amounts from real conditions at times.

Determinations of V_d by the use of S and T amplitudes may be very useful for two purposes. First, the determined value of V_d for an event permits the normalization of the S signal amplitude to zero wind conditions by

$$log\ A' = log\ A_s - k\, V_d \qquad (4)$$

where A' is the normalized amplitude. This normalization is necessary to permit interpretation of any signal.

Second, the determination of values of V_d from signals at various times in the CTBT infrasonic network would permit an improved statistical basis for the global stratospheric wind, especially in the areas of the network stations. Of course this improvement would be cumulative over time but could be done with any sources which provide both S and T signals such as those from earthquakes.

VI. Summary

The examples provided for T signals are based upon the first-bounce location of Bishop. It will be important to understand whether the results also apply to longer distances. At the present time this work has not been extended to greater distances but an effort will be made to do this. Unfortunately data for T signals at greater distances may be somewhat sparse because of the emphasis upon the generally stronger S signals.

There are some indications of T signals characteristics at larger distances. A detection by us of S and T signals at a distance of 517 km (about a two-bounce distance) from a high explosive test gives excellent agreement with the amplitude predicted on the basis of the first-bounce data. A study of the modeling of signals from a 1 kT surface burst by Dighe et al (1999) shows that T signals are expected at a distance of 1175 km. However the average velocity of the principal T signal is higher than we find at first-bounce locations. In another study ReVelle et al (1999) have examined evidence for T signals at larger distances from surface explosions. In this work the existence of high-frequency T signals is emphasized.

Clearly, T signals can be an important aspect of CTBT monitoring by providing confirmation of S signal results. It is noteworthy that the T signal amplitudes apparently would not require the normalization for wind effects needed by S signal amplitudes. Useful byproducts of the analysis of pairs of S and T signals are an estimate of the distance to the source from a one-station observation and a determination of the effective value of the directed stratospheric velocity, V_d. Further work will be required to better understand T signals at long distances.

Acknowledgements

The work was supported by the U.S. Department of Energy Office of Non-Proliferation and National Security.

References

Dighe, Kalpac A., Rodney W. Whitaker and William T. Armstrong, 1998 , Modeling Study of Infrasonic Detection of 1 KT Atmospheric Blast, Proceedings for the 20th Annual Seismic Research Symposium on Monitoring a Comprehensive Test Ban Treaty (CTBT), U.S. Department of Energy.

Mutschlecner, J.Paul, Rodney W. Whitaker and Lawrence H. Auer,1999, An Empirical Study of Infrasound Propagation, Los Alamos National Laboratory Report LA-13620-MS

Reed, Jack W., 1969, Climatology of Airblast Propagations from Nevada Test Site Nuclear Airbursts, Sandia Laboratories Report SC-RR-69-572.

ReVelle, D. O., R. W. Whitaker, S.N. Kulichkov and O. M. Raspopov, 1999, On High-frequency Thermospheric Arrivals at Long Distances from Surface Explosions, to be published in the Proceedings of the Infrasound Workshop for CTBT Monitoring (Winnipeg, Canada).

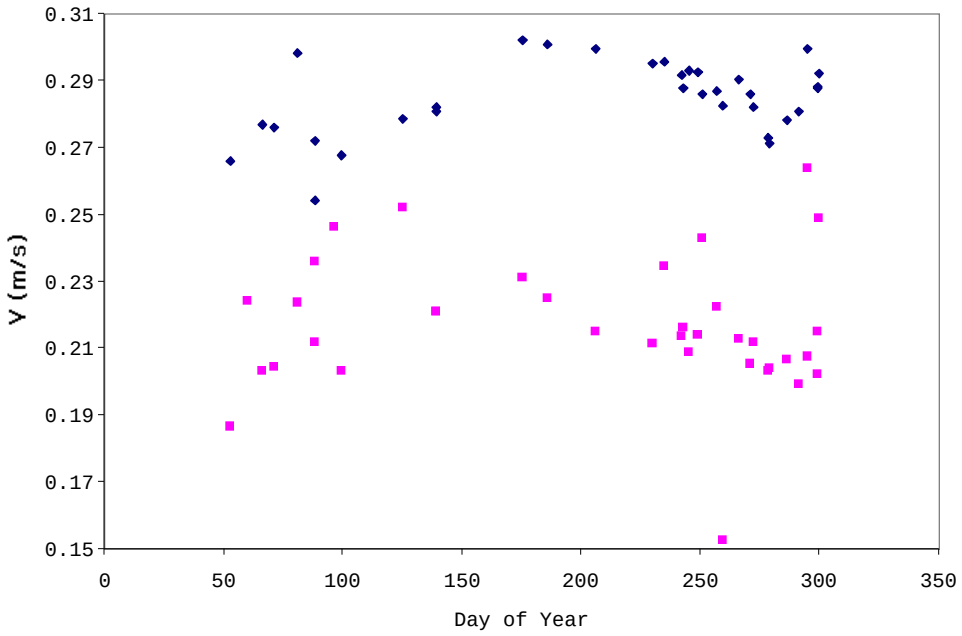


Figure 1. Observations at Bishop of the average propagation velocity of stratospheric signals (diamonds) and thermospheric signals (squares).

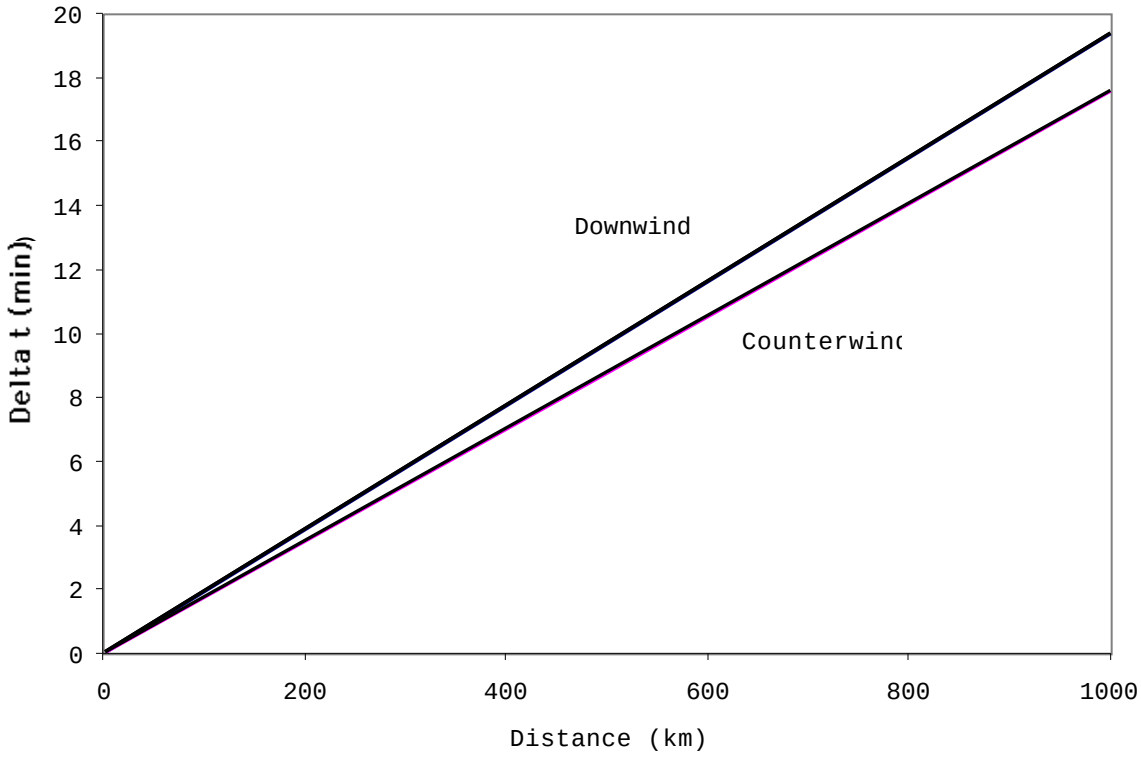


Figure 2. The time difference between stratospheric and thermospheric signal returns as a function of distance.

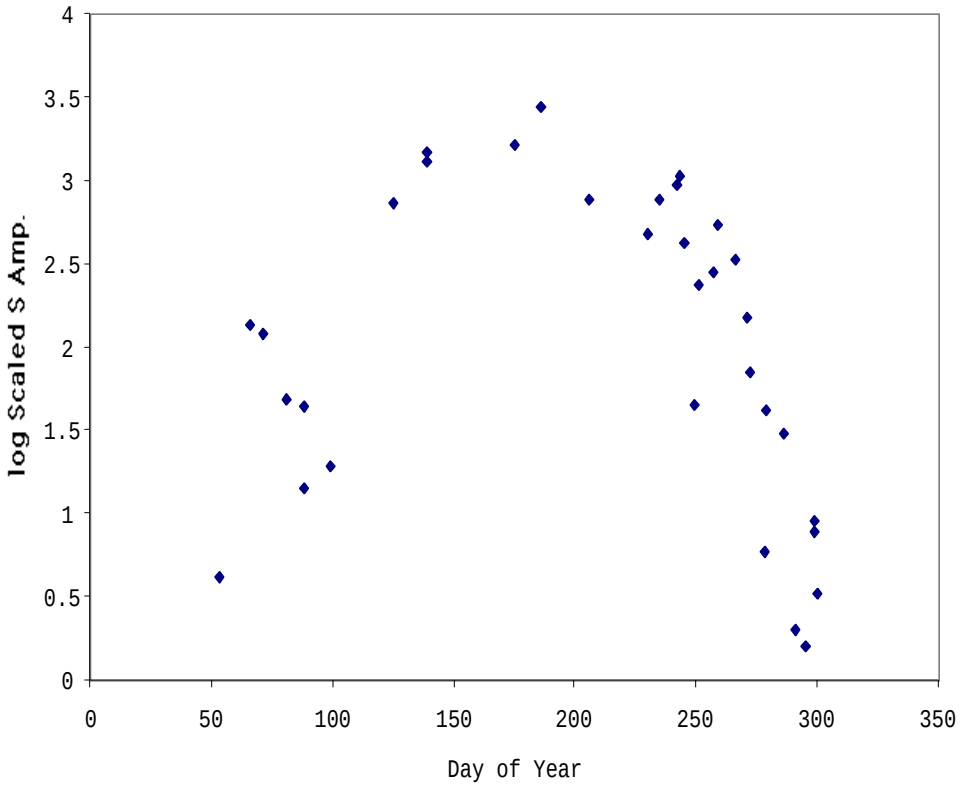


Figure 3. The logarithm of yield-scaled stratospheric signal amplitudes versus day of the year as observed at Bishop, California.

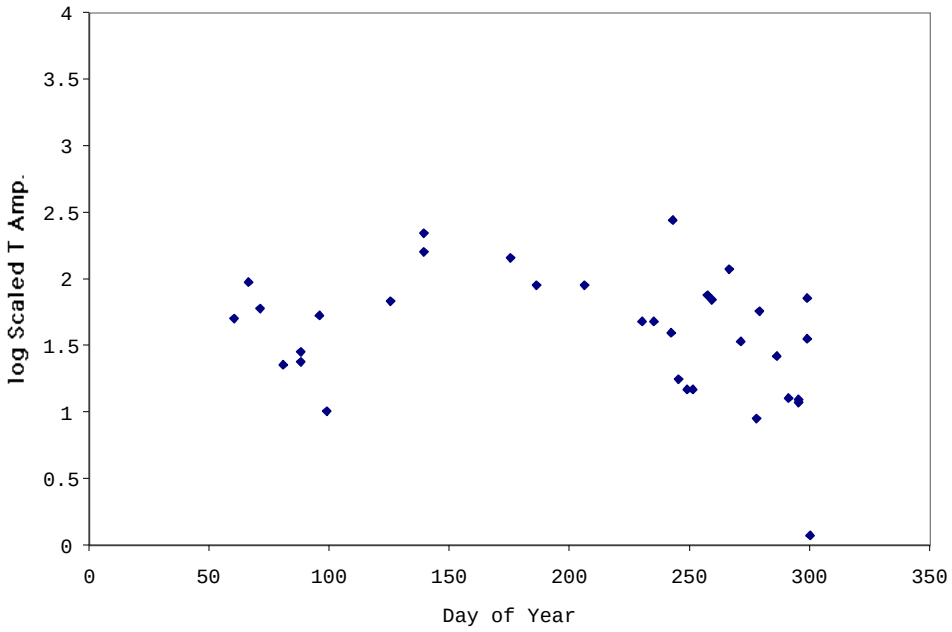


Figure 4. The logarithm of yield-scaled thermospheric signal amplitudes versus day of year as observed at Bishop, California.

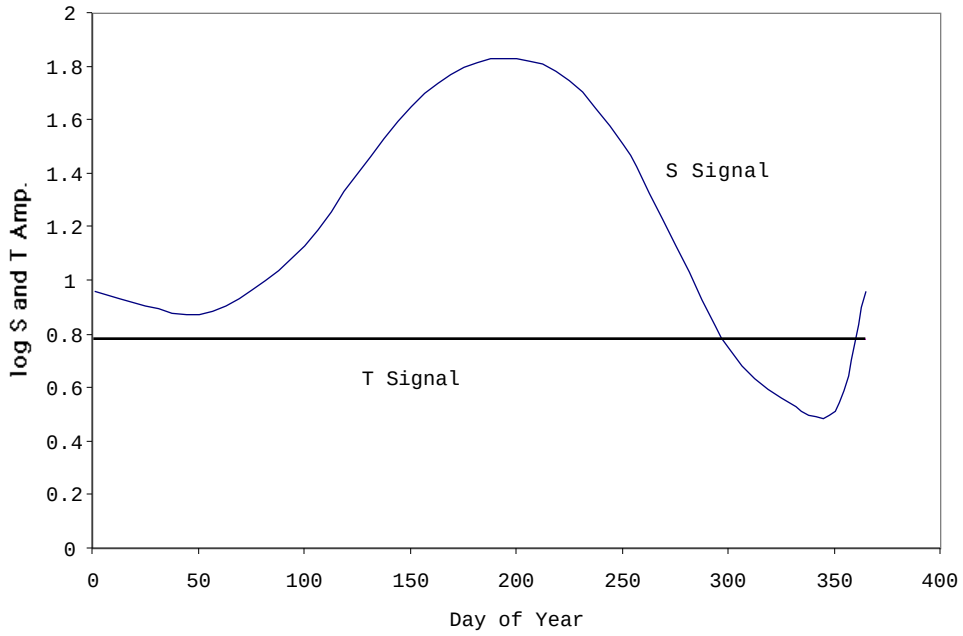


Figure 5. A comparison of the logarithm of amplitude for stratospheric signals (curve) and thermospheric signals (line) as a function of day of the year. Predictions are for a 1 kT atmospheric burst at a distance of 500 km. with signals propagating directly to the west at mid-northern latitudes.

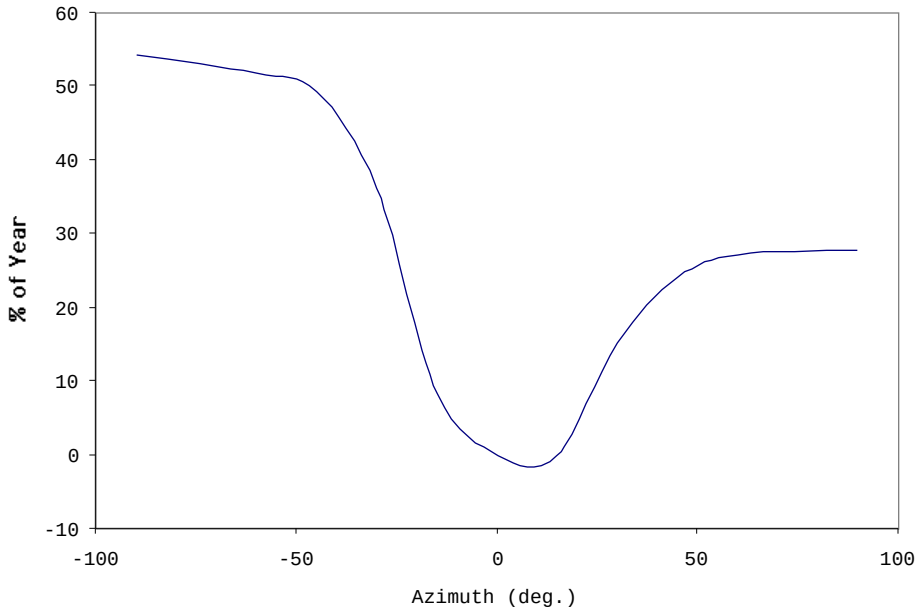


Figure 6. Percentage of the year during which thermospheric signal amplitudes are competitive with stratospheric signal amplitudes versus azimuth. Azimuths are positive to the east and negative to the west.

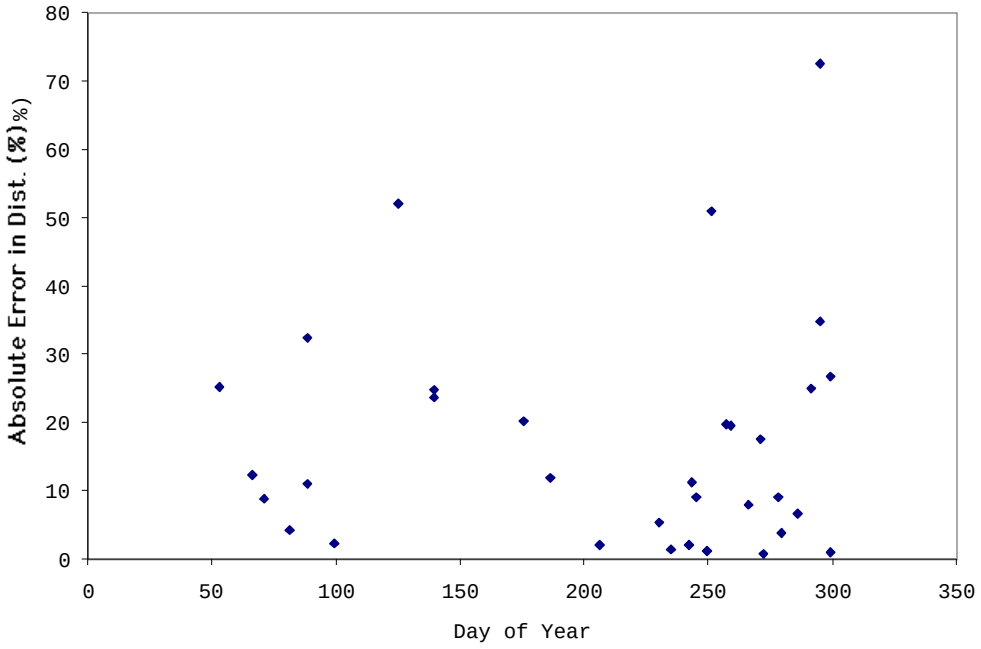


Figure 7. Absolute values of percentage error in the determination of distance for stratospheric-thermospheric signal pairs at Bishop, California versus day of the year.

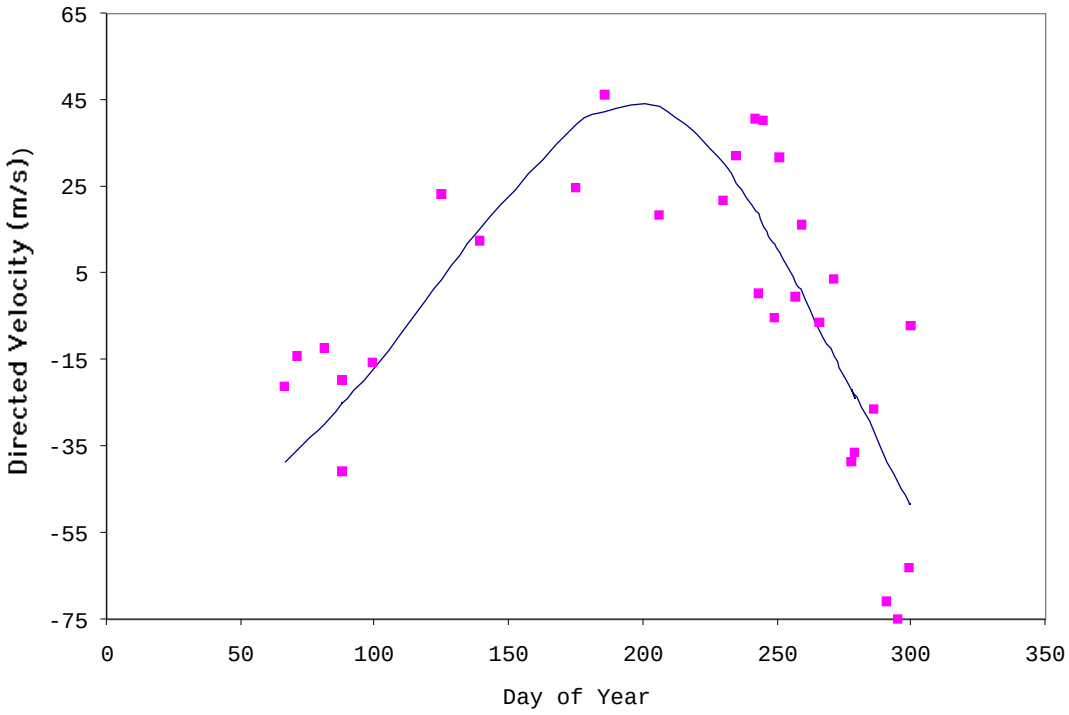


Figure 8. A comparison of the stratospheric directed velocity from a statistical model with the velocity derived from pairs of stratospheric and themosoheric signal amplitudes observed at Bishop, California. The statistical model is shown as a line and the dervived values as squares

ADAPTATION OF AN UNDERWATER ACOUSTIC PROPAGATION MODEL TO INFRASONIC ATMOSPHERIC PROPAGATION

Guy V. Norton and Wayne A. Kinney
Ocean Acoustics Branch, Naval Research Laboratory
Jorge C. Novarini, Planning Systems Inc.
Dan J. Ramsdale, Neptune Sciences, Inc.
Rodney W. Whitaker, Los Alamos National Laboratory

Sponsored by U. S. Department of Energy
Office of Nonproliferation and National Security
Office of Research and Development and
Contract No. DE-AI04-98AL79805

ABSTRACT

For decades, the U. S. Navy has been engaged in the development of underwater acoustic propagation models to aid in the design and effective use of underwater sonar systems. Much of the expertise created in this development is applicable (directly or by modification) to challenges associated with the use of infrasonic arrays to monitor CTBT compliance. We will report on the results of the modification and adaptation of a parabolic-equation underwater propagation model to predict and analyze acoustic-gravity wave signals in both a range-independent and a range-dependent atmosphere. Examples are given that include the effects of range-dependent winds on signal strength for the case of an airborne explosive source and a ground-based infrasonic receiver. Frequencies of interest are in the band from 0.02 to 10 Hz, and ranges of interest are 1000 km or less.

Key Words: infrasound monitoring

1. Introduction

The issues relating to infrasonic propagation in the atmosphere, although long standing, have remained relatively unexplored within the acoustic community. The subject has however acquired renewed interest due to the Comprehensive Test Ban Treaty (CTBT) [1]. Infrasound monitoring is one of the main tools for detecting distant nuclear explosions. The detected signals are the low frequency components (roughly between 0.02 to 10 Hz) of the shock wave produced by an atmospheric nuclear burst. They can be detected at ranges up to a few thousand kilometers by virtue of the waveguide created by ground reflections and refraction in the atmosphere. The problem is essentially that of propagation in a range dependent environment, similar to that occurring in other branches of acoustics. In particular, attention must be given to upper (>10 km) atmospheric winds, the speeds of which can be a significant fraction of the acoustic propagating sound speed [2].

Modeling infrasonic propagation in a realistic environment would provide a useful tool for the test ban treaty monitoring community. However there appears to be a lack of ready-to-use models capable of high fidelity modeling. By high fidelity modeling we mean modeling the propagation of the acoustic energy in an environment which includes all of the nuances and intricacies of the real environment. This would include the range and altitude dependent sound speed due to temperature and density variations, the range and altitude dependent atmospheric winds as well as the range dependent terrain over which the acoustic field propagates. Not only would this range dependent terrain contain variations in such things as density and porosity but also changes in terrain type. Since infrasonic propagation occurs over such large distances, the type of terrain over which the signal propagates could change for example from grassland to forests to mountains, and finally across water. The propagation model should be capable of not only maintaining the correct amplitude (i.e. conserve energy) of the signal but also maintaining the correct phase as it propagates the signal in this complex and dynamic environment.

The underwater acoustic community has, over the years, developed propagation models that are capable of determining the correct amplitude and phase of the acoustic field in very sophisticated and complex environments. These underwater environments are just as complex and dynamic as the atmospheric environments. The propagation models developed are based on a variety of mathematical and physical concepts. The most familiar are those models that solve the reduced wave equation or Helmholtz equation (thus implicitly assuming a point harmonic source i.e. operating in the frequency domain). Among them are; the normal mode solution to the Helmholtz equation; reduction of the Helmholtz equation to a parabolic equation (PE methods); wavenumber integration methods and ray tracing techniques. They each have their strong and weak points. The nearly universal assumption made by each model is that azimuthal coupling is assumed unimportant. The consequence is that the models operate in cylindrical coordinates, assume azimuthal symmetry (i.e. ignore azimuth), which results in a 2-dimensional (r, z) model. When the environment is weakly range-dependent (i.e. the environment does not change rapidly over a short-range interval) the normal mode models give adequate results. If however the environment changes rapidly with range, resulting in mode coupling (energy transferring between modes) then PE models and some wavenumber integration models are more appropriate, since they are marching algorithms and they naturally include the ability to handle range dependence.

This paper is concerned with taking a model, which is widely known to the underwater acoustics community as the split-step Pade´ solution of the Finite Element Parabolic Equation (EFEPE) model developed by Collins [3], and adapting it to infrasonic atmospheric propagation. There are PE [4], normal mode and FFP-based [5,6] atmospheric propagation models in the community, with some of them developed specifically for outdoor propagation, such as that of White and Gilbert [4], where a range independent case was analyzed. Other models have their origin in underwater acoustics. In particular, Franke and Swenson [5] and Gudesen [6] have taken well-known underwater acoustic propagation models (FFP and SAFARI) and adapted them to atmospheric propagation. However, none have addressed the infrasonic frequency regime. In this work, several important enhancements to the EFEPE model were incorporated, such as the altitude and range dependent atmospheric winds, as well as a starter appropriate for a point source over a plane reactive interface. The theory behind these additions as well as the theory for PE will be included. Finally, both frequency domain and time domain results will be presented. At the lower end of the frequency range of interest, acoustic gravity waves may play a role. Since the basic

component of the current model (EFEPE) does not account for acoustic gravity waves, they are not included in the current adaptation. Their inclusions will be the subject of future work.

2. Parabolic Equation Theory

The following description is based on the work by Collins [3]. For a more in-depth description, the reader is directed to the original body of work. Recently Lingevitch *et.al.* [7] has developed an acousto-gravity PE. We start with the Helmholtz equation in cylindrical coordinates and assume azimuthal symmetry. Where z is the height above the air-ground interface and r is the horizontal distance from the source located at r=0, z=z_0. We assume that kr >> 1 and remove the spreading factor $r^{-1/2}$ from the acoustic pressure *p*. The PE method is by definition a boundary value problem, thereby requiring that we provide the starting field. In addition, the boundary conditions at the air-land interface (if allowing for geo-acoustic bottom and thus bottom penetration, at the end of the numerical grid) and at the top of the numerical grid (maximum height of the problem). Range dependency is made up through many different range independent regions. In each range-independent region, the acoustic pressure satisfies the farfield equation,

$$\frac{\partial^2 p}{\partial r^2} + \rho \frac{\partial}{\partial z} \frac{1}{\rho} \frac{\partial p}{\partial z} + k^2 p = 0 \tag{1}$$

Where ρ is the density, $k = (1 + i\eta\beta)\omega / c$ is the complex wavenumber, $\eta = (40\pi \log_{10} e)^{-1}$
β is the attenuation (in dB per wavelength), c is the sound speed, and ω is the circular frequency. Note that Eq. (1) does not account for gravity waves, this will be handled at a later time. Since c, r, and β depend only on z, Eq. (1) factors as follows:

$$\left(\frac{\partial}{\partial r} + ik_0\sqrt{1+X} \right)\left(\frac{\partial}{\partial r} - ik_0\sqrt{1+X} \right) p = 0\,, \tag{2}$$

$$X = k_0^{-2}\left(\rho \frac{\partial}{\partial z} \frac{1}{\rho} \frac{\partial}{\partial z} + k^2 - k_0^2 \right), \tag{3}$$

where c_0 is the reference sound speed and $k_0 = \omega/c_0$. The following approximation is valid if the outgoing component of *p* dominates the incoming component:

$$\frac{\partial p}{\partial r} = ik_0\sqrt{1+X}\, p\,. \tag{4}$$

Removing the factor exp (ik_0r) from *p*, we obtain

$$\frac{\partial p}{\partial r} = ik_0\left(-1+\sqrt{1+X}\right)p\,. \tag{5}$$

To obtain the split-step Pade´ solution, Eq. (5) is solved analytically before applying a Pade´ approximation. Given the field over *z* at an arbitrary range *r*, the solution of Eq. (5) at the range $r+\Delta r$ is

$$p(r+\Delta r) = \exp[i\sigma\left(-1+\sqrt{1+X}\right)]p(r) \tag{6}$$

where $\sigma = k_0\Delta r$. Now imposing a Pade´ approximation to the RHS of Eq. (6) we obtain,

$$\exp[i\sigma(-1+\sqrt{1+X})] \cong 1+\sum_{j=1}^{n}\frac{a_{j,n}X}{1+b_{j,n}X}, \tag{7}$$

Substituting Eq. (7) into Eq. (6), we obtain the split-step Pade´ solution,

$$p(r+\Delta r) = p(r)+\sum_{j=1}^{n} a_{j,n}\left(1+b_{j,n}X\right)^{-1} X\,p(r) \tag{8}$$

The depth operator is discretized-using finite-differences. The resulting matrices are tridiagonal.

3. Modification of the basic PE model

There are four major changes made to EFEPE resulting in the atmospheric version (Air-EFEPE). First the sound speed is complex through the entire vertical extent of the problem. Second, the starting field incorporated is based on the reflection of a spherical wave from a locally reacting boundary. Third, the inclusion of altitude dependent atmospheric winds, and lastly a new bottom boundary condition is imposed. For an in depth discussion of each modification the reader is directed to a paper by Norton *et.al.* [8]. However since the effect of wind is examined by an example, the method of including wind into the model will be presented.

Atmospheric Winds

For the model under consideration, any environmental effect in the fluid mass (atmosphere) has to be included through the index of refraction. However, the wind is a directional phenomenon while temperature (main parameter controlling the sound velocity) is a scalar. Therefore, wind speed cannot be simply added to the local sound speed. A more rigorous approach is required. Nijs and Wapenaar [9] treated the wind speed as a vector quantity resulting in a modified propagation wavenumber. Assuming air to be an ideal gas and sound propagation to be an adiabatic process, one can write, $K=\gamma P_0$, where P_0 is the static pressure, and $\gamma = C_p/C_v$ (the ratio of the specific heats). With these assumptions, the wavenumber can be rewritten. Introducing the Mach vector **m** (which is altitude dependent), we have

$$c^2 = \gamma P_0 / \rho_0 \tag{9a}$$

$$m_x = w_x / c, \text{ and } m_y = w_y / c, \tag{9b}$$

$$k = \omega / c, \tag{9c}$$

$$k_m = \omega / c - m_x k_x - m_y k_y. \tag{9d}$$

The local wind speed c incorporates the effects of temperature while **m** stands for the wind effect. The first variable is a scalar and the second is a vector. w_x and w_y denote the local wind speed. The wavenumber k of Eq. (9c) is now replaced by k_m of Eq. (9d). Now a determination of k_x and k_y is required. k_x and k_y are the horizontal components of the wavenumber in the x and y direction. Since PE is a 2-Dimensional model (range and altitude) k_x and k_y have the following description,

$$k_x = k\left(\frac{\frac{\partial p}{\partial r}}{\sqrt{\left(\frac{\partial p}{\partial r}\right)^2+\left(\frac{\partial p}{\partial z}\right)^2}}\right)\cos(\theta) \qquad k_y = k\left(\frac{\frac{\partial p}{\partial r}}{\sqrt{\left(\frac{\partial p}{\partial r}\right)^2+\left(\frac{\partial p}{\partial z}\right)^2}}\right)\sin(\theta) \tag{10}$$

where θ is the angle that *r* makes to the x-axis. The derivative of *p* with respect to *z* is performed using a central difference stencil, while the derivative with respect to *r* utilizes a backward difference stencil, which requires saving the pressure at the previous range.

To reduce the execution time, the model is parallelized via use of the "DOACROSS" commands available on Silicon Graphics Incorporation (SGI) multi-processor platforms.

4. Examples

Two examples will be presented showing some of the capabilities of the model. The first example shows a time domain result for the propagation of the infrasonic pulse resulting from a nuclear explosion in the atmosphere. The environment for this case is very simple. The sound speed is constant with height (300 m/s) and there are no winds. The source location is at a height of 5 m with the receiver location at a height of 1 m. The model was run for 140 frequencies starting at a frequency of .05 Hz**,** with a frequency increment of .05 Hz. Initially each frequency had equal weighting**.** A pressure signature commonly used to investigate the excitation of infrasonic modes by nuclear explosions is the so-called Glasstone pulse [10]. It represents the pressure history of the blast wave. It has the form

$$\frac{p_G(t)}{\Delta p_{ref}} = \left(1 - \frac{t}{T_+}\right) e^{-(t/T_+)} U\left(\frac{t}{T_+}\right), \tag{11}$$

with

$$T_+ = 0.33\left[1 + 0.047 \ln\left(\frac{R}{R_{ref}}\right)\right]^{1/2} \tag{12}$$

and t is measured from the onset of the shock. U (*) is the Heaviside step function. The parameter Δp_{ref} is the shock overpressure at a reference distance R_{ref} from a 1KT burst in the standard atmosphere. The shock overpressure at a reference distance of 5.84 $\Lambda_{0\ ref}$, (where $\Lambda_{0\ ref}$ = 256m) is 34mbar**.** The spectral amplitude for the Glasstone pulse is given by

$$A_G(\omega) = \frac{-i}{2\pi\left(i\omega - \frac{1}{T_+}\right)^2} \tag{13}$$

For each frequency, since we are dealing with a cw model, weights determined from Eq. (13) were applied to the output of Air-EFEPE. The resulting time signal is then obtained via an inverse FFT. Figure 1 depicts the comparison of the Air-EFEPE model along with the Glasstone pulse at a range of 1000km. The widths of the two pulses are approximately the same as are the over pressure and role-off. The main difference is that the Glasstone pulse does not show the large over pressure excursion that the synthesized signal does. The reason for the difference was believed to be due to the fact that the analytic expression for the Glasstone pulse knows nothing about the source receiver geometry or about the complex impedance of the land. Therefore, a simplified expression for the pressure near grazing, based on work by Attenborough [11], was used to synthesize a signal. This signal was compared to the Air-EFEPE result. Figure 2 depicts the comparison. Note that the widths of the two signals are a better match than that shown in Fig. 1a. The overpressure that occurs after the large negative excursion does not compare as well as the Glasstone pulse did. However there is an overpressure occurring prior to this negative excursion. It is not as large as the synthesized signal but this could be due to the fact that it is an approximate solution.

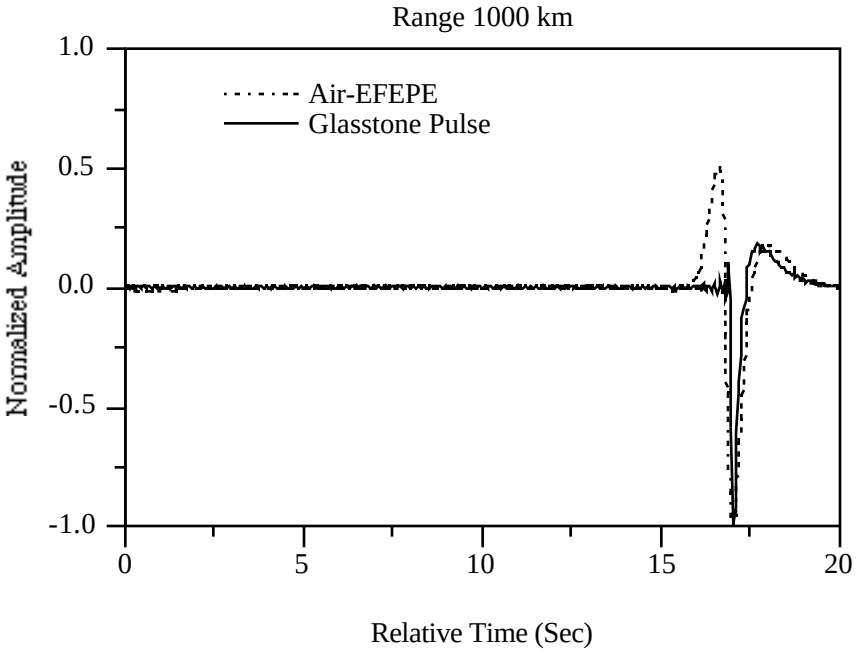


Figure 1. Comparison of the pulse generated by the Air-EFEPE model and the analytic expression for the Glasstone pulse.

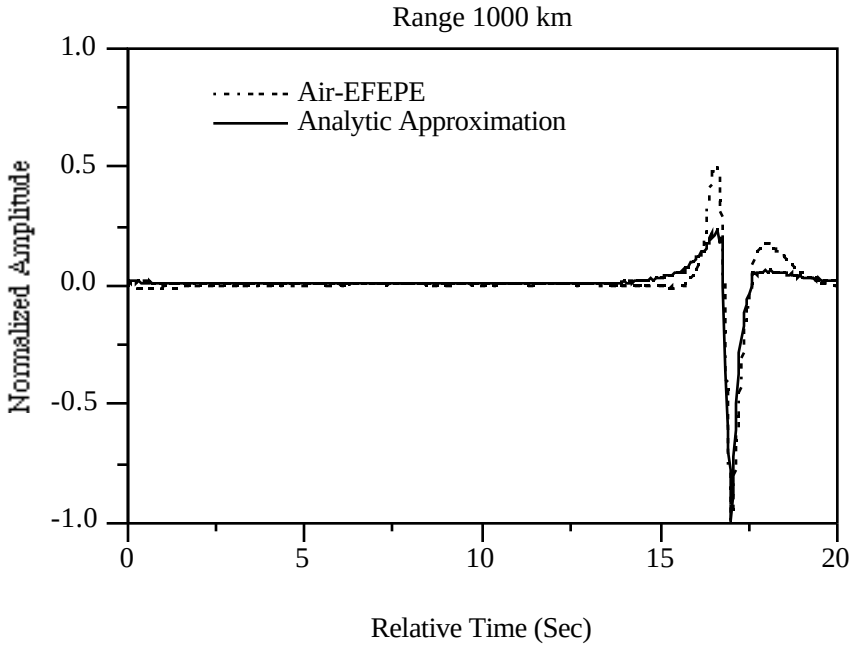


Figure 2. Comparison of the pulse generated by the Air-EFEPE model and the analytic approximation for the pulse from Attenborough.

The second example depicts a frequency domain result. This example is not meant to be realistic. It is used to show that range dependence is included for both sound speed and atmospheric winds. The environment initially consists of an isovelocity sound speed (330 m/s) from the ground to an altitude of 300 km. A 5 Hz source is placed at 150 km. Five separate cases were run. For the first case the environment did not change with range, or in other words this represents a range independent case. This case was run so that the results from the next four cases could be compared to this range independent (baseline environment) environment. Figure 3 depicts the result.

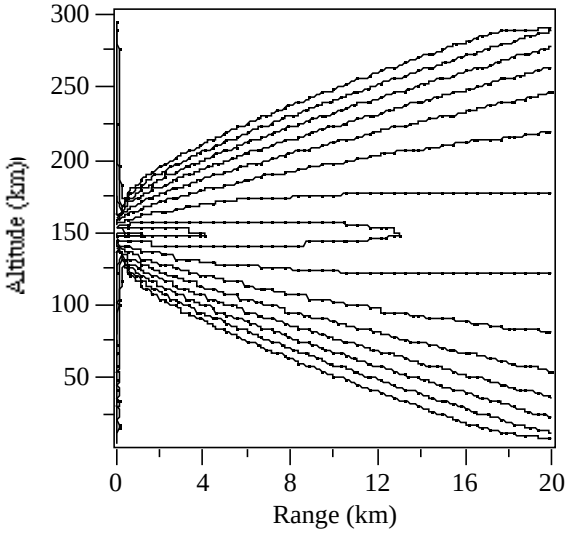


Figure 3. Contour plot of the acoustic field, altitude vs. range for the isovelocity sound speed. Contour levels are 30 to 150 dB in steps of 10 dB.

The sound speed varies with range for the second environment. For this case the sound speed had a minimum at 150 km, while the sound speed at the surface and at 300 km remains at 330 m/s. This minimum becomes more extreme at each kilometer out to 10 km where the minimum is 180 m/s. Beyond 10 km the minimum sound speed reverses until at 20 km the sound speed is once again isovelocity (constant 330 m/s). This results in a sound speed gradient that increases with range, to 10 km and then reverses until at 20 km the gradient disappears. The change in the minimum sound speed is 15 m/s at every km. See Fig. 4 for the resulting sound speed profiles.

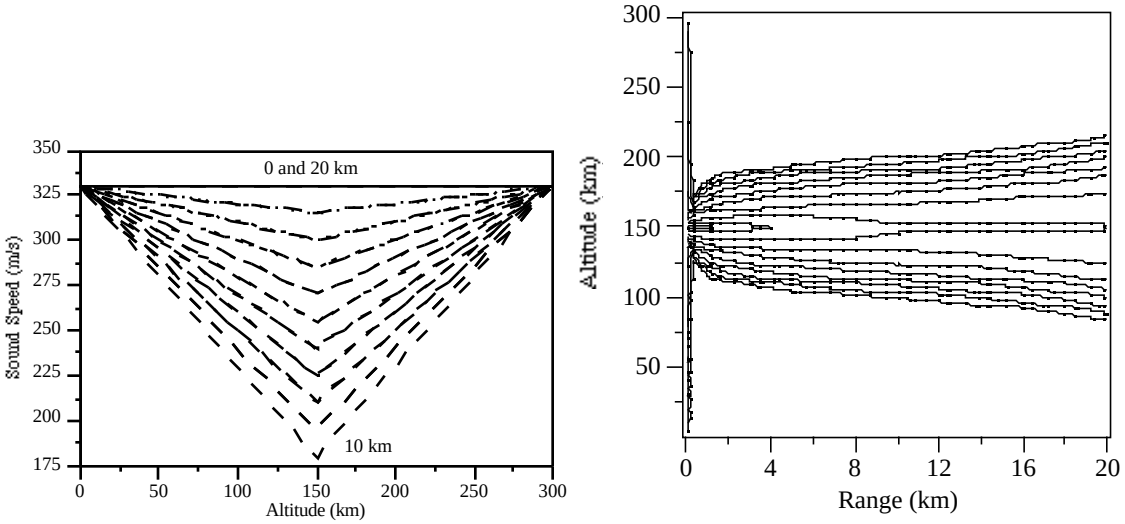


Figure 4a. Sound speed profiles for environment 2. Figure 4b. Contour plot of the acoustic field, altitude vs. range for the 2nd environment (sound speed shown in Fig. 4a). Contour levels are 30 to 150 dB in steps of 10 dB.

Figure 4b depicts the intensity of the acoustic field (expressed in dB) versus altitude and range. Notice that compared to the isovelocity case (Fig. 3) the field is very focused. This is the result of the sound speed gradients. From 10 km to 20 km the strengths of the gradients become less, resulting in a gradual spreading of the acoustic field.

The sound speed profiles used for the 3rd environment are depicted in Fig. 5a. Now instead of having a minimum at an altitude of 150 km there is a maximum. At each kilometer in range, starting at 1km the maximum increases at a rate of 15 m/s out to 10 km (Maximum sound speed is 480 m/s). From 11 km to 20 km in range the maximum decreases by 15 m/s at each kilometer, until at 20 km the sound speed is once again constant (330 m/s). See Fig. 5a.

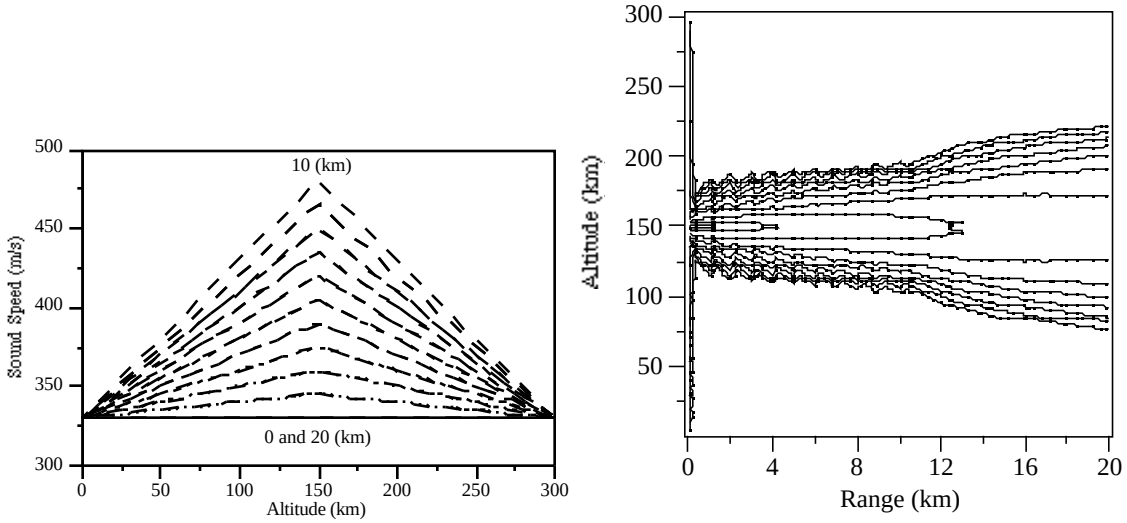


Figure 5a. Sound speed profiles for environment 3. Figure 5b. Contour plot of the acoustic field, altitude vs. range for the 3rd environment (sound speed shown in Fig. 5a). Contour levels are 30 to 150 dB in steps of 10 dB.

Figure 5b depicts the result for this environment. Notice that this result is significantly different from the last result and from the isovelocity result (Fig. 3). The field is very focused and there appears to be some symmetric structure out to 10 km. This structure is due to the fact that the gradient increases only at discrete ranges (and remaining constant until the next increase) and not continuously with range. After 10 km the strengths of the gradients decrease, allowing the acoustic field to spread in height.

The next two environments consist of an isovelocity sound speed (330 m/s) with a range dependent atmospheric wind field. The wind speed profiles used for the 4th environment is depicted in Fig. 6a. This environment is similar to environment 2 (Fig. 4a) except the wind speed x-axis component (at 150 km height) increases in the negative x direction. At each kilometer in range, starting at 1km the wind speed increases at a rate of 15 m/s out to 10 km (Maximum wind speed is 150 m/s in the negative x direction). From 11 km to 20 km in range the wind speed decreases by 15 m/s at each kilometer, until at 20 km the wind speed is once again constant (0 m/s). See Fig. 6a.

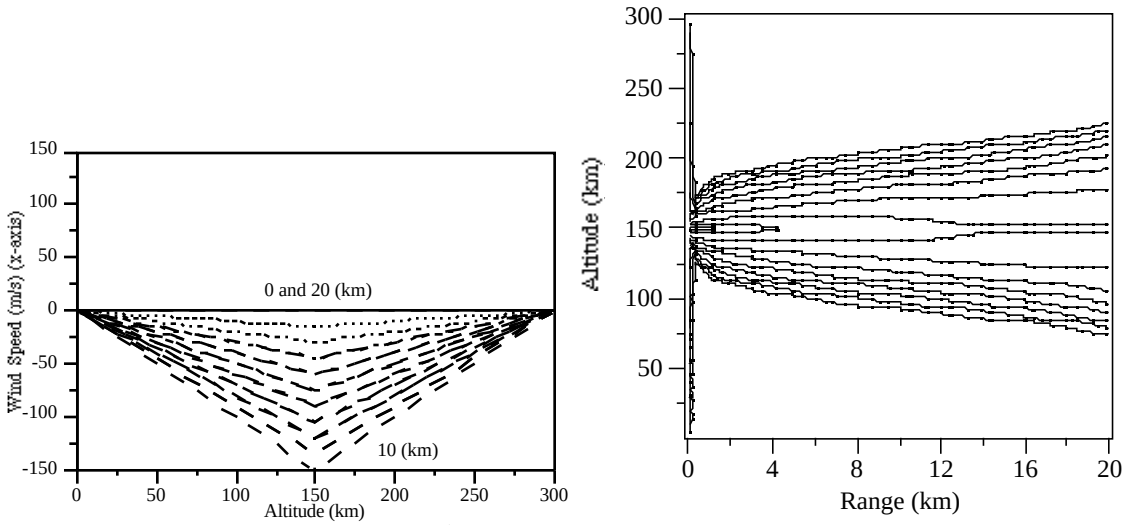


Figure 6a. Wind speed profiles used in 4th environment. Figure 6b. Contour plot of the acoustic field, altitude vs. range for the 4th environment (wind speed shown in Fig. 6a). Contour levels are 30 to 150 dB in steps of 10 dB.

Figure 6b depicts the intensity of the acoustic field (expressed in dB) versus altitude and range. Notice that compared to the results from first environment (Fig. 4b) the two are nearly identical. The differences are noticeable at the maximum range, where field has spread out more in height than when the sound speed changed. This result is not surprising, since the act of changing the local sound speed, results in a change of the local wavenumber, where as including the wind field results in a direct change of the wavenumber while not changing the sound speed. Again we see that from 10 km to 20 km the strengths of the gradients become less, resulting in a gradual spreading of the acoustic field.

The wind speed profiles used for the 5th environment is depicted in Fig. 7a. This environment is similar to environment 3 (Fig. 5a) except the wind speed x-axis component (at 150 km height) increases in the positive x direction. At each kilometer in range, starting at 1km the wind speed increases at a rate of 15 m/s out to 10 km (Maximum wind speed is 150 m/s in the positive x direction). From 11 km to 20 km in range the wind speed decreases by 15 m/s at each kilometer, until at 20 km the wind speed is once again constant (0 m/s). See Fig. 7a.

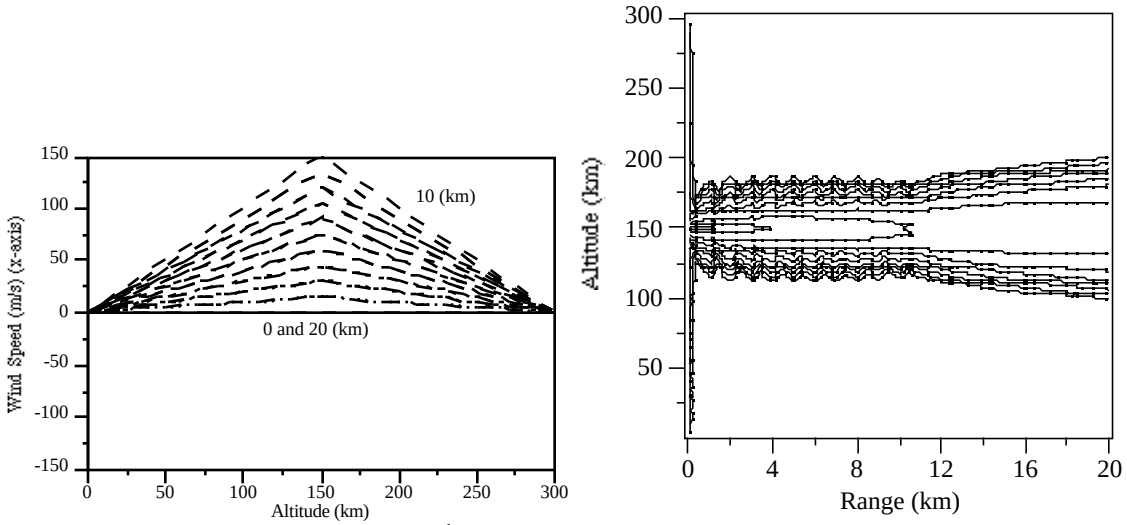


Figure 7a. Wind speed profiles used in 5th environment. Figure 7b. Contour plot of the acoustic field, altitude vs. range for the 5th environment (wind speed shown in Fig. 7a). Contour levels are 30 to 150 dB in steps of 10 dB.

Figure 7b depicts the intensity of the acoustic field (expressed in dB) versus altitude and range. Notice that compared to the results from 3rd environment (Fig. 5b) the two again are nearly identical. Differences are noticeable throughout the range of propagation. The reason is again due to the fact that changing the local sound speed, results in a change of the local wavenumber, where as including the wind field results in a direct change of the wavenumber while not changing the sound speed. It is apparent that the field is more focused in range compared to Fig. 5b.

5. Concluding remarks

A prototype atmospheric acoustic propagation model for infrasonics has been introduced whose genesis is in underwater acoustic propagation. This prototype model includes range and altitude dependent atmospheric winds, and accounts for attenuation in the atmosphere. A starting field is incorporated based on the reflection of a spherical wave from a locally reacting boundary, and lastly a new bottom boundary condition appropriate for an air-ground interface is imposed. The inclusion of the gravity term in the wave equation will be the subject of future work.

Acknowledgements

This work was sponsored by the U. S. Department of Energy and the Los Alamos National Laboratory under contract No. DE-AI04-98AL79805.

References

[1] Sullivan, J. D., "The Comprehensive Test Ban Treaty," (March 1998), *Physics Today*, 24-29.
[2] Whitaker, R. W., "Infrasonic Monitoring," 1995, Phillips Laboratory Monitoring Symposium, Scottsdale, Arizona, USA.
[3] Collins, M. D., "A split-step Pade´ solution for the parabolic equation method," J. Acoust. Soc. Am.; 1993, **93**, 1736-1742.
[4] White, M. J., Gilbert, K. E., "Application of the parabolic equation method to the Outdoor Propagation of Sound," Applied Acoustics, 1989; **27**, 227-238.
[5] Franke, S. J., Swenson, Jr. G. W., "A brief tutorial on the Fast Field Program (FFP) as applied to sound propagation in the air;" Applied Acoustics, 1989, **27**, 203-215.
[6] Gudesen, A., "Application of the SAFARI model to sound propagation in the atmosphere," J. Acoust. Soc. Am.; 1990, **87**, 1968-1974.
[7] Lingevitch, J. F., Collins, M. D. and Siegmann, W. L., "Parabolic equations for gravity and acousto-gravity waves," J. Acoust. Soc. Am.; 1993, **105**, (6) 3049-3056.
[8] Norton, G. V. and Novarini, J. C., "Modeling infrasonic atmospheric propagation via a finite element parabolic equation model," submitted to Applied Acoustics.
[9] Nijs, L., Wapenaar, C. P. A., "The influence of wind and temperature gradients on sound propagation, calculated with two-way wave equation," J. Acoust. Soc. Am.; 1990, **87**, 1987-1998.
[10] Posey, J. W., Application of Lamb Edge Mode Theory in the Analysis of Explosively Generated Infrasound, Ph. D. Thesis, Department of Mechanical Engineering, Massachusetts Institute of Technology, Cambridge, MA, August 1971.
[11] Attenborough, K., Review of ground effects on outdoor sound propagation from continuous broadband sources, Applied Acoustics; 1988, **24**, 289-319.

SIMULTANEOUS COMPARISON OF THREE CO-LOCATED PIPE SYSTEMS FOR WIND-NOISE REDUCTION FOR USE WITH MODEL #4 CHAPARRAL INFRASONIC MICROPHONES AT FAIRBANKS, ALASKA

John V. Olson and Charles R. Wilson, Geophysical Institute, University of Alaska
Fairbanks, Alaska, USA

Sponsored by the U.S. Department of Energy
Contract No. DE-FC04-98AL79802

ABSTRACT

Three identical Chaparral Model No. 4 microphones were used for the simultaneous testing of three different co-located wind-noise reduction pipe systems in a forested area in Fairbanks, Alaska. The first pipe system was a standard 305 meter long Daniels tapered steel pipe that is vented with a hypodermic needle every 1.5 meters. The second noise reduction system tested was the Los Alamos National Laboratory/Comprehensive Nuclear-Test-Ban-Treaty (LANL/CTBT) prototype system consisting of twelve radial porous hoses, each with a length of 15 meters to give a total aperture of 30 meters for the array. The third system was suggested by Doug Christie of the Provisional Technical Secretariat (CTBTO) at the Infrasonic Workshop at Bruyeres-Le-Chatel, France, in July 1998. This third system is a hexagonal array of six 30-meter long linear sections of 2-inch diameter rigid pipe. The six chords of the hexagon array are vented every 1.5 meters with a hypodermic needle and are separately connected to the microphone, at their centers, by _-inch diameter rigid pipe. The total aperture of the hexagonal array is 70 meters. Located at a common site in a wooded area near the University of Alaska, the microphone outputs are digitized at a 100-hertz rate using a 24-bit digitizer and transmitted using a spread-spectrum radio link back to the Geophysical Institute. There the data are logged to a network accessible computer disk in files that contain 10-minute segments of the data. Daily plots of the rms levels from each microphone are produced on a regular basis. Detailed analysis of the microphone responses is performed using power spectral density estimates based upon the Welch method. In general, it is found that during almost all wind conditions the hexagonal array achieved the lowest noise power. The LANL/CTBT array noise levels were usually the highest and the Daniels pipe produced intermediate levels of noise reduction.

Key Words: infrasonic wind noise reduction

OBJECTIVE

One of the four primary sensor systems identified as part of the Comprehensive Nuclear-Test-Ban-Treaty (CTBT) program is a worldwide array of infrasonic detection systems. Each infrasonic system is based upon an array of at least four microphones, including noise-reducing arrays, arranged in an isosceles triangle with 1-3 km sides with one sensor in the center. It is well known that the primary source of pressure fluctuations near the ground is produced by wind-generated turbulence. In order to reduce the background levels of this wind noise, arrays of pipes are often used in an attempt to average the wind turbulence over some area near the microphone. The pipe systems are vented to the atmosphere at regular intervals and connected to each microphone.

Several pipe configurations for wind-noise reduction have been proposed. The objective of this study is to test three commonly used noise-reducing arrays under arctic conditions using co-located microphones. Through these tests we will be able to identify the noise-reducing array that is the most efficient in reducing wind noise. We will also be able to describe the performance of each system over a variety of climatic conditions ranging from warm, calm intervals through rain and frost conditions and, finally, to the frigid arctic conditions with an accompanying snow pack covering the array. The three noise reduction arrays that we have chosen to study include: 1) a 305 meter long Daniels tapered steel pipe that is vented with hypodermic needles every 1.5 meters; 2) a system of twelve radial porous "soaker" hoses, each with a length of 15 meters; 3) a hexagonal array of six 30-meter long sections of 2-inch diameter rigid pipe.

Once we have identified the most efficient of the noise-reduction systems we plan to deploy the microphones in the standard CTBT geometry in order to test the array itself under arctic conditions at a high-latitude site. In time we plan to add a fifth microphone placed several kilometers from the central array in order to estimate the coherence length of the various infrasound signals. A wealth of natural infrasound is present in the interior of Alaska that includes microbaroms, mountain associated waves, auroral infrasound, earthquakes and volcanic eruptions. A review of these signals and their analysis is given at our home page: http://maxwell.gi.alaska.edu/~crw.

RESEARCH ACCOMPLISHED

While our research encompasses a sequence of ongoing tasks and goals we have begun to gather data on microphone and noise-reduction array performance during summer conditions. After acquiring and deploying the microphones and data-logging equipment we began to collect data in early May, 1999. Our data is sampled at a rate of 100 samples per second giving a 50 hertz Nyquist frequency. Upon analysis the data are low-pass filtered and decimated by a factor of 5 to give a 10 hertz Nyquist frequency. In the first phase of microphone comparison we have collected data continuously in order to compare the microphone responses to a variety of signals and weather conditions.

Three microphones with three different noise-reducing arrays were installed side-by-side at the Ballaine Lake site near the University of Alaska. The first noise-reduction array is a 305 meter long Daniels tapered steel pipe that is vented with a hypodermic needle every 1.5 meters. The pipe axis lies roughly east-west. The second array is the Los Alamos National Laboratory/Comprehensive Nuclear-Test-Ban Treaty (LANL/CTBT) prototype. This array consists of twelve radial porous "soaker" hoses, each 15 meters in length giving a total aperture of 30 meters. The third system is a hexagonal array of six 30 meter long linear sections of 2 inch diameter rigid pipe. The six chords of the hexagon are vented every 1.5 meters with a hypodermic needle and each chord is separately connected to the microphone by a 3/4 inch diameter rigid pipe from the center of the chord. The total aperture of the array is 70 meters.

Figure 1 shows a typical 24 hour segment of data in which the rms variation is computed over 10 minute segments from each microphone.

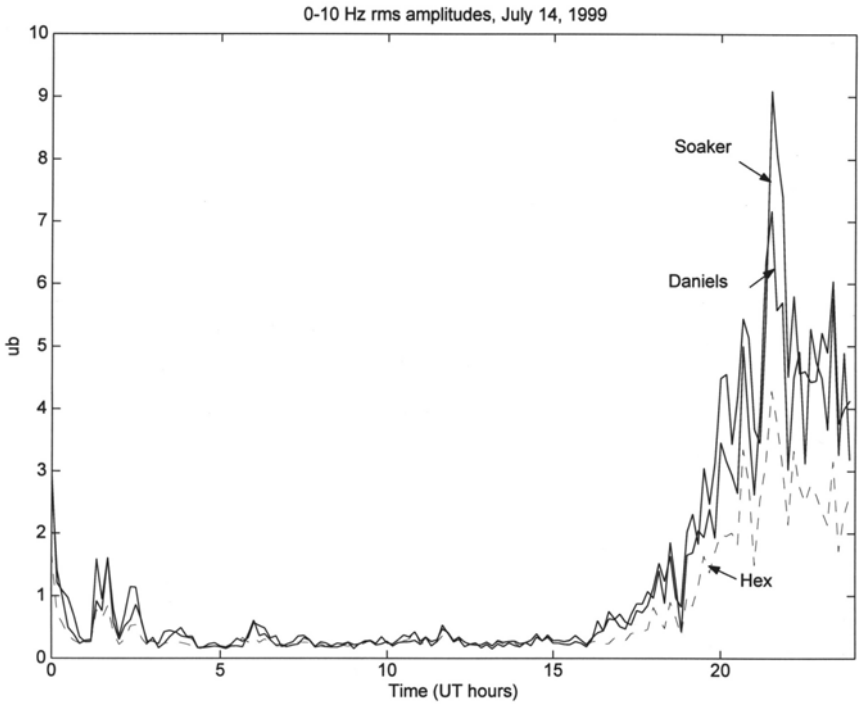


Figure 1. Rms signal levels computed from 10 minute segments for July 14, 1999. 0000 UT is 1600 local time. Typical of the data observed, the quietest intervals occur after midnight and the largest during the afternoons, local time. Note that through all wind conditions the hex array is the most effective noise reducer.

In this figure it can be seen that there is a diurnal variation in the rms signal level from each sensor. It should be noted that 0000 UT is 1600 local time. Generally speaking, the quietest intervals occur after midnight near 1200 UT and the noisiest during the windiest portion of the day which is usually the local afternoon. Figure 1 shows a consistent pattern found for all times and wind conditions and that is the relative efficiency in reducing the noise by each array. Almost always we have found that the hexagonal array is the most efficient in cancelling wind noise, followed by the Daniels array with the LANL "soaker" array the least efficient.

In order to evaluate the relative effectiveness of each of the noise-reducing arrays in more detail, we operated for a period with one of the three microphones open to the atmosphere with no noise-reducing array attached. This allowed us to compare the effectiveness of two of the noise-reducing arrays directly against an open microphone. Through the period the various arrays were swapped to give relative comparisons of all arrays against eachother and an open microphone. This procedure was necessitated since we have only three microphones. If a fourth microphone were available we could operate all three noise reducers simultaneously in comparison with an open microphone. Figure 2 shows a spectrum taken on July 7, 1999 at 0000 UT during which time one microphone was open to the atmosphere with only a 2-meter section of hose between the manifold and the outside atmosphere. The other two microphones were attached to the Daniels and hexagonal arrays. The wind conditions were moderate and the rms signal levels from the microphones ranged from 5 to 10 microbars.

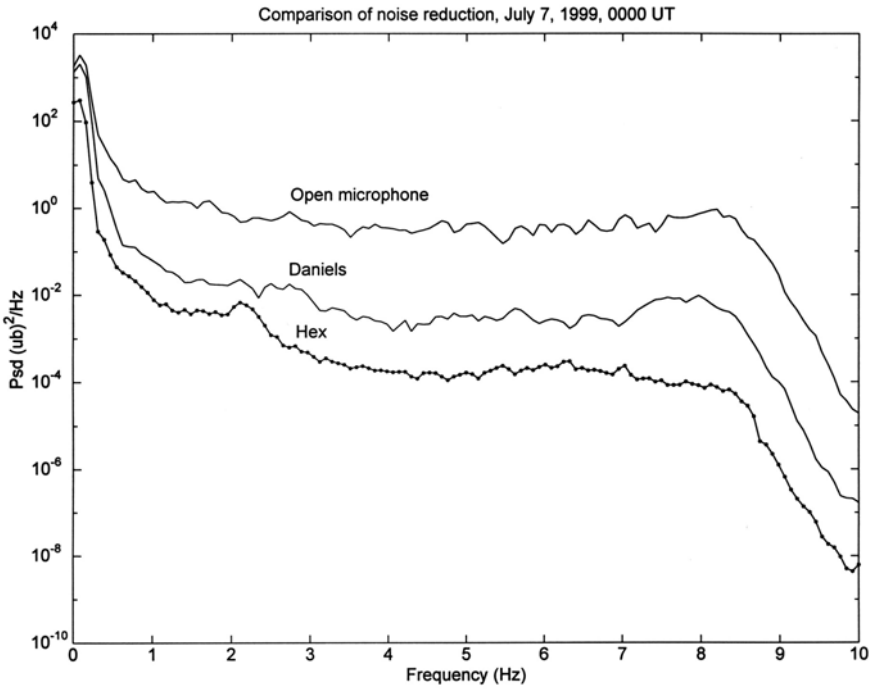


Figure 2. This figure shows power spectral density estimates of wind noise taken at 0000 UT on 7 July 1999. Noise levels produced by the Daniels and hexagonal noise-reducing arrays can be compared to the noise from an open microphone. It can be seen that the hex array is more effective than the Daniels array across the entire 0-10 hertz spectrum.

As can be seen the spectrum is dominated by variations at very low frequencies. While both noise-reducers are effective it can be seen that at all frequencies across the band from 0 to 10 hertz the hexagonal array is the most efficient in reducing the wind noise reaching levels a full order of magnitude less than the Daniels. Note the small increase near 2 hertz in the hexagonal response. This is characteristic of the hex array itself. The presence of resonances in the spectrum of the response of various acoustic filters was shown by Alcoverro, 1998.

Figures 3 and 4 show spectra with the other two possible combinations of microphones compared to an open microphone. Figure 3 shows a spectrum taken on June 29, 1999 at 0000 UT during which time the hexagon and "soaker" arrays were connected to microphones. Again, moderate winds of a few miles per hour were present. Again the hexagonal array is more efficient in reducing the wind noise at all frequencies between 0 and 10 hertz. Note also the continued presence of the resonance near 2 hertz. Figure 4 shows a spectrum taken on July 12, 1999 at 0000 UT. In this case the Daniels and "soaker" arrays were connected to microphones. In this case the responses are similar with the Daniels showing increased rejection of wind noise near 4 hertz.

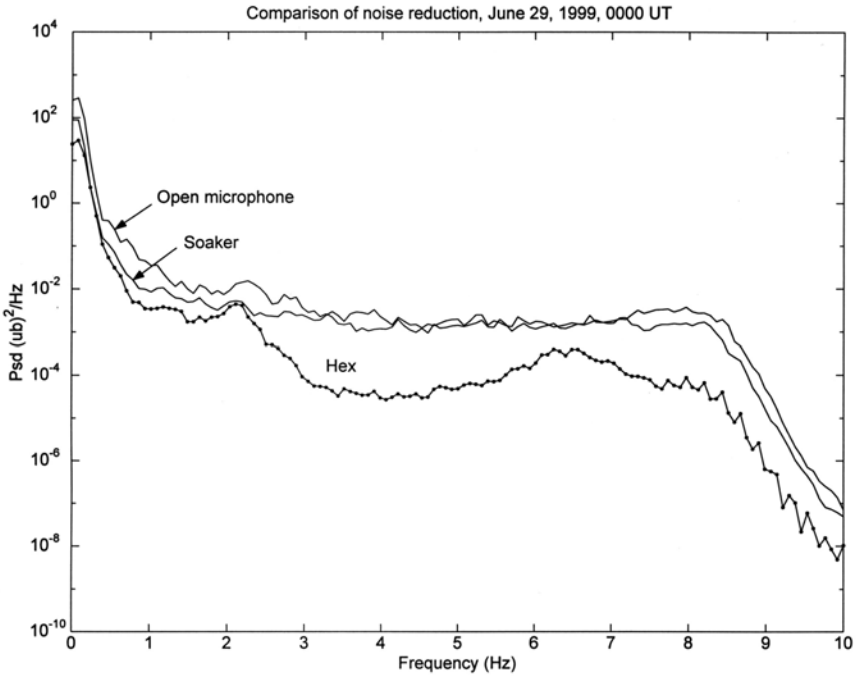


Figure 3. This figure shows power spectral density estimates of wind noise taken at 0000 UT on 29 June 1999. Noise levels produced by the LANL prototype ("soaker") and hexagonal noise-reducing arrays can be compared to the noise from an open microphone. It can be seen that the hex array is more effective than the "soaker" array across the entire 0-10 hertz spectrum. Note the spectral increase near 2 and 6 hertz in the hexagonal array. These are probably due to resonances in the array.

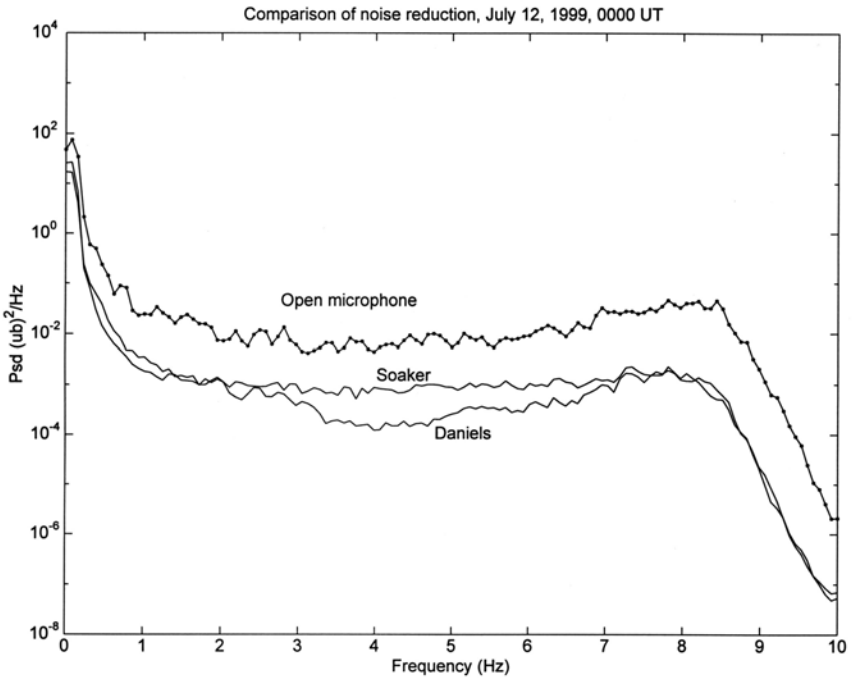


Figure 3. This figure shows power spectral density estimates of wind noise taken at 0000 UT on 12 July 1999. Noise levels produced by the Daniels and LANL prototype ("soaker") noise-reducing arrays can be compared to the noise from an open microphone. It can be seen that the Daniels array is more effective than the "soaker" array across the entire 0-10 hertz spectrum.

CONCLUSIONS AND RECOMMENDATIONS

The examples given above show a consistent result: the hexagonal array is the most efficient in reducing wind noise when compared to a linear Daniels pipe or the LANL/CTBT array of "soaker" hoses. Under most conditions data from the hexagonal array show power spectral density levels that are generally two orders of magnitude lower than those from an open microphone and usually an order of magnitude below those shown by the Daniels and LANL/CTBT "soaker" arrays.

With these data in hand we intend to proceed to the second phase of our research program that includes installing four microphones in a triangular array with one microphone at the center of the triangle as prescribed by CTBT specifications. It is our intention to install the hexagonal noise reducing array at each of the microphone sites.

REFERENCES

Alcoverro, B., Acoustic Filters Design and Experimental Results, Proceedings of the Informal Workshop on Infrasounds held in Bruyeres-le-Chatel, France, Published by Department Analyse et Surveillance de L'Environment, July 1998.

ESTIMATION AND LOCATION USING MULTIPLE INFRASOUND ARRAYS

Robert H. Shumway
Sung-Eun Kim
University of California, Davis

Defense Threat Reduction Agency, DOD
Contract DSWA01-97-0150

ABSTRACT

Integrating or *fusing* array data from various sources will be extremely important in making the best use of networks for detecting infrasonic signals and for estimating their velocities and azimuths. In addition, studying the size and shape of location ellipses that use velocity, azimuth and travel time information from an integrated collection of small arrays to locate the event will be critical in evaluating our overall capability for monitoring a CTBT.

In the first phase of this study, we have developed a small-array theory that characterizes the uncertainty in estimated velocities and azimuths for different infrasonic array configurations and levels of signal correlation. The performance of simple beam forming and a generalized likelihood beam that is optimal under signal correlation have been compared. Empirical work to establish plausible signal frequencies and coherence levels for small arrays has concentrated on several events in the Pacific.

The second phase of the study develops statistical methods for integrating information from a collection of small arrays in order to obtain unified estimators for the location of an event as well as the predictive region that best characterizes location uncertainty. We derive optimal methods based on a nonlinear Bayesian approach to combining wavenumber parameters and their uncertainties into an uncertainty ellipse for the location. The methodology is capable of combining uncertainties for the overall input variances with observed data from small arrays to get posterior predictive regions for locations. Several contrived examples are used to compute ellipses that might be expected from a typical set of small infrasonic arrays.

Key Words: *Detection, Location, Infrasound, Multiple array processing, Nonlinear estimation, Bayesian methods*

OBJECTIVES

The first phase of this study focused on completely characterizing the statistical detection and estimation capabilities of small infrasonic arrays, as contemplated by the Prototype International Data Centre (PIDC). For a multivariate correlated signal model, we developed the statistical approaches for (i) maximum likelihood detection, (ii) estimation of velocity and azimuth parameters, (iii) estimation of noise spectra and the signal spectral matrix and (iv) performance of various array configurations. Applications of the results to several events, coupled with theoretical calculations based on the Mack-Flinn distance-coherence model, gave predicted azimuthal standard deviations ranging from 1 to 5 degrees, depending on the center frequency of the signal, array configuration and signal to noise ratio. Summaries of the results obtained can be found in Shumway and Kim (1998) and in Shumway et al (1999).

In the second phase of this study, we are examining the implications that the results of the first phase have for location uncertainty using estimated wave-number parameters from more than one array. In general, there may be a small number of arrays that detect any given event and we look at different methods for estimating the uncertainty of locations derived from these kinds of data. The results take wave-number coordinates from multiple arrays and combine or *fuse* them into an overall location for the common event and obtain an associated uncertainty region for the location. As has been observed by numerous authors, the assumptions made about the variances of the observed errors in estimated wave-numbers or travel times will influence the size of the uncertainty region. In this analysis, we focus on three assumptions regarding the unknown variances, namely that they are (A) known exactly (Evernden, 1969), (B) completely unknown (Flinn, 1965) and (C) subject to a prior distribution (Jordan and Sverdrup, 1981, Bratt and Bache, 1988). We give several examples involving small arrays and an event location similar to what might be expected from a subset of arrays recording an event on the proposed PIDC network of infrasonic stations .

RESEARCH ACCOMPLISHED

Model Development

In the case of an infrasonic array, it is convenient to assume that observed data at sensor $j = 1, 2, \ldots, N$ for array $k = 1, 2, \ldots, n$ records

$$y_{jk}(t) = s_{jk}(t - T_{jk}) + n_{jk}(t) \tag{1}$$

as signal plus noise, where the time delays

$$T_{jk}(\boldsymbol{\theta}) = -\frac{\mathbf{r}'_{jk}\boldsymbol{\theta}_k}{\nu} \tag{2}$$

depend on the array coordinates $\mathbf{r}_{jk} = (r_{jk1}, r_{jk2})'$ and a wave-number vector $\boldsymbol{\theta}_k = (\theta_{1k}, \theta_{2k})'$ and ν is the center frequency. It should be noted that the wave-numbers can be related to the velocity and azimuth of the propagating signal that is of interest (see Shumway et al, 1999) . We will not express the equations here in those terms but will simply note that $\boldsymbol{\theta}_k = \boldsymbol{\theta}_k(\boldsymbol{x})$ is related to the event location $\boldsymbol{x} = (x_1, x_2)'$ through

$$\boldsymbol{\theta}_k(\boldsymbol{x}) = \frac{\nu}{V}\frac{(\mathbf{c}_k - \boldsymbol{x})}{d_k(\boldsymbol{x})} \tag{3}$$

where $\mathbf{c}_k = (c_{1k}, c_{2k})'$ denotes the coordinates of the center of the k^{th} array and V is the velocity of the signal with ν and V generally taken as being fixed and known. The signs of the two components of $\boldsymbol{\theta}_k(\boldsymbol{x})$

change, depending on where the event is located relative to the center coordinates of the array. The distance term in the denominator is obviously also a function of the location, given by

$$d_k(\boldsymbol{x}) = \|\boldsymbol{c}_k - \boldsymbol{x}\|. \tag{4}$$

There will usually be estimators available for the n wave-number vectors, say $\hat{\boldsymbol{\theta}}_1, \hat{\boldsymbol{\theta}}_2, \ldots, \hat{\boldsymbol{\theta}}_n$, available from each of the n arrays, along with the asymptotic covariance matrices, say $\Sigma_k, k = 1, \ldots, n$. These have been determined in Shumway et al (1999) for both beam-forming and correlated beam-forming frequency wave-number estimators.

In order to give a concrete example, consider the three arrays in Figure 1, with centers at $\boldsymbol{c}_1 = (0,0)', \boldsymbol{c}_2 = (0,-1000)', \boldsymbol{c}_2 = (-1000,0)'$, observing an hypothetical event at $\boldsymbol{x} = (-2366,-2366)'$, with all distances measured in km.

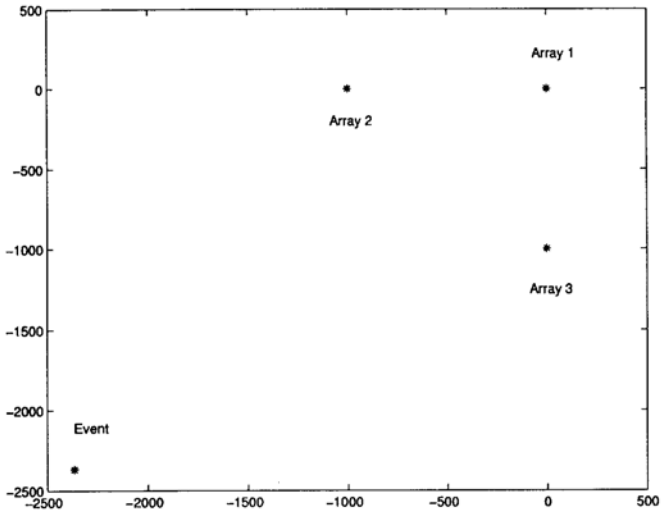


Figure 1: Hypothetical array centers for location example

Each of the arrays, centered at their respective values, will generate an estimator for the wave-number parameters relative to the event. Since this particular event is in the third quadrant for all of the arrays the coefficients of the two components of (3) will all be negative. In this case, the location is $\boldsymbol{x} = (-2366,-2366)'$ and the true wave-numbers become are $\boldsymbol{\theta}_1(\boldsymbol{x}) = (-.0733,-.1270)'$, $\boldsymbol{\theta}_2(\boldsymbol{x}) = (-.1037,-.1037)'$ and $\boldsymbol{\theta}_3(\boldsymbol{x}) = (-.1270,-.0733)'$, as can be computed from (3), with $\nu = .044$ Hz and $V = .3$ km/sec.

The above discussion suggests that we might assume a model for the estimated wave-number vectors that takes the form

$$\hat{\boldsymbol{\theta}}_k = \boldsymbol{\theta}_k(\boldsymbol{x}) + \boldsymbol{e}_k \tag{5}$$

where the errors are assumed to have 2×2 covariance matrices of the form

$$\text{cov } \boldsymbol{e}_k = \sigma^2 \Sigma_k, \tag{6}$$

and σ^2 denotes the variance parameter. The problem is to estimate the location vector, given a sample of 2×1 wave-number estimators $\hat{\boldsymbol{\theta}}_1, \ldots, \hat{\boldsymbol{\theta}}_n$ and the covariance matrices $\Sigma_1, \ldots, \Sigma_n$. The model (5) is is nonlinear in the location parameter vector $\boldsymbol{x}$ because of (3) and (4).

It should be noted, at this point, that travel times may also be known from considerations apart from the wave-number estimation methodology discussed in Shumway et al (1999). For example, travel times may also be determined by cross correlating elements in the array, using onset times read by an analyst or monitoring the ratio of short-term to long-term mean squares. While such information cannot be completely independent of the wavenumber analysis, it may present a more global solution in the sense that the observations do not depend on focusing on a given frequency band. If such estimated travel times are available, the model in (5) might be augmented by one expressing the estimated travel times , say $\hat{t}_1, \ldots, \hat{t}_n$ in a form analgous to (5) where

$$t_k(\boldsymbol{x}) = \frac{d_k(\boldsymbol{x})}{V} \tag{7}$$

is again a nonlinear function of the location vector $\boldsymbol{x}$.

Wave-number Estimation and Uncertainty

Shumway et al (1999) have investigated optimal detection and estimation of the wave-number vector and its uncertainty. They develop the F-statistic for detection under perfect signal correlation and a generalized beam for detection when the signal correlation degrades with distance. Under the model given in (1) and (2), they obtain the maximum likelihood estimators of the wave-number vector, say $\hat{\boldsymbol{\theta}}$. The asymptotic covariance matrix, in the case of beamforming and perfect signal correlation, is given by

$$\Sigma \approx \frac{1}{2(2\pi)^2} \frac{1}{L} \frac{r}{N} \left(1 + \frac{r}{N}\right) R^{-1} \tag{8}$$

where N is the array size, L is the number of frequencies smoothed for the detector (time-bandwidth product), R is the covariance matrix of the array coordinates and r is inverse of the signal to noise ratio.

The estimated wave-numbers from n arrays, say $\hat{\boldsymbol{\theta}}_1, \ldots, \hat{\boldsymbol{\theta}}_n$ and their asymptotic covariance matrices, $\Sigma_1, \ldots, \Sigma_n$ serve as natural inputs for the fused locations given in the next section.

Fused Locations: Classical and Bayesian Methods

We extend the classical methods first to the case where we observe wave-number parameters and their covariance matrix from n arrays and wish to combine or *fuse* the information into an overall lcoation. The nonlinear model (5) can be treated in the usual way. That is, expand $\boldsymbol{\theta}_k(\boldsymbol{x})$ around some initial value, say $\boldsymbol{x} = \boldsymbol{x}_0$ and write a linearization as

$$\hat{\boldsymbol{\theta}}_k - \boldsymbol{\theta}_k(\boldsymbol{x}_0) = A_k(\boldsymbol{x}_0)(\boldsymbol{x} - \boldsymbol{x}_0) + \boldsymbol{e}_k, \tag{9}$$

where

$$A_k(\boldsymbol{x}) = \frac{\partial \boldsymbol{\theta}_k(\boldsymbol{x})}{\partial \boldsymbol{x}} \tag{10}$$

is the usual 2×2 matrix of partial derivatives of $\boldsymbol{\theta}_k(\boldsymbol{x})$. Then, stacking the n, 2×1 wave-number vectors and minimizing the weighted sum of squared errors can be done by sucessively estimating $\boldsymbol{\beta} = \boldsymbol{x} - \boldsymbol{x}_0$. This leads to

$$\hat{\boldsymbol{x}} = \hat{\boldsymbol{x}}_0 + C^{-1}(\boldsymbol{x}_0) \sum_{k=1}^{n} A_k(\boldsymbol{x}_0)' \, \Sigma_k^{-1} [\hat{\boldsymbol{\theta}}_k - \boldsymbol{\theta}_k(\boldsymbol{x}_0)], \tag{11}$$

where

$$C(\boldsymbol{x}_0) = \sum_{k=1}^{n} A_k(\boldsymbol{x}_0)' \; \Sigma_k^{-1} A_k(\boldsymbol{x}_0). \tag{12}$$

It follows that the approximate covariance matrix of the final estimator is

$$\text{cov } \hat{\boldsymbol{x}} = \sigma^2 C^{-1}(\hat{\boldsymbol{x}}). \tag{13}$$

Equations (10) and (11) exhibit the *fusion estimators* at each stage as pooled estimators over the n arrays as long as the variances are known. We may also develop a confidence ellipse for the fusion estimators under assumptions (A), (B) and (C) mentioned earlier.

(A) **Variance Known:** We may assume that the variance σ^2 is known, either from the statistical variances of the computed wave-number estimators or from a combination of factors including the statistical wave-number variances. In this case, the generalization of the usual chi-squared ellipse considered by Evernden (1969) can be computed from the fact that

$$\big(\boldsymbol{x} - \hat{\boldsymbol{x}}\big)' C(\hat{\boldsymbol{x}}) \big(\boldsymbol{x} - \hat{\boldsymbol{x}}\big) \sim \sigma^2 \chi_2^2, \tag{14}$$

where $\sim$ denotes *is distributed as* and χ_2^2 denotes a chi-squared distribution with 2 degrees of freedom. Note that the statistical uncertainty of the wave-number estimators is already in the matrix Σ_k so that a plausible estimator for σ^2 in the absence of other factors might by unity.

(B) **Variance Unknown:** If variances are known only up to the constant σ^2, it must be estimated. are completely unknown and must be determined from the small-array data. For the Gaussian case, the maximum likelihood estimator is proportional to the unbiased estimator

$$s^2 = \frac{1}{2(n-1)} \sum_{k=1}^{n} \big(\hat{\boldsymbol{\theta}}_k - \boldsymbol{\theta}_k(\hat{\boldsymbol{x}})\big)' \; \Sigma_k^{-1} \big(\hat{\boldsymbol{\theta}}_k - \boldsymbol{\theta}_k(\hat{\boldsymbol{x}})\big). \tag{15}$$

This case, originally considered in Flinn(1965), leads to a confidence interval based on the F-distribution, namely

$$\big(\boldsymbol{x} - \hat{\boldsymbol{x}}\big)' C(\hat{\boldsymbol{x}}) \big(\boldsymbol{x} - \hat{\boldsymbol{x}}\big) \sim 2 s^2 F_{2,2(n-1)}, \tag{16}$$

where $F_{2,2(n-1)}$ denotes the F-distribution with 2 and $2(n-1)$ degrees of freedom.

(C) **Variance Subject to Prior Distribution:** It is often the case that it is unrealistic to assume that the variance is known exactly because (14) becomes too small. For a small number of arrays, the ellipse based on the F-statistic (16) is often much too large. A useful compromise, introduced by Jordan and Sverdrup (1981)and continued by Bratt and Bache (1988), is to quantify the initial uncertainty about σ^2 by assigning it a prior distribution with density function $\pi(\sigma^2)$. It is convenient to use the inverted chi-squared distribution with parameters m, representing the equivalent sample size embodied in the prior information and σ_0^2, representing a prior centering value for the variance. For the form of the density function, see Anderson (1984). Figure 2 plots the density function for the standard deviation σ for $\sigma_0 = .02$ and $m = 10, 30$. We note that the two values put the standard deviation between .01 and .05 for $m = 10$ and between .015 and .03 for $m = 30$ For a fully Bayesian approach, we assume a non-informative prior on $(-\infty < x_1, x_2 < \infty)$ for the location $\boldsymbol{x}$ and compute the posterior distribution,

given the wave-number observations, as a bivariate t-distribution with 2 and $2(n-1)+m$ degrees of freedom. The posterior estimator for the variance is

$$\sigma'^2 = \frac{2(n-1)s^2 + m\sigma_0^2}{2(n-1)+m} \tag{17}$$

implying that the best approach is simply to pool the initial variance σ_0^2 and the sample variance s^2, weighted by their degrees of freedom. The quadratic form involving the location vector $\boldsymbol{x}$ in the multivariate t has an F-distribution, making the 95% posterior probability ellipse for the location expressible as

$$(\boldsymbol{x}-\hat{\boldsymbol{x}})'C(\hat{\boldsymbol{x}})(\boldsymbol{x}-\hat{\boldsymbol{x}}) \sim 2\sigma'^2 F_{2,2(n-1)+m} \tag{18}$$

It is interesting that the form of the posterior probability ellipse (18) is similar to (16) but will be tighter because of the additional degrees of freedom for the F-statistic. Hence, the Bayesian solution represents a compromise between (14) and (16), the methods of (A) and (B).

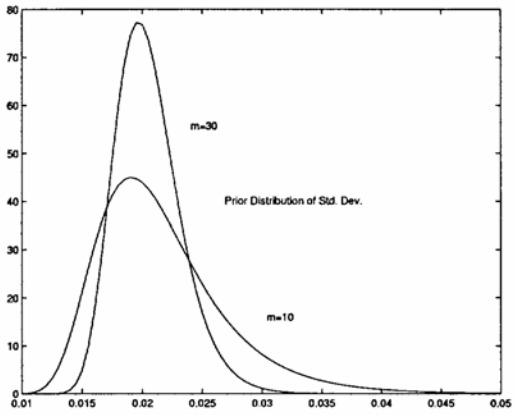


Figure 2: Possible prior distributions for standard deviation of wavenumber estimates

Preliminary Data Analysis

We illustrate some of the potential of the equations derived in the previous section with the contrived array given in Figure 1. We consider two possible configurations of recording arrays, namely all three arrays recording or only the two arrays centered at $\boldsymbol{c}_1 = (0,0)'$ and $\boldsymbol{c}_3 = (0,-1000)'$ recording. This gives a comparison between a wider and more narrow aperture.

The known location of the event in question was taken to be $\boldsymbol{x} = (-2360, -2360)$, as shown in Figure 1. The wavenumber estimates were simulated by computing $\boldsymbol{\theta}_k$ form (3) and adding random noise, according to (5), with the covariance matrix as computed from (8) . The array was assumed to have $N = 4$ elements arranged in a triangle with 1 km sides and a center element. The signal to noise ratio was taken as 3 and the degrees of freedom as $L = 17$. Locations were computed using the random inputs and a covariance matrix computed from (8). Ten Gauss-Newton iterations were performed using the approach in (9)-(12)

The overall performance of subsets of arrays recording various events within this region is being studied using simulated data and reasonable expected performance parameters for infrasonic arrays

Finally, it has been found that the locations are susceptible to perturbations in the derivatives involved in the nonlinear methodology implied by Equations (9)-(12). The Bayesian approach may be helpful in this context. Note that, in the Bayesian approach, we assume that $\hat{\boldsymbol{\theta}}_k$ is normally distributed with mean $\boldsymbol{\theta}_k(\boldsymbol{x})$ where the distribution is conditional on $\boldsymbol{x}$ and σ^2, which are jointly distributed as a uniform and inverted chi-squared distribution respectively. The posterior distribution of the location $\boldsymbol{x}$, conditional on the data $\hat{\boldsymbol{\theta}}$ will be of the form

$$P(\boldsymbol{x}|\hat{\boldsymbol{\theta}}_1, \ldots, \hat{\boldsymbol{\theta}}_n) \propto [Q(\boldsymbol{x})]^{-(m+2n)/2} \tag{19}$$

where

$$Q(\boldsymbol{x}) = \sum_{k=1}^{n} \left(\hat{\boldsymbol{\theta}}_k - \boldsymbol{\theta}_k(\boldsymbol{x})\right)' \Sigma_k^{-1} \left(\hat{\boldsymbol{\theta}}_k - \boldsymbol{\theta}_k(\boldsymbol{x})\right) \tag{20}$$

Then, whether (19) is regarded as a posterior distribution in the Bayesian sense or an integrated likelihood, in the sense of Berger et al (1999), we seek $\hat{x}$ as the minimizer of the quadratic form $Q(\boldsymbol{x})$. This is exactly the objective function considered in the conventional approach using (11). Expanding $Q(\boldsymbol{x})$ about the resulting minimizer $\hat{\boldsymbol{x}}$ leads to the same solution. However, it may be possible to develop a derivative-free approach to treating the nonlinearity of $\hat{\boldsymbol{\theta}}_k(\boldsymbol{x})$ using resampling techniques and we are looking at this possibility in the sequel.

to get the final estimated locations, which turned out to be $\hat{x} = (-2330, -2344)'$ for the full array and $\hat{x} = (-2233, -2282)'$ for the reduced array.

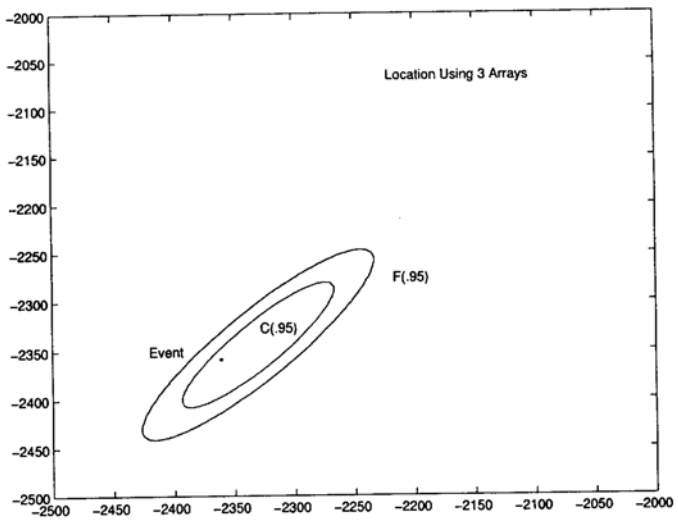


Figure 3: Location of hypothetical event at (-2366,-2366) using all three arrays in Figure 1

Figures 3 and 4 show the confidence ellipses, computed by methods (A) and (B), with the smaller ellipse being the chi-squared ellipse with known variance. Depending on the prior assumptions as to the distribution of the variance, the Bayesian posterior probability ellipse would like somewhere between the chi-squared and F ellipses. The contrived example gives an idea as to the relative sizes of the ellipses expected under different variance assumptions and under the different array configurations. Note that the case where only two arrays recorded gives a much larger ellipse and that both ellipses reflect the fact that the observing arrays had a relatively narrow aperture (30 degrees for $n = 3$ and 15 degrees for $n = 2$).

CONCLUSIONS AND RECOMMENDATIONS

The detection and location of events depends on a number of parameters that can be varied to develop plausible performance measures for different configurations of recording arrays and event locations . Optimum detection and estimation of wave-number parameters, including velocity and azimuth, and the uncertainty of such estimators has been covered during the first year of this contract and appears in Shumway et al (1999). In the present phase of the study , we have developed expressions for the location and its uncertainty using an optimum fusion of wave-number parameters from an arbitrary configuration of recording arrays. These estimators and uncertainty regions, given in the previous section, allow us to compute the expected performance as a function of the configurations of both the small recording arrays and the geometry of the multiple arrays recording the event.

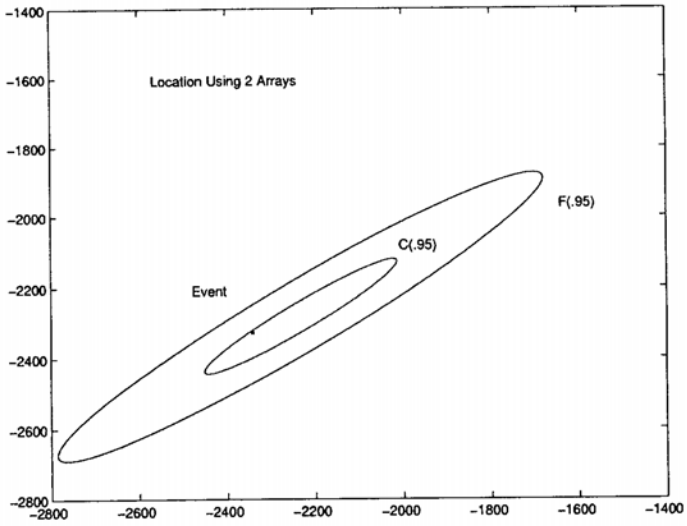


Figure 4: Location of hypothetical event at (-2366,-2366) using two arrays (0,0) and (0,-1000) Figure 1

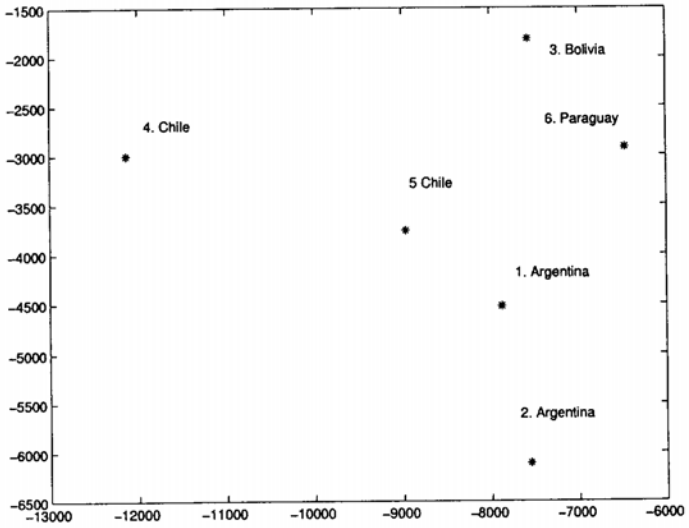


Figure 5: A subset of infrasonic arrays planned for the Prototype International Data Center

However, our primary focus is to characterize the location performance of combinations of infrasonic arrays in the PIDC network. Figure 5 shows a small area and the locations of arrays planned for that area.

REFERENCES

Anderson, T.W. (1984). *An Introduction to Multivariate Statistical Analysis.* New York: Wiley.

Berger, J.O, B. Liseo and R.L. Wolpert (1999). Integrated likelihood methods for eliminating nuisance parameters. *Statistical Science*, **14**, 1-28.

Bratt, S.R. and T.C. Bache (1988). Locating events with a sparse network of regional arrays. *Bull. Seismolog. Soc. Amer*, **78**, 780-798.

Evernden, J.F. (1969). Precision of epicenters obtained by small numbers of world-wide stations. *Bull Seismolog. Soc. Amer.*, **59**, 1365-1398.

Flinn, E.A. (1965). Confidence regions and error determinations for seismic event location. *Rev. Geophys.*, **3**, 157-185.

Jordan, T.H. and K.A. Sverdrup (1981). Teleseismic location techniques and their application to earthquake clusters in the South-Central Pacific, *Bull Seismolog. Soc. Amer*, **71**, 1105-1130.

Shumway, R.H., S.E. Kim and R.R. Blandford (1999). Nonlinear estimation for time series observed on arrays. Chapter 7, Ghosh ed. *Asymptotics, Nonparametrics and Time Series*, 227-258. New York: Marcel Dekker.

Shumway, R.H. and S.E. Kim (1998). Detection and estimation on small infrasonic arrays. In *Proceedings of 20th Annual Seismic Research Symposium on Monitoring a Comprehensive Test Ban Treaty (CTBT)*, ed. J. Fantroy D. Heatley, J. Warren, F. Chavez and C. Meade, Dept. of Defense, Nuclear Treaty Programs and U.S. Dept. of Energy, Office of Nonproliferation and National Security.

INFRASOUND SCALING AND ATTENUATION RELATIONS FROM SOVIET EXPLOSION DATA AND INSTRUMENT DESIGN CRITERIA FROM EXPERIMENTS AND SIMULATIONS

Jeffry L. Stevens, David A. Adams, G. Eli Baker, Heming Xu, and John R. Murphy,
Maxwell Technologies, Systems Division
Igor Divnov, V. N. Bourchik, and Ivan Kitov, Institute for the Dynamics of the Geospheres, Moscow, Russia

Sponsored by U. S. Department of Defense
Defense Threat Reduction Agency
Contract No. DSWA01-97-C-0129

ABSTRACT

This project has two distinct parts:

1. modeling of infrasound signals from atmospheric explosions and evaluation of International Monitoring System network performance using data from historic Russian nuclear tests and other infrasound data sources; and
2. analysis of infrasound instrumentation through a program of experimentation and theoretical modeling.

The Institute for the Dynamics of the Geospheres (IDG) in Moscow, Russia, has an archive of infrasound recordings from Soviet atmospheric nuclear tests that were conducted in 1957 and 1961, and has recently digitized the highest quality records from this data set. We have measured the infrasound signals from these records and compared them with previously developed scaling and attenuation relations. We find that the data are in best agreement with a scaling and attenuation relation developed by Los Alamos National Laboratory (LANL) which can be written as

$$\log P = 3.37 + 0.68 \log W - 1.36 \log R$$

where P is zero to peak pressure amplitude in Pascals, W is the yield in kilotons, and R is the source-to-receiver distance in kilometers. We use the scaling relations to define an infrasound magnitude, and to estimate the detection capability of the International Monitoring System (IMS) being developed as part of the Comprehensive Nuclear-Test-Ban Treaty (CTBT). Network capability is predicted using the network simulation programs NetSim and XNICE. The detection threshold for the proposed 60-station IMS network is estimated to be slightly higher than the design goal of 1 kT required by the CTBT.

We have developed the capability to numerically simulate the response to infrasound signals and a variety of noise models, of an arbitrary arrangement of porous hoses or of pipes with acoustic inlets. We performed experiments to assess different physical models of signal propagation in a cylindrical conduit to determine an appropriate basis for the model. The experiments also provide data for comparison with simulation results. We have run a series of simulations to assess the effect of different parameters on signal propagation, and to assess the performance of different instrument configurations in improving signal-to-noise ratios.

Key Words: infrasound, scaling relation, attenuation, atmospheric explosion, instrument

OBJECTIVE

The objective of this project is to develop a better understanding of infrasound excitation, propagation, and recording in order to be able to predict the capability of the IMS network to detect and identify atmospheric explosions. To accomplish this, we are gathering a data set of infrasound recordings from historical Soviet explosions, modeling these data and using them to develop improved scaling and attenuation relations. In addition, we are using experimental and numerical methods to model the response of infrasound recording instrumentation.

RESEARCH ACCOMPLISHED

Part 1: Infrasound scaling and attenuation relations and IMS detection capability

The International Monitoring System (IMS) required by the Comprehensive Nuclear Test Ban Treaty (CTBT) will include sixty infrasound stations designed to detect atmospheric nuclear explosions. A design requirement is that the system be able to detect and locate explosions as small as one kiloton anywhere in the world. In order to estimate the capability of the infrasound network, it is necessary to be able to predict the amplitude of an infrasound signal at any location, and to evaluate whether the signal would be detectable above noise levels. In this paper, we use a data set of infrasound recordings from a set of Soviet explosions to put constraints on infrasound scaling relations and to estimate the detection capability of the IMS.

Scaling and attenuation relations are empirical and/or theoretical equations that relate the amplitude and period of infrasound signals to the explosion yield and source to receiver distance. Several different relations have been developed based on theoretical infrasound modeling, and on recordings of atmospheric nuclear and chemical explosions. We examine scaling and attenuation relations from Pierce and Posey (1971), Clauter and Blandford (1998), Whitaker (1995), and a set of relations derived by Russian scientists described by Stevens et al (1998). These scaling relations can be written as:

$\log P = -1.54 + \log W - 0.5 \log(R \sin \Delta)$ Pierce and Posey (1971) (1)

$\log P = 0.92 + 0.5 \log W - 1.47 \log \Delta$ AFTAC (Clauter and Blandford, 1998) (2)

$\log P = 3.37 + 0.68 \log W - 1.36 \log R$ LANL (Whitaker, 1995) (3)

$\log P = 3.00 + 0.33 \log W - \log R$ Russian – Crosswind (4)

$\log P = 3.30 + 0.33 \log W - \log R$ Russian – Downwind (5)

where P is zero to peak pressure in Pascals, W is yield in kilotons, R is distance in kilometers, and Δ is distance in degrees. The LANL relation uses a wind-corrected pressure.

The different scaling relations predict very different detection thresholds. Yield estimates for the threshold pressure level differ by several orders of magnitude, even though each relation was constrained by some infrasound data set. Table 1 shows the calculated yield at a nominal detection threshold of 0.1 Pascal for each of the scaling relations. The most important factor is the exponent in the pressure/yield relation. With the Pierce/Posey relation, which has a yield exponent of 1, pressure drops off much more rapidly with yield than with the other relations leading to a very high threshold level. The 0.33 yield exponent in the Russian relations, however, implies a very slow decrease in pressure with yield and leads to very low threshold levels. The Whitaker and Clauter/Blandford relations, which have yield exponents of 0.68 and 0.5, respectively, predict intermediate threshold levels.

	10	20	30	40	50	60
Clauter/Blandford	0.13	0.97	3.2	7.4	14	24
Whitaker	0.46	1.8	4.2	7.4	11	17
Russia Crosswind	0.0014	0.01	0.037	0.088	0.17	0.30
Russia Downwind	0.0002	0.0014	0.0046	0.011	0.02	0.037
Pierce/Posey	47	93	140	180	220	260

Table 1. Detection capability for a nominal detection threshold of 0.1 Pascal. The table shows yield in kilotons for each scaling relation and source to receiver distances from 10-60 degrees.

Soviet Infrasound Data

The Institute for the Dynamics of the Geospheres (IDG) in Moscow, Russia, has an archive of approximately 300 recordings from 34 Soviet atmospheric nuclear tests that were conducted in 1957 and 1961. 20 of these explosions were located at the Novaya Zemlya test site, 12 at Semipalatinsk, and 2 at Kapoustin Yar (see Figure 1). Of these, 178 recordings from 15 of the tests recorded at stations from 1000 to 5000 km were found to be of adequate quality for analysis. The yields of these tests range from 8 KT to 58 MT. IDG has digitized 65 of these waveforms to date. The data set includes one high altitude explosion and the largest atmospheric explosion ever detonated. The explosions corresponding to this data set are listed in Table 2. The number of records listed in the table is the number of records digitized. There are additional waveforms from several of the explosions that will be digitized at a later date. Paths to 17 recording stations are also shown on Figure 1.

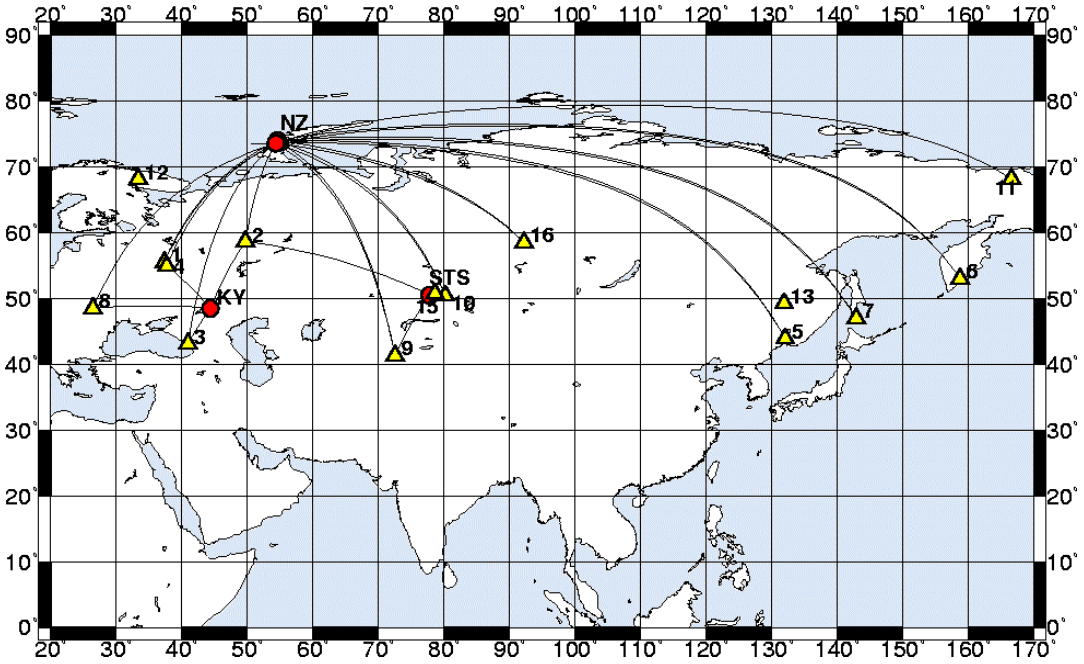


Figure 1. Stations recording infrasound signals from atmospheric explosions at three Soviet nuclear test sites Semipalatinsk (STS), Kapoustin Yar (KY), and Novaya Zemlya (NZ).

Test Site	Explosion Number	Date	Time (Moscow)	Latitude	Longitude	Height of Burst (m)	Yield (KT)	Number of Records
STS	088	09/04/61	08:00:27	50.45	77.74	730	7-9	2
STS	089	09/05/61	09:00:05	50.45	77.74	710	12-16	3
KY	091	09/06/61		48.45	44.30	20000	10-11	6
NZ	095	09/10/61	12:00:14	73.52	54.30	2500	2400	23
NZ	116	10/02/61	13:30:50	73.92	54.55		250-330	13
NZ	125	10/20/61	11:07:03	73.52	54.30		1450	16
NZ	133	10/30/61	11:33:27	73.52	54.30	3500	58000	2

Table 2. Soviet atmospheric nuclear explosions and the number of records for each event that are currently being digitized. STS is the Semipalatinsk test site, KY is Kapoustin Yar, and NZ is Novaya Zemlya.

Measurement of Russian data

All of the Russian data were carefully measured in a consistent manner. The data were first filtered to remove long and short period noise outside the frequency band of the data. A Butterworth filter was used with corner frequencies of .01 and .2 Hz for events with yield less than 100 kilotons, .002 and .1 Hz for events with yields between 100 kilotons and 2 megatons, and .001 and .1 Hz for events with yield greater than 2 megatons. The amplitude and period were measured as half the maximum peak to peak amplitude and twice the time difference between the peak and trough, respectively. Measurements were made on both the acoustic wave and the low

frequency Lamb wave if possible. Only data with known instrument responses were measured, and a digital correction for the instrument response was made at the observed period.

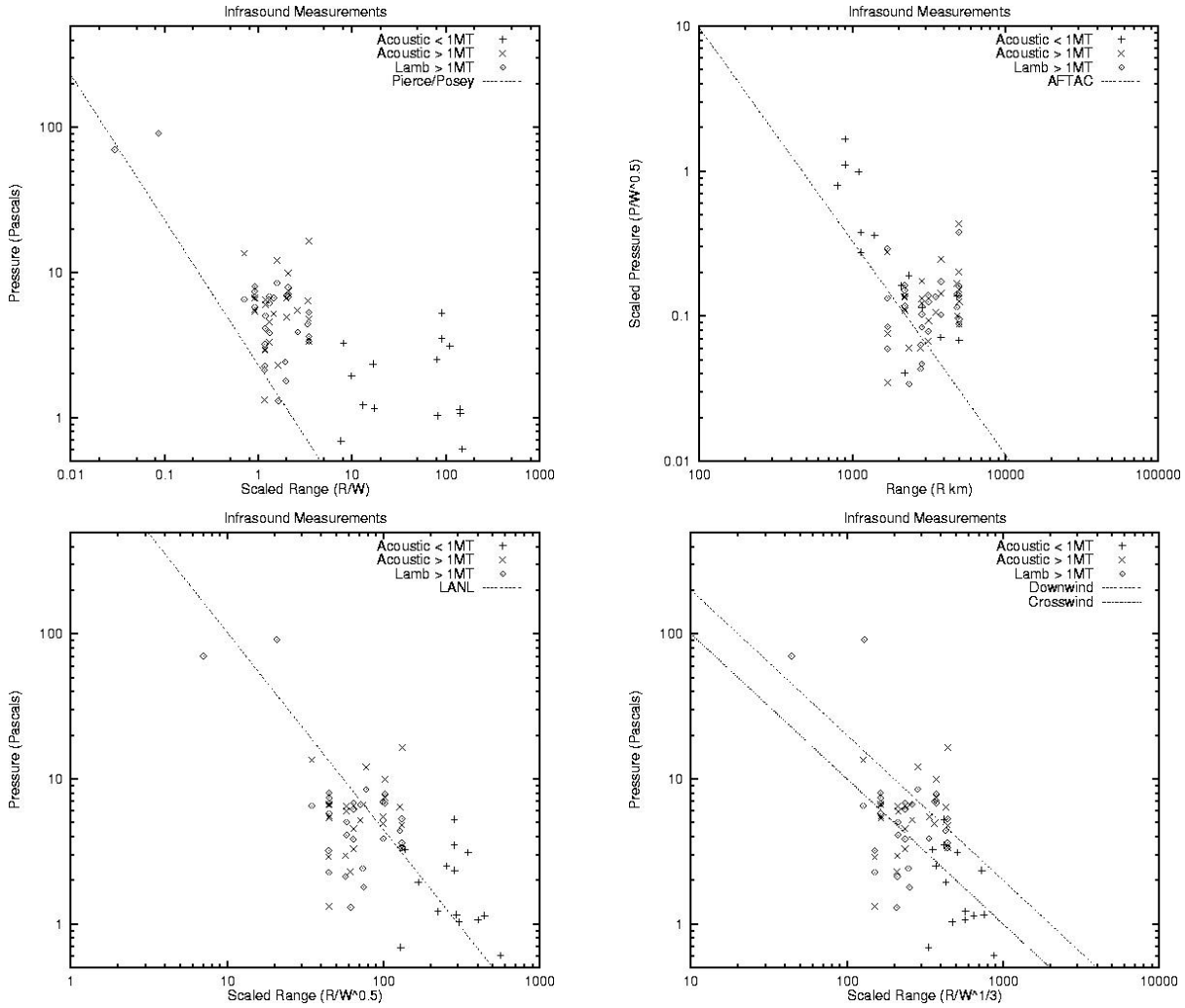


Figure 2. Comparison of Russian data with scaling relations. Top left is the Pierce/Posey relation equation 1, top right the AFTAC relation (Clauter and Blandford) equation 2, bottom left is the LANL relation (Whitaker) equation 3, and bottom right are the Russian relations equations 4 and 5.

Figure 2 shows a comparison between pressure measurements made from the Russian data and equations 1-5. It is not possible to put them all on the same plot because the scaling relations have different functional forms. The AFTAC relation (equation 2) fits the lower yield data and some of the higher yield data quite well. The Pierce/Posey relation (equation 1) is a fairly good fit to the high yield Lamb wave data, but does not fit the acoustic wave data, particularly for the lower yield events. The LANL relation (equation 3) appears to fit the data very well over the entire scaled range, although there is considerable scatter about the line. The pressure measurements have not been wind corrected since we do not have information about wind conditions at the time of the tests. The Russian relations (equations 4-5) also fit the data fairly well with the crosswind equations matching the lower amplitude data and the downwind equations matching the higher amplitude data, however the observed data falls below the predicted curves for larger scaled ranges, and the data points for the largest yield events are well above the curve, while the lower yield events lie below the curve. This suggests that the pressure/yield slope of 0.33 is too small.

The LANL relation has recently been adopted as the basis for an infrasound magnitude by the International Data Center (IDC) (Brown, 1999). The magnitude equation is $M_i = \log_{10} P + 136 \log_{10} R - 0019\ \nu$ where ν is stratospheric wind velocity in m/sec. Infrasound magnitudes for the Russian data set (without wind correction),

were calculated for the seven Soviet explosions. In calculating these magnitudes, we used the largest of the Lamb and acoustic arrival if both were measured. Figure 3 shows M_i plotted vs. yield. Also shown is the LANL relation, equation 3, rewritten as a magnitude/yield relation $M_i = 068 \log W + 337$. This equation fits the data over this very wide yield range very well. The exception is the high altitude explosion at Kapoustin Yar which lies above the curve by about 0.5 magnitude units.

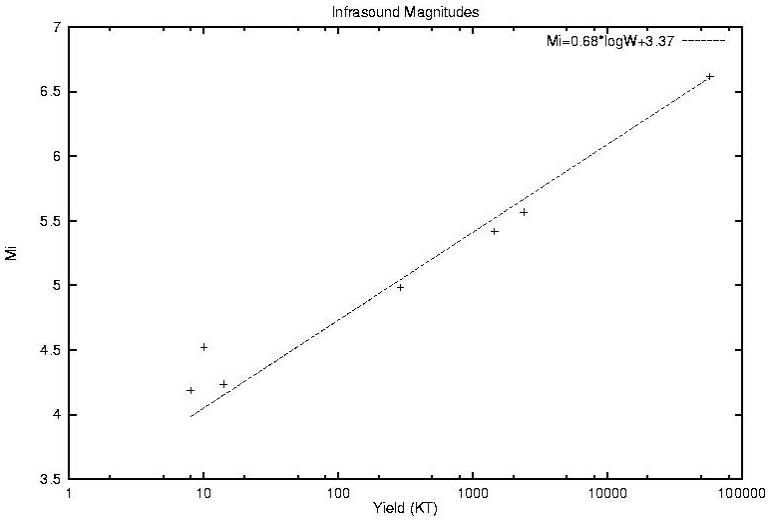


Figure 3. Infrasound magnitude plotted vs. yield for seven Soviet explosions.

Spectral Measurements

Some additional insight into the scaling laws can be obtained by examining the spectra of arrivals with different yields at the same station. Station 7, at Yuzno-Sakhalinsk, recorded four atmospheric explosions with yields of 250, 1450, 2400, and 58000 kilotons. The spectra of these four arrivals are shown in Figure 4. The shape of the spectra change dramatically over this yield range, with much more low frequency energy at higher yields.

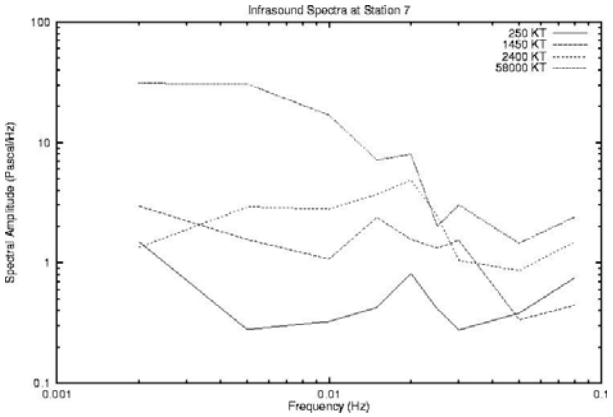


Figure 4. Spectra of four infrasound signals recorded at station 7 with yields of 250, 1450, 2400, and 58000 kilotons.

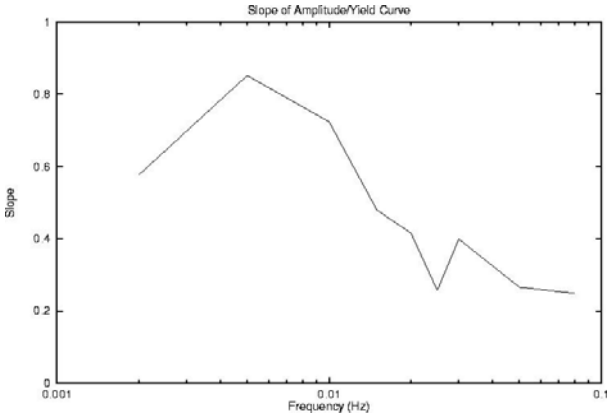


Figure 5. The slope of the log amplitude vs. log yield curve plotted as a function of frequency.

Figure 5 shows the slope of the amplitude vs. yield curve plotted as a function of frequency. This figure shows that the slope of the amplitude/yield curve is strongly frequency dependent, and that the slope is close to 1, as in the Pierce/Posey model, at very low frequencies, but declines to approximately 1/3, as in the Russian scaling laws, at higher frequencies.

Network Detection Simulations

In order to predict the performance of the proposed 60 station IMS infrasound network, we modified the network simulation program NetSim (Sereno et al., 1990) to include the models of infrasound propagation described in equations 10-14. NetSim uses these equations to calculate the pressures as a function of yield and range. These are used together with station locations, a noise model, a minimum signal to noise ratio for reliable measurement, and the number of stations required for a signal to be reported, to determine the network detection threshold as a function of position on the earth. We have calculated detection thresholds for the proposed IMS network under the following assumptions:

1. Noise estimates were taken from Blandford and Clauter (1995). The amplitude of background noise is log normally distributed with log mean value of –1.1 (Pascals) and log standard deviation of 0.33. The noise distribution is taken to be geographically uniform.
2. The minimum signal to noise ratio for detection is 2.
3. Two stations detect infrasound signals at a 90% confidence level.
4. Four element infrasound arrays increase signal to noise ratio by a factor of 2.
5. Propagation error has a log standard deviation in log signal of 0.2.

Detection threshold maps were calculated for the AFTAC and LANL scaling relations. We did not calculate the detection threshold for the Pierce Posey or Russian models because they are clearly unrealistic for yields near the detection threshold. The results are shown in Figures 6-7. For the LANL models, the detection threshold is predicted to be between 0.7 and 3.2 kilotons depending on location. For the AFTAC model, the detection threshold is between 0.3 and 2.3 kilotons. Since other factors are uniform in these simulations, the variations in threshold level are determined by station coverage. These scaling relations with the conditions listed above predict, therefore, that the infrasound detection threshold for the IMS network is somewhat higher than the design goal of one kiloton, and that explosions near this limit could escape detection at some locations.

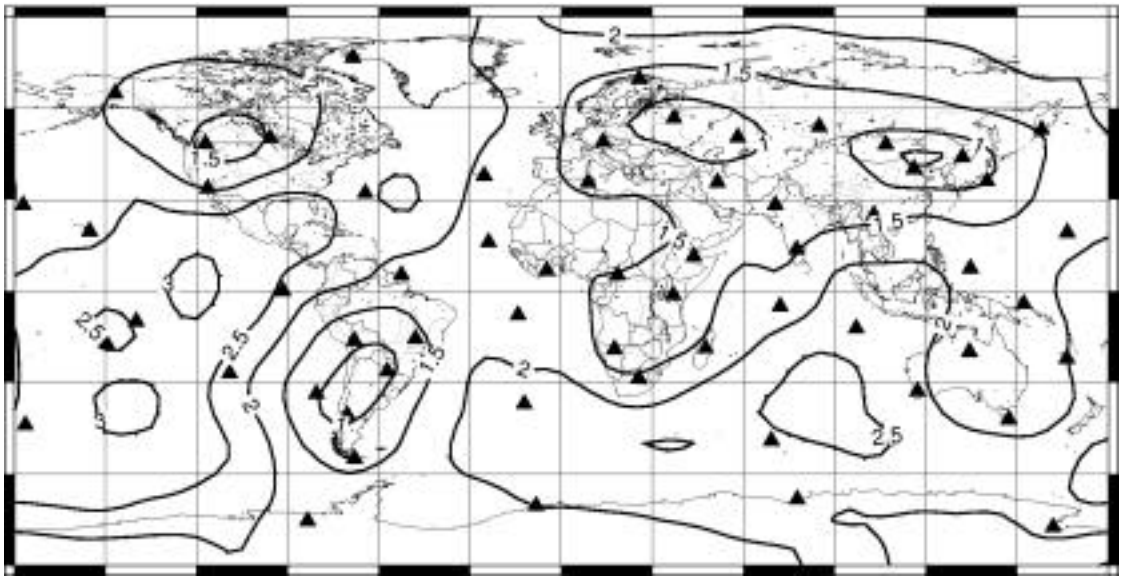


Figure 6. Contours showing detection thresholds with a 90% level of confidence for detection at 2 infrasound stations. The intervals are logarithmically spaced with labels in kilotons. The model is from Whitaker (1995).

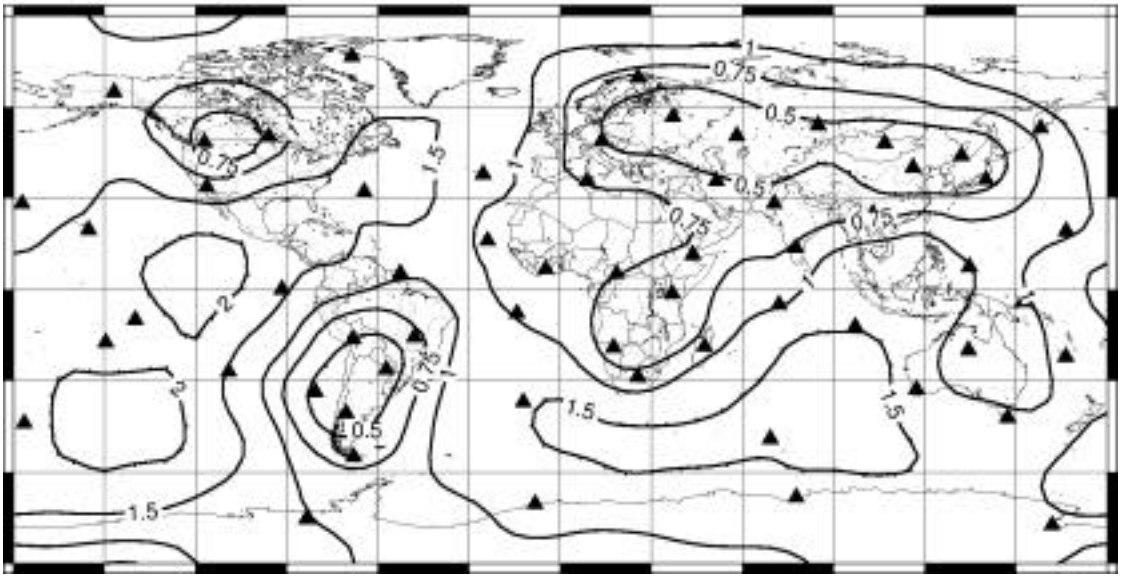


Figure 7. Contours showing detection thresholds with a 90% confidence level for detection at 2 infrasound stations. The intervals are logarithmically spaced with labels in kilotons. The model is from Clauter and Blandford (1998).

Part 2: Infrasound instrumentation research

The goal of the instrumentation work is the accurate simulation of the response of any configuration of pipes and inlets used as a spatial filter for a microbarograph. Such a capability will enable the optimization of instrument designs and the separation of instrument from source and propagation effects. Initial experiments performed to ensure that the simulations have a valid physical basis are described in Stevens et al (1998). Additional experiments are described below. We also describe the numerical method used to perform the simulations, present results of simulations that compare the performance of different configurations, and discuss the remaining experimental and theoretical work that must be performed.

We measured the dispersion of infrasound signals between approximately 0.1 and 10 Hz at amplitudes of 1 to 5 Pascals, the typical range for infrasound signals (Figure 8). These results are consistent with the physical model of acoustic wave propagation in a cylindrical conduit, which provides the basis for our numerical model.

No proposed physical models that we have considered accurately predict attenuation. This lack of a theoretical understanding of the attenuation requires that the model use an empirically determined exponential decay factor for acoustic wave propagation in a cylindrical conduit. Furthermore, to provide meaningful and accurate numerical simulations, the attenuation of each material used to construct spatial filters must be determined empirically.

The numerical simulations use a propagator method, developed and detailed by Burridge (1971), to obtain the pipe response. The flux-pressure vector $\begin{pmatrix} f \\ p \end{pmatrix}$ is propagated through an impermeable section of pipe of length l by

$$\begin{pmatrix} f(x+l) \\ p(x+l) \end{pmatrix} = \begin{pmatrix} \cosh\Gamma l & -\frac{1}{Z_0}\sinh\Gamma l \\ Z_0 \sinh\Gamma l & \cosh\Gamma l \end{pmatrix} \begin{pmatrix} f(x) \\ p(x) \end{pmatrix} = M \begin{pmatrix} f(x) \\ p(x) \end{pmatrix}, \quad (6)$$

where $p(x)e^{i\omega t}$ is a harmonic pressure fluctuation and $f(x)e^{i\omega t}$ is a harmonic volume flux at a distance x from the left end of the pipe. Γ and Z_0 are the propagation constant and characteristic impedance of the pipe, both dependent in a complicated way upon frequency, radius of the pipe, and other variables (Burridge, 1971; Benade, 1939). The resulting flux-pressure vector from an inlet at x with impedance Z_k is propagated by

$$\begin{pmatrix} f(x_+) \\ p(x_+) \end{pmatrix} = \begin{pmatrix} 1 & -\frac{1}{Z_k} \\ 0 & 1 \end{pmatrix} \begin{pmatrix} f(x_-) \\ p(x_-) \end{pmatrix} + \begin{pmatrix} Pe_k / Z_k \\ 0 \end{pmatrix} = N \begin{pmatrix} f(x_-) \\ p(x_-) \end{pmatrix} + \begin{pmatrix} Pe_k / Z_k \\ 0 \end{pmatrix} \tag{7}$$

where, $x_\pm$ are the right and left side of the location x, and Pe is the pressure disturbance at the inlet. Therefore, the flux-pressure vectors at x_1 and x_2, two locations along the pipe, are related by

$$\begin{aligned} \begin{pmatrix} f(x_2) \\ p(x_2) \end{pmatrix} &= M_{Nb+1} \prod_{i=Nb}^{1} N_i M_i \begin{pmatrix} f(x_1) \\ p(x_1) \end{pmatrix} + M_{Nb+1} \left[\begin{pmatrix} Pe_{Nb} / Z_{Nb} \\ 0 \end{pmatrix} + \sum_{j=2}^{Nb} \prod_{i=Nb}^{j} N_i M_i \begin{pmatrix} Pe_{j-1} / Z_{j-1} \\ 0 \end{pmatrix} \right] \\ &= A \begin{pmatrix} f(x_1) \\ p(x_1) \end{pmatrix} + B \end{aligned} \tag{8}$$

where Nb is the number of inlets between x_1 and x_2, the inlets are numbered as 1, 2, …, Nb from x_1 and x_2, N's are the propagator matrices at the inlets, M_1, M_{Nb+1} as defined in equation (6) correspond to the propagator matrices between x_1 and the first inlet and between x_2 and the last inlet, $M_k, k=2,Nb$ are the propagator matrices between the k'th and (k+1)'th inlets, and A and B are the propagator matrices from x_1 and x_2. The method is extended to derive the response of multiple pipe arrays.

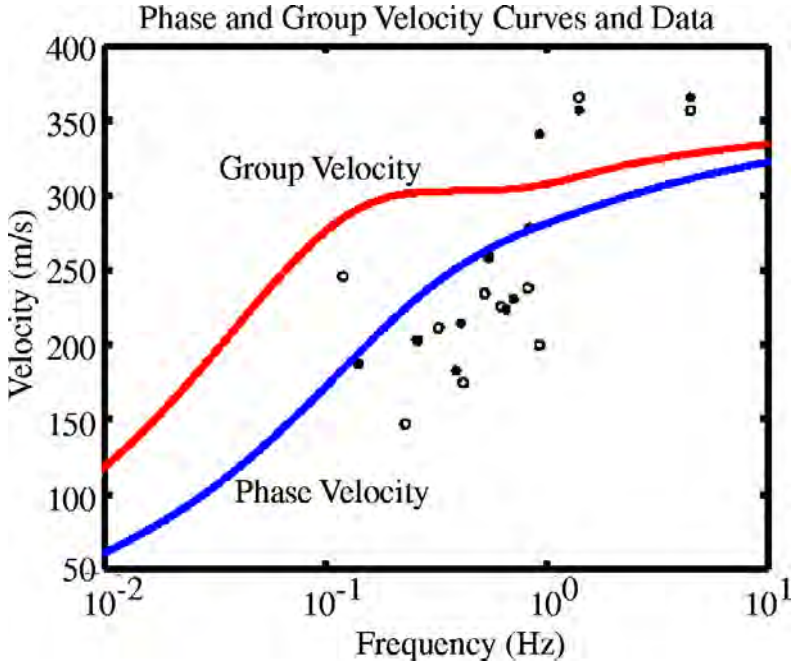


Figure 8: Theoretical dispersion curves for acoustic waves in cylindrical conduits (from Haak and de Wilde, 1998), and group velocity measurements.

Three configurations used to reduce noise interference are considered (Figure 9). One is a simple 20 m radius star system, in which several identical pipes with inlets join at the center. The second is a 30 m star with the inner 10 m of each pipe impermeable, to reduce the effect of spatially correlated noise. The last is a hexagonal system, in which the 20 m transverse pipes are composed of pipes with inlets and the 20 m radial pipes are impermeable.

For the star receiver system, we compute the pressure response for a few cases. Figure 10 (left) shows that the response to a vertically propagating signal varies with the length of the pipe. The number of inlets in each pipe is held constant. The response is nearly flat at lower frequency, decreases in the intermediate frequency range, but exhibits peaks corresponding to the resonance frequencies of the pipe. The decay at higher frequencies is associated with the increase of the propagation constant in the pipe. To avoid resonant peaks in the frequencies of interest, the pipe length will be limited. For CTBT monitoring from 0.01 to 4 Hz, the maximum length is approximately 30 meters. For pipes of the same length the response varies with the number of the inlets, as shown in Figure 10 (right) for the case of vertical incidence. Using more inlets flattens the response curve at

higher frequencies and thus increases the bandwidth. At still higher frequency the signal decays rapidly and is interfered with by resonance peaks. The response is similar for the hexagonal configuration.

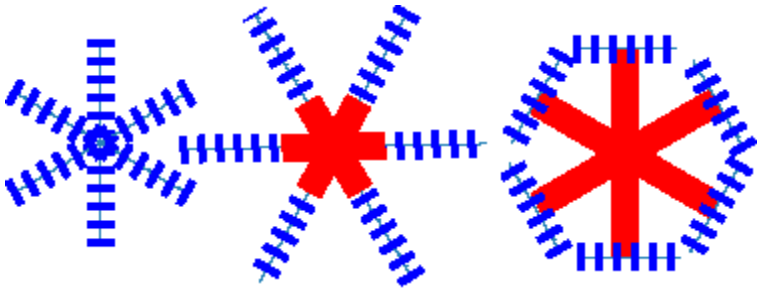


Figure 9: Dashed lines represent pipes with 100 acoustic ohm inlets at 1 meter spacing. Solid lines represent impermeable pipes. The pressure is measured in the center of each configuration.

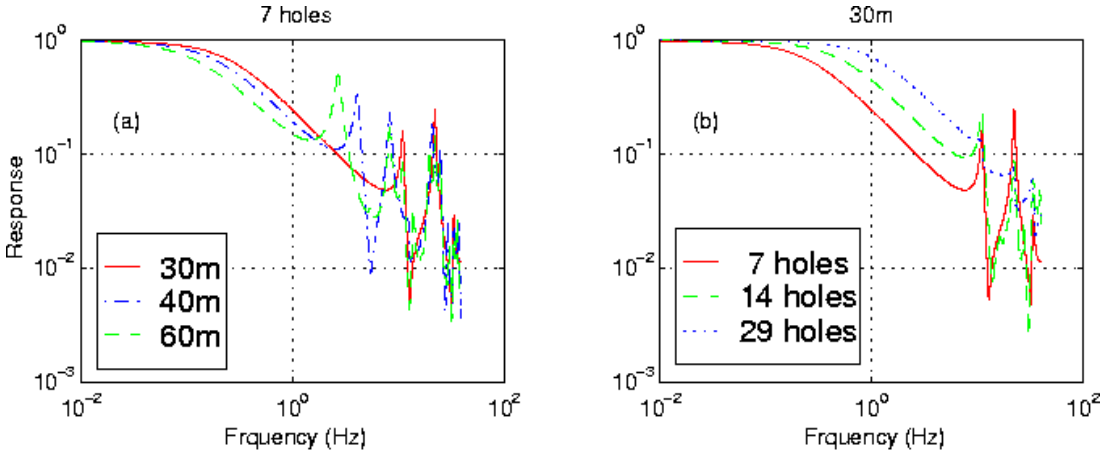


Figure 10: Response of star pipe systems of different lengths (left) and number of inlets (right).

The advantage one configuration has over another will likely occur in its noise suppression characteristics. The permeable pipes are in different locations relative to the center of the two configurations, and the noise, mainly from wind, may correlate over some length, so the systems examined may exhibit different noise reduction capabilities. This may be offset by the greater loss in signal amplitude for configurations in which the signal must propagate further. We use Gaussian noise with 0, 2, 5, and 10 meter correlation lengths to simulate infrasonic noise and assess noise reduction, which is much greater for less well-correlated noise for each configuration (e.g. Figure 11, left). There is little enhancement of S/N by any of the configurations, for 10 and 5 m correlation length noise, while for the uncorrelated and 2 m correlation length noise, there is significant improvement in S/N, and better performance by both of the star configurations.

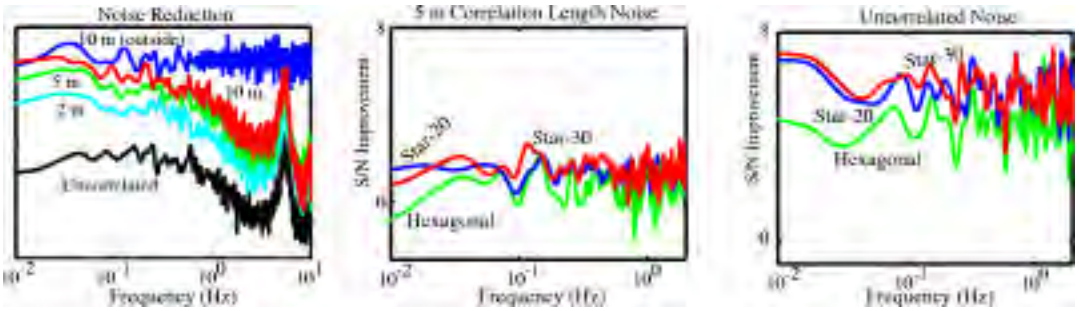


Figure 11: At left are noise spectra before (upper spectral line) and after spatial filtering by a 30 m star configuration (Figure 9, center) for 10m, 5m , 2m, and uncorrelated noise (successively lower spectral lines). Input frequency spectra are flat and the same amplitude for each noise type. The increase in S/N for a vertically incident plane wave and 5 m correlation length noise (center), and uncorrelated noise (right), are shown for different configurations.

CONCLUSIONS AND RECOMMENDATIONS

In the analysis above, we used a data set of infrasound waveforms from Soviet atmospheric tests ranging in yield from 8 kilotons to 58 megatons to place constraints on infrasound scaling relations and to estimate the detection threshold of the future International Monitoring System. Analysis of 42 waveforms shows that measured pressures are consistent with yield and attenuation scaling relations developed at LANL for HE tests, and also fairly consistent with a scaling relation developed by AFTAC. The scaling relations developed by Pierce and Posey are consistent with Lamb waves from very large explosions, but not with acoustic waves from smaller explosions.

The network simulation results indicate that the detection threshold of the future IMS infrasound network may be somewhat higher than the one-kiloton design goal. This result depends, of course, on a number of assumptions that went into the simulations. The most important of these is the background noise level. While we have used the same noise level worldwide, clearly the noise levels will vary depending on location. Blandford et al (1995) made threshold estimates using station dependent noise estimates derived from average wind values and found significantly lower threshold levels. The accuracy of the simulation could be improved considerably by using noise measurements gathered from each infrasound station location, a process which is still in its early stages. We also made the assumptions that a four element array leads to a factor of two improvement in signal/noise ratio, and that a signal can be identified with a signal to noise ratio of 2. Both of these assumptions are probably optimistic. Improvements could also be made in the signal modeling, particularly by including stratospheric winds, which will have the effect of improving detection in some directions and degrading it in others. Excitation and propagation, however, appear to be modeled quite well by the LANL relation, equation 3, over a wide range of explosion yields and distance ranges, and this relation can be used to predict infrasound amplitudes in network simulations.

Our experimental work confirms that acoustic waves in a cylindrical conduit provide an appropriate physical basis for numerical simulations of infrasound instrument response. We have developed an accurate and computationally efficient numerical model, which permits determination of the response of any pipe configuration. Three configurations tested show distinctly different S/N performance. Determination and incorporation of realistic noise models and empirical measures of attenuation for the particular materials used will be necessary to ensure that the simulations are relevant to instruments that will be deployed as part of the IMS. This will be the focus of future instrumentation efforts.

REFERENCES

Benade, A. H., 1968, On the propagation of sound waves in a cylindrical conduit, *J. Acoust. Soc. Am.*, 2, 616-623.

Blandford, R. R. and D. A. Clauter (1995), "Capability Estimation of Infrasound Networks", AFTAC report.

Blandford, R. R., D. A. Clauter, R. W. Whitaker, and T. Armstrong (1995), "Infrasound Network Options," AFTAC/DOE White Paper presented at VMTF meeting.

Brown, D. J. (1999) "Summary of Infrasound Source Location Meeting: San Diego, November 9-10, 1998, Center for Monitoring Research Technical Report CMR-99/02, January.

Burridge, R., 1971, The acoustics of pipe arrays, *Geophys. J. R. Astroc. Soc.*, 6, 53-69.

Clauter, D. A. and R. R. Blandford (1998), "Capability Modeling of the Proposed International Monitoring System 60-Station Infrasonic Network," proceedings of the Infrasound workshop for CTBT monitoring, Santa Fe, New Mexico, August 25-28, 1997, LANL report number LA-UR-98-56.

Haak, H.W. and G.J. de Wilde (1998), "On the Propagation of Low Frequency Sound Waves in Porous Hoses used in Infrasound Detection Systems, pre-print

Pierce, A. D. and J. W. Posey (1971), "Theory of the Excitation and Propagation of Lamb's Atmospheric Edge Mode from Nuclear Explosions," *Geophys. J. R. astr. Soc.*, **26**, 341-368.

Sereno, T. J., S. R. Bratt, and G. Yee (1990), "NetSim: A computer program for simulating detection and location capability of regional seismic networks," SAIC Annual Technical Report to DARPA, SAIC 90/1163, March.

Stevens, J. L., G. E. Baker, J. R. Murphy, J. Morris, and I. I. Divnov (1998), "Infrasound Excitation and Propagation Research," Proceedings of the 20th Seismic Research Symposium on Monitoring a Comprehensive Test Ban Treaty, 21-23 September, 1998.

Whitaker, R. W. (1995), "Infrasonic Monitoring," proceedings of the 17th annual Seismic Research Symposium in Scottsdale, AZ, September 12-155, 1995, 997-1000.

AN INTRODUCTION TO THE ASCENSION ISLAND SYNERGY EXPERIMENT

Rod Whitaker and Tom Sandoval, Los Alamos National Laboratory

Phil Harben and Donald Rock, Lawrence Livermore National Laboratory

Sponsored by U. S. Department of Energy
Office of Nonproliferation and National Security
Office of Research and Development
Contract No. W-7405-ENG-48

ABSTRACT

Early in the DOE CTBT program, Lawrence Livermore National Laboratory (LLNL) had promoted a synergy experiment wherein data from multiple technologies would be combined, for common events, to demonstrate improvements in derived products over single technology results. The initial plans suggested work off the California coast, but due to a variety of problems (no longer remembered), the focus changed to Ascension Island, which is an IMS infrasound site and one of the hydroacoustic MILS sites. LLNL remains the lead lab for this experiment with LANL providing the infrasound capability.

This presentation will provide an overview of the Ascension Island environment and working conditions. In May of this year, we deployed one three component seismometer and a four element infrasound array in the region known as Butt Crater. During this period, LLNL also made contacts and arrangements to use some of the MILS data for certain events. We will provide good photographic coverage of the sensor sites and other Ascension views as well as provide discussion of some of the finer logistic points that need to be appreciated in working at this location, including data handling.

Key Words:: infrasound, seismic, hydroacoustic, synergy

OBJECTIVE

The objective of the synergy experiment is to demonstrate the utility of multi-technology data in improving the derived information from measured events. Ascension Island, a British territory, is the site of one US Missile Impact Locator System (MILS), a set of hydrophones around the island. It is also a planned infrasound site in the International Monitoring System, thus having two of the three waveform technologies. LLNL proposed deploying a three component seismic sensor and an infrasound array on the island for a one to two year to gather cooperative data, including MILS data, from natural and manmade sources.

RESEARCH ACCOMPLISHED

In March, 1999, personnel from LLNL and LANL went to the island to establish sites for the seismic and infrasound sensors, as well as establish locations for the seismic sensors to be used in the early May air-gun experiment (Harbin et. al., this volume). Arrangements were made with Merlin Communications to provide maintenance/operation support along with transfer of data tapes back to LLNL. We also briefed the Administrator of the island, Mr. R. C. Huxley, on the experiment plan and goals. This visit coincided with the start of the IMS infrasound site survey undertaken by Dr. Michael Hedlin and Chris Say of the University of California San Diego. We assisted them on getting their equipment to the field which allowed examination of several possible sites. With consideration of prevailing winds, logistics and costs, we chose an area in Butt Crater for the synergy deployment.

Figure 1 shows a map of the island, which is dominated by volcanic rock of various types and sizes, with several good examples of cinder cones. Trade winds blow most of the time and finding really quiet sites was not possible. Our experience indicates that Ascension is an excellent candidate for added elements in the future IMS infrasound installation. There is one large peak, Green Mountain, at 2871 ft elevation, and Figure 2 shows a view looking into Butt Crater from part way up Green Mountain. The near equatorial location ensures warm to quite hot temperatures most of the time, and Butt Crater is certainly warm.

In May 1999, LLNL and LANL personnel returned to install the seismic sensor and infrasound array. The four element infrasound array was deployed with nominal 100m interelement separations. This allowed for cost savings through the used of hard cable connections. Power is supplied with solar panels and battery backup. The seismic sensor is close to the infrasound array and in the general area of the IRIS seismic installation. We used Chaparral Physics Model 2 sensors (essentially the same as the former Globe 100C) for the infrasound array and are recording at 20 sps. The three component seismic sensor is a Springnether S-6000 two hertz free period unit, sampling at 250 sps. The seismic sensor was located on a large concrete pad that had been used a cable tie-down for a former radio tower. The pad provided the best possibility for coupling to the rock as it extended to a depth of at least 10 feet.

Figure 3 shows one of the infrasound array elements and gives a view of the terrain at the array site. Figure 4 shows Don Rock at the solar panel pole. The utility box houses the Ref Tek recorder and battery backup. The diagram in Figure 5 gives the layout of the infrasound array and seismic sensor.

CONCLUSIONS AND RECOMMENDATIONS

The deployment was completed as planned, and we now enter the data collection phase. Analysis of the data will begin soon. Ascension may be a site where added elements in the IMS infrasound array will provide improved performance through increased signal to noise.

REFERENCES

Ascension Island has an excellent web site with rather good information on the island and it's history. The web site is: http://www.ascension-island.gov.ac

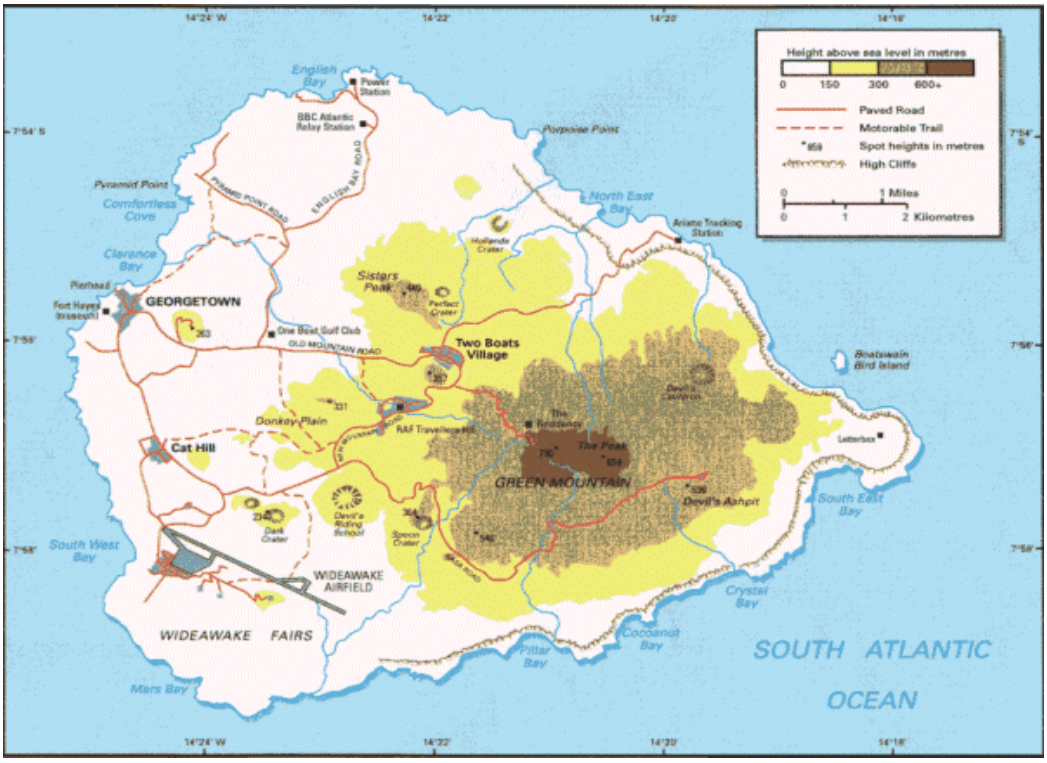


Figure 1: A map of Ascension Island.

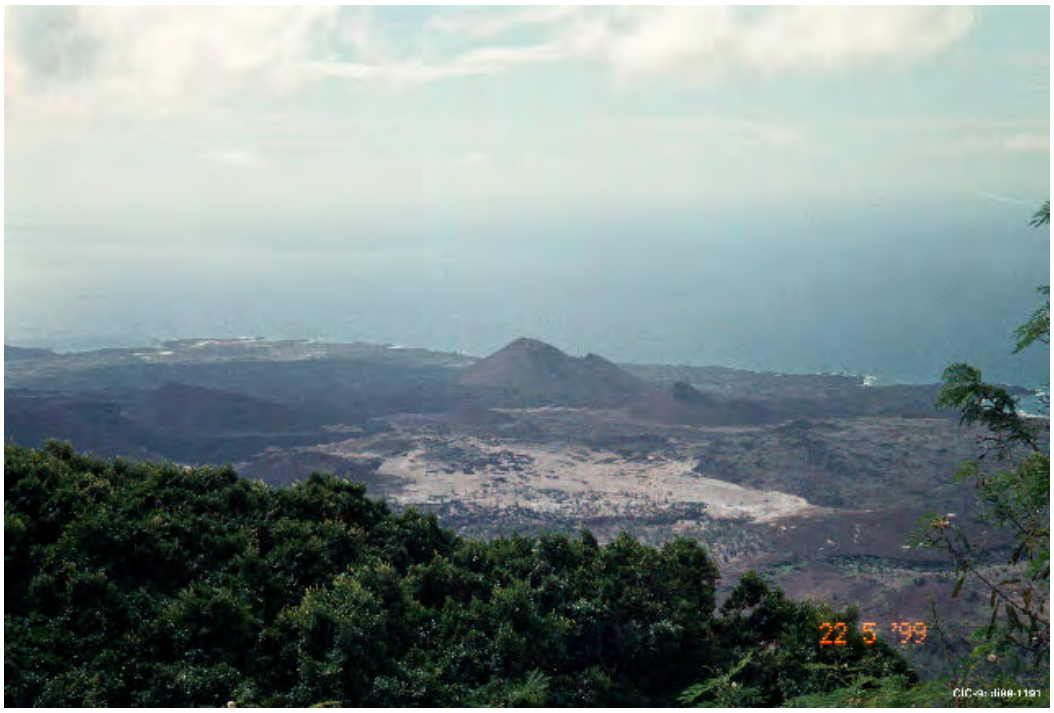


Figure 2: Looking into Butt Crater from midway up Green Mountain. Two cinder cones are clearly visible.

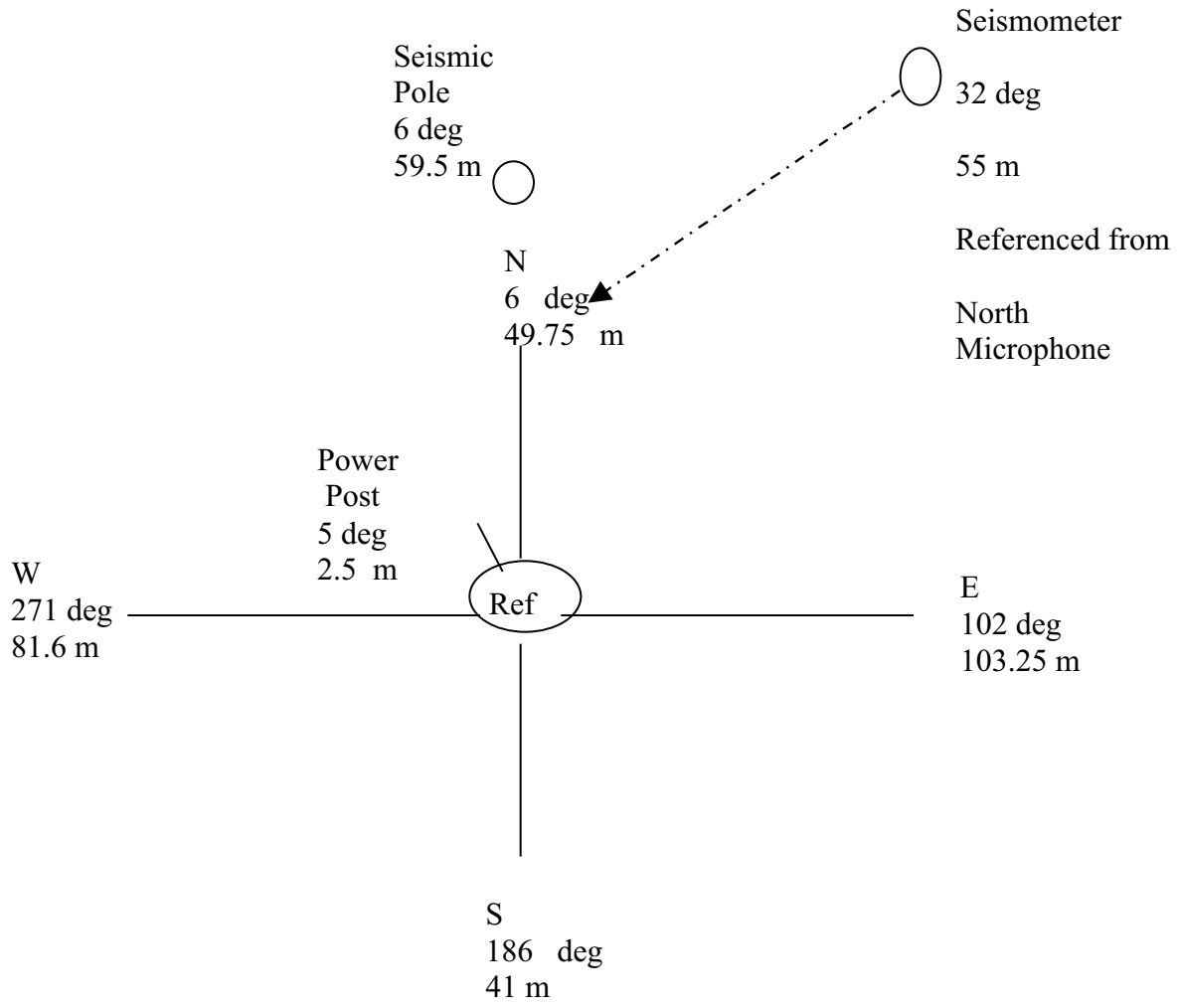


Figure 3: In Butt Crater showing the white microphone cover with the South microphone just to the right. One porous hose is seen just left of center in the foreground.



Figure 4: Don Rock at the solar panel, battery box installation, which supplies power to the infrasound array. It is hotter than it looks, and the wind is blowing.

Figure 5: Schematic layout of infrasound array. Bearings are with respect to magnetic north.



RADIONUCLIDE MONITORING

MEDICAL INDUSTRY INTERFERENCE WITH CTBT MONITORING OF ATMOSPHERIC RADIONUCLIDES

K. M. Foltz Biegalski, S. R. Biegalski, and Dwight L. Williams, Center for Monitoring Research

Sponsored by the U.S. Department of Defense
Defense Threat Reduction Agency
Contract No. DTRA01-99-C-0031

ABSTRACT

The prototype International Data Center (pIDC) has been processing radionuclide data since 1995 to support the development of technology required for verification of the Comprehensive Nuclear-Test-Ban-Treaty (CTBT). This data contains gamma-ray spectra of environmental aerosol and gas samples collected from over 20 radionuclide stations. The gamma-ray spectra are analyzed resulting in the quantification of nuclide-specific atmospheric activity concentrations. Most of the radionuclides detected originate from natural sources. However, some result from nuclear weapons tests and releases from nuclear reactors, nuclear accelerators, and medical isotope production facilities. For nuclear-test-ban verification, it is important to be able to identify the type of source for anthropogenic radionuclide measurements.

Medical industry use of radioisotopes in the diagnosis and treatment of diseases has grown dramatically in the past 20 years. Medical radioisotopes are currently used in over 13 million procedures a year. As therapeutic isotope technology advancements reveal new modalities of treatment, this number may increase further resulting in a higher probability of the detection of such nuclides in environmental samples.

The pIDC has detected a number of radionuclides originating from the medical industry. These radionuclides include ^{123}I, ^{131}I, ^{99m}Tc, and ^{201}Tl. Other radionuclides used in the medical industry have been detected (e.g., ^{137}Cs and ^{133}Xe), but are believed to originate from other sources. Some of these nuclides are the same as those considered to be highly indicative of a nuclear weapons test. Since high accuracy is desired in monitoring compliance to the CTBT, it is crucial to understand the potential for radionuclides released from medical facilities to interfere with signals from nuclear weapons tests.

Key Words: radionuclide monitoring, aerosol, prototype International Data Centre, medical radionuclides, ^{123}I, ^{131}I, ^{99m}Tc, and ^{201}Tl

OBJECTIVE

The purpose of the Comprehensive Nuclear-Test-Ban Treaty (CTBT) is to cease "all nuclear weapons test explosions and all other nuclear explosions" thereby preventing nuclear weapons proliferation and enhancing international peace and security [CTBT]. Verification of the Treaty is achieved by a network of seismic, hydroacoustic, infrasound, and radionuclide stations that continuously monitor for indicators of a nuclear weapons blast.

The prototype International Data Center (pIDC) plays a pivotal role in the development and deployment of the required technology for the International Monitoring System (IMS). Since the beginning of 1996, the pIDC has received data from at least eight radionuclide monitoring stations [Mason et al., 1996]. Today, that number has increased to twenty [Bohner and Mason, 1998]. (See Table 1 for a listing of the current radionuclide monitoring stations and Figure 1 for a map showing their locations.) As a result, the pIDC has a large, comprehensive database of international atmospheric radionuclide data. The complete future radionuclide monitoring system (RMS) will contain 80 stations [CTBT].

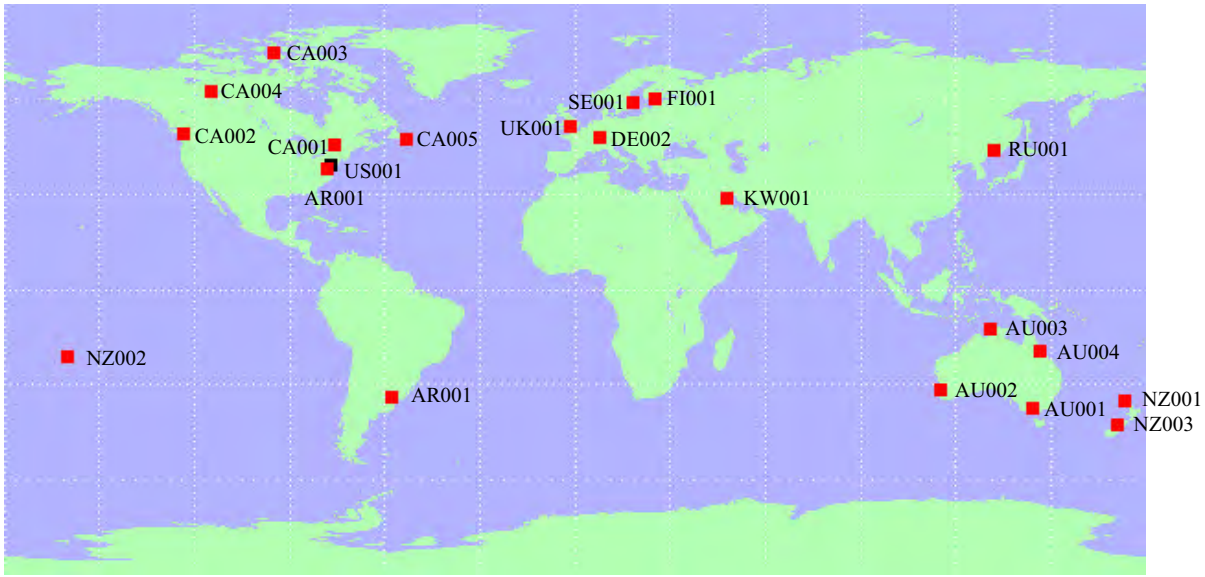


Figure 1. Current Operating Radionuclide Monitoring Stations of the pIDC

Challenges to the successful monitoring of compliance to the CTBT can be identified by studying the aerosol data stored at the pIDC. Radionuclides from various sources other than nuclear weapons tests have been detected by the Radionuclide Monitoring System (RMS) including nuclear power reactors, accelerators, medical isotope production facilities, factories, re-entrainment of fall-out, and natural sources. The objective of this paper is to identify the radionuclides detected by the RMS that have been determined to originate from the medical industry, and to discuss the effects of these interference signals in the context of CTBT verification.

RESEARCH ACCOMPLISHED

Radioactive isotopes are used in more than 38,000 diagnostic medical procedures each day in the United States [DOE, 1999]. Over 100 different radionuclides are currently administered for such purposes [NMRC, 1999]. The production of radioactive medical isotopes and the waste generated from their use are potential sources of atmospheric radioaerosols and gases. Although there are strict procedures in place for the disposal of radiopharmeceuticals and generated refuse, some of the activity is not properly disposed

because it is carried internally by patients outside of the appropriate medical departments [Beretta et. al, 1997]. Incineration of medical wastes is also a potential source for radionuclides in the atmosphere.

Table 1. Radionuclide Stations Currently Contributing Data to the pIDC

Station Code	Location	Start of Data Processing in pIDC Operations
AR001	Buenos Aires, Argentina	January, 1996
AU001	Melbourne, Australia	September, 1995
AU002	Perth, Australia	January, 1997
AU003	Darwin, Australia	February, 1997
AU004	Townsville, Australia	February, 1997
CA001	Ottawa, Canada	December, 1995
CA002	Vancouver, Canada	April, 1996
CA003	Resolute, Canada	May, 1996
CA004	Yellowknife, Canada	May, 1996
CA005	St. John's, Canada	June, 1996
DE002	Schauinsland, Germany	January, 1996
FI001	Helsinki, Finland	January, 1996
KW001	Kuwait City, Kuwait	September, 1995
NZ001	Kaitaia, New Zealand	May, 1995
NZ002	Rarotonga, New Zealand	May, 1996
NZ003	Hokitika, New Zealand	May, 1996
RU001	Ussuriysk, Russia	November, 1995
SE001	Stockholm, Sweden	September, 1995
UK001	Chilton, England	June, 1996
US001	Charlottesville, USA	December, 1995

The pIDC has identified signals from the following medical radioisotopes in atmospheric aerosol samples: ^{123}I, ^{131}I, ^{99m}Tc, ^{201}Tl, ^{137}Cs, and ^{133}Xe. Although both ^{137}Cs and ^{133}Xe are used in the medical industry and have been detected numerous times by the RMS, the sources of these nuclides have been determined to be resuspension of fallout from nuclear weapons and Chernobyl as well as from nearby nuclear power reactors, respectively. Some detection instances for the other radionuclides listed have been directly correlated to releases from medical facilities. The implications of this phenomenon on the efficacy of monitoring compliance to the CTBT are addressed in this paper.

^{123}I ($t_{1/2}$ = 13.2 hours)

This medical radioisotope is used mainly for diagnosis purposes. Depending upon test protocols, ^{123}I may be ingested or injected. By observing the absorption of ^{123}I in the body, malfunctions of the brain, thyroid, and kidney can be determined. The predominate γ-line of ^{123}I at 159 keV (83.3%) can also be utilized for myocardial and cerebral imaging.

^{123}I is cyclotron-produced by proton bombardment of ^{123}Cs by the reaction:

$$^{124}_{54}Xe(p,2n)^{123}_{55}Cs \overset{5.94m}{\blacklozenge} {}^{123}_{54}Xe \overset{2.08h}{\blacklozenge} {}^{123}_{53}I.$$

Although ^{123}I has been observed at only one station in the RMS, signal detection of this radiophameceutical occurs on a frequent basis as shown in Table 2 below.

Table 2. ^{123}I Detections at RMS Station CA002 in Vancouver, Canada from 1996 Until 14 June 1999

^{123}I							
Station	Total Spectra Reviewed at Station	Number of Spectra with ^{123}I	Percent of Spectra with ^{123}I	Average (_Bq/m ^{3})	Standard Deviation (_Bq/m ^{3})	Minimum (_Bq/m ^{3})	Maximum (_Bq/m ^{3})
CA002	1104	342	30.98	334.4	744.1	5.09	6202

Due to the high detection frequency and periodicity of ^{123}I, a source term investigation for this nuclide was initiated at the pIDC. It was found that a commercial radioisotope production facility is located 2 km southeast of the CA002 monitoring site [Mason and Williams, 1999]. Operational data was obtained from the facility and compared to the detections of ^{123}I. The results are displayed in Figure 2. A temporal correlation between the facility's production schedule and the detection of ^{123}I is evident.

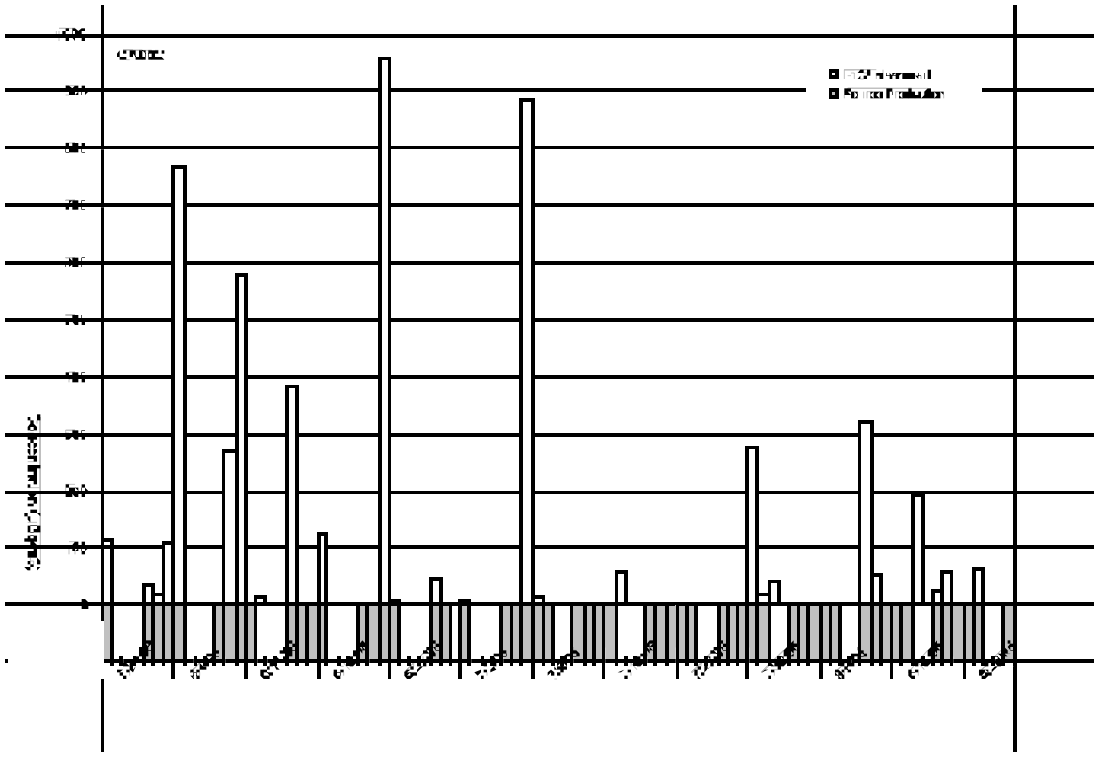


Figure 2. Dates of ^{123}I Production and Detection at CA002 [Mason and Williams, 1997]

Because ^{123}I is not considered a relevant isotope for CTBT monitoring, and because it doesn't interfere with signals from relevant CTBT isotopes, the detection of this medical isotope should not impact the efficacy of the RMS in achieving its monitoring goals.

^{131}I ($t_{1/2}$ = 8.020 days)

This radiopharmeceutical is utilized in many radiotherapy protocols and diagnostic procedures. One of the most popular medical uses of ^{131}I is for the treatment of hyperthyroidism. Others include various imaging techniques; use for antibody lab biochemistry in mental illness; locating infections, tumors, and metastatic lesions; radiolabeling; and treatment of the following medical conditions: carcinoma of the thyroid, graves disease, goiters, prostate cancer, hepatocellular carcinoma, melanoma, spinal tumor, neuroblastoma [NMRC, 1999].

^{131}I is a fission product and is produced in reactors for the medical industry. Unlike ^{123}I, this isotope is considered a relevant fission product in monitoring compliance of the CTBT. Its release from sources other than a nuclear weapons test will reduce the sensitivity of the RMS to this particular radionuclide.

Table 3 displays incidences when ^{131}I was observed in RMS atmospheric samples. Some of these detections are more likely from reactor releases, especially those from stations FI001 in Helsinki, Finland and SE001 in Stockholm, Sweden.

Table 3. ^{131}I Detections at RMS Stations from 1996 until 14 June 1999

^{131}I							
Station	Total Spectra Reviewed at Station	Number of Spectra with ^{131}I	Percent of Spectra with ^{131}I	Average (_Bq/m^3)	Standard Deviation (_Bq/m^3)	Minimum (_Bq/m^3)	Maximum (_Bq/m^3)
AR001	363	17	4.7	12.3	13.0	2.57	49.4
CA002	1104	1	0.1	3.51	-	-	-
DE002	187	1	0.5	0.305	-	-	-
FI001	415	12	2.9	0.403	0.232	0.151	0.945
KW001	999	6	0.6	5.27	3.10	2.30	9.95
NZ001	143	1	0.7	1.05	-	-	-
NZ003	151	2	1.3	1.04	0.315	0.819	1.27
SE001	718	4	0.6	1.37	0.538	0.681	1.98
UK001	162	1	0.6	0.411	-	-	-
US001	1132	2	0.2	21.6	7.46	16.3	26.8

There are several ways to determine the source of ^{131}I. First, the station history must be researched and studied. If ^{131}I has never been observed at a station, its detection at that station should arouse suspicion, especially when observed in conjunction with other relevant fission products. If other fission products are identified and quantified within the same _-ray spectrum, the source is likely not medical and radionuclide ratios may be utilized to discriminate between nuclear power emissions and a nuclear weapons test. If ^{131}I has been detected on occasion or frequently at a station, a source investigation like the one described for ^{123}I is extremely useful. In most cases, this results in the identification of a legitimate radionuclide source. The placement of stations upwind or far from possible sources of ^{131}I can greatly reduce interferences from this isotope.

^{99m}Tc ($t_{1/2}$ = 6.01 hours)

^{99m}Tc is used in over 80 percent of medical procedures requiring the administration of radionuclides [DOE, 1999]. It is estimated that 675 MBq of ^{99m}Tc were released to the environment in 1994 alone [Beretta et al., 1997].

Many characteristics of this isotope add to its versatility. For example, the half-life is long enough to examine metabolic processes yet short enough to minimize the patient's dose. The patient's dose is further reduced because there are no high-energy beta emissions to damage surrounding tissues. In addition, the low energy γ-rays of ^{99m}Tc easily escape the body and can be accurately detected by a γ-camera. The chemistry of technicium allows it to be incorporated into a range of biomolecules, which concentrate in different organs such as the brain, heart, liver, lungs, bones, thyroid, and kidney.

^{99m}Tc is produced on-site in generators. Hospitals and other medical facilities are supplied with such generators directly from the production reactor. A ^{99m}Tc generator is comprised of a lead container enclosing a chromatography column to which ^{99}Mo (the parent of ^{99m}Tc) is adsorbed [MDS Nordion S.A., 1997]. ^{99}Mo is a fission product with a half-life of 65.9 hours. ^{99m}Tc is eluted from the generator by a saline solution when required for use in a procedure. After two weeks or less, the generator is spent and must be returned to the production facility for recharging.

As shown in Table 4, this radiopharmeceutical has been detected at seven RMS stations in fifty spectra. The predominant _-line of ^{99m}Tc at 140.5 keV (89.0%) is difficult to differentiate from that of ^{75m}Ge (139.7 keV at 38.8%). Before Feb. 4, 1998 the pIDC would generally identify signals at ~140 keV as ^{75m}Ge. This is because the key _-line energy used by the pIDC for ^{75m}Ge (139.9 keV) was slightly higher than the value in the most recent decay data library from Brookhaven National Laboratory (139.7 keV). This problem has since been corrected, but earlier spectra have not yet been reanalyzed. Therefore, it is possible that ^{99m}Tc is present in other samples but not identified.

Table 4. Positive ^{99m}Tc Detections at RMS Stations from 4 Feb. 1998 Until 14 June 1999

^{99m}Tc							
Station	Total Spectra Reviewed at Station	Number of Spectra with ^{99m}Tc	Percent of Spectra with ^{99m}Tc	Average (_Bq/m ^{3})	Standard Deviation (_Bq/m ^{3})	Minimum (_Bq/m ^{3})	Maximum (_Bq/m ^{3})
AR001	363	10	2.8	756	508	287	1980
AU001	799	14	1.8	227	120	89.9	448
CA002	1104	16	1.5	189	126	101	609
DE002	187	4	2.1	1.62E+05	1.88E+05	142	4.01E+05
KW001	999	4	0.4	169	102	34.3	279
RU001	498	1	0.2	4.44E+04	-	-	-
US001	1132	1	0.1	339	-	-	-

^{75m}Ge is produced by neutron bombardment of ^{74}Ge within the detector by the following reaction:

$$^{74}_{32}Ge(n,\gamma)^{75m}_{32}Ge.$$

There are several ways to differentiate between ^{75m}Ge and ^{95m}Tc when a peak is observed near 140 keV. The first is to attempt nuclide identification by peak centroid energy alone. The difference in the line energies, as provided in the Brookhaven National Laboratory library, is 0.8 keV. However, this method is not always reliable due to uncertainties of peak centriod locations and uncertainties of the energy calibration. A second approach includes utilizing both the preliminary (4 hour) spectrum and the full spectrum (~24 hours) of a particular sample. By using both spectra, the half-life of the radionuclide at ~140 keV can be determined. Since ^{75m}Ge would be continually produced throughout the gamma-ray acqusition, the decay rate would be nearly constant (assuming a constant cosmic-ray flux). The calculated half-life of ^{75m}Ge would consequently be very large. In comparison to the half-life of ^{99m}Tc at 6.01 hours or its parent, ^{99}Mo, at 2.75 days, it is easy to discriminate between the nuclides by employing this test.

Once ^{99m}Tc has been positively identified by one or both of the methods above, the most probable source of the nuclide may then be determined. The sample is first checked for the presence of ^{99}Mo. The detection limit for this nuclide is lower than that of ^{99m}Tc because it's primary γ–line at 739.5 keV is only 12.2% abundant. However, if ^{99}Mo is present, then the likelihood of the ^{99m}Tc originating from a medical source is very low. This is because ^{99m}Tc is chemically separated from its parent during elution from a generator. Determination of the nuclide's half-life, as previously described, can also be used for nuclide source determination. If the half-life matches that of ^{99}Mo, then the two nuclides are in secular equilibrium and possibly originate from the direct fission product release of a nuclear reactor or weapons blast. If the half-life matches that of ^{99m}Tc, then the nuclide is likely from a medical industry source.

There is one station in Table 4 that does not send preliminary spectra: AR001 in Buenos Aires, Argentina. Therefore, the half-life test cannot be performed on samples from this station. However, samples from this station have been checked for ^{99}Mo and none show any evidence of this nuclide. Correspondence with station personnel indicates the presence of five potential nearby sources of ^{99m}Tc, all of which are medical centers and laboratories. The list includes:

1. Tecnuar (3 km W),
2. Bacon (5 km NW),
3. Vilela Medical Center (3.3 km S),
4. Diagnostico Maipu (2.3 km N), and
5. Fernandez Hospital (5.6 km S).

Consequently, the likelihood of ^{99m}Tc detected at AR001 originating from a medical source is very high.

^{99m}Tc is a relevant fission product for monitoring CTBT compliance. The presence of this nuclide from medical sources will decrease the station sensitivity towards ^{99m}Tc from other sources. However, methods are available to determine the source of the nuclide.

^{201}Tl ($t_{1/2}$ = 3.04 days)

This radionuclide is used for myocardial scintigraphy in the evaluation of coronary perfusion and cellular viability. It is also used for scintigraphy of muscles in cases of peripheral vascular disorders, parathyroid scintigraphy, and tumor visualization in different organs, especially the brain and thyroid. ^{201}Tl is cyclotron-produced by proton bombardment of ^{203}Tl by the reaction:

$$^{203}_{81}Tl(p,3n)^{201}_{82}Pb \xrightarrow{9.4\,hr} {}^{201}_{81}Tl.$$

Only one RMS station, AR001, has had confirmed detections of this radiopharmeceutical. Considering the location of the station near so many medical centers, this phenomenon is not surprising. However, earlier detections of ^{201}Tl could have been missed by the pIDC because it was initially not included in the software radionuclide library. This problem has since been corrected, but earlier spectra have not yet been reanalyzed. Table 5 summarizes data on the detection instances at AR001.

Table 5. ^{201}Tl Detections at RMS Station AR001 from 1996 Until 14 June 1999

^{201}Tl							
Station	Total Spectra Reviewed at Station	Number of Spectra with ^{201}Tl	Percent of Spectra with ^{201}Tl	Average (_Bq/m ^{3})	Standard Deviation (_Bq/m ^{3})	Minimum (_Bq/m ^{3})	Maximum (_Bq/m ^{3})
AR001	363	4	1.1	212	206	22.5	466

^{201}Tl is not considered a relevant anthropogenic nuclide for monitoring compliance to the CTBT, nor does any of its decay photons interfere with any major lines of relevant nuclides. Therefore, the presence and detection of this nuclide by RMS stations should not impact the analysis of γ s pectra.

CONCLUSIONS AND RECOMMENDATIONS

Based on international aerosol data compiled at the pIDC from the current RMS network, it is evident that several stations have detected radionuclides originating from medical sources. It has been shown that the detection of ^{123}I and ^{201}Tl have little effect on the ability of the RMS to monitor compliance of the CTBT. In contrast, the detection of other radiopharmeceuticals, like ^{99m}Tc and ^{131}I, can complicate the analysis of RMS data. To address this problem, methods have been devised to aid in nuclide and source identification.

When the RMS becomes fully operational with 80 international stations, the detection instances of medical isotopes will undoubtedly increase. It is also expected that radiophameceuticals other than those previously identified will be detected. (Table 6 lists radionuclides that are both radiopharmeceuticals and potentially indicative of a nuclear weapons test.) Depending on station location and local meteorological conditions, stations will observe varying amounts of interference from medical isotopes.

To reduce the impact of medical isotopes on RMS operations, local siting of stations should be optimized. When available, historical sample data should be used as an important source of information for nuclide and source identification. By determining the sources of radionuclides, we develop a good understanding of the environment and maintain awareness of possible interferences with nuclear weapons test detections.

Table 6. Radiopharmeceuticals that Are Also Potentially Indicative of a Nuclear Weapons Test

Nuclide	Half-Life	Medical Uses [NMRC, 1998]
Am-241	432 y	Osteoporosis detection, heart imaging.
As-74	17.8 d	Biomedical applications.
Au-198	2.69 d	Cancer treatment using mini-gun ; treating ovarian, prostate, and brain cancer.
Ce-141	32.5 d	Gastrointestinal tract diagnosis, measuring regional myocardial blood flow.
Co-57	272 d	Gamma camera calibration, radiotracer, and source for X-ray fluorescence spectroscopy.
Co-60	5.27 y	Destroy cancer cells, disinfect surgical equipment and medicines, external radiation cancer therapy.
Cr-51	27.7 d	Cell labeling and dosimetry.
Cs-137	30.2 y	Blood irradiators, PET imaging, tumor treatment.
Cu-64	12.7 h	PET scanning, planar imaging, SPECT imaging, dosimetry studies, cerebral and myocardial blood flow, treating colorectal cancer.
Eu-152	13.4 y	Medical.
Eu-155	4.73 y	Osteoporosis detection.
Fe-59	44.5 d	Medical.
I-131	8.04 d	See text, page 3.
Ir-192	73.8 d	Treatment of cancers of the prostate, brain, breast, gynecological cancers.
Mo-99	65.9 h	Parent for ^{99m}Tc.
Nb-95	35.0 d	Myocardial tracer and PET imaging.
Pb-203	2.16 d	SPECT and PET planar imaging (used with Bi-212), monoclonal antibody immunotherapy, cellular dosimetry.
Pd-109	13.4 h	Potential therapeutic agent.
Rh-105	35.4 h	Potential therapeutic agent.
Ru-103	39.3 d	Myocardial blood flow, radiolabeling microspheres, PET imaging.
Sc-46	83.8 d	Regional blood flow studies, PET imaging.

Table 6. CTBT-Relevant Radionuclides Used in the Medical Industry (continued)

Nuclide	Half-Life	Medical Uses [NMRC, 1998]
Sc-47	3.34 d	Cancer treatment and diagnostics, monoclonal antibodies, radioimmunotherapy.
Sm-153	2.00 d	Cancer treatment and diagnosis, monoclonal antibodies, bone cancer pain relief, treatment of leukemia.
Tc-99m	6.01 h	See text, page 4.
Tm-170	129 d	Portable blood irradiations for leukemia, lymphoma treatment, power source.
Xe-133	5.25 d	Lung imaging, regional cerebral blood flow, liver imaging, SPECT imaging of brain, lesion detection.
Y-88	107 d	Cancer tumor therapy.
Y-91	58.5 d	Cancer treatment, cellular dosimetry.
Zn-65	244 d	Medical.
Zr-95	64.0 d	Medical.

REFERENCES

A. Beretta, L. Conte, M. Monciardini, and L. Bianchi. Radiation Protection Dosimetry Vol. 71, No. 3, pp. 223-226 (1997).

CTBT Text.

DOE. "Medical Isotopes Production Project: Molybdenum-99 and Related Isotopes Availability of Draft Environmental Impact Statement and Public Hearings" http://apollo.osti.gov/html/doe/notice.html (1995).

G. F. Knoll, Radiation Detection and Measurement, 2nd ed., John Wiley & Sons, New York (1989).

L.R. Mason, D.W. Williams. *Ultra-Sensitive Environmental Monitoring of Emissions from a Radioisotope Production Facility* Proceedings to the 11th Pacific Basin Nuclear Conference in Banff, Canada, May 3-7 (1998).

L.R. Mason, W.C. Evans, J.B. Bohlin, and G.R. Shipman. Radionuclide Monitoring Operations Report of the Prototype International Data Center, First Quarter 1996, Pacific-Sierra Research Corp. Technical Report No. 2651 (1996).

J.D. Bohner, L.R. Mason. Radionuclide Monitoring Operations Report of the Prototype International Data Center, Third Quarter 1998 , Pacific-Sierra Research Corp. Technical Report No. 2794 (1999).

MDS Nordion S.A. http://www.bmedia.be/nordion/Radiopharmaceuticals_products.html (1997).

NMRC. "Medical Isotope Applications" http://www.cbvcp.com/nmrc/mia.html (1998).

CESIUM-137 DISTRIBUTIONS AND TRENDS AT CTBT RADIONUCLIDE MONITORING STATIONS AND THEIR IMPLICATIONS ON CTBT MONITORING

S. R. Biegalski, J. Bohner, L. R. Mason, Center for Monitoring Research

Sponsored by the U.S. Department of Defense
Defense Threat Reduction Agency
Contract No. DTRA01-99-C-0031

ABSTRACT

As part of the development support for the Comprehensive Nuclear-Test-Ban Treaty (CTBT), the prototype International Data Center (pIDC) has been processing radionuclide data since 1995. Radionuclide data received from field stations includes gamma-ray spectra, meteorological data, and state of health (SOH) information. To date over 20 radionuclide monitoring stations have transmitted data to the pIDC. The radionuclide monitoring system collects both aerosol and gas samples. Gamma-ray spectral analyses are performed on the samples to determine if they contain anthropogenic radionuclides indicative of nuclear debris.

A key radionuclide monitored by this system is ^{137}Cs [WP.224]. This radionuclide has a large fission yield and is produced in large quantities during a nuclear explosion [Vladimirski et al., 1998]. Due to the half-life of ^{137}Cs (30.17 years), amounts of this nuclide from past nuclear tests and reactor releases are still present in the soil and atmosphere. Cesium-137 from these sources is routinely detected in the prototype CTBT radionuclide monitoring system.

The pIDC has analyzed and reviewed gamma-ray spectra from over 7500 samples collected by the radionuclide monitoring network. Eight per cent of these samples contain the fission product ^{137}Cs. Samples from northern Europe have the highest percentage of ^{137}Cs detections due to the re-suspension of fall-out from the Chernobyl accident [Hötzl et al., 1992]. At most stations, ^{137}Cs concentrations follow a seasonal trend with high levels being detected in the spring and fall. This trend is similar to what is expected for aerosols from crustal origin. It is important to understand the behavior of this fission product in the monitoring environment for accurate characterization in the context of nuclear test ban verification.

Key Words: radionuclide monitoring, ^{137}Cs, aerosol, and pIDC

OBJECTIVE

The objective of this research is to examine the distribution, trends, and sources of airborne ^{137}Cs measured at radionuclide stations contributing data to the PDIC. Multiple sources contribute to atmospheric activity concentrations of ^{137}Cs measured at different sampling stations. The primary source of ^{137}Cs is the resuspension of fallout from past nuclear weapons tests and the Chernobyl event in 1986. Other airborne ^{137}Cs sources include reactor releases, industrial accidents, and laboratory contamination.

The spectra received at the pIDC are characterized with respect to their content [Bohner, 1998; Evans, 1996]. The characterization algorithm assumes either a normal, log-normal, or square-root distribution for the radionuclide atmospheric activity concentrations. Initial studies of radionuclide data indicated that a square-root distribution was a good assumption. Now that the network has acquired more data, ^{137}Cs distributions are re-examined to determine the best distribution for characterization modeling.

Seasonal trends are also observed in this data set. These trends are the result of meteorological influences on crustal resuspension and atmospheric transport. Understanding these seasonal influences is important for determining the sources of ^{137}Cs.

RESEARCH ACCOMPLISHED

Table 1 lists the stations that have contributed radionuclide data to the pIDC, their locations, date at which the pIDC began processing station data in operations, and the station's sampling methodology. Most stations have continued to send data to the pIDC on a regular basis with some data gaps due to routine maintenance and equipment failures. Most stations contributing to the pIDC operate on a long sampling methodology. A long sampling methodology is one in which the time from the beginning of the aerosol sample collection to the end of the gamma-ray spectrum acquisition is longer than a week. For compliance with the CTBT International Monitoring System standards, stations must adhere to a sampling methodology where the time between the beginning of the aerosol sample collection and the end of the gamma-ray spectrum acquisition is less than or equal to 72 hours.

Measurements of airborne ^{137}Cs have been made at 9 of the 20 stations listed in Table 1. These stations are shown in Figure 1 along with their respective percent of samples containing ^{137}Cs at detectable levels. Stations in Europe have the highest percentage of ^{137}Cs detections due to the re-suspension of fallout from the Chernobyl event. The DE002 (Schauinsland, Germany) station has the highest ^{137}Cs detection percentage. This is largely due to the fact that the long sampling methodology at the DE002 station equates to lower ^{137}Cs detection limits. It is very likely that ^{137}Cs is present in all European aerosol samples at some level. Detection of ^{137}Cs is dependent on the station's sampling methodology, gamma-ray spectroscopy system, and other factors that affect the detection limit. ^{137}Cs detections in the current Southern Hemisphere stations are virtually non-existent. An exception to this are the ^{137}Cs detections made at the AR001 (Buenos Aires, Argentina) station. The source of the AR001 ^{137}Cs is yet to be completely determined, but it is likely due to local detector/laboratory contamination or local medical industry sources.

Figure 2 is a plot of the ^{137}Cs atmospheric activity concentrations. Multiple years of the aerosol data are plotted in a "box and whisker" format. A line in the box represents the mode of the air concentrations. The range of the box depicts the bounds of the 25th and 75th percentiles of the data. The whiskers extending from the box represent the bounds of the 10th and 90th percentile of data. Data points that extend beyond the 10th and 90th percentiles are plotted individually. The highest ^{137}Cs airborne activity concentrations were measured at the KW001 (Kuwait City, Kuwait) station at levels above 100 _Bq m $^{-3}$. The detections of ^{137}Cs at KW001 are strongly correlated to sandstorm activity and consequently to significant sand deposits on the filters. An investigation is currently being performed coorelating the ^{137}Cs concentrations in the Kuwait soil with those found in the sand collected on the filters. Figure 2 shows that a good portion of all the ^{137}Cs concentrations are in the 1 to 10 _Bq m $^{-3}$ range. Detections of ^{137}Cs at lower levels are observed at the DE002 (Schauinsland, Germany) and UK001 (Chilton, England) stations since their long sampling methodology equates to lower detection limits. No special treatment was given to this data for values below the limit of detection. All ^{137}Cs atmospheric activity concentrations measured at the pIDC are well below levels those that would adversely affect human health.

Table 1
Radionuclide Stations Contributing Data to the pIDC

Station Code	Location	Start of Data Processing in pIDC Operations	Sampling Methodology
AR001	Buenos Aires, Argentina	January, 1996	Short
AU001	Melbourne, Australia	September, 1995	Short
AU002	Perth, Australia	January, 1997	Long
AU003	Darwin, Australia	February, 1997	Long
AU004	Townsville, Australia	February, 1997	Long
CA001	Ottawa, Canada	December, 1995	Long
CA002	Vancouver, Canada	April, 1996	Short
CA003	Resolute, Canada	May, 1996	Long
CA004	Yellowknife, Canada	May, 1996	Long
CA005	St. John's, Canada	June, 1996	Long
DE002	Schauinsland, Germany	January, 1996	Long
FI001	Helsinki, Finland	January, 1996	Long/Short*
KW001	Kuwait City, Kuwait	September, 1995	Short
NZ001	Kaitaia, New Zealand	May, 1995	Long
NZ002	Rarotonga, New Zealand	May, 1996	Long
NZ003	Hokitika, New Zealand	May, 1996	Long
RU001	Ussuriysk, Russia	November, 1995	Short
SE001	Stockholm, Sweden	September, 1995	Short
UK001	Chilton, England	June, 1996	Long
US001	Charlottesville, USA	December, 1995	Short

* Station has maintained both long and short sampling methodologies.

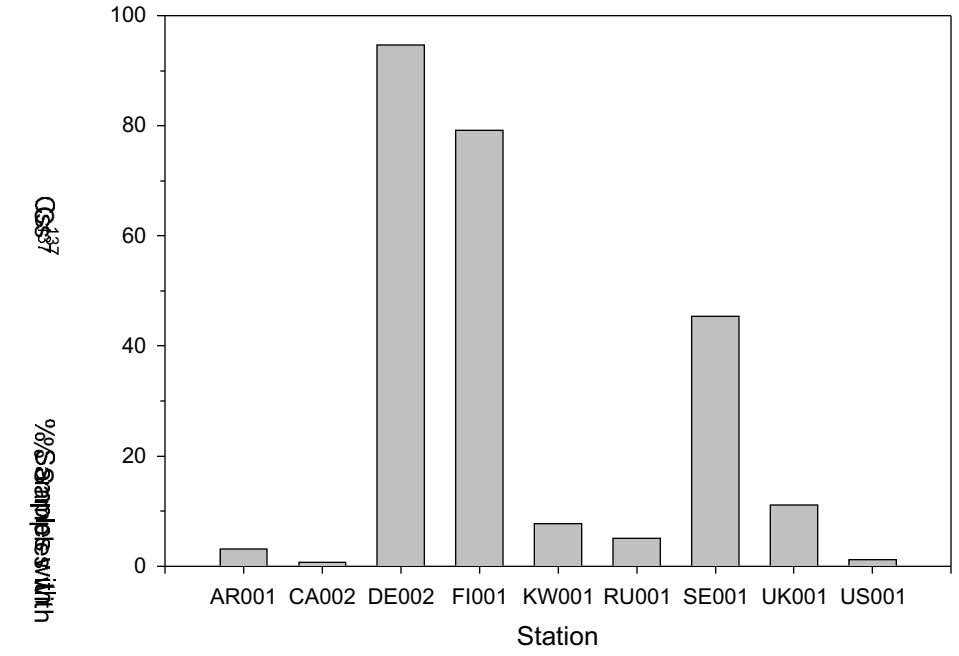


Figure 1. Percent of samples with detectable levels of ^{137}Cs.

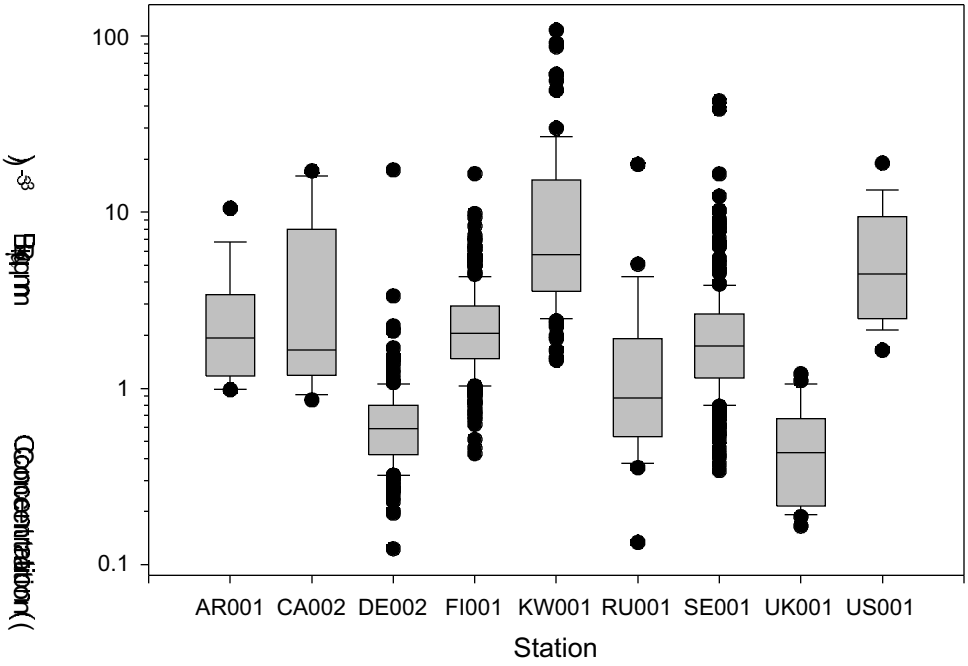


Figure 2. Box plot of all airborne ^{137}Cs measurements made at the pIDC.

Distribution of ^{137}Cs Atmospheric Activity Concentrations

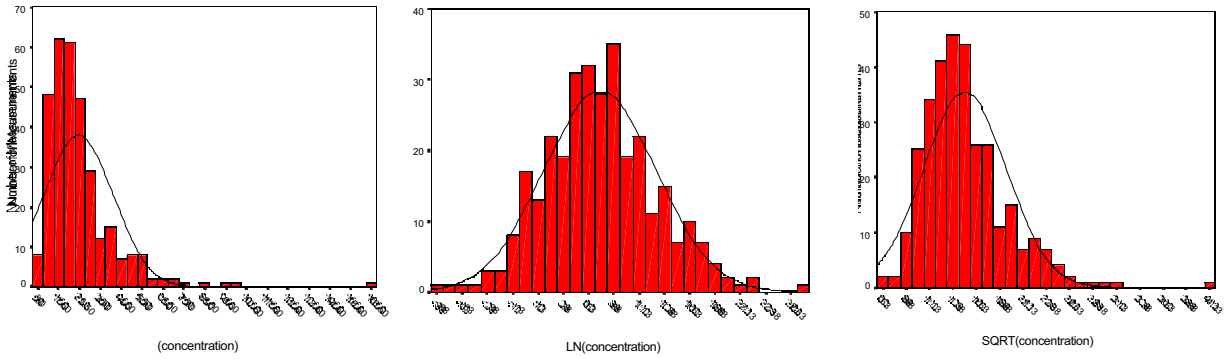
The radionuclide characterization algorithm utilized at the pIDC assumes the atmospheric activity concentrations follow a normal, log-normal, or square-root distribution [Evans, 1996]. Thus, the distribution type affects the prediction limits of the characterization code. Three methods were utilized in this research to examine how well the three different distribution types fit the ^{137}Cs data: histograms, cumulative probability plots, and the Kolmogorov-Smirnov test. Table 2 summarizes the results of the three methods utilized to determine the best distribution fit to the ^{137}Cs data. The results shown in this table indicate that the three methods produce very similar conclusions.

Table 2
^{137}Cs Distribution Fits

Station	Histogram	Cumulative Probability Plot	Kolmogorov-Smirnov Test	Best Distribution Fit
AR001	(Log-Normal)	(Log-Normal)	(Log-Normal)	(Log-Normal)
CA002	(Log-Normal)	(Log-Normal)	(Log-Normal)	(Log-Normal)
DE002	Log-Normal	Log-Normal	Log-Normal	Log-Normal
FI001	Log-Normal	Log-Normal	Log-Normal	Log-Normal
KW001	Log-Normal	Log-Normal	Log-Normal	Log-Normal
RU001	Log-Normal	Log-Normal	Log-Normal	Log-Normal
SE001	Log-Normal	Log-Normal	Log-Normal	Log-Normal
UK001	(Log-Normal)	(Log-Normal)	(Log-Normal)	(Log-Normal)
US001	(Log-Normal or Square-Root)	(Log-Normal or Square-Root)	(Square-Root)	(Square-Root)

Values in parentheses are for sample sets smaller than 20. These values should be viewed with caution since the sample set is small.

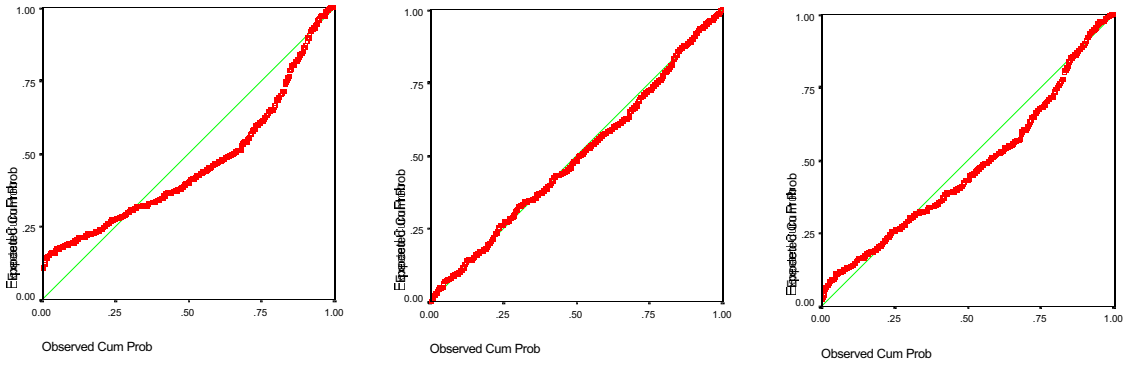
Histograms were made to visually display the ^{137}Cs activity concentration distributions. Figure 3 shows the ^{137}Cs histograms for the FI001 (Helsinki, Finland) Station. A plot of a normal distribution was plotted over each histogram to provide visual guidance. These plots clearly show that the best fit for this data is with the natural log transform. Thus, the log-normal distribution would be best suited for modeling ^{137}Cs at the FI001 (Helsinki, Finland) station. Similar plots were examined for each distribution type for each station where ^{137}Cs was detected. Table 2 contains a summary of the results of the histogram plotting method. The results for stations with small data sets should be interpreted with caution. For the US001 station, it was difficult to judge with the histogram method if the log-normal or square-root distribution best fit the data.



3a 3b 3c

Figure 3. Histograms of FI001 (Helsinki, Finland) ^{137}Cs atmospheric activity concentrations (_Bq m $^{-3}$) with normal distribution overlay. Figure 3a is the data with no transform. Figure 3b is the data with a natural log transform. Figure 3c is the data with a square-root transform.

Cumulative probability plots were also utilized to visually display the fit of the data to a normal distribution. Figure 4 displays the cumulative probability plots for the FI001 ^{137}Cs activity concentrations. A perfect correlation between the expected distribution and the observed data would result in a straight line at 45 degrees. Similar to the histograms shown in Figure 3, the cumulative probability plots show that the data with a natural log transform best fits the FI001 ^{137}Cs data. Table 2 contains a summary of the results of the cumulative probability plot method. Again, the results for stations with small data sets should be interpreted with caution. For the US001 station, it was difficult to judge with the cumulative probability plot method if the log-normal or square-root distribution best fit the data.



4a 4b 4c

Figure 4. Cumulative probability plots of FI001 (Helsinki, Finland) ^{137}Cs atmospheric activity concentrations. Figure 4a is the data with no transform. Figure 4b is the data with a natural log transform. Figure 4c is the data with a square-root transform.

The Kolmogorov-Smirnov test procedure was also applied to the ^{137}Cs data. This test compares the observed cumulative distribution function for a variable with a specified theoretical distribution. The Kolmogorov-Smirnov factor, Z, is computed from the largest difference (in absolute value) between the observed and theoretical distribution function. The goodness-of-fit test determines how well the observations conform to the theoretical distribution. For this testing, the normal distribution was utilized as the theoretical distribution to which the observed data is compared. Natural log and square-root transformations were applied to the data to test the goodness-of-fit with the log-normal and square-root distributions, respectively. In contrast to the histogram and cumulative probability plot graphical methods, the Kolmogorov-Smirnov test provides a quantitative value by which the comparison may be judged, Z. Basically, the lower the Z, the better the fit. However, one must also take the sample set size into account since the Kolmogorov-Smirnov Z value is a sum of differences and does not normalize to sample set size. The results of the Kolmogorov-Smirnov test provide similar conclusions to the plotting methods. However, the Z value allows for a more quantitative comparison.

Table 3
Kolmogorov-Smirnov Test for ^{137}Cs Distributions

Station	Sample Set Size	Normal Distribution Z	Log-Normal Distribution Z	Square-Root Distribution Z	Best Distribution Fit
AR001	11	(0.863)	(0.528)	(0.709)	(Log-Normal)
CA002	8	(1.136)	(0.759)	(0.992)	(Log-Normal)
DE002	176	4.347	1.020	2.401	Log-Normal
FI001	316	2.963	0.890	1.907	Log-Normal
KW001	77	2.432	1.073	1.846	Log-Normal
RU001	25	1.491	0.569	1.114	Log-Normal
SE001	324	4.989	1.112	2.517	Log-Normal
UK001	18	(0.861)	(0.574)	(0.604)	(Log-Normal)
US001	13	(0.705)	(0.657)	(0.645)	(Square-Root)

Values in parentheses are for sample sets smaller than 20. These values should be viewed with caution since the sample set is small.

The conclusions reached from the histogram, cumulative probability plot and Kolmogorov-Smirnov test are similar. The graphical methods require some subjective interpretation of the plots whereas the Kolmogorov-Smirnov test provides a Z value from which a comparison may be made. With the exception of the US001 station, all of the station's ^{137}Cs concentrations are best fit with a log-normal distribution. However, the US001 data set is small and the square-root distribution is only marginally better than the square-root distribution at fitting the data.

^{137}Cs Atmospheric Activity Concentration Trends

Trace element trends were investigated with the aid of both box and whisker plots and bar graphs. The objective of these plots is to reveal the existing annual trends present in ^{137}Cs atmospheric activity concentrations. In general, ^{137}Cs measurements at the stations may be broken down into about five source categories: 1) local resuspension of weapons and accident fallout, 2) remote resuspension of weapons and accident fallout, 3) deposition of stratospheric ^{137}Cs injected at the time of the initial weapon explosion or nuclear accident, 4) local reactor, medical, or other nuclear facilities, and 5) laboratory contamination. The first three of these source categories are dependent on meteorological factors. These meteorological influences vary by season and affect the atmospheric ^{137}Cs activity concentrations accordingly. Understanding the seasonal trends of the measured atmospheric ^{137}Cs activity concentrations aids in the modeling of the data as well as with the determination of the ^{137}Cs sources.

Figure 5 contains a box and whisker plot of ^{137}Cs at the FI001 (Helsinki, Finland) station. The mode values observed as lines within the box show that ^{137}Cs atmospheric activity concentrations are highest in winter and lowest in the summer. This is a similar trend observed at other European stations. The high ^{137}Cs in the winter is suspected to be a result of the increased probability of transport for resuspended Chernobyl

fallout from heavily contaminated regions. The seasonal low found in July is the result of decreased atmospheric pressure differentials occurring during this month and, consequently, the reduced crustal resuspension. The summer lows are commensurate with trends observed in other crustal materials (Biegalski *et al.*, 1998).

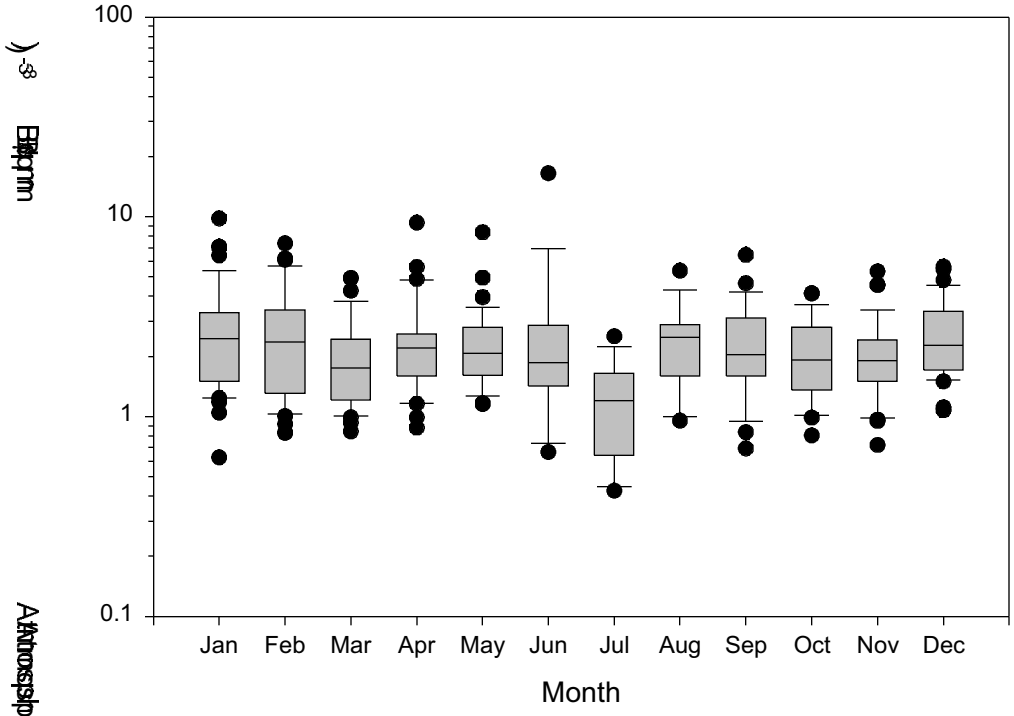


Figure 5. ^{137}Cs atmospheric activity concentrations at FI001 (Helsinki, Finland) as a function of month. Data accumulated from January, 1996 through June, 1999.

For stations with a reduced number of ^{137}Cs measurements, a bar chart was found to be more useful than a box and whisker plot for determining seasonal trends. Figure 6 is a bar chart showing the number ^{137}Cs detections at KW001 (Kuwait City, Kuwait) as a function of month. The majority of detections occurred during the spring. These detections strongly corresponded to the sandstorm activity reported in the local vicinity. These data support the assumption that ^{137}Cs detections at the KW001 station are a result of local resuspension.

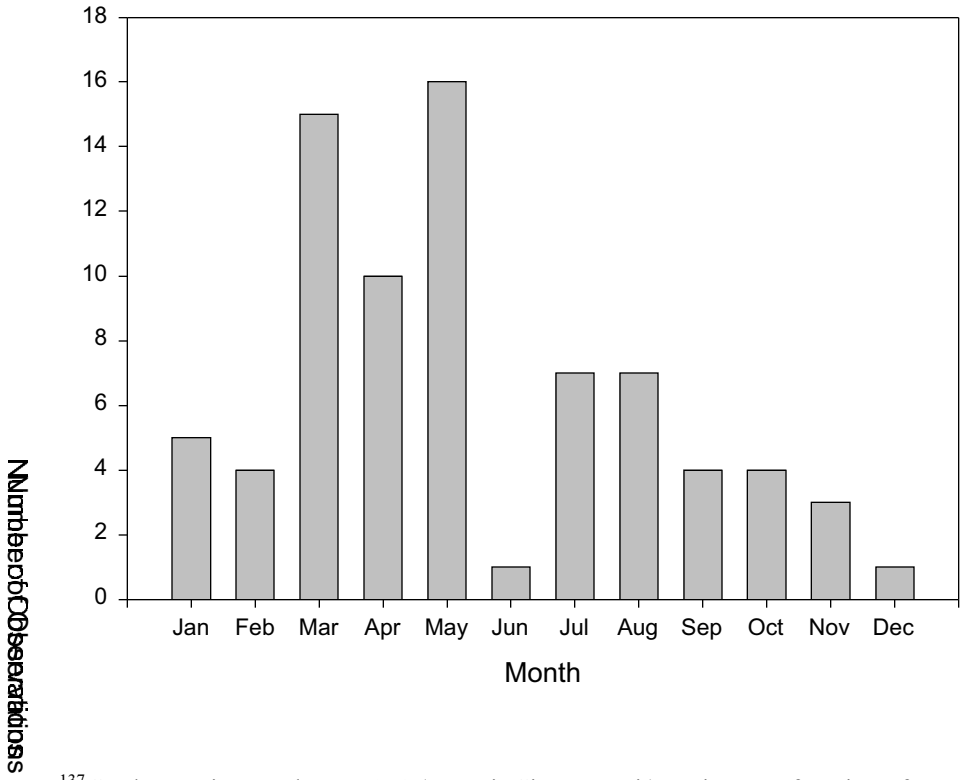


Figure 6. ^{137}Cs observations at the KW001 (Kuwait City, Kuwait) station as a function of month. Data accumulated from September, 1995 to June, 1999.

CONCLUSIONS AND RECOMMENDATIONS

Data presented in this paper show the atmospheric activity concentration distributions and seasonal trends for ^{137}Cs. All of the ^{137}Cs atmospheric activity concentrations follow a log-normal distribution with the exception of the US001 (Charlottesville, USA) station where the sample set is small. Most of the data exhibit seasonal trends with lows in the summer months. The seasonal tends are the result of meteorological influences on the resuspension of crustal material to the atmosphere. This phenomenon is very common with crustal material and the relationship between crustal particle suspension and wind speed is well documented [Gillette and Porch, 1978; Gillette and Passi, 1988].

These data can be used for modeling ^{137}Cs atmospheric activity concentrations at different stations and calculating prediction intervals. The prediction intervals may then be used to characterize radionuclide samples and determine if the atmospheric activity concentrations are at normal levels. Samples with radionuclide atmospheric activity concentrations at abnormally high levels should be examined in more detail than normal analysis, and an effort should be placed to determine the origin of the aerosol.

Similar studies will be performed for new stations that are brought on-line in the radionuclide monitoring system. It is important to understand the specific environment being monitored with special attention given to the distribution, trends, and sources of fission products within that environment. Such studies are vital to differentiating normal measurements from abnormal ones.

REFERENCES

Biegalski, S. R.; Landsberger, S.; Hoff, R. M.(1998), "Source-Receptor Modeling Using Trace Metals in Aerosols Collected at Three Rural Canadian Great Lakes Sampling Stations," *J. Air & Waste Manage. Assoc*., Vol. 48, pp. 227-237.

Bohner, J (1998) " Comparison of the Current and Proposed Characterization Approaches for Radionuclide Measurements", CMR Technical Report CMR-98/35.

Hötzl, H; Rosner, G.; Winkler, R. (1992) "Sources of present Chernobyl-derived cesium concentrations in surface air and deposition samples," *Science of the Total Environment*, Vol. 119, pp. 231-242.

Evans, W. C.(1996) "Automated Categorization of Airborne Radioactivity Measurements for CTBT Monitoring," PSR Technical Note 1091.

Gillette, D.A.; Proch W. M. (1978) *Journal of Geophysical Research*, Vol. 83, pp. 409-415.

Gillette, D. A.; Passi, R. (1988) *Journal of Geophysical Research*, Vol. 93, pp. 14,233-14,241.

Vladimirskiy, L.; L. R. Mason, M. Zähringer, J. D. Bohner, "Optimizing the Fission Product Library for Verification of the Comprehensive Nuclear-Test-Ban Treaty," CMR Technical Report CMR-98/29, June 1998.

WP.224, Working Group 1 - Verification, "International Monitoring System Expert Group Report based on Technical Discussions held from 6 February to 3 March 1995," 16 March 1995.

DISTRIBUTION AND TRENDS OF NATURAL RADIONUCLIDE CONCENTRATIONS AT CTBT RADIONUCLIDE MONITORING STATIONS

S. R. Biegalski, Center for Monitoring Research

Sponsored by the U.S. Department of Defense
Defense Threat Reduction Agency
Contract No. DTRA01-99-C-0031

ABSTRACT

The Atmospheric Radionuclide Monitoring Program at the prototype International Data Center (pIDC) began developing technical support for the Comprehensive Nuclear-Test-Ban-Treaty (CTBT) in October 1995. Since then, over 20 particulate monitoring stations have transmitted data to the pIDC. The data include gamma-ray spectra of aerosol samples collected with high-volume air samplers. Sampling methodology (e.g., sampling time, volume of air sampled, decay time, gamma-ray acquisition time) currently varies from station to station, but will soon be standardized.

Successful environmental monitoring in support of the CTBT requires a detailed knowledge of the natural radionuclide concentrations that dominate the background. Natural radionuclides can both help and hinder monitoring efforts. On the positive side, they may be utilized for quality assurance/quality control (QA/QC) measures. However, significantly high natural radionuclide background levels will adversely affect a station's detection capabilities.

Natural radionuclides may originate from interactions of cosmic-rays with matter or from the singular event at the beginning of the universe (primordial). This study characterizes the natural radionuclide concentrations and seasonal trends of four naturally measured radionuclides: ^{7}Be, ^{210}Pb, ^{212}Pb, and ^{40}K. This information is necessary to model natural radionuclide concentration levels for station characterization.

Key Words: radionuclide monitoring, aerosol, pIDC, natural radionuclides, ^{7}Be, ^{210}Pb, ^{212}Pb, and ^{40}K

OBJECTIVE

While the focus of the radionuclide monitoring effort at the pIDC is to monitor the environment for radioactive aerosols and gas representative of a nuclear weapon test, the overwhelming majority of radionuclide measurements are those of natural origins. The presence of these natural radionuclides can both help and hinder the pIDC's monitoring efforts. On the positive side, the natural radionuclides may be utilized in system performance monitoring, station QA/AC measures, and provide information about the local environment of the station. On the negative side, the signal from the natural radionuclides increase the Compton continuum background of the spectrum and interfere with the detection of anthropogenic radionuclides expected to be produced in a nuclear weapon test.

To optimize our benefits from the presence of natural radionuclides within the gamma-ray spectrum, an increased understanding of their occurrence rates, distributions, and trends needs to be achieved. This information may then be utilized to enhance detector calibrations, monitor the performance of the detection equipment, and provide QA/QC guidance on the sampling metrics. The information may be included in models that calculate prediction intervals for the expected natural radionuclide concentrations. If a natural radionuclide is measured outside the predicted range, then a flag is raised indicating that the sample should be reviewed with increased scrutiny.

The modeling of expected radionuclide concentrations at the pIDC is referred to as sample characterization. Samples with natural radionuclides present at normal levels and have no anthropogenic radionuclides indicative of a nuclear test are characterized as Level 1. Natural radionuclides present at abnormal levels and have no anthropogenic radionuclides indicative of a nuclear test are characterized as Level 2. Detailed descriptions of the sample characterization methods may be found in Evans (1996) and Bohner (1998). Within the current software, radionuclide concentrations may be modeled as having normal, log-normal, or square-root distributions. This research will demonstrate which distributions best represent the radionuclides at the different stations.

The natural radionuclides considered in this research include ^{7}Be, ^{210}Pb, ^{212}Pb, and ^{40}K. These are the most common natural radionuclides that may be quantitatively determined. Many radionuclides are detected within the radon and thoron decay series that can only be qualitatively identified. The pIDC is currently evaluating methods to accurately determine activity concentrations of radionuclides within a decay series, but no such method is in place at the current time. Numerous other natural radionuclides are observed less predictably; many generated through interactions with cosmic radiation.

^{7}Be is a cosmogenically produced radionuclide that decays with a 53.28 day half-life. It is produced as a result of cosmic-ray interactions with nitrogen and oxygen atoms in the stratosphere and upper troposphere. The magnitude of the ^{7}Be production is affected by the energy level of the bombarding cosmic radiation and the atmospheric density of nitrogen and oxygen targets. Maximum production of ^{7}Be occurs in the stratosphere [Koch *et al*., 1996]. This production is also a function of longitude and the 11-year solar cycle. To be detected on the ground by the radionuclide monitoring system contributing data to the pIDC, vertical atmospheric mixing must occur to transport the ^{7}Be to lower altitudes. While the production of ^{7}Be does not vary with seasons, the meteorological influences on vertical atmospheric transport does. Thus, seasonal trends are often observed with ground-based ^{7}Be atmospheric activity concentration measurements. ^{7}Be may be quantified through its 477.6 keV gamma-ray with 10.3% abundance.

^{210}Pb is a terrestrial radionuclide in the radon decay series. Many other radon daughters are also found within the spectra evaluated at the pIDC including ^{214}Pb and ^{214}Bi. Radon concentrations vary with respect to geographical regions and are a function of local crustal uranium concentrations and soil permeability. Following production, radon daughters attach indiscriminately to available aerosol and therefore spread evenly with respect to area over the ambient aerosol size distribution [Koch *et al*., 1996]. The 22.6 year half-life of ^{210}Pb allows for substantial geographical distribution. Therefore, ^{210}Pb atmospheric activity concentrations are less regionally dependent than radon concentrations. This nuclide may be quantified

through its 46.50 keV gamma-ray with 4.1 % abundance. However, within International Monitoring System (IMS) specifications, there is no requirement to analyze spectra at energies as low as this. ^{212}Pb is another terrestrial radionuclide but it is in the thoron decay series. Other radionuclides in the thoron decay series measured at the pIDC are ^{212}Bi and ^{208}Tl. Unlike ^{210}Pb, the ^{212}Pb atmospheric activity concentrations are more closely tied to the concentrations of its parent, thoron. This is largely a function of this radionuclide's half-life of 10.6 hours. ^{212}Pb may be quantified through its primary decay line at 238.63 keV with 43.60 % abundance.

^{40}K is a radionuclide of primordial origin. It has a long half-life of 1.3×10^9 years and is widely distributed throughout the environment. Its natural abundance is 0.0119 %. This radionuclide is present not only in atmospheric aerosols, but also in the aerosol filters used to collect samples as well as in the surrounding building materials. ^{40}K may be quantified through its 1460.75 keV line with 10.67 % abundance.

RESEARCH ACCOMPLISHED

Table 1 lists the stations that have contributed radionuclide data to the pIDC, their locations, date at which the pIDC began processing the station data in operations, and the station's sampling methodology. Most stations have continued to send data to the pIDC on a regular basis through the present time with some data gaps due to routine maintenance and equipment failures. Most of the stations contributing to the pIDC operate on a long sampling methodology. A long sampling methodology is one in which the time from the beginning of aerosol sample collection to the end of gamma-ray spectrum acquisition is longer than a week. For compliance with CTBT International Monitoring System standards, stations must adhere to a sampling methodology in which the time between the beginning of aerosol sample collection and end of the gamma-ray spectrum acquisition is less than or equal to 72 hours. Stations with long sampling methodologies are not able to detect certain short-lived radionuclides including ^{212}Pb.

Table 1
Radionuclide Stations Contributing Data to the pIDC

Station Code	Location	Start of Data Processing in pIDC Operations	Sampling Methodology
AR001	Buenos Aires, Argentina	January, 1996	Short
AU001	Melbourne, Australia	September, 1995	Short
AU002	Perth, Australia	January, 1997	Long
AU003	Darwin, Australia	February, 1997	Long
AU004	Townsville, Australia	February, 1997	Long
CA001	Ottawa, Canada	December, 1995	Long
CA002	Vancouver, Canada	April, 1996	Short
CA003	Resolute, Canada	May, 1996	Long
CA004	Yellowknife, Canada	May, 1996	Long
CA005	St. John's, Canada	June, 1996	Long
DE002	Schauinsland, Germany	January, 1996	Long
FI001	Helsinki, Finland	January, 1996	Long/Short*
KW001	Kuwait City, Kuwait	September, 1995	Short
NZ001	Kaitaia, New Zealand	May, 1995	Long
NZ002	Rarotonga, New Zealand	May, 1996	Long
NZ003	Hokitika, New Zealand	May, 1996	Long
RU001	Ussuriysk, Russia	November, 1995	Short
SE001	Stockholm, Sweden	September, 1995	Short
UK001	Chilton, England	June, 1996	Long
US001	Charlottesville, USA	December, 1995	Short

* Station has maintained both long and short sampling methodologies.

Distribution of Atmospheric Activity Concentrations

As stated, the pIDC utilizes a modeling code to calculate confidence intervals of atmospheric activity concentrations. The confidence intervals are then used to determine if the measured atmospheric activity concentration is within normal bounds. A user may choose one of three distribution types in the initial model set-up procedure. Initial research was conducted in this area [Evans, 1996; Shen, 1998]. However, this work examines all the stations, includes a larger data set, and utilizes a more comprehensive approach in determining the best distribution fits and seasonal trends.

Three methods are utilized to investigate the best distribution fits to the data: the first method includes plotting the data on a histogram, the second method includes plotting the data on a cumulative probability plot, and the third method is the Kolmogorov-Smirnov test. The first two methods are graphical methods that require a visual comparison of the data fit to a given distribution. The third method, the Kolmogorov-Smirnov test, compares the observed cumulative distribution function for a variable with a specified theoretical distribution. The Kolmogorov-Smirnov variable, Z, is computed from the largest difference (in absolute value) between the observed and theoretical distribution function. The goodness-of-fit test determines how well the observations conform to the theoretical distribution. Basically, the lower the Z-value, the better the fit. For this test, the normal distribution is utilized as the theoretical distribution to which the observed data is compared. Natural log and square-root transformations are applied to the data to test the goodness-of-fit with the log-normal and square-root distributions, respectively. However, one must also take the sample set size into account because the Kolmogorov-Smirnov Z-value is a sum of differences and does not normalize to sample set size. The results of the Kolmogorov-Smirnov test provide similar conclusions to the plotting methods, however, the Z value allows for a more quantitative comparison.

Table 2 contains the Kolmogorov-Smirnov test results for ^{7}Be at all the radionuclide monitoring stations. Out of the twenty stations, four were best fit with a normal distribution, seven were best fit by a log-normal distribution, and nine were best fit with a square-root distribution. For many of the stations, large differences were seen between the quality of fit between the distribution types. The data sets were all large enough to provide adequate representation of the atmospheric activity concentration distribution. The results for the KW001 (Kuwait City, Kuwait) station indicate that a square-root distribution best fits the ^{7}Be data. This is commensurate with the results of an initial study reported in Evans (1996). The ^{7}Be data for the DE002 (Schauinsland, Germany) station is best fit by the square-root distribution. This is in contrast to data reported by Winkler *et al*. (1998) for another rural sampling location in southern Germany (about 10 km north of the city of Munich) that is best fit by a log-normal distribution. The Winkler *et al*. data set consists of 46 10-day samples collected from December, 1994 through March, 1996.

Table 2 contains the Kolmogorov-Smirnov test results for ^{210}Pb at all the radionuclide monitoring stations. Out of the twenty stations, four are best fit with a normal distribution, nine are best fit by a log-normal distribution, six are best fit with a square-root distribution, and one station did not have ^{210}Pb measurements available. The 46.50 keV gamma-ray was not always detectable on all gamma-ray spectroscopy systems. The electronic noise was often high in this energy region and some systems had their lower-level energy discriminator set above this energy. As a result, the ^{210}Pb data set is not as complete as the ^{7}Be data set. Also, one should view the results from the NZ001 (Kaitaia, New Zealand), NZ002 (Rarotonga, New Zealand), and NZ003 (Hokitika, New Zealand) stations with caution because the data sets are small. No data is available for the AU001 (Melbourne, Australia) station. ^{210}Pb atmospheric activity concentrations are not normally modeled at the pIDC for sample characterization, so no previous studies have been performed at the pIDC on the ^{210}Pb atmospheric activity concentration distributions. A comparison can be made between the DE002 (Schauinsland, Germany) data and the data reported by Winkler *et al*. (1998). Both data sets show that a log-normal distribution best fits the ^{210}Pb atmospheric activity concentrations within the southern Germany region.

Table 2
^{7}Be Atmospheric Activity Concentration Distributions

Station	Sample Set Size	Normal Distribution K-S Z-Value	Log-Normal Distribution K-S Z-Value	Square-Root Distribution K-S Z-Value	Best Distribution Fit
AR001	363	0.830	1.876	0.881	Normal
AU001	799	1.882	1.732	0.542	Square-Root
AU002	117	1.132	0.603	0.809	Log-Normal
AU003	120	1.160	0.774	0.741	Square-Root
AU004	117	0.690	0.571	0.414	Square-Root
CA001	170	1.242	1.194	1.073	Square-Root
CA002	1104	4.063	1.549	1.945	Log-Normal
CA003	121	1.164	1.145	0.733	Square-Root
CA004	127	1.043	0.606	0.806	Log-Normal
CA005	75	0.641	0.926	0.713	Normal
DE002	187	0.912	0.790	0.336	Square-Root
FI001	409	2.096	0.568	1.286	Log-Normal
KW001	999	1.162	1.929	0.698	Square-Root
NZ001	143	0.964	0.702	0.780	Log-Normal
NZ002	135	0.796	0.974	0.647	Square-Root
NZ003	151	1.105	0.400	0.678	Square-Root
RU001	498	1.030	3.110	1.520	Normal
SE001	718	3.027	1.315	1.515	Log-Normal
UK001	162	0.909	0.486	0.523	Log-Normal
US001	1132	1.234	4.124	1.762	Normal

Table 4 contains the Kolmogorov-Smirnov test results for ^{212}Pb at all the radionuclide monitoring stations. Due to ^{212}Pb's 10.6 hour half-life, only stations that employ short counting methodologies are considered for studying the ^{212}Pb atmospheric concentration distributions. Out of these eight stations, none are best fit with a normal distribution, six are best fit by a log-normal distribution, and two are best fit with a square-root distribution. The ^{212}Pb data set utilized for the FI001 (Helsinki, Finland) station has been abbreviated to include only those samples that adhered to a short sampling methodology. The ^{212}Pb atmospheric activity distribution at KW001 is best fit by a square-root distribution similar to what was shown in an earlier evaluation [Evans, 1996].

Studies on ^{40}K atmospheric activity concentrations indicate that the majority of the counts under the 1460.75 keV peak result from ^{40}K within the filter blank and detector background. While histograms, cumulative probability plots, and the Kolmogorov-Smirnov test are all applied to the ^{40}K data, these results have little meaning because no blank subtraction has been performed on the data. Figure 1 shows the ^{40}K count-rates for the US001USA1 detector at the US001 (Charlottesville, USA) station. The shifts in count-rates are due to changes in the aerosol filter batches. Thus, one can see that for a given batch of aerosol filters, the ^{40}K count-rate remains relatively constant. This phenomenon is often utilized at the pIDC as a QA/QC check on gamma-ray spectrum acquisition time.

Table 3
^{210}Pb Atmospheric Activity Concentration Distributions

Station	Sample Set Size	Normal Distribution K-S Z-Value	Log-Normal Distribution K-S Z-Value	Square-Root Distribution K-S Z-Value	Best Distribution Fit
AR001	72	1.396	2.260	1.517	Normal
AU001	-	-	-	-	
AU002	107	2.040	0.817	1.444	Log-Normal
AU003	112	0.834	0.744	0.546	Square-Root
AU004	109	1.708	0.565	1.203	Log-Normal
CA001	149	1.263	2.979	2.105	Normal
CA002	310	9.145	6.279	9.13	Log-Normal
CA003	106	1.124	0.999	0.728	Square-Root
CA004	109	1.345	0.849	0.878	Log-Normal
CA005	72	1.277	2.200	1.762	Normal
DE002	108	1.107	0.663	0.770	Log-Normal
FI001	288	2.085	1.764	1.698	Square-Root
KW001	199	4.862	1.098	1.785	Log-Normal
NZ001	17	(0.409)	(0.898)	(0.629)	(Normal)
NZ002	5	(0.748)	(0.611)	(0.682)	(Log-Normal)
NZ003	15	(0.778)	(0.986)	(0.690)	(Square-Root)
RU001	227	7.117	2.308	5.412	Log-Normal
SE001	661	3.712	1.346	2.627	Log-Normal
UK001	83	1.181	0.774	0.445	Square-Root
US001	424	7.950	3.010	2.625	Square-Root

Values in parentheses are for sample sets smaller than 20. These values should be viewed with caution since the sample set is small.

Seasonal Trends

Seasonal trends are observed at most of the stations for ^{7}Be, ^{210}Pb, and ^{212}Pb. Since the ^{40}K signals in the gamma-ray spectra are dominated by the blank, no seasonal variations are observed (nor expected) for ^{40}K. The best tool for observing the seasonal trends is the box plot. A box plot of ^{7}Be at the KW001 station (Kuwait City, Kuwait) is shown in Figure 2. Multiple years of the aerosol data are sorted by month and each month's data are plotted in a "box and whisker." A line in the box represents the mode of the monthly air concentrations. The range of the box depicts the bounds of the 25th and 75th percentiles of the data. The whiskers extending from the box represent the bounds of the 10th and 90th percentile of data. Data points that extend beyond the 10th and 90th percentiles are plotted individually. The seasonal trend in this data is obvious with the peak ^{7}Be concentrations occurring in the summer months.

Table 5 shows the months with the highest median atmospheric activity concentration. If no seasonal trend is observed, the space in the table is left empty. This is often the result of insufficient data. ^{212}Pb is not quantified at stations with a long-decay sampling methodology and no seasonal trend is observed for this radionuclide at these stations. While most stations exhibited 12-month cycles in their natural radionuclide concentrations, some stations display trends with two distinct peaks in atmospheric activity concentrations. Figure 3 contains a box plot of the ^{7}Be atmospheric activity concentrations at the RU001 (Ussuriysk, Russia) station. Clear seasonal highs are seen for ^{7}Be during the months of April and September. Since variations in ^{7}Be atmospheric activity concentrations at a given station are largely a function of meteorological influences on vertical atmospheric mixing, it is no surprise that highs are seen both in the spring and fall.

Table 4
^{212}Pb Atmospheric Activity Concentration Distributions

Station	Sample Set Size	Normal Distribution K-S Z-Value	Log-Normal Distribution K-S Z-Value	Square-Root Distribution K-S Z-Value	Best Distribution Fit
AR001	361	1.858	0.869	0.962	Log-Normal
AU001	799	3.540	1.725	1.760	Log-Normal
AU002	-	-	-	-	
AU003	-	-	-	-	
AU004	-	-	-	-	
CA001	-	-	-	-	
CA002	1104	4.199	1.428	2.566	Log-Normal
CA003	-	-	-	-	
CA004	-	-	-	-	
CA005	-	-	-	-	
DE002	-	-	-	-	
FI001	248	4.750	1.214	2.740	Log-Normal
KW001	971	2.934	2.451	1.214	Square-Root
NZ001	-	-	-	-	
NZ002	-	-	-	-	
NZ003	-	-	-	-	
RU001	497	4.322	0.788	2.761	Log-Normal
SE001	713	12.045	1.046	6.146	Log-Normal
UK001	-	-	-	-	
US001	1131	2.654	1.854	0.877	Square-Root

* FI001 sample set size reduced to samples from 01-Sept-1998 to 10-June-1999 that adhere to short-decay sampling methodology.

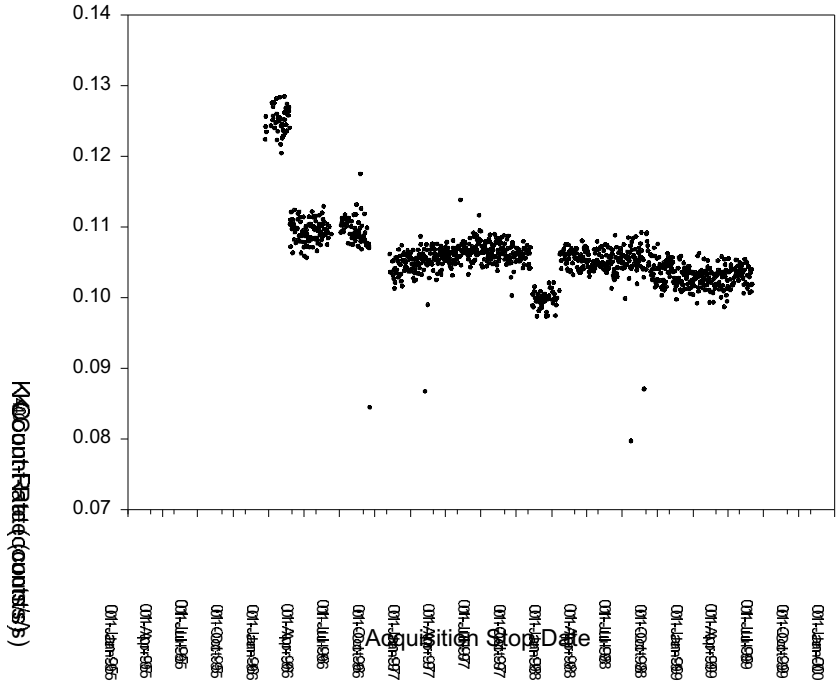


Figure 1. ^{40}K count-rates in sample spectra for US001USA1 detector at US001 (Charlottesville, USA) station. Data from December, 1995 through June, 1999.

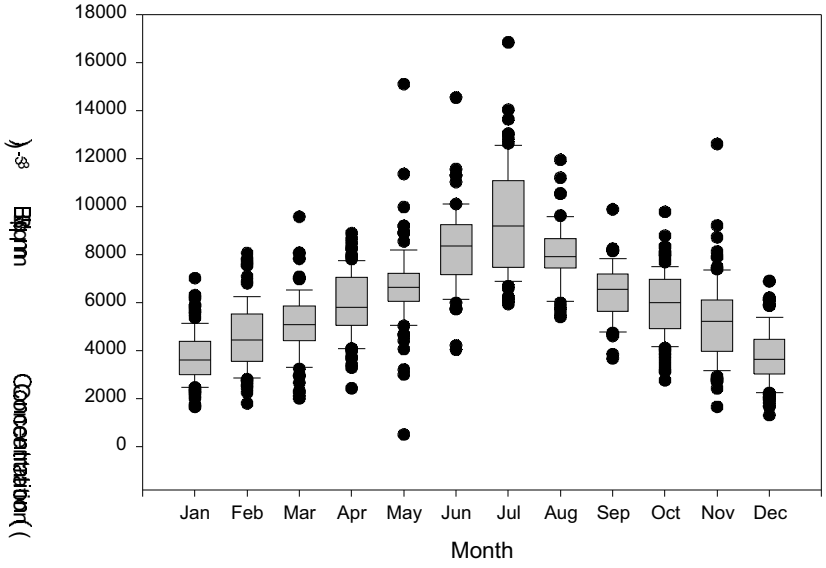


Figure 2. Box plot of ^{7}Be at KW001 (Kuwait City, Kuwait) station. Data from September, 1995 to June, 1999.

Table 5
Seasonal Peaks of Natural Radionuclide Activity Concentrations

Station	^{7}Be	^{210}Pb	^{212}Pb	^{40}K
AR001	December	(December)	(September)	-
AU001	February		March	-
AU002	March	May		-
AU003	October	June		-
AU004	October	May/October		-
CA001	July	February		-
CA002	April/September	August	August	-
CA003	March	February		-
CA004	March/July	February		-
CA005	March/August	(January)		-
DE002	June	September		-
FI001	June	March		-
KW001	July	June	November	-
NZ001	January			-
NZ002	November			-
NZ003	February			-
RU001	April/September	January	April/November	-
SE001	June	December	August	-
UK001	April/October	March/October		-
US001	April/July	September	September	-

Months in parentheses were for data with only a marginal seasonal trend.

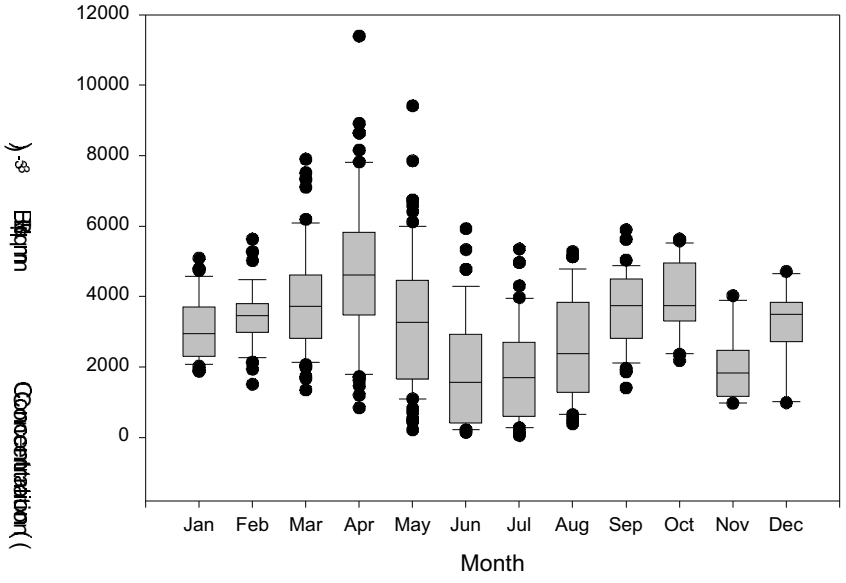


Figure 3. Box plot of ^{7}Be at RU001 (Ussuriysk, Russia) station. Data from November, 1995 to July, 1998.

CONCLUSIONS AND RECOMMENDATIONS

This research shows the distributions and trends of natural radionuclides monitored at twenty stations. These distributions and trends will be utilized to model the expected ranges of the natural radionuclide concentrations at these stations. If an abnormal measurement is detected, a flag will be created to alert radionuclide analysts that the natural radionuclide concentration is out of the expected range. The radionuclide analyst may then pay special attention to sampling metrics like sampling time, decay time, gamma-ray spectrum acquisition time, and sampler flow-rate. Monitoring the levels of these radionuclides in all analyzed samples is an excellent form of performance monitoring.

At many stations the ^{7}Be concentrations fluctuate largely with season. Knowledge of these fluctuations is beneficial to monitoring the atmosphere for fission products from nuclear weapon tests because detection is highly dependent on atmospheric transport. A large degree of vertical mixing in the atmosphere enhances the station's ability to capture fission product aerosols from a nuclear test.

The fluctuations of ^{210}Pb provide some indication of the crustal resuspension at the station. At times of the year when ^{210}Pb concentrations are high, the resuspension of old nuclear weapons fallout and resuspension of fallout from previous nuclear accident releases should also be high. As more data is collected in Europe, correlations should be made between the resuspension of Chernobyl fallout and ^{210}Pb concentrations.

Similar studies should continue to be performed as more stations are brought on-line. This information will help in our understanding of the environment that the station is monitoring. Such information may then be advantageous to the monitoring system as a basis for performance monitoring and other QA/QC measures.

REFERENCES

Bohner, J (1998) " Comparison of the Current and Proposed Characterization Approaches for Radionuclide Measurements", CMR Technical Report CMR-98/35.

Evans, W. C.(1996) "Automated Categorization of Airborne Radioactivity Measurements for CTBT Monitoring," PSR Technical Note 1091.

Koch, D. M.; Jacob, D. J.; Graustein, W. C. (1996) "Vertical transport of tropospheric aerosols as indicated by ^{7}Be and ^{210}Pb in a chemical tracer model," *Journal of Geophysical Research*, Vol. 101, No. D13, pp. 18,651-18,666.

Shen, X. (1998) "Natural Radionuclide Concentration Distribution and Seasonal Trend Analysis Report," CMR Technical Report CMR-98/31.

Winkler, R.; Dietl, F.; Frank, G.; Tschiersch, J. (1998) "Temporal Variation of ^{7}Be and ^{210}Pb size Distributions in Ambient Aerosol" *Atmospheric Environment*, Vol. 32, No. 6, pp. 983-991.

HIGH-SENSITIVITY DETECTION OF XENON ISOTOPES VIA BETA-GAMMA COINCIDENCE COUNTING

Ted W. Bowyer, Justin I. McIntyre, Paul L. Reeder
Pacific Northwest National Laboratory

Sponsored by U. S. Department of Energy
Office of Nonproliferation and National Security
Office of Research and Development
Contract No. DE-AC06-76RLO 1830

ABSTRACT

Measurement of xenon fission product isotopes is a key element in the global network being established to monitor the Comprehensive Nuclear-Test-Ban Treaty. Pacific Northwest National Laboratory has developed an automated system for separating Xe from air which includes a beta-gamma counting system for ^{131m}Xe, ^{133m}Xe, ^{133}Xe, and ^{135}Xe. Betas and conversion electrons are detected in a plastic scintillation cell containing the Xe sample. The counting geometry is nearly 100% for beta and conversion electrons. The resolution in the pulse height spectrum from the plastic scintillator is sufficient to observe distinct peaks for specific conversion electrons. Gamma and X-rays are detected in a NaI(Tl) scintillation detector which surrounds the plastic scintillator sample cell. Two-dimensional pulse height spectra of gamma energy versus beta energy are obtained. Each of the four xenon isotopes has a distinctive signature in the two-dimensional energy array. The details of the counting system, examples of two-dimensional beta-gamma data, and operational experience with this counting system will be described.

Key Words: Xenon Fission Products, Beta-Gamma Coincidence Counting, CTBT Monitoring

OBJECTIVE

1. Relevance to CTBT

Clandestine underground nuclear tests are likely to vent Xe fission product gases into the atmosphere. As called for by the Comprehensive Nuclear-Test-Ban Treaty (CTBT), the International Monitoring System includes xenon monitoring systems to detect any such releases [1]. These systems must be extremely sensitive because of the dilution of the Xe gases during atmospheric transport to the monitoring station. Present requirements specify that the four isotopes ^{131m}Xe, ^{133m}Xe, ^{133}Xe, and ^{135}Xe be measured, that ^{133}Xe be measured with a sensitivity of <1 mBq/m^3, and that the measurement system be suitable for automatic operation in remote locations.

2. Significance of each isotope

The four isotopes of Xe to be measured for CTBT have varying degrees of usefulness as indicators of a nuclear weapons explosion [2]. However, any or all of them may be present in routine air samples so it is important to quantify them so that anomalous concentrations can be evaluated.

The nuclide ^{131m}Xe ($t_{1/2}$ = 11.93 d) is produced in low yield from nuclear explosions - several orders of magnitude below that of ^{133}Xe and ^{135}Xe. However, it is formed as a by-product of ^{133}Xe production for use in medical procedures. It can be present in airborne samples as a result of accidental releases from medical facilities, during operation of nuclear reactors, or from dissolution of spent reactor fuel. Although it is not a major indicator of a nuclear explosion, it is a potential interference in measurements of the other Xe isotopes. It is can also be used as a convenient source to calibrate the beta-gamma counting system. In those cases where there is a long time delay between a nuclear explosion and collection of the sample, an elevated level of ^{131m}Xe may be the only indicator of a weapons violation because the ^{131m}Xe half-life is longer than the other Xe fission products.

The ^{133m}Xe is present in air samples primarily as the result of a process involving its independent fission yield - most likely, the result of a nuclear explosion. Because ^{133m}Xe is produced in only 2.9% of ^{133}I decays, its cumulative fission yield relative to ^{133}Xe is quite small. Most of the Xe released during reactor operations or fuel reprocessing results from decay of the precursor I isotopes (cumulative yield) which results in low ratios of ^{133m}Xe to ^{133}Xe. Also, the method of thermal neutron capture on stable Xe isotopes used to produce ^{133}Xe for medical purposes yields almost 10 times as much ^{133}Xe as ^{133m}Xe. Thus, a high quantity of ^{133m}Xe as well as a high ratio of ^{133m}Xe to ^{133}Xe in a given air sample is a key indicator of a nuclear weapons test.

The most likely Xe nuclide seen in ambient air samples is ^{133}Xe. This is often observed in locations downwind from nuclear power plants or perhaps from medical facilities. Its 5.25 d half-life and large cumulative fission yield are factors contributing to its detectability. The PNNL Xe monitoring system routinely observed ^{133}Xe in samples of New York City air and occasionally in samples of air taken in central Florida [3]. The yields of ^{133}Xe seen in these locations are highly variable depending on weather conditions. At our laboratory in eastern Washington state, we rarely observe ^{133}Xe in ambient air as we are upwind of the only reactor in our area. At island locations in the southern hemisphere, levels of ^{133}Xe in ambient air should be negligible. Thus, it will be essential to monitor the baseline levels of ^{133}Xe at each monitoring station. A large increase in ^{133}Xe concentrations above typical fluctuations would be an indication of a possible treaty violation.

Both the independent and the cumulative fission yields of ^{135}Xe are quite large. However, the short half-life for ^{135}Xe ($t_{1/2}$ = 9.14 h) imposes restrictions on the distance over which this nuclide can travel between its source and the Xe sampling station. In the absence of any near-by sources such as nuclear power reactors, the presence of ^{135}Xe is another clear indication of a nuclear weapons test.

3. Isotopic signatures

The four Xe isotopes of interest for CTBT have distinctive radioactive decay properties which allow them to be distinguished from each other in a suitably designed detection system. These decay properties are given in Table 1 along with their radioactive half-lives and fission yields. The independent fission yields are more likely to be associated with nuclear weapons explosions whereas the cumulative fission yields are more closely associated with reactor operations or spent fuel operations.

Table 1. Half-lives, fission yields, principal radiations and abundances of Xe fission products.[a,b]

Nuclide	^{131m}Xe	^{133m}Xe	^{133}Xe	^{135}Xe
Half-life	11.93 d	2.19 d	5.25 d	9.14 h
Fission yield				
Independent (%)	2.41×10^{-7}	4.23×10^{-3}	1.46×10^{-3}	1.20×10^{-1}
Cumulative (%)	4.51×10^{-2}	1.98×10^{-1}	6.72×10^{0}	6.60×10^{0}
Photon Emission				
Energy (keV)	163.9	233.2	81.0	249.8
Abundance (%)	1.96	10.3	37.0	90.0
X-ray Emission				
(K-shell)				
Energy (keV)	30.	30.	31.	31.
Abundance (%)	54.05	56.3	48.9	5.2
(L-shell)				
Energy (keV)	4.3	4.3	4.5	4.5
Abundance (%)	7.2	6.8	5.2	0.6
Beta Spectrum				
Max. Energy (keV)			346.	905.
Ave. Energy (keV)			99.	300.
Abundance (%)			99.	97.
Conversion. Electrons				
(K-shell)				
Energy (keV)	129.	199.	45.	214.
Abundance (%)	60.7	63.1	54.1	5.7
(L-shell)				
Energy (keV)	159.	229.	75.	245.
Abundance (%)	37.4	26.9	8.4	1.1

[a]Half-lives and decay data are from the Table of Radioactive Isotopes [4] .
[b]Fission yields are for fast fission of ^{235}U [5] .

The nuclide ^{131m}Xe is an isomeric state which decays to the ground state of ^{131}Xe by a 163.9-keV transition. The 163.9-keV gamma is highly converted and can not be seen in gamma singles counting above the normal backgrounds. However, the coincidence between the 129-keV conversion electrons and the 30-keV X-rays of Xe provides a unique signature in a beta-gamma counting system. With a low-noise NaI(Tl) detector, the 4.3-keV X-rays can be observed in coincidence with the 159-keV conversion electrons.

The nuclide ^{133m}Xe has a similar decay scheme as ^{131m}Xe. Its 233.2-keV gamma is also difficult to see in gamma singles counting, but the 30-keV X-rays in coincidence with its conversion electrons at 199 keV are efficiently detected in a beta-gamma counting system. . With a low-noise NaI(Tl) detector, the 4.3-keV X-rays can be observed in coincidence with the 229-keV conversion electrons.

The dominant beta decay branch (99.2%) of ^{133}Xe populates the first excited state of ^{133}Cs which deexcites by emission of an 81-keV gamma or by internal conversion producing conversion electrons and Cs X-rays. The coincidence between the beta particles and the 81-keV gamma is a distinctive signature for ^{133}Xe. However, the 81-keV gamma appears in only 37% of the ^{133}Xe decays due to internal conversion. The conversion electrons are counted along with the preceding betas by the beta detector. A second signature for ^{133}Xe is the coincidence between the betas plus conversion electrons with the 31-keV X-rays of the Cs daughter.

The distinctive signature for ^{135}Xe is its 249.8-keV gamma in coincidence with the preceding beta particle.

To make use of these individual signatures, it is necessary to measure the energy spectrum of the gamma and X-rays in coincidence with the energy spectrum of the betas and conversion electrons as described below.

II. RESEARCH ACCOMPLISHED

In support of the CTBT monitoring program, the Pacific Northwest National Laboratory (PNNL) has developed an automated system for separating Xe from air and counting the Xe fission-product nuclides [3][6] . The system is called ARSA which stands for Automated Radioxenon Sampler-Analyzer. The PNNL system extracts the few cm^3 of Xe contained in 48 m^3 of air by use of cryogenic techniques and selective adsorption on charcoal as described elsewhere in this symposium. The Xe samples are counted with a beta-gamma coincidence system which has high sensitivity for ^{131m}Xe, ^{133m}Xe, ^{133}Xe, and ^{135}Xe [7] [8] [9]. Samples are contained in hollow plastic scintillation cells surrounded by two NaI(Tl) detectors. Pulse height spectra for beta particles and/or conversion electrons detected by the plastic scintillator are recorded in coincidence with the pulse height spectra of gammas and X-rays detected by the NaI(Tl) scintillator. These pulse height data are stored in a two-dimensional array of gamma (photon) energy versus beta (electron) energy as described below. Each of the four Xe isotopes of interest occupies a distinctive location within the two-dimensional array. Background radiations are largely eliminated by the coincidence requirement between the plastic scintillator and the NaI(Tl) scintillator. The use of beta-gamma coincidence counting provides identification of each isotope under very low-background conditions and thus gives the required high sensitivity for detection of Xe fission products.

1. Description of detector

    a. Hardware

The beta-gamma counting system contains two rectangular NaI(Tl) detectors sandwiched together in a single aluminum can with a light barrier between them. Each crystal is viewed by two 7.62-cm diam. photomultiplier tubes (PMTs). The outputs of the two PMTs are gain matched and summed to provide uniform pulse height resolution over the long dimension of the crystal. The arrangement of crystals and PMTs is illustrated in Fig. 1.

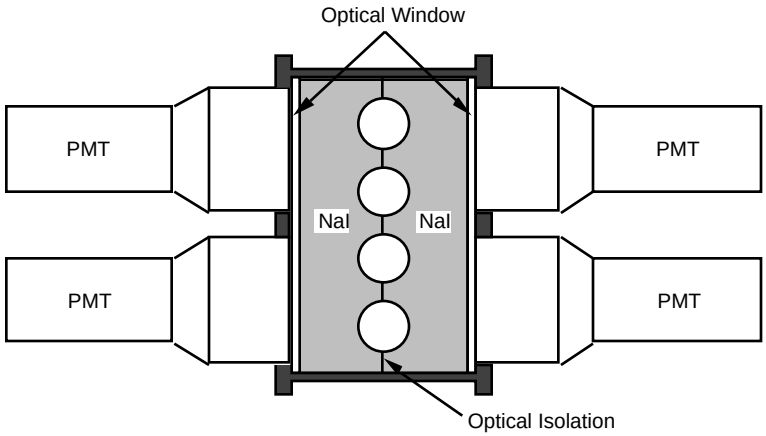


Fig. 1. NaI(Tl) scintillation detectors for Xe monitoring system. Plastic scintillator sample cells occupy the four holes in the NaI(Tl) detectors.

Four holes with diameters of 3.175 cm are machined in the plane defined by the light barrier between the two crystals. These holes contain the plastic scintillation cells that contain the Xe samples and detect the beta particles. This detector package allows the simultaneous counting of four samples. The scintillation cells are cylinders with outside dimensions of 5.08-cm length by 1.51-cm diam. having 0.12-cm thick walls and 0.10-cm thick end plugs giving an internal volume of 6.18 cm^3. The arrangement of sample cell and phototubes is illustrated in Fig. 2. A single gas transfer line is used to insert and remove the Xe sample. The figure does not show the additional transfer tubes which allow an external calibration source to be moved to the midpoint of the cell.

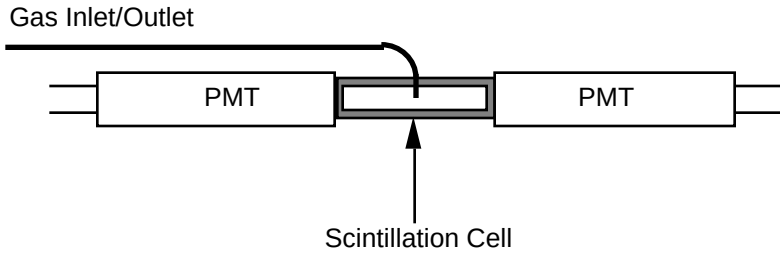


Fig. 2. Schematic representation of plastic scintillation sample cell and photomultiplier tubes.

The plastic scintillator walls are thick enough to completely stop all betas from ^{133}Xe. The ends of the scintillation cells are viewed by 1.90-cm diam. Thorn 9078SA PMTs. The two PMTs are operated in coincidence so that PMT dark current pulses are rejected.

b. Electronics

The electronics described in our previous publications were designed to provide beta-gated gamma spectra only [3][7][8][9]. These electronics have now been modified to provide both the gamma spectra and the beta spectra in a two-dimensional histogram array. The pulse height spectra from the two halves of the NaI(Tl) detector are gain matched and multiplexed together to provide a single gamma pulse height spectrum. However, logic pulses are generated for events in each half of the NaI(Tl) detector. Valid events are those for which only one of the two halves has an event. This requirement allows the rejection of Compton scattering events in which a gamma scatters from one half of the detector into the other half and also allows the rejection of cosmic ray events which traverse both detectors.

The pulses from the two PMTs at each end of a single beta cell are summed together before being shaped for pulse height analysis. Gain matching of these two PMTs must be performed to optimize the pulse height resolution for the beta spectrum. Logic pulses are created for each of the four xenon sample cells. The beta pulses are multiplexed to a single analog-to-digital converter (ADC). However, the beta logic pulses are used to route the pulse height data to four separate gamma versus beta two-dimensional arrays in the computer. Multiplexing of the beta and gamma signals to a single gamma ADC and a single beta ADC simplifies the electronics and is possible because of the low count rates in all the detectors. Typical gamma singles count rates are about 50 to 100 cps when the detector is within the 5.08-cm thick lead shield whereas the beta count rates in a single cell are about 1 cps.

All of the electronics used for the radiation detection are commercial NIM modules except for the interface module which transfers the two gamma logic pulses, the four beta logic signals, the gamma pulse height address, and the beta pulse height address to the computer. Currently, the data acquisition computer is the same QNX-based computer which controls the xenon collection and purification process.

c. Calibrations

For relatively simple decay schemes, the efficiency of a particular detector can be determined by coincidence counting without knowing the absolute disintegration rate of the source. The counting rate in the beta detector (R_β) is given by the source strength (R_o) times the beta detection efficiency (ε_β) times the abundance of the beta (A_β). The beta-gamma coincidence rate ($R_{\beta\gamma}$) is given by the source strength times the beta efficiency times the beta abundance times the gamma efficiency (ε_γ) times the gamma abundance (A_γ). Thus the beta efficiency is determined from the following expression.

$$\frac{R_{\beta\gamma}}{R_\gamma} = \frac{R_o * \varepsilon_\beta * A_\beta * \varepsilon_\gamma * A_\gamma}{R_o * \varepsilon_\gamma * A_\gamma} = \varepsilon_\beta * A_\beta \qquad \text{Eq. (1)}$$

Thus, the beta efficiency is determined simply by measuring the beta-gamma coincidence rate and the gamma singles rate. The beta abundance is known from the decay scheme.

Calibration of the beta efficiency for ^{133}Xe is best done with a spike sample of pure ^{133}Xe available from commercial suppliers. The number of counts in the beta-gated gamma peak at 81 keV divided by the

number of counts in the ungated 81-keV gamma peak is the beta efficiency associated with that gamma peak. Note that the beta abundance as given in Table 1 is essentially 100%. The same procedure gives the beta counting efficiency for the betas and conversion electrons in coincidence with the 31-keV X-rays. The counting efficiency for the combined betas plus conversion electrons is greater than the counting efficiency for the betas alone because the extra pulse height contributed by the conversion electrons puts more of the events above the low-level discriminator threshold. Experimentally, we measure a counting efficiency for the betas associated with the 81-keV gamma from ^{133}Xe of about 75% whereas the betas and conversion electrons associated with the 31-keV X-rays have an efficiency of 97%. Although we do not have experimental efficiencies for the conversion electrons associated with ^{131m}Xe and ^{133m}Xe, the energies of the conversion electrons from these two isotopes are greater than most of the betas from ^{133}Xe so we expect the conversion electron counting efficiencies to be greater than 95%. For ^{135}Xe, the beta spectrum extends to a maximum energy about 3x the maximum energy of the ^{133}Xe beta spectrum so we expect beta efficiencies greater than 90% for ^{135}Xe.

The calibration of the gamma efficiencies for ^{133}Xe could be done in a similar fashion. However, an extra correction factor is required to account for the fact that not all beta events have the same counting efficiency and the gamma abundances are not unity. This correction factor is dependent on knowing the beta efficiencies for each of the beta processes and the gamma abundance factor. For ^{133}Xe, the efficiency for the 81-keV gamma is the number of counts in the beta-gated 81-keV gamma peak divided by the number of counts in the ungated beta spectrum times the correction factor. The experimental value for this efficiency is 84% for the sum of the two NaI(Tl) detectors. This efficiency value includes the small iodine escape peak at 52 keV. Without the escape peak, the efficiency is 80%. The efficiency for the 31-keV X-ray peak is the number of counts in the beta-gated 31-keV peak divided by the number of counts in the ungated beta spectrum times a different correction factor. The experimental efficiency for the 31-keV X-ray is 67%. It is not surprising that the 31-keV X-rays are less efficient than the 81-keV gamma because the X-rays have a higher absorption probability while traversing the plastic scintillator cell, the sample cell holder, and the hermetic can surrounding the NaI(Tl) detector. It is expected that the gamma detection efficiency will first increase as a function of gamma energy and then decrease at energies above 100 keV. Thus the gamma detection efficiency for the 249.8-keV gamma from ^{135}Xe should be about 30% less than the efficiency for the 81-keV gamma. As an alternative procedure, we are currently calibrating the gamma efficiencies using a mixed isotopic source with calibrated intensities.

2. Rn interference

A major requirement of the xenon collection and purification system is to provide a xenon sample free of radon gas. The ^{238}U found naturally throughout the world decays through a chain of alpha and beta decays to ^{222}Rn which has a 3.8 d half-life. The amount of ^{222}Rn present in ambient air is variable depending on location and weather conditions but normally is in far greater concentration than the desired xenon isotopes. If any ^{222}Rn is transferred into the xenon sample cell, it produces two beta-decaying daughter isotopes, ^{214}Pb and ^{214}Bi, which are readily observed by the beta-gamma counting system and interfere with measurements of the xenon radioactivities.

An example of a two-dimensional (2D) histogram array of gamma pulse height versus beta pulse height is shown in the left hand plot of Fig. 3 for a sample containing ^{222}Rn gas and no radioactive Xe gas. The energy scale of the gamma axis has been adjusted to include the 609.3-keV gamma ray following beta decay of ^{214}Bi. The gain on the beta axis has also been adjusted to see the maximum pulse heights produced by the betas from ^{214}Pb and ^{214}Bi.

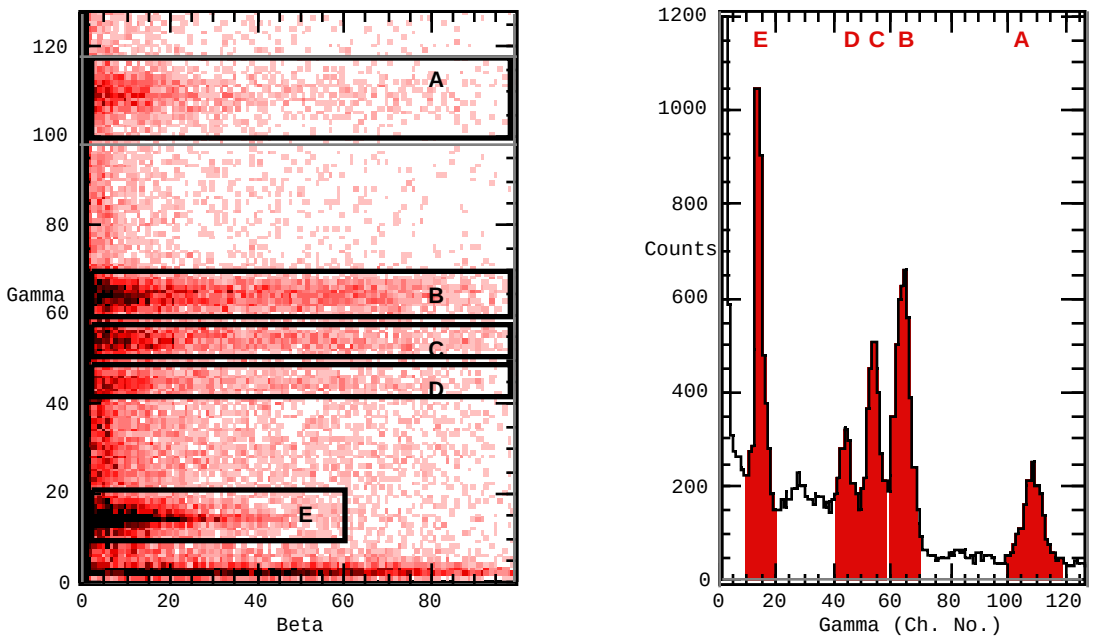


Fig. 3. Left hand plot is two-dimensional array of gamma pulse height versus beta pulse height for Rn sample. Axes are labeled with channel numbers. Gray scale indicates relative number of counts. Right hand plot is gamma spectrum obtained from the same data by integration along the beta axis.

These pulse heights are greater than the pulse heights observed for the xenon isotopes. The right hand plot of Fig. 3 shows the one-dimensional gamma spectrum obtained by integrating the counts along the beta axis between beta channels 2 through 99. The regions of interest labeled A - E in the 2-D array of Fig. 3 correspond to the following radiations.

A. 609.3-keV gamma ray following beta emission from ^{214}Bi.
B. 351.9-keV gamma ray following beta emission from ^{214}Pb.
C. 295.1-keV gamma ray following beta emission from ^{214}Pb.
D. 241.9-keV gamma ray following beta emission from ^{214}Pb
E. X-rays with energies between 75- and 90-keV from ^{214}Pb plus a small contribution (≈10%) of X-rays between 77- and 92-keV from ^{214}Bi.

The shaded areas and labels in the right hand plot of Fig. 3 correspond to the regions of interest defined in the left hand plot.

The 241.9-keV gamma from ^{214}Pb interferes with observation of the 249.8-keV gamma from ^{135}Xe while the X-rays from Pb and Bi decays interfere with observation of the 81-keV gamma from ^{133}Xe. Fortunately the areas of each peak in these spectra are constant relative to each other so knowing the area under the 351.9-keV peak, for example, in an actual xenon spectrum allows one to calculate the counts due to ^{214}Pb and ^{214}Bi corresponding to their X-ray peak and the 241.9-keV peak. These calculated areas can then be used to correct the observed areas in the xenon spectra. Because the beta pulse height spectra for the desired xenon isotopes have lower amplitudes than the beta pulse height spectra for the interferences, we can choose regions of interest in the 2-D arrays which minimize the contribution from the interferences.

3. 2-D spectrum of Xe from U fission

An experiment to measure Xe gases from fission of ^{235}U was conducted. A thin sample of ^{235}U was irradiated at a reactor and allowed to cool in a sealed container for about 1 day. Then a syringe was inserted into the gas space surrounding the sample and a small volume of gas was removed. This gas was then injected without further purification into a xenon sample cell and counted at 4 hour intervals over several days. A typical 2D histogram array is shown in Fig. 4 along with the same data integrated to give the gamma spectrum gated by betas of all energies.

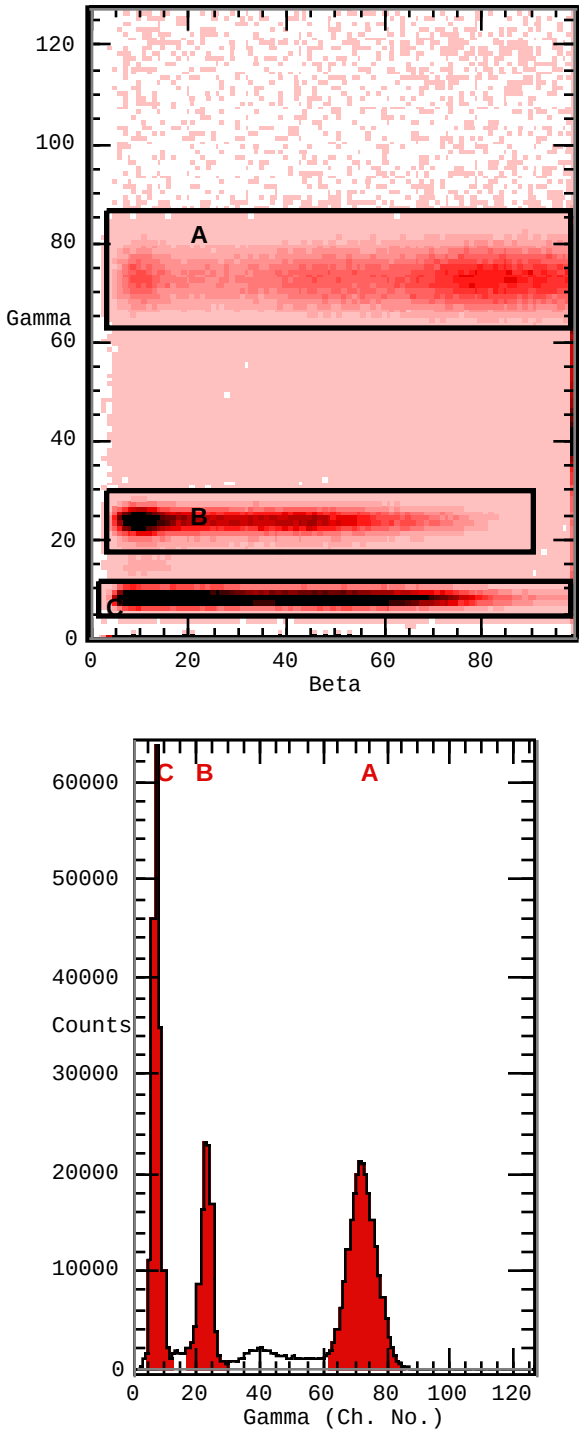


Fig. 4. Left hand plot is two-dimensional array of gamma pulse height versus beta pulse height for Xe fission gas sample. Axes are labeled with channel numbers. Gray scale indicates relative number of counts. Right hand plot is gamma spectrum obtained from the same data by integration along the beta axis.

a. Identification of ROI's

The boxes labeled A, B, and C in the 2D plot in Fig. 4 correspond to regions of interest for particular Xe isotopes. Region A is centered on the gamma peak at 250 keV and the beta spectrum corresponding to the 905-keV betas from ^{135}Xe. The energy scale for this particular experiment did not allow observation of the highest energy beta pulses for this isotope. Region B is centered on the 81-keV gamma and 346-keV betas from ^{133}Xe. Region C is centered on the 31-keV X-rays and betas plus conversion electrons also from ^{133}Xe. Note that the betas and conversion electrons from ^{133}Xe are observed simultaneously in the plastic scintillator so that the energy of the conversion electrons shifts the beta spectrum to somewhat greater pulse heights than for the beta spectrum observed with the 81-keV gamma.

The shaded areas in the gamma spectrum shown in the right hand plot of Fig. 4 indicate the corresponding regions of interest. The small peak at about channel 40 on the gamma axis is the result of the fortuitous overlap of the Compton edge and Compton backscatter peaks for an incident gamma energy of 250 keV. The conclusion that this peak is associated with ^{135}Xe is confirmed by the half-life analysis described below.

Because of the time delay before collecting the xenon gas sample, much of the ^{133}I had decayed to ^{133}Xe thus increasing the abundance of the ^{133}Xe at the expense of ^{133m}Xe. As a consequence, the conversion electron peak at 200 keV in coincidence with the 30-keV X-rays for ^{133m}Xe was somewhat obscured. Likewise, the signature for ^{131m}Xe is not expected for this set of data because of the low independent yield of ^{131}Xe. The long half-life of ^{131}I (8 days) prevents it from contributing to the cumulative yield of ^{131m}Xe in this experiment.

b. Half-life analysis

Two-dimensional pulse height spectra were obtained for the xenon fission products as a function of time over a period of about 7 days. Various regions of interest like those illustrated in Fig. 4 were integrated to obtain the number of counts as a function of time. These data were analyzed using a least squares fitting program which accounted for growth and decay and branchings for all xenon isotopes. For gamma energies greater than 100 keV, all the regions of interest could be fitted with just two components corresponding to decay of ^{135}Xe and a flat background. Regions of interest restricted to gamma energy of 80 ± 20 keV were fitted using 4 components – decay of ^{133}Xe, growth and decay of ^{133}Xe from decay of ^{133m}Xe, a small contribution from ^{135}Xe, and a flat background. The decay curves corresponding to 30 ± 10 keV-gamma energy were quite complex as ^{133m}Xe, ^{133}Xe, and ^{135}Xe all contribute X-rays in this region. From the initial activities calculated from a fit to the 30 ± 10-keV region which included all beta energies, we calculated that the xenon fission gas sample at the time of extraction from the ^{235}U target had 13% ^{133m}Xe, 75% ^{133}Xe, and 12% ^{135}Xe (atom %) which is in rough agreement with expectations based on cumulative fission yields. As expected, when the same region of interest was limited to only the highest beta energy (channels 95 - 99 in Fig. 4), the decay curve could be fitted with only a ^{135}Xe component and a flat background component.

Normally, the ARSA system will not perform half-life analysis. Identification of specific isotopes will be based on relative numbers of counts within a specific region of interest associated with individual signatures. However, the 2D spectra and half-life analysis performed in this experiment illustrates that the ARSA counting system does measure all the xenon isotopes of interest for CTBT purposes.

5. Factors affecting performance

The 2D histogram arrays of gamma energy versus coincident beta energy provide a highly selective and sensitive technique for identification and quantification of particular xenon isotopes. However, there are several factors which degrade the performance and which should be avoided whenever possible.

The only radioactive gas which interferes is ^{222}Rn. The signatures from the ^{214}Pb and ^{214}Bi daughters were shown above in Section II.2. If ^{222}Rn is not completely removed by the xenon separation system, the daughter signatures will be observed in the counting data. However, using the regions of interest defined in Fig. 3, the number of counts in region B (352-keV gamma) will be in a fixed ratio to the number of counts in regions D and E. These fixed ratios can be used with the observed number of counts in region B to

provide an accurate correction for the Rn daughters that might interfere with the xenon isotopes whose signatures occur near regions D and E. Because of possible errors in making such corrections, it is desirable to minimize any contamination of the xenon sample with radon.

Another factor affecting performance is the incomplete removal of one xenon sample before inserting a new xenon sample. We have observed that a small fraction (≈5%) of a xenon sample remains in the sample cell even after prolonged pumping on the cell. Thus, if a low activity xenon sample is counted after a preceding sample with high activity levels, the residual activity can bias the result for the low activity sample. To correct for this effect, we always take a background count before each sample count and use any residual xenon activity in the background count to correct the sample count.

A third factor affecting performance is the variability of the concentrations of xenon radioisotopes in ambient air due to human activities related to medical uses of xenon isotopes or to reactor operations. These variations will be dependent on the location of the sampling station, weather conditions, and the human activities. It will be necessary to establish baseline concentrations of each of the four isotopes at each of the sampling stations and to observe these concentrations over some period of time to establish normal variations in these concentrations. In any case, a high concentration of ^{133m}Xe would be immediate cause for further investigation.

III. CONCLUSIONS AND RECOMMENDATIONS

1. Minimum detectable concentrations

The data shown in Section II.3 for xenon fission gas are for a laboratory test and are not representative of typical counting data for ambient air. Results from ambient air samples taken over several months in New York City have been described in our previous publication [3]. ^{135}Xe was observed only on a few occasions as a result of releases from nearby reactors. Variable concentrations of ^{133}Xe up to 60 mBq/m^3 were observed routinely as a result of reactor releases or medical usage. The counting system used during the New York tests did not involve measurement of the beta spectra so the concentrations of ^{131m}Xe and ^{133m}Xe could not be separated from each other. However, the combined concentration was always weak or not observed.

The results of the New York tests lead to the estimates of minimum detectable concentrations (MDC) shown in Table 2 for the various isotopes[10] . These values are based on 16 hours of counting per sample and stable xenon yields of about 1 cm^3. The range of MDCs for ^{133}Xe is primarily due to memory effects following intentional spike samples.

Table 2. Minimum detectable concentrations of xenon fission product isotopes based on 2σ uncertainties.

Isotope	MDC (mBq/m^3)
^{131m}Xe + ^{133m}Xe	0.8
^{133}Xe	0.14 to 0.34
^{135}Xe	0.18

More recently, the ARSA system gives about 2 cm^3 of Xe and samples are counted for 24 h instead of 16. Thus the MDCs now are even lower than those given in Table 2. Samples are collected for about 8 h so these results are available three times per day. The current specification for CTBT monitoring for ^{133}Xe is 1 mBq/m^3 so the ARSA system easily meets this requirement. The CTBT specifications are not defined for the other Xe isotopes because they depend critically on the detection system used. The 2D counting data for the ARSA system reported here will enable determination of all four Xe isotopes, but we do not yet have results for the MDCs of ^{131m}Xe and ^{133m}Xe separately.

2. Program status and directions

The ARSA system has been developed over the past few years with several prototype systems of increasing sophistication. The development program is continuing with the goal of reducing the size and power requirements of the system. One of the requirements of the earlier prototypes was to use commercial NIM electronics wherever possible. We are currently designing dedicated counting electronics which will minimize the electronics package. At present, there are two copies of the latest ARSA system. One is in

operation at PNNL and the other is at DME Corp. in Orlando, FL. DME Corp. has been given the task of producing a commercial version of the ARSA system based on the current PNNL prototype.

a. Monte Carlo modeling

Recently, we have begun a program of Monte Carlo calculations to model the response of the plastic scintillator and NaI(Tl) detectors to various radiations. Because of the unusual shape of the xenon sample cell, its response to internal xenon beta and conversion electrons is of great interest. In addition, the response to the external calibration sources is needed. Previously, we have used an external source containing equal amounts of ^{154}Eu and ^{155}Eu to establish amplifier gains for the beta detectors and to monitor the detector performance over time. We now plan to use an external source containing ^{154}Eu and ^{207}Bi. The ^{207}Bi calibration source has conversion electrons at 482 keV and 976 keV which greatly simplify adjusting the beta amplifier gains. The 482-keV conversion electrons lose much of their energy in the first wall of the sample cell and the rest of their energy in the second wall. The conversion electrons at 976 keV have enough energy to pass completely through both walls of the sample cell. However, electrons can undergo large angle scattering in the plastic and thus the 976 keV electrons could deposit all of their energy some fraction of the time. This complicated response will be modeled and compared to the response observed experimentally.

b. Phase I, II, III testing

The CTBT Preparatory Commission has requested a test of xenon analysis systems to assess the state-of-the-art for current technology. Currently there are four countries (France, Russia, Sweden, and USA) which have systems designed to meet the CTBT requirements for xenon monitoring. The proposed schedule calls for a three phase test which should be completed by the end of the year 2000. The first phase will allow development and completion of the Russian and Swedish systems. Phase two will involve installation and simultaneous testing of all four systems at the Institute for Atmospheric Research in Freiburg, Germany. It is expected that this phase will take one or two months and be completed in early 2000. The third phase will be a test of xenon systems at future International Monitoring System (IMS) sites at locations yet to be chosen. The purpose of this phase is to demonstrate long-term, unattended operation to gain experience on measurements without highly skilled technical operators in attendance.

The ARSA system developed by PNNL is ready now to participate in these tests and we are confident that the ARSA system will satisfy all the requirements for xenon monitoring for CTBT verification.

REFERENCES

[1] L. R. Mason, J. D. Bohner, D. L. Williams, Int. Conf. Meth. and Appl. of Radioanal. Chem., Kailua-Kona, HI, April 6-11, 1997, J. Radioanal. Nucl. Chem. 235, 65 (1998).

[2] T. W. Bowyer, R. W. Perkins, K. H. Abel, W. K. Hensley, C. W. Hubbard, A. D. McKinnon, M. E. Panisko, P. L. Reeder, R. C. Thompson, and R. A. Warner, Xenon Radionuclides, Atmospheric: Monitoring, Encyclopedia of Environmental Analysis and Remediation, Robert A. Myers, Ed., John Wiley and Sons, 1998, pp. 5299-5314.

[3] T. W. Bowyer, K. H. Abel, C. W. Hubbard, M. E. Panisko, P. L. Reeder, R. C. Thompson, and R. A. Warner, J. Radioanal. Nucl. Chem. 240, 109 (1999).

[4] E. Browne and R. B. Firestone, "Table of Radioactive Isotopes", John Wiley and Sons, Inc., New York, 1986.

[5] ENDF/B-VI, National Nuclear Data Center, Brookhaven, NY.

[6] T. W. Bowyer, K. H. Abel, C. W. Hubbard, A. D. McKinnon, M. E. Panisko, R. W. Perkins, P. L. Reeder, R. C. Thompson, and R. A. Warner, Int. Conf. Meth. and Appl. of Radioanal. Chem., Kailua-Kona, HI, April 6-11, 1997, J. Radioanal. Nucl. Chem. 235, 77 (1998).

[7] P. L. Reeder, T. W. Bowyer, and R. W. Perkins, Int. Conf. Meth. and Appl. of Radioanal. Chem., Kailua-Kona, HI, April 6-11, 1997, J. Radioanal. Nucl. Chem. 235, 89 (1998).

[8] P. L. Reeder and T. W. Bowyer, Nucl. Instrum. Meth. Phys. Res. A 408, 573 (1998).

[9] P. L. Reeder and T. W. Bowyer, Nucl. Instrum. Meth. Phys. Res. A 408, 582 (1998).

[10] P. L. Reeder, T. W. Bowyer, and K. H. Abel, "Analysis of Beta-Gated Gamma Spectra for the PNNL ARSA and Estimate of Minimum Detectable Activities for (^{131m}Xe+^{133m}Xe), ^{133}Xe, and ^{135}Xe", PNNL-11784-Rev. 1, March 1998.

A TAGGED AEROSOL GENERATOR FOR TESTING CTBT ATMOSPHERIC RADIONUCLIDE AEROSOL SAMPLERS

Alfred J. Cavallo and Colin G. Sanderson, Environmental Measurements Laboratory

Sponsored by the U.S. Department of Energy
Office of Nonproliferation and National Security
Office of Research and Development
Project Number GC0402

ABSTRACT

Gamma-ray spectrometry of air particulates collected on filter paper can be a very useful technique for determining the presence of nuclear fission products in the environment. Such airborne fission products could indicate clandestine nuclear weapons testing, nuclear fuel reprocessing or the catastrophic failure of a nuclear reactor. These atmospheric aerosols are collected and analyzed by high-volume air sampler/analyzers at many locations around the world to monitor compliance with the Comprehensive Nuclear-Test-Ban Treaty (CTBT).

For airborne radionuclide samplers, the CTBT specifications require a total collection efficiency of 80% or greater for 0.2-µm particles as well as a total collection efficiency of 60% or greater for 10-µm particles. To verify that CTBT samplers meet these specifications, a Tagged Aerosol Generator will produce aerosol particles with two known size distributions: a polydisperse distribution with diameters around ***0.25*** µm and a monodisperse distribution with a diameter of 10 µm. For calibration, one size distribution is generated; these particles are tagged with short-lived radon progeny (^{218}Po), then injected into the apparatus to be tested. Sampler collection efficiency for a given aerosol can be determined by measuring the activity of the radon progeny deposited on the air filter.

Particles of the required diameter are generated by commercially available instruments (Palas AGF 2.0 for the 0.25-µm diameter particles, and the TSI 3450 Vibrating Orifice Generator for the 10-µm diameter particles). These particles are neutralized in a TSI 3054 high-flow neutralizer and injected into a 100 l Attachment Volume, along with radon gas from a 1.5-MBq radon source. The Attachment Volume is a cylinder 150 cm tall and 30 cm in diameter; the major design constraint is provided by the requirement to produce 10-µm diameter tagged particles. The settling velocity of such particles is 18 cm min^{-1}; given the attachment rate of ^{218}Po, this implies a tall attachment vessel with low flow rates. Assuming a particle concentration of 10^5 cm^{-3} for the 0.25-µm diameter particles and 50 cm^{-3} for the 10-µm diameter particles (Liu et al., 1974), the attached fractions are 0.98 and 0.55, respectively. This is computed using standard attachment theory (Fuchs, 1964; Postendörfer, 1979, Raabe, 1969) using a diffusion coefficient of 0.07 cm^2 sec^{-1}, which is appropriate for neutral polonium dioxide (Goldstein and Hopke, 1998). A screen (Cheng, et al., 1980) at the exit of the attachment volume is used to remove the unattached aerosol from the air stream. For a sample time of 15 minutes, this should produce an activity on the sampler filter of 140 Bq and 70 Bq, for each particle size, respectively (Evans, 1969).

Key Words: radioactive aerosol, tagged aerosol, radon, aerosol sampler

Introduction

Radionuclide-labeled particles are often used as tracers in lung deposition, pharmacokinetic, and scientific studies. For example, Smith and Cheng (1998) used monodisperse silver particles ($10<d_p<40$ nm) tagged with ^{212}Pb, a decay product of ^{220}Rn with a 10.6 hr half life, for gamma scintigraphy in respiratory tract deposition studies. The decay products of ^{222}Rn also emit gamma rays (Table 1) and can also be used as tracers for calibration and research. Given their high activity and short half-lives, which minimizes counting time and any possibility of contamination, they are a reasonable choice in this application where gamma detection is already used to measure airborne radionuclides.

Methodology

Fig. 1 shows a schematic of a proposed instrument, which consists of the following components:

- ♦ the aerosol generator(s), used to create aerosols with a known particle size distribution,
- ♦ the charge neutralizer, needed to produce high, stable aerosol concentrations,
- ♦ the radon source, used to produce a short lived radioactive element (^{218}Po) to tag the aerosol,
- ♦ and the attachment chamber, in which the ^{218}Po becomes attached to the aerosol particles.

The characteristics of each of these components will be examined in some detail.

Aerosol Generators

The aerosol material is sebacic acid dioctyl ester doped with fluorescine, a fluorescent dye. The aerosol would be tagged with both ^{218}Po and fluorescine, providing two independent methods of verifying the sampler efficiency (assuming that the filter material could be removed from the instrument). Using the radioactive aerosol would test both the aerosol collection efficiency and the gamma counting efficiency of the sampler, while a fluorescence measurement would verify aerosol collection efficiency only.

No one piece of equipment can be used to generate particles over the size range of interest (***0.2*** to 10 μm). A vibrating orifice will be used to generate large particles and a nebulizer to generate small diameter particles. Each is sufficiently simple so that having two different aerosol generators is not a design issue.

A vibrating orifice generator, in this case the TSI Model 3450, produces a monodisperse aerosol by applying a periodic disturbance to a liquid jet. Droplet diameters between 10 μm and 200 μm are possible and are determined by the orifice diameter, the flow rate of the fluid through the orifice and the vibration frequency of the orifice plate. The liquid is a mixture of solvent (propanol), which evaporates rapidly from the droplet, and solute (sebacic acid), which remains. Final particle diameter is determined by the solute to solvent ratio. The generator has been tested with a pure propanol solution using both a 20 μm orifice and a 10 μm orifice. The former is easier to use but operates at a lower frequency and generates fewer particles (lower particle concentration). Concentration of the 10 μm particles (N, cm^{-3}) is:

$$N = \frac{f \cdot 60 \cdot e}{Q_V}$$

f = orifice vibration frequency (275 kHz)

e =efficiency (0.5)

Q_V = volumetric flow rate (25 lpm)

For the parameters listed above, the particle concentration in the attachment volume is expected to be about 330 cm^{-3}, well above the value of 50 cm^{-3} assumed in the design study.

Droplet diameter (d) is:

$$d = \left(\frac{6 \cdot Q}{\pi \cdot f} \right)^{\frac{1}{3}}$$

Q =liquid flow rate (0.08 $cm^3 min^{-1}$)

f = vibrating orifice frequency (275 kHz)

which for the listed parameters is 20.97 μm. This implies a solvent to solute ratio (equal to the ratio of the generated particle diameter to the desired particle diameter to the third power) of 9.24:1. Using a syringe with a 20 cm^3 capacity gives an operating time of 4 hrs, which is more than adequate to perform the calibration.

An atomizer (nebulizer) produces a polydisperse aerosol with a count mean diameter of ***0.25*** μm and a geometric standard deviation ≤2. In the atomizer, compressed air is used to form a high velocity jet flowing over a tube leading to the liquid reservoir. Liquid is drawn up through the tube and atomized by the jet of air. Large particles are removed from the air stream by impaction and in a cyclone, and the resulting aerosol leaves the atomizer through a fitting at the top of the reservoir. A commercially available instrument, the Palas AGF 2.0, has been tested for this application; for a flow rate of 15 lpm, particle concentrations of $>10^6$ cm^{-3} are easily obtained. Once again, final particle size is controlled by the solvent to solute ratio.

Radon Source

Sources with activities of up to 3700 kBq are available commercially, and can be transported without special permits. A source with an activity of 3000 kBq would be sufficiently large for this application. At a flow rate of 25 lpm in the attachment chamber, such a source would produce an average radon concentration of 15 kBq m^{-3}. Assuming 50 percent attachment of the ^{218}Po, this will provide a signal far above background. For example, the activity of a NIST calibration source for an NaI well detector using ^{137}Cs at 662 keV, half life of 30.17 years, is 164 Bq. For comparison, the maximum activity of ^{214}Pb in the instrument to be tested would be about 800 Bq, assuming a ^{218}Po concentration of 3700 Bq m^{-3} on the attached aerosol, a flow rate of 25 lpm, and a run time of 120 minutes (Evans, 1969).

Neutralizer

Both the nebulizer and the vibrating orifice produce particles that are charged or multiply charged, and thus have lower diffusion coefficients than uncharged particles. Particle charge depends on many factors, such as particle diameter and composition; high particle charge can cause drastically reduced particle output and unstable particle concentration. Neutralizers using ^{85}Kr in a sealed stainless steel tube for flow rates up to 150 lpm are available commercially, and routinely used to produce an aerosol of known charge distribution, and high, stable particle concentrations.

Attachment Volume

The attachment coefficient β (cm^3 sec^{-1}) can be written as (Postendorfer et al., 1979):

$$\beta = \frac{\pi v_{avg} d^2 (\Delta + 0.5d) D}{4D(\Delta + 0.5d) + 0.25 v_{avg} d^2}$$

Here d is the target aerosol diameter, v_{avg} is the average velocity and D the diffusion coefficient of the ultrafine polonium aerosol, and Δ the mean apparent free path, modified for diffusion effects at larger particle diameters (Fuchs, 1964). For aerosol particles with diameters greater than 1 μm, the attachment coefficient is proportional to dD while for particles with diameters less than 0.1 μm, the coefficient is proportional to $d^2 v_{avg}$.

For these calculations the diffusion coefficient (D) of the polonium aerosol is taken to be 0.07 cm^2 sec^{-1}, 34 nm ≤ Δ ≤ 63nm, and v_{avg} is 1.30×10^4 cm sec^{-1}. The attached fraction of the aerosol (A) as a function of residence time in the attachment chamber is given by (Raabe, 1969):

$$A = 1 - [\frac{\lambda_1}{\lambda_1 + \lambda_a} \cdot (1 - \exp - (\lambda_1 + \lambda_a)t)] .$$

Here λ_1 is the decay constant for ^{218}Po (0.227 min^{-1}), and λ_a is the attachment constant for polonium-aerosol attachment (ß•N, the attachment coefficient times the aerosol concentration). For the system parameters quoted above, ß•N>2.5 min^{-1} for both the 300 μm and the 10 μm distributions, indicating high attachment fraction (>0.8) and excellent system performance.

A 100 mesh screen at the end of the attachment chamber would serve as a filter to remove from the exiting flow the unattached aerosol which has a particle size (0.5 nm) far outside the operating range of the sampler. The high diffusivity ultrafine aerosol would be captured on the screen while the larger diameter particles pass through into the instrument.***[; it must be removed since its diameter of 0.5 nm]*** Aerosol losses from impaction and interception on the screen can be computed (Cheng et al., 1980) as follows:

Interception efficiency (n_r) is given by:

$$n_r = (2k)^{-1}[(1+R)^{-1} + (1+R) + 2(1+R)\ln(1+R)]$$

while impaction efficiency (n_i) is given by:

$$n_i = (2k)^{-2} I \cdot St;$$

$$I = (29.6 - 28a^{0.62})R^2 - 27.5R^{2.8}$$

$$St = \frac{2ra_p^2 CU}{9ma}$$

For the system under consideration, k=0.22, St≈0.068, I≈0.1, and $n_r \approx 0.04$, $n_i = 0.03$.

One problem with using radon progeny to tag the aerosol is that, given the high flow rates of the atmospheric samplers (8000 lpm) the activity from the radon progeny normally in the atmospheric may, under some circumstances, approach that of the tagged aerosol on the filter. This will need to be determined for each sampler being tested; it can be handled either by taking a background measurement before and after the calibration, or by supplying filtered air to the sampler itself. While this complicates the measurement, it does not make it significantly more complex or less accurate.

CONCLUSION

By using commercially available equipment the design and assembly of the tagged aerosol generator is greatly simplified. Generator stability and running time appears to be more than adequate for this application. This provides a simple and cost effective solution to the problem of performance verification of the atmospheric aerosol samplers.

REFERENCES

Cheng, Y.S., J. A. Keating, and G. M. Kanapilly, Theory and Calibration of a Screen Type Diffusion Battery. *J. Aerosol Sci.* **11**: 549-556; 1980.

Evans, R.B. Engineers Guide to the Elementary Behavior of Radon Daughters. Health Phys. **17:** 229-252; 1969. Fuchs, N.A. (1964) *The Mechanics Of Aerosols*, Pergamon Press: The Macmillan Company, New York, NY.

Goldstein, S. D. and P. K. Hopke, Environmental Neutralization of Po-218. *Environ. Sci Techno.* **19**:146-151; 1985.

Liu, B.H., R. N. Berglund, J. K. Agarwal, Experimental Studies of Optical Particle Counters. *Atmospheric Environment* **8:** 717-732; 1974.

Postendorfer, J., G. Robig, and A. Ahmed, Experimental Determination of the Attachment Coefficients of Atoms and Ions on Monodisperse Aerosols. *J. Aerosol Sci.* **10**: 21; 1979.

Raabe, O.G. Concerning The Interactions That Occur Between Radon Decay Products And Aerosols. *Health Phys.* **17:** 177-185; 1969.

Smith, S. and Y.S. Cheng, Generation of 212Pb Attached Ultrafine Particles for Deposition Experiments. *Aerosol Sci. andTech.* **29**: 442-448; 1998.

Table 1. Gamma Ray Emission From Radon Progeny

Gamma Ray Energy (keV)	Radionuclide	Emission Probability
242	^{214}Pb	0.04
295	^{214}Pb	0.19
352	^{214}Pb	0.36
609	^{214}Bi	0.46
1120	*^{214}Bi*	*0.15*
1765	*^{214}Bi*	*0.16*

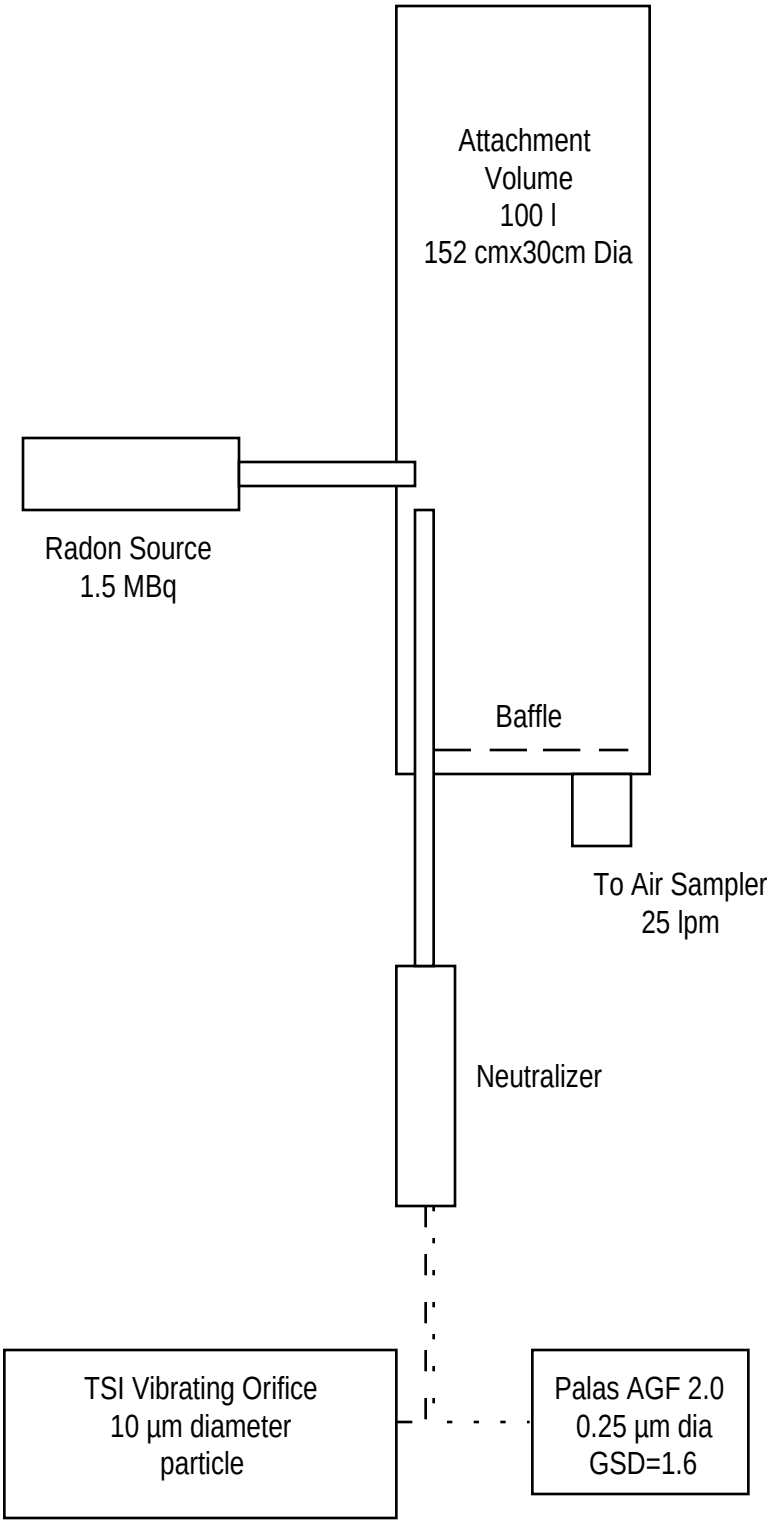


Figure 1. Schematic of the Tagged Aerosol Sampler, showing the particle generators, neutralizer, radon source and attachment volume.

INTEGRATING THE RADIONUCLIDE NETWORK DATA INTO THE INTERNATIONAL VERIFICATION REGIME

Mona Dreicer, U.S. Department of State
Roland Draxler, U. S. National Oceanographic and Atmospheric Administration
Michel Jean, Canadian Meteorological Centre

ABSTRACT

Throughout the final stages of the Comprehensive Nuclear-Test-Ban Treaty (CTBT) negotiations, radioactivity unambiguously characteristic of a nuclear weapons explosion, collected from the 80-station-station International Monitoring System (IMS) radionuclide network, was seen by many as being the "smoking gun" of nuclear-test-ban verification. Carried by global atmospheric transport, radionuclides released into the atmosphere would be detected and identified in areas far away from the source. The detected radioactivity could then be linked to anomalous events detected by the seismic, infrasonic or hydroacoustic IMS networks, through the use of existing geo-location capabilities based on meteorological transport modeling. If a clandestine test were to occur, ideally, the event location and associated error ellipses from the different IMS networks would overlap and delineate in which region of the world a States Party might wish to call an On-Site Inspection. Use of one of any number of technically acceptable meteorological transport models could point to quite different regions as probable sources of the detected radioactivity. That is why it is important to understand the uncertainties inherent in these models and to use the radionuclide data in concert with data from the other three monitoring technologies. Within the context of the Preparatory Commission's Working Group B, we are investigating mechanisms for providing CTBT Signatories with an international consensus on meteorological geo-location results that reflects the inherent uncertainties that must be taken into account in evaluating a particular event and deciding on an appropriate response to that event.

Key Words: radionuclide network, meteorological back tracking, data fusion

OPERATIONS OF THE AUTOMATED RADIOXENON SAMPLER/ ANALYZER - ARSA

James C. Hayes, Keith H. Abel, Theodore W. Bowyer, Tom R. Heimbigner,
Mark E. Panisko, Paul L. Reeder,
Justin I. McIntyre, Robert C. Thompson, Lindsay C. Todd, Ray A. Warner
Pacific Northwest National Laboratory

Sponsored by U.S. Department of Energy
Office of Nonproliferation and National Security
Office of Research and Development
Contract No. DE-AC-76RL0-1830

ABSTRACT

The Automated Radioxenon Sampler/ Analyzer (ARSA), designed and built by Pacific Northwest National Laboratory (PNNL), for the Department of Energy, has exceeded measurement requirements for noble gas measurement systems established by the Comprehensive Nuclear-Test-Ban Treaty. Two units, one at PNNL and a second, sent to DME Corp. of Florida, were built and extensively tested. Both systems have successfully demonstrated stable xenon yields greater than 1.5 cm^3 for an eight-hour collection period, corresponding to minimum detectable concentrations for ^{133}Xe on the order of 0.1 mBq/m^3 three times per day. High stable xenon yields are critical in obtaining these low minimum detectable concentrations.

A history of testing and results that led to the high xenon yields of the ARSA system is presented. A compilation of field tests, laboratory tests and baseline tests that led to cost reduction, power savings and size reduction of the ARSA are also discussed. Lastly, the type of data generated from the ARSA of interest to data center personnel are discussed.

Key Words: noble gas, xenon, radionuclides, collection, ARSA, CTBT.

OBJECTIVES

The Automated Xenon Sampler/ Analyzer (ARSA) was designed and built by the Pacific Northwest National Laboratory with support and guidance from the Department of Energy's Comprehensive Nuclear-Test-Ban-Treaty (CTBT) Research and Development Office and called out by the CTBT for detecting and quantifying radioactive xenon, a key signature of a nuclear detonation. The function of the ARSA is to aid other international monitoring systems, hydroacoustic, infrasound and seismic, in determining if an explosion originated from a nuclear or a conventional detonation. As authorized by the CTBT for radionuclide monitoring systems, the ARSA detects ^{131m}Xe, ^{133}Xe, ^{133m}Xe as well as ^{135}Xe[1]. The minimum required detectable concentration (MDC) for ^{133}Xe was outlined by the CTBTO to be < 1 mBq/ m^3 for 24-hour samples. The ARSA has established the minimum detectable activity for ^{133}Xe near the level of 0.1mBq/m^3 using a NaI(Tl)-based beta-gamma coincidence spectrometer for 8-hour samples, and hence meets the specifications called out by the CTBT by more than an order-of-magnitude. The spectrometer was designed at PNNL and subsequently the concept adopted and a spectrometer built at the FOA in Sweden to measure the energy-energy correlation distributions of low energy x-rays and gamma-rays emitted in coincidence with betas and conversion electrons for all the Xe isotopes listed above. The low MDC is achievable not only because of the low background counting but also in part due to the large quantity of stable Xe collected during the 8-hour sampling cycle. Two units built by PNNL have consistently collected and isolated 1.5 cc of stable Xe from an 8-hour cycle resulting in the impressive Xe collection figure of merit ≥ 0.1875 cc/hr.

ARSA Operations

The ARSA operates on three basic principles, (1) Xe collection (2) Xe purification and (3) Xe quantification (see figure 1). The Xe collection and purification processes are based on adsorption of Xe onto an adsorbent (charcoal) held at cryogenic temperatures. During the 8-hour Xe collection phase, 48 m^3 of compressed atmospheric gas is driven through a set of pressure swing dryers that entrap and eliminate CO_2 and water vapor from the process stream. The dry air is then driven through an air chiller that cools the air to less than -110º C. The cold air is in turn used to self-cool a radon trap (PreRT) to less than –95° C, and is then used to self-cool a larger main charcoal trap (MCT) to less than –90° C. The gas that passes through the PreRT, including the Xe, is stripped of radon, exits the trap and directed through the MCT. Xenon is then collected on the cold charcoal within the MCT. During collection of Xe, other atmospheric gases also adsorb on the charcoal. At – 90° C, however, only small amounts of O_2, N_2, Ar, CH_4, Kr, and CO and even less He, H_2 and Ne remain on the charcoal of the MCT after collection. To eliminate the residual atmospheric gases that do collect on the MCT, vacuum is applied to the cold MCT for approximately 1-hour. Additional cooling occurs in the MCT when vacuum is applied due to the reduction of pressure in the trap and from the heat of evaporation of the condensed gases as they evaporate from the charcoal. The temperature drops from –90° C to less than –110° C and subsequently begins to warm. At the end of the vacuum step the temperature of the charcoal in the MCT is less than –80° C. This vacuum technique is effective in removing most of the aforementioned atmospheric gases while leaving the Xe on the trap. Removal of atmospheric gases prior to chemical and cryogenic manipulation is critical not only for optimization of chemical separation but also for quantification of Xe since these gases interfere with transport and composition gas measurements.

The collection efficiency of the adsorbent depends on the vapor pressure of Xe at the collection temperature in relation to the partial pressure of Xe in the gas stream[2]. The resulting collection efficiency is improved by either lowering the temperature of the collection adsorbent or by increasing the partial pressure of the gas to be collected, in this case Xe. The collection traps temperatures are based on the output temperature of the chiller. An output temperature of -110º C results in the charcoal trap temperatures of nominally -90º C. Since the temperature of the traps are as low as the cooling system can maintain, the partial pressure of Xe must be increased to effect the collection efficiency of Xe on the adsorbent. An equally important function of the vacuum step is the removal of oxygen from the MCT as heat is applied to the MCT during the purification phase of operation.

In order to increase the vapor pressure of Xe in the gas stream and reduce competition for adsorption sites on the charcoal, the ARSA was designed to remove the interfering atmospheric gases during the Xe collection phase of operation. Some small amount of radon, however, can pass through the PreRT and collect on the MCT. Also, CO_2 can be present on the charcoal from the collection phase or can be introduced into the gas process stream during the Xe purification phase from a gas leak in the system. Cautionary steps have been taken for assurance that neither gas makes its way through the purification phase. After vacuum has been applied to the MCT, it is externally heated to 175° C. To elute Xe from the charcoal, nitrogen (240 cc/ min, >99 % purity) is passed through the heated charcoal for 180 min. After exiting the MCT, the nitrogen stream is passed through a trap filled with decarbite (a NaOH based chemical), the only expendable chemical in the system, to remove any remaining CO_2. The process stream is then routed through a post radon trap (PRT). The PRT is a second radon trap filled with 1/8", 5Å molecular sieve and is thermostatically cooled to a temperature in the range of -50^{o} C by opening and closing a valve from the cold waste gas stream that exits the collecting MCT into a cooling loop inside the PRT. At this point in the process, the gas stream is primarily nitrogen and Xe. The gas is then passed through a final charcoal trap (FCT) that contains approximately 0.5 g of charcoal. The FCT is cooled externally to less than -95° C from the process gas stream as it exits the chiller. Elution of Xe from the MCT has been timed to insure all of the Xe has been removed from the MCT. After 180 min of Xe concentration onto the FCT, vacuum is applied to the trap to remove most of the nitrogen. The MCT could not be cooled while vacuum is applied since the trap is cooled by the gas process stream as it flows through the trap. Cooling of the FCT, however, is maintained during the entire vacuum step.

Sample transfer from the FCT to the counting cell is accomplished by heating the FCT to 275° C then volumetrically expanding the gas into a detector cell. Recently we have experimented with the use of a syringe transfer pump to recover the sample that remains in the FCT after the expansion step, see below. Once in the cell, the gas is counted for 24 hours. After a 24-hour count in the nuclear detector system, the gas is volumetrically expanded into a calibrated volume where the quantity of Xe is determined with a thermal conductivity detector (TCD).

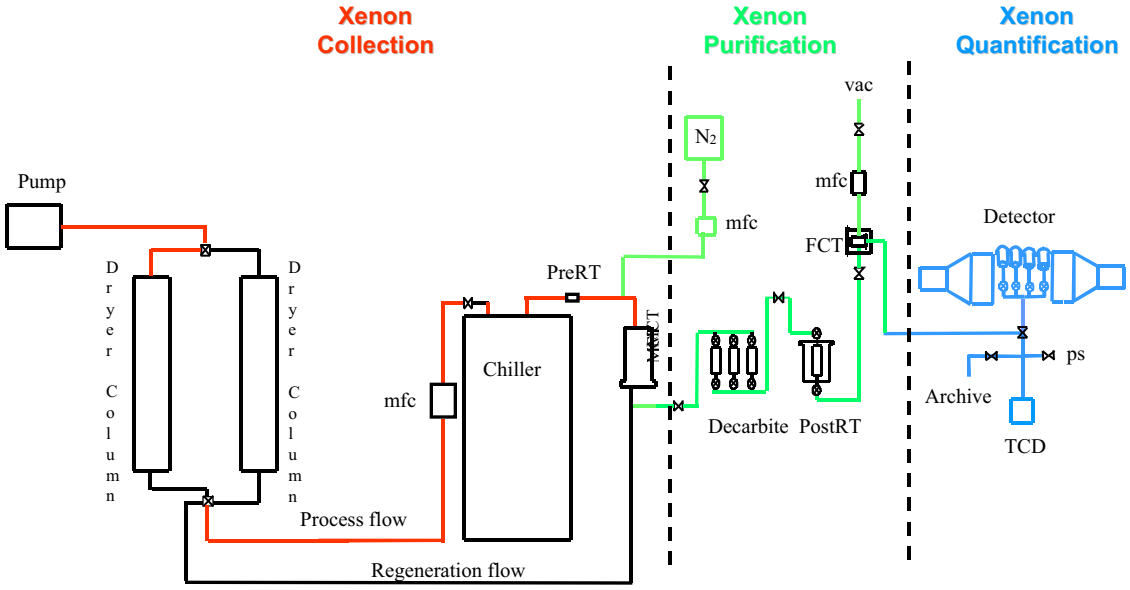


Figure 1. Simplified flow schematic depicting Xe collection, Xe Purification and Xe Quantification.

The objectives of the experimentation described herein were to optimize the operating efficiency of a functional ARSA unit for the end purpose of increasing the stable Xe yield. Although the ARSA is heralded for the low MDC, a measure of the nuclear detector, the yield of stable Xe not only indicates how well the system operates, but also assists in lowering the MDC of the system. The MDC of the nuclear detector is proportional to the volume of Xe and inversely proportional to the square-root of the background, and therefore, an increase in the Xe yield has a large impact towards lowering the MDC of the ARSA system. In order to optimize the Xe yield, we recently concentrated on two areas. First was removal of CO_2 from the gas stream in order to eliminate flow obstructions (due to CO_2 freezing in the lines), reduce the amount of decarbite used in the system and to reduce interference during quantification of stable Xe. Second was to increase the transfer efficiency of the gas from the FCT to the detector cell using a transfer pump. We also report on the quantification of stable Xe using a TCD.

RESEARCH ACCOMPLISHED

Pressure Swing Dryers

Since water vapor and carbon dioxide are the major adsorption interference of Xe on activated charcoal, they are the most important to remove from the gas stream prior to cryogenic collection. The atmospheric abundance of CO_2 is nominally 300 to500 ppmv. With a relatively high sublimation temperature of -79º C, up to 2.4 m^3 of CO_2 can adsorb on the –90° C main charcoal trap during an 8-hour collection cycle. Although charcoal has a large surface area, the adsorption capacity of Xe on charcoal is diminished from atmospheric levels of CO_2 competitively adsorbing on the charcoal. It is postulated that CO_2 and water vapor bond to the charcoal by Van der Waals forces[3]. In addition, water bonds to an available oxygen atom

on the surface of the charcoal via hydrogen bonding. Additional water molecules then bond to the bonded water molecule, again by hydrogen bonding, causing microscopic liquefaction to occur at the surface of the charcoal. When enough water and CO_2 bond to the surface of the charcoal through repeat of these mechanisms, the micro-capillaries within the charcoal become blocked. Blockage of the capillaries results in reduction of the vast surface area within the matrices of capillaries and pores in the charcoal such that Xe adsorption becomes greatly reduced. Additionally, the ARSA operates at temperatures low enough to freeze CO_2 in the chiller lines and the transfer lines between traps. If CO_2 freezes in the process lines, flow to the traps will be reduced and eventually will stop, resulting in automatic shutdown of the system[4]. Additionally, if high enough concentrations of CO_2 reach the TCD, the calculated Xe yield will be impacted. The effect of CO_2 in the TCD will be discussed below.

While several variations of dryers that both remove water and CO_2 have been constructed and tested, the most successful to date have been pressure swing regenerative dryers. Pressure swing dryers consist of two drying columns operating in tandem. A high-pressure stream of gas flowing through the column removes water vapor and CO_2 while a low-pressure stream of waste-dry air that exits the MCT flowing through the second column, regenerates the adsorbent.

Two different adsorbents were tested within the drying columns. In the first test system, mixed columns of 13X molecular sieve and activated aluminum oxide (alumina) were used. Generally, low CO_2 levels and low dew points were obtained from operating conditions of 100 slpm and 100-psig (700 kPa) as observed by dew point sensor and gas chromatography/ TCD (GC/ TCD) analyses. The CO_2 level was determined from the dryer outputs to exceed 2 ppmv, however, a total of 96 cc of CO_2 was collected on the MCT during 8-hour runs. To eliminate all of the CO_2 in the gas stream after the MCT, the stream was passed through a decarbite trap prior to collection on the final charcoal trap. The regeneration of the dryer columns required heating the columns to nominally 400° C for several hours with a flow of CO_2-free air. The heat given off to the room and the power consumption (a few hundred Watts) from the dryers made regenerative heating prohibitive. The molecular sieve columns were field tested at the Environmental Measurements Laboratory (EML) on the ARSA system[5]. During these tests, dryer reliability was problematic, as was high CO_2 levels in the counting cell. Xenon yields at EML were on the order of 1.0 to 1.2 cc for an 8-hour run.

An improved version of the pressure swing regenerative dryers using pure alumina as the adsorbent was then tested. This configuration provided superior CO_2 removal and eliminated the need for heating to regenerate the adsorbent. The operation, however, was the same as described above for a pressure swing dryer. The CO_2 levels from the exit of the dryers were below 1 ppmv, and in fact could not be observed in the TCD response of a calibrated GC/TCD used independently for analyzing the air stream composition (see below). Figure 2 shows the CO_2 concentration in the final gas product from Xe samples collected from automated running of the ARSA at PNNL during the latter part of June, 1999. The low concentrations of the CO_2 levels observed were indicative of the dryer performance.

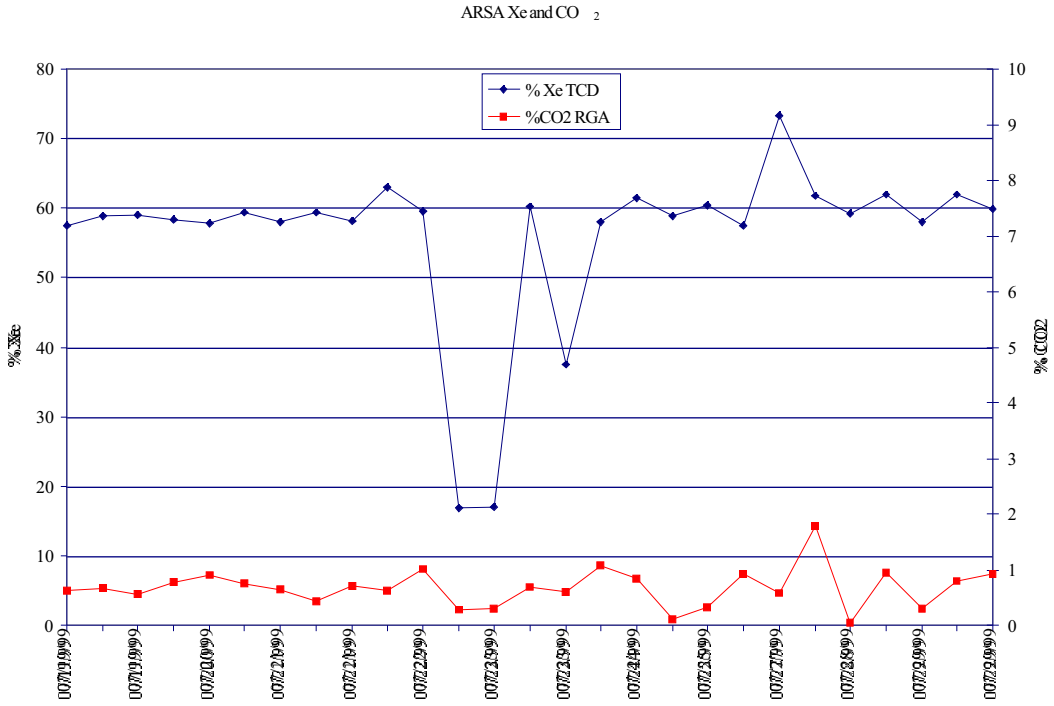


Figure 2. Xenon and CO_2 levels for ARSA final gas samples obtained from operating condition for the dates between 7/19/99 and 7/29/99. Carbon dioxide below the 1% levels are typical.

The method for analyzing the CO_2 was created in the Vapor Analytical Laboratory at PNNL[6]. Passivated SUMMA™ canisters (850 cc) were utilized for sample collection. Aliquots of the collected vapor were analyzed using a GC/TCD. The analytes were identified by matching the sample peak retention time with that of a traceable gas standard mixture. The instrument was calibrated at five different concentrations for CO_2 over a range of 17 to 2100 ppmv. An average response factor from the calibration was used for quantification. Quality control objectives were achieved using both initial and continuing calibration verifications. Blank samples were run to detect the presence of any contamination and carryover. Samples were collected at the beginning and end of each pressure swing cycle and cycle times were varied from 5 to 10 min.

The dryer testing was conducted using the dryer columns that were attached to an operating ARSA. Gas was collected from the gas stream that originated after the process air had been dried and scrubbed of CO_2, and was collected into the SUMMA canisters. After the sample was collected, the SUMMA canister was connected to a gas manifold that contained a sample port, a pressure sensor, an inert gas line and a vacuum port. The sample valve was opened to the evacuated gas manifold and a pressure reading of the sample was obtained. The pressure in the SUMMA canister was adjusted to approximately 1400 torr, using vacuum for high-pressure samples, or by dilution with ultra-high purity nitrogen for samples that were less than atmospheric pressure. A 5-cc aliquot was drawn out of the pressure-adjusted SUMMA canister using a valved gas-tight syringe. The sample was then injected into a 1-cc sample loop on a HP 5980 GC/TCD. The 1-cc sample loop is open on both ends to allow for excess sample from the 5-cc syringe to flush the loop. The sample was then directed from the 1 cc sample loop to a fused silica precolumn, via a 6-port valve, where heavy components (organics) are removed from the gas stream. The remaining gas was passed onto a GS-Q column where CO_2 is retained. Using a two-valve system on the GC, the samples are eluted and measured with an on-board TCD.

Transfer Pump

Transfer of Xe from the FCT to the nuclear detector cell in the ARSA system was accomplished by simple volumetric expansion of the gas that collected on the charcoal to an evacuated cell that is part of the nuclear counting system (see elsewhere in these proceedings[7]). The final charcoal trap is heated to 275° C for several minutes until the trap is completely heated then three valves are opened to allow the hot gas to expand into the transfer tubing and into the cell. The cell volume is 6.4 cc, the volume of the transfer tubing is 1.8 cc, and the FCT filled with charcoal has an estimated 1.5 cc volume. It was determined through liquid nitrogen collection of the gas from the FCT that 35% of the sample was left in the lines and the FCT. Addition of a syringe transfer pump to aid in the transfer of the Xe from the FCT into the cells has increased the Xe yield over 25 %. As shown in figure 3, after addition of the syringe transfer pump, the Xe yield in the cell increased from nominally 1.4 to 1.5 cc to near 2.0.cc resulting in an improved figure of merit ≥ 0.25.

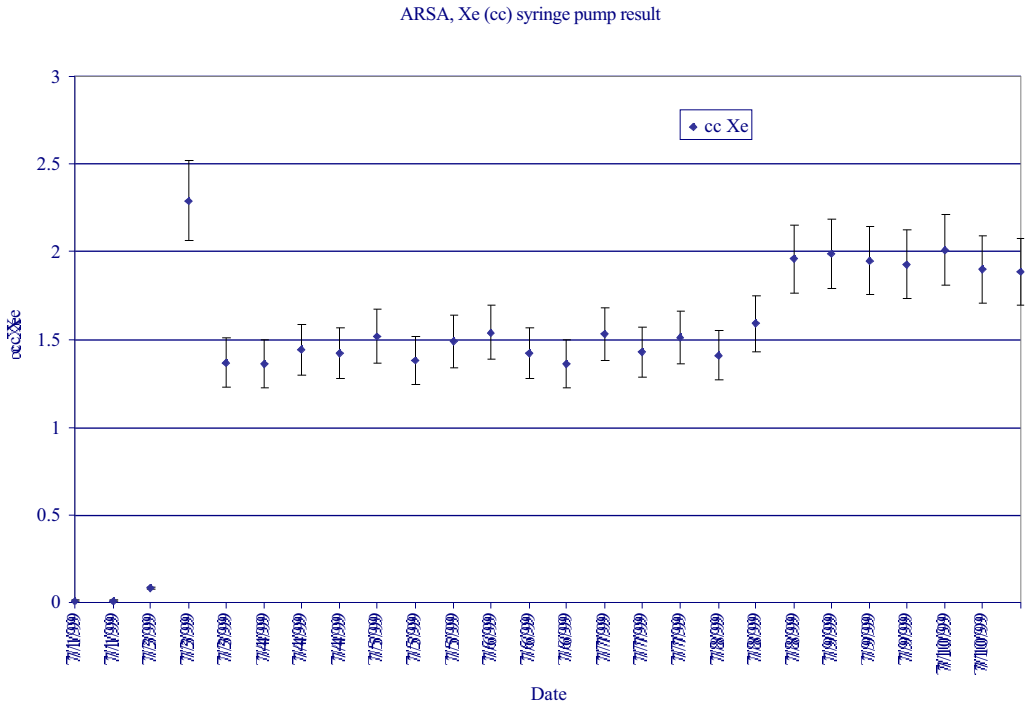


Figure 3. Stable Xe yields for the month of July. The increase in yield on the 9th was due to addition of a syringe transfer pump.

The transfer pump was operational on July 8, 1999, however, the stable Xe results in an operating ARSA are not determined until 24 hours after the transfer. Therefore, the results for the transfer on the 8th are determined on the 9th. The Xe yields that are low, less than 1 cc, and high, up to 5 cc, can be typical for a startup of the ARSA. The yields during the startup state depend on the system state just prior to the system shutting down and the time when the system is started. In order to achieve 100% duty cycle, the ARSA was designed with duplicate collection moieties and a partial duplicate purification train. This arrangement allows the system to collect gas on a MCT for a chosen time on one moiety while the other moiety (a duplicate MCT) proceeds with purification and quantification. The low yields that result from the startup are due to the ARSA software control program starting the purification process on one side and the collection process on the other. The MCT from the initial purification process does not have any collected gas on the trap resulting in a low, or no Xe yield (figure 3). Conversely, during the initial collection, the software that controls the gas processing is designed to wait for a time synchronization to allow the three daily samples to be processed and recorded at the same time each day. The control program enters a wait

state until 2:00, 10:00 or 18:00 GMT (or other programmable time) depending on when the system finishes the first cycle of the control program. The wait state often will create a situation where the collecting MCT may collect gas for up to 16 hours. The extended collection times are evident in a high Xe yield on the first cycle after a system restart (see Xe > 2.3 cc in figure 3.)

Considering the effect on the Xe yield of the extended collection time, we ran experiments collecting gas on one main charcoal trap for up to 4 days, continuously and intermittently. The results (figure 4) are even more pronounced than the startup collection shown in figure 3. The results of our extended collection studies show some yields near 5 cc of Xe. The yields at 4.2, 5.2 and 4.8 cc were from extended runs over a minimum of 4 days. Although these yields were not obtained in an 8-hour collection cycle, we are confident that the ARSA traps are sized large enough so an increase in flow rate will have similar effects on the Xe yield for an 8-hour cycle. We are also confident that the capacity of the final charcoal trap (FCT) is over-sized for 8-hour collections.

The results throughout the time frame shown in figure 4 represent an extended testing period. Often the ARSA was shut down for testing or upgrade of both software and hardware, or occasionally shutdown from hardware failures. The shutdowns are indicated, as described above, as a low yield (typically < 0.6 cc) followed by a high yield (typically > 2.5 cc). The low yields from 6/16/99 to 6/21/99 were due to a leak in the transferline caused during construction of the transfer pump. Time frames where the yields were stable for more than three or four days were results from typical stable ARSA operation. It should also be noted that up to 7/99 the ARSA ran on 60 Hz power. After 7/1/99 and until 7/18/99 the ARSA ran on 50 Hz power to test the system for world-wide power compatibility. As shown in figure 2, the Xe yields were averaging 1.6 to 1.7 cc until the system was converted to 50 Hz. After the conversion, the yields dropped to around 1.4 to 1.5 cc (operating without the transfer pump). After 7/18/99, the gas-processing portion of the ARSA was converted back to 60 Hz. The results are evident in the Xe yields as they surpassed the 2.3-cc mark. Several factors may aid to the increased yield when the system is run at 60 Hz. It was clearly evident that the output of the chiller had raised from –113° C to –110° C. The effect of the warmer chiller output air was also observed in the trap temperatures. The cooling of the PreRT, the MCT, and the FCT was increased at least 5° C. The effect of the temperature increase may not, however, explain the decreased in Xe yield when the system is run at 50 Hz. During the Xe collection phase we pull vacuum on the MCT as described earlier. Changing from 60 to 50 Hz may decrease the vacuum power enough to effect the removal of interfering gases.

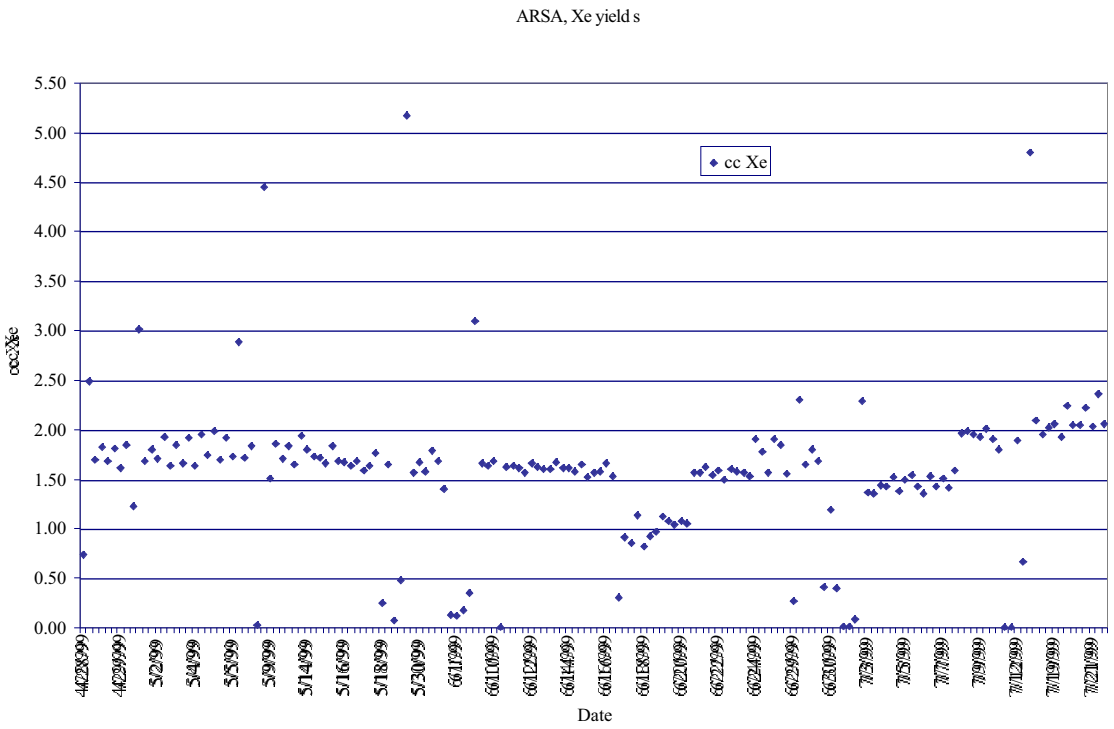


Figure 4. Xe yields (cc Xe) for the months of 4/99 through 7/99.

Thermal Conductivity Detector (TCD)

The TCD is the tool chosen to analyze the composition of gas for the ARSA for several reasons. First, the TCD is relatively inexpensive compared to other methods such as a residual gas analyzer (RGA) - a mass spectrometer used in the first ARSA system field tested at EML[5]. Second, the TCD is small, and uses far less power compared to other measurement systems. The final reason is the long-term stability of the TCD unit. The thermal conductivity detector is calibrated for 0 to 100 % Xe in nitrogen and comes as a commercial-off-the-shelf instrument. The stable Xe yield is then calculated from the percent Xe, pressure and the analyze volume. The thermal conductivity detector has recently been modified to include a non-dispersive infrared detector (NDIR) to detect CO_2 in the Xe/ N_2 gas mixture and is currently being tested in the ARSA. Using the CO_2 monitor, we will be able to determine when the decarbite trap is spent or when the dryers are not functioning. Currently, the ARSA's operation is so stable that CO_2 is not expected to interfere appreciably with stable Xe measurements even without decarbite, unless there are severe problems with the operation of the dryers.

The calibration of the TCD was verified within the ARSA system at varying pressures as shown in figure 5. To verify the calibration, the TCD was connected to the gas analysis volume and a detector cell then evacuated to 20 mbar. Xenon (40% in N2) was expanded into the evacuated cell and a calibrated analyze volume to the desired pressure. The pressure and TCD reading were recorded then the valve between the cell and the TCD was closed and the analyze volume was again evacuated. The contents of the cell were expanded into the analyze volume and the pressure and TCD values were recorded. This procedure was repeated until the pressure was below 90 torr. The data in figure 5 indicates accurate, sort-term stable operation of the TCD for various pressures.

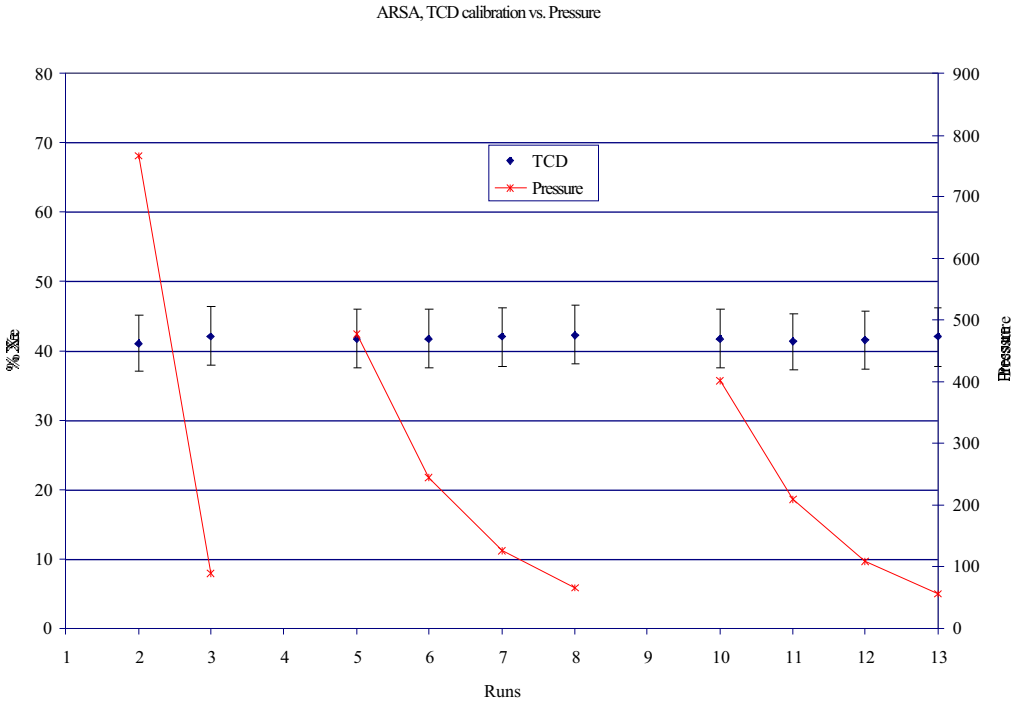


Figure 5. Thermal conductivity detector calibration verification with varying pressure. Readings were recorded from a TCD that was connected to an operating ARSA. Error bars are ±10% relative error.

The ARSA field model that was tested at EML used an RGA for determining Xe yield. The advantage of an RGA over the TCD is that the gas analyses included all of the atmospheric gases. As mentioned earlier, CO_2 breakthrough was problematic at EML. It was necessary to analyze the entire mixture of gas to determine how much of the mixture was Xe using an RGA. The technique used at EML for gas analysis with the RGA was well established and was used on the ARSA at PNNL to verify the TCD readings of actual gas samples. Figure 6 shows the TCD and RGA readings from 7/19/99 through 7/29/99. The RGA was calibrated using a gas standard that included Xe, Kr, CO_2, CO and N_2 (all nominally 3%) in a balance of Ar. The calibration was verified using the same Xe (40%) in N_2 standard that was used to verify the TCD calibration. The RGA spectrum was run concurrently with the TCD during normal operating conditions.

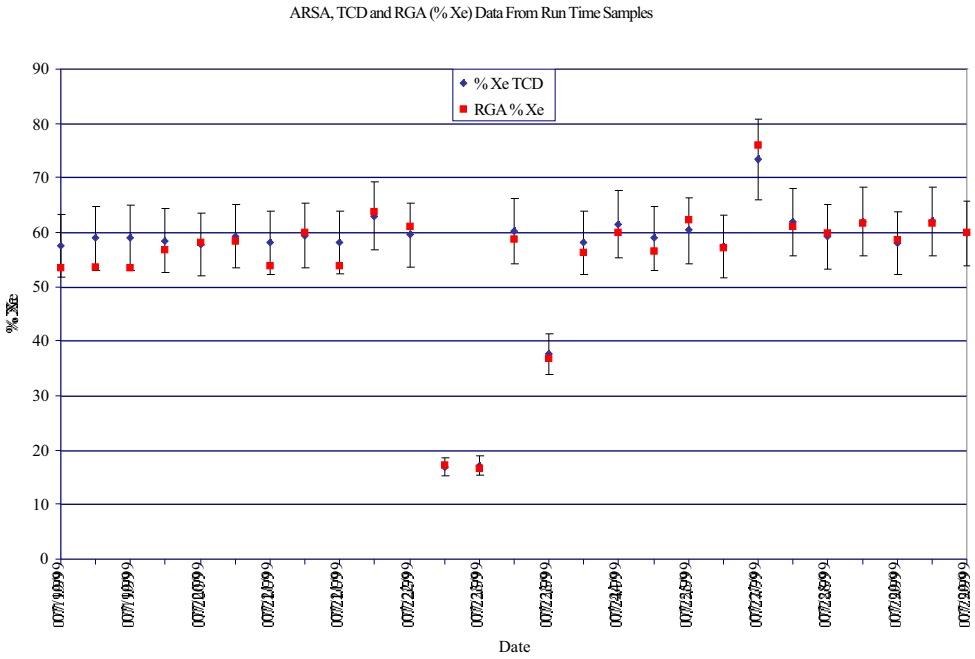


Figure 6. Thermal conductivity detector and residual gas analyzer readings for ARSA samples during typical operation. Error bars are ±10% relative error.

CONCLUSIONS AND RECOMMENDATIONS

Although the ARSA prototypes have been in functional for over a year, we are continuing to enhance the operation processes, add QA/QC checks and determine long term failure modes. We have achieved near complete removal of CO_2 and water from the gas process stream using pressure swing dryers. An added benefit to improving the dryer technology was power savings and increased reliability. Addition of the transfer pump has increased the transfer efficiency by 25% of the sample from the FCT to the detector cell. Additional testing to improve the pump efficiency is planned. The TCD analyzer has proven to be robust and reliable with the added benefit of a cost reduction of an ARSA unit by approximately $20,000.

The significance of the data presented in this paper, however, reaches beyond simply testing components of the ARSA. We have not only presented tests that increase the operation efficiency of the ARSA through experimentation, we have also presented results that typify the quality of data that is obtained from a PNNL ARSA.

REFERENCES

(1) Reeder, P., T. Bowyer, K. Abel, C. Hubbard, M. Panisko, R. Thompson, R. Warner, "Observation of 135Xe with the PNNL ARSA System, PNNL-11654", August 1997.

(2) Scarpitta Charles, S., Harley, Naomi H., "Adsorption and desorption of Noble Gases on Activated Charcoal: I. ^{133}Xe Studies in a Monolayer and Packed Bed", *Health Physics*, **Vol 59**, No. 4 (October 1990), pp.383-392.

(3) Underhill, D.W., "The adsorption of Argon, Krypton and Xenon on Activated Charcoal", *Health Physics*, **Vol 71**, No. 2 (August 1996), pp. 160-166.

(4) Abel, K.H., T.R. Heimbigner, T.W. Bowyer, M.E. Panisko, "ARSA Safety Systems", PNNL internal report PNNL-2142, February 1999.

(5) Bowyer, T.W., K.H. Abel, C.W. Hubbard, M.E. Panisko, P.L. Reeder, R.C. Thompson, R.A. Warner, "Field Collection and Measurement of Radioxenon for the Comprehensive Test Ban Treaty", *Journal of Radioanalytical and Nuclear Chemistry* **Vol 240**, No 1 (1999).

(6) PNNL. 1996. *Analysis Method for the Determination of Permanent Gases in Hanford Waste Tank Vapor Samples Collected in SUMMA™ Passivated Stainless Steel Canisters,* PNL-TVP-05 Rev. 2, Pacific Northwest National Laboratory, Richland, Washington.

(7) Ted W. Bowyer, Justin I. McIntyre, and Paul L. Reeder, "High Sensitivity Detection of Xe Isotopes via Beta-Gamma Coincidence Counting", 21st Seismic Research Symposium: Technologies for Monitoring The Comprehensive Nuclear-Test-Ban, In Print.

EVALUATION OF FISSION PRODUCT ISOTOPES FOR FIELD OR LABORATORY DETECTION

H.S. Miley and R.J. Arthur, E.A. Lepel, S.L. Pratt, C.W. Thomas, Pacific Northwest National Laboratory

Sponsored by U.S. Department of Energy
Office of Nonproliferation and National Security
Office of Research and Development
DE-AC06-76RLO 1830

ABSTRACT

An International Monitoring System (IMS) is being created to monitor the Comprehensive Nuclear-Test-Ban Treaty (CTBT). Radionuclide aerosols will be monitored to provide positive proof of an atmospheric explosion. In addition, a group of laboratories will perform quality assurance and confirmatory analyses of samples of interest. The field and laboratory systems will perform gamma-ray spectrometric analysis of air filters. While laboratories may undertake additional analysis such as chemical separation and beta counting, the scope of this work is to make evaluations with respect only to gamma-ray spectrometry.

Short lived fission product spectra have been acquired on gamma-ray spectrometers appropriate for both field and laboratory measurements of compliance with the Comprehensive Nuclear Test Ban Treaty. These spectra simulate a reasonable CTBT sample indicative of a small atmospheric explosion occurring at continental distance from a monitoring station. The radionuclides can be ranked by the measurement uncertainty, signal-to-noise ratio, and other means. Additional isotopes may be ranked by using simulated spectra from individual isotopes in a variational method. The results of this ranking are shown and could contribute to the formation of a list of reasonable isotopes to trigger a CTBT bulletin.

Key Words: Radionuclide, Aerosol, Fission, Isotope, Atmospheric

OBJECTIVE

This work seeks to experimentally establish a ranked list of isotopes observable in a challenging scenario: a 1 kt explosion in the atmosphere at about 10,000 km upwind.

The function of the IDC requires a library of radionuclides for automated aerosol spectral analysis, and a library of relevant radionuclides is needed to screen spectra into a multi-level categorization scheme. In particular, a list of fission products typical of an atmospheric explosion is required to highlight events of increased importance. The categorization scheme requires detection of one relevant fission-product isotope for Level 4 designation, and two relevant fission-product isotopes for Level 5 designation. Samples that generate Level 5 spectra may be sent to a laboratory for confirmatory analysis. The case for xenon isotopes is substantially different and will not be discussed here.

RESEARCH ACCOMPLISHED

A given radionuclide should rank highly if it has several favorable criteria. These include:

- Good $T_{1/2}$ or product of another isotope with good $T_{1/2}$
- Good decay characteristics
- Good branching ratio
- Good gamma-ray energy
- No or few interferences with natural isotopes
- No or few interferences with calibration isotopes
- No or few interferences among fission products

Most of these criteria lend themselves well to simple calculation. Even the influence of the natural background may be trivially calculated by computing minimum detectable concentrations based upon a reasonable atmospheric sample [1]. Unfortunately, potential interferences with other fission products are not so easily resolved.

Computation methods do exist for synthetically creating spectra [2], and this would allow for the cross interferences among fission isotopes. However, to provide a close simulation of reality we would first need to correct the fission product lists for differing deposition rates of chemical species in the atmosphere and other effects. Given that this data is unknown and potentially varies in specific regions, detonation environments, and times of year, the simplest approach is to physically create the sources in a rapid reactor irradiation. The spectra that are produced may contain certain anomalies that can be ignored:

- Relatively high 1001 keV (^{234m}Pa) and 185 keV (^{235}U)
- Minimal loss of iodine isotopes

To experimentally take all the above parameters (except fractionation) into consideration, we created a fission product source experimentally by irradiating ampoules containing an enriched-uranium solution. Quartz ampoules containing 1.2 micrograms of uranium solution were exposed to a thermal neutron flux at the University of Washington reactor to produce a total of 1.58×10^9 fissions per ampoule. The liquid was calibrated for fission product content, and a small quantity was introduced as a source into a detector of very low background. The liquid was diluted and a sample representing a simulated atmospheric explosion detection filter was created. The activity was selected using data from historic atmospheric sampling at PNNL [3], specifically 11 samples where an atmospheric detonation at Lop Nor was detected in Richland, WA (yield: ~20 kt, range: ~10,000 km, travel time: ~12 days). Variation between reactor fission product yields and weapon fission product yields was ignored, since the results are essentially qualitative.

Table 1. Original Fission Product Library for Automated Analysis

Be-7	Cd-115	Cs-134
K-40	Cd-115m	Cs-136
Sr-89	Sn-123	Cs-137
Sr-91	Sn-125	Ba-140
Y-91	Sb-125	La-140
Y-93	Sb-126	Ce-141
Zr-95	Sb-127	Ce-143
Zr-97	Sb-128	Ce-144
Nb-95	Te-127	Nd-147
Nb-97	Te-132	Pm-149
Mo-99	Te-127m	Pm-151
Tc-99m	Te-129m	Sm-153
Ru-103	Te-131m	Sm-156
Rh-105	I-130	Eu-155
Rh-106	I-131	Eu-157
Pd-109	I-132	Tb-161
Ag-111	I-133	
Ag-112	I-135	

The number of sample fission atoms was determined from 1-week samples acquired with high-volume displacement pumps and 1-week measurements on high-efficiency, multi-parameter sodium iodide counting systems. In order to adapt this for use in the CTBT measurement regime, the fissions/sample were adjusted to 3.8×10^8 fissions to reflect the daily volume collected (20,000 m3) by the Radionuclide Aerosol Sampler/Analyzer (RASA) [4]. Sample splitting is expected to occur before measurement of a sample at a laboratory, but since the degree of splitting has not been determined at the time of this writing, no sample splitting has been assumed.

The spectrum obtained from this sample was evaluated using an automated analysis code, RAYGUN [5], which has many functional similarities to the code used by the IDC and treaty signatories. The library used for the automated RAYGUN analysis was reasonably comprehensive (see Table 1), containing 53 isotopes and 273 gamma-rays.

This library was derived from fission product libraries previously considered for a relevant radionuclide list [6], with several additions and deletions. The nuclear decay information that makes up this library (gamma-ray energies, half life, and branching ratios) was compiled from various sources and adjusted to maximize the likelihood of detection.

Simulated 14-day Detection Results

In order to gain some idea of the effectiveness of various isotopes in detection, selected isotopes were ranked using several methods. The aggregate ranking is shown in Table 2. This ranking also includes isotopes that were below the level of detection. This allows us to determine which isotopes would be the next likely list entries.

Direct spectral comparison of the 14-day-old fission spectra and a typical daily filter on a RASA in Richland, WA indicated that the normal atmospheric isotopes and background signals (radon daughters, K-40, Be-7) did not play a significant role. Therefore, no daily filter spectral data were added in.

The appearance of Cs-137 on this list is slightly surprising, given the long half-life. Since Cs-137 may be re-suspended from old weapons debris or from Chernobyl fallout, this isotope will not add great confidence if it is one of only two detected isotopes.

Since only particulate forms of iodine isotopes are expected to be captured by aerosol filters, the technique used to create the test sample probably contained artificially elevated iodine levels. For this reason, iodine isotopes were deleted from this list. This is a judgement based on the fact that the chemical form of iodine may vary and the measured quantity will be highly dependent on the percentage of iodine in particulate form. It could be argued that this deletion represents a lost detection capability, and certain iodine isotopes may need to be added to the list, although the evidence above indicates that it is not likely needed to detect an atmospheric explosion. It was also noted that the many lines of iodine isotopes could cause difficulty with the data reduction algorithms.

Effects of Decay Time

One might argue that the list derived above will only be applicable at the 14-day decay time, since the growth and decay of isotopes may greatly adjust the relative worth of an isotope. For this reason, spectral data from the same sample at a short decay time (2 days) was also analyzed in the same way. This spectrum is not a logical extension of the original scenario: it has 2-days worth of decay but 14-days worth of dilution. It is intended only to show the effects of decay on the table generated from the 14-day measurement.

Table 2. Ranking of 14-day-old sample of fission products.

Ranking	Radionuclide/Pair	T 1/2	Energy (keV)	Comments
1	Ce-141	32.5 d	145.4	
2	Ba-140/La-140	12.7 d	537.3/487.0	
3	Mo-99	2.75 d	140.5/739.6	140.5 most intense, but low energy attenuates
4	Zr-95/Nb-95	64 d	756.7/765.8	
5	Ce-144	285 d	133.5	
6	Nd-147	11 d	531	Interference on all peaks
7	Sm-153	1.9 d	103.2	
8	Pd-112/Ag-112	0.88 d	617.5	
9	Cs-137	11000 d	661.7	
10	Sr-89	50.5 d	910.3	Te-131m interferes with the only peak
11	Cs-136	13.2 d	1048.1	Not seen in spectrum
12	Cs-134	752 d	604.7/795.8	Not seen in spectrum
13	Zr-97/Nb-97	0.70 d	743.4/657.9	Not seen in spectrum
14	Tb-161	6.9 d	57.1	Not seen in spectrum
15	Eu-156	15.2 d	1230.7	Not seen in spectrum
16	Pd-111/Ag-111	7.5 d	342.1	Not seen in spectrum
17	Cd-115	2.2 d	336.2	Not seen in spectrum
18	Cd-115m	45 d	933.8	Not seen in spectrum

Note: Radionuclides 1-10 are ranked according to number of net counts in the preferred peak and/or the statistical uncertainty assigned by the reduction software (based on counts in peak, interference, attenuation, etc.) Radionuclides 11-18 were either not visible in the spectrum or were not clearly identified by the reduction software. Synthetic spectra [5] were added until the software identified the radionuclide, in which case ranking is by the activity level required to achieve software identification.

The two-day ranking is so similar to the 14-day list, it is clear that decay times between 2 and 14 days are not greatly significant.

Table 3. Ranking of 2-day-old sample of fission products.

Ranking	Radionuclide/Pair	T 1/2	Energy (keV)	Comments
1	Mo-99	2.75 d	140.5/739.6	140.5 is most intense, but low energy attenuates
2	Ba-140/La-140	12.7 d	537.3/487.0	
3	Zr-97/Nb-97	0.70 d	743.4/657.9	
4	Ce-141	32.5 d	145.4	
5	Zr-95/Nb-95	64 d	756.7/765.8	
6	Tb-161	6.9 d	57.1	
7	Sm-153	1.9 d	103.2	
8	Ce-144	285 d	133.5	
9	Nd-147	11 d	531	Interference on all peaks
10	Pd-112/Ag-112	0.88 d	617.5	
11	Sr-89	50.5 d	910.3	Te-131m interferes with the only peak
12	Cs-134	752 d	604.7/795.8	Not seen in spectrum
13	Eu-156	15.2 d	1230.7	Not seen in spectrum
14	Cs-136	13.2 d	1048.1	Not seen in spectrum
15	Cs-137	11000 d	661.7	Not seen in spectrum
16	Pd-111/Ag-111	7.5 d	342.1	Not seen in spectrum
17	Cd-115m	45 d	933.8	Not seen in spectrum
18	Cd-115	2.2 d	336.2	Not seen in spectrum

Note: Radionuclides 1-11 are ranked according to number of net counts in the preferred peak and/or the statistical uncertainty assigned by the reduction software (based on counts in peak, interference, attenuation, etc.) Radionuclides 12-18 were either not visible in the spectrum or were not clearly identified by the reduction software. Synthetic spectra [5] were added until the software identified the radionuclide, in which case ranking is by the activity level required to achieve software identification.

CONCLUSIONS AND RECOMMENDATIONS

While a human analyst could have adjusted the data analysis to glean more from these spectra, the list of automatically detected radionuclides in Table 2 represents the easily detectable isotopes in the spectra. This list should therefore be adequate for normal event screening into a multi-level scheme. Given that the current concept of the screening system contains only 1 or 2 fission products corresponding to Level 4 or Level 5, a list of the 10 most likely isotopes should be adequate under all circumstances. With the exception of iodine isotopes, the detection of other fission products not on this list (for instance from Table 1 but not Table 2) without some or all of the isotopes in Table 2 is highly unlikely, and may constitute a pathological sample requiring special consideration.

For example, elevated Be-7 is likely due to unusually high cosmic-ray spallation in the atmosphere. Cosmic ray neutrons can spoof the detection of Mo-99, due to neutron reactions in the germanium crystal. On the other hand,
the high volatility of iodine may allow the observation of only iodine isotopes from a leaky underground test. This scenario argues for the addition of iodine isotopes as appropriate to Table 2.

There is little recurring cost in maintaining a large library for automated data processing. One possible pitfall is that radon daughter gamma-ray lines may be at similar energies and if efficiency data are in error, an isotope may be erroneously detected. Otherwise, there is no cost in allowing States Parties subscribers to create custom screening algorithms based on custom data flags developed for the IDC.

Although this simulated 1 kt detection is statistically unquestionable, it should be noted that the only intra-element isotopic ratio that can be formed of these detected isotopes is Ce-141/Ce-144, which is not the

most desirable. This general result supports the conclusions previously established concerning the difficulty in broadly applying fission product ratios [7].

Table 4. Total Fission Product vs. Total Activation Product Activity in ORIGEN Calculations in Underground, Underwater, and Atmospheric Activation Scenarios.

	3 days	10 days	30 days
U-235 FP	1.3E+17	3.5E+16	1.0E+16
UG AP	1.2E+16	3.7E+14	2.1E+14
UW AP	2.1E+15	1.3E+14	1.0E+14
ATM AP	3.8E+12	3.4E+12	2.6E+12

Note: All values in Bq.

Concerning activation products: since a reasonable 1 kt detection at 10,000 km after 14 days leaves a large signal, there is no need to use activation products in the Relevant Radionuclide List. Table 4 compares gross activity from several activation scenarios with fission products [8]. It could be argued that these isotopes should be in the automated data processing library, thereby allowing data-product subscribers to flag these isotopes. However, while this may be useful for States Parties purposes, it is not necessary for detection of a test ban treaty violation.

REFERENCES

[1] L. Vladimirskiy, et al, CMR Technical Report CMR-98/29 (1998).
[2] W.K. Hensley, et al, IEEE NSS 1993 Conference Proceedings, 672-675., H.S. Miley, IEEE NSS 1993 Conference Proceedings, 240-243.
[3] C.W. Thomas, et al, PNL-3826, UC-11 (1981).
[4] S.M. Bowyer, et al, IEEE Transactions on Nuclear Science, Vol. 44, No. 3 (1997) 551-556.
[5] W.K. Hensley, et al, J of Radioanalytical and Nuclear Chemistry, Articles, Vol 124, No. 2 (1988) 481-499
[6] L-E. DeGeer, Preparatory Commission for the Comprehensive Nuclear Test Ban Treaty Organization, Technical Report, PRT/IDC-1999/02 (1999).
[7] H.S. Miley, et al, PNNL-SA-31186 (1998).
[8] Perkins, et al, PNNL-11554 (1997).

EVALUATION OF LABORATORY DETECTION SYSTEMS FOR FISSION PRODUCT DETECTION

Miley and R.J. Arthur, E.A. Lepel, S.L. Pratt, C.W. Thomas
Pacific Northwest National Laboratory
Sponsored by U.S. Department of Energy

Office of Nonproliferation and National Security
Office of Research and Development
Contract Number: DE-AC06-76RLO 1830

ABSTRACT

To effectively monitor the Comprehensive Nuclear-Test-Ban Treaty (CTBT), an International Monitoring System (IMS) is being constructed which will encircle the Earth with explosion detection technology [1]. Radionuclide measurements will be carried out for aerosols and for radioactive xenon isotopes. The radionuclide portion of the IMS requires a group of laboratories to perform quality assurance measurements on the radionuclide stations and to perform confirmatory analyses of samples of interest. The goal of the re-analysis is greater confidence in the detection of fission products, which are potential proof of a CTBT violation. The selection of laboratory technology for this mission can critically affect the confidence level attainable in a fixed measurement time.

Short lived fission product spectra have been created to evaluate several instrumentation approaches for laboratory measurements of the Comprehensive Nuclear Test Ban Treaty. Modest germanium detectors of several types and in shields of varying background have been used to acquire daily spectra from a hypothetical CTBT detection scenario: A group of sources was designed to simulate a CTBT sample acquired at continental distance from a small, atmospheric explosion. These spectra have been analyzed to determine what additional confidence may be expected from confirmatory laboratory measurements.

The performance of the diverse group of detectors was estimated in several ways and as a function of time. In addition, the number of isotopes detected was tabulated for certain detectors as a function of source strength. These performance estimations should provide a clear indication of the trade-off between cost and measurement quality.

Key Words: Radionuclide, Aerosol, Fission, Isotope, Atmospheric

OBJECTIVE

While chemical dissolution of the filters may be an optional approach to laboratory analysis, high-sensitivity gamma-ray spectroscopy will be the best choice for sample re-analysis because it is relatively inexpensive, non-destructive, and the most easily adapted to diverse samples. While bBeta-gamma coincidence is probably the best choice for xenon isotopes, options in high-resolution gamma-ray spectroscopy with germanium detectors for aerosol samples are considered in this work.

The simulation scenario selected has been based upon experience gathered from actual atmospheric detonations measured at PNNL during the 1960's and 1970's. Although PNNL routinely monitored the atmosphere for nuclear detonations [2], the explosions listed in Table 1 were chosen because of the interesting down-wind distances (~10,000 km) and the range of explosion sizes (~20 kilotons).

Predicting probable downwind travel time of an atmospheric plume is not within the scope of this work. The average downwind travel time reported for the detonations shown above was chosen for the pre-sampling decay (12 days). An additional 3 days of decay in the CTBT station was added and finally an additional 3 days of sample-shipment time was allowed. The total pre-measurement decay time for this scenario is therefore 18 days.

The sample fissions reported in Table 1 were determined from 1-week samples acquired with high-volume displacement pumps and 1-week measurements on high-efficiency, multi-parameter sodium iodide counting systems. In order to adapt this for use in the CTBT measurement regime, the fissions/sample were adjusted to reflect the daily volume collected (20,000 m^3) by the Radionuclide Aerosol Sampler/Analyzer (RASA) [3]. Sample splitting is expected to occur before measurement of a sample at a laboratory, but since the degree of splitting has not been determined at the time of this writing, no sample splitting has been assumed.

Table 1.Historical Explosion Data and Equivalent RASA Sample

Explosion Date	Putative Yield	Sample fissions	RASA fissions
10-16-64	20 kt	7.54×10^9	4.43×10^{10}
5-14-65	>20 kt	3.60×10^9	3.35×10^9
10-27-66	<20 kt	7.67×10^{10}	7.14×10^{10}
12-24-67	15-20 kt	1.10×10^{10}	1.02×10^{10}
11-18-71	20 kt	1.47×10^9	2.45×10^9
1-7-72	<20 kt	2.03×10^9	3.38×10^9
1-23-76	<20 kt	2.57×10^8	4.28×10^8
9-17-77	15 kt	6.05×10^9	1.01×10^{10}
3-15-78	<20 kt	3.33×10^{10}	5.55×10^{10}
12-14-78	<20 kt	3.30×10^9	5.50×10^9
10-16-80	<20 kt	3.62×10^8	6.08×10^8

Quartz ampoules containing 1.2 micrograms of uranium solution were exposed to a thermal neutron flux at the Washington State University reactor to produce a total of 1.58×10^9 fissions per ampoule. Samples of this solution were stippled onto media representing two basic expected sample configurations: the cylindrical geometry of the RASA and the essentially point-like geometry of compressed filters.

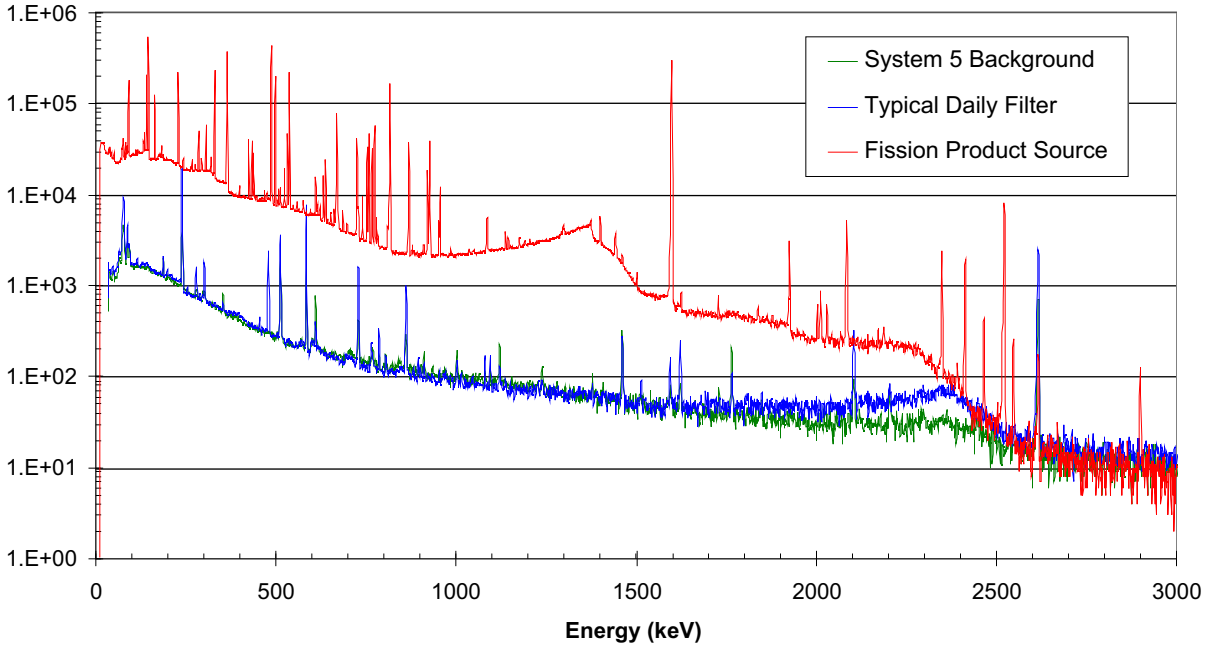


Figure 1. Fission Product Spectra (System 5)

The relatively challenging scenario selected for the experiment is a small detonation at a great distance. The CTBT laboratories will only need to fulfill basic requirements through certified procedures, and may therefore have different measurement approaches. The approaches selected for this experiment were selected to typify the CTBT lab approaches and to determine their expected performance.

The procedure expected of a CTBT lab will primarily consist of gamma-ray spectroscopy of samples already measured at a radionuclide station. Regular quality checks of the radionuclide stations are expected to constitute the majority of analyses performed. However, the ultimate mission of the laboratory is to enhance confidence in radionuclide results in the case of a suspected weapon violation. Thus laboratory samples will be mostly filters with natural isotopes only.

For these reasons, the laboratory detection procedure must exceed the sensitivity of the radionuclide stations by approximately an order of magnitude. This can be achieved by a combination of longer counting times, larger detectors, and lower backgrounds. Low background detectors are an excellent approach since the radon daughter activity in the filter will be much lower after a few days of decay provided by the sample transport time, provided the sample has been properly handled. Longer counting time is facilitated by allowing up to one week for the results of the lab measurement.

Several detection approaches have been evaluated, and are shown in Table 2. These systems are all in regular use at PNNL either in a typical counting-room or within a RASA. The MDA listed for these systems is derived from a 24-hour system background blank.

Table 2. Evaluated detection systems

No.	Relative Eff. HPGE Type	Shielding	MDA(Bq) ^{140}Ba	FWHM
1	90% P type	10-cm Pb, Passive	0.122	1.9 keV
2	36% P type	10-cm Pb, Passive	0.804	2.2 keV
3	47% N type	10-cm Pb, Passive	0.705	2.1 keV
4	41% P type	10-cm Pb, Passive	0.511	1.8 keV
5	29% P type	15-cm Pb, Active	0.044	2.8 keV

System 1 is a mechanically cooled P-type detector of 90% relative efficiency. This detector is similar to the detectors specified for use in the RASA. In this experiment, it is encased in a 10-cm thick lead cave with an inner copper lining. The source material was stippled onto a filter similar to a RASA filter and counted in a RASA geometry, i.e. wrapped around the detector. The detector resolution was measured to be 1.9 keV FWHM at 1332 keV.

System 2 is a 36% relative efficiency P-type detector in a 10-cm thick lead shield with an inner iron lining. The source was created in a point-like geometry and measured at a distance of 10 cm from the detector face, to minimize summing effects. System 2 has a measured resolution of 2.2 keV FWHM at 1332 keV.

System 3 is a 47% relative efficiency N-type detector in a shield similar to System 2 with a point-like source at 10 cm. System 3 has a thin Be entrance window and a resolution of 2.1 keV FWHM at 1332 keV.

System 4 is a commercial extra low-background detector encased in a low-background commercial shield. The detector is a 41% relative efficiency P-type detector and has a measured resolution of 1.8 keV at 1332 keV. The shield is a large diameter, 10 cm lead shell lined with copper. The point-like source was positioned 10 cm from the detector face.

System 5 is a custom built 29% relative efficiency P-type detector [4]. The construction materials have all been selected for low background. The shield is 15 cm of lead. The inner 5-cm is 160-year-old lead recovered from a sunken freighter. A 10-cm, active cosmic anti-coincidence system surrounds the entire shield. System 5 has a measured resolution of 2.8 keV FWHM at 1332 keV. The point-like source prepared for this system was placed at a distance of 1.9 cm from the side of the detector, making the geometry factor similar to System 1.

To fairly evaluate the systems under consideration, it may seem necessary to mathematically add in the signals expected from the measurement of atmospheric filters decayed to appropriate age. Figure 1 shows the comparison of a 14-day-old fission product spectrum to appropriately decayed high-volume aerosol filters. Besides the ^{208}Tl peak at 2614.47 keV, there is little impact. In actual fact, the fission product signal could be substantially smaller before radon daughters become important.

Automated gamma-ray analysis using RAYGUN [5] was chosen as the ultimate comparison of the detection approaches, and the results are tabulated in Table 3. All uncertainties, upper-limit values, and net peak areas determined by RAYGUN are based on a background continuum that RAYGUN computes for all regions of any given data spectrum. The RAYGUN data reduction code currently uses an algorithm to compute upper-limit values that is based on the branching fraction, the detection efficiency at the given energy and the computed background continuum in the region of the gamma-ray used to quantify a particular radionuclide. The reported upper-limit corresponds to a 95% Confidence Interval for the Minimum Detectable Amount (MDA) when using an integrating window that is ±1.4 FWHM around the centroid. (An integrating region-of-interest that is 1.4 FWHM-units wide is optimal for MDA calculations in cases where the presence of the radionuclide is low enough to be in question. A wider integrating

window is used by RAYGUN when a peak is definitely present and net counts are required to compute a quantitative activity level.)

Table 3. Spectral Analysis Results

	Fission Product	System 1		System 2		System 3		System 4		System 5	
	Isotopes	(Bq)	% Error	(Bq)	% Error	(Bq)	% Error	(Bq)	% Error	(Bq)	% Error
1	Cerium-141	230	1.0%	200	1.0%	250	1.0%	200	1.2%	250	1.2%
2	Barium-140	420	2.8%	350	3.3%	430	5.6%	400	2.1%	330	11.5%
3	Lanthanum-140	460	3.9%	420	2.3%	480	0.7%	460	0.7%	300	10.8%
4	Zirconium-95	42	3.1%	41	1.4%	36	6.6%	69	1.8%	52	5.1%
5	Molybdenum-99	40	9.9%	51	6.5%	58	14.7%	54	4.4%	65	21.3%
6	Ruthenium-103	81	1.0%	71	1.0%	77	1.1%	75	1.4%	57	1.2%
7	Neodymium147	110	6.2%	110	2.8%	110	3.2%	110	2.8%	56	28.5%
8	Iodine-131	130	2.5%	81	3.1%	84	2.7%	90	1.2%	85	6.8%
9	Tellurium-132	53	1.4%	61	1.0%	58	2.2%	59	1.4%	72	3.5%
10	Cerium-144	38	2.1%	24	3.7%	45	2.8%	32	7.9%	43	4.3%
11	Iodine-133	< 3.1		< 6.1		< 17		< 43		5.9	60.1%
12	Antimony-126	< 0.28		0.19	21.1%	< 1.3		< 2.0		0.4	74.9%
13	Antimony-127	2.3	9.8%	4.1	16.4%	3.7	9.4%	4	17.7%	< 2.7	
14	Cesium-137	1.2	5.8%	1.3	9.0%	< 0.84		< 1.4		0.5	41.2%
15	Cadmium-115	< 0.81		< 0.96		< 2.9		< 4.6		< 1.9	
16	Cesium-136	< 0.28		< 0.41		< 1.3		< 2.0		< 0.56	
17	Rhodium-105	< 1.7		< 2.0		< 5.8		< 11		8.0	36.7%
18	Silver-111	< 4.3		< 5.1		< 14		< 26		< 9.3	
19	Tellurium-129m	15	11.8%	< 30		< 84		< 130		< 39	
20	Zirconium-97	< 2.8		< 8.1		< 11		< 32		< 9.3	
21	Europium-156	< 4.1		< 6.1		< 14		< 33		< 7.0	
22	Ruthenium-106	22000	38.8%	25000	29.5%	11000	67.0%	150000	20.9%	19000	17.0%
23	Technetium-99m	< 0.62		-0.81		< 2.0		< 3.5		< 1.3	
24	Niobium-95	16	1.1%	13	1.3%	13	1.7%	15	2.3%	13	1.9%
25	Europium-155	< 0.90		< 1.2		< 3.0		< 4.6		< 2.8	
26	Antimony-125	< 1.2		< 2.0		< 5.0		< 9.8		< 2.8	
27	Yttrium-91	110	17.4%	< 111		< 290		< 500		< 150	
28	Tin-125	< 4.8		< 6.6		< 18		< 36		< 8.5	
29	Cerium-143	5.8	3.8%	5.57	4.0%	5.9	5.3%	5	16.5%	5.5	17.7%
30	Tellurium-131m	< 1.6		< 2.5		< 7.7		< 13		< 3.6	
31	Samarium-153	0.84		< 1.5		< 2.8		< 4.1		2.9	29.1%
32	Promethium-151	< 4.1		< 5.6		< 16		< 29		< 8.9	
33	Palladium-112	< 7.8		< 14		< 40		< 65		< 19	
34	Terbium-161	140	18.6%	< 220		110	7.0%	17	22.1%	310	4.5%
35	Cadmium-115m	< 19		< 46		< 98		< 160		< 69	
36	Silver-112	< 7.8		< 14		< 40		< 65		< 19	
37	Tin-123	< 32		< 54		< 130		< 220		< 74	
38	Strontium-89	< 150		220	68.4%	< 770		< 1100		210	71.9%
39	Cesium –134	< 0.44		< 0.71		< 2.4		< 3.2		< 0.88	
40	Palladium-111	< 4.3		< 5.1		< 14		< 26		< 9.3	
41	Strontium-91	< 1.4		2.0	30.0%	< 6.9		< 11.3		2.3	25.4%
42	Yttrium-93	51	3.9%	46	4.8%	53	6.1%	59	14.3%	52	12.4%
43	Palladium-109	83	5.3%	< 13		34	13.9%	< 45		< 27	
44	Tellurium-127m	<2700		< 3000		< 210		< 270		< 370	
45	Tellurium-127	< 47		< 71		< 210		< 360		< 113	
46	Antimony-128	< 0.62		< 1.3		< 3.0		< 6.0		< 1.7	
47	Iodine-130	< 0.51		< 1.0		< 2.7		< 4.9		< 1.5	
48	Iodine-135	< 4.6		< 5.6		< 13		< 32		< 7.8	
49	Promethium-149	< 6.3		< 8.1		20	27.5%	< 40		< 13	
50	Samarium-156	< 3.7		< 6.1		< 13		< 26		< 8.4	
51	Europium-157	< 6.7		< 10		< 29		< 50		< 15	
52	Iodine-132	250	5.1%	300	10.5%	370	4.6%	380	3.5%	250	3.5%

While the absolute efficiency of the counting geometries was not known exactly (it isn't needed for detection), variations in the loss of iodine isotopes in sample preparation may still be noted. Iodine isotopes represent a special challenge in this type of sample simulation. Since 1/3 to 1/2 of iodine in the atmosphere

from an explosion will be in a form suitable for filtration trapping, the iodine in the irradiated quartz ampoule was clearly at least twice what should be expected relative to, say, ^{99}Mo. On the other hand, after the sample has been diluted and stippled onto a substrate, then dried under heat lamps in a hood, the volatile iodine isotopes may be reduced.

CONCLUSIONS AND RECOMMENDATIONS

The data in Table 3 may be manipulated in several ways to evaluate the different detection approaches. The most trivial would be to count the number of detected isotopes for each system. Additional isotopes, particularly if in reasonable ratios, would constitute enhanced confidence that a marginal IMS radionuclide detection is defensible. One may require, however, that only the higher quality isotopes should be used for this determination. Table 4 shows the cumulative number of isotopes for each system with error bars at or below a range of threshold values.

The comparison between the systems is approximately a tie between System 1 and System 4 when very restrictive limits are placed on isotopic detections. Where any detection is counted, System 5 is superior, and System 4 is worst. However, it is clear that this measure does not strongly differentiate the systems.

A Figure of Merit (FOM) is desired which more directly captures the enhanced confidence that the laboratory measurement provides. The first concept that was considered by the authors was to estimate the average confidence in a hit by a given system, then multiply by the number of isotopes detected by that system.

Assuming that one could construct the confidence level of a detection from a RAYGUN output, however, it is obvious that the result of this exercise would be simply the sum of the confidence of each isotope. Thus, one need only construct a relative measure of confidence for each isotope, sum all for a given system, then compare. The same thresholds may be applied to judge the systems only on the best isotopes, all isotopes, or any threshold between.

A candidate for detection confidence may be simply formed by inverting the magnitude of the error bar. Thus, an isotope with a 50% uncertainty would have a confidence FOM of 2, while an isotope detected with a 1% uncertainty would have a confidence FOM of 100. Table 5 shows this FOM computed for the same thresholds shown in Table 4.

This measure shows System 4 to be superior regardless of how restrictive the acceptance criteria. This information can be interpreted in several ways and there are several implications. Firstly, modestly lowered background reduction with a modestly sized detector are superior to a larger (x2) detector in a simple shield or an elaborate shield but smaller (x0.7) detector.

The failure of System 5 to exceed the other systems is due to the fact that the sample-associated background dominates the spectrum. In fact, even the radon daughters in the filter were not important. So with the low background masked by the source, the only remaining important feature of the detector was its small size. This shows that a lower MDA for ^{140}Ba computed from system background may be a deceptive measure of system value.

The recommendation that may be drawn from this experiment is that there is more than one way to adequately configure laboratory hardware to perform a confirmatory measurement on a CTBT aerosol sample. The best results for samples with significant fission-product content will come from simultaneously reducing background and increasing detector size. Ultra-low-background detectors will not have an impact on this problem. Extremely large detectors will also not improve the detection greatly.

In fact, it is the interference of the different fission products that limits the confidence FOM. In this light, it would seem that greater selectivity might be the way to increase the FOM, if increases were desired. Improved resolution or coincidence techniques could be employed to increase selectivity, but the immediate advantage would only be to shorten the time needed to reach the required sensitivity, and thus increase the throughput of the laboratory.

On the other hand, large or ultra-low background detectors (Systems 1 and 5) can fill an important role for samples that have no significant fission product content, which have several days of radon-daughter decay, and which have been handled in a manner that does not add contamination. In this case, the ^{140}Ba MDA listing in Table 2 is more indicative of system performance. It should be remembered that the vast majority of samples are expected to be of this type.

The final conclusion is all CTBT parties would be best served by well equipped laboratories which can have procedures in place for both low and high activity samples.

Table 4. System Comparison by Isotopes Detected

Max Error %	System 1	System 2	System 3	System 4	System 5
2%	4	5	4	6	3
3%	8	9	8	9	3
5%	11	12	9	11	7
10%	17	15	15	12	9
20%	20	16	17	15	14
30%	20	19	18	17	18
50%	21	19	18	17	20
100%	21	20	19	17	23

Table 5. System Comparison by Confidence FOM

Max Error %	System 1	System 2	System 3	System 4	System 5
2%	362	448	393	508	219
3%	486	528	511	635	219
5%	596	663	564	686	322
10%	688	689	657	699	356
20%	707	705	671	717	394
30%	707	717	675	727	409
50%	710	717	675	727	415
100%	710	718	676	727	419

REFERENCES

[1] CTBT text available at www.acda.gov

[2] C.W. Thomas, et al, PNL-3826, UC-11 (1981)

[3] S.M. Bowyer, et al, IEEE Transactions on Nuclear Science, Vol. 44, No. 3 (1997) 551-556

[4] H.S. Miley, et al., J of Radioanalytical and Nuclear Chemistry, Articles, Vol 160, No. 2 (1992) 371-385, RJ Arthur et al, J of Radioanalytical and Nuclear Chemistry, Articles, Vol 160, No. 2 (1992) 297-304

[5] W.K. Hensley, et al, J of Radioanalytical and Nuclear Chemistry, Articles, Vol 124, No. 2 (1988) 481-499

DATA PROCESSING AND ANALYSIS

USING MULTICAST IN THE GLOBAL COMMUNICATIONS INFRASTRUCTURE FOR GROUP COMMUNICATION

Deborah A. Agarwal, Information and Computing Sciences Division,
Ernest Orlando Lawrence Berkeley National Laboratory

Sponsored by U. S. Department of Energy
Office of Nonproliferation and National Security
Office of Research and Development
Contract No. DE-AC03-76SF00098

ABSTRACT

International Monitoring System (IMS) stations and the International Data Centre (IDC) of the Preparatory Commission for the Comprehensive Nuclear-Test-Ban Treaty Organization generate data and products that must be transmitted to one or more receivers. The application protocols used to transmit the IMS data and IDC products will be CD-x and IMS-x and the World Wide Web (WWW). These protocols use existing Internet applications and Internet protocols to send their data. The primary Internet applications in use are electronic mail (e-mail) and the file transfer protocol (ftp). The primary Internet communication protocol in use is the Transmission Control Protocol (TCP), which provides reliable delivery to the receiver. These Internet applications and protocol provide *unicast* (point-to-point) communication. A message sent using unicast has a single recipient; any message intended for more than one recipient must be sent to each recipient individually. In the current design, the IDC and the National Data Centres (NDC's) provide data forwarding to the appropriate receivers. The overhead associated with using unicast to transmit messages to multiple receivers either directly or through a forwarder increases linearly with the number of receivers. In addition, using a forwarding site introduces possible delays and possible points of failure in the path to the receivers.

Reliable multicast provides communication services similar to TCP but for a group of receivers. The reliable multicast protocol provides group membership services and message delivery ordering. If an IMS station were to send its data using reliable multicast instead of unicast, only sites that are members of the multicast group would receive the data at approximately the same time. This might provide an efficient means of disseminating station data or IDC data products to all receivers and eliminate or greatly reduce the need for data forwarding.

Several commercial and research reliable multicast protocols exist for the Internet. Each of these protocols is designed to serve a specific community of users and applications. The author has undertaken a study to determine if reliable multicasting is appropriate for use in the Global Communication Infrastructure (GCI).

Key Words: communications, multicast, reliable

OBJECTIVE

Reliable multicast is a basic capability that has been proposed for use as a communication mechanism in the Global Communication Infrastructure (GCI). A study has been undertaken by the author to determine whether reliable multicast can be used in the Comprehensive Nuclear Test-Ban Treaty (CTBT) monitoring network. There are two aspects to providing reliable multicast in the GCI network. The reliable multicast capability would need to be available in the network and the International Data Center (IDC) application protocols would need to be converted to make use of the reliable multicast capability before any benefits would be realized.

The Global Communication Infrastructure (GCI)

The International Monitoring System (IMS) under the Comprehensive Nuclear Test-Ban Treaty (CTBT) comprises 321 IMS stations and 16 radionuclide laboratories worldwide. The International Data Center (IDC) in Vienna will collect, store, and process the monitoring data from these stations. The IDC is responsible for distribution of the data and the data products to the National Data Center (NDC) of each interested Member State. The closed and secure data network under construction to carry this data is called the Global Communications Infrastructure (GCI). The GCI will provide data communication links for the IMS stations, the NDC's and the IDC. When the network is in full operation, it is expected to carry approximately 10 gigabytes per day.

Topologically, the GCI is a private network composed of frame relay and satellite links configured as a two-level tree rooted at the IDC. The major network nodes are the IDC in Vienna and four (or more) satellite hubs in Germany, Italy (2) and the United States. High-speed terrestrial Frame Relay private virtual circuits (PVC) with integrated services digital network (ISDN) backups connect the IDC to each of the hubs. There are four space satellites; each VSAT hub provides communication for a different satellite. Typically, an IMS station is connected by a VSAT (Very Small Aperture Terminal earth station) to one of the satellites and thus one of the four hubs. The NDC's are connected to the GCI via VSAT, frame relay, or the Internet. There are also three methods of connecting IMS stations to the GCI. These methods are called respectively the Basic Topology, Partitioned Subnetwork and Independent Subnetwork. In the Basic Topology, the monitoring data originating at an IMS station uses a GCI VSAT satellite link to a VSAT hub, and from there, it travels a GCI Frame Relay PVC to the IDC. In a Partitioned Subnetwork, the physical connection of the GCI at the IMS stations is the same as in the Basic Topology except that data from the IMS stations is routed through the NDC before going to the IDC. In an Independent Subnetwork, the GCI does not have a direct connection to the IMS stations. The network between the IMS stations and the NDC is installed and operated by the Member State. Data from the IMS stations in an Independent Subnetwork is routed through the NDC before going to the IDC. The GCI is expected to meet stringent performance requirements. For example, the one-way delay target is 5 seconds or less for at least 99.5% of the time. The virtual circuit availability is set at 99.5% over one year.

The protocols and applications that have been developed for the general Internet will be used by the GCI to send the CTBT data and data products through the GCI network. The Internet protocols are implemented in the hosts and routers of the network and they define a method for sending data through the network. The Internet protocols come standard on routers and hosts and provide a standard and effective means of communicating in diverse environments. The Transmission Control Protocol (TCP) and the User Datagram Protocol (UDP) are the Internet protocols used to provide unicast (point-to-point) communication0. The TCP protocol provides reliable transmission of messages, error detection, and flow control. The TCP protocol uses an explicit connection between the sender and receiver to send the data. The two ends of the connection explicitly coordinate to determine connection parameters, what has been received, buffer space, and lost messages. UDP provides an unreliable, unregulated message transmission capability. UDP provides no coordination between the sender and the receiver. The Internet protocols are used to exchange data across the network. They transport the data to its destination; they do not attempt to interpret the data inside the messages.

The Internet applications use the underlying Internet protocols (primarily TCP) to provide higher level capabilities like electronic mail (e-mail), file transfer protocol (ftp), and World Wide Web (WWW). By using the already existing Internet standards as the GCI communication mechanisms, the GCI is able to

utilize all of the capabilities of the general Internet but in its own private network. These applications come standard in most operating systems and are interchangeable across different implementations.

The IMS data will be transmit across the GCI using proprietary IDC application protocols. These application protocols are the CD-x and IMS-x protocols (the x when replaced by a number identifies a particular version of the protocol). The CD-x protocol will provide reliable transmission of continuous data from primary seismic, hydroacoustic, and infrasound sensors. Non-continuous data from the IMS stations and the IDC will likely be sent using the IMS-x protocol. The IMS-x protocol will use a combination of conventional e-mail, ftp, and WWW.

The CD-1 protocol, which is already implemented, uses the TCP protocol to send data. The CD-2 protocol is being designed now and is expected to eventually replace the CD-1 protocol. The CD-2 protocol will provide many enhancements including authentication and a more advanced data format. It is being designed to be able to run over either the TCP or UDP protocol. The reliability mechanisms in CD-2 will provide application level reliability and provide reliable delivery beyond what is available in TCP. The TCP reliable message delivery works only while there is a connection between the sender and the receiver. The CD-2 protocol will provide the mechanisms for determining what the receiver is missing and recovering the missing data. CD-2 will also add mechanisms for making sure that the data reaches stable storage at the receiver. In addition, the CD-2 protocol will be responsible for forwarding data at the IDC and the NDC's of Independent Subnetworks and Partitioned Subnetworks.

All of the IMS data must be received at the IDC regardless of whether it is via the Basic Topology, a Partitioned Subnetwork, or an Independent Subnetwork. The IDC is also responsible for forwarding this data to Member States that request the data or data product. Since the CTBT monitoring network implementation is only just underway, the number of NDC's that will request data and particular data products from the IDC is not well known. Many of the Member States will have relatively low data rate connections from the IDC to their NDC, so it is unlikely that they are expecting to request significant amounts of continuous data. However, at least one Member State has requested all the continuous and non-continuous data from the IDC.

Multicast

As the Internet has grown so has the need for additional communication protocols. In particular a new class of applications has emerged that require the ability to send messages to a large group of receivers efficiently. This need has led to the development of the IP multicast capability in the Internet. IP multicast provides an unreliable communication mechanism that allows a single message to be sent to a group of receivers. IP multicast is a service implemented in the hosts and routers of the network. The multicast addresses are a separate address range recognized by the routers as multicast groups. Multicast packets are sent addressed to a multicast address. Applications that wish to receive the multicast packets open a connection to the multicast address and their host automatically transmits a join message to the nearest router. The router then adds the host to the multicast dissemination tree for the group. The multicast tree is dynamic and provides an efficient means of transmitting the packet through the network to reach all the receivers without traveling any link more than once. The routers at branch points in the tree duplicate the packet and send it down all the tree branches. For more detail regarding the multicast routing protocols, see 0and 0.

The IP multicast communication mechanisms are gradually becoming a standard part of the Internet protocol suite and they co-exist with the TCP and UDP mechanisms. The IP multicast mechanisms do not replace the unicast mechanisms; they instead provide an additional service. Since IP multicast is still a relatively new technology routers do not come with IP multicast enabled by default. The router administrator must enable it before it can be used in the network. Unfortunately, not many commercial applications are making use of IP multicast so many Internet Service Providers (ISP) have not yet enabled the capability.

IP multicast messaging is an unreliable service similar to UDP; it provides unreliable message delivery. Reliable multicast is effectively the multicast equivalent to the TCP protocol. Reliable multicast provides reliable delivery of messages to multiple receivers. Reliable multicast uses IP multicast to provide the actual message dissemination capability and it adds reliable delivery mechanisms. A reliable multicast

protocol provides several potential advantages over TCP when there are in fact multiple receivers. With reliable multicast the receivers in a group can be reached by sending a single message. Using TCP the messages would need to be sent to each receiver individually by the original sender or a site acting as a forwarder. In the case of the CTBT network the forwarding site is the IDC (and the NDC in the case of a Partitioned or Independent Subnetwork).

Reliable multicast is not yet a standard communication protocol that is part of the operating systems of hosts but it can run on the hosts. Reliable multicast is an end-to-end protocol that is run at each of the senders and receivers participating in a reliable multicast session. It usually uses IP multicast for its underlying communication mechanism. There are several commercial and freeware reliable multicast protocols available today. Some of the available reliable multicast protocols are described in [1-3], [6-10], and [12].

The reliable multicast protocols are not yet standard on the Internet. One reason is that there are competing views regarding what reliable message delivery guarantees an application should be provided. The types of applications that are supported by the reliable multicast protocols range from distributed databases to multicast ftp so they do not have a uniform set of requirements. The reliable multicast protocols are each designed for use in a particular class of applications. The application classes differ in the message delivery reliability and ordering properties required and the number of participants in a multicast group. The reliable multicast protocols also differ in their methods of indicating message loss, determining membership, and retransmitting lost messages. The underlying mechanisms and message formats of each reliable multicast protocol are different; so the different implementations can not communicate with each other. This means that sites participating in the same reliable multicast session need to run the same reliable multicast protocol. The network routers do not participate in the reliable multicast protocol; they only need to handle IP multicast messages.

RESEARCH ACCOMPLISHED

Reliable multicast can only provide benefits to the CTBT if it is implemented in the GCI network and it is used by the IDC application protocols such as CD-x and IMS-x. The potential benefits of using reliable multicast in the network could be increased reliability from eliminating data forwarding operations, network bandwidth savings and improved scalability to multiple receivers. The reliability of the continuous data collection and dissemination might be improved by eliminating the forwarding operations. But, eliminating some or all of the forwarding operations may be disallowed by the CTBT. Determination of whether particular multicasting uses are allowed by the treaty is an important issue but it is outside the scope of this paper. The legal and political issues of multicasting in the GCI will not be addressed by this paper. This paper will instead focus only on the technical issues of multicasting. Since the IDC application protocols can only make use of reliable multicast if it is provided in the GCI network, this section start with a description of how IP multicast and reliable multicast would be implemented in the GCI network.

IP Multicast in the GCI

As with the Internet, the IP multicast capabilities of the GCI are implemented in the routers and the end hosts. In order for IP multicast to work in the network the routers at the satellite hubs and in the frame relay network would need to have IP multicast enabled. The broadcast nature of the satellite portion of the GCI network provides some relatively natural multicast mechanisms. The satellite hub already broadcasts all unicast and multicast data it sends to its remote VSAT sites. If the data in a message is not addressed to any of the machines located at a particular VSAT then the VSAT throws the message away after receiving it; the VSAT passes messages sent to a multicast address. Multicasts from the satellite hub are sent once over the satellite link and received by all the remote VSAT sites connected to that hub. In the other direction the satellite link is not broadcast; multicasts sent by a remote VSAT site are received only at the satellite hub. If there are other VSAT located members of the multicast group on that same satellite hub then the hub retransmits the multicast to the remote VSAT's. This retransmission is handled by the router located at the satellite hub. Since a multicast from a VSAT to the hub reaches only the hub, no network bandwidth on this piece of the route will be saved. However, a multicast in the direction from the hub to the VSAT reaches all the VSAT's with hosts joined to the multicast group; the multicast uses only

the network bandwidth required to reach one VSAT. The network bandwidth savings from using multicast increase with the number of receivers located at VSAT sites connected to the same satellite hub.

The routers in the frame relay network are located at the ends of the frame relay PVC's. These routers would also need to be configured to allow IP multicast before IP multicast would work in the frame relay portion of the GCI network. The PVC's between the routers simply act as ordinary network links. Multicast operates in a frame relay network the same way it does on the Internet; the routers build a message dissemination tree and forward multicast messages down this tree. The principle savings IP multicast could provide are from avoiding sending data down any network link more than once. In the case of transoceanic or transcontinental links this may produce significant savings. The frame relay network can also be configured to contain a multicast mesh. Enabling a multicast mesh effects only the multicast traffic, it has no effect on the unicast traffic in the frame relay network. The unicast messages travel through the frame relay PVC's and the multicast traffic uses the mesh. The benefit of using a multicast mesh is realized when a more efficient multicast dissemination tree can be built. The mesh allows the tree to branch at any place in the frame relay network rather than only at the ends of the PVC's. The decision of whether to share the unicast PVC's or define a multicast mesh in the frame relay network is an engineering design decision that does not effect the external behavior of the network.

The GCI Integration Laboratory within the IDC contains a test network composed of all the essential components of the GCI but isolated from the GCI so that it can be used for testing without impacting the GCI. The GCI Integration Laboratory is composed of three remote sites that are connected via VSAT to a satellite hub. The satellite hub is connected to the IDC using a frame relay PVC. The routers and software in the GCI Integration Laboratory network are the same types and versions as is used in the rest of the GCI. The IP multicast capabilities were enabled on the GCI Integration Laboratory routers temporarily for feasibility tests to allow testing of IP multicast.

Extensive tests measuring throughput, loss, round trip time, and packet size were conducted in the GCI Integration Laboratory. The test software was designed to allow packets of a designated size to be generated and sent using a periodic rate. The software had the ability to send the data either one-way or with the receiver(s) bouncing the traffic back using another IP multicast address to allow round trip times to be measured. The tests indicate that the GCI Integration Laboratory components are able to pass IP multicast traffic at the full capacity of the links without problem.

One difficulty encountered is that the hosts located at the end of the frame relay link are located behind a firewall. The firewall does not allow IP multicast packets to pass through it so these machines cannot exchange IP multicast messages with the VSAT connected hosts. If the GCI network will contain firewalls between machines that must exchange IP multicasts, a way to get multicasts through the firewall will need to be determined. Most firewall products do not directly recognize IP multicast packets. The successful tests of the IP multicast capabilities and performance in the GCI Integration Laboratory were conducted by placing a machine on a LAN directly connected to the frame relay link. This machine was outside of the firewall and was thus able to exchange IP multicast messages with the VSAT located hosts.

CTBT Application Protocols

The IDC application protocols (CD-x and IMS-x) were also studied to determine feasibility of using reliable multicast as their transport mechanism. The overall data rate in the GCI is expected to be on the order of 10 gigabytes per day. Approximately 8.5 gigabytes per day of this data is continuous data sent using the CD-x protocol. Since the CD-1 protocol is already in use and is expected to be phased out the study instead focused on the CD-2 protocol, which is still in the design phase.

The current CD-2 design specifications assume that data will be transmitted using unicast. This assumption is most apparent in the specification of the connection setup and termination. With unicast connections there is only one sender and one receiver so the connection is either up or down. Multicast introduces the concept of multiple receivers and a multicast group. The members of the group are notified of membership changes and the current membership of the group. The determination of whether the sender or a specific receiver is in the group is made by examining the group membership rather than the connection state. The CD-2 protocol design would likely require minor modifications to accommodate this change. The other aspect of the CD-2 design that would be affected by reliable multicast is the reliable

delivery of frames. Acknowledgements and retransmission requests would be coming from multiple receivers if reliable multicast were used under CD-2. This may affect the specification but it will need to be considered in the CD-2 protocol implementation. Since there are relatively few subscribers to the CD-2 data from the IMS stations reliable multicast is unlikely to provide any scaling benefits. The benefits would more likely be from bandwidth savings and any improvements in reliability that can be achieved by removing forwarding operations.

The IMS-x protocol will likely be used to disseminate the data products generated by the IDC and to transmit any non-continuous IMS station data. The e-mail, ftp and WWW services will likely be provided by the standard Internet applications available in most operating systems today. The Internet standard versions of these applications are based on unicast communication. There are, however, commercial and research versions of ftp and WWW that are based on reliable multicast. The network news application also has versions available that support reliable multicast and it could potentially be used instead of e-mail. But, in order to use reliable multicast-based services in the IMS-x protocol the reliable multicast-based versions of each of these reliable multicast enabled applications would need to be installed at each of the sites participating in IMS-x data exchanges. Currently the only data that will likely be transmitted using IMS-x and have a significant number of recipients is the data products generated by the IDC. These data products are sent to only to NDC's subscribed to the data product. The connections from the IDC to the various NDC's subscribed to a particular data product are likely to be a combination of Internet, satellite and frame relay links. Thus, the network bandwidth savings may not turn out to be significant. More information than is available today about the subscription list of each of the data products would be needed to make this determination. In addition, it may take a while to get IP multicast enabled between the IDC and the NDC's connected via the Internet depending on the Internet Service Providers involved.

Reliable Multicast in the GCI

The reliable multicast protocols were also evaluated to determine whether an existing reliable multicast protocol could serve the needs of the CTBT. One of the critical delineators between different reliable multicast protocols is whether they support coordination between multiple senders in a group. The IMS-x and CD-x would not require coordination between different sites sending messages so the reliable multicast protocol would only need to support a single sender per reliable multicast group. The reliable multicast group sizes (receiver set) will also likely be relatively small (less than 200) for all IDC applications and quite small (less than 10) for the CD-x application protocol.

Some of the existing reliable multicast protocols that provide the characteristics described in the paragraph above are the Multicast Dissemination Protocol (MDP)0 and the Reliable Multicast Transport Protocol (RMTP)0. These protocols are available, they are deployed in applications, and they have on-going development projects. Many characteristics differentiate the above protocols and these characteristics could be used to narrow the choices. If the decision to use a reliable multicast protocol in the GCI is made, then additional criteria such as membership, congestion control, and security will also need to be considered in determining which reliable multicast protocol to use.

The MDP protocol which is a freely available protocol was obtained via the WWW and installed in the GCI Integration Laboratory to test the basic capability of the reliable multicast protocols to run in the GCI network. Reliable multicast transfers of jpeg images were performed using the MDP protocol. The images were transferred back and forth between remote VSAT located sites and an IDC located machine. The MDP protocol provided reliable multicast over these GCI links without requiring any modification or tuning to account for the satellite links. The other reliable multicast protocols were not tested in the GCI Integration Laboratory. The MDP is source code available and free making it a prime candidate for use in the GCI. The RMTP protocol is a commercial product so it has associated licensing fees and is not source code available. In addition, the RMTP protocol contains mechanisms for scaling to exceedingly large groups. These mechanisms would not be needed in the GCI but, they would require additional configuration and maintenance.

CONCLUSIONS AND RECOMMENDATIONS

Reliable multicast protocols provide a capability to send a single message to multiple receivers. Using reliable multicast protocols can sometimes improve scalability, efficiency or reliability of an application. This paper reports on a study that has been undertaken by the author to determine whether use of reliable multicast can benefit the CTBT monitoring network. Since the CTBT monitoring network is not yet fully established there are many details of the networks and protocols that have not been finalized. This made studying the possible effect of reliable multicast in the CTBT monitoring network more difficult. The study was, however, able to determine that IP multicast and reliable multicast can run in the GCI network. Some candidate reliable multicast protocols for use in the network were presented and a likely candidate, the MDP protocol, was tested in the GCI Integration Laboratory.

The CD-2 protocol may be able to gain benefits from using reliable multicast in the GCI. But, a determination of what uses of reliable multicast are allowed under the CTBT would need to be made. If reliable multicast is to be used in the GCI, then a final decision regarding which reliable multicast protocol to use would need to examine the detailed needs of the application protocol.

REFERENCES

D. Agarwal, P. Melliar-Smith, L. Moser, and R. Budhia, "Reliable Ordered Delivery Across Interconnected Local-Area Networks," Transactions on Computer Systems, vol. 16, no. 2 (May 1998).

Y. Amir and J. Stanton, "The Spread Wide Area Group Communication System," Johns Hopkins University Technical Report, CNDS-98-4, available from ftp://ftp.cnds.jhu.edu/pub/papers/spread.ps.

K. Birman and T. Joseph, "Reliable communication in the presence of failures," ACM Transactions on Computer Systems, vol. 5, no. 1, pp. 47-76, February 1987.

D. Comer, *Internetworking with TCP/IP: Principles, Protocols, and Architecture*, 2nd ed, Volume I, New Jersey: Prentice-Hall, 1991.

D. Estrin, D. Farinacci, A. Helmy, D. Thaler, S. Deering, M. Handley, V. Jacobson, P. Sharma, L. Wei, "Protocol Independent Multicast," IETF RFC 2362, available from ftp://ftp.isi.edu/in-notes/rfc2362.txt

S. Floyd, V. Jacobson, C. Liu, S. McCanne, and L. Zhang, "A Reliable Multicast Framework for Light-weight Sessions and Application Level Framing," IEEE/ACM Transactions on Networking, December 1997, Volume 5, Number 6, pp. 784-803.

J. Lin and S. Paul, "RMTP: A Reliable Multicast Transport Protocol," IEEE INFOCOM '96, March 1996, pp. 1414-1424.

J. Macker and W. Dang, "The Multicast Dissemination Protocol version 1 (mdpv1) Framework," Technical white paper, US Naval Research Laboratory, available from http://tonnant.itd.nrl.navy.mil/docs/mdpv1.ps.

K. Miller, K. Robertson, A. Tweedly, M. White, "StarBurst Multicast File Transfer Protocol (MFTP) Specification," IETF Draft Specification, draft-miller-mftp-spec-03.txt, dated April 1998.

W. Strayer, S. Gray, and R. Cline, Jr., "An Object-Oriented Implementation of the Xpress Transfer Protocol," Proceedings of the Second International Workshop on Advanced Communications and Applications for High-Speed Networks (IWACA), Heidelberg, Germany, September 26-28, 1994.

D. Waitzman, C. Partridge, S. Deering, "Distance Vector Multicast Routing Protocol," IETF RFC 1075, available from ftp://ftp.isi.edu/in-notes/rfc1075.txt

B. Whetten, M. Basavaiah, S. Paul, T. Montgomery, N. Rastogi, J. Conlan, T. Yeh, "The RMTP-II Protocol," Internet Draft, draft-whetten-rmtp-ii-00.txt and draft-whetten-rmtp-ii-app-00.txt, dated April 1998.

A SIMPLE PROCEDURE FOR KRIGING LEFT-CENSORED DATA

Kevin K. Anderson, Pacific Northwest National Laboratory
W. Scott Phillips, Los Alamos National Laboratory

Sponsored by U.S. Department of Energy
Office of Nonproliferation and National Security
Office of Research and Development
Contract Nos. DE-AC06-76RLO 1830

ABSTRACT

Kriging is a widely applied geostatistical prediction methodology. Many forms of kriging are used to obtain accurate predictions from observed spatial data. This paper discusses the problem of kriging spatial data that include some left-censored values. Limitations of measurement instruments or high noise levels may censor some observations so that one only knows that the values are less than reported thresholds. Naively ignoring this type of data typically over-predicts the spatial surfaces. Stein (1992) presented a Monte Carlo method for estimating the high-dimensional integrals required to calculate the predictive, conditional distributions. This paper presents a simple procedure that can be used with existing complete-data kriging algorithms. We present an analysis of seismic Lg-phase amplitude residuals from Chinese earthquakes. The final results yield a broadened low-amplitude zone across Tibet, increasing predicting power in areas from which poor Lg are observed. We anticipate the method will be useful for creating amplitude correction surfaces for use in estimating magnitudes and evaluating Comprehensive Test Ban discriminants.

Key Words: imputation, Lg phase amplitudes, spatial statistics

OBJECTIVE

Regional seismic characterization is a major research area of the Comprehensive Nuclear-Test-Ban Treaty Program. Kriging techniques are being used to produce spatial corrections for travel times, and various amplitudes. The objective of this research is to produce a two-stage kriging algorithm, which could incorporate poor signal- to-noise data or below-detection-threshold (left-censored) data.

The two-stage kriging algorithm is demonstrated using amplitudes of seismic Lg phases recorded in China. Lg is a collection of shear modes trapped in the earth's crust and is often found in seismograms collected at distances between 300 and 2000 km from the source. Lg is known to exhibit dramatic variations in behavior in tectonically complex areas and can be severely attenuated or blocked by transitions between oceanic and continental crust (Press and Ewing 1952) or by continental structures such as the edge of the Tibetan plateau (Ruzaikin et al. 1977). Because good signal-to-noise data originating behind a blockage zone is rare, our ability to map propagation efficiency is greatly reduced in these areas. The inclusion of left-censored data information will increase the number of constraining data points in such areas, leading to better prediction and less reliance on unconstrained extrapolation. Corrections based on propagation maps will be important for estimating magnitudes (Nuttli 1986) and reducing the scatter in phase and spectral ratios used to discriminate between natural and man-made seismic events (Pomeroy et al. 1982); thus, such corrections will be useful for monitoring the Comprehensive Nuclear-Test-Ban Treaty.

RESEARCH ACCOMPLISHED

This paper presents a simple procedure that can be used with one's favorite complete-data Kriging algorithm. Stein's (1992) procedure obviates existing algorithms and software when faced with left-censored data. We formulate a two-stage procedure under the Simple Kriging assumptions; however, application to Ordinary Kriging situations is immediate. For comparison, we present examples of simulated data sets with just one left-censored datum, with much left-censored data (Stein's 1992 simulated data), and with Lg-phase amplitude residuals from Chinese earthquakes (Phillips 1999). This research has been submitted for publication in The Journal of Computational and Graphical Statistics, and is available as a PNNL technical report (PNNL-12206).

CONCLUSIONS AND RECOMMENDATIONS

The application of the procedure to Chinese seismic data produced broadened regions of poor Lg efficiency, which would not have been seen had left-censored data been ignored. The most efficient raypaths originate from northwest, northeast and southeast quadrants, the Baikal Rift in particular. These paths cross older and geologically stable regions, consistent with the observed efficient propagation. Little Lg is observed for Tibet events (a well-known blockage). Shallow trench events on either side of Taiwan, whose raypaths cross oceanic crust, also produce little Lg. Regions of poor Lg efficiency are broadened by the procedure. In particular, central and western areas of Tibet are characterized by lower Lg values because of the influence of censored data. Previously, predictions for these areas were solely based on extrapolation because too few events were large enough to produce Lg exceeding the signal-to-noise threshold.

REFERENCES

Nuttli, O.W. (1986), “Yield Estimates of Nevada Test Site Explosions Obtained from Seismic Lg Waves”, Journal of Geophysical Research, 91, 2137-2151.

Phillips, W.S. (1999), “Empirical Path Corrections for Regional Phase Amplitudes”, Bulletin of the Seismological Society of America, in press.

Pomeroy, P.W., W.J. Best, and T.V. McEvilly (1982), “Test Ban Treaty Verification with Regional Data: A Review”, Bulletin of the Seismological Society of America, 72, S89-S129.

Press, F., and M. Ewing (1952), “Two Slow Surface Waves Across North America”, Bulletin of the Seismological Society of America, 42, 219-228.

Ruzaikin, A.I., I.L. Nersesov, V.I. Khalturin, and P. Molnar (1977), “Propagation of Lg and Lateral Variations in Crustal Structure in Asia”, Journal of Geophysical Research, 82, 307-316.

Stein, M.L. (1992), “Prediction and Inference for Truncated Spatial Data”, Journal of Computational and Graphical Statistics, 1, 91-110.

CLUSTER ANALYSIS FOR CTBT SEISMIC EVENT MONITORING

Dorthe B. Carr and Chris J. Young, Sandia National Laboratories
Richard C. Aster and Xioabing Zhang, New Mexico Institute of Mining and Technology

Sponsored by U.S. Department of Energy
Office of Nonproliferation and National Security
Office of Research and Development
Contract No. DE-AC04-94AL85000

ABSTRACT

Mines at regional distances are expected to be continuing sources of small, ambiguous events which must be correctly identified as part of the Comprehensive Nuclear-Test-Ban Treaty (CTBT) monitoring process. Many of these events are small enough that they are only seen by one or two stations, so locating them by traditional methods may be impossible or at best leads to poorly resolved parameters. To further complicate matters, these events have parametric characteristics (explosive sources, shallow depths) which make them difficult to identify as definite non-nuclear events using traditional discrimination methods. Fortunately, explosions from the same mines tend to have similar waveforms, making it possible to identify an unknown event by comparison with characteristic archived events that have been associated with specific mines.

In this study we examine the use of hierarchical cluster methods to identify groups of similar events. These methods produce dendrograms, which are tree-like structures showing the relationships between entities. Hierarchical methods are well-suited to use for event clustering because they are well documented, easy to implement, computationally cheap enough to run multiple times for a given data set, and because these methods produce results which can be readily interpreted. To aid in determining the proper threshold value for defining event families for a given dendrogram, we use cophenetic correlation (which compares a model of the similarity behavior to actual behavior), variance, and a new metric developed for this study.

Clustering methods are compared using archived regional and local distance mining blasts recorded at two sites in the western U.S. with different tectonic and instrumentation characteristics: the three-component broadband DSVS station in Pinedale, Wyoming and the short period New Mexico Tech (NMT) network in central New Mexico. Ground truth for the events comes from the mining industry and local network locations, respectively. The clustering techniques prove to be much more effective for the New Mexico data than the Wyoming data, apparently because the New Mexico mines are closer and consequently the signal to noise ratios (SNR's) for those events are higher. To verify this hypothesis we experiment with adding gaussian noise to the New Mexico data to simulate data from more distant sites. Our results suggest that clustering techniques can be very useful for identifying small anomalous events if at least one good recording is available, and that the only reliable way to improve clustering results is to process the waveforms to improve SNR. For events with good SNR that do have strong grouping, cluster analysis will reveal the inherent groupings regardless of the choice of clustering method.

Key Words: cluster analysis, discrimination, mining events

OBJECTIVE

One way to determine if an event is from a particular mine is for an analyst to compare known waveforms from that mine to the unknown waveform. This can be done by eye, and for an analyst who knows a region well, events from certain mines can be easily identified by visual inspection. However, with the large volume of data that can be expected when monitoring the Comprehensive Nuclear-Test-Ban Treaty (CTBT), we want to find a way to automate comparing unknown waveforms to archived events associated with specific mines. In this study, we investigate the use of cluster analysis techniques to facilitate this comparison. Previous seismic event studies have used cluster analysis to classify event catalogues (Isrealsson, 1990; Riviere-Barbier and Grant, 1993), but have only provided a cursory view of the richness of the discipline.

Using data from three mines in Wyoming and four mines in New Mexico, we compare different waveform processing methods and cluster analysis techniques to determine what processing parameters and cluster analysis techniques do the best job of clustering known events. To help determine which methods give the best results, we use two metrics. The first is cophenetic correlation and the second is a metric based on separation of known events from different mines and the formation of clusters of events from the same mine.

RESEARCH ACCOMPLISHED

Cluster Analysis

The term cluster analysis refers to a variety of techniques for grouping similar entities in such a way that their interrelationships are revealed. Most of the work in the area comes from taxonomy, a discipline of biology, where researchers seek to classify organisms based on sets of measurements (e.g. various measurements of types of bones). The first step in any method of cluster analysis is to quantify the similarity, or conversely, the dissimilarity between the entities to be categorized. Because the mathematical equations involved are typically given using dissimilarity, we follow that convention. A measure of dissimilarity could easily be developed for seismic waveforms (e.g. parameters could be arrival times, signal to noise ratio (SNR), etc.), but this would involve a subjective choice of the parameters which we would prefer to avoid. Instead we choose to base our measure of dissimilarity on waveform correlation, by forming the complement of the correlation coefficient. This quantity conveniently ranges from 0 to 1, but this is not necessary for cluster analysis; any measure of dissimilarity will do.

Cluster Analysis Techniques

There are many different types of cluster analysis techniques, but most fall into one of four general types (Davis, 1986): partitioning methods (e.g. factor analysis), arbitrary origin methods (e.g. K-means method), mutual similarity methods, and hierarchical clustering methods. The choice of the type to use depends on various characteristics including the user's mathematical competency, the computational resources available, and of course the manner in which the results are to be used. For this study we choose to use hierarchical cluster methods, because these methods are well-documented, easy to implement, computationally cheap enough to run multiple times for a given data set, and because these methods produce results which can be readily interpreted for our data sets (seismic events). Hierarchical clustering methods form *dendrograms*, which are tree-like structures showing the relationships between the entities. Dendrograms can be built either by division, i.e. from the top down, or agglomeration, i.e. from the roots up. Agglomerative methods are much more common and are generally computationally less expensive. In this study we use agglomerative methods.

There are many methods to agglomeratively build the dendrogram, but all of them follow the same basic process. Note that in the following the term "pair" refers to any two entities that are being joined; each of these entities can be either an original data entity or a cluster formed from data entities and/or other clusters. The generalized process is as follows:

1. find the minimum dissimilarity pair (i.e most similar) in the dissimilarity matrix
2. remove the rows and columns corresponding to each member of the pair from the matrix

3. by some means add a new row and column corresponding to the dissimilarities between the newly formed pair and all remaining entities (either original entities or clusters).
4. repeat steps #1-3 until the matrix has been reduced to 2x2 whereupon the last pairing is the only pair left and no further updates are necessary.

The trick, of course, is in step #3 where one must generate dissimilarities for the new pair with all other entities. There are several methods for doing this. In our study we tested six methods. Nearest neighbor or **single linkage** is a method based on the minimum dissimilarity, i. e. the best pair of all possible pairs. On the other end of the spectrum is the furthest neighbor or **complete linkage** method where linkage is based on the maximum dissimilarity, i.e. the worst pair. With the **group average** method, linkage is based on the average of the dissimilarities. For the **centroid** method, linkage is based on the squared Euclidean distance between the centroids of each entity. Linkage is based on the "between-group sum of squares" for two entities with the **minimum variance** method. At each stage in this method, variance within clusters is minimized with respect to variance between clusters. The last method is the **flexible** method. The dissimilarities are weighted with three constants that add to 1. The values we use are 0.625, 0.625 and -0.25.

Dendrogram Interpretation

Once the dendrogram has been formed, it can be interpreted. However, there can be many ways to group the events into different clusters and the decision is always subjective. In some cases, the groups may be obvious, but this is certainly not always the case. For complex dendrograms, the question of where to "cut the stems" of the tree-like structure is not easily answered and so we have investigated methods to aid in the decision.

Cophenetic Correlation

One method which has been proposed to help with this problem is the use of cophenetic correlation. Cophenetic correlation is the correlation between the actual dissimilarities as recorded in the original dissimilarity matrix, and the dissimilarities which can be read off of the dendrogram. In essence, this is a measure of how well the dendrogram, which is a model of the similarity behavior, models the actual behavior. Notice that the cophenetic correlation can be calculated at each step of the building of the dendrogram, "scoring" only the dissimilarities between entities which have been built into the tree to that point. Thus, one can make a simple plot of cophenetic correlation vs. pair number. Sudden decreases in the cophenetic correlation indicate that the cluster just formed has made the dendrogram less faithful to the data and thus may suggest that the decision line should lie between this cluster and the previous one (Ludwig and Reynolds, 1988). Similarly, one can look for sudden increases in variance at each cycle for a suggestion that a "bad" group has been formed. For our implementation, the variance increase at each cycle is computed as the variance of the newly formed group less the variances for each of the two groups which were combined to form the group. Both of these methods are easy to implement and we have built them into our standard dendrogram package to aid in interpretation. In general, we find the cophenetic correlation to be much more robust.

SNL Metric

In the case where the grouping is already known and the method and any waveform processing parameters are being chosen to achieve the best separation, we found that it is desirable to develop a metric to score the success of the produced dendrogram at separating the groups. We found no such metrics in the literature and so developed one of our own. Our metric rewards two properties. First, separation, which we define to be the tendency to place entities from different groups into their own clusters. Thus dendrograms which put all of the objects of a certain type in clusters which have few if any objects of other types will score well. Second, in order to promote the formation of clusters, we reward fusion, that is the tendency to have fewer clusters for each group. This constraint must be added because otherwise the unclustered original data entities will score perfectly for separation and this will always be the preferred solution.

Data

We compare waveform processing methods and group similarity calculation methods using archived regional and local distance mining blasts recorded at two sites in the western U.S. with different tectonic and instrumentation characteristics. Both sites are located within regional distances of regular mining activity, so data is readily available.

In Wyoming, data was collected with the Deployable Seismic Verification System (DSVS) installed at the Pinedale Seismic Research Facility (PSRF) near Boulder, Wyoming. DSVS records three component high frequency data (0.5-50 Hz) on a Teledyne Geotech S3 seismometer and a 24-bit digitizer. The sample rate is 200 samples per second. The data can be considered accurate up to 40 Hz and the average background noise is close to the USGS-Peterson low noise model (Carr, 1993). Three mining operations in Wyoming provided origin times and total tonnage of ripple fired events detonated at their sites in 1991 and 1992. Archived DSVS data was searched for events and 175 usable signals were found. Both timing problems and poor signal-to-noise made it difficult to find signals at DSVS. The origin times supplied often did not produce a signal at the predicted P-time at DSVS, so many events were assumed to be from a particular mine if they started close to the predicted P-time. Most events were small, because the ripple-fire technique is used to reduce ground motion and minimize damage.

Mining data in New Mexico was collected with the New Mexico Tech (NMT) network, a collection of 19 stations throughout New Mexico. All the seismometers are 1 Hz, critically damped geophones with an upper corner of about 15 Hz. The sampling rate is 100 Hz. For this study we are using station CAR, a single vertical component instrument. Data was collected over a 4 month period in 1997 when mining activity was high in western New Mexico and eastern Arizona. The events were located using the NMT network. Even though the mines are located outside the network, we feel the locations are good enough to associate specific events to each mine. And the fact that the NMT data comes from a network provides us with a means to compare our clusters, which are derived using only a single station of the network, with the locations determined from the entire network using traditional methods.

Table 1 lists characteristics of the data from the mines in Wyoming and New Mexico. Mines W1 and W2 are at similar distances from DSVS and both have poor SNR. Mines NM1 and NM3 are at similar distances from station CAR in New Mexico. Examples of signals from all of the mines are in Figure 1.

Table 1: Characteristics of Wyoming and New Mexico mines

mine	distance	azimuth	Lg-P (range)	Lg -P (ave)	SNR
W1	359 km	75 degrees	38-50 sec	43.6 sec	poor
W2	322 km	90 degrees	36-47 sec	43.0 sec	poor
W3	144 km	217 degrees	17-22 sec	20.6 sec	good
NM1	179 km	224 degrees	17-24 sec	22.6 sec	good
NM2	211 km	226 degrees	25-27 sec	26.3 sec	good
NM3	144 km	336 degrees	20-25 sec	22.9 sec	good
NM4	257 km	249 degrees	28-37 sec	31.3 sec	good

Waveform Processing

Before cluster analysis is done we process the waveforms. Six parameters, (1) time window, (2) sample rate, (3) phase type, (4) tapering, (5) Hilbert enveloping and (6) filtering are varied to see the effects on the resulting dendrograms.

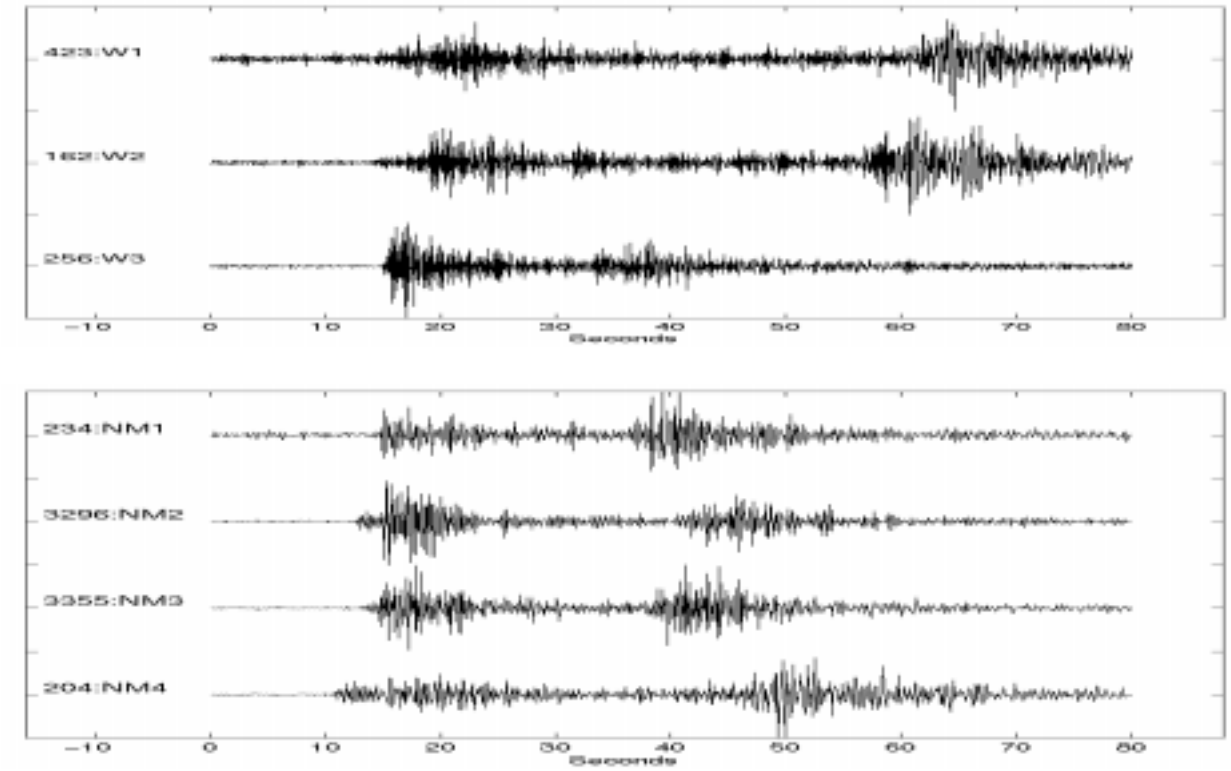


Figure 1. Sample waveforms from the Wyoming mines (top) and New Mexico mines (bottom)

Rivier-Barbier and Grant (1993) found that the Lg - P time is the characteristic of the waveform that best clustered their data, and we also found this to be true. A time window starting right before the picked P arrival and long enough to see the secondary arrival worked better than shorter windows or windows centered on the secondary arrival. The sample rate did not have much affect on the dendrograms, and so we choose to downsample the data in order to minimize the computer memory needed to calculate the dissimilarities.

Tapering the traces was done to remove any edge effects that could result from ending in the middle of a cycle. The taper cannot be too large however, or important features of the waveform will no longer contribute to the correlation. A slight taper of 5% works well. Using a Hilbert envelope removes negative values in the waveform and acts as a low pass filter. Without the envelope, the sorting focusses on small details in the waveforms that cause events from the same mine to be split into different clusters. The enveloping also causes the resemblance values to increase and separates the clusters better, so we always use a Hilbert envelope when doing cluster analysis. Filtering affects the results only if the waveforms from different mines have different frequency content. In most cases, filtering the data does not have much effect on the dendrogram.

We started by using the flexible method to do cluster analysis. Once we determined the best processing parameters using this method, we used the same parameters and tested the other five cluster analysis techniques. All methods cluster the events, although there are slight differences in the pairing of events. We found that if the waveform processing parameters are picked correctly and are robust, it really doesn't matter which cluster analysis method is used. Since we like the look of the dendrogram created using the flexible method the best, that is the method of choice.

Cluster Analysis Results

Dendrograms of the Wyoming and New Mexico data are in Figures 2 and 3. For both data sets, dendrograms are calculated using a time window starting just before the picked P arrival and long enough to see any secondary arrivals, a

5% taper, a Hilbert envelope and the flexible method. In Wyoming the events separate into three clusters, one of W3 events and two with W1 and W2 events mixed together. The decision line along the left side of the clusters is where we picked the solution, using the metrics which are illustrated beneath the dendrogram. Mines W1 and W2 are approximately the same distance from DSVS, and it appears that the Lg -P time alone cannot effectively separate the two mines into distinct clusters. We experimented with just the W1 and W2 events to see if it is possible to separate them into two clusters. Filtering the data helps, but we cannot find a characteristic feature in the W1 and W2 waveforms that clusters the two mines into two distinct groups effectively and robustly.

However, in New Mexico the events separate into four clusters, each corresponding to a specific mine. There are three events that are misclustered, but they have abnormally low P amplitudes compared to the other signals from the same mines, so we believe that is why they are misclustered. The two mines in New Mexico at similar distances from the station CAR, mines NM1 and NM3, clearly separate into two groups, unlike the Wyoming data. Mines W1 and W2 are both over 300 km away from the recording station, and the SNR is not very good. Mines NM1 and NM3 are less than 180 km away from the recording station and have good SNR. We hypothesize that since the SNR is better for the mines in New Mexico, there is correlation on other features of the waveforms besides the Lg - P time that is separating the events into two clusters. In Wyoming the SNR is not good enough to correlate on any other features in the waveforms.

In order to investigate the effects of changing SNR on the groupings provided by cluster analysis, we use the New Mexico data, which has excellent SNR in its raw form. We simulate noisy data by adding noise to the data to decrease the SNR. One common means to add noise to an event recording is to capture a sample of noise ahead of the first arrival, scale it as desired, and then add it to the event waveform. Unfortunately, for our data set this cannot always be done because the data is segmented and so each waveform does not always include a sufficient pre-event noise sample. Instead, we choose a single pre-event noise sample spanning 27 seconds from one of the event recordings, randomize the phase information to prevent correlation, and dilate/contract it as needed to generate the noise samples which were added to each of the waveforms. To do this, for each signal waveform to which we added noise, we took the fft of our master noise sample, resampled the amplitude spectra at the appropriate frequency spacing for the signal waveform's time length (recall that the length of the time interval spanned by a waveform determines the frequency discretization for the fft in the spectral domain), generated new random phase information at the new frequency discretization using a white distribution, transferred the new spectral series back to the time domain using the inverse fft to generate the new noise waveform, scaled the new noise waveform for the specified SNR, and then added it to the signal waveform. For the scaling, we use SNR to specify the relationship between the maximum value of the signal waveform and the maximum value of the generated noise waveform which will be added to the signal waveform. Thus, an SNR of 2 implies that the generated noise waveform is scaled to half of the signal waveform before it is added to the signal waveform.

We add noise to the New Mexico data in gradual steps, starting with a value of SNR = 10 and decreasing to a value of SNR = 0.5. What this means is that when SNR = 10, we added noise to the traces which has a maximum value of 0.10 of the maximum signal. Using a value of SNR = 0.5 means adding noise which has a value of 2 times the maximum signal. The dendrograms produced when SNR = 10 and SNR = 5 show no noticeable differences from the dendrogram with no noise (Figure 3). There are four clusters, each corresponding to one mine with the same misclustered events as with the raw data. Changes in the dendrogram start occurring when we get to noise levels with SNR = 3, SNR = 2 and SNR = 1. In Figure 4 we see the dendrogram resulting when SNR = 2. Sample traces without noise and with the added noise are in Figure 5. There are four clusters in the dendrogram. Mines NM2 and NM4 still make distinct clusters, but the other two clusters consist of events from both mines NM1 and NM3. These two mines are at similar distances from the station CAR (Table 1). We have added enough noise to the signals, that the characteristics in the waveforms that separated the two mines when the SNR was good can no longer be recognized by the cluster analysis. When we decrease the value of SNR to 0.5, we add so much noise that not even the Lg - P times can cluster the events, and we end up with the events from the four mines all mixed together.

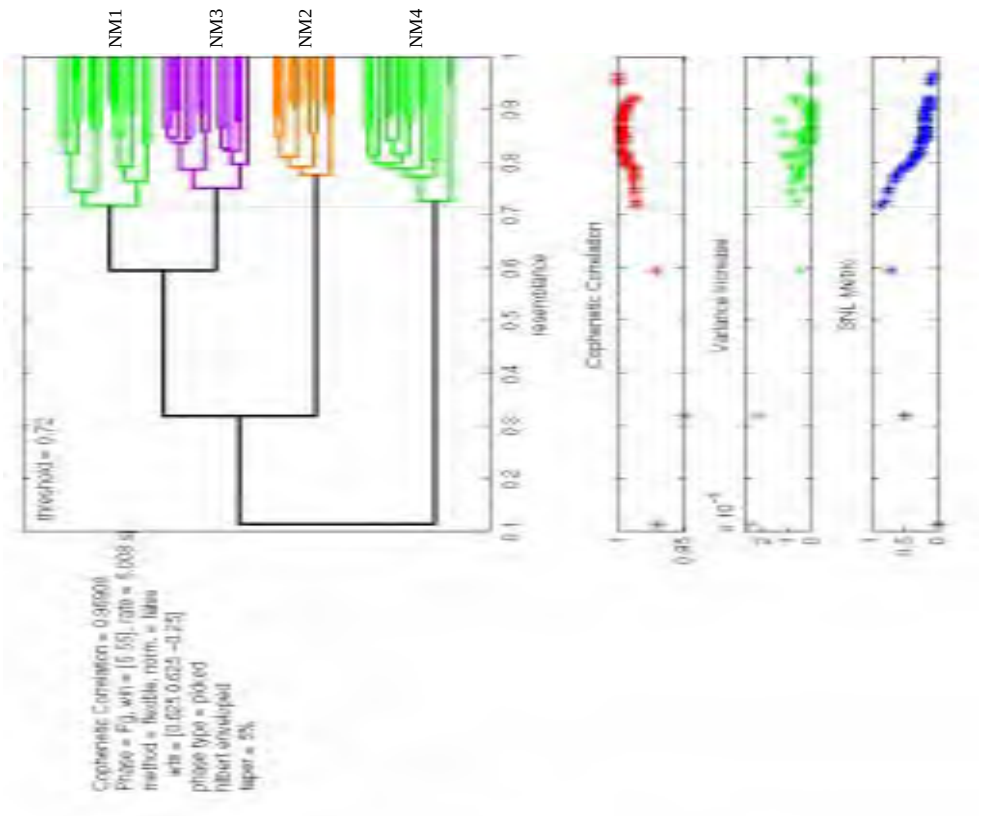


Figure 3. Dendrogram using the events from mines in New Mexico. There are four clusters corresponding to each of the four mines.

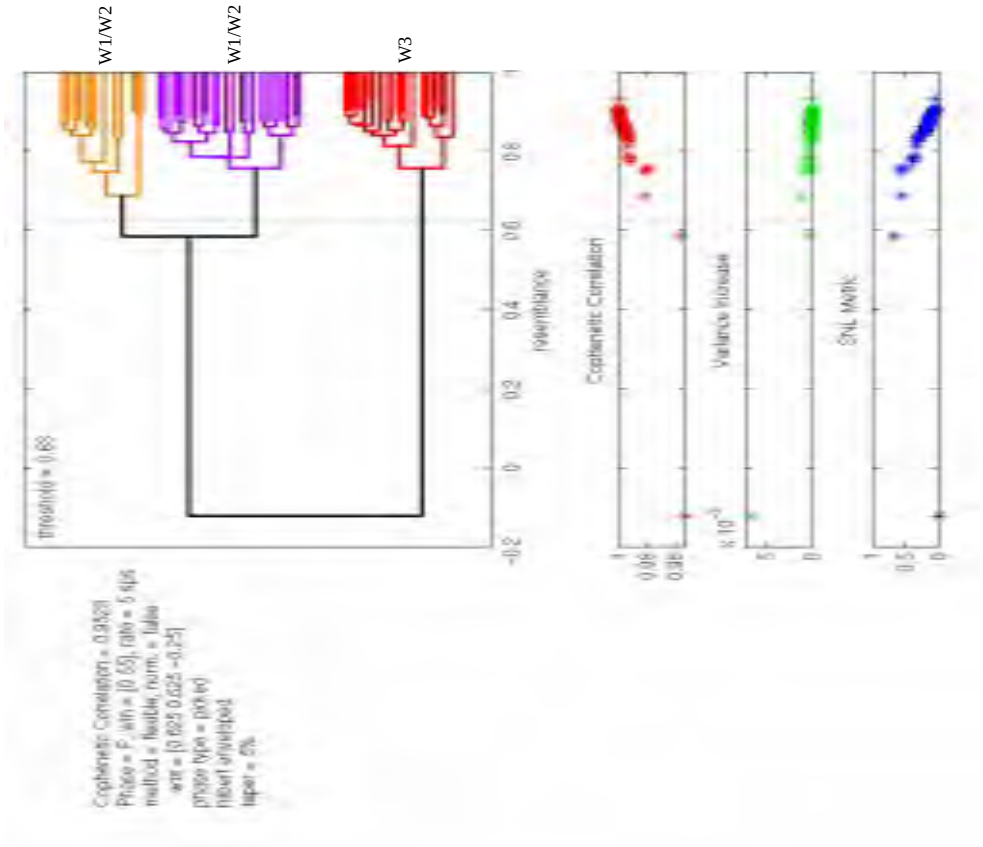


Figure 2. Dendrogram using the events from mines in Wyoming. There are three clusters, but the top two clusters both have W1 and W2 events. Only W3 events are in the bottom cluster.

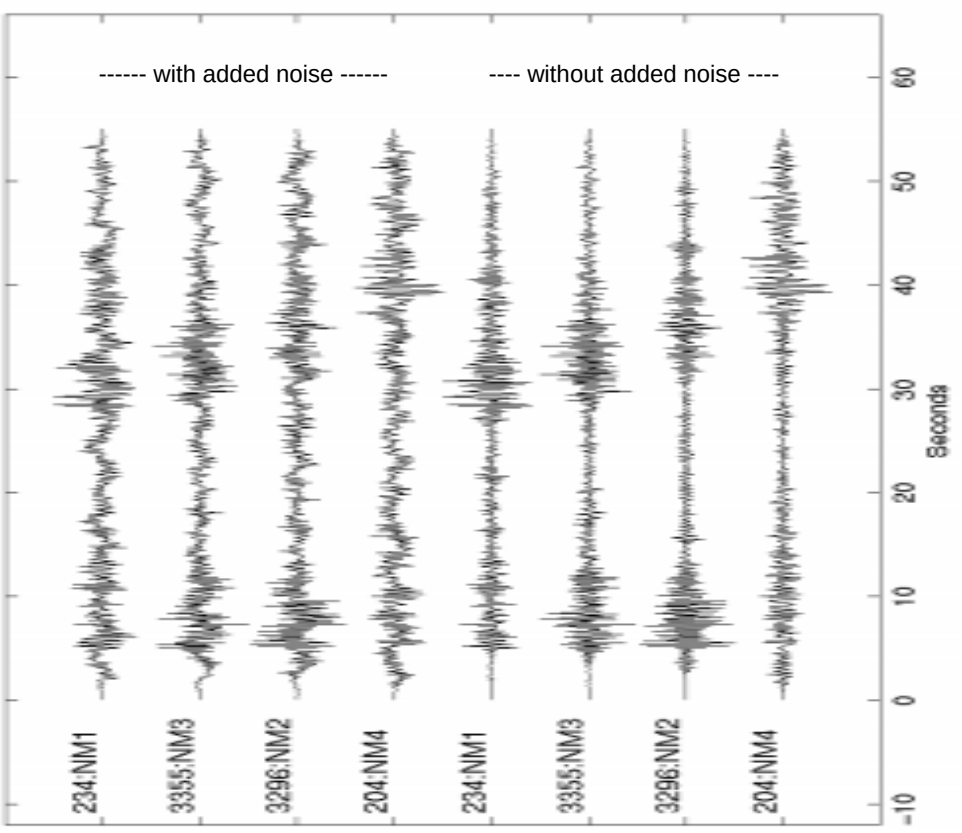


Figure 5. Sample traces from the New Mexico data. The four traces on the bottom are the raw traces, i.e. without added noise. The four traces on top are the same events where noise with a maximum value of 1/2 of the maximum signal was added to the traces.

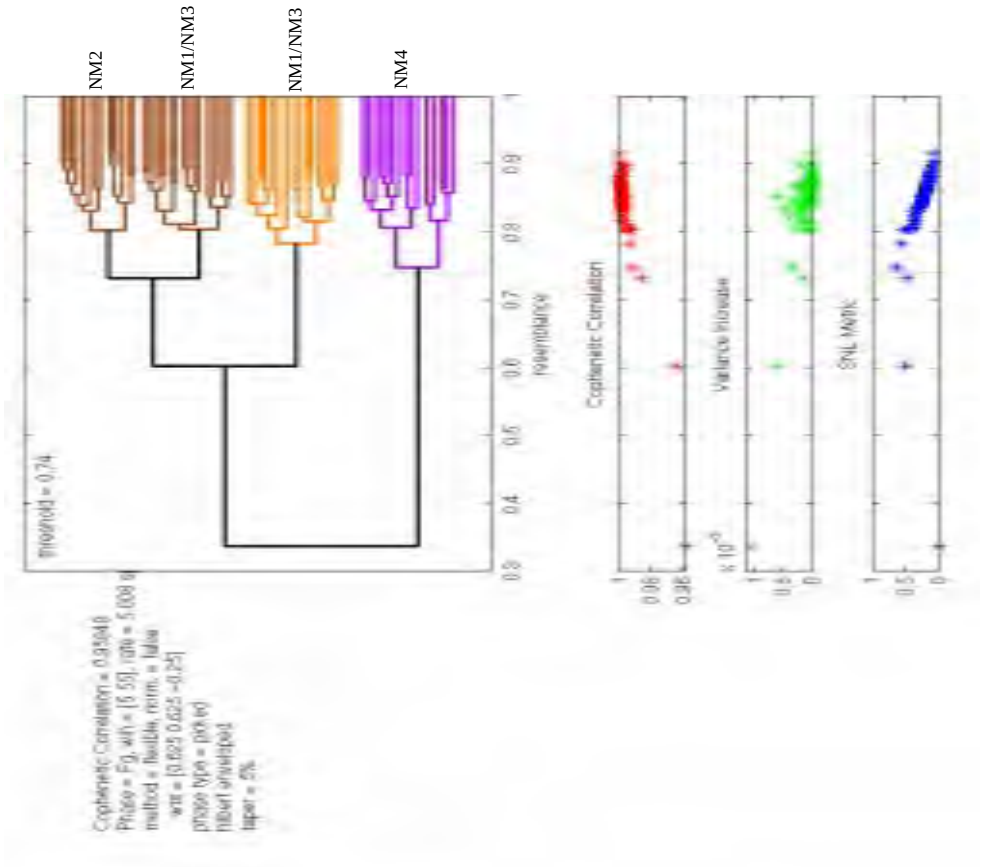


Figure 4. Dendrogram using the events from mines in New Mexico after noise was added to the raw waveforms. There are still four clusters, but the middle two both have events from mines NM1 and NM3 mixed together.

CONCLUSIONS ANDRECOMMENDATIONS

As we have shown, it is easy to calculate dendrograms for a given data set, and if appropriate waveform processing is done, events from specific mines will cluster. The waveform processing is important, and some specific parameters affect the resulting dendrogram more than others. One characteristic of the waveform that is important for creating distinct clusters is the Lg - P time, so the time window used to calculate the dendrogram must include both the P and secondary arrivals. Using a Hilbert envelope can also improve the clustering, because it smooths out some of the details in the waveforms that can cause events from the same mine to be broken into more than one cluster.

In Wyoming, no matter how much pre-processing of the waveforms we do, we are not able to clearly separate events from mines W1 and W2. We concluded at first that if the Lg - P times for two mines are virtually identical, then clustering analysis would not work. However, calculating a dendrogram with the New Mexico data proved that events from mines at similar distances can cluster in distinct groups. The difference between the Wyoming and New Mexico data is the SNR of the events. The New Mexico data had very good SNR, but the Wyoming data, for a variety of reasons, had poor SNR. By adding noise to the New Mexico data, we are able to show that clustering deteriorates as the noise level increases. When we add noise that has a maximum value of 1/2 of the maximum signal, the events from mines NM1 and NM3 which had clearly clustered with the raw data, are starting to mix together. The dendrogram from New Mexico calculated with the added noise (Figure 4) looks similar to the dendrogram calculated using the Wyoming data (Figure 2).

If the waveforms have poor SNR, then the other features that can be used to cluster events such as the shape of the different arrivals or the frequency content, cannot be discerned. In fact, the production of a dendrogram is very much a “garbage in, garbage out” process; none of the cluster analysis methods can extract information where there is none available. Typically, if an analyst cannot discern similarities between the entities, then a dendrogram will not help. However, if the preparatory work is properly done, and the data do have strong grouping, the choice of cluster analysis method will make little difference. We believe cluster analysis can be useful in comparing unknown waveforms with archived data from known mines. It should be fairly simple to implement an automated process to do the comparison.

REFERENCES

Carr, D. B. (1993). **Evaluation of the Deployable Seismic Verification System at the Pinedale Seismic Research Facility**, SAND93-1696.

Davis, J. C. (1986). **Statistics and data analysis in geology**, J. Wiley & Sons, New York.

Isrealson, H. (1990). **Correlation of Waveforms from Closely Spaced Regional Events**, Bull. Seism. Soc. Am., vol 80, pp. 2177-2193.

Ludwig, J. A. and J. F. Reynolds (1988). **Statistical ecology**, J. Wiley & Sons, New York.

Riviere-Barbier F. and L. T. Grant (1993). **Identification and Location of Closely Spaced Mining Events**, Bull. Seism. Soc. Am., vol. 83, pp. 1527-1546.

Sandia is a multiprogram laboratory operated by Sandia Corporation, a Lockheed Martin Company, for the United States Department of Energy under contract DE-AC04-94AL85000.

PROTOTYPING REGIONAL DISCRIMINATION TOOLS WITH MATSEIS

Eric Chael, Mark Harris, Chris Young, Sandia National Laboratories
Kevin Mayeda, William Walter, Lawrence Livermore National Laboratory
Steve Taylor, Aaron Velasco, Los Alamos National Laboratory

Sponsored by U. S. Department of Energy
Office of Nonproliferation and National Security
Office of Research and Development
Contract No. DE-AC04-94AL85000

ABSTRACT

To facilitate the development, testing and comparison of regional seismic discriminants, we have implemented some of the most promising techniques in Matseis, a Matlab-based seismic processing tool kit. The existing Matseis package provides graphical tools for analyzing seismic data from a network of stations. It can access data via a CSS 3.0 database, or from static files in a format defined by the user. Waveforms are displayed in a record-section format, with overlays for IASPEI91 travel-time curves. The user can pick arrivals and locate events, then show the results on a map. Tools are available for spectral and polarization measurements, as well as beam forming and f-k analysis with array data. Additionally, one has full access to the Matlab environment and any functions available there, as well as to portions of the U.S. Department of Energy Knowledge Base.

Recently, we have added some new tools to Matseis for calculating regional discrimination measurements. The first of these performs Lg coda analysis as developed by Mayeda and coworkers at Lawrence Livermore National Laboratory (LLNL). Lg coda magnitudes are calculated from the amplitudes of the coda envelopes in narrow frequency bands. Ratios of these amplitudes between high- and low-frequency bands provide a spectral-ratio discriminant for regional events.

The second tool we have implemented measures P/Lg phase ratios, using the MDAC technique of Taylor (Los Alamos National Laboratory) and Walter (LLNL). P and Lg amplitudes are obtained at select frequencies, then corrected for source magnitude and propagation path. Finally, we added a tool for analyzing long-period Rayleigh and Love arrivals, useful for moment:magnitude and LQ:LR discrimination. Because all these tools have been written as Matlab functions, they can be easily modified to experiment with different processing details. The performance of the discriminants can be evaluated using any event available in the database.

Key Words: data processing and analysis, regional discrimination

OBJECTIVE

Effective verification of the CTBT will require the implementation of reliable regional seismic discriminants. Processing details for event identification – including algorithms, their parameters and the decision thresholds – will certainly vary with geologic setting. The Knowledge Base effort of the DOE CTBT Research Program will provide a mechanism for storing and retrieving such region-specific information. Software tools which an analyst employs to characterize a seismic event will connect to the Knowledge Base to obtain the appropriate information based on the source location and the stations available.

We have begun adding some of the more promising regional discriminants to MatSeis, a seismic analysis toolkit based on MATLAB®. The objectives of this effort are twofold. First, it should facilitate the testing and refinement of the routines. Graphical interfaces will make the discriminants easier to use and accessible to a wider audience; the inherent flexibility and openness of MATLAB will simplify the process of modifying and tuning the functions. Second, MatSeis will provide the connection to the Knowledge Base, so that the discriminants can be properly configured for a given region.

RESEARCH ACCOMPLISHED

The MatSeis seismic processing toolkit was developed at Sandia to support CTBT R&D on improving event association and location (Harris and Young, 1997). Through menus in the MatSeis user interface, a researcher can connect to a CSS 3.0 database and select events, arrivals and waveforms for analysis. Once the desired data have been obtained, the waveforms can be displayed as a record section, with signals from the various stations organized vertically based on their epicentral distance (Figure 1). Selected travel-time

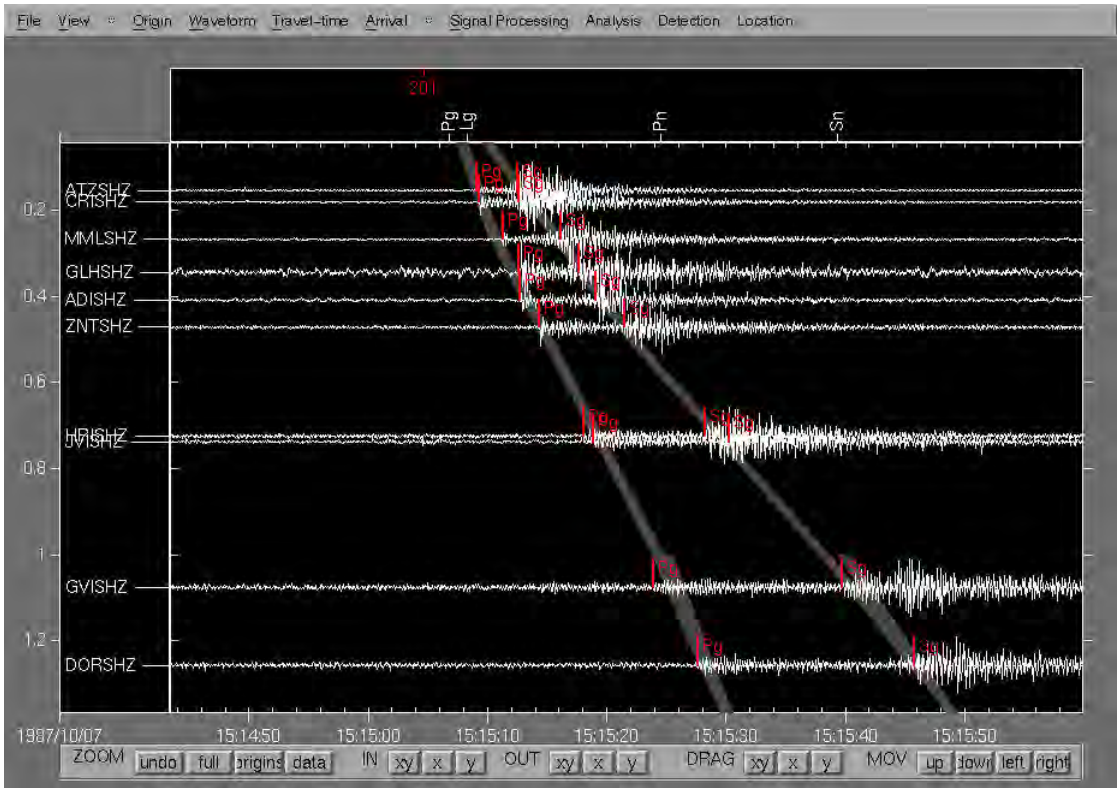


Figure 1. The main MatSeis screen.

curves may be overlaid on the plot, to assist in identifying phases. The package then provides a wide assortment of functions which the user can employ to assist in interpreting the signals and hence characterizing the event. A variety of filters can be applied to the signals. Arrivals can be picked or retimed, then their amplitude and period may be measured. The user may relocate the event via an interface to a location routine descended from TTAZLOC (Bratt and Bache, 1988), and display station and event positions on a map through an interface to the M_Map mapping toolbox (Pawlowicz, 1998). Modules are included for spectrum estimation, waveform correlation, polarization analysis, beamforming and frequency-wavenumber analysis. MatSeis serves as a key tool for developing and testing the DOE Knowledge Base, a system for storing and accessing region-specific information. Thus the analysis functions in MatSeis can exploit the contents of the Knowledge Base to optimize their performance in a given geographic area.

Written in the MATLAB® language, MatSeis can be readily modified or extended to include new functionality, so it serves as a very convenient prototyping platform for developing and testing new algorithms. Because of this inherent flexibility, and the developing access to region-specific information in the DOE Knowledge Base, we believe that MatSeis provides a suitable platform for testing and comparing regional discrimination algorithms. We have incorporated new modules for three candidate discriminants into MatSeis. These modules provide easy-to-use interfaces for performing the required measurements, with consistent implementation of common processing steps such as defining time windows and selecting frequency bands. The discriminants included so far include Lg coda analysis of Mayeda and coworkers, the P/Lg phase ratio technique of Taylor and Walter, and long-period Rayleigh and Love wave interpretation.

Mayeda has developed an approach for obtaining stable single-station Lg magnitudes from the decay of the Lg coda (Mayeda, 1993; Mayeda and Walter, 1996). A regional seismogram is filtered with a series of narrowband Butterworth filters and envelope functions are generated from each filter output. The coda behind the Lg onset is then modeled for each band using either a parametric form or an empirical envelope based on prior data from the station. The median log difference between the modeled and observed envelopes across the coda window then provides a spectral estimate at the center frequency of each filter. The energy in this source spectrum between 1.2 and 2.2 Hz is converted to an Lg coda magnitude. Finally, the ratio between the energy densities at low and high frequencies provides a discrimination measure (Mayeda and Walter, 1995). At the Nevada Test Site, explosions tend to produce weaker high-frequency Lg signals than earthquakes with similar low-frequency content.

To begin Lg coda analysis in MatSeis, the user first selects from the main screen an event and one or more stations at regional distance. When the Lg coda tool is chosen from the menu, the Lg coda GUI appears (Figure 2). The waveform window of this tool displays a seismogram, with default time intervals for Lg coda and pre-P noise highlighted. These time intervals can be modified as desired by dragging the highlight boxes along the waveform. From the interface, the analyst selects the desired station, channel and frequency bands. Additional parameters for the analysis are adjusted by editing a setup file. As parameters change, the coda spectral estimates and the magnitude and discrimination results are automatically updated.

The most promising regional discriminants appear to be those based on comparing the Lg arrival to either Pn or Pg (Walter *et al.*, 1995; Taylor, 1996). Taylor and Hartse (1998) have shown that corrections for source magnitude and the propagation path improve the ability of P/Lg ratios to separate earthquakes and explosions. More recently, Taylor *et al.* (1999) have refined the procedures for calculating these discriminants. Their method is known as Magnitude and Distance Amplitude Corrections, or MDAC. Smoothed spectral estimates are obtained for each arrival window. Corrections for event magnitude and the source-receiver path are then applied to the measurement for each phase at each desired frequency. The magnitude correction accounts for the change in corner frequency with event size. The path correction assumes frequency-independent geometric spreading, and attenuation due to a Q that varies as a power of frequency. Parameters for the source and propagation models in any region are empirically derived. The discriminant value is subsequently obtained by ratioing the corrected P and Lg amplitudes for a given frequency.

The MatSeis tool for P/Lg discrimination is shown in Figure 3. As with the Lg coda tool, one begins by selecting an event and some regional stations in the main MatSeis window. Arrival and noise windows are extracted for analysis, and the resulting discrimination ratios are calculated. The interface shows the seismogram for a selected station and the spectra obtained from its arrival and noise windows. The Pn/Lg and Pg/Lg ratios

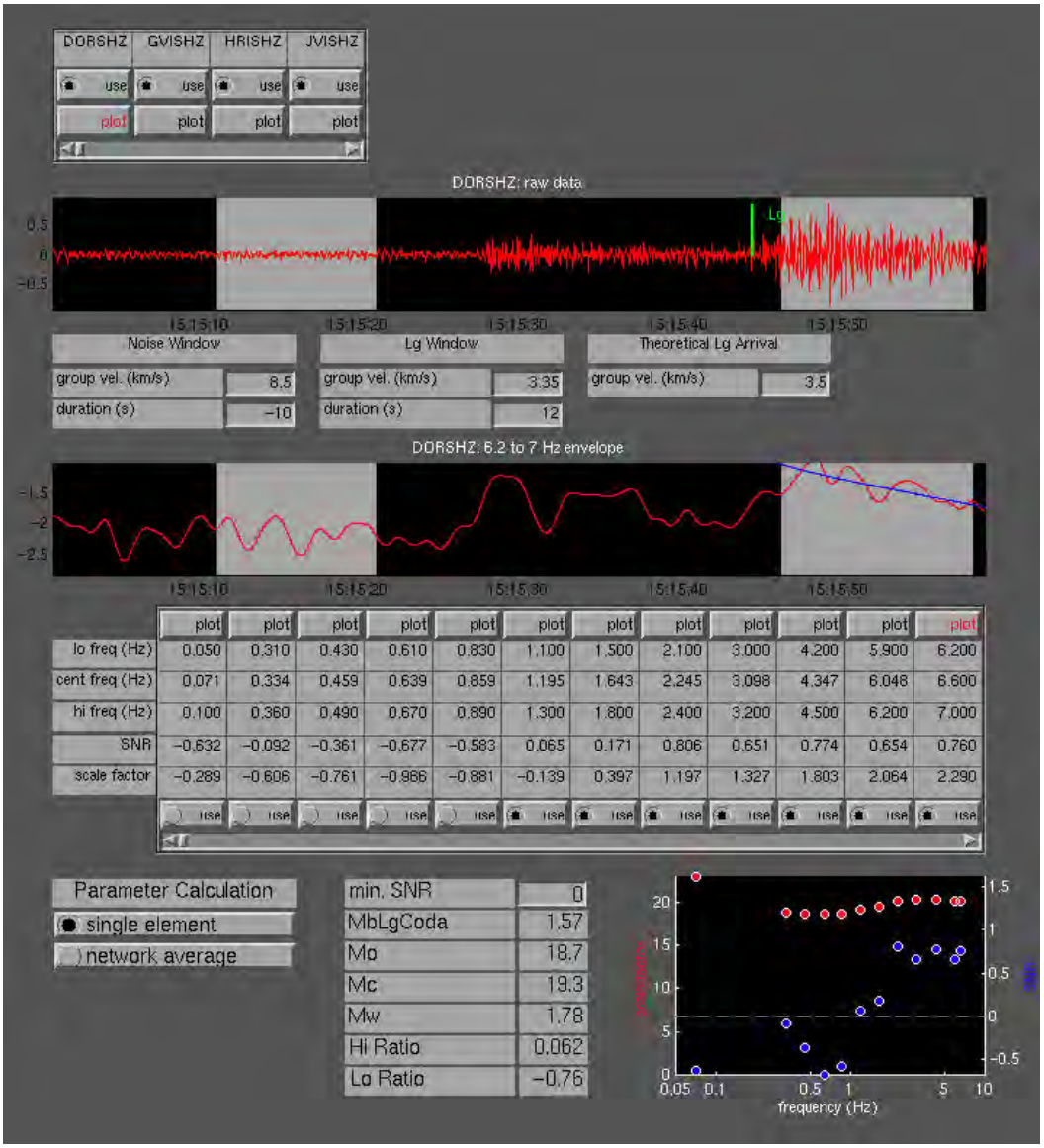


Figure 2. User interface for Lg coda analysis.

for specified frequency bands are displayed in two plots, one for the current station, another for average results among multiple stations. Calculations can be performed in either the time domain, using narrowband filters and mean squared amplitudes, or the frequency domain, using FFTs.

The third discrimination tool we have implemented facilitates the analysis of long-period Love and Rayleigh arrivals. This tool has no distance restrictions, but can be invoked for any station with three-component, long-period or broadband records. For a selected station, the horizontal channels are first rotated to radial and transverse directions. Love (LQ), Rayleigh (LR) and noise windows are denoted using appropriate group velocities. The routine next calculates envelope functions for the bandpass-filtered records, then measures the peak amplitudes over the specified arrival windows. Signal-to-noise ratios for LQ and LR are determined, and the discrimination measure is simply the log of the ratio of the LQ and LR amplitudes. Explosive sources typically produce low values for this discriminant, because of their weak Love waves.

A primary motivation for adding these discriminants to MatSeis is to enable easy modification of processing parameters, and even of the algorithms themselves. This capability should simplify the task of optimizing the discrimination procedures for different regions. With multiple methods available in a common environment, one can more readily compare and contrast them, to understand their relative strengths. Combining the evidence from a variety of discriminants should improve the reliability of regional event identification.

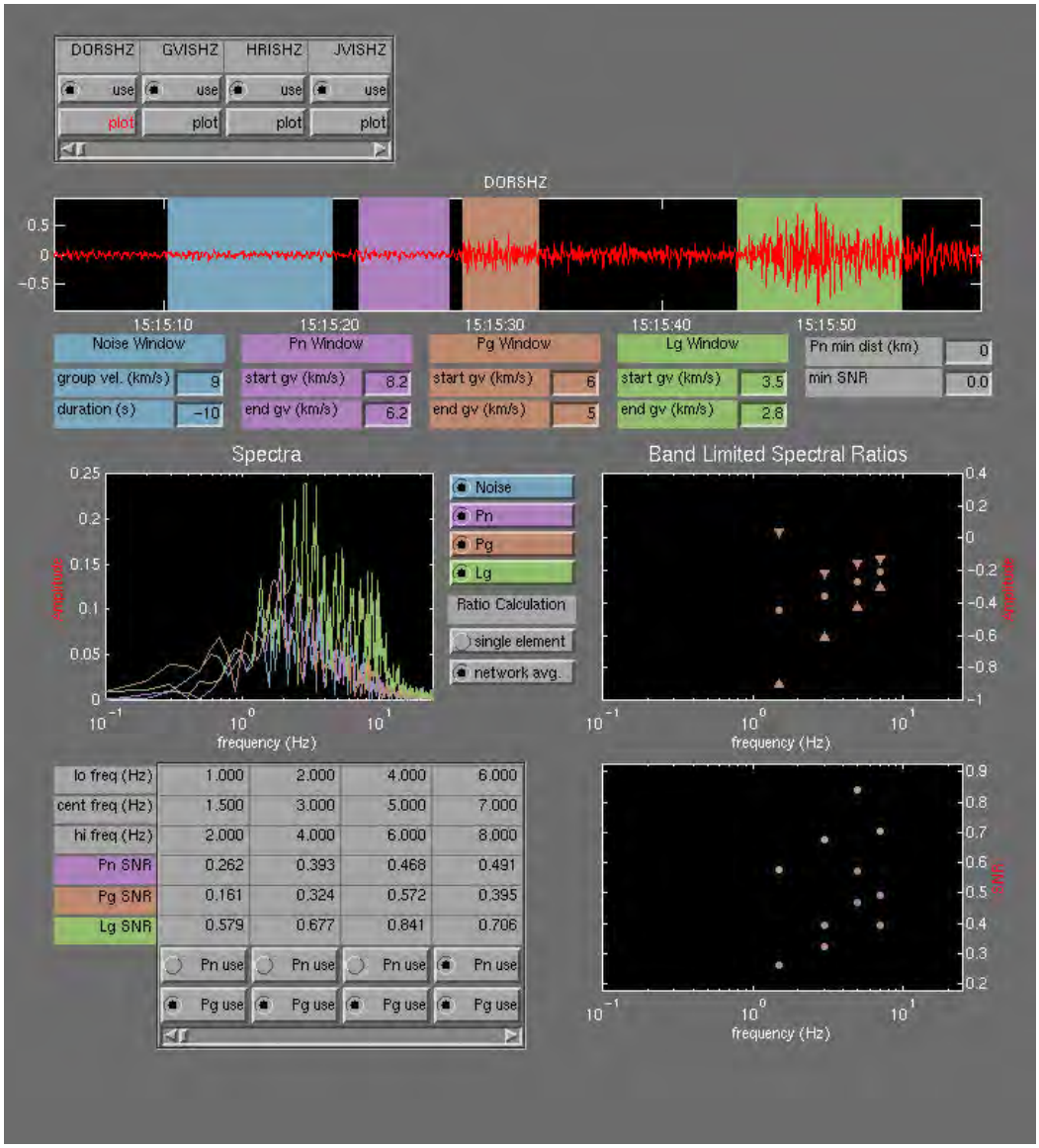


Figure 3. User interface for the P/Lg discriminant.

CONCLUSIONS AND RECOMMENDATIONS

We have implemented some promising regional discrimination algorithms as MATLAB functions, and developed easy-to-use graphical interfaces which can be invoked from MatSeis. As a result, a user can apply these discriminants to any event available in a CSS database, and exploit the appropriate region-specific information stored in the DOE Knowledge Base. We plan to add the capability to show results from selected reference events, so that one may observe a new event's relationship to prior activity in the region. As the Knowledge Base matures, we will enhance these tools to take advantage of more of the information stored there.

REFERENCES

Bratt, S. R. and T. C. Bache, Locating events with a sparse network of regional arrays, *Bull. Seism. Soc. Am.*, **78**, 780-798, 1988.

Harris, M. and C. Young, MatSeis: a seismic GUI and toolbox for Matlab, *Seism. Res. Lett.*, **68**, 267-269, 1997.

Mayeda, K., mb(Lg coda): a stable single-station estimator of magnitude, *Bull. Seism. Soc. Am.*, **83**, 851-861, 1993.

Mayeda, K. and W. R. Walter, Lg coda moment rate spectra and discrimination using Lg coda envelopes, in *Proceedings: Symposium on the Non-Proliferation Experiment: results and implications for test-ban treaties, Rep. LLNL Conf-9404100*, 202-212, Lawrence Livermore Natl. Lab., Livermore, CA, 1995.

Mayeda, K. and W. R. Walter, Moment, energy, stress drop, and source spectra of western United States earthquakes from regional coda envelopes, *J. Geophys. Res.*, **101**, 11195-11208, 1996.

Pawlowicz, R., M_Map: a mapping package for Matlab, http://www.ocgy.ubc.ca/~rich/map.html, 1998.

Taylor, S. R., Analysis of high-frequency Pg/Lg ratios from NTS explosions and western U. S. earthquakes, *Bull. Seism. Soc. Am.*, **86**, 1042-1053, 1996.

Taylor, S. R. and H. E. Hartse, A procedure for estimation of source and propagation amplitude corrections for regional seismic discriminants, *J. Geophys. Res.*, **103**, 2781-2789, 1998.

Taylor, S. R., A. A. Velasco, H. E. Hartse, W. S. Phillips, W. R. Walter and A. J. Rodgers, Amplitude corrections for regional seismic discriminants, submitted to *Pure Appl. Geophys.*, 1999.

Walter, W. R., K. M. Mayeda and H. J. Patton, Phase and spectral ratio discrimination between NTS earthquakes and explosions, part I: empirical observations, *Bull. Seism. Soc. Am.*, **85**, 1050-1067, 1995.

Sandia is a multiprogram laboratory operated by Sandia Corporation, a Lockheed Martin Company, for the United States Department of Energy under contract DE-AC04-94AL85000.

PROBABILISTIC INTEGRATION OF SEISMIC, HYDROACOUSTIC AND INFRASONIC DATA USING THE DEMPSTER-SHAFER RULES FOR COMBINING EVIDENCE

Zoltan A. Der and Matthew W. McGarvey, Ensco Inc

Robert H. Shumway, University of California at Davis

Sponsor; Defense Threat Reduction Agency
Contract DSWA01-98-C-0145

ABSTRACT

Identification of suspicious events as nuclear explosions or events of other types is commonly based on incomplete and contradictory data. Although in CTBT monitoring most of the evidence comes from seismic sources, other types of data (hydoacoustic, infrasonic) are often helpful in the classifying an event. The major issue how to merge information from such diverse sources. The Dempster-Shafer (DS) calculus has been implemented as a vehicle for merging information in this application. The reason for this that, unlike full Bayesian calculus, it does not require full knowledge of the conditional probabilities or priors in the problem, it accepts various combinations of joint probability estimates, it merges the information form various independent source regardless of the order of the merging of the data. The final outcome of such calculations is an evidential interval consisting of the support (evidence for) and the plausibility (1-the support against) of simple and composite propositions. Propositions (hypotheses in the parlance of DS) are either simple (the event is an earthquake) or composite, (the event is some kind of explosion). The development of the solutions can be followed as the algorithm processes the various discriminants successively.

The key inputs in the application of the DS calculus are probability masses derived for the various propositions (simple or composite) appropriate to the various (seismic and non-seismic) discriminants. We are in the process of finding the best ways to produce probability masses for the various standard discriminants. Although statistical discriminants based on Gaussian-distributed are often effective, we do not depend solely on such models. Instead, we incorporated several approaches from the general pattern-recognition literature into the estimation of probability masses. Since the seismic discriminants use various aspects of seismograms they can be assumed to furnish independent information as required by the merging process in DS calculus. The same is true for other types of discriminants. The total process is being implemented in MATLAB and includes a graphical user interface. We have found that the output of the process imitates human reasoning quite well for various hypothetical scenarios.

Key Words: data fusion, discrimination, inference

INTRODUCTION

Identifying various types of observed events in the context of a Comprehensive Nuclear Test Ban Treaty (CNTBT) is a classical pattern recognition and data fusion problem. The actual task involves the collection of available observations and the application of various proven dicriminants. Presently, the latter come mostly from seismic observations, but other types of data, such as hydroacoustic, infrasonic and radionuclide observations may contribute. Unless the event is very large (in such cases discrimination is a relatively easy task) the set of available observation is limited and often contradictory. The other basic question is how to combine the available information in an objective manner. Studies of poorly identified events (e.g. Ryall et al 1996) typically involve lengthy discussions and weighting all of the available information with discriminatory value. It happens frequently that different investigators come to drastically different conclusions because they attach different weight to various kinds of observations.

There are various basic issues that have to be addressed in applying discriminants. Typically, most seismic discriminants are affected by the variability of propagation through the Earth. Thus transportability of discriminants cannot be assumed a priori. In applying discriminants one needs data for various types of events, preferably from the same region involving similar propagation paths. The prior data are in the form of populations of data points with poorly defined statistical distributions. Assumption of normality is merely convenient and mathematically tractable, but in most cases there is not enough data to prove normality, often the distribution is visibly not normal. Nevertheless, statistical discrimination methods seem to be appropriate in many cases as long as not much emphasis is placed on the computed 'confidence limits' and 'linear discriminants'. The aura of precision and rigor that is often attached to statistical discrimination studies is rarely justified.

Simply comparing the *available* data to new data has its own pitfalls. A famous old Ms-mb discrimination study has found that nuclear explosions and earthquakes can be reliably discriminated in western North America. Closer examination of the data showed that all the *available* explosions had higher magnitudes than the available earthquakes and the formal separation was mostly based on magnitude. Once the magnitude difference was removed, or smaller explosions were included the discrimination capability was found to be much reduced. On the other hand, one could argue that large events must be explosions since large earthquakes are rare in the region, thus magnitude has a discriminant value. Whether to accept this premise or not is a matter of personal taste. This argument implicitly considers *a priori* probabilities, that most people prefer to disregard, otherwise 95% of all events could be reliably classified as earthquakes without any data analysis at all.

Therefore, when depending on previous experience in a given region for discrimination one must make sure that discrimination does not depend on the limited extent of previous data. If the physical factors playing role in a discriminant are well understood, then it is possible, through physical modeling, to characterize the nature of possible data sets even though the amount of available data is limited (e. g. Barker 1996). Unfortunately, the physical basis of many of the regional discriminants is poorly understood.

Another issue is what discriminants can be considered as independent pieces of information. Clearly the M0-mb and related discriminants and the Pn/Sn spectral ratios can be considered to be independent pieces of information. On the other hand, the numerous values of the latter in various frequency bands are not, since they are similar and seem to furnish the same kind of information. For such redundant information a reduction in the dimensionality by combining such evidence is appropriate, as we shall demonstrate below.

DEMPSTER-SHAFER RULES FOR COMBINATION OF EVIDENCE

Dempster-Shafer (DS) calculus is a generalization of Bayesian methods of inference (Dempster 1968, Shafer 1976). In order to differentiate it from standard statistical methods DS has its own version of terminology. In DS parlance hypotheses are called propositions, the equivalents of probabilities are termed probability masses. In typical usage of DS each knowledge source (KS) contributes a set of single or combined propositions (so called general propositions that have probability masses assigned to disjunctions of several single propositions). Generally such sets are incomplete (not all combinations of propositions are represented).

For instance, Proposition 1 may be that a given event is an earthquake (single proposition) while Proposition 2 may be that the given event is either a quarry blast or nuclear explosion (combined or general proposition). Prior to processing by the DS method all the available probability masses, single and combined, are normalized such that they sum to unity. The uncertainty in a proposition A is reflected by the evidential interval defined by its support and plausibility. Support is defined as the sum of probability masses m for propositions that include A and the plausibility is unity minus the sum of probability that do not include A, that is the support for its negation, 1-s(~A).

The following equations define the DS rule for combining information from two independent knowledge sources (Dillard 1982). The combined probability mass of the general proposition B is

$$m(B) = \sum_{B' \& B'' = B} m_1(B')\, m_2(B')/\, C \qquad (1)$$

where B' and B'' vary over the general propositions supported by KS1 and KS2, respectively, and

$$C = \sum_{B' \& B'' \neq \sim \Theta} m_1(B')\, m_2(B'') \qquad (2)$$

Letting F(B) denote the numerator of equation (1) [i.e. F(B)=C *m(B)], we can write

$$C = \sum F(B) \qquad (3)$$

where the sum is over all valid general propositions. The resulting support for the general proposition B is

$$s(B) = \sum_{B' \& B = B'} m(B'). \qquad (4)$$

Equation (4) also needed in the calculation of the plausibility p (not probability!) of the single proposition A_i which is

$$p(A_i) = 1 - s(\sim A_i) \qquad (5)$$

Similar, more complex, equations may be written for multiple independent sources KS1, KS2…. KSn. Because the combining of the evidence from independent sources by DS rules is commutative and associative, i.e. the order and grouping is immaterial, we chose to combine sources in pairs, each new source to the previously combined sources. This not only makes the combination of evidence simpler, but allows one to follow the development of the solution easier. It is also easy see how the addition of another piece of evidence changes the reliability of combined solution.

Even though in the notation shown above the combining process may appear complex, it is quite straightforward as a worked numerical example published by Cleckner (1985) demonstrates.

DISCRIMINANTS

We have implemented a simple prototype demonstration system for identifying seismic events that incorporates the following discriminants.

1) P wave complexity
2) Modulation
3) S/P spectral ratios
4) Lg-P spectral ratios
5) Ms-mb
6) Lg spectral ratio

These individual discriminants are described briefly below.

P wave complexity has been found to be effective in dicriminating earthquakes from quarry blasts in Scandinavia (Blandford 1993). P wave from earthquakes tend to have more gradual onset of amplitudes that explosions. These observations were made visually. In order to parameterize complexity we have computed the ratio of the first moment of the seismogram Pn power centered on the arrival time to that of the total power all within the time interval between the arrival time and two seconds after the arrival. This gave us a complexity parameter of 0.7 for impulsive arrivals that decayed after the arrival, 0.9 for arrivals that started abruptly but remained at constant amplitude and 1.5 for arrivals that built up gradually (as unity minus exp(at)) in amplitude from arrival onset within the following 2 second interval.

Spectral modulation distinguishes single explosions and earthquakes from multiple mining explosions and underwater explosions. The cause for spectral modulation in multiple mining explosions is ripple firing (Baumgardt and Ziegler 1986, Smith 1993, Kim et al 1994) while spectra of underwater explosions are modulated because of multiple bubble pulses and water reverberations (Baumgardt and Der 1999). This discriminant was parameterized as the maximum cepstral amplitude, this spectral modulation parameter varied between zero to 0.7 in our simulations, the latter value was assigned as the mean value for underwater explosions and quarry blasts. Other possibilities for modulation-based discriminants exist however (Hedlin 1998).

S/P spectral ratios are commonly given as vectors of values for various frequency bands, the remarks with regards to the reduction of dimensionality made above apply to this discriminant as well. Because their values depend only weakly on frequency the values in various bands but are similar for the same events these can be combined to form a univariate discriminant. This can be accomplished by the standard procedure of computing the covariance matrix between the vector components for a large data set (containing all kind of events) and projecting the individual event vectors along the eigenvector corresponding to the largest eigenvalue. This is done in the system automatically for this types of discriminants. Sn/Pn discriminant tends to separate single explosions on one hand from earthquakes and multiple mining explosions (Sereno et al 1998). Some studies indicate that mine bursts are less earthquake-like than most earthquakes.

Lg/P spectral ratios are employed similarly to the Sn/Pn ratios. They are also commonly given as vectors of values in several frequency bands which need to be reduced in dimensionality also. Typically this discriminant is expected to have larger values for earthquake-like events than for explosions.

Ms-mb. This is a member of a family of discriminants that essentially compare the spectral energy of seismograms in the short and long period bands. Its various versions (mb-ML, mb-M0) are effective discriminants that can separate earthquakes from all kinds of explosions over wide magnitude ranges.

Lg spectral ratio was found to be effective in the western United States and New England (Li et al 1996).

It is easy to add more discriminants to the system. In the near future we plan to include probability estimates for hydroacoustic and infrasonic measurements The role of the discriminants is to provide probability masses for the various single and combined propositions based on the data from a given new event by using the statistical parameters derived the pre-existing data from the given, presumably homogeneous with respect to propagation characteristics, region. We assume that propagation anomalies, distance corrections and transportability were adequately considered before entering into the DS merging scheme.

With regards to event type single propositions were assumed
1) Single explosion on land
2) Single underwater explosion
3) Mining explosion (multiple)
4) Mine burst
5) Earthquake

Note that nuclear explosions are not mentioned as a separate category in this case. It is not possible to discriminate nuclear explosions from large single chemical explosions using the discriminants listed here.

In all cases the discriminants will provide probability masses to the DS fusion process based on past experience in the region. Mathematically the most expedient way to define probability masses is to evaluate Gaussian probability densities at the parameter values corresponding to the event to be classified and this was done in this report. The Gaussian densities (single or multiple dimensional) would be fitted to sets of data points for the various available event types accumulated from past experience in the region. Naturally, the sets of probability masses, which will be incomplete with regards to all the possible propositions, will have to be normalized prior to entering into the DS fusion process. The various discriminants generally do not always provide probability masses for each individual simple proposition, but often give those appropriate to compound propositions. For example, modulation characterizes both quarry blasts and underwater explosions, quarry blasts (multiple explosions) and single explosions tend to have P waves with low complexity. Moreover, if the parameter populations are distinctly non-Gaussian then one has to use other methods for computing probability masses. The pattern recognition literature provides numerous approaches to the problem, it includes methods such as the nearest neighbor classification, potential functions, smoothed empirical distributions and neural networks (e.g. Tou and Gonzalez 1974, Theodoridis and Koutroumbas 1999).

IMPLEMENTATION OF THE SYSTEM

A simple prototype system for merging information from various sources was implemented in MATLAB utilizing the GUI generating software (GUIMAKER) by Marchand (1996). The system processes the information by stepping through all the available discriminants, presenting the supporting regional data, estimates the probability masses for the new event. The probability masses are merged with those of the preceding discriminants in each step. Discriminants that are not available for a given event are simply skipped in combining the evidence.

The system assumes that we have previous experience (data populations) for various single and multiple types of events in the area. The discriminants for a given new event are read in and the probability masses for the various appropriate single and compound propositions are computed by comparing it with the previous experience. The method of comparison can be selected for each discriminant, in this report we assumed Gaussian probability distributions for the data. The probability masses are merged with the previous merged results as the new discriminant is considered. Finally, the time evolution of the support (belief) for all user-selected single and multiple propositions can be displayed. A file is written to record the history of the reasoning process. This file includes all the input data for the event, the probability masses, all the beliefs for the set of all available single and combined propositions.

EXAMPLES

In order to demonstrate the workings of the system, we have generated synthetic data and 'previous experience' for the set of discriminants listed above. In order to have sufficient realism in these simulations, the synthetic data were made conform with the published results by a number of investigators (Li et al 1996, Sereno et al 1998, Fisk 1994, Fisk et al 1994, Bennett et al 1994, Barker 1996, Barker et al 1993). In most areas no results are available for all the discriminants above. In actual applications, ideally, standardized reference data sets should be accumulated within geophysically well defined regions. The 'new data' for one synthetic set displays consistently the properties of a single explosion. The other set has contradictory characteristics in the various discriminants. We must remind the reader, however, that these are totally made-up data.

Working with the first set, we show the Ms-mb data and the data point in **Figure 1** (top). The Sn/Pn spectral ratio data is assumed to be available for five frequencies (Figure 1 bottom). The latter is reduced to a single dimensional Gaussian distribution in the process as described above. As we step through the various discriminants the probability mass for the proposition 1 (EX single explosion) steadily increases (**Figure 2**).
On the other hand the probability mass for the proposition 5 (EQ earthquake) steadily diminishes as more and more evidence merged contradicting it (Figure 2).

The second data set, combined with the same 'previous experience' gives a much less consistent result (displays of the system for Ms-mb and Sn/Pn spectral ratios are shown in **Figure 3**). The history of the proposition 1 (EX) shows an increase for modulation and Sn/Pn which support it, followed by a sharp

decline as conflicting data for the Lg/Pg spectral ratios, Ms-mb and Lg spectral ratios are merged. The best fit is to the properties of a mine tremor but with a low probability (**Figure 4**).

CONCLUSIONS AND FUTURE PLANS

The work presented shows that the DS rules for combining evidence from multiple independent sources provide a natural framework for identifying events on the basis of various types of seismic, infrasonic and hydroacoustic observations. The methodology naturally accommodates incomplete and contradictory data and overlapping propositions. The development of belief and plausibility estimates as more discriminants are added reflect the internal consistency of the data set. In the cases where conflicting pieces of information must be reconciled a widening of the evidential interval and the lowering of belief indicates a reduction in the reliability of the conclusions. The next step is to formulate probability mass computations for non-seismic data using sources such as Brown et al 1998, Chael and Lohr 1998, Dighe et al 1998, and Herrin 1998.

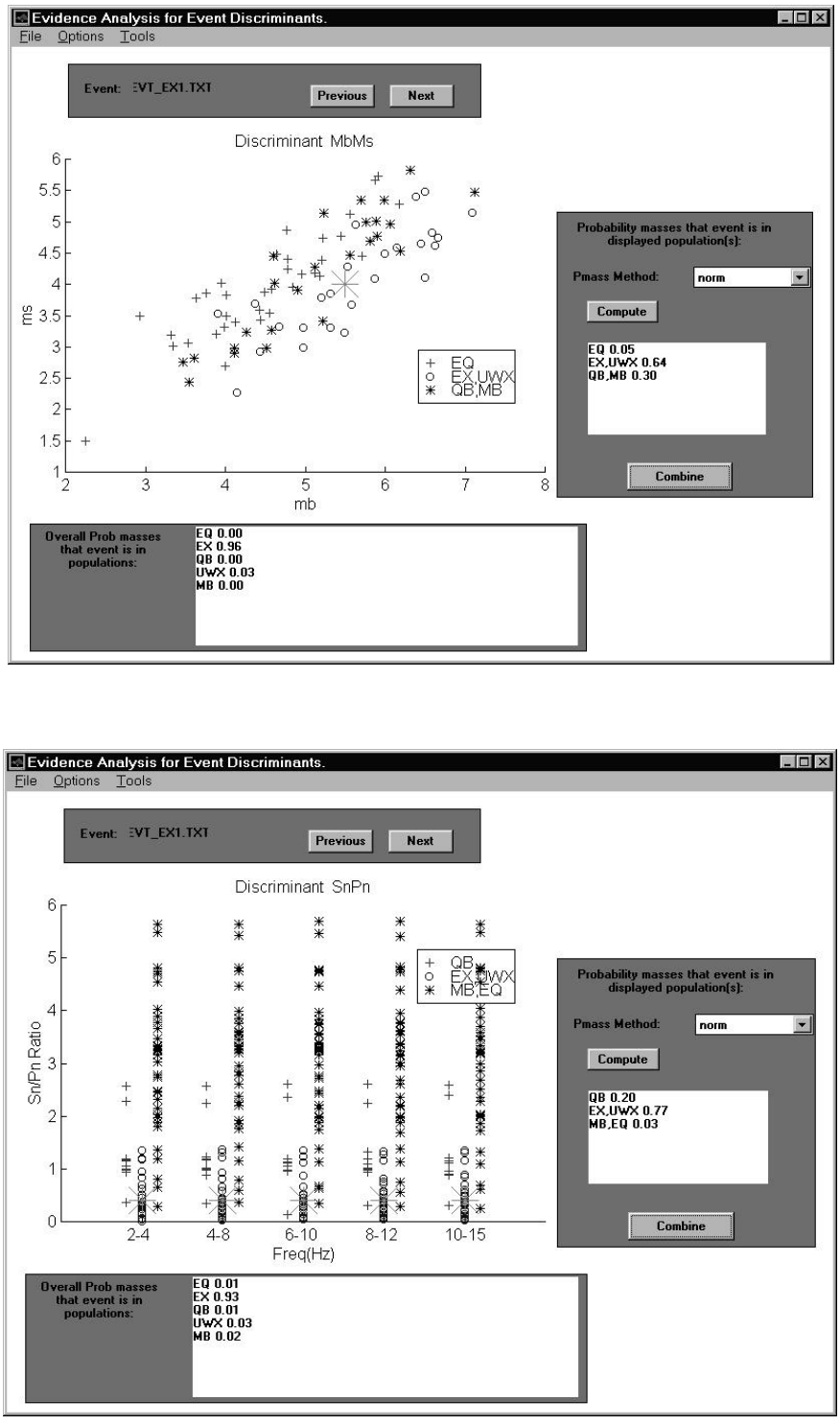
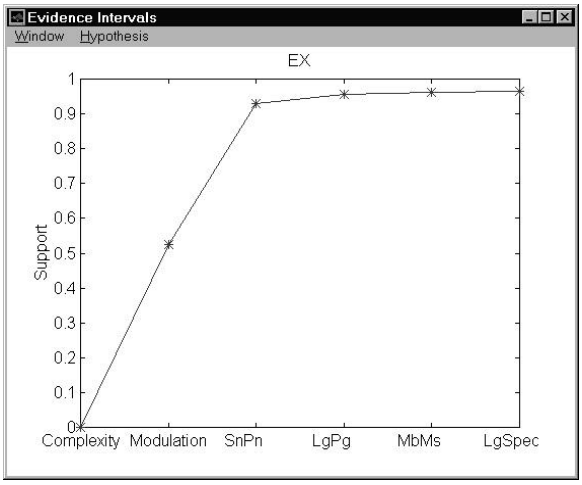


Figure 1. Synthetic Ms-mb (top) and Sn/Pn spectral ratio (bottom) populations. The Ms-mb were assumed to be well separated for earthquakes and single explosions but mixed for quarry blasts and mine bursts. The large stars correspond to the assumed data. The panels show the GUI presentation, allowing the combination of evidence (Compute button), changing of the method for computation of probability masses.



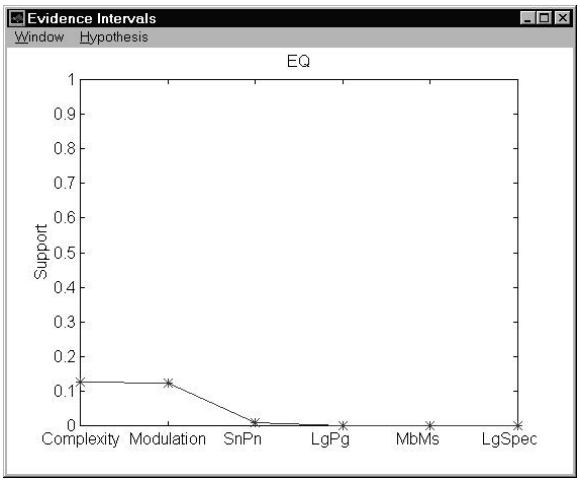
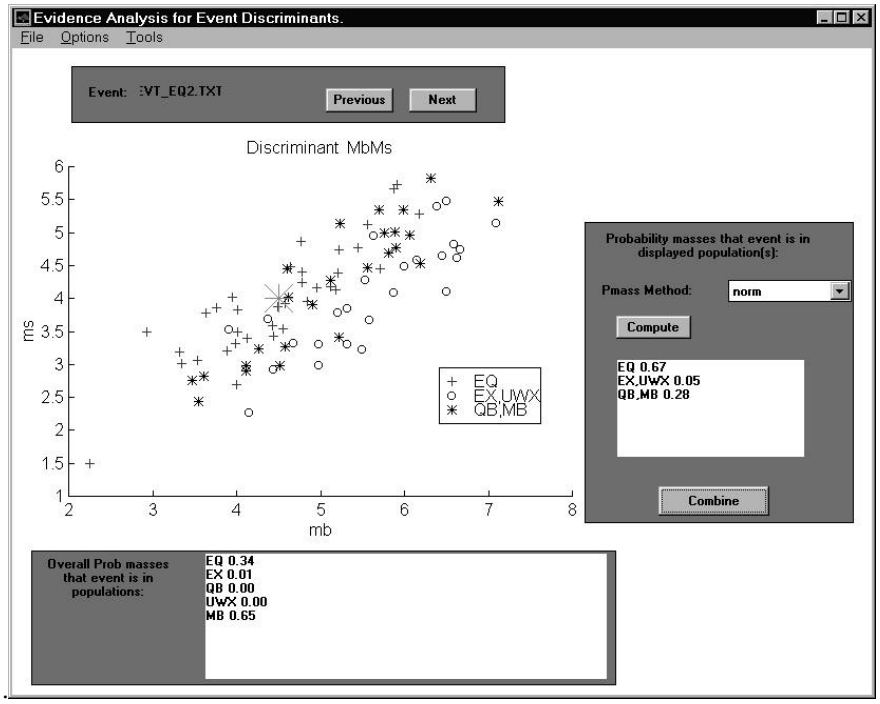


Figure 2. The time histories of supports for the #1 proposition (EX single explosion) and those for the proposition #5 (EQ earthquake). Note the monotonous increase of the first and the decrease of the second. This is due to the fact that all the data support proposition #1.



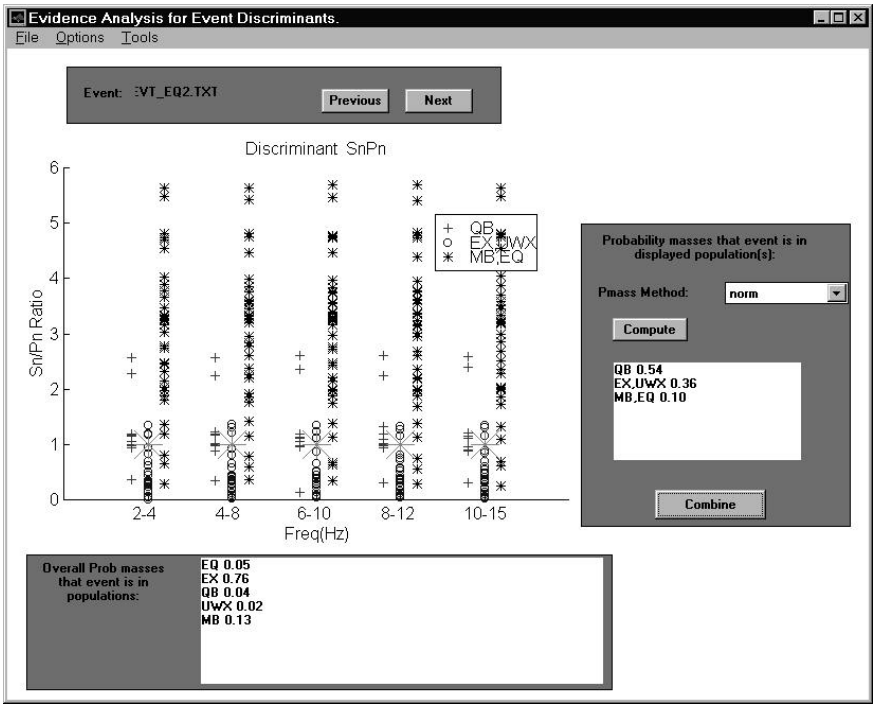


Figure 3. Synthetic Ms-mb (top) and Sn/Pn spectral ratio (bottom) populations. The Ms-mb were assumed to be well separated for earthquakes and single explosions but mixed for quarry blasts and mine bursts. The large stars correspond to the assumed data. Not that in this case there is a conflict between these two sets of data.

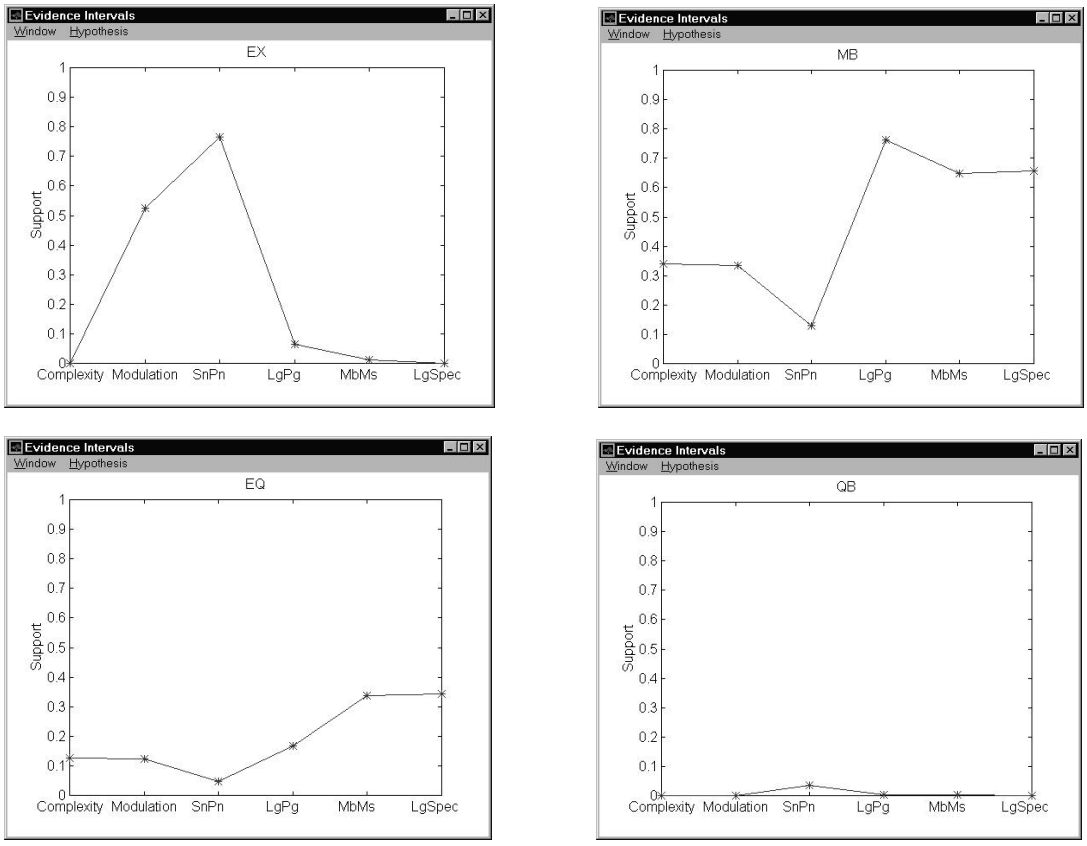


Figure 2. The time histories of supports (belief) for the #1 proposition (EX single explosion), #4 (MT mine tremor), #5 (EQ earthquake) and #2 (QB quarry blast or multiple explosion) for the second set of assumed data. Because of the conflicting data the support for each is changing non-monotonously and none reach a high value.

REFERENCES

Barker, T.G., McLaughlin, K.L. and J.L. Stevens (1993), Numerical simulation of quarry blast sources. Maxwell Laboratories, S-Cubed, La Jolla, CA. Technical Report prepared for Phillips Laboratory, Kirtland AFB, NM.

Baumgardt, D.R. and K. A. Ziegler (1988). Spectral evidence for source multiplicity in explosions, application to regional discrimination of earthquakes and explosions, Bull. Seism. Soc. Am. 78, 1773-1795.

Barker, T. G. (1996), XNICE: A system for assessing network identification performance. PL-TR-96-2087. Prepared for the Phillips Laboratory. Hanscom AFB, MA, by S-Cubed, Division of Maxwell Laboratories, La Jolla, CA.

Bennett, T. J., Marshall, M. E., McLaughlin, K. L., Barker, B. W. and J. R. Murphy (1994), Seismic investigations of rockbursts. Proceedings of the 18-th Annual Seismic Research Symposium on Monitoring a Comprehensive test Ban Treaty. Annapolis, MD.

Blandford, R. R. (1993), Discrimination of earthquakes and explosions at regional distance using complexity. AFTAC-TR-93-044. Air Force Technical Applications Center, Patrick AFB, FL.

Brown, D. J., Katz, C. N, LeBras, R., Wang, J., and A. Gault (1998), Infrasonic processing at the Prototype International Data Center. In 'On Monitoring a Comprehensive Test Ban Treaty' Proceedings of the 20th Annual Seismic Research Symposium, sponsored by the US Department of Defense and the US Department of Energy, September 21-24 1998, Santa Fe, NM.

Chael, E. P., and R. D. Lohr (1998), Infrasound records from US atmospheric tests. In 'On Monitoring a Comprehensive Test Ban Treaty' Proceedings of the 20th Annual Seismic Research Symposium, sponsored by the US Department of Defense and the US Department of Energy, September 21-24 1998, Santa Fe, NM.

Cleckner, W. H. (1985), Tactical Evidential Reasoning: An application of the Dempster-Shafer theory of evidence. M.S. Thesis. Naval Postgraduate School, Monterey, CA.

Dempster, A. P. (1968), A generalization of Bayesian inference. J. Roy. Stat. Soc., Series B., 30, 205-247.

Dighe, K.A., Whitaker, R. W., and W. T. Armstrong (1998), Modeling study of infrasonic detection of a 1 kt atmospheric blast. In 'On Monitoring a Comprehensive Test Ban Treaty' Proceedings of the 20th Annual Seismic Research Symposium, sponsored by the US Department of Defense and the US Department of Energy, September 21-24 1998, Santa Fe, NM.

Dillard, R. A. (1982), Computing probability masses in rule-based systems. Technical Document 545, Naval Ocean Systems Center, San Diego, CA.

Dillard, R. A. (1983), Computing confidences in tactical rule-based systems by using the Dempster-Shafer theory. Technical Document 649, Naval Ocean Systems Center, San Diego, CA.

Fisk, M. D. (1994), Identification and event characterization; Getting down to outliers. CTBT Monitoring Technologies Conference, San Diego, CA.

Fisk, M. D., Gray, H. L. and McCartor, G. L. (1994), Statistical framework for seismic event discrimination and preliminary assessment of CTBT monitoring capability. CTBT Monitoring Technologies Conference, San Diego, CA.

Hedlin, M. A. (1998), A global test of a time-frequency small-event discriminant. Bull. Seism. Soc. Am., 88, 973-988.

Herrin, E., (1998)m, Reducing false alarms with seismo-acoustic synergy. In 'On Monitoring a Comprehensive Test Ban Treaty' Proceedings of the 20th Annual Seismic Research Symposium, sponsored by the US Department of Defense and the US Department of Energy, September 21-24 1998, Santa Fe, NM.

Kim, W.Y., Simpson, D.W. and P.G. Richards (1994), High frequency spectra and regional phases from earthquakes and chemical explosions. Bull. Seism. Soc. Am., 84, 1365-1386.

Li, Y., Toksöz, M. N., and Rodi, W. L. (1996), Discrimination of small earthquakes and explosions. Proceedings of the 18-th Annual Seismic Research Symposium on Monitoring a Comprehensive test Ban Treaty. Annapolis, MD.

Marchard, P. (1996), Graphics and GUIs with MATLAB. CRC Press.

Ryall, A., S., Baumgardt, D. R., Fisk, M. D., and Riviere-Barbier, F. (1996), Resolving regional discrimination problems. In "Monitoring a Comprehensive Test Ban Treaty.", NATO ASI Series, Series E: Applied Sciences. Kluwer Academic Publishers.

Sereno, T. J., Jenkins, R. D. and Bache, T. C. (1998), Discrimination of Asian explosions with range-corrected S/P ratios. In Proceeding of the 20th Annual Seismic Research Symposium on Monitoring a Comprehensive Test Ban Treaty. Santa Fe, NM.

Shafer, G. (1976), A Mathematical Theory of Evidence. Princeton University Press.

Smith, A.T. (1993), Discrimination of explosions from simultaneous mining blasts. Bull. Seism. Soc. Am., 83, 160-179.

Sereno, T. J., Jenkins, R. D and Bache, T. C. (1998), Discrimination of Asian explosions with range-corrected S/P ratios. In 'On Monitoring a Comprehensive Test Ban Treaty' Proceedings of the 20th Annual Seismic Research Symposium, sponsored by the US Department of Defense and the US Department of Energy, September 21-24 1998, Santa Fe, NM.

Tou, J. T., and Gonzalez, R. C. (1974), Pattern Recognition Principles. Addison-Wesley.

RECENT DEVELOPMENTS IN SAC2000: ENHANCED PROCESSING, DATABASE INTERACTION, AND COMPATIBILITY WITH OTHER TOOLS

Mike Firpo, Doug Dodge, Peter Goldstein, Lawrence Livermore National Laboratory

Sponsored by U. S. Department of Energy
Office of Nonproliferation and National Security
Office of Research and Development
Contract No. W-7405-Eng-48

ABSTRACT

Development of the Department of Energy Comprehensive Nuclear-Test-Ban Treaty Research and Development (DOE CTBT R&D) Knowledge Base is a complex, evolutionary process involving a large number of signal processing and data analysis tasks and tools. Our efforts have been focused on the development of signal processing and data analysis enhancements that help facilitate this process. We have also developed database access and data management capabilities that improve access to data and facilitate the utilization of multiple tools. These developments have been used to address a number of knowledge-base-related tasks including:

- Data selection, inspection, and quality control
- Phase picking and amplitude measurements
- Magnitude estimation
- Discrimination studies
- Depth and mechanism estimation
- Geophysical model development using waveform modeling

Recent developments in SAC2000 include a number of capabilities needed by the DOE CTBT R&D program. These developments include a mixture of relatively new capabilities and enhancements to existing capabilities. All of these capabilities resulted from direct requests from researchers at Lawrence Livermore National Laboratory and in the monitoring community. A sample of some of these capabilities is given below.

- READCSS and WRITECSS, which have been completely rewritten so that they are 100% compatible with CSS3.0; thus, a user can read in CSS3.0 data, process it, and pass it back out in CSS3.0 without losing any of the relevant CSS3.0 parameters. This provides improved access to CSS3.0 parameter data and significantly improved compatibility with other tools.
- COMMIT, ROLLBACK, and RECALLTRACE, which allow the user to combine parameters calculated from processed data with unprocessed waveforms, undo the effects of processing on seismic waveforms, and commit process data to an input/output buffer for future processing.
- READGSE and WRITEGSE, which read and write GSE2.0 format, and a READSUDS command which reads PC SUDS data.
- TRAVELTIME, which has been modified to allow the user to save model travel times in the SAC headers and use general 1-D velocity models to compute travel times.
- TRANSFER, which has been updated to read instrument responses from an Oracle database and to allow the use of FAP files.
- SORT command, which allows users to sort their data based on SAC header fields.
- WHITEN command, which flattens the spectrum of a user's data.
- FILTERDESIGN, which has been updated to allow the user to save the results to files so that they can be used with other processing.
- PRINT options, which have been added to a number of commands.

Key Words: database, knowledge base, data processing, data analysis

INTRODUCTION

SAC2000 or SAC, as many users refer to it, is a fundamental signal processing and analysis tool for a large portion of the international seismological community including academic, government, and business institutions. SAC has attained this popularity for a variety of reasons. Foremost, are its extensive, well-documented, well-tested, and well-maintained mathematical capabilities, its macro programming language which allows users to develop new analysis techniques and customized processing programs, and its ability to do both batch and interactive processing. SAC's Strengths also include its ability to process a diverse range of data types and its extensive usage (> 400 institutions worldwide) which has made it much easier for researchers to develop collaborative research projects. SAC is relatively easy to use and is available on a variety of hardware platforms. Much of its popularity is probably due to its user oriented development philosophy which has led to consistent, backward compatible development guided by users input and needs.

SAC2000's extensive signal processing capabilities include: data inspection, signal correction, and quality control, unary and binary data operations, travel-time analysis, spectral analysis including high-resolution spectral estimation, spectrograms and binary sonograms, and array and three-component analysis (Figure 1). These capabilities have proved useful for solving a number of geophysical problems including, estimation and analysis of strong ground motions, earthquake, explosion, volcanic source studies, seismic discrimination and identification studies, magnitude estimation, travel-time analysis, studies of wave propagation phenomena such as path and site effects, and investigations of Earth structure. It has also proved useful for analysis of other geophysical data such as measurements of electromagnetic or hydro-acoustic phenomena.

OVERVIEW OF RECENT DEVELOPMENTS

Over the last few years, our focus has been on enhancing the ability to combine and utilize data and results from a variety of tools and data sources. A number of processing and analysis tools have been incorporated such as more powerful TRANSFER and TRAVELTIME capabilities and an interface to MATLAB. Table 1 lists new or enhanced processing and analysis tools.

I/O has been overhauled to make SAC2000 completely fluent in the CSS 3.0 schema. SAC2000 can read and write CSS 3.0 flat files, and our new CSS 3.0 binary file; it also reads CSS 3.0 data from an Oracle™ database. Other I/O improvements include the ability to read and write GSE 2.0 data, and to read PC SUDS and IRIS/PASSCAL SEGY data. Table 2 lists the new or enhanced I/O capabilities.

Table 3 lists a number of features that have been added to make SAC2000 more convenient. These features include a SORT command, the ability to delete selected files from memory (DELETECHANNEL), a unix-style history capability (HISTORY), and an in-memory cut command (CUTIM).

Table 4 describes new features that provide for more efficient processing of data, and Table 5 displays features that allow custom software development: integrating the user's software into SAC or integrating SAC's I/O functions into the user's software.

Some of these functions are described below. For more details on any function, get the latest version of SAC2000 from our ftp site, and use the HELP command.

Powerful Tools

The following table lists recent enhancements to SAC2000's processing and analysis capabilities. More details are also available in the HELP facility built into SAC.

Table 1. Recent Additions to SAC's Processing and Analysis Capabilities.

TRANSFER FROM EVALRESP	Utilizes Tom McSweeney's evalresp library to correct for instrument response
TRANSFER FROM FAP	Utilizes a frequency/amplitude/phase (FAP) file to correct for instrument response
TRANSFER FROM DBASE	Finds an evalresp, fap, or polezero file from an Oracle database to correct for instrument response
TRAVELTIME TAUP	Reads traveltime curves produced by TauP (Crotwell et. al. 1998)
TRAVELTIME PICKS	Stores arrival information in T0 - T9 headers
WHITEN	Applies a linear filter to the input signal to "whiten" or "flatten" the signal's spectrum
FILTERDESIGN FILE	Saves the responses from FILTERDESIGN to a set of SAC files for analysis
GMTMAP/MAP	Mapping display using Generic Mapping Tool
3C	MATLAB based three component analysis tool
MAT	A general interface between MATLAB and SAC

TRANSFER
SAC's TRANSFER command has long been used to remove instrument responses from waveform data. Three new options bring it up to date with modern instrument response technology:

The EVALRESP option enables the user to apply transfer functions extracted from SEED data volumes using the evresp code (Version 3.2.11) by Thomas J. McSweeney. The RESP files must be in the current directory or must be specified by full path and name. The EVALRESP option uses the STATION-CHANNEL-NETWORK-DATE-TIME information in the SAC headers to identify the correct RESP file and extract the proper transfer function from that file. However, it is possible to override the header values by specifying additional options to TRANSFER. The possible options are: STATION, CHANNEL, NETWORK, DATE, TIME, TYPE, and FNAME. Each option must be followed by an appropriate value.

The FAP option uses instrument response information from a frequency-amplitude-phase (FAP) file in the standard format used at the Center for Monitoring Research (pIDC). FAP files have five columns: frequency, amplitude, phase, amplitude error, and phase error.

The DBASE option searches an Oracle™ database for the applicable instrument response file which must be of type EVALRESP, POLEZERO, or FAP. The file found is used in the calculations of the TRANSFER command. Note: In order to use the DBASE option, the user must have access to an Oracle™ database with links to the applicable files, the database must be formatted as described in the HELP TRANSFER documentation, and the user must have the Oracle™ version of SAC2000.

TRAVELTIME
The TRAVELTIME command has been a part of SAC's Signal Stacking Subprocess (SSS) for a number of years now. It allows the user to produce traveltime curves from the iasp91 model, or to read curves in from text files. These curves can be overlain on a record section plot using command PRS TTIME ON. Now the PICKS option allows the times where the curves intersect the waveforms to be stored in the header fields T0 - T9.

TauP is a very flexible traveltime estimator developed by Philip Crotwell at the University of South Carolina (Crotwell et. al. 1998). It allows the user to produce traveltime curves from a model of the user's

design. The TRAVELTIME command in SAC2000 now takes a TAUP option which allows it to read the traveltime curves generated with TauP. Used in conjuction with PRS TTIME ON, this allows the display of TauP curves on record section plots in SAC. Used in conjunction with the PICKS option, it puts TauP traveltimes into the T0 - T9 header fields in SAC files.

MATLAB Three-Component Data Analysis Tool
We have developed a new, MATLAB-based tool for interactive and batch mode analysis of 3-component seismic data. This tool will improve a user's ability to detect and identify seismic phases, especially secondary phases. It has also helped us process data and identify problems with data such as incorrect sensor orientation information.

This tool has a number of capabilities including: graphical data selection and filter design, automatic back-azimuth and incidence angle estimation, interactive, graphical, three-component particle motion analysis, and maximum-likelihood probability estimates of selected wavetypes (Christoffersson et al., 1988).

Figure 2 displays a selected example of the interactive version of this three-component data analysis tool. Interactive data/window selection, phase picking, and signal rotation are done in the main window. Popup windows are used to: filter the data (no windows shown), interactively analyze particle motions (Particle motion module), and compute maximum-likelihood probabilities for selected wavetypes (ML-polarization analysis module).

I/O

Table 2 displays new I/O commands which make SAC useful on a wider range of data files and formats.

Table 2. Recent Additions to SAC's I/O Capabilities.

READCSS/WRITECSS	Complete CSS 3.0 compliance; reads and writes both CSS 3.0 flatfiles, and a CSS 3.0 binary formats
READDB	Access CSS 3.0 data from an Oracle database
READGSE/WRITEGSE	GSE 2.0 I/O
READSUDS	Reads PC SUDS with automatic byte conversion
READ SEGY	Reads IRIS/PASSCAL version of SEGY files
READ ALPHA	Reads SAC formatted Alpha files (replaces CONVERT)
READTABLE	This is the old READALPHA command, renamed to avoid confusion with READ ALPHA

With the release of version 0.58, SAC2000 now has two parallel internal data buffers: the original buffer which houses the data in traditional SAC format, and a second buffer which stores the data in CSS 3.0 tables. As needed, SAC2000 can seamlessly move the data between the two buffers, allowing fully compliant CSS 3.0 reading and writing capability. The READDB command allows SAC to read CSS 3.0 data directly from a properly configured Oracle™ database.

This data storage modification has dramatically improved SAC's ability to read other relational formats, enabling the reading and writing of GSE 2.0 files and the reading of PC SUDS files. Also, SEGY files of the type available through IRIS/PASSCAL can now be read with the SEGY option to the READ command.

The READ command now has a new ALPHA option which reads SAC formatted alphanumeric text files (those produced by WRITE ALPHA). READ ALPHA replaces the old CONVERT command which could only handle one file at a time and didn't take the MORE option. To avoid confusion, the one-word command READALPHA – which reads columns of data – has been given an alternative name: READTABLE.

Added Convenience

Most of the recent ease-of-use enhancements to SAC2000 are highlighted in Table 3. Those changes involving process management are listed in Table 4.

Table 3. Recent Enhancements to SAC's Ease-of-use.

SORT	Sort files based on header values
CUTIM	Cut files in memory, can make multiple cuts
PRINTHLP	Prints the specified HELP file
PRINT option	An option to most plotting command, sends plot to printer
PRINT command	Prints the most recent SGF file
SGF OVERWRITE	Allows SGF files to over-write previous SGF files
DELETECHANNEL	Removes specified files from memory
FILENUMBER	Tags most plots with filenumbers, for use with DELETECHANNEL
PICKAUTHOR	Specifies preferred authors when reading picks from CSS data
PICKPHASE	Specifies preferred phases when reading picks from CSS data
MERGE	MERGE can now merge overlapping files
HISTORY	View prior SAC commands. Reissue commands with ! or !! (as in UNIX)
maximum file number	SAC can now hold 1000 files in memory

SORT allows the user to sort files in memory based on header fields. Up to five fields can be selected, and for each field the sort can be in ascending (default) order or descending order.

CUTIM is similar to CUT, except that while CUT simply sets the parameters and lets the cut happen on the following READs, CUTIM cuts the data in memory, and has no effect on subsequent READs. CUTIM also allows files to be cut into multiple pieces, so that if you start with two files, and specify three cut segments, you will end up with six files in memory – three segments from each of the original two files.

DELETECHANNEL allows the user to remove specified files from memory. For example, one can read large sets of data from relational files or large directories of SAC files, sort them on a particular header field, and then delete those files which don't match desired criteria. The command FILENUMBER is helpful for determining the file numbers of files to be deleted.

HISTORY works much like the UNIX history command. It lists previous SAC commands given in the current session. The exclamation point (!) can be used to reissue commands in three ways: !! reissues the previous command, !n (n denotes a number) reissues command n as listed by the HISTORY command, and !s (s denotes a character string) reissues the most recent command which begins with the string s.

Table 4. Process Management Commands

COMMIT	Protect changes from being undone with ROLLBACK or REACALLTRACE
ROLLBACK	Undo changes since last COMMIT
RECALLTRACE	Commit the header, rollback the waveform

The process management capability is made possible by the dual data storage buffers mentioned in the section about I/O. ROLLBACK undoes all the changes since the last COMMIT (or the READ). COMMIT protects changes from being undone. RECALLTRACE (RECALL) rolls back the waveform along with those header fields which are tightly bound to the waveform (such as npts, delta, etc.) and commits the header fields which are not tightly bound to the waveform (such as picks and event information).

Incorporating Your Own Code

The following table lists features which allow the user to incorporate code into SAC, or to read and write SAC data files from his/her own code.

Table 5. Software Interface Enhancements

command interface	Allows users to write commands in C or FORTRAN and add them to SAC
sacio.a	A library with SAC's I/O routines callable from stand-alone FORTRAN or C programs

For more details regarding the external command interface, use HELP EXTERNAL_INTERFACE and HELP LOAD at the SAC> prompt.

For details about the sacio.a library, use HELP INPUT_OUTPUT, HELP BLACKBOARD, and HELP APPENDIX at the SAC> prompt.

CONCLUSIONS

We have implemented a number of new processing capabilities and enhancements in SAC2000 that will improve users' efficiency and their ability to accurately interpret data. We have also developed a new, flexible data structure for SAC2000 that will allow us to access, modify, and output all the information in CSS3.0-based Oracle™ databases or CSS3.0 flat files. Other data schemas can now be read. Among them, GSE can also be written. These new capabilities are essential for efficient processing and analysis of the large amounts of seismic data that are currently being collected. A number of conveniences have been added to SAC2000 including SORT, DELETECHANNEL, and HISTORY which make the process flow more smoothly from the human perspective. Also, facilities are in place which allow SAC to interface with other software.

REFERENCES

Christoffersson, A.,E.S. Husebye, and S.F. Ingate, 1988, Wavefield decomposition using ML probabilities in modeling single-site 3-component records, Geophys. Journal Int., 93, 197-213.

Goldstein, P., Doug Dodge, and Mike Firpo, 1997, Recent developments in SAC2000, Proceedings of the 19th annual seismic research symposium on monitoring a CTBT, Orlando, FL, September 23-25.

Wessel, P. and W. H. F. Smith, Free software helps map and display data, EOS Trans. AGU, 72, 441, 1991

Goldstein, P, et. al. 1998, What's new in SAC2000? Enhanced Processing and Databse Access, Seismological Research Letters, 69:3, 202-204

Crotwell, H. P., et. al., 1999, The TauP Toolkit: Flexible Seismic Travel-time and Ray-path Utilities, Seismological Research Letters. 70:2, 154-160

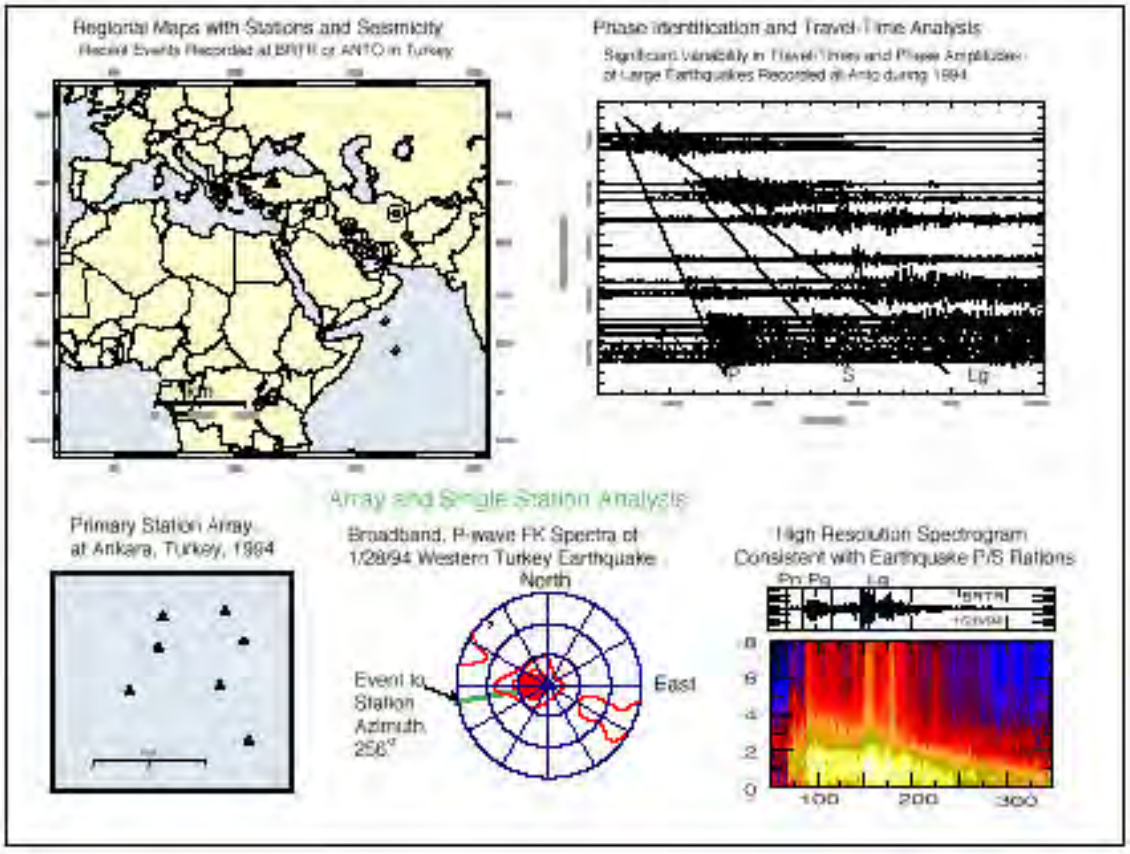


Figure 1. Selected signal processing and analysis capabilities in SAC2000.

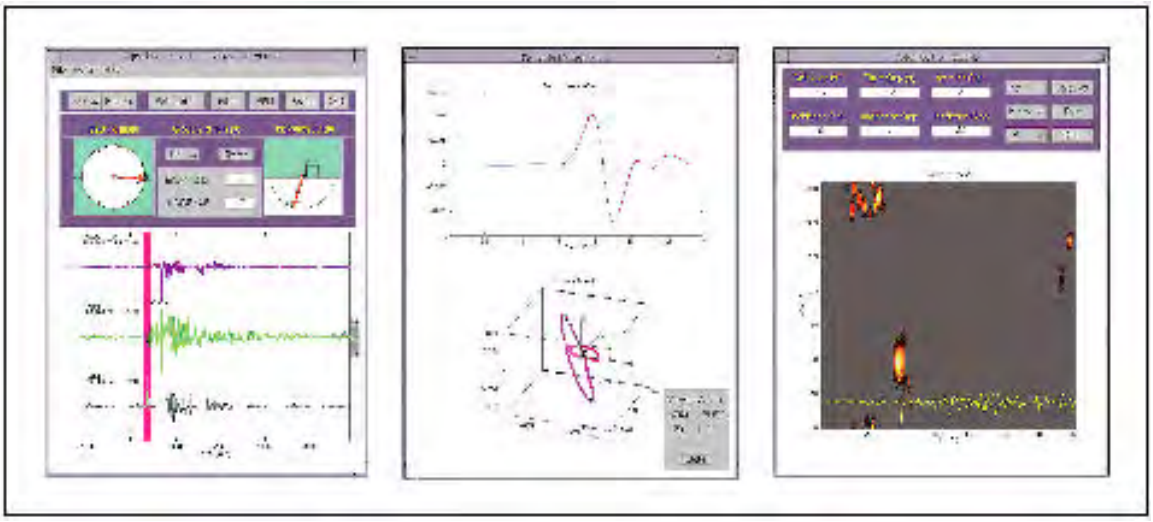


Figure 2. Interactive version of SAC2000's 3-component datainspection and analysistool.

ASSESSMENT OF DATA QUALITY OF SELECTED DATA SETS IN THE DEPARTMENT OF ENERGY/COMPREHENSIVE NUCLEAR TEST-BAN-TREATY KNOWLEDGE BASE

D. N. Hagedorn, C. A. LoPresti, R. F. O'Brien, S. A. Hartley, B. G. Amidan
Pacific Northwest National Laboratory

Sponsored by U.S. Department of Energy
Office of Nonproliferation and National Security
Office of Research and Development
Contract No. DE-AC06-76RLO 1830

ABSTRACT

The U.S. Department of Energy's (DOE) Comprehensive Nuclear Test-Ban-Treaty (CTBT) Knowledge Base (KB) contains detailed regional data, from which corrections to seismic, hydroacoustic, and infrasonic signals will be generated. As the KB is populated with information and data sets detailing regional geological and geophysical structures and reference event data, questions of "How good is the information?" and "What confidence can I have in the corrections?" arise. This report documents work to-date at the Pacific Northwest National Laboratory on the development of a "toolbox" of statistically-based algorithms which may be used to assess the quality of individual data sets, and consistency across multiple data sets, both on data in the KB and prior to including new data in the KB.

Thirteen data sets (consisting of metadata, header, projection, and data files), supplied by Sandia National Laboratories, from the KB were used in this preliminary examination. The metadata files were reviewed before analysis of the data sets began. We noted that some fields were not filled in, others had very brief entries, while yet others were quite complete and informative. Comparing metadata files across data sets, we noted that the quality of the information was not consistent, there were problems with the accuracy/ precision of the numerical data, processing audit trails were poor to nonexistent, and when compared to the headers in the data files, some discrepancies were noted.

Several methods were employed to evaluate the individual data sets for spurious data. We believe that because these gridded data sets in the KB are composites created from multiple sources and have been processed and smoothed, no outlier data was found. We did discover in some of the data sets that areas of constant value (algorithm default values) existed, which are not geologically reasonable. We believe that these areas were created as a result of the processing and are not valid data.

Problems with agreement between data sets were also identified. Comparing data sets was problematic because of the different grid sizes and cell locations. As an example of what can be done to evaluate agreement between data sets, we examined three Mohorovicic (Moho) Discontinuity depth maps, which contained regions in common to two or all three data sets. Depths to, and trends in, the Moho in the data sets did not agree with each other, and in some instances depths at the same location had differences of up to 20 km.

These are all serious problems, which must be rectified prior to using this KB data to generate seismic corrections. The effects of the noted discrepancies on the corrections have not yet been assessed, but we believe that corrections derived from using the different data sets would be significantly different. The cumulative effects of multiple errors could be more drastic. Certain needs for the overall KB were also identified, such as a need for well-defined criteria for accuracy of data, estimates of uncertainty to be associated with individual data, a consistent schema for gridding and combining data sets, and tolerance limits for agreement between data sets.

Treatment of uncertainty in the data and understanding the effects of that error on the correction estimates that result from using the KB data is essential. The data sets from the KB used in this study are not raw data. They have been generated from multiple sources, processed, interpolated, and smoothed, and have no estimates of error or uncertainty. Uncertainty estimates cannot be confidently derived from processed and smoothed data, as from raw data. Any estimates of error and uncertainty will need to be inferred from ground-truth events.

Key Words: Knowledge Base, Data Quality

OBJECTIVE

This work seeks to develop Matlab-based tools, in the form of an easily accessed Matlab toolbox, which can be used to assess the overall quality of the data contained in the KB and data destined for inclusion in the KB. These tools can be used both to assess the confidence in the present KB data and to make certain that future additions or "loads" (i.e., additions to or replacement of data) to the KB are both consistent with the contained data and have an understandable effect on future interpretations based on the KB data. Additionally, this 'toolbox' will facilitate the identification of areas that would benefit most from efforts to gather additional high-quality data for inclusion in the KB. This work benefits the CTBT monitoring program by building confidence in the KB, allowing identification of problem areas with poor/little data, and supporting efforts to optimize additional data collections that will enhance the KB.

RESEARCH ACCOMPLISHED

To accomplish the development of the Data Quality Assessment Toolbox (DQAT), PNNL is performing evaluations on 13 data sets currently in the KB. Data presently in the KB were obtained from many diverse sources and some data are of unknown quality. The KB data include geological and geophysical measurements and maps, seismic records, topological data, political boundaries, metadata used to qualify "hard" data, and other types of data. Multiple data sets, containing similar and overlapping data, are also a part of the KB. For this preliminary report, we examined both the individual data sets for obvious or hidden problems (inconsistencies, outlier data, mislocation errors, etc.) and the degree to which these data exhibit reasonable agreement.

Data are of two primary types: gridded data and vector data. The gridded data represent three-dimensional surfaces (i.e., contour maps), while the vector data represent two-dimensional features, such as boundary descriptions, rivers, and, in some instances, single-point features. PNNL requested representative data and SNL delivered 13 data sets: 10 gridded and 3 vector. The data sets cover the MidEast/North Africa (MENA) and/or central Asia. The data sets investigated are listed in Table 1. (Note: All references to data sets in this report are noted by use of capital letters.)

Discussion of Metadata

The metadata were examined for internal inconsistencies and for inconsistencies with the headers in the ASCII data, as well as for erroneous entries in the text. The metadata are a very important component of the KB, containing information about where the data came from, the processing that has occurred, the reference list, the geographic boundary data, the accuracy information, and other information.

Examination of the metadata files and cross-checking that information with the information contained in the headers of the associated data files resulted in the following problems being revealed and many questions being raised:

- differences in precision - In the boundary data, some are integers, some have eight decimal places, some three, and some one. Consistency within a single data set is often not present. Is precision to eight decimal places to be believed (i.e., to the nearest millimeter)?
- differences in overall quality - Original data were of varying quality and were often digitized from maps (already processed and smoothed), combined with data from various other sources in poorly-documented ways, and smoothed again. The resulting grid was then resampled to create the data sets received by PNNL.
- metadata not consistently filled in - Some descriptions are very complete, others are less so, and some are totally blank.
- interpolation of gridded data - All gridded data are interpolated (according to the associated metadata files); some are smoothed to a greater degree than others.
- data discrepancies with headers - One gridded set (Bouguer gravity for MENA) uses a different geodetic datum. This is contradicted by information in the header of the data set. Also, a number of columns of data in Bouguer gravity for the MENA dataset (BOUGUER) disagree with information in the header of the data file (398 vs. 460).
- incorrect interval date – The beginning interval date is wrong in the GVOLCANOES data set.

- missing data-acquisition dates - Dates referencing when original data were acquired are usually missing. For some data, this is quite important, since measurement techniques have vastly improved over the years.
- missing references - References are missing for two Cornell data sets (CORN_BASM, and MOHO).

Some of the fields lacking from the metadata files are, for our work, critical. These include locations of the raw data, estimates of the uncertainty of the raw data, contribution to the uncertainty by the processing stream, descriptive statements about how the data was processed (the steps and algorithms used), and the models used to create the final data values. Some of the fields contained in the metadata are essentially useless to the end-user from a data quality perspective.

Investigation of Individual Data Sets

Since most of the provided data sets were developed by combining and smoothing other, possibly derived, sets of data, extensive analysis of each set of data yields little information. Lack of access to the original raw data prevents this evaluation from tracing anomalies back to their sources, and thus can not be attributed to the original source or to processing, modeling, or other causes. The data sets used in this study are derived from other data sets, which may be composed of multiple sources and are processed and smoothed. Furthermore, the criteria for transforming and/or deriving each raw data set, as well as combining data sets, are unknown; therefore, the accuracy, representiveness, uncertainty, and quality of each data set are unknown.

Several types of anomalous data detection operators were applied and very little outlier data was found. This is attributed to the fact that these data have been multiply processed and smoothed, thus eliminating spurious values. One interesting observation did emerge from examination of the Bouguer gravity map: areas with constant values were discovered. We have concluded that these areas are not geologically-feasible, and are artifacts of processing and should be removed from the data sets.

Comparison of Data Sets

One problem encountered in analyzing the gridded data sets for consistency appeared when using Matlab to overlay the data with coastlines and political boundaries. The two Matlab vector data sets are not identical. While this is not an apparent problem with the gridded data sets from the KB currently under evaluation, the situation is exactly analogous to problems contained in the KB, according to reports from SNL. PNNL plans to address the KB problem in future work.

From out initial overview examination we noted that of the 13 data sets, three contained depth-to-Moho data, and there was a single area in common to all three (MOHO, COL_MOHO, and CORN_MOHO). This was an ideal area to evaluate the 'fit', or agreement, of the data in the KB. Figure 1 illustrates the geographic extent and overlap of the three Moho depth data sets.

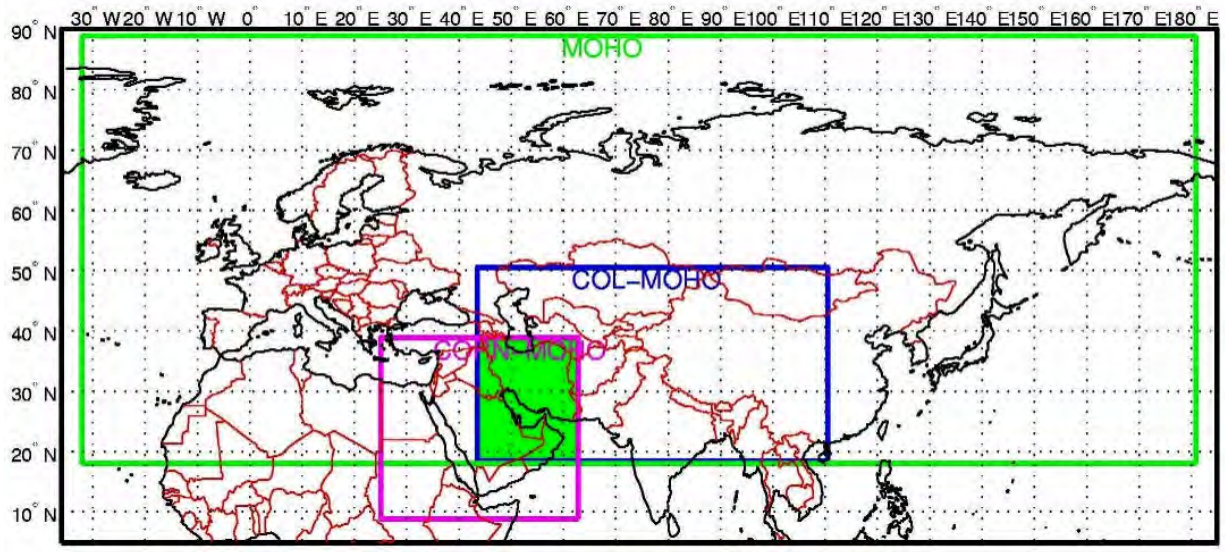


Figure 1. Geographic areas covered by data in MOHO, COL_MOHO, and CORN_MOHO depth-to-Moho data sets.

The first problem in trying to compare the different data sets was that each data set had different cell sizes and cell locations in the map system. Two of the data sets, MOHO and CORN_MOHO, had 0.0920762274019710^{o} and 0.09^{o} square cells, respectively. The third data set, COL_MOHO, was sampled on a 1^{o} square cell size. This means that there are roughly 121 cells from each MOHO and CORN_MOHO grid that refer to the same area as one cell in the COL_MOHO data set. Furthermore, none of the three data sets had locations (cell centers) in common. To compare the data sets, it was first necessary to create a common cell grid system. The COL_MOHO data set was used as the baseline. This eliminated problems associated with creating a finely spaced grid from a coarse one and was sufficient for this overview of the data. In the areas that overlapped the three data sets, the MOHO and CORN_MOHO data sets were sub-sampled to match the COL_MOHO map coordinates as closely as possible. This was done by a "nearest-neighbor" approach: simply locating the nearest cell location in both the MOHO and CORN_MOHO data sets, coordinating with a cell location in the COL_MOHO data set, and assigning the value in that "neighboring" cell to the new grid. In Figures 2a and 2b, observe the original CORN_MOHO data set and the same data set resampled to represent 1^{o} square cells. It can easily be seen that while some of the smaller features are absent, as expected, the sub-sampling scheme represents the original data fairly well.

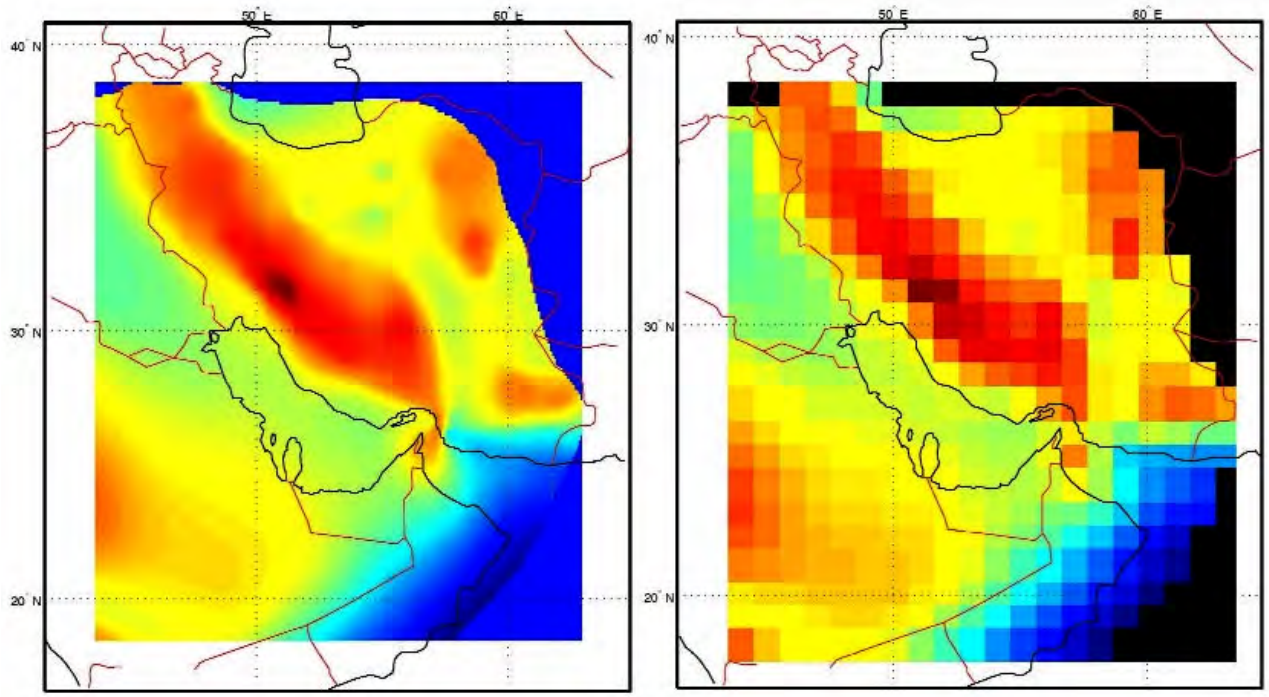


Figure 2. The CORN_MOHO data set at its original resolution (a) and the same data set resampled to represent 1° square cells (b).

Perspective maps of the three data sets that correspond to the overlapping green area in Figure 1 are presented in Figure 3 (parts a, b, and c). Note that the perspective maps for the CORN_MOHO and MOHO data sets represent the sub-sampled points from those data sets that are closest to the cell centers of the COL_MOHO data set. It is apparent from these perspective maps that the data sets differ greatly: both the MOHO and CORN_MOHO data sets have a deep trench in the Moho trending in the northwest-southeast direction, whereas the COL_MOHO data set has a bowl-like depression in the center of the map. This difference may be real (derived from the raw data) or may be an artifact reflecting how the data sets were processed and smoothed. We cannot determine the reason unless raw data are available. The degree of difference that is acceptable is not presently known and must be defined before the data are used.

Cell-by-cell pair-wise comparisons of overlapping areas of CORN_MOHO (Cornell University), MOHO (Cornell University), and COL_MOHO (University of Colorado) reveal cell value differences ranging from approximately -17,000 to +17,000 meters. While these differences appear large, the mean and median cell differences were negligible. Using exploratory analysis techniques, it appears that while both mean and median differences (biases) between Moho depths (over large areas: 16° of longitude and 19° of latitude) between maps may be small, there are smaller areas of the maps where values differ significantly and may be of concern.

Differences in the maps may be due to different methods used to derive the map data (original data), possible errors or inaccuracies of measurements, different smoothing algorithms used for each map, and/or the effect of combining different data sets into each of the individual data sets. Determination of the origin of the errors was beyond the scope of this study, as the raw data are not available.

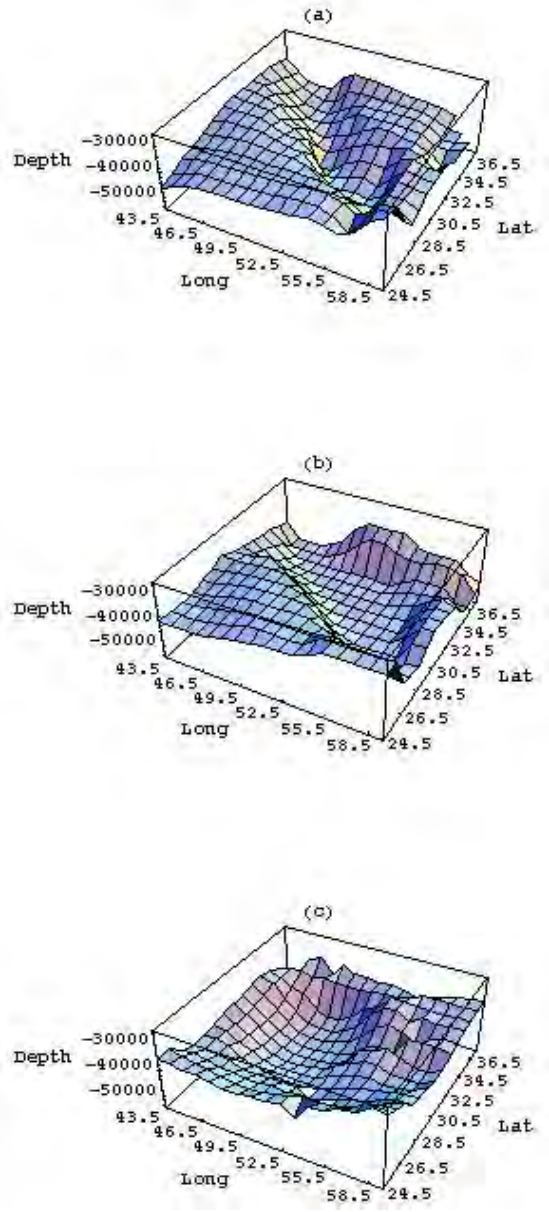


Figure 3. Perspective plots of the depth-to-Moho values in: (a) CORN_MOHO, (b) MOHO, and (c) COL_MOHO.

Histograms of the depth-to-Moho values, made for each of these data sets, are shown in Figure 4. The most striking feature of these histograms is seen in Figure 4 (b), representing the MOHO data set. The figure shows several abnormally large bars at 30,000, 35,000, 40,000, 45,000, and 50,000 meters. It is postulated that these values are the result of digitizing a contour map from the Institute of Physics of the Earth, Moscow, Russia. Such anomalies appearing at 5000-meter intervals are likely due to data inside artificial contour boundaries that are local minima or maxima areas of Moho depth. That is, after smoothing the data sets, local minima or maxima within the contour remain constant. Simply knowing that these regions exist can help explain some of the anomalies that were observed. It can also be noted that the spread of the histograms differs, mainly due to the truncation of the MOHO data at 25,000 and 45,000 meters.

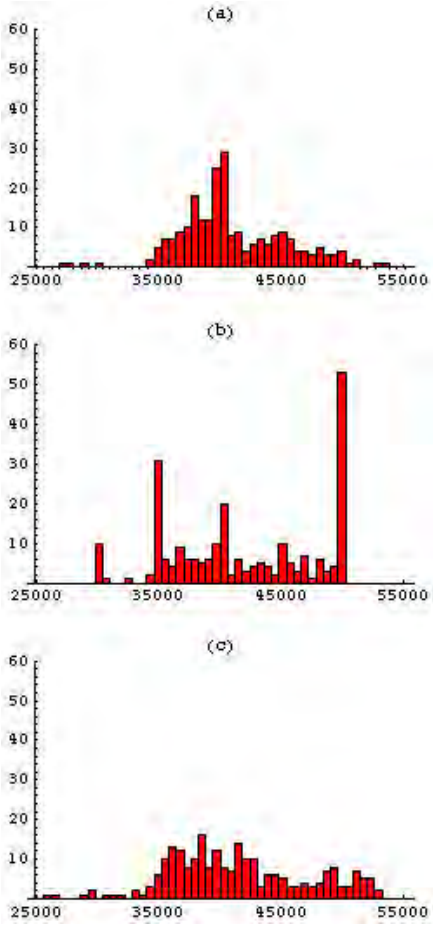


Figure 4. Histograms of the depth-to-Moho values in: (a) CORN_MOHO, (b) MOHO, and (c) COL_MOHO.

Summary statistics for each of the data sets in Table 1 reveal that mean Moho depth in the three maps differs by up to 1000 meters, while the median differs by at most about 550 meters. Notice also, that while the range of the MOHO data set is smaller than the others; its standard deviation is larger due to the large number of values at the extreme truncation points of 30,000 and 45,000 meters.

Maps	CORN_MOHO	MOHO	COL_MOHO
Mean	40,927.7	41,979.0	41,435.4
Median	40,128.0	40,680.0	40,674.0
25% Quantile	38,100.0	36,590.0	37,237.0
75% Quantile	43,857.0	48,790.0	45,261.0
Standard Deviation	4,318.7	6,146.6	5,625.4
Range	26,623.0	20,150.0	27,112.0
Interquartile Range	5,757.0	12,200.0	8,024.0

Table 1. Summary Statistics of COL_MOHO, Sub-Sampled CORN_MOHO, and MOHO Data Sets

Cell-by-cell differences demonstrate the magnitude of the differences that exist between the maps. Table 2 gives brief summary statistics of the differences. The overall mean cell-by-cell differences are only slightly biased, ranging from in value -1,015 to +543 meters. However, while the mean difference in cell-by-cell differences of Moho depth between maps is small, this does not imply that the maps are similar. The

dissimilarity in the maps is suggested by the rather large variability of the differences, as can be seen by examination of the histograms and the standard deviations of differences.

Mapped Differences	Mean (km)	Median (km)	Standard Deviation
CORN_MOHO - COL_MOHO	-507.7	-197.0	5,724.6
MOHO - COL_MOHO	543.6	356.0	7,145.4
CORN_MOHO - MOHO	-1,015.3	-146.0	4,505.6

Table 2. Cell-by-Cell Relative Differences of Moho Depth Between Maps

It can be determined from the data that roughly 50% of all relative differences are off by more than 10% of the baseline value. The largest relative differences seem to occur at the lower and upper values of the baseline data sets, while the maximum differences seem to occur most frequently at roughly the 30,000- and 50,000-meter depths. Thus, bias between all maps appears to be a function of depth to the Moho.

The reasons for the differences in the data sets are certainly varied and may be due to accuracy of the actual measurements used, the smoothing techniques used, and other modeling assumptions (both documented and undocumented). The determination of which data set is most accurate at this point is not a statistical issue, but one of basic geological science.

Detailed Comparison of MOHO Versus COL_MOHO Data Sets

In this section, we examine a larger geographic area than the area in common to all three Moho depth data. We sought to discover whether the disagreements observed in the smaller region extended to larger areas. To do so, we examined the agreement between the MOHO and COL_MOHO data sets.

For reasons described earlier, a map of 1° cell size was created from the MOHO data set, with cell locations corresponding to those in the COL_MOHO data set. A nearest-neighbor approach was again used. The MOHO value located closest, in a great-circle distance, to the mapped location in the COL_MOHO data set, was taken as the value at that new mapped location. As may be observed in Figure 1, the region of overlap is quite substantial, covering about 28° of latitude and about 65° of longitude, which is nearly all of the COL_MOHO region and approximately 16% of the region covered by the MOHO data set. The regions in common that were used in this analysis are presented in Figure 5 (MOHO, binned to a 1° grid) and Figure 6 (COL_MOHO).

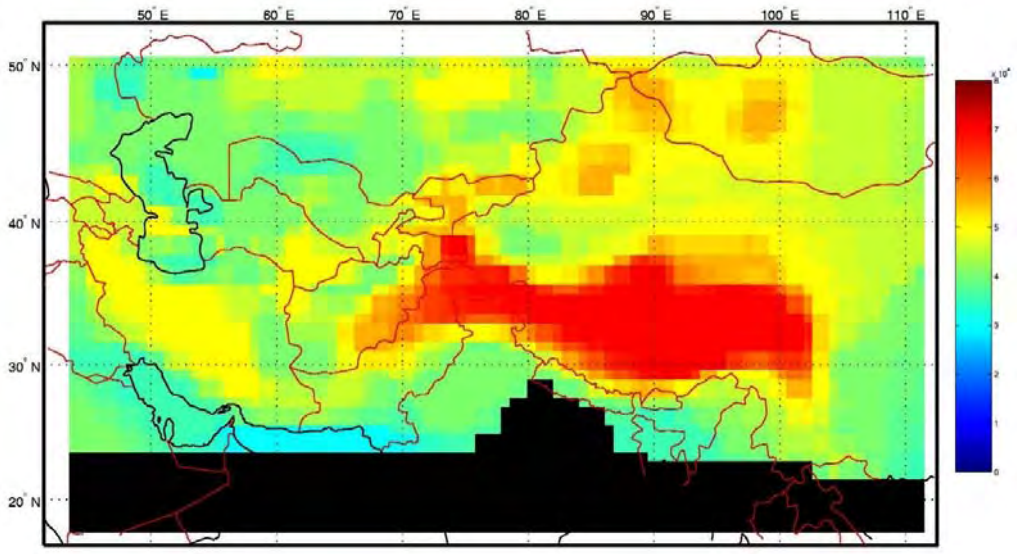


Figure 5. Depth-to-Moho values in MOHO data set, binned to a 1° grid.

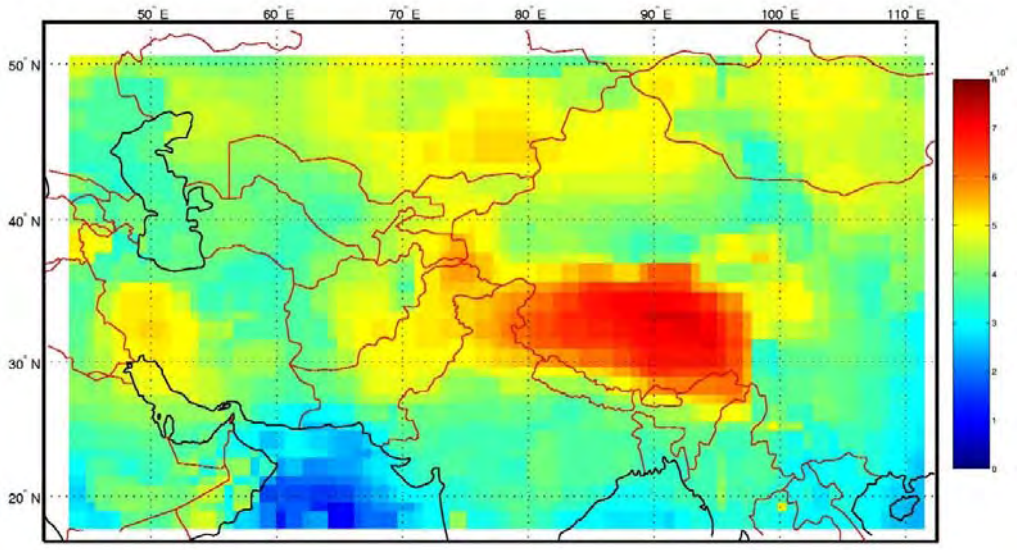


Figure 6. Depth-to-Moho values in COL_MOHO data set, at the original 1° grid.

The two areas were differenced and percentages created from those residuals. Figure 7 shows the spatial distribution of the relative percent differences. The red area, at the bottom of the map, represents missing values. Residuals range from -16 km to +35 km, and relative percent difference ranges from -30% to over +100%. Notably, different geographic regions show patterns of "underprediction" or "overprediction" relative to the reference map. For instance, over the Persian Gulf, the dark blue shows that the MOHO map claims a shallower depth-to-Moho than does the COL_MOHO map. The raw MOHO map indicates a typical depth-to-Moho in that region of 34 to 38 km, and the COL_MOHO map indicates 45 to 50 km. Figure 7 shows a few orange and reddish areas; in these areas, the MOHO map suggests Moho depths up to twice that suggested by the COL_MOHO map.

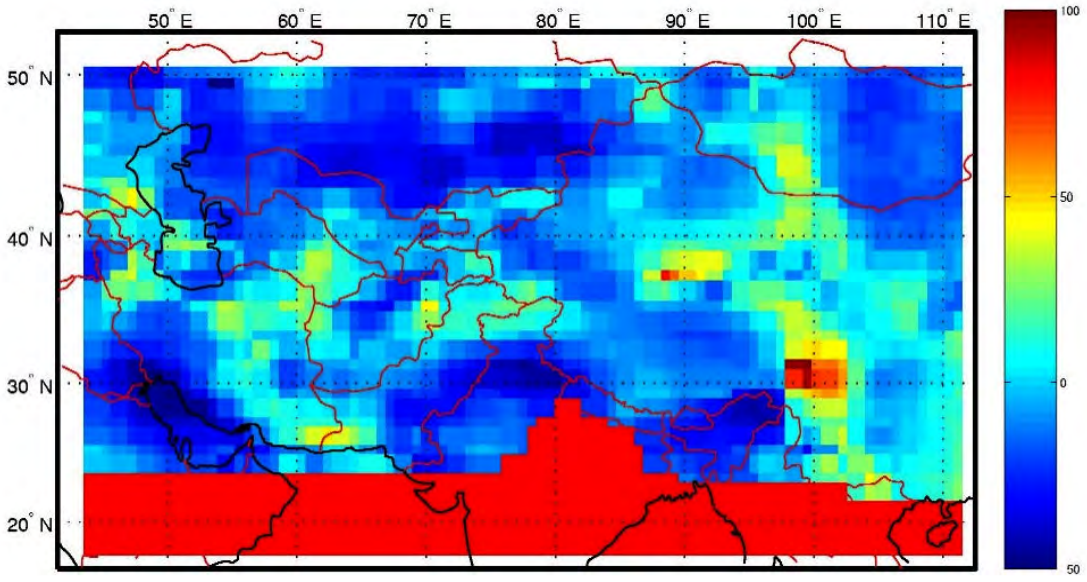


Figure 7. Spatial distribution of the relative percent differences in depth-to-Moho values resulting from MOHO - COL_MOHO.

Figure 8 presents the distribution of relative percent differences as a histogram. Although the center of the distribution is around 0% difference, a large fraction of the differences is substantially different from 0 km. Table 3 presents a statistical summary of the raw differences. Significant variations are apparent: the mean of the MOHO data is nearly 4600 km deeper than the mean of the COL_MOHO data, and the range of depths for MOHO is 8,565 to 70,140 km versus COL_MOHO depths of 29,930 to 73,697 km. While these statistics are enlightening, they are only a summary of the facts.

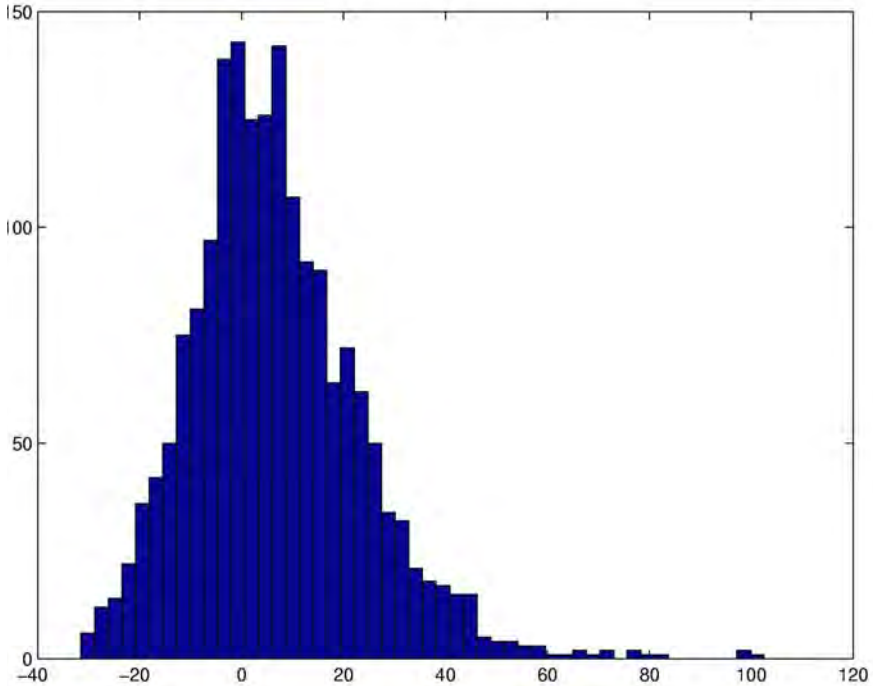


Figure 8. Histogram of Relative Percent Residuals Resulting from MOHO - COL_MOHO. Note the skewness to the distribution.

	MOHO, 1° grid	**COL_MOHO**
Mean	46,804 km	42,207 km
Median	45,000 km	41,524 km
Standard Deviation	8,998 km	9,118 km
Maximum	70,140 km	73,697 km
Minimum	8,565 km	29,930 km

Table 3. Results from statistical analysis of the two Moho depth data sets (MOHO and COL_MOHO)

Table 4 presents the percentiles of residuals and the relative percent differences between the MOHO and COL_MOHO maps. With regard to Moho depths greater than COL_MOHO depths, 10% of the data pairs have a raw difference of +10.9 km or greater, which translates to a relative percent difference of +27.5% or greater. On the other side of the distribution, with MOHO values less than COL_MOHO values, 10% of the data pairs have a raw difference of at least -6 km, which also translates to a relative percent difference of at least -12.6%. To illustrate the extent of these differences, observe that only 25% of the data pairs have a residual of less than ±2 km (24th to 49th percentiles), and only 27% of data pairs have a relative percent difference of less than ±5% (23rd to 51st percentiles). This large area comparison shows significant disagreements between the MOHO and COL_MOHO maps. The amount of variation observed when comparing all three Moho depth data sets over a small region in common to all three appears to extend to the entire data set. The amount of disagreement exhibits a geographic dependence. Certain geographic

regions are systematically overpredicted while others are underpredicted. We present a short example of this type of analysis below.

Percentile	Difference (km)	Relative Difference (%)
Minimum	-16.2	-31.5
1	-13.4	-25.9
5	-8.7	-18.0
10	-6.0	-12.6
25	-1.9	-4.3
50	+2.2	4.8
75	+6.7	15.9
90	+10.9	27.5
95	+13.8	36.1
99	+22.4	55.9
Maximum	+35.4	102.5

(a) For corresponding plots, see Figure 23 for distributions of residuals and Figure 24 for relative differences between MOHO map depths versus COL_MOHO map depths.

Table 4. Percentiles of distributions of residuals and relative differences between depths of MOHO data set versus COL_MOHO data[a]. Total number of cells, 1832.

Analysis of MOHO and COL_MOHO Data Sets by Subregion

The MOHO and the COL_MOHO maps differ in important respects in various geographical subregions over the overlapping portions. Explanations for these differences no doubt lie in the different pedigrees of each map and possibly even the definitions of the physical measures used to calculate estimates of the values for depth-to-Moho.

To further understand the observed spatial inconsistencies between the MOHO and COL_MOHO depth-to-Moho data sets, the region in common to both data sets was subdivided into 32 subregions, and each of these was then statistically examined for agreement. Two of the subregions contained too few data pairs for analysis. Table 5 presents correlation coefficients for equally sized subregions of the overlap, in terms of numbers of 1° cells. The higher the value of $|r|$, the more closely the two surfaces agree with each other. Recall that correlation coefficients indicate tendency of variables to vary in step with each other, but say nothing about equality of values being compared.

	Longitudes							
Latitudes	**43.5° – 50.5°**	**51.5° - 58.5°**	**59.5° - 66.5°**	**67.5° - 74.5°**	**75.5° - 82.5°**	**83.5° - 90.5°**	**91.5° - 98.5°**	**99.5° - 106.5°**
42.5° - 49.5°	*-0.14*	0.11	0.37	*-0.18*	*-0.20*	0.24	*-0.11*	*-0.06*
34.5° - 41.5°	0.41	*-0.16*	*-0.13*	0.80	0.88	0.82	0.79	0.55
26.5° - 33.5°	0.47	0.02	0.72	0.67	0.82	0.96	0.46	0.60
18.5° - 25.5°	***-0.80***	0.74	*-0.23*	0.54	NaN[b]	NaN[b]	0.29	0.10

(a) Each cell (subregion) in the northernmost three rows represents 64 depth pairs. Each cell (subregion) in the bottom row represents from 16 to 29 data pairs.
The highlighted cells indicate those subregions that are statistically similar (strong correlations).
The significance of the correlation coefficient, r, at $p < 0.01$, is dependent on the number of data in the regression. $|r| > 0.33$ for the top three rows.
(b) Not enough data pairs for a reliable correlation coefficient.

Table 5. Product-Moment Correlation Coefficients, r, over 30 Equal-Sized Subregions of the Region of Overlap Between COL_MOHO and MOHO Data[a]

Table 5 indicates substantial spatial variation in the tendency of the two maps to indicate similar trends in Moho depths. Although many of the subregions show strong positive correlations, indicating that the two depth surfaces more or less follow each other, at least 13 of the 30 subregions do not have statistically significant correlation coefficients. The significance of the correlation coefficient, ***r***, is dependent on the number of data in the regression, thus the values in Table 5 should not be viewed as absolute indicators of fit. Small coefficients indicate that, the two surfaces vary independently of each other. The subregion in the extreme southwest corner is negatively correlated ***(-0.80)*** indicating opposite surface trends with respect to Moho depth. The problem with this subregion may be related to the quality of the data near the edge of the COL_MOHO data set. This region may contain sparse raw data, and thus the uncertainty may be extremely high. This is only a hypothesis and cannot be proved or disproved without associated error estimates or by examination of the raw data. In spite of this regional variation and disagreements, the overall correlation coefficient (***r)*** for all 30 of the data pairs was very strong at +0.67 (n=1832).

Interpretation of the significance of the correlation coefficients may be guided by the following: for the northernmost subregions with 64 data pairs, a value of $|r| > 0.33$ would be considered statistically significant at the 1% level (two-sided test). The cells in the bottom row represent 16 to 29 pairs, such that $|r|$ needs to be >0.45 to 0.60 to indicate statistical significance at 1%. The critical values of ***r*** are presented as general guidelines rather than as formal statistical tests. These subregions also were not optimized to the detected features of disagreement. A more in-depth examination should reveal more detail about the nature of the disagreement, whether region-dependant, artifacts of the method for data set generation, or resulting from the types of processing applied to the data.

CONCLUSIONS AND RECOMMENDATIONS

The preliminary investigation into what "tools" would be of most use in assessing the quality and consistency of the data in the KB has resulted in more questions and new directions, which should be pursued. The initial premise that statistical tools could be used to examine individual data sets for erroneous values became less important as we began to understand the genesis of these data. Most of the gridded measurement data has been highly processed and smoothed. Thus, erroneous values have been either eliminated prior to processing or have been averaged away by the processing and smoothing. Additional data sets, based directly upon and containing raw data, that will be added in the future, will be more receptive to the use of statistical tools.

Problems were found within and among data sets, identified by several methods, and include the following:

- metadata incompleteness and disagreement with header file data,
- significant disagreements among overlapping data sets reporting the same parameter,
- a lack of any error/uncertainty estimates accompanying data sets,
- different data sets reporting the same parameter receiving vastly different processing and smoothing operators,
- missing values and constant values that complicate analysis and bias results,
- a need for a consistent schema for gridding and combining data sets and a lack of any consistent reference points,
- a need for well-defined criteria for: the accuracy of data, the degree of error that is tolerable for correction calculations, and tolerance limits for agreement among data sets.

Key future tasks will address the following questions:

- What measures of uncertainty or error estimates need to be included with the data?
- What are the issues associated with assessing data in light of cultural and geologic features (rivers, cities, roads, faults, coastlines, topography, etc.)?
- What issues are associated with sequential kriging, and multiple sampling and smoothing of the data?
- What are the problems associated with combining vector and gridded data types?
- What is the optimum method for fusing multiple maps into a single data set?
- How do we best propagate and estimate the cumulative uncertainties in the KB-based corrections?

The tools under development are being designed to enable evaluation of the degree of agreement between different data sets, sequential "loads" (updated data sets), and adjacent data sets. The tools will:

- be easy to use and provide understandable graphical/textural results,
- provide robust evaluations of the status of the KB,
- be built upon statistical tools designed to accurately describe the completeness, uncertainties, and limitations of the state of the KB and/or input data "loads",
- help identify what data would be most beneficial to include in future data sets,
- assist in the development of data-quality criteria for the incorporation of future data, based upon the current content of the KB (i.e., the new data needs to be able to be "melded" or "fused" into the existing data), and
- provide a basis for prioritizing data improvement efforts.

REFERENCES

(none)

DATA AUTHENTICATION DEMONSTRATION FOR RADIONUCLIDE STATIONS

Mark Harris and Pres Herrington, Sandia National Laboratories
Harry Miley, J. Edward Ellis, David McKinnon, and Devon St. Pierre, Pacific Northwest National Laboratory

Sponsored by U.S. Department of Energy
Office of Nonproliferation and National Security
Office of Research and Development
Contract No. DE-AC04-94AL85000

ABSTRACT

Data authentication is required for certification of sensor stations in the International Monitoring System (IMS). Authentication capability has been previously demonstrated for continuous waveform stations (seismic and infrasound). This paper addresses data surety for the radionuclide stations in the IMS, in particular the Radionuclide Aerosol Sampler/Analyzer (RASA) system developed by Pacific Northwest National Laboratory (PNNL).

Radionuclide stations will communicate data by electronic mail using formats defined in IMS 1.0, Formats and Protocols for Messages. An open message authentication standard exists, called S/MIME (Secure/Multipurpose Internet Mail Extensions), which has been proposed for use with all IMS radionuclide station message communications. This standard specifies adding a digital signature and public key certificate as a MIME attachment to the e-mail message. It is advantageous because it allows authentication to be added to all IMS 1.0 messages in a standard format and is commercially supported in e-mail software. For command and control, the RASA system uses a networked Graphical User Interface (GUI) based upon Common Object Request Broker Architecture (CORBA) communications, which requires special authentication procedures.

We have modified the RASA system to meet CTBTO authentication guidelines, using a FORTEZZA card for authentication functions. We demonstrated signing radionuclide data messages at the RASA, then sending, receiving, and verifying the messages at a data center. We demonstrated authenticating command messages and responses from the data center GUI to the RASA. Also, the particular authentication system command to change the private/public key pair and retrieve the new public key was demonstrated. This work shows that data surety meeting IMS guidelines may be immediately applied to IMS radionuclide systems.

Key Words: authentication, radionuclide

Sandia is a multiprogram laboratory operated by Sandia Corporation, a Lockheed Martin Company, for the United States Department of Energy under Contract DE-AC04-94AL85000.

OBJECTIVE

All monitoring stations in the International Monitoring System (IMS) must include data authentication equipment before certification [1]. Authentication technology has previously been demonstrated for seismic and infrasound stations [2], and is becoming commercially available. Authentication has not yet been implemented on radionuclide station hardware. This work was conducted to clarify the specifications issued by the PTS and demonstrate the feasibility of implementing data and command authentication at radionuclide stations.

RESEARCH ACCOMPLISHED

The protocols used within the IMS for radionuclide data use the standard Internet electronic mail system for delivery. Radionuclide data is formatted as text messages as specified in IMS 1.0 [3] and simply emailed to its recipient. With the global computer network capability available today, this has proven to be a flexible and powerful data communication mechanism, as is evidenced by the success of AutoDRM systems for waveform data retrieval. Basing user protocols upon standard industry protocols also allows commodity software products to be used for at least some elements of the system, reducing development cost.

Building upon this, the PTS has specified that radionuclide data messages should be authenticated using protocols of the Secure/Multipurpose Internet Mail Extensions (S/MIME) [4]. S/MIME is a developing standard of the Internet Engineering Task Force (IETF) S/MIME working group [5], which has been widely adopted in industry. S/MIME specifies procedures for signed and/or encrypted data and X.509 public key certificates to be transmitted as MIME attachments [6]. Feghhi et al. [7] thoroughly describes the complexities of using digital certificates and the associated public-key infrastructure (PKI) in the Internet environment. The overall key management structure needed for the use of public key certificate technology by the IMS has been addressed in previous demonstrations and is well understood [2,4]. Note that with this technology, all public key information needed to verify digital signatures is embodied within X.509 certificates.

Other PTS authentication specifications are also required for radionuclide stations. Briefly, these specify that all IMS data must be signed at the stations and all commands generated remote from the station must be verified. The Digital Signature Standard (DSS) [8] must be used, with public key size of 1024 bits. The signature function must be performed in a dedicated, tamper indicating hardware device. This device must be capable of self-generating a private key and communicating the new public key. The system must also support a remote key change command with transmission of the new public key to IMS authorities.

A hardware cryptographic token that meets these PTS requirements has been used in previous demonstrations. This token (the U.S. Government developed Fortezza Card) isolates cryptographic operations and private key material on a PCMCIA processor card. At least one company (SPYRUS, http://www.spyrus.com/) now offers a Fortezza-compatible card with only authentication functions installed, making it free of U.S. export restrictions on strong encryption.

Many commercial products support the S/MIME standards employed here (to varying degrees, since some parts of the current standards are considered drafts and are actively being developed). Conformance to S/MIME is generally good enough so that various commercial and open source products work together reliably. This is a great advantage, as it limits the extent of custom software that must be developed and distributed to the community. Any user with access to the certificates distributed by the IDC can verify signatures on data using a standard electronic mail software package, such as *Netscape Messenger*.

A radionuclide monitoring station: RASA

To investigate the feasibility of implementing data and command authentication at a radionuclide monitoring station, we have developed a demonstration of this technology using the PNNL-developed RASA station equipment (see Figure 1). The RASA provides ultrasensitive field measurement of short-lived fission products in near real time. This permits detection at great distances from nuclear detonation sites. The analyzer passes air through a large-area, low-pressure-drop filter at a high flow rate for selectable time periods; then seals, barcodes and performs a gamma-ray analysis of the filter. The gamma-ray spectrum

is automatically transmitted to appropriate organizations. Filter samples are retained for subsequent analysis. The RASA operates automatically and all functions are remotely programmable. The RASA is now being manufactured commercially.

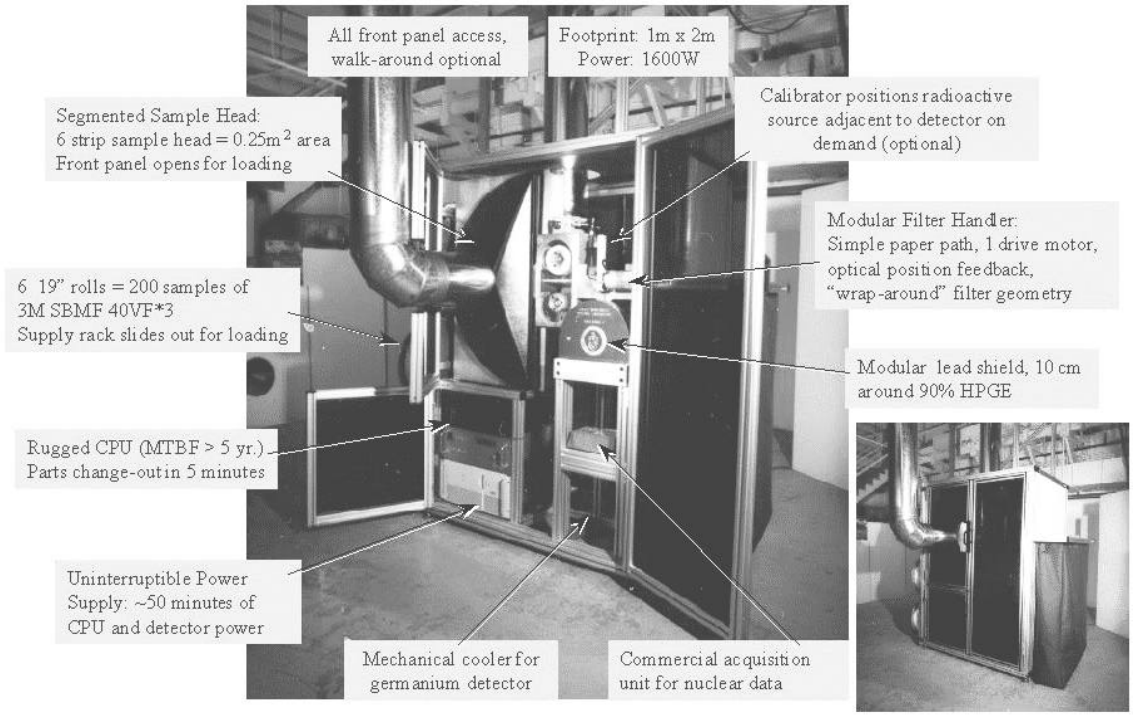


Figure 1. RASA radionuclide monitoring equipment.

Authentication software developed

To support this demonstration, the prototype RASA system at PNNL was modified to perform authentication functions internally. A PC Card reader was integrated into the computer system within the RASA so that a Fortezza card could be installed. The standard driver software for the Fortezza card (the CI Library) was ported to the operating system of the RASA computer. This allowed software that already uses the Fortezza card with CI Library to be easily ported and used on the RASA.

We have adapted the *authd* software, used in past authentication demonstrations, to run on the RASA computer. This authentication server program manages interactions with a Fortezza card and maintains a database of public key certificates for use in verifying signed messages. Applications connect to *authd* using a socket interface and can request signature and verification operations on blocks of data. Standard key management issues may also be handled using this interface, such as requesting a new key pair be generated. We extended *authd* to perform tasks related to message authentication: X.509 certificate handling and PKCS #7 signature generation [9]. The OpenSSL software package [10] is used as the basis library for certificate processing. An *authd* client library is provided so that operations may be easily integrated into other software applications.

For this demonstration a system was assembled to simulate all relevant components of the IMS: the radionuclide station itself, a receiving data center, and certification equipment used by a PTS Key Management Authority. This system is illustrated here and described below.

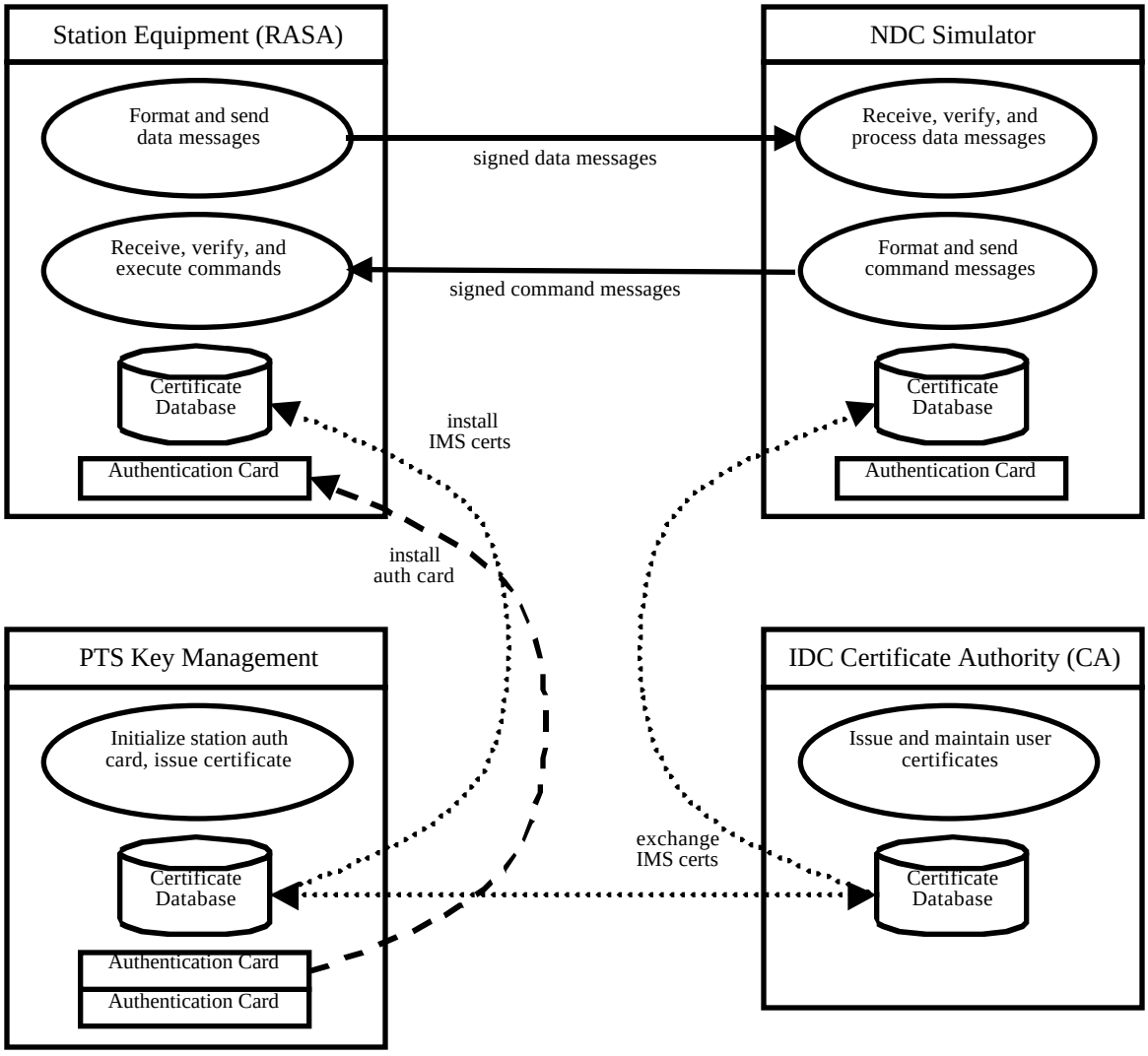


Figure 2. Demonstration system overview.

A realistic procedure was developed to initialize the authentication unit and install public keys at the station. This simulates the actions performed by a PTS Key Management Authority (also referred to as a certification observer) during an initial IMS certification visit. This initial secure transaction is the basis of trust for the station from that point on. The observer certifies that the public key information obtained for the station is trustworthy by issuing the station public key certificate and signing it. The observer further certifies that the public keys for remote users of the station are securely installed. After this transaction, authenticated messages may be transmitted between station and data center on an open network and reliably verified, until some event (such as tampering at the station) breaks the chain of trust.

For this demonstration, a certificate authority (CA) was simulated for the IDC using functions in OpenSSL. The CA serves as the root of trust in PKI systems, and must be administered in a very secure manner (security of the CA is not addressed here). The CA certifies all user certificates (either by signing them directly or indirectly) and distributes them to other users. Users can load these certificates into their message authentication software (e.g. *authd* or *Netscape*). Users need the certificate of the CA (and any indirect authorities) to verify messages under this structure. In the case of this demonstration, the simulated IDC CA certifies the observer, which certifies the station. Initially, users need both the CA and observer

public-key certificates to authenticate the station certificate. Once the station certificate has been securely transmitted to the CA by the observer, the CA may certify it directly and distribute it to users.

To support standard message data authentication, S/MIME formatting software was developed and integrated into the RASA data processing flow (see Figure 3). Since radionuclide stations already use email messages, formatting and transmission capabilities were already available. An extra step was introduced to take each standard email message and convert it to an S/MIME message with attached digital signature calculated by the authentication card. The *authd* program creates a standard PKCS #7 signedData attachment, including the X.509 certificate for the station, which contains the public key. Then the S/MIME format data message is sent to the recipient in the usual way (in this case to the NDC Simulator). Normally the message would be automatically verified and processed at the data center. For this demonstration we simply view the message and verify the signature in *Netscape*.

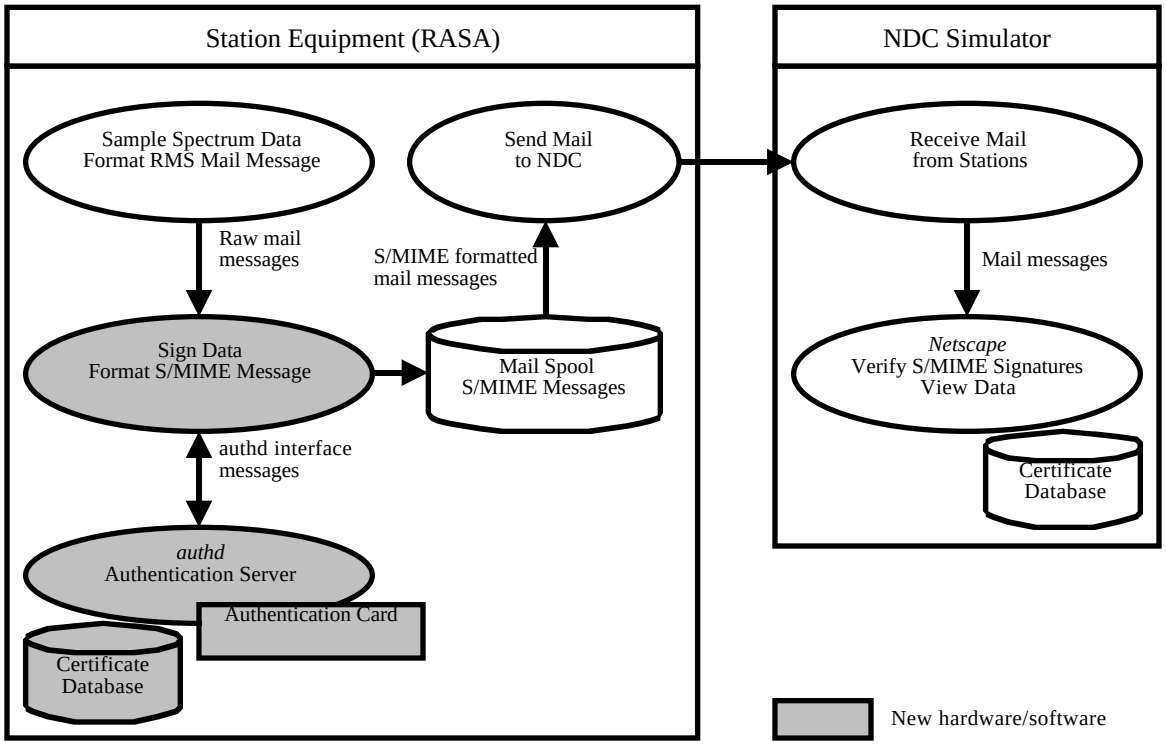


Figure 3. Data authentication flow diagram.

Originally, software for remote command and control of the RASA equipment was tightly integrated between the client (remote user) and server (RASA computer) software. This type of communication is difficult to operate in a highly secured manner on an open network (though some products are becoming available to secure individual TCP/IP connections end-to-end on a network that could be applied here). To illustrate command authentication with the RASA, a new command mode was developed which limits communications to discrete signed and verified transactions. Again, *authd* is used for authentication functions (see Figure 4). S/MIME format is used for the command message signatures in this demonstration. Two commands are demonstrated: a command to generate an interim spectrum measurement and a command to change the key pair on the authentication unit within the RASA. The first command results in a data message being generated and sent from the RASA in the usual manner. The second command causes the authentication software in the RASA to generate a new key pair in the authentication card, generate a new X.509 public key certificate (signed using the original key), and forward this new certificate to recipients as part of the next data message.

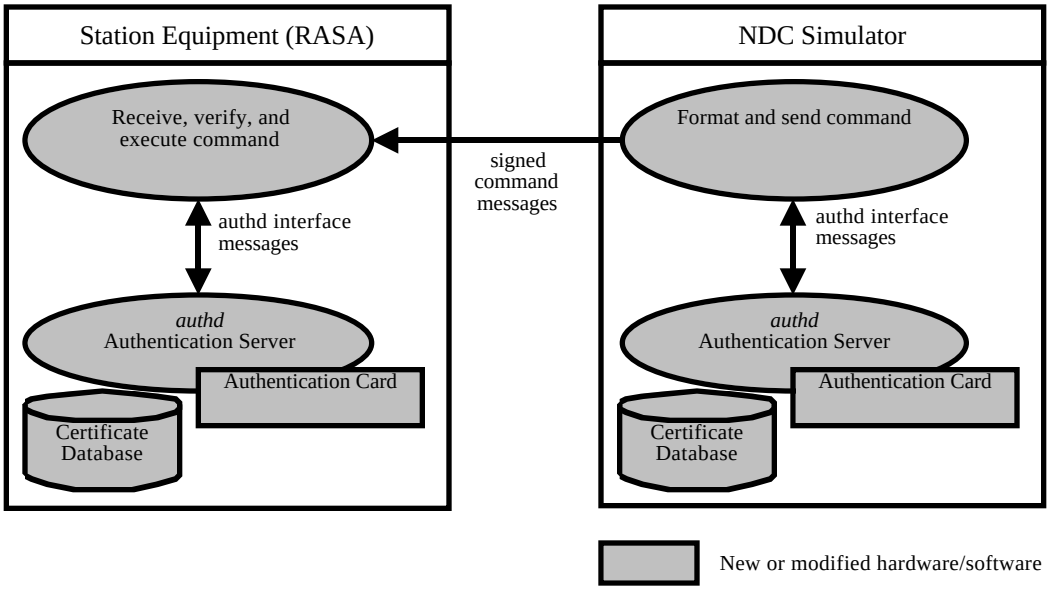


Figure 4. Command authentication flow diagram.

Authentication operations demonstrated on the RASA

We conducted a demonstration of all aspects of data surety at a radionuclide station: system initialization and key management, data authentication using S/MIME messages, and remote command authentication. The procedures used in this demonstration are summarized here.

Initialization operations at the IDC for the PTS Key Management Authority (the observer) were:
1. Obtained an authentication unit (e.g. a hardware authentication card).
2. Initialized authentication unit, generate a new key pair and public key certificate.
3. Certified public key certificate with IDC certificate authority (CA).
4. Obtained relevant public key certificates (for remote command users) for distribution to the station.

Initialization operations at the station were:
1. Observer obtained the station authentication card.
2. Observer initialized the authentication card with standard parameters and instructed it to generate a new key pair.
3. Observer generated a public key certificate for the authentication card and signed it with his own private key. The observer is known as the issuer of the station certificate. [At this point a chain of trust exists from the IDC CA through the observer to the station authentication unit.]
4. Observer installed the authentication card in the station equipment.
5. Observer installed relevant public key certificates (IDC, NDC, and station) in the station equipment.
6. Station began using new private and public keys.
7. Observer securely transferred new station certificate to the IDC for certification and distribution.

During normal operation, a radionuclide station periodically transmits a data message to the receiving data center. Once the station authenticator is initialized, all data and status messages are signed. The procedure for demonstrating this function was:
1. Wait to receive email data or status messages from the station on the NDC Simulator.
2. View the messages on the NDC Simulator (using Netscape), noting the status of the signature verification.

- Note that public key certificates must be installed into Netscape for the IDC CA and the observer that issued the station certificate.

Command authentication involves sending signed command messages from the NDC Simulator to the station:

1. Format a command message on the NDC Simulator.
2. Send the command message to the RASA.
3. RASA software verifies the message signature and completes the command.
4. In the case of the Key Change command, after the key pair has been changed by *authd* and a new certificate generated, an email message is queued to be signed and sent to the standard recipients, in order to propagate the new public key.

CONCLUSIONS AND RECOMMENDATIONS

We have demonstrated authentication technology for radionuclide stations using the required formats and protocols. Industry standards have been followed, allowing this system to work with existing software products. The demonstrated system should meet IMS certification requirements for authentication, and will be further developed and integrated into the RASA system for operational use.

This work is also applicable to other parts of the IMS where message authentication is needed. In particular, auxiliary seismic stations that use an email-based AutoDRM data communication method could use the demonstrated hardware and software to provide authenticated data transmission to the IDC. Automated signature verification on incoming data could be performed using this software, though performance limits of the hardware authentication card could be restrictive. The IDC itself (as well as the NDCs) could adapt this software to provide authenticated data products to users. Once the required certificate management system is in place signature verification will be available for all data users.

Some operational issues were not known while this demonstration was being prepared, and should be addressed if they have not been already. For example, the S/MIME protocol is flexible with regard to the number and details of the certificates that are attached to the signature. These details should be specified to ensure compatibility of software throughout the IMS and IDC.

REFERENCES

1. *Procedures for IMS Station Certification*, CTBT/PTS/INF.144/Rev.1, 13 May 1999.

2. Draelos, T., M. Harris, P. Herrington, and D. Kromer, Data Surety Demonstrations, *20th Seismic Research Symposium on Monitoring a CTBT*, September 1998.

3. *Formats and Protocols for Messages – IMS 1.0*, IDC-3.4.1Rev1, March 1999.

4. *Task Leader Paper on Authentication*, CTBT/WGB/TL-6/4/Rev.4, 12 February 1999.

5. S/MIME Working Group, http://www.imc.org/ietf-smime/, 1999.

6. Galvin, J., S. Murphy, S. Crocker, and N. Freed, *Security Multiparts for MIME: Multipart/Signed and Multipart/Encrypted*, RFC 1847, October 1995.

7. Feghhi, J., J. Feghhi, and P. Williams, Digital Certificates: Applied Internet Security, Addison Wesley Longman, 1999.

8. *Digital Signature Standard (DSS)*, FIPS PUB 186, 1994.

9. Kaliski, B., *PKCS #7: Cryptographic Message Syntax Version 1.5*, RFC 2315, March 1998.

10. OpenSSL: The Open Source toolkit for SSL/TLS, http://www.openssl.org/, 1999.

A GROUND TRUTH DATABASE FOR REGIONAL SEISMIC RESEARCH

Ivan Henson, Indra Gupta, and Robert Wagner, Multimax, Inc., Largo, Maryland

Sponsored by Defense Threat Reduction Agency
Contract No. DSWA01-98-C-0156

ABSTRACT

The main objective of this project is the formation of databases providing ground truth for regional seismic research conforming to the latest Center for Monitoring Research (CMR) schema. These ground truth data sets will be incorporated into the contractor's existing Ground Truth Database (GTDB), and the "event directories" will be made available for use at CMR. The effort focuses on events in the CMR Calibration Event Bulletin (CEB) from China, the former Soviet Union, and North America. Events are carefully re-analyzed by using *geotool* and following procedures established at the CMR for the Reviewed Event Bulletin (REB). Revisions consist mostly of re-timing phase arrivals and, whenever possible, adding missed phases. Waveform data from available Incorporated Research Institutions for Seismology (IRIS) stations are retrieved and analyzed; the criteria for selecting the IRIS stations are primarily to collect data within 25 degrees distance, then to reduce any azimuthal gap for distances beyond 25 degrees (up to about 50 or 60 degrees), and to obtain data at PKP distances. A modified version of *LocSAT*, called *Locate*, which uses a graphical interface and allows interactive processing to generate location results, is used to locate the CEB events. Two sets of location results per event are derived: the first by using only the revised International Data Centre (IDC) arrivals, and the second by using, both the IRIS and revised IDC data.

All (70) events in China from the CMR Calibration Event Bulletin (CEB) have been re-analyzed by using waveform data from over 140 IDC stations contributing over 4000 arrivals. By analyzing data from over 130 IRIS stations, nearly 3800 waveforms were retained and nearly 2300 arrivals added. The most important contribution of the IRIS data is the addition of a large number of arrivals from regional phases. As an example, for epicentral distances less than 17 degrees (about 1900 km), the regional phases (Pn, Pg, Sn, and Lg) in the three datasets consisting of combined IRIS and revised IDC, only the revised IDC, and the original CEB arrivals, total 1362, 225, and 140, respectively. Analysis of all CEB events in China has been completed and the results delivered to the CMR. Similar analysis of CEB events in the former Soviet Union, based on the use of both IDC and IRIS stations, is in progress.

For the Chinese database of 70 events, a comparison of the CEB locations with those derived by using the revised IDC arrivals and the combination of IRIS and revised IDC data showed generally small differences (average less than 9 km in each case). However, a similar comparison of source depths showed the CEB estimates to be significantly larger than each of the other two estimates, suggesting that the CEB source depths have probably been overestimated. This is supported by the remarkably good agreement observed between depth estimates based on the combined use of IRIS and revised IDC data and those available from the International Seismological Centre (ISC) for a large number of common events.

Key Words: database, ground truth, Calibration Event Bulletin, CMR, CTBT, regional seismic research

OBJECTIVE

Monitoring the Comprehensive Nuclear-Test-Ban Treaty (CTBT) requires the ability to detect, locate and identify seismic events effectively. Once a suspicious event has been detected, its location must be accurately determined as a precursor to event identification and potential on-site inspections. The Calibration Event Bulletin (CEB) database was initiated at the Center for Monitoring Research (CMR) in June 1996 in response to recommendations by the Group of Scientific Experts (Bondar, 1998a). The main purpose of the CEB database is to collect data routinely for the calibration of the International Monitoring System (IMS) network so that locations can be improved. The selection of CEB events is made from the Reviewed Event Bulletin (REB) events by meeting certain criteria, such as a body wave magnitude between 4 and 6. Soon after the calibration effort began at the PIDC it was recognized that that not all calibration events can be accepted as ground truth (Bondar,1998b). A primary objective of this project is the formation of databases which provide improved ground truth for events in China, former Soviet Union, and North America, as selected from the CMR Calibration Event Bulletin (CEB). Several studies have demonstrated the usefulness of such databases for improved monitoring of the CTBT (e.g., Grant *et al.*, 1997; Bondar *et al*., 1998). Re-analysis of the IDC data combined with retrieval and analysis of selected IRIS data leads to improved location and depth estimates of CEB events.

RESEARCH ACCOMPLISHED

(a) Formation of Databases

Analysis and relocation of all (70) events in China from the CMR Calibration Event Bulletin (CEB) have been completed by using waveform data from over 140 IDC stations and over 130 IRIS stations. The CEB epicentral locations of these 70 events are shown in Figure I along with the locations of both IDC and IRIS stations which recorded these events. Note the large number of IRIS stations at regional distances for most of the 70 Chinese events.

Analysis procedures followed are basically the same as for the REB bulletin. Most revisions consist of minor re-timings with emphasis on defining phase types, and missed phases are added whenever possible. At far regional distances, most later crustal phase types Sn and Lg are often made non-defining due to large residuals that result from using IASP91 travel times. Occasionally, a CEB event undergoes significant changes when, for example, improper depth phases or multiple events occur. The analysis made use of waveform data from over 140 IDC stations contributing, over 4000 arrivals. A total of 132 IRIS stations contributed nearly 3800 waveforms and 2300 arrivals. The criterion for acquiring data from IRIS stations is primarily to collect data within 25 degrees distance, then to reduce any azimuthal gap for distances beyond 25 degrees (up to about 50 or 60 degrees), and to obtain data at PKP distances. The most important contribution of the IRIS data is the addition of a large number of arrivals from regional phases. For epicentral distances less than 17 degrees (about 1900 km), the regional phases (Pn, Pg, Sn, and Lg) in the three datasets consisting of combined IRIS and revised IDC, only the revised IDC, and the original CEB arrivals, total 1374, 230, and 140, respectively. A comparison of the propagation paths available in the original CEB dataset and the IRIS and revised IDC dataset for Pn and Lg, shown in Figures 2 and 3, respectively, clearly demonstrates the significant contribution the IRIS data have made in providing additional regional phases.

A modified version of *LocSAT*, called *Locate*, which uses a graphical interface and allows interactive processing to generate location results, is used to locate the CEB events. The location time residuals for each arrival are displayed, and the residuals that exceed the CMR limit for allowable defining phases are highlighted. Relocations can be computed quickly for different defining arrivals to assess the effect of adding arrivals, such as those measured from IRIS data, to the original CMR data set.

Two sets of location results per event are derived: the first by using only the revised IDC arrivals, and the second by using both the IRIS and revised IDC data. As an example, the recording stations, which provided data used in determining the epicentral location and depth of the Chinese seismic event of 12 March 1996, are shown in Figure 4a. For this seismic event near the borders of Mongolia and former Soviet Union, the original CEB solution was based on the use of only 44 IDC stations, whereas the solution based on the

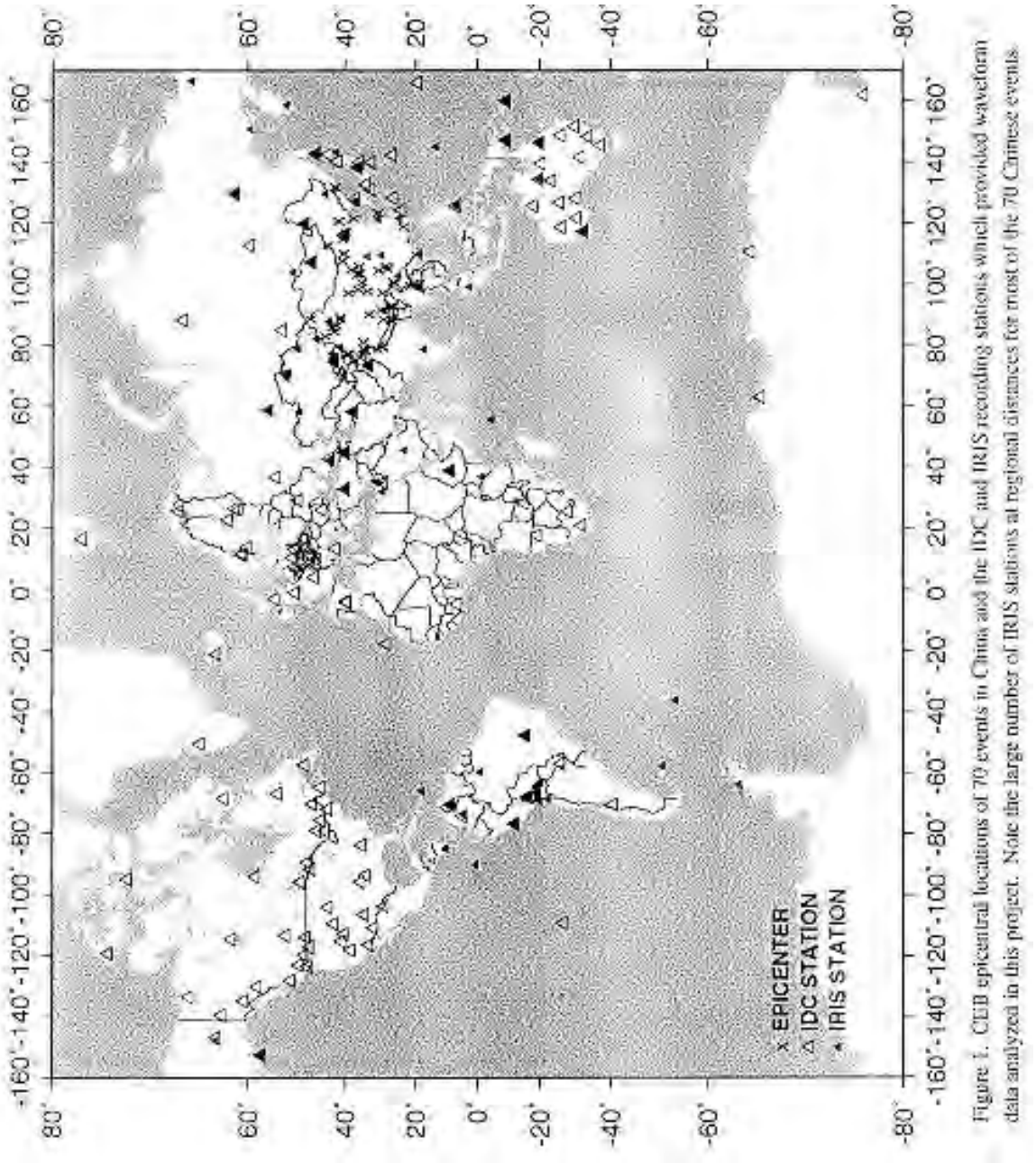


Figure 1. CEB epicentral locations of 70 events in China and the IDC and IRIS recording stations which provided waveform data analyzed in this project. Note the large number of IRIS stations at regional distances for most of the 70 Chinese events.

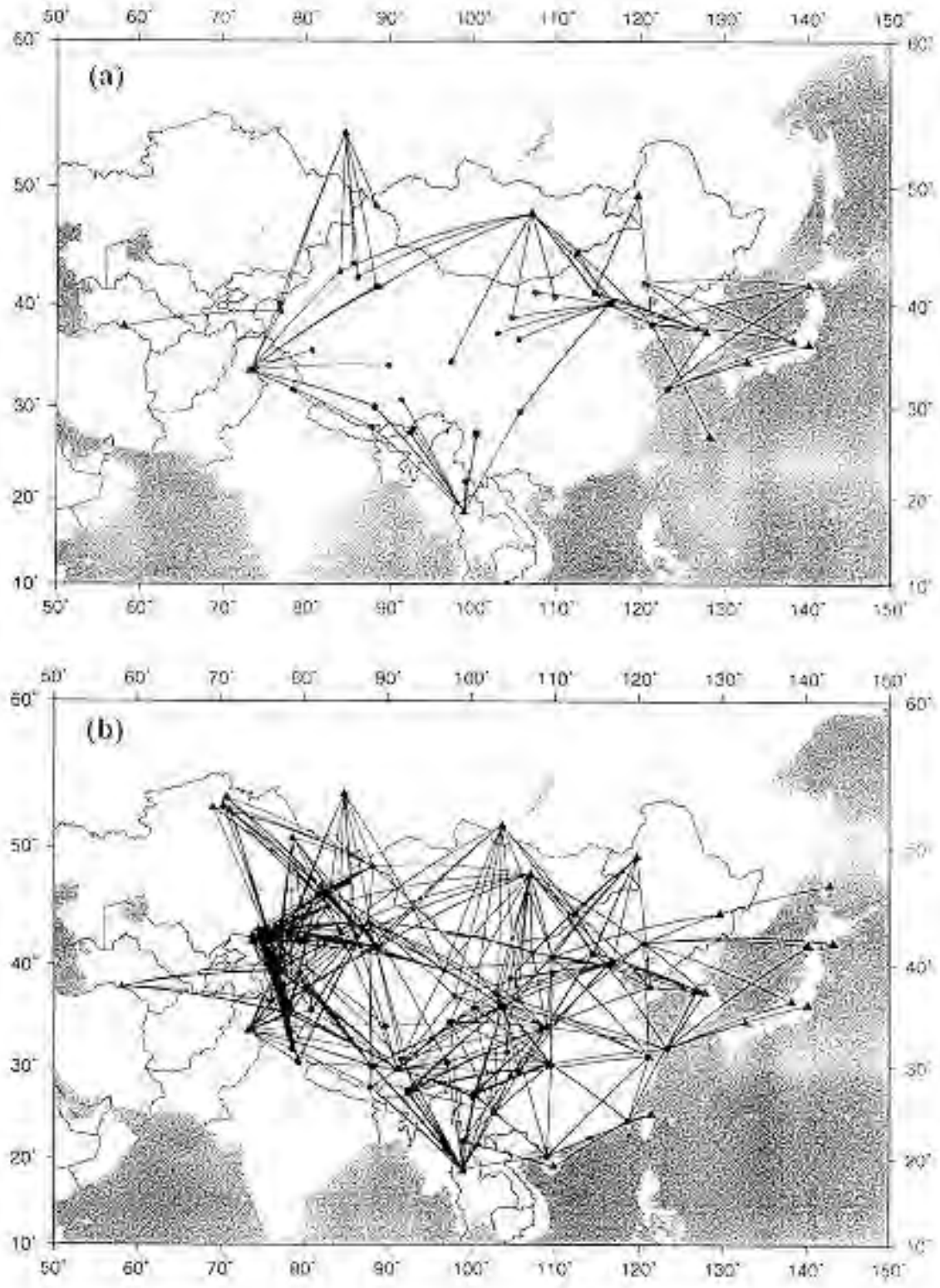


Figure 2. Comparison of Pn phases and corresponding propagation paths available in (a) original CEB dataset showing 42 events and 74 paths, and (b) IRIS and revised IDC dataset showing 66 events with 592 paths. The IRIS data provide a large number of additional Pn arrivals.

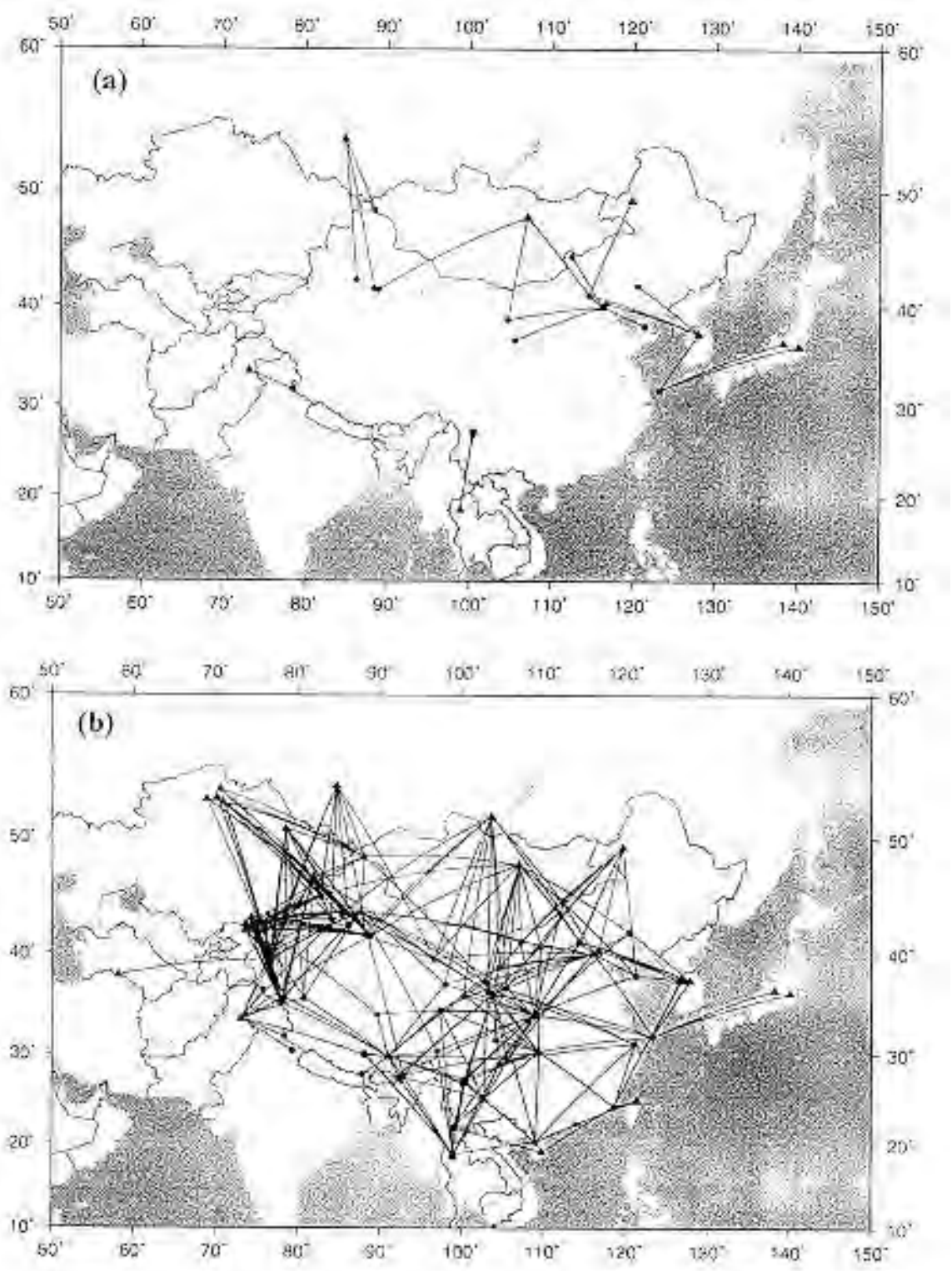


Figure 3. Comparison of Lg phases and corresponding propagation paths available in (a) original CEB dataset showing 18 events and 24 paths, and (b) IRIS and revised IDC dataset showing 62 events with 414 paths. The IRIS data provide a large number of additional Lg arrivals.

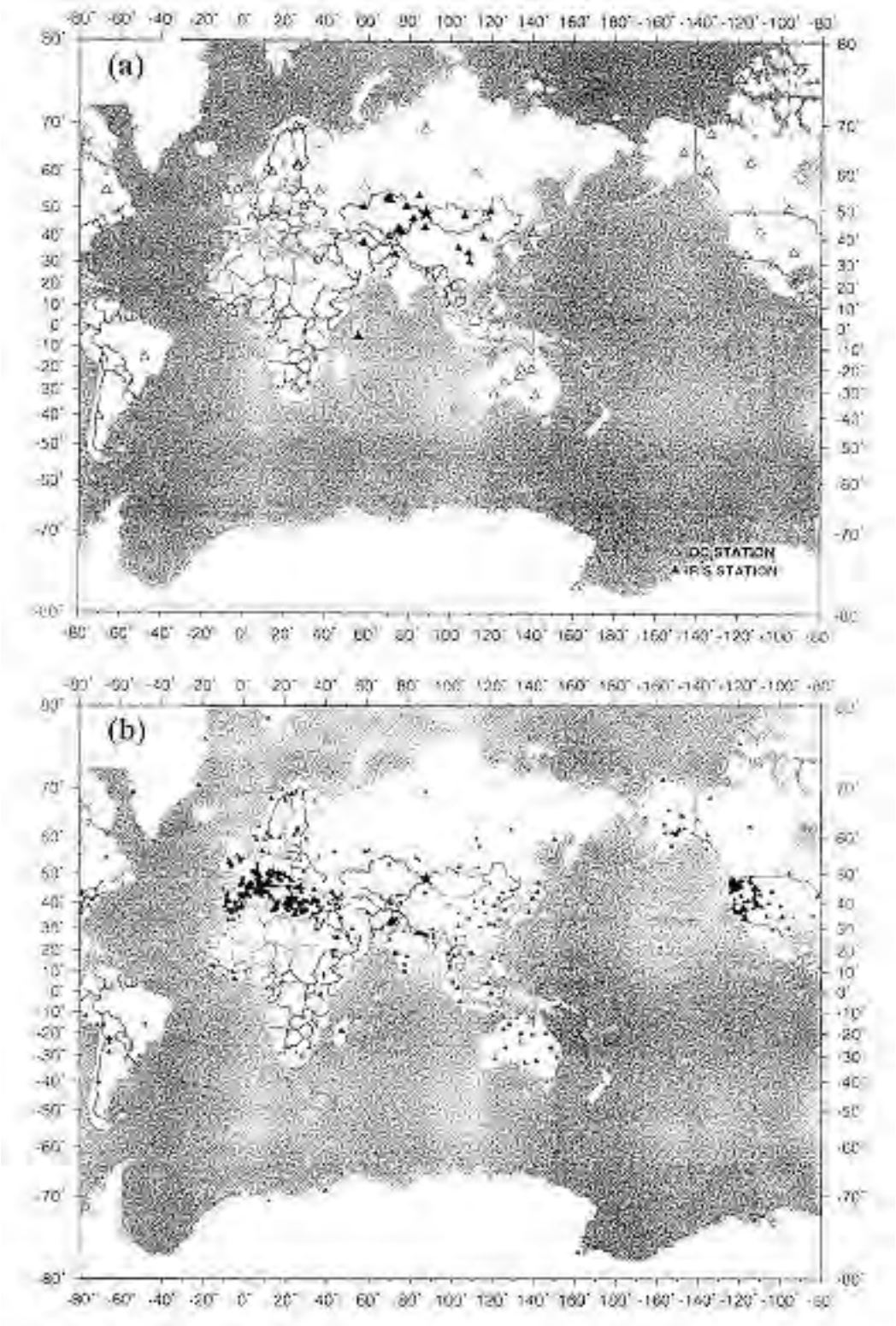


Figure 4. Comparison of recording stations providing data used in determining the epicentral location and depth of the seismic event of 12 March 1996, shown by a star; (a) 44 IDC stations used in the original CEB solution and the additional 23 IRIS stations, and (b) 586 recording stations used in the ISC solution. Note the significantly larger number of stations used by the ISC.

combined use of IRIS and revised IDC data made use of 23 IRIS stations in addition to the 44 IDC stations. For the same event, the epicentral location determined by the International Seismological Centre (ISC) used data from a much larger number (586) of recording stations (Figure 4b). A comparison of the epicentral location and depth for this seismic event, as obtained from seven different sources: (1) the original CEB, (2) revised IDC, (3) combination of IRIS and revised IDC, (4) ISC, (5) National Earthquake Information Center, USGS, (6) BJI (State Seismological Bureau, Beijing, China), and (7) MOS (institute of Physics of the Earth, Moscow, Russia), is shown in Figure 5. Location error ellipses from the first four sources are also shown. The solutions from BJI and MOS networks, based on the use of numerous stations at local and regional distances, are likely to be more accurate than that in the original CEB. It is interesting to note that the epicentral location based on the combined use of IRIS and revised IDC (No. 3 in Figure 5) lies somewhere in the middle of the BJI and MOS determinations and the CE9 location. The derived source depth also lies between the BJI and MOS determinations. It seems therefore that the solution based on the use of both IRIS and revised IDC data provides improved estimates of both epicentral location and depth in comparison to the original CEB solution.

For the entire Chinese database of 70 events, a comparison of the CEB locations with those derived by using the two methods mentioned above show no systematic trend and generally small differences (average less than 9 km in each case). Figure 6 shows differences in epicentral location between the original CEB and those derived by the combined use of both IRIS and revised IDC for all 70 Chinese events. The arrows point from the CEB location to the new location and the location differences range between 0.8 and 28.3 km with an average value of 8.5 km. However, a similar comparison of source depths shows the CEB estimates to be significantly larger than each of the other two estimates, suggesting that the CEB source depths may have been overestimated. The differences in source depth between the

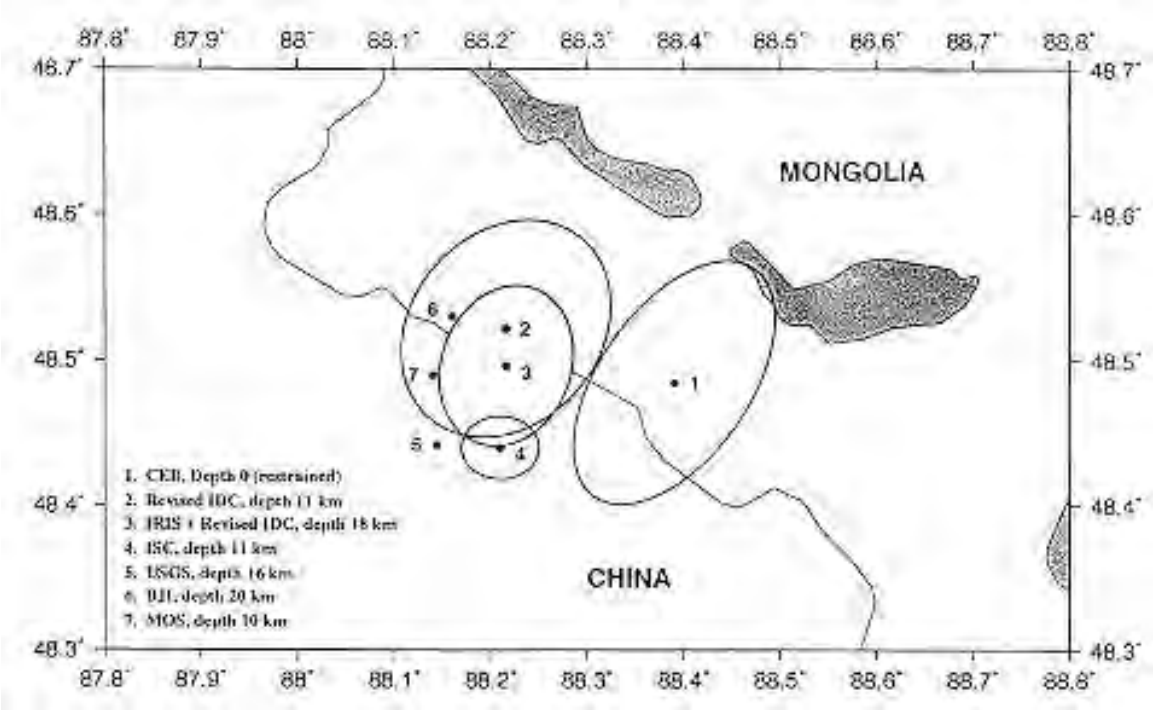


Figure 5. Comparison of epicentral location and depth for seismic event of 12 March 1996 from seven different sources: original CEB, Revised IDC, IRIS + Revised IDC, ISC, USGS, BJI, and MOS. Location error ellipses from the first four sources are also shown. Results based on the use of both IRIS and revised IDC data (No. 3) appear to provide improved estimates of both epicentral location and depth.

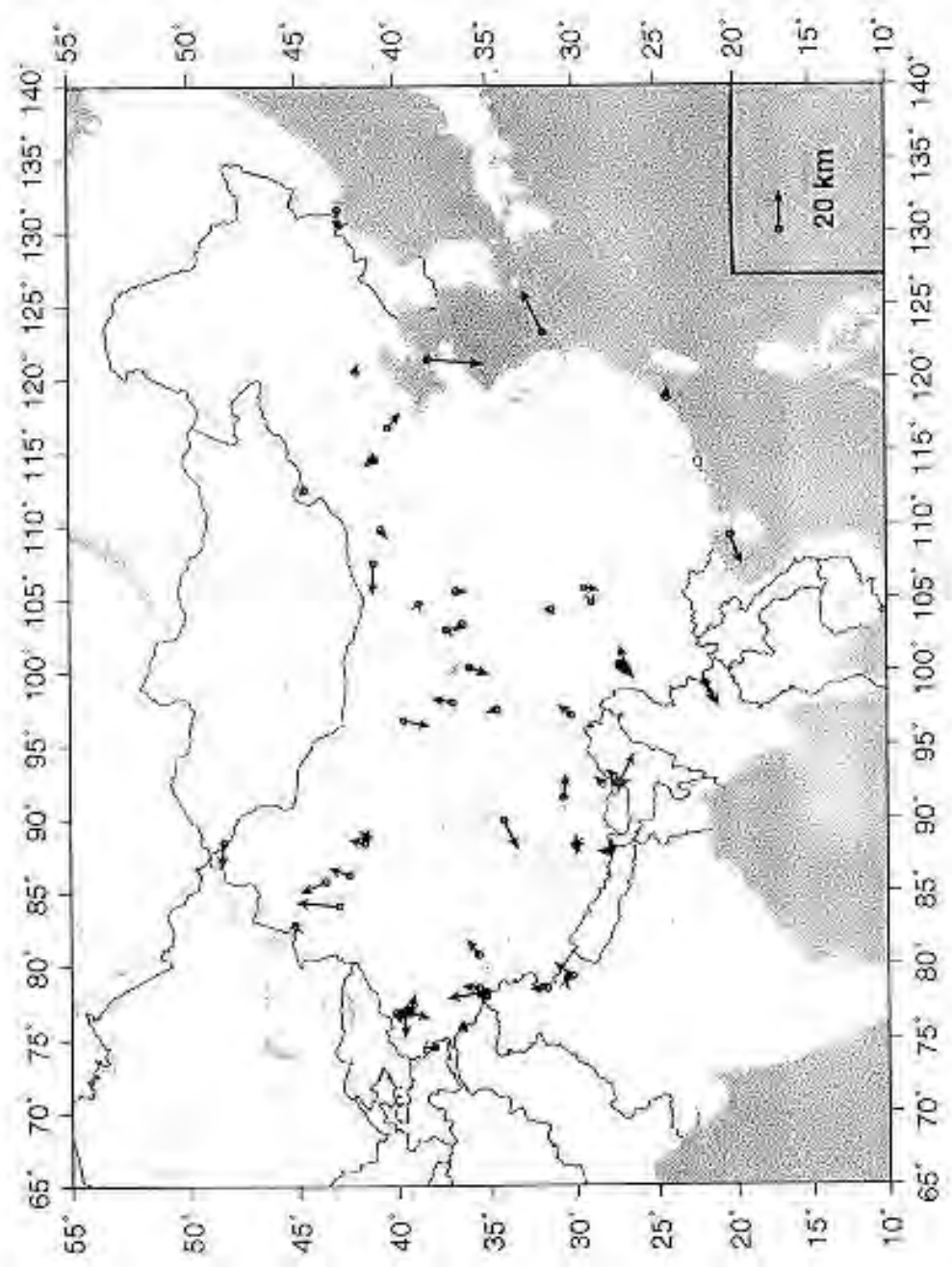


Figure 6. Differences in epicentral location between the original CEB and those derived by the combined use of both IRIS and revised IDC for all 70 Chinese events. The arrows point towards the new location and the average difference between the two locations is 8.5 km.

original CEB and those derived by the combined use of both the IRIS and revised IDC data, shown in Figure 7, have an average value of about 17 km, indicating that for most events the new depths are significantly smaller than those in the original CEB. Results from only 49 events are shown since, out of 70 Chinese events, source depths for both sets of data were available for only 49 events. These differences in source depths are supported by the remarkably good agreement observed between depth estimates based on the combined use of IRIS and revised IDC data and those available from the ISC for a large number of common events. According to Storchak (1999), epicentral locations from the ISC, derived from a much larger dataset and covering a larger range of azimuths than those by the IDC, are probably more accurate than the IDC locations. It should however be noted that the ISC determinations are generally over two years behind real time and may therefore be of only limited use for monitoring the CTBT.

The results obtained from analysis of all (70) CEB events in China were delivered to the CMR. Each event location consists of four CSS3.0 files, including the origin, origerr, arrival, and assoc database tables. Therefore, a total of 560 such database files were delivered to CMR ready for installation into their CEB database. All IRIS waveform data which contributed to the above 70 CEB events in China were also delivered to the CMR on one 8 mm archive tape in CSS3.0 format. Analysis, similar to that carried out for the Chinese events, has been completed for 43 CEB events in the former Soviet Union by using waveform data from both IDC and IRIS stations.

(b) Analysis of Several Other Datasets

We are also analyzing near-field, local, and regional data from the 1997 Depth of Burial Experiments at the former Soviet test site at Balapan in eastern Kazakhstan. More recent (1998) data from the Degelen test site are also being retrieved and examined.

CONCLUSIONS AND RECOMMENDATIONS

Formation of databases with significantly improved ground truth can be accomplished by a combination of re-analysis of the IDC data and retrieval and examination of data from other available sources such as the IRIS. For the Chinese dataset, the most important contribution of the IRIS data is the addition of a large number of arrivals from regional phases, so that solutions based on the combined use of both IRIS and IDC data provide improved estimates of both epicentral location and depth in comparison to the original CEB solution. Such analysis should also be carried out for other regions of the world.

REFERENCES

Bondar, I. (1998a). PIDC Calibration Event Bulletin Technical Reference, CMR-98/16, Center for Monitoring Research, Arlington, Virginia.
Bondar, I. (1998b). PIDC Ground Truth Event Bulletin Technical Reference, CMR-98/21, Center for Monitoring Research, Arlington, Virginia.
Bondar, I., X. Yang, J. Wang, M. Bahavar, H. Israelsson, and K. McLaughlin (1998). Tuning, and calibration activities at the PIDC, Proc. of the 20,h Annual Seismic Research Symposium on Monitoring a Comprehensive Test Ban Treaty (CTBT), U. S. Department of Energy, Washington, DC, 1-10.
Grant, L., R. Wagner, F. Ryall, and I. Henson (1997). Ground truth database for regional seismic discrimination research, Proc. of the 19th Annual Seismic Research Symposium on Monitoring a Comprehensive Test Ban Treaty, U. S. Department of Energy, Washington, 867-876.
Storchak, D. A. (1999). Reasons for pIDC mislocations: a view from the ISC, oral presentation at the 1999 General Assembly of the IUGG, 30 July 1999 (EG 12/LT4).

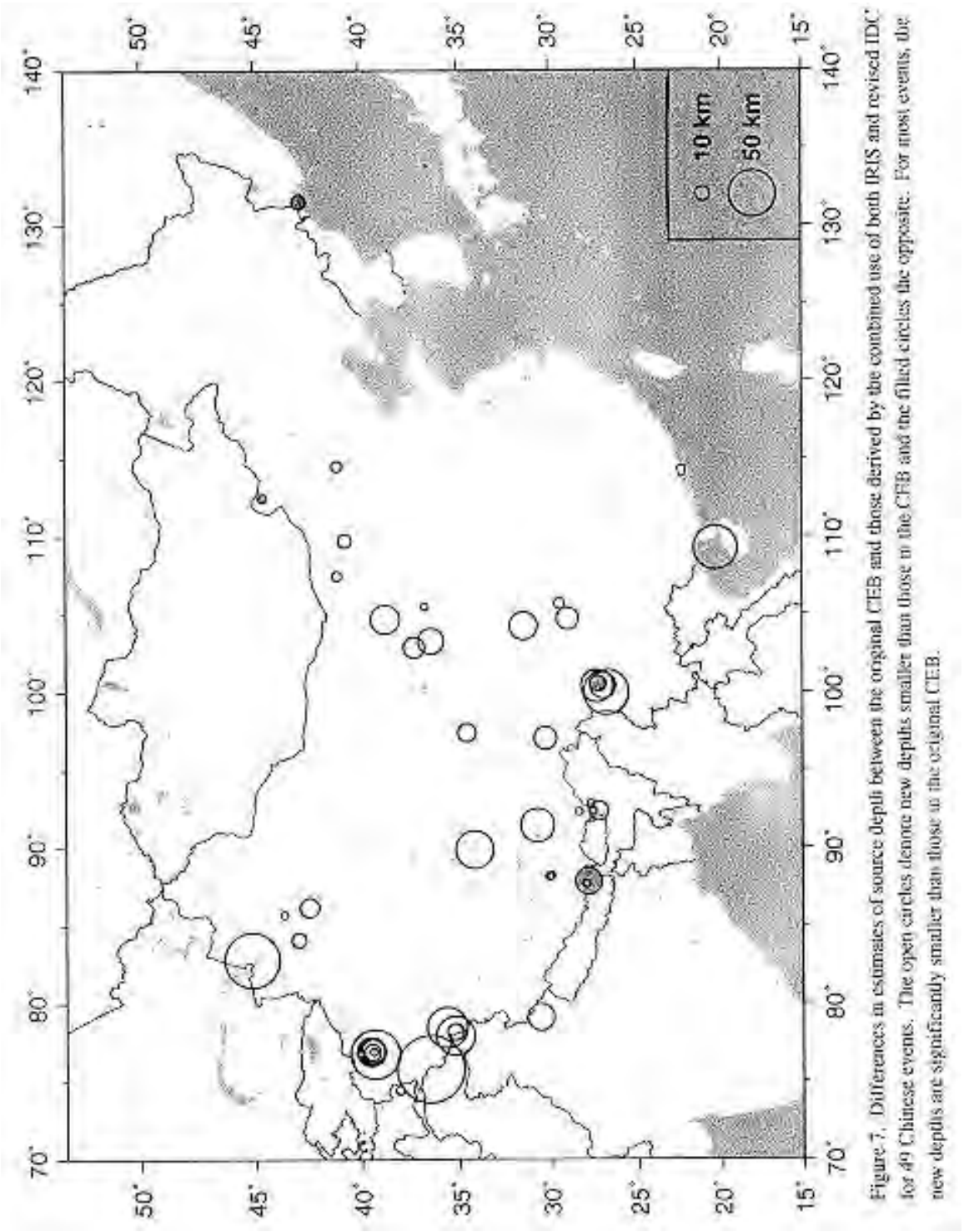


Figure 7. Differences in estimates of source depth between the original CEB and those derived by the combined use of both IRIS and revised IDC for 49 Chinese events. The open circles denote new depths smaller than those in the CEB and the filled circles the opposite. For most events, the new depths are significantly smaller than those in the original CEB.

THE KNOWLEDGEBASE INTERFACE FOR PARAMETRIC GRID INFORMATION

James R. Hipp, Chris J. Young, Randall W. Simons, Sandia National Laboratories

Sponsored by U.S. Department of Energy
Office of Nonproliferation and National Security
Office of Research and Development
Contract No. DE-AC04-94AL85000

ABSTRACT

The parametric grid capability of the Knowledge Base (KBase) provides an efficient, robust way to store and access interpolatable information that is needed to monitor the Comprehensive Nuclear Test Ban Treaty. To meet both the accuracy and performance requirements of operational monitoring systems, we use an approach which combines the error estimation of kriging with the speed and robustness of Natural Neighbor Interpolation. The method involves three basic steps: data preparation, data storage, and data access. In past presentations we have discussed in detail the first step. In this paper we focus on the latter two, describing in detail the type of information which must be stored and the interface used to retrieve parametric grid data from the Knowledge Base.

Once data have been properly prepared, the information (tessellation and associated value surfaces) needed to support the interface functionality, can be entered into the KBase. The primary types of parametric grid data that must be stored include: (1) generic header information; (2) base model, station, and phase names and associated ID's used to construct surface identifiers; (3) surface accounting information; (4) tessellation accounting information; (5) mesh data for each tessellation; (6) correction data defined for each surface at each node of the surfaces owning tessellation; (7) mesh refinement calculation set-up and flag information; and (8) kriging calculation set-up and flag information. The eight data components not only represent the results of the data preparation process but also include all required input information for several population tools that would enable the complete regeneration of the data results if that should be necessary.

Data retrieval and subsequent client processing are handled by a library of C++ KBase interface routines known as libKBI_grid (library Knowledge Base Interface for gridded information). Specific function calls can be inserted into client source code to make requests from the libKBI_grid API during execution. The libKBI_grid functionality can be divided into six specific tasks including: (1) database connection, (2) surface fetch initialization, (3) data cluster fetch size initialization, (4) surface association, (5) location initialization, and (6) surface interpolation.

Key Words: Knowledge Base interface, parametric grid, tessellation, surface

OBJECTIVE

To improve the U.S. National Data Center (USNDC) capability to monitor a Comprehensive Test Ban Treaty (CTBT), researchers at the U.S. Department of Energy (DOE) national laboratories are collaborating to develop a collection of data and associated access tools collectively known as the Knowledge Base. The Knowledge Base (hereafter KBase) will consist of many types of information which will improve the performance of the four principle monitoring technologies -- seismic, hydroacoustic, infrasonic, and radionucleic -- at various regions of interest around the world. The number of different data sets in the KBase is expected to be huge, but viewed from an information representation perspective, there are only four basic types of data: reference event information, parametric grid information, contextual information, and supporting information (Shepherd et al., 1998). In this report parametric grid information is the primary focus.

Parametric grid information is interpolatable data associated with particular geographic locations (i.e. a grid) on the earth. The interpolation part of the definition is important: not all data sets which have geographic coordinates should be interpolated. Examples of proper, interpolatable parametric grid data sets are travel-time corrections for any of the sensor technologies. The grid of locations for which information has been specified may be regular or irregular, depending on the method of collection or generation of data. Regardless, the KBase information derived from these grids must meet certain requirements, i.e. the interpolated values must: 1) include a robust error estimate; 2) be first and second order continuous; and 3) be delivered to applications "quickly" (the precise speed requirement depends on the application).

In previous papers we discussed methods of preparing parametric grid data including the mesh refinement methodology (Hipp 98), for obtaining rigorous representations of the data, and methods for interpolating the data quickly and accurately (Hipp 97). In this paper we shall concentrate on the type of information that must be stored, and more importantly, on the description of the interface used to retrieve parametric grid data from the Knowledge Base.

RESEARCH ACCOMPLISHED

Stored Parametric Grid Information

After the parametric grid has been determined, which accurately represents the data value and modeling error surfaces, the information (tessellation and associated value surfaces) can be entered into the KBase. The primary types of parametric grid data that must be stored in a database regardless of format include:

1. **Generic header information including the date of creation, the version numbers of the kriging and mesh refinement software used to generate the data, and the maximum tessellation, basemodel, station and phase ID's used to construct the surface identifier hashing function;**
2. **Basemodel, Station, and Phase names and associated ID's used to construct data surface identifiers;**
3. **Surface accounting information including the number of surfaces, and for each surface, the surface id, the basemodel, station, and phase names from which the surface was formed, the back-ground modeling error used by the surface, and the tessellation id of the tessellation upon which the surface is represented;**
4. **Tessellation accounting information including the number of tessellations, and for each tessellation, the tessellation id, the number of nodes, triangles, and represented surfaces, and the tessellation's modified-gradient parameter flag;**
5. **Mesh data for each tessellation including a description of all nodes that comprise the tessellation and the connectivity of the tessellation in the form of**

triangle information. Each node is defined by an ID, a location that includes the longitude, latitude, and depth of the node, and a type flag that indicates specific node type information. Each triangle is defined by an ID, a set of three node ID's that are the triangle's vertices, and a type flag that gives additional triangle specific information;

6. **Correction data defined for each surface at each node of the surface's owning tessellation. This data includes a correction value, a longitudinal and latitudinal derivative, and a modeling error value (this is travel-time specific… other data types, such as hydro-acoustic or infrasound, may have different data storage requirements).**
7. **Mesh refinement calculation setup and flag information which is necessary to reliably regenerate the mesh data that is contained within the database; and**
8. **Kriging calculation setup and flag information which is necessary to completely regenerate the kriged surfaces from which the refined mesh was evaluated.**

In the list above the concept of a surface is introduced which refers to the actual stored data defined at all nodes of a specific tessellation for a unique identifying basemodel, station, and phase set. Each surface is owned by a single tessellation. That is, each surface only uses one tessellation's node-set to tie its values to. Surfaces are not multiply defined across many tessellations. However, it is possible to include more than one tessellation in the data storage. Each tessellation has its own node and connectivity (triangles) definition and owns some subset of the surfaces defined in the database.

In the next section we shall discuss how the application interface software (libKBI_grid) uses stored data to provide requesting client applications with interpolated results.

Data Access Methodology: Application Interface

Once data have been processed and stored, they are ready to be accessed and used by client applications. The access and use of the data consists of three primary steps: data retrieval from the KBase, containing triangle search via the walking triangle method, and the Natural-Neighbor Interpolation (NNI) calculation to return results. Each of these functional steps are executed by the libKBI_grid software which serves as the implementor of the Data Access process.

This section will begin by discussing briefly the functional interface of libKBI_grid. Subsequent sections will describe each of the three data access steps including data retrieval, which defines the methodology and format for extracting data from the KBase; the containing triangle search which refers to the searching method used by libKBI_grid to find the client requested interpolation point within the tessellation(s) connectivity structure; and, the NNI including the gradient-modification used to ensure that the NNI is differentiable at all node points.

libKBI Functionality

Parametric grid data retrieval and subsequent processing is handled by a library of C++ KBase interface routines known as libKBI_grid (library Knowledge Base Interface for Gridded Information). Specific function calls can be inserted into client source code to make requests from the libKBI_grid API during execution. The libKBI_grid functionality can be divided into six specific tasks including:

1. **database connection,**
2. **surface fetch initialization (SFI),**
3. **data cluster fetch size initialization,**
4. **surface association,**

5. **location initialization, and**
6. **surface interpolation**

The first task, database connection, is simply a call to establish a connection to the KBase through a database manager such as Oracle, SDE, or even a flat-file representation. This call is a standard request providing the names of the server, database, password, and other pertinent information required to make a proper connection.

The second task, surface fetch initialization (SFI), refers to the manner in which DA is restricted, or enveloped, to include only a subset of the data available in the KBase. DA is restricted to optimize data retrieval performance by minimizing the amount of data that must be retrieved from the KBase and stored in-core. This is generally accomplished by eliminating data (surfaces) from retrieval consideration if they are not necessary for the current problem defined by the client application accessing libKBI_grid. As discussed above, the concept of a surface, used here and throughout the remainder of this paper, refers to the data that comprise travel-times, magnitudes, amplitudes, etc., and their derivative and modeling error values for a specific basemodel, station and phase assignment. The concept of a surface, as well as the methodologies and software abstractions used to enable the data access restrictions are discussed in the next section on data retrieval.

The third task, data cluster fetch size initialization, defines another restriction on the amount of data from particular surfaces that can be loaded at one time. The data cluster is best viewed as a spatial cookie-cutter that only retrieves data from requested surfaces whose nodes lie within the boundaries of a pre-defined polygon (the cookie-cutter). This concept is also described in detail in the next section.

The fourth task, surface association, allows restriction of which surfaces are actually interpolated to a subset of those that were loaded based on the SFI prescription. Like the previous two tasks, this one is also described in more detail in the next section.

The fifth task, location initialization, simply sets the longitude and latitude of an interpolation request from the client application. Once libKBI_grid receives this information it is able to perform a containing triangle search which is prerequisite to calculating the interpolated values at the provided location.

Finally, the sixth task, surface interpolation, refers to the actual NNI calculation at the current location specified by the client.

As noted above, past reports have been written that document the formation and population of parametric grid data (Hipp 1996, and Hipp 1998) and provide examples of the use of the entire method for performing quality event location (Young 1998). In those reports the methods and techniques for performing the containing triangle search and natural-neighbor interpolation on a Delaunay tessellation (Delaunay, 1934) were discussed. The interested reader should consult Lawson (1977) or Sambridge (1995) for a discussion of the triangle-walk location algorithm or Watson (1992) or Sambridge (1995) for more information concerning the natural-neighbor interpolation technique. Those topics will not be discussed further in this paper. Here we will concentrate on data retrieval tasks only (tasks 2 through 4 above).

Data Retrieval

We have just seen that libKBI_grid handles all issues associated with retrieving data from the KBase. Specifically, it accomplishes the data retrieval by restricting the amount of information that is loaded in-core and by further restricting interpolation calculations on a surface-specific basis. The amount of data retrieved is restricted in two different ways. First, the available surfaces in the KBase are culled to a predefined subset as defined by the client application. Second, a spatial data cluster (cookie cutter) is used to further restrict the amount of data loaded to that which lies within the boundary of the data cluster. We shall describe each of these methods of restricting the accessed and processed data in the paragraphs below. But

first we need to define the abstract representation of a tessellation object to fully understand how libKBI_grid accesses the data and makes it available for use by a client application.

Tessellation And Surface Object Abstraction

We discovered above that the KBase, regardless of implementation, must store surface, node, and triangle information within the database. We also saw that the KBase was capable of storing many tessellations and that each tessellation, in turn, could have many surfaces assigned to it. Figure 1 illustrates this concept abstractly with an imaginary KBase that includes 4 tessellations. Each tessellation contains the nodes and triangles that define spatial location and connectivity information for that tessellation. In addition, each tessellation contains one or more surfaces that utilize the spatial information of the tessellation (the nodes) as locations to define its values on. For example, assume that "surface 1" is travel-time information which consists of a single travel-time value for each and every node defined within the tessellation. The assembly of all such values over their respective nodes forms a discrete surface. Using an interpolation function one can define a continuous interpolated surface over the entire range of the tessellation.

In our imaginary KBase of Figure 1 we see that "tessellation 1" has 4 surfaces, "tessellation 2" has 5 surfaces, "tessellation 3" has 2 surfaces, and "tessellation 4" has 3 surfaces. Notice that the index number of each surface is unique regardless of which tessellation owns the surface. This is an intended data requirement of the KBase. The KBase does not allow a surface to be represented by more than one tessellation. One can imagine the trouble that would undoubtedly occur if libKBI_grid tried to access the surface assigned to say basemodel 'AK135', station 'CMAR', and phase 'P' only to find that the surface index existed in two different tessellations. Which one would be used?

The relationship between a tessellation and the surfaces that it owns can be made clearer by examining Figure 2. Figure 2 shows constituent parts of "tessellation 4" of the imaginary KBase. The parts of a tessellation consist of geometry information (nodes and triangles) and value information (surfaces). Notice that all geometric spatial location information is provided by the nodes of the tessellation. A node is, quite simply, the latitude, longitude, and depth of some point on the earth. In and of itself it has no other attributes assigned to it. The triangles, on the other hand, are a means of tracking the mesh connectivity of a tessellation. A triangle is simply the indices of each of the three nodes that comprise the triangle.

The node indices are always ordered in a counter-clockwise fashion relative to an outward pointing normal on the surface of the Earth. Triangle connectivity provides a means for determining node neighbors and is vital for performing the containing triangle search and the node neighbor calculation both of which are required to perform NNI.

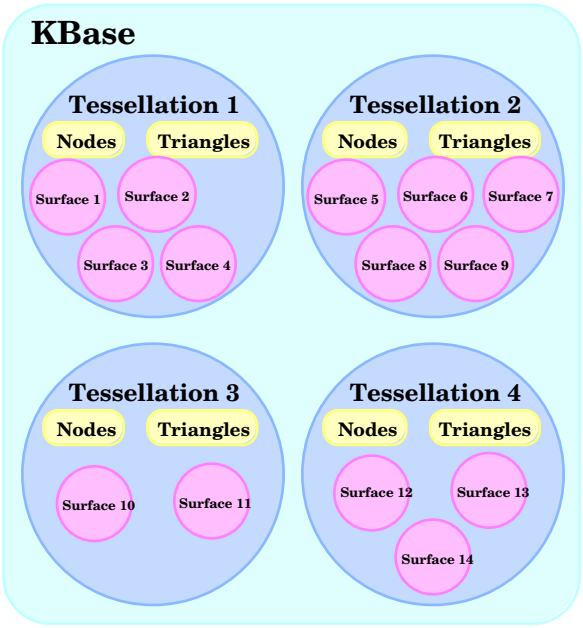


FIGURE 1. Abstraction of KBase storage for multiple tessellations

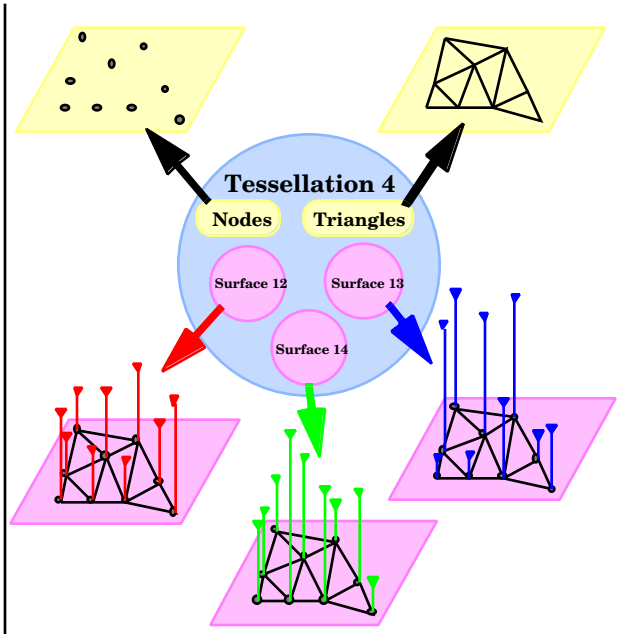


FIGURE 2. Abstraction of KBase tessellation components

The actual data values that are to be interpolated are contained within the surface object representations. In Figure 2 three surfaces are shown; 12, 13, and 14. Notice that all three use the tessellations' nodes as the spatial location upon which their values are defined. The only difference between one surface and the next is the magnitude of the value at each of the tessellation's fixed nodes and not its location.

Surface Fetch Initialization (SFI)

Now that we have examined the abstract nature of the tessellation object relative to how it is represented in libKBI_grid we are ready to investigate the three primary data retrieval tasks of libKBI_grid. Recall from above that the first data retrieval task following database connection was surface fetch initialization (SFI). The purpose of SFI is to define a specific set of surfaces that are defined as necessary and required by the calling client application to properly perform its intended function. By restricting the number of surfaces accessed by libKBI_grid to a subset of those available in the KBase a substantial performance gain may be noticed. Also, computer resources (memory) may be in short supply and minimizing the amount of in-core data can help to alleviate this problem.

Figure 3 depicts a surface fetch subset from the imaginary KBase. In the example presented in Figure 3 surfaces 1, 2, and 3 of "tessellation 1", surfaces 5, 7, and 9 of "tessellation 2", surface 10 of "tessellation 3", and surface 14 of "tessellation 4" are designated for access while surfaces 4, 6, 8, 11, 12, and 13 of their respective tessellations are restricted from access. In this example we have reduced the number of surfaces required for access by almost 50%. In reality the number of surfaces may be in the thousands while the fetch

subset is generally in the single or double digits. Real problems can see savings of a factor of 10 to 100 in access performance.

As an example of the use of SFI, consider the location of a seismic event with a small subset of the station/phase combinations available in the KBase, e.g. only P phases for the stations at regional distances. Once the event is ready to be located, the relevant station/phase combinations are known, so SFI can be used to limit the scope of the queries to the KBase in the data access step and thereby improve the speed of the KBase access.

Data Cluster Access

The next data retrieval task performed by the libKBI_grid API is data cluster fetch size initialization. Defining a data cluster fetch size is also a method of minimizing the amount of data that must be acquired and stored in-core. Recall that the data cluster was best viewed as a spatial cookie-cutter that only retrieves the requested surface data from nodes that lie within the confines of a pre-defined polygon (the cookie-cutter). The need for this type of functionality may provide the best reason to use a sophisticated commercial product for DS rather than a simple flat-file: for example, the ESRI product SDE, which operates on top of an ORACLE relational database, directly supports this type of retrieval.

Figure 4 depicts this concept where the data cluster is an imaginary circle centered over a region of interest for the client application. The figure shows two separate data clusters and the resulting nodes and triangles accessed by both clusters. Notice that the data cluster method is intelligent and only loads data that is the set difference between the current accessing cluster and all other clusters that were defined before it. For the example given in Figure 4, cluster 1 is used to access some data from a surface. At a later time cluster 2 is defined to access additional data. The data returned by cluster 2 is the set difference of the data between cluster 2 and cluster 1 (cluster 2- cluster 1). This process is repeated every time a new cluster is designated, initialized, and its data are loaded. In this way only the difference in data between the current cluster and all previously loaded clusters are retrieved from the database which can substantially reduce the data throughput from the KBase to the libKBI_grid software. Additionally, minimizing the radius, or spatial range, of the data cluster to a size that is reasonable for the current problem can also significantly reduce the total amount of data transferred from the KBase to libKBI_grid.

When data are fetched using the data cluster, all surfaces defined in the SFI are accessed. Figure 5 depicts this process and shows (abstractly) how three subsequent data cluster accesses are made from all surfaces designated for access by the SFI task of the libKBI_grid software. By way of the imaginary example the total data retrieval from the KBase following the three data cluster accesses is the sum of the data contained in the union of the three data clusters as retrieved from each accessible surface.

Surface Association

The last task to be discussed concerning data retrieval is surface association. Surface association is a means of restricting which surfaces are actually interpolated from those that were loaded based on the SFI prescription. In many cases, the list of surfaces would be the same, but not always. For instance, in a batch mode event location run, it may be known up front that all events were detected by a given network, hence the SFI call can limit access to that network. However, for a given event, the particular subset of network stations that actually recorded may well be different. This means that libKBI_grid would have to load additional data (surfaces) beyond the initial SFI prescription.

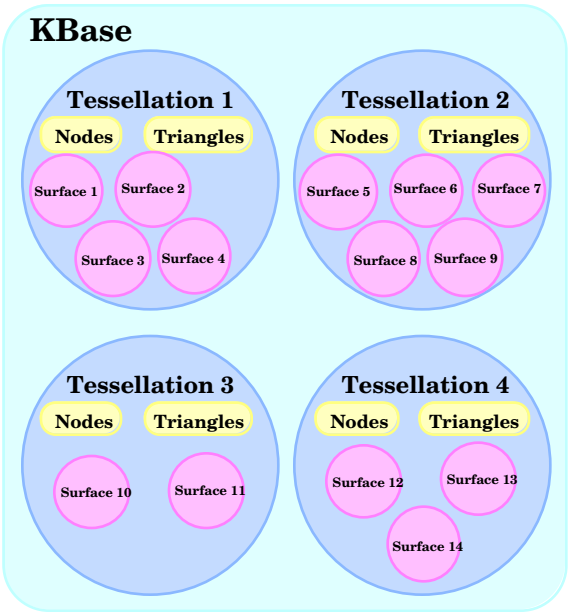


FIGURE 3. Surface Fetch Initialization (SFI)

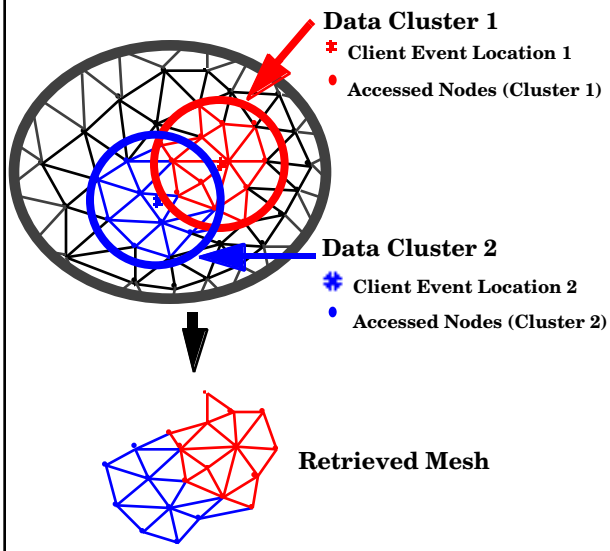


FIGURE 4. Data Cluster Access

The purpose of surface association is to define a specific set of surfaces for which results are required for the current event location being processed by the calling client application. This set is generally a subset of those defined in the SFI task but may include all surfaces defined by the SFI, and in some cases, even surfaces that were designated not to be accessed by the SFI. This could happen if a user simply forgot or left out important surfaces from their SFI specification. Under those circumstances libKBI_grid simply loads the new surface into its SFI specification and loads all necessary data for the new surface as determined by the union of all accessed data clusters.

Figure 6 shows an example of surface association using our imaginary KBase where surfaces 3, 7, 9, and 14 are designated as surfaces associated with the current event being processed by the client application. Given this specification only surfaces 3, 7, 9, and 14 will be processed for performing interpolation calculations at client specified locations.

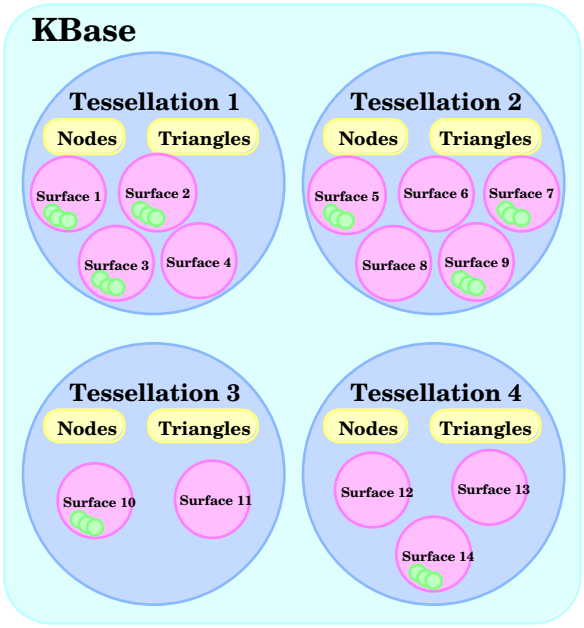


FIGURE 5. SFI Surface Data Cluster Access

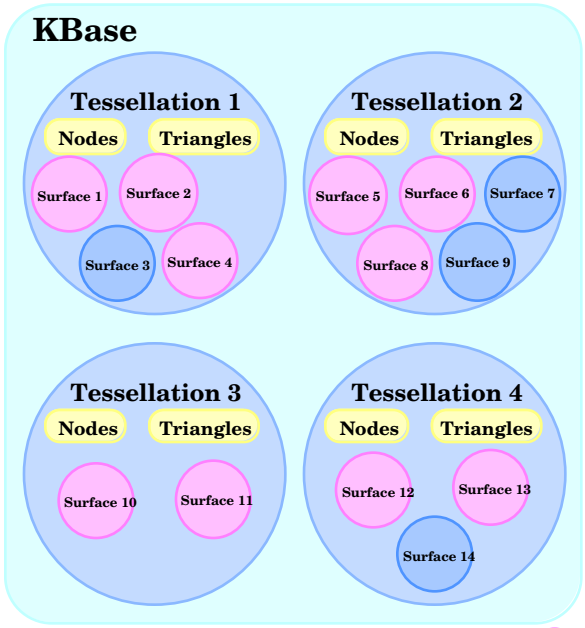


FIGURE 6. Surface Association

CONCLUSIONS

In this paper we have presented the Knowledge Base interface for parametric grid data (libKBI_grid), focusing on the storage and access information. The storage information includes eight data components that represent the results of the data preparation process and also include all required input data for several population tools. This enables complete reprocessing of the storage data whenever necessary.

When information is requested by a client through libKBI_grid, data from the KBase is extracted using a surface fetch initialization (SFI) prescription to restrict the number of accessible surfaces and a representative data cluster size to restrict the amount of data accessed per SFI surface. This set of data is further restricted from interpolation processing on a per event basis by the client through a surface association prescription. The remaining surfaces are processed to find the containing triangles of all locations as prescribed by the client applications. Then a NNI calculation is performed and all interpolated values are returned to the client for each of the final surfaces defined in the event's surface association set.

REFERENCES

Delaunay, B.N. (1934). ***Sur la sphere vide***, Bull. Acad. Science USSR VII: Class. Sci. Math., 793-800.

Hipp, J. R., Keyser, R. G., Young, C. J, Shepherd, E., Chael, E. P., (1996). ***Knowledge Base Interpolation of Path- Dependent Data Using Irregularly Spaced Natural Neighbors***, 18th Annual Seismic Research Symposium On Monitoring a CTBT, PL-TR-96-2153, pp 1014-1025.

Hipp, J. R., Young, C. J, Shepherd, E., Moore, S. G., (1998). ***The DOE Knowledge Base Methodology for the Creation of an Optimal Spatial Tessellation***, 20th Annual Seismic Research Symposium On Monitoring a CTBT, pp 717-726.

Lawson C. L., 1977, ***Software for C1 surface interpolation***, Mathematical Software III, ed. Rice. J., Academic Press, New York.

Sambridge, M., J. Braun, and H. McQueen (1995). ***Geophysical Parameterization and Interpolation of Irregular Data Using Natural Neighbors***, Geophys. J. Int.

Watson, D. F., (1992). ***Contouring: A Guide to the Analysis and Display of Spatial Data***, Pergamon, ISBN 0-08- 040286-0, 321 pp.

Young, C. J., Hipp, J. R., Shepherd, E., Moore, S., G., (1998). ***The DOE Model For Improving Seismic Event Locations Using Travel Time Corrections: Description and Demonstration***, 20th Annual Seismic Research Symposium On Monitoring a CTBT, PL-TR-96-2153, pp 782-790.

SCIENTIFIC MEETINGS DATABASE: A NEW TOOL FOR CTBT-RELATED INTERNATIONAL COOPERATION

Jerzy F. Knapik, Chief of International Cooperation Section, Provisional Technical Secretariat
Mary L. Girven, Decision Support Systems Software Engineering Department, Sandia National Laboratories

Sponsored by:
CTBTO PrepCom/PTS and
U.S. Department of Energy,
Office of Nonproliferation and National Security,
Office of Research and Development
Contract No. DE-AC04-94AL85000

ABSTRACT

The mission of international cooperation is defined in the Comprehensive Nuclear-Test-Ban Treaty (CTBT). Ways and means of implementation were the subject of discussion during the International Cooperation Workshop held in Vienna in November 1998, and during the Regional Workshop for CTBTO International Cooperation held in Cairo, Egypt, in June 1999.

In particular, a database of "Scientific and Technical Meetings Directly or Indirectly Related to CTBT Verification-Related Technologies" was developed by the CTBTO PrepCom / PTS / International Cooperation section and integrated into the organization's various web sites in cooperation with the U.S. Department of Energy CTBT Research and Development Program. This database, the structure and use of which is described in this paper/presentation, is meant to assist the CTBT-related scientific community in identifying worldwide expertise in the CTBT verification-related technologies and should help experts, particularly those of less technologically advanced States Signatories, to strengthen contacts and to pursue international cooperation under the Treaty regime.

Specific opportunities for international cooperation, in particular those provided by active participation in the use and further development of this database, are presented in this paper and/or presentation.

Key Words: international cooperation, scientific meetings, meetings database, opportunities for international cooperation

Introduction

Albert Einstein wrote in a letter, dated 2 August 1939, to President Franklin D. Roosevelt:

> *"In the course of the last four months it has been made probable - through the work of Joliot in France as well as Fermi and Szilard in America - that it may become possible to set up a nuclear chain reaction in a large mass of uranium, by which vast amounts of power and large quantities of new radium-like elements will be generated. (...) This new phenomenon would also lead to the construction of bombs, and it is conceivable – though much less certain – that extremely powerful bombs of a new type may thus be constructed. A single bomb of this type, carried by boat and exploded in a port, might very well destroy the whole port together with some of the surrounding territory. However, such bombs might very well prove to be too heavy for transportation by air."* [1]

Personal correspondence of this kind gives some insight into the human relations behind our history. Einstein's prediction, as cited above, has been proven wrong only with regard to the last sentence. He was right in all his other points. Also, later in the letter Einstein drew the President's attention to the fact that in some areas relevant to the use of science for peace rather than war, international cooperation had already been stopped and that it would probably be blocked completely in the near future as war became imminent, a dire prediction that also proved true.

After more than half a century in which "*extremely powerful bombs of a new type*" (nuclear bombs) were developed, tested, and used, a Comprehensive Nuclear-Test-Ban Treaty (CTBT) banning all nuclear explosions was finally negotiated, and as of 4 August 1999, has been signed by 152 countries, including five nuclear weapon states, and ratified by 42 States Signatories. It appears likely that nuclear explosion testing is over, after more than 2090 nuclear explosions have been conducted by countries around the world.

At the same time, verification of compliance with the CTBT (also with the previous nuclear arms treaties) has become one of the major concerns of many nations. Credible verification requires vigorous cooperation in order to enhance internationally reliable capabilities to identify possible violations, minimize false alarms, and thus maintain confidence in compliance. Development and maintenance of the **International** Monitoring System (IMS) as well as the **International** Data Centre (IDC), and the preparatory work for the conduct of **internationally** assembled On-Site Inspections, are the main tasks of a new **international** organization directly dedicated to this mission and provided for in the Treaty, the Comprehensive Nuclear-Test-Ban Treaty Organization (CTBTO).

Fully reliable verification (by the world community) of total compliance of all states with their nuclear-test-ban obligations requires international cooperation. Remember that, in the broadest sense of the term *international cooperation*, there will be 321 internationally maintained monitoring stations and 16 laboratories located within the territory of 90 sovereign states. Also, international cooperation, in terms of the Treaty, abides by the principle that the Treaty gives equal rights and obligations to all States Signatories. This includes, in particular, the right to access the data collected by the IMS, as well as their sovereign right to use data received from the IDC for strengthening their national verification measures, in addition to possible application of these data for other peaceful purposes. However, it may be difficult for some States to take advantage of the possible "direct" benefits resulting from their status as signatories and even members of the Treaty without these important international links and cooperation.

Achievement of the political goals of the Treaty requires continuous interaction among experts working in specific areas of science and technology. It requires strengthening cooperation among researchers representing different countries but working in the same field of science. These fields of science are related to the four main components of the IMS, enumerated in the Protocol to the Treaty as: seismological,

[1] Courtesy of the Franklin D. Roosevelt Library, Hyde Park, New York.

radionuclide, hydroacoustic and infrasound monitoring. Another very broad area of cooperation encompasses developers of very sophisticated computer systems and new methods of transmission, processing and analysis of data.

Furthermore, some common tasks and final products are only possible when experts from diverse areas of science and technology are working in concert. Experts representing different technologies are encouraged to arrange, broaden and strengthen interdisciplinary contacts and international cooperation among experts representing different branches of CTBT verification-related science. Such international cooperation might enhance interdisciplinary expertise and prove to be a unique technological advantage for the scientific community to be gathered around the CTBTO mission and CTBTO personnel.

A good example of such an interdisciplinary CTBT-related meeting of researchers is the Seismic Research Symposium holding its 21st meeting this year in Las Vegas. In spite of its title, which by tradition has its roots in seismology, it, in fact, draws together representatives of each of the monitoring techniques from many different research centers and countries around the world.

International scientific cooperation, if addressing the sensitive areas related to the issues of international/national security matters, over its strictly professional and very substantive output, also has an additional aspect: It is a carrier of values, which should be numbered among the international confidence-building measures.

Because of the specific characteristics pointed out above, implementation of the CTBT is as much related to human relations as it is to technical verification. Both aspects are especially conducive to the development of international cooperation. And it is in strong opposition to any clandestine nuclear weapons' development programs - subject of the verification regime, which particularly do not want international publicity. This view is corroborated by an historical perspective of the last half-century.

Mission of international cooperation

The popular meaning of the phrase "international cooperation" is extremely broad. It is in very common use today in various contexts and with diverse connotations. However, in our paper/presentation, when we use this term, our meaning will be as it is defined by Paragraph 12 of Article IV of the Treaty, which states:

> "*The States Parties undertake to promote cooperation among themselves to facilitate and participate in the fullest possible exchange relating to technologies used in the verification of this Treaty in order to enable all States Parties to strengthen their national implementation of verification measures and to benefit from the application of such technologies for peaceful purposes."* [2]

Many attempts to elaborate on the meaning of the phrase "international cooperation," in terms of the CTBT, have brought us to the conclusion that it is practically impossible to improve the concise wording that was finally agreed to by the distinguished representatives of States and their experts who negotiated the text of the Treaty. Therefore, when explaining the mission of international cooperation to the general public on the International Cooperation home page of the CTBTO Open Web Site, the decision was made to simply use the literal text of this paragraph, represented in all six official languages of the Treaty (see URL: http://www.ctbto.org/ctbto/ic_mission.shtml).

[2] Full official text of the Comprehensive Nuclear-Test-Ban Treaty (see http://www.ctbto.org/ctbto/treaty.shtml for full information about Treaty from the CTBTO Home Page or http://www.ctbto.org/ctbto/treaty/treatytext.ic.html#P152 for specific paragraph in context).

Ways and means to promote cooperation among States Signatories

The Treaty gives equal rights and obligations to all member States. In particular, this refers to the cooperation promoted among themselves in the terms of the quoted paragraph from the Treaty. However, there are, obviously, different needs, requirements and national priorities, in particular because the whole spectrum of large and small countries, with very different levels of economic and technological development, is represented among all States Signatories of the Treaty.

From the very beginning there have been three priority tasks for the international cooperation team at CTBTO PrepCom:

1. to discuss expectations of individual States regarding ways and means of international cooperation under the Treaty regime;
2. to define the role, which is expected by State Signatories, of the Provisional Technical Secretariat in this matter;
3. to identify as early as possible the most efficient ways/forms of its maintenance.

These tasks became the objectives of an extended set of bilateral and multilateral contacts with representatives of many States, in particular with many developing countries. These contacts also provide good opportunities for representatives of States Signatories that are less active in the PrepCom to work with updated information on recent developments of the technical and organizational infrastructure of the Treaty verification system, on the training activities offered by the PTS verification divisions, etc.

During discussions with representatives of States Signatories, it has been recognized that CTBT-related international cooperation issues are a vital interest of many States, particularly those which are developing. It has strengthened and expanded recognition that *"International cooperation under the CTBT regime is an element in broadening Treaty support and participation, thereby contributing to an early establishment and the efficient operation of the Treaty verification regime. (…) Facilitating and promoting cooperation among member States would, therefore, enhance national implementation of verification measures and peaceful application of such technologies, for example natural hazard mitigation, etc., but also assist the process of broadening Treaty participation."* [3]

This political spin-off of the international cooperation activities, which are focused in the terms of the Treaty on the science and technology development and cooperation issues, was confirmed during the two international workshops organized by the PTS for the purpose of multilateral reviews and discussions of:

- ways and means to promote cooperation among States Signatories so as to facilitate and participate in the fullest possible exchange relating to technologies used in the verification of the Treaty; and

- methods for strengthening national implementation of verification measures with maximum benefit from the application of such technologies for peaceful purposes.

The first of these two meetings, the "International Cooperation Workshop," which was held 16-17 November 1998, brought together in the Vienna International Centre representatives of 58 States Signatories from all geographical regions. The second meeting, a follow-up of the Vienna Workshop's discussions, focused on regional cooperation opportunities. Held in Cairo, Egypt, 1 - 3 June 1999, the "Regional Workshop for CTBTO International Cooperation" was attended by participants from 22 African States (including 3 non-signatory States) and representatives of the Organization of African Unity (OAU). Some participants of the first workshop who were from African States were invited to present papers at the second workshop. France and the United States, as well as the PTS also provided speakers for the Cairo Workshop.

[3] Masabumi Sato, CTBTO PrepCom/PTS; Significance and potential benefits of the CTBT; CTBT/IC/WS-I/CRP.6. Published in a compendium of documents "International Cooperation Workshop", CTBTO PrepCom, Vienna, January 1999.

The main points discussed and some conclusions formulated during these two workshops may be summarized as follows: [4]

- The purpose of the CTBTO is to assist its member States to monitor Treaty compliance;
- The CTBT verification system involves technologies which require expertise and qualified man-power for its effective operation;
- The CTBT can be a highly effective technological tool that can generate wide-ranging data, which can be used for peaceful purposes. The more we understand it, the better we can use it and the more benefits can be derived and offered to member States. Access to data should be as open as possible;
- The CTBTO should be a catalyst in promoting cooperation/helping to identify areas of need, acting as an information clearinghouse for cooperation;
- The regional programs/fora, if possible also to be open to non-signatory States, received particular support for information sharing/exchange of experience;
- Regional "centres of excellence" were suggested as a possible format for information sharing; the establishment of such centres in R&D institutions and universities could provide a visible means for regional cooperation, and local industries may be able to provide support;
- Regional cooperation in CTBT verification-related technologies could be promoted through the establishment of regional data centres (RDC); RDCs could be significant tools for data sharing, scientific research, training programs, and coordination, and thus strengthen participation and cooperation between all States;
- **Active participation in scientific meetings and propagation of CTBT ideals and work thereon, is a way to advance understanding of and support for the Treaty;**
- **CTBTO could receive and disseminate information concerning relevant issues in a database.**

The potential role of the CTBTO PrepCom in assisting developing countries, e.g. in the area of seismology, was a subject of very interesting considerations by one of the invited discussion initiators and included into his paper [5] presented at the Regional Workshop in Cairo. In particular, the tasks to be performed at a CTBT national data centre (NDC), from the most elementary in the early stages to a full range of activities, were outlined by the author of this paper in the context of non-CTBT-related *"questions of seismic hazard/risk being essential for a country that wishes to address its future development in a cost-effective and responsible manner.*" [6] However, with reference to the very small countries, a relevant observation was made in Cairo by another speaker, who brought to participants' notice, that *"the issues of defining seismic activity or atmospheric radionuclide disparity (...) become intricate or meaningless when it comes to acquiring national data for a small country."* [7] Creation of the Regional Data Centre(s) was then proposed and discussed, as an efficient solution e.g. for the groups of neighboring countries in the Africa Region.

In light of the success of the first regional workshop for the African region recently held in Cairo, the next two regional workshops (SEAPFE- South East Asia, the Pacific and the Far East, and LAC – Latin America and Caribbean) are already proposed by the PTS for the year 2000. Working Group A (WGA),

[4] For more details see Summaries of both Workshops distributed with the PTS documents CTBT/PTS/INF.80 and CTBT/PTS/INF.173/Rev.1, accordingly. A compilation of all papers presented during the Vienna '98 ICW was published by the PTS in the form of a booklet in January 1999; an appropriate set of documents of the Cairo Regional Workshop will be published in September 1999.

[5] Robi .J. Kleywegt, Council for Geoscience, South Africa; Regional Co-operation Mechanisms in CTBT Verification-Related Monitoring Technologies; paper presented at the Regional Workshop for CTBTO International Cooperation, Cairo, Egypt, 1999, to be published by the PTS.

[6] Ibid.

[7] John Odeke Ilukor, Ministry of Energy and Mineral Development, Makerere University, Uganda; A Discussion on "Regional Data Centres"; paper presented at the Regional Workshop for CTBTO International Cooperation, Cairo, Egypt, 1999, to be published by the PTS.

during its twelfth session held in June 1999, expressed support for holding these regional workshops. [8] These workshops will create additional opportunities for the PTS to strengthen/broaden relations with many countries from the next two geographical regions and should become new sources of ideas on how to promote international cooperation among the States Signatories in accordance with the expectations and specific needs of their particular region.

Role of science in CTBT monitoring and verification efforts

The researchers working in the pertinent areas of CTBT-related science and technology are fully aware of the extremely great potential for scientific developments in the areas of research related to the implementation of the Treaty regime. Also, there is no need today to convince the majority of politicians and national R&D policy makers, who are well-versed in the CTBT verification-related matters, of the key role science plays in the successful accomplishment by the Treaty's historic mission.

It is hard to overestimate the importance of the establishment in 1976 of the international scientific task force, called the Group of Scientific Experts (GSE), and/or the contribution of the successful maintenance and results of the GSETT-3 (Group of Scientific Experts Third Technical Test) to the ultimate success of CTBT. "*GSET-3 demonstrated the feasibility and the capability of the global, seismological verification system and (...) has been a 'global training course' that has developed verification expertise in a large number of countries."* [9] Results of such efforts, which have been made to review and to coordinate multiple CTBT-related individual research tasks encompassing all four verification technologies and data processing (see e.g. DOE CTBT R&D Programs [10]), confirm the general assertion of the important role of science made above. There is also no doubt that the ability to immediately apply developments resulting from the ongoing technological progress in many fields directly (but also indirectly) related to CTBT verification, might in the future be a very critical factor for the improvements in the quality of the CTBT verification regime which are necessary *"in order to create a significant deterrent against those who may be tempted to try to evade detection. (...) Successful fulfillment of this responsibility will increase confidence in the performance of the monitoring system by reducing the number of false alarms to the lowest level consistent with effective detection of Treaty violations."* [11]

An attempt to give a comprehensive review and/or to systematize all aspects of the role of science for CTBT monitoring and verification efforts is a task exceeding both the ambition of the authors and the range of this paper. Nevertheless, two points will be briefly highlighted in this section. In our opinion, these two issues are stronger than other ones related to the mission of international cooperation and, in particular, are most directly related to development of the database of CTBT-related scientific meetings. In both cases, a short citation is borrowed from the reference source/paper where much broader consideration of the issue by other authors may be found.

The first point to be stressed here is an awareness of the complexity of scientific issues associated with nuclear test monitoring. *"It is important to recognize that the role of science is multifaceted, particularly for monitoring technologies associated with complex Earth systems. For example, the efforts to understand seismic or acoustic signals from nuclear explosions should not be conducted in isolation from understanding such signals resulting from earthquakes, quarry blasts, landslides, or other sources of wave*

[8] See: Report of Working Group A to the Ninth Session of the Preparatory Commission for the Comprehensive Nuclear-Test-Ban Treaty Organization; document CTBT/WGA-12/1; item 7.14.

[9] Ola Dahlman, Defense Research Establishment (FOA) Sweden; Group of Scientific Experts Third Technical Test (GSETT-3) experiences; CTBT/IC/WS-I/CRP.10; Published in a compendium of documents "International Cooperation Workshop", CTBTO PrepCom, Vienna, January 1999; p. 143.

[10] Comprehensive Test Ban Treaty Research and Development FY 95-96 Program Plan; document DOE/NN-0003, see also the DOE CTBT R&D Program Web Site at http://www.ctbt.rnd.doe.gov/ .

[11] Ibid.

motions, some of which have properties similar to those of nuclear explosions. Similarly, one cannot simply study sources in one part of the world and generalize the results to the entire globe. Geological processes have produced great heterogeneity in the planet's interior that influences the propagation of seismic and acoustic energy on each path from source to receiver. Similarly, wind patterns, ocean currents, and ocean floor topography vary from place to place, and human activities are region dependent. There is an intrinsic need to attain an understanding of the source and propagation effects for all monitoring technologies for all significant source types and specific regions of the world." [12]

The second point concerns the potential for "dual-use" of elements of the verification system. It is, in fact, a specific aspect and a consequence of the first point brought up above. *"There will be many benefits from the CTBT if this system can be used for other scientific and technical applications. (...) When complete, the IMS and IDC will be the foundation for an unprecedented global test ban verification system. These same capabilities can also support a broad range of international scientific and technical cooperation. Specifically, the verification system is designed to detect and identify nuclear explosions over the entire Earth, yet it also will monitor considerable background "noise" from large numbers of earthquakes, volcanoes, atmospheric disturbances and conventional explosions. To screen these signals from potential Treaty violations, the conventional system will analyze all of these events. For these reasons, the data and information produced by this system will be useful both to States Parties for CTBT verification and to organizations concerned with geophysical monitoring (e.g. for scientific research, earthquake monitoring, weather forecasting)."* [13] A broad list of examples of possible dual-use applications of each of the four CTBT verification technologies is presented in the paper quoted above, as well as in another invited paper [14] delivered at the first International Cooperation Workshop held in Vienna in November 1998.

Both points mentioned above are of special importance for the better understanding of the role of science in CTBT monitoring and verification efforts and for understanding the potential non-CTBT verification-related practical benefits for States Parties (including those which, according to the Protocol of the Treaty, are not hosting IMS monitoring stations). These benefits are the result of spin-offs from the Treaty's implementation-oriented research and cooperation.

Varying aspects of the issues listed above were also discussed when considering the idea of and basic guidelines for the development of the "Database of Scientific and Technical Meetings **Directly or Indirectly** Related to the CTBT Verification-Related Technologies." It should assist the CTBT-related scientific community, as well as the staff of the PTS, in identifying worldwide expertise in the relevant, but reasonably broad, area of science and technology. Easily accessible to experts of the States Signatories, it should help them, in particular those of less technologically advanced States, to strengthen contacts and to develop international cooperation under the Treaty regime.

Scientific meetings – a window on international cooperation

When opening a discussion in Cairo on the proposals for regional cooperation in Africa, Professor G.K.King'oriah (Kenya) numbered a mobilization of local and regional knowledge and capabilities to enhance understanding of the CTBT among the important ways to promote technical cooperation. According to his paper delivered to the Workshop, "*this involves active participation in scientific meetings and propagation of CTBT at national and regional level, which can be done through the organization of*

[12] Research Required to Support Comprehensive Nuclear Test Ban Treaty Monitoring; Panel's Report; Published by the US National Research Council, National Academy Press, Washington D.C. 1997.

[13] Charles E. F. Meade, Defense Threat Reduction Agency, USA; Dual-use benefits of the CTBT verification system; CTBT/IC/WS-I/CRP.9; Published in a compendium of documents, "International Cooperation Workshop," CTBTO PrepCom, Vienna, January 1999, p.135.

[14] Peter D. Marshall, AWE Blacknest, UK; Benefits from an exchange of knowledge in the Treaty-related science and technologies: A personal perspective; CTBT/IC/WS-I/CRP.11; Published in a compendium of documents, "International Cooperation Workshop," CTBTO PrepCom, Vienna, January 1999, p.153.

regional seminars and conferences for exchanging notes on technologies and implementation strategies. Doing this automatically leads to efficient utilization of the regional capacity for the exchange of experiences and sharing of information." [15]

Early on, the PTS began formulating the idea of developing a database of CTBT verification-related scientific meetings to cover the relevant national and international scientific meetings organized by the various institutions and research centres of States Signatories and/or by international organizations. Experts participating in the Second On-Site Inspection Workshop organized by the PTS in Vienna in February 1998, were the first representatives of the CTBT-related international scientific community who were asked for their cooperation in providing initial meeting data as well as comments and ideas to assist in the database's development.

At the same time, the PTS's International Cooperation section started collecting meeting data based on generally accessible Internet resources (announcements of the annual meetings of the international/national R&D organizations, special home pages developed, for example, by the organizing committees of forthcoming meeting, etc.), as well as on the information provided by the PTS's experts working in all the verification technologies.

One of the preliminary assumptions of the developers was that the list of relevant meetings encompassed by the new database would start, if possible, from the beginning of 1998.

In March 1999, 57 meetings were included in the first version of the "Database of Scientific and Technical Meetings Directly and Indirectly Related to CTBT Verification-Related Technologies," which was presented by the PTS in the paper CTBT/PTS/INF.126. In May 1999, the next version of the meetings database, which by then included 72 meetings, was distributed with the document CTBT/PTS/INF.126/Rev.1 during the Working Group B (WGB) ninth session. All States Signatories have been encouraged to actively cooperate with this development effort by contributing relevant meeting information, as well as their observations and advice, all of which can greatly assist the PTS in building the most comprehensive and up-to-date database of meetings possible. One result of this cooperation was the proposal that this database be made widely accessible to as many interested parties as possible via the Internet on CTBTO's various web sites.

Database of Scientific and Technical Meetings … "Goes Live" on the Internet

In April 1999, shortly before the WGB meeting in May, the U.S. Department of Energy (US DOE) proposed that the "Database of Scientific and Technical Meetings Directly and Indirectly Related to CTBT Verification-Related Technologies" be made available to the general public on the CTBTO Open Web Site as well as incorporated into the meetings list of the username/password controlled Experts Communication System (ECS) and the Documents Distribution System (DDS) [16]. There was already a central database of meetings that was visible on each of these web sites, and the basic tools to display and manage it already existed. As the new database contained more fields of information (e.g. organizing institution, point of contact, web site URL, topics, etc.), it was proposed that the original tools be updated to incorporate the new fields and include the new concept of individually controlling visibility (which meeting is visible on which web site). A mock-up version was created at Sandia National Laboratories [17], linked to from the new International Cooperation home page on the CTBTO PrepCom Open Web Site and reported to the WGB ninth session in May.

[15] George K. King'oriah, National Council for Science and Technology, Kenya; Regional CTBTO Cooperation; paper presented at the Regional Workshop for CTBTO International Cooperation, Cairo, Egypt, 1999, to be published by the PTS.

[16] The DDS is another password controlled web system for missions and it has not yet been launched by the PTS.

[17] Sandia is a multiprogram laboratory operated by Sandia Corporation, a Lockheed Martin Company, for the Untied States Department of Energy under Contract DE-AC04-94AL85000.

During this session, "*WGB agreed that the CTBTO open home page would be a useful medium for the dissemination of science and technology information and all research organizations and programme managers should be encouraged to make available any relevant web site addresses. The International Cooperation Section could include these addresses in its database of scientific meetings indicating the links to specific topics such as the proceedings of scientific symposia and workshops."* [18]

In June the first set of necessary changes were completed and incorporated into all of the CTBTO Web Sites in Vienna. Anyone who has a current web browser (e.g. Netscape Navigator or Communicator or MS IE) and access to the Internet may access the International Cooperation view of this database of meetings at http://www.ctbto.org/cgi-bin/ic_meetings.cgi (or from the main CTBTO PrepCom Open Web Site's Home Page, go to "Opportunities," then "International Cooperation"). Also open to the public is the PrepCom list of meetings which are officially sponsored by the PTS at http://www.ctbto.org/cgi-bin/ctbto_meetings.cgi (or from the main Home Page, go to "Organization," then "CTBTO PrepCom Meetings"). The remainder of this paper deals specifically with the International Cooperation view of the central meetings database and delineates how to use this tool.

There are four types of web pages that deal with meetings:

1. **Main Meetings Page (see example in Figure 1), is where users can list meetings, decide how they want to limit, order and/or display meeting information, propose a new meeting, or review recent changes that have been made to the contents of the database;**

   If the default settings are used, when the user clicks the "**List Meetings**" button with a mouse or other pointing device, a page displays listing in chronological order the set of all meetings that are currently underway or will begin sometime in the future.

   But users don't have to accept the default settings. Those who wish to see the information displayed differently may modify the default settings for limiting, ordering and displaying meeting information maintained in this database.

   For example, users can: (defaults are in **bold** font)

   - Limit meetings: (default is not to limit meetings)
     - to a specific meeting group or forum (e.g. Seismic Research Symposium, used in the examples)
     - to a selected technology (Seismic, Radionuclide, Hydroacoustic or Infrasound)
     - by searching for a word or phrase (users may enter text here)
   - Limit timeframe:
     - to specific time range (**Future**, Forthcoming, Recent, Archived or No Limit, which is used in the example below); for convenience a checkbox labeled "Anytime" is provided to easily override the default action.
     - or specify year or month/year (valid years or month/year combinations are selectable)
   - Order meetings:
     - by date (**chronologically** or reverse chronologically)
     - or group sessions by alphabetically sorted meeting groups or forums
   - Select display view: (**Standard HTML**, Wide HTML, or Print-formatted (same as Wide HTML view but formatted without navigation bar and with a different footer)

[18] Report of Working Group B to the Ninth Session of the Preparatory Commission for Comprehensive Nuclear-Test-Ban Treaty Organization; document CTBT/WGB-9/1, pages 6-7.

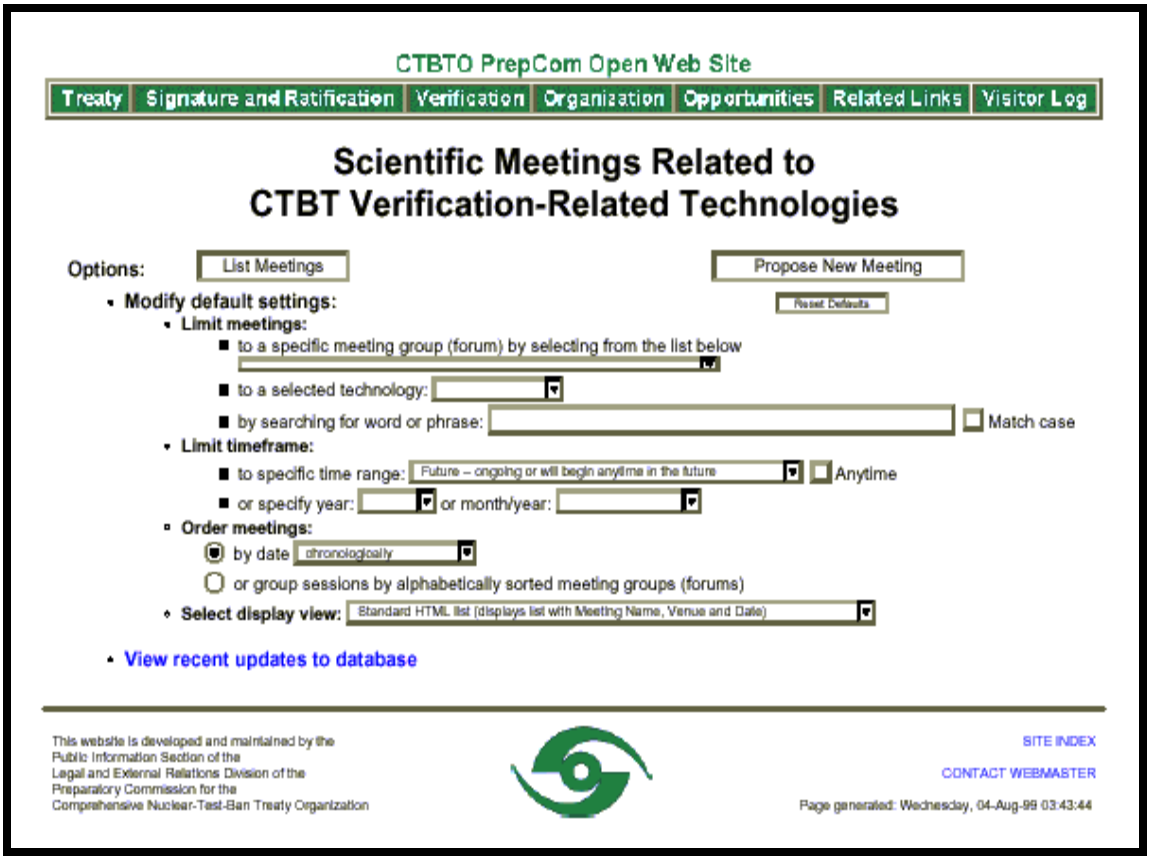


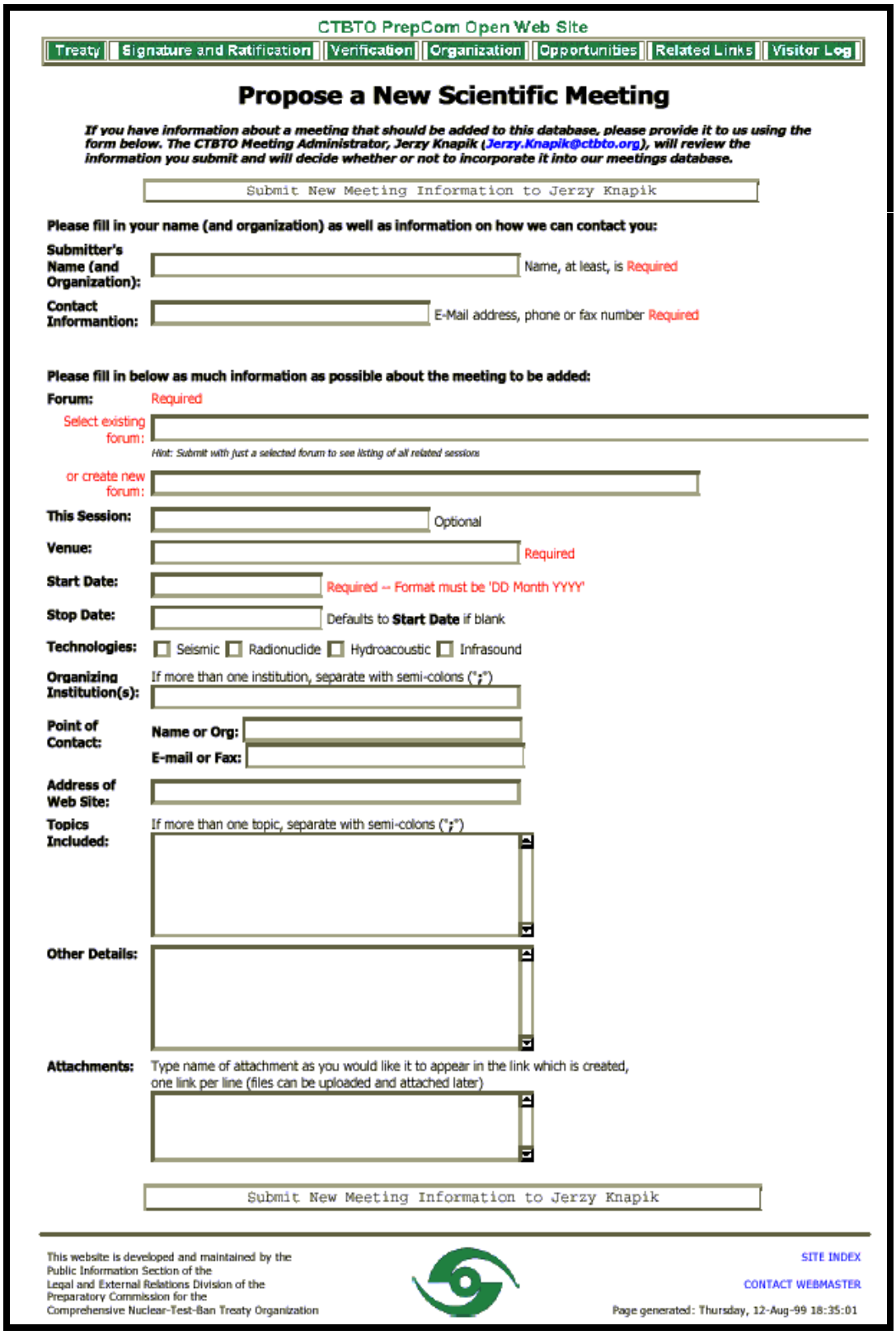
Figure 1 – Main Meetings Page

Suppose a user is looking for the last hydroacoustic meeting held in Berlin (that's all they remember). Just limit the technology to "hydroacoustic", type "Berlin" in the "by searching for a word or phrase" text area, limit timeframe to "Anytime", "Recent" or "Archived", and click the "**List Meetings**" button.

An additional option users have on the Main Meeting Page is to "**Review recent updates to database**". This log file displays additions, updates or changes that have been made to the contents of the database. For the CTBTO PrepCom Open Web Site and DDS views, changes made in the previous 30 days are displayed; for ECS, this function displays meeting database updates since the last time the user checked.

2. Form page (see Figure 2) to enter information about a new meeting to add to database

The PTS's Meeting Administrator maintains this database of meeting information through Administrator tools on the ECS. Anyone wishing to contribute information about a meeting that they believe would be beneficial to have added to this database may "**Propose a New Meeting**" by filling in the on-line form (see Figure 2) which is displayed when a user clicks on this link from the main meetings page. The information provided is sent to the Meeting Administrator who will then decide whether it is appropriate to make the addition. Comments or corrections should be e-mailed to the Meeting Administrator at Jerzy.Knapik@ctbto.org or the CTBTO Webmaster at ctbto_webmaster@ctbto.org.



CTBTO PrepCom Open Web Site

Treaty | Signature and Ratification | Verification | Organization | Opportunities | Related Links | Visitor Log

Propose a New Scientific Meeting

If you have information about a meeting that should be added to this database, please provide it to us using the form below. The CTBTO Meeting Administrator, Jerzy Knapik (Jerzy.Knapik@ctbto.org), will review the information you submit and will decide whether or not to incorporate it into our meetings database.

Submit New Meeting Information to Jerzy Knapik

Please fill in your name (and organization) as well as information on how we can contact you:

Submitter's Name (and Organization): Name, at least, is Required

Contact Informantion: E-Mail address, phone or fax number Required

Please fill in below as much information as possible about the meeting to be added:

Forum: Required

Select existing forum:

Hint: Submit with just a selected forum to see listing of all related sessions

or create new forum:

This Session: Optional

Venue: Required

Start Date: Required -- Format must be 'DD Month YYYY'

Stop Date: Defaults to **Start Date** if blank

Technologies: Seismic Radionuclide Hydroacoustic Infrasound

Organizing Institution(s): If more than one institution, separate with semi-colons (";")

Point of Contact: **Name or Org:** **E-mail or Fax:**

Address of Web Site:

Topics Included: If more than one topic, separate with semi-colons (";")

Other Details:

Attachments: Type name of attachment as you would like it to appear in the link which is created, one link per line (files can be uploaded and attached later)

Submit New Meeting Information to Jerzy Knapik

This website is developed and maintained by the Public Information Section of the Legal and External Relations Division of the Preparatory Commission for the Comprehensive Nuclear-Test-Ban Treaty Organization

SITE INDEX

CONTACT WEBMASTER

Page generated: Thursday, 12-Aug-99 18:35:01

Figure 2 – Form Page, to propose a new meeting be added to database

3. List Pages (see examples in Figures 3, 4, 5 and 6) display the results of a query when the "List Meetings" button is clicked;

If the default settings are used, a page displays listing in chronological order the set of all meetings that are currently underway or will begin in the future.

Figure 2 below is one example of a list page (with meeting group limited to "Seismic Research Symposium," time-frame set to "Anytime" or "No Limit" so both meetings (one in the past and one on the future) will display, and the "Standard HTML" display view selected):



Figure 3 – List Page: Meetings ordered by date

If "Standard HTML" is selected as the display view (the default setting) the following columns of information display:

- Meeting Name (*: Session*)
  This field is usually a combination of meeting group name/forum and session separated by a colon if a session exists.
  This field is always a link to the data page for this particular meeting. The data page contains the full set of information available for a meeting and is described later.
- Venue
  The location of the meeting or workshop (usually city, country or city/state, country).
- Date(s)
  A character string that represents the beginning through ending dates (e.g. 21-24 September 1999).

If the user decides to "group sessions by alphabetically sorted meeting groups or forums" from the "Order by" section, meetings are first sorted alphabetically by group name or forum, then individual session names are listed sorted by date. Figure 4 is an example where meetings are grouped by session:



Figure 4 – List Page: Sessions grouped by meeting name/forum

With either the "Wide HTML" or "Print-formatted" display view, more information is available horizontally on the page. It may be useful with these views to use a smaller font and/or print the output in landscape mode to avoid having to scroll horizontally or having data overflow the right margin when printing.

As you can see in Figure 5 (Wide HTML view) and Figure 6 (Print-formatted view), two additional columns of information are displayed:

- Organizing Institution
- Topics Include

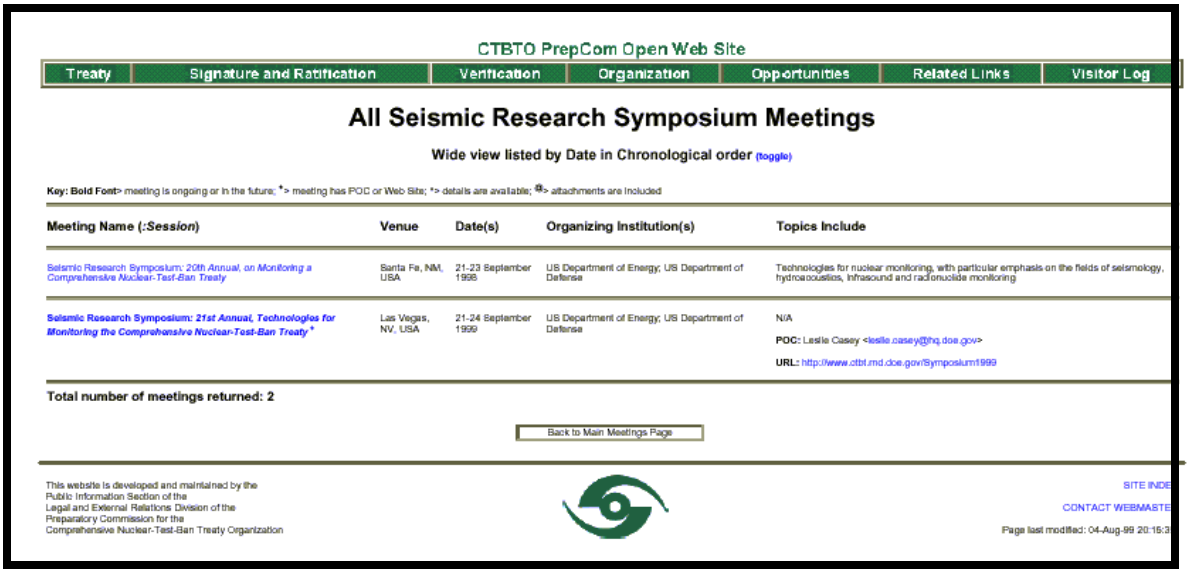


Figure 5 – List Page: Wide HTML view

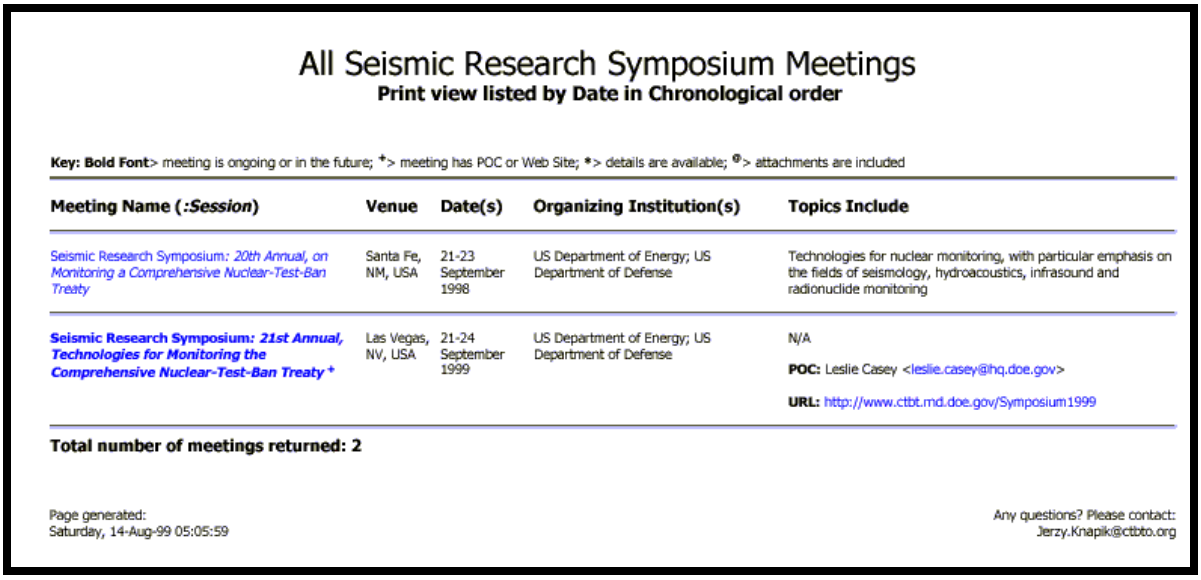


Figure 6 – List Page: Print-formatted view

4. Data Pages (see example in Figure 7) display as much information as possible about a meeting.

When a user clicks on a meeting name and/or optional session from a list page, the corresponding data page displays all available information about the meeting, including the following fields:

- Meeting Name
- Venue
- Date(s)
- Technologies
- Organizing Institution(s)
- Point of Contact
- Web site URL
- Topics Include
- Details
- Attachments

Figure 7 is an example of a data page for the 21st Annual Seismic Research Symposium, Technologies for Monitoring the Comprehensive Nuclear-Test-Ban Treaty:

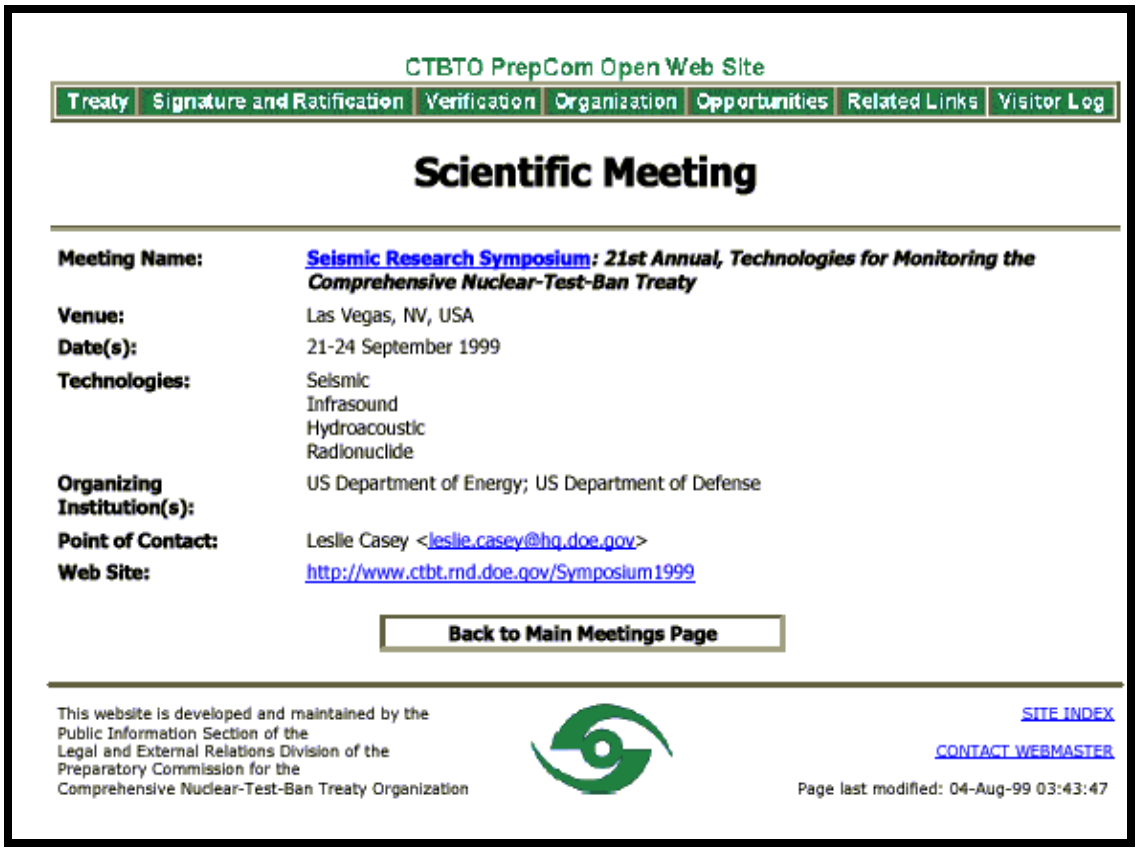


Figure 7 – Data Page

Note that fields only display if they contain information. In the example above, the "Details" and "Attachments" fields are not listed because no information is available.

The "Meeting Group" portion of the "Meeting Name" field (the text which precedes the colon), is clickable. Use this link to list all sessions of a particular meeting group/forum. In the example above, clicking on the "**Seismic Research Symposium**" link would redisplay the list page in Figure 4. Of course, all e-mail addresses and web site URLs are also clickable and can be used to send messages to meeting POCs and access additional information on a web site provided by the meeting organizer.

What's next?

Use it! Contribute to it! And increase confidence in CTBT through International Cooperation!!

In addition, consider the question, "How can we make this database more comprehensive and useful to CTBT-related researchers and the scientific community at large?"

Over time, the PTS hopes to receive more and more proposals to add new meetings of regional, national and even local interest to this database from States Signatores' research centers, universities, etc.

New ideas on how to further develop this database are already under consideration, e.g. how to collect, process and correspondingly archive technical information such as proceedings and reports which are available to participants to make them also available to other interested parties. If properly developed, as well as continuously updated, the PTS's database can become a unique, consolidated source of references on verification-related technological developments, a tool to assist scientists worldwide.

In the spirit of "International Cooperation," anyone having ideas for possible enhancements or improvements to this new tool is strongly encouraged to contact either or both of the authors: Jerzy Knapik, Chief of the International Cooperation section at CTBTO/PrepCom/PTS (Jerzy.Knapik@ctbto.org) and Mary Girven, former CTBTO PrepCom Webmaster and developer of these web tools, at Sandia National Laboratories (mlgirve@sandia.gov).

OPTIMIZED THRESHOLD MONITORING

Tormod Kværna, Lyla Taylor, Frode Ringdal and Johannes Schweitzer, NORSAR

Sponsored by U. S. Department of Defense
Defense Threat Reduction Agency
Contract No. DSWA01-97-C-0128

ABSTRACT

We have continued our efforts to develop a fully automated tool for continuous threshold monitoring of a given target area. Several case studies have been conducted for the Indian, Pakistani, and Novaya Zemlya (NZ) test sites. Specifically, we have demonstrated the benefit of including the large aperture NORSAR array (NOA) for optimized threshold monitoring. After introducing so-called time delay corrections in the beam forming process, most of the beam signal amplitude is retained. However, the main benefit of including the NORSAR array is its excellent ability to suppress signals from events located outside the target area. Because of the large array aperture of about 60 km, the array response has a very narrow main lobe and relatively small side lobes.

Signals from events located outside the target area often cause a temporary degradation of the monitoring capability, resulting in peaks in the network threshold trace. Our approach is that if we are able to confidently associate these short-duration peaks with events located *outside* the target area, it is highly unlikely that an event simultaneously took place *within* the target area.

The first step in an automatic analysis of the threshold traces is to identify significant threshold peaks. In order to accommodate both undulations in the long-term background noise level and noise variability, we have developed a peak detection method based on estimates of the noise variance and the long-term trend of the threshold trace. For the NZ test site, the peak detection threshold is typically around m_b 2.0. Secondly, we have developed a procedure for association of network threshold peaks with arrivals detected at each individual station. If we can confidently state that these arrivals originated outside the target area, the corresponding threshold peak can be discarded from further consideration.

For arrivals detected at array stations, the estimated azimuth and apparent velocity can effectively be used as criteria for sorting out arrivals originating outside the target area. An additional criterion for sorting out non-critical arrivals is a confident association with an event located outside the target area. Such phase associations are currently available in the PIDC Reviewed Event Bulletin (REB) and the NORSAR automatic regional bulletin based on the Generalized Beam Forming algorithm.

Key Words: data processing and analysis

OBJECTIVE

The objective of this work has been to improve the Threshold Monitoring (TM) algorithm for use in monitoring compliance with the Comprehensive Test Ban Treaty. In particular, we have investigated improvements associated with the use of optimized bandpass filters, station-specific travel-time and slowness/azimuth corrections for sites to be monitored. Through integration of the TM results with traditional detector and event information we have further extended the automatic monitoring utility of the TM method.

RESEARCH ACCOMPLISHED

Seismic events occurring at or near the former underground nuclear test site on Novaya Zemlya have been subjected to extensive investigation over the last four decades, as monitoring of the events in this region has been of special interest to the international community. Following the developments of sensitive regional arrays in northern Europe (see **Fig. 1**), events with magnitudes as low as 2.5 have been successfully detected and located in this region.

The development of the Threshold Monitoring (TM) method (Kværna and Ringdal, 1999; Ringdal and Kværna, 1989, 1992) has further improved the monitoring capability of this area. By optimizing the processing parameters from recordings of previous events in the region, the joint TM processing of the regional arrays ARCES, SPITS, FINES, and NORES place an upper bound on possible events in this area, which during normal noise conditions fluctuates around magnitude 2.0. A typical example is shown in **Fig. 2,** where the upper trace shows the combined magnitude threshold for the four arrays processed. There are, however, often instances when the monitoring threshold is temporarily increased because of signals from events located outside the region of interest. For complete monitoring, we have until recently manually investigated the cause of these threshold peaks. The procedure used has been to compare the time intervals of the short duration threshold peaks to event and signal detection information found in standard event bulletins or signal detection lists. If a threshold peak could confidently be associated with an event located outside the target area, we considered it highly unlikely that another event simultaneously took place within the target area.

The current research has focused on the development of a fully automatic peak explanation facility for analysis of the magnitude threshold traces. In this way we intend to minimize the need for manual classification of the threshold peaks such that manual analysis will only be necessary when events within the actual target region occur. Although the focus of this paper is the Novaya Zemlya test site, the method will be directly applicable to any geographical areas like the other underground nuclear test sites.

Automatic detection of peaks in the network threshold trace

The first step in the automatic analysis of threshold traces is to identify significant threshold peaks. Our approach has been to develop a peak detection method based on estimates of the noise variance and the long term trend of the threshold trace. From experiments with various data sets, we have developed a method which comprises the following steps:

- Calculate the long-term-median (LTM) of the threshold trace with a typical window length of 30 minutes and a sampling interval of 5 minutes.
- Calculate the overall standard deviation (SIGMA) of the threshold trace around the long-term-median after removing the upper 10% of the data values. The removal of the upper 10% of the data values is done to reduce the influence of the threshold peaks on the estimate of the standard deviation.
- Define the peak detection limit as LTM + 5 * SIGMA
- Alternatively, the peak detection limit is defined separately for each threshold trace using a predefined shift above the LTM. For the Novaya Zemlya network threshold trace we have initially found that LTM + 0.35 provides a reasonable peak detection limit, whereas the individual station/phase threshold traces show a somewhat larger variability, and LTM + 0.4 was consequently used.

Fig. 3 shows a panel with threshold traces for 18 May 1999 with predefined peak detection limits superimposed. Notice that six peaks are identified on the network threshold trace which we have to investigate in more detail.

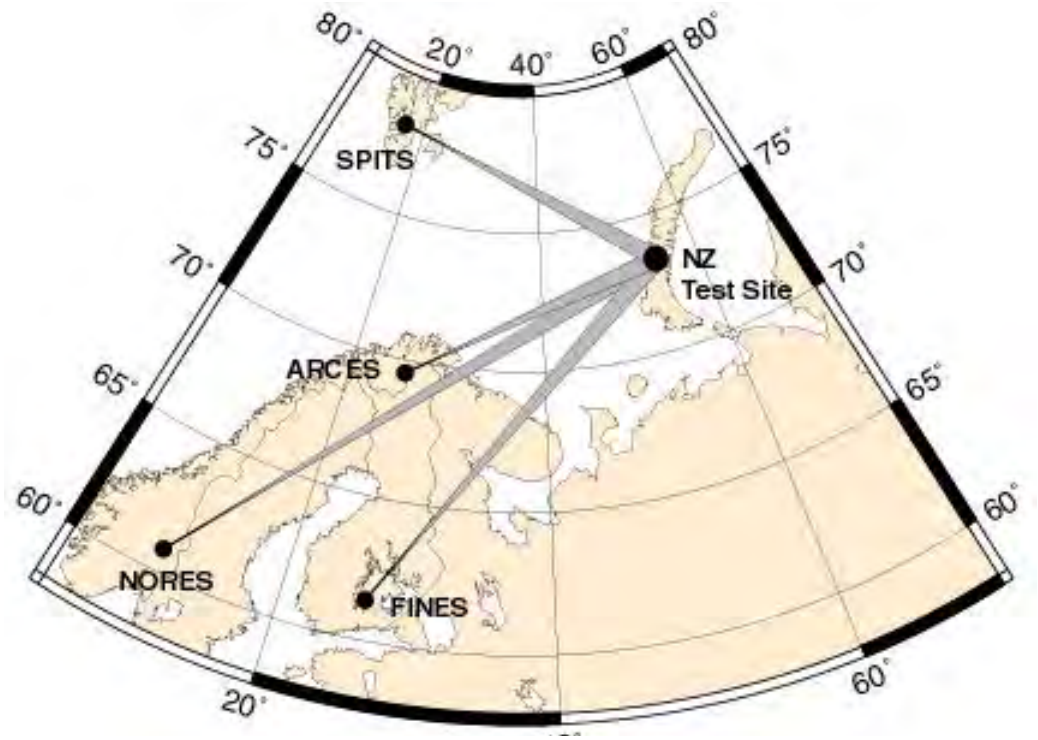


Fig. 1. Map of Novaya Zemlya and the locations of the four arrays (SPITS, ARCES, FINES, and NORES) used to monitor the region around the former underground nuclear test site.

Association of network threshold peaks with signals detected at each individual array

In order to relate the peaks of the network threshold trace to information obtained by traditional signal processing at each array, we first have to determine the time intervals associated with each network threshold peak. Through experiments, the following procedure has been established:

- Detect peaks on the threshold traces calculated for each individual phase. Examples are given in the lower panels of **Fig. 3**.
- For each phase considered, find the peak detection intervals overlapping the peak detection intervals of the network threshold trace, and use the union as the time interval of interest. See **Fig. 4** for details.
- The x-axes of the threshold traces show origin times at the NZ test site. When searching the detection lists for signals associated with the threshold peaks, we have to shift the detection times in accordance with the expected phase travel time from the NZ test site to the actual array.
- From statistics on the distribution of slowness and azimuth estimates, we define for each phase a critical azimuth and slowness range for events in the vicinity of the NZ test site. The numbers used are given in **Table 1**. Detected signals with azimuth and slowness estimates falling outside the critical ranges are assumed to be caused by events located outside the NZ testing area, otherwise, further offline analysis will be required to determine the cause of the threshold peak. Examples of array signal detections associated with the network threshold peaks are shown in **Fig. 5** and **Fig. 6**.

- An overview of the results after associating the network threshold peaks with signals detected at each individual array is given in **Fig. 3**. For each of the P-phase threshold traces we have only considered threshold peaks associated with a network threshold peak. In the four lower panels, an arrow indicates that we have found one or more signal detections with azimuth and slowness estimates within the critical ranges.
  For the peaks of the network threshold trace shown on top of the figure, an arrow indicates that at least one of the arrays has a detection with azimuth and slowness estimates within the critical ranges. The causes of these threshold peaks have to be investigated in more detail, e.g. by comparing to existing event bulletins or by offline analysis of the raw seismic data.
- In order to investigate the threshold peaks having phase observations with slownesses and azimuths typical for NZ events, we have introduced the functionality of comparing the critical signals to phases associated to events reported in the NORSAR bulletin of events in northern Europe (Kværna et al., 1999). The critical threshold peak at 20:20 on 18 May 1999 (see **Fig. 3**) is in this way found to be caused by an m_b 4.5 event located north of Severnaya Zemlya. For this location, P-phases observed at FINES and NORES have azimuths and slownesses comparable with P-phases from events at the NZ test site. Detailed information on the critical detections is given in **Table 2**.

There will still be a few situations when we have threshold peaks that cannot be explained by the procedures outlined above. In such situations we have to carry out additional manual analysis to determine the cause of the event. Typical situations may be signal detections in the coda of larger teleseismic events.

Array	Phase	Expected Azimuth (degrees)	Lower Azimuth (degrees)	Higher Azimuth (degrees)	Expected Slowness (sec/deg)	Lower Slowness (sec/deg)	Higher Slowness (sec/deg)
ARCES	P	62.2	47.2	77.2	11.22	10.59	17.11
ARCES	S	64.3	49.3	79.3	23.21	19.86	31.77
SPITS	P	97.6	77.6	117.6	13.24	10.59	19.86
SPITS	S	97.6	77.6	117.6	23.16	19.86	34.75
FINES	P	29.6	11.6	47.6	11.63	10.59	14.83
NORES	P	33.6	18.6	48.6	10.85	9.27	14.26

Table 1: Definition of critical azimuth and slowness ranges for phases from events near the NZ test site

CONCLUSIONS AND RECOMMENDATIONS

Concerning optimized site-specific threshold monitoring it is important to be aware that the main purpose of the method is to call attention to any time instance when a given threshold is exceeded. Through the development of the automatic explanation function for threshold peaks we have further reduced the need for manual analysis. This will enable analysts to focus their efforts on those events that are truly of interest in a continuous monitoring situation.

Through the integration of threshold monitoring with the results provided in traditional detection lists and event bulletins we have further improved the automatic monitoring capability of a given target area. For the Novaya Zemlya test site the monitoring threshold fluctuates around magnitude 2.0 during normal noise conditions, and we plan to evaluate the procedure in more detail by accumulating processing statistics for a longer time interval.

For the primary seismic stations of the International Monitoring System (IMS) for verifying compliance with the CTBT, we have available optimized processing parameters for the Indian and Pakistani test sites, and we plan to derive processing parameters for the former Chinese, French, and US test sites. There is, however, a need to further investigate the integration of three-component stations into the automatic explanation facility for threshold peaks.

Configuration	**Edge 1**	**Edge 2**	**Duration (sec)**	**Max. mag.**
Network	1999-138:20.21.28	1999-138:20.28.23	416	2.87
FINES P	1999-138:20.22.09	1999-138:20.28.16	367	3.78
NORES P	1999-138:20.21.27	1999-138:20.22.53	87	3.74

Station Phase	Arid	Arrival time (Origin time)	SNR	App. Vel. (km/s)	Azim. (deg)	R.pwr.	dS (s/deg)
FINES P	91336	1999-138:20.25.56.125 *(1999-138:20.22.11.925)*	45.1	10.3	12.7	0.98	3.40
FINES P	91339	1999-138:20.26.13.800 (*1999-138:20.22.29.600)*	2.9	8.7	15.9	0.97	3.13
NORES P	91473	1999-138:20.26.27.393 (*1999-138:20.21.45.993)*	3.0	11.6	23.3	0.93	2.22

Table 2: Definition of the critical threshold peaks shown in Fig. 3. The phases with critical slownesses and azimuths are given in the lower part of the table. These phases are all associated with a magnitude 4.5 event located north of Severnaya Zemlya

REFERENCES

Kværna, T. and F. Ringdal (1999): Seismic Threshold Monitoring for Continuous Assessment of Global Detection Capability, accepted for publication in BSSA.

Kværna, T., J. Schweitzer, L. Taylor and F. Ringdal (1999): Monitoring of the European Arctic using regional generalized beamforming. In: *NORSAR Semiannual Tech. Summ. 1 October 1998 - 31 March 1999, NORSAR Sci. Rep. 2-98/99*, Kjeller, Norway

Ringdal, F. & T. Kværna (1989): A multichannel processing approach to real time network detection, phase association and threshold monitoring, *Bull. Seism. Soc. Am.*, 79, 1927-1940.

Ringdal, F. & T. Kværna (1992): Continuous seismic threshold monitoring, *Geophys. J. Int.*, 111, 505-514.

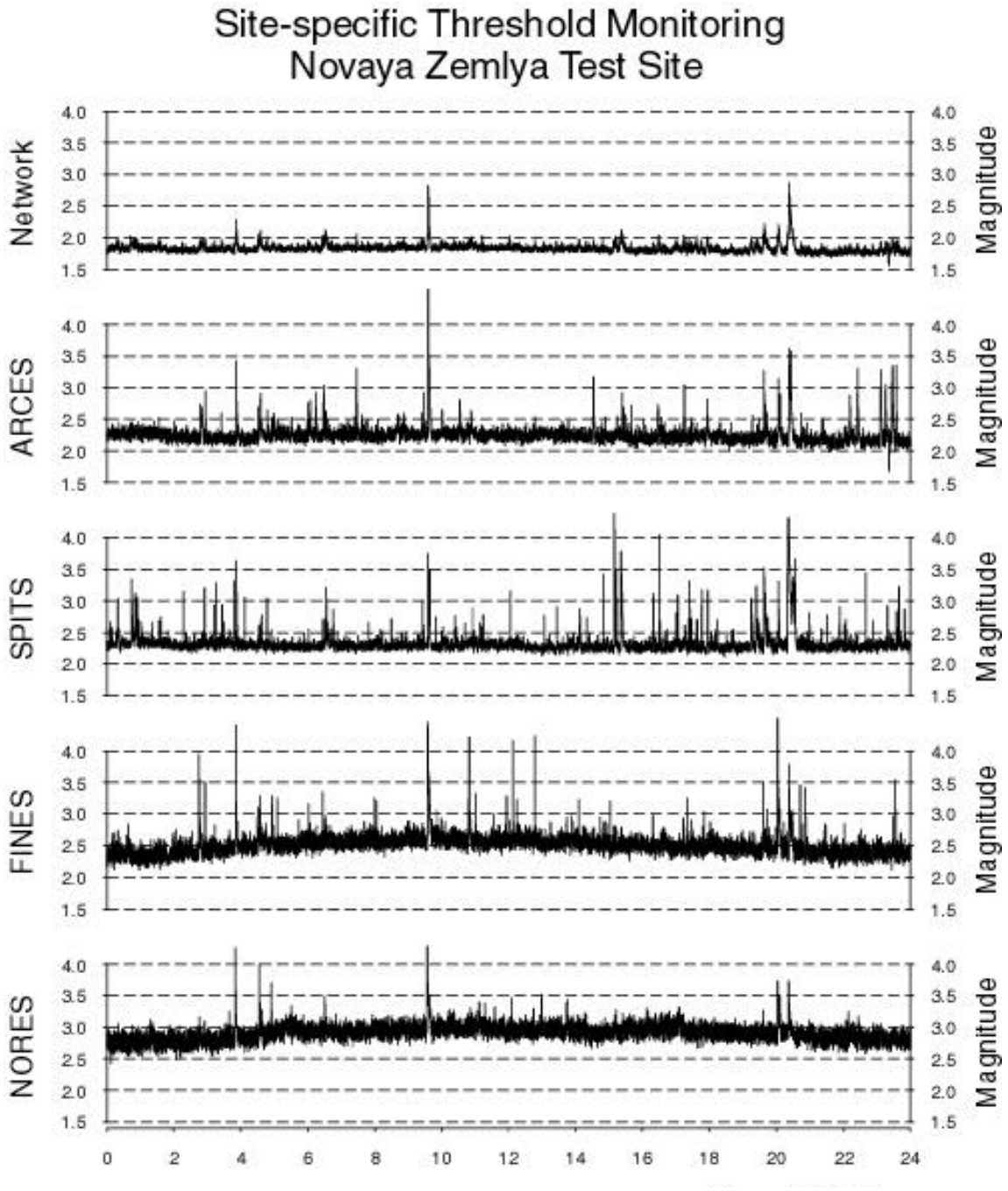


Fig. 2. Results from threshold monitoring of the Novaya Zemlya Test Site for 18 May 1999. The network trace on top is the combined threshold trace, using P phases for all arrays and in addition S phases for ARCES and SPITS. The traces for each of the four stations (P phases only) are shown below the network trace.

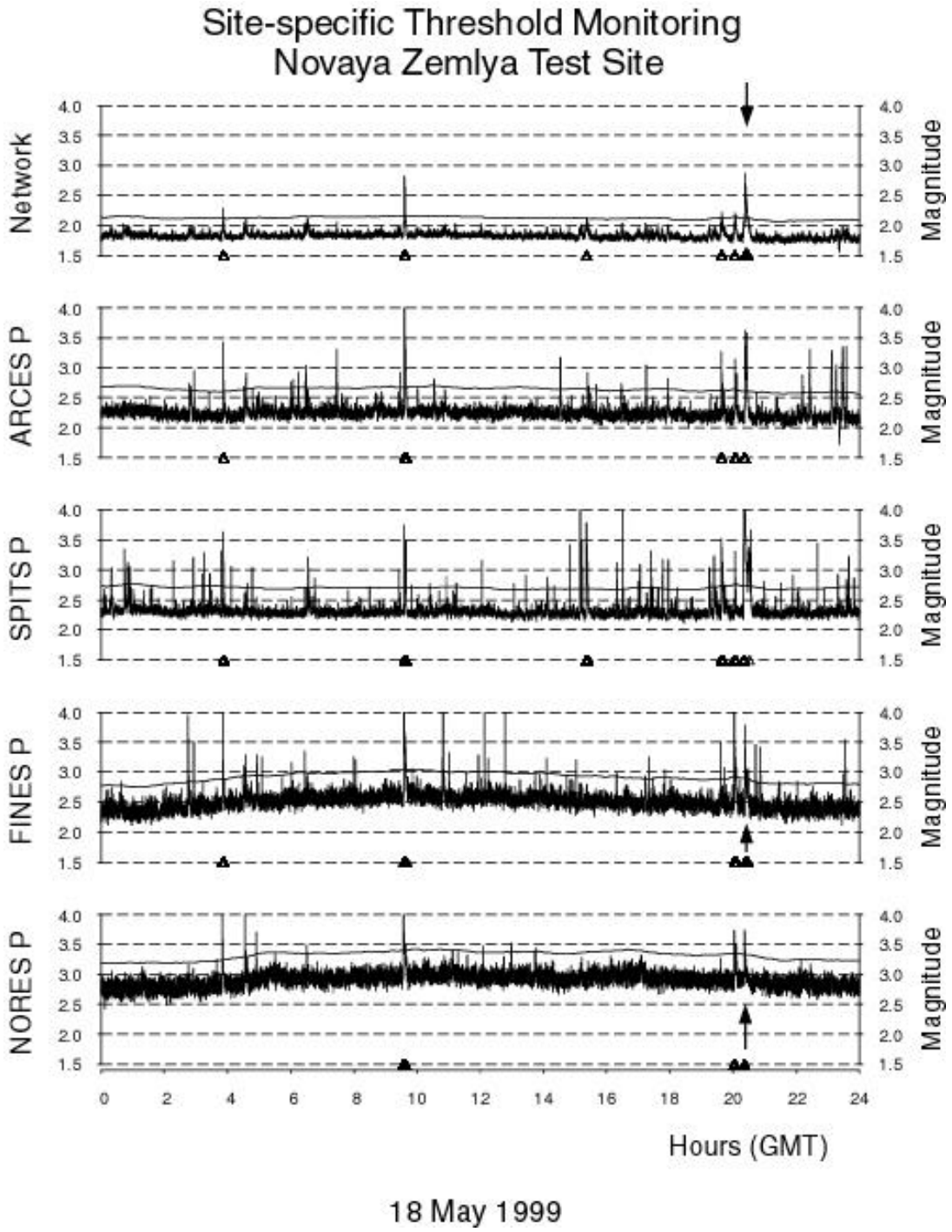


Fig. 3. Results from threshold monitoring of the Novaya Zemlya Test Site for 18 May 1999 with predefined peak detection limits superimposed. For each of the P-phase threshold traces we have only considered threshold peaks associated with a network threshold peak. In the four lower panels, an arrow indicates that we have found one or more signal detections with azimuth and slowness estimates within the critical ranges.

For the peaks of the network threshold trace shown on top of the figure, an arrow indicates that at least one of the arrays has a detection with azimuth and slowness estimates within the critical

ranges. The network threshold peak around 20:20, marked by the arrow, is caused by an mb 4.5 event located north of Severnaya Zemlya.

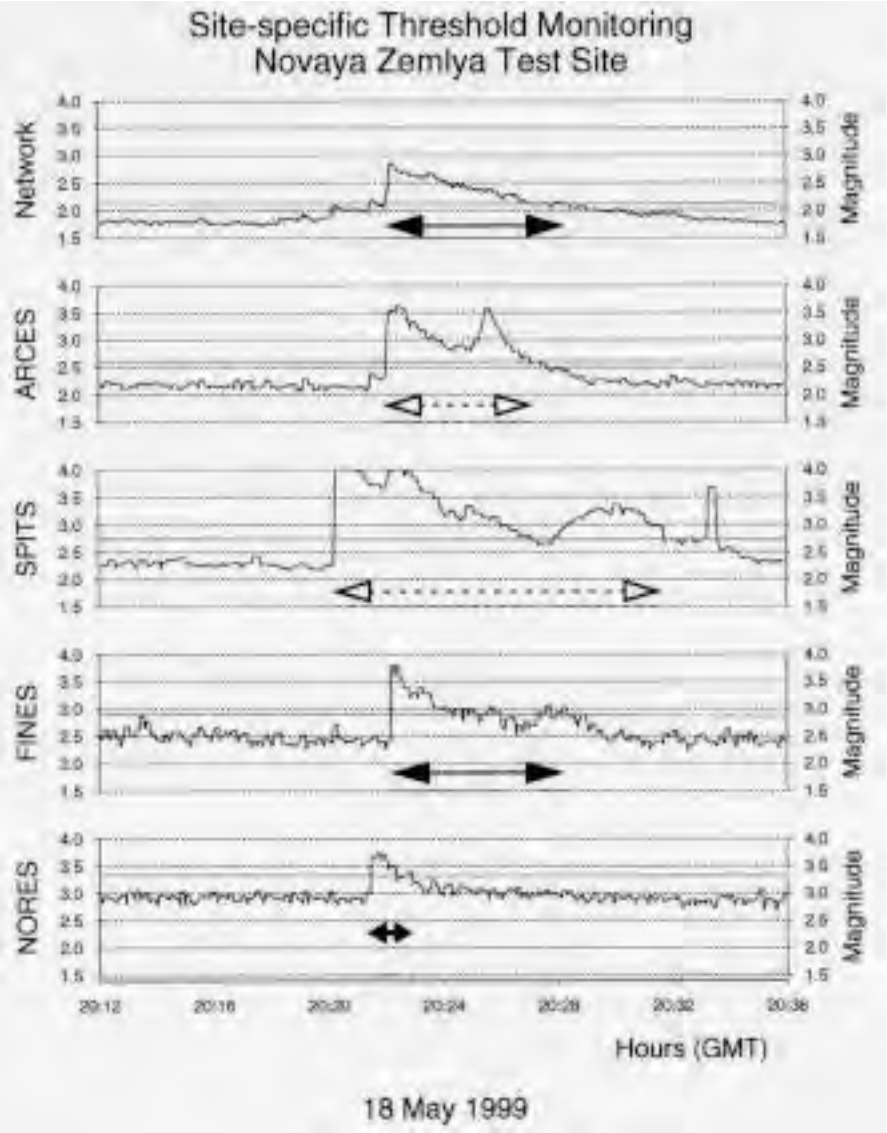


Fig. 4. Illustration of the procedure for defining the time intervals used for finding matching detections. For each phase considered, we find the peak detection intervals overlapping the peak detection intervals of the network threshold trace, and use the <u>union</u> as the searching time interval for each station. When searching the detection lists for signals associated with the threshold peaks, we have to shift the detection times in accordance with the expected phase travel time from the NZ test site to the actual array.

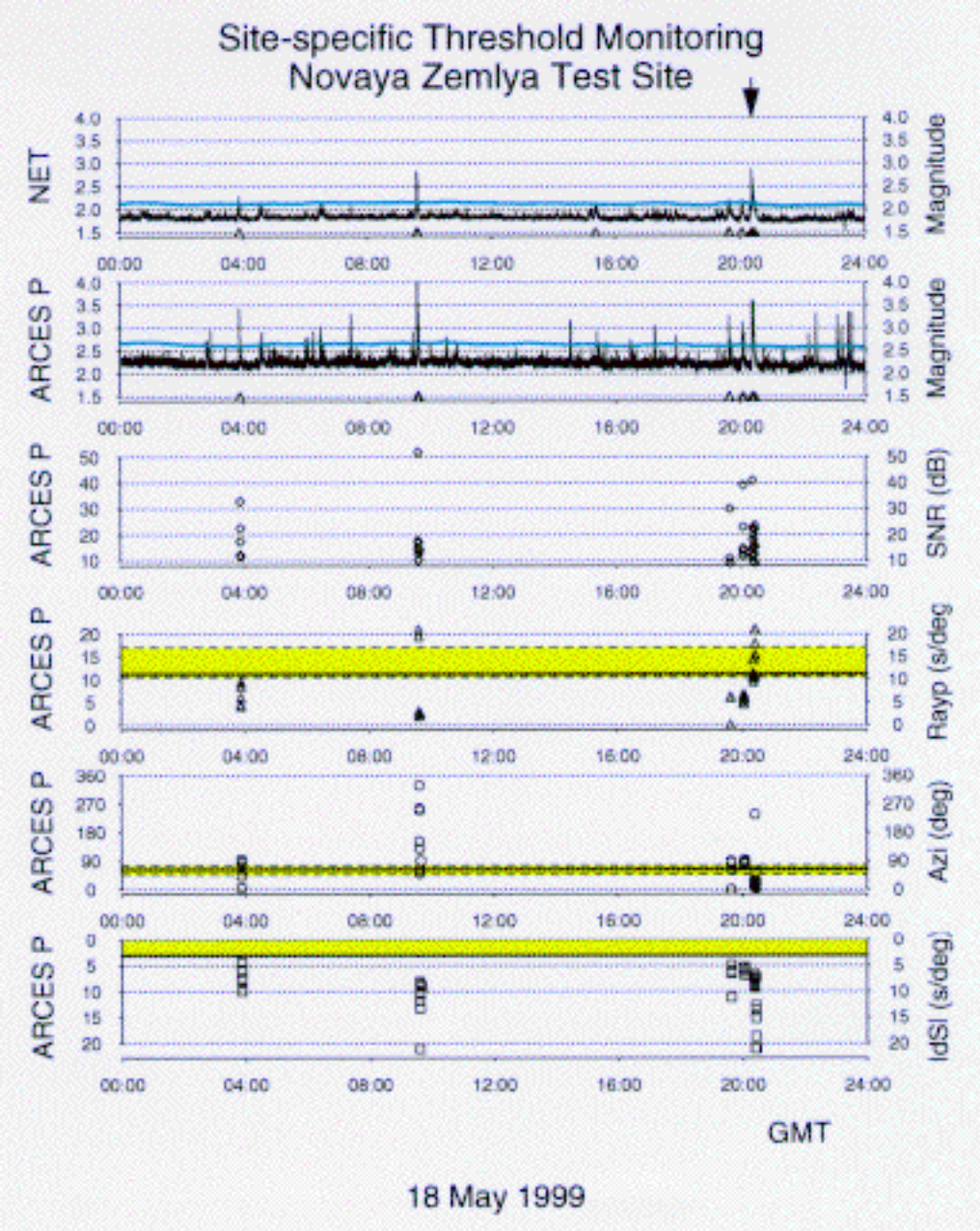


Fig. 5. Results from correlating peaks of the NZ magnitude thresholds with information from the signal detector at ARCES. The two upper panels show the threshold traces for the network and for the ARCES P-phase. The peak detection limits are superimposed. Information about the signal detections associated with the network threshold peaks is displayed in the four lower panels. The critical ranges of slowness (ray parameter) and azimuth are shaded grey in panels 4 and 5, and the bold dashed lines indicate the expected values of P-phases from the NZ test site. The panel at the bot-

tom indicates the differences in horizontal slowness estimates between the detected signals and the expected value for P-phases from the NZ test site (in s/deg). The shaded region within 3 s/deg indicates the approximate range of interest for NZ P-phases. Signals satisfying both the azimuth and slowness criteria are shown by filled symbols. Notice that no ARCES detections satisfies both the azimuth and slowness criteria.

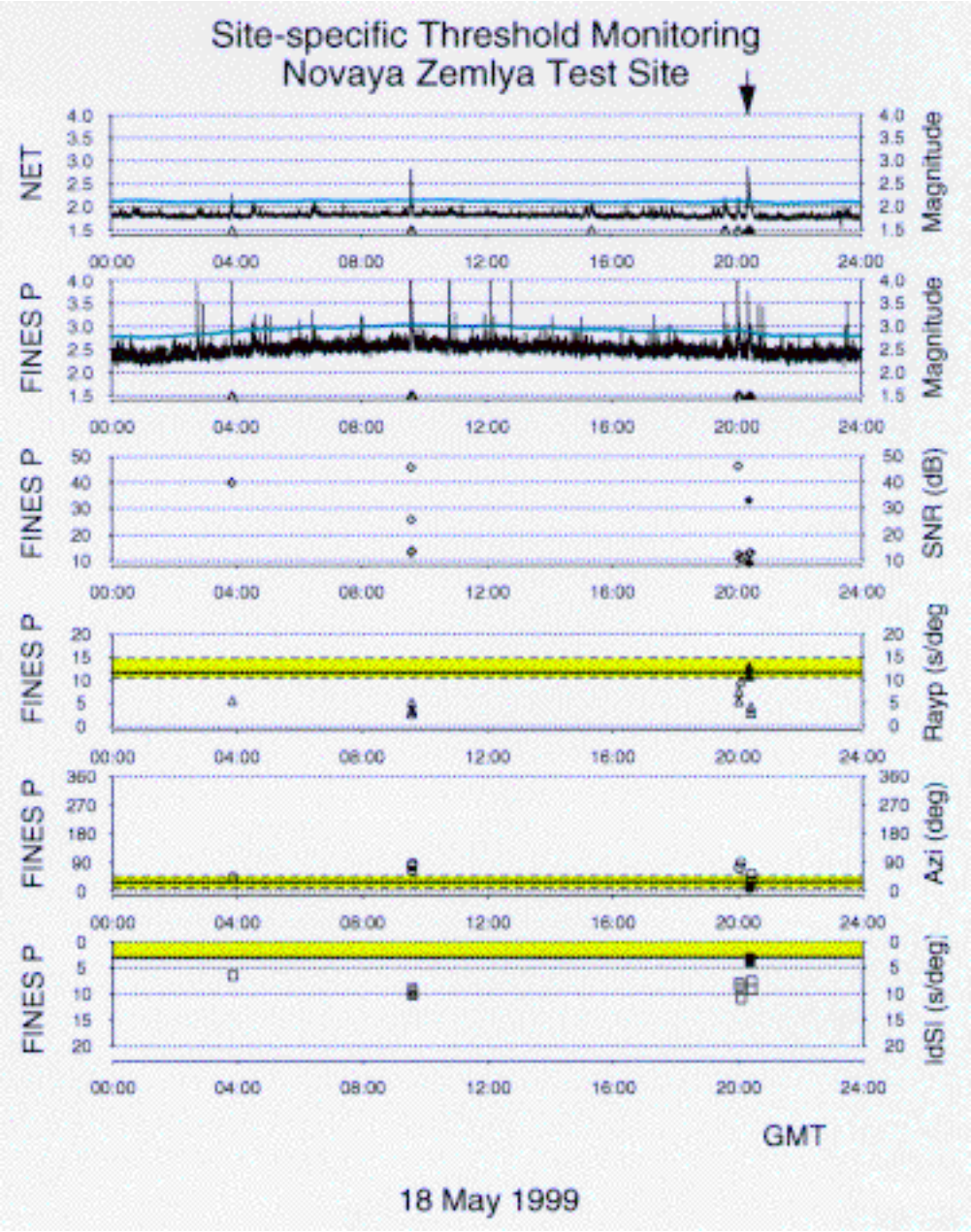


Fig. 6. Results from correlating peaks of the NZ magnitude thresholds with information from the signal detector at FINES. A detailed explanation of the figure content is given in the caption of Fig. 5. Notice that for the network threshold peak around 8:20 p.m. there are two FINES detections with azimuth and slowness estimates that fall within the critical range for P-phases from NZ events. This is because the event location near Severnaya Zemlya is at about the same azimuth from

FINES as NZ, and with a similar expected phase velocity. However, when combined with other stations (e.g. ARCES, see Fig. 5), it becomes clear that the signal cannot be from the NZ test site

INTEGRATION OF SEISMIC, HYDROACOUSTIC, INFRASOUND AND RADIONUCLIDE PROCESSING AT THE PROTOTYPE INTERNATIONAL DATA CENTRE

Ronan J. Le Bras, Jerry A. Guern, Doug A. Brumbaugh, Jeff A. Hanson, Tom J. Sereno
Monitoring Systems Operation, Science Applications International Corporation

Sponsored by U. S. Department of Defense
Defense Threat Reduction Agency
Contract No. DASG60-96-C-0151

ABSTRACT

The Comprehensive Nuclear-Test-Ban Treaty (CTBT) calls for the establishment of networks of seismic, hydroacoustic, infrasound, and radionuclide sensors to monitor the earth for underground, underwater, and atmospheric nuclear tests.

Seismic processing at the prototype International Data Center (pIDC) has been operating continuously since the GSETT-3 experiment that took place throughout 1995. Seismic is the most mature of the four monitoring technologies for automatic processing and interactive analysis.

Since late 1996, efforts have been made, under the Multi-Sensor Data Fusion project funded by the Defense Threat Reduction Agency (DTRA), to integrate hydroacoustic and infrasound monitoring technologies into the existing automatic processing and interactive review framework. The project has contributed to the integration of the single-sensor signal processing of hydroacoustic and infrasound waveform data within the operational system and has enhanced network processing to include two hydroacoustic phase types, *H*-phase (in-water generated) and *T*-phase (underground generated) and one additional infrasound phase, *I*. A joint bulletin including the three technologies is produced at the pIDC on a continuous basis. The bulletin includes arrivals from natural and man-made events recorded at all three sensor types. Enhancements have been made to the travel-time handling system to take into account temporal variations which may be significant for both acoustic technologies.

Case studies have also been conducted under the project, involving marine and atmospheric ground-truth or near ground-truth explosions. A set of low-yield marine explosions off the coast of Japan has increased confidence in the path-dependent velocity and attenuation models used in hydroacoustic processing. Atmospheric explosions from the White Sands Missile Range were recorded at two infrasound stations, and we conducted automatic and interactive processing on that data set to gain knowledge about infrasound propagation and test our system on this ground-truth data. Mining explosions have been analyzed in the context of joined seismic and infrasound processing, showing the improved location accuracy expected when azimuth determined from the infrasound data is added to the seismic data.

Efforts are currently under way to extract azimuth information at multi-hydrophone hydroacoustic stations and to prototype joined automatic processing of radionuclide detection data.

Key Words: data fusion, seismic, hydroacoustic, infrasound, radionuclide, operational system, case studies.

OBJECTIVE

The Multi-Sensor Data Fusion Project, sponsored by the Defense Threat Reduction Agency (DTRA) was initiated in the fall of 1996 in support of the prototype International Data Center's (pIDC) effort to integrate operational processing of the four monitoring technologies, seismic, hydroacoustic, infrasound and radionuclide. The main objective of the project was to bring as much processing of the acoustic technologies into pIDC operations as the existing networks would allow, by integrating newly developed single-technology processing modules *DFX* and *StaPro* for hydroacoustic and infrasound as well as upgrading the seismic network processing module, *GA*, into a multi-technology network processing module. We also wanted to analyze the operational results of the joint processing of the different technologies to learn about single technology and multiple event detection and statistics from this initial implementation. To achieve the objective of upgrading the network processing software in the absence of fully implemented networks and to satisfy the need for its thorough testing, a synthetic detections generator, *SynGen*, has been developed to allow simulations of planned large size networks. To calibrate the processing parameters and evaluate earth models, several case studies were undertaken involving hydroacoustic and infrasound data.

RESEARCH ACCOMPLISHED

Introduction

At the initiation of the project, the seismic processing capability was by far the most developed, and the approach taken to integrate the additional technologies was a progression where first the hydroacoustic data was integrated into the processing suite, then the infrasound and finally the radionuclide, following an approach where the technologies closer in kind to seismic were integrated first.

Hydroacoustic and infrasound sensors record pressures on continuous waveform traces and measure physical phenomena similar to seismic data. For both technologies, the single-sensor processing suite adopted the same general approach as in seismic processing. Two distinct modules perform single-sensor processing. The first module, *DFX*, performs the detection and feature extraction on the waveforms and the second one, *StaPro*, uses the features extracted from the waveforms to classify detections among different types. This project served as the integrator of the single-sensor modules, developed under separate efforts (*Laney et al., 1996, Willeman et al., 1996*) into pIDC operations. Within this project, network processing for the acoustic technologies has been closely integrated with seismic network processing and detections of all three types are processed jointly within the same module. The initial phase type identification of seismic and acoustic phases is used to guide network processing.

The initial implementation of the single-sensor hydroacoustic signal processing detector and initial phase identifier, developed in a separate effort as well as an upgraded network processing module were integrated into pIDC operations in January 1997. The experimental pIDC network has received signals on a semi-regular basis from a limited set of five stations, among which three of them (WK30, ASCN and VIB) are located at the International Monitoring System (IMS) sites specified by the Treaty. In this initial implementation, the station processing module used a set of feature-based default rules to differentiate between three types of hydroacoustic detections: noise (*N*), in-water explosion (*H*), or mostly earthquake-generated underground source (*T*). A neural-net approach to perform initial phase identification has been later tested and adopted at hydroacoustic stations PSUR and WK30. The neural net process performs the same differentiation between *N*, *H* and *T* arrivals.

Infrasound processing was first introduced in January 1998. All infrasound stations of the pIDC experimental network consist of an array of four microbarographs, most with separations of a few hundreds of meters, smaller than the standard IMS design. The detector in place at the pIDC is a combined coherency and signal to noise ratio detector. Both coherency and amplitude measures have to exceed a threshold for a detection to be declared. Station processing simply differentiates between noise arrivals (*N*) and signal (*I*) based on the value of the trace (or phase) velocity measured by the detector and feature extractor.

At the time of publication of this paper, the three waveform technologies are processed operationally at the pIDC for all available stations, including publication of automatic and analyst-reviewed bulletins containing arrivals from all three sensor types.

We have developed a plan to integrate the radionuclide detections into a bulletin fusing all four monitoring technologies. The plan calls for fusion processing of radionuclide detections at and above level 4 (anomalous level of anthropogenic radionuclides). An analysis will be conducted, using atmospheric transport results to determine the likelihood that an individual radionuclide detection has the same origin as a Seismic-Hydroacoustic-Infrasound (SHI) event.

Figure 1 is a schematic representation of the current set of three automated processing pipelines at the pIDC, with, in addition, the planned fourth pipeline envisioned to process radionuclide detections.

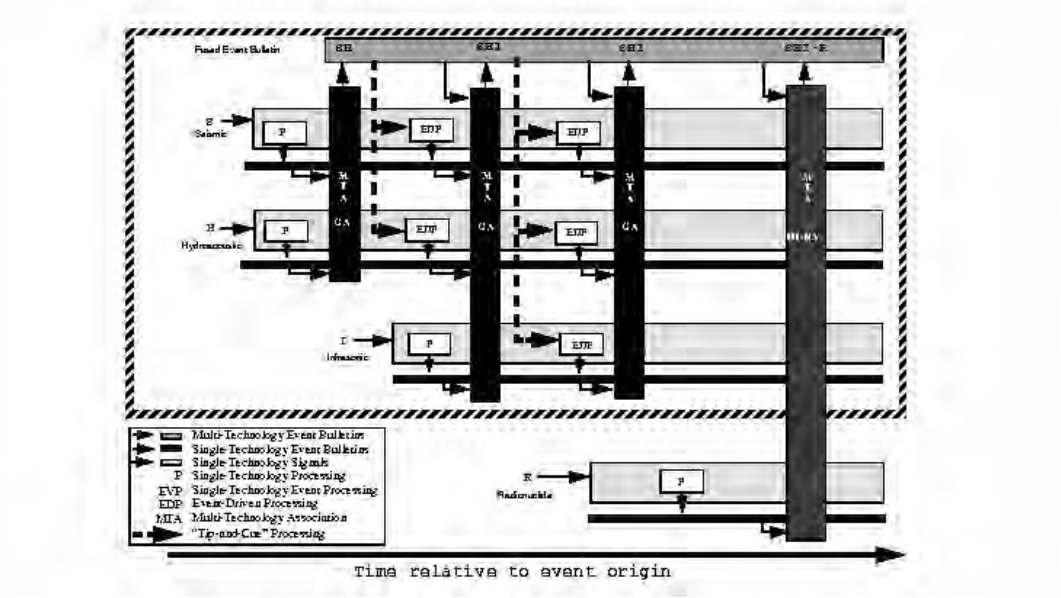


Figure 1. This schema represents the four pipeline processing configuration accomplishing fusion of all four monitoring technologies. The first three pipelines represented by the black vertical bars are currently implemented in pIDC operations by the GA system and produce multi-technology bulletins SEL1, SEL2 and SEL3, in order of increasing time. The fourth pipeline (in gray) represents the planned SHI-R fusion that will be done by a processing module to be developed, called SHI-RPA.

In the course of testing the different processing modules, we have gathered data from events of interest for all waveform technologies and performed a number of case studies. These case studies include sets of marine explosions from seismic refraction experiments in the Western Pacific, two atmospheric explosions with ground truth origin time and location, and mining events recorded at co-located seismic and infrasound arrays in Western Texas (TXIAR and TXAR). The marine explosions have provided useful data to test the hydroacoustic station processing module and in particular have allowed us to evaluate the phase identification module and test a cepstral-based bubble pulse delay extractor. Examination of the data from the atmospheric events in the White Sands Missile Range, for which ground-truth origin data is available, allowed evaluation of the detector and location modules. The mining events generated both seismic and infrasound arrivals and provided an opportunity to evaluate the usefulness of processing these two data types jointly.

Operational Plans and Implementation at the pIDC

Hydroacoustic

The principal mission of the hydroacoustic network is to detect underwater explosions and help in detecting lower atmospheric explosions. A large number of detections are recorded daily at the hydroacoustic stations when the current short-term average to long-term average (STA/LTA) signal to noise ratios are used in the detector. In the absence of discrimination between different types of arrivals, and of azimuthal information, since the current stations consist of single hydrophones, this large number of detections would lead the current network processing system to an unmanageably large proportion of false events (*Le Bras and Sereno, 1996*). Fortunately, station processing cuts down the number of detections to be considered by network processing by differentiating between underwater explosions (*H*), underground sources, mostly earthquake-generated (*T*), and noise detections (*N*). Whereas single-sensor seismic processing classifies individual detections based on their path of propagation, the approach taken by the single-sensor processing of hydroacoustic signals includes the source characteristics into the classification, thus performing some level of source discrimination at the level of single-station processing. A large number of features are measured on the hydroacoustic waveforms, for each of up to eight frequency bands. Classification into the three types of phases is performed either using a default set of rules on the frequency-dependent features or neural network weights adapted for individual stations. The default rules attempt to first identify positively the *T* phases mostly through their main characteristics of a long duration and low relative frequency content. Noise phases (*N*) are the next set of phases to be identified. Their frequency content characteristics overlap the *T* phase's frequency content, but they usually have a shorter duration. Finally, phases that do not fit into the *T* or *N* class are identified as in-water explosions (*H*). The main feature differentiators are a large ratio of high frequency to low frequency content and a short duration.

Network processing has been adapted to process hydroacoustic phase types. One of the main characteristics of hydroacoustic phases is that they propagate efficiently in the water column and that they can be blocked by significant continental masses after a few kilometers of underground propagation. To take this into account, blockage maps have been developed for individual hydroacoustic stations. They are taken into account by network processing to determine whether an association is expected or not given the blockage constraints on the path. The maximum distance of propagation in a given azimuthal direction obtained from the blockage maps is compared against the distance between source and station in every hydroacoustic association. Associations that are found to be along blocked paths are disallowed.

Blockage is taken into account at several stages of the automatic association process (or network processing). This includes an initial grid-based exhaustive search where the phase list attached to each grid point takes it into account for every station. Blockage is also checked after location to verify the legitimacy of each hydroacoustic association. Finally, blockage maps are first checked at the prediction stage before adding a hydroacoustic phase to an association set. An interactive tool has also been developed and presents either an alphanumeric window indicating whether a path is blocked or clear or a map showing the great circle path color-coded according to its blockage status.

At the time of the initial implementation of hydroacoustic processing, travel time for hydroacoustic phases was handled using a simple constant velocity (1485 m/s) model. This has been upgraded starting with release PIDC_6.0 where path-dependency was introduced. The travel time handler was further upgraded with release PIDC_6.1 to allow for seasonal dependency in addition to path-dependency. In addition, this last improvement included the capability to specify path-specific modeling errors for acoustic phases. The season and path-specific travel times can be generated for any hydroacoustic station with known location. Each station is user-configurable where the travel time uses by default the constant velocity model unless it is specified that the season and path-specific set of tables exist for the station and should be used. The path and season-dependent tables are generated using a ray-mode computation software, the Active Sonar Performance Model (ASPM), with DBDB5, a standard 5 minute bathymetry US Navy-provided oceanic velocity database. The theoretical travel time differences between a constant velocity model and these path-dependent travel times reaches a few tens of seconds and it is expected that their implementation will improve the fit with observed travel times. This has been observed and confirmed for a few specific paths (see section on case studies, in particular Figure 2). The seasonal dependence on a given path is not as

significant as the difference between the constant velocity travel time and the path-dependent travel time and so far we have not put found any systematic variation with the seasons on pIDC hydroacoustic data.

The season and path-specific travel times are used for both *T* and *H* phases, however two differences are worth noting in the current configuration between these phase types. The first is that the travel time for *T* phases includes an underground path, usually short in length compared to the total distance between source and receiver, but undetermined. This is taken into account by adding a coupling term to the modeling errors for *T* phases. The second and most significant difference is that the *T* phases's travel time is not taken into account in the location as opposed to the *H* phase's travel time. The system is capable of locating a purely hydroacoustic event provided *H* arrivals have been detected and identified at a minimum of three stations. In the current configuration, *T* phases alone cannot form an event and they are always associated to pre-existing seismic events as non-defining phases and acquired by travel time prediction based on the origin time and location of the seismic event.

The vast majority of hydroacoustic phases associated to pIDC events are earthquake-generated *T* phases. A statistical analysis of the hydroacoustic results at the pIDC shows that for a two-year period starting in May 1997, the Reviewed Event Bulletin (REB) contains 13,532 *T* phases that are associated to 8,437 events. The number of events possessing a hydroacoustic *T* phase is about 25% of the total number of REB events when taking into account hydroacoustic stations down time.

At press time of this paper, no explosive marine events have been automatically detected and formed by the system, although there have been examples of automatic detections emanating from two series of small-yield marine explosions. Because of the low number of stations, the automatic detections were made at one or two stations and correctly identified as explosion-generated. The arrivals at the stations missing the detections had too low a signal to noise ratio to be detected. The fact that automatic processing correctly identified some of the arrivals as originating from in-water explosions incited the analyst into looking for additional detections and thus later completing the association set to a total of three stations. In both cases, the occurrence of the small yield explosions was independently confirmed.

A serious drawback of the current hydroacoustic network is that, although two existing stations (Wake Island and Ascension) as well as planned IMS stations consist of multiple hydrophones, no advantage is currently taken from that multiple hydrophone configuration. We are in the process of developing this capability and we are planning to include it within release PIDC_7.0.

Infrasound

The planned IMS infrasonic network is intended to detect unannounced atmospheric explosions anywhere on the globe. The design for IMS infrasound stations consists of an array of four microbarographs in a triangular pattern with a center element. Array processing for infrasound sensors is most similar to seismic array processing with the exception that the detections are based on a more sophisticated hybrid algorithm that takes into account a measure of waveform coherency in addition to the usual STA/LTA signal to noise measure. For a detection to be declared at an infrasound station, both measures must coincidently exceed a threshold specific to each measure.

The atmosphere is traditionally divided into different layers with altitude: the troposphere, stratosphere, mesosphere and thermosphere, in order of increasing altitude. Propagation of sound in the atmosphere is complex even in the absence of winds, due to the presence of two low velocity zones. For an atmosphere at rest, this sound velocity structure gives rise to three main groups of arrivals: the tropospheric, stratospheric and thermospheric arrivals. We are currently not attempting to differentiate between these different arrival types at the station processing level, although we are collecting a large set of feature measurements for each detection, which should help us in the future to identify these arrivals. In the current implementation of the initial phase identification module, a very simple phase velocity-based rule is used to differentiate detections between noise detections which are called *N* and signals of interest, which are all indiscriminately assigned the generic phase type *I*. Detections are considered to be signal of interest (*I*) when their phase velocity is between two bounding values, currently set at 290 m/s and 660 m/s.

The current version of network processing (PIDC_6.1) has integrated the infrasound phase type by modeling the infrasound propagation as a single phase with a large time modeling error to account for the possibility that a given observed phase may be one of the three arrival types. The azimuth measurement is very precise and contributes the most to event location. The location algorithm will always locate an event at the surface if it includes an infrasound arrival (either purely infrasound or mixed event). There is currently an upper limit of 60 degrees on the range at which infrasound arrivals will be associated.

The travel time handling system has the capability to use station-specific and path-dependent travel times calculated using average seasonal wind patterns and we are in the process of integrating such tables for operational stations into the PIDC_7.0 release.

The operational results at the PIDC show on average a low number of automatic infrasound associations (492) and automatic pure infrasound events (57) since implementation of release PIDC_6.1, between December 2, 1998 and August 2, 1999. The main characteristic of the distribution of pure infrasound events is its extreme irregularity with time. We observed a large number of automatic events in early December 1998, including one that was later confirmed and included in the REB.

Radionuclides

Twenty-two radionuclide stations currently exist and are operational, with an additional 58 stations planned to reach the total of 80 stations proposed in the CTBT. At each station, particles are collected continuously from the passing airmass for 24 hours. Each sample is then allowed to age for another 24 hours so that "background" radionuclides that may interfere with measurement can decay away. The radionuclide content of the sample is then determined through gamma ray spectroscopy. If anthropogenic radionuclides are detected, the sample is assigned a level 4 or 5 (respectively single or multiple anthropogenic radionuclides) alert status.

Meteorological measurements from the NOAA database and meteorological modeling software are used to determine the trajectories covered by the airmass. This locus of points in time and space from which the detected radionuclides might have been released is called the Field of Regard (FOR) of the sample. The NOAA data set consists of wind velocity measurements gathered at 24-hour intervals at points on a regular grid covering the globe. OMEGA is a weather modeling prediction program used to calculate wind velocities at the grid points to a temporal resolution of 1 hour by modeling the airflow between the two endpoints that bound the 24-hour interval.

This information is used to simulate particle releases from each grid point at 1-hour intervals for a period of 3-14 days before a given sampling period. The locus of points from which a particle released a certain period of time before a sampling period has a significant probability of being detected in the sample is called the sample's Field of Regard for that time period used to calculate high resolution FORs and several other related data products. A radionuclide detection with a level 4 or 5 alert status triggers OMEGA to calculate 72, 48 and 24 hour FORs for the detecting station and sampling period. Automating radionuclide association to SHI events, then, consists simply of searching for events from the Standard Screened Events Bulletin (SSEB) whose error ellipse has an intersection with a field of regard for a level 4-5 alert sample and whose origin time is compatible with the FOR's time period.

Particle trajectories could also be used to improve on the 24-hour granularity of the FORs, however the size of the FORs is usually of the order of at most a few error ellipses and the added complication of performing trajectory interpolation may not be worth the small gain in resolution. Unlike the other three technologies in the Fused Event Bulletin, radionuclide detections represent direct physical evidence of a nuclear reaction at least, possibly of an explosion. Hence, greater care must be taken when publishing data relevant to this technology to avoid the appearance of making an accusation. In the context of the automated IDC system, an association drawn between a radionuclide detection and an SSEB event should not and cannot be construed as a claim that the SSEB event was indeed the source of the radionuclides. The association must be understood to indicate only that a detection of anthropogenic radionuclides was made at a station and that if such nuclides had been released from the location/time of the SSEB event, the probability of their being detected at that station in that sample is significant. Neither

of these offers any basis on which to calculate the probability that such radionuclides *actually were* released from the location/time of the SSEB event.

Case studies

Marine explosions

In the course of testing hydroacoustic signal processing algorithms to characterize explosion sources from earthquake-generated *T* phases, a series of over 100 distinct signals were identified at the two Pacific hydroacoustic stations: Point Sur, California (PSUR), and Wake Island (WK30). The distance between the two stations is about 41°. The signals were grouped in three distinct 8- to 10-hour long subsets from September 6 to 10, 1996, and clearly emanated from in-water explosions because of the presence of bubble pulses identifiable in their spectrum, cepstrum and autocorrelation. Furthermore, individual events could be correlated between the two stations and the time separation between them was quasi-constant (12-15 minutes). These characteristics pointed to human activity, and more specifically, to a seismic refraction survey as the source of these events. Since PSUR and WK30 were the only stations that recorded the series of explosions, no definite location was attempted. The locus of possible locations was a line crossing the Pacific Ocean from the coast of Antarctica, passing between Australia and New Zealand up to Northern Japan.

After some investigation, we established that the signals observed at these two stations emanated from a seismic refraction survey conducted by a Japanese scientific crew offshore northern Honshu, Japan (*Ryota Hino, 1998, personal communication*). The underwater explosions ranged from 20 to 400 *kg* in size, and were detonated at approximately 28° from WK30 and 71° from PSUR. The comparatively small size of these explosions, and the fact that they were recorded with good signal to noise ratios at cross-oceanic distances illustrate the extremely good propagation characteristics of the oceans. An explosion of interest to the monitoring community would be detected at long distance ranges provided that there exists an oceanic path between the location of the source and the hydrophone. The signals generated by the refraction survey allowed us to evaluate the performance of automated processing programs and partially validate path-dependent hydroacoustic travel times tables. Marine refraction surveys such as this are now rare in the oceans and this ground truth data set is of great interest to validate propagation models and processing techniques.

Knowledge of the ground truth information for this set of marine explosions allowed us to establish the reliability of our detection and phase identification processes as well as of the cepstral delay time measurements. We established the extreme consistency of the delay times between the two stations that recorded the explosions. While variations from explosion to explosion were found to vary by about 0.02 seconds, likely due to differences in yield and depth, the difference between measurements at the two stations for the same explosion are within 0.002 second of each other. This makes the cepstral delay a suitable attribute to use as an association criterion. We were able to evaluate and validate path-dependent hydroacoustic travel times derived from a standard database of US Navy measurements. Synthetic travel times computed with the 2D station-specific travel time model were within five seconds of the observed travel times, whereas travel times generated assuming a constant hydroacoustic velocity were up to 40 seconds too early. Clearly, the predicted travel times benefit from using path-dependent travel time tables for each station, rather than a constant velocity model.

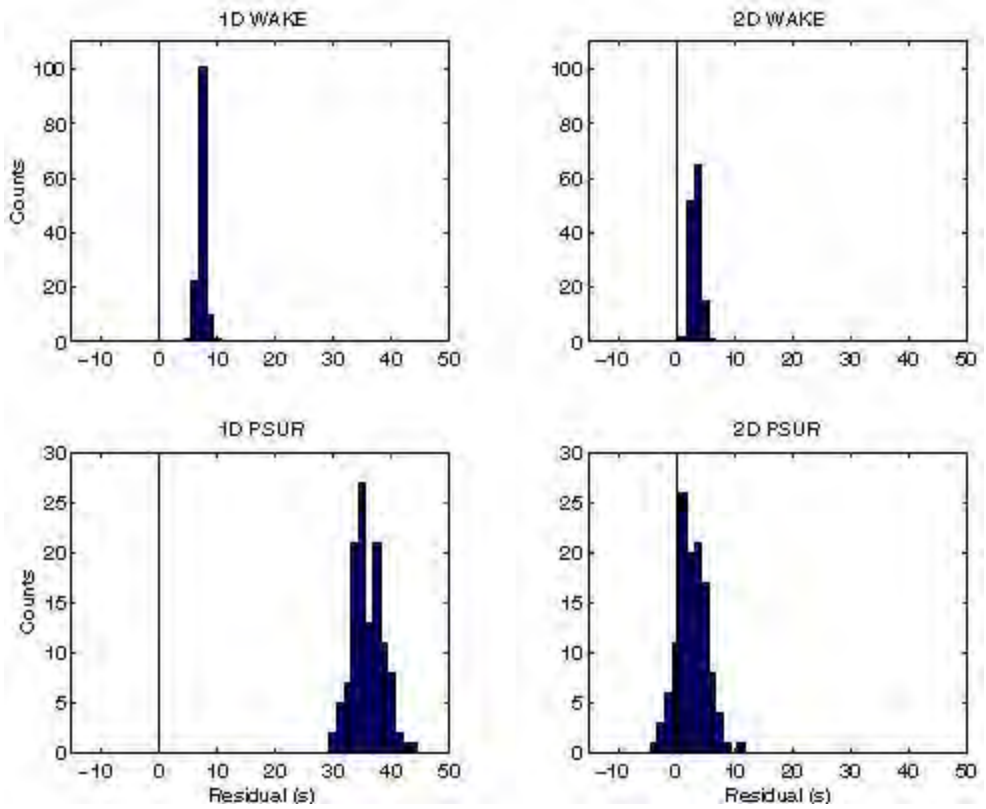


Figure 2. Histograms of travel time residuals (observed minus predicted travel times) computed at WK30 and PSUR using both the 1D constant velocity model and the 2D travel time tables. Note the vertical scale on the histograms differs between WK30 and PSUR. A significant improvement in travel time accuracy is obtained when the 2D travel time tables are employed, particularly for PSUR detections.

Low altitude atmospheric explosions

Two lower atmospheric explosions at the White Sands Missile Range in November 1997 provided us with ground truth data against which to test our infrasound processing modules and propagation models. A detailed study (*Jenkins et al., 1998*) of these two explosions, which occurred at one week interval from each other, pointed out variations in travel time (17 seconds difference at station LSAR for the first arrivals) and character of the waveforms between the two events. There were however similarities in the duration of the wavetrain within which individual arrivals can be correlated from one event to the other at both stations. A general observation is that the phase velocities of arrivals show an increasing trend with time within the wavetrain, consistent with the interpretation that they are sampling higher and higher layers of the atmosphere.

Mining events

Examination of two mining events for which both seismic and infrasound waveforms were available has yielded information on infrasound propagation at close regional distances. Both events were recorded at seismic station TXAR and infrasound station TXIAR and the data were provided to us by J. Bonner from Southern Methodist University (*Sorrels et al., 1997*). One of the events occurred on October 4, 1996 in the Micare coal-mining district in Northern Mexico and is referred to as the Micare event. The other event occurred on October 11, 1996 in a mining district in New Mexico and is referred to as the Tyrone event. A detailed study of the events is available in *Flanagan et al. (1999)*.

The observed lone infrasonic arrival from the Micare event is likely a thermospheric arrival. The infrasound arrival from that event has a total travel time of 20 m 18.3 s, is more consistent with the expected wave group velocity from thermospheric arrivals (around 245 m/s) than for tropospheric arrivals (around 320 m/s). This is further confirmed by its high phase velocity (376 m/s). The Tyrone event, with its seven separate infrasound arrivals, yields a variety of phase velocities, but it is difficult to observe a strong trend of increasing phase velocities with increasing travel time, such as was observed for the White Sands ground-truth explosions in *Jenkins et al.* (1998), as the quality of the arrivals for this event is not as high. The main conclusion of this study is the apparent ability of the infrasound sensors to contribute significantly to the location process by decreasing the size of the error ellipses when infrasound detections are combined with seismic detections, as illustrated by Figure 3. The default modeling errors for azimuth currently in place at the PIDC (0.102 s/km) were used in the locations and were found to lead to location solutions that include our best estimates of the ground-truth locations.

Another significant conclusion is that processing of infrasound data may benefit from using an approach complementary to the classical F-K analysis. An envelope function approach to slowness-azimuth determination was successful in determining a more accurate azimuth than a classical F-K approach. This suggests that envelope functions may be more reliable for characterizing infrasound data when a lack of signal coherency across the array prevents a classical FK analysis.

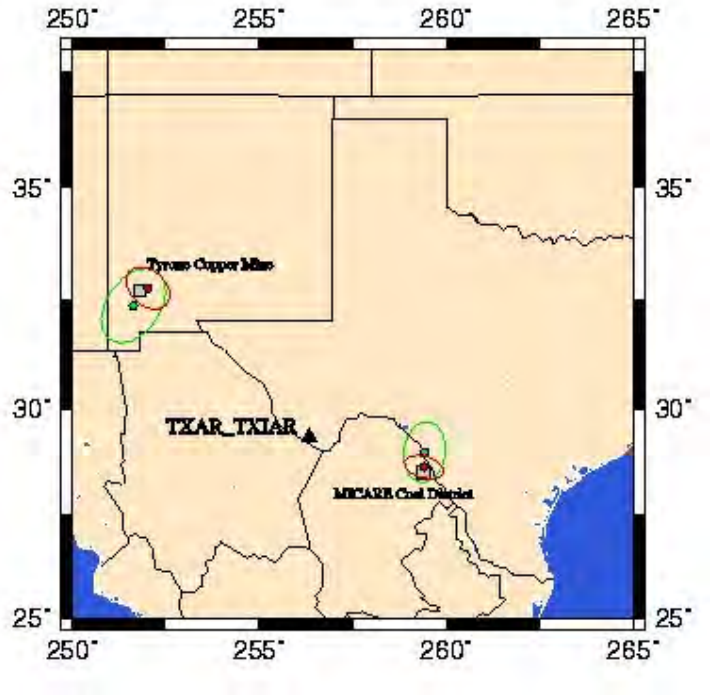


Figure 3. Estimated locations of October 4 and October 11, 1996 explosions. The circles on which the larger error ellipses (green) are centered indicate locations estimated using the Pn and Lg arrivals only while the centers of the smaller error ellipses (red) indicate the final locations estimated using the first infrasound arrival, I, together with Pn and Lg to form the location. The 90% error ellipses are computed in all cases. Note the improvement in the azimuth and reduced area error ellipse of the combined seismic-infrasound location. The actual mine locations are represented by the gray squares.

CONCLUSIONS AND RECOMMENDATIONS

We have implemented in pIDC operations a processing suite that demonstrates the feasibility of doing joint network processing of detections from the three waveform technologies, seismic, hydroacoustic and

infrasound. We have also analyzed a few examples of waveform data from events of interest to the monitoring community to show the validity of our processing suite on these special events.
More work remains to be done to take full advantage of the acoustic data types. For instance, the hydroacoustic stations of the IMS are planned to consist of groups of multiple hydrophones. To take advantage of this configuration and enhance the usefulness of hydroacoustic arrays, we are in the process of developing a module to jointly process hydroacoustic arrivals to obtain an azimuth at hydroacoustic stations.

While the hydroacoustic propagation model in place takes into account blockage as well as path-dependent and seasonal variations and is thus quite elaborate, infrasound is still using a constant velocity model. This implies that the modeling errors are large, leading to potentially erroneous associations. One of the goals of planned enhancements to the infrasound propagation model is to match travel times better and allow for smaller travel time modeling errors.

Case studies have proven quite useful in evaluating the pIDC processing software and more should be conducted to evaluate the planned enhancements, for example comparison of ground truth infrasonic travel time data with existing models.

REFERENCES

Hanson, J., R. Le Bras, P. Dysart, D. Brumbaugh, A. Gault and J. Guern, Operational Processing and Special Studies of Hydroacoustics at the Prototype International Data Center, submitted to *P. A. Geoph.*

Flanagan, M., R. Le Bras, J. Hanson and R. Jenkins, Analysis of Two Mining Explosions Recordings at the TXAR Seismic and Infrasound Arrays, *SAIC Tech. Report, 99/3002,* 25pp., (1999).

Jenkins, R., C. N. Katz, R. Le Bras, and T. Sereno. Ground-Truth Analysis of Explosions Recordings at LSAR and TXIAR Infrasound Arrays, *SAIC Tech. Report 98/3035*, 25pp., (1998).

Laney, H., P. Dysart, H. Freese and R. Willemann, An automated system for detecting and classifying in-water explosions and T-phases, *J. Acoust. Soc. Am., 100, 2641,* (1996).

Le Bras, R. and T. Sereno, Monitoring the Earth for Nuclear Testing in Underground and Underwater Environments, *Processings of the 1996 AGU Fall Meeting* (1996).

Sorrells, G. G., E. T. Herrin, and J. L. Bonner, Construction of regional ground-truth databases using seismic and infrasound data, *Seism. Res. Lett.*, *vol. 68, no. 5,* 743-752, (1997).

Willeman, R., H. Laney, P. Dysart and H. Freese, A global monitoring system for a nuclear test ban treaty, *J. Acoust. Soc. Am., 100, 2642,* (1996).

OPERATION AND RECENT DEVELOPMENT OF THE PROTOTYPE INTERNATIONAL DATA CENTRE

Stephen G. Mangino

SAIC, Center for Monitoring Research, Arlington, VA
Sponsored by U.S. Department of Defense, DTRA
Contract No. DTRA01-99-C-0025

ABSTRACT

The Prototype International Data Center (PIDC) in Arlington, Virginia is now in its fifth year of full-scale operation. It continues to evolve through a series of software 'releases' that incorporate advanced physical and computer science technologies. After testing on the operational system at the PIDC, the software is delivered to the CTBT Organization in Vienna. The second release of software to the IDC was installed in May 1999, and provides that facility with a capability for data acquisition, automatic processing, analysis and product dissemination that is essentially identical to that of the PIDC.

The network currently used by the PIDC consists of 36 primary and 37 auxiliary seismic stations; 4 hydroacoustic stations. 6 infrasonic and 20 radionuclide stations that together yield on average 4.2 Gb of data per day. These data are forwarded to the Vienna IDC which at present (May 1999) does not have any independent data sources. The PIDC continues to publish multiple automated event listings and a Reviewed Event Bulletin (REB) for every day of the year. Over the past year, enhancements of the application software, data services and system utilities have refined the ability to detect and locate events. In the latest version of the software these include:

- routine automatic and interactive processing of infrasound data
- seasonally varying hydroacousitc travel times and improved hydroacoustic analysis tools
- 'Filed of Regard" images for radionuclide measurements
- source specify station corrections (SSSC's) for northwestern Eurasia
- improved coefficients for M_L determinations, to closer match m_b
- new M_s computation, including regional-distances
- Threshold monitoring, assessing seismic station and network detection capability
- expanded bulletin formats that include maximum-likelihood and upper-bound magnitudes.

In addition to this new functionality, there have been many improvements in such areas as the stability of the distributed application and control processing system, and better error-handling capabilities. Data and products from the PIDC continue to be made available by subscription (regular mail messages), on demand through an 'AutoDRM' service, and via the PIDC Web page (www.pidc.org)l

Key Words; International Data Centre, bulletin

ENHANCEMENTS IN AUTOMATED PROCESSING SYSTEMS

The operability of IMS systems was significantly enhanced with the replacement of ISIS, a distributed application control processing system (DACS), by Tuxedo, a more robust queue-based DACS. Tuxedo 'middle-ware' has been in use for several years, for example, by the banking industry in Automated Teller Machines (ATM's). Operability of the system was also improved with the new DACS controller GUI '*Tuxpad*'. *Tuxpad* was developed to enable an IMS system operator the ability to monitor and control the entire automated processing system via a handy GUI interface. *Tuxpad* features include online modifications to the timely execution individual process or entire groups of processes, re-distribution of processing load, etc. A similar advancement incorporated within the WorkFlow GUI enables an operator to examine in detail the status of a individual process within the 'pipeline', identify problems that may exist, and if necessary re-process the interval via a simple mouse command. Although such modifications may appear subtle, they have enhanced the error handling capability and significantly improved the operability of the automated processing system.

INFRASONIC SIGNAL PROCESSING

Infrasonic signal processing is a routine part of interactive analysis at the PIDC. Infrasonic waves can originate in the atmosphere or as seismic waves that couple with the atmosphere. The signals typically have a duration from 10-100 seconds, in general a dominant frequency from 0.01-3.0 Hz and can display a strong coherence across an array of sensors. An infrasonic 'detection' is declared by the automated system when the spatial coherence of the waveforms exceeds a pre-determined threshold, where the spacial coherence of the waveforms is calculated in a two-dimensional slowness plane for a set of frequency bands. Although 60 IMS infrasonic stations are scheduled to be deployed, 6 are currently available at the PIDC. For the tuning of existing and the testing of new algorithms and parameter configurations an interactive GUI analysis tool has been developed (Wang, 1999). Improvements pertaining to the kinds of features of a detection that should be extracted as well as the methodology of extraction are active research topics.

HYDROACOUSTIC INTERACTIVE ANALYSIS TOOLS

Hydoacousitc processing includes signal detection, feature measurement, phase identification and association. Among the many new features introduced into the Analyst Review Subsystem (ARS) several of these features that specifically address processing and displaying hydroacoustic data are in standard use. Hydroacoustic functionality includes and allows users to:

- select whether to display the peak or probability weighted arrival time;
- display the onset/termination times for a hydro arrival;
- modify the onset/termination times;
- send the modifications to DFX (Detection and Feature Extraction) for processing;
- display the new onset/termination and arrival times and;
- save these new parameters to the database.

The addition of hydroacoustic as well as atmospheric infrasound data as input has extended ARS' processing requirements. Previously ARS could safely assume all seismic arrivals occurred within 40 minutes of an event, however, acoustic phases may arrive hours later. ARS' has been modified to handle time-extension waveform loading for a given analysts' allocation.

FIELD OF REGARD IMAGERY

The PIDC generates products to support radionuclide monitoring operations and to support the location of radionuclide sources using atmospheric transport modeling (Zuzola et al., 1998). One such product, the field of regard (FOR) identifies an area within which air has a non-zero probability of moving forward over a specific time interval and arriving at a site or a point location. The area identified is based on the release of air parcels at grid point locations from which the air parcels grow by diffusion/dispersion and move with the

atmospheric flow. If the parcels grow in size and move over the site or point location, and have grown large enough to impact the site at a user defined minimum concentration (minimum detection level), then that particular parcel contributes to the probability distribution. The area enclosing the union of all parcels over a period of time which impact the site defines the FOR. The ratio of the parcels from any particular grid point that arrive/impact at a station to the total number of air parcels released from all grid points that arrive/impact at that station taken from all releases for all the grid points in the region of interest determines the probability distribution needed to define the most likely source area, or the FOR. The time specified for the field of regard is the initial time of release of air parcels from any of the grid points. If the FOR is a 48-hour FOR, air parcels require 48 hours or less travel time from any grid point to arrive at (or pass through) the site or point location. Detailed sample information, measurement categorizations, processing results and FOR images are available for 48- and 72-hour timesteps via the PIDC website.

SOURCE SPECIFIC STATION CORRECTIONS

It is well known that IASPEI91 global travel time curves deviate from observed travel times in shields and platforms at regional distances. One of the objectives of the PIDC is to improve event locations using regional travel time corrections for IMS stations relative to IASPEI91. The PIDC incorporated source specific station corrections (SSSC's) into the IMS during the spring of 1999 for the Fennoscandian region. In addition, SSSC's are under testing for more than 20 seismic stations in the US and Canada (Yang and McLaughlin, 1999b). Preliminary results presented in Yang et al., (1999b) show event locations are improved and error ellipses are reduced when such corrections are utilized.

IMPROVED ML DETERMINATION OF IMS STATIONS

In the spring of 1999, station-specific correction curves for M_L estimation were installed into the PIDC operational system. This was the first significant upgrade since 1995 (Israelsson, 1995) to reduce the discrepancy between M_L and m_b on a station by station basis. Better station M_L magnitude estimates result in better network M_L. Improved curves were determined from two years (1997-1998) data recorded at 85 stations or about 13,000 arrivals. Comparisons and results discussed in detail in (Yang et al., 1999) show a significant reduction in biases and scatter for many of the IMS stations.

MS COMPUTATION INCLUDING REGIONAL-DISTANCES

Computation of M_s was modified by replacement of the Prague distance formula with the formula of Rezapour and Pierce (1998) and Stevens and McLaughlin (1997) in order to increase accuracy, reduce uncertainty and decrease M_s thresholds. Since the beginning of GSETT-3 surface wave processing was limited to the range of 20-100 degrees, primarily because M_s calculated at distances less than 20 degrees is consistently lower than M_s at greater distances. Modifications discussed in McLaughlin and Stevens (1999) show this is no longer the case, hence, the distance range for measuring surface waves was extended to 2-100 degrees. These enhancements significantly improve the PIDC's ability to estimate M_s.

THRESHOLD MONITORING

Threshold Monitoring (TM) provides an ability to assess the detection performance of the primary IMS seismic network using hourly summaries of each station's data availability, noise levels and average and worst-case global detection capability. Graphical results in the form of PostScript files are accessible via the PIDC website and via pointers in the fileproduct table which provides a framework for distributing TM results through the Subscription system. TM has been included within the SEL3 pipeline which runs approximately 12 hours behind real time. Several applications comprise TM (Kvaerna, 1998) and include: TMthreshold, which calculates global detection thresholds using DFX, and TMprod which creates hourly summary plots and updates the fileproduct table. The three kinds of TM plots available are:

- 'detplot' provides average and worst-case network detection capability by the hour;
- 'status' provides the noise level, signal, and data gaps for primary seismic stations;

- 'uptime' displays a world map with information on station availability.

IMS1.0, MAXIMUM-LIKELIHOOD AND UPPER-BOUND MAGNITUDES

The Reviewed Event Bulletin (REB) is a list of events and event parameters obtained by analyst review of automated processing results of data from Primary and Auxiliary SHI stations. IMS1.0 format is now the standard publication format for PIDC products. Perhaps the most significant new feature of IMS1.0 is the inclusion of maximum likelihood magnitude measurements.

The PIDC has routinely estimated maximum likelihood m_b and M_s magnitudes and stored the values as mb_mle and ms_mle in the REB netmag tables since April 1998. These magnitudes are published as mbmle and msmle in the IMS1.0-format REB and represent the maximum likelihood estimate for m_b and M_s, based on associated P-wave and LR measured at primary stations plus the noise amplitudes measured at primary stations at the predicted times for P- waves and LR. In general, the maximum likelihood values will be slightly less than the network average magnitudes published as m_b and M_s. Because large events have few stations that do not have detections, the maximum likelihood values will be nearly the same. In the case that there are no associated P-waves in the epicentral distance range 20 to 100 degrees or LR detections in the epicentral distance range 2 to 100 degrees, 95% confidence upper bounds are estimated for m_b and M_s respectively, based on the measured noise values at respective predicted times at primary stations. These 95% confidence upper bounds are published as mbub and msub in the IMS1.0-format REB and represent the magnitude which 95% probability no station would detect given the observed noise levels. Recent results are discussed in Israelsson (1999).

This is the first application of routine publication of automated maximum likelihood and upper bound magnitudes. While all possible P-waveforms are reviewed by analysts, M_s and M_s noise estimates are detected, associated, and measured automatically without analyst review. M_s upper bounds reflect the results of the automated detection of LR amplitudes. Note, some legitimate LR measurements may not have been associated by the automated system and are treated as noise.

REFERENCES

Israelsson, H., (1995), Update of parameters for M_L determination, CCB-PRO-95/18.

Israelsson, H., (1999), MLE Magnitudes, Initial Results in CMR Technical Report CMR-99/12.

Kvaerna, T., (1998), Threshold Monitoring System, CCB-PRO 98/32.

Rezapour, M. and R. G. Pearce (1998), Bias in surface-wave magnitude Ms due to inadequate distance corrections, *Bull. Seism. Soc. Am.*, 88. 43-61.

Stevens, J.L. and K.L. McLaughlin (1997), Improved methods for regionalized surface wave analysis', PL-TR-97- 2135, MFD-TR-97-15887.

Wang, J. (1999), A GUI Tool for Infrasonic Signal Processing in MATLAB, CMR Technical Report 99/12.

Yang, X. and K. McLaughlin (1999a), SSSC's for regional phases at Fennoscandian and other stations, CCB memo, CCB-PRO-99/03.

Yang, X, K. McLaughlin and R. North (1999b), Source Specific Station Corrections for regional phases at International Monitoring Systems (this issue).

Zuzolo, P., A. Powell, C. Powell, E. Brooks, D. Bacon, R. Sarma, T. Dunn and M. Turner (1998), Initiation of Atmospheric Transport and Visual Analysis Operations at the PIDC, CCB-PRO 98/

RESEARCH AND DEVELOPMENT OF A GEOGRAPHICAL INFORMATION SYSTEM (GIS) FOR NUCLEAR TREATY MONITORING

David N. Steer, Dogan Seber, Eric Sandvol, Christine Orgren,
Carrie Brindisi, and Muawia Barazangi
Institute for the Study of the Continents, Cornell University

Sponsored by U. S. Department of Defense
Defense Threat Reduction Agency
Grant No. DSWA 0 1 -97-0006

ABSTRACT

Research and development of a Geographical Information System (GIS) with global and regional coverage is underway at Cornell University. This GIS is being designed to provide essential data and research products required for successful monitoring of the Comprehensive Nuclear-Test-Ban Treaty (CTBT). This system will support the National Data Center (NDC) and the International Monitoring System (IMS) by providing a common frame of reference in which to merge the results of the four monitoring technologies (seismic, hydroacoustic, infrasound, and radionuclide). The GIS under development is intended to improve monitoring capabilities by providing rapid access and visualization of seismic and non-seismic databases in an interactive way. The data and analysis tools will also assist in ongoing calibration and location studies during the implementation of the CTBT and serve the verification readiness objectives of the CTBT.

All available geologic, geophysical, and imagery databases must be fused with bulletins produced from NDC and IMS data to better calibrate a given region and for improved location of events. These complementary data are also essential for verification and discrimination between nuclear explosions and other types of similar events such as mine blasts or collapses, rock bursts, large chemical explosions, or anomalous seismic events. Research and development is focused on creating and evaluating solid earth databases required for calibration and discrimination of events in the Middle East, North Africa, and the United States. A tectonic map of the North Africa region has been finalized and 1:5,000,000 scale or better digital geologic data have been added for Africa, the Middle East, and South Asia. Mosaics of Thematic Mapper imagery for much of North Africa and the Middle East has been assembled from individual scenes, registered, and entered into the database.

An exhaustive review of scientific literature resulted in the most complete database of focal mechanisms available for North Africa and the Middle East, in addition to that available in the Harvard database. Database research and development for the United States has resulted in assembly of all available digital geology. These data include the 1:2,500,000 U.S. Geological Survey digital geology map of the continental U.S. as well as high-resolution geology (1:500,000 scale) for Arizona, Colorado, Idaho, Illinois, Minnesota, Montana, Nevada, New Mexico, Oregon, Utah, Washington, and Wyoming. The entire USGS National Atlas (high-resolution geographic data) was also added to the database.

Research is underway to create an updated, digital map of depth-to-basement for the continental United States and North America. We are also developing and improving the design of menu-driven, custom analysis tools, as well as metadata for all digital data sets. When fully implemented, the GIS will provide a rapid analysis tool to assist in discrimination of nuclear from non-nuclear events. These analyses will be improved by placing suspect events in spatially registered displays of topography, geology, tectonic zones, faults, historical seismicity, focal mechanisms, cultural landmarks, and Landsat imagery. A JAVA-based interactive application program that runs under Web browsers has been developed to access Cornell's GIS system. The CTBT community and other interested researchers can access the application at http://atlas.geo.cornell.edu.

Key Words: GIS, Middle East, North Africa, United States, geophysics, imagery, geology

OBJECTIVE

The main objective of this work is to facilitate and enhance the location and calibration capability of the International Monitoring System (IMS) and to assist the US National Data Center (NDC) by providing digital databases used for monitoring the CTBT. The research and development are focused on the Middle East, North Africa, and the United States. The databases being developed include diversified geological, geophysical, geographical, and imagery information that are pertinent to compliance provisions of the treaty. Regional digital geology and tectonic maps are being added to the system as they become available or are being scanned and digitized at Cornell. Geophysical data such as depth-to-basement, crustal thickness, and crustal and upper-most mantle velocity structure are being derived from compilations of the existing literature. Geographical data of the highest available resolution are also being added to the system to assist in monitoring activities. Digital imagery are being added to assist in locating mines and for geologic interpretations that may provide information pertinent to CTBT monitoring. We are developing and improving the design of menu-driven, custom-made display and analysis tools and the accompanying metadata for all data sets housed in the system. The metadata provide the necessary information about the quality, resolution, accuracy, and techniques used to develop the data. This research and development is critical to both the verification and compliance provisions of the Comprehensive Nuclear-Test-Ban Treaty.

RESEARCH ACCOMPLISHED

Middle East and North Africa Databases

Research and development of databases for the Middle East and North Africa resulted in a regional tectonic map, a study of focal mechanism solutions, and registration of a large volume of imagery data. The regional tectonic map of North Africa (Figure 1) was completed by digitizing, registering, and adding attributes to maps of Algeria, Tunisia, Egypt, Libya, and Morocco. These data are important for placing an event in its proper tectonic setting during analysis. Digital geologic data that cover all of Africa, the Middle East, and South Asia were acquired from the USGS (USGS 470 series data), simplified, and added to the GIS database. The data for Africa (Persits et al., 1997) that cover the entire African continent were synthesized from UNESCO maps of approximately 1:5 million scale. Data for the Arabian Peninsula (Pollastro et al., 1998) were compiled from UNESCO 1:5 million and 1:2 million USGS maps. The digital database for South Asia (Wandrey and Law, 1998) was compiled from 1:5 and 1:10 million scale UNESCO maps. Geologic data for the Asia Pacific (Steinshouer et al., 1999) region were derived from regional 1:5 million scale maps and data for the Former Soviet Union (Persits et al., 1998) were derived from 1:7.5 million maps. These data are accurate to approximately 5000 meters (based on a 1:5 million scale map) and provide essential information about the surface geology that is needed when rapidly researching an area of interest. References that describe seismic events with focal mechanism solutions for the Middle East and North Africa were located. A total of ~800 events, primarily with magnitudes between 4-5.5, were added to the database (Figure 2). This database expands on the global Harvard CMT focal mechanism database and provides another important resource for analyzing regional events.

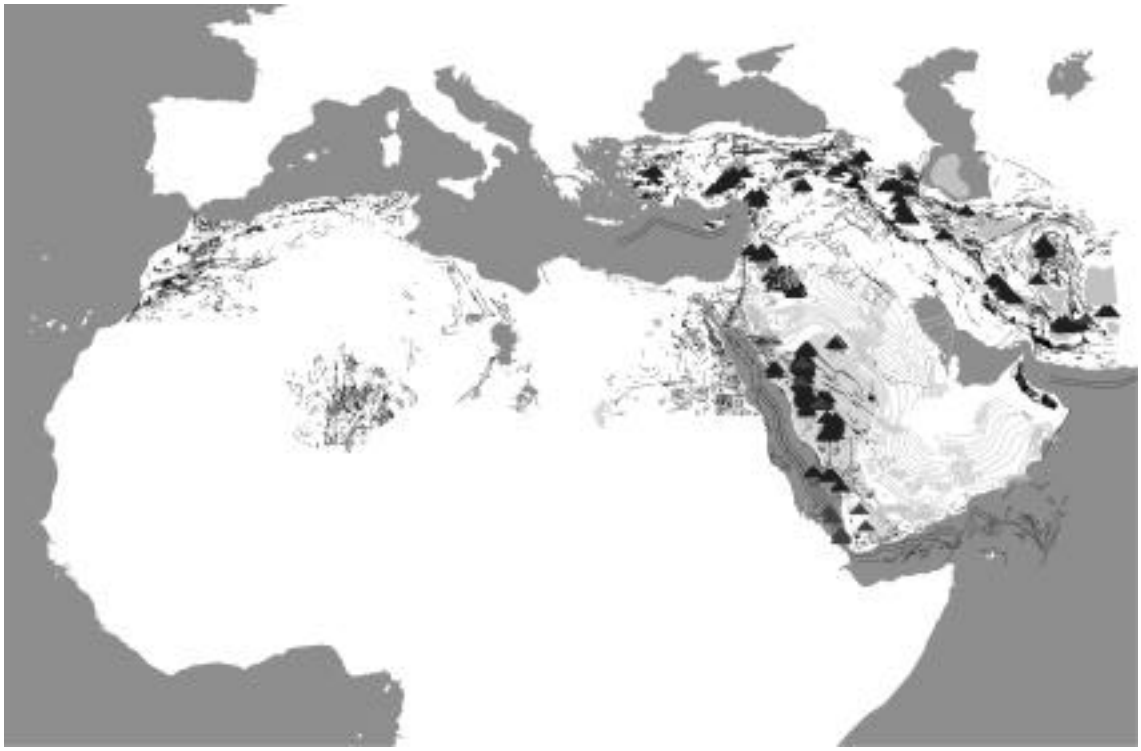


Figure 1. Tectonic map of the Middle East and North Africa compiled from detailed research of the literature and original research completed at Cornell University.

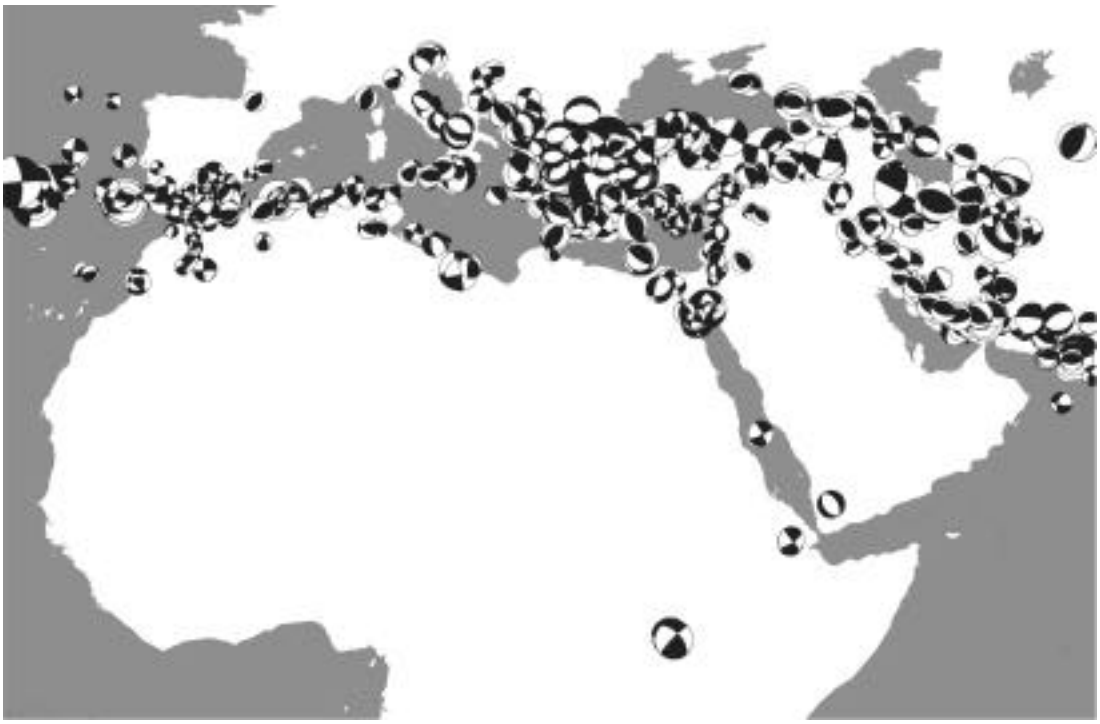


Figure 2. Focal mechanism solutions for the Middle East and North Africa as derived from a search of the scientific literature. These solutions are in addition to those found in the global Harvard CMT focal mechanisms database.

A revised Bouguer gravity anomaly map for the entire Middle East and most of the African continent was developed using new data obtained from the Defense Mapping Agency. These data can be used to model crustal structure when analyzing a specific path of interest. Cornell also expanded the library of Thematic Mapper imagery available for the Middle East and North Africa. The data span Northwest Africa and most of the Middle East including Israel, Palestine, Lebanon, Syria, eastern Turkey and most of Iran and Iraq (Figure 3). These data are being used to locate possible active mine locations and for geologic interpretations of the Middle East and North Africa.

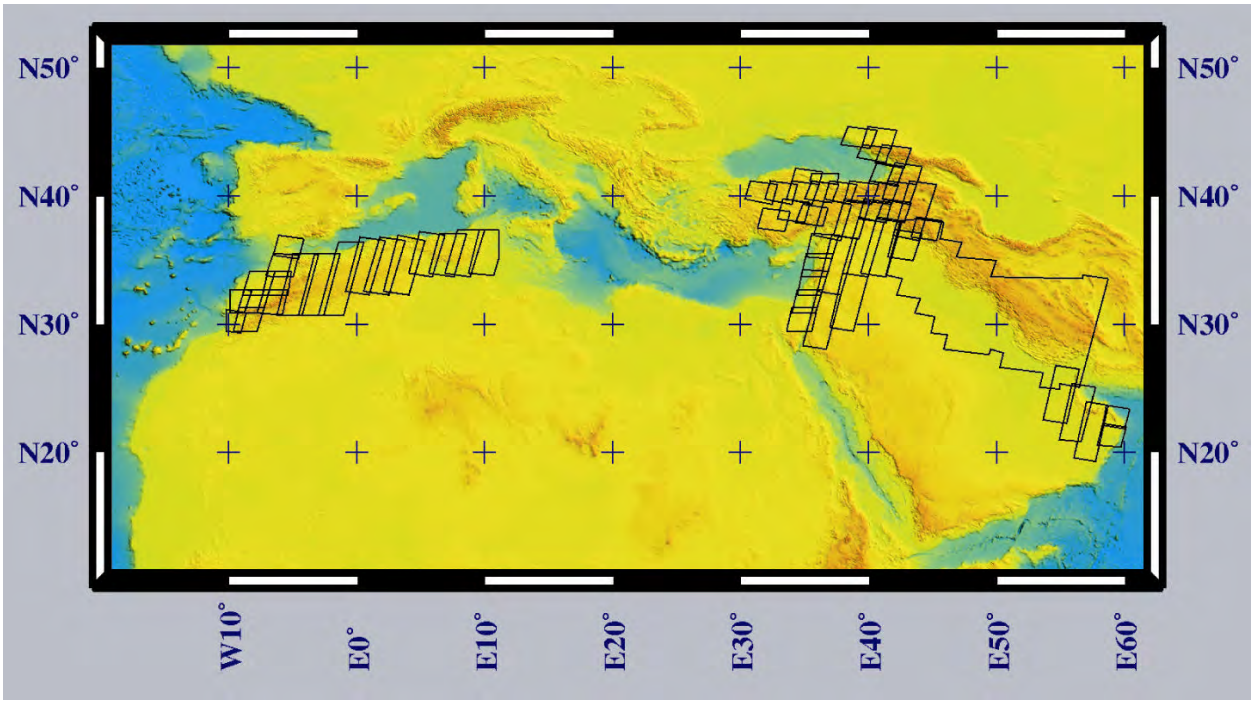


Figure 3. Map showing Landsat Thematic Mapper imagery that are processed, geographically registered and available at Cornell

United States Databases

High-resolution digital geophysical and geological databases for the United States were researched, downloaded, and reformatted for inclusion to the Cornell database. Detailed geology and fault data were obtained from the USGS or state geologic surveys for *Arizona*, *Arkansas*, Colorado, *Idaho*, *Illinois*, *Kentucky*, *Minnesota*, Montana, *Nevada*, New Mexico, *Oregon*, Utah, *Washington*, and Wyoming (states in italics include fault data). Additionally, regional geologic data were located and downloaded for the Lake Superior, Northwest, and Pacific Northwest regions. These data are at 1:500,000 scale with a variety of projections. Due to the complexity of the geology represented by these data, a time period attribute is added to each data set and the data are then projected to geographic coordinates. This allows all the detailed data to be displayed simultaneously with correct, uniform geologic color symbology while retaining all detailed information. Other geologic information pertinent to analyzing an event in the United States include the mine database from the former US Bureau of Mines. This global database includes over 220,000 mines with over 70 attributes for each mine.

In order to assist in ongoing calibration efforts in the United States, the 1:2,500,000 basement maps for the central United States of Sims et al. (1991) and Sims (1990) were merged. These data were converted to three-dimensional grids (Figure 4) with an associated statistical confidence interval using the kriging technique. Additional data covering other regions of the United States were identified, digitized and are

being combined with other data to complete a basement map of the United States. Analog maps of basement contours for the Pacific margin of the United States (Gardner et al., 1993) were located and digitized. These data were combined with previously entered data for the Great Valley and Sierra Nevada (Wentworth et al., 1995). For other areas of California, the Smith (1964) map of basement exposures was digitized. Similar maps of basement exposures were located for portions of Texas (Vlissides, 1964) and the Appalachians (Drake et al., 1988).

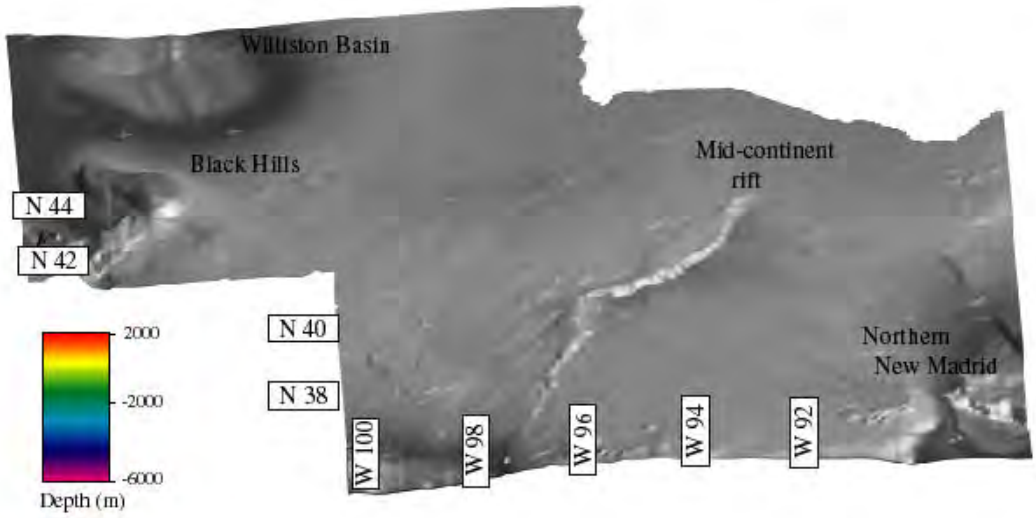


Figure 4. A perspective view of the depth-to-basement grid of the US mid-continent region. This grid was generated using the kriging interpolation technique. Contour data were digitized from regional maps, converted to point data and then interpolated.

Other data added to the Cornell database include seismic event locations and geographic data. The complete Center for a National Seismic System (CNSS) seismic database was added to the Cornell database. The CNSS composite catalog is created and stored at the Northern California Earthquake Data Center (NCEDC). This is a global database that includes over 700,000 events (1940-present). Contributions to the CNSS catalog are made on a regional basis and include many very small events (magnitude 1-2) that are not reported in any other catalog. Each seismic network that contributes catalog data to the CNSS composite catalog is assigned a geographic region where that network's solution (location and magnitude) is considered authoritative. If more than one network supplies a solution for the same earthquake, only one solution for that earthquake is included in the composite catalog. The complete USGS digital National Atlas database was identified and downloaded for inclusion to the database. This large database contains detailed geographic

data for the continental Unites States. It includes airport locations, aquifers, cities and urban areas, counties, federally protected land and watershed boundaries, hydrologic data, roads, and railroads.

Metadata

To provide consistency for users with datasets from other sources, the Federal Geographic Data Committee (FGDC) Content Standard for Digital Geospatial Metadata is being applied to all data that are entered into the Cornell GIS system. Metadata standards facilitate data sharing through time and space. The standard specifies the information content of metadata for digital geospatial data; its purpose is to provide a common set of terminology and definitions for documentation related to these metadata. The standard establishes the names of data elements and groups of data elements, the definitions of these data elements and groups, and information about the values that are to be provided for the data elements.

The FGDC data elements are as follows: Identification Information - this is the basic information about the data set. Examples include the title, the geographic area covered, vintage, and rules for acquiring or using the data. Data Quality Information - this is the assessment of the quality of the data set. Examples include the positional and attribute accuracy, completeness, consistency, the sources of information, and methods used to produce the data. Spatial Data Organization Information - this is the mechanism used to represent spatial information in the data set. Examples include the method used to represent spatial positions directly (such as raster or vector) and the number of spatial objects in the data set. Spatial Reference Information - this attribute is a description of the reference frame, means of encoding, and coordinates of the data set. Examples include the name of and parameters for map projections or grid coordinate systems, horizontal and vertical datum, and the coordinate system resolution. Entity and Attribute Information - this is information about the content of the data set, including the entity types, their attributes and the domains from which attribute values may be assigned. Examples include the names and definitions of features, attributes, and attribute values. Distribution Information - this contains information about obtaining the data set. Examples include a contact for the distributor, available formats, information about how to obtain data sets online or on physical media (such as cartridge tape or CD-ROM), and fees for the data. Metadata Reference Information - this is information on the vintage of the metadata information and the responsible party. Examples include update data and information about the organization that provided the metadata.

Development of New Web Site

A new, sophisticated web site that is interactive, easy-to-use, and gives complete access to data sets available at Cornell University is now operational. The application is written using the Java language. The Java applet acts as an interface to our ArcInfo data sets that are kept on the server side. ArcInfo is a Geographic Information System software package from Environmental Systems Research Inc. Once a user selects data and/or entries and click on the "Submit Request ..." button, a URI is sent within Java to the server, which is received by a CGI script that creates Arc Macro Language (AML) files that are run in ArcInfo. The resultant map is then served back to the client and registered with the application so that the user can get latitude and longitude information. Once a new map is displayed, a user can download postscript or jpeg versions of the maps within the application. The projection used in all mapping applications is Equirectangular centered at 30 degree North (or South) latitudes. Equirectangular is a simple projection that allows displaying data sets in both local and global scales. The web site now allows users to enter their own data as well the ability to query existing databases. The interactive site includes a graphical user interface that permits the user to zoom and change display properties. This resource is now available for the entire CTBT research community to assist in their research and development efforts. The site includes all metadata and a comprehensive users manual and is located at **http://atlas.geo.cornell.edu**.

CONCLUSIONS AND RECOMMENDATIONS

The geology, geophysical, geographic and imagery data contained in the Cornell GIS database are essential for CTBT monitoring and compliance. The data contained in the system provide ancillary information essential for regional calibration and discrimination studies as well as for possible On-Site Inspections.

Research and development of GIS databases to support compliance and verification provisions of the CTBT must continue. Though much work has been accomplished in acquiring, researching, and evaluating data for the Middle East, North Africa, and the United States, much remains to be completed. Existing databases must routinely be updated and new regions must be added as information becomes available. Metadata, though time consuming to create, are an essential element of the database and must be created for those databases added to the system or updated as needed. In order to disseminate CTBT research results to the broader scientific community, Cornell will continue to provide public access to data through an open web site. With cooperation from contributing scientists, data and results of research can be added to the system such that signatories to the treaty, researchers, and interested scientists can view the data, make maps, and compare results. Cornell will also continue to develop new components to its GIS that will provide additional analysis tools and simpler access to the data.

REFERENCES

Drake, A., Hall, L., Nelson, A., 1988, Basement and basement-cover relation map of the Appalachian Orogen in the United States, Miscellaneous Investigations Series - U. S. Geological Survey, OPF I-1655, 1:1,000,000 scale, U. S. Geological Survey, Reston, VA.

Gardner, J., Cacchione, D., Drake, D., Edwards, B., Field, M., Hampton, M., Karl, H., Kenyon, N., Masson, D., McCulloch, D., and Grim, M., 1993, Map showing depth to basement in the deep-sea basins of the Pacific continental margin, Strait of Juan de Fuca to Cape Mendocino, Miscellaneous Investigations Series - U. S. Geological Survey, 1:1,000,000 scale, U. S. Geological Survey, Reston, VA.

Persits, F., Ahlbrandt, T, Tuttle, M., Charpentier, R., Brownfield, M., and Takahashi, K., 1997, *Maps showing geology, oil, and gas fields and geological provinces of Africa*, USGS OPF 97-470A, US Dept. Interior, Washington, D.C., 1 CDROM.

Persits, F., Ulmishek, G.F., and Steinshauer, D. W., 1998, *Maps showing geology, oil and gas fields, and geologic provinces of the Former Soviet Union*, USGS OPF 97-470E, US Dept. Interior, Washington, D.C., 1 CDROM.

Pollastro, R.M., Karshbaum, A.S., and Viger, R.J., 1998, *Map showing geology, oil, and gas fields and geological provinces of the Arabian Peninsula*, USGS OPF 97-470B, US Dept. Interior, Washington, D.C., 1 CDROM.

Sims, P.K., Precambrian basement map of the northern Midcontinent, U.S.A., U. S. Geological Survey, OPF I-1853-A, 1:1,000,000 scale, U. S. Geological Survey, Reston, VA.

Sims, P.K., Peterman, Z.E., Hildenbrand, T.G., and Mahan, S., Precambrian basement map of the Trans-Hudson Orogen and adjacent terranes, Northern Great Plains, U.S.A., U. S. Geological Survey, OPF I-2214, 1:1,000,000 scale, U. S. Geological Survey, Reston, VA.

Smith, M., 1964, Map showing distribution and configuration of basement rocks in California, Oil and Gas Investigations Map, U. S. Geological Survey, Reston, VA,

Steinshauer, D. W., Qiang, J., McCabe, P.J., and Ryder, R.T., 1999, *Maps showing geology, oil and gas fields, and geologic provinces of the Asia Pacific region*, USGS OPF 97-470F, US Dept. Interior, Washington, D.C., 1 CDROM.

Vlissides, S.,1964, Map of Texas showing oil and gas fields, pipelines, and areas of exposed basement rocks, Oil and Gas Investigations Map, OPF OM-0214, 1:1,000,000 scale, U. S. Geological Survey, Reston, VA.

Wandry, C.J., and Law, B.E., 1998, *Maps showing geology, oil, and gas fields and geological provinces of South Asia*, USGS OPF 97-470C, US Dept. Interior, Washington, D.C., 1 CDROM.

Wentworth, C., Fisher, G., Reid, L., and Jachens, R., 1995, The surface of crystalline basement, Great Valley and Sierra Nevada, California, Miscellaneous Investigations Series - U. S. Geological Survey, OPF 95-0096, U. S. Geological Survey, Reston, VA.

STATUS OF THE INTERNATIONAL MONITORING SYSTEM

STATUS OF THE INFRASOUND COMPONENT OF THE INTERNATIONAL MONITORING SYSTEM, COMPREHENSIVE NUCLEAR-TEST-BAN TREATY

Douglas Christie,
International Monitoring System Division, Provisional Technical Secretariat,
Comprehensive Nuclear-Test-Ban Treaty Organization

ABSTRACT

The infrasound component of the International Monitoring System (IMS) for verification of the Comprehensive Nuclear-Test-Ban Treaty will consist of 60 ultra-sensitive array stations distributed as uniformly as possible over the surface of the globe. This network will be capable of detecting and locating any atmospheric nuclear explosion with yields of 1 kT or more. The detection threshold will be significantly less than 1 kT in many parts of the world.

All of the infrasound stations in the IMS network are new stations. The establishment of each of these array stations requires a careful site survey to ensure that the station is located in a low-noise environment, the installation of equipment at each array element, and a testing and evaluation period followed by station certification. The infrasound site survey program is well advanced. The establishment of equipment is underway or has been completed at a number of IMS stations, and a few of these stations are now undergoing testing and evaluation. It is expected that 15% or more of the infrasound stations in the global network will be in operation by the end of this year.
Many of the technical issues related to station installation have now been resolved. The remaining issues are primarily concerned with station certification requirements, station performance evaluation and operational and maintenance procedures for certified stations.

Key Words: infrasound stations, International Monitoring System

INTERNATIONAL MONITORING SYSTEM: TASK LEADER VIEW FROM VIENNA

J Alwyn Davies, Working Group B Task Leader
Comprehensive Nuclear-Test-Ban Treaty Technical Advisor
Permanent Mission of the United Kingdom Mission to United Nations Agencies
Embassy of the United Kingdom
Vienna, Austria

ABSTRACT

An independent view from that of the Provisional Technical Secretariat (PTS) of the Comprehensive Nuclear-Test-Ban Treaty Organisation (CTBTO) is given on how the commissioning of the International Monitoring System (IMS) is planned and resourced. The presentation describes briefly the main policy-making organs of the CTBTO and also gives a brief description of the CTBTO's International Monitoring System (IMS) regime. It also looks at the progress made by the PTS in meeting the goals of the 1997, 1998, and, as far as possible, the 1999 work programmes. The presentation identifies some of the problems encountered by the CTBTO, both politically and technically. Consideration is made to the future financial resourcing of the CTBTO, in particular the IMS major programme, future IMS-related issues that need addressing, and attempts to predict when the Entry-into-Force criteria might be met.

Key Words: International Monitoring System, Provisional Technical Secretariat, Comprehensive Nuclear-Test-Ban Treaty Organisation

AIM

The aim of this presentation is to give an overview of PTS progress on commissioning the International Monitoring System (IMS), which is part of the verification regime necessary for the Comprehensive Nuclear-Test-Ban Treaty (CTBT). The purpose is to show how the commissioning is planned, what progress is being made, to give an indication of the difficulties that have been encountered, and what I see as the future.

This is a personal view and does not represent the views of the United Kingdom Mission in Vienna nor that of the British Government.

BACKGROUND

Although there have been negotiations on a CTBT that stretch back over 40 years, the Treaty that was eventually signed resulted from negotiations held at the Conference of Disarmament in the period January 1994 through June 1996. The Treaty was opened for signature in September 1996, and currently it has over 150 Signatories and almost 40 ratifiers. In order to bring the Treaty into effect, a Preparatory Commission (PrepCom) was set up in November 1996 with its home in Vienna. The PTS was established there in March 1997 in offices occupying three then-empty floors of one of the tower blocks of the Vienna International Centre.

Various bodies or organs were established during the PrepCom phase. There is the parent body itself and its subsidiary organs of Working Group A (WGA), Working Group B (WGB) and the Advisory Group. PrepCom is the governing body, somewhat similar to the International Atomic Energy Agency (IAEA) Board of Governors. WGA deals with nontechnical issues, whereas WGB is technical, dealing with all issues associated with verification, not just the IMS. The Advisory Group, formerly called the financial AG, deals mainly with financial and procedural matters. Each meets for various durations three time a year in Vienna. The chair of PrepCom rotates periodically on a geographical basis, whereas the terms of the Chairs of the other bodies are not defined.

Under the Chairmanship of Dr. Ola Dahlman WGB is structured with five programme coordinators who have responsibilities for each of the five major verification programmes.

THE INTERNATIONAL MONITORING SYSTEM

The IMS, as defined in the Treaty, comprises 321 monitoring stations employing four separate monitoring technologies: seismic in the earth, hydroacoustic in and above the oceans, and infrasound and radionuclide in the atmosphere. The stations are distributed world wide. The radionuclide stations are supported by up to 16 radionuclide laboratories, again distributed on a wide geographical basis. This monitoring system will the largest associated with any international treaty. It will also surpass any national capability.

Though many seismic stations already exist, most will require some upgrading. Several new arrays are required and several three-component stations need to be upgraded to arrays. Digitization and communication at many need to be increased considerably. The hydroacoustic system is almost new: the only two existing ones being the US MILS arrays at Wake and Ascension Islands whose conditions are not yet up to the IMS standards. The infrasound system, which is almost entirely new, requires 4-element arrays to be installed at a minimum. Although there are many radionuclide stations existing worldwide their suitability for IMS purposes is not good. Perhaps one-fourth of the required particulate stations exist but almost all need some upgrading. Virtually no noble gas capability exists at IMS locations. For many, noble gas detection is seen as a particularly important monitoring capability.

ENTRY INTO FORCE

For this Treaty to enter into force, two criteria must be met. The first is political in that 44 named States not only have to sign this Treaty but also have to ratify it. The Treaty can enter into force 180 days after the deposition of the 44th instruments of ratification. The second requirement is not

so exact but it requires that an operational verification system must be capable of meeting the verification requirements of the Treaty. Some States take this to mean, *inter alia*, that all 321 IMS stations need to be established. This view is not subscribed to by all, including some powerful States.

COST

The IMS will be costly. The early estimates at Geneva were US$80-100M with the belief that these estimates might prove to be too low. This is certainly the case and recent estimates total about US$145-180M. As the PTS get a better understanding of the tasks required and various technical organisations or institutions are approached, it is becoming apparent that even the current updated cost estimates are probably too low, especially when stations in the most remote arrears are addressed. It is possible that the costs of logistics may outweigh the instrument costs in some cases. Even when established, the IMS alone will be expensive to operate and maintain.

PLANNING OF THE COMMISSIONING PROGRAMME

In mid-1997 the question was asked: which stations should be commissioned first? At that time there was virtually no technical staff in the PTS; rather, it was composed of political, administrative and legal branches. Thus, WGB had to define the technical work programme. WGB's recommendation was adopted for the 1998 and 1999 work programmes. WGB also tried to cost the programme, although in reality it was not the best possessor of accurate information. When it came to the 2000 programme and budget, which is still under active debate, a different approach was adopted. It was felt that the PTS had come of age and therefore should be given the responsibility of developing its own programme, following closely the guidelines given to it by WGB. In all cases the final programme is agreed and approved by PrepCom. The whole process has been unpleasant at times since extreme positions are taken by some delegations. There are those who wish to see expeditious progress being pursued and realise that this requires high financial resourcing, while others for whatever reason are advocating very low levels of spending and are willing to accept slower progress. Some delegations have called for Zero Real Growth even in the second or third years of a large capital investment programme.

The outcome of this difference of opinion is that so far the programmes have been modest concentrating perhaps in the first few years on surveying sites. This is consistent with the concept of "preparedness" advocated by the WGB chairman. As time passes, it is hoped the emphasis will move from surveying to upgrading leading eventually to certification and operation.

The PTS runs on annual budgets that have risen from $28M in the partial year of 1997 to $75M in the year 1999. The PTS have shown that when this organization is completely established, some $85M/yr will be required. To date the IMS element has consistently been just under 50% of the total.

PROGRESS TO DATE

Progress in implementing the IMS commissioning plans so far has not been good, although 1999 has seen a dramatic improvement. With hindsight it is easy to say that some States Signatories have been too demanding and too unrealistic in their expectations. 1997 was a poor year with little being achieved; 1998 was slightly better in that some surveys but virtually no installations or upgrades were conducted other than those carried out by a few countries using their own funding and resources. However, 1999 has seen a vast improvement and the PTS remain confident of completing the combined 1997/8/9 work programmes in a timely fashion.

The reasons for poor progress are many, ranging from the absence of an existing infrastructure, slow staff recruitment, lack of legal basis for work to be done, poor cooperation by some States Signatories, costs higher than expected, lack of decisions by WGA and WGB in some cases, and lack of project management experience in an international regime. One particular problem concerns the exact locations of the stations as specified by geographical coordinates in the Treaty. When the networks were being developed by the technical experts at Geneva, there was an understanding that

the locations could be accurate to perhaps 50-100 km without adversely affecting monitoring capability. However, when the Treaty came to be drafted, some nontechnical diplomat decided that precision was called for and identified the stations by geographical coordinates. However, this was not too exact and, as a result, the locations listed for several stations are essentially wrong.

FUTURE INVESTMENTS TO MEET TARGETS

Up to now, there has been much debate on the annual budgets, which have risen each year, as is expected for a programme that has a large capital investment programme. One of the problems for many delegations is that they had no indication to what level the annual budgets might rise. In developing programmes the two guidelines required, namely an end-date or an annual financial limit, have not been given. Following calls from many delegations in early 1999, the PTS produced what was called their 5-year plan (CTBT/PTS/INF.98). In this they gave indications of what they saw as annual budgets to complete the capital investment programme by certain dates. They took the year 2004 as the mean, with accelerated and decelerated programmes for completion in 2002 or 2006 as alternatives. Delegations regarded this document as an information document and accepted its contents on the understanding that it was not to dictate the pace of progress. That was for the State Signatories to determine. The figures show that annual budgets over $100M are required in some years dropping to a steady state value of about $85M after completion of the verification regime. This figure is required to keep the organisation running and does not include any recapitalisation. So far, annual budgets have been well below the steady state value.

MAIN ISSUES FOR FUTURE CONSIDERATION

Many technical issues remain outstanding, and some require urgent resolution. In particular there is a need to get the IMS operational manuals sorted out. Another important issue is the degree to which IMS data and International Data Centre products are confidential and not available to the world at large. There are very opposing views on this. One delegation wants the information to be freely available to all, while a second delegation believes it should be embargoed for three months before being released. There is also much to be resolved associated with the radionuclide laboratories and transportation of IMS samples from stations to the laboratory.

THE FUTURE

A question often asked is “when will this Treaty enter into force?” There is no simple answer. Each can make individual judgments against the two criteria, namely the political and technical criteria. Even with adequate funding, it will be at least five years before all the requirements are met. Without adequate funding it is impossible to answer exactly, but one possible answer is “never.”

STATUS OF THE SEISMIC NETWORKS OF THE INTERNATIONAL MONITORING SYSTEM, COMPREHENSIVE NUCLEAR-TEST-BAN TREATY

Holly Given
International Monitoring System Division, Provisional Technical Secretariat,
Comprehensive Nuclear-Test-Ban Treaty Organisation

ABSTRACT

The Comprehensive-Nuclear-Test Ban Treaty calls for the establishment of two seismic networks as part of the International Monitoring System (IMS): a primary network of 50 stations (30 arrays and 20 three-component stations), and an auxiliary network of 120 stations (113 three-component stations and 7 arrays). This abstract gives an overview of the progress achieved during the first three years of work by the Provisional Technical Secretariat.

By the end of 1999, site surveys will be completed for about 90% of the primary network. At that time, about 50% of the primary seismic network will substantially meet the minimum requirements for seismic stations established by the Preparatory Commission. This early completion rate is partially due to incorporation into the IMS of many stations from GSETT-3 that required only minor upgrading. By the end of 2000, site surveys for the primary network should be finished and the network at nearly 70% completion, with emphasis on the completion of 8 new arrays in Eurasia.

A recent assessment of the operational status of the auxiliary network found that 32% of auxiliary stations substantially meet the minimum requirements, 56% require either a new seismometer or digital acquisition system (or both), and 12% require new station construction and installation. Work is underway at many auxiliary stations but at a lower investment level than for the primary network.

Aside from the principal task of station installation and upgrading, other areas of effort involve incorporation of authentication, instrument testing, station certification, monitoring station performance, training host country operators, and defining procedures for the operational phase of the IMS.

Key Words: primary seismic stations, auxiliary seismic stations

STATUS OF THE HYDROACOUSTIC NETWORK OF THE INTERNATIONAL MONITORING SYSTEM, COMPREHENSIVE NUCLEAR-TEST-BAN TREATY

John Newton
International Monitoring System Division, Provisional Technical Secretariat,
Comprehensive Nuclear-Test-Ban Treaty Organization

ABSTRACT

To verify compliance with the Comprehensive Nuclear-Test-Ban Treaty (CTBT), the Provisional Technical Secretariat (PTS) of the CTBT Organisation (CTBTO) is establishing the International Monitoring System (IMS), a global network of seismic, infrasound, hydroacoustic and radionuclide sensors to detect, identify, and locate the signals generated by a nuclear explosion. The IMS hydroacoustic network, designed to monitor the major world oceans, contains eleven stations located with an emphasis on the vast ocean areas of the Southern Hemisphere. Two quite different sensing techniques are employed in the hydroacoustic network; hydrophone sensors, which effectively cover large ocean areas but are quite complex and expensive, and seismic detectors on small islands which are less effective, but considerably simpler and cheaper.

Presently three of the planned hydroacoustic network stations exist, while the remaining eight stations will be new installations. The establishment of each hydroacoustic station requires a survey to ensure the suitability of the site, the installation of new equipment or the upgrade of existing facilities, and finally a period of testing and certification. The site survey requirements have been completed for four of the stations, and two additional surveys are planned to begin during 1999. Equipment for two new hydrophone stations and one new island seismometer station is under development with installation and initial operational testing scheduled for early in 2000.

Key Words: hydroacoustic station, International Monitoring System

STATUS OF THE RADIONUCLIDE COMPONENT OF THE INTERNATIONAL MONITORING SYSTEM, COMPREHENSIVE NUCLEAR-TEST-BAN TREATY

Joachim Schulze
International Monitoring System Division, Provisional Technical Secretariat,
Comprehensive Nuclear-Test-Ban Treaty Organization

ABSTRACT
The radionuclide component of the International Monitoring System (IMS) for verification of the Comprehensive Nuclear-Test-Ban Treaty will consist of 80 stations to detect radioactive particulates transported from the source through the atmosphere to the station. Forty of these 80 stations will be equipped with the capability to detect radioactive Xenon isotopes, a nuclear explosion indicator difficult to contain. Sixteen radionuclide laboratories will support the stations with further analysis of samples on request.

The radionuclide network will be capable of detecting and locating atmospheric nuclear explosions with yields down to 1 kT or even lower. A strong point of the radionuclide system is its ability to differentiate between a nuclear explosion and other types of explosions.

To install a radionuclide station, a site survey is performed to ensure that the site is coupled to the upper airflow, that infrastructure is available, and that no radionuclide background lowers the sensitivity. About half of all the site surveys have been done or are underway. The equipment installation at 18 stations is underway or finished. It is expected that at least 10 radionuclide stations will be operating by the end of this year.

Procedures for certifying laboratories and operating/maintaining stations are under discussion. Recently developed Xenon detection systems are in the operational test phase.

Key Words: xenon, radionuclide stations, radionuclide laboratories